Oil & Natural Gas Technology

DOE Award No.: DE-FE0010667

Final Scientific/Technical Report

Liquid-Rich Shale Potential of Utah's Uinta and Paradox Basins: Reservoir Characterization and Development Optimization

Project period: October 1, 2012 to September 30, 2015 (extended to March 31, 2017)

Submitted by:
Utah Geological Survey
1594 W. North Temple, Suite 3110
Salt Lake City, UT 84116
DUNS # 176871572

Principal Investigator: Michael D. Vanden Berg
michaelvandenberg@utah.gov, 801-538-5419

Prepared for:
United States Department of Energy
National Energy Technology Laboratory

Submitted: August 31, 2017

U.S. DEPARTMENT OF ENERGY | NATIONAL ENERGY TECHNOLOGY LABORATORY

Office of Fossil Energy

NETL DISCLAIMER

This report was prepared as an account of work sponsored by an agency of the United States Government. Neither the United States Government nor any agency thereof, nor any of their employees, makes any warranty, express or implied, or assumes any legal liability or responsibility for the accuracy, completeness, or usefulness of any information, apparatus, product, or process disclosed, or represents that its use would not infringe privately owned rights. Reference herein to any specific commercial product, process, or service by trade name, trademark, manufacturer, or otherwise does not necessarily constitute or imply its endorsement, recommendation, or favoring by the United States Government or any agency thereof. The views and opinions of authors expressed herein do not necessarily state or reflect those of the United States Government or any agency thereof.

UGS DISCLAIMER

Although this product represents the work of professional scientists, the Utah Department of Natural Resources, Utah Geological Survey, makes no warranty, expressed or implied, regarding its suitability for a particular use. The Utah Department of Natural Resources, Utah Geological Survey, shall not be liable under any circumstances for any direct, indirect, special, incidental, or consequential damages with respect to claims by users of this product.

TABLE OF CONTENTS

LIST OF APPENDICES

EXECUTIVE SUMMARY

The enclosed report is the culmination of a multi-year and multi-faceted research project investigating Utah's unconventional tight oil potential. From the beginning, the project team focused efforts on two different plays: (1) the basal Green River Formation's (GRF) Uteland Butte unconventional play in the Uinta Basin and (2) the more established but understudied Cane Creek shale play in the Paradox Basin.

The 2009-2014 high price of crude oil, coupled with lower natural gas prices, generated renewed interest in exploration and development of liquid hydrocarbon reserves. Following the success of the mid-2000s shale gas boom and employing many of the same well completion techniques, petroleum companies started exploring for liquid petroleum in shale formations. In fact, many shales targeted for natural gas include areas in which the shale is more prone to liquid production. In Utah, organic-rich shales in the Uinta and Paradox Basins have been the source of significant hydrocarbon generation, with companies traditionally targeting the interbedded sands or carbonates for their conventional resource recovery. Because of the advances in horizontal drilling and hydraulic fracturing techniques, operators in these basins started to explore the petroleum production potential of the shale units themselves.

The GRF in the Uinta Basin has been studied for over 50 years, since the first hydrocarbon discoveries. However, those studies focused on the many conventional sandstone reservoirs currently producing oil and gas. In contrast, less information was available about the more unconventional crude oil production potential of thinner carbonate/shale units, most notably the basal Uteland Butte member.

The Cane Creek shale of the Paradox Basin has been a target for exploration periodically since the 1960s and produces oil from several small fields. The play generated much interest in the early 1990s with the successful use of horizontal drilling. Recently, the USGS assessed the undiscovered oil resource in the Cane Creek shale of the Paradox Basin at 103 million barrels at a 95 percent confidence level and 198 million barrels at a 50 percent confidence level. Nonetheless, limited research was available or published to further define the play and the reservoir characteristics.

The specific objectives of the enclosed research were to (1) characterize geologic, geochemical, and geomechanical rock properties of target zones in the two designated basins by compiling data and by analyzing available cores, cuttings, and well logs; (2) describe outcrop reservoir analogs of GRF plays (Cane Creek shale is not exposed) and compare them to subsurface data; (3) map major regional trends for targeted intervals and identify "sweet spots" that have the greatest oil potential; (4) reduce exploration costs and drilling risks, especially in environmentally sensitive areas; (5) improve drilling and fracturing effectiveness by determining optimal well completion design; and (6) reduce field development costs, maximize oil recovery, and increase reserves. These objectives are all addressed in a series of nine publications that resulted from this extensive research project. Each publication is included in this report as an independent appendix.

Appendix I: *Shale Oil Resource Play Potential of the Green River Formation, Uinta Basin, Utah*

- Schamel, S.
- Published as Utah Geological Survey Open-File Report 639
- Fulfills the requirements of Task 3.1, 3.2, 4.4, 7.1, 8.1, and 8.2

The Green River Formation in the Uinta Basin has many characteristics typical of an ideal shale oil resource play. It is a world-class oil-prone source rock. In nearly all parts of the basin there are many thousands of net feet of Type-I and Type-II kerogen-rich calcareous mudstones, many intervals of which have average total organic carbon (TOC) of 5–10% or greater. In the north-central and western parts of the basin a substantial part of the formation is in the oil-generative window. A large volume of the formation has reached "peak oil". Furthermore, organic maturation simulations done in this study using PRA BasinView-3D™ indicates early entry into the oil-generative window. In the northwest parts of the basin the lower Green River Formation was generating oil even before the end of the Eocene and slowing of

sediment accumulation in the basin. Anomalous formation pressures are observed in the lower Green River Formation across much of the basin. In the area of the greater Altamont-Bluebell field in the northwest of the basin, the abnormal pressures are nearly lithostatic (0.6 to 0.8 psi/ft). The Green River Formation is unquestionably a superb petroleum system responsible for very large cumulative production of oil and associated natural gas, and an even larger potential oil sand resource.

This assessment of the shale oil resource play potential of the Green River Formation is based on the integration of:

- basin-wide stratigraphy and facies distributions;
- programmed pyrolysis and other geochemical data from organic-rich calcareous mudstone in fourteen wells, most of which are in the northern and western quadrants of the basin;
- new basin-wide BasinView 3D™ numerical modeling of thermal maturation at a 1.0 km resolution;
- the known distribution of oil and oil sand accumulations in Green River Formation and age-equivalent reservoirs; and
- the current revitalization of oil production from Green River–Wasatch reservoirs.

Typical shale oil resource plays are self-contained petroleum systems having ineffective carrier systems that severely restrict migration of oil generated in the source rocks from migrating outward or upward into traps in reservoirs marginal to the oil kitchens. Consequently, the oil backs up into any and all pore space in the source rock succession, even creating fracture storage space where anomalous pressures occur. Relatively tight rocks that would normally never be considered reservoirs can have very high oil saturations and oil-in-place. In a shale oil resource play, these are what are exploited by horizontal wells and hydraulic fracture stimulation.

As more of the shale oil plays receive close scrutiny, it is becoming clear that no two are the same with regards to character of source rock or reservoir. What they all have in common, however, is (1) an organic-rich source rock capable of generating large volumes of oil, (2) interbedded or proximal reservoir intervals that, although tight, have sufficient porosity and/or natural fractures to be capable of hosting commercially significant volumes of the producible oil, and (3) inefficient carrier systems resulting in the oil generated remaining in proximity to the oil-generative source rock. The presence of anomalous formation pressures appears necessary to drive the oil from reservoir to well bore, even when fracture stimulated. These are “self-sourcing” petroleum systems only when viewed on a scale that encompasses the entire source rock formation and its immediately adjacent strata, or a significant portion thereof. And so, it is with the Green River Formation, which has both an internal “self-sourcing” continuous oil play within the oil generative window and conventional oil accumulations on its periphery. Due to the lenticular character of the sandstone and carbonate beds in the Green River Formation and the underlying Wasatch Formation, some beds trap oil locally, while others carry the oil up-dip into traps at a distance from the oil generative window.

Only a few years after the discovery of the Altamont field, it was described as an “oil accumulation near the center of a deep basin”, an example of a then newly-recognized “group of deep-basin, organic-shale-related, overpressured accumulations” having significant hydrocarbon potential. Altamont-Bluebell field characteristics subsequently have come to identify a basin-centered, continuous resource play. These characteristics include:

- difficulty in defining field limits laterally and vertically because the trap is stratigraphic with no simple down-dip water levels or facies boundaries to the productive horizons,
- multiple thin productive zones with abnormally high fluid pressures, and
- very low matrix porosities enhanced by post-lithification fractures.

The companies now using fracture stimulation and horizontal wells to produce oil from Green River–Wasatch sandstone and carbonate reservoirs have merely rediscovered this basin-centered, continuous shale oil resource play.

Appendix II: *Geological, Geochemical, and Reservoir Characterization of the Uteland Butte Member of the Green River Formation, Uinta Basin, Utah*

- Birdwell, J., Vanden Berg, M.D., Johnson, R.C., Mercier, T.J., Boehlke, A.R., and Brownfield, M.E.
- Published in Dolan, M.P., Higley, D.K., and Lillis, P.G., editors, Hydrocarbon Source Rocks in Unconventional Plays, Rocky Mountain Region: Rocky Mountain Association of Geologists
- Fulfills the requirements of Task 3.1, 3.2, 4.1, 4.2, 4.4, 5.1, 5.2, 7.1, 7.2, 8.1, and 8.2

The informal Uteland Butte member of the lower part of the Green River Formation was deposited in a major transgressive phase of the early freshwater stage of Eocene Lake Uinta, in the Uinta Basin. It ranges in thickness from around 50 to over 300 ft and contains primarily limestone, dolostone, and organic-rich mudstone and siltstone, with sandstone and ostracodal limestone in marginal areas. The Uteland Butte member is age-equivalent to part of the freshwater Cow Ridge Member of the Green River in the Piceance Basin of Colorado and may correspond to the freshwater Luman Tongue of the Green River in the Greater Green River Basin of Wyoming and Colorado. Of these intervals, only the Uteland Butte was buried deep enough to have resulted in a major petroleum system. Since late 2010, the Uteland Butte has become a successful tight-oil play, with total cumulative oil production of about 4.38 million barrels (as of December 2014) and initial well production ranging from less than 100 up to 1,700 barrels of oil equivalent per day, all produced through the use of horizontal drilling, hydraulic fracturing, and acid treatment in dolomite-rich target zones. Most horizontally drilled laterals in the Uteland Butte average about 5,000 ft, but a few of the more recent wells have reached over 11,000 ft. Organic-rich mudstone, siltstone, and limestone are likely the source of oil in the Uteland Butte, and thin, highly porous dolostones are the primary reservoirs targeted with horizontal drilling. Uteland Butte oils are generally very waxy and have API gravities ranging between 30° and 40°. The oils are also low in sulfur (<0.3 wt. %) and isotopically light with $\delta^{13}C$ values for saturate and aromatic fractions between -29 and -33 ‰. Molecular parameters show that the Uteland Butte oils are derived from similar organic material as other Green River Formation oils produced in the Uinta Basin. Immature outcrop samples from the eastern and western margins of the basin were examined to obtain estimates of original organic content and kerogen quality for Uteland Butte source rocks. The organic matter in these outcrop samples is predominantly Type I kerogen, but is somewhat less hydrogen-rich than the kerogen present in overlying oil shale deposited during brackish- to saline-lake phases of the Green River Formation based on Rock-Eval hydrogen indices. In core samples, Uteland Butte rocks are in the oil generation window based on a variety of thermal maturity indicators. Basinwide organic richness was examined using historical Fischer assay data. The samples with the highest oil yields occur just to the west of an overpressured region. Chloroform-extractable organic matter content from high-porosity samples from dolomitic intervals is up to four times that of the adjacent mudstones. The thickness of dolomite beds in the Uteland Butte is nonuniform through the stratigraphic interval and is an important factor for production potential due to its high porosity and petroleum content, as determined by Rock-Eval parameters and soxhlet extraction. Formation pressures vary from normal to possibly underpressured in shallow areas, to moderately overpressured along the deep basin trough. In general, wells in the overpressured area are the most productive. Assessment units were defined using basinwide data on organic richness, thermal maturity, and dolomite content, including an overpressured sweet spot in the most productive part of the basin.

Appendix III: *Lithofacies, Deposition, Early Diagenesis, and Porosity of the Uteland Butte Member, Green River Formation, Eastern Uinta Basin, Utah and Colorado*

- Logan, S.K., Sarg, J.F., and Vanden Berg, M.D.
- Published as Utah Geological Survey Open-File Report 652
- Fulfills the requirements of Task 3.1, 3.2, 4.1, 4.2, 5.1, 5.2, 5.4, 7.2, 8.1, and 8.2

The Uteland Butte member of the lower Green River Formation in the eastern part of Utah's Uinta Basin was correlated and mapped from outcrop to the subsurface using lithofacies and sequence-stratigraphic boundaries. The study area extends from the outcrop on the western side of the Douglas Creek Arch where lake-margin sediments occur, to cores from the Greater Natural Buttes natural gas field in central Uintah County, where sublittoral facies are predominant.

Eighteen facies and eight facies associations were described in the Uteland Butte section. Facies were identified based on lithology, grain size, texture, sedimentary structures, bed thickness, bed boundaries, and geometries and include: (F1) grey/green siltstone, (F2) lime to dolomitic mudstone, (F3) ostracod lime mudstone-wackestone, (F4) molluscan lime wackestone-packstone, (F5) oolitic lime mudstone-wackestone, (F6) intraclastic-ostracod lime packstone-grainstone, (F7) ostracod lime packstone-grainstone, (F8) oolitic lime packstone-grainstone, (F9) oncolite-ooid lime packstone-grainstone,(F10) ooid-pisolite lime packstone-grainstone, (F11) bioclastic lime floatstone to rudstone, (F12) ostracod-bearing sandstone, (F13) structureless to laminated sandstone, (F14) cross-stratified sandstone, (F15) carbonaceous shale, (F16) laminated illitic claystone, (F17) argillaceous mudstone, and (F18) laminated silty oil shale. Sedimentary facies are grouped into eight facies associations based on lateral and vertical relationships of depositional environments, energy level of the lake water, and relative water depth and include: (FA-A) fluvial-deltaic deposits, (FA-B) shoreline carbonate mudstone, (FA-C) littoral to sublittoral claystone to sandstone, (FA-D) carbonate shoal, (FA-E) microbial carbonate, (FA-F) littoral to sublittoral bioclastic mudstone to wackestone, (FA-G) littoral to sublittoral oil shale, and (FA-H) laminated oil shale.

On the eastern edge of the lake basin, where a ramp margin persisted and deltaic and fluvial influences were minor, outcrops show lake-margin environments that underwent four major flooding events. These cycles are correlated into the deeper regions of the lake using cores from the Greater Natural Buttes natural gas field area. Sublittoral successions from deeper in the lake are 30% thicker than the marginal Uteland Butte successions and are lean in silt and richer in dolomite—nearly every bed deposited in the sublittoral environment contains greater than 25% dolomite.

The Uteland Butte member contains rare stromatolites and lacks evaporites and analcime, but bivalves, gastropods, and ostracods are abundant across the study area, indicating a fresh water lake environment. Mud occurs in three forms: calcite, dolomite, and clay. Dolomite displays intercrystalline porosity averaging between 7 and 17%. Dolomitic mud found in packstones and grainstones occurs primarily as grain coatings, intraclasts, and peloids.

Appendix IV: *Dolomitization in the Uteland Butte Member of the Eocene Green River Formation, Uinta Basin, Utah*

- Rueda, F., and Machel, H.
- Included in final report, but currently unpublished. This is a nearly complete draft of F. Rueda's M.S. thesis. A final version of the thesis will be completed by December 2017.
- Fulfills the requirements of Task 3.1, 3.2, 4.1, 4.2, 5.1, 5.2, 5.4, 7.1, 7.2, 8.1, and 8.2

The lacustrine Green River Formation (GRF) is an important oil-producing formation in the Uinta Basin, Utah (USA). In recent years, the unconventional carbonate reservoirs in the Uteland Butte member (UBM) at the base of the GRF have been targeted because of their petrophysical properties and their estimated resource of 214 million barrels of oil and 329 billion cubic feet of gas. The stratigraphic interval

of interest is within the middle of the UBM, defined at the bottom and top by the D and C shales, respectively. Within this interval, there are three regionally extensive dolomite layers named PZ2, PZ1', and PZ1, consisting of up to 100% dolomite. These beds vary from 1.5 to 8 feet in thickness and are interbedded with organic-rich limestones and shales. They have up to 30% porosity but only a maximum of 0.1 mD permeability.

The main objectives of this study are to characterize the facies types and determine how they are related to dolomitization, elucidate the dolomitization process and how porosity and permeability are related this process, and delineate the regional geometry of the dolomite layers. This study employed several methods including outcrop and core descriptions; petrographic analysis by means of transmitted light, cathodoluminescence microscopy, and scanning electron microscopy petrography; mineralogical identification and ordering of dolomites through X-ray diffractometry; elemental compositions by means of X-ray spectrometry (EDS in SEM) and electron microprobe; trace element analysis using inductively coupled plasma mass spectrometry; and conventional and clumped oxygen and carbon isotope analysis.

Deposition of the UBM took place during transgressive-regressive cycles that were driven by climate variations. The ancient Uinta Lake water level was high during cooler and rainy periods that alternated with warmer and drier periods, which led to lower lake levels caused by reduced fluvial input and/or evaporative drawdown. The three PZ layers were deposited in littoral environments as intraclastic grainstones and ooid ostracod grainstone-packstones, and also in littoral to sublittoral environments as mudstones, peloidal bioturbated mudstones, and ostracod wackestones. There is no discernible relationship between dolomitization and depositional environments.

Dolomitization took place syndepositionally from lake water that was moderately evaporated and also enriched in Mg during drier periods. These conditions formed dolomite crystals characterized by a wide range of %Ca from 50% to 59% with a strong mode in 52 to 55%, and low cation ordering that ranges from 0.2 to 0.5. The %Ca range and the low cation ordering are interpreted as results of variable and incomplete recrystallization in a closed system during burial under considerable hydrologic overpressure. The $\delta^{13}C$ values for dolomite range from 6‰ to -5.4‰ (VPDB) suggesting high organic activity and/or organic matter decay, coupled with organic matter oxidation by sulfate reducing bacteria. The $\delta^{18}O$ values for dolomite range from 0.9 to -7.3‰ (VPDB) interpreted as elevated lake water temperatures. The calculated fluid temperature of dolomitization is between 14 to 36°C. Furthermore, there is a strong correlation between %Ca and cation ordering, and Sr and Mn concentration with depth. The %Ca increases in depth, whereas cation ordering decreases; the Sr concentration decreases in depth, whereas Mn concentration increases. This trend may be related to dolomitizing fluid flow.

Increased fresh water input during more humid climate periods stopped dolomitization and facilitated deposition of lime mud layers. $\delta^{13}C$ for calcites range from 1‰ to -1‰ (VPDB), and the $\delta^{18}O$ for calcites range from -5.8 to -10.1‰ (VPDB). The calculated temperature for calcite precipitation is between 3 and 12°C.

The dolomite crystal sizes range from 0.25 to 6 μm and porosity is mainly intercrystal. Dolomite layers PZ1, PZ1', and PZ2 display four dolomite textures: planar e, planar s, nonplanar-a, and planar-c. Planar-e and planar-s are associated with higher porosity. However, there is no defined trend or distribution of texture versus porosity. Permeability is low due to irregular and commonly disconnected pore throats. Also, diagenetic products after dolomitization, such as chert nodules (length-slow chalcedony), isopachous quartz cement, blocky ferroan calcite and equant to blocky calcite cement, reduced porosity and permeability.

Appendix V: *Assessment of Undiscovered Oil and Gas Resources in the Uteland Butte Member of the Eocene Green River Formation, Uinta Basin, Utah*

- Johnson, R.C., Birdwell, J.E., Mercier, T.J., Brownfield, M.E., Charpentier, R.R., Klett, T.R., Leathers, H.M., Schenk, C.J., and Tennyson, M.E.
- Published as U.S. Geological Survey Fact Sheet 2015-3052
- Assessment was performed using data from this DOE project supplied by the PI
- Fulfills the requirements of Task 7.1, 7.2, 8.1, and 8.2

Using a geology-based assessment methodology, the U.S. Geological Survey estimated mean undiscovered resources of 214 million barrels of oil, 329 billion cubic feet of associated/dissolved natural gas, and 14 million barrels of natural gas liquids in the informal Uteland Butte member of the Green River Formation, Uinta Basin, Utah.

Appendix VI: *Characterization and Horizontal-Drilling Potential of Oolitic and Ostracodal Limestone Reservoirs in the Eocene Green River Formation, Northeastern Uinta Basin, Utah*

- Morgan, C.D., and Stimpson, R.W.
- Included in final report, but currently unpublished. Will soon be published as a Utah Geological Survey Special Study.
- Fulfills the requirements of Task 3.1, 3.2, 4.1, 4.2, 4.5, 7.1, 7.2, 8.1, and 8.2

Oolitic and ostracodal limestone reservoirs in the Eocene Green River Formation have been oil productive in Utah's Uinta Basin for many decades. Wonsits Valley field, one of the only fields in the basin with a thick and laterally extensive oolitic/ostracodal limestone reservoir—the G1 interval, was discovered in 1962 and has produced more than 52 million barrels of oil and 137 billion cubic feet of gas (through 2015). The G1 interval, in the lower Douglas Creek Member, is a limestone and calcareous sandstone with a maximum combined thickness of more than 90 feet. Most of Wonsits Valley is produced from vertical wells, but in the early 2000s, QEP Resources began drilling and completing horizontal laterals in the G1.

Laterally-extensive oolitic/ostracodal limestone beds were deposited in high energy shoreface environments of Lake Uinta. These beds have been described in the structurally deep Bluebell field associated with the north shore of paleo-Lake Uinta and in outcrop and core along the southern and eastern shores. Most oolitic/ostracodal limestone beds in the basin are thin, typically 1 to 5 feet thick such as in the Brennan Bottom field; Wonsits Valley field is the exception.

Oolitic/ostracodal limestone beds typically contain calcite cement with intergranular, intragranular, and rare moldic porosity. The beds commonly have more porosity than associated sandstone beds – 18% average porosity in G1 limestone versus 12% average porosity for G1 sandstone. The sandstone beds commonly contain quartz overgrowths that reduce reservoir quality. In some cases, ostracods and ooids are a component of the sandstone beds, reducing the potential for quartz overgrowths and therefore improving reservoir quality. Oolitic/ostracodal limestone beds have become a horizontal drilling target in the Uinta Basin because of their good reservoir quality and generally laterally consistent distribution. As of 2015, at least 35 horizontal wells have been drilled in the northeastern Uinta Basin exploiting the G1 bed in Wonsits Valley and neighboring fields as well as the stratigraphically lower H4 limestone.

Appendix VII: *Geological Characterization of the Pennsylvanian Paradox Formation Cane Creek Shale and Other Paradox Shales, Paradox Basin, Utah*

- Morgan, C.D., and Stimpson, R.W.
- Included in final report, but currently unpublished. Will soon be published as a Utah Geological Survey Special Study.
- Fulfills the requirements of Task 3.1, 3.2, 4.1, 4.2, 4.4, 4.5, 7.1, 7.2, 8.1, and 8.2

The Cane Creek shale (clastic cycle 21) is a hydrocarbon source rock and reservoir in the lower part of the Pennsylvanian Paradox Formation in Paradox Basin of southeast Utah. The Cane Creek is overlain and underlain by beds of salt and is divided into A, B, and C zones (in descending order). The B zone is the primary hydrocarbon source rock and productive interval consisting of black organic-rich shale, dolomite, siltstone to fine-grain sandstone, and some anhydrite. Total organic carbon is more than 20% wt. in many of the thin shale beds. The siltstone/sandstone beds, the primary reservoir facies have significant porosity (up to 15%). Permeability is generally low (~0.1 mD), so naturally occurring fractures are an

important component of the reservoir. Productive dolomite and siltstone beds are rarely encountered in the A and C zones which mostly consist of anhydritic dolomite and bedded anhydrite along with the halite, providing overlying and underlying seals to the reservoir. The reservoir is over pressured having fluid gradients ranging from 0.75 to 0.95 psi/ft. Traps are formed by seismically defined local anticlines and fault closures, combined with facies and permeability variations.

Oil production was first established from the Cane Creek shale in the 1960s but only one well was economic until horizontal drilling renewed the play in the 1990s. The most successful Cane Creek field is the Big Flat field which has produced more than 5 million barrels of oil from 21 active wells. The U.S. Geological Survey's mean estimate of undiscovered resources in the Cane Creek and other Paradox Formation shale beds basin-wide is 471 million barrels of oil, 472 million barrels of natural gas liquids, and 11,418 billion cubic feet of gas.

Excellent oil shows and some minor production have also been encountered in clastic cycle 19 of the Paradox Formation in the Greentown area, in the northern part of the play. This clastic interval may have potential as a future exploration target. Upper Paradox shales, Chimney Rock, Gothic, and Hovenweep, are the source rocks for the Desert Creek and Ismay reservoirs in the Blanding Basin, south of the main Cane Creek play area. Although not currently oil-productive, these shales may be good horizontal targets in the future.

Appendix VIII: *Potential Oil-Prone Areas in the Cane Creek Shale Play, Paradox Basin, Utah, Identified by Epifluorescence Microscopy Techniques*

- Chidsey, T.C., and Eby, D.E.
- Published as Utah Geological Survey Special Study 160
- Fulfills the requirements of Task 3.1, 3.2, 4.2, 4.3, 7.1, 7.3, 8.1, and 8.2

The Cane Creek shale of the Pennsylvanian Paradox Formation has produced over 7.8 million barrels of oil and about 7.9 billion cubic feet of gas from 18 fields in the Paradox Basin of southeastern Utah. Potential oil-prone areas in the Cane Creek play area were identified in the northern part of the basin based on hydrocarbon shows recognized using non-destructive epifluorescence (EF) microscope techniques on cuttings, core chips, and uncovered thin sections. Approximately 2650 individual cuttings samples and core chips were evaluated from 31 wells penetrating the Cane Creek shale throughout the region. The wells include seven producers, one having cumulative production of >1 million barrels of oil from the Cane Creek since its completion in 1962.

The Cane Creek shale is divided into three intervals, based on wireline geophysical well-log characteristics and lithology, referred to as the A, B, and C intervals; the B interval is the primary oil producer. Finely crystalline dolomites and sandstones in the B interval have been the main targets of horizontal drilling. The dolomites in these intervals display intercrystalline porosity and microbial constructional pores whereas sandstones exhibit intergranular porosity; both rock types contain microporosity and fracture porosity. A new, qualitative visual EF rating was developed and applied to the group of samples from each cuttings sample interval in each well. The highest, average highest, highest average, and average of the sample averages of the EF ratings from each well were plotted and mapped for the entire Cane Creek as well as the A, B, and C intervals.

As expected, productive wells (fields) are distinguished by their generally higher EF ratings. However, an area of moderate to good fluorescence (indicating probable capacity of some oil production if there is adequate porosity and permeability) is indicated within a northwest- to southeast-oriented curvilinear fairway in the Cane Creek shale of the Paradox fold and fault belt. In contrast, the northeastern area shows a regional trend of low EF. This implies that hydrocarbon migration in Cane Creek dolomite, sandstone, and other porous lithologies was along regional northwest-trending folds, faults, and fracture zones, and created a potential oil-prone area that to date is relatively untested.

Appendix IX: *Geomechanical Characterization of the Uteland Butte and Cane Creek Tight Oil Plays*

- McLennan, J., and Zannoni, J.
- Included in final report, but currently unpublished.
- Fulfills the requirements of Task 3.1, 3.2, 4.1, 4.6, 6.1, 6.2, 6.3, 6.4, 6.5, 6.6, 6.7, 7.2, 8.1, and 8.2

One aim has been to explore methodologies for predicting brittle rock behavior and considering the consequences during well stimulation. By comprehending a reservoir's characteristics, a second goal has been to use hydraulic fracturing simulations to suggest potentially appropriate treatment methods for application in the Cane Creek and Uteland Butte plays. The rocks encountered in these two plays are relatively brittle and industry has become casually comfortable with terms such as brittleness and fracability. While inferences on brittleness and fracability can be useful for selecting landing zones and qualitatively assessing barriers, incorporating them into numerical simulations is still challenging. In fact, one might still ask "What is fracability?" The answer might be that fracability is a colloquial slang that suggests that tensile fracturing may dominate, and that expended energy on failure goes to creation of open, extensive, conductive fractures (although maintenance of conductivity is not guaranteed). There is confusion as to whether this implies a dominant single discontinuity or a complex network of fractures. There is confusion as to whether this implies a contained or vertically extensive fracture. Presume that those (complexity and containment) are separate criteria that need to be dealt with in order for a stimulation to be effective. Presume further that brittleness can help in the determination of fracability.

Brittleness and Fracability

Conventional methods for determining brittleness were summarized. One problem with the concept of brittleness is that most definitions do not take into account the plastic deformation that takes place. Plastic deformation is non-recoverable. It occurs after the regime in which elastic properties such as Young's modulus and Poisson's ratio - commonly used in brittleness assessments - are determined. In fact, by its very nature, brittleness must imply consideration of behavior after yield of a material has initiated - well after conditions where elastic moduli are determinant. By ignoring non-recoverable (plastic) deformation, the energy that needs to continue being put into more plastic rocks versus more brittle ones is completely ignored. How can we improve?

1. As several authors have pointed out, large scale geological controls - in particular stress conditions and major geologic structural defects - need to be explicitly considered. In most cases, little effort is made to determine what these stress conditions are. Brittle-ductile behavior is governed by in-situ stresses. It should be a priority to measure stresses or infer from them logs at the least.
2. For core-based measurements of brittleness, newer interpretation methods should be considered. Several techniques for assessing brittleness have been evaluated in this report, with particular emphasis on considering how a rock fails, and how it deforms after it starts to yield. This is the implicit discriminator between brittle and ductile behavior. Several new techniques are suggested. Consider post-peak behavior in brittleness predictions.
3. Most brittleness predictions cannot readily be put into hydraulic fracturing simulators. How is mechanical stratigraphy (fracture frequency and mechanical and hydraulic character, in particular) used to predict fracture growth? How do we represent brittleness in standard models? Some possibilities are simulations that take into account post-peak behavior (strain softening or hardening). Continue to improve models for propagation along/through weaknesses.
4. As is evident, all of these effects are overshadowed by what role natural discontinuities play in fracture propagation. The industry has come a long way in terms of developing models that

incorporate these discontinuities - their detection and mechanical characterization - is still challenging. Use these discontinuities in simulations. Figure i illustrates these challenges.

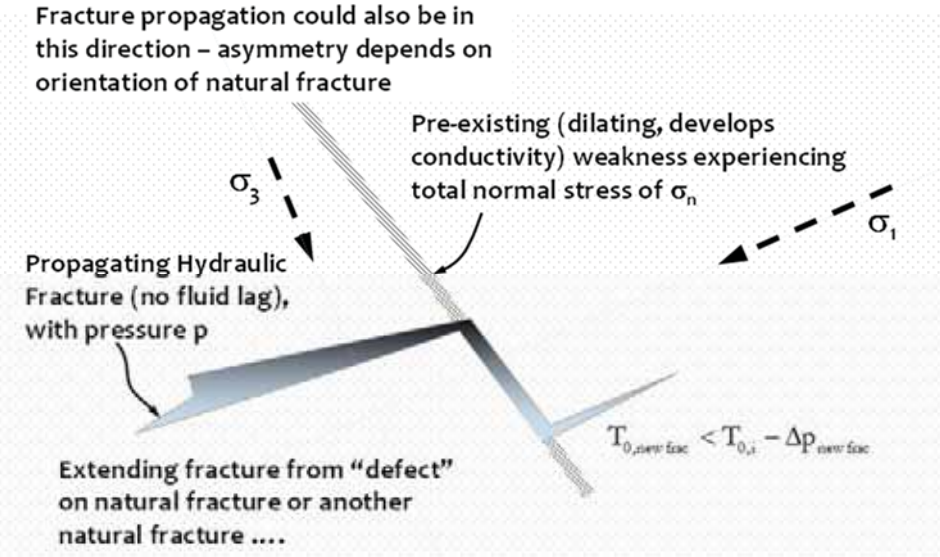

Figure i. *A hydraulic fracture propagates from a weak point along the opposite face of a natural fracture offset. We have a semi-quantitative appreciations of fracture propagation under conditions such as these. The challenges are designation of the discontinuities in-situ and inference of their mechanical and hydraulic resistances. Even more complicated for researchers will be to struggle with the recognition that process zones, loading rates, and non-elastic fracture mechanics may invalidate instinctual appreciations, such as the one shown here.*

The move towards incorporating brittleness is exciting because it recognizes lithologic, structural, and stress-related control of fracture propagation. To improve assessment of brittleness, several new calculation methods have been tried on the wells available for this project. In all cases, the governing premise is that an energy balance is relevant. For example, a certain amount of energy is consumed by quasi-static deformation of a particular formation. This consumption may be more for a ductile material. Alternatively, a certain amount of energy is released after a rock starts to lose its ability to absorb the energy input into it (this input is from geologic events, hydraulic fracturing, production …). The magnitude and the rate at which this extraneous energy is ultimately released can be taken to indicate brittle versus ductile behavior. The premise then is to consider energy stored, energy released, and the rate/magnitude of energy release during a "failure". Five new methods were proposed and have been tested in a preliminary fashion. These are:

- **Zone 1 - Ratio of secant modulus to Young's modulus:** The premise here is that an appropriately picked secant modulus incorporates non-recoverable deformation and Young's modulus manifests elastic, recoverable deformation. The premise is that the lower the ratio of the secant modulus to Young's modulus, the more ductile the failure will be because energy has been consumed/expended even before strain softening. This might be called a Deformation Index.

- **Zone 2 - Ductility Index - Amount of plasticity or strain hardening:** This index quantifies the amount of perfect plasticity or strain hardening in advance of stronger localization and reduction in load bearing capacity.

- **Zone 3a - Tang and Kaiser (axial)**: Tang and Kaiser (1998) provided a very insightful relationship for failure of coal pillars. One measure of this is the amount of energy released when failure occurs. This can be approximated as follows, as modified by Bereskin and McLennan (2008).

$$E_f = \frac{1}{2E}(\Delta\sigma_f)^2 V_f \quad \text{(i)}$$

$$V_f = \underbrace{\varepsilon_a(1-2\nu)}_{\text{Volumetric Strain Based on Axial strain}} \underbrace{\frac{\pi}{4}D^2L}_{\text{Sample Volume}} \quad \text{(ii)}$$

where:

E_f ..... energy released by failure
E ..... Young's modulus
$\Delta\sigma_f$ ..... stress drop after brittle failure
V_f ..... failed volume (reported here for triaxial testing)
ε_a ..... axial strain occurring during strain softening (energy release)
ν ..... Poisson's ratio
D ..... sample diameter
L ..... sample length

- **Zone 3b - Tang and Kaiser (volumetric):** This is similar to the technique described above with the exception that the bulk modulus is used instead of Young's modulus and the volume is based on the measured volumetric strain (rather than the axial strain and Poisson's ratio).

- **Zone 4 - Peak to Residual Strength Ratio:** This is the ratio of the peak to residual stresses and provides an indication of the energy released with catastrophic failure.

- **Zone 5 - Ratio of Stored to Expended Energy:** This method involves integration under a stress-strain curve. This ratio of energies can provide indications of brittleness versus ductility.

Field Assessments

In conjunction with these evaluations of brittleness, data from six wells were processed. Three of these wells targeted the Uteland Butte formation. These wells are: Bill Barrett 14-1-46, Bill Barrett 14-3-45, and Newfield Cesspooch 15-21-3-3W. The other three wells accessed the Cane Creek formation. These wells are Cane Creek 26-3, Cisco State 36-13, and Cane Creek 7-1. All of these wells have well logs available except Cane Creek 7-1. Core was available for all six of the wells for triaxial testing but the Cane Creek 7-1 well was not available for other core testing. Other than the Cane Creek 7-1 well, the other five cores provided measurements of porosity, permeability, TOC, oil maturity, and fracture toughness. Representative sections were created for fracture modelling.

Comparative fracture modeling was carried out to determine what additional treatment optimization may be relevant. Recognizing the absence of well-specific data, generic surrogate wells were assessed in some instances, especially for representing horizontal wells. For the horizontal wells evaluated, logging data, mechanical properties and the limited stress data were incorporated into representative type sections

penetrated by the horizontal drilling. Fracture modeling was carried out with commercial stimulation software.

Vertical completions were evaluated first since the legacy wells were mostly straight hole. Planar 3D hydraulic fracturing treatment simulations were carried out using E-StimPlanTM. The two wells simulated were Bill Barrett well 14-3-45 in the Uteland Butte and the Cisco State 36-13 well in the Cane Creek. In each case, vertical height growth was problematic. In the Cane Creek wells, the problem related to penetration into adjacent salts. Alternatively, for Uteland Butte scenarios, predicted vertical growth and unrealistic perforating scenarios limited production. Figure ii suggests that the predictions were reasonable. This figure also emphasizes why vertical completions will not be economic.

The production history (real and simulated), and current industry practice endorsed changing from a vertical drilling trajectory in both of these plays. This was already starting to happen when this study was initiated. Horizontal type wells were developed for this study. After compiling the laboratory and logging data for the two generic locations, type reservoirs were developed, by amalgamating the various sources of information. In either scenario - Uteland Butte or Cane Creek, the key issue was containment of the fracture in a discrete pay zone/intervals.

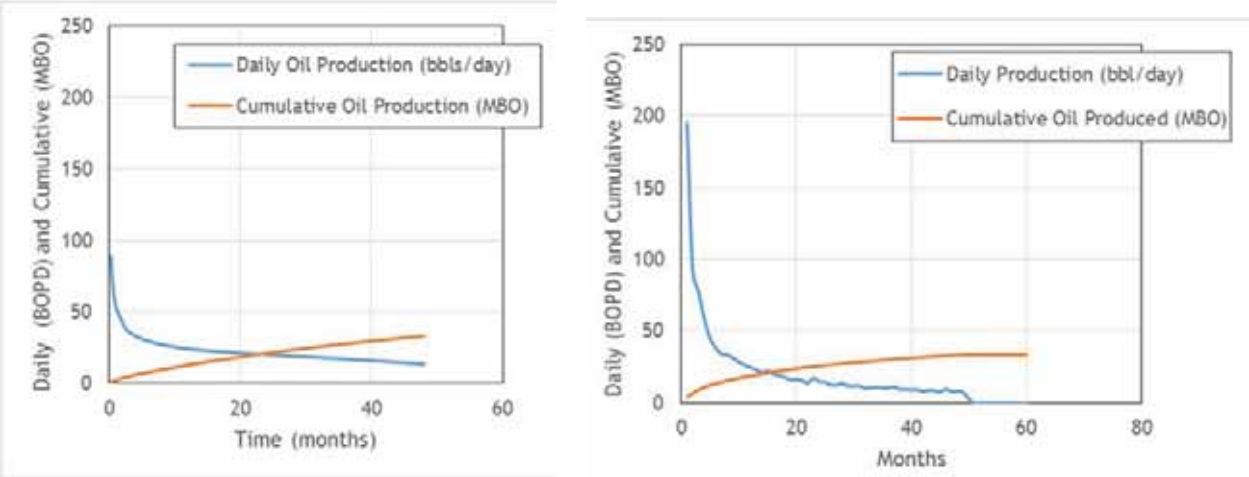

Figure ii. *This is predicted (left panel) versus actual (right panel) oil production for Bill Barrett 14-3-45. Large length perforated - counterproductive. Significant upward growth was also an issue. These forecasts were based on the simulated fracture geometries.*

In the case of the Cane Creek play, salt immediately adjacent to the pay is particularly challenging. Penetration of a water-based treatment fluid into saline zones will result in subsequent salt precipitation and loss of productive capacity. In the case of the Uteland Butte, upward growth out of pay jeopardizes the effectiveness of the stimulation by limiting in-zone surface area.

Horizontal Completions in Cane Creek

Legacy wells completed in the Cane Creek (vertical or horizontal) were marginally productive. There was some evidence and inference that fracturing treatments used in these wells were penetrating into the over- and underlying salt zones and causing salt to block fractures and perforations, thereby reducing the productivity of the well, if not killing it. This would be even more exaggerated for situations where the well wandered out of the pay. Regardless, it was decided to prioritize horizontal wells in the treatment simulations. Generically, the fluids considered were as follows.

Oil-Based Fluid: To their credit, a previous operator treated the formation with mineral oil. Lease crude would have been another possibility but the synthetic oil is likely more biodegradable and easier to justify with regulators and the public. The benefit of this fluid genre is the limited reaction with the adjacent salt formations. A viscosity of nominally 2 cP was used for the oil - relatively low and this inhibits proppant carrying.

Gelled Oil: This is another possible fluid that would minimize interaction with adjacent salt. The drawback is perceived to be out-of-zone growth with the higher viscosity. However, the treating fluids themselves will not interact with the salt. Other issues could be environmental and safety.

Water Based Fluid: Both slickwater and a 50 lb pptg (per thousand gallons) borate crosslinked fluid were evaluated. The slickwater was assumed to have a viscosity of nominally 0.64 cP at reservoir temperature. The properties of the crosslinked were taken from the simulator database. Two extreme fluid scenarios were assessed to comprehend height growth. An intermediate situation might be a low loading linear gel (a viscoelastic surfactant was also evaluated). Obviously there are pros and cons for all of the viscosified fluids including expense, failure to break, and residual polymer damage. The purpose was to assess the role of rate and rheology and presume that good treatment design (proper breaker systems and loading, customized for the play) could overcome residual damage. The disadvantages of the slickwater relate to proppant carrying capacity.

Composite: One of the observations with the crosslinked fluid was screenout when proppant (other than 80/100 mesh) reached the perforations - particularly when rate was reduced to avoid upwards growth. At the other extreme, proppant from the low viscosity treatments would settle. Cyclic injection was evaluated to consider the possibility of fracture placement with proppant acting as an in-fracture diverter and inhibiting height growth. This concept is not new. Diversion treatments for height containment were described in the 1980s. One relevant publication is Greener, 1994. Cyclic injection would seem to offer some possibilities.

The basis for the composite/cyclic treatments was low viscosity fluid pumped in small stage volumes with sand concentrations of 0.5 followed by 1.0 ppg. This was followed by displacement with higher viscosity fluid to push the proppant to the top and the bottom of the pay and to nominally extend the fracture. This was followed by a final cycle of low viscosity fluid with the same low proppant concentrations. The same concept could be applied by fingering the low viscosity fluid through a proppant carrying more viscous fluid or simply running cycled proppant concentrations. Figure iii is an example. More clusters and smaller alternating/cyclic fluids seemed to be desirable. Oil based fluids were most appropriate. Of course, smaller fracture treatments implies more stages are required and wells will need to be drilled closer together. Economic optimization will be necessary.

Horizontal Completions in the Uteland Butte

Until less than a decade ago, wells in the Uteland Butte member of the Green River formation were vertical wells that completed the Uteland Butte section as a secondary target. Recently, operators have targeted the Uteland Butte member specifically, with varying success - much more success with horizontal completions. As with the Cane Creek, horizontal wells were simulated, using Schlumberger's Kinetix Stimulation Software suite.

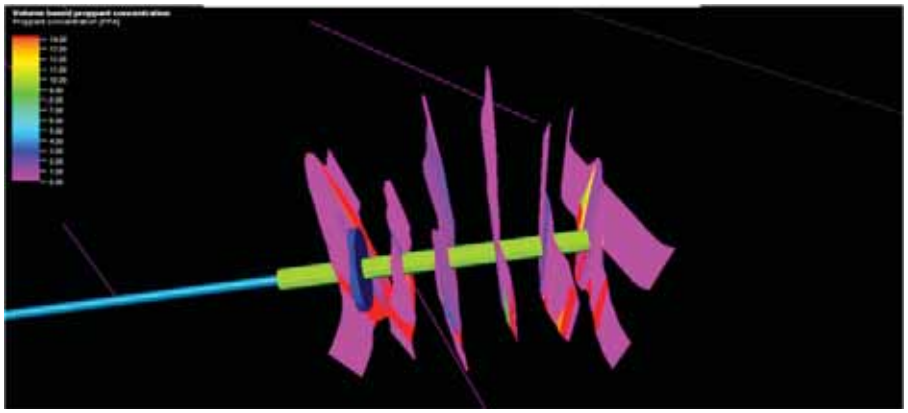

Figure iii. *This is an EOJ view of the extent of six fracture systems (one from each perforation cluster) with cycled water based fluids having different viscosities. The contours are for proppant concentration from 0 to 14 ppa. Proppant coverage is poor but there appears to be moderate containment.*

As with the Cane Creek, vertical containment is important. Options that merit further consideration include reduced rate, low viscosity treatments, cyclic injection (could be favorable), and dramatically reduced tactical treatments similar to fracpacks. The latter were simulated to be effective but may not be practical because of the consequence of screenout. Smaller treatments mandate closer well spacing.

In either case (Cane Creek or Uteland Butte) the recommendations might seem to be contrary to industry practice. The philosophy is that significant volumes of fluid and proppant are wasted at best for noncontributing pay. At worst, as for salt precipitation in the Cane Creek, larger treatments can be catastrophic.

In either situation, simulations at least support more clusters (or more stages), smaller fluid volumes, aggressive sand schedules where feasible and smaller well spacing (economic justification and optimization of spacing is beyond the scope of this project). Cyclic fluid injection merits consideration.

TECHNOLOGY TRANSFER ACTIVITIES

UGS Website

UGS has maintained a project website detailing the progress of the project. The website includes all project-related abstracts, reports, and presentations. This site will also host the final report.

https://geology.utah.gov/resources/energy/oil-gas/shale-oil/

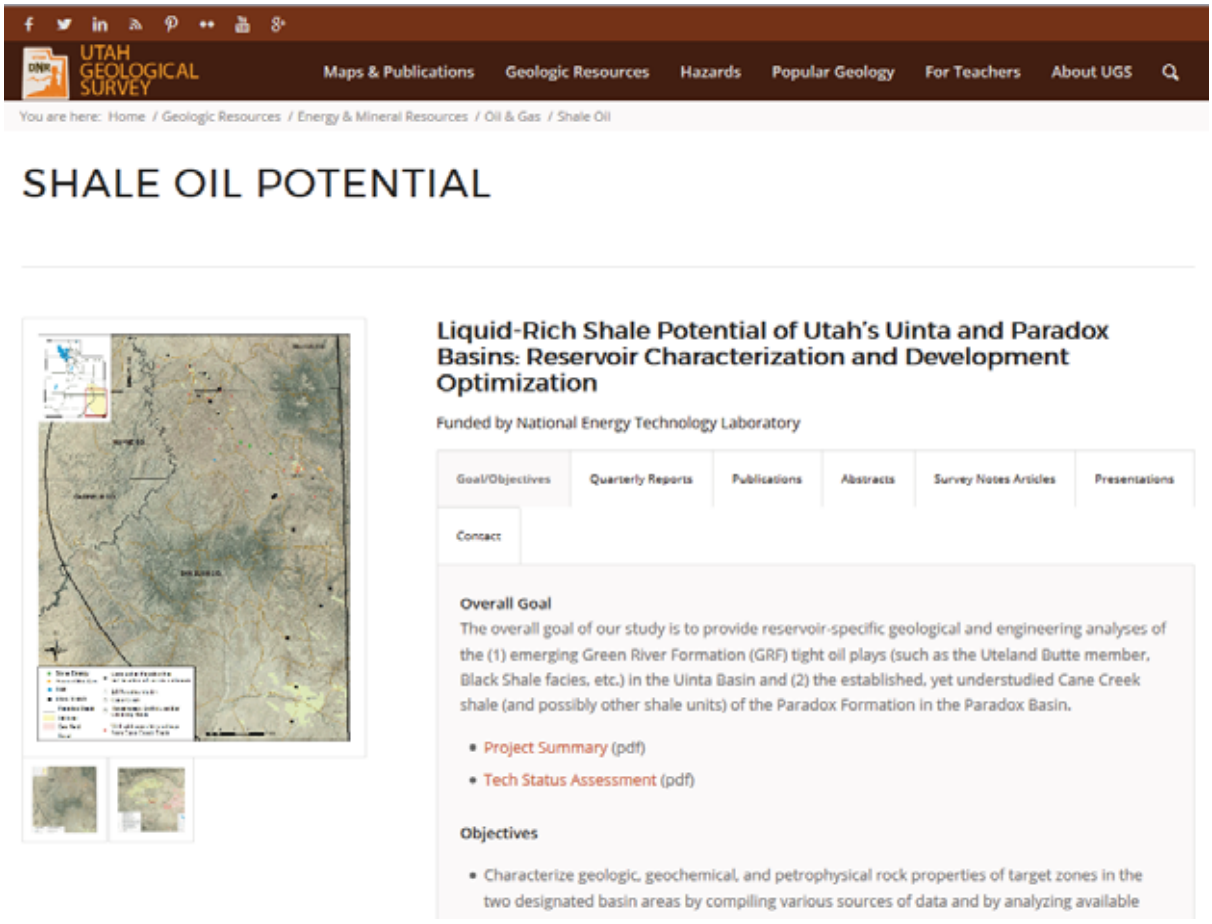

Articles in UGS *Survey Notes* Newsletter

The PI wrote an article titled "Liquid-rich Shale Potential of the Uinta and Paradox Basins" for the May 2013 *Survey Notes* newsletter (Volume 45, Number 2) describing the project and its goals. *Survey Notes* is published by the UGS and distributed to over 5000 individuals interested in Utah geology.

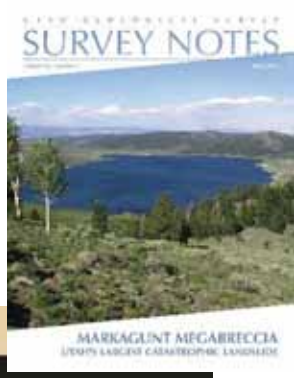

ENERGY NEWS

LIQUID-RICH SHALE POTENTIAL OF

by Michael Vanden Berg

The National Energy Technology Laboratory, part of the U.S. Department of Energy, recently funded the Utah Geological Survey to analyze and characterize the potential of Utah's shale formations for liquid hydrocarbon production. In particular, this new three-year study will research organic-rich units within the Green River Formation of the Uinta Basin in northeastern Utah and the Paradox Formation of the Paradox Basin in southeastern Utah.

The current high price of crude oil, coupled with lower natural gas prices, has generated renewed interest in exploration and development of liquid hydrocarbon reserves. Following the success of the recent shale gas boom (e.g., Barnett shale in Texas, Woodford shale in Oklahoma, Marcellus shale in Pennsylvania and surrounding states) and employing many of the same well completion techniques (e.g., horizontal drilling and hydraulic fracturing), petroleum companies are now exploring for liquid petroleum in shale formations (e.g., Bakken shale in North Dakota, Eagle Ford shale in Texas). In fact, many shales targeted for natural gas also include areas in which the shale is more prone to liquid production. In Utah, organic-rich shales in the Uinta and Paradox Basins have been the source of significant hydrocarbon generation; companies have traditionally targeted the interbedded porous sands or carbonates with conventional recovery techniques (e.g., vertical or near-vertical wells). However, with the advances in horizontal drilling and hydraulic fracturing, operators in these basins are now starting to explore the potential of the shale units themselves.

The Green River Formation in the Uinta Basin has been studied for over 50 years since the first hydrocarbon discoveries. However, early studies focused on the many conventional sandstone reservoirs

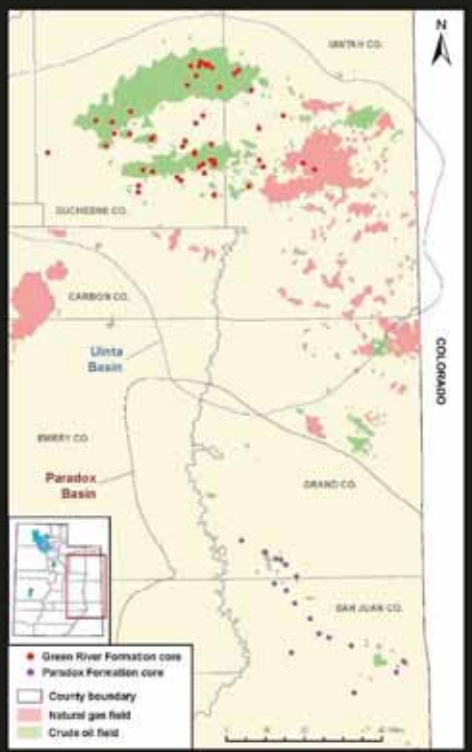

Map of the Uinta and Paradox Basins showing the location of cores available for this study.

Core from the Uteland Butte Member of the Green River Formation, Uinta Basin, Utah (Bill Barrett Corp., 14-1-46). One of the productive horizontal targets is the roughly 5-foot-thick tan dolomitic bed with porosities ranging from 20 to 30%. The oil is sourced from the surrounding darker gray organic-rich limestones, which contain abundant shell fossils, indicating that these layers were deposited in a freshwater lake.

6 SURVEY NOTES

THE UINTA AND PARADOX BASINS

currently producing large quantities of oil and gas. In contrast, little information exists on the more unconventional crude oil production potential of thinner, organic-rich shale/carbonate units such as the Uteland Butte member, black shale facies, and deep Mahogany zone. For information on the distinction between shale oil and oil shale, which also occurs in the Green River Formation, see article by Thomas Chidsey, *Survey Notes*, September 2012, v. 44, no. 3 (in short, oil shale refers to rock that contains immature organic material called kerogen, while shale oil has experienced sufficient heat/pressure, converting organic matter into crude oil, which is still trapped in the micro-pores of the shale).

The Paradox Formation in the Paradox Basin consists of multiple layers of salt interbedded with clastic deposits (sands, silts, clays, or carbonates), many of which contain organic-rich shales. One such clastic interval, the Cane Creek shale, has been a target for exploration on and off since the 1960s and produces oil from several small fields. The play generated much interest in the early 1990s with successful use of horizontal drilling in a handful of wells. Despite this limited success, little research has been conducted or published to further define the play and its reservoir characteristics.

Over the next three years, the UGS plans to characterize the geology of these prospective shale formations to better predict the areas, or "sweet spots," with the greatest production potential. In addition, our research partners at the Energy and Geoscience Institute at the University of Utah will investigate the geomechanical properties (rock strength, brittleness, elasticity, etc.) of these rocks to help determine the best drilling and well completion strategies. A more complete understanding of the geology and geomechanical properties of these formations will help maximize potential recoverable reserves and limit the drilling of nonproductive wells, which in turn will help reduce environmental impacts.

Geologist recording rock properties from an outcrop of the Uteland Butte Member of the Green River Formation in Ninemile Canyon.

Core from the Cane Creek shale of the Paradox Formation (right), Paradox Basin, Utah (Union Pacific Resources Company, Remington 21-11). The source of the oil is the dark gray to black, organic-rich shale intervals, which are interbedded with mottled anhydrite (lightest gray).

Project team member, Craig Morgan, wrote an article titled "Understanding Southeast Utah's Cane Creek Oil, A Continuing Challenge" for the May 2015 *Survey Notes* newsletter (Volume 47, Number 2). This public-friendly article summarized historical Cane Creek production and included initial results of our new Cane Creek research study.

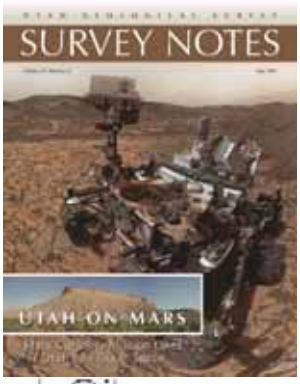

Understanding Southeast Utah's Cane Creek Oil, A Continuing Challenge

BY Craig D. Morgan

INTRODUCTION

The Cane Creek shale of the Paradox Formation in southeastern Utah has been a challenging oil reservoir to develop. As part of a three-year U.S. Department of Energy-funded study, the Utah Geological Survey (UGS) has been researching the Cane Creek shale, characterizing its geologic, geomechanical, and geochemical properties throughout the Paradox Basin. The goal of improved reservoir characterization is to identify potential exploration areas outside the current Cane Creek unit near Dead Horse Point State Park, as well as improve drilling and production techniques to reduce costs and environmental impacts.

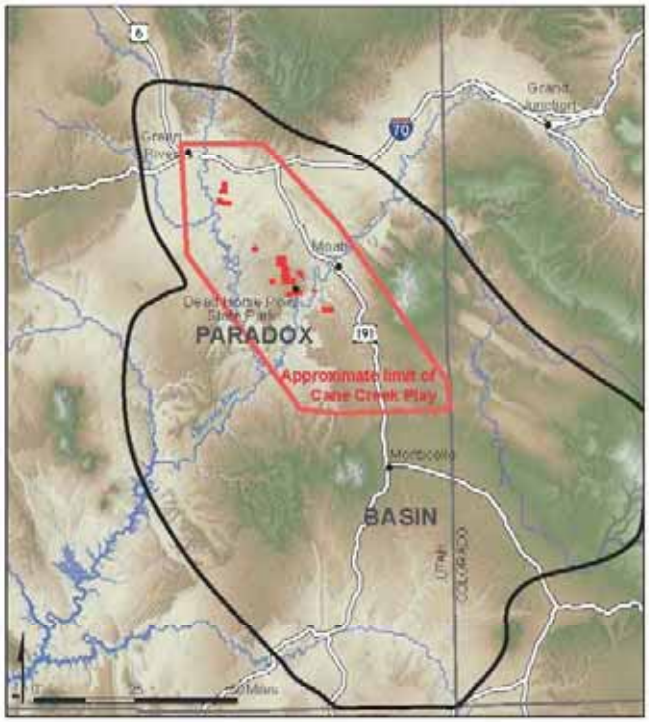

Paradox Basin in southeast Utah and southwest Colorado. The approximate limit of the Cane Creek play is based on the mapped extent of the Cane Creek shale in Utah. Red boxes are areas with Cane Creek oil production.

DRILLING HISTORY

Over the past decade, the Moab area of the Paradox Basin has seen a large increase in drilling and subsequent oil production. The first oil discovery in the Moab area occurred in the 1920s from the 300-million-year-old (Pennsylvanian-aged) Paradox Formation. Drilling equipment and building materials were loaded on barges and floated down the Colorado River to where the first discovery was drilled on the axis of the Cane Creek anticline near the current site of the Moab potash mine. While drilling, the well blew out at a depth of 2028 feet and the rig was destroyed by the resulting fire. Several additional wells were drilled on the anticline, but only a minor amount of oil was produced. Later, the equipment was floated farther down the river to Shafer dome, which resulted in drilling a dry hole.

In 1957, drilling up on Big Flat, near present-day Dead Horse Point State Park, resulted in the discovery of oil in the Mississippian Redwall Limestone. This was the first discovery of oil from Mississippian-aged rocks in Utah. Ultimately, three oil wells and four dry holes were drilled in the Big Flat field, which was abandoned in 1971 after producing more than 83,000 barrels of oil (BO).

The early 1960s saw the discovery of the Shafer Canyon, Bartlett Flat, and Long Canyon fields. The Shafer

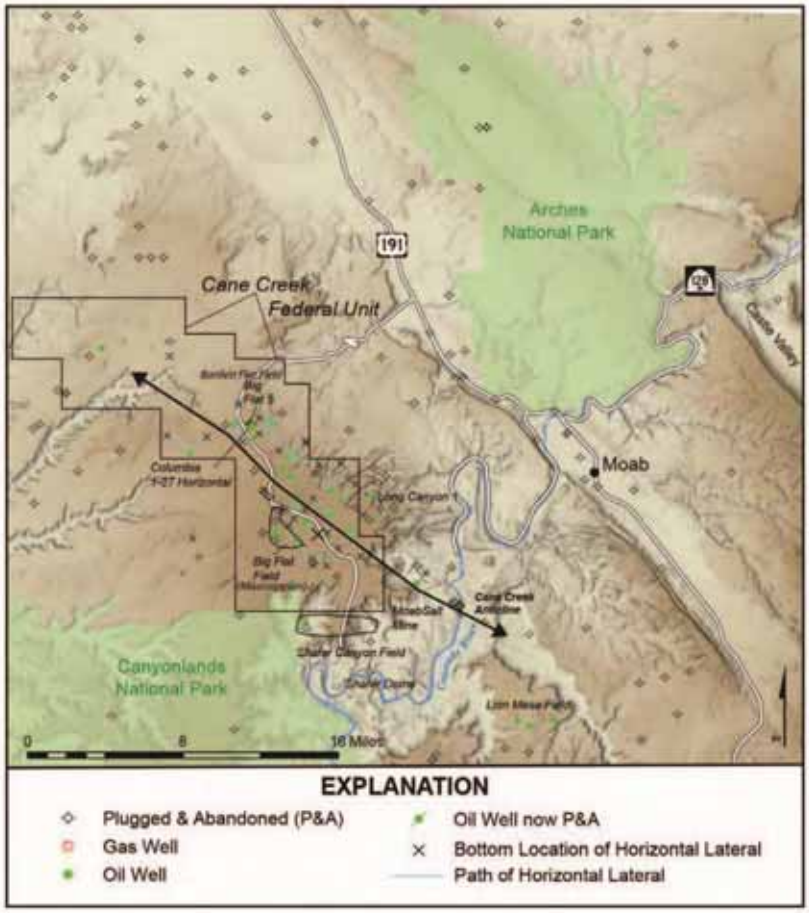

Oil and gas wells in the Moab region, some dating back to the 1920s. Current oil drilling and production is from wells in the Cane Creek Federal unit. Many of the wells in the unit were drilled horizontally in the Cane Creek shale, and some horizontal laterals are thousands of feet in length.

Canyon field consisted of two wells, one on each side of Dead Horse Point State Park, which produced from the Cane Creek shale. The wells were plugged and abandoned in 1969 after producing over 67,000 BO, mostly from one well. Bartlett Flat (Big Flat 5 well) and Long Canyon (Long Canyon 1 well) fields (both one-well fields) also produced from the Cane Creek shale. The casing collapsed in the Big Flat 5 well and the field was abandoned after producing 39,000 BO. Several additional wells unsuccessfully attempted to establish production at Bartlett Flat. The Long Canyon well was the most successful well in the area drilled during the 1960s. The well has produced more than 1 million BO and is still producing. Lion Mesa field was discovered in 1980, but has only produced a minor amount of oil from the Cane Creek shale.

Exploration continued in the Moab area, but significant success did not occur until Columbia Gas Development Corporation formed the Cane Creek Federal unit in 1991 and drilled a horizontal well (1-27) in the Cane

RESERVOIR CHARACTERIZATION

The Cane Creek shale is a difficult oil reservoir to develop. In the Big Flat area, about 3500 feet of interbedded sandstone, shale, and limestone overlie the Paradox Formation. From the top of the Paradox to the Cane Creek, there is about 3500 to 4000 feet of salt with thin, interbedded shale beds. Under the pressure and temperature of deep burial, salt will often flow, like squeezing a tube of toothpaste. Salt flowage can ruin a well by collapsing the well casing and plugging well perforations and tubing.

Mapping seismic data can identify faults and structural highs at the Cane Creek shale horizon. These deep structures are often the drilling targets, but identifying where good reservoir-quality porous beds and natural fractures occur is much more difficult. On the surface the formations are generally flat-lying to gently inclined, but the salt deposits of the Paradox Formation are often highly deformed. Movement of thousands of feet of salt from one location to another formed large salt anticlines; when the salt pushed through or intruded into the overlying formations it created salt diapirs. Moab–Spanish Valley, Castle Valley, and Salt Valley in Arches National Park are all examples of large diapiric salt anticlines. The Big Flat area sits atop the Cane Creek anticline, which is the result of more subdued salt movement. The movement of salt formed a broad, gentle anticline but did not penetrate the overlying formations. Additionally, smaller-scale deformation within the individual Paradox salt cycles often resulted in folding the Cane Creek shale into "wavy folds." These folds typically have a wave height of several feet to tens of feet and are spaced hundreds of feet apart. This smaller-scale folding can make it very difficult to keep the drill bit within the Cane Creek reservoir when drilling a horizontal lateral several thousand feet long.

Naturally occurring open fractures in the Cane Creek shale are important permeability pathways for oil to move from the formation into the well bore. Core from the Cane Creek contains many types of fractures; some are thin with limited length and are filled with anhydrite, calcite, or clay, and some are wider and filled with halite. Open fractures tend to be near vertical but are confined to individual brittle sandstone or carbonate beds. An important part of predicting where oil-productive fractures might exist involves understanding when both the filled and open fractures formed, what forces caused the fracturing, and what fluid flow conditions resulted in mineral-filled fractures versus open fractures. Another key exploration element is understanding the timing of oil generation. Were the mineral-filled fractures sealed before or after oil was generated and were the open fractures formed before or during the time of peak oil generation? We are using organic-matter maturity data and burial history studies to determine when, and at what temperature, oil was generated. Also, fluid inclusions found in the fracture-fill minerals are being used to help determine at what temperature, and therefore what time during burial, minerals formed in the fractures. As minerals form within a fracture, microscopic bubbles of liquid and gas can

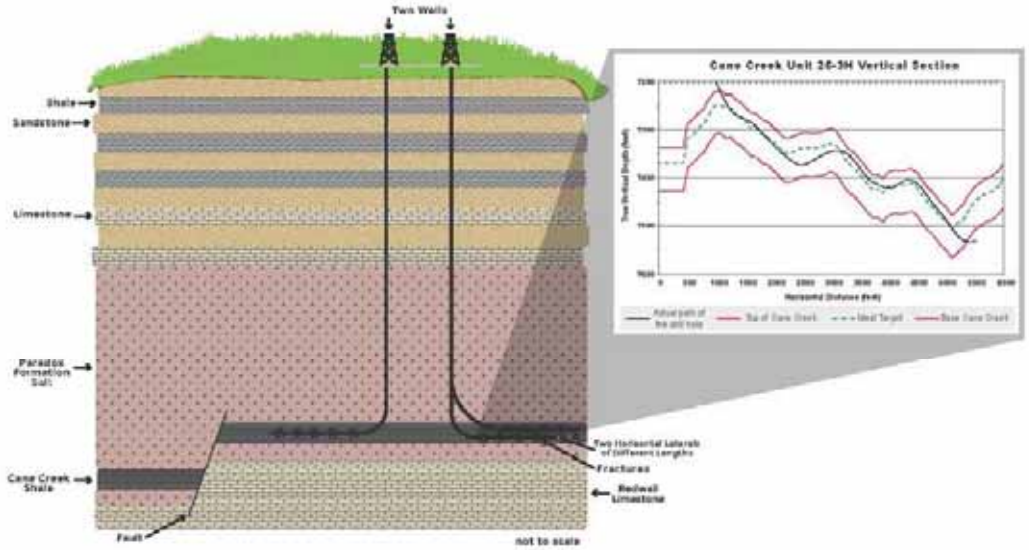

Diagram illustrating horizontal drilling in the Cane Creek shale of the Paradox Formation. In some wells multiple laterals are drilled. The Cane Creek is often gently folded and rarely ever level. The smaller diagram shows the actual path of a horizontal lateral and the difficulty of staying within the Cane Creek reservoir target (from Utah Division of Oil, Gas and Mining well records).

CANE CREEK UNIT

SHAFER DOME | PRODUCTION FACILITIES | DRILLING WELL

Drilling along the Colorado River at Shafer dome (A) and Cane Creek anticline (B) in the 1920s. Material was floated down the river on barges and the buildings and derrick were constructed on site. Photographs courtesy of Utah Historical Society. Present-day oil production from the Cane Creek shale is from horizontal wells. Producing facilities and drilling well photographs by Ammon McDonald (Utah Division of Oil, Gas and Mining).

become trapped within the crystal structure. Heating and cooling of the bubbles reveals the composition of the fluids, gases, and the temperature at which they formed. When in geologic history the fractures formed can be determined by comparing temperature data generated from a burial history curve to the fluid inclusion temperatures. Burial history curves also help us determine when oil was generated within the Cane Creek.

STATUS OF UGS STUDY

Ongoing work includes mapping regional thickness, structure, organic content, and organic thermal maturity of the Cane Creek shale and associated salt deposits using well logs and cores to determine the extent of the reservoir and hopefully identify additional exploration areas. Improved reservoir characterization leads to more efficient development which can reduce the number of wells needed to be drilled and reduce the overall environmental impact of drilling. The UGS is currently in the final phase of the study and is preparing the final technical report.

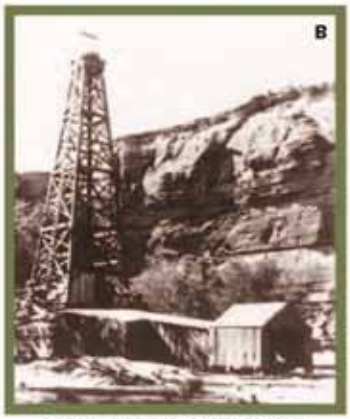

CANE CREEK ANTICLINE

Additional information on the Cane Creek reservoir characterization study, including quarterly technical reports and presentations, can be found on the project website at http://geology.utah.gov/resources/energy/oil-gas/shale-oil/

ABOUT THE AUTHOR

Craig Morgan is a senior geologist in the Energy and Minerals Program at the Utah Geological Survey (UGS). Craig started his career working as a well-site mudlogger and went on to work in oil and gas exploration for a decade before joining the Utah Department of Natural Resources, first as a water rights specialist in the Division of Water Rights, and then as a petroleum geologist with the UGS. Craig's work has primarily focused on reservoir characterization studies for exploration and improved hydrocarbon recovery, as well as studies for carbon sequestration and produced-water management.

Articles in Industry Magazines

AAPG Explorer

The AAPG EXPLORER is the monthly tabloid magazine of the American Association of Petroleum Geologists that covers news of interest to the AAPG membership. Contents include coverage of the entire span of energy interest, with emphasis on exploration for hydrocarbons and energy minerals. Breaking news stories, features, profiles of personalities, comment columns and Association information is included. The AAPG EXPLORER is read by more than 42,000 members and friends of the Association in 129 countries.

June 2013 – "Unconventional Uteland Butte Sparks New Utah Activity"

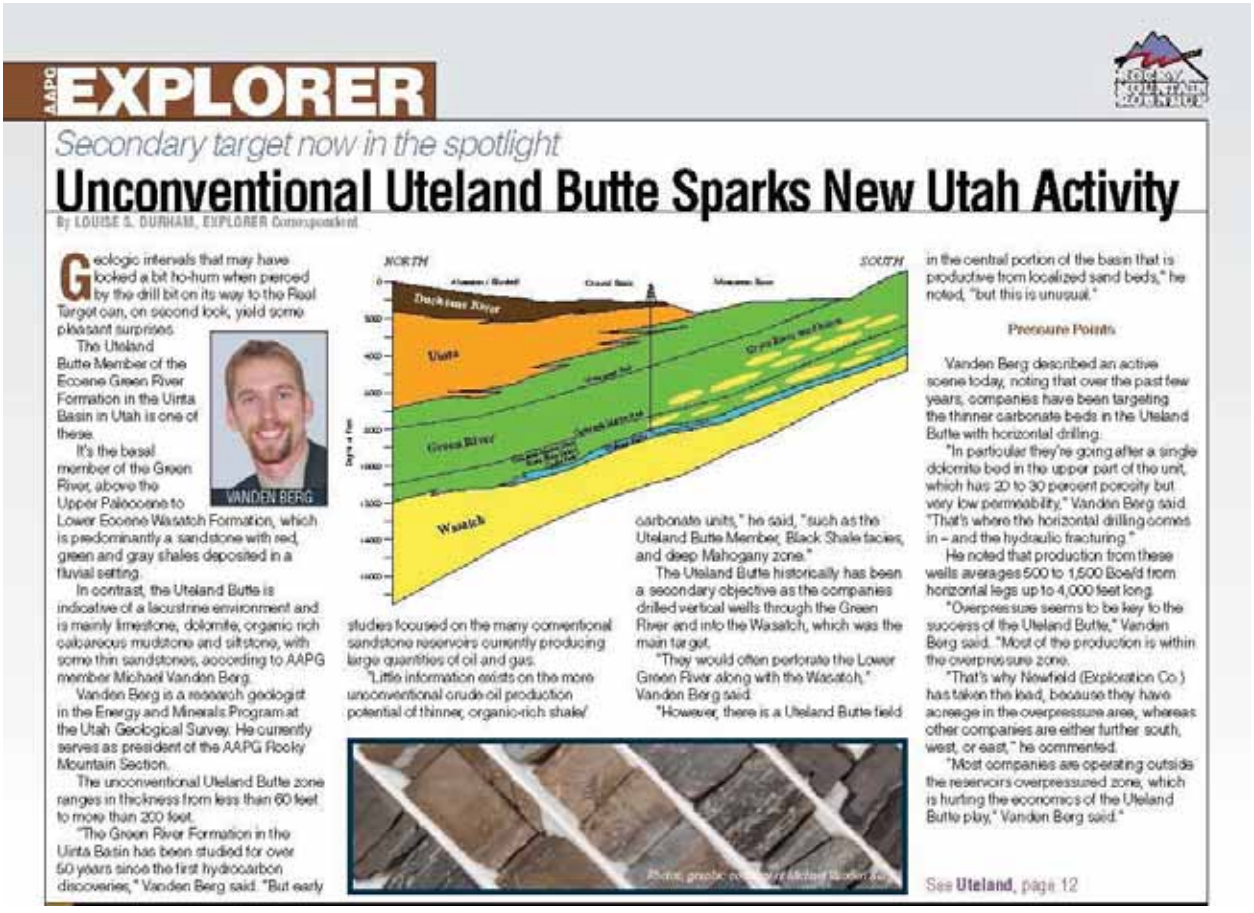

AAPG EXPLORER

Secondary target now in the spotlight

Unconventional Uteland Butte Sparks New Utah Activity

By LOUISE S. DURHAM, EXPLORER Correspondent

Geologic intervals that may have looked a bit ho-hum when pierced by the drill bit on its way to the Real Target can, on second look, yield some pleasant surprises.

The Uteland Butte Member of the Eocene Green River Formation in the Uinta Basin in Utah is one of these.

VANDEN BERG

It's the basal member of the Green River, above the Upper Paleocene to Lower Eocene Wasatch Formation, which is predominantly a sandstone with red, green and gray shales deposited in a fluvial setting.

In contrast, the Uteland Butte is indicative of a lacustrine environment and is mainly limestone, dolomite, organic rich calcareous mudstone and siltstone, with some thin sandstones, according to AAPG member Michael Vanden Berg.

Vanden Berg is a research geologist in the Energy and Minerals Program at the Utah Geological Survey. He currently serves as president of the AAPG Rocky Mountain Section.

The unconventional Uteland Butte zone ranges in thickness from less than 60 feet to more than 200 feet.

"The Green River Formation in the Uinta Basin has been studied for over 50 years since the first hydrocarbon discoveries," Vanden Berg said. "But early studies focused on the many conventional sandstone reservoirs currently producing large quantities of oil and gas.

"Little information exists on the more unconventional crude-oil production potential of thinner, organic-rich shale/carbonate units," he said, "such as the Uteland Butte Member, Black Shale facies, and deep Mahogany zone."

The Uteland Butte historically has been a secondary objective as the companies drilled vertical wells through the Green River and into the Wasatch, which was the main target.

"They would often perforate the Lower Green River along with the Wasatch," Vanden Berg said.

"However, there is a Uteland Butte field in the central portion of the basin that is productive from localized sand beds," he noted, "but this is unusual."

Photo: geologic outcrop by Michael Vanden Berg

Pressure Points

Vanden Berg described an active scene today, noting that over the past few years, companies have been targeting the thinner carbonate beds in the Uteland Butte with horizontal drilling.

"In particular they're going after a single dolomite bed in the upper part of the unit, which has 20 to 30 percent porosity but very low permeability," Vanden Berg said. "That's where the horizontal drilling comes in – and the hydraulic fracturing."

He noted that production from these wells averages 500 to 1,500 Boe/d from horizontal legs up to 4,000 feet long.

"Overpressure seems to be key to the success of the Uteland Butte," Vanden Berg said. "Most of the production is within the overpressure zone.

"That's why Newfield (Exploration Co.) has taken the lead, because they have acreage in the overpressure area, whereas other companies are either further south, west, or east," he commented.

"Most companies are operating outside the reservoirs overpressured zone, which is hurting the economics of the Uteland Butte play," Vanden Berg said."

See Uteland, page 12

Overlooked by past operators – and even some geologists – the Uteland Butte is indicative of a lacustrine environment and is mainly limestone, dolomite, organic rich calcareous mudstone and siltstone, with some thin sandstones. It also has become a hot target "with significant potential" in Utah, and the subject of intense research and investigation.

Uteland

from page 10

Making It Better

Right now, the Utah Geological Survey is evaluating how to make these fringe areas of the Uteland Butte more productive.

"We see significant potential in the fringe area," Vanden Berg noted. "The question we want to answer is what is the best way to complete these horizontal wells to unlock that potential."

There's a whole lotta research going on.

Vanden Berg is principle investigator for a newly launched three-year-long program funded by the National Energy Technology Laboratory – Liquid-Rich Shale Potential of Utah's Uinta and Paradox Basins: Reservoir Characterization and Development Optimization.

The overall goal of the study is to provide reservoir-specific geological and engineering analyses of:

- Emerging Green River Formation tight oil plays, such as the Uteland Butte Member, Black Shale facies and others in the Uinta Basin.
- Established yet understudied Cane Creek shale (and possibly other shale units) of the Pennsylvanian-age Paradox Formation in the Paradox Basin.

Hands-On Experience

If you were on the scene during the recent AAPG Annual Convention and Exhibition in Pittsburgh, you may have examined a Uteland Butte core that Vanden Berg transported in for a core poster session.

The core, which is from the productive carbonate zone in the Uteland Butte, was acquired from the Bill Barrett 14-3-45 BTR well in southwestern Altamont Field.

"The horizontal drilling objective, as analyzed in the core, is a five-foot interval of fractured dolomite, with porosities between 14 and 26 percent, interbedded with organic-rich limestone," Vanden Berg noted.

"The TOC values for the 60 feet of recovered core range between 2 and 5 percent, while Ro (vitrinite reflectance) values range between 0.7 and 1.1, indicating these rocks are self-sourcing."

Not to worry if you missed the Uteland Butte core-viewing opportunity in Pittsburgh. Word has it that you'll have another chance during a session at the upcoming AAPG Rocky Mountain Section meeting in Salt Lake City in September.

June 2014 – "Cane Creek Shale Keeping Utah in Energy Mix"

AAPG EXPLORER

ROCKY MOUNTAIN ROUNDUP

UGS multi-year study continues

Cane Creek Shale Keeping Utah in Energy Mix

By LOUISE S. DURHAM, EXPLORER Correspondent

Industry interest and activity in shale reservoirs continues to escalate.

The big headline-makers, such as the Barnett, Haynesville, Marcellus, comprise only some chapters of the big story.

The less familiar names also are beginning to make their mark.

Count the Cane Creek shale in the Pennsylvanian-age Paradox formation in the Paradox Basin in southeast Utah among those receiving considerable attention.

`The Cane Creek is a transgressive-regressive sequence in the lower portion of the Paradox,` said AAPG member Stephanie Carney, geologist at the Utah Geological Survey (UGS).

`It's tens of feet to nearly 200 feet thick, over-and underlain by salt beds,` Carney said.

She noted that it's divided into the A, B and C intervals, in descending order.

- B interval is the primary hydrocarbon source rock and productive zone, comprised of black organic-rich shale, dolomite, dolomitic sandstone and some anhydrite. Naturally occurring fractures are essential for economic production.
- A and C intervals are principally dolomite and anhydrite and act as seals for the B interval.


VANDEN BERG

> "This is where our study goes beyond studies done in the past. It's access to all of the new cores from wells drilled in the last couple of years."

`There's been activity in the Cane Creek since the 1960s, but just vertical wells with limited production,` said AAPG member Mike Vanden Berg, senior geologist and petroleum section manager at the UGS. `In the 1990s, operators started drilling horizontal wells but with short laterals, which hindered success.

`Recently, they're drilling much longer laterals with much more success,` Berg emphasized.

A Big Deal

The UGS is in the midst of implementing a multi-year study of the shale oil potential of the Cane Creek shale formation. The effort is being funded by the U.S. Department of Energy.

This is a big deal.

The USGS recently assessed the undiscovered oil resource in the Cane Creek shale in the Paradox Basin at 103 MMb (95-percent confidence level) and 198 MMb (50-percent confidence level).

Most of the operators and explorers in the play are small independents who are not in a position to conduct their own detailed basin-wide research, which is needed to truly understand the tight oil potential of this shale formation.

Carney pinpointed the goals of the UGS study:

- Gain insight into the geological, geochemical and geomechanical rock properties of the Cane Creek shale.
- Further define the play and the reservoir characteristics.

`The Big Flat field (near Moab) in the central portion of the play area is where

See **Cane Creek**, page 22

Cane Creek

from page 20

most of the current production is taking place," Berg said. "We're trying to determine what is the production potential to the north and south, where there's been very limited drilling.

"We think there's still potential (in these areas)," he emphasized. "The differences could be as simple as better structure in the Big Flat that has caused more fracturing.

"We do see that the thermal maturity changes from south to north," he said. "The organic matter is still kind of in the early oil window, but in the central to north – it's in the peak oil window.

"This may have something to do with why there's pretty good production in the central portion."

Looking for Fractures

Because they have cores from the south and the Big Flat field, they can see lithology and facies change between the two areas. Carney noted that this could contribute to the area productivity.

"This is where our study goes beyond studies done in the past," Berg noted. "It's access to all of the new cores from wells drilled in the last couple of years.

"We can map the three intervals using geophysical logs," he said, "but the question has always been: Has the facies changed across the basin?

"It's hard to tell from geophysical logs," he said, "and that's where the cores come in."

Carney noted there is significant work yet to be done, including a more detailed look at the fractures.

"We'll do fluid inclusion work on the fractures to figure out timing, whether the fractures occurred before or after oil migration," she said. "We'll look at more cores to do geomechanical work on a lot of the cores to help come up with strategies for well completions."

The outcome of just one of the wells drilled by Fidelity E&P in 2010 in the Big Flat field makes a profound statement about the production that can be attained.

After the first year of production, no other well in the lower 48 states had produced as much as that one well, according to Jayne Gates, asset team manager for the Paradox Basin at Fidelity.

The Cane Creek 12-1 reportedly produced between 600,000 and 700,000 barrels of oil during its first year in operation. The oil continues to free-flow to the surface today, meaning it doesn't yet require a pumping unit.

GEO ExPro magazine

GEO ExPro is an interdisciplinary magazine and online publication which explains, clarifies, and discusses geoscience and technology in an easy-to-read manner, allowing busy professionals to rapidly catch up on industry developments within the disciplines of Geology, Geophysics and Reservoir Engineering. The magazine is enjoyed by explorers, managers, and decision makers over 60 countries throughout the world. Half of these come from oil and gas operating companies, with the rest working in service companies, research organizations and a wide range of consultancies.

2016 - Volume 13, Number 2

"Identifying Potential Oil Zones in Tight Reservoirs: Low-cost epifluorescence microscope techniques have delineated a prospective, relatively untested oil-prone fairway in the Cane Creek shale play, Paradox Basin, Utah"

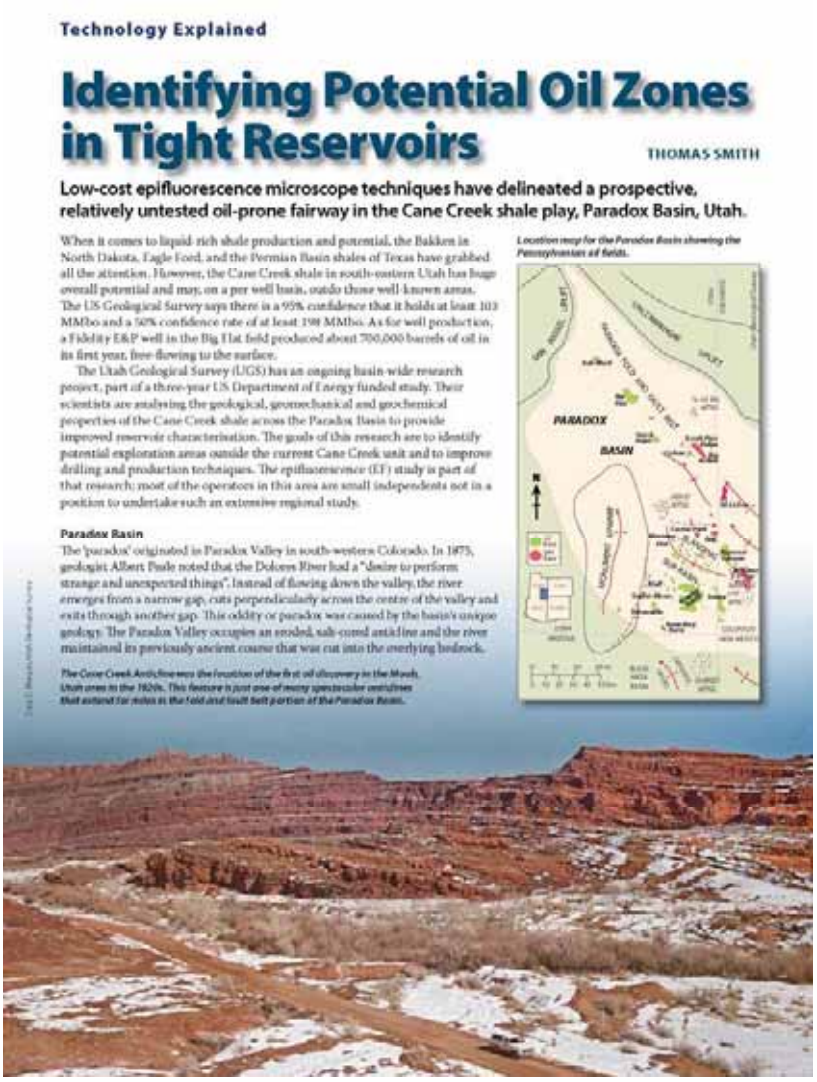

Technology Explained

Identifying Potential Oil Zones in Tight Reservoirs

THOMAS SMITH

Low-cost epifluorescence microscope techniques have delineated a prospective, relatively untested oil-prone fairway in the Cane Creek shale play, Paradox Basin, Utah.

When it comes to liquid-rich shale production and potential, the Bakken in North Dakota, Eagle Ford, and the Permian Basin shales of Texas have grabbed all the attention. However, the Cane Creek shale in south-eastern Utah has huge overall potential and may, on a per well basis, outdo those well-known areas. The US Geological Survey says there is a 95% confidence that it holds at least 103 MMbo and a 50% confidence rate of at least 198 MMbo. As for well production, a Fidelity E&P well in the Big Flat field produced about 700,000 barrels of oil in its first year, free-flowing to the surface.

The Utah Geological Survey (UGS) has an ongoing basin-wide research project, part of a three-year US Department of Energy funded study. Their scientists are analysing the geological, geomechanical and geochemical properties of the Cane Creek shale across the Paradox Basin to provide improved reservoir characterisation. The goals of this research are to identify potential exploration areas outside the current Cane Creek unit and to improve drilling and production techniques. The epifluorescence (EF) study is part of that research; most of the operators in this area are small independents not in a position to undertake such an extensive regional study.

Location map for the Paradox Basin showing the Pennsylvanian oil fields.

Paradox Basin

The 'paradox' originated in Paradox Valley in south-western Colorado. In 1875, geologist Albert Peale noted that the Dolores River had a "desire to perform strange and unexpected things". Instead of flowing down the valley, the river emerges from a narrow gap, cuts perpendicularly across the centre of the valley and exits through another gap. This oddity or paradox was caused by the basin's unique geology. The Paradox Valley occupies an eroded, salt-cored anticline and the river maintained its previously ancient course that was cut into the overlying bedrock.

The Cane Creek Anticline was the location of the first oil discovery in the Moab, Utah area in the 1920s. This feature is just one of many spectacular anticlines that extend for miles in the fold and fault belt portion of the Paradox Basin.

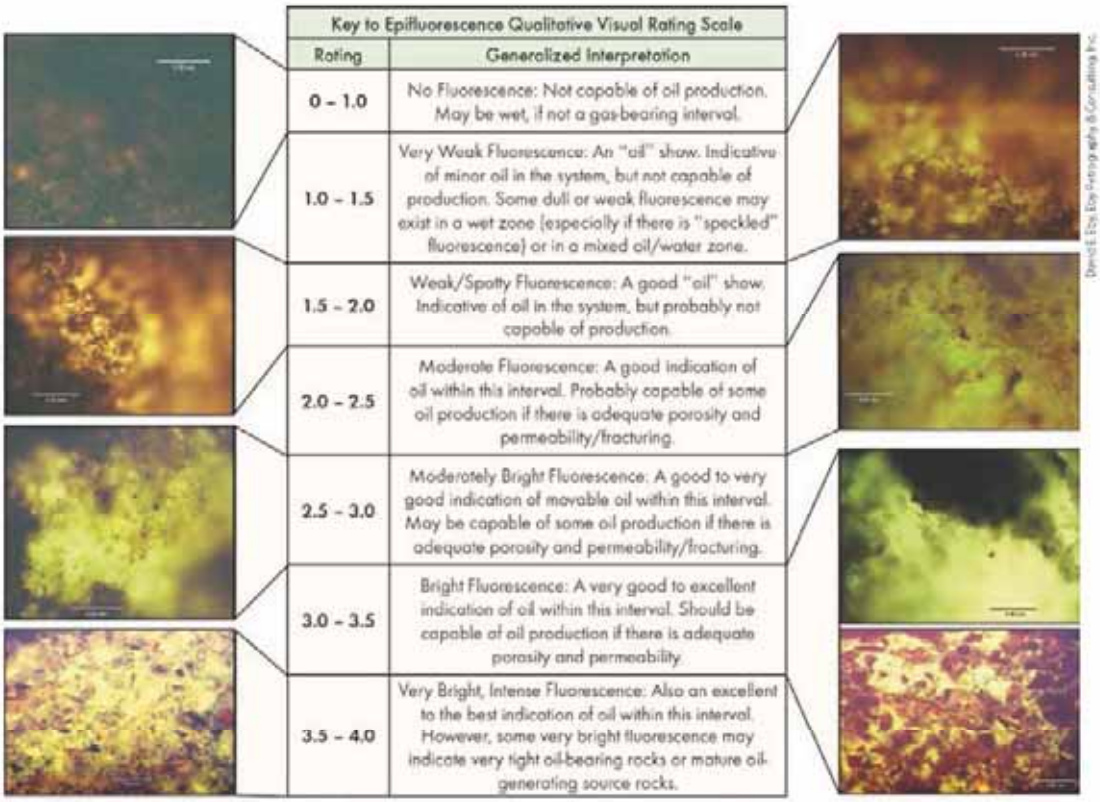

Micrographs showing examples of visually rated epifluorescence in the Cane Creek shale zone.

Moab Valley (Spanish Valley) located to the west in Utah has a similar geological history and is bisected by the Colorado River.

The Paradox Basin covers 85,470 km², primarily in south-east Utah and south-west Colorado, but extends into northern Arizona and New Mexico. The basin formed during Pennsylvanian (Late Carboniferous) time about 330 to 310 million years ago, when a series of fault-bounded uplifts and basins developed from Utah to Oklahoma as a result of continental collisions that formed the Ancestral Rockies. The Paradox Basin received a thick succession of cyclic carbonates, evaporites and organic-rich shales, now known as the Paradox Formation. The basin is divided into three areas: the fold and fault belt in the north, the Aneth platform in the south, and the Blanding sub-basin located between those two areas. Deposition in the northern portion of the basin (the Moab area) was in a highly restricted marine bay. Fluctuations in sea level left alternating thick deposits of halite and minor amounts of potassium and magnesium salts during low sea levels, while carbonates and siltstones with thin organic-rich shales were deposited during the high stands. There are 29 cycles in the Moab area; the Cane Creek shale was deposited in the highstand portion of cycle 21 in the lower Paradox Formation.

The first well in Utah was drilled in the northern end of the Paradox Basin near the town of Green River in 1891. Greater Aneth, Utah's largest oil field, is located in the southern end of the basin. Discovered in 1956, the field has produced over 470 MMbo.

The Study

The first oil discoveries in the Pennsylvanian Cane Creek shale play occurred in the early 1960s. The most successful well drilled during this period was at Long Canyon field, which has produced over 1 MMbo, although most wells produced less than 70,000 bo before being plugged and abandoned. Exploration continued but significant success did not occur until Columbia Gas Development Corporation formed the Cane Creek Federal unit in 1991 and drilled a horizontal well, the first long-reach horizontal well in Utah. The company drilled six horizontal wells that have delivered over 1.4 MMbo and are still producing. Recently, Fidelity Exploration & Production Company took ownership of the field and has drilled 17 additional wells in the Cane Creek Federal unit. Now, with longer laterals and improved completions, well rates have dramatically increased and are expected to ultimately produce about 1.7 MMbo each.

The horizontal target is the B interval where the reservoir is primarily comprised of dolomite, sandstone and siltstone with both intercrystalline and microporosity. This interval is sandwiched by the A and C zones, consisting of organic-rich shale, anhydrite and silty dolomite which serve as both

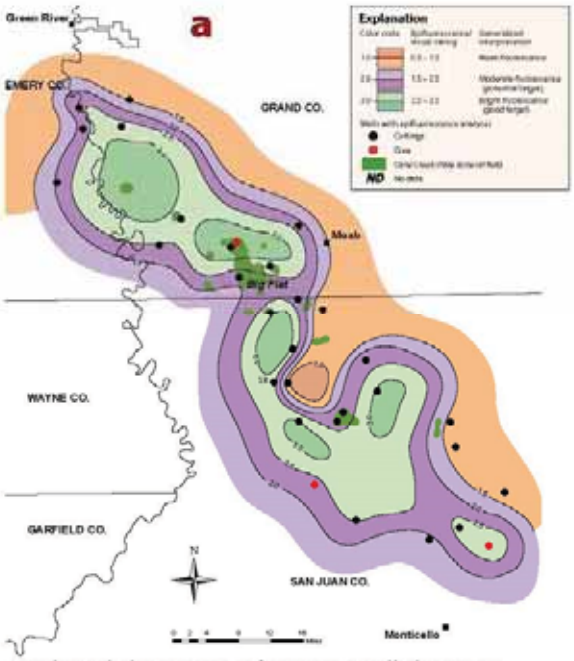

Maps showing highest maximum epifluorescence (a) and highest average epifluorescence (b) for Cane Creek B interval. A well-defined fairway with ratings 2.0 and higher (purple and greens) follows the same general trend as the total Cane Creek shale highest rating. All existing Cane Creek fields lie within this trend. Very prospective, largely untested B interval sections are present in lobes to the north-west and south-east of the Big Flat field, indicating the interval may not have uniform prospectivity along the favourable fairway. High-risk, less prospective areas occur to the north-east and south-west of the prospective fairway.

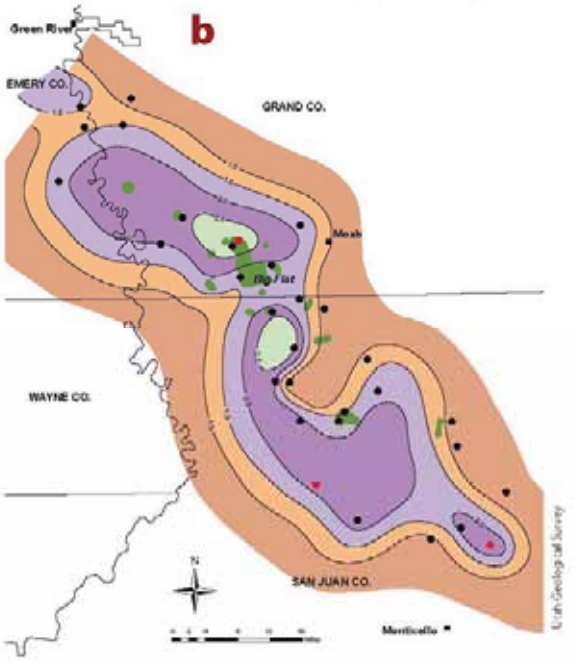

the hydrocarbon source and as seals for the B interval. The entire Cane Creek interval is naturally fractured and overpressured. Production occurs in the fractured dolomites, sandstones and siltstones, usually on subtle subsidiary structural noses found associated with the major structures that trend south-east to north-west across the northern portion of the Paradox Basin. This area, known as the Paradox fold and fault belt, is crossed by large spectacular anticlines that are cored by salt.

Locating these subtle traps usually requires expensive, 3D seismic acquisition in often environmentally sensitive areas. To help high grade this large area outside the existing unit for lease acquisition and more detailed seismic mapping that could lead to exploratory drilling, UGS scientists working with Dr. David E. Eby, from Eby Petrography & Consulting, Inc., Denver, Colorado, have used the area's extensive collection of cuttings, core chips and a limited number of thin sections to conduct this study. EF microscope techniques gave them a low-cost, non-destructive way to characterise the reservoir properties and organic matter including live hydrocarbons.

"Approximately 2,650 cuttings samples and core chips from the collection at the Utah Core Research Centre were evaluated from 31 wells penetrating the Cane Creek shale, including several producers," explains Tom Chidsey, senior scientist at the UGS. "Cuttings were examined under a binocular microscope and representative samples were selected over the Cane Creek interval. Four to ten samples were analysed over each depth interval from each well. The cuttings or core chips were placed on Petrologs™, a small plastic, self-adhesive compartmentalised cuttings storage unit that made sample preparation quick and inexpensive for EF examination. All Petrologs used in this study are stored at the Utah Core Research Centre and are available to the public."

Qualitative Mapping

"EF petrography makes it possible to clearly identify hydrocarbon shows in the Cane Creek cuttings," says Chidsey. "The best images are obtained at relatively high magnifications (greater than 100x). A qualitative visual rating scale (a range and average) based on EF evaluation was applied to the group of cuttings or core chips. Using the qualitative visual rating scale, a variety of EF readings for each well were plotted and mapped. We mapped highest maximum and highest average for the total Cane Creek shale zone and then separated out the A, B, and C intervals. All the maps use the same ratings. Areas considered highly prospective for oil have ratings 2.0 or higher." As expected, the EF ratings for productive Cane Creek wells were generally highest and served as a baseline in identifying potential.

"The Cane Creek interval is a difficult reservoir to explore and develop," explains Chidsey. "Seismic mapping can identify potential drilling targets; however, identifying where good quality reservoirs exist is extremely difficult. Using low-cost EF analysis and

Epifluorescence Microscopy

EF microscopy enables better imaging of poorly preserved textures and grains in sandstone, siltstone and carbonate rocks, particularly the type of dolomites encountered in the Cane Creek play. Information on the diagenesis, pore types and organic matter (including 'live' hydrocarbons) within sedimentary rocks are gained using EF microscopy. Samples are analysed using a rapid and non-destructive procedure employing a petrographic microscope equipped with reflected-light capabilities, a high pressure mercury vapour lamp for EF evaluation, appropriate filtering and a film imaging system. For the Cane Creek samples, magnification ranges for examination and image-documentation were between 130 and 320x, and it was found that broad-band, blue-light EF was the most helpful in observational work on the dolomites. The greater depth of investigation into a sample by the reflected fluorescence technique over that provided by either polarised or other forms of reflected light makes it possible to resolve grain boundary and compositional features that are normally not appreciated in cuttings or thin-section petrography.

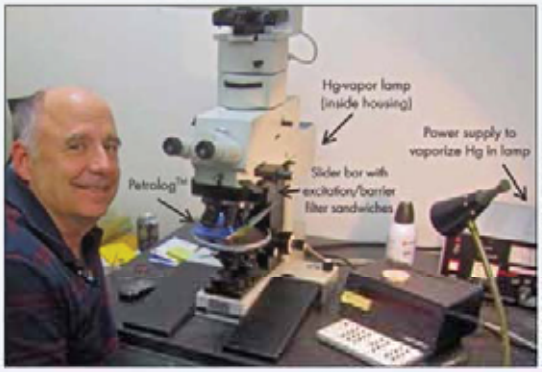

mapping has identified a prospective north-west to south-east oriented fairway in the Cane Creek shale zone, whereas the north-eastern part of the Paradox fold and fault belt shows low EF values. The implication is that hydrocarbon migration in the Cane Creek dolomite beds was along regional north-west trending folds, faults and fracture zones, creating this relatively untested oil-prone area.

"EF analysis represents a low-cost method that can help quantify and delineate the 'sweet spots' and the potential areas in emerging tight oil plays around the world just as it has in the Cane Creek shale."

The UGS and Eby previously conducted a similar EF study on the Mississippian Leadville Limestone, also in the Paradox Basin, which also showed areas with untested potential. ■

Project Presentations at National and Regional Conferences

All abstracts and most presentations can be downloaded from the UGS project website.

Birdwell, J.E., Vanden Berg, M.D., and Johnson, R.C., 2017, Geochemistry and mineralogy of the Eocene Green River Formation petroleum system, Uinta Basin, Utah. AAPG meeting, Houston, TX.

Birdwell, J.E., Vanden Berg, M.D., Johnson, R.C., and Boehlke, A.R., 2016, Geochemistry and mineralogy of the Uteland Butte member of the Green River Formation, Uinta Basin, Utah. AAPG-RMS-PS meeting, Las Vegas, NV.

Rueda, F., Machel, H.G., and Vanden Berg, M.D., 2016, Origin of petroliferous dolomitic beds in the Uteland Butte member, Lower Green River Formation, Uinta Basin, Utah. AAPG-RMS-PS meeting, Las Vegas, NV.

Rueda, F., Vanden Berg, M.D., and Machel, H., 2016, Dolomitization in the Uteland Butte member of the Eocene Green River Formation, Uinta Basin, Utah: Implications for petroleum production potential. AAPG meeting, Calgary, Alberta, Canada.

Logan, K., and Sarg, R., 2016, Lacustrine lithofacies, depositional processes, and diagenesis of the Uteland Butte member, Uinta Basin. AAPG meeting, Calgary, Alberta, Canada.

Eby, D., Chidsey, T., Vanden Berg, M.D., Carney, S., Boden, T., Wood, R., and Hurlbut, W., 2015, Potential oil-prone areas in the Cane Creek shale play, Paradox Basin, Utah, U.S.A., identified by epifluorescence techniques. AAPG meeting, Denver, CO.

Vanden Berg, M.D., Morgan, C., and Chidsey, T., 2015, Analyzing core from two emerging tight oil plays in Utah: The Uteland Butte member of the Green River Formation in the Uinta Basin and the Cane Creek shale within the Paradox Formation in the Paradox Basin. AAPG meeting, Denver, CO.

Vanden Berg, M.D., Wood, R., Carney, S., and Morgan, C., 2014, Geological characterization of the Uteland Butte member of the Eocene Green River Formation: An emerging unconventional carbonate tight oil play in the Uinta Basin, Utah. AAPG-RMS meeting, Denver, CO.

Morgan, C., Carney, S., Nielsen, P., Vanden Berg, M.D., and Wood, R., 2014, Play analysis of the Cane Creek shale, Pennsylvanian Paradox Formation, Paradox Basin, southeast Utah. AAPG-RMS meeting, Denver, CO.

Carney, S., Nielsen, P., and Vanden Berg, M.D., 2014, Geological evaluation of the Cane Creek shale, Pennsylvanian Paradox Formation, Paradox Basin, southeastern Utah. AAPG meeting, Houston, TX.

Nielsen, P., Morgan, C., and Vanden Berg, M.D., 2013, Detailed sedimentology and stratigraphy of the Remington 21-1H Cane Creek shale core, Pennsylvanian Paradox Formation, southeastern Utah: Implications for unconventional hydrocarbon recovery. AAPG-RMS meeting, Salt Lake City, UT.

Nielsen, P., Morgan, C., and Vanden Berg, M.D., 2013, Current understanding of the sedimentology, stratigraphy, and liquid-oil potential of the Pennsylvanian Cane Creek shale of the Paradox Formation, southeastern Utah. AAPG-RMS meeting, Salt Lake City, UT.

Vanden Berg, M.D., Morgan, C.D., Chidsey, Jr., T.C., and Nielsen, P., 2013, The Uteland Butte member of the Eocene Green River Formation: An emerging unconventional carbonate tight oil play in the Uinta Basin, Utah. AAPG, Pittsburgh, PA.

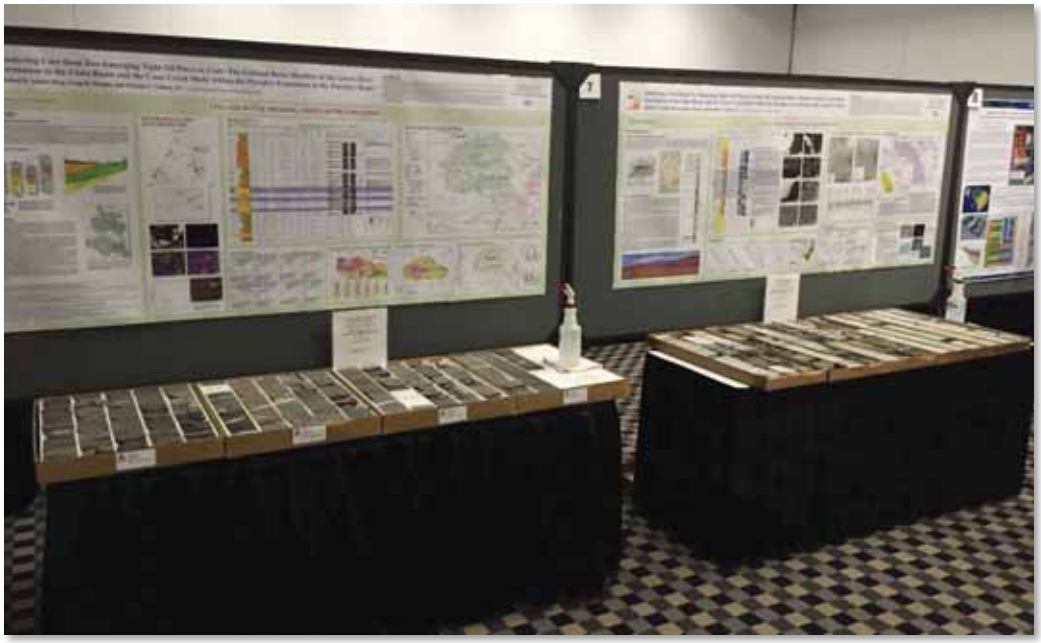

Uteland Butte and Cane Creek core poster presented at the 2015 AAPG annual meeting in Denver, CO

Project team members Tom Chidsey (left) and David Eby (second from left) present a poster on the Cane Creek shale at the 2015 AAPG annual meeting in Denver, CO.

AAPG Energy Minerals Division Annual Reports

Project team member Tom Chidsey wrote articles summarizing the geology and current drilling and research activities of the Uteland Butte, Cane Creek, and other tight oil plays in Utah for inclusion in the 2014, 2015, and 2016 AAPG-EMD Shale Gas and Liquids Committee annual reports.

http://www.aapg.org/about/aapg/overview/committees/emd/articleid/26349/committee-emd-shale-gas-liquids#141872236-activity--reports

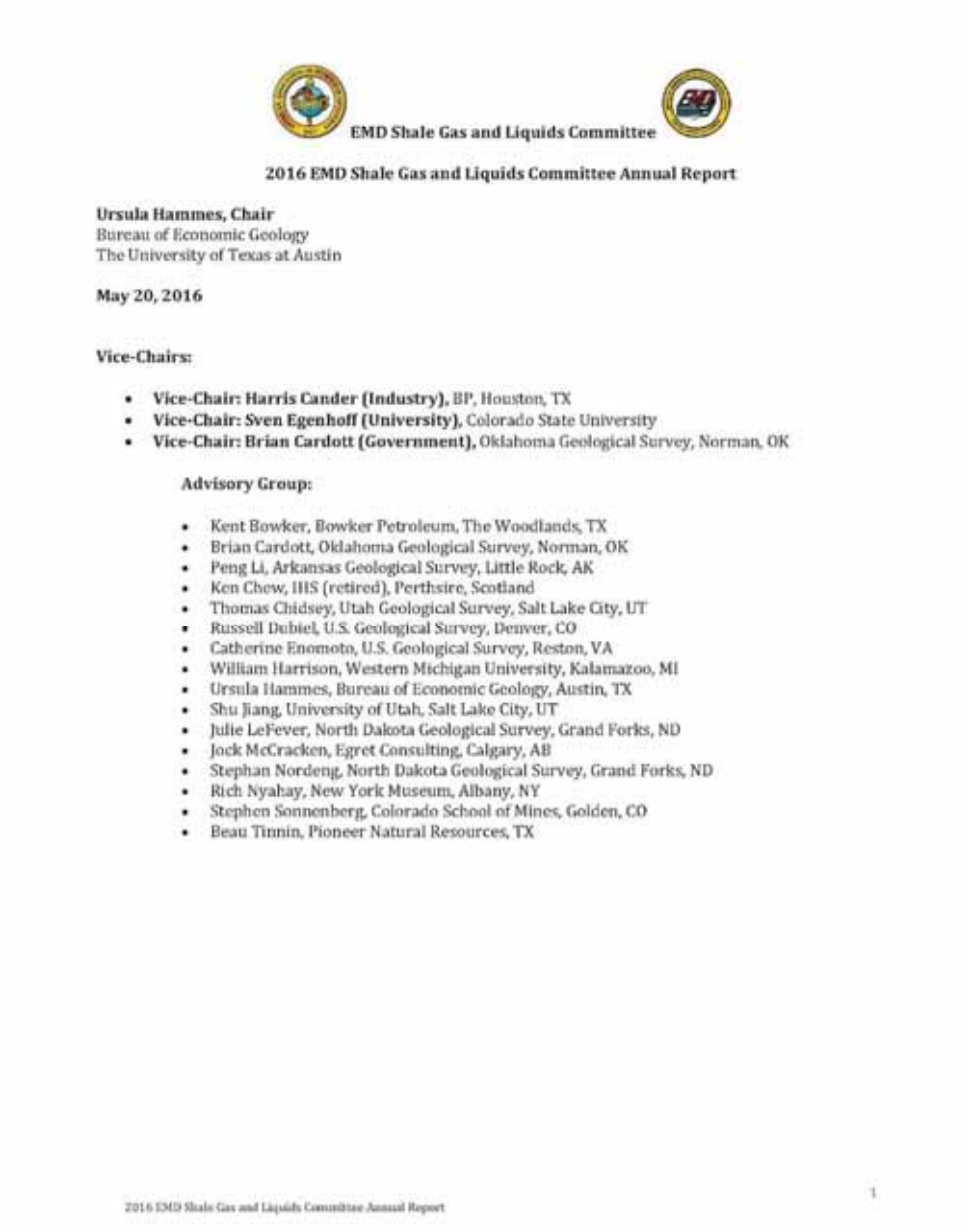

EMD Shale Gas and Liquids Committee

2016 EMD Shale Gas and Liquids Committee Annual Report

Ursula Hammes, Chair
Bureau of Economic Geology
The University of Texas at Austin

May 20, 2016

Vice-Chairs:

- **Vice-Chair: Harris Cander (Industry),** BP, Houston, TX
- **Vice-Chair: Sven Egenhoff (University),** Colorado State University
- **Vice-Chair: Brian Cardott (Government),** Oklahoma Geological Survey, Norman, OK

Advisory Group:

- Kent Bowker, Bowker Petroleum, The Woodlands, TX
- Brian Cardott, Oklahoma Geological Survey, Norman, OK
- Peng Li, Arkansas Geological Survey, Little Rock, AK
- Ken Chew, IHS (retired), Perthsire, Scotland
- Thomas Chidsey, Utah Geological Survey, Salt Lake City, UT
- Russell Dubiel, U.S. Geological Survey, Denver, CO
- Catherine Enomoto, U.S. Geological Survey, Reston, VA
- William Harrison, Western Michigan University, Kalamazoo, MI
- Ursula Hammes, Bureau of Economic Geology, Austin, TX
- Shu Jiang, University of Utah, Salt Lake City, UT
- Julie LeFever, North Dakota Geological Survey, Grand Forks, ND
- Jock McCracken, Egret Consulting, Calgary, AB
- Stephan Nordeng, North Dakota Geological Survey, Grand Forks, ND
- Rich Nyahay, New York Museum, Albany, NY
- Stephen Sonnenberg, Colorado School of Mines, Golden, CO
- Beau Tinnin, Pioneer Natural Resources, TX

2016 EMD Shale Gas and Liquids Committee Annual Report 1

Industry Outreach Activities/Workshops

- Utah Governor's Annual Energy Development Summit – January 10-11, 2013

  Tom Chidsey, UGS Senior Scientist and project participant, delivered a presentation about Utah shale gas and oil potential, including an overview of this project's goals and objectives. The summit was attended by over 1400 people from Utah and other states and countries. The summit also included a trip for interested participants to the Utah Core Research Center where several cores were on display including a Uteland Butte core and the project exhibit booth panel.

- Uinta Basin Oil and Gas Collaborative Group (UBOGCG) quarterly meeting – January 17, 2013

  The PI presented an overview of the project at the UBOGCG meeting in Vernal, UT. This meeting typically hosts ~100 attendees including oil and gas operators, government officials, and the general public.

- RPSEA-sponsored conference and field trip, hosted by the Utah Geological Survey – September 10-11, 2014

  The UGS hosted a RPSEA-sponsored conference and field trip on September 10-11, 2014. The agenda included presentations on the Uteland Butte and Cane Creek tight oil plays and the field trip included a stop in Nine Mile Canyon to view the Uteland Butte in outcrop. The conference was attended by over 70 individuals from the private sector, academia, and state and federal government agencies. The conference also included Uteland Butte and Cane Creek core displays.

- Core workshop for Shell Oil Company - June 3, 2014

  The PI led a lacustrine systems core workshop for Shell Oil Company that included Uteland Butte core and a discussion of our project.

- Core workshop for the 3rd Annual Utah Governor's Energy Development Summit – June 4, 2014

  The PI led a core workshop for Summit attendees. The workshop included cores from several different producing fields in Utah, including the Cane Creek and the Uteland Butte tight oil plays.

- AAPG Lacustrine Basin Exploration field course – Core Workshop – September 16, 2014

  The PI helped organize a core workshop for an AAPG field course focusing on lacustrine rocks of the Green River Formation, including the Uteland Butte member.

- Core workshop for a delegation of Chinese energy scientists – October 2, 2014

  The workshop included Uteland Butte and Cane Creek cores and the PI gave a presentation describing the project's goals and objectives.

- Core workshop and field trip for oil and gas industry geologists – April 28-30, 2015

  The PI led a core workshop and field trip for several oil and gas industry geologists in April 2015, highlighting the petroleum geology of the Green River Formation in the Uinta Basin, Utah, including the unconventional Uteland Butte member.

- Core workshop for a delegation of Chinese government energy scientists – August 25, 2015

  A delegation of about 15 Chinese government energy scientists toured the Utah Core Research Center. On display were Uteland Butte and Cane Creek cores and the PI gave a presentation describing the project's goals and objectives.

- Core workshop for geologists from SM Energy – December 9, 2015

  The PI lead a core workshop for geologists from SM Energy focused on the Uteland Butte play.

- Core workshop for oil and gas industry geologists – January 30-31, 2017

  The PI hosted a Green River Formation core workshop for 25 geologists from 11 different companies (Ultra, Axia, Finley, Bayless, Crescent Point, Sinclair, Wexpro, Newfield, Badlands, Anschutz, and Summit Mudlogging). The PI gave several presentations on the Green River Formation, including results of research performed as part of this project. The PI also presented cores examined as part of this project.

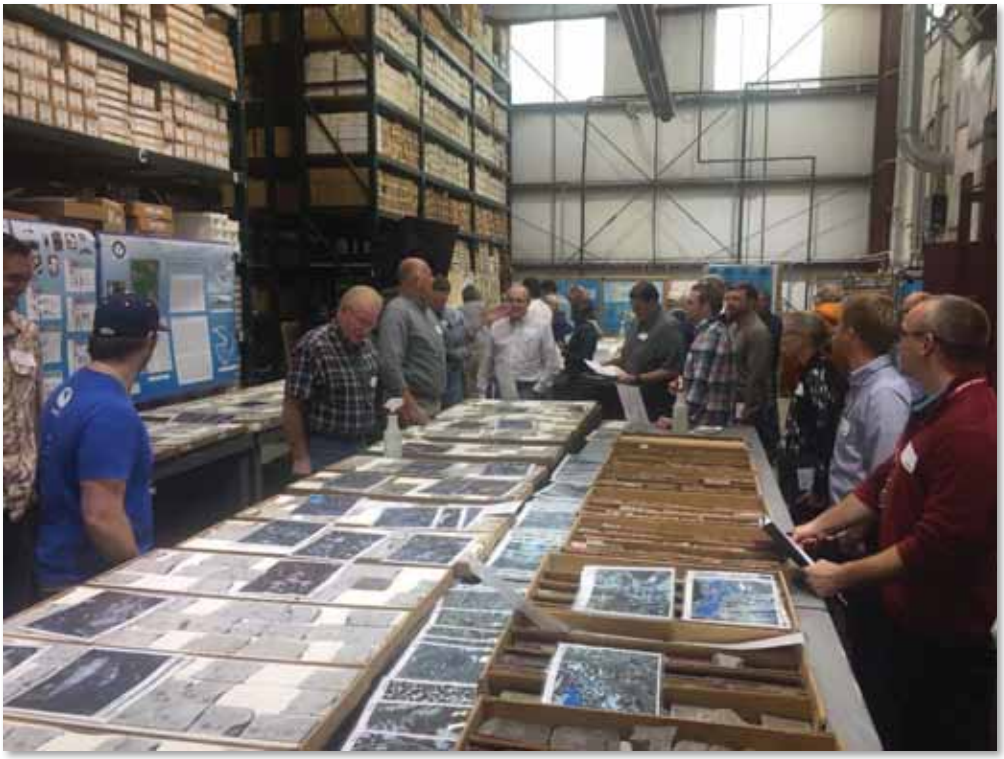

Core workshop at the Utah Core Research Center

Quarterly Reports

The PI wrote and distributed 18 quarterly reports, each highlighting the project's progress from the previous quarter. All quarterly reports can be downloaded from the UGS project website.

Project Displays at American Association of Petroleum Geologists Conferences

Project materials, plans, objectives, and results were displayed at the UGS exhibit booth during the following meetings of the AAPG:

AAPG Annual Convention, May 19-22, 2013, Pittsburgh, Pennsylvania
AAPG Rocky Mountain Section Meeting, September 22-24, 2013, Salt Lake City, Utah
AAPG Annual Convention, April 6-9, 2014, Houston, Texas
AAPG Rocky Mountain Section Meeting, July 20-22, 2014, Denver, Colorado
AAPG Annual Convention, May 31-June 3, 2015, Denver, Colorado

Field Trips

Several fieldtrips were run as part of various conferences and workshops. Stops were made at classic Green River Formation Uteland Butte outcrops in the southern Uinta Basin.

- Field trip and core workshop for Repsol and Statoil – June 2-5, 2013
- AAPG-RMS field trip – September 25, 2013
- Field trip and core workshop for Pertamina – April 16-21, 2014
- RPSEA-sponsored conference and field trip – September 10-11, 2014
- Field trip and core workshop for oil and gas industry (Ultra, Wexpro, Encana, Endeavour, Bayless, Sinclair) geologists – April 28-30, 2015
- Utah Geological Association field trip – September 17-19, 2015

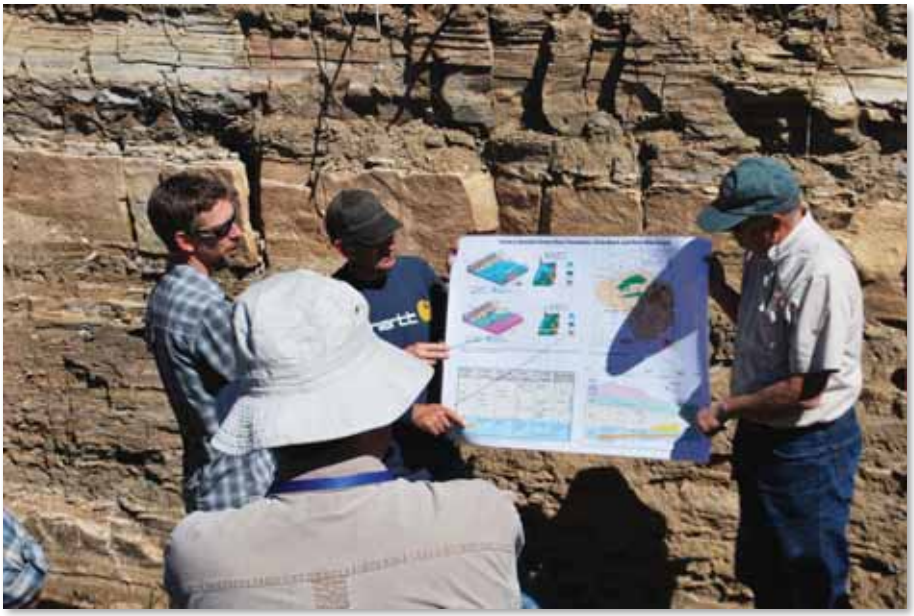

Final Publications

Published papers:

Schamel, S., 2015, Shale Oil Resource Play Potential of the Green River Formation, Uinta Basin, Utah: Open-File Report 639.

Schamel, S., 2015, Rediscovered Shale Oil Resource Play Potential of the Green River Formation, Uinta Basin, Utah: Associated with Energy Resource Development, *in* Vanden Berg, M.D., Ressetar, R., and Birgenheier, L.P., editors, Geology of Utah's Uinta Basin and Uinta Mountains: Utah Geological Association Publication 44, p. 275-303.

Johnson, R.C., Birdwell, J.E., Mercier, T.J., Brownfield, M.E., Charpentier, R.R., Klett, T.R., Leathers, H.M., Schenk, C.J., and Tennyson, M.E., 2015, Assessment of Undiscovered Oil and Gas Resources in the Uteland Butte Member of the Eocene Green River Formation, Uinta Basin, Utah: USGS Fact Sheet 2015-3052.

Logan, S.K., Sarg, J.F., and Vanden Berg, M.D., 2016, Lithofacies, Deposition, Early Diagenesis, and Porosity of the Uteland Butte Member, Green River Formation, Eastern Uinta Basin, Utah and Colorado: UGS Open-File Report 652.

Birdwell, J., Vanden Berg, M.D., Johnson, R.C., Mercier, T.J., Boehlke, A.R., and Brownfield, M.E., 2016, Geological, Geochemical, and Reservoir Characterization of the Uteland Butte Member of the Green River Formation, Uinta Basin, Utah, *in* Dolan, M.P., Higley, D.K., and Lillis, P.G., editors, Hydrocarbon Source Rocks in Unconventional Plays, Rocky Mountain Region: Rocky Mountain Association of Geologists.

Chidsey, T.C., and Eby, D.E., 2017, Potential Oil-Prone Areas in the Cane Creek Shale Play, Paradox Basin, Utah, Identified by Epifluorescence Microscopy Techniques: UGS Special Study 160.

Papers included in the final report, but not yet published:

Characterization and Horizontal Drilling Potential of Oolitic and Ostracodal Limestone Reservoirs in the Eocene Green River Formation, Northeastern Uinta Basin, Utah – Craig D. Morgan and Rebekah W. Stimpson, Utah Geological Survey.

> *Status: The report is finished and has undergone internal review; it will be published as a UGS Special Study after an extensive peer-review process.*

Dolomitization in the Uteland Butte Member of the Eocene Green River Formation, Uinta Basin, Utah – Federico Rueda (M.S. student) and Dr. Hans Machel (Professor of geology at University of Alberta).

> *Status: Rueda is finishing his M.S. thesis and plans to defend in December 2017. A nearly complete draft of his thesis is included in the final report. After his thesis is finalized, Machel and Vanden Berg will summarize the research into one or two journal articles.*

Geological Characterization of the Pennsylvanian Paradox Formation Cane Creek Shale and Other Paradox Shales, Paradox Basin, Utah – Craig D. Morgan and Rebekah W. Stimpson, Utah Geological Survey.

> *Status: The report is finished and has undergone internal review; it will be published as a UGS Special Study after an extensive peer-review process.*

Geomechanical Characterization of the Uteland Butte and Cane Creek Tight Oil Plays – Dr. John McLennan (Chemical engineering professor at the University of Utah and researcher at the Energy and Geoscience Institute) and Josh Zannoni (PhD student).

Status: The report is finished and included in the final report, but it has not undergone peer review. The PI and McLennan will work to review the report and prepare it for publication.

Appendix I

Shale Oil Resource Play Potential of the Green River Formation, Uinta Basin, Utah

Steven Schamel

GeoX Consulting Inc., Salt Lake City, UT

Utah Geological Survey Open-File Report 639

SHALE OIL RESOURCE PLAY POTENTIAL OF THE GREEN RIVER FORMATION, UINTA BASIN, UTAH

by Steven Schamel

OPEN-FILE REPORT 639
UTAH GEOLOGICAL SURVEY
a division of
UTAH DEPARTMENT OF NATURAL RESOURCES
2015

Shale Oil Resource Play Potential of the Green River Formation, Uinta Basin, Utah

by Steven Schamel

Cover photo: *Outcrop of the middle Green River Formation, Willow Creek Canyon. Photo by Michael Vanden Berg.*

OPEN-FILE REPORT 639
UTAH GEOLOGICAL SURVEY
a division of
UTAH DEPARTMENT OF NATURAL RESOURCES
2015

STATE OF UTAH
Gary R. Herbert, Governor

DEPARTMENT OF NATURAL RESOURCES
Michael Styler, Executive Director

UTAH GEOLOGICAL SURVEY
Richard G. Allis, Director

PUBLICATIONS
contact
Natural Resources Map & Bookstore
1594 W. North Temple
Salt Lake City, UT 84114
telephone: 801-537-3320
toll-free: 1-888-UTAH MAP
website: mapstore.utah.gov
email: geostore@utah.gov

UTAH GEOLOGICAL SURVEY
contact
1594 W. North Temple, Suite 3110
Salt Lake City, UT 84114
telephone: 801-537-3300
website: geology.utah.gov

CONTENTS

SHALE OIL RESOURCE PLAY POTENTIAL OF THE GREEN RIVER FORMATION, UINTA BASIN, UTAH

by Steven Schamel

ABSTRACT

The Green River Formation in the Uinta Basin has many characteristics typical of an ideal shale oil resource play. It is a world-class oil-prone source rock. In nearly all parts of the basin there are many thousands of net feet of Type-I and Type-II kerogen-rich calcareous mudstones, many intervals of which have average total organic carbon (TOC) of 5–10% or greater. In the north-central and western parts of the basin a substantial part of the formation is in the oil-generative window. A large volume of the formation has reached "peak oil". Furthermore, organic maturation simulations done in this study using PRA BasinView-3D™ indicates early entry into the oil-generative window. In the northwest parts of the basin the lower Green River Formation was generating oil even before the end of the Eocene and slowing of sediment accumulation in the basin. Anomalous formation pressures are observed in the lower Green River Formation across much of the basin. In the area of the greater Altamont-Bluebell field in the northwest of the basin, the abnormal pressures are nearly lithostatic (0.6 to 0.8 psi/ft). The Green River Formation is unquestionably a superb petroleum system responsible for very large cumulative production of oil and associated natural gas, and an even larger potential oil sand resource.

This assessment of the shale oil resource play potential of the Green River Formation is based on the integration of:

- basin-wide stratigraphy and facies distributions;
- programmed pyrolysis and other geochemical data from organic-rich calcareous mudstone in fourteen wells, most of which are in the northern and western quadrants of the basin;
- new basin-wide BasinView 3D™ numerical modeling of thermal maturation at a 1.0 kilometer resolution;
- the known distribution of oil and oil sand accumulations in Green River Formation and age-equivalent reservoirs; and
- the current revitalization of oil production from Green River–Wasatch reservoirs.

Typical shale oil resource plays are self-contained petroleum systems having ineffective carrier systems that severely restrict migration of oil generated in the source rocks from migrating outward or upward into traps in reservoirs marginal to the oil kitchens. Consequently, the oil backs up into any and all pore space in the source rock succession, even creating fracture storage space where anomalous pressures occur. Relatively tight rocks that would normally never be considered reservoirs can have very high oil saturations and oil-in-place. In a shale oil resource play these are what are exploited by horizontal wells and hydraulic fracture stimulation.

As more of the shale oil plays receive close scrutiny, it is becoming clear that no two are the same with regards to character of source rock or reservoir. What they all have in common, however, is (1) an organic-rich source rock capable of generating large volumes of oil, (2) interbedded or proximal reservoir intervals that, although tight, have sufficient porosity and/or natural fractures to be capable of hosting commercially significant volumes of the producible oil, and (3) inefficient carrier systems resulting in the oil generated remaining in proximity to the oil-generative source rock. The presence of anomalous formation pressures appears necessary to drive the oil from reservoir to well bore, even when fracture stimulated. These are "self-sourcing" petroleum systems only when viewed on a scale that encompasses the entire source rock formation and its immediately adjacent strata, or a significant portion thereof. And so it is with the Green River Formation, which has both an internal "self-sourcing" continuous oil play within the oil generative window and conventional oil accumulations on its periphery. Due to the lenticular character of the sandstone and carbonate beds in the Green River Formation and the underlying Wasatch Formation, some beds trap oil locally, while others carry the oil up-dip into traps at a distance from the oil generative window.

Only a few years after the discovery of the Altamont field, it was described as an *"oil accumulation near the center of a deep basin"*, an example of a then newly-recognized *"group of deep-basin, organic-shale-related, overpressured accumulations"* having significant hydrocarbon potential. Altamont-Bluebell field characteristics subsequently have come to identify a basin-centered, continuous resource play. These characteristics include:

- difficulty in defining field limits laterally and vertically because the trap is stratigraphic with no simple down-dip water levels or facies boundaries to the productive horizons,

- multiple thin productive zones with abnormally high fluid pressures, and
- very low matrix porosities enhanced by post-lithification fractures.

The companies now using fracture stimulation and horizontal wells to produce oil from Green River–Wasatch sandstone and carbonate reservoirs have merely *rediscovered* this basin-centered, continuous shale oil resource play.

1. INTRODUCTION

The Uinta Basin (Fig. 1-1) is a mature oil and gas province (USGS, 2003). Through the beginning of 2015, the two counties producing nearly all of the hydrocarbons from the basin, Duchesne and Uintah, had cumulative life-time production of 712 million barrels of oil and 5438 billion cubic feet of natural gas (Utah Division of Oil, Gas, and Mining [DOGM]). All, or virtually all, of the oil, constituting 45% of the state's total, is sourced from the Green River Formation and extracted from what have been considered to be conventional reservoirs in this or immediately adjacent formations (Fouch and others, 1994). The principal oil fields in the Uinta Basin are shown with green overprint in Figure 1-2. Their cumulative production and recent annual production are presented in Table 1-1. Production rates of oil and associated gas have been increasing recently through the adoption of various enhanced recovery strategies. With the increasing interest in finding and developing unconventional shale oil and shale gas resources in North America and elsewhere, it is natural to inquire into the possibility for a shale oil resource play in the Green River Formation in the Uinta Basin. An earlier study (Schamel, 2005) supported by the Utah Geological Survey UGS) had concluded that the possibility of a successful shale gas play was small due to low thermal maturity for gas, but a potential shale oil resource play was not considered, nor was it investigated.

A shale oil resource has all of the characteristics of a viable petroleum system except one: the presence of an efficient network of carrier beds linking the source rock with reservoir traps. In a petroleum system with conventional oil plays, hydrocarbons generated in a source rock migrate out of the source rock (primary migration; Mann, 1994) through an interacting combination of molecular diffusion through the source rock's kerogen network and Darcy flow within the micro-pore network. On encountering more porous and permeable laminae, distinct beds and/or fracture networks, the oil can enter a carrier system (secondary migration; England, 1994) that leads either to discrete traps or eventually to the surface. In situations where the carrier system does not exist or is ineffective relative to the rate of hydrocarbon generation, the oil backs up within the source rock formation filling all available pore space. When organic-rich rock layers are intercalated with organic-lean, but more porous, layers, the

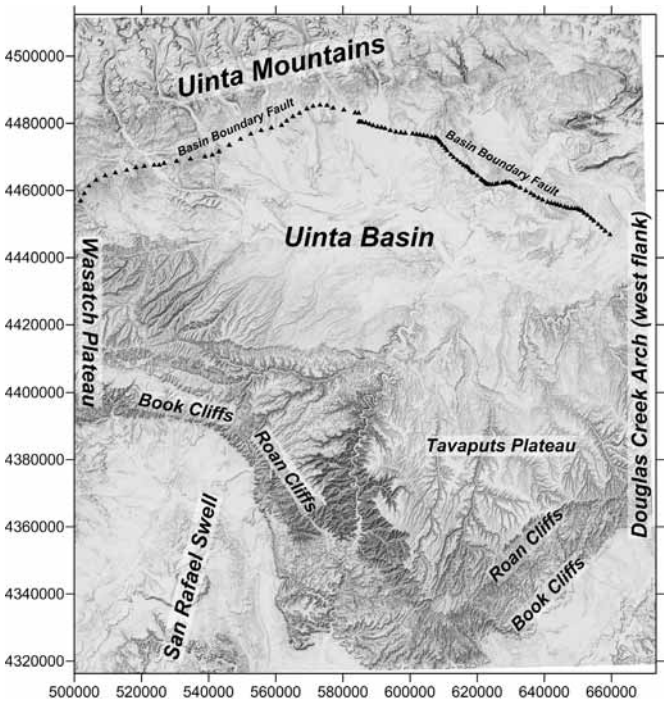

Figure 1-1: *Shaded relief map of the Uinta Basin and bounding structural uplifts: Uinta Mountains, Douglas Creek Arch, San Rafael Swell, and Wasatch Plateau. The Tavaputs Plateau is a southern extension of the basin, which is bounded on the south by its erosional limits in the Roan Cliffs (lower Tertiary) and Book Cliffs (Upper Cretaceous). The geographic coordinates are meters in UTM NAD83, Zone 12.*

oil tends to concentrate in the more porous strata. This is true even when the "reservoir" is a micropore or a sub-micropore system. If sufficiently thick, porous and permeable, these are the targets ("sweet spots") on which the shale oil play is based. In contrast to a shale gas reservoir, which normally is the source rock, the shale oil reservoirs are strata immediately adjacent to and/or interbedded with the primary source rock. In the Williston Basin it is the silty, but organic carbon-lean, Middle Bakken Member and silty beds of the Sanish and Three Forks Formations below the organic carbon-rich Lower Bakken Member. In the Niobrara Formation shale oil play throughout the eastern Rockies, it is chalks intercalated within and totally enclosed by the source rock that is the micropore reservoir. The Bakken Shale and the Niobrara Formation are actually hybrid, dual-reservoir, systems.

The general characteristics of a successful shale oil reservoir drawn from Sonnenberg (2010) for the Bakken Shale and from general knowledge of other shale oil plays include:

- a "world-class" source rock containing abundant oil-prone kerogen,
- within the oil-generative window such that oil has been generated and retained,
- oil saturations high enough to permit expulsion from the rock matrix into a system of fractures and micro-fractures,

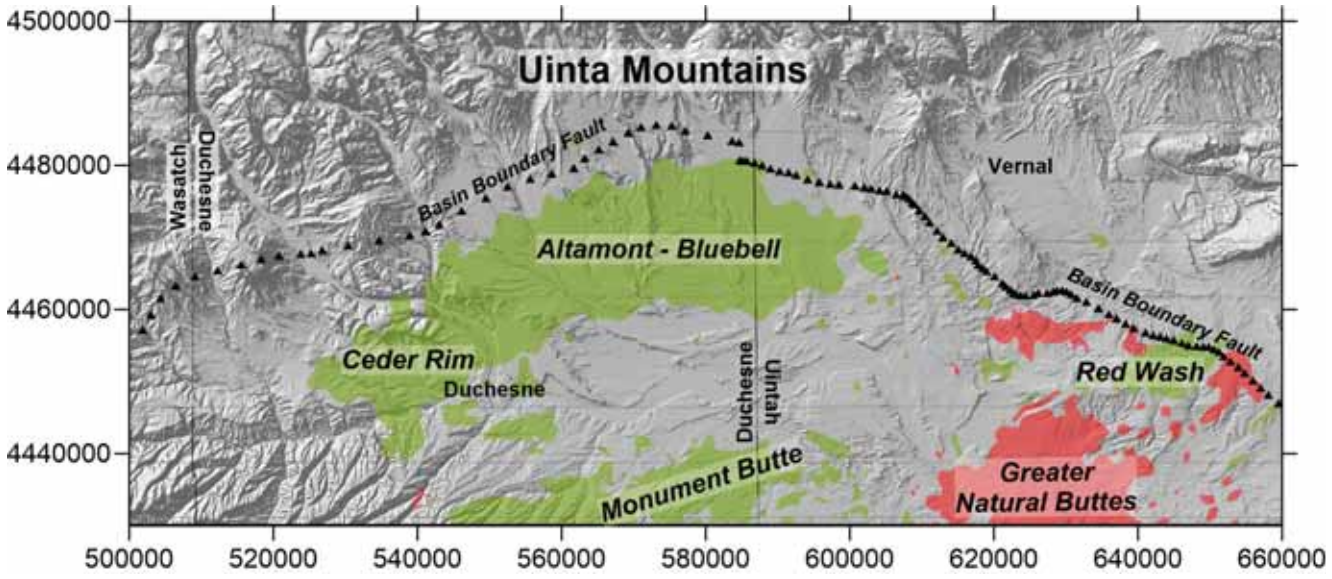

Figure 1-2: *The principal oil fields (green, natural gas fields in red) in the Uinta Basin that produce Green River-sourced oil from Green River Formation and stratigraphically proximal conventional reservoirs. County lines and two of the major towns in the basin are indicated for geographic reference. The geographic coordinates are meters in UTM NAD83, Zone 12.*

Table 1-1: *Cumulative and annual production of oil and natural gas from significant fields in the Uinta Basin producing hydrocarbons sourced dominantly from the Green River Formation. Cumulative production includes January 2014. Data from Utah DOGM.*

Fields	Cumulative Oil	Cumulative Natural Gas	Oil annual production (barrels)				Natural gas annual production (mcf)			
			2013	*2012*	*2011*	*2010*	*2013*	*2012*	*2011*	*2010*
ALTAMONT	137,197,157	299,180,399	4,297,355	3,343,734	2,627,584	2,265,728	12,376,431	10,266,582	8,298,294	5,860,603
ANTELOPE CREEK	7,878,325	16,648,174	682,449	490,980	319,155	278,107	843,854	623,143	390,761	314,392
BLUEBELL	177,233,246	249,065,474	3,038,817	2,677,485	2,312,062	2,005,642	4,663,075	4,138,947	3,614,384	3,226,331
BRENNAN BOTTOM	3,409,391	3,337,841	434,477	289,115	208,361	256,352	266,595	151,809	147,176	182,540
BRUNDAGE CANYON	19,583,962	118,277,192	1,501,765	1,147,654	1,222,258	1,247,192	10,477,530	9,535,775	12,051,108	12,475,577
CEDAR RIM	15,403,691	36,258,555	419,331	681,205	494,921	356,076	1,385,808	1,656,282	1,196,972	794,471
DUCHESNE	1,693,012	3,619,765	71,444	67,055	56,088	72,003	178,403	129,852	121,035	161,608
EIGHT-MILE FLAT	614,380	7,262,708	118,897	104,831	74,165	12,067	542,337	550,433	596,459	759,264
HORSESHOE BEND	2,232,303	28,912,625	51,119	42,426	43,285	40,907	305,869	321,919	320,740	405,694
LAKE CANYON	1,422,988	7,061,515	482,574	453,427	131,183	77,528	1,805,405	1,331,572	634,750	728,883
MONUMENT BUTTE	63,337,441	137,818,755	5,078,350	5,313,430	4,946,775	5,043,418	7,920,771	10,106,427	9,467,740	10,013,766
N MYTON BENCH	4,416,549	5,076,251	2,101,854	1,369,038	364,100	77,274	2,615,199	1,403,846	330,287	107,084
PARIETTE BENCH	1,885,842	46,660,646	72,407	98,840	119,449	129,748	4,218,894	4,773,217	5,331,734	5,555,566
RED WASH	87,145,167	385,941,002	375,336	343,832	392,406	379,295	12,714,842	9,246,892	4,185,771	2,603,713
SOUTH MYTON BENCH	2,256,216	18,907,657	185,825	287,825	662,916	845,493	3,340,534	4,522,616	5,671,716	3,782,840
UTELAND BUTTE	1,963,845	9,378,239	150,771	119,361	83,398	63,331	933,906	927,861	998,520	1,058,743
WALKER HOLLOW	19,901,521	34,490,387	144,685	156,592	160,937	166,319	217,471	245,535	255,606	259,869
WEST WILLOW CREEK	1,127,578	11,995,905	7,261	8,535	9,918	12,936	118,430	156,089	210,000	273,768
WHITE RIVER	3,068,967	14,886,277	27,344	27,275	27,971	38,314	378,441	404,951	499,536	652,153
WINDY RIDGE	4,581,345	7,179,336	1,000,293	841,247	914,013	348,822	1,963,165	1,617,790	1,129,994	368,959
WONSITS VALLEY	52,103,370	132,341,530	253,939	231,116	258,088	276,685	3,609,907	4,032,357	4,471,751	5,370,324
	608,456,296	**1,574,300,233**	**20,496,293**	**18,095,003**	**15,429,033**	**13,993,237**	**70,876,867**	**66,143,895**	**59,924,334**	**54,956,148**

- commonly associated with abnormally high fluid pressure gradients; as high as 0.73 psi/ft in the Bakken Shale, but just greater than 0.50 psi/ft is more normal, and
- a mudstone or siltstone reservoir host rock that is naturally fractured or capable of fracture stimulation.

It is clear from the large volume of oil and associated natural gas trapped in conventional clastic and porous limestone reservoirs within and rimming the Uinta Basin, that the Green River Formation has, or has had, a very efficient carrier system that guided the hydrocarbons from the source kitchen in the basin center to the productive reservoirs.

This study has sought evidence for conditions that could support a shale oil play in the stratigraphy, organic geochemistry, and simulated history of organic maturation of the Green River Formation.

2. STRATIGRAPHY

The Uinta Basin is a strongly asymmetric intracratonic depression formed by crustal loading beneath the rising Uinta Mountains anticlinorium (Fig. 1-1). Pre- and synorogenic strata within the basin dip uniformly northward towards the Uinta Basin Boundary Fault, which borders the deepest part of the basin. The south flank of the basin is elevated by two Laramide uplifts, the San Rafael Swell on the southwest and the reactivated Uncompaghre Uplift (Stone, 1977) on the southeast. Douglas Creek Arch, a north-south trending Laramide uplift, forms the eastern flank of the basin immediately east of the Utah-Colorado state line. The south rim of the basin is formed by the Book (Cretaceous) and Roan (Paleocene) Cliffs capped by a high plateau rising to elevations of 8000 to 10,000 feet.

The stratigraphy of the Uinta Basin records an evolution from a passive margin basin through the Paleozoic and most of the Mesozoic to a foreland basin east of the Sevier Thrust Belt in the Late Cretaceous, to finally a Laramide intracratonic depression in the latest Cretaceous through late Eocene. It was during this last phase that large lakes formed throughout the region that previously was an extensive foreland basin, the Western Interior Seaway (Franczyk and others, 1992). In northeast Utah, in the general area of the Uinta Basin, there were two major lakes (Fig. 2-1), Lake Flagstaff of Paleocene age and Lake Uinta of Eocene age (Ryder and others, 1976; Fouch and others, 1992). Light gray and varicolored biomicrites of the Flagstaff Limestone are the record of Lake Flagstaff and organic-rich lacustrine shales of the Green River Formation were deposited in Lake Uinta (Fouch and others, 1994). During the dry period between Lake Flagstaff and Lake Uinta time, 800 to 1200 ft of continental red mudstone and sandstones were deposited in a fluvial-flood plain setting. This is the Wasatch Formation, which in part interfingers with both the underlying Flagstaff Limestone and the overlying Green River Formation. As Lake Uinta expanded during Green River time, the fluvial-flood plain setting was replaced by periodic sandy delta systems that emptied northward across marginal lacustrine carbonate muds and limestones (Ryder and others, 1976; Castle, 1990). These deltaic and shoreline sandstones are the reservoirs for the heavy oil and bitumen on the south flank of the Uinta Basin (Schamel, 2013).

In the Uinta Basin, conventional oil and associated natural gas are produced principally from sandstones and bioclastic limestones in the Green River Formation and the upper Wasatch Formation (Morgan, 2003; Morgan and others, 2003; Kelso and Eherenzeller, 2008; Morgan, 2008). Natural gas is produced from a variety of Paleocene through Jurassic sandstone reservoirs. In a few fields, biogenic methane is extracted from the upper Eocene Uinta Formation. The immobile oil and bitumen are reservoired in many of these same units (Fig. 2-2). The Uinta Basin oil is sourced from the Green River Formation (Fouch and others, 1994; Ruble and others, 2001; Lillis and others, 2003) and the natural gas is sourced from the organic-rich Mancos Shale and/or Mowry Shale, as well as coals within the Frontier Formation and Mesaverde Group (Rice and others, 1992).

Green River Formation

The basal Green River Formation represents the initiation of Lake Uinta as a single, large lake. For much of the Eocene, the lake occupied only a small part of the basin along the northern margin of the structural depression (Fig. 2-1). The lake was ringed by a 'marginal lacustrine' mudflat that was periodically inundated by lake waters. Beyond the shoreline were alluvial fans and delta complexes that sometimes encroached on the lake and at other times were flooded. The consequence was a broad region in which reservoir and carrier-bed sandstones and shoreline bioclastic carbonates are intimately intercalated with organic-rich lacustrine source rocks (Keighley and others, 2002; Keighley and Flint, 2008). The basin continued to receive sediments as long as the basin subsided, driven by the Laramide orogeny and uplift of the Uinta Mountains. However, in the middle Eocene to earliest Oligocene, the basin filled in with red fluvial mudstone, sandstones, and conglomerates of the Uinta and Duchesne River Formations. There must have been a climatic factor to the end of Lake Uinta. The main lacustrine period coincided with the Early Eocene Climatic Optimum (Smith and others, 2008a), a period of a historically hot global climate. This was followed by a long period of increasing aridity.

The most important Tertiary source rocks in the Uinta Basin are the kerogen-rich calcareous claystones and marlstones deposited as the open-lacustrine facies of the Green River Formation (Katz, 1995; Ruble and Philp, 1998). A distinction is drawn between those open-lacustrine facies assembledges that are *offshore* and continuously subaqueous and those that are *nearshore* and subjected to shoreline influences, including periodic subaerial exposure. The offshore open-lacustrine facies

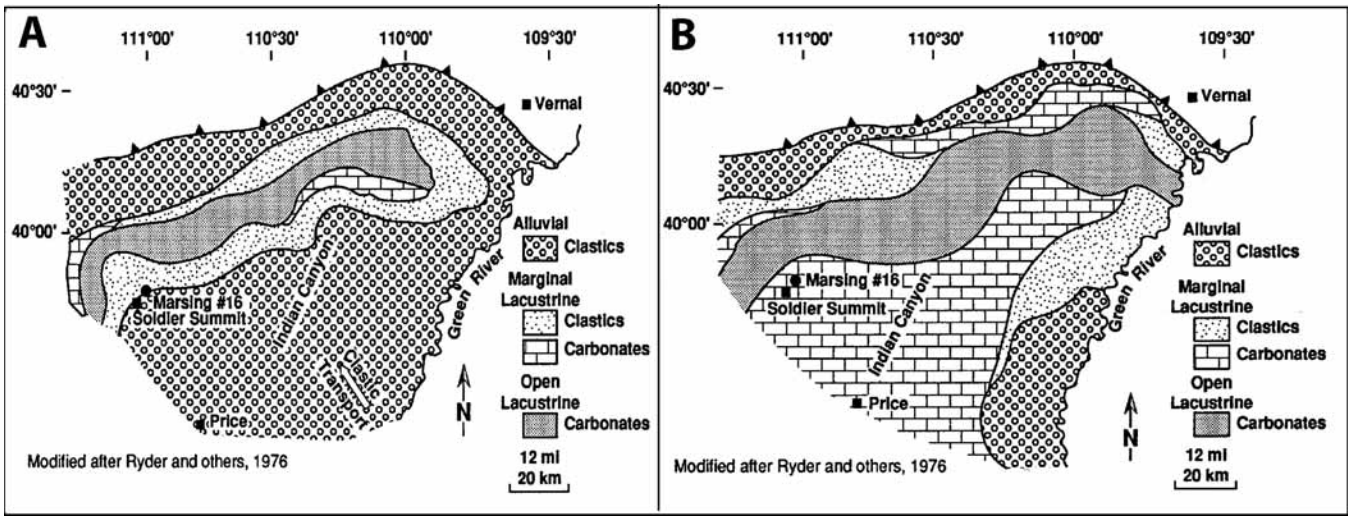

Figure 2-1: *Green River Formation facies distributions in western Lake Uinta, the part of the Uinta Basin west of the Green River (Schamel, 2005, after Wiggins and Harris, 1994). A. Late Paleocene – at this time the lacustrine facies had relatively limited extent in the foredeep immediately to the south of the Uinta thrust. B. Early Eocene – time of expanded open and marginal lacustrine deposition.*

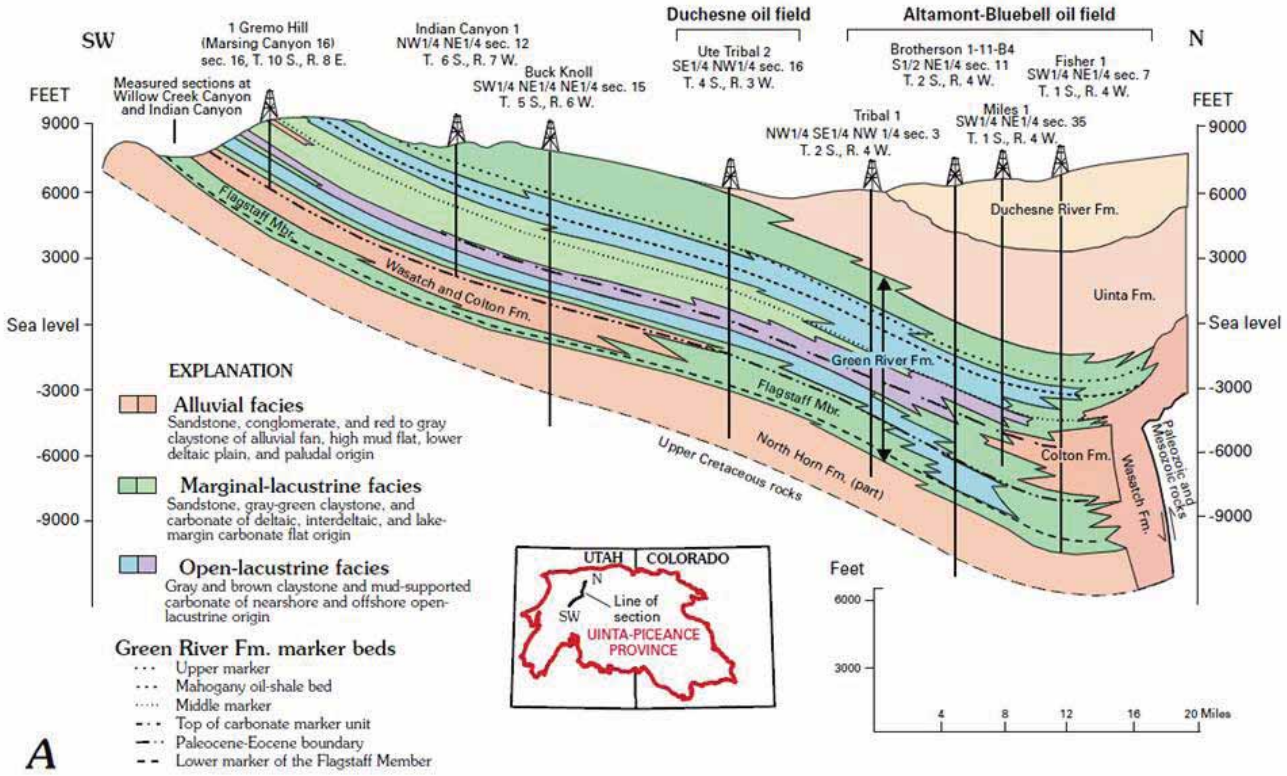

Figure 2-2: *Structural cross section from Soldier Summit (Marsing 16 well) northeast to the Altamont –Bluebell field and South Uinta thrust fault near the structural and depositional axis of the Uinta Basin (Wiggins and Harris, 1994). The open lacustrine facies, blue in the cross section, constitute the main body of 'black shales' in the Green River Formation.*

is characterized by black to beige, laminated or very thinly bedded calcareous claystone and shaly carbonate. The kerogen in these high-grade *"oil shales"* is Type I. They formed in relatively deep, quiet anoxic lake waters as alternating laminae of bacterial/algal ooze (Ruble and others, 1994) and algae-derived low-Mg calcite. The clay content is minor. The nearshore open-lacustrine facies is lithogically diverse and includes weakly laminated, organic-rich, mud-supported carbonate containing large Unionid pelecypods with black laminated mudstone and coal beds, and scattered thin sandstone-siltstone beds. Present also are beds of wackestone/packstone rich in ostracods and gastropod fragments (Wiggins and Harris, 1994). The siliciclastics accumulated mainly in offshore bars related spatially to deltas (Castle, 1990; Remy, 1992) entering the lake. In the interdeltaic portions of the shoreline (marginal lacustrine facies) were carbonate mudflats, ephem-

eral ponds, and small peat mires that may or may not have preserved organic matter (Ryder and others, 1976).

The open-lacustrine (black shale) facies rocks are distributed in two principal zones (Figs. 2-3 and 2-4) representing extended periods of lake flooding. The lower interval, the Black Shale facies (Thompson, 1971; Picard and others, 1973) is at or near the base of the Green River Formation (Fig. 2-3). The upper black shale is the Parachute Creek Member, which contains the exceptionally organic-rich Mahogany Zone. Near the paleo-axis of the lake, the two black shale intervals merge (Ryder and others, 1976; Fig. 2-3, Duchesne section).

With deltas and fan deltas entering the basin from the basin margins, broad mudflats that rapidly cycle between subaerial and subaqueous, and a relatively limited perennial lake that with a longer cyclicity flooded nearly the entire basin, it is understandable that the stratigraphic nomenclature of the Green River Formation is complex and, in part, contradictory. Fortunately, there were several episodes of maximum lake flooding that deposited stratigraphic markers that can be followed in wells and outcrop across large portions of the basin (Fig. 2-2). These markers serve to permit the formation to be divided into three members. The ages of several of the markers can be dated by intercalated tuffs (Smith and others, 2008b; Birgenheier and Vanden Berg, 2011).

The base of a persistent ostracod-rich limestone (55.3 Ma) marking the earliest widespread flooding of Lake Uinta, the Uteland Butte Limestone, is the base of the Green River Formation and the Lower Member. The top of the Lower Member is another distinctive limestone, the "Carbonate Marker" (53.9 Ma). The Long Point Bed (54.0 Ma) is a marker within the Lower Member. The Lower Member encompasses the Black Shale facies unit. The Middle Member extends from the top of the Carbonate Marker to the Mahogany Zone (49.3 – 48.9 Ma), an exceptionally organic-rich shale marker representing a wide-spread persistent flooding event. In some nomenclatures the Middle Member is equivalent in its entirety to the Douglas Creek Member, but Johnson and Roberts (2003) place the base of the younger Parachute Creek Member (Fig. 2-2) at the base of the organic-rich R-4 interval (51.6 Ma), well below the Mahogany Zone (R-7). The Upper Member begins at the top of the Mahogany Zone and extends to the top of the formation. The uppermost parts of the lacustrine succession, the organic-carbon-lean "saline facies" and the "limestone and sandstone facies", are placed in the Upper Member.

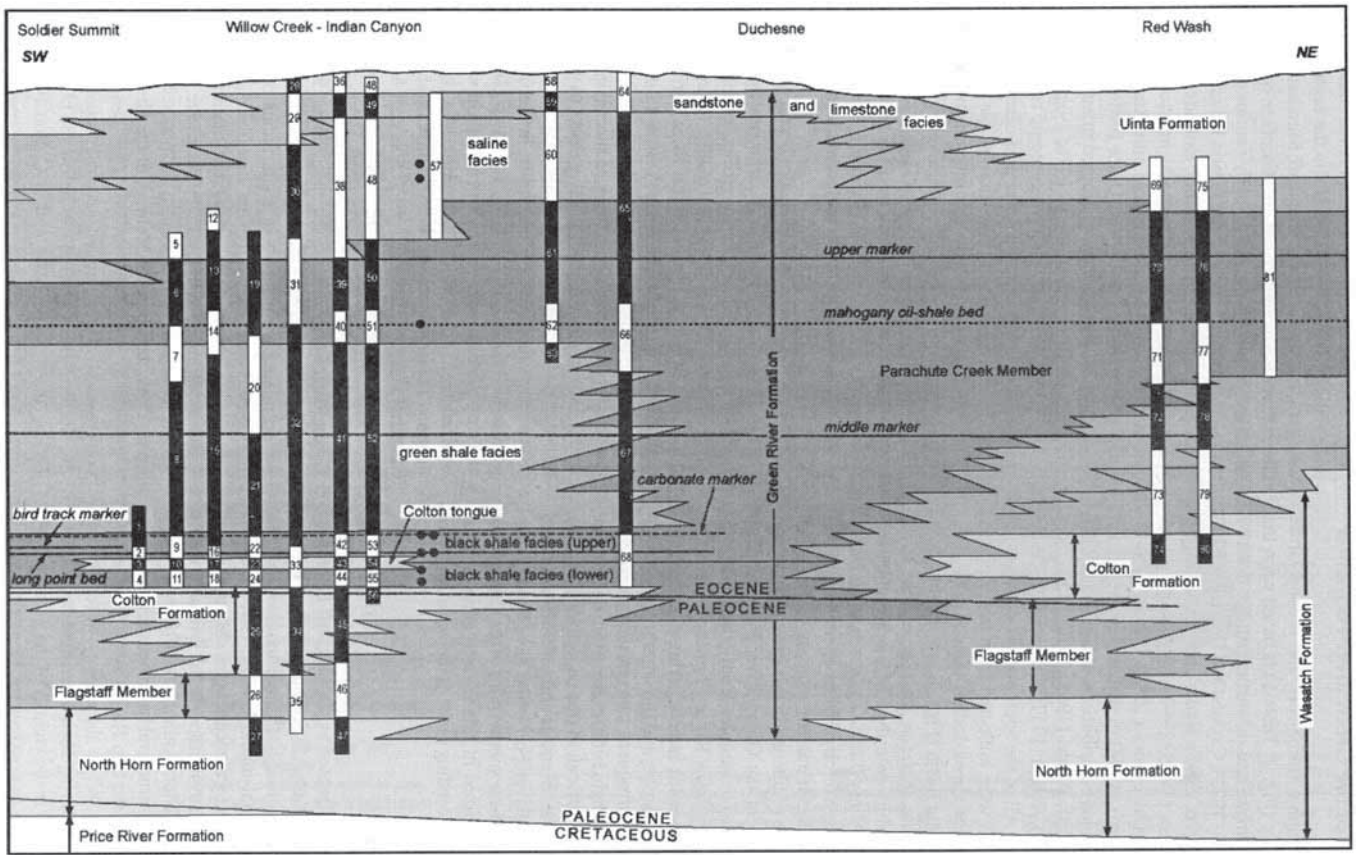

Figure 2-3: *Stratigraphic cross section from Soldier Summit northeast across the Uinta Basin to the Red Wash field, just east of the Green River south of Vernal (Ruble and Philp, 1998, redrawn after Ryder and others, 1976). The section illustrates temporal expansions and contractions of the open lacustrine (dark gray) and marginal lacustrine (medium gray) facies associations. In the basin depocenter (Duchesne) the open lacustrine facies merge into a continuous organic-rich mudstone succession.*

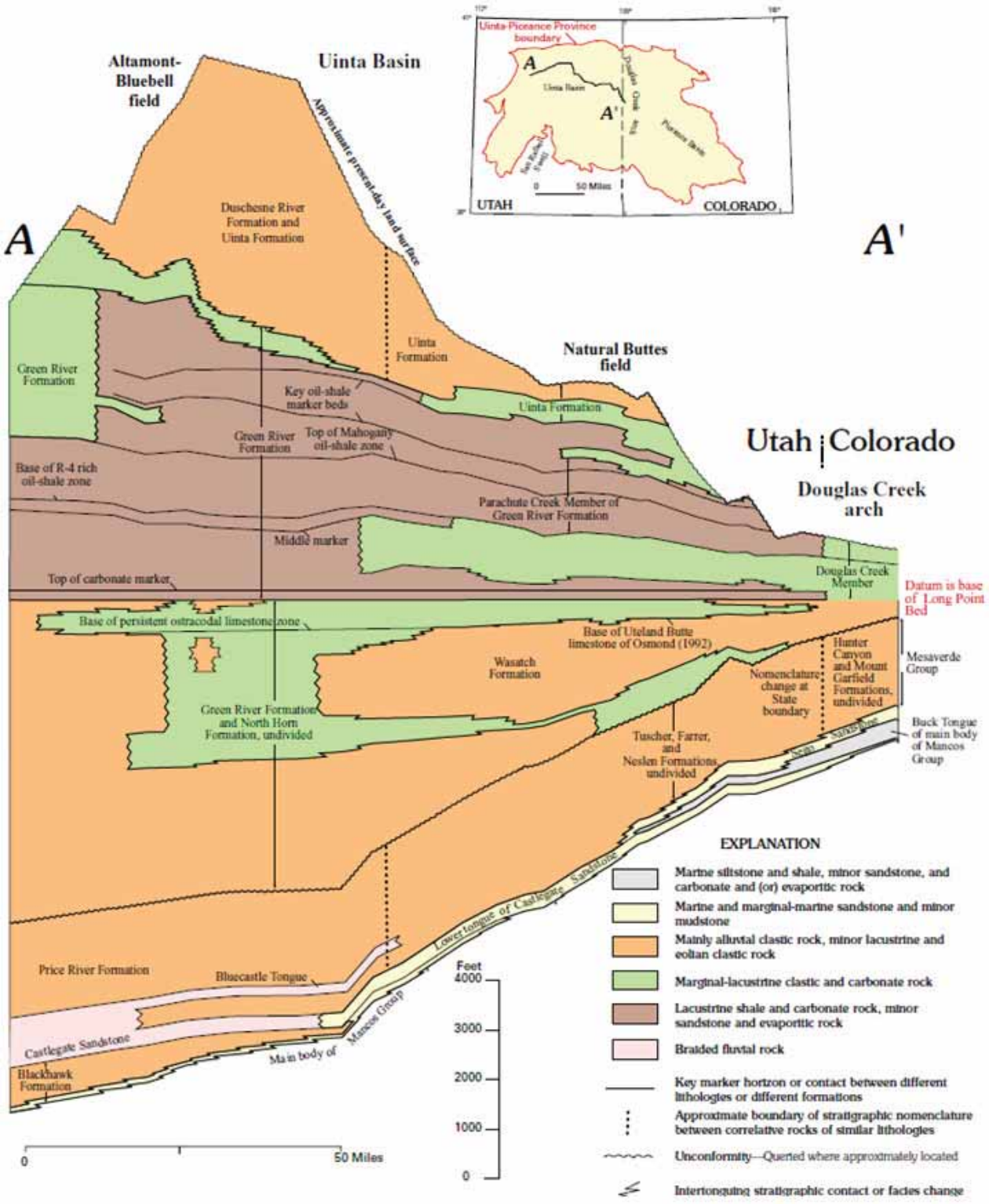

Figure 2-4: *Stratigraphic correlations and marker beds of the Green River Formation and adjacent dominantly siliciclastic formations (modified after Johnson and Roberts, 2003). Key to lithologies: orange, mainly alluvial siliciclastic rock; green, marginal-lacustrine siliciclastic and carbonate rock; brown, lacustrine mudstone and carbonate rock.*

An alternative, and perhaps more useful, division of the formation in the parts of the basin where open and marginal lacustrine facies dominate is to divide it based on the degree of organic richness (Ryder and others, 1976; Fig. 2-3), separating organic-rich and organic-lean intervals based on bulk density or sonic log signatures or direct measurement of organic content (Vanden Berg, 2008; Fig. 2-5).

The Marsing 16 core (Fig. 2-6; Wiggins and Harris, 1994) samples the cyclic marginal lacustrine facies of the Green Shale facies (Middle Green River Formation), open and marginal lacustrine rocks of the Black Shale facies (Lower Green River Formation), and a short interval of the underlying Wasatch (Colton) deltaic sandstones. The core hole twins the Gremo Hill Fee 1 well (16-10S-8E; API 435130002). A set of core photographs

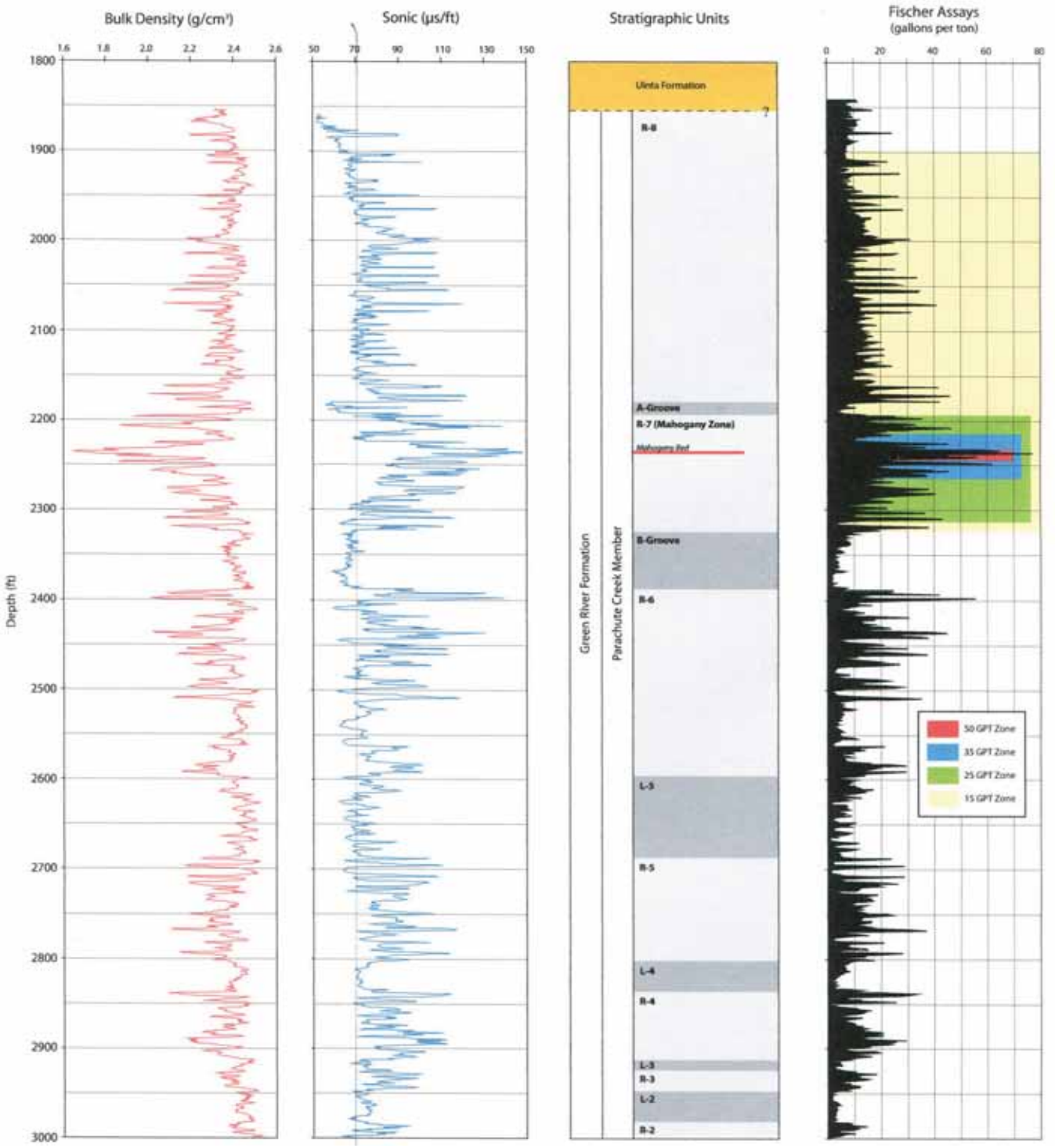

Figure 2-5: *Stratigraphy of the Middle and Upper Green River Formation showing organic-rich (R-) and organic-lean (L-) alternations (Vanden Berg, 2008).*

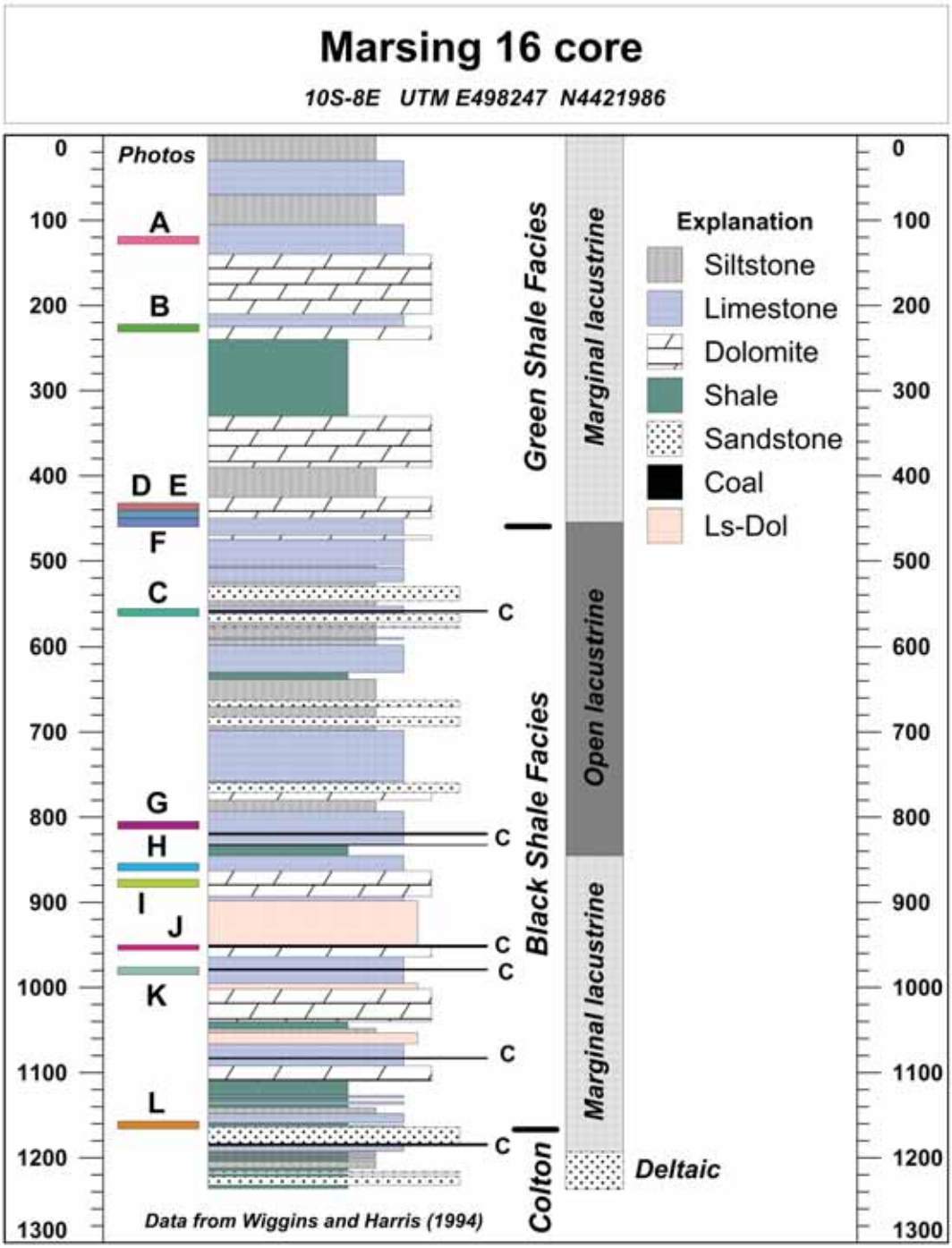

Figure 2-6: *Marginal and open lacustrine lithologies in the Marsing 16 core (Wiggins and Harris, 1994). The letter "C" indicates coal beds observed in core. Core depths in feet. See text for description of the core.*

of selected segments are in Figures 2-7 and 2-8. Near the top of the core is a thick, uniform limestone, the "Middle Marker" (Fig. 2-7, A). The remainder of the section is thinly laminated alternations of gray-green claystone and carbonates deposited on a carbonate flat (Fig. 2-7, B, D-F). The open lacustrine rocks of the Black Shale facies are cyclically alternating siliciclastics and carbonates (Figure 2-7, C; note algal coal at 563 ft). The silt and sand is thought to have been transported into the deep lake from shoreline deltaic deposits by wind- generated currents. The carbonate intervals are black, laminated limy mudstone commonly with abundant pelecypods, ostracods, and coals (Figs. 2-8, G-K). Fractured oil-saturated sandstone beds are observed (Fig. 2-8, L), as are numerous subvertical open and partially-open fractures (Fig. 2-8, J).

In stratigraphically equivalent strata to the east of Marsing 16, fine-grained, cross-bedded sandstone fills fluvial channels incised into cyclically laminated claystone and carbonates (Figs. 2-9 and 2-10). These channels provide carrier systems from the organic-rich basin center to thicker alluvial sand-

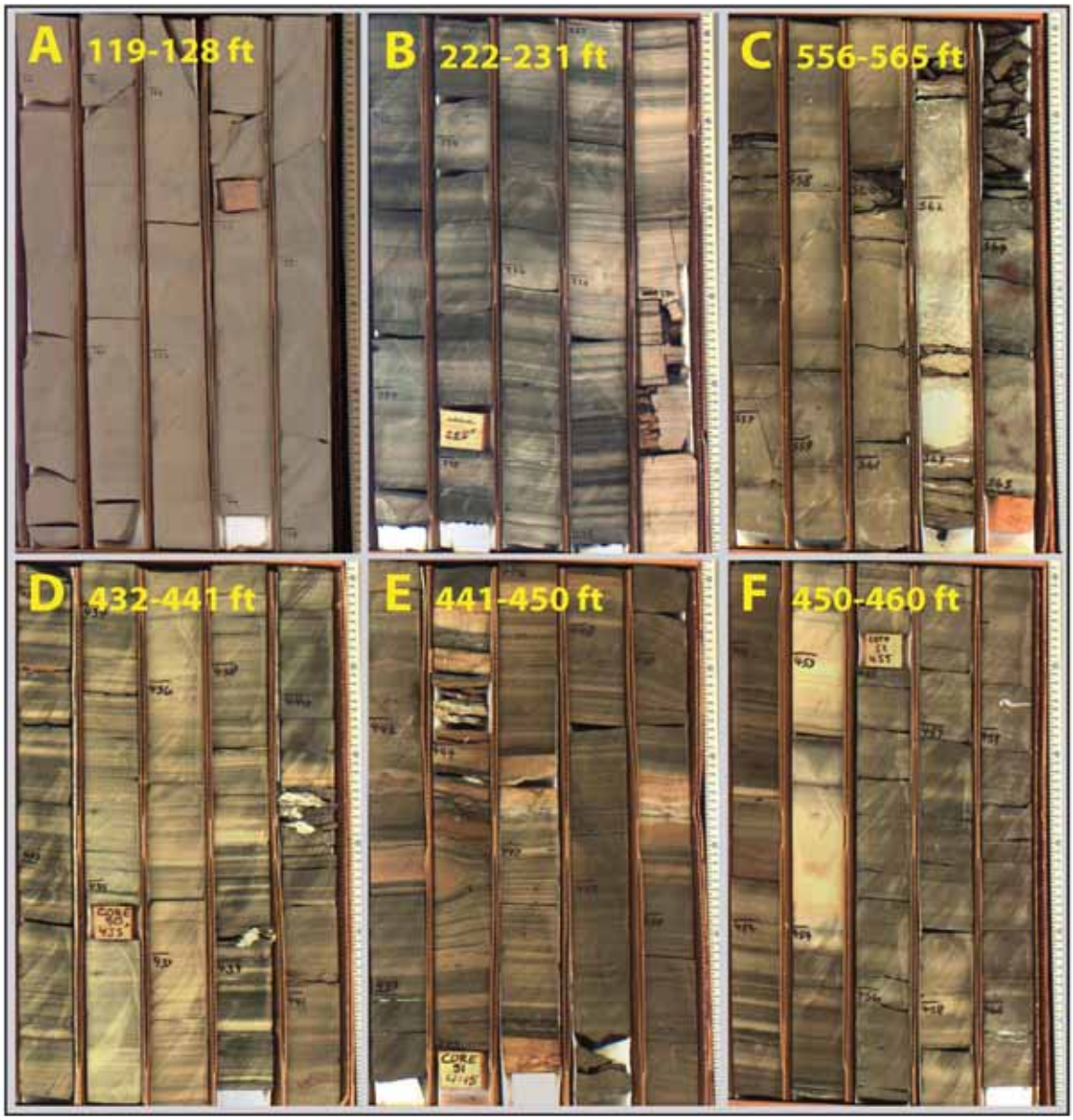

Figure 2-7: *Photographs of segments of the Marsing 16 core showing the variety of lithotypes and bedding characteristics in the Green Shale facies The locations of each panel are indicated in Figure 2-6. See text for description.*

stone bodies on the basin margins. In the basin center, however, there appear to be relatively thick intervals of monotonous laminated gray to black claystone lacking siliciclastics (Figs. 2-11 and 2-12) that are not connected to carrier systems supporting secondary migration of hydrocarbons. The Virgil Mecham 1-11A2 well tested (DSTs) over 125 barrels of "highly gas-cut oil" from the interval depicted in Figure 2-11.

The total thickness of the Green River Formation varies from less than 2000 feet in the southeast against the Douglas Creek Arch to over 7500 feet thick in the west near Duchesne (Fig. 2-13). The isopach thick delineates the basin depocenter paralleling the Basin Boundary Fault. The isopachs for each of the portions of the Green River Formation and structure maps for selected markers are shown in Figures 2-14 through 2-24. Figure captions describe the content of the individual maps.

Post-Green River Overburden

In the Uinta Basin south of the Basin Boundary Fault, the Green River Formation is presently overlain by just two formations, the Uinta Formation of late middle Eocene age and the later Eocene-earliest Oligocene Duchesne River Formation. Due to erosional beveling of the post-Green River overburden, just the Uinta Formation is present in the central part of the basin (Fig. 2-25), but both formations are found to the north up to and even beneath the Basin Boundary Fault. The total thickness of the post-Green River overburden exceeds 7000 ft in the extreme northwest (Fig. 2-25), adjacent to the fault, and thins southward to the present outcrop edge of the Uinta Formation. Due to late Neogene erosion, the full original thickness of the Duchesne River Formation is nowhere preserved south of the fault. The original thickness of the Uin-

Figure 2-8: *Photographs of segments of the Marsing 16 core showing the variety of lithotypes and bedding characteristics in the Black Shale facies. The locations of each panel are indicated in Figure 2-6. See text for description.*

Figure 2-9: *Twenty-foot wide fluvial sandstone channel incised into cyclic marginal lacustrine sediments at Indian Canyon (11S-10E) on Rt. 191 southwest of Duchesne and close to the Marsing 16 well (10S-8E).*

Figure 2-10: *Twenty-foot thick fluvial sandstone channel incised into marginal lacustrine Black Shale facies at Indian Canyon (11S-10E) southwest of Duchesne.*

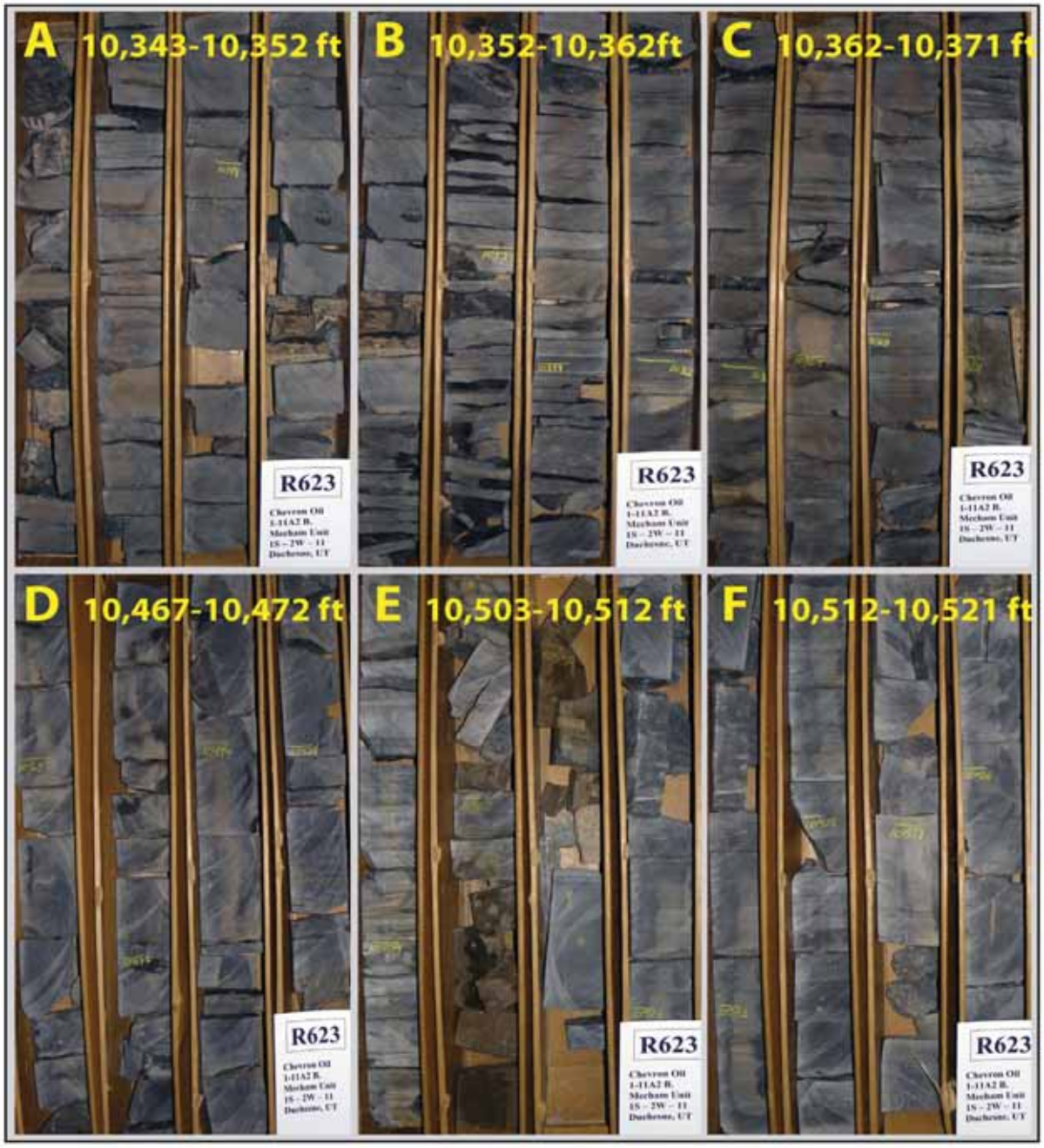

Figure 2-11: *Photographs of lower Green River Formation (Black Shale facies) open lacustrine organic-rich sediments in core from the Virgil Mecham 1-11A2 well (API 4301330009; 1S-2W). See text for description.*

ta Formation is preserved only north of the Duchesne River outcrop edge (blue line in Figure 2-25).

In order to assess the degree of thermal maturation of the Green River Formation source rocks, the spatial variation in maturity levels, and the times at which these levels are reached in different parts of the basin, it is essential to reconstruct, as best as possible, the full original thickness of the overburden, the times of deposition of the various units, and the history of exhumation. The procedures for doing this are presented in Chapter 4. However, this section discusses what is firmly known about the overburden succession.

Perhaps driven by the onset of glaciations in the Antarctic (Berggren and Prothero, 1992), global cooling and increased aridity began in the late middle Eocene, ending the Early Eocene Climatic Optimum, and continued into the earliest Oligocene. In middle Eocene time, Lake Uinta experienced a gradual transition from wet to increasingly arid climates. This was observed in the Upper Green River Formation by the progression from oil shales of the R-8 interval (humid) to the "saline facies" and the "limestone and sandstone facies" (arid playa and alluvial). The Uinta Formation (late middle Eocene) records the encroachment of alluvial sedimentation on the remaining playas in the basin depocenter. Based on magneto-

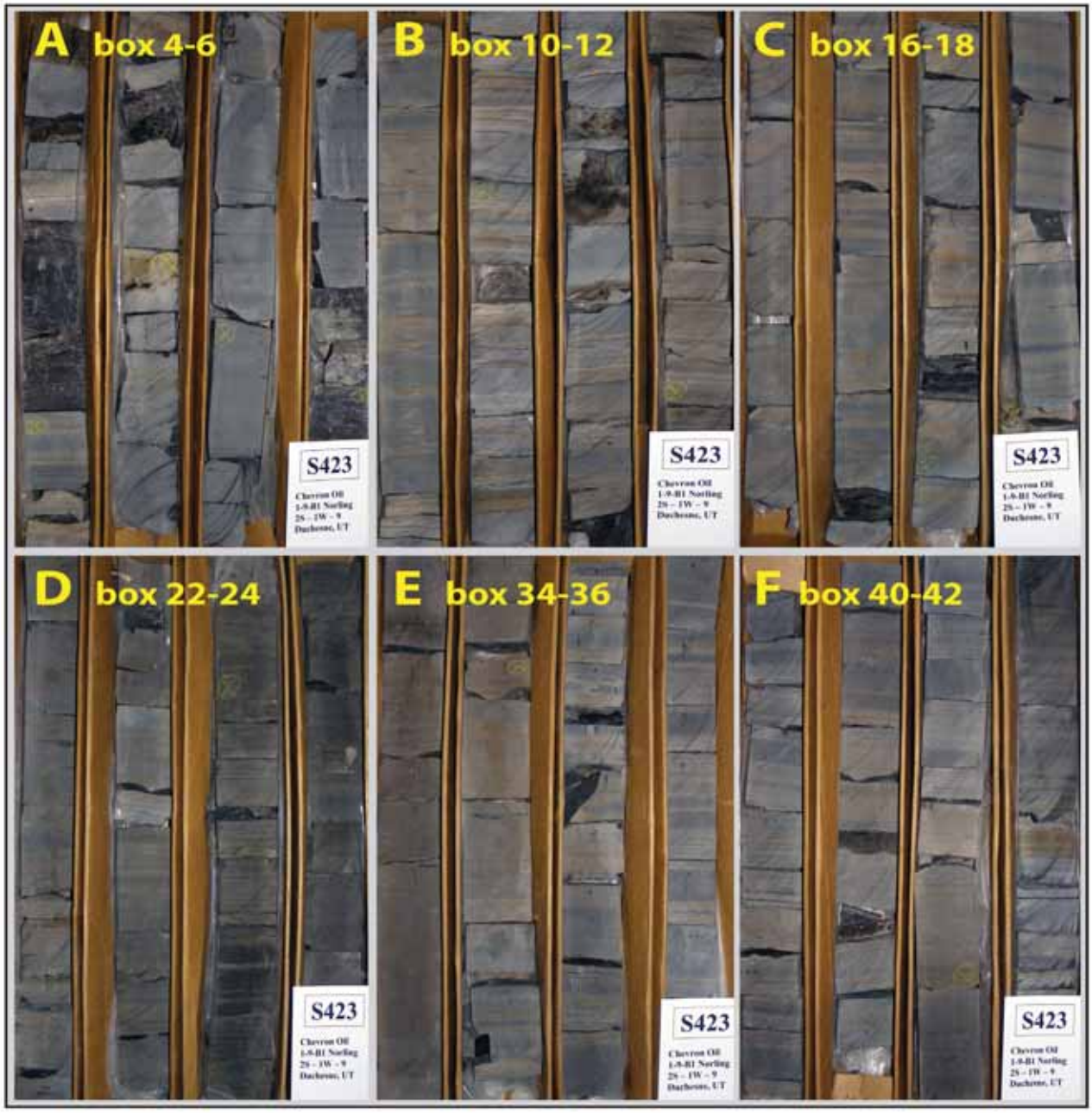

Figure 2-12: *Photographs of lower Green River Formation (Black Shale facies) open lacustrine organic-rich sediments in core from the Norling 1-9B1 well (API 4301330315; 2S-1W). See text for description.*

stratigraphy, Prothero (1996) dates the base of the Uinta Formation as 47.0 Ma, but more convincingly Smith and others (2008a, 2008b) consider the contact to be time-transgressive, ranging in age from 47 Ma in the east to 44 Ma in the western basin depocenter where the playas lingered longest. The Uinta Formation is fluvial variegated mudstone and fine-grained sandstone with minor conglomerate and volcanic tuffs. In the extreme north of the basin, the formation is reported to be 3100 to 3200 feet thick, but in the southeast it is just 1300 to 1400 feet thick (Sprinkel, 2007, Plate 3).

The Duchesne River Formation has been divided into four members, the first three of which are distinguished by differing proportions of varicolored sandstone and mudstone with minor conglomerate. The depositional setting is fluvial with minor interfluvial lakes (Murphey and others, 2011). The highest unit, the Starr Flat Member, stands apart for its abundance of conglomerate with minor sandstone and mudstone (Sprinkel, 2006). In the northern Uinta Basin, the Duchesne River Formation is reported to be about 3650 feet thick (Sprinkel, 2007, Plate 3). The Lapoint ash bed at the base of the third highest member (Lapoint Member) has been dated as 39.74 ± 0.07 Ma (Prothero and Swisher, 1992). The Duchesne River Formation is the stratotype for the Duchesnean North American Land Mammal Age (NALMA) which records a major faunal replacement in North America during which there

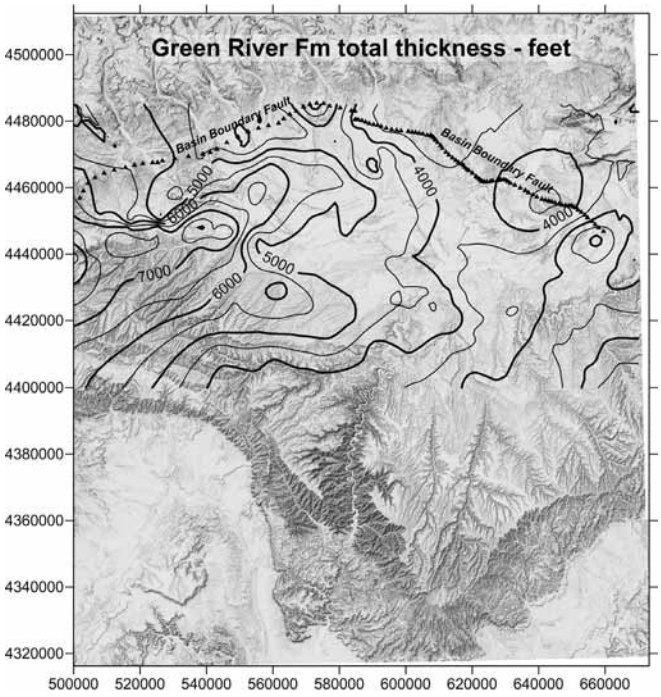

Figure 2-13: *Isopach for the entire Green River Formation from the base of the Uteland Butte member to the top of the formation. For the areas of the basin where the formation is not erosionally truncated, thickness varies from less than 3000 feet in the southeast against the Douglas Creek Arch to over 7500 feet in the northeast-trending basin depocenter in the western part of the basin. There is a secondary thick trending eastward from the depocenter. These large differences in formation thickness will influence the spatial distribution of thermal maturity of the Green River source rocks. The geographic coordinates are meters in UTM NAD83, Zone 12. Contour interval: 500 feet.*

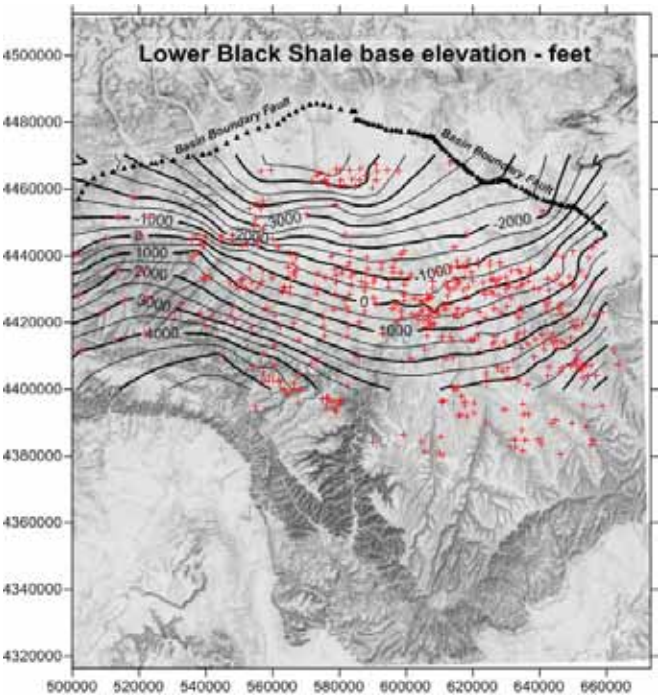

Figure 2-14: *Elevation (msl) of the base of the Uteland Butte Limestone and Lower Black Shale. This is the base of the Green River Formation. Red crosses indicate wells with elevation control; gridding of well tops was limited to the central and northern basin. Contour interval: 500 feet.*

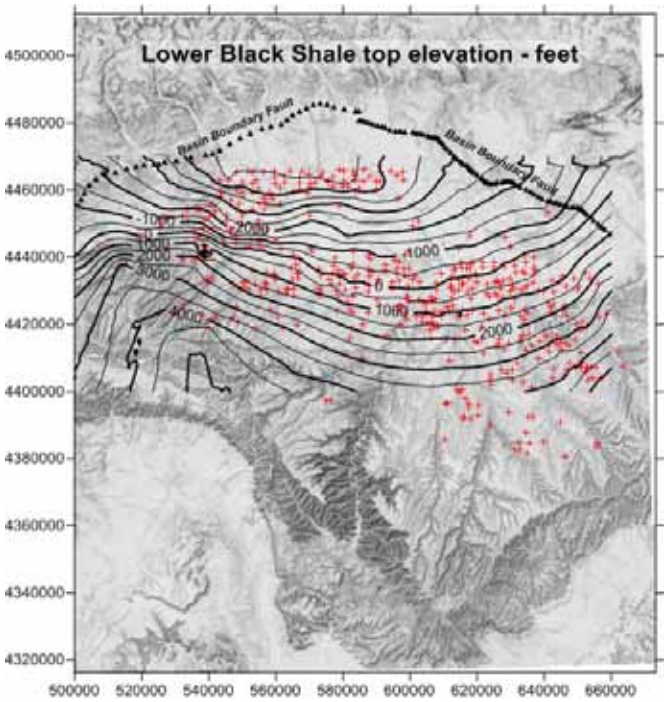

Figure 2-15: *Elevation of the top of the Carbonate Marker or the top of the Lower Green River Formation and the lower Black Shale facies. Red crosses indicate wells with elevation control. Contour interval: 500 feet*

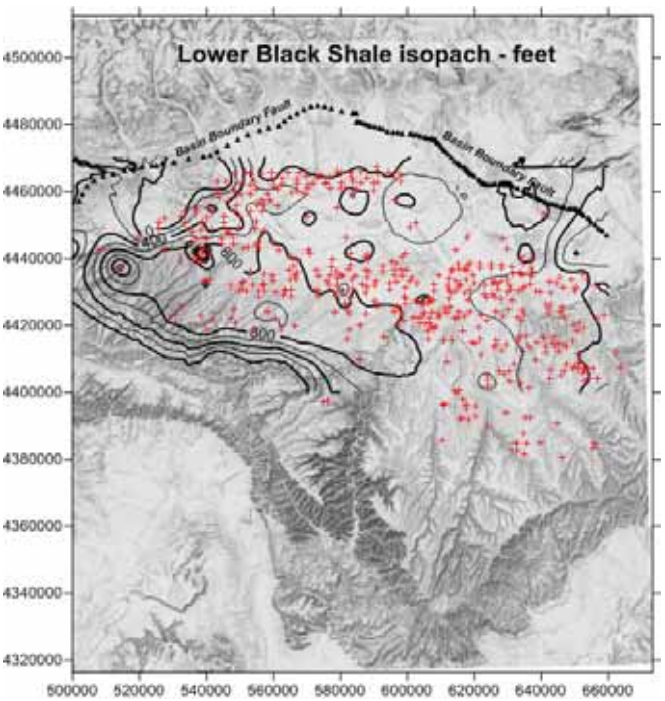

Figure 2-16: *Isopach of the lower Black Shale unit, the Lower Green River Formation. The 800+ foot thick trends east-west along the present south erosional edge of the southwest part of the basin. The rapid thinning to the south is an artifact of erosional thinning in the Roan Cliffs. The isopach thick coincides with the known distribution of the Wasatch (Colton) tongue within the Black Shale unit as mapped. Red crosses indicate wells with interval thickness control. Contour interval: 200 feet.*

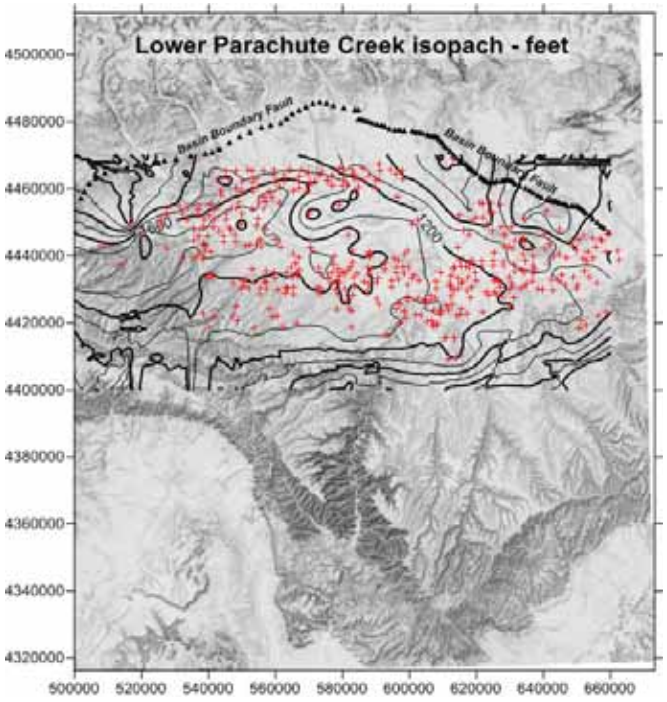

Figure 2-17: *Isopach of the lower Parachute Creek Member, the interval from the top of the Carbonate Marker to the base of the R-4 interval. This is the lower part of the Middle Green River Formation, commonly correlated with the Douglas Creek Member. Thickness exceeds 1800 feet in the northeast-trending basin depocenter and is between 1200 to 1600 feet over a broad east-west trending area in the southern part of the basin. Red crosses indicate wells with interval thickness control. Contour interval: 200 feet.*

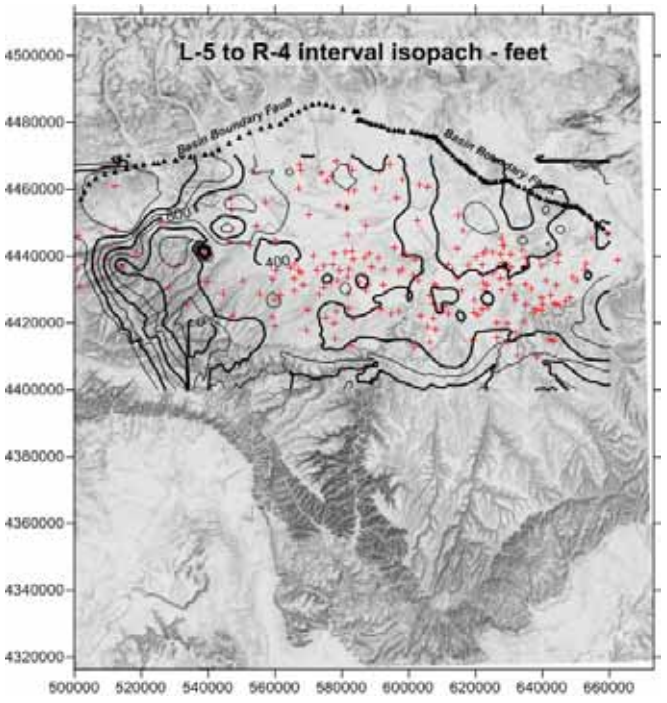

Figure 2-18: *Isopach of the portion of the Parachute Creek Member between the base of the R-4 interval to the top of the L-5 interval (refer to Figure 2-5; Vanden Berg, 2008). Thickness is relatively uniform across the basin. Red crosses indicate wells with interval thickness control. Contour interval: 200 feet.*

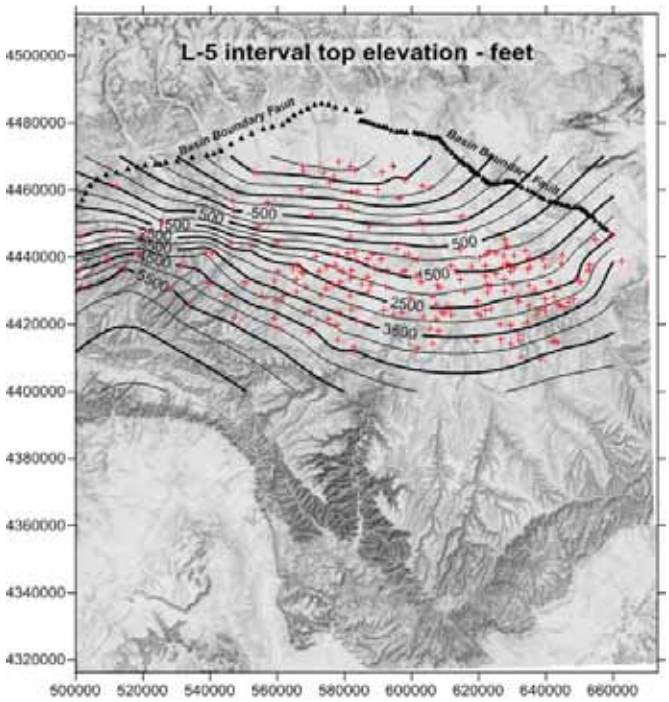

Figure 2-19: *Elevation (msl) of the top of the L-5 interval (refer to Figure 2-5; Vanden Berg, 2008). Red crosses indicate wells with elevation control. Contour interval: 250 feet.*

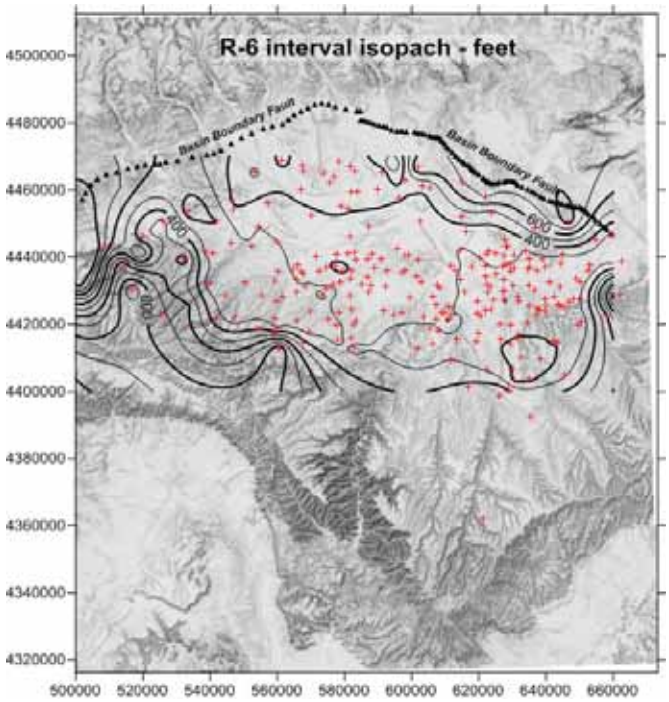

Figure 2-20: *Isopach of the R-6 and B-groove intervals (refer to Figure 2-5; Vanden Berg, 2008) between the top of the L-5 interval and the base of the Mahogany Zone (top of B-groove). Across most of the basin this interval is less than 400 feet thick. Red crosses indicate wells with interval thickness control. Contour interval: 100 feet.*

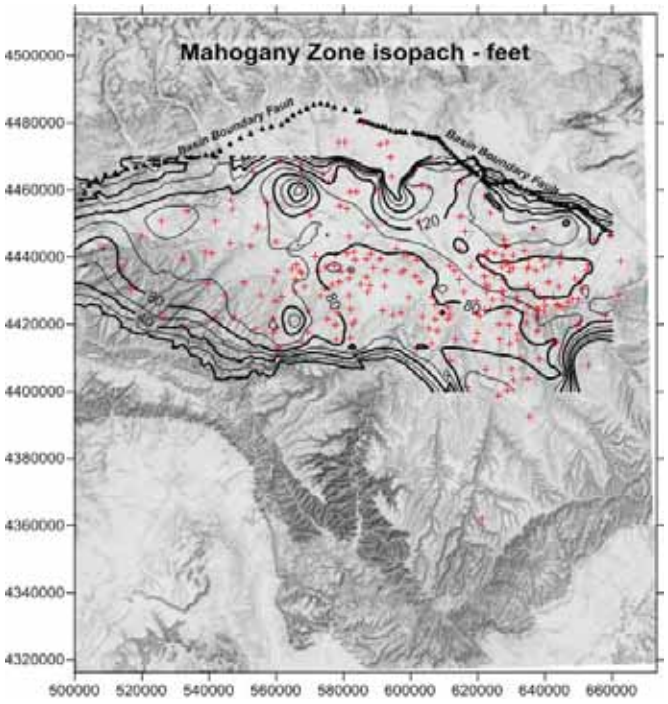

Figure 2-21: *Isopach for the Mahogany Zone, the R-7 interval (refer to Figure 2-5; Vanden Berg, 2008). Across the greater part of the basin, this exceptionally organic-rich zone is 80 to 120 feet thick. However, it is observed to be thickening towards the Basin Boundary Fault. Red crosses indicate wells with interval thickness control. Contour interval: 20 feet.*

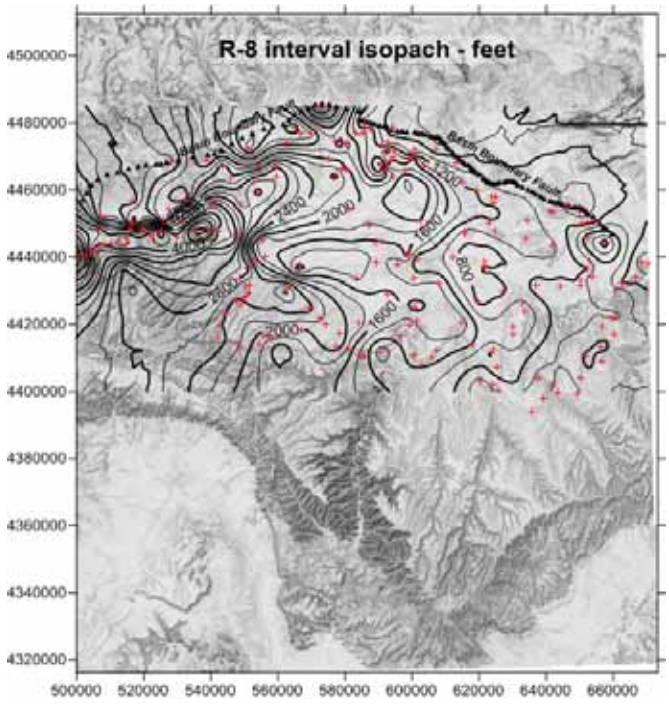

Figure 2-23: *Isopach of the Upper Green River Formation above the Mahogany Zone. Thickness increases dramatically from east to west, from less than 400 feet in the southeast to more than 4000 feet in the basin depocenter in the west. Some portion of the irregularities in this isopach may relate to the difficulty in accurately determining the top of the Green River Formation. Red crosses indicate wells with interval thickness control. Contour interval: 200 feet.*

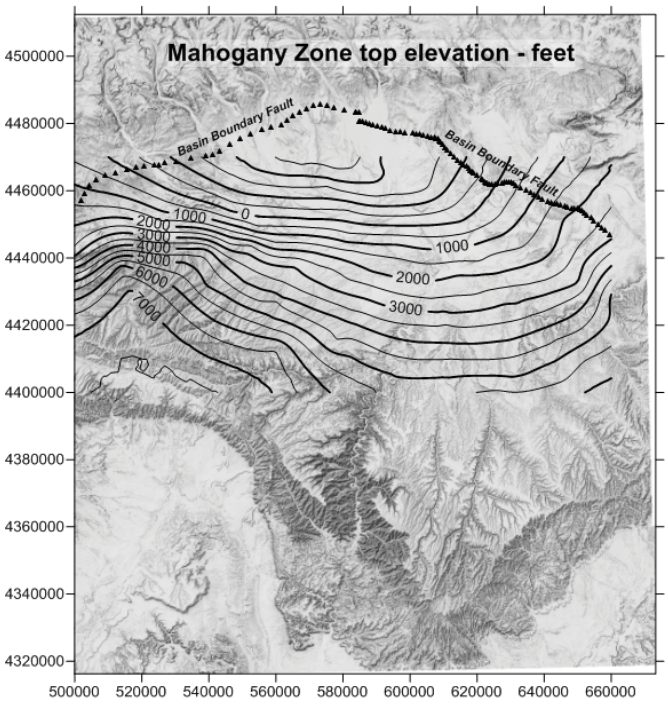

Figure 2-22: *Elevation (msl) of the top of the Mahogany Zone, R-7, the base of the Upper Green River Formation (refer to Figure 2-5; Vanden Berg, 2008). The control wells are the same as those shown in Figure 2-21. Contour interval: 500 feet.*

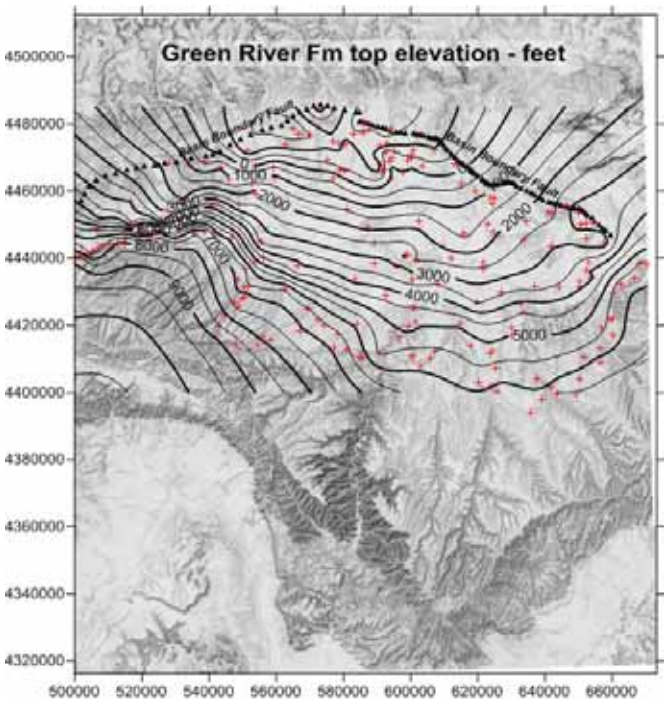

Figure 2-24: *Elevation (msl) of the top of the Green River Formation. Red crosses indicate wells with elevation control. Contour interval: 500 feet.*

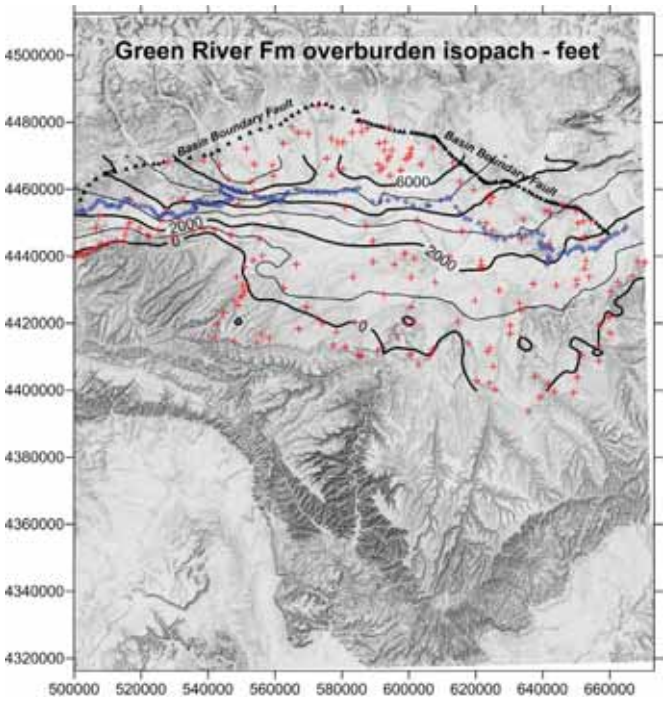

Figure 2-25: *Isopach of the post-Green River Formation overburden, the combined Uinta and Duchesne River Formations. The thickness ranges from zero at the southern erosion edge of the base of the Uinta Formation to over 7000 feet along the Basin Boundary Fault in the extreme northwest of the basin. This isopach was constructed by subtracting the top of the Green River Formation (Fig. 2-24) from the present ground surface at each of the wells indicated by the red cross. The zero isopleth is the outcrop edge of the Uinta Formation on geologic maps (Bryant, 2010; Weiss and others, 2003; Sprinkel, 2007; Sprinkel, 2009). The blue dotted line indicates the present south outcrop edge of the Duchesne River Formation. Contour interval: 1000 feet.*

were large numbers of last and first occurrences of land mammal genera (Murphey and others, 2011).

Along the south flank of the Uinta Mountians, and capping the Diamond Mountain and the Blue Mountain plateaus, there are erosional remnants of a poorly-sorted boulder to pebble conglomerate (Rowley and others, 1985; Sprinkel, 2006; Bryant, 2010), the Bishop Conglomerate. In nearly all instances the mapped Bishop Conglomerate rests conformably on the conglomeratic Starr Flat Member of the Duchesne River Formation. Kowallis and others (2005) have dated tuffs in the Bishop Conglomerate on the Diamond Mountain Plateau as 30.54 ± 0.22 Ma using $^{40}Ar/^{39}Ar$ laser fusion methods. Furthermore, they argue that the Bishop Conglomerate and Starr Flat Member are the same stratigraphic unit and propose dropping the name Starr Flat.

The end of the Eocene was apparently the time in which the Laramide orogeny was ending, thus permitting regionally extensive pedimentation of the mountains flanking the Uinta Basin. The Gilbert Peak erosion surface was formed by this episode of pedimentation (Hansen, 1986). This surface forms the top (depositional and/or erosional) of the Duchesne River Formation. The Bishop Conglomerate-Starr Flat Member was deposited on top of and basinward of the Gilbert Peak surface (Pedersen and Hadder, 2005).

Until the mid-Tertiary, the modern Green River existed in two segments separated by the Uinta Mountains–White River Uplift. The upper Green River drained eastward well north of the mountain range and the lower Green River was just a minor tributary to the Colorado River south of the mountains. In the early Miocene, extension on the north flank of the Uinta Mountains was instrumental in capturing the upper Green River and diverting it along the graben into northwest Colorado (Hansen, 1986). The river deposited the Miocene Browns Park Formation in this newly-formed, structurally-controlled basin. At the time of early Miocene (20.3 Ma) crustal extension, the Gilbert Peak erosion surface tilted northward, thus ending deposition of the Bishop Conglomerate (Hansen, 1986). Due perhaps to infilling of the Browns Park basin or headward erosion of the lower Green River, in the late Neogene the two segments of the Green River eventually connected, either through the Gates of Lodore (Hansen, 1986) or the Canyons of Lodore (Pedersen and Hadder, 2005). The incision of entrenched meander canyons into plateaus capped and rimmed by the Gilbert Peak surface suggests that the connection occurred in the Pleistocene (Hansen, 1986). The widespread occurrence of gravels dated as middle Pleistocene resting with minor erosion on the Bishop Conglomerate strongly implies that little erosion occurred in the Uinta Basin before about 0.5 Ma (Sprinkel and others, 2013).

Based on the discussion above and in consultation with Douglas Sprinkel, Utah Geological Survey, the following scenario is proposed for the post-Green River Formation stratigraphy and geomorphic development of the Uinta Basin.

- Accompanying a period of global cooling and increasing aridity from the late middle Eocene through the earliest Oligocene, deposition in the Uinta Basin laid down a very thick succession of fluvial sediments, up to 3200 feet of Uinta Formation and 3600 feet of the three lower members of the Duchesne River Formation.
- An interval of tectonic quiescence near the Eocene-Oligocene boundary accompanied by extensive pedimentation creating the Gilbert Peak erosion surface that in the Uinta Basin forms the top of the Duchesne River Formation.
- Beginning in early Oligocene time (30.5 Ma), deposition on the Gilbert Peak surface of coarse proximal alluvium of the Bishop Conglomerate and age-equivalent Starr Flat Member. Alluvium continues to accumulate into the earliest Miocene.
- Early Miocene (20.3 Ma) crustal extension leading to grabens on the north flank of the Uinta Mountains is accompanied by northward tilting of the Gilbert Peak erosion surface and its sedimentary cover, effectively turning off sediment accumulation on the high arid plateau across the structural Uinta Basin.

- Starting in the late Miocene, approximately 10 Ma, low-energy streams in the headwaters of the lower Green River drainage begin cutting into the high plateau. Erosion rates are very slow.
- In the middle Quaternary (0.5 Ma), the upper Green and Yampa Rivers join with the lower Green River resulting in very rapid incision of the high plateau and lowering of Green River tributary base levels in the Uinta Basin. It was in this half million year period that the major part of the present landscape was carved, exhuming many thousands of feet of post-Green River overburden.

3. ORGANIC GEOCHEMISTRY

Lacustrine basins are ideal settings for the accumulation and preservation of organic matter, especially large volumes of hydrogen-rich kerogens (Fleet and others, 1988; Carroll and Bohacs, 2001; Katz, 1990; Carroll and Wartes, 2003; Bohacs and others, 2003). The Eocene Green River Formation is widely recognized as a world-class source-rock succession for conventional oil resources and for having the potential for unconventional oil (Fouch and others, 1994; Katz, 1995; Dubiel, 2003; Lillis and others, 2003; among many others). The purpose of this study is not to re-establish the quality of the Green River source rocks, but rather to determine if they have characteristics common to known shale oil resource plays, such as the marine Niobrara Formation and Bakken Shale.

All lacustrine basins have a diversity of depositional settings that shift back and forth with the climatically-driven rise and fall of the lake system. Lake Uinta was not exceptional. As discussed in the previous chapter, fluvial delta and alluvial plains rimmed the outer parts of the lake basin. Broad and ever-changing mudflats formed the ever-migrating lake shoreline, and the near-perennial lake itself was subject to cyclic sedimentation that was influenced by internal and external drivers. Therefore, it is not surprising that the kerogen types found in the Green River Formation (Fig. 3-1) are wide-ranging from humic and algal coals to exceptionally hydrogen-rich sapropel, each characteristic of a different part of the total lake system (Fig. 3-2).

The wells for which organic geochemical analyses are presented in this chapter are identified in Table 3-1 and located on a map (Fig. 3-3). The data reported in Anders and Gerrild (1984) are from cuttings; all other analyses are from core material. With the exception of the analyses tabulated in Dean and Anders (1991), all of the analyses are new to the public domain and are being presented herein perhaps for the first time. Data from the recently drilled Bill Barrett Corporation 16X-23D-36 and 14X-22-46 cores were donated to the UGS in March 2012. In early 2010, Dan Jarvie (Texas Christian University) graciously donated a large set of analyses for the Marsing 16 core. In addition, El Paso E & P contributed analyses from six deep Green River Formation cores drilled in the Altamont-Bluebell field. The cores, housed at the U.S. Geological Survey Core Research Center (USGS CRC) in Denver, date from the late 1960s to early 1980s, but the analyses are very recent.

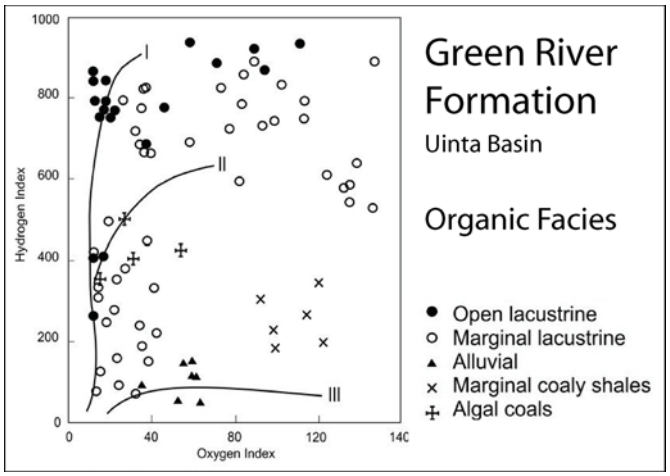

Figure 3-1: *Organic facies of the Green River Formation as indicated by fields on a van Krevelen plot. Kerogens range from high-HI algal-rich organics in the open lacustrine sediments to algal and humic coals and carbonaceous sediments in an alluvial setting on the extreme margins of the lacustrine basin. Data from Anders and Gerrild (1984).*

Programmed Pyrolysis Source Rock Characterization

Programmed pyrolysis (Peters and Cassa, 1994, Appendix D) refers to an analytical technique by which a known weight of dry source rock is heated in a specially designed micro-oven at a programmed rate, such as 15°C/min to drive off and measure with a gas detector initially the free hydrocarbons in the rock that can be volatized without cracking the kerogen (S1 peak), then at higher temperatures the hydrocarbons pyrolysates generated by kerogen cracking (S2 peak), and finally at the highest temperature the CO_2 generated by the burning of carbon with the oxygen within the remaining kerogen or char (S3 peak). The S1 peak is a measure of the residual liquid hydrocarbons already in the rock in units of mg HC/g dry rock. The S2 peak is a measure of the rock's capacity for generating new hydrocarbons by thermal cracking, also in units of mg HC/g rock. The sum of these two peaks (S1+S2) indicates the total oil generating capacity, the *genetic potential* (GP). The oven temperature at which the maximum generation of S2 pyrolysate is measured is the *Tmax* parameter, which can be related to the thermal maturity of the source rock. The higher the Tmax, the larger the quantity of hydrocarbons that had been generated already in the rock (higher transformation ratio), therefore, the greater the thermal maturity. The parameters also can be used to calculate pseudo-values of hydrogen index (HI) and oxygen index (OI). The formulas are: HI = (S2/TOC) x 100, in units of mg HC/ g TOC and OI = (S3/TOC) x 100, in units of mg CO2/g TOC. RockEval™ is just

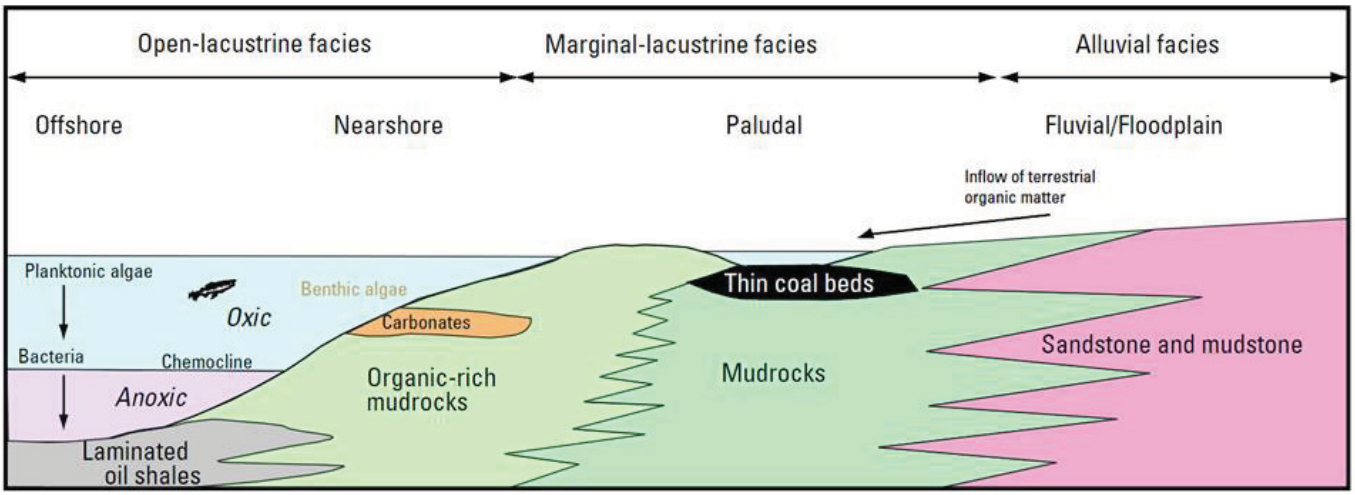

Figure 3-2: *Generalized depositional settings for the several organic facies of Lake Uinta. Dubiel (2003), modified from Ruble and others (2001).*

Table 3-1: *Wells for which programmed pyrolysis analyses were available to and used in this study.*

Well API	Well name	T-R	UTM E	UTM N	Depth range, ft	Data source
4301350623	16X-23D-36BTR	3S-6W	540518	4450034	3887-5150	UGS file
4301350351	14X-22-46DLB	4S-6W	537941	4440231	5480-5625	UGS file
4305130002	Marsing 16	10S-8E	498247	4421986	57-1223	UGS file
4301330030	Chasel 1-81A1	1S-1W	581901	4472569	10639-10705	USGS CRC file
4301330031	Olsen U1-12A2	1S-2W	580308	4773988	10495-10603	USGS CRC file
4304731470	DR Long 2-19A1E	1S-1W	591251	4470045	9163-9716	USGS CRC file
4301330036	Lamiq-Urrity 1-8A2	1S-2W	573084	4473208	10833-10951	USGS CRC file
4301330009	Virgil Mecham 1-11A2	1S-2W	578696	4474035	10348-10634	USGS CRC file
4301330315	Norling 1-9B1	2S-1W	535097	4464443	7497-7618	USGS CRC file
na	WOSCO EX-1	9S-20E	619749	4426824	2181-2963	Dean and Anders (1991)
na	Coyote Wash 1	9S-23E	644159	4431387	571-1043	Dean and Anders (1991)
4301330114	Ute Tribal 1-16	4S-7W	527471	4442295	7030-8110	Anders and Gerrild (1984)
4301330040	Cedar Rim 3	3S-6W	533730	4450740	4600-7400	Anders and Gerrild (1984)
4301330122	Dustin 1	2S-3W	567013	4460465	8500-14080	Anders and Gerrild (1984)
4301330113	Daniel Uresk Fee 1	4S-1W	581626	4446093	5030-11080	Anders and Gerrild (1984)

one of several patented analytical devices for conducting programmed pyrolysis of source rocks. All others work on the same basic principles as the original RockEval™.

Cross plots of programmed pyrolysis derived HI vs. TOC and HI vs. OI taken together are standard measures of both source rock organic richness and kerogen types. The HI vs. OI is a version of the industry-standard van Krevelen plot. A cross plot of genetic potential (GP) vs. TOC is a standard tool for evaluating overall source rock quality. Commonly used threshold values for all of these parameters are tabulated in Peters and Cassa (1994).

Noble and others (1997) introduced a technique developed at ARCO for rapid assessment of the effectiveness of shale seals, those with sufficiently high capillary pore pressures to inhibit the penetration of oil upward out of a "shale-sealed" oil pool. The method used programmed pyrolysis data, which at the time was widely available to industry. The parameter introduced as a measure of oil saturation in the shale is (S1/TOC) x 100, in units of mg HC/g TOC. The logic was that a highly effective shale seal would have low values of oil saturation, whereas a "leaky" shale would have high values. Shales with values of 120 mg HC/g TOC or greater clearly would contain non-indigenous hydrocarbons that leaked in from the underlying oil pool.

This same parameter, referred to as the "oil saturation index" (OSI) is now gaining popularity in the search for shale oil resource plays. Most of the geochemical service companies include this parameter in their standard programmed pyrolysis reports. Jarvie (2012) has identified any shale with an index

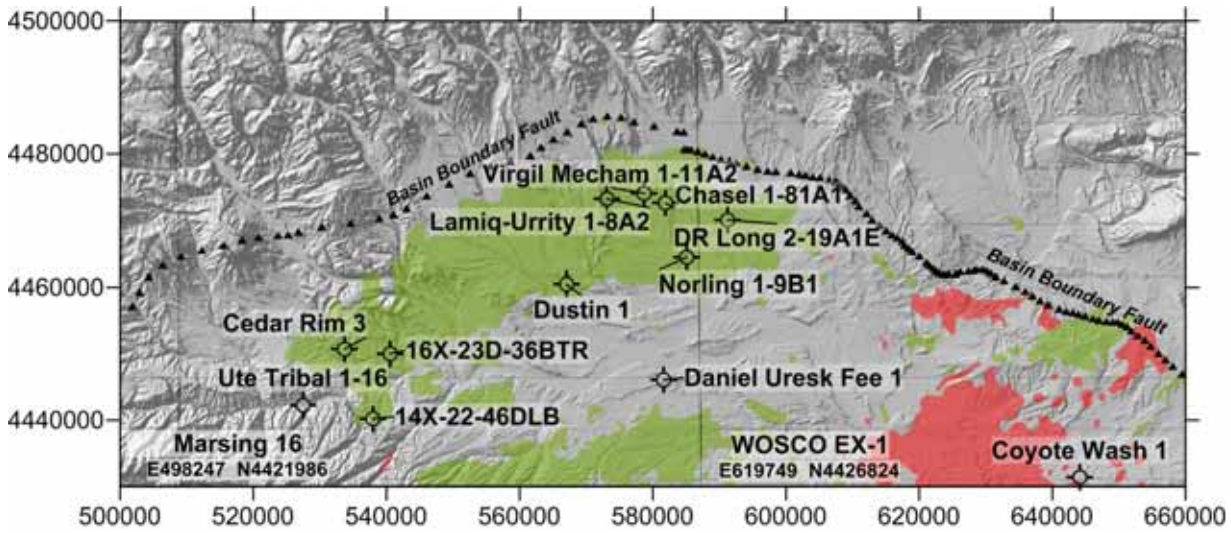

Figure 3-3: *Location of cored wells having programmed pyrolysis data used in this study. Refer to Table 3-1 for the well coordinates, API numbers and data sources. Marsing 16 and WOSCO EX-1 lie immediately to the southwest and south, respectively, of the map. The geographic coordinates are meters in UTM NAD83, Zone 12.*

greater than 80 to 100 mg HC/g TOC as having the potential to be a commercial shale oil resource. In the absence of natural fractures, organic-rich mudstones retain as much as 70–80 mg of hydrocarbons per gram of TOC. Oil at these levels of concentration is bound by the organic-matter by adsorption and solvation (absorption) and is not mobile (Jarvie, 2012). Potentially productive source-rock intervals are either those with very high values of OSI, such as the Eagle Ford Formation in southeast Texas (Figure 3-4), or intercalated or proximal low-TOC strata that have been charged with oil from adjacent productive beds, as in the Bakken (Figure 3-5) and Niobrara Formations.

The OSI is an effective predictor of potential shale oil reservoirs only for rocks within the oil-generative window. As the gas-generative window is reached, the residual oil is cracked, reducing the value of S1. This is what is observed in organic-rich mudstone of the Paradox Formation in the Paradox Basin. In the oil-generative window in the Paradox Formation in Utah, both the GP and OSI values are high relative to TOC, but both parameters are lower in southwest Colorado which is in the gas-generative window (Figs. 3-6 and 3-7). The Paradox Formation organic-rich mudstones produce oil in Utah and gas with minor gas-liquids in Colorado (Schamel, 2009).

For each group of Green River Formation core samples, this chapter presents four cross plots of programmed pyrolysis data: TOC vs. HI, HI vs. OI, GP vs. TOC, and finally S1 vs. TOC, an x-y representation of the OSI that displays more information than just the index itself. Where a large amount of data is available for a single core, these key parameters are also displayed in a geochemical log.

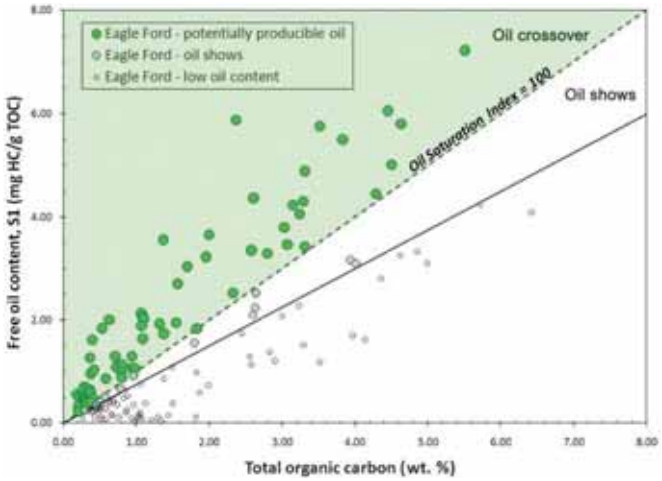

Figure 3-4: *Total organic carbon (TOC) plotted against S1 for Eagle Ford Formation mudstones with a range of oil contents as evidenced in well tests. Figure is modified from Jarvie (2012). AAPG©2012, reprinted by permission of the AAPG whose permission is required for further use.*

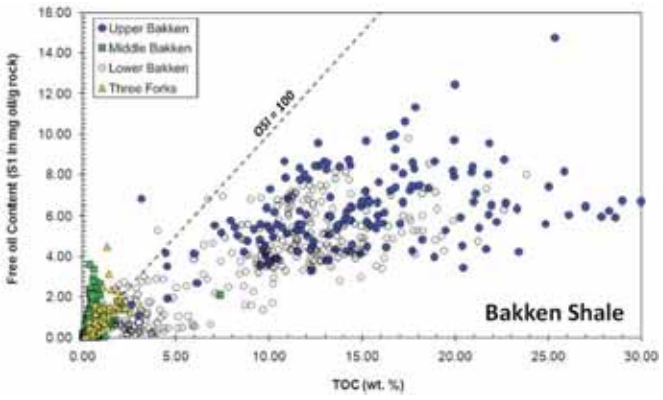

Figure 3-5: *TOC plotted against S1, a measure of residual oil in the rock, for the Bakken Shale. The values with low TOC and very high S1 are Middle Bakken "reservoir" samples in an oil-impregnated, but non-source rock portion of the Bakken Shale. The Three Forks Formation commonly plays a similar role as a non-source oil reservoir. Figure modified after Jarvie (2012). AAPG©2012, reprinted by permission of the AAPG whose permission is required for further use.*

The 1237-foot-long Marsing 16 core samples a large segment of the Green River Formation immediately southwest of its depocenter in the western part of the basin. The upper part contains the "Middle Marker" and the Green Shale facies of the lower Middle Green River Formation (refer to Figure 2-6). The lower part samples the entire Lower Green River Black Shale facies and the uppermost deltaic sandstones of the underlying Wasatch (Colton) Formation. The full range of kerogen types known in the Green River Formation are present in this core (Figs. 3-8 and 3-9). Note that there are both algal and humic coals. Source-rock quality ranges from poor to excellent (Fig. 3-10), with the majority of the samples being very good and excellent. It is interesting that the Green Shale facies is a consistently better source rock than the Black Shale

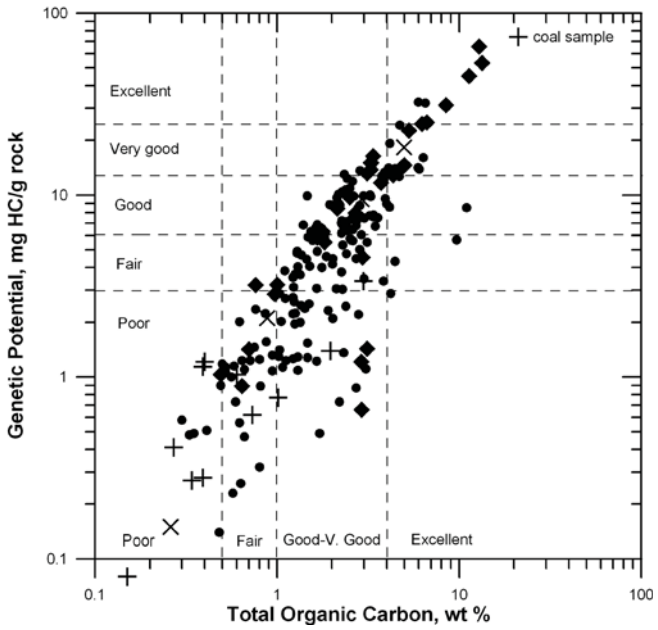

Figure 3-6: *TOC plotted against genetic potential (S1+S2) for various Paradox Formation shales in the Paradox Basin of Utah. This plot serves to indicate general source rock quality, as indicated in the figure. Data reported in Schamel (2009).*

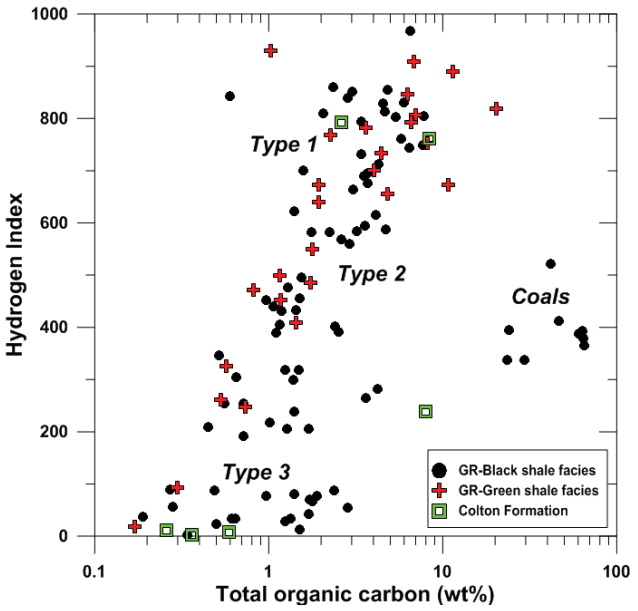

Figure 3-8: *For Marsing 16 core samples, TOC plotted against hydrogen index (HI) showing that except for the coals, hydrogen content of the kerogen increases with increased organic richness. The most oil prone source rocks are also the richest. This 1237 ft core sampled the Lower Green River Formation in the southwest Uinta Basin. Data from UGS CRC files.*

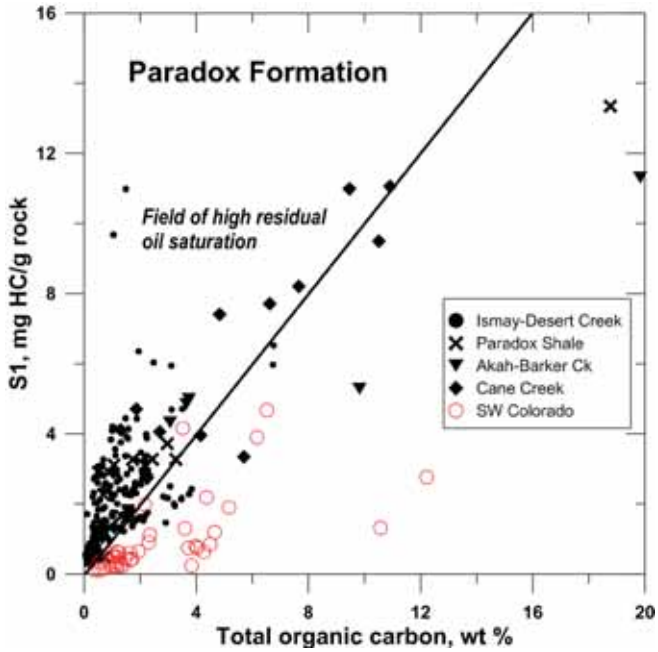

Figure 3-7: *TOC plotted against S1 from programmed pyrolysis for Paradox Formation shales in oil-producing Utah (black symbols) and natural gas-producing southwest Colorado (red circles). Data from Schamel (2009) and GeoX Consulting Inc internal files.*

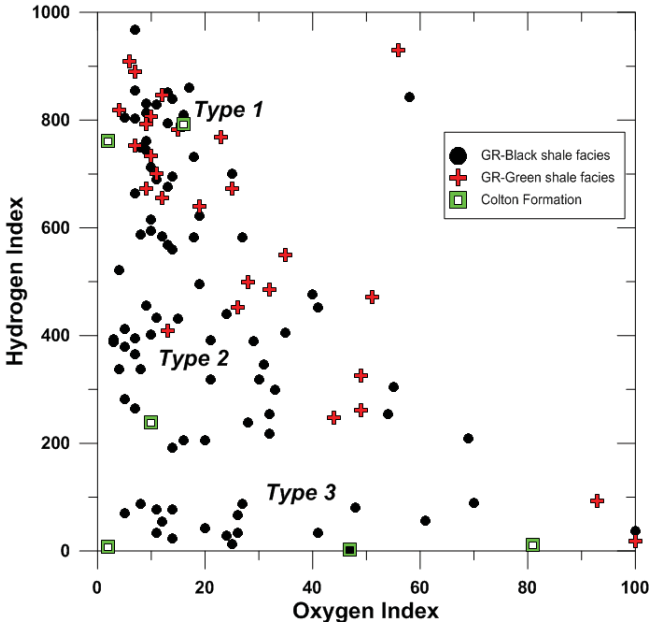

Figure 3-9: *A van Krevelen plot showing the wide range of kerogen types found in the lower Green River Formation sampled in the Marsing 16 core. The diversity of kerogen types exists in each of the three stratigraphic units cored. Data from UGS CRC files.*

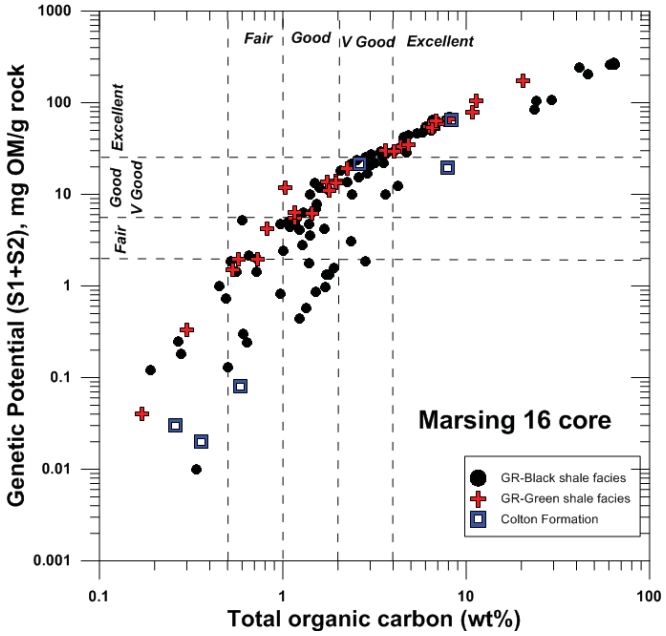

Figure 3-10: *TOC vs. genetic potential plot for Marsing 16 core samples indicating the high quality of source rocks in the Black Shale and the Green Shale facies. Note the very large range in values of both TOC and GP. This reflects the large diversity of the cyclically-interbedded organic facies. Data from UGS CRC files.*

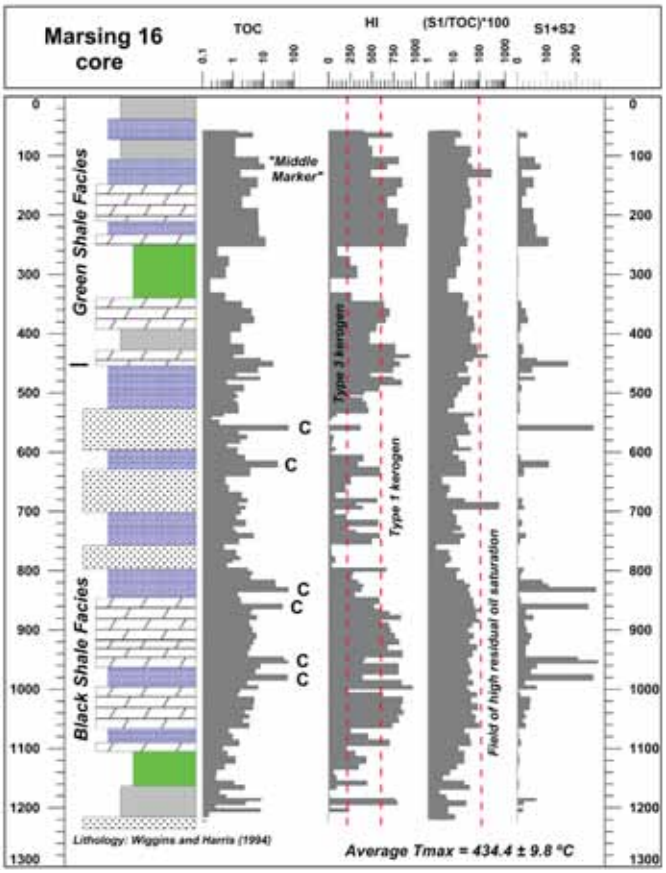

Figure 3-11: *Organic geochemical log of the lower Green River Formation in the Marsing 16 core in the southwest Uinta Basin. Depth in feet; "C" indicates coal beds. Data from Wiggins and Harris (1994) and UGS CRC files. See text for discussion.*

facies. The geochemical logs for the Marsing 16 core (Fig. 3-11), which plot the values in the cross plots as a function of depth, show interesting patterns. Most obvious are the four cycles expressed in values of TOC, HI, and the OSI. These cycles match only in part the stratigraphic subdivisions of Wiggins and Harris (1994); refer to Figure 2-6. The most organic carbon- and hydrogen-rich rocks are associated with the intervals identified as marginal lacustrine. These intervals also have the higher residual oil saturations. Note that TOC and (S1/TOC)x100 are displayed on log scales. The siliciclastics-carbonate, open-lacustrine succession has only Type II and Type III kerogens and low oil saturation index. There are just three instances of OSI higher than 100, and these spikes are in the 200 to 600 range (Fig. 3-11). Examination of the core photographs for these spikes failed to disclose their source. Examination of the actual core would be needed. It is clear, however, that the residual oil saturations are not sufficiently high to characterize the Green River Formation sampled by this core as a potential shale oil resource. The low OSI values could indicate low thermal maturity of the source rocks, related to their shallow depth of burial, or migration of once-present mobile oil out of the rock. The average Tmax (see Fig. 3-11) is just at the lower oil-generative window threshold.

Core samples from the southeast part of the basin are primarily from the Middle and lowest Upper Green River Formation. The samples are very hydrogen-rich and dominantly Type I kerogens (Figs. 3-12 and 3-13) and their TOC content is exceptionally high. Consequently, these Middle and Upper Green River strata are very good to excellent source rocks (Fig. 3-14). A few of the samples from the WOSCO EX-1 and

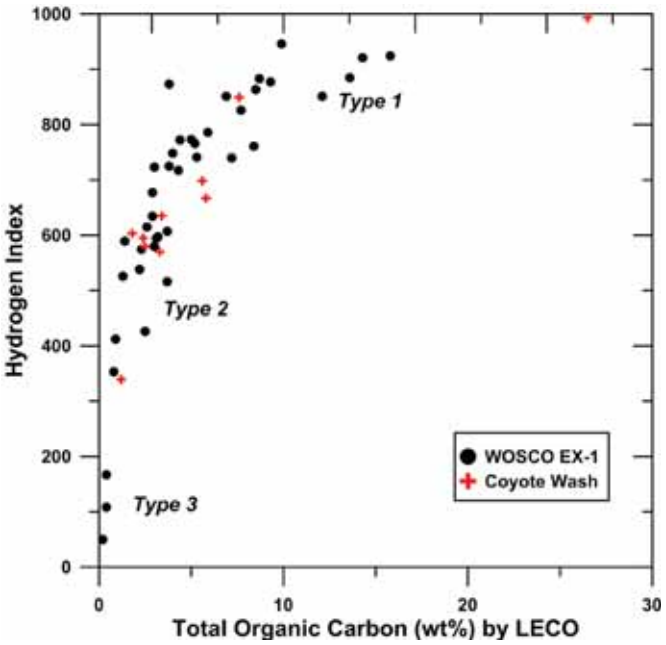

Figure 3-12: *TOC vs. hydrogen index for Parachute Creek Member samples in cores from the southeast Uinta Basin. Data from Dean and Anders (1991).*

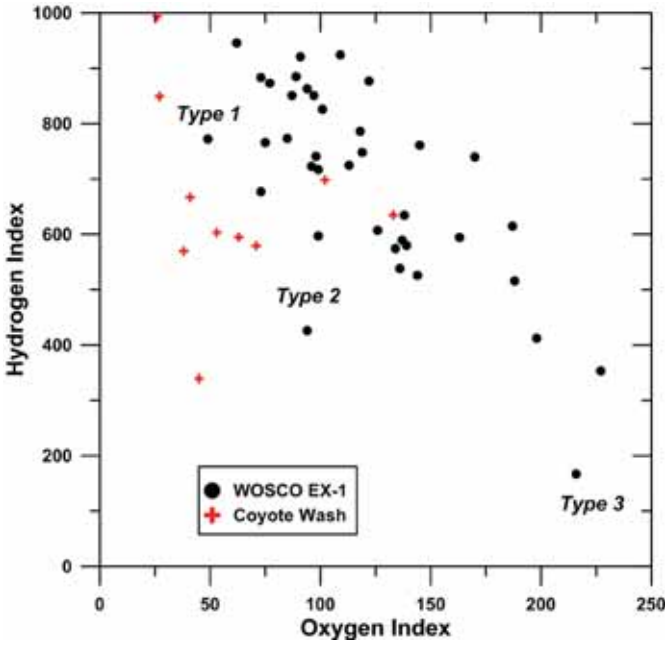

Figure 3-13: *Van Krevelen plot for the Parachute Creek Member core samples in the southeast basin. Note the predominance of Type I and Type II kerogens at this higher stratigraphic level, at least in this axial part of the basin. Data from Dean and Anders (1991).*

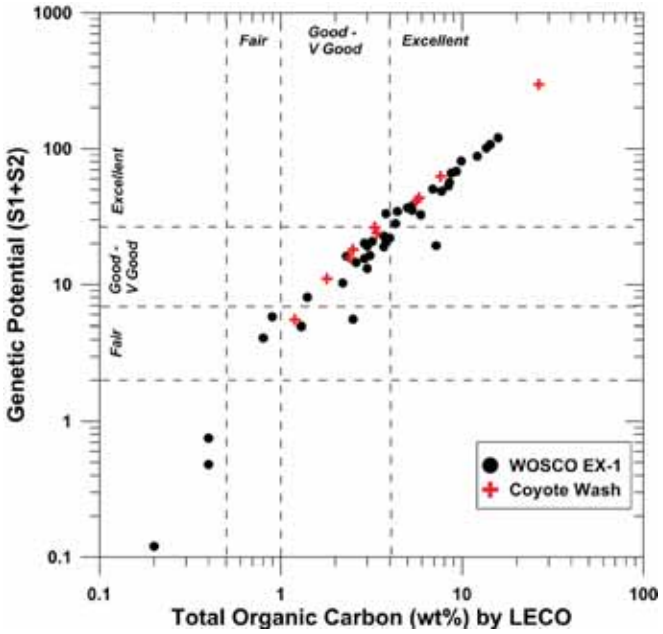

Figure 3-14: *TOC vs. genetic potential of the Parachute Creek Member core samples indicating the overall good to excellent quality of the source rocks. It is known that these are low maturity rocks, although Tmax or R_o measurements are not available for the samples. Data from Dean and Anders (1991).*

Coyote Wash cores even have elevated values of OSI (Fig. 3-15). The geochemical log of the WOSCO EX-1 core (Fig. 3-16) shows a cyclic variation in geochemical parameters that corresponds to the alternating "rich-" and "lean-" intervals. In the intervals in which TOC is greatest, the HI and genetic potentials (S1+S2) are greatest. The OSI is uniformly low except in one two-sample interval centered at a depth of 2,415 feet (Fig. 3-16) in which the index exceeds 200 mg HC/g TOC. These samples are in the B-groove interval (Fig. 2-5) lacking quality source rock. Bitumen-saturated tuff beds, such as that observed in a nearby well (Fig. 3-17) are described throughout the core (Robinson and Cook, 1975), but this is not one of them. Dean and Anders (1991) appear not to have sampled any of the bitumen-impregnated tuffs since no such units appear in the programmed pyrolysis data in the geochemistry log. The very high oil saturation suggests the tuff bed is a conventional reservoir bed.

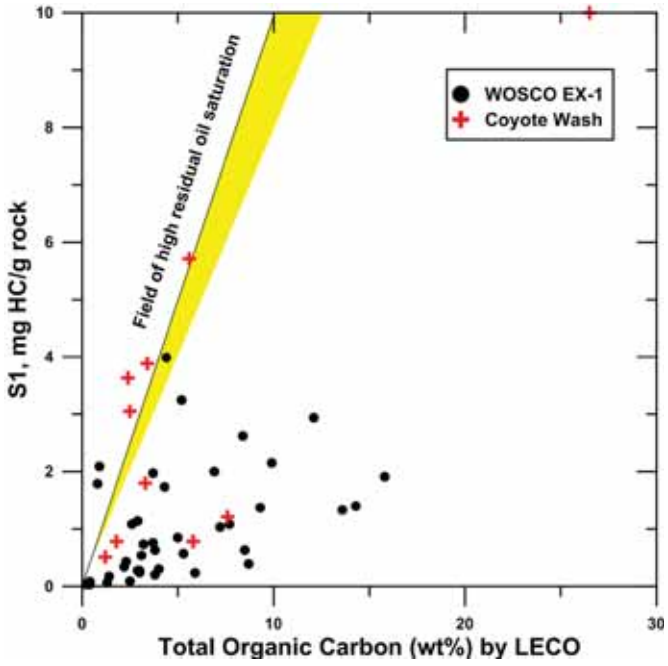

Figure 3-15: *TOC vs. S1 for Parachute Creek Member core samples in the southeast basin. Note that a few of the EX-1 and Coyote Wash samples have values of oil saturation index (OSI) greater than 100. The yellow field indicates OSI values in the range 80-100 mg HC/g TOC. Data are from Dean and Anders (1991). See text for discussion.*

Robinson and Cook (1975) extracted oil from the WOSCO EX-1 core with solvents and analyzed the oil to determine its principal liquid chromatography fractions, the Saturate-Aromatic-Resin-Asphaltine (SARA) components. They found that the quantity of solvent-extracted oil ranged from negligible to 5.1 wt%. In the bitumen-impregnated tuffs, the solvent-extracted oil quantity was in the 2.9 to 7.5 wt% range, with one exceptional sample at 93.9 wt%. The oils are richest in resins (55.4% average), branched alkanes (25.7%), and aspaltines (11.9%). Normal alkanes and aromatics, generally dominant components in normal oils, are unusually low at 3.8% and 3.2%, respectively. These oils appear very immature. The relatively low concentration of solvent-extractable oil makes the

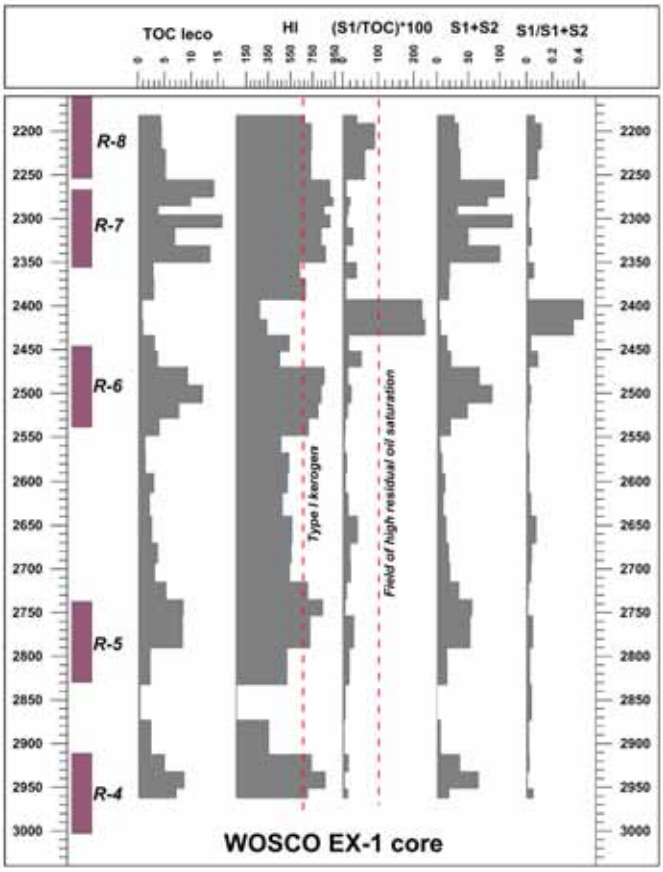

Figure 3-16: *Organic geochemical log for the upper Green River Formation in the WOSCO EX-1 core in the southeast Uinta Basin. Depths in feet. See text for the description.*

Figure 3-17: *Bitumen impregnated tuff bed in the upper R-6 oil shale interval in the Skyline 16 core. The tuff bed is just 2 inches thick. The core is southeast of the WOSCO EX-1 core in 10-11S-25E; UTM E 661445, UTM N 4415109.*

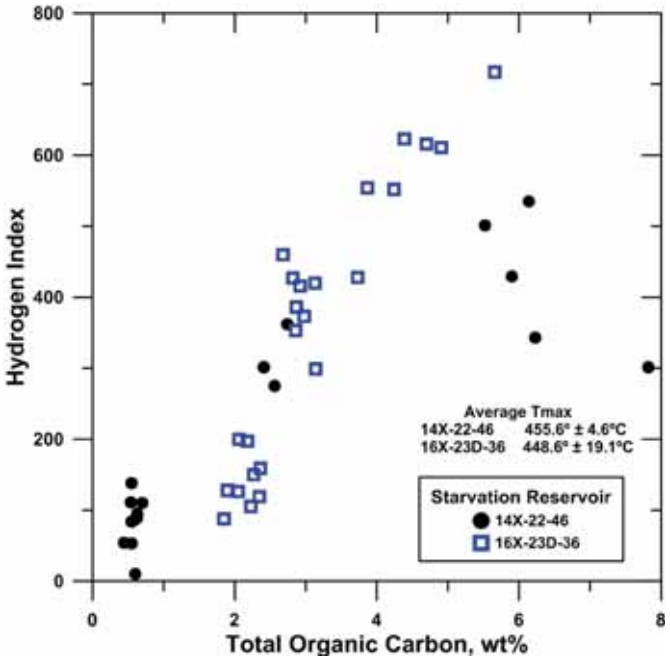

Figure 3-18: *TOC vs. hydrogen index for fresh Green River Formation core samples from two wells near Starvation Reservoir in the southwest basin. Data from UGS CRC files.*

rock, despite the high TOC and HI, a poor candidate for a shale oil resource given the current level of thermal maturity.

Dean and Anders (1991) published independently measured LECO TOC and Fischer assays of oil yield in gallons per ton (GPT) for the WOSCO EX-1 core. A regression analysis of these data yields an algorithm for converting Fischer assay values to organic richness:

$$TOC = 0.42308\ (GPT) + 0.34154 \qquad R^2 = 0.9934$$

The 14X-22-46 and 16X-23D-36 cores from the Starvation Reservoir area (Fig. 3-3) west of Duchesne capture select intervals from the middle and upper Green River Formation. The 14X-22-46 core samples the Black Shale facies and the 16X-23D-36 core samples portions of the interval from the lower R-8 through R-5, including the Mahogany Zone (R-7). The cores have a mix of kerogen types, and relative to other core samples, lower than expected HI and TOC (Figs. 3-18 and 3-19). These low values could relate to thermal maturity, which is indicated to be in or near "peak oil". Nevertheless, the rocks are good to excellent source rocks (Fig. 3-20). Several of the core samples have OSI values that approach and even exceed 100 (Fig. 3-21). The one sample in Figure 3-21

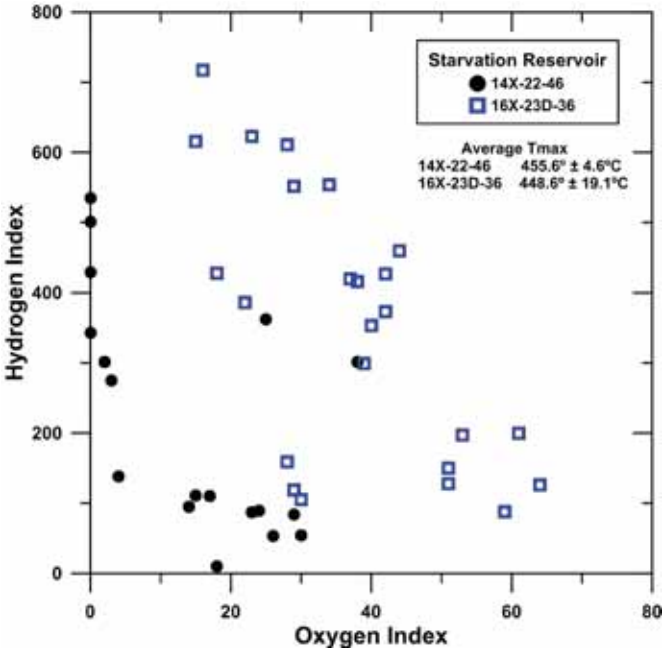

Figure 3-19: *Van Krevelen plot for fresh Green River Formation core samples from two wells near Starvation Reservoir in the southwest basin. The samples represent a broad range of kerogen types, but dominantly Type II kerogens. Data from UGS CRC files.*

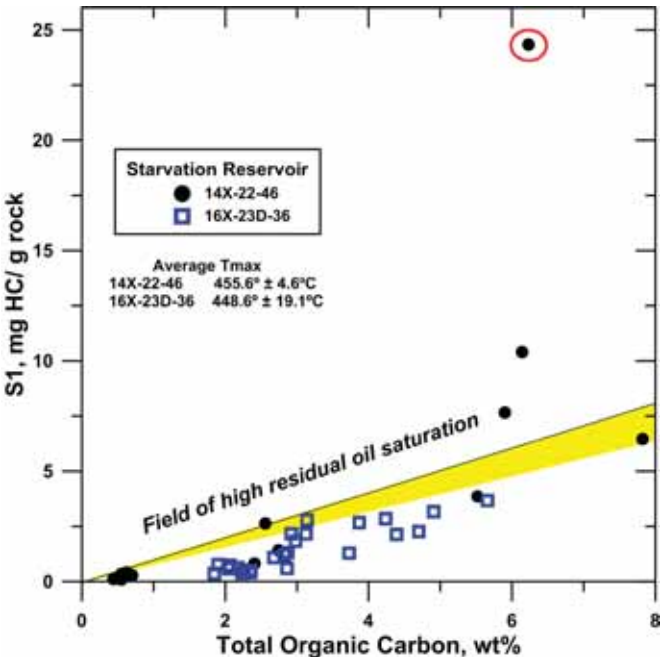

Figure 3-21: *TOC vs. S1 from programmed pyrolysis analysis for Green River cores in the vicinity of Starvation Reservoir. Note that three of the samples have OSI values greater than 100, but other samples fall into the 80-100 field, shown in yellow. One sample (red circle) has an exceptionally high value. See text for discussion. Data from UGS CRC files.*

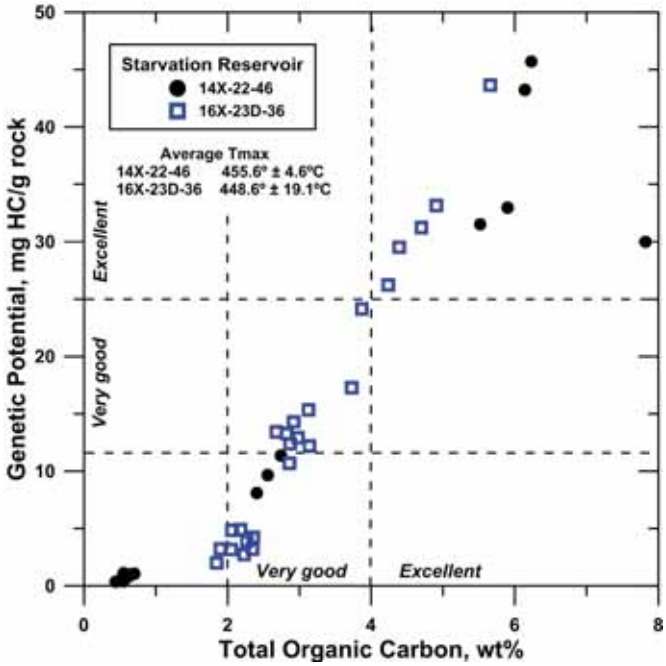

Figure 3-20: *TOC vs. genetic potential for Green River Formation core from wells near Starvation Reservoir. The samples are of good and very good to excellent source rocks. Data from UGS CRC files.*

circled in red has an OSI value of 390 suggesting an oil-impregnated reservoir bed, but without further information on the 14X-22-48 core, it is not possible to know with certainty.

The cores from the six wells in the Altamont-Bluebell field have been in storage for several decades since the wells were drilled and the present condition of the core is not known, except for Norling 1-9B1 and Virgil Mecham 1-11A2, both of which are still in good condition. Well reports contain limited information about the stratigraphic level of the Green River Formation cored. However, for the limited tops reported, the Norling 1-9B1 core samples appear to be in the Mahogany Zone. Note the large number of samples with Type I kerogen (Fig. 3-22 and 3-23). The same is possibly true of the DR Long 2-19A1E core, however these samples are primarily Type II kerogen. The Olsen U1-12A2, Virgil Mecham 1-11A2, Chasel 1-81A1 and Lamiq-Urrity 1-8A2 cores sample the lower Green River Black Shale facies. Programmed pyrolysis values indicate that the kerogen is dominantly Type II (Figs. 3-22 and 3-23), with the exception of many samples from the Norling 1-9B1 and Virgil Mecham 1-11A2 cores. Source rock quality is fair to very good (Fig. 3-24); only the Norling 1-9B1 core is an excellent source rock. Despite the relatively low quality of the source rock compared to other cores presented above, many of the core samples from a variety of wells have elevated residual oil saturations, several with an OSI in excess of 100 (1:1 line in Figure 3-25).

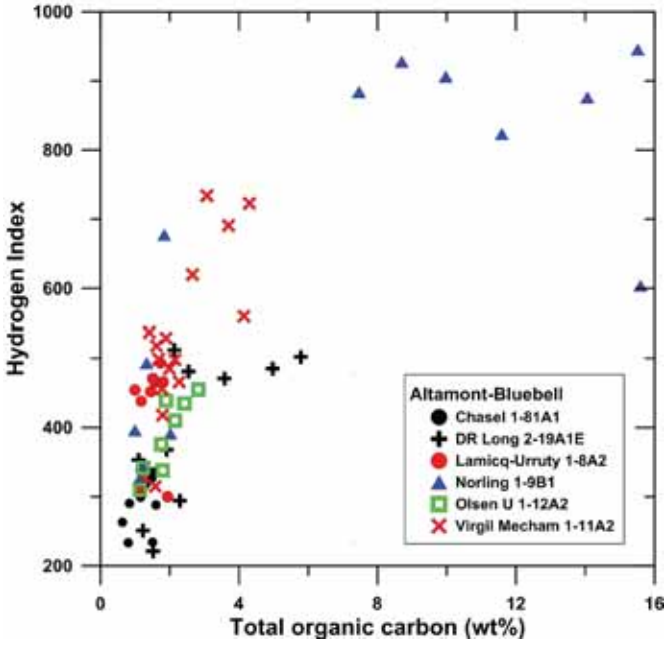

Figure 3-22: *TOC vs. hydrogen index for six older cores of apparent open lacustrine facies Green River Formation from wells in the northern Altamont and Bluebell fields. Data from USGS CRC files.*

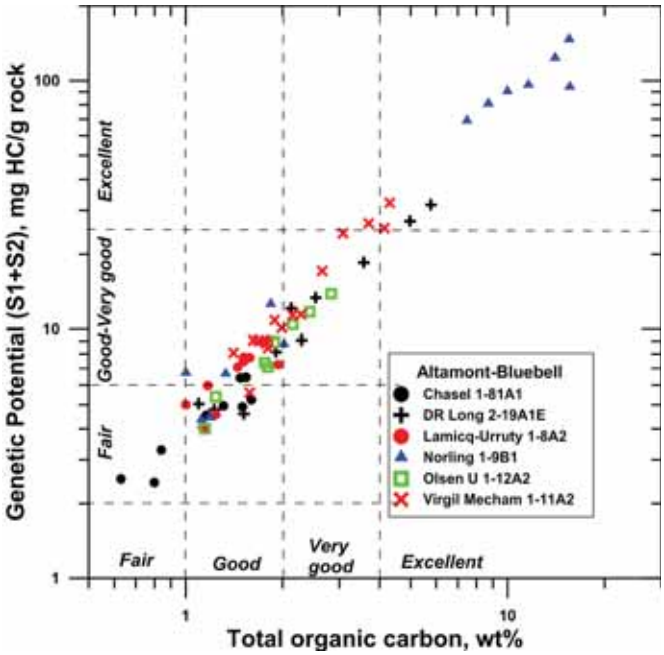

Figure 3-24: *TOC vs. genetic potential for deep core samples from the northern Altamont and Bluebell fields. The core samples are rocks having fair to excellent source potential. The Norling 1-9B1 well, which is to the southwest of the others, has sampled rocks with the highest source potential. Data from USGS CRC files.*

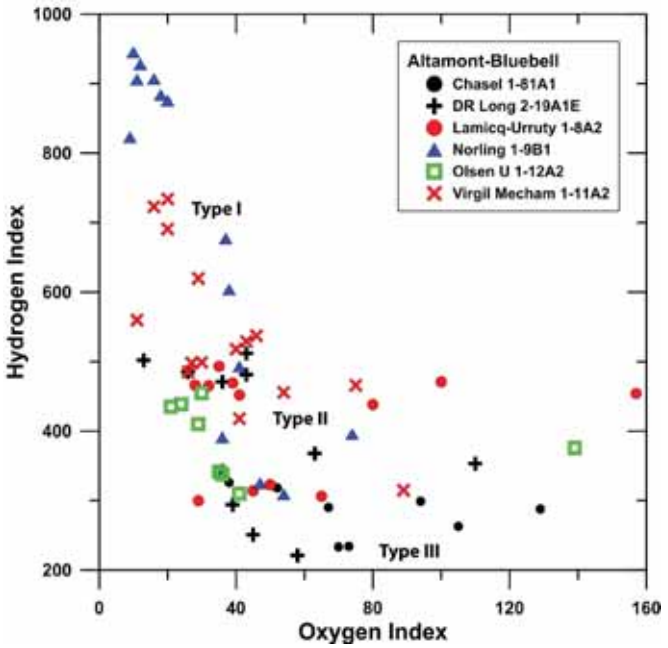

Figure 3-23: *Van Krevelen plot of core samples in the deep northern Altamont and Bluebells fields. It is noteworthy that no Type III kerogen is observed in this sample suite in apparent open lacustrine facies rocks from near the basin axis. The kerogens are predominantly Type II, with Type I represented in just two wells. Data from USGS CRC files.*

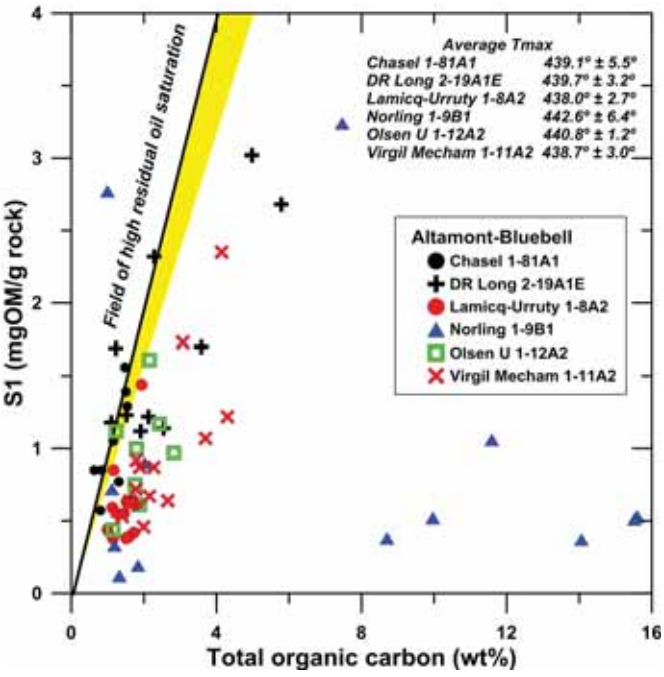

Figure 3-25: *TOC vs. S1 for deep core samples from the northern Altamont and Bluebell fields. Many of the core samples have OSI values greater than 80 (yellow field), but only a few exceed 100. These rocks could have potential for a shale oil resource play. Data from USGS CRC files.*

In the Norling 1-9B1 core (Mahogany), free or mobile oil occurs in bioclastic limestone or sandstone lenses and in open fractures (Fig. 3-26). The fractures are commonly short and strata bound, as depicted in Figure 3-26, but oil also fills many long subvertical fractures that are partially closed by calcite. Similar fractures are not observed in the Virgil Mecham 1-11A2 core (lower Black Shale).

Organic Maturity and Anomalous Formation Pressure

It is generally accepted that even in the deeper part of the Uinta Basin at the Altamont-Bluebell field, the Mahogany oil shale bed is situated above the normal oil generative window for a Type II kerogen, whereas the pre-Eocene portions of the basal Green River Black Shale have thermal maturities of about 1.1–1.2% vitrinite reflectance (R_o) (Anders and others, 1992; Nuccio and others, 1992), sufficient for generation of oil and associated gas. Closer to the basin margins, the level of thermal maturity in the Green River Formation decreases such that in the western Natural Buttes area it is merely 0.75% R_o at the Eocene-Paleocene boundary beneath the Black Shale. All but the lower Black Shales of the Green River Formation in the deeper parts of the Uinta Basin are immature with respect to hydrocarbon generation. It should be noted that the Green River Formation has a limited number of actual measurements of vitrinite reflectance, so prior basinwide thermal maturity estimates are poorly constrained.

The programmed pyrolysis data gathered for this study suggest a different situation, at least for the western part of the basin in the area of the greater Altamont-Bluebell field. Here cores that sampled the upper parts of the Green River Formation have Tmax values characteristic of the "early mature" oil window (Fig. 3-27). In wells near the Starvation Reservoir, core samples from all levels of the Green River Formation have Tmax values indicating "peak oil" levels of maturity, equivalent to R_o of 0.65% to 0.9% (Peters and Cassa, 1994).

What is certain is that the maturity levels at the base of the Green River Formation (lower Eocene) will not exceed those determined from measured R_o (Fig. 3-28) at the base of the underlying Mesaverde Formation (Upper Cretaceous). Thermal maturation simulations for a limited number of wells in the Uinta Basin (Nuccio and Roberts, 2003) predict maturities for the lower part of the Green River Formation in the northwest half of the basin in the oil, and even, the dry gas, window (Fig. 3-29). Entry into the oil window is modeled earlier than 20 Ma (Fig. 30).

As presented above, a large portion of the kerogen in the Green River Formation can be characterized as Type I. Therefore, thermal maturity of the hydrogen-rich source rocks may be

Figure 3-26: *The occurrence of oil in Norling 1-9B1 core as fracture filling and/or oil-impregnated lenses of bioclastic limestone or sandstone with relatively higher porosity than the adjacent lime mudstone source rock. The core was photographed in October 2012 at the USGS CRC, Denver.*

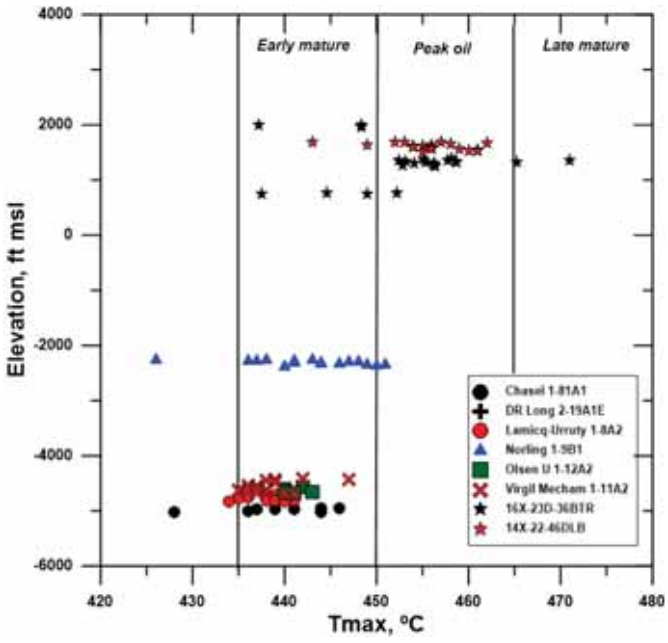

Figure 3-27: *Measured values of Tmax plotted against the elevation, not depth, of the core samples from wells in the greater Altamont-Bluebell field. There is a counterintuitive relationship in which the samples with highest elevations have the highest Tmax values and the presently deepest samples have the lower values of Tmax. See text for discussion. Data from USGS CRC files.*

constrained if closed-system, hydrous pyrolysis experiments on the Green River Black Shale (Ruble and others, 2001; Lewan and Roy, 2010) provide the best description of the reaction kinetics of this source rock (Fig. 3-31). The very large activation energy determined from the experiments of 68.7 kcal/mole and relatively small frequency factor (Ao) of 1.65 x 10^{32} my^{-1} suggest that the onset of oil generation from the Green River Black Shales will be delayed to about 0.75% R_o. The peak of oil generation would be at the equivalent of about 1.0 R_o and oil and gas generation would occur together over a relatively narrow generative window. A separate gas generative window, if even relevant in the Green River Black Shales, would have been reached only in the very deepest parts of the Uinta basin, if at all.

At normal depths of production, overpressuring occurs throughout the Uinta Basin (Nelson, 2002, 2003). The highest overpressures (Figs. 3-32 and 3-33) are encountered in the Altamont-Bluebell district at depths greater than 10,000 ft (Bredehoeft and others, 1994). As this also is the basin center, the top of the overpressured region is within the lower Green River/Wasatch Formation. In this part of the basin the interval of maximum pressure gradient (0.60–0.80 psi/ft) is about 4000 ft thick and extends to near the top of the Upper Cretaceous. This overpressured zone is considered to be associated with the active generation of oil and associated gas from the Lower Black Shale of the Green River Formation (Bredehoeft and others, 1994). There may be an alternative explanation for the observed overpressures, as will be discussed in the final chapter.

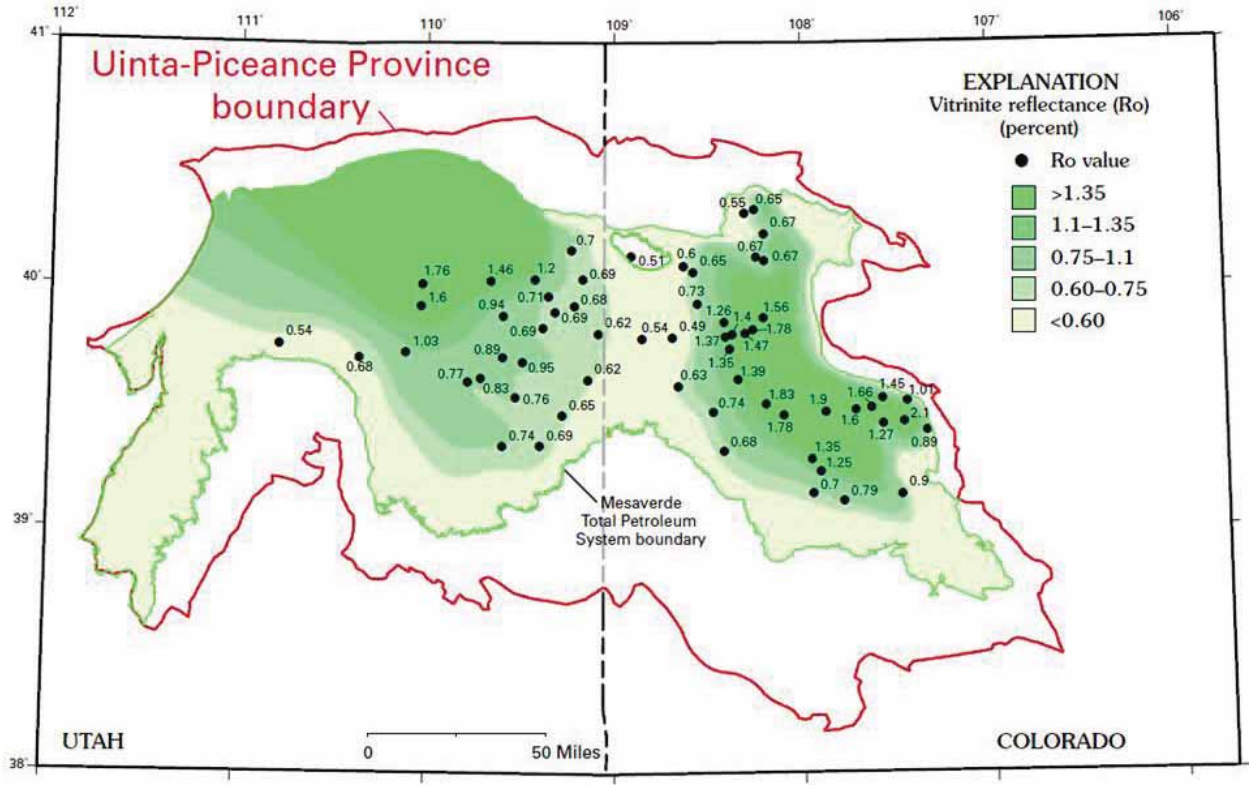

Figure 3-28: *Measured vitrinite reflectance (R_o) values from near the base of Mesaverde-top of Mancos Shale contact in the Uinta and Piceance Basins (Nuccio and Roberts, 2003). These values from thousands of feet below the base of the Green River Formation establish a floor on R_o in this younger source rock.*

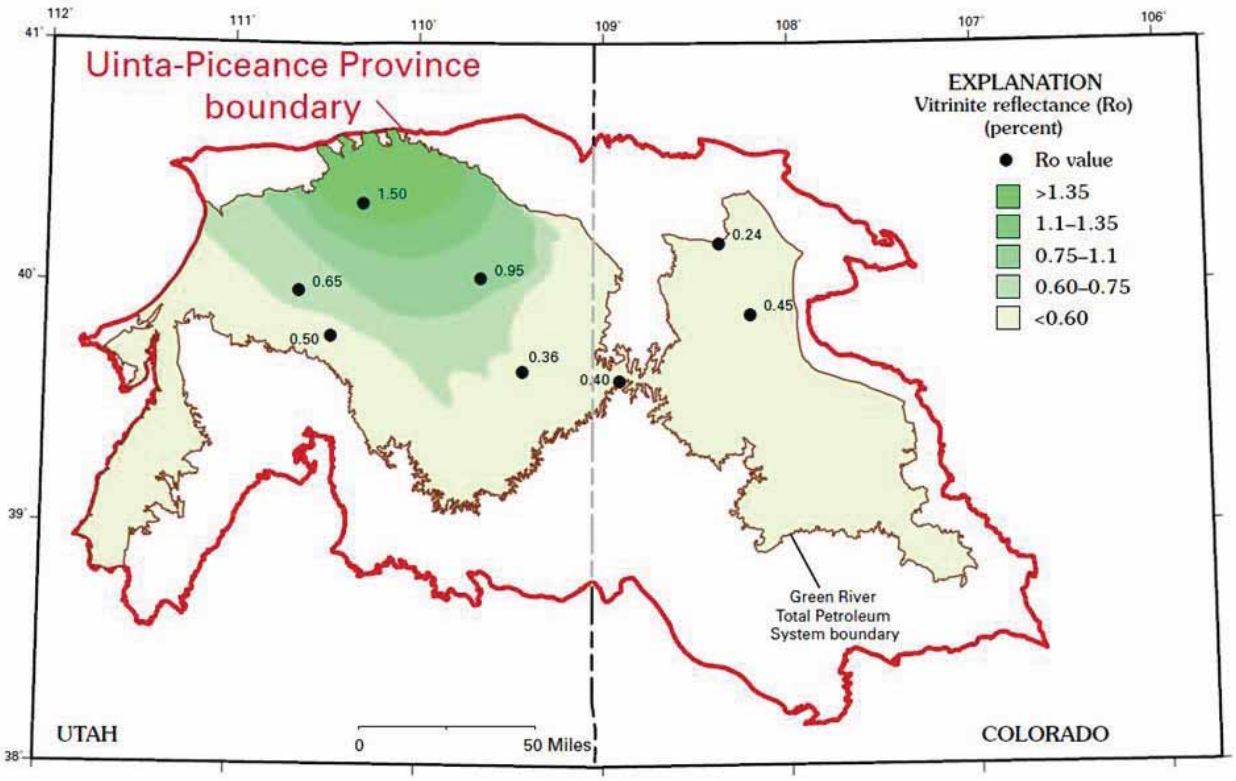

Figure 3-29: *Simulated vitrinite reflectance (R_o) values for the lower Green River Formation based on five modeled deep wells in the Uinta Basin (Nuccio and Roberts, 2003). Note that the R_o isopleths are constructed to generally conform to those for the deeper base Mesaverde Group. Considering the small number of simulated wells (5), there is only limited geologic justification for such a construction.*

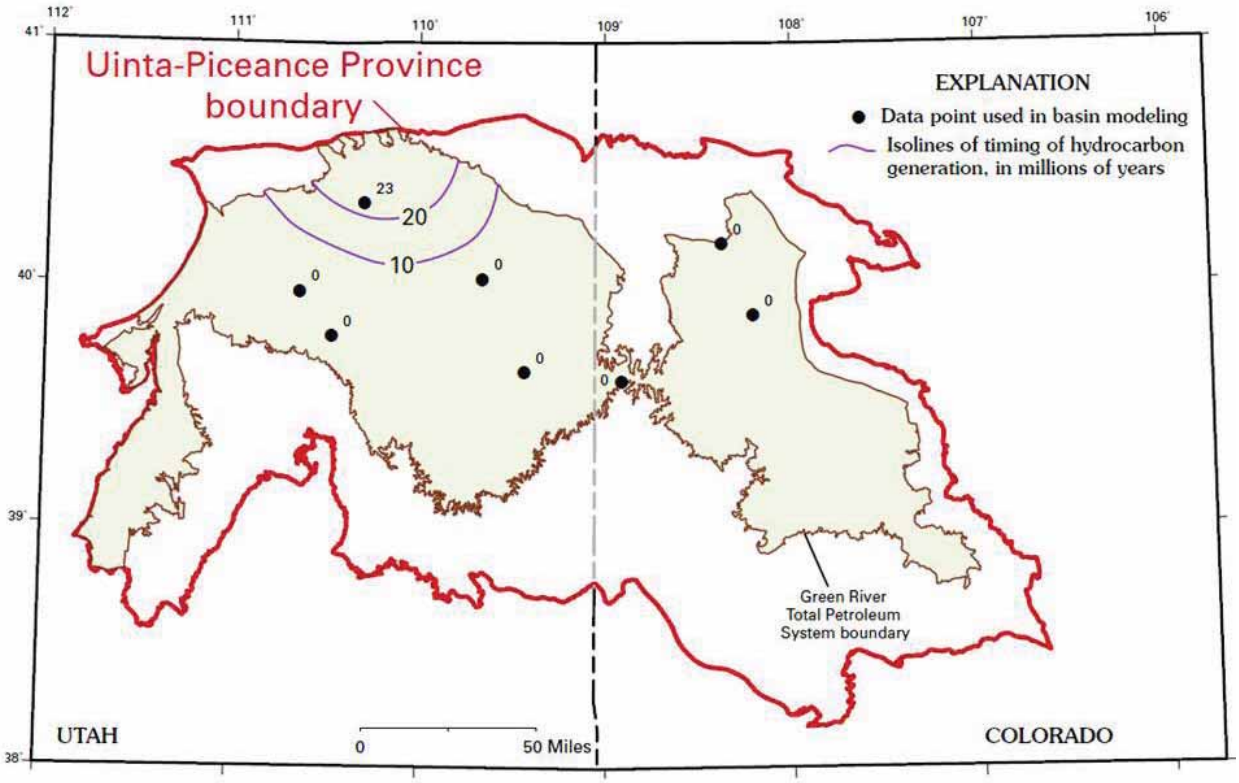

Figure 3-30: *Simulated "time-triggers" representing the time in millions of years before the present for entry of the lower Green River Formation into a thermal maturity window representing "significant oil and gas generation" (Nuccio and Roberts, 2003). The simulations would suggest earliest entry into the oil generative window in the Neogene for only a small portion of the Uinta Basin.*

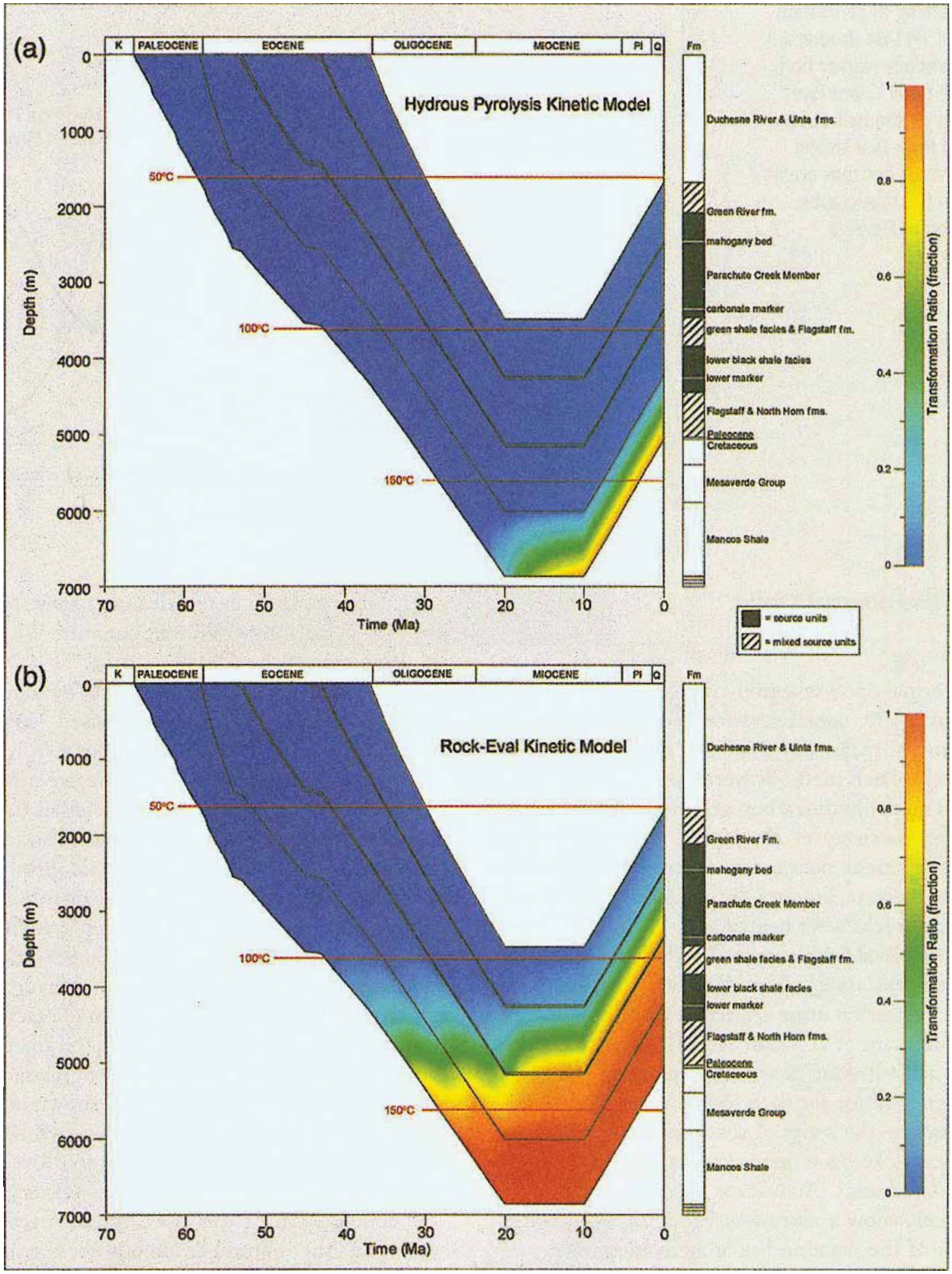

Figure 3-31: *Burial history curves and organic maturity simulations for two alternative models for the Brotherson 1-11-B4 well (API 4301330052) in township 2S-4W (Ruble and others, 2001). This is the northernmost of the modeled wells shown in Figure 3-27. The UTM coordinates of the well are E 559583 N 4464084. See text for the full description. AAPG©2001, reprinted by permission of the AAPG whose permission is required for further use.*

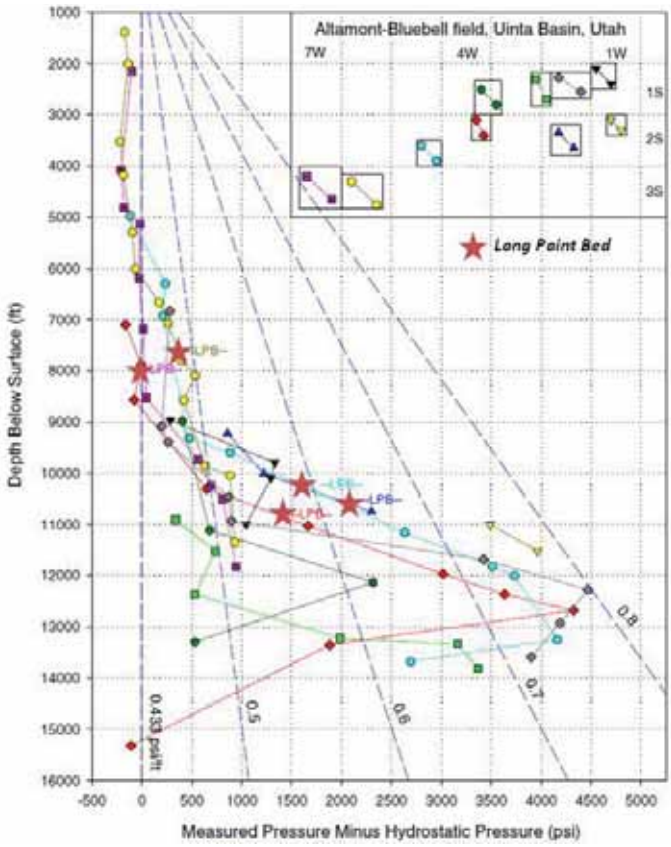

Figure 3-32: *Overpressure-depth profiles determined from drill-stem test data in deep wells in the northern Altamont field (Nelson, 2003). Many of the wells have anomalous pressures approaching lithostatic (0.8 psi/ft). These anomalous pressures are observed in the Lower Member of the Green River Formation and down into the Wasatch (Colton) Formation. The red stars indicate the position of the Long Point Bed, a marker within the Lower Member, along each excess pressure curve. The highest overpressures are within the Wasatch (Colton) Formation.*

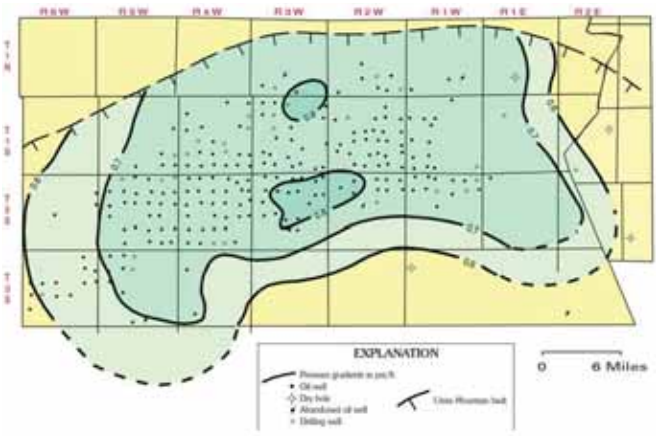

Figure 3-33: *Map showing values of anomalous formation pressure gradients (psi/ft) measured in drill-stem tests in the Altamont-Bluebell field reported by Lucas and Drexler (1975). The fault bounding the area of anomalous formation pressures on the north is the Uinta Basin Boundary Fault. The figure is from Dubiel (2003).*

4. NUMERICAL SIMULATIONS OF ORGANIC MATURATION

Given the limited number of direct measurements (R_o) of organic maturation of the Green River Formation in the Uinta Basin, it was considered prudent to undertake numerical simulation using the Platte River AssociatesBasinView-3D™ modeling software. This highly sophisticated and versatile simulator was loaned to this UGS-sponsored research project by Dr. Jay Leonard, President of Platte River Associates (PRA).

In a normal 1-D numerical simulation (Waples, 1994) using a program such as the PRA BasinMod-1D™ there are three principal components.

1. By assigning measured depths and presumed geologic ages to formation tops encountered in a well, it is possible to construct a *burial history curve*. This is the trajectory of burial of the formation boundaries as a function of time. With the assignment of sediment intervals deposited, but subsequently removed by erosion, the trajectory also captures the "uplift" of the formation tops.

2. With the assignment of a value of heat flow, or alternatively the geothermal gradient, the burial history curve is converted to a *temperature history curve* that plots against geologic time the increase in ambient temperature of stratigraphic markers during burial and crustal cooling accompanying exhumation.

3. The thermal trajectories provide ambient temperatures for calculation of thermal maturities for the various stratigraphic markers (or intervals) using the Arrhenius equation. This semi-empirical expression characterizes the quasi-first-order chemical reactions involved in the conversion of kerogen to liquid hydrocarbons and natural gas. The *rate* of the organic reactions (cracking of large molecules in kerogen to the smaller molecules in hydrocarbons) is a function of temperature; the higher the temperature, the faster the reactions proceed. Thus, the conversion of kerogen to hydrocarbons is a function of both temperature and time. This is what the simulations are calculating and expressing as *transformation ratios* or equivalent measures of thermal maturation of organic matter in the buried sediments.

When wells with stratigraphic tops are not available in a part of the basin where an organic maturation simulation is desired, modelers will construct a "synthetic well" with tops reflecting the known formation thicknesses for the region. This is the principal behind the PRA BasinView-3D™ simulator.

BasinView-3D™ uses either structure surfaces or isopach maps for each of the stratigraphic horizons in the basin (or

part of a basin) to construct an array of "synthetic wells" that then are modeled individually as normal 1-D simulations. The results of the simulations for each of the "synthetic wells" are then gridded and expressed as isopleth maps. This way the modeler can rapidly simulate the spatial variations in organic maturity and other model output parameters for a very large area and at a very fine resolution. Typically, the model runs for this study involved over 9000 nodes or "synthetic wells" with a one kilometer spacing taking just over ten minutes each to generate. The time involved in generating the simulations is short, but the time involved building and refining the models can be considerable.

Simulations were carried out for just the northern half to two-thirds of the Uinta Basin, the area bounded by UTM (NAD83) Eastings 500000 and 660000 and Northings 4430000 and 4485000 (Fig. 4-1). To the extent possible, the area of the basin simulated is south of the Basin Boundary Fault. This is the deepest part of the basin, and the part with a highest proportion of open lacustrine facies source rocks.

Model Input Parameters

The set of input parameters used in these particular simulations are: (1) the *structure surface and isopach grids* (in meters) that define the stratigraphic units constructed using Surfer 10™ and Surfer 11™, (2) the absolute age of bounding surfaces of the stratigraphic units and/or geologic events, (3) *kerogen kinematics* from Ruble and others (2001) and default kerogen parameters built into BasinMod-1D™ and BasinView-3D™, (4) *initial TOC* of the designated "source rock" units determined from the information presented in Chapter 3, (5) *heat flow values* for the Uinta Basin reported in Chapman and others (1984), and (6) generalized *lithology* mixes for the individual model intervals. The simulators allow a variety of other variables, such as petrophysical properties of the rock units, to be specified by the modeler. In all instances, the PRA default values of these second-tier parameters were accepted. The model-specific input parameters are described below.

The Green River Formation is divided into seven model elements designated GR-1 to GR-7. The bounding surfaces for each of the units is shown in Table 4-1 along with the ages assigned to each surface. Most of the surfaces are defined by presumed basin-wide events making them everywhere the same age. A few, most notably the top of the Green River Formation (GR-1), are time-transgressive. For the purpose of the simulations, all surfaces are treated as time-constant. The source of the data for constructing the surface and determining its absolute age is presented in the figure captions for each of the surface maps (Figs. 4-2 through 4-9).

In earlier trial model simulations the grids used were constructed with Surfer 10™. In general, these grids extended beyond the region of well top control in the data sets gridded. The result was large regions lying north of the Basin Boundary Fault having clearly meaningless simulation results. So for the final set of five simulations (iterations using the same input surfaces and ages) presented in this report, a new set of Green River Formation grids was constructed using a feature in Surfer 11™ (beta), *"blank convex hull when gridding"*, that limits the grid nodes to just the region containing control values. The new grids reduce the area covered by the simulations, but they should assure more accurate output. The surface maps in Figures 4-2 through 4-9 were constructed using these same Surfer 11™ grid files. These input Surfer grid files can be found in the Digital Appendix C.

In the Uinta Basin, the strata overlying the Green River Formation have little commercial value for fossil fuels. Nevertheless, it is surprising how little information exists on the regional stratigraphy of this "overburden" succession. Well tops have been compiled for many of the marker beds within

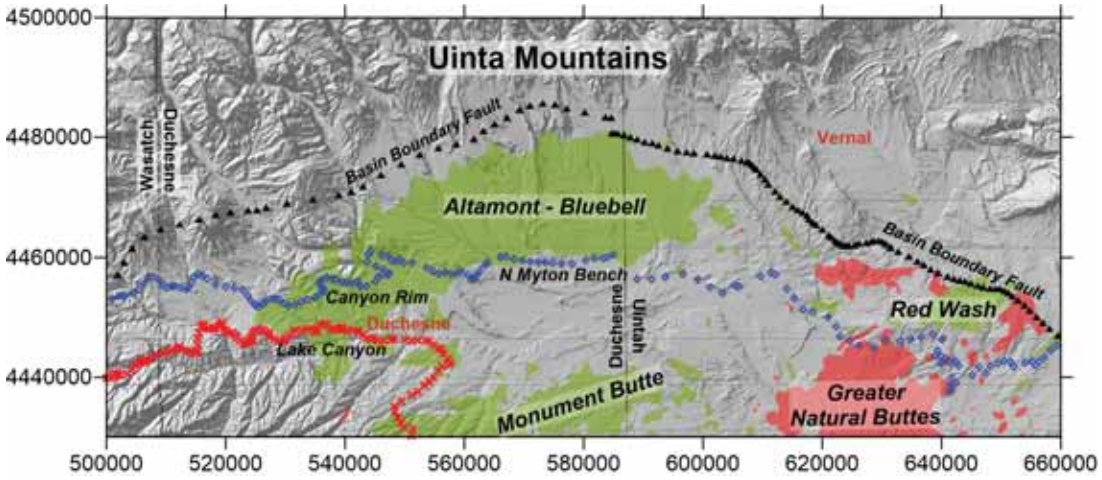

Figure 4-1: *Basemap for the modeled portion of the Uinta Basin showing the location of the Basin Boundary Fault, the larger fields producing oil from the Green River Formation (green areas, red areas are natural gas fields), the county lines, and major towns. The blue line marks the southern erosional edge of the Duchesne River Formation and the red line marks the southern erosional edge of the Uinta Formation, south of which the uppermost Green River Formation is exposed at the surface. The geographic coordinates are meters in UTM NAD83, Zone 12.*

Table 4-1: *Organic maturation model events*

Age/*Duration*	Unit/Haitus	Surface or *Interval*
0.0 Ma		Present-day ground surface
0.50–0.0 Ma	*E-2*	*Erosion II isopach (high rate; 70% of total erosion)*
10.0–0.50 Ma	*E-1*	*Erosion I isopach (slow rate; 30% of total erosion)*
20.3–10.0 Ma		*Post- Bishop Conglomerate pediment lag or hiatus*
20.3 Ma	---------- Tbc	Top of Bishop Conglomerate surface (reconstructed)
30.5 Ma	---------- Tdr	Gilbert Peak geomorphic surface (projected; age: Kowallis and others, 2008)
40.0 Ma	---------- Tu	Top of Uinta Fm surface (age: Prothero, 1996)
47.0 Ma	---------- GR-1	Top Green River Fm surface (age: Prothero, 1996)
48.9 Ma	---------- GR-2M	Top of Mahogony Zone surface
49.3 Ma	---------- GR-3	Top of B-groove (base Mahogony Zone) surface
50.3 Ma	---------- GR-4	Top of L-5 interval surface
51.6 Ma	---------- GR-5	Base of R-4 interval surface
53.9 Ma	---------- GR-6	Top of Carbonate Marker surface (top lower Black Shale)
54.0 Ma	---------- GR-7	Base of Long Point Bed surface (base Douglas Creek Mbr)
55.3 Ma	----------	Base of Ostracodal Limestone surface (base lower Black Shale)

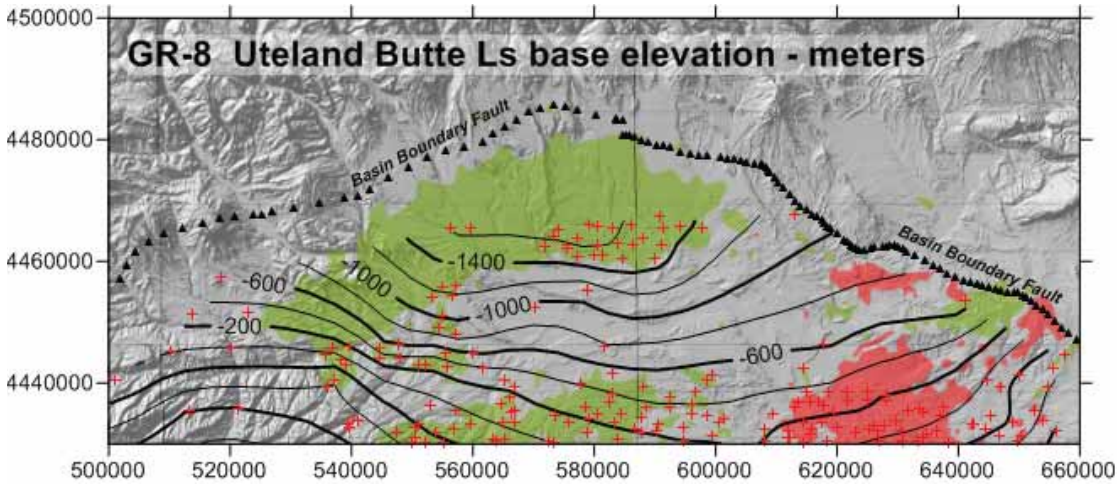

Figure 4-2: *Structure map relative to mean sea level (msl) of the base of the Ostracodal Limestone or Uteland Butte Limestone. This is the effective base of the Green River Formation. This surface forms the bottom of the model. Red crosses indicate well locations with surface tops. Well tops source: U.S. Geological Survey; refer to Johnson and Roberts (2003). The contour interval (CI) is 200 meters.*

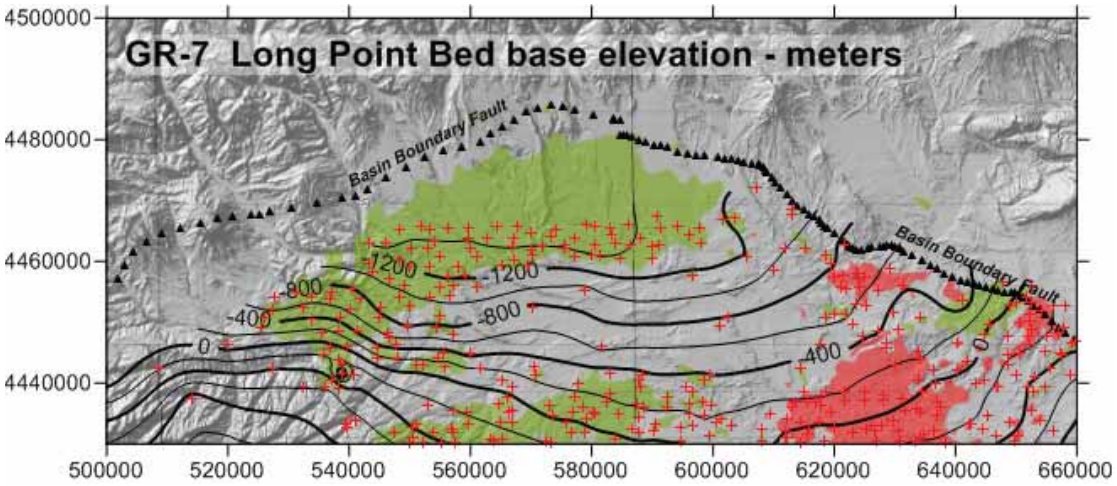

Figure 4-3: *Structure map (msl) of the base of the Long Point Bed, the base of the Douglas Creek Member. This is the top of the GR-7 model element. Red crosses indicate well locations with surface tops. Well tops source: U.S. Geological Survey; refer to Johnson and Roberts (2003). CI = 200 m*

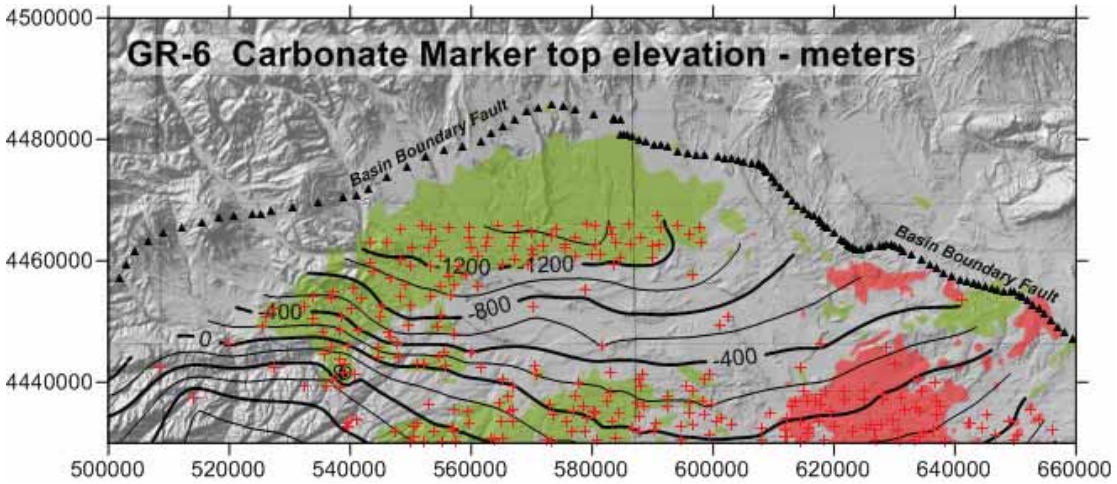

Figure 4-4: *Structure map (msl) of the top of the Carbonate Marker, the effective top of the Black Shale Facies or Lower Green River Formation. This is the top of the GR-6 model element. Red crosses indicate well locations with surface tops. Well tops source: U.S. Geological Survey; refer to Johnson and Roberts (2003). CI = 200 m*

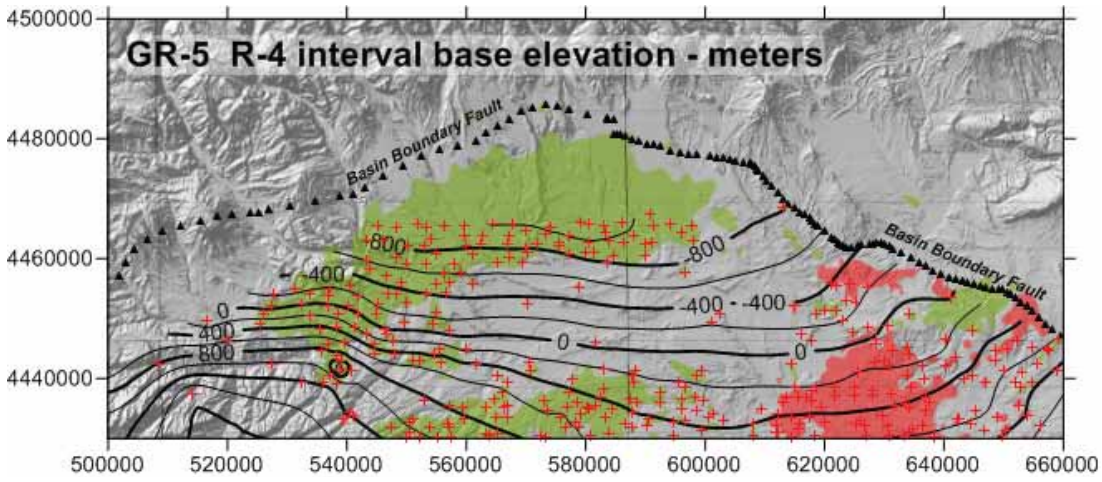

Figure 4-5: *Structure map (msl) of the base of the R-4 interval of the Parachute Creek Member and top of the GR-5 model element. Red crosses indicate well locations with surface tops. The age of the surface is 51.6 Ma (Birgenheier and Vanden Berg, 2011). Well tops source: Utah Geological Survey. CI = 200 m*

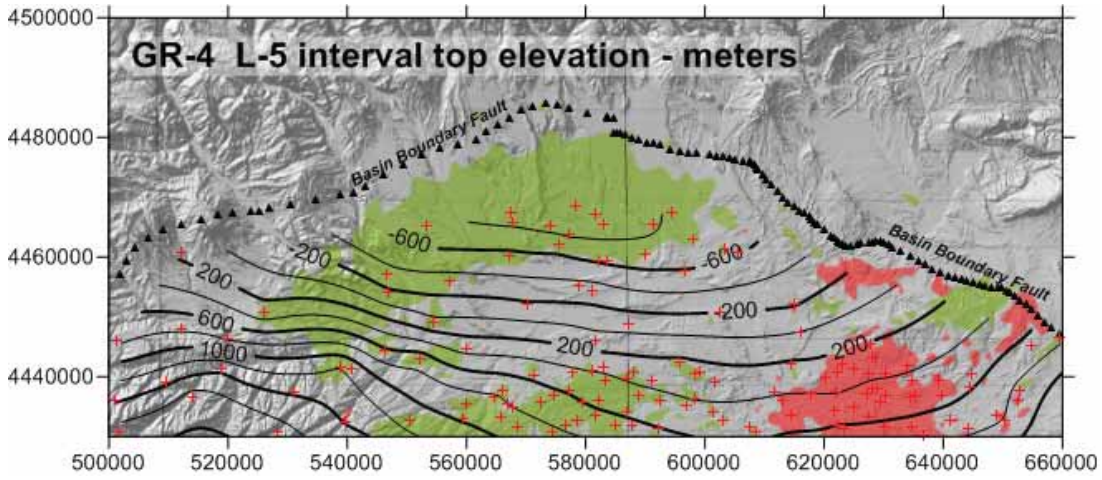

Figure 4-6: *Structure map (msl) of the top of the L-5 interval of the Parachute Creek Member and top of the GR-4 model element. Red crosses indicate well locations with surface tops. The age of the surface is 50.3 Ma (Birgenheier and Vanden Berg, 2011). Well tops source: Utah Geological Survey. CI = 200 m*

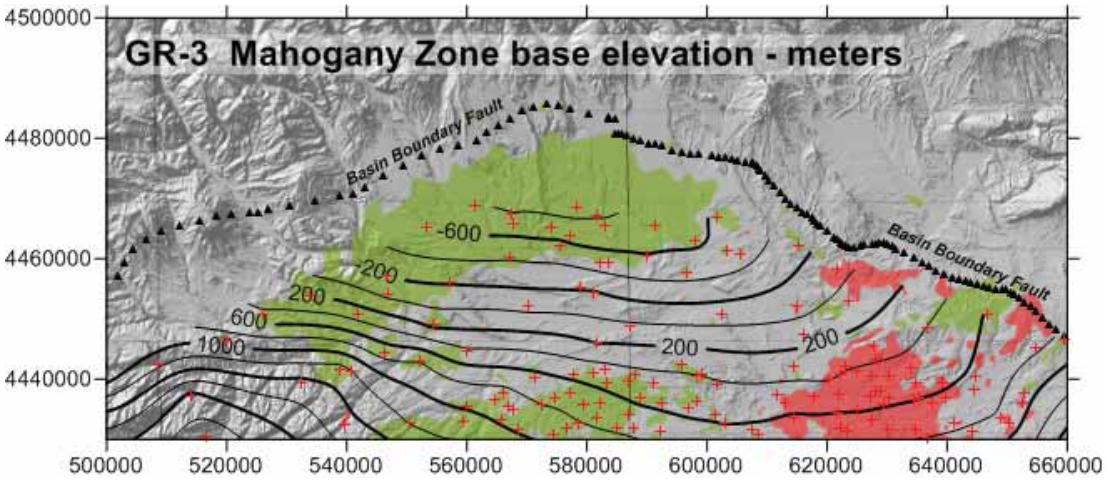

Figure 4-7: *Structure map (msl) of the top of the B-groove interval of the Parachute Creek Member, which is the base of the Mahogany Zone (GR-2M), and top of the GR-3 model element. Red crosses indicate well locations with surface tops. The age of the surface is 49.3 Ma (Birgenheier and Vanden Berg, 2011). Well tops source: Utah Geological Survey. CI = 200 m*

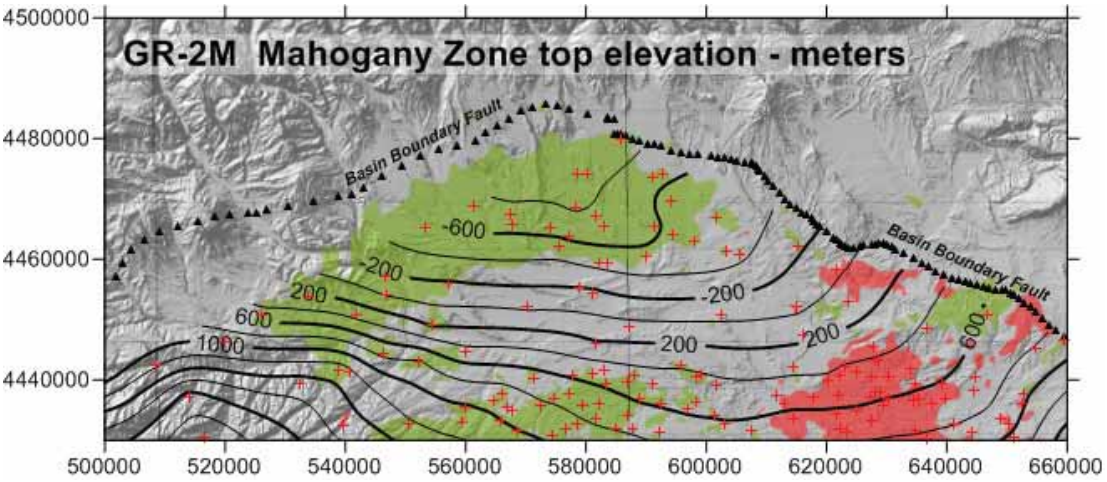

Figure 4-8: *Structure map (msl) of the top of the Mahogany Zone (R-7) interval of the Parachute Creek Member and top of the GR-2M model element. Red crosses indicate well locations with surface tops. The age of the surface is 48.9 Ma (Birgenheier and Vanden Berg, 2011). Well tops source: Utah Geological Survey. CI = 200 m*

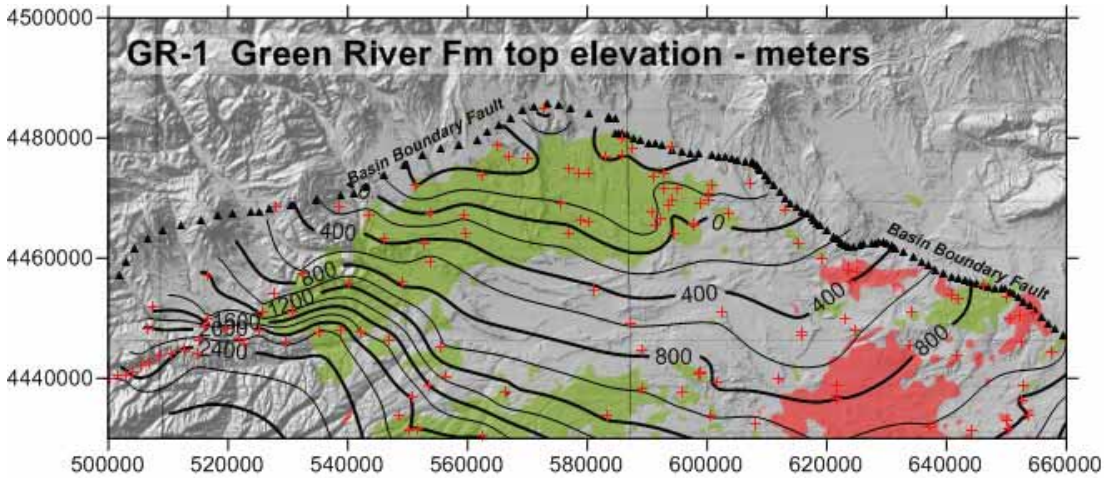

Figure 4-9: *Structure map (msl) of the top of the Green River Formation and top of the GR-1 model element. Red crosses indicate well locations with surface tops. The age of the surface reported by Prothero (1996) to be 47.0 Ma, but Smith and others (2008b) indicate that it is a time-transgressive surface ranging in age from 47 Ma in the eastern part of the basin to 44 Ma in the west, where lacustrine conditions lingered longest. Well tops source: Utah Geological Survey. CI = 200 m*

the Green River Formation, but there are no such compilations for the formations overlying the Green River Formation or even the top of the Green River itself. The overburden is an essential stratigraphic element driving thermal maturation, so it was necessary for this project to construct structure maps for this succession, starting with the top of the Green River Formation.

The transition from lacustrine-playa strata of the uppermost Green River Formation into the overlying fluvial mudflat red mudstone and channel sands of the Uinta Formation is gradual. The tops of Green River Formation recorded in well completion reports are commonly inconsistent, even between adjacent wells. As explained in Chapter 2, the structure map for the top of the Green River Formation was constructed from tops extracted from published tops tables (Sprinkel, 2007), cross sections (Johnson, 2003), interpretation of plotted LAS files (see Digital Appendix A), as well as heavily edited tops compilations from DOGM well completion reports. An additional constraint on the top of the Green River Formation surface is the elevation of the mapped southern outcrop edge of the Uinta Formation on the Duchesne (Bryant, 2010), Price (Weiss and others, 2003), Seep Ridge (Sprinkel, 2009) and Vernal (Sprinkel, 2007) geologic maps. This diverse data set was used to construct the structure surface map in Figure 4-9.

The same sources were used to attempt construction of pre-erosion isopach maps for the overlying Uinta and Duchesne River Formation. However, here the control was even sparser. Early attempts at constructing conventional isopleth maps yielded unacceptable results. Consequently, indirect methods were adopted that in the end may be more reasonable. It was noted that the cluster of reliable thicknesses for the Uinta Formation in the Red Wash field area are in the range of 500–550 m (1640–1800 ft), whereas a similar cluster in the Bluebell and eastern Altamont fields are from 900–950 m (2950–3100 ft) thick. These values were used to create the synthetic isopach shown in Figure 4-10. The isopach grid was added to the grid for the top of Green River Formation (Fig. 4-9) to yield the structure surface for the top of the Uinta Formation (Tu; Fig. 4-11). The surface elevations were checked for consistency with the elevations of the southern outcrop edge of the Duchesne River Formation (blue line in Figure 4-10) observed on the Duchesne (Bryant, 2010) and Vernal (Sprinkel, 2007) geologic maps, and they were remarkably close.

The Duchesne River Formation is partly to completely eroded across nearly all of the Uinta Basin. Only along the south flank of the Uinta Mountains are there remnants where the Lapoint Member is overlain by the Starr Flat Member-Bishop Conglomerate. These are the only areas where there is the full, pre-erosion thickness of the formation preserved. Unfortunately, these are areas largely north of the Basin Boundary Fault where wells are few and far between. Hanson (1986) describes the base of the Starr Flat Member as the Gilbert Peak geomorphic surface, and the projection of this surface southward across the basin defines the top of the Duchesne River Formation. This surface was modeled by projecting the elevations of the base of the Starr Flat Member and/or the Bishop Conglomerate (Table 4-2), where remnant on the south flank of the Uinta Mountains, Little Mountain, Diamond Mountain plateau, and Blue Mountain plateau, gradually downward and outward across the basin. It is imagined that the Gilbert Peak surface was an arid-climate pediment like those of the modern Basin and Range Province. This reconstructed Gilbert Peak geomorphic surface is taken to be the same as the top of the Duchesne River Formation (Fig. 4-12).

The isopach for the Bishop Conglomerate (Fig. 4-13) is considered to be a conservative estimate of its original thickness. It is constructed by taking the thickness observed for the formation in the erosional remnants and projecting those

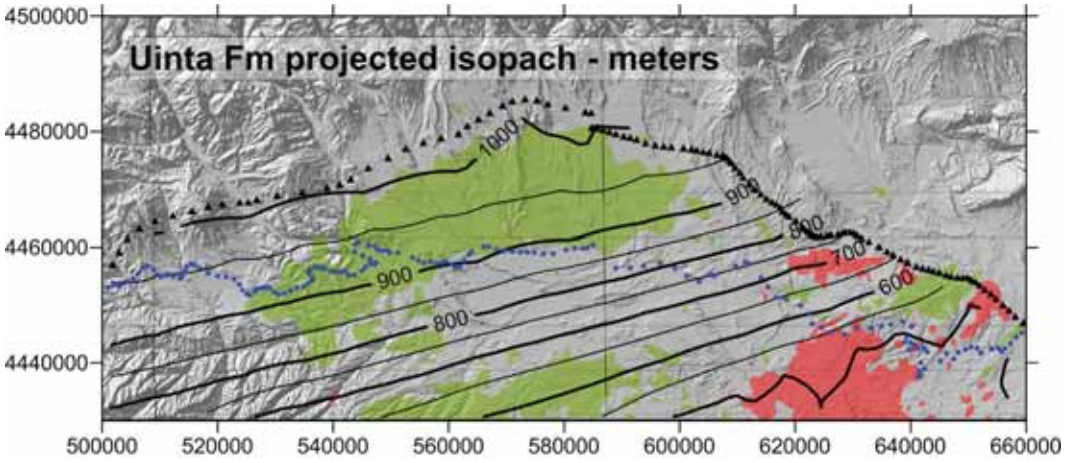

Figure 4-10: *Generalized pre-erosion thickness of the Uinta Formation projected from areas of relatively reliable well control in the Red Wash and northeast Altamont-Bluebell fields where thicknesses are in the range of 500-550 m and 900-950 m, respectively. The blue line indicates the south outcrop edge of the Duchesne River Formation. South of this line to the outcrop edge of the Uinta Formation (red line) the observed thicknesses are reduced by erosional beveling. CI = 50 m*

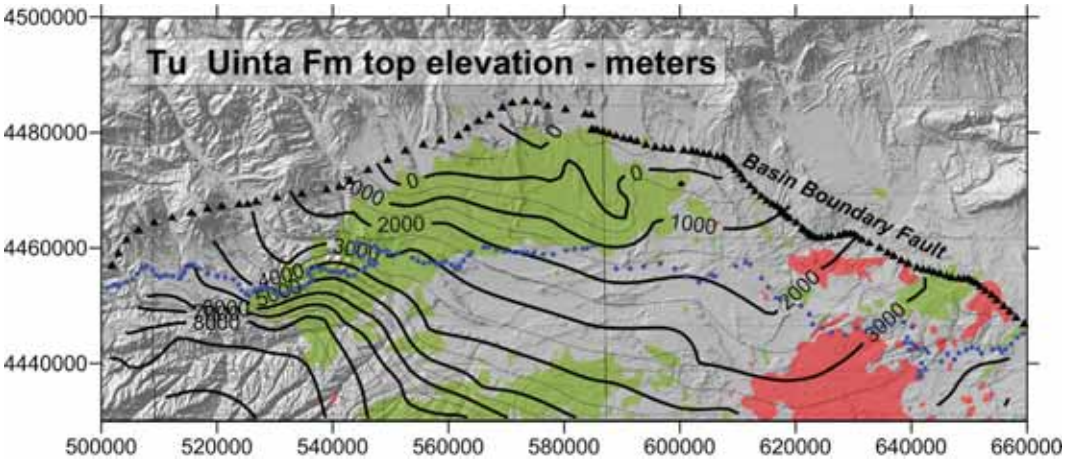

Figure 4-11: *Structure map (msl) for the top of the Uinta Formation constructed by adding the pre-erosion isopach in Figure 4-10 to the top of Green River Formation structure surface (Figure 4-9). South of the Duchesne River Formation outcrop edge this surface projects southward above the present ground surface. Extensions of the surface north of the Basin Boundary Fault are artifacts of gridding that should be ignored. The age of the surface is 40.0 Ma (Prothero, 1996). CI = 500 m*

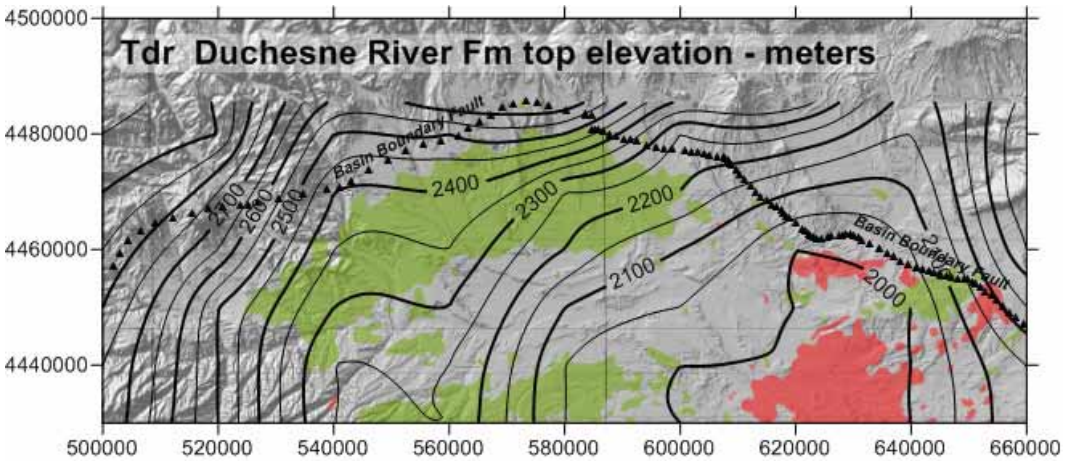

Figure 4-12: *Generalized structure map (msl) for the surface representing the pre-erosion top of the Duchesne River Formation constructed by projecting the present elevations of the Gilbert Peak surface across the basin as though it were an arid-climate pediment flanking the Uinta and Split Mountain uplifts. As this surface is considered to post-date uplift of the mountains flanking the Uinta Basin, the extension of the surface north of the Basin Boundary Fault is intentional. The Duchesne River Formation does everywhere overlap this fault. The age of the surface is radiometrically dated as 30.5 Ma (Kowallis and others, 2005). See text for further discussion of the surface. CI = 50 m*

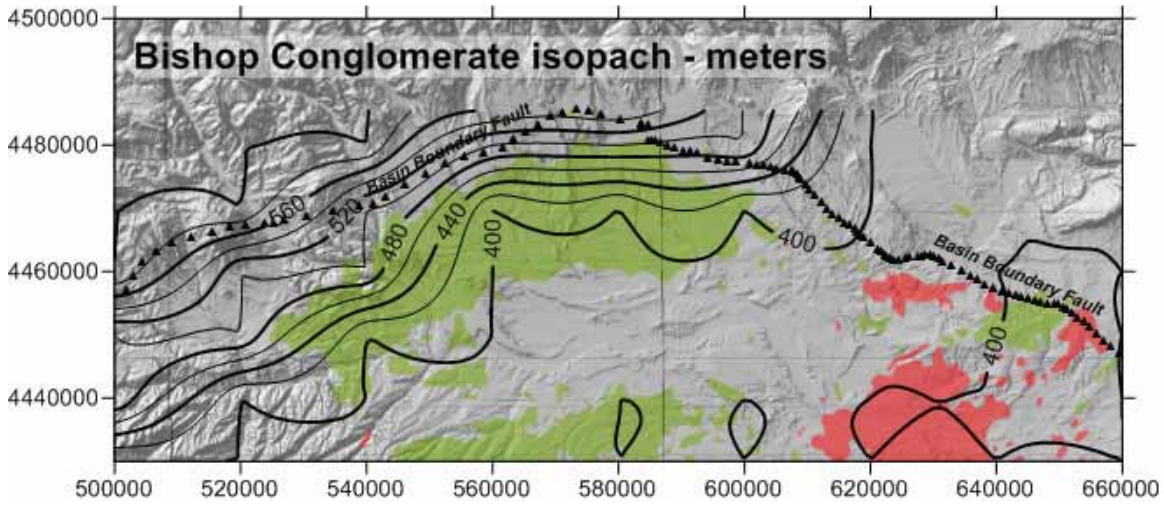

Figure 4-13: *Generalized thickness of the pre-erosion Bishop Conglomerate constructed by projecting the maximum thickness of the Bishop Conglomerate-Starr Flat Member where preserved on the south flank of the Uinta Mountains southward into the basin as an arid-climate alluvial fan deposit. It is presumed that the unit was accumulating through the entire Oligocene and into the earliest Miocene, until about 20.3 Ma (Ogg and others, 2008). CI = 20 m*

Table 4-2: *Elevations in meters of the Gilbert Peak geomorphic surface and estimated thicknesses of the Starr Flatt Member-Bishop Conglomerate determined from mapped contacts in erosional remnants in the Duchesne-Kings Peak (Bryant, 2010), Dutch John (Sprinkel, 2006), and Vernal (Rowley and others, 1985) geologic quadrangle maps. One meter = 3.28 feet.*

Site	Name	Gilbert Peak elev, m	Bishop Congl. thick, m
A	Tabby Mtn W	2850	
B	Tabby Mtn	2750	
C	Dry Mtn	2250	
D	Round Mtn	3000	
E	Dry Ridge	2500	500
F	Lake Fort Mtn	2500-2750	500
G	Starr Flat	2750	650
H	Pole Mtn	2500-2750	500
I	Mosby Mtn	2500	450
J	Little Mtn	2250	400
K	Taylor Mtn	2750	
L	Diamond Mtn	2250	150
M	Jones Hole	2300	150
N	Blue Mtn plateau	2400	<100

thicknesses across the basin with minimal thinning. Again an intermountain arid-climate pediment deposit is envisioned, one that thins slightly away from the basin margins. The thickness in meters (Table 4-2) was determined by the difference in elevation between the base of the Starr Flat Member and the highest point underlain by the Bishop Conglomerate. Nearly everywhere patches of middle Pleistocene alluvium are mapped directly overlying the Bishop Conglomerate (Bryant, 2010; Sprinkel, 2006; Sprinkel, 2007). South of the Basin Boundary Fault, the Bishop Conglomerate has been completely removed by erosion.

For each formation with substantial erosion, BasinView-3D™ requires input of a grid representing the isopach of the portion of the formation lost to erosion. For the Uinta Formation, this isopach grid was constructed by substracting the present-day ground surface (Fig. 4-14) from the top of Uinta Formation (Tu) surface (Fig. 4-11). The same procedure was used to calculate the isopach for the portion of the Duchesne River Formation lost to erosion. For this isopach it was necessary to add back the eroded Uinta Formation south of the Duchesne River outcrop limit. These two isopachs are displayed in Figures 4-15 and 4-16.

The total erosion after 10 Ma was determined by subtracting the present-day ground surface from the reconstructed top of the Bishop Conglomerate. The total erosion is separated into two separate isopach grids: Erosion 1 (Fig. 4-17) during the period 10–0.5 Ma representing 30% of the total erosion and Erosion 2 (Fig. 4-18) during the period 0.5 to 0 Ma representing the remaining erosion.

After running a variety of trial models to check the functioning of the simulator, five project models were run having the sets of variables indicated in Table 4-3. The models, designated A through E, were all identical except for the specific combination of variables related to the value of heat flow and the specific kerogen kinematics, as shown in the table. All models shared the same input surface elevation and isopach grids, model limits and node spacing, lithology mixes for the various stratigraphic units, initial TOC values for the designated source rock units, and a uniform surface temperature of 20°C.

Nearly all levels of the Green River Formation have potential to generate hydrocarbons. However, just four of the model units were treated as “source rock” units and assigned kerogen types with kinematics and values of “initial TOC”. The “initial TOC” values in all models are 15% for GR-2M, 10%

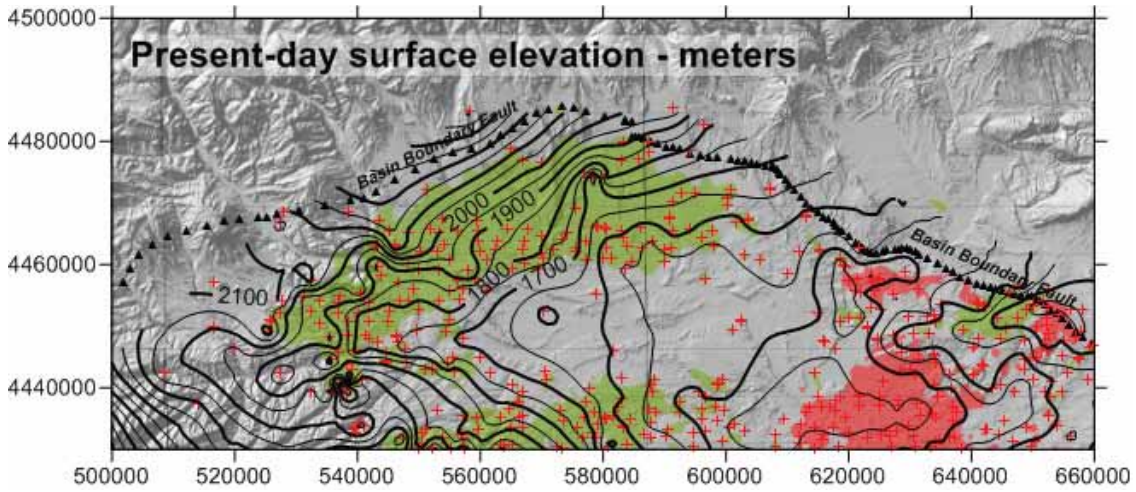

Figure 4-14: *Generalized elevation (msl) of the present-day ground surface constructed from the ground elevations of wells used to construct the Green River Formation surfaces, rather than DEM data, in order to avoid potential simulation artifacts resulting from a large mismatch in grid densities. Data from Utah Geological Survey and Utah Division of Oil, Gas, and Mining. CI = 50 m*

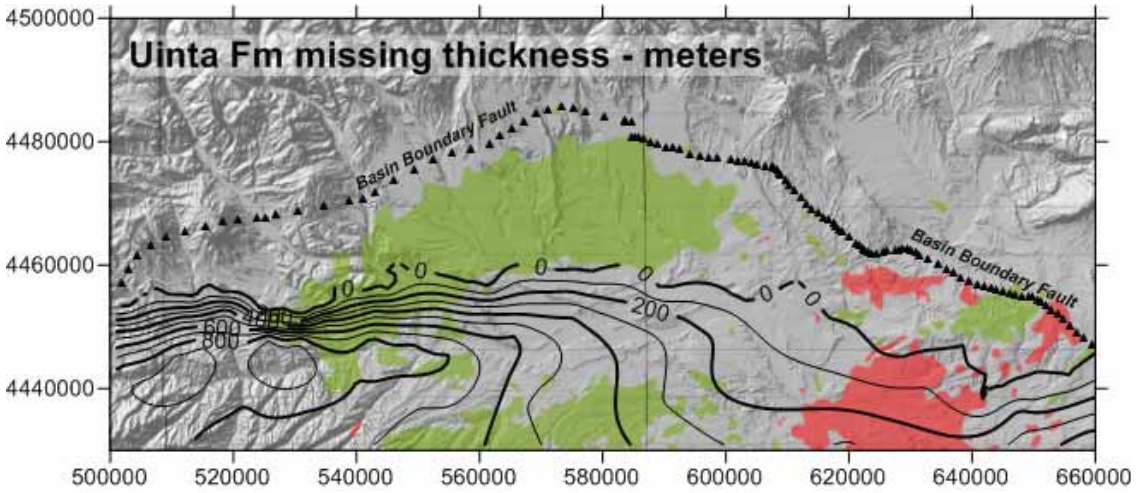

Figure 4-15: *Thickness of the Uinta Formation removed by erosion after 10 Ma. The isopach grid was constructed by subtracting the present-day ground surface (Fig. 4-14) from the generalized top of Uinta Formation surface (Fig. 4-11). CI = 100 m*

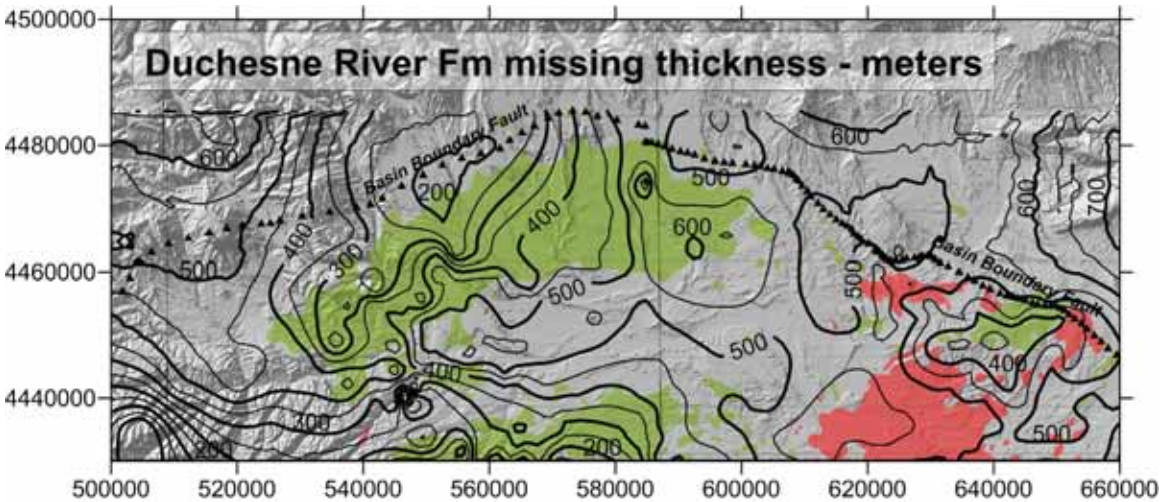

Figure 4-16: *Thickness of the Duchesne River Formation removed by erosion after 10 Ma. The isopach grid was constructed by subtracting the present-day ground surface (Fig. 4-14) from the generalized top of the Duchesne River Formation (Fig. 4-12), then adding back the eroded Uinta Formation isopach (Fig. 4-15). CI = 50 m*

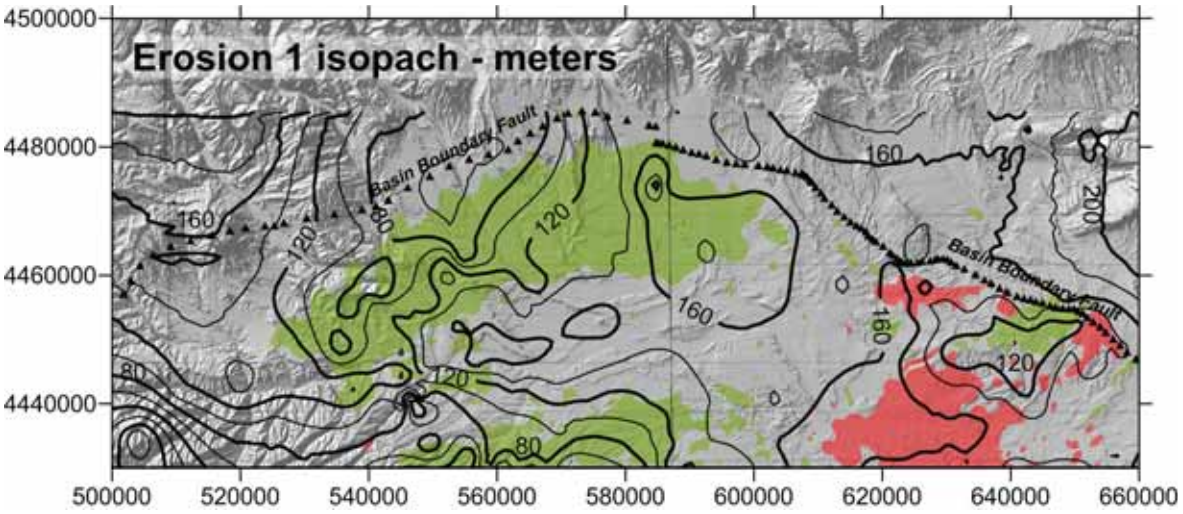

Figure 4-17: *Model thickness of the erosion occurring between 10 and 0.5 Ma. This isopach represents 30% of the total erosion determined by subtracting the present-day ground surface (Fig. 4-14) from the reconstructed top of the Bishop Conglomerate. CI = 20 m*

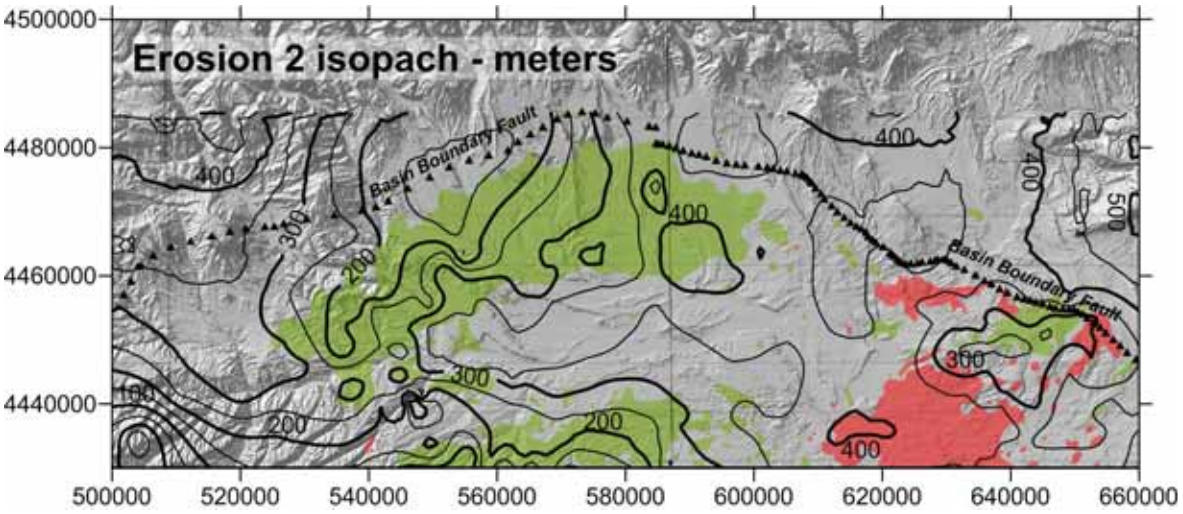

Figure 4-18: *Model thickness of the erosion occurring between 0.5 and 0.0 Ma. This isopach represents 70% of the total erosion determined by subtracting the present-day ground surface (Fig. 4-14) from the reconstructed top of the Bishop Conglomerate. CI = 50 m*

Table 4-3: *Input variables for each of the five project models simulated, Model A through Model E. Model kinematics: RE and LLNL are from programmed pyrolysis, HP is from hydrous pyrolysis.*

	Heat flow	***Surface T, °C***	***GR-2M***	***GR-4***	***GR-6/7***
Model A	52 mW/m^2	20	Mahogany RE	Mahogany RE	Black Shale RE
Model B	52 mW/m^2	20	Mahogany HP	Mahogany HP	Black Shale RE
Model C	52 mW/m^2	20	Type I, LLNL	Type I, LLNL	Type II, LLNL
Model D	57 mW/m^2	20	Mahogany RE	Mahogany RE	Black Shale RE
Model E	57 mW/m^2	20	Mahogany HP	Mahogany HP	Black Shale RE

for GR-4, and 5% for GR-6 and GR-7. Units GR-1, GR-3 and GR-5 are treated as "non-source rock" having no initial TOC.

Calculations requiring physical properties of rocks, such as thermal conductivity or average petrophysical properties, can draw on a set of default values related to standard lithologies. Alternatively, the user can specifically assign physical values to each rock unit when creating the model. Where the actual physical properties are not known, the user has the option of creating lithology mixes of the default lithologies. The lithology mixes used in all of the five project models are:

Tdr: 60% sandstone + 20% siltstone + 20% shale

Tu: 30% sandstone + 40% siltstone + 30% shale

GR-n "source rock": 10% siltstone + 50% shale + 40% dolomite

GR-n "non-source rock": 30% siltstone + 20% shale + 50% dolomite

The kerogen kinematics associated with the various kerogen types reported in Table 4-3 are specified in Table 4-4. The kerogen designated Type I, LLNL and Type II, LLNL are widely used kerogens published by the Lawrence Livermore National Laboratory and included in the kerogen type library in BasinView-3D™ and BasinMod-1D™. The other kerogen kinematics were determined by either RockEval programmed pyrolysis methods (RE) or hydrous pyrolysis (HP). They are published in Ruble and others (2001).

Chapman and others (1984) calculated geothermal gradients and heat flows across the Uinta Basin. They observed heat flow to decrease monotonically from 64 mW/m^2 in the southeast of the basin to 40 mW/m^2 in the extreme north along the Basin Boundary Fault. The average heat flow of 57 mW/m^2 (approximately equivalent to a geothermal gradient of 25°C/km) has been adopted in previous thermal maturation models (Sweeney, 1988; Ruble and others, 2001; Nuccio and Roberts, 2003) and is used in Models D and E in this study. However, this average heat flow is thought to be an artifact of high Quaternary erosion rates and unrealistically high for the Tertiary. The rapid exhumation of the basin in the mid and late Pleistocene would have the effect in the parts of the basin with major erosion of increasing geothermal gradients from which the heat flow is calculated. Rapid exhumation in recent time will have its greatest effect exactly where the higher heat flows are reported (Chapman and others, 1984). Models A, B and C used a more reasonable 52 mW/m^2. In hindsight, even this value may be too high.

The geographic limits for all models were from UTM (NAD83, Zone 12) Easting 500000 to 660000 and from Northing 4430000 to 4485000, with a node spacing of one kilometer. This resulted in over 9000 nodes (pseudowells) calculated for each simulation and a grid resolution of one kilometer.

Table 4-4: *Kerogen kinematics used in the various project models; see Table 4-3. E is the activation energy and Ao is the frequency factor, both variables in the Arrhenius equation used to calculate the rate of thermally- driven conversion of kerogen to hydrocarbons. Different values of the parameters, in particular the activation energy, may apply to different mole fractions of the kerogen.*

	fraction	*E*	*Ao*
Mahogany Shale	0.06	46	3.788 x 10^{26} /my
RockEval	0.16	48	3.788 x 10^{26} /my
	0.26	49	3.788 x 10^{26} /my
	0.36	50	3.788 x 10^{26} /my
	0.04	51	3.788 x 10^{26} /my
	0.12	52	3.788 x 10^{26} /my
Mahogany Shale	1.00	69	1.6505x 10^{29} /my
Hydrous pyrolysis			
Black Shale facies	0.02	47	1.139 x 10^{26} /my
RockEval	0.04	48	1.139 x 10^{26} /my
	0.83	51	1.139 x 10^{26} /my
	0.07	53	1.139 x 10^{26} /my
	0.03	58	1.139 x 10^{26} /my
Type I LLNL	0.07	49	1.6 x 10^{27} /my
BMOD-1D	0.9	53	1.6 x 10^{27} /my
	0.03	54	1.6 x 10^{27} /my
Type II LLNL	0.05	49	9.5 x 10^{26} /my
BMOD-1D	0.2	50	9.5 x 10^{26} /my
	0.5	51	9.5 x 10^{26} /my
	0.2	52	9.5 x 10^{26} /my
	0.05	53	9.5 x 10^{26} /my

Numerical Simulation Output Parameters

BasinView-3D™ is capable of generating a very large range of output parameters, each of which can be calculated in the simulation for any of the model stratigraphic units and associated times. Each parameter can be viewed as a graphic representation, a map, within the simulator, or exported as an array of x-y-z values formatted for any of several types of data mapping programs. Spatial variations in the burial history of different parts of the model can be visualized in synthetic 1-D burial history curves (Figures 4-19 and 4-20) that can be extracted as output graphics.

For this project, just five parameters were exported as Surfer™ grids: (1) transformation ratio, (2) vitrinite reflectance, (3) excess pressure (pressure in excess of hydrostatic), (4) oil generated (barrels per acre), and (5) time-triggers indicating time of entry of a specific stratigraphic unit into a particular

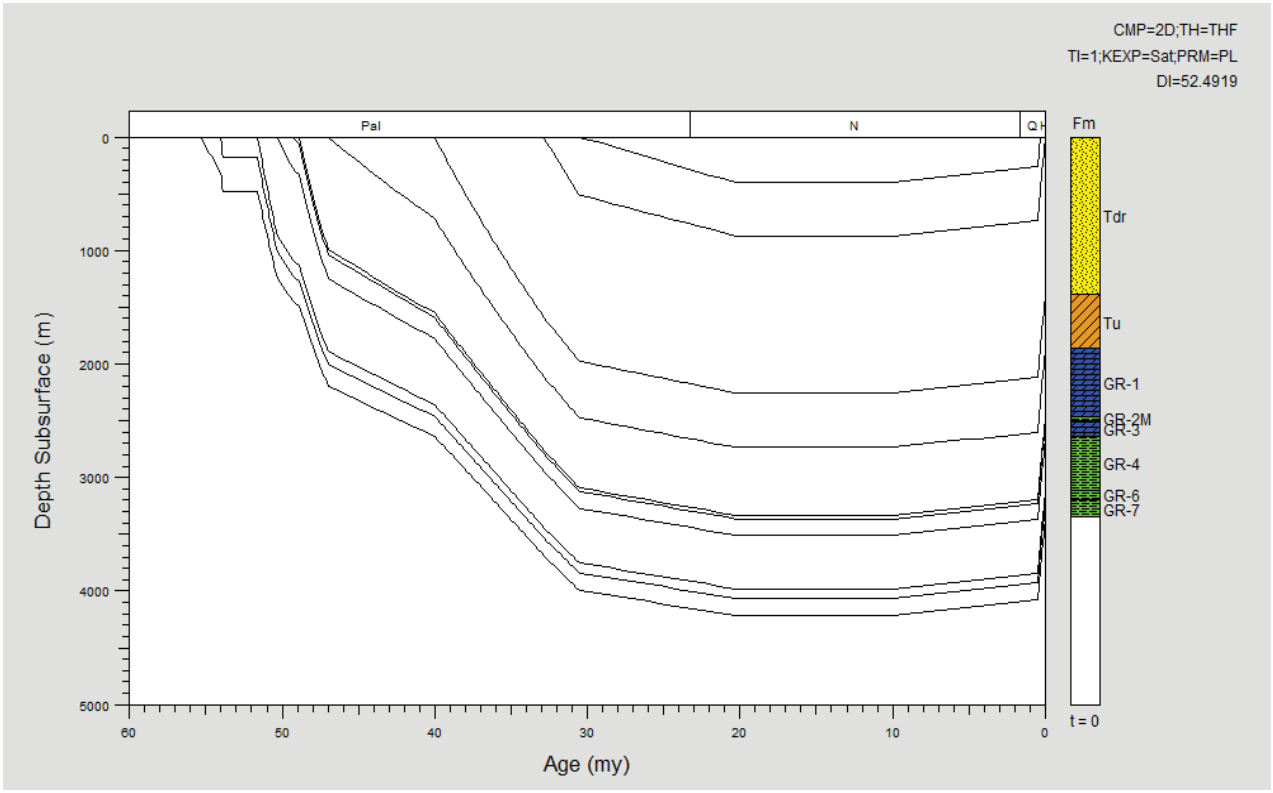

Figure 4-19: *Burial history curves for a synthetic well in the northern Altamont-Bluebell field extracted from the BasinView-3D model. The base of the Green River Formation reaches a depth greater than 4000 m (13,000 ft). The well coordinates are Easting 579573, Northing 4468449.*

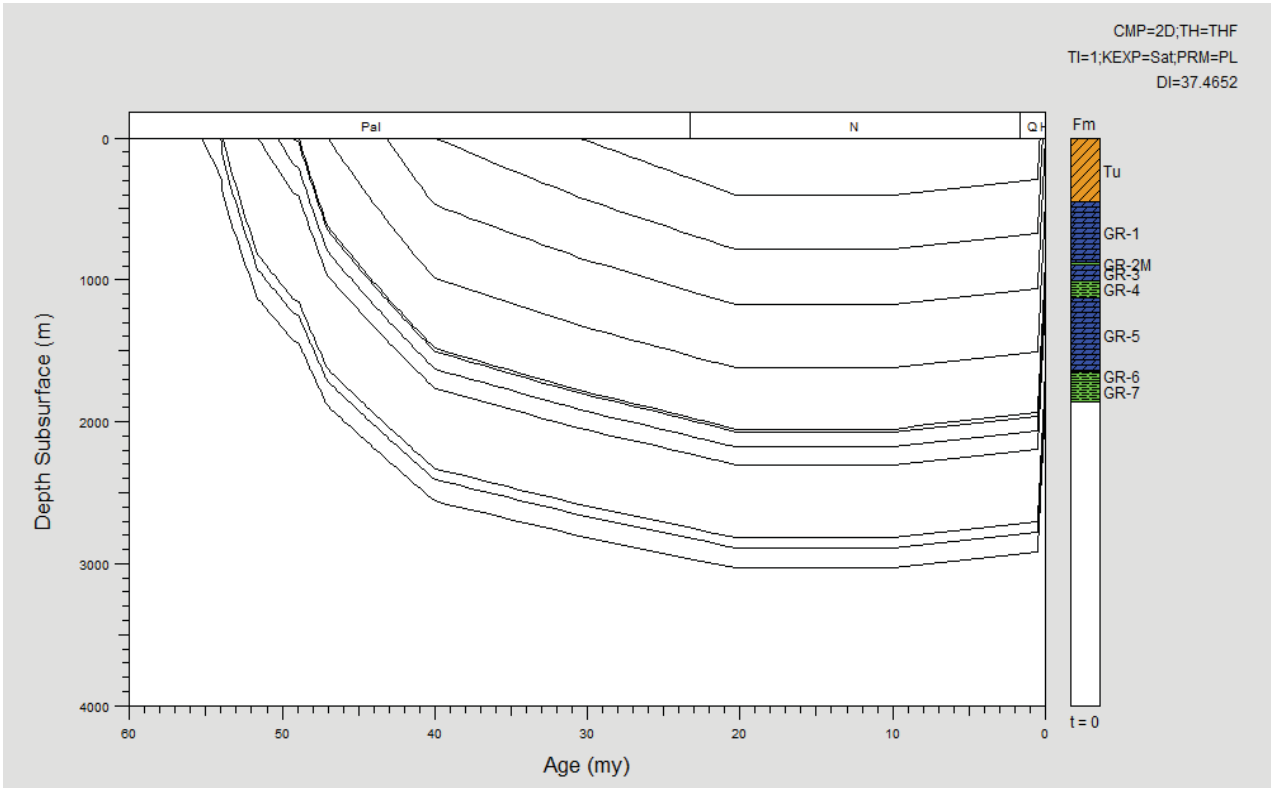

Figure 4-20: *Burial history curves for a synthetic well in the northern Monument Butte field extracted from the BasinView-3D model. The base of the Green River Formation reaches a depth approaching 3000 m (10,000 ft). The well coordinates are Easting 585768, Northing 4434659.*

organic maturity window. These parameters have been extracted for the assigned source rock units for various times (see Table 4-5).

The time-trigger maps provide a very direct means for visualizing the time of entry of different parts of the basin for a specific stratigraphic horizon into a particular maturity threshold. Figures 4-21 through 4-32 compare the simulations for Model A (52 mW/m^2) with Model D (57 mW/m^2). Understandably, the maturation threshold entry times are earlier by a few million years for the model run at the higher heat flow value. The simulations are shown for three stratigraphic horizons: (1) the top of the Mahogany Zone, (2) the base of the Parachute Creek Member, and (3) the middle of the Black Shale facies in the Lower Green River Formation. What stands out in all simulation maps is that the time of entry into the oil window is very early, considerably earlier by as much as 30 million years compared to the simulation by Nuccio and Roberts (2003; Figure 3-29). Also the trend of the oil kitchen is parallel to the northwest segment of the Basin Boundary Fault and parallel to the isopach thick of the Green River Formation in Figure 2-12. Entry into all maturity thresholds is later in what is now the deepest part of the basin, the extreme north, compared with the areas to the southwest and especially near Duchesne.

Table 4-5: *Chart of simulation output parameters exported as Surfer gird files for each of the models simulated, Model A through Model E. The grid files generated by the simulation can be found in Digital Appendix C in the folders for each individual model.*

Transformation ratio	0 Ma	10.0 Ma	20.3 Ma	30.5 Ma
GR-2M	A B C D E	A B C D E	A B C D E	A B C D E
GR-4	A B C D E	A B C D E	A B C D E	A B C D E
GR-7	A B C D E	A B C D E	A B C D E	A B C D E

Vitritnite reflectence LLNL	0 Ma	10.0 Ma	20.3 Ma	30.5 Ma
GR-2M	A B C D E	A B C D E	A B C D E	A B C D E
GR-4	A B C D E	A B C D E	A B C D E	A B C D E
GR-7	A B C D E	A B C D E	A B C D E	A B C D E

Excess pressure (psi)	0 Ma	10.0 Ma	20.3 Ma	30.5 Ma
GR-2M	A B C D E	A B C D E	A B C D E	A B C D E
GR-4	A B C D E	A B C D E	A B C D E	A B C D E
GR-7	A B C D E	A B C D E	A B C D E	A B C D E

Oil generated (bbls per acre)	0 Ma
GR-2M	A B na D E
GR-4	A B na D E
GR-6	A B na D E
GR-7	A B na D E

Time triggers	Early mature	Mid-mature	Peak oil	Main gas
GR-2M	A B C D E	na B C D E	A na C D E*	
GR-4	A B C D E	na B C D E	A B* C D E*	
GR-7	A B C D E	na B C D E	A B C D E	A B C D E

* or Late mature

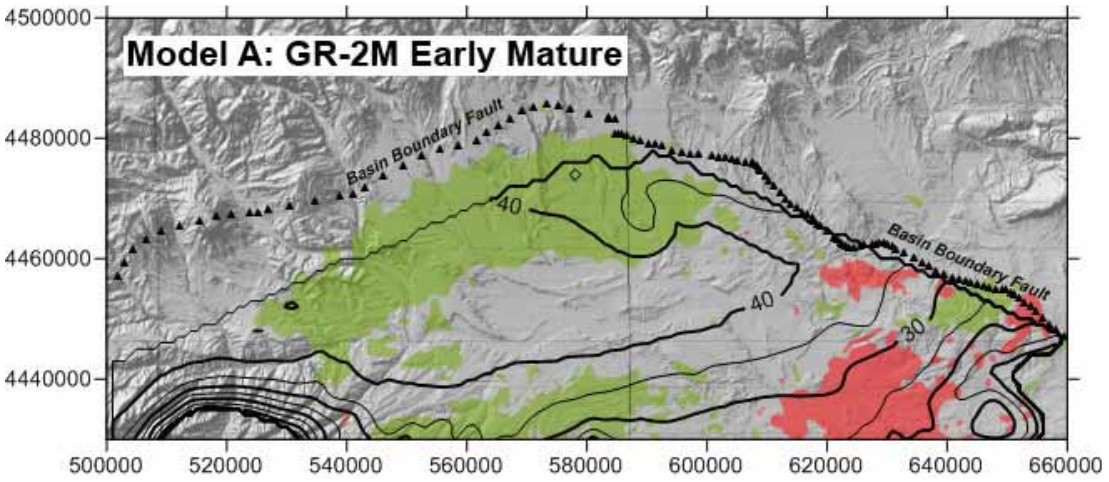

Figure 4-21: *Time-trigger for entry of the Mahogany Zone (GR-2M) into the Early Mature oil window in Model A in which the heat flow is specified as the preferred 52 mW/m². Note that a large portion of the GR-2M unit has entered the oil window even before end of deposition of the Uinta Formation. Early Mature is equivalent to vitrinite reflectance of 0.6–0.65% and Tmax of 435°–445°C (Peters and Cassa, 1994). CI = 5 Ma*

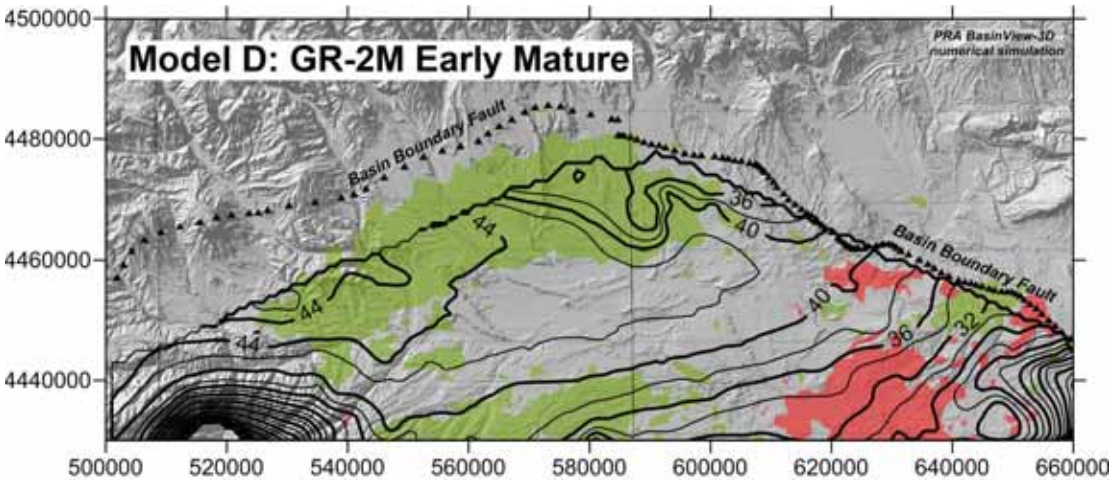

Figure 4-22: *Time-trigger for entry of the Mahogany Zone (GR-2M) into the Early Mature oil window in Model D in which the heat flow is specified as the Uinta Basin average 57 mW/m² (Chapman and others, 1984). Note that at the slightly higher heat flow the entry into the oil window is a few million years earlier throughout the region modeled. It is possible that the simulation fails in the extreme southwest of the model area. CI = 2 Ma*

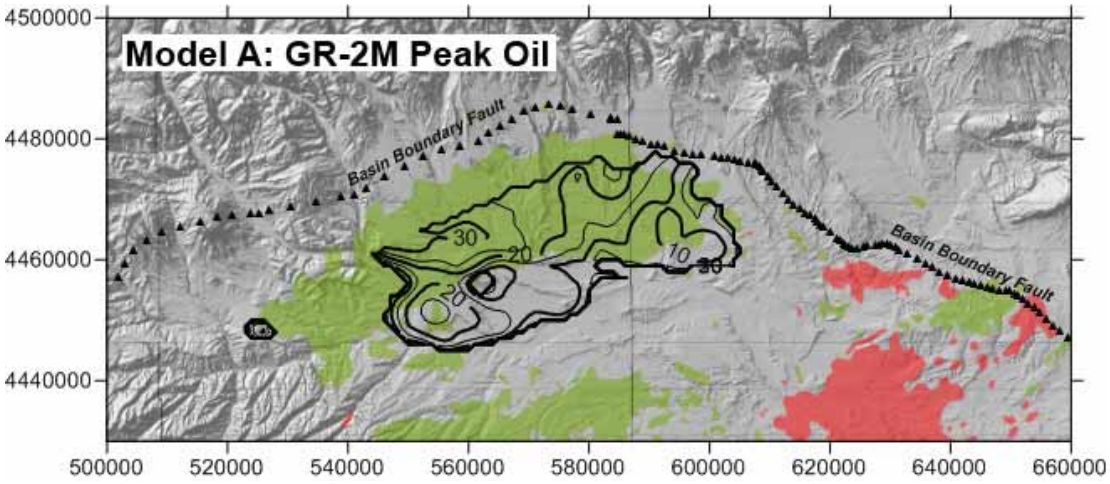

Figure 4-23: *Time-trigger for entry of the Mahogany Zone (GR-2M) into the Peak Oil maturity window in Model A in which the heat flow is specified as the preferred 52 mW/m². This area is spatially constrained to the deep axis of the basin in the region of the Altamont-Bluebell field. Peak Oil is equivalent to vitrinite reflectance of 0.65–0.9% and Tmax of 445°–450°C (Peters and Cassa, 1994). CI = 5 Ma*

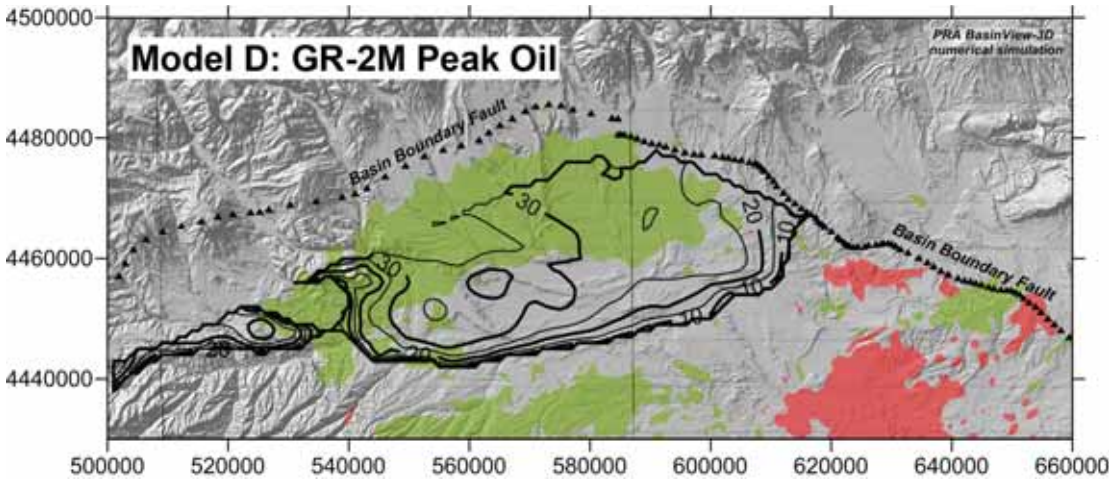

Figure 4-24: *Time-trigger for entry of the Mahogany Zone (GR-2M) into the Peak Oil maturity window in Model D in which the heat flow is specified as the Uinta Basin average 57 mW/m^2 (Chapman and others, 1984). At this slightly higher heat flow the region of entry is larger and the time of entry is as much as 10 Ma earlier than for the lower value of heat flow. CI = 5 Ma*

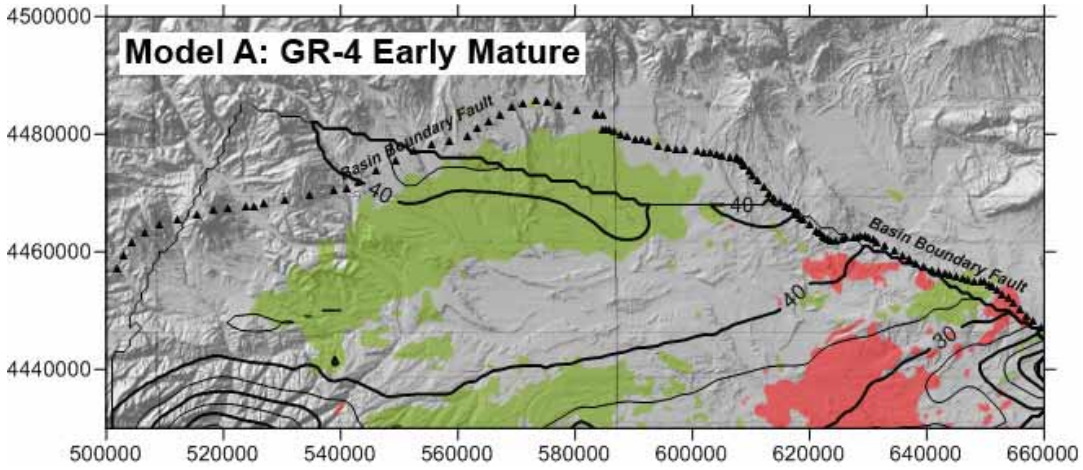

Figure 4-25: *Time-trigger for entry of the lower Parachute Creek Member (GR-4) into the Early Mature oil window in Model A in which the heat flow is specified as the preferred 52 mW/m^2. Virtually all of the north and central Uinta Basin is in the oil generative window at this stratigraphic level. Note that a single outlier "placed well" is pulling the simulation across the Basin Boundary Fault in the northwest. Isopleths north of the fault should be ignored. CI = 5 Ma*

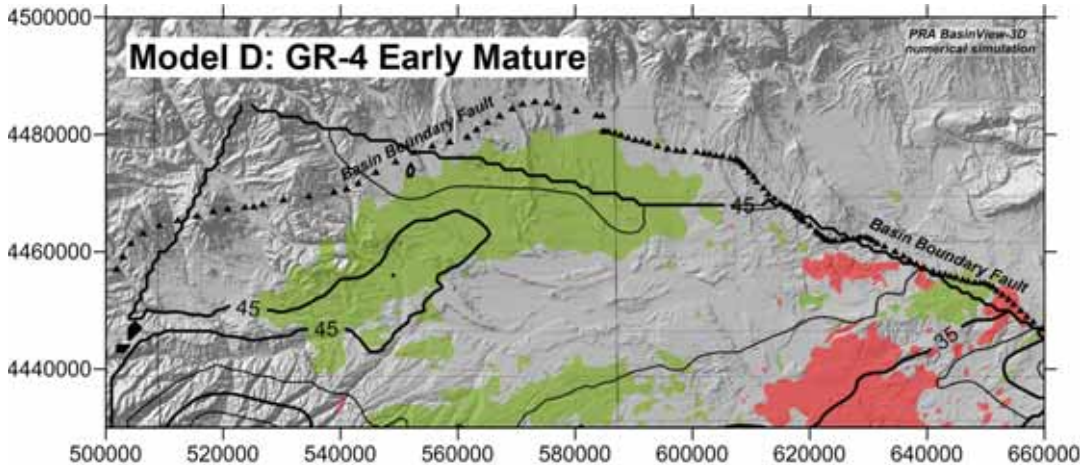

Figure 4-26: *Time-trigger for entry of the lower Parachute Creek Member (GR-4) into the Early Mature oil window in Model D in which the heat flow is specified as the Uinta Basin average 57 mW/m^2 (Chapman and others, 1984). Note that the earliest entry into Early Mature in the southwest portion of the greater Altamont field, not the presently deepest part of the basin. CI = 5 Ma*

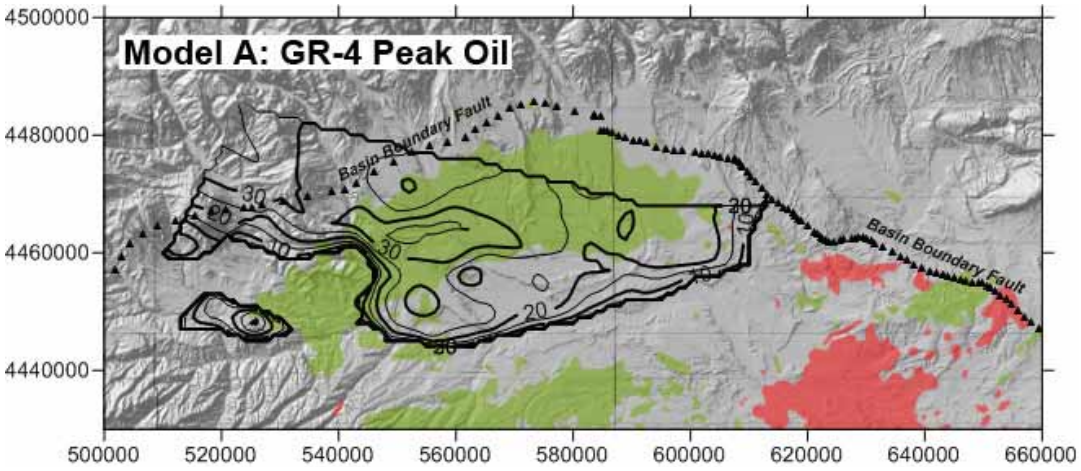

Figure 4-27: *Time-trigger for entry of the lower Parachute Creek Member (GR-4) into the Peak Oil maturity window in Model A in which the heat flow is specified as the preferred 52 mW/m². This area is spatially constrained to the deep axis of the basin in the region of the Altamont-Bluebell field, the portion of the field where anomalous formation pressures are observed (see figure 3-32). The 30 Ma isopleths might project across the gap in the simulation west of Duchesne. CI = 5 Ma*

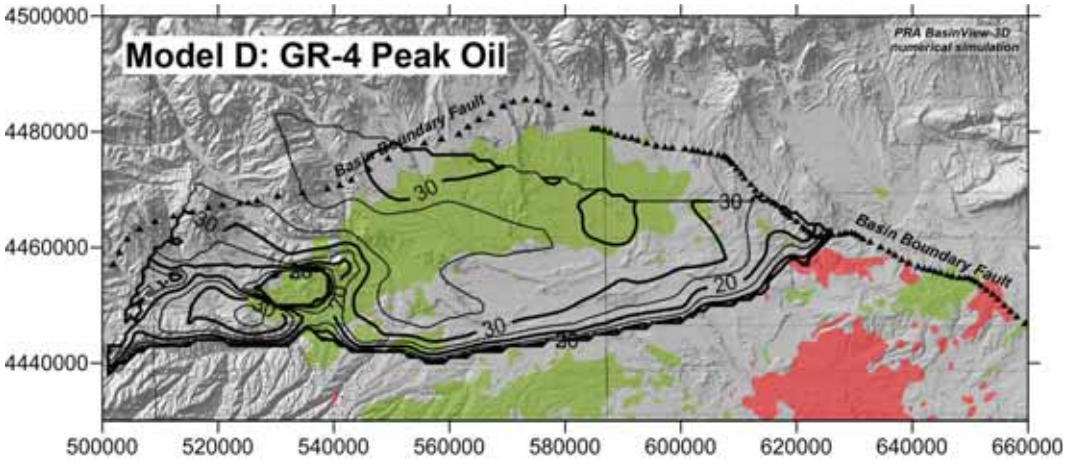

Figure 4-28: *Time-trigger for entry of the lower Parachute Creek Member (GR-4) into the Peak Oil maturity window in Model D in which the heat flow is specified as the Uinta Basin average 57 mW/m² (Chapman and others, 1984). A possible flaw in the surfaces defining the GR-4 unit, possibly a small cross-over of the surfaces, is resulting in a hole in the simulation results for an area on the west side of the map. It could be acceptable to project the 35 Ma isopleths across the hole. CI = 5 Ma*

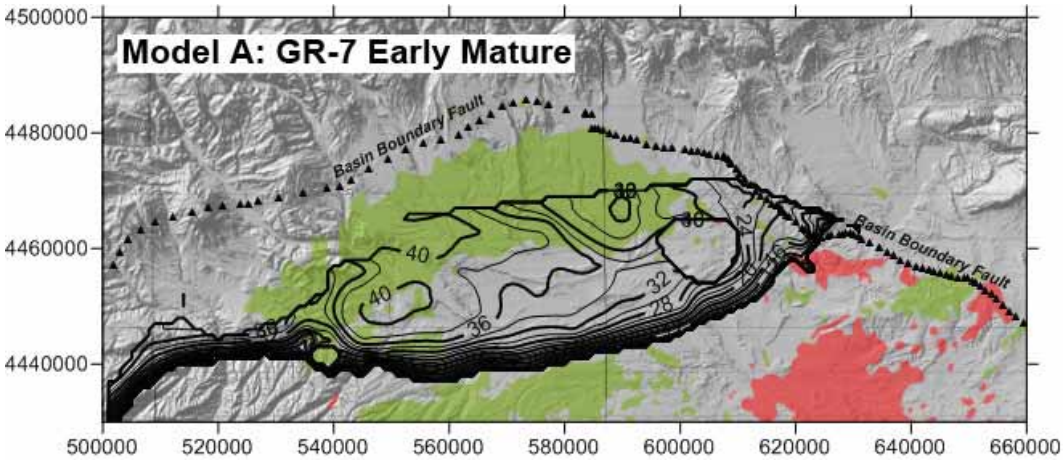

Figure 4-29: *Time-trigger for entry of the Lower Green River Formation (Black Shale facies, GR-7) into the Early Mature oil window in Model A in which the heat flow is specified as the preferred 52 mW/m². The circular void in the simulation east-central part of the map is due to a cross-over of model surfaces. CI = 2 Ma*

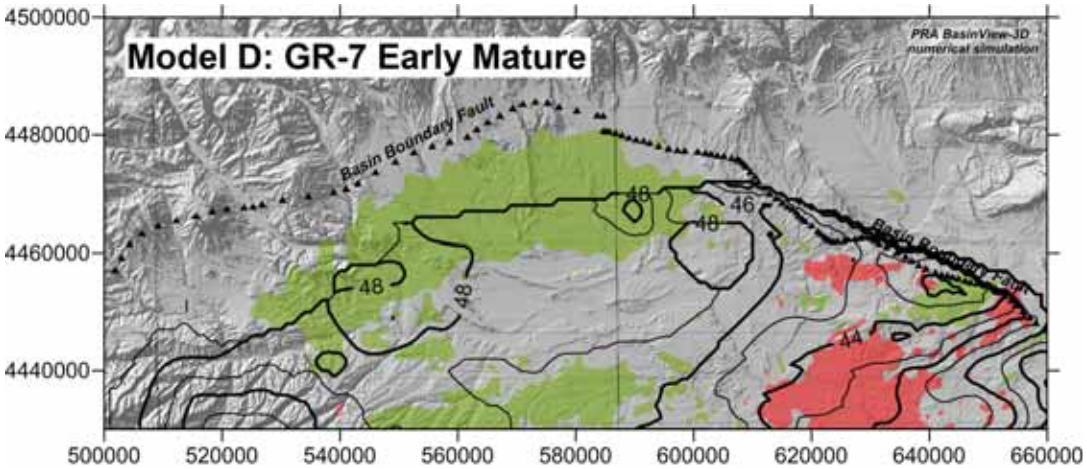

Figure 4-30: *Time-trigger for entry of the Lower Green River Formation (Black Shale facies, GR-7) into the Early Mature oil window in Model D in which the heat flow is specified as the Uinta Basin average 57 mW/m² (Chapman and others, 1984). At this higher heat flow the deepest stratigraphic level of the Green River Formation is entering the oil generative window while the uppermost part of the very thick formation is still being deposited. Refer to Table 4-1. The circular void in the simulation in the east-central part of the map is due to a cross-over of model surfaces. CI = 2 Ma*

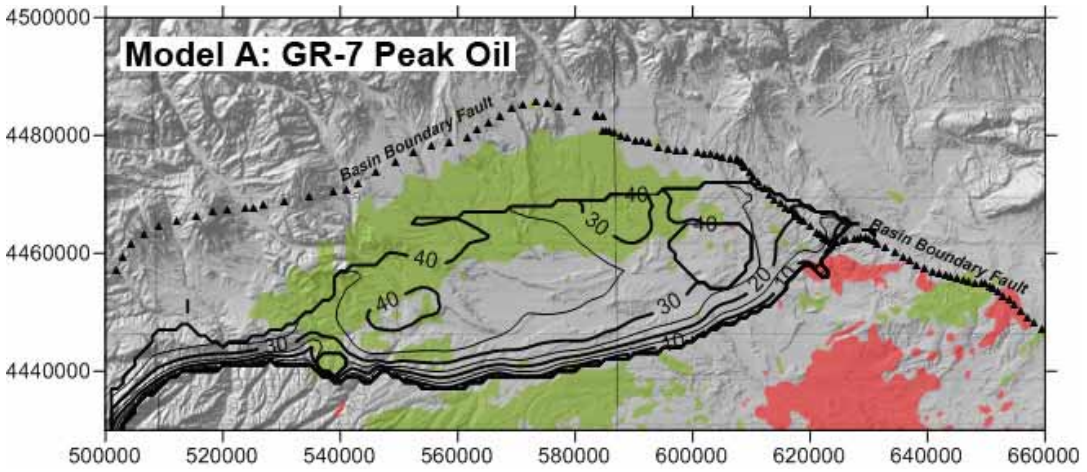

Figure 4-31: *Time-trigger for entry of the Lower Green River Formation (Black Shale facies, GR-7) into the Peak Oil maturity window in Model A in which the heat flow is specified as the preferred 52 mW/m². The circular void in the simulation in the east-central part of the map is due to a cross-over of model surfaces. CI = 5 Ma*

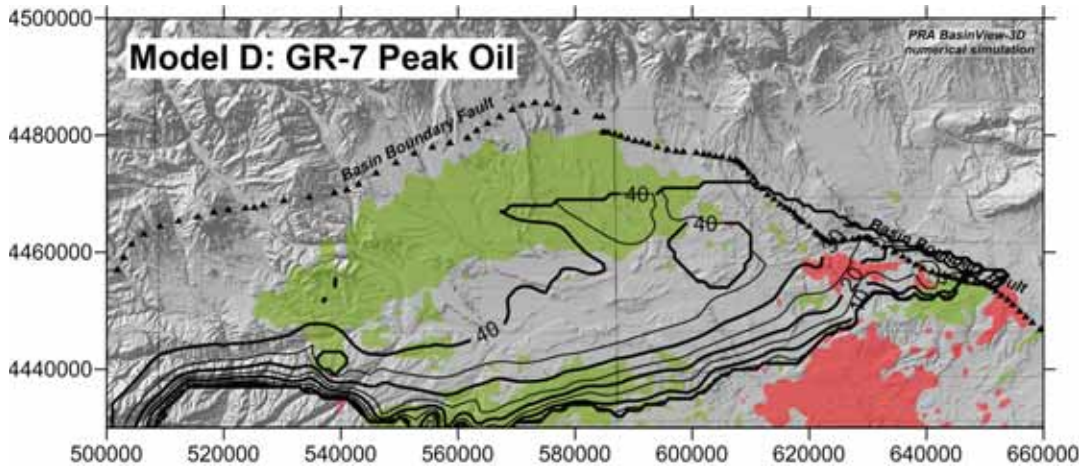

Figure 4-32: *Time-trigger for entry of the Lower Green River Formation (Black Shale facies, GR-7) into the Peak Oil maturity window in Model D in which the heat flow is specified as the Uinta Basin average 57 mW/m² (Chapman and others, 1984). The circular void in the simulation in the east-central part of the map is due to a cross-over of model surfaces. CI = 5 Ma*

The vitrinite reflectance (R_o-LLNL) maps (Figs. 4-33 to 4-44) depict the spatial distribution of simulated R_o using transformation ratio to R_o equivalencies developed at the Lawrence Livermore National Laboratory. The simulations were determined for the three stratigraphic horizons and four different times, 0 Ma, 10 Ma, 20.3 Ma and 30.5 Ma. The simulations are shown only for Model A, which generally match the R_o values in Anders and Gerrild (1984). Model D simulations are thought to be too high. As with the time-trigger maps, the oil kitchen is shown trending northeast, parallel to the northwest segment of the Basin Boundary Fault.

The maturity maps appear to be relatively insensitive to different model kerogen kinematics. Recall that Ruble and others (2001) propose that their Mahogany Shale activation energy would delay active oil generation of the Type I kerogen until a R_o maturity-equivalency of 0.75% is reached. However, it is definitely possible to see the effect of using the different kerogen kinematics in the simulations of oil generated. The results from using different kerogen kinematics are summarized in Table 4-6. The simulations using activation energies for Type I kerogen based on programmed pyrolysis (RE) derived data predict large quantities of oil generated, whereas simulations using the activation energy for Type I kerogen based on hydrous pyrolysis predict only minimal oil generation. These are the results found by Ruble and others (2001) in their alternative 1-D simulations shown in Figure 3-31. If we accept the hydrous pyrolysis activation energy as the better descriptor for Green River Type I kerogen, the source rocks rich in Type I kerogen have just recently begun entering the oil generative window, which has significant implications for the Green River petroleum system.

Simulations of the excess (anomalous) pressure offer another way of looking at the question of time of entry into the oil generative window. The calculations of this parameter are very poor. Better calculations would have required assigning petrophysical properties, currently unknown, to the Green River rocks. However, what is observed in all of the simulations is that the area of anomalous pressures is large for the 0 Ma time

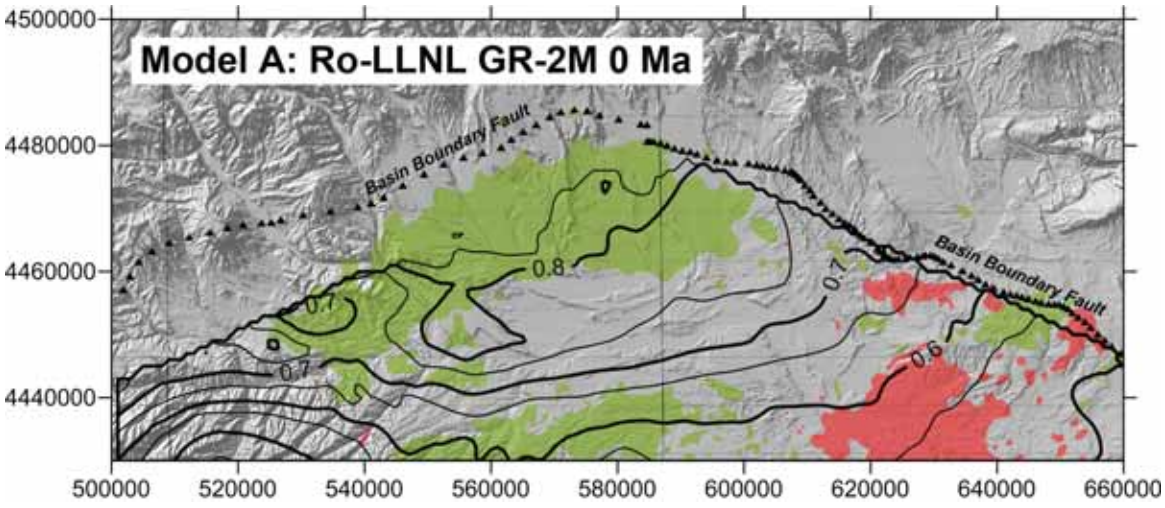

Figure 4-33: *Simulated vitrinite reflectance values for the Mahogany Shale (GR-2M) at the present-time (0 Ma). CI = 0.05% R_o*

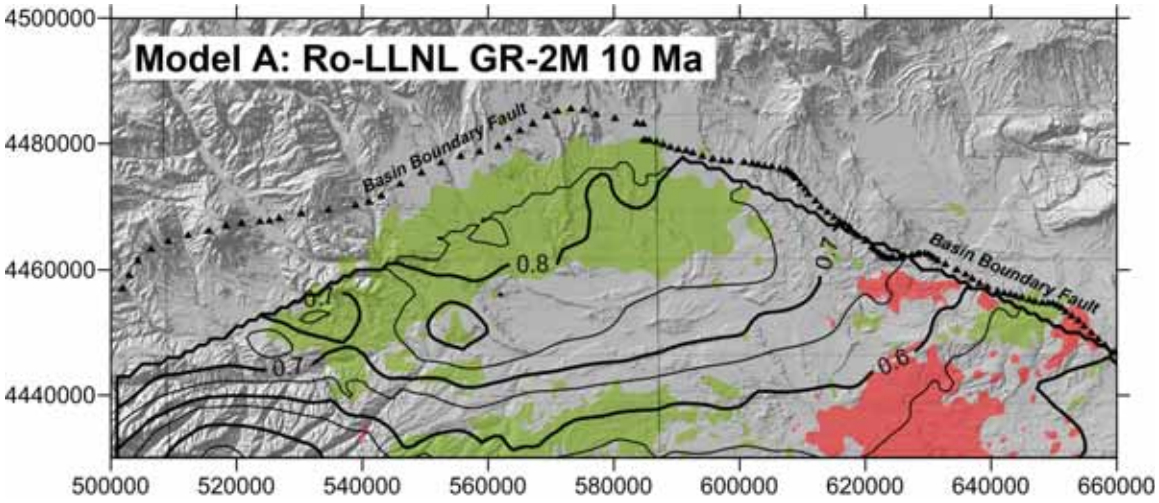

Figure 4-34: *Simulated vitrinite reflectance values for the Mahogany Shale (GR-2M) at 10 Ma. CI = 0.05% R_o*

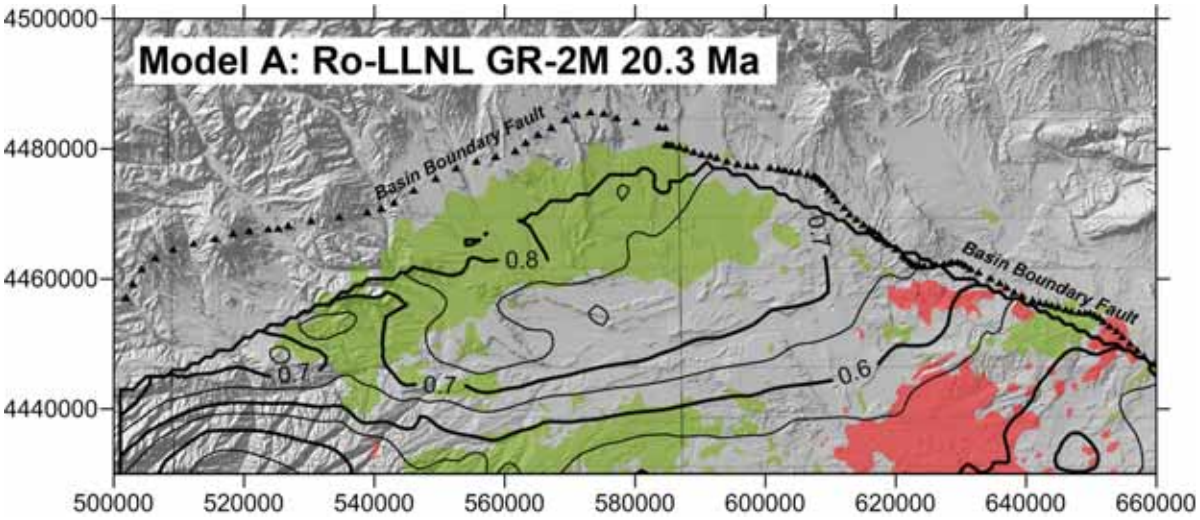

Figure 4-35: *Simulated vitrinite reflectance values for the Mahogany Shale (GR-2M) at 20.3 Ma. CI = 0.05% R_o*

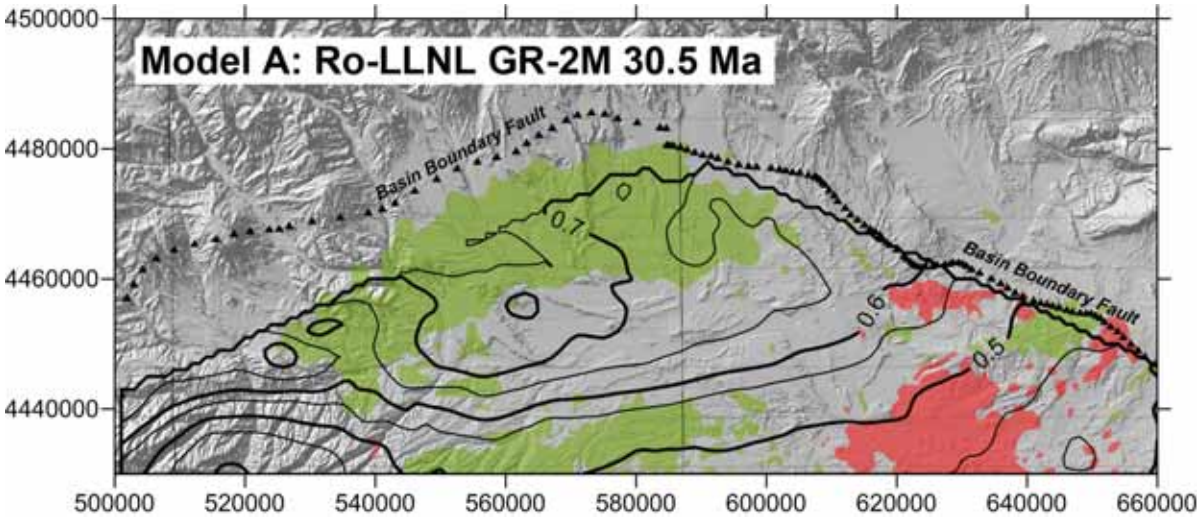

Figure 4-36: *Simulated vitrinite reflectance values for the Mahogany Shale (GR-2M) at 30.5 Ma. CI = 0.05% R_o*

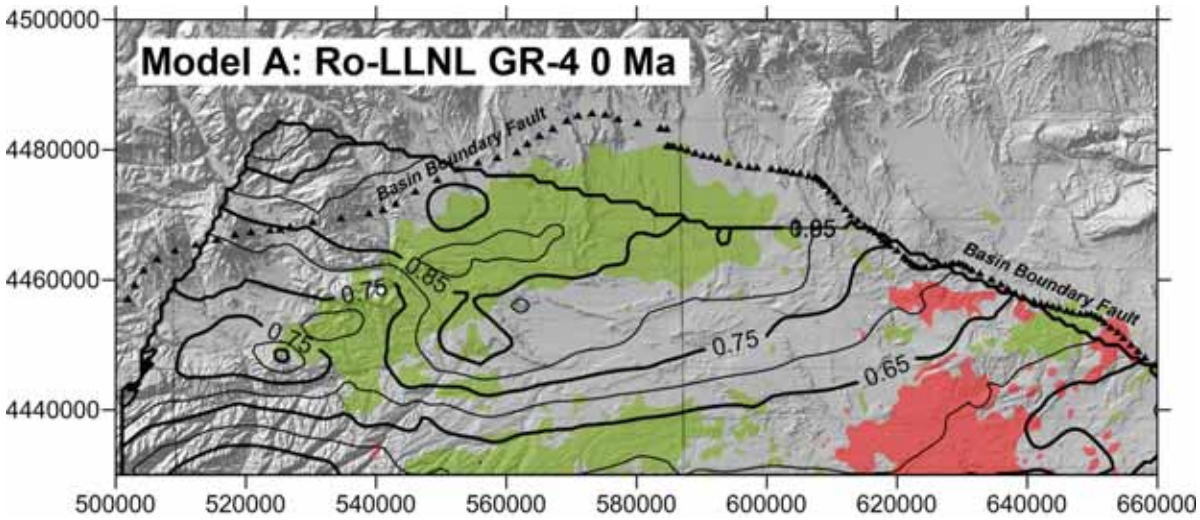

Figure 4-37: *Simulated vitrinite reflectance values for the lower Parachute Creek Member (GR-4) at the present-time (0 Ma). Note that a single outlier "placed well" is pulling the simulation across the Basin Boundary Fault in the northwest. Isopleths north of the fault should be ignored. CI = 0.05% R_o*

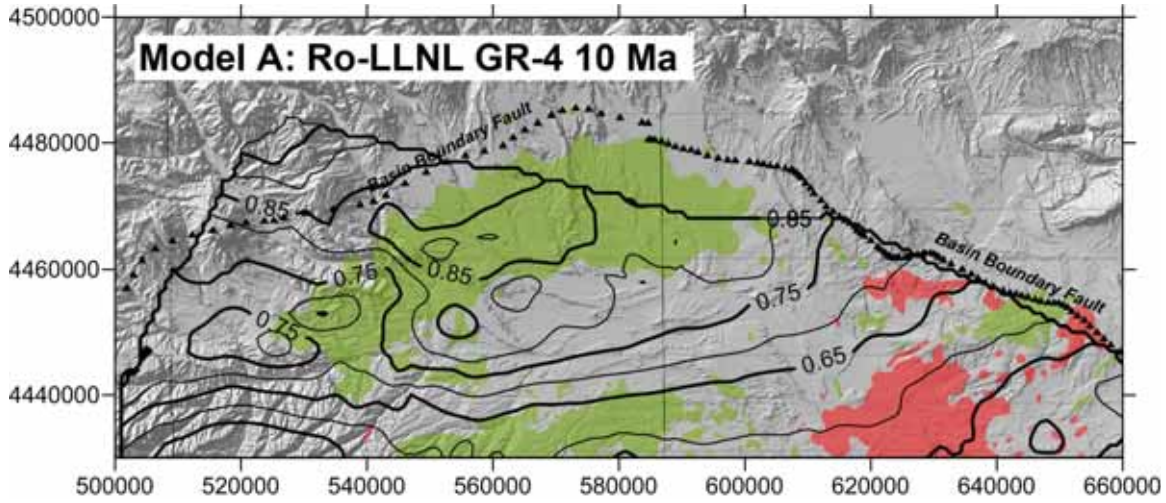

Figure 4-38: *Simulated vitrinite reflectance values for the lower Parachute Creek Member (GR-4) at 10 Ma. Note that a single outlier "placed well" is pulling the simulation across the Basin Boundary Fault in the northwest. Isopleths north of the fault should be ignored. CI = 0.05% R_o*

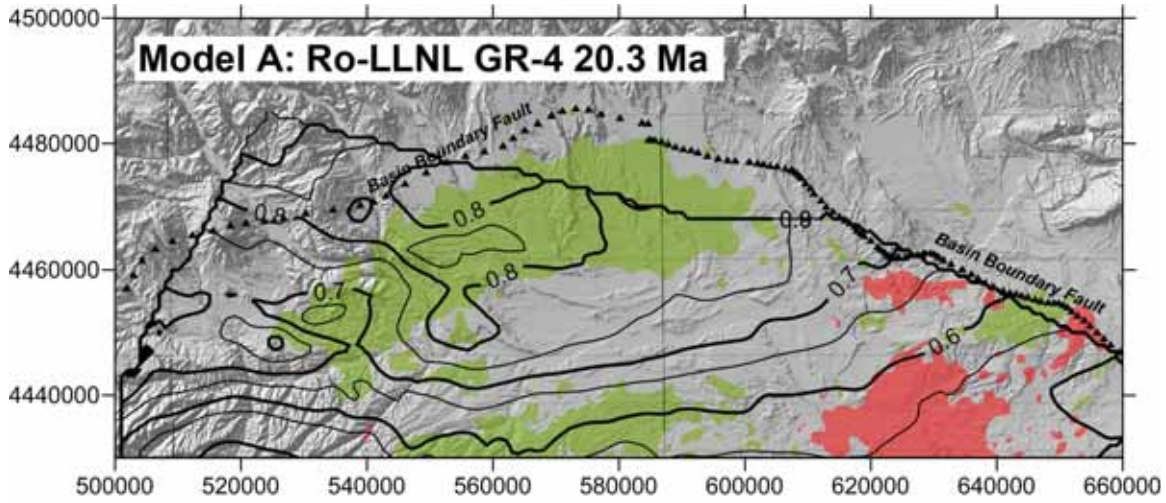

Figure 4-39: *Simulated vitrinite reflectance values for the lower Parachute Creek Member (GR-4) at 20.3 Ma. Note that a single outlier "placed well" is pulling the simulation across the Basin Boundary Fault in the northwest. Isopleths north of the fault should be ignored. CI = 0.05% R_o*

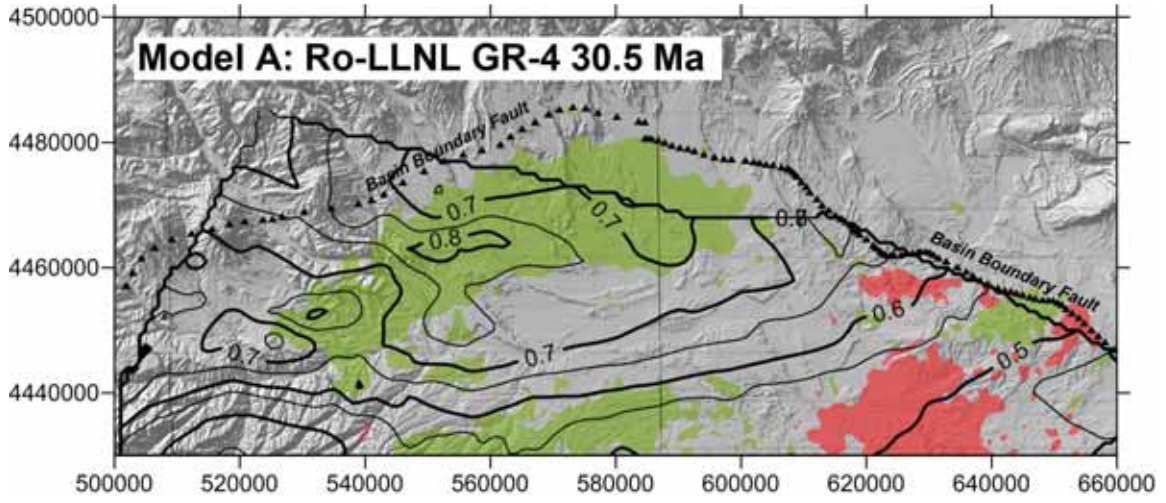

Figure 4-40: *Simulated vitrinite reflectance values for the lower Parachute Creek Member (GR-4) at 30.5 Ma. Note that a single outlier "placed well" is pulling the simulation across the Basin Boundary Fault in the northwest. Isopleths north of the fault should be ignored. CI = 0.05% R_o*

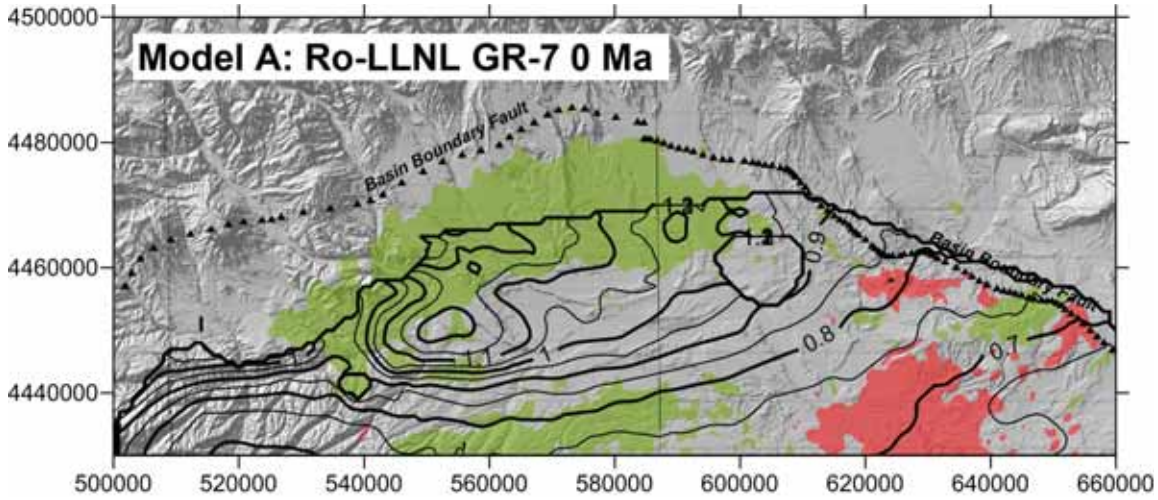

Figure 4-41: *Simulated vitrinite reflectance values for the Black Shale facies (GR-7) at the present-time (0 Ma). The circular void in the simulation in the east-central part of the map is due to a cross-over of model surfaces. CI = 0.05% R_o*

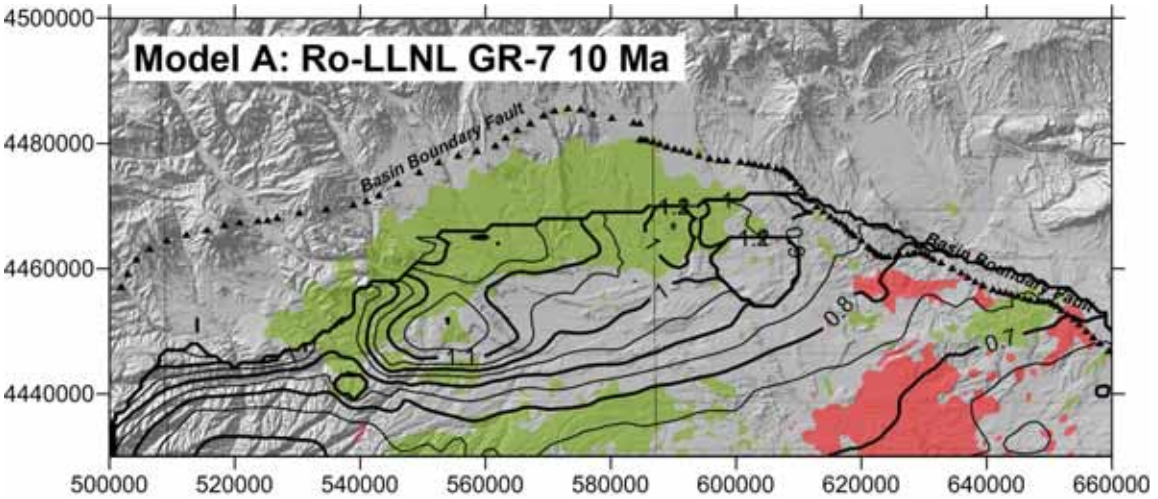

Figure 4-42: *Simulated vitrinite reflectance values for the Black Shale facies (GR-7) at 10 Ma. The circular void in the simulation in the east-central part of the map is due to a cross-over of model surfaces. CI = 0.05% R_o*

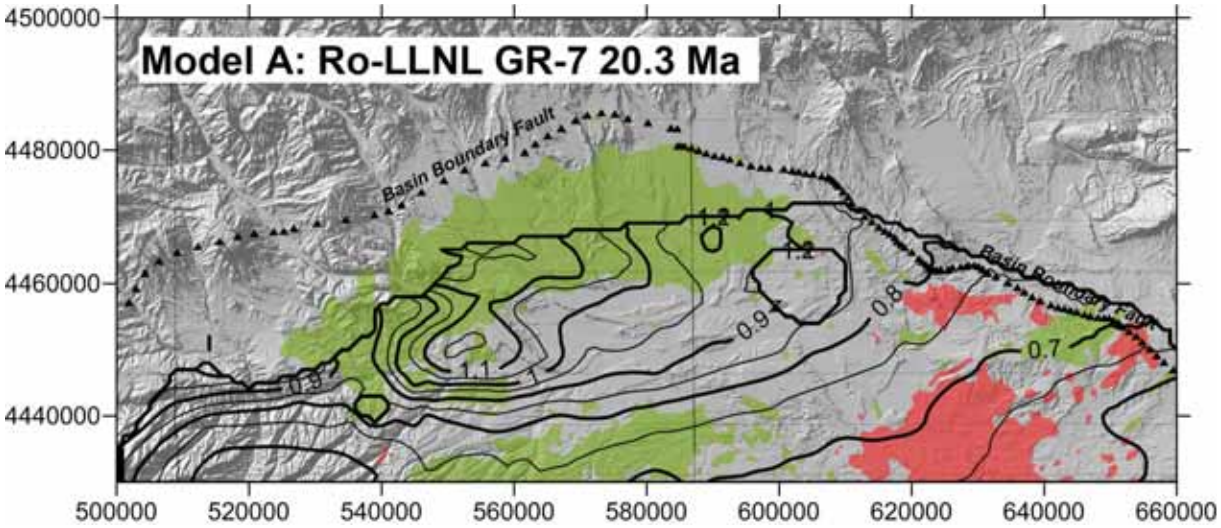

Figure 4-43: *Simulated vitrinite reflectance values for the Black Shale facies (GR-7) at 20.3 Ma. The circular void in the simulation in the east central part of the map is due to a cross-over of model surfaces. CI = 0.05% R_o*

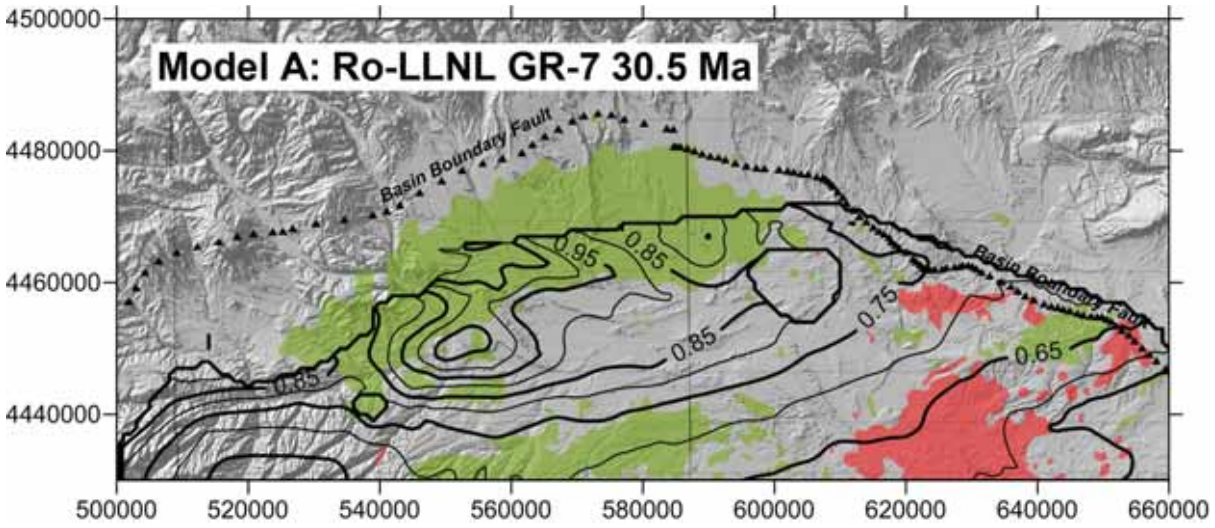

Figure 4-44: *Simulated vitrinite reflectance values for the Black Shale facies (GR-7) at 30.5 Ma. The circular void in the simulation in the east central part of the map is due to a cross-over of model surfaces. CI = 0.05% R_o*

Table 4-6: *The maximum values of oil generated in barrels of oil per acre in simulations for the different models. Note that Model A and B and D and E use different kinematics, Type 1 kerogen kinematics determined from open-system programmed pyrolysis (RockEval) versus closed system hydrous pyrolysis. The kerogen kinematics are identified by stratigraphic interval and source: RE (open-system RockEval) and HP (closed-system hydrous pyrolysis) from Ruble and others (2001) and LLNL (a commonly used BasinView 3-D default). MBO is units of thousand barrels per acre.*

	Oil generated - maximum value, MBO				Model kerogen kinematics			
	GR-2M	GR-4	GR-6	GR-7	GR-2M	GR-4	GR-6/7	Heat flow
Model A	7,000	5,600	420	650	Mahogany RE	Mahogany RE	Black Shale RE	52 mW/m^2
Model B	0.0013	0.014	420	650	Mahogany HP	Mahogany HP	Black Shale RE	52 mW/m^2
Model C	na	na	na	na	Type I, LLNL	Type I, LLNL	Type II, LLNL	52 mW/m^2
Model D	8,000	6,500	480	850	Mahogany RE	Mahogany RE	Black Shale RE	57 mW/m^2
Model E	0.0125	0.15	480	850	Mahogany HP	Mahogany HP	Black Shale RE	57 mW/m^2

(Fig. 4-45) and quite small for previous times (Figs 4-46 and 4-47). There are two ways to interpret this observation. Either the higher anomalous pressure at the present is due to volume expansion of reservoired hydrocarbons related to the recent and rapid exhumation (unloading) of the basin, or it relates to the relatively recent entry of the Type I kerogens into the oil generative window.

5. DISCUSSION

In a conventional petroleum system, oil moves by buoyancy drive from source to trap through a carrier system, a network of permeable carrier beds, faults and fractures, and/or along unconformities. The oil generated in the "kitchen" leaves the tight source rocks by pressure-driven diffusion and Darcy flow (England, 1994), commonly aided by local fracturing caused by volume expansion of kerogen converting to bitumen and oil. The volume of oil that moves in this "primary" migration is just that portion generated that is not held in the source rock by sorption on and within the organic matter present or trapped behind nanno-size pore throats. Not all of the oil generated is free to migrate into the carrier network, only that portion that is not "irreducible" (Pepper, 1991).

Where the carrier system is non-existent or highly inefficient, the oil remains entrapped in the source-rock succession. This situation results in an unconventional continuous petroleum accumulation, a potential shale oil resource play. Typical shale oil resource plays are self-contained petroleum systems having ineffective carrier systems that severely restrict oil generated in the source rocks from migrating outward or upward into traps in reservoirs external to the oil kitchens. Consequently, oil backs up into any and all pore space in the source rock succession, even creating fracture storage space where over-pressures approaching lithostatic (0.8 psi/ft) occur. Relatively tight rocks that normally never would be considered reservoirs can have high oil saturations and oil-in-place. Hydrocarbon charge is pervasive across a large area, but one with poorly delineated boundaries. No distinct oil-water contacts are recognized and there is little water production, yet water occurs up dip from the oil accumulation. Normally, shale oil plays have low recovery factors (< 10%),

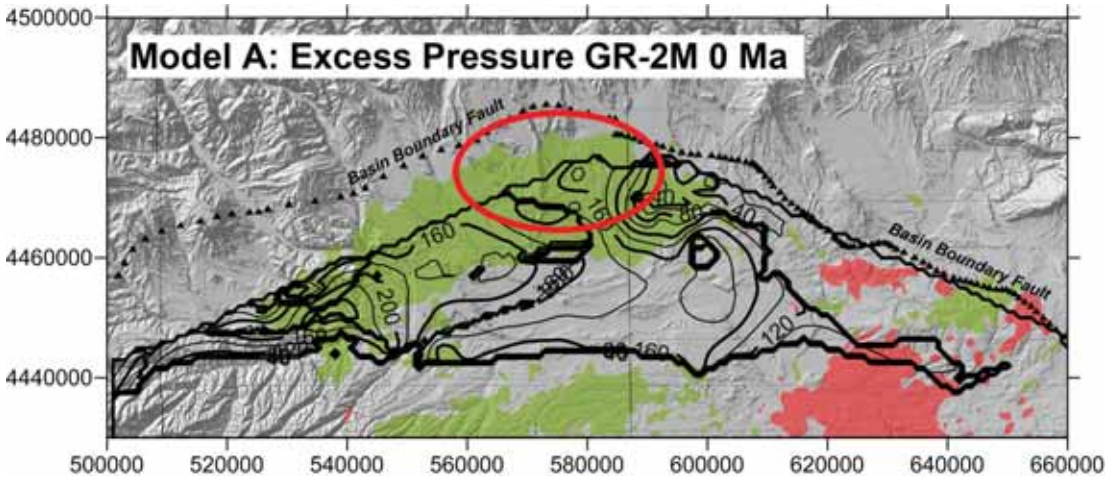

Figure 4-45: *Field of Excess Pressure (pressure in excess of hydrostatic) in the Mahogany Zone (GR-2M) at the present, 0 Ma. Units are pounds per square inch (psi). Calculation of this parameter is sensitive to the petrophysical properties of the lithologies assigned. Consequently, the map should be seen as a qualitative representation of anomalous pressures. The red ellipse encloses the region of very high anomalous pressures reported by Lucas and Drexler (1975) and Nelson (2002). Contour interval is 20 pounds per square inch (psi).*

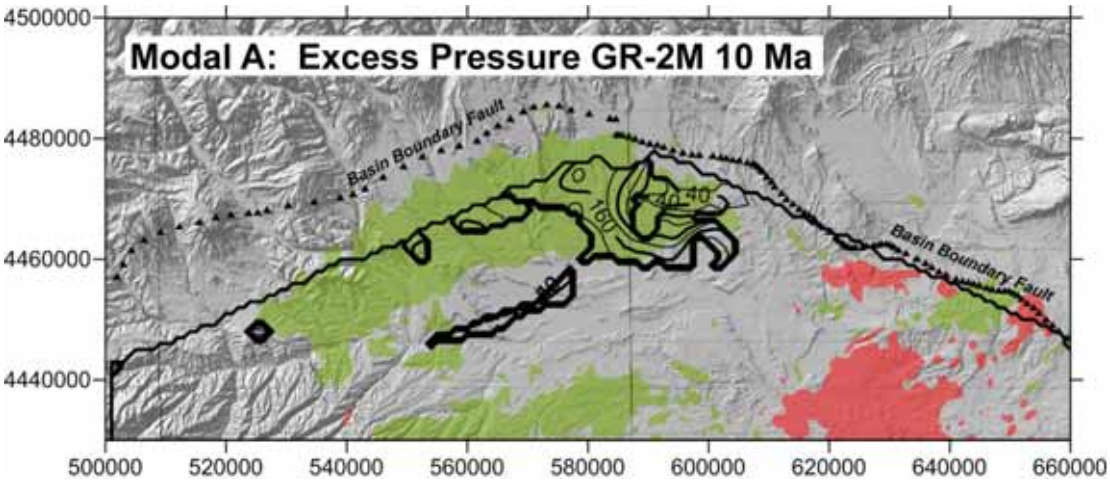

Figure 4-46: *Field of Excess Pressure (pressure in excess of hydrostatic) in the Mahogany Zone (GR-2M) at the onset of exhumation, 10 Ma. Units are pounds per square inch (psi). CI = 20 psi*

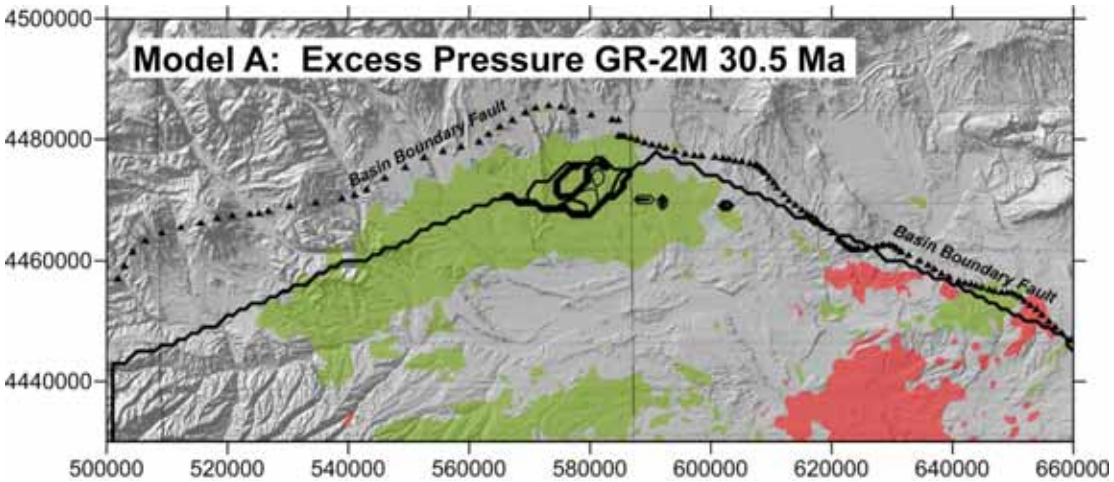

Figure 4-47: *Field of Excess Pressure (pressure in excess of hydrostatic) in the Mahogany Zone (GR-2M) at the end of deposition of the Duchesne River Formation, 30.5 Ma. Units are pounds per square inch (psi). Although the Mahogany Zone is generating liquid hydrocarbons at this time, there is very limited area with overpressure. CI = 10 psi*

despite the very large oil resource in-place. This is due to the very low permeability of the tight rocks that serve as the reservoirs. In a shale oil resource play these tight oil reservoirs are what are exploited by horizontal wells and hydraulic fracture stimulation. The universal characteristics of a shale oil resource play are (1) oil saturations in excess of irreducible and (2) formation pressures in excess of hydrostatic (0.43 psi/ft), but commonly approaching lithostatic (Jarvie, 2012). Otherwise, the plays, or even parts of the same play, can be quite distinct.

Although the actual source-rocks can yield commercial quantities of oil, as in the Eagle Ford play (Fig. 3-4), it is commonly the case that the productive reservoir intervals are interbedded within or are in proximity to the mature source rocks. This is the situation in the Bakken (Fig. 3-5) and Niobrara plays (Jarvie and others, 2011; Sonnenberg, 2011), where the target reservoirs for well completion are the organic matter-poor and slightly more porous carbonates and siliciclastics adjacent to the organic-rich source beds. The source rocks are commonly too tight to yield high oil rates and they retain the residual oil too tenaciously. These low-TOC reservoirs have high oil saturations compared to their organic carbon content, that is, high values of OSI. Additionally, they are characterized by low S1, S2 and HI values.

The Green River Formation in the Uinta Basin has many characteristics typical of an ideal shale oil resource play. It is a world-class oil-prone source rock. In nearly all parts of the basin there are many thousands of net feet of Type-I and Type-II kerogen-rich calcareous mudstones, many intervals which have average total organic carbon contents of 5–10%, or greater. In the north-central and western parts of the basin, a substantial part of the formation is currently in the oil-generative window. A large volume of the formation has reached "peak oil". Furthermore, organic maturation simulations done in this study using PRA BasinView-3D™ (see Chapter 4) indicate early entry into the oil-generative window. In the northwest parts of the basin, the lower Green River Formation was generating oil even before the end of the Eocene and slowing of sediment accumulation in the basin. Anomalous formation pressures are observed in the Green River Formation across much of the basin. In the area of the greater Altamont-Bluebell field in the northwest of the basin, the abnormal pressures are nearly lithostatic (0.6 to 0.8 psi/ft). The Green River Formation is, unquestionably, a superb petroleum system responsible for very large cumulative production of conventional oil and associated natural gas, and an even larger unexploited, immobile, heavy-oil resource (Schamel, 2013). But that very fact may limit its prospects as a significant shale oil resource play.

The pattern of cyclical, climate-driven lacustrine deposition of the Green River Formation was such that porous siliciclastics and shoreline bioclastic carbonates extend across most of the basin, even into the basin depocenter in the north and northwest. These relatively porous strata, in part, served as effective carrier beds for oil generated in this kitchen area to migrate laterally up dip to the south and east to charge the producing Green River oil fields (Monument Butte, Red Wash, among many others) and the vast oil sand deposits of the Tavaputs Plateau (Schamel, 2013). These oil accumulations are outside of the Green River oil-generative window. In contrast, oil production in the northwest quadrant (Altamont-Bluebell field and its southwest extensions) is from thick porous sandstone and carbonate (Uteland Butte) beds intercalated with thermally-mature source rocks.

The northwest depocenter of the Uinta Basin is where Green River open-lacustrine facies rocks dominate (Fig. 2-1), the formation is thickest (Fig. 2-13), the greatest part of the formation is in the oil generative window (Figs. 4-33 to 4-44), and the lower parts of the formation are overpressured (Figs. 3-32 and 3-33). Cores in this area have sandstone and porous carbonate lenses within the organic-rich calcareous mudstone that consistently are oil impregnated (Figs. 2-12 and 3-26). It is here that the Green River Formation has potential as a shale oil resource play, especially in intervals isolated from effective oil carrier systems.

A central element of this study is the basinwide modeling of thermal maturation carried out using BasinView-3D™ to create a grid of numerical simulations for synthetic wells with one kilometer spacing. Simulations were done for the northern two-thirds of the basin, the deeper and known petroleum generative area. The formation tops for generating the synthetic wells are derived from the contour map grids displayed in the structure maps in Chapter 2. The surfaces are constrained by a large number of wells up through the Mahogany Zone across the region modeled. However, the configuration of higher surfaces, partially eroded in the south, was reconstructed from a combination of well tops and surface projections, or by other means described in Chapter 4. The burial history model of the basin incorporated into the simulations has the following phases.

- Rapid sediment accumulation of the Green River, Uinta, and Duchesne River Formations during the Eocene, coincident with the Laramide uplift of the Uinta Mountians.

- A brief period of peneplanation in the early Oligocene (30.5 Ma) during which the Gilbert Peak geomorphic surface formed. This surface then was buried beneath a thin veneer of Bishop Conglomerate, laid down slowly until the early Miocene (20.3 Ma). There is no indication that the thick Oligocene-age volcaniclastic deposits found west of the Uinta Mountains ever reached the Uinta Basin.

- A long period (20.3 to 10.0 Ma) during which pediments covered the basin at the extreme northern extent of the southern segment of the Green River drainage and little sediment was added or removed.

- Exhumation of the basin began slowly at about 10.0 Ma, but then accelerated 500,000 years ago when the southern Green River segment captured its northern segment, thus dramatically lowering the local base level. Stream capture and greatly accelerated erosion rates are both likely tied to the onset of mountain glaciation in the region.

The Green River Formation was deposited rapidly in the early Eocene, buried under a thick succession of fluvial sediments (Uinta and Duchesne River Formations) by the end of the Eocene-early Oligocene, and then remained buried until the middle Pleistocene. The details of this scenario, with documentation, are presented in Chapter 2.

As described in Chapter 4, the numerical simulation of organic maturation is based on temperature history curves for a grid across the basin. These, in turn, are derived from the measured depths and known or estimated geologic ages of basin-wide stratigraphic markers, and from plausible heat-flow values at the time of basin infilling. At each grid node, the Arrhenius equation is used to calculate the rates of conversion of kerogen to bitumen, liquid hydrocarbons, and natural gas from the temperature history curves. The rates of conversion, in turn, are integrated into transformation ratios in space and time. The transformation ratio expresses the portion of initial kerogen converted to hydrocarbons (0.0 for no hydrocarbons to 1.0 for complete conversion of the kerogen, leaving only a pyrobitumen or graphite residue). BasinView-3D™ converts the transformation ratio to conventional measures of organic maturity, such as vitrinite reflectance equivalent or time-of-entry of a specific stratigraphic datum into a maturity threshold, "time-triggers" such as entry into the "peak-oil" window.

In order to visualize the variations in thermal maturation throughout the thick Green River Formation, simulations were run for three surfaces at the bottom, middle and top of the source-rock bearing part of the formation. These surfaces are: (1) the base of the lower Black Shale or Uteland Butte Limestone (55.3 Ma); (2) the base of the R-4 or the lower Green Shale interval (51.6 Ma); and (3) the top of the Mahogany Zone (48.9 Ma). In order to visualize the changes in thermal maturation of each of these three reference horizons over time, simulations were run for four times in the past: 1) 35.5 Ma, the end of basin infilling marked by the early Oligocene Gilbert Peak geomorphic surface; 2) 20.3 Ma, the end of Bishop Conglomerate deposition in the early Miocene; 3) 10.0 Ma, the estimated initial onset of basin exhumation; and 4) 0.0 Ma or the present-day. Thermal maturations were calculated for each of the three reference horizons at each of the four times in five different simulations run using different heat flow values and kerogen kinematics (see Table 4-3). The simulations are displayed either as times of entry into different thermal maturation windows, such as "early oil" or "peak oil" (Figures 4-21 through 4-32) or as equivalent vitrinite reflectance (R_o) values (Figures 4-33 through 4-44).

In general, the simulations indicate that in the area of the greater Altamont-Bluebell field, the lower Black Shale enters the "peak oil" window already by 40 Ma to 30 Ma. By present-day in the same area, the lower Black Shale has reached the "late oil" or early "wet gas" window. A similar pattern is observed for the lower Green Shale and the Mahogany Zone, only the maturation windows are slightly lower and the times of entry are slightly later, as would be expected. Generation of oil in the Green River source rocks is occurring close to or shortly following the end of sediment infilling of the Uinta Basin, and after that time there is only a slight increase in thermal maturation. Given that thermal maturation is a function of both time and temperature, the generation of hydrocarbons would have continued, albeit at slow rates, up into the Pleistocene and the onset of very rapid exhumation of the basin.

The active generation of hydrocarbons commonly is considered to be a cause of abnormal formation pressure (Spencer, 1987; Law and Spencer, 1998; Swarbrick and others, 2002). However, as noted by Osborne and Swarbrick (1997), it is the rapid generation and/or desorption of natural gas that is the more effective cause of large excess pressures. Furthermore, overpressures are inherently unstable and will dissipate unless continuously maintained. In the more thermally mature portions of the Uinta Basin, in particular the greater Altamont-Bluebell field (Fig. 3-33), late generation of natural gas by cracking of kerogen and residual oil, together with gas expansion due to rapid exhumation, may be the cause of the extremely high abnormal formation pressures observed in the lower Black Shale and underlying Wasatch Formation (Figure 3-32). If true, the overpressure is a recent and transient phenomenon related to sudden unroofing of a gas-charged petroleum system.

Lacustrine basins are ideal settings for the accumulation and preservation of organic matter, especially large volumes of hydrogen-rich kerogen, and Lake Uinta was no exception. The Green River Formation is widely recognized as a world-class source-rock succession for conventional oil and associated natural gas resources. Nevertheless, there is a general paucity of standard organic geochemical analyses of Green River source rocks in the public domain. For this study, there were only 15 wells for which programmed pyrolysis data were available from the literature and from UGS and USGS files (Table 3-1). However, from these 15 wells, nearly all with core samples, there were a total of 312 separate programmed pyrolysis analyses. Fortunately, 222 of the geochemical analyses from 9 cores (Table 5-1) in the western half of the basin had been run within the past five years by the same highly-reliable laboratory. The other analyses are more than a decade old and perhaps less reliable. Given that the cores are from all portions of the basin (Fig. 3-1) and sampled virtually all of the organic-rich portions of the Green River Formation, these analyses form a reliable basis for characterizing the source rocks.

There are two salient aspects of the organic geochemistry of the Green River Formation. The first relates to the wide range

Table 5-1: *Summary of average values and standard deviations for selected geochemical parameters measured on Green River Formation core samples in the western part of the Uinta Basin. The values presented are for the data plotted in Figures 5-1 to 5-3. Township-Range is Salt Lake meridian.*

Well name	T-R	TOC	HI	Tmax	OSI	OSI max	#	Depth range, ft
Chasel 1-81A1	1S-1W	1.2 ± 0.4	287.4 ± 37.6	439.1±5.5	86.5 ± 27.7	135	9	10639 - 10705
DR Long 2-19A1E	1S-1W	2.6 ± 1.6	381.5 ± 112.5	439.7 ± 3.2	80.0 ± 37.1	138	11	9163 - 9716
Olsen U1-12A2	1S-2W	1.9 ± 0.6	388.1 ± 54.3	440.8 ± 1.2	52.0 ± 14.9	90	8	10495 - 10603
Lamiq-Urrity 1-8A2	1S-2W	1.4 ± 0.3	412.6 ± 76.5	438.0 ±2.7	42.3 ± 16.9	73	12	10833 - 10951
Virgil Mecham 1-11A2	1S-2W	2.0 ± 1.0	536.6 ± 115.2	438.7 ± 3.0	38.5 ± 10.6	57	15	10348 - 10634
Norling 1-9B1	2S-1W	8.4 ± 7.9	654.0 ± 254.2	442.6 ± 6.4	32.3 ± 76.5	277	18	7497 - 7618
16X-23D-36BTR	3S-6W	3.2 ± 1.0	377.0 ± 187.4	453.6 ± 7.7	46.4 ± 21.0	89	22	3887 - 5150
14X-22-46DLB	4S-6W	2.5 ± 2.6	215.4 ± 166.7	455.6 ± 4.6	79.7 ± 86.9	391	18	5480 - 5625
Marsing 16 BkSh	10S-8E	3.4 ± 4.9	440.8 ± 280.6	437.1 ± 4.5	46.9 ± 88.8	580	82	460 - 1165
Marsing GrSh	10S-8E	4.2 ± 4.6	599.4 ± 249.2	433.6 ± 5.5	50.5 ± 61.0	292	27	57 - 450

of kerogen types present within organic-carbon-rich mudstones in the formation (Fig. 3-1). These vary from humic and algal coals to exceptionally hydrogen-rich sapropel, each characteristic of a different part of the lake environment from shoreline to near-perennial lake center. Despite the range of kerogen types observed, cross-plots of total organic carbon (TOC) vs. genetic potential (GP) indicate that, on the whole, the rocks are good to excellent source rocks (Figures 3-10, 3-14, 3-20, and 3-24). Average TOC values for the nine cores in the western part of the basin are in the range 1.2 wt% to 8.4 wt% (Table 5-1), all in the good to excellent range (Peters and Cassa, 1994). Only a few of the samples analyzed would be classified as fair or poor. Furthermore, the kerogens generally are quite hydrogen-rich with average values of hydrogen index (HI) in the range 287 to 654 mg HC/g TOC, but with large standard deviations indicative of the variability in kerogen type (Table 5-1).

The second notable aspect of the geochemistry is the widespread cyclicity of geochemical properties (Figs. 3-11 and 3-16), particularly TOC and HI. The range of kerogen types is indicated in the large values of standard deviation associated with the average HI values (Table 5-1). Climatically driven rise and fall of Lake Unita drove the expansion and contraction of the shoreline to lake center depositional settings that, in turn, determined the dominant kerogen types preserved. Indeed, it is this cyclicity, alternating organic-rich and organic-lean intervals, that is used as the basis for delineating Green River Formation stratigraphy in the central portions of the basin (Vanden Berg, 2008).

Given the paucity of measured vitrinite reflectance (R_o) values for the Green River Formation, Tmax from programmed pyrolysis is the only widely available indicator of thermal maturity. Tmax values for cores in the western half of the basin are in the "early oil" and "peak oil" maturity windows (Fig. 3-27) as delimited by Peters and Cassa (1994). Just a few samples fall into the "late oil" field. Average Tmax values for the cores, other than Marsing 16, are in the range 486°C to 456°C (Table 5-1). The Green and Black Shale intervals in Marsing 16 with average values of 434°C and 437°C, respectively, are at the threshold into the "early oil" generative window. Tmax values from cuttings reported by Anders and Gerrild (1984) from the greater Altamont-Bluebell area (Fig. 3-3) are in the same range as the more recent analyses from cores: Dustin 1 (451°C), Cedar Rim 3 (451°C), and Ute Tribal 1-6 (453°C).

In Figure 3-27, we observe a curious, counterintuitive inversion of Tmax values in that the shallower samples (higher elevations) are the more mature, whereas the deeper samples are less mature. It is significant that the wells with the shallower and more mature Tmax values are in the southwest portion of the basin close to the Book Cliffs. What we are seeing is evidence for northward tilting of the Green River section following the imprint of maximum thermal maturity. Given that generation of hydrocarbons is simulated to have continued into the late Pliocene-Pleistocene, this tilting and erosional stripping of the southwest corner of the basin presumably is very recent. One plausible explanation for this northward tilt is isostatic rebound of the entire northern portion of the Colorado Plateau, including the San Rafael Swell and the present south rim of the Uinta Basin, due to exhumation of all or large parts of the thick Mesozoic section once burying the area south of the Uinta Basin.

The thermal maturity indicated from Tmax values is lower than that predicted from the thermal maturation simulations presented in Chapter 4 and discussed above. It is possible that the heat flow value of 52 mW/m^2 used for the simulations was unrealistically high, even though it represented the low end of present-day measured heat flow in the Uinta Basin. A lower paleo-heat flow for the rapidly filling sedimentary basin is plausible, as would be a higher value during the present. Recent, rapid erosional unroofing of the basin would result in a temporarily distorted thermal profile that would yield a higher-than-historic heat flow value.

Alternatively, the Tmax value thresholds for the thermal maturation windows from Peters and Cassa (1994) might not be relevant for the lacustrine source rocks of the Green River

Formation. For instance, it has been shown that the onset of oil generation for the hydrogen-rich (Type I-II) Bakken Shale is reached at Tmax of 425°C, and that by 450°C, the source rock is passing into the wet gas generative window (Jin and Sonnenberg, 2012). The onset of oil generation in the marine Type 2-S Monterey Shale kerogen is at even lower maturities, Tmax in the 410° to 425° range (Jarvie, 2012). However, as discussed in Chapter 3, the reaction kinetics for the Green River hydrogen-rich (Type I) source rocks may be such that the onset of oil generation is delayed to about 0.75% R_o (Ruble and others, 2001: Lewan and Roy, 2010). The peak of oil generation would be at the equivalent of about 1.0 R_o and oil and gas generation would occur together over a relatively narrow generative window. A separate gas generative window, if even relevant in the Green River organic-rich mudstones, would have been reached only in the very deepest parts of the Uinta Basin, if at all. If, indeed, Green River Type I kerogens have a delayed entry into the oil generative window, then the maturity windows would be expected to shift towards higher Tmax thresholds, not lower ones.

When the thermal maturity of a Type I or Type II kerogen increases, the HI decreases. As oil is generated, hydrogen is concentrated in the hydrocarbon phase, which generally is expelled from the source rock, thus depleting its hydrogen. The decrease in HI tracks the increase in transformation ratio to the point where the remaining kerogen and any residual oil cracks into natural gas. Low HI values are associated with the gas generative window. This is reflected in the maturity trajectories commonly shown in Van Krevelen plots (Fig. 3-1) for the different kerogen types. A cross plot of Tmax vs. HI is a convenient tool for examining the decline in HI with increasing source rock maturation. However, such a plot for the 222 core analysis in the western basin (Fig. 5-1) fails to demonstrate any obvious decrease in HI with increasing thermal maturity, as measured by Tmax. There is a very large scatter in HI values. The very high HI values in the "early mature" window are from cores (Marsing 16 and Norling 1-9B1) that have generated at least some petroleum.

As discussed in Chapter 3, very few samples of Green River core have OSI values greater than the 80–100 range, the empirical threshold for oil to be readily expelled from the source rock (Jarvie, 2012). At lower OSI values, liquid hydrocarbon is retained in the rock, largely by sorption to kerogen or trapped behind nanno-pore throats. However, a majority of the core samples have OSI values that fall just below this threshold (Fig. 5-2). The average OSI for the cores in Table 5-1 range from 32 to 86, but with large standard deviations. This observation raises the interesting possibility that during programmed pyrolysis runs this residual oil is advancing the appearance of the S2 peak, thereby resulting in a lower than expected Tmax value. The "bound oil" is not expelled as "free oil" at lower temperatures to form the S1 peak, but it could be released during kerogen pyrolysis that forms the S2 peak. Such "bound oil" could also result in a larger S2 peak and thereby a larger HI value than what would be generated

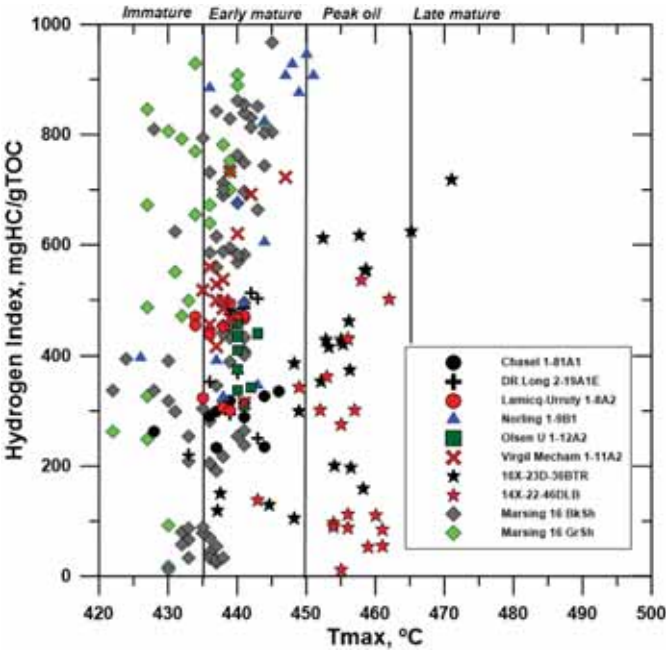

Figure 5-1: *Programmed pyrolysis Tmax values plotted against hydrogen index for core samples of Green River Formation source rocks in the western Uinta Basin. The vertical lines are thermal maturity thresholds for Tmax values reported in Peters and Cassa (1994).*

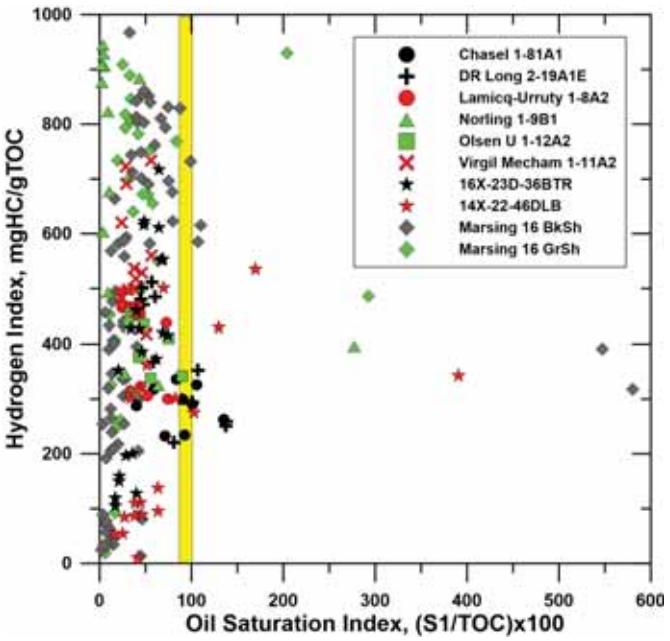

Figure 5-2: *Programmed pyrolysis oil saturation index (OSI) values plotted against hydrogen index for core samples of Green River Formation source rocks in the western Uinta Basin. The vertical yellow bar is the empirical threshold for retention of oil in tight source rocks (Jarvie, 2012). Higher OSI values are one of the key characteristics of productive shale oil plays.*

by the kerogen alone. If so, this could also account for the anomalously low Production Index (PI) readings, less than 0.1, for many of the Green River core samples (Fig. 5-3). HI derived from programmed pyrolysis is (S2/TOC) x 100; PI = S1/(S1 + S2). Larger S2 values increase HI, but decrease PI. Jin and Sonnenberg (2012) also report substantial quantities of residual oil in the organic-rich mudstones of the Bakken Shale. In the absence of an independent measure of thermal maturity, such as vitrinite reflectance, this explanation for slightly lower than expected Tmax thermal maturities remains a "working hypothesis". However, it is possible that due to the presence of "bound oil", Tmax values of 425° and 450°C approximate the actual limits for the oil generative window in the Green River Formation. This would be more consistent with the known petroleum characteristics of the formation and the thermal maturation simulations using the heat flow value of 52 mW/m^2.

A very important observation derived from the programmed pyrolysis data (Fig. 5-2 and Table 5-1) is that the Green River organic-rich mudstones have OSI values that are too low to make them candidates for a self-sourcing shale oil reservoir. What oil they contain is "bound oil", not free to migrate readily from rock to well, even when the rock is fracture stimulated. As discussed in Chapter 3, the few high values of OSI (Table 5-1) are likely associated with thin, relatively porous, commonly-fractured, oil-impregnated interbeds within the source rock intervals, as shown in Figures 3-17 and 3-26. These more porous, permeable and brittle beds are the potentially productive oil reservoirs.

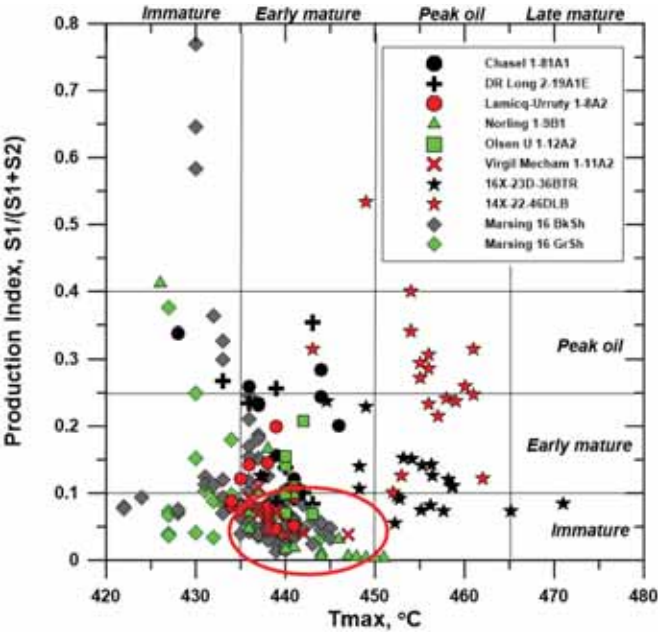

Figure 5-3: *Programmed pyrolysis Tmax values plotted against production index (PI) for core samples of Green River Formation source rocks in the western Uinta Basin. The vertical and horizontal lines are thermal maturity thresholds for Tmax and PI values, respectively, as reported in Peters and Cassa (1994). The red ellipse highlights the cluster of anomalously low PI values.*

Typically, shale oil resource plays are discovered by drilling and appropriate well completions, not through the study of cores. The scientific investigations follow production and serve the purpose of targeting "sweet spots" and enhancing recovery. This is likely to be the situation with the Green River Formation in the Uinta Basin as well. Within and along the margins of the greater Altamont-Bluebell field, several operators have been finding success with intensive hydraulic fracture completions and have begun to exploit specific reservoir targets with horizontal wells, even within what can be regarded as "source rock" intervals. If the formation responds in a way that would be expected of a typical shale oil resource play, for all intents and purposes, it is one.

The Cedar Rim and Altamont fields (Fig. 5-4) were delineated in 1969 and 1970; the Bluebell field is just a decade older. Only a few years later, Lucas and Drexler (1973) identified the Altamont-Bluebell field as an *"oil accumulation near the center of a deep basin"*, an example of a then newly-recognized *"group of deep-basin, organic-shale-related, overpressured accumulations"* having significant hydrocarbon potential. They attribute to the Altamont-Bluebell field characteristics that subsequently have come to identify a basin-centered, continuous resource play. These include:

- difficulty in defining field limits laterally and vertically because the trap is stratigraphic with no simple down-dip water levels or facies boundaries to the productive horizons,
- multiple thin productive zones with abnormally high fluid pressures, and
- very low matrix porosities enhanced by post-lithification fractures.

The initial development of the Altamont-Bluebell field was by vertical wells targeting sandstone lenses encased in red mudstone in the Wasatch Formation and lacustrine carbonate and sandstone beds intercalated with organic-rich dark mudstone in the lower Green River Formation. On 320 acre spacing, wells were completed by perforating target horizons and using light acid treatments to stimulate flow. Typically, 12 to 35 Wasatch and 10 to 20 Green River intervals, each 3 to 30 feet thick, were perforated in a section totaling 1800 to 3000 feet thick (Smouse, 1993). The reservoir targets have low porosity, averaging 10%, very low permeability, and required natural fractures for both storage and good deliverability. The wells produced a medium to light high-wax oil and large quantities of associated natural gas comingled from the many completed intervals. Solution gas drive was aided by the abnormally high initial formation pressures. Regardless of the number of zones perforated and acid treated in each well, production tests indicated that generally fewer than 10 beds actually produce (Montgomery and Morgan, 1998). The Cedar Rim field has the same naturally-fractured Wasatch and lower Green River reservoirs and general characteristics as the western Altamont field, but production is shallower and the GORs are

higher, up to 13,000 (Eckels, 1993). In the greater Altamont-Bluebell district, all wells drilled through the lower Green River Formation and into the overpressured interval were producers (Smouse, 1993). However, within a decade or two, the fields were in decline and had been abandoned by their initial operators.

Over the past decade, several mid-size independent petroleum companies, new players in the Uinta Basin, have rediscovered the Green River-Wasatch continuous oil play. They have entered the basin armed with new technologies, massive slickwater fracture stimulation and horizontal drilling. In the four years beginning 2010, the year this study was first proposed, there has been a boom in oil and associated gas development within and along the southern margins of the Altamont-Bluebell fields (Fig. 5-4). Most, but certainly not all, of the new activity has been focused in the region of anomalous formation pressure in the range of 0.5 to 0.7 psi/ft. Activity has been most intense in two new fields, Lake Canyon, established in 2006, and North Myton Bench, formed in 2009. In this period (through September 2013), a total of 617 new wells have either gone into production (231 wells), been spudded (64 wells), or have been approved (322 wells). The result has been a dramatic increase in oil and associated natural gas production (Table 5-2). The greater Altamont-Bluebell fields have had a 154% increase in oil production. The North Myton Bench field has grown from no production in 2009 to over 2.1 million barrels in just four years. In just five years, there was more than a thousand-fold increase in the Lake Canyon field. In large measure, the increase in production has been made

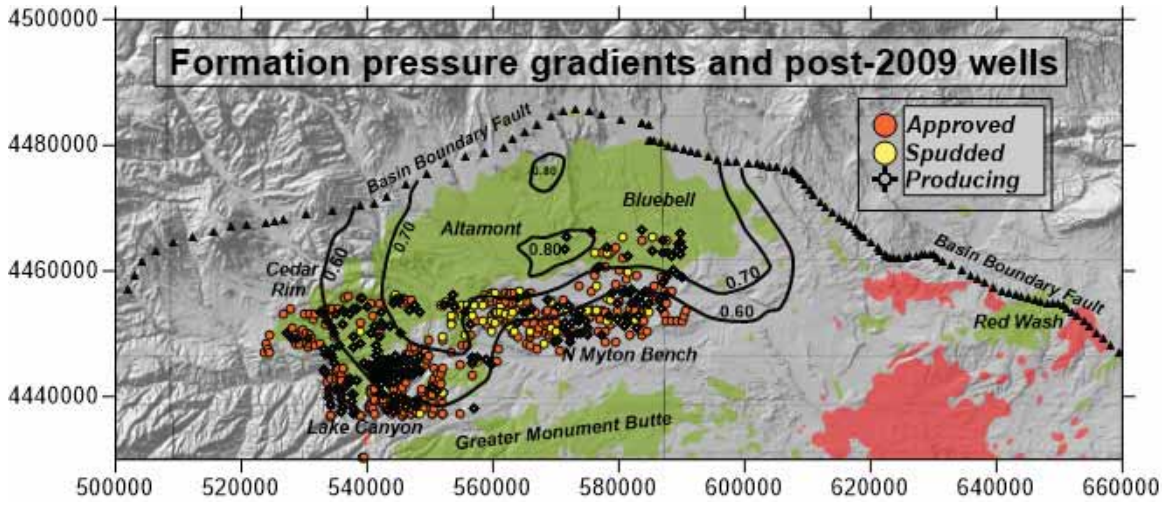

Figure 5-4: *Distribution of wells that were brought into production, spudded or approved in the period 2010 through mid-2013 in 12 townships along the south and southwest margin of the overpressured greater Altamont-Bluebell field. The new wells shown are mainly in the North Myton Bench, the Lake Canyon, and the Blacktail Ridge portion of the Cedar Rim fields. The overpressure isopleths (psi/ft) are from Lucas and Drexler (1973) and the well locations and status as of June 2013 are from Utah DOGM. The geographic coordinates are meters in UTM NAD83, Zone 12.*

Table 5-2: *Contrasting annual oil production 2009 to 2013 for the group of fields within the region of elevated formation pressures (greater Altamont-Bluebell) and those to the south (greater Monument Butte) that produce from essentially the same general Green River–Wasatch reservoirs. The 2013 natural gas production as barrels-of-oil equivalent (BOe) show the relative contributions of gas in the two groups of fields. Data from Utah DOGM.*

Field	*2013*	*2009*	*%diff*	*Gas: 2013 BOe*	*O+G: 2013 BOe*	*%gas*
Altamont	4,297,355	1,707,755	151.6	2,133,867	6,431,222	33.2
Bluebell	3,038,643	2,216,758	37.1	803,978	3,842,621	20.9
Cedar Rim	419,331	113,779	268.5	238,932	658,263	36.3
Lake Canyon	482,574	30,303	1492.5	311,277	793,851	39.2
N Myton Bench	2,101,854	0		450,896	2,552,750	17.7
Total	***10,339,757***	***4,068,595***	***154.1***	***3,938,951***	***14,278,708***	***27.6***
Monument Butte	5,078,350	4,647,015	9.3	1,365,650	6,444,000	21.2
Brundage Canyon	1,501,768	1,155,487	30	1,806,471	3,308,239	54.6
Antelop Creek	682,449	180,993	277.1	143,940	826,389	17.4
S Myton Bench	185,825	54,461	241.2	575,954	761,779	75.6
Total	***7,448,392***	***6,037,956***	***23.4***	***3,892,015***	***11,340,407***	***34.3***

possible by the expansion in the number of drill sites occupied due to progressive down-spacing from 320 acre to 160 acre and, more recently, to 80 acre. These fields also produce substantial quantities of natural gas. In 2013, on a barrels-of-oil equivalence (BOe), natural gas contributed over a quarter of the production from the greater Altamont-Bluebell fields and a third of the production from the greater Monument Butte fields (Table 5-2).

Fracture stimulation completions are being made in fewer, more carefully selected, intervals than were perforated in the older wells. Still, the new wells are being completed in many of the same multiple zones within the Green River and Wasatch Formations. For instance, the vertical Bar F 1-20-3-2 well (API 4301350009) in the North Myton Bench field was completed with six fracture stimulation stages, two in Wasatch sandstone intervals, two in the Uteland Butte limestone-sandstone, and two in the Castle Peak limestone-sandstone (source: DOGM well file). The geologic report for the Evans 1-4-3-3 well (API 4301350561), also in the North Myton Bench field, identifies multiple fractured "oil shale" oil shows on the order of many tens of feet thickness in the Middle and Lower Green River Members, shows in the Bar F Sandstone (15 ft of pay, 13% porosity) and Uteland Butte beds (19 ft of pay, 14% porosity) in the Lower Green River Member, and 65 ft of net pay (13% porosity) in Wasatch sandstones. The pay zones were identified from logs and resistivity values greater than 40 ohms. As in the past, the porous and brittle Uteland Butte carbonate-siliciclastic interval at the base of the Green River Formation is a favored reservoir target for both vertical and horizontal well completions (Vanden Berg and others, 2013).

Virtually all of the recent vertical wells are completed in both the lower Green River Formation, generally the Uteland Butte member and a few other relatively porous and/or brittle intervals, and the underlying Wasatch sandstones. The presence of overpressured reservoir targets appears to be a requisite for locating and designing the well. All wells are fracture stimulated, normally with multistage, large slickwater treatments, but after a year or so of natural flow, the wells must be put on artificial lift production of oil and associated natural gas from all intervals is comingled, making it impossible to associate production with specific completed intervals. It is observed that within one to three years, a well's production rates drop off by an order of magnitude or more. The decline curves are hyperbolic, as would be expected of fractured, but otherwise tight, reservoir intervals. The decline curves for the recent, fracture-stimulated wells are similar to the older, pre-2000 wells, at least as far as can be observed in the shorter time of record (source: randomly selected DOGM records for groups of wells listed in Digital Appendix D). Production characteristics are similar by other measures, as well. For instance, the gas-oil ratios (GOR) and water-oil ratios (WOR) of the older and younger group of wells are indistinguishable (Fig. 5-5). The very recent horizontal wells may, in time, display different declines, but after two years of production, for instance, the 14-3-45 BTR well (API 4301350676) cited by Vanden Berg and others (2013) has seen an order of magnitude decrease in both oil and gas rates, similar to the recent vertical wells.

As more of the shale oil plays receive close scrutiny, it is becoming clear that no two are the same with regards to character of source rock or reservoir. What they all have in common,

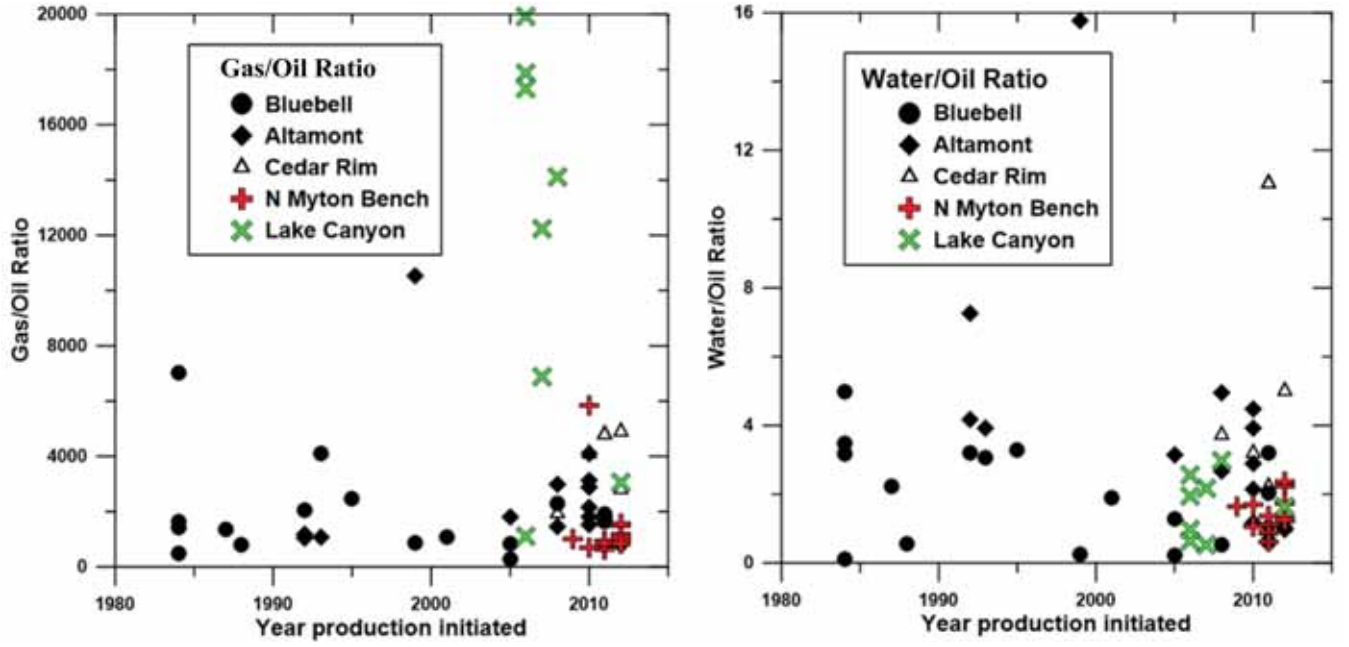

Figure 5-5: *Gas/oil and water/oil ratios for representative production wells drilled over a 30-year period of time from 1984 to 2013. The cumulative ratios through mid-2013 are plotted against the year that production was initiated. The very high gas/oil ratios observed in the Lake Canyon field are also reflected in the very high portion of total production from this field that is natural gas (see Table 5-2). Data is from Utah DOGM; see Digital Appendix D for the data for specific wells.*

however, is (1) an unusually organic-carbon-rich source rock capable of generating large volumes of oil, (2) interbedded or proximal reservoir intervals that, although tight, have sufficient porosity and/or natural fractures to be capable of hosting commercially significant volumes of the producible oil, and (3) inefficient carrier systems resulting in the oil generated remaining in proximity to the oil-generative source rock. The presence of anomalous formation pressures appears necessary to drive the oil from reservoir to well bore, even when fracture stimulated. These are "self-sourcing" petroleum systems only when viewed on a scale that encompasses the entire source rock formation and its immediately adjacent strata, or a significant portion thereof. And so it is with the Green River Formation, which has both an internal "self-sourcing" continuous oil play within the oil generative window and conventional oil accumulations on its periphery. Due to the lenticular character of the sandstone and carbonate beds in the Green River Formation and the underlying Wasatch Formation, some beds trap oil locally, while others carry the oil up-dip into traps at a distance from the oil generative window.

In the short-run, at least, the success of the newly rediscovered Green River continuous oil play may be due more to downspacing to a higher density of wells than to the application of new well completion technologies, such as fracture stimulation and horizontal drilling. As has been observed in other "shale oil" plays with wells having similar hyperbolic declines, such as the Eagle Ford and Bakken, the pace of drilling activity must be maintained in order to support high overall field production. It remains to be seen if the application of the new technologies results in higher ultimate recoveries per well than has been observed in the first group of vertical wells drilled in the Altamont-Bluebell field over three decades ago. It could be that fracture stimulated horizontal wells are necessary to compensate for the lower anomalous formation pressures along the outer margins of the Green River shale oil play.

ACKNOWLEDGMENTS

This study received generous matching funds from the Utah Geological Survey's *Characterization of Utah's Hydrocarbon Reservoirs, Metals, and Industrial Minerals* – FY 2012 solicitation. Michael Vanden Berg was the Survey's contract manager for the project.

Many persons aided the study with valuable advice and data: Jim Borer (Cimarex Energy), Marc Eckels (Wind River Resources), Dan Jarvie (Texas Christian University), Michael Lewan (U.S. Geological Survey), Tim Ruble (Weatherford), Doug Sprinkel (Utah Geological Survey), Michael Vanden Berg (Utah Geological Survey), and Stephen Wells (El Paso E&P).

Special gratitude is expressed to Dr. Jay Leonard, President of Platte River Associates for the temporary loan of licenses for BasinMod-1D and BasinView-3D to use for simulating the thermal maturity of the Green River Formation. Access to these powerful analytical tools greatly enhanced the project. Nancy Hunter and Michelle Hayhurst, both with Platte River Resources, provided essential technical and logistic support during the basin modeling phase of the study.

REFERENCES

Anders, D.E., and Gerrild, P.M., 1984, Hydrocarbon generation in lacustrine rocks of Tertiary age, Uinta Basin, Utah—Organic carbon, pyrolysis yield, and light hydrocarbons, *in* Woodward, J., Meissner, F.F., and Clayton, J.L., editors, Hydrocarbon Source Rocks of the Greater Rocky Mountain Region: Rocky Mountain Association of Geologists, p. 513–529.

Anders, D.E., Palacas, J.G., and Johnson, R.C., 1992, Thermal maturity of rocks and hydrocarbon deposits, Uinta Basin, Utah, *in* Fouch, T.D., Nuccio, V.F., and Chidsey, T.C., Jr., editors, Hydrocarbon and Mineral Resources of the Uinta Basin, Utah and Colorado: Utah Geological Association 1992 Field Symposium, p. 53–76.

Bergenheier, L.P., and Vanden Berg, M.D., 2011, Core-based integrated sedimentologic, stratigraphic, and geochemical analysis of the oil shale bearing Green River Formation, Uinta Basin, Utah: U.S. Department of Energy National Energy Technology Laboratory, Document DE-FE0001243, p. 19.

Berggren, W.A., and Prothero, D.R., 1992, Eocene-Oligocene climatic and biotic evolution—an overview, *in* Prothero, D.R., and Berggren, W.A., editors, Eocene-Oligocene Climatic and Biotic Evolution: Princeton University Press, p. 1–28.

Bohacs, K.M., Carroll, A.R., and Neal, J.E., 2003, Lessons from large lake systems—thresholds, nonlinearity, and strange attractors, *in* Chan, M.A., and Archer, A.W., editors, Extreme Depositional Environments: Mega End Members in Geologic Time: Geological Society of America Special Paper 370, p. 75–90.

Bredehoeft, J.D., Wesley, J.B., and Fouch, T.D., 1994, Simulation of the origin of fluid pressure, fracture generation, and the movement of fluids in the Uinta basin, Utah: American Association of Petroleum Geologists Bulletin, v. 78, p. 1729–1747.

Bryant, B., 2010, Geologic map of the east half of the Salt Lake City 1° x 2° quadrangle (Duchesne and Kings Peak 30′ x 60′ quadrangles), Duchesne, Summit, and Wasatch Counties, Utah, and Uinta County, Wyoming (1:125,000): Utah Geological Survey Miscellaneous Publication 10-1DM, 2 sheets.

Carroll, A.R., and Bohacs, K.M., 2001, Lake-type controls on petroleum source rock potential in nonmarine basins: American Association of Petroleum Geologists Bulletin,

v. 85, p. 1033–1053.

Carroll, A.R., and Wartes, M.A., 2003, Organic carbon burial by large Permian lakes, northwest China, *in* Chan, M.A., and Archer, A.W., editors, Extreme Depositional Environments: Mega End Members in Geologic Time: Geological Society of America Special Paper 370, p. 91–104.

Castle, J.W., 1990, Sedimentation in Eocene Lake Uinta (lower Green River Formation), northeastern Uinta Basin, Utah, *in* Katz, B.J., editor, Lacustrine Basin Exploration—Case Studies and Modern Analogues: American Association of Petroleum Geologists Memoir 50, p. 243–263.

Chapman, D.S., Keho, T.H., Bauer, M.S., and Picard, M.D., 1984, Heat flow in the Uinta Basin determined from bottom hole temperature (BHT) data: Geophysics, v. 49, p. 453–466.

Dean, W.E., and Anders, D.E., 1991, Effects of source, depositional environment, and diagenesis on characteristics of orgainic matter in oil shale from the Green River Formation, Wyoming, Utah, and Colorado, *in* Tuttle, M.L., editor, Geochemical, Biogeochemical, and Sedimentological Studies of the Green River Formation, Wyoming, Utah, and Colorado: U. S. Geological Survey Bulletin 1973, p. F1–F16.

Dubiel, R.F., 2003, Geology, depositional models, and oil and gas assessment of the Green River Total Petroleum System, Uinta-Piceance Province, eastern Utah and western Colorado, Petroleum Systems and Geologic Assessment of Oil and Gas in the Uinta-Piceance Province, Utah and Colorado: U.S. Geological Survey Digital Data Series DDS-69-B, Chapter 5, p. 1–41.

Eckels, M.T., Cedar Rim, 1993, *in* Hill, B.G., and Bereskin, S.R., editors, Oil and Gas Fields of Utah: Utah Geological Association, Salt Lake City, Utah, unpaginated.

England, W.A., 1994, Secondary migeration and accumulation of hydrocarbons, *in* Magoon, L.B., and Dow, W.G., editors, The Petroleum System—from Source to Trap: American Association of Petroleum Geologists Memoir 60, p. 211–217.

Fleet, A.J., Kelts, K.R., and Talbot, M.R., 1988, Lacustrine Petroleum Source Rocks: Geological Society of London Special Publication 40, 391 p.

Fouch, T.D., Nuccio, V.F., Anders, D.E., Rice, D.D., Pitman, J.K., and Mast, R.F., 1994, Green River (!) petroleum system, Uinta Basin, Utah, U.S.A. *in* Magoon, L.B., and Dow, W.G., editors, The Petroleum System—from Source to Trap: American Association of Petroleum Geologists Memoir 60, p. 399–421.

Fouch, T.D., Nuccio, V.F., Osmond, J.C., MacMillan, L., Cashion, W.B., and Wandrey, C.J., 1992, Oil and gas in uppermost Cretaceous and Tertiary rock, Uinta Basin, Utah, *in* Fouch, T.D., Nuccio, V.F., and Chidsey, T.C., Jr., editors, Hydrocarbon and Mineral Resources of the Uinta Basin, Utah and Colorado: Utah Geological Association 1992 Field Symposium, p. 9–47.

Franczyk, K.J., Fouch, T.D., Johnson, R.C., Molenaar, C.M., and Cobban, W.A., 1992, Cretaceous and Tertiary paleogeographic reconstructions for the Uinta-Piceance basin study area, Colorado and Utah, Evolution of Sedimentary Basins—Uinta and Piceance Basins: U.S. Geological Survey Bulletin 1787, p. Q1–Q37.

Hansen, W.R., 1986, Neogene tectonics and geomorphology of the eastern Uinta Mountains in Utah, Colorado, and Wyoming: U.S. Geological Survey Professional Paper 1356, 78 p.

Jarvie, D.M., 2012, Shale resource systems for oil and gas: Part 2—Shale-oil resource systems, *in* Breyer, J.A., editor, Shale reservoirs—Giant resources for the 21st century: American Association of Petroleum Geologists Memoir 97, p. 89–119.

Jarvie, D.M., Coskey, R.J., Johnson, M.S., and Leonard, J.E., 2011, The geology and geochemistry of the Parshall area, Mountrail County, North Dakota, *in* Robinson, J.W., LeFever, J.A., and Gaswirth, S.B., editors, Bakken-Three Forks Petroleum System in the Williston Basin: Rocky Mountain Association of Geologists, p. 229–281.

Jin, H., and Sonnenberg, S.A., 2012, Source rock potential of the Bakken Shales in the Williston Basin, North Dakota and Montana: American Association of Petroleum Geologists Annual Convention and Exhibition, Long Beach, CA, April 22–25, 2012, www.searchanddiscovery.com/documents/2012/20156jin/nix_jin.pdx.

Johnson, R.C., 2003, Northwest to southeast cross section of Cretaceous and Lower Tertiary rocks across the eastern part of the Uinta Basin, Utah, Petroleum Systems and Geologic Assessment of Oil and Gas in the Uinta-Piceance Province, Utah and Colorado: U. S. Geological Survey Digital Data Series DDS-69-B, Chapter 11, p. 1–6.

Johnson, R.C., and Roberts, L.N.R., 2003, Depths to selected stratigraphic horizons in oil and gas wells for Upper Cretaceous and Lower Tertiary strata of the Uinta basin, Utah, Petroleum Systems and Geologic Assessment of Oil and Gas in the Uinta-Piceance Province, Utah and Colorado: U. S. Geological Survey Digital Data Series DDS-69-B, Chapter 13, p. 1–30.

Katz, B.J., 1990, Lacustrine Basin Exploration: American Association of Petroleum Geologists Memoir 50, 340 p.

Katz, B. J., 1995, The Green River Shale: an Eocene carbonate lacustrine source rock, *in* Katz, B.J., editor, Petroleum Source Rocks: Berlin, Springer Verlag, p. 309–324.

Keighley, D.G., and Flint, S.S., 2008, Fluvial sandbody geometry and connectivity in the middle Green River Formation, Nine Mile Canyon, southwestern Uinta basin, *in* Longman, M.W., and Morgan, C.D., editors, Hydrocarbon Systems and Production in the Uinta Basin, Utah: Rocky Mountain Association of Geologists – Utah Geological Association Publication 37, p. 101–119.

Keighley, D., Flint, S., Howell, J., Andersson, D., Collins, S., Moscariello, A., and Stone, G., 2002, Surface and subsur-

face correlation of the Green River Formation in central Nine Mile Canyon, SW Uinta Basin, Carbon and Duchesne Counties, east-central Utah: Utah Geological Survey Miscellaneous Publication 02-1, unpaginated.

Kelso, B.S., and Eherenzeller, J.L., 2008, Petroleum geology of the Brundage Canyon oil field, Southern Tertiary Oil Trend, Uinta basin, *in* Longman, M.W., and Morgan, C. D., editors, Hydrocarbon Systems and Production in the Uinta Basin, Utah: Rocky Mountain Association of Geologists – Utah Geological Association Publication 37, p. 283–302.

Kowallis, B.J., Christiansen, E.H., Balls, E., Heizler, M.T., and Sprinkel, D.A., 2005, The Bishop Conglomerate Ash Beds, south flank of the Uinta Mountains, Utah—Are they pyroclastic fall beds from the Oligocene ignimbrites of western Utah and eastern Nevada?, *in* Dehler, C.M., Pederson, J.L., Sprinkel, D.A., and Kowallis, B.J., editors, Uinta Mountain Geology: Utah Geological Association Publication 33, p. 131–145.

Law, B.E., and Spencer, C.W., 1998, Abnormal pressure in hydrocarbon environments, *in* Law, B.E., Ulmshek, G.F., and Slavin, V.I., editors, Abnormal Pressures in Hydrocarbon Environments: American Association of Petroleum Geologists Memoir 70, p. 1–11.

Lewan, M.D., and Roy, S., 2010, Role of water in hydrocarbon generation from Type-I kerogen in Mahogany oil shale of the Green River Formation: Organic Geochemistry, v. 42, p. 31–41.

Lillis, P.G., Warden, A., and King, J.D., 2003, Petroleum systems of the Uinta and Piceance basins—Geochemical characteristics of oil types, Petroleum Systems and Geologic Assessment of Oil and Gas in the Uinta-Piceance Province, Utah and Colorado: U. S. Geological Survey Digital Data Series DDS-69-B, Chapter 3, p. 1–25.

Lucas, P.T., and Drexler, J.M., 1975, Altamont-Bluebell—A major fractured and overpressured stratigraphic trap, Uinta Basin, Utah, in Bolyard, D.W., editor, Symposium on Deep Drilling Frontiers in the Central Rocky Mountains: Rocky Mountain Association of Geologists, p. 265–273.

Mann, U., 1994, An integrated approach to the study of primary petroleum migration, *in* Parnell, J., editor, Geofluids: Origin, Migration and Evolution of Fluids in Sedimentary Basins: Geological Society of London Special Publication 78, p. 233–260.

Montgomery, S.L., and Morgan, C.D., 1998, Bluebell field, Uinta Basin—reservoir characterization for improved well completion and oil recovery: American Association of Petroleum Geologists Bulletin, v. 82, p. 1113–1132.

Morgan, C.D., 2003, The Bluebell Oil Field, Uinta Basin, Duchesne and Uintah Counties, Utah: Characterization and Oil Well Demonstration: Utah Geological Survey Special Study 106, 95 p.

Morgan, C.D., 2008, Greater Monument Butte oil field: Infill drilling results and potential CO_2 enhanced oil recovery, *in* Longman, M.W., and Morgan, C.D., editors, Hydrocarbon Systems and Production in the Uinta Basin, Utah: Rocky Mountain Association of Geologists – Utah Geological Association Publication 37, p. 303–318.

Morgan, C.D., Chidsey, T.C., Jr., McClure, K.P., Bereskin, S.R., and Deo, M.D., 2003, Reservoir characterization of the Lower Green River Formation, Uinta Basin, Utah: Utah Geological Survey Open-File Report 411, 140 p.

Murphey, P.C., Townsend, K.E.B., Friscia, A.R., and Evanoff, E., 2011, Paleontology and stratigraphy of middle Eocene rock units in the Bridger and Uinta Basins, Wyoming and Utah, *in* Lee, J., and Evans, J.P., editors, Geologic Field Trips to the Basin and Range, Rocky Mountains, Snake River Plain, and Terranes of the U.S. Cordillera: Geological Society of America Field Guide 21, p. 125–166.

Nelson, P.H., 2002, Subsurface fluid pressures from drill-stem tests, Uinta basin, Utah: The Mountain Geologist, v. 39, p. 17–26.

Nelson, P.H., 2003, Subsurface pressures from drill-stem tests, Uinta and Piceance Basins, Utah and Colorado, Petroleum Systems and Geologic Assessment of Oil and Gas in the Uinta-Piceance Province, Utah and Colorado: U.S. Geological Survey Digital Data Series DDS-69-B, Chapter 14, p. 1–32.

Noble, R.A., Kaldo, J.G., and Atkinson, C.D., 1997, Oil saturation in shales—Applications in seal evaluation, *in* Surdam, R.C., editor, Seals, Traps, and the Petroleum System: American Association of Petroleum Geologists Memoir 67, p. 13–29.

Nuccio, V.F., and Roberts, L.N.R., 2003, Thermal maturity and oil and gas generation history of petroleum systems in the Uinta-Piceance Province, Utah and Colorado, Petroleum Systems and Geologic Assessment of Oil and Gas in the Uinta-Piceance Province, Utah and Colorado: U. S. Geological Survey Digital Data Series DDS-69-B, Chapter 4, p. 1–35.

Nuccio, V.F., Schmoker, J.W., and Fouch, T.D., 1992, Thermal maturity, porosity, and lithofacies relationships applied to gas generation and production in Cretaceous and Tertiary low-permeability (tight) sanstone, Uinta basin, Utah, *in* Fouch, T.D., Nuccio, V.F., and Chidsey, T.C., Jr., editors, Hydrocarbon and Mineral Resources of the Uinta Basin, Utah and Colorado: Utah Geological Association Guidebook 20, p. 77–93.

Ogg, J.G., Ogg, G., and Gradstein, F.M., 2008, The Concise Geologic Time Scale: Cambridge University Press, 177 p.

Pederson, J.L., and Hadder, K.W., 2005, Revisiting the classic conundrum of the Green River's integration through the Uinta uplift, *in* Dehler, C.M., Pederson, J.L., Sprinkel, D.A., and Kowallis, B.J., editors, Uinta Mountain Geology: Utah Geological Association Publication 33, p. 149–154.

Pepper, A.S., 1991, Estimating the petroleum expulsion behavior of source rocks: a novel quantitative approach, *in*

England, W.A., and Fleet, A.J., editors, Petroleum Migration: Special Publication of Geological Society London, v. 59, p. 9–31.

Peters, K.E., and Cassa, M.R., 1994, Applied source rock geochemistry, *in* Magoon, L.B., and Dow, W.G., editors, The Petroleum System—from Source to Trap: American Association of Petroleum Geologists Memoir 60, p. 93–120.

Picard, M.D., Thompson, W.D., and Williamson, C.R., 1973, Petrology, geochemistry and stratigraphy of Black Shale Facies of Green River Formation (Eocene), Uinta Basin, Utah: Utah Geological and Mineralogical Survey Bulletin 100, 52 p.

Prothero, D.R., 1996, Magnetic stratigraphy and biostratigraphy of the middle Eocene Uinta Formation, Uinta Basin, Utah, *in* Prothero, D.R., and Emry, R.J., editors, The Terrestrial Eocene-Oligocene Transition in North America: Cambridge University Press, p. 3–24.

Prothero, D.R., and Swisher, III, C.C., 1992, Magnetostratigraphy and geochronology of the terrestrial Eocene-Oligocene transition in North America, *in* Prothero, D.R., and Berggren, W.A., editors, Eocene-Oligocene Climatic and Biotic Evolution: Princeton University Press, p. 46–73.

Remy, R.R., 1992, Stratigraphy of the Eocene part of the Green River Formation in the south-central part of the Uinta Basin, Utah: U.S. Geological Survey Bulletin 1787, p. BB1–BB25.

Rice, D.D., Fouch, T.D., and Johnson, R.C., 1992, Influence of source rock type, thermal maturity, and migration of composition and distribution of natural gases, Uinta Basin, Utah, *in* Fouch, T.D., Nuccio, V.F., and Chidsey, T.C., Jr., editors, Hydrocarbon and Mineral Resources of the Uinta Basin, Utah and Colorado: Utah Geological Association 1992 Field Symposium, p. 95–109.

Robinson, W.E., and Cook, G.L., 1975, Compositional variations of organic material from Green River oil shale—WOSCO EX-1 core (Utah): U.S. Bureau of Mines Report of Investigations 8017, 40 p.

Rowley, P.D., Hansen, W.R., Tweto, O., and Carrara, P.E., 1985, Geologic map of the Vernal 1° x 2° quadrangle, Colorado, Utah, and Wyoming (1:250,000): U.S. Geological Survey.

Ruble, T.E., Bakel, A.J., and Philp, R.P., 1994, Compound-specific isotopic variability in Uinta Basin native bitumens: paleoenvironmental implications: Organic Geochemistry, v. 21, p. 661–671.

Ruble, T.E., Lewan, M.D., and Philp, R.P., 2001, New insights on the Green River petroleum system in the Uinta basin from hydrous pyrolysis experiments: American Association of Petroleum Geologists Bulletin, v. 85, p. 1333–1371.

Ruble, T.E., and Philp, R.P., 1998, Stratigraphy, depositional environments and organic geochemistry of source-rocks in the Green River petroleum system, Uinta basin, Utah, *in* Pitman, J.K., and Carroll, A.R., editors, Modern and Ancient Lake Systems—New Problems and Perspectives: Utah Geological Association Guidebook 25, p. 289–328.

Ryder, R.T., Fouch, T. D., and Elison, J. H., 1976, Early Tertiary sedimentation in the western Uinta Basin, Utah: Geological Society of America Bulletin, v. 87, p. 496–512.

Schamel, S., 2005, Shale Gas Reservoirs of Utah: Survey of an Unexploited Potential Energy Resource: Utah Geological Survey Open-File Report 461, 114 p.

Schamel, S., 2009, Shale gas potential of the Paradox Basin, Colorado and Utah, *in* Houston, W.S., Wray, L.L., and Moreland, P.G., editors, The Paradox Basin Revisited—New Developments in Petroleum Systems and Basin Analysis: Rocky Mountain Association of Geologists Special Publication, p. 568–603.

Schamel, S., 2013, Unconventional oil resources of the Uinta Basin, Utah, *in* Hein, F.J., Leckie, D., Larter, S., and Suter, J.R., editors, Heavy-Oil and Oil-Sand Petroleum Systems in Alberta and Beyond: American Association of Petroleum Geologists Studies in Geology 64, p. 437–480.

Smith, M.E., Carroll, A.R., and Mueller, E.R., 2008a, Elevated weathering rates in the Rocky Mountains during the Early Eocene Climatic Optimum: Nature Geoscience, p. 370–374.

Smith, M.E., Carroll, A.R., and Singer, B.S., 2008b, Synoptic reconstruction of a major ancient lake system: Eocene Green River Formation, western United States: Geological Society of America Bulletin, v. 120, p. 54–84.

Smouse, D., 1993, Altamont-Bluebell, *in* Hill, B.G., and Bereskin, S.R., editors, Oil and Gas Fields of Utah: Utah Geological Association, Salt Lake City, Utah, unpaginated.

Sonnenberg, S.A., 2010, The Bakken petroleum system of the Williston Basin—a tight oil resource play: Hart Energy Shale Oil Webinar, March 2, 2010.

Sonnenberg, S.A., 2011, The Niobrara petroleum system—a new resource play in the Rocky Mountain Region, *in* Estes-Jackson, J.E., and Anderson, D.S., editors, Revisiting and Revitalizing the Niobrara in the Central Rockies: Denver, Colorado, Rocky Mountain Association of Geologists, p. 13–32.

Spencer, C.W., 1987, Hydrocarbon generation as a mechanism for overpressuring in Rocky Mountain region: American Association of Petroleum Geologists Bulletin, v. 71, no. 4, p. 368–388.

Sprinkel, D.A., 2006, Interim geologic map of the Dutch John 30′ x 60′ quadrangle, Daggett and Uintah Counties, Utah, Moffat County, Colorado, and Sweetwater County, Wyoming (1:100,000): Utah Geological Survey Open-File Report 491DM, 3 Plates.

Sprinkel, D.A., 2007, Interim geologic map of the Vernal 30′ x 60′ quadrangle, Uintah and Duchesne Counties, Utah, and Moffat and Rio Blanco Counties, Colorado

(1:100,000): Utah Geological Survey Open-File Report 506DM, 3 Plates.

Sprinkel, D.A., 2009, Interim geologic map of the Seep Ridge 30′ x 60′ quadrangle, Uintah, Duchesne, and Carbon Counties, Utah, and Rio Blanco and Garfield Counties, Colorado (1:100,000): Utah Geological Survey Open-File Report 549DM, 3 Plates.

Sprinkel, D.A., Sharp, W., and Schamel, S., 2013, New insights into the timing of exhumation of the Uinta Basin and mountain-front retreat of the Uinta Mountains, Utah: 2013 American Association of Petroleum Geologists Rocky Mountain Section Meeting, Salt Lake City, Utah, 22–24 September, 2013.

Stone, D.S., 1977, Tectonic history of the Uncompaghre uplift, in Exploration Frontiers of the Central and Southern Rockies: Denver, Rocky Mountain Association of Geologists Guidebook, p. 23–30.

Swarbrick, R.E., Osborne, M.J., and Yardley, G.S, 2002, Comparison of overpressure magnitude resulting from the main generating mechanisms, *in* Huffman, A.R., and Bowers, G.L., editors, Pressure Regimes in Sedimentary Basins and Their Prediction: American Association of Petroleum Geologists Memoir 76, p. 1–12.

Sweeney, J.J., 1988, Application of maturation indicators and oil reaction kinetics to put constraints on thermal history models for the Uinta Basin, Utah, U.S.A.: Organic Geochemistry, v. 13, p. 199–205.

Thompson, W.D., 1971, Stratigraphy of black-shale facies of Green River Formation (Eocene), Uinta Basin, Utah: M.S. Thesis, University of Utah, 122 p.

USGS Uinta-Piceance Assessment Team, 2003, Petroleum systems and geologic assessment of oil and gas in the Uinta-Piceance Province, Utah and Colorado: US Geological Survey Digital Data Series DDS-69-B.

Vanden Berg, M.D., 2008, Basin-wide evaluation of the uppermost Green River Formation's oil-shale resource, Uinta Basin, Utah and Colorado: Utah Geological Survey Special Study 128, 19 p.

Vanden Berg, M.D., Morgan, C.D., Chidsey, T.C, Jr., and Nielsen, P., 2013, The Uteland Butte Member of the Eocene Green River Formation—an emerging unconventional carbonate tight oil play in the Uinta Basin, Utah: American Association of Petroleum Geologists Annual Convention & Exhibition, May 19–22, 2013, Pittsburgh, PA.

Waples, D.W., 1994, Maturity modeling: Thermal indicators, hydrocarbon generation, and oil cracking, *in* Magoon, L.B., and Dow, W.G., editors, The Petroleum System—from Source to Trap: American Association of Petroleum Geologists Memoir 60, p. 285–306.

Weiss, M.P., Witkind, I.J., and Cashion, W.B., 2003, Geologic map of the Price 30′ x 60′ quadrangle, Carbon, Duchesne, Uintah, Utah, and Wasatch Counties, Utah (1:100,000): Utah Geological Survey Map 198DM.

Wiggins, W.D., and Harris, P.M., 1994, Lithofacies, depositional cycles, and stratigraphy of the lower Green River Formation, southwestern Uinta Basin, Utah Notes for SEPM Core Workshop: Lacustrine Source-Rock Depositional Environments, American Association of Petroleum Geologists Annual Convention, Denver, June 11, 1994, SEPM, p. 105–141.

Appendix II

Geological, Geochemical, and Reservoir Characterization of the Uteland Butte Member of the Green River Formation, Uinta Basin, Utah

Justin E. Birdwell[1], Michael D. Vanden Berg[2], Ronald C. Johnson[1], Tracey J. Mercier[1], Adam R. Boehlke[1], and Michael E. Brownfield[1]

[1]U.S. Geological Survey, Denver, CO
[2]Utah Geological Survey, Salt Lake City, UT

Published in:
Dolan, M.P., Higley, D.K., and Lillis, P.G., editors, Hydrocarbon Source Rocks in Unconventional Plays, Rocky Mountain Region: Rocky Mountain Association of Geologists

Geological, Geochemical, and Reservoir Characterization of the Uteland Butte Member of the Green River Formation, Uinta Basin, Utah[1]

JUSTIN E. BIRDWELL[2], MICHAEL D. VANDEN BERG[3], RONALD C. JOHNSON[2], TRACEY J. MERCIER[2], ADAM R. BOEHLKE[2], MICHAEL E. BROWNFIELD[2]

1. Manuscript received March 18, 2015; Accepted June 29, 2015
2. U.S. Geological Survey, Central Energy Resources Science Center, Denver, CO 80225
3. Utah Geological Survey, 1594 W. North Temple, Suite 3110, Salt Lake City, UT 84114

ABSTRACT

The informal Uteland Butte member of the lower part of the Green River Formation was deposited in a major transgressive phase of the early freshwater stage of Eocene Lake Uinta, in the Uinta Basin. It ranges in thickness from around 50 to over 300 ft and contains primarily limestone, dolostone, and organic-rich mudstone and siltstone, with sandstone and ostracodal limestone in marginal areas. The Uteland Butte member is age-equivalent to part of the freshwater Cow Ridge Member of the Green River in the Piceance Basin of Colorado and may correspond to the freshwater Luman Tongue of the Green River in the Greater Green River Basin of Wyoming and Colorado. Of these intervals, only the Uteland Butte was buried deep enough to have resulted in a major petroleum system. Since late 2010, the Uteland Butte has become a successful tight-oil play, with total cumulative oil production of about 4.38 million barrels (as of December 2014) and initial well production ranging from less than 100 up to 1,700 barrels of oil equivalent per day, all produced through the use of horizontal drilling, hydraulic fracturing, and acid treatment in dolomite-rich target zones. Most horizontally drilled laterals in the Uteland Butte average about 5,000 ft, but a few of the more recent wells have reached over 11,000 ft. Organic-rich mudstone, siltstone, and limestone are likely the source of oil in the Uteland Butte, and thin, highly porous dolostones are the primary reservoirs targeted with horizontal drilling.

Uteland Butte oils are generally very waxy and have API gravities ranging between 30° and 40°. The oils are also low in sulfur (<0.3 wt. %) and isotopically light with $\delta^{13}C$ values for saturate and aromatic fractions between -29 and -33 ‰. Molecular parameters show that the Uteland Butte oils are derived from similar organic material as other Green River Formation oils produced in the Uinta Basin. Immature outcrop samples from the eastern and western margins of the basin were examined to obtain estimates of original organic content and kerogen quality for Uteland Butte source rocks. The organic matter in these outcrop samples is predominantly Type I kerogen, but is somewhat less hydrogen-rich than the kerogen present in overlying oil shale deposited during brackish- to saline-lake phases of the Green River Formation based on Rock-Eval hydrogen indices. In core samples, Uteland Butte rocks are in the oil generation window based on a variety of thermal maturity indicators. Basinwide organic richness was examined using historical Fischer assay data. The samples with the highest oil yields occur just to the west of an overpressured region. Chloroform-extractable organic matter content from high-porosity samples from dolomitic intervals is up to four times that of the adjacent mudstones. The thickness of dolomite beds in the Uteland Butte is nonuniform through the stratigraphic interval and is an important factor for production potential due to its high porosity and petroleum content, as determined by Rock-Eval parameters and soxhlet extraction. Formation pressures vary from normal to possibly underpressured in shallow areas, to moderately overpressured along the deep basin trough. In general, wells in the overpressured area are the most productive. Assessment units were defined using basinwide data on organic richness, thermal maturity, and dolomite content, including an overpressured sweet spot in the most productive part of the basin.

INTRODUCTION

The informal Uteland Butte member (Osmond, 1992) of the Eocene Green River Formation in the Uinta Basin of northeastern Utah resulted from a major transgression of an early freshwater stage of Lake Uinta. This lacustrine interval was deposited prior to the main saline-lacustrine oil shale sequence of the Green River Formation and was not included as part of the recently completed Uinta Basin oil shale assessment (Johnson et al., 2010). The successful development of the Uteland Butte as a tight-oil play using modern horizontal drilling and hydraulic fracturing combined with acid treatment (Anderson and Roesink, 2013; Durham, 2013; Vanden Berg et al., 2014) has led to renewed interest in the unconventional resource potential of lacustrine basins and provides a potential analog for other lacustrine plays. Prior to the recent horizontal drilling, the Uteland Butte was a commonly perforated interval along with many other zones in the Green River Formation, but was rarely a primary target for drilling. Based on production data from late 2010 through the end of 2014, the Uteland Butte has produced approximately 4.38 million barrels of high-API gravity, paraffinic crude oil and 7.34 billion cubic ft of natural gas using these new production techniques (5.65 million barrels of oil equivalent, MMBOE; Utah Division of Oil, Gas, and Mining, 2015).

This study incorporates a wide range of data relevant to production from the Uteland Butte member in order to better characterize this little-studied interval of the Green River Formation in the Uinta Basin and to assess the factors that influence oil production. Fischer assay oil-yield data for the Uteland Butte member in the U.S. Geological Survey (USGS) Oil Shale Assessment database (Johnson et al., 2010) are used to identify the organic-rich areas of the unit. Literature data on the thermal maturity of hydrocarbon deposits in the Uinta Basin (Anders et al., 1992) are examined and compared with recent data collected on Uteland Butte cores and then utilized to delineate areas where Uteland Butte member organic-rich shale can be expected to be thermally mature. Pressure data from drillstem tests for wells completed in the Uteland Butte and in adjacent units were collected and are utilized along with recently published mud weight data (Anderson and Roesink, 2013) to estimate the distribution of overpressure within the Uteland Butte play (Johnson, 2014). Production histories from horizontal wells collected by the Utah Division of Oil, Gas, and Mining (2015) have been examined as part of a recent USGS assessment of the Uteland Butte play (Johnson et al., 2015a) and are used to help define assessment units (AUs) and possible areas of higher production or "sweet spots" in order to relate other properties to that production. It should be noted that the historical vertical drilling data in this area is of little use for examining the producibility of the Uteland Butte, as these tests were completed in multiple lacustrine intervals and it is unclear how much oil was produced from any particular reservoir rock.

Analysis of Uteland Butte member rock characteristics (e.g., porosity, permeability, lithology and mineralogy, and organic geochemistry) derived from core samples obtained from companies operating Uteland Butte wells and the Utah and U.S. Geological Surveys provide the basis for this report. Produced-oil samples from wells and extractable organic matter (EOM) collected from Uteland Butte rocks were also examined, characterized and compared to other Uinta Basin oils. Results from this work are used to evaluate the importance of dolomitic intervals within the Uteland Butte to the productivity of the play.

Although the Piceance and Greater Green River Basins contain freshwater lacustrine rocks similar to those of the Uteland Butte member, only in the Uinta Basin was

subsidence after deposition of the organic-rich lacustrine interval sufficient to have facilitated the creation of a substantial petroleum system. In addition to the unique high thermal maturity of the freshwater Uteland Butte member, it also contains porous dolomite intervals that serve as reservoirs and horizontal drilling targets and may not be present in equivalent sequences in the other principal basins of the Green River Formation.

METHODS

Two Uteland Butte cores, 14-1-46 BTR (sec. 1, T. 4 S., R. 6 W.) and 14-3-45 BTR (sec. 3, T. 4. S., R. 5 W.), were donated along with geochemical and geophysical data to the Utah Geological Survey by the Bill Barrett Corporation (Denver, CO). The data from these cores are presented herein, supplemented with additional analyses conducted on samples collected from these cores by USGS personnel. Rock porosity, permeability, and X-ray diffraction (XRD) analyses of samples from these cores were performed by Core Laboratories (Houston, TX). Conventional plug-analysis protocols were used to determine porosity, using a Boyle's Law technique in which grain volume was measured at ambient conditions and pore volume under confining stress, and permeability to air was measured on plugs using an unsteady-state method under confining stress. XRD analyses were conducted on two size-fractions, greater than and less than 20 microns (μm), to determine bulk mineralogy and clay mineralogy using a Core Laboratories in-house method. Rock-Eval and total organic carbon (TOC) analyses were conducted by Geomark Research Ltd. (Humble, TX) using a Rock-Eval 2 instrument (Delsi Inc., Houston, TX) and a LECO® C230 analyzer (LECO® Corporation, St. Joseph, MI), respectively.

Outcrop samples collected by USGS personnel in August 2014 at the White River section (Colorado, sec. 11, T. 1 N., R. 103 W.) were screened using infrared spectroscopy to obtain qualitative information on organic richness and mineralogy. Selected samples were then submitted for Rock-Eval and TOC analysis. Organic geochemistry data for another outcrop sample (930922-1) from the Willow Creek–Indian Canyon outcrop (Utah, sec. 27, T. 11 S., R. 10 E.; Ruble and Philp, 1998) were reported by Ruble (1996) and Ruble et al. (2001) and are included herein for comparison with data from the White River outcrop. The sample from Willow Creek and all of the White River samples were characterized using whole-pattern XRD and analysis of clay separates. Mineral phases were quantified using the Jade® and ClaySim® software packages (Material Data, Inc., Livermore, CA). Whole-pattern fitting in Jade® was used to estimate major and minor mineral weight percentages based on Rietveldt refinement with an internal 20 wt. % corundum standard. Clay mineral phases were identified by XRD analysis of oriented mounts of the <2-μm fraction from each sample following treatment with sodium hypochlorite to remove organic matter. ClaySim® was then used to quantify the amount of each clay mineral present in the whole-rock samples.

Extractable organic matter (EOM) was collected from pulverized core samples using soxhlet extraction with chloroform. Four Uteland Butte member and two Green River Formation (one comingled and one from the Parachute Creek Member of the Green River) oil samples were donated to the USGS by the Bill Barrett Corporation. The oils and EOM samples were characterized to determine C_{15+} saturate-aromatic-resin-asphaltene (SARA) fractions and whole-oil, saturate, and aromatic fraction gas chromatograms and carbon-13 isotopic compositions. API gravity, total C_{15-} volatiles, and sulfur content were also determined on the oil samples. All analyses were performed by the USGS Organic Geochemistry Laboratory (Denver, CO) using methods available online (U.S. Geological Survey Energy Resources Program, 2015).

Fischer assay analyses conducted on samples from the Uteland Butte member were extracted from the USGS Oil Shale Assessment database for the Uinta Basin (Johnson et al., 2010). The Fischer assay method is a standardized laboratory tool for determining oil, water, and gas yield from oil shale (Stanfield and Frost, 1949; American Society for Testing Materials, 1984). A source rock or oil shale sample is crushed and sieved to -8 mesh (<2.38 mm) and a 100 g (0.22 lbs.) aliquot is heated to 500 °C (932 °F) at a rate of 12 °C/min and held at that temperature for 40 minutes. Oil and water vapor generated during pyrolysis are cooled and collected along with the spent shale. Gas generation is determined by the difference between the original sample mass and the sum of the oil, water, and spent rock collected and is designated as gas+loss. When sufficient oil is generated the specific gravity is measured and used to determine the oil yield in gallons per ton (GPT).

GEOLOGIC SETTING AND BACKGROUND

The Paleocene and Eocene Flagstaff Member of the Green River Formation underlies the Uteland Butte and is the oldest lacustrine unit in the Uinta Basin that may have potential as an unconventional petroleum resource play. The Uteland Butte and Flagstaff are separated by the fluvial Colton Formation in marginal areas of the lacustrine interval. Organic-rich shale in the Flagstaff Member is considered to be one of the sources for oil produced out of the Altamont-Bluebell field (Tissot et al., 1978; Fouch et al., 1994; Morgan et al., 2003a) and marginal lacustrine rocks from the Flagstaff Member are productive in that field. The Flagstaff phase of Lake Uinta formed through the coalescence of isolated lakes in the underlying and intertonguing alluvial and paludal Upper Cretaceous to Eocene North Horn Formation (Fouch, 1975). The first descriptions of the Flagstaff Member were on the Wasatch Plateau by Spieker and Reeside (1925) and Spieker (1946, 1949). The Flagstaff Member has been traced in outcrop in the western part of the Uinta Basin (Spieker, 1949) and eastward to near outcrops of the Upper Cretaceous and lower Tertiary strata along the Green River (Fischer et al., 1960). Farther to the east, the Flagstaff appears to grade into sandstone and shale. The Flagstaff has been traced in the subsurface throughout much of the western Uinta Basin by Ryder et al. (1976) and the eastern part of the basin by Johnson (1985) where, at maximum transgression, it extended to within a few miles of the crest of the Douglas Creek arch. Throughout most of its history, however, the lake during Flagstaff time was confined to the trough of the Uinta Basin south of the rising Uinta uplift. The Flagstaff Member in the western Uinta Basin depositionally grades from the lake margins to lake center and lithologically from (1) interbedded sandstone, siltstone, gray calcareous claystone, algal coal, and oncolytic carbonate, to (2) gray, highly fossiliferous mud- and grain-supported limestone, and then to (3) dark-gray, mud-supported limestone (Ryder et al., 1976).

The freshwater lacustrine interval, later informally named the Uteland Butte limestone by Osmond (1992), was first studied by Bradley (1931) when he measured and described a detailed section of these rocks at an exposure in Indian Canyon in the western part of the Uinta Basin. The "basal tongue of the Green River Formation" was the informal name that was applied to this interval by Bradley (1931). There are about 200 ft of Uteland Butte rocks at Indian Canyon, consisting primarily of flaky shales and marlstones containing ostracodes, pelecypods, and gastropods, and are separated from overlying lacustrine rocks by a 380 ft-thick tongue of fluvial Wasatch or Colton Formations.

The majority of the recent horizontal drilling in the Uinta Basin has targeted the Uteland Butte member. This interval represents the most expansive period of the freshwater lacustrine phase of Lake Uinta. It is believed to be equivalent to the most expansive period of the freshwater Cow Ridge Member of the Green River Formation in the Piceance Basin (Johnson, 1985) and the Luman Tongue of the Green River Formation in the Greater Green River Basin (Horsfield et al., 1994). The freshwater lacustrine unit was referred to as the "Uteland Butte limestone" in the subsurface after the Uteland Butte field (Osmond, 1992) and has subsequently been designated the Uteland Butte member. Folsom (1968) also used the term Uteland Butte member to describe a gas-productive, lower Tertiary interval that sourced the Uteland Butte field, but did not attribute it to the Green River Formation. Lithologies found in the Uteland Butte include limestone, dolostone, calcareous mudstone, and occasional sandstone (Morgan et al., 2003b). It has been suggested that the lack of sandstone may have been caused by rapid lake-level rise leading to siliciclastic sediments being deposited in proximal stream channels (Morgan et al., 2003b).

The approximate maximum extent of the offshore carbonate and shale facies of the Uteland Butte member is shown in Figure 1. The true maximum extent of the lake during deposition of the Uteland Butte is not currently known. The resemblance of the marginal lacustrine facies to floodplain rocks has made it difficult to map the extent of that facies based on geophysical logs and the limited availability of lithological descriptions. Figure 2 provides a simplified well log and core log that includes the Uteland Butte interval.

The Uteland Butte member has been described in detail at three localities in the Uinta Basin where it crops out west of the crest of the Douglas Creek arch (Cashion, 1967; Johnson et al., 1988). Two of these locales, the Evacuation Creek and White River sections (Fig. 1), were revisited in August 2014 and the White River section was described as a new outcrop that was better exposed than the one previously studied (Johnson et al., 1988). The lower part (19.5 ft) of the White River section consists of dark-brown, organic-rich

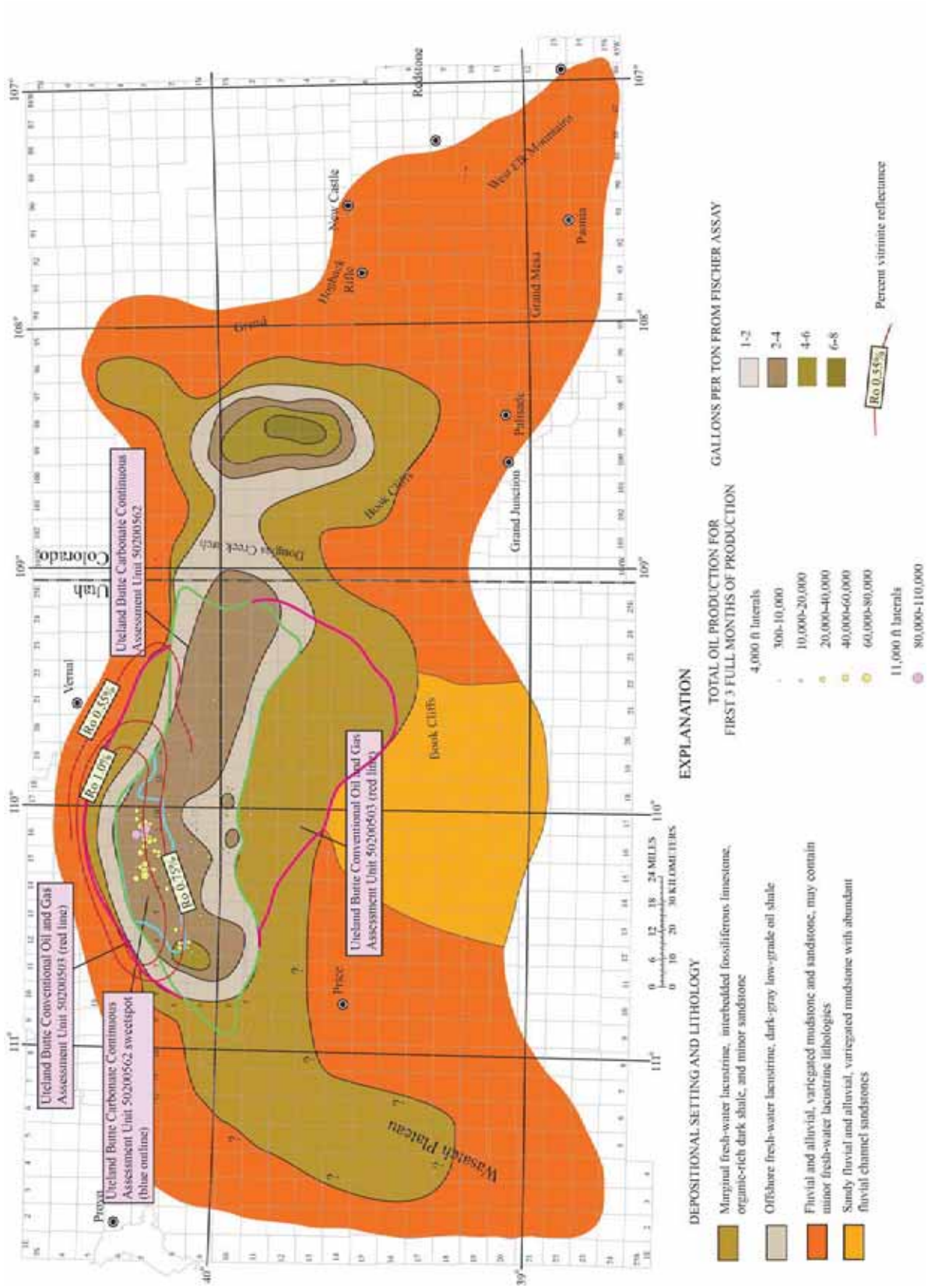

Figure 1. Map of Uteland Butte assessment units showing major lithologies, outcrop features, production data, organic richness (based on Fischer assay), thermal maturity (Ro isopach contours in feet [red line]), overpressured area (shaded pink), and assessment units (thick green and pink lines). ft, feet

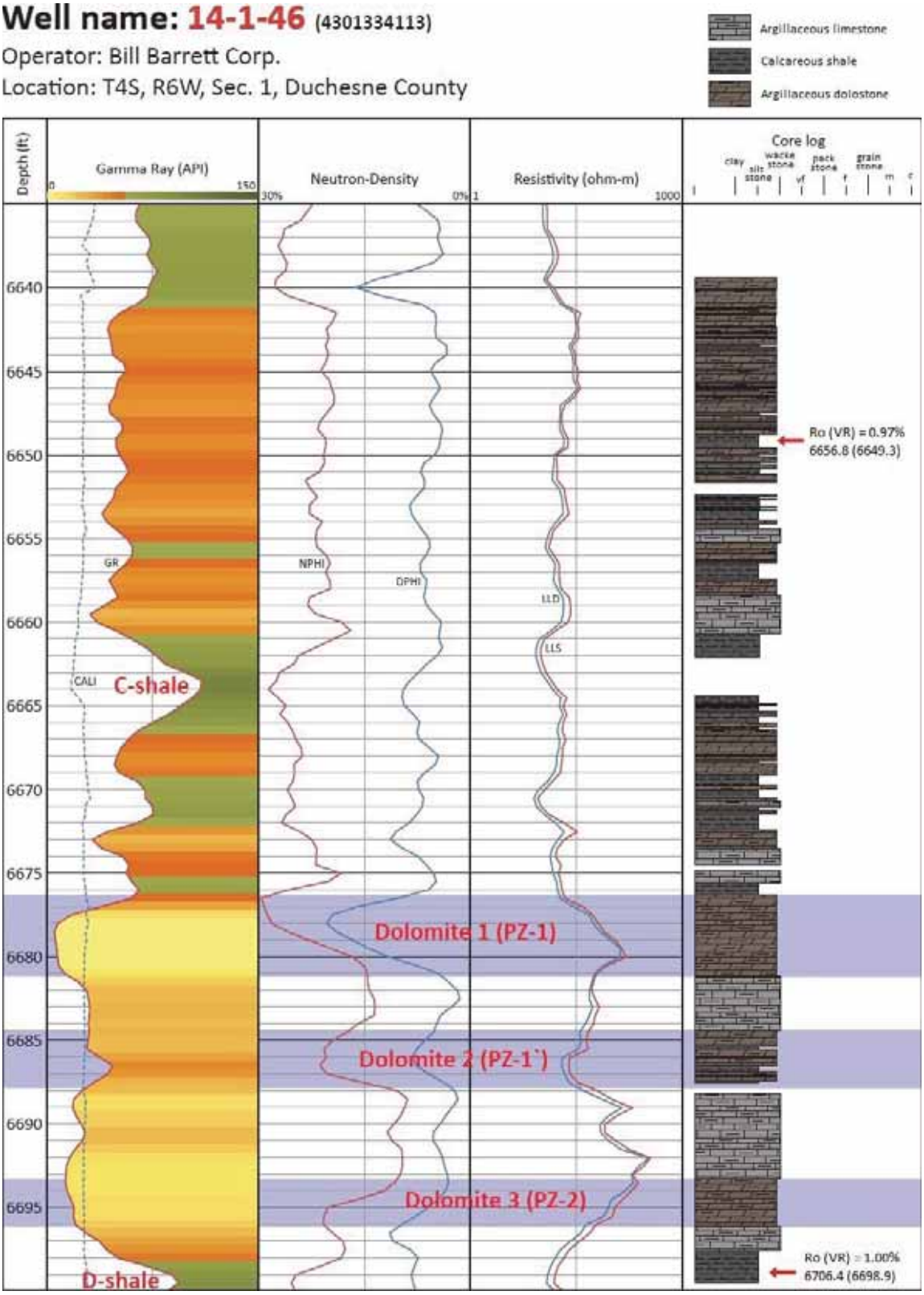

Figure 2. Well logs (gamma-ray, density, neutron porosity, and resistivity) for Uteland Butte well 14-1-46 (API 43-013-34113).

shale, white shell beds of freshwater mollusks, and one discontinuous stromatolite bed. This interval appears to directly overlie variegated mudstones deposited in an alluvial plain environment and was not exposed at the original site described by Johnson et al. (1988). It has been noted that oolite and oncolite beds are common in the freshwater lacustrine interval of the Uinta Basin (Johnson, 1985) and that occasionally stromatolite beds are observed in marginal rocks of the Uteland Butte member. Because stromatolites generally do not develop in the presence of grazing gastropods like those identified in beds adjacent to the stromatolite bed at the White River section, this observation indicates that shell beds found in the Uteland Butte member may represent periodic mortality events as the water in the lake varied from fresh to brackish during deposition.

A slightly thicker interval (32.5 ft) of primarily even-bedded ostracode- and mollusk-rich limestone interbedded with gray mudstone overlies the basal interval at the recently described White River section. From around 50 ft to just under 100 ft above the base of the section, intervals of dark limestone interbedded with gray mudstone are present. There is a very fine to fine-grained sandstone layer located between 99 and 112 ft above the base of the section that is the only significant sandstone in the Uteland Butte. A mostly covered interval of medium-gray mudstone and ostracode- and mollusk-bearing limestone is located above the sandstone. The section description ends 112 ft above the base at the approximate top of the lacustrine rock interval. Above this point are mainly variegated mudstones leading up to the Long Point Bed at the base of the R-0 oil shale zone of the Garden Gulch Member of the Green River Formation (Johnson et al., 2010).

Within the Evacuation Creek section there are interbedded limestones, dark shales, and thin very fine to fine-grained sandstones. Limestone beds are commonly micritic and contain ostracodes, oolites, pisolites, gastropods, pelecypods, and other fossil remains. The base of the Uteland Butte at this location consists of an interval of thin, interbedded sandstone and dark shale beds overlying Wasatch Formation variegated mudstones.

CHARACTERIZATION OF CORE AND OUTCROP ROCKS

A summary of the porosity, permeability, mineralogical, and organic geochemical data collected on the Uteland Butte member cores donated by the Bill Barrett Corp. are shown in Figures 3 through 5. Data collected on outcrop samples are summarized in Tables 1 and 2 and included with or alluded to in Figures 4 and 5. In general, the cores consisted of interbedded calcareous shale, limestone, and dolomite. Core samples are representative of distal facies of the Uteland Butte, while the outcrop samples represent proximal facies. The target dolomitized beds (PZ-1 and similar beds, Fig. 2) for most if not all of the horizontal Uteland Butte wells in the basin are highlighted in the figures and located at depths between 6,680 and 6,710 ft in the 14-1-46 BTR core and 7,370 and 7,380 ft in the 14-3-45 BTR core.

Porosity, Permeability, and Mineralogy

A total of 84 porosity and 61 permeability measurements were performed on samples from the two cores. Porosities varied between 1 and 31 volume percent (vol. %) with the majority of samples (n = 58) having values ranging between 3 and 10 vol. %. Permeability values ranged over six orders of magnitude (~20 nanodarcies to 8.59 millidarcies) and were roughly log-normal in their distribution, with a median and average of 0.004 and 0.337 millidarcies (mD), respectively. The permeability cutoff between conventional and continuous petroleum systems is considered to be around 0.1 mD and good overpressure seals are expected to be in the 10^{-5} to 10^{-4} mD range (Williams, 2012). The Uteland Butte permeability values were, for the most part, at or below the 0.1 mD level and several intervals had sufficiently low permeability to be potential overpressure seals.

Figure 3 clearly shows that within the interval of the Uteland Butte examined in these two cores, dolomite and calcite alternate as the dominant mineralogical phases with few exceptions. Total carbonate content ranged from 33 to 96 wt. %, in all but one sample at the bottom of the 14-1-46 BTR core (15.1 wt. %), and the average carbonate content in samples for the two wells was around 70 wt. %. Dolomite and calcite content were inversely related to each other, with most samples showing a clear dominance of one carbonate mineral over the other.

The porosity and permeability variability is reflected between lithofacies as determined by XRD. Figure 3 shows that the highest porosity samples (>20% porosity, n = 3) were all located within the PZ-1 dolomitic interval (66-85% dolomite). Porosity and permeability data were sorted by lithofacies according to dominant mineralogy (calcite, dolomite, or other) for sample depths that included both types of

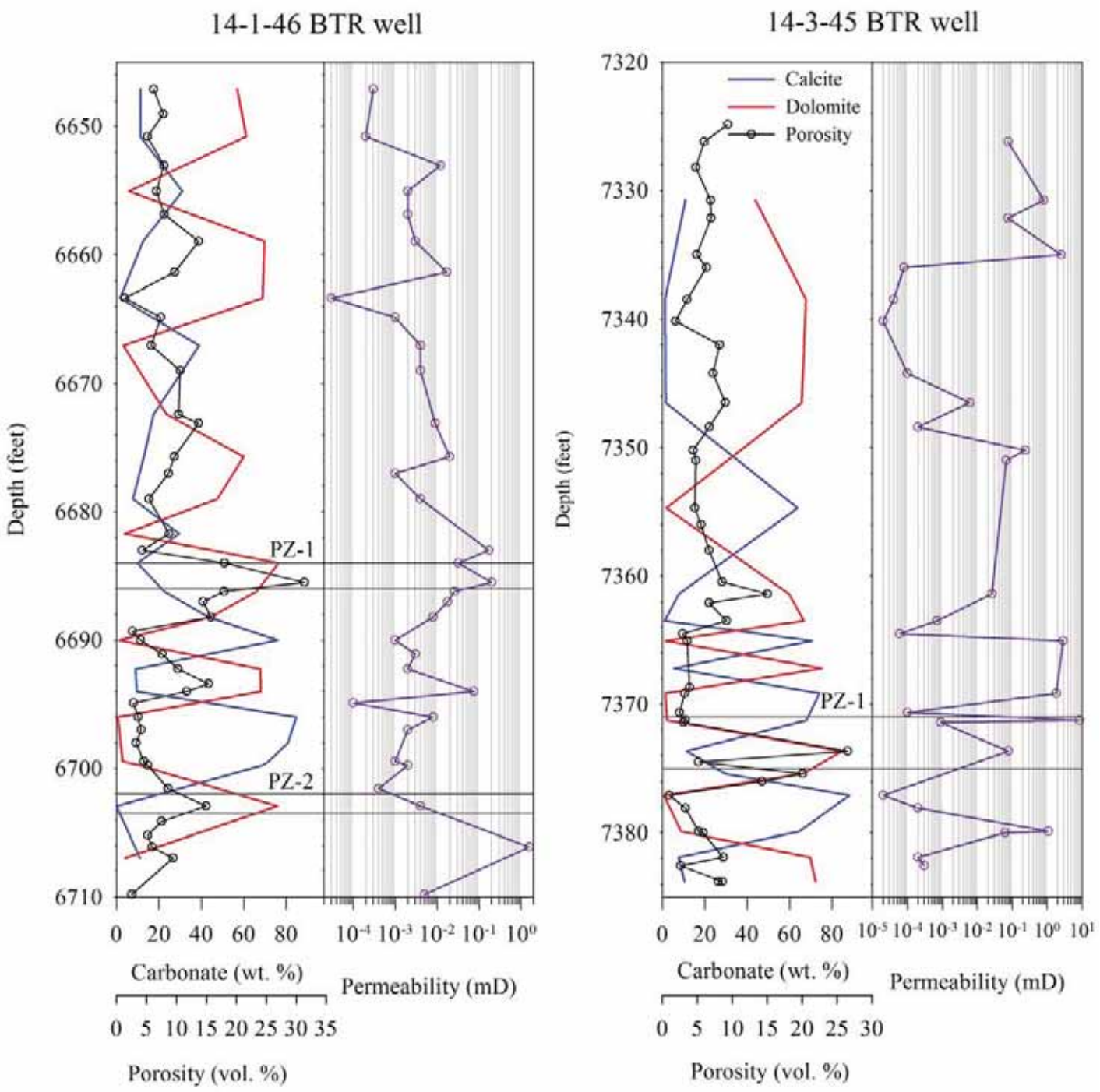

Figure 3. Porosity, permeability, and carbonate mineralogy logs for informal Uteland Butte member cores. mD, millidarcies; vol. %, volume percent; wt. %, weight percent.

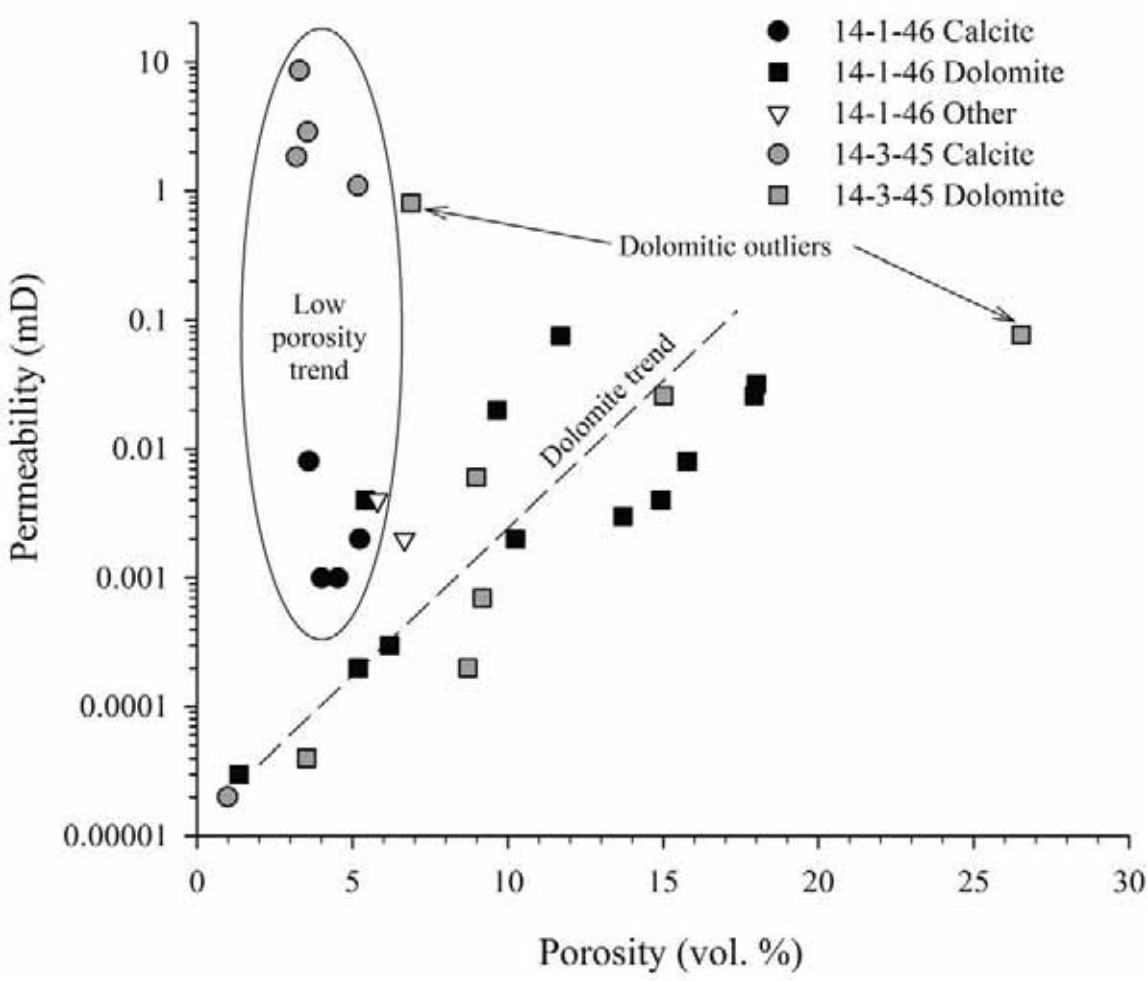

Figure 4. Porosity and permeability data sorted by dominant mineralogy of the sample; the only samples shown are for those depths that included all three measurements. "Other" is the sum of quartz, feldspar, and total clay. mD, millidarcy; vol. %, volume percent void or fluid-filled space.

data. When plotted (Fig. 4), the results indicate two general trends, one with dolomitic samples showing a range of permeability values from 10^{-5} to 0.1 mD and porosity from 1 to 26 %, and calcareous shales showing another range from 10^{-5} to 10 mD, and 1 to 5% porosity. Samples falling into the "other" category (dominated by quartz + feldspar + total clay) plotted in the overlap area between the calcareous and dolomitic trends. All of the high-permeability samples (>0.1 mD, including one dolomitic sample) were from the 14-3-45 BTR well; it is unclear due to the limited sample size if this observation is significant.

The mineralogy of the outcrop samples showed a mix of carbonate and clays, along with quartz and feldspar (Table 1), similar to that observed in the cores. Detailed clay mineralogy showed the common presence of kaolinite, chlorite, and montmorillonite minerals that are generally rare in the saline-brackish phase of the Green River Formation. The presence of these minerals is expected to be related to the particular lake conditions during Uteland Butte time (Dyni, 1976; Yuretich, 1988), but the significance of the mineralogical differences between the freshwater and saline stages of Lake Uinta is currently unclear and requires further study.

Organic Geochemistry

Geochemical logs for the two Uteland Butte member cores are shown in Figure 5 and include XRD mineralogy,

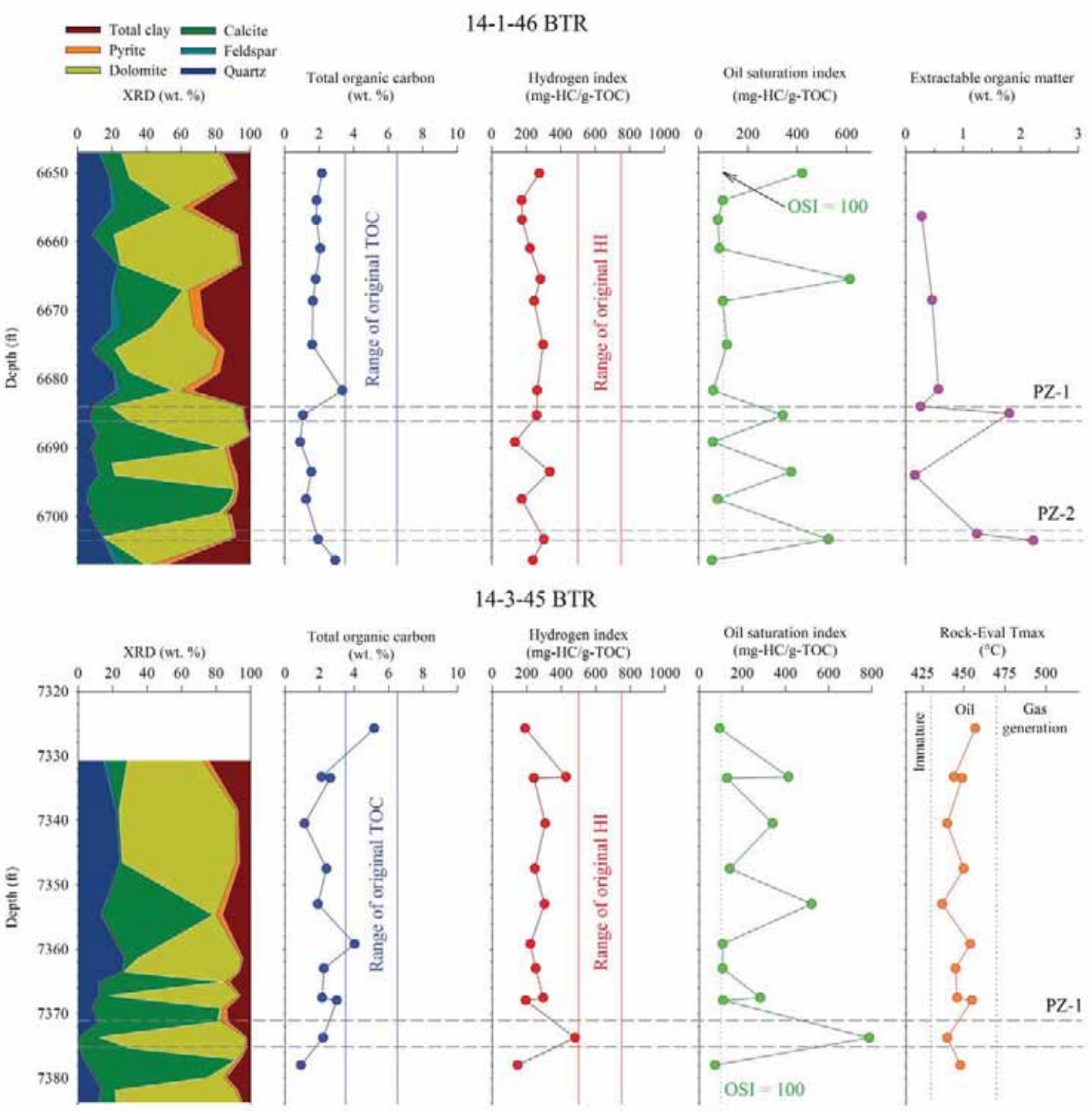

Figure 5. Uteland Butte member core geochemical logs showing quantitative mineralogy (X-ray diffraction, organic-free basis), total organic carbon (TOC) content, Rock-Eval Hydrogen index (HI = S2/TOC×100), Rock-Eval Oil saturation index (OSI = S1/TOC×100), and extractable organic matter content (14-1-46 BTR), and Rock-Eval Tmax (14-3-45 BTR). PZ-1 and PZ-2 are dolomitic intervals targeted for horizontal drilling (see Fig. 2). ft, feet, wt %, weight percent; mg, milligrams.

TABLE 1.

Mineralogy determined by whole-pattern X-ray diffraction and clay separates analysis of thermally immature samples of the informal Uteland Butte member from the White River and Willow Creek–Indian Canyon outcrops. [1]All values are reported as mineral weight percentages on an organic-free basis; [2]illite polytypes; Ca, calcium; Fe, iron; Mg, magnesium; ml, milliliter; no., number.

Sample no.	Quartz[1]	Microcline	Calcite	Aragonite	Mg-Calcite	Dolomite	Pyrite	Gypsum
82614-1-1	21	15	2			7		4
82614-1-2	28	11	7			1		
82614-1-3	20	11	5			16		
82614-1-4	17	8	34			2		
82614-1-5	10	3				71		
82614-1-6	15	6				50		
82614-1-7	24	19				3		2
82614-1-9	14	6	12					1
82614-1-10	24	11	15			2		
82614-1-11	12	1	2			74		
82614-1-13	7	2	85					1
930922-1	8		12	12	58		1	
Sample no.	Kaolinite	Ca-Montmorillonite	Illite 1md[2]	Illite 2m1[2]	Fe-Chlorite	Total Carbonate	Total non-clay	Total clay
82614-1-1	7	17	19	2	7	9	49	52
82614-1-2	11	20	16	1	6	8	47	54
82614-1-3	6	15	19	2	6	21	52	48
82614-1-4	6	12	16	2	5	35	60	40
82614-1-5	3	11		2		71	84	16
82614-1-6	4	13	6	4	3	50	70	30
82614-1-7	7	15	21	3	7	3	48	52
82614-1-9		26	20	11	9	12	33	67
82614-1-10	2	18	21	2	6	17	52	48
82614-1-11		8		3		76	89	11
82614-1-13	1	1	2			85	95	5
930922-1		2	3	2	2	82	90	10

TOC, hydrogen index (HI = S2/TOC×100), oil saturation index (OSI = S1/TOC×100), EOM content (14-1-46 BTR only), and Tmax (14-3-45 BTR only). Data from immature outcrop samples were analyzed to determine the original TOC and HI ranges indicated (Table 2). The immature samples are generally good quality, oil-prone source rocks with TOC contents ranging between ~3 and 6 wt. %, and HI values >500 mg-HC/g-TOC. Based on these initial conditions, the mature core samples retain some residual oil-generating potential and are approaching the end of the oil generation window.

Rock OSI values in both cores were high (~100 mg/g) to very high (>200 mg/g), reflecting excellent oil producibility (Jarvie, 2012). These high-OSI values were consistent with the EOM content for samples from similar depths (up to 2 wt. %). In general, the dolomitic intervals contained around 4 times more EOM than the calcareous beds, consistent with the lower porosity of the calcite-rich samples. Production index (PI = S1/S1+S2) values (Table 2)

TABLE 2.

Total organic carbon (TOC) content and Rock-Eval measured and calculated values for thermally immature samples of the Uteland Butte member from the White River and Willow Creek-Indian Canyon (930922-1) outcrops. HC, hydrocarbons; [1]hydrogen index (HI = S2/TOC×100); [2]oxygen index (OI = S3/TOC×100); [3]oil saturation index (OSI = S1/TOC×100); [4]production index (PI = S1/S1+S2); wt. %, weight percent; mg, milligram; g, gram.

Sample No.	TOC (wt. %)	S1 (mg-HC/g-rock)	S2 (mg-HC/g-rock)	S3 (mg-CO2/g-rock)	Tmax (°C)	HI[1] (mg-HC/g-TOC)	OI[2] (mg-CO2/g-TOC)	OSI[3] (mg-HC/g-TOC)	PI[4]
82614-1-1	3.46	0.86	24.02	1.39	435	694	40	0.25	0.03
82614-1-2	3.77	0.63	27.23	1.49	431	722	40	0.17	0.02
82614-1-3	3.33	0.82	24.95	1.34	437	749	40	0.25	0.03
82614-1-4	2.87	0.74	18.23	1.26	431	635	44	0.26	0.04
82614-1-5	2.25	0.87	15.45	1.12	432	687	50	0.39	0.05
82614-1-6	2.58	0.92	17.02	1.13	438	660	44	0.36	0.05
82614-1-7	2.42	0.68	14.60	1.06	437	603	44	0.28	0.04
82614-1-9	2.40	0.51	14.14	1.37	442	589	57	0.21	0.03
82614-1-10	6.03	0.72	53.83	2.28	441	893	38	0.12	0.01
82614-1-11	1.29	0.39	7.13	1.17	441	553	91	0.30	0.05
82614-1-13	1.77	0.17	11.36	1.25	441	642	71	0.10	0.01
930922-1	5.86	0.65	43.04	2.73	438	734	47	0.11	0.01

were generally 0.3 or higher and followed the trends in OSI. Tmax values were highly variable and ranged between 430 and 457 °C with no consistent trend in either core, and do not appear to provide useful information on the thermal maturity of the source rocks in the Uteland Butte. Vitrinite reflectance measurements, on a very limited number of core samples, consistently had Ro values of approximately 1%, indicating that the Uteland Butte is currently in the oil window. Using an estimated original HI of 680 mg-HC/g-TOC and PI of 0.03 (average values for outcrop samples), the transformation ratio (or fractional conversion to petroleum; Peters et al., 2005, page 99) of the Uteland Butte core samples approaches 80%. This result indicates that the petroleum generation potential of the Uteland Butte source rocks at depth is nearly exhausted.

Thermally immature outcrop samples had the expected low OSI, PI, and Tmax values. HI and oxygen index (OI = S3/TOC×100) values for the outcrop rocks are plotted (Fig. 6, left panel) along with those from the core samples on a pseudo van Krevelen diagram (Espitalié et al., 1977). The results indicate that the outcrop rocks and core samples contain Type II kerogen. However, a plot of S2 vs. TOC (Fig. 6, right panel; Dembicki, 2009) yields a borderline Type I trend that is more consistent with other Green River Formation shales. The lower hydrogen content of the Uteland Butte mudstones is likely an indication of differences in the preservation of organic matter in the freshwater stage of the lake. Elemental ratios were determined on isolated kerogen from one sample (8261-1-10) collected at the White River section and the Willow Creek–Indian Canyon outcrop sample (Ruble, 1996) and H/C ratios were 1.50 and 1.35, respectively, and O/C ratios were less than 0.1. These results indicate that the Uteland Butte member contains a Type I kerogen with similar or lower hydrogen content to other Green River Formation kerogen (H/C ~1.5).

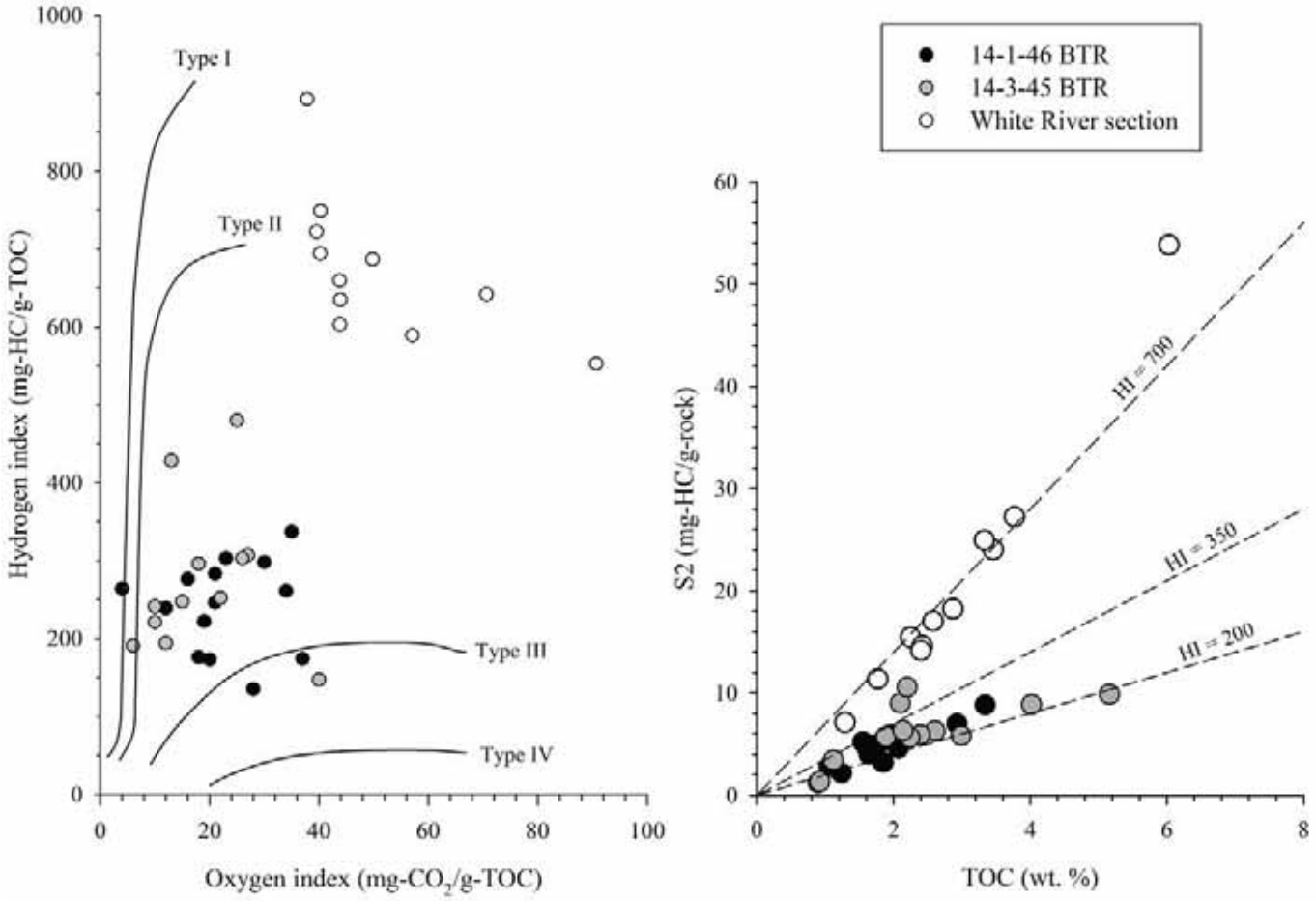

Figure 6. Left plot: pseudo van Krevelen diagram showing Rock-Eval hydrogen index (HI = S2/TOC×100) and oxygen index (OI = S3/TOC×100) data compared with standard kerogen trends. Right plot: Rock-Eval S2 vs. total organic carbon (TOC) content. mg, milligrams; wt. %, weight percent.

CHARACTERIZATION OF OILS AND EXTRACTABLE ORGANIC MATTER

Four oil samples donated by the Bill Barrett Corp. were sourced to the Uteland Butte member based on oil assignments using the respective completion intervals of each well. Oil samples were waxy and ranged from bright yellow to brownish-yellow and black. All Uteland Butte oil samples examined for this study are highly paraffinic, resembling shoe polish at room temperature, with API gravities ranging between 30° and 40°. Table 3 provides a summary of bulk and molecular properties for the Bill Barrett Corp. samples.

The very light isotopic signatures ($\delta^{13}C$ < -30 ‰) of the oils indicate the expected non-marine source. All samples had low sulfur content (≤0.03 wt. %), and high hydrocarbon/polar ratios (>6.4). Pristane (Pr) to phytane (Ph) ratios of the whole-oils and saturates fractions were 1.50 or greater, consistent with a freshwater lacustrine source (Mello et al., 1995). Figure 7 (bottom panel, C) shows a typical Uteland Butte oil saturate fraction trace measured by gas chromatography with a flame ionization detector (GC-FID). Published (Lillis et al., 2003) and unpublished data from a wide range of Uinta Basin oil samples characterized by the USGS Organic Geochemistry Laboratory in Denver were compared with the Uteland Butte oil results. Recognized oil types that were sourced from the Green River Formation in the Uinta Basin include Green River A and Green River B (Lillis et al., 2003). Green River A (GR-A) has been attributed to the "black shale facies," which includes the Uteland Butte member. Green River B (GR-B)

has been attributed to the Mahogany zone oil shale, but could also be described as Parachute Creek Member oil so as to include other potential source rocks with similar organic geochemical properties to the Mahogany zone. Another type, Green River "W" (GR-W), is a category including oils that were until recently attributed to reservoirs in the Wasatch Formation, but are now considered to be related to the Uteland Butte oils (Birdwell et al., 2014; Lillis and Cumming, 2014). GR-A oils are the most common Uinta Basin oil type and have high wax contents, carbon preference indices (CPI; Hunt, 1979) < 1.10, and low β-carotane content (Lillis et al., 2003). The GR-B oils typically have higher odd-carbon predominance (CPI > 1.2) and higher β-carotane content than GR-A oils. In general, the Uteland Butte and GR-W oils more closely resemble the GR-A oils, due to their high wax content, low CPIs (~1.0), and minimal β-carotane content. However, comparison of the Pr/n-C_{17} and Ph/n-C_{18} ratios for all of the Uinta Basin lacustrine oils, including the Uteland Butte, showed a consistent trend for oils sourced from various Green River Formation lacustrine facies, indicating a similar organic matter source for Green River Formation oils throughout the lacustrine interval (Fig. 8). The Uteland Butte and GR-W oils consistently had lower Pr/n-C_{17} and Ph/n-C_{18} ratio values than most of the GR-A and GR-B samples, indicating that they are more thermally mature than many of the other Uinta Basin oils (Tissot et al., 1971).

Data on EOM from eight rock samples from the 14-1-46 BTR core are summarized in Table 4 and a plot of the saturate fraction GC-FID trace for two representative samples are shown in Figure 7 (top and middle panels, A and B). Some EOM samples had chromatogram peak distributions that were roughly bimodal (Fig. 7 panel A), with intense peaks between n-C_{13} and n-C_{15} and in the mid C_{20}'s. Other EOM samples had bell-shaped distributions of normal alkanes, with maximum peak intensities in the mid C_{20}'s that were depleted of nearly all hydrocarbons below n-C_{15} (Fig. 7 panel B). A similar observation is reported by Jarvie et al. (2011) in a comparison

TABLE 3.

Bulk and molecular parameters measured for Bill Barrett Corp. oil samples. Gas chromatography parameters determined on saturates fraction. [1]Well information available from the Utah Division of Oil, Gas, and Mining (2015); [2]API standard deviations (stdev.) all ≤ 0.2; [3]Carbon-13 stdev. ≤ 0.11; [4]Carbon preference index (Hunt, 1979); [5]Pristane/phytane ratio; [6]sulfur content stdev. ≤ 0.02 wt. %; [7]ND = not detected. °API, American Petroleum Institute inverse measure of oil density; wt. %, weight percent; ‰, parts per thousand.

Well[1]	Source	API gravity (°)[2]	Saturates (wt. %)	Aromatics (wt. %)	Resins (wt. %)	Asphaltenes (wt. %)	C_{15-} volatiles (wt. %)	Whole oil $\delta^{13}C$ (‰)[3]	Saturates $\delta^{13}C$ (‰)	Aromatics $\delta^{13}C$ (‰)	CPI[4]	Pr/Ph[5]	Pr/ n-C_{17}	Ph/ n-C_{18}	Sulfur (wt. %)[6]
Aurora 4-21d-720	Comingled?	23.0	48.8	17.8	4.4	5.0	24	-31.24	-31.76	-30.76	1.06	1.02	0.83	0.89	0.06
Aurora 5-32	Parachute Creek	21.1	36.4	23.3	24.8	8.0	7.5	-30.87	-32.03	-30.82	1.40	1.17	1.54	2.90	0.29
RU 7-20	Uteland Butte	32.2	64.7	10.9	1.5	10.0	13	-31.43	-31.37	-30.03	1.00	1.56	0.37	0.23	0.03
13H-33-46 BTR	Uteland Butte	33.3	65.2	9.2	1.3	10.2	14.1	-32.41	-32.63	-30.97	1.02	1.58	0.25	0.16	0.03
13H-13-46 BTR	Uteland Butte	37.0	68	5.7	1.3	7.8	17.3	-32.29	-32.43	-30.52	0.99	1.51	0.19	0.13	ND[7]
9H-4-45 BTR	Uteland Butte	39.1	70.4	3.3	0.9	5.8	19.6	-32.36	-32.35	-30.16	0.98	1.60	0.16	0.10	ND

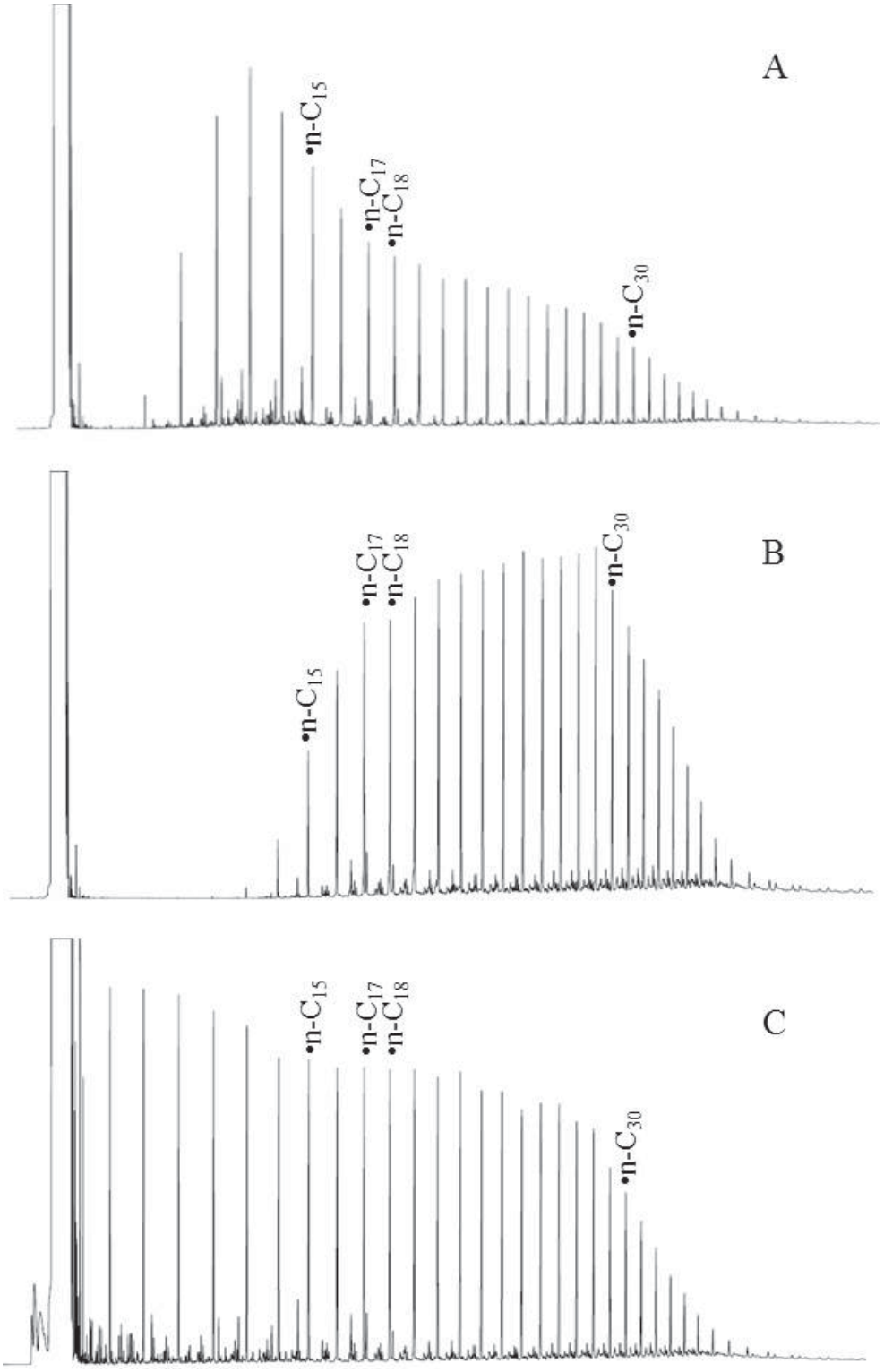

Figure 7. Chromatograms of extractable organic matter (EOM) from the 14-1-46 core (panels A, B) and Uteland Butte member oil from the 9H-4-45 BTR well (panel C). Extractable organic matter (EOM) sample shown in panel A is from a depth of 6,681.5 ft (calcareous shale) and the EOM shown in panel B is from 6,703.5 ft (dolomitic PZ-2; see Figures 2 and 5). Several normal alkanes (n-C) are indicated.

of EOM samples from the low-porosity upper and high-porosity middle members of the Bakken Formation in the Williston Basin. Although the chromatograms show some obvious differences between the EOM samples and Uteland Butte oils, which is attributed to volatilization during core storage (depleted in C_{15-} hydrocarbons), the carbon isotope, SARA, and molecular parameters determined on the EOM samples are consistent with those of the Uteland Butte oils discussed previously, as demonstrated in the plot of Pr/n-C_{17} vs. Ph/n-C_{18} (Fig. 8). The differences in the two EOM chromatograms were related to the mineralogy of the rocks from which they were extracted. Of the eight EOM samples collected, two were from dolomite-rich rocks (about 76 wt. %) and the other six were from rocks with low dolomite content (< 6 wt. %) and high calcite and total clay. The dolomitic samples were also high in porosity (15 – 20 vol. %), contained the highest concentrations of EOM (~2 wt. %) overall, and had bell-shaped distributions in the saturates fraction (and whole-oil, not shown) chromatograms. The non-dolomitic samples had lower porosities (< 9 vol. %) with EOM contents of less than 0.6 wt. % and bimodal distributions in their GC traces. Permeability for all samples examined for EOM content ranged within an order of magnitude (0.002 – 0.032 mD), and due to the limited number of samples, it was unclear if permeability varied systematically with lithofacies among this subset of samples. The higher porosity of the dolomitic samples may explain their greater depletion in light hydrocarbons during core storage.

PRODUCTION HISTORY

The Uteland Butte member is oil productive throughout a large area of the Uinta Basin (i.e., the play is not isolated to any one field, but is nearly basinwide). Until recently the Uteland Butte was not a primary drilling objective (Morgan et al., 2003b). The current focus on Uteland Butte development has targeted thin, regionally extensive dolomite beds with more than 20 percent porosity but low permeability (0.01 – 0.1 mD). These dolomite beds (designated PZ-1, PZ-1′, and PZ-2 along with other unnamed beds by Bill Barrett Corp.; Fig. 2), in particular the PZ-1, are being targeted by horizontal drilling and hydraulic fracturing; the latter of which could connect several dolomitic reservoir beds (Anderson and Roesink, 2013; Vanden Berg et al., 2014). Production data from 84 horizontal wells that produce from the Uteland Butte were extracted from the Utah Division of Oil, Gas, and Mining database (2015). These records were compared with information from individual well files to confirm

TABLE 4.

Bulk and molecular parameters for extractable organic matter (EOM) samples from the 14-1-46 BTR core. Gas chromatography parameters were determined on saturates fraction.

[1]Carbon-13 standard deviation ≤ 0.72; [2]Carbon preference index (Hunt, 1979); [3]Pristane/phytane ratio.

Sample depth (ft)	Lithofacies	EOM (wt. %)	Saturates (wt. %)	Aromatics (wt. %)	Resins (wt. %)	Asphaltenes (wt. %)	Saturates $\delta^{13}C$ (‰)[1]	Aromatics $\delta^{13}C$ (‰)[1]	CPI[2]	Pr/Ph[3]	Pr/n-C_{17}	Ph/n-C_{18}
6668.5	Calcareous shale	0.46%	76.5	9.1	5.8	8.6	-32.17	-30.67	0.98	1.60	0.16	0.12
6681.5	Low carbonate shale	0.57%	74.0	11.4	5.1	9.5	-32.00	-31.07	1.00	1.51	0.14	0.10
6703.5	Shaley dolomite	2.22%	87.4	6.1	2.3	4.3	-32.35	-31.04	0.98	1.44	0.16	0.11
6656.3	Shale (some dol/cal)	0.28%	73.0	12.8	5.6	8.6	-31.34	-30.64	0.98	1.43	0.20	0.15
6684-6686	Dolomite	1.80%	90.6	4.3	1.9	3.2	-31.77	-30.44	1.03	1.22	0.26	0.19
6694	Calcareous shale	0.16%	65.6	15.6	8.4	10.4	-31.79	-30.34	0.99	2.05	0.14	0.08
6702-6703.5	Shaley dolomite	1.24%	83.1	6.9	3.3	6.6	-32.13	-30.90	0.99	1.40	0.19	0.12
6684	Low carbonate shale	0.26%	74.1	13.3	6.7	5.9	-32.80	-30.82	0.97	1.94	0.18	0.13

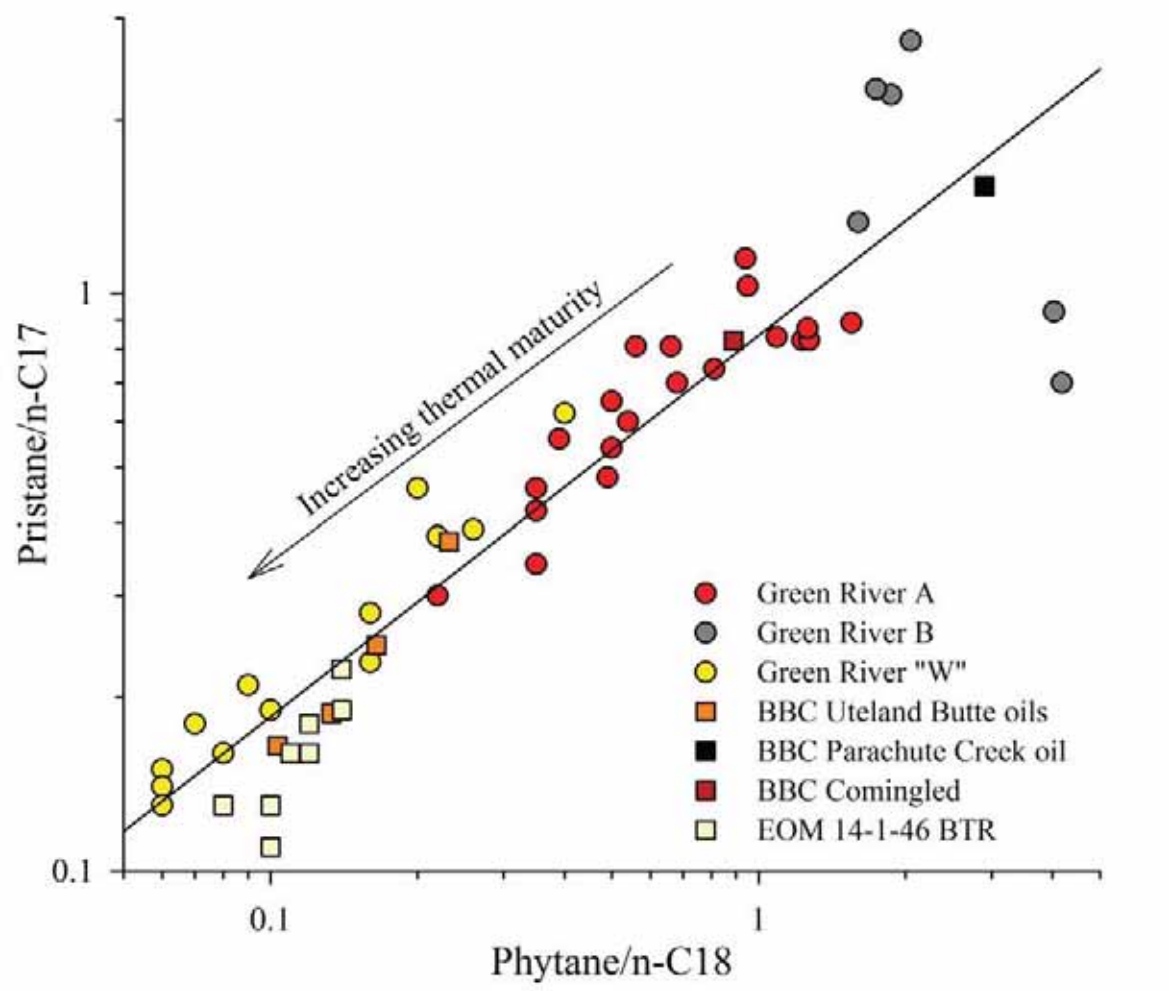

Figure 8. Plot of pristane/n-C_{17} vs. phytane/n-C_{18} for Uinta Basin Green River A and Green River B oil samples (Lillis et al., 2003), Green River "W" oils (previously attributed to Wasatch Formation reservoirs), oils donated by the Bill Barrett Corporation (BBC) from Uteland Butte member (4), Parachute Creek Member (1), and "comingled" oils (1) wells; and extractable organic matter from Uteland Butte core samples (14-1-46 BTR). Scatter in the Green River B samples is due to high variability in n-C_{17} and n-C_{18} content.

that the stratigraphic interval being produced is the Uteland Butte. Data were examined with emphasis on production during the first month (average reporting period 36 days) and first three full months reported as barrels of oil equivalent (BOE), which includes natural gas production (one BOE is equivalent to 5,800 cu. ft of natural gas). Wells were sorted into three categories: (1) forty-two 5,000-ft laterals outside of the overpressured region ("normal-pressured") shown in Figure 1 (discussed further in a later section); (2) thirty-four 5,000-ft laterals within the overpressured region; and (3) eight extra-long laterals (approximately 11,000 ft) within the overpressured region. Two recently drilled wells of the 84 do not yet have any reported production data.

Histograms showing total production for the first month (sorted by average daily production in BOE) and the first three full months (sorted by total BOE produced from each well) are presented in Figure 9 (top and bottom panels, respectively). Separate distributions for normal-pressured, overpressured, and extra-long lateral wells are shown. The sum of all production for all wells during the first month of operation was 1.14 MMBOE, or about 20% of the total production from the Uteland Butte as of December 2014 (Utah Division of Oil, Gas, and Mining, 2015).

The most common type of producing well was normal-pressured with the first month's production less than 100 and up to 200 BOE/day (n = 32). Among the 5,000-ft laterals in the overpressured area, typical first month's production was between 400 and 800 BOE/day (20 wells). Total production from all wells during their first three full months operating was 1.96 MMBOE; this represents about 35% of all production from the Uteland Butte to date (5.65 MMBOE). All but one of the normal-pressured wells produced less than 20,000 BOE during this timeframe, while 27 of the overpressured wells yielded more than 20,000 and as much as 70,000 BOE (one well). The wells with extra-long laterals in the overpressured area show the greatest initial production by far. All of the wells with 11,000-ft laterals (6 total with data) had first month's production over 1,000 BOE/day and the four with first three months production data all produced over 67,000 BOE during that period, which when combined (503,124 BOE), were more than the sum of all production from the normal-pressured wells during their first three months (342,877 BOE).

Declines in production from Uteland Butte horizontal wells with time-online are typical of unconventional tight-oil plays in that production decreases rapidly when compared to most conventional oil wells. Vanden Berg et al. (2014) compared production rates (BOE/day) for the overpressured and normal-pressured wells with 5,000-ft laterals from the time just after completion to a little more than two years online. A typical normal-pressured well with an initial production rate of about 300 BOE/day had dropped to one-tenth of that after 28 months. An overpressured well, with initial production of around 760 BOE/day, showed a similar decline (to 100 BOE/day) after 32 months. Data for an extra-long lateral, with a timeframe from completion to six-months online, showed a two-thirds reduction in production rate (1,500 to 500 BOE/day)

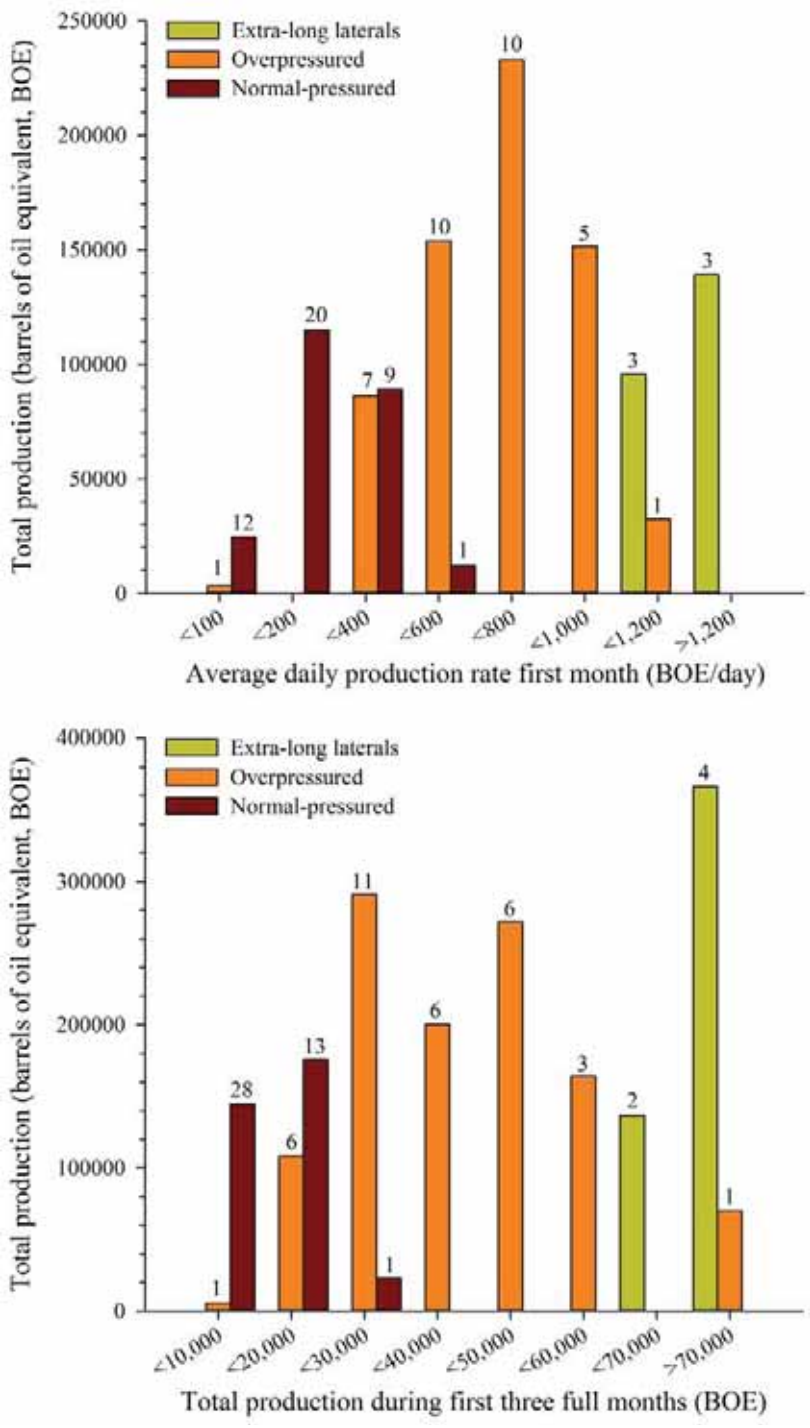

Figure 9. Histograms summarizing first month's average production rate (top, BOE/day) and first three full months of production (bottom, BOE) from normal-pressure (0.433 ft/psi to 0.5 ft/psi), overpressured (greater than 0.5 psi/ft), and extra-long (11,000 ft) lateral wells. Numbers above bars indicate how many wells are represented by each bar. BOE, barrels of oil equivalent; psi, pounds per square inch per foot.

and was consistent with the decline curves for the shorter horizontals wells.

Data on gas-oil (GOR, thousand cubic ft/barrel, MCF/bbl) and oil-water (OWR, barrel/barrel) ratios were also examined for 71 Uteland Butte wells using first 3 full months and first 12 months production data from IHS ENERDEQ (IHS Energy, 2015). In the first three months of production, GOR values were typically around 1 MCF/bbl, with average, median, and maximum values of 1.56, 0.88, and 14.95 MCF/bbl, respectively. Over the first year of production, the values increased slightly, with typical values between 1.25 and 2.25 MCF/bbl, and average, median, and maximum respective values of 2.11, 1.54, and 15.82 MCF/bbl. Correlation of first 3 months and first 12 months GORs showed a moderately high correlation coefficient ($R^2 = 0.864$) and a slope of 1.18, indicating a slight increase in gas production with increasing production time. Water production varied widely for Uteland Butte wells, with OWR values ranging between 1 and 3 bbl/bbl for most wells for both the first 3 full months and first 12 months of production. Average, median, and maximum OWR were also similar during the two production periods (5.70, 5.98; 2.22, 2.18; 76.05, 85.66 bbl/bbl) and a strong correlation between 3- and 12-month OWRs was observed ($R^2 = 0.963$) with a near unity slope, indicating little change in relative water production with time online. In general, there was no discernible difference in GOR values between overpressured and normal-pressured wells. However, the normal-pressured wells showed a bimodal distribution of OWRs, with about half ranging between 0.3 and 3 bbl/bbl and the other half varying from 6 to 130 bbl/bbl, while the overall distribution for the overpressured wells was normally distributed between 0.4 and 9.2 bbl/bbl It should be noted that initial water production is expected to be higher in unconventional oil wells due to flow-back waters used during hydraulic fracturing, but there is no evidence for this in the Uteland Butte wells based on trends in the first 3- and 12-month OWR values.

BASINWIDE FACTORS RELATED TO PRODUCTION

Organic Richness

Fischer assay data was generated by the U.S. Bureau of Mines during the 1960s and 1970s on samples of cuttings from drill holes as part of an examination of oil shale resources in the Uinta Basin. In the Uinta Basin Oil Shale database, there were 24 drill holes with Fischer assay data on samples from the Uteland Butte member (Johnson et al., 2010). However, there are a few potential issues with this Fischer assay data because the sampling interval can be 10 ft or more for cuttings used in these analyses, and some thin, organic-rich shale beds may not be detected. Another potential concern with Fischer assay data is that analytical errors in samples with low oil yields may be significant (Stanfield and Frost, 1949) and unlike Rock-Eval, the method does not differentiate between generated oil present in the rock and oil generated during kerogen pyrolysis. Despite these caveats, the Fischer assay results do provide a basinwide dataset that allows for assignment of an approximate extent of the organic-rich rocks in the Uteland Butte member. Figure 1 shows the extent of Uteland Butte samples that exceeded Fischer assay oil yields of one gallon of oil per ton of rock (GPT). Of the 417 Fischer assay samples processed, 257 generated sufficient oil to report oil yield, and of these 67% (n = 172) had yields greater than 1 GPT. Only 3% (8) had yields greater than 5 GPT and the thickest, richest interval based on these data has an oil yield of 3.6 GPT over a thickness of 280 ft. Nearly every well shown on Figure 1 that is producing out of the Uteland Butte member is located within the >1 GPT area.

Overpressure

Abnormal pressure is a common phenomenon in continuous or basin-centered petroleum systems in Rocky Mountain basins (Law and Spencer, 1998). Pressure gradients are determined using pressure measurements with depth and normal formation pressure is defined by the hydrostatic gradient (0.433 psi/ft). Reservoirs in Rocky Mountain basins are considered to be significantly overpressured if the pressure gradient exceeds 0.5 psi/ft (Spencer, 1987). Formations in communication with a regional groundwater system are expected to display normal pressure, unless recharge areas are much higher in elevation than the overall basin. Pressures can exceed the hydrostatic gradient in lithologic units that are isolated or encased by impermeable barriers within subsiding basins where compaction of the lithologic column prevents fluid migration out of the unit. Another mechanism, one that has been invoked to explain overpressure in Rocky Mountain basins, is hydrocarbon generation. Conversion of solid kerogen to oil and gas

leads to a net increase in volume of the organic phase (Gies, 1984; Spencer, 1987; Law and Spencer, 1998). Overpressure has been identified as an important factor driving many of the high-production rates for wells in the Uteland Butte horizontal play (Anderson and Roesink, 2013; Vanden Berg et al., 2014).

Downhole pressure within the wellbore can be measured using drillstem tests or from variations in mud weights used during drilling. Drillstem tests do not provide a direct measure of formation pressure, but are considered to be one of the better estimation methods (Holm, 1998). Mud weights are also useful for this purpose, but lack the reliability and precision of drillstem tests for defining overpressure. In this study, we have used data derived from both methods to define overpressured areas within the Uteland Butte member. The reliability of drillstem test data was determined by comparing the initial shut-in pressure with the final shut-in pressure; similar values generally indicate that the test was run long enough to permit equilibration between the well bore and formation pressure.

Drillstem tests from 42 intervals in or near the Uteland Butte were determined to be reliable based on our criterion and within 6 of those intervals the pressure gradients were 0.50 psi/ft or greater defined here as significant overpressure. The mud weights used in five drill holes were added to the drillstem data in defining the overpressured part of the play, and were particularly useful in areas where information from drillstem tests was unavailable. Mud weights used in four of the drill holes indicated significant overpressure; the remaining drill hole was normally pressured. The overpressured area (>0.5 psi/ft) in the Uteland Butte member defined by the drillstem test and mud weight data is shown within the light-pink shaded portion of Figure 1 and is generally comparable to a map of overpressure defined using only mud weight data (Anderson and Roesink, 2013). The majority of drillstem tests within this area indicate significant overpressure, but some do not. The tests within the shaded area that did not indicate overpressure could be due to poorly run tests within an overpressured interval or could reflect that there are some normally pressured zones within a generally overpressured area. Comparison of the production rates plotted in Figure 1 show that the horizontal wells within the overpressured area are the most productive wells in the Uteland Butte, as indicated in previous studies (Anderson and Roesink, 2013; Vanden Berg et al., 2014; Johnson et al., 2015b).

Thermal Maturity

The majority of organic matter identified in the Green River Formation is described as Type I kerogen, which indicates that it is oil-prone with high hydrogen content compared to other kerogen types; this is also true for the Uteland Butte. For Type I kerogen, the onset of oil generation is thought to correspond to a vitrinite reflectance (Ro) of between 0.6 and 0.7%, with oil generation complete between a Ro of 1.2 to 1.3% (Baskin and Peters, 1992; Ruble et al., 2001). Vitrinite measurements on samples rich in Type I kerogen can be difficult to obtain, as the terrestrial-sourced vitrinite maceral will be mixed with and diluted by the more prominent algal organic matter. Therefore, variations in vitrinite reflectance may only indirectly indicate thermal maturity of the largely amorphous Type I kerogen in Green River Formation rocks.

A small number of vitrinite reflectance measurements (n = 11) from within or near the Uteland Butte member were published by Anders et al. (1992). The values in that study generally define an area of high thermal maturity near and just to the south of the basin trough. Isomaturity lines are shown on Figure 1, highlighting regions with Ro values of 0.75%, beyond the onset of oil generation for Type I organic matter, and 1.0% or greater. An incomplete line for values of 0.55% Ro or higher is also plotted, but insufficient data were available to enclose the area representative of this level of thermal maturity. The majority of productive wells are located within the 0.75% Ro line, and the wells with the highest rates of production are within the most mature area (Fig. 1).

The Rock-Eval and vitrinite reflectance data collected on samples from cores 14-1-46 BTR and 14-3-45 BTR were also considered in examining thermal maturity of the Uteland Butte. A limited number of vitrinite measurements (n = 3), available from the Bill Barrett Corp. cores were added to those from Anders et al. (1992) to help determine the variations in thermal maturity. Average Ro values were 0.97% at 6,656.8 ft and 1.00% at 6,706.35 ft in the 14-1-46 BTR core and 0.99% at 7,363 ft in the 14-3-45 BTR core. All were consistent with the Anders et al. (1992) data.

Dolomite Intervals

The total thickness of carbonate beds within the Uteland Butte member has been examined in the subsurface using electric logs and any available Amstrat logs available from the USGS Core Research Center in Denver. Resistant

intervals on the electric logs were considered to be carbonate-rich, due to the rarity of sandstones in the Uteland Butte. Figure 10 shows the thickness of the PZ-1 dolomite bed in the Uteland Butte member (numbered isopach) which is one of the primary drilling targets. Figure 2 shows a sample well and core log for one Uteland Butte well with several identifying intervals noted, including the three main dolomite targets (PZ-1, PZ-1′, and PZ-2) and the C- and D-shales, which can be used to locate the interval of the Uteland Butte that contains the dolomite-rich beds. The carbonate map was generated based on core descriptions and well logs and therefore differs somewhat from the Anderson and Roesink (2013) map that was derived solely from log data. The maximum thickness of dolomite-rich beds is about 16 ft in the carbonate-rich area within the thickest part of the Uteland Butte; this is about one-third of the maximum thickness reported previously (Anderson and Roesink, 2013); they indicated that the total thickness of dolomite-rich beds drops off rapidly to the north and this is generally consistent with our map (Fig. 10). This decrease in dolomite-rich thickness was used to help delineate the northern boundary of the Uteland Butte tight-oil play.

The results shown in Figure 10 include all lacustrine rocks containing some carbonate-rich beds and are thicker than the main carbonate-rich interval of the Uteland Butte member isopached by Morgan et al. (2003b). We assumed that all intervals with carbonate content could produce some oil, particularly when fractured along with the main carbonate-rich interval. The thickness of this interval varies from less than 50 ft in the southeast part of the basin, where it consists of a single ostracodal and oolitic limestone, to more than 400 ft thick along the basin trough, where it directly overlies older lacustrine rocks and directly underlies the R-0 zone of the Garden Gulch Member. The Uteland Butte could not be identified with certainty north of the isopached area shown in Figure 1 and therefore the northern limit of the Uteland Butte is not clearly defined. In this area, the Uteland Butte grades into a thick, complex mix of intertonguing facies, including the offshore lacustrine, marginal lacustrine, and alluvial rocks that form the stratigraphic trap for the Altamont-Bluebell field, making it difficult to define a distinct boundary. It is clear from the production data shown in Figure 1 and the PZ-1 thickness isopach in Figure 10 that many of the most productive wells are located where the dolomite-rich beds are present, but all highly productive wells are not necessarily associated with the dolomites.

Assessment Units

Figure 1 outlines the assessment units (AUs) designated by the USGS to be within the Uteland Butte tight-oil play (Johnson et al., 2015a). Two AUs and one "sweet spot" were assigned based on the available geological, geochemical, and production data and are briefly described herein. The Uteland Butte Carbonate Continuous AU lies within the area bounded by the green line on Figure 1 and encompasses much of the deep, central portion of the Uinta Basin. This AU contains most of the wells currently producing from the Uteland Butte member. A sweet spot, containing most of the highest producing wells is included within this AU. The sweet spot is defined by the presence of overpressure (>0.5 psi/ft), coincides with the thickest part of the offshore phase of the Uteland Butte, and includes high levels of organic richness with thermal maturities within the oil window.

The southern margin of the Continuous Carbonate AU is defined by the transition from organic-rich offshore lacustrine carbonate and shale to more marginal sandstone, siltstone, and mudstone of the Uteland Butte Marginal Lacustrine Conventional Oil and Gas AU, outlined by the pink line on Figure 1. The southern contact between the two AUs is gradational in terms of lithofacies, thus the line between them was assigned based on Fischer assay oil-yield data, specifically where the organic richness of the Uteland Butte is less than 1 GPT. At the northern boundary of the Continuous Carbonate AU, it is also gradational into the marginal lithofacies and extends into the northern area of the Marginal Lacustrine AU. This boundary was defined using both the lithofacies map of carbonate thickness and the Fischer assay oil-yield isopachs for 1 and 2 GPT cutoffs. The eastern boundary for the Continuous Carbonate AU was difficult to define due to the limited availability of core or production data. The boundary was placed a few miles from outcrop.

CONCLUSIONS

This paper has summarized the geology and various geochemical and mineralogical properties related to tight-oil production from the continuous resource play in the Uteland Butte member of the Green River Formation in the Uinta Basin. Based on our examination of the Green River Formation basins, only the Uinta Basin possesses the combination of interbedded organic-rich shale and brittle carbonate lithologies at sufficient thermal maturity to have

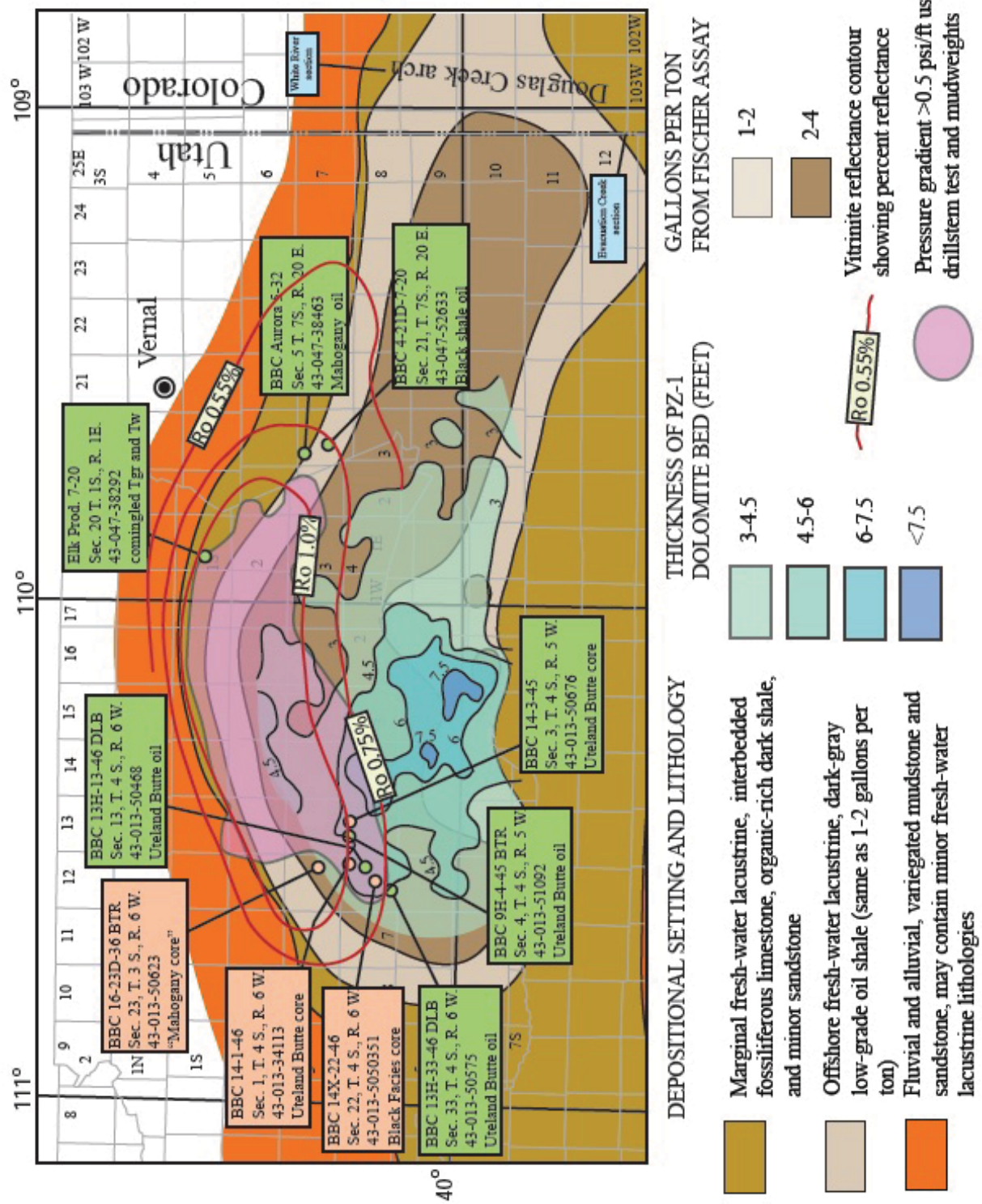

Figure 10. General Uteland Butte member map showing thickness in ft of the PZ-1 bed (numbered isopachs) and locations of cores (salmon-colored boxes), oil wells (green boxes), and outcrops (blue boxes) are also indicated. See Figure 1 for additional legend information.

generated large quantities of oil to produce a viable tight-oil play. The high thermal maturities in the Green River Formation in the Uinta Basin are related to the tremendous subsidence that took place after the main organic-rich interval was deposited; this burial was far greater than in the other Green River basins during the same period.

The organic geochemistry and mineralogy of the Uteland Butte member vary somewhat from that of the overlying saline-brackish oil shale intervals of the Douglas Creek, Garden Gulch, and Parachute Creek Members of the Green River Formation. Lower TOC and HI values in immature samples relative to the overlying oil shales may be related to lower organic productivity or poor preservation in the freshwater lacustrine phase of Lake Uinta when compared to the more saline and alkaline conditions that dominated later. The mineralogy of the Uteland Butte, both in core and outcrop, is also different from other freshwater lacustrine intervals of the Green River Formation in the Piceance and Greater Green River Basins, in that carbonates are common and often the dominant mineral component. The common occurrence of clays, such as kaolinite, montmorillonite, and chlorite, in the Uteland Butte also differentiates it from other stages of Lake Uinta's history, in that the dominant aluminosilicates in later intervals are feldspar minerals and analcime.

The most productive area of the Uteland Butte member is located where the following standard criteria are met: (1) organic-rich based on Fischer assay yields, (2) presence of overpressure, and (3) high thermal maturity. The high-porosity, brittle and dolomite-rich intervals provide targets for horizontal drilling and are potentially important reservoir rocks, but their presence does not appear to be essential for high productivity. The relationship between overpressure and well productivity has been noted previously for Uteland Butte wells (Anderson and Roesink, 2013; Vanden Berg et al., 2014) and based on production data is shown to be the primary driving factor for differences in well performance. Future development in the Uteland Butte member is expected to emphasize the use of extended 11,000-ft laterals that should lead to substantially higher production rates, particularly in the overpressured area of the basin.

ACKNOWLEDGEMENTS

The authors thank the Bill Barrett Corporation (Jason Anderson, John Conner, and Dan Moore) for sample and data access, the Utah Geological Survey Core Facility (Peter Nielsen, Tom Dempster) for assistance with core sampling, the U.S. Geological Survey Organic Geochemistry Laboratory in Denver (Augusta Warden, Zach Lowry, Mark Dreier, and Tammy Hannah) for performing much of the analytical work presented in this paper, and Paul Lillis for guidance during outcrop sampling and oil and EOM characterization. We also thank Tom Judkins (USGS retired) for geologic names review and Craig Morgan (Utah Geological Survey) and Debra Higley (USGS) for technical review of the manuscript. Any use of trade, product or firm names is for descriptive purposes only and does not imply endorsement by the U.S. Government.

REFERENCES

American Society for Testing Materials, 1984, Designation D 388-80, Standard test method for oil from oil shale: Annual Book of ASTM Standards, 1984, p. 513–525.

Anders, D.E., Palacas, J.G., and Johnson, R.C., 1992, Thermal maturity of rocks and hydrocarbon deposits, Uinta Basin, Utah: *in* Fouch, T.D., Nuccio, V.F., and Chidsey, T.C. Jr. eds., Hydrocarbon and mineral resources of the Uinta Basin, Utah and Colorado: Utah Geological Association Guidebook 20, p. 53–76.

Anderson, J.G., and Roesink, J.G., 2013, Reservoir characterization of the Uteland Butte Formation in the Uinta Basin: American Association of Petroleum Geologists Search and Discovery Article #50888, 2 oversized sheets.

Baskin, D.K., and Peters, K.E., 1992, Early generation characteristics of a sulfur-rich Monterey kerogen: American Association of Petroleum Geologists Bulletin, v. 76, p. 1–13.

Birdwell, J.E., Johnson, R.C., Lillis, P.G., and Brownfield, M.E., 2014, Differentiating Green River Formation oils sourced from freshwater and saline lacustrine facies in the eastern Uinta Basin, Utah: American Association of Petroleum Geologists Search and Discovery Article #90193, 21 p.

Bradley, W.H., 1931, Origin and microfossils of the oil shale of the Green River Formation of Colorado and Utah: U.S. Geological Survey Professional Paper 168, 58 p.

Cashion, W.B., 1967, Geology and fuel resources of the Green River Formation southeastern Uinta Basin Utah and Colorado: U.S. Geological Survey Professional Paper 548, 48 p.

Dembicki, H., 2009, Three common source rock evaluation errors made by geologists during prospect or play appraisals: American Association of Petroleum Geologists Bulletin, v. 93, p. 341-356.

Durham, L.S., 2013, Unconventional Uteland Butte sparks new Utah activity: American Association of Petroleum Geologists Explorer, June 2013, p. 10-12.

Dyni, J.R., 1976, Trioctahedral smectite in the Green River Formation, Duchesne County, Utah: U.S. Geological Survey Professional Paper 967, 14 p.

Espitalié, J., Madec, M., Tissot, B., Menning, J.J., and Leplat, P., 1977, Source rock characterization methods for petroleum exploration: Proceedings of the Ninth Offshore Technology Conference, Houston, Texas, v. 3, p. 439-443.

Fischer, D.J., Erdmann, C.E., and Reeside, J.B., Jr., 1960, Cretaceous and Tertiary formations of the Book Cliffs, Carbon, Emery, and Grand Counties, Utah, and Garfield and Mesa Counties, Colorado: U.S. Geological Survey Professional Paper 332, 80 p.

Folsom, L.W., 1968, Economic aspects of Uinta Basin gas development, *in* Beebe, B.W., and Curtis, B.F., eds., Natural gases of North America – A symposium: American Association of Petroleum Geologists Memoir 9, v. 1, p. 199-208.

Fouch, T.D., 1975, Lithofacies and related hydrocarbon accumulations in Tertiary strata of the western and central Uinta Basin, Utah, *in* Bolyard, D.W., ed., Symposium of deep drilling frontiers in the central Rocky Mountains: Rocky Mountain Association of Geologists Guidebook, p.163-173.

Fouch, T.D., Nuccio, V.F., Anders, D.E., Rice, D.D., Pitman, J.K., and Mast, R.F., 1994, Green River (!) petroleum system Uinta Basin, Utah, U.S.A., *in* Magoon, L.B., and Dow, W.G., eds., The petroleum system—From source to trap: American Association of Petroleum Geologist Memoir 60, p. 399-421.

Gies, R.M., 1984, Case history for a major Alberta Deep Basin gas trap, the Cadomin Formation, *in* Masters J.A., ed., Elmsworth, case study of a deep basin gas field: American Association of Petroleum Geologists Memoir 38, p. 115-140.

Holm, G.M., 1998, Distribution and origin of overpressure in the Central Graben of the North Sea, *in* Law, B.E., Ulmischek, G.F., and Slavin, V.I. , eds., Abnormal pressures in hydrocarbon environments: American Association of Petroleum Geologists Memoir 24, p. 123-144.

Horsfield, B., Curry, D.J., Bohacs, K., Littke, R., Rullkötter, J., Schenk, H.J., Radke, M., Schaefer, R.G., Carroll, A.R., Isaksen, G., and Witte, E.G., 1994, Organic geochemistry of freshwater and alkaline lacustrine sediments in the Green River Formation of the Washakie Basin, Wyoming, U.S.A: Organic Geochemistry, v. 22, p. 415-440.

Hunt, J.M., 1979, Petroleum geochemistry and geology: W.H. Freeman and Company, San Francisco, 617 p.

IHS Energy, 2015, ENERDEQ U.S. Production Data: IHS Energy Group Online Database, (accessed February 25, 2015, at http://energy.ihs.com/).

Jarvie, D.M., 2012, Shale resource systems for oil and gas: Part 2 – Shale-oil resources systems, *in* Breyer, J.A., ed., Shale reservoirs – Giant resources for the 21st century: American Association of Petroleum Geologists Memoir 97, p. 89-119.

Jarvie, D.M., Coskey, R.J., Johnson, M.S., and Leonard, J.E., 2011, Chapter 9: The geology and geochemistry of the Parshall area, Mountrail County, North Dakota, *in* Estes-Jackson, J.E., and Anderson D.S., eds., Revisiting and revitalizing the Niobrara in the central Rockies: Rocky Mountain Association of Geologists, p. 229-281.

Johnson, R.C., 2014, Detailed north-south cross section showing environments of deposition, organic richness, and thermal maturities of lower Tertiary rocks in the Uinta Basin, Utah: U.S. Geological Survey Scientific Investigations Map 3304, 12 p., 1 sheet, http://dx.doi.org/10.3133/sim3304

Johnson, R.C., 1985, Early Cenozoic history of the Uinta and Piceance Creek Basins, Utah and Colorado, with special reference to the development of Eocene Lake Uinta, *in* Flores, R.M., and Kaplan, S.S., eds., Cenozoic paleogeography of the west-central United States, Rocky Mountain paleography symposium 3: The Rocky Mountain Section, Society of Economic Paleontologists and Mineralogists p. 247-276.

Johnson, R.C., Nichols, D.J., and Hanley, J.H., 1988, Stratigraphic sections of Lower Tertiary strata and

charts showing palynomorph and mollusc assemblages, Douglas Creek arch area Colorado and Utah: U.S. Geological Survey Miscellaneous Field Investigations Map MF-1997, two large foldouts.

Johnson, R.C., Mercier, T.J., Brownfield, M.E., and Self, J.G., 2010, Assessment of in-place oil shale resources of the Eocene Green River Formation, Uinta Basin, Utah and Colorado: Oil shale resources of the Uinta Basin, Utah and Colorado: U.S. Geological Survey Digital Data Series DDS-69-BB, Chapter 1, 153 p. http://pubs.usgs.gov/dds/dds-069/dds-069-bb/

Johnson, R.C., Birdwell, J.E., Mercier, T.J., Brownfield, M.E., Charpentier, R.R., Klett, T.R., Leathers, H.M., Schenk, C.J., and Tennyson, M.E., 2015a, Assessment of undiscovered oil and gas resources in the Uteland Butte Member of the Eocene Green River Formation, Uinta Basin, Utah: U.S. Geological Survey Fact Sheet 2015–3052, 2 p.

Johnson, R.C., Birdwell, J.E., Mercier, T.J., and Brownfield, M.E., 2015b, Geology of shale oil and potential shale oil reservoirs in the lower part of the Green River Formation, Uinta, Piceance and Greater Green River basins: 2015 American Association of Petroleum Geologists Search and Discovery Article #90216.

Law, B.E., and Spencer, C.W., 1998, Abnormal pressure in hydrocarbon environments, *in* Law, B.E., Ulmischek, G.F., and Slavin, V.I., eds., Abnormal pressures in hydrocarbon environments: American Association of Petroleum Geologists Memoir 24, p. 1-11.

Lillis, P.G., Warden, A., and King, J.D., 2003, Petroleum systems of the Uinta and Piceance basins— Geochemical characteristics of oil types, Chapter 3, *in* Petroleum systems and geologic assessment of oil and gas in the Uinta-Piceance Province, Utah and Colorado: U.S. Geological Survey Digital Data Series DDS-69-B, 25 p.

Lillis, P.G., and Cumming, V.M., 2014, Correlation of oils and tar sands in the Green River Petroleum System, Uinta Basin, Utah: American Association of Petroleum Geologists Rocky Mountain Section Meeting, July 20-22, 2014, Program with abstracts, p. 33.

Mello, M.R., Telnaes, N., and Maxwell, J.R., 1995, The hydrocarbon source potential in the Brazilian marginal basins: a geochemical and paleoenviromental assessment, *in* Huc, A.Y., ed., American Association of Petroleum Geologists Studies in Geology, v. 40, p. 233–272.

Morgan, C.D., Gwynn, J.W., Allison, M.L., Curtice, Richard, Deo, M.D., Jarrard, Richard, Morris, T.H., and Tripp, C.N., 2003a, Characterization of the Bluebell oil field, Uinta Basin, Duchesne and Uintah Counties, Utah: Utah Geological Survey Special Study 106, 95 p.

Morgan, C.D., Chidsey, T.C. Jr., McClure, K.P., Bereskin, S.R., and Deo, M.D., 2003b, Reservoir characterization of the lower Green River Formation, Uinta Basin, Utah: Utah Geological Survey Open-File Report, 411, 140 p.

Osmond, J.C., 1992, Greater Natural Buttes gas field, Uintah County, Utah, *in* Fouch, T.D., Nuccio, V.F., and Chidsey, T.C. Jr. eds., Hydrocarbon and mineral resources of the Uinta Basin, Utah and Colorado: Utah Geological Association Guidebook 20, p. 143-163.

Peters, K.E., Walters, C.C., and Moldowan, J.M., 2005, The biomarker guide: Biomarkers and isotopes in the environment and human history, Volume 1: Cambridge University Press, 2nd edition, 1155 p.

Ruble, T.E., 1996, Geochemical investigations of the mechanisms of hydrocarbon generation and accumulation in the Uinta Basin, Utah: Ph.D. dissertation, University of Oklahoma, Norman, Oklahoma, 333 p.

Ruble, T.E., and Philp, R.P., 1998, Stratigraphy, depositional environments and organic geochemistry of source-rocks in the Green River petroleum system, Uinta Basin, Utah, *in* Pitman, J.K. and Carroll, A.R., eds., Modern and ancient lake systems-new problems and perspectives: Utah Geological Association Guidebook 26, p. 289-328.

Ruble, T.E., Lewan, M.D., and Philp, R.P., 2001, New insights on the Green River petroleum system in the Uinta Basin from hydrous pyrolysis experiments: American Association of Petroleum Geologist Bulletin, v. 85, p. 1333–1371.

Ryder, R.T., Fouch, T.D., and Elison, J.H., 1976, Early Tertiary sedimentation in the western Uinta Basin, Utah: Geological Society of America Bulletin, v. 87, p. 496-512.

Spencer, C.W., 1987, Hydrocarbon generation as a mechanism for overpressuring in Rocky Mountain region: American Association of Petroleum Geologists Bulletin, v. 71, p. 368-388.

Spieker, E.M., 1946, Late Mesozoic and Early Cenozoic history of central Utah: U.S. Geological Survey Professional Paper 205-D, p. 117-161.

Spieker, E.M., 1949, The transition between the Colorado Plateau and the Great Basin in central Utah: Utah Geological Society Guidebook 4, 106 p.

Spieker, E.M., and Reeside, J.B., Jr., 1925, Cretaceous and Tertiary formations of the Wasatch Plateau, Utah: Geological Society of America Bulletin, v. 36, p. 435-454.

Stanfield, K.E., and Frost, I.C., 1949, Method of assaying oil shale by a modified Fischer retort: U.S. Bureau of Mines Report of Investigations 4477, 13 p.

Tissot, B.P., Califet-Debyser, Y., Deroo, G., and Oudin, J.L., 1971, Origin and evolution of hydrocarbons in Early Toarcian shales, Paris Basin, France: American Association of Petroleum Geologists Bulletin, v. 55, p. 2177-2193.

Tissot, B., Deroo, G., and Hood, A., 1978, Geochemical study of the Uinta Basin—Formation of petroleum from the Green River Formation: Geochimica et Cosmochimica Acta, v. 42, p. 1469-1485.

U.S. Geological Survey Energy Resources Program, 2015, Geochemistry laboratories methods: http://energy.usgs.gov/GeochemistryGeophysics/GeochemistryLaboratories/GeochemistryLaboratoriesMethods.aspx (accessed February 28, 2015).

Utah Division of Oil, Gas, and Mining, 2015, Online Oil and Gas Information System – Production Data: http://oilgas.ogm.utah.gov/Data_Center/LiveData_Search/production.htm (accessed March 2015).

Vanden Berg, M.D., Wood, R.E., Carney, S.M., and Morgan, C.D., 2014, Geological characterization of the Uteland Butte Member of the Eocene Green River Formation: an emerging unconventional carbonate tight oil play in the Uinta Basin, Utah: 2014 Rocky Mountain Section of the American Association of Petroleum Geologists Annual Meeting, July 20-22, 2014, Program with Abstracts, p. 44.

Williams, K.E., 2012, The permeability of overpressure shale seals and of source rock reservoirs is the same: American Association of Petroleum Geologists Search and Discover Article #40935.

Yuretich, R.F., 1988, Possible relationships of stratigraphy and clay mineralogy to source rock potential in lacustrine sequences, *in* Fleet, A.J., Kelts, K., and Talbot, M.R., eds., Lacustrine petroleum source rocks: Geological Society of London Special Publications v. 40, p. 139–151.

BIOGRAPHIES

Justin Birdwell is a research environmental engineer and geochemist with the Central Energy Resources Science Center of the U.S. Geological Survey in Denver, Colorado. He received B.S. and Ph.D. degrees in chemical engineering from Louisiana State University in Baton Rouge. His research focuses on estimation of recoverable oil shale resources in the Green River Formation, geochemical aspects of unconventional petroleum resource assessment, environmental impacts of energy development, development and application of new methods for characterizing source rocks and petroleum, and development of energy-related geochemical reference materials.

Michael Vanden Berg is the Petroleum Section Manager for the Utah Geological Survey in Salt Lake City, Utah. He has a M.S. degree in geology from the University of Utah and a B.S. degree in geology from Calvin College in Grand Rapids, Michigan, and is a licensed professional geologist. Mike has worked in the Energy and Minerals section of the Utah Geological Survey for over 10 years evaluating oil shale and petroleum resources.

Ronald Johnson is a research geologist with the Central Energy Resources Science Center of the U.S. Geological Survey in Denver, Colorado, and has worked for more than 40 years with the USGS. He received his undergraduate and advanced degrees from the University of Buffalo in Buffalo, New York. Ron is currently working on a variety of projects related to unconventional petroleum resources in Rocky Mountain basins. He served as the project chief for the recent Green River Formation Oil Shale Assessment and was the lead geologist in the USGS assessment of the Uteland Butte petroleum resource play.

Tracey Mercier is a geographer and spatial analysis expert with the Central Energy Resources Science Center of the U.S. Geological Survey in Denver, Colorado. He received a B.A. degree in geographic information systems from Metropolitan State University in Denver in 1997. From 1996 to 2008, he was a consultant to the USGS. Since 2008, he has been a geographic information and database analyst for the USGS working on energy-related issues.

Adam Boehlke is a physical scientist with the Central Energy Resources Science Center of the U.S. Geological Survey in Denver, Colorado. He received a B.S. in environmental science from Metropolitan State University in Denver and a M.S. degree in environmental science from the University of Colorado, Boulder. His work focus is sedimentary diagenesis, clay mineralogy, and mudrock characterization by means of ion bean and X-ray analysis.

Michael Brownfield is a Scientist Emeritus geologist with the U.S. Geological Survey in Denver, Colorado. He received B.S. and M.S. degrees in geology from the University of Oregon. His research has focused on coal geology, geochemistry, and sedimentology utilizing data from petrographical, mineralogical, and geological analysis of coal and coal-bearing rocks. Mick has worked extensively in both domestic and foreign coal and petroleum systems, with particular focus on regional stratigraphic studies of Cretaceous and Tertiary coal-bearing sequences in northwest Colorado to support resource evaluation. He was a key member of the National Coal Assessment, National Oil and Gas Assessment for the northwestern United States, the 2012 World Petroleum Assessment, and the Green River Formation Oil Shale Assessment. He has been involved in USGS programs designed to provide technical assistance to foreign countries in defining and developing their resources, including Mauritania and Bulgaria and a multiyear project in Armenia, where he served as a consultant to Armenian geologists on coal exploration and resource assessment. Currently he is conducting assessments for the National and Global Assessment of Petroleum Resources Project on basins in Sub-Saharan Africa.

Appendix III

Lithofacies, Deposition, Early Diagenesis, and Porosity of the Uteland Butte Member, Green River Formation, Eastern Uinta Basin, Utah and Colorado

S. Katherine Logan[1], J. Frederick Sarg[1], and Michael D. Vanden Berg[2]

[1]Colorado School of Mines, Golden, CO
[2]Utah Geological Survey, Salt Lake City, UT

Utah Geological Survey Open-File Report 652

LITHOFACIES, DEPOSITION, EARLY DIAGENESIS, AND POROSITY OF THE UTELAND BUTTE MEMBER, GREEN RIVER FORMATION, EASTERN UINTA BASIN, UTAH AND COLORADO

S. Katherine Logan, J. Frederick Sarg, and Michael D. Vanden Berg

OPEN-FILE REPORT 652
UTAH GEOLOGICAL SURVEY
a division of
UTAH DEPARTMENT OF NATURAL RESOURCES
in cooperation with the
U.S. GEOLOGICAL SURVEY
2016

LITHOFACIES, DEPOSITION, EARLY DIAGENESIS, AND POROSITY OF THE UTELAND BUTTE MEMBER, GREEN RIVER FORMATION, EASTERN UINTA BASIN, UTAH AND COLORADO

S. Katherine Logan[1], J. Frederick Sarg[1], and Michael D. Vanden Berg[2]

[1] Department of Geology & Geological Engineering,
Colorado School of Mines, Golden, CO; corresponding author, jsarg@mines.edu

[2] Utah Geological Survey, Salt Lake City, UT

Cover photo: *Transition from the fluvial Wasatch Formation (red slope) to the lacustrine carbonates and mudstones of the Uteland Butte member of the Green River Formation, eastern Uinta Basin.*

OPEN-FILE REPORT 652
UTAH GEOLOGICAL SURVEY
a division of
UTAH DEPARTMENT OF NATURAL RESOURCES
in cooperation with the
U.S. GEOLOGICAL SURVEY
2016

STATE OF UTAH
Gary R. Herbert, Governor

DEPARTMENT OF NATURAL RESOURCES
Michael Styler, Executive Director

UTAH GEOLOGICAL SURVEY
Richard G. Allis, Director

PUBLICATIONS
contact
Natural Resources Map & Bookstore
1594 W. North Temple
Salt Lake City, UT 84114
telephone: 801-537-3320
toll-free: 1-888-UTAH MAP
website: mapstore.utah.gov
email: geostore@utah.gov

UTAH GEOLOGICAL SURVEY
contact
1594 W. North Temple, Suite 3110
Salt Lake City, UT 84114
telephone: 801-537-3300
website: geology.utah.gov

CONTENTS

FIGURES

TABLES

LITHOFACIES, DEPOSITION, EARLY DIAGENESIS, AND POROSITY OF THE UTELAND BUTTE MEMBER, GREEN RIVER FORMATION, EASTERN UINTA BASIN, UTAH AND COLORADO

S. Katherine Logan, J. Frederick Sarg, and Michael D. Vanden Berg

ABSTRACT

The Uteland Butte member of the lower Green River Formation in the eastern part of Utah's Uinta Basin was correlated and mapped from outcrop to the subsurface using lithofacies and sequence-stratigraphic boundaries. The study area extends from the outcrop on the western side of the Douglas Creek Arch where lake-margin sediments occur, to cores from the Greater Natural Buttes natural gas field in central Uintah County, where sublittoral facies are predominant.

Eighteen facies and eight facies associations were described in the Uteland Butte section. Facies were identified based on lithology, grain size, texture, sedimentary structures, bed thickness, bed boundaries, and geometries and include: (F1) grey/green siltstone, (F2) lime to dolomitic mudstone, (F3) ostracod lime mudstone-wackestone, (F4) molluscan lime wackestone-packstone, (F5) oolitic lime mudstone-wackestone, (F6) intraclastic-ostracod lime packstone-grainstone, (F7) ostracod lime packstone-grainstone, (F8) oolitic lime packstone- grainstone, (F9) oncolite-ooid lime packstone-grainstone, (F10) ooid-pisolite lime packstone-grainstone, (F11) bioclastic lime floatstone to rudstone, (F12) ostracod-bearing sandstone, (F13) structureless to laminated sandstone, (F14) cross-stratified sandstone, (F15) carbonaceous shale, (F16) laminated illitic claystone, (F17) argillaceous mudstone, and (F18) laminated silty oil shale. Sedimentary facies are grouped into eight facies associations based on lateral and vertical relationships of depositional environments, energy level of the lake water, and relative water depth and include: (FA-A) fluvial-deltaic deposits, (FA-B) shoreline carbonate mudstone, (FA-C) littoral to sublittoral claystone to sandstone, (FA-D) carbonate shoal, (FA-E) microbial carbonate, (FA-F) littoral to sublittoral bioclastic mudstone to wackestone, (FA-G) littoral to sublittoral oil shale, and (FA-H) laminated oil shale.

On the eastern edge of the lake basin, where a ramp margin persisted and deltaic and fluvial influences were minor, outcrops show lake-margin environments that underwent four major flooding events. These cycles are correlated into the deeper regions of the lake using cores from the Greater Natural Buttes natural gas field area. Sublittoral successions from deeper in the lake are 30% thicker than the marginal Uteland Butte successions and are lean in silt and richer in dolomite—nearly every bed deposited in the sublittoral environment contains greater than 25% dolomite.

The Uteland Butte member contains rare stromatolites and lacks evaporites and analcime, but bivalves, gastropods, and ostracods are abundant across the study area, indicating a fresh water lake environment. Mud occurs in three forms: calcite, dolomite, and clay. Dolomite displays intercrystalline porosity averaging between 7 and 17%. Dolomitic mud found in packstones and grainstones occurs primarily as grain coatings, intraclasts, and peloids.

INTRODUCTION

The Uinta Basin, located in northeastern Utah and northwestern Colorado, is recognized for its organic-rich, Eocene-aged, lacustrine deposition (Bradley, 1931; Cole and Picard, 1978; Dyni and Hawkins, 1981; Hasiotis and Honey, 2000). Lacustrine systems are widely known to be sensitive to minor changes in accommodation and climate because of the smaller volumes of water and sediment compared to marine systems (Bohacs and others, 2000). Fluctuations in lake water levels can be rapid and are preserved in lake sediments that show distinctive vertical and lateral variations in stratigraphic units like the Green River Formation.

This study focuses on the lacustrine lithofacies, depositional processes, and diagenesis of the eastern portion of the Uteland Butte member of the lower Green River Formation; the formation's first major, widespread lacustrine unit. This interval is characterized by limestone, dolomite, organic-rich-calcareous mudstone, siltstone, and rare sandstone beds (Morgan and others, 2003). Dolomitized sections in the western portion of the basin act as hydrocarbon reservoirs which have porosity values commonly above 20% but low permeability due to very fine to microcrystalline fabric, and are targeted via horizontal drilling (Vanden Berg and others, 2014; Birdwell and others, in press).

The main goal of this study was to develop an integrated, subsurface to outcrop, sequence-stratigraphic framework for the depositional systems and lateral facies relationships of the

carbonates and siliciclastics in the Uteland Butte on the eastern, non-productive, side of the Uinta Basin. In addition, this study includes a cursory characterization of the distribution and timing of dolomitization, including a description of pore types, dimensions, geometry, and distribution within the facies of the Uteland Butte member.

Previous Work

The Uteland Butte member represents the initiation of a lake environment at the end of deposition of the alluvial Wasatch Formation (Morgan and Bereskin, 2003). Bradley (1931) first described this unit on the western side of the Uinta Basin in Indian Canyon as the basal tongue of the Green River Formation. He considered this interval to be the first sediments of ancient Lake Uinta. The Uteland Butte member is equivalent to the basal limestone facies of Little (1988) and the Uteland Butte limestone of Osmond (1965). More recent work has been completed on the lower Green River Formation in the southwestern and western regions of the basin (Ryder and others, 1976; Remy, 1992; Wiggins and Harris, 1994; Keighley and others, 2003; Morgan and Bereskin, 2003; Taylor and Ritts, 2004; Burton and others, 2014), but little research has been completed on the eastern area where extensive outcrop exposures exist. Publications that focus on the eastern Uinta Basin are limited to general basin wide studies (Johnson, 1985a; Johnson, 1985b; Franczyk and others, 1992; Rosenberg and others, 2015). Johnson (1985a) completed a detailed study of the depositional history of the Piceance and Uinta Basins. The Green River tongue or Uteland Butte member in the eastern basin area is mentioned as a lime section rich in mollusks and ostracods (Johnson, 1985b). Most recently, the western portion of the Uteland Butte, which has been the target of significant hydrocarbon exploration, has been studied by Burton and others (2014), Vanden Berg and others (2014), and Birdwell and others (in press).

Tectonic Setting

The Uinta Basin is a structural and sedimentary basin formed in Late Cretaceous through early Tertiary time when rising Laramide uplifts broke up the Rocky Mountain foreland area into a number of smaller basins (Johnson, 1985a). These basins were separated by basement cored uplifts including the Uinta Mountains, Douglas Creek Arch, Uncompahgre Uplift, and the San Rafael Swell (figure 1). Laramide tectonism remained active throughout the Paleocene-Eocene depositional time interval of the Wasatch-Green River Formations (Franczyk and others, 1992). This tectonic activity, in combination with climatic changes, controlled lacustrine development in the early Eocene (Bohacs and others, 2000; Carroll and others, 2006; Davis and others, 2008, 2009).

The Uinta Basin is an asymmetrical foreland basin, with the largest sediment accumulations (greater than 4 km) close to the Uinta Uplift along the northern margin of the basin where subsidence was greatest (Fouch and others, 1992; Keighley and others, 2003). The more gently dipping southern margin of the basin experienced less subsidence and abundant sediment influx throughout the Paleocene and Eocene. The basins containing Green River sediments, including the Uinta Basin, are considered examples of ponded basins (Dickinson and others, 1988). During periods of high lake levels, the Uinta Basin on the west and the Piceance Basin on the east were connected into one large lake.

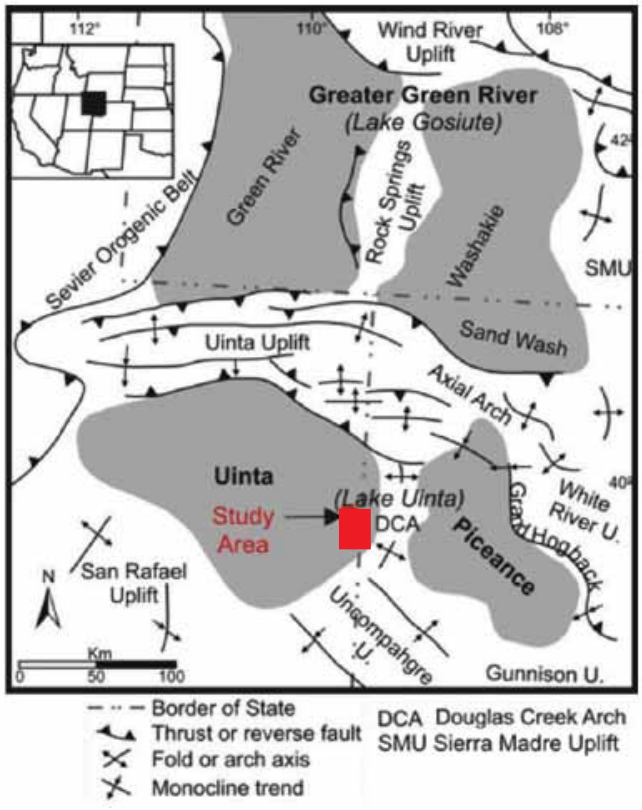

Figure 1. *Eocene intermountain lake basins and associated bounding uplifts in Colorado, Utah, and Wyoming (modified after Dickinson and others, 1988). Study area is outlined with red square.*

Field Area

The Uinta Basin is located in northeastern Utah and northwestern Colorado on the western edge of the Rocky Mountains. The basin lies almost entirely within the state of Utah and is separated from the related Piceance Basin by the Douglas Creek Arch (figure 1). The study area lies within Rio Blanco County, Colorado, and eastern Uintah County, Utah, in four main canyons: Hells Hole Canyon, Evacuation Creek, Texas Creek, and Missouri Creek, an area covering about 150 km^2 (figure 2). The outcrop locations are approximately 105 km southeast of Vernal, Utah, and run north-south along the Utah-Colorado state border.

Two Uteland Butte cores were made available to this project courtesy of Anadarko Petroleum Corporation. The addition of these cores from the Greater Natural Buttes natural gas field, approximately 60 km northwest of the outcrop areas, allowed

for a depositional and stratigraphic transect from the eastern margin toward the basin center (figure 2). The drilling of the NBU 921-22M-GR well included recovery of 28 m of core, from 4826 to 4919 feet drill depth, with a 3.6 foot upward shift to match the geophysical logs, and covers nearly the entire Uteland Butte section. The NBU 921-18C4BS core consists of four recovered intervals in the lower Green River Formation. The lowest core, core 4, captures the upper 14.6 meters of the Uteland Butte, from about 5080 to 5128 feet drill depth, with a 1.5 foot downward shift to match the geophysical logs.

Stratigraphy

Deposition of the Green River Formation lacustrine sediments in Lake Uinta occurred over a roughly 10 million year period between about 54 to 44 Ma (Picard, 1957; Ryder and others, 1976; Smith and others, 2008, 2010; Davis and others, 2010). The Green River Formation lies above and is interbedded with the uppermost variegated shale, sandstone, and conglomerate fluvial deposits of the Wasatch Formation in the east and the Colton Formation in the west (figure 3). Overall thickness of the Green River Formation varies across the Uinta Basin. The thickest sediment accumulations (>2000 m) are to the west-northwest, the location of the early paleo-depocenter and the longest lived portion of the lake. In contrast, the eastern-southeastern edge, closer to the outcrop, has an average lacustrine sediment thickness of 900 m (Ryder and others, 1976; Schamel, 2015).

The lower Green River Formation, in the southern basin area, is subdivided into two main stratigraphic intervals bounded by regionally correlative carbonate units. The oldest interval is the Uteland Butte member, a bioclast-bearing unit that represents the first widespread lake system in the Unita Basin. In

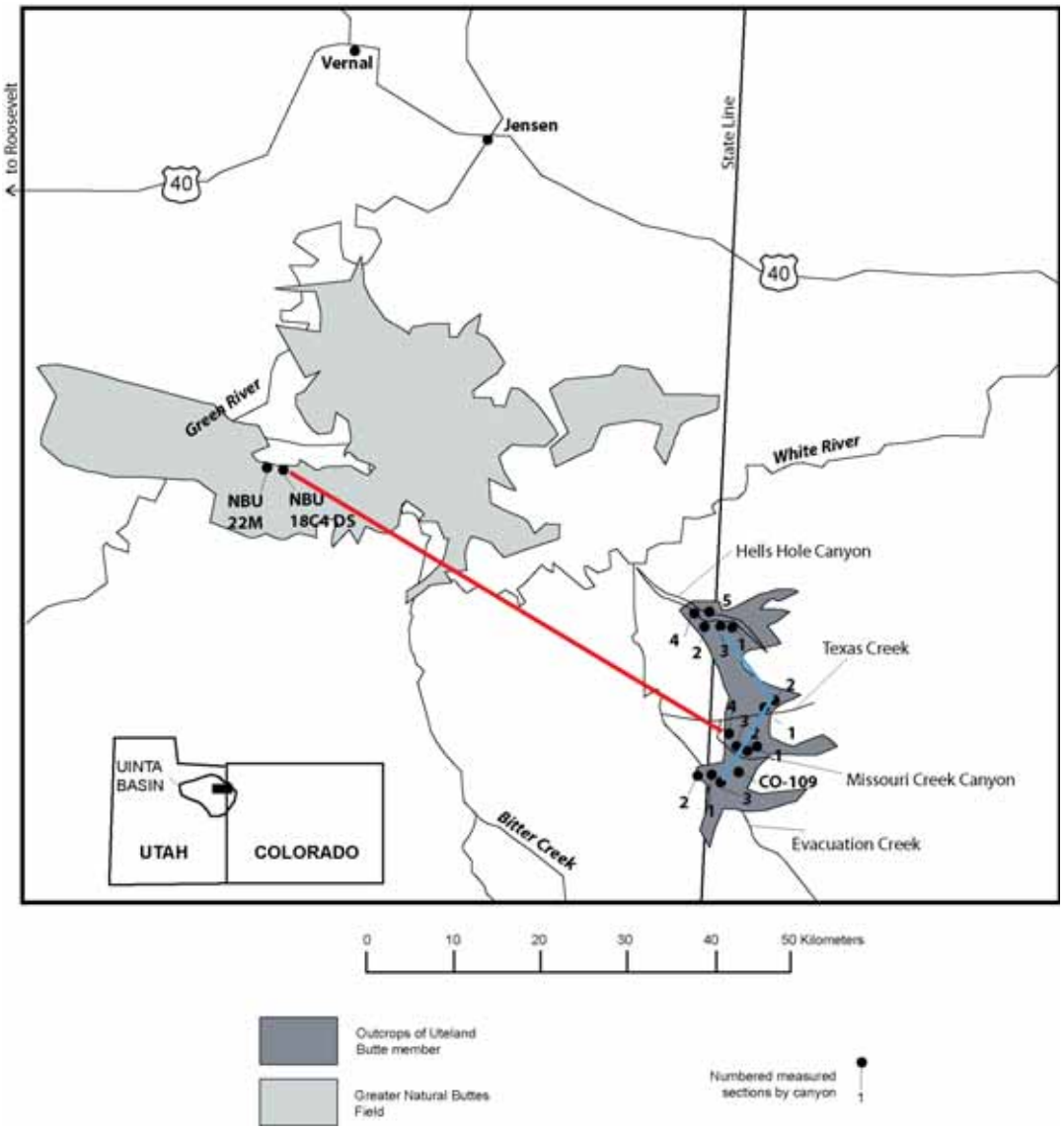

Figure 2. *Location map for eastern Uinta Basin study area, from eastern lake margin where outcrops lie along the Colorado-Utah border to cores from the Greater Natural Buttes natural gas field. A cross section along strike follows the blue line; a dip cross section from Missouri Creek to the Natural Buttes cores follows the red line.*

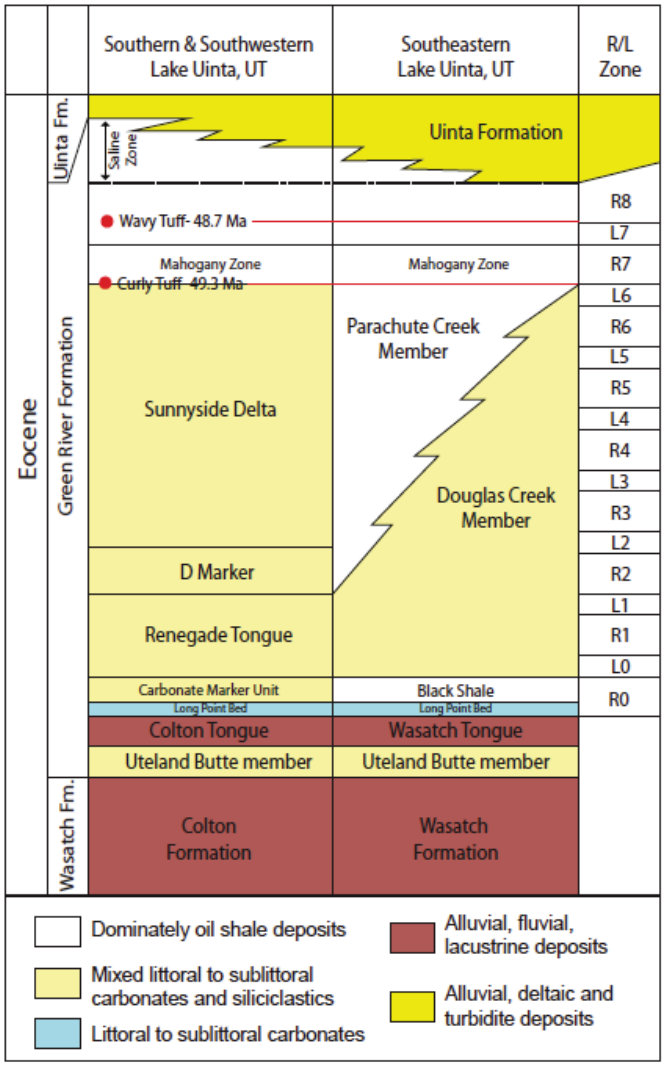

Figure 3. *Lithostratigraphic subdivision of the lower and middle Eocene deposits and correlation with kerogen-rich (R) and kerogen-poor (L) zones in the Uinta Basin (figure modified after Pitman, 1996; Dyni, 2006; Johnson and others, 2010; Self and others, 2010a, b; Tänavsuu-Milkeviciene and Sarg, 2012; Vanden Berg, 2008; rich and lean zones after Cashion and Donnell, 1972, 1974; Long Point Bed after Johnson, 1984). Rich and lean zones apply only for the deep lake deposits and cannot be used for correlation in the shallow marginal areas. Wavy and Curly Tuff numbers represent million years ago (Smith and others, 2010).*

the southern basin margin area, the Uteland Butte interfingers above and below with the alluvial-fluvial-lacustrine Wasatch Formation (figure 3). The upper Wasatch tongue in the east and the Colton tongue in the west are overlain by the second carbonate interval, the Carbonate Marker Unit which contains the Long Point Bed (Johnson, 1985a; Johnson, 1985b; Schomacker and others, 2010). The Long Point Bed overlies the Wasatch tongue in the study area and forms a distinctive bioclastic coquina interval that marks the beginning of the next transgression. The Black Shale Facies, which overlies the Long Point Bed, is equivalent to the upper portion of the Carbonate Marker Unit found farther to the west. Overlying the Black Shale Facies is the Douglas Creek Member of the Green River Formation, which is characterized by interbedded fluvial-deltaic and carbonate deposits (Abbott, 1957; Ryder and others, 1976). The Parachute Creek Member of the upper Green River Formation intertongues with these more proximal units and consists of finely laminated calcite and dolomite-rich mudstones deposited in alternating organic-rich (R) and lean (L) zones. These zones are interbedded with sparse siltstone and sandstone beds (Cashion and Donnell, 1972, 1974). The most consistent marker bed in the Green River Formation is the Mahogany oil-shale bed (within the R7), which lies within the Parachute Creek Member and represents Lake Uinta's highest water level (Johnson and others, 2010).

Uteland Butte Member

In the study area, the Uteland Butte member unconformably overlies a thick, variegated paleosol interval in the upper Wasatch Formation and is overlain by an alluvial pulse that comprises the uppermost Wasatch Formation or Wasatch tongue (Bradley, 1931; Ryder and others, 1976; Remy, 1992). The Uteland Butte member ranges in thickness from 15 to 65 m and consists of limestone, dolomite, organic-rich calcareous mudstone, siltstone, coquina, and occasional sandstone (figure 4). Along the eastern lake-margin, the Uteland Butte deposits are up to 22 m thick and consist of intermixed carbonate grainstone and mudstone beds. Ostracod and oolite-bearing grainstone beds, as thick as 2.5 m, are commonly interbedded with mixed mudstone and siltstone. The Uteland Butte member is a highly cyclic interval with centimeter to decimeter scale changes in outcrop and core (figure 4). The interval shows an overall coarsening upwards through time, and carbonate grainstone replaces the light green claystone and siltstone that dominate early lake deposits. The presence of ostracod and mollusks in the Uteland Butte member indicate that this unit was deposited in relatively clear and fresh lake waters that had little clastic input (Picard, 1957).

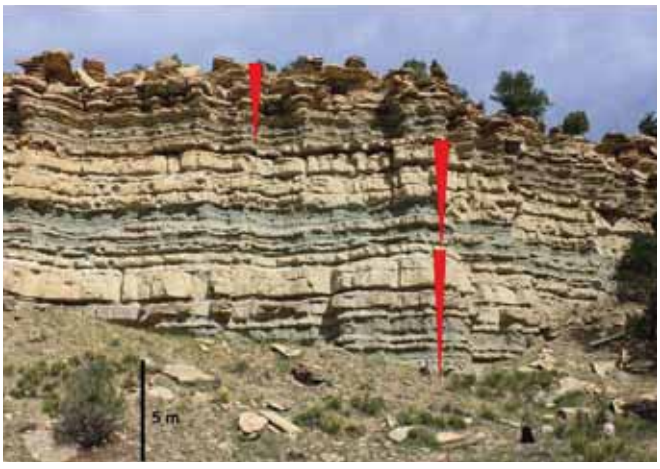

Figure 4. *White Face Butte outcrop at the Evacuation Creek 1 measured section (see figure 2) showing grey/green siltstone interbedded with light tan, bioclastic, lime packstones and grainstones. Red triangles indicate three shallowing up intervals in the Uteland Butte member.*

Depositional Cyclicity

A cycle is used to describe repetitive sedimentary successions interpreted to represent lacustrine expansion and contraction (Pietras and others, 2003). Several cycles are present within the Uteland Butte member (figure 4). Cycles in the lake margin region show shallowing upward sequence; a similar trend has been observed in other units of the Green River Formation on the southern and western side of the Uinta Basin (Eugster and Hardie, 1978; Smoot, 1983; Little, 1988). The cycles in the Uteland Butte range from 4 to 7 m thick on the margin and between 7 and 13 m in the deeper basin. These cycles are bounded by flooding surfaces in the form of littoral, lean oil shale and laminated ostracod siltstones along the eastern edge, and by black, laminated oil shale in the basin center. Flooding surfaces are commonly marked by intraclastic rudstone above, usually a few centimeters thick.

METHODOLOGY

This study integrated outcrop with subsurface data to construct a sub-regional correlation of the Uteland Butte member in northwestern Colorado and northeastern Utah. Fifteen outcrop sections were measured over 150 km^2 between Evacuation Creek and Hells Hole Canyon along the Colorado-Utah border. Sections range from 15 to 22 m in thickness and were measured on a centimeter scale to define lake level fluctuations and associated sedimentary cyclicity. The Uteland Butte is exposed in five canyons in this area including Evacuation Creek, Missouri Creek, Texas Creek, and Hells Hole Canyon (figure 2). In Hells Hole, the outcrops are continuous for about 8 km until they dip into the subsurface. Along strike variations can be assessed with a cross section transect from White Face Butte in the south to Missouri Creek, then Texas Creek, and finally to Hells Hole Canyon in the north. Sections in each respective canyon are anywhere from a 0.5 to 2 km apart, and distances between canyons vary between 3 and 24 km. Detailed descriptions identified lithology, nature of contacts, presence of fossils, organic-richness, and bed architecture.

Lithofacies and facies associations were defined for the outcrop sections and the two cores. Facies are primarily based on grain-size, depositional texture, fossil or bioclast abundance, and sedimentary structures. Facies associations were defined to represent distinctive depositional settings and are based on Gierlowski-Kordesch (2010).

Petrographic description was completed on thin sections from 41 outcrop samples within the Uteland Butte member and the Wasatch Formation. Thin sections, prepared for Anadarko by Weatherford Laboratories, from the core were also described. Descriptions include observations of porosity character, carbonate grain identification (calcite vs. dolomite), estimation of mineral percentages, and examination of rock microstructures.

Dip and strike cross sections were constructed from the outcrop into the subsurface (figure 2, red line is a depositional dip cross section and blue line represents a depositional strike cross section). This project focused only on an eastern to central basin correlation. In addition, these cross sections integrate data into a sub-regional depositional model and provide regional context on the nature of the facies changes and dolomite relationship in the basin. Correlative surfaces helped identify major cycles and were mapped using flooding surfaces.

Characterization of microporosity was undertaken using the QEMSCAN (***Q****uantitative* ***E****valuation of* ***M****inerals by* ***SCAN****ing* electron microscopy) analysis tool. QEMSCAN is an integrated system that consists of a Scanning Electron Microscope (SEM), four nitrogen-free Energy-Dispersive X-ray spectroscopy (EDS) detectors, and proprietary software to capture a wide spectrum of elemental abundance data on a pixel basis and to image pore size and architecture. Twelve samples, representing a distribution of lithofacies identified in outcrop and core were analyzed at the Colorado School of Mines for quantitative mineralogy, porosity, and grain size. These analyses provided information about dolomite distribution, clay mineralogy, porosity distribution, and pore geometry.

LITHOFACIES

Eighteen sedimentary facies are recognized in the Uteland Butte member within the study area. Facies were identified based on lithology, grain size, and sedimentary structures (table 1). Additional criteria for lithofacies identification include bed thickness, bed boundaries, and geometries. These facies are grouped into eight facies associations based on lateral and vertical relationships between the facies (table 2). Rock texture is based upon Dunham's classification (1962), with the Embry and Klovan (1971) modification (e.g., rudstone, floatstone). Classification of mixed siliciclastic-carbonate rocks containing between 10 to 50% terrigenous admixtures were distinguished in nomenclature from pure carbonates. Grains were not incorporated into the rock name until they compose >20% (for intraclasts, oncoids, or ooids) or >40% (for fossils and peloids) of the rock (Strohmenger and Wirsing, 1991).

Lacustrine zones in Lake Uinta have been defined by energy levels as: (1) the littoral zone above fair-weather wave base; (2) the sublittoral zone between fair weather wave base and storm wave base; and (3) the profundal zone below storm wave base (after Reading and Collinson, 1996; Cohen, 2003; Renaut and Gierlowski-Kordesch, 2010). The relative water depth is defined after Renaut and Gierlowski-Kordesch (2010) and Tänavsuu-Milkeviciene and Sarg (2012), where a shallow lake is described as a lake with only littoral and sublittoral zones and a deep lake is described as a lake with littoral, sublittoral, and profundal zones.

Table 1. *Lithofacies in the Uteland Butte member of the Green River Formation.*

	Lithofacies	Texture/lithology/ grain types	Structure	Thickness	Geometries and Contacts	Location	FA
1	Grey/Green Siltstone	Siliciclastic clay to silt	Laminated to massive	Laminated to very thick bed	Laterally continuous, sharp basal non-erosive contact	Littoral to sublittoral	A, C
2	Lime to Dolomitic Mudstone	Lime mud	Structureless, commonly graded or laminated	Medium to very thick bed	Laterally continuous, sharp contact	Littoral	A, B, F
3	Ostracod Lime Mudstone-Wackestone	Lime mud, ostracods, siliciclastic quartz particles, microbial	Ostracods, massive, graded, plane-parallel, cross-stratified	Very thin to thick	Laterally continuous, Sharp basal non-erosive contact	Littoral to sublittoral	B, C, E, F, G
4	Molluscan Lime Wackestone-Packstone	Lime mud, shells, siliciclastic clay particles	Bivalves, gastropods, structureless, wavy, plane-parallel	Laminated to thick	Sharp basal non-erosive contact, undulatory, gradational	Littoral to sublittoral	B, C, F, G
5	Oolitic Lime Mudstone- Wackestone	Lime mud, oolites, pisolites	Massive, plane-parallel	Thin bed	Sharp basal non-erosive contact	Littoral	B, C, F, G
6	Intraclastic-Ostracod Lime Packstone-Grainstone	Carbonate mud clasts, ostracods	Ostracod, mud clasts, structureless, ripple cross-laminations	Very thin to medium bed	Thin and undulatory, gradational	Littoral to sublittoral	C, D
7	Ostracod Lime Packstone-Grainstone	Ostracods, peloids, lime mud	Massive, plane-parallel, ripple cross-laminations	Very thin to very thick bed	Laterally continuous, sharp base, gradational, gravity flows	Littoral to sublittoral	C, D, F
8	Ooid Lime Packstone-Grainstone	Oolites, peloids, lime mud	Oolites, peloids, massive, plane-parallel	Very thin to very thick bed	Laterally continuous, sharp base	Littoral	D, E
9	Oncolite-Ooid Lime Packstone-Grainstone	Oncoids, lime mud, ostracod grains	Oncolites, lime mud, ostracod grains, quartz, massive	Thin	Gradational	Littoral	C, D, E
10	Ooid-Pisolite Lime Packstone-Grainstone	Pisoids, ostracods, lime mud	Pisolites, peloids, massive or plane-parallel	Thin to medium bed	Thin and discontinuous, gradational	Littoral	D
11	Bioclastic Lime Floatstone to Rudstone	Ostracods and shells, lime mud	Bivalves and gastropods >2mm, structureless or wavy	Very thin to thin bed	Sharp to gradational, laterally continuous	Littoral to sublittoral	D
12	Ostracod-Bearing Sandstone	Fine to medium sand, ostracods, shells, calcite	Ripple cross-laminations, massive	Medium to thick bed	Laterally continuous, sharp base, discontinuous	Littoral	C
13	Structureless to Laminated Sandstone	Fine to coarse grained sand	Structureless, graded, calcite	Thin to thick	Thick and discontinuous, sharp base	Littoral to sublittoral	A, C
14	Cross-Stratified Sandstone	Medium to coarse grained	Planar cross-stratified, high angle	Thick	Sharp lower contact	Shoreline	A
15	Carbonaceous Shale	Lignite	Finely laminated fine sediment, plant and organic material	Thin bed	Thin and continuous	Marshes and swamps	B
16	Laminated Illitic Claystone	Kerogen-rich mud, clay-rich	Parallel-laminated, occasionally ostracod rich, some silt to sand layers and lenses	Laminated to medium bed	Transitional, continuous	Littoral to sublittoral	F, G, H
17	Argillaceous Mudstone	Dolomitic mudstone with siliciclastic clay	Wavy, plane-parallel laminated	Thin to thick bed	Transitional to sharp base	Sublittoral	B, C, F, G, H
18	Laminated Silty Oil Shale	Dominantly dolomitic, kerogen-rich, with silt to very fine sand	Parallel-laminated, silt to sand layers and lenses	Laminated to medium bed	Transitional	Sublittoral to Profundal	G, H

Table 2. *Facies associations of the Uteland Butte member of the Green River Formation.*

FA	Facies Association	Description	Lithofacies
A	Fluvial-Deltaic Deposits	Sandstone channel and tabular bodies laterally and vertically associated with littoral to sublittoral siltstone and sandstone (FA-C), and laterally associated with shoreline mudstone (FA-B) and carbonate shoals (FA-D).	F1, F2, F12, F13, F14, F17
B	Shoreline Carbonate Mudstone	Calcareous and dolomitic mudstones are vertically associated with carbonate shoals (FA-D) and littoral to sublittoral siltstone (FA-C). In association with delta deposits (FA-A).	F2, F3, F4, F5, F15
C	Littoral to Sublittoral Claystone to Sandstone	Large, massive siltstones located down-dip from delta systems (FA-A), sandstones, thin and discontinuous.	F1, F2, F3, F4, F5, F6, F7, F8, F12, F13, F17
D	Carbonate Shoal	Laterally extensive marginal grainstone beds largely ostracod, intraclast and bivalve rich. Vertically and laterally associated with littoral to sublittoral siltstones (FA-C), and laterally associated with FA-A and FA-B.	F6, F7, F8, F9, F10, F11
E	Microbial Carbonate	Thin, wavy laminated, dominantly found mixed with dolomitic mud and ostracod shell beds in sublittoral environments. Vertically associated with littoral to sublittoral oil shale (FA-G), sublittoral siltstones and littoral to sublittoral bioclastic wackestone to mudstone (FA-F).	F3, F8, F9
F	Littoral to Sublittoral Bioclastic Mudstone to Wackestone	Distal carbonate and dolomite deposits with varying amounts of ostracod and bivalve grains. Laminated and laterally continuous. Laterally associated with littoral to sublittoral oil shale (FA-G), laminated oil shale (FA-H) and carbonate shoals, generally ostracod accumulations (FA-D).	F2, F3, F4, F7, F16, F17
G	Littoral to Sublittoral Oil Shale	Laminated silt-rich and kerogen poor oil shale. Laterally continuous. Laterally and vertically associated with carbonate shoals (FA-D), microbial deposits (FA-E) and littoral to sublittoral siltstones and sandstones (FA-C), and FA-F mudstones and wackestones.	F3, F4, F16, F17, F18
H	Laminated Oil Shale	Laterally extensive laminated oil shale with higher kerogen content and low silt percentages. Most distal deposit. Associated with FA-F.	F16, F17, F18

Lithofacies F1: Grey/Green Siltstone

Lithofacies F1 consists of greyish green, fissile mud to silt with varying organic material and includes ostracod and bivalve shells. Beds range from massive to thin and thick plane-laminated and range in thickness from 1 cm to thicker than 3 m. Calcareous content and concretions are found locally and compose up to 20% of this facies. Siliciclastic grains are angular to subrounded and range in size from fine silt to fine sand (figure 5A). Horizontal and vertical burrows are present and can be abundant.

Lithofacies F1 represents a unit mainly deposited from suspension fall-out in a quiet environment away from the higher energy shoreline, in the deeper littoral and sublittoral region. These beds contain abundant ostracods. Abundance of ichnofossils suggests a well-oxygenated lake bottom area. F1 is laterally adjacent to bioclastic rudstone beds, carbonate shoals, and sublittoral to littoral distal sandstone deposits. This facies is persistent throughout the outcrop area.

Lithofacies F2: Lime to Dolomitic Mudstone

Lithofacies F2 is dominantly microcrystalline calcite or dolomite, with between 10 to 30% clay to fine quartz silt, minor amounts of calcite spar, ostracods, pelecypod shells, and accessory minerals (figure 5B). F2 is structureless with some grading into coarser grained rock types. Microcrystalline calcite accounts for 90 to 95% of this facies. Undifferentiated bioclast grains are randomly oriented and angular to subangular in shape. Identifiable ostracod valves and bivalve shells account for less than 3% of matrix and are commonly broken and isolated. There are trace amounts of organic material and fish scales. Bed thickness ranges from 5 mm to >1m. Porosity in this facies is dominantly microporosity and is 1% or less.

Lithofacies F2 is interpreted to have been deposited by precipitation from the water column in calm shoreline environments and on carbonate mud flats. The fine-grained nature of this facies suggests a low-energy depositional environment and the bioclasts suggest oxic conditions with increased water circulation. The low influx of quartz grains suggests relatively great distances from deltaic and fresh water surface inputs into the lake.

Lithofacies F3: Ostracod Lime Mudstone-Wackestone

Lithofacies F3 is dominantly a microcrystalline lime mud with ostracod shells, minor amounts of siliciclastic quartz, and organic material (figure 5C). Beds generally exhibit massive, plane-parallel or cross-stratified laminations in coarser intervals. Ostracod shells are broken and whole and show random orientation, while quartz grains are randomly dispersed, subrounded to rounded, and silt to very fine sand in size. Beds are non-erosive and have a sharp base, and the bed thickness ranges from very thin to thick (1–100 cm).

This facies represents an environment with varying energy activity. The microcrystalline calcite material likely precipitated from the water column in calm water conditions. Ostracods are planktonic and fall out of suspension after death. Deposits in deeper water environments show fining upward

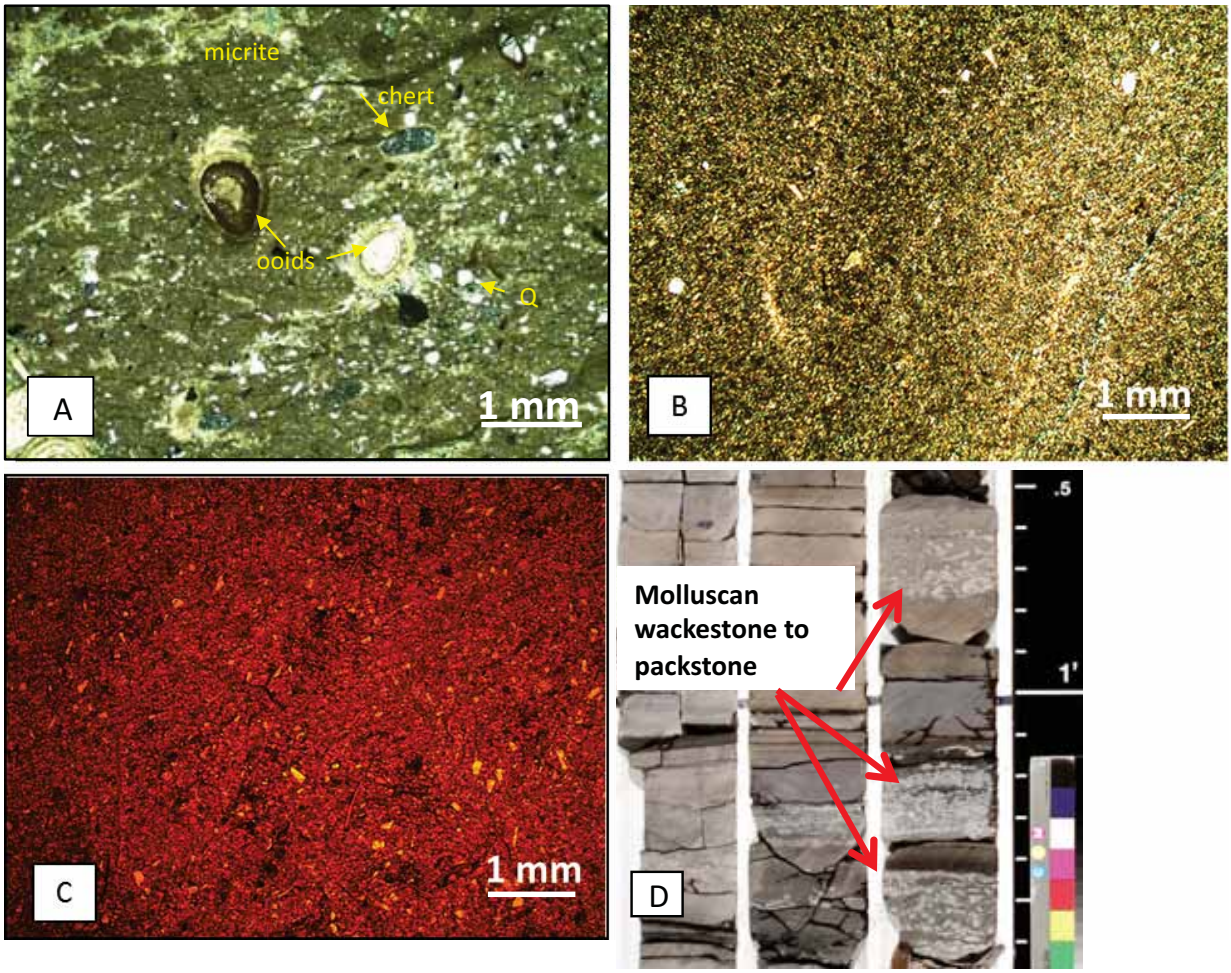

Figure 5. A. *F1 grey/green siltstone with superficial ooid grains, angular quartz (Q), chert, and micrite (Evacuation Creek 2);* ***B.*** *F2 lime to dolomitic mudstone (Evacuation Creek 2);* ***C.*** *F3 ostracod lime mudstone-wackestone (red alizarin stain) with black organic material and yellow quartz grains (Evacuation Creek 2);* ***D.*** *F4 molluscan lime wackestone-packstone from Anadarko NBU 921-22M core, depth range 4870 to 4872.2 feet.*

patterns in places and may have been brought into the distal littoral to sublittoral environment by turbidity flows, which can occur over mudflat (F2) areas extending out to deeper waters in the littoral to sublittoral regions where calm water persists. F3 beds are laterally adjacent to carbonate shoal deposits (F6, F7, F8, and F9), delta deposits (F12, 13, 14, and 17), and carbonate mudflats (F2).

Lithofacies F4: Molluscan Lime Wackestone-Packstone

Lithofacies F4 has a mineralogically homogeneous microcrystalline calcite matrix with bivalve, gastropod, and ostracod grains, and trace amounts of quartz and organic material (figure 5D). Beds are structureless to wavy, plane-parallel laminated, and the pelecypod shells are usually broken and oriented parallel to bedding. Siliciclastic material occurs as angular to subangular silt-sized grains. Beds are very thin to medium (1–30 cm) and have sharp, undulatory, non-erosive basal contacts.

F4 represents an environment with varying energy activity. Again, the microcrystalline calcite material is likely precipitated from the water column in calm water conditions. The biogenic shells suggest an oxic environment. This facies is interpreted to occur in two main areas, along the shoreline in a mudflat area where mollusks flourished or in distal littoral to sublittoral regions where calm water persists. F4 is laterally adjacent to carbonate shoals (F6, F7, F8, and F9) and carbonate mudflats (F2) and is observed in outcrop and core. This facies is dolomite-rich in the two basin center cores.

Lithofacies F5: Oolitic Lime Mudstone-Wackestone

Lithofacies F5 consists of calcareous and dolomitic microcrystalline mud with 5 to 15% sub-spherical ooids and trace amounts of ostracod remains and organic material (lens in figure 6A). F5 shows massive or plane-parallel laminations that are interlaminated with organic material. Bed thickness varies from 2 to 35 cm and displays sharp basal contacts.

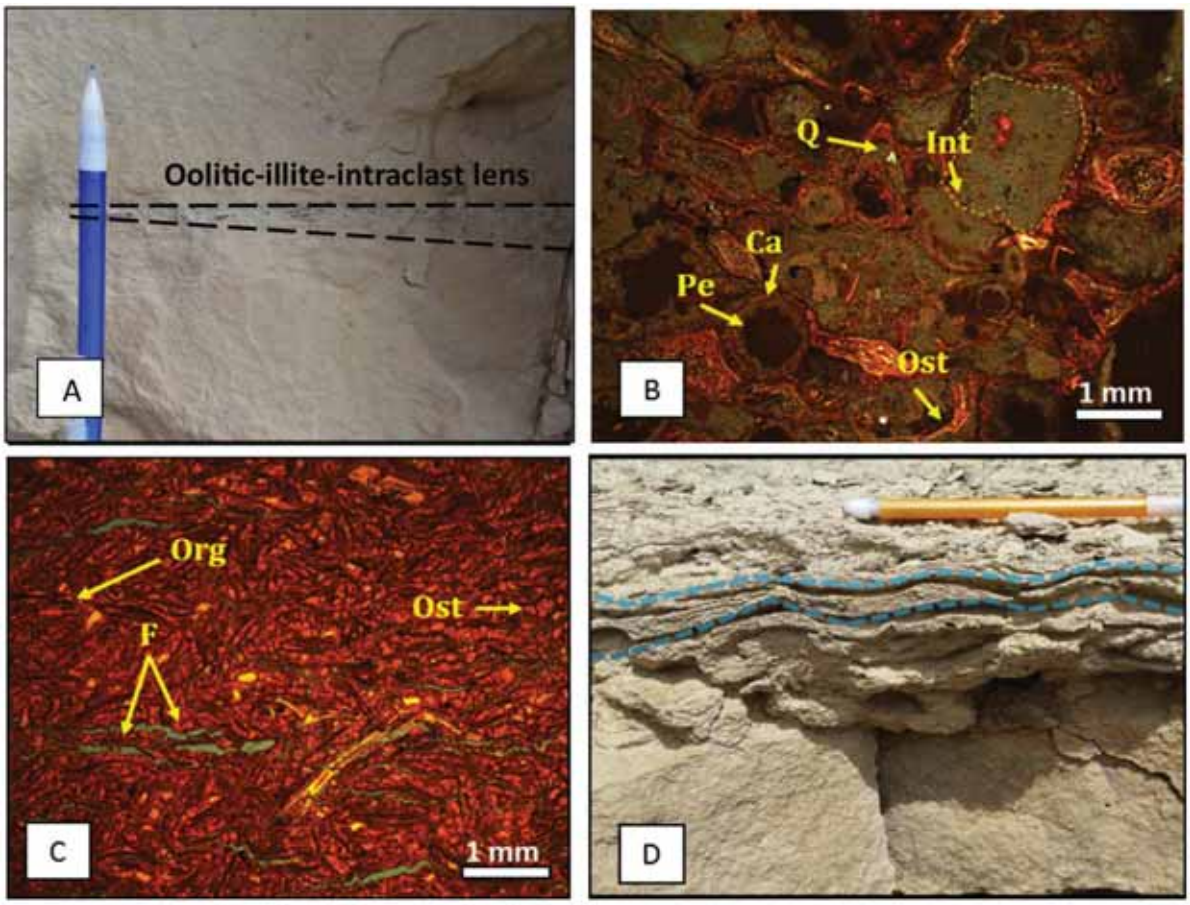

Figure 6. A. *F5 oolitic lime mudstone-wackestone with illite-intraclast lens in lime to dolomite mudstone (F2) (Hells Hole 3);* ***B.*** *F6 Intraclast-ostracod lime packstone-grainstone with intraclasts (Int), ostracods (Ost), quartz (Q), peloids (Pe), and lithified carbonate coating (Ca) (Texas Creek 1);* ***C.*** *F7 ostracod lime packstone-grainstone laminated with fractures (F), organic material (Org), and ostracods (Ost) (Evacuation Creek 3);* ***D.*** *F8 oolitic lime packstone-grainstone with wave-ripple laminations at the top of the bed (Texas Creek 2).*

This facies represents a moderate energy environment. Similar to lithofacies F2, F3, and F4, the calcareous mud is likely deposited as a precipitate from the supersaturated water column in a lower energy environment. Ooids require more energy to form and were probably carried into the system during storms or higher energy events from nearby grainstone deposits (F6, F7, F8, and F9) and are intermixed with F2 mudstone.

Lithofacies F6: Intraclastic Ostracod Lime Packstone-Grainstone

Lithofacies F6 is predominantly composed of intraclast and ostracod grains, with minor amounts of siliciclastic quartz, peloids, and ooids (figure 6B). The intraclasts are poorly sorted, closely packed, angular to subrounded, and range in size from medium sand to gravel (>2 mm) and are dominantly composed of microcrystalline dolomite (figure 6B). The associated ostracods shells are typically filled with dolomicrite and are whole or broken. These clasts are usually deposited with oncoids and broken ostracod pieces. Intraclasts and ostracods have high intraparticle and moldic porosity, with low associated permeability. Siliciclastic grains are rare in F6 and are silt (0.05 mm) in size. Calcite spar occurs as cement between intraclasts and ostracod grains. Beds are thin to medium (3–30 cm) in thickness and have gradational to sharp contacts with other grainstones.

The intraclasts are interpreted to have been broken and transported from carbonate mud flat areas that were partially lithified and dry. These clasts probably formed when a storm or sudden rise in lake level overtook these dried flats and ripped up the carbonate mud material, reworking the pieces to form well-rounded clasts or only moving the clasts short distances leaving them angular. These clasts also appear to have undergone dolomitization prior to their formation. This facies formed along near-shore and sublittoral areas in a moderate energy environment with other carbonate shoal deposits and adjacent to low energy carbonate sediments.

Lithofacies F7: Ostracod Lime Packstone-Grainstone

This lithofacies is an ostracod-bearing limestone with minor amounts of organic material and the rare oncoid (figure 6C).

Beds display massive, wavy, or plane-parallel laminations with grains oriented along laminations. Ostracod valves are closely packed, both broken and whole, and are commonly filled with dolomicrite. Ostracod grains commonly have minor coatings around shells and hold broken ostracod valve pieces inside a larger-whole shells intermixed with dolomite mud. Siliciclastic quartz, when present, is subangular to subrounded and silt sized. Organic material and fish scales display random orientations. F7 beds range from 2 cm to >1 m in thickness and are laterally continuous with sharp bases.

F7 represents a high energy environment with large grains and little mud. F7 is found in marginal to sublittoral areas. Finer-grained muds and silts were likely winnowed and redeposited in calmer environments. F7 beds are laterally associated with other carbonate shoal deposits and carbonate mudflats. These deposits are observed in core and outcrop where they are laterally adjacent to intraclastic packstones (F6), bioclastic packstones (F4) and interbedded with finely laminated oil shale (F18).

Lithofacies F8: Oolitic Lime Grainstone-Packstone

Lithofacies F8 is dominated by calcitic ooids with varying amounts of siliciclastic quartz, organic fragments, and ostracod shells. Beds are massive, plane-parallel laminated or wave-rippled (figure 6D) and ooids are sub-spherical to spherical and superficial. Ooid cores vary in composition and include ostracods, peloids, quartz grains, or host intraparticle porosity. Grains are closely packed and range in size from 0.5 to 2 mm, with a median size of 1.25 mm. F8 is typically associated with ostracod fragments that are lightly coated with calcite and range in size from 0.5 to 1 mm. Intraparticle and oomoldic porosity are dominant in the 1 cm- to >1 m-thick beds that are moderately continuous laterally and have sharp basal contacts. F8 is primarily observed in outcrop.

This facies is interpreted to have been deposited in a high-energy littoral environment. Ooid grainstones possibly formed near an inlet for fluvial systems or areas influenced by wave and wind activity in areas along the eastern margin of Lake Uinta. These deposits accumulate where wave energy and precipitation of carbonate are active in the water column. F8 is a carbonate shoal and occurs laterally adjacent to carbonate mudflat deposits.

Lithofacies F9: Oncolite-Ooid Lime Packstone-Grainstone

Lithofacies F9 is dominantly composed of oncoid grains that have irregular, micritic concentric laminations mixed with ooid grains characterized by even, concentric laminations (figure 7A). The irregular micritic laminations are thought to result from microbial-induced precipitation of calcite. Grains commonly possess both types of laminations. Oncoid-ooid grains are commonly mixed with ostracods, molluscan fragments, and microcrystalline lime mud. Beds show overall lack of structure and are thin from a few cm to 10 cm thick. Grains are ellipsoidal to sub-spherical in shape and range in size from 2 to 6 mm in diameter. Grain nuclei are composed of ostracods, peloids, bivalve fragments, and quartz grains. Porosity is interparticle, intraparticle, intercrystalline, and oomoldic. Beds were generally locally deposited and are not laterally continuous.

F9 is formed through microbial induced precipitation of calcite. These deposits are subrounded and are interpreted to form in episodic wave action that partially rounded the grains. Grains accumulate in partially restricted areas and are intermixed with ostracods.

Lithofacies F10: Ooid-Pisolite Lime Packstone-Grainstone

Lithofacies F10 is dominantly composed of pisoid grains >2 mm and peloid grains with varying amounts of ostracod fragments, molluscan shells, and microcrystalline dolomite (figure 7C). Beds are massive to plane-parallel or wavy laminated, though a lack of structure is most common. Pisoids are subspherical to spherical in shape and range in size from 2 to 4.5 mm in diameter. Pisoid cores are composed of ostracods, peloids, shells, and quartz grains. Porosity is interparticle, intercrystalline, and moldic. F10 beds are very thin to thin (1–10 cm) with gradational bed contacts. Beds are local deposits and not laterally continuous.

This facies formed in lower energy environments than ooids, but higher energy than the carbonate flat muds. The grain support fabric of these pisoid grains suggests episodic energy to move grains and allow coating to precipitate. These deposits accumulated in areas along shorelines extending offshore into a few meters of water depth. F10 is laterally adjacent to carbonate shoal grainstones (F7, 8, 9, 11), which formed in high energy environments, and carbonate mudflat (F2) deposits, which accumulated in low energy environments. This facies is primarily observed in outcrop.

Lithofacies F11: Bioclastic Lime Floatstone to Rudstone

Facies F11 is a molluscan, ostracod-rich crystalline limestone with varying amounts of siliciclastic quartz grains and organic material (figure 7B). Beds in this facies grade from a floatstone to a rudstone lacking mud and show wavy to structureless bedding. The bivalve and ostracod shells present are both broken and whole, and range from 2 to >25 mm in size, with the average grain about 5 mm. Siliciclastic quartz grains are minor and range from very fine to fine sand and are angular to subangular. F11 beds are thin (1–10 cm) and have both gradational and sharp basal contacts.

F11 is a high-energy deposit. The gradational contacts and chaotic nature of these beds supports a storm or singular event

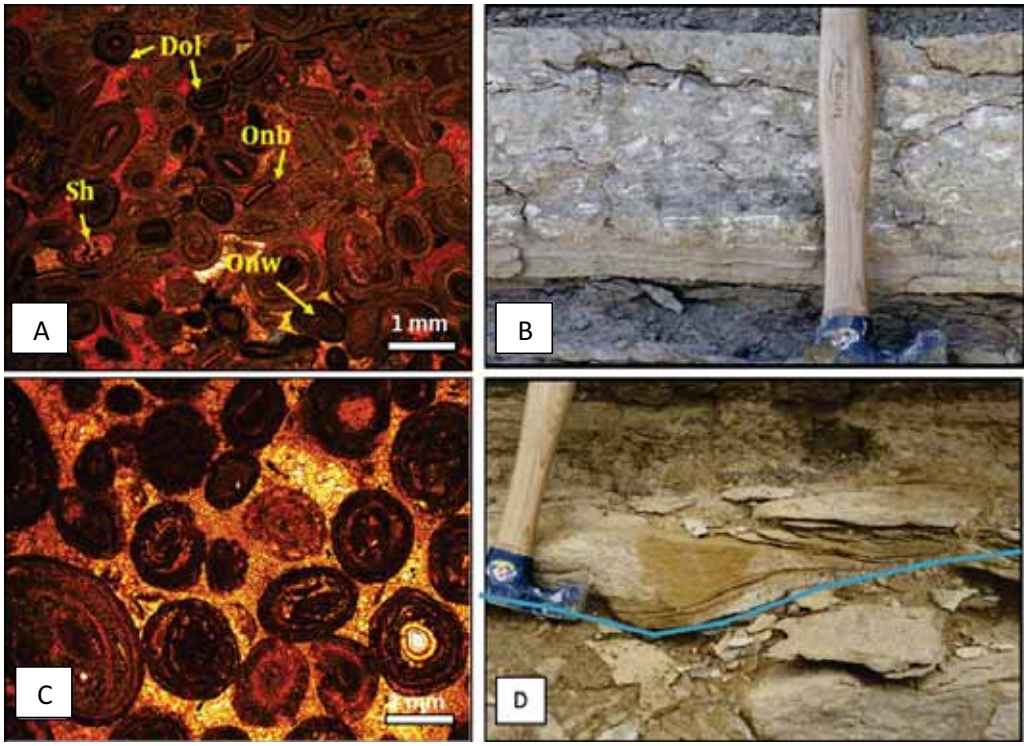

Figure 7. A. *F9 oncolite lime packstone-grainstone with broken ostracod shells (Onb) and whole ostracod shells (Onw), shelter porosity (Sh), and dolomite mud (Dol) (Texas Creek 2, sample #15, PPL). Blue epoxy shows pore space in B and E;* ***B.*** *F11 bioclastic lime floatstone to rudstone with bivalves (Hells Hole 3);* ***C.*** *F10 ooid-pisolite lime packstone-grainstone with ostracod shells (Hells Hole 2);* ***D.*** *F12 ostracod bearing sandstone (Missouri Creek 2).*

deposit. These coarse grainstones are found in distal littoral to sublittoral regions of the lake, primarily down-dip from an area rich in packstones and grainstones where oxygen levels are high and biota flourish. F11 is associated with illitic oil shale (F16), littoral to sublittoral siltstones (F1), and argillaceous dolomudstone (F17).

Lithofacies F12: Ostracod Bearing Sandstone

Lithofacies F12 is an ostracod-bearing, fine- to medium-grained quartz sandstone with varying amounts of detrital grains (clay and feldspar) and organic material. Beds are thin to very thick (3–100+ cm), well sorted, and contain varying amounts of ostracods. They are current ripple cross-laminated or are massive. The quartz is well sorted, subangular to subrounded, ranges from fine to medium grain size, and is well sorted. Ostracod grains are whole or broken and occur in thin bands within the sandstone beds. This facies occurs in limited locations on the eastern margin of the study area (figure 7D).

The ripples in this facies suggest a high energy environment along the margin of the lake. This sand could also be from deeper littoral to sublittoral regions of the lake deposited offshore during storm events when high wave energy was present. The sand was transported into the system through rivers and streams from the Douglas Creek Arch just a few kilometers to the east. These beds are laterally adjacent to carbonate shoal deposits and littoral to sublittoral siltstone deposits.

Lithofacies F13: Structureless to Laminated Sandstone

Lithofacies F13 sandstone beds are fine to medium grained, quartz-rich with varying amounts of feldspar and plagioclase (figure 8A). Grains are angular to subrounded and poorly sorted. Beds are structureless to laminated and laterally continuous in outcrop with no channelization or change in bed thickness over tens of meters. F13 bed contacts have sharp bases.

Facies F13 represents sediments which were probably deposited as distal stream mouth bars along the lake margin. Sediment inputs were from local river systems during periods of high discharge. These beds are associated with littoral to sublittoral siltstones and illitic oil shale and occur in littoral to sublittoral depositional environments.

Lithofacies F14: Cross-Stratified Sandstone

Lithofacies F14 is fine- to medium-grained, well-sorted, tan to yellow sandstone with half-meter scale cross-stratified laminations, cut and fill structures, and current ripples (figure 8B). This facies forms within a sandstone unit that has a sharp base and is channelized. This unit locally occurs in association with green-grey siltstones and claystones and laminated sandstones. This sandstone filled channel can be traced for 30 meters to both edges of the channel body.

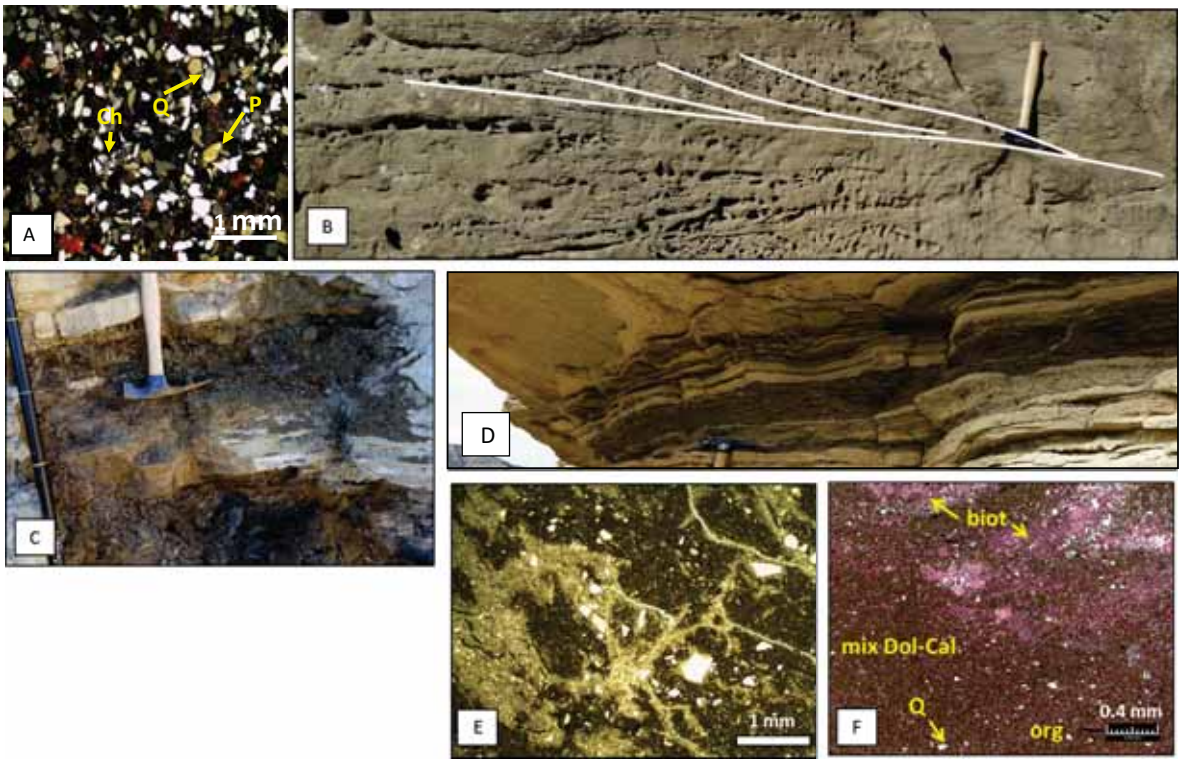

Figure 8. A. *F13 structureless to laminated sandstone, Ch-chert, Q-quartz and P-pyrite (Texas Creek 2);* ***B.*** *F14 cross-stratified sandstone (Evacuation Creek 3);* ***C.*** *F15 carbonaceous shale (Texas Creek 2);* ***D.*** *F16 laminated illite claystone (Missouri Creek 2);* ***E.*** *F17 argillaceous mudstone with micrite and angular quartz grains (white), (Texas Creek 1);* ***F.*** *F18 laminated silty oil shale, containing possible bioturbation (biot), lime mud (Dol-Cal), organic material (org), and silt size quartz (Q), sample from Anadarko NBU 921-22M core, photomicrograph prepared by Weatherford Labs.*

Facies F14 cut and fill features, ripples, and cross-stratification represent a high energy directional system. The well-sorted material suggests that sand was transported over some distance. This facies is interpreted as fluvial channel-fill sediment that fed into the basin.

Lithofacies F15: Carbonaceous Shale

Facies F15 is a thinly laminated organic accumulation. This bed is tabular, 10 to 20 mm thick, and rich in plant material and organic fragments (figure 8C).

This facies represents a backwater environment that was not in the main lake body, but just outside of the lake along the shoreline. This facies represents a swamp environment that likely formed in quiet, protected areas along the lake shore.

Lithofacies F16: Laminated Illitic Claystone

Lithofacies F16 is distinguishable by brown and tan color in outcrop and is a dolomitic clay-rich deposit dominated by illite, montmorillonite, and chlorite clay (QEMSCAN® results, see Calcite, Dolomite, and Porosity section below). This facies is parallel-laminated and sheet-like in geometry (figure 8D). Clay beds, intermixed with thin dolomite layers, are lean in organic content. Rare ostracods are associated with these units. Beds are thin to medium in thickness (3–30 cm) and occur in the upper portion of the Uteland Butte member in the Missouri Creek area along the eastern margin of Lake Uinta.

F16 is a distal littoral to proximal sublittoral deposit that is relatively rich in kerogen compared to surrounding facies, but lean compared to the sublittoral oil shale from the distal cores. This facies represents a low energy environment that received sediment probably through suspension from the water column. F16 is laterally adjacent to bioclastic lime floatstone and rudstone deposits (F11), and argillaceous mudstones (F17).

Lithofacies F17: Argillaceous Mudstone

Lithofacies F17 is a calcareous mudstone with ostracod shells, minor amounts of authigenic calcite, and siliciclastic grains (figure 8E). These beds show fine parallel-laminations that are rich in organic material. Ostracods found in F17 consist of fragments that show minor variability in orientation and are locally concentrated within dolostone (<3 cm thick). Horizontal burrows are present. Silt grains often occur in lenses and range in size from very fine to coarse silt and are subangular to subrounded. F17 bed thickness ranges from 2 mm to >1 m and contacts are sharp or gradational.

This facies represents a moderate energy depositional environment that experienced increased siliciclastic input. The facies likely occurred in a more proximal sublittoral environment than the laminated oil shale (F18) and closer to the siliciclastic input areas. F17 is also associated with ostracod and mollusk wackestones (F3 and F4) and ostracod packstones (F7). This facies is only observed in cores.

Lithofacies F18: Laminated Silty Oil Shale

Facies F18 beds are aphanocrystalline to very fine crystalline, authigenic dolomite that has replaced an original calcareous and clay-rich matrix (figure 8F). These kerogen-rich beds have parallel-laminations which are dominantly matrix-rich with a few grain-rich laminations. Rare, small, horizontal burrows occur within F18. Sparse siliciclastic grains within these beds are subangular to subrounded and range in size from fine silt to fine sand. Beds have sharp, discontinuous contacts which occasionally host load structures and are 3 mm to >1 m thick.

F18 is a low energy facies that represents a depositional environment supplied with sediment from suspension fall-out and precipitation from the water column. These beds are far from fluvial influx. F18 is found in the distal-sublittoral to shallow profundal area of the lake where anoxic conditions preserve the kerogen-rich beds and where bioturbation from organisms is rare. This facies is only observed in core.

FACIES ASSOCIATIONS

The Uteland Butte sedimentary facies (F) as defined by sedimentary structures, textures, and composition are grouped into eight facies associations (FA) based on lateral and vertical relationships (table 2). Facies associations are grouped into lacustrine environments or zones based on energy level and relative water depth. During deposition of the Uteland Butte member, Lake Uinta consisted of littoral, sublittoral, and perhaps shallow profundal environments.

Littoral deposits, observed mainly in outcrop, are rich in siliciclastic and carbonate material. Siliciclastic deposits are predominantly fluvial sandstone to littoral and sublittoral siltstones characterized by low-angle cross-stratification and plane-parallel cross-stratification. These deposits are primarily found at the base of the Uteland Butte member. Deeper lacustrine zones rarely have thick silt and sand accumulations.

Laterally continuous carbonate shoal facies persist along the eastern margin of Lake Uinta. Shoal deposits vary widely in thickness, have sharp bases and are rich in ostracods, dolomitic intraclasts, oolites, oncoids, and bivalve shells. These deposits are typically interbedded cyclically with littoral siltstones. Microbial carbonates are rare and occur as 2 to 3 cm thick capping deposits on ostracod and intraclast grainstones.

Littoral to sublittoral oil shale deposits occur in outcrop in the upper portions of the Uteland Butte member and in association with littoral to sublittoral siltstones and littoral to sublittoral bioclastic mudstone to wackestone deposits.

Sublittoral deposits were observed mainly in core. These beds are mostly bioclastic-rich packstones and wackestones and laminated deposits of littoral to sublittoral oil shale that show large variations in kerogen content.

Facies Association A: Fluvial-Deltaic Deposits

Facies Association A (FA-A) is a fluvial-deltaic deposit containing mixed channel-form sandstones with cross-stratification and scour and fill (F14), as well as structureless sandstone (F13) (figure 9). Color ranges from light tan to yellow or grey-black. F14 bodies vary in thickness from 2 to 5 m and contain concave-up scours, no bioturbation, climbing ripples, high-angle cross-stratification, and plane-parallel laminations. In places, F13 sandstones are bioturbated and contain ostracod shells. Sandstone deposits are laterally discontinuous and the average width is around 15 m. Sand bodies are associated with grey/green siltstone (F1) and have medium to fine-grained subangular clasts that are well sorted. Channel orientation indicates flow from the east and southeast.

The presence of ostracods and moderate sorting of subangular grains of medium to fine sand in the large channel deposits suggest a locally sourced fluvial channel deposit that formed at the edge of a standing water system (Schomacker and others, 2010). Downstream fining is suggested from tracing the channel fill deposit outcrop (figure 9A) in the lakeward direction (figure 9B). The velocity of the discharge in this channel dropped significantly upon contact with a water body the size of Lake Uinta, depositing medium- to coarse-grained material along the shoreline and finer grained sediments in more distal regions.

Areas with large delta influence show increased amounts of sand and silt deposition and less carbonate shoal accumulation. These deltaic deposits were dominantly sourced from the southeast near Evacuation Creek. Minor fluvial influence was observed to the north in the Texas Creek area and no large sand deposits were identified in the northern Hells Hole Canyon area. FA-A is not present in the cores.

FA-A is overlain by ostracod grainstones (F7) and grey/green siltstones (F1) that are interbedded with dolomitic pelodial mudstones (F2) and bioclastic wackestone (F5).

Facies Association B: Shoreline Carbonate Mudstones

Shoreline carbonate mudstones (FA-B) consist of fine-grained micritic to dolomicritic mud associated with calm, oxic water conditions (figure 10). This facies association commonly

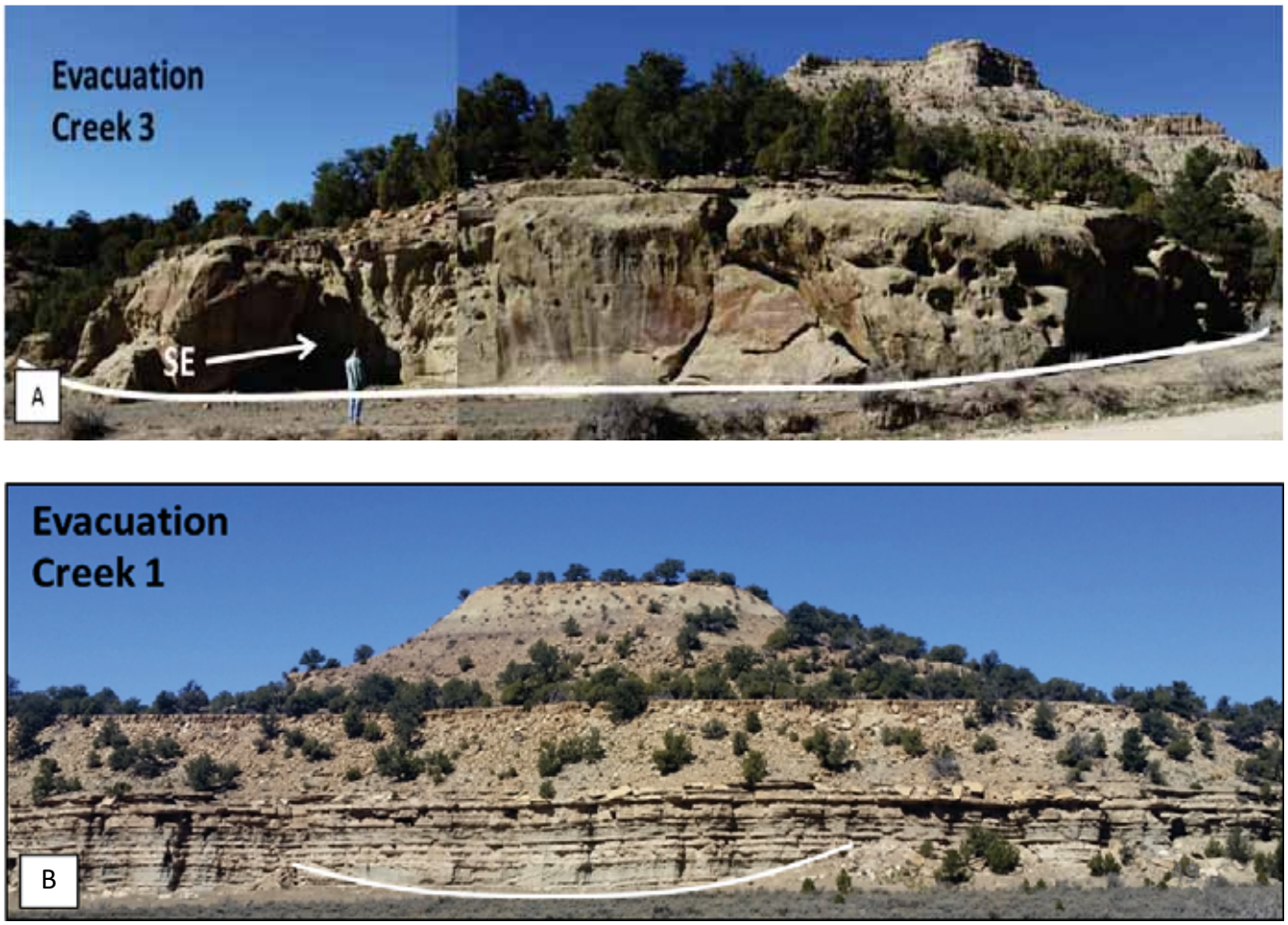

Figure 9. *Facies Association A.* ***A.*** *Channel body in middle Uteland Butte in southern Evacuation Creek; the channel is 30 m wide and 6 m high;* ***B.*** *F1 grey/ green siltstone and thin F13 structureless to laminated sandstones filling channel farther lakeward of (A).*

contains ostracods and is found along the shoreline (figure 10A, B, C, D) and extends into the deeper littoral and proximal sublittoral regions where oxic and low energy conditions are maintained.

This association occurs throughout the entire Uteland Butte member along the eastern portion of the Uinta Basin and in the cores farther to the northwest. These beds can be traced laterally hundreds of meters along the outcrop. FA-B occurs interbedded with carbonates composed of floatstone to rudstone, grainstone to packstones, and carbonate mudstones that are structureless or contain cross-stratification, ripple cross-lamination, and horizontal lamination. Grains include oolites, pisolites, oncoids, encrusted intraclasts, and bioclasts.

FA-B includes calcareous dolomitic mudstone (F2) (figure 10A, B, E), ostracod wackestone to packstone (F3) (figure 10C), molluscan mudstone to wackestone (F4), oolitic mudstone to wackestone (F5), and is associated with the grainstone facies (F6, F7, F8, F9). This facies association is also commonly found interbedded with fluvial-deltaic deposits (FA-A), littoral to sublittoral claystones to sandstones (FA-C), or carbonate shoals (FA-D).

Facies Association C: Littoral to Sublittoral Claystone to Sandstone

Facies Association C (FA-C) is a grouping of facies characterized by grey to green clay to silt size grains that are well sorted within homogeneous and laminated beds (figure 11A, B). Facies in this association include ostracod bearing sands (F12), grey/green siltstones (F1) (figure 11C, D), thin structureless sands (F13), and argillaceous mudstones (F17). Ostracods and preserved organic matter are common in these facies. Contacts are both gradational and sharp. Interbedded facies include calcareous mudstone (F2), ostracod, intraclast-ostracod and peloidal shoals (F6, F7, F8), and bioclastic wackestones (F3, F4, F5). Facies in this association contain burrows filled with carbonate material (FA-D) from overlying beds (figure 11E).

FA-C is genetically related to fluvial systems entering the basin carrying in siliciclastic sediment. This association is closely related to FA-A fluvial-deltaic deposits. FA-C sands represent a more distal sheet-like, down-dip deposit of coarser material. FA-C lacks wave modification features.

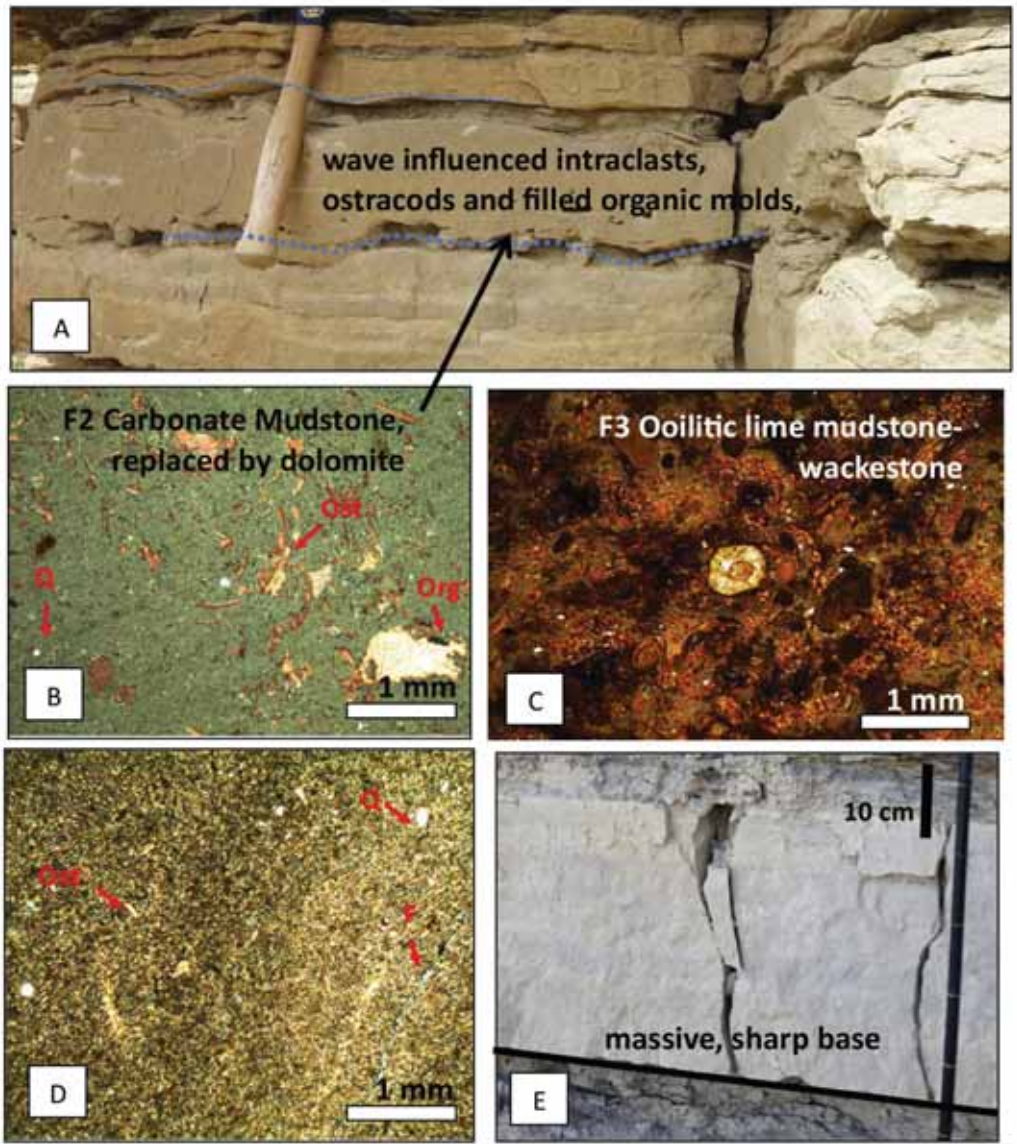

Figure 10. *Facies Association B.* ***A.*** *and* ***B.*** *F2 wave influenced lime to dolomitic mudstone with its associated thin section, Q-quartz, Ost-ostracod, Org-organic material from measured section CO 109, sample #5;* ***C.*** *F3 oolitic lime mudstone-wackestone that is a lens within a calcareous mudstone (Hells Canyon 2, sample #4;* ***D.*** *F2 lime to dolomite mudstone with quartz (Q), ostracod (ost), and fractures (F), (Evacuation Creek 2, sample #8);* ***E.*** *Sharp based F4 molluscan lime wackestone-packstone.*

Facies Association D: Carbonate Shoal

Facies Association D (FA-D) is a marginal littoral deposit of grainstones and packstones composed of oolites, oncoids, pisolites, ostracods, bivalves, and intraclastic carbonates (figures 7A, 12, and 13). Bioclasts and ostracods are the most common constituents. Sedimentary structures are present in the grainstones and packstones and include wave ripples, cross-stratification, and parallel lamination. Beds generally coarsen upward, range in thickness from millimeters up to 2 m, and are laterally consistent along the eastern margin of Lake Uinta (figure 12D).

This association is indicative of a high-energy depositional environment along the carbonate ramp in the littoral zone of the lake, typically accumulating in water along the shoreline. Pisoid and oncoid deposits are indicative of high energy, heavily reworked shallow-water areas of the littoral zone (Renaut and Gierlowski-Kordesch, 2010). This level of agitation is characteristic of shoal deposits and requires strong, persistent waves and currents. These are likely sourced from wind driven currents along the eastern margin of the lake. The presence of wave-rippled grainstones also indicates wave-influence along the lake margin. This association, in combination with FA-A and FA-B, can be used to approximate the shoreline geometry.

Shoals are usually interbedded with littoral to sublittoral claystones and sandstones (FA-C) and laterally associated with shoreline carbonate mudstones (FA-B) and fluvial-deltaic deposits (FA-A). FA-D deposits were formed in higher energy environments than FA-B, which is associated with calmer shoreline areas.

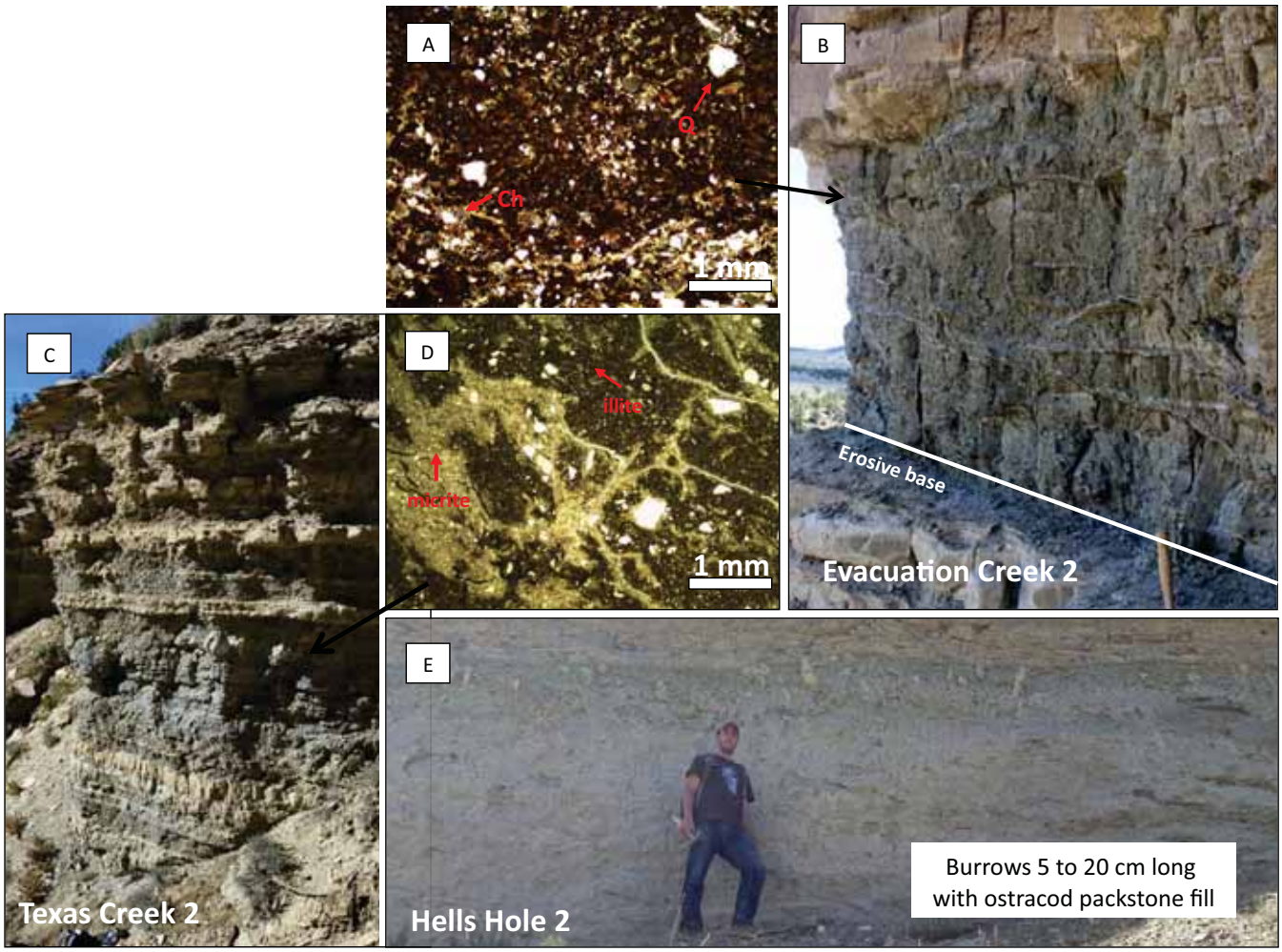

Figure 11. *Facies Association C.* ***A.*** *F1 faintly laminated grey/green-siltstone (F1) with subangular medium-sized quartz grains and chert (Evacuation Creek 2, sample #3);* ***B.*** *Thick grey/green siltstone (F1) bed with erosive base and gradational top, (Evacuation Creek 2);* ***C.*** *Outcrop with low net-to-gross, photomicrograph shown in (D) occurs along a transition zone between grey/green siltstone (F1) and calcareous mudstone (F2), (Texas Creek 2);* ***D.*** *F2 lime to dolomite mudstone with green silt, ooids, intraclast and subangular quartz grains, faintly laminated (Texas Creek 1, sample #3);* ***E.*** *grey/green siltstone (F1) burrowed at contact, burrows are 5 to 20 cm long and filled with the overlying ostracod packstone (Hells Hole 2).*

Facies Association E: Microbial Carbonates

The microbial carbonate facies association (FA-E) consists of minor growth in the form of very thin microbial films, oncoid packstones and grainstones (F9) (figures 7A and 14A, B, D), and within ostracod wackestone (F3) (figure 14C) observed in core and outcrop. These beds are thin, between one to ten centimeters, and occur in association with rip-up clasts and dolomite filled ostracod shells. Algal mat accumulation is wavy and made up of millimeter-size laminations visible only petrographically from core samples suggesting they accumulate in sublittoral lake regions. No dome features, heads, or well-developed biohermal mound features were observed. Overall the Uteland Butte member lacks microbial deposits. The poor development of microbial structures and the abundance of ostracods, bivalves, and gastropods suggest a freshwater lake containing consumers that prevented preservation.

Facies Association F: Littoral to Sublittoral Bioclastic Mudstone to Wackestone

Facies Association F (FA-F) consists of fine carbonate mudstones (F2), mollusk, intraclast, and ostracod wackestones (F2-F5), and argillaceous mudstones (F17) (figure 15). FA-F is characterized by light grey to tan brown beds that contain bioclastic material and are between centimeter and meter scale in outcrop and core. These units are interpreted to have been deposited in moderate- to low-energy depositional environments that occurred above the oxic/anoxic boundary within the littoral and sublittoral region.

FA-F occurs interbedded with littoral to sublittoral oil shale (FA-G), and littoral to sublittoral siltstones to claystone (FA-C). Vertically, FA-F is associated with FA-D and FA-E in more proximal littoral regions and associated with FA-H in the deepest region of the basin.

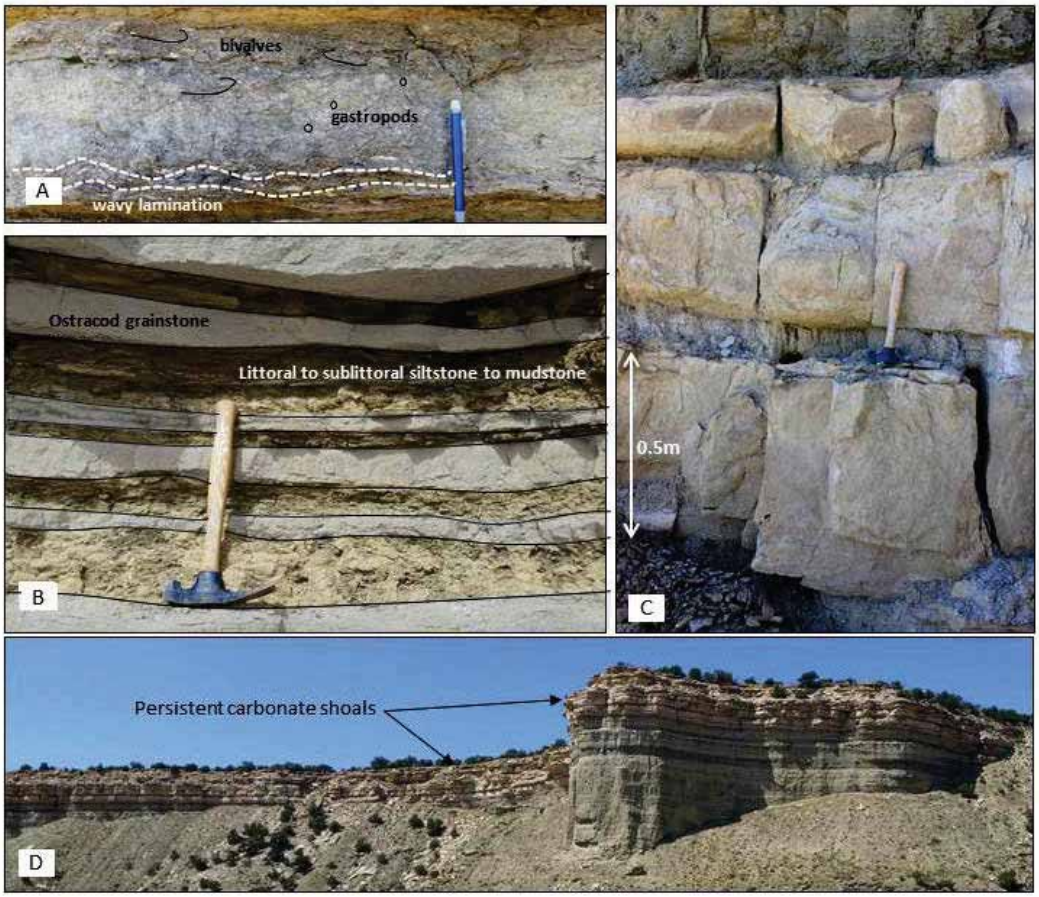

Figure 12. *Relationship of FA-C littoral to sublittoral mudstones to sandstones and FA-D carbonate shoal.* ***A.*** *Wave influenced bioclastic lime floatstone to rudstone (F11), 10 cm thick bed is contained within FA-C (Hells Hole 1);* ***B.*** *Thin, centimeter-scale cyclicity between FA-C and FA-D (CO109);* ***C.*** *Thick, meter-scale cyclicity between FA-C (recessive beds) and FA-D (thick, light tan beds) (Evacuation Creek 2);* ***D.*** *Persistent beds of FA-D across the outcrop in the uppermost Uteland Butte member, view to west towards the Hells Hole 3 (HH3) outcrop.*

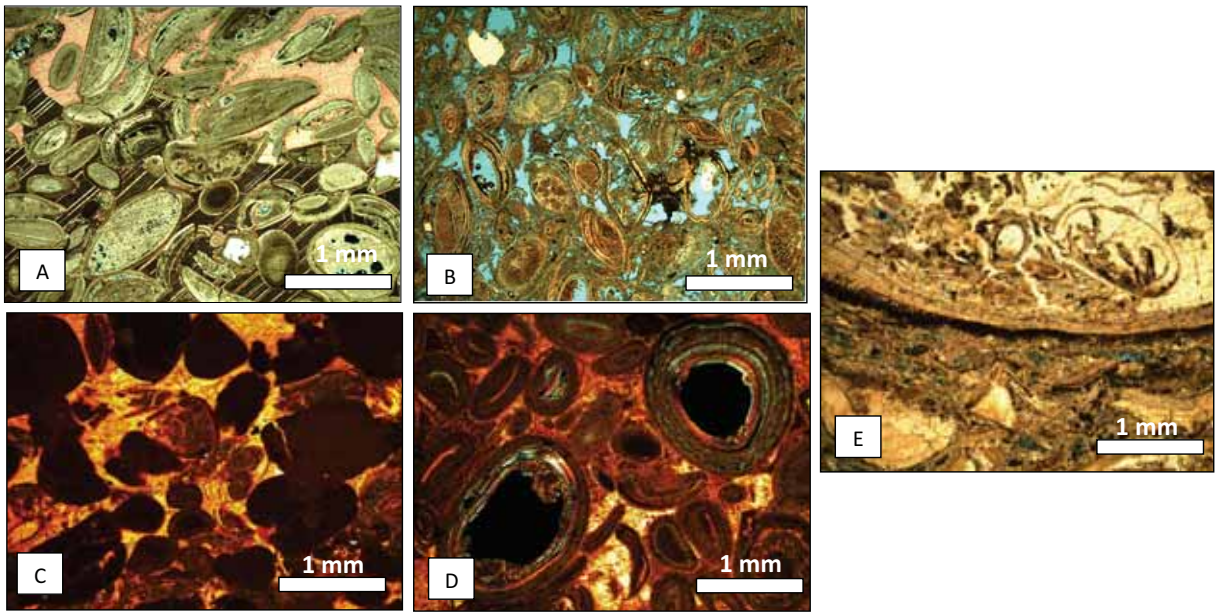

Figure 13. *Facies Association D.* ***A.*** *Ostracod lime packstone-grainstone (F7) with isopachous calcite cement and dissolution porosity (CO109, sample #17, XPL);* ***B.*** *Coated ostracod lime packstone-grainstone (F7) with inter and intraparticle porosity (CO 109, sample #18, PPL);* ***C.*** *Intraclastic-ostracod lime packstone-grainstone (F6), (Evacuation Creek 2, sample #16, 4x PPL);* ***D.*** *Oolitic-lime packstone-grainstone (F8) with calcite cement and intraparticle porosity (Evacuation Creek 3, sample #17, PPL);* ***E.*** *Bioclastic lime floatstone to rudstone (F11), (Hells Hole 3 sample #18, PPL).*

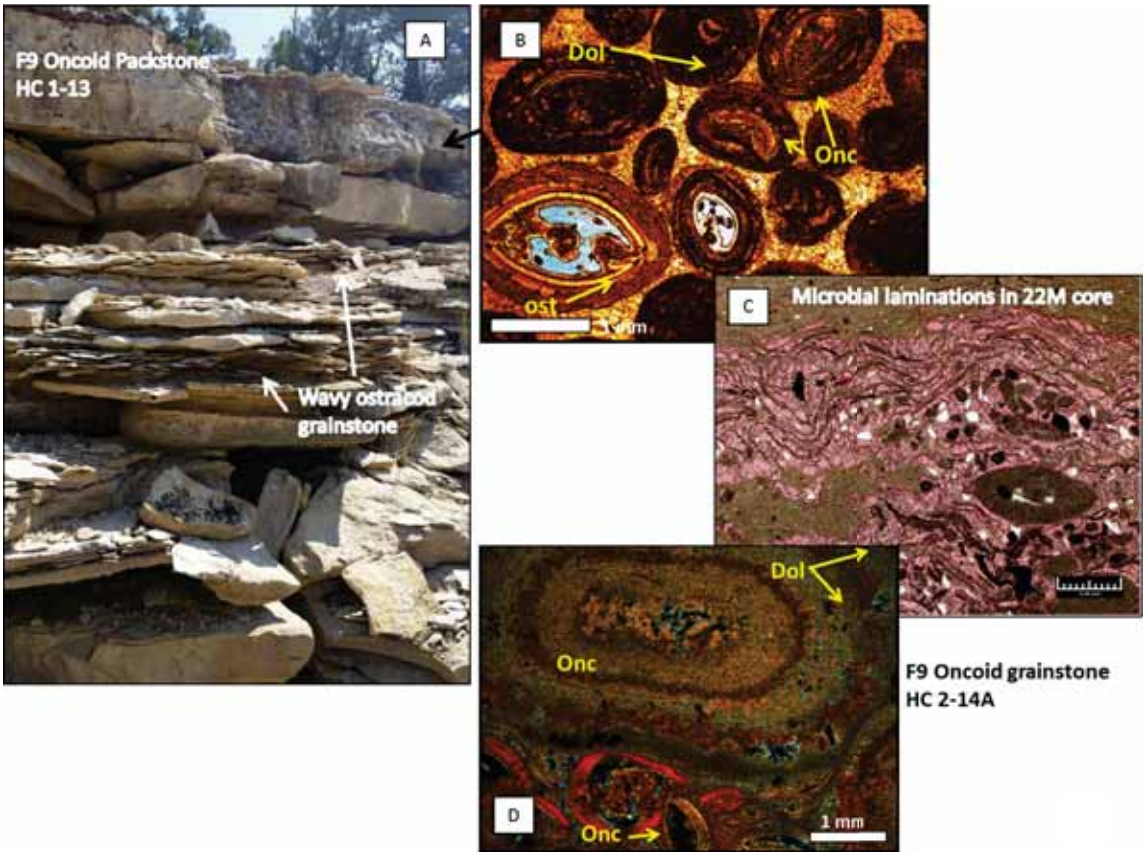

Figure 14. *Facies Association E.* ***A.*** *F9 oncolite lime packstone-grainstone in outcrop, unit is uniform thickness in outcrop and caps the top (Hells Hole 1);* ***B.*** *Photomicrograph of bed in (B), oncoid grains contain ostracod valves and are filled with lime mud (Hells Hole 1, sample #13);* ***C.*** *Microbial laminations in an ostracod lime mudstone-wackestone (F3) with subrounded silt grains, photomicrograph from NBU 921-22M core at 4907.6 foot depth. Black scale bar is 0.4 mm in length, photomicrograph prepared by Weatherford Labs;* ***D.*** *F9 oncolite lime packstone-grainstone; oncoid grain here is 5 mm in width (Hells Hole 1, sample #13).*

Facies Association G: Littoral to Sublittoral Oil Shale

Facies Association G (FA-G) consists of laterally laminated, organic-rich, illitic claystone (F16), laminated ostracod wackestone (F3), and argillaceous mudstones (F17) (figure 16). This oil shale is light tan to dark brown in color and is observed mainly in deeper lake environments, though it is also present in marginal to sublittoral areas. Fish remains and ostracods are commonly present in this facies association. Along the lake margin, organic richness is moderate to low. Beds are relatively thin in outcrop, about 0.5 m, and are thicker in the deeper subsurface deposits, about 2 m.

This association is interpreted as a low-energy environment in the distal littoral to sublittoral regions where oxygen levels are low and bioturbation is rare. These organic-rich carbonate and silty oil shales and mudstones were deposited in a large range of depths along the ramp-slope with low wave energy (Renaut and Gierlowski-Kordesch, 2010). These units are interbedded with littoral and sublittoral claystones to sandstones (FA-C) and littoral to sublittoral bioclastic mudstones and wackestones (FA-F). Beds are associated with laminated oil shale (FA-H) deeper in the basin and sublittoral ostracod packstones (FA-D) towards the margin. FA-G is present in both core and outcrop.

Facies Association H: Laminated Oil Shale

Facies Association H (FA-H) is made up of finely laminated, organic-rich oil shale (F18) (figures 8F, 17). This association is only present in core and is interpreted to represent the deepest depositional environment in the study area. Color ranges from dark-grey to black and has a higher organic content than shale in FA-G, which is more argillaceous. This association is typically plane-parallel, and bivalve fossils are occasionally present. Beds are several centimeters to a half-meter thick.

FA-H is interpreted as a deep, open-water deposit in the profundal portion of the lake where plankton and algal production is high, macrofauna populations are low, and organic preservation rates outpace carbonate production (Ryder and others, 1976; Renaut and Gierlowski-Kordesch, 2010). This facies is laterally and vertically associated with littoral to sublittoral oil shale (FA-G), littoral to sublittoral claystones to sandstones (FA-C), and littoral to sublittoral bioclastic mudstones to wackestones (FA-F).

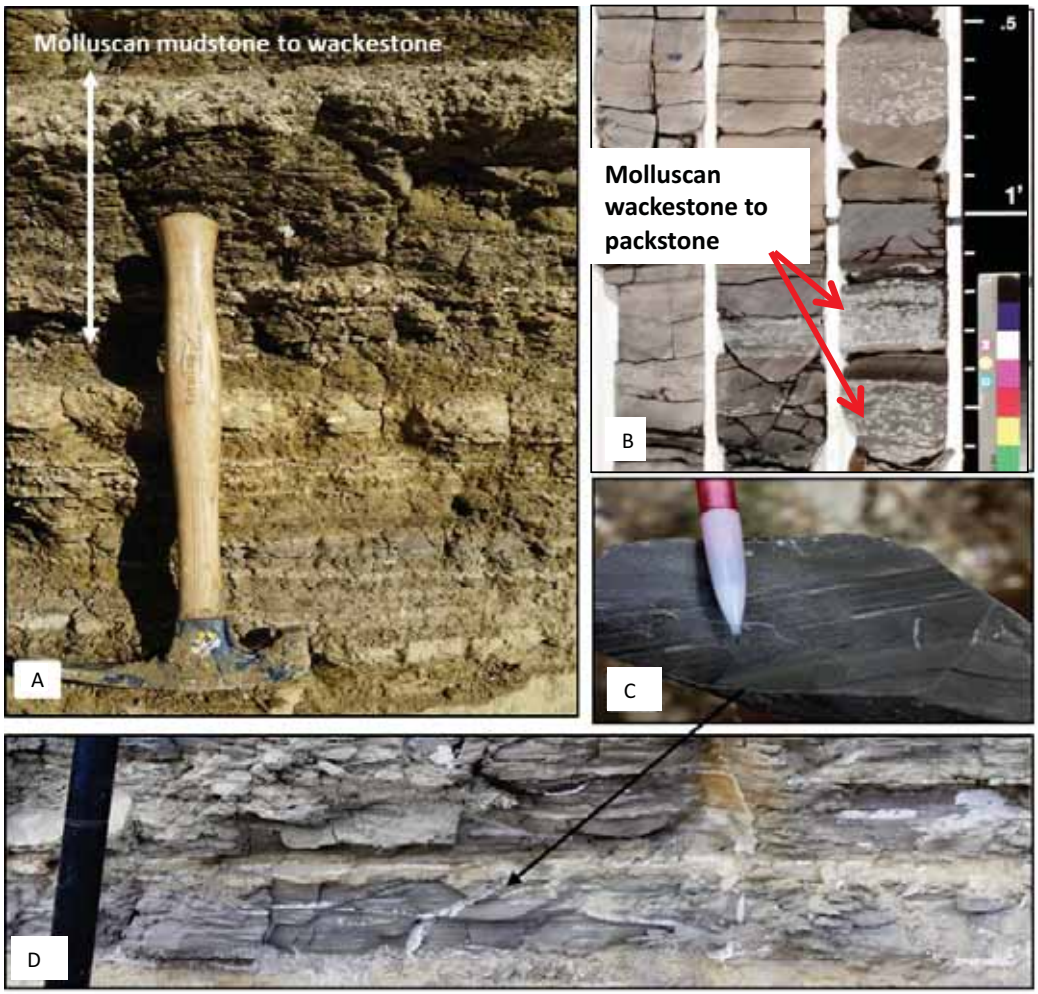

Figure 15. *Facies Association F.* ***A.*** *F17 and F4 interbedded, argillaceous mudstone and molluscan lime wackestone-packstone (Hells Hole 1);* ***B.*** *F4 molluscan lime wackestone-packstone in NBU 921-22M core, 4870 to 4872.2 feet depth;* ***C.*** *Silt/sand lenses interlaminated with organic-rich mudstone (Evacuation Creek 1);* ***D.*** *Argillaceous grey-lime mudstone with silt lens (Evacuation Creek 1).*

DEPOSITIONAL MODEL AND SEQUENCE STRATIGRAPHY

The facies and facies associations described above were used to build a depositional model for the Uteland Butte member. The model illustrates the lateral distribution of the carbonate and siliciclastic facies extending from the ancient lake's southeast shoreline into the deeper part of the lake to the northwest (figure 18). Fluvial-deltaic (FA-A) and shoreline mudstones (FA-B) deposits are located in the backwater and shoreline area and are interbedded with lake units. The shoreline region of the lake is characterized by littoral to sublittoral claystones to sandstones (FA-C) that extend out into the basin and are interbedded with carbonate shoals (FA-D). Shoals containing ooids, pisoids, oncoids, and coated ostracod grainstones occur off axis from fluvial systems in areas with episodic waves and currents. Carbonate shoals (FA-D) also occur in deeper littoral environments where current energy is high. Carbonate shoals are commonly interbedded with littoral to sublittoral oil shale (FA-G), littoral to sublittoral bioclastic mudstones and wackestones (FA-F), and microbial carbonates (FA-E). These associations also interfinger with one another along strike. Farther into the deep sublittoral and profundal zones, organic-rich, laminated oil shale (FA-H) was deposited in a dysoxic to anoxic environment and interfingers with silty littoral to sublittoral oil shale (FA-G).

This depositional model was applied to measured sections and cores through analysis of thin section photos, bed character, and stacking patterns. A stratigraphic framework was compiled for each section to ensure consistency in interpretation before correlation. Figure 19 is an example of data from one outcrop, County Rd 109, with interpretations on lithofacies, facies associations, and stacking patterns. Facies were used to make interpretations about depositional environments and facies associations. The facies associations were used to predict the shallowing and deepening cycles of Lake Uinta—these cycles are represented as black (short-term) and red (longer-term) triangular cones. An example of these cycles is displayed on the outcrop image to the left of the measured section in figure 19. A lower, deeper littoral to sublittoral oil shale occurs interbedded with ostracod packstones, and this

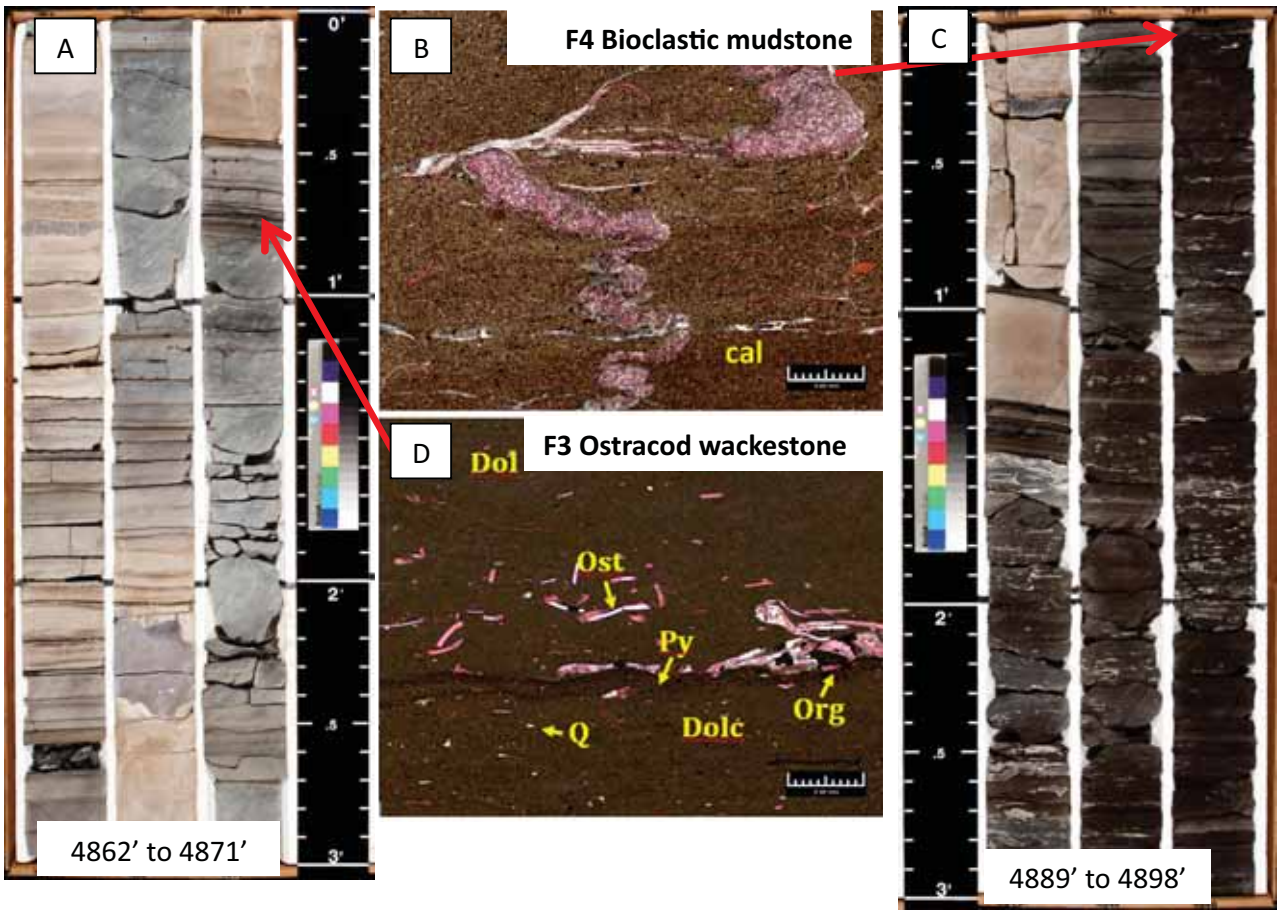

Figure 16. *Facies Association G.* ***A.*** *Core location of photomicrograph (D), this laminated ostracod lime mudstone-wackestone (F3) is interbedded with ostracod lime packstone-grainstone (F7), from 921-22M core at 4862 to 4871 feet depth;* ***B.*** *F4 molluscan lime wackestone-packstone with laminated mud (cal), organic material, and large compressed burrows, from NBU 921-22M core sample depth 4895.75 feet;* ***C.*** *Red arrow from (B) notes location of photomicrograph in NBU 921-22M core, F4 is dark grey, faintly laminated, and overlain by mollusk wackestones, sample depth 4889 feet to 4898 feet;* ***D.*** *F3 ostracod lime mudstone-wackestone, ostracod (Ost) grains concentrated in dolomitic mud laminations with organic material (Org) and pyrite (Py), 921-22M core sample depth 4868.65 feet; Black scale bars in (B) and (D) are 0.4 mm, photomicrographs prepared by Weatherford Labs.*

unit shallows upward into a mixed FA-D and FA-C littoral to sublittoral claystone to sandstone deposits and carbonate shoal. The section is capped by a thick carbonate shoal deposit (FA-D) (figure 19A-C). Figures 19D and 19E illustrate green grey siltstone (F1) and littoral to sublittoral oil shale (FG) that occurs at the base of cycles.

A sequence stratigraphic interpretation was constructed for the Uteland Butte member based on observations from this study and previous research completed by Cole and Picard (1978) and Little (1988). The framework shows a ramp lake environment for the Uteland Butte dipping westward into deeper Lake Uinta (figures 20 and 21). Shallow-marginal lacustrine environments are subject to episodic subaerial exposure, significant facies variations, and ultimately a very complex lateral and vertical facies-sequence history (Tucker and Wright, 1990; Platt and Wright, 1991; Bustillo and others, 2002). The stratigraphic interpretation presented below is based on facies association distribution, stacking patterns, organic richness of deposits, and depositional processes.

Littoral Lake Margin

Littoral to sublittoral siltstones and carbonate grainstone facies dominate in the shallow lake environment of Lake Uinta (figure 20). Shoal or shoreline grainstone facies reflect the wave and current energy in the lake system, which resulted in thick beds of abundant intraclast, ostracod, mollusk, and pelodial grainstones. Littoral carbonates grade laterally into floodplain or fluvial clastic deposits as energy changed along the shoreline. Carbonate facies were deposited in areas of low fluvial clastic input.

Figure 20 is a 20-km-long strike cross section along the eastern lake-margin of Lake Uinta, from Evacuation Creek in the south to Hells Hole Canyon in the north. The Uteland Butte is divided into four cycles based on significant flooding surfaces (dotted lines) at the top of overall shallowing upward cycles. The basal Uteland Butte contact is marked by an abrupt transition from Wasatch Formation paleosols to delta deposits, which represents the basal sequence boundary

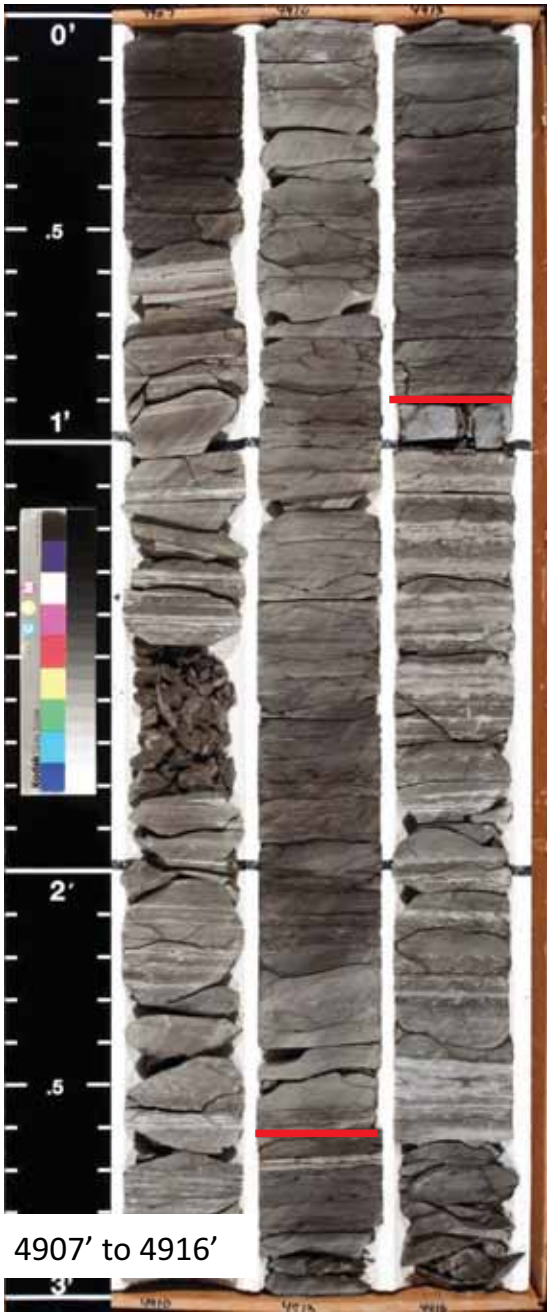

Figure 17. *Facies Association H. Black, laminated oil shale facies in NBU 921-22M core from 4907 to 4916 feet depth, between red bars.*

of the Uteland Butte in the study area. The basal delta sands have a uniform thickness where exposed in outcrop, contain ostracods, and show no channelization. These basal deltaic deposits signify an initial increase in runoff and early lake level rise (Tänavsuu-Milkeviciene and Sarg, 2012). As the lake continues to deepen, these delta deposits are overlain by littoral to sublittoral claystone to sandstone (FA-C). The lake then shallows upward through cycle 1 into carbonate shoals (FA-D) (section CO 109).

The base of the second cycle is marked by littoral to sublittoral claystones to sandstones (FA-C) and a thin rip-up-clast bed in Texas Creek 2 and Hells Hole 1. Second cycle ostracod packstones in the Texas Creek 1 and 2 outcrops contain notable amounts of quartz, indicating a nearby fluvial source and contributing to the thick littoral to sublittoral claystone to sandstone (FA-C) accumulations. Cycle 2 shallows upward into widespread carbonate shoal facies (FA-D) rich in mollusks, ostracods, and intraclasts.

Cycle 3 commences with widespread littoral to sublittoral claystone to sandstone (FA-C) and littoral to sublittoral bioclastic mudstone to wackestone (FA-F). The lake then shallows, depositing thick packages of ostracod shoals (F7, FA-D) at CO 109, Missouri Creek, and Hells Hole Canyon. This cycle contains the most continuous grainstone units and is richest in mollusks. These shoals are interbedded with thin accumulations of shoreline carbonate mudstone (FA-B) and littoral to sublittoral claystone to sandstone (FA-C). A large sandstone channel, six meters thick, is present in the Evacuation Creek area in cycle 3. This channel likely influenced the large quantity of silty accumulation seen in cycle 3 to the north.

The final flooding surface, the top of cycle 3, is marked by intraclastic rudstones in Evacuation Creek 3, CO 109, and Missouri Creek 1; by littoral to sublittoral oil shale (FA-G) in Texas Creek 1; and by littoral to sublittoral claystone to sandstone (FA-C) in Hells Hole Canyon 1 and Texas Creek 2. The Texas Creek 1 deposits above cycle 3 are littoral to sublittoral oil shale (FA-G) interbedded with intraclastic grainstones and coquinas (FA-D). Cycle 3, in the remaining sections is overlain by deeper littoral to sublittoral claystone to sandstone (FA-C), which gradually transitions into thick carbonate shoals (FA-D) that are interbedded in some areas with deeper littoral oil shales (FA-G), littoral to sublittoral claystone and sandstone (FA-C) (Texas Creek 2), and shoreline carbonate mudstones (FA-B) (Hells Hole 1). The carbonate shoal (FA-D) accumulations are thickest at CO 109 and Hells Hole Canyon 1 suggesting a lack of fluvial influence in these areas during cycle 4 deposition.

Sublittoral Lake

Uteland Butte sediments from deeper, open water lake settings are laminated; show some bioturbation; contain silt, ostracods and bivalve shells; and lack evidence of in situ vegetation (i.e., autochthonous coal). Figure 21 is a dip cross section correlating outcrops at Missouri Creek in the southeastern Uinta Basin to the NBU 921-22M core from the Greater Natural Buttes natural gas field to the northwest. The four outcrops in Missouri Creek are composed of FA-A fluvial-deltaic deposits, FA-B shoreline carbonate mudstones, FA-C littoral to sublittoral claystone to sandstone, FA-D carbonate shoals, FA-F littoral to sublittoral bioclastic mudstone to wackestone, and FA-G littoral to sublittoral oil shale. The core contains FA-C littoral to sublittoral claystone to sandstone, FA-D carbonate shoals, FA-F littoral to sublittoral mudstones, FA-G littoral to sublittoral oil shales, and FA-H laminated oil shales. Cycle

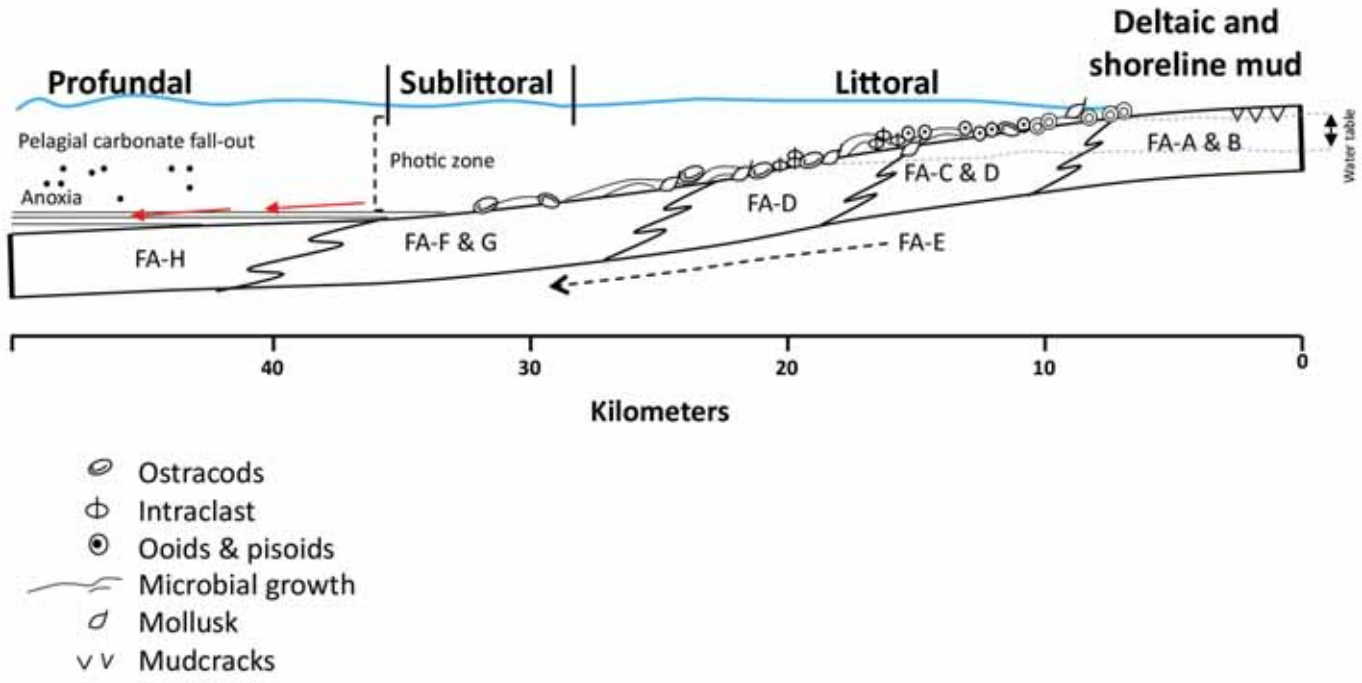

Figure 18. *Depositional model illustrating the lateral distribution of the limestone and siliciclastic facies associations deposited during Uteland Butte time in Lake Uinta's lacustrine (F1-F18) environment. The facies association distribution of the Uteland Butte member highlights the prominence of ostracods, intraclasts, peloids, and siltstones through the littoral and sublittoral regions. FA-E (microbial carbonate, dotted arrow below model) is minor and occurs in association with oncolite lime packstone-grainstone (F9) and ostracod lime mudstone-wackestone (F3).*

initiation was identified and correlated using rip-up lag deposits and the presence of deep lake oil shale facies overlying shallower facies. This cross section shows significant down ramp thickening and facies changes from lake-margin littoral environments in Missouri Creek to sublittoral mud-rich environments in the core. The basin core is dominated by the littoral to sublittoral mudstone to wackestone (FA-F) and littoral to sublittoral oil shale (FA-G).

DISCUSSION AND SUMMARY

The Uteland Butte member contains laterally persistent lacustrine lithofacies along the eastern basin outcrop area. The eastern edge of Lake Uinta was a gently dipping ramp (figures 20 and 21) subject to minor deltaic and fluvial influences, except in the Evacuation Creek area to the south. The outcrops display lake-margin, mixed siliciclastic and carbonate shoreline deposition composed of four major cycles. These cyclic deposits near the lake margin range from 3 to 7 m thick. Cycles are initially rich in sublittoral siliciclastic facies that shallow up to littoral carbonate shoals. Cycles 2 through 4 experienced similar regressions within each cycle where water levels were persistently in wave-dominated environments, but not proximal enough to accumulate terrestrial successions of clay or sand. In core, sublittoral cycle sediment accumulation ranges from as great as 3 to 12.5 meters. Laminated oil shale shallows upward into bioclastic wackestones and silty laminated oil shale in the sublittoral and distal littoral environment.

The fresh water environment of Lake Uinta hosted abundant populations of bivalves, gastropods, and ostracods during each cycle. The mollusk populations are particularly abundant to the north in Hells Hole Canyon where no fluvial influence was recorded. Hells Hole also hosted the thickest and most continuous successions of grainstones, with only minor thin units of silt. Mollusks are most abundant in the third cycle in the sublittoral areas, and it is possible that the third transgression was more nutrient-rich and fresher relative to other lake cycles.

Grainstone and packstone successions are prominent in both sublittoral and littoral settings, but the thickness of these beds are different. The thin, gradational and interbedded nature of the sublittoral packstones supports a different depositional process than the thick, meter-scale grainstones observed in lake-margin environments. The marginal grainstones also have a more laterally continuous nature within these facies over the entire 21 km N-S lateral transect studied. Although facies persist, lateral continuity of beds is not widely observed, as even outcrops that are only 0.5 km apart show little evidence to support bed-to-bed correlation. This is true for the two cores as well. Though the cores are located near one another, they do not display lateral continuity between grainstone and packstone beds. The sublittoral grainstones and packstones are possibly the result of high productivity during lake freshening periods when the deeper sublittoral to profundal lake environments were more oxic. In contrast, oxic fresh water persisted along the lake margin resulting in thick shoal deposits.

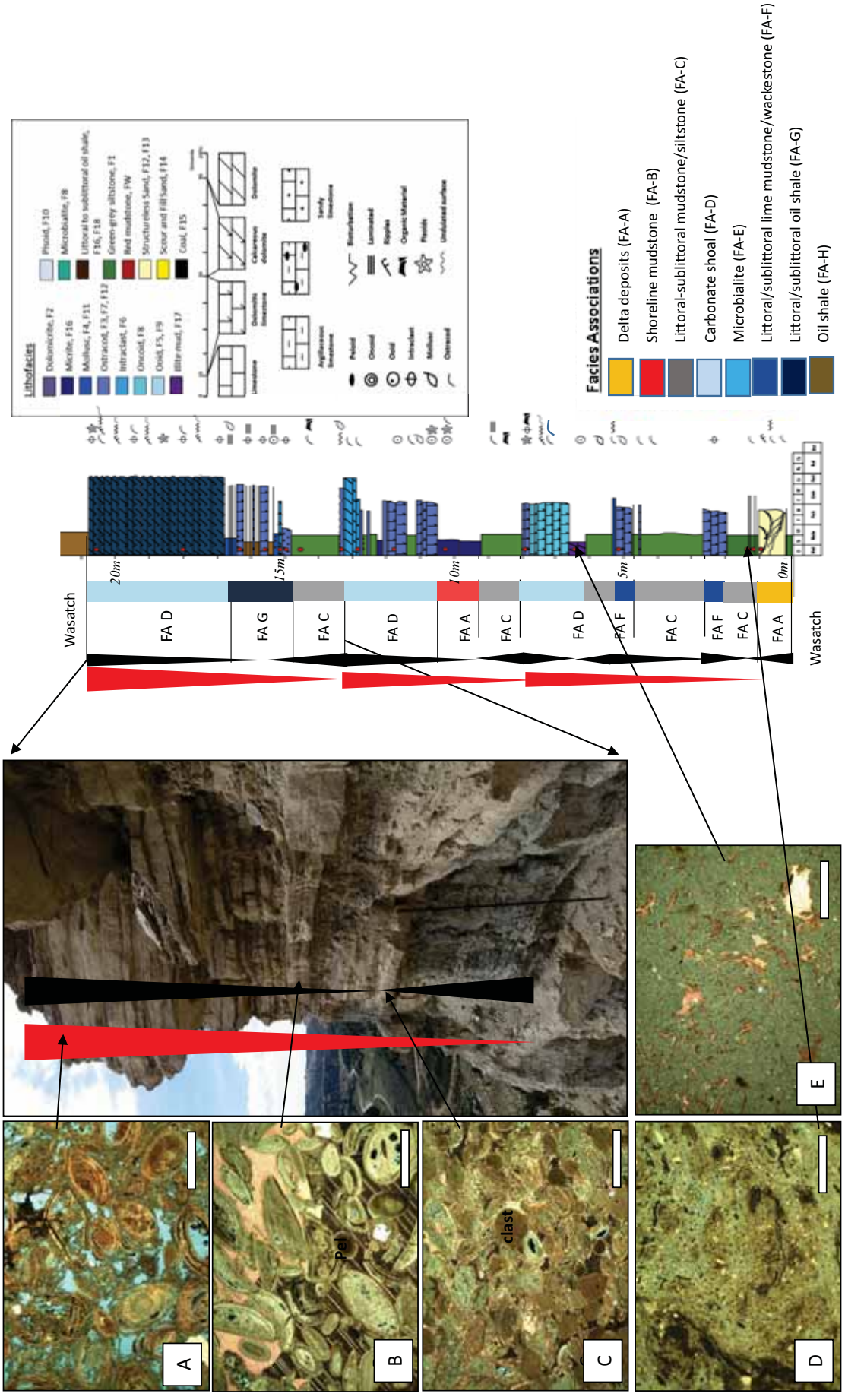

Figure 19. *Outcrop from CO109 measured section showing lithofacies and facies associations; **A.** F7 ostracod lime packstone-grainstone, with intraparticle and interparticle porosity, sample 18 (red dot on section) PPL 4x; **B.** F7 ostracod packstone, ostracod grains are coated, peloids (Pel), sample 17; **C.** F7 ostracod lime packstone-grainstone, sample 16; **D.** F1 grey/green siltstone with quartz grains and micrite, sample 12; **E.** F2 lime to dolomitic mudstone, massive with ostracod valves, sample 5. Cones represent shallowing (widening upward) or deepening (narrowing upward) trends, red cones are lower order sequences and black are higher order cycles. Black rod in outcrop photo is 1.5 m long. Graphic section in middle shows facies associations on left and lithofacies on right. Grain size and carbonate texture scale for measured section, lower right.*

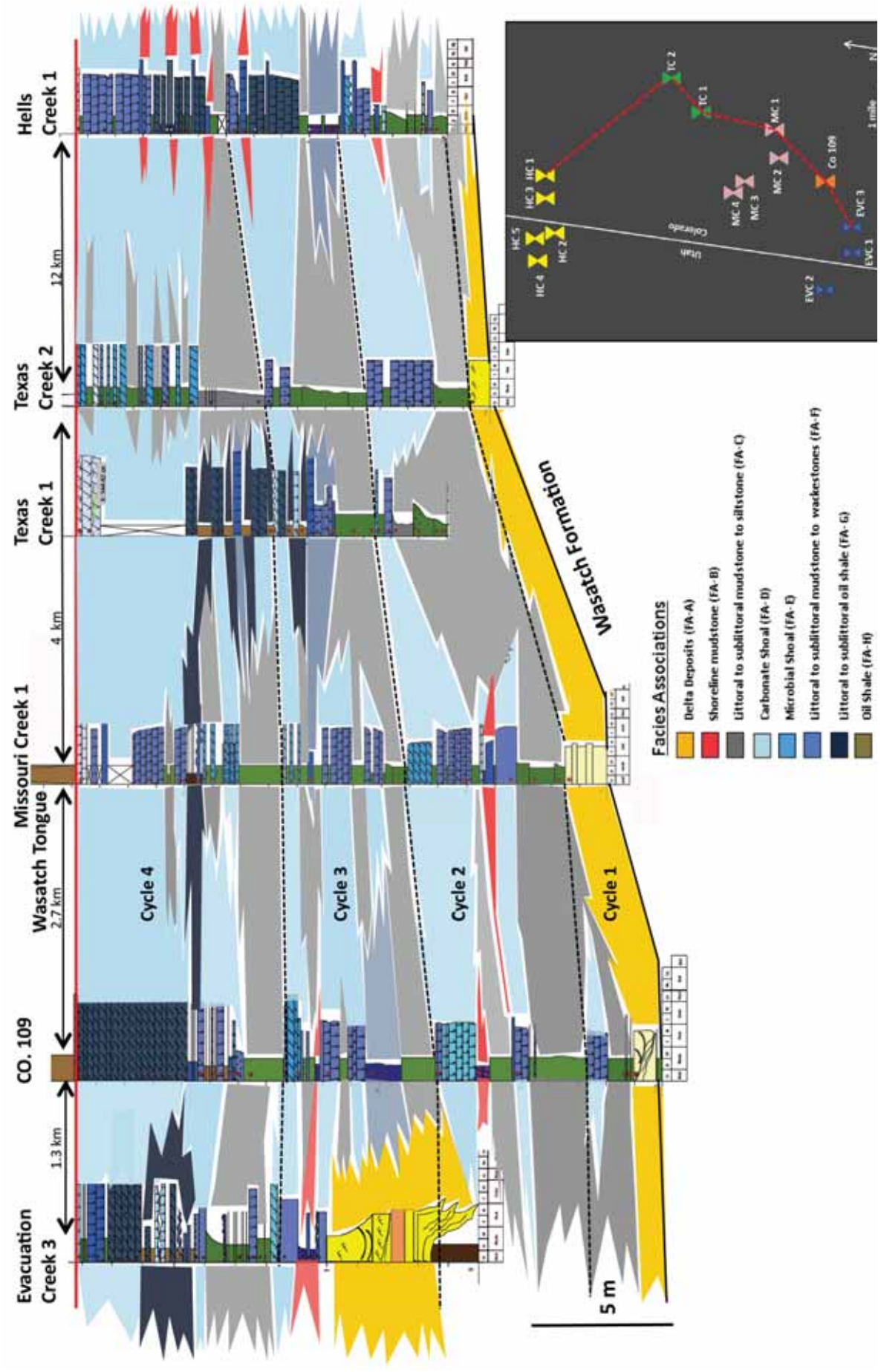

Figure 20. *Strike cross section along the eastern margin of Lake Uinta from south to north, Evacuation Creek 3 to Hells Hole 1. Individual measured sections are colorized and textured by facies (see figure 19), and lateral facies interpretation is colorized by facies association (grain size and carbonate textures, legend in figure 19). Predominant facies association trends are the laterally extensive carbonate shoals and littoral to sublittoral siltstones.*

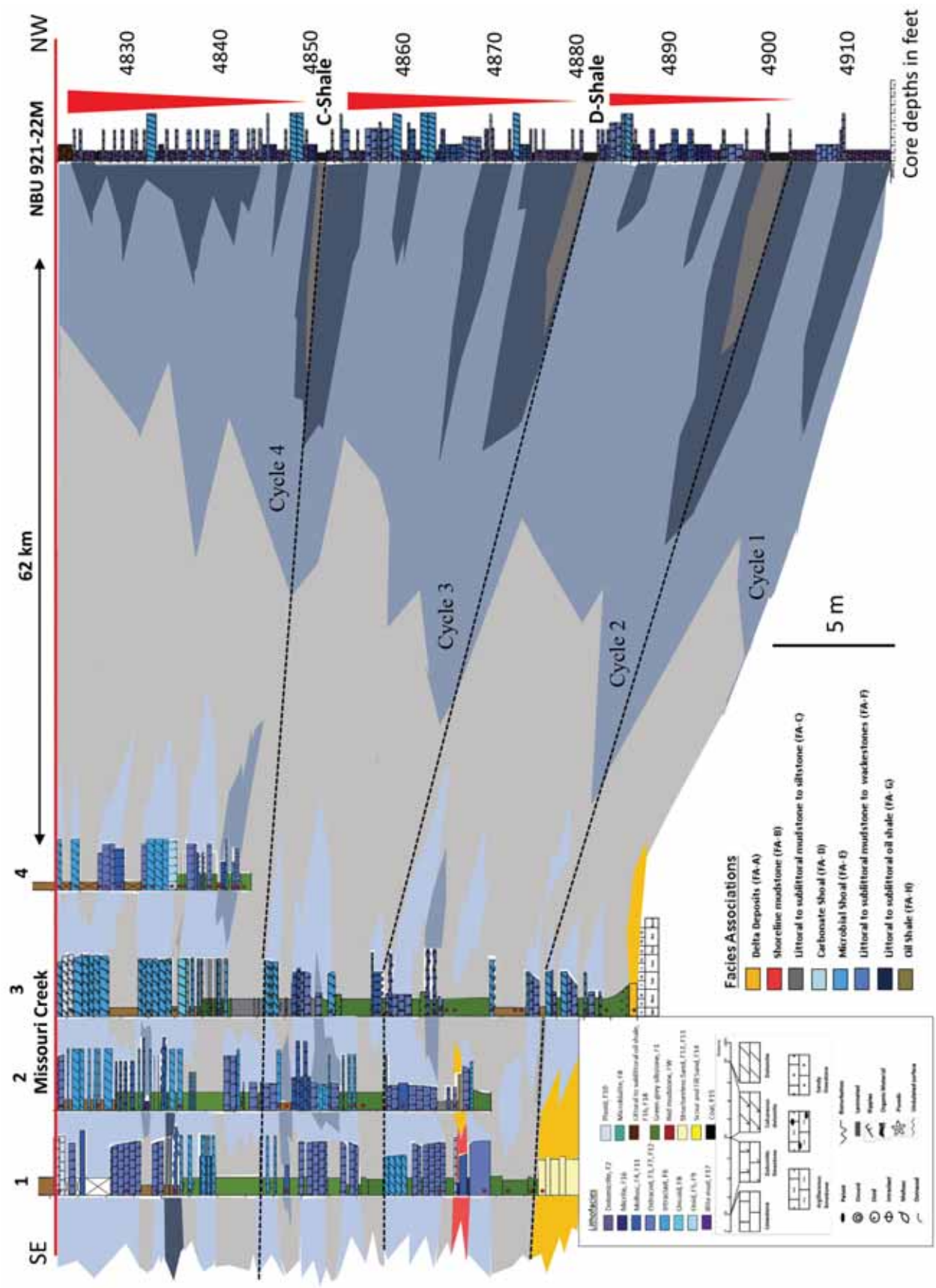

Figure 21. *Dip cross section from Missouri Creek Canyon to the NBU 921-22M core in the Greater Natural Buttes natural gas field. Major shallowing upward cycles are represented by red triangular cones next to core section. C- and D-shales are per Utah Geological Survey and oil company nomenclature. Individual measured sections are colorized and textured by facies (see figure 19) and lateral facies interpretation is colorized by facies association (grain size and carbonate textures as in legend on figure 19).*

Stratigraphic interpretations were based upon flooding surfaces marked by thin intraclastic rudstones and abrupt shift to deeper sublittoral mudrock. These correlations were made on the sub-regional scale between lake-margin environments as they changed laterally from calm backwater environments indicated by mud deposition to moderate energy, wave-influenced carbonate shoal settings, to fluvial environments that are preserved as sandy channel fill. Depositional cycles appear aggradational suggesting that sedimentation and accommodation were in balance. Correlation is possible from the lake margin into the deeper sublittoral basin where facies are highly laminated, organic rich, and thinly bedded. Facies showed major changes over the 62 km, but the four cycles are persistent into the deeper regions of the lake. Sublittoral successions are 30% thicker than the lake-margin Uteland Butte and are leaner in silt and richer in dolomite, nearly every bed contains >25% dolomite. The lakeward, and along depositional strike (Little, 1988), persistence of these cycles suggest an allocyclic control on deposition that can be tested as work on Uteland Butte is extended across the greater Lake Uinta area.

DIAGENESIS: CALCITE, DOLOMITE, AND POROSITY

Reservoir quality is an important issue in the Uteland Butte carbonates and this study included a preliminary examination of the early diagenesis that affected these carbonates. The following section summarizes the two most important early diagenetic changes to the Uteland Butte sediments, calcite cementation and dolomitization, which have had major impacts on the porosity in these rocks.

Calcite Cementation

Calcite is observed as cementation throughout the Uteland Butte in littoral facies and in some sublittoral facies. Two cement textures occur in the Uteland Butte samples, mosaic or granular cement and equant crystals. Cementation occurs between oolite, oncoid, and ostracod grains (figure 7C, figure 13A and B, figure 14B); in dissolved moldic pore spaces; as syntaxial overgrowths between peloids, ellipsoidal oncoids, and ostracod valves (figure 13E); and as equant mosaic calcite cementation in intraparticle pores (figure 13A). Cementation has significantly reduced porosity in packstones and grainstones. These cements are interpreted to represent early meteoric cementation in a lake environment undergoing lake level changes and fluvial input where carbonate-rich waters were present.

Dolomite

Dolomite/calcite ratios were determined through petrographic analysis and by QEMSCAN mineralogy scans. Varieties of Mg-rich carbonate range from stoichiometric dolomite to Mg-calcite, minerals that are very abundant in the Uteland Butte member (figure 22). The Uteland Butte carbonates typically contain between 25 to 50% dolomite with an average of 35%, most commonly as carbonate mud. The dolomudstone in the small QEMSCAN samples (1.5 cm X 1.5 cm areas) show a high percentage of dolomite (66–79%) and occur as intraclasts and peloids (figure 22). The intraclasts contain remnants of calcite. In both samples, calcite occurs as Mg-calcite and calcite. In figure 22B Mg-bearing calcite makes up 10.6% and calcite accounts for 9.7%. The same is the case for figure 22C where Mg-calcite is 23.5% and calcite is only 9.7%. Calcite occurs as bioclasts of bivalves and ostracods, and as calcite cement. In addition, dolomite is observed replacing ooid, oncoids, pisoids, and replacing the lime mud fill between ostracod shells. Dolomitic mud is rarely associated with mollusk and gastropod rudstones and floatstones.

Dolomite is also observed in core (figure 23). The F13 sublittoral oil shale is dolomite rich with laminations that host calcite ostracod shells and pyrite (figure 23A) and F7 intraclasts host green dolomite mud (figure 23B). Dolomitic bioclastic packstone to wackestones contain calcitic bivalve grains in a dolomitic mud matrix (figure 23C). F18 laminated dolomitic oil shales have possible burrows filled with calcite (pink), organic material (black), and silt size quartz (figure 23D).

The presence of dolomitic intraclasts in both the lake-margin and deeper lake area suggests early pre-burial replacement of lime mud in Mg-rich water with high organic content.

Porosity

FEI QEMSCAN 650F-Back Scatter Electron (BSE) system was the primary analysis tool used to evaluate microporosity within the facies of the Uteland Butte member. Initial estimates made from petrographic analysis underestimate porosity values, especially in fine-grained material where microporosity dominates. This is a result of the lower resolution of an optical microscope. The QEMSCAN-BSE detects and maps porosity and pore values as small as one micro-meter.

The QEMSCAN-BSE porosity analysis is run over several small areas (1.5 cm X 1.5 cm) to get a range and average porosity for each sample. Each scan produces three values, a porosity value, a porosity+mineral transition value, and a mineral amount. BSE relative intensity thresholds used to determine these values are: 0 to 27 porosity, 27 to 35 porosity+mineral transition, 35 + mineral. The porosity+mineral transition records porosity values detected between clear porosity and clearly defined mineral. In other studies (Jobe, 2013; Al-Suwaidi, 2015), other porosity measures such as CMS helium injection and mercury injection analyses indicate that this transition is dominantly porosity. Values discussed below are a sum of porosity and porosity/mineral transition values.

The Uteland Butte outcrop samples show varying amounts of micro- to nanoporosity. Porosity occurs in interparticle and in-

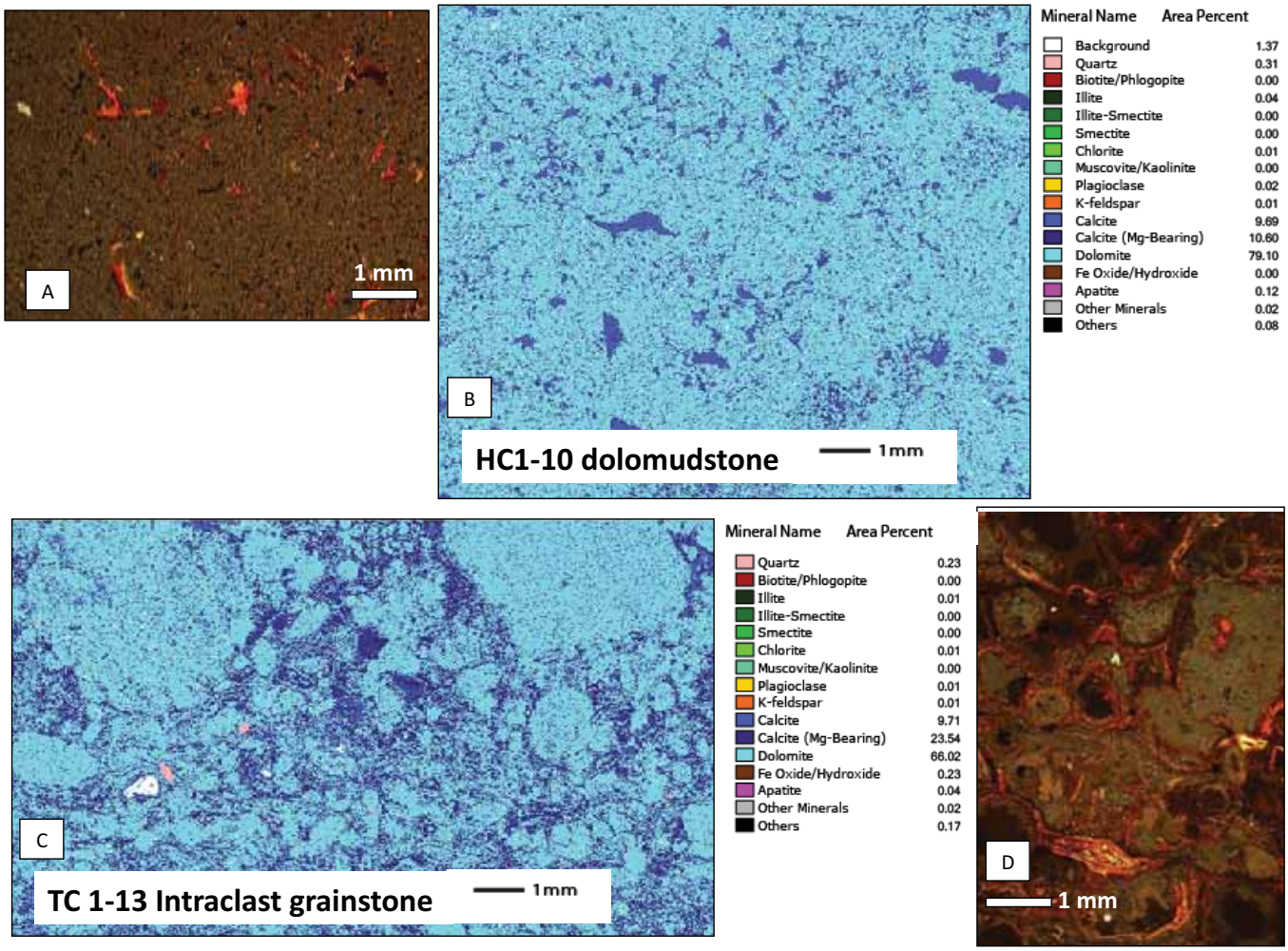

Figure 22. *Dolomite is most commonly observed in the Uteland Butte as a green to brown fine mud;* ***A.*** *Photomicrograph of (F2) lime to dolomite mudstone, organic rich with ostracod shells;* ***B.*** *QEMSCAN mineralogical scan of (A), dolomite composes 79.1% of the sample, and calcite ostracod shells and cement make up the remaining rock composition;* ***C.*** *Diagenesis did not completely alter calcite, intraclasts still contain some Mg-bearing calcite, though they are predominantly dolomitic. Clasts are coated in calcite cement (QEMSCAN mineral scan);* ***D.*** *Photomicrograph for (C), intraclast-peloid grainstone. Calcite fills interparticle pores and has occurred after dolomitization and rip-up of intraclast grains.*

traparticle pores and in dolomite mud as intercrystalline porosity. Dolomitic mud generally shows intercrystalline porosity, which ranges from 7 to 22%, and in size, from <1 to 5 micrometers (figure 24; F2, F7, and F9). Fracture and interparticle porosity is dominant in packstones, grainstones, rudstones, and floatstones, ranging from less than 1 to 8% (figure 24; F6, F8, and F10). Grainstones composed of peloid, ostracod, ooid, and oncoids also contain a wide variety of macroporosity types (figure 13B and D, figure 14B) from shelter to intraparticle in oncoids and some moldic porosity from bioclasts. Green siltstones (F1) have very low porosity (≤ 1%).

Although QEMSCAN-BSE scans were not run on core samples, the high concentration of fine-grained dolomite material supports a basic assumption that intercrystalline porosity may be common (figure 24; F2). Weatherford Labs measured porosity and permeability data using core plugs for several facies in the NBU-921-22m core. Porosity values and pore types are comparable to the outcrop estimates (table 3). Pore types are also consistent with the outcrop. The ostracod-intraclast packstone (F7) has primarily microporous intercrystalline porosity. The burrowed dolowackestone (F2) has intercrystalline microporosity with variable interconnectivity and a small amount of moldic pores and secondary pores. The argillaceous molluscan dolowackestone (F4) has intraparticle and intercrystalline porosity.

Despite the variety of facies analyzed, the pore size distribution observed was generally consistent across the eastern field area. Pore size distribution was calculated from digital pore extraction that calculates pore size with shape distribution. Isolated large macropores were avoided to keep from skewing QEMSCAN results. Pore size distribution for the eight facies displayed in figure 24 fell almost entirely into the range of 1 to 5 micro-meters. In dolomitic-mudrocks, <1 to 5 micro-meters represented about 90% of the pore size distribution. In calcareous mudstones, and coarser grained carbonate shoal facies, 5 to 10 micro-meters represented 15 to 25% of the pore size

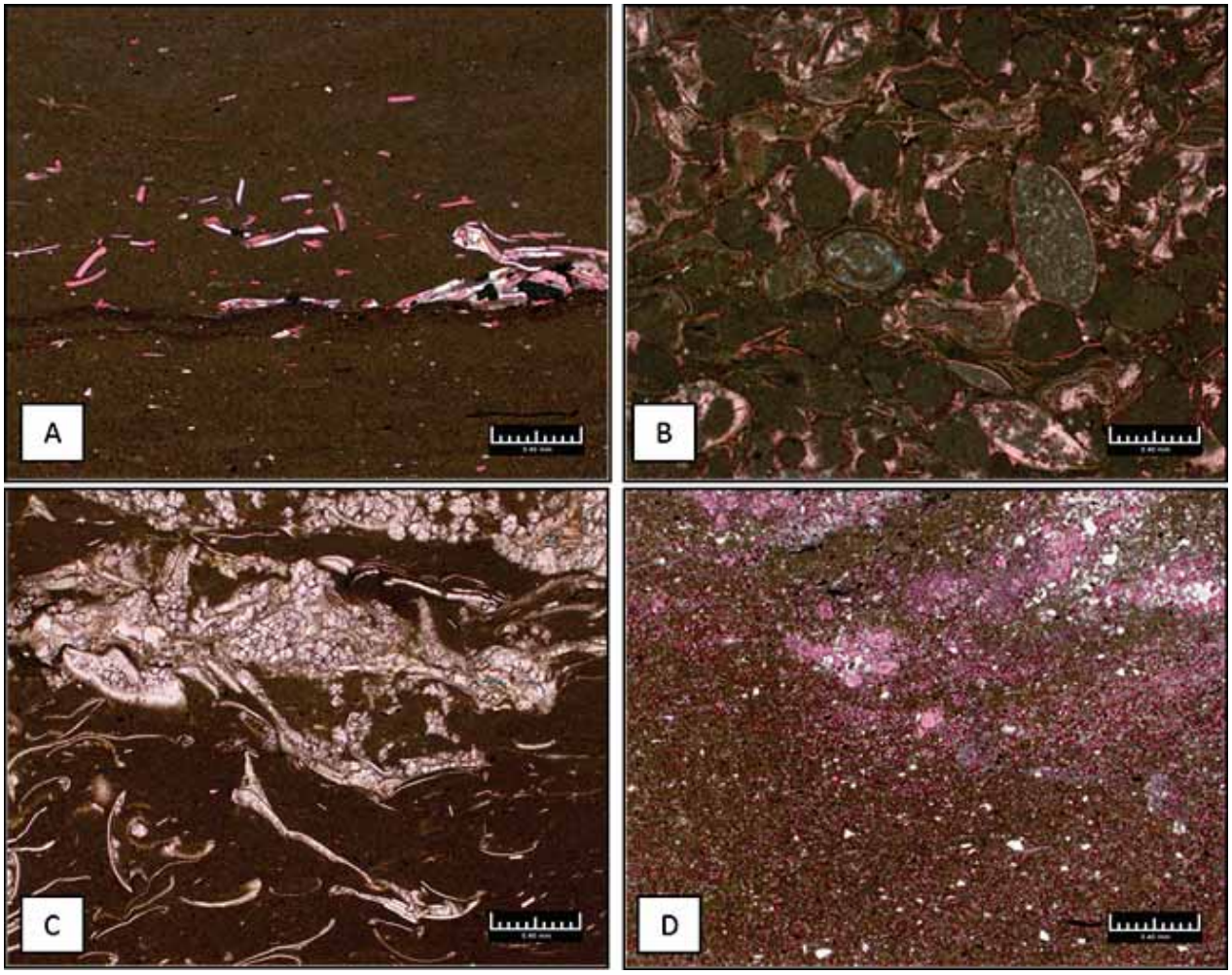

Figure 23. *Dolomite diagenesis seen in core, all samples from NBU 921-22M, Anadarko Petroleum Company.* ***A.*** *F3 ostracod lime mudstone-wackestone, argillaceous with black organic material, sample depth of 4868.65'; **B.** F7 ostracod lime packstone-grainstone, brown-green peloids are diagenetically replaced and commonly preserved within ostracod shells, calcite cement fills in between grains, sample depth of 4856.80 ft; **C.** F4 molluscan lime wackestone-packstone, mud is dolomitic while shell remains and grains around shells are calcite, sample depth of 4869.10 ft; **D.** Laminated oil shale with calcite replacement within interpreted burrowed sections, organic material and silt size quartz grains, sample depth of 4915 ft. Black scale bar is 0.40 mm.*

distribution, and <1 to 5 micro-meters represented the majority of the pore size distribution.

CONCLUSIONS

(1) The first major transgression of ancient Lake Uinta in the Uinta Basin was a highly cyclic, climatically driven, fresh, ostracod-rich, and molluscan-rich lake in which sediments underwent significant early dolomitization.

(2) The Uteland Butte lake-margin sediment is rich in silt and grainstone deposits, and the sublittoral deposits are thicker, highly laminated, finer grained, and contain more diagenetic dolomite. Dolomite mud is abundant, making up 25% to 50% of carbonate material, in marginal and sublittoral deposits.

(3) Four main cycles are preserved within the Uteland Butte member and are correlative from the lake margin into the deeper basin.

(4) Among the represented facies, porosity ranges between 1% and 20%, and permeability is usually below 1 md.

ACKNOWLEDGMENTS

This project was funded by the Utah Geological Survey via a grant from the U.S. Department of Energy, National Energy Technology Laboratory (DE-FE0010667). Funding was also provided by the Colorado School of Mines Green River Industrial Associates Consortium. The authors would like to thank the UGS reviewers who spent significant time editing this report and markedly improved the manuscript.

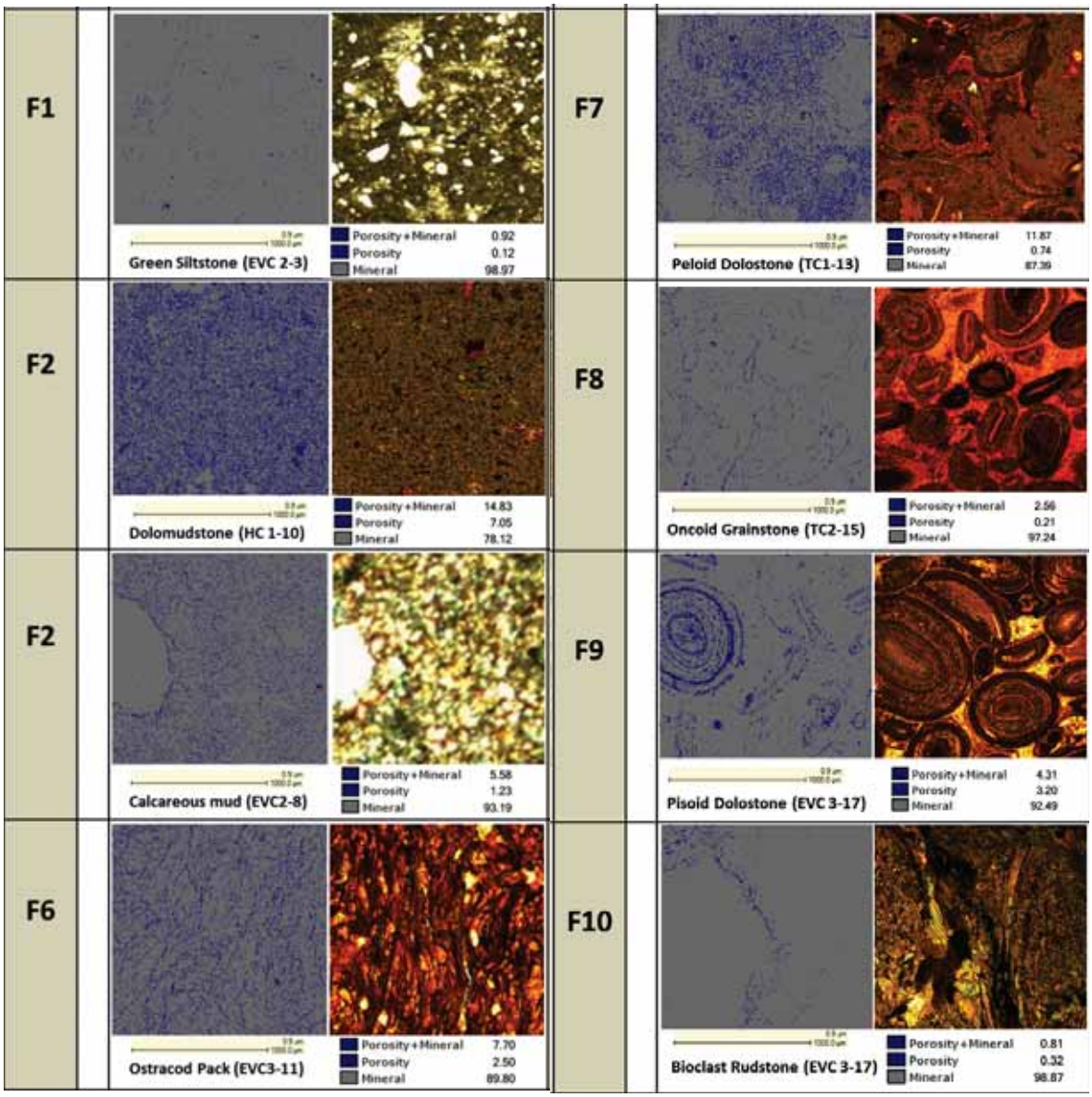

Figure 24. *Left is QEMSCAN images of F1, F2, and F6 displaying porosity >1 micro-meter and associated thin section photos. Right is QEMSCAN images of F7 through F10 displaying porosity >1 micro-meter and associated thin section photos. Porosity+mineral records an intensity transition from open pores to 100% mineral. Previous work shows that this transition is dominantly porosity.*

Table 3. *Porosity and permeability for Uteland Butte core samples (Weatherford analysis for Anadarko Petroleum).*

Lithofacies	Porosity (%)	Permeability (md)
Ostracod dolowackestone (F3)	12.2	1.23
Bioclastic dolowackestone (F4)	7.1	0.0053
Burrowed dolowackestone (F4)	2.8	0.092
Argillaceous molluscan dolowackestone (F4)	4.4	0.0001
Ostracod-intraclast packstone (F6)	6.9	0.0054
Dolograinstone (F6)	7.2	0.044
Bioclastic packstone (F11)	2.7	0.0001
Argillaceous dolomudstone (F17)	1.8	0.0011

REFERENCES

Abbott, W., 1957, Tertiary of the Uinta Basin: Utah Geological Association, Guidebook to the Geology of the Uinta Basin, eighth annual conference, 1957, p. 102–109.

Al-Suwaidi, M.E., 2015, Lower Bab Member (A0)— A study of sequence stratigraphy, porosity characterization, and tight reservoir development, Abu Dhabi, UAE: Golden, Colorado School of Mines, Ph.D. dissertation, 147 p.

Birdwell, J.E., Vanden Berg, M.D., Johnson, R.C., Mercier, T.J., Boehlke, A.R., and Brownfield, M.E., in press, Geological, geochemical, and reservoir characterization of the Uteland Butte member of the Green River Formation, Uinta Basin, Utah: Rocky Mountain Association of Geologists, Source Rock Compendium.

Bohacs, K.M., Carroll, A.R., Neal, J.E., and Mankiewicz, P.J., 2000, Lake-basin type, source potential, and hydrocarbon character—an integrated sequence-stratigraphic-geochemical framework, *in* Gierlowski-Kordesch, E.H., and Kelts, K.R., editors, Lake Basins through space and time: American Association of Petroleum Geologists Bulletin, v. 83, p. 3–34.

Bradley, W.H., 1931, Origin and microfossils of the oil shale of the Green River Formation of Colorado and Utah: U.S. Geological Survey Professional Paper 168, p. 58.

Burton, D., Woolf, K., and Sullivan, R., 2014, Lacustrine depositional environments in the Green River Formation, Uinta Basin—Expression in outcrop and wireline logs: American Association of Petroleum Geologists Bulletin, v. 98, no. 9, p. 1699–1715.

Bustillo, M.A., Arribas, M.E., and Bustillo, M., 2002, Dolomitization and silicification in low-energy lacustrine carbonates (Paleogene, Madrid Basin, Spain): Sedimentary Geology, v. 151, p. 107–126.

Carroll, A.R., Chetel, L.M., and Smith, M.E., 2006, Feast to famine—Sediment supply control on Laramide basin fill: Geology, v. 34, p. 197–200.

Cashion, W.B., and Donnell, J.R., 1972, Chart showing the correlation of selected key units in the organic-rich sequence of the Green River Formation, Piceance Creek basin, Colorado and Uinta basin, Utah: U.S. Geological Survey Bulletin B-1394-G, 9p.

Cashion, W.B., and Donnell, J.R., 1974, Revision of nomenclature of the upper part of the Green River Formation, Piceance Creek Basin, Colorado, and eastern Uinta Basin, Utah: U.S. Geological Survey Bulletin B-1396-G, 9p.

Cohen, A.S., 2003, Paleolimnology: Oxford University Press, Oxford, p. 500.

Cole, R.D., and Picard, M.D., 1978, Comparative mineralogy of nearshore and offshore lacustrine lithofacies, Parachute Creek Member of the Green River Formation, Piceance Creek Basin, Colorado, and eastern Uinta Basin, Utah: Geological Society of America Bulletin, v. 89, p. 1441–1454.

Davis, S.J., Wiegard, B.A., Carroll, A.R., and Chamberlain, C.P., 2008, The effect of drainage reorganization on paleoaltimetry studies—an example from the Paleogene Laramide foreland: Earth and Planetary Science Letters 275, p. 258–268.

Davis, S.J., Mulch, A., Carroll, A.R., Horton. T.W., and Chamberlain, C.P., 2009, Paleogene landscape evolution of the central North America Cordillera—developing topography and hydrology in the Laramide foreland: Geological Society of America Bulletin, v. 120, p. 100–133.

Davis, S.J., Mix, H.T., Weigand, B.A. Carroll, A.R., and Chamberlain, C.P, 2010, Synorogenic evolution of large-scale drainage patterns—isotope paleohydrology of sequential Laramide basins: American Journal of Science, v. 309, p. 549–602.

Dickinson, W.R., Klute, M.A., Hayes, M.J., Janecke, S.U., Lundin, E.R., McKittrick, M.A., and Olivares, M.D., 1988, Paleogeographic and paleotectonic setting of Laramide sedimentary basins in the central Rocky Mountain region: Geological Society of America Bulletin, v. 100, p. 1023–1039.

Dunham, R.J., 1962, Classification of carbonate rocks according to depositional textures: American Association of Petroleum Geologists Memoir 1, p. 108–121.

Dyni, J.R., and Hawkins, J.E., 1981, Lacustrine turbidites in the Green River Formation, northwestern Colorado: Geological Society of America Bulletin, v. 9, no. 5, p. 235–238.

Dyni, J.R., 2006, Geology and resources of some world oil-shale deposits: U.S. Geological Survey Scientific Invest. Rep. 2005-5294, 42 p.

Embry, A.F., and Klovan, J.E., 1971, A Late Devonian reef tract on northeastern Banks Island, N.W.T.: Bulletin of Canadian Petroleum Geology, v. 19, p. 730–761.

Eugster, H.P., and Hardie, L.A., 1978, Saline lakes, *in* Lermand, A., editor, Lakes—Chemistry, geology, physics: Springer, Berlin, p. 238–293.

Fouch, T.D., Nuccio, V.F., Osmond, J.C., MacMillan, L., Cashion, W.B., and Wandrey, C.J., 1992, Oil and gas in uppermost Cretaceous and Tertiary rock, Uinta Basin, Utah, *in* Fouch, T.D., Nuccio, V.F., and Chidsey, T.C., editors, Hydrocarbon and mineral resources of the Uinta Basin, Utah and Colorado: Utah Geological Association, Guidebook 20, p. 9–47.

Franczyk, K.J., Fouch, T.D., Johnson, R.C., Molenaar, C.M., and Cobban, W.A., 1992, Cretaceous and Tertiary paleogeographic reconstructions for the Uinta-Piceance Basin study area, Colorado and Utah: U.S. Geological Survey Bulletin B-1787-Q, p. 1–37.

Gierlowski-Kordesch, E.H., 2010, Lacustrine carbonates, *in* Alonso-Zarza, A.M., and Tanner, L.H., editors, Carbonates in continental settings—Facies, environments, and processes: Elsevier, Developments in Sedimentology 61, p. 1–101.

Hasiotis, S.T., and Honey, J.G., 2000, Paleohydrologic and stratigraphic significance of crayfish burrows in continental deposits—examples from several Paleocene Laramide basins in the Rocky Mountains: Journal of Sedimentary Research, 70, p. 127–139.

Jobe, T.D., 2013, Sedimentology, chemostratigraphy and quantitative pore architecture in microporous carbonates—examples from a giant oil field offshore Abu Dhabi, UAE: Golden, Colorado School of Mines, Ph.D. dissertation, 143 p.

Johnson, T.C., 1984, Sedimentation in large lakes: Annual Review of Earth and Planetary Sciences 12, p. 179–204.

Johnson, R.C., 1985a, New names for units in the lower part of the Green River Formation, Piceance Creek Basin, Colorado: U.S. Geological Survey Bulletin 1529-I, p. 20.

Johnson, R.C., 1985b, Early Cenozoic history of the Uinta and Piceance Creek Basins, Utah and Colorado, with special reference to the development of Eocene Lake Uinta, *in* Flores, R.M., and Kaplan, S.S., editors, Cenozoic paleogeography of the west-central United States: Rocky Mountain Section, Society of Economic Paleontologists and Mineralogists, Denver, CO., p. 247–276.

Johnson, R.C., Mercier, T.J., Michael, B.E., and Self, J.G., 2010, Assessment of in-place oil shale resources in the Eocene Green River Formation, Uinta Basin, Utah and Colorado: U.S. Geological Survey, Chapter 1, p. 4–162.

Keighley, D., Flint, S., Howell, J., and Moscariello, A., 2003, Sequence Stratigraphy in Lacustrine Basins—A model for part of the Green River Formation (Eocene), southwest Uinta Basin, Utah, U.S.A.: Journal of Sedimentary Research, v. 73, no. 6, p. 987–1006.

Little, T.M., 1988, Depositional environments, petrology, and diagenesis of the basal limestone facies, Green River Formation (Eocene), Uinta basin, Utah: Salt Lake City, University of Utah, M.S. thesis, 154 p.

Morgan, C.D., and Bereskin, S.R., 2003, Characterization of petroleum reservoirs in the Eocene Green River Formation, central Uinta Basin, Utah: The Mountain Geologist, v. 39, no. 4, p. 111–127.

Morgan, C.D., Chidsey, T.C., Jr., McClure, K.P., Bereskin, S.R., and Deo, M.D., 2003, Reservoir characterization of the lower Green River Formation, Uinta Basin, Utah: Utah Geological Survey Open-File Report, 411, 140 p.

Osmond, J.C., 1965, Geologic history of site of Uinta Basin, Utah: American Association of Petroleum Geologists Bulletin, v. 49, no. 11, p. 1957–1973.

Picard, M. D., 1957, Green River and Lower Uinta Formations—Subsurface stratigraphic changes in central and eastern Uinta Basin, Utah: Utah Geological Association Guidebook, p. 116–130.

Pietras, J.T., Carroll, A.R., Singer, B.S., and Smith, M.E., 2003, 10 k.y. depositional cyclicity in the early Eocene—Stratigraphic and $^{40}Ar/^{39}Ar$ evidence from the lacustrine Green River Formation: Geological Society of America, v. 31, no. 7, p. 593–596.

Pitman, J.K., 1996, Origin of primary and diagenetic carbonates in the lacustrine Green River Formation (Eocene), Colorado and Utah: U.S. Geological Survey Bulletin 2157, p. 1–16.

Platt, N.H., and Wright, V.P., 1991, Lacustrine carbonates—facies models, facies distributions and hydrocarbon aspects, *in* Anadon, P., Cabrera, L., Kelts, K., editors, Lacustrine facies analysis: International Association of Sedimentologists Special Publication, v. 13, p. 57–74.

Reading, H.G., and Collinson, J.D., 1996, Clastic coasts, *in* Reading, H.G., editor, Sedimentary Environments: Processes, Facies and Stratigraphy, 3rd edition, Blackwell Science, Oxford, p. 154–231.

Remy, R.R., 1992, Stratigraphy of the Eocene part of the Green River Formation in the south-central part of the Uinta Basin, Utah: U.S. Geological Survey Bulletin B-1787-BB, p. 1–69.

Renaut, R.W., and Gierlowski-Kordesch, E.H., 2010, Lakes, *in* James, N.P., and Dalrymple, R.W., editors, Facies Models: Geological Association of Canada, IV Series, GEOtext 6, p. 541–575.

Rosenberg, M.J., Birgenheier, L.P., and Vanden Berg, M.D., 2015, Facies, stratigraphic architecture, and lake evolution of the oil shale bearing Green River Formation, eastern Uinta Basin, Utah, *in* Smith, M.E., and Carroll, A.R., editors, Stratigraphy and paleolimnology of the Green River Formation, western USA: Springer, DOI 10.1007/978-94-017-9906-5, p. 211–249.

Ryder, R.T., Fouch, T.D., and Elison, J.H., 1976, Early Tertiary sedimentation in the western Uinta Basin, Utah: Geological Survey of America Bulletin, v. 87, p. 496–512.

Schamel, S., 2015, Rediscovered shale oil resource play potential of the Green River Formation, Uinta Basin, Utah—Associated with energy resource development, *in* Vanden Berg, M.D., Ressetar, R., and Birgenheier, L.P., editors, Geology of Utah's Uinta Basin and Uinta Mountains: Utah Geological Association Publication 44, p. 275–303.

Schomacker, E.R., Kjemperud, A.V., Nystuen, J.P., and Jahren, J.S., 2010, Recognition and significance of sharp-based mouth-bar deposits in the Eocene Green River Formation, Uinta basin, Utah: Sedimentology, v. 57, p. 1069–1087.

Self, J.G., Brownfield, M.E., Johnson, R.C., and Mercier, T.J., 2010a, Fischer assay histograms of oil shale drill cores and cuttings from the Uinta basin, Utah and Colorado:

U.S. Geological Survey, Digital Data Series DDS–69–BB, chapter 5, 8 p.

Self, J.G., Brownfield, M.E., Johnson, R.C., and Mercier, T.J., 2010b, Fischer assay histograms of oil shale drill cores and cuttings from the Piceance Basin, northwestern Colorado: U.S. Geological Survey, Digital Data Series DDS–69–Y, chapter 7, 9 p.

Smith, M.E., Carroll, A.R., and Singer, B.S., 2008, Synoptic reconstruction of a major ancient lake system—Eocene Green River Formation, western United States: Geological Society of America Bulletin, v. 120, n. 1, p. 1–54.

Smith, M.E., Chamberlain, K.R., Singer, B.S., and Carroll, A.R., 2010, Eocene clocks agree—coeval $^{40}Ar/^{39}Ar$, U-Pb, and astronomical ages from the Green River Formation: Geology, v. 38, p. 527–530.

Smoot, J.P., 1983, Depositional subenvironments in an arid closed basin—the Wilkins Peak Member of the Green River Formation, western United States: Geological Society of America Bulletin, v. 120, p. 54–84.

Strohmenger, C., and Wirsing, G., 1991, A proposed extension of Folk's (1959, 1962) textural classification of carbonate rocks: Carbonate and Evaporites, Springer Link, v. 6, p. 23–28.

Tänavsuu-Milkeviciene, K., and Sarg, J.F., 2012, Evolution of an organic-rich lake basin—stratigraphy, climate and tectonics—Piceance Creek Basin, Eocene Green River Formation: Sedimentology, v. 59, p. 1735–1768.

Taylor, A.W., and Ritts, B.D., 2004, Mesoscale heterogeneity of fluvial lacustrine reservoir analogues—examples from the Eocene Green River Formation and Colton Formations, Uinta Basin, Utah, USA: Journal of Petroleum Geology, v. 27, p. 3–25.

Tucker, M.E., and Wright, V.P., 1990, Carbonate sedimentology: Blackwell Scientific Publications, Oxford, 482 p.

Vanden Berg, M.D., 2008, Basin-wide evaluation of the uppermost Green River Formation's oil-shale resource, Uinta basin, Utah and Colorado: Utah Geological Survey Special Study 128, p. 1–23.

Vanden Berg, M.D., Wood, R.E., Carney, S.M., and Morgan, C.D., 2014, Geological characterization of the Uteland Butte Member of the Eocene Green River Formation—an emerging unconventional carbonate tight oil play in the Uinta Basin, Utah: 2014 Rocky Mountain Section of the American Association of Petroleum Geologists Annual Meeting, July 20–22, 2014, Program with Abstracts, p. 44.

Wiggins, W.D., and Harris, P.M., 1994, Lithofacies, depositional cycles, and stratigraphy of the lower Green River Formation, southwestern Uinta Basin, Utah: Society for Sedimentary Geology, Core Workshop No. 19, p. 105–141.

Appendix IV

Dolomitization in the Uteland Butte Member of the Eocene Green River Formation, Uinta Basin, Utah

Federico Rueda and Hans Machel

University of Alberta, Edmonton, Canada

Dolomitization in the Uteland Butte Member of the Eocene Green River Formation, Uinta Basin, Utah.

by

Federico Rueda Chaparro

A thesis submitted in partial fulfillment of the requirements for the degree of

Master of Science

Earth and Atmospheric Science Department

University of Alberta

ABSTRACT

The lacustrine Green River Formation (GRF) is an important oil-producing formation in the Uinta Basin, Utah (USA). In recent years, the unconventional carbonate reservoirs in the Uteland Butte member (UBM) at the base of the GRF have been targeted because of their petrophysical properties and their estimated resource of 214 million barrels of oil and 329 billion cubic feet. The stratigraphic interval of interest is within the middle of the UBM, defined at the bottom and top by the D and C Shales, respectively. Within this interval, there are three regionally extensive dolomite layers named PZ2, PZ1', and PZ1, consisting of up to 100% dolomite. These beds vary from 1.5 to 8 feet in thickness and are interbedded with organic-rich limestones and shales. They have up to 30% porosity but only a maximum of 0.1 mD permeability.

The main objectives of this study are to characterize the facies types and determine how they are related to dolomitization; elucidate the dolomitization process and how porosity and permeability are related this process; delineate the regional geometry of the dolomite layers. This study employed several methods including outcrop and core descriptions; petrographic analysis by means of transmitted light, cathodoluminescence microscopy, and scanning electron microscopy petrography; mineralogical identification and ordering of dolomites through X-ray diffractometry; elemental compositions by means of X-ray spectrometry (EDS in SEM) and electron microprobe; trace element analysis using inductively coupled plasma mass spectrometry; conventional and clumped oxygen and carbon isotope analysis.

Deposition of the UBM took place during transgressive-regressive cycles that were driven by climate variations. The ancient Uinta Lake water level was high during cooler and

rainy periods that alternated with warmer and drier periods, which led to lower lake levels caused by reduced fluvial input and/or evaporative drawdown. The three PZ layers were deposited in littoral environments as intraclastic grainstones and ooid ostracod grainstone-packstones, and also in littoral to sublittoral environments as mudstones, peloidal bioturbated mudstones, and ostracod wackestones. There is no discernible relationship between dolomitization and depositional environments.

Dolomitization took place syndepositionally from lake water that was moderately evaporated and also enriched in Mg during drier periods. These conditions formed dolomite crystals characterized by a wide range of %Ca from 50% to 59% with a strong mode in 52 to 55%, and low cation ordering that range from 0.2 to 0.5. The %Ca range and the low cation ordering are interpreted as results of variable and incomplete recrystallization in a closed system during burial under considerable hydrologic overpressure. The $\delta^{13}C$ values for dolomite range from 6‰ to -5.4‰ (VPDB) suggesting high organic activity and/or organic matter decay, coupled with organic matter oxidation by sulfate reducing bacteria. The $\delta^{18}O$ values for dolomite range from 0.9 to -7.3‰ (VPDB) interpreted as elevated lake water temperatures. The calculated fluid temperature of dolomitization is between 14 to 36 °C. Furthermore, there is a strong correlation between %Ca and cation ordering, and Sr and Mn concentration with depth. The %Ca increase in depth, whereas cation ordering decrease; the Sr concentration decrease in depth, whereas Mn concentration increase. This trend may be related to dolomitizing fluid flow.

Increased fresh water input during more humid climate periods stopped dolomitization and facilitated deposition of lime mud layers. $\delta^{13}C$ for calcites range from 1‰ to -1‰ (VPDB), and the $\delta^{18}O$ for calcites range from -5.8 to -10.1‰ (VPDB). The calculated temperature for calcite precipitation is between 3 and 12 °C.

The dolomite crystal sizes range from 0.25 to 6 μm and porosity is mainly intercrystal. Dolomite layers PZ1, PZ1', and PZ2 display four dolomite textures: planar e, planar s, nonplanar-a, and planar-c. Planar-e and planar-s are associated to higher porosity. However, there is no defined trend or distribution of texture versus porosity. Permeability is low due to irregular and commonly disconnected pore throats. Also, diagenetic products after dolomitization, such as chert nodules (length-slow chalcedony), isopachous quartz cement, blocky ferroan calcite and equant to blocky calcite cement, reduced porosity and permeability.

TABLE OF CONTENTS

Page

LIST OF TABLES

Page

LIST OF FIGURES

CHAPTER ONE

INTRODUCTION

Lacustrine basins around the world are host to significant accumulations of hydrocarbons. For example, the fluvial-lacustrine Bohay Bay Basin in China is responsible for about one third of the country's total petroleum production (Hao et al., 2009). In Brazil, roughly 85% of oil produced from continental margin fields is sourced from lacustrine rocks (Mello and Maxwell 1990). In the United States, the lacustrine Green River Formation (GRF) in the Uinta Basin, Utah, hosts a very large accumulation of conventional oil and gas, as well as one of the largest immature oil shale resources, with an estimated 1.32 trillion barrels of initial oil in place (Johnson et al. 2010). While most drilling efforts in the Uinta Basin target more conventional sandstone reservoirs, the thin carbonates in the informal named Uteland Butte member at the base of the GRF has gained interest in recent years as an unconventional reservoir targeted with horizontal drilling. Recently, Johnson et al. (2015) estimated that the Uteland Butte contains a mean undiscovered resource of 214 million barrels of oil and 329 billion cubic feet.

The Uinta Basin is part of a cluster of lake basins that is located near the junction of Utah, Wyoming, and Colorado (Figure 1.1). The geological evolution of these lake basins started with the Sevier orogeny during Jurassic through early Cenozoic times (Johnson, 1985) that defined the western margin by uplifting of the Sevier Thrust Belt. Once the Sevier orogeny stopped, the Laramide Orogeny deformed the ancient foreland basin into smaller sedimentary basins during mid Cretaceous to early Paleogene, thus creating the lacustrine basins (Johnson, 1985) at the central area of the ancient Rocky Mountains foreland basin. The Laramide orogeny

created the physiographic boundaries of the lake basins as we know them today, including those of the Uinta Basin. The east-west trend Uinta Uplift likely rose prior to the end of the Cretaceous (Hansen, 1965) and was a source of sediments for Paleocene formations (Johnson, 1985). The NW-SE trend Uncompahgre uplift and the NE-SW San Rafael Swell uplifting started in the Maastrichtian (Johnson, 1985; Fouch, 1983). The north-south trend anticline Douglas Creek Arch likely started to rise at the end of Cretaceous (Tweto, 1975). The three lakes developed in the Laramide foreland basin and were filled with up to several thousand meters of deposits during early Tertiary times.

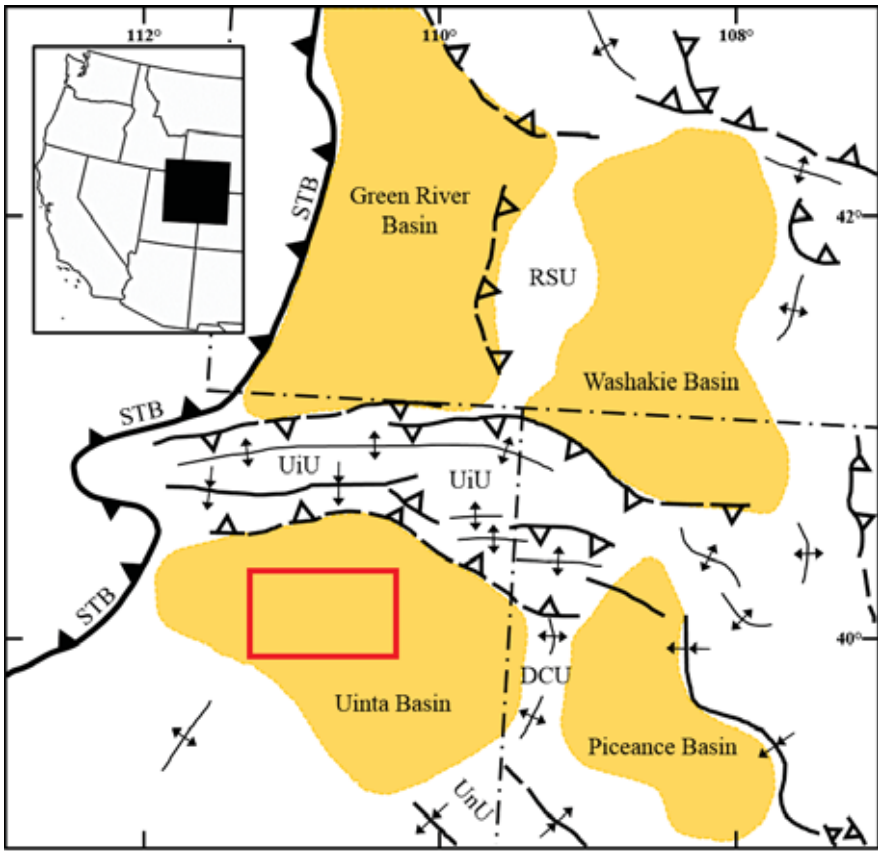

Figure 1.1: Eocene intermountain lake basins and associated uplifts. Modified from Dickinson et al (1988). Study area highlighted by red rectangle. DCU: Douglas Creek Uplift, RSU: Rock Springs Uplift, STB: Sevier Thrust Belt, UiU: Uinta Uplift, UnU: Uncompahgre Uplift.

The GRF was deposited in the Eocene epoch between 53 and 45 Ma (Smith, 2007; Smith et al. 2008). The basal parts of the GRF are thought to be deposited in fresh water environments, as evidenced by an abundance of fresh water molluscs (Johnson, 1985; Smith, 2007; Smith et al., 2008) and it is represented by the Uteland Butte member (Johnson et al., 2010). The middle intervals of the GRF contain layers of 'oil shale' that were likely deposited in brackish lake water environment generated by regression of lake water (Johnson et al., 2010). The upper section of the GRF were deposited in much shallower water level and hypersaline environments, as evidenced by halite and sodium carbonate salt beds with thickness reaching up to 5.8 meters (Dyni et al., 1985; Johnson, 1985; Long, 2006; Smith et al., 2008; Johnson et al., 2010).

The Uteland Butte member ranges in thickness from about 15 to 120 meters, being thickest near the depositional center of the Uinta Basin to the north and west (Vanden Berg et al., 2014; Johnson et al., 2016). This member represents the first 'transgression' of ancient Lake Uinta (Vanden Berg et al., 2013; Johnson et al., 2016) and is composed of a succession of interbedded limestones, dolostones, organic-rich calcareous mudstones, siltstones, and a few sandstones (Bereskin et al., 2004; Vanden Berg et al., 2014; Johnson et al., 2016).

Pusca (2003) defined the depositional environments for the Uteland Butte member as shallow lake to playa environments for the carbonate rocks, and as distal lake for the shales. In the so far most comprehensive study on facies and depositional environments of the Uteland Butte member, Logan (2015) identified depositional environments ranging from littoral, sublittoral, to profundal, based on outcrops and core well descriptions located at the eastern boundary of the Uinta Basin.

This study focuses on the distal Uteland Butte facies in the deeper portion of the basin mostly in Duchesne County, (Utah); and of particular interest to understand the origin of thin

dolomite beds (<0.5 to 2.5 m) that exhibit very high porosity, but low permeability (Figure 1.3), and act as significant hydrocarbon reservoirs, which are targeted with horizontal drilling and hydraulic fracturing techniques.

1.1 Research objectives

This project pursues solutions to several questions related to the dolomitization process(es) within the Uteland Butte and how this relates to petroleum production potential. The specific objectives of this study include:

1) Characterization and analysis of facies types for the Uteland Butte member as they relate to dolomitization;
2) Determination of the process(es) of dolomitization;
3) Investigation of how porosity and permeability are related to dolomitization;
4) Characterization of the geometry (lateral and vertical extent) of the dolomite layers across the western Uinta Basin;
5) Possible implications for petroleum reservoir development.

1.2 Previous work

There is a substantial body of literature on the Uinta Basin and the GRF (e.g., Picard, 1955; Johnson, 1985; Remy, 1992; Smith, 2007; Johnson et al., 2016; Tänavsuu-Milkeviciene et al., 2017), which cover a large range of aspects that includes the tectonic evolution, sedimentology, paleoclimate, and several others. However, only a few studies have dealt with dolomitization.

The first notable attempt to explain dolomitization in the GRF was by Eugster and Surdam (1973), who invoked evaporation in playa flats as the chief cause and location of dolomitization. Implicit to their 'playa model' is that the lake margin was very shallow and even drying up during times of prolonged evaporation. In their own words (Eugster and Surdam 1973, Abstract): *"In these playa flats alkaline brines evolved through evaporation and precipitation of calcium carbonate and protodolomite in the capillary zone near the ground-water table. Dolomitic mudstones, marlstones, and calcareous and siliciclastic sandstones were the products of occasional floods on the playa."*

Williamson and Picard (1974) identified dolomite as a replacement of the microcrystalline and fine-crystalline calcite matrix (micrite and sparite) of certain layers and concluded that dolomitization took place very early in the diagenetic history, prior to lithification. These authors did not identify any specific relationship between facies and dolomitization but nevertheless concluded that dolomitization was promoted by episodic evaporation coupled with high Mg/Ca ratios in the lake water. In addition, they argued that the Mg necessary for dolomitization was likely flushed in by river drainage in the form of admixed clay minerals. However, they did not find a correlation between acid-insoluble residues and dolomite contents (Williamson and Picard, 1974).

Ryder et al. (1976) differentiated two genetic types of dolomite associated with depositional environments: (i) an open lacustrine (profundal) environment in which dolomite formed from Mg that was released from interbedded algae-rich laminites; and (ii) near shore (littoral) environments where the fine-grained carbonate sediments were dolomitized as a result of pumping of brines enriched in Mg by evaporation. The latter conforms to the "playa-lake" by Eugster and Surdam (1973).

Desborough (1978) proposed that dolomitization took place in organic-rich (oil shale to-be) layers when the lake was chemically stratified. While he worked mainly in the Parachute Creek Member of the Green River Formation of the Piceance Basin (Figure 1.1), he also applied this 'model' to the Uinta Basin. Accordingly, cyanobacteria concentrated Mg through their metabolism, which was released during post-mortem degradation near the water-sediment interface, thereby promoting dolomitization.

Cole and Picard (1978), working in the Parachute Creek Member on the eastern side of the Uinta Basin and in the neighboring Piceance Basin, did more detailed mineralogical work than previous studies. They reported that dolomite is abundant throughout the Parachute Creek Member and most abundant in the oil shale lithofacies. In the Uinta Basin, the dominant carbonate minerals were found to be dolomite, ankerite, and calcite, and analcime, potassium feldspar, quartz, and albite were also found in the nearshore facies. Cole and Picard (1978) suggested that dolomite formed as the result of biological and chemical conditions of the lake water.

Pitman (1996) was the first researcher to systematically apply stable isotope geochemistry to the dolomite problem in the GRF for both the Douglas Creek and Parachute Creek Members. Based on carbon isotope data, Pitman (1996) identified two types of dolomite: 'primary' and 'diagenetic'. The primary dolomites have $\delta^{13}C$ values ranging from about -2 to +2 ‰ PDB (Pee Dee Belemnite), whereas the diagenetic dolomites have $\delta^{13}C$ values ranging from about +2 to +4 ‰ PDB. According to Pitman (1996), the primary dolomites were formed by gradual increases in the dissolved bicarbonate concentration (carbonate alkalinity) when the lake evolved from hydrologically 'open' to hydrologically 'closed', catalyzed by increased photosynthetic activity. In contrast, Pitman (1996) interpreted the origin of the diagenetic

dolomite as mediated by bacterial sulfate reduction. Pitman (2006) did not differentiate between direct formation of dolomite from aqueous solution and replacement of carbonate mud.

Long (2006) investigated dolomitization in several intervals of the Green River Formation and identified two different dolomite crystals based on their lithology occurrence. The first dolomites are related to the oil shale layers. Long (2006) interpreted these dolomites as result of bacterial methanogenesis process that promoted dolomite precipitation. The second dolomites are related to micrite layers in the "Tgl member", which correlates with the Uteland Butte. Long (2006) interpreted these dolomites formed as a replacement of lime mud under evaporitic conditions.

Logan et al (2016) completed a comprehensive facies analysis of the Uteland Butte member located on the eastern side of the Uinta Basin. The Uteland Butte in this area contains more proximal facies (e.g., grainstones, deltaic and mouth-bar sand units, etc.) and little dolomite, compared to the more distal Uteland Butte on the west side of the basin (the focus of this study), where the unit is a productive oil and gas reservoir.

In summary, previous studies agree on one point: the dolomite(s) in the GRF, and more specifically in the Uteland Butte member, formed syndepositionally and/or very early diagenetically. However, these studies offered several possibilities for the source of Mg, the driving mechanism for dolomitization (hydrologically and/or geochemically), with some disagreement as the dolomite(s) being primary or a replacement product of lime mud.

1.3 Study area and stratigraphic interval of interest

The study area covers the central to southwestern parts of the Uinta Basin, mostly in Duchesne County (Figure 1.2). The stratigraphic interval of interest is within the middle portion of the Uteland Butte member, defined at the bottom and top by the informally named D Shale and C Shale, respectively. Within this interval there are three prominent and regionally extensive dolomite layers named PZ1, PZ1', and PZ2 (operator designations). These dolomite beds, as well as numerous other thin dolomite beds throughout the Uteland Butte, have significant reservoir potential due to their high porosity and lateral extent (Figure 1.3).

1.4 Dolomite theoretical framework

Dolomite, $CaMg(CO_3)_2$, is a rhombohedral carbonate mineral of Mg and Ca, commonly found in sedimentary rocks. When a rock consists of more than 90% dolomite, it is commonly referred to as dolostone, although many authors refer to such rocks also with the mineral name dolomite.

The origin of the mineral dolomite has been a focus of a large number of investigations for more than 200 years. Dolomites are important for several reasons including: (1) dolomite is a common carbonate mineral in ancient carbonate successions yet rare in recent carbonate sediments; (2) dolomite has not been synthetized in laboratories at low-diagenetic temperatures (less than about 30°C) inorganically or organically; and (3) most natural dolomites formed via replacement of pre-existing limestones, and many dolomitized carbonates form prolific reservoir rocks for hydrocarbons (Tucker and Wright, 1990; McKenzie, 1991; Purser et al., 1994

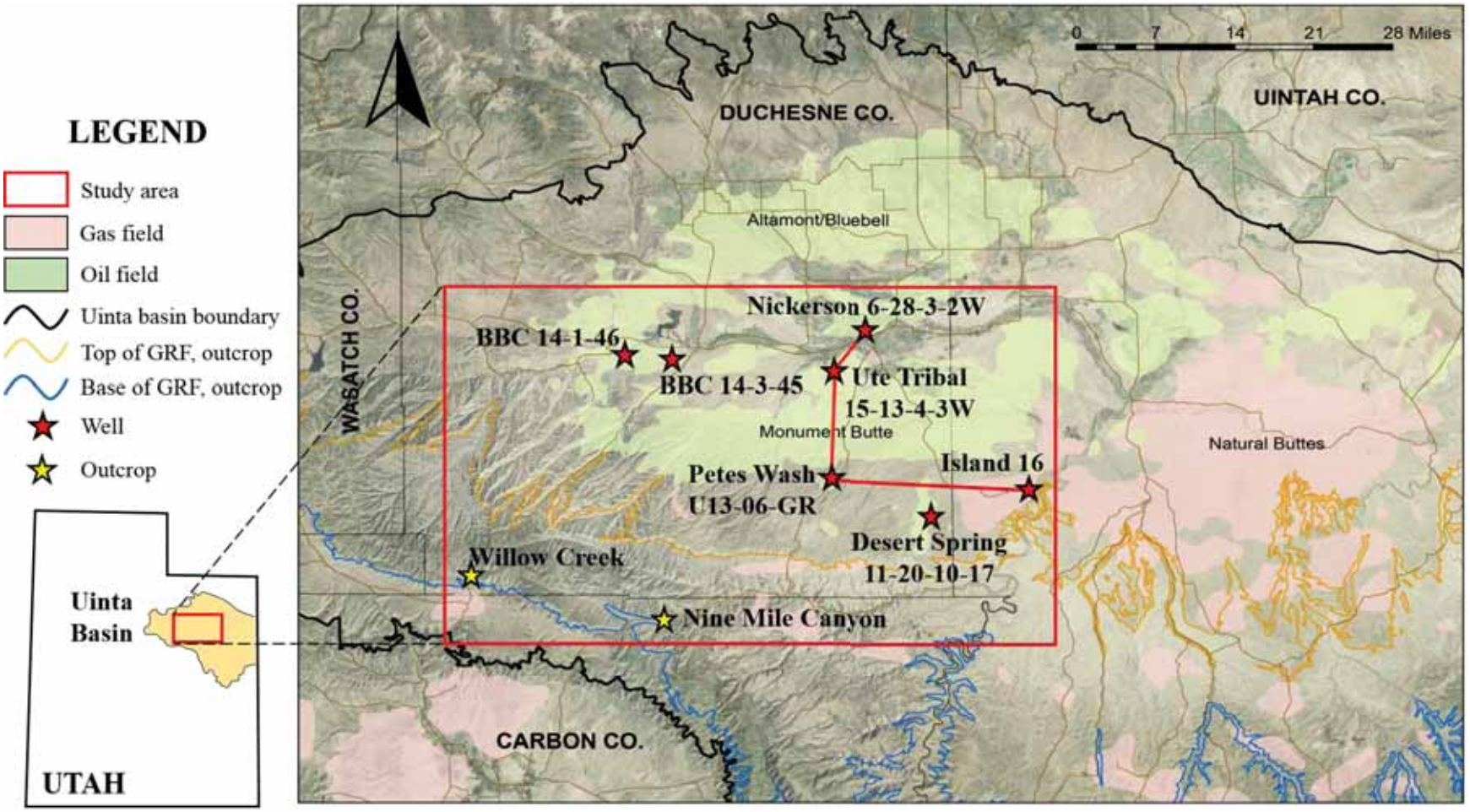

Figure 1.2: Location of study area (red outline). Modified from Vanden Berg et al. (2014). The red line connects the wells chosen for cathodoluminescence microscopy, see chapter 3 for further description.

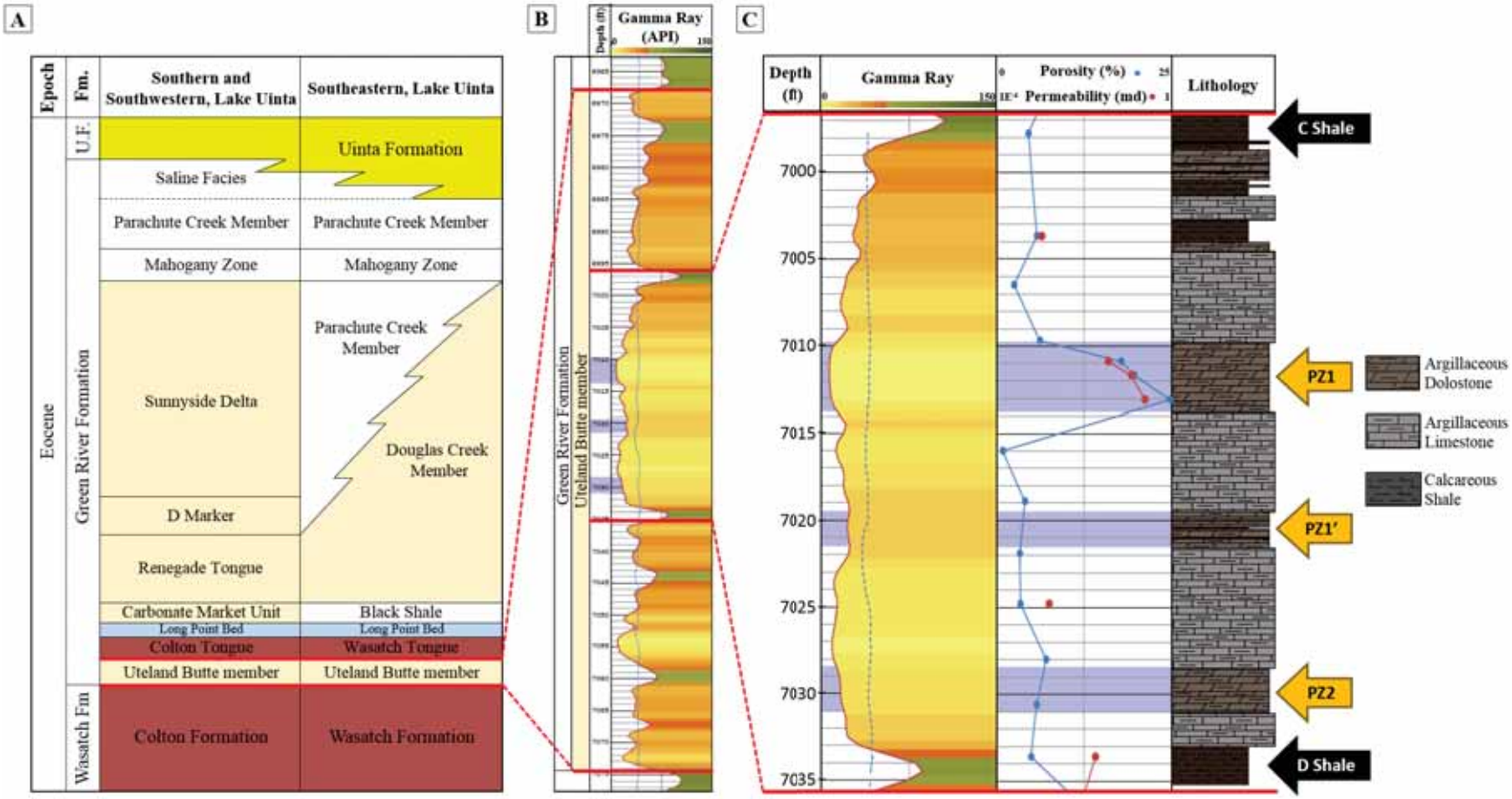

Figure 1.3: (A) Stratigraphic chart of the GRF modified from Logan et al. (2016) and stratigraphic interval of interest (B, C). (B) is a gamma ray and porosity logs from the Ute Tribal 15-13-4-3W Uteland Butte core drilled by Newfield. The interval of interest is the central part of the Uteland Butte member (enlarged in C). (C) is a composite of gamma ray, porosity, permeability, and lithology logs of the interval of interest.

Warren, 2000; Machel 2004; Gregg et al. 2015; Kaczmarek et al 2017). In natural diagenetic environments, dolomite most commonly forms via dolomitization, which is the replacement of calcite by dolomite, or subordinately via direct precipitation from aqueous solution in the form of cements that line or fill pores (e.g., Machel, 2004). In addition, dolomite can also form at the sediment-water interface as mud. The latter type is also known as 'penecontemporaneous' dolomite, the former two as 'post-depositional' dolomites (Budd 1997).

Over the years many models of dolomitization have been proposed, most of them with the aim to explain the genesis of reservoir-sized geobodies of dolostones, among them the microbial model, the mixing zone model, the related reflux and sabkha models, several seawater models, the compaction model, two thermal convection models, a topography driven model, a tectonic model, and the hydrothermal model (Machel, 2004). In addition, there are viable models for dolomitization that do not form reservoir-sized dolomite/dolostone geobodies, such as the Coorong and playa models (Eugster and Surdam, 1974; Warren, 2000). This study attempts to explain dolomitization of the GRF Uteland Butte member within the framework of these models. A new model would arise in case none of the existing models provides a satisfactory genetic interpretation.

CHAPTER TWO

GEOLOGICAL FRAMEWORK

2.1 Basin and lake evolution

The formation of the Uinta Basin began in the Jurassic up to the early Cenozoic by the development of the Sevier Orogenic belt that resulted from the collision of the Farallon and the North American plate. (Johnson, 1985).The uplifted Sevier Orogenic belt became the west boundary of the Lake Uinta.

Later, during late Cretaceous to early Paleocene, the Laramide Orogeny caused retreat of the Rocky Mountains foreland basin and formed a series of regional uplifts (Johnson, 1985; Johnson et al., 2016) that transformed the epicontinental foreland basin into several smaller basins that filled with lakes in the early Eocene (Dickinson et al., 1988) (Figure 2.1C and D).

In the early Eocene, tectonic and climatic conditions allowed the development of four lacustrine basins: the Uinta Basin that occupied the area between Sevier and Laramide structures; the Gosiute Basin to the north in what is now southwest Wyoming; the Piceance Basin to the east in what is now Colorado; and the Claron Basin to the south (Figure 2.1 C, D).

The Uinta Basin is a structural, asymmetric basin located in the northeastern part of Utah, bounded in the north by the Uinta Mountains, in the east by the Douglas Creek Arch, in the south by the San Rafael Swell and the Uncompahgre Uplift, and in the west by the Wasatch Mountains.

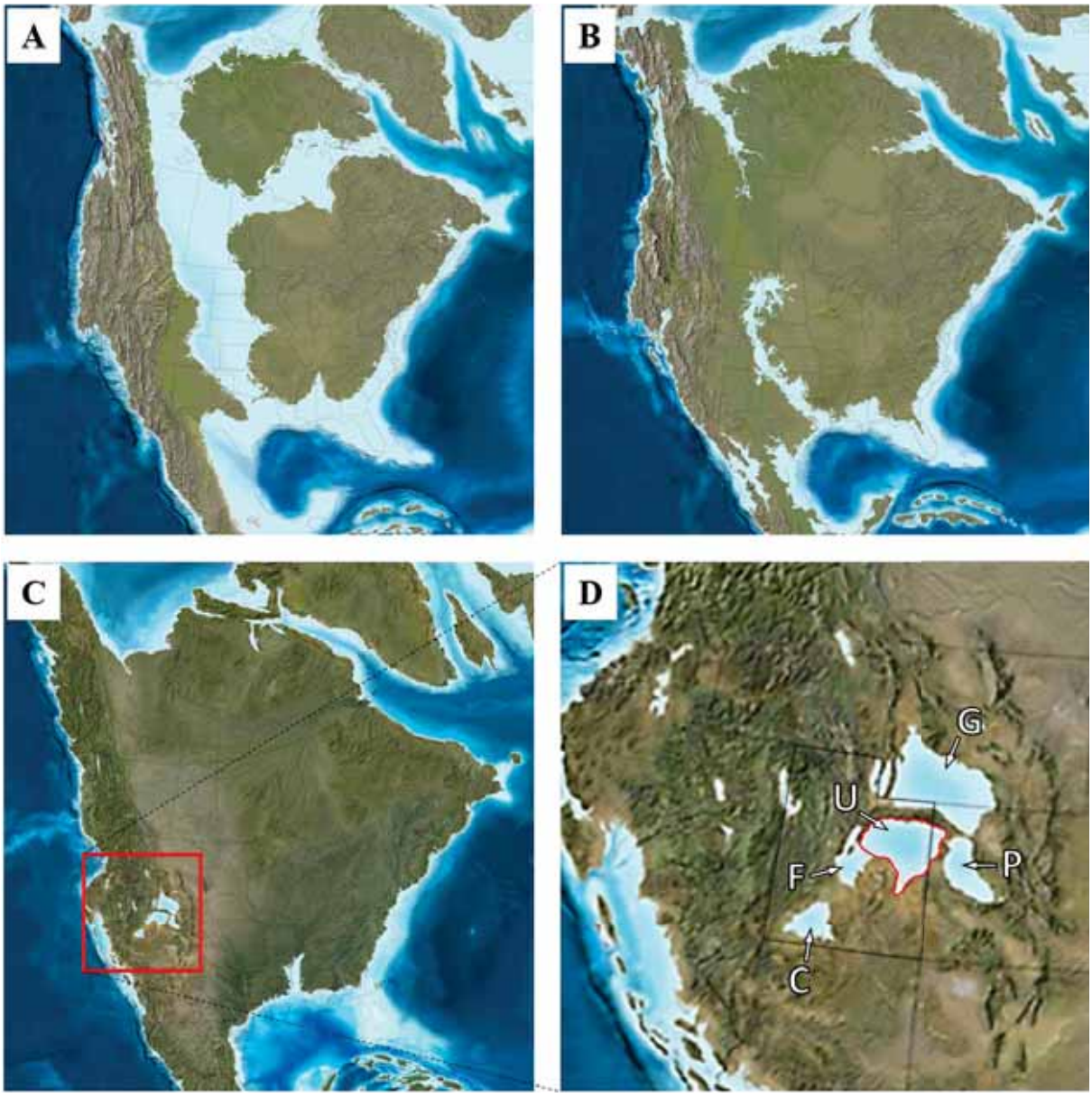

Figure 2.1: Paleogeographic evolution of North America during the Laramide Orogeny (A and B). (A) Late Cretaceous. (B) Early Paleocene. Both images retrieved from Ron Blakey website at http://deeptimemaps.com/wp-content/uploads/2016/05/NAM_key-75Ma_LateK.png. C and D) Early Eocene: Intermountain and coexisting lacustrine basins; (D) enlargement of (C) showing Lake Gosiute (G), Uinta (U), Piceance (P), and Flagstaff (F) basins, and Claron lakes. The boundary between Uinta and Flagstaff basins is outlined in red, image retrieved from Ron Blakey website at http://deeptimemaps.com/wp-content/uploads/2016/05/NAM_key-50Ma_Eocene.png

2.2 Paleohydrology

The tectonic events of the late Paleocene to early Eocene controlled the extent of drainage within the catchment area, and thereby sizes and connections of the Uinta and Gosiute lakes therein.

Ancient Lake Uinta was fed by streams from the surrounding paleo-highs. The basin received water from the Uinta Mountains to the north, and thereby sediments from the erosion of Precambrian to Cretaceous bedrock, including large deposits of Paleozoic carbonates (Hansen, 1965; Pusca, 2003).

From the west, sediment was supplied by the Wasatch Mountains (Sevier Thrust Belt), from erosion of Paleozoic and Mesozoic carbonates (Davis, 2008; Gierlowski-Kordesch et al., 2008).

The drainage from the south came from the San Rafael Swell, eroding mostly Paleozoic sedimentary rocks that ranged from marine shales of the Mancos Shale Formation to alluvial plains and fluvial clastics of the Morrison Formation (Doelling, 2002), and from the Mojave region transported by the California paleoriver (Dickinson et al., 2012). Drainage and sediments were also derived from the Uncompahgre Uplift in the southeast (Cashion, 1967; Dickinson et al., 1988; Davis et al. 2009; Johnson et al. 2010; Smith et al. 2008), mostly composed of Proterozoic metamorphic rocks (Case, 1991) (Figure 2.2).

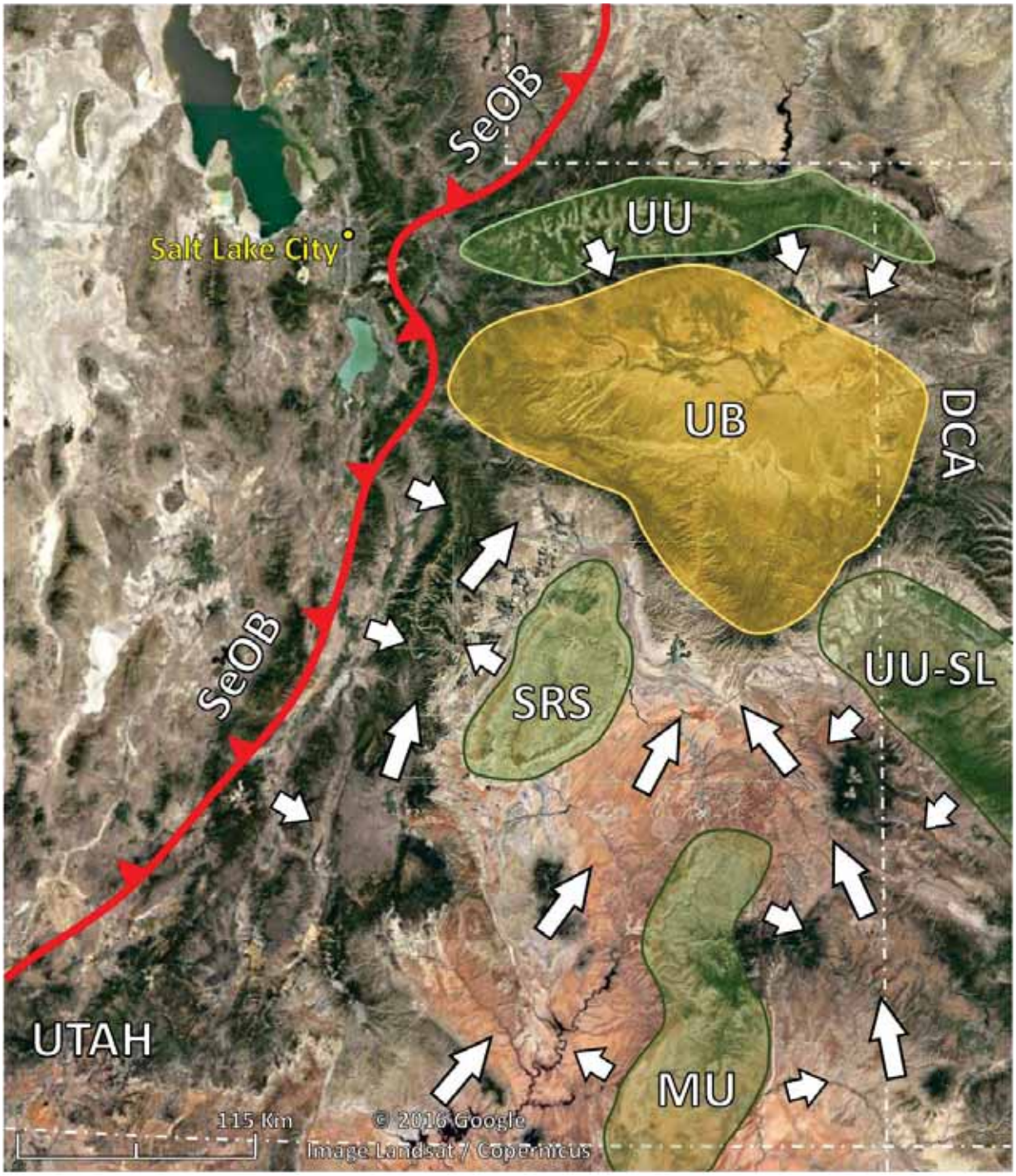

Figure 2.2: Paleogeographic location of the Uinta Basin and surrounding uplifts. Arrows represent the potential paleocurrents that likely fed Lake Uinta. UB - Uinta Basin (Foreman et al., 2012; Vanden Berg et al., 2014), UP - Uinta Uplift (Baars and Stevenson, 1981; Foreman et al., 2012), UU–SL - Uncompahgre Uplift (Sweet and Soreghan, 2012) – San Luis Mountains (Kluth, 1986), MU - Monument Upwarp (Hintze et al., 2000), SRS - San Rafael Swell (Doelling, 2002), SeOB - Sevier Orogenic Belt (Hintze et al., 2000).

2.3 Sedimentology

The sedimentological evolution of these lakes was governed by climatic and tectonic factors that defined depositional settings and facies associations. Carroll and Bohacs (1999) established a lake classification based on facies associations: overfilled, balanced, and underfilled lake (Figure 2.3). According to Carroll and Bohacs (1999), the most common associations are fluvial-lacustrine, fluctuating profundal, and evaporite facies, which are the result of climate (sediment supply) and tectonism (accommodation rate) fluctuations.

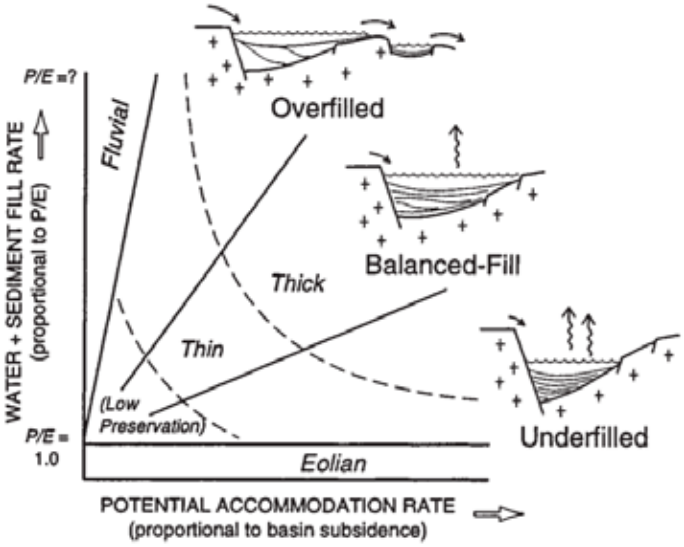

Figure 2.3: Schematic representation of lake types according to sediment and water supply (controlled by climate) versus accommodation rate (controlled by tectonism) (Carroll and Bohacs, 1999). Deposition of the Uteland Butte member most likely took place within the overfilled to balanced-fill lake type. Image from Carroll and Bohacs (1999).

The overfilled lakes are characterized by marlstone and fresh water coquinas interbedded with thin coal seams. Balanced-fill lakes record the flooding and desiccation phases by organic rich calcareous mudstone and dolomitic grainstone with evidences of subaerial exposure. The underfilled lake types display a wide variety of facies association from alluvial-

fan, laminated oil shales, and evaporite minerals such trona and halite (Carroll and Bohacs, 1999).

Based on the lithologic characteristics and facies associations, sedimentation in Lake Uinta during deposition of the Uteland Butte member was controlled mainly by periodic lake water level fluctuations and a balance between accommodation space and sediment infill. The Uteland Butte member is characterized by shallowing upward sequences defined by organic rich shales, molluscan limestones and coquina, and dolomudstone to ooidal dolograinstones. Therefore, as defined by Carroll and Bohacs' (1999) lakes classification, deposition of the Uteland Butte member most likely took place between the underfilled and balanced-fill lake types (Figure 2.3).

2.4 Stratigraphy

The Green River Formation (GRF) is conformably bound at the base by the late Paleocene to early Eocene Wasatch Formation (Roehler, 1991) in the east and the Colton Formation in the west. The overlying Uinta Formation represents the fluvial sediments that eventually filled Lake Uinta. The age of deposition is between ca. 54 and 45 million years (Smith, 2007) corresponding to the early and middle Eocene epoch (Eugster et al., 1973; Ryder et al., 1976; Johnson, 1985). The Green River Formation varies in thickness from about 2200 m in the center to northwestern area of the basin to about 600 m in the southeastern area (Schamel, 2015).

The Uteland Butte is the basal member of the GRF (Cashion, 1964; Davis et al., 2009; Johnson et al., 2016). Its thickness also varies according to its location within the Uinta Basin,

with about 120 m being thickest in the north close to the Uinta Uplift, and thinning to about 15 m in the southeastern portion (Johnson et al., 2016). The age of deposition for the Uteland Butte member was estimated as ca. 54-52 m.y. based on paleontological evidence (Remy, 1992).

The GRF was first divided into four members (from top to base) by Bradley (1931) as follows: (1) Douglas Creek, (2) Garden Gulch, (3) Parachute Creek, and (4) Evacuation Creek. Since then, several other authors have provided differing and in parts overlapping subdivisions for the GRF. Morgan and Bereskin (2003) were the first to identify and define the Uteland Butte member at the base of the GRF. Logan et al. (2016) summarized the stratigraphic nomenclature of the GRF based on previous studies. In this project, the stratigraphic nomenclature of Logan et al. (2016) will be used, as shown in Figure 1.3.

2.5 Facies and Depositional Environments

The lithofacies of the Uteland Butte member generally consists of interbedded limestones, dolostones, calcareous mudstones, siltstones, and a few sandstones. The main allochem particles in the limestones are ostracods, ooids, fresh water molluscs (disarticulated pelecypods or tubiform gastropods), algae, fish fragments, peloids, and intraclasts (Morgan et al., 2003; Bereskin et al., 2004). In outcrops located in the southern margin of the Uinta Basin, Long (2006) identified cyclic intercalations of massive biomicrites with ostracods, gastropods, bivalves, and charophytes at the base, dark organic rich micrites with nodules in the middle, then grading into shales toward the top. Most recently, based on outcrops and cores located on the eastern side of the basin, Logan et al. (2016) described the Uteland Butte member as intercalations of grey to green siltstones, dolomudstone to dolograinstone with abundant peloids,

ostracods, and rock fragments, molluscan lime wackestone to mudstone, sandstones, coal seams, and oil shale.

Bereskin et al. (2004) interpreted the GRF as deposits from two main environments: (1) marginal lacustrine carbonates flats, deltaic, and inter-deltaic environments; and (2) open, deeper lacustrine facies. Similarly, Ruble and Philp (1998) identified three main environments: (1) open lacustrine; (2) marginal lacustrine deltaic and inter-deltaic mudflats and paludal; and (3) alluvial deltaic plain, high mud flat, and alluvial fan, based on outcrop observations and well logs from the lower section of the GRF. Logan et al. (2016) interpreted the depositional environments of the Uteland Butte member as a fresh water ramp margin with minor influence of fluvial systems, based on the absence of stromatolites, lack of evaporite minerals, and abundance of bivalves, gastropods, and ostracods with in the limestone beds.

CHAPTER THREE

METHODOLOGY

This study investigates the depositional, diagenetic, and geochemical characteristics of the dolomites PZ layers of the Uteland Butte member of the lower GRF as a means to better understand the inherent dolomitization processes. This study employed a wide variety of investigative methods including: 1) outcrop and core descriptions; 2) petrographic analysis by means of transmitted light and cathodoluminescence microscopy; 3) scanning electron microscopy (SEM); 4) mineralogical identification via semi-quantitative major element analysis and ordering of dolomites through X-ray diffractometry (XRD); 5) elemental composition by X-ray spectrometry (EDS coupled with SEM); 6) electron microprobe analysis (EPMA); 7) trace element analysis using inductively coupled plasma mass spectrometry (ICP-MS), and 8) conventional and clumped oxygen and carbon stable isotope analysis.

3.1 Field work: Outcrops

Two Uteland Butte outcrops were studied in the spring of 2015, located in the southwestern portion of the Uinta Basin: Nine Mile Canyon and Willow Creek Canyon (Figures 1.2 and 3.1). A stratigraphic column was created for each outcrop area based on detailed descriptions of lithology, fossils, sedimentary structures, and contact types. The Willow Creek Canyon section covers a thickness of 175.7 ft (53.5 m) and contains the entire Uteland Butte member (Appendix 1). The Nine Mile Canyon section covers a thickness of 34.6 ft (10.5 m) and

includes only the upper portion of the Uteland Butte member (Appendix 1). Table 3.1 contains detailed location information for each outcrop section.

3.1.1 Core description and sampling

Core selection was based on three main features: well location, recovery of the Uteland Butte member, and core accessibility. Located in the west-central area of the Uinta Basin, the selected cores cover the interval of interest (excluding the BBC 14-3-45 well that only captured the PZ1 dolomite layer) from shallow (south) to deep (north) depositional environments, and incorporate geologic characteristics of the basin center not exposed at outcrop (Figure 3.1). Table 3.1 contains detailed location information for the cores included in this study.

Once the wells were chosen, first those cores were logged and sampled that are housed at the Utah Geological Survey (UGS) in Salt Lake City, UT, from November 11th to November 14th, 2014. The remainder of the chosen cores were located in a private storage facility in Denver, CO, and where logged there from February 15th to February 20th, 2015.

The fundamental criteria for sampling was the ability to cover the entirety of dolomite layers PZ1, PZ1' and PZ2 from base to top, one sample per foot. In addition, interbedded layers of limestone and dolostones below, between, and above the three layers of interest were also sampled, but with less coverage. A total of 167 samples were taken from the cores for further analysis. Stratigraphic columns were built for each described core (Appendix 2) in base of previous core descriptions (Vander Berg, personal communication, 2015) complemented with own core descriptions and information obtained from thin section petrography.

Code	Operator at time of drilling (current operator)	Well/Outcrop name	Well/Outcrop location	Current location of core
BBC 14-1	Bill Barrett Corp. (Rig II)	14-1-46	N 40° 9' 26.5" W 110° 30' 48.1"	Utah Core Research Center, Salt Lake City
BBC 14-3	Bill Barrett Corp. (Rig II)	14-3-45	N 40° 9' 23.7" W 110° 26' 17.4"	Utah Core Research Center, Salt Lake City
N 6-28	Newfield	Nickerson 6-28-3-2W	N 40° 11' 40.8" W 110° 7' 1.6"	Newfield facility in Houston
UT 15-13	Newfield	Ute Tribal 15-13-4-3W	N 40° 7' 45.5" W 110° 10' 7.9"	Newfield facility in Houston
PW 13-06	EOG Resources (QEP Energy)	Petes Wash 13-06 GR	N 39° 58' 44.1" W 110° 10' 7.2"	Utah Core Research Center, Salt Lake City
WDS 11-20	Chandler (QEP Energy)	West Desert Spring 11-20-10-17	N 39° 55' 39.0" W 110° 1' 54.2"	Utah Core Research Center, Salt Lake City
IU 16	Wexpro (QEP Energy)	Island Unit 16	N 39° 57' 24.2" W 109° 51' 49.8"	Utah Core Research Center, Salt Lake City
WC		Willow Creek Canyon	N 39° 50' 17.2" W 110° 47' 3.3"	
NMC		Nine Mile Canyon	N 39° 46' 35.5" W 110° 28' 58.5"	

Table 3.1: Detailed location, operator and core location of selected wells, and outcrops used in this research.

3.2 Petrography

3.3 Transmitted light microscopy

A total of 140 polished thin sections were investigated using a Zeiss Jenapol Polarizing Microscope under 3.2X, 10X, and 20X magnifications. All thin sections were partially stained, for easier determination of calcite versus dolomite mineralogy, by dipping them halfway into a solution of 1.5% HCl acid + 0.2 g of Alizarin red solution + 2.0 g of Potassium ferricyanide, following a procedure proposed by Dickson (1965). Detailed descriptions were generated for each thin section using rock classifications of Dunham (1962), with modifications by Embry and Klovan (1971), and focused on mineralogical composition as well as identification of bioclasts, coated grains, sedimentary structures, and bioturbation (Appendix 3). In addition, the carbonate grains were classified according to Flügel (2010) and semi-qualitative estimates of matrix, carbonate grains, and siliciclastic material were made using charts by Baccelle and Bosellini (1965).

3.4 Cathodoluminescence microscopy

Cathodoluminescence microscopy was performed using an Olympus BH-2 microscope coupled with a cold cathode Premier American Technologies Luminoscope Model ELM-3R. Each thin section was placed in the vacuum chamber with the pressure reduced to about 0.07 Torr, then irradiated by an electron beam with a voltage of 10-15 kV and a current of about 0.5 mA. Luminescent images were recorded using a digital camera Pentax K-5.

Twenty-one thin sections from the PZ1, PZ1', PZ2 dolomite layers were selected from four wells: Nickerson 6-28-3-2W, Ute Tribal 15-13-4-3W, Petes Wash 13-06 GR, and Island Unit 16, which are located along a traverse that stretches from distal (north) to proximal (south) parts of the ancient lake (Figure 1.2).

3.5 Scanning electron microscopy (SEM)

A total of ten polished thin sections were selected for SEM petrography and energy dispersive X ray spectroscopy (EDS) analysis (Appendix 4). All samples were coated with a carbon film to improve conductivity and thus image resolution. The equipment used was a Zeiss EVO LS15 EP using an electron beam with an accelerating voltage of 25.0 kV, located in the SEM laboratory at the Department of Earth and Atmospheric Sciences (EAS Department), University of Alberta.

3.6 X-Ray diffractometry

A total of 76 powder samples were analyzed in the X-ray diffractometry laboratory, EAS Department, University of Alberta. Approximately 1 g of each sample was mixed with an internal quartz standard, then mounted on a zero-background plate. Samples were powdered using a low speed micro-drill with tungsten carbide and diamond bits. The equipment used was an Ultima IV Rigaku X-ray Diffractometer, which uses a cobalt tube with a radiation wavelength (λ) value of 1.78899Å, run at 40 kV and 35 mA. All scans were run from 2° to 100° 2θ, using a 0.02° 2θ step size with a scan speed of 2° 2θ per minute. The resulting peaks were then corrected

with the quartz internal standard *d*101 peak (31.035° 2θ). Identification of minerals was done by Jade 9 software. The results are tabulated in Appendix 5.

As part of collaborative work, a total of 21 powdered samples were analyzed at the X-Ray diffractometry laboratory in the EAS Department at Indiana University Bloomington, and a total of 47 powdered samples were analyzed at the X-Ray diffractometry laboratory in the Department of Geosciences at Western Michigan University. All powders were acquired using a low speed micro-drill with tungsten carbide and diamond bits. The equipment used at the Indiana University laboratory was a Bruker D8 X-ray Diffractometer, which uses a copper tube with a radiation wavelength (λ) value of 1.540562 Å, run at 45 kV and 35 mA. All scans were run from 2° to 70° 2θ, using a 0.02° 2θ step size with a step time of 0.6°2θ per minute. The equipment used at the Western Michigan University laboratory was a Second Generation Bruker D2 Phaser X-ray Diffractometer, which uses a copper tube with a radiation wavelength (λ) value of 1.5406 Å. All scans were run from 20° to 60° 2θ, using a 0.008° 2θ step size with a step time of 0.48°2θ per minute. The results are presented in Appendix 5.

3.7 Major and Trace Elements Analysis

3.7.1 Electron microprobe analysis (EMPA)

Given the microcrystalline size of dolomite crystals identified with SEM (see detailed explanation in chapter 6, section 6.3), electron microprobe analysis was selected to obtain quantitative dolomite chemical values.

A total of four highly polished thin sections of PZ1, PZ1', and PZ2 were analysed using the Electron Micro Probe Cameca SX100 equipped with five wavelength dispersive spectrometer (WDS) of the Electron Microprobe Laboratory, EAS Department, University of Alberta. Operating conditions were: 40° takeoff angle; beam energy of 15 keV; 20 nA beam current; and 3 μm beam diameter. Prior to analysis, each thin section was coated with carbon film to enhance conductivity over the polished thin section surface. For data corrections, a series of standard measurements (dolomite, siderite, strontianite, and K-253 NIST RM glass) were conducted before the analysis. The results are summarized in Appendix 6.

3.7.2 Inductively coupled plasma mass spectrometry (ICP-MS) analysis

A total of 50 samples from the PZ1, PZ1', and PZ2 dolostones and interbedded limestones were analyzed for major and trace element concentrations in the Canadian Centre for Isotopic Microanalysis laboratory at the University of Alberta. The measurements were carried out using a Perkin-Elmer Elan 6000 Inductively Coupled Plasma – Mass Spectrometer (ICP-MS) with a cross-flow nebulizer, a 40 MHz RF-generator, with a working power between 600 and 1600 W.

Powdered samples of 200 mg were digested overnight in 10 ml of nitric acid 8N. After digestion, solid and liquid phases were separated by centrifuge. Concentrations were determined for 10 elements: Mg, Ca, Al, Si, Fe, Mn, Na, Zn, Sr, and Pb. The results are presented in Appendix 7.

3.7.3 Stable Isotope Analysis

3.7.4 Conventional carbon and oxygen stable isotope analysis

A total of 74 samples were selected for conventional carbon and oxygen stable isotope analysis, including 18 samples from PZ1, 9 from PZ1', and 12 from PZ2. The rest of the samples are form interbedded layers of limestone and dolostones below, between, and above the three layers of interest. All samples were analyzed in the Isotope Science Laboratory at the University of Calgary. Calcite and dolomite were analyzed by a continuous flow isotope ratio mass spectrometry (CF-IRMS) using a Thermo Finnigan GasBench coupled to a DeltaV^{Plus}. The powders were created using a low speed micro-drill with tungsten carbide and diamond bits. A powdered sample of approximately 300 μg was then weighted into a vial and approximately 200 μl of anhydrous phosphoric acid was added for digestion at 25ºC for a specific time. The evolved CO_2 was then sampled automatically by the Gas Bench and introduced into the DeltaV^{Plus} stable isotope ratio mass spectrometer for analysis of $\delta^{13}C$ and $\delta^{18}O$ ratios (Applied Geochemistry Group, 2014).

Since previous XRD analyses revealed that many samples contain variable mixtures of calcite and dolomite (with generally very minor contributions of quartz and silicates), the bimineralic carbonate samples were subjected to a selective chemical separation as follows: first, an aliquot of CO_2 was sampled at variable times of about 2-8 hours and deemed to represent calcite only; a second aliquot of CO_2 was retrieved after about 72 hours, at which time all carbonates had been digested, and deemed to represent dolomite. Unexpectedly, and unfortunately, it turned out that the first aliquot also contains some CO_2 from dolomite (further discussed below). Internal lab reference materials were run at the beginning and the end of each

set of samples (nine samples per set) and were used to normalize the data and to correct any equipment deviation. All results are reported in the permil notation (‰) relative to the international VPDB scale for $\delta^{13}C$ and $\delta^{18}O$ (Applied Geochemistry Group, 2014).

While it is common practice in stable isotope research to separate calcite and dolomite through differential phosphoric acid digestion, commonly 1-2 hours for calcite and >8-12 hours for dolomite (Degens & Epstein, 1964; Al-Aasm et al., 1990; Ray & Ramesh 1998; Walters, et al., 1972; McCrea, J. M., 1950; Swart, Burns, & Leder, 1991), these acid digestion times could not be used in our work due to the automated system in operation at the University of Calgary. As a consequence, the maximum acid digestion time (hours) was exceeded, which resulted in variable amounts of dolomite dissolved along with the calcite (to produce the first aliquot of CO_2, as described previously). Therefore, many isotopic values from bimineralic carbonate samples, and initially deemed to be valid for calcite, are not trustworthy.

The problem was identified by comparing the calcite:dolomite ratios determined by XRD with the calcite:dolomite ratios determined by the amounts of CO_2 of the first and second aliquots. Once this problem was identified many of the samples previously deemed to represent calcite were excluded from the data analysis and/or flagged as calcite-dolomite mixtures. The only values deemed to reliably represent calcite are those that fulfill the following requirements: (1) monomineralic calcite samples (100% calcite), and (2) samples with calcite/dolomite ratios less than 5% (maximum error allowed) based on XRD data. Moreover, samples with >5% dolomite also contain minor amount of quartz, illite, albite, and/or muscovite. Therefore, dolomite contamination is considered negligible. The results are presented in Appendix 8.

3.7.5 Clumped isotopes

The clumped isotope technique was applied to a small subset of samples because it allows for estimation of the temperature of carbonate mineral formation regardless of fluid chemical composition. (e.g., Ghosh et al., 2006; Eiler, 2007). The relation between ^{13}C and ^{18}O of dolomite crystals is totally independent of the isotopic composition from dolomite precursor fluid (Millán et al., 2016; Ghosh et al., 2006).

A total of 26 samples from the PZ1, PZ1', and PZ2 dolostones, as well as the interbedded limestones (splits of the powdered samples previously drilled for XRD and conventional isotope analysis), were selected to be run on a collaborative basis at the Department of Earth Sciences at Swiss Federal Institute of Technology (ETH). The analytical procedure is described in Millán et al. (2016). At the time of this writing, only a small subset of these 26 samples had been run with an insufficient number of duplicate and re-runs. Hence, the data presented in this research have to be considered preliminary and not sufficiently verified.

CHAPTER FOUR

FACIES

The facies deposited in lake basins are controlled by a number of independent and partially interdependent external factors such as: drainage area, type of surrounding rock outcrop, topography, tectonism, and climate, as well as internal agents, such as oxygen availability, nutrients, water chemistry, etc. (Gierlowski-Kordesch, 2010; Barron, 1990). In some cases, even small changes in these factors can impact depositional environments creating disproportionate variations in lateral and vertical facies architecture. Conversely, changes in facies allow, within limits, conclusions about the aforementioned internal and external agents.

Facies types were identified and characterized using outcrop, core, and thin section descriptions from the stratigraphic interval between the D and C shales, located in the middle section of the Uteland Butte member at the base of the Green River Formation. These facies types were created based on detailed and systematic descriptions of: (1) depositional rock textures: rock type, grain size, sorting, and packing; (2) bioclasts; (3) other carbonate grains - coated grains, peloids, and intraclasts; (4) sedimentary structures: stratification, bedding, laminations, and bioturbation; and (5) siliciclastic material. The facies were numbered from 1 to 8 in the order of overall shallowing depositional environments (Table 4.1).

	FACIES NAME	LITHOLOGY	BIOCLASTS	OTHER CARBONATE GRAINS	SEDIMENTARY STRUCTURES	CLASTIC MATERIAL	ENVIRONMENT
1	Silty mudstone	Silty mudstone	Ostracod shell fragments	-	Planar parallel, wavy discontinuous	Clay	Distal sublittoral to profundal
2	Lime mudstone	Dolomudstone	Scarce ostracod shell fragments	Scarce peloids	Structureless	Coarse silt subangular quartz grains and clay	Distal littoral - sublittoral carbonate mud flats
3	Ostracod wackestone	Dolowackestone	Ostracod shells, scarce fish bones and charophytes	Peloids	Massive, plane parallel	Scarce silt quartz grains	Littoral
4	Peloid wackestone-packstone	Silty dolowackestone - dolopackstone	Scarce ostracods and fish bones	Peloids	Wavy discontinuous, plane parallel	Coarse silt subangular quartz grains and clay	Littoral
5	Mollusc mudstone-wackestone-floatstone	Wackestone - floatstone	Pelecypods, gastropods, and ostracods	-	Massive	Scarce silt quartz grains	Littoral - Sublittoral
6	Intraclast grainstone-packstone	Dolograinstone - dolopackstone	Scarce ostracod shell fragments	Intraclasts	Structureless	-	Littoral shoreline
7	Ooid grainstone-packstone	Dolograinstone - dolopackstone	Ostracods and rare charophytes	Ooids, scarce peloids, oncoids and intraclasts	Massive, cross lamination	-	Littoral Shoreline
8	Ostracod grainstone-packstone	Dolograinstone - dolopackstone	Ostracods	Scarce ooids and peloids	Structureless, wavy discontinuous	Coarse silt to fine sand, subangular quartz grains	Littoral near shore and shoreline
9	Brown claystone	Arenaceous claystone	Scarce ostracod shell fragments and fish bones	-	Plane parallel	Coarse silt rounded quartz grains	Distal littoral
10	Coal	Coal	Plant fragments	-	-	-	Supralittoral swamps

Table 4.1: Summary of lithofacies identified between the D and C shales.

In the most detailed work on depositional facies in the entire section of the Uteland Butte member, Logan et al. (2016) defined a total of 18 lithofacies types, which are based on outcrops near the eastern margin of the Uinta Basin complemented by the core from central Uintah County (central-east side of basin). Table 4.2 provides a correlation of facies types from Logan et al. (2016) with those established in this study. Several of Logan et al. (2016) facies types are not found in the central-west part of the basin because the east part of the basin contains more proximal facies, and also the stratigraphic interval of interest is just part of the entire section of the Uteland Butte member.

This research		Logan (2015)	
	Facies Name		**Facies Name**
1	Silty oil shale	18	Laminated silt-rich oil shale
2	Lime mudstone	17	Argillaceous mudstone
3	Ostracod wackestone	3	Ostracod Lime Wackestone/ Mudstone
4	Peloidal wackestone - packstone	5	Oolitic Lime Mudstone/ Wackestone
5	Molluscan mudstone - wackestone - floatstone	4	Molluscan Lime Mudstone/ Wackestone
		11	Bioclastic Floatstone to Rudstone
6	Intraclast grainstone - packstone	6	Intraclasic-ostracod Lime Packstone/ Grainstone
7	Ooid grainstone - packstone	9	Oolitic packstone/ grainstone
8	Ostracod grainstone - packstone	7	Ostracod Packstone/ Grainstone
9	Brown claystone	W	Green, Brown & Maroon
10	Coal	15	Coal
-	-	1	Grey/ Green
-	-	2	Calcareous to Dolomitic Mudstone
-	-	8	Oncolite-ostracod grainstone
-	-	10	Pisolite packstone/ grainstone
-	-	12	Ostracod Sandstone
-	-	13	Structureless Sandstone
-	-	14	Cross-Stratified Sandstone
-	-	16	Illitic Oil Shale

Table 4.2: Lithofacies correlation between Logan et al. (2016) and this project.

4.1 Lithofacies

This following section provides descriptions and images of the most distinctive facies types encountered in the study area. Diagenetic features are mostly excluded and were not considered in the subsequent interpretations of the depositional environments, unless these features appear to be integral parts of the depositional setting. For example, pyrite that formed syndepositionally and thus indicates an anoxic depositional setting, or syndepositionally formed lutecite (length-slow chalcedony) that suggests an evaporitic depositional setting. Dolomitization is included in this exclusion.

4.1.1 Silty mudstone - F1

The silty mudstone lithofacies (F1) is a finely laminated, black to dark gray, organic-rich silty mudstone with up to 10% quartz particles, which range from coarse to fine silt size and are subangular, poorly sorted, and erratically distributed (Figure 4.1). Bioclasts are mostly thin, disarticulated ostracod shell fragments, many with preserved fish-hook shape terminations (Scholle and Ulmer-Scholle, 2003), 0.3 to 0.5 mm in length, aligned parallel to stratification. These shells form densely packed coquinas with thicknesses of 0.5 to 1 mm (Figure 4.1B). These layers are interbedded with lean, organic-poor clay layers and laminae that appear light gray in hand specimens. Scarce dewatering structures truncate some laminations (Figure 4.1C).

Depositional environment. Clay sized material was deposited in a low-energy setting below fair-weather wave base, probably in a distal sublittoral to profundal environment, allowing for accumulation of sediment from suspension. This environment is not susceptible to seasonal changes. The high degree of preservation of organic matter and the absence of bioturbation suggest an anoxic depositional environment likely developed by thermal and/or chemical lake water stratification (Collinson, 1979; Boehrer and Schultze, 2008; Tucker and Wright, 2009; Long, 2006), whereby deposition of the organic-rich layers took place below the chemocline. On the other hand, the lean clay laminae represent periods of low organic matter production and/or vertical fluctuations of the chemocline, likely in response to changes in climate and/or the amount of river input and outflow.

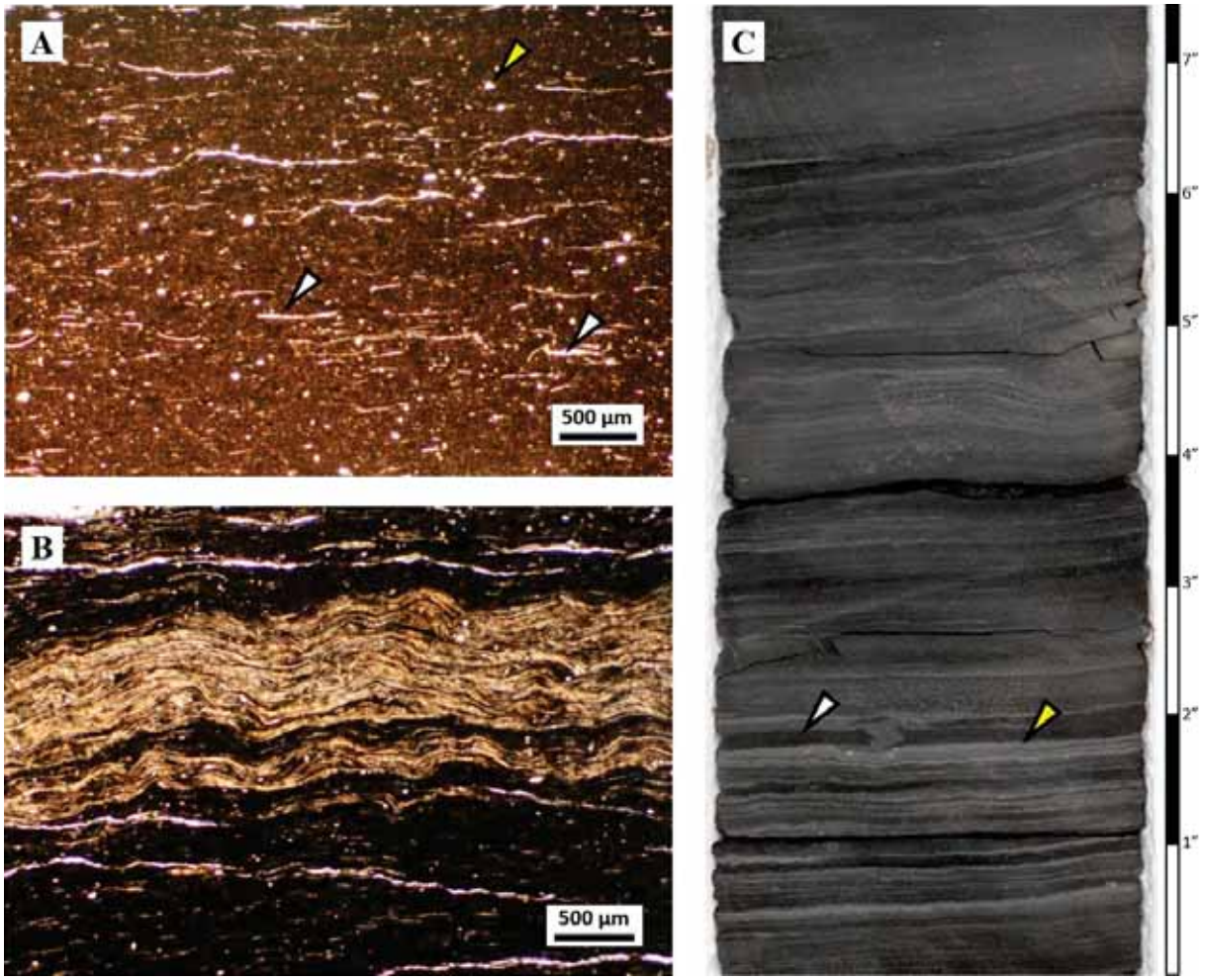

Figure 4.1: Facies F1 - Silty mudstone. (A) Transmitted light microphotograph of an organic poor clay bed with ostracod shell fragments aligned parallel to stratification (horizontal axis) (white arrows); silt material is composed of quartz (yellow arrow); 14-1-46, sample 24, 6672.8 ft., plane polarized light (PPL). (B) Transmitted light microphotograph of densely packed shell fragments (light yellow) interbedded with organic-rich mudstone (dark areas); 14-1-46, sample 7, 6705.3 ft., PPL. (C) Core photograph of silty mudstone facies interbedded with organic-rich laminae (white arrow), densely packed shell laminae (yellow arrow), and organic-poor silt laminae (light gray); 14-1-46, 6705'4" to 6705'11".

4.1.2 Lime mudstone – F2

The lime mudstone lithofacies (F2) is light brown, commonly homogeneous, microcrystalline lime mudstone that is completely dolomitized except for relatively rare bioclasts, with up to about 3% clay minerals and rounded, poorly sorted grains of quartz ranging from fine to medium silt (Figure 4.2). Accessory minerals are microcrystalline pyrite (less than 3%), occasional authigenic, euhedral, prismatic, microcrystalline quartz (less than 1%) and lutecite (length-slow chalcedony) crystals filling intraparticle pores. Bioclast content is low, generally less than 3%, and is mainly composed of articulated or fragmented ostracod shells ranging in size from 0.05 to 0.2 mm (Figure 4.2A). This facies shows massive to planar parallel stratification and rare bioturbation structures are present in core. This facies is occasionally interbedded with thin laminae consisting of irregular or lenticular carbonate grains transported from different environments (likely from nearshore areas), such as peloids (likely steinkerns) and scarce ooids, forming small lenses of peloidal grainstones (Figure 4.2B).

Depositional environment. The microcrystalline matrix that makes up most of this facies type probably crystallized directly from lake water as lime mud, and then dolomitized. Excellent preservation of disarticulated ostracod shells (Figure 4.2A) suggests a low-energy environment with quiet water below fair-weather wave base. Furthermore, the low argillaceous contribution suggests that the depositional environment was located relatively far away from the source of siliciclastic input (river mouth) and/or represents times of significantly reduced input of river water. Episodic storm events disrupted the generally calm setting. The presence of lutecite likely represents brief periods of subaerial exposure with evaporation, as discussed in Chapters 5 and 6.

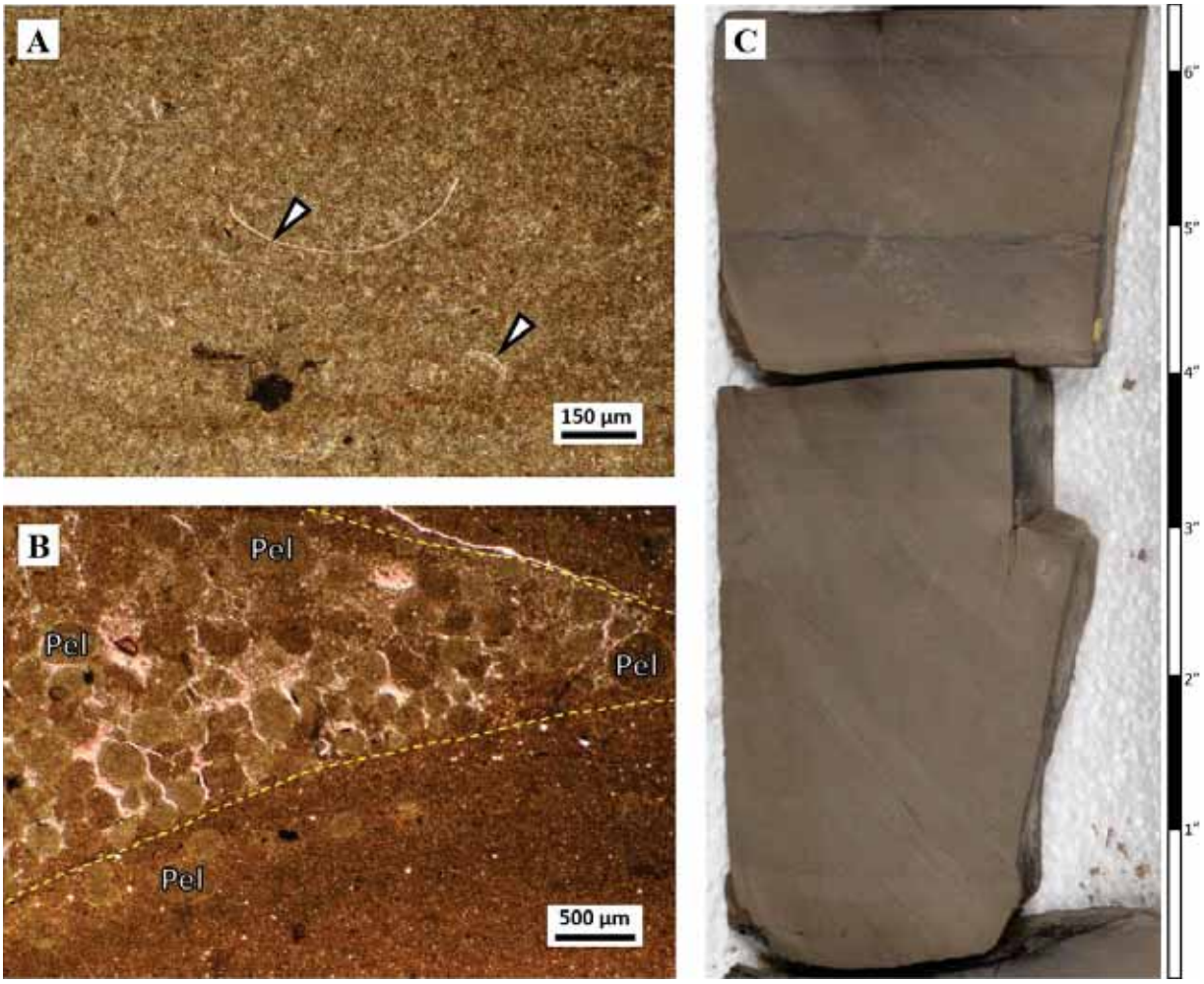

Figure 4.2: Facies F2 - Lime mudstone. (A) Transmitted light microphotograph of lime mudstone with scarce and well preserved disarticulated ostracods shells (white arrows); bitumen impregnated (black spots); 14-1-46, sample 17, 6692.6 ft, PPL. (B) Transmitted light microphotograph of interbedded lenses (yellow dashed lines) of dolomitized peloids (Pel) embedded in microsparitic calcite cement (stained pink); some bitumen impregnation between peloids (dark areas); Nickerson 6-28-3-2W, sample 3, 8205.6 ft., PPL. (C) Core photograph of lime mudstone facies characterized by massive and planar stratification; 14-1-46, 6702'8" to 6703'4".

4.1.3 Ostracod wackestone – F3

The ostracod wackestone lithofacies (F3) is brown, microcrystalline matrix with <10 vol-% of siliciclastic material. Fragmented ostracod shells are abundant (Figure 4.3A), fish bones and minor to rare elliptical gyronites [charophytes female reproduction organ (Flügel, 2010)] with size ranging from 0.02 to 0.05 mm (Figure 4.3B). Dolomitized peloids are also relatively common and range from 0.01 to 0.05 mm in size. Stratification is mostly planar or slightly wavy, whereas some layers are bioturbated. Accessory minerals are microcrystalline pyrite (less than 1 vol-%), occasionally authigenic, euhedral, prismatic, microcrystalline quartz, ranging from 10 to 20 μm in size. This facies hosts conspicuous chert nodules with irregular shapes and sizes, commonly with cm-dimensions and elongated parallel to bedding (Figure 4.3C).

Depositional environment. Facies F3 is similar to Facies F2, which suggests that they were deposited in adjacent and partially overlapping depositional environments. The most important differences between these two facies types is the relative abundance of peloids and ostracods, and the chert nodules that appear to be absent in Facies F2. Again, the microcrystalline matrix that makes up most of this Facies F3 probably crystallized directly from lake water as lime mud, and then recrystallized and/or dolomitized. The setting probably was distal littoral, above fair-weather wave base. In-situ deposition of benthic ostracod shells indicates an oxygenated environment. Furthermore, gyrogonites (Figure 4.3B) also points to shallow water depths within a littoral setting (Håkanson and Jansson, 1983, Flügel, 2010), whereas the association of ostracods with charophytes (gyrogonites) suggests brackish lake water (Flügel, 2010). Chert nodules with lutecite suggests episodic evaporitic conditions (Folk and Pittman 1971, Pittman and Folk, 1971; Eugster and Hardie, 1978; Scholle and Ulmer-

Scholle, 2003; Warren, 2006; Flügel, 2010). The chert nodules thus can be interpreted as an integral part of the depositional setting even though, in the strictest sense, they are a diagenetic feature (as is the dolomite that now makes up the matrix).

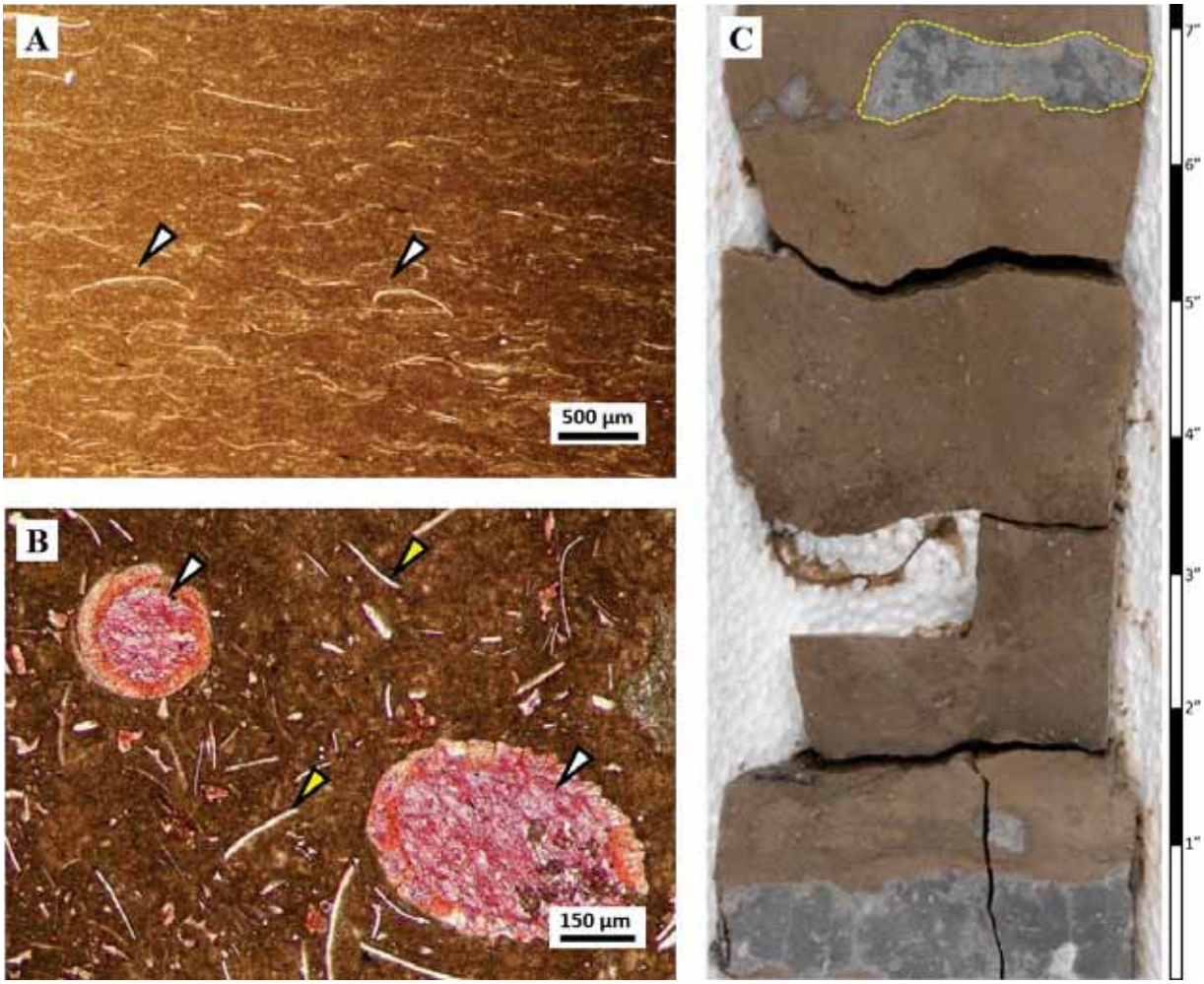

Figure 4.3: Facies 3 - Ostracod wackestone-packstone. (A) Transmitted light microphotograph of ostracod wackestone with disarticulated ostracods shells (white arrows) aligned sub-parallel to bedding; Ute Tribal 15-13-4-3W, sample 12, 7016.4 ft.; PPL. (B) Transmitted light microphotograph of gyrogonite (white arrows) associated with ostracod shell fragments (yellow arrows), random distribution of carbonate grains; 14-3-45, sample 27, depth: 7373.65 ft.; PPL. (C) Core photograph of typical ostracod wackestone facies characterized by massive stratification and elongated chert nodules/bed (yellow dashed outline); 14-1-16, 6685'4" to 6686'.

4.1.4 Peloid wackestone – packstone – F4

The peloid wackestone – packstone lithofacies (F4) is light brown, dolomitized matrix, wackestone – packstone with less than 5% of well sorted particles of quartz. These particles are fine silt in size. The most abundant carbonate grains are peloids, which are light green to gray in color and elongated in shape, with grain size from 0.05 to 1 mm (Figure 4.4A and B). Bioclast are mostly disarticulated and fragmented ostracod shells and fish bones. Euhedral, prismatic, and microcrystalline authigenic quartz is present as accessory mineral. F4 hosts chert nodules with irregular shapes and sizes, commonly with cm-dimensions parallel to bedding. Pyrite is present as very fine and scattered crystals. Frequent bioturbation structures.

Depositional environment. Similar sedimentary structures between Facies F4 and Facies F3 suggests a partially overlapping depositional environments. The most important differences between these two facies types is the lack of gyronites and the relative abundance of peloids. This environment probably was exposed to periodic energy changes that imported angular peloids from different depositional settings within the lake. Bioturbation reflects oxygenated environments. Similar to F3, this facies presents scarce and scattered authigenic euhedral quartz associated with chalcedony chert nodules, suggesting evaporitic environments. Peloidal wackestone – packstone facies is laterally associated with ostracod wackestone – packstone facies (F3), deposited in a depositional environment probably located in the littoral setting above the fair-weather wave base.

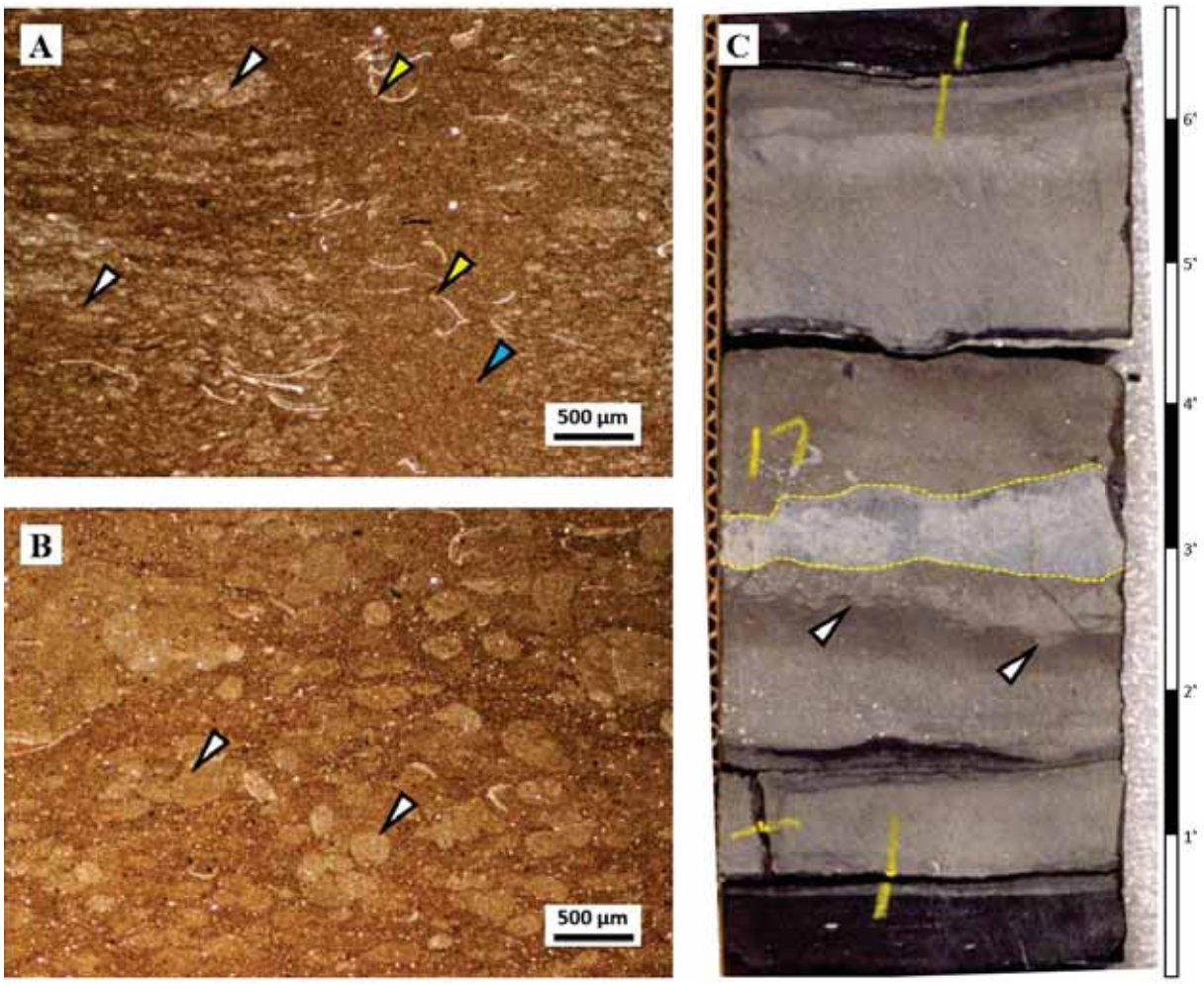

Figure 4.4: Facies F4 - Peloidal wackestone-packstone. (A) Transmitted light microphotograph of peloidal (white arrows) wackestone with scarce and disarticulated ostracods shells (yellow arrows); stratification disrupted by biological activity (blue arrow); Nickerson 6-28-3-2W, sample 9, 8542.5 ft.; PPL. (B Transmitted light microphotograph of peloids (white arrows) within a microcrystalline dolomite matrix and clay material (dark brow area); Ute Tribal 15-13-4-3W, sample 13, 7017.4 ft.; PPL. (C) Core photograph of peloidal wackestone - packstone facies showing bioturbation structures (white arrow) and chert nodule (yellow dashed outline); Ute Tribal 15-13-4-3W, 7017'1" to 7017'8".

4.1.5 Mollusc wackestone – floatstone – F5

The mollusc wackestone - floatstone lithofacies (F5) is characterized by light to dark gray color, wackestone to floatstone with micrite in matrix. Bioclasts are mainly elongated and tubiform gastropods, centimeter-size pelecypods, and ostracods shells usually broken and aligned sub-parallel to bedding. Gastropods are the most abundant fossil in this facies. Pelecypod shells range from 0.1 to 3 cm. Disarticulated and fragmented ostracods shells are smaller versus molluscan bioclasts (Figure 4.5A and B). There are frequent thin coquinas layers displaying good preservation of shells (some complete) distributed aleatory (Figure 4.5C). F5 displays a gray dark color due to high organic matter content. Accessory minerals are microcrystalline pyrite and anhedral microcrystalline dolomite (less than 5%). Scarce quartz detritus particles (<3%) range from medium to very fine silt size and are poor to moderate sorted. Beds are typically structureless and usually have sharp non-erosive contacts at the top.

Depositional environment. F5 represents an environment variable in energy. Lacustrine pelecypods and gastropods are usually distributed in nearshore or flood plain settings (Cohen, 2003; Flügel, 2010). In contrast, microcrystalline calcite (probably crystallized directly from lake water) suggests a calm setting. Interbedding molluscan wackestone and coquina layers points to rapid water energy change caused by storms. Molluscan wackestone – floatstone lithofacies F5 probably was deposited in the littoral environment with well oxygenated water, above the fair-weather wave base, close to the shoreline. Additionally, gastropods fossils indicates fresh water conditions (Picard, 1955; LaRocque, 1956; Williamson and Picard, 1974).

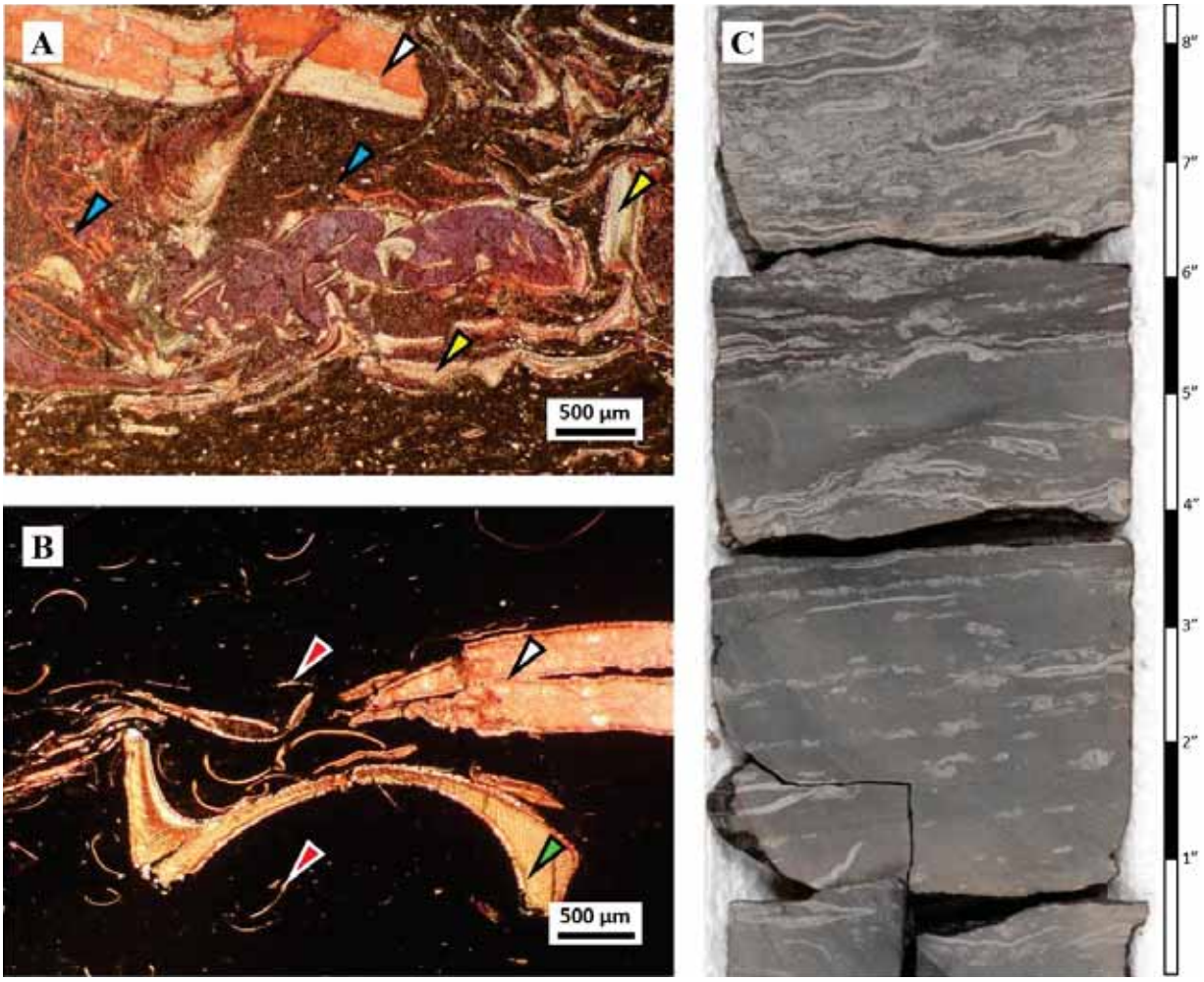

Figure 4.5: Facies F5 - Molluscan bearing wackestone-floatstone. (A) Transmitted light microphotograph of molluscan bearing floatstone with centimetre-size shells of pelecypods (white arrow), gastropods (yellow arrows), and disarticulated ostracods shells (blue arrows); Petes Wash 13-06 GR, sample 5, 5537.3 ft.; PPL. B) Transmitted light microphotograph of organic rich wackestone with pelecypods (white arrow), gastropods (green arrow); and ostracods (red arrows); black colour in matrix due to high organic matter content; Nickerson 6-28-3-2W, sample 8, 8234.6 ft.; PPL. (C) Core photograph of interbedding coquina layer (at the top) with molluscan floatstone (at the base); 14-1-46, 6696'1" to 6697'1".

4.1.6 Intraclast packstone- grainstone – F6

The intraclast packstone – grainstone lithofacies (F6) is a light brown packstone to grainstone composed mainly by dolomitic intraclasts and peloids, and minor ooids. Bioclasts are mainly ostracods shells fragments erratically distributed (Figure 4.6A and B). Intraclasts are angular to well-rounded in shape and poorly sorted. The intraclasts are composed by microcrystalline dolomite in matrix and shells (likely ostracods). Furthermore, intraclasts show circumgranular cracks that defines irregular to globular particles of microcrystalline dolomite. Cracks are filled with blocky calcite cement (Figure 4.6A). Peloids are composed exclusively by microcrystalline dolomite and display elongated shapes. Bioclasts are mainly disarticulated and fragmented ostracod shells (Figure 4.6B). Rare (1%) quartz particles with fine silt size.

Depositional environment. Rock texture and carbonate grains are characteristic of a high energy environment. Intraclast particles were deposited, dolomitized, and partially lithified in a different area (likely in the littoral environment). Moreover, the intraclasts were exposed to eogenetic process that created circumgranular cracks (Esteban and Klappa, 1983; Freytet and Verrecchia, 2002; Flügel, 2010). After exposure, these hard rocks were ripped out by storms. Part of this material was subjected to reworking by wave action which caused them to evolve into well rounded particles (Figure 4.6B). Finally, these particles were transported to the current environment of deposition. Lithofacies F6 was probably located in near shore areas affected by wave action.

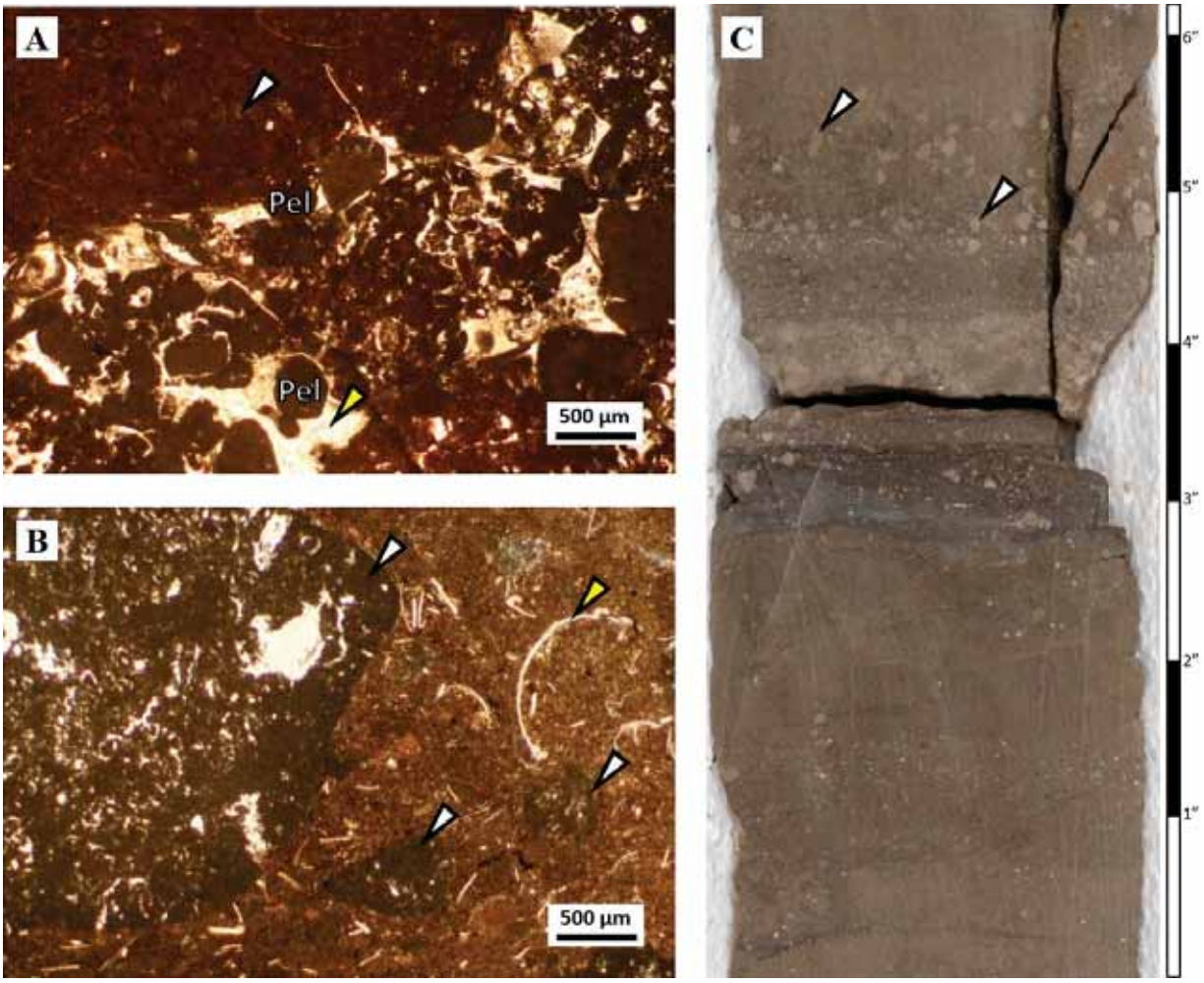

Figure 4.6: Facies F6 - Intraclast peloid packstone-grainstone. (A) Transmitted light microphotograph of centimetre-size dolomitized intraclasts (white arrow), and peloids (Pel) within a blocky calcite cement (yellow arrow); 14-1-46, sample 12, 6683.95 ft.; PPL. (B) Transmitted light microphotograph of well-rounded intraclasts (white arrows), ostracods shell fragments (yellow arrow) within a dolomitized micrite (?) matrix; 14-1-46, sample 13, 6684.90 ft.; PPL. (C) Core photograph of intraclastic peloidal facies. Rip-up intraclast particles (white arrows) within a dolomitized micrite (?) matrix; 14-1-16, 6684'11" to 6685'5".

4.1.7 Ooid grainstone – packstone – F7

The ooid grainstone – packstone lithofacies (F7) is a dark brown grainstone to packstone mainly composed by well-sorted and completely dolomitized ooids, peloids, and intraclasts, and rare (<2%) ostracods shells. Ooids show spherical to sub-spherical shapes with concentric layers of dolomitized micrite (?) (Figure 4.7A). Some ooids present micritization (Figure 4.7B); however, these ooids consist of microcrystalline dolomite. The ooids' core is composed of bioclast (ostracod shell fragments), quartz particles, peloids, and intraclasts. Ooids size ranges from 0.2 to 1.5 mm. Accessory minerals are euhedral, microcrystalline, double-terminated, authigenic quartz and microcrystalline pyrite. F7 facies present massive stratification (Figure 4.7C).

Depositional environment interpretation. Ooid grainstone – packstone layers were deposited in a shallow and high energy environment likely close to the shore area, or a mudflat influenced by wave agitation with low input of siliciclastic material, above the fair-weather wave base.. Lack of siliciclastic material and micritization of ooids might indicate a high microbe activity environment. Additionally, authigenic, euhedral and double-terminated quartz precipitated within the interparticle open space indicating saline environments (Flügel, 2010)

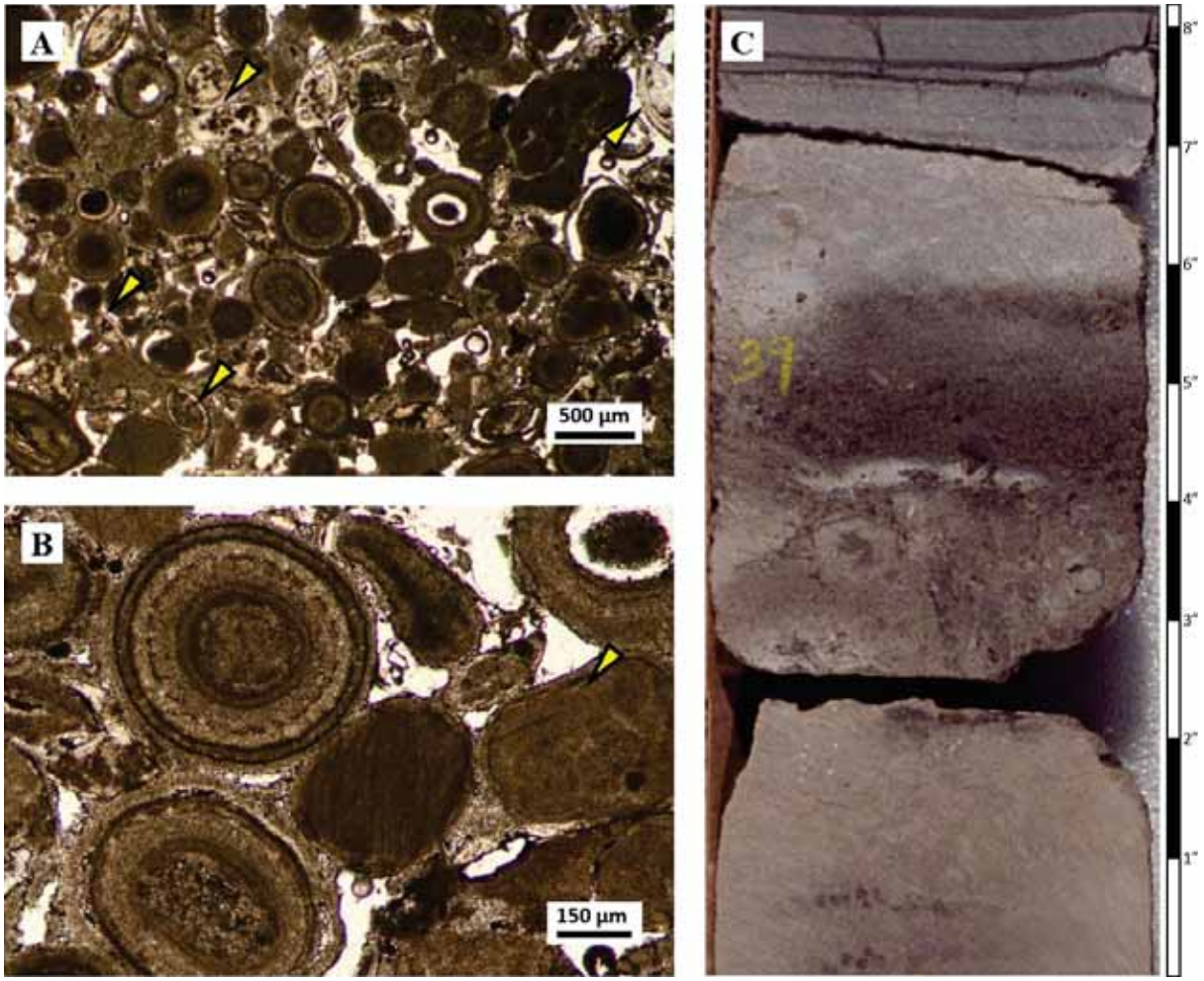

Figure 4.7: Facies F7 - Ooid grainstone - packstone. (A) Transmitted light microphotograph of ooid grainstone with partially dissolved ooids and scarce articulated ostracods shells (yellow arrows); Petes Wash 13-06 GR, sample 6, 5539.5 ft.; PPL. (B) Detail of microphotograph (A) that shows micritization of ooids (yellow arrow). Note ooids are completely dolomitized; PPL. (C) Core photograph of ooid grainstone facies with massive stratification; Petes Wash 13-06 GR, 5539'3" to 5539'11".

4.1.8 Ostracod grainstone – packstone – F8

The ostracod grainstone – packstone lithofacies (F8) is characterized by a light brown ostracod bearing grainstone – packstone. Carbonate grains are mainly ostracod shells (40 – 50%), which are densely packed, articulated and deformed shells; minor dolomicrite pellets, and scarce peloids. Moreover, internal cavity of ostracods is filled with dolomitized micrite (?) and pellets (Figure 4.8A). Some ostracods shells present constructive micritization. Siliciclastic material is scarce (<2%) and is mainly composed by medium silt to very fine subangular quartz. Microcrystalline pyrite is present as accessory mineral. F8 hosts chert nodules, mainly composed by lutecite, with elongated shapes and variable sizes, commonly with cm-dimensions, parallel to bedding (Figure 4.8C). In core, F8 presents parallel and massive stratification.

Depositional environment. The depositional environment of ostracod grainstone - packstone lithofacies (F8) is interpreted as shallow setting with moderate to high energy, probably located in mud flats within littoral environments. The abundance of ostracods was likely promoted by optimal lake water conditions that boosted ostracod reproduction rate. Additionally, shell constructive micritization was probably generated by algae (Flügel, 2010) attached to the shell's surface. In this case, this environment must be located at euphotic zone with high nutrient concentration (Scholle and Ulmer-Scholle, 2003; Flügel, 2010). Lutecite in chert nodules suggests evaporitic conditions (Folk and Pittman 1971, Pittman and Folk, 1971; Eugster and Hardie, 1978; Scholle and Ulmer-Scholle, 2003; Warren, 2006; Flügel, 2010)

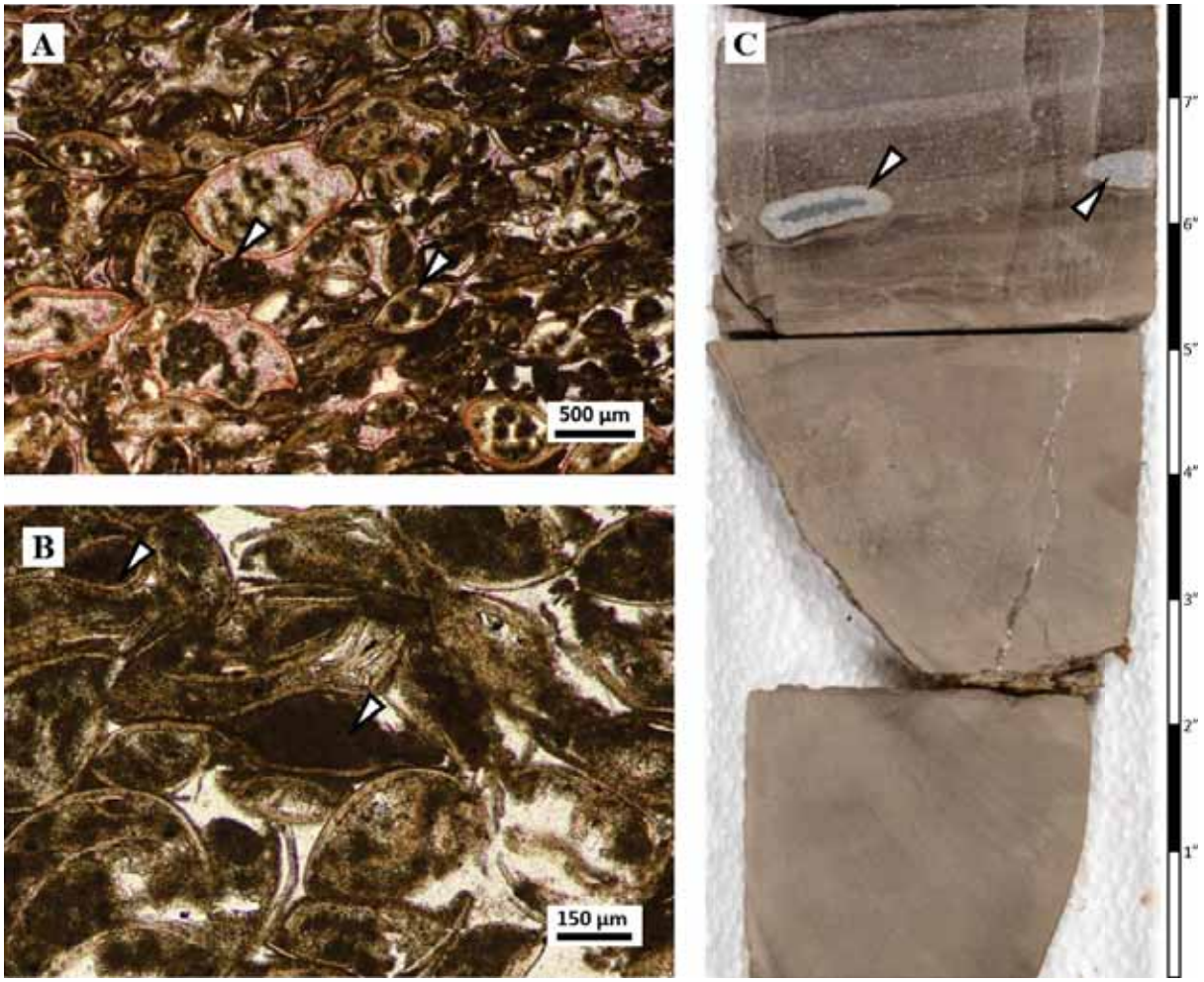

Figure 4.8: Facies F8 - Ostracod grainstone - packstone. (A) Transmitted light microphotograph of ostracod grainstone. The internal voids of ostracods were partially filled with dolomitized pellets and micrite (white arrows); the resting voids were filled with blocky ferroan calcite cement (pale purple areas); West Desert Spring 11-20-10-17, sample 11, 4998.5 ft.; PPL. (B) Transmitted light microphotograph of ostracod grainstone facies. Microcrystalline dolomite is within the internal cavity of articulated ostracods shells (white arrows); West Desert Spring 11-20-10-17, sample 11, 4998.5 ft.; PPL. (C) Core photograph of ostracod grainstone facies with chert nodules (white arrows); 14-1-16, 6680'0" to 6680'8".

4.1.9 Brown claystone – F9

The brown claystone facies (F9) is characterized by light brown to grey arenaceous claystone, in places fissile, with quartz particles up to 15 %. These particles are well sorted, subangular to rounded, with size that range from very fine to fine sand. Bioclasts are thin and disarticulated fragments of shells (likely ostracod shells) and fish bones with particle sizes varying from 0.05 to 0.3 mm (Figure 4.9A). This facies is interbedded with laminae of ostracod coquinas (Figure 4.9B). F9 show plane parallel and wavy stratification; thicknesses vary from about 0.1 to 2.5 m. Scarce bioturbation structures are present Facies F9.

Depositional environment. Arenaceous claystone facies is vertically associated with thin coal seams and is present mainly at the landward area of the basin (Willow Creek outcrop). This association suggests a low energy environment close to the shoreline settings (Ryder et al., 1976) and close to the siliciclastic input areas (deltas). Interbedded claystone and coquina layers indicate episodic ostracod blooms. Bioturbation indicates an oxygenated environment.

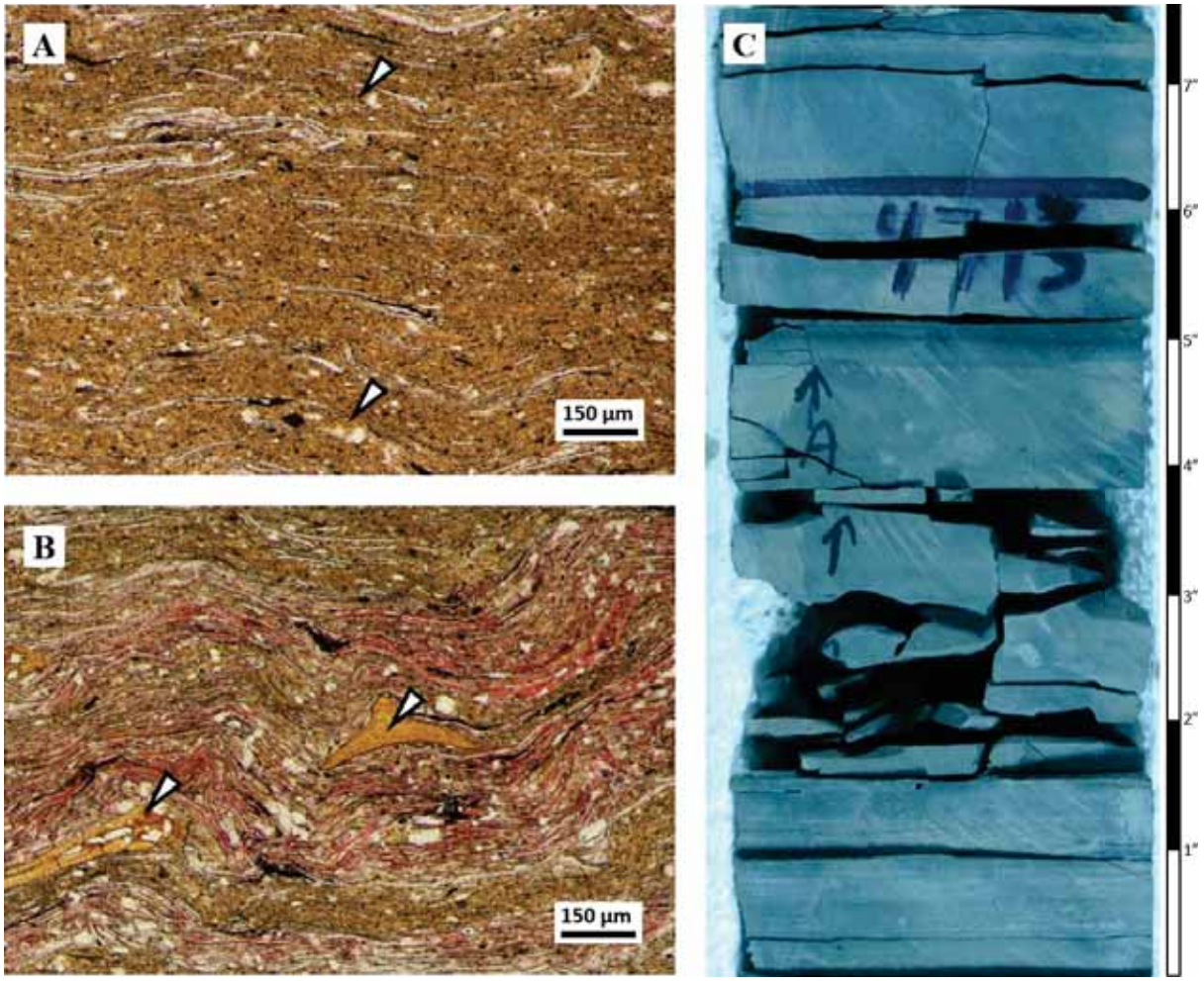

Figure 4.9: Facies F9 - Brown arenaceous claystone. (A) Transmitted light microphotograph of brown mudstone with disarticulated ostracod shell fragments aligned subparallel to bedding, with subangular to rounded and very fine sand quartz grains (white arrows); Island Unit 16, sample 16, 4713.2 ft.; PPL. (B) Transmitted light microphotograph of interbedded laminae of coquinas (pink-red) and arenaceous claystone (light brown area); fish bones are associated with coquina; Island Unit 16, sample 16, 4713.2 ft.; PPL. (C) Core photograph of brown and fissile claystone; Island Unit 16, 4712'11" to 4712'6".

4.1.10 Coal - F10

Coal facies (F10) is defined by dark brown to black thin coal seams with average bed thickness of 0.03 m (Figure 4.10). There is presence of some recognizable plant structures. Coal seams are associated vertically with brown arenaceous claystone facies (F9) and ostracod wackestone (F3). This facies is present only in Willow Creek outcrop.

Depositional environment. The coal seam facies represents a swamp environment close to the lacustrine basin (Uinta Basin). This setting is likely the in-land expression of cyclic rising of water table caused by transgression events (Reinson, 1992; Keighley et al., 2003; Catuneanu, 2006).

Figure 4.10: Facies F11 - Coal. Thin coal seam in Willow Creek outcrop. Seam coals are vertically associated with claystone (F9) (at the base) and dolowackestone (F3) (at the top).

4.2 Facies associations

Facies grouping into genetically related units is based on vertical and lateral association, rock textures and sedimentary structures. Facies association are summarized in Table 4.3. Facies association allows for the recognition of lacustrine depositional environments in larger scale depending on water agitation levels and relative water depth (Tanavsuu-Milkeviciene and Sarg, 2012). According to the facies associations, the lake water column is subdivided into three main depositional environments: (1) littoral zone, which is highly influenced by wave activity and limited at the base by the fair-weather wave base (FWWB); (2) sublittoral zone, which is between the FWWB and the storm wave base (SWB); and (3) profundal zone that is below the SWB (Tanavsuu-Milkeviciene and Sarg, 2012) (Figure 4.11). The littoral and sublittoral zones are located within the photic zone.

Facies associations			
Code	**Name**	**Facies**	**Environment**
A	Laminated mudstones	F1	Profundal
B	Massive carbonates	F2, F3, F4, F5	Littoral to sublittoral
C	Marginal carbonates	F2, F6, F7, F8	Littoral to sublittoral
D	Marginal swamps	F9, F2, F10	Supralittoral

Table 4.3: Facies associations regarding to genetic vertical and horizontal relation, sedimentary structures, and rock textures.

4.2.1 Marginal swamp

Marginal swamp environment is defined by vertical association of brown claystone (F9), ostracod dolowackestone (F3), and coal (F10) facies. The paleogeographic location for this association could be placed out of the lake basin (landward), bordering the coastal line. Moreover, coal seam and lacustrine deposit (F3 and F5) associations were created by transgression events that covered the swamps leading deposition of ostracod wackestone and fresh water molluscan wackestone – floatstone lacustrine facies (Figure 4.11).

4.2.2 Marginal carbonates

Marginal carbonates environments are defined by lateral association of ooid grainstone (F7), intraclast grainstone – packstone (F6) and ostracod grainstone – packstone (F8) facies, which indicate high energy environment influenced by wave action (Gierlowski-Kordesch, 2010). Eventually, part of this zone was subaerial exposed by lake water level regression events. The exposure areas were subjected to weathering and erosion that generated intraclastic carbonate grains. This facies association occurs at the top of dolomite layer PZ1 in well Petes Wash 13-06 GRsouthern of the Uinta Basin (landward) as well as at the top of dolomite layer PZ1 in well 14-1-46 at the center of the Uinta Basin (basin ward), suggesting an isolated, extensive, and flat carbonate littoral setting with very low or no interaction with siliciclastic sediments. Based on ooids and pisoids abundance, cycle thickness, and comparing with modern lacustrine stromatolites, Ryder et al. (1976) estimate the water depth for this environment ranging from 10 cm to 9 m (Figure 4.11).

4.2.3 Massive carbonates

This facies association is composed by lime mudstone (F2), ostracod wackestone (F3), and peloid wackestone – packstone (F4). It is characterized by massive carbonates with fine size carbonate grains and scarce to moderate ostracods shell fragments and fish bones. Grain size of carbonate grains and increment of matrix percentage suggest and environment of moderate to low energy, favoring deposition of organic matter. This environment was ideal for benthic organisms (ostracods mainly) that reworked sediments. These organic activity partially obliterated primary sedimentary structures. Biological activity indicates an oxygenated setting. This environment was influenced by episodic storms that formed lenses of peloidal within the lime mudstones (F2) (Figure 4.11).

4.2.4 Laminated oil rich mudstones

This facies association is characterized by laminated oil rich mudstones interbedded with laminaes of lean silty mudstone and coquinas laminaes. The high organic matter content values suggests an anoxic environment located below the SWB within the aphotic zone where lack of oxygen and light create adverse condition for living organisms. However, this setting changed periodically toward more oxygenated depositing light gray, poor-organic mudstone likely promoted by water level regressions.

A

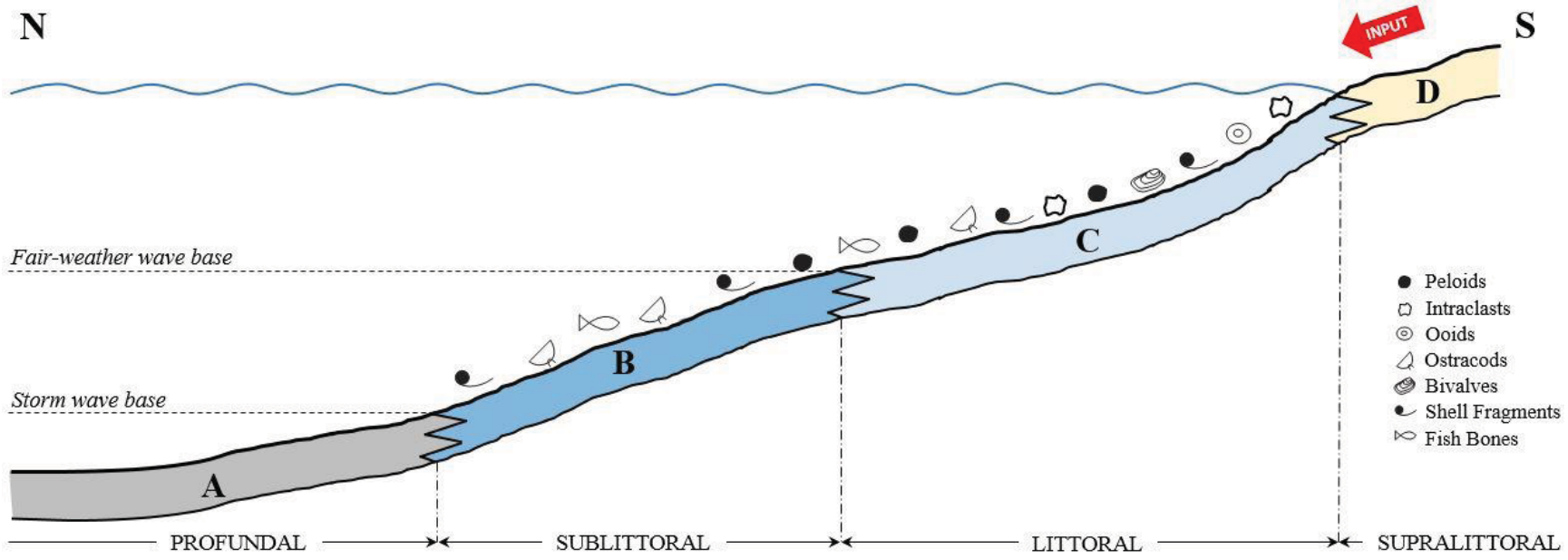

B

Vertical facies associations distribution				
Code	Profundal	Sublittoral	Littoral	Supralittoral
A	———	—		
B		———	- - - -	—
C		- -	———	—
D				———

Figure 4.11: (A) Schematic representation of facies association and their geographical location within the Uinta Basin profile; modified from Logan (2015). (B) Vertical occurrence of the facies association. Note some facies were deposited in several depositional environments.

4.3 Facies successions and cyclicity

Individual facies are arranged vertically, defining repetitive cycles or successions that help to determine the Uinta Basin evolution throughout deposition of the interval of interest. Thickness of this interval ranges from 7 m (22.9 ft) landward up to 12 m (39 ft) basinward. Fluctuations in lake level was recorded by vertical variation of facies

The idealized cycle is defined at the base by oil rich mudstone, following at the middle of the cycle with a molluscan wackestone – floatstone layer, and top of each cycle with an intraclastic dolograinstone, ooid dolograinstone, or an ostracod dolograinstone – dolopackstone (Figure 4.12). This cycle is interpreted as result of a transgression event, in which the oil rich mudstone (F1) is considered as the flooding surface and the intraclast grainstone – packstone facies (F6) is considered as the regressive surface. The cycle is repeated three times between D and C shales, showing local variations.

The idealized cycle composed by silty mudstone at the base, molluscan wackestone – floatstone, and dolograinstone – dolopackstone at the top describes a shallowing upward sequence. The silty mudstone deposits represent a period of flooding promoted by either a water input rate higher than output rate (climate) or by a higher accommodation rate than sediment supply rate (tectonism) (Ryder et al., 1976; Carrolls and Bohacs, 1999). As result, deposition of silty mudstone facies occurred landward (Ryder et al., 1976). At the same time, wackestone and floatstone facies moved landward. Due to the water table increment, the supralittoral zone might have inundated establishing supralittoral swamps, which favoured deposition of lenticular coal seams. After flooding, a gradual water table drop moved back the depositional environments basinward, exposing in some places already deposited grainstone – packstone layers to subaerial

conditions. Pedogenesis characteristics, such as circumgranular cracks, were developed at the top of layer PZ1 in well Petes Wash 13-06 GR, which supports this interpretation.

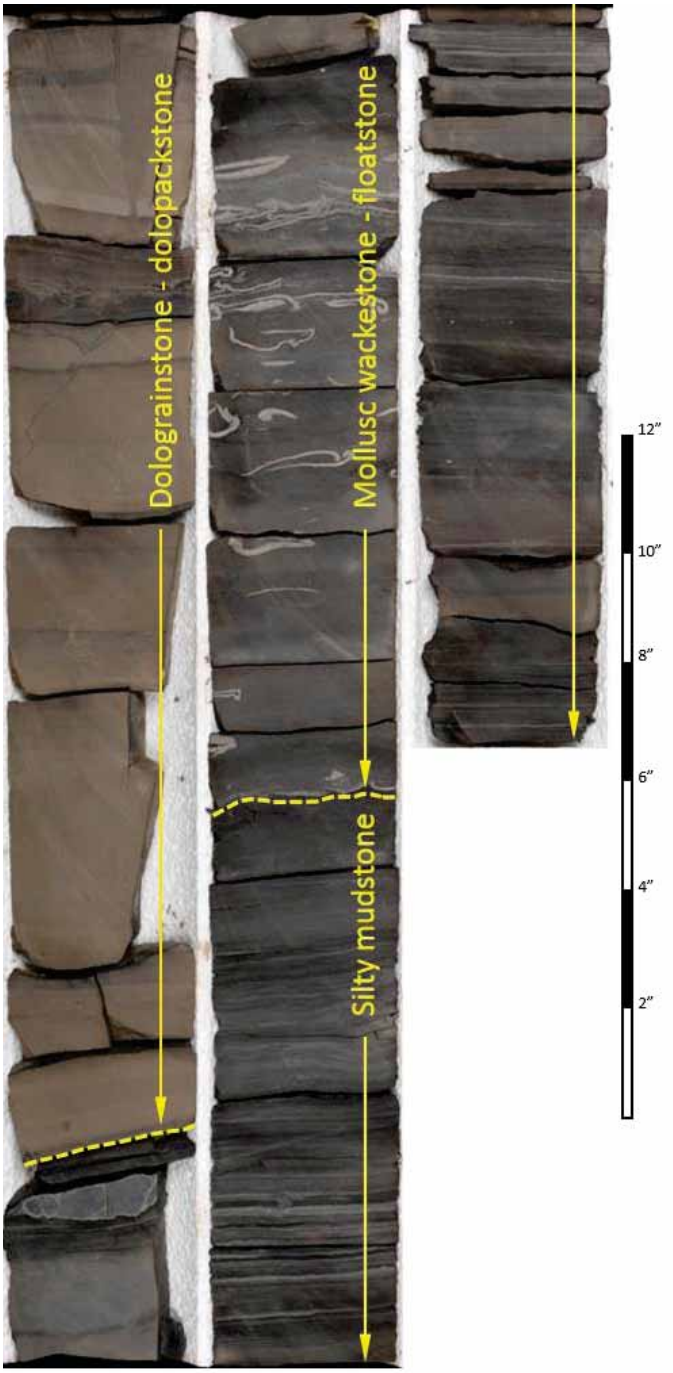

Figure 4.12: Core photograph of the idealized cycle. At the base is the oil rich mudstone facies (F1); followed by mollusc wackestone – floatstone facies (F5); and dolograinstone – dolopackstone facies at the top (F6); 14-1-16, 6702' to 6706'1".

The idealized depositional cycle constitutes a shallowing upward sequence. The silty mudstone deposits represent a period of flooding promoted either by a water inflow rate higher than the outflow rate (driven by climate) or by an accommodation rate higher than the sediment supply rate (driven by tectonism) (Ryder et al., 1976; Carrolls and Bohacs, 1999). As a result, depositional environment of silty mudstone facies moved southward (Ryder et al., 1976). Furthermore, raising water table would has expanded the supralittoral environments southward, leading to the development of swamps and the deposition of lenticular coal seams.

After maximum flooding, water table dropped and moved the depositional environments basinward, exposing some areas of grainstone – packstone layers to subaerial conditions. Pedogenic characteristics, such as circumgranular cracks, were developed at the top of layer PZ1 in well Petes Wash 13-06 GR.

This interpretation is consistent with the findings by Tänavsuu-Milkeviciene et al. (2017) who defined three major depositional cycles for the entire section of the Green River Formation. The section of interest here might be correlated with the first depositional cycle defined by Tänavsuu-Milkeviciene et al. (2017), which was controlled by shorter climate variations of that interpreted by Tänavsuu-Milkeviciene et al. (2017). During high humidity episodes (high inflow rate), water lake level rose up pushing the marginal facies associations landward. In contrasts, dry episodes (low inflow rate) caused a lake water drop moving back the marginal facies basinward (Tänavsuu-Milkeviciene et al., 2017).

The idealized depositional cycles represent a period of deposition of about 10 to 16 thousand of years (ky.) (Table 4.4), based on the average calculated sediment accumulation rate defined by Smith et al. (2008) at the basin-margin areas of the Uinta basin, of about 150 mm/ky. The low sediment accumulation rate of the pre-dolomitization lime mud sediments (at the top in the idealized cycle) probably was caused by low sediment supply, which in turn was promoted

by low water inflow (dryer periods). The cyclicity was likely controlled by periodic climate variations of about 10 to 15 ky. (Table 4.4). In the section of interest, there are five cycles, which can be correlated laterally with thickness variation (Table 4.4 and Figure 4.13).

Cycle	Well								Time (ky)
	BBC 14-1	BBC 14-3	N 6-28	UT 15-13	PW 13-06	DS 11-20	IU 16	TAve	
C5	8.0	6.4	6.2	6.0	3.4	1.5	3.0	4.9	10.0
C4	3.9	5.8	5.7	5.8	4.8	7.3	8.0	5.9	12.0
C3	8.0	9.6	6.5	9.7	11.5	3.2	7.4	8.0	16.2
C2	8.8	-	11.4	9.1	2.9	3.6	4.9	6.8	13.8
C1	7.3	-	7.5	6.8	7.5	6.0	3.6	6.5	13.1

Table 4.4: Thickness and calculated time of deposition for each idealized cycles identified within D and C shales. TAve: Thickness average of each cycle; thickness expressed in ft.

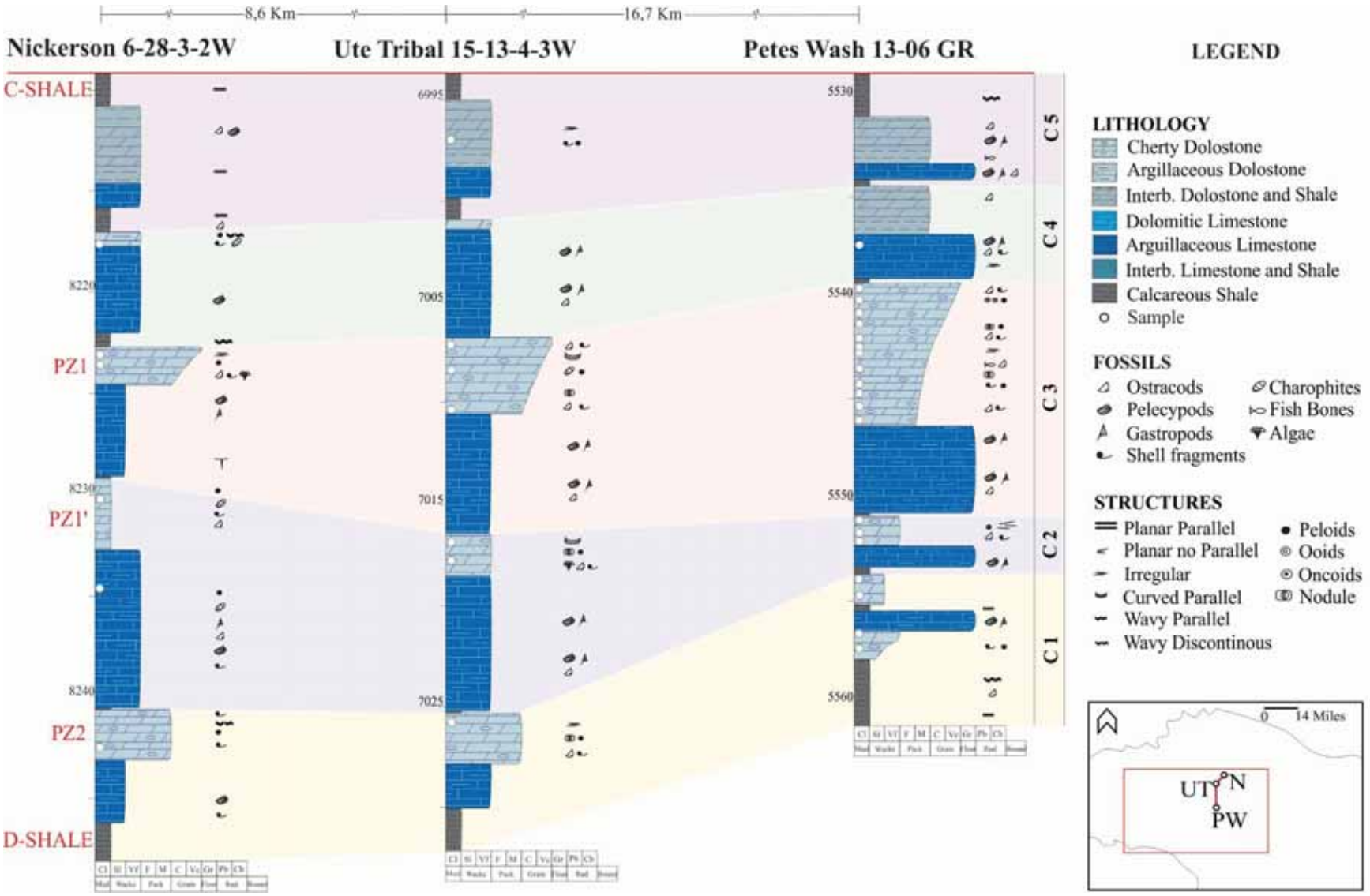

Figure 4.13: Correlation of stratigraphic cycles C1 to C5 (right column) within D and C shales. In the inset map, N: Nickerson 6-28-3-2W, UT: Ute Tribal 15-13-4-3W, and PW: Petes Wash 13-06 GR

4.4 Facies and dolomitization

Facies and dolomitization relationship show three main factors: (i) dolomitization took place at the top of each cycle; (ii) pervasive matrix dolomitization occurred in facies F2, F3, F4, F6, F7 and F8; and (iii) mollusc wackestone – floatstone facies (F5) was not dolomitized (Figure 4.14).

Dolomitization occurred only the top of the idealized cycle when the regression surface was reached. At this period of time, water became supersaturated in dolomite (likely promoted by evaporation) allowing dolomitization, in which the dense fluids percolated through the already deposited and unconsolidated calcium carbonate mud (F2, F3, F4, F6, F7, and F8). In contrasts, molluscan wackestone – floatstone facies was not dolomitized by either low porosity and permeability values for molluscan wackestone – floatstone facies (F6), which did not allow percolation of dolomitizing fluids through this facies or decrease of the Mg^{2+}/Ca^{2+} ratio of the dolomitizing fluid, or a combination of both.

CHAPTER FIVE

DIAGENESIS

The stratigraphic interval of study shows a composite of diagenetic events from near-surface to deep burial diagenetic settings. Special attention was paid to dolomitization, i.e., how this process is related to the petrophysical properties (porosity and permeability) of petroliferous dolomite layers PZ1, PZ1', and PZ2. Additional diagenetic processes such as mechanical compaction, cementation, dissolution, fracturing, and stylolitization are also considered because they also affected the reservoir properties.

Fifteen diagenetic events were identified based on thin section petrographic descriptions. The relative timing of the diagenetic features was interpreted based on textural relationships. However, the duration of some event remains uncertain because of diagenetic complexity. A summary of diagenetic events and their temporal relationship are given in the Table 5.1, a paragenetic sequence chart (Section 5.1.2).

5.1 Diagenetic history from core and thin section petrography

5.1.1 Petrographic observations

Dolomite textural description and classification were completed following Gregg and Sibley's (1984) and Sibley and Gregg's (1997) dolomite textural classification modified by

Wright (2001) (Figure 5.1). Four types of dolomite textures were identified using thin section and scanning electron microscopy (SEM). These were classified as planar-e, planar-s, nonplanar-a, and cement categories. Detailed descriptions of texture and crystal size on the SEM scale are presented in Section 5.2.1.1 and 5.2.1.2.

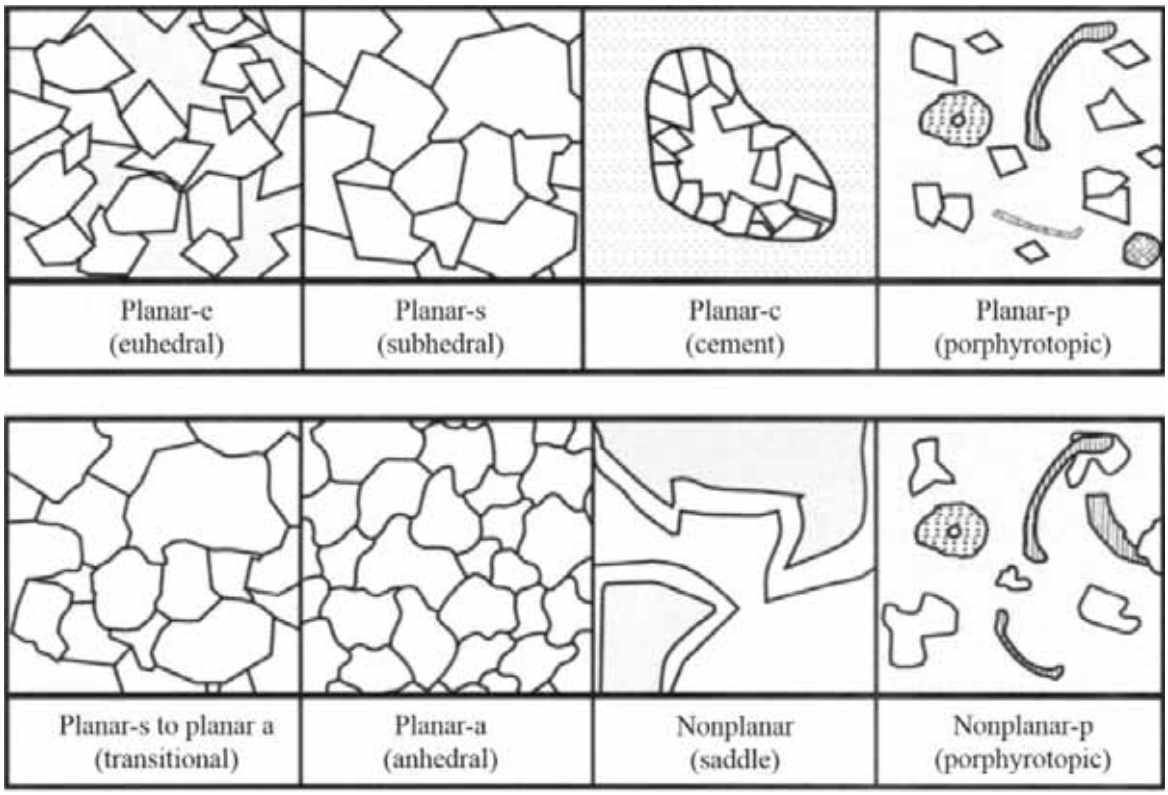

Figure 5.1: Dolomite textural classification proposed by Gregg and Sibley (1984), Sibley and Gregg (1987) and modified by Wright. Image modified from Machel (2004).

Additionally, mineral crystal size and carbonate grain size follow the classification proposed by Folk (1962) (Figure 5.2).

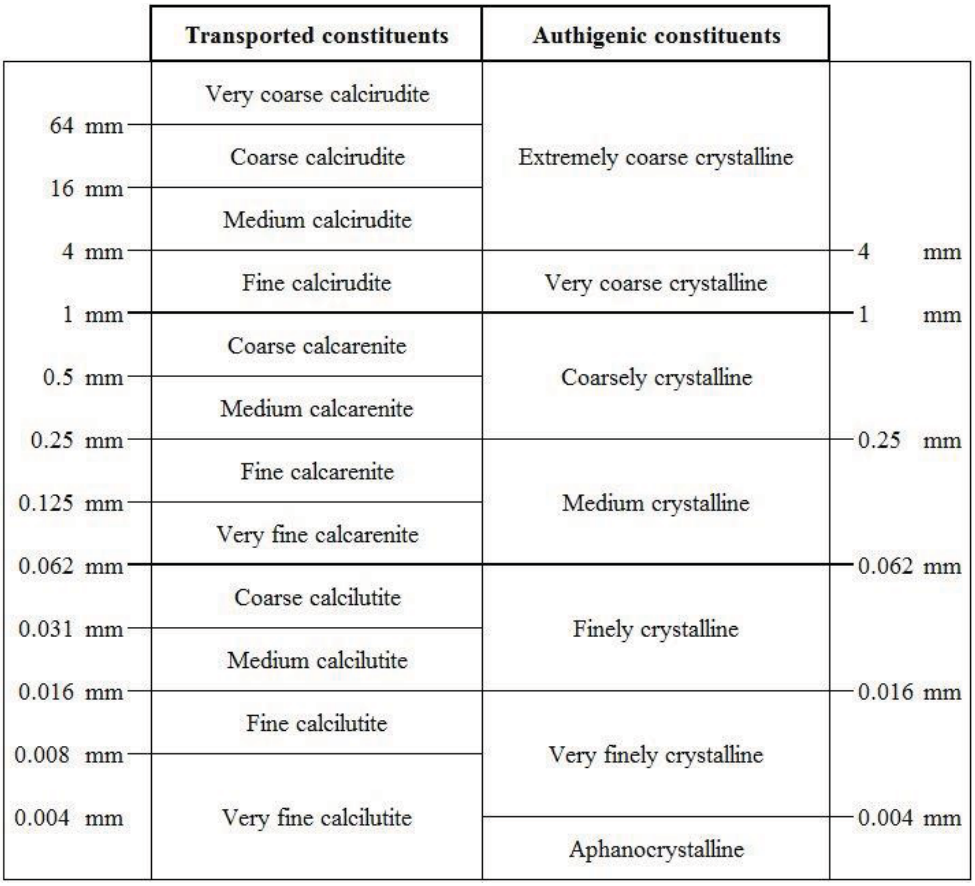

Figure 5.2: Carbonate grain size and mineral crystal size classification; Folk, 1962.

5.1.1.1 Cracks - Phase 1a

Cracks are usually random with no preferential direction and are polygonal in shape. Cracks do not crosscut but rather preferentially skirt carbonate grains, becoming circumglanular cracks (Figure 5.3A). Sub-millimetre sized cracks are present in dolomitized micrite rock fragments (Figure 5.3A to C) and are filled with calcite cement (Figure 5.3C). These intraclasts are exclusively present at the top of layer PZ1 toward the basin center in wells BBC 14-1, BBC 14-3, and N 6-28. Larger and wider cracks are present exclusively in the Nine Mile outcrop in ostracod dolopackstone (Figure 5.3D) and show the same pattern as the smaller scale features.

5.1.1.2 Meniscus cement - Phase 1b

Meniscus cement precipitated at carbonate grain contacts (Figure 5.3E), partially filling interparticle pores. Meniscus cement shows a geographical variation in its relative abundance as follows: in nearshore areas, meniscus cement is preferentially developed within intraclastic grainstone, ooid grainstone, and ostracod grainstone facies (F6, F7, and F8), in which the meniscus cement is more abundant in well PW 13-06 at the top of layer PZ1. Basinward meniscus cement is not present. The original carbonate mineral that precipitated as meniscus cement was replaced by dolomite, which obliterated the original texture of meniscus cement.

5.1.1.3 Molds I- Phase 2a

Molds were created by dissolution of mainly mollusk shells (Figure 5.3F). Such molds are present only within dolomitized intraclasts (Facies F6) and are completely filled with calcite cement. These molds have preserved the original shapes without any evidence of mechanical deformation (Figure 5.3F).

5.1.1.4 Blocky calcite cement - Phase 2b

Blocky calcite crystal ranges from medium to coarse crystalline in size. This cement fills moldic porosity and cracks (Figure 5.3A to D) in intraclastic grainstone and ostracod grainstone facies (F6 and F8).

Figure 5.3

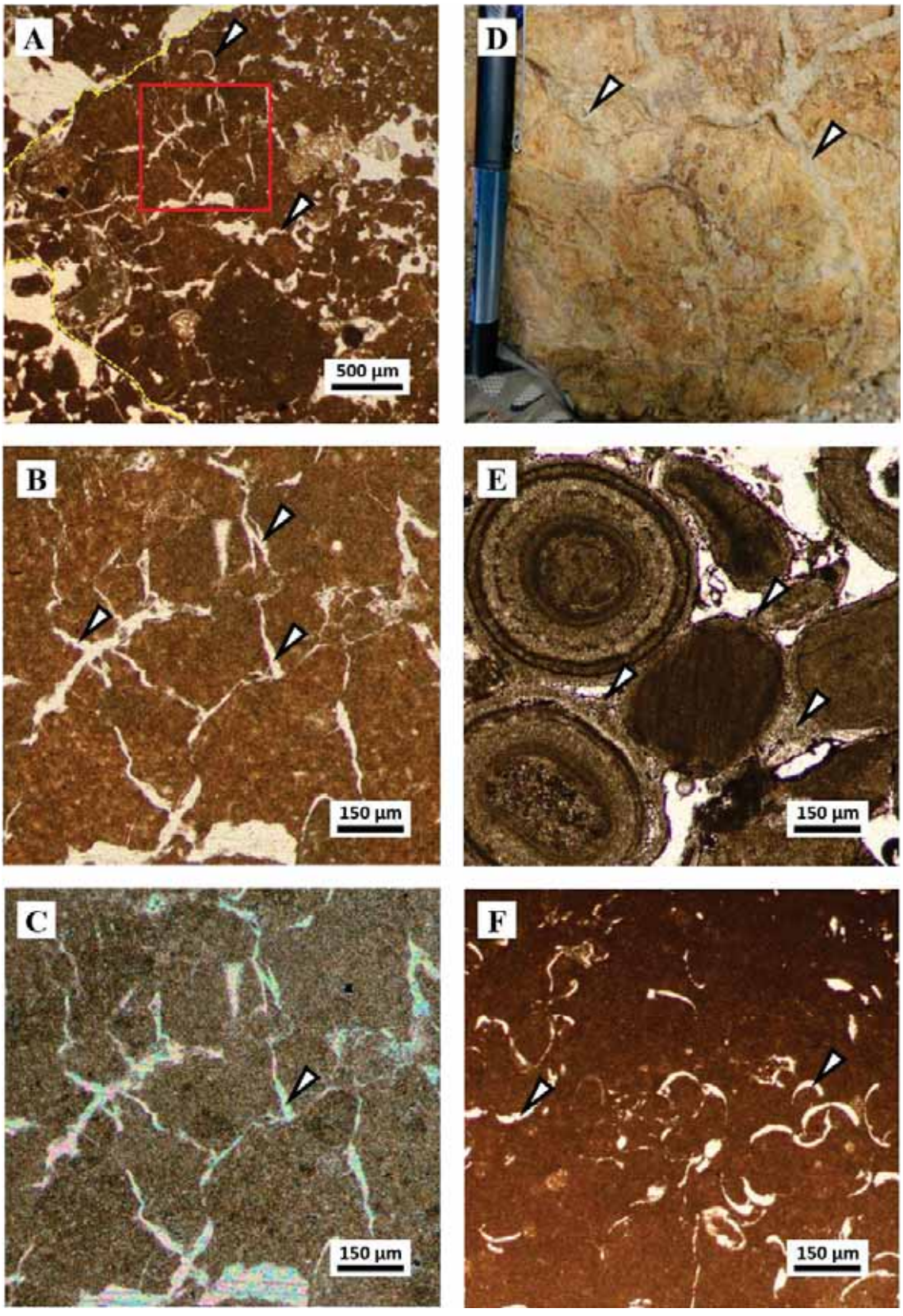

Figure 5.3

(A) Photomicrograph of intraclast (yellow dash outline) with cracks that surrounded peloids (arrow) and crosscut dolomitized matrix; well: N 6-28, sample: 5, depth: 8223.2 ft.; plane polarized light (PPL).

(B) Detail of photomicrograph (A). Polygonal micro-cracks (arrows) that crosscut microcrystalline dolomitized matrix (dark brown area). Cracks are completely filled with blocky calcite cement; PPL.

(C) Crossed-polarized photomicrograph (B). Blocky calcite cement fills cracks (arrow). Calcite cement is represented by pale pink to green colours areas; crossed polarized light (XPL).

(D) Cracks present in the near-shore area filled with blocky calcite cement (arrows); Nine Mile outcrop, pen for scale.

(E) Photomicrograph of ooid dolograinstone with microcrystalline meniscus cement at grains contacts (arrows); well: PW 13-06, sample 6, depth: 5539.5 ft.; PPL.

(F) Molds of bioclasts (likely mollusc shell fragments) filled with blocky calcite cement (arrow); well: UT 15-13, sample 5, depth: 6982.2 ft.; PPL

5.1.1.5 Variably lithified sediment – Phase 2c

Sediment variably compacted by early meniscus and blocky calcite cement.

5.1.1.6 Replacive dolomite - Phase 3a

This section provides petrographic observations on the thin section scale, however, characterization of individual dolomite crystals is not possible using the petrographic microscope because the crystals are too small. This characterization was therefore conducted by virtue of SEM images (see Sections 5.2.1.1 and 5.2.2.1 for further analysis). Replacive dolomite is brown to green in colour, with crystal size ranges from aphanocrystalline to very finely crystalline. Replacive dolomite is found in the matrix (Figure 5.4A), as well in peloids, intraclasts (Figure 5.4B), ooids, and pellets; however, dolomite generally do not replace bioclasts (Figure 5.4C).

5.1.1.7 Dolomite cement - Phase 3b

Dolomite cement is clean microcrystalline crystals and partially fills intraparticle pores, usually present as overgrowth of dolomitized internal sediment (Figure 5.4D to F). Most crystals are euhedral to subhedral, crystal size varies from 10 to 20 μm. Dolomite cement (Phase 3b) is preferentially developed at nearshore areas within the ostracod grainstone and ooid grainstone facies (F8 and F9). In contrast, the basinward facies (F3, F4, and F5) do not display this type of dolomite cement.

Figure 5.4

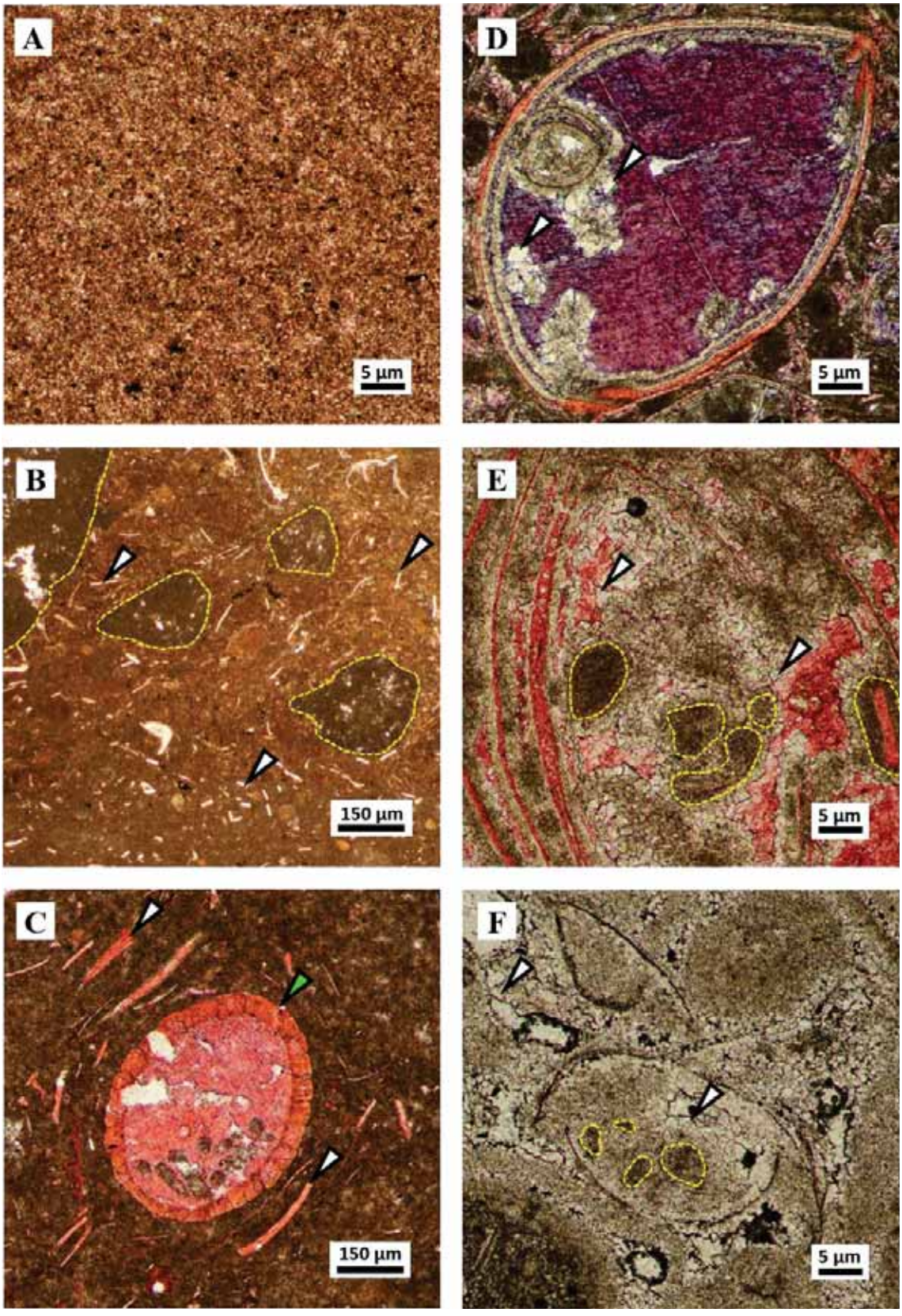

Figure 5.4

(A) Very fine crystalline dolomite in matrix (brown colour area); black spots are pyrite crystals and hydrocarbon droplets; well: BBC 14-1, sample: 17, depth: 6692.6 ft.; PPL.

(B) Very fine crystalline dolomite in matrix (light brown area) and dolomitized intraclasts (dark brown, outlined by yellow dashed lines). Bioclasts (arrows) were not dolomitized; well: BBC 14-1, sample: 13, depth: 6684.9 ft.; PPL.

(C) Matrix-selective dolomitization (dark brown colour area). Note shell fragments (white arrows) and gyrogonite bioclast (green arrow) are not dolomitized; well: BBC 14-3, sample: 27, depth: 7373.65 ft.; PPL.

(D) Planar-c dolomite cement (arrows) characterized by euhedral crystals with light green colour; partially filling intraparticle pore; well: IU 16, sample: 14, depth: 4729.9 ft.; PPL.

(E) Rims of planar-c dolomite cement (arrows) grow around dolomitized peloids (?) and ooids (yellow dashed outlines); well: DS 11-20, sample 12, depth: 4999.35 ft.; PPL.

(F) Planar-c dolomite cement (arrows) around dolomitized peloids (?) within ostracod shells; well: PW 13-06, sample: 6, depth: 5539.5 ft.; PPL.

5.1.1.8 Molds II – Phase 4

Molds developed by partial to complete dissolution of calcite bioclasts (Figures 5.5A to C). Dissolution of bivalves not previously filled with mud were later filled with fibrous chert (Figures 5.5A and B), whereas bivalves filled with mud formed molds only as narrow as the shells (Figure 5.5C).

5.1.1.9 Isopachous quartz cement rims – Phase 5a

Quartz crystals of Phase 5 have a size range from 5 to 20 μm, with bladed to equant shapes. This quartz cement lines interparticle pores (Figures 5.5D and E), and in rare cases intraparticle pores (Figure 5.5F). This cement is preferentially developed in the nearshore area within the intraclast, ostracod, and ooid grainstone facies (F6, F7, and F8).

5.1.1.10 Chert nodules – Phase 5b

Silica forms elongated and irregular chert nodules (up to several decimetres in dimension) within dolomite layers PZ1, PZ1' and PZ2. The nodules are composed of assorted silica varieties: length-fast and length-slow (quartzine) chalcedony (Flöerke et al., 1991), megaquartz (Folk and Weaver, 1952), and granular microcrystalline quartz (Knauth, 1994). Colourless, fibrous, and aphanocrystalline chalcedony cement also fills intraparticle pores (Figures 5.5A and B) and vugs.

Figure 5.5

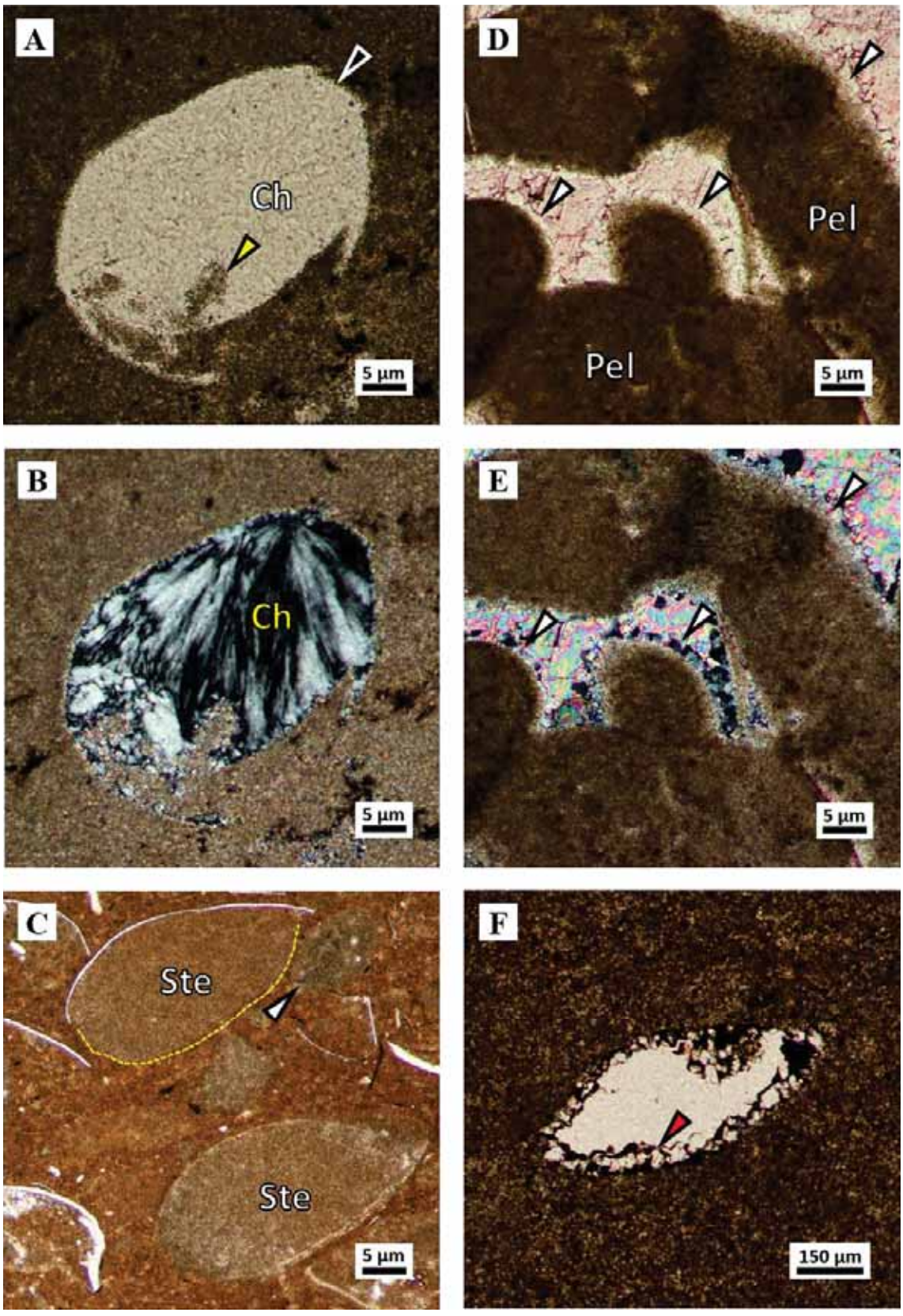

Figure 5.5

(A) Ostracod mold (black arrow) filled with dolomite (yellow arrow) and chalcedony (Ch); well: PW 13-06, sample: 8, depth: 5543.5 ft.; PPL.

(B) Crossed-polarized light image of (A). Feathered texture of the chalcedony that fills internal ostracod (?) pore; XPL.

(C) Partial (yellow dashed line) and complete dissolution (arrow) of ostracod shells; and steinkerns (Ste) within an aphanocrystalline dolomitized matrix; well BBC 14-1, sample: 9, depth: 6680.1 ft.; PPL.

(D) Rims of very fine crystalline quartz as cement (arrows) around dolomitized peloids (Pel); well: BBC 14-1, sample: 12, depth: 6683.95 ft.; PPL.

(E) Crossed-polarized light image of (D). Quartz cement (arrows), and calcite cement (yellow, green, and blue area); XPL.

(F) Rims of equant quartz cement (arrow) in intraparticle pore. Dark brown and black spots are hydrocarbons; well: N 6-28, sample: 7, depth: 8230.2 ft.; PPL.

Both length-slow (Figures 5.6A to C) and length-fast (Figures 5.6D and E) chalcedony display a spherulitic fibrous habit and/or a radial fibrous to feathered habit (Figures 5.5B, 5.6B and E), nucleated along pore walls. Megaquartz crystals show a polygonal crystal habit with irregular interlocking crystals, located at the centers of voids, filling remaining space (Figure 5.6F). Granular microcrystalline quartz (anhedral quartz crystals around bioclast in Figure 5.6A to D) composes the majority volume of the chert nodules.

5.1.1.11 Euhedral quartz – Phase 5c

Quartz of Phase 5c is colourless, clean, commonly hexagonal and double–terminated euhedral crystals of quartz that vary in size from 5 to 20 μm. Euhedral quartz crystals contain very fine crystalline dolomite inclusions (Figure 5.7A). They formed around chert nodules and within bioclasts (Figures 5.7B and C), overall in random distribution within the dolomitized matrix of facies F2, F3, and F4.

5.1.1.12 Pyrite – Phase 6

Very fine crystalline pyrite is comprised of octahedral crystals associated with calcite within chert nodules (Figure 5.7D). Crystal size varies from 10 to 100 μm. Some pyrite crystals encase very fine crystalline and planar-e dolomites (Figure 5.7E). There are also disseminated crystals of very fine to fine crystalline framboidal pyrite within very fine crystalline dolomite (matrix) (Figure 5.7F). Framboidal pyrite crystals range in size from 5 to 10 μm.

Figure 5.6

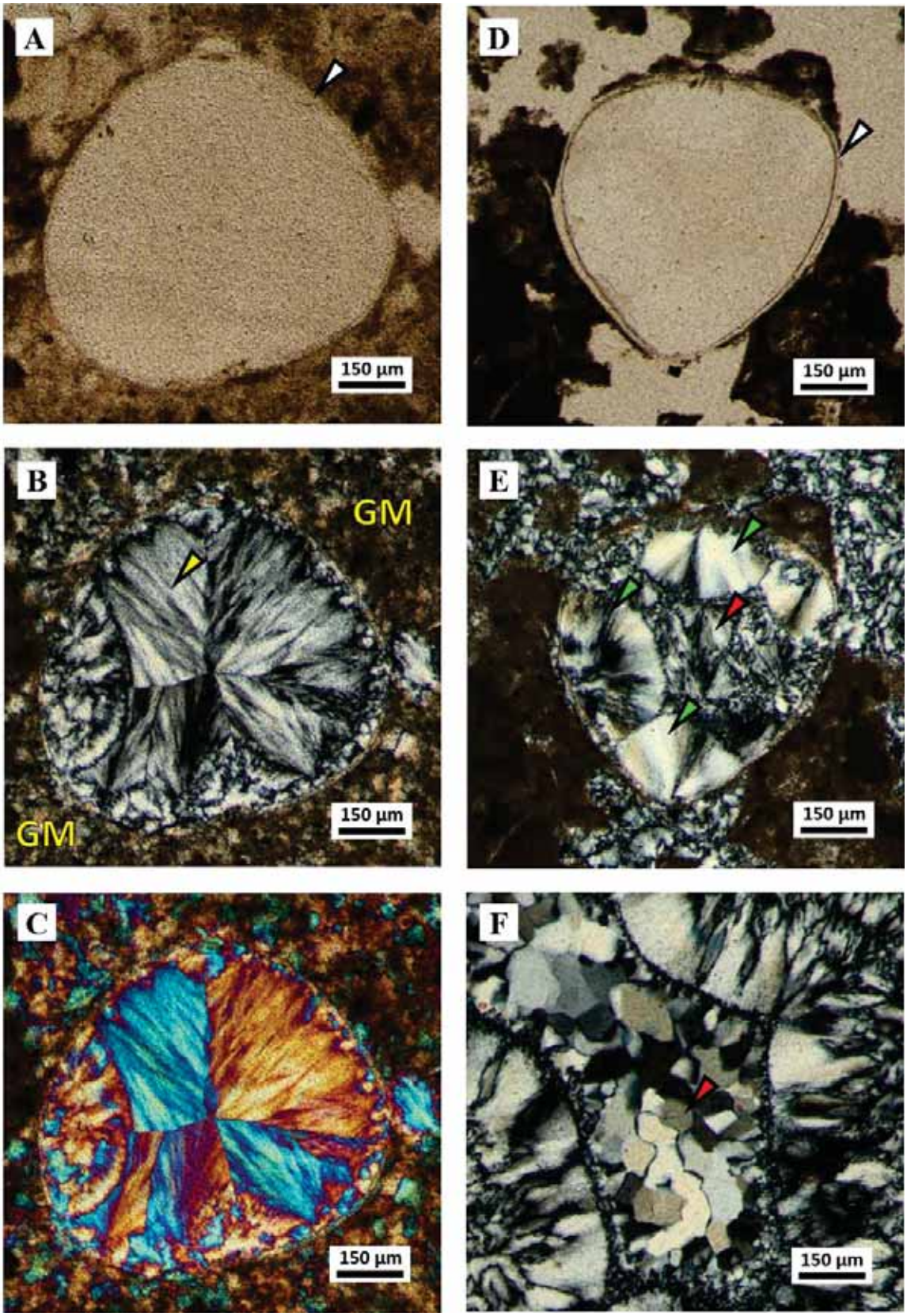

Figure 5.6

(A) Photomicrograph of part of a chert nodule. Ostracod shells (arrow) are mimetically replaced by microcrystalline quartz. Internally the ostracod is filled by chalcedony (light brown area); well: BBC 14-3, sample: 28, depth: 7374 ft.; PPL.

(B) Crossed-polarized light image of (A). Quartzine with feathered habit (arrow) nucleated at the ostracod shells. Granular microcrystalline quartz (GM) precipitated around bioclasts (dark brown, and grey area around ostracod shells); XPL.

(C) Same sample as in (A) and (B); XPL with gypsum plate.

(D) Photomicrograph of part of a chert nodule with an articulated ostracod (arrow), which is partially replaced by quartz and dolomite. Internal void filled with chalcedony; well: BBC 14-3, sample: 29, depth: 7375 ft.; PPL.

(E) Crossed-polarized light image of (D). Several arrays of chalcedony nucleated at the internal walls of the ostracod shell (green arrows); some chalcedony have radial fibrous to feathered habit (center of the ostracod, red arrow); XPL.

(F) Megaquartz crystals (center, red arrow) fill a void post-dating chalcedony cement (fibrous and feathered crystals); well: BBC 14-3, sample: 29, depth: 7375 ft.; XPL.

Figure 5.7

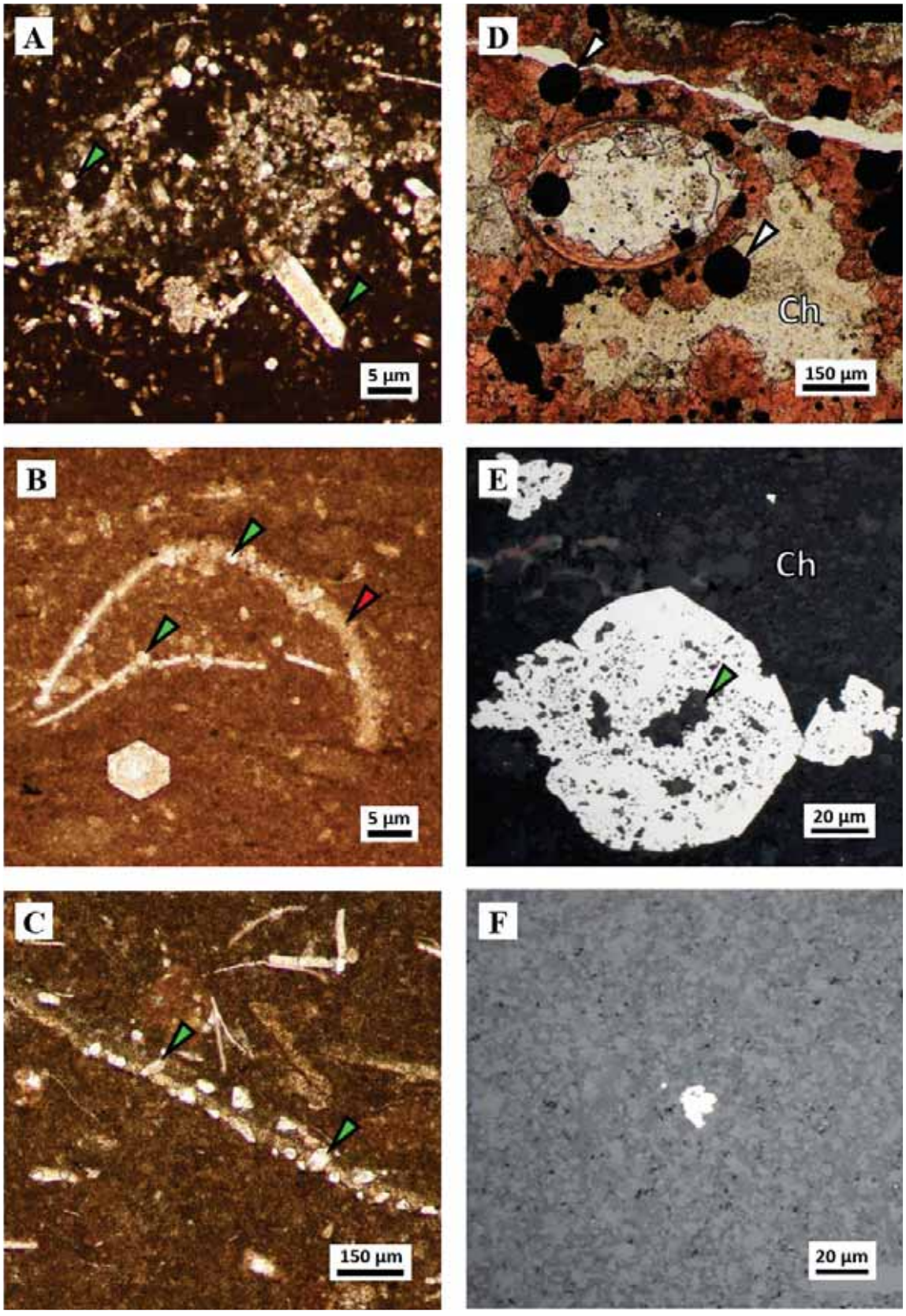

Figure 5.7

(A) Euhedral quartz (arrows) within an aphanocrystalline dolomite matrix (dark brown area). Quartz crystals have dolomite inclusions (small light brown crystals within quartz); well: UT 15-13, sample: 11, depth: 7009.9 ft.; PPL.

(B-C) Euhedral quartz (arrows) within an aphanocrystalline dolomite matrix (light brown area). Some quartz (green arrows) crystallized preferentially along ostracod (?) shells (red arrow); (B) Well: UT 15-13, sample: 11, depth: 7009.9 ft.; PPL. (C) Well: BBC 14-3, sample: 28, depth: 7374.05 ft.; PPL.

(D) Fine crystalline pyrite crystals with cubic and octahedral shape (arrows) associated with calcite (red areas) within a chert nodule (Ch); well: PW 13-06, sample: 11, depth: 5552.3 ft.

(E) Reflected light photomicrograph of medium to coarse crystalline pyrite with octahedral shapes (bright area) that enclose very fine crystalline planar-e dolomite (arrow) within a chert nodule (Ch); well: N 6-28, sample: 6, depth: 8223.7 ft.

(F) Reflected light photomicrograph of very fine crystalline and framboidal pyrite (bright white area) within dolomitized matrix (light grey and brown area); well: PW 13-06, sample: 10, depth: 5545.3 ft.

5.1.1.13 Mechanical compaction features – Phase 7

Several mechanical compaction features are present: (i) Broken and flattened bioclasts (Figures 5.8A, 5.9A and B); (ii) peloids elongated and/or amalgamated parallel to bedding (Figure 5.8B); (iii) concavo-convex contacts between grains; and (iv) breakage of ooids and peloids.

5.1.1.14 Equant calcite – Phase 8

Equant calcite forms mosaics of mostly anhedral crystals with size varying from 10 to 50 μm. This calcite also fills interparticle pores as cement. It is more abundant toward nearshore areas (facies F6, F7, and F8), especially within the ostracod grainstone facies (F8) (Figure 5.8C). Equant calcite cement is not present toward the basin center (F2, F3, and F4 facies).

5.1.1.15 Molds and vugs – Phase 9

Partial dissolution of equant calcite cement created vugs, which were completely filled with ferroan calcite cement in Phase 10 (Figures 5.8D and E). Partial dissolution of bioclasts (preferentially pelecypods and gastropods) created moldic pores, which was also filled by ferroan calcite cement (Figure 5.8F).

Figure 5.8

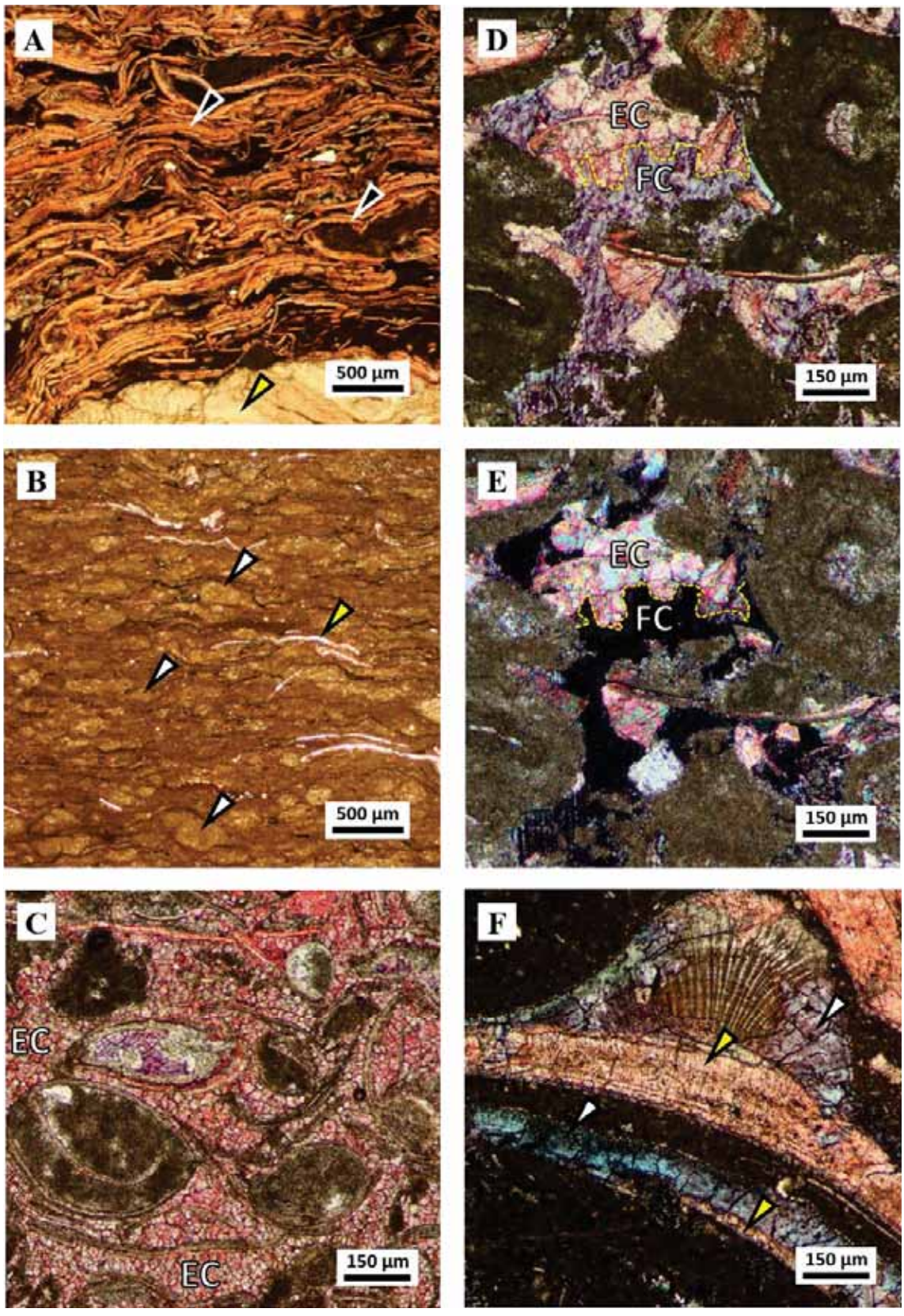

Figure 5.8

(A) Transmitted light photomicrograph of densely packed ostracod (black arrows) and gastropod shell (green arrow); well: DS 11-20, sample 14, depth: 5017 ft.; PPL.

(B) Transmitted light photomicrograph of elongated and dolomitized peloids (steinkerns?) (white arrows), and flattened ostracod shells (blue arrow) aligned parallel to bedding; well: UT 15-13, sample: 7, depth: 6989 ft.; PPL.

(C) Transmitted light photomicrograph of equant calcite (EC) in interparticle pores. Crystal size ranges from 10 to 20 μm; well: IU 16, sample: 14, depth: 4729.9 ft.; PPL.

(D) Transmitted light photomicrograph of equant calcite cement (EC) and ferroan calcite cement (FC) in contact along a possible dissolution front (yellow dashed line); well: DS 11-20, sample: 13, depth: 5000.3 ft.; PPL.

(E) Crossed-polarized image of (D).

(F) Partial dissolution of bioclast. Original metastable calcium carbonate of gastropod shell fragments (white arrows), which was partially dissolved and then filled by blocky ferroan calcite cement (yellow arrows); well: PW 13-06, sample: 14, depth: 5565.9 ft.

5.1.1.16 Blocky ferroan calcite cement– Phase 10

Blocky ferroan calcite is a cement with crystals that vary in size from 50 to 200 μm. Ferroan calcite cement mainly fills intraparticle and interparticle pores and it is normally associated with equant calcite cement of Phase 8 (Figures 5.9A and B). In some cases this type of cement fills pores that resulted from the dissolution of shells of pelecypods and gastropods (Figure 5.9C).

5.1.1.17 Subhorizontal stylolites and sutured seams– Phase 11

Subhorizontal stylolites and sutured seams are nearly parallel to bedding. Subhorizontal stylolites have an irregular to hummocky shape (Logan and Semeniuk, 1976) with amplitudes up to 20 μm. In some cases, a set of stylolites composes an irregular anastomosing set (Figure 5.9D). Swarms of microstylolites or sutured seams are common in dolostones (Figure 5.9E).

5.1.1.18 Oil impregnation– Phase 12

Black oil (liquid phase) fills intercrystal, interparticle, and moldic pores (Figure 5.9F), fractures, stylolites, and solution seams. Oil is present in all carbonate facies (F2 to F8). Textural relationship between oil impregnation and blocky calcite cement (phase 15) does not clarify the time occurrence between these phases.

Figure 5.9

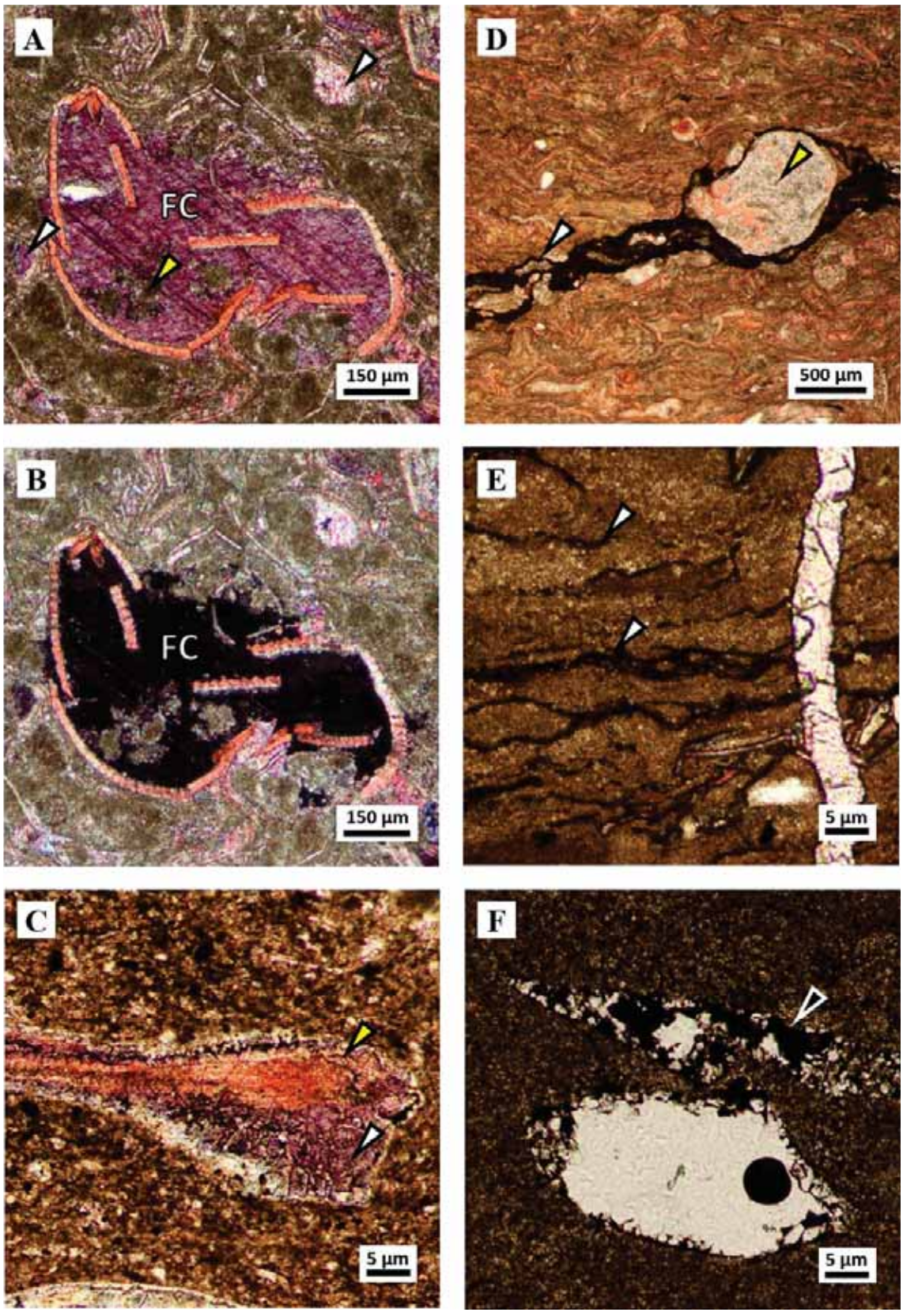

Figure 5.9

(A) Transmitted light photomicrograph of blocky ferroan calcite cement (FC) in ostracod intraparticle pores (dark purple centre and white arrow), encasing patches/clusters of microcrystalline dolomite (yellow arrow); well: IU 16, sample: 14, depth: 4729.9 ft.; PPL.

(B) Crossed-polarized light image of (A).

(C) Transmitted light photomicrograph of blocky ferroan calcite cement (white arrow) in space developed by partial dissolution of shell fragment (green arrow); well: BBC 14-1, sample: 6, depth: 6666.5 ft.; PPL.

(D) Transmitted light photomicrograph of irregular to hummocky subhorizontal stylolites forming an anastomosing set (arrow); well: IU 16, sample: 16, depth: 4733.2 ft.; PPL.

(E) Transmitted light photomicrograph of swarms of microstylolites or sutured seams (arrows) in dolowackestone. Subvertical fracture (green arrow) post-dates the stylolites and is filled by blocky calcite cement (Phase 15); well: UT 15-13, sample: 6, depth: 6983.9 ft.; PPL.

(F) Hydrocarbon in intercrystal pores in dolomitized matrix (black spots within dark brown area), and in moldic pores as droplets (arrow); well: N 6-28, sample: 7, depth: 8230.2 ft.; PPL.

5.1.1.19 Subvertical stylolites and solution seams– Phase 13

Vertical stylolites are characterized by sharp to wavy boundaries, and commonly columnar to wave-like peak stylolites (Logan and Semeniuk, 1976) with amplitudes up to 2500 μm, which crosscut bedding planes and carbonate grains (Figure 5.10A). Subvertical stylolites are associated with subvertical fractures (Figure 5.10A) and occur in both limestones and dolostones. Insoluble material has thicknesses ranging from 50 to 200 μm (Figure 5.10B). These stylolites are preferentially developed toward the basin center in wells BBC 14-1, BBC 14-3, N 6-28, and UT 15-13.

5.1.1.20 Vertical fractures– Phase 14

Single or cluster vertical fractures are characterized by straight, branching, and stepped profiles nearly perpendicular to stratification (Figure 5.10C). Fractures display apertures (space between walls) up to 50 μm. Fractures crosscut carbonate grains, chert nodules, and stylolites. Fractures are partially to completely filled with calcite cement of Phase 15. There is no evidence of relative movement between fracture walls.

5.1.1.21 Drusy calcite cement– Phase 15

Fibrous to bladed calcite crystals that vary from medium crystalline to blocky and very coarse crystalline in size (center of the void), with well-defined twining (Figures 5.10D and E). Calcite cement fills vertical fractures (Phase 14) and stylolites (Phase 13). These calcite crystals commonly contain hydrocarbons (oil) in fluid inclusions (Figure 5.10F).

Figure 5.10

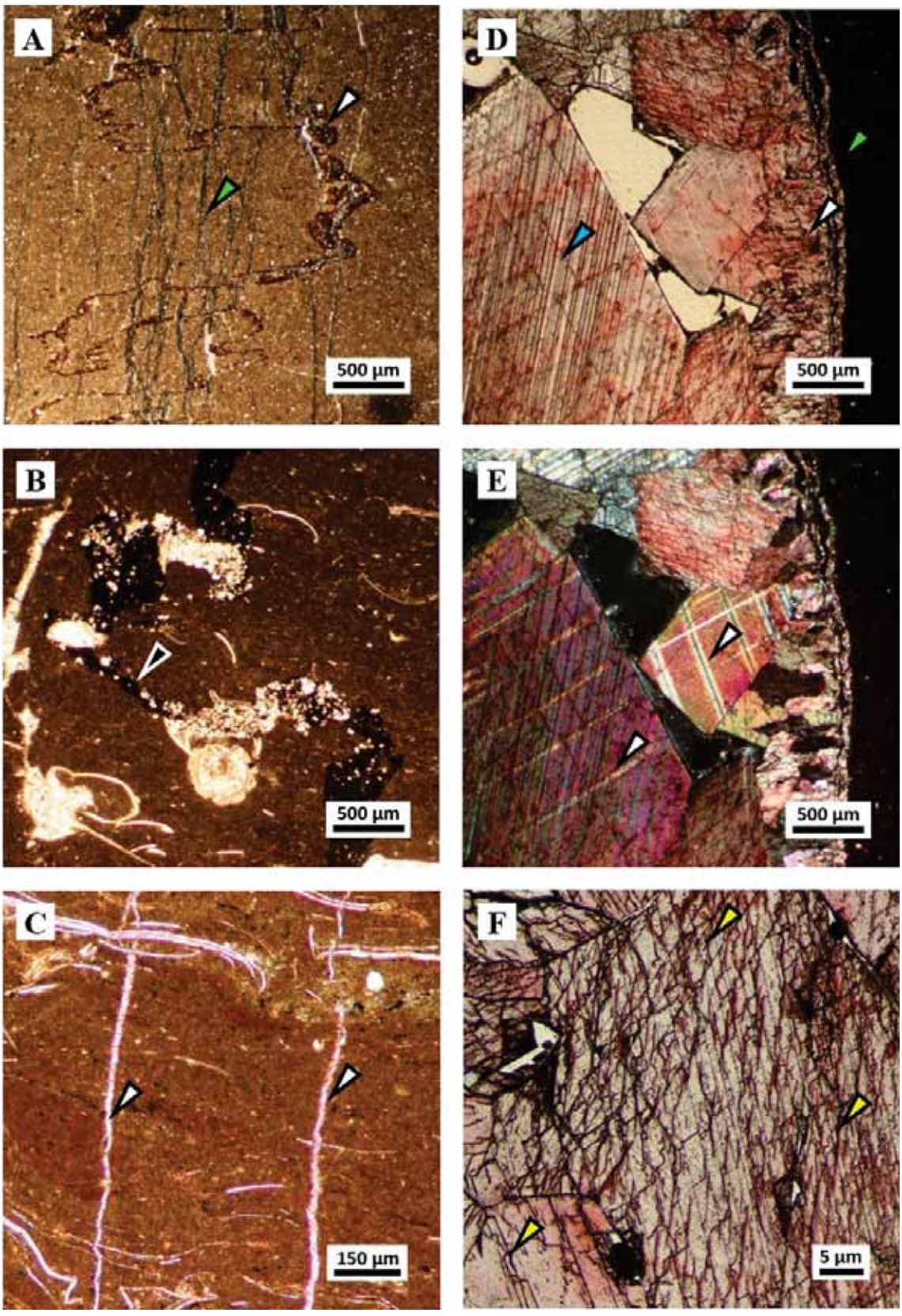

Figure 5.10

(A) Transmitted light photomicrograph of subvertical serrated stylolites (white arrow) with amplitude up to 2500 μm. These stylolites are associated to subvertical fractures (green arrow); well: N 6-28, sample: 1, depth: 8199.3 ft.; PPL.

(B) Transmitted light photomicrograph of anastomosing sutured seam (black arrow) that crosscuts stratification (horizontal in photomicrograph). Undissolved material is mainly quartz (bright spots within sutured seam) and clay; well: N 6-28, sample: 8, depth: 8234.6 ft.; PPL.

(C) Transmitted light photomicrograph of straight subvertical fractures (arrows) that crosscut stratification (horizontal in photomicrograph) and ostracod shells. Fractures contain blocky calcite cement of Phase 15 (red colour within fractures); well: BBC 14-1, sample: 20, depth: 6701.4 ft.; PPL.

(D) Transmitted light photomicrograph of drusy calcite cement with crystal size increasing from medium crystalline (white arrow) at the stylolite wall (green arrow) toward a very coarse crystalline (blue arrow) in the center. Calcite crystals have well-defined twining; well: N 6-28, sample: 12, depth: 8267.4 ft.; PPL.

(E) Crossed-polarized light image of (A), characterized by well-defined twining (arrows).

(F) Hydrocarbon fills (yellow arrows) fractures in blocky calcite crystals (entire area of the photomicrograph); well: N 6-28, sample: 12, depth: 8267.4 ft.

5.1.2 Interpretation

The paragenetic sequence defined in Table 5.1 chronologically lists the products that were formed over the entire stratigraphic section of interest. The top of the table shows timing from early (after deposition) to late (present). Additionally, the base of the table shows diagenesis environments that correlate diagenetic setting as proposed by Machel (1999). The near-surface diagenetic setting is located at depths of zero to maximum a few meters and is controlled by surface waters, be they marine, fresh or evaporitic. The shallow burial diagenetic setting is located below the near-surface diagenetic setting down to about 1000 m, still heavily influenced, if not controlled by, surface-derived waters. The intermediate burial diagenetic setting is located between about 1000 and 3000 m in depth, the bottom being defined as coinciding with the top of the liquid oil window, which varies in depth and it is controlled by geothermal gradient and kerogen type. Finally, the deep burial diagenetic setting encompasses the liquid oil window and reaches down to the top of the metamorphic realm (Machel 1999).

This section interprets the diagenetic processes that created the various diagenetic products described in the previous section. The term ‘phase’ is defined here as the time interval during which a particular diagenetic process created the product(s) listed in Table 5.1.

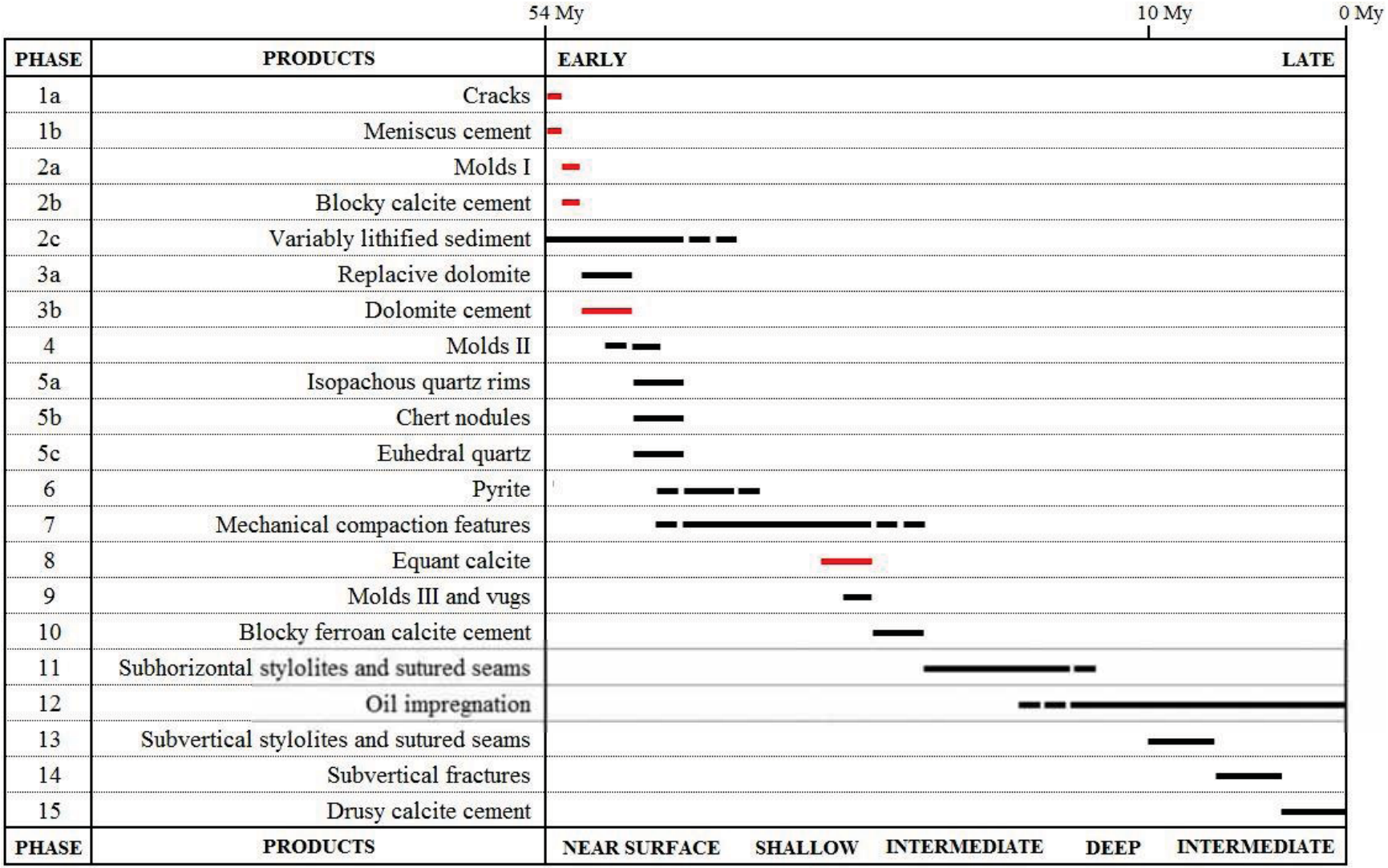

Table 5.1: Paragenetic sequence. Phases 1 (cracks and meniscus cement), 2 (molds and equant-blocky calcite cement), 3b (dolomite cement), and 8 (equant calcite cement) took place along the near shoreline area only. These diagenetic products are highlighted red.

5.1.2.1 Phase 1a – 1b

Diagenesis transformed precursor lime sediments just after deposition in the near-surface diagenetic setting. The first diagenetic processes formed two products: cracks (phase 1a) and meniscus cement (phase 1b). These features were likely developed by subaerial exposure of unlithified sediment, in which, due to pore water evaporation, soft sediment shrinkage produced crack networks and/or circumgranular cracks (Esteban and Klappa, 1983). This process took place along the shoreline area, presumably during periods of subaerial exposure, although the observed cracks may also have formed subaqueously due to syneresis.

The progressive evaporation of pore water in the vadose zone allowed crystallization of calcite as meniscus cement (James and Choquette, 1984) at or near carbonate grain boundaries. Vadose diagenesis took place only along the shore belt area located near the southern limits of the study area.

5.1.2.2 Phase 2a – 2b – 2c

Vertical fluctuations in the water table formed several diagenetic products. In phase 2a, meteoric water probably promoted dissolution of metastable carbonate minerals (Scholle and Ulmer-Scholle, 2003), forming molds and vugs. Cracks that had formed in Phase 1 as well as molds and vugs of Phase 2a were then filled with equant calcite cement, commonly completely. The dissolution of bioclasts and subsequent precipitation of equant and blocky calcite cement suggest early diagenesis within the meteoric-phreatic zone (Pingitore, 1976; Scholle and Ulmer-Scholle, 2003), which overlaps the near-surface and shallow burial diagenetic settings defined by Machel (1999).

Also during Phase 2, lime mud likely was partially lithified to limestone (here identified as Phase 2c), perhaps only partially and variably depending on proximity to the fluctuating lake shore line, thereby forming semi-lithified carbonate material by virtue of an interplay of recrystallization (stabilization of metastable aragonite and/or high-Mg calcite) and minor intergranular cementation (Tucker and Wright, 1990; Flügel, 2010). The petrographic evidence currently available does not permit to judge the degree of mineralogical stabilization and induration of the sediments prior to Phase 3.

5.1.2.3 Phase 3a – 3b

Dolomite was formed by two different processes: the replacement of the precursor micrite matrix (phase 3a), and crystallization as cement (phase 3b). Moreover, dolomite cement crystals overgrew dolomite replacement crystals. This relationship suggests that lime(stone) replacement and dolomite cementation were nearly contemporaneous processes, and the products (replacement and cements) precipitated from the same parental dolomitized fluid. Furthermore, the fact that dolomitization was stratiform and created layers PZ1, PZ1', and PZ2 that alternate with limestone layers suggests that dolomitization was a nearly synsedimentary process in the near-surface diagenetic environment. As such the Uteland Butte dolomite layers conform to the type of dolomite known as penecontemporaneous (Budd, 1977; Warren, 2000; Machel 2004). Dolomite formation likely was driven by slight to moderate degrees of evaporation, as further discussed in Section 5.3.

5.1.2.4 Phase 4

Molds were created by the dissolution of bioclasts. This process occurred in the near-surface diagenetic environment where fluids dissolved ostracod shells and fragments (Figures 5.5A to C). The dissolution of bioclasts may have been a by-product of dolomitization. Alternatively, and perhaps more likely, incursions of relatively fresh lake water and/or rain water during periods of subaerial exposure facilitated dissolution of non-dolomitized bioclasts.

5.1.2.5 Phase 5a – 5b – 5c

Bioclast dissolution and quartz crystallization likely took place at the same time (Maliva and Siever, 1989) and nearly contemporaneously with dolomitization and/or very soon thereafter. Furthermore, considering that silicified bioclasts do not show any reworking (disarticulated shells) or mechanical deformation (broken shells), silicification likely took place prior to mechanical compaction, thus also in the near-surface diagenetic environment. Primary calcium carbonate matrix and carbonate grains (intraclasts and peloids) now contained within chert nodules consist of dolomite, which indicates that dolomitization predated silicification.

Quartzine within chert nodules suggest that the silicification process probably was driven by evaporation (Folk and Pittman, 1971; Siedlecka, 1972; Heaney, 1995; Warren, 2006). The source of silica likely was the river water that fed the lake, and thereby from the eroding hinterland.

5.1.2.6 Phase 6

Pyrite can be formed as a by-product of either bacterial sulfate reduction (BSR) or thermochemical sulfate reduction (TSR) (Machel 2001). TSR occurs at in deep burial diagenetic settings at temperatures between 100 ºC to 140 ºC. In the Uteland Butte member pyrite formation must have taken place within the near-surface to shallow burial diagenetic settings. This interpretation is based on the textures and the occurrence of pyrite in the paragenetic sequence, as well as on the recognition that the maximum burial temperature of the study area, likely was near 110 ºC based on Schamel (2015) burial history curves, was too low for thermochemical sulfate reduction. The fact that pyrite is overall very low in abundance likely reflects that the lake water had a very low sulfate concentration, rather than low concentrations of iron or organic matter, both of which were abundant.

5.1.2.7 Phase 7

Mechanical compaction deformed the entire stratigraphic section of interest, generating densely packed mollusk layers, broken bioclasts, and elongation parallel to the bedding of semi-lithified components. Mechanical compaction likely took place throughout the near-surface and shallow burial diagenetic settings. The fact that many bioclasts show evidence of breakage further suggests that early diagenetic lithification was rather 'weak' overall, thus leaving many semi-plastic sedimentary layers into the shallow burial diagenetic setting (see Phase 2c above). Phase 7 might have overlapped with dolomitization (Phase 2a and 2b), pyritization (phase 5), and silicification (phases 6a, 6b, and 6c)

5.1.2.8 Phase 8

Equant calcite cement was created during and after mechanical compaction. The temporal interpretation of this calcite cement is based on crystal morphology and superposition with other diagenetic products.

5.1.2.9 Phase 9

A third generation of mold formed along with some vugs during Phase 8, considering the types of cements that are found filling them (Figures 5.8D to F), notably ferroan calcite. The cause for this phase of dissolution cannot be ascertained but may well have been yet another temporary freshening of the pore water after previous phases of evaporation that had formed dolomite and/or chert.

5.1.2.10 Phase 10

Soon after Phase 9 equant ferroan calcite cement of Phase 10 filled the remaining pores (Figures 5.9A to C). The precipitation of ferroan calcite cement requires a reducing environment, which preferentially develops within intermediate and deep burial diagenetic settings (Machel 1999; Scholle and Ulmer-Scholle, 2003, Flügel, 2010). The textural relationship of ferroan calcite cement with previous diagenetic products confirms this interpretation.

5.1.2.11 Phase 11

Continuous burial led to the development of subhorizontal stylolites and sutured seams caused by chemical compaction. Stylolitization took place in the intermediate and deep burial diagenetic settings.

5.1.2.12 Phase 12

Oil was generated likely in the upper levels of the deep burial diagenetic setting, considering the (lacustrine) type of kerogen [types I and II, Schamel, 2015)] contained in the Green River Basin. According to Schamel (2015), the stratigraphic interval of interest underwent differential burial, in which the maximum depth for the northern part of the study area (depocenter) is estimated at 3700 m, and for the southern part of the study area (near-shore line) is around 2550 m. Schamel (2015) estimated that the northern part of the study area is nowadays within the wet gas window.

5.1.2.13 Phase 13

The subvertical stylolites likely were created by a tectonic compressive event (Ebner et al., 2010), in which direction of the maximum compressive stress was subhorizontal.

5.1.2.14 Phase 14

Vertical fractures may have formed during tectonic compression in a tri-axial stress field, or during uplift and/or the erosion that took place 0.5 Mya (Schamel, 2015). Considering

the current post-uplift depth of the strata of interest, Phase 14 must be placed into the intermediate burial diagenetic environment.

5.1.2.15 Phase 15

Drusy calcite cement partially filled some open subvertical fractures and stylolites (Figures 5.10D to F). Calcite crystal sizes and texture variation suggest an intermediate burial diagenetic setting (Machel, 1999). Along the walls of subvertical stylolites and/or fractures, calcite crystals are characterized by medium crystalline in size with bladed texture, whereas at the center of the void, calcite crystals are characterized by very coarse crystalline in size with blocky texture.

5.1.3 Burial history

Schamel (2015) designed a burial history model for the Green River Formation. In this model the base of the Green River Formation is defined by the Uteland Butte member, which is located at the base of the GR-7 unit (Figure 5.11). The maximum temperature that unit GR-7 reached was between 95 ^{o}C and 120 ^{o}C at a geothermal gradient of 25 ^{o}C/km. However, the highest temperature of 120 ^{o}C does not apply to the current study area because it was calculated for a synthetic well located farther north, representing the region of maximum burial.

Considering that the current study area is located between the depocenter and the nearshore settings of the Uinta Basin, the maximum burial temperature in the current study area is estimated to be ~110 ^{o}C [based on extrapolation of Schamel's (2015) model] (Figure 5.11).

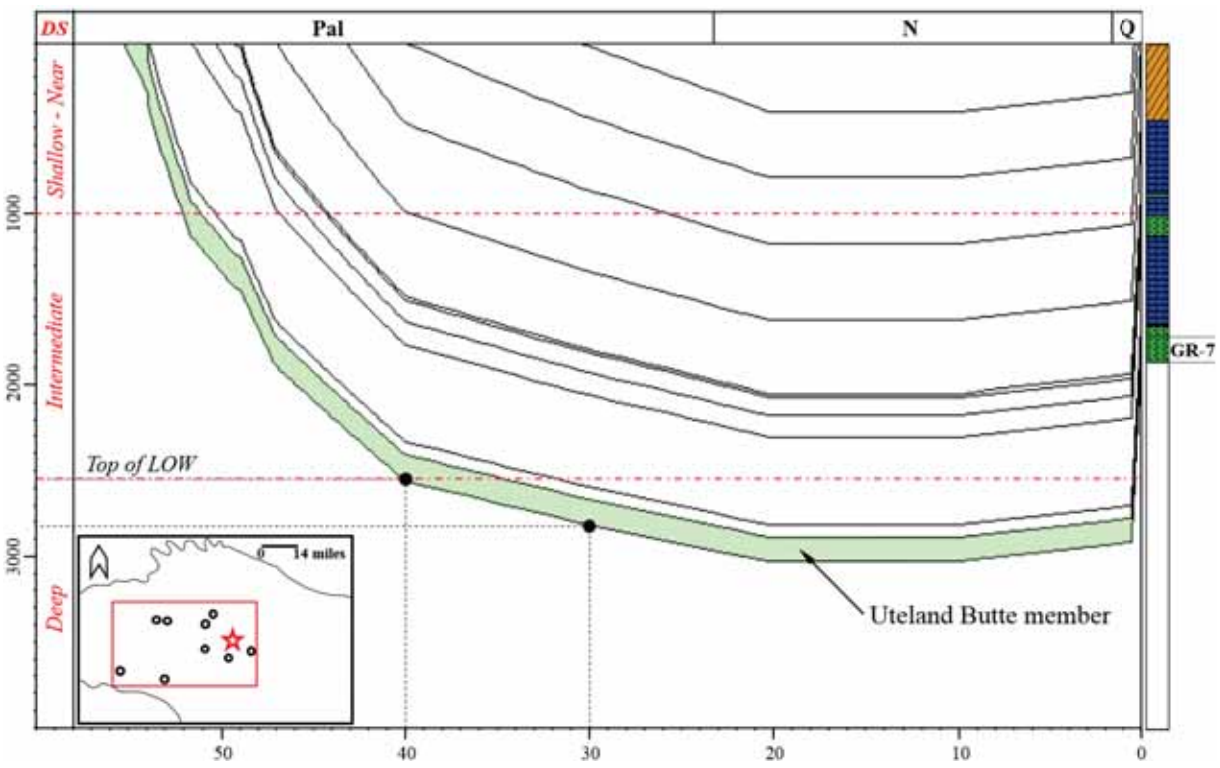

Figure 5.11: Burial curve of a synthetic well located within the study area (red star in the inset map) correlated with diagenetic environments as identified in this study (left column), modified from Schamel (2015); DS: Diagenetic settings (left column) based on Machel's (1999) diagenetic environments classification; Pal: Paleogene, N: Neogene, Q: Quaternary, LOW: Liquid oil window.

The burial curve (Figure 5.11) describes a high burial rate in the time interval from 55 to 40 Mya. Most of the identified diagenetic phases took place in the near-surface and shallow diagenetic settings from phase 1 up to phase 9 between the time of deposition at about 55 Mya and 52 Mya; all of them in the first three My of the deposition. Later on, phases 10 and 11 occurred in in the intermediate diagenetic setting between about 52 and 40 Mya. Thereafter, the burial rate decreased, as defined by reduction of the negative slope at 40 Mya, reaching the maximum burial depth around 3050 m at 20 Mya. Schamel (2015) estimated that the liquid oil window (phase 12) has passed between about 40 and 30 Mya (black dots in Figure 5.11). Oil

generation window defines the intermediate – deep diagenetic settings boundary (Machel, 1999) located around 2550 and 2850 m; followed by an extended period of no additional burial, as described by the horizontal contours between 20 and 10 Mya. Uplift of the basin started at about 10 Mya with an abrupt slope change at around 0.5 Mya, likely generated by high erosion rates (Schamel, 2015).

5.2 Dolomite

5.2.1 Observations

This section presents petrographic characteristics obtained by means of scanning electron microscopy (SEM) and cathodoluminescence microscopy, as well as compositional data of the dolomite(s), such as Ca^{2+} content and cation ordering, stable isotope and elemental composition data.

5.2.1.1 Crystal shapes

Petrographic observation using a transmitted light microscope (Zeiss Jenapol Polarizing Microscope) was not able to offer sufficient detail because of the less than 10 μm crystal sizes of the dolomites. Therefore, scanning electron microscopy was used to characterized crystal shapes and size.

A dip cross-section was selected to identify variations dolomite textures from the nearshore areas toward the basin center (Figure 5.12), composed of wells N 6-28, UT 15-06, and PW 13-06. Three thin sections were selected for PZ1, four thin sections were selected for PZ1', and three thin sections were selected for PZ2. Thin sections were carbon coated to enhance image quality.

Dolomite layers PZ1, PZ1', and PZ2 display four dolomite textures: planar-e (Figure 5.13A), planar-s (Figure 5.13B), nonplanar-a (Figure 5.13C), and planar-c (Figure 5.13D). Intercrystal voids are present in planar-s and nonplanar-a dolomites, probably from dissolution of calcium carbonate cores in Phase 3 and/or Phase 8 (Table 5.1).

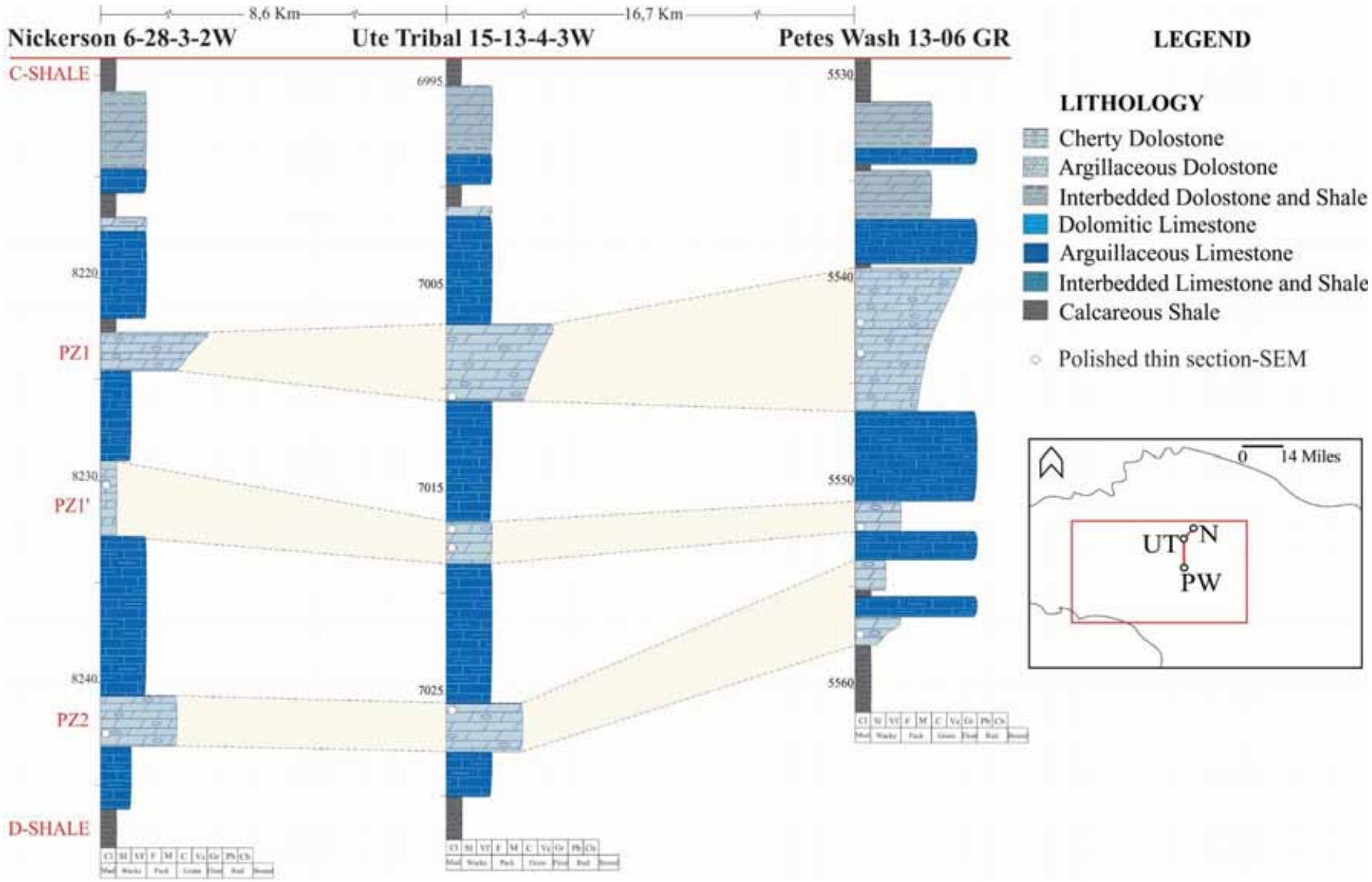

Figure 5.12: Stratigraphic correlation of PZ layers with location (depth) of selected polished thin section for layers PZ1, PZ1', and PZ2. In the inset map, N: Nickerson 6-28-3-2W, UT: Ute Tribal 15-13-4-3W, and PW 13-06 GR.

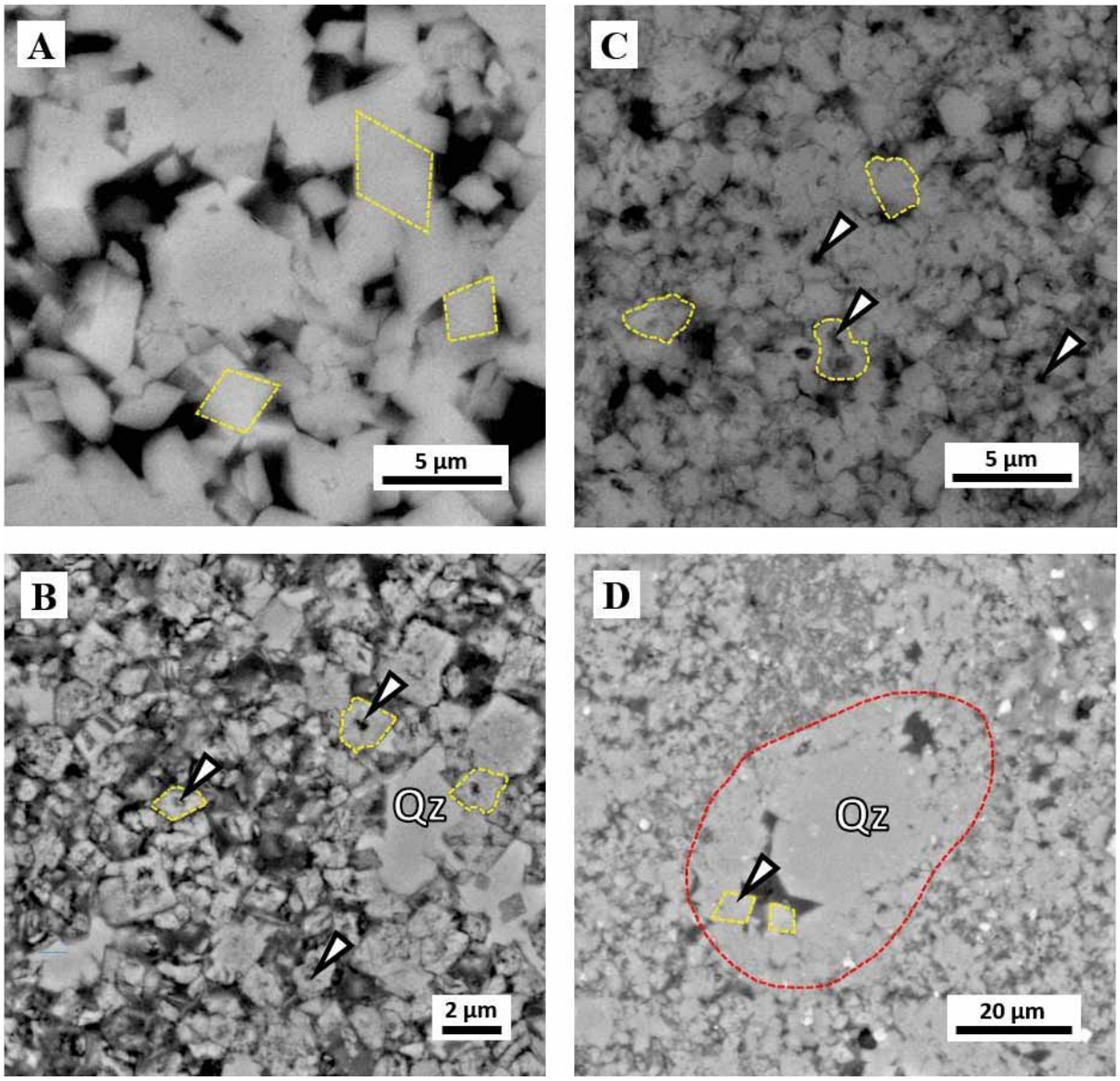

Figure 5.13: (A) SEM image of planar-e dolomite texture. Note the straight dolomite faces and well defined rhombohedral habit (yellow dashed lines); well: N 6-28, sample: 7, depth: 8230.2 ft. (B) SEM image of planar-s dolomite, some dolomite crystals have irregular faces (yellow dashed lines); holes within dolomite crystals (white arrows) were created by dissolution; post-dolomitization authigenic quartz (Qz) encases some dolomite crystals; well: PW 13-06, sample: 12, depth: 5557.4 ft. (C) SEM image of nonplanar-a dolomite, dolomite crystals have irregular and lobate crystal faces (yellow dashed outlines); internal holes in dolomite crystals (white arrows) created by dissolution; well: UT 15-13, sample: 11, depth: 7009.9 ft. (D) SEM image of planar-c dolomite; interparticle pore (likely an articulated ostracod shell, red dashed line) partially filled by dolomite cement (yellow dashed outlines) and authigenic quartz (Qz); well: N 6-28, sample: 9, depth: 8242.5 ft.

These textures display a distinctive distribution across the study area. For layer PZ1, planar-e dolomite is predominant in well PW 13-06 located nearshore, while nonplanar-a dolomite is more common in well UT 15-13 located in an intermediate zone. PZ1' consists entirely of planar-e dolomite in the near-shore area (Well PW 13-06) and near the basin center (Well N 6-28), while nonplanar-a and planar-s dominate at an intermediate zone. PZ2 layer presents a different pattern in which the most abundant texture is planar-s dolomite in all three locations (Figure 5.14).

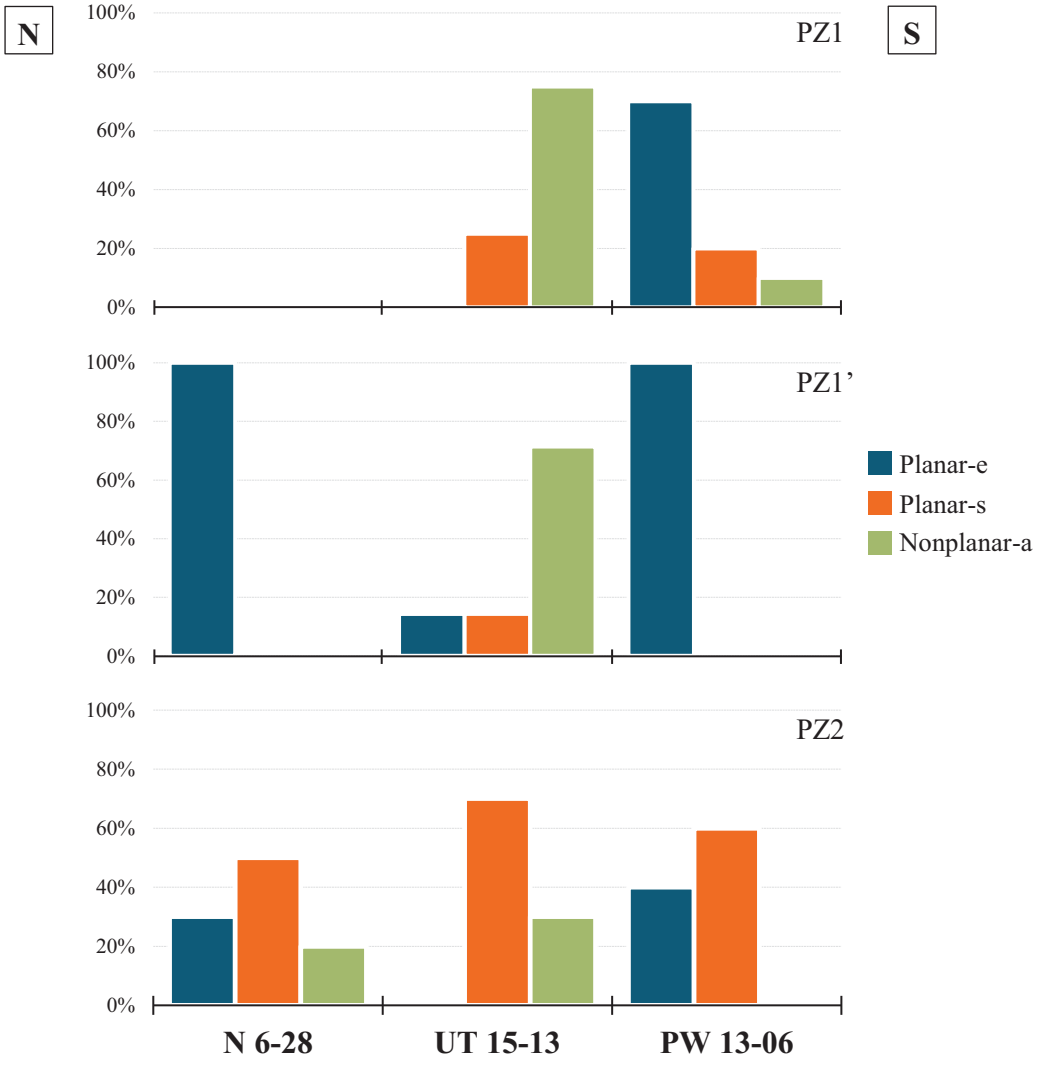

Figure 5.14: Distribution of dolomite textures for each PZ layer. N: North, S: South. The cross section is shown in Figure 5.12.

5.2.1.2 Crystal sizes

Identification of dolomite crystal sizes was based on the following steps: First, individual dolomite crystal size was measured according to crystal shape. For euhedral and subhedral crystals, two of the straight edges of the rhomb were measured. For anhedral crystals, the largest and shortest crystal diameter were measured. Secondly, the crystal sizes were grouped according to crystal size frequency distribution. Clustering dolomite crystal sizes using frequency distribution shape was inconclusive because the histograms do not show natural breaks (valleys). The Jenks natural breaks classification method was used because it minimizes the standard deviation of the selected group and maximizes the standard deviation between groups (Jenks, 1967).

As a result, three dolomite crystal populations emerged: population one (POP 1), ranging from 0.25 to 1.5 μm; population two (POP 2), ranging from 1.5 to 3.0 μm; and population three (POP 3), ranging from 3.0 to 6.0 μm. POP 1 is the most abundant with 53.7%, followed by POP 2 with 37.7%, and POP 3 with 8.6 % (Figure 5.15). These three dolomite populations are present in all measured samples in about the same relative proportion. The means and standard deviations of the measured crystals are summarized in Table 5.2, grouped by dolomite layer. The dolomite crystal size populations do not present any preferential distribution along the N-S cross-section of Figure 5.12.

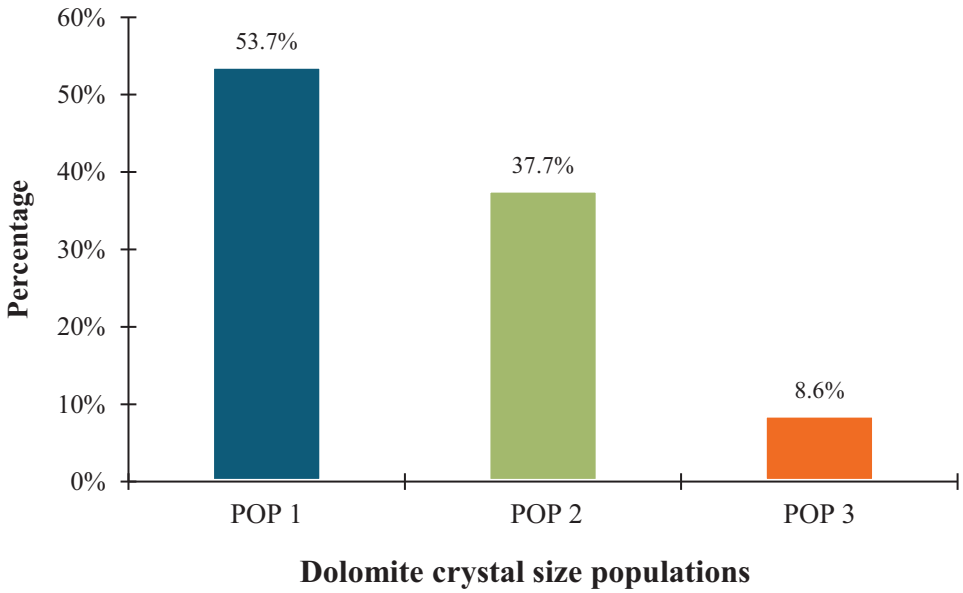

Figure 5.15: Percentage distribution of dolomite crystal size populations. POP 1: 0.25 µm to 1.5 µm, POP 2: 1.5 µm to 3.0, POP 3: 3.0 µm to 6.0 µm.

Well	Sample	Depth (ft)	Layer	Mean size (µm)	St.Dev (µm)	n
UT 15-13	11	7009.9	PZ1	1.3	0.67	193
PW 13-06	7	5541.9	PZ1	2.4	0.94	80
PW 13-06	8	5543.5	PZ1	2.2	0.98	86
N 6-28	7	8230.2	PZ1'	2.0	0.90	78
UT 15-13	12	7016.4	PZ1'	1.6	0.80	125
UT 15-13	13	7017.4	PZ1'	1.5	0.50	54
PW 13-06	11	5552.3	PZ1'	2.7	1.11	19
N 6-28	9	8242.5	PZ2	1.7	0.78	100
UT 15-13	14	7025.2	PZ2	1.4	0.65	128
PW 13-06	12	5557.4	PZ2	1.3	0.54	124

Table 5.2: Mean size and standard deviation (St.Dev) of dolomite crystals.

The dolomite crystal size distribution (CSD) shows a right-skewed distribution with major crystal size concentration around the lowest values (0.25 µm to 2.5 µm) and a tail located at the highest values (6 µm) (Figure 5.16). The peak around 0.25 µm to 2.5 µm is composed of POP 1 and POP 2, whereas the tail (3 µm to 6 µm) is composed mainly of POP3. All dolomite PZ layers display the same distribution.

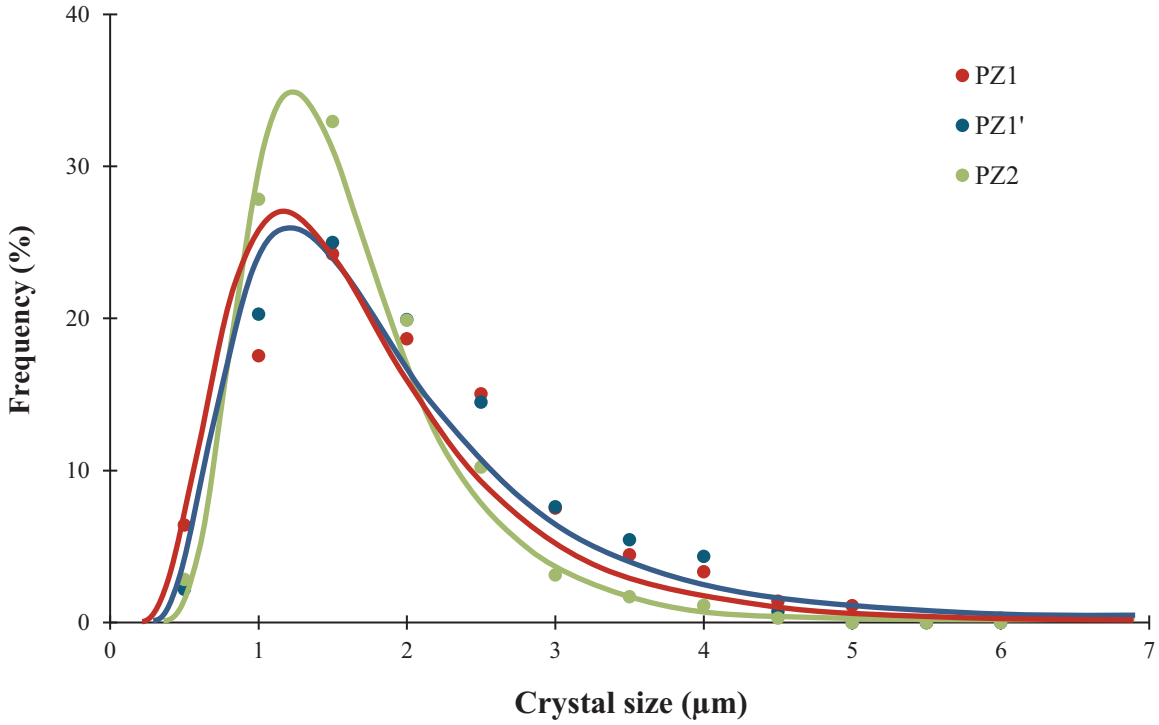

Figure 5.16: Dolomite crystal size distribution for each PZ layer. All PZ layers present a right-skewed and left tail distribution.

Validation of the right-skewed and left tail distribution was validated through the Anderson-Darling statistical test (Anderson and Darling, 1954), considering the normal distribution as the null hypothesis. In Figure 5.17A, the data (red dots) deviate from the normal probability (blue line), obtaining an AD (Anderson-Darling) value of 16.301. In contrast, in Figure 5.17B most of data (red dots) fit with the lognormal probability (blue line), with an AD

value of 1.617. Comparing AD values of both settings (A and B), the normal distribution has the highest AD value. In this case, the null hypothesis (CDS as normal distribution) is rejected. Dolomite CSD for PZ layers presents a better approach to a lognormal distribution.

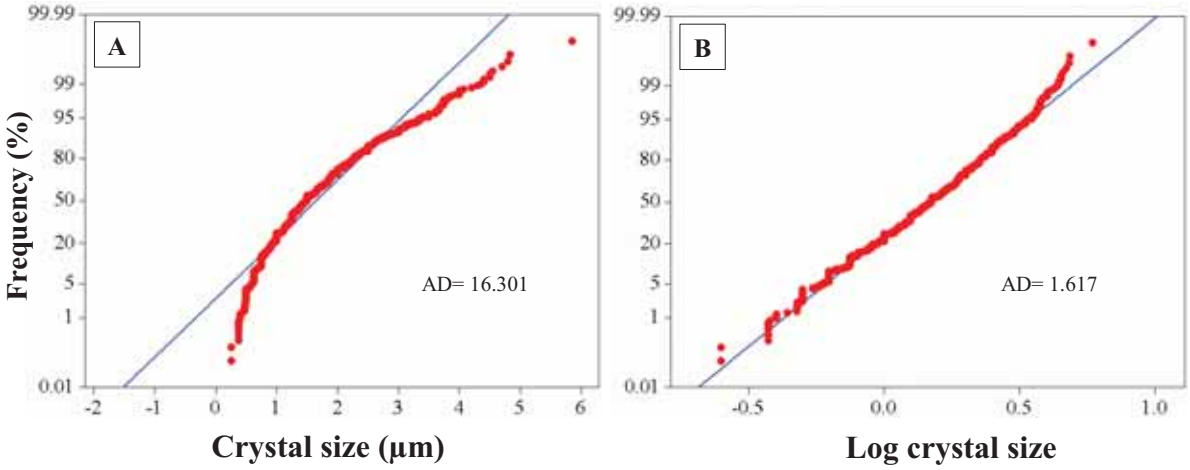

Figure 5.17: Validation of dolomite CSD: (A) Normal and (B) lognormal distributions. AD: Anderson-Darling value.

5.2.1.3 Cathodoluminescence

The electron beam excitation on the surface of dolomite crystals do not display any visible luminescence characteristics either through a microscope (Figure 5.18) or through the cathodoluminescence (CL) detector attached to the SEM.

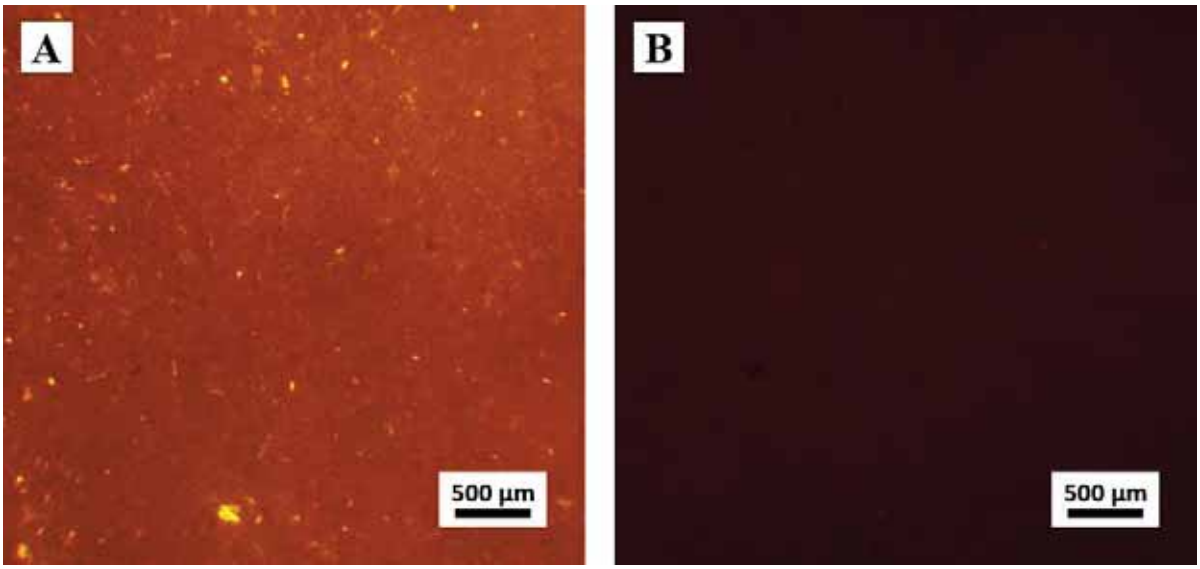

Figure 5.18: (A) Transmitted light Photomicrograph of dolomudstone at the base of PZ1 with dolomite crystals in matrix (dark red area); well: PW 13-06, sample: 10, depth: 5545.3 ft. (B) Cathodoluminescence Photomicrograph of the same area in (A) with no visible luminescence contrast.

5.2.1.4 Stoichiometry

Dolomite stoichiometry was identified by means of XRD and EMPA data. This section compares the dolomite calcium mole percentage from XRD, EMPA. The XRD data considered here is from Indiana University laboratories because it has the highest resolution. Comparison and discussion of XRD data from different laboratories is detailed in Appendix 4.

The high resolution diffractograms from Indiana University display three remarkable characteristics: (i) a d_{104} dolomite peak is displaced toward lower 2θ values relative to the ideal dolomite peak; (ii) the d_{104} dolomite peak is usually split into "subpeaks" with side humps (asymmetrical peak); and (iii) the d_{104} dolomite peak shows is rather broad (Figure 5.19). All dolomite samples run at Indiana University (14 samples) show the same or similar pattern. The other two labs do not resolve the split peaks and/or asymmetries but the means of the d104

peaks have been calibrated against those from the Indiana University (the same 20 samples were run in all three XRD labs, see Appendix 4).

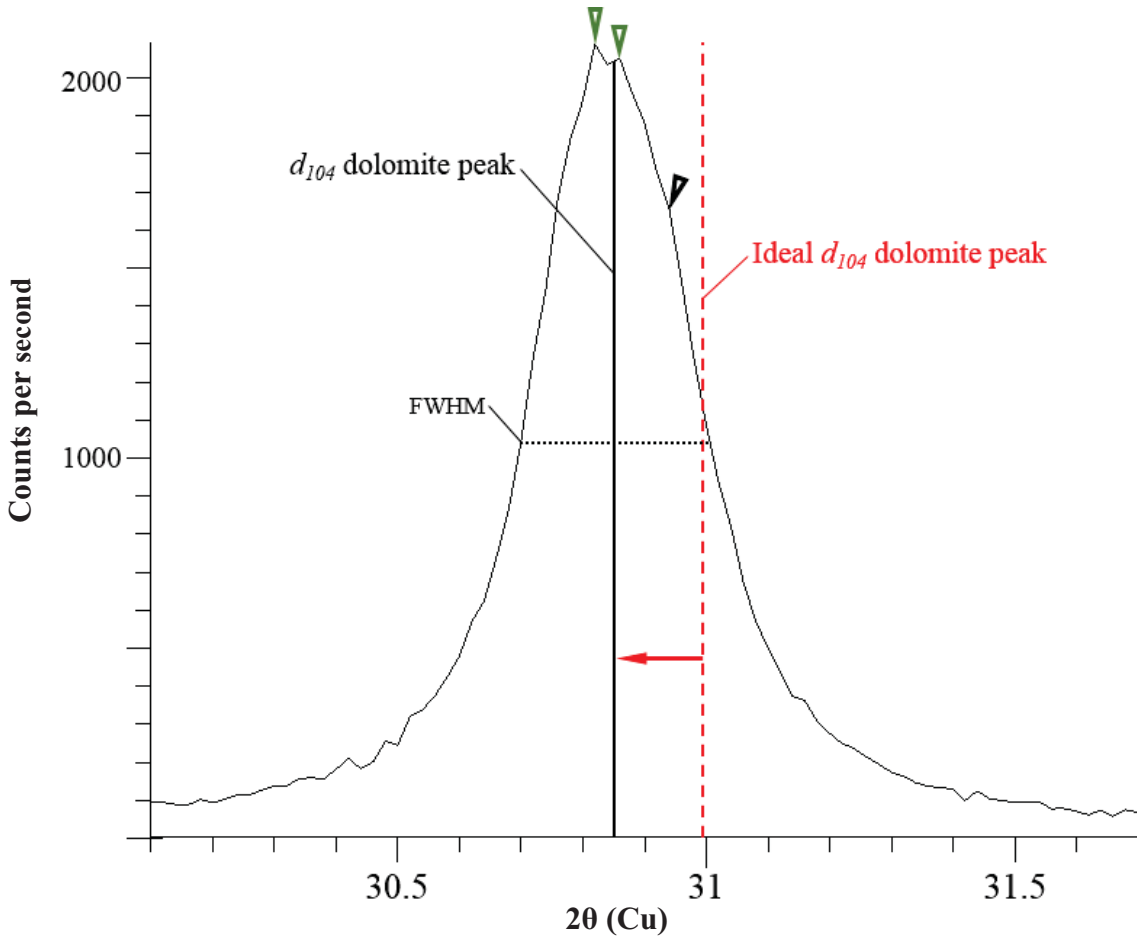

Figure 5.19: High-resolution diffractogram of the d_{104} dolomite peak that displays three remarkable characteristics: (i) d_{104} peak (30.86°2θ represented by vertical black line) shifted toward lower 2θ values (ideal dolomite d_{104} peak, red dashed line), in this particular sample = 0.13°2θ (left red arrow); (ii) split d_{104} peak (green arrows) and side humps (black arrow) that define an asymmetrical d_{104} reflection; and (iii) wide peak with a full width of half maximum intensity (FWHM) of 0.31°2θ, higher that the ideal dolomite [FWHM= 0.155°2θ for Eugui dolomite (Jones et al., 2001)]. Well PW 13-06, sample: 8, depth: 5543.5 ft. XRD diffractogram from Indiana University (Cukα radiation).

The observed XRD diffraction pattern could be related to: (i) iron substituting for magnesium, (ii) calcium substituting for magnesium, and/or (iii) different dolomite chemical populations (Kaczmarek and Sibley, 2011). Both Fe^{2+} and excess Ca^{2+} cations within the crystals lattice causes a shift of the d_{104} dolomite peak toward lower 2θ values.

The possibility of Fe^{2+} causing the observed broadening and/or the shifting of the d_{104} peak can be discounted in the basis of energy-dispersive X-ray spectroscopy (EDS), EMPA, and ICP-MS data (Appendix 3, 5, and 6 respectively), none of the which showed Fe^{2+} values higher than 1 %Fe (EDS = 0.2%, EMPA = 0.2%, ICP-MS = 0.9%; all values are arithmetic means). Hence, the observed patterns are interpreted as resulting from Ca^{2+} excesses. Furthermore, the split in the d_{104} dolomite peak is likely generated by at least two calcian dolomite populations (e.g., Jones et al., 2001).

The dolomite calcium mole percentage (%Ca_{Dol}) was calculated using the equation proposed by Lumsden (1979), in which there is a direct correlation between the Ca^{2+} mole percentage and the position of the d_{104} peak of dolomite crystals (Equation 1):

$$NCaCO_3 = 333.33 * d - 911.99 \quad \text{(Equation 1)}$$

where $NCaCO_3$ is the dolomite calcium content in mole percentage, and d is the d-spacing of the d_{104} peak, calculated using the Bragg law (Equation 2):

$$\text{Sin } \theta = \lambda/2d \quad \text{(Equation 2)}$$

where θ is the reflected angle, λ is the wavelength of Cu Kα radiation, and d is the spacing value between crystal lattices. Equation 2 in 1:

$$NCaCO_3 = [333.33 * (\lambda/2*\text{Sin } \theta)] - 911.99 \quad \text{(Equation 3)}$$

The resulting $\%Ca_{Dol}$ values for all samples analyzed are listed in Appendix 4. The calculated $\%Ca_{Dol}$ values, obtained using Lumsden's equation, are subject to errors as neither Equations 1 nor 3 consider other features that affect the d-spacing. These features include heterogeneous cation replacement that causes and estimated error between 1 to 2.5 $\%Ca_{Dol}$ (Reeder and Sheppard, 1984). However, the error could be even larger given the presence of several dolomite populations, each of them with a different $\%Ca_{Dol}$ composition (Reeder and Sheppard, 1984).

For the dolomites of the Uteland Butte member, an estimation of the $\%Ca_{Dol}$ error using the Lumsden equation was realized by comparing the $\%Ca_{Dol}$ values calculated from XRD data to the $\%Ca_{Dol}$ values measured from EMPA data (Table 5.3 and Figure 5.20). The EMPA $\%Ca_{Dol}$ values were taken as base of reference because (1) the precision and accuracy (0.4 to 0.5 $\%Ca_{Dol}$) is considerably smaller than the XRD data and (ii) EMP is capable to measure individual dolomite crystals. Previous to the measurement, the EMPA was calibrated against dolomite (internal) standard for Ca, Mg, Sr, Fe, and Mn. The calculated $\%Ca_{Dol}$ values from EMPA data were determined by the relationship between the Ca and Mg molar fraction as defined in Equation 4:

$$\%Ca_{Dol} = ({}^{m}Ca / ({}^{m}Ca + {}^{m}Mg)) \times 100 \quad \text{(Equation 4)}$$

where ^{m} is the molar fraction.

The frequency distribution of the EMPA data was plotted for each sample (Figure 5.20B). Each bin represents a different $\%Ca_{Dol}$ population (Bin in Table 5.3). The arithmetic mean of each bin was compared to the probable correlative $\%Ca_{Dol}$ population (from XRD data) represented by sub-peaks and humps recorded in each diffractogram (blue vertical lines in

Figure 5.20A). The calculated difference of $\%Ca_{Dol}$ (arithmetic mean) between EMPA and XRD (by mean of Lumsden (1979) equation] is 0.5 %Ca. As result, the difference between EMPA and XRD data from Indiana University laboratory is considered negligible.

This affirmation is additionally confirmed by the strong positive correlation (R^2=0.7) between the $\%Ca_{Dol}$ (EMPA data) versus the d_{104} spacing (calculated from XRD data using equation 2) (Figure 5.21). As result, the XRD data from Indiana University laboratory is considered the base of reference between the University of Alberta and Western Michigan University laboratories.

	XRD			**EMPA**			**Δ**
	Subpeak	d_{104} (2θ)	$\%Ca_{Dol}$	Bin	n	$\%Ca_{Dol}$	EMPA-XRD
6-28-7	P1	30.92	51.22	B4	48	52.6	1.4
	P2	30.88	52.43	B5	60	53.3	0.9
	P3	30.86	53.04	B6	4	54.3	1.3
15-13-14	P1	30.90	51.83	B3	8	51.7	-0.1
	P2	30.88	52.43	B4	28	52.5	0.1
	P3	30.84	53.65	B5	4	53.8	0.1
	P4	30.82	54.27	B7	1	55.8	1.5
13-06-8	P1	30.94	50.61	B2	1	50.9	0.3
	P2	30.90	51.83	B3	5	51.6	-0.2
	P3	30.85	53.35	B4	9	52.7	-0.6
	P4	30.82	54.27	B5	22	53.5	-0.7
	P5	30.78	55.49	B6	22	54.4	-1.1
	P6	30.75	56.41	B7	1	55.0	-1.4
13-06-11	P1	30.86	53.04	B7	6	55.5	2.5
	P2	30.82	54.27	B8	18	56.5	2.2
	P3	30.78	55.49	B9	22	57.5	2.0
	P4	30.74	56.72	B10	4	58.3	1.6

Table 5.3: Comparison of $\%Ca_{Dol}$ values obtained from XRD (Indiana University) and EMPA. The difference of the %Ca between XRD and EMPA (Δ) was calculated taking as base of reference the values from EMPA data. EMPA-XRD arithmetic mean = 0.5.

Figure 5.20

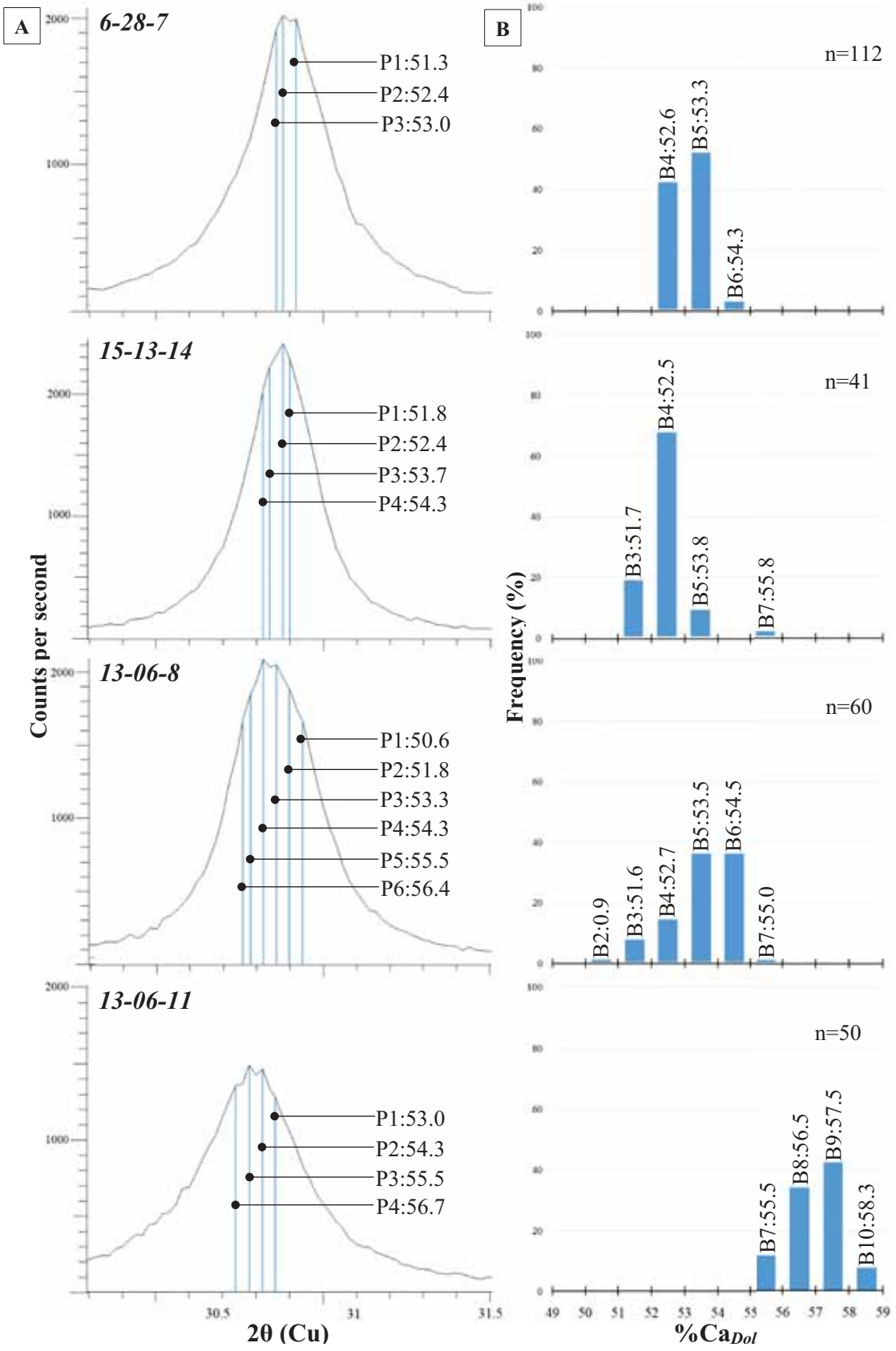
A
6-28-7
P1:51.3
P2:52.4
P3:53.0
15-13-14
P1:51.8
P2:52.4
P3:53.7
P4:54.3
13-06-8
P1:50.6
P2:51.8
P3:53.3
P4:54.3
P5:55.5
P6:56.4
13-06-11
P1:53.0
P2:54.3
P3:55.5
P4:56.7
Counts per second
2000
1000
30.5
31
31.5
2θ (Cu)
B
n=112
B4:52.6
B5:53.3
B6:54.3
n=41
B3:51.7
B4:52.5
B5:53.8
B7:55.8
n=60
B2:0.9
B3:51.6
B4:52.7
B5:53.5
B6:54.5
B7:55.0
n=50
B7:55.5
B8:56.5
B9:57.5
B10:58.3
Frequency (%)
100
80
60
40
20
0
49
50
51
52
53
54
55
56
57
58
59
%Ca$_{Dol}$

Figure 5.20: Graphic comparison between the %Ca$_{Dol}$ values calculated from (A) XRD data [using the Lumsden (1979) equation] and (B) EMPS data. (A) Diffractogram for each sample. All samples show a split d_{104} peak with one or several humps, each of them possibly representing a different %Ca$_{Dol}$ population with a unique d_{104} at different 2θ value. Each d_{104} "subpeak" is represented by a blue line. The calculated value of %Ca$_{Dol}$ for each inferred population is indicated at the right side of each d_{104} "subpeak". (B) %Ca$_{Dol}$ frequency distribution for each sample measured by EMPA. The %Ca$_{Dol}$ arithmetic mean for each population is indicated at the top of each bin.

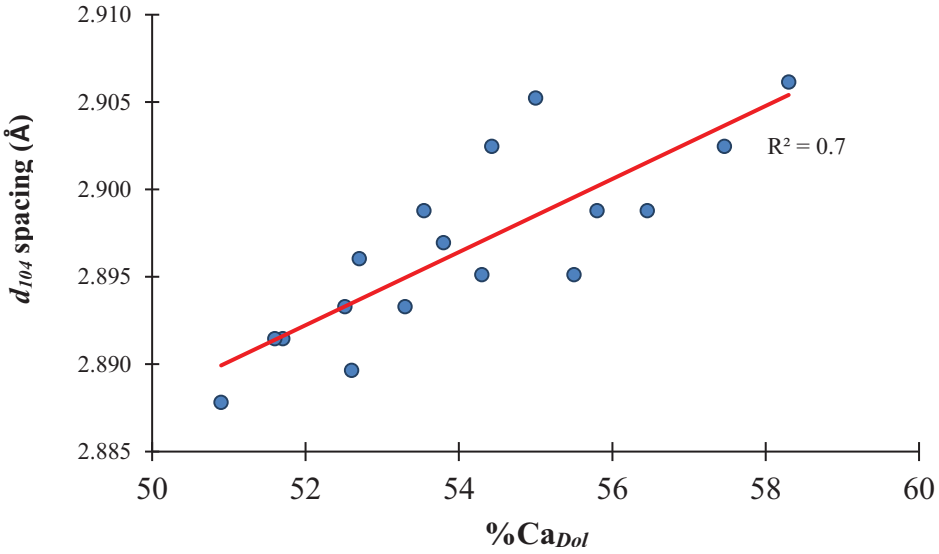

Figure 5.21: Correlation between d_{104} (vertical axis) calculated from XRD data and %Ca$_{Dol}$ (horizontal axis) calculated from EMPA data. Red line: linear regression.

The Uteland Butte dolomites display a wide range of %Ca$_{Dol}$, from 49% to 59%. The %Ca$_{Dol}$ distribution for each PZ layer is shown in Figure 5.22. Each dolomite layer displays a different frequency distribution. PZ1 has a multimodal %Ca$_{Dol}$ distribution with the near stoichiometric mode between 49 and 52 %Ca$_{Dol}$ (14%), followed by a strong mode between 53 and 55 %Ca$_{Dol}$ (83%), and a third mode between 58 and 59 %Ca$_{Dol}$ (3%). PZ1' displays a multimodal % Ca$_{Dol}$ distribution with three different modes: a near stoichiometric mode between 51 and 54 %Ca$_{Dol}$ (65%), a second mode between 55 and 56 %Ca$_{Dol}$ (23%), and a third

one between 57 and 58 %Ca_{Dol} (12%). In contrast, PZ2 describes a bimodal distribution with a broad mode between 51 and 55 %Ca_{Dol} (85%) and a second mode between 56 and 58 %Ca_{Dol} (15%) (Figure 5.22).

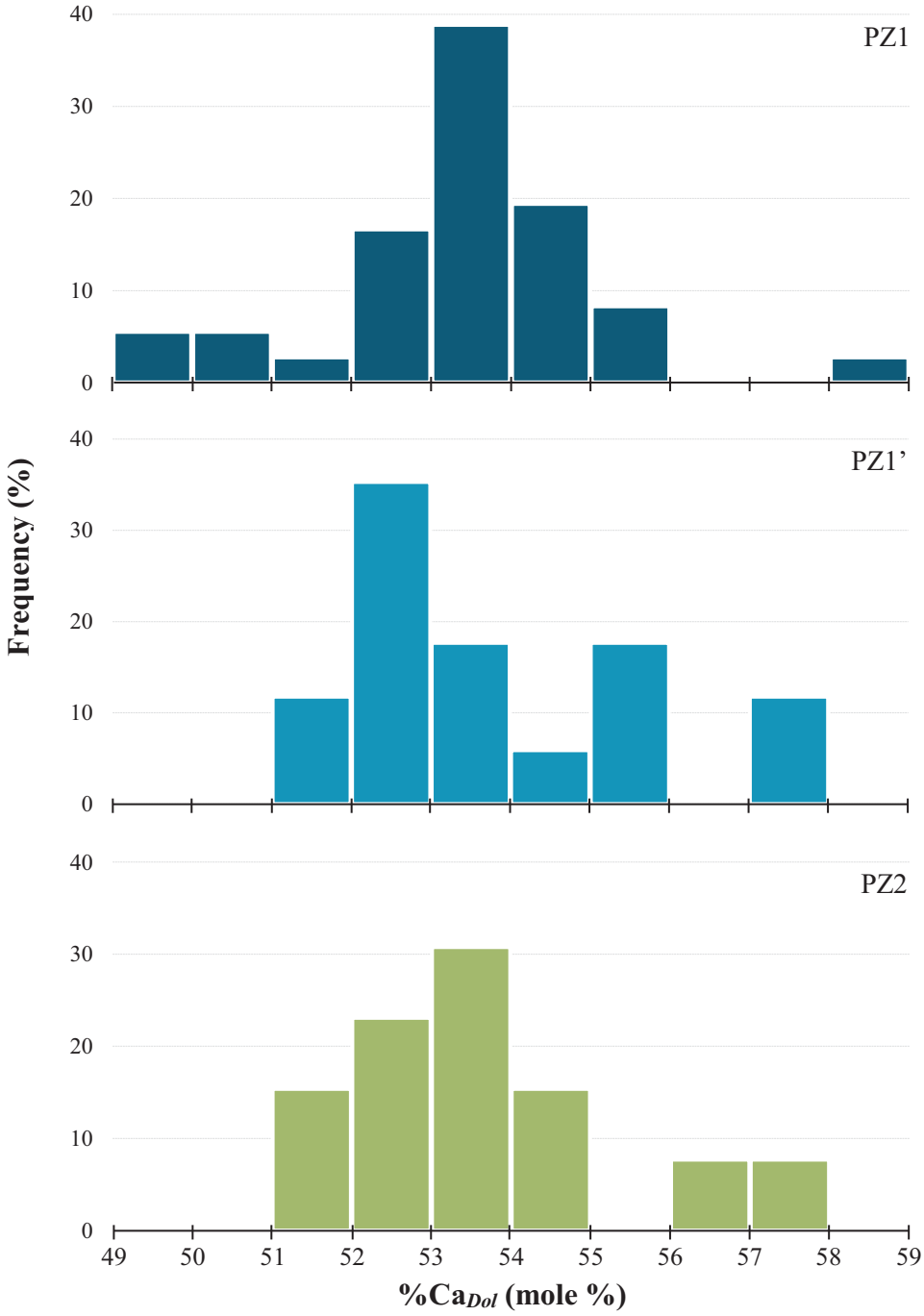

Figure 5.22: Frequency distribution of calcium mole percentage in dolomite crystals (%Ca_{Dol}) for each PZ layer. %Ca_{Dol} calculated by mean of the equation by Lumsden (1979).

Combining all data, the dolomites form two major populations: (i) Population 1 ($POP1_{\%Ca}$) varies in a wide range from 49 to 56 $\%Ca_{Dol}$, and (ii) Population 2 ($POP2_{\%Ca}$) ranges from 57 to 59 $\%Ca_{Dol}$ (Figure 5.23). $POP1_{\%Ca}$ contains 92% of all data. These dolomites are calcium-rich (or calcian) dolomites according to the Gregg et al. (2015) definition.

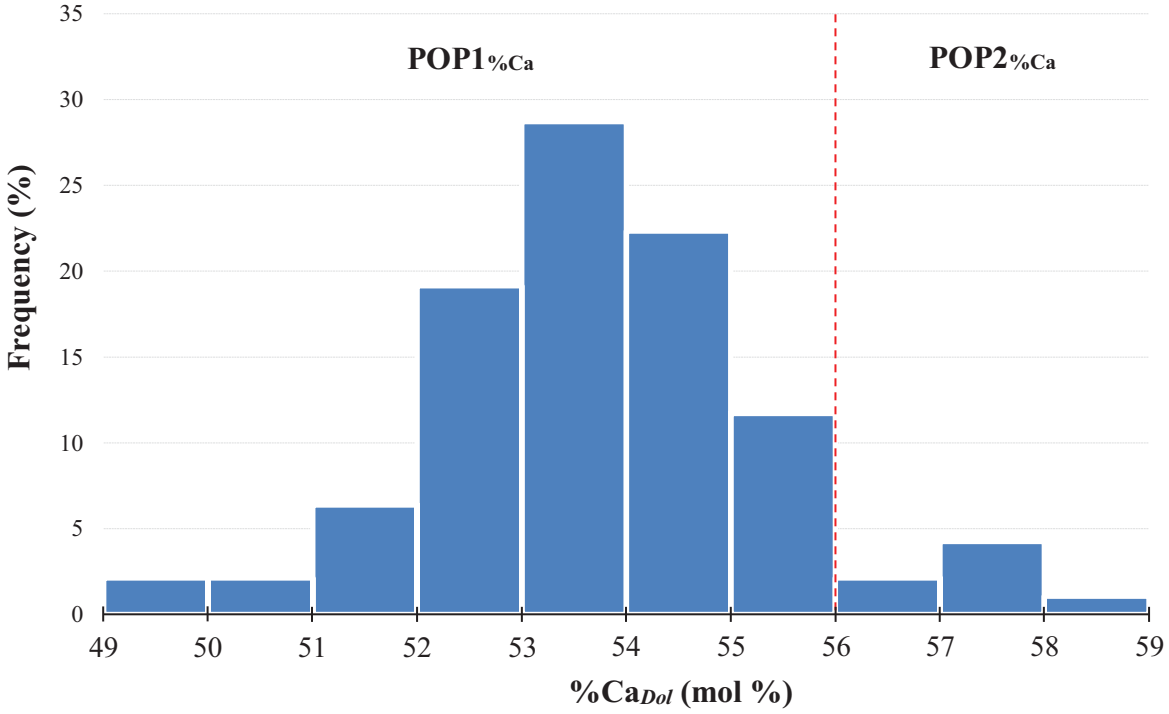

Figure 5.23: $\%Ca_{Dol}$ populations. $POP1_{\%Ca}$ fluctuates between 49 to 56.5 %Ca and $POP2_{\%Ca}$ fluctuates between 56.5 to 59 %Ca. $POP1_{\%Ca}$ is the most abundant (92%).

Calcium excess in dolomite crystals also displays a vertical trend in which the more stoichiometric dolomite are located preferentially at the tops pf the PZ layers, whereas the non-stoichiometric dolomite crystals are preferentially located at the bases of the PZ layers (Figure 5.24). This trend is remarkable in the PZ1 layer, well PW 13-06, in which there is a strong correlation between $\%Ca_{Dol}$ and depth (R^2=0.8) (Figure 5.25).

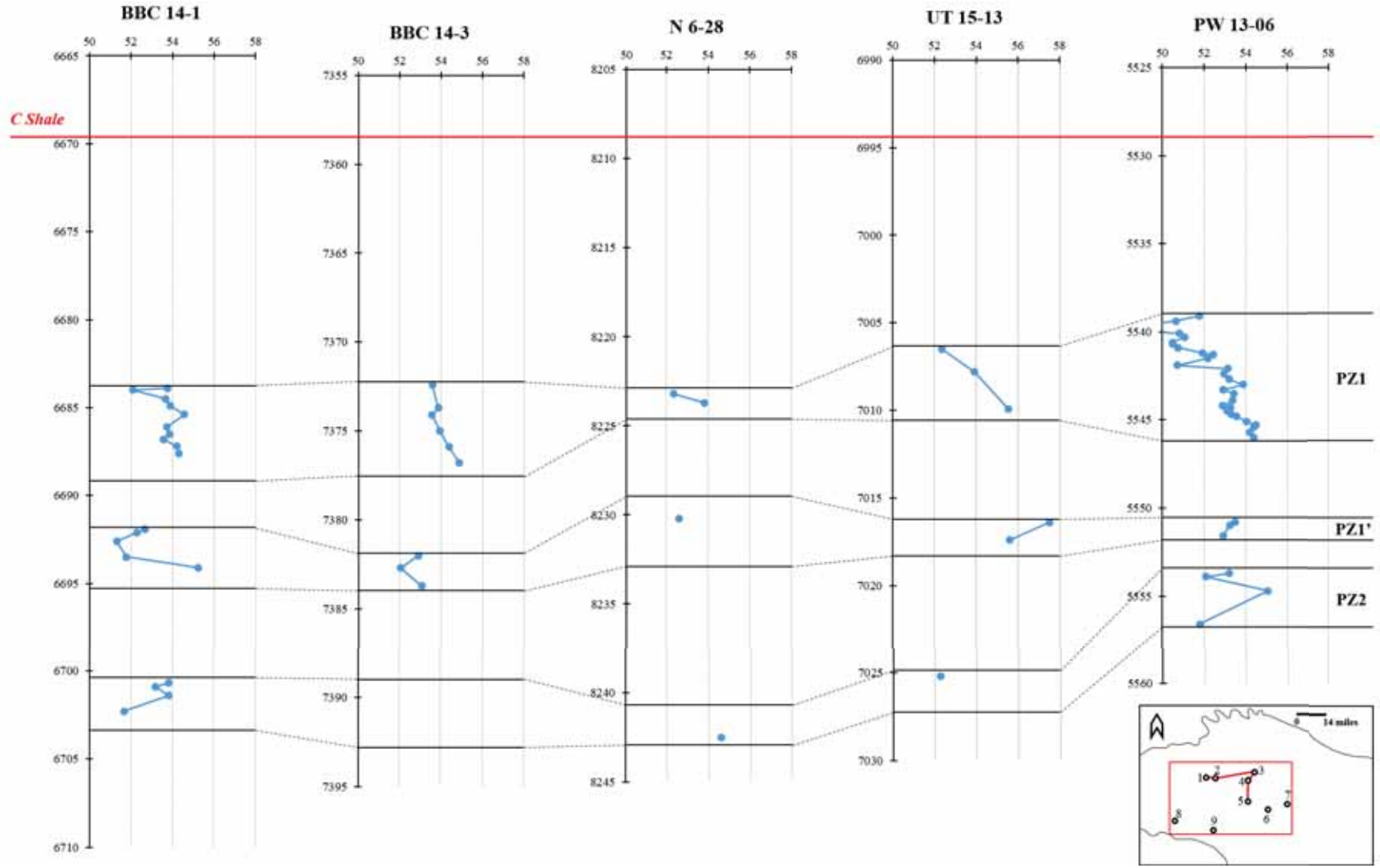

Figure 5.24: Dolomite stoichiometry variation in depth; horizontal axe: $\%Ca_{Dol}$ (%), vertical axe: depth (ft). See map inset for well locations; numbers in the inset map stand for wells/outcrops as 1: BBC 14-1, 2: BBC 14-3, 3: N 6-28, 4: UT 15-13, 5: PW 13-06, 6: DS 11-20, 7: UI 16, 8: WC, and 9: NMC.

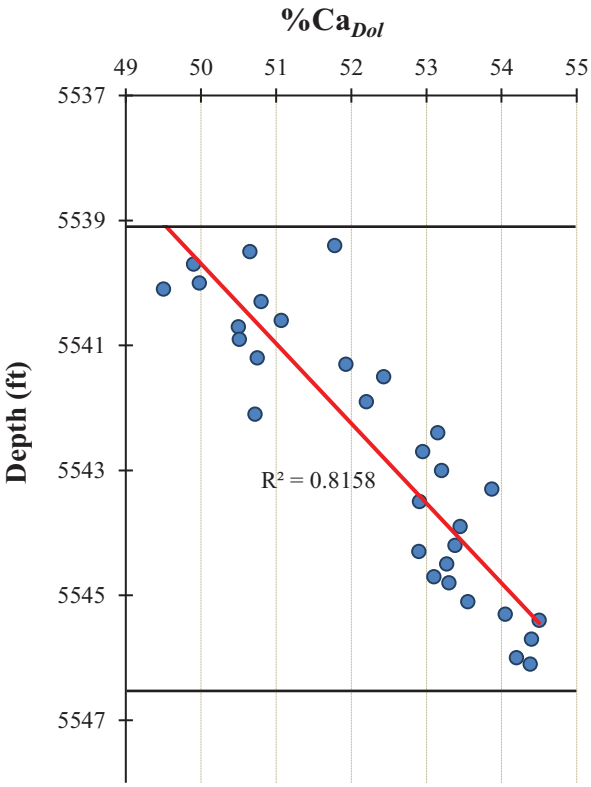

Figure 5.25: %Ca$_{Dol}$ variation with depth. Data for PZ1 layer, well PW 13-06. Black horizontal lines: top and base of the PZ layer, red line: linear regression.

5.2.1.5 Ordering

The XRD diffractogram also offers information on dolomite cation ordering characteristics. Goldsmith and Graf (1958) defined a calcium-magnesium bearing carbonate mineral as dolomite if the crystal displays d_{110}, d_{015}, and d_{021} ordering peaks relative to the 100% of d_{104} dolomite peak with relative intensities of 1.2% for the d_{110} peak, 9.6% for the d_{015} peak, and 6.3% for the d_{021} peak (Eugui dolomite values (www.rruff.info)]. The degree of cation ordering was calculated according to the Goldsmith and Graf's (1958) definition (d_{015} / d_{101}).

Intensities of d_{015} and d_{101} peaks were obtained from XRD data (Appendix 4). Dolomites are thus characterized by low cation ordering values varying from 0.1 to 0.5, with a

mean of 0.27 and standard deviation of 0.03 (Table 5.4). The dolomite cation ordering and $\%Ca_{Dol}$ relationship shows a trend, in which the highest cation ordering values (>0.3) are from nearly stoichiometric dolomites (49 to around 54 %Ca), whereas the lowest cation ordering values (0.1 to 0.3) are from calcium-rich dolomite (around 54 to 58 %Ca) (Figure 5.26).

		Ordering		
Well	**PZ**	**Mean**	**St.Dev**	**n**
BBC 14-1	PZ1	0.21	0.05	10
	PZ1'	0.34	0.06	5
	PZ2	0.28	0.06	4
BBC 14-3	PZ1	0.21	0.01	6
	PZ1'	0.25	0.03	3
N 6-28	PZ1	0.27	0.03	2
	PZ1'	0.30		1
	PZ2	0.24		1
UT 15-13	PZ1	0.29	0.08	3
	PZ1'	0.24		1
	PZ2	0.33		1
PW 13-06	PZ1	0.32	0.09	12
	PZ1'	0.25	0.03	3
	PZ2	0.33	0.03	3
DS 11-20	PZ1	0.27		1
	PZ1'	0.22		1
	PZ2	0.20		1
I16	PZ1	0.23	0.03	2
	PZ1'	0.27	0.00	2
	PZ2	0.24	0.04	2

Table 5.4: Cation ordering and $\%Ca_{Dol}$ by well and PZ layer (n = 64). Data from XRD.

Ordering also varies with depth in which the more ordered dolomites are located at the tops pf the PZ layers, whereas the disordered dolomites are preferentially located at the bases of the PZ layers. This trend is remarkable in the PZ1 layer, well PW 13-06, in which there is a strong correlation between ordering and depth (R^2=0.7) (Figure 5.27).

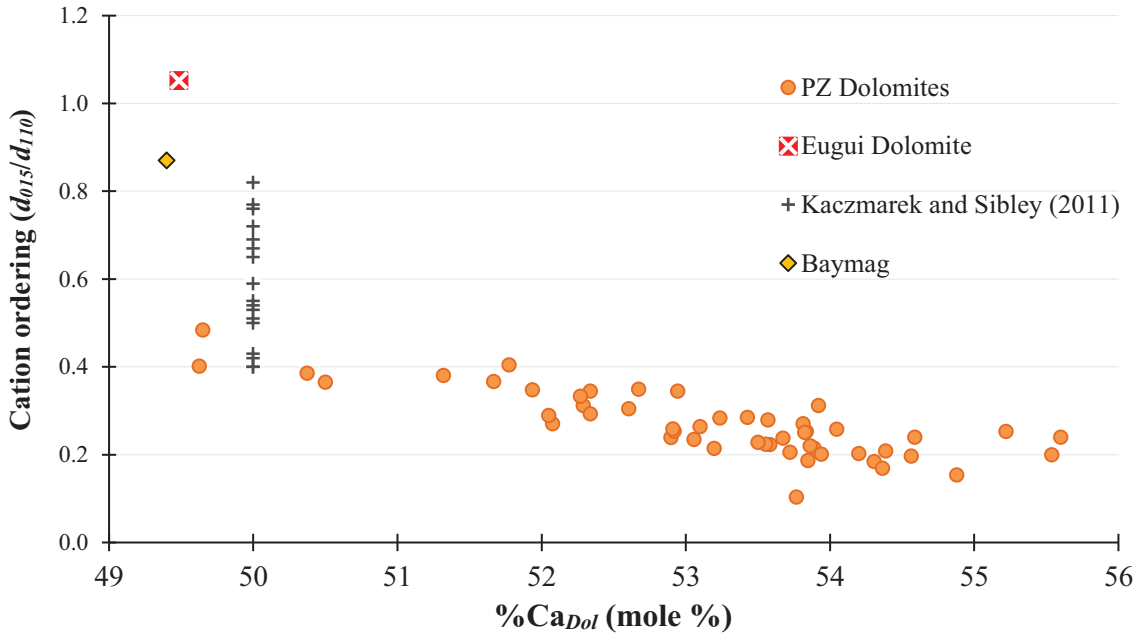

Figure 5.26: Correlation between cation ordering and %Ca$_{Dol}$ populations for all PZ layers combined. Baymag dolomite, synthetic dolomites (Kaczmarek and Sibley, 2011), and Eugui dolomite (www.rruff.info) values plotted as reference.

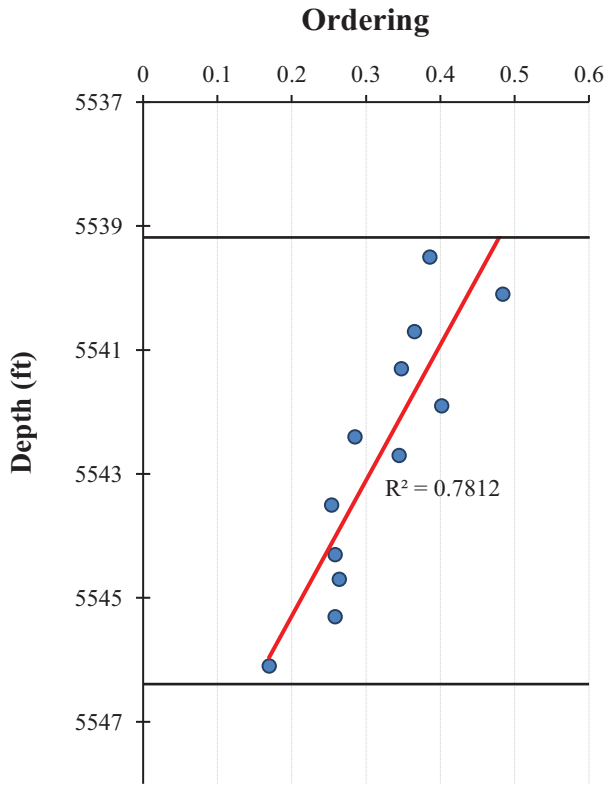

Figure 5.27: Ordering variation with depth. Data for PZ1 layer, well PW 13-06. Black horizontal lines: top and base of the PZ layer, red line: linear regression.

5.2.1.6 Conventional carbon and oxygen isotope data

The carbon and oxygen isotope values for all dolomite PZ layers (n = 39) display a wide spectrum. $\delta^{13}C$ of dolomite ($\delta^{13}C_{Dol}$) varies from 6.0‰ to -5.2‰ (VPDB), and $\delta^{18}O$ of dolomite ($\delta^{18}O_{Dol}$) varies from 0.9‰ to -10.4‰ relative to Vienna Pee Dee Belemnite (VPDB). In contrast, carbon and oxygen isotopic values for the selected limestone samples (n = 8) show smaller ranges: $\delta^{13}C$ of calcite ($\delta^{13}C_{Cal}$) varies from -1.0‰ to 1.0‰ (VPDB), and $\delta^{18}O$ of calcite ($\delta^{18}O_{Cal}$) varies from -10.1‰ to -5.8‰ (VPDB). Table 5.5 shows the summary of the isotopic composition for each dolomite layer and limestone samples.

		$\delta^{13}C$ (VPDB)			**$\delta^{18}O$ (VPDB)**		
Layer	Mineral	Values (‰)	Range	Mean	Values (‰)	Range	Mean
PZ1	Dolomite	-5.4 to 4.8	10.2	1.8	-7.3 to 0.9	8.2	-2.6
PZ1'	Dolomite	-3.3 to 5.2	8.5	1.5	-6.2 to 0.1	6.3	-2.9
PZ2	Dolomite	-1.1 to 6.0	7.1	1.3	-6.0 to -0.7	5.3	-3.4
Limestone	Calcite	-1.0 to 1.0	2.0	-0.3	-10.1 to -5.8	4.3	-7.7

Table 5.5: Isotopic signatures for PZ layers and interbedded limestone layers.

Assuming isotopic equilibrium, the broad $\delta^{13}C_{Dol}$ distribution can be separated in two groups: (i) a set of $\delta^{13}C_{Dol}$ values depleted by 1‰ to 6‰ relative to $\delta^{13}C_{Cal}$ (left arrow Figure 5.28), and (ii) a set of $\delta^{13}C_{Dol}$ values enriched by 1‰ to 6‰ relative to $\delta^{13}C_{Cal}$ (right arrow Figure 5.28).

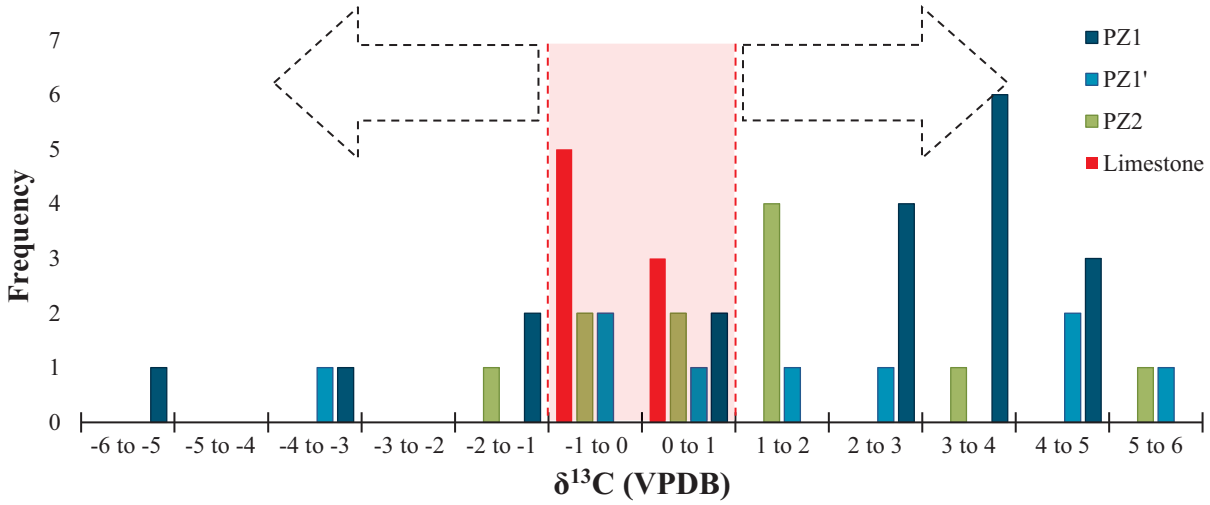

Figure 5.28: $\delta^{13}C$ frequency distribution for dolomites (all PZ dolomite layers) and calcites (interbedded limestones).

The $\delta^{18}O_{Dol}$ values are generally significantly less depleted than those from the limestones (Figure 5.29). Moreover, dolomites of PZ1 display the highest $\delta^{18}O_{Dol}$ mean value (-2.6‰ VPDB), whereas dolomites in PZ2 show the lowest $\delta^{18}O_{Dol}$ mean value (-3.4‰ VPDB). However, the $\delta^{18}O_{Dol}$ values range of the PZ1 is broader (8.2‰) than those from PZ2 (5. 3‰).

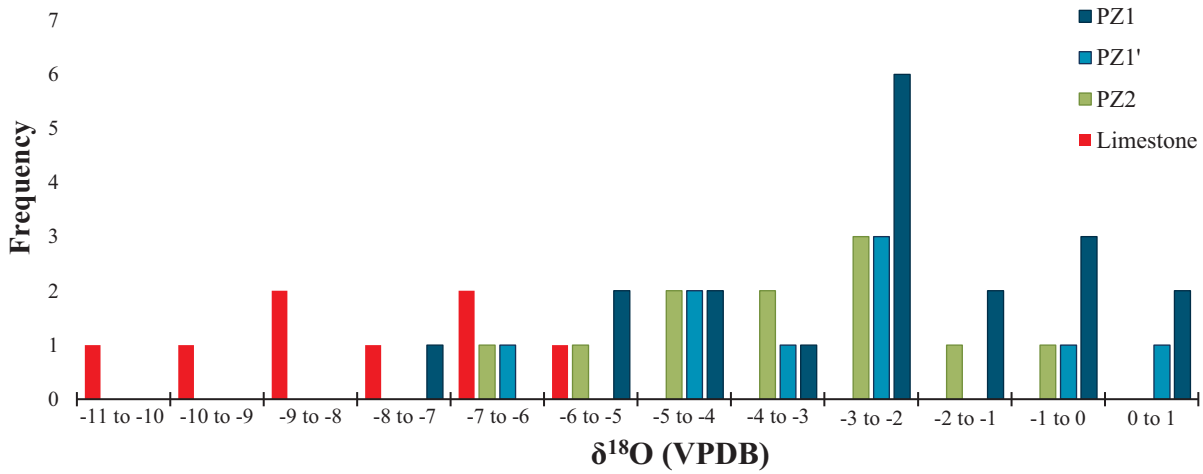

Figure 5.29: $\delta^{18}O$ frequency distribution of dolomite (all PZ dolomite layers) and calcite (interbedded limestone). $\delta^{18}O_{Dol}$ increment from parental $\delta^{18}O$ calcite between -5‰ and 1‰ (VPDB).

5.2.1.7 Clumped-isotopes thermometry

One method for determining the temperature of dolomitization is from the clumped-isotopes technique. The calculated temperature of formation for the dolomite samples varies from 59 to 30°C. Furthermore, the calculated temperature of formation for the calcite samples are higher that dolomite temperature and varies from 84 to 79 °C (Table 5.6).

Sample	Depth	Litho	PZ Layer	%Dol	$\delta^{13}C$ (VPDB)	$\delta^{18}O$ (VPDB)	Δ_{47}	T (°C)
13-06-5	5537.3	L		1.8%	-0.46 -0.51	-9.74 -9.77	0.555	79
13-06-7	5541.9	D	PZ1	100%	3.30 3.31 3.30	-4.54 -4.43 -4.37	0.679	30
13-06-12	5557.4	D	PZ2	100%	1.34	-4.60	0.599	59
6-28-1	8199.3	D		100%	0.55 0.58	-2.39 -2.36	0.609	55
6-28-7	8230.2	D	PZ1’	100%	4.57 4.56	-2.30 -2.22	0.627	48
6-28-8	8234.6	L		5.3%	0.72 0.72	-10.40 -10.36	0.545	84

Table 5.6: Calculated dolomitizing fluid temperature (T) for PZ layers in wells PW 13-06 and N 6-28. Litho: Lithology, L: Limestone, D: Dolostone, %Dol: Dolomite percentage in the carbonate fraction.

5.2.1.8 Elemental compositions

The major elements Ca and Mg and the trace elements Na, Al, Fe, Mn, Si, Zn, Sr, and Pb were measured in 43 dolomite samples (from dolostones) and seven calcite samples (from limestones). The Na, Al, Fe, Mn, Si, Zn, Sr, and Pb concentration values are presented graphically in Figure 5.30 and tabulated in Appendix 6.

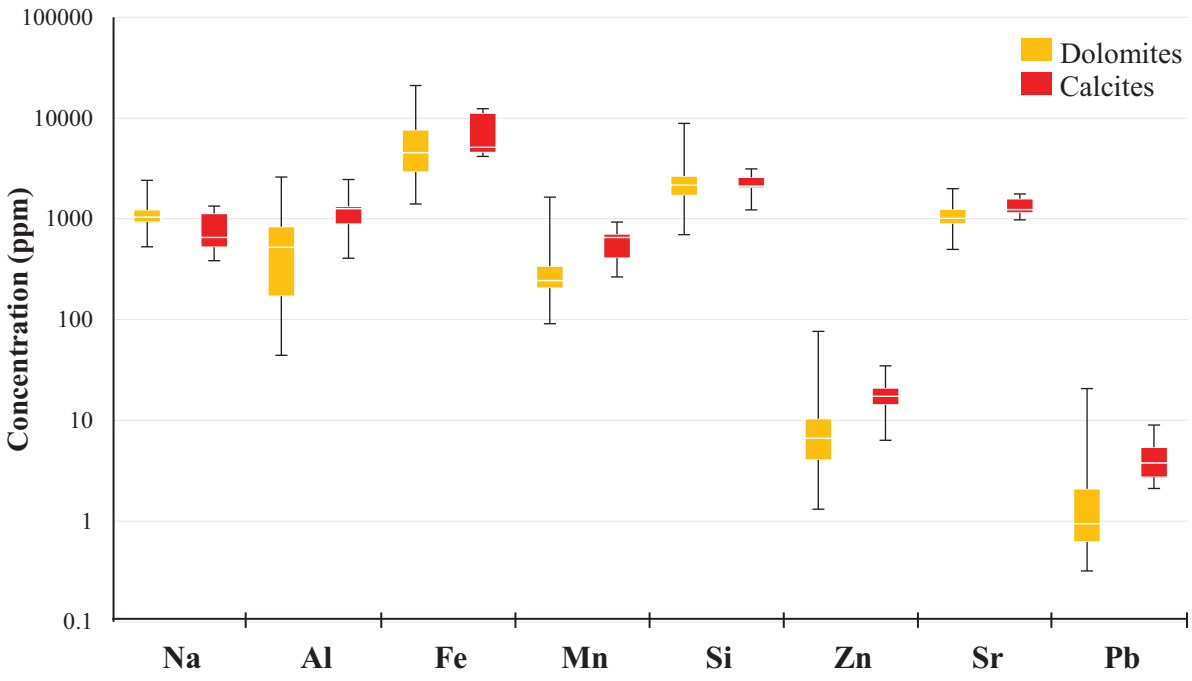

Figure 5.30: Elemental compositions of dolomites and calcites.

Sodium: Dolomites have higher Na values than calcites. Dolostones values range from 528 to 2412 ppm (average 1113 ppm), and calcite values range from 348 to 1338 ppm (average 812 ppm) (Figure 5.30). Furthermore, the higher Na values are located toward the near shore area (Figure 5.32A).

Strontium: Dolomites show lower Sr values than calcites. Dolomites values range from 497 to 1991 ppm (average 1092 ppm), and calcites values range from 977 to 1765 ppm (average 1348 ppm) (Figure 5.30). There is an Sr trend in which the highest values are located toward the centre of the basin in wells N 6-28, UT 15-13, and PW 13-06 (Figure 5.32B).

Iron: Dolomites have lower Fe values than calcites. Dolostones values range from 1404 to 21044 ppm (average 5861 ppm), and calcites values range from 4162 to 12397 ppm

(average 7598 ppm) (Figure 5.30). There is no discernible geographical distribution for Fe (Figure 5.32C).

Manganese: Dolomites have lower Mn values than calcites. Dolomites values range from 91 to 1642 ppm (average 322 ppm), and calcite values range from 265 to 929 ppm (average 583 ppm) (Figure 5.30). There is no discernible geographical distribution for Fe (Figure 5.32D).

Aluminium: Dolomites have relatively lower Al values than calcites. Dolomites values range from 44 to 2599 ppm (average 664 ppm), and calcite values range from 407 to 2456 ppm (average 1224 ppm) (Figure 5.30). Furthermore, there is an Al trend in which the higher values are located toward the near shore area (Figure 5.33A).

Silicon: Dolomites have around the same Si values as calcites. Dolomites values range from 697 to 8856 ppm (average 2475 ppm), and calcites values range from 1227 to 3131 ppm (average 2241 ppm) (Figure 5.30). There is no discernible geographical distribution for Si (Figure 5.33B).

Zinc: Dolomites show lower Zn values than calcites. Dolomites values range from 1.3 to 76.4 ppm (average 12.09 ppm), and calcites values range from 6.3 to 34.8 ppm (average 18.4 ppm) (Figure 5.30). There is no discernible geographical distribution for Zn (Figure 5.33C).

Lead: Dolomites show lower Pb values than calcites. Dolomites values range from 0.32 to 20.67 ppm (average 2.12 ppm), and calcites values range from 2.11 to 8.98 ppm (average 4.45 ppm) for calcite (Figure 5.30). There is no discernible geographical distribution for Zn (Figure 5.33D).

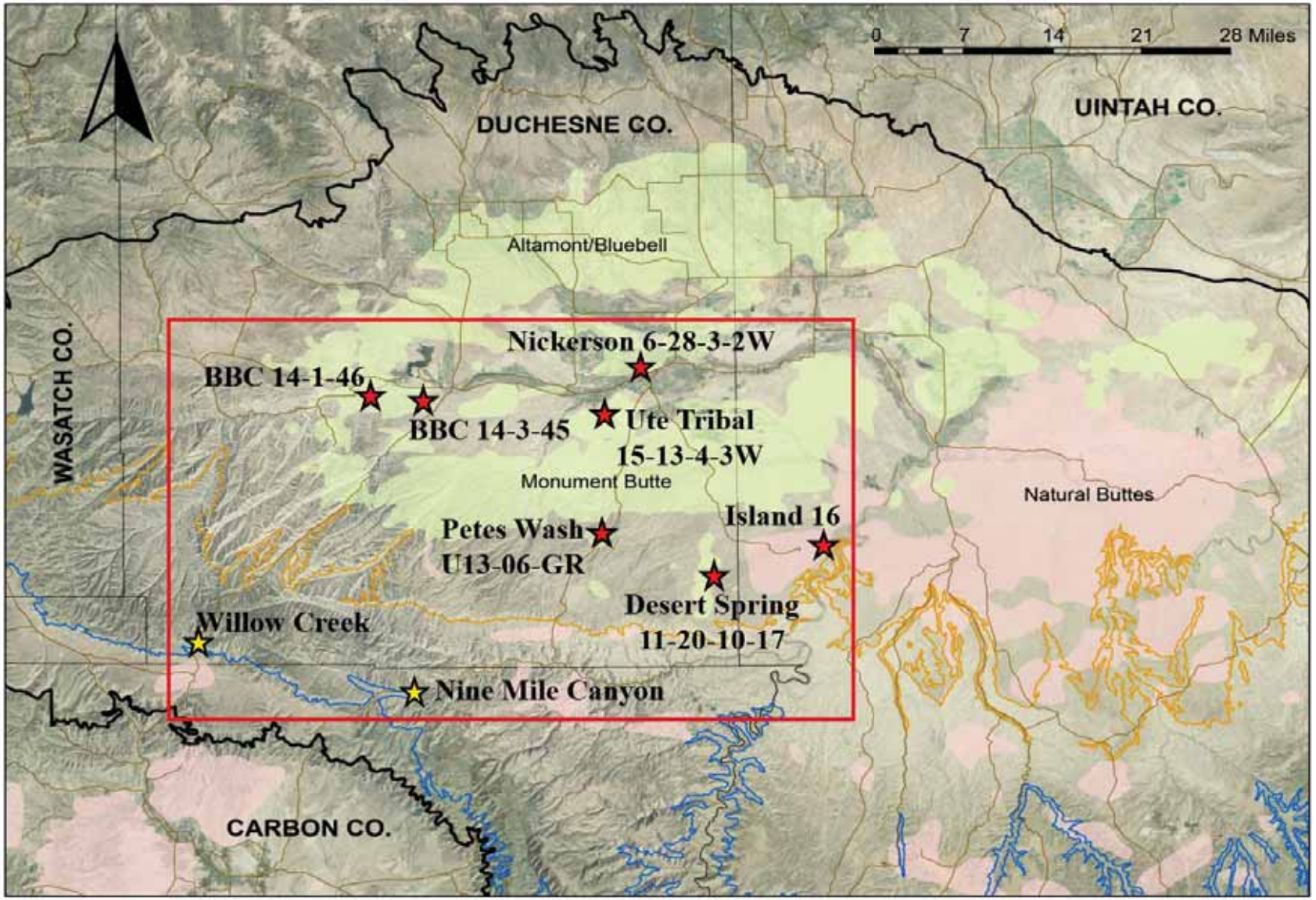

Figure 5.31: Location map of well and outcrops. Image modified from Vanden Berg, et al. (2014).

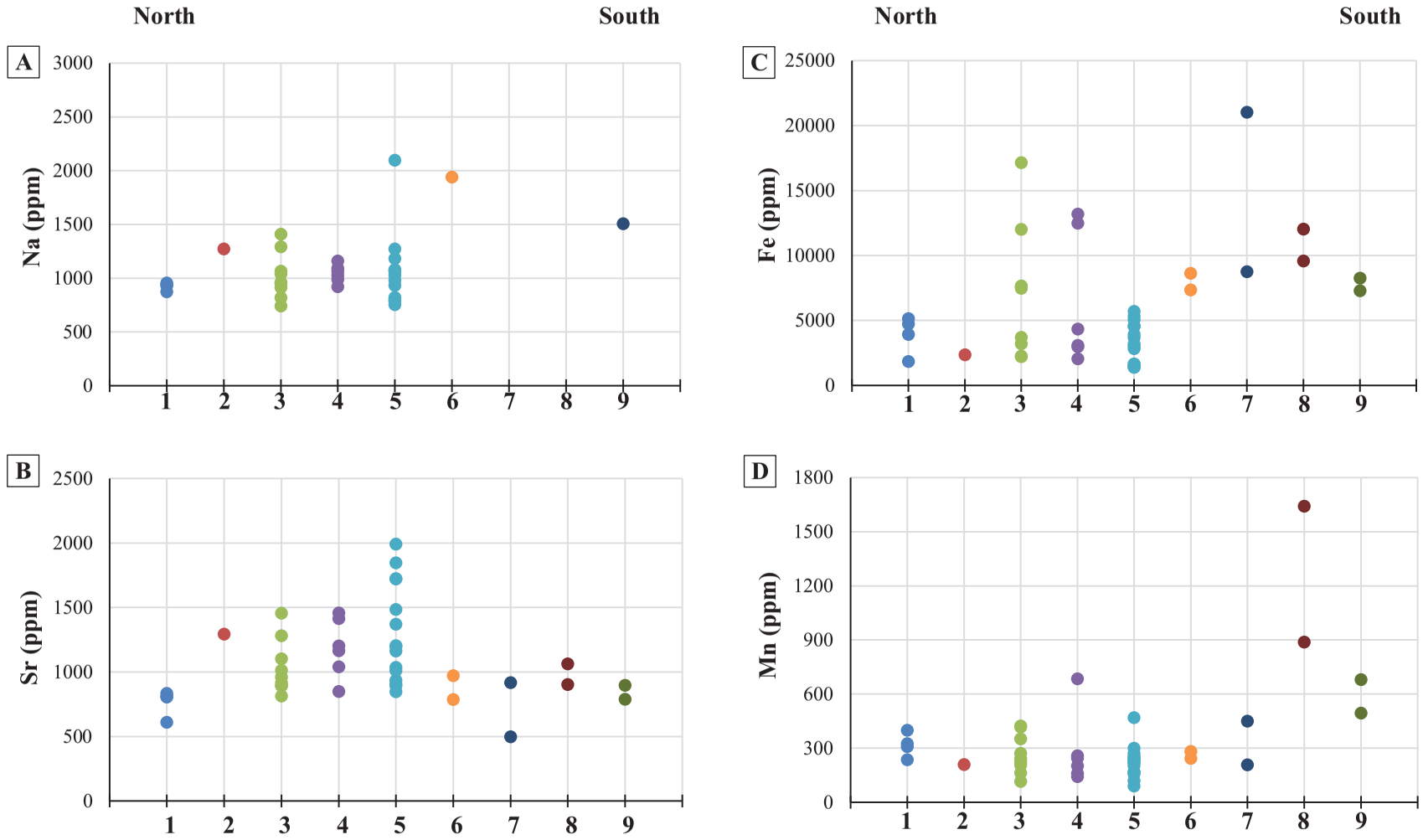

Figure 5.32: Na, Sr, Fe, and Mn concentration in dolomites and geographical distribution. Numbers in the horizontal axis represent wells and outcrops data; 1: BBC 14-1, 2: BBC 14-3, 3: N 6-28; 4: UT 15-13; 5: PW 13-06; 6: DS 11-20; 7: I 16; 8: NMC; 9: WC. For wells/outcrops locations, see Figure 5.31.

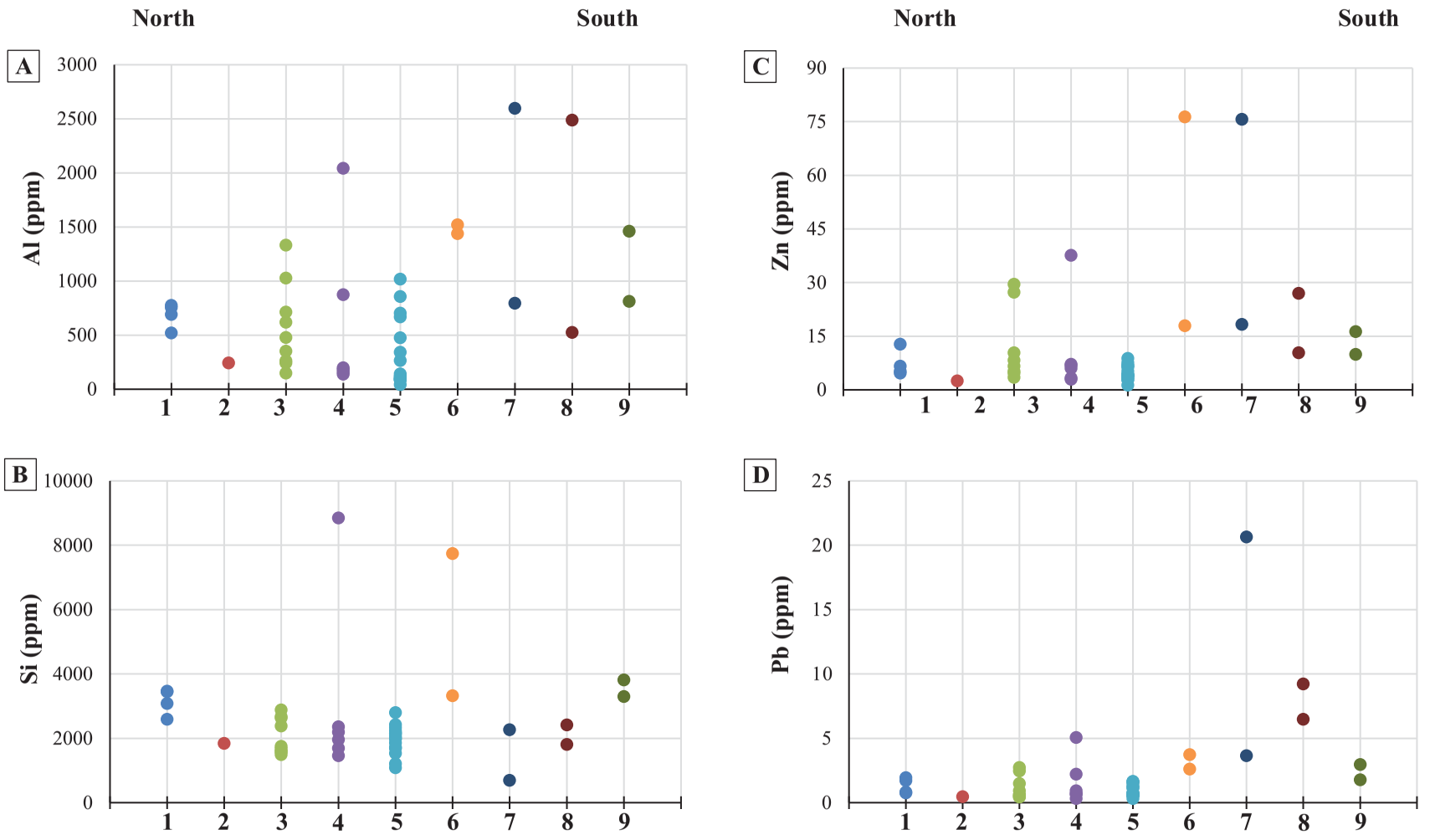

Figure 5.33: Al, Si, Zn, and Pb concentration in dolomites and geographical distribution. Numbers in horizontal axis represent wells and outcrops data; 1: BBC 14-1, 2: BBC 14-3, 3: N 6-28; 4: UT 15-13; 5: PW 13-06; 6: DS 11-20; 7: I 16; 8: NMC; 9: WC. For wells/outcrops locations, see Figure 5.31.

5.2.2 Interpretations

5.2.2.1 Crystal shapes

Proper identification of dolomite texture and crystal size is very important for making interpretations about dolomitizing fluid characteristics (Machel, 2004; Warren, 2000; Sibley and Gregg, 1987; Gregg and Sibley, 1984). The coexistence of planar-e, planar-s, and nonplanar-a textures suggests either a variation over time in the composition of the dolomitizing fluid (Sibley and Gregg, 1987), or a different dolomitization phases, each from different fluid (Sibley and Gregg, 1987; Machel 2004), or inheritance of crystal size variations from the lime(stone) precursors.

Sibley and Gregg (1987) recognized that the dolomite crystal shapes correlate with supersaturation of dolomitizing fluids with the temperature of dolomitization. Straight crystal faces in planar-e dolomite commonly tend to develop at "low supersaturation and/or low temperatures" (Sibley and Gregg, 1987, p. 968). In contrast, nonplanar-a textures tend develop from highly supersaturated fluids and/or at "high" temperatures (Sibley and Gregg, 1987), for example, at temperatures higher than the so-called "critical roughening temperature", which is around 50 to 100 °C for dolomite (Sibley and Gregg, 1987).

Regional distribution of dolomite textures (planar-s, nonplanar-a, and planar-e) (Figure 5.14), can be interpreted to be the result of geographic variations in the chemical composition of the dolomitizing fluid. In nearshore areas, the fluid composition may has been only slightly supersaturated developing mainly planar-e textures, whereas in the intermediate zone between the nearshore and basin center areas the dolomitizing fluid was probably more highly

concentrated, thus creating planar-s textures. However, more data must be acquired to confirm this interpretation.

5.2.2.2 Crystal size

Dolomite crystal sizes and populations offer important information about the history of diagenesis related to dolomitization events or recrystallization. Dolomite crystal size populations may inherited or controlled by the crystal sizes of the precursor limestone, by recrystallization of metastable dolomite precursor mineral phases, or by different dolomitization events (Sibley and Gregg, 1987; Sibley et al., 1993; Machel, 2004).

The right-skewed dolomite crystal size distribution (Figure 5.16) probably was created by recrystallization, which involves an increase of crystal size (Gregg, and Shelton, 1989). Increment of crystal size can develop a right-skewed CSD for dolomite (Gregg et al., 1992; Sibley et al., 1983). This is likely the case of the dolomite in all PZ layers, in which the original crystal size was modified from small crystals size (POP1 and POP2) to larger crystals size (POP3).

5.2.2.3 Cathodoluminescence

According to Machel et al. (1991), luminescence in the carbonate minerals is the emission of light (photons) from certain elements (mainly Mn^{2+}, Rare Earth Elements, and Pb^{2+}). Photon emission is produced when an external source of energy (such as an electron beam) excites an electron, moving it toward a higher energetic band. When the exited electrons

lose energy, they return to lower energy levels and release energy difference as photons (Boggs and Krinsley, 2006).

The lack of luminescence in the dolomite crystals of this study can be attributed to either or both of the following:

(i) Low concentrations of activator Mn^{2+} and sensitizer Pb^{2+} elements (Machel, 1985; Machel and Burton, 1991; Machel, 2000) coupled with a high concentration of quencher Fe^{2+}. Machel (1995) indicates that luminescence is related to the activator-sensitizer and quenchers concentration ratio up to the point that high concentrations of Fe^{2+} (principal quencher) may constrain luminescence behaviour. To identify luminescence using a standard luminescence microscope, Machel (2000) suggests a minimum concentration of 10 to 20 ppm for Mn^{2+} coupled with a concentration of 150 ppm for Fe^{2+} (Mn/Fe = 0.1). A higher Fe^{2+} concentration creates a lower Mn/Fe ratio, which quenches luminescence. The Mn/Fe ratio was calculated from EMPA data with a value of 0.05, and from ICP-MS data with a value of 0.06. The low Mn/Fe ratio likely is the reason for the observed absence of cathodoluminescence.

(ii) A later recrystallization event that destroyed the initial activator-sensitizer and quenchers zonation (Machel, 2000).

5.2.2.4 Stoichiometry

Dolomite calcium percentages can be related to environments of dolomitization (Lumsden and Chimahusky, 1980; Searl, 1994; Gregg et al, 1992). In general, evaporitic settings correlate with nearly stoichiometric dolomites (50 - 52 $\%Ca_{Dol}$) and non-evaporitic

settings correlate with non-stoichiometric dolomites (55 - 56 $\%Ca_{Dol}$). However, a potential recrystallization event, which is probably reflected by the left-skewed CSD (Figure 5.16), might has altered the original $\%Ca_{Dol}$ chemical signature (Mazzullo, 1992; Machel, 1997; Gregg, et al., 2015) from non-stoichiometric dolomite ($POP2_{\%Ca}$) to nearly stoichiometric dolomite ($POP1_{\%Ca}$).

5.2.2.5 Ordering

Based on experimental data (synthetic dolomite), Kaczmarek and Sibley (2011) concluded that dolomite cation ordering and stoichiometry characteristics are related to parental fluid composition. They argue that the more supersaturated dolomitizing fluid is, the higher the Mg content in dolomite, despite variable dolomite cation ordering. Some of the synthetic dolomite crystals resulting from the Kaczmarek and Sibley experiments are plotted in Figure 5.24. These dolomite crystal series precipitated from supersaturated fluids (Mg/Ca molar ratio ≥1) with a wide range of cation ordering from about 0.4 to 0.8 (Figure 5.24).

Cation ordering values are relatively low (0.27 ±0.07) compared to those of ideal dolomite (~0.87 in Figure 5.24 for Baymag dolomite). According to Kaczmarek and Sibley (2011), the first replacement phase during dolomitization (very high magnesium calcite or protodolomite) invariable displays very low degree of cation ordering. If these metastable phases are allowed to recrystallize over time, they assume increasingly higher degrees of ordering (and lower Ca^{2+} excess). Hence, it is reasonably inferred that the observed ranges in cation ordering represents various “stages” of progressive recrystallization, which did not go to completion, except for the nearly stoichiometric $POP1_{\%Ca}$.

5.2.2.6 Conventional carbon and oxygen isotope data

Environmental interpretations are based on calcite (matrix) and dolomite isotopic composition relationships. For dolomite formation interpretations, the baseline of reference is the $\delta^{13}C$ and $\delta^{18}O$ values of calcite (matrix) of the limestone. This assumption is valid only if the calcite (matrix) in limestone did not undergo recrystallization.

$\delta^{13}C$ values of calcite ($\delta^{13}C_{Cal}$) are close to the Vienna Pee Dee Belemnite standard with a narrow variation (±1‰ PDB) (Figure 5.25). Assuming isotopic equilibrium, this value can be taken to represent the dissolved organic carbon of the lake water (DIC_W).

On the other hand, the $\delta^{13}C_{Dol}$ enrichment (from 1‰ to 6‰ PDB, Figure 5.25) is interpreted to have resulted from one or both of the following two processes:

(i) A $\delta^{13}C_{Dol}$ enrichment can be caused by high organic activity. In this process organisms preferentially take up ^{12}C, which increases the $\delta^{13}C$ values of the DIC_W. Consequently, dolomite formed in isotopic equilibrium with the lake water has elevated $\delta^{13}C_{Dol}$ values. This interpretation is supported by the total organic carbon (TOC) and S2 values in the dolomite PZ layers (Figure 5.30). In Well N 6-28, taken as representative of the other wells, there is a remarkable contrast between the limestone and dolomite PZ layers, in which the dolomite layers consistently have higher TOC and S2 values than the interbedded limestones. The dolomite layers reach the highest TOC values, expressed as wt% HC (see Figure 5.34).

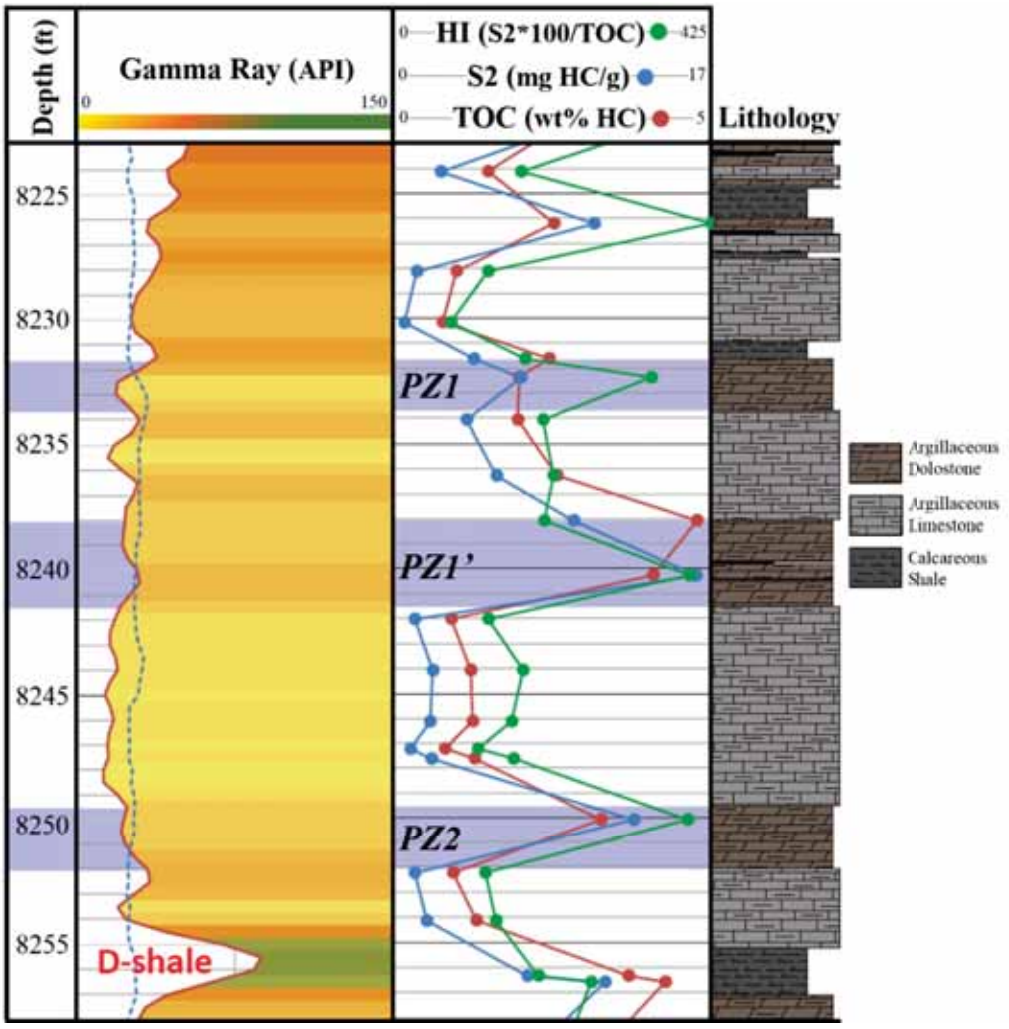

Figure 5.34: Total organic carbon (TOC) and S2 logs of well N 6-28. Dolomite PZ layers are highlighted in blue. Logs courtesy of Michael Vanden Berg, 2015.

(ii) Organic matter decay may also play an important role in the $\delta^{13}C_{Dol}$ enrichment. This process could be represented by Equation 5 (Irwin et al., 1977), in which the organic matter (acetate) is fermented to carbon dioxide and methane with a significant isotopic fractionation between the two products (e.g., Tucker and Wright, 1990).

$$CH_3COOH \rightarrow CO_2 + CH_4 \quad \text{(Equation 5)}$$

According to Irwing and Curtis (1977), acetate fermentation releases CO_2 with $\delta^{13}C$ values around +15‰ PDB, while the concomitantly formed CH_4 may have $\delta^{13}C$ values around -50‰ PDB. Consequently, dolomite formed in isotopic equilibrium with CO_2 from acetate fermentation may be significantly enriched in ^{13}C, whereby the amount of enrichment depends on the relative proportions of DIC_W and CO_2 from fermentation.

In contrast, six samples have $\delta^{13}C_{Dol}$ values significantly depleted relative to the calcite (Figure 5.28). This depletion is here interpreted as the result of organic matter oxidation as represented by Equations 6 and 7:

$$CH_4 + SO_4^{2-} \rightarrow HCO_3^- + HS^- + H_2O \quad \text{(Equation 6)}$$

$$2CH_2O + SO_4^{2-} \rightarrow H_2S + 2HCO_3^- \quad \text{(Equation 7)}$$

Biochemical methane (CH_4) oxidation, as represented by Equation 6 (Tucker and Wright, 1990) and carbohydrates ($2CH_2O$) oxidation by sulphate-reducing bacteria (Berner et al., 1985; Machel 2001) described by Equation 7 (Berner et al., 1985) leads to the simultaneous formation of ^{13}C-depleted carbonates (from the HCO_3^-) and pyrite (from the HS^-) (Figure 5.35), if Ca^{2+}, Mg^{2+} and Fe^{2+} are available. The carbohydrates oxidation process, products (Equation 7), and by-products are represented in Figure 5.35.

In either case (Equation 6 or 7), the source of oxygen is the dissolved sulfate (SO_4^{2-}) present in the lake water. Tuttle and Goldhaber (1993), working in the depocenter area of the Uinta Basin, suggested that sulfate anions were supplied by river input and derived from weathering of Jurassic marine evaporite minerals.

This interpretation is supported by the occurrence of framboidal pyrite crystals associated to the dolomite crystals (Figure 5.7F).

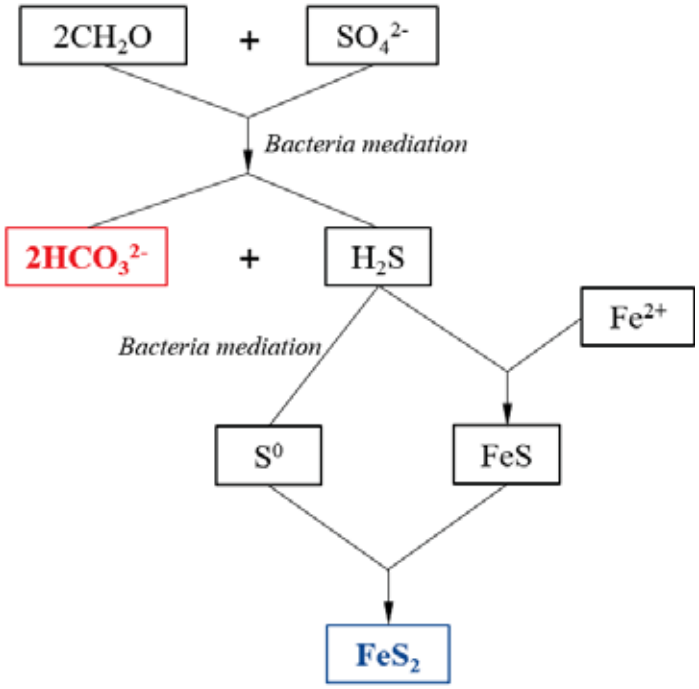

Figure 5.35: Idealized processes that may created low $\delta^{13}C$ values in dolomites: Oxidation of low $\delta^{13}C$ organic matter [-25 to -30‰ PDB (e.g., Tucker and Wright, 1990; Machel 2001)] created ^{13}C-depleted bicarbonate anions (red rectangle). Pyrite (blue rectangle) formed as by-product from the hydrogen sulfide and detrital iron (Fe^{2+} in lake water) reaction. Modified from Berner et al., 1985.

$\delta^{18}O$ values of dolomite ($\delta^{18}O_{Dol}$) can provide information concerning the temperature of dolomite formation, whereas $\delta^{13}C$ of dolomite can indicate meteoric water inflow with soil-derived CO_2, organic activity, organic matter degradation, and/or sulphate reduction (Tucker and Wright, 1990; Talbot and Kelts, 1990; Machel, 2004).

The low $\delta^{18}O_{Cal}$ values suggests that calcite crystallized in isotopic equilibrium from fresh lake water. This interpretation is supported by fossil associations presented in the limestone facies (F6). According to La Roque (1956), the pelecypod and gastropod fossils recorded at the base of the Green River Formation (correlated to the UBM) are fresh water mollusc species. Moreover, the wide range of the $\delta^{18}O_{Cal}$ values (from -10.1 to -5.8‰ VPDB,

mean: -7.7‰, range: 4.3‰) suggests fluctuations on fluvial inflow rates, variable degrees of rock-water interaction, or variable temperature during subsequent burial recrystallization, or a combination of all three processes/factors.

MacGinite (1969) described the fossil floral record in the Green River Formation and calculated the average temperature for the coldest months as 12 °C, with a minimum temperatures of about 3 °C. Assuming lake water temperatures from 3 °C to 12°C and precipitation in isotopic equilibrium, the oxygen isotopic composition of the lake water ($\delta^{18}O_W$) might have fluctuated between -13.13‰ and -6.38‰ SMOW (Standard Mean Oceanic Water) (Table 5.7), with an arithmetic mean of -9.55 ±1.9‰.

Well	Sample	$\delta^{18}O_{Cal}$ (PDB)	$\delta^{18}O_W$ @ 3°C (SMOW)	$\delta^{18}O_W$ @ 12°C (SMOW)
BBC 14-1	14-1-19	-9.28	-12.27	-10.00
N 6-28	6-28-8	-8.02	-10.97	-8.71
PW 13-06	13-06-4	-8.39	-11.35	-9.09
PW 13-06	13-06-5	-7.48	-10.42	-8.16
PW 13-06	13-06-14	-10.11	-13.13	-10.86
PW 13-06	13-06-18	-6.42	-9.32	-7.06
DS 11-20	11-20-2	-6.47	-9.37	-7.11
I 16	16-5	-5.76	-8.64	-6.38

Table 5.7: Calculated $\delta^{18}O$ of lake water ($\delta^{18}O_W$) for calcite precipitation, assuming lake water temperatures between 3 °C and 12°C (MacGinite, 1969).

The isotopic water composition was calculated using the temperature equation for the calcite–water system proposed by Friedman and O'Neil (1977) (Equation 8).

$$10^3 \ln\alpha = 2.78 * (10^6/T^2) - 2.89 \quad \text{(Equation 8)}$$

A variation from the $\delta^{18}O$ values of calcites to the higher $\delta^{18}O$ values in dolomites (Figure 5.26) was probably caused by a combination of temperature increase and/or evaporation. During evaporation, the water composition is controlled by equilibrium and kinetic effects (Tucker and Wright, 1990; Gat, 1995; Davis et al., 2009). For the kinetic effect, the lighter water molecules ($^{1}H^{16}O$) diffuse more easily to the atmosphere. For the equilibrium effect, the lighter water molecules have higher vapor-pressure values, which makes it easier for them to pass into the atmosphere. As a result, the lake water becomes enriched in D and ^{18}O. Consequently, dolomite crystals that form in isotopic equilibrium with lake water are also enriched in ^{18}O.

The lake water temperatures calculated for dolomitization are listed in Table 5.8, calculated based on the measured $\delta^{18}O$ of dolomites and the estimated $\delta^{18}O$ isotopic composition, using the dolomite-water system isotopic fractionation proposed by Sheppard and Schwarcz (1970) (Equation 9).

$$10^{3}Ln\alpha = 3.23 * (10^{6}/T^{2}) - 3.29 \quad \text{(Equation 9)}$$

Pitman (1996), working in the depocenter of the Uinta Basin, estimated the $\delta^{18}O$ values of fresh lake water setting (for calcite precipitation) between -12‰ and -6‰ SMOW, which are close to the range calculated for the calcites in this study (see Table 5.7). Furthermore, Pitman (1996) estimates that the $\delta^{18}O_W$ was around -5‰ SMOW for a slightly evaporated environment. By comparison, Long (2006), working in the southwest margin of the Uinta Basin, estimated the $\delta^{18}O_W$ of fresh lake water setting (calcite precipitation) around -9‰ and -2‰ SMOW, and the $\delta^{18}O_W$ for evaporated setting (dolomite precipitation) around -11‰ and -4.5‰ (SMOW).

Long (2006) calculated these values assuming a constant temperature of 25 °C for calcite and dolomite precipitation.

Estimation of the $\delta^{18}O_W$ during dolomitization considers the $\delta^{18}O_W$ values proposed by Pitman (1996), but enlarging the $\delta^{18}O_W$ range in ±5‰ SMOW, from -10‰ to 0‰ SMOW. The calculated $\delta^{18}O_W$ values proposed by Long (2006) are not included in this analysis because he estimated the calcite and dolomite precipitation at the same temperature of 25 °C. This cannot be accurate because a number of reasons, one of them flagged by his assertion that the $\delta^{18}O_W$ for dolomitization was lower than $\delta^{18}O_W$ for calcite precipitation.

On the contrary, the higher $\delta^{18}O$ values of dolomite versus calcite suggest that dolomitization was probably caused by somewhat evaporated lake water with higher $\delta^{18}O_W$ from evaporation. Therefore, the temperature of dolomitization must also has been higher than that of the fresh water setting (12 °C).

Based on these considerations, the lake water $\delta^{18}O$ isotopic composition during dolomitization is evaluated here in three different $\delta^{18}O_W$ settings: (i) $\delta^{18}O_W$ = -10‰ (SMOW), (ii) $\delta^{18}O_W$ = -5‰ (SMOW), and (iii) $\delta^{18}O_W$ = 0‰ (SMOW) (Table 5.8).

$\delta^{18}O_W$ = -10‰ (SMOW) was not a probable alternative during dolomitization because the majority of the calculated temperatures are lower than 13 °C (values in red, Table 5.8), with some values below 0 °C. Similarly, $\delta^{18}O_W$ = 0‰ (SMOW) was not a probable water isotopic composition during dolomitization because the majority of the calculated temperatures are higher than 40 °C (values in red, Table 5.8). On the other hand, an intermediate $\delta^{18}O_W$ = -5‰ (SMOW) yields reasonable temperatures between 13 °C to 36°C with four exceptions (in red, Table 5.8).

Current lakes around the Uinta Basin have similar temperatures (variably throughout seasons) (Belovsky et al., 2011; Eardley, 1938), and the calculated temperatures (in Table 5.8) are similar to the estimated paleo-temperatures of the Uinta Lake based on paleo-biological and paleo-climate studies (Ramussen et al. 1999; MacGinite, 1969).

Well	Sample	$\delta^{18}O_{Dol}$ (PDB)	T (°C) @ $\delta 18O_W$ = -10‰ SMOW	T (°C) @ $\delta 18O_W$ = -5‰ SMOW	T (°C) @ $\delta 18O_W$ = 0‰ SMOW
			PZ1		
BC 14-1	14-1-14	-2.71	6.3	24.9	47.8
BBC 14-1	14-1-15	-5.05	14.8	35.3	60.9
N 6-28	6-28-5	-2.06	4.0	22.2	44.4
N 6-28	6-28-6	0.87	-5.3	10.8	30.4
UT 15-13	15-13-9	0.04	-2.8	13.9	34.1
UT 15-13	15-13-10	-1.63	2.6	20.4	42.2
UT 15-13	15-13-11A	-7.30	23.8	46.4	75.1
UT 15-13	15-13-11B	-2.59	5.8	24.3	47.1
PW 13-06	13-06-6	-1.55	2.3	20.1	41.8
PW 13-06	13-06-6B	-0.39	-1.4	15.5	36.2
PW 13-06	13-06-7	-2.62	6.0	24.5	47.3
PW 13-06	13-06-7B	-0.69	-0.4	16.7	37.6
PW 13-06	13-06-8	-2.85	6.8	25.5	48.5
PW 13-06	13-06-9	-2.18	4.4	22.6	45.0
PW 13-06	13-06-10	-4.33	12.1	32.0	56.7
PW 13-06	13-06-10A	-3.26	8.2	27.2	50.7
DS 11-20	11-20-4	-0.84	0.0	17.3	38.3
I 16	16-3	-5.61	17.0	37.9	64.3
I 16	16-4	-4.42	12.4	32.4	57.2
			PZ1'		
BBC 14-1	14-1-17	-2.37	5.1	23.5	46.0
N 6-28	6-28-7	-0.26	-1.8	15.0	35.6
UT 15-13	15-13-12	-4.63	13.2	33.3	58.4
UT 15-13	15-13-13	-4.83	13.9	34.2	59.5
PW 13-06	13-06-10B	-6.16	19.1	40.6	67.6
PW 13-06	13-06-11	-10.39	37.6	63.8	98.1
DS 11-20	11-20-5	-2.44	5.3	23.7	46.3
I 16	16-7	0.06	-2.8	13.8	34.1
I 16	16-8	-3.00	7.3	26.1	49.3

			PZ2		
BBC 14-1	14-1-20	-2.69	6.2	24.8	47.7
BBC 14-1	14-1-21	`	-0.3	16.8	37.7
N 6-28	6-28-9	-2.11	4.2	22.4	44.6
UT 15-13	15-13-14	-1.31	1.5	19.1	40.6
PW 13-06	13-06-11A	-5.37	16.0	36.8	62.8
PW 13-06	13-06-11B	-4.84	14.0	34.3	59.6
PW 13-06	13-06-11C	-2.90	6.9	25.7	48.7
PW 13-06	13-06-12	-6.03	18.6	40.0	66.8
DS 11-20	11-20-8	-4.80	13.8	34.1	59.4
DS 11-20	11-20-9	-3.47	9.0	28.1	51.8
I 16	16-10	-3.62	9.5	28.8	52.7
I 16	16-11	-2.02	3.9	22.0	44.2

Table 5.8: Calculated temperatures (T °C) of dolomitizing fluids based on estimated lake water $\delta^{18}O$ composition varying from -10‰ to 0‰ SMOW and measured $\delta^{18}O_{Dol}$ values from conventional isotopes analysis. Temperatures values that deemed unreasonable for dolomitization are highlighted in red color; temperatures calculated using the dolomite-water system isotopic fractionation equation proposed by Sheppard and Schwarcz (1970). See text for discussion.

A different estimation of the temperature along dolomitization is based on a comparison between the current lake water temperatures of the Great Salt Lake (Utah, USA) and the estimated temperatures of the Eocene epoch in the study area. The Great Salt Lake was chosen because it is located around the same latitude as the ancient Uinta Lake. The reported maximum water temperature in the summer of Great Salt Lake varies between 26 °C and 32 °C (Belovsky et al., 2011; Eardley, 1938; www.usclimatedata.com). Furthermore, the relationship between lake water and air temperatures is positive and strong (high R^2) for the highest lake water-air temperatures (McCombie, 1959). On the other hand, Ramussen et al. (1999), using fossil of mammals estimated that the coolest temperature in the middle Eocene was at least 4 °C higher than current temperatures. Therefore, it is reasonable to assume that the water

temperature of the ancient Uinta Lake could have reached at least 30 °C. This temperature supports the notion that the lake water $\delta^{18}O$ isotopic composition fluctuated during dolomitization between -10‰ and 0‰ (SMOW), and most likely was close to -5‰ SMOW.

5.2.2.7 Clumped-isotopes thermometry

The clumped-isotopes results (Table 5.6), supplement the conventional oxygen isotope results as follows:

(i) The dolomite PZ1 layer presents a dolomitization temperature of 30 °C (sample 13-06-7), which is close to its temperature of around 24 °C estimated from conventional oxygen isotope geothermometry (see previous section). However, the dolomite PZ1' and PZ2 layers show much higher dolomitization temperatures of 48 °C (sample 6-28-7) and 59 °C (sample 13-06-12), respectively. The discrepancy between the estimated temperature from conventional oxygen isotopes and clumped-isotopes may due to the following reasons: (1) analytical error (Bernasconi, personal communication, 2016); or (2) the higher "clumped" temperatures do not reflect the dolomitization process, but are due to recrystallization.

(ii) Dolomitization temperature in the two limestone samples analyzed are significantly higher than those calculated temperatures for dolomite samples (79 °C for sample 13-06-5 and 84 °C for sample 6-28-8).These temperatures cannot possibly reflect the lake water at the time of calcite formation and/or deposition, but must be due to recrystallization during burial.

Considering that the calculated clumped-isotopes temperatures are in the range of the estimated maximum burial temperatures (from north to south) in the study area (see Section 5.1.3), it appears that the calcites for the limestones layers were prone to isotopic re-equilibrium during recrystallization near maximum burial whereas the dolomites of the dolostones were not.

5.2.2.8 Elemental compositions

Trace element concentration in dolomite crystals can be used for interpretations about the dolomitizing fluid, dolomitization environment, and/or recrystallization. The concentration of trace elements concentration in minerals is defined by (i) trace element fluid concentration, (ii) water/rock ratio of the system, and (iii) the distribution coefficient (*D)* (Tucker and Wright, 1990). If an element has a *D* value >1, the resulting crystal is enriched (higher $^{m}Te/^{m}Ca$) than the parental fluid. In contrast, if an element has a *D* value <1, the resulting crystal is impoverished (low $^{m}Te/^{m}Ca$) than the parental fluid (McIntire, 1963). However, distribution coefficients are not constant. Rather they might vary with the composition of the solid phase, temperature, pressure, and kinetic factors (Veizer, 1983; McIntire, 1963).

The trace element concentration in dolomite is defined by Equation 10 (Gregg and Shelton, 1989), which correlates the molar ratio of the trace element to that of Ca^{2+} and Mg^{2+} as follows:

$$[^{m}Te/(^{m}Ca + {}^{m}Mg)]_{s} = D * [^{m}Te/(^{m}Ca+{}^{m}Mg)]_{l} \quad \text{(Equation 10)}$$

where “m” is the molar concentration, “Te” stands for trace element, “*s*” represents the solid phase (calcite), “*D*” stands for the distribution coefficient, and “*l*” represents the liquid phase

(or dolomitizing lake/pore water in this case). This equation is valid for systems in equilibrium and homogeneous distribution of trace elements during precipitation (Veizer, 1983).

The Sr and Na concentrations of the dolomitizing fluids are compared to two specific reference waters composition: (i) a saline setting represented by the current Great Salt Lake concentration, and (ii) a fresh water setting represented by the average concentration of several lakes. Calculation was based on the distribution coefficients for dolomite proposed by Veizer (1983) (D_{Sr} = 0.025 to 0.07, D_{Na} = $2x10^{-5}$ to $2x10^{-4}$), the current Ca. Mg, Sr, and Na concentration of Great Salt Lake water (Whitehead and Feth, 1961); and the Ca, Mg, Sr, and Na average concentration of current fresh lake water [Majid, 1983 in Veizer (1983)] (Table 5.9 and Figure 5.35).

	Dolomitizing fluids	**Freshwater - Lakes**	**Saline water - Great Salt Lake**
Sr (ppm)	1300	0.07	15
Na (ppm)	1420	50	83600
Ca (ppm)	245701	8	241
Mg (ppm)	133081	6	7200
$^{m}Sr/(^{m}Ca+^{m}Mg)$	$2.66x10^{-2}$	$1.79x10^{-3}$	$5.66x10^{-4}$
$^{m}Na/(^{m}Ca+^{m}Mg)$	$9.69x10^{1}$	$1.28x10^{0}$	$3.16x10^{0}$

Table 5.9: Sr and Na concentrations and ratios to Ca^{2+} of calculated dolomitizing fluid compared to current fresh water from lakes in the region and saline water form Great Salt Lake.

Sr and Na are associated with the degree of salinity of the dolomitization fluids (Land and Hoops, 1973; Tucker and Wright, 1990). Assuming partition equilibrium during dolomitization and no recrystallization, the probable calculated Sr and Na concentrations of the dolomitizing fluid (ancient Uinta Lake or pore waters derived from it) were greater than the

waters references (Figure 5.36), suggesting an evaporitic dolomitizing fluid. This interpretation is valid only if the Na is incorporated within the dolomite lattice. Furthermore, the geographical variation of this data, with somewhat elevated values located toward the near-shore area (Figure 5.31A), suggests that the lake/pore water had elevated salinities at least temporarily toward the near shore areas.

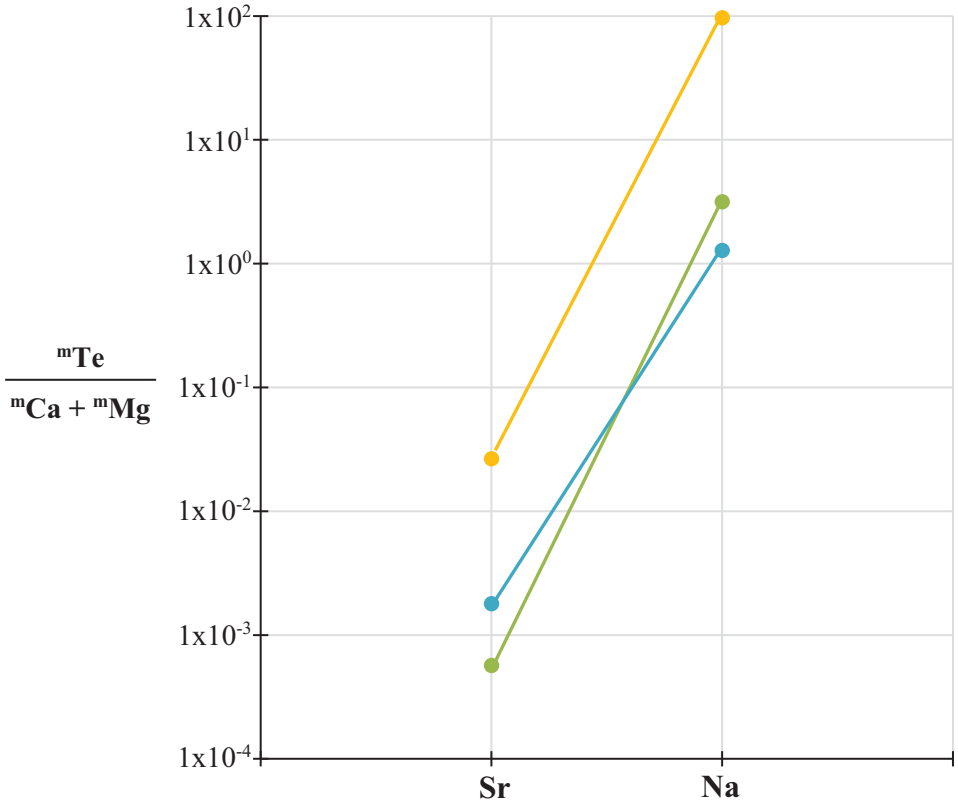

Figure 5.36: Calculated Sr/Ca and Na/Ca molar concentration of the ancient Uinta Lake (yellow line), the Great Salt Lake (green line), and fresh lakes waters (blue line).

On the other hand, the Sr concentration in dolomites may be an indicator of dolomitizing fluid flow and Sr/Ca ratio of the dolomitizing fluid. In figure 5.37, the Sr

concentration decrease with depth, which probably represent an upward dolomitizing fluid directions (see Chapter six, section 6.1.3 for further discussion).

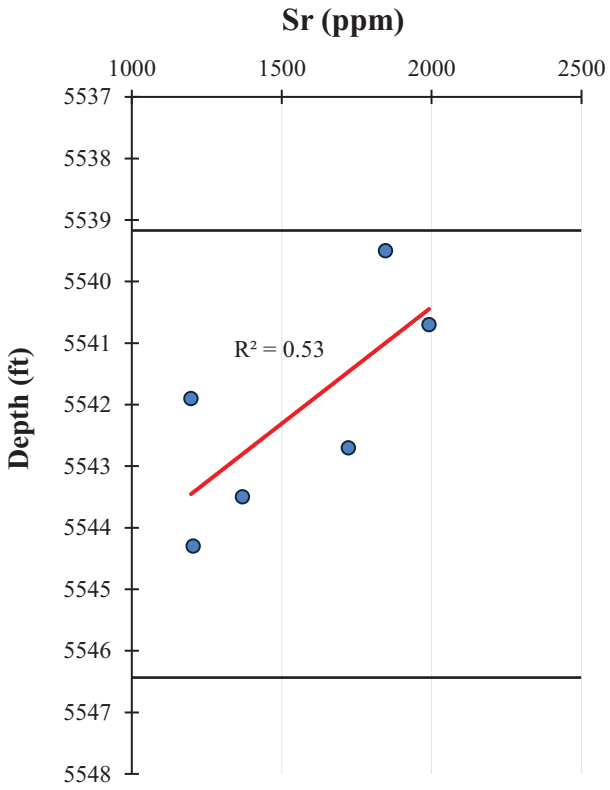

Figure 5.37: Sr concentration variation of dolomite crystals with depth. PZ1 layer, well PW 13-06. Horizontal black lines: top and base of the PZ layer, red line: linear regression line.

The Fe and Mn concentrations are indicators of the reduction-oxidation potential of the dolomitization fluid (Davison, 1993; Tucker and Wright, 1990; Machel and Burton, 1991) and the availability of these elements (Budd, 1997). For these elements to be incorporated into the dolomite lattice must be in their divalent forms, which requires a reducing redox potential (Machel and Burton, 1991). Fe and Mn concentrations higher than 1000 ppm and 50 ppm, respectively, suggests reducing pore waters and Fe-Mn external source (Budd, 1997). The average Fe and Mn concentration (5216 pp and 322 ppm, respectively) in the dolomite samples

of this study (see also Figures 5.31C and D), suggest a reducing lake/pore water setting. This interpretation is valid only if the current Fe and Mg concentrations in dolomite crystals are the original signature.

The Al and Si concentrations are taken as a proxy for the amount of "insoluble residue", i.e., essentially the clay mineral content in the samples because these elements cannot be incorporated into dolomite at low diagenetic temperatures (Weber, 1964). In the samples of this study, the Al concentrations have a spatial distribution in which the higher values are preferentially located in the near-shore area (Figure 5.32A). This distribution was probably caused by deposition of most of the suspended sediment in the near-shore areas, which led to a consequent decrease of clay sediments toward the basin center. In contrast, the Si concentration shows roughly the same concentration along the basin (Figure 5.32B).

The Zn and Pb concentrations are commonly elevated in basinal brines (e.g., Morrow, 1982), and dolomites formed from them often are associated with galena and/or sphalerite. The PZ layers of the Uteland Butte member do not have any of these characteristics. In contrast the average Zn and Pb concentrations are low (12 ppm, and 2 ppm, respectively) (Figures 5.30C and D) in comparison with known basinal dolomites, which reach values up to 14 ppm and 50 ppm respectively (Luczaj et al., 2016).

5.3 Porosity

5.3.1 Observations

This section analyzes dolomitization and porosity characteristics from different perspectives. First, it describes dolomite layer porosity features, then it describes porosity according to its geographical (lateral) and vertical (depth) distribution using well core plug data (from companies), and finally, it describes porosity values (from SEM images analysis) associated to dolomite textures.

Dolomitization and porosity are closely related but there is no general rule that describes this relationship. Machel (2004) defines six potential sources of porosity enhancement related to dolomitization: mole-per-mole replacement, calcite dissolution, dolomite dissolution, pH reduction in pore water, fluid mixing, and thermochemical sulfate reduction (Machel, 2004). For PZ layers, porosity development may have been formed by mole-per-mole replacement and dolomite dissolution processes. There is no evidence of pore water pH reduction, fluid mixing with different chemical compositions, or thermochemical sulfate reduction processes that could have enhanced porosity in PZ layers. Additionally, the current porosity may have been partially or largely inherited from the lime precursor.

Mole-per-mole replacement enhanced porosity due to volume loss. Volume loss can be described by the chemical reaction that describes dolomitization, in which two moles of calcite are replaced by one mole of dolomite (Machel 2004). Dolomite dissolution further enhances porosity. Many dolomite crystals in the PZ layers show a hole within them near the center, interpreted here as result of dissolution of metastable dolomite (Figures 5.13B and C).

Core, thin sections, and SEM image petrographic descriptions show fabric and non-fabric selective porosity types (e.g. Figures 5.5C, 5.4A). For fabric selective porosity, four different types are present: intercrystal (IC), moldic (MO), interparticle (IEP), and intraparticle (IAP); and for non-fabric selective, two different types are present: vug (VG) and fractures (FR).

IC is considered primary because it was likely developed syndepositional (Choquette and Pray, 1970) and is present only in grain-supported facies (ooid grainstone, F7). However, some of these pores were occluded by calcite cement (phases 1b, 2b, and 8 in Table 5.1) before oil migration (phase 12). Therefore, IC is considered negligible as it is restricted to a specific facies (F7), and additionally, it was occluded by post-diagenetic products.

On the other hand, secondary porosity types are the result of diagenetic events (Choquette and Pray, 1970). MO, IAP, and VG were created previously to hydrocarbon generation by dissolution events (phases 2a, 4, and 9 in Table 5.1), whereas FR was developed after hydrocarbon generation by stress. Most of these pore types were partially occluded by carbonate and silica cementation phases (phases 2a, 4, 5a, 5b and 9 in Table 5.1). Among the secondary pore types developed by dissolution, IAP has the highest porosity values up to 20% (thin section estimation percentage); however, this porosity is exclusively present within the ooid grainstone facies (F7). In contrast, IC is the most abundant in all PZ layers. According to the porosity classification proposed by Luo and Machel (1995), the pore size of IC is between microporosity and mesoporosity types. On the other hand, FR porosity represents a very low porosity percentage (<1%) and most of the fractures are partially to completely filled by calcite cement (phase 15).

The geographic distribution of porosity was established based on core plug data (Vanden Berg, personal communication, 2015). Based on the abundance of pore types, the

author assumed that measured porosity values from core plugs were generated mainly by intercrystal porosity type. PZ1 displays a wide porosity variation; however, it has the highest porosity values of all PZ layers with an average of 17.7% (σ: 7.1%). Wells BBC 14-1, BBC 14-3, and N 6-28 have higher porosity variability in comparison with well UT 15-13. PZ1' and PZ2 have the lowest porosity values with an average of 9.4% (σ: 5.9%) and 12.3% (σ: 7.1%) respectively.

Lateral distribution of porosity in the PZ layers shows a poor trend. For PZ1, the correlation line (red dashed line in Figure 5.38) between the average porosity values (white line within boxes) is roughly horizontal, but the maximum porosity values (high whiskers in Figure 5.38) are located at toward the basin center (north). Porosity distribution in PZ2 shows a similar trend, in which the highest porosity values are preferentially located at the basin center (north) (Figure 5.38).

Moreover, vertical distribution of porosity also show a poor trend; in which the highest porosity values are preferentially located near the tops of the PZ layers, whereas the lowest porosity values are preferentially located near the bases of the PZ layers (Figure 5.39).

A different porosity characterization was made using SEM images. Porosity values were measured using APS Assess 2.0 image analysis software. The colour threshold that represent the pore area was variable and was selected according to the bright gray colour of the dolomite crystals (Figure 5.40). Three thin sections were selected for PZ1, four thin sections for PZ1', and three thin sections for PZ2 (Figure 5.12). A total of 36 SEM images was used to measure porosity.

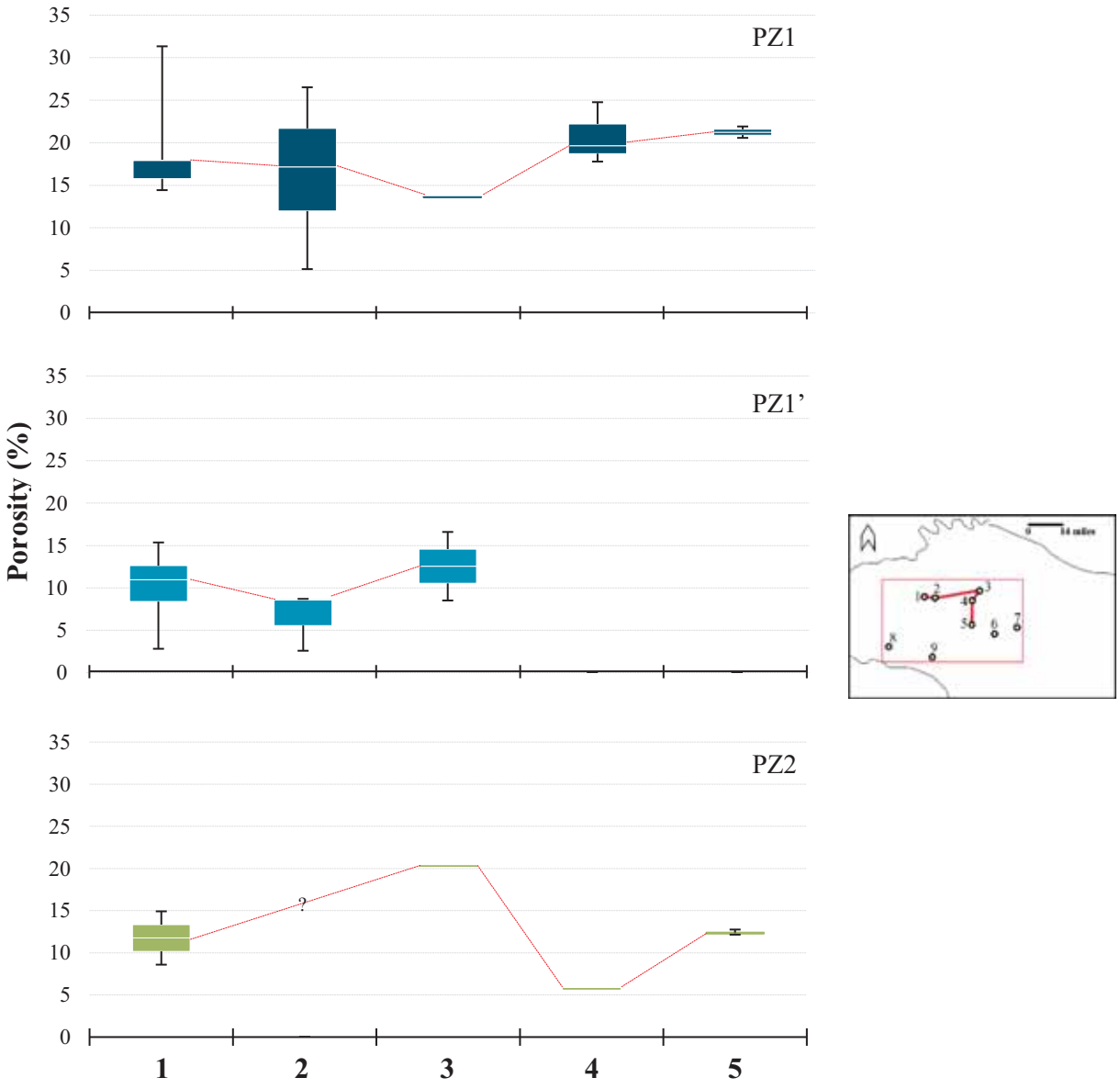

Figure 5.38: Horizontal porosity variation for each PZ layer. Porosity values measured from core plug samples. Red dashed line represents porosity average correlation between wells. 1: BBC 14-1, 2: BBC 14-3, 3: N 6-28, 4: UT 15-13, 5: PW 13-06.

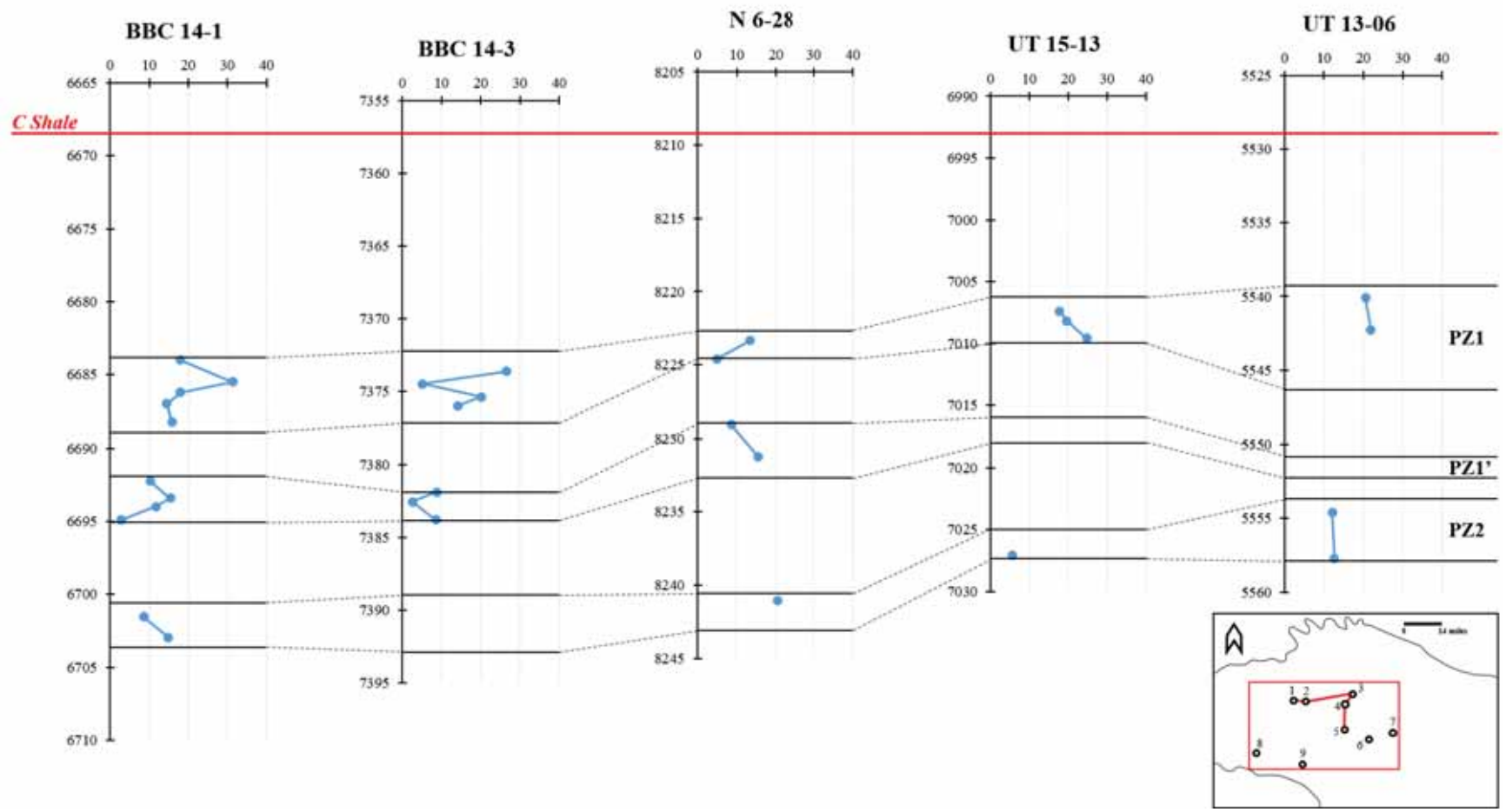

Figure 5.39: Porosity variation with depth. Porosity values measured from core plugs; horizontal axis: porosity (%), vertical axis: depth (ft). Number in the inset map 1: BBC 14-1, 2: BBC 14-3, 3: N 6-28, 4: UT 15-13, 5: UT: 13-06.

Figure 5.40

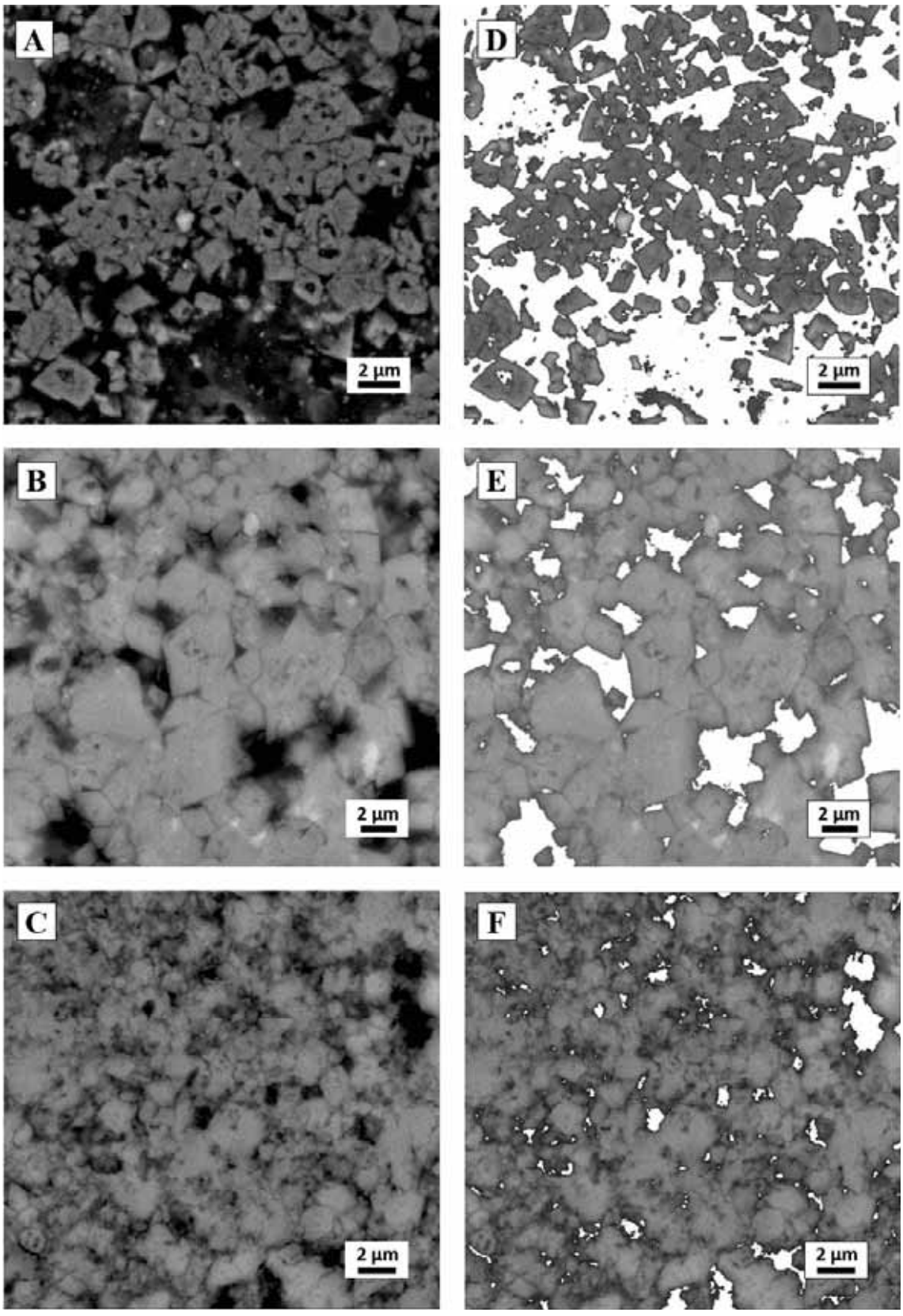

Figure 5.40:

(A) SEM image of planar-e texture characterized by straight dolomite crystal faces; well: UT 15-13, sample: 13, depth: 7017.4 ft, PZ1' layer.

(B) SEM image of planar-s texture characterized by straight and irregular dolomite crystal faces; well: N 6-28, sample: 9, depth: 8242.5 ft, PZ2 layer.

(C) SEM image of non-planar texture characterized by irregular dolomite crystal faces and more densely packed crystals; well: UT 15-13, sample: 11, depth: 7009.9 ft, PZ1 layer.

(D) Same image as (A) showing porosity area (white irregular area). Calculated porosity: 43.38%.

(E) Same image as (B) showing porosity area (white irregular area). Calculated porosity: 12.4%.

(F) Same image as (C) showing porosity area (white irregular area). Calculated porosity: 7.82%.

CHAPTER SIX

PRELIMINARY DRAFT ONLY

At the time of completion of this document Chapter Six could be supplied only as a first draft. This Chapter will be revised and expanded for the final version of the thesis, which is scheduled for the defense on September 19, 2017.

CHAPTER SIX

DISCUSSION AND INTERPRETATION OF DOLOMITIZATION

This chapter provides an interpretation of dolomitization to account for the occurrence of petroliferous dolomite layers on various scales: (i) Individual dolomite layers; (ii) stratigraphic interval between D and C Shales; and (iii) the context of regional paleogeography. It also attempts to correlate with reservoir characteristics.

6.1 Individual dolomite layers

6.1.1 Dolomite: Replacement

The dolomite crystals in the PZ layers originated as replacement of the lime mud and/or at least partially lithified lime mud. This is shown by distinctive petrographic textural features such as partial or complete matrix-selective replacement, and occurrence of microvugs and moulds (Tucker and Wright, 1990; Machel 2004).

All dolomite replacement characteristics are present in the PZ dolomite layers. The original texture of the parental limestone is still preserved in these layers (Figures 5.4C to F); and microvugs (Figure 5.4A) and moulds (Figure 5.5C) are present in all PZ layers. These pores were probably generated by dissolution of metastable carbonate crystals.

6.1.2 Mg^{2+} source

Dolomitization is favoured by several factors such as high Mg^{2+}/ Ca^{2+} ratio, high alkalinity, and high temperatures (Machel and Mountjoy, 1986; Machel and Mountjoy, 1987; Machel, 2004). Lacustrine environments generally have a low magnesium contents between 2.4 ppm (Turkana Lake) to 756 ppm (Caspian Lake) (Nikanorov and Brazhnikova, 2004). Freshwater lakes can have Mg^{2+} concentrations below 1 ppm (Nikanorov and Brazhnikova, 2004), when the water inflow rate is higher than the water outflow in the absence of evaporation (Renaut and Gierloswki-Kordesch, 2010).

The most probable source of magnesium for dolomite formation in the Uteland Butte member is from weathering of surrounding magnesium-rich igneous rocks (pyroxenes and amphiboles) that released magnesium ions, which were then transported by rivers and groundwater. Igneous rocks that supply relatively high amount of Mg^{2+} are gabbros, norites, pyroxenites, harzburguites and dunites and their analogous. Such mafic rocks have high magnesium oxide contents that vary between 6.73% for gabbro and 37.94% for dunite (Best, 1982). These magnesium sources are located within the drainage catchment areas that supplied sediment and ions to Uinta Lake at the time of the Uteland Butte member deposition.

Therefore, the Mg^{2+} source likely came from the magnesium-rich igneous rocks are located at the southwestern region of the Uinta Basin (Hunt, 1954;), notably a Proterozoic metapyroxenite body located within the probable catchment area at the northwestern part of the Uncompahgre Plateau, with magnesium oxide (weight percent) as high as 19.4 % (Case, 1991) (Figure 6.1).

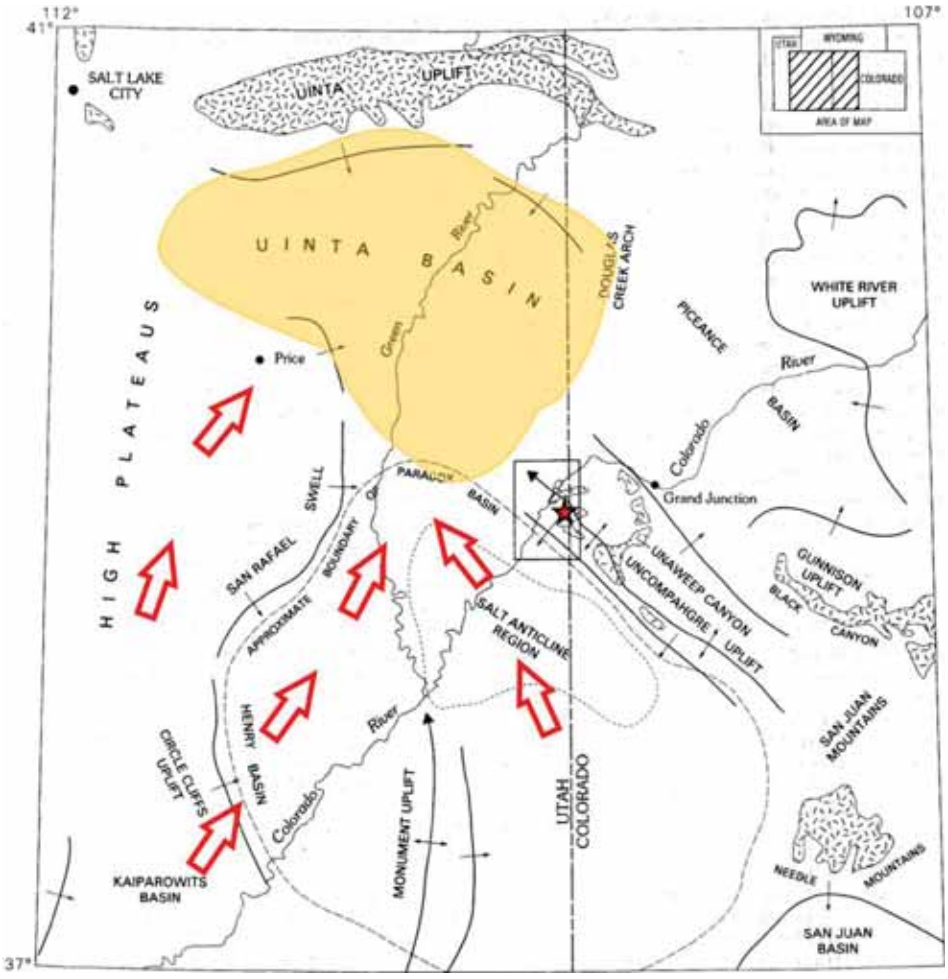

Figure 6.1: Location of metapyroxenite (red start) and the Uinta basin (yellow area). Additional potential sources of Mg^{2+} were located toward south/southwest of the Uinta Basin (see Chapter 2, Section 2.2). Red arrow represents the probable paleocurrent. Figure modified from Case (1991).

Chemical weathering is the main process that provides magnesium to surface waters (Nikanorov and Brazhnikova, 2004). An example of this process can be represented by Equation 11 (Broecker, 1971), in which enstatite ($MgSiO_3$), a common component of mafic an ultramafic intrusive rocks (Nesse, 1991), weathers in a subaerial environment as follows:

$$2CO_2 + 3H_2O + MgSiO_3 \rightarrow Mg^{2+} + H_4SiO_4 + 2HCO_3^- \quad \text{(Equation 11)}$$

Chemical weathering of igneous bodies during deposition of the Uteland Butte member may have been favoured by climate changes, specifically relatively short term (10^3 to 10^5 years) global warming with elevated atmospheric CO_2 values [higher than 2000 ppm (Pearson and Palmer, 2000)] that took place in the Early Eocene epoch (Zachos et al., 2001) and likely enhanced the rate of the chemical weathering of igneous rocks in the region. In this global climate short-term changes, the rate of rain increased during cool periods (Robert and Kennett, 1992), whereas the carbon dioxide values increased during warming periods such as the Early Eocene Climatic Optimum (EECO), with CO_2 concentrations almost nine times the current values (Pearson and Palmer, 2000; Zachos et al., 2001).

6.1.3 Dolomitizing environment

Most dolomite crystals (about 91%; see Chapter 5, section 5.2.1.2) are classified as aphanocrystalline, ranging between 0.25 to 3 μm in size. Dolomite crystal size is controlled by nucleation and growth rates, which are directly regulated by temperature (Gregg and Sibley, 1984; Sibley and Gregg, 1987). The overall very small dolomite crystal size likely was caused by high nucleation rates which commonly are associated with evaporitic (syndepositional) environments. Folk and Siedlecka (1974) stated that very fine dolomite crystals are an indicator of an evaporite cycle in schizohaline environments. Warren (2000) characterized syndepositional dolomite in the evaporite settings very fine in size (< 10 μm). Budd (1997) interpreted Holocene dolomite as direct precipitation from seawater, also characterized by very fine crystals (< 10 μm), and classified them as penecontemporaneous dolomite.

In all these situations, dolomitization was driven by evaporation that also favoured crystallization of evaporite minerals (such as quartzine and gypsum). While sulfates are not formed in the Uteland Butte member, quartzine and other silica varieties are common (Figures 5.6A to F). The mineralogical association dolomite-silica and lack of gypsum crystals suggest that the dolomitizing fluids in the Uteland Butte member was the Uinta Lake water with very low sulfate concentration paired with relatively high Mg^{2+} concentration.

On the other hand, preferential distribution of dolomite textures (Figure 5.14) suggest that the chemical composition of dolomitizing fluids and temperature changed over time. Low dolomite supersaturated fluids and low temperature may lead to the development of rhombohedral dolomite crystals with planar-e texture, whereas high dolomite supersaturated fluids and high temperature may lead to the development of planar-s and nonplanar textures (Sibley and Gregg, 1987). Hence, the observed textural distribution may have been generated by variations in dolomite fluid saturation, temperature, and lake water level.

Temperature and lake water level were probably controlled by climate changes, whereby increased lake water temperature and evaporation promoted the lake water level to drop. These changes generated variations in the chemical composition of the lake water as well, including supersaturation with respect to dolomite that overcame the kinetic barriers to dolomitization.

An idealized representation of lake water levels, dolomite texture variations, and interpretation of dolomite fluid composition is summarized in Figure 6.2. This interpretation contemplates the variation of the supersaturation with respect to dolomite and temperature at different time intervals (t_0, t_1, t_2, t_3, and t_4 in Figure 6.2A and B) and correlates them with dolomite textures.

In the freshwater stage (t_0), the lake water was undersaturated for dolomite and the temperature was below 12 °C (see Chapter 5, Section 5.2.2.6). In this setting the lime mud deposits remained as calcium carbonates. In the next stage (t_1), the lake water reached and/or exceeded dolomite supersaturation and the lake water temperature increased promoting dolomitization. This setting was developed by evaporation and low fresh water inflow. Dolomite crystals formed in this stage were probably characterized by a planar-e to planar-s textures. At an advanced stage (t_2), the lake water reached its maximum supersaturation with respect to dolomite, allowing the formation of dolomite crystals characterized by nonplanar-a and planar-s textures, which likely overprinted at least some of the earlier formed planar-e dolomites. Then (t_3), when the climate turned cooler, the level of supersaturation decreased progressively probably due to higher river water inflow (that caused lake water rose up also) and the temperature also decrease. Consequently, the dolomite crystals formed in this stage were likely characterized by planar-e textures and probably overprinted the earlier dolomites. Finally (t_4), the climate changed to a cooler and raining period with high fresh water inflow, thus decreasing the lake water temperature and driving the lake/pore water to shift toward undersaturated in dolomite. In this final stage dolomitization ceased.

Parallel to the fluctuation of the lake water level, lake water density also changed. Because of evaporation, lake water became denser, which forced it to move downward dolomitizing the already deposited calcium carbonate sediments. The dolomitization model that describes this setting is the reflux model (Adams and Rhodes, 1960) in which the metastable calcium carbonate crystals were replaced by dolomite as the brine passed through the unconsolidated lime mud.

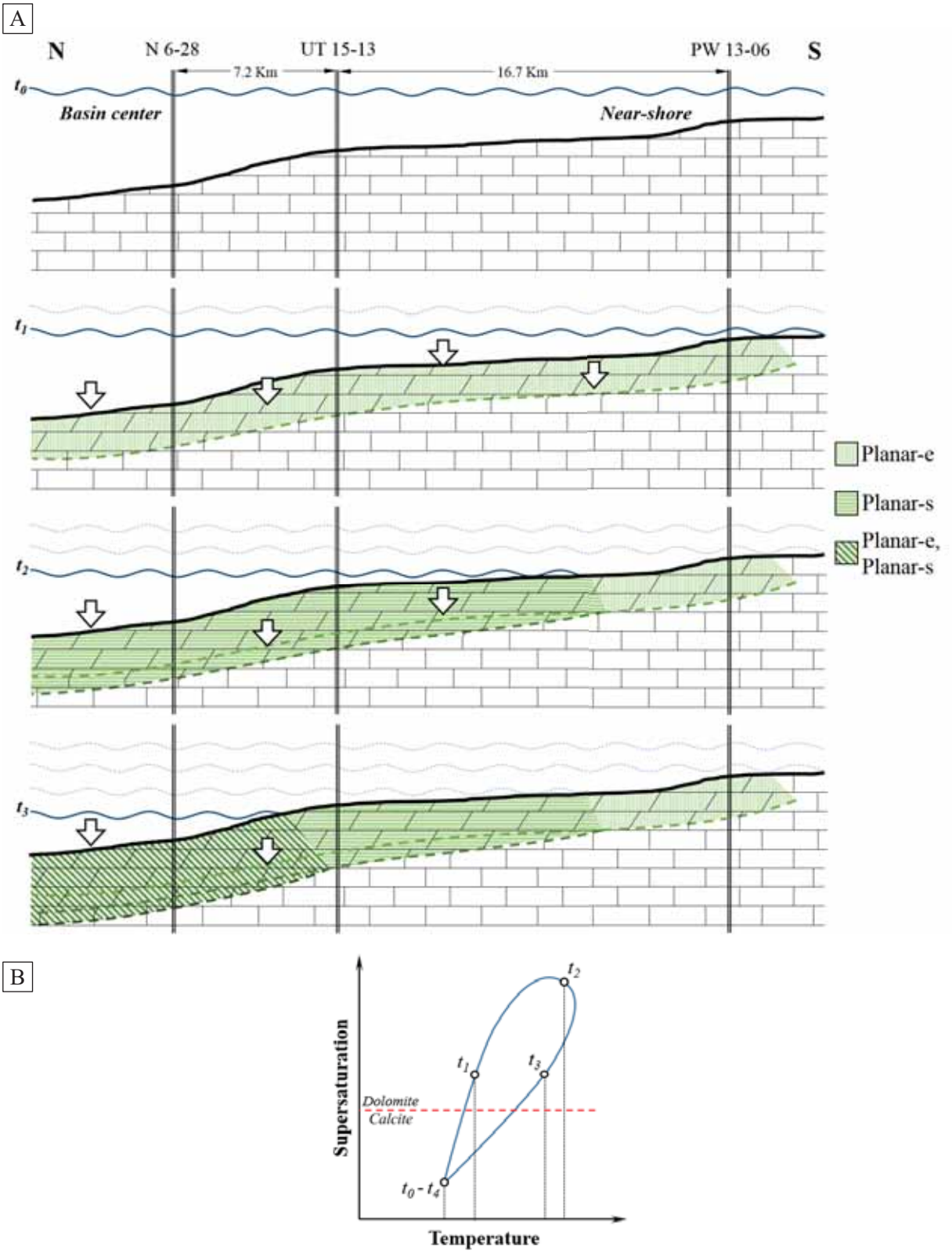

Figure 6.2: (A) Schematic representation of seepage reflux dolomitizing model. Arrows indicate direction of dolomitizing fluids flow. (B) Schematic representation of variation of lake water supersaturation versus temperature.

This interpretation is supported by the observed variation of calcium excess in the dolomites with depth. In this pattern, the near stoichiometric dolomite are preferentially located near the tops of the PZ layers, whereas the calcium-rich dolomites are preferentially located near the bases of PZ layers (Figures 5.24 and 5.25). The $\%Ca_{Dol}$ variations in depth are thus interpreted as generated by changes in dolomitizing fluid composition. At the initial stage of dolomitization, the evaporated lake water had the highest level of supersaturation, allowing formation of nearly stoichiometric dolomite crystals near the tops of the PZ layers. As lake water percolated more deeply through the parental lime mud sediments, the level of supersaturation decreased. Consequently, the dolomite crystals formed lower and at the bases of the PZ layers were increasingly calcium enriched.

Furthermore, the ordering of the dolomite crystals also display a correlation with depth in which the most ordered dolomites are preferentially located near the top of the PZ layers, whereas the disordered dolomite crystals are located near the bases of the PZ layers (Figure 5.27). Differential reaction time could had created dolomite cation ordering variation with depth. If so, the lime mud sediments at the tops of the PZ layers interacted with the dolomitization fluid for a longer period of time, more than the lime mud sediments located at the bases of the PZ layers. This interpretation is in accordance with the Kaczmarek and Sibley (2011) findings related to cation ordering. They stated that the first dolomite crystals that formed are characterized by low cation ordering values independent of the dolomitizing fluid composition and, moreover, cation ordering increases with reaction time. However, the time that has passed since initial dolomite formation (~54-52 Mya.) and the burial history (maximum burial depth ~3 Km and maximum temperature ~100° C) should have modified the original dolomite composition and degree of ordering.

The occurrence of low cation ordering coupled with a wide stoichiometry range is highly unusual for rocks of this age and burial history which calls for unusual interpretation. The most likely cause for this apparent compositional and structural immaturity of the dolomites of the Uteland Butte member is that the stratigraphic interval is and has been overpressured. Bridwell et al. (2016) measured the pressure in 42 intervals (in or near) of the Uteland Butte member and found six intervals with pressure gradients equal or greater than 0.5 psi/ft. Anderson and Roesink (2013) calculated the Uteland Butte member pressure gradient with maximum values of 0.65 psi/ft. According to the calculated and measured pressures of the Uteland Butte member, the stratigraphic interval of interest is then characterized as overpressured reservoir [based on Dickinson (1953) overpressure definition] with values equal of higher than 0.5 psi/ft.

The reflux model for dolomite formation of the Uteland Butte member implies a progressive increment in thickness of the dolomite PZ layers basin ward related to the lake water drop and lake water supersaturation. However, the expected geometry of the dolomite PZ layers does not correlate with the current geometry, in which dolomite PZ layers display a tabular geometry although they vary in thickness that pitch out basinward (north) and landward (south) (further discussion in section 6.1.4). Therefore, the geometry of the PZ layers is likely the result of a combination of two diachronous dolomitizing processes. Additional to the variation of the lake water supersaturation respect to dolomite, the evaporative pumping model may explain the particular characteristics of the dolomites in the Uteland Butte member.

The evaporative pumping model probably took place when the partially dolomitized sediments were exposed to subaerial conditions. Evaporation of the pore water may caused a vertical hydraulic gradient that allowed pore fluids to move upward (Hsü and Siegenthaler, 1969), thus allowing recrystallization of the previous dolomitized sediments (Figure 6.3).

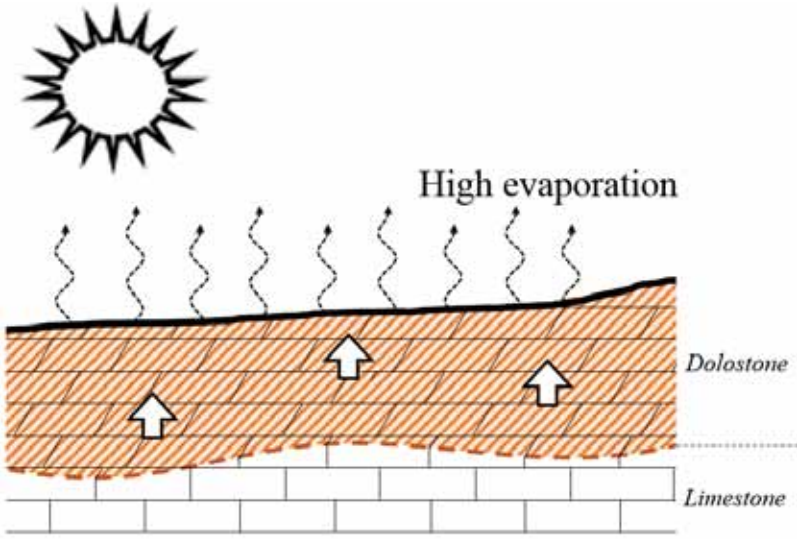

Figure 6.3: Schematic representation of the evaporative pumping model. White arrows indicate the direction of the dolomitizing fluids flow.

The Sr concentration of the dolomite crystals probably recorded the dolomitizing fluids flow, which developed the Sr concentration variation with depth (Figure 5.36). According to Machel (1999), Sr concentration variation of replacement dolomites depends on the Sr/Ca ratio of the dolomitizing fluid relative to that of the parental limestone. If the dolomitizing fluid has a Sr/Ca ratio equal or lower than that of the limestone, the Sr concentration in dolomite should increase downflow. In contrast, if the dolomitizing fluid has a Sr/Ca ratio higher than that of the limestone, the Sr concentration in dolomite should decrease downflow. Applying this concept, the evaporated and upward pore fluid probably had a Sr/Ca ratio equal or smaller than that of the parental lime mud sediments.

Dolomitization (seepage reflux and evaporative pumping) process probably took place several time during the dryer climate conditions, which was alternated with short raining periods. This model describes the formation of one single dolomite layer. In the stratigraphic section of interest, this cycle was repeated five times (Figure 4.13).

6.1.4 Geometry of the dolomite PZ layers

Dolomite PZ layers display a tabular geometry (variable in thickness) that pitch out basinward (north) and landward (south) (Figures 6.6 to 6.8). PZ1 thickness varies from 1.9 ft (0.6 m) to 7.1 ft (2.2 m); PZ1' from 1.5 ft (0.5 m) to 7.1 ft (1.2 m); and PZ2 from 1.5 ft (0.5 m) to 4 ft (1.2 m). The PZ1, PZ1' and PZ2 layers tend to be thicker in the intermediate zone between the near-shore area and the basin center (Figures 6.4 to 6.6). The thickness variation in the PZ layers was probably controlled by the paleobathymetry of the Uinta Lake, by the availability of dolomitizing fluid, by the porosity of the unconsolidated lime mud, by a barrier (thin mudstone laminae) deposited at the top of each limestone layer that may has acted as an aquitard, or a combination of these alternatives.

The probable paleobathymetry of the Uinta Lake during dolomite formation was depicted as a very shallow and extensive flat (Eugster and Surdam, 1973) between the coastal line and the basin center, probably isolated from the basin center by a carbonate shoal that was occasionally subaerial exposed. In this setting, the maximum depth was probably located in the central area, in which the thicker section of the dolomite PZ layers was formed. This setting is the same proposed by and Eugster and Surdam (1973) to explain the origin of the dolomites in the Green River Formation.

Coorong and sabkha dolomitization models generate thin stratiform dolomite layers (Warren, 2000; Machel 2004). Therefore, the expected geometry for these models fits pretty well with the current dolomite PZ layer geometry, suggesting a dolomitization model similar to the Coorong and sabkha settings.

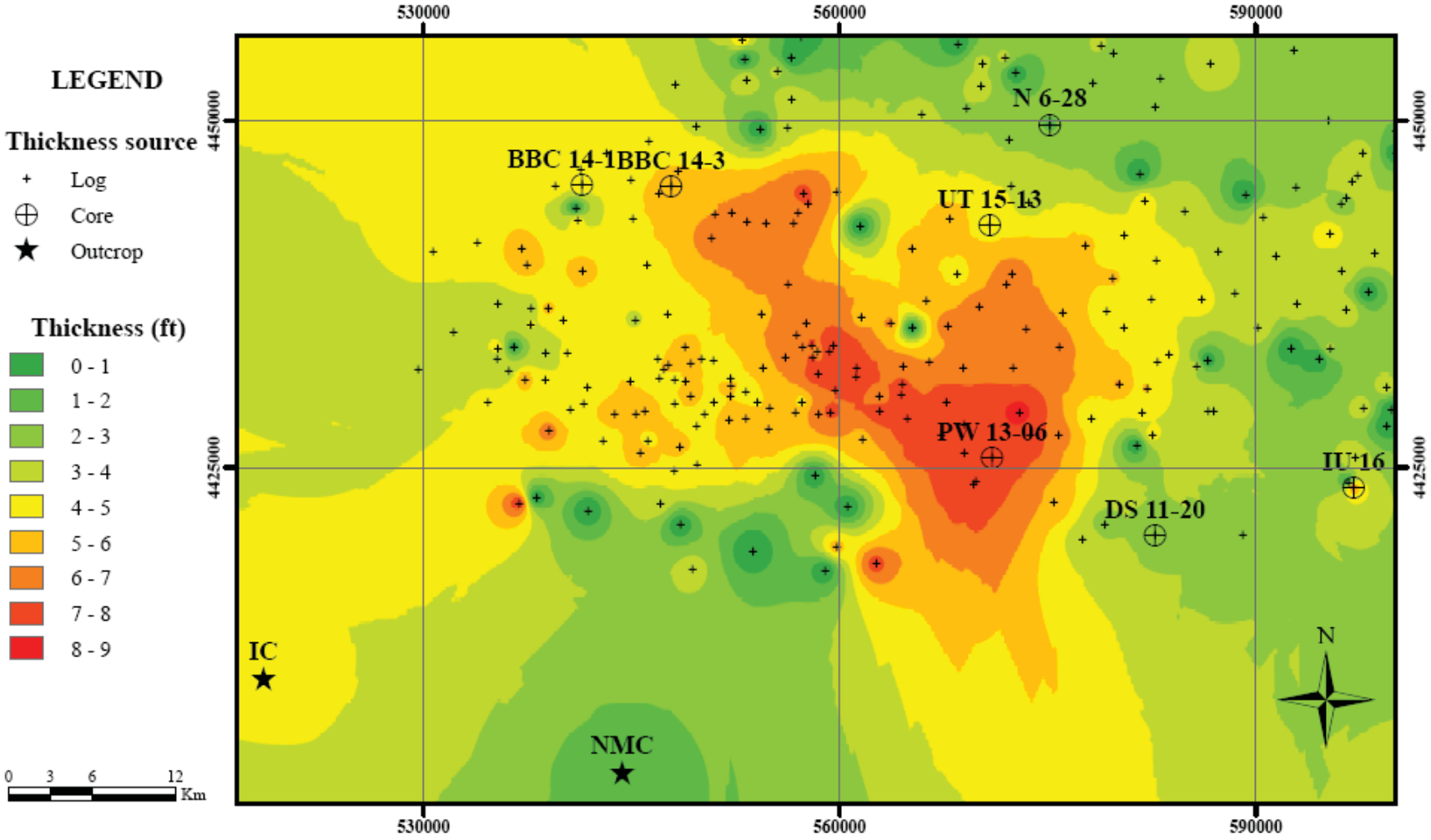

Figure 6.4: Isopachous map for PZ1 layer. Thickness measured from logs (data courtesy of Michael Vanden Berg, 2015), cores, and outcrops.

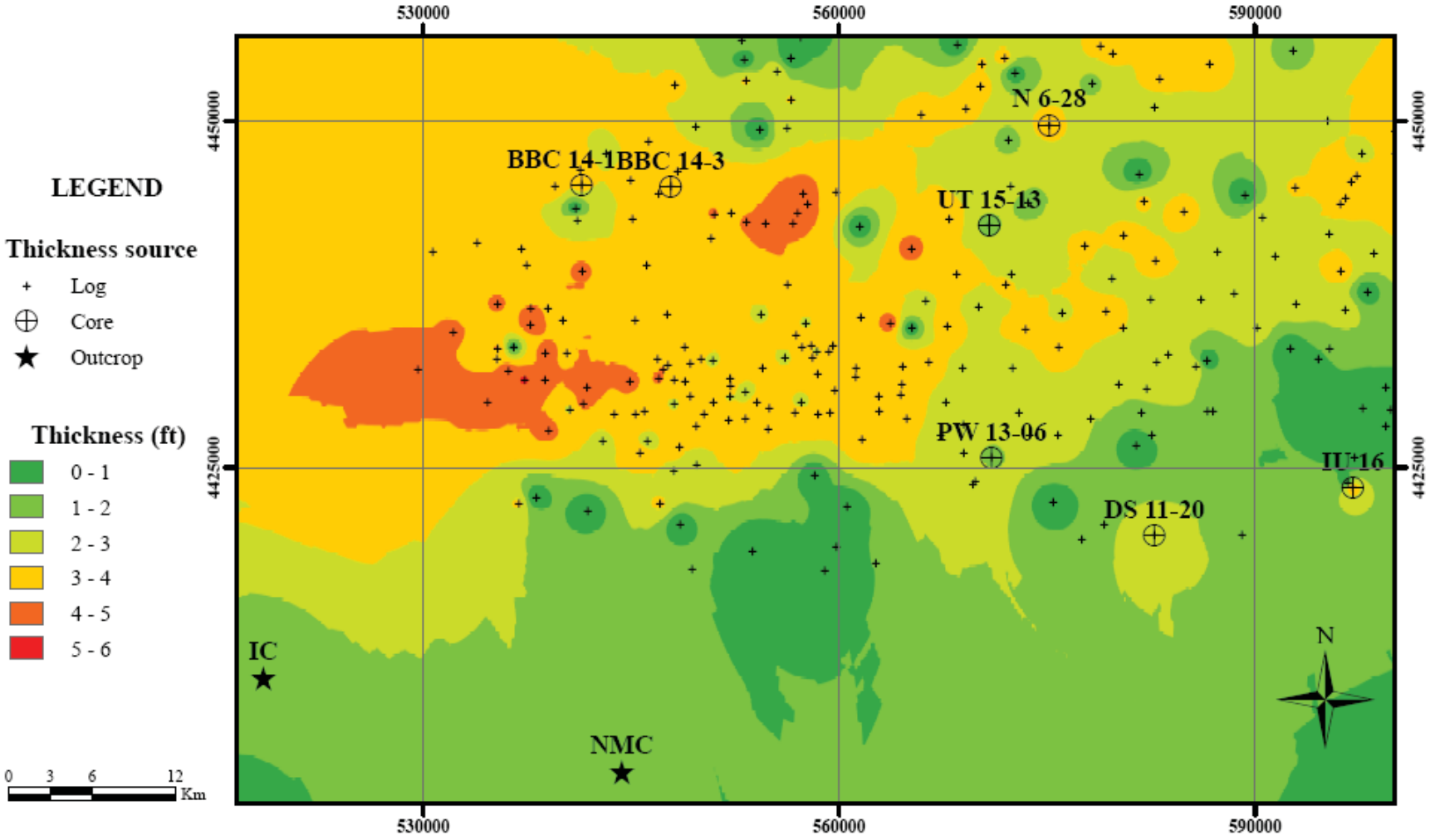

Figure 6.5: Isopachous map for PZ1' layer. Thickness measured from logs (data courtesy of Michael Vanden Berg, 2015), cores, and outcrops.

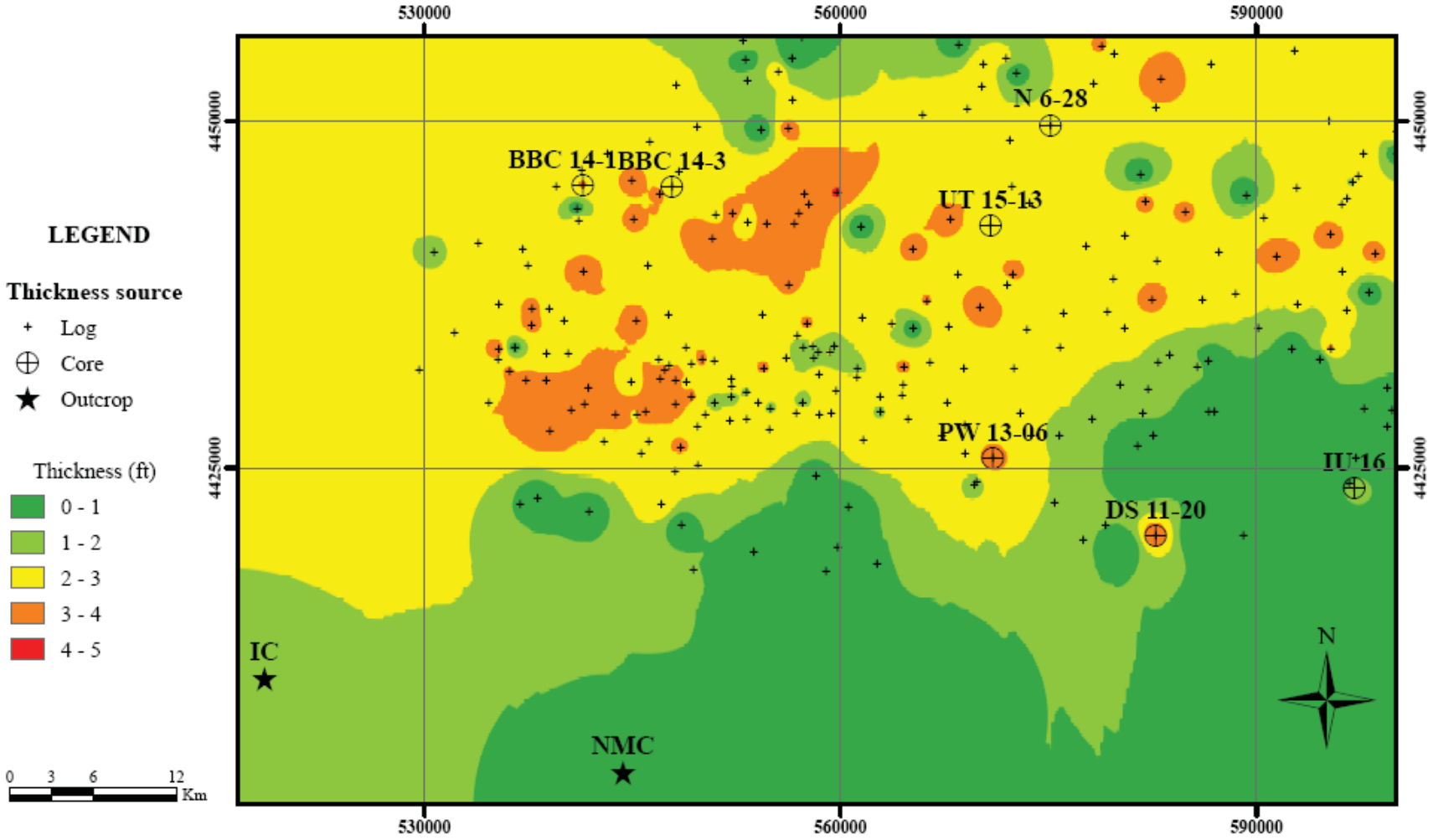

Figure 6.6: Isopachous map for PZ2 layer. Thickness measured from logs (data courtesy of Michael Vanden Berg, 2015), cores, and outcrops.

6.1.5 Calcite – Dolomite – Chert: Lake water evolution

The variation in the chemical composition of the lake water can be further characterized by the mineral association and timing between calcite, dolomite, and chert occurrence. The diagenesis of these minerals can be briefly described as: (i) calcite precipitation (deposition of lime mud), (ii) dolomitization of calcite (lime mud sediment and/or limestone), and (iii) chert formation within PZ layers. During the freshest water and relatively low temperature settings precipitation of calcium carbonate was promoted. Dolomite formation was caused by variations in the chemical composition of lake water coupled with increased temperature. Increased lake water temperature coupled with promoted dolomitization. According to the estimation of lake water temperatures by $\delta^{18}O$ geothermometry, the calcite-dolomite mineral association suggests a gradual increase of the lake water temperature from 12°C (calcite precipitation) to 36° to 40°C (dolomitization). This temperature increase was correlated with the lake water regression: as the lake water level decreased, the temperature increased.

In the fresh water setting, calcite precipitated likely promoted by a decrease in CO_2 concentration either due to photosynthesis (high organic activity) or by lake water degassing (Eugster and Hardie, 1978; Tucker and Wright, 1990). Calcite precipitation led to an increase in the Mg/Ca ratio, which favoured dolomitization.

Eugster and Hardie (1978) defined the fluid evolution of a hydrologically closed system, in which the evaporation products depend on lake water chemical composition. They propose three main possible evolution pathways based on HCO_3^- / Mg^{2+} + Ca^{2+} ratio. Lack of sodium carbonates and calcium sulfates within the stratigraphic interval of interest suggests a lake water with equal bicarbonate (HCO_3^-) and Mg^{2+}+ Ca^{2+} ratio. The HCO_3^- / Mg^{2+} + Ca^{2+}

ratio changed because of mineral crystallization. Depletion of alkaline metals (mainly Mg and Ca) due to calcite (precipitation) and dolomite (replacement) generated pH to increase, which kept the silica in solution. Occasional fresh water input diluted the lake water and decreased the pH of the lake water (Eugster, 1967) hence promoting chert crystallization within the already dolomitized lime mud sediment/limestone. Furthermore, the lack of sodium carbonates and calcium sulfates suggest a lake water salinity below seawater, probably a hyposaline composition.

6.1.6 Applicable models of dolomitization

Most models of dolomitization involve seawater and/or derivatives of the seawater as the dolomitizing fluid (e.g. Machel, 2004). However, none of these models can be applied to explain the origin of the dolomites in the Uteland Butte member, which were deposited in a lacustrine environment. Therefore, the models that remain as possibilities are (i) the mixing model, and two models linked with evaporated water, (ii) the seepage reflux model, and (iii) the evaporative pumping model. These models are here correlated with the characteristics of the dolomites of the Uteland Butte member (Table 6.1).

It appears that the evaporative reflux and the evaporative pumping models are equally likely alternatives. In the evaporative reflux model, the sediments would have been submerged and the evaporated water moved downward due to lake water density. In the case of the evaporative pumping, the lake water level would has been lowered so as to expose the lake sediments to the atmosphere, allowing pore water to move up through sediments (Figure 6.2).

Furthermore, while evaporation likely was a key factor for dolomitization, the salinity of the lake water likely was relatively high. Without direct evidence and in the noted absence of evaporite minerals, it is safe to speculate that the salinity of the lake water, and the pore water derived from it, ranges from fresh during the cooler periods to brackish during warmer and dryer periods.

In either scenario, dolomitization was controlled by climate. In the warmest periods, freshwater input was diminished and lake water evaporation was promoted, allowing dolomite PZ layers to form. In the coolest periods, freshwater input increased, diluting lake water, hence inhibiting dolomitization. The interpreted freshwater – brackish water changes are also recorded by the fossils associations: freshwater molluscs (pelecypods and gastropods) in the floatstone layers, more salinity tolerant organisms (ostracods and gyronites) and lack of fresh water molluscs in the dolomite layers.

Additionally to the evaporative models (reflux and pumping), there is a playa-lake model proposed by Eugster and Surdam (1973), which offers an explanation for dolomite formation in the Green River Formation, Gosiute Lake, Wyoming (USA). This model is genetically associated to the evaporative pumping model, in which a high evaporation rate caused dolomitization throughout a wide and flat "playa" and very shallow littoral settings (Eugster and Surdam, 1973).

As conclusion, the origin of the dolomite formation of the Uteland Butte member is a combination of diachronous dolomitization processes that involves evaporative reflux and pumping models, which took place in a flat playa-lake setting (Figure 6.7).

Dolomite characteristics	Dolomitization models			
	Mixing zone	Evaporative pumping	Evaporative reflux	Playa-Lake
Aphanocrystalline dolomite		✓	✓	✓
Low ordering	✓	✓	✓	✓
Broad %Ca spectrum	✓	✓	✓	✓
Lack of evaporite minerals	✓	✓	✓	
Small scale dolomite-limestone interbedding		✓	✓	✓
Tabular geometry		✓	✓	✓

Table 6.1: Dolomite characteristics for each probable dolomitization model that explain the origin of dolomite in the Uteland Butte member.

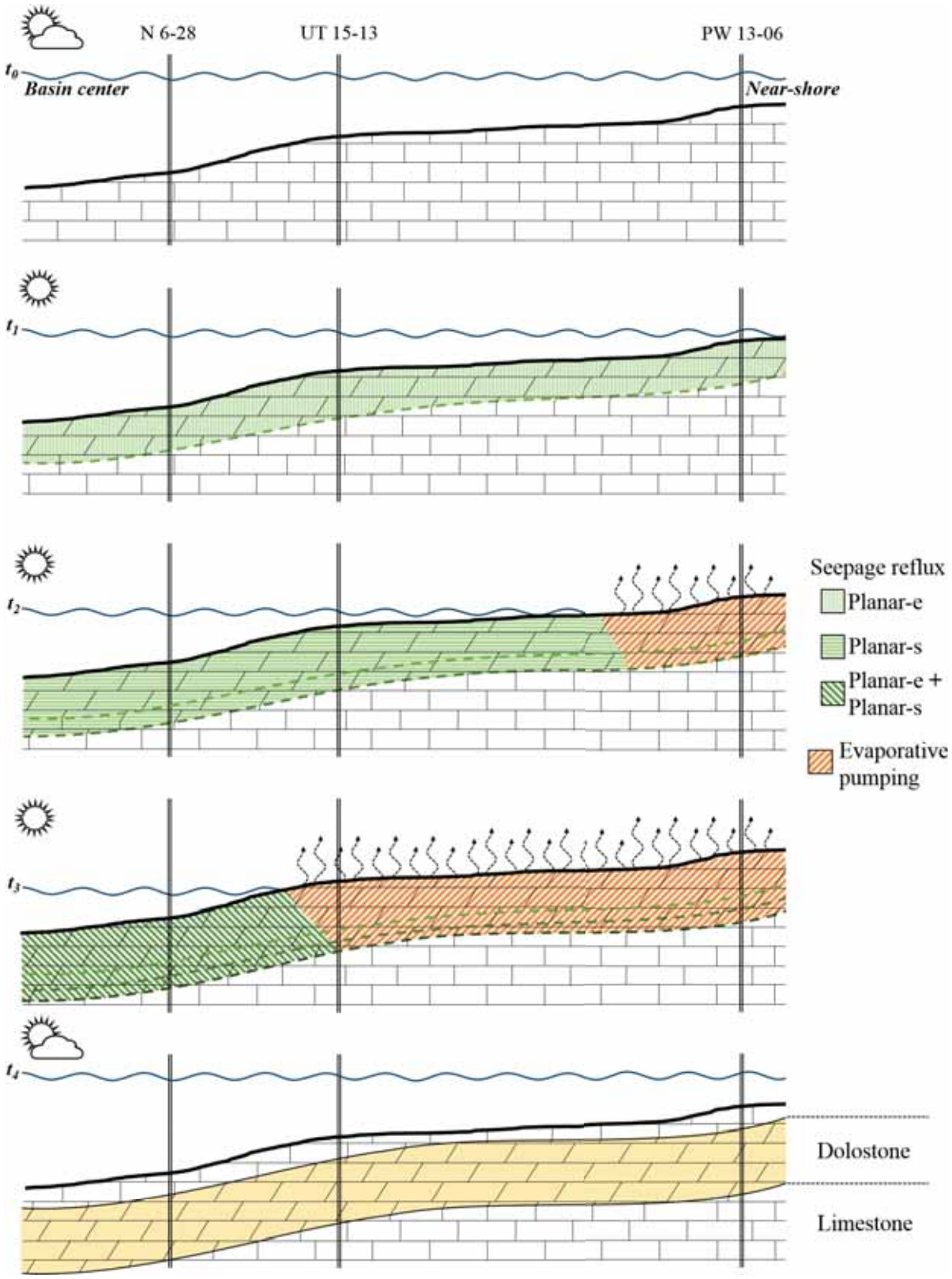

Figure 6.7: Schematic representation of the diachronous dolomitizing processes that took place in the playa-lake setting.

6.2 Stratigraphic interval D and C Shales

Periodic variations on climate was recorded by the repetition of the idealized cycle, which is present five times in the interval of interest (see Chapter 4, section 4.3). Dolomitization took place at the top of the cycles when climatic conditions, characterized by high temperatures and high evaporation rates, promoted dolomitization. However, dolomite formation could has been not possible without evolution of the Uinta lake from the fresh water setting, that took place at the base of the cycles (represented by the silty mudstone and limestone layers), toward an arid and dry setting. In the fresh water period, the drainage (rivers and groundwater) feed the Uinta Lake with Mg^{2+} ions that make possible dolomitization during the later dry periods. As summary, dolomitization is the result of cyclic changes of the Uinta Lake characteristics driven by climate.

6.3 Regional paleogeography

Sedimentation pattern of lacustrine basins is controlled by climate and tectonism (Tucker and Wright, 1990; Gierlowski-Kordesch, 2010; Tänavsuu-Milkeviciene et al., 2017). Changes in depositional settings caused by climate occur during short periods of time, whereas changes driven by tectonism take longer periods of time (Tänavsuu-Milkeviciene et al., 2017). The stratigraphic section of interest in the study area was basically controlled by climate variations, however, the entire section of the Green River Formation records depositional changes caused by tectonism.

Davis et al. (2009) interpreted the evolution of the catchment area of the lacustrine intermountain and coexisting basins of Claron Lake, Lake Flagstaff, and Uinta Lake. Davis et

al. (2009) identified a negative slope shift of the $\delta^{18}O_{Cal}$ values, which is interpreted as result of changes in the hydrology that in turn was controlled by height increment of the catchment area. Accordingly, altitude of the catchment area of the Uinta Lake at the time of deposition of the Uteland Butte member was lower than at the top of the Green River Formation (saline facies), which probably reached highness of about 2500 to 3000 m (Davis et al., 2009).

6.4 Dolomitization and porosity

Dolomite PZ layers are characterized by high porosity values of up to 30% and low permeability values that ranges from 10^{-1} to up to 10^{-3} mD (see Chapter 5, section 5.3). Dolomite textures and porosity values show a positive correlation (Woody et al., 1996; Lucia, 1999; Moore, 2001). Woody et al. (1996) correlated planar-e textures with high porosity and high permeability values. Figure 6.14 shows the correlation between dolomite texture and porosity.

There is a weak positive correlation between dolomite texture and porosity (Figure 6.8). However, planar textures (planar-e and planar-s) preferentially show the highest porosity values in contrast with a non-planar texture, which shows the lowest porosity values.

There is not a discernible relationship between dolomite texture and porosity and texture relationship ($R^2 < 0.2$). The poor correlation was probably generated by recrystallization events that might have created increment of dolomite crystal size and/or changes in crystals shape.

On the other hand, dolomite crystals packing is related with porosity values. In planar-e textures, dolomite crystals have straight crystal boundaries associated with more open space between crystals. In contrast, non-planar texture dolomite crystals are irregular in shape and

closely packed (Figure 5.39), which significantly reduces the open space between dolomite crystals.

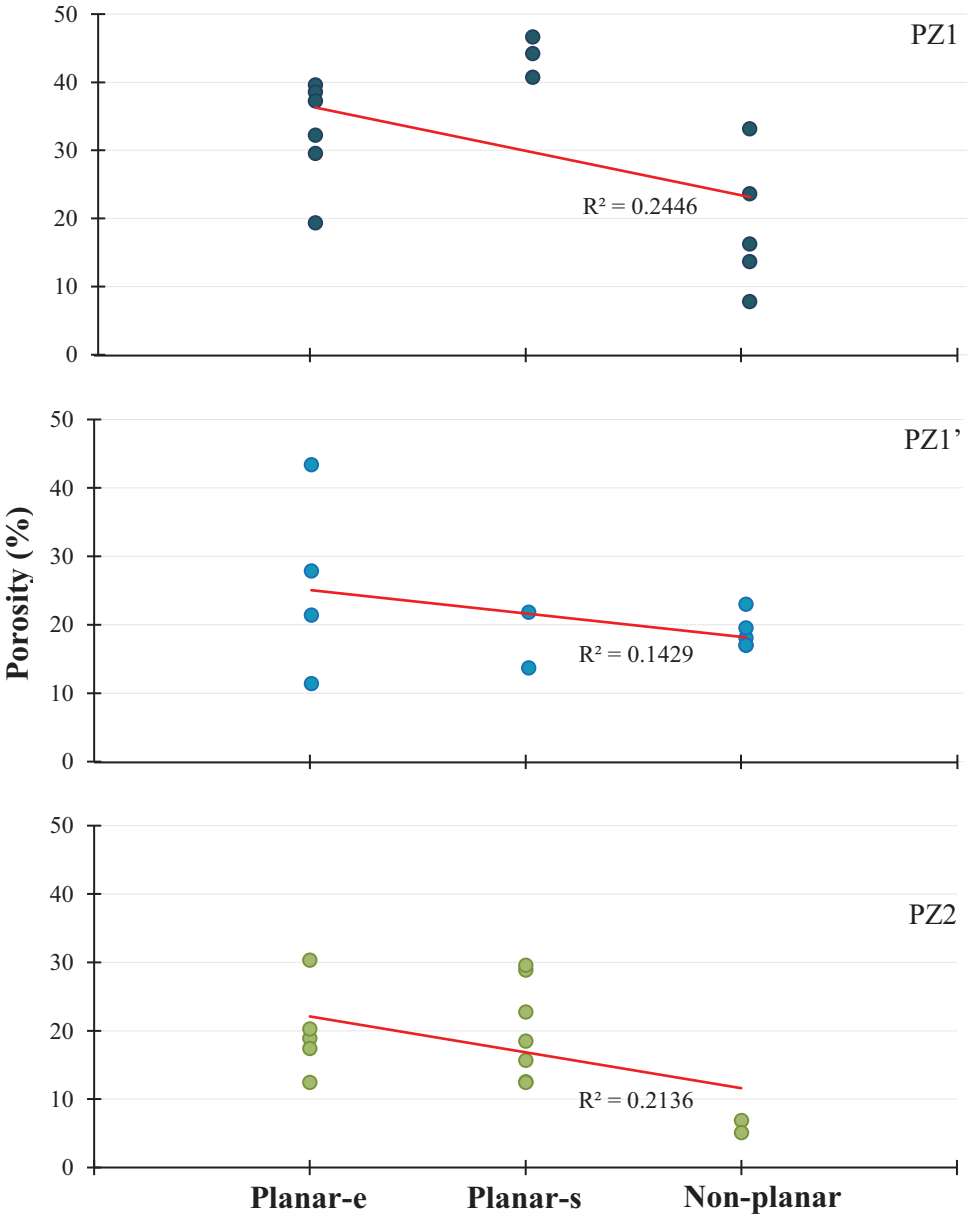

Figure 6.8: Dolomite texture versus porosity for each PZ layer. Dolomite texture determined from SEM image and porosity calculated from SEM image analysis software.

CHAPTER SEVEN

PRELIMINARY DRAFT ONLY

This Chapter summarizes the main findings of this work with reference to the objectives outlined in Chapter One, and also lists avenues for future work.

CHAPTER SEVEN

CONCLUSIONS AND FUTURE WORK

7.1 Conclusions

This project provides new insights into the dolomitization process of the Uteland Butte member and it relationship with porosity of the unconventional PZ layers, and successfully addressed the five specific objectives as follows:

Objective 1

Characterization and analysis of facies types for the Uteland Butte member as they relate to dolomitization. The UTB were deposited between the littoral and sublittoral settings. However, there is no recognizable relationship between facies and dolomitization. Pervasive and matrix selective dolomitization crosscut all facies boundaries, since the distal sublittoral setting (basin ward) toward the near-shore area.

Objective 2

Determination of the process of dolomitization. Dolomite PZ layers were originated by replacing the lime mud parental sediments, mainly characterized by distinctive petrographic textural features such as partial or complete matrix-selective replacement, vugs and moulds pores, two dolomite populations, and dolomite cementation. Furthermore, dolomites conform to the type of dolomite known as penecontemporaneous due to the aphanocrystalline crystal size that ranges from 0.5 to 6 μm, wider range of %Ca content that varies from 50% to 59%,

and low cation ordering that range from 0.1 to 0.5. Dolomitization was controlled by climate in which in the driest periods increased the evaporation that shifted the lake water from freshwater (calcite precipitation) toward a more saline (dolomitization).

Objective 3

Dolomitization and porosity-permeability: There is not a discernible control of dolomitization over porosity permeability. However, dolomite textures e and s present higher porosity values. The geographic distribution of the primary texture of the dolomite PZ layers was apparently controlled by changes in dolomitizing fluid chemical composition, however, recrystallization partially obliterated this preferential distribution.

Objective 4

Geometry of the dolomite layers across the western Uinta Basin: Thickness of the PZ layers is highly variable and it was probably controlled by the availability of dolomitizing fluid, density of dolomitizing fluid, porosity features of the partially consolidated and underlying lime mud sediment, or a combination of all. Furthermore, there is a trend in which the thicker section of the PZ layers are located between the near-shore area and the basin center.

Objective 5

Possible implications for petroleum reservoir development: Dolomitization created intercrystal and vug porosity as the most abundant porosity types. However, dolomite recrystallization changed the primary petrophysical characteristic of these layers that converted the in the current heterogeneous PZ reservoirs.

7.2 Future work

There are new questions that raised during the development of this study, which will help to understand better the dolomitization of the Uteland Butte member. This questions are:

1) Stoichiometry and cation ordering of dolomite. The wide range of the %Ca coupled with the low cation ordering is a conspicuous characteristic of the dolomite PZ layers. The diagenetic history in which the dolomite PZ layer reached maximum burial of around 3000 m with temperatures around 100 °C would modified these features. However, the features are still printed in the dolomites, and especially remarkable is the cation ordering with an average of 0.27 and a maximum value of 0.48.

2) The discrepancy between the temperatures calculated from the conventional oxygen isotopes and clumped isotopes thermometry could be investigated deeper. The clumped isotopes temperature for calcite is much higher than for dolomite from layers within the same stratigraphic interval of interest. Based on this difference, it appears that calcite is more prone to recrystallization that dolomite, however both layers underwent the same burial history.

REFERENCES

Adams, J. E., and Rhodes, M. L., 1960, Dolomitization by seepage refluxion: AAPG Bulletin, v. 44, no. 12, p. 1912-1920, http://archives.datapages.com/data/bulletns/1957-60/images/pg/00440012/1900/19120.pdf.

Al-Aasm, I. S., Taylor, B. E., and South, B, 1990, Stable isotope analysis of multiple carbonate samples using selective acid extraction: Chemical Geology: Isotope Geoscience Section, v. 80, no. 2, p. 119-125, https://doi.org/10.1016/0168-9622(90)90020-D.

---------Analysis of ^{13}C and ^{18}O of carbonate minerals by CF-IRMS, http://www.ucalgary.ca/uofcisl/techniques.

Anderson, J. G., and Roesink, J. G., 2013, Reservoir characterization of the Uteland Butte Formation in the Uinta Basin, American Association of Petroleum Geologists Search and Discovery Article #50888, http://www.searchanddiscovery.com/pdfz/documents/2013/50888anderson/ndx_anderson.pdf.html

Anderson, T. W., and Darling, D. A., 1954, A test of goodness of fit: Journal of the American statistical association, v. 49, no. 268, p. 765-769, DOI:10.1080/01621459.1954.10501232

Baars, D. L., and Stevenson G. M, 1981, Tectonic evolution of western Colorado and eastern Utah, *in* R. C. Epis and J. F. Callender, eds., Western Slope (Western Colorado) - New Mexico Geological Society 32nd Annual Fall Field Conference Guidebook: New Mexico Geological Society, p. 105-112.

Baccelle, L. and Bosellini, A, 1965, Diagrammi per la stima visiva della composizione percentuale nelle rocche sedimentary: Annali dell'Univrsità di Ferrara (Nuova Serie), Sezione 9, Scienze Geologiche e Paleontologiche, v. 1, no. 3, p. 59-62.

Banner, J. L., 1995, Application of the trace element and isotope geochemistry of strontium to studies of carbonate diagenesis: Sedimentology, v. 42, no. 5, p. 805-824, DOI:10.1111/j.1365-3091.1995.tb00410.x.

Barron, E. J, 1990, Climate and Lacustrine Petroleum Source Prediction, *in* Katz, B. J., ed., Lacustrine Basin Exploration, AAPG Memoir 50: The American Association of Petroleum Geologists, p. 1-18.

Belovsky, G. E., et al., 2011, The Great Salt Lake Ecosystem (Utah, USA): long term data and a structural equation approach: Ecosphere, v.2, no. 3, 1-40, DOI:10.1890/ES10-00091.1.

Bereskin, S. R., Morgan, C. D., and McClure, K. P, 2004, Descriptions, petrology, photographs, and photomicrographs of core from the Green River Formation, south-central Uinta Basin, Utah: Utah Geological Survey Miscellaneous Publication, v. 4, p. 1 – 38, http://archives.datapages.com/data/utah-geological-survey/data/mp-04-2.pdf

Berner, R. A., De Leeuw, J. W., Spiro, B., Murchison, D. G., and Eglinton, G., 1985, Sulphate reduction, organic matter decomposition and pyrite formation [and discussion]: Philosophical Transactions of the Royal Society of London A: Mathematical, Physical and Engineering Sciences, v. 315, no. 1531, p. 25-38, http://www.jstor.org/stable/37702.

Best, M.G, 1982, Igneous and Metamorphic Petrology: San Francisco, W. H. Freeman and Company.

Bhat, H. L, 2015, Introduction to crystal growth: principles and practice: Boca Raton, CRC Press.

Birdwell, J. E., Berg, M. D. V., Johnson, R. C., and Brownfield, M. E., 2016, Geological, geochemical and reservoir characterization of the Uteland Butte member of the Green River Formation, Uinta Basin, Utah, in Michael P. D., Debra K. H., and Paul G. L., eds., Hydrocarbon Source Rocks in Unconventional Plays, Rocky Mountain Region: Rocky Mountain Association of Geologists, p. 352-378,

https://www.researchgate.net/profile/Justin_Birdwell/publication/311296330_Geological_geochemical_and_reservoir_characterization_of_the_Uteland_Butte_member_of_the_Green_River_Formation_Uinta_Basin_Utah/links/584f111308aeb989252cb31c.pdf.

Birdwell, J. E., Vanden Berg, M. D. V., Johnson, R. C., and Brownfield, M. E., 2016, Geological, geochemical and reservoir characterization of the Uteland Butte member of the Green River Formation, Uinta Basin, Utah, *in* Michael P. D., Debra K. H., and Paul G. L., Hydrocarbon Source Rocks in Unconventional Plays, Rocky Mountain Region: The Rocky Mountain Association of Geologist, p. 352-378.

Boehrer, B., and Schultze, M, 2008, Stratification of lakes: Reviews of Geophysics, v. 46, no. 2, 1-27, http://onlinelibrary.wiley.com/doi/10.1029/2006RG000210/epdf.

Boggs, S. J., and Krinsley, D, 2006, Application of cathodoluminescence imaging to the study of sedimentary rocks: New York, Cambridge University Press, 165 p.

Bradley, W. H, 1931, Origin and Microfossils of the Oil Shale of the Green River Formation of Colorado and Utah: U.S. Geological Survey Professional Paper 168, p. 1-58, https://pubs.usgs.gov/pp/0168/report.pdf.

Broecker, W. S, 1971, A kinetic model for the chemical composition of sea water: Quaternary Research, v. 1, no.2, p. 188-207, https://doi.org/10.1016/0033-5894(71)90041-X.

Budd, D. A, 1997, Cenozoic dolomites of carbonate islands: their attributes and origin: Earth-Science Reviews, v. 42, no 1-2, p. 1-47, https://doi.org/10.1016/S0012-8252(96)00051-7.

Carroll, A. R., and Bohacs, K. M, 1999, Stratigraphic classification of ancient lakes: Balancing tectonic and climatic controls: Geology, v. 27, no. 2, p. 99-102, DOI:10.1130/0091-7613(1999)027<0099:SCOALB>2.3.CO;2.

Case, J. E, 1991, Geologic Map of the Northwestern Part of the Uncompahgre Uplift, Grand County, Utah, and Mesa County, Colorado, with Emphasis on Proterozoic Rocks. U.S. Geological Survey.

Cashion, W. B, 1967, Geology and fuel resources of the Green River Formation, southeastern Uinta basin, Utah and Colorado: U.S. Geological Survey Professional Paper 548, p. 1-48, https://pubs.usgs.gov/pp/0548/report.pdf.

Cashion, W. B, 1995, Stratigraphy of the Green River Formation, Eastern Uinta Basin, Utah and Colorado - A Summary: Grand Junction Geological Society, p. 15 – 21, http://archives.datapages.com/data/grand-junction-geo-soc/data/013/013001/pdfs/15.pdf.

Choquette, W., and Pray, L. C, 1970, Geologic nomenclature and classification of porosity in sedimentary carbonates: American Association of Petroleum Geologist Bulletin, v. 54, no. 2, p. 207-250, http://archives.datapages.com/data/bulletns/1968-70/images/pg/00540002/0200/02070.pdf.

Cohen, A. S, 2003, Paleolimnology: the history and evolution of lake systems: New York, Oxford University Press, 500 p.

Cole, R. D., and Picard, M. D, 1978, Comparative mineralogy of nearshore and offshore lacustrine lithofacies, Parachute Creek Member of the Green River Formation, Piceance Creek Basin, Colorado, and eastern Uinta Basin, Utah: Geological Society of America Bulletin, v. 89, no. 10, p. 1441-1454, DOI:10.1130/0016-7606(1978)89<1441:CMONAO>2.0.CO;2.

Davis, S. J, 2008, Synorogenic evolution of large-scale drainage patterns: Isotope paleohydrology of sequential laramide basins [Ph.D. thesis]: Stanford, Stanford University, 204 p., http://login.ezproxy.library.ualberta.ca/login?url=http://search.proquest.com/docview/304471073?accountid=14474.

Davis, S. J., Mulch, A., Carroll, A. R., Horton, T. W., and Chamberlain, C. P, 2009, Paleogene landscape evolution of the central North American Cordillera: Developing topography and hydrology in the Laramide foreland: Geological Society of America Bulletin, v. 121, no. 1-2, p. 100-116, DOI:10.1130/B26308.1.

Davis, S. J., Mulch, A., Carroll, A. R., Horton, T. W., and Chamberlain, C. P., 2009, Paleogene landscape evolution of the central North American Cordillera: Developing topography and hydrology in the Laramide foreland: Geological Society of America Bulletin, v. 121, no. 1-2, p. 100-116, DOI:10.1130/B26308.1.

Davison, W., 1993, Iron and manganese in lakes: Earth-Science Reviews, v. 34, no. 2, p. 119-163, DOI: 10.1016/0012-8252(93)90029-7.

Degens, E. T., and Epstein, S, 1964, Oxygen and carbon isotope ratios in coexisting calcites and dolomites from recent and ancient sediments: Geochimica et Cosmochimica Acta, v. 28, no. 1, p. 23-44, https://doi.org/10.1016/0016-7037(64)90053-5.

Desborough, G. A, 1978, A biogenic-chemical stratified lake model for the origin of oil shale of the Green River Formation: An alternative to the playa-lake model: Geological Society of America Bulletin, v. 89, no. 7, p. 961-971, DOI:10.1130/0016-7606(1978)89<961:ABSLMF>2.0.CO;2.

Dickinson, G., 1953, Geological aspects of abnormal reservoir pressures in Gulf Coast Louisiana: AAPG Bulletin, v. 37, no. 2, p. 410-432, http://archives.datapages.com/data/bulletns/1953-56/images/pg/00370002/0400/04100.pdf.

Dickinson, W. R., Klute, M. A., Hayes, M. J., Janecke, S. U., Lundin, E. R., McKittrick, M. A., and Olivares, M. D, 1988, Paleogeographic and paleotectonic setting of Laramide sedimentary basins in the central Rocky Mountain region: Geological Society of America Bulletin, v. 100, no. 7, p. 1023-1039, DOI:10.1130/0016-7606(1988)100<1023:PAPSOL>2.3.CO;2.

Dickinson, W. R., Lawton, T. F., and Inman, K. F, 1986, Sandstone detrital modes, central Utah foreland region: stratigraphic record of Cretaceous-Paleogene tectonic evolution: Journal of Sedimentary Research, v. 56, no. 2, p. 276-293, http://archives.datapages.com/data/sepm/journals/v55-58/data/056/056002/pdfs/0276.pdf.

Dickinson, W. R., Lawton, T. F., Pecha, M., Davis, S. J., Gehrels, G. E., and Young, R. A., 2012, Provenance of the Paleogene Colton Formation (Uinta Basin) and Cretaceous–Paleogene provenance evolution in the Utah foreland: Evidence from U-Pb ages of detrital zircons, paleocurrent trends, and sandstone petrofacies: Geosphere, v. 8, no. 4, p. 854, DOI:10.1130/GES00763.1.

Dickson, J. A. D, 1965, A modified staining technique for carbonates in thin section. Nature, v. 205, no. 4971, p. 587, http://dx.doi.org/10.1038/205587a0.

Doelling, H. H, 2002, Interim Geologic Map of the San Rafael Desert 30' x 60' Quadrangle, Emery and Grand Counties, Utah.

Dunham, R. J, 1962, Classification of carbonate rocks according to depositional textures: The American Association of Petroleum Geologists Memoir 1, p. 108-121, http://archives.datapages.com/data/specpubs/carbona2/images/a038/a0380001/0100/01080.pdf.

Dyni, J.R., Milton, C., and Cashion, W.B, 1985, The saline facies of the upper part of the Green River Formation near Duchesne, Utah, *in* Picard, M.D, ed., Geology and Energy Resources, Uinta Basin of Utah. Salt Lake City: Utah Geological Association, Publication, p. 51-60, http://archives.datapages.com/data/uga/data/055/055001/pdfs/51.pdf.

Eardley, A. J., 1938, Sediments of Great Salt Lake, Utah: AAPG Bulletin, v. 22, no. 10, p. 1305-1411, http://archives.datapages.com/data/bulletns/1938-43/images/pg/00220010/1300/13050.pdf.

Ebner, M., Toussaint, R., Schmittbuhl, J., Koehn, D., and Bons, P., 2010, Anisotropic scaling of tectonic stylolites: A fossilized signature of the stress field?: Journal of Geophysical Research: Solid Earth, v. 115, no. B6, DOI:10.1029/2009JB006649.

Embry III, A. F., and Klovan, J. E., 1971, A late Devonian reef tract on northeastern Banks Island, NWT: Bulletin of Canadian Petroleum Geology, v. 19, no. 4, p. 730-781, http://archives.datapages.com/data/cspg/data/019/019004/pdfs/0730.pdf.

Esteban, M., Klappa, C. F., 1983, Subaerial exposure environment, *in* Scholle, P.A., Bebout, D. G., and Moore, C. H., eds., Carbonate depositional environments: American Association of Petroleum Geologists, Memoir, 33, p. 1-54.

Eugster, H. P., 1967, Hydrous sodium silicates from Lake Magadi, Kenya: Precursors of bedded chert: Science, v. 157, no. 3793, p. 1177-1180, DOI: 10.1126/science.157.3793.1177.

Eugster, H. P., and Hardie, L. A., 1978, Saline lakes, *in* Lerman A. and Baccini P., Lakes: Chemistry, Geology, Physics, p. 237-293, New York: Springer-Verlag.

Eugster, H. P., and Surdam, R. C., 1973, Depositional environment of the Green River Formation of Wyoming: A preliminary report: Geological Society of America Bulletin, v. 84, no. 4, p. 1115-1120, DOI:10.1130/0016-7606(1973)84<1115:DEOTGR>2.0.CO;2.

Flöerke, O. W., Graetsch, H., Martin, B., Röeller, K., and Wirth, R., 1991, Nomenclature of micro- and non-crystalline silica minerals, based on structure and microstructure: Neues Jahrbuch Fuer Mineralogie. Abhandlungen, v. 163, no. 1, p. 19-42.

Flügel, E., 2010, Microfacies of carbonate rocks: Analysis, interpretation and application. 2nd edition: Berlin, Springer, 984 p.

Folk, R. L., and Land, L. S., 1975, Mg/Ca ratio and salinity: two controls over crystallization of dolomite: American Association of Petroleum Geologists Bulletin, v. 59, no. 1, p. 60-68, http://archives.datapages.com/data/bulletns/1974-76/images/pg/00590001/0050/00600.pdf.

Folk, R. L., and Pittman, J. S., 1971, Length-slow chalcedony; a new testament for vanished evaporites: Journal of Sedimentary Petrology, v. 41, no, 4, p. 1045-1058. DOI:10.1306/74D723F1-2B21-11D7-8648000102C1865D.

Folk, R. L., and Siedlecka, A., 1974, The “schizohaline” environment: Its sedimentary and diagenetic fabrics as exemplified by Late Paleozoic rocks of Bear Island, Svalbard: Sedimentary Geology, v. 11, no. 1, p. 1-15, DOI:10.1016/0037-0738(74)90002-5.

Folk, R. L., and Weaver, C. E., 1952, A study of the texture and composition of chert: American Journal of Science, v. 250, p. 498-510, DOI:10.2475/ajs.250.7.498.

Foreman, B. Z., Heller, p. L., and Clementz, M. T., 2012, Fluvial response to abrupt global warming at the Palaeocene/Eocene boundary: Nature, v. 49, no. 7422, p. 92-95, doi:10.1038/nature11513.

Fouch, T. D., 1976, Revision of the lower part of the Tertiary System in the central and western Uinta basin, Utah: Geological Society Bulletin 1405-C, p. C1-C7, https://pubs.usgs.gov/bul/1405c/report.pdf.

Freytet, p., and Verrecchia, E. P, 2002, Lacustrine and palustrine carbonate petrography; an overview. *Journal of Paleolimnology, 27*(2), p. 221-237.

Friedman, I., and O'Neil, J. R., 1977, Data of geochemistry: Compilation of stable isotope fractionation factors of geochemical interest: US Geological Survey Bulletin Vol 440-KK, https://pubs.usgs.gov/pp/0440kk/report.pdf.

Gat, J. R., 1995, Stable isotopes of fresh and saline lakes, *in* Lerman, A., Imboden, D. M., and Gat, J. R., eds., Physics and chemistry of lakes: Springer-Verlag Heidelberg, p. 139-165.

Ghosh, P., Adkins, J., Affek, H., Balta, B., Guo, W., Schauble, E. A., Scharg, D., and Eiler, J. M., 2006, 13 C–18 O bonds in carbonate minerals: A new kind of paleothermometer: Geochimica et Cosmochimica Acta, v. 70, no. 6, p. 1439-1456, https://doi.org/10.1016/j.gca.2005.11.014.

Gierlowski-Kordesch, E. H., 2010, Lacustrine carbonates, in Alonso-Zarzs A. M. and Tanner L. H, eds., Carbonates in continental settings: Facies, environments, and processes, Developments in Sedimentology 61: Oxford, Elsevier, p. 1-101.

Gierlowski-Kordesch, E. H., Jacobson, A. D., Blum, J. D., and Garćes, B. V., 2008, Watershed reconstruction of a Paleocene–Eocene lake basin using Sr isotopes in carbonate rocks: Geological Society of America Bulletin, v. 120, no. 1-2, p. 85-95, DOI:10.1130/B26070.1.

Goldsmith, J. R., and Graf, D. L., 1958, Structural and compositional variations in some natural dolomites: The Journal of Geology, v. 66, no. 6, p 678-693, http://www.jstor.org/stable/30056855.

Gregg, J. M., 1985, Regional epigenetic dolomitization in the Bonneterre Dolomite (Cambrian), southeastern Missouri: Geology, v. 13, no. 7, p. 503-506, DOI:10.1130/0091-7613(1985)13<503:REDITB>2.0.CO;2.

Gregg, J. M., and Shelton, K. L. (1989). Minor-and trace-element distributions in the Bonneterre Dolomite (Cambrian), southeast Missouri: Evidence for possible multiple-basin fluid sources and pathways during lead-zinc mineralization: Geological Society of America Bulletin, v. 101, no. 2, p. 221-230, DOI:10.1130/0016-7606(1989)101<0221:MATEDI>2.3.CO;2.

Gregg, J. M., and Sibley, D. F, 1984, Epigenetic dolomitization and the origin of xenotopic dolomite texture: Journal of Sedimentary Research, v. 54, no. 3, p. 908-931, http://archives.datapages.com/data/sepm/journals/v51-54/data/054/054003/pdfs/0908.pdf.

Gregg, J. M., Bish, D. L., Kaczmarek, S. E., and Machel, H. G., 2015, Mineralogy, nucleation and growth of dolomite in the laboratory and sedimentary environment: A review: Sedimentology, v. 62, no. 6, p. 1749-1769, DOI:10.1111/sed.12202.

Gregg, J. M., Howard, S. A., and Mazzullo, S. J., 1992, Early diagenetic recrystallization of Holocene (< 3000 years old) peritidal dolomites, Ambergris Cay, Belize: Sedimentology, v. 39, no. 1, p. 143-160, DOI:10.1111/j.1365-3091.1992.tb01027.x.

Håkanson, L., and Jansson, M, 1983, Principles of Lake Sedimentology: Berlin: Springer-Verlag, 387 p.

Hansen, W. R., 1965, Geology of the Flaming Gorge area Utah – Colorado – Wyoming U. S. Geological Survey Professional Paper 490: Washington, United States Government Printing Office, p. 1-196, https://pubs.usgs.gov/pp/0490/report.pdf.

Hao, F., Zhou, X., Zhu, Y., Bao, X., and Yang, Y., 2009, Charging of the Neogene Penglai 19-3 Field, Bohai Bay Basin, China; oil accumulation in a young trap in an active fault zone: AAPG Bulletin, v. 93, no. 2, p. 155-179, doi:10.1306/09080808092

Hardy, R, and Tucker, M. E., 1988, X-Ray powder diffraction of sediments, *in* Tucker M., ed., Techniques in sedimentology: Oxford: Blackwell Scientific Publications. p. 191-228.

Heaney, P. J., 1995, Moganite as an indicator for vanished evaporites; a testament reborn?: Journal of Sedimentary Research, Section A: Sedimentary Petrology and Processes, v. 65, no. 4, pp. 633-638, DOI: 10.1306/D4268180-2B26-11D7-8648000102C1865D.E

Hintze, L. F., Willis, G. C., Laes, D. Y., Sprinkel, D. A., and Brown, K. D., 2000, *Digital geologic map of Utah*. Utah Geological Survey, Utah Department of Natural Resources.

Hsü, K. J., and Siegenthaler, C., 1969, Preliminary experiments on hydrodynamic movement induced by evaporation and their bearing on the dolomite problem: Sedimentology, v. 12, no. 1-2, p. 11-25, DOI: 10.1111/j.1365-3091.1969.tb00161.x.

Hudson, J. D., 1977, Stable isotopes and limestone lithification: Journal of the Geological Society, v. 133, no. 6, p. 637-660, http://DOI:10.1144/gsjgs.133.6.0637.

Hunt, C. B., 1956, Cenozoic Geology of the Colorado Plateau: US Geological Survey Professional Paper 279, p. 1-99, https://pubs.usgs.gov/pp/0279/report.pdf.

Irwin, H., Curtis, C., and Coleman, M., 1977, Isotopic evidence for source of diagenetic carbonates formed during burial of organic-rich sediments: Nature, v. 269, p. 209-213, DOI:10.1038/269209a0.

James, N., P., and Choquette, P. W., 1984, Diagenesis 9. Limestones - The Meteoric Diagenetic Environment: Geoscience Canada, v. 11, no. 4, p. 161-194, https://journals.lib.unb.ca/index.php/GC/article/view/3395/3909.

Johnson, R. C., 1985, Early Cenozoic history of the Uinta and Piceance Creek basins, Utah and Colorado, with special reference to the development of Eocene Lake Uinta, *in* Flores R. M. and Kaplan, S. S., eds., Cenozoic Paleogeography of the West-Central

United States. Rocky Mountain Section (SEPM): Silers Printing, p. 247-276, http://archives.datapages.com/data/rocky_sepm/data/023/023001/pdfs/247.pdf.

Johnson, R. C., Birdwell, J. E., Mercier, T. J., and Brownfield, M. E., 2016, Geology of tight oil and potential tight oil reservoirs in the lower part of the Green River Formation, Uinta, Piceance, and Greater Green River Basins, Utah, Colorado, and Wyoming: U.S. Geological Survey Scientific Investigations Report 2016–5008, 63 p., https://pubs.usgs.gov/sir/2016/5008/sir20165008.pdf.

Johnson, R. C., Birdwell, J. E., Mercier, T. J., Brownfield, M. E., Charpentier, R. R., Klett, T. R., Leathers, H. M., Schenk, C. J., and Tennyson, M. E., 2015, Assessment of undiscovered oil and gas resources in the Uteland Butte Member of the Eocene Green River Formation, Uinta Basin, Utah: U.S. Geological Survey Fact Sheet 2015–3052, p. 1-2. http://dx.doi.org/10.3133/fs20153052.

Johnson, R., Mercier, T., Brownfield, M., and Self, J., 2010, Assessment of in-place oil shale resources in the Eocene Green River Formation, Uinta Basin, Utah and Colorado: U.S. Geological Survey Digital Data Series DDS–69–BB, https://pubs.usgs.gov/dds/dds-069/dds-069-y/REPORTS/69_Y_CH_1.pdf.

Jones, B., Luth, R. W., and MacNeil, A. J., 2001, Powder X-ray diffraction analysis of homogeneous and heterogeneous sedimentary dolostones: Journal of Sedimentary Research, v. 71, no. 5, p. 790-799, http://archives.datapages.com/data/sepm/journals/v71/071005/pdfs/0790.pdf.

Kaczmarek, S. E., 2005, Crystal growth mechanisms in natural and synthetic dolomite: Insight into dolomitization kinetics [Ph.D. thesis]: East Lansing, Michigan State University, 230 p., http://search.proquest.com/pqdtglobal/docview/305457408/F463BEBFAEEE4574PQ/1?accountid=14474.

Kaczmarek, S. E., and Sibley, D. F., 2011, On the evolution of dolomite stoichiometry and cation order during high-temperature synthesis experiments: an alternative model for the geochemical evolution of natural dolomites: Sedimentary Geology, v. 240, no. 1, p. 30-40, https://doi.org/10.1016/j.sedgeo.2011.07.003.

Keighley, D., Flint, S., Howell, J., and Moscariello, A., 2003, Sequence stratigraphy in lacustrine basins: a model for part of the Green River Formation (Eocene), southwest Uinta Basin, Utah, USA: Journal of Sedimentary Research, v. 73, no. 6, p. 987-1006, http://archives.datapages.com/data/sepm/journals/v73/data/073/073006/pdfs/0987.pdf .

Kile, D. E., Eberl, D. D., Hoch, A. R., and Reddy, M. M., 2000, An assessment of calcite crystal growth mechanisms based on crystal size distributions: Geochimica et Cosmochimica Acta, v. 64, no. 17, p. 2937-2950, https://doi.org/10.1016/S0016-7037(00)00394-X.

Kluth, C. F., 1986, Plate tectonics of the ancestral Rocky Mountains, *in* Peterson, J.A., ed., Paleotectonics and Sedimentation in the Rocky Mountain Region, United States: American Association of Petroleum Geologists Memoir 41, p. 353-369, Tulsa: The American Association of Petroleum Geologist, http://archives.datapages.com/data/specpubs/structu1/images/a155/a1550001/0350/03530.pdf.

Knauth, L. P, 1994, Petrogenesis of chert, *in* Heaney, P. J., Prewitt, C. T., and Gibbs, G. V., eds., Silica: physical behavior, geochemistry and materials applications: Mineralogical Society of America, p. 233-258.

Land, L. S., and Hoops, G. K., 1973, Sodium in carbonate sediments and rocks: a possible index to the salinity of diagenetic solutions: Journal of Sedimentary Research, v. 43, no. 3, p. 614-617, DOI:10.1306/74D7281A-2B21-11D7-8648000102C1865D.

Land, L.S., 1980, The isotopic and trace element geochemistry of dolomite: the state of the art, *in* Zenger, D. H., Dunham, J. B., and Ethington, R. L., eds., Concepts and Models of Dolomitization, SEPM Society for Sedimentary Geology, no. 28, p. 87-110, DOI:10.2110/pec.80.28.0087.

LaRocque, A., 1956, Tertiary mollusks of central Utah, *in* Peterson, J. A., ed., Geology and Economic Deposits of East Central Utah: Intermountain Association of Petroleum Geologist, p. 140-145, http://archives.datapages.com/data/uga/data/006/006001/pdfs/140.pdf.

Logan, B. W., and Semeniuk, V., 1976, Dynamic metamorphism; processes and products in Devonian carbonate rocks, Canning Basin, Western Australia: Special Publication - Geological Society of Australia, v. 6, p. 1-138.

Logan, S. K, 2015, Lacustrine lithofacies, depositional processes, and diagenesis of the Uteland Butte Member, Green River Formation, eastern Uinta Basin, Utah and Colorado [M.Sc. thesis]: Denver, Colorado School of Mines, 143 p., http://search.proquest.com/pqdtglobal/docview/1696048147/C9108BE9E31481DPQ/1?accountid=14474.

Logan, S. K., Sarg, J. F., and Vanden Berg, M. D., 2016, Lithofacies, deposition, early diagenesis, and porosity of the Uteland Butte member, Green River Formation, eastern Uinta Basin, Utah and Colorado: Utah Geological Survey Open File Report 652, 32 p., http://ugspub.nr.utah.gov/publications/open_file_reports/ofr-652.pdf

Long, M., 2006, Origin of the Dolomite on the Green River Formation [Ph.D. thesis]: Houston, University of Houston, 336 p., http://search.proquest.com/pqdtglobal/docview/305320777/fulltextPDF/23BA6849E07A4872PQ/1?accountid=14474.

Lucia, F. Jerry, 1999, Carbonate reservoir characterization: An integrated approach: Berlin, Springer, 227 p.

Luczaj, J. A., McIntire, M. J., and Olson Hunt, M. J.,2016, Geochemical Characterization of Trace MVT Mineralization in Paleozoic Sedimentary Rocks of Northeastern Wisconsin, USA: Geosciences, v. 6, no. 2, p. 1-29, DOI:10.3390/geosciences6020029.

Lumsden, D. N., 1979, Discrepancy between thin-section and X-ray estimates of dolomite in limestone: Journal of Sedimentary Research, v. 49, no. 2. p. 429-436, http://archives.datapages.com/data/sepm/journals/v47-50/data/049/049002/pdfs/0429.pdf.

Lumsden, D. N., and Chimahusky, J. S., 1980, Relationship between dolomite nonstoichiometry and carbonate facies parameters: Special Publication - Society of

Economic Paleontologists and Mineralogists, v.28, p. 123-137, http://archives.datapages.com/data/sepm_sp/SP28/Relationship_Between_Dolomite.pdf.

Luo, P., and Machel, H. G., 1995, Pore size and pore throat types in a heterogeneous dolostone reservoir, Devonian Grosmont Formation, Western Canada sedimentary basin: American Association of Petroleum Geologist Bulletin, v. 79, no. 11, p. 1698-1719, http://archives.datapages.com/data/bulletns/1994-96/images/pg/00790011/1650/1698.pdf.

MacGinitie, H. D., 1969, The Eocene Green River flora of northwestern Colorado and northeastern Utah: University of California Publications in Geological Sciences, v. 83, p. 1-203.

Machel, H. G, 1995, Magnetic mineral assemblages and magnetic contrasts in diagenetic environments - with implications for studies of palaeomagnetism, hydrocarbon migration and exploration: Geological Society, London, Special Publications, v. 98, vo. 1, p. 9-29, doi:10.1144/GSL.SP.1995.098.01.02.

Machel, H. G, 1997, Recrystallization versus neomorphism, and the concept of ‘significant recrystallization in dolomite research: Sedimentary Geology, v. 113, no. 3-4, p. 161-168, https://doi.org/10.1016/S0037-0738(97)00078-X.

Machel, H. G, 1999, Effects of groundwater flow on mineral diagenesis, with emphasis on carbonate aquifers: Hydrogeology Journal, v. 7, no. 1, p. 94-107, DOI:10.1007/s100400050182.

Machel, H. G, 2001, Bacterial and thermochemical sulfate reduction in diagenetic settings - old and new insights: Sedimentary Geology, v. 140, no. 1, p. 143-175, https://doi.org/10.1016/S0037-0738(00)00176-7.

Machel, H. G., 1985, Cathodoluminescence in Calcite and Dolomite and Its Chemical Interpretation: Geoscience Canada, v. 12, no. 4, p. 139-147, https://journals.lib.unb.ca/index.php/GC/article/view/3427/3941

Machel, H. G., 1988, Fluid flow direction during dolomite formation as deduced from trace-element trends: Special Publication - Society of Economic Paleontologists and Mineralogists, v. 43, p. 115-125, http://archives.datapages.com/data/sepm_sp/SP43/Fluid_Flow_Direction_During_Dolomite_Formation.htm.

Machel, H. G., 2000, Application of cathodoluminescence to carbonate diagenesis, *in* Pagel, M., Barbin,V., Blanc, P., and Ohnenstetter, D., eds., Cathodoluminescence in Geosciences: Springer-Verlag, p. 271-301.

Machel, H. G., and Mountjoy, E. W, 1987, General constraints on extensive pervasive dolomitization - and their application to the Devonian carbonates of western Canada: Bulletin of Canadian Petroleum Geology, v. 35, no. 2, p. 143-158, http://archives.datapages.com/data/cspg/data/035/035002/pdfs/0143.pdf

Machel, H. G., and Mountjoy, E. W., 1986, Chemistry and environments of dolomitization - A reappraisal: Earth-Science Reviews, v. 23, no. 3, p. 175-222, https://doi.org/10.1016/0012-8252(86)90017-6.

Machel, H. G., Mason, R. A., Mariano, A. N., and Mucci, A., 1991, Causes and emission of luminescence in calcite and dolomite, *in* Barker, C. E. and Kopp, O.C., eds., Luminescence Microscopy and Spectroscopy: Qualitative and Quantitative Applications. SEPM Short Course Notes, 25: Society of Sedimentary Geology, p. 9-25.

Machel, H.G. and Burton, E.A., 1991, Factors governing cathodoluminescence in calcite and dolomite, and their implications for studies of carbonate diagenesis, *in* Barker, C. E. and Kopp, O. C., eds., Luminescence Microscopy and Spectroscopy: Qualitative and Quantitative Applications. SEPM Short Course Notes, 25: Society of Sedimentary Geology, p. 37-57.

Machel, H.G., 2004, Concepts and models of dolomitization: a critical reappraisal, *in* Braithwaite, C. J. R., Rizzi, G., and Darke, G., eds., The Geometry and Petrogenesis of dolomite hydrocarbon reservoirs: London, Geological Society, p. 7-63.

Maliva, R. G., and Siever, R, 1989, Nodular chert formation in carbonate rocks: The Journal of Geology, v. 97, no. 4, p. 421-433, https://doi.org/10.1086/629320.

Mazzullo, S. J., 1992, Geochemical and neomorphic alteration of dolomite; a review. Carbonates and Evaporites, v. 7, no. 1, p. 21-37, DOI: 10.1007/BF03175390.

McCombie, A. M., 1959, Some relations between air temperatures and the surface water temperatures of lakes: Limnology and Oceanography, v. 4, no. 3, p. 252-258, http://dx.doi.org/10.4319/lo.1959.4.3.0252.

McCrea, J. M., 1950, On the isotopic chemistry of carbonates and a paleotemperature scale: The Journal of Chemical Physics, v. 18, no. 6, p. 849-857, http://dx.doi.org/10.1063/1.1747785.

McKenzie, J.A., 1991, The dolomite problem: An outstanding controversy, *in* Mueller, D. W., McKenzie, J. A., and Weissert, H., eds., Controversies in modern geology; Evolution of geological theories in sedimentology, Earth history and tectonics: Academic Press, p. 35-54, http://dx.doi.org/10.1063/1.1747785.

Millán, M. I., Machel, H., and Bernasconi, S. M., 2016, Constraining Temperatures of Formation and Composition of Dolomitizing Fluids in the Upper Devonian Nisku Formation (Alberta, Canada) with Clumped Isotopes: Journal of Sedimentary Research, 86(2), p. 107-112, DOI:10.2110/jsr.2016.6.

Moore, C. H., 2001, Carbonate reservoirs: Porosity evolution and diagenesis in a sequence stratigraphic framework: Amsterdam: Elsevier, 461 p.

Morgan, C. D., and Bereskin, S. R., 2003, Characterization of Petroleum Reservoirs in the Eocene Green River Formation, Central Uinta Basin, Utah: The Mountain Geologist, v. 39, p. 111-127, http://archives.datapages.com/data/rmag/mg/2003/morgan.pdf.

Morrow, D. W., 1982, Diagenesis 2. Dolomite-Part 2 Dolomitization Models and Ancient Dolostones: Geoscience Canada, v. 9, no. 2, p. 95-107, https://journals.lib.unb.ca/index.php/GC/article/view/3299/3816.

Nesbitt, B. E., and Muehlenbachs, K., 1994, Paleohydrogeology of the Canadian Rockies and origins of brines, Pb-Zn deposits and dolomitization in the Western Canada

Sedimentary Basin: Geology, v. 22, no. 3, p. 243-246, DOI:10.1130/0091-7613(1994)022<0243:POTCRA>2.3.CO;2.

Nesse, W. D, 1991, Introduction to Optical Mineralogy: New York, Oxford University Press.

Nikanorov, M., and Brazhnikova, L.V., 2004, Water chemical composition of rivers, lakes and wetlands, *in* M. G. Khublaryan, ed., Types and Properties of Waters, Encyclopedia of Life Support Systems (EOLSS): Oxford, Eolss Publishers Co., p. 42-79.

Pearson, P. N., and Palmer, M. R., 2000, Atmospheric carbon dioxide concentrations over the past 60 million years: Nature, v. 406, no. 6797, p. 695-9, DOI: 10.1038/35021000.

Picard, M. D, 1971, Petrographic criteria for recognition of lacustrine and fluvial sandstone, PR Spring oil-impregnated sandstone area, southeast Uinta Basin, Utah: Utah Geological and Mineralogical Society, Special Studies, p 1-24, http://repository.icse.utah.edu/dspace/bitstream/123456789/5335/1/Utah-Tar-360.pdf.

Picard, M. D., 1955, Subsurface stratigraphy and lithology of Green River Formation in Uinta Basin, Utah: American Association of Petroleum Geologists Bulletin, v. 39, no. 1, p. 75-102. DOI:10.1306/5CEAE0E5-16BB-11D7-8645000102C1865D.

Pingitore, N. J., 1976, Vadose and phreatic diagenesis; processes, products and their recognition in corals: Journal of Sedimentary Petrology, v. 46, no. 4, p. 985-1006, http://archives.datapages.com/data/sepm/journals/v42-46/data/046/046004/pdfs/0985.pdf.

Pitman, J. K., 1996, Origin of primary and diagenetic carbonates in the lacustrine Green River Formation (Eocene), Colorado and Utah: US Geological Survey Bulletin 2157, p. 1-17, https://pubs.usgs.gov/bul/2157/report.pdf.

Pittman, J. S., and Folk, R. L, 1971, Length-slow chalcedony after sulphate evaporite minerals in sedimentary rocks. Nature Physical Science, v. 230, no. 11, p. 64-65, https://www.nature.com/nature-physci/journal/v230/n11/pdf/physci230064a0.pdf.

Purser, B. H., Tucker, M. E., and Zenger, D. H., 1994, Problems, progress and future research concerning dolomites and dolomitization, *in* Purser, B. H., Tucker, M. E., and

Zenger, D. H., eds., Dolomites: A volume in honour of Dolomieu: Blackwell Scientific Publications, p. 3-21.

Pusca, V. A., 2003, Wet/dry, terminal fan-dominated sequence architecture: A new, outcrop-based model for the Lower Green River Formation, Utah [Ph.D. thesis]: Laramie, University of Wyoming, 175 p., http://search.proquest.com/docview/305284786/513A6C6E6A9942C6PQ/1?accountid=14474.

Rasmussen, D. T., Conroy, G. C., Friscia, A. R., Townsend, K. E., and Kinkel, M. D., 1999, Mammals of the middle Eocene Uinta Formation, *in*, Gillete, D. D., ed., Vertebrate paleontology in Utah: Salt Lake, Utah State Geological Survey, p. 401-420.

Ray, J. S., and Ramesh, R, 1998, Stable carbon and oxygen isotope analysis of natural calcite and dolomite mixtures using selective acid extraction: Journal-Geological Society of India, 52, p. 323-332, http://www.geosocindia.org/index.php/jgsi/article/view/68815.

Reeder, R. J., and Sheppard, C. E., 1984, Variation of lattice parameters in some sedimentary dolomites: American Mineralogist, v. 69, no. 5-6, p. 520-527, https://doi.org/10.1086/626547.

Reinson, G. E., 1992, Transgressive barrier island and estuarine systems, *in* Walker, R. G, and James, N. P, eds., Facies models: response to sea level change: Geological Association of Canada, p. 179-194.

Remy, R. R., 1992, Stratigraphy of the Eocene Part of the Green River Formation in the South-Central Part of the Uinta Basin, Utah: U.S. Geological Survey Bulletin, 1787 - BB, p. 1-79, https://pubs.usgs.gov/bul/1787bb/report.pdf.

Renaut, R. W., and Gierloswki-Kordesch, E. H., 2010, Lakes, *in* James, N. P. and Dalymple, R. W., eds., Facies Models: Geological Association of Canada, p. 541-575.

Robert, C., and Kennett, J. P., 1992, Paleocene and Eocene kaolinite distribution in the South Atlantic and Southern Ocean: Antarctic climatic and paleoceanographic implications: Marine Geology, v. 103, no. 1-3, p. 99-110, https://doi.org/10.1016/0025-3227(92)90010-F.

Roehler, H. W, 1991, Revised stratigraphic nomenclature for the Wasatch and Green River formations of Eocene age, Wyoming, Utah, and Colorado. U.S. Geological Survey Professional Paper 1506-B, https://pubs.usgs.gov/pp/1506b/report.pdf.

Ruble, T. M., and Philp, R. P, 1998, Stratigraphy, Depositional Environments and Organic Geochemistry of Source-Rocks in the Green River Petroleum System, Uinta Basin, Utah, *in* Pitmand, J. K. and Carroll, A. R., eds., Modern and Ancient Lake Systems, Utah Geological Association Guidebook 26: Utah Geological Association Publication, p. 289-328, http://archives.datapages.com/data/uga/data/069/069001/pdfs/289.pdf.

Ryder, R. T., Fouch, T. D., and Elison, J. H., 1976, Early Tertiary sedimentation in the western Uinta basin, Utah: Geological Society of America Bulletin, v. 87, no. 4, p. 496-512, DOI:10.1130/0016-7606(1976)87<496:ETSITW>2.0.CO;2.

Schamel, S, 2015, Shale oil resource play potential of the Green River Formation, Uinta Basin, Utah: Utah Geological Survey Open-File Report 639, 65 p., http://ugspub.nr.utah.gov/publications/open_file_reports/ofr-639/ofr-639.pdf

Scholle, P. A., and Ulmer-Scholle, D. S., 2003, A Color Guide to the Petrography of Carbonate Rocks: Grains, Textures, Porosity, Diagenesis, AAPG Memoir 77, v. 77: Tulsa, American Association of Petroleum Geologist, 459 p.

Searl, A., 1994, Discontinuous solid solution in Ca-rich dolomites: the evidence and implications for the interpretation of dolomite petrographic and geochemical data, *in* Purser, B., Tucker, M., and Zenger, D., eds., Dolomites, A Volume in Honour of Dolomieu: International Association of Sedimentologists, Special Publication 21: Blackwell Scientific Publications, p. 361-376.

Sheppard, S. M., and Schwarcz, H. P, 1970, Fractionation of carbon and oxygen isotopes and magnesium between coexisting metamorphic calcite and dolomite: Contributions to Mineralogy and Petrology, v. 26, no. 3, p. 161-198, DOI: 10.1007/BF00373200.

Sibley, D. F., and Gregg, J. M, 1987, Classification of dolomite rock textures: Journal of Sedimentary Petrology, v. 57, no. 6, p. 967-975,

http://archives.datapages.com/data/sepm/journals/v55-58/data/057/057006/pdfs/0967.pdf.

Sibley, D. F., Gregg, J. M., Brown, R. G., and Laudon, P. R., 1993, Dolomite crystal size distribution, *in* Rezak, R. and Lavoie, D. L., eds., Carbonate microfabrics: Springer-Verlag, p. 195-204.

Siedlecka, A., 1972, Length-slow chalcedony and relicts of sulphates; evidences of evaporitic environments in the Upper Carboniferous and Permian beds of Bear Island, Svalbard: Journal of Sedimentary Petrology, v. 42, no. 4, pp. 812-816, DOI:10.1306/74D7263A-2B21-11D7-8648000102C1865D.

Smith, M. E, 2007, The stratigraphy and geochronology of the Green River Formation, Western U.S [Ph.D. thesis]: Madison, University of Wisconsin-Madison, 318 p., http://search.proquest.com/docview/304776713/A64EEBCAC5A64C64PQ/2?accountid=14474.

Smith, M. E., Carroll, A. R., and Singer, B. S,, 2008, Synoptic reconstruction of a major ancient lake system: Eocene Green River Formation, western United States: Geological Society of America Bulletin, v. 120, no. 1-2, p. 54-84, DOI:10.1130/B26073.1.

Smith, M. E., Carroll, A. R., Scott, J. J., and Singer, B. S., 2014, Early Eocene carbon isotope excursions and landscape destabilization at eccentricity minima: Green River Formation of Wyoming: Earth and Planetary Science Letters, v. 403, p. 393-406, DOI:10.1016/j.epsl.2014.06.024.

Swart, p. K., Burns, S. J., and Leder, J. J., 1991, Fractionation of the stable isotopes of oxygen and carbon in carbon dioxide during the reaction of calcite with phosphoric acid as a function of temperature and technique: Chemical Geology: Isotope Geoscience section, v. 86, no. 2, p. 89-96, https://doi.org/10.1016/0168-9622(91)90055-2.

Sweet, D. E, and Soreghan, G. S., 2012, Late Paleozoic tectonics and paleogeography of the ancestral Front Range: Structural, stratigraphic, and sedimentologic evidence from

the Fountain Formation (Manitou Springs, Colorado): Geological Society of America Bulletin, v. 122, no. 3/4, p. 575-594, DOI:10.1130/B26554.1.

Symcox, C., 2015, Facies, stratigraphy, and mineralogy of the Carbonate marker and D marker units, lower Green River Formation, Uinta Basin, Utah [M.Sc. thesis]: Denver, Colorado School of Mines, 162 p., http://search.proquest.com/docview/1720262797/E8F7EDE79523463CPQ/1?accountid=14474.

Talbot, M. R., and Kelts, K., 1990, Palaeolimnological signatures from carbon and oxygen isotopic ratios in carbonates from organic-rich lacustrine sediments, *in* Katz B. J., ed., Lacustrine exploration: Case studies and modern analogs, American Association of Petroleum Geologists Memoir 50: Tulsa, American Association of Petroleum Geologists, p. 99-112.

Tänavsuu-Milkeviciene, K., and Frederick Sarg, J., 2012, Evolution of an organic-rich lake basin; stratigraphy, climate and tectonics; Piceance Creek basin, Eocene Green River Formation: Sedimentology, v. 59, no. 6, p. 1735-1768, DOI:10.1111/j.1365-3091.2012.01324.x.

Tänavsuu-Milkeviciene, K., Sarg, J. F., and Bartov, Y., 2017, Depositional Cycles and Sequences in an Organic-Rich Lake Basin: Eocene Green River Formation, Lake Uinta, Colorado and Utah, USA: Journal of Sedimentary Research, v. 87, no. 3, p. 210-229, http://archives.datapages.com/data/sepm/journals/087/087003/pdfs/210.pdf.

Tucker, M. E., and Wright, V. P., 1990, Carbonate sedimentology: Oxford, Blackwell Scientific Publications.

Tuttle, M. L., and Goldhaber, M. B., 1993, Sedimentary sulfur geochemistry of the Paleogene Green River Formation, western USA: implications for interpreting depositional and diagenetic processes in saline alkaline lakes: Geochimica et Cosmochimica Acta, v. 57, no. 13, p. 3023-3039, https://doi.org/10.1016/0016-7037(93)90291-4.

Tweto, O., 1975, Laramide (late Cretaceous-early Tertiary) orogeny in the southern Rocky Mountains: Memoir - Geological Society of America, v. 144, p. 1-44, https://dx.doi.org/10.1130/MEM144-p1.

Vanden Berg, M. D., Morgan C. D., Chidsey, T. C., and Nielsen, P., 2013, The Uteland Butte Member of the Eocene Green River Formation: An Emerging Unconventional Carbonate Tight Oil Play in the Uinta Basin, Utah: Poster presented at the AAPG Eastern Section Meeting, Pittsburgh, PA, September 6-10.

Vanden Berg, M. D., Wood, R. E., Carney, S. M, and Morgan C. D., 2014, Geological Characterization of the Uteland Butte Member of the Eocene Green River Formation: An Emerging Unconventional Carbonate Tight Oil Play in the Uinta Basin, Utah. Paper presented at Rocky Mountain Section AAPG Annual Meeting, Denver, CO.

Veizer, J., Lemieux, J., Jones, B., Gibling, M. R., and Savelle, J., 1978, Paleosalinity and dolomitization of a Lower Paleozoic carbonate sequence, Somerset and Prince of Wales Islands, arctic Canada: Canadian Journal of Earth Sciences, v. 15, no 9, p. 1448-1461.

Walters, L. J., Claypool, G. E., and Choquette, P. W., 1972, Reaction rates and $\delta^{18}O$ variation for the carbonate-phosphoric acid preparation method: Geochimica et Cosmochimica Acta, v. 36, no. 2, p. 129-140, https://doi.org/10.1016/0016-7037(72)90002-6

Warren, J. K., 2006, Evaporites: Sediments, Resources, and Hydrocarbons: New York, Springer Berlin Heidelberg, 1035 p.

Warren, J., 2000, Dolomite: occurrence, evolution and economically important associations: Earth-Science Reviews, 52(1), p. 1-81, https://doi.org/10.1016/S0012-8252(00)00022-2.

Weber, J. N., 1964, Trace element composition of dolostones and dolomites and its bearing on the dolomite problem: Geochimica et Cosmochimica Acta, v. 28, no. 10-11, p. 1817-1832, DOI:10.1016/0016-7037(64)90023-7.

Weiss, M., P., Witkind, I. J., and Cashion, W. B., 1981, Geologic map of the Price 30'X60' Quadrangle, Carbon, Duchesne, Uintah, Utah, and Wasatch Counties, Utah. U.S.

Geological Survey Miscellaneous Investigations Series Map I-1981, 1 sheet, 1:100,000.

Whitehead, H. C., and Feth, J. H., 1961, Recent chemical analyses of waters from several closed-basin lakes and their tributaries in the western United States: Geological Society of America Bulletin, .v 72, no. 9, p. 1421-1425, DOI: 10.1130/0016-7606(1961)72[1421:RCAOWF]2.0.CO;2

Williamson, C. R., and Picard, M. D., 1974, Petrology of carbonate rocks of the Green River Formation (Eocene): Journal of Sedimentary Research, v. 44, no. 3, p. 738-759, http://archives.datapages.com/data/sepm/journals/v42-46/data/044/044003/pdfs/0738.pdf.

Willis, G.C, 1999, The Utah thrust system - An overview: Utah Geological Association Publication 27, p. 1-9, http://archives.datapages.com/data/uga/data/070/070001/pdfs/1.pdf.

Woody, R. E., Gregg, J. M., and Koederitz, L. F., 1996, Effect of texture on petrophysical properties of dolomite: evidence from the Cambrian-Ordovician of southeastern Missouri: Association of Petroleum Geologist Bulletin, v. 80, no. 1, p. 119-131, http://archives.datapages.com/data/bulletns/1994-96/images/pg/00800001/0100/0119.pdf

Zachos, J., Pagani, M., Sloan, L., Thomas, E., and Billups, K., 2001, Trends, rhythms, and aberrations in global climate 65 Ma to present: Science, v. 292, no. 5517, p. 686-693, DOI:10.1126/science.1059412.

APPENDIX 1: Stratigraphic columns and cores

BBC 14-13-1

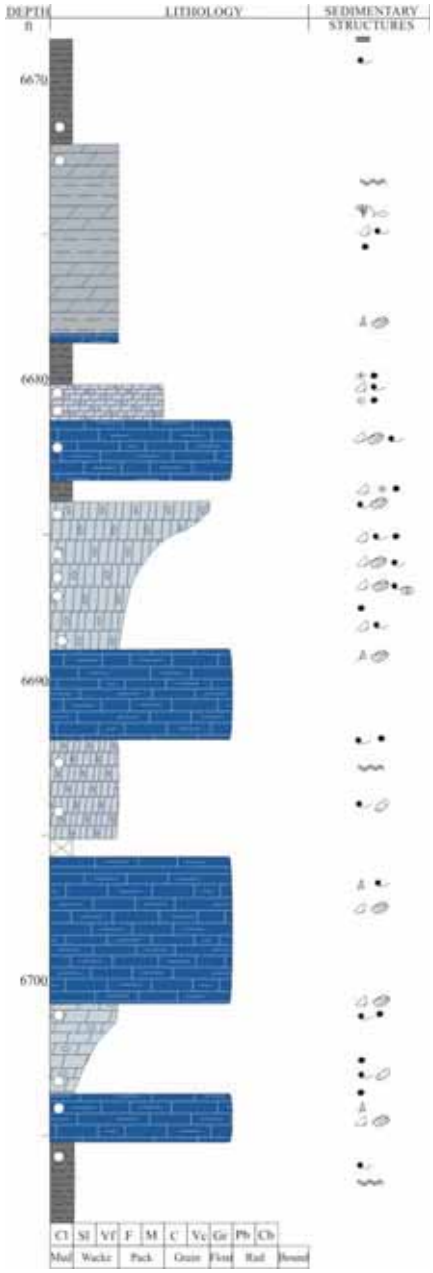
DEPTH
ft
LITHOLOGY
SEDIMENTARY
STRUCTURES
6670
6680
6690
6700
Cl
Si
Vf
F
M
C
Vc
Gr
Pb
Ch
Mud
Wacke
Pack
Grain
Flint
Rud
Bound

BBC 14-3-45

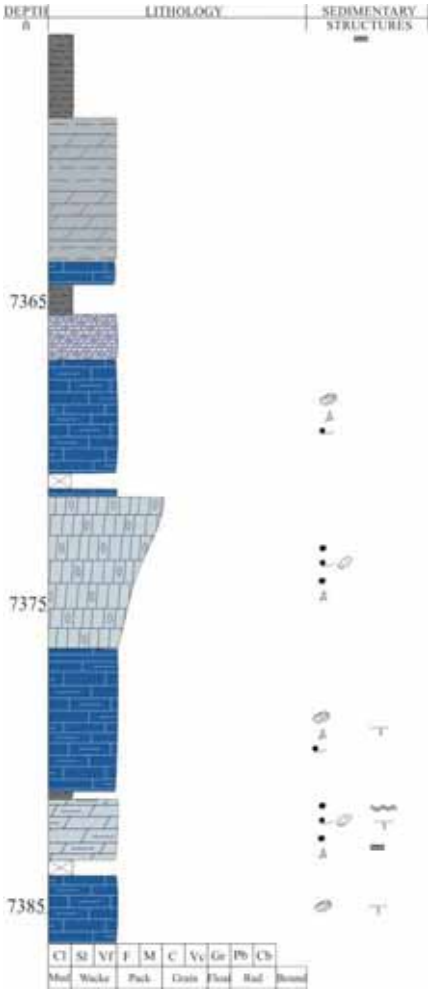
DEPTH
ft
LITHOLOGY
SEDIMENTARY
STRUCTURES
7365
7375
7385
Cl
Si
Vf
F
M
C
Vc
Gr
Pb
Cb
Mud
Wacke
Pack
Grain
Float
Rud
Bound

Nickerson 4-26-3-2W

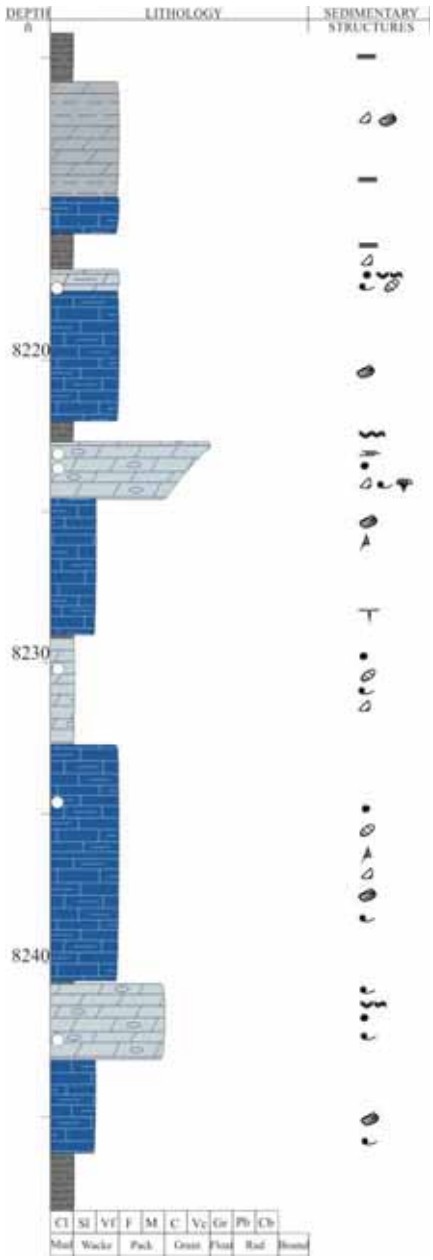

Ute Tribal 15-13-4-3W

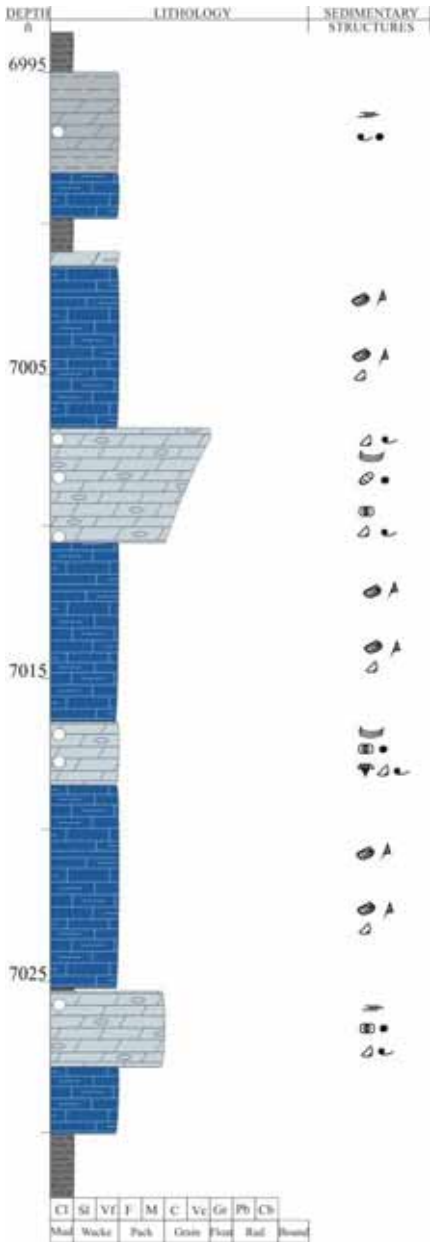

Petes Wash 13-06 GR

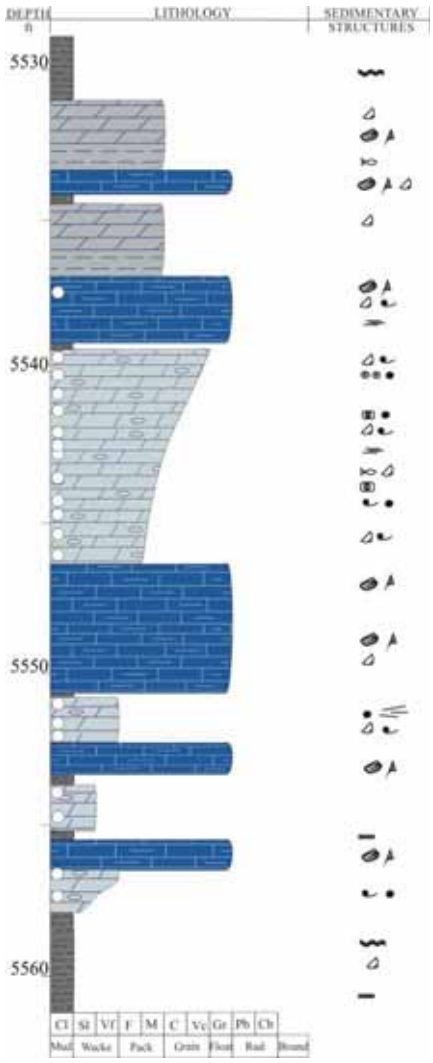

West Desert Spring 11-20-10-17

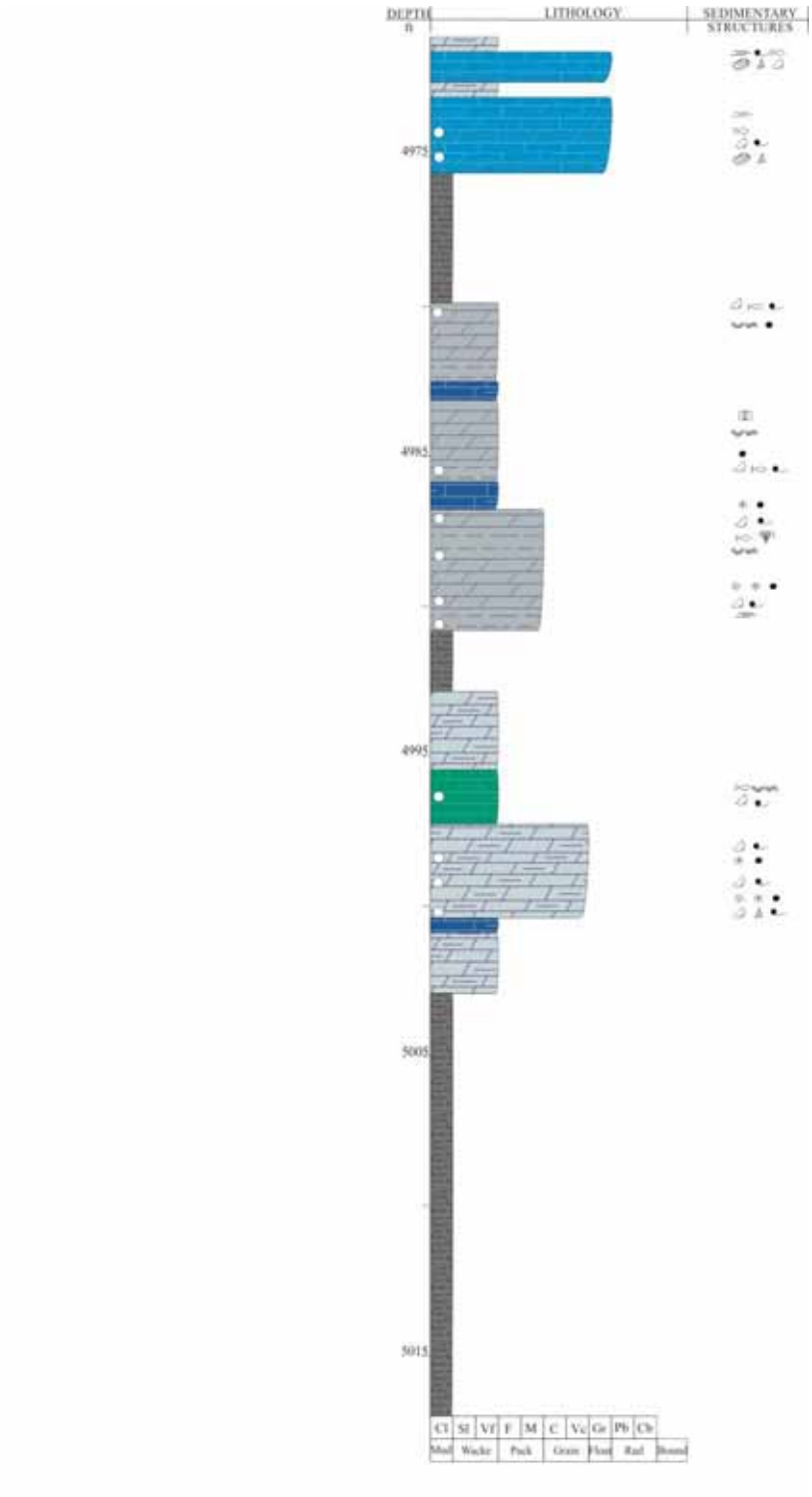

Island Unit 16

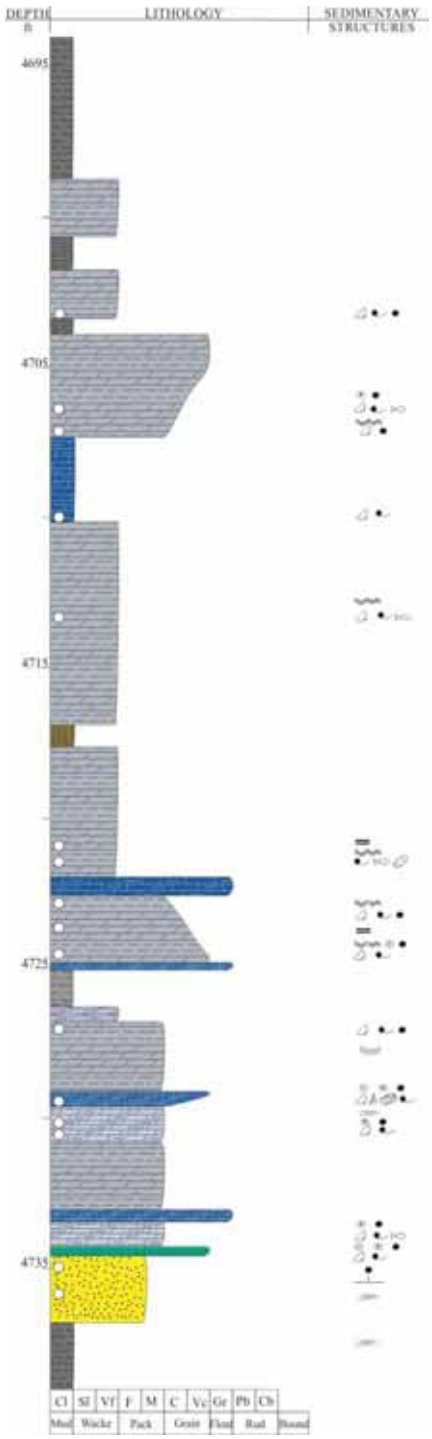

Willow Creek Canyon

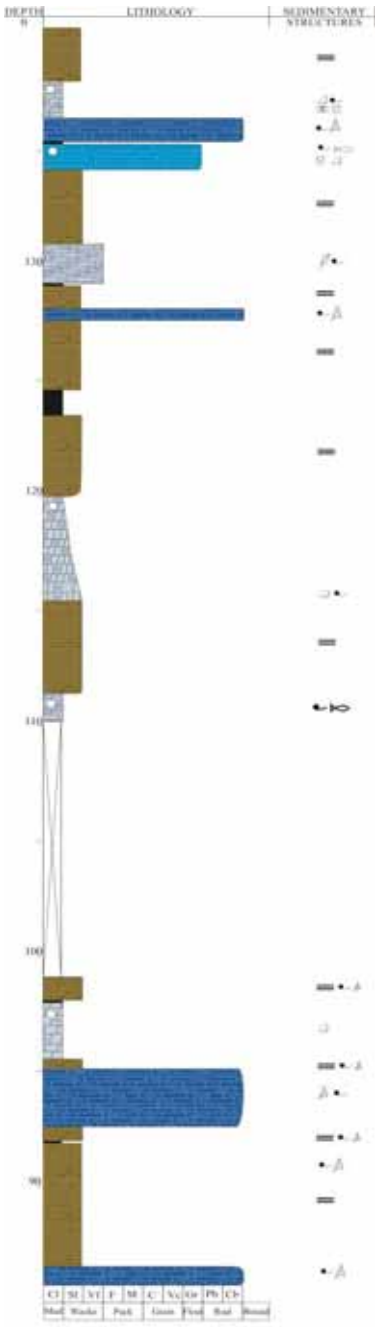

Nine Mila Canyon

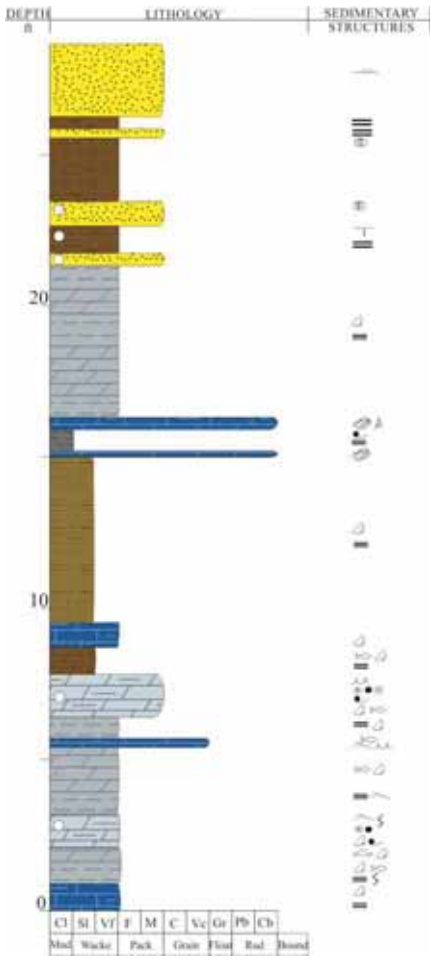

APPENDIX 2: Thin section description

ROCK TYPE CLASSIFICATION	
D	Dolomitized (>75% of Dolomite)
M	Mudstone
W	Wackestone
P	Packstone
G	Grainstone
F	Floatstone
R	Rudstone
d	Dolomitic (<75% Dolomite)
S	Silty
SS	Siltstone
Mud	Mudstone
A	Arenaceous
SSt	Sandstone
Ar	Arguillaceous
C	Calcareous
Sh	Shale
CL	Claystone

MINERALOGY	
Cal	Calcite
FCal	Ferroal Calcite
Dol	Dolomite
Sil	Silice
Pyr	Pyrite
Gyp	Gypsum

BIOCLASTS	
O	Ostracods
P	Pelecypods
G	Gastropods
SF	Shell fragments
FS	Fish scales
CH	Charophyte
FB	Fish Bones (Undefined)
AM	Alga Mats
MAB	More abundant Bioclast

CARBONATE GRAINS (CG)	
RF	Rock fragmnets
On	Oncoids
Oo	Ooids
Pel	Peloids
Cor	Corticoids
MAA	Most Abundant CG

NON CARBONATE GRAINS	
Qz	Quartz
Cla	Clay
Sil	Silt
San	Sand
VF	Very Fine
F	Fine
M	Medium
C	Coarse
VC	Very coarse

FABRIC	
MS	Matrix Supported
GS	Grain Supported
Ratio	MS/GS

SORTING	
MS	Moderately sorted
WS	Well sorted
PS	Poorly sorted
VWS	Very well sorted

ROUNDING	
S	Subrounded
R	Rounded
SA	Subangular
A	Angular

STRATIFICATION	
I	Irregular stratification
M	Massive (lack)
PP	Plana Paralell
PW	Paralell wavy
WD	Wavy discontinous
CP	Curved Parallel
SL	Structureless
WN	Wavy non parallel
PNP	Planar non parallel
PD	Planar discontinuous

LAYER THICKNESS	
TNL	Thinly laminated
TCL	Thickly laminated
VTB	Very thinly bedded
TB	Thinly bedded

GRADATION	
A	Agradational
CU	Coarsening upward
FU	Fining upward

		MINERALOGY						BIOCLASTS									OTHERS CABONATE GRAINS								NON CARBONATES GRAINS					FABRIC					STRATIFICATION					
Thin Section	Depth - core	Cal	FCal	Dol	Sil	Pyr	Ox	O	P	G	SF	FS	FB	CH	AM	%	MAB	RF	On	Oo	Pel	Cor	%	MACG	CG %	Cla	Sil	San	Qz	NCG%	MS	GS	Ratio	Sorting	Rounding	Bedding	Thickness	Bioturbation	A	CU	FU
14-1-1	6652.80	5	1	45	45	4	0	1	0	0	1	1	0	0	0	13	O	0	0	0	0	0	5	Pel	18	0	M	0	1	3	1	0	80/20	MS	S	PP	VTB	0	1	0	0
14-1-2	6657.75	1	0	50	44	5	0	1	0	0	1	0	0	0	0	5	SF	0	0	0	1	0	25	Pel	30	1	M	0	1	15	1	0	60/40	MS	S	PP	VTB	1	1	0	0
14-1-3	6658.75	15	1	50	29	5	0	1	0	0	1	0	0	0	0	7	SF	0	1	0	1	0	5	Pel	12	0	C	0	1	7	1	0	70/30	WS	S	M	VTB	1	1	0	0
14-1-4	6665.50	5	0	45	45	5	0	1	0	0	1	0	0	0	0	1	O	0	0	0	0	0	0	0	1	0	M	0	1	5	1	0	95/5	WS	R	M	VTB	0	1	0	0
14-1-5	6666.00	5	1	5	50	15	0	1	0	0	1	0	0	0	0	5	SF	0	0	0	0	0	0	0	5	1	C	0	1	30	0	1	40/60	MS	SA	WD	VTB	1	1	0	0
14-1-6	6666.50	15	1	5	45	5	1	1	1	1	1	0	0	0	0	30	G	0	0	0	0	0	0	0	30	0	M	0	1	2	1	0	60/40	MS	R	M	VTB	0	1	0	0
14-1-7	6672.80	10	0	0	10	0	0	0	0	0	1	0	0	0	0	1	SF	0	0	0	0	0	0	0	1	1	C	0	1	4	1	0	80/20	WS	S	PP	VBT	0	1	0	0
14-1-8	6675.30	5	1	65	20	4	5	1	0	0	1	0	1	0	1	5	SF	0	0	0	1	0	25	Pel	30	0	M	0	1	5	1	0	80/20	WS	S	PP-W	VBT	0	0	1	0
14-1-9	6680.10	5	3	75	10	2	5	1	0	0	1	0	0	0	0	5	SF	0	1	0	1	0	25	Pel	30	0	C	VF	1	5	0	1	30/70	WS	S	PNP	VBT	0	1	0	0
14-1-10	6680.35	1	3	80	15	1	0	1	0	0	1	0	0	0	0	5	SF	0	0	1	1	0	15	Pel	20	0	M	0	1	3	1	0	50/50	MS	S	M	VBT	0	1	0	0
14-1-11	6683.15	74	1	5	20	0	0	1	1	0	1	0	0	0	0	40	P	0	0	0	0	0	0	0	40	0	M	0	1	10	1	0	60/40	PS	SA	I	VBT	0	1	0	0
14-1-12	6683.95	2	40	50	8	0	0	1	0	0	1	0	0	0	0	3	SF	1	1	0	1	1	30	Pel	33	0	0	0	1	0	0	1	30/70	-	-	M	VBT	0	1	0	0
14-1-13	6684.90	2	3	80	10	1	4	1	0	0	1	0	0	0	0	15	SF	1	0	0	1	0	25	Pel	40	0	F	0	1	1	0	1	40/60	-	-	M	VBT	0	1	0	0
14-1-14	6685.40	3	5	77	10	5	0	1	1	0	1	0	0	0	0	10	SF	0	0	0	1	0	3	Pel	13	0	M	0	0	3	1	0	80/20	-	-	M	VBT	0	1	0	0
14-1-15	6686.80	5	3	80	10	2	0	1	1	0	1	0	0	0	0	15	SF	0	0	0	1	0	20	Pel	35	0	M	0	0	5	1	0	70/30	-	-	I	VBT	1	1	0	0
14-1-16	6688.35	3	1	89	5	1	1	1	0	0	1	0	0	0	0	5	SF	0	0	0	1	0	3	Pel	8	0	M	0	1	1	1	0	90/10	-	-	M	VBT	0	1	0	0
14-1-17	6692.60	30	0	60	4	3	3	0	0	0	1	0	0	0	0	1	SF	0	0	0	1	0	30	Pel	31	0	F	0	1	3	1	0	50/50	PS	SA	PP-W	TCL	0	1	0	0
14-1-18	6693.50	1	0	95	3	1	0	0	0	0	1	0	0	1	0	1	SF	0	0	0	0	0	0	0	1	0	M	0	1	2	1	0	95/5	WS	R	M	VTB	0	1	0	0
14-1-19	6696.10	90	5	3	2	0	0	1	1	1	1	0	0	0	0	45	G	0	0	0	0	0	0	0	45	0	M	0	1	7	1	0	50/50	MS	S	M	VTB	0	1	0	0
14-1-20	6701.40	5	3	85	5	1	1	1	1	0	1	0	0	0	0	10	SF	0	0	0	1	0	15	Pel	25	0	M	0	1	7	1	0	80/20	WS	S	CP	VTB	1	1	0	0
14-1-21	6703.10	0	0	79	20	1	0	0	0	0	1	0	0	1	0	1	SF	0	0	0	1	0	1	Pel	2	0	M	0	1	2	1	0	99/1	WS	R	M	VTB	0	1	0	0
14-1-22	6703.75	4	0	0	95	1	0	0	0	0	0	0	0	0	0	30	P	0	0	0	1	0	0	0	30	0	M	0	1	5	1	0	50/50	MS	S	M	VTB	0	1	0	0
14-1-23	6704.50	90	1	0	8	1	0	1	1	0	1	0	0	0	0	30	P	0	0	0	0	0	0	0	30	0	M	0	1	5	1	0	50/50	MS	S	M	VTB	0	1	0	0
14-1-24	6705.30	70	0	0	20	1	0	0	0	0	1	0	0	0	0	50	SF	0	0	0	0	0	0	0	50	0	F	0	1	10	0	1	30/70	PS	A	PW	VTB	0	1	0	0
14-1-25	7343.90	2	0	80	15	3	0	0	0	0	1	0	0	1	0	1	SF	0	0	0	1	0	0	0		0	F	0	1	1	1	0	95/5	MS	S	WD	VTB	0	1	0	0
14-1-26	7372.35	5	0	70	20	5	0	1	0	0	1	0	0	0	0	10	SF	0	0	0	1	0	2	Pel	12	0	F	0	0	1	1	0	75/25	-	-	M	VTB	0	1	0	0
14-1-27	7373.65	6	1	70	20	3	0	1	0	0	1	0	0	1	0	10	SF	0	0	0	1	0	1	Pel	11	0	F	0	0	1	1	0	60/30	-	-	M	VTB	0	1	0	0
14-1-28	7374.05	10	5	30	50	3	2	1	0	0	1	0	0	1	0	15	O	0	0	0	1	0	2	Pel	17	1	F	0	0	1	1	0	70/30	-	-	WD	VTB	0	1	0	0
14-1-29	7375.00	5	2	70	20	3	0	1	0	0	1	0	0	1	0	15	SF	0	0	0	1	0	20	Pel	35	1	F	0	0	1	1	0	70/30	-	-	M	VTB	0	1	0	0
6-28-1	8199.30	1	0	84	10	5	0	0	0	0	1	0	0	0	0	5	SF	0	0	0	1	0	25	Pel	30	1	M	0	1	20	1	0	70/30	MS	S	PP	VTB	0	0	1	0
6-28-2	8203.60	2	0	90	6	2	0	1	0	0	1	0	0	1	0	1	O	0	0	0	1	0	30	Pel	31	1	M	0	1	10	1	0	80/20	WS	R	PP	VTB	0	1	0	0
6-28-3	8205.60	1	0	90	7	2	0	1	0	0	1	0	0	1	0	1	SF	0	0	0	1	0	30	Pel	31	0	F	0	0	1	1	0	90/10	-	-	WD	VTB	0	0	1	0
6-28-4	8217.60	1	0	90	7	2	0	0	0	0	1	0	0	1	0	0	0	0	0	0	1	0	30	Pel	30	1	M	0	1	5	1	0	80/20	-	-	WD	VTB	1	0	0	1
6-28-5	8223.20	40	0	40	15	5	0	1	0	0	1	0	0	0	0	1	SF	0	0	0	1	0	20	Pel	21	0	0	0	0	0	1	0	90/10	-	-	M	VTB	0	1	0	0
6-28-6	8223.70	15	0	70	10	5	0	1	0	0	1	0	0	0	1	3	O	0	0	0	1	0	5	Pel	8	1	M	0	0	3	1	0	80/20	-	-	SL	VTB	1	1	0	0
6-28-7	8230.20	1	0	80	18	1	0	1	0	0	1	0	0	1	0	1	O	0	0	0	1	0	20	Pel	21	1	M	0	0	1	1	0	95/5	-	-	M	VTB	0	1	0	0
6-28-8	8234.60	90	0	8	1	1	0	1	1	1	1	0	0	1	0	15	O	0	0	0	1	0	0	0	15	0	M	0	0	10	1	0	80/20	-	-	M	VTB	0	1	0	0
6-28-9	8242.50	3	0	75	20	2	0	0	0	0	1	0	0	0	0	5	SF	0	0	0	1	0	50	Pel	55	1	M	0	1	2	1	0	50/50	WS	R	WD	VTB	0	1	0	0
6-28-10	8248.90	10	0	80	8	2	0	1	0	0	1	0	0	0	0	20	SF	0	0	0	0	0	0	0	20	0	F	0	0	3	1	0	60/30	-	-	WD	VTB	0	1	0	0
6-28-11	8256.00	5	0	85	5	5	0	1	0	0	1	0	0	1	0	2	SF	0	0	0	1	0	5	Pel	7	0	M	0	1	10	1	0	75/25	MS	S	SL	VTB	0	0	1	0
6-28-12	8267.40	20	0	5	10	5	0	0	0	0	1	0	0	0	0	5	SF	0	0	0	0	0	0	0	5	1	C	0	1	20	1	0	70/30	MS	R	WD	VTB	0	1	0	0
6-28-13	8270.30	5	0	88	5	2	0	0	0	0	1	0	0	0	0	1	SF	0	0	0	1	0	30	Pel	31	1	C	0	1	3	1	0	85/15	WS	S	WD	VTB	0	1	0	0

		MINERALOGY						BIOCLASTS										OTHERS CABONATE GRAINS								NON CARBONATES GRAINS						FABRIC				STRATIFICATION						
Thin Section	Depth - core	Cal	FCal	Dol	Sil	Pyr	Ox	O	P	G	SF	FS	FB	CH	AM	%	MAB	RF	On	Oo	Pel	Cor	%	MACG	CG %	Cla	Sil	San	Qz	NCG%	MS	GS	Ratio	Sorting	Rounding	Bedding	Thickness	Bioturbation	A	CU	FU
15-13-2	6965.20	5	0	90	5	5	0	1	0	0	0	0	0	0	1	5	O	1	0	0	1	0	7	Pel	13	1	M	0	0	1	1	0	60/40	-	-	SL	VTB	1	1	0	0
15-13-3	6966.40	70	0	15	10	4	0	1	1	1	1	0	0	0	0	10	O	0	0	0	0	0	0	0	30	0	F	0	1	20	1	0	60/40	MS	S	WD	VTB	0	1	0	0
15-13-4	6974.50	1	0	89	8	2	0	0	0	0	1	0	0	0	0	1	SF	0	0	0	1	0	50	Pel	66	1	C	0	1	15	1	0	80/20	MS	S	WD	VTB	0	0	1	0
15-13-5	6982.20	0	0	95	4	1	0	0	0	0	1	0	0	1	0	30	SF	0	0	0	1	0	5	Pel	45	1	M	0	1	10	1	0	90/10	WS	S	WD	VTB	0	1	0	0
15-13-6	6983.90	15	0	80	4	1	0	0	0	0	1	0	0	1	0	3	SF	0	0	0	1	0	30	Pel	38	1	M	0	1	5	1	0	60/40	WS	S	WD	TCL	0	1	0	0
15-13-7	6989.00	20	0	70	8	2	0	1	0	0	1	0	0	0	0	3	SF	0	0	0	1	0	40	Pel	53	1	C	0	1	10	1	0	50/50	MS	S	WD	TCL	1	1	0	0
15-13-8	6996.40	5	0	85	9	1	0	0	0	0	1	0	0	0	0	1	SF	0	0	0	1	0	20	Pel	31	1	M	0	1	10	1	0	70/30	WS	S	PD	TCL	0	1	0	0
15-13-9	7006.50	0	0	80	18	2	0	1	0	0	1	0	0	0	0	5	SF	1	1	0	1	0	40	Pel	52	0	C	0	1	7	1	0	55/45	-	-	CP	TCL	0	1	0	0
15-13-10	7007.80	1	0	90	8	1	0	0	0	0	0	0	0	1	0	1	CH	0	0	0	1	0	1	Pel	3	1	F	0	0	1	1	0	95/5	-	-	M	VTB	1	1	0	0
15-13-11	7009.90	1	0	80	18	1	0	1	0	0	1	0	0	0	0	1	SF	0	0	0	1	0	10	Pel	16	1	F	0	1	5	1	0	80/20	-	-	M	VTB	1	1	0	0
15-13-12	7016.40	2	0	80	10	8	0	1	0	0	1	0	0	0	0	20	O	0	0	0	1	0	10	Pel	32	1	M	0	0	2	1	0	60/40	-	-	PW	VTB	0	1	0	0
15-13-13	7017.40	5	0	80	13	2	0	1	0	0	1	0	0	0	1	7	O	0	0	0	1	0	5	Pel	13	1	F	0	0	1	1	0	90/10	-	-	CP	VTB	1	1	0	0
15-13-14	7025.20	3	0	85	10	2	0	1	0	0	1	0	0	0	0	5	SF	0	0	0	1	0	15	Pel	20	0	0	0	0	0	1	0	70/30	-	-	SL	VTB	1	1	0	0
15-13-15	7031.80	0	0	90	8	2	0	0	0	0	1	0	0	1	0	1	SF	0	0	0	1	0	15	Pel	21	1	M	VF	1	5	1	0	80/20	MS	S	SL	VTB	0	1	0	0
15-13-16	7036.60	80	0	10	9	1	0	1	1	1	1	0	0	0	0	30	G	0	0	0	0	0	0	0	40	0	M	0	1	10	1	0	60/40	WS	S	SL	VTB	0	1	0	0
15-13-17	7051.80	5	0	90	3	2	0	0	0	0	1	0	0	0	0	2	SF	0	0	0	1	0	50	Pel	62	1	M	0	1	10	1	0	70/30	MS	S	PNP	TCL	0	1	0	0
15-13-18	7053.20	70	0	5	20	5	0	1	1	0	1	0	0	0	0	10	O	0	0	0	0	0	0	0	20	1	F	0	1	10	1	0	70/30	MS	S	PD	VTB	0	1	0	0
15-13-19	7067.70	5	0	90	3	2	0	0	0	0	1	0	0	0	0	2	SF	0	0	0	1	0	5	Pel	12	1	M	0	1	5	1	0	90/30	-	-	SL	VTB	1	1	0	0
15-13-20	7070.40	50	0	0	5	0	0	0	0	0	0	0	0	0	0	0	0	0	0	0	0	0	0	0	7	1	F	0	1	7	-	-	-	-	-	PP	TCL	0	1	0	0
13-06-1	5524.20	15	0	75	7	3	0	1	0	0	1	0	0	1	0	30	SF	0	0	0	1	0	10	Pel	45	0	M	0	1	5	1	0	70/30	WS	S	PNP	VTB	0	1	0	0
13-06-2	5524.70	1	0	95	3	1	0	0	0	0	1	0	0	1	0	1	SF	1	0	0	0	0	0	0	6	1	F	0	0	5	1	0	95/5	-	-	SL	VTB	0	1	0	0
13-06-3	5527.30	10	0	65	20	5	0	1	0	0	1	0	0	0	0	2	SF	0	0	0	1	0	20	Pel	23	1	M	0	0	1	1	0	60/40	-	-	WD	VTB	1	1	0	0
13-06-4	5528.30	70	5	5	15	0	0	1	1	1	1	0	0	0	0	45	O	0	0	0	0	0	0	0	60	0	C	VF	1	15	0	1	50/50	VWS	S	SL	VTB	0	1	0	0
13-06-5	5537.30	70	5	5	15	0	0	1	1	1	1	0	0	0	0	40	O	0	0	0	0	0	0	0	48	0	C	VF	1	8	0	1	50/51	WS	S	SL	VTB	0	1	0	0
13-06-6	5539.50	20	0	55	25	0	0	1	0	0	0	0	0	0	0	5	O	1	1	1	1	0	50	Ooids	55	0	0	0	0	0	0	1	30/70	-	-	SL	VTB	0	1	0	0
13-06-7	5541.90	3	0	55	40	2	0	1	0	0	1	0	0	0	0	5	SF	0	0	0	1	0	10	Pel	17	1	F	0	1	2	1	0	80/20	-	-	SL	VTB	0	1	0	0
13-06-8	5543.50	5	0	50	40	4	1	1	0	0	1	0	1	0	0	5	O	0	0	0	1	0	5	Pel	11	0	F	0	0	1	1	0	95/5	-	-	SL	VTB	1	1	0	0
13-06-9	5544.30	3	0	90	5	2	0	0	0	0	1	0	0	0	0	1	SF	0	0	0	1	0	1	Pel	3	1	0	0	0	1	1	0	100	-	-	SL	VTB	1	1	0	0
13-06-10	5545.30	5	0	75	15	5	0	1	0	0	1	0	0	0	0	5	SF	0	0	0	1	0	50	Pel	56	1	0	0	0	1	1	0	80/20	-	-	SL	VTB	1	1	0	0
13-06-11	5552.30	5	0	75	15	5	0	1	0	0	1	0	0	0	0	5	SF	0	0	0	1	0	10	Pel	17	1	M	0	0	2	1	0	70/30	-	-	I	VTB	0	1	0	0
13-06-12	5557.40	0	0	80	15	5	0	0	0	0	1	0	0	0	0	1	SF	0	0	0	1	0	2	Pel	18	1	M	0	1	15	1	0	95/5	MS	S	M	VTB	1	1	0	0
13-06-13	5563.30	10	5	80	3	2	0	1	0	0	1	0	0	1	0	15	SF	0	1	0	1	0	10	Pel	26	1	F	0	1	1	1	0	80/20	-	-	WD	VTB	0	1	0	0
13-06-14	5565.90	65	20	4	10	1	0	1	1	1	1	0	0	0	0	60	G	0	0	0	0	0	0	0	62	0	M	0	1	2	1	0	50/50	MS	S	SL	VTB	0	1	0	0
13-06-15	5580.80	5	0	0	80	0	0	0	0	0	0	0	0	0	0	0	0	0	0	0	0	0	0	0	90	1	C	F	1	90	0	1	10/90	MS	S	SL	VTB	0	1	0	0
13-06-16	5595.40	0	0	85	10	5	0	0	0	0	0	0	0	0	0	0	0	0	0	0	1	0	15	Pel	20	1	M	0	1	5	1	0	95/5	MS	S	PP	VTB	1	1	0	0
13-06-17	5596.00	0	0	90	8	2	0	0	0	0	0	0	0	0	0	0	0	0	0	0	1	0	30	Pel	32	1	M	0	1	2	1	0	60/40	MS	R	PNP	VTB	0	1	0	0
13-06-18	5603.40	85	5	2	5	3	0	1	1	1	1	0	0	0	0	10	O	0	0	0	0	0	0	0	13	1	F	0	1	3	1	0	70/30	WS	S	SL	VTB	0	1	0	0
13-06-19	5607.80	5	0	88	5	2	0	1	0	0	1	0	1	0	0	5	SF	0	0	0	1	0	30	Pel	40	1	M	0	1	5	1	0	60/40	WS	S	WD	TCL	1	1	0	0
13-06-20	5617.40	0	0	0	1	3	0	1	0	0	1	0	0	0	0	2	SF	0	0	0	0	0	0	0	4	1	F	0	1	2	-	-	-	MS	R	PP	VTB	0	1	0	0
11-20-1	4972.50	40	10	20	25	3	1	1	1	1	1	0	1	0	0	20	G	0	0	0	0	0	0	0	30	1	M	0	1	10	1	0	60/40	WS	SA	SL	VTB	0	0	1	0
11-20-2	4974.50	45	10	20	20	3	1	1	1	1	1	0	1	0	0	50	G	0	0	0	0	0	0	0	55	1	F	0	1	5	1	0	50/50	WS	S	SL	VTB	0	1	0	0
11-20-3	4975.40	40	0	15	30	5	0	1	1	1	1	0	0	0	0	40	O	0	0	0	0	0	0	0	47	1	F	0	1	7	1	0	60/30	WS	S	SL	VTB	0	1	0	0
11-20-4	4980.10	20	0	70	8	2	0	1	0	0	1	0	1	0	0	30	SF	0	0	0	1	0	5	Pel	50	1	M	0	1	15	0	0	50/50	MS	S	WD	TCL	1	1	0	0
11-20-5	4985.50	25	0	60	10	5	0	1	0	0	1	0	1	0	0	15	SF	0	0	0	1	0	5	Pel	30	1	M	0	1	10	1	0	70/30	WS	S	WD	TCL	1	1	0	0
11-20-6	4986.50	20	0	70	8	2	0	1	0	0	1	0	1	0	1	10	SF	1	1	0	1	0	15	Pel	28	1	M	0	1	3	1	0	70/30	WS	S	WP	TCL	1	1	0	0
11-20-7	4987.90	20	0	75	4	1	0	1	0	0	1	0	1	0	1	15	SF	0	0	0	1	0	15	Pel	33	1	M	0	1	3	1	0	80/30	WS	S	PNP	TCL	1	1	0	0
11-20-8	4989.50	25	0	60	14	1	0	1	0	0	1	0	0	0	0	3	SF	0	1	1	1	0	20	Ooids	26	1	M	0	1	3	1	0	70/30	WS	S	WD	VTB	0	1	0	0
11-20-9	4990.45	40	0	55	4	1	0	1	0	0	1	0	0	0	0	5	SF	0	1	1	1	0	25	Ooids	31	1	F	0	1	1	0	1	50/50	-	-	SL	VTB	0	1	0	0
11-20-10	4996.35	30	0	40	10	10	0	1	0	0	1	0	1	0	0	5	SF	0	0	0	0	0	0	0	20	1	M	0	1	15	1	0	50/50	WS	S	WD	VTB	0	1	0	0
11-20-11	4998.50	10	30	50	5	5	0	1	0	0	1	0	0	0	0	15	O	0	1	0	1	0	60	Oncoids	75	0	0	0	0	0	0	1	20/80	-	-	M	VTB	0	1	0	0
11-20-12	4999.35	10	25	55	5	5	0	1	0	0	1	0	0	0	0	15	O	1	1	1	1	0	60	Ooids	75	0	0	0	0	0	0	1	40/60	-	-	M	VTB	0	1	0	0
11-20-13	5000.35	20	20	50	5	5	0	1	0	1	1	0	0	0	0	14	O	1	1	1	1	0	60	Ooids	74	0	0	0	0	0	0	1	40/60	-	-	M	VTB	0	1	0	0
11-20-14	5017.00	80	10	1	8	1	0	1	1	1	1	0	1	0	0	50	O	0	0	1	1	0	10	Ooids	65	1	C	0	1	5	0	1	40/60	MS	R	SL	VTB	0	1	0	0
11-20-15	5020.00	10	20	69	0	1	0	1	0	0	1	0	0	0	0	10	O	0	1	1	0	0	60	Ooids	70	0	0	0	0	0	0	1	30/70	-	-	SL	VTB	0	1	0	0
11-20-16	5021.30	60	5	13	20	2	0	1	1	1	1	0	0	0	0	40	SF	0	1	1	1	0	10	Ooids	65	0	C	F	1	15	0	1	40/60	MS	S	SL	VTB	0	1	0	0
11-20-17	5022.15	15	10	60	10	5	0	1	1	0	1	0	0	0	0	5	SF	1	1	1	1	0	20	Ooids	45	0	C	VF	1	20	0	1	50/50	PS	R	SL	VTB	0	1	0	0

		MINERALOGY						BIOCLASTS										OTHERS CABONATE GRAINS								NON CARBONATES GRAINS						FABRIC					STRATIFICATION					
Thin Section	Depth - core	Cal	FCal	Dol	Sil	Pyr	Ox	O	P	G	SF	FS	FB	CH	AM	%	MAB	RF	On	Oo	Pel	Cor	%	MACG	CG %	Cla	Sil	San	Qz	NCG%	MS	GS	Ratio	Sorting	Rounding	Bedding	Thickness	Bioturbation	A	CU	FU
16-1	4701.30	0	0	5	15	5	0	0	0	0	1	0	1	0	0	3	SF	0	0	0	0	0	0	0	18	1	M	F	1	15	1	0	85/15	WS	R	WD	VTB	0	1	0	0
16-2	4705.40	5	0	70	20	4	1	1	0	0	1	0	0	0	0	1	O	0	0	0	1	0	15	Pel	16	1	0	0	0	0	1	0	90/10	-	-	M	VTB	1	1	0	0
16-3	4706.30	60	2	30	5	1	1	1	0	0	1	0	1	0	0	40	SF	1	1	0	1	0	30	Pel	75	0	F	0	1	5	0	1	30/70	-	-	WP	VTB	0	1	0	0
16-4	4707.00	5	2	70	20	3	0	1	0	0	0	0	0	0	0	7	O	0	0	0	1	0	40	Pel	52	1	M	0	0	5	1	0	90/10	-	-	WP	VTB	0	1	0	0
16-5	4710.00	75	1	10	10	4	0	1	0	0	1	0	0	0	0	2	SF	0	0	0	0	0	0	0	9	1	M	0	1	7	1	0	95/5	WS	R	M	VTB	0	1	0	0
16-6	4713.20	20	0	0	10	10	2	1	0	0	1	0	1	0	0	10	SF	0	0	0	0	0	0	0	15	1	F	0	1	5	1	0	70/30	WS	R	WP	VTB	0	1	0	0
16-7	4720.80	5	0	80	10	5	0	0	0	0	1	0	1	0	0	2	SF	0	0	0	1	0	15	Pel	27	1	M	0	1	10	1	0	80/20	MS	S	PP	TNL	0	0	1	0
16-8	4721.25	15	0	75	8	2	0	0	0	0	1	0	1	1	0	10	SF	0	0	0	1	0	10	Pel	25	1	F	0	1	5	1	0	60/40	WS	R	WP	VTB	0	1	0	0
16-9	4722.50	15	0	80	3	2	0	1	0	0	1	0	0	0	0	10	SF	0	0	0	1	0	25	Pel	40	1	F	0	1	5	1	0	55/45	WS	R	WD	TNL	0	1	0	0
16-10	4723.30	5	0	83	10	2	0	1	0	0	1	0	0	0	0	5	SF	0	0	0	1	0	5	Pel	13	1	F	0	1	3	1	0	80/20	WS	S	PP	VTB	0	1	0	0
16-11	4724.20	40	0	53	5	2	0	1	0	0	1	0	0	0	0	1	O	0	0	1	1	0	60	Pel	61	1	0	0	0	0	0	1	40/60	-	-	WD	TCL	0	0	1	0
16-12	4726.60	20	0	70	8	2	0	1	0	0	1	0	0	0	0	20	SF	0	0	0	1	0	25	Pel	47	1	M	0	0	2	1	0	60/40	-	-	CP	VTB	0	1	0	0
16-13	4729.05	60	10	30	0	0	0	1	1	1	1	0	0	0	0	30	G	0	1	1	1	1	20	On	50	0	0	0	0	0	0	1	20/80	-	-	SL	VTB	0	1	0	0
16-14	4729.90	15	9	70	5	1	0	1	0	0	1	0	0	0	0	15	O	0	1	0	1	0	30	On	45	0	0	0	0	0	0	1	30/70	-	-	SL	VTB	0	1	0	0
16-15	4730.20	25	10	60	4	1	0	1	0	0	1	0	0	0	0	10	O	0	1	0	1	0	40	Pel	50	0	0	0	0	0	0	1	30/71	-	-	SL	VTB	0	1	0	0
16-16	4733.20	60	5	30	4	1	0	1	0	0	1	0	1	0	0	20	O	0	1	0	1	0	30	On	50	1	0	0	0	0	0	1	30/70	-	-	SL	VTB	0	1	0	0
16-17	4734.05	0	40	25	34	1	0	1	0	0	1	0	0	0	0	1	SF	1	1	1	1	0	40	Pel	61	0	C	M	1	20	0	1	20/80	MS	SA	SL	VTB	0	1	0	0
16-18	4734.95	30	10	5	55	0	0	0	0	0	0	0	0	0	0	0	0	0	0	0	1	0	0	0	70	1	C	F	1	70	0	1	30/70	PS	SA	SL	VTB	0	1	0	0
16-19	4735.80	20	25	5	50	0	0	0	0	0	0	0	0	0	0	0	0	0	0	0	0	0	0	0	70	1	C	F	1	70	0	1	30/70	PS	SA	SL	VTB	0	1	0	0
16-20	4747.50	10	20	68	0	3	0	1	0	0	1	0	0	0	0	5	SF	0	1	1	1	0	40	Pel	50	1	F	0	1	5	0	1	30/70	-	-	SL	TCL	0	1	0	0
16-21	4748.80	15	5	75	1	4	0	1	0	0	1	0	0	0	0	10	SF	0	0	0	1	0	10	Pel	27	1	M	0	1	7	1	0	70/30	-	-	SL	VTB	0	1	0	0
16-22	4750.70	9	30	60	0	1	0	0	0	0	1	0	0	0	0	5	O	1	1	1	1	0	60	Pel	66	0	M	0	0	1	0	1	30/70	-	-	SL	VTB	0	1	0	0
16-23	4751.10	30	20	24	25	1	0	1	0	0	1	0	0	0	0	30	SF	0	1	1	1	0	30	Oncoids	80	0	C	F	1	20	0	1	30/70	WS	SA	SL	VTB	0	1	0	0
16-24	4770.90	20	8	70	2	0	0	1	0	0	0	0	0	0	0	25	O	1	1	0	1	0	40	Oncoids	70	1	F	0	0	5	0	1	30/70	-	-	SL	VTB	0	1	0	0
16-25	4771.30	0	30	69	0	1	0	1	0	0	0	0	0	0	0	1	O	0	0	0	1	0	2	Pel	4	1	F	0	0	1	1	0	95/5	-	-	SL	VTB	0	1	0	0
I8	-	80	0	0	15	5	0	1	1	1	1	0	1	0	0	60	G	0	0	0	0	0	0	0	60	1	F	0	1	5	0	1	10/90	-	-	SL	VBT	0	1	0	0
I7	-	5	0	60	30	5	0	1	0	0	1	0	0	0	0	5	SF	0	0	0	0	0	0	0	5	1	F	0	1	3	1	0	80/20	WS	R	WD	VBT	1	1	0	0
I6	-	82	0	15	0	2	1	1	1	0	1	0	1	0	0	15	SF	0	0	0	0	0	0	0	15	1	F	0	1	3	1	0	60/40	-	-	SL	VBT	0	1	0	0
I5	-	3	0	90	3	1	3	1	0	0	1	0	0	0	0	2	SF	0	0	0	0	0	0	0	2	1	F	0	1	3	1	0	90/10	WS	S	SL	VBT	1	1	0	0
I4	-	5	0	90	3	1	2	0	0	0	1	0	1	0	0	1	FB	0	0	0	0	0	0	0	1	1	F	0	1	3	1	0	90/10	WS	R	SL	VBT	1	1	0	0
I3	-	5	0	90	3	2	0	1	0	0	1	0	0	0	0	5	SF	0	0	0	0	0	0	0	5	1	F	0	1	3	1	0	90/10	-	-	SL	VBT	1	1	0	0
I2	-	45	0	50	4	1	0	1	0	0	1	0	0	0	0	20	O	1	1	0	1	0	50	On	70	0	F	0	0	1	0	1	10/90	-	-	SL	VBT	0	1	0	0
I1	-	1	24	65	5	2	3	1	0	0	1	0	1	0	0	5	SF	0	1	0	0	0	1	On	6	1	M	0	1	1	1	0	70/30	-	-	SL	VTB	1	1	0	0
S3	-	10	0	45	40	5	0	0	0	0	0	0	0	0	0	0	0	1	0	0	0	0	0	0	0	1	C	F	1	60	1	0	60/40	VWS	R	SL	VTB	0	1	0	0
S4-1	-	2	28	5	60	0	5	0	0	0	0	0	0	0	0	0	0	1	0	0	0	0	0	0	0	1	C	F	1	80	1	0	50/50	WS	S	SL	VTB	0	1	0	0
S4-2	-	1	24	5	65	0	5	0	0	0	0	0	0	0	0	0	0	1	0	0	0	0	0	0	0	1	C	F	1	80	1	0	50/50	WS	S	SL	VTB	0	1	0	0
S4-3	-	1	19	5	70	0	5	0	0	0	0	0	0	0	0	0	0	1	0	0	0	0	0	0	0	1	C	F	1	80	1	0	50/50	WS	S	SL	VTB	0	1	0	0
S4-4	-	1	3	10	80	1	5	0	0	0	0	0	0	0	0	0	0	1	0	0	0	0	0	0	0	1	C	F	1	60	1	0	50/50	WS	S	SL	VTB	0	1	0	0
S4-5	-	1	0	40	50	4	5	0	0	0	0	0	0	0	0	0	0	0	0	0	0	0	0	0	0	1	C	VF	1	50	1	0	70/30	PS	R	SL	VTB	0	1	0	0
S2	-	25	2	60	10	3	0	1	0	0	1	0	0	0	1	20	O	0	1	1	1	0	40	Pel	60	1	C	0	1	10	1	0	40/60	MS	SA	WN	VTB	0	1	0	0
S1	-	15	0	79	5	1	0	1	0	0	1	0	0	0	0	20	O	0	1	0	1	0	60	On	80	1	C	0	1	5	0	1	20/80	MS	S	PW	VTB	0	1	0	0

APPENDIX 3: EDS – SEM

		Atomic %							
Sample	**Spot**	**O**	**Mg**	**Al**	**Si**	**S**	**Cl**	**K**	**Ca**
6-28-7	6-28-7_ 1.spx	71.8	10.5		1.0				16.7
6-28-7	6-28-7_ 10.spx	65.4	12.9		3.3				18.3
6-28-7	6-28-7_ 11.spx	66.9	12.3		2.6				18.1
6-28-7	6-28-7_ 2.spx	71.7	10.7		1.3				16.2
6-28-7	6-28-7_ 3.spx	71.8	10.8		1.1				16.2
6-28-7	6-28-7_ 4.spx	67.4	12.7		2.3				17.6
6-28-7	6-28-7_ 5.spx	66.8	13.3		2.1				17.7
6-28-7	6-28-7_ 6.spx	66.9	12.6		2.0				18.4
6-28-7	6-28-7_ 7.spx	66.7	13.7		2.0				17.6
6-28-7	6-28-7_ 8.spx	66.7	12.5		2.7				18.1
6-28-7	6-28-7_ 9.spx	68.0	11.4		3.5				17.1
6-28-7	6-28-9_ 1.spx	66.3	9.2	1.5	3.3	0.2	3.4	0.4	15.4
6-28-7	6-28-9_ 2.spx	57.1	15.1	0.4	2.8	0.1	2.7	0.1	21.4
6-28-7	6-28-9_ 3.spx	63.5	14.3		1.5		1.5		18.9
6-28-7	6-28-9_ 4.spx	61.4	13.8		1.5		2.0		21.2
6-28-7	6-28-9_ 5.spx	63.1	13.7		1.5		2.3		19.2
6-28-7	6-28-9_ 6.spx	64.8	5.2		19.3		1.4		9.3
6-28-7	6-28-9_ 7.spx	59.3	11.0		12.1		2.0		15.5
6-28-7	6-28-9_ 8.spx	59.0	14.4		4.2		2.4		19.7
6-28-7	6-28-9_ 9.spx	61.1	7.0		17.3		2.0		12.4
13-06-7	13-06-07_ 1.spx		41.1						58.7
13-06-7	13-06-07_ 2.spx		38.8						61.1
13-06-7	13-06-07_ 3.spx		44.4						55.5
13-06-7	13-06-07_ 4.spx		37.9						62.0
13-06-7	13-06-07_ 5.spx		42.5						57.3
13-06-7	13-06-07_ 6.spx		43.7						56.1
13-06-7	13-06-07_ 7.spx		44.4						55.5
13-06-8	13-06-08_Ccoated_ 21.spx		39.6						59.7
13-06-8	13-06-08_Ccoated_ 15.spx		45.7						53.5
13-06-8	13-06-08_Ccoated_ 14.spx		46.5						52.7
13-06-8	13-06-08_Ccoated_ 20.spx		41.6						57.7
13-06-8	13-06-08_Ccoated_ 9.spx		45.5						53.9
13-06-8	13-06-08_Ccoated_ 13.spx		42.8						56.7
13-06-8	13-06-08_Ccoated_ 18.spx		43.8						55.8
13-06-8	13-06-08_Ccoated_ 19.spx		40.5						59.1
13-06-8	13-06-08_Ccoated_ 8.spx		40.3						59.3
13-06-8	13-06-08_Ccoated_ 17.spx		45.7						54.0
13-06-8	13-06-08_Ccoated_ 4.spx		47.7						52.0
13-06-8	13-06-08_Ccoated_ 5.spx		43.7						56.0
13-06-8	13-06-08_Ccoated_ 11.spx		44.8						55.0
13-06-8	13-06-08_Ccoated_ 10.spx		42.0						57.9

		Atomic %							
Sample	**Spot**	**O**	**Mg**	**Al**	**Si**	**S**	**Cl**	**K**	**Ca**
13-06-8	13-06-08_ 6.spx	69.0	6.5		12.3	0.2	1.3		10.7
13-06-8	13-06-08_ 7.spx	70.7	10.3		1.3	0.1	1.0		16.4
13-06-8	13-06-08_Ccoated_ 12.spx		44.2						55.7
13-06-8	13-06-08_ 8.spx	69.0	11.7		0.9	0.1	0.8		17.5
13-06-8	13-06-08_Ccoated_ 7.spx		39.7						60.2
13-06-8	13-06-08_Ccoated_ 6.spx		39.8						60.2
13-06-8	13-06-08_Ccoated_ 26.spx		41.8						58.2
13-06-8	13-06-08_Ccoated_ 25.spx		43.4						56.6
13-06-8	13-06-08_Ccoated_ 24.spx		38.1						61.9
13-06-8	13-06-08_Ccoated_ 22.spx		41.6						58.4
13-06-8	13-06-08_Ccoated_ 16.spx		43.9						56.1
13-06-8	13-06-08_Ccoated_ 1.spx		40.7						59.3
13-06-8	13-06-08_Ccoated_ 3.spx	64.9			35.1				
13-06-8	13-06-08_Ccoated_ 2.spx	63.5		0.1	32.6		2.6		
13-06-8	13-06-08_ 9.spx	65.8	3.2		23.5	0.2	0.8		6.5
13-06-8	13-06-08_ 4.spx	68.1	12.6		0.4		0.9		17.9
13-06-8	13-06-08_ 3.spx	61.9	4.3	6.0	13.0		0.9	5.3	8.2
13-06-8	13-06-08_ 2.spx	63.0	3.5	6.2	13.6		0.9		6.9
13-06-8	13-06-08_ 12.spx	67.2	4.2		18.9	0.2	0.9		8.7
13-06-8	13-06-08_ 11.spx	65.8	3.6		23.3	0.1	0.8		6.4
13-06-8	13-06-08_ 10.spx	65.6	3.4		23.1	0.2	0.9		6.8
13-06-8	13-06-08_ 1.spx	61.7	3.0	7.4	15.5		0.8		4.8
13-06-11	13-06-11_ 1.spx		37.6						61.6
13-06-11	13-06-11_ 10.spx		39.2						60.6
13-06-11	13-06-11_ 2.spx		38.3						61.4
13-06-11	13-06-11_ 3.spx		39.8						59.6
13-06-11	13-06-11_ 4.spx		36.7						61.6
13-06-11	13-06-11_ 5.spx		40.7						59.1
13-06-11	13-06-11_ 6.spx		36.5						63.5
13-06-11	13-06-11_ 7.spx		35.1						64.7
13-06-11	13-06-11_ 8.spx		42.2						57.4
13-06-11	13-06-11_ 9.spx		36.7						61.9
13-06-12	13-06-12_ 1.spx		43.2						56.8
13-06-12	13-06-12_ 10.spx		41.7						57.8
13-06-12	13-06-12_ 11.spx		41.7						58.3
13-06-12	13-06-12_ 2.spx		39.5						60.0
13-06-12	13-06-12_ 3.spx		41.2						58.8
13-06-12	13-06-12_ 4.spx		39.3						59.9
13-06-12	13-06-12_ 5.spx		43.2						56.8
13-06-12	13-06-12_ 6.spx		45.4						54.2
13-06-12	13-06-12_ 7.spx		43.4						56.6
13-06-12	13-06-12_ 8.spx		41.4						58.3
13-06-12	13-06-12_ 9.spx		42.4						57.3
15-13-13	15-13-13_ 1.spx		39.4						60.2
15-13-13	15-13-13_ 2.spx		40.6						59.1
15-13-13	15-13-13_ 3.spx		43.0						57.0

		Atomic %							
Sample	**Spot**	**O**	**Mg**	**Al**	**Si**	**S**	**Cl**	**K**	**Ca**
15-13-13	15-13-13_ 5.spx		38.8						61.2
15-13-13	15-13-13_ 6.spx		39.8						60.2
15-13-13	15-13-13_ 7.spx		39.3						60.6
15-13-13	15-13-13_ 8.spx		39.1						60.8
15-13-13	15-13-13_ 9.spx		38.9						61.1
15-13-14	15-13-14_ 1.spx	65.8			34.2				
15-13-14	15-13-14_ 10.spx		44.0						56.0
15-13-14	15-13-14_ 11.spx		41.1						57.7
15-13-14	15-13-14_ 12.spx		42.3						57.0
15-13-14	15-13-14_ 13.spx		43.1						56.9
15-13-14	15-13-14_ 14.spx		45.6						54.4
15-13-14	15-13-14_ 15.spx		43.4						56.1
15-13-14	15-13-14_ 16.spx		44.1						55.9
15-13-14	15-13-14_ 17.spx		44.1						55.9
15-13-14	15-13-14_ 18.spx		42.1						57.8
15-13-14	15-13-14_ 19.spx		43.4						56.3
15-13-14	15-13-14_ 2.spx		43.6						56.4
15-13-14	15-13-14_ 20.spx		43.0						56.5
15-13-14	15-13-14_ 21.spx		42.5						57.2
15-13-14	15-13-14_ 3.spx		42.0						58.0
15-13-14	15-13-14_ 4.spx		43.6						56.2
15-13-14	15-13-14_ 5.spx		43.6						56.2
15-13-14	15-13-14_ 6.spx		43.8						56.2
15-13-14	15-13-14_ 7.spx		41.4						58.3
15-13-14	15-13-14_ 8.spx		41.8						57.2
15-13-14	15-13-14_ 9.spx		42.6						56.5

APPENDIX 4: XRD

				%CaCO3		
Well	Sample code	depth	Litho	Indiana University	University of Alberta	Western Michigan University
BBC 14-1	14-1-2	6657.8	D		55.2	
BBC 14-1	14-1-4	6665.5	D		53.4	
BBC 14-1	14-1-8	6675.3	D		55.5	
BBC 14-1	14-1-12	6684.0	PZ1			53.8
BBC 14-1	14-1-12B	6684.5	PZ1			52.1
BBC 14-1	14-1-13	6684.9	PZ1			53.7
BBC 14-1	14-1-14	6685.4	PZ1		55.2	53.9
BBC 14-1	14-1-14A	6686.1	PZ1			54.6
BBC 14-1	14-1-14B	6686.5	PZ1			53.7
BBC 14-1	14-1-15	6686.8	PZ1		55.5	53.8
BBC 14-1	14-1-15A	6687.2	PZ1			53.6
BBC 14-1	14-1-15B	6687.6	PZ1			54.2
BBC 14-1	14-1-16	6688.4	PZ1			54.3
BBC 14-1	14-1-16A	6692.1	PZ1'			52.7
BBC 14-1	14-1-17	6692.6	PZ1'		54.2	52.3
BBC 14-1	14-1-18	6693.5	PZ1'			51.3
BBC 14-1	14-1-18A	6694.1	PZ1'			51.8
BBC 14-1	14-1-18B	6694.9	PZ1'			55.2
BBC 14-1	14-1-19A	6700.9	PZ2		53.3	53.8
BBC 14-1	14-1-20	6701.4	PZ2		54.8	53.2
BBC 14-1	14-1-20A	6702.3	PZ2			53.8
BBC 14-1	14-1-21	6703.1	PZ2		53.7	51.7
BBC 14-3	14-3-26	7372.4	PZ1		55.3	53.6
BBC 14-3	14-3-27	7373.7	PZ1			53.9
BBC 14-3	14-3-28	7374.1	PZ1			53.6
BBC 14-3	14-3-29	7375.0	PZ1			53.9
BBC 14-3	14-3-30	7375.9	PZ1			54.4
BBC 14-3	14-3-31	7376.8	PZ1			54.9
BBC 14-3	14-3-32	7382.0	PZ1'			52.9
BBC 14-3	14-3-33	7382.7	PZ1'			52.1
BBC 14-3	14-3-34	7383.7	PZ1'			53.1
N 6-28	6-28-1	8199.3	D	55.2	52.7	
N 6-28	6-28-2	8203.6	D		53.7	
N 6-28	6-28-3	8205.6	D		52.1	
N 6-28	6-28-4	8217.6	D	55.8	53.3	
N 6-28	6-28-5	8223.2	PZ1		52.3	
N 6-28	6-28-6	8223.7	PZ1	54.9	53.8	
N 6-28	6-28-7	8230.2	PZ1'	51.8	52.6	
N 6-28	6-28-9	8242.5	PZ2	54.9	54.6	
N 6-28	6-28-10	8248.9	D		55.5	
N 6-28	6-28-12	8267.4	D		51.0	
N 6-28	6-28-13	8270.3	D		54.7	

				%CaCO3		
Well	Sample code	depth	Litho	Indiana University	University of Alberta	Western Michigan University
UT 15-13	15-13-5	6982.2	D		53.7	
UT 15-13	15-13-6	6983.9	D		54.7	
UT 15-13	15-13-7	6989.0	D		53.7	
UT 15-13	15-13-9	7006.5	PZ1		52.3	
UT 15-13	15-13-10	7007.8	PZ1		53.9	
UT 15-13	15-13-11B	7009.9	PZ1	55.5	55.5	
UT 15-13	15-13-12	7016.4	PZ1'		57.5	
UT 15-13	15-13-13	7017.4	PZ1'	55.2	55.6	
UT 15-13	15-13-14	7025.2	PZ2	52.7	52.3	
PW 13-06	13-06-1	5524.2	D		55.0	
PW 13-06	13-06-2	5524.7	D		55.5	
PW 13-06	13-06-3	5527.3	D		52.6	
PW 13-06	13-06-6	5539.5	PZ1		51.6	50.4
PW 13-06	13-06-6A	5540.1	PZ1			49.7
PW 13-06	13-06-6B	5540.7	PZ1		51.8	50.5
PW 13-06	13-06-6C	5541.3	PZ1			51.9
PW 13-06	13-06-7	5541.9	PZ1	52.7	51.1	49.6
PW 13-06	13-06-7A	5542.4	PZ1		53.1	53.4
PW 13-06	13-06-7B	5542.7	PZ1			52.9
PW 13-06	13-06-8	5543.5	PZ1	53.3	54.2	52.9
PW 13-06	13-06-9	5544.3	PZ1			52.9
PW 13-06	13-06-9A	5544.7	PZ1		54.9	53.1
PW 13-06	13-06-10	5545.3	PZ1	55.5	53.1	54.0
PW 13-06	13-06-10A	5546.1	PZ1		56.0	54.4
PW 13-06	13-06-10B	5551.0	PZ1'		55.7	53.5
PW 13-06	13-06-10C	5551.6	PZ1'		55.5	53.2
PW 13-06	13-06-11	5552.2	PZ1'	55.2	54.6	52.9
PW 13-06	13-06-11A	5553.9	PZ2		53.9	53.2
PW 13-06	13-06-11B	5554.7	PZ2		53.4	52.1
PW 13-06	13-06-11C	5556.6	PZ3			55.1
PW 13-06	13-06-12	5557.4	PZ2	54.3	55.7	51.8
PW 13-06	13-06-13	5563.3	D		55.0	
PW 13-06	13-06-14	5565.9	L		53.9	
PW 13-06	13-06-15	5580.8	D		50.3	
PW 13-06	13-06-16	5595.4	D		54.2	
PW 13-06	13-06-17	5596.0	D		54.2	
PW 13-06	13-06-18	5603.4	L		53.1	
PW 13-06	13-06-19	5607.8	D		54.9	
DS 11-20	11-20-1	4972.5	D		56.2	
DS 11-20	11-20-2	4974.5	L		54.0	
DS 11-20	11-20-4	4980.1	PZ1		56.0	
DS 11-20	11-20-5	4985.5	PZ1'		55.5	
DS 11-20	11-20-8	4989.5	PZ2		52.2	
DS 11-20	11-20-9	4990.5	PZ2		57.7	

				%CaCO3		
Well	**Sample code**	**depth**	**Litho**	**Indiana University**	**University of Alberta**	**Western Michigan University**
I 16	16-2	4705.4	D		55.5	
I 16	16-3	4706.3	PZ1	57.0	58.2	
I 16	16-4	4707.0	PZ1		55.2	
I 16	16-7	4720.8	PZ1'		54.9	
I 16	16-8	4721.3	PZ1'		57.1	
I 16	16-10	4723.3	PZ2		56.5	
I 16	16-11	4724.2	PZ2		55.0	

APPENDIX 5: EMPA

		Concentration (WT%)						
SAMPLE	Point	Fe	Mn	Mg	Ca	Sr	C	O
13-06-11 traverse1A	1	0.06	0.00	11.46	23.41	0.10	12.71	50.78
13-06-11 traverse1A	2	0.52	0.00	10.89	23.90	0.07	12.66	50.61
13-06-11 traverse1A	3	0.49	0.00	11.12	23.71	0.09	12.72	50.82
13-06-11 traverse1A	4	0.51	0.02	11.18	23.72	0.08	12.76	51.00
13-06-11 traverse1A	5	0.10	0.00	10.86	24.55	0.08	12.76	50.98
13-06-11 traverse1A	6	0.56	0.04	11.11	23.87	0.08	12.78	51.08
13-06-11 traverse1A	7	0.37	0.00	11.42	23.71	0.08	12.84	51.31
13-06-11 traverse1A	8	0.55	0.00	10.93	24.25	0.08	12.80	51.15
13-06-11 traverse1A	9	0.35	0.00	6.22	31.01	0.10	12.46	49.77
13-06-11 traverse1A	10	0.52	0.00	11.51	23.71	0.07	12.92	51.63
13-06-11 traverse1A	11	0.14	0.00	10.91	24.85	0.12	12.89	51.49
13-06-11 traverse2	1	0.26	0.07	10.76	24.22	0.10	12.66	50.59
13-06-11 traverse2	2	0.61	0.00	10.62	24.24	0.06	12.65	50.56
13-06-11 traverse2	3	0.31	0.00	11.45	23.57	0.09	12.80	51.15
13-06-11 traverse2	4	0.18	0.00	10.97	24.33	0.09	12.77	51.02
13-06-11 traverse2	5	0.37	0.03	11.28	23.83	0.08	12.81	51.20
13-06-11 traverse2	6	0.34	0.00	11.00	24.31	0.07	12.80	51.17
13-06-11 traverse2	7	0.73	0.00	10.54	24.62	0.09	12.76	50.99
13-06-11 traverse2	8	0.59	0.00	10.77	24.48	0.07	12.79	51.13
13-06-11 traverse2	9	0.05	0.02	12.75	22.48	0.00	13.05	52.15
13-06-11 traverse3	1	0.41	0.00	11.11	23.66	0.07	12.68	50.67
13-06-11 traverse3	2	0.40	0.00	11.08	23.80	0.04	12.70	50.75
13-06-11 traverse3	3	0.51	0.00	10.99	23.93	0.07	12.72	50.85
13-06-11 traverse3	4	0.55	0.02	11.02	23.90	0.07	12.74	50.93
13-06-11 traverse3	5	0.29	0.00	10.80	24.49	0.10	12.75	50.96
13-06-11 traverse3	6	0.06	0.00	11.08	24.30	0.10	12.79	51.10
13-06-11 traverse3	7	0.37	0.00	11.35	23.92	0.07	12.87	51.42
13-06-11 traverse3	8	0.43	0.00	11.10	24.31	0.08	12.88	51.46
13-06-11 traverse3	9	0.52	0.04	11.11	24.20	0.09	12.88	51.46
13-06-11 traverse4	1	0.40	0.00	11.06	23.70	0.07	12.66	50.61
13-06-11 traverse4	2	0.44	0.00	11.14	23.58	0.07	12.68	50.66
13-06-11 traverse4	3	0.43	0.00	11.16	23.58	0.12	12.69	50.71
13-06-11 traverse4	4	0.49	0.00	11.00	23.79	0.07	12.68	50.67
13-06-11 traverse4	5	0.53	0.00	11.48	23.35	0.05	12.79	51.11
13-06-11 traverse4	6	0.33	0.00	10.78	24.47	0.09	12.74	50.92
13-06-11 traverse4	7	0.24	0.00	11.18	24.04	0.10	12.80	51.14
13-06-11 traverse4	8	1.36	0.00	10.26	24.46	0.05	12.70	50.75
13-06-11 traverse4	9	0.74	0.00	10.51	24.69	0.08	12.76	51.01
13-06-11 traverse4	10	0.68	0.00	11.03	24.15	0.06	12.84	51.33

		Concentration (WT%)						
SAMPLE	Point	Fe	Mn	Mg	Ca	Sr	C	O
13-06-11 traverse5	2	0.95	0.05	10.78	23.79	0.04	12.68	50.66
13-06-11 traverse5	3	0.35	0.03	10.66	24.49	0.10	12.70	50.77
13-06-11 traverse5	4	0.48	0.02	10.72	24.33	0.10	12.71	50.78
13-06-11 traverse5	5	0.30	0.02	11.16	23.94	0.09	12.77	51.05
13-06-11 traverse5	6	0.38	0.02	10.77	24.46	0.10	12.75	50.97
13-06-11 traverse5	7	0.39	0.03	10.83	24.38	0.10	12.76	51.00
13-06-11 traverse5	8	0.13	0.00	10.95	24.44	0.14	12.78	51.08
13-06-11 traverse5	9	0.17	0.00	11.06	24.29	0.13	12.80	51.15
13-06-11 traverse5	10	0.14	0.03	11.35	24.06	0.07	12.87	51.42
13-06-11 traverse5	11	0.48	0.00	10.92	24.41	0.08	12.83	51.25
13-06-11 traverse5	12	0.40	0.00	11.40	23.86	0.08	12.88	51.47
13-06-11 traverse5	13	0.16	0.00	3.78	34.75	0.13	12.33	49.29
13-06-8 traverse1	1	0.06	0.04	11.74	23.03	0.10	12.74	50.89
13-06-8 traverse1	2	0.09	0.04	12.02	22.68	0.09	12.77	51.05
13-06-8 traverse1	3	0.07	0.06	11.83	22.92	0.11	12.76	50.99
13-06-8 traverse1	4	0.06	0.04	11.58	23.33	0.10	12.75	50.97
13-06-8 traverse1	5	0.10	0.00	11.95	22.85	0.08	12.79	51.10
13-06-8 traverse1	6	0.08	0.04	11.77	23.11	0.09	12.78	51.07
13-06-8 traverse1	7	0.08	0.03	12.08	22.69	0.08	12.80	51.17
13-06-8 traverse1	8	0.09	0.06	12.02	22.73	0.11	12.80	51.15
13-06-8 traverse1	9	0.09	0.04	12.26	22.43	0.10	12.82	51.24
13-06-8 traverse1	10	0.06	0.05	11.71	23.29	0.12	12.81	51.18
13-06-8 traverse1	11	0.10	0.05	12.49	22.20	0.11	12.87	51.44
13-06-8 traverse1	12	0.09	0.03	11.81	23.22	0.09	12.83	51.28
13-06-8 traverse1	13	0.10	0.04	11.93	23.06	0.10	12.85	51.35
13-06-8 traverse1	14	0.07	0.04	12.00	23.00	0.09	12.86	51.39
13-06-8 traverse1	15	0.05	0.03	11.76	23.37	0.09	12.85	51.34
13-06-8 traverse1	16	0.08	0.06	11.99	23.02	0.11	12.87	51.43
13-06-8 traverse1	17	0.12	0.03	11.91	23.17	0.09	12.87	51.43
13-06-8 traverse1	18	0.12	0.03	12.01	23.16	0.10	12.92	51.64
13-06-8 traverse2	1	0.09	0.05	12.00	22.65	0.11	12.76	50.99
13-06-8 traverse2	2	0.08	0.03	11.92	22.78	0.12	12.75	50.97
13-06-8 traverse2	3	0.06	0.04	11.83	22.91	0.14	12.75	50.96
13-06-8 traverse2	4	0.08	0.04	11.74	23.06	0.10	12.75	50.95
13-06-8 traverse2	5	0.09	0.03	12.26	22.41	0.11	12.82	51.22
13-06-8 traverse2	6	0.07	0.05	11.76	23.13	0.10	12.78	51.09
13-06-8 traverse2	7	0.05	0.05	12.13	22.67	0.10	12.82	51.24
13-06-8 traverse2	8	0.12	0.03	11.97	22.91	0.08	12.82	51.25
13-06-8 traverse2	9	0.06	0.03	11.73	23.29	0.10	12.81	51.19
13-06-8 traverse2	10	0.06	0.06	11.65	23.40	0.10	12.81	51.19
13-06-8 traverse2	11	0.09	0.04	11.79	23.22	0.08	12.82	51.25
13-06-8 traverse2	12	0.11	0.03	12.02	22.87	0.11	12.84	51.32
13-06-8 traverse2	13	0.10	0.06	12.13	22.76	0.12	12.87	51.42
13-06-8 traverse2	14	0.09	0.04	12.63	22.12	0.13	12.92	51.62

		Concentration (WT%)						
SAMPLE	Point	Fe	Mn	Mg	Ca	Sr	C	O
13-06-8 traverse2	16	0.10	0.06	12.13	22.81	0.11	12.88	51.48
13-06-8 traverse2	17	0.05	0.05	11.70	23.56	0.13	12.88	51.48
13-06-8 traverse2	18	0.10	0.03	12.09	23.01	0.11	12.92	51.62
13-06-8 traverse2	19	0.09	0.04	12.16	22.94	0.09	12.93	51.65
13-06-8 traverse2	20	0.06	0.04	11.88	23.59	0.10	12.97	51.85
13-06-8 traverse3	1	0.07	0.03	12.57	21.83	0.13	12.79	51.12
13-06-8 traverse3	2	0.07	0.04	11.90	22.79	0.12	12.75	50.95
13-06-8 traverse3	3	0.06	0.06	11.76	23.01	0.09	12.75	50.94
13-06-8 traverse3	4	0.10	0.04	12.25	22.44	0.10	12.83	51.25
13-06-8 traverse3	5	0.12	0.02	12.52	22.13	0.10	12.86	51.41
13-06-8 traverse3	6	0.08	0.04	12.04	22.93	0.09	12.86	51.39
13-06-8 traverse3	7	0.11	0.03	12.29	22.59	0.11	12.89	51.49
13-06-8 traverse3	8	0.10	0.05	11.90	23.33	0.11	12.92	51.62
13-06-8 traverse3	9	0.07	0.04	12.32	22.81	0.08	12.96	51.79
13-06-8 traverse4	1	0.07	0.05	12.15	22.42	0.10	12.76	51.00
13-06-8 traverse4	2	0.08	0.05	12.44	22.10	0.11	12.81	51.19
13-06-8 traverse4	3	0.09	0.06	11.80	23.14	0.09	12.81	51.20
13-06-8 traverse4	4	0.34	0.05	11.89	22.84	0.09	12.82	51.22
13-06-8 traverse4	5	0.07	0.04	11.72	23.30	0.14	12.81	51.21
13-06-8 traverse4	6	0.07	0.00	12.80	21.90	0.15	12.92	51.64
13-06-8 traverse4	7	0.10	0.03	11.84	23.26	0.10	12.86	51.39
13-06-8 traverse4	8	0.07	0.03	12.17	22.90	0.11	12.91	51.60
13-06-8 traverse4	9	0.09	0.00	12.35	22.73	0.08	12.94	51.72
13-06-8 traverse5	1	0.14	0.07	12.19	22.34	0.06	12.77	51.04
13-06-8 traverse5	2	0.05	0.06	11.82	23.07	0.13	12.80	51.13
13-06-8 traverse5	3	0.25	0.03	12.20	22.59	0.11	12.87	51.44
13-06-8 traverse5	4	0.09	0.04	12.11	23.20	0.10	12.98	51.87
15-13-14 traverse1	1	0.04	0.00	12.41	22.11	0.10	12.78	51.07
15-13-14 traverse1	2	0.10	0.00	12.37	22.18	0.10	12.79	51.13
15-13-14 traverse1	3	0.11	0.00	12.20	22.41	0.09	12.78	51.08
15-13-14 traverse1	4	0.23	0.04	12.12	22.41	0.08	12.77	51.04
15-13-14 traverse1	5	0.08	0.00	12.35	22.42	0.09	12.85	51.35
15-13-14 traverse1	6	0.08	0.00	12.52	22.38	0.09	12.93	51.65
15-13-14 traverse1	7	0.08	0.00	12.55	22.62	0.12	13.01	52.01
15-13-14 traverse2	1	0.05	0.00	12.46	22.16	0.09	12.82	51.24
15-13-14 traverse2	2	0.11	0.00	12.30	22.34	0.08	12.81	51.19
15-13-14 traverse2	3	0.02	0.00	12.57	22.03	0.10	12.83	51.29
15-13-14 traverse2	4	0.05	0.00	12.70	21.86	0.10	12.85	51.35
15-13-14 traverse2	5	0.04	0.00	12.21	22.57	0.09	12.82	51.23
15-13-14 traverse2	6	0.05	0.00	12.49	22.16	0.13	12.84	51.31
15-13-14 traverse2	7	0.00	0.00	11.48	23.89	0.00	12.84	51.30
15-13-14 traverse2	8	0.09	0.00	12.47	22.49	0.11	12.94	51.70

		Concentration (WT%)						
SAMPLE	Point	Fe	Mn	Mg	Ca	Sr	C	O
15-13-14 traverse3	2	0.11	0.00	12.27	22.31	0.07	12.78	51.07
15-13-14 traverse3	3	0.05	0.00	12.43	22.11	0.10	12.79	51.13
15-13-14 traverse3	4	0.04	0.03	12.03	22.67	0.11	12.77	51.03
15-13-14 traverse3	5	0.07	0.00	12.32	22.37	0.08	12.82	51.23
15-13-14 traverse3	6	0.08	0.00	12.37	22.32	0.09	12.84	51.29
15-13-14 traverse3	7	0.10	0.00	12.15	22.67	0.06	12.83	51.25
15-13-14 traverse3	8	0.04	0.00	12.28	22.58	0.09	12.85	51.37
15-13-14 traverse3	9	0.11	0.00	12.22	22.64	0.12	12.86	51.39
15-13-14 traverse3	10	0.17	0.00	12.28	22.54	0.06	12.87	51.44
15-13-14 traverse3	11	0.03	0.00	12.35	22.82	0.04	12.95	51.76
15-13-14 traverse3	12	0.16	0.04	12.48	22.47	0.07	12.95	51.77
15-13-14 traverse4	1	0.05	0.00	12.31	22.47	0.11	12.84	51.31
15-13-14 traverse4	2	0.19	0.00	12.34	22.32	0.10	12.84	51.31
15-13-14 traverse4	3	0.46	0.00	12.27	22.19	0.10	12.83	51.27
15-13-14 traverse4	4	0.00	0.00	12.58	22.39	0.10	12.94	51.71
15-13-14 traverse4	5	0.10	0.00	12.42	22.59	0.09	12.94	51.72
15-13-14 traverse4	6	0.09	0.00	12.44	22.72	0.07	12.99	51.90
15-13-14 traverse5	1	0.10	0.00	12.15	22.49	0.07	12.77	51.04
15-13-14 traverse5	2	0.10	0.00	12.33	22.38	0.07	12.83	51.27
15-13-14 traverse5	3	0.18	0.00	12.13	22.60	0.09	12.81	51.21
15-13-14 traverse5	4	0.05	0.00	12.45	22.37	0.09	12.88	51.46
15-13-14 traverse5	5	0.26	0.00	12.01	22.91	0.08	12.87	51.41
15-13-14 traverse5	6	0.09	0.00	12.33	22.60	0.08	12.90	51.54
15-13-14 traverse5	7	0.04	0.00	12.33	22.80	0.08	12.95	51.74
15-13-14 traverse5	8	0.08	0.00	12.53	22.65	0.06	13.01	51.99
6-28-7 traverse1	1	0.00	0.03	12.26	22.36	0.07	12.77	51.05
6-28-7 traverse1	2	0.11	0.00	12.26	22.30	0.07	12.77	51.05
6-28-7 traverse1	3	0.00	0.00	12.18	22.52	0.07	12.78	51.06
6-28-7 traverse1	4	0.00	0.00	12.05	22.68	0.09	12.77	51.02
6-28-7 traverse1	5	0.03	0.00	12.36	22.27	0.05	12.79	51.13
6-28-7 traverse1	6	0.00	0.00	12.10	22.68	0.06	12.78	51.08
6-28-7 traverse1	7	0.13	0.00	11.94	22.78	0.11	12.77	51.03
6-28-7 traverse1	8	0.06	0.00	11.96	22.83	0.09	12.78	51.06
6-28-7 traverse1	9	0.07	0.00	12.13	22.56	0.12	12.79	51.11
6-28-7 traverse1	10	0.06	0.00	12.02	22.77	0.08	12.79	51.10
6-28-7 traverse1	11	0.09	0.00	12.10	22.66	0.07	12.80	51.14
6-28-7 traverse1	12	0.00	0.00	12.23	22.56	0.06	12.81	51.21
6-28-7 traverse1	13	0.04	0.00	12.01	22.83	0.07	12.79	51.13
6-28-7 traverse1	14	0.03	0.00	12.31	22.48	0.04	12.83	51.28
6-28-7 traverse1	15	0.05	0.00	12.37	22.39	0.07	12.84	51.33
6-28-7 traverse1	16	0.08	0.00	12.05	22.83	0.07	12.82	51.25
6-28-7 traverse1	17	0.04	0.00	12.09	22.80	0.09	12.83	51.27
6-28-7 traverse1	18	0.03	0.00	12.19	22.71	0.09	12.85	51.34

		Concentration (WT%)						
SAMPLE	Point	Fe	Mn	Mg	Ca	Sr	C	O
6-28-7 traverse1	20	0.11	0.00	12.19	22.71	0.06	12.86	51.39
6-28-7 traverse1	21	0.00	0.00	12.23	22.78	0.05	12.88	51.47
6-28-7 traverse1	22	0.08	0.00	12.21	22.74	0.05	12.88	51.46
6-28-7 traverse1	23	0.04	0.00	12.44	22.48	0.05	12.90	51.55
6-28-7 traverse1	24	0.04	0.00	12.24	23.01	0.06	12.96	51.80
6-28-7 traverse2	1	0.04	0.00	12.24	22.37	0.06	12.77	51.03
6-28-7 traverse2	2	0.08	0.00	12.11	22.50	0.08	12.76	50.99
6-28-7 traverse2	3	0.12	0.00	11.26	23.68	0.06	12.69	50.73
6-28-7 traverse2	4	0.02	0.00	12.00	22.72	0.07	12.76	50.98
6-28-7 traverse2	5	0.06	0.00	12.15	22.53	0.06	12.77	51.05
6-28-7 traverse2	6	0.00	0.00	12.24	22.47	0.07	12.79	51.12
6-28-7 traverse2	7	0.00	0.00	12.29	22.47	0.04	12.81	51.20
6-28-7 traverse2	8	0.05	0.00	12.05	22.74	0.06	12.79	51.11
6-28-7 traverse2	9	0.09	0.00	12.16	22.61	0.05	12.81	51.19
6-28-7 traverse2	10	0.05	0.00	12.18	22.62	0.06	12.82	51.21
6-28-7 traverse2	11	0.02	0.00	12.45	22.31	0.03	12.85	51.34
6-28-7 traverse2	12	0.00	0.00	12.12	22.76	0.10	12.82	51.24
6-28-7 traverse2	13	0.00	0.00	12.21	22.74	0.08	12.86	51.40
6-28-7 traverse2	14	0.09	0.00	12.16	22.76	0.07	12.86	51.40
6-28-7 traverse2	15	0.04	0.00	12.40	22.60	0.06	12.92	51.63
6-28-7 traverse2	16	0.03	0.02	12.25	22.80	0.06	12.91	51.58
6-28-7 traverse2	17	0.00	0.00	12.13	23.06	0.08	12.92	51.62
6-28-7 traverse2	18	0.11	0.00	12.27	22.84	0.07	12.94	51.72
6-28-7 traverse2	19	0.00	0.00	12.08	23.18	0.09	12.93	51.68
6-28-7 traverse2	20	0.21	0.00	11.93	23.36	0.06	12.95	51.74
6-28-7 traverse3	1	0.15	0.00	12.02	22.65	0.05	12.77	51.02
6-28-7 traverse3	2	0.02	0.00	12.31	22.34	0.08	12.79	51.12
6-28-7 traverse3	3	0.03	0.00	12.09	22.66	0.06	12.78	51.07
6-28-7 traverse3	4	0.07	0.00	12.09	22.63	0.06	12.78	51.07
6-28-7 traverse3	5	0.13	0.00	12.06	22.62	0.09	12.78	51.06
6-28-7 traverse3	6	0.05	0.00	12.25	22.42	0.07	12.80	51.14
6-28-7 traverse3	7	0.05	0.00	12.24	22.48	0.07	12.80	51.16
6-28-7 traverse3	8	0.03	0.00	12.33	22.39	0.03	12.81	51.20
6-28-7 traverse3	9	0.03	0.00	12.13	22.66	0.04	12.80	51.15
6-28-7 traverse3	10	0.03	0.00	12.25	22.53	0.05	12.82	51.23
6-28-7 traverse3	11	0.11	0.00	12.13	22.60	0.11	12.81	51.17
6-28-7 traverse3	12	0.07	0.00	12.13	22.67	0.06	12.81	51.19
6-28-7 traverse3	13	0.06	0.00	12.23	22.53	0.09	12.82	51.22
6-28-7 traverse3	14	0.07	0.00	12.20	22.59	0.07	12.83	51.26
6-28-7 traverse3	15	0.02	0.02	12.11	22.76	0.06	12.82	51.25
6-28-7 traverse3	16	0.03	0.00	12.16	22.81	0.07	12.86	51.39
6-28-7 traverse3	17	0.30	0.03	11.66	23.28	0.07	12.82	51.21
6-28-7 traverse3	18	0.04	0.00	12.29	22.62	0.10	12.88	51.45
6-28-7 traverse3	19	0.09	0.00	12.27	22.65	0.06	12.88	51.47

		Concentration (WT%)						
SAMPLE	Point	Fe	Mn	Mg	Ca	Sr	C	O
6-28-7 traverse3	21	0.14	0.00	12.29	22.63	0.07	12.89	51.53
6-28-7 traverse3	22	0.00	0.00	12.01	23.21	0.10	12.90	51.57
6-28-7 traverse3	23	0.06	0.00	12.26	22.99	0.05	12.97	51.82
6-28-7 traverse3	24	0.37	0.00	11.94	23.30	0.04	12.97	51.82
6-28-7 traverse4	1	0.00	0.00	12.39	22.20	0.09	12.79	51.09
6-28-7 traverse4	2	0.04	0.00	12.09	22.60	0.06	12.77	51.02
6-28-7 traverse4	3	0.11	0.00	11.95	22.81	0.05	12.77	51.05
6-28-7 traverse4	4	0.07	0.00	12.13	22.59	0.08	12.79	51.11
6-28-7 traverse4	5	0.16	0.00	11.86	22.91	0.08	12.77	51.05
6-28-7 traverse4	6	0.07	0.00	12.28	22.43	0.06	12.81	51.20
6-28-7 traverse4	7	0.14	0.00	12.22	22.47	0.10	12.82	51.23
6-28-7 traverse4	8	0.10	0.00	12.25	22.52	0.05	12.83	51.27
6-28-7 traverse4	9	0.00	0.00	12.40	22.41	0.07	12.85	51.36
6-28-7 traverse4	10	0.05	0.03	12.09	22.77	0.09	12.83	51.27
6-28-7 traverse4	11	0.04	0.00	12.25	22.62	0.07	12.85	51.35
6-28-7 traverse4	12	0.04	0.02	12.29	22.57	0.04	12.86	51.38
6-28-7 traverse4	13	0.11	0.00	12.13	22.78	0.07	12.85	51.36
6-28-7 traverse4	14	0.08	0.02	12.19	22.71	0.08	12.86	51.39
6-28-7 traverse4	15	0.00	0.00	12.38	22.55	0.06	12.88	51.49
6-28-7 traverse4	16	0.06	0.00	12.20	22.75	0.07	12.87	51.43
6-28-7 traverse4	17	0.03	0.00	12.27	22.76	0.12	12.91	51.58
6-28-7 traverse4	18	0.05	0.00	12.36	22.69	0.08	12.92	51.65
6-28-7 traverse4	19	0.00	0.00	12.13	23.04	0.10	12.91	51.60
6-28-7 traverse4	20	0.21	0.00	12.36	22.58	0.09	12.93	51.68
6-28-7 traverse4	21	0.10	0.00	12.20	23.08	0.07	12.98	51.87
6-28-7 traverse4	22	0.06	0.02	12.60	22.57	0.05	13.02	52.02
6-28-7 traverse5	1	0.05	0.00	12.07	22.62	0.04	12.76	50.99
6-28-7 traverse5	2	0.03	0.00	12.26	22.42	0.06	12.79	51.13
6-28-7 traverse5	3	0.06	0.00	12.14	22.56	0.08	12.78	51.09
6-28-7 traverse5	4	0.03	0.00	12.26	22.48	0.06	12.81	51.20
6-28-7 traverse5	5	0.05	0.00	12.20	22.57	0.08	12.82	51.21
6-28-7 traverse5	6	0.12	0.00	11.93	22.92	0.05	12.80	51.14
6-28-7 traverse5	7	0.05	0.00	12.24	22.57	0.08	12.83	51.27
6-28-7 traverse5	8	0.16	0.00	12.02	22.82	0.00	12.81	51.21
6-28-7 traverse5	9	0.00	0.00	12.27	22.61	0.08	12.85	51.35
6-28-7 traverse5	10	0.09	0.00	12.13	22.80	0.05	12.85	51.36
6-28-7 traverse5	11	0.03	0.00	12.22	22.75	0.06	12.87	51.44
6-28-7 traverse5	12	0.03	0.00	12.11	22.93	0.07	12.87	51.44
6-28-7 traverse5	13	0.00	0.00	12.24	22.78	0.07	12.89	51.50
6-28-7 traverse5	14	0.03	0.00	12.17	22.89	0.07	12.89	51.50
6-28-7 traverse5	15	0.03	0.00	11.98	23.16	0.08	12.88	51.46
6-28-7 traverse5	16	0.13	0.00	12.13	22.87	0.09	12.89	51.51
6-28-7 traverse5	17	0.04	0.00	12.27	22.79	0.06	12.91	51.59
6-28-7 traverse5	18	0.04	0.00	12.21	22.89	0.06	12.91	51.59

		Concentration (WT%)						
SAMPLE	Point	**Fe**	**Mn**	**Mg**	**Ca**	**Sr**	**C**	**O**
6-28-7 traverse5	20	0.05	0.00	12.35	22.73	0.08	12.94	51.71
6-28-7 traverse5	21	0.07	0.00	12.35	22.80	0.06	12.96	51.79
6-28-7 traverse5	22	0.04	0.00	12.07	23.35	0.06	12.98	51.87

APPENDIX 6: ICP-MS

				Concentration (ppm)									
W/O	Sample	Litho	Depth	Ca	Mg	Na	Al	Si	Fe	Mn	Zn	Sr	Pb
2	14-1-4	D	6665.5	248675	149442	931.8	693.4	3451.7	5149.6	399.6	5.2	833.2	0.8
2	14-1-14	PZ1	6685.4	225617	120877	955.7	777.3	3089.6	4748.1	308.6	12.8	608.5	1.9
2	14-1-17	PZ1'	6692.6	244420	126593	873.3	755.8	3467.8	3924.9	326.2	6.7	803.9	1.7
2	14-1-19	L	6696.1	372918	15518	425	951	2675	4271	705	17.3	1662	2.69
2	14-1-21	PZ2	6703.1	267000	140463	942.2	522.4	2597.5	1848.3	236.3	4.7	811.4	0.8
3	14-1-26	PZ1	7372.35	263715	141876	1273.1	243.7	1850.0	2359.4	209.5	2.6	1292.4	0.5
4	6-28-1	D	8199.3	208594	107159	1065.5	1334.8	2885.7	17164.6	207.1	29.6	1012.4	2.5
4	6-28-2	D	8203.6	214855	108400	914.0	621.2	2636.0	7671.4	243.5	10.4	916.8	0.6
4	6-28-3	D	8205.6	254435	130130	741.4	714.2	2678.1	12020.6	352.6	8.3	893.6	1.5
4	6-28-4	D	8217.6	244175	122682	954.0	1029.2	2386.0	7492.0	417.4	27.3	813.8	2.7
4	6-28-6	PZ1	8223.7	252341	137474	1293.9	150.5	1582.8	3205.8	224.4	6.6	1454.9	0.5
4	6-28-7	PZ1'	8230.2	269703	141954	962.5	264.6	1751.3	2224.1	116.1	3.5	892.6	0.6
4	6-28-9	PZ2	8242.5	278704	135641	1042.6	353.6	1683.1	3713.8	423.6	4.7	960.3	0.5
4	6-28-10	D	8248.9	282808	120591	820.3	480.4	1604.9	7606.9	272.8	5.3	1101.1	0.9
4	6-28-13	D	8270.3	254046	136813	1409.5	244.6	1500.7	2255.5	163.2	3.2	1280.7	0.3
5	15-13-1	L	6945.9	353004	11190	623	1264	2115	12397	929	34.8	1135	8.98
5	15-13-5	D	6982.2	221106	112451	1161.3	2044.1	2362.7	12491.5	258.6	37.7	848.2	5.1
5	15-13-7	D	6989	268080	148742	1065.7	200.3	1964.1	13188.6	684.5	6.9	1039.9	0.7
5	15-13-9	PZ1	7006.5	232123	149330	1094.3	181.7	2199.3	4354.4	202.8	7.2	1412.3	2.2
5	15-13-10	PZ1	7007.8	255347	161219	922.5	159.7	1693.4	2990.9	142.8	3.0	1456.6	0.7
5	15-13-11B	PZ2	7009.9	253364	129550	988.4	139.3	1462.7	2054.7	245.1	3.4	1200.8	0.3
5	15-13-14	PZ2	7025.2	232868	147531	1025.4	874.4	8855.6	3092.5	160.1	6.0	1164.7	0.9
6	13-06-1	D	5524.2	269433	101397	935.1	344.3	1540.2	4600.1	225.3	4.0	935.0	1.6
6	13-06-2	D	5524.7	277323	115555	1028.8	476.6	2012.0	4545.6	221.9	6.8	1483.2	0.6
6	13-06-3	D	5527.3	276877	130559	808.1	142.2	1694.0	5340.8	234.9	4.2	905.9	0.3
6	13-06-4	L	5528.3	407091	6315	384	407	1227	11547	709	13.4	1765	2.11
6	13-06-6	PZ1	5539.5	282515	164765	822.0	44.2	2159.1	1429.8	91.1	1.3	1846.2	1.4
6	13-06-6B	PZ1	5540.7	245014	161206	2098.7	119.8	1718.3	1669.5	241.8	7.7	1991.5	0.8
6	13-06-7B	PZ1	5542.7	264659	146416	1274.0	113.0	1985.0	1439.0	299.8	6.3	1722.1	0.6
6	13-06-8	PZ1	5543.5	261192	132692	787.6	94.2	2236.8	3932.4	469.9	2.9	1368.8	1.7
6	13-06-9	PZ1	5544.3	248924	131320	755.4	88.6	1863.8	1626.1	271.5	4.1	1204.2	0.7
6	13-06-10B	PZ1'	5551	246686	132581	1184.6	1020.0	2426.3	5077.2	254.0	8.9	1161.6	1.6
6	13-06-11	PZ1'	5552.2	246342	134757	982.1	857.1	2162.5	5715.4	203.2	6.8	1011.2	1.2
6	13-06-11B	PZ2	5554.7	236416	124624	1061.2	670.7	2080.4	3197.3	158.0	4.4	846.0	0.7
6	13-06-14	L	5565.9	370285	6392	654	1291	2050	10833	654	22.4	1500	5.34

				Concentration (ppm)									
W/O	**Sample**	**Litho**	**Depth**	**Ca**	**Mg**	**Na**	**Al**	**Si**	**Fe**	**Mn**	**Zn**	**Sr**	**Pb**
6	13-06-17	D	5596	250691	150098	792.8	98.0	1214.8	2831.3	169.3	3.7	1034.6	0.6
6	13-06-18	L	5604	312560	16660	1168	2456	3131	5129	364	19.5	1237	5.46
6	13-06-19	D	5607.8	233885	129379	1074.3	267.2	2337.2	3696.5	245.1	2.9	892.3	0.6
7	11-20-2	L	4974.5	381082	8069	1338	824	2002	4851	451	6.34	1159	2.77
7	11-20-4	PZ1	4980.1	215128	106155	1942.4	1520.6	3328.7	8627.6	282.7	18.0	785.6	3.7
7	11-20-5	PZ1'	4985.5	234295	107464	1421.2	1440.7	7746.7	7353.1	244.2	76.4	969.8	2.6
8	16-5	L	4710	343576	17018	1090	1371	2488	4162	265	15.2	977	3.78
8	16-7	PZ1'	4720.8	238937	116240	1507.8	796.6	2271.8	8757.7	208.7	18.3	916.4	3.7
10	I-4	D	-	243544	136852	1310.1	814.0	3299.8	7302.2	495.0	10.0	896.9	1.8
10	I-5	D	-	237415	115591	1122.3	1463.0	3815.5	8262.6	680.5	16.3	787.0	3.0
		Detection limit		10	0.5	0.7	0.1		7	0.02	0.05	0.01	0.02

APPENDIX 7: Carbon and oxygen isotopes

Well	Sample	Depth	$\delta^{13}C$ (VPDB)	$\delta^{18}O$ (VPDB)	%Calcite	%Dolomite
BBC 14-1	14-1-2	6657.75	-0.2	-2.8	22.3	77.7
BBC 14-1	14-1-4	6665.5	1.5	-1.5	1.2	98.8
BBC 14-1	14-1-8	6675.3	-1.1	-5.1	15.6	84.4
BBC 14-1	14-1-14	6685.4	-3.3	-2.7	7.0	93.0
BBC 14-1	14-1-17	6692.6	-3.3	-2.4	0.0	100.0
BBC 14-1	14-1-19	6696.1	-1.2	-8.3	99.2	0.8
BBC 14-1	14-1-20	6701.4	1.2	-2.7	16.2	83.8
BBC 14-1	14-1-21	6703.1	1.9	-0.7	1.4	98.6
N 6-28	6-28-1	8199.3	1.4	-0.8	0.0	100.0
N 6-28	6-28-2	8203.6	5.2	-0.1	10.0	90.0
N 6-28	6-28-3	8205.6	6.4	-2.0	0.0	100.0
N 6-28	6-28-4	8217.6	4.1	-1.9	0.0	100.0
N 6-28	6-28-5	8223.2	0.3	-2.1	13.4	86.6
N 6-28	6-28-6	8223.7	2.4	0.9	6.8	93.2
N 6-28	6-28-7	8230.2	5.2	-0.3	0.0	100.0
N 6-28	6-28-8	8234.6	1.3	-7.3	94.7	5.3
N 6-28	6-28-9	8242.5	3.7	-2.1	2.8	97.2
N 6-28	6-28-10	8248.9	2.7	-4.0	7.1	92.9
N 6-28	6-28-11	8256	2.3	-4.9	21.9	78.1
N 6-28	6-28-12	8267.4	3.0	-7.3	21.0	79.0
N 6-28	6-28-13	8270.3	-0.3	-1.3	4.4	95.6
UT 15-13	15-13-1	6945.9	0.1	-7.2	90.4	9.6
UT 15-13	15-13-5	6982.2	2.9	0.1	0.0	100.0
UT 15-13	15-13-6	6983.9	2.0	-2.8	22.4	77.6
UT 15-13	15-13-7	6989	3.5	-2.1	4.0	96.0
UT 15-13	15-13-9	7006.5	4.8	0.0	0.0	100.0
UT 15-13	15-13-10	7007.8	2.1	-1.6	0.0	100.0
UT 15-13	15-13-11A	7009.9	2.9	-7.3	0.0	100.0
UT 15-13	15-13-11B	7009.9	3.9	-2.6	6.1	93.9
UT 15-13	15-13-12	7016.4	4.7	-4.6	14.9	85.1
UT 15-13	15-13-13	7017.4	4.7	-4.8	12.6	87.4
UT 15-13	15-13-14	7025.2	6.0	-1.3	0.0	100.0
PW 13-06	13-06-1	5524.2	2.5	0.5	8.2	91.8
PW 13-06	13-06-2	5524.7	2.3	-4.7	7.3	92.7
PW 13-06	13-06-3	5527.3	3.4	1.1	2.0	98.0
PW 13-06	13-06-5	5537.3	0.4	-6.5	100.0	0.0

Well	Sample	Depth	$\delta^{13}C$ (VPDB)	$\delta^{18}O$ (VPDB)	%Calcite	%Dolomite
PW 13-06	13-06-6	5539.5	4.3	-1.5	1.6	98.4
PW 13-06	13-06-6B	5540.7	3.7	-0.4	0.0	100.0
PW 13-06	13-06-7	5541.9	4.3	-2.6	0.0	100.0
PW 13-06	13-06-7B	5542.7	3.7	-0.7	0.0	100.0
PW 13-06	13-06-8	5543.5	3.5	-2.8	0.0	100.0
PW 13-06	13-06-9	5544.3	2.7	-2.2	0.0	100.0
PW 13-06	13-06-10	5545.3	3.3	-4.3	15.5	84.5
PW 13-06	13-06-10A	5546.1	3.5	-3.3	12.9	87.1
PW 13-06	13-06-10B	5551	2.2	-6.2	6.3	93.7
PW 13-06	13-06-11A	5553.9	1.1	-5.4	68.3	31.7
PW 13-06	13-06-11B	5554.7	1.0	-4.8	0.9	99.1
PW 13-06	13-06-11C	5556.6	1.2	-2.9	48.6	51.4
PW 13-06	13-06-12	5557.4	1.9	-6.0	0.0	100.0
PW 13-06	13-06-13	5563.3	1.1	-4.1	20.2	79.8
PW 13-06	13-06-14	5565.9	-0.9	-9.6	98.4	1.6
PW 13-06	13-06-15	5580.8	-0.9	-6.5	40.1	59.9
PW 13-06	13-06-16	5595.4	-0.5	-1.5	0.0	100.0
PW 13-06	13-06-17	5596	2.9	-2.2	0.0	100.0
PW 13-06	13-06-18	5603.4	0.1	-6.1	98.2	1.8
PW 13-06	13-06-19	5607.8	2.5	-1.4	3.4	96.6
DS 11-20	11-20-1	4972.5	-3.0	-3.8	36.7	63.3
DS 11-20	11-20-2	4974.5	-0.7	-5.3	98.5	1.5
DS 11-20	11-20-4	4980.1	-2.0	-0.8	3.5	96.5
DS 11-20	11-20-5	4985.5	-1.0	-2.4	9.5	90.5
DS 11-20	11-20-8	4989.5	-0.1	-4.8	97.5	2.5
DS 11-20	11-20-9	4990.45	-1.1	-3.5	31.9	68.1
I 16	16-1	4701.3	-0.8	0.5	0.0	100.0
I 16	16-2	4705.4	3.1	-4.0	13.3	86.7
I 16	16-3	4706.3	0.9	-5.6	30.5	69.5
I 16	16-4	4707	-1.3	-4.4	13.1	86.9
I 16	16-7	4720.8	-0.9	0.1	4.3	95.7
I 16	16-8	4721.25	0.5	-3.0	28.0	72.0
I 16	16-10	4723.3	0.2	-3.6	14.1	85.9
I 16	16-11	4724.2	-1.0	-2.0	35.7	64.3
I 16	16-19	4735.8	-2.1	-4.6	4.6	95.4

IAEA values used to normalize data

	^{13}C	^{18}O
NBS 18	-5.1 ± 0.1	-23.2 ± 0.1
NBS 19	1.95 (b.d.)	-2.2 (b.d.)
IAEA CO-1	2.5	-2.4 ± 0.1
IAEA CO-8	-5.8	-22.7 ± 0.2
IAEA CO-9	-47.1	-15.6 ± 0.2
LSVEC	-46.6 ± 0.15	

Precision and accuracy as 1 sigma of (n=10) lab std

0.2	for $\delta^{13}C$
0.2	for $\delta^{18}O$

Appendix V

Assessment of Undiscovered Oil and Gas Resources in the Uteland Butte Member of the Eocene Green River Formation, Uinta Basin, Utah

Ronald C. Johnson, Justin E. Birdwell, Tracey J. Mercier, Michael E. Brownfield, Ronald R. Charpentier, Timothy R. Klett, Heidi M Leathers, Christopher J. Schenk, and Marilyn E. Tennyson

U.S. Geological Survey, Denver, CO

U.S. Geological Survey Fact Sheet 2015-3052

USGS
science for a changing world

National and Global Petroleum Assessment

Assessment of Undiscovered Oil and Gas Resources in the Uteland Butte Member of the Eocene Green River Formation, Uinta Basin, Utah

Using a geology-based assessment methodology, the U.S. Geological Survey estimated mean undiscovered resources of 214 million barrels of oil, 329 billion cubic feet of associated/dissolved natural gas, and 14 million barrels of natural gas liquids in the informal Uteland Butte member of the Green River Formation, Uinta Basin, Utah.

Introduction

The U.S. Geological Survey (USGS) recently completed a geology-based assessment of conventional and continuous (unconventional) oil and gas resources of the informal Uteland Butte member (Osmond, 1992) of the Eocene Green River Formation, Uinta Basin, Utah (fig. 1). The recent successful development of a tight oil play in the informal Uteland Butte member, using modern horizontal drilling and hydraulic fracturing techniques (Durham, 2013; Anderson and Roesink, 2013; Vanden Berg and others, 2014), has spurred a renewed interest in the tight oil potential of lacustrine rocks.

Assessment Units

The USGS defined a Green River Total Petroleum System (TPS) and two assessment units (AU) within the TPS: (1) the Uteland Butte Carbonate Continuous Oil Assessment Unit; and (2) the Uteland Butte Conventional Oil and Gas Assessment Unit (fig. 1). Key input data used to assess the informal Uteland Butte member are in table 1.

The Uteland Butte Carbonate Continuous Oil AU covers much of the deep central part of the Uinta Basin (fig. 1) and consists largely of organic-rich offshore lacustrine carbonate and shale. The most productive reservoir rock and the main target for horizontal drilling is highly porous, largely impermeable dolomite beds, but significant oil is also present in adjacent organic-rich shale and micritic limestone beds. The Uteland Butte Carbonate Continuous Sweet Spot or area with unusually high estimated ultimate recoveries (EURs), is present in the north-central part of the AU in an area of abnormally high formation pressures. Overpressure appears to be the most important factor in predicting Uteland Butte production, but other factors also play a role including: (1) total thickness of the Uteland Butte member; (2) total thickness of dolomite beds; (3) organic richness; and (4) thermal maturity. The overpressured sweet spot was defined using drilling mud weights (Anderson and Roesink, 2013) and drill stem tests.

The Uteland Butte Conventional Oil and Gas AU is divided into two areas, one along the north margin of the basin and the other in the south-central part of the basin (fig. 1). The two areas are in quite different geologic settings. The north area is in marginal lacustrine rocks along the deep basin trough where thermal maturities are high and overpressure is locally encountered. Oil is trapped by the updip pinch out of marginal lacustrine clastic and carbonate reservoirs into offshore lacustrine carbonate and shale of the Uteland Butte Carbonate Continuous Oil AU to the south.

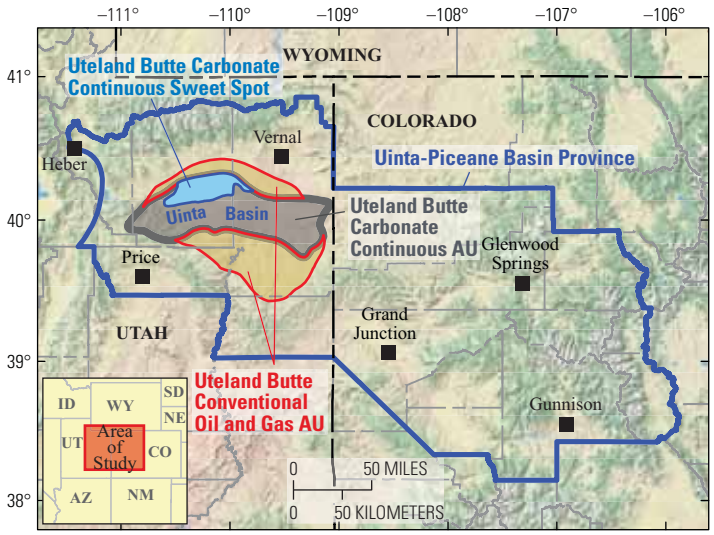

Source: National Park Service (2015)

Figure 1. U.S. Geological Survey Uinta-Piceance Basin Province of Utah and Colorado, the Uteland Butte Conventional Oil and Gas Assessment Unit (AU), the Uteland Butte Carbonate Continuous Oil Assessment Unit and the geologic sweet spot within the assessment unit.

The south area of the Uteland Butte Conventional Oil and Gas AU, in contrast, is in marginal lacustrine rocks along the south margin of the basin where thermal maturity is low and formation pressures are near normal. Trapping mechanism in the south segment is probably the updip pinch out of individual marginal lacustrine clastic units into alluvial mudstone.

The Uteland Butte Conventional Oil and Gas AU consists largely of sandstone, siltstone, carbonate, and mudstone deposited in a marginal lacustrine setting. Oil migrated into this AU from thermally mature, organic-rich offshore lacustrine rocks of the informal Uteland Butte member. The Uteland Butte Conventional Oil and Gas AU is thought to contain mainly undiscovered oil fields but some gas fields are also likely to be present. There is abundant evidence for vertical migration of gas in the basin from deeper, gas-prone source rocks in the underlying Upper Cretaceous interval (Rice and others, 1992). Some of this gas has migrated into the marginal lacustrine facies of the informal Uteland Butte member and may be trapped where an adequate seal is present.

Resource Summary

The USGS assessed undiscovered, technically recoverable continuous (unconventional) and conventional resources in the informal Uteland Butte member. Mean resources for the Uteland Butte Carbonate Continuous Oil AU are 177 million barrels of oil (MMBO); 218 billion cubic feet of gas (BCFG); and 10 million barrels of natural gas liquids (MMBNGL) (table 2). Mean resources for the Uteland Butte Conventional Oil and Gas AU are 37 MMBO; 111 BCFG; and 4 MMBNGL (table 2).

Table 1. Key assessment input data for one continuous and one conventional assessment unit in the informal Uteland Butte member, Uinta-Piceance Basin Province.

[EUR, estimated ultimate recovery per well; MMBO, million barrels of oil; BCFG, billion cubic feet of gas; AU, assessment unit; %, percent. The average EUR input is the minimum, median, maximum, and calculated mean]

Assessment input data–continuous AU				
Uteland Butte Carbonate Continuous Oil AU	Minimum	Mode	Maximum	Calculated mean
Potential production area of AU (acres)	400,000	700,000	1,373,000	824,333
Average drainage area of wells (acres)	120	160	200	160
Percentage of total AU area that is untested (%)	98	99	99.5	98.8
Success ratio (%) in sweet spots	80	95	100	91.7
Average EUR (MMBO) in sweet spots	0.06	0.085	0.14	0.088
Success ratio (%) in nonsweet spots	30	50	70	50.0
Average EUR (MMBO) in nonsweet spots	0.03	0.044	0.09	0.046
AU probability	1.0			
Assessment input data–conventional AU				
Uteland Butte Conventional Oil and Gas AU	Minimum	Median	Maximum	Calculated mean
Number of oil fields	1	12	40	12.93
Number of gas fields	1	4	10	4.19
Sizes of oil fields (MMBO)	0.5	2	30	2.86
Sizes of gas fields (BCFG)	3	12	180	17.08
AU probability	1.0			

Table 2. Assessment results for continuous and conventional oil and gas resources in the informal Utland Butte member, Uinta-Piceance Basin Province.

[MMBO, million barrels of oil; BCFG, billion cubic feet of gas; MMBNGL, million barrels of natural gas liquids; TPS, total petroleum system; AU, assessment unit. Results shown are fully risked estimates. For gas accumulations, all liquids are included under the NGL (natural gas liquids) category. F95 represents a 95 percent chance of at least that amount tablulated. Other fractiles are defined similarly. Fractiles are additive under the assumption of perfect positive correlation. Shading indicates not applicable]

Total Petroleum System (TPS) and Assessment Units (AUs)	AU probability	Accumulation type	Total undiscovered resources											
			Oil (MMBO)				Gas (BCFG)				NGL (MMBNGL)			
			F95	F50	F5	Mean	F95	F50	F5	Mean	F95	F50	F5	Mean
Green River TPS														
Uteland Butte Carbonate Continuous Oil AU	1.0	Oil	104	170	272	177	98	205	383	218	4	9	20	10
Total unconventional resources			104	170	272	177	98	205	383	218	4	9	20	10
Green River TPS														
Uteland Butte Conventional Oil and Gas AU	1.0	Oil	15	34	70	37	15	35	74	39	1	1	3	2
		Gas					27	63	148	72	1	1	3	2
Total conventional resources			15	34	70	37	42	98	222	111	2	2	6	4
Total undiscovered resources			119	204	342	214	140	303	605	329	6	11	26	14

References Cited

Anderson, J.G., Roesink, J.G., 2013, Reservoir characterization of the Uteland Butte Formation in the Uinta Basin: American Association of Petroleum Geologists, Search and Discovery Article #50888, 2 oversized sheets.

Durham, L.S., 2013, Unconventional Uteland Butte sparks new Utah activity: American Association of Petroleum Geologists Explorer, June 2013.

Osmond, J.C., 1992, Greater Natural Buttes gas field, Uintah County, Utah, *in* Fouch, T.D., Nuccio, V.F., and Chidsey, T.C., Jr., eds., Hydrocarbon and mineral resources of the Uinta Basin, Utah and Colorado: Utah Geological Association Guidebook No. 20, p. 143–163.

Rice, D.D., Fouch, T.D., and Johnson, R.C., 1992, Influence of source rock type, thermal maturity, and migration on composition and distribution of natural gases, Uinta Basin, Utah, *in* Fouch, T.D., Nuccio, V.F., and Chidsey, T.C. Jr., eds., Hydrocarbon and mineral resources of the Uinta Basin, Utah and Colorado: Utah Geological Association Guidebook No. 20, p. 95–110.

Vanden Berg, M.D., Wood, R.E., Carney, S.M., Morgan, C.D., 2014, Geological characterization of the Uteland Butte Member of the Eocene Green River Formation—An emerging unconventional carbonate tight oil play in the Uinta Basin, Utah: *in* Program and Abstracts, Rocky Mountain Association of Geologist—American Association of Petroleum Geologists Annual Meeting, July 20–22, 2014, p. 44.

Uteland Butte Assessment Team

Ronald C. Johnson, Justin E. Birdwell, Tracey J. Mercier, Michael E. Brownfield, Ronald R. Charpentier, Timothy R. Klett, Heidi M. Leathers, Christopher J. Schenk, and Marilyn E. Tennyson.

ISSN 2327-6916 (print) ISSN 2327-6932 (online) http://dx.doi.org/10.3133/fs20153052

Appendix VI

Characterization and Horizontal Drilling Potential of Oolitic and Ostracodal Limestone Reservoirs in the Eocene Green River Formation, Northeastern Uinta Basin, Utah

Craig D. Morgan and Rebekah W. Stimpson

Utah Geological Survey, Salt Lake City, UT

CHARACTERIZATION AND HORIZONTAL-DRILLING POTENTIAL OF OOLITIC AND OSTRACODAL LIMESTONE RESERVOIRS IN THE EOCENE GREEN RIVER FORMATION, NORTHEASTERN UINTA BASIN, UTAH

Craig D. Morgan

and

Rebekah W. Stimpson

Utah Geological Survey, Salt Lake City, UT

TABLE OF CONTENTS

LIST OF FIGURES

LIST OF TABLES

ABSTRACT

Oolitic and ostracodal limestone reservoirs in the Eocene Green River Formation have been oil productive in Utah's Uinta Basin for many decades. Wonsits Valley field, one of the only fields in the basin with a thick and laterally extensive oolitic/ostracodal limestone reservoir—the G1 interval—was discovered in 1962 and has produced more than 52 million barrels of oil and 137 billion cubic feet of gas (through 2015). The G1 interval, in the lower Douglas Creek Member, is a limestone and calcareous sandstone with a maximum combined thickness of more than 90 feet. Most of Wonsits Valley is produced from vertical wells, but in the early 2000s, QEP Resources began drilling and completing horizontal laterals in the G1.

Laterally-extensive oolitic/ostracodal limestone beds were deposited in high energy shoreface environments of Lake Uinta. These beds have been described in the structurally deep Bluebell field associated with the north shore of paleo-Lake Uinta and in outcrop and core along the southern and eastern shores. Most oolitic/ostracodal limestone beds in the basin are thin, typically 1 to 5 feet thick such as in the Brennan Bottom field; Wonsits Valley field is the exception.

Oolitic/ostracodal limestone beds typically contain calcite cement with intergranular, intragranular, and rare moldic porosity. The beds commonly have more porosity than associated sandstone beds – 18% average porosity in G1 limestone versus 12% average porosity for G1 sandstone. The sandstone beds commonly contain quartz overgrowths that reduce reservoir quality. In some cases, ostracods and ooids are a component of the sandstone beds, reducing the potential for quartz overgrowths and therefore improving reservoir quality. Oolitic/ostracodal limestone beds have become a horizontal drilling target in the Uinta Basin because of their good reservoir quality and generally laterally consistent distribution. As of 2015, at least 35 horizontal wells have been drilled in the northeastern Uinta Basin exploiting the G1 bed in Wonsits Valley and neighboring fields as well as the stratigraphically lower H4 limestone.

INTRODUCTION

The Uinta Basin is a major oil producing basin in northeastern Utah (figure 1). Most of the oil production is from the lower and middle portions of the lacustrine Eocene Green River Formation (figure 2). Oil is also produced from the Colton (Wasatch) Formation and Flagstaff Member of the Green River Formation in the deep basin (e.g., Cedar Rim, Altamont, and Bluebell fields).

Deposits of the Green River Formation in the northeastern portion of the Uinta Basin are prolific oil producers from both conventional and unconventional reservoirs. Most of the conventional production is from multiple stacked sandstone beds deposited in deltaic, littoral, and fluvial environments associated with paleo-Lake Uinta river systems and are typically laterally discontinuous. In contrast, many of the limestone beds are laterally continuous over many miles and were deposited in the shallow shoreface environment of Lake Uinta. The limestones are composed of ostracods and/or ooids and are usually cemented with calcite. Despite their mostly limited thickness, these limestone beds are ideal targets for horizontal drilling. The oolitic/ostracodal limestone beds typically have good porosity but low matrix permeability. The most productive oolitic/ostracodal unit in the northeast Uinta Basin is the lower Douglas Creek Member G1 limestone (informal operator designation) (figure 2) in the Wonsits Valley and neighboring oil fields.

In this study, we characterize the G1 limestone, and underlying G1 sandstone, and discuss the horizontal drilling potential of oolitic/ostracodal limestone reservoirs in the Uinta Basin.

GEOLOGIC SETTING

The Uinta Basin in northeastern Utah is a latest Cretaceous and Paleogene asymmetric foreland basin that is deepest in the north near the basin boundary fault along the Uinta Mountains. The Wasatch Uplift forms the western boundary of the Uinta Basin, and the San Rafael Swell and Uncompahgre uplift

form the southern boundary. The Douglas Creek Arch forms the eastern boundary separating the Uinta Basin from the Piceance Basin in Colorado (figure 1).

During much of the Cretaceous, eastern Utah was dominated by the Western Interior Seaway. The seaway withdrew as regional uplift occurred during the latest Cretaceous. Collision of the Cordilleran volcanic arc to the west with the North American Craton resulted in the Cordilleran orogenies (Hintze and Kowallis, 2009) with eastward directed Sevier thrusts and development of Laramide interior basins such as the Uinta and Piceance Basins, and basement-cored uplifts such as Uinta, San Rafael, and Uncompahgre uplifts (Smith and others, 2008; Dickinson and others, 2012). Lake Uinta formed within the subsiding Uinta and Piceance Basins. The Uinta Basin received siliciclastic sediments from the Mojave region along the south shore of the lake and from the Uinta Mountains along the north shore (figure 3), resulting in extensive north- and south-shore non-coincident margins (Renaut and Owen, 1991; Borer, 2016). The subsiding basin formed in a complex system of interfingering fluvial and lacustrine environments deposited along the shores of the lake. Repeated expansion and contraction of the lake during more than 10 million years of deposition resulted in a thick sequence of interbedded hydrocarbon source rocks, complex reservoirs, and seals preserved within the Green River Formation. The Green River dips northward toward the basin axis at about 4 to 6 degrees; the maximum depth to the base of the formation is over 20,000 feet in the Altamont and Bluebell oil fields along the northern extent of the Uinta Basin (figure 4) (Fouch and others, 1994).

During the Eocene (33.9 to 55.8 Ma) the continents were in about the same position as today, just 5 to 8 degrees latitude south of their present position (Roehler, 1993). Prevailing west to east paleowinds were also similar to present day (Roehler, 1993) and produced west to east longshore currents along both the northern and southern shores of Lake Uinta, building up and converging in the eastern portion of the basin where the lake narrowed and the depth decreased toward the Douglas Creek Arch. During maximum lake level, the downwind (eastern) side of Lake Uinta probably had more than 100 miles of fetch (Borer, 2016). The currents developed a higher energy environment in this area which resulted in better sorting and winnowing of fines in the oolitic/ostracodal limestone and sandstone sediments (Borer, 2016). Subsequently, many of the reservoir beds have more porosity and permeability in the northeastern Uinta Basin compared to similar reservoirs in the western portion of the basin.

Oolitic/ostracodal limestone beds are conventional oil reservoirs found throughout much of the Uinta Basin. Oolitic/ostracodal outcrops have been described in Nine Mile Canyon (Remy, 1992; Keighley and others, 2002; Morgan, 2003; Morgan and others, 2003a), Desolation Canyon (Morgan, 2003; Ford and others, 2016), and Raven Ridge (Borer, 2016). Oolitic/ostracodal reservoirs have been described in core from Greater Monument Butte field (Bereskin and others, 2004) and in the deep Bluebell field (Morgan and others, 2003b). Oolitic/ostracodal beds described in core and outcrop are generally only a few feet thick (Remy, 1992; Keighley and others, 2002; Morgan, 2003; Bereskin and others, 2004). Borer (2016) described the carbonate beds at Raven Ridge as turn-around transgressive deposits along the outer edge (lakeward) of landward-stepping siliciclastic shoreface cycles. During lake-level rise, terrigenous material is deposited updip due to increasing accommodation. Borer (2016) described the beds as shoal-crest zones rich in coated allochems stepping landward until the shoal is drowned displaying a “keep-up” then “give-up” motif (Neumann and Macintyre, 1985; Sarg, 1988).

STUDY AREA

The study area covers portions of T. 6 S. through T. 9 S., and R. 19 E. through R. 22 E., Salt Lake Base Line and Meridian (SLB&M), and portions of T. 2 S. through T. 5 S., and R. 2 E. through R. 3 E., Uinta Base Line and Meridian (UB&M), Uintah County, Utah (figure 5). The primary area of interest is in the Wonsits Valley, Gypsum Hills, and Brennan Bottom fields, where QEP Resources has drilled and completed numerous vertical and horizontal wells principally targeting the informally-named G1 reservoir, in particular the oolitic/ostracodal limestone beds within the G1. The thinner H2 and H4 limestones below the G1 also have been targeted for production. Wonsits Valley is the only large oil field (>5 MMBO) in the Uinta Basin where most of the production is from an oolitic/ostracodal limestone bed.

PRODUCTION BACKGROUND

The G1 reservoir In the Wonsits Valley field was described by Schuh (1993a) as "medium grained ostracodal or calcareous quartz arenites, and fine grained sandy ostracodal limestone." Porosity ranges from 8 to 19% (averaging 12%) in the sandstone and 8 to 28% (averaging 18%) in the limestone, and permeability measurements from 1 to 50 md (Schuh, 1993a). Schuh (1993a) reported that based on chromatography analysis of the oil, 80% of the production was coming from the limestone.

The Wonsits Valley field was discovered in 1962 with the completion of the Stout Federal Unit 1 well (Section 8, T. 8 S., R. 22 E., SLB&M) drilled to a depth of 5762 feet and completed at 5578 feet in the G1. Many of the Green River Formation oil fields neighboring Wonsits Valley were also discovered and developed in the 1960s. The early wells were drilled vertically, completed through perforated casing, and stimulated with high-pressure hydrochloric acid (HCl). Wells in Wonsits Valley field were drilled on 40-acre spacing in an area encompassing more than 6000 acres (Schuh, 1993a).

The Brennan Bottom field approximately 6 miles northwest of Wonsits Valley field produces from numerous thin beds in the Green River and Wasatch Formations. Green River production is from thin (<10-ft thick) limestone beds including the G1 and H4 (Schuh, 1993b). Schuh (1993b) described the limestones as having 8 to 20% porosity and 0.5 to 20 md.

The Brennan Bottom field was discovered in 1954 with the completion of the Brennan Bottom Federal 1 well (Section 13, T. 7 S., R. 20 E., SLB&M) drilled to a depth of 8000 feet and completed from 6870 to 7328 feet (gross perforated interval) in numerous Green River limestones and Wasatch sandstones. The early wells were drilled vertically, cased, perforated, and treated with HCl.

Throughout the Uinta Basin, various oolitic/ostracodal beds were perforated in vertical wells along with numerous sandstone, other carbonate, and mudstone beds. The typical completion technique until a decade ago was to fracture stimulate with HCl and no proppant, but since then, many of the wells in the deep basin have been fracture stimulated with slick water and proppant. The production contribution from oolitic/ostracodal beds in wells with 5 to more than 50 perforated zones is rarely known, and Wonsits Valley is the only field in the basin where the oolitic/ostracodal bed is thick enough to be profitable as a single-producing reservoir in a vertical well.

Throughout most of the Uinta Basin, the oolitic/ostracodal beds are thin (1-5 ft) but laterally continuous, similar to the Brennan Bottom field. Horizontal drilling can expose thousands of feet of a thin reservoir to the well bore. As a result, oolitic/ostracodal beds have become a primary reservoir target. Previously, wells in Brennan Bottom were typically completed by perforating eight or more beds in the Green River and Wasatch Formations including several thin limestones (Schuh, 1993b). Some of the recent completions are in laterals drilled from older vertical wells and others are newly drilled horizontal wells. The wells are cased, perforated, and stimulated with HCl.

METHODS

Core Description

We described the lithology, facies, sedimentary structures, and fracturing in 396 feet of core from three wells that penetrated the G1 interval in the eastern Uinta Basin—195.5 feet from Wonsits Valley 101-2, 159.3 feet from Wonsits Valley 128, and 41.5 feet from Whiton 1-19-3C (figure 5). These three cores are housed at the Utah Core Research Center in Salt Lake City.

Eight thin sections of the G1 interval from the above-mentioned cores were prepared by Wagner Petrographic located in Lindon, Utah. The blue epoxy visible in the photomicrographs reveals the porosity in each sample. We classified the lithologies observed in the sections using Dunham's (1962) carbonate rock classification system.

Mapping the G1 Interval

Identifying oolitic/ostracodal limestone beds using only geophysical well logs can be difficult because they are generally thin. The log characteristics of an oolitic/ostracodal bed and thin sandstone or other carbonate can be very similar, especially since many sandstone beds contain some ostracods and/or ooids (Longman and others, 2003). Density-neutron and photo electric (PE) logs used for lithology identification are questionable at best when trying to determine the lithology of thin beds that share some compositional similarities. Sample and mud logs with detailed descriptions are not publicly available for most wells in the basin, and they often are unreliable when trying to identify thin oolitic/ostracodal beds. Most well cutting samples are 10-foot composites and cannot be used to differentiate thin oolitic/ostracodal, sandstone, and carbonate beds. Most of the publicly available sample logs describe sandstone and carbonate beds with minor ooids or ostracods over tens to hundreds of feet. A description that includes ooids or ostracods as part of a heterolithic sample may contain thin oolitic/ostracodal limestone beds or sandstone/muddy carbonate with some ooids/ostracods as part of the bed. If the description does not mention ostracods or ooids then the interval probably does not contain any. Many of the sandstone beds do not have the lateral continuity and horizontal drilling potential of most limestone beds, so it is important to differentiate between the two.

Despite the above-mentioned difficulties, a thickness map of the G1 limestone was prepared for a portion of the Wonsits Valley and Gypsum Hills fields (T. 8 S., R. 21 E., SLB&M) (figure 6). We were able to distinguish between limestone and sandstone in the G1 interval in wells that have good quality gamma-ray, density, and neutron (DN) logs (figure 7). An attempt was made to have at least one data point in each quarter section resulting in a spatially representative sample of data points for contouring.

CORE DESCRIPTIONS

Cores containing the G1 were recovered from the Wonsits Valley 128, Wonsits Valley 101-2, and Gypsum Hills Whiton 1-19-3C wells (figures 6 and 7). All three wells were vertically drilled and completed in the G1 interval and overlying beds and are excellent resources for better understanding the oolitic/ostracod limestones. In addition, QEP Resources provided porosity and permeability data for the three cores (figure 8).

Eight thin sections of the G1 limestone beds were made from the three cores described above. Dominant grain types are ooids and ostracods, and most of the samples are true packstones, though the G1 also contains wackestones and limestones according to Dunham's (1962) classification system.

Wonsits Valley 101-2

The Wonsits Valley 101-2 well was cored from 5200 to 5332 feet terminating in the G1 interval (figures 9 and 10). Four lake cycles were cored above the G1 in ascending order, F5, F4, F2, and E5. Each cycle begins with open-lacustrine dark brown to dark gray shale and coarsens upward into interbedded siltstone and shale, topped with very fine grained sandstone. Porosity and permeability were measured from core plugs from all of the cored cycles (figure 11). All of the cycles have some samples with permeability above 1 mD; some with 100s mD are due to high interparticle porosity (Mark Longman, Questar Exploration and Production, personal communication, May 2017).

G1 Interval

The G1 interval was cored from 5397 to 5426 (29 feet) and encountered a thin (5-ft) G1 limestone overlying a horizontal to low-angle cross-bedded sandstone (figures 9 and 10). The lower G1 consists of 19 feet of oil saturated, very fine grained sandstone with thin interbedded siltstone and shale. The limestone is

light brown (highly oil stained) and generally massive, with only rare bedding. The limestone is mostly ostracods with some ooids and calcite cement. Some visible vuggy porosity is seen in the core samples. The limestone is overlain by a 5 feet of fining upward, horizontally bedded siltstone to shale with some thin interbedded oolitic/ostracodal limestones. Porosity values from 15 core plugs range from 3.4 to 13.4% with an average of 7.4%. Permeability ranges from 0.01 to 29.4 mD (figure 11).

Two thin sections were cut and described from the Wonsits Valley 101-2 core at 5400 and 5402 feet (figure 12). The matrix-supported wackestone to packstone at 5400 feet, near the upper transition of the G1, preserves some intragranular porosity between ooid rings and in ostracod interiors. Ooids commonly contain quartz nuclei in this sample (figure 12a, b). Abundant ostracods and minor ooids form a coarse-grain packstone at 5402 feet with some intraparticle porosity in many of the ostracods (figure 12c). The dark brown coloring in the photomicrographs is a result of oil staining.

F5 Interval

The F5 interval overlies the G1 interval and was cored from 5358 to 5398 feet (40 feet thick). The interval begins with gray to dark gray shale with an upward increase in burrowing. The F5 is transitional with the G1 and grades upward to interbedded shale and light gray siltstone, topped with light brown, oil saturated very fine grained sandstone. Porosity values from 15 core plugs range from 2.0 to 9.6% with an average of 5.5%, permeability ranges from 0.01 to 30.3 mD (figure 11).

F4 Interval

The F4 interval was cored from 5325 to 5358 feet (33 feet thick). The F4 consists of a thin gray to dark gray shale at the base overlain by light gray siltstone that is oil saturated and bioturbated with horizontal and vertical burrows. The upper portion of the bed is dominantly siltstone with some thin sandstone beds. Porosity from 32 core plugs range from 1.6 to 12.9% with an average of 8.7%; permeability ranges from 0.01 to 135 mD with an average of 25.3 mD (figure 11). The average permeability is 17.2 mD without the two highest values 135 and 125 mD, which may be the result of fractures.

F2 Interval

The F2 interval was cored from 5266 to 5325 feet (59 feet thick). The F2 consists of lower dark gray to black, horizontally laminated shale transitioning upward to siltstone and sandstone, very fine grained, with some oil saturation, and some horizontal and vertical burrowing. Porosity from 43 core plugs ranges from 2.1 to 12.8% with an average of 8.2%; permeability ranges from 0.01 to 121.5 mD with an average of 9.8 mD (figure 11). The average permeability is 4.6 mD without the two highest values 121.5 and 113.0 mD, which may be the result of fractures.

E5 Interval

The E5 interval was cored from 5200 to 5266 feet (66 feet thick). The E5 consists of lower black shale and siltstone and a 1-foot light gray, cryptocrystalline limestone overlain by light gray to light brown shale and thinly laminated siltstone. The upper portion of the interval is interbedded shale, siltstone, and sandstone. Some bioturbation and siltstone clasts are present, along with disturbed bedding, sandstone-filled injection features, rare oil saturation, and some fractures. Porosity from 17 core plugs ranges from 2.0 to 13.9% with an average of 8.8%; permeability ranges from 0.01 to 161.0 mD (figure 11). Eight samples have permeability greater than 50 mD possibly due to fractures. The average permeability is 0.7 mD without the eight possibly fractured-enhanced values.

Wonsits Valley 128

The Wonsits Valley 128 well was cored from 5241 to 5402 feet (figure 13) and terminates in the G1 interval. Four lake cycles above the G1 in ascending order, F5, F4, F2, and E5, were cored. Lake cycles F4, F2, and E5 begin with open-lacustrine dark brown to dark gray shale and coarsen upward with interbedded siltstone and shale, and topped with very fine grained sandstone. Lake cycle F5 is an incomplete cycle lacking a well-developed upper sandstone facies. Porosity and permeability were measured from core plugs from all of the cored cycles. The sandstone beds have a steeper porosity/permeability slope, possibly due to fracturing, whereas the G1 limestone has a much gentler slope (figure 14).

G1 Interval

The limestone unit of the G1 interval in Wonsits Valley 128 is 22.5 feet thick; the core recovered the upper 20.5 feet of the G1, but well logs indicate an additional 2.0 feet of limestone. The limestone recovered in this well is overlain by thinly-laminated shale with thin stringers of ostracods. The G1 limestone is light brown, oil saturated, and has no visible bedding. The limestone is mostly composed of tightly packed ostracods and some ooids with calcite cement. Some visible vuggy porosity is seen in the core samples. The core has vertical to near vertical open fractures that are confined to the limestone bed. Most (all?) of the fractures are drilling induced (figure 15). Porosity from 21 core plugs ranges from 9.0 to 22.7% with an average of 14.5%; permeability ranges from 0.02 to 11.0 mD.

Three thin sections were prepared from the Wonsits Valley 128 core (figure 16). The uppermost thin section from 5380 feet displays a wackestone to packstone composed of loosely compacted ostracods and ooids in a calcite-cemented limestone with some intragranular and intergranular porosity (figure 16 a, b). No porosity is visible within the calcite cement. Photomicrographs of a thin section from 5390 feet reveal a limestone with intra- and intergranular porosity, collapsed ostracod shells, and little to no cement (figure 16c, d). Ooids within the limestone at this depth commonly contain quartz nuclei. Photomicrographs from 5399 feet display compacted ostracods within a calcite cement; many of the ostracods exhibit intraparticle porosity as their interiors have been dissolved, and no visible porosity exists within the cement (figure 16e, f).

F5 Interval

The F5 interval was cored from 5347 to 5381 feet (34 feet thick) and consists of gray to black shale and some dolomitic to silty dolomitic mudstone. The upper portion of the interval consists of interbedded light gray siltstone with vertical and horizontal burrows, and gray to dark gray shale. The top of the interval is lacking a well-developed sandstone facies. Porosity from 18 core plugs ranges from 0.5 to 7.8% with an average of 3.1%; permeability ranges from 0.02 to 8.7 mD (figure 14).

F4 Interval

The F4 interval was cored from 5322 to 5347 feet (25 feet thick) and consists of lower gray to dark gray shale with interbedded bioturbated siltstone. The interval coarsens upward to interbedded siltstone and very fine grained sandstone. The sandstone is oil saturated with vertical fractures. Porosity from 21 core plugs ranges from 2.1 to 10.8% with an average of 7.4%; permeability ranges from 0.02 to 6.7 mD with an average of 3.2 mD (figure 14).

F2 Interval

The F2 interval was cored from 5270 to 5322 feet (52 feet) and consists of dark gray shale, some with large vertical burrows, and interbedded siltstone coarsening upward to interbedded siltstone and very

fine grained sandstone. Some light brown oil saturation is also present. The upper sandstone facies is again poorly developed. Porosity from 24 core plugs ranges from 2.2 to 11.3% with an average of 6.9%; permeability ranges from 0.02 to 8.5 mD (figure 14).

E5 Interval

Only the lower portion of the E5 interval was cored from 5241 to 5270 feet. The E5 consists of dark gray to black, bioturbated shale interbedded with thinly laminated siltstone, coarsening upward with increasing laminated siltstone. The top of the core has a small (0.4-ft) stromatolite overlain by 0.6 feet of dark gray to black shale. Porosity and permeability data were not measured in the E5 interval.

Gypsum Hills Whiton 1-19-3C

The Gypsum Hills Whiton 1-19-3C well was cored from 5229 to 5271 feet and terminates in the G1 interval (figure 17). The core includes 22 feet of mudstone and shale of the lower F5 interval.

G1 Interval

The limestone within the G1 interval in Gypsum Hills Whiton 1-19-3C well is 14.3 feet thick, light to dark brown, highly oil saturated, and exhibits some low-angle cross-bedding though it is generally massive (figures 17 and 18). Core plug measurements from the G1 limestone have a porosity range of 3.7 to 20.8% with an average of 12.8%. Permeability values range from 0.01 to 3.65 mD (figure 8).

The core transitions upward from siltstone and silty limestone with some ostracods and thin wavy laminations into packstone, which is composed of ostracods and some ooids cemented with calcite. Some visible vuggy porosity is seen in the core samples. The core has low-permeability; thin, gray, silty shale interbeds; and silty shale rip-up clasts throughout the G1. Vertical to near-vertical drilling-induced open fractures are confined to the limestone bed. The prominent vertical fracture from 5269.2 to 5269.7 feet (figure 18) is probably drilling induced and demonstrates the potential for hydraulically induced fracturing in the dense limestone bed. The limestone gradually transitions upward into silty shale.

Three thin sections were prepared and described from the G1 interval in the Gypsum Hills Whiton 1-19-3C core (figure 19). Tightly packed ostracods partially suspended in a muddy matrix at 5251 feet exhibit intragranular porosity (figure 19a). Conventional core analysis from 5250 to 5251 feet and 5251 to 5252 feet has 4.7% porosity with 0.05 mD permeability, and 8.3% porosity with 0.04 mD permeability, respectively. The thin section from 5260 feet exhibits intragranular porosity from dissolved ooid layers, intergranular porosity, and abundant tightly-packed ostracods, many of which are collapsed (figure 19b, c). Conventional core analysis from 5259 to 5260 feet and 5260 to 5261 feet has 21% porosity with 3.31 mD permeability and 19.7% porosity with 10.0 mD permeability, respectively. Ooids commonly have quartz nuclei at this depth. The limestone at 5263 feet is composed almost entirely of ostracods with few ooids. Many of the ostracods have preserved porosity between the valves commonly aligned along their long axes (figure 19d). Conventional core analysis from 5262 to 5263 feet (deepest interval analyzed) has 3.7% porosity with <0.01 mD permeability.

REGIONAL MAPPING OF OOLITIC/OSTRACODAL LIMESTONE BEDS

Well log correlations (figures 20 and 21) show that the G1 and H4 intervals are in the lower Douglas Creek Member of the middle Green River Formation (figure 2). Facies within the lower Douglas Creek at Wonsits Valley transition to the northwest into thinner and deeper lake deposits (black shale facies on many of the well completions reports). The thickness of the G1 interval trends southwest to northeast and is slightly thicker on the southeast side (figure 6). Log characteristics can be correlated for many miles,

but it is unclear if the correlative beds are limestones or sandstones. The lower Douglas Creek thins to the northwest where the lake was deeper and sedimentation rates were lower in the profundal zone; thinning occurs to the southwest where accommodation space was decreasing landward (figure 20). The lower Douglas Creek and G1 is thickest in the shoreface environment where there is relatively large accommodation and abundant sediment supply. The northwest portion of the cross section B to B' (figure 20) is approaching the northern shore, and the southeastern portion of the cross section is approaching the southern shore. The axis of the lake and associated shorelines constantly shifted through time.

HYDROCARBON PRODUCTION FROM OOLITIC/OSTRACODAL LIMESTONES IN THE STUDY AREA

We gathered production data from the Utah Division of Oil, Gas and Mining website for horizontally drilled wells in the Wonsits Valley field, as well as 35 horizontal wells, including Brennan 15 and BBS 15G, targeting the G1 (31 wells) or H4 (4 wells) interval (appendix). We generated decline curves for oil and gas production in the Brennan 15 and BBS 15G wells using IHS Petra® software.

Cumulative production from the Wonsits Valley field through 2015 is 53 MMBO and 138 BCFG, but the percentage currently from the oolitic/ostracodal limestone beds cannot be determined from public data. The more recent increase in gas is from reservoirs in the underlying Wasatch Formation and Mesaverde Group. The 31 wells with horizontal laterals in the G1have produced a total of 3 MMBO and 2 BCFG for an average of 100 MBO and 73 MMCFG per well (table 1 and appendix). The four wells with horizontal laterals in the H4 have produced a total of 140 MBO and 145 MMCFG for an average of 35 MBO and 36 MMCFG per well (table 1 and appendix). The horizontal wells have been on production for a few years compared to decades of production for most of the vertical wells in the Wonsits Valley field.

Figure 22 shows when perforations and re-perforations were made in the G1 interval for the vertical Gypsum Hills 1-19-3C, Wonsits Valley 128, and Wonsits Valley 101-2 wells and the oil, gas, and water production. These wells were perforated in multiple beds and were not limited to the G1 interval. Wonsits Valley 101-2 was plugged and abandoned in 1997 with a total production of 46,697 BBLs oil and 5085 MCF gas, and Wonsits Valley 128 and Gypsum Hills 1-19-3C are still active and have produced 259,475 BBLs oil and 41,725 MCF gas and 218,207 BBLs oil and 97,522 MCF gas, respectively, as of December 2015.

Laterals in the study area measured from the surface location to the bottom hole location range from 1700 to 4550 feet and average 3400 feet. Lateral measurements were made from the map; the actual lateral distance within the pay zone is less. Many of the well reports available from the Utah Division of Oil, Gas and Mining do not have a directional survey report or include in the well completion report the net pay or the amount of lateral within the pay zone. The density of horizontal wells drilled in the oolitic/ostracodal limestone beds is very low, and the production history is limited. However, many horizontals have produced tens of MBO and some more than 100 MBO (figures 23 and 24 and Table 1). Two examples from the Brennan Bottom field, one completed in the G1 and one completed in the H4a, are discussed in the following paragraphs.

The Brennan 15 (SWSE Section 13, T. 7 S., R. 20 E., SLB&M) (figure 5) is completed in two laterals drilled in the G1 limestone. The north lateral is more than 3000 feet long with a true vertical depth of 6747 feet. The south lateral is more than 1000 feet long with a true vertical depth of 6801 feet. Both laterals have a 4.5-inch slotted liner and both were treated with 15% HCl. The north lateral was treated in five stages: stages 1 to 4 were treated with 5000 gals HCl each, and the fifth stage was treated with 4400 gals. The south lateral was treated in eight stages: stages 2, 3, and 7 were treated with 5000 gals of HCl while stages 1, 4, 6, and 8 were treated with 7500 gallons of HCl. The well was completed in February 2009 with an initial daily production flowing 349 BO, 4 MCFG, and 105 BW and has produced 144 MBO and 81 MMCFG in 83 months, an average of 1735 BO/month. Decline curve analysis indicates the well could produce a total of 209 MBO and 160 MMCFG assuming a life of 20 years (from completion) with a daily average of 3 BO and 4 MCFG at the end of the 20 years (figure 25). Total water production is less than 18

MBW (as of December 31, 2016). Monthly water production is sporadic indicating the reservoir lacks a strong water drive.

Well BBS 15G (SWSE Section 22, T. 7 S., R. 21 E., SLB&M) (figure 5) was drilled and completed as a vertical well in the H4a limestone in February 2007 with an initial daily production of 163 BO, 0 MCFG, and 36 BW. The well produced 14 MBO in 33 months and averaged 433 BO/month. A horizontal lateral was drilled in the H4a and completed in December 2009 at 10,054 feet (mechanical depth) and 6419 feet (true vertical depth) for an initial production of 142 BO, 0 MCFG, and 77 BW. Production from the lateral in 71 months is 44 MBO, an average of 619 BO/month. Decline curve analysis indicates that over 20 years the well could produce 132 MBO and 110 MMCFG (from completion) with a daily average of 2 BO and 2 MCFG at the end of the 20 years (figure 26). Total water production is less than 21 MBW (as of December 31, 2016). Monthly water production has averaged about 150 BW for more than two years, and lacks any obvious long-term trend.

DISCUSSION

The G1, F, and E units are a series of shallowing-upward depositional cycles, some complete, some with multiple pulses, and some incomplete cycles. A typical cycle consists of shale coarsening upward to silty shale, thin interbedded siltstone and shale, and capped with very fine grained sandstone or mixed oolitic sandstone and rare oolitic/ostracodal limestone. The capping sandstone or limestone is interpreted as a transgressive deposit representing the turnaround from falling lake level to rising lake level (Borer, 2016). Many of the individual beds within the depositional cycles are thin and lack distinct bedding features. Cycles identified in the cores are interpreted to have been deposited on the littoral shelf to sublittoral, although some shales and siltstones may have been deposited in the profundal zone. The cycles represent transitions from possible profundal/deep sublittoral to littoral settings. The sandstone/limestone bed capping the depositional cycle is typically overlain by silty shale often with very thin layers of oolites; the overlying flooding surface is generally a gradational transition and not a sharp contact. There is no evidence in the three cores examined of exposure such as soil horizons, mud cracks, or rooting in the G1 or overlying F and E cycles, indicating the cycles are subaqueous deposits. Some cycles are capped with thin rip-up clasts indicating a transgressive lag deposit during a flooding event. Most beds are highly bioturbated and exhibit both horizontal and vertical burrows. The relatively thin capping sandstone or limestone beds in each cycle suggest deposition in a shallow shelf to shore break setting with low sand input.

The southwest to northeast thickness trend of the G1 interval in the Wonsits Valley area is interpreted to result from a shallow shelf break associated with one of the many fluctuating shorelines, with the deepest portion of Lake Uinta to the northwest during G1 deposition (figures 20, 27, 28). This shelf break may have provided a location for the local buildup of ostracods and ooids that comprise the G1 limestone. The limestone directly overlies a sandstone bed in several wells, though this sandstone was only recovered in the Wonsits Valley 101-2 core (figures 9 and 10). The sandstone is cross-bedded, grading upward to horizontal bedding and is interpreted as a shallowing shoreface deposit (figure 28). The prevailing paleowind was west to east, which exerted longshore currents along the shore of Lake Uinta. The narrowing of the lake near the Utah-Colorado border caused a convergence and increased intensity of the currents (figure 27). The energy of the currents increased sorting and winnowing of fines helping to build up sandstone and oolitic/ostracodal deposits with better reservoir quality (porosity and permeability) than found in many other parts of the basin.

Core plug analyses from the G1 in Whiton 1-19-3C, Wonsits Valley 101-2, and Wonsits Valley 128 reveals good porosity but marginal permeability (figure 8); some of the outlier data points may represent enhanced fracture permeability. The highly cemented, tightly compacted limestones are dense, which is ideal for natural fracture development and artificial hydraulic fracture development.

CONCLUSIONS

Description and mapping of the laterally-continuous oolitic/ostracodal limestone unit within the G1 interval of the lower Douglas Creek Member of the Green River Formation in the Uinta Basin, reveals thickness variations of 0 to 25 feet. The limestone unit trends southwest to northeast for more than 6 miles. Based on the underlying and overlying deposits from Lake Uinta and the composition of the limestone, the G1 interval was deposited along a shelf break of the southeastern margin of Eocene-aged Lake Uinta as lake level rose from a lowstand level.

As of 2015 and according to publicly available data, 31 horizontal wells have targeted the G1 interval and have produced at least 3 MMBO and 2 BCFG, making this unit an important hydrocarbon reservoir. The underlying H4 limestone has also been targeted with at least four horizontal drilling projects and produced 140 MBO and 145 MMCFG through 2015.

Oolitic/ostracodal limestone reservoirs are a unique reservoir in the Uinta Basin due to their lateral continuity and commonly contain higher porosity than most sandstone beds. Oolitic/ostracodal beds that are a few tens of feet thick, such as in Wonsits Valley field, are rare, but can contain sufficient reserves to be economic as a single reservoir in a vertical well. Wonsits Valley field has been extensively drilled and has undergone a secondary waterflood, therefore horizontal wells have been drilled only along the margins of the field.

Oolitic/ostracodal beds that are less than 10 feet thick are more common throughout the basin. These thinner beds are not typically the only target of a vertical well, but can be exploited as horizontal targets due to their lateral continuity if the vertical well(s) did not deplete the reservoir and/or only drained a very limited area. Many of the older vertical wells nearing their economic limit have the potential to be re-entered to drill laterals in limestone units. Using established well bores with sufficient diameter and quality of casing greatly reduces the cost and improves the economics of exploiting these horizontal targets.

ACKNOWLEDGMENTS

This study would not have been possible without the well core and well data from QEP Resources of Denver, Colorado, and helpful discussions with QEP Resources geologists. Funding for this project was provided by Total SA via a grant through the University of Utah. Additional funding was provided by the Utah Geological Survey and the National Energy Technology Laboratory, U.S. Department of Energy, grant DE-FE0010667, titled Liquid-rich Shale Potential of Utah's Uinta and Paradox Basins: Reservoir Characterization and Development Optimization. Helpful review comments were provided by Mark Longman with QEP Resources in Denver, Colorado.

REFERENCES

Bereskin, S.R., Morgan, C.D., and McClure, K.P., 2004, Descriptions, petrology, photographs, and microphotographs of core from the Green River Formation, south-central Uinta Basin, Utah: Utah Geological Survey Miscellaneous Publication 04-2, 208 p.

Blakey, R. and Ranney, W., 2008, Ancient landscapes of the Colorado Plateau: Grand Canyon, Grand Canyon Association, 156 p.

Borer, J.M., 2016, High-resolution stratigraphy of the lower portion of the Green River Formation at Raven Ridge and Red Wash field, NE Uinta Basin, Utah, Colorado, USA: Facies and stratigraphic patterns in a high-gradient, high-energy lacustrine system: Rocky Mountain Association of Geologists, The Mountain Geologist, v. 53, no. 3, p. 119-223.

Dickinson, W.R., Lawton, T.F., Pecha, M., Davis, S.J., Gehrels, G.E., and Young, R.A., 2012, Provenance of the Paleogene Colton Formation (Uinta Basin) and Cretaceous-Paleogene provenance evolution in the Utah foreland: evidence from U-Pb ages of detrital zircons, paleocurrent trends, and sandstone petrofacies; Geological Society of America Geosphere, v 8, no. 4, p. 854-880.

DOGM, Utah Division of Oil, Gas and Mining, http://oilgas.ogm.utah.gov/

Dunham, R. J., 1962, Classification of carbonate rocks according to depositional texture. In: Ham, W.E., editor, Classification of carbonate rocks: American Association of Petroleum Geologists Memoir 1, p. 108-121.

Ford, G.L., Dechesne, M., and Phyles, D.R., 2016, Stratigraphic architecture of the fluvial-lacustrine basin-fill succession at Desolation Canyon, Uinta Basin, Utah: Reference to Walthers' law and implications for the petroleum industry: Rocky Mountain Association of Geologists, The Mountain Geologist, v. 53, n. 1, p. 5-27.

Fouch, T.D., Nuccio, V.F., Anders, D.E., Rice, D.D., Pitman, J.K., and Mast, R.F., 1994, Green River petroleum system, Uinta Basin, Utah, U.S.A., in Magoon, L.B., and Dow, W.G., editors, The petroleum system-from source to trap: American Association of Petroleum Geologists Memoir 60, p. 399-421.

Hintze, L.F., and Kowallis, B.J., 2009, Geologic history of Utah: Brigham Young University Geology Studies, Special Studies 9, 225 p.

Keighley, D., Flint, S., Andersson, D., Collins, S., Moscariello, A., and Stone, G., 2002, Surface and subsurface correlation of the Green River Formation in central Nine Mile Canyon, SW Uinta Basin, Carbon and Duchesne Counties, east-central Utah: Utah Geological Survey Miscellaneous Publication 02-1, 66 p.

Longman, M., Basse, R., and Pope, J., 2003, Characteristics of the Glen Bench sandstone reservoir, Eocene Green River Formation, Glen Bench field, Uintah County, Utah: Rocky Mountain Association of Geologists, The Mountain Geologist, v. 39, n. 4, p. 129-141.

Morgan, C.D., 2003, Geologic guide and road logs of the Willow Creek, Indian, Soldier Creek, Nine Mile, Gate, and Desolation Canyons, Uinta Basin, Utah: Utah Geological Survey Open-File Report 407, 57 p.

Morgan, C.D., Chidsey, Jr., T.C., McClure, K.P., Bereskin, S.R., and Deo, M.D., 2003a, Reservoir characterization of the lower Green River Formation, Uinta Basin, Utah: Utah Geological Survey Open-File Report 411, CD ROM 140 p.

Morgan, C.D., Gwynn, J.W., Allison, M.L., Curtice, R., Deo, M.D., Morris, T.H., and Tripp, C.N., 2003b, Characterization of the Bluebell oil field, Uinta Basin, Duchesne and Uintah Counties, Utah, in Morgan, C.D., editor, The Bluebell oil field, Uinta Basin, Duchesne and Uintah Counties, Utah: characterization and oil well demonstration: Utah Geological Survey Special Study 106, 104 p.

Neumann, A.C., and Macintyre, I., 1985, Reef response of sea level rise: keep-up, catch-up or give-up, *in* Gabric, C., Toffart, J.L., and Salvat, B., editors, Proceedings of the fifth International Coral Reef Congress: Tahiti, French Polynesia, Antenne Museum-EPHE, v. 3, p. 105-110.

Remy, R.R., 1992, Stratigraphy of the Eocene part of the Green River Formation in the south-central part of the Uinta Basin, Utah: U. S. Geological Survey Bulletin 1707-BB, 79 p.

Renaut, R.W., and Owen, R.B., 1991, Shore-zone sedimentation and facies in a closed rift lake: the Holocene beach deposits of Lake Bogoria, Kenya *in* Anadon, P., Cabrera, L1, and Kelts K., editors, Lacustrine facies analysis: International Association of Sedimentologists Special Publication 13, p. 175-195.

Roehler, H.W., 1993, Eocene climate, depositional environments, and geography, greater Green River Basin, Wyoming, Utah, and Colorado: U.S. Geological Survey Professional Paper 1506-F, 82 p.

Sarg, J.F., 1988, Carbonate sequence stratigraphy *in* Wilgus, C.K., Hastings, B.S., Kendall, C.G., Posamentier, H., Van Ross, C.A., and Van Wagoner, J., editors, Sea-level changes: an integrated approach: SEPM Society for Sedimentary Geology Special Publication 42, p. 155-181.

Schuh, M.L., 1993a, Wonsits Valley *in* Hill, B.G., and Bereskin, S.R., editors, Oil and Gas Fields of Utah: Utah Geological Association publication 22, unpaginated.

Schuh, M.L., 1993b, Brennan Bottom *in* Hill, B.G., and Bereskin, S.R., editors, Oil and Gas Fields of Utah: Utah Geological Association publication 22, unpaginated.

Smith, M.E., Carroll, A.R., and Singer, B.S., 2008, Synoptic reconstruction of a major ancient lake system: Eocene Green River Formation, western United States: Geological Society of America Bulletin, v. 20, p. 54-84.

USGS Uinta-Piceance Assessment Team, 2003, Petroleum systems and geologic assessment of oil and gas in the Uinta-Piceance Province, Utah and Colorado: U.S. Geological Survey Digital Data Series DDS-69-B.

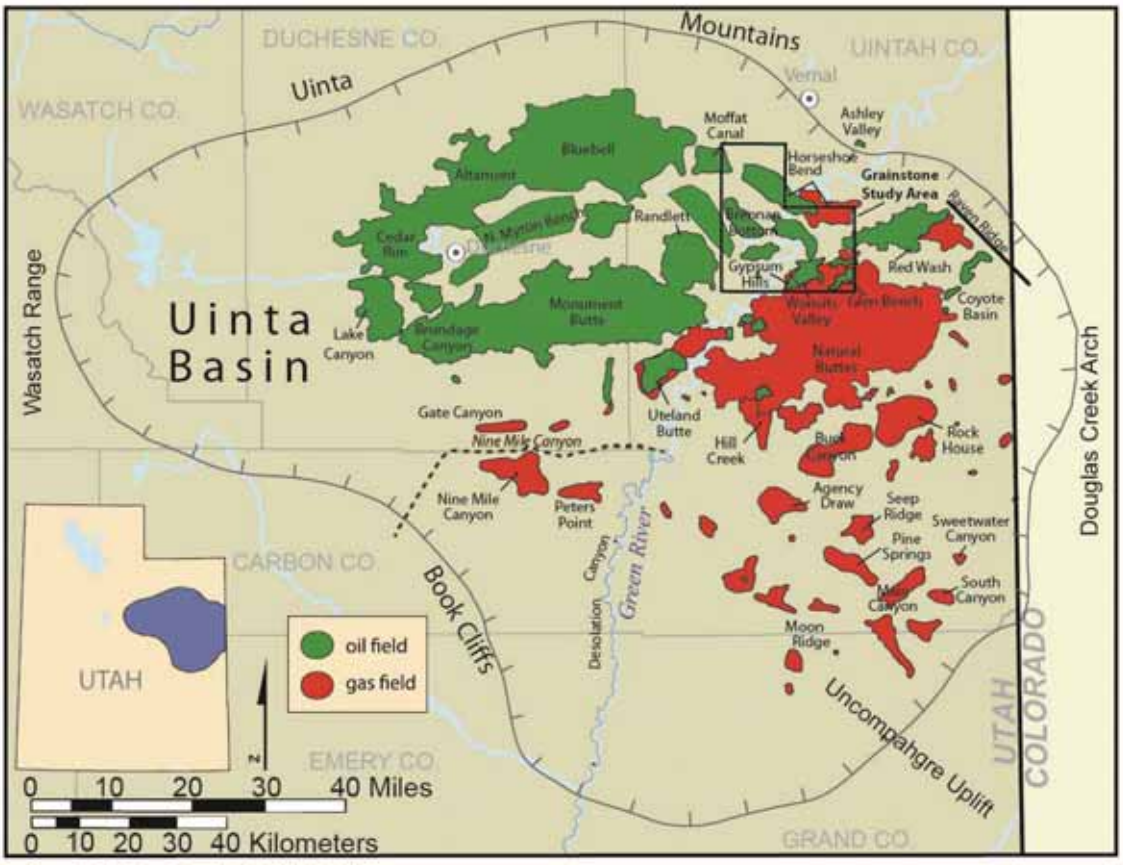

Figure 1. *Map of the Uinta Basin in northeastern Utah showing major oil and gas fields. The study area is outlined in black.*

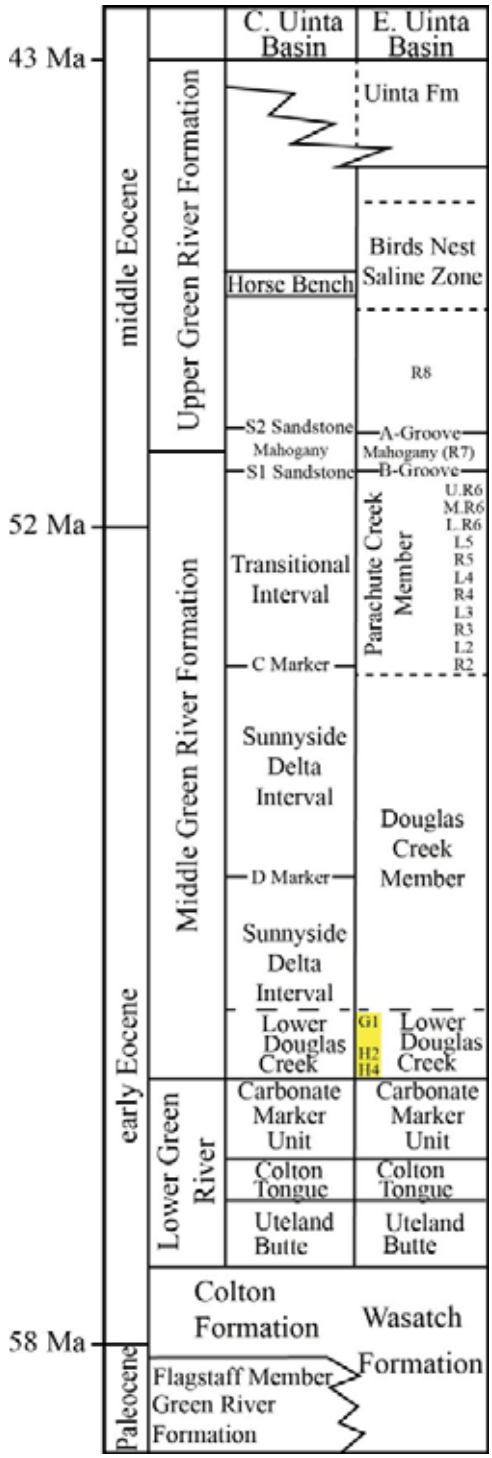

Figure 2. *Green River Formation stratigraphic chart for the central and eastern Uinta Basin. The G1, H2, and H4 limestones are located in the lower Douglas Creek Member of the middle Green River Formation. Oolitic/ostracodal limestone beds are found throughout the basin in the middle and lower Green River, as well as the Flagstaff Member.*

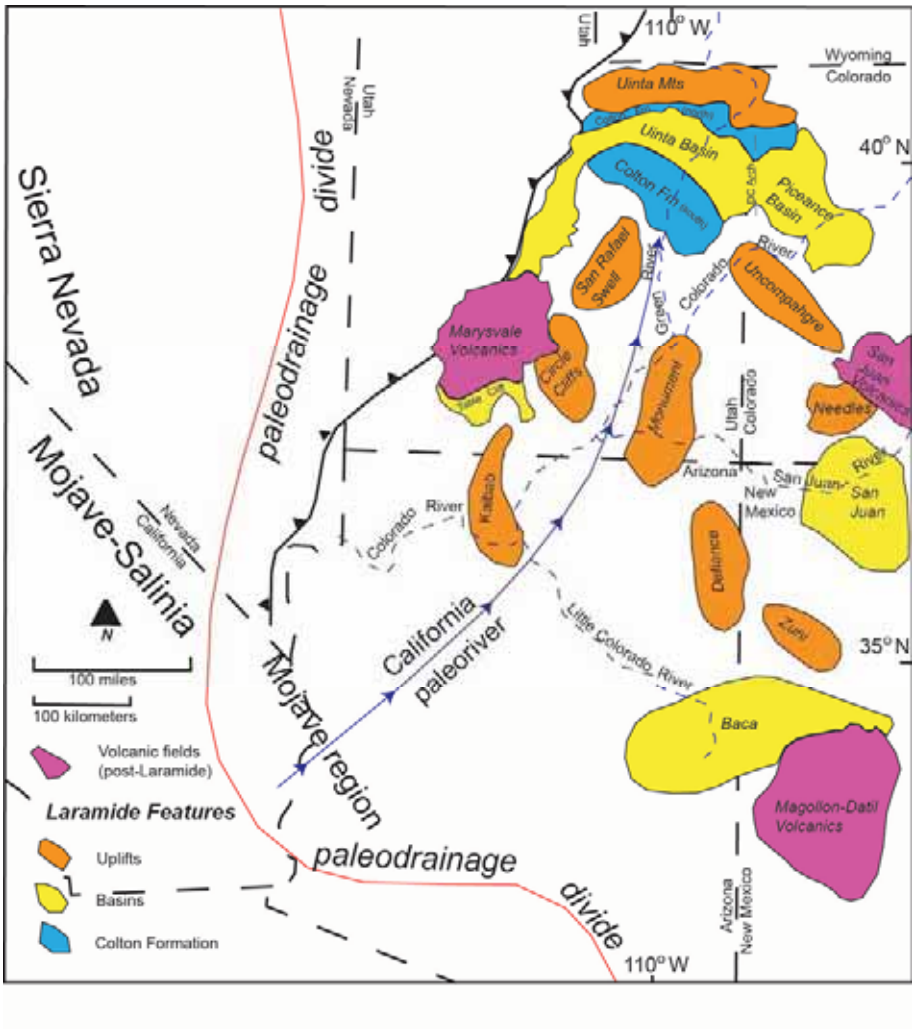

Figure 3. *Late Paleocene to early Eocene paleogeographic map depicting the California paleoriver system from the Mojave region to the Uinta Basin. The river was a major source for siliciclastics carried into the Uinta Basin from the southern shore. Sediments from the Uinta Mountains were carried into the lake from the north. The Uinta and Piceance basins are separated by the Douglas Creek Arch (DC Arch). Modified from Dickinson and others, 2012.*

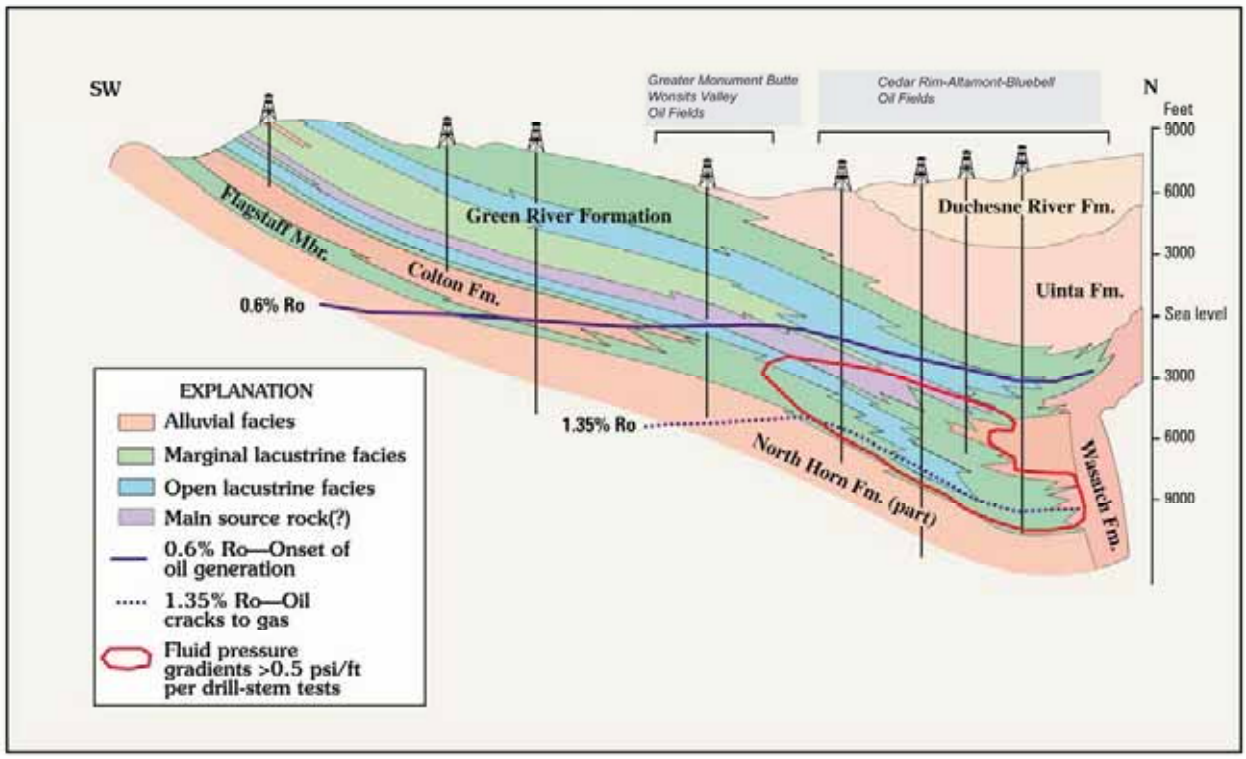

Figure 4. *Generalized cross section of the Uinta Basin showing interfingering of alluvial and open to marginal lacustrine facies. From USGS Uinta-Piceance Assessment Team (2003).*

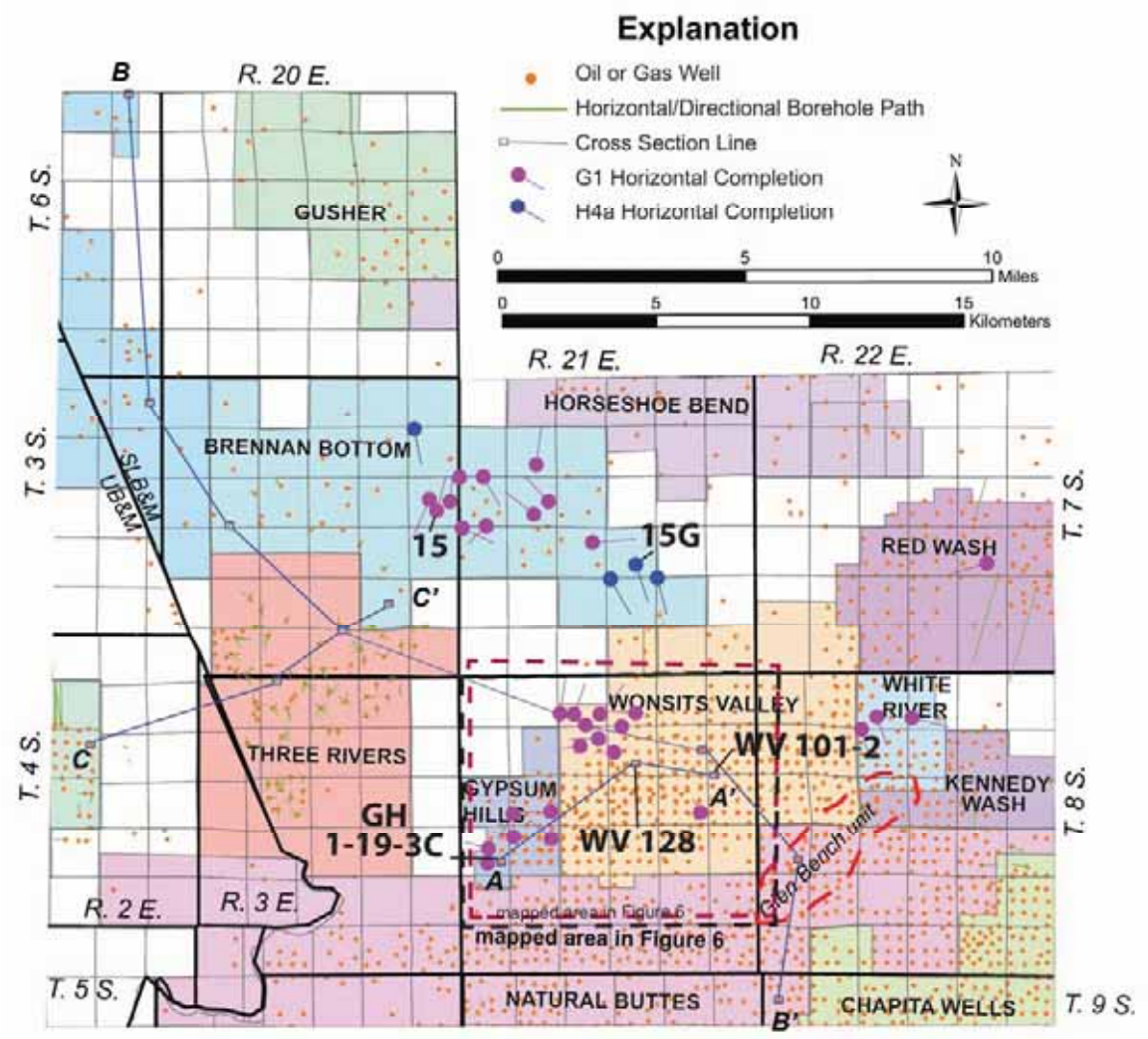

Figure 5. *Map of the study area showing all wells, oil fields (DOGM defined boundaries), and G1 and H4 horizontal completions. Cross section A-A' is figure 7, B-B' is figure 20, and C-C' is figure 21. Brennan 15 and Brennan 15G are discussed as examples of production from each of the reservoirs. The dashed rectangle is the mapped area in figure 6. Cores from Gypsum Hills Whiton 1-19-3C (GH 1-19-3C), Wonsits Valley 128 (WV 128), and Wonsits Valley 101-2 (WV 101-2) are discussed in the text. Well data and field boundaries are from Utah Automated Geographic Reference Center (AGRC) SGID Data http://gis.utah.gov/.*

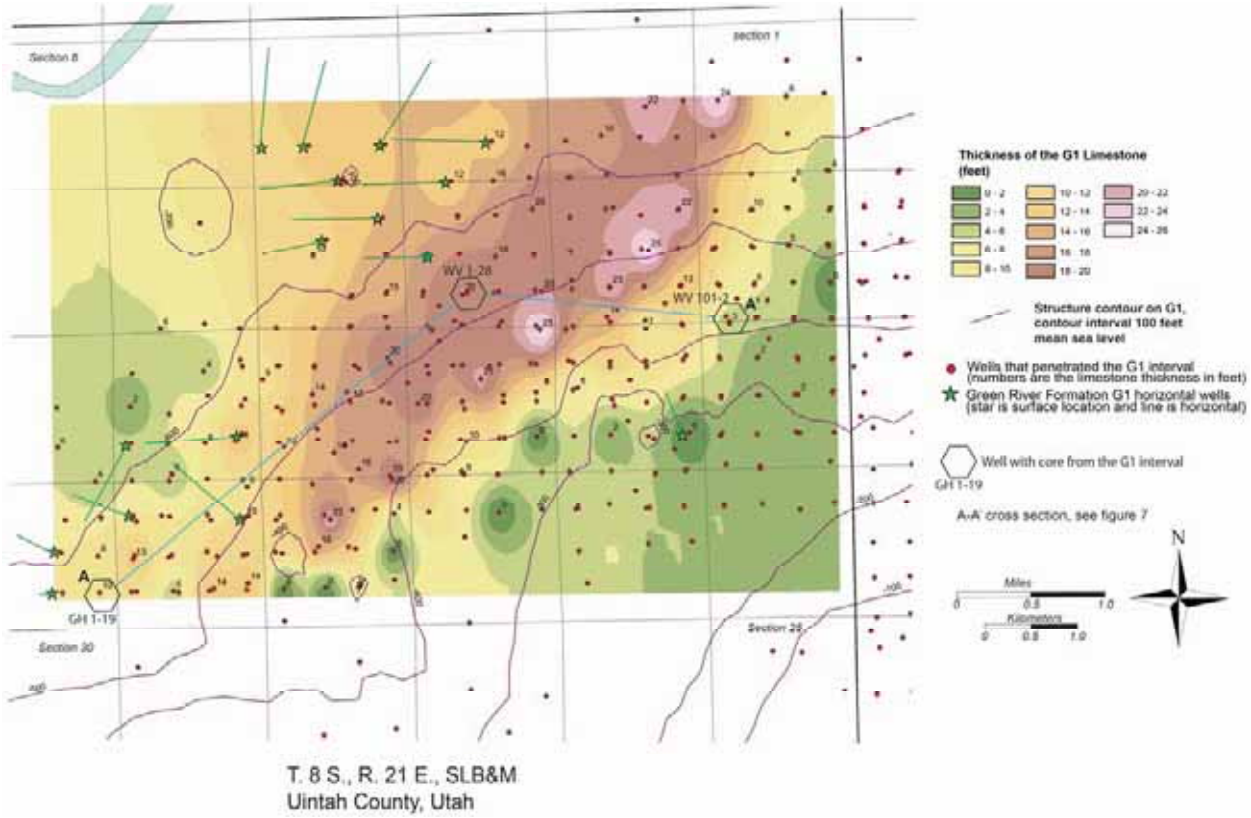

Figure 6. *Map of the Wonsits Valley field showing structure contours of the top of the G1 and thickness of the limestone. Structure contours are 100-foot intervals, datum mean sea level. Thickness contours are 2-foot intervals. Cross section A-A' is figure 7.*

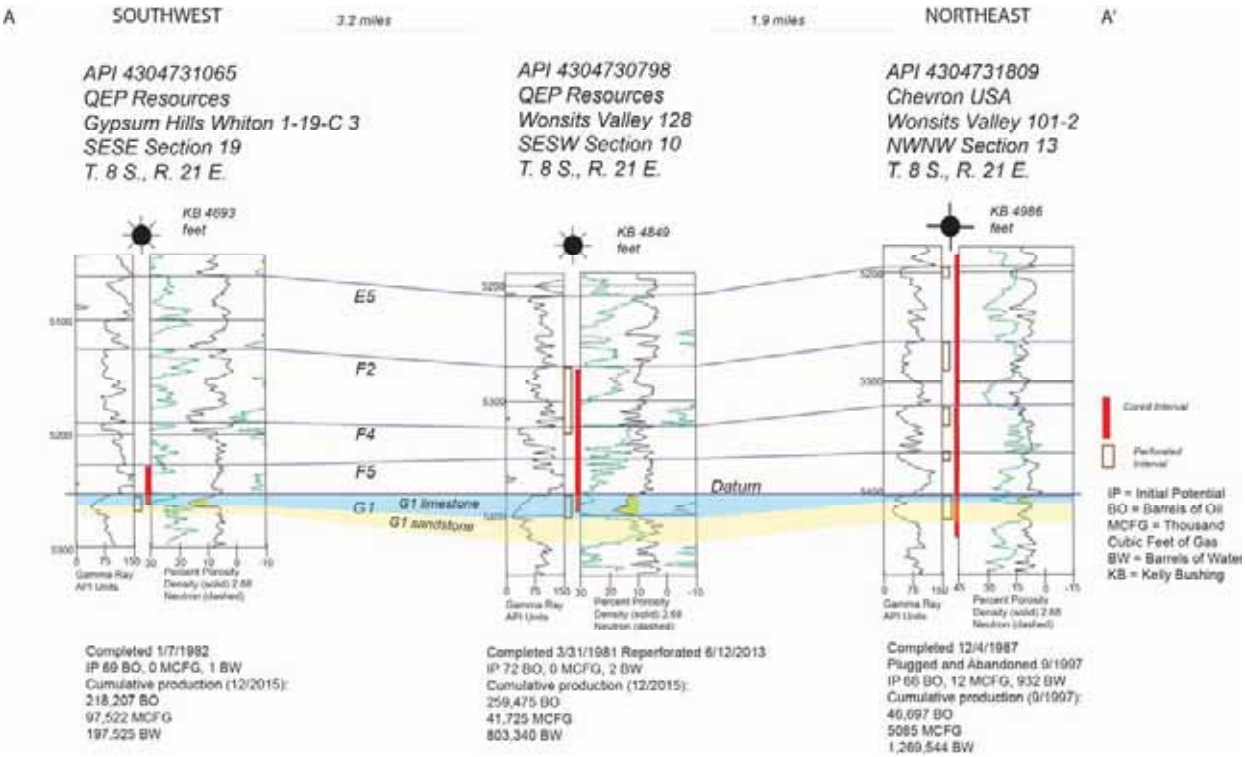

Figure 7. *Stratigraphic well-log cross section A to A' of three cored wells in the Gypsum Hills and Wonsits Valley fields. Correlation zones E5 through G1 are informal operator designations. Well data are from Utah Division of Oil, Gas and Mining http://oilgas.ogm.utah.gov/. See figure 6 for location of cross section.*

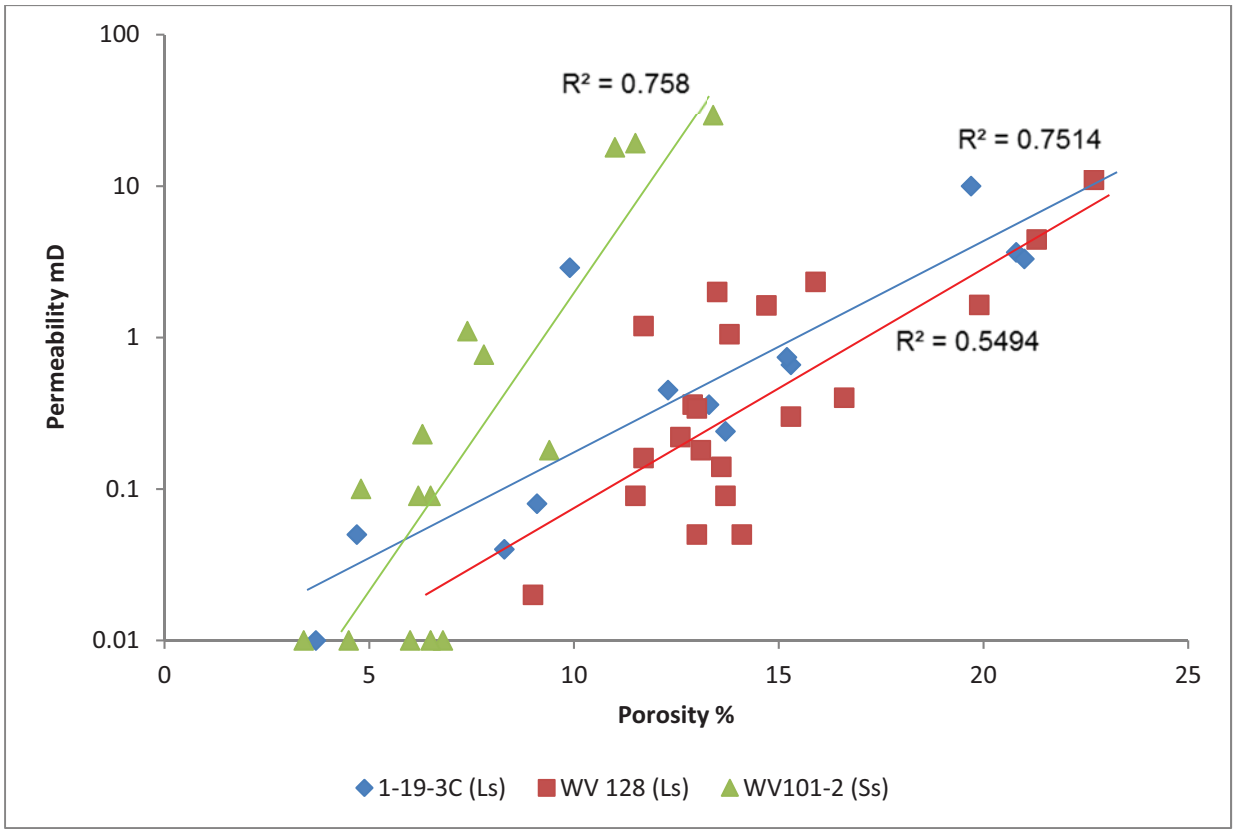

Figure 8. *Plot of core plug porosity and permeability data of the G1 interval only, from the Gypsum Hills Whiton 1-19-3C, Wonsits Valley 128, and Wonsits Valley 101-2 wells. The data from the 1-19-3C and 128 come from the G1 limestone and have a similar slope. The 101-2 data are from the underlying G1 sandstone and the porosity/permeability line has a much steeper slope.*

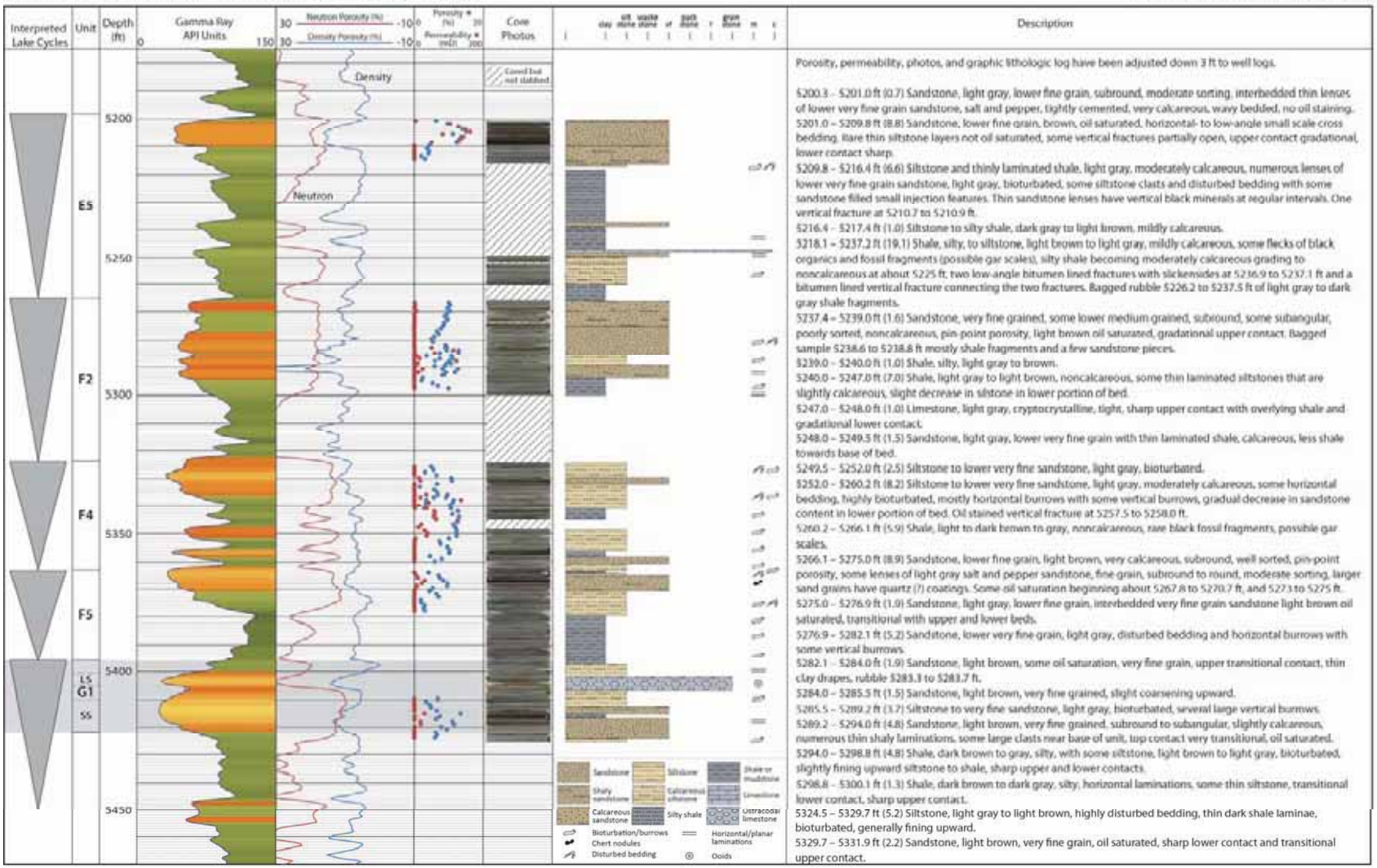

Figure 9. *Core log for the Wonsits Valley 101-2 well. Porosity and permeability measurements were obtained from core plugs. See figure 6 for location of well.*

Description (cont.)
5331.9 – 5341.0 ft (9.1) Siltstone, light gray, highly bioturbated and disturbed bedding, some thin beds of sandstone, very fine grained, light brown, oil saturated, transitional upper and lower contacts, overall coarsening upward. 5341.0 – 5345.0 ft (4.0) Shale, brown to gray, silty, some siltstone, bioturbated, transitional upper and lower contacts. 5349.5 – 5353.8 ft (4.3) Siltstone, light gray, highly bioturbated. 5353.8 – 5355.0 ft (1.2) Siltstone, light brown, no visible bedding, oil saturated. 5355.0 – 5356.0 ft (1.0) Siltstone, light gray, highly bioturbated with horizontal and vertical burrows. 5356.0 – 5358.1 ft (2.1) Shale, gray to dark gray, some minor siltstone light gray, burrowing, noncalcareous. 5358.1 – 5360.8 ft (2.7) Sandstone, very fine grain, light brown, oil saturated, lower portion of unit has some thin shale, upper contact transitional, lower contact unknown. 5360.8 – 5363.2 ft (2.4) Siltstone and shale, light gray, highly bioturbated with horizontal and vertical burrows, bioturbated bedding, generally coarsening upward, transitional upper (?) and lower contacts. 5363.2 – 5364.0 ft (0.8) Shale, gray to dark gray, noncalcareous. 5364.0 – 5364.8 ft (0.8) Siltstone, light gray, some thin shale, disturbed bedding, transitional upper and lower contacts. 5364.8 – 5370.6 ft (5.8) Sandstone, very fine grain, subangular to subround, light brown, siliceous, trace of chert grains, very slightly calcareous, slight coarsening upward appearance (but still very fine grain) some darker frosted grains upper portion of unit. 5370.6 – 5379.6 ft (9.0) Siltstone, light gray, interbedded gray shale, highly bioturbated with mostly horizontal but some vertical burrows, disturbed and reworked bedding, coarsening upward with some thin (0.1 to 0.3 ft) very fine grain sandstone beds, oil saturated, transitional upper and lower contacts. 5379.6 – 5383.0 ft (3.4) Shale, light gray, massive, rare burrows, noncalcareous, upward increase in burrows and some siltstone, transitional upper and lower contacts. 5383.0 – 5390.5 ft (7.5) Shale, to silty shale, gray to dark gray, highly bioturbated with horizontal and some vertical burrows. 5390.5 – 5397.4 ft (6.9) Shale, gray to dark gray, noncalcareous, massive, rare bioturbation, transitional upper and lower boundaries. 5397.4 – 5402.0 ft (4.6) Siltstone, light gray, calcareous, Shale, dark gray, noncalcareous, thin horizontal bedding, some thin ostracodal/oolitic deposits, overall fining upward with decreasing limestone and siltstone. 5402.0 – 5407.0 ft (5.0) Limestone (G1), ostracodal with some ooids, light brown, oil saturated, less oil staining in upper 1-foot of unit, transitional upper and lower contacts, upper portion some thin siltstone and increasing ooids. 5407.0 – 5412.5 ft (5.5) Siltstone to very fine grain sandstone, light gray, some cross bedding, mostly highly bioturbated, transitional upper and lower contacts. 5412.5 – 5423.2 ft (10.7) Sandstone very fine grain, light brown, oil saturated, some thin streaks of siltstone and shale, generally horizontally bedded, transitional upper and lower contacts. 5423.2 – 5423.8 ft (0.6) Sandstone, very fine grain, light gray, with minor cross bedding. 5423.8 – 5424.4 ft (0.6) Sandstone, very fine grain, light gray to light brown, oil saturated, subround to subangular, slightly calcareous. 5424.4 – 5425.6 ft (1.2) Siltstone, light gray, bioturbated, slightly calcareous.

Figure 9. *Continued*

Figure 10. *Photograph of core from Wonsits Valley 101-2, from 5390 to 5414 feet. See figure 6 for location of well. The G1 limestone (5399 to 5404 ft) has gradational upper and lower boundaries. The G1 is oil saturated but with less saturation in the upper 1-foot. The G1 overlies a very-fine grained sandstone, light gray, with minor cross-bedding. See figure 9 for detailed core log.*

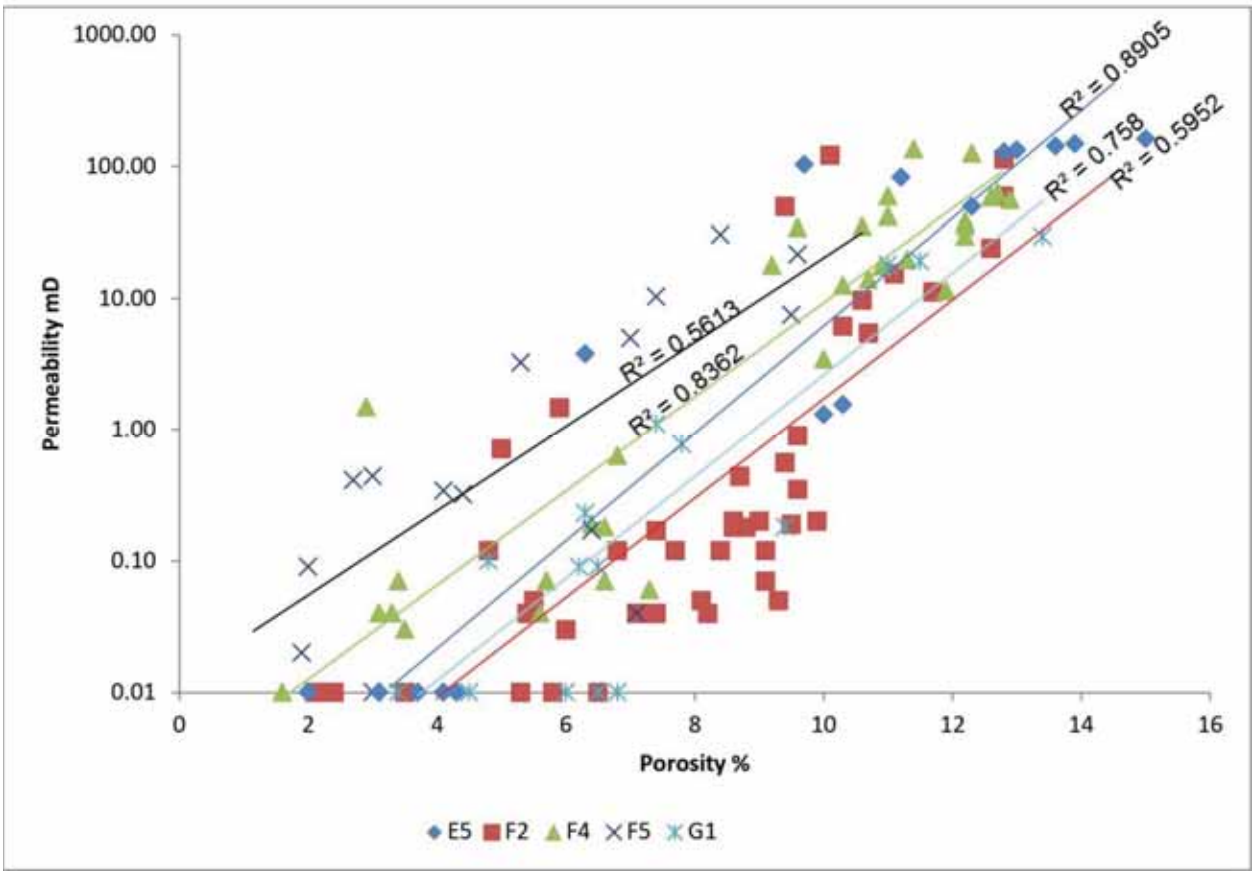

Figure 11. *Wonsits Valley 101-2 porosity and permeability plot. All of the cycles, including the G1, are sandstone to siltstone facies. Each cycle has a different but poorly defined slope, but all of the cycles have some permeability above 1 mD; highest values are probably due to microfracturing. Each cycle has a similar range except F5, which has slightly higher permeability per porosity. This is different than in the Wonsits Valley 128 where each cycle has much more of a distinct grouping pattern (see figure 14). See figure 9 for correlation of interpreted lake cycles.*

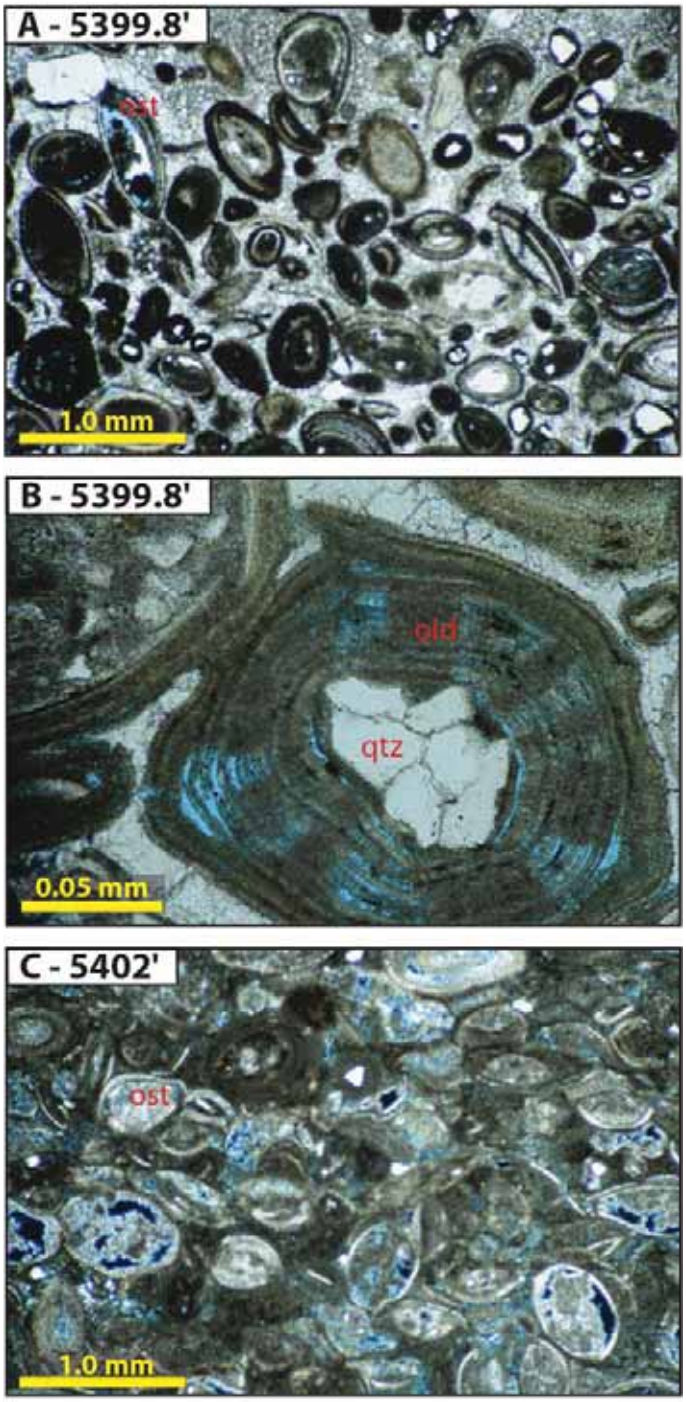

Figure 12. *Photomicrographs from G1 limestone recovered in Wonsits Valley 101-2. A-5399.8 feet, plane-polarized light (PPL), medium- to coarse-grained ooid and ostracod (ost) packstone to wackestone with calcite cement; B-5399.8 feet, PPL, fine-grained ooid grainstone with quartz (qtz) nuclei and equant calcite cement, dissolution along ooid (oid) layers creating minor intraparticle porosity. This is a poor reservoir facies. C-5402 feet, cross-polarized light (XPL), coarse-grained ostracodal packstone with intraparticle porosity within micrite.*

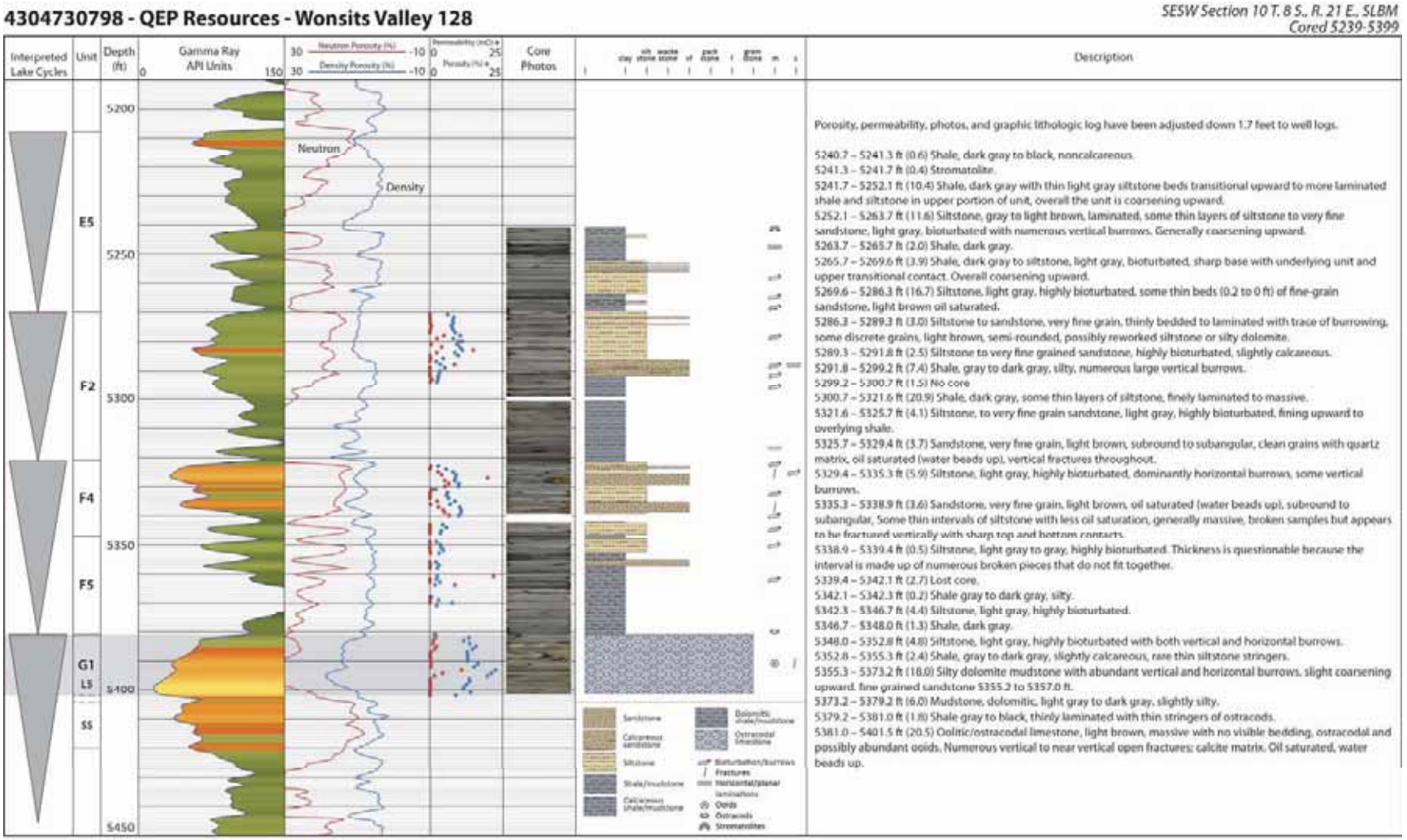

Figure 13. *Core log of the Wonsits Valley 128. Porosity and permeability measurements were obtained from core plugs. See figure 6 for location of well.*

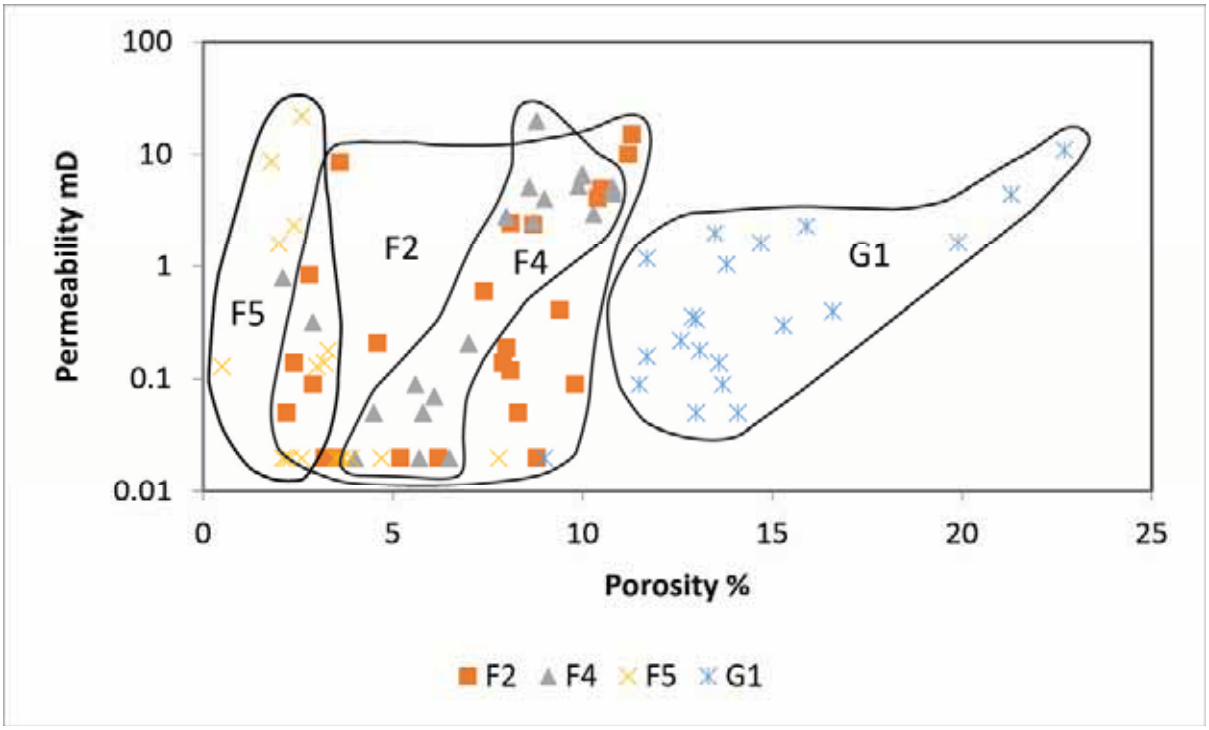

Figure 14. *Wonsits Valley 128 porosity and permeability plot. Cycles F2, F4, and F5 are data from sandstone/siltstone facies whereas the G1 is from the limestone facies. Each cycle has a different slope but the sandstone beds have a steeper slope than the G1 limestone. The near-vertical pattern for the F5 cycle indicates fractures dominate over matrix porosity and permeability. See figure 13 for correlation of interpreted lake cycles.*

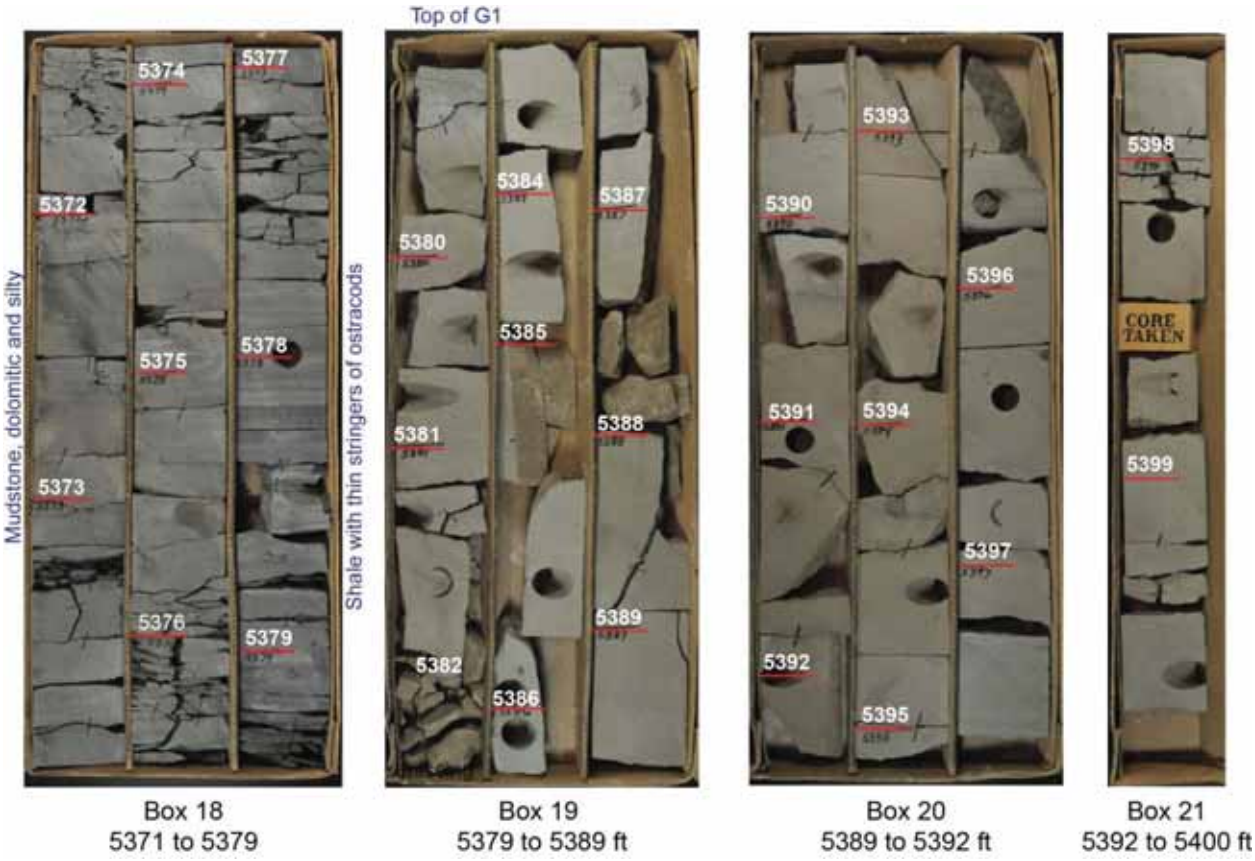

Figure 15. *Photograph of core from Wonsits Valley 128, from 5371 to 5400 feet. See figure 6 for location of well. Boxes 19 - 21 display the G1 limestone with abundant ostracods and ooid, no visible bedding. Numerous vertical to near vertical fractures are mostly (all?) drilling induced. G1 is mostly light brown and highly oil saturated. See figure 13 for detailed core log.*

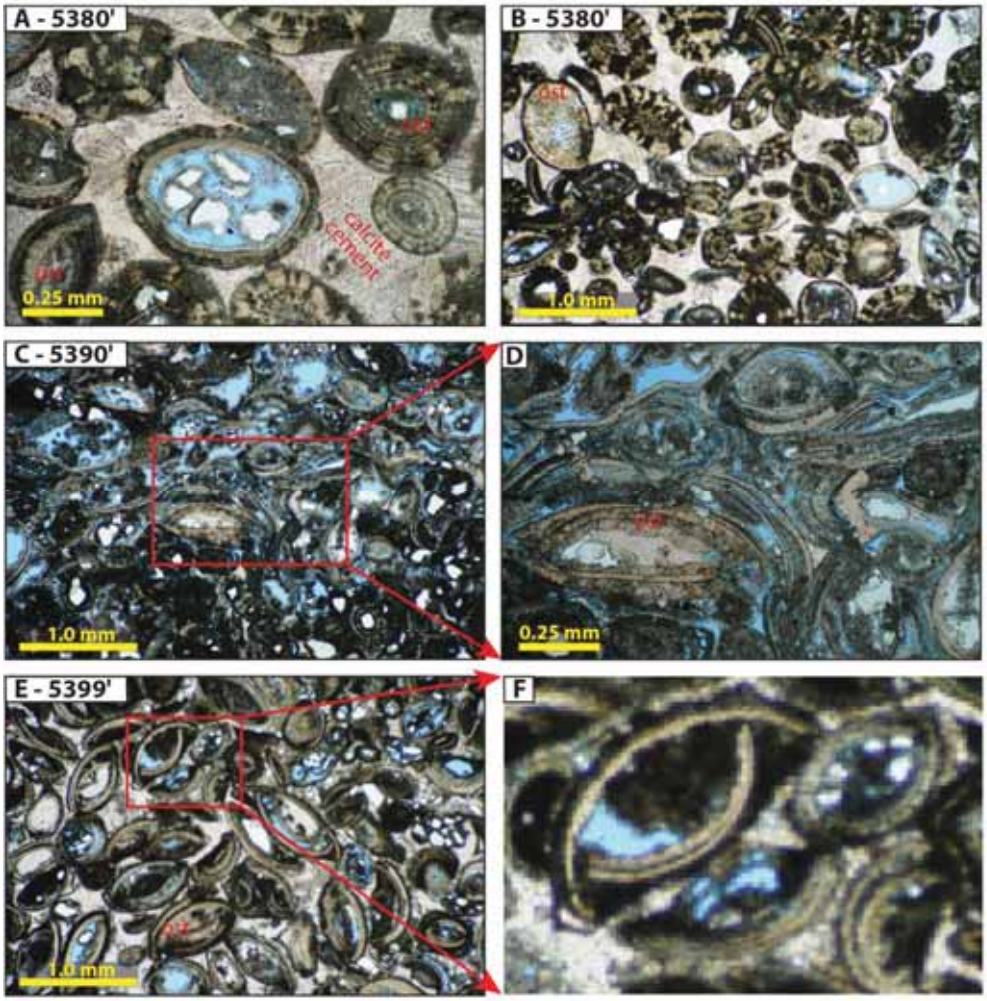

Figure 16. *Photomicrographs from Wonsits Valley 128; A-5380 ft, PPL, ooid (oid) wackestone to packstone with ostracods (ost), some intragranular porosity, and calcite cement; B-5380 ft, PPL, intragranular porosity within an ostracod and ooid grainstone; C-5390 ft, PPL, packed ostracods and ooids with intra- and intergranular porosity with little to no matrix or cement; A close up view of C shows intergranular and intraparticle porosity (blue) between broken ostracod shells; E-5399 ft, PPL, intraparticle porosity within ostracod shells with little to no porosity between the grains due to calcite cement. A close up view of E shows intraparticle porosity within the ostracod shells.*

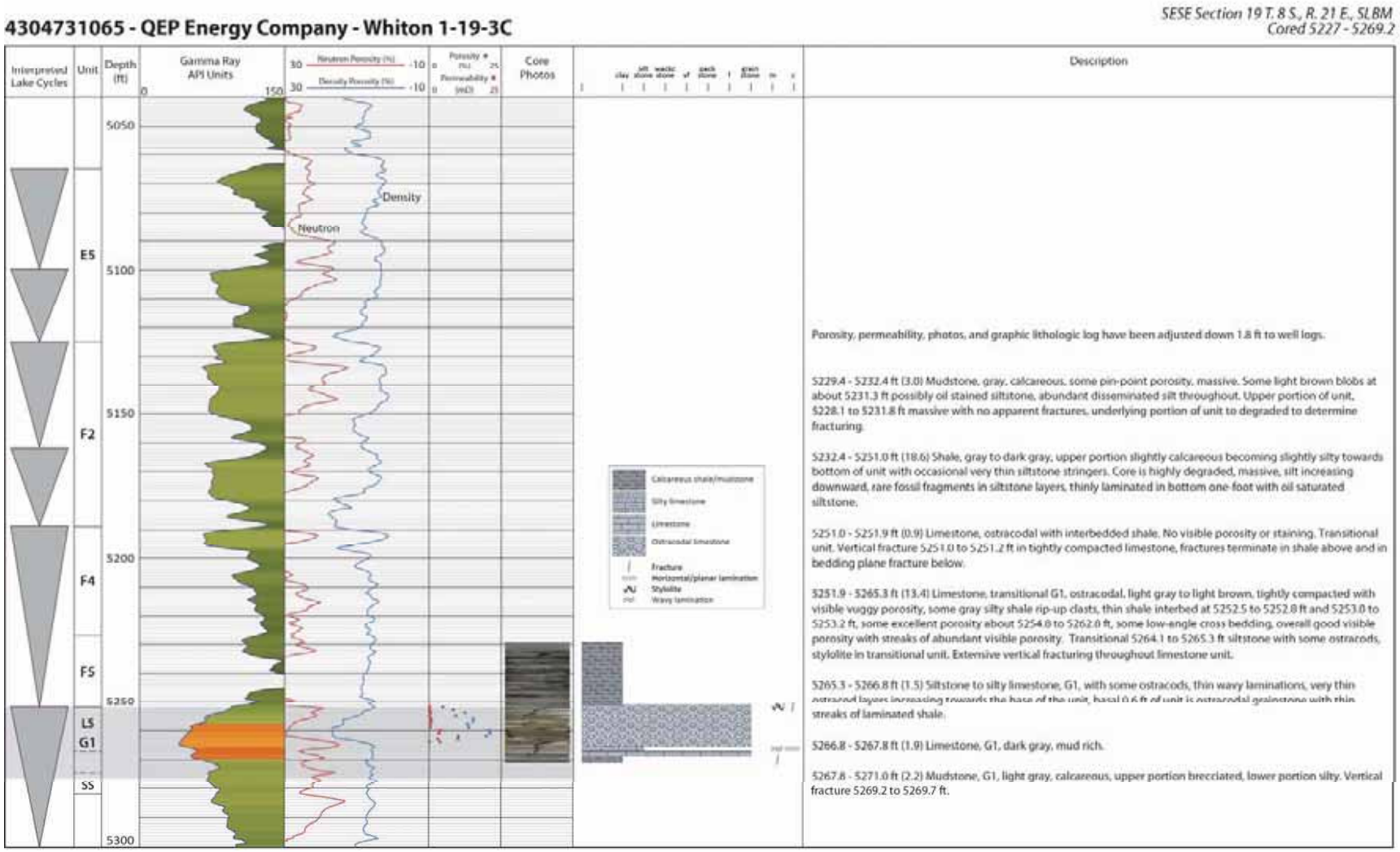

Figure 17. *Core log of the Gypsum Hills Whiton 1-19-3C well. Porosity and permeability were obtained from core plugs. See figure 6 for location of well.*

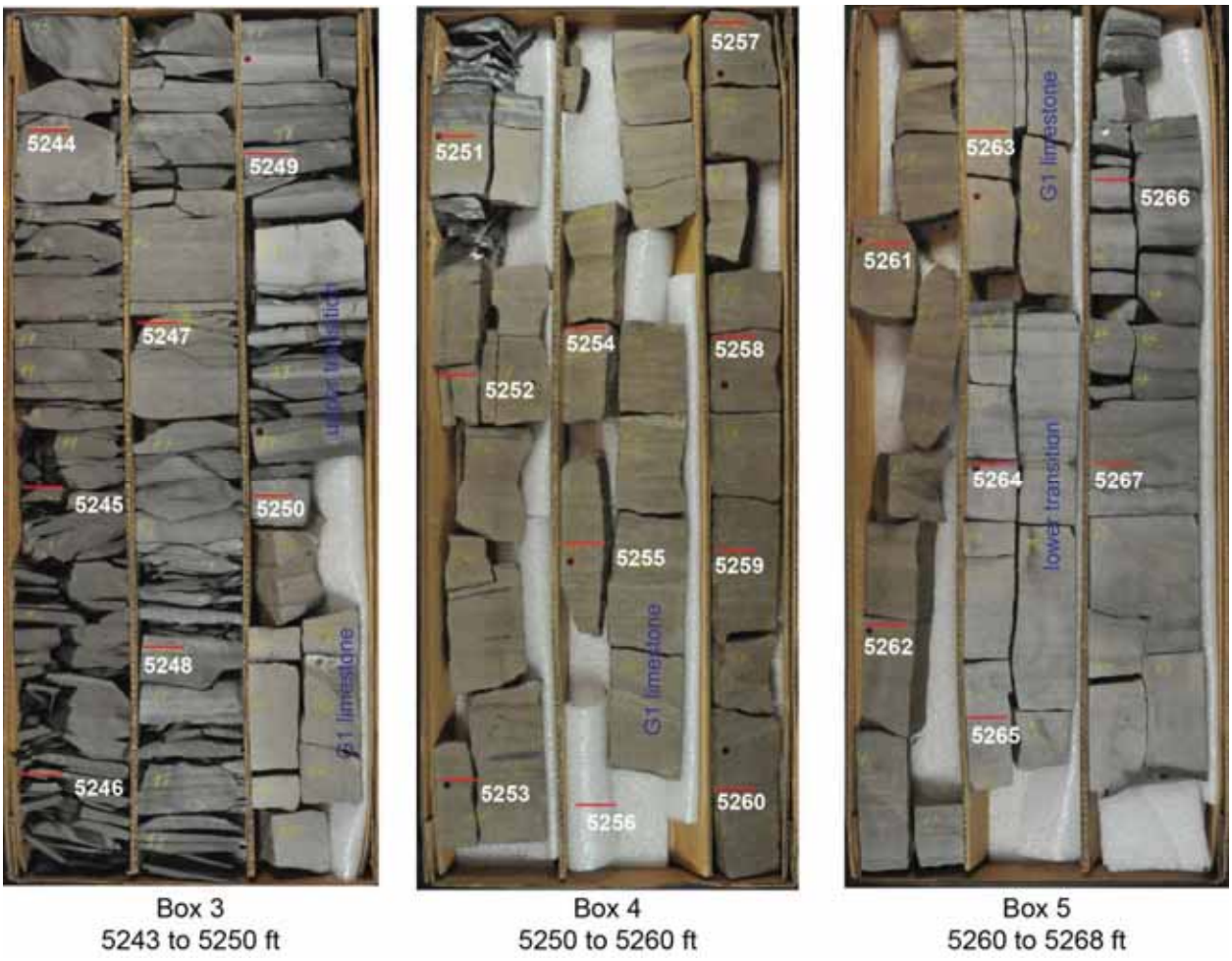

Figure 18. *Photograph of core from Gypsum Hills Whiton 1-19-3C, from 5243 to 5268 feet. See figure 6 for location of well. G1 limestone with gradational upper boundary at 5250 feet, some low-angle cross-bedding, gradational lower boundary from 5263.5 to 5265 feet consists of a silty limestone with some ostracods becoming mud rich below 5265 feet. Light to dark brown, highly oil saturated. Most (all?) vertical fractures are drilling induced. See figure 17 for detailed core log.*

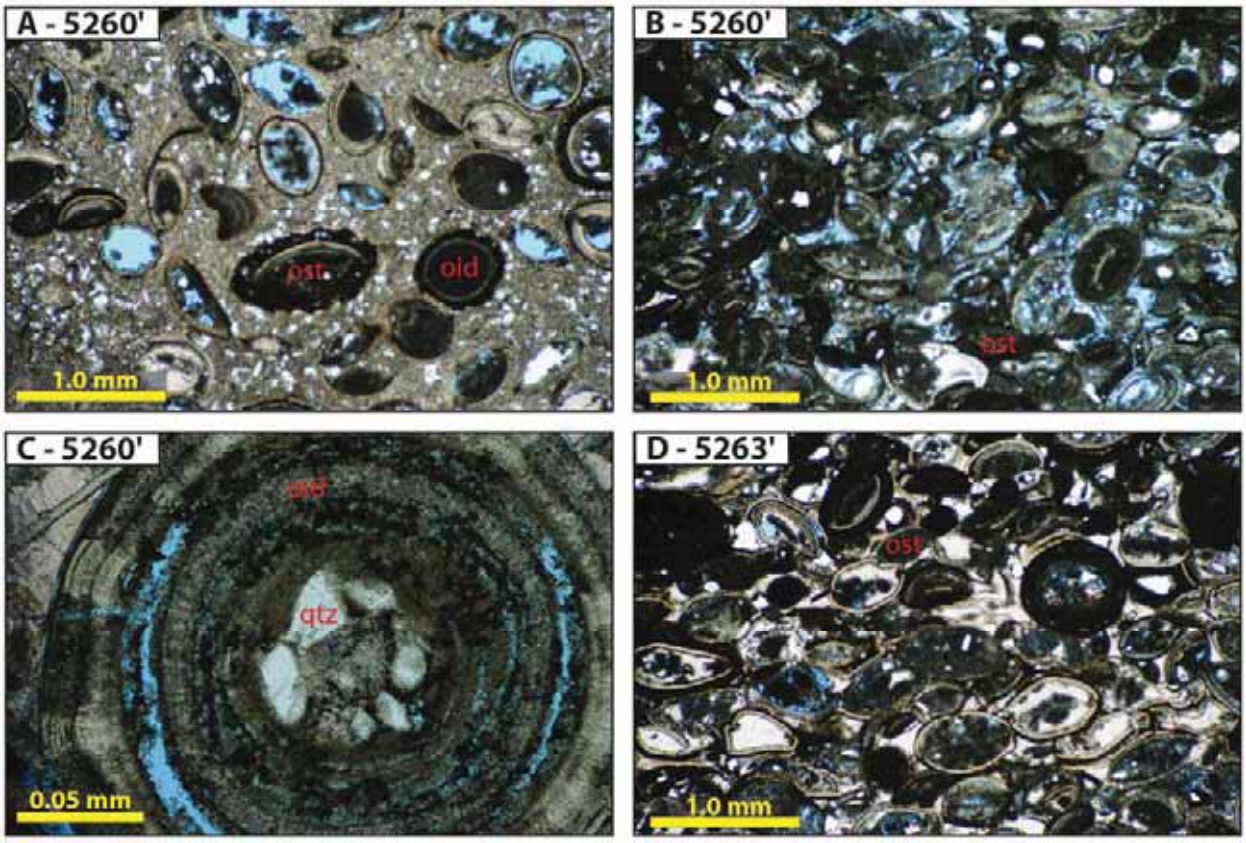

Figure 19. *Photomicrographs from Gypsum Hills Whiton 1-19-3C; A-5251 ft, PPL, mud supported ostracods (ost) and sparse ooids (oid) with intragranular porosity and rare microporosity within the wackestone; B-5260 ft, PPL,good reservoir facies of grain-supported ostracods and ooids with intragranular and matrix porosity in blue. C-5260 ft, PPL, dissolution created porosity along intraparticle layers of an ooid with a quartz (qtz) nucleus; D-5263 ft, PPL, grain supported ostracods and ooids with intragranular porosity.*

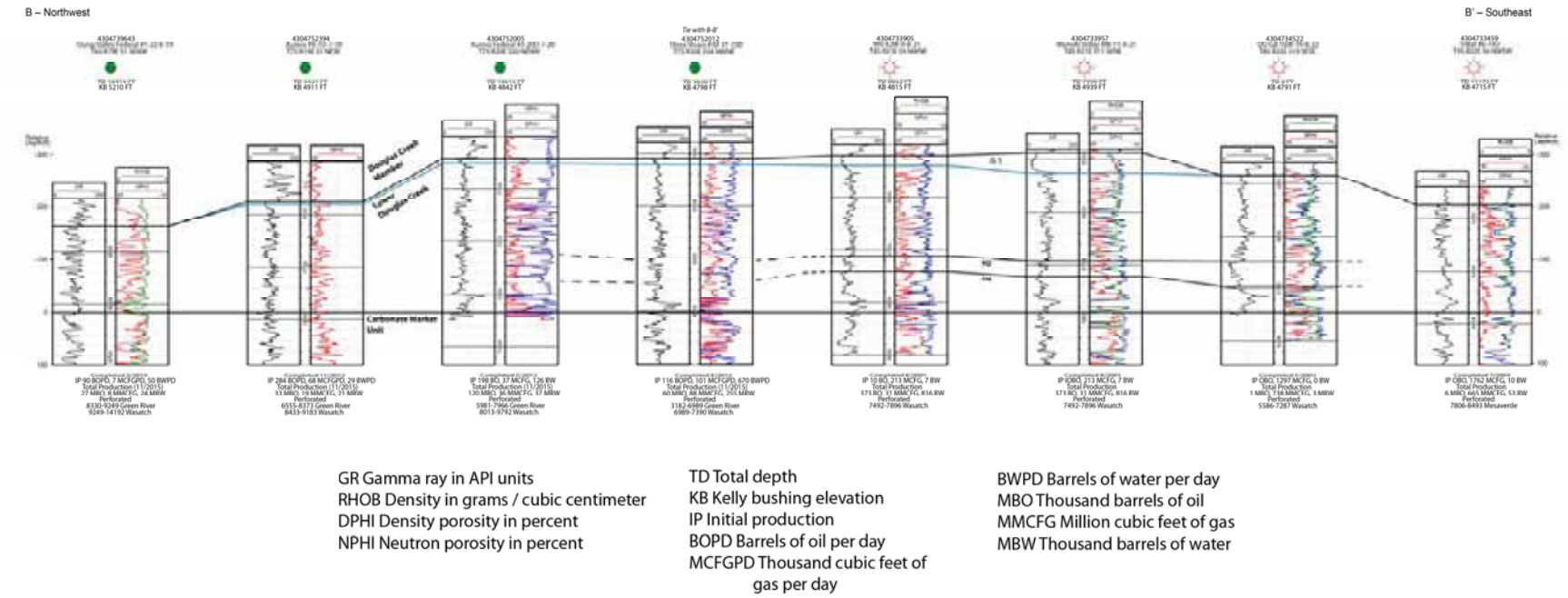

Figure 20. *Northwest to southeast well-log cross section B to B' of the lower Douglas Creek Member (Black Shale facies in many well reports) of the Green River Formation. G1, H2, and H4 beds are shown but difficult to correlate laterally. See figure 5 for location of cross section.*

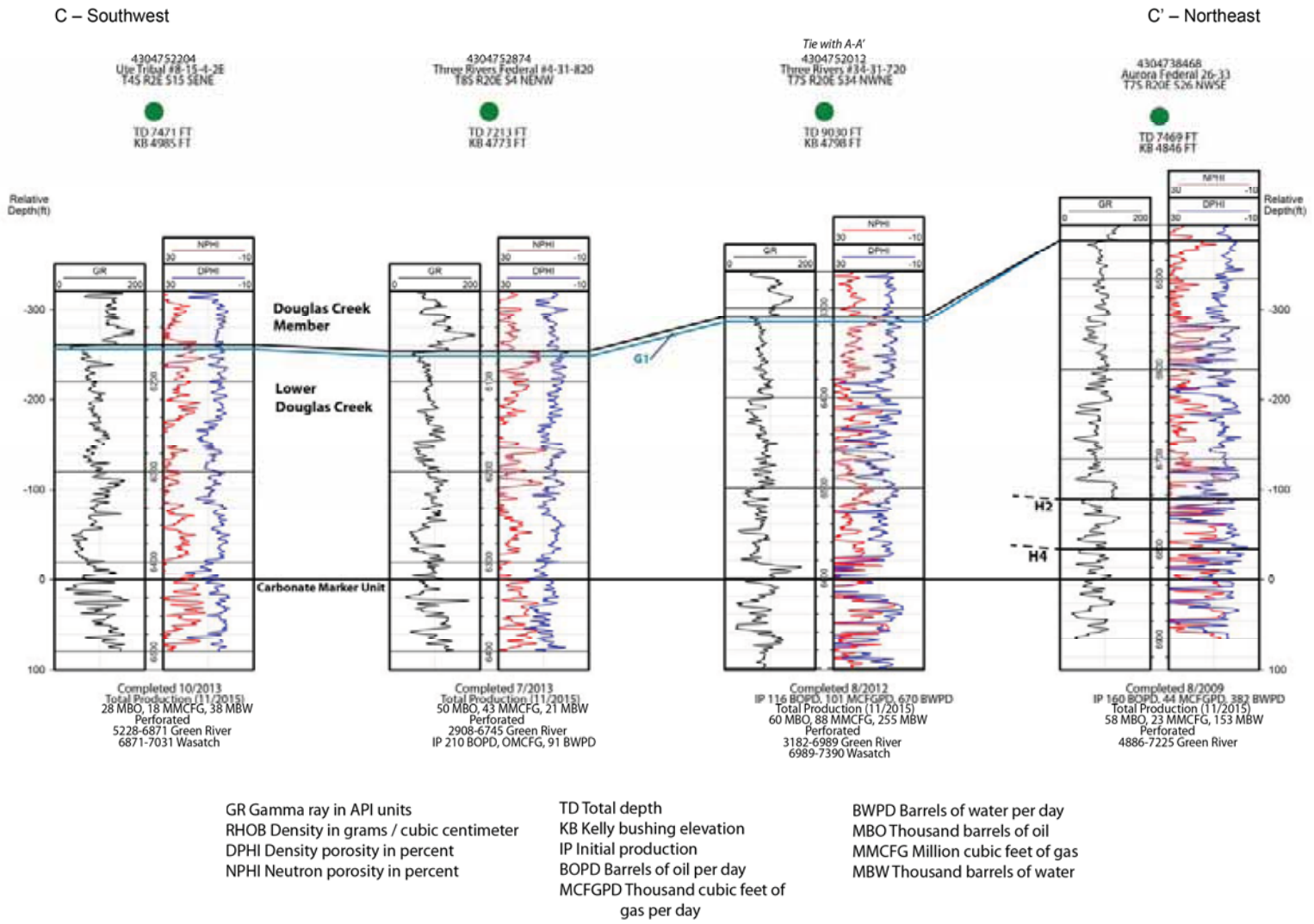

Figure 21. *Southwest to northeast well-log cross section C to C' of the lower Douglas Creek (black shale facies in many well reports) of the Green River Formation. The cross section is roughly along depositional strike of the lower Douglas Creek. See figure 5 for location of cross section*

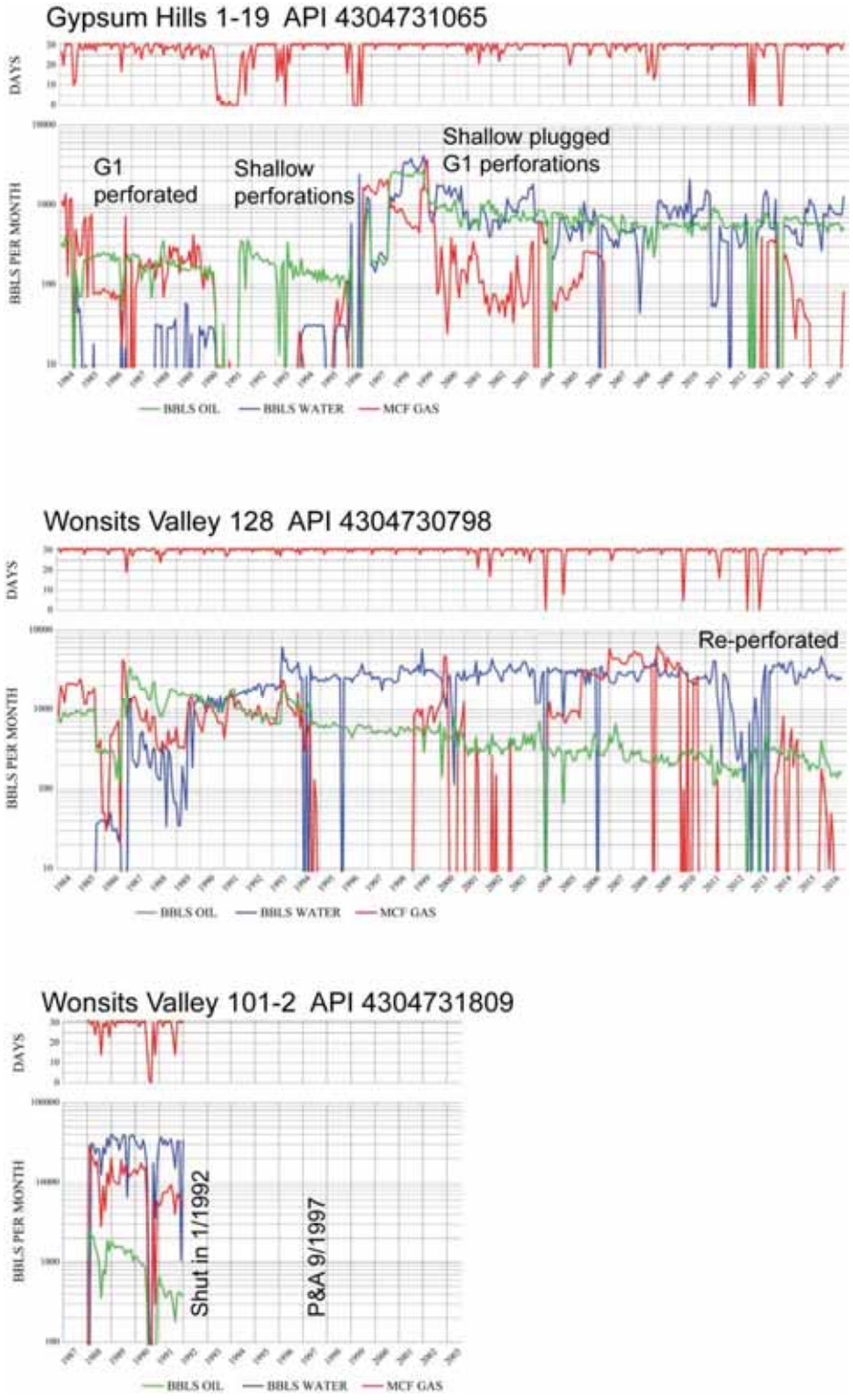

Figure 22. *Production decline curves for the three cored wells in figure 7. All three are vertical wells completed in the G1, but the Wonsits Valley 128 and 101-2 are also perforated in other zones. Curves are from Utah Division of Oil, Gas and Mining http://oilgas.ogm.utah.gov/. See figure 6 for well locations.*

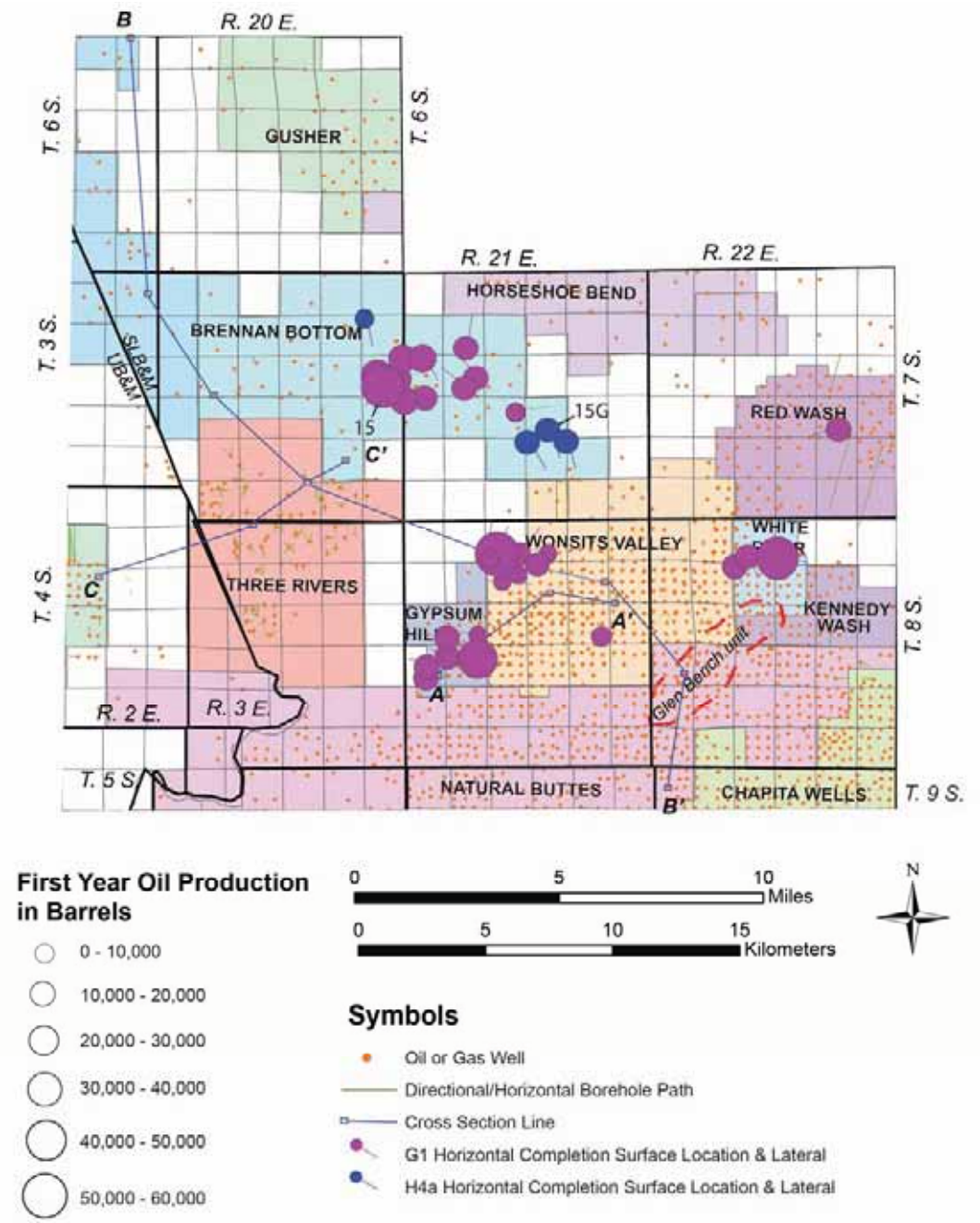

Figure 23. *Bubble map illustrating the volume of oil produced during the first year of the well for horizontal completions in the G1 and H4 beds.*

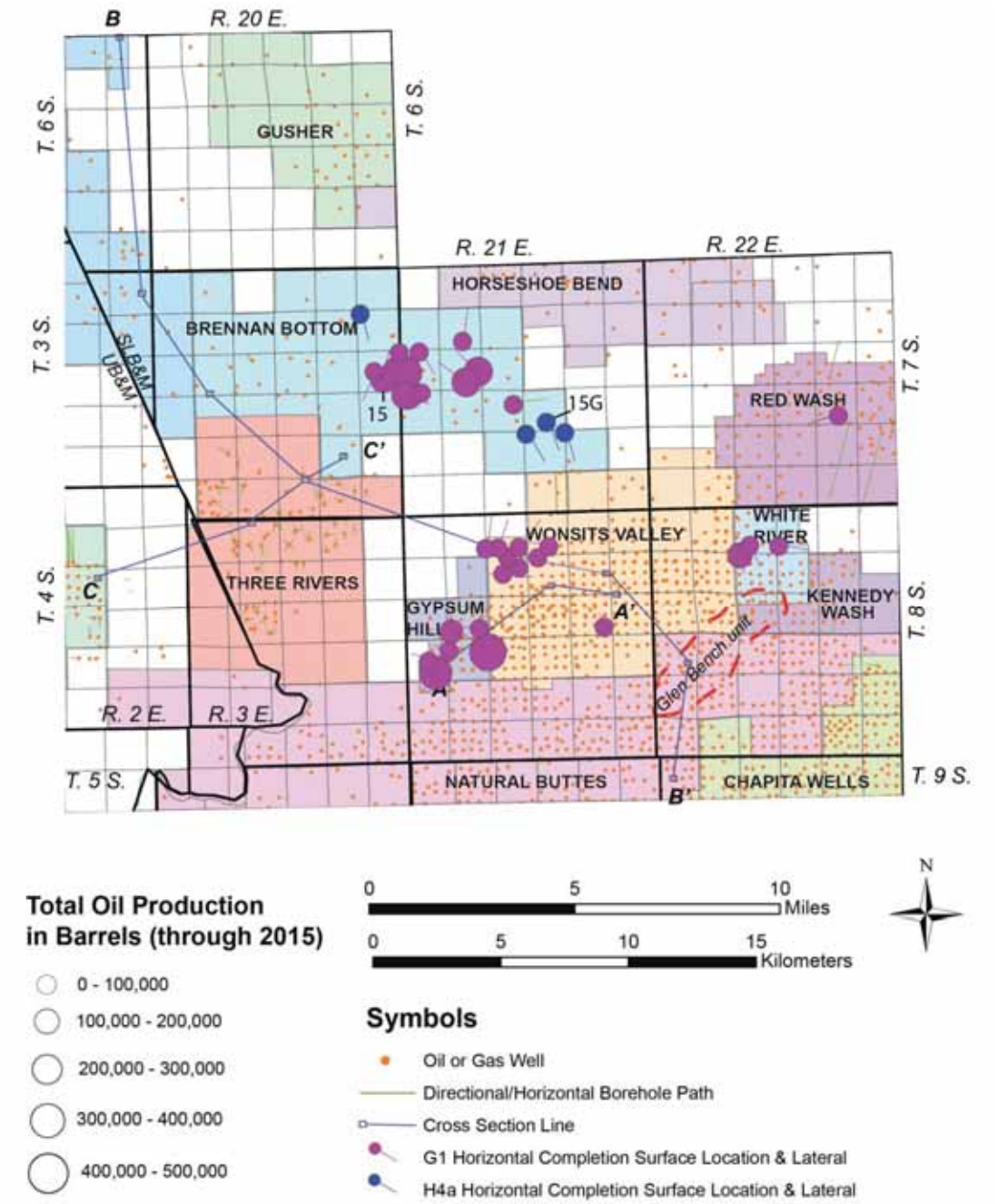

Figure 24. *Bubble map illustrating the total volume of oil produced from horizontal wells completed in the G1 and H4 beds.*

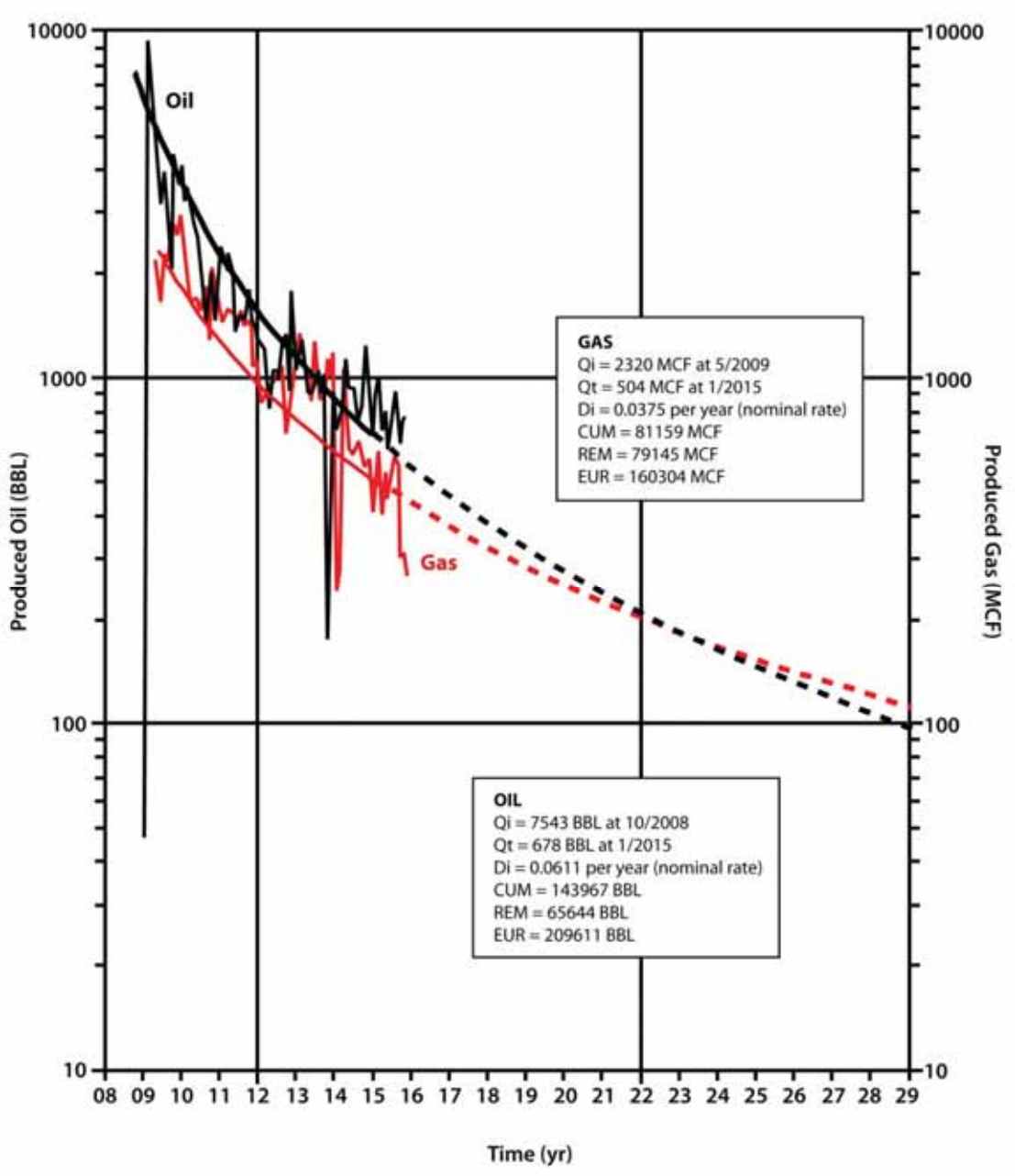

Figure 25. *Decline curve analysis of the Brennan 15 well (SW1/4SE1/4 section 13, T. 7 S., R. 20 E., SLB&M) in the Brennan Bottom field. The well is completed in two horizontal laterals drilled in the G1 limestone. Decline curve analysis indicates the well could produce 209 MBO and 160 MMCFG in 20 years. Qi = initial production rate, Qt = current production rate, Di = annual decline rate, Cum = cumulative production, REM = remaining potential production, and EUR = estimated ultimate recovery. Production values in barrels (BBL) and thousand cubic feet (MCF). Water production is sporadic and is less than 18 MBW (as of December 31, 2015). Future water production was not evaluated.*

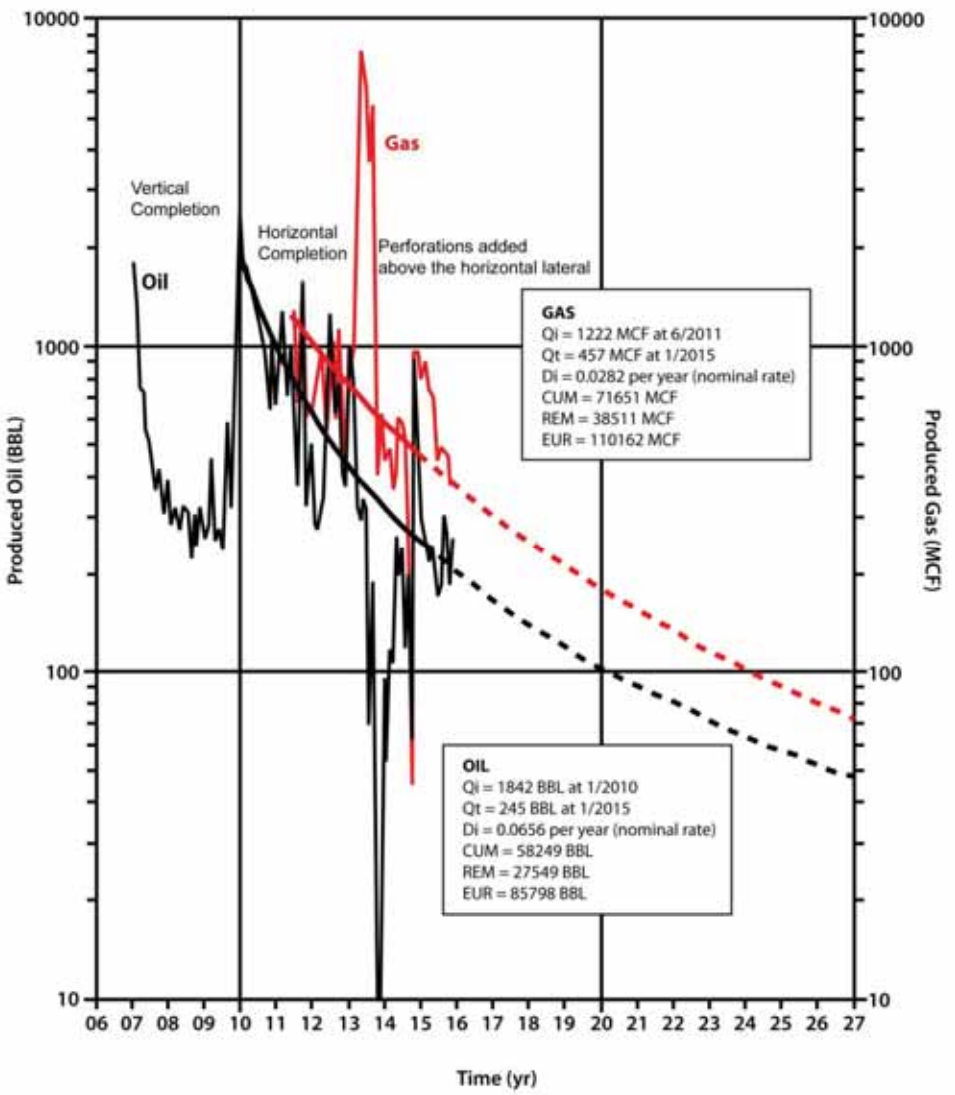

Figure 26. *Decline curve analysis of the BBS 15 G well (SW1/4SE1/4 section 22, T. 7 S., R. 21 E., SLB&M) in the Brennan Bottom field. The well was drilled and completed as a vertical well in the H4a limestone. After five years of production a lateral was drilled. Shallow perforations in the vertical portion of the well were added to the horizontal perforations. The well has produced 14 MBO from the vertical completion and 44 MBO from the horizontal lateral and shallow perforations. Decline curve analysis indicates the well could produce 132 MBO and 110 MMCFG in 20 years. Qi = initial production rate, Qt = current production rate, Di = annual decline rate, Cum = cumulative production, REM = remaining potential production, and EUR = estimated ultimate recovery. Production values in barrels (BBL) and thousand cubic feet (MCF). Produced water is less than 21 MBW (as of December 31, 2015) with around 150 BW per month for the past two years. Future water production was not evaluated.*

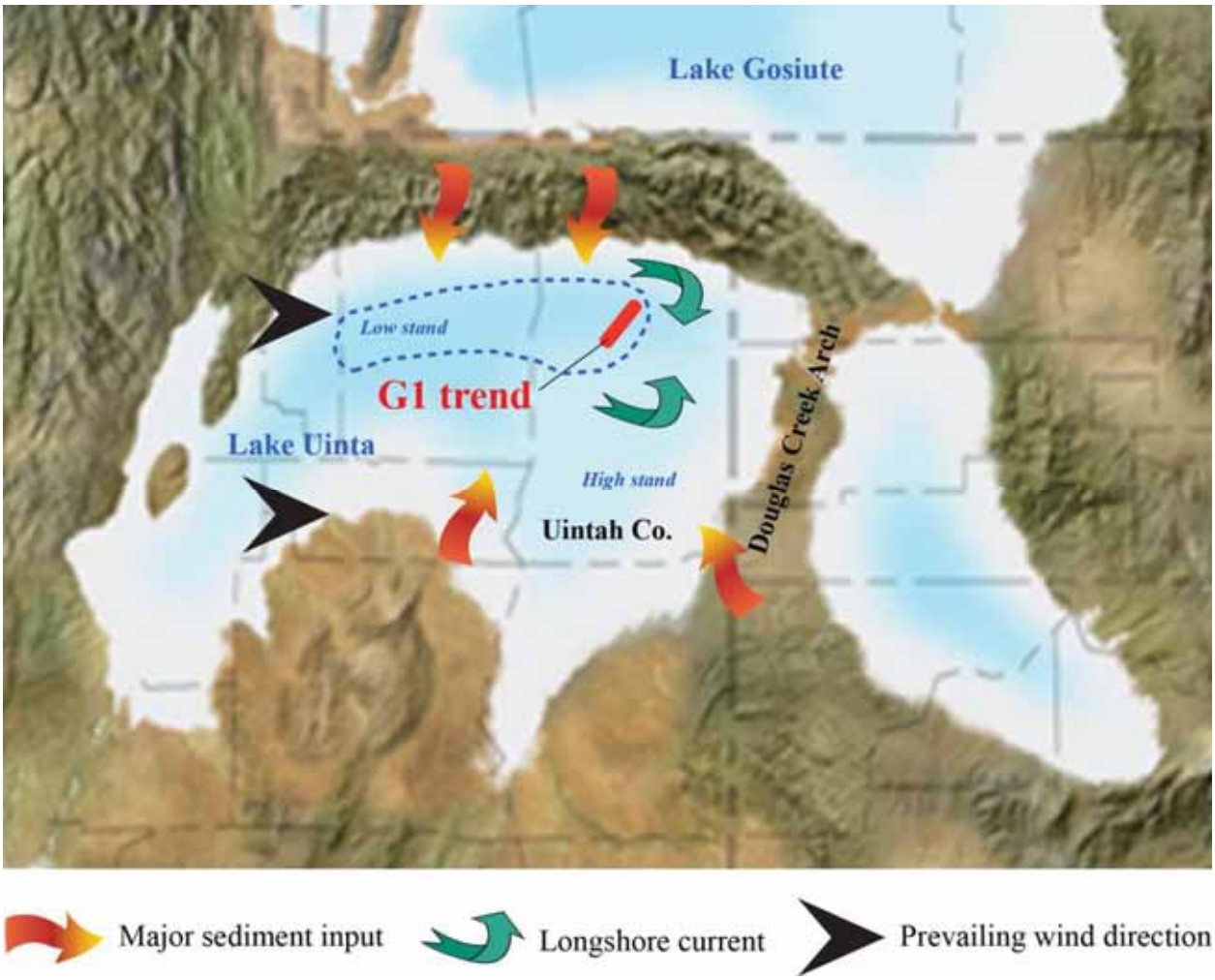

Figure 27. *Paleogeographic map of Lake Uinta. Ostracodal/oolitic limestone and sandstone reservoirs in the eastern Uinta Basin typically have more porosity due to better sorting and winnowing of fines by strong longshore currents. Modified from Blakey and Ranney (2008).*

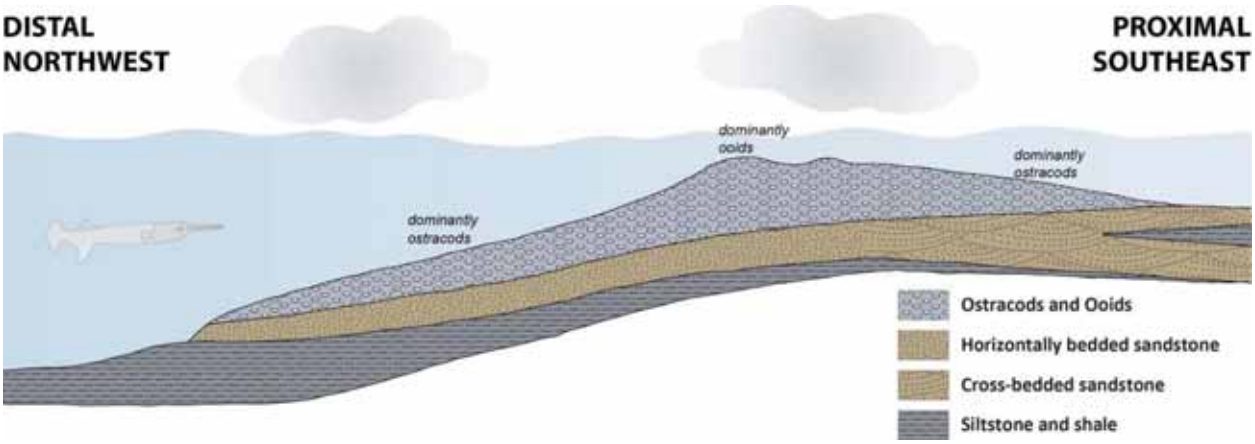

Figure 28. *Highly generalized paleodepositional cross section diagram northwest to southeast across the Wonsits Valley field illustrating the facies of the G1. During the lake lowstand, sandstone is deposited over deeper lake siltstone and shale deposits. During the transgressive turnaround, limestone with ostracod shells and ooids is deposited on the shore break as a bar until lake level rise exceeds the rate of deposition. Ooids dominate the bar crest with ostracods dominant on the flanks (Mark Longman, Questar Exploration and Production, personal communication, April 2017). Eventually the limestone bar is overlain by deeper lake muds during the maximum flood.*

Table 1. *Summary production of horizontally drilled wells completed in the G1 and H4a limestones. Cumulative production data through December 31, 2015.*

	G1 Grainstone 30 wells	**H4a Grainstone 4 wells**
Total BOE Year 1	667,202	58,069
Average BOE/Well Year 1	22,240	14,517
Average BOE/D/Well Year 1	61	40
Cumulative Oil	3,073,141	139,801
Average Cumulative Oil/Well	102,438	34,950
Cumulative Gas	2,248,033	144,625
Average Cumulative Gas/Well	74,934	36,156
Cumulative BOE	3,460,733	164,736
Average Cumulative BOE/Well	115,358	41,184
Average BW/Well Year 1	16,575	8107
Average Cumulative BW/Well	117,023	24,180

BOE = Barrels of oil equivalent (MCFG/5.8) + BO
BO = Barrels of oil
MCFG = Thousand cubic feet of gas
BW = Barrels of water

APPENDIX

Horizontally drilled wells completed in the G1 or H4a limestone, API number, operator, well name. Production data from DOGM through December 2015

API	COMPANY NAME	WELL NAME	FIELD NAME	prod_unit	oil_year1	gas_year1	wtr_year1	days	BOE_year1	BOE_D_year1	TOTCUM_OIL	TOTCUM_GAS		TOTCUM_WTR	
4304730028	QEP ENERGY COMPANY	GH 4	GYPSUM HILLS	G1	17059	5955	1052	362	18,086	50	349602	292443		45397	
4304732304	QEP ENERGY COMPANY	GH 9	GYPSUM HILLS	G1	48526	1487	81634	365	48,782	134	340834	21120		446309	
4304715419	QEP ENERGY COMPANY	BRENNAN 3	BRENNAN BOTTOM	G1	17573	19042	595	382	20,857	55	263044	206648		106765	
4304730109	QEP ENERGY COMPANY	BRENNAN 6	BRENNAN BOTTOM	G1	29440	22084	8427	363	33,248	92	241086	122817		38815	
4304731509	QEP ENERGY COMPANY	BRENNAN 8	BRENNAN BOTTOM	G1	19972	4165	2555	360	20,690	57	229906	383356		125605	
4304740198	QEP ENERGY COMPANY	BRENNAN 15	BRENNAN BOTTOM	G1	51612	18417	1285	365	54,788	150	143967	81159		17350	
4304734723	QEP ENERGY COMPANY	GHX 13HG-17-8-21	GYPSUM HILLS	G1	13835	1655	64281	362	14,120	39	140228	57622		265720	
4304734208	QEP ENERGY COMPANY	WRU GB 4WRG-9-8-22	WHITE RIVER	G1	16867	333	6141	364	16,924	46	110748	138592		72150	
4304735668	QEP ENERGY COMPANY	RW 34-23AG	RED WASH	G1	12748	1445	128879	367	12,997	35	98766	20300		1045046	
4304738436	QEP ENERGY COMPANY	SSU 14G-4-8-21	WONSITS VALLEY	G1	57586	0	707	376	57,586	153	92668	115001		4468	
4304715417	QEP ENERGY COMPANY	BRENNAN 1	BRENNAN BOTTOM	G1	34671	0	634	378	34,671	92	92659	36045		8328	
4304739792	QEP ENERGY COMPANY	WRU GB 13G-3-8-22	WHITE RIVER	G1	53565	23823	19470	366	57,673	158	90839	105786		48160	
4304734106	QEP ENERGY COMPANY	WV 3G-10-8-21	WONSITS VALLEY	G1	18307	2751	3752	375	18,781	50	89906	14421		29277	
4304733566	QEP ENERGY COMPANY	GH 10G-19-8-21	GYPSUM HILLS	G1	14114	5446	4916	380	15,053	40	85896	45124		64959	
4304732774	QEP ENERGY COMPANY	BRENNAN 14	BRENNAN BOTTOM	G1	29165	7521	2888	365	30,462	83	85324	54685		93717	
4304732771	QEP ENERGY COMPANY	BRENNAN 10	BRENNAN BOTTOM	G1	19004	0	4540	365	19,004	52	71882	14792		26185	
4304740197	QEP ENERGY COMPANY	BRENNAN 7R	BRENNAN BOTTOM	G1	33667	24432	9976	364	37,880	104	68800	67439		16011	
4304731272	QEP ENERGY COMPANY	BRENNAN FED 15-8	BRENNAN BOTTOM	G1	10873	2819	1214	361	11,359	31	64093	157997		4168	
4304732651	QEP ENERGY COMPANY	GH 19	GYPSUM HILLS	G1	10381	32040	2708	371	15,906	43	55035	65154		27241	
4304732779	QEP ENERGY COMPANY	BRENNAN 12	BRENNAN BOTTOM	G1	20079	11943	9137	356	22,139	62	53549	56666		93717	
4304737990	QEP ENERGY COMPANY	SSU 2G-9-8-21	WONSITS VALLEY	G1	21430	0	582	370	21,430	58	46748	22323		27505	
4304737993	QEP ENERGY COMPANY	GH 16G-17-8-21	GYPSUM HILLS	G1	6346	0	85	364	6,346	17	41881	2823		149	
4304736736	QEP ENERGY COMPANY	SSU 8G-9-8-21	WONSITS VALLEY	G1	8062	0	1832	350	8,062	23	35963	9341		8283	
4304734109	QEP ENERGY COMPANY	WV 15G-3-8-21	WONSITS VALLEY	G1	8893	2719	7255	365	9,362	26	35609	24236		43607	
4304734283	QEP ENERGY COMPANY	WV 16G-14-8-21	WONSITS VALLEY	G1	4155	15	114507	351	4,158	12	34450	3191		809172	
4304740097	QEP ENERGY COMPANY	WRU GB 14G-4-8-22	WHITE RIVER	G1	18224	0	4800	350	18,224	52	29629	0		11374	
4304738415	QEP ENERGY COMPANY	SSU 16G-4-8-21	WONSITS VALLEY	G1	10471	4506	0	365	11,248	31	24044	46097		8714	
4304740613	QEP ENERGY COMPANY	JB 8G-21-7-21	BRENNAN BOTTOM	G1	9976	8804	6734	375	11,494	31	20288	33755		10389	
4304740199	QEP ENERGY COMPANY	SSU 13G-4-8-21	WONSITS VALLEY	G1	8287	18256	3177	359	11,435	32	18642	41986		5429	
4304737991	QEP ENERGY COMPANY	SSU 11G-9-8-21	WONSITS VALLEY	G1	4433	0	3499	368	4,433	12	17055	7114		6685	
4304733660	QEP ENERGY COMPANY	WV 12G-10-8-21	WONSITS VALLEY	G1	1693	9730	47344	365	3,371	9	31481	20369		629943	
							Wtr_Year1		*BOE_year1*	*BOE_D_year1*	*TOTCUM_OIL*	*TOTCUM_GAS*	*BOE*	*TOTCUM_WTR*	
							544,606		*670,573*	*1,829*	*3,104,622*	*2,268,402*		*4,140,638*	*SUM*
							17,568		*21,631*	*59*	*100,149*	*73,174*		*133,569*	*AVERAGE*
4304737443	QEP ENERGY COMPANY	BBS 15G-22-7-21	BRENNAN BOTTOM	H4a	16595	0	4552	364	16,595	46	58249	71651		18537	
4304752468	QEP ENERGY COMPANY	JB 4G-26-7-21	BRENNAN BOTTOM	H4a	17503	2293	14427	365	17,898	49	30429	12626		57344	
4304740482	QEP ENERGY COMPANY	OP 4G-12-7-20	BRENNAN BOTTOM	H4a	7714	3769	6114	375	8,364	22	29171	25171		12345	
4304739180	QEP ENERGY COMPANY	JB 4G-27-7-21	BRENNAN BOTTOM	H4a	14151	6149	7335	364	15,211	42	21952	35177		8495	
							Wtr_Year1		*BOE_year1*	*BOE_D_year1*	*TOTCUM_OIL*	*TOTCUM_GAS*	*BOE*	*TOTCUM_WTR*	
							32,428		*58,069*	*159*	*139,801*	*144,625*	*164,736*	*96,721*	*SUM*
							8,107		*14,517*	*40*	*34,950*	*36,156*	*41,184*	*24,180*	*AVERAGE*

Appendix VII

Geological Characterization of the Pennsylvanian Paradox Formation Cane Creek Shale and Other Paradox Shales, Paradox Basin, Utah

Craig D. Morgan and Rebekah W. Stimpson

Utah Geological Survey, Salt Lake City, UT

GEOLOGIC CHARACTERIZATION OF THE PENNSYLVANIAN PARADOX FORMATION CANE CREEK SHALE AND OTHER PARADOX SHALES, PARADOX BASIN, UTAH

By

Craig D. Morgan and Rebekah Stimpson

Utah Geological Survey

2017

TABLE OF CONTENTS

LIST OF FIGURES

LIST OF TABLES

APPENDICES

ABSTRACT

The Cane Creek shale (clastic cycle 21) is a hydrocarbon source rock and reservoir in the lower part of the Pennsylvanian Paradox Formation in Paradox Basin of southeast Utah. The Cane Creek is overlain and underlain by beds of salt and is divided into A, B, and C zones (in descending order). The B zone is the primary hydrocarbon source rock and productive interval consisting of black organic-rich shale, dolomite, siltstone to fine-grained sandstone, and some anhydrite. Total organic carbon is more than 20% wt. in many of the thin shale beds. The siltstone/sandstone beds, the primary reservoir facies, have significant porosity (up to 15%). Permeability is generally low (~0.1 mD), so naturally occurring fractures are an important component of the reservoir. Productive dolomite and siltstone beds are rarely encountered in the A and C zones which mostly consist of anhydritic dolomite and bedded anhydrite along with the halite, providing overlying and underlying seals to the reservoir. The reservoir is over pressured having fluid gradients ranging from 0.75 to 0.95 psi/ft. Traps are formed by seismically defined local anticlines and fault closures, combined with facies and permeability variations.

Oil production was first established from the Cane Creek shale in the 1960s but only one well was economic until horizontal drilling renewed the play in the 1990s. The most successful Cane Creek field is the Big Flat field which has produced more than 5 million barrels of oil from 21 active wells. The U.S. Geological Survey's mean estimate of undiscovered resources in the Cane Creek and other Paradox Formation shale beds basin-wide is 471 million barrels of oil, 472 million barrels of natural gas liquids, and 11,418 billion cubic feet of gas.

Excellent oil shows and some minor production have also been encountered in clastic cycle 19 of the Paradox Formation in the Greentown area, in the northern part of the play. This clastic interval may have potential as a future exploration target. Upper Paradox shales, Chimney Rock, Gothic, and Hovenweep, are the source rocks for the Desert Creek and Ismay reservoirs in the Blanding Basin, south of the main Cane Creek play area. Although not currently oil-productive, these shales may be good horizontal targets in the future.

INTRODUCTION

The Cane Creek shale oil and gas play is in the fold and fault belt of the Paradox Basin in southeast Utah and southwest Colorado (figure 1). This study focuses on the Cane Creek play in the Utah part of the Paradox Basin (figure 2). The Cane Creek is a thin heterolithic unit consisting of interbedded shale, carbonate, clastic, and evaporite rocks in the thick predominantly halite Pennsylvanian Paradox Formation which is part of the Pennsylvanian Hermosa Group (figure 3). The Paradox Basin was a marine restricted basin resulting in deposition of thousands of feet of evaporite beds with interbedded thin carbonate, sand, and shale during marine high stands (figure 4). The Paradox Formation is bounded by shallow open-marine shelf carbonates of the underlying Pinkerton Trail and overlying Honaker Trail Formations.

The Paradox Formation has been an exploration target since the 1920s when oil was first produced from the formation. Exploration has waxed and waned spurred on by exciting discoveries followed by dry holes. Increases in oil pricing and improved horizontal drilling technology have driven the most recent activity. The Cane Creek has produced more than 7.6 million barrels of oil (MMBO) (table 1) and 29 wells produced 58 thousand barrels of oil (BO) during December 2015 (table 2). The U.S. Geological Survey calculated the Cane Creek has a mean undiscovered resource of 215 MMBO and 4723 billion cubic feet of gas (BCFG) (table 3 and appendix A).

The Cane Creek "shale" is not truly a shale but rather a very heterolithic unit composed of interbedded anhydrite, anhydritic dolomitic mudstone, dolomite, silty dolomite, very fine-grain sandstone to siltstone, and thin (inches) organic-rich shale beds. The thin shale beds are the primary source for hydrocarbons within the Cane Creek shale. The primary reservoir is the sandstone and to a lesser degree the silty dolomite beds. The reservoir has low matrix permeability and naturally occurring fractures are

essential to economic production. Other heterolithic units within the Paradox are often referred to as clasts within an evaporite cycle consisting of the clastic bed and an overlying halite bed. The cycles and associated clastic units are numbered from top to bottom following Hite (1960) (figure 3).

Production from the Cane Creek is typically from seismically defined structures. Faulting of the underlying Mississippian and older rocks formed blocks where the lower Paradox Formation, including the Cane Creek, was deposited and draped over the fault blocks. Some of the faults continued to move during the Pennsylvanian causing displacement of the Cane Creek and other lower Paradox cycles (Grove and others, 1993). Deposition of Permian and Early Triassic sediments shed from the Uncompahgre uplift created heavy loading on the Paradox salt. The loading caused the salt to move forming diapiric salt anticlines such as Moab-Spanish Valley, Castle Valley, and Salt Valley within Arches National Park (Doelling and others, 1988) (figure 5). Salt welds formed in the intervening synclines. The Cane Creek and many other anticlines in the Paradox Basin are the result of a buildup of salt that did not intrude the overlying sediments. Secondary folding within the salt developed wave-like structures with amplitudes of 15 to 100 feet and wavelengths of 300 to 3000 feet (Grove and others, 1993). The complex structural history caused numerous periods of fracturing and fracture filling within the Cane Creek and other Paradox clastics. Recent 3-dimensional (3D) seismic surveys have greatly improved the definition of these Mississippian fault blocks. However, structure alone does not guarantee successful production; sandstone quality, open fractures, and the timing of oil generation all play a critical role.

The success rate using horizontal drilling in the Cane Creek reservoir has been good in the Cane Creek unit in the Big Flat area (figure 6 and appendix B). However, the well costs are very high and many of the wells are sub- to marginally economic. The Cane Creek unit has been owned by several companies; the most active operators were Columbia Gas Development Corporation (Columbia Gas) who drilled the first horizontal wells in the unit and Fidelity Exploration and Production Company (Fidelity E&P) who significantly increased the number of wells and production from the unit. Fidelity E&P sold the Cane Creek unit to Wesco Operating Company in 2016. Work by Fidelity E&P in the Cane Creek unit included drilling vertical pilot holes and taking core from the Cane Creek before drilling horizontal laterals. Cores were extensively evaluated using the most up to date petrophysical, geochemical, and geomechanical analyses to characterize the reservoir. Fidelity E&P acquired 3D seismic over much of the unit to map the complex structure more accurately. But even with all the new reservoir characterization, the Cane Creek play has not developed into a typical resource play where the drilling program is simply designed to fill in a spacing pattern. Each new Cane Creek location is like a wildcat well requiring special attention to structure and reservoir quality. Additionally, exploration outside of the Cane Creek unit has not resulted in any new high yielding oil discoveries.

GOAL AND OBJECTIVES

The Cane Creek shale in the Paradox Basin has been a target for oil and gas exploration on and off since the 1960s and oil is produced from several fields. The play generated renewed interest in the early 1990s with the successful application of horizontal drilling. Drilling activity increased in the 2000s because of rising oil prices and continued until 2014 when prices collapsed.

Whidden and others (2012) assessed the undiscovered oil resource in the Cane Creek shale of the Paradox Basin at 103 MMBO with a 95% confidence level, 198 MMBO with a 50% confidence level, and a mean of 215 MMBO (table 3 and appendix A). Nonetheless, limited research has been conducted or published to further define the play and the reservoir characteristics.

Goal

The goal of our study is to provide reservoir-specific geological and engineering analyses of the oil producing Cane Creek shale (and other potential hydrocarbon producing clastic/shale units) of the

Paradox Formation in the Paradox Basin, southeast Utah. Increased drilling activity associated with the rise in oil prices resulted in new core, core analysis, and completion and production data.

This research project provides detailed geologic and geochemical information that will hopefully help reduce drilling risk and possibly increase hydrocarbon production and recorded reserves. In addition to the Cane Creek, several other organic-rich shales in the Paradox Formation have the potential for significant reserve–base additions.

Objectives

The main objectives of this project were to:

- characterize geologic, geochemical, and petrophysical rock properties of the Cane Creek shale by compiling various sources of data and analyzing available well cores, cuttings, and logs;
- map major regional trends, structure, thickness of the Cane Creek and informal lithologic zones within the Cane Creek and overlying and underlying straitigraphic units to identify areas of greatest oil production potential;
- evaluate drilling and completions techniques to determine best practices that reduce exploration costs and drilling risks, especially in environmentally sensitive areas; and
- identify other shale intervals within the Paradox Formation that may have economic oil potential needing further study.

Additional Objectives

Additional objectives of the project conducted by others were to:

- map potential-prone areas in the Cane Creek play using epifluorescence evaluation of cuttings (Chidsey and Eby, 2017); and
- study the geomechanics of the Cane Creek reservoir (McLennan, in progress).

PREVIOUS STUDIES

Geologic studies of the Paradox Basin are extensive and span over the last 80 years. The basin has attracted geologists with its scenic geology, complex stratigraphy, and structural attributes as well as economic geologists interested in hydrocarbons, uranium, potash, and copper. The following is a brief overview of the available publications that are the most relevant to this project.

Recent publications on the petroleum geology of the Paradox Basin are presented in the Rocky Mountain Association of Geologists volume on the Paradox Basin (Houston and others, 2009) which includes an extensive bibliography by Rasmussen and others (2009). Anna and others (2014) and Whidden and others (2014) present preliminary work completed for the U.S. Geological Survey resource assessment currently in final preparation.

Basin-wide studies of the stratigraphy and tectonics of the Paradox Basin include Baker and others (1933), Wengerd and Matheny (1958), Mallory (1972), Szabo and Wengerd (1975), Baars and Stevenson (1981), Goldhammer and others (1991), Montgomery (1992), and Blakey (2009). Studies specific to the Paradox Formation were published by Hite (1960), Peterson and Hite (1969), Hite and Buckner (1981), and Hite and others (1984).

Papers on the structure of the Paradox Basin were published by Kelley (1958), Baars (1966), Kluth and Coney (1981), Barbeau (2003), Kluth and DuChene (2009), and Trudgill (2011). Cater (1970), Hite and Cater (1972), Doelling (1988), Doelling and others (1988), and Rasmussen (2014) all discuss the salt tectonics in the basin.

Papers specifically dealing with the petroleum system within the Paradox Basin were published by Montgomery (1992), Whidden and others (2012), Anna and others (2014), Stevenson and Wray (2014), and Whidden and others (2014). Petroleum geochemistry is discussed by Nuccio and Condon (1996), Guthrie and Bohacs (2009), and Rasmussen and Rasmussen (2009).

Smith (1978a, 1978b, 1978c, 1978d, 1978e) published papers on Bartlett Flat, Big Flat, Cane Creek, Long Canyon, and Shafer Canyon fields. Morgan and others (1991, 1992a, 1992b), and Grove and others (1993) discuss the geology of the Bartlett Flat-Big Flat (Kane Springs unit) fields, and Grove and Rawlins (1997) discuss the Cane Creek shale exploration play in the Big Flat and neighboring area.

GEOLOGIC SETTING

Structure

The Paradox Basin is a Pennsylvanian-age structural basin in the Four Corners area of southeast Utah and southwest Colorado and a smaller part of northeast Arizona and northwest New Mexico (figure 1).

Prior to development of the Paradox Basin, the Four Corners area was part of a regionally extensive, stable cratonic shelf dominated by shallow marine carbonate deposition (figure 7) (Nuccio and Condon, 1996; Blakey, 2009). Regional uplift during the Late Mississippian and Early Pennsylvanian resulted in exposure and karstification of the Mississippian carbonates (Nuccio and Condon, 1996).

At the beginning of the Pennsylvanian, the collision of the Gondwana and Laurentia plates (Barbeau, 2003; Kluth and Duchene, 2009) resulted in the rise of the Uncompahgre uplift of the Ancestral Rocky Mountains and subsidence of the Paradox Basin (Blakey, 2009) which Baars and Stevenson (1981) described as a pull-apart basin (figure 8). The area subsided along a series of northwest-trending faults forming an asymmetrical oval-shaped basin deepest along the boundary with the Uncompahgre uplift of the ancestral Rocky Mountains (figure 4). Faulting was strongly influenced by rejuvenation of pre-existing late Precambrian northwest-trending structures (Baars and Stevenson, 1981).

The Paradox Basin is commonly divided into the Paradox fold and fault belt, Blanding sub-basin, and Aneth platform within the Blanding sub-basin (figure 1) (Whidden and others, 2014). The Paradox basin is separated from the Uncompahgre uplift on the east and northeast by a high-angle fault with thousands of feet of displacement (figure 4). The uplift had a maximum elevation of 12,000 to 15,000 feet (Stokes, 1986). The basin is bounded to the south and southwest by the Defiance-Zuni platform. The Emery shelf to the west separated the basin from the open marine shelf environment (figure 8) (Herman and Sharp, 1956; Hintze and Kowallis, 2009).

The Paradox Basin was located in a subtropical, arid environment and is commonly defined by the maximum extent of the salt in the Paradox Formation of the Hermosa Group (figure 1) (Condon, 1997), although deposits of the Paradox and overlying Honaker Trail Formations extend beyond the limits of the salt. The Middle to Upper Pennsylvanian Hermosa Group consists of, from oldest to youngest, the Pinkerton Trail, Paradox, and Honaker Trail Formations (figure 3). The saline deposits of the Paradox are bounded by normal shallow marine deposits of the underlying Pinkerton Trail and overlying Honaker Trail.

Glacial and interglacial climatic cycles in the southern hemisphere of the Pangean continent caused cyclic fluctuations in relative sea level and salinity (Hite and Buckner, 1981; Goldhammer and others, 1991; Whidden and others, 2014). The cyclicity in the highly restricted Paradox Basin resulted in a series of upward-shoaling, disconformity-bounded deposits of marine, organic-rich, black shale through carbonate to hypersaline salt. The cycles are considered fourth-order depositional cycles (cyclothems of 0.2-0.5 m.y. [Mitchum and Van Wagoner, 1990]) (Anna and others, 2014). The 20+ cycles resulted in deposition of thousands of feet of evaporites, mainly halite, with lesser amounts of potassium and magnesium salt and anhydrite. The salt beds are interbedded with thin clastic beds consisting of anhydrite, anhydritic-dolomitic mudstone, silty dolomite, dolomite, very-fine grain sandstone and

siltstone, and thin (inches) organic-rich shale (Peterson and Hite, 1969; Hite and others, 1984). The faulted terrain within the basin partly controlled deposition of the lower cyclic units and the development of salt-cored anticlines that are dominant structural features in the Paradox Basin fold and fault belt (Kelly, 1958). The stacked sequences of shale and salt that compose most of the Paradox Formation is referred to as the saline facies of the Paradox (Hite, 1960). The salt and shale sequences interfinger with clastics to the northeast that were shed off the Uncompahgre uplift and with penesaline and normal marine carbonates to the southwest (figure 4).

Clastic beds represent condensed sedimentation deposited during relative sea-level rise and highstand (global greenhouse conditions) (figure 8) and evaporites were deposited during marine lowstands (global icehouse conditions) (figure 9) (Goldhammer and others, 1991; Whidden and others, 2014). Clastic beds range in thickness from 10 to 200 feet and are generally overlain by 200 to 400 feet of halite. The clastic beds are used as markers for regional correlation (Hite and Buckner, 1981; Goldhammer and others, 1991; Nuccio and Conden, 1996; Trudgil and Arbuckle, 2009; and Massoth, 2012). Twenty-nine fourth-order depositional cycles have been described in the Moab area (Hite, 1960; Hite and Buckner, 1981). Hite and Cater (1972) and Reid and Berghorn (1981) divided the Paradox Formation into informal production zones, in ascending order, Alkali Gulch, Barker Creek, Akah, Desert Creek, and Ismay (figure 3). The Cane Creek is within cycle 21 in the Alkali Gulch zone (Hite, 1960; Hite and Cater, 1972; Reid and Berghorn, 1981). Rassmussen and Rassmussen (2009) defined 80 depositional cycles in the Paradox Basin; 59 cycles are within the Hermosa Group and 21 cycles are in the overlying Elephant Canyon Formation of the Cutler Group.

Siliciclastics shed off the Uncompahgre uplift eventually filled the Paradox Basin and red-bed continental deposition dominated from the Permian through Jurassic time (figure 10). The sediment loading in the Paradox Basin caused the Paradox salt to flow laterally and vertically during the Middle Pennsylvanian (late Desmoinesian) reaching a peak in Late Pennsylvanian time (Missourian and Virgilian) resulting in numerous northwest-trending, salt-cored anticlines (figure 5) (Anna and orthers, 2014). Significant salt movement continued into the Early Triassic (Rasmussen and Rasmussen, 2009). The breakup of Pangaea and the resulting Cretaceous Interior Seaway to the east caused deposition of thick marine shales and sandstones in the basin (figure 11). The Paleogene was a time of major Laramide uplift in the western interior with gentle epeirogenic uplift of the Colorado Plateau and Paradox Basin. The Paradox Basin was deeply incised during the Neogene by the present-day Colorado and Green Rivers and their tributaries. The erosion created canyons and plateaus exposing the salt anticlines and eolian deposits of the Triassic and Jurassic Glen Canyon Group throughout much of the Paradox Basin (figure 12).

Cane Creek Shale

The Cane Creek shale is mostly dolomite, silty dolomite, and mixed dolomite with some limestone, often with abundant mottled anhydrite displacing dolomite. Sandstone/siltstone beds are part of the Cane Creek in a few locations within the Paradox Basin. Thin organic-rich shale beds are the source for hydrocarbons in the Cane Creek. The Cane Creek is informally divided into zones A, B, and C, in descending order (figure 13). The A and C zones are transitional with the overlying and underlying salt beds and typically contain interbedded and nodular anhydrite with dolomite. The B zone is the primary productive unit in the Cane Creek. The average total organic carbon of the thin black shales in the B zone is 15% with some samples up to 28% (Grumman, 1993).

Core Laboratories (Core Labs) studied the Cane Creek 26-3 well core and described the following diagenetic sequence for the Cane Creek shale (appendix C): (1) early pyrite, (2) finely crystalline dolomite cement, (3) quartz overgrowth, (4) partial dissolution of less stable feldspar grains, (5) dolomitization, (6) calcite cement, (7) anhydrite cement and replacement and, (8) late stage halite fracture filling. Eby Petrography and Consulting studied thin sections from the Remington 21-1H well core (appendix D) and described some calcite in the dolomitic muds, indicating incomplete dolomitization.

Anhydrite replaced some dolomite grains and dolomitic muds. Some anhydrite crystals were replaced by Fe-sulfide crystals indicating some later stage pyrite. Some microfractures and anhydrite-filled vugs are lined with bitumen.

Siltstone to very fine-grain sandstone beds within the B zone are the primary horizontal drilling target in the Big Flat area. The sandstone has generally higher porosity than the carbonates and therefore greater storage capacity. Core plug data from the Cane Creek 26-3 well averages 10% porosity in the sandstone (24 samples) and 5% porosity in the carbonates (46 samples). The sandstone is composed of mostly very fine-grain, sub-round to sub-angular, well sorted quartz with some very fine dolomite grains interpreted as wave modified eolian deposits that accumulated on paleo highs within the basin.

Fault-associated anticlines are the primary drilling targets (Grove and others, 1993) and are believed to have the highest density of fracturing. These faults are not reflected on the surface and must be seismically identified. Second-order folds due to salt movement have amplitudes of 15 to 100 feet and apparent wavelengths of 300 to 600 feet (Grove and Rawlins, 1997). Fracture data from orientated cores in the Cane Creek shale show a regional northwest to southeast, near vertical, open extensional fracture system that is not significantly affected by the orientation of local folds (Grove and Rawlins, 1997).

The Cane Creek was deeply buried but is now as much as 9000 feet shallower than maximum burial due to uplift of the Colorado Plateau and subsequent erosion (Rasmussen and Rasmussen, 2009). The thick overlying and underlying salt provide an excellent seal for the hydrocarbons and fluid pressure. The fluid gradients in the Cane Creek at Big Flat range from 0.75 to 0.95 psi/ft. The oil is sweet paraffinic crude with 36º to 43º API gravity and a 40º to 45ºF pour point (Grove and others, 1993). The associated gas has a heating value of 1200 to 1400 British Thermal Units (Btu per cubic feet) with a trace of carbon dioxide (CO_2) and no hydrogen sulfide (H_2S) (Grove and others, 1993).

EXPLORATION HISTORY

The first oil discovery in the Moab area occurred in the 1920s from Paradox Formation. The first discovery well was drilled on the axis of the Cane Creek anticline near the current site of Intrepid's potash mine (Smith, 1978c). Drilling equipment and building materials were loaded on barges and floated down the Colorado River to the drill site. The well blew out while drilling at a depth of 2028 feet and the rig was destroyed by the resulting fire (figure 14). Later, equipment was floated farther down the river to Shafer dome, where drilling resulted in a dry hole (figure 15). Over the years, several additional wells were drilled on the Cane Creek anticline near the site of the 1920s blow out, but only a minor amount of oil was ever produced. A summary of the early history of drilling on the Cane Creek anticline is given by Smith (1978c). A summary of Cane Creek wells with location, completion, and production data is compiled in appendix B.

The search for oil in the Moab area has continued sporadically since the 1920s. The discovery of oil in the Mississippian Redwall Limestone at Big Flat brought numerous explorers to the area leading to the discovery of the Lisbon and Salt Wash fields (figure 16 and table 4). While drilling to the Redwall many of the wildcat wells encountered oil shows in the overlying Pennsylvanian Paradox Formation, particularly the Cane Creek shale. The Long Canyon well (figure 17) established the first commercial production from the Cane Creek, but additional drilling in the area resulted in disappointing results. The Cane Creek became a target again in the 1990s with the successful completion of the Kane Springs 1-27 horizontal well (figure 18). More recently (approximately 2000 to 2014) with rising oil prices, the Moab area has experienced a significant increase in horizontal drilling in the Cane Creek and subsequent oil production. The collapse of oil prices in late 2014 resulted in the cessation of drilling in the area.

Big Flat Area

The Big Flat area which includes the Cane Creek unit, is the most successful area within the Cane Creek play. The early 1960s saw the discovery of the Shafer Canyon (Smith, 1978e), Bartlett Flat (Smith, 1978a; Grove and others, 1993), and Long Canyon (Smith, 1978d) fields. The Shafer Canyon field consisted of two wells, one on each side of Dead Horse Point State Park that produced from the Cane Creek shale (figure 19). The wells were plugged and abandoned in 1969 after producing over 67 MBO, mostly from one well. Bartlett Flat (Big Flat 5) and Long Canyon (Long Canyon 1) fields (both one-well fields) also produced from the Cane Creek shale. The casing collapsed in the Big Flat 5 well and the field was abandoned after producing 39 MBO. Several additional wells unsuccessfully attempted to established production at Bartlett Flat until 1991 when the first horizontal well was drilled (Grove and others, 1993). The Long Canyon 1 well was the most successful well in the area drilled during the 1960s. The well has produced more than 1 MMBO and is still producing. Lion Mesa field was discovered in 1980, but only produced a minor amount of oil from the Cane Creek shale.

Big Flat Field (Mississippian)

In 1957, drilling on Big Flat resulted in the discovery of oil in the Mississippian Redwall Limestone (Preston, 1961; Smith, 1978b). This was the first discovery of oil from Mississippian-age rocks in Utah. Ultimately, three oil wells and four dry holes were drilled in the Big Flat field, which was abandoned in 1971 after producing about 83 MBO. The field was drilled on a faulted, seismically defined structure with four-way closure. Although not a large field, it brought attention to the area and highlighted the potential of the Redwall, which lead to the discovery of the larger Lisbon and Salt Wash fields.

Big Flat Field (Pennsylvanian)

Columbia Gas Development Corporation: Exploration continued in the Moab area but significant success did not occur until Columbia Gas formed the Kane Springs federal unit in 1991 and drilled a horizontal well (1-27) in the Cane Creek shale in the abandoned Bartlett Flat field (Grove and others, 1993). This was the first long-reach horizontal well drilled in Utah. Drilling horizontally in the Cane Creek shale allows wells to penetrate 1000+ feet of reservoir rock, versus 10 to 30 feet in a vertical well, and greatly increases the probability of encountering natural fractures essential to economic production. Columbia Gas drilled six horizontal wells that have produced more than 1.4 MMBO and are still producing. Columbia Gas sold the unit to Aviara Energy in 1996; the unit changed ownership several times, Hunt Petroleum in 2002, Intrepid in 2003, Bobcock and Brown in 2006, and Fidelity E&P in 2008 who then conducted an active drilling program and greatly expanded the field.

Fidelity Exploration & Production Company: Fidelity E&P took ownership of the former Kane Springs unit and formed the Cane Creek federal unit in 2007, covering the same acreage. The unit includes Hell Roaring field and Big Flat field. The Bartlett Flat and Park Road fields were combined with Big Flat field in 1991. Fidelity E&P has drilled 17 horizontal wells in the unit, many of which have horizontal legs exceeding 5000 feet in length. Total production from the Cane Creek unit through December 2015 is 5.7 MMBO, and 3.9 BCFG, with 54,072 BO and 28,642 MCFG produced during the month of December 2015 (figure 20). Many of the wells have multiple horizontal laterals and some drill pads contain two wells, helping to reduce the surface footprint of development (figure 21). Fidelity E&P sold their interest in the Cane Creek play to Wesco Operating Inc. in 2016.

Lion Mesa Field

The Lion Mesa field was discovered in 1980 with the completion of the 27-1A well (section 27, T. 27 S., R. 21 E.) (Quigley, 1983). The field is a seismically defined fault closure mapped at the top of the Mississippian; closure at the Cane Creek horizon is minor (figure 22). The 27-1A well was perforated

in the Cane Creek shale with an initial production of 75 BOPD. The well produced a total of 1888 BO and 0 MCFG and was plugged and abandoned in 2016. Three additional vertical wells were drilled and all failed to establish any production. The Hatch Point 22-33H well was completed in a horizontal lateral in the Cane Creek with an initial production of 10 BOPD. The well never produced and was abandoned in 1991. The Lion Mesa field is similar to the Big Flat field; it lies along the Cane Creek anticline and appears to have been a paleo-high with some sandstone accumulation in the Cane Creek. The lack of economic hydrocarbon accumulation at Lion Mesa may be due to the lack of a local structural closure at the Cane Creek horizon.

Lisbon Area Exploration

The Lisbon area southeast of Big Flat has been explored over the years with both vertical and horizontal wells. Minor amounts of oil and gas have been produced from the Cane Creek in the Hatch Point and Wilson Canyon fields and from the La Sal 29-28 well. Wells drilled in the area encounter good quality source rocks, black organic-rich shales, and silty dolomites (often anhydritic) but lack well-developed sandstone beds similar to the reservoir rock in Big Flat field.

Wilson Canyon Field

The Wilson Canyon field has one Cane Creek producer, the Chevron Federal 1 well (section 24, T. 29 S., R. 23 E.). The Federal 1 was completed in 1968 as a vertical Cane Creek well and produced for many years before a horizontal lateral was drilled in the reservoir in 2002. The vertical well produced 89,667 BO and 133,267 MCFG from 1968 to 2002. From 2002 to 2015, the well has produced only 1231 BO and 25,330 MCFG from the horizontal lateral (figure 23).

Hatch Point Field

The Threemile unit was formed in 2008 and lies in T. 29 S., R.21–22 E. Four wells were drilled in the unit and two were completed as Cane Creek producers. The Hatch Point field consists of two Cane Creek wells and the Hatch Point 1 well completed in 1992 producing from the Redwall Limestone. Total production through December 2015 from the Cane Creek wells, Threemile 12-7 and Threemile 43-18H, is 65 MBO and 24 MMCFG; production for the month of December 2015 is 121 BO and 0 MCFG.

Greentown Area

Salt Wash Field

Salt Wash field is an asymmetrical east- to west-trending anticline discovered in 1961 (figure 24). Production is from the Mississippian Redwall Limestone (Smouse, 1993; Morgan, 1994). Total production from the field through December 2015 is 1.6 MMBO and 11.7 BCFG, December 2015 production was 1 BO. The gas from the Redwall is low BTU and is used on-site or vented. The Cane Creek was drill-stem tested in the 1-16A State well (section 16, T. 23 S., R. 17 E.) and recovered 600 feet of oil, but a Cane Creek completion was never attempted. The 18-2 Government well (section 18, T. 23 S., R. 17 E.) was perforated in shallower Paradox shales (3-9, 11, and 16-19) in 1981 but only produced intermittently a total of 2042 BO and 629 MCFG through December 2015. A horizontal well in the Cane Creek has not been drilled in the Salt Wash field.

Greentown Field

Beginning in 2005 and continuing through 2008, Delta Petroleum Corporation (Delta) drilled nine wells south of the town of Green River to test the hydrocarbon potential in numerous Paradox Formation clastic beds. Delta Petroleum employed a different strategy than that typically used in the Big Flat area where wells (vertical and horizontal) are commonly completed in a single clastic bed (Cane Creek) with little to no stimulation. In the Greentown area, Delta perforated and fracture stimulated numerous clastic intervals in separate stages. Most fracture stimulations used slick water with sand while some were diesel and sand.

A great deal of optimism was created when clastic 19 (operator O zone) in the Greentown State 36-11 well was perforated and fracture treated. The initial flow pressure was 6150 psi at the surface but quickly increased to 8000 psi, more pressure than Delta Petroleum was prepared to handle. The operator called in a service company specializing in pressure control. They flowed the well for a month drawing down the pressure to a manageable level (figure 25). Delta then set a bridge plug above the clastic 19 perforations and perforated and fracture stimulated shallower clastic beds in the Paradox Formation. Delta was never able to get back to clastic 19 due to mechanical problems in the wellbore. The well was completed in 2007 in shallower beds above clastic 19 and soon after was plugged and abandoned having produced only 364 BO with no reported gas or water.

Two wells were completed as oil wells and were designated as the Greentown field. The Greentown 32-42 well (section 32, T. 22 S., R. 17 E.) was completed in 2007 but plugged and abandoned in 2009 due to casing collapse; the well produced 1374 BO. The Federal 28-11 well (section 28, T. 22 S., R. 17 E.) penetrated a recumbent fold in the Cane Creek (figures 26 and 27). The well is perforated in clastic 19 and in a steeply folded and overturned part of the Cane Creek as well as the normal Cane Creek below the associated thrust fault (figure 28). The Federal 28-11 was completed in 2008 and has produced about 71 MBO and 266 MMCFG through December 2015 (figure 29). The gas-to-oil ratio (GOR) for the total production through December 2015 is 3725 cubic feet of gas per barrel of oil (CFG/BO) and 5271 CFG/BO for the month of December 2015. During the month of December 2015, the well produced 789 BO and 4159 MCFG.

Based on well logs and testing, clastic 19 and the Cane Creek shale (clastic 21) appear to have the most hydrocarbon potential in the Greentown unit. Neither clastic (19 or Cane Creek) have been cored in the Greentown area greatly limiting the reservoir characterization. At the Big Flat field the principle reservoir lithology in the Cane Creek is very fine-grain sandstone mostly within the B zone. The Cane Creek in the Greentown unit is similar in total thickness to Big Flat but appears to have a thinner B zone and thicker A and C zones. The B zone does not exhibit any density-neutron porosity cross over (limestone matrix), possibly indicating a lack of sandstone reservoir. Core of the Cane Creek in the Greentown unit is needed to accurately determine the reservoir quality. Cuttings were not examined for this report. Numerous other clastic beds were tested by Delta and resulted in oil shows but no economic production.

Clastic 19 generally thickens from Big Flat to Greentown (south to north) and has more density - neutron cross over in the Greentown area indicating possible sandstone lithology but can also be an indicator of gas in the reservoir (figure 30). Delta drilled the Greentown 36-24H, near the Greentown State 36-11, as a vertical well and then made two attempts to drill a horizontal leg in clastic 19, but mechanical problems in both of the legs prevented any completion attempts.

All of the wells drilled by Delta experienced some mechanical problem such as salt plugging and/or collapsed casing. As a result, the oil and gas potential of the Greentown area is difficult to evaluate. The two-well Greentown field was approved in 2009. Delta sold their interest in the Greentown area to Pacific Energy and Mining who, in 2013, formed the Greentown Exploratory unit covering 31,383 acres but has not drilled any wells.

DRILLING AND COMPLETION TECHNIQUES

Drilling Techniques

The Cane Creek shale and other Paradox Formation clastic beds often display good oil shows when drilled but are difficult to establish long term production. Drilling in the Big Flat area during the 1950s and 1960s was focused on the Mississippian Redwall Limestone, but when a well failed to establish production from the Redwall, the operators would often attempt to complete the well in the overlying Cane Creek. Although many wells tested small volumes of oil, only one well, Long Canyon 1, was an economic success.

Drilling is complicated due to the unique challenges presented by the thick accumulations of salt in the Paradox Formation. Best practices involve drilling to the top of the salt and setting casing. The sedimentary sequence above the salt is low pressure due to exposure along the canyons of the Colorado River. The salt has very high fluid pressure requiring weighted mud that would be lost into the lower pressure formations above. Most operators drill with an oil-base mud to prevent dissolving the salt and creating large wash outs in the drill hole. To complete a well, high-strength casing is required in the Paradox salt section otherwise the casing can collapse by the plastic movement of the ductile salt.

Renewed interest in the Cane Creek shale came with the development of horizontal drilling, which greatly increases the volume of the reservoir exposed in the well bore and increases the potential to encounter fractures. A horizontal well was completed in 1991 by Columbia Gas in the Kane Springs unit, establishing economic production from the Cane Creek in what would become the Big Flat field. Fidelity E&P purchased the Columbia Gas assets in the Cane Creek play. Fidelity E&P shot 3D seismic, drilled vertical pilot holes, collected core from the Cane Creek, then moved uphole and began drilling at an angle to intersect the Cane Creek horizontally. Wells are drilled on seismically defined local structures and fault closures.

Natural fractures are an important reservoir characteristic for economic completion in the Cane Creek shale and can provide high volume oil production without artificial stimulation of the reservoir. Drilling horizontally greatly increases the probably of intersecting open fractures. The orientation of the fractures in the area is northwest to southeast with a smaller conjugate set of fractures trending northeast to southwest (figure 31 and appendix C). Most fractures are steeply dipping and those cemented with halite and/or anhydrite are generally the widest (table 5). The direction of the horizontal wellbore is based on the dip of the structure being tested, the available surface location, and lease and reservoir drainage models. The orientation and length of each horizontal well is different. Comparison of horizontal lengths and direction to the flush production (first six months) of the wells displays no correlation (figure 32). For example, some short laterals parallel to the regional fracture trends have out produced long reach laterals drilled in a similar direction or perpendicular to the fracture trend. Each well location is structurally unique; each location has unique lease and drainage objectives, greatly complicating development of the area.

The objective of horizontal drilling in the Cane Creek shale is to penetrate the Cane Creek with the drill bit horizontal to the bedding plane. The Cane Creek is not a flat lying bed so the trajectory of the well bore can be very complex (figure 33). It is generally desirable to drill the bed at low dip (up or down) so the drill string can slide through the horizontal section. The Cane Creek has structural dip and secondary folding due to salt movement. These folds generally have a wave height of 300 feet and distance of 1000 feet (Grove and others, 1993). As a result, a horizontal lateral in the Cane Creek has a wavy pattern in a structural dip.

Completion Techniques

The Cane Creek and other Paradox Formation clastic intervals are overlain and underlain by anhydrite and thick salt (halite) deposits (figure 3). Inducing fractures through artificial stimulation runs the risk that the fractures will extend into the overlying and underlying salt and, along with saturated brine

within the formation, mobilize the salt and redeposit it in the main reservoir, perforations, and production tubing.

Several of the wells in the Greentown area were treated with a slick-water and proppant stimulation. Many of the treated wells reported salt plugging during testing. However, the casing collapsed in those wells, unrelated to the stimulation, so without long term production it is unknown if salt plugging would have persisted or if it was only a temporary problem. The Federal 28-11 well was perforated and treated with a slick-water and proppant stimulation in repeated sections of the Cane Creek and clastic 19 (figure 28) and is the only producing well in the Greentown field. The well records show salt plugging during production testing but it is not publicly known if plugging continues to be a problem.

The Greentown 36-24H well was first drilled as a vertical well. The Cane Creek and lower clastic intervals were perforated and treated with an oil-based proppant stimulation. Oil-base fluid is used to prevent dissolving and mobilizing the formation salt. Some frac-sand fill problems were reported during production testing but there was no report of salt plugging. The well was swabbed recovering minor shows of oil and gas but never fully recovered the treatment volume (load). The Greentown 36-24H was plugged and abandoned after two unsuccessful attempts were made to drill horizontally in the clastic 19 interval.

The Fidelity E&P Cane Creek 32-1-25-19 horizontal well (SWSW section 35, T. 25 S., R. 19 E.) was completed (May 2014) as a low volume oil well in the Cane Creek shale. The well produced 18 MBO and 10 MMCFG in 7 months and averaged 94 BOPD. The well was then treated with about 200 to 400 barrels of mineral oil with proppant per stage, in 6 stages (November 2014). After treatment, the well produced 26 MBO, 13 MMCFG in 7 months averaging 128 BOPD (figure 34). The increase in production is minor but this was a poor producing well to begin with; high-volume producing wells may respond better to fracture stimulation.

HYDROCARBON PRODUCTION FROM THE CANE CREEK SHALE AND CLASTIC 19

The Cane Creek shale is the most oil productive clastic bed in the Paradox Formation. The shallower clastic 19 bed has produced some minor volumes of hydrocarbons from the Big Flat and Greentown areas. Attempts have been made to complete in other clastic intervals but have only resulted in very minor production in one well. The Paradox Formation resource potential is described by Anna and others (2014) and Widden and others (2014) as part of the U.S. Geological Survey Resource Assessment of the Paradox Basin (in preparation). They divided the Cane Creek into two Assessment Units (AUs) based on percent vitrinite reflectance (%Ro) values from Nuccio and Condon (1996) and Rasmussen and Rasmussen (2009). The Cane Creek oil AU has Ro <1.1% and the Cane Creek gas AU has Ro >1.1%. There are very few data points in the deeper part of the basin defining the gas AU. Currently, the Greentown Federal 28-11 well (NWNW section 28, T. 22 S., R. 17 E.) is the only Cane Creek producing well in the gas AU.

Cane Creek Oil Production

Oil produced from the Cane Creek shale was described by Grove and others (1993) as sweet, paraffinic crude. The oil has an API gravity of 36º to 43º, and a specific gravity of 0.811 to 0.844 at 60º F. The pour point ranges from 40º to 44.6º F with an oil formation volume of factor 1.32 to 1.34. Cane Creek oil is trucked from individual wells to refineries in Utah and Colorado. There are currently no central facilities or oil pipelines in the area.

As of the end of December 2015, 35 wells in the Cane Creek study area have produced more than 7.6 million BO (MMBO) (8.5 MMBOE) (table 1). Total production of barrels of oil equivalent (BOE) per well ranges from 2 MBOE to 1,325 MBOE, with a mean of 300 MBOE/well (figure 35). The ratio of cubic feet of gas produced per barrel of oil (GOR) ranges from 0 to 3.7 MCFG/BO with a mean of 0.7

MCFG/BO. Removing the Greentown field well data, which is the highest gas producer and in the gas AU, the range is 0 to 1.8 MCFG/BO with a mean of 0.6 MCFG/BO (figure 36). The volume of water produced per barrel of oil ranges from 0 to 53 MBOE/BW with a mean of 1.7 MBOE/BW. After removing the two highest BOE/BW producing wells, the range is 0 to 0.8 MBOE/BW with a mean of 50 BOE/BW (figure 37).

Most of the wells, including all the high-volume producers, are in the Big Flat area. Total production through December 2015 from the Cane Creek unit, Big Flat and Hell Roaring fields, is 5.6 MMBO and 3.9 BCFG. Production for the month of December 2015 was 800 MBO and 388 MMCFG (figure 20). The most productive well is the Cane Creek 12-1, which was completed in September 2012 and has already produced 867 MBO (0.9 MMBOE) (figures 38 and 39) and should easily surpass the Long Canyon well as the biggest Cane Creek producer. The BW/BO for the total production in this area is 0.1 BW/BO and 0.3 BW/BO for the month of December 2015. The BO/BW ratio is low but will increase as wells mature, but probably not significantly since the reservoir drive is primarily gas expansion and not a strong water drive. Produced water is disposed at the Kane Springs 16-1 injection well or the commercial Danish Flats facility in Grand County. The GOR for the total production is 697 CFG/BO and 485 CFG/BO for the month of December 2015.

The Federal 28-11 well in the Greentown field has produced more than 100 MBOE (71 MBO and 266 MMCFG) (figure 29) and is completed in clastic 19 and a repeated section of Cane Creek. The well is in the U.S. Geological Survey Cane Creek gas AU and produces a much higher GOR than the wells in the Big Flat area (USGS Cane Creek oil AU) to the south, due to the greater depth and therefore greater thermal maturity in the Greentown area (figure 2). Production in Federal 28-11 is commingled; therefore it is unknown how much of the volume is coming from clastic 19 versus the Cane Creek shale.

Cane Creek wells in the Lisbon area have produced less than 100,000 BOE. The Chevron Federal was drilled and completed in the Cane Creek from a vertical well bore in 1968. The vertical well produced 89 MBO and 121 MMCFG. In 2002 a horizontal lateral was drilled in the Cane Creek and produced an additional 25 MBO and 36 MMCFG as of December 31, 2015, but the well has been shut in since October 2008 (figure 23).

Cane Creek Gas Production

Analysis of the associated gas from nine Cane Creek wells has an average heating value of 1473 British thermal units (Btu) per cubic foot with a range of 1190 to 1627 Btu per cubic foot. The gas has a trace of CO_2 and no H_2S (table 6). Based on total production through December 2015 the gas-to-oil ratio for the Cane Creek unit is 697 CFG/BO.

For decades the associated gas was used on site or flared due to the high cost of building a natural gas line from the Big Flat area. All of the natural gas produced (>1 BCFG) from the Long Canyon well has been flared. Columbia Gas who first began drilling horizontal Cane Creek wells in the Big Flat area, considered constructing both gas and oil pipelines. Columbia Gas planned to lay two lines along State Highway 313 from Big Flat to the mouth of Seven Mile Canyon, approximately 17 miles. The gas line would tie into the Rocky Mountain pipeline at the junction of Seven Mile Canyon and Highway 191. The other line would deliver oil to storage tanks stationed behind the hogback ridge at the mouth of Seven Mile Canyon. The oil line would have eliminated oil tanker traffic in the Big Flat area. The lines would have been built within the Utah Department of Transportation (UDOT) right of way for Highway 131. However, Highway 131 has a switch back with tight turns, not suitable for a pipeline, requiring the proposed lines to cross approximately 600 feet of Bureau of Land Management (BLM) administered lands. Columbia Gas could not get approval to cross BLM lands and the route was dropped from consideration. The BLM did approve the Right of Way (ROW) for a gas line from the Big Flat area north along the Dubinky well road in 1992, but due to low gas prices and the low volume of gas production, Columbia Gas did not feel it would be economical.

Fidelity E&P took ownership of the original Columbia Gas wells in 2008 and drilled additional horizontal Cane Creek wells. Production reached a volume where they determined it was economical to build a gas pipeline along the longer (approximately 29 miles), but BLM preferred, route. The BLM approved construction of the Dead Horse Lateral Pipeline (DHLP) and the Blue Hills gas processing plant, in November 2013, construction began in December 2013. The system of gas gathering lines connecting individual wells to the DHLP was approved in June of 2014. The DHLP pipeline follows SR 313 from Big Flat to the junction with the Dubinky Well road, a well-graded unpaved road. The pipeline follows the Dubinky Well road north to the Blue Hills road where it ties into the Pacific pipeline, which follows the Blue Hills road to the southeast tying into the Rocky Mountain pipeline (figure 40). The Pacific pipeline had recently been completed to transport gas from the Greentown field to the Rocky Mountain pipeline. Approximately 25 miles of gathering lines connect 19 producing wells at Big Flat to the DHPL. A booster station about 14 miles north of Big Flat maintains the pressure in the pipeline. The Blue Hills Gas Processing Facility was constructed where the DHLP ties into the Pacific pipeline. The processing plant extracts natural gas liquids, primarily a mix of ethane, propane, and butane, for sale and then puts the remaining methane gas back into the pipeline. Table 7 shows gas gathered from the DHPL at the Blue Hills plant, NGL produced, and gas shipped to the Rocky Mountain pipeline. The first reported production of gas liquids from the Blue Hills gas plant began March 2015.

Production from Clastic 19

There have been several attempts to produce oil from the clastic 19 bed. In the Big Flat area three wells have produced from clastic 19. The three wells are the Kane Springs 16-1 (section 16, T. 25 S., R. 18 E.), Cane Creek 36-3H (section 36, T. 25 S., R. 19 E.), and the vertical Cane Creek 1-1 (section 1, T. 26 S., R. 19 E.) (figure 41). The 16-1 was drilled horizontally in clastic 19 and completed in 1993 producing 93 BOPD. The well was converted to a water disposal well in 1998 after producing a total of 15,589 BO, 27,465 MCFG, and 2368 BW. Produced water from the Cane Creek wells is disposed of in the Cutler Group at a depth of 1490 to 1520 feet. Water analysis from the KS 16-1 in the Utah Division of Oil, Gas and Mining well files show the produced water has 226,000 total dissolved solids (TDS) and the injection zone has 54,000 TDS. A total of 714 MBW have been disposed of in the 16-1 well, about 2 MBW per month (figure 42). The Cane Creek 1-1 well is a vertical completion and the best clastic 19 producing well. The well was completed in 2008 producing 439 BOPD and 262 MCFGPD. Total production through December 2015 is 133 MBO and 135 MMCFG, in November 2015 the well was shut in. The 36-3H was completed in 2014 producing 54 BOPD and 50 MCFGPD. Total production through December 2015 is 2978 BO and 2329 MCFG, production for the month of December 2015 was 1 BO.

CORRELATION AND MAPPING

Correlation of the Cane Creek Shale

The Pennsylvanian Paradox Formation Cane Creek shale is part of cycle 21 of Hite (1960). In the Paradox Basin, individual shale or clastic interbeds are easily correlated over long distances. Each cycle consists of a clastic bed and a thick salt bed that are number from the top of the formation down (figure 3) (Massoth, 2012). Correlations can be carried many miles in the northwest to southeast paleodepositional direction but less so in the southwest and northeast directions. Down dip to the northeast is where the thickest salt was deposited (figure 4) and where the greatest loading from the overlying Cutler Group occured, resulting in large northwest- to southeast-trending diapiric anticlines (figure 5). The massive movement of the salt and associated shales combined with few well penetrations, make correlation of individual cycles within the deep basin very difficult. To the southwest, the Cane Creek and other clastic

deposits onlap onto the carbonate shelf, quickly losing their individual identities without the bounding salt beds.

The Cane Creek is divided into three informal zones in descending order, A, B, and C (figure 13) (Grove and others, 1993). The tops of the informal zones are described as sequence boundaries by Rasmussen and Rasmussen (2009) and Rasmussen and others (2009). The boundaries are typically easily identified on a gamma-ray log especially if combined with one or more porosity curves such as sonic, density, or neutron.

Structure Mapping

The Paradox Basin is an asymmetric basin that dips to the northeast and the deepest part is near the Uncompahgre uplift. The basin shallows to the southwest as shown by the structure of the Mississippian Red Wall Limestone (figure 43). Regional structures affecting the basin are the north plunging Monument upwarp and the east to southeast plunging structure off the San Rafael Swell, converging at the Big Flat area. Structure mapping of the Cane Creek shows a northwest to southeast strike with the plunging Monument upwarp in the Big Flat area. The Cane Creek plunges steeply to the north in the Greentown area (figure 44). A detailed structure map of the Cane Creek in the Big Flat area shows a complex set of faulted anticlines on the regional high (figures 45 and 46). The faults do not offset surface rocks and are identified in wells and on 3D seismic data gathered by Fidelity E&P and presented in many of the Division of Oil, Gas and Mining (DOGM) well files. Well log correlation and structure mapping in the Greentown field indicate a recumbent fold in the lower Paradox (figures 26 and 28). Seismic data is not available to the UGS so the structural interpretation is based solely on well data, published papers, and public DOGM records.

Thickness Mapping

The Cane Creek thins from northeast to southwest although local thickening and thinning is very common (figure 47). Some local thickness anomalies are the result of folding and faulting of the Cane Creek. The strike of the thickness trend for the Cane Creek is generally northwest to southeast with deposition of the Cane Creek controlled by the regional structure of the Paradox Basin. The Cane Creek is thickest to the northeast near the basin center, although the lack of penetrations does not clearly demonstrate the thickening, and is thinnest to the southwest on the shallowing shelf of the basin. Thickness mapping of the Cane Creek intervals show slight regional thinning of the C and B zones (figures 48 and 49) from southeast to northwest and general uniform thickness of the A zone (figure 50). The thickness mapping may be somewhat biased because the data set is dominantly along the depositional strike of the Cane Creek with limited data perpendicular to the depositional strike. Thickness of the B zone does not distinguish productive areas from nonproductive areas in the Cane Creek.

Thickness mapping from the top of the Paradox salt to the base of the salt reveals regional salt structures formed by the movement of the salt due to loading of sediment during Permian and Triassic time (figure 51). The valleys east of the Cane Creek play such as Lisbon, Moab, and Castle Valley, were formed by large northwest-southeast trending salt diapirs controlled by basement faulting (figure 5). In the Cane Creek play area there are numerous salt anticlines where the salt did not penetrate overlying statra. The Cane Creek, Big Flat, and Shafer Dome fields lie along the crest of the Cane Creek and Shafer Dome anticlines respectively, which are expressed on the surface. Many of the Greentown wells have a thickened salt section. The salt anticline structures do not reveal the structure deeper in the formation at the Cane Creek level, which is controlled by the underlying structure on the Redwall Limestone. A map of the thickness of the Paradox salt below the Cane Creek shows thinning at Salt Wash, Big Flat, Lion Mesa, and the west flank of Lisbon anticline, indicating these were Mississippian highs when the Cane

Creek was deposited (figure 52). These paleo highs may have been locations for accumulation of wind-blown sand, an important reservoir lithology in the B zone.

DESCRIPTION, TOTAL ORGANIC CONTENT, AND POROSITY AND PERMEABILITY ANALYSES OF CORE FROM THE CANE CREEK SHALE

Of the seven wells that have core in the Cane Creek (figure 2), the UGS described and analyzed five cores: Cane Creek 26-3, Cane Creek 7-1, Skyline 1, Remington 21-1H, State 36-13, and Gibson Dome 1. The Cane Creek 26-3 well core was made available to the UGS as well as the analyses of the core from Core Labs (appendix C). The Cane Creek 26-3 is a high volume producing well in the Big Flat field. The Skyline 1 is a dry hole northeast of the Big Flat field; the core is housed at the USGS Core Center in Denver, Colorado. Cisco State 36-13 and Remington 21-1H are from exploration wells in the southeast part (Lisbon area) of the Cane Creek trend,. Gibson Dome 1 was a research well drilled by the U.S. Department of Energy in 1982 and cored the Paradox Formation to evaluate the potential for nuclear disposal. The core is housed at the University of Texas in Austin. The Cane Creek in the Gibson Dome 1 well was described by a UGS geologist and analyses from oil exploration companies were provided to the UGS. Photographs of the core from the Cane Creek 7-1 well were provided to the UGS, but we did not have the opportunity to inspect and describe the core. The core from the Cane Creek State 1-36 was not available to the UGS but whole core analyses are in the DOGM well file and are discussed in this chapter. There are no cores from the Greentown area in the northwest part of the trend.

Cane Creek 26-3

The Cane Creek 26-3 (NESW section 26, T. 25 S., R. 19 E.) was drilled and completed by Fidelity E&P as a vertical well in the Cane Creek shale. The Cane Creek was cored from 7388 to 7474 feet beginning in the top of the A zone, through all of the B and C zones, and ending in the underlying salt (figure 53). The core is housed at the UGS Utah Core Research Center (UCRC) in Salt Lake City. The vertical well was completed October 2012 flowing 27 BO, 0 MCFG, and 43 BW. The well produced 2993 BO, 663 MCFG, and 1 BW in 6 months. Fidelity E&P drilled a horizontal leg in the Cane Creek and completed the well in November 2013, flowing 276 BO, 222 MCFG, and 0 BW. As of December 31, 2015, the well has produced 373,714 BO, 217,574 MCFG, and 6720 BW from the horizontal lateral.

A Zone

The A zone was cored from 7388 to 7409 feet. The zone is highly heterolithic with limestone, dolomitic mudstone, and some thin siltstone and organic-rich shale beds. Much of the zone is dolomite mudstone with abundant anhydrite (figure 54). Minor attributes include pin-point porosity in dolomite, highly bioturbated limestone, and finely laminated (possibly algal) shale. Numerous thin fractures are filled with clay or anhydrite and wider fractures are filled with halite (figure 55). The zone has a strong petroliferous odor but is not perforated due the abundant anhydrite.

Core Labs prepared and analyzed 13 thin sections from the A zone; the following descriptions are from the Core Labs report (appendix C). Their samples included sandstone, siltstone, dolomitic siltstone, dolomite, limestone, and anhydrite. The sandstones are well sorted with an average grain size range from 0.059 to 0.074 mm, coarse silt to very-fine grain sandstone. The carbonate samples are bioturbated with mudstone, wackestone, packstone, and boundstone textures. The thin sections contain microfractures cemented by anhydrite, halite, or calcite. Open fractures were described in the thin sections but it was not known if they are natural or induced.

B Zone

The B zone was cored from 7409 to 7446 feet and is the primary productive facies in the Cane Creek. The zone consists of limestone, dolomite, silty dolomite, black organic-rich shale, and siltstone to very fine-grain sandstone (figures 56 and 57). The dolomitic mudstone in the B zone contains much less anhydrite than in the A and C zones. The abundant siltstone to very fine sandstone is the dominant reservoir facies in the B zone. Pin point porosity was observed in the dolomitic mudstones, some mudstones are brecciated and contain limestone clasts. Vertical to near-vertical thin to wide fractures were observed in all facies and are generally filled with anhydrite, halite, or calcite (figure 58) and some have crystal growth and bitumen. The widest fractures are mostly halite filled. The siltstone is light gray, dolomitic, and bioturbated with some pin-point porosity visible. The transition from dolomitic siltstone to overlying silty dolomite is gradational.

Core Labs prepared and analyzed 18 thin sections from the B zone; the following descriptions are from the Core Labs report (appendix C). Their samples included argillaceous sandstones, sandstones, dolomitic argillaceous siltstones, and silty dolostone (figure 59). The samples are well sorted coarse silt to very fine sand, most are bioturbated, some with distinct burrows. Microfractures were observed in the thin sections filled with halite, anhydrite, and calcite. Peloids and quartz silt grains are common in the dolomites. The siltstones/sandstones are mostly feldspathic litharenite with some samples classified as litharenite, sublitharenite, lithic arkose, and subarkose. The siltstones/sandstones contain moderate amounts of potassium feldspar, minor amounts of limestone and dolomite rock fragments, minor to trace amounts of calcite replacement grains and muscovite. Other minor to rare grains include plagioclase, volcanic rock fragments, heavy minerals, and elongate plant fragments. Cement in the siltstones/sandstones is commonly quartz overgrowth and dolomite.

C Zone

The C zone was cored from 7446 to 7471 feet, an additional 3 feet of core is from the underlying cycle and consists of massive anhydrite. The zone consists of dolomitic mudstone with abundant anhydrite, sandstone, black organic-rich shale, and massive and laminated anhydrite (figure 60). The sandstone is very fine grain grading to siltstone, is bioturbated, and has fine minor laminations and near vertical halite fractures (figure 61). Sandstone in the C zone are similar to the sandstone in the B zone and are good quality reservoir rock, but generally thinner.

Core Labs prepared and analyzed 11 thin sections from unit C and the underlying anhydrite; the following descriptions are from the Core Labs report (appendix C). The thin section samples included dolomitic sandstone, dolomitic siltstone, argillaceous siltstone, dolomite, dolomitic anhydrite, and anhydrite (figures 62). The siltstone/sandstone is moderately well to well sorted coarse silt to very fine sand. Samples are bioturbated with some microfractures. Quartz overgrowths are moderate in abundance in the siltstone and minor to rare in the sandstone. There are minor occurrences of pore-filling dolomite and pyrite and trace amounts of feldspar overgrowths, calcite, anhydrite, titanium oxides, and halite cement.

Cane Creek 7-1

Fidelity E&P drilled, cored and completed the Cane Creek 7-1 well (NENE section 7, T. 26 S., R. 20 E.) as a vertical hole and no subsequent horizontal lateral was drilled. The Cane Creek was cored from 7590 to 7671 feet beginning in the lower half of the A zone, through the B zone, and most of the C zone (figure 63). The well was completed February 2014 flowing 337 BO, 176 MCFG, and 0 BW. As of December 31, 2015, the well has produced 36,169 BO, 14,170 MCFG, and 5244 BW from the horizontal lateral. Average production during December 2016 was 6.6 BOPD, 1.7 MCFGPD, and 0.3 BWPD.

The UGS was not provided access to the core but was given photographs. The description is from viewing the photographs and geophysical well logs, and making some assumptions, such as dolomite versus limestone, based on experience gained studying the Cane Creek 26-3 core.

A Zone

The lower half of the A zone was cored in the Cane Creek 7-1 well. The zone is dominantly dolomitic mudstone (possible some limestone), dark gray to dark brown, with some thin dolomitic black shale beds. Most of the dolomite has abundant nodular anhydrite. Most of the dolomite appears to be bioturbated with some anhydrite-filled burrows and some thin laminations of possible algal origin. Some near vertical fractures appear to be halite and anhydrite-filled, and a few open fractures may be induced.

B Zone

The majority of the B zone appears to be dolomitic mudstone, dark gray to dark brown, some with abundant nodular anhydrite. The zone has numerous thin beds of black dolomitic (?) shale, gradational with the dolomitic mudstone, and some shale beds with sharp upper and lower contacts. The lower portion of the B zone has some gray to light gray silty dolomite (?). There does not appear to be any siltstone or sandstone beds in the 7-1 B or C zone, the primary reservoir facies in the Cane Creek 26-3 core. Schmidt and Spencer (2014) did not identify any siltstone or sandstone in the cuttings samples in the vertical pilot hole or the horizontal lateral.

C Zone

The majority of the C zone appears to be dolomitic mudstone and possibly silty dolomite with some thin black shale beds. The gray to light gray silty dolomite is highly bioturbated, may have anhydrite dispersed throughout, and some fractures possibly filled with halite and anhydrite. Dolomitic mudstone has abundant nodular anhydrite and some thin laminations of possible algal origin.

Skyline 1

The Skyline 1 (NWSE section 5, T. 26 S., R. 20 E.) was a vertical well drilled by Davis Oil Company in 1981 to test the Cane Creek and was plugged and abandoned in December 1981. The Cane Creek Shale C zone was cored from 7501 to 7521 feet (figure 64). A UGS geologist went to the USGS core center in Denver and described the core. The well was perforated from 7455 to 7508 feet (Cane Creek A, B, and C zones) and 7538 to 7550 feet (clastic 22). After fracture stimulation, the well was swabbed tested and produced an initial potential of 10 BOPD from the Cane Creek, with no gas or water reported.

A and B Zones

Cane Creek Shale A and B zones were not cored in the Skyline 1 well. Descriptions of the cuttings in the DOGM well file describe the zones as dolomite and anhydrite, no siltstone or sandstone was identified.

C Zone

The cored interval in the C zone was described as mostly light to medium gray dolomitic siltstone with wavy and horizontal laminations and some convoluted bedding (figures 64 and 65). X-ray diffraction (XRD) data from the USGS indicates a high percentage of quartz in the samples. Fractures in the

siltstones are salt filled. There are some thin organic-rich shales and mottled anhydrite in the lower portion of the core.

Remington 21-1H

Union Pacific Resources Company drilled and cored the vertical Remington 21-1H well (SESE section 21, T. 31 S., R. 23 E.), and then drilled two horizontal laterals in the Cane Creek. The Cane Creek was cored from 7435 to 7496 feet beginning in the lower part of the A zone and through the B and C zones (figure 66). The core is housed at the UCRC. The well was plugged and abandoned after production testing the second lateral through a pre-perforated liner. Oil and water were recovered but volumes or rates from the production testing were not reported.

A Zone

The A zone was cored from 7435 to 7440 feet. The cored interval is mostly dolomite and shaley dolomite, typically dark gray to black with some thinly laminated shale beds. The dolomite has abundant mottled anhydrite throughout. Minor fractures are calcite and halite filled with possible bitumen. Some small pyrite crystals were observed in the core.

Two thin sections from the A zone were examined by Eby Petrography & Consulting, Inc. (appendix D). A thin section from 7435.5 feet is described as finely crystalline dolomite with no visible matrix porosity (figure 67A). Some matrix is composed of grain-supported fine peloids, possibly some burrows and organic remnants and traces of microfractures along thin organic seams. These are some disseminated quartz-rich silt grains with rounded outlines, consistent with possible eolian delivery system, and some remnant limestone and diagenetic pyrite. A thin section from 7437.3 feet is described as anhydrite with some dolomite (figure 67C). The anhydrite has distinctive palmate structures indicative of subaqueous sulfate mineral growth which displaces the dolomite. The anhydrite has a felted ground mass within the palmate nodules. The dolomite patches contain relicts of peloids, organic matter, and some anhydrite-filled microfractures.

B Zone

The entire B zone was cored from 7440 to 7469 feet (figure 66). The zone is composed of dolomite, silty dolomite, thin black shale to silty shale, and one thin (1.6 feet) highly bioturbated siltstone near the base of the unit. Many of the dolomite beds have anhydrite blebs and highly mottled anhydrite (figure 68 and 69). The dolomite is gray to dark gray but some beds are dark brown possibly indicating increasing silt content. The dolomite also has some thin shaley laminations, indications of bioturbation, and minor thin anhydrite- and salt-filled fractures and rare pyrite throughout. Thin layers of rip-up clasts or brecciation are present indicating possible exposure surfaces. The zone appears to be organic rich but lacks any good quality siltstone to sandstone reservoir, and the reservoir quality of silty dolomite beds is greatly reduced by the abundant anhydrite.

Fracture analysis by TerraTek a Schlumberger Co. describes numerous mineralized and partially mineralized fractures as well as a number of open fractures (table 8 and appendix E). Partially open fractures are more abundant in silty dolomite intervals, and low-angle open fractures are in the shale zones. The shale and clean silty dolomite beds are thin and bounded above and below by anhydritic dolomites. As a result, the fracture network may not be well connected. Production testing indicates a much lower effective permeability than these data indicate.

Five thin sections were examined by Eby Petrography & Consulting, Inc. (appendix D). A thin section from 7445.6 feet is described as dolomite with some vaguely laminated fabric that may be microbial in origin. Rare large pores and vugs are partially filled with anhydrite and lined with bitumen. Calcite- and anhydrite- filled fractures are cross cut by stylolites filled with insoluble residues. A thin

section from 7446.7 feet contains nodular anhydrite in a dolomite matrix indicating a hypersaline sabka depositional setting. Iron sulfide crystals line most of the contacts between the anhydrite and dolomitic mudstone which has some bitumen-filled vugs. The thin section from 7448 feet is described as anhydritic dolomite with microbial laminations (figure 70A). Laminations consist of alternating mud-rich and grain-rich (peloids) laminae. The thin section from 7450.0 is described as a dolomitic mudstone with some patches of anhydrite (figure 70C). The mudstone has some detrital quartz silt grains, rare patches of bitumen, and some fractures filled with calcite, anhydrite, and bitumen. Small disseminated pyrite crystals are also present in the matrix. The thin section from 7450.7 feet is described as vaguely laminated dolomite with some mottling and contains some relict laminae with an overprint of either haloturbation or bioturbation. Pyrite and bitumen form numerous patches in the matrix as well as fill several microfractures.

Two thin sections were examined by TerraTek a Schlumberger Co. (appendix E). A thin section from 7456.2 feet is described as silty, carbonate mudstone with variably sized anhydrite nodules and anhydritic intraclasts. The sample has two sets of calcite-filled fractures and a larger calcite- and anhydrite-filled fracture which is crosscut by a stylolite. The sample contains terrigenous silt, disseminated pyrite and some calcite signifying incomplete dolomitization. Porosity is rare consisting of porosity within partially mineralized microfractures and rare patches of porosity within the micritic matrix. The thin section at 7463.1 feet is described as a silty dolomitic mudstone with both anhydrite- and halite-filled fractures. Fine crystalline anhydrite is present as vein filling and nodules throughout the sample. The sample contains terrigenous silt composed of quartz, feldspar, and mica, as well as rare peloids, phosphate, pyrite, and glauconite. The thin section has sparse patches of intercrystalline microporosity and rare dissolution pores and fracture porosity.

C Zone

The entire C zone was cored from 7469 to 7492 feet (figure 66). The zone is composed of dark gray to dark brown shaley dolomite and calcareous dolomite, most with abundant anhydrite and rare thin black shale. Some beds are highly bioturbated with some anhydrite- and salt-filled fractures (figure 71). No thin sections were made from the core of the C zone.

Cisco State 36-13

Patara Oil & Gas drilled the vertical Cisco State 36-13 well (NWNE section 36, T. 31 S., R. 24 E.) in 2011. The well was perforated in the Cane Creek and later abandoned; test recoveries were not reported. The Cane Creek was cored from 7586 to 7654 feet beginning in the upper part of the A zone through the B and C zones and ending in the underlying anhydrite (figure 72). Patara Oil & Gas had the core analyzed by Core Labs and provided the report to the UGS (appendix F). The core is housed at the UCRC. The Cisco State well has adequate source rock but lacks good quality reservoir because there are only a few thin dolomitic siltstone beds and much of the carbonate contains anhydrite.

A Zone

The A zone was cored from 7586 to 7600 feet (figure 72). The zone consists of dolomite and dolomitic mudstone with some thin black laminated shale, abundant mottled anhydrite, and traces of pyrite (figure 73). There are some salt-filled fractures with bitumen and rare vugs.

B Zone

The B zone was cored from 7600 to 7626 feet (figure 72). The zone consists of dolomite, silty dolomite, dolomite with abundant mottled anhydrite, and some thin shale and dolomitic siltstone beds

(figure 74). There are some salt- and anhydrite-filled fractures but no visible bitumen and only traces of pyrite.

C Zone

The C zone was cored from 7626 to 7655 feet (figure 72). The zone consists of dolomite with abundant mottled anhydrite, black shale, and bedded anhydrite (figure 75). There are some salt- and anhydrite-filled fractures throughout the unit.

Gibson Dome 1

Gibson Dome 1 (SESE section, 21T. 30 S., R. 21 E.) was drilled as part of the U.S. Department of Energy's National Waste Terminal Storage Program (NWTS). Gibson Dome was evaluated as a potential high-level radioactive-waste storage site. The geologic manager for the Paradox Basin study was Woodward-Clyde Consultants (1982a, 1982b). A continuous 4-inch-diameter core was taken from below surface to a total depth of 6384 feet. The Cane Creek was cored from 5220 to 5310 feet (figure 76) and is housed at the University of Texas in Austin. The Gibson Dome well is the most southwest well that has Cane Creek core. The Gibson Dome has relatively thin siltstone and dolomite beds compared to other cores examined, has much more anhydrite, and is a very poor reservoir. The shales are also very thin but organically rich. Weatherford Labs conducted Rock Eval analysis on 5 samples for the UGS, (table 9, Appendix G) and Chesapeake Energy Corporaton also conducted Rock Eval analysis on 5 samples (table 9).

A Zone

The A zone was cored from 5220 to 5238 feet and consists of dolomitic siltstone, silty limestone and bedded anhydrite. Fractures and sedimentary structures were not observed in the zone due to the abundance of anhydrite. Four samples had 1.24 to 10.30% TOC and averaged 4.14% (table 9).

B Zone

The B zone was cored from 5238 to 5280 feet and consists of calcareous siltstone, silty limestone, and bedded anhydrite. The zone is thinly laminated to massive with minor thin fractures and rare pyrite. Chesapeake Energy Corporation performed tight rock analysis on numerous shale intervals in the Gibson Dome core; one sample taken in the Cane Creek had 10.0% porosity and >1000 nanoDarcys (>0.001 mD) permeability. TOC analysis of four samples ranged from 3.09 to 20.80% with an average of 9.19% (table 9).

C Zone

The C zone was cored from 5280 to 5310 feet and consists of calcareous siltstone with moderate fracturing, faint laminations, and abundant anhydrite. TOC analysis of two samples recorded 2.72% and 5.59% with an average of 4.16% (table 9).

Cane Creek State 1-36

Chevron USA drilled and cored the vertical Cane Creek State 1-36 (NWSE section 36, T. 27 S., R. 20 E.) well and subsequently drilled a horizontal lateral in the Cane Creek Shale in 1991. A drill-stem test in the Cane Creek lateral recovered 1200 feet of drilling mud. The drilling mud was then displaced

with nitrogen blowing the hole dry but no formation fluid entered the wellbore. The well was plugged and abandoned. The Cane Creek was cored from 7026 to 7095 feet beginning in the upper part of the B zone and ending in the lower part of the C zone. The UGS has not seen the core and there are no descriptions in the State records, but the porosity and permeability analyses are available in the DOGM well file (table 10 and figure 77). Full diameter Dean-Stark analyses were performed on one-foot segments of the core. Horizontal permeability was measured in the north-south and east-west directions as well as in the vertical direction. The results show a strong anisotropy in several of the samples demonstrating the significance that the vertical to near-vertical fractures can have in the reservoir (table 10). The core analyses show several feet of core with very permeable fractures, but based on the production test results these fractures must be very limited and lack significant connectivity.

Core Analyses

Organic Carbon Content

Total organic carbon (TOC) was measured on samples from five of the cored wells studied (table 11). These samples were collected by various researchers and well operators over time. As a result, the criteria used for sampling is unknown and undoubtedly not uniform. The lithology of each sample is not known for certain, we assigned the dominant bed lithology to the sample based on the depth of the sample, but this could be incorrect. For example, a dolomite bed may have very thin (< 1-ft) interbedded shale and it is unknown if the sample was taken from a thin shale or the dolomite. Comparing data from different wells should be done with caution; samples of only the most promising looking shale may have been collected in one well while samples of much more variable lithology may have been collected in another well. Using TOC to determine the oil generating potential of a well is difficult when it is uncertain how thick and extensive the sampled bed is; a very high TOC from a limited and thin (1-2 inch) bed may not be as significant as a moderate TOC value from a thick (feet) and laterally extensive bed. But with all these uncertainties general trends and values can help define an oil play area.

A total of 53 samples from Cane Creek cores were taken in five wells and have a range of TOC from 0.04% to 20.8%. The Cane Creek has good source rocks in all five wells and in all three of the Cane Creek zones (A, B, and C) (table 12). The ranges and average TOC values for each unit are: A zone ranges from 2.19% to 10.3% with an average of 5.39%, B zone ranges from 0.14% to 20.29% with an average of 5.54%, and C zone ranges from 0.04% to 12.52% with an average of 4.66%. The ranges and average TOCs by lithology are: shale ranges from 0.04% to 20.29% with an average of 6.84%, carbonate ranges from 0.11% to 13.01% with an average of 4.28%, and siltstone ranges from 0.06% to 6.20% with an average of 1.63%. Both the carbonate and siltstone have a high outlier value that may actually indicate thin shale beds, if the outliers are removed the carbonate averages 3.93% and the siltstone averages 0.10%. The ranges and average TOCs by well are: Skyline 1 ranges from 0.06% to 7.89% with an average of 1.66%, Cisco State 36-13 ranges from 0.04% to 17.60% with an average of 2.69%, Cane Creek 26-3 ranges from 3.71% to 12.52% with an average of 6.81%, Remington 21-1H ranges from 0.97% to 20.29% with an average of 8.43%, and Gibson Dome 1 ranges from 2.72% to 20.80% with an average of 9.73% .

The large range of TOC values for lithology type and for well may be biased by sampling procedure focused on black organic-rich appearing shales. Average values are of limited value due to the large range of data. The ranges for the three zones, A, B, and C, may be biased by sampling procedure as well, but the greater range in the B zone may be representative of greater heterogeneity within the zone.

Porosity and Permeability

Conventional porosity and permeability (P&P) analyses are available for three of the cored wells examined, Cane Creek 26-3, Cisco State 36-13, and Remington 21-1H (figure 77 and table 13). The Cane Creek State 1-36 core is not public but the results of whole core porosity and permeability analyses are available from the DOGM well file; this data provides additional insight into the Cane Creek reservoir.

A plot of P&P data from all four of the wells shows multiple trends (figure 77). The trend for Cane Creek 26-3 and Cisco State 36-13 are nearly a match even though the producing 26-3 has well developed sandstone facies which is lacking in the 36-13 dry hole. The Remington 21-1H has a higher trend line than the 26-3 and 36-3 but this is not reflective of a better reservoir. The 26-3 analyses were measured at 2280 psi confining pressure and the 36-3 was measured at 2310 psi, to reflect downhole conditions. The 21-1H was measured at 400 psi confining pressure. The reduction from the 21-1H trend to the 26-3 and 36-3 trends might represent the reduction in porosity and permeability due to depth of burial.

A plot of the P&P data for the four wells based on lithology demonstrates the difficulty of using a variety of data sources. Some anhydrite, anhydritic dolomite, and shale beds have unexpectedly high permeability (figure 78A). This could be the result of taking plugs in thin beds that are not the same lithology as the general bed description, for example a thin porous dolomite within bedded anhydrite or anhydritic dolomite. As a result, the P&P plot based on lithology may be of limited value. A P&P plot based on grain density was equally questionable since anhydritic dolomite and dolomite have similar grain densities, and silty (quartz grains) dolomite and siltstone/sandstone with both quartz and dolomite grains will have similar grain densities. A P&P plot of samples described as dolomite or sandstone show two populations, a low permeability group and a higher permeability group (figure 78B). The percent of dolomite and sandstone that populates each group is nearly equal. We were unable to determine what causes the two separate populations, but it might be due to unrecognized microfracturing.

The Cane Creek 26-3 is the only producing well of the four wells discussed. The siltstone and very fine-grain sandstone in the B zone of the 26-3 is the main reservoir and primary horizontal target for wells in the Big Flat area. A P&P plot by zone (A, B, and C) shows higher porosity (storage) and permeability (transmissibility) in the B zone compared to A and C (figure 79). A P&P plot of sandstone (including siltstone) and carbonate (limestone and dolomite) data from Cane Creek 26-3 has two populations with the high permeability population dominated by carbonates, perhaps indicating greater fracturing (figure 80A). Within the low permeability population, the sandstone has generally higher porosity (figure 80B). The carbonate has a higher trend line than the sandstone but a lower slope, indicating permeability increases in the sandstone facies with increasing porosity at a higher rate than in the carbonate facies. The sandstone has better storage capacity and therefore is an important facies for economic oil production. The difference in reservoir quality between the sandstone and some of the dolomites is subtle, therefore the dolomite, particularly the silty dolomites, should not be overlooked as a potential reservoir. Many of the carbonate beds have anhydrite which is not reflected in core plugs because sampling will often avoid the anhydrite, but this anhydrite can greatly reduce the overall storage capacity and permeability of the bed.

The P&P trend for the Cane Creek State 1-36 has a much lower slope than the other three wells (figure 77). The P&P data for the State 1-36 well are from whole core (1-foot segments) analysis measured in a N-S, E-W, and vertical direction (table 10). All of the samples are described as sandstone in the TerraTek a Schlumberger Co. core analysis report in the DOGM well file. For the P&P plot, the lowest value for each 1-foot segment was used to avoid fracture permeability. The three directions clearly show the influence of fracturing on permeability. Several samples with fractures have permeability <0.1 mD in one or two directions but 100s mD in the third direction. For example, in sample 1 (7026 to 7027 feet) the permeability in the N-S direction is 0.03 mD, in the E-W direction it is 0.27 mD, and in the vertical direction it is 981 mD (table 10). We interpret this as a high-permeability, open vertical fracture that is oblique to the N-S and E-W directions. The E-W direction may have some enhanced permeability by crossing through the vertical fracture.

GENERATION, MIGRATION, AND TRAPPING OF HYDROCARBONS IN THE CANE CREEK SHALE

The Paradox Formation Cane Creek shale is generally organically rich and thermally mature enough to have generated a significant volume of hydrocarbons. Other Paradox shales that have significant source rock potential are the Chimney Rock, Gothic, and Hovenweep (figure 3) (Nuccio and Condon, 1996; Schenk, 2002; Ramussen and Rasmussen, 2009; Whidden and others, 2012). Whidden and others (2012) calculated a mean total undiscovered resource for the Cane Creek shale of 215 MMBO, 193 BCFG, and 15 million barrels of natural gas liquids (MMBNGL) (table 3; appendix A).

Burial history charts, which show the depth of burial and later uplift of a formation or source rock being studied, were produced for the Cane Creek shale. Burial is shown over time and includes periods of non-deposition and erosion. Incorporating heat flow into the burial history allows for the interpretation of the catagenesis of kerogen including beginning and peak oil generation and beginning and peak expulsion of hydrocarbons from the source rock. The timing of generation and expulsion when combined with the knowledge of the basin structure, and development of potential reservoirs and traps, can identify oil migration pathways and areas of potential accumulations.

Burial and thermal history studies show the Cane Creek began generating hydrocarbons in the deep fold and fault belt, near the ancestral Uncompahgre uplift, and proceeded over time to the southwest in shallower parts of the basin (Nuccio and Condon, 1996; Ramussen and Rasmussen, 2009).

Hydrocarbon Generation

The thin organic-rich shales in the Cane Creek have high TOC values, some greater than 20% wt. The dolomite has TOC values generally less than 10% but still high enough to contribute to petroleum generation and expulsion. Time and temperature are critical factors for kerogen to generate hydrocarbons.

Vitrinite reflectance (%Ro) is a measure of the percentage of incident light reflected from the surface of vitrinite particles. The maturation of vitrinite is a kinetic process and is used to determine the maximum temperature the rock has been exposed to, a critical factor in determining the hydrocarbon generation potential. The %Ro is divided into diagenesis, catagenesis, and metagenesis, to define stages of maturation. During diagenesis ($Ro < 0.5\%$) mild temperatures and pressures resulting from early burial and compaction cause the organic matter to form new structures that comprise a waxy material known as kerogen. Kerogen produces petroleum during catagenesis ($0.5\% < Ro < 2.0\%$). During metagenesis ($2.0\% < Ro < 4.0\%$) the remaining kerogen and hydrocarbons in the rock are altered to methane (Horsfield and Rullkotter, 1994). The relationship of %Ro and hydrocarbon generation is dependent on the type of kerogen in the source rock (figure 81) (Tissot and Welte, 1984).

Heat flow is a critical component in modeling burial history and hydrocarbon generation. Henrikson and Chapman (2002) studied 511 bottom-hole temperatures (BHT) from 181 oil and gas wells throughout Utah which were then grouped into 88 sites. The BHTs were corrected for cooling effects from drill mud circulation. Previous data and the new 88 sites were used to prepare a heat flow map of the State of Utah (Henrikson and Chapman, 2002). The mean heat flow for the Colorado Plateau is 62 W/m^{-2} with a probability error of 15%. The average thermal gradient for the Colorado Plateau is 26º C km^{-1} (figure 82).

After deposition of the marine Hermosa Group, siliciclastics of the Cutler Group shed from the Uncompahgre uplift began filling the basin. Loading from the thick deposits of the Cutler caused the salt to begin to move forming diapirs, salt walls, intervening salt welds, salt anticlines, and recumbent folding within the Paradox Formation. The area of salt tectonics is known as the fold and fault belt of the Paradox Basin (figures 1 and 5). The early loading placed the Cane Creek within the oil generative and expulsion window in the deep part of the basin. Southwest of the deep basin the Paradox salt is thinner and the overlying Cutler thins dramatically. As a result, the area didn't generate and expulse hydrocarbons from the Cane Creek until much later.

Rasmussen and Rasmussen (2009) conducted burial and thermal history modeling on 29 wells in the Paradox fold and fault belt. Their modeling showed oil generation beginning near the ancestral Uncompahgre uplift as early as late Desomoinesian, 304 Ma (table 14 and figure 83) when the Honaker

Trail Formation of the Hermosa Group was still being deposited in the southwest part of the basin. Expulsion of hydrocarbons began 259 Ma in the Paradox Basin 1 well. The Long Canyon 1 well in the Big Flat area began oil generation 249 Ma with expulsion beginning 77 Ma (table 14). Many of the wells modeled by Rasmussen and Rasmussen (2009) in the Big Flat and Lisbon areas reached peak oil generation about 76 to 82 Ma (figure 83 and table 14). Uplift of the Colorado Plateau began in Late Miocene and resulted in as much as 9000 feet of overburden being removed. The uplift and erosion was sufficient to stop oil generation and expulsion in the Paradox Basin (Rasmussen and Rasmussen, 2009).

Migration and Trapping of Hydrocarbons

Moore (2015) studied fluid inclusions from three wells: Cane Creek 26-3, Cisco State 36-13, and Remington 21-1H. The following discussion is from his report which is available in full in appendix H. Samples were taken from fractures with dolomite, anhydrite, and salt filling and all are characterized by similar mineral and fluid relationships. The samples are dominated by one-phase liquid-rich inclusions which indicate a trapping temperature of <50ºC, some two-phase inclusions contain liquid and a small vapor bubble, and rare three-phase inclusions contain liquid or vapor bubble and halite (figures 84, 85, 86, and 87). Two- and three-phase inclusions could have formed at low temperatures as well but re-equilibrated as the rocks were progressively buried. Contemporaneous migration of both saline water and oil is indicated by the presence of both aqueous and oil inclusions within the same growth zones, healed fractures, and rarely the same fluid inclusion, and occurred during and after vein filling. The majority of the inclusions contain liquid with a salinity of ~30 wt% NaCl + $CaCl_2$ indicative of interaction with evaporites. Fluoresce indicates an API gravity of about 35º.

A burial history chart (figure 88) and temperature gradient curve (figure 89) for the Cane Creek 26-3 show that the oil in the fluid inclusions could not have been generated locally in the Big Flat area. The 50ºC temperature would have been reached at 304 Ma at a depth of about 1400 meters (4600 ft). Rasmussen and Rasmussen (2009) show oil generation in the Long Canyon 1 well, near the 26-3, began at 249 Ma and expulsion began at 77 Ma. Rasmussen and Rasmessen (2009) show oil generation in the Paradox Basin 1 well in the deep portion of the basin beginning at 304 Ma. The oil in the fluid inclusions would have migrated from the deep basin to the Big Flat area. England (1994), using an extensive world-wide petroleum basin database, modeled migration distances and determined the migration occurred over an average distance of 6 miles. Sluijk and Nederlof (1984) found that in a significant number of basins migration exceeded 50 miles. The distance from Paradox Basin 1 to Long Canyon 1 is about 25 miles, but the shale and anhydritic dolomite would have been poor carrier beds for long distance migration. Some oil may have migrated into the underlying Mississippian Redwall Limestone, southwest of the Big Flat area, and then moved vertically along faults from the Redwall into the Cane Creek, an equally unlikely path. The abundance of aqueous fluid and rare oil content of the inclusions indicates that, as expected, early long-distance migration from the deep basin, represents a very minor volume of oil. Salt tectonics within the fold and fault belt would have eliminated migration pathways shortly after expulsion began.

The Cane Creek shale is overlain and underlain by thick beds of halite. Rock salt is one of the best reservoir seals having a permeability of about 10^{-21} m^2 (10^{-20} ft^2) (Bredehoeft, 1988; Peach and Spiers, 1996; Popp and others, 2001), within the range that Deming (1994) showed was needed for a bed to retain pressure for more than 1 million years. As a result, the Cane Creek reservoir has retained much of the pressure developed at maximum burial resulting in a highly overpressured reservoir at the present post-uplift depth. The retention of the pressure indicates the majority of the oil was generated in-situ, and long distance migration, which would have provided a release for the pressure, did not occur.

Overpressuring can occur due to “disequilibrium compaction particularly during rapid subsidence of low-permeability sediments” (Osborne and Swarbrick, 1997). Overpressuring that involves a change in volume (e.g., after kerogen produces hydrocarbons) must be well sealed or pressure leak-off will occur (Osborne and Swarbrick, 1997). Both scenarios for overpressuring apply to the Cane Creek shale. At some point during burial the permeability will decrease to a point where the bed will begin to retain fluid,

this is known as the fluid isolation point (Osborne and Swarbrick, 1997). In rock salt the in-situ permeability and porosity is very low at a burial depth of just 230 feet (Casas and Lowenstein, 1989; Schoenherr and others, 2007). The burial history chart of the Cane Creek 26-3 shows the maximum burial of the Cane Creek was 4200 meters (14,000 ft) which at a normal pressure gradient of 0.45 psi/ft would have resulted in a minimum of 6200 psi, and additional pressure could have been created by the volumetric conversion of kerogen to hydrocarbon. Uplift and erosion has placed the B zone at a depth of 7416 feet; if 100% of the hydrostatic pressure was retained the reservoir would have a pressure gradient of 0.84 psi/ft., which is within the reported range of 0.75 to 0.95 psi/ft for the Cane Creek at Big Flat (Grove and others, 1993).

GEOCHEMICAL CHARACTERIZATION OF THE CANE CREEK SHALE

The Pennsylvanian Paradox Formation Cane Creek shale preserves a marine flooding event that deposited dolomite, dolomitic siltstone, anhydrite, fine-grain sandstone, and black shale between evaporative cycles composed chiefly of anhydrite and halite (Goldhammer and others, 1991; Morgan and others, 2014; Widden and others, 2014). In order to interpret the evolution and maturity of the organic matter within the unit, we analyzed Rock-Eval data from five well cores and cuttings from ten wells (figure 90 and table 15).

The Rock-Eval data are from a variety of sources resulting in limited interpretations of the data set. Organic richness, hydrocarbon generation, and remaining potential are a function of TOC and the bed thickness and lateral extent. Records do not indicate whether a sample from core is representative of a whole bed or of a thin black shale within a larger bed. Cuttings are often collected every ten feet while drilling and can be a mix of lithologies from thin beds plus cavings from above. TOC values derived from cuttings can underrate the TOC content if the sample contains both organic-rich and organic-poor beds. The TOC values can be biased if shale is carefully selected from the cuttings for analysis because the samples may be from a very thin bed or plus shale cavings from above. These sampling biases should not adversely affect thermal maturity analysis. Although data from multiple sources has its limitations, general trends derived from the data can be useful in interpreting general organic richness, thermal maturity, hydrocarbon generation, and remaining hydrocarbon potential.

Organic Quality and Type

Each well analyzed had 1 to 21 samples taken, and we calculated the average TOC of all of the samples run per well; average TOC values range from 0.60 to 17.07 weight % (table 15). Average values should be considered with caution because one or two high or low outlier values can skew the average. Most of the samples are mature for oil and have good to very good source rock quality (figure 91). Maximum TOC values from the study wells range from 0.6 to 17.6 weight % (figure 92); hopefully the best potential source rock (black shale) was sampled. Anomalies or outlier data can occur due to differences in sampling and number of samples in the dataset.

TOC data from five well cores were evaluated for each Cane Creek Shale zone and lithology (table 12). All five wells have some high TOC values indicating good source rock; average TOC per well is strongly influenced by the number of organic poor beds analyzed. The average TOC is similar for each of the Cane Creek zones (A, B, and C) (table 12), although the B zone has more potential source rock beds and greater thickness than the A or C zones.

Hydrogen index (HI) and oxygen index (OI) were calculated for six of the wells. HI values from these wells range from 74.13 to 496 mg HC/g TOC and OI values range from 8 to 116 mg CO_2/g TOC (table 16). Based on the van Krevelen plot most of the samples fall into Type II kerogen which is sourced from marine plankton and can produce oil and gas (figure 93).

Thermal Maturity and Productivity

Vitrinite reflectance (R_o) was examined in seven wells by Nuccio and Condon (1996) (table 17). All of the samples are within the oil window (0.6 to 1.3 %Ro) or early gas window (1.3 to 1.85 %Ro). The highest values are from the Salt Wash 1 and Grand Fault 14-25 wells, both in the USGS Cane Creek gas assessment unit. R_o values in the 0.60 to 1.40% range are most likely to have petroleum liquid generation (Jarvie, 2012).

Type I and type II kerogen with a Rock-eval pyrolysis Tmax value less than 435ºC are immature, values between 435ºC and 455ºC (Type I) or 456ºC (Type II) are in the oil window, values above 455/456ºC indicate the kerogen is in the gas window (Tissot and others, 1987). (table 15) (figure 94). Maximum Tmax values from 15 wells range from 430 to 462.6°C (figure 95), and of these 15 wells, one well plots in the immature organic matter range, twelve wells are in the mature or oil window, and four wells are in the over-mature gas window

A cross plot of production index (PI) and thermal maturity (Tmax) show 10 of 17 samples within the oil window (Nuccio and Condon, 1996) (figure 96). Maximum production values (PI) from the study wells range from 0.09 to 0.73 (figure 97), and PI values at Tmax range from 0.05 to 0.67 (figure 98).

Geochemical data from the Cane Creek shale show the organic carbon is primarily from a marine setting, is good to very good quality, and has the potential for oil generation. Oil potential within the Cane Creek shale generally improves to the north and east, which correlates with the deeper sea level adjacent to the Uncompahgre uplift (Blakey and Ranney, 2008).

FRACTURES IN THE CANE CREEK SHALE

Naturally occurring fractures are important for permeability in the Cane Creek reservoir. The regional structural trend seen on surface fractures is northwest to southeast paralleling the Pennsylvanian Paradox Basin and associated salt anticlines and Uncompahgre uplift. Local and regional structure at the Cane Creek horizon can be complex, but the dominant fracture trend is northwest to southeast with a less pronounced conjugate northeast to southwest trend (Grove and others, 1993; Grove and Rawlins, 1997).

Fractures in the core from the Remington 21-1H well were studied by TerraTek a Schlumberger Co. (table 8 and appendix E) and those in the Cane Creek 26-3 well by Core Labs (table 5 and appendix C). Most fractures in the Cane Creek are completely to partially filled with calcite/dolomite, anhydrite, and/or halite. Many fractures terminate at bedding contacts.

The Cane Creek 26-3 core was not oriented, so Core Labs measured all fractures oriented to a line drawn on the core and then rotated all data based on orientation determined by the imaging log and well bore deviation. The dominant fracture trend measured by Core Labs in the Cane Creek 26-3 core is northwest to southeast with a conjugate northeast to southwest trend (figure 31). The fractures are mostly cemented with calcite/dolomite, anhydrite, and/or halite. An open fracture from 7422 to 7424 feet is coated with pyrobitumen. The best developed fractures are in the dolomitic siltstone/sandstone beds (figure 53). Fractures cemented with anhydrite are near or connected to anhydrite beds. The fractures described by Core Labs are summarized in table 5. The fractures with the most potential for production are the partially open fractures in the dolomitic siltstone/sandstone.

The Remington 21-1H oriented core was analyzed by TerraTek a Schlumberger Co. (appendix E). The cored interval consisted of moderately to well-fractured silty argillaceous dolomite, interbedded with poorly fractured anhydrite and anhydritic dolomite. Fractures in anhydrite and anhydritic dolomite are mostly completely mineralized while open- and partially-mineralized fractures are in the silty dolomite beds. In shale beds both low-angle open and filled fractures are present. Completely mineralized fractures are the most abundant type in the core. Fracture orientation is northwest to southeast with a

secondary set northeast to southwest. Cross cutting relationships show the fractures filled with anhydrite formed before fractures filled with halite.

Fluid inclusion study by Dr. Joe Moore at EGI (2015) (appendix H) show fracture development and filling occurred very early after deposition at less than 6500 ft (2000 m) depth. We were unable to determine the age of the open fractures, generally in the silty dolomites to siltstone/sandstone beds, which rarely had any mineralization. The open fractures may have developed during or just prior to, maximum burial and peak oil generation when most water would have already been expelled, so no mineralization occurred. The older mineralized fractures may have acted as a ductile unit causing new fractures to develop in the more brittle siliclastic beds.

CHIMNEY ROCK, GOTHIC, AND HOVENWEEP SHALES

Depositional cycles in the Paradox Formation are defined by a salt and associated clastic (Hite and Buckner, 1981). Most Paradox clastics are very thin and contain only minor amounts of total organic carbon (TOC). Clastics other than the Cane Creek shale (cycle 21) and cycle 19 clastic, that have sufficient thickness and organic content to be considered hydrocarbon source and possibly reservoir are: Chimney Rock shale (cycle 5, base of lower Desert Creek), Gothic shale (cycle 3, base of lower Ismay), and Hovenweep shale (cycle 2, base of upper Ismay) (figure 99). The shales are bounded above and below by carbonates and some thin interbedded anhydrite. In the Blanding Sub-basin some of the carbonate rocks are porous algal mounds that form the Desert Creek and Ismay conventional reservoirs.

The upper Paradox shales are divided into the Chimney Rock, Gothic, and Hovenweep oil or gas assessment units based on Ro <1.1% for oil and Ro >1.1% for gas (Anna and others, 2014; Whidden and others, 2014). Ro data is from Nuccio and Condon (1996) and Rasmussen and Rasmussen (2009).

The Chimney Rock, Gothic, and Hovenweep shales are similar to the Cane Creek. The upper Paradox shales are described as “black laminated, organic-rich calcareous to dolomitic mudstone, shaley carbonate grading upward to intercalated dolostone and laminated with minor black shale and anhydrite capped by thin halite beds” (Anna and others, 2014). They contain moderate to high TOC and are the source for the oil produced from the Desert Creek and Ismay algal mound deposits in the Blanding Sub-basin.

The Chimney Rock shale has a mean thickness of about 30 feet but is more than 100 feet thick in a narrow section along the Uncompahgre uplift (figure 100) (Anna and others, 2014; Whidden and others, 2014). The thickness trend is northwest to southeast paralleling the basin structure. Samples from outcrop have 0.2 to 8.7% TOC with a mean of 4.5% and samples from core have 0.4 to 8.6% TOC with a mean of 3.6% (Anna and others, 2014). There is currently no production from the Chimney Rock shale.

The thickness of the Gothic shale ranges from <20 to more than 200 feet. The shale is thickest near the Uncompahgre uplift and is typically 20 to 50 thick in the Blanding Sub-basin (figure 101) (Anna and others, 2014; Whidden and others, 2014). Samples from the outcrop have 0.1 to 4.0 TOC with a mean of 1.8%; samples from core range from 0.3 to 6.7% TOC with a mean of 2.6% (Anna and others, 2014). Eight wells in the Chimney Rock, Gothic, and Hovenweep gas AU, have produced from the Gothic in the southwest portion of the fold and fault belt, but only six have produced more than 20 MMCFG. A ninth well in the Chimney Rock, Gothic, and Hovenweep oil AU, produced a minor amount of oil in the Blanding Sub-basin.

The Hovenweep is about 20 feet thick in most of the Paradox Basin but can be 50 to 100 feet in portions of the fold and fault belt and Blanding Sub-basin. The Hovenweep reaches a maximum thickness over 200 feet near the Uncompahgre uplift (figure 102) (Anna and others, 2014; Whidden and others, 2014). There is currently no production from the Hovenweep.

The upper Paradox shales are not overpressured like the Cane Creek shale. The shales are typically overlain and underlain by carbonates that provide migration pathways to conventional reservoirs in the Desert Creek and Ismay zones. As a result, much of the oil generated in the upper Paradox shales may have migrated to other reservoirs. Anna and others (2014) calculated at 50% probability the

undiscovered oil and gas resource to be 238 MMBO for the Chimney Rock, Gothic, and Hovenweep oil AU, and 6075 BCFG for the gas AU (table 3; appendix A).

SUMMARY

The Paradox Basin is a Pennsylvanian-age northwest- to southeast-oriented pull-apart basin that is asymmetrical with the deep axis to the northeast near the ancestral Uncompahgre uplift. The restricted marine basin was located in a subtropical, arid environment where thick salt beds were deposited during marine lowstands and interbedded clastics were deposited during transgressive to high-stand events. Nearly 6 MMBO have been produced from the Cane Creek shale, mostly in the Big Flat area. The U.S. Geological Survey calculates the mean total undiscovered resource basin-wide for the Cane Creek to be 869 MMBO and 11,020 BCFG.

The Pennsylvanian Paradox Formation Cane Creek shale is a heterolitic unit composed of thin, black laminated organic-rich shales, silty dolomite, dolomitic mudstones that often contain moldic to nodular anhydrite, siltstone to very fine sandstone having both quartz and dolomite grains, and bedded anhydrite. The Cane Creek is informally divided into three zones from top to bottom, A, B and C. The A and C zones are transitional to overlying and underlying halite deposits, respectively. These zones are mostly anhydritric dolomitic mudstone and bedded anhydrite with minor thin black shale, and siltstone/sandstone beds may occur in the C zone. The B zone is the primary reservoir and is composed of siltstone/sandstone, silty dolomite, dolomitic mudstone, and some anhydritic dolomite.

The Cane Creek shale is organically rich, having total organic carbon (TOC) >20% wt. in the thin shales and generally >1% but <10% wt. TOC in many of the dolomitic mudstone beds. The Cane Creek is mostly thermally mature and has generated a significant volume of oil in the Paradox Basin. The oil is sweet paraffinic crude with 36º to 43º API gravity, 40º to 45º pour point, and 1200 to1400 BTU associated gas. The Cane Creek is sealed above and below by thick beds of halite which has preserved much of the fluid pressure developed during maximum burial and peak oil generation. As a result, the Cane Creek is a highly over-pressured reservoir with pressure gradients ranging from 0.75 to 0.95 psi/ft.

The Cane Creek is well sealed, acting as both a hydrocarbon source rock and reservoir. The siltstone/sandstone beds have the most effective porosity for hydrocarbon storage, some storage is in the silty dolomites. Permeability is low in both the siltstone/sandstone and dolomite beds but is often enhanced by open fractures.

The Cane Creek play area is an elongated northwest to southeast trend following the structure and paleo-depositional trend of the Pennsylvanian Paradox Basin. The play is limited to the northeast where the basin is deeper and dominated by diapiric salt anticlines and welds. Salt flow in this area has distorted the shales so their depth and lateral continuity are nearly impossible to predict. The play is limited to the southwest where the Cane Creek laps onto the Pennsylvanian-age carbonate shelf forming the southeast border of the basin.

Cane Creek traps are typically locally closed and faulted structures that are not identified at the surface. Seismic surveys, particularly 3D seismic, are needed to identify potential drilling targets.

The reservoir facies in the Cane Creek is thin (feet to a few tens of feet maximum) and has low permeability. One vertical well (Long Canyon 1) produced economic quantities of oil, but it is an exception. To produce large quantities of oil, horizontal wells are needed to encounter sufficient reservoir and increase the potential of encountering open fractures. A vertical pilot hole should be drilled through the Cane Creek to confirm the structural location of the shale and determine the quality of the reservoir. Then drill a lateral well, the direction of which is often based on structure (slight down-dip direction is needed) and lease and drainage area considerations. Drilling perpendicular to the fracture trend does not appear to increase the chances of success. Staying in zone is greatly complicated by folding due to salt flowage and small unrecognized faults.

Horizontal laterals are cased and typically completed natural because fracture stimulating shales in the Paradox Formation can easily create communication with the overlying and underlying salt beds.

Several wells in the Greentown area were given slick-water fracture treatments but experienced salt plugging in the production tubing. Oil-based fracture fluid has been used on a couple of poor performing wells with marginal success.

Several attempts have been made to complete in the cycle 19 clastic, particularly in the Greentown area. Attempted completions of clastic 19 in the Big Flat area have been unsuccessful, but one marginal well in the Greentown area is producing from both the clastic 19 and the Cane Creek shale. Clastic 19 thickens from Big Flat to the Greentown area, but no cores have been taken so the reservoir quality is poorly understood. Many wells in the Greentown area had impressive shows in clastic 19 but encountered mechanical problems during drilling and/or completion. Most of the Greentown wells that were completed as producing wells had the casing collapse before or shortly after production began.

The upper Paradox shales, Chimney Rock, Gothic, and Hovenweep, are organically rich and are the source of oil produced from the Desert Creek and Ismay algal mound reservoirs in the Blanding Sub-basin. Some minor gas has been produced from the Gothic in the southeast portion of the fold and fault belt, but otherwise this shale is not currently a producing reservoir.

CONCLUSIONS AND RECOMEMDATIONS

The Cane Creek shale is a high-quality source rock and potential reservoir. Structural closure is necessary for trapping and 3D seismic is required to identify deep subtle structures. Fault structures formed during the Mississippian and early Pennsylvanian provided paleo-highs where wind-blown clastic and dolomite grains accumulated resulting in good quality reservoir beds. Significant recoverable reserves may still exist, especially in the Big Flat area. Economic deposits in the Lisbon area to the south and Greentown area to the north have not yet been found, but source rock quality, thermal history of the areas, and abundant oil shows make these areas good territory for prospecting. Additional studies on the oil generation and migration in the areas may help define a more detailed play for exploration. Clastic 19 in the Greentown area appears to have significant potential, but attempts to exploit the reservoir have encountered numerous mechanical problems during drilling, completion, or early production stages. Clastic 19 is much less prospective south of Greentown in the Big Flat and Lisbon areas where it thins dramatically. The upper Paradox shales, Chimney Rock, Gothic, and Hovenweep, are good source rocks that are highly speculative as economic reservoirs. These shales are not over-pressured and much of the oil generated has migrated out of the shale to Deseret Creek and Ismay carbonate reservoirs. Very little core from the upper Paradox shales has been taken, but based on logs it appears that the shales lack any siliciclastic beds that could host significant volumes of oil.

The following recommendations should be considered when oil prices once again support additional drilling for the Cane Creek shale in the Paradox Basin:

- Acquire 3D seismic over the prospect to identify subtle structures and faults.
- Focus on areas with good local anticlinal or fault structures and areas with siltstone/sandstone beds in the reservoir.
- Drill a vertical pilot hole to confirm the structure and depth of the target bed and evaluate the reservoir potential.
- Take core in the vertical pilot hole of the target shale if nearby core is not available.
- Drill a horizontal lateral in the most porous bed, in the Cane Creek this is usually a siltstone/sandstone in B zone.
- Consider oil-based fracture stimulation as production declines, perhaps multi-stage small volume treatments.

The following recommendations are for the clastic 19 play in the Greentown area:

- Conduct a detailed study of the casing program to determine how to avoid casing collapse.
- Conduct a detailed study of previous vertical and horizontal drilling practices in the Greentown area.

- Develop improved drilling and completion best practices for the Greentown area.
- Drill a vertical well near the Greentown State 36-11 well (controlled blow out in cycle 19 clastic) and core clastic 19.
- Drill a horizontal lateral in clastic 19 if the core shows porous reservoir rock.
- Acquire 3D seismic over the area to identify additional drilling locations if a horizontal lateral is successful.

REFERENCES

Anna, L.O., Whidden, K.J., and Pearson, K.M., 2014, Assessment of continuous oil and gas reservoirs, Paradox Basin, Utah, Colorado, New Mexico, and Arizona: Rocky Mountain Association of Geologists The Mountain Geologist, v. 51, no. 2, p. 139–160.

Baars, D.L., 1966, Pre-Pennsylvanian paleotectonics—Key to basin evolution and petroleum occurrences in paradox Basin, Utah and Colorado: American Association of Petroleum Geologists Bulletin, v. 50, p. 2082-2111.

Baars, D.L., and Stevenson, G.M., 1981, Tectonic evolution of the Paradox Basin—Utah and Colorado, *in* Wiegard, D.L., editor, Geology of the Paradox Basin: Rocky Mountain Association of Geologists Field Conference Guidebook, p. 23-31.

Baker, A.A., Dane, C.H., and Reeside, J.B., Jr., 1933, Paradox Formation of eastern Utah and western Colorado: American Association of Petroleum Geologists Bulletin, v. 17, p. 963-980.

Barbeau, D. L., 2003, A flexural model for the Paradox Basin—Implications for the tectonics of the Ancestral Rocky Mountains: Basin Research v. 15, p. 97-115.

Birdwell, J.E., Vanden Berg, M.D., Johnson, R.C., Mercier, T.J., Boehlke, A.R., and Brownfield, M.E., 2015, Geological, geochemical, and reservoir characterization of the Uteland Butte member of the Green River Formation, Uinta Basin, Utah, *in* Vanden Berg, M.D., Ressetar, R., and Birgenheier, L.P., editors, Geology of Utah's Uinta Basin and Uinta Mountains: Utah Geological Association Publication 44.

Blakey, R.C., 2009, Paleogeography and geologic history of the western Ancestral Rocky Mountains, Pennsylvanian-Permian, southern Rocky Mountains and Colorado Plateau, *in* Houston, W.S., Wray, L.L., and Moreland, P.G., editors, The Paradox Basin revisited—new developments in petroleum systems and basin analysis: Rocky Mountain Association special Publication, p. 222-264.

Blakey, R., and Ranney, W., 2008, Ancient landscapes of the Colorado Plateau: Grand Canyon Association Special Publication, p. 222-264.

Bredehoeft, J.D., 1988, Will salt repositories be dry?: American Geophysical Union Eos Transacttions, , v. 69, p. 121-131.

Casas, E., and Lowenstein, T.K., 1989, Diagenesis of saline pan halite—comparison of petrographic features of modern, Quaternary and Permian halites: Journal of Sedimentary Petrology, v. 59, p. 724-739.

Cater, F.W., 1970, Geology of the Salt Anticline Region in southwestern Colorado: U.S. Geological Survey Professional Paper 637, 80 p.

Chidsey, T.C., Jr., editor, 2009, The Mississippian Leadville Limestone exploration play, Utah and Colorado-exploration techniques and studies for independents: Final Report, U.S. Department of Energy DE-FC26-03NT15424, 432 p.

Chidsey, T.C., Jr., and Eby, D.E., 2017, Potential oil-prone areas in the Cane Creek shale play, Paradox Basin, Utah, identified by epifluorescence microscope techniques: Utah Geological Survey Special Study 160, 178 p.

Condon, S.M., 1997, Geology of the Pennsylvanian and Permian Cutler Group and Permian Kaibab Limestone in the Paradox Basin, southeastern Utah and southwestern Colorado: U.S. Geological Survey Bulletin 2000-P, 46 p.

Deming, D., 1994, Factors necessary to define a pressure seal: American Association of Petroleum Geologists Bulletin, v. 78, p. 1005-1009.

Doelling, H.H., 1988, Geology of Salt Valley anticline and Arches National Park, Grand County, Utah: Utah Geological and Mineralogical Survey Bulletin 122, 58 p.

Doelling, H.H., Oviatt, C.G., and Huntoon, P.W., 1988, Salt deformation in the Paradox region: Utah Geological and Mineral Survey Bulletin 122, 93 p.

England, W.A., 1994, Secondary migration and accumulation of hydrocarbons, chapter 12, *in* Magoon, L.B., and Dow, W.G., editors, The petroleum system from source to trap: American Association of Petroleum Geologists, Memoir 60, p. 211-217.

Goldhammer, R.K., Oswalk, E.J., and Dunn, P.A., 1991, Hierarchy of stratigraphic forcing—example from Middle Pennsylvanian shelf carbonates of the Paradox Basin *in* Franseen, E.K., Watney, W.L., Kendall, C.G., and Ross, W., editors, Sedimentary modeling—computer simulations and methods for improved parameter definition: Kansas Geological Survey Bulletin, v. 233, p. 361-413.

Grove, K.W., Horgan, C.C., Flores, F.E., and Bayne, R.C., 1993, Bartlett Flat, Big Flat (Kane Springs Unit), *in* Hill, B.G., and Bereskin, S.R., editors, Oil and Gas fields of Utah: Utah Geological Association Publication 22, unpagenated.

Grove, K.W., and Rawlins, D.M., 1997, Horizontal exploration of oil and gas-bearing natural fracture systems in the Cane Creek clastic interval of the Pennsylvanian Paradox Formation, Grand and San Juan Counties, Utah, *in* Close, J., and Casey, T., editors, Natural fracture systems in the southern Rockies: Four Corners Geological Society, p. 133-134.

Grummon, M.L., 1993, Cane Creek shale member of the Paradox Formation, exploiting a self-sourced reservoir with horizontal well bores: American Association of Petroleum Geologists Bulletin, p. 1449-1450.

Guthrie, J.M., and Bohacs, K.M., 2009, Spatial variability of source rocks—a critical element for defining the petroleum system of the Pennsylvanian carbonate reservoirs of the paradox Basin, SE Utah, *in* Houston, W.S., Wray, L.L., and Moreland, P.G., editors, The Paradox Basin revisited—new developments in petroleum systems and basin analysis: Rocky Mountain Association of Geologists, Special Publication, p. 95-130.

Henrikson, A., and Chapman, D.S., 2002, Terrestrial heat flow in Utah: University of Utah, 47 p.

Herman, G., and Sharp, S.L., 1956, Pennsylvanian and Permain stratigraphy of the Paradox salt embayment, *in* Peterson, J.A., editor, Geology and economic deposits of east central Utah: Intermountain Association of Petroleum Geologists Seventh Annual Field Conference, p. 77-86.

Hintze, L.F., and Kowallis, B.J., 2009, Geologic history of Utah: Brigham Young University Geology Studies Special Publication 9, 225 p.

Hite, R.J., 1960, Stratigraphy of the saline facies of the Paradox Member of the Hermosa Formation of southeastern Utah and southwestern Colorado, *in* Smith, K.G., editor, Geology of the Paradox Basin fold and fault belt: Four Corners Geological Society Guidebook, Third Annual Conference, p. 86-89.

Hite, R.J., Anders, D.E., and Ging, T.G., 1984, Organic-rich source rocks of Pennsylvanian age in the Paradox Basin of Utah and Colorado, *in* Woodward, J., Meissner, F.F., and Clayton, J.L., eds., Hydrocarbon source rocks of the greater Rocky Mountain region: Rocky Mountain Association of Geologist, p. 255-274.

Hite, R.J., and Cater, F.W., 1972, Pennsylvanian rocks and salt anticlines, Paradox Basin, Utah and Colorado, *in* Mallory, W.W., editor, Geologic atlas of the Rocky Mountain region: Rocky Mountain Association of Geologist, p. 133-138.

Hite, R.J., and Buckner, D.H., 1981, Stratigraphic correlations, facies concepts and cyclicity in Pennsylvanian rocks of the Paradox Basin, *in* Wiegand, D.L., editor, Geology of the Paradox Basin: Rocky Mountain Association of Geologists Field Conference, p. 147-159.

Horsfield, B., and Rullkotter, J., 1994, Diagenesis, catagenesis, and metagenesis of organic matter, *in* Magoon, L.B., and Dow, W.G., editors, The petroleum system—from source to trap, Chapter 10—part III, Processes: American Association of Petroleum Geologists Special Volume, p. 189-199.

Houston, W.S., Wray, L.L., and Moreland, P.G., editors, 2009, The Paradox Basin revisited—new developments in petroleum systems and basin analysis: Rocky Mountain Association of Geologists Special Publication, 852 p.

Jarvie, D.M., 2012, Shale resource systems for oil and gas—part 2—shale-oil resource systems: *in* Breyer, J.A., editor, Shale reservoirs—giant resources for the 21st century: American Association of Petroleum Geologists Memoir 97, p. 89-119.

Kelly, V.C., 1958, Tectonics of the region of the Paradox Basin, *in* Sanborn, A.F., editor, Guidebook to the geology of the Paradox Basin: Intermountain Association of Petroleum Geologists, Ninth Annual Field Conference, p. 31-38.

Kluth, C.F., and Coney, P.J., 1981, Plate tectonics of the Ancestral Rocky Mountains: Geology, v. 9, p. 10-15.

Kluth, C.F., and DuChene, H.R., 2009, Late Pennsylvanian and Early Permian structural geology and tectonic history of the Paradox Basin and Uncompahgre Uplift, Colorado and Utah, *in* Houston, W.S., and Wray, L.L., and Mooreland, P.G., editors, The Paradox Basin revisited—New developments in petroleum systems and basin analysis: Rocky Mountain Association of Geologists Special Publication—The Paradox Basin, p. 178-197.

Mallory, W.W., 1972, Pennsylvanian System—regional synthesis, *in* Mallory, W.W., editor, Geologic atlas of the Rocky Mountain region: Rocky Mountain Association of Geologists, p. 111-128.

Massoth, T.W., 2012, Well database and maps of salt cycles and potash zones of the paradox Basin, Utah: Utah Geological Survey Open-File Report 600, 13 p.

McCarthy, K., Rojas, K., Niemann, M., Palmowhi, D., Peters, K., and Stankiewicz, A., 2011, Basic petroleum geochemistry for source rock evaluation: Schlumberger Oilfield Review, v. 23, p. 32-43.

McLennan, J., in progress, Study of the geomechanics of the Cane Creek reservoir.

Mitchum, R.M., Jr., and Van Wagoner, J.C., 1990, High-frequency sequences and eustatic cycles in the Gulf of Mexico basin: Proceedings Gulf Coast Section SEPM 11th Annual Research Conference, p. 257-267.

Montgomery, S., 1992, Paradox Basin—Cane Creek play, *in* Cheney, T., Cain, D., editors, Petroleum Frontiers: Petroleum Information Corporation, 66 p.

Moore, J., 2015, A fluid inclusion investigation of selected samples from the Cane Creek oil field, Utah: Utah Geological Survey contract report, 18 p.

Morgan, C.D., 1992a, Horizontal drilling potential of the Cane Creek shale, Paradox Formation, Utah, *in* Schmoker, J.W., Coalson, E.B., and Brown, C.A., editors, Geological studies relevant to horizontal drilling in western North America: Rocky Mountain Association of Geologists Guidebook, p. 257-265.

Morgan, C.D., 1992b, Cane Creek exploration play area Emery, Grand, and San Juan Counties, Utah: Utah Geological Survey Open-File Report 232, 5 p., 9 pl., scale 1:500,000.

Morgan, C.D., 1994, Exploring for new oil in old fields, Salt Wash field—a case study: Utah Geological Survey Open-File Report 307, 128 p.

Morgan, C.D., Carney, S.M., Nielsen, P.J., Vanden Berg, M.D., Wood, R.E., 2014, Play analysis of the Cane Creek shale, Pennsylvanian Paradox Formation, Paradox Basin, southeast Utah: American Association of Petroleum Geologist Rocky Mountain Section program with abstracts, Poster available at: http://geology.utah.gov/resources/energy/oil-gas/shale-oil/ accessed August 2015.

Morgan, C.D., Yonkee, W.A., and Tripp, B.T., 1991, Geological considerations for oil and gas drilling on State Potash leases at Cane Creek Anticline, Grand and San Juan Counties, Utah: Utah Geological Survey Circular 84, 24 p.

Nuccio, V.F., and Condon, S.M., 1996, Burial and thermal history of the Paradox Basin, Utah and Colorado, and petroleum potential of the Middle Pennsylvanian Paradox Formation: U. S. Geological Survey Bulletin 2000-O, 41 p.

Osborne, M.J., and Swarbrick, R.E., 1997, Mechanisms for generating overpressure in sedimentary basins—a reevaluation: American Association of Petroleum Geologists Bulletin, v. 81, no. 6, p. 1023-1041.

Peach, C.J., and Spiers, C.J., 1996, Influence of crystal plastic deformation on dilatancy and permeability development in synthetic salt rock: Tectonophysics, v. 256, p. 101-128.

Peterson, J.A., and Hite, R.J., 1969, Pennsylvanian evaporite-carbonate cycles and their relation to petroleum occurrence, southern Rocky Mountains: American Association of Petroleum Geologists Bulletin, v. 53, p. 884-908.

Popp, T., Kern, H., and Schulze, O., 2001, Evolution of dilatancy and permeability in rock salt during hydrostatic compaction and triaxial deformation: Journal of Geophysical Research, v. 106, p. 4061-4078.

Preston, D., 1961, Big Flat field, *in* Preston, D., editor, Oil and Gas Fields of Utah—A Symposium: Utah Geological Association Guidebook, unpagenated.

Quigley, W.D. 1983, Lion Mesa *in* Fassett, J.E., editor, Oil and gas fields of the Four Corners area: Four Corners Geological Society, v. 2, p. 1089-1091.

Rasmussen, D.L., 2014, Namakiers in Triassic and Permian formations in the Paradox Basin (USA) with comparisons to modern examples in the Zagros Fold Belt, Iran, *in* MacLean, J.S., Biek, R.F., and Huntoon, J.E., editors, Geology of Utah's far south: Utah Geological Association Publication 43, p. 689-756.

Rasmussen, L., and Rasmussen, D.L., 2009, Burial history analysis of the Pennsylvanian petroleum system in the deep Paradox fold and fault belt, Colorado and Utah, *in* Houston, W.S., Wray, L.L., and Moreland, P.G., editors, The Paradox Basin revisited – new developments in petroleum systems and basin analysis: Rocky Mountain Association of Geologists Special Publication, p. 24-94.

Rasmussen, D.L., Rasmussen, L., Rasmussen, G.J., and Longman, M.W., 2009, Selected bibliography—Paradox Basin and Four Corners region, *in* Houston, W.S., Wray, L.L., and Moreland, P.G., editors, The Paradox Basin revisited—new developments in petroleum systems and basin analysis: Rocky Mountain Association of Geologists Special Publication, p. 780-852.

Reid, F.S., and Berghorn, C.E. 1981, Facies recognition and hydrocarbon potential of the Pennsylvanian Paradox Formation, *in* Wiegand, D.L., editor, Geology of the Paradox Basin: Rocky Mountain Association of Geologists, p. 111-117.

Schenk, C.J., 2002, Assessment of undiscovered oil and gas resources in selected Rocky Mountain provinces for the Energy Policy and Conservation Act of 2000 (EPCA 2000): U.S. Geological Survey Fact Sheet FS-149-02, 2p.

Schmidt, H., and Spencer, S., 2014, Cane Creek Unit 7-1H: Fidelity Exploration & Production CO., Unpublished geologic report in DOGM well files, 23 p.

Schoenherr, J., Urai, J.L., Kula, P.A., Littke, R., Schleder, Z., Larroque, J., Newall, M.J., Al-Abry, N., Al-Siyabi, H.A., and Rawahi, Z., 2007, Limits to the sealing capacity of rock salt—a case study of the infra-Cambrian Ara Salt from the South Oman salt basin: American Association of Petroleum Geologists, Bulletin v. 91, no. 11, p. 1541-1557.

Sluijk, D., and Nederlof, M.H., 1984, A worldwide geological experience as a systematic basis for prospect appraisal, *in* Demaison, G., and Morris, J.R., editors, Petroleum geochemistry and basin analysis: American Association of Petroleum Geologists Memoir 35, p. 15-26.

Smith, K.T., 1978a, Bartlett Flat, *in* Fassett, J.E., editor, Oil and gas fields of the Four Corners area: Four Corners Geological Society, v. 2, p. 1061-1063.

Smith, K.T., 1978b, Big Flat, *in* Fassett, J.E., editor, Oil and gas fields of the Four Corners area: Four Corners Geological Society, v. 2, p. 596-598.

Smith, K.T., 1978c, Cane Creek, *in* Fassett, J.E., editor, Oil and gas fields of the Four Corners area: Four Corners Geological Society, v. 2, p. 624-626.

Smith, K.T., 1978d, Long Canyon, *in* Fassett, J.E., editor, Oil and gas fields of the Four Corners area: Four Corners Geological Society, v. 2, p. 676-678.

Smith, K.T., 1978e, Shafer Canyon, *in* Fassett, J.E., editor, Oil and gas fields of the Four Corners area: Four Corners Geological Society, v. 2, p. 700-702.

Smouse, D., 1993, Salt Wash, *in* Hill, B.G., and Bereskin, S.R., editors, Oil and gas fields of Utah: Utah Geological Association Publication 22, unpagenated.

Stevenson, G.M., and Wray, L.L., 2014, History of petroleum exploration of Paleozoic targets in the Paradox Basin, *in* Houston, W.S., Wray, L.L., and Moreland, P.G., editors, The Paradox Basin revisited—new developments in petroleum systems and basin analysis: Rocky Mountain Association of Geologists, Special Publication, p. 1-23.

Stokes, W.L., 1986, Geology of Utah: Utah Museum of Natural History, Occassional Paper Number 6, 280 p.

Szabo, E., and Wengerd, S.A., 1975, Stratigraphy and tectogenesis of the Paradox Basin *in* Fassett, J.E., editor, Canyonlands country: Four Corners Geological Society Guidebook 8th field conference, p. 193-210.

Tissot, B.P., and Welte, D.H., 1984, Petroleum formation and occurrence—Second edition: New York, Springer-Verlag, 699 p.

Tissot, B.P., Pelet, R., and Ungerer, P.H., 1987, Thermal history of sedimentary basin, maturation indices, and kinetics of oil and gas generation: American Association of Petroleum Geologists Bulletin v. 71, p. 1445-1466.

Trudgil, B.D., 2011, Evolution of salt structures in the northern Paradox Basin—controls on evaporate deposition, salt wall growth and supra-salt stratigraphic architecture basin research: Basin Research, v. 23, p. 208-238.

Trudgil, B.D., and Arbuckle, W.C., 2009, Reservoir characterization of clastic cycle sequences in the Paradox Formation of the Hermosa Group, Paradox Basin, Utah: Utah Geological Survey Open-File Report 543, 106 p.

Utah Division of Oil, Gas and Mining (DOGM) website, http://oilgas.ogm.utah.gov/. accessed March 2017.

Wengerd, S.A., and Matheny, M.L., 1958, Pennsylvanian system of the Four Corners region: American Association of Petroleum Geologists Bulletin, v. 42, p. 2048-2106.

Whidden, K.J., Anna, L.O., Pearson, K.M., and Lillis, P.G., 2012, Assessment of undiscovered oil and gas resources in the Paradox Basin province, Utah, Colorado, New Mexico, and Arizona: U. S. Geological Survey Fact Sheet 2012-3031, 4 p.

Whidden, K.J., Lillis, P.G., Anna, L.O., Pearson, K.M., and Dubiel, R.F., 2014, Geology and total petroleum systems of the Paradox Basin, Utah, Colorado, New Mexico, and Arizona: Rocky Mountain Association of Geologists The Mountain Geologist, v. 51, no. 2, p. 119-138.

Woodward - Clyde Consultants, 1982a, Geologic characterization report of the Paradox Basin study region, Utah study areas: Report ONWI 290, prepared for the Office of Nuclear Waste Isolation, Battelle Memorial Institute, Columbus, Ohio, v. 1 regional overview and v. II Gibson Dome.

Woodward - Clyde Consultants, 1982b, Gibson Dome No. 1 Borehole, Gibson Dome study area of the Paradox Basin region, San Juan County, Utah: Report ONWI 388, prepared for the Office of Nuclear Waste Isolation, Battelle Memorial Institute, Columbus, Ohio, v. 1 thru VI.

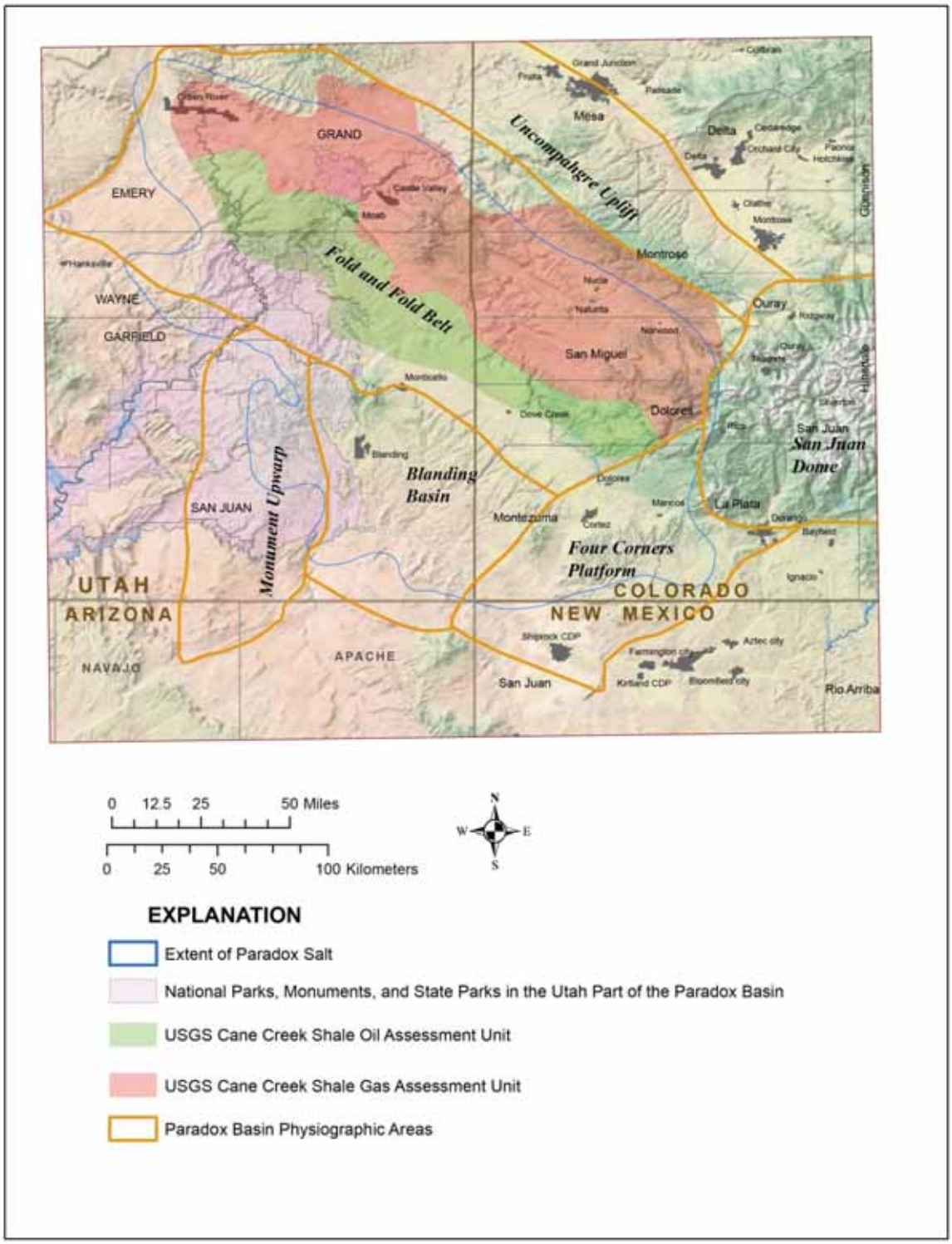

Figure 1. *Paradox Basin in the Four Corners area of Utah, Colorado, Arizona, and New Mexico. The basin is defined by the extent of the Paradox Formation salt. Physiographic areas and Cane Creek assessment units from Anna and others (2014) and Whidden and others (2014). The Cane Creek play lies within the fold and fault belt of the basin.*

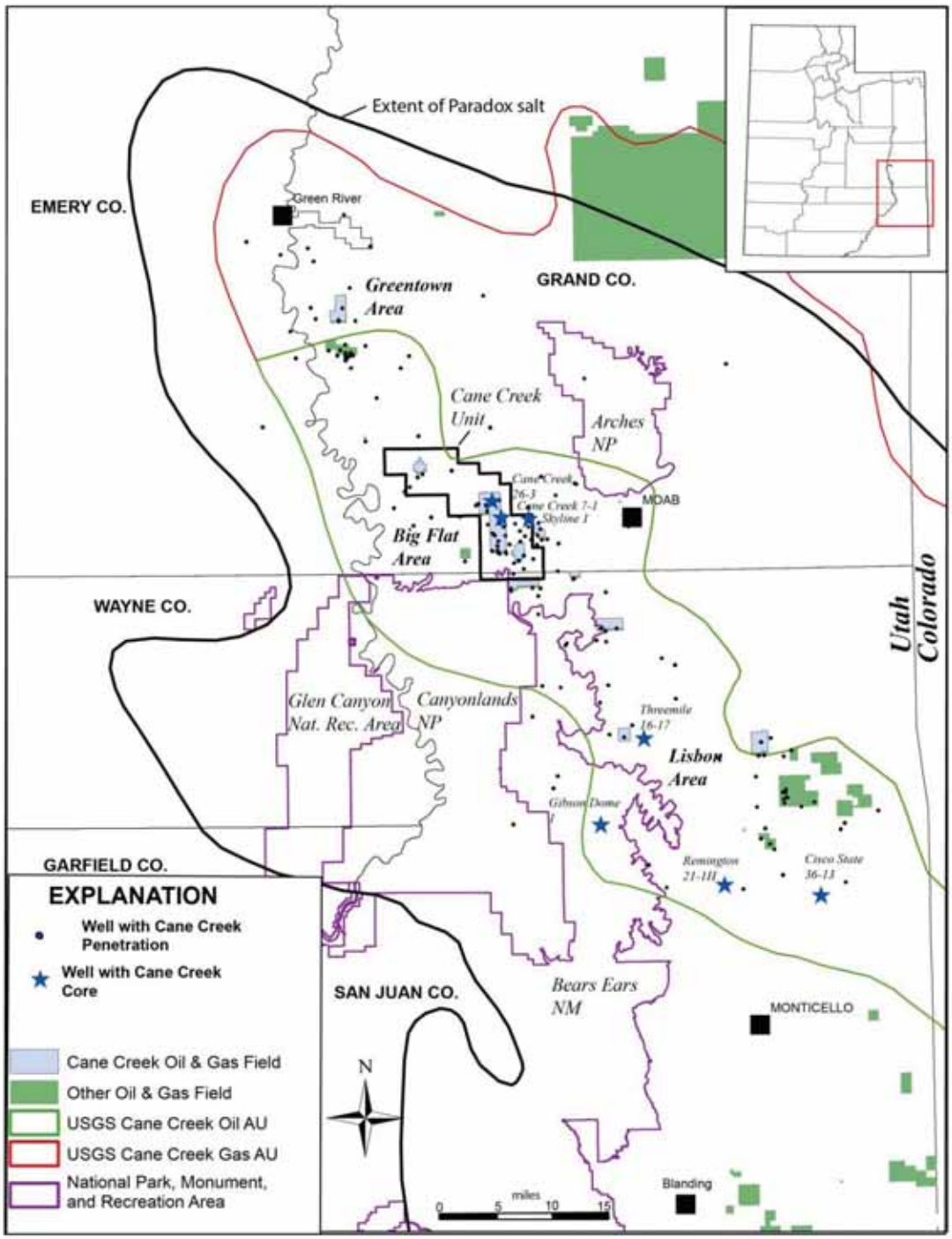

Figure 2. *Utah part of the Paradox Basin defined by the extent of the Paradox Formation salt. The Cane Creek play defined by the U.S. Geological Survey oil and gas assessment units (AU) from Anna and others (2014) and Widden and others (2014). They play area is further divided into informal Greentown, Big Flat, and Lisbon areas in this report. NP is National Park, NM is National Monument, and Nat Rec is National Recreation.*

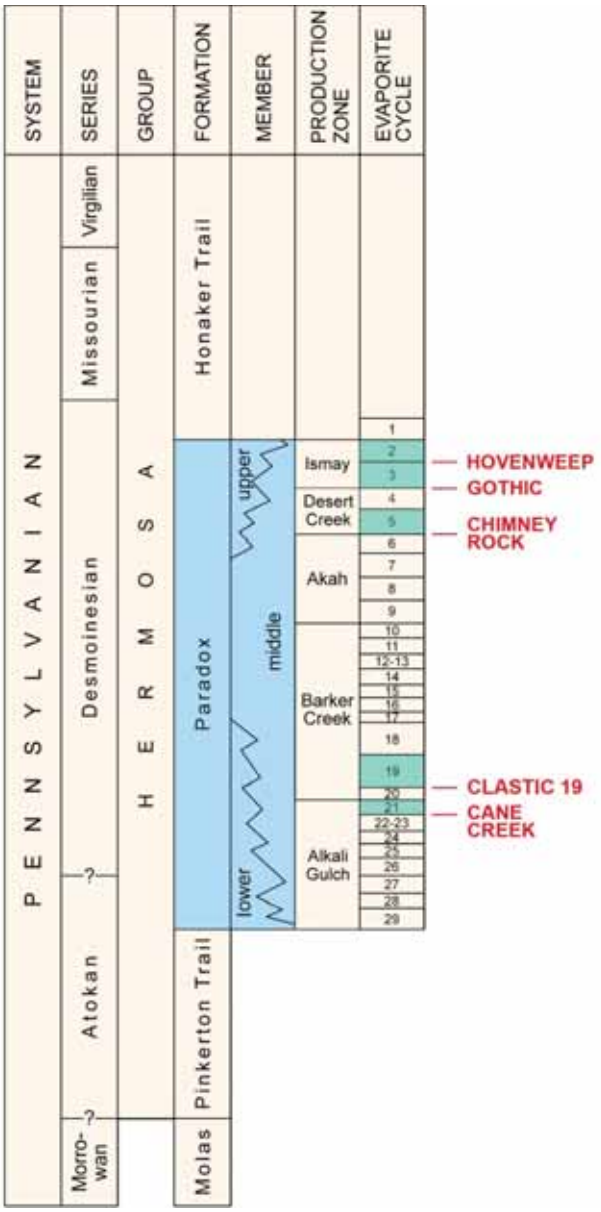

Figure 3. *Pennsylvanian nomenclature for the Paradox Basin based on Hite, 1960. The Hermosa Group consists of shallow marine carbonate and sandstone deposits of the Pinkerton Trail and Honaker Trail Formations which underlie and overlie the Paradox Formation. The Paradox is divided into oil field production zones and further divided into evaporite cycles numbered from top to bottom. The Cane Creek shale is part of cycle 21. Other organic-rich deposits with potential for oil and gas production are clastic 19 (cycle 19), Chimney Rock Shale (cycle 5), Gothic Shale (cycle 3) and Hovenweep Shale (cycle 2).*

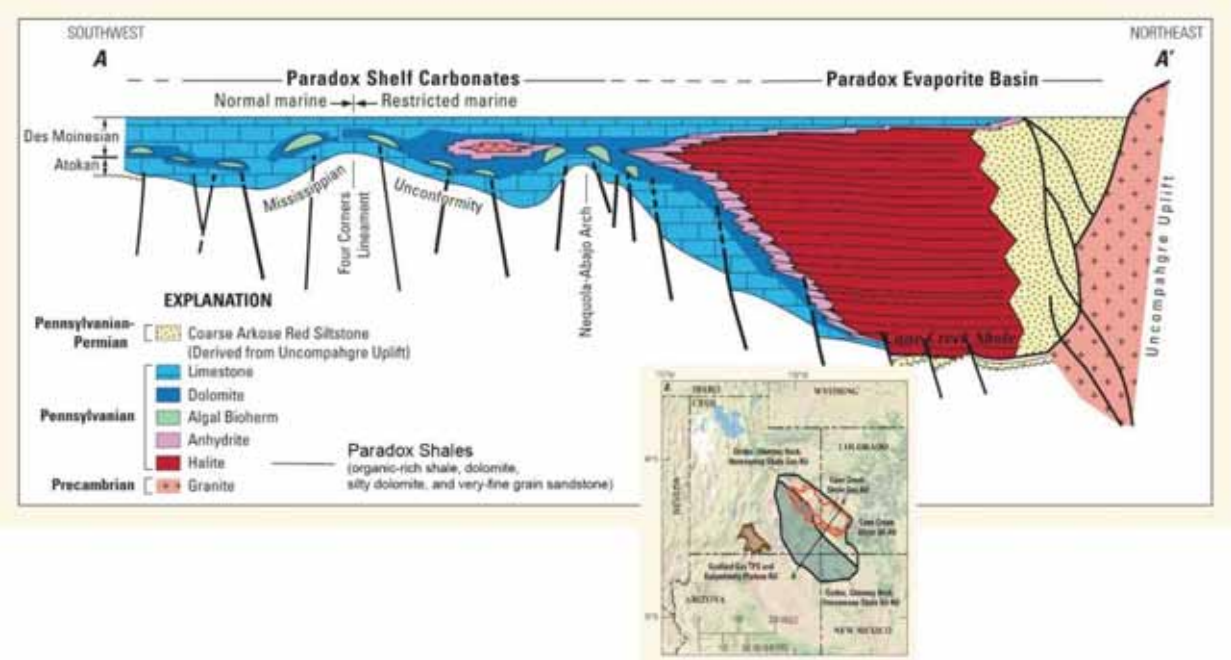

Figure 4. *Southwest to northeast cross section of the Paradox Basin. The evaporative basin consists of a series of depositional cycles of shale and salt. The Cane Creek shale is the lower most faulted cycle in this diagram. Modified from Whidden and others (2014).*

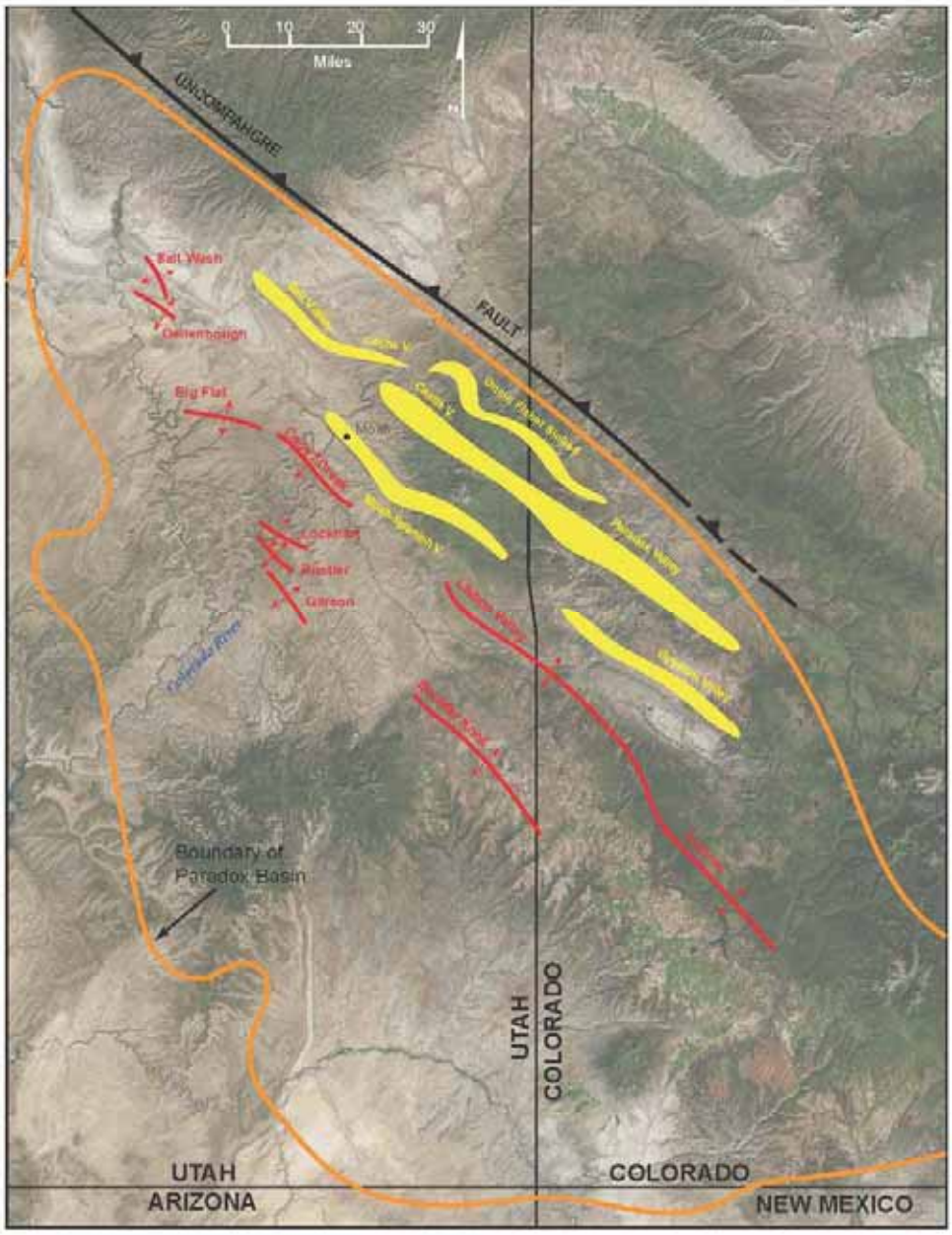

Figure 5. *Map of Paradox Basin showing the principal structures. Salt valley anticlines, shown in yellow, are a result of diapiric salt movement in the Paradox Formation. Other anticlines (red) are the result of salt movement that did not penetrate the formations overlying the Paradox. Modified from Doelling and others (1988).*

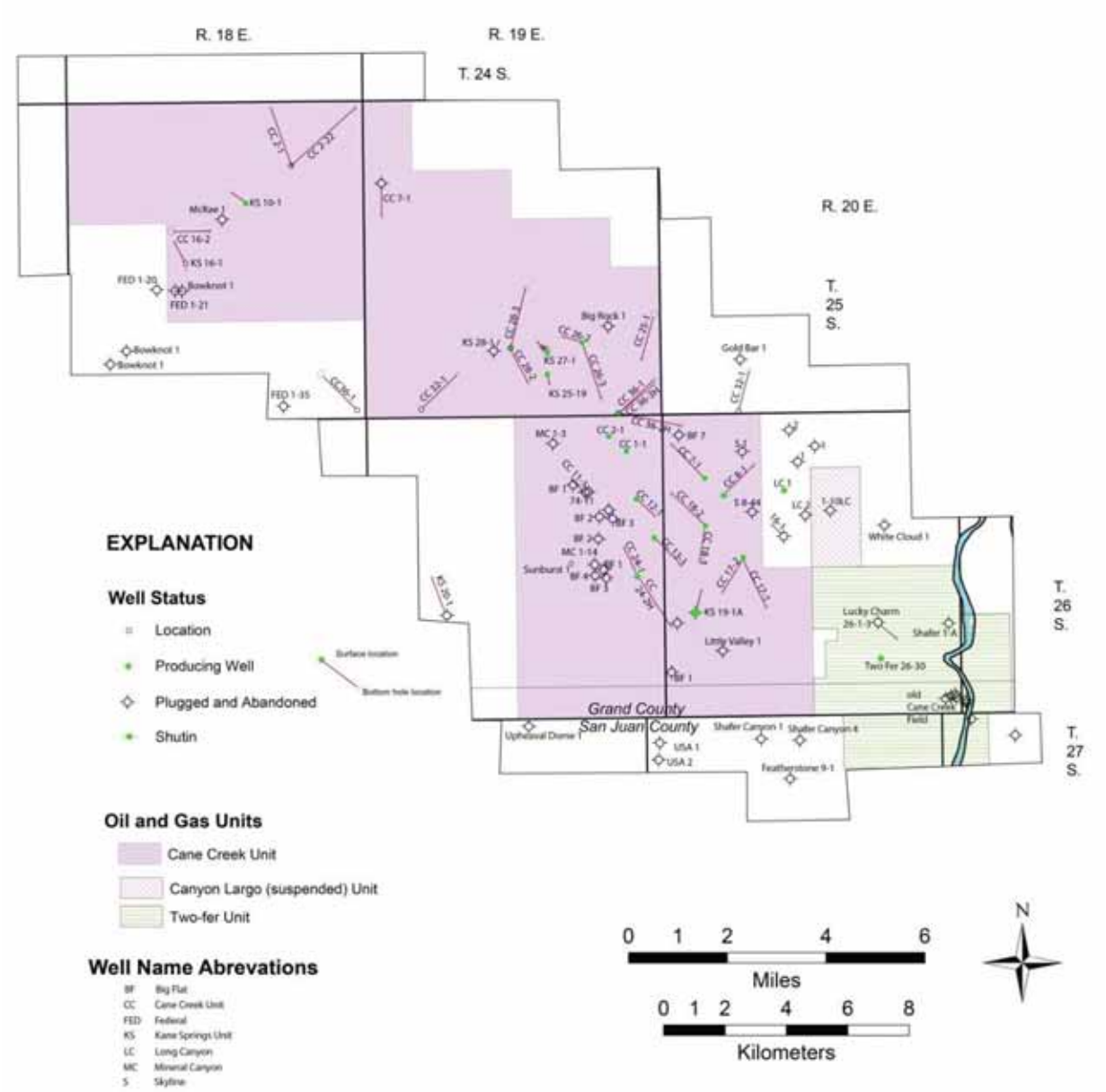

Figure 6. *Cane Creek federal unit and neighboring units. Columbia Gas and Development originally formed the Kane Springs unit and drilled the first horizontal Cane Creek well, the KS 27-1. Fidelity Exploration and Production Company purchased the unit and established a new unit named Cane Creek covering the same acreage.*

Figure 7. *Paleogeography during the Mississippian Period (340Ma) interpreted by Blakey and Ranney (2008). The Colorado Plateau including the Paradox Basin was dominated by shallow marine carbonate deposition with deeper open-marine deposition to the west. Modified from Blakey and Ranney (2008).*

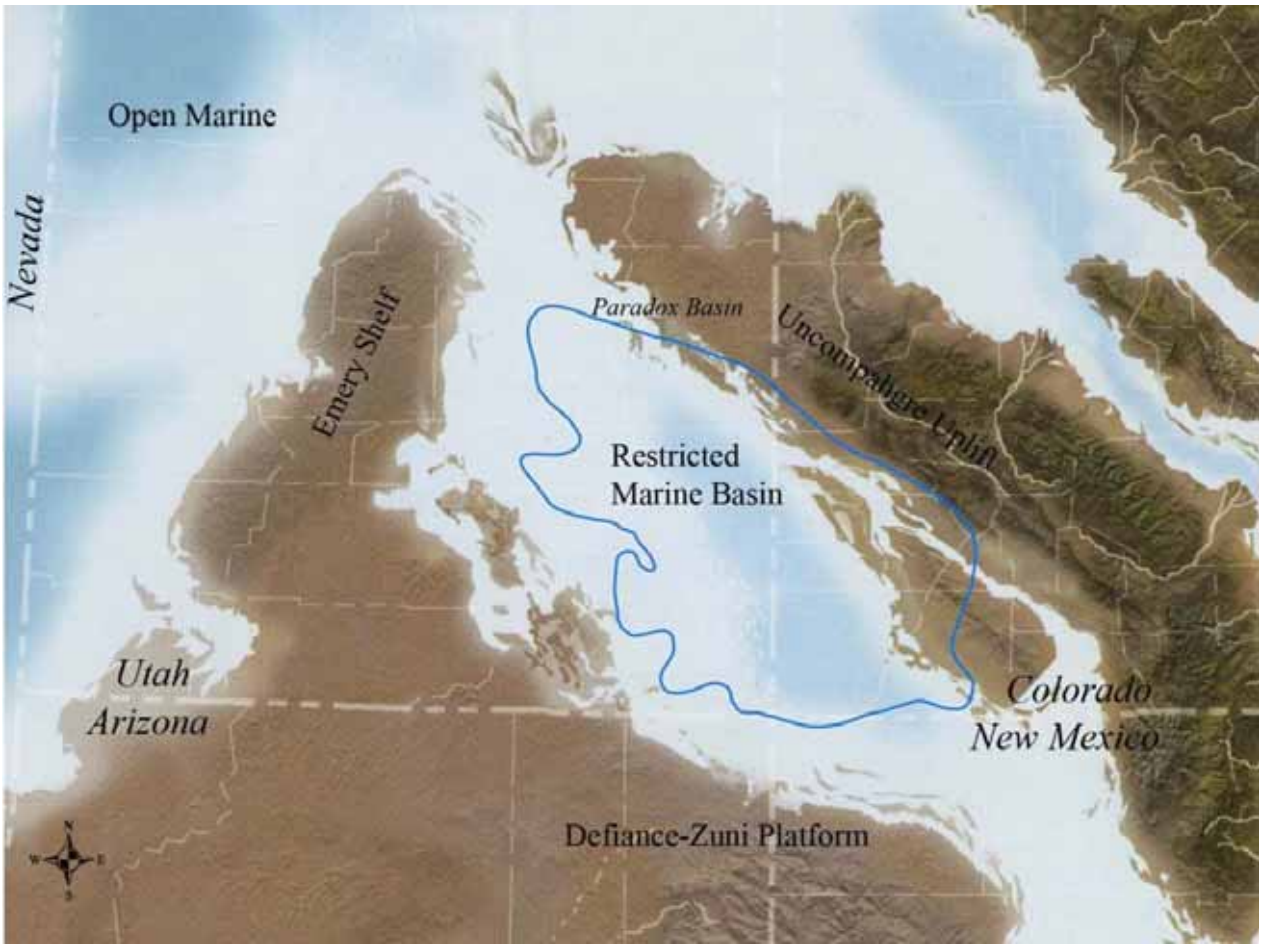

Figure 8. *Paleogeography of the Colorado Plateau and Paradox Basin (outlined in blue) during the Middle Pennsylvanian (308 Ma) illustrating a highstand depositional cycle. The basin formed as a pull-apart basin along a series of northwest-trending faults forming an asymmetrical basin bounding the Uncompahgre uplift, part of the ancestral Rocky Mountains. The basin was bounded to the south by the Defiance-Zuni platform and the Emery shelf to the west. Modified from Blakey and Ranney (2008).*

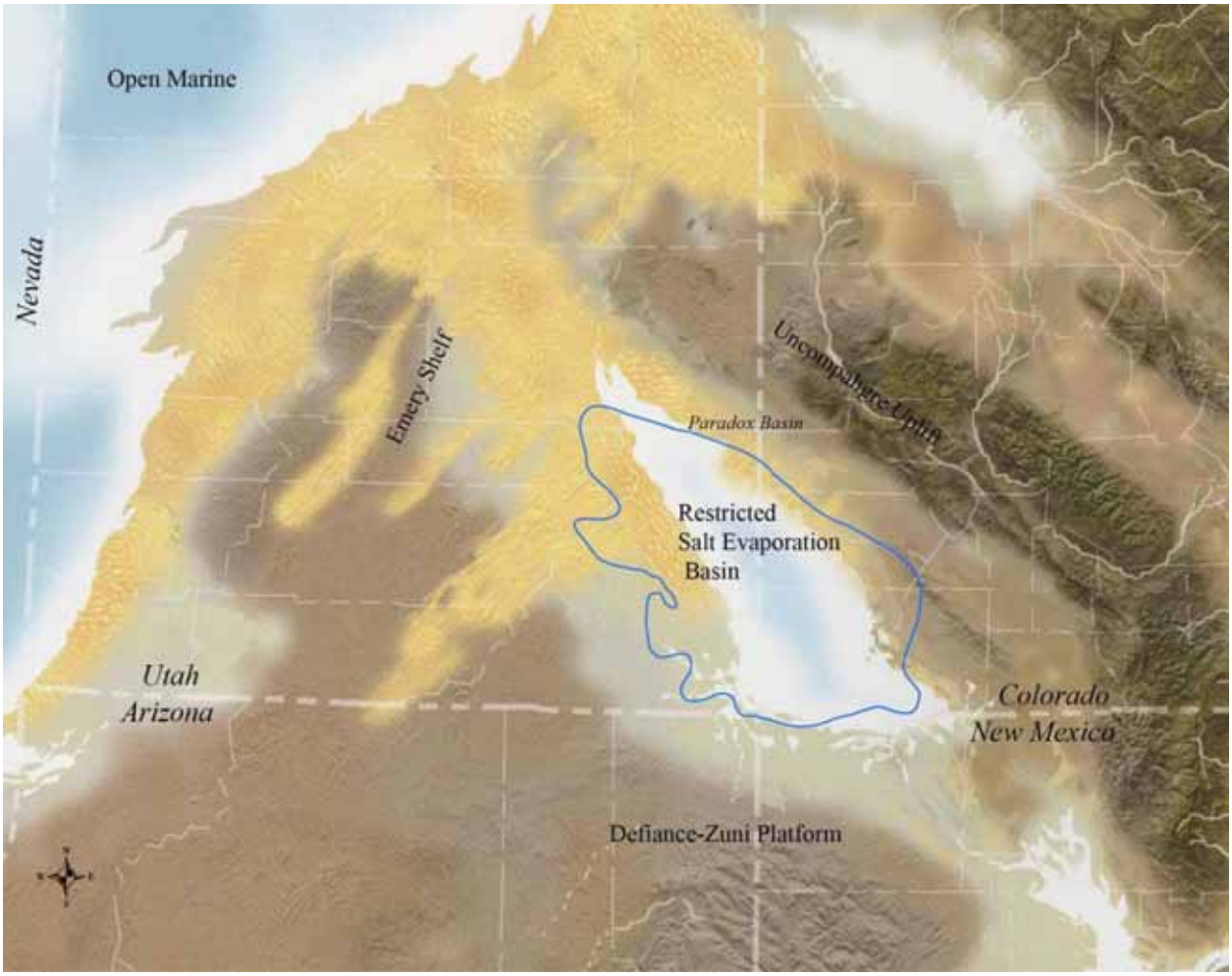

Figure 9. *Paleogeography of the Colorado Plateau and Paradox Basin (outlined in blue) during the Middle Pennsylvanian (308 Ma) illustrating a lowstand depositional cycle. Dominant deposition during lowstand was evaporites, anhydrite and halite. The basin formed as a pull-apart basin along a series of northwest-trending faults forming an asymmetrical basin bounding the Uncompahgre uplift, part of the ancestral Rocky Mountains. The basin was bounded to the south by the Defiance-Zuni platform and the Emery shelf to the west. Modified from Blakey and Ranney (2008).*

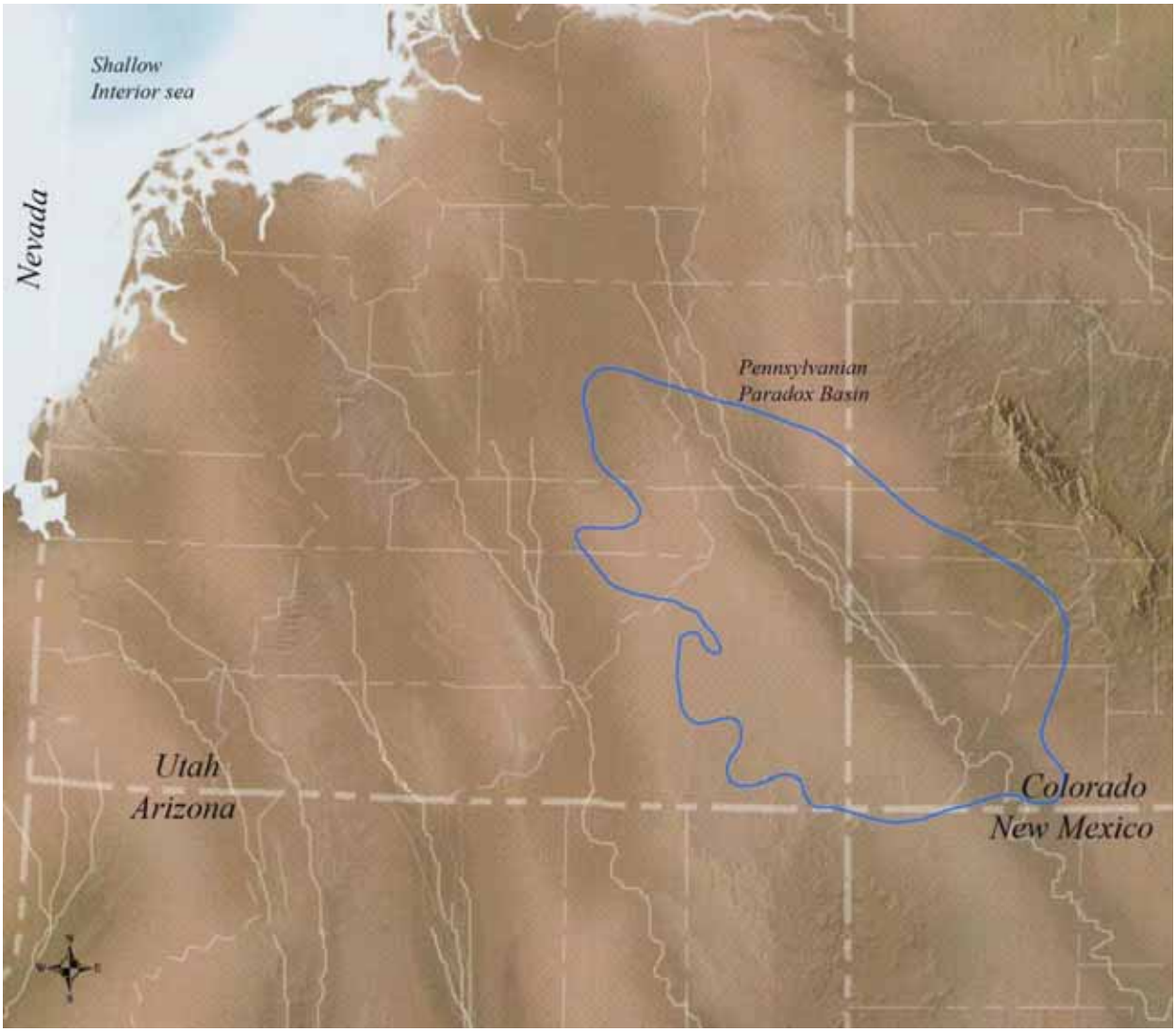

Figure 10. *Paleaogeography of the Colorado Plateau and Paradox Basin (outlined in blue) during the Middle Triassic (240 Ma). The area was dominantly a low-lying arid environment with channel and floodplain deposits. The Paradox Basin is completely filled in and sediment loading during the Permian and Triassic initiated movement of salt and development of salt anticlines. Modified from Blakey and Ranney (2008).*

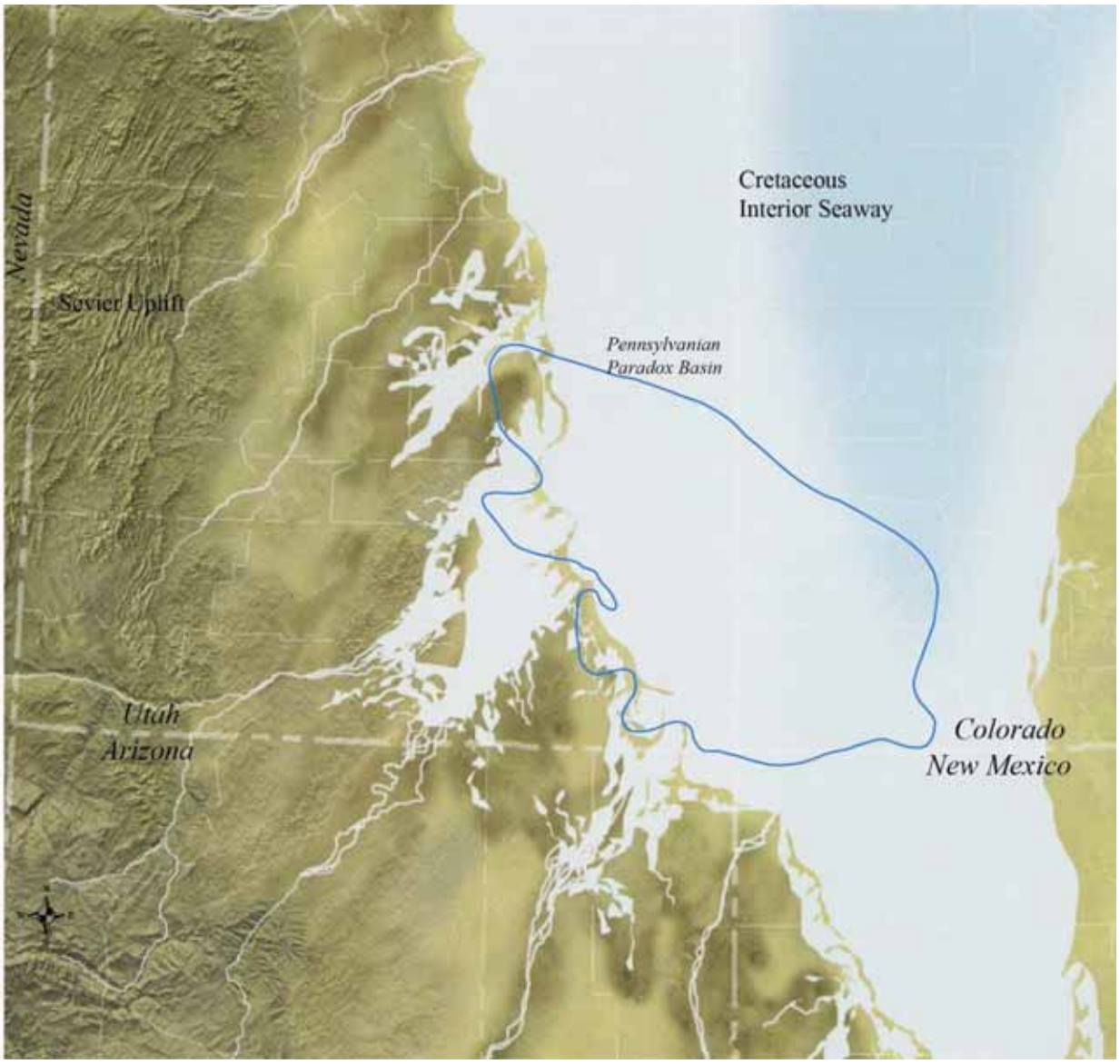

Figure 11. *Paleogeography of the Colorado Plateau and Paradox Basin (outlined in blue) during the Early Cretaceous Albian time (105 Ma). With the Sevier Orogeny to the west, the Colorado Plateau subsided and the Cretaceous Interior Seaway advanced from the north into the plateau area depositing deltas, shorelines swamps, and open-marine sediment. Much of the Cretaceous deposits were removed from the Paradox Basin during uplift of the Colorado Plateau. Modified from Blakey and Ranney (2008).*

Figure 12. *View south from Dead Horse State Park. View area and mesas in the background are formed by eolian Triassic Wingate Sandstone and typically topped by the Jurassic Navajo Sandstone. At this location, the Colorado River has incised the Early Permian Cutler Group. Photograph by Gregg Beukelman.*

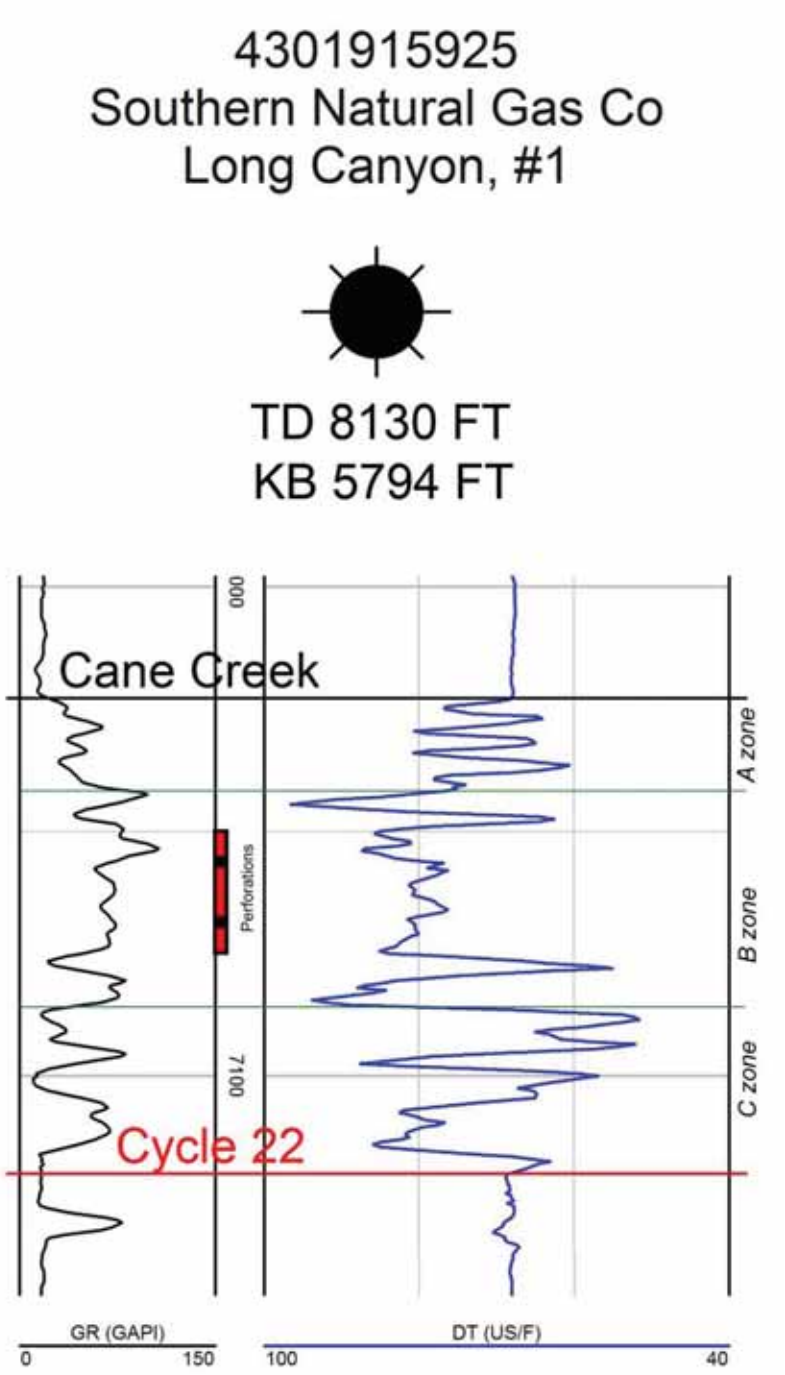

Figure 13. *Gamma ray and sonic travel time (sonic) curves through the Cane Creek shale from the Long Canyon 1 well. The Cane Creek is informally divided into A, B, and C zones. The A and C zones are transitional with the overlying and underlying salt beds and contain abundant interbedded and nodular anhydrite. The B zone is the primary productive interval in the Cane Creek containing silty dolomite and very fine-grain sandstone.*

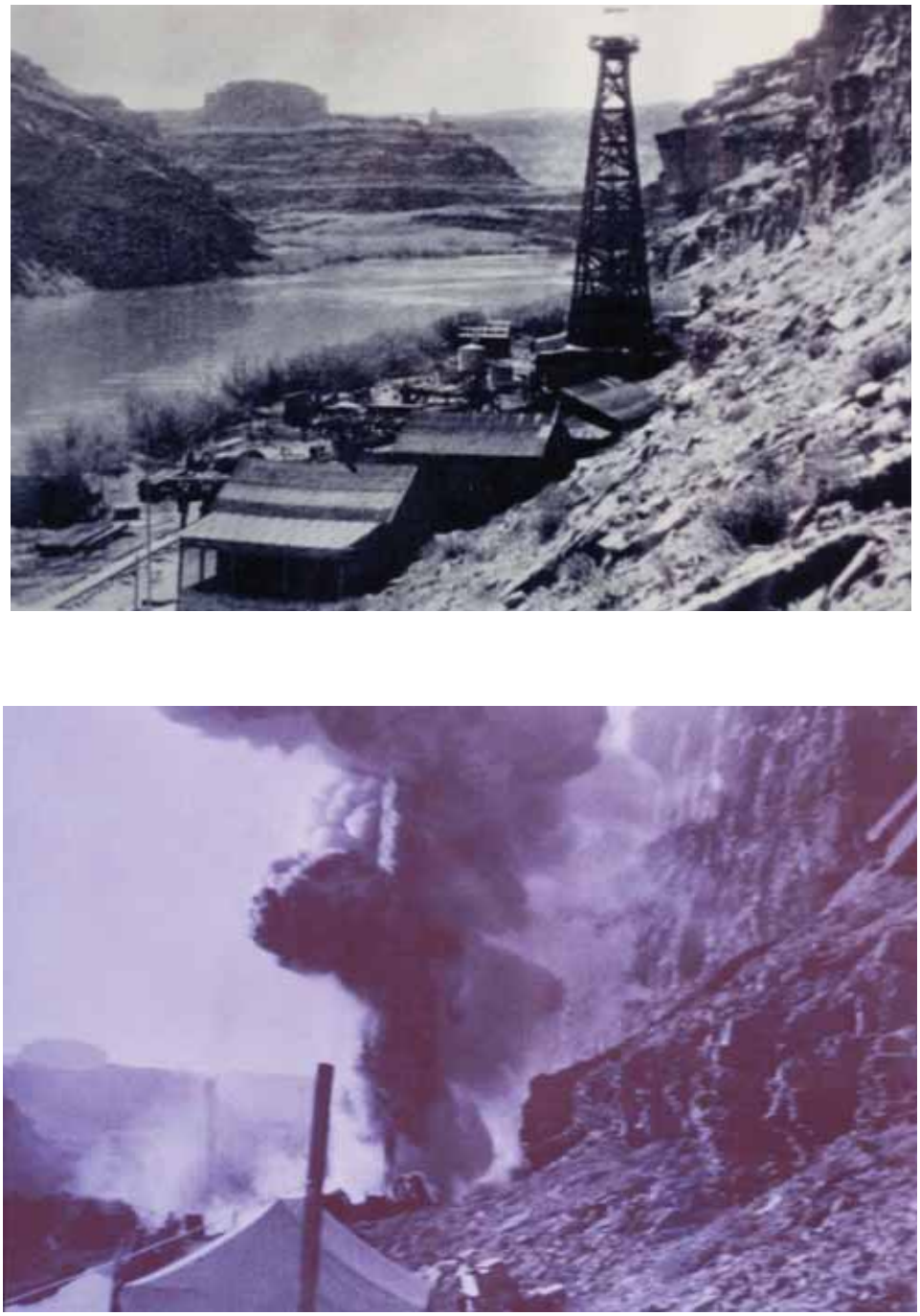

Figure 14. *Drilling on the axis of the Cane Creek anticline along the banks of the Colorado River in the 1920s. Material was floated down the river on barges and the rig and houses were constructed on site. The well blew out while drilling in the upper Paradox Formation. Photographs from the Utah Historical Society.*

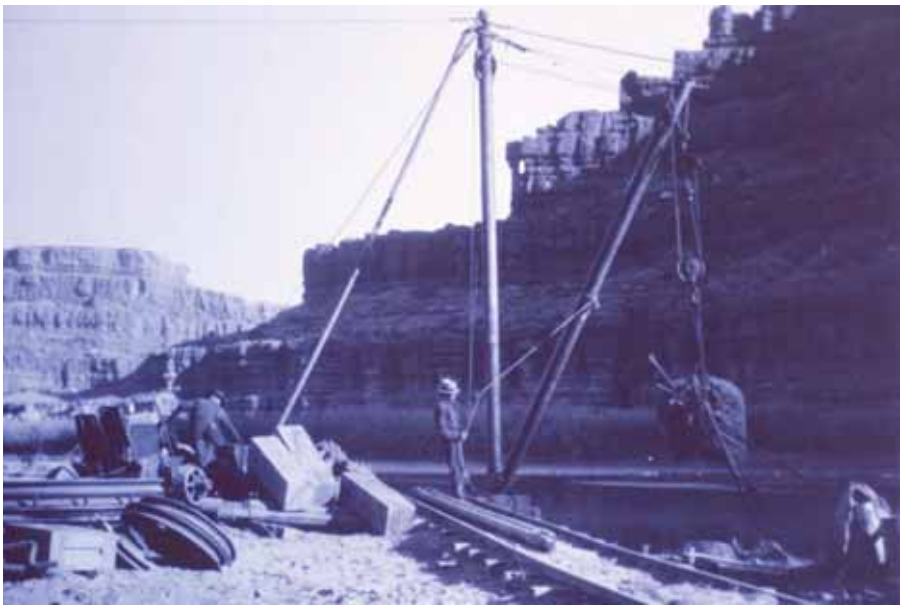

Figure 15. *Unloading material at Shafer Dome to drill for oil in the 1920s. After an unsuccessful drilling attempt at Cane Creek anticline the equipment was floated farther down the Colorado River to the Safer Dome site. Drilling resulted in a dry hole. Photographs from the Utah Historical Society.*

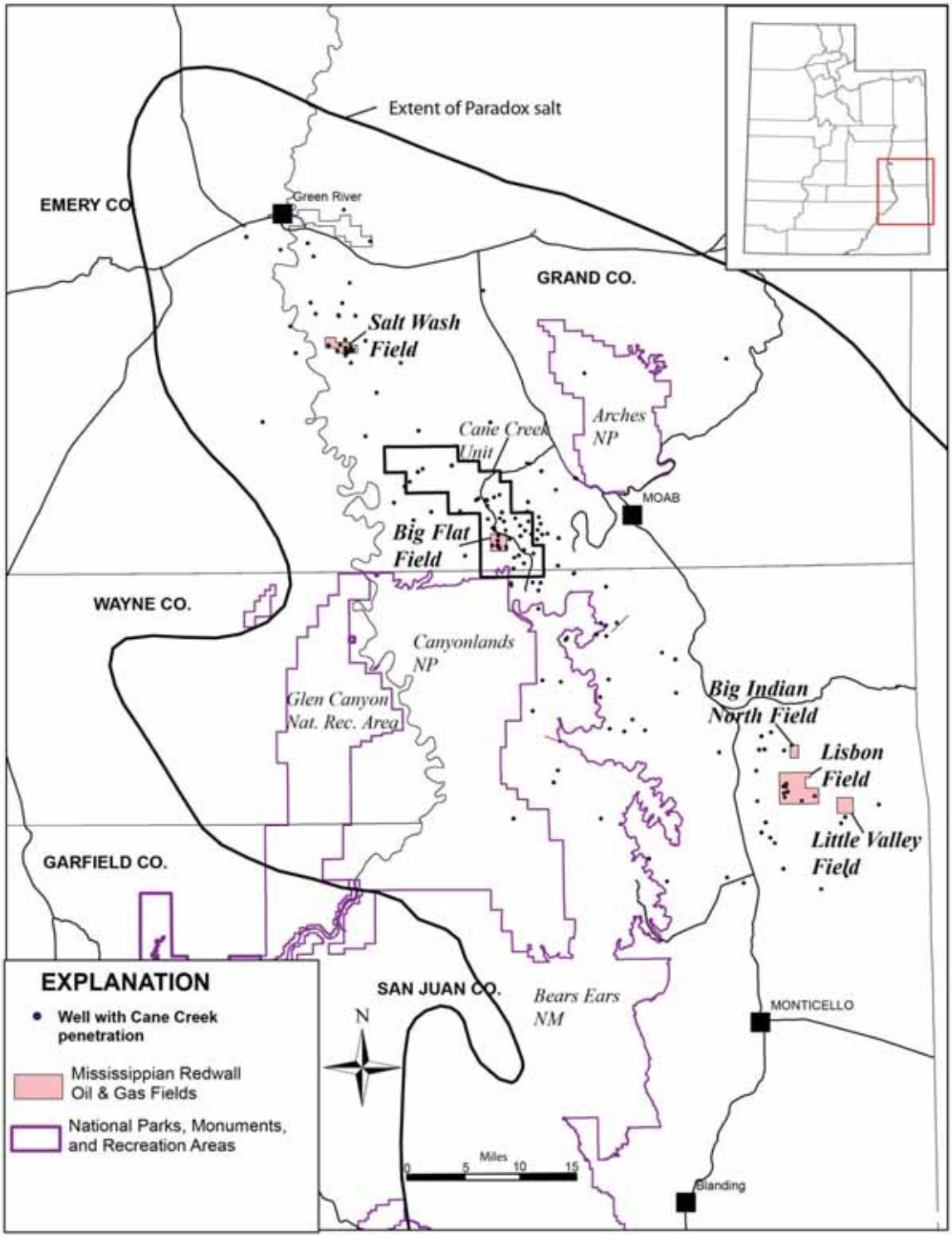

Figure 16. *Oil and gas fields in the Paradox Basin that produced from the Mississippian Redwall Formation. Wells drilling to the Redwall penetrated the Cane Creek shale which was often a secondary objective if the Redwall was unproductive. See table 4 for production details about each field. Field boundaries from Utah Division of Oil, Gas and Mining.*

Figure 17. *The Long Canyon 1 well (SENW section 9, T. 26 S., R. 20 E.) was completed in 1962 producing from the Cane Creek shale. The well has produced more than 1.1 MMBO. View is to the southeast with the La Sal Mountains in the background.*

Figure 18. *Kane Springs 1-27 well (NWSE section 27, T. 25 S., R. 19 E.) completed in 1991, was the first horizontal well in the Cane Creek shale. The direction of the horizontal lateral is towards the location of the photographer, beneath the dry hole marker in the top photograph. The well has produced more than 500 MBO.*

Figure 19. *Shafer Canyon field discovered in 1962 consisted of two wells completed in the Cane Creek shale drilled on opposite sides of Dead Horse Point. The field was abandoned in 1969 after producing more than 67 MBO. The top photograph is a view to the northwest of the Shafer Canyon unit 1 well (SENW section 4, T. 27 S., R. 20 E.) with Dead Horse Point in the background. The lower photograph is a view to the southwest of the USA 1 well (SENW section 6, T. 27 S., R. 20 E.) with the north flank of Shafer Dome in the middle ground.*

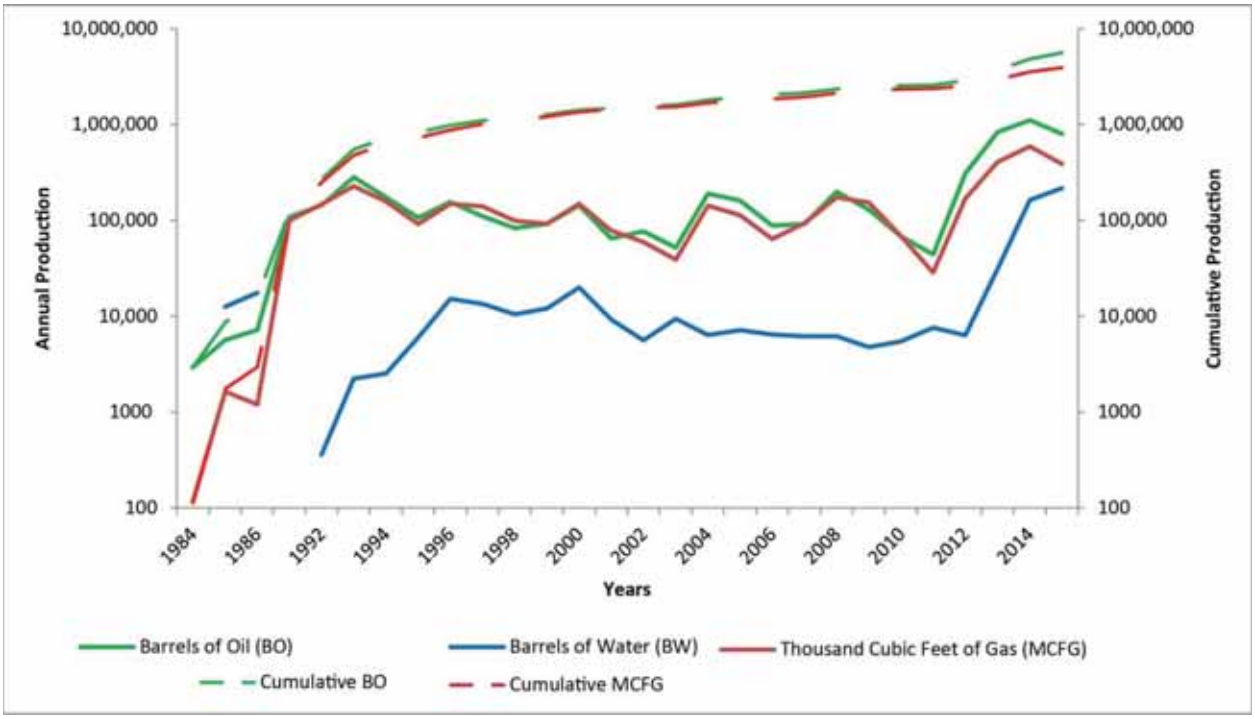

Figure 20. *Production curves from the Cane Creek unit; Big Flat and Hell Roaring fields. The unit has produced more than 5.6 MMBO and 3.9 MMCFG from 22 wells through December 2015. Data from Utah Division of Oil, Gas and Mining.*

Figure 21. *Cane Creek 28-2 and 28-3 wells (NESE section 28, T. 25 S., R. 19 E.) drilled from the same drill pad to reduce surface disturbance. The 28-2 well was drilled to the southeast and bottomed in NENW section 34. The 28-3 well was drilled to the northeast and bottomed in the NWSW section 22.*

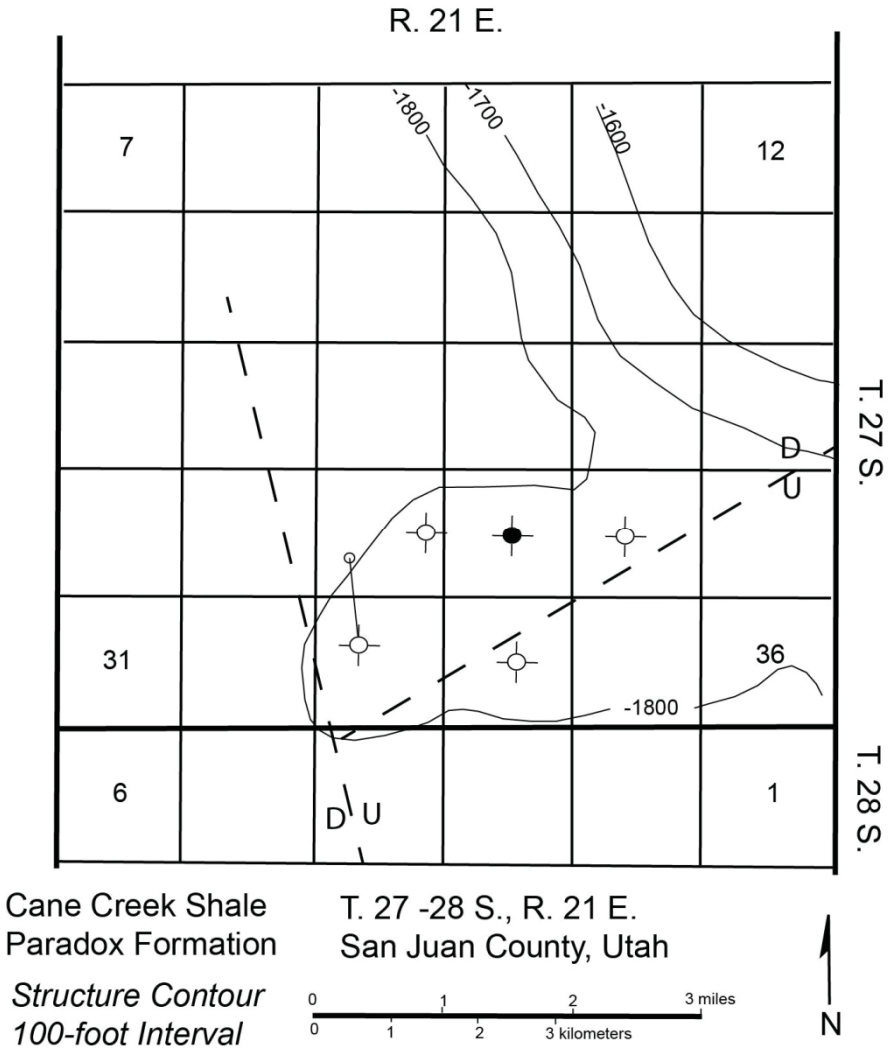

Figure 22. *Cane Creek structure at Lion Mesa field. The field was drilled based on fault closure at the Mississippian Redwall Formation horizon. Faults are from Quigley (1983) and may not extend upward to the Cane Creek horizon.*

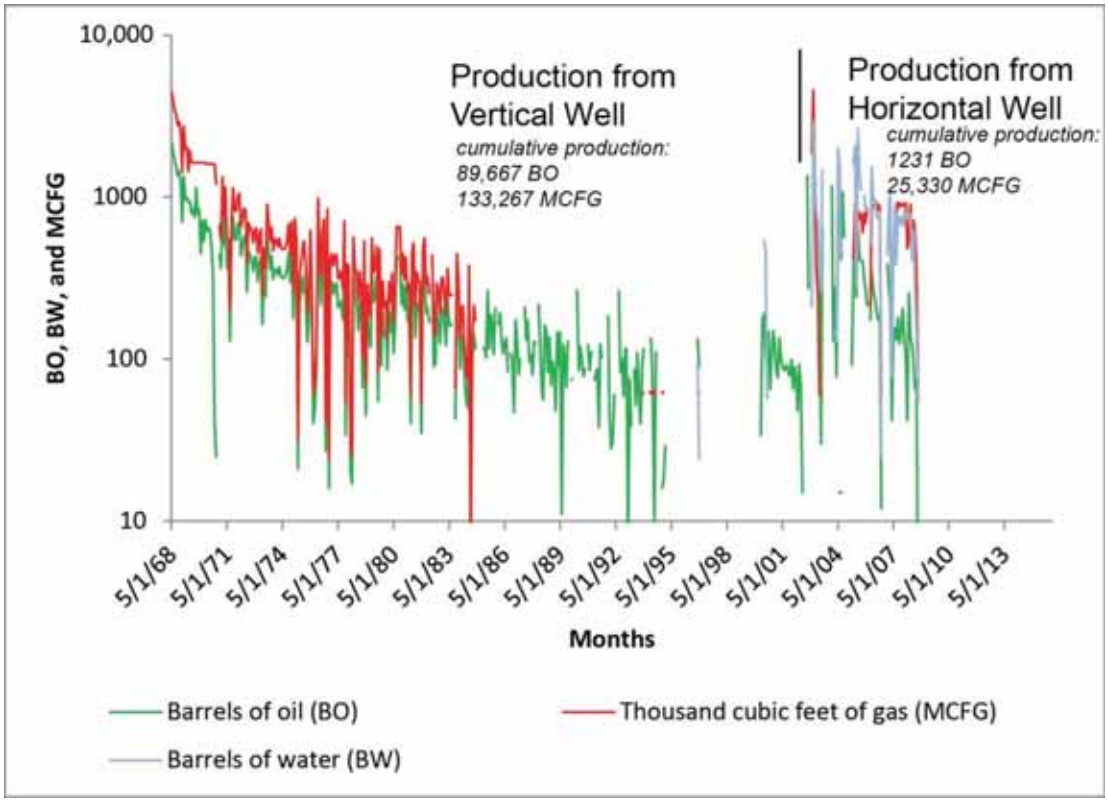

Figure 23. *Monthly production from the Chevron Federal 1 (section 24, T. 29 S., R. 23 E.). The well produced from a vertical wellbore until a horizontal lateral was drilled in the Cane Creek in 2002. The horizontal has produced a large volume of water and only a small amount of oil.*

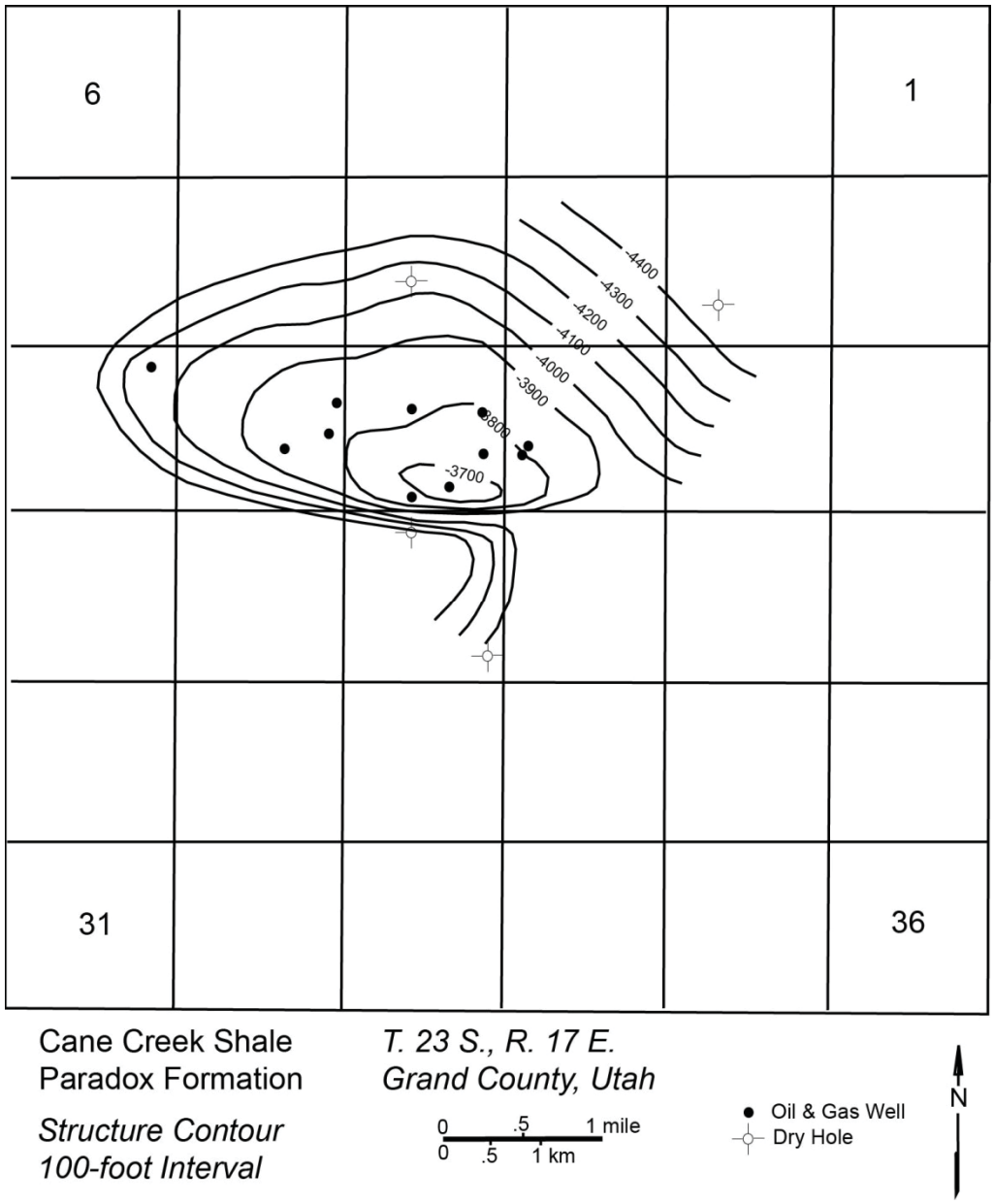

Figure 24. *Cane Creek structure at Salt Wash field. The field produces from the underlying Mississippian Redwall Formation. A horizontal Cane Creek completion has not been attempted at Salt Wash. Contour interval 100 feet mean sea-level elevation. Modified from Morgan (1994).*

Figure 25. *Greentown State 36-11 well testing perforations in the Paradox Formation clastic 19; view to the north. The well encountered high-pressure gas during production testing and had to be flared for a month to draw the pressure down before the operator could re-enter the hole and set a bridge plug above the perforations. The operator was never able to remove the bridge plug and get back to the clastic 19 perforations. Notice flare to the right of the building.*

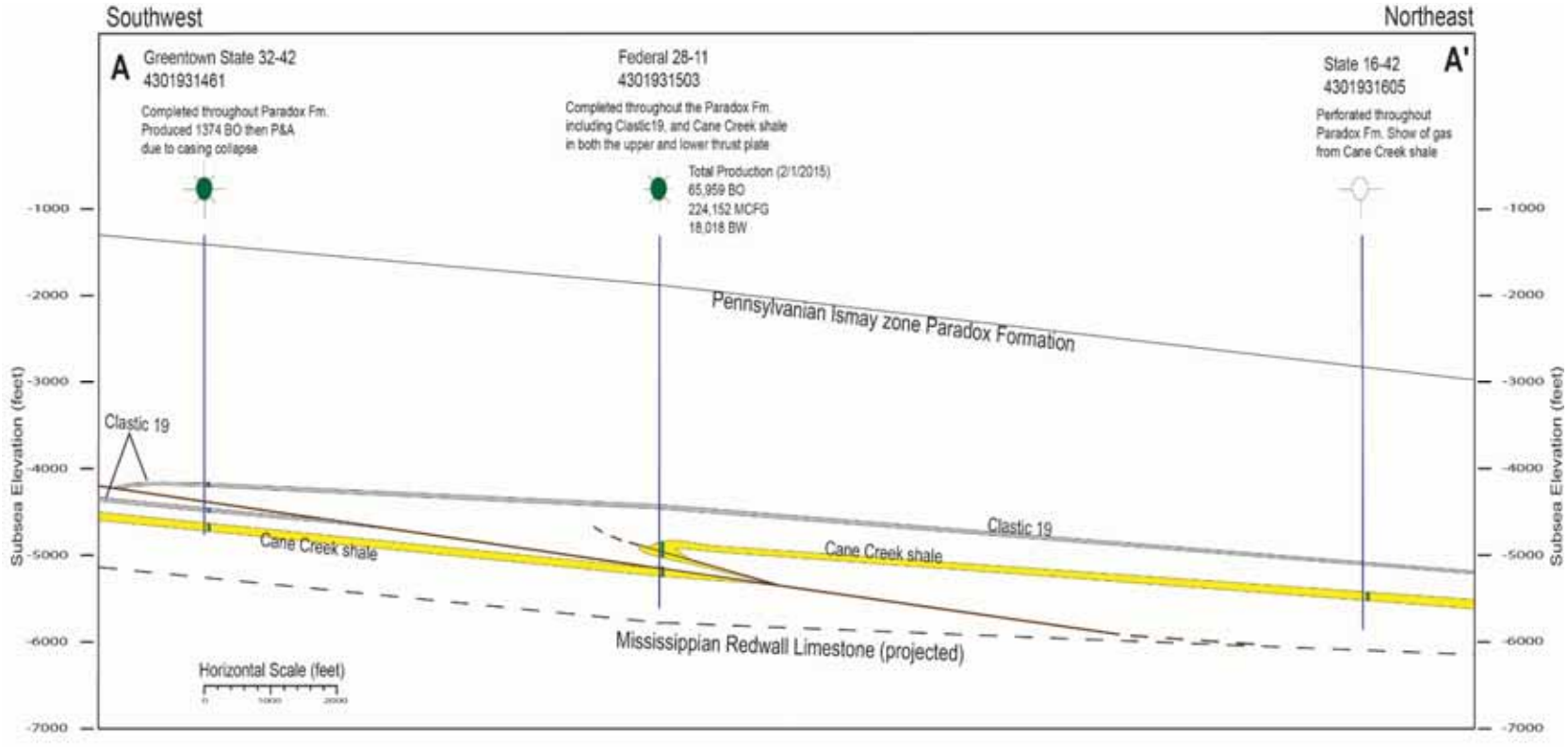

Figure 26. *Southwest to northeast cross section through the Greentown field. The State 32-42 well penetrated a repeated clastic 19 bed and the Federal 28-11 well is perforated in the Cane Creek shale, overturned Cane Creek, and a repeated Cane Creek bed. See figure 27 for location of cross section.*

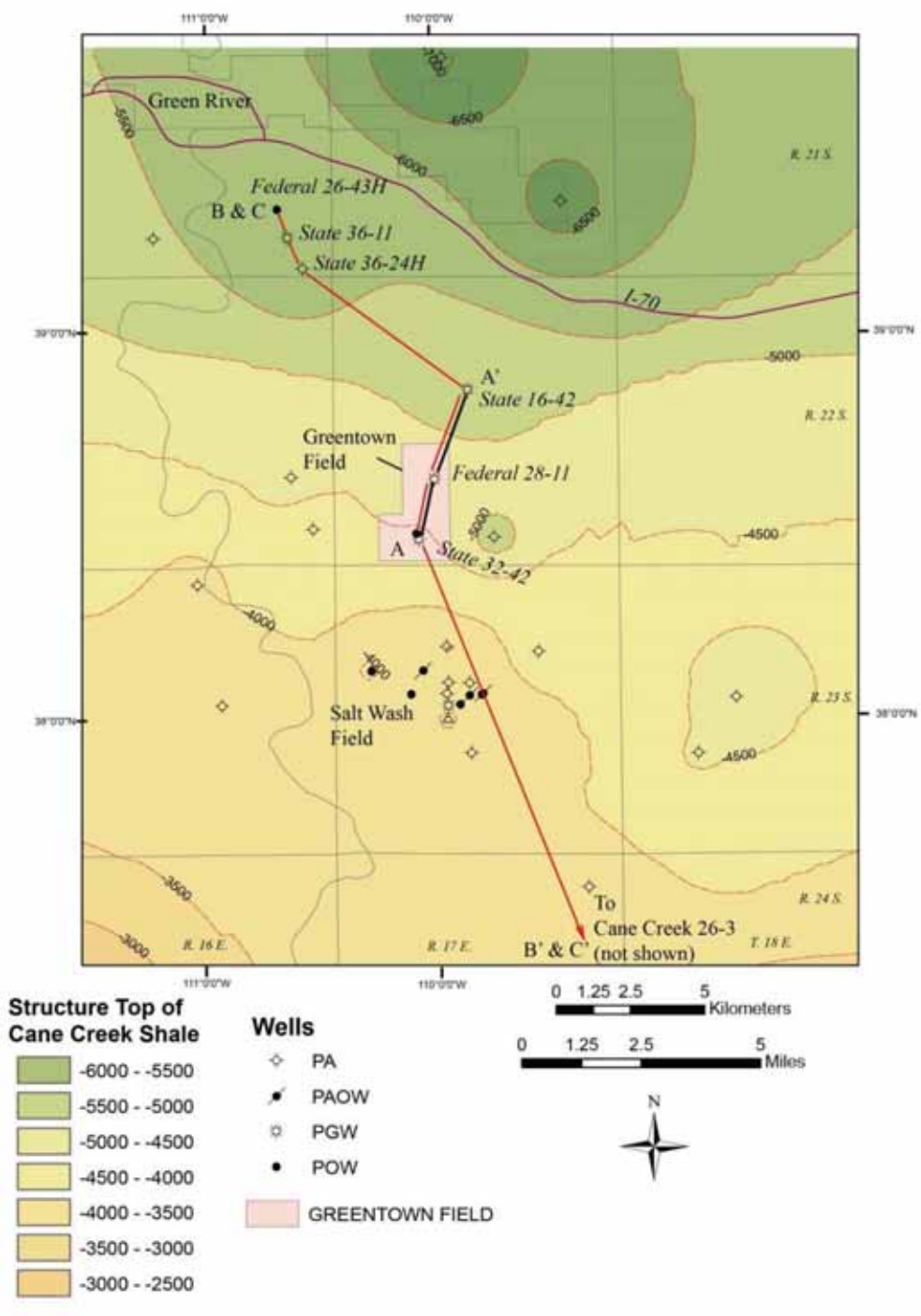

Figure 27. *Cane Creek shale structure, 500-foot contour interval, mean sea-level datum. Cross section A-A' is figure 26 structural cross section, B-B' is figure 30 clastic 19 well log cross section, and C-C' is figure 28 Cane Creek shale well log cross section.*

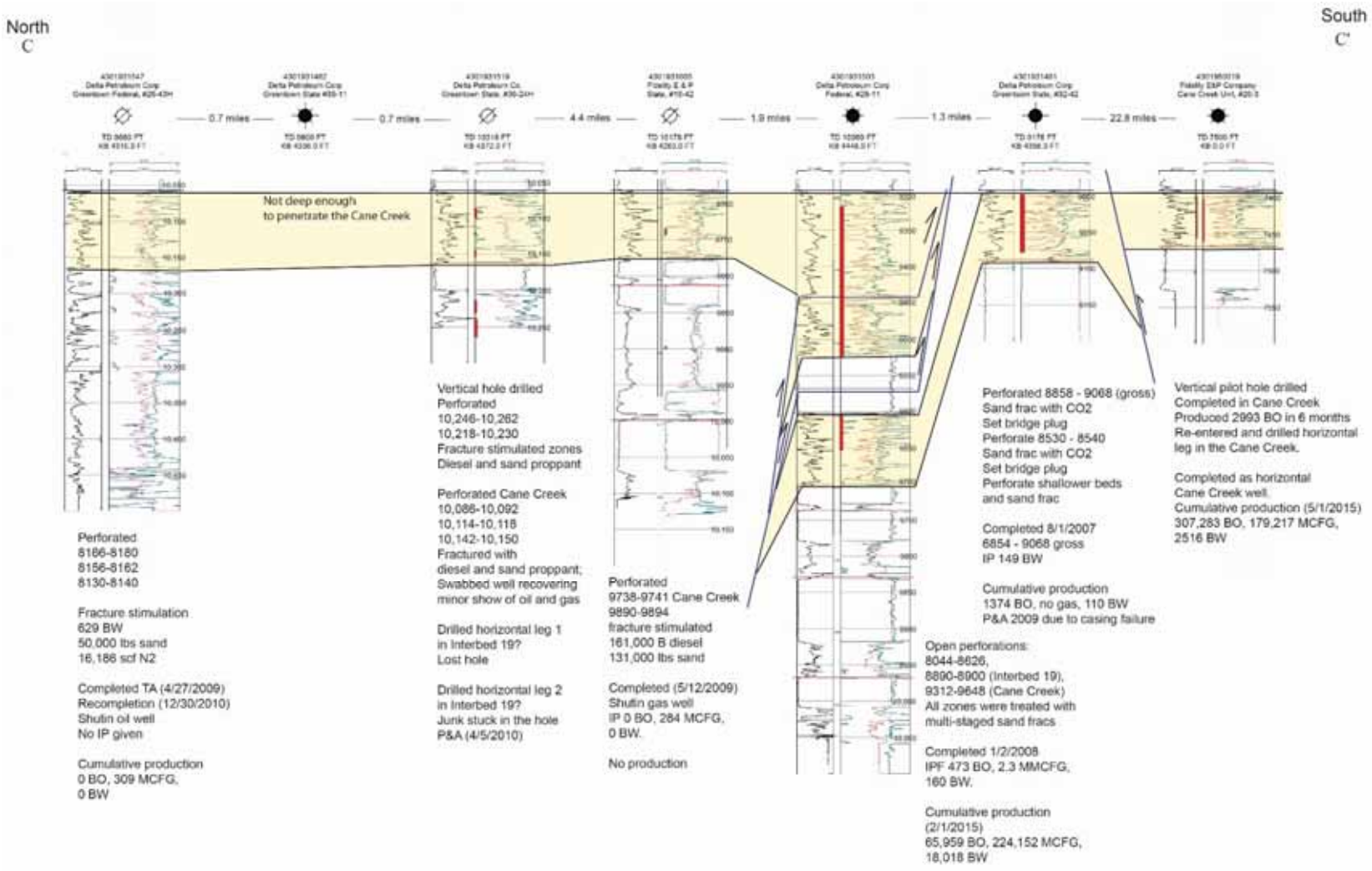

Figure 28. *North to south well log cross section of the Paradox Formation Cane Creek shale in the Greentown area. The Cane Creek thickness doesn't vary significantly from the Big Flat area to the south. But the Cane Creek in Greentown does appear to have more interbedded anhydrite and lacks the fine-grain sandstone facies that is productive in Big Flat. Core is needed to confirm the differences in the lithology of the Cane Creek. See figure 27 for cross section location.*

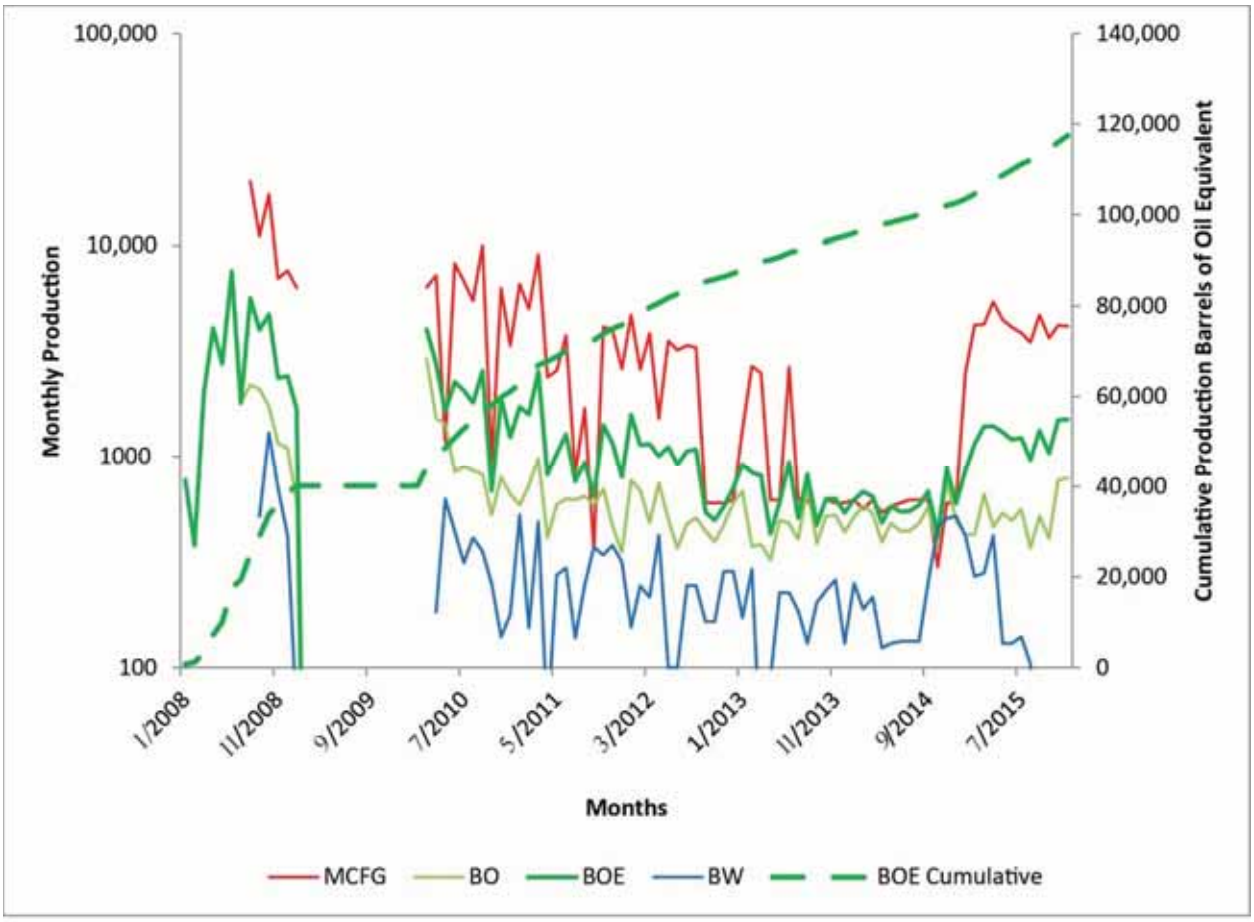

Figure 29. *Monthly and cumulative production curves for the Federal 28-11 in the Greentown field. The field is in the USGS Cane Creek gas assessment unit and produces a higher gas-to-oil ratio than wells in the Big Flat area. MCFG = thousand cubic feet of gas, BO = barrels of oil, BOE = barrels of oil equivalent, BW = barrels of water. Through December of 2015 the well has produced more than 71,000 BO and 266,000 MCFG, a BOE of 117,477.*

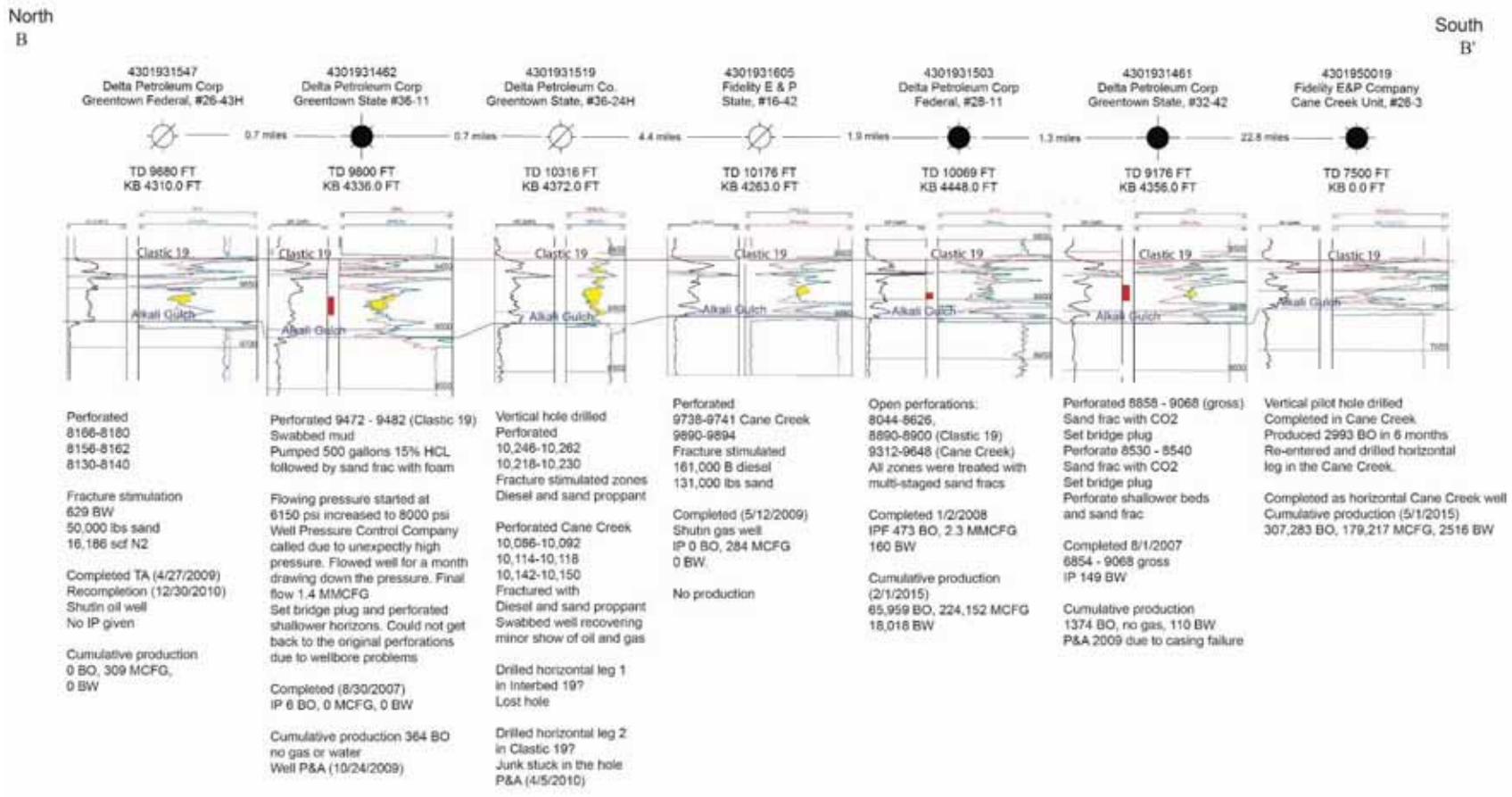

Figure 30. *North to south well log cross section of the Paradox Formation clastic 19 in the Greentown area. The bed thickens from south in the Big Flat area northward to the Greentown area. Cross over of the neutron curve to the density curve is common in the Greentown area indicating a higher gas concentration and/or possibly some sandstone in the shale. Datum is top of clastic 19, sea-level elevation shown in feet. TD = total depth and KB = elevation of the kelly bushing. See figure 27 for location of cross section.*

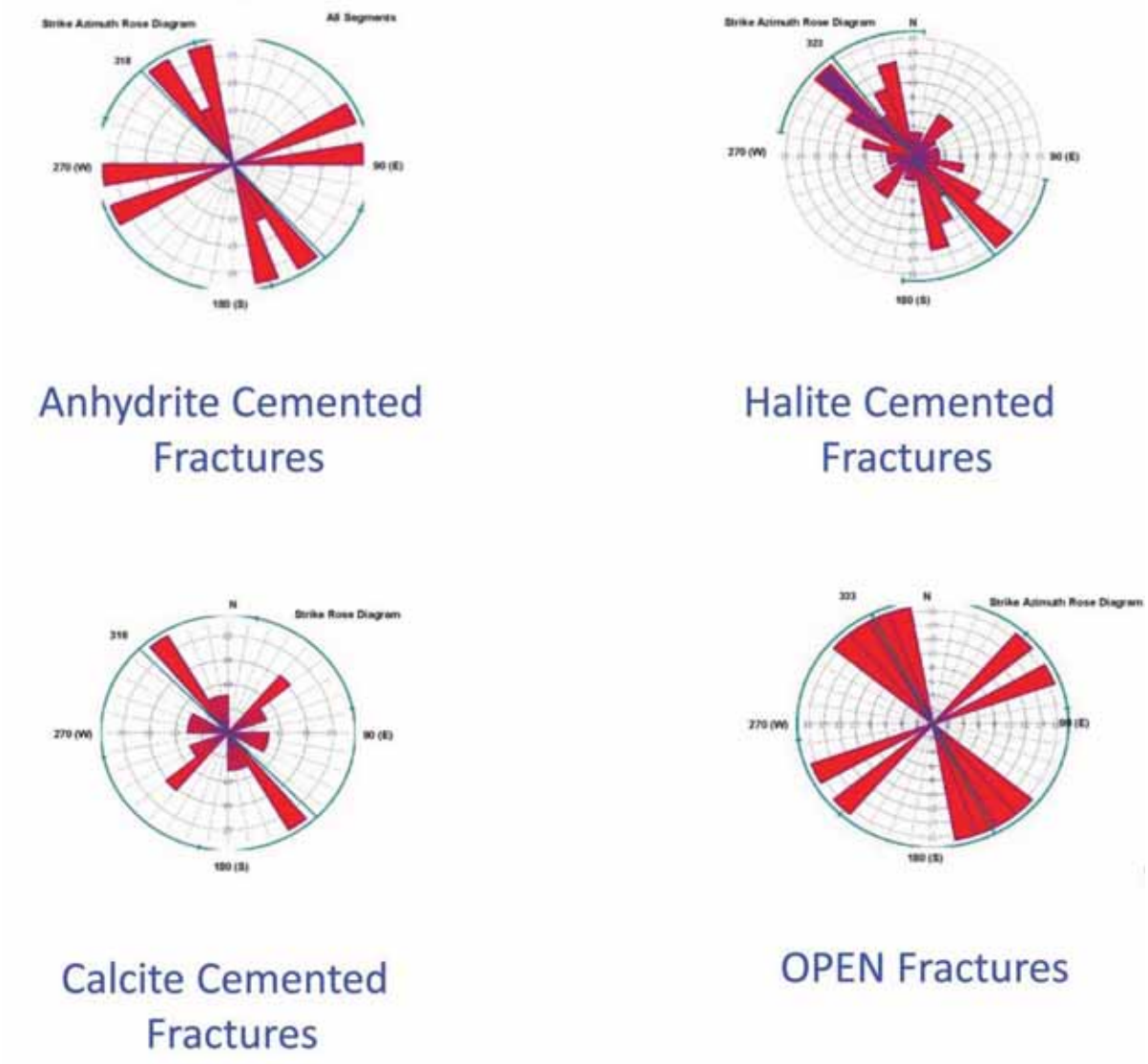

Figure 31. *Rose diagrams for fractures in the Cane Creek unit 26-3 well. Fracture orientation, regardless of cementing material or no cement, is dominantly northwest-southeast parallel to the regional structure and depositional trend of the Paradox Formation. Figure is from Core Laboratories, Inc., Houston, Texas, prepared in 2013 for Fidelity Exploration & Production Inc., and provided to the UGS (appendix C).*

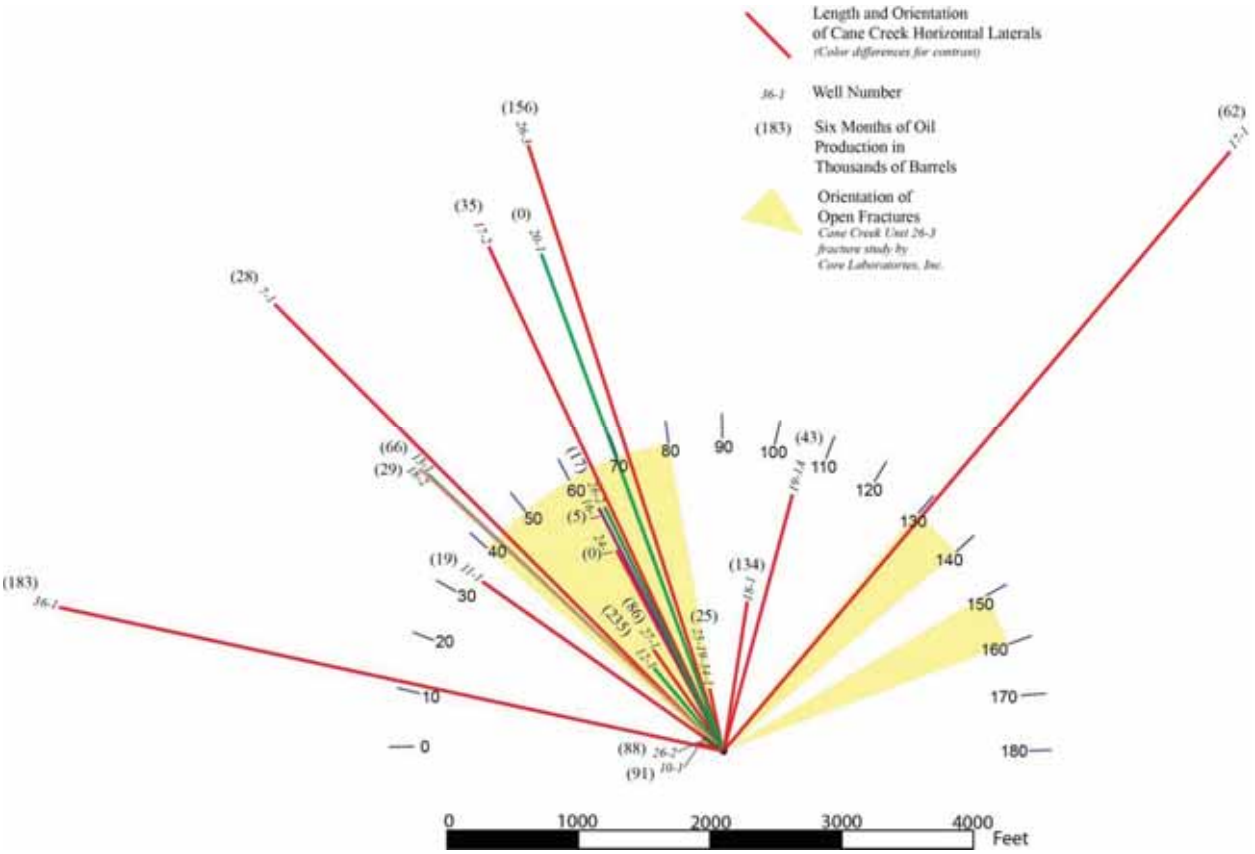

Figure 32. *Comparison of length and azimuth of horizontal laterals in the Cane Creek shale drilled in the Cane Creek unit. The first six months of production for each lateral is shown in parentheses in thousands of barrels of oil. The yellow highlights show the general trends of fractures in the Cane Creek (see figure 31). Most laterals were drilled nearly parallel to the fracture trend. There does not appear to be any correlation between the length or the direction of the lateral to the productivity of the well.*

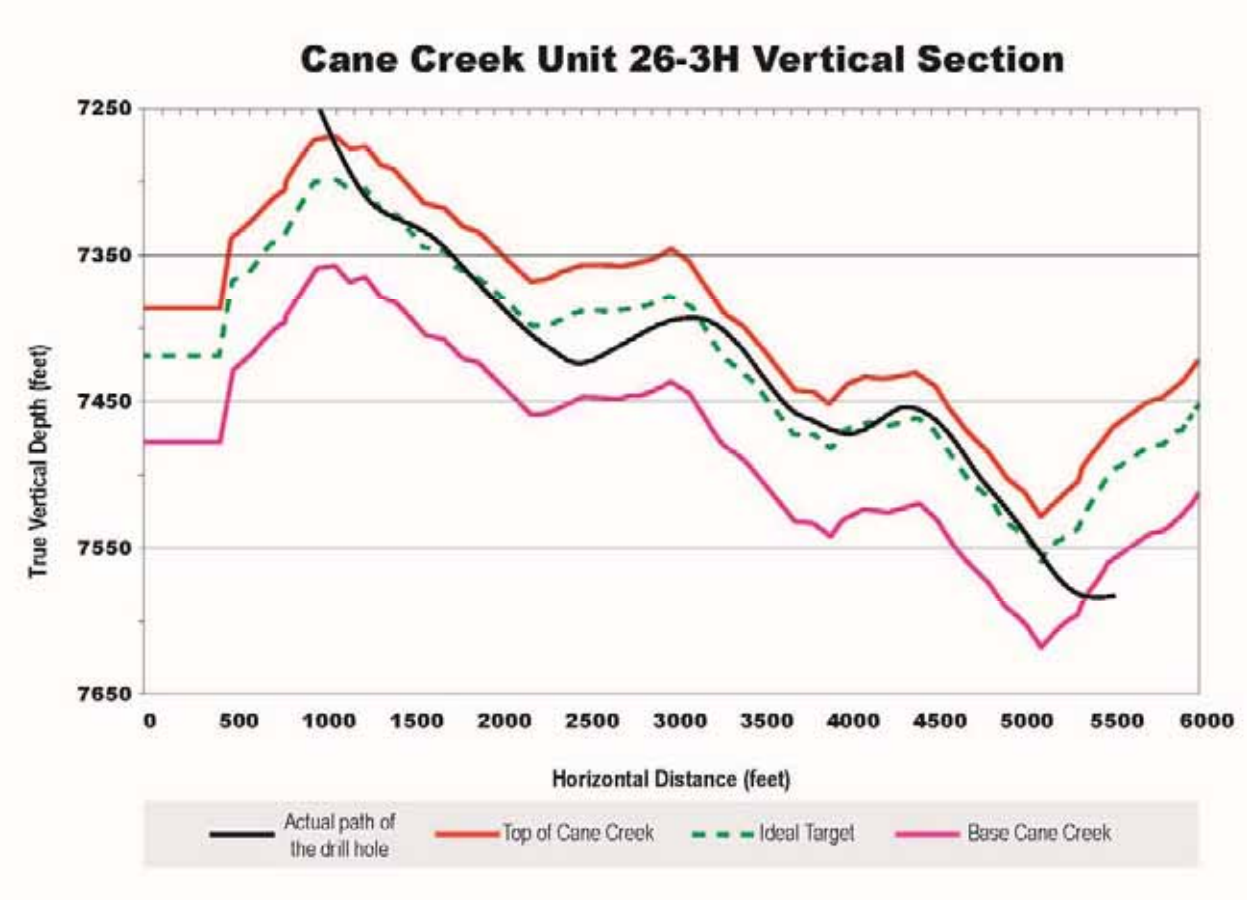

Figure 33. *Horizontal profile of the lateral drilled in Cane Creek unit 26-3H well (NESW section 26, T. 25 S., R. 19 E.; BHL SWNW section 25). The lateral was drilled in a down dip direction and encountered secondary salt folding that add to the difficulty of keeping the well bore in the target zone. The well bottomed in the underlying salt after encountering an apparent dip reversal. Data from Utah Division of Oil, Gas and Mining well records. The vertical exaggeration of the profile is about 9 times.*

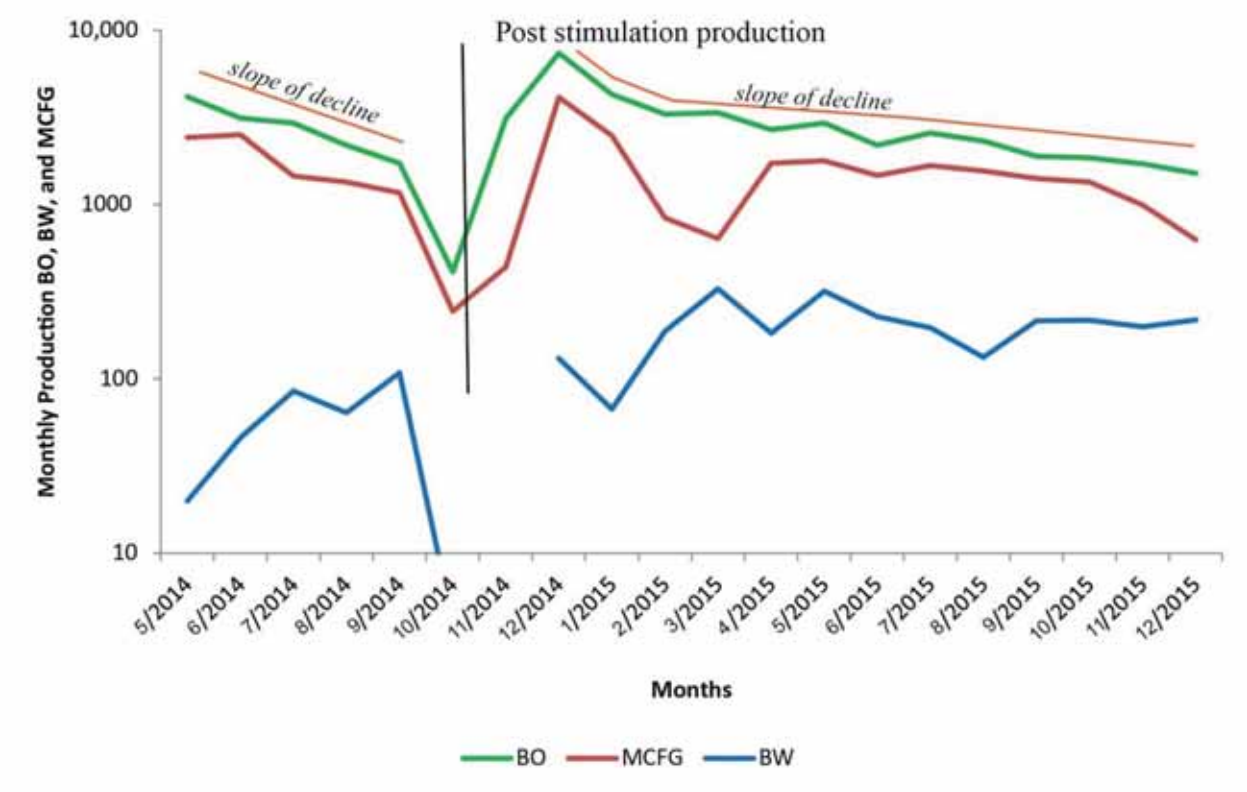

Figure 34. *Production curves for the Cane Creek 32-1-25-19 well (SWSW section 32, T. 25 S., R. 19 E.). The well was a poor producer from the beginning, so in November 2014 the operator stimulated the Cane Creek reservoir with 200 to 400 barrels of mineral oil with proppant per stage, in six stages. The stimulation did increase the monthly production and reduce the slope of decline.*

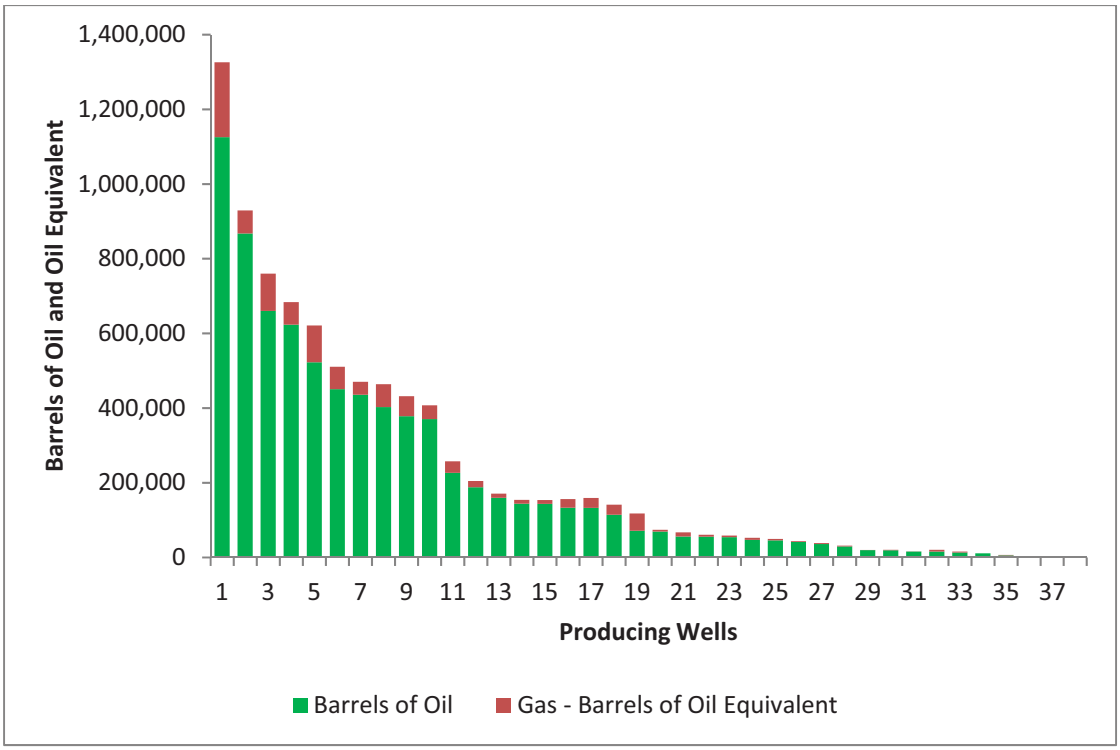

Figure 35. *Total production by well from largest to smallest as of December 31, 2015. Barrels of oil plus barrels of oil equivalent based on 5.8 mcfg = 1 BO. Range is from 2035 BOE to 1,325,935 BOE from 38 wells; mean 229,276 BOE, median 95,688 BOE. Production data from Utah Division of Oil, Gas and Mining.*

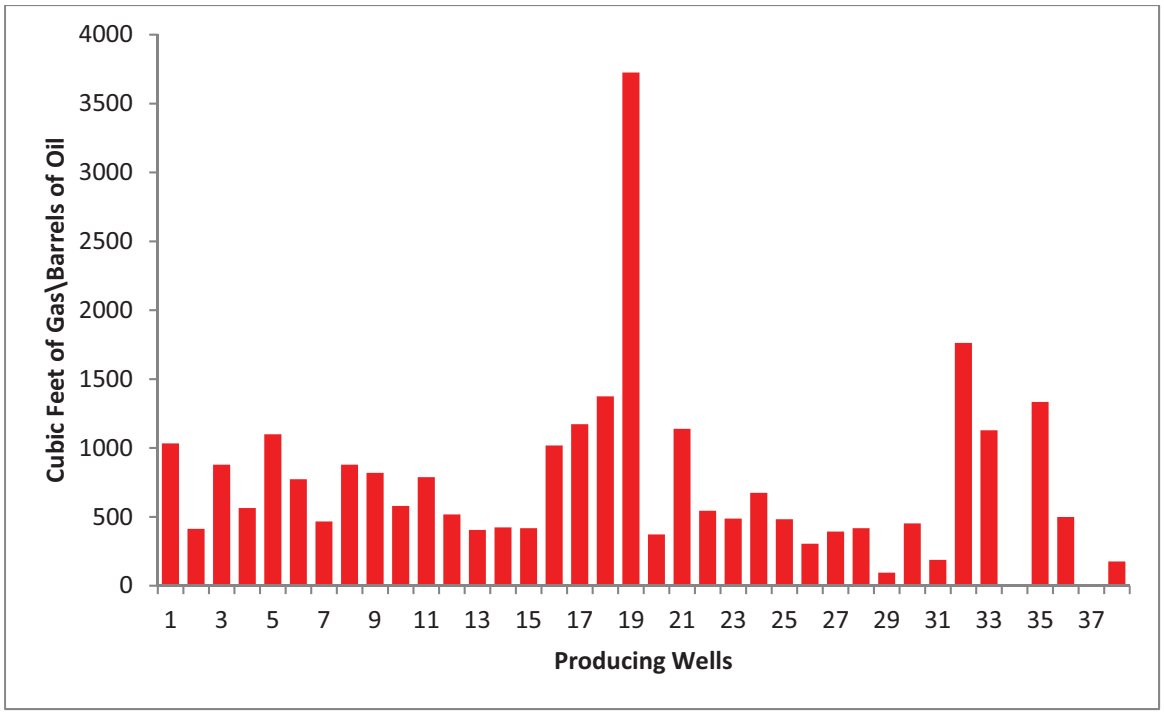

Figure 36. *Cubic feet of gas per barrel of oil produced (GOR) per well, based on total production as of December 31, 2015. The range is from 0 to 3725 CFG/BO, mean of 731 CFG/BO. Production data from Utah Division of Oil, Gas and Mining.*

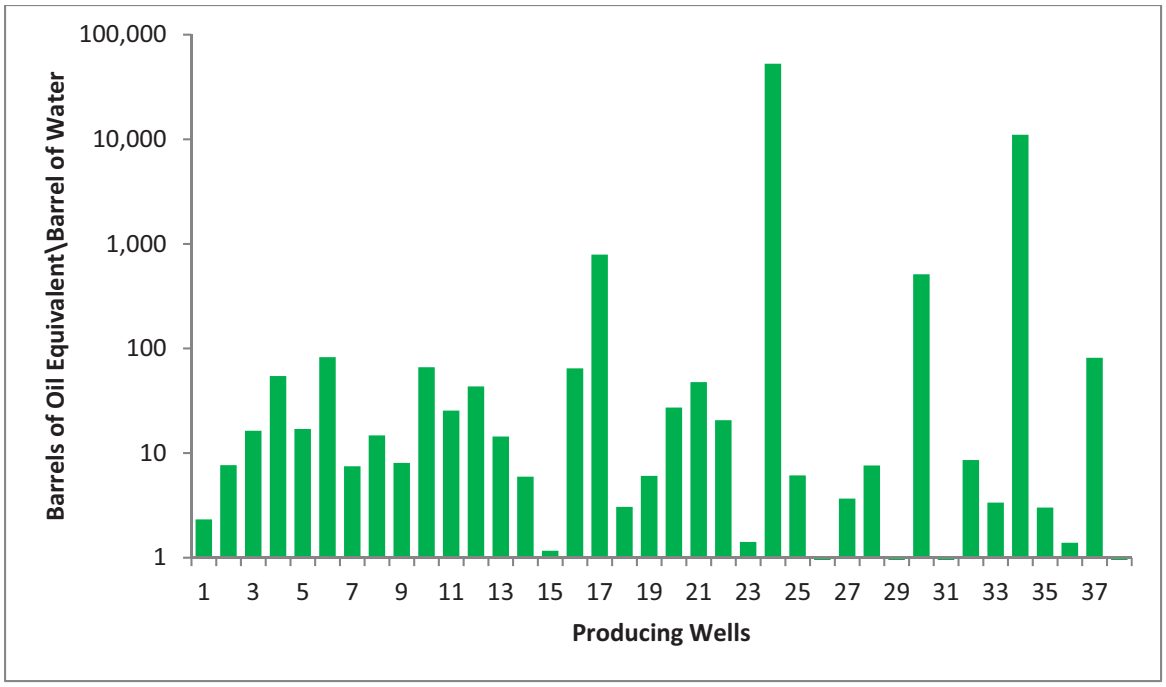

Figure 37*. Barrels of oil equivalent per barrel of water produced per well, based on total production as of December 31, 2015. The range is 0 to 52,628 BOE/BW, mean of 1727 BOE/BW. Production data from Utah Division of Oil, Gas and Mining.*

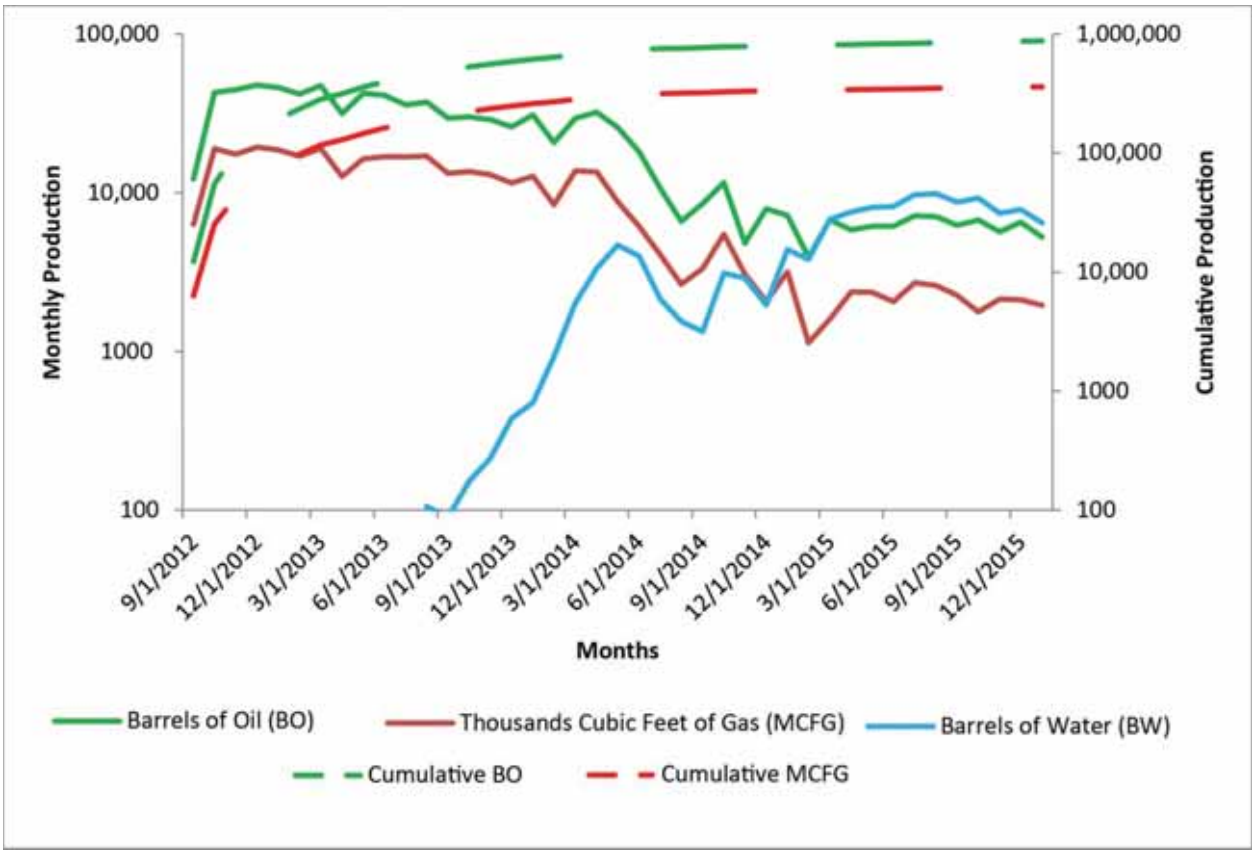

Figure 38. *Production curves for Cane Creek 12-1 (section 12, T. 26 S., R. 19 E.) the most productive well in the Cane Creek unit. In 41 months, the well has produced more than 872 MBO and 360 MMCFG. Production data from Utah Division of Oil, Gas and Mining.*

Figure 39. *Cane Creek 12-1 well (section 12, T. 26 S., R. 19 E.), the most productive well in the Cane Creek unit. As of December 2015, the well has produced more than 872 BO and 360 MMCFG. Production data from Utah Division of Oil, Gas and Mining.*

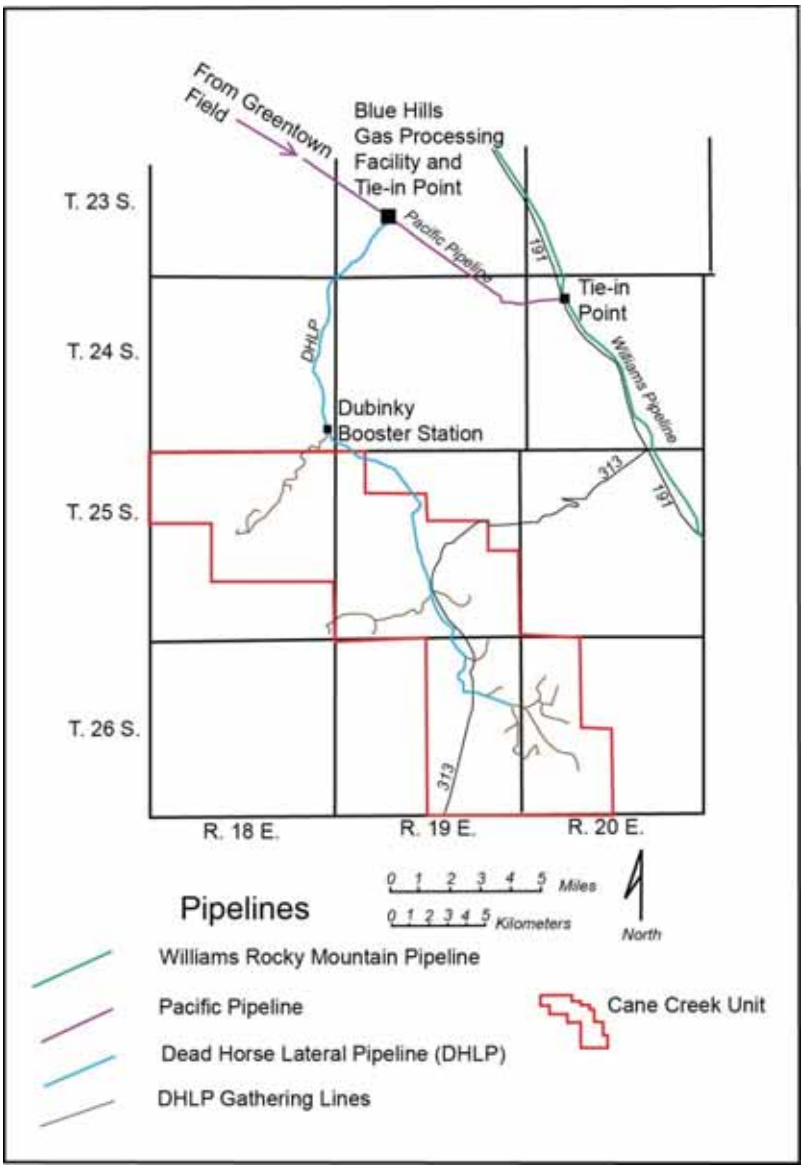

Figure 40. *Gas pipeline map showing gathering lines and the Dead Horse lateral that delivers gas from the Cane Creek unit to the Blue Hills gas processing facility. Gas from the processing facility is delivered to the Williams Rocky Mountain pipeline via the Pacific pipeline coming from the Greentown field.*

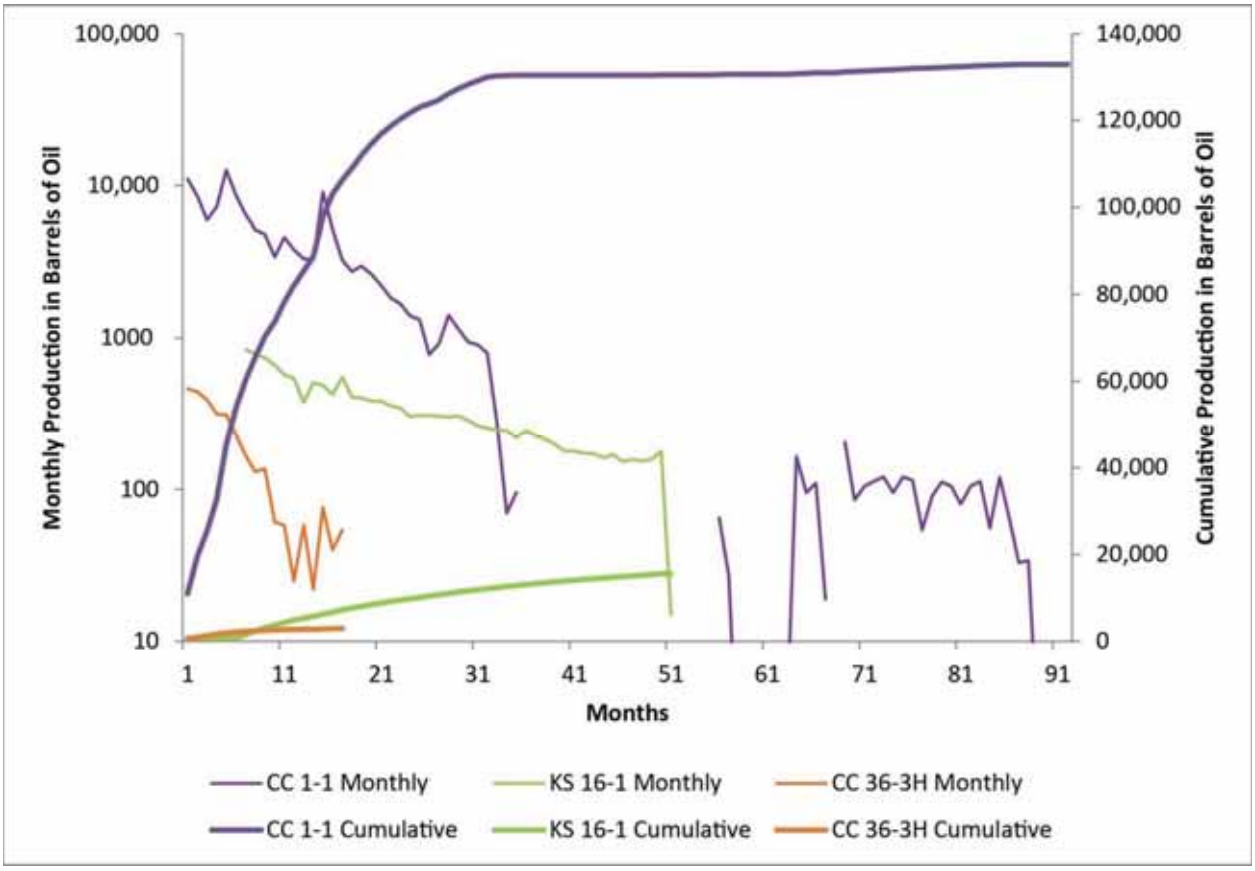

Figure 41. *Oil production curves for Cane Creek 1-1 well (section 1, T. 26 S., R. 19 E.), Kane Springs 16-1 well (section 16, T. 25 S., R. 18 E.) and Cane Creek 36-3H well (section 36, T. 25 S., R. 19 E.). All three wells produced from the Paradox Formation clastic 19. KS 16-1 and CC 36-3H are horizontal wells, CC 1-1 produced from a vertical borehole. Each well was completed at different times but the production for all wells as shown starting at month 1 for easy comparison. Data from Utah Division of Oil, Gas and Mining.*

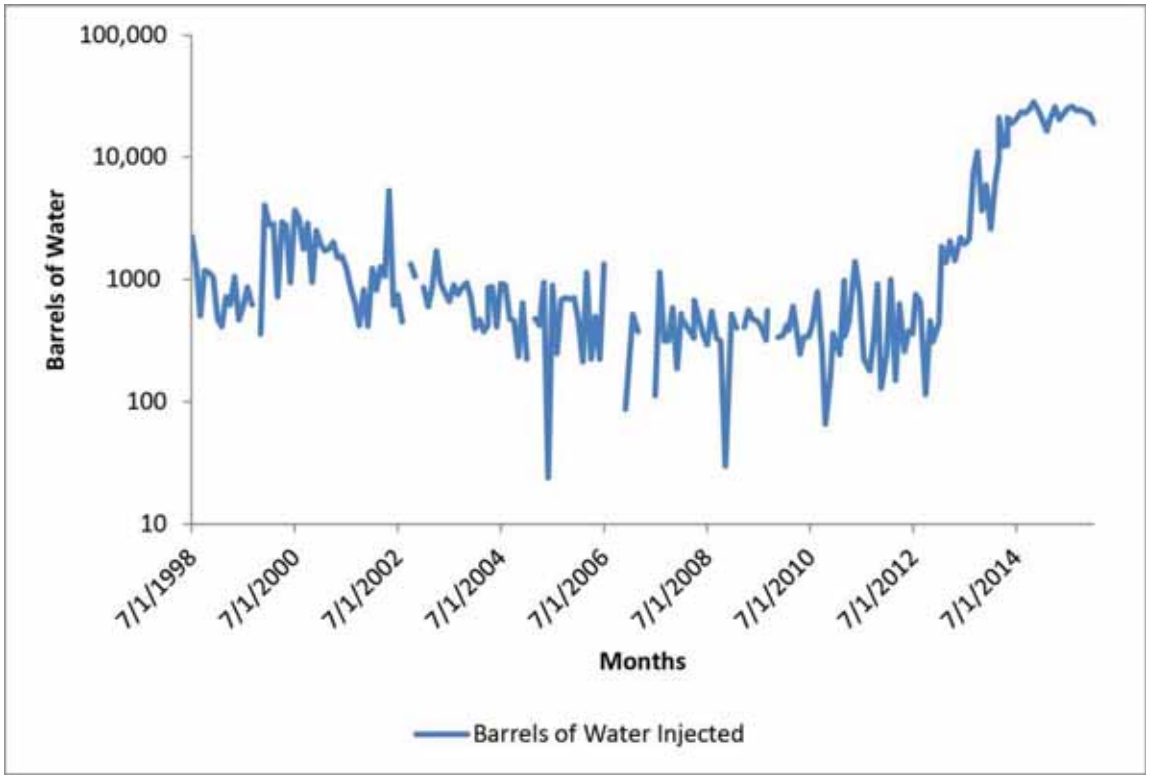

Figure 42. *Barrels of produced water injected into the Kane Springs 16-1 well (section 16, T. 25 S., R. 18 E.). Volumes greatly increased in 2013 when several new wells were completed in the Cane Creek unit. Water is injected into the Cutler Group at a depth of 1490 to 1520 feet. Injection data from Utah Division of Oil, Gas and Mining.*

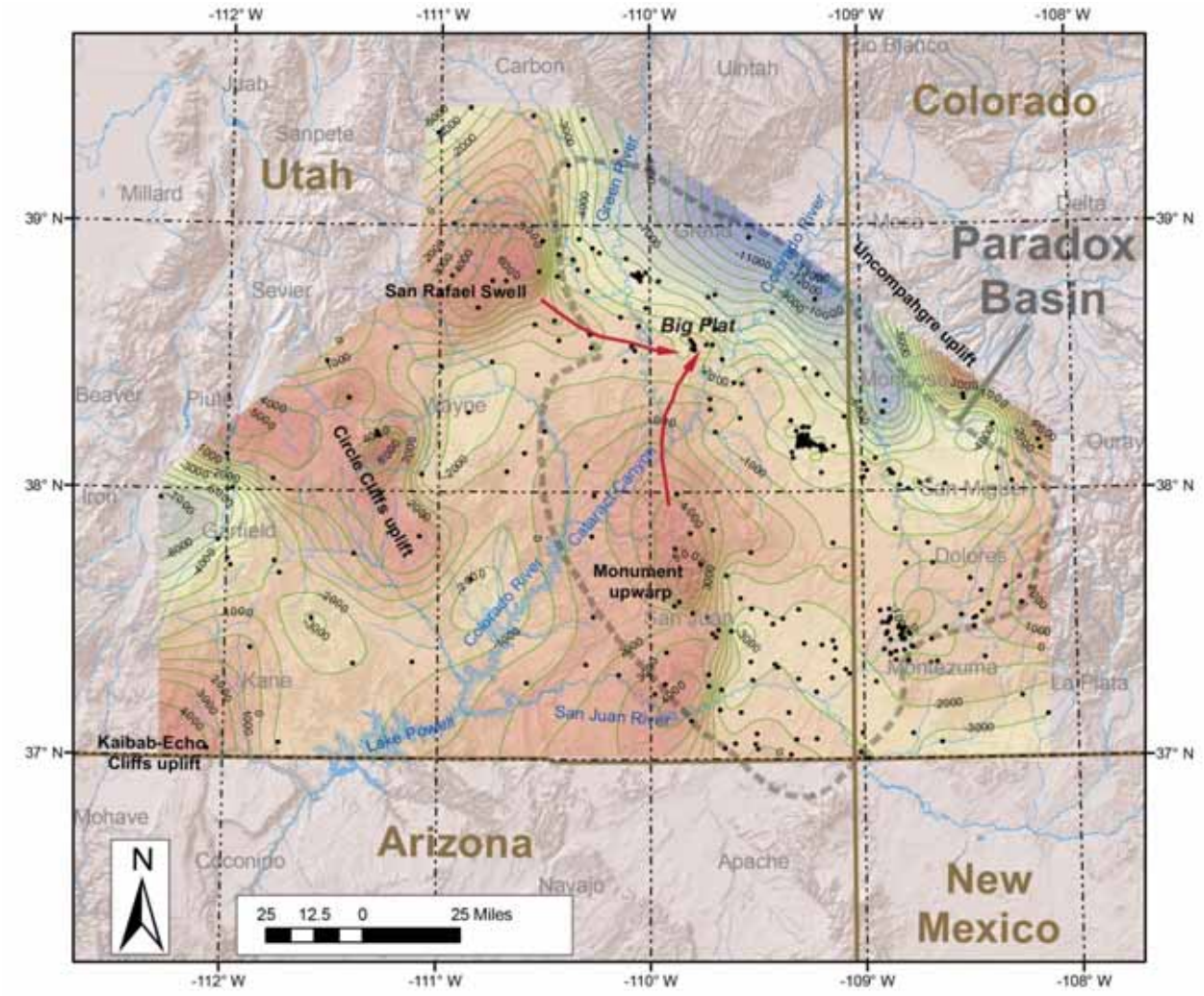

Figure 43. *Structure contour of the Mississippian Red Wall Limestone based on well penetrations (black dots). The Mississippian structure controls most of the structure in the overlying Cane Creek shale. The Big Flat area lies at the convergence of the plunging Monument upwarp and a plunging nose from the San Rafael Swell. Contour interval 1000 feet mean sea level datum. Modified from Chidsey (2009).*

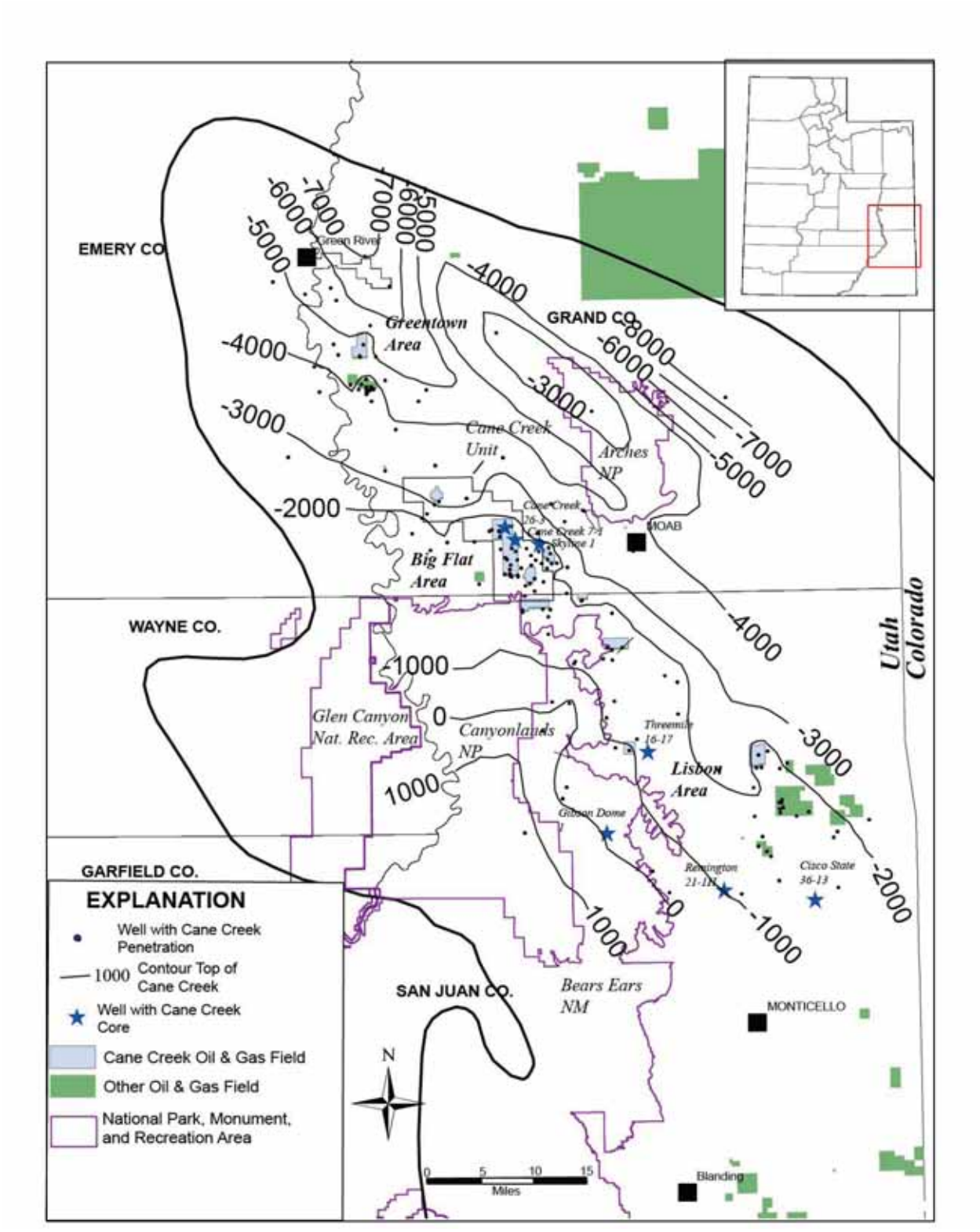

Figure 44. *Structure of the Cane Creek shale based on well penetrations, no faults shown. Contour interval 1000 feet, mean sea level datum.*

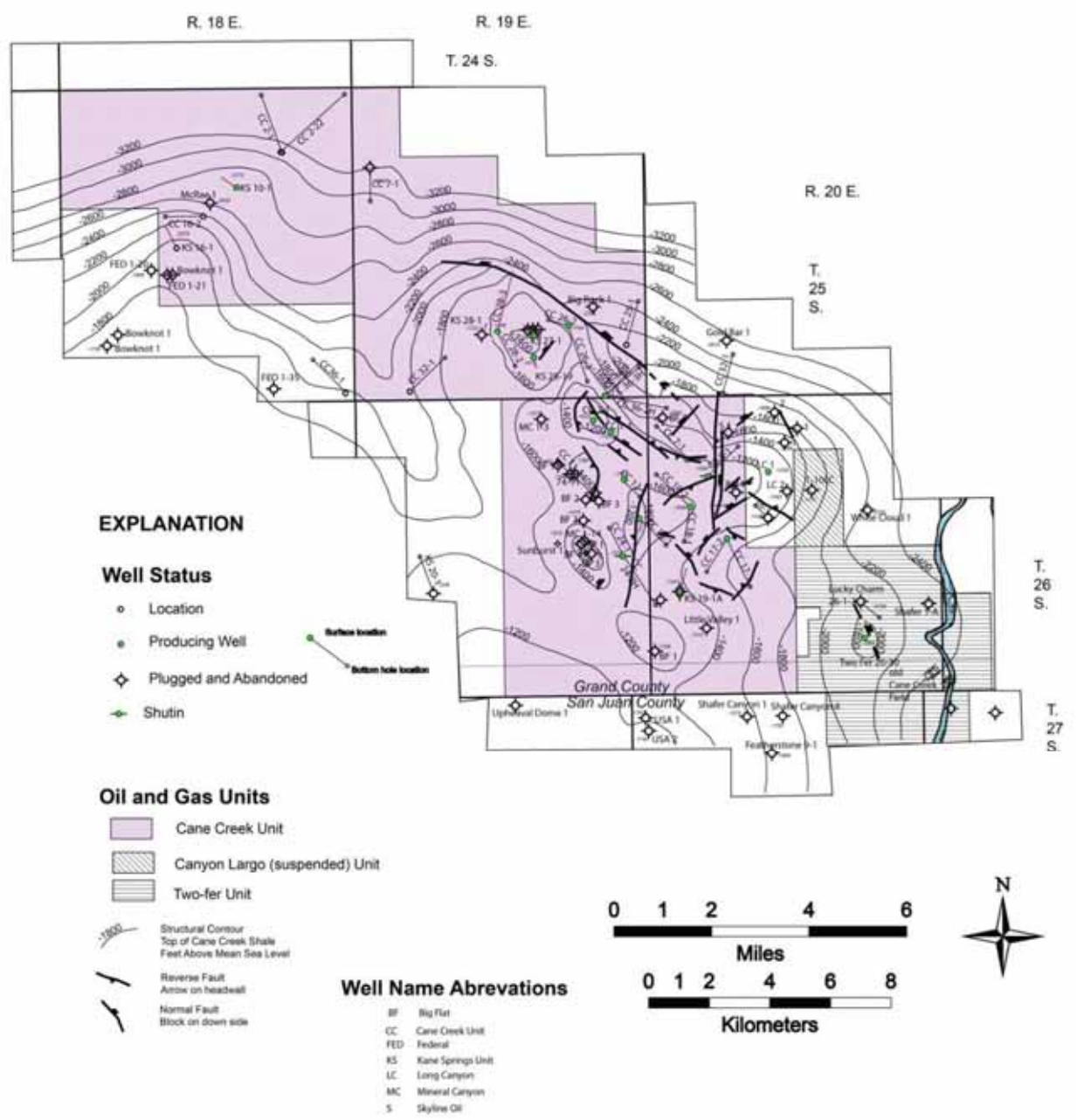

Figure 45. *Structure of the Cane Creek shale in the Big Flat area. Faulting is based on well file exhibits submitted by Fidelity E&P to Utah Division of Oil, Gas and Mining. Fidelity E&P acquired 3D seismic to define the structure. Contour interval is 200 feet mean sea level datum.*

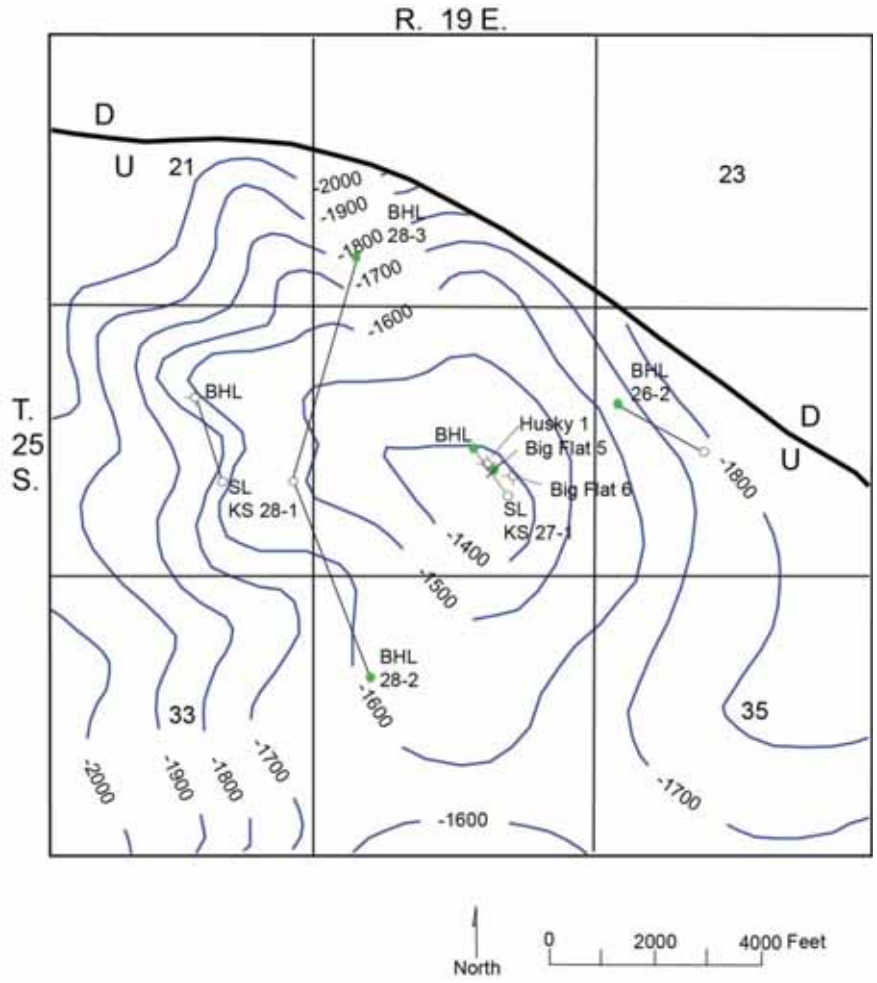

Figure 46. *Structure on top of the Cane Creek. The KS 27-1well was the first Cane Creek horizontal well drilled. Big Flat 5 was a vertical Cane Creek well that produced until the casing collapsed. Fault displacement is about 400 feet. KS = Kane Springs, SL = surface location, BHL = bottom hole location. Modified from Grove and others (1993).*

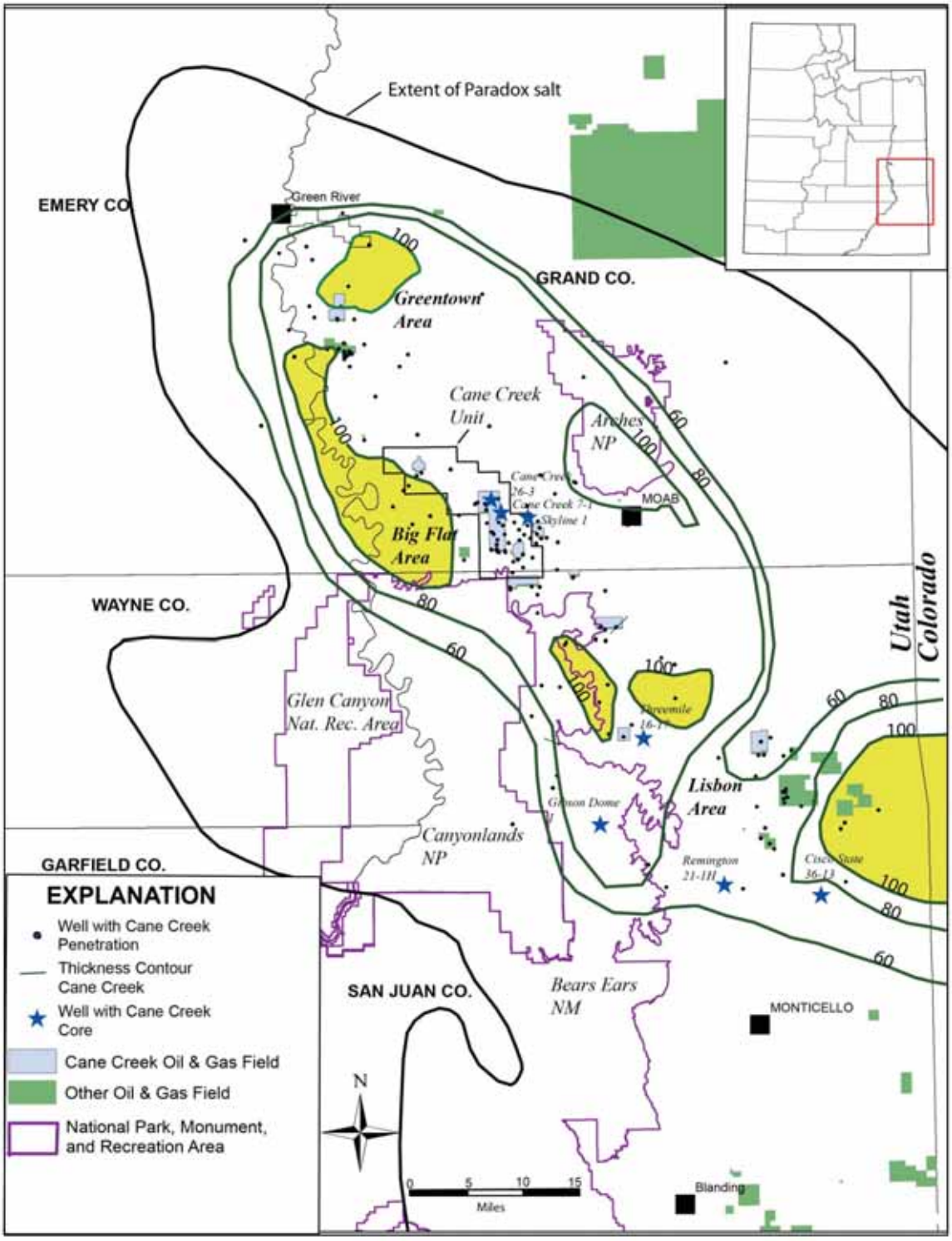

Figure 47. *Thickness contour of the Cane Creek shale. Areas of local thickening are highlighted in yellow. Some thickening may be due to tectonics. Contour interval 20 feet.*

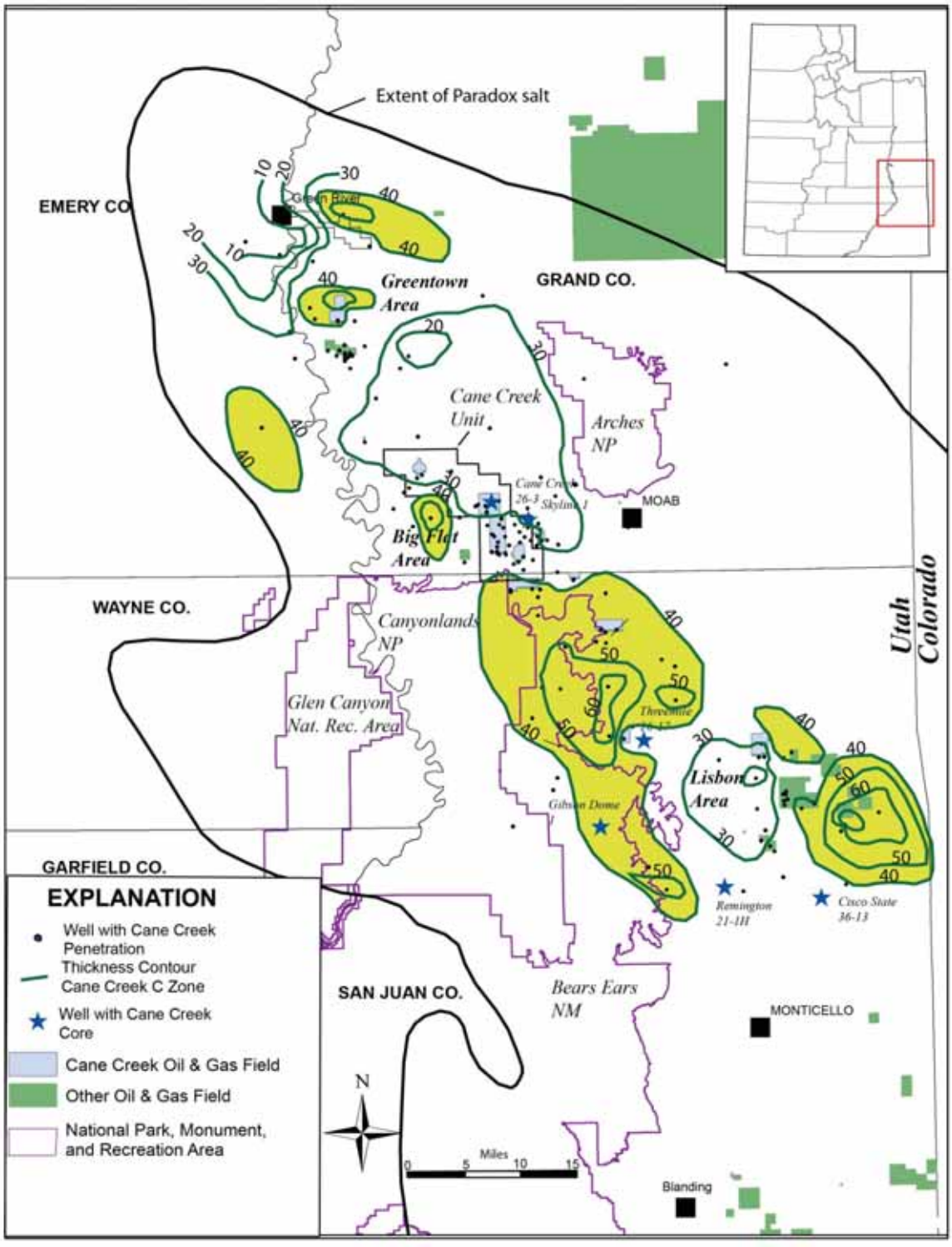

Figure 48. *Thickness contour of Cane Creek C zone, see figure 13 for definition of zones. Areas of local thickening are highlighted in yellow (more than 40 feet). Some thickening may be due to tectonics. Contour interval 10 feet.*

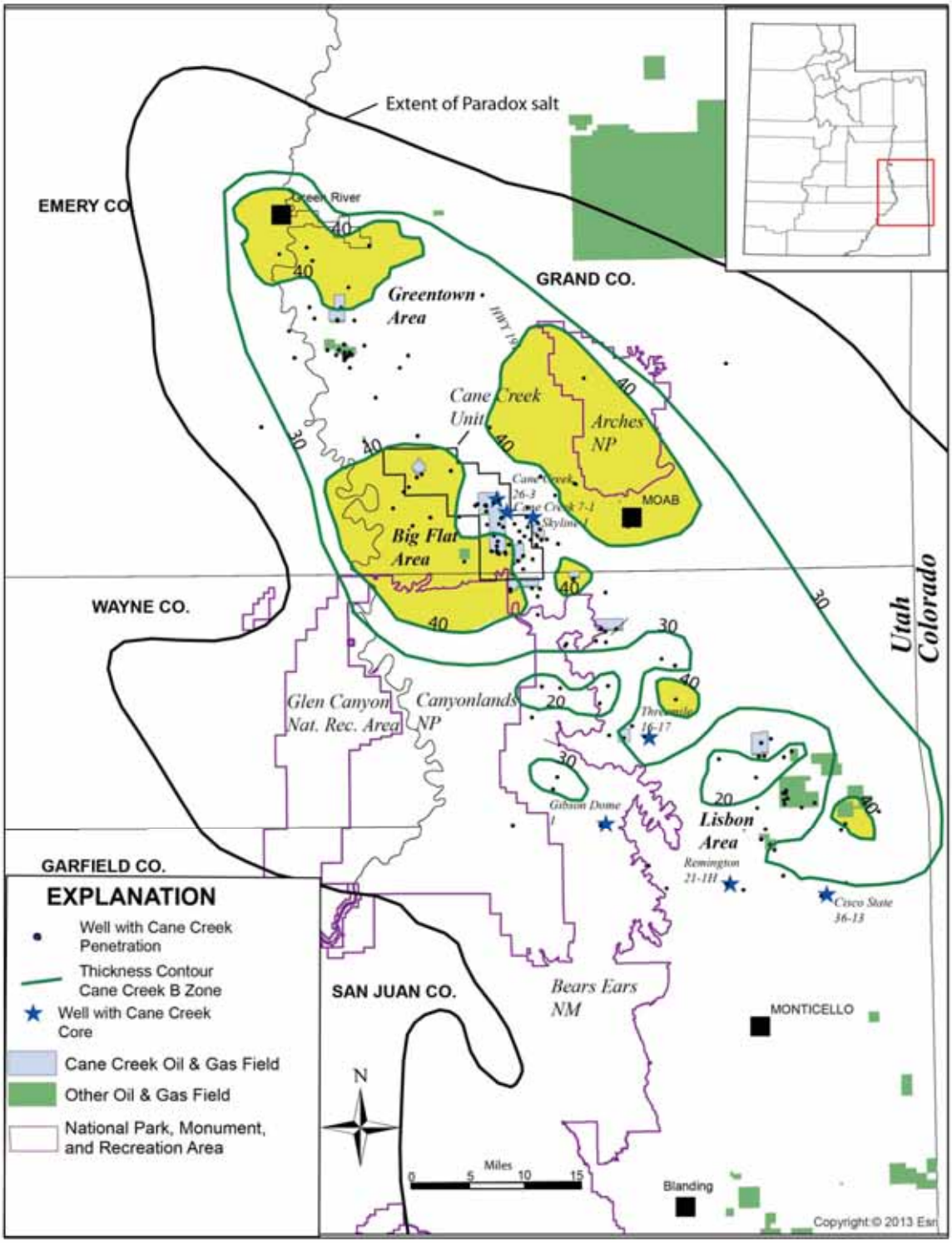

Figure 49. *Thickness contour of Cane Creek B zone, see figure 13 for definition of zones. Areas of local thickening are highlighted in yellow (more than 40 feet). Some thickening may be due to tectonics. Contour interval 10 feet.*

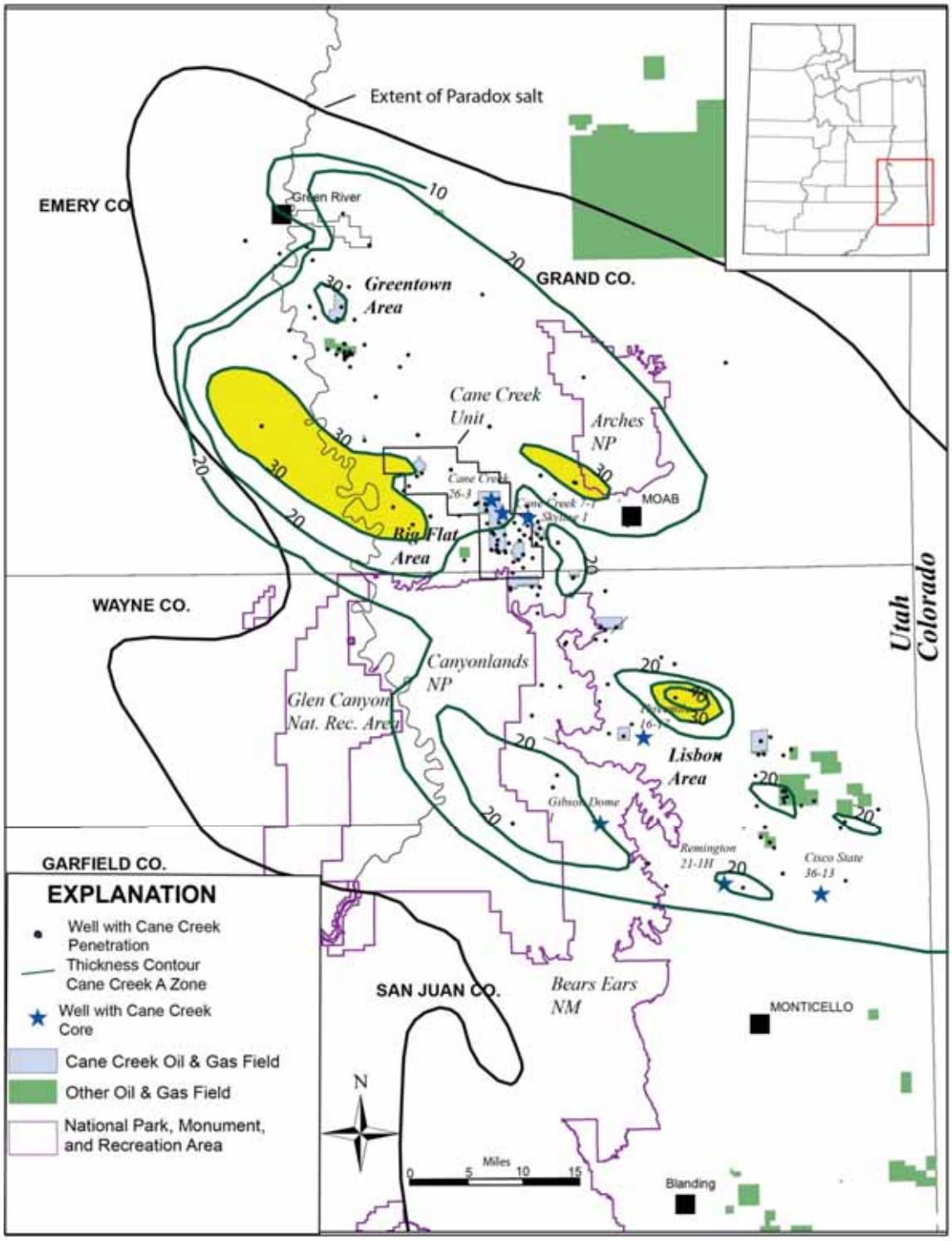

Figure 50. *Thickness contour of the Cane Creek A zone, see figure 13 for definition of zones. Areas of local thickening are highlighted in yellow (more than 30 feet). Some thickening may be due to tectonics. Contour interval 10 feet.*

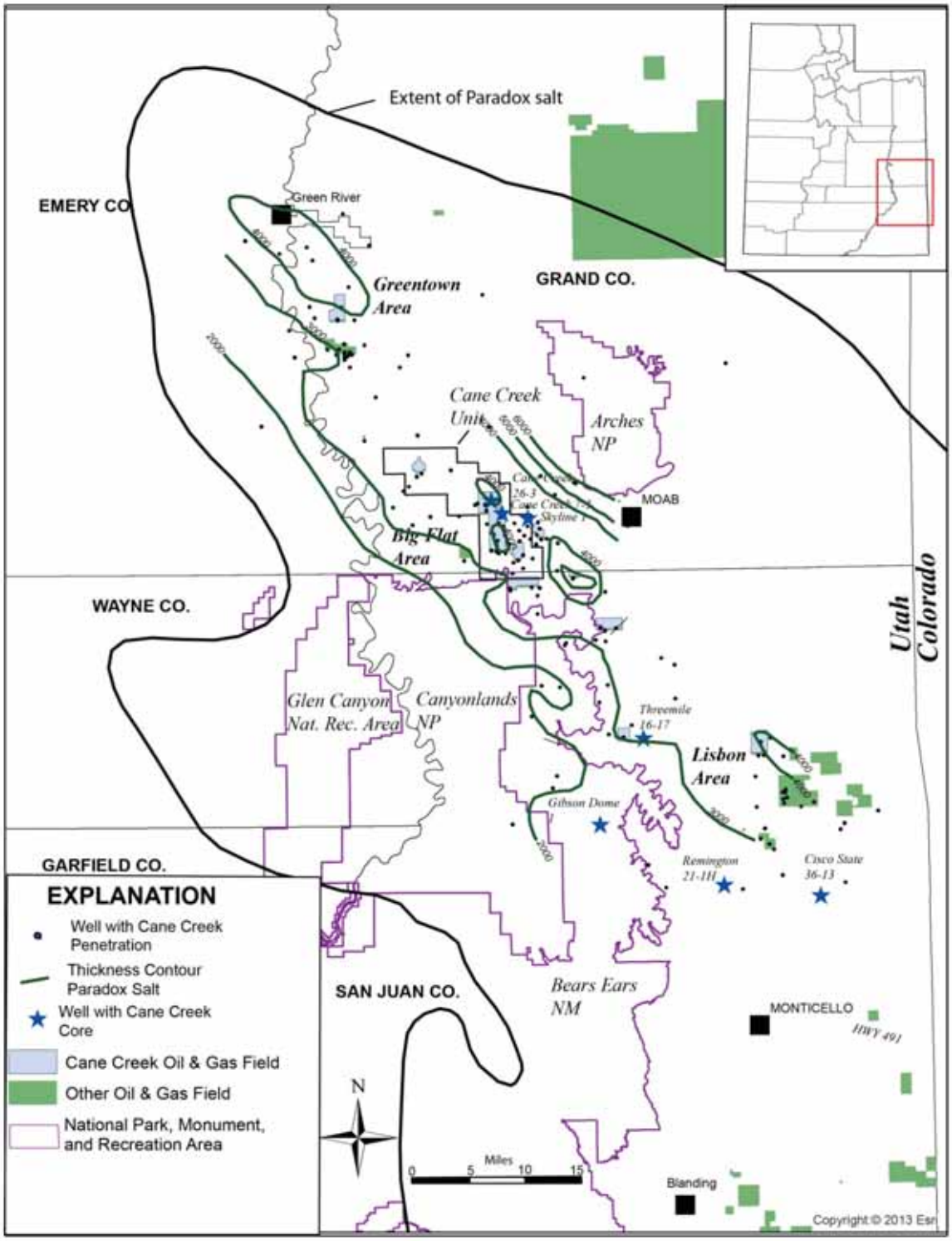

Figure 51. *Thickness of the Paradox salt (middle member figure 3) from the top of the stratigraphically highest salt to the base of the lowest salt. Contour interval 1000 feet.*

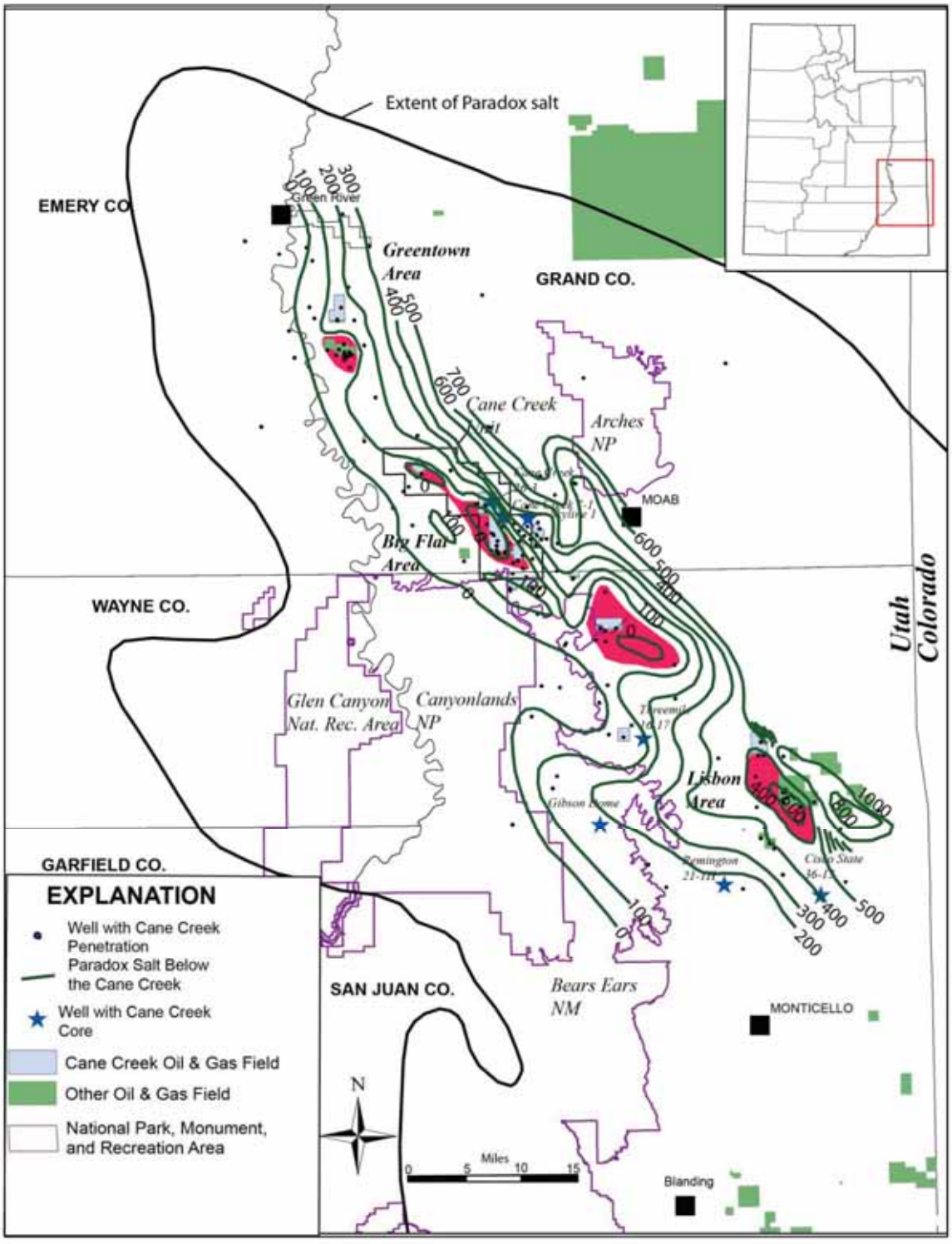

Figure 52. *Thickness of the salt below the Cane Creek shale. Areas of localized thinning are highlighted in red and may be an indication of structural highs during deposition of the Cane Creek.*

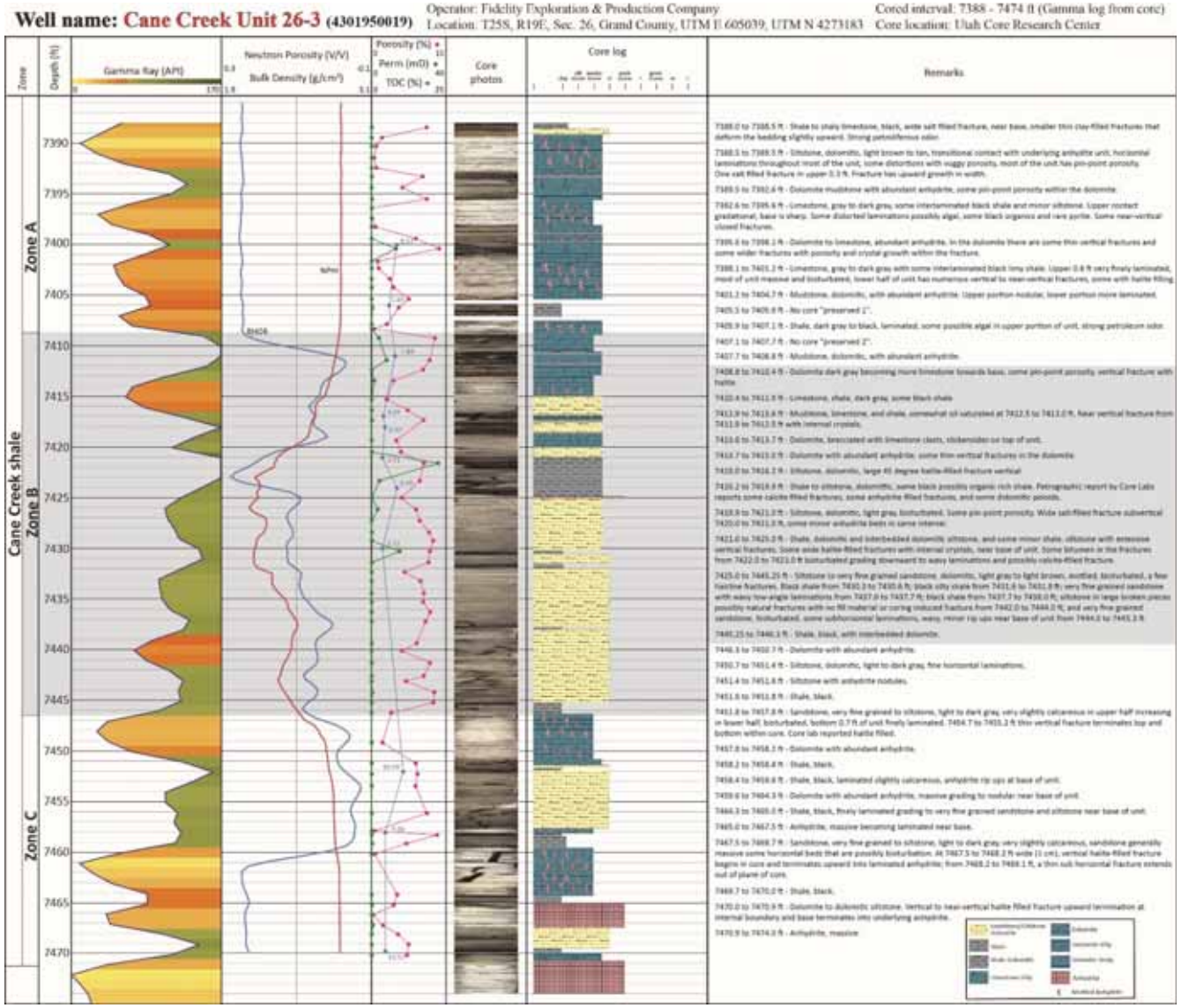

Figure 53. *Core log of the Cane Creek 26-3 well. A vertical pilot hole was cored and then a horizontal lateral was drilled and completed in the Cane Creek B zone. The well has produced more than 370 BO and 214 MCFG through December 2015 (Utah Division of Oil, Gas and Mining).*

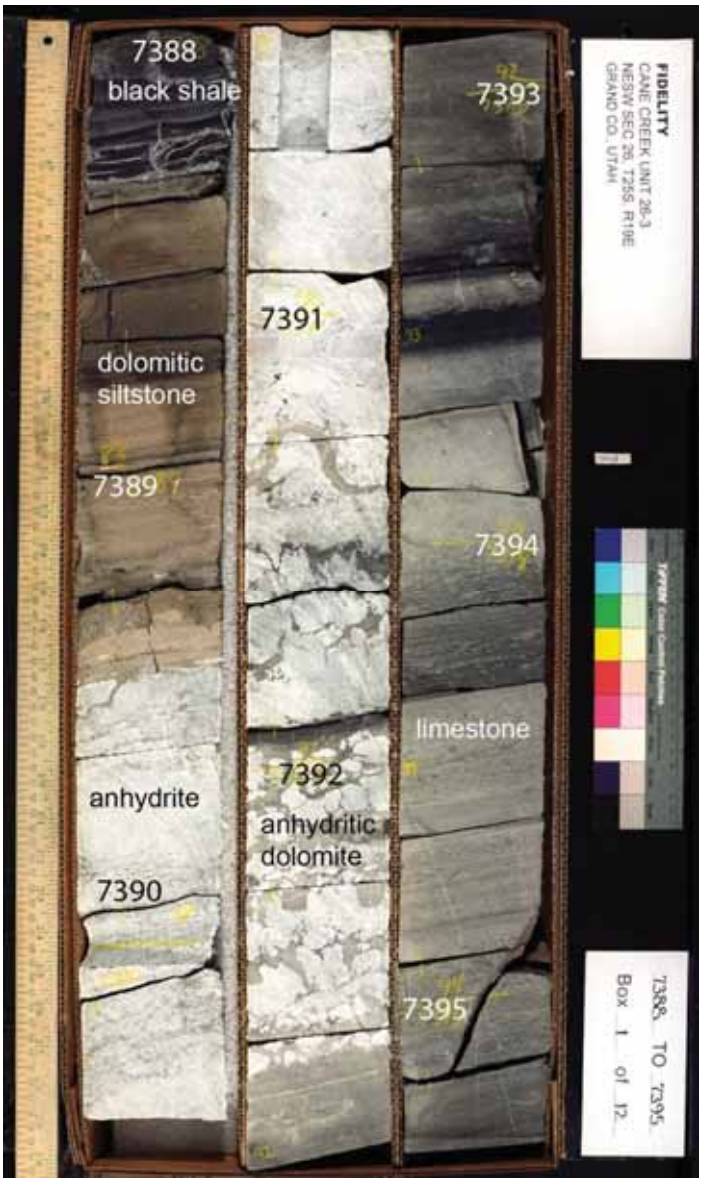

Figure 54. *Photograph of core from the Cane Creek shale A zone in the Cane Creek 26-3 well. Thin interbedded black shale, dolomitic siltstone, anhydrite and limestone. Limestone is bioturbated and thinly laminated in part.*

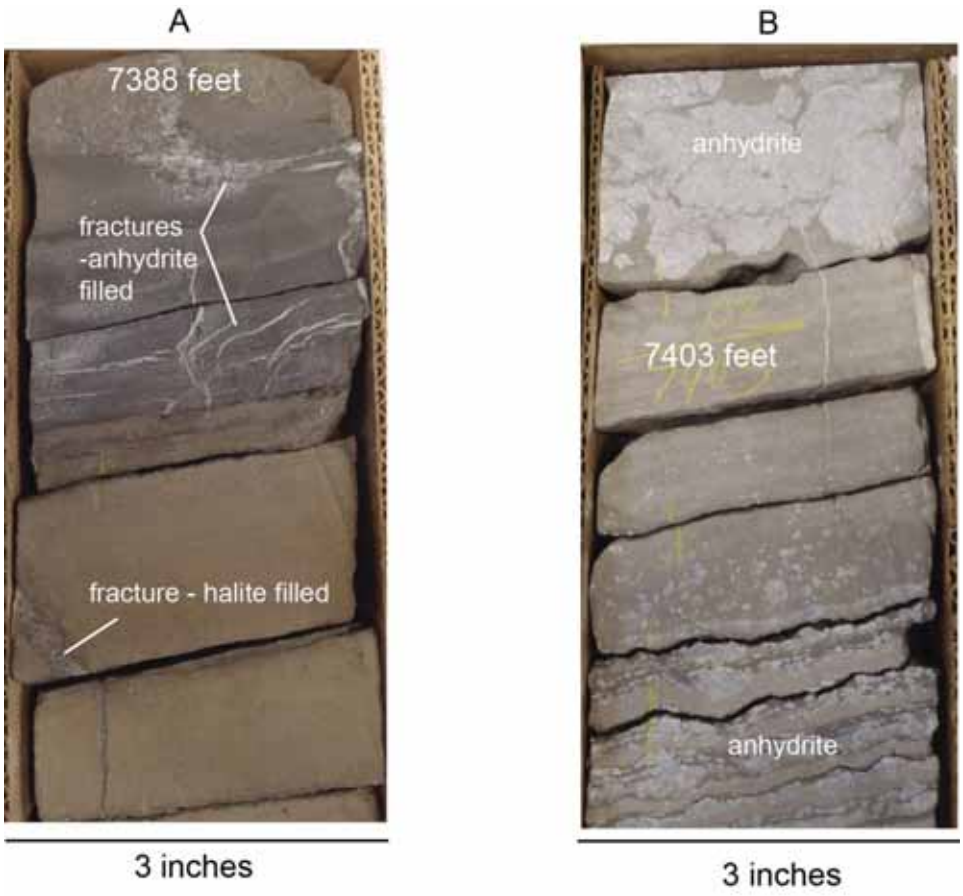

Figure 55. *Photographs of Cane Creek shale A zone core from Cane Creek 26-3. A) Dolomitic mudstone (gray) and dolomitic siltstone (light brown) with thin anhydrite-filled fractures and thicker halite-filled fractures (7388 ft). B) Dolomitic mudstone with abundant anhydrite and very fine anhydrite-filled fractures (7403 ft).*

Figure 56. *Photograph of Cane Creek shale B zone in the Cane Creek 26-3 well. Thin bedded fractured limestone and brecciated dolomite overlying anhydritic dolomite. Dolomitic siltstone with halite-filled fracture overlying silty dolomitic black shale.*

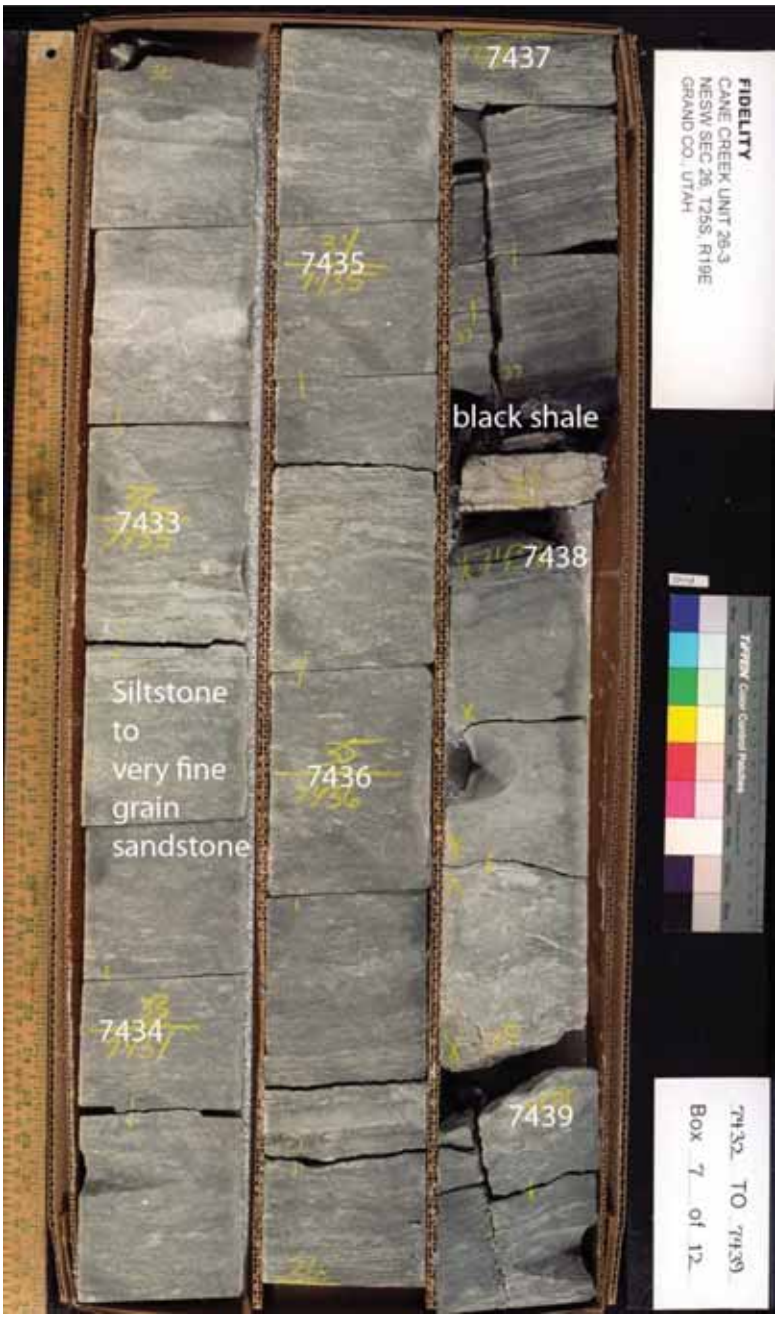

Figure 57. *Photograph of Cane Creek shale B zone in the Cane Creek 26-3 well. Siltstone to very fine grain sandstone, the main reservoir facies. Dolomitic, bioturbated, with interbedded black shale.*

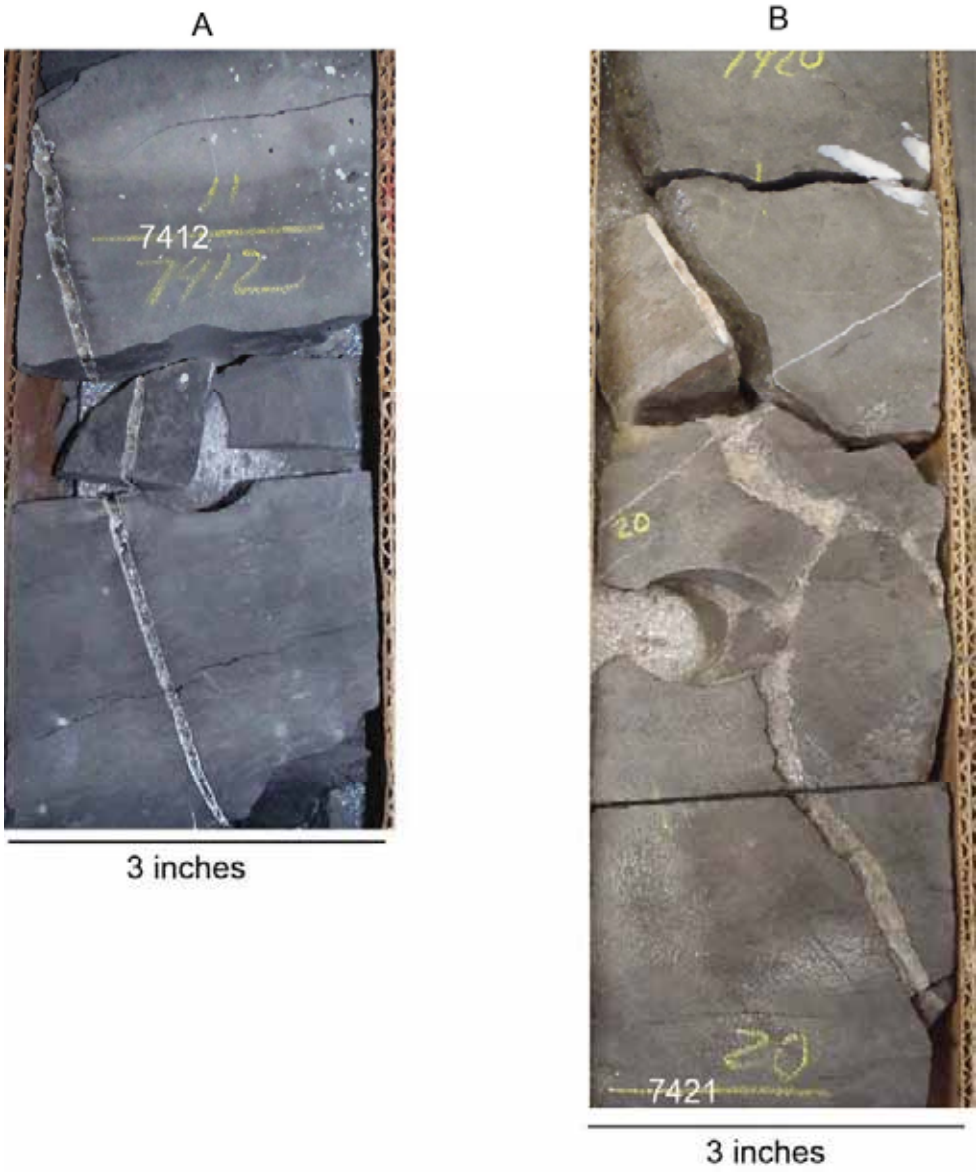

Figure 58. *Photographs of Cane Creek shale B zone core from Cane Creek 26-3. A) Micritic limestone with near vertical calcite-filled fracture. B) Dolomitic siltstone with wide salt-filled fracture cutting much thinner anhydrite(?)-filled fracture.*

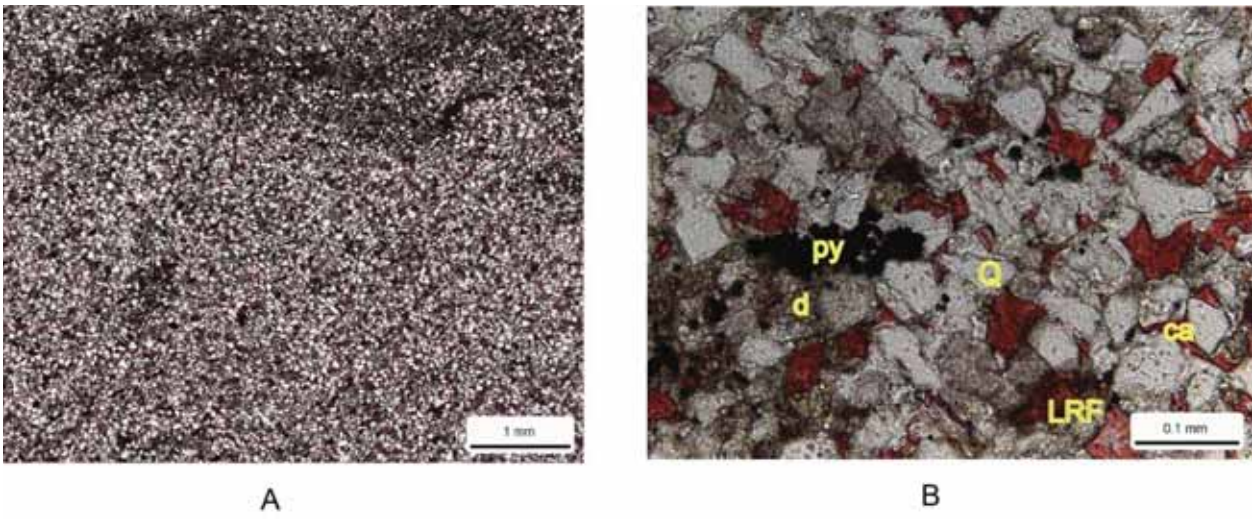

Figure 59. *Photomicrographs from Cane Creek 26-3 B zone at 7426.0 feet. A) Very fine-grain argillaceous sandstone (feldspathic litharenite) with 8.9% porosity and 3.28 mD permeability from core analysis. B) Well sorted, bioturbated with abundant quartz (Q) and common dolomite rock fragments (d). Minor amounts of other rock fragments (LRF) and calcite (ca) replacement grains, minor quartz overgrowths and pyrite (py). From Core Laboratories, Inc., petrographic analysis report (appendix C).*

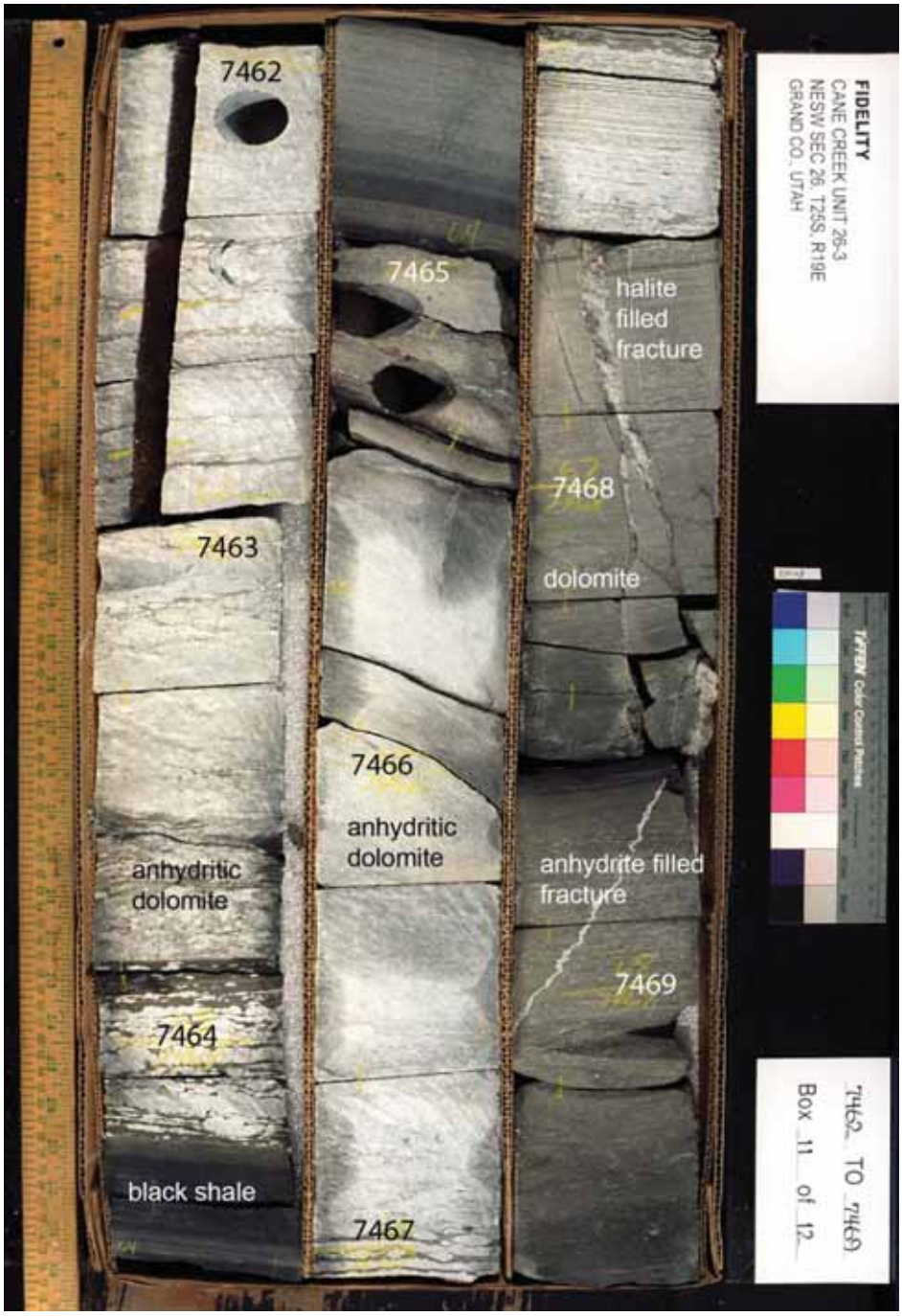

Figure 60. *Photograph of Cane Creek shale C zone in the Cane Creek 26-3 well. Dolomite with abundant anhydrite, thin interbedded black shale, halite- and anhydrite-filled fractures.*

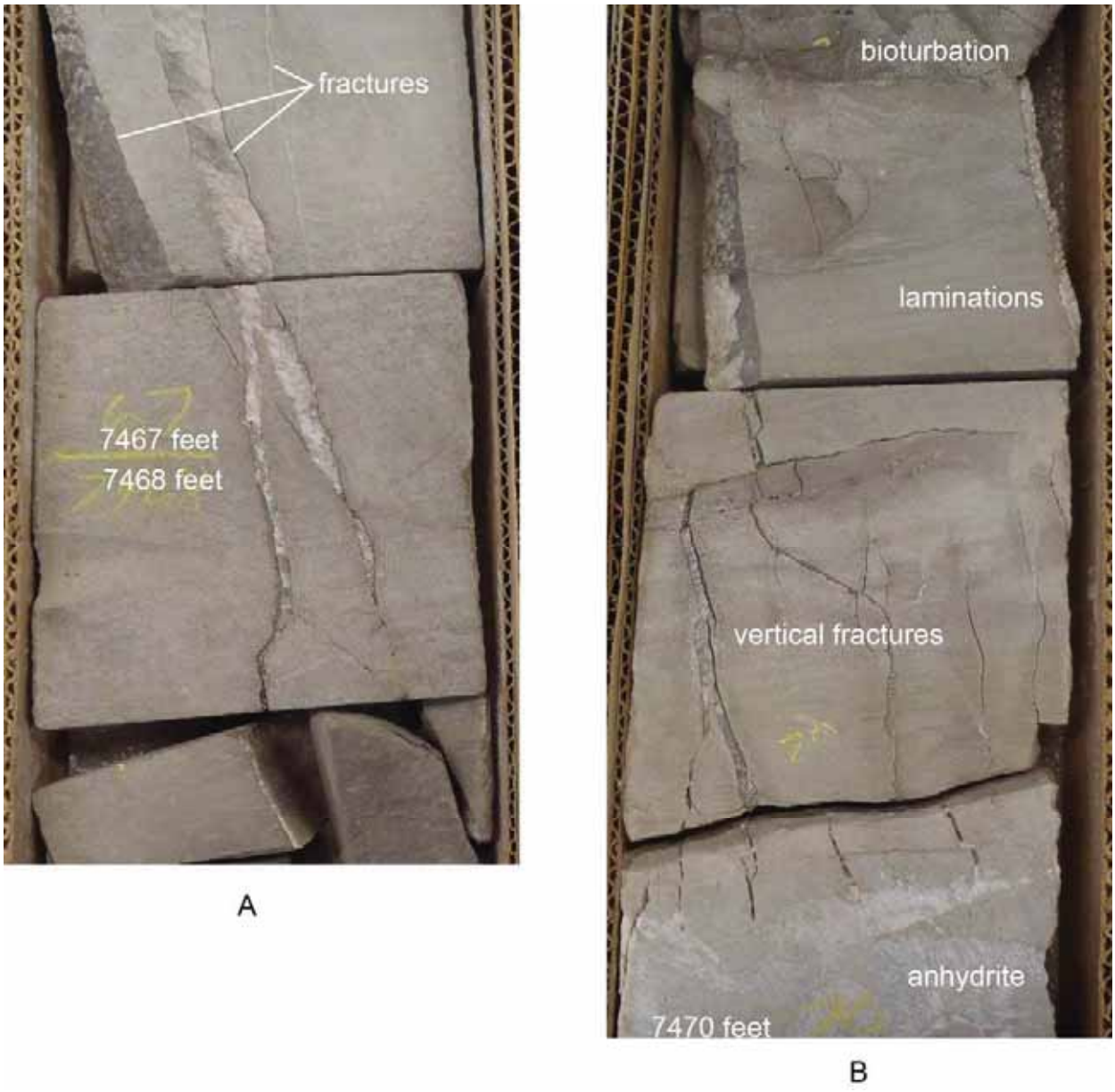

Figure 61. *Photographs of Cane Creek shale C zone core from Cane Creek 26-3. A) Very fine-grain, bioturbated sandstone with wide halite-filled and thinner clay(?)-filled fractures (7468 ft). B) Dolomitic siltstone with some horizontal laminations and bioturbation. Near vertical halite-filled fractures, some terminate upward at an internal bedding boundary and terminate downward into anhydritic dolomitic mudstone (7470 ft).*

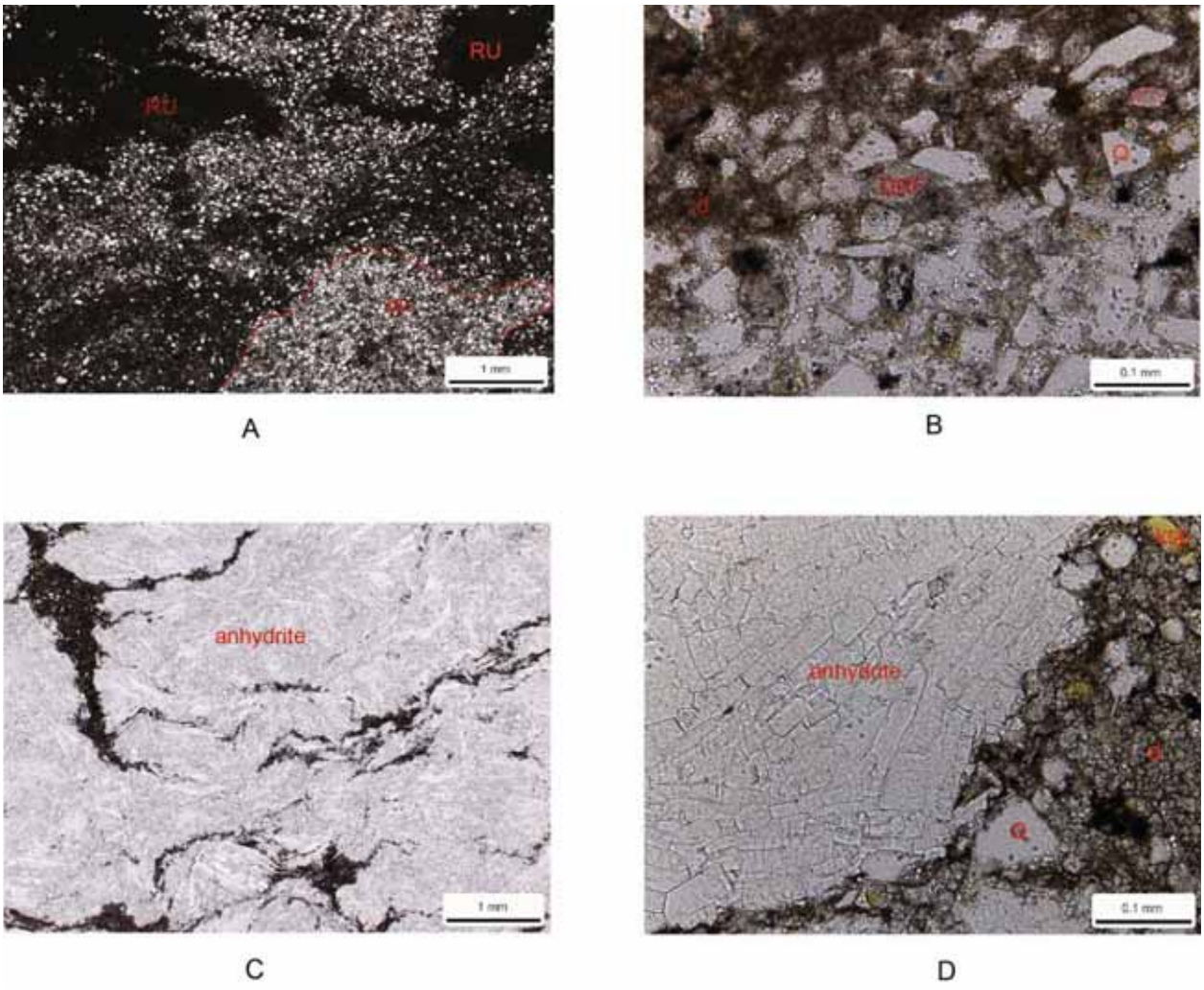

Figure 62. *Photomicrographs from Cane Creek 26-3 C zone. A) and B) Very fine-grain bioturbated (bu) dolomitic argillaceous sandstone (litharenite). Mostly quartz (Q) but also contains dolomite rock fragments (DRF) in a dolomitic (d) mudstone matrix. Core analysis from this depth indicates 9.2% porosity and 0.009 mD permeability (7452 ft). C) and D) Nodular anhydrite in a dolomitic mudstone. The mudstone contains quartz (Q) and potassium feldspar (ksp) as well as organic matter in a dolomitic mudstone matrix (d). Core analysis from this interval indicates 0.63% porosity and 0.001 mD permeability (7460 ft). From Core Laboratories, Inc., petrographic analysis report (appendix C).*

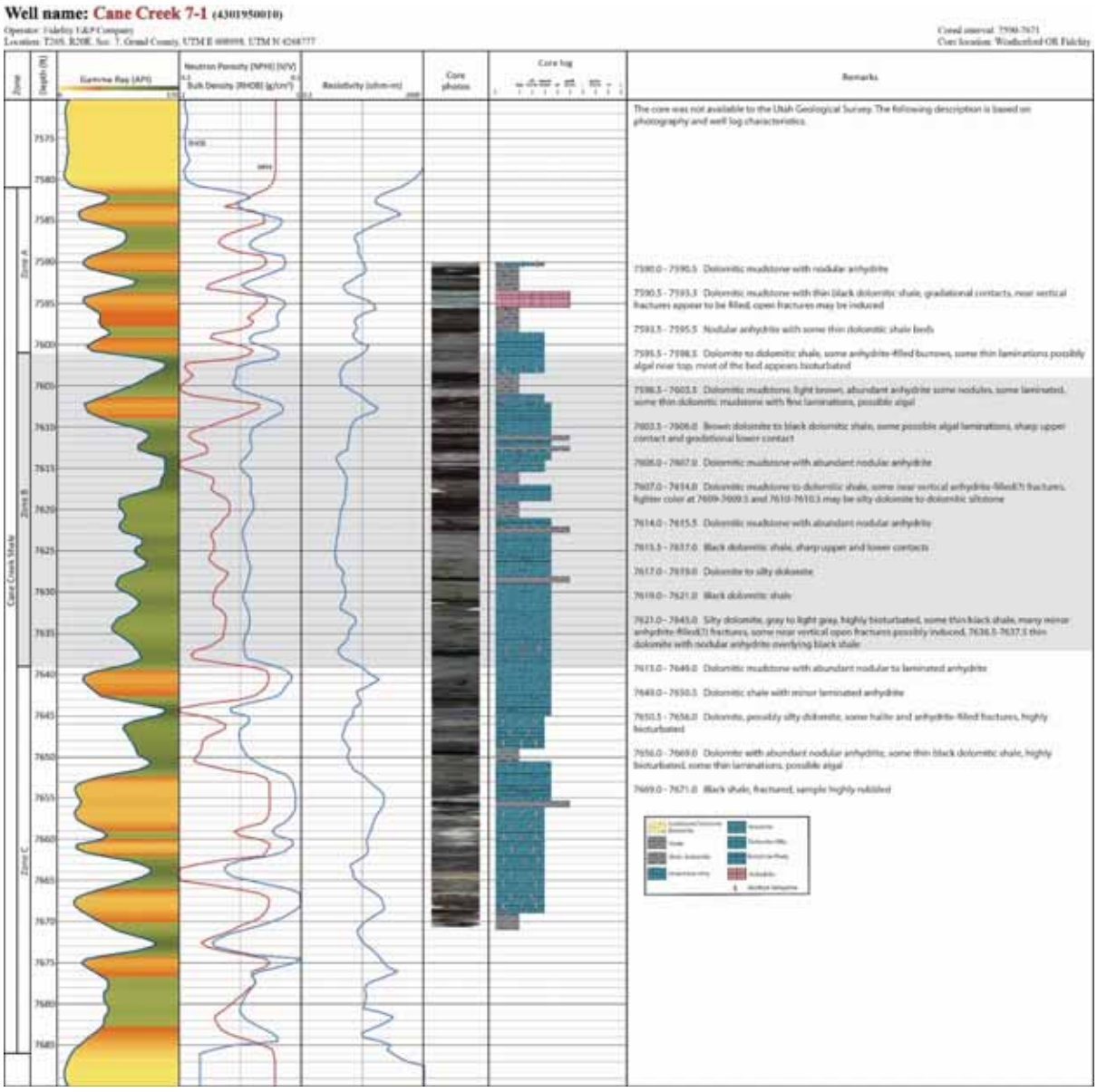

Figure 63. *Core log of the Cane Creek 7-1 well. A pilot hole was cored and then a horizontal lateral was drilled and completed in the Cane Creek shale B zone. The well has produced more than 36 MBO and 14 MMCFG through December 2015 (Utah Division of Oil, Gas and Mining).*

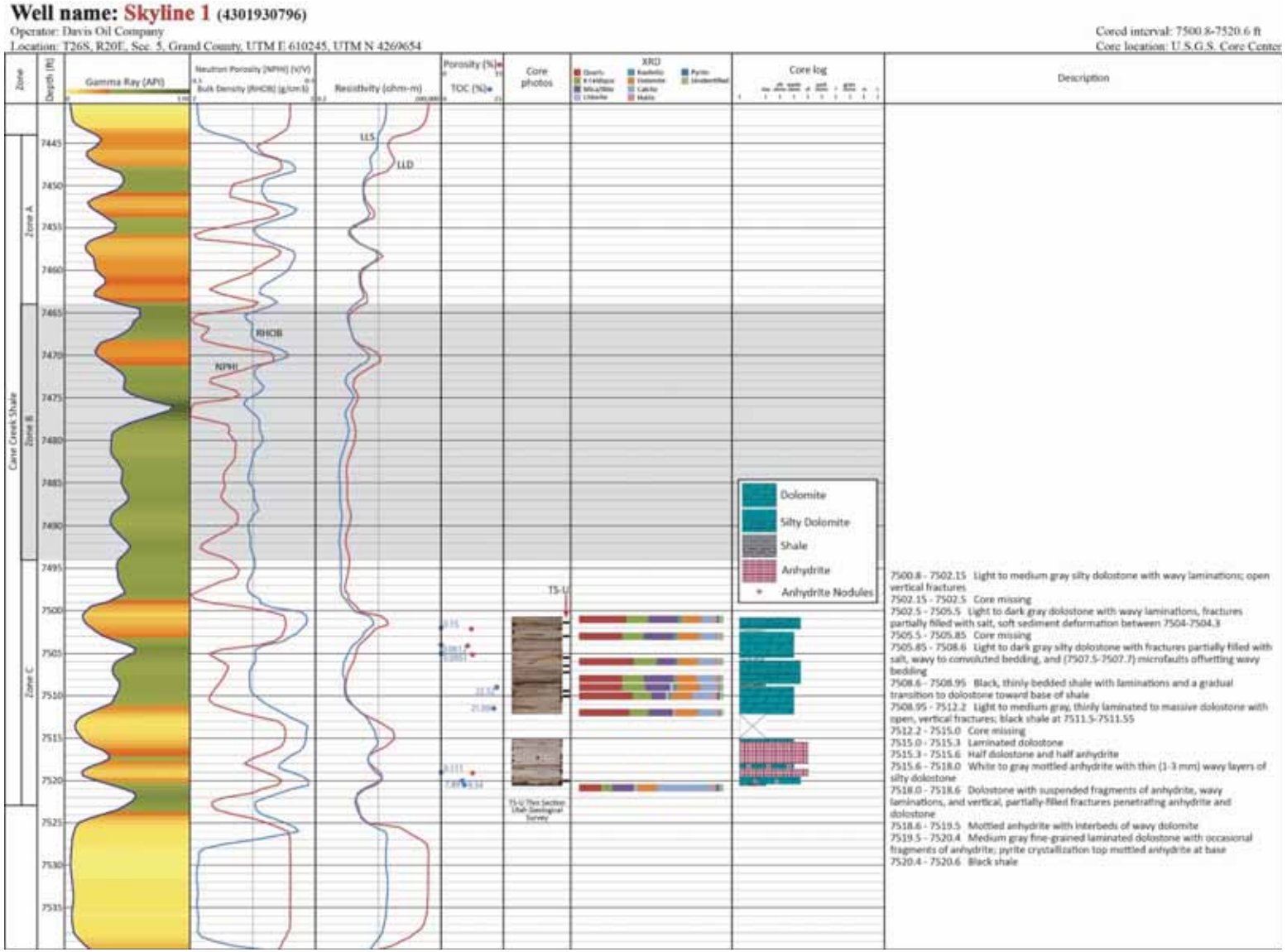

Figure 64. *Core log of Skyline 1 well, a vertical test of the Cane Creek shale. The well was cased and perforated in A, B, and C zones and swab tested at a rate of 10 BOPD. The well never produced and was plugged and abandoned in 1981.*

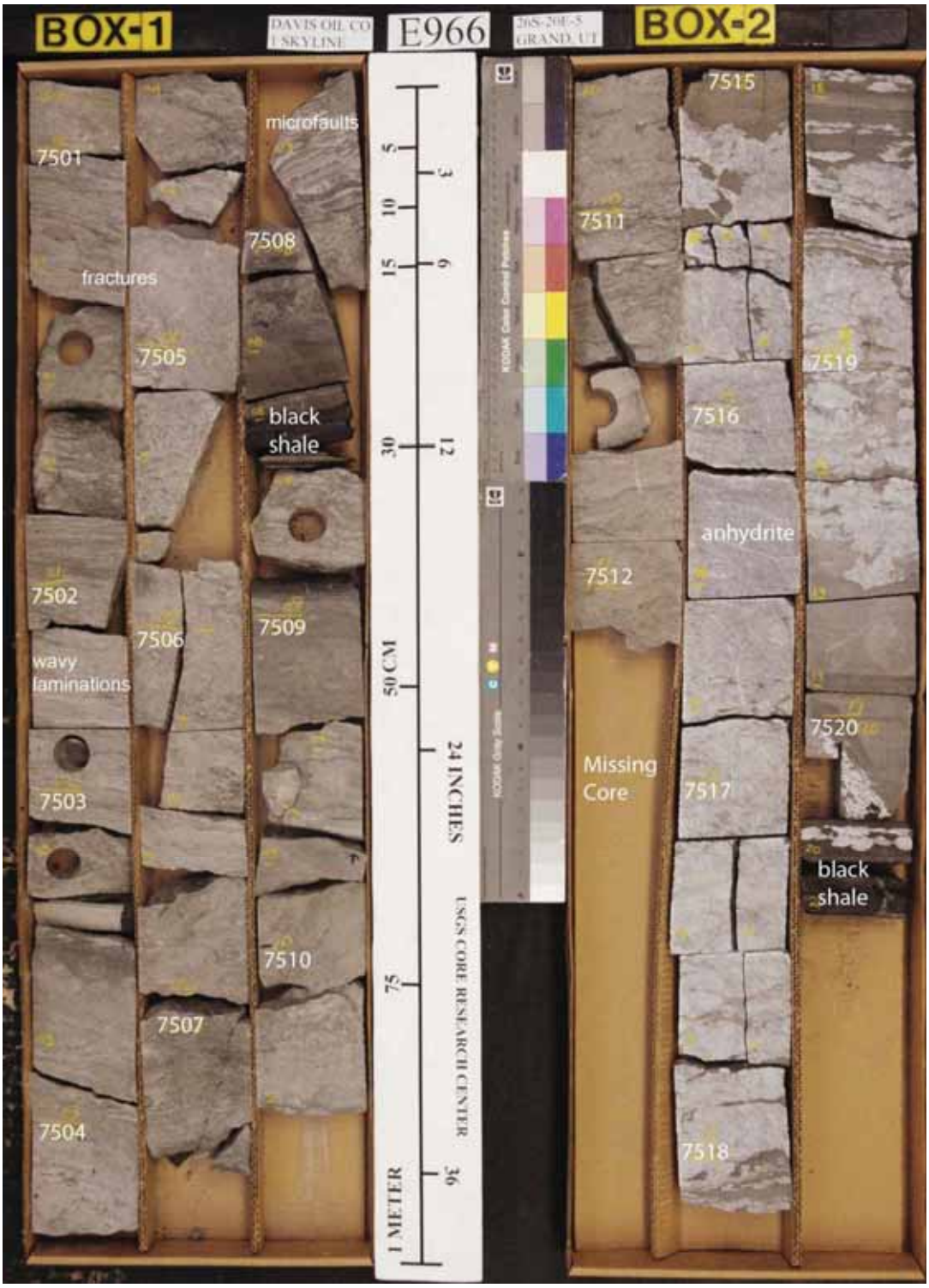

Figure 65. *Photograph of the Skyline 1 core, Cane Creek shale C zone. Primarily siltstone with thin black organic-rich shale and mottled anhydrite. Near vertical open fractures are drilling induced.*

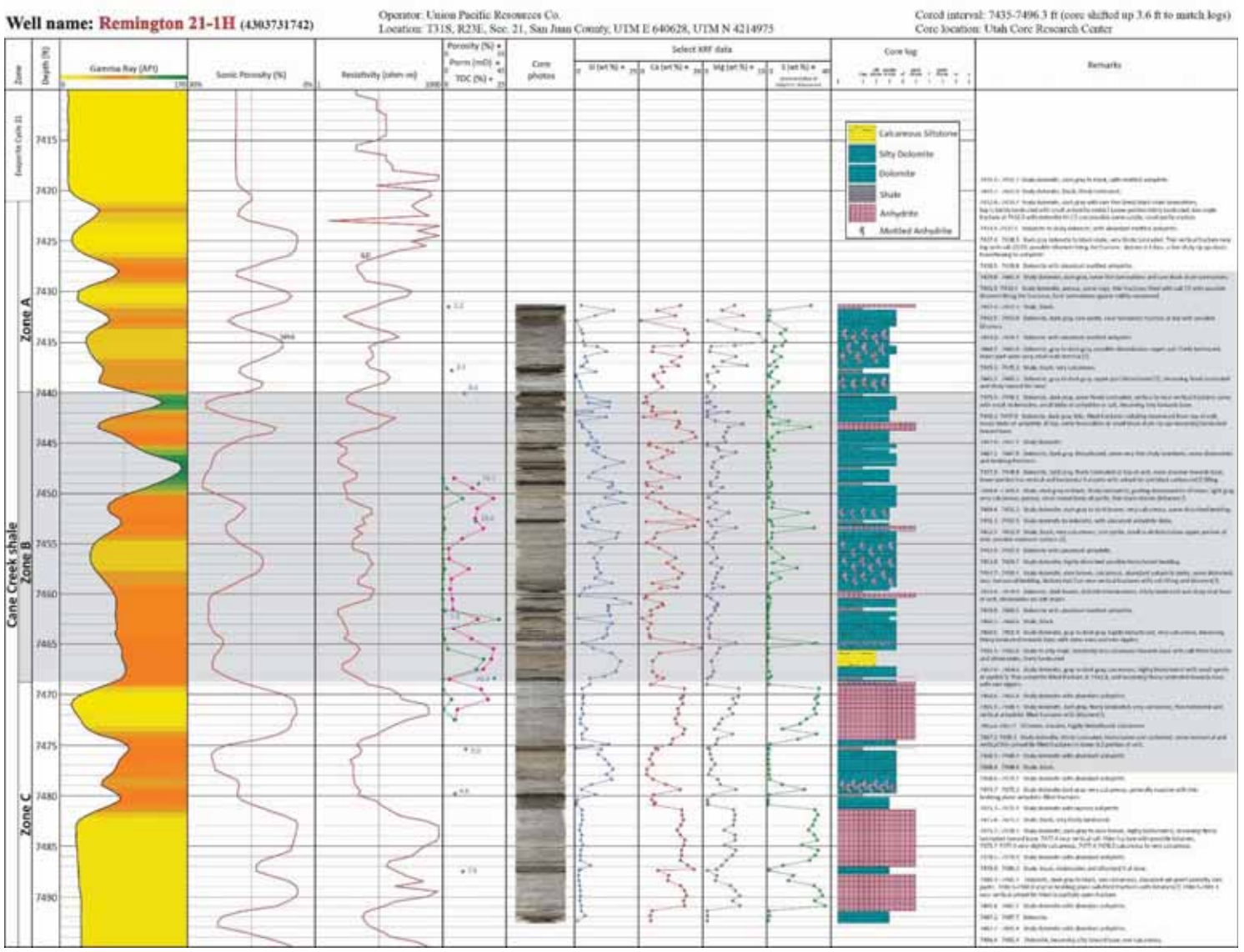

Figure 66. *Core log of the Remington 21-1H well. A pilot hole was cored in lower A zone, all of B and C zones, and then two horizontal laterals were drilled. The well was plugged and abandoned after production testing minor amounts of oil.*

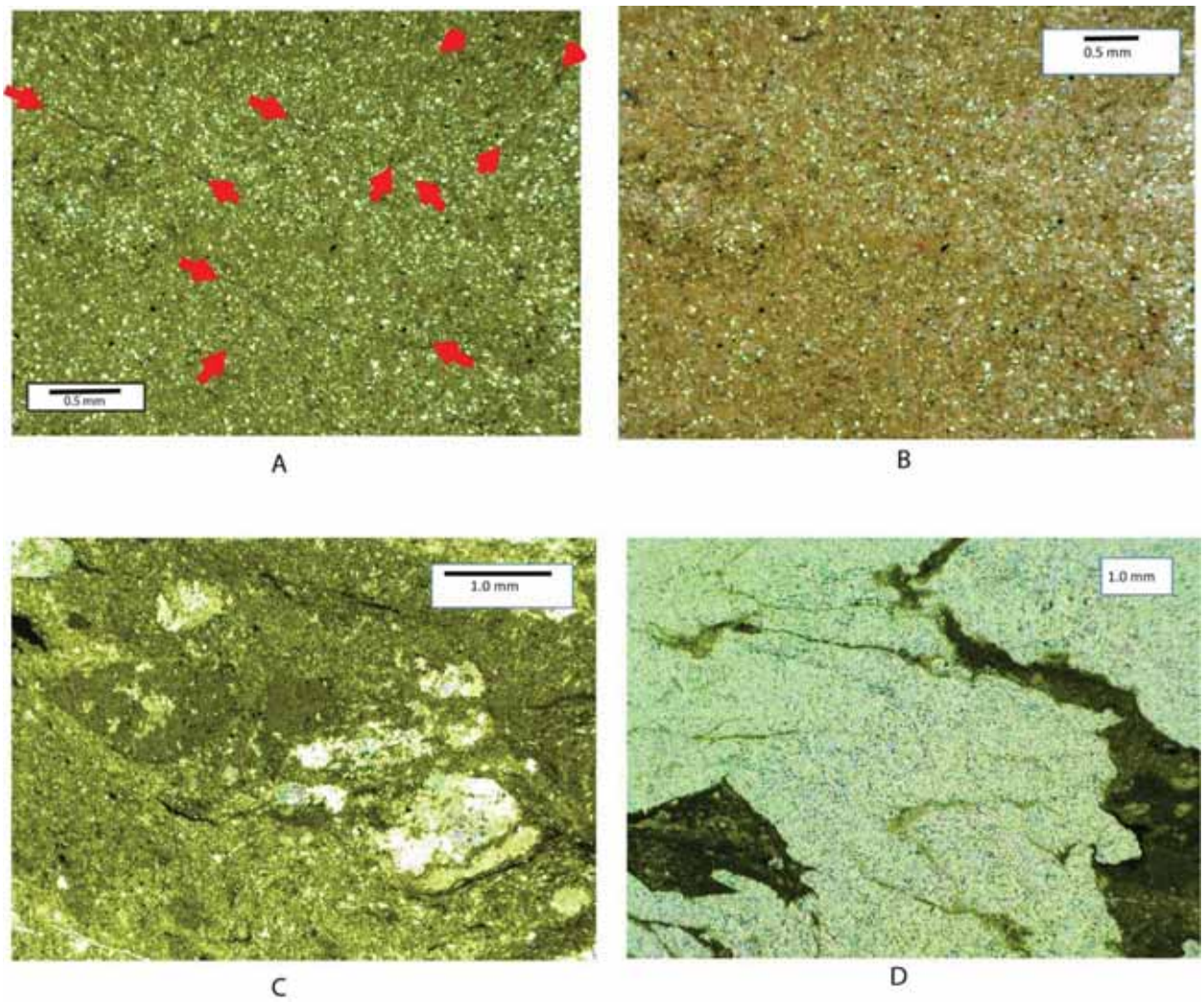

Figure 67. *Photomicrographs of the Cane Creek shale A zone from Remington 21-1H well. A) Finely crystalline dolomite contains small peloids and a significant amount of silt grains (white specks. Intersecting conjugate set of microfractures (red arrows) that appear to be open. Cross polarized light (7435 ft). B) Dolomite stained with Alizaren Red-S solution showing small but abundant patches of red to pink, indicating some calcite that has not been dolomitized. Quartz-rich silt grains and opaque diagenetic pyrite. Cross polarized and reflected light (7435 ft). C) Dolomitic matrix with small patches of white anhydrite, relicts of peloids, small intraclasts and black organic matter. Mottled pattern of dolomite is the result of bioturbation or haloturbation. Plane light (7437.3 ft). D) Anhydrite with felted micro fabric. Wispy dark-colored organic-rich dolomite. Cross polarized (7427.3 ft), From internal report by Eby Petrography and Consulting Inc. (appendix D).*

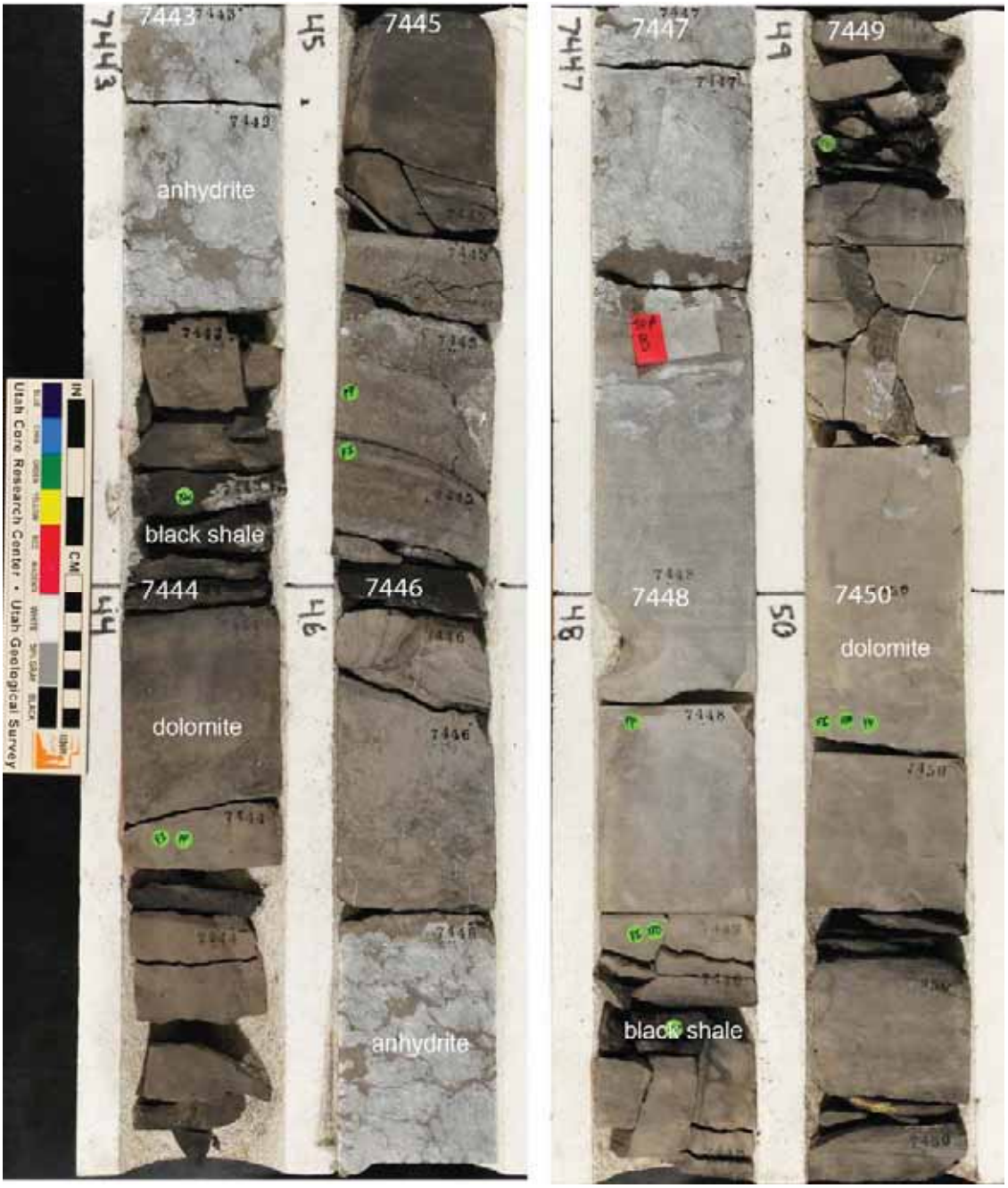

Figure 68. *Photographs of core from Cane Creek shale B zone in the Remington 21-1H well. Dolomite with thin black organic-rich shales and dolomite with anhydrite. Core depths are 3.6 feet deeper than log depths.*

Figure 69. *Photographs of core from the Cane Ceek shale B zone in the Remington 21-1H well. Dolomite and anhydritic dolomite with thin black shale, and thin siltstone. Massive anhydrite of the C zone. Core depths are 3.6 feet deeper than log depths.*

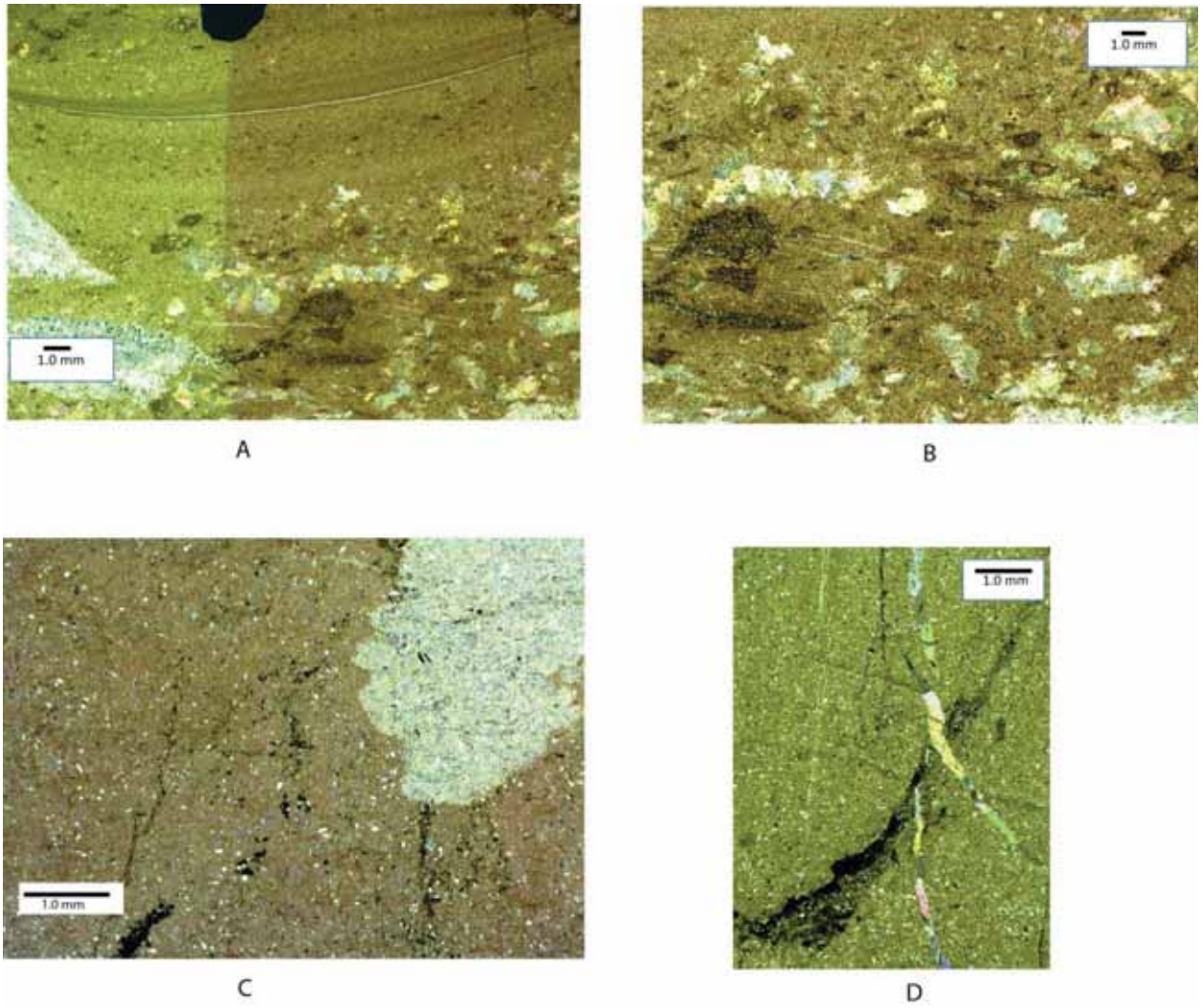

Figure 70. *Photomicrographs of Cane Creek shale B zone from Remington 21-1H. A) Dolomite with alternating mud-rich and grain-rich laminae that may be part of a stromatolitic microbialite. Anhydrite replacement white, gray, and multicolored patches. Viewed under cross polarized light (7448 ft). B) Dolomite with scattered anhydrite replacement (light pastel colored areas). Remnants of original grains and peloids and possible thin-shelled skeletal fragments (7448 ft). C) Dolomite with mottled anhydrite (upper right) and abundant white detrital silt grains. Some black bitumen, pyrite crystals (opaque), and microfractures partially lined with black bitumen (7450 ft). D) Dolomite matrix with disseminated white and gray specks of silt-sized detrital grains. Fractures in pastel colors are calcite and anhydrite filled, black bitumen-filled fracture. Cross polarized light (7450 ft). From internal report by Eby Petrography and Consulting Inc. (appendix D).*

Figure 71. *Photographs of core from Cane Creek shale C zone in the Remington 21-1H well. Dolomite with abundant anhydrite. Core shown wet to highlight the texture in the anhydrite beds.*

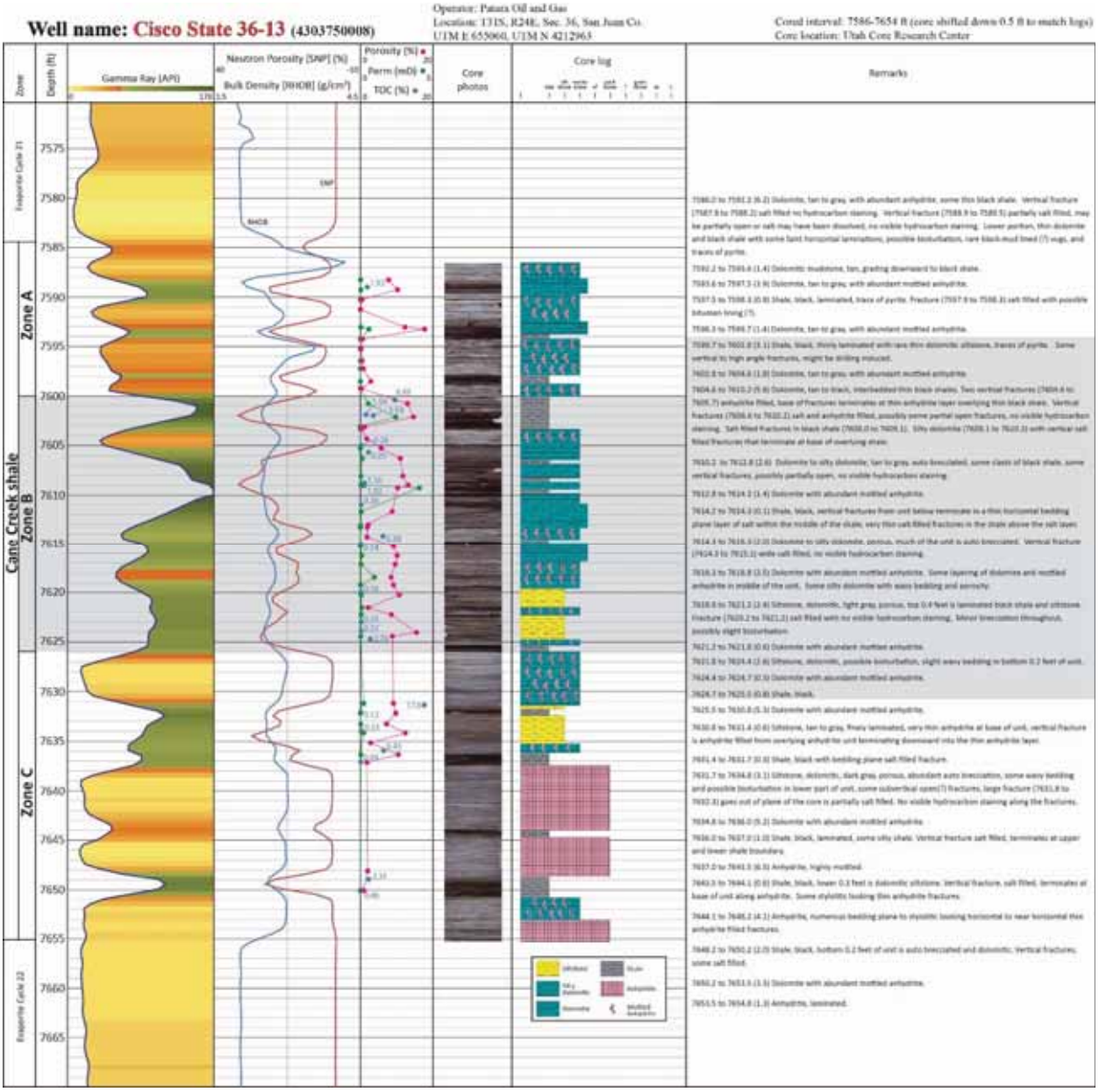

Figure 72. *Core log of the vertical Cisco State 36-13 Cane Creek test. The well was cased and tested (results not reported) and then plugged and abandoned.*

Figure 73. *Photographs of core from Cane Creek shale A zone in the Cisco State 36-13 well. Dolomitic mudstone with abundant anhydrite, some thin organic-rich black shales. Core shown wet to highlight the texture in the anhydrite beds.*

Figure 74. *Photographs of core from Cane Creek shale B zone in the Cisco State 36-13 well. Dolomitic mudstone with abundant anhydrite with interbedded dolomitic siltstone and thin organic-rich black shales. Core shown wet to highlight the texture in the anhydrite beds.*

Figure 75. *Photographs of core from the Cane Creek shale C zone in the Cisco State 36-13 well. Mostly anhydrite in a dolomitic mudstone matrix with some interbedded dolomitic siltstone and organic-rich black shale. Core shown wet to highlight the texture in the anhydrite beds.*

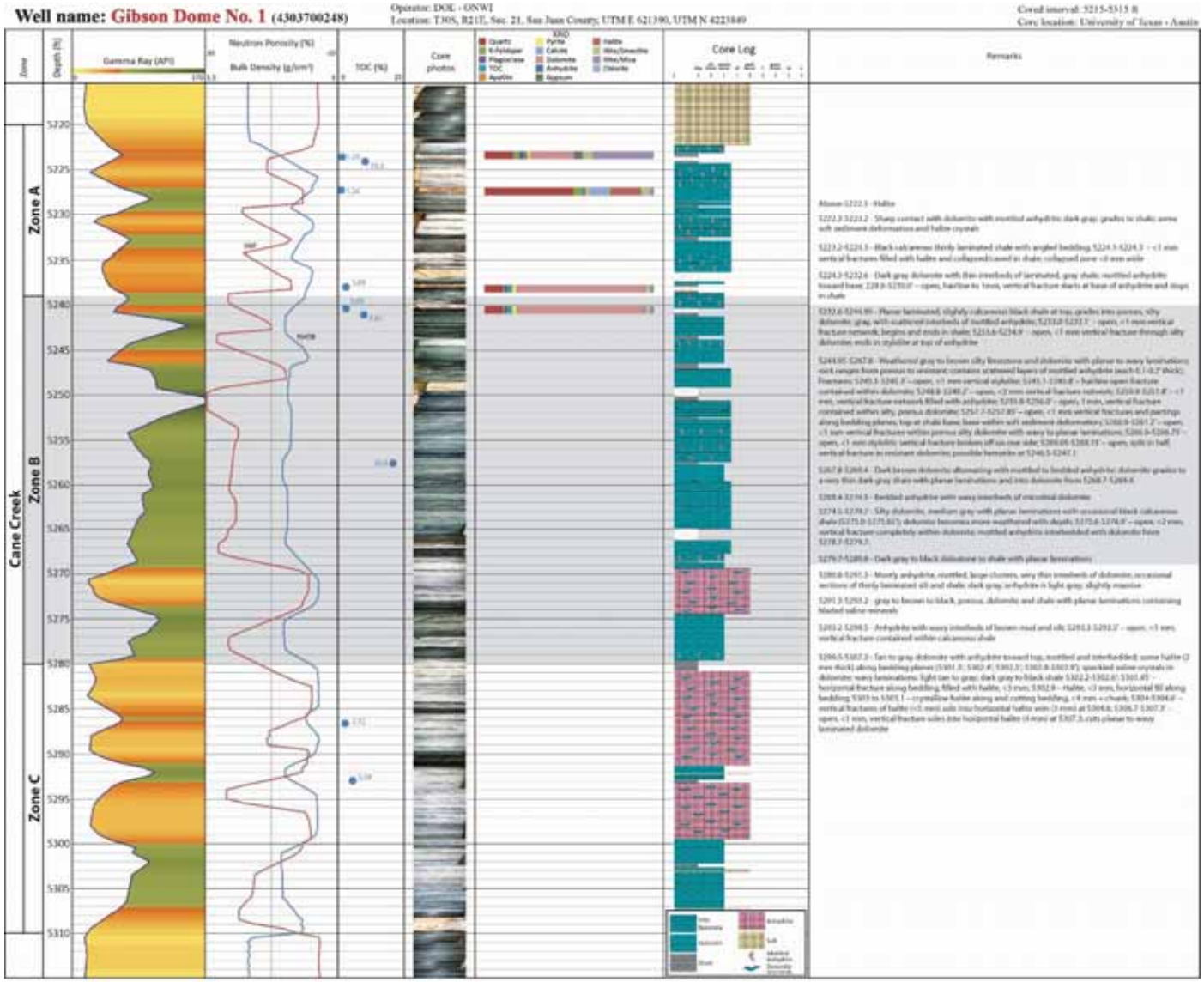

Figure 76. *Core log of the Gibson Dome 1 well. The U. S. Department of Energy cored the Paradox Formation to evaluate the formation's potential for high-level radioactive-waste storage. The well's oil potential was not tested.*

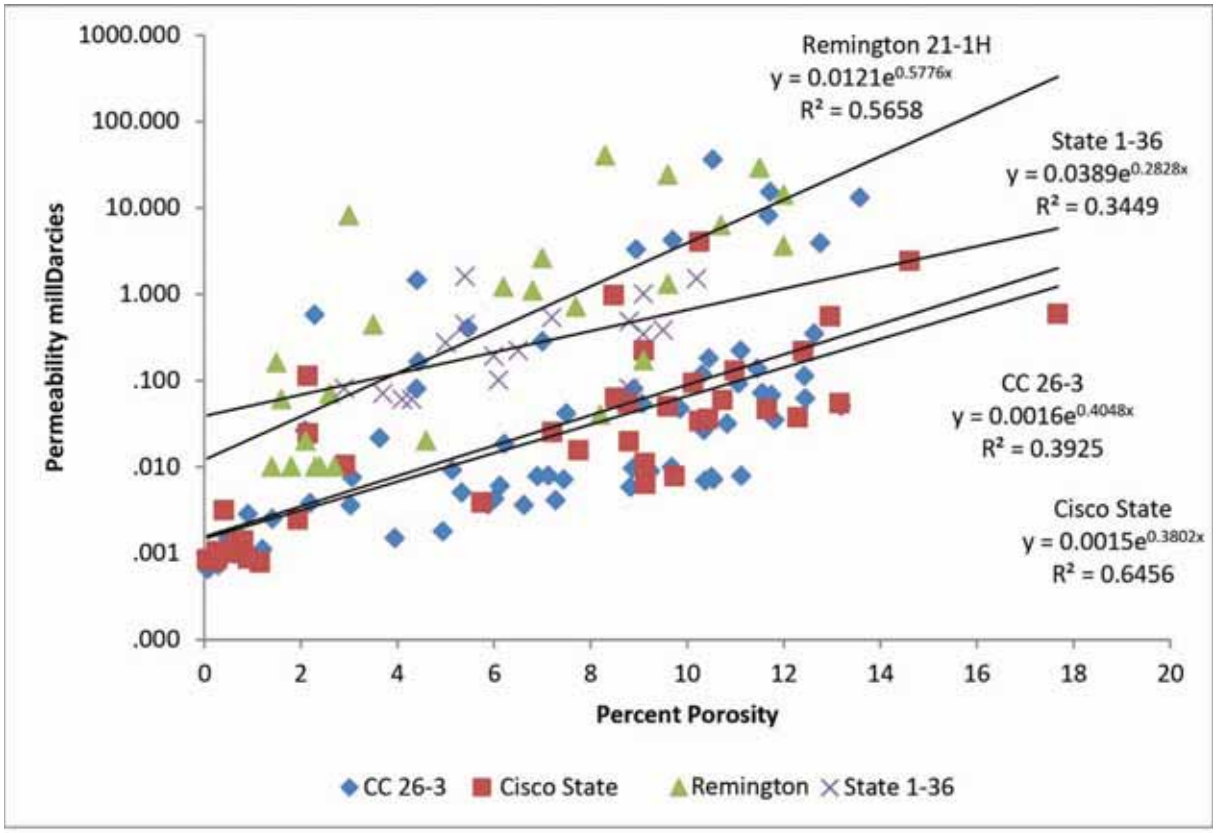

Figure 77. *Plot of Cane Creek shale porosity versus permeability from core plug analyses of four wells. CC 26-3 and State 1-36 are from the Big Flat area. The Cisco State and Remington 21-1H are from the Lisbon area. Remington and Chevron appear to have better reservoir quality but Remington was measured at 400 psi confining pressure, Chevron confining pressure was not reported. CC 26-3 data was measured at 2280 psi and Cisco State at 2310 psi confining pressure. See figure 2 for location of wells. CC 26-3 = Cane Creek unit 26-3.*

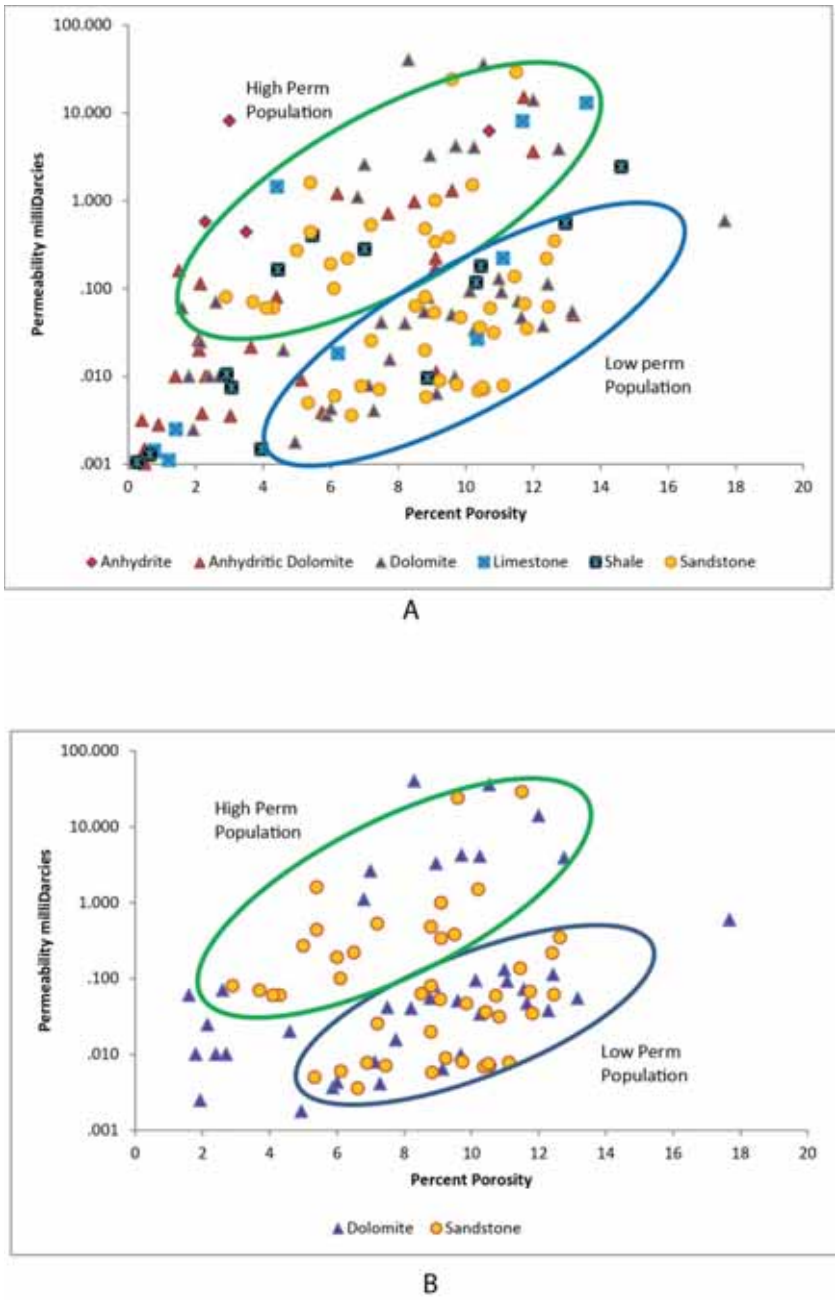

Figure 78. *Porosity and permeability cross plots based on lithology from CC 26-3, State 1-36, Cisco State 36-13, and Remington 21-1H. A) The data is grouped into two populations; the high perm population may be plugs with microfractures. All lithologies are represented in both populations except anhydrite. B) Same data set as in (A) but only dolomite and sandstone samples, the primary reservoir facies are plotted. The two reservoir facies are about equally represented in each population.*

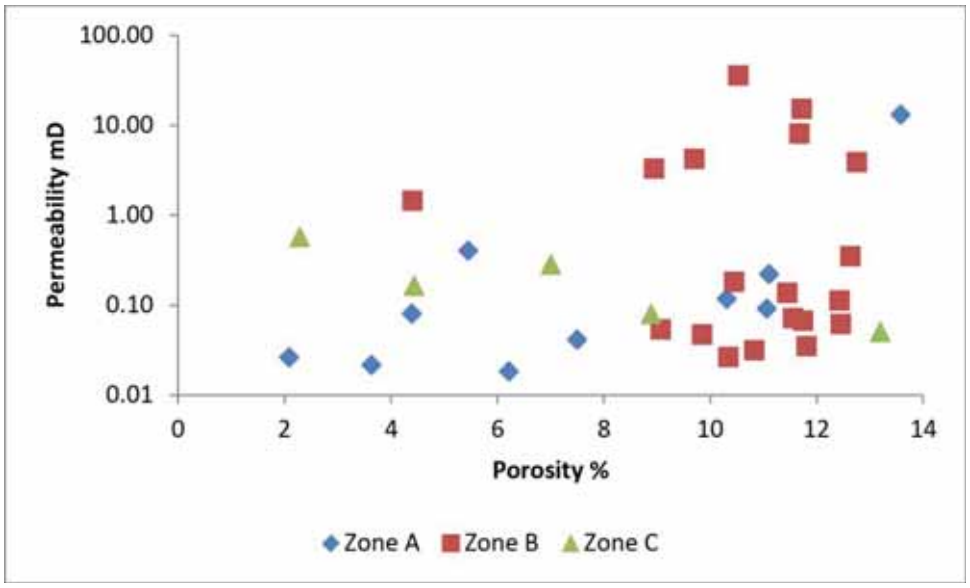

Figure 79. *Porosity and permeability core plug analysis for the Cane Creek shale A, B, and C zones from the Cane Creek 26-3 well. The B zone is the primary reservoir, and B zone samples have higher porosity and therefore greater storage capacity than the A or C zones.*

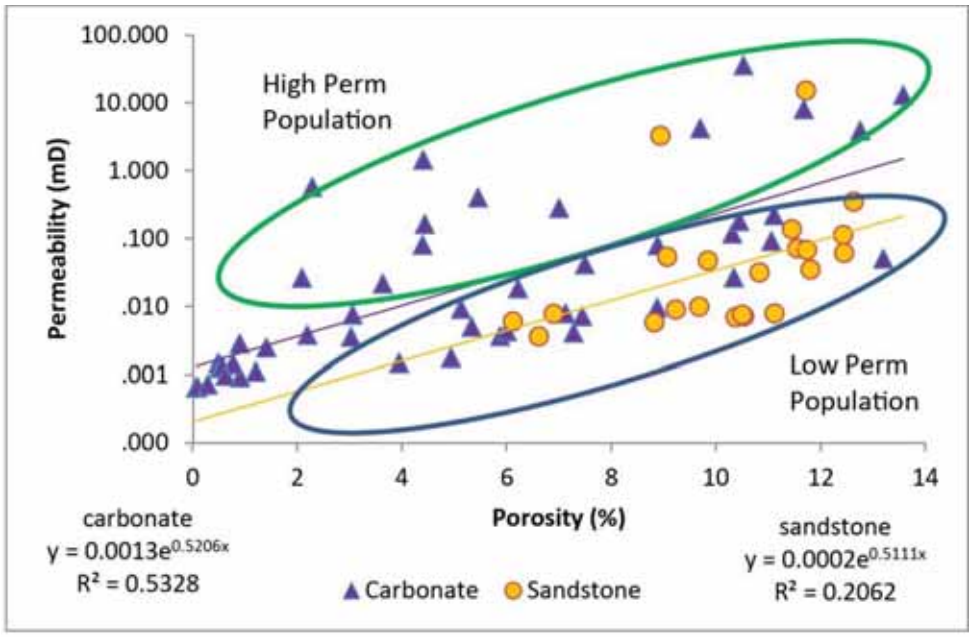

A

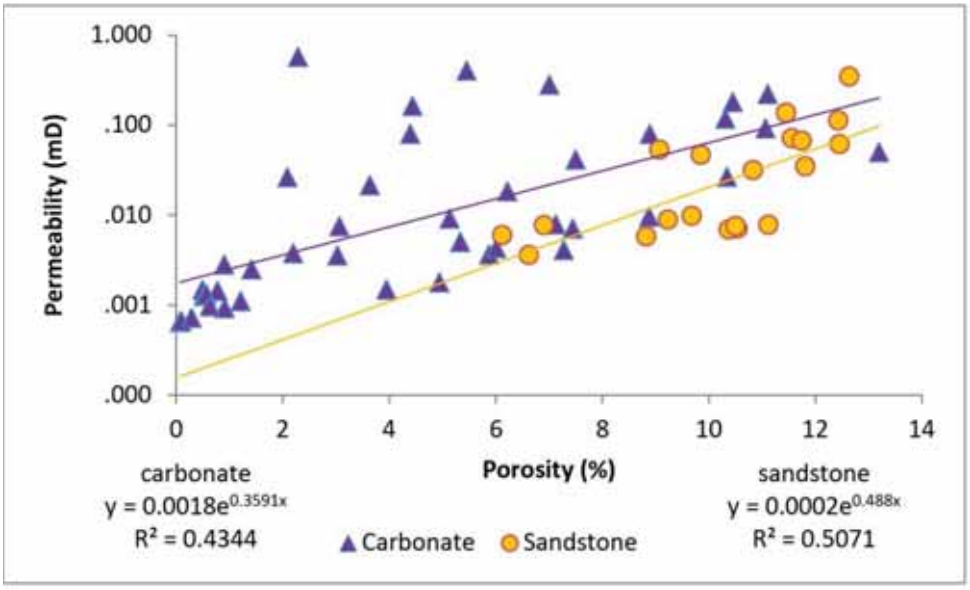

B

Figure 80. *Porosity versus permeability data from the Cane Creek 26-3 well plotted by lithology. A) Displays all of the data, higher permeability may be the result of fractures. B) Data above 1 mD is eliminated focusing on the lower permeability population. The carbonate has higher permeability than sandstone at lower porosity, but the sandstone has more data points above 8% porosity.*

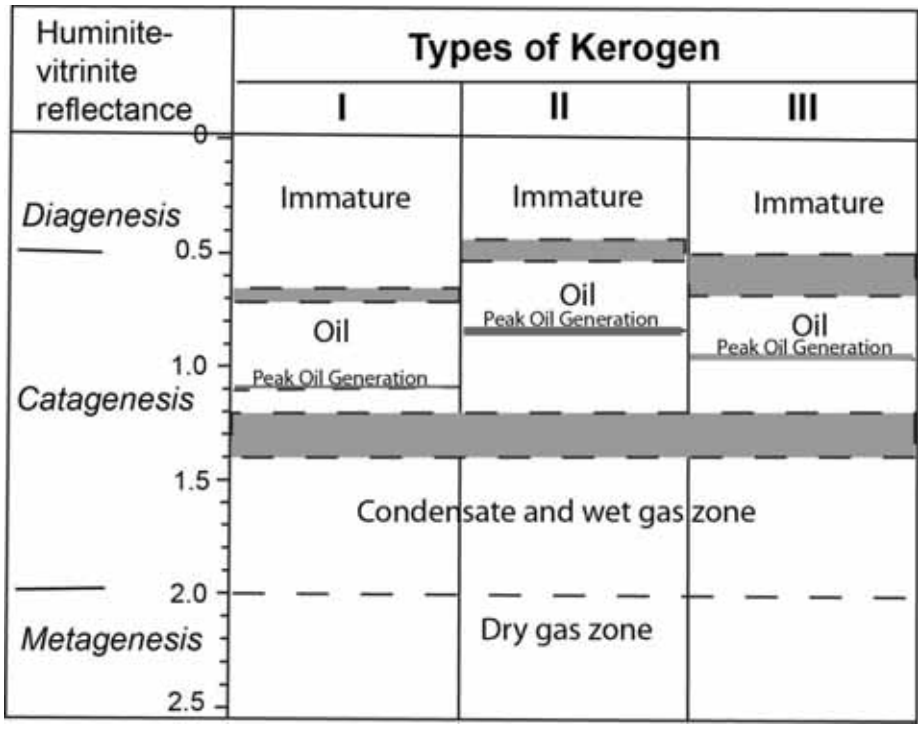

Figure 81. *Stages of kerogen maturation based on vitrinite reflectance (%Ro). Cane Creek shale has mostly type I and II kerogens. Modified from Tissot and Welte (1984).*

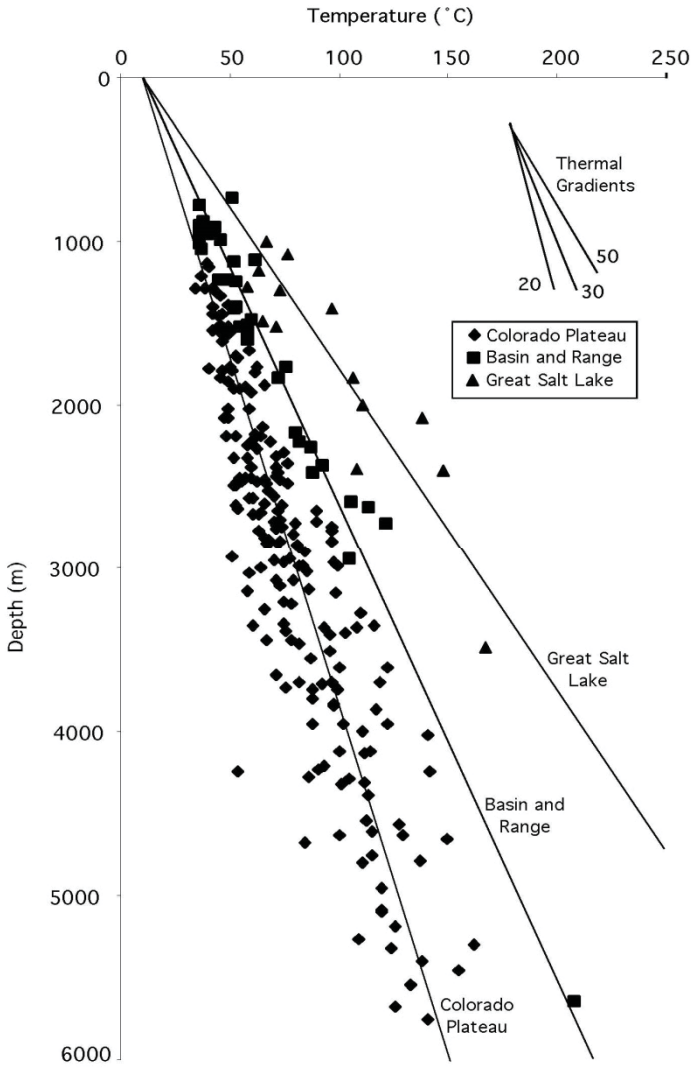

Figure 82. *Temperature versus depth throughout the state of Utah. The average thermal gradient for the Colorado Plateau is 26° C km^{-1}. From Henrikson and Chapman (2002).*

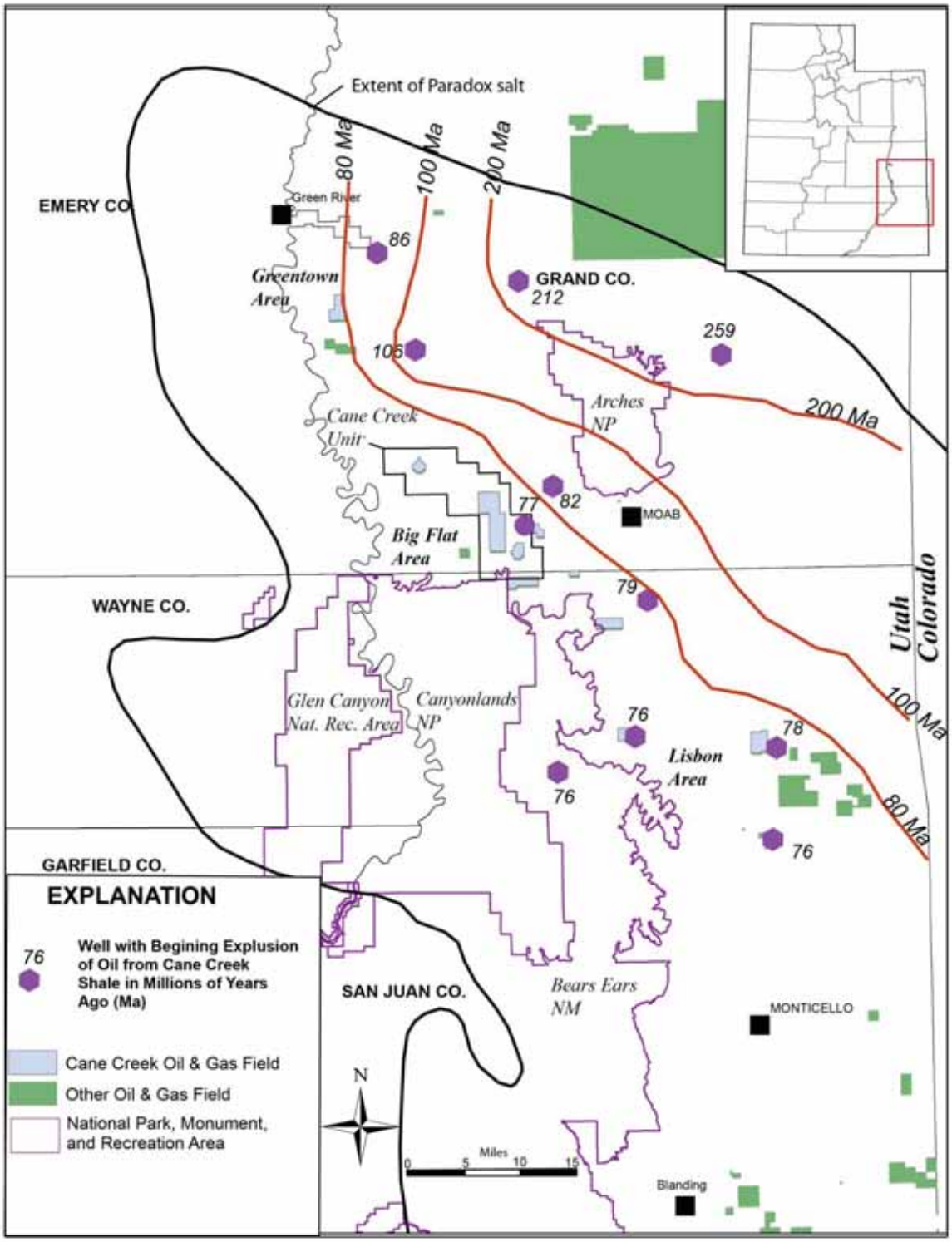

Figure 83. *Map showing when oil expulsion from the Cane Creek shale began. Generation began in the deep basin near the Uncompahgre uplift and progressed to the southwest. Data from Rasmussen and Rasmussen (2009).*

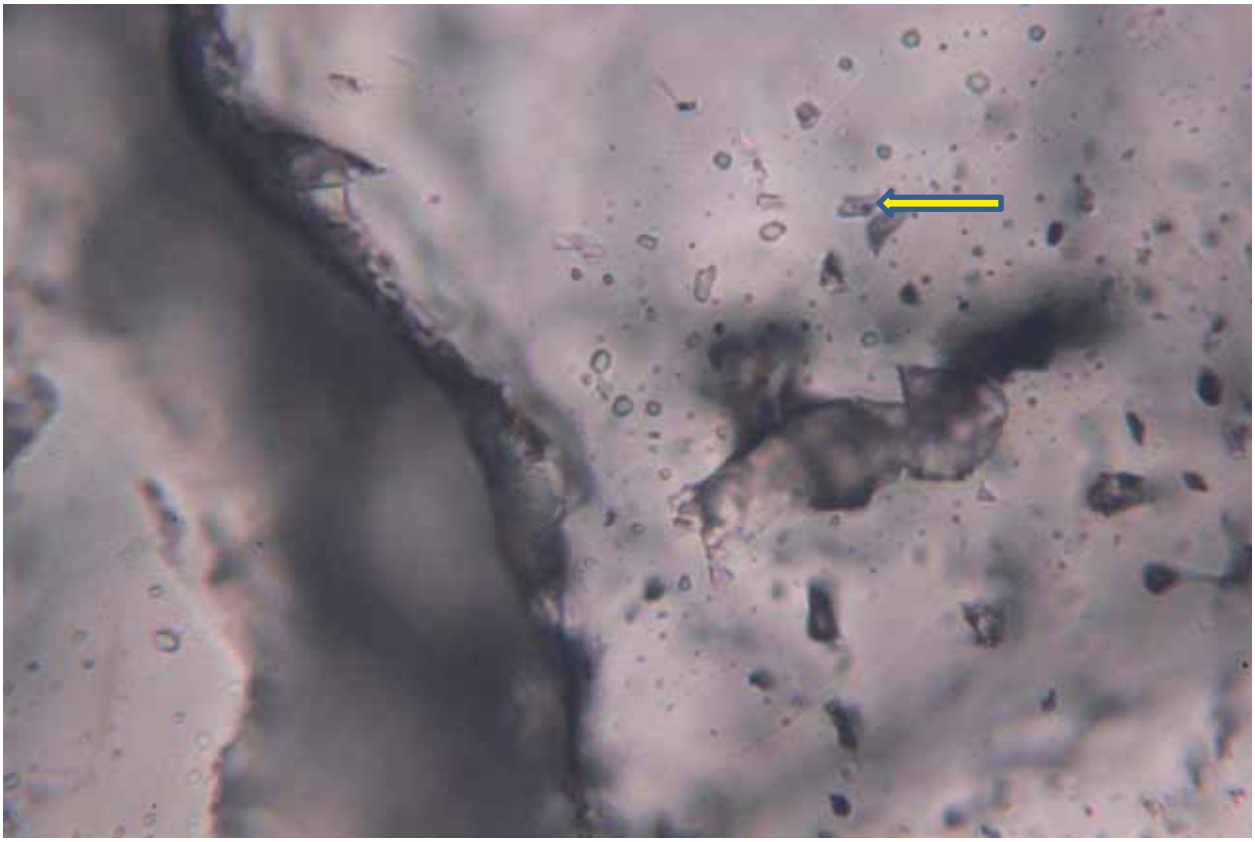

Figure 84. *Thin section from Cisco State 36-13 at a depth of 7360.9 feet showing primary aqueous fluid inclusions in dolomite. The majority of inclusions contain only liquid. The arrow points to a two-phase inclusion. The image was taken under plane polarized light and the field of view is 0.3 mm.*

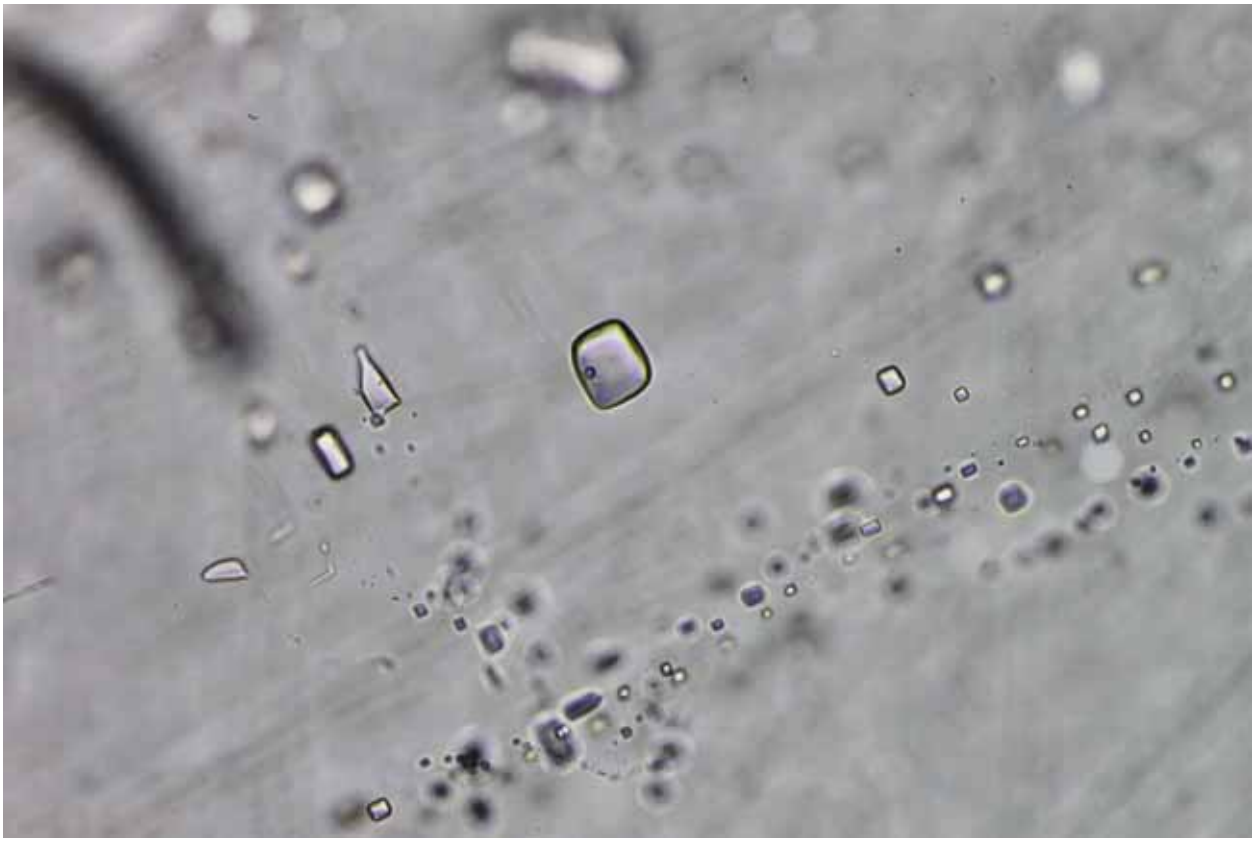

Figure 85. *Thin section from Cisco State 36-13 at a depth of 7630.9 feet showing one- and two-phase aqueous fluid inclusions in halite. The large central inclusion contains a small vapor bubble; the other inclusions contain only liquid. The image was taken under plane polarized light and the field of view is 1 mm.*

Figure 86. *Thin section from Cane Creek 26-3 well from a depth of 7420 feet showing three-phase aqueous fluid inclusion containing liquid, a vapor bubble and a halite crystal (at point of arrow). The inclusion is 61 micrometers long, exceptionally large. The dissolution temperature of the halite indicates a NaCl content of 29 wt%.*

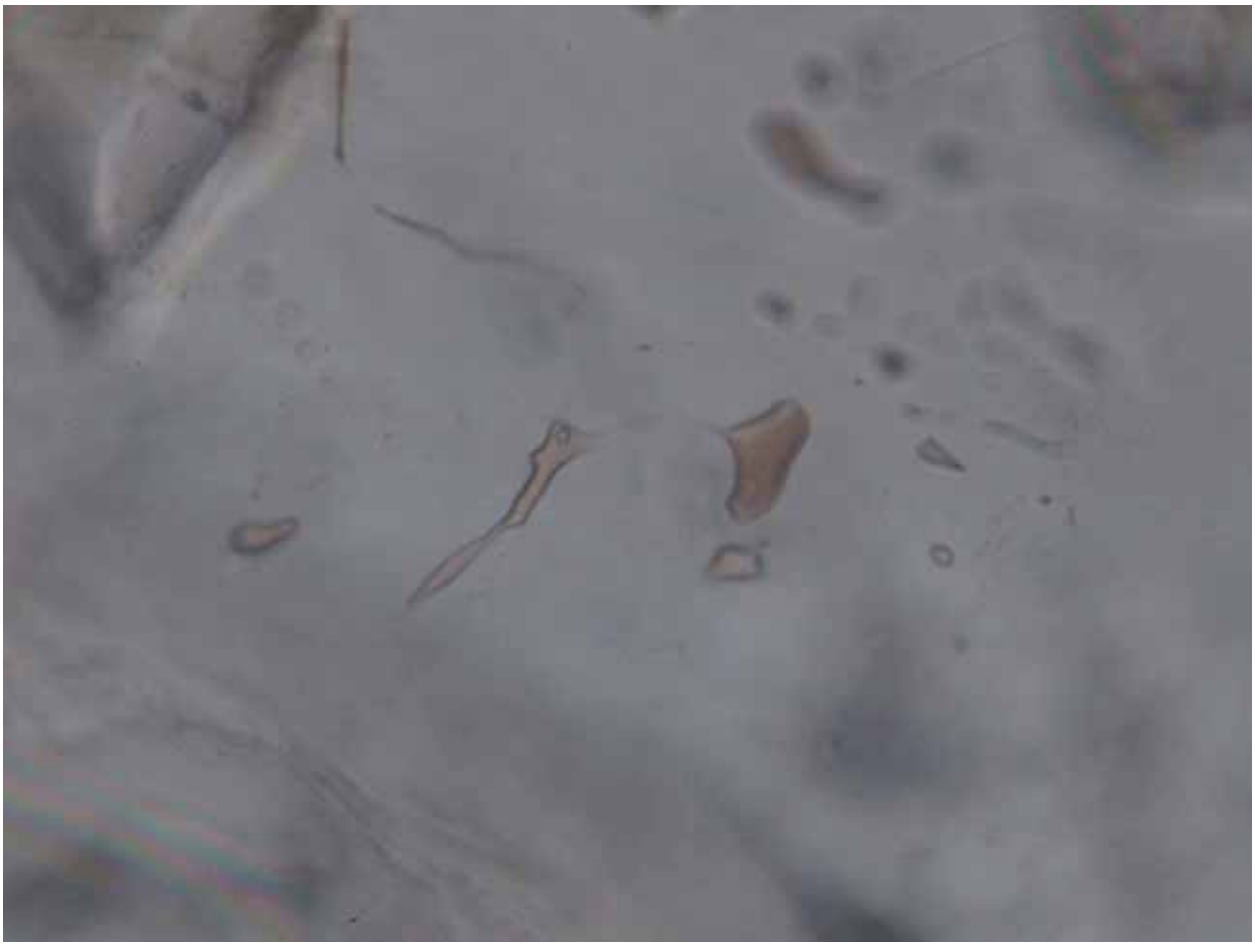

Figure 87. *The thin section from Cisco State 36-13 well from a depth of 7630.9 feet showing one- and two-phase secondary oil inclusions in dolomite. The central inclusion contains a small vapor bubble. The image was taken under plane polarized light and the field of view is 0.3 mm.*

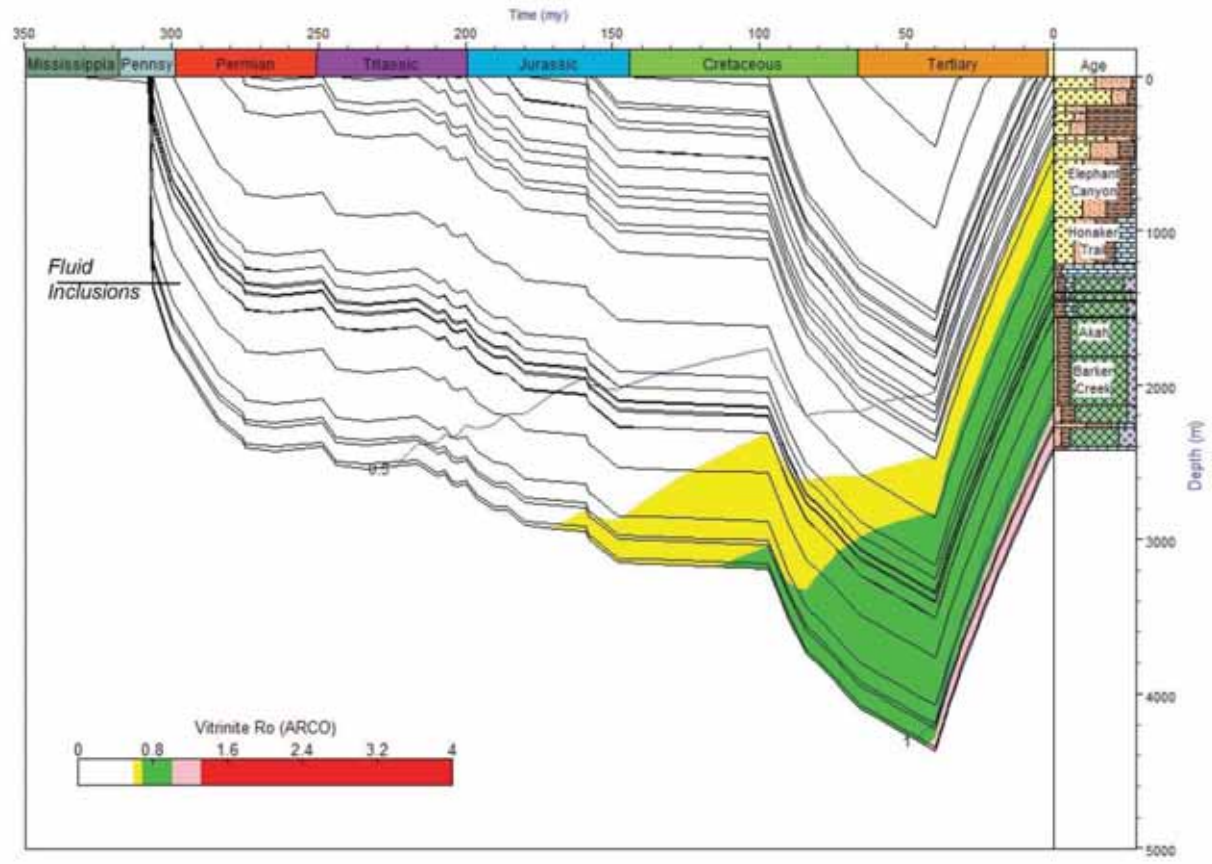

Figure 88. *Burial history chart for the Cane Creek 26-3 well using the Genesis 5.5 program. Time of early oil generation is shown as 0.5% Ro with peak oil generation shown in green. Fluid inclusions from the Cane Creek shale have a 50° C temperature, equivalent to 1400 meters (4600 feet), and must have migrated from deeper in the basin.*

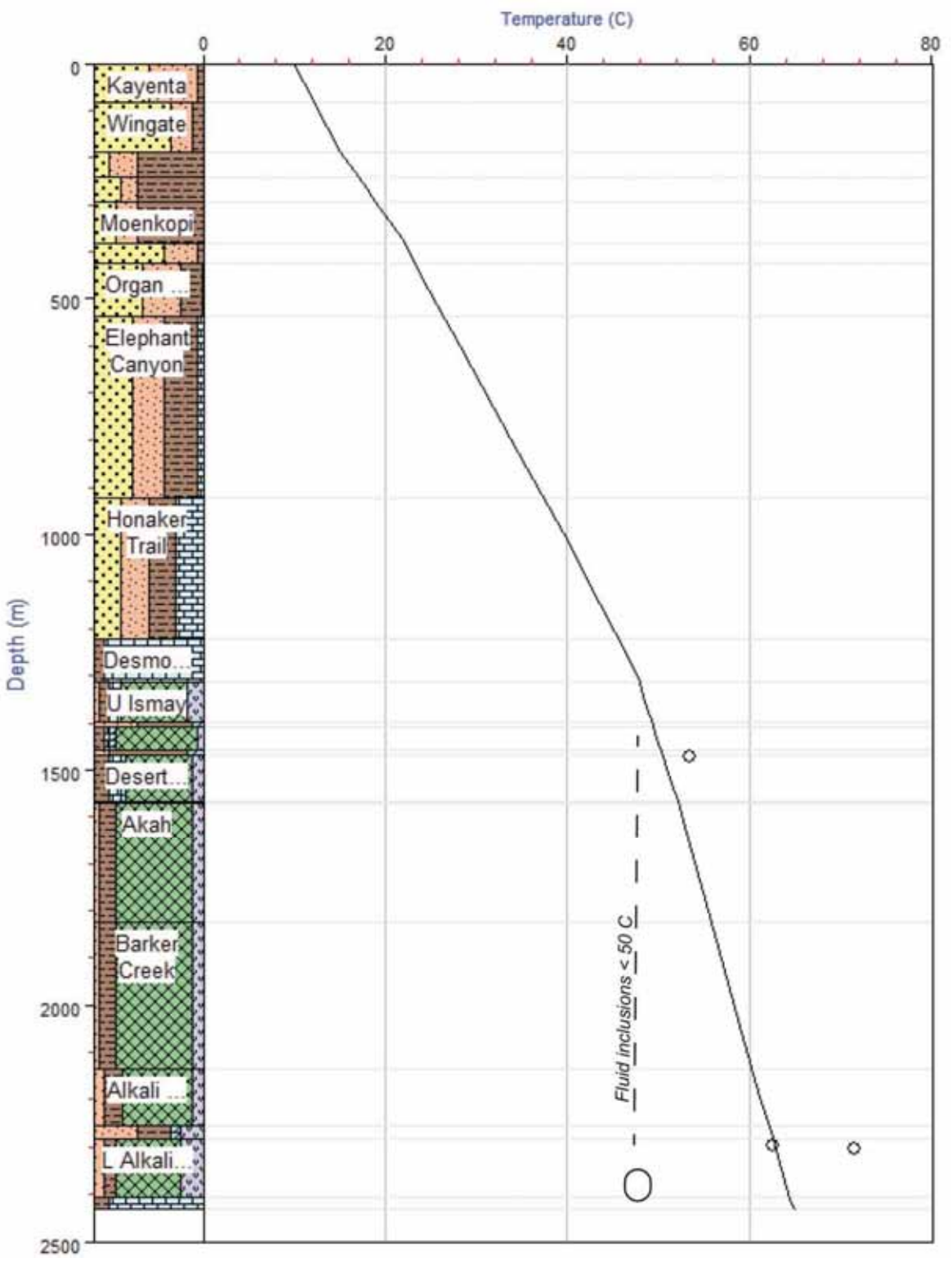

Figure 89. *Temperature gradient for the Cane Creek 26-3 well using the Genesis 5.5 program. Temperature of fluid inclusions in the Cane Creek shale are less than 50□ indicating a depth of about 1400 meters (4600 feet) (Moore, 2015).*

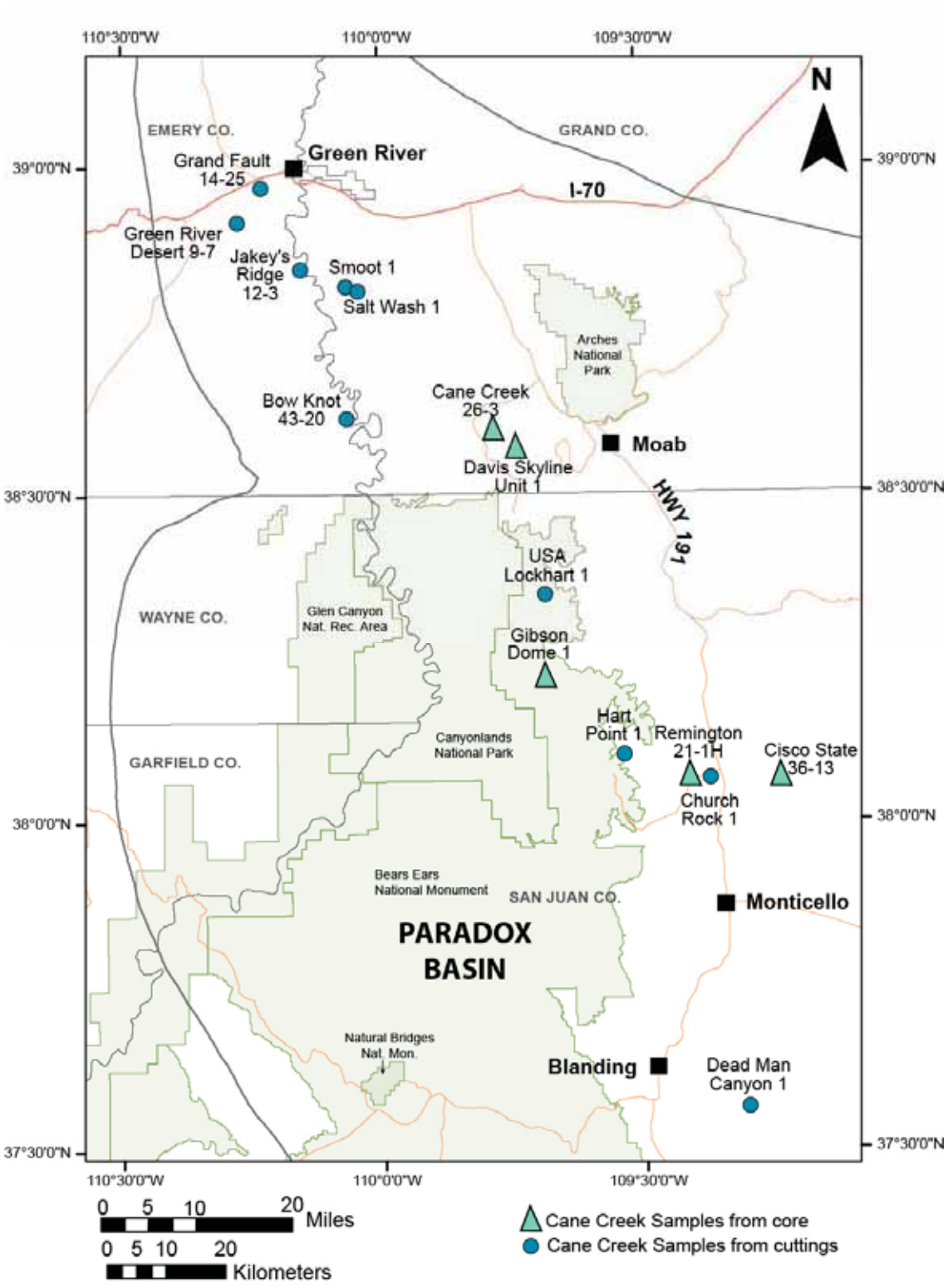

Figure 90. *Index map of 15 wells used in the geochemical analyses, see table 15.*

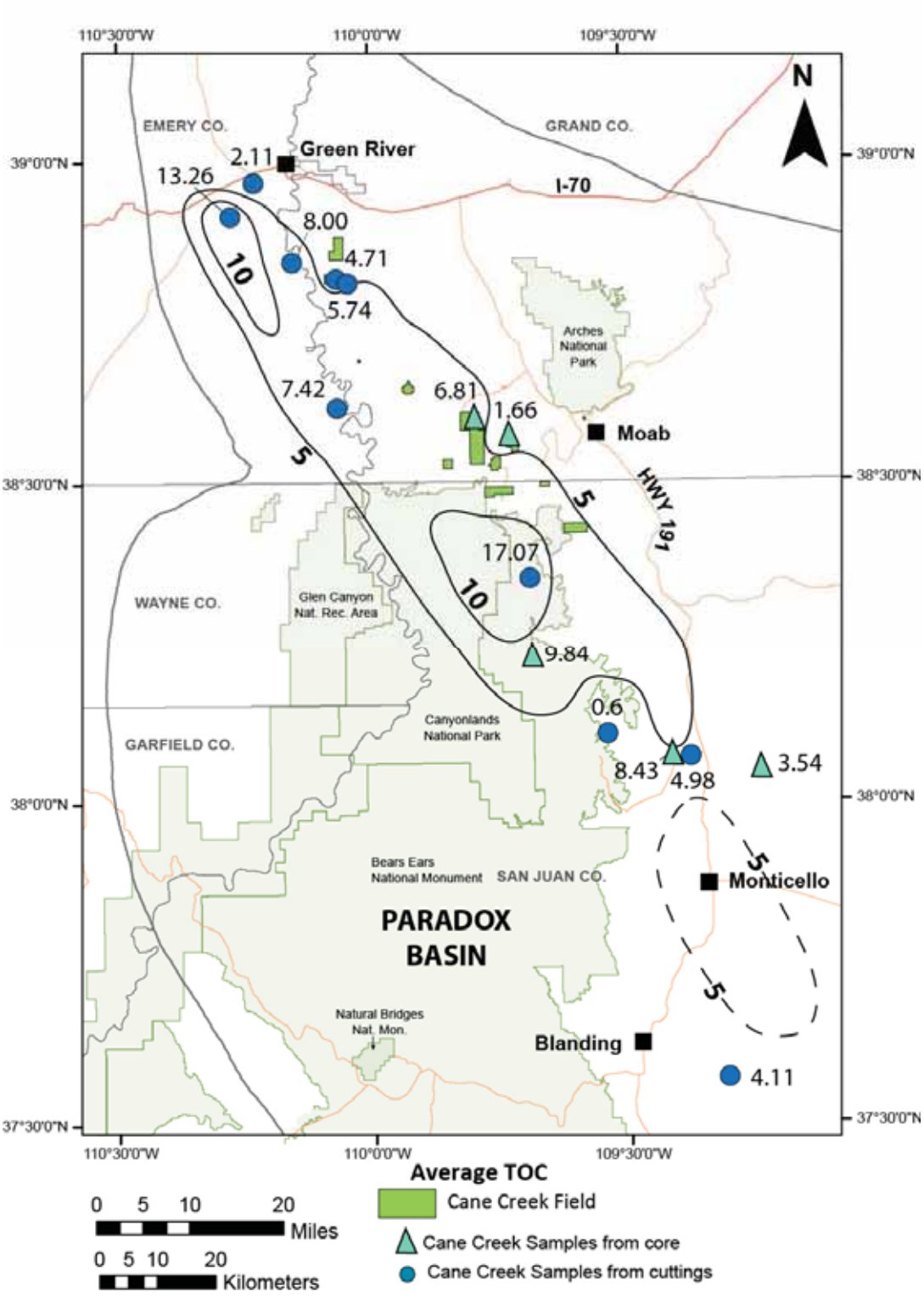

Figure 91. *A map of the average total organic carbon (TOC) for 15 wells penetrating the Cane Creek shale in the Paradox Basin. Average TOC values for the mapped wells range from 0.60 to 17.07 units. The well with the highest value is USA Lockhart 1 and is roughly centered in the linear trend of wells.*

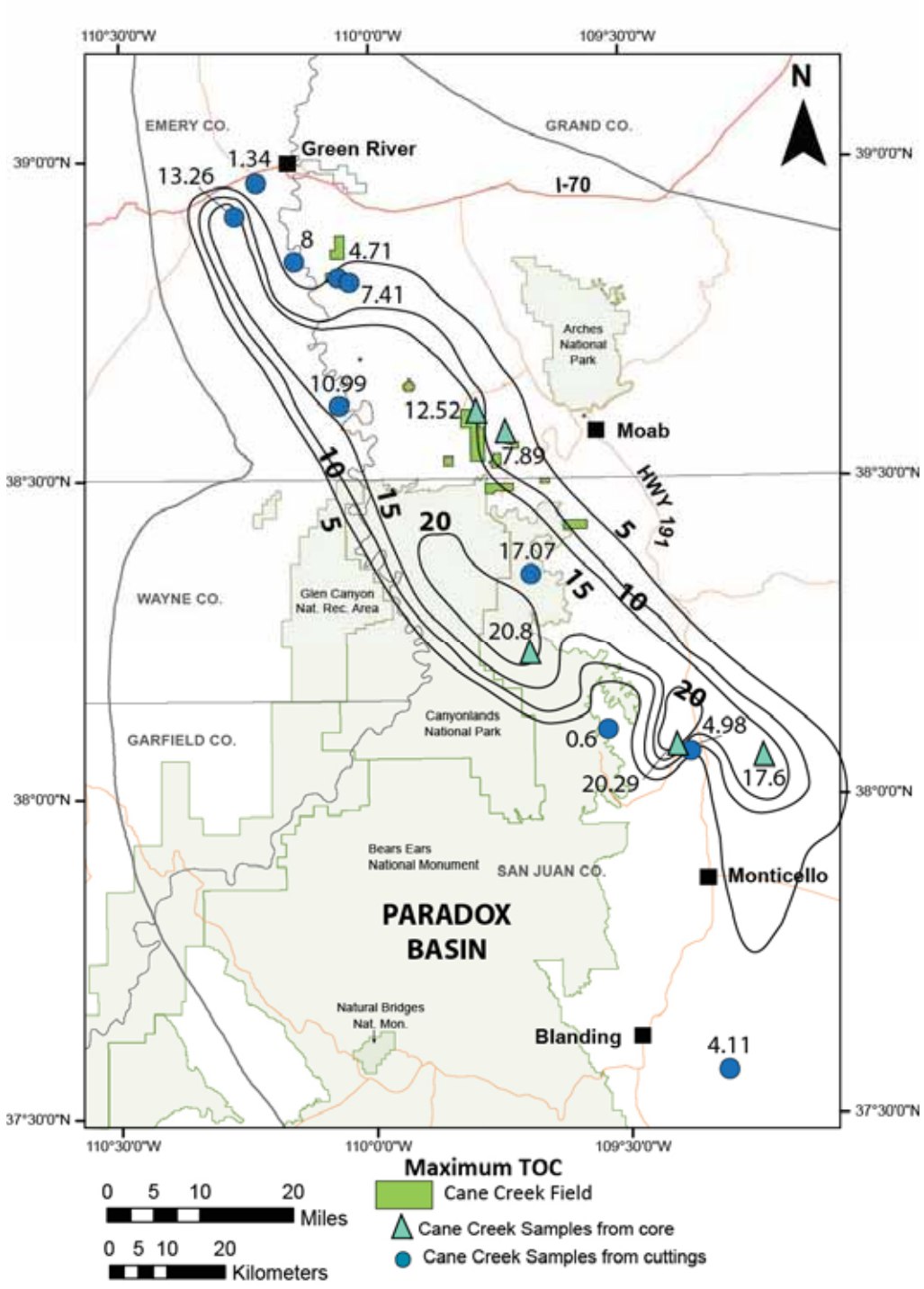

Figure 92. *Maximum TOC values from the Cane Creek shale in the Paradox Basin generally increase toward the center of the Paradox Basin and values range from 1.34 to 20.29. These measurements indicate the source rock quality for Cane Creek shale production is best in the central region of the basin, trending northwest-southeast.*

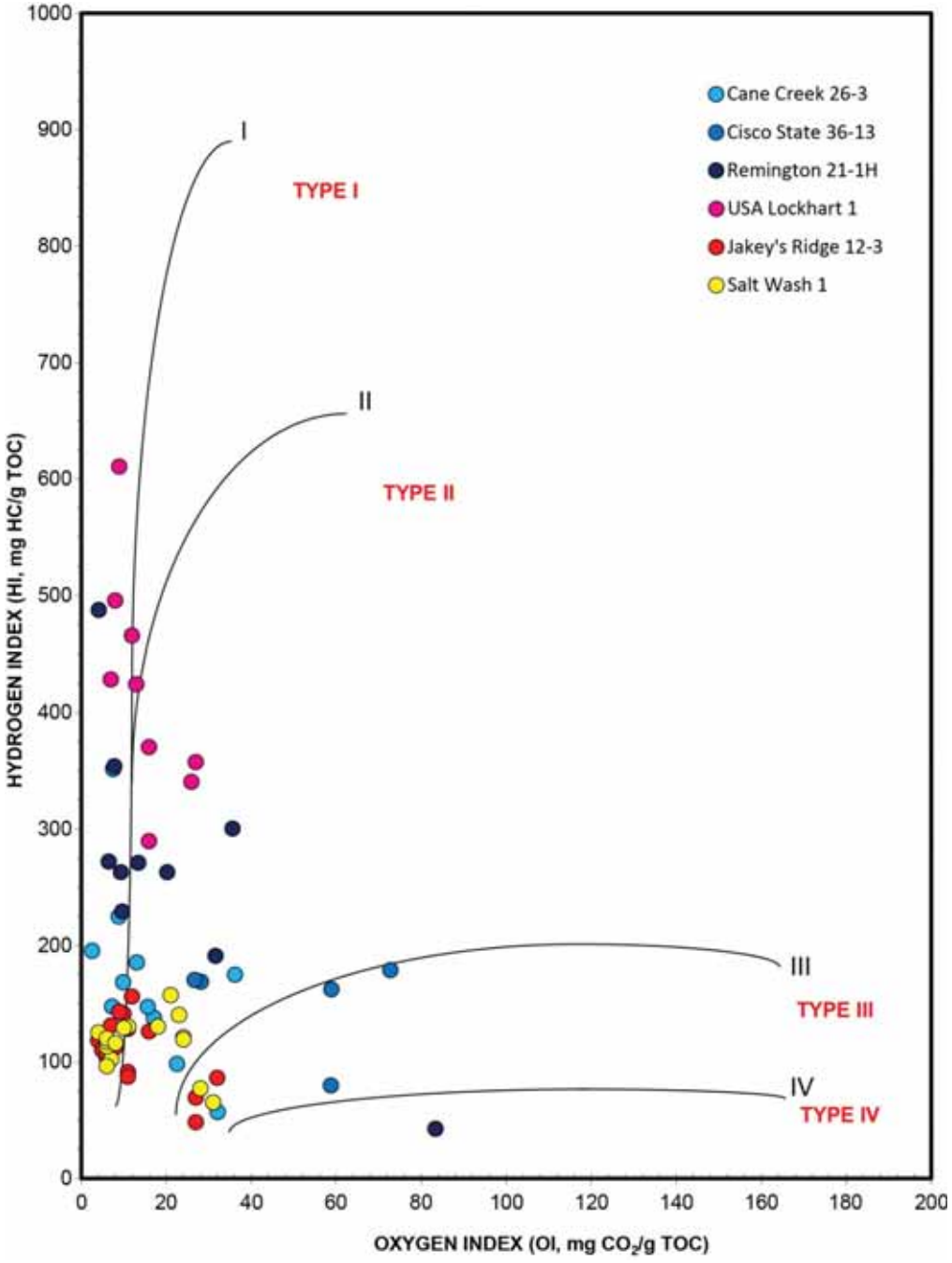

Figure 93. *A van Krevelen plot for six wells penetrating the Cane Creek shale in the Paradox Basin. Kerogen types include Type I kerogen, which is mainly algal-sourced and is oil prone but can also produce gas; Type II kerogen, sourced from plankton and algae and can produce oil and gas; Type III kerogen, sourced from terrestrial plants and can produce dry gas; and Type IV kerogen, sourced from reworked residual organic matter and likely does not generate oil or gas (McCarthy and others, 2011).*

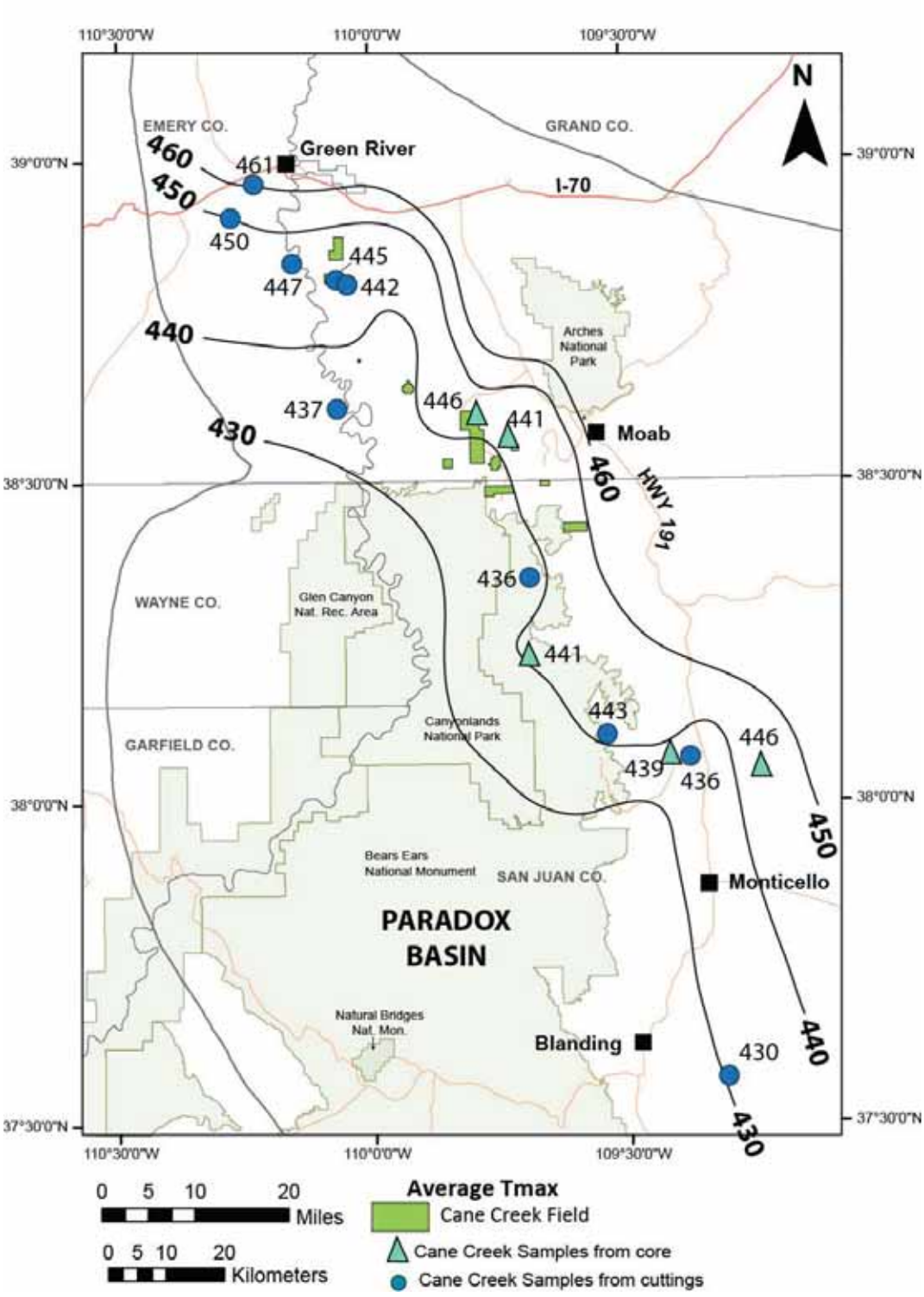

Figure 94. *Average Tmax values from the Cane Creek shale range from 418 to 461°C and increase eastward in a similar trend as average PI shown in figure 97. The values cover all of the corresponding kerogen types typically indicated by Tmax values. The overall average is ~440°C which would indicate a terrestrial kerogen source (type III kerogen) (McCarthy and others, 2011).*

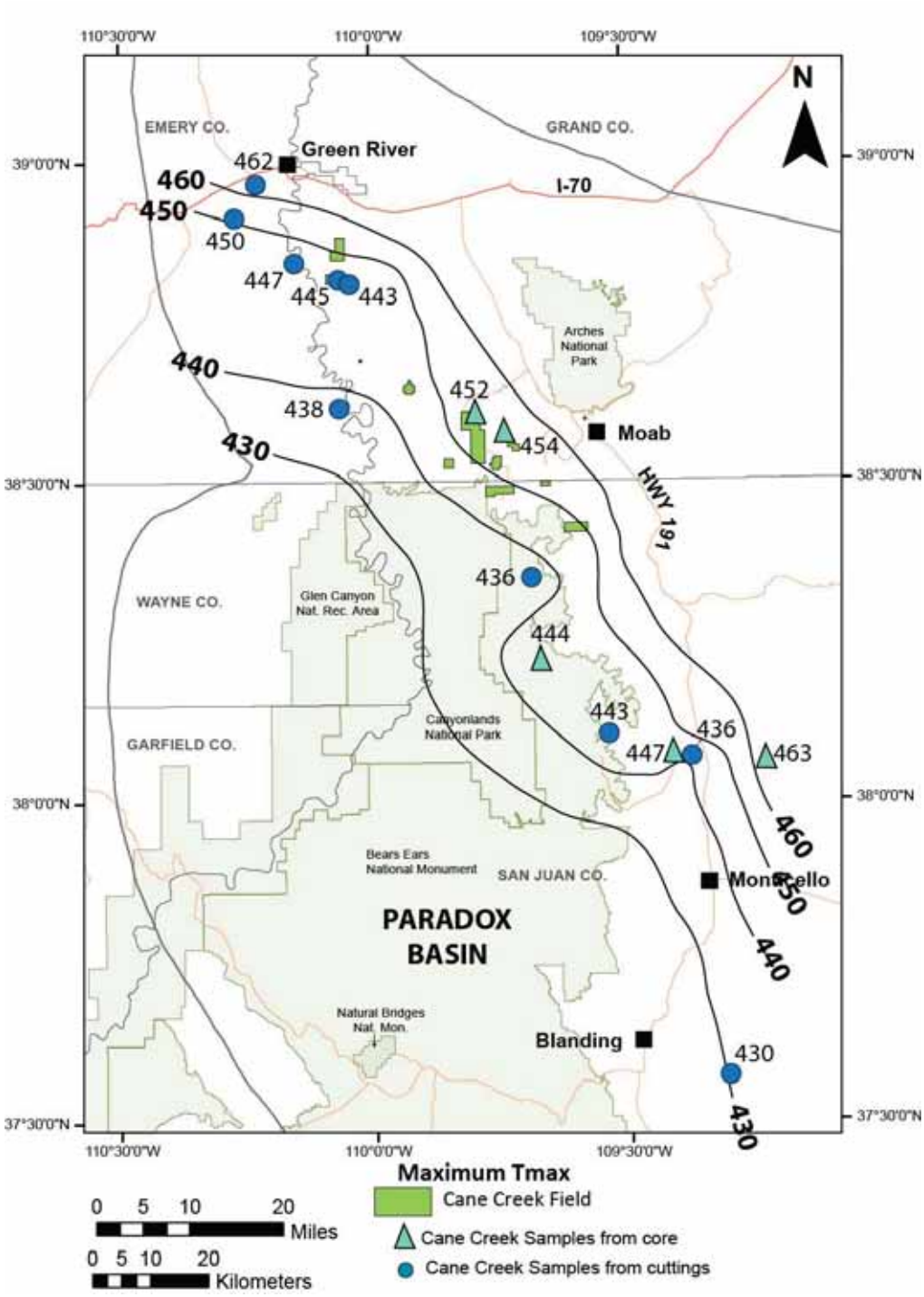

Figure 95. *Maximum Tmax (the temperature at which the maximum amount of hydrocarbons are generated during pyrolysis), values for the Cane Creek shale show a trend of increasing maturity to the north and northeast ranging from 430°C to 463°C.*

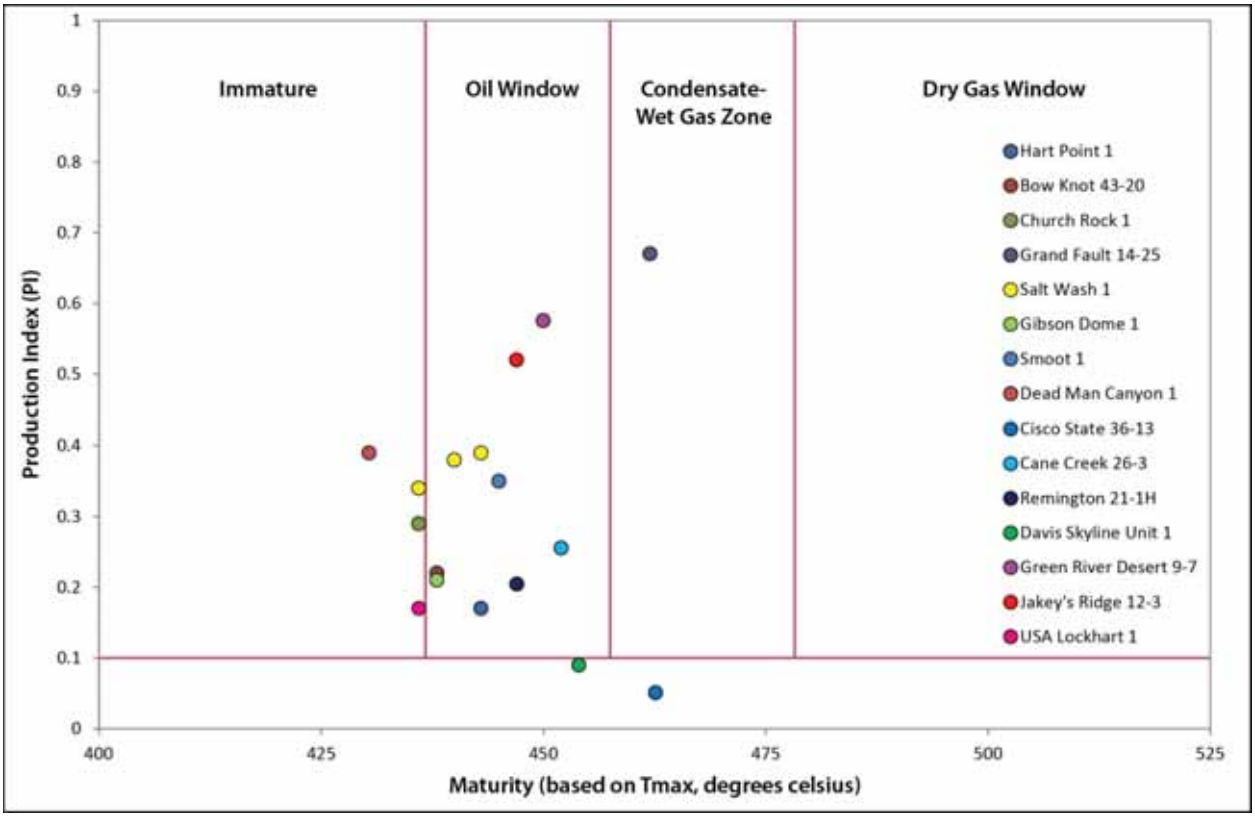

Figure 96. *Thermal maturity of samples from the Cane Creek shale derived from Tmax and PI show 10 of 17 samples plot within the oil window, 4 are immature, and 1 is in the condensate-wet gas zone.*

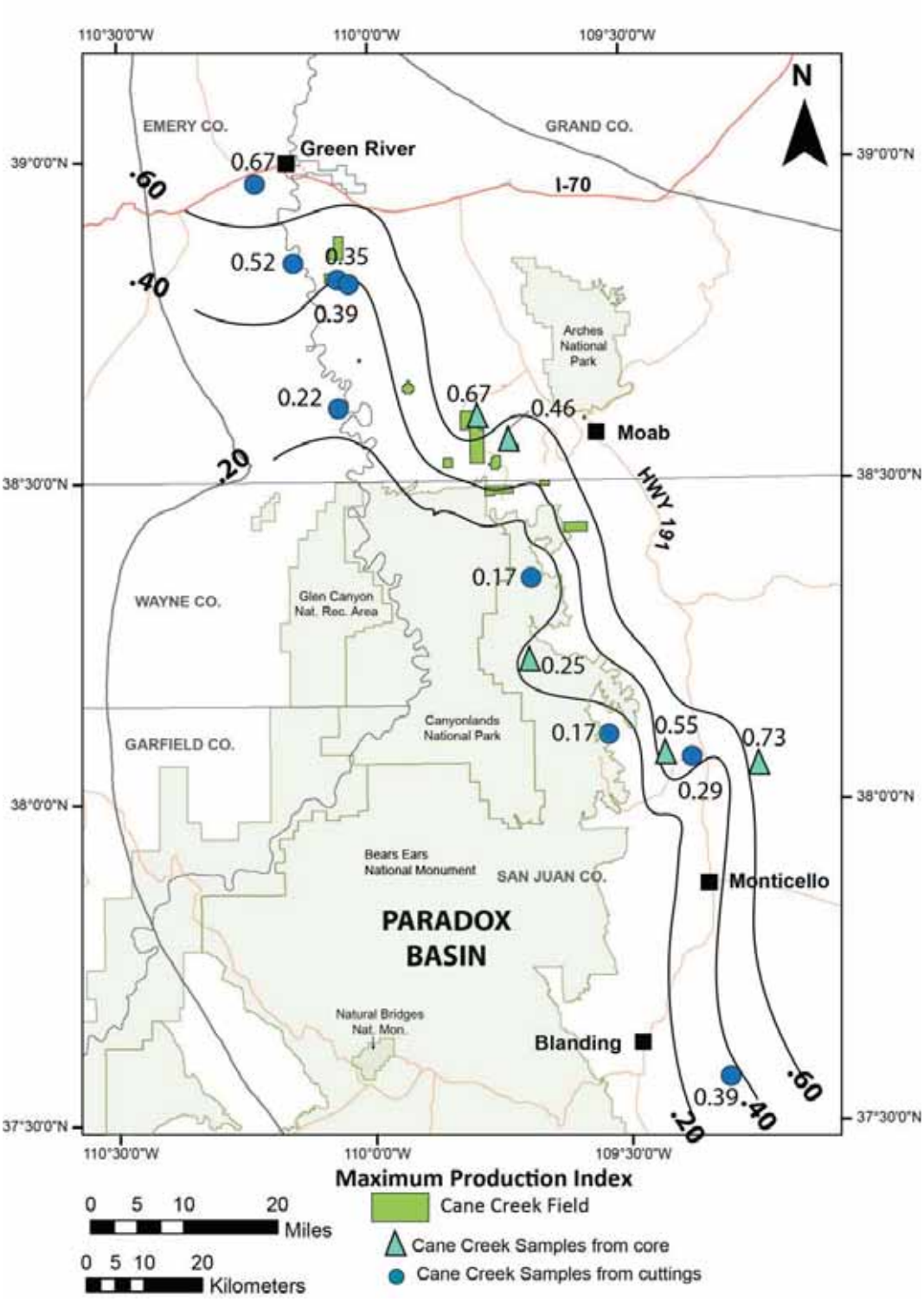

Figure 97. *Maximum production index (PI) values from the Cane Creek interval of the Paradox Basin Formation generally increase to the northeast.*

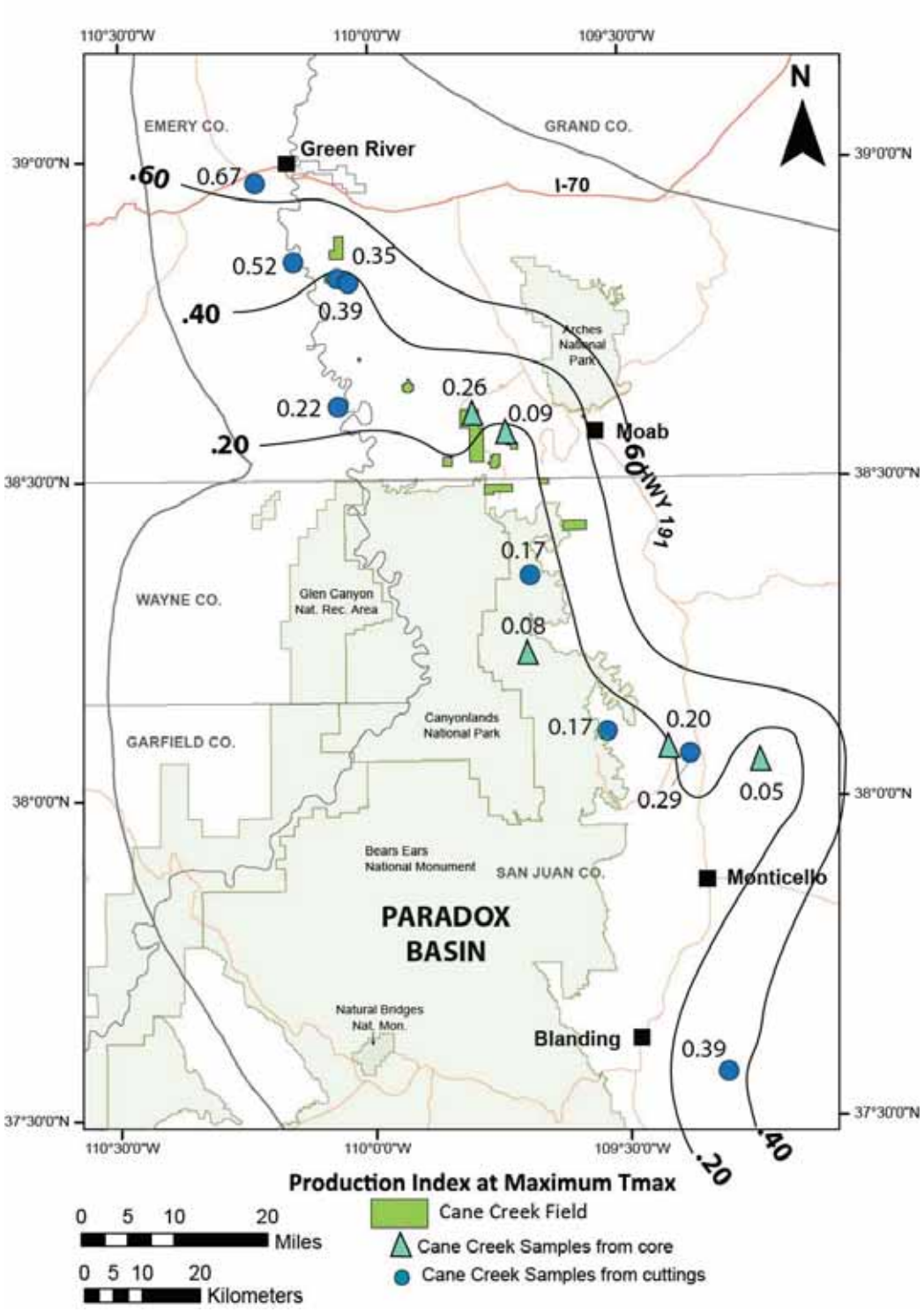

Figure 98. *A map of production index (PI) values at maximum Tmax from 14 wells penetrating the Cane Creek shale in the Paradox Basin generally increase to the northeast.*

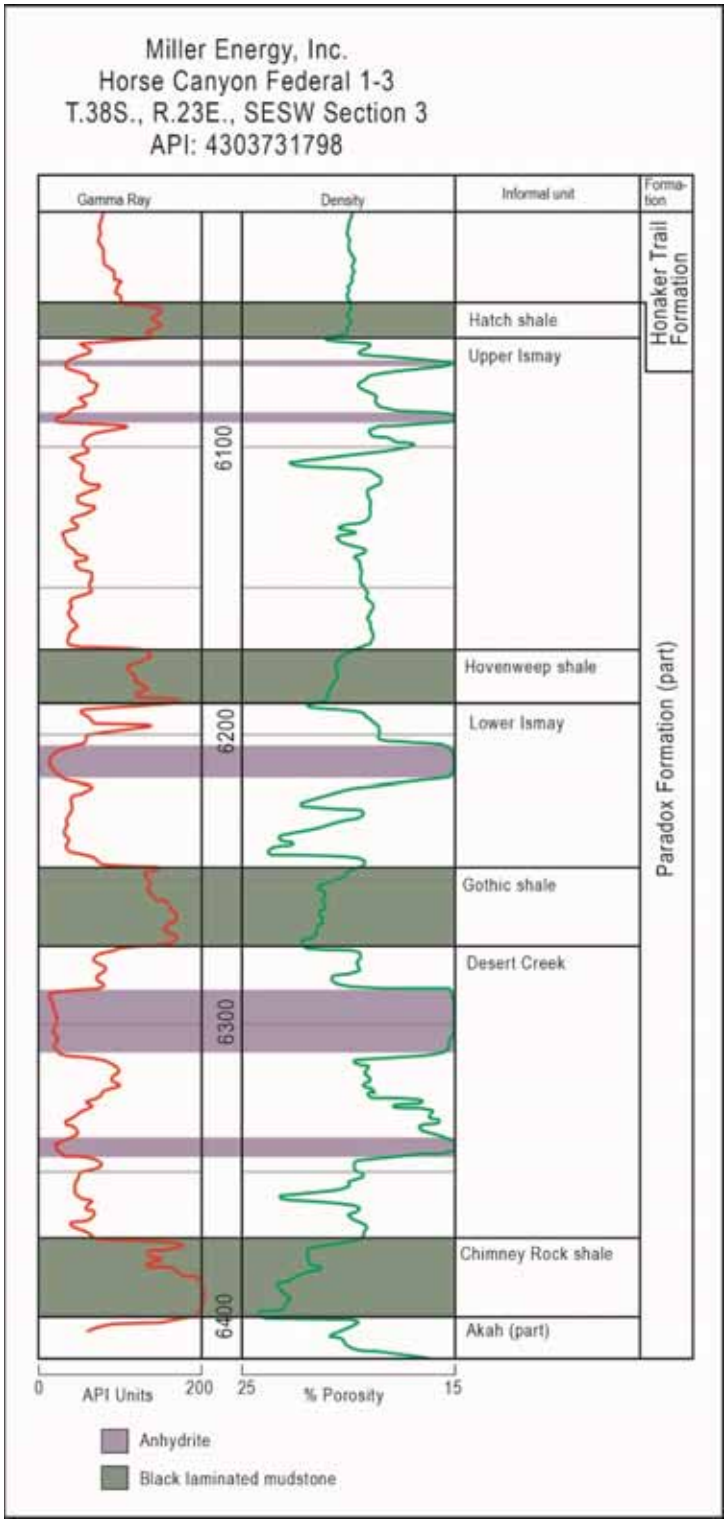

Figure 99. *Well log through the Chimney Rock, Gothic, and Hovenweep shales all of which have exhibited potential for hydrocarbon production. Shales are bounded above and below by carbonate and thin interbedded anhydrite. Modified from Anna and others (2014).*

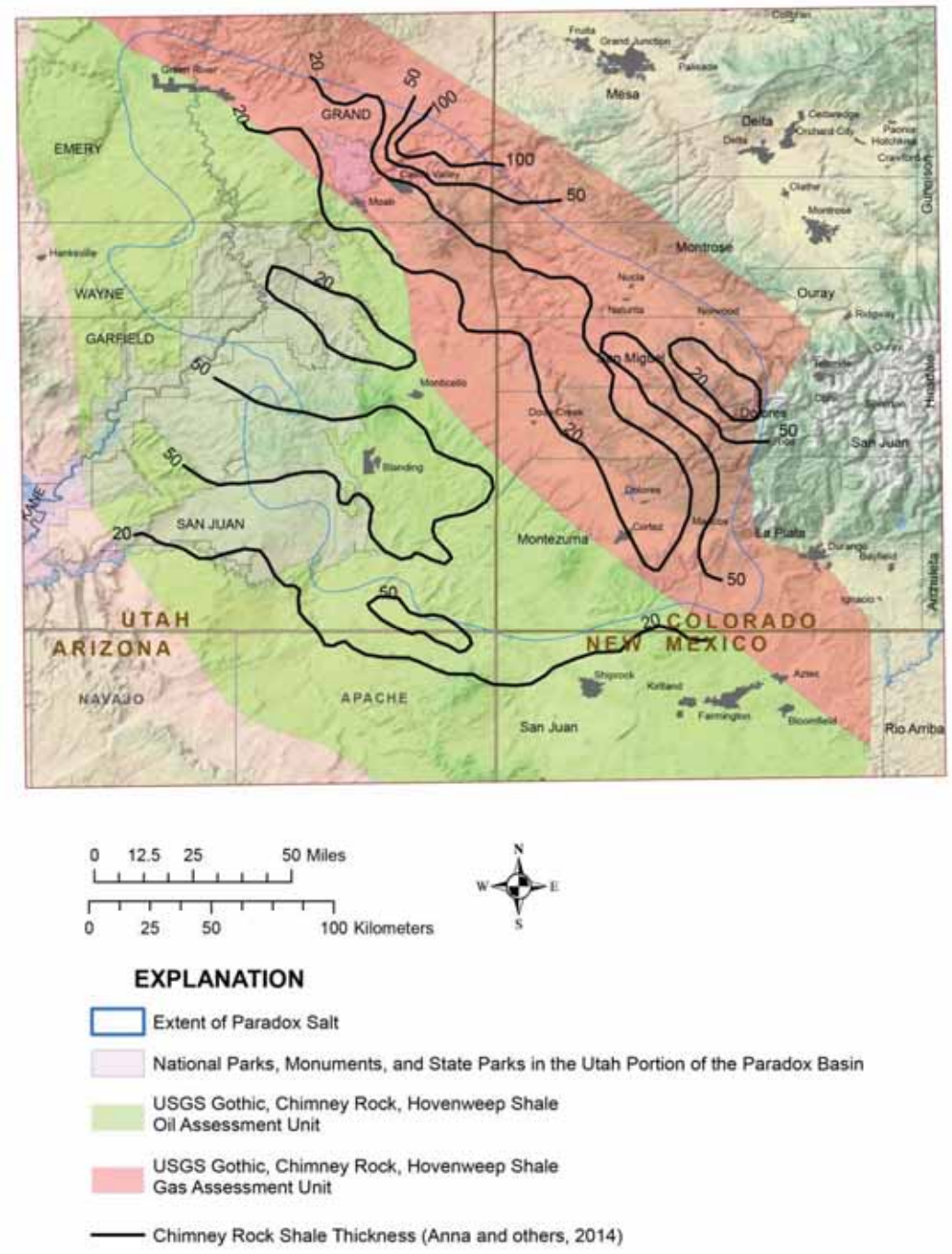

Figure 100. *Thickness of the Chimney Rock shale of the Paradox Formation. Variable contour intervals in feet. Oil and gas assessment units and contours are from Anna and others (2014).*

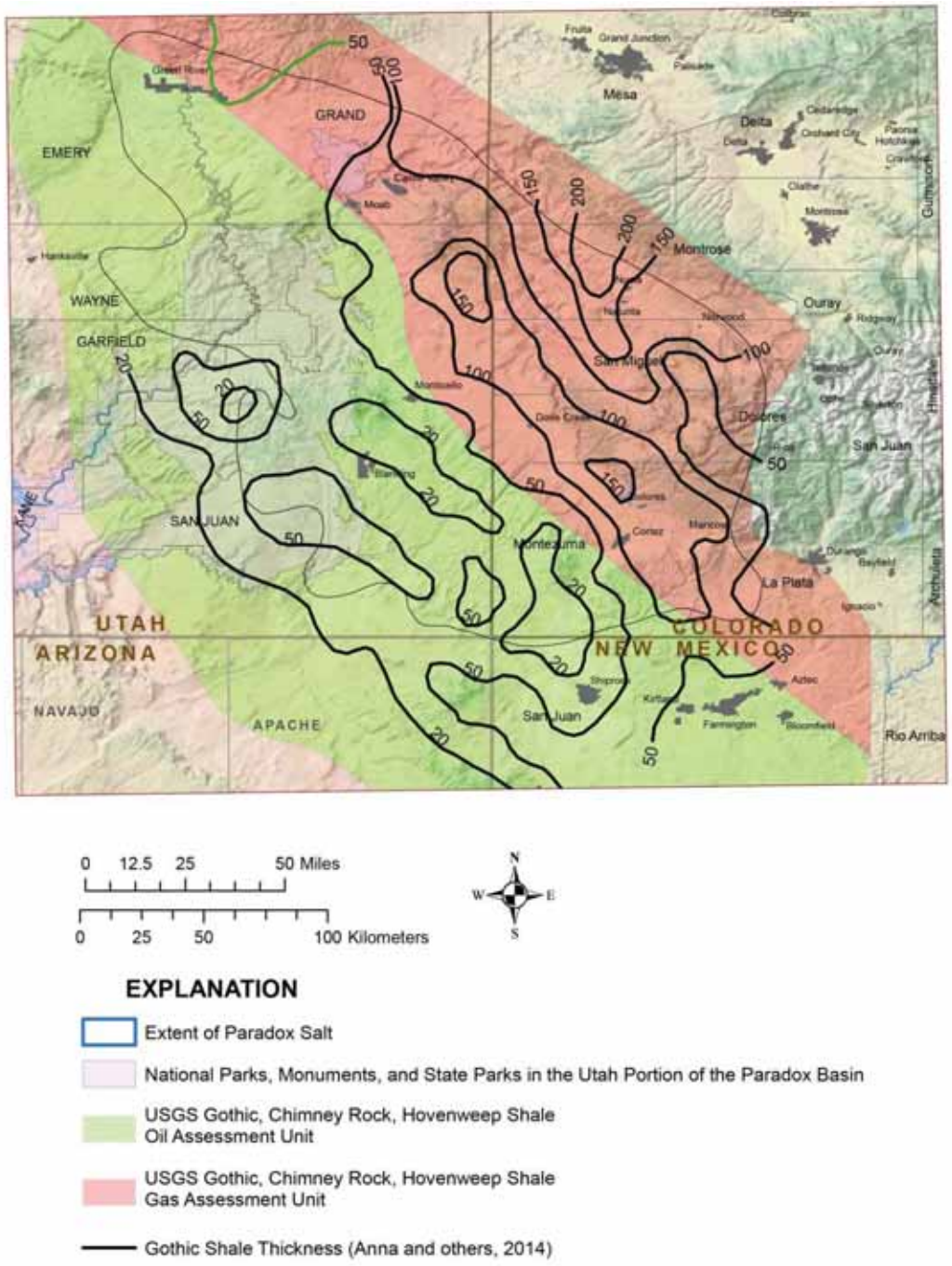

Figure 101. *Thickness of the Gothic shale of the Paradox Formation. Variable contour intervals in feet. Oil and gas assessment units and contours are from Anna and others (2014).*

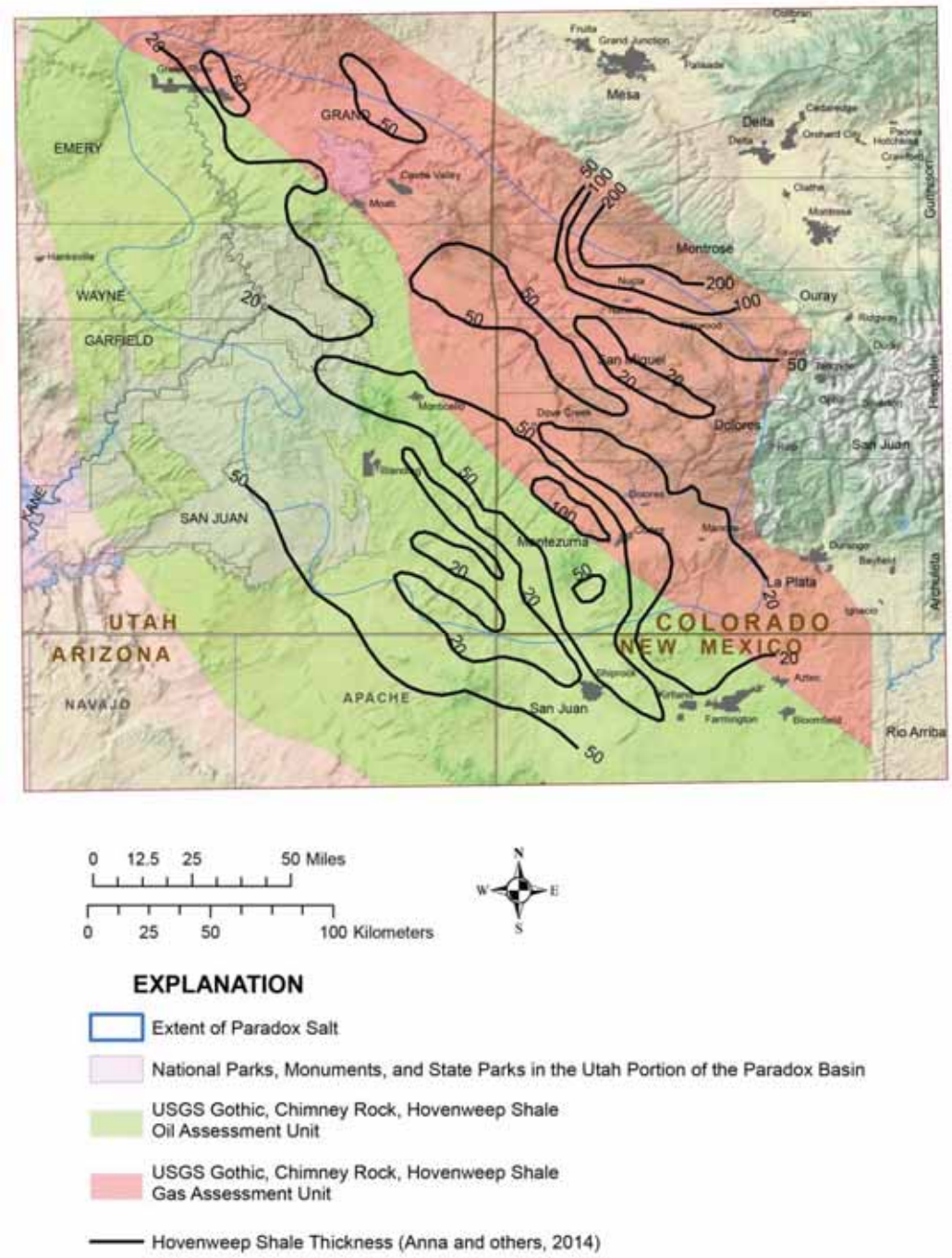

Figure 102. *Thickness of the Hovenweep shale of the Paradox Formation. Variable contour intervals in feet. Oil and gas assessment units and contours are from Anna and others (2014).*

Table 1. *Total production through December 2015 from fields that produce from the Cane Creek shale. Data source Utah Division of Oil, Gas and Mining monthly production by field http://oilgas.ogm.utah.gov/Publications/Publications.htm*

Field Name	***Location (TR)***	***No. of Wells***	***Thousand Barrels of Oil (MBO)***	***Million Cubic Feet Gas (MMCFG)***	***Comments***
Bartlett Flat	T25-26S, R19E	1	39		Original Big Flat 5 well. Combined with Big Flat field
Big Flat	T26S, R19E	21	5035	3385	Cane Creek unit
Greentown	T22S, R17E	2	73	266	One active well
Hatch Point	T29S, R21E	3	65	24	Threemile unit, one well completed in 2016 (not included in production)
Hell Roaring	T25S, R18E	1	659	579	Cane Creek unit One well
Cane Creek	T26S, R20-21E	?	None reported		Original exploration 1920s and 1950s
Lion Mesa	T27S, R21E	1	2		Abandoned
Long Canyon	T26S, R20E	1	1152	1199	One well
Park Road	T26S, R20E	2	489	299	Cane Creek unit
Shafer Canyon	T27S, R20E	2	67		Two wells now abandoned
Wilson Canyon	T29S, R23E	1	89	39	
Undesignated	Variable	3	30	0	Gold Bar 1 Two Fer 26-30 La Sal 29-28
Total		38	7700	5791	

Table 2. *Production for the month of December 2015 from fields producing from the Cane Creek shale. Wilson Canyon and Long Canyon still produce intermittently. Data source Utah Division of Oil, Gas and Mining monthly production by field http://oilgas.ogm.utah.gov/Publications/Publications.htm*

Field Name	*Location (TR)*	*No. of Wells*	*Barrels of Oil (BO)*	*Thousand Cubic Feet Gas (MCFG)*	*Comments*
Big Flat	T26S, R19E	21	53,450	28,494	Cane Creek unit
Greentown	T22S, R17E	1	789	4,159	
Hatch Point	T29S, R21E	2	45	0	Threemile unit
Hell Roaring	T25S, R18E	1	622	148	Cane Creek unit
Long Canyon	T26S, R20E	1	0	0	
Park Road	T26S, R20E	2	3,369	1,760	Cane Creek unit
Wilson Canyon	T29S, R23E	1	0	0	
Total		29	58,275	34,561	

Table 3. *Total undiscovered resources for the Paradox Formation total petroleum system. From Whidden and others (2012). See appendix A.*

Total petroleum systems (TPS) and assessment units (AU)	Field type	Total undiscovered resources											
		Oil (MMBO)				Gas (BCFG)				NGL (MMBNGL)			
		F95	F50	F5	Mean	F95	F50	F5	Mean	F95	F50	F5	Mean
Paradox Formation TPS													
Cane Creek Shale Oil AU	Oil	103	198	382	215	84	175	364	193	6	14	31	15
Cane Creek Shale Gas AU	Gas					2,473	4,284	7,420	4,530	88	168	319	181
Gothic, Chimney Rock, Hovenweep Shale Oil AU	Oil	126	238	449	256	91	186	382	205	7	15	32	16
Gothic, Chimney Rock, Hovenweep Shale Gas AU	Gas					3,342	6,075	11,042	6,490	120	238	472	260

Table 4. *Oil and gas fields in the Paradox Basin that produced from the Mississippian Redwall Formation.*

Field Name	***Location (TR)***	***No. of Wells***	***Thousand Barrels of Oil (MBO)***	***Million Cubic Feet Gas (MMCFG)***	***Comments***
Big Flat	T26S, R19E	3	83		Abandoned, gas vented
Big Indian North	T29S, R24E	1	178	26,420	
Lisbon	T30S, R24E	20	54,403	808,602	Much of the gas production is recycled
Little Valley	T30S, R25E		137	17,312	Abandoned
Salt Wash	T23S, R17E	3	1,653	11,751	Low Btu gas is vented

Table 5. *Fracture strike, dip, and width by fracture type from the Cane Creek 26-3 well. Data is from Core Laboratories, Inc., Houston, Texas, prepared in 2013 for Fidelity Exploration & Production Inc., and provided to the UGS (appendix C).*

Fracture Type	***Strike Average (azimuth)***	***Dip Average (degrees)***	***Width Average (mm)***	***Number of Samples***
Halite Cemented	323°	71°	1.2	31
Calcite/Halite Cemented	316°	76°	0.77	13
Anhydrite Cemented	318°	79°	3.5	5
Fracture with Slickenside	314°	13°	0.02	19
Open Fracture	333°	75°	0.60	6
Artificial Petal	324°	74°	0.01	7

Table 6. *Gas analysis from wells in the Cane Creek unit. Data from Utah Division of Oil, Gas and Mining hearing files, Docket 2013-011, cause 196-44.*

Well No.	Propane	IsoButane	Butane	IsoPentane	Pentane	Hexane+	Methane	Ethane	Hexane	Nitrogen	BTU
28-2	12.32	1.49	4.30	0.74	1.02	0.69	59.44	19.15	0.69	0.85	1541
26-3	7.78	1.19	3.55	0.73	0.96	0.57	70.64	13.38	0.00	1.18	1396
26-2	9.52	0.94	1.98	0.25	0.26	0.17	67.40	18.63	0.17	0.83	1374
10-1	13.50	1.61	4.52	0.77	10.6	0.89	56.70	20.38	0.89	0.57	1588
19-1	12.25	1.54	5.14	1.13	1.78	1.68	56.42	18.90	1.67	1.14	1627
34-1	12.17	1.34	3.80	0.63	0.88	0.70	59.77	19.67	0.70	1.03	1519
2-1	11.15	1.18	3.12	0.49	0.64	0.46	62.73	19.27	0.46	0.96	1462
18-1	4.01	0.40	1.20	0.25	0.39	0.38	80.06	10.40	0.38	2.90	1190
12-1	13.13	1.33	3.62	0.56	0.78	1.00	56.46	22.30	1.00	0.81	1558
17-2	10.89	1.10	2.67	0.47	0.64	0.55	63.30	19.28	nr	1.08	1448
7-1	15.30	1.55	3.86	0.68	0.92	0.89	52.17	24.03	nr	0.60	1619
36-1	9.21	1.03	2.48	0.49	0.63	0.73	67.48	17.13	nr	0.81	1411
17-1	12.16	1.46	4.05	0.83	1.19	1.09	59.55	18.66	nr	0.99	1550
Averages	11.03	1.24	3.41	0.62	0.86	0.75	62.47	18.55	0.66	1.06	1483

Hydrogen Sulfide (H_2S) is zero
Carbon Dioxide (CO_2) is 0.01 or less
nr = not reported

Table 7. *Gas received, processed, and sold from the Blue Hills Gas Plant from the first day of operation through December 2015. Data from Utah Division of Oil, Gas and Mining.*

Report Date	Gas Gathered	Wet Gas	Gas In	Plant Fuel	Vent/ Flare	Shrinkage	Gas Sold	BTU Sold	NGL Produced
March	24,012	0	24,012	4,200	6,478	1,201	12,133	1,504	64,353
April	36,791	0	36,791	4,500	12,082	5,519	14,690	1,815	68,699
May	39,652	286	39,366	3,912	6,388	5,905	23,161	2,866	133,368
June	32,761	330	32,431	3,349	5,345	4,914	18,823	1,234	136,839
July	39,715	341	39,374	3,549	7,119	5,906	22,800	1,203	176,889
August	39,875	341	39,534	4,028	2,918	9,883	22,705	1,243	160,729
September	36,383	330	36,053	4,194	1,396	6,784	23,679	1,238	156,821
October	33,718	330	33,388	4,240	1,355	6,590	21,203	1,235	135,196
November	31,010	330	30,680	4,313	1,380	7,771	17,216	1,235	117,298
December	29,613	341	29,727	4,211	1,740	6,139	17,182	1,235	113,320
Averages	34,353	263	34,090	4,050	4,620	6,061	19,359	1,480	126,351

All gas volumes reported in thousand cubic feet (MCFG)
Gas Gathered = gas received by the plant that was metered at the well
Wet Gas = natural gas liquids removed from the gathering system prior to entering the plant
Gas In = gas metered as it enters the plant
Plant Fuel = gas consumed as part of the normal operation of the plant
Vent/Flare = gas vented or flared due to lack of market
Shrinkage = gas volume loss due to extracting the natural gas liquids
Gas Sold = gas sold to the pipeline after processing
BTU Sold = the heating value in British Thermal Units (BTU) of the gas sold
NGL Produced = natural gas liquids (mixed) produced in gallons at 60 F

Table 8. *Average fracture parameters in Cane Creek core from the Remington 21-1H well. From TerraTek contract report (appendix E).*

Fracture Type	Avg Length (cm)	Avg Fill width (mm)	Avg Aperture (mm)	Avg Spacing (mm)	Total Number of Fractures	Avg Intensity (fracs/ft)
Totally Open	10.4			47.6	51	0.8
Partially Open Penetrative	11.0		0.05	*	3	0.05
Partially Open Non-penetrative	5.9		0.05	16.8	32	0.5
Partially Mineralized	9.9	1.45	0.07	25.9	95	1.6
Completely Mineralized	7.1	0.61		16.2	341	5.6

*Fractures occur singly in 1-foot interval

Table 9. *Rock-Eval data from Cane Creek shale in the Gibson Dome 1 well (section 21, T. 30 S., R. 21 E.).*

Client	Lab	ID	Depth	Unit	TOC	S1	S2	S3	Tmax	HI	OI	S2/S3	S1/TOC*100	PI
Chesapeake	V248	14	5223.6	A	1.59	0.81	1.83		446.7					
UGS	Weatherford	1	5224.1	A	10.30	8.55	32.45	0.96	438	315	9	34	83	0.21
Chesapeake	V248	15	5227.3	A	1.24	0.99	2.61		438.3					
Chesapeake	V248		5227.5	A	3.42	4.14	7.83	0.85	429	229	25	9.21	120	0.35
Chesapeake	V248	16	5238.0	B	3.09	5.18	12.83		440.6	415				
Chesapeake	V248	16	5240.4	B	3.09	5.18	12.83		440.6	415				
UGS	Weatherford	2	5241.1	B	9.81	3.50	16.16	0.77	442	165	8	21	36	0.18
UGS	Weatherford	3	5257.6	B	20.80	8.52	101.91	0.63	444	490	3	162	41	0.08
UGS	Weatherford	4	5286.7	C	2.72	3.09	9.47	0.70	437	348	26	14	114	0.25
UGS	Weatherford	5	5293.0	C	5.59	3.86	16.16	0.56	443	289	10	29	69	0.19

Table 10. *Full diameter porosity and permeability analysis of the Cane Creek B and C zones in the Cane Creek State 1-36 well (section 36, T. 27 S., R. 20 E.). Samples with strong anisotropy are highlighted in yellow and may indicate open fractures.*

		Permeability			Porosity	Saturation			
Sample Number	**Depth (feet)**	**N-S (mD)**	**E-W (mD)**	**Vertical (mD)**	**Percent (%)**	**Oil (%)**	**Water (%)**	**Grain Density (gm/cc**	**Zone**
1	7026-27	.03	.27	981	5.0	31.1	54.2	2.74	B
2	7028-29	.61	.38	2.5	9.5	22.5	61.1	2.73	B
3	7031-32	.03	.08	.02	8.8	23.9	45.9	2.76	B
4	7034-35	.42	.48	.03	8.8	33.2	54.5	2.70	B
5	7036-37	1088	.50	395	10.9	18.1	63..2	2.73	B
6	7040-41	.53	3.2	227	7.2	16.0	65.2	2.73	B
7	7045-46	.15	.10	.05	6.1	38.2	51.7	2.72	B
8	7047-48	.19	.34	.12	9.1	27.6	54.8	2.72	B
9	7049-50	1.7	1.0	.22	9.1	25.0	49.5	2.68	B
10	7052-53	.99	1.5	.13	10.2	14.3	54.6	2.70	B
11	7055-56	.85	.22	.10	6.5	24.7	49.2	2.76	B
12	7059-60	.36	1.6	27	5.4	29.5	56.0	2.69	C
13	7067-68	.15	.07	.05	3.7	12.0	55.3	2.79	C
14	7077-78	.37	.44	95	5.4	33.7	56.4	2.70	C
15	7079-80	.05	.08	.96	2.9	35.7	44.8	2.69	C
16	7084-85	.19	1468	8948	6.0	32.2	57.1	2.67	C
17	7086-87	.07	.06	.01	4.3	31.0	56.0	2.66	C
18	7094-95	.06	.06	.03	4.1	39.0	50.7	2.64	C

Table 11. *Total organic carbon (TOC) in the Cane Creek shale from the five wells studied. All samples were collected from core. LS = limestone, SH = shale, DOL = dolomite, and SLT = siltstone.*

Well	Depth (feet)	Zone	Lithology	TOC (%)
Cane Creek 26-3	7400	A	LS	8.52
Cane Creek 26-3	7406	A	SH	5.89
Cane Creek 26-3	7411	B	SH	7.88
Cane Creek 26-3	7417	B	DOL	4.03
Cane Creek 26-3	7418	B	DOL	4.92
Cane Creek 26-3	7421	B	SH	3.71
Cane Creek 26-3	7424	B	DOL	8.49
Cane Creek 26-3	7430	B	DOL	3.73
Cane Creek 26-3	7452	C	SH	10.59
Cane Creek 26-3	7458	C	DOL	4.66
Cane Creek 26-3	7470	C	SH	12.52
Skyline 1	7502	C	SLT	0.15
Skyline 1	7504	C	SLT	0.06
Skyline 1	7505	C	SLT	0.09
Skyline 1	7519	C	DOL	0.11
Skyline 1	7520	C	DOL	7.89
Remington 21-1H	7432	A	SH	2.19
Remington 21-1H	7438	A	SH	3.51
Remington 21-1H	7440	B	DOL	8.56
Remington 21-1H	7449	B	SH	14.06
Remington 21-1H	7453	B	DOL	13.01
Remington 21-1H	7462	B	SH	0.97
Remington 21-1H	7469	B	SH	20.29
Remington 21-1H	7476	C	SH	9.04
Remington 21-1H	7480	C	DOL	4.78
Remington 21-1H	7488	C	DOL	7.90
Cisco State 36-13	7589	A	DOL	1.92
Cisco State 36-13	7600	B	SH	9.49
Cisco State 36-13	7602	B	SH	3.59
Cisco State 36-13	7602	B	SH	1.54
Cisco State 36-13	7605	B	DOL	0.26
Cisco State 36-13	7606	B	DOL	2.25
Cisco State 36-13	7609	B	DOL	1.16
Cisco State 36-13	7609	B	DOL	1.02
Cisco State 36-13	7611	B	DOL	0.26
Cisco State 36-13	7614	B	SH	6.20
Cisco State 36-13	7615	B	DOL	0.14
Cisco State 36-13	7620	B	DOL	0.16
Cisco State 36-13	7623	B	DOL	0.25
Cisco State 36-13	7624	B	DOL	0.22
Cisco State 36-13	7625	B	DOL	2.76
Cisco State 36-13	7631	C	DOL	17.60
Cisco State 36-13	7632	C	SH	0.12
Cisco State 36-13	7634	C	DOL	0.23
Cisco State 36-13	7636	C	DOL	6.43
Cisco State 36-13	7637	C	SH	0.04
Cisco State 36-13	7649	C	SH	2.31
Cisco State 36-13	7650	C	SH	0.46
Gibson Dome 1	5224	A	SH	1.59
Gibson Dome 1	5224	A	SH	10.30

Well	Depth (feet)	Zone	Lithology	TOC (%)
Gibson Dome 1	5227	A	DOL	1.24
Gibson Dome 1	5228	A	DOL	3.42
Gibson Dome 1	5238	B	DOL	3.09
Gibson Dome 1	5240	B	DOL	3.09
Gibson Dome 1	5241	B	SH	9.81
Gibson Dome 1	5258	B	SH	20.80
Gibson Dome 1	5287	C	SH	2.72
Gibson Dome 1	5293	C	SH	5.59

Table 12. *Total organic carbon (TOC) by Cane Creek zone, lithology, and by well. All zones and lithologies have some source rock potential.*

Zone	Number of Samples	TOC (%) Range
A	9	1.24-10.30
B	29	0.14-20.80
C	20	0.04-12.52

Lithology	Number of Samples	TOC (%) Range	Average TOC (%)	Adjusted Average TOC (%)*
Shale	24	0.04-20.8	6.84	
Carbonate	30	0.11-17.6	4.28	3.93
Siltstone	4	0.06-6.20	1.63	0.10

*Highest outlier value removed, possible shale based on TOC value.

Well Name	Number of Samples	TOC (%) Range
Cane Creek 26-3	11	3.73-12.52
Skyline 1	5	0.06-7.89
Remington 21-1H	10	0.97-20.29
Cisco State 36-13	22	0.04-17.60
Gibson Dome 1	10	1.24-20.80

Table 13. *Porosity and permeability of plugs from Cane Creek core. The B zone (highlighted) is the primary target for horizontal drilling.*

			Range		Average	
Well Name	**Zone**	**Number of Samples**	**Porosity (%)**	**Permeability (mD)**	**Porosity (%)**	**Permeability (mD)**
Cane Creek 26-3	A	23	0.07-13.58	0.001*-13.00	4.07	0.611
Cane Creek 26-3	B	32	3.03-12.76	0.001*-35.65	9.26	2.27
Cane Creek 26-3	C	16	0.29-13.20	0.001*-0.572	5.86	0.25
Cisco Sate 36-13	A	12	0.07-17.68	0.009-0.592	4.48	0.0582
Cisco Sate 36-13	B	25	0.06-15.42	0.0001*-4.060	8.08	0.03496
Cisco Sate 36-13	C	9	0.91-12.40	0.0001*-0.223	6.79	0.200
Remington 21-1H	A	0				
Remington 21-1H	B	21	1.4-11.5	<0.01*-40.00	5.8	5.62
Remington 21-1H	C	4	3.0-10.7	0.17-8.10	6.6	3.73

* = lower limit of analysis

Table 14. *Time of oil generation from the Cane Creek shale. Gen = generation, Expul = expulsion, Ro = vitrinite reflectance. From Rasmussen and Rasmussen (2009).*

Well	Time @ Gen (ma)	%Ro @ Gen	Time @ Peak Gen (ma)	%Ro @ Peak Gen	Time @ Expul (ma)	Time @ Peak Expul (ma)
Federal 1-26	258	0.46	84	0.79	86	83
Crescent 1	302	0.46	243	0.69	212	206
Federal 1-21	279	0.46	86	0.85	106	83
Paradox Basin 1	304	0.45	273	0.66	259	244
Gold Bar 2	259	0.46	83	0.75	82	81
Long Canyon 1	249	0.46	82	0.69	77	65
Bridger Jack Mesa 1	239	0.46	82	0.73	79	78
Hatch Point 1	269	0.46	82	0.73	76	76
La Sal 1	270	0.46	82	0.73	78	78
Gibson Dome 1	258	0.46	82	0.72	46	75
Hatch Wash 1	244	0.46	82	0.72	76	75

Table 15. *Maximum temperature (Tmax), production index (PI), and total organic carbon (TOC) from Rock-Eval data from the cores and cuttings of the Cane Creek shale.*

API Number	Operator	Well	Sec.	T.	R.	Latitude	Longitude	Depth (ft)	Tmax	PI	TOC	Source
4301511182†	Superior Oil	Grand Fault 14-25	14	21S	15E	38.9667	-110.22561	8990	462	0.67	1.34	Nuccio & Condon, 1996
								9020	460	0.63	2.87	
4301510021†	Amax	Green River Desert 9-7	9	22S	15E	38.9142	-110.27225	7670	450	NA	13.26	USGS
4301510736†	Mobil Oil	Jakey's Ridge 12-3	15	23S	16E	38.8422	-110.14959	8060	447	0.52	8	USGS
4301910831†	Pan American Oil	Salt Wash 1	15	23S	17E	38.8087	-110.03904	8150	436	0.34	2.29	USGS
4301910831†	Pan American Oil	Salt Wash 1	15	23E	17E	38.8087	-110.03904	8100	440	0.38	7.41	Nuccio & Condon, 1996
								8150	443	0.39	4.06	
4301916047†	Texaco	Smoot 1	17	23S	17E	38.8158	-110.06213	8230	445	0.35	4.71	Nuccio & Condon, 1996
4301911187†	Superior Oil	Bow Knot 43-20	20	25S	17E	38.6142	-110.06209	5670	437	0.2	8.21	Nuccio & Condon, 1996
								5780	438	0.22	2.75	
								5830	436	0.19	10.99	
								5850	437	0.19	7.71	
4301950019*	Fidelity	Cane Creek 26-3	26	25S	19E	38.6009	-109.79373	7400	442	0.5	8.52	Fidelity
								7406	446	0.47	5.89	
								7411	445	0.47	7.88	
								7417	441	0.56	4.03	
								7418	447	0.59	4.92	
								7421	445	0.67	3.71	
								7424	449	0.55	8.49	
								7430	450	0.39	3.73	
								7452	452	0.26	10.59	
								7458	443	0.42	4.66	
								7470	443	0.53	12.52	
4301930796*	Davis Oil	Davis Skyline Unit	5	26S	20E	38.5685	-109.73452	7502	444	0.45	0.15	USGS

		1										
								7504	428	0.46	0.06	
								7505	444	0.38	0.09	
								7519	434	0.39	0.11	
								7520	454	0.09	7.89	
4303710849†	Pan American Oil	USA Lockhart 1	23	28S	20E	38.3462	-109.68156	4380	436	0.17	17.07	Nuccio & Condon, 1996
NA*	USDOE	Gibson Dome 1	21	30S	21E	38.2238	-109.68839	5224	438	0.21	10.3	UGS
								5241	442	0.18	9.81	
								5258	444	0.08	20.8	
								5287	437	0.25	2.72	
								5293	443	0.19	5.59	
4303710438†	Gulf Oil Co	Hart Point 1	8	31S	22E	38.0995	-109.53245	7090	443	0.17	0.6	Nuccio & Condon, 1996
4303731742*	Union Pacific Resources	Remington 21-1H	21	31S	23E	38.0716	-109.39676	7432	431	0.48	2.18	Union Pacific Resources
								7438	438	0.38	3.51	
								7440	441	0.35	8.56	
								7449	447	0.2	14.06	
								7453	446	0.15	13.01	
								7462	433	0.55	0.97	
								7469	441	0.27	20.29	
								7476	439	0.25	9.04	
								7480	440	0.34	4.78	
								7488	438	0.38	7.9	
4303711128†	Skelly Oil	Church Rock 1	26	31S	23E	38.0634	-109.36804	7940	436	0.29	4.98	Nuccio & Condon, 1996
4303750008*	Patara Oil & Gas	Cisco State 36-13	36	31S	24E	38.0511	-109.23273	7589	439	0.55	1.92	Patara O&G
								7602	443	0.67	1.54	
								7609	430	0.73	1.02	
								7624	370	0.63	0.22	
								7632	408	0.68	0.12	

								7650	419	0.7	0.46	
4303750008*	Patara Oil & Gas	Cisco State 36-13	36	31S	24E	38.0511	-109.23273	7600	461	0.1	9.49	UGS
								7602	447	0.2	3.59	
								7605	438	0.38	0.26	
								7606	434	0.37	2.25	
								7609	440	0.36	1.16	
								7611	429	0.38	0.26	
								7614	459	0.11	6.2	
								7615	429	0.35	0.14	
								7620	455	0.22	0.16	
								7623	444	0.45	0.25	
								7625	458	0.14	2.76	
								7631	463	0.05	17.6	
								7634	432	0.42	0.23	
								7636	449	0.14	6.43	
								7649	451	0.23	2.31	
4303710842†	Pan American Oil	Dead Man Canyon 1	20	37S	24E	37.5612	-109.3024	7630	430	0.39	4.11	Nuccio & Condon, 1996

*Core
†Cuttings
NA No API number is assigned to the USDOE well (U.S. Department of Energy)
USGS Core Center geology.cr.usgs.gov/crc/index.html
UGS Utah Geological Survey (Weatherford Laboratories)
Patara O&G, Fidelity, Union Pacific Resources, well operators who provided geochemical reports to UGS

Table 16. *HI and OI values for available wells.*

Well	Sample Depth or Depth Range (ft)	HI	OI
Gibson Dome 1	5,239	*415.29*	NA
Cisco State 36-13	7,589-7,650.1	*127*	*116*
Cane Creek 26-3	7,452	351.45	7.55
Remington 21-1H	7,435.25-7,491.2	*266.87*	*22.15*
Davis Skyline Unit 1	7,520	381.24	NA
Green River Desert 9-7	7,670	74.13	NA
Jakey's Ridge 12-3	8,060	91	11
Salt Wash 1	8,150	130	18
USA Lockhart 1	4,380	496	8

Italicized values are average over the Cane Creek interval

Table 17. *Vitrinite reflectance data for the Cane Creek shale from Nuccio and Condon, 1996. Samples below 6200 feet are within the oil window (0.6 to 1.3 %R_o) and those deeper than 6600 feet are in the gas window (1.3 to 3.0 %R_o). Two outliers are the samples from Church Rock 1 and Hatch Point 1 wells, which are both within the oil window and are from over 7100 feet. Tmax data from Rock-Eval pyrolysis indicates the Church Rock and Hatch Point wells are in the oil window as well (Nuccio and Condon, 1996).*

Well Name	Location Section-T-R	Depth (feet)	Vitrinite reflectance %R_o
Grand Fault 14-25	14-21S-15E	8,840	1.72
		9,080	1.82
		9,250	1.72
Salt Wash 1	15-23S-15E	7,620	1.49
		8,100	1.85
45-5-G	5-24S-15E	6,180	1.24
		6,681	1.49
Bow Knot 43-20	20-25S-17E	5,580	1.08
		5,670	1.07
		5,830	1.03
Gibson Dome 1	21-30S-21E	5,256	1.09
Hatch Point 1	8-31S-22E	7,180	0.63
Church Rock 1	26-31S-23E	7,940	0.73

Appendix A:

U.S. Geological Survey Fact Sheet

USGS
science for a changing world

National Assessment of Oil and Gas

Assessment of Undiscovered Oil and Gas Resources in the Paradox Basin Province, Utah, Colorado, New Mexico, and Arizona, 2011

Using a geology-based assessment methodology, the U.S. Geological Survey estimated means of 560 million barrels of undiscovered oil, 12,701 billion cubic feet of undiscovered natural gas, and 490 million barrels of undiscovered natural gas liquids in the Paradox Basin of Utah, Colorado, New Mexico, and Arizona.

Introduction

The U.S. Geological Survey (USGS) recently completed a geology-based assessment of the undiscovered, technically recoverable oil and gas resources in the Paradox Basin, which extends into parts of Utah, Colorado, Arizona, and New Mexico (fig. 1). Figure 1 shows the Paradox Basin Province boundary, as defined by Gautier and others (1996), as part of the 1995 USGS National Assessment. The assessment was based on the geologic elements that define a total petroleum system (TPS), which include petroleum source rocks (source rock maturation, petroleum generation and migration), reservoir description (reservoir presence and quality), and petroleum traps (trap type, timing of trap formation, and timing of seal deposition). Using this framework, seven TPSs were identified in the Paradox Basin. Four conventional assessment units (AU), four continuous AUs, and one coalbed gas AU were quantitatively assessed.

Geologic Summary

The Paradox Basin formed in the Pennsylvanian as a response to large intraplate stresses that have been attributed to the collision of Gondwana and Laurentia (Barbeau, 2003; Kluth and DuChene, 2009). The basin is asymmetric, with the deepest part along the north margin, adjacent to the Uncompahgre uplift in Utah and Colorado (fig. 2). Interbedded salt and black shales were deposited close to the north basin margin, along with clastics shed off the Uncompahgre uplift. Penesaline and normal marine carbonates developed along the gently dipping southwest basin margin and interfingered with the salt and black shales.

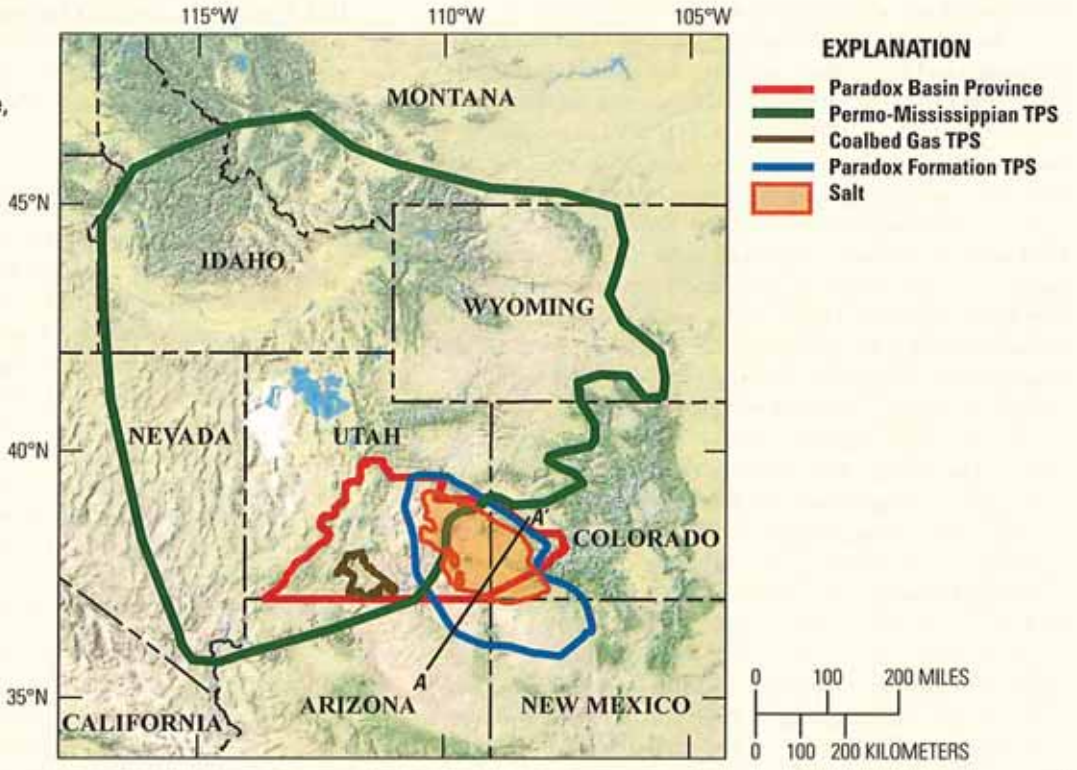

Figure 1. Location of Paradox Basin with the Permo-Mississippian, Coalbed Methane, and Paradox Formation Total Petroleum System (TPS) boundaries and the Paradox Basin Province boundary. The orange polygon delineates the boundary of salt deposition. Hypothetical assessment units not shown on map.

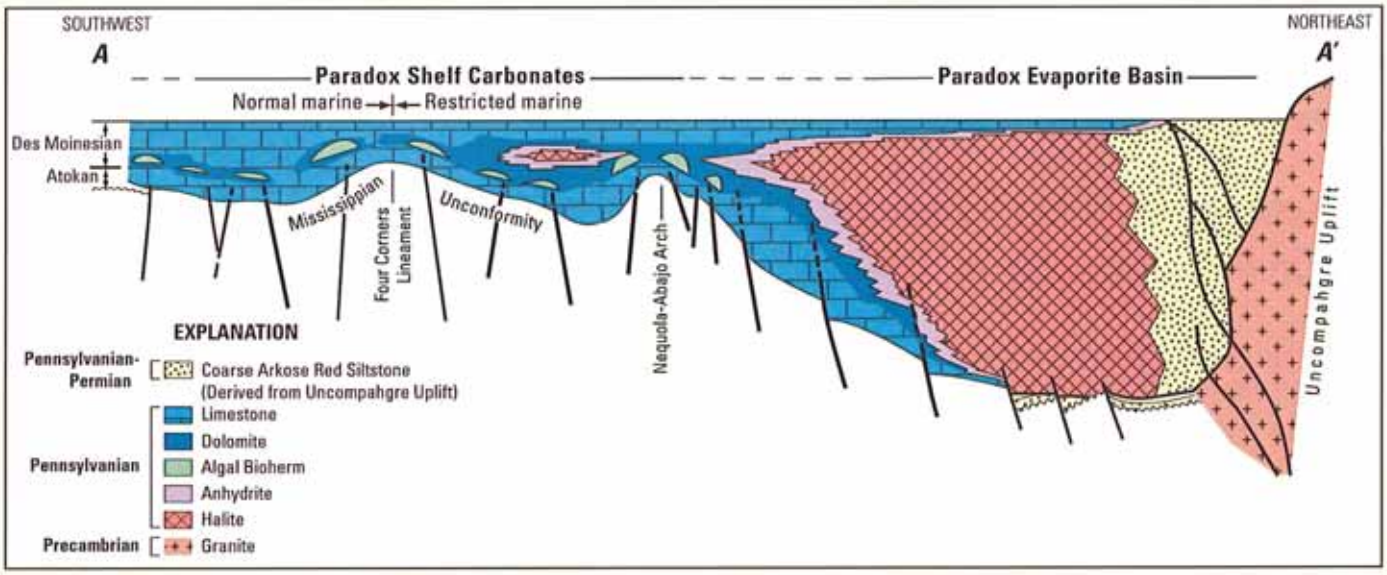

Figure 2. Northeast to southwest cross-section of the Paradox Basin (modified from Goldhammer and others, 1991).

Paradox Formation Total Petroleum System

The Paradox Formation TPS (fig. 1) is defined by hydrocarbons sourced from Middle Pennsylvanian (Desmoinesian) black dolomitic shales of the Paradox Formation that were deposited in the subsiding basin (fig. 2). These shales are interbedded with thick salt deposits. Petroleum from these source rocks is present in three conventional AUs (fig. 3a): (1) Leadville McCracken; (2) Pennsylvanian Carbonate Buildups and Fractured Limestone, and (3) Upper Paleozoic – Mesozoic Reservoirs. Conventional accumulations are defined as those that have well-defined boundaries and hydrocarbon-water contacts, and tend to have adequate porosity and permeability.

The Leadville McCracken AU consists of Mississippian limestones and Devonian sandstones that are interpreted to have undergone hydrothermal fluid flow since the Oligocene (Chidsey and others, 2009), which created localized reservoir-quality porosity and permeability. Migration of hydrocarbons from the overlying Paradox Formation was along through-going faults. The Pennsylvanian Carbonate Buildups and Fractured Limestone AU consists of phylloid algal mounds that developed along topographic highs on the shallow southwest flank of the Paradox Basin, with micritic open-marine limestones deposited in the intervening lows and farther basinward. Phylloid algal mounds possess excellent reservoir properties; furthermore, tectonic fracturing, produced from the movement of underlying salt, may have enhanced porosity and permeability in the micritic limestones. The source and reservoir facies are in close stratigraphic juxtaposition, and short-distance lateral and vertical migration was along faults and fractures. Traps are mainly stratigraphic, controlled by porosity and permeability trends in the algal mound facies and by fracturing due to salt movement. Seals are provided by overlying tight dolomite facies. The Upper Paleozoic–Mesozoic Reservoirs AU contains stacked reservoirs of mixed continental, lacustrine, and fluvial clastic rocks of Late Pennsylvanian through Jurassic age. Hydrocarbons sourced from the Paradox Formation likely migrated into overlying reservoirs through vertical faults and extensive fracture networks that are associated with salt structures. Traps are provided by salt anticlines, ridges and walls, and nonreservoir quality units (intraformational and interformational) act as seals.

Four unconventional AUs also were defined as part of the Paradox Formation TPS (fig. 3b): (1) Cane Creek Shale Oil AU; (2) Cane Creek Shale Gas AU; (3) Gothic, Chimney Rock, Hovenweep Shale Oil AU; and(4) Gothic, Chimney Rock, Hovenweep Shale Gas AU. Continuous reservoirs are defined as those with diffuse boundaries and lacking obvious traps and seals. Production from these reservoirs is typically enhanced or controlled by fractures. The Cane Creek Shale Oil and Shale Gas AUs and the Gothic, Chimney Rock, Hovenweep Shale Oil and Shale Gas AUs are differentiated by a maturation boundary of vitrinite reflectance = 1.1 percent, with the more mature strata (gas) in the deeper part of the basin near the Uncompahgre uplift.

Permo-Mississippian Total Petroleum System

The Permo-Mississippian TPS (fig. 1) is defined by the presence of oils from either the Permian Phosphoria Formation or the Mississippian Delle Phosphatic Member of Chainman Shale and equivalents, or both. Geochemical data support the interpretation that the oils originated from the Phosphoria Formation, but do not exclude their origin from the Delle. The Permian–Mesozoic Reservoirs AU (fig. 3a) includes many of the same clastic reservoirs as the Upper Paleozoic–Mesozoic Reservoirs AU, but these reservoirs contain Permo-Mississippian TPS hydrocarbons. The Manning Canyon Continuous Gas AU was not quantitatively assessed.

Coalbed Gas Total Petroleum System

The Coalbed Gas TPS is in the south-central part of Utah (fig. 1). The Kaiparowits Plateau AU (fig. 3b) was assessed for coalbed methane from the Upper Cretaceous Straight Cliffs Formation. The Henry Mountains Coalbed Gas AU was not quantitatively assessed.

Figure 3a. Location of four conventional assessment units (AUs) in the Paradox Basin.

Figure 3b. Location of five continuous assessment units (AUs) in the Paradox Basin. TPS, total petroleum system.

Hypothetical Total Petroleum Systems

Two TPSs were recognized in the Paradox Basin that do not have any known resources and could not be quantitatively assessed. The Precambrian Chuar Group contains shales with up to 10 percent total organic carbon that could have generated technically recoverable hydrocarbons within the Precambrian Chuar Self-Sourced Reservoirs AU. The Devonian Aneth Formation is described as having black shale intervals and because the Devonian is one of the major source rock intervals worldwide (Klemme and Ulmishek, 1991), the formation is recognized as having some potential for technically recoverable hydrocarbons within the Devonian Self-Sourced Reservoirs AU.

Resource Summary

The USGS assessed undiscovered, technically recoverable oil and gas resources in nine assessment units in the Paradox Basin (table 1). Four conventional AUs were assessed to contain means of 89 million barrels of oil (MMBO), 833 billion cubic feet of gas (BCFG), and 18 million barrels of natural gas liquids (MMBNGL). Four unconventional AUs were assessed to contain means of 471 MMBO, 11,868 BCFG, and 472 MMBNGL. The Kaiparowits Plateau Coalbed Gas AU was assessed to contain a mean of 450 BCFG. The assessment was based on 2011 IHS well and production data (IHS Energy Group, 2011).

For Further Information

Supporting studies of the geologic models and the methodology used in the 2011 Paradox Basin assessment are in progress. Assessment results are available at the USGS Central Energy Resources Science Center website: *http://energy.cr.usgs.gov/oilgas/noga/*.

References Cited

Barbeau, D.L., 2003, A flexural model for the Paradox Basin—Implications for the tectonics of the Ancestral Rocky Mountains: Basin Research, v. 15, p. 97–115.

Chidsey, T.C., Jr., Morgan, C.D., Eby, D.E., Moore, J.N., Taylor, L.H., and Humphrey, J.D., 2009, Diagenetic analysis of the Leadville Limestone, Lisbon case-study field, *in* Chidsey, T. C., Jr., ed., The Mississippian Leadville Limestone exploration play, Utah and Colorado—Exploration techniques and studies for independents: Final Report for DOE Award, no. DE-FC26-03NT15424, p. 4-1–4-20.

Gautier, D.L., Dolton, G.L., Takahashi, K.I., and Varnes, K.L., 1996, 1995 National assessment of United States oil and gas resources—Results, methodology, and supporting data: U.S. Geological Survey Digital Data Series DDS–30, Release 2.

Goldhammer, R.K., Oswald, E.J., and Dunn, P.A., 1991, Hierarchy of stratigraphic forcing—Example from Middle Pennsylvanian shelf carbonates of the Paradox Basin, *in* Franseen, E.K., Watney, W.L., Kendall, C.G.St.C., and Ross, W., eds., Sedimentary modeling—Computer simulations and methods for improved parameter definition: Kansas Geological Survey Bulletin 233, p. 361–414.

IHS Energy Group, 2011, PI/Dwights PLUS U.S. production data: Englewood, Colo., database available from IHS Energy Group.

Klemme, H.D., and Ulmishek, G.F., 1991, Effective petroleum source rocks of the world; stratigraphic distribution and controlling depositional factors: American Association of Petroleum Geologists Bulletin, v. 75, p. 1809–1851.

Kluth, C.F., and DuChene, H.R., 2009, Late Pennsylvanian and Early Permian structural geology and tectonic history of the Paradox Basin and Uncompahgre Uplift, Colorado and Utah, *in* Houston, W.S., Wray, L.L., and Moreland, P.G., eds., The Paradox Basin revisited—New developments in petroleum systems and basin analysis: Rocky Mountain Association of Geologists Special Publication – The Paradox Basin, p. 178–197.

Assessment Team

Paradox Basin Assessment Team: Katherine J. Whidden (Task Leader; *kwhidden@usgs.gov*), Lawrence O. Anna, Krystal M. Pearson, and Paul G. Lillis.

Review Committee: Ronald R. Charpentier, Troy A. Cook, Timothy R. Klett, Richard M. Pollastro, Russell F. Dubiel, and Christopher J. Schenk.

Table 1. Paradox Basin Province assessment results.

[MMBO, million barrels of oil; BCFG, billion cubic feet of gas; MMBNGL, million barrels of natural gas liquids. Results shown are fully risked estimates. For gas accumulations, all liquids are included as NGL (natural gas liquids). F95 represents a 95-percent chance of at least the amount tabulated; other fractiles are defined similarly. Fractiles are additive under the assumption of perfect positive correlation. TPS, total petroleum system; AU, assessment unit. Gray shading indicates not applicable]

Total petroleum systems (TPS) and assessment units (AU)	Field type	Total undiscovered resources											
		Oil (MMBO)				Gas (BCFG)				NGL (MMBNGL)			
		F95	F50	F5	Mean	F95	F50	F5	Mean	F95	F50	F5	Mean
Paradox Formation TPS													
Leadville McCracken AU	Oil	6	19	39	20	16	54	124	60	2	7	17	8
	Gas					16	47	105	52	0	0	1	1
Pennsylvanian Carbonate Buildups and Fractured Limestone AU	Oil	15	51	102	54	21	74	162	81	2	6	14	6
	Gas					147	509	987	530	0	1	1	1
Upper Paleozoic-Mesozoic Reservoirs AU	Oil	2	4	10	5	6	17	41	20	0	1	2	1
	Gas					27	81	164	87	0	1	2	1
Permo-Mississippian TPS													
Permian-Mesozoic Reservoirs AU	Oil	2	9	25	10	1	2	8	3	0	0	0	0
	Gas					0	0	0	0	0	0	0	0
Total conventional resources		**25**	**83**	**176**	**89**	**234**	**784**	**1,591**	**833**	**4**	**16**	**37**	**18**
Paradox Formation TPS													
Cane Creek Shale Oil AU	Oil	103	198	382	215	84	175	364	193	6	14	31	15
Cane Creek Shale Gas AU	Gas					2,473	4,284	7,420	4,530	88	168	319	181
Gothic, Chimney Rock, Hovenweep Shale Oil AU	Oil	126	238	449	256	91	186	382	205	7	15	32	16
Gothic, Chimney Rock, Hovenweep Shale Gas AU	Gas					3,342	6,075	11,042	6,490	120	238	472	260
Precambrian Chuar Group TPS													
Precambrian Chuar Self-Sourced Reservoirs AU	Oil	Not quantitatively assessed											
Devonian TPS													
Devonian Self-Sourced Reservoirs AU	Oil	Not quantitatively assessed											
Permo-Mississippian TPS													
Manning Canyon Continuous Gas AU	Gas	Not quantitatively assessed											
Coalbed Gas TPS													
Kaiparowits Plateau Coalbed Gas AU	Gas					205	411	824	450	0	0	0	0
Henry Mountains Coalbed Gas AU	Gas	Not quantitatively assessed											
Total continuous resources		**229**	**436**	**831**	**471**	**6,195**	**11,131**	**20,032**	**11,868**	**221**	**435**	**854**	**472**
Total undiscovered oil and gas resources		**254**	**519**	**1,007**	**560**	**6,429**	**11,915**	**21,623**	**12,701**	**225**	**451**	**891**	**490**

Appendix B:

Summary of Cane Creek Wells

INDEX

Cane Creek Well Summary

API	Well Name	Township	Range	Section
4301931547	Greentown Federal 26-43H	21S	16E	26
4301931462	Greentwon State 36-11	21S	16E	36
4301931519	Greentown State 36-24H	21S	16E	36
4301950002	Gunnison Valley 22-9	21S	17E	9
4301931569	Greentown State 31-362216H	22S	16E	36
4301931605	State 16-42	22S	17E	16
4301931503	Federal 28-11	22S	17E	28
4301931461	Greentown State 32-42	22S	17E	32
4301950031	Greentown 32-42-1A	22S	17E	32
4301930679	Government 18-2	23S	17E	18
4301931331	Kane Springs 10-1	25S	18E	10
4301931341	Kane Springs 16-1	25S	18E	16
4301931363	Cane Creek Federal 7-1	25S	19E	7
4301950011	Cane Creek 26-2	25S	19E	26
4301950019	Cane Creek 26-3	25S	19E	26
4301911333	Big Flat 5	25S	19E	27
4301931310	Kane Springs 27-1	25S	19E	27
4301931325	Kane Springs Federal 28-1	25S	19E	28
4301950020	Cane Creek 28-2	25S	19E	28
4301950045	Cane Creek 28-3	25S	19E	28
4301950037	Cane Creek 32-1-25-19	25S	19E	32
4301950061	Cane Creek 32-2-25-19	25S	19E	32
4301931334	Kane Springs 25-19-34-1	25S	19E	34
4301950030	Cane Creek 36-1	25S	19E	36
4301950033	Cane Creek 36-2H	25S	19E	36
4301950035	Cane Creek 36-3H	25S	19E	36
4301930795	Gold Bar 1	25S	20E	29
4301950049	Cane Creek 32-1-25-20	25S	20E	32
4301931446	Cane Creek 1-1	26S	19E	1
4301931396	Cane Creek 2-1	26S	19E	2
4301931364	Cane Creek 11-1	26S	19E	11
4301950009	Cane Creek 12-1	26S	19E	12
4301931156	Mineral Canyon 1-14	26S	19E	14
4301950014	Cane Creek 13-1	26S	19E	18
4301931332	Kane Springs 20-1	26S	19E	20
4301931447	Cane Creek 24-1	26S	19E	24
4301950034	Cane Creek 24-2H	26S	19E	24
4301930796	Skyline 1	26S	20E	5
4301950010	Cane Creek 7-1	26S	20E	7
4301950051	Cane Ceek 7-2-26-20	26S	20E	7
4301931591	Cane Creek 7-1	26S	20E	7
4301931449	Cane Creek 8-1	26S	20E	8
4301915925	Long Canyon 1	26S	20E	9
4301931567	Utah State 16-1	26S	20E	16
4301950028	Cane Creek 17-1	26S	20E	17
4301950032	Cane Creek 17-2	26S	20E	17

INDEX

Cane Creek Well Summary

API	Well Name	Township	Range	Section
4301950012	Cane Creek 18-1	26S	20E	18
4301950027	Cane Creek 18-2	26S	20E	18
4301931324	Kane Springs 19-1A	26S	20E	19
4301931452	Two Fer 26-30	26S	20E	26
4301931624	Lucky Charm 26-1-3	26S	20E	26
4303715925	Shafer Canyon 1	27S	20E	4
4303731631	Cane Creek State 1-36	27S	20E	36
4303730617	Federal 4-26	27S	21E	26
4303730518	Hatch Point 27-1A	27S	21E	27
4303730650	Lion Mesa 5-28	27S	21E	28
4303731630	Hatch Point 22-33H	27S	21E	33
4303730559	Lion Mesa 2-34	27S	21E	34
4303750069	Threemile 12-2-29-21	29S	21E	12
4303750001	Threemile 12-7	29S	21E	12
4303731857	Threemile 43-18H	29S	22E	18
4303730005	Chevron Federal 1	29S	23E	24
4303750002	La Sal 29-28	29S	23E	29
4303700248	Gibson Dome 1 (DOE)	30S	21E	21
4303731742	Remington 21-1H	31S	23E	21
4303750008	Cisco State 36-13	31S	24E	36

Greentown Federal 26-43H

API Number	4301931547
Well Name and Location	Greentown Federal 26-43H, T. 21 S., R. 16 E., section 26
KB and TD	4310 ft KB; 10,587 ft TD Pilot hole
Pilot Hole (yes or no)	Yes
Surface Location	2363 FSL 606 FEL NESE section 26
Top of pay Location	
Bottom Hole Location	2321 FNL 1927 FEL; TD 11,609 MD/10,175 TVD in Cane Creek
Top of Cane Creek	9626 Pilot hole
Pay Zone	
Horizontal Leg	Plugged and Abandoned 6/4/2008
BHL Lateral 2	2648 FSL 1017 FEL
Top of pay L2	"O zone" Shale 19, Plugged and Abandoned 9/17/2008
Pay Zone L2	
TD L2	10,107 MD/9531 TVD
Horizontal Leg	627-ft Azumith 307 degrees
BHL Lateral 3	2248 FNL 1567 FEL
Top of pay L3	"O zone" Shale 19, Plugged and Abandoned 10/16/2008
TD L3	10,610 MD/9733 TVD
Horizontal Leg	1407-ft Azumith 313 degrees
Comments	Unable to drill out cementing ball
BHL Lateral 4	2501 FSL 990 FEL
Top of pay L4	"O zone" Shale 19, Plugged and Abandoned 1/14/2009
TD L4	9855 MD/9740 TVD
Horizontal Leg	
Comments	Fish left in hole
Completion Date & IP	4/27/2009 No IP reported. Shut in 11/7/2011
Total Production (12-31-2015)	0 BO, 403 MCFG, 0 BW
COMMENTS	First horizontal completion attempted in the Cane Creek, horizontal side tracks 2 through 4 were in Shale 19.

Greentown State 36-11

API Number	4301931462
Well Name and Location	Greentown State 36-11, T. 21 S., R. 16 E., section 36
KB and TD	4336 ft KB; 9800 ft TD
Pilot Hole (yes or no)	Vertical well
Surface Location	955 FNL 468 FWL NWNW section 36
Top of pay Location	
Bottom Hole Location	
Top of Cane Creek	Not deep enough
Pay Zone	9472-9482 ("O zone" Shale 19)
Horizontal Leg	
BHL Lateral 2	
Top of pay L2	
Top of Cane Creek L2	
Pay Zone L2	
TD L2	
Horizontal Leg	
Completion Date & IP	8/30/2007, IP 6 BO, 0 MCFG, 0 BW; Plugged and Abandoned 10/24/2009
Total Production (12-31-2015)	364 BO, no gas or water reported
COMMENTS	Drilled four hundred feet of salt below Shale 19 without encountering the Cane Creek.

Greentown State 36-24H

API Number	4301931519
Well Name and Location	Greentwon State 36-24H, T. 21 S., R. 16 E., section 36
KB and TD	4372 ft KB; 10,316 ft TD in vertical hole
Pilot Hole (yes or no)	Yes
Surface Location	1108 FSL 2158 FWL SESW section 36
Top of pay Location	
Bottom Hole Location	2280 FNL 1573 FWL
Top of Cane Creek	10,063 ft in vertical hole
Pay Zone	
Horizontal Leg	1980 ft lateral NW
BHL Lateral 2	1021 FNL 1071 FWL at 12,600 ft
Top of pay L2	
Top of Cane Creek L2	
Pay Zone L2	
TD L2	12,651 MD/9606 TVD
Horizontal Leg	3333 feet long, direction NW
Completion Date & IP	4/5/2010, Plugged and Abandoned
Total Production	
COMMENTS	Openhole treated shale below Cane Creek 10,246-10,230, no results reported. Perforated and treated Cane Creek 10,086-10,150, tested minor shows of oil and gas. Two laterals attempted in shale 19, lost both holes and unable to test.

Gunnison Valley Fee 22-9

API Number	4301950002
Well Name and Location	Gunnison Valley Fee 22-9, T. 21 S., R. 17 E., section 9
KB and TD	4342 ft KB; 11,430 ft TVD
Pilot Hole (yes or no)	Yes to 8626 ft
Surface Location	1980 FNL 1981 FWL SENW section 9
Top of pay Location	
Bottom Hole Location	12,971 ft MD 11,430 TVD
Top of Cane Creek	11,345 ft
Pay Zone	
Horizontal Leg	About 2500 ft long
BHL Lateral 2	10875 ft MD 8639 ft TVD
Top of pay L2	Gothic Shale
Top of Cane Creek L2	Gothic 8746 ft
Pay Zone L2	
TD L2	1857 FS 1729 FE from surface
Horizontal Leg	133 degree azumith, approximately 3600 ft long
Completion Date & IP	11/15/2013 Plugged and Abandoned
Total Production	None
COMMENTS	Two laterals: one in the Cane Creek (Fidelity) produced 84 BO, perforated multiple interclasts in vertical section (Liberty) with no production, drilled horizontal lateral in Gothic Shale (Anadarko) with no production

Greentown State 31-36-2216H

API Number	4301931569
Well Name and Location	Greentwon State 31-362216H, T. 22 S., R. 16 E., section 36
KB and TD	4238 ft KB, 9210 ft vertical well
Pilot Hole (yes or no)	Yes
Surface Location	1025 FNL 2290 FEL NWNE Section 36
Top of Cane Creek	8602 ft in vertical well
Pay Zone	8602 to 8702 ft gross Cane Creek
BHL Lateral 1	1439 FNL 1183 FEL
Top of pay L2	
Top of Cane Creek L2	
Pay Zone L2	Cane Creek
TD L2	10,200 ft MD, 8674 ft TVD
Horizontal Leg	Collapsed lateral
BHL Lateral 2	1830 FSL 725 FEL
Top of pay L2	
Top of Cane Creek L2	
Pay Zone L2	Cane Creek
TD L2	11,475 ft MD, 8628 ft TVD
Horizontal Leg	
BHL Lateral 3	1498 FNL 1908 FEL
Top of pay L3	
Top of Cane Creek L3	
Pay Zone L3	O zone AKA Clastic 19
TD L3	8498 ft MD, 8177 ft TVD
Horizontal Leg	
BHL Lateral 3 Sidetrack 1	3229 FNL 834 FEL
Top of pay L3 ST1	
Top of Cane Creek L3 ST1	
Pay Zone L3 ST1	Clastic 19
TD L3 ST1	10,605 ft MD, 8302 ft TVD
Horizontal Leg	
BHL Lateral 3 Sidetrack 2	4050 FNL 857 FEL
Top of pay L3 ST2	
Top of Cane Creek L3 ST2	
Pay Zone L3 ST2	Clastic 19
TD L3 ST2	11,415 ft MD, 8333 ft TVD
Horizontal Leg	

BHL Lateral 4	1224 FSL 857 FEL
Top of pay L4	
Top of Cane Creek L4	
Pay Zone L4	
TD L4	11,414 ft MD, 8333 ft TVD
Horizontal Leg	
Completion Date & IP	Vertical Mississippian test completed 4/15/2008
Total Production	Never produced
COMMENTS	Other completion dates listed by DOGM: Deepen 10,200 ft P&A 5/13/2008: Deepen 11,475 ft P&A 6/15/2008: Deepen 8498 ft P&A 7/1/2008: Deepen 10,605 ft TA 7/14/2008: Deepen 11,414 ft TA 8/3/2008: Deepen 11,415 ft TA 8/3/2008
Additional Comments	Greentwon State 31-362216 (4301931555) P&A TD 40 ft: Greentown State 31-362216B (4301931570 P&A TD 40 ft.

API Number	4301931605
Well Name and Location	State 16-42, T. 22 S., R. 17 E., section 16
KB and TD	4263 ft KB; 10,176 ft TD
Pilot Hole (yes or no)	Vertical well
Surface Location	2108 FNL 559 FEL SENE section 16
Top of pay Location	
Bottom Hole Location	
Top of Cane Creek	9683 ft
Pay Zone	Perforated and treated Cane Creek 9738-9894 ft
Horizontal Leg	
BHL Lateral 2	
Top of pay L2	
Top of Cane Creek L2	
Pay Zone L2	
TD L2	
Horizontal Leg	
Completion Date & IP	5/12/2009, IP 0 BO, 284 MCFG, 0 BW
Total Production (12/31/2015)	Shut in with no production
COMMENTS	

API Number	4301931503
Well Name and Location	Federal 28-11, T. 22 S., R. 17 E., section 28
KB and TD	4448 ft KB, 10,069 ft TD
Pilot Hole (yes or no)	Vertical hole
Surface Location	800 FNL 726 FWL NWNW section 28
Top of pay Location	
Bottom Hole Location	
Top of Cane Creek	9295 ft
Pay Zone	8044-9648 ft (gross)
Horizontal Leg	
BHL Lateral 2	
Top of pay L2	
Top of Cane Creek L2	
Pay Zone L2	
TD L2	
Horizontal Leg	
Completion Date & IP	1/2/2008, IP 473 BO, 2.3 MMCFG, 160 BW
Total Production (12/31/2015)	71,535 BO, 266,462 MCFG, 19,455 BW
COMMENTS	Perforated and multi-stage fracture treatment Shale 19 and Cane Creek repeated in recumbent fold

Greentown State 32-42

API Number	4301931461
Well Name and Location	Greentown State 32-42, T. 22 S., R. 17 E., section 32
KB and TD	4356 ft, 9176 ft
Pilot Hole (yes or no)	Vertical well
Surface Location	2190 FWL 1068 FEL SENE section 32
Top of pay Location	
Bottom Hole Location	
Top of Cane Creek	8820 ft
Pay Zone	
Horizontal Leg	
BHL Lateral 2	
Top of pay L2	
Top of Cane Creek L2	
Pay Zone L2	
TD L2	
Horizontal Leg	
Completion Date & IP	8/1/2007 , IP 149 BW, Plugged and Abandoned 2009 due to casing failure
Total Production	1374 BO, no gas, 110 BW
COMMENTS	Perforated and fracture treated 6854-9068 (gross)

API Number	4301950031
Well Name and Location	Greentown 32-42-1A, T. 22 S., R. 17 E., section 32
KB and TD	4360 ft KB; 9200 ft TD
Pilot Hole (yes or no)	Vertical well
Surface Location	2190 FNL 1109 FEL, SENE section 32
Top of pay Location	
Bottom Hole Location	
Top of Cane Creek	9142 ft
Pay Zone	
Horizontal Leg	
BHL Lateral 2	
Top of pay L2	
Top of Cane Creek L2	
Pay Zone L2	
TD L2	
Horizontal Leg	
Completion Date & IP	8/4/2014 IPF 0 BO, 63 MCFG, 0 BW Clastic 19
Total Production	Never produced
COMMENTS	Reverse fault repeating clastic 20, TD in Cane Creek, based on mud log, was unable to run open-hole geophysical well logs past 8850, cement bond log to 9100 ft.

API Number	4301930679
Well Name and Location	Government 18-2, T. 23 S., R. 17 E., NENE 18
KB and TD	4219 ft Graded, 9340 ft TD
Pilot Hole (yes or no)	Vertical well
Surface Location	785 FNL 1075 FEL section 18
Top of pay Location	
Bottom Hole Location	
Top of Cane Creek	8250 ft (-4-31)
Pay Zone	Cane Creek B zone 8280-8310 ft (not tested or produced)
Horizontal Leg	
BHL Lateral 2	
Top of pay L2	
Top of Cane Creek L2	
Pay Zone L2	
TD L2	
Horizontal Leg	
Completion Date & IP	8/17/1981 IP 0 BO and 0 MCFG, Plugged and abandoned 8/14/2008
Total Production	2042 BO, 629 MCFG, 651 BW
COMMENTS	Completed in clastic 19 and numerous other intervals above 19, Cane Creek not tested. Clastic 19 has 12 feet of density/neutron cross over

Kane Springs 10-1

API number	4301931331
Well Name and Location	Kane Springs 10-1; T. 25 S., R. 18 E., section 10
KB and TD	5297 ft; 9080 MD/8109 TVD
Pilot Hole (yes or no)	no
Surface Location	2333 FSL 2112 FEL NWSE section 10
Top of pay Location	723 North and 1074 West of surface location
Bottom Hole Location	3918 FSL 3341 FEL
Top of Cane Creek	8069 TVD (-2772)
Pay Zone	8948 MD/8083 TVD to 9080 MD/8109 TVD
Horizontal Leg	SL to BHL 1483 feet; horizontal pay 132 ft N56W
BHL Lateral 2	NA
Top of pay L2	
Top of Cane Creek L2	
Pay Zone L2	
Horizontal Leg	
Completion Date & IP	11/19/1992; IP 1273 BO, 757 MCF, 47 BW
Total Production (12/31/2015)	659,883 BO, 579,732 MCFG, 46,464 BW
COMMENTS	Horizontal leg slight updip, short lateral due to high pressure encountered within a short distance in horizontal leg

API Number	4301931341
Well Name and Location	Kane Springs 16-1; T. 25 S., R. 18 E., section 16
KB and TD	5164 ft; TD 9424 MD/7426 TVD
Pilot Hole (yes or no)	no
Surface Location	960 FSL 1960 FWL SESW section 16
Top of pay Location	4400 FSL 1715 FWL
Bottom Hole Location	3018 FSL 949 FWL
Top of Cane Creek	7239 TVD (-2075)
Pay Zone	7389 MD/7180 TVD to 9424 MD/7426 TVD
Horizontal Leg	SL to BHL 2293 ft; horizontal pay 2035 ft N27W
BHL Lateral 2	
Top of pay L2	Clastic 19 6830 to 6878 MD
Top of Cane Creek L2	
Pay Zone L2	
Horizontal Leg	IP 93 BO, 113 BW
Completion Date & IP	Completed shallower clastic (19) 11/1/1993; Converted to water disposal 7/1/1998
Total Production	15,589 BO, 27,465 MCFG, 2368 BW
COMMENTS	Surface location on directional survey is wrong

Cane Creek Federal 7-1

API Number	4301931363
Well Name and Location	Cane Creek Federal 7-1; T. 25 S., R. 19 E., section 7
KB and TD	5180 ft; 8416 MD/8372 TVD
Pilot Hole (yes or no)	no
Surface Location	1596 FNL 2040 FWL SENW section 7
Top of pay Location	
Bottom Hole Location	
Top of Cane Creek	8421MD/8330 TVD (-3150) from Rassmussen in DOGM well file
Pay Zone	
Horizontal Leg	3000 feet, south (180 degree)
BHL Lateral 2	660 FSL 2264 FWL
Top of pay L2	
Top of Cane Creek L2	8498 MD/8348 TVD (-3168)
Pay Zone L2	
TD L2	9810 MD/8374 TVD
Horizontal Leg	8524 to 9810 MD
BHL Lateral 2	660 FSL 2264 FWL
Top of pay L2	
Top of Cane Creek L2	
Pay Zone L2	
TD L2	TD 11115 MD/8370 TVD
Horizontal Leg	9208 to 11115 MD
Completion Date & IP	9/8/2003 P&A
COMMENTS	Horizontal with no directional survey. Original plus two side tracks. First hole encountered Cane Creek at to low of an angle. Difficulity encountoring Cane Creek and staying in zone.

Cane Creek 26-2

API Number	4301950011
Well Name and Location	Cane Creek 26-2, T. 25 S., R. 19 E., section 26
KB and TD	5676 feet, TD 8685 MD, 7261 TVD
Pilot Hole (yes or no)	yes
Surface Location	2615 FSL 2101 FWL NESW section 26
Top of pay Location	
Bottom Hole Location	2165 FSL 570 FWL
Top of Cane Creek	7380 (-1704) in pilot hole
Pay Zone	8422 MD/8582 TVD to 7275 MD/7262 TVD
Horizontal Leg	SL to BHL 1610 feet, horizontal leg 160 feet, N72W
BHL Lateral 2	
Top of pay L2	
Top of Cane Creek L2	
Pay Zone L2	
TD L2	
Horizontal Leg	
Completion Date & IP	4/1/2012 IP 239 BO, 127 MCFG, 0 BW
Total Production (12/31/2015)	226,489 BO, 178,490 MCFG, 10,095 BW
COMMENTS	

API Number	4301950019
Well Name and Location	Cane Creek 26-3, T. 25 S., R. 19 E., section 26
KB and TD	5675 feet, TD 12466 MD/7583 TVD ending in clastic 22 below Cane Creek
Pilot Hole (yes or no)	yes
Surface Location	2615 FSL 2141 FWL NESW section 26
Top of pay Location	1669 FSL 2377 FWL section 26
Bottom Hole Location	2544 FNL 1241 FWL section 25
Top of Cane Creek	7384 (-1709) vertical pilot hole; 7884 MD/7251 TVD (-1576) in horizontal
Pay Zone	7884 to 12,466 MD
Horizontal Leg	SL to BHL 5526 feet, horizontal lateral 4582 feet, S72E:
BHL Lateral 2	
Top of pay L2	
Top of Cane Creek L2	
Pay Zone L2	
TD L2	
Horizontal Leg	
Completion Date & IP	10/26/2012 vertical well IP 27 BO, 0 MCFG, 43 BW; 11/1/2013 horizontal IP 276 BO, 222 MCFG, 0 BW
Total Production	370,517 BO, 214,150 MCFG, 6172 BW
COMMENTS	Twin to 26-2: Vertical completion made 2995 BO in 6 months.

API Number	4301911333
Well Name and Location	Big Flat 5, T. 25 S., R. 19 E., section 27
KB and TD	5767 ft KB, 7632 ft TD
Pilot Hole (yes or no)	Vertical well
Surface Location	1980 FSL 1980 FEL NWSE section 27
Top of pay Location	
Bottom Hole Location	
Top of Cane Creek	7190 ft
Pay Zone	7220 to 7250 ft
Horizontal Leg	
BHL Lateral 2	
Top of pay L2	
Top of Cane Creek L2	
Pay Zone L2	
TD L2	
Horizontal Leg	
Completion Date & IP	Completed 11/28/1961 IP 454 BO, 282 MCFG, no water reported
Total Production	39,000 BO in four years but 36,000 BO was produced was in one year.
COMMENTS	Plugged and abandoned 12/3/1963 after casing collapsed

Kane Springs 27-1

API number	4301931310
Well Name and Location	Kane Springs 27-1 T 25 S., R 19 E., section 27
KB and TD	KB 5792 ft, 8244 MD/7248 TVD
Pilot Hole (yes or no)	No
Surface Location	1700 FEL 1650 FSL NWSE section 27
Top of pay Location	1989 FSL 1072 FEL
Bottom Hole Location	2600 FSL 2380 FEL
Top of Cane Creek	7233 MD/7165 TVD (-1373)
Pay Zone	7510 MD/7269 TVD to 8244 MD/7248 TVD
Horizontal Leg	SL to BHL 1169 ft, Horizontal pay zone 734 ft
BHL Lateral 2	NA
Top of pay L2	
Top of Cane Creek L2	
Pay Zone L2	
Horizontal Leg	
Completion Date & IP	4/8/1991; IP 914 BO, 290 MCFG, 0 BW
Total Production (12/31/2015)	522,351 BO, 573,785 MCFG, 36,612 BW
COMMENTS	Horizontal leg near zero to slight down dip. Difference between BHL structure and reported structure at BHL = 17 feet.

Kane Springs Federal 28-1

API Number	4301931325
Well Name and Location	Kane Springs Federal 28-1: T. 25 S., R. 19 E., section 28
KB and TD	5602 ft; 7254 ft in vertical well, first directional 8685 MD/7368 TVD
Pilot Hole (yes or no)	Yes
Surface Location	1900 FSL 1900 FEL NWSE section 28
Top of pay Location	
Bottom Hole Location	
Top of Cane Creek	7252 ft (-1618) estimated in vertical
Pay Zone	
Horizontal Leg	
BHL Lateral 2	2416 FSL 1374 FEL
Top of pay L2	
Top of Cane Creek L2	
Pay Zone L2	7673 MD/7336 TVD to 9012 MD/7233 TVD
TD L2	9012 MD 7232 TVD
Horizontal Leg	
Completion Date & IP	Completed 2/24/1992 for 0 BO and 0 MCFG
Total Production	Never produced
COMMENTS	Plugged and abandoned 5/12/2005

API Number	4301950020
Well Name and Location	Cane Creek 28-2, T. 25 S., R. 19 E., section 28
KB and TD	5692 ft KB, TD 10,501 MD/7388 TVD
Pilot Hole (yes or no)	yes
Surface Location	2004 FSL 284 FEL NESE section 28
Top of pay Location	965 FSL 250 FWL section 27
Bottom Hole Location	1198 FNL 1363 FWL NENW section 34
Top of Cane Creek	7148 (-1456) vertical pilot hole
Pay Zone	8479 to 10501 MD
Horizontal Leg	SL to BHL 3601 feet, horizontal leg 2022 feet, S64E
BHL Lateral 2	Completed lateral see data above and comments
Top of pay L2	
Top of Cane Creek L2	
Pay Zone L2	
TD L2	
Horizontal Leg	
Completion Date & IP	12/24/2012 IP 225 BO, 93 MCFG, 0 BW
Total Production (12/31/2015)	69,446 BO, 25,827 MCFG, 2713 BW
COMMENTS	First lateral crossed a fault at 7990 MD so they continued drilling to determine if above or belwo Cane Creek, eventually encountering the clastic above the Cane Creek. Second lateral encountered the fault at 7916 MD/7152 TVD about 100 feet from surface location.

Cane Creek 28-3

API Number	4301950045
Well Name and Location	Cane Creek 28-3, T. 25 S., R. 19 E., section 28
KB and TD	5687 ft KB, 11,894 MD 7571 TVD TD
Pilot Hole (yes or no)	No
Surface Location	2000 FSL 288 FEL NESE section 28
Top of pay Location	1326 FNL 274 FWL
Bottom Hole Location	1545 FSL 926 FWL NWSW section 22
Top of Cane Creek	1326 FNL 274 FWL
Pay Zone	8900 to 11,700 ft MD
Horizontal Leg	14 degree azimuth
BHL Lateral 2	
Top of pay L2	
Top of Cane Creek L2	
Pay Zone L2	
TD L2	
Horizontal Leg	
Completion Date & IP	Completed 12/17/2014, IPF 296 BO, 235 MCFG, 0 BW
Total Production (12/31/2015)	187,805 BO, 97,015 MCFG, 4719 BW
COMMENTS	Surface location same as 28-2 (4301950020).

Cane Creek 32-1-25-19

API Number	4301950037
Well Name and Location	Cane Creek 32-1-25-19, T. 25 S., R. 19 E., section 32
KB and TD	KB 5686 ft, TD 12,025 ft MD, 7562 ft TVD
Pilot Hole (yes or no)	Yes
Surface Location	1114 FSL 858 FWL, SWSW section 32
Top of pay Location	6576 FWL 1539 FSL
Bottom Hole Location	861 FNL 897 FEL NENE section 32
Top of Cane Creek	7476 TVD
Pay Zone	7860 - 12,025 MD
Horizontal Leg	Length approximately 4827 ft, azumith 47 degrees, flat to gental NE dip
BHL Lateral 2	
Top of pay L2	
Top of Cane Creek L2	
Pay Zone L2	
TD L2	
Horizontal Leg	
Completion Date & IP	5/5/2014 IP 181 BO, 182 MCFG
Total Production	55,536 BO, 30,196 MCFG, 2946 BW
COMMENTS	Fractured stimulated 11/19/2014 in 6 stages total 1912 frac oil (mineral oil with 30/50 proppant) and 66,500 bbls diesel

Cane Creek 32-2-25-19

API Number	4301950061
Well Name and Location	Cane Creek 32-2-25-19, T. 25 S., R. 19 E., section 32
KB and TD	
Pilot Hole (yes or no)	
Surface Location	1114 FSL 893 FWL
Top of pay Location	
Bottom Hole Location	
Top of Cane Creek	
Pay Zone	
Horizontal Leg	
BHL Lateral 2	
Top of pay L2	
Top of Cane Creek L2	
Pay Zone L2	
TD L2	
Horizontal Leg	
Completion Date & IP	July 2015, permit approved but not yet spudded.
COMMENTS	Surface location same as 32-1-25-19 (4301950037).

Kane Springs 25-19-34-1

API number	4301931334
Well Name and Location	Kane Springs 25-19-34-1; T. 25 S., R. 19 E., section 34
KB and TD	5849 ft; TD 7377 TVD
Pilot Hole (yes or no)	No
Surface Location	934 FNL 1678 FEL
Top of pay Location	1314 FNL 1652 FEL
Bottom Hole Location	1694 FNL 1513 FEL
Top of Cane Creek	7530 MD/7321 TVD (-1472 TVD)
Pay Zone	7580 MD/7339 TVD to 7988 MD/7377 TVD
Horizontal Leg	SL to BHL 777 ft; horizontal pay 408 ft S12E
BHL Lateral 2	NA
Top of pay L2	
Top of Cane Creek L2	
Pay Zone L2	
Horizontal Leg	
Completion Date & IP	5/21/1993; IP 731 BO, 328 MCF, 0 BW
Total Production (12/31/2015)	378,283 BO, 309,938 MCFG, 53,669 BW
COMMENTS	

Cane Creek 36-1

API Number	4301950030
Well Name and Location	Cane Creek 36-1, T. 25 S., R. 19 E., section 36
KB and TD	5820 Ft KB, TD 12,073 MD/7959 TVD
Pilot Hole (yes or no)	yes TD 7521 salt 23
Surface Location	267 FSL 774 FWL SWSW section 36
Top of pay Location	608 FSL 1197 FWL SWSW
Bottom Hole Location	1501 FNL 896 FEL SENE section 36
Top of Cane Creek	7308 ft (-1498)
Pay Zone	7690 MD/7308 TVD to 12073 MD/7399 TVD
Horizontal Leg	4383 feet, N46E
BHL Lateral 2	
Top of pay L2	
Top of Cane Creek L2	
Pay Zone L2	
TD L2	
Horizontal Leg	
Completion Date & IP	9/24/2013 IP 113 BO, 0 MCFG, 0 BW
Total Production (12/31/2015)	623,209 BO, 351,064 MCFG, 12,542 BW
COMMENTS	lateral drilled in downward dipping Cane Creek

Cane Creek 36-2H

API Number	4301950033
Well Name and Location	Cane Creek 36-2H, T. 25 S., R. 19 E., section 36
KB and TD	5818 ft KB: 11,482 ft MD/7681 TVD TD
Pilot Hole (yes or no)	No
Surface Location	267 FSL 754 FWL SWSW section 36
Top of pay Location	
Bottom Hole Location	737 FNL 286 FEL section 1, T. 26 S., R. 20 E.
Top of Cane Creek	7302 ft TVD; 7464 ft MD
Pay Zone	7325 to 7670 ft TVD; 7525 to 11,398 ft MD
Horizontal Leg	103 degrees azimuth
BHL Lateral 2	
Top of pay L2	
Top of Cane Creek L2	
Pay Zone L2	
TD L2	
Horizontal Leg	latreral path about 7 degrees down dip.
Completion Date & IP	8/26/2014 IPF 200 BO, 48 MCFG, 1 BW
Total Production (12/31/2015)	29,547 BO, 12,311 MCFG, 4169 BW
COMMENTS	Surface location same as 36-1 (4301950030)

Cane Creek 36-3H

API Number	4301950035
Well Name and Location	Cane Creek 36-3H, T. 25 S., R. 19 E., section 36
KB and TD	5818 ft KB; 8400 ft MD/7046 TVD TD
Pilot Hole (yes or no)	No
Surface Location	267 FNL 734 FWL SWSW section 36
Top of pay Location	Clastic 18/19 497 FSL 908 FWL section 36
Bottom Hole Location	1287 FSL 1927 FWL section 36
Top of Cane Creek	7101 ft MD Clastic 81/19
Pay Zone	Clastic 18/19 7101 to 8320 ft MD
Horizontal Leg	
BHL Lateral 2	
Top of pay L2	
Top of Cane Creek L2	
Pay Zone L2	
TD L2	
Horizontal Leg	1299 ft length 49 degree azimuth
Completion Date & IP	8/16/2014 IPF 54 BO, 50 MCFG, 0 BW
Total Production (12/31/2015)	2978 BO, 1484 MCFG, 2329 BW (Clastic 18/19)
COMMENTS	Surface location same as 36-1 (4301950030) BHL very close to 36-1 BHL.

Gold Bar 1

API Number	4301930795
Well Name and Location	Gold Bar 1 T. 25 S., R. 20 E., section 29
KB and TD	5325 ft KB; 8279 ft TD
Pilot Hole (yes or no)	Vertical well
Surface Location	720 FSL 2010 FEL SWSE section 29
Top of pay Location	
Bottom Hole Location	
Top of Cane Creek	7939 ft
Pay Zone	7945 to 7996 ft and 8082 to 8098 ft
Horizontal Leg	
BHL Lateral 2	
Top of pay L2	
Top of Cane Creek L2	
Pay Zone L2	
TD L2	
Horizontal Leg	
Completion Date & IP	1/15/1982 IP 53 BO, 0 MCFG, 24 BW
Total Production	13,125 BO, 14,800 MCFG, 4674 BW
COMMENTS	Plugged and Abandoned 10/27/1984

Cane Creek 32-1-25-20

API Number	4301950049
Well Name and Location	Cane Creek 32-1-25-20 T. 25 S., R. 20 E., section 32
KB and TD	5251 ft KB, 11405 ft MD, 7856 ft TVD
Pilot Hole (yes or no)	Yes to salt 18
Surface Location	452 FSL 2312 FEL SESE section 32 T. 25 S., R. 20 E.
Top of pay Location	
Bottom Hole Location	
Top of Cane Creek	
Pay Zone	
Horizontal Leg	
BHL Lateral 2	
Top of pay L2	
Top of Cane Creek L2	7665 ft MD, 7398 TVD
Pay Zone L2	7750 to 11310 ft
TD L2	11405 ft MD; 7856 ft TVD
Horizontal Leg	Gross length approximately 4150 ft, azumith 17 degrees,
Completion Date & IP	8/24/2014 IPF 120 BO, 1 MCFG, 45 BW
Total Production 12/31/2015)	1996 BO, 351 MCFG, 2457 BW
COMMENTS	First horizontal encountered fault at 9340 ft placing lateral below Cane Creek. Side track 1 encountered fault at 9330 ft placing lateral above Cane Creek. Side track 2 successfully drilled Cane Creek B

Cane Creek 1-1

API Number	4301931446
Well Name and Location	Cane Creek 1-1, T. 26 S., R. 19 E., section 1
KB and TD	5914 ft KB; 7355 ft TD
Pilot Hole (yes or no)	Vertical well
Surface Location	2240 FSL 1317 FWL, NWSW section 1
Top of pay Location	
Bottom Hole Location	
Top of Cane Creek	7237 ft
Pay Zone	Shale 18 - 6904 to 6915 ft, Shale 19 - 6934 to 6952 ft.
Horizontal Leg	
BHL Lateral 2	
Top of pay L2	
Top of Cane Creek L2	
Pay Zone L2	
TD L2	
Horizontal Leg	
Completion Date & IP	5/4/2008 IPF 439 BO, 262 MCFG, 0 BW
Total Production (12/31/2015)	132,960 BO, 135,246 MCFG, 2421 BW Clastic 18/19
COMMENTS	No geophysical logs below 4000 ft. Cane Creek perfs squeezed 7239 to 7311 ft are not productive.

Cane Creek 2-1

API Number	4301931396
Well Name and Location	Cane Creek 2-1, T. 26 S., R. 19 E., section 2
KB and TD	5947 ft GL, 7220 ft TD
Pilot Hole (yes or no)	Vertical hole
Surface Location	2289 FNL 518 FEL SENE section 2
Top of pay Location	
Bottom Hole Location	
Top of Cane Creek	6964 ft
Pay Zone	Perforated 6968 to 7038 ft
Horizontal Leg	
BHL Lateral 2	
Top of pay L2	
Top of Cane Creek L2	
Pay Zone L2	
TD L2	
Horizontal Leg	
Completion Date & IP	5/18/2004 IPF 513 BO, 657 MCFG, 0 BW
Total Production (12-31-2015)	450,555 BO, 348,090 MCFG, 6179 BW
COMMENTS	No geophysical well logs past 4000 ft

Cane Creek 11-1

API Number	4301931364
Well Name and Location	Cane Creek 11-1; T. 26 S., R. 19 E., section 11
KB and TD	6170 ft; TD 9893 MD/7554 TVD (-1384)
Pilot Hole (yes or no)	no
Surface Location	2220 FNL 2060 FWL
Top of pay Location	2350 FNL 2322 FWL
Bottom Hole Location	3766 FNL 3989 FWL
Top of Cane Creek	7587 md/7521 tvd (-1351)
Pay Zone	7702 MD/7582 TVD to 9892 MD/7554 TVD
Horizontal Leg	SL to BHL 2472 feet, Horizontal leg 2190 feet, S35W
BHL Lateral 2	
Top of pay L2	
Top of Cane Creek L2	
Pay Zone L2	
Horizontal Leg	
Completion Date & IP	Shut-in oil well 7/15/2002 IP 1100 BO, 560 MCFG, 0 BW; P&A 5/18/2005.
Total Production	19,015 BO, 8592 MCFG, 40 BW
COMMENTS	Dip near vertical in lower part of horizontal leg

Cane Creek 12-1

API Number	4301950009
Well Name and Location	Cane Creek 12-1, T. 26 S., R. 19 E., section 12
KB and TD	6188 ft KB; TD 10196 MD/7747 TVD
Pilot Hole (yes or no)	Yes
Surface Location	2194 FSL 2497 FWL NESW section 12
Top of pay Location	2390 FEL 2157 FSL
Bottom Hole Location	1350 FSL 1651 FEL
Top of Cane Creek	7735 ft (-1547)
Pay Zone	8096 to 8886 MD
Horizontal Leg	SL to BHL 1500 feet, horizontal leg 790 feet. S50E
BHL Lateral 2	
Top of pay L2	
Top of Cane Creek L2	
Pay Zone L2	
TD L2	
Horizontal Leg	
Completion Date & IP	9/10/2012 IP 165 BO, 0 MCFG, 118 BW
Total Production (12/31/2015)	867,263 BO, 358,052 MCFG, 121,243 BW
COMMENTS	

API Number	4301931156
Well Name and Location	Mineral Canyon 1-14, T. 26 S., R. 19 E., section 14
KB and TD	6047 ft KB; 8082 ft TD
Pilot Hole (yes or no)	Vertical well
Surface Location	720 FSL 2010 FEL SWSE section 29
Top of pay Location	
Bottom Hole Location	
Top of Cane Creek	7332 ft
Pay Zone	Perforated 6055 to 6063 ft, shallow interclast
Horizontal Leg	
BHL Lateral 2	
Top of pay L2	
Top of Cane Creek L2	
Pay Zone L2	
TD L2	
Horizontal Leg	
Completion Date & IP	12/1/1984 IPF 197 BO, 139 MCFG, 0 BW
Total Production (12/31/2015)	15,750 BO, 2949 MCFG, 30,098 BW
COMMENTS	Plugged and Abandoned 3/13/1986

Cane Creek 13-1

API Number	4301950014
Well Name and Location	Cane Creek 13-1, T. 26 S., R. 19 E., section 13
KB and TD	6111 ft KB, TD 11291 MD/7644 TVD
Pilot Hole (yes or no)	Yes
Surface Location	2071 FNL 880 FEL SENE section 13
Top of pay Location	2511 FSL 200 FWL NESW section 13
Bottom Hole Location	342 FSL 1895 FWL SWSE section 18
Top of Cane Creek	7926 ft (-1815)
Pay Zone	8254 MD/7644 TVD to 11291 MD/7854 TVD
Horizontal Leg	SL to BHL 4023 feet, horizontal leg 3037 feet, S43E
BHL Lateral 2	
Top of pay L2	
Top of Cane Creek L2	
Pay Zone L2	
TD L2	
Horizontal Leg	
Completion Date & IP	5/11/2013 IP 255 BO, 0 MCFG, 0 BW
Total Production (12/31/2015)	143,470 BO, 59,802 MCFG, 132,015 BW
COMMENTS	

Kane Springs 20-1

API number	4301931332
Well Name and Location	Kane Springs 20-1; T. 26 S., R. 19 E., section 20
KB and TD	5658 ft KB; TD 10936 MD/7479 TVD
Pilot Hole (yes or no)	No
Surface Location	2400 FWL 1000 FWL SESW section 20
Top of pay	7420 MD/7194 TVD (-1536)
Bottom Hole Location	513 FNL 1049 FWL NENW section 20
Top of Cane Creek	7420 MD/7194 TVD (-1536)
Pay Zone	not reported on completion report
Horizontal Leg	SL to BHL 4002 ft; N70E
BHL Lateral 2	NA
Top of pay L2	
Top of Cane Creek L2	
Pay Zone L2	
Horizontal Leg	
Completion Date & IP	Plugged & Abandoned; 8/11/1993
COMMENTS	No directional survey submitted to DOGM

Cane Creek 24-1

API Number	4301931447
Well Name and Location	Cane Creek 24-1, T. 26 S., R. 19 E., section 24
KB and TD	6078 ft KB; TD 8294 MD/7657 TVD
Pilot Hole (yes or no)	No
Surface Location	682 FNL 2829 FEL NENW section 24
Top of pay Location	
Bottom Hole Location	1284 FNL 2414 FEL
Top of Cane Creek	7590 ft (-1512)
Pay Zone	7650 to 8100 ft MD
Horizontal Leg	
BHL Lateral 2 sidetrack 1	2112 FSL 196 FWL section 13, T. 26 S., R. 19 E.
Top of pay L2	
Top of Cane Creek L2	
Pay Zone L2	7967 MD/7613 TVD to 9659 MD/7716 TVD
TD L2	9659 MD/7716 TVD
Horizontal Leg	Length 1692 feet, N28W
BHL Lateral 3 sidetrack 2	2371 FSL 1085 FWL section 13, T. 26 S., R. 19 E.
Top of pay L3	129 FSL 2341 FWL section 13
Top of Cane Creek L3	7590 ft
Pay Zone L3	7626 MD/8000 MD to 7689 MD/10425 TVD
TD L3	11614 MD/7683 TVD
Horizontal Leg	
BHL Lateral 4 sidetrack 3	2506 feet North and 1300 feet West of surface location
Top of pay L4	
Top of clastic 19 L4	
Pay Zone L4	
TD L4	9552 MD/7120 TVD
Horizontal Leg	
Completion Date & IP	11/8/2007 completed Cane Creek IP 590 BO, 588 MCFG, 0 BW. Temporarily abandoned 5/15/2012.
Total Production (12/31/2015)	132,482 BO, 155,246 MCFG, 202 BW.
COMMENTS	Drilled three laterals in Cane Creek (original leg and sidetrack 1 and 2) and a fourth lateral in clastic 18/19.

Cane Creek 24-2H

API Number	4301950034
Well Name and Location	Cane Creek 24-2H, T. 26 S., R. 19 E., section 24
KB and TD	6074 ft KB; TD 13,400 MD, 7291 TVD
Pilot Hole (yes or no)	No
Surface Location	650 FNL 2829 FEL NENW section 24
Top of pay Location	
Bottom Hole Location	5439 FSL 3427 FEL OF section 24; 807 FNL 598 FWL section 30 T. 26 S., R. 20 E.
Top of Cane Creek	8586 MD, 7748 TVD
Pay Zone	9877 to 13,280 ft
Horizontal Leg	Approximte length 6428 ft, azimuth 148 degrees, dip 6 degrees
BHL Lateral 2	
Top of pay L2	
Top of Cane Creek L2	
Pay Zone L2	
TD L2	
Horizontal Leg	
Completion Date & IP	6/5/2014 IP 227 BO, 106 MCFG, 0 BW
Total Production (12/31/2015)	159,709 BO, 64,472 MCFG, 11,862 BW
COMMENTS	Same location as 24-1 (4301931447). No open hole logs.

Skyline 1

API Number	4301930796
Well Name and Location	Skyline 1 T. 26 S., R. 20 E., section 5
KB and TD	7538 ft KB; 7670 ft TD
Pilot Hole (yes or no)	Vertical well
Surface Location	1968 FSL 2000 FEL NWSE section 5
Top of pay Location	
Bottom Hole Location	
Top of Cane Creek	7444 ft
Pay Zone	
Horizontal Leg	
BHL Lateral 2	
Top of pay L2	
Top of Cane Creek L2	
Pay Zone L2	
TD L2	
Horizontal Leg	
Completion Date & IP	11/1/1981; Plugged and abandoned
Total Production	
COMMENTS	Perforated Cane Creek 7455 to 7508 ft and clastic 22 7538 to 7550 ft. Stimulated with 70,000 gals salt water, 8000 lbs 100 mesh sand, 130,000 lbs 20/40 mesh sand, and 900,000 scf nitrogen. Swab tested, final reported rate 10 BOPD.

Cane Creek 7-1

API Number	4301950010
Well Name and Location	Cane Creek 7-1, T 26 S., R. 20 E., section 7
KB and TD	5980 ft KB; TD 11941 MD, 7765 TVD
Pilot Hole (yes or no)	Yes
Surface Location	823 FNL 874 FEL NENE section 7
Top of pay Location	163 FSL 1227 FEL section 6
Bottom Hole Location	2754 FSL 912 FWL section 6 UTMX 607956 UTMY 4269856
Top of Cane Creek	7580 ft
Pay Zone	7515 to 5894 ft TVD; 7920 to 11,870 ft MD
Horizontal Leg	Drilled to 9281 , pulled back and drilled sidetrack hole
BHL Lateral 2	2791 FSL 906 FWL section 6
Top of pay L2	163 FSL 1227 FEL
Top of Cane Creek L2	7515 MD 5894 MD
Pay Zone L2	7920 to 11890 ft MD
TD L2	
Horizontal Leg	Approximately 5000 feet length, azimuth 316 degrees
Completion Date & IP	1/27/2014 IPF 337 BO, 176 MCFG, 0 BW
Total Production (12/31/2015)	36,050 BO 14,139 MCFG, 10,481 BW
COMMENTS	

API Number	4301950051
Well Name and Location	Cane Ceek 7-2-26-20, T. 26 S., R. 20 E., section 7
KB and TD	
Pilot Hole (yes or no)	
Surface Location	854 FNL 875 FEL
Top of pay Location	
Bottom Hole Location	
Top of Cane Creek	
Pay Zone	
Horizontal Leg	
BHL Lateral 2	
Top of pay L2	
Top of Cane Creek L2	
Pay Zone L2	
TD L2	
Horizontal Leg	
Completion Date & IP	12/31/2015, DOGM lists as operation suspended
COMMENTS	Surface location same as 7-1 (4301950010).

Cane Creek 7-1
Abandoned Location

API Number	4301931591
Well Name and Location	Cane Creek 7-1, T. 26 S., R. 20 E., section 7
KB and TD	
Pilot Hole (yes or no)	
Surface Location	823 FNL 874 FEL
Top of pay Location	
Bottom Hole Location	
Top of Cane Creek	
Pay Zone	
Horizontal Leg	
BHL Lateral 2	
Top of pay L2	
Top of Cane Creek L2	
Pay Zone L2	
TD L2	
Horizontal Leg	
Completion Date & IP	Location abandoned
COMMENTS	Can be confused with Cane Creek 7-1 API 4301950010 which is a completed oil well

Cane Creek 8-1

API Number	4301931449
Well Name and Location	Cane Creek 8-1, T. 26 S., R. 20 E. section 8
KB and TD	6017 ft KB; TD 7720 MD
Pilot Hole (yes or no)	Yes
Surface Location	2563 FNL 1429 FWL SENW section 8
Top of pay Location	
Bottom Hole Location	
Top of Cane Creek	7571 ft (-1554)
Pay Zone	7580 to 7655 perforations
Horizontal Leg	NA
BHL Lateral 2	2370 FNL 1310 FWL reported in DOGM as lateral 1
Top of pay L2	
Top of Clastic 18/19 L2	
Pay Zone L2	
TD L2	8424 MD/7747 TVD
Horizontal Leg	N34W
BHL Lateral 3	Reported DOGM as lateral 2
Top of pay L3	
Top of Clastic 18/19 L3	
Pay Zone L3	
TD L3	8395 MD/7854 TVD
Horizontal Leg	N56W
BHL Lateral 4	465 FSL 921 FEL section 5, T. 26 S., R. 20 E. Reported DOGM lateral 3
Top of pay L4	
Top of Clastic 10 L4	
Pay Zone L4	
TD L4	5955 TVD
Horizontal Leg	N46E
Completion Date & IP	7/14/2008 Completed as shut in oil well no IP reported
COMMENTS	Vertical Cane Creek test with laterals in shallower clastics. L2 listed as shut in Paradox well , no production as of 12/31/2015

Long Canyon 1

API Number	4301915925
Well Name and Location	Long Canyon 1, T. 26 S., R. 20 E., section 9
KB and TD	5794 ft KB; TD 8132
Pilot Hole (yes or no)	Vertical Well
Surface Location	2339 FNL 2473 FWL SENW section 9
Top of pay Location	
Bottom Hole Location	
Top of Cane Creek	7024
Pay Zone	7042-7076
Horizontal Leg	
BHL Lateral 2	
Top of pay L2	
Top of Cane Creek L2	
Pay Zone L2	
TD L2	
Horizontal Leg	
Completion Date & IP	8/24/1963 IP 600 BO no gas and no water reported
Total Production (12/31/2015)	1,125,446 BO, 1,162,735 MCFG, 571,991 BW
COMMENTS	Shut in since 11/2014

Utah State 16-1

API Number	4301931567
Well Name and Location	Utah State 16-1, T. 26 S., R. 20 E., section 16
KB and TD	6017 ft KB; TD 7650
Pilot Hole (yes or no)	Cane Creek vertical test
Surface Location	1749 FNL 2117 FWL SENW section 16
Top of pay Location	
Bottom Hole Location	
Top of Cane Creek	7355 (-1338)
Pay Zone	perforated 7355 to 7405 and 7527 to 7595 feet
Horizontal Leg	NA
BHL Lateral 1	710 FNL 1084 FWL
Top of pay L1	
Top of Cane Creek L1	
Pay Zone L1	Clastic 18
TD L1	8436 MD/7314 TVD
Horizontal Leg	
Completion Date & IP	Completed 1/31/2009; Plugged and abandoned 5/18/2010
Total Production	246 BO, no gas or water reported
COMMENTS	Vertical Cane Creek test, lateral drilled in Clastic18/19

Cane Creek 17-1

API Number	4301950028
Well Name and Location	Cane Creek 17-1, T. 26 S., R. 20 E., section 17
KB and TD	6113 ft KB, TD 11602 MD/7729 TVD
Pilot Hole (yes or no)	Yes TD 7910 ft in salt 22
Surface Location	935 FSL 2047 FEL SWSE section 17
Top of pay Location	449 FSL 1675 FEL section 17
Bottom Hole Location	2592 FNL 62 FEL section 20
Top of Cane Creek	7711 ft (-1598)
Pay Zone	8074 MD/7746 TVD to 11,602 MD/7882 TVD
Horizontal Leg	3500 feet, S62E
BHL Lateral 2	
Top of pay L2	
Top of Cane Creek L2	
Pay Zone L2	
TD L2	
Horizontal Leg	
Completion Date & IP	6/21/2013 IP 386 BO, 0 MCFG, 0 BW
Total Production (12/31/2015)	143,763 BO, 60,851 MCFG, 25,986 BW
COMMENTS	Same surface location as 17-2 (4301950032). May have crossed a fault, entered into salt at 10,680 MD and were uncertain if above or below the Cane Creek. As of 12/31/2015, DOGM well files available but not the well logs.

API Number	4301950032
Well Name and Location	Cane Creek 17-2, T. 26 S., R. 20 E., section 17
KB and TD	6112 FT kb; TD 11,620 MD, 7768 TVD
Pilot Hole (yes or no)	No
Surface Location	975 FSL 2047 FEL SWSE section 17
Top of pay Location	715 FSL 2150 FEL
Bottom Hole Location	SWNW section 20, T. 26 S., R. 20 E.
Top of Cane Creek	7892 MD, 7718 TVD
Pay Zone	7950 to 11,420 ft MD
Horizontal Leg	Length approximately 4000 ft, azimuth 214 degrees
BHL Lateral 2	
Top of pay L2	
Top of Cane Creek L2	
Pay Zone L2	
TD L2	
Horizontal Leg	
Completion Date & IP	2/17/2014 IPF 294 BO, 130 MCFG, 0 BW
Total Production (12/31/2015)	54,097 BO, 26,304 MCFG, 41,445 BW
COMMENTS	Horizontal leg slightly downward dipping @ 11,300 an abrupt steep upward dip was encountered.

Cane Creek 18-1

API Number	4301950012
Well Name and Location	Cane Creek 18-1, T. 26 S., R. 20 E., section 18
KB and TD	6018 ft KB; 9272MD/7692TVD
Pilot Hole (yes or no)	Yes
Surface Location	721 FNL 766 FEL NENE section 18
Top of pay Location	
Bottom Hole Location	1503 FSL 1161 FEL
Top of Cane Creek	7666 ft (-1648)
Pay Zone	8118 MD/7706 TVD to 9272 MD/7693 TVD
Horizontal Leg	SL to BHL 1863 feet, horizontal leg 1154 feet, S9W
BHL Lateral 2	
Top of pay L2	
Top of Cane Creek L2	
Pay Zone L2	
TD L2	
Horizontal Leg	Sidetrack 1
BHL Lateral 3	415 feet west and 3109 feet South of surface location
Top of pay L3	
Top of Cane Creek L3	
Pay Zone L3	
TD L3	10633 MD/7604 TVD
Horizontal Leg	Sidetrack 2, S10W, 3134 feet
Completion Date & IP	5/22/2012 original horizontal IP 254 BO, 133 MCFG, 9 BW. 3/20/2013 second sidetrack-lateral 3 IP 403 BO, 105 MCFG, 0 BW.
Total Production (12/31/2015)	435,467 BO, 203,062 MCFG, 62,891 BW
COMMENTS	

Cane Creek 18-2

API Number	4301950027
Well Name and Location	Cane Creek 18-2, T. 26 S., R. 20 E., section 18
KB and TD	6018 ft KB, TD 11,958 MD/9143 TVD
Pilot Hole (yes or no)	Yes
Surface Location	741 FNL 720 FEL NENE section 18
Top of pay Location	690 FSL 2145 FEL section 7
Bottom Hole Location	2391 FNL 941 FEL section 7
Top of Cane Creek	7666 ft (-1648) in horizontal
Pay Zone	8879 to 11,958 ft MD
Horizontal Leg	SL to BHL 5071 feet, horizontal 3079 feet, N47W
BHL Lateral 2	
Top of pay L2	
Top of Cane Creek L2	
Pay Zone L2	
TD L2	
Horizontal Leg	
Completion Date & IP	4/8/2013 IP 30 BO, 0 MCFG, 188 BW
Total Production (7/1/2015)	41384 BO, 12,577 MCFG, 48,831 BW
COMMENTS	Surface location 45 feet east of 18-1

Kane Springs 19-1A ST

API number	4301931324
Well Name and Location	Kane Springs 19-1A; T. 26 S., R. 20 E., section 19
KB and TD	5990 ft KB; 9825 MD/7420 TVD (Side Track (ST hole))
Pilot Hole (yes or no)	No
Surface Location	800 FSL 1918 FEL
Top of pay	NA
Bottom Hole Location	1890 N 475 E of surface location
Top of Cane Creek	NA
Pay Zone	NA
Horizontal Leg	1949 ft length, N14E
BHL Lateral 2	Kane Springs 19-1A ST; T. 26 S., R. 20 E., section 19 (Side Tract - prod. lateral)
Top of pay L2	1710 FSL 1713 FEL
Top of Cane Creek L2	7815 MD/7337 TVD (-1347)
Pay Zone L2	7824 MD/7340 TVD to 9825 MD/7420 TVD
Horizontal Leg	SL to BHL 2922 ft; Horizontal pay 2001 ft; N15E
Completion Date & IP	11/13/1999; IP 1158 BO, 234 MCFG, 0 BW
Total Production (12/31/2015)	402,710 BO, 353,653 MCFG, 31,473 BW
COMMENTS	Drilled leg down dip

API Number	4301931452
Well Name and Location	Two Fer 26-30, T. 26 S., R. 20 E., section 26
KB and TD	4562 ft KB; TD 6508 ft (6499 TVD)
Pilot Hole (yes or no)	
Surface Location	588 FSL 1864 FWL SESW section 26
Top of pay Location	
Bottom Hole Location	
Top of Cane Creek	6226 (-1664)
Pay Zone	
Horizontal Leg	
BHL Lateral 2	
Top of pay L2	
Top of Cane Creek L2	
Pay Zone L2	
Horizontal Leg	
Completion Date & IP	8/14/2009 IP 319 BO, 287 MCFG, 0 BW.
Total Production (12/31/2015)	11,028 BO, no gas or water
COMMENTS	Near vertical hole drilled on salt mine property

Lucky Charm 26-1-3

API Number	4301931624
Well Name and Location	Lucky Charm 26-1-3, T. 26 S., R. 20 E., section 26
KB and TD	4242 ft KB; TD 7803 MD/5870 TVD
Pilot Hole (yes or no)	No
Surface Location	1048 FNL 2021 FWL NENW section 26
Top of pay Location	
Bottom Hole Location	2487 FNL 1573 FWL
Top of Cane Creek	
Pay Zone	
Horizontal Leg	TD clastic 19 by mistake
BHL Lateral 1	
Top of pay L1	
Top of Cane Creek L1	7220 MD/6367 TVD (-2125)
Pay Zone L1	
TD L1	7548 MD/6604 TVD
Horizontal Leg	Drilled at approximately 45 degree angle S43E 330-foot lateral
BHL Lateral 2	
Top of pay L2	
Top of Cane Creek L2	mostly salt no Cane Creek
Pay Zone L2	
TD L2	7402 MD/6483 TVD
Horizontal Leg	S42E length 1194 feet
BHL Lateral 3	
Top of pay L3	
Top of Cane Creek L3	7423 MD no sandstone
Pay Zone L3	
TD L3	8436 MD/6493 TVD
Horizontal Leg	S44E length 2694 feet, salt at 8165 MD
BHL Lateral 4	
Top of pay L4	
Top of Cane Creek L4	dolomite then salt at end of lateral
Pay Zone L4	
TD L4	7725 MD/6421 TVD
Horizontal Leg	S43E length 1943 feet, parallel ST 3 but 20 feet lower
Completion Date & IP	4/3/2010 P&A
COMMENTS	Drilled on salt mine property

Shafer Canyon 1

API Number	4303715925
Well Name and Location	Shafer Canyon 1, T. 27 S., R. 20 E., section 4
KB and TD	4534 ft KB; 6198 ft TD
Pilot Hole (yes or no)	Vertical well
Surface Location	2295 FNL 1830 FWL SENW section 4
Top of pay Location	
Bottom Hole Location	
Top of Cane Creek	6108 ft
Pay Zone	6138 to 6163 ft
Horizontal Leg	
BHL Lateral 2	
Top of pay L2	
Top of Cane Creek L2	
Pay Zone L2	
TD L2	
Horizontal Leg	
Completion Date & IP	4/20/1963 IP 98 BO, 0 MCFG, 0 BW
Total Production	67,556 BO, 63,807 MCFG Plugged and abandoned 7/1/1969
COMMENTS	A minor portion of the production is from Shafer 2

Cane Creek State 1-36

API Number	4303731631
Well Name and Location	Cane Creek State 1-36
KB and TD	KB 5883 ft; TD 9267 ft (MD), 6983 ft (TVD)
Pilot Hole (yes or no)	Yes
Surface Location	2442 FEL 1728 FSL section 36
Top of pay Location	1608 FSL 2587 FEL section 36
Bottom Hole Location	554 FSL 1043 FWL
Top of Cane Creek	7018 ft (vertical); 7078 ft (horizontal)
Pay Zone	
Horizontal Leg	
BHL Lateral 2	
Top of pay L2	
Top of Cane Creek L2	
Pay Zone L2	
TD L2	
Horizontal Leg	
Completion Date & IP	Completed 12/3/1991 Plugged and Abandoned
Total Production	
COMMENTS	Drilled by Chevron near the Lion Mesa field

Federal 4-26

API Number	4303730617
Well Name and Location	Federal 4-26, T. 27 S., R. 21 E., section 26
KB and TD	5480 ft KB; 7800 ft TD
Pilot Hole (yes or no)	Vertical well
Surface Location	1940 FNL 1900 FWL SENW section 26
Top of pay Location	
Bottom Hole Location	
Top of Cane Creek	7253 ft
Pay Zone	7253 to 7336 gross Cane Creek
Horizontal Leg	
BHL Lateral 2	
Top of pay L2	
Top of Cane Creek L2	
Pay Zone L2	
TD L2	
Horizontal Leg	
Completion Date & IP	7/13/1981 IPF 20 BO, 0 MCFG, 150 BW Shallow clastics in Paradox
Total Production	16 BO, 0 MCFG, 0 BW
COMMENTS	Plugged and abandoned 10/14/2014

Hatch Point 27-1A

API Number	4303730650
Well Name and Location	Hatch Point 27-1A, T. 27 S., R. 21 E., section 27
KB and TD	5604 ft KB; 8030 ft TD
Pilot Hole (yes or no)	Vertical well
Surface Location	2027 FSL 1837 FWL NESW section 27
Top of pay Location	
Bottom Hole Location	
Top of Cane Creek	7396 ft
Pay Zone	7396 to 7460 ft gross Cane Creek
Horizontal Leg	
BHL Lateral 2	
Top of pay L2	
Top of Cane Creek L2	
Pay Zone L2	
TD L2	
Horizontal Leg	
Completion Date & IP	6/10/1980 IP 75 BO, 50 MCFG, 0 BW
Total Production	1888 BO, 0 MCCFG, 0 BW
COMMENTS	Plugged and abandoned 5/8/2016

API Number	4303730650
Well Name and Location	Lion Mesa 5-28, T. 27 S., R. 21 E., section 28
KB and TD	5535 ft KB; 7858 ft TD
Pilot Hole (yes or no)	Vertical well
Surface Location	1960 FNL 680 FEL SENE section 28
Top of pay Location	
Bottom Hole Location	
Top of Cane Creek	7320 ft
Pay Zone	7320 to 7408 ft gross Cane Creek
Horizontal Leg	
BHL Lateral 2	
Top of pay L2	
Top of Cane Creek L2	
Pay Zone L2	
TD L2	
Horizontal Leg	
Completion Date & IP	5/28/1981 IP not reported completed Mississippian
Total Production	Never produced
COMMENTS	Plugged and abandoned 9/15/2014. Cane Creek was perforated and swab tested, no oil or gas reported.

Hatch Point 22-33H

API Number	4303731630
Well Name and Location	Hatch Point 22-33H, T. 27 S., R. 21 E., section 33
KB and TD	5617 ft KB, 10,200 ft MD/7381 ft TVD TD
Pilot Hole (yes or no)	No
Surface Location	2595 FNL 2070 FWL SENW section 33
Top of pay Location	
Bottom Hole Location	2966 ft 351 degree azimuth
Top of Cane Creek	7545 ft MD/7381 ft TVD
Pay Zone	
Horizontal Leg	Gross length 2966 ft
BHL Lateral 2	
Top of pay L2	
Top of Cane Creek L2	
Pay Zone L2	
TD L2	
Horizontal Leg	
Completion Date & IP	10/3/1991 Plugged and abandoned
Total Production	
COMMENTS	Horizontal test on the Lion Mesa structure

API Number	4303730559
Well Name and Location	Lion Mesa 2-34, T. 27 S., R. 21 E., section 34
KB and TD	5485 ft KB, 8426 ft TD
Pilot Hole (yes or no)	Vertical well
Surface Location	2000 FSL 1850 FWL NESW section 34
Top of pay Location	
Bottom Hole Location	
Top of Cane Creek	7255 ft
Pay Zone	7255 to 7346 ft gross Cane Creek
Horizontal Leg	
BHL Lateral 2	
Top of pay L2	
Top of Cane Creek L2	
Pay Zone L2	
TD L2	
Horizontal Leg	
Completion Date & IP	9/23/1980 Plugged and abandoned
Total Production	
COMMENTS	

Threemile 12-7

API Number	4303750001
Well Name and Location	Threemile 12-7, T. 29 S., R. 21 E., section 12
KB and TD	6209 ft; 10724 MD/7661 TVD
Pilot Hole (yes or no)	Yes
Surface Location	2140 FSL 1925 FEL NWSE section 12
Top of pay Location	
Bottom Hole Location	2409 FSL 1593 FWL section 7
Top of Cane Creek	7548 ft TVD
Pay Zone	10,328-10,652 MD
Horizontal Leg	3528 ft length, azimuth 88 degreees
BHL Lateral 2	
Top of pay L2	
Top of Cane Creek L2	
Pay Zone L2	
TD L2	
Horizontal Leg	
Completion Date & IP	1/13/2011, IP 795 BO, 2406 MCFG, 0 BW
Total Production (12/31/2015)	45,852 BO, 22,106 MCFG, 8138 BW
COMMENTS	

Three Mile Unit 12-2-29-21

API Number	4303750069
Well Name and Location	Three Mile Unit 12-2-29-21, T. 29 S., R. 21 E., section 12
KB and TD	6186 feet graded elevation, TD not reported
Pilot Hole (yes or no)	
Surface Location	2103 FSL 1924 FEL NWSE section 12
Top of pay Location	
Bottom Hole Location	
Top of Cane Creek	
Pay Zone	
Horizontal Leg	
BHL Lateral 2	
Top of pay L2	
Top of Cane Creek L2	
Pay Zone L2	
TD L2	
Horizontal Leg	
Completion Date & IP	Completed 10/14/2016 no IP reported
Total Production	
COMMENTS	Logs and well files are confidental as of January 2017

Threemile 43-18H

API Number	4303731857
Well Name and Location	Threemile 43-18H, T. 29 S., R. 22 E., section 18
KB and TD	5961 ft KB; 13,475 MD/7499 TVD
Pilot Hole (yes or no)	Yes
Surface Location	1857 FSL 771 FEL
Top of pay Location	1128 FSL 748 FEL section 18
Bottom Hole Location	2386 FWL 682 FEL section 6
Top of Cane Creek	7563 ft
Pay Zone	7910-12621 MD ft
Horizontal Leg	6291 ft length, due north
BHL Lateral 2	
Top of pay L2	
Top of Cane Creek L2	
Pay Zone L2	
TD L2	
Horizontal Leg	
Completion Date & IP	8/16/2009 Initial Potential 72 BO, 38 MCFG, 196 BW
Total Production (12/31/2015)	19,402 BO, 1821 MCFG, 70,686 BW
COMMENTS	Hatch Point field

Chevron Federal 1

API Number	4303730005
Well Name and Locatio	Chevron Federal 1, T. 29 S., R. 23 E., section 24
KB and TD	6522 ft KB; 9955 ft TD
Pilot Hole (yes or no)	Originally vertical, horizontal drilled 2002
Surface Location	1980 FNL 660 FEL, SENE section 24
Top of pay Location	1530 FNL 1007 FEL
Bottom Hole Location	1089 FNL 3002 FEL
Top of Cane Creek	8445 ft
Pay Zone	8817 to 10,896 ft (8490 to 8404 ft TVD)
Horizontal Leg	
BHL Lateral 2	
Top of pay L2	
Top of Cane Creek L2	
Pay Zone L2	
TD L2	
Horizontal Leg	
Completion Date & IP	5/9/1968 IP 147 BO, 299 MCFG, 308 BW: Horz 12/8/2002 424 BO, 302 MCFG, 90 BW
Total Production (12/31/2015)	114,214 BO, 156,978 MCFG, 46,308 BW: Horz prod 25,330 BO, 35,770 MCFG, 44,188 BW
COMMENTS	Shut in since 10/2008, Wilson Canyon field

API Number	4303750002
Well Name and Location	La Sal 29-28, T. 29 S., R. 23 E., section 29
KB and TD	5847 ft KB; 12,900 ft MD 8111 TVD TD
Pilot Hole (yes or no)	Yes
Surface Location	743 FSL 738 FEL SESE section 29
Top of pay Location	
Bottom Hole Location	2344 FNL 1319 FEL section 28
Top of Cane Creek	8165 ft
Pay Zone	10,580 to 12,820 ft
Horizontal Leg	5627 ft from wellhead, azmuth 64 degrees
BHL Lateral 2	
Top of pay L2	
Top of Cane Creek L2	
Pay Zone L2	
TD L2	
Horizontal Leg	
Completion Date & IP	5/16/2011 IPF 248 BO, 320 MCFG, 0 BW
Total Production (12/31/2015)	5458 BO, 7280 MCFG, 2227 BW
COMMENTS	Shut in since 10/2012: Mud log available but no geophysical well logs

Gibson Dome 1 (DOE)

API Number	4303700248
Well Name and Location	Gibson Dome 1, T. 30 S., R. 21 E., section 21
KB and TD	4966 ft; 6384 ft
Pilot Hole (yes or no)	vertical hole
Surface Location	SESESE section 21
Top of pay Location	
Bottom Hole Location	
Top of Cane Creek	5220 ft
Pay Zone	5220-5310 ft gross interval
Horizontal Leg	
BHL Lateral 2	
Top of pay L2	
Top of Cane Creek L2	
Pay Zone L2	
TD L2	
Horizontal Leg	
Completion Date & IP	1/7/1981
Total Production	
COMMENTS	The API is an unofficial number used only by the UGS. The DOE drilled Gibson Dome as a stratigraphic core hole to evaluate potential nuclear storage in the Paradox Formation salt, the well does not appear in the DOGM databases.

Remington 21-1H

API Number	4303731742
Well Name and Location	Remington 21-1H, T. 31 S., R. 23 E., section 21
KB and TD	6403 ft KB; 9615 MD/7574 TVD ft
Pilot Hole (yes or no)	Yes
Surface Location	1068 FSL 995 FEL SESE section 21
Top of pay Location	
Bottom Hole Location	232 FNL 291 FWL section 27
Top of Cane Creek	7422 ft TVD
Pay Zone	
Horizontal Leg	9813 MD/7441 TVD
BHL Lateral 2	663 FSL 1174 FWL section 22
Top of pay L2	
Top of Cane Creek L2	
Pay Zone L2	
TD L2	9615 MD/7574 TVD
Horizontal Leg	
Completion Date & IP	4/6/1995 Plugged and Abandoned
Total Production	
COMMENTS	

Cisco State 36-13

API Number	4303750008
Well Name and Location	Cisco State 36-13, T. 31 S., R. 24 E., section 36
KB and TD	6012 ft KB; 7947 ft
Pilot Hole (yes or no)	Vertical well
Surface Location	1158 FNL 1543 FEL NWNE section 36
Top of pay Location	
Bottom Hole Location	
Top of Cane Creek	7584 ft
Pay Zone	Perforated 7621-7626
Horizontal Leg	
BHL Lateral 2	
Top of pay L2	
Top of Cane Creek L2	
Pay Zone L2	
TD L2	
Horizontal Leg	
Completion Date & IP	Temporaliy abandoned 9/23/2011; Plugged and abandoned 7/28/2014
Total Production	
COMMENTS	

Appendix C:

Cane Creek 26-3

Core Analysis Report by Core Laboratories, Inc.

Core Lab
RESERVOIR OPTIMIZATION

PETROLEUM SERVICES

Petrographic Analysis of Conventional Core Samples

Cane Creek 26-3 Well
Grand County, Utah
Fidelity Exploration

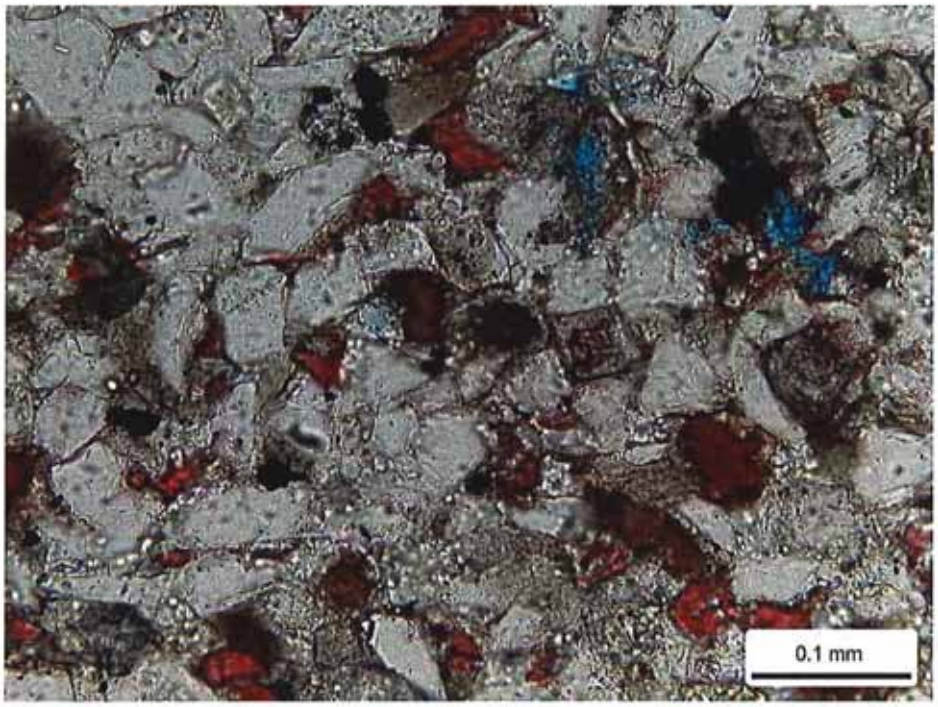

Houston ATC Job File No.: 121467G

February 2013

Core Laboratories, Inc.
Houston Advanced Technology Center
6316 Windfern Road
Houston, Texas 77040

TABLE OF CONTENTS

Introduction

This report presents the results of thin section, SEM, and XRD analyses of conventional core samples from the Cane Creek 26-3 well in Grand County, Utah. The objectives of this study are to evaluate the composition, diagenetic features, paragenesis, clay type and distribution, and pore system characteristics of the selected samples. This was accomplished through XRD analysis of 86 samples, thin section point-count of 43 samples, and SEM analysis of 10 samples. Two additional samples were added to the study to identify any water-soluble minerals or otherwise sensitive components. One sample was taken from material that was soaked overnight in 7% KCl and the other sample came from untreated material. The samples were analyzed by XRD, thin section point-count, and SEM combined with EDX. A list of the analyzed samples including depth, lithology, tests performed, and core analysis data (where available) is presented in Table 1. XRD data are provided in Table 2. Thin section and SEM descriptions and photomicrographs are provided in Plates 1 through 45.

Results

Unit A (7389.15-7414.20 feet):

Lithology/Texture

Sixteen samples were selected from Unit A of the Cane Creek well. These samples include five clastic rocks (two argillaceous sandstones, one argillaceous calcareous sandstone, one argillaceous siltstone, and one dolomitic argillaceous siltstone), six carbonates (five dolostones and one limestone), four anhydrites, and one sample with both anhydrite and dolostone lithologies. The argillaceous sandstones and siltstones are well sorted and average grain size ranges from 0.059 to 0.074 mm (coarse silt to lower very fine sand). These samples are often bioturbated and contain microfractures. Some of the microfractures are cemented by anhydrite, halite, and/or calcite, while others remain open. It is unclear if some of the open microfractures (yellow arrow, Plate 15A) are natural or induced.

Texture varies widely among the carbonates, and includes mudstone, wackestone, packstone, and boundstone textures. The dolostones contain varying amounts of silt and anhydrite. Many contain wavy laminations, and some are bioturbated or contain distinct burrows. Open and cemented microfractures are present; cements filling the microfractures include anhydrite (anh, Plate 9A), halite (red arrows, Plate 13B), calcite, quartz (qa, Plate 1A), and dolomite. Anhydrite (anh, Plate 11B) also occurs as nodules in some of the dolostones. Organic matter (om, Plate 12B) is concentrated along microstylolites in the limestone. The anhydrite samples often have a nodular texture, but can be massive.

Framework/Allochemical Grains

Quartz grains are abundant and potassium feldspar and dolomite rock fragments (DRF, Plate 14B) are generally found in moderate amounts in the argillaceous sandstones and siltstones. Limestone rock fragments (LRF, Plate 14B) and volcanic rock fragments are generally minor in abundance. Other minor to rare grains include argillaceous rock

fragments, mica (mostly muscovite and rare biotite), plant fragments, and calcite replaced grains (ca-rg). Rare plagioclase and heavy minerals are also observed at some depths. Samples are classified as feldspathic litharenites and litharenites (Figure 1).

Detrital silt grains are common in the anhydritic silty dolostones at 7403.15 and 7404.00 feet and minor to rare in the other carbonates. Most of the silt grains are quartz; potassium feldspar and dolomite rock fragments are less common, and argillaceous rock fragments and mica are rare. Discrete plant fragments are minor in abundance in the dolostones. Intraclasts (yellow arrows, Plate 13A) are the most common allochemical grain in the dolowackestone at 7407.65 feet and are minor in abundance in the dolomudstone at 7401.40 feet. Peloids are moderate in abundance in the dolowackestone and minor to rare in the other dolostones. Quartz, potassium feldspar, and dolomite rock fragments are also present in the small carbonate zone remaining in the anhydrite sample at 7414.20 feet. Allochems in the dolostone part of the anhydrite/dolostone sample at 7392.15 feet are mostly peloids (p, Plate 3B), with less common ooids (oo, Plate 3A) and rare intraclasts.

Matrix/Clay Minerals

Detrital matrix is common to abundant in the argillaceous sandstones and siltstones, and consists of detrital clay intermixed with varying amounts of micrite (microcrystalline calcite). The matrix is also rich in organic matter in the dolomitic argillaceous siltstone at 7412.15 feet. Dolomite partially replaces the matrix in all samples, but dolomite replacement is more extensive in the dolomitic argillaceous siltstone at 7412.15 feet. Total clay (based on XRD) ranges from 8.9 to 21.1%. Most of the clay is illite & mica (6.5-16.3%). Minor amounts of mixed-layer illite/smectite (1.3-2.5%) and chlorite (1.0-2.1%) are also present. Most of the clay in these samples comes from the detrital matrix, but in some samples argillaceous rock fragments, mica grains, and authigenic clay rims also contribute to total clay values.

Dolomite replaced matrix is abundant in the dolostones, and contains varying amounts of detrital clay intermixed with the dolomite. Organic-rich micrite matrix is abundant in the limestone, and has been neomorphosed to microspar. The calcite matrix also contains a minor amount of detrital clay intermixed with the organic matter and microspar. Thin zones of carbonate and clay matrix remain in the anhydrite samples at 7391.15 and 7414.20 feet. Total clay in the carbonates ranges from 0 to 4.2%. Virtually all of the clay is illite and mica; traces (<1%) of mixed-layer illite/smectite and chlorite are present in some of the dolostones. Less than one percent total clay (illite and mica) was detected in the anhydrite samples.

Cements

Because most intergranular pores are filled with detrital matrix, pore-filling cements are generally minor in abundance in the argillaceous sandstones and siltstonesPyrite (yellow arrow, Plate 8B) is observed in minor to moderate amounts, typically as small framboids and occasionally as larger aggregates scattered throughout. Quartz overgrowths have developed on some of the detrital quartz grains. Quartz overgrowths are better developed in the samples with the least amount of matrix, or within “clean” burrows, and less well developed in the matrix-rich argillaceous calcareous sandstone and the dolomitic argillaceous siltstone. Calcite, dolomite, and anhydrite cements are found in minor to trace amounts (except at 7394.10 feet, which contains a moderate amount of

calcite cement), and typically fill intergranular pores and cement microfractures. Titanium oxides and halite (NaCl, Plate 14B) are rarely observed.

Anhydrite is common to abundant in three of the dolostones (7401.40, 7403.15, and 7404.00 feet), where it occurs as nodules and filling microfractures. Anhydrite is minor in abundance in the remaining dolostones and the limestone. A minor amount of pyrite is dispersed throughout the matrix in the carbonates. Halite fills microfractures in two of the dolostones (7389.15 and 7407.65 feet).

Tightly interlocking, tabular crystals of anhydrite (anh, Plate 6B) are the dominant authigenic mineral in the anhydrite samples. Pyrite framboids are scattered throughout some of the anhydrite samples, but typically concentrated in the dolomitic zones. Calcite cement fills microfractures in the dolostone part of the anhydrite/dolostone sample. Rare quartz replaces the anhydrite at 7397.15 feet.

Paragenesis

A generalized paragenetic sequence of events (Table 4) for Unit A was determined through relationships of cements and replacement minerals in thin section and SEM. Early pyrite and titanium oxides were followed by relatively finely crystalline dolomite cement and replacement. The precipitation of quartz overgrowths followed dolomitization, as evidenced by dolomite crystals engulfed in quartz cement. Similarly, calcite inclusions within anhydrite cement suggests calcite cement filled intergranular pores and secondary pores and fractures prior to anhydrite cement and replacement/displacement. Late-stage halite filled intergranular pores and microfractures.

Porosity

Core analysis data from the argillaceous sandstones and siltstones indicates these samples contain 6.22 to 13.58% porosity and permeability ranges from 0.0183 to 13.0125 md. The fractured sample at 7400.15 feet has the highest permeability; values are under 0.2205 md for all other depths. Grain density ranges from 2.704 to 2.782 g/cc. Visible pores found in some samples include rare intergranular pores, secondary intragranular pores within partially dissolved feldspar grains, and partially open microfractures (although it is unclear if the fractures are natural or induced). Some of the porosity comes from micropores associated with the matrix.

Measured porosity for the dolostones and the limestone ranges from 1.21 to 5.45% and permeability ranges from 0.0011 to 0.4015 md. Grain density ranges from 2.718 to 2.925 g/cc in the dolostones. The variability is associated with the amount of anhydrite present in the sample. The limestone has a grain density of 2.628 g/cc. The low grain density in the limestone is associated with the abundance of organic matter at that depth. The sample with the greatest amount of visible pores in thin section is the doloboundstone at 7389.15 feet. This sample contains a minor amount of intercrystal pores (BC, Plate 1B) and fenestral pores (yellow arrow, Plate 1A), as well as rare microfractures. Intercrystal pores are rarely observed in the peloidal dolowackestone at 7407.65 feet. Secondary intracrystal pores have developed within partially dissolved anhydrite cement at 7401.40 feet and at 7403.15 feet, but are rare overall. No visible pores were observed in the limestone.

The very low porosity and permeability values in the anhydrite samples range from 0.09 to 0.91% and 0.0007 to 0.0015 md, respectively. Grain density ranges from 2.890 to 2.962 g/cc. Rare intercrystal pores within dolomitic areas are the only visible pores observed in thin section.

Unit B (7416.15-7443.00 feet):

Lithology/Texture

Fourteen samples were selected from Unit B of the Cane Creek well. These samples include nine argillaceous sandstones, two sandstones, two dolomitic argillaceous siltstones, and one silty dolostone. These samples are well sorted and average grain size ranges from 0.051 to 0.083 mm (coarse silt to lower very fine sand). Most samples are bioturbated or contain distinct burrows. Some samples contain uneven, wavy, or discontinuous laminae. Cross-laminations are observed in the argillaceous sandstone at 7424.85 feet. Many samples also contain open microfractures (yellow arrow, Plate 19B), typically oriented parallel to subparallel to bedding. Some of the microfractures are partially filled with halite. It is unclear if some or all of the microfractures are natural or induced. A natural calcite and anhydrite cemented microfracture (ca/anh, Plate 17A) is observed in the dolostone. The dolostone has a wackestone texture.

Framework/Allochemical Grains

Quartz grains are abundant and potassium feldspar is typically found in moderate amounts in the argillaceous sandstones, sandstones, and dolomitic argillaceous siltstones. Limestone rock fragments and dolomite rock fragments (DRF, Plate 20A) vary in abundance, from minor to common. Calcite replaced grains and mica (mostly muscovite) are also observed in minor to trace amounts. Other minor to rare grains found at some depths include plagioclase, volcanic rock fragments (VRF, Plate 29B), argillaceous rock fragments, heavy minerals, elongate plant fragments, and rip-up clasts (RU, Plate 20A). Samples form a cluster on the ternary diagram (Figure 1), with most falling into the feldspathic litharenite category. Some samples extend into litharenite, sublitharenite, lithic arkose, and subarkose categories (Figure 1).

Peloids are the most common allochemical grain in the silty dolostone. Silt-size clastic grains are mostly quartz; potassium feldspar, dolomite rock fragments, volcanic rock fragments, mica, and plant fragments are much less common.

Matrix/Clay Minerals

Detrital matrix is abundant in the dolomitic argillaceous siltstones, moderate to common in the argillaceous sandstones, and rare or absent from the sandstones. The matrix consists of detrital clay intermixed with micrite. Dolomite partially replaces the matrix in all samples, but a much larger proportion of the matrix has been replaced in the dolomitic argillaceous siltstones. Total clay (based on XRD) ranges from 6.4 to 6.7%. Most of the clay is illite & mica (4.3-12.1%). Other minor to rare clay minerals include mixed-layer illite/smectite (0.8-2.7%), chlorite (1.0-2.9%), and kaolinite (0.0-0.5%). Most of the clay comes from the detrital matrix, but minor to rare argillaceous rock fragments, mica grains, and authigenic clay rims present at some depths also contribute to total clay values.

Dolomite replaced matrix is abundant (59.6%) in the silty dolostone, and is intermixed with a minor to moderate amount of detrital clay (5.2% based on XRD). Most of the clay is illite and mica. Mixed-layer illite/smectite and chlorite are rare (<1%).

Cements

Quartz overgrowths (qo, Plate 29D) are minor to moderate in abundance in the sandstones and argillaceous sandstones, and rare or absent in the dolomitic argillaceous siltstones and the silty dolostone. Quartz overgrowths are most common in the sandstones and within "cleaner" parts of the argillaceous sandstones, where they had room to develop within intergranular pores. Pore-filling dolomite is minor to moderate in abundance in the sandstones and argillaceous sandstones, except in the argillaceous sandstone at 7424.85 feet, where it is common. Dolomite cement is rare or absent in the dolomitic argillaceous siltstones. Pore-filling calcite cement (ca, Plate 21B) is also present in minor to moderate amounts, except in the dolomitic argillaceous siltstone at 7421.40 feet, where it is absent. Pyrite framboids (py, Plate 21B) are scattered throughout all samples. Other minor to rare cements found at some depths include halite (NaCl, Plate 26D), titanium oxides, anhydrite, and celestine.

Calcite and anhydrite cement fill a microfracture in the silty dolostone. Pyrite is also observed in minor amounts.

Paragenesis

The paragenetic sequence of events (Table 4) for Unit B, as best determined through thin section and SEM observations begin with early pyrite and titanium oxides that were followed by dolomite cement and replacement. The precipitation of quartz overgrowths occurred after dolomitization. Partial dissolution of less stable feldspar grains preceded calcite cementation, as evidenced by the precipitation of calcite (ca, Plate 19D) within these secondary pores. Remnants of calcite cement are engulfed by anhydrite, suggesting the calcite was present prior to the anhydrite. Late-stage halite filled intergranular pores and microfractures.

Porosity

Core analysis data from the sandstones, argillaceous sandstones and dolomitic argillaceous siltstones indicates these samples contain 4.94 to 12.43% porosity and permeability ranges from 0.0018 to 35.65 md. Two samples have significantly higher permeability values, the dolomitic argillaceous siltstone at 7421.40 feet (35.65 md) and the argillaceous sandstone at 7426.00 feet (3.279 md). Permeability is under 0.1368 md for all other samples. The elevated permeabilty in these two samples is likely associated with fractures. Intergranular pores (ig, Plate 30D) are minor to rare in the sandstones and present in trace amounts in some of the argillaceous sandstones. Secondary intragranular pores (ip, Plate 19D) within partially dissolved feldspar grains are present in several samples. A portion of the measured porosity comes from micropores associated with the matrix. Grain density ranges from 2.679 to 2.752 g/cc.

Measured porosity for the silty dolostone is 7.28% and permeability is 0.0041 md. Grain density is 2.809 g/cc. No open pores were identified in the silty dolostone. The measured porosity must come from micropores associated with the matrix.

Supplemental samples

Two additional samples were analyzed by thin section point-count, XRD, and SEM combined with EDX to identify any water soluble minerals or otherwise sensitive components. Both samples are from 7438.00 feet. One sample was taken from material that was soaked overnight in 7% KCl and the other sample came from untreated material.

These samples contain mostly quartz and feldspar grains in a detrital clay matrix. Dolomite (d, Plate 44E), calcite, quartz overgrowths, and pyrite (py, Plate 44B) cements are also present. No salts (in the form of halite or sylvite cement) were observed in thin section, XRD, or SEM analysis of the untreated sample. However, the EDX spectrum (Plate 44D) of this sample shows chlorine is associated with the detrital clay.

Both the outer surface of the KCl treated sample, as well as a fresh surface from the interior of the same sample were evaluated. As expected, KCl is prevalent in the outer surface of the treated sample (Plate 45E). However, the fresh surface from the interior of the KCl treated sample (Plate 45C/D) did not contain any salt, or chlorine peak when analyzed by EDX.

Unit C (7446.15-7473.10 feet):

Lithology/Texture

Thirteen samples were selected from Unit A of the Cane Creek 26-3 well. These samples include three dolomitic argillaceous sandstones, one dolomitic argillaceous siltstone, one argillaceous siltstone, one organic-rich dolostone, four dolomitic anhydrites, and three anhydrites. The argillaceous sandstones and siltstones are moderately well to well sorted and average grain size ranges from 0.057 to 0.078 mm (coarse silt to lower very fine sand). These samples are bioturbated and some contain open microfractures. It is unclear if some of the open microfractures are natural or induced.

The organic-rich dolostone has a mudstone texture. Silty laminations are observed, as well as silt-filled burrows. Open microfractures are also observed in the organic-rich dolostone. Both microfractures and lamina are displaced by a microfault. Some of the anhydrite samples have a nodular texture, and others are more massive.

Framework/Allochemical Grains

Quartz grains (Q, Plate 36B) are abundant and dolomite rock fragments are moderate to common in the argillaceous sandstones and siltstones. Less common grains include potassium feldspar (Ksp, stained yellow), mica, and plant fragments. Minor to rare rip-up clasts (RU, Plate 34A), polycrystalline quartz, volcanic rock fragments, limestone rock fragments, argillaceous rock fragments, heavy minerals, and calcite replaced grains are also present in some samples. These samples plot on the ternary diagram as feldspathic litharenites, with rare litharenites and subarkoses (Figure 1).

Most of the silt grains in the organic-rich dolostone are quartz; rare potassium feldspar and mica are also present. The anhydrite samples contain minor to rare quartz and potassium feldspar. Mica, organic matter (om, Plate 32B), and dolomite rock fragments are also present at some depths.

Matrix/Clay Minerals

Matrix is common to abundant in the dolomitic argillaceous sandstones and the dolomitic argillaceous siltstone. The matrix likely originally consisted of detrital clay intermixed with micrite, but a large portion of the original matrix appears to have been replaced by dolomite. The argillaceous siltstone contains a minor to moderate amount of detrital clay matrix, which is unevenly distributed in the sample. Total clay, based on XRD, ranges from 5.7 to 17.8%. Most of the clay is illite & mica (3.5-12.9%). Minor to trace amounts of chlorite (1.7-2.7%) and mixed-layer illite/smectite (0.5-2%) are also present. Most of the clay in these samples comes from the detrital matrix, but argillaceous rock fragments, mica grains, and rare authigenic clay rims present in some samples also contribute to total clay values.

The organic-rich dolostone contains abundant dolomite, detrital clay, organic-rich matrix. XRD detected 14.7% total clay. Most of the clay (10.0%) is illite and mica. Minor amounts of chlorite (2.8%) and mixed-layer illite/smectite (1.9%) are also present.

Little to no clay was detected in the anhydrite samples (0.0-2.8% total clay, based on XRD). Specific clay minerals identified by XRD include illite and mica (0.0-1.9%), mixed-layer illite/smectite (0.0-0.5%), and chlorite (0.0-0.5%). When present, the clay is associated with dolomitic zones in the anhydrite samples.

Cements

Quartz overgrowths are moderate in abundance in the dolomitic argillaceous siltstone and the argillaceous siltstone, and minor to rare in the dolomitic argillaceous sandstones. Pore-filling dolomite and pyrite cements are generally minor in abundance. Other cements found in minor to trace amounts at some depths include potassium feldspar overgrowths, calcite, anhydrite, titanium oxides, and halite.

The only cement found in the organic-rich dolostone is pyrite. Occurring in minor amounts, pyrite is typically associated with the organic-rich matrix. Cements (other than anhydrite) are minor to rare in the anhydrite and dolomitic anhydrite samples. Cements found at some depths include dolomite, celestine, and pyrite.

Paragenesis

The generalized paragenetic sequence for Unit C, as best determined through thin section and SEM analysis begins with early pyrite and titanium oxides, followed by dolomite cement and replacement. Quartz overgrowths engulf some dolomite crystals, suggesting they precipitated after the dolomite. Calcite cement later filled open intergranular pores and replaced some grains. Late-stage cements include anhydrite and halite.

Porosity

Core analysis data (where available) from the dolomitic argillaceous sandstones and siltstones indicates these samples contain 3.95 to 11.12% porosity and permeability ranges from 0.0015 to 0.0089 md. Grain density ranges from 2.682 to 2.754 g/cc. Rare intergranular pores (ig, Plate 41B) are observed in the dolomitic argillaceous siltstone at 7454.00 feet, and are absent from the other samples. Secondary intragranular pores (ip, Plate 36D) within partially dissolved feldspar grains and lithic fragments are rare, but noted at several depths. Most of the measured porosity likely comes from micropores within the matrix.

No visible pores are observed in the organic-rich dolostone. Measured porosity is 13.20% and permeability is 0.0500 md. Grain density is 2.65 g/cc. The low grain density is associated with the abundance of organic matter at this depth. Micropores within the matrix must account for the measured core analysis porosity.

No pores were observed in thin section for the anhydrites and dolomitic anhydrites. Core analysis porosity ranges from 0.39 to 0.96%. Permeability is only available for the sample at 7460.15 feet, and is 0.0010 md. Grain density ranges from 2.896 to 2.959 g/cc.

Please feel free to contact me if you have any questions or comments concerning this report.

Sincerely,

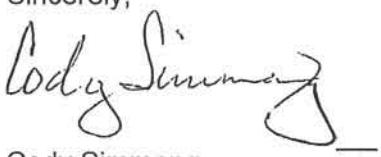

Cody Simmang
Geologist
Core Laboratories
cody.simmang@corelab.com

DETAILED ANALYTICAL PROCEDURES

Thin Sections

Thin sections were prepared by first impregnating the samples with epoxy to augment cohesion and to prevent loss of material during grinding. Blue dye was added to the epoxy to highlight the pore spaces. Each thinly sliced sample was mounted on a frosted glass slide and then cut and ground in water to an approximate thickness of 30 microns. Selected thin sections were stained with the following: Alizarin Red-S to differentiate calcite (stains red) from clear dolomite (does not stain); potassium ferricynanide to identify ferroan dolomite (stains medium blue) and ferroan calcite (stains purple); and sodium cobaltinitrite to distinguish feldspars (potassium feldspar stains yellow and plagioclase does not stain). In an effort to avoid sample damage, samples containing large amounts of clay minerals were not stained. The thin sections were analyzed using standard petrographic techniques. Detailed thin section analysis included of a count of 300 points per sample.

Scanning Electron Microscopy (SEM)

Each sample was mounted on an aluminum stub with silver paste so that a freshly broken surface was exposed. The samples were coated with gold/palladium (Au/Pd) alloy using a Hummer Jr. Coating Unit. The SEM photomicrographs are secondary electron images taken digitally with a camera attached to a FEI Scanning Electron Microscope operating at approximately 20 kV. Qualitative elemental data on selected minerals observed during the SEM study were obtained through the use of an interfaced Energy Dispersive Spectroscope (EDS) equipped with a Si (Li) detector. Recognition of any authigenic clays was based on the criteria proposed in Wilson and Pittman (1977).

X-ray Diffraction Analysis (XRD)

Sample Preparation

Samples submitted for whole-rock and clay-fraction XRD mineral analyses are first cleaned of obvious drilling contaminants and then disaggregated in a mortar and pestle. Approximately five grams of each sample are transferred to isopropyl alcohol and pulverized using a McCrone micronizing mill. The resultant powders are dried, disaggregated, and packed into aluminum sample holders to produce random whole-rock mounts. A separate split of each sample is dispersed in a dilute sodium phosphate solution using a sonic probe. The suspensions are then centrifugally size-fractionated to isolate clay-size (<4 micron ESD) materials for a separate clay-fraction mount. The suspensions are then vacuum-deposited on silver membrane filters to produce oriented clay mineral aggregates. Membrane mounts are attached to stainless steel slugs and exposed to ethylene glycol vapor for a minimum of 24 hours.

Analytical Procedures

XRD analyses of the samples are performed utilizing Scintag (for clay analysis) and Philips (for bulk powder analysis) automated powder diffractometers equipped with a copper source (40kV, 40mA) and a solid state or scintillation detector. The whole rock samples are analyzed over an angular range of 2-60 degrees 2-theta at a scan rate of one degree/minute. The glycol-solvated clay-fraction mounts are analyzed over an angular range of 2-50 degrees 2-theta at a rate of 1.5 degrees/minute.

Semi-quantitative determinations of whole-rock and phyllosilicate mineral amounts are done utilizing integrated peak areas (derived from peak-decomposition / profile-fitting methods) and empirical reference intensity ratio (RIR) factors determined specifically for the diffractometer used in data collection. The total clay mineral (including mica) abundance of each sample is determined from the whole-rock XRD patterns using combined {00l} and {hkl} clay mineral reflections and suitable empirical RIR factors.

XRD patterns from glycol-solvated clay-fraction samples are analyzed using techniques similar to those described above. Determinations of mixed-layer clay ordering and expandability are done by comparing experimental diffraction data from the glycol-solvated clay mineral aggregates with simulated one dimensional diffraction profiles generated using the program NEWMOD written by R.C. Reynolds.

APPENDIX A

THIN SECTION & SEM PHOTOMICROGRAPHS & DESCRIPTIONS

PLATES 1 - 45

TABLE 1

ANALYTICAL PROGRAM & PETROGRAPHIC SUMMARY

Fidelity E & P, Cane Creek 26-3 Well, Grand Co., Utah

Plate #	Depth (ft):	Thin Section	SEM	XRD	Unit	Lithology	Porosity (%)	Perm. (md)	Grn. Den. (g/cc)	Oil Sat. (%)	Water Sat. (%)	Net Conf. Stress (psig)
1	7389.15	X	-	X	A	Dolostone	2.09	0.0263	2.718	16.4	39.7	2280
2	7391.15	X	-	X	A	Anhydrite	0.49	0.0015	2.962	0.0	40.2	2280
3	7392.15	X	-	X	A	Anhydrite / Dolostone	0.91	0.0009	2.890	13.6	32.4	2280
4	7394.10	X	X	X	A	Argillaceous Calcareous Sandstone	6.22	0.0183	2.716	27.3	57.8	2280
5	7395.25	X	-	X	A	Argillaceous Siltstone	11.11	0.2205	2.717	25.4	60.5	2280
6	7397.15	X	-	X	A	Anhydrite	0.09	0.0007	2.931	6.7	14.8	2280
7	7398.00	X	-	X	A	Anhydrite	0.78	0.0014	2.937	8.4	24.8	2280
8	7400.15	X	-	X	A	Argillaceous Sandstone	13.58	13.0125	2.704	29.1	59.5	2280
9	7401.40	X	-	X	A	Anhydritic Dolostone	1.21	0.0011	2.925	35.1	21.0	2280
10	7403.15	X	-	X	A	Anhydritic Silty Dolostone	3.64	0.0214	2.884	60.4	22.2	2280
11	7404.00	X	-	X	A	Anhydritic Silty Dolostone	4.40	0.0799	2.859	39.1	44.4	2280
12	7406.00	X	-	X	A	Organic-Rich Limestone	5.46	0.4015	2.628	41.4	25.9	2280
13	7407.65	X	-	X	A	Dolostone	3.06	0.0075	2.909	37.7	12.3	2280
14	7410.00	X	X	X	A	Argillaceous Sandstone	n/a	n/a	n/a	n/a	n/a	n/a
15	7412.15	X	-	X	A	Dolomitic Argill. Siltstone	10.34	0.0265	2.782	33.0	50.1	2280
16	7414.20	X	-	X	A	Anhydrite	0.73	-	2.957	1.3	11.0	Ambient
17	7416.15	X	-	X	B	Silty Dolostone	7.28	0.0041	2.809	25.1	50.9	2280
18	7419.15	X	-	X	B	Dolomitic Argill. Siltstone	4.94	0.0018	2.752	34.4	59.3	2280
19	7421.40	X	X	X	B	Dolomitic Argill. Siltstone	10.53	35.6485	2.749	27.7	63.7	2280
20	7424.85	X	-	X	B	Argillaceous Sandstone	6.01	0.0043	2.704	32.8	59.3	2280
21	7426.00	X	X	X	B	Argillaceous Sandstone	8.94	3.2788	2.722	24.7	67.7	2280
22	7427.10	X	-	X	B	Argillaceous Sandstone	9.68	0.0098	2.687	38.4	58.9	2280
23	7429.10	X	X	X	B	Argillaceous Sandstone	12.43	0.1123	2.685	27.9	59.1	2280
24	7431.25	X	-	X	B	Argillaceous Sandstone	11.45	0.1368	2.699	30.2	68.4	2280
25	7433.10	X	-	X	B	Argillaceous Sandstone	9.85	0.0469	2.704	22.7	66.3	2280
26	7435.15	X	X	X	B	Argillaceous Sandstone	10.38	0.0069	2.684	25.5	67.2	2280
27	7437.10	X	-	X	B	Argillaceous Sandstone	10.83	0.0314	2.683	22.5	64.9	2280
28	7439.25	X	-	X	B	Argillaceous Sandstone	9.07	0.0534	2.707	19.9	68.5	2280

TABLE 1

ANALYTICAL PROGRAM & PETROGRAPHIC SUMMARY

Fidelity E & P, Cane Creek 26-3 Well, Grand Co., Utah

Plate #	Depth (ft):	Thin Section	SEM	XRD	Unit	Lithology	Porosity (%)	Perm. (md)	Grn. Den. (g/cc)	Oil Sat. (%)	Water Sat. (%)	Net Conf. Stress (psig)
29	7441.20	X	X	X	B	Sandstone	11.74	0.0670	2.686	33.4	48.5	2280
30	7443.00	X	X	X	B	Sandstone	6.90	0.0077	2.679	22.7	53.6	2280
31	7446.15	X	-	X	C	Dolomitic Argill. Sandstone	3.95	0.0015	2.710	31.2	63.0	2280
32	7448.15	X	-	X	C	Anhydrite	0.54	-	2.943	12.4	15.2	Ambient
33	7450.10	X	-	X	C	Anhydrite	0.94	-	2.896	35.4	26.0	Ambient
34	7452.20	X	-	X	C	Dolomitic Argill. Sandstone	9.24	0.0089	2.754	40.9	36.1	2280
35	7454.00	X	-	X	C	Dolomitic Argill. Sandstone	n/a	n/a	n/a	n/a	n/a	n/a
36	7456.10	X	X	X	C	Argillaceous Siltstone	11.12	0.0078	2.682	30.6	61.8	2280
37	7458.25	X	-	X	C	Organic-Rich Dolostone	13.20	0.0500	2.658	28.9	37.5	2280
38	7460.15	X	-	X	C	Dolomitic Anhydrite	0.63	0.0010	2.950	8.7	37.1	2280
39	7461.15	X	-	X	C	Anhydrite	0.39	-	2.959	2.4	20.7	Ambient
40	7463.10	X	-	X	C	Dolomitic Anhydrite	0.91	-	2.937	13.6	44.7	Ambient
41	7469.10	X	X	X	C	Dolomitic Argill. Siltstone	7.45	0.0071	2.688	37.2	43.7	2280
42	7471.20	X	-	X	C	Dolomitic Anhydrite	0.97	-	2.933	0.0	64.8	Ambient
43	7473.10	X	-	X	C	Dolomitic Anhydrite	0.46	-	2.953	0.0	45.2	Ambient
44	7438- untreated "C"	X	X	X	-	Argillaceous Sandstone	-	-	-	-	-	-
45	7438-KCl "A"	X	X	X	-	Argillaceous Sandstone	-	-	-	-	-	-

TABLE 2
THIN SECTION POINT-COUNT PETROGRAPHIC DATA
Fidelity E & P, Cane Creek 26-3 Well, Grand Co., Utah

	Framework Grains																									Matrix						Authigenic Minerals											Porosity							
Depth (ft)	Monocrystalline quartz	Polycrystalline quartz	Potassium feldspar	Plagioclase	Volcanic rock fragment	Metamorphic rock fragments	Limestone rock fragments	Dolomite rock fragments	Argillaceous rock fragments	Chert rock fragments	Micas	Heavy minerals, undif.	Coid-dolomite	Peloid-calcite	Plant fragments	Peloid-dolomite	Rip-up/intraclast	Glauconite	Dolomite replaced grains	Calcite replaced grains	Pyrite replaced grains	Total Framework Constituents	Detrital clay matrix	Mixolite matrix	Dolomitic matrix	Clay and carbonate matrix	Organic matrix	Total detrital matrix	Authigenic clay	Quartz overgrowths/replacement	Potassium feldspar overgrowths	Dolomite	Calcite	Anhydrite	Celestine	Pyrite	Titanium oxides	Halite	Total authigenic minerals	Intergranular	Intercrystalline	Intragranular	Intracrystalline	Moldic	Fracture	Fenestral	Total visible porosity
7389.15	0.0	0.0	0.0	0.0	0.0	0.0	0.0	0.0	0.0	0.0	0.0	0.0	0.0	0.0	1.6	3.2	0.0	0.0	0.0	0.0	0.0	**4.8**	0.0	0.0	84.0	0.0	0.0	**84.0**	0.0	1.2	0.0	0.0	0.0	1.6	0.0	1.2	0.0	1.6	**5.6**	0.0	3.6	0.0	0.0	0.0	0.0	0.4	1.6	**5.6**
7391.15	0.0	0.0	0.0	0.0	0.0	0.0	0.0	0.0	0.0	0.0	0.0	0.0	0.0	0.0	0.8	0.0	0.0	0.0	0.0	0.0	0.0	**0.8**	0.0	1.2	0.4	0.0	0.0	**1.6**	0.0	0.0	0.0	0.0	0.0	96.8	0.0	0.8	0.0	0.0	**97.6**	0.0	0.0	0.0	0.0	0.0	0.0	0.0	0.0	**0.0**
7392.15	0.0	0.0	0.0	0.0	0.0	0.0	0.0	0.0	0.0	0.0	0.0	0.0	3.6	8.0	2.0	0.8	0.8	0.0	0.0	0.0	0.0	**15.2**	0.0	0.0	26.0	0.0	0.0	**26.0**	0.0	0.0	0.0	0.0	1.6	56.0	0.0	1.2	0.0	0.0	**58.8**	0.0	tr	0.0	0.0	0.0	0.0	0.0	0.0	**0.0**
7394.10	32.0	0.0	6.0	0.0	0.0	0.0	2.4	8.4	0.4	0.0	0.4	0.0	0.0	0.0	2.0	0.0	0.0	0.0	0.0	1.6	0.0	**55.2**	0.0	0.0	9.2	22.0	0.0	**31.2**	0.0	2.0	tr	1.6	6.0	1.2	0.4	2.4	tr	0.0	**13.7**	0.0	0.0	tr	0.0	0.0	tr	0.0	0.0	**0.0**
7395.25	34.4	0.0	8.0	0.4	0.0	0.0	7.6	8.8	2.0	0.4	1.2	0.4	0.0	0.0	4.4	0.0	0.0	0.0	0.0	1.2	0.0	**70.0**	0.0	0.0	2.8	15.2	0.0	**18.0**	0.8	2.4	0.0	0.4	3.2	tr	0.0	4.8	0.0	0.0	**11.6**	tr	0.0	tr	0.0	0.0	0.0	0.4	0.0	**0.4**
7397.15	0.0	0.0	0.0	0.0	0.0	0.0	0.0	0.0	0.0	0.0	0.0	0.0	0.0	0.0	0.4	0.0	0.0	0.0	0.0	0.0	0.0	**0.4**	0.0	0.0	0.0	0.0	0.0	**0.0**	0.0	0.4	0.0	0.4	0.0	98.8	0.0	0.0	0.0	0.0	**99.6**	0.0	0.0	0.0	0.0	0.0	0.0	0.0	0.0	**0.0**
7398.00	0.0	0.0	0.0	0.0	0.0	0.0	0.0	0.0	0.0	0.0	0.0	0.0	0.0	0.0	0.0	0.0	0.0	0.0	0.0	0.0	0.0	**0.0**	0.0	0.0	0.0	0.0	0.0	**0.0**	0.0	0.0	0.0	0.0	0.0	100.0	0.0	0.0	0.0	0.0	**100.0**	0.0	0.0	0.0	0.0	0.0	0.0	0.0	0.0	**0.0**
7400.15	44.0	0.0	10.0	0.0	0.0	0.0	3.6	5.2	1.6	0.0	1.6	tr	0.0	0.0	1.6	0.0	0.0	0.0	0.0	0.4	0.0	**69.6**	0.0	0.0	1.6	16.8	0.0	**18.4**	1.2	2.4	0.8	1.2	1.2	0.0	0.0	5.2	0.0	tr	**12.0**	tr	0.0	0.0	0.0	0.0	0.0	0.0	0.0	**0.0**
7401.40	2.8	0.0	0.4	0.0	0.0	0.0	0.0	0.0	0.0	0.0	0.4	0.0	0.0	0.0	1.2	2.4	2.0	0.0	0.0	0.0	0.0	**9.2**	0.0	0.0	63.2	0.0	0.0	**63.2**	0.0	0.0	0.0	0.0	0.0	24.4	0.0	2.4	0.0	0.0	**26.8**	0.0	0.0	0.0	0.8	0.0	0.0	0.0	0.0	**0.8**
7403.15	13.6	0.0	4.4	0.0	0.0	0.0	0.0	1.2	0.8	0.0	0.4	0.0	0.0	0.0	2.4	0.8	0.0	0.0	0.0	0.0	0.0	**23.6**	4.4	0.0	47.2	0.0	0.0	**51.6**	0.0	0.0	0.0	0.0	0.0	21.6	0.0	2.8	0.0	0.0	**24.4**	0.0	0.0	0.0	0.4	0.0	0.0	0.0	0.0	**0.4**
7404.00	12.0	0.0	1.6	0.0	0.0	0.0	0.0	6.0	0.0	0.0	1.2	0.0	0.0	0.0	1.6	2.8	0.0	0.0	0.0	0.0	0.0	**25.2**	0.0	0.0	53.6	0.0	0.0	**53.6**	0.0	0.0	0.0	0.0	0.0	16.8	0.0	4.4	0.0	0.0	**21.2**	0.0	0.0	0.0	0.0	0.0	0.0	0.0	0.0	**0.0**
7406.00	0.8	0.0	0.0	0.0	0.0	0.0	0.0	0.0	0.0	0.0	0.0	0.0	0.0	0.0	0.0	0.0	0.0	0.0	0.0	0.0	0.0	**0.8**	0.0	72.0	0.0	0.0	23.2	**95.2**	0.0	0.0	0.0	0.0	0.0	1.2	0.0	2.8	0.0	0.0	**4.0**	0.0	0.0	0.0	0.0	0.0	0.0	0.0	0.0	**0.0**
7407.65	1.6	0.0	tr	0.0	0.0	0.0	0.0	0.4	0.0	0.0	0.0	0.0	0.0	0.0	2.4	6.8	15.2	0.0	0.0	0.0	0.0	**26.4**	0.0	0.0	65.2	0.0	0.0	**65.2**	0.0	0.0	0.0	0.0	0.0	4.4	0.0	1.2	0.0	2.8	**8.4**	0.0	tr	tr	0.0	0.0	0.0	0.0	0.0	**0.0**
7410.00	47.6	0.0	8.0	0.4	0.0	0.0	5.2	5.6	0.4	0.0	0.8	tr	0.0	0.0	0.8	0.0	0.0	0.0	0.0	0.4	0.0	**70.8**	0.0	0.0	1.6	14.8	0.0	**16.4**	0.4	3.2	0.4	1.2	1.2	0.8	0.0	5.6	tr	tr	**12.9**	0.0	0.0	0.0	0.0	0.0	0.0	0.0	0.0	**0.0**
7412.15	28.0	tr	6.4	0.0	0.0	0.0	2.0	18.4	0.8	0.0	1.2	0.0	0.0	0.0	2.0	0.0	0.0	0.0	0.0	1.2	0.0	**61.2**	0.0	0.0	17.6	7.6	5.2	**30.4**	0.0	0.4	tr	0.4	1.2	0.0	0.0	6.0	tr	0.4	**8.5**	0.0	0.0	0.0	0.0	0.0	tr	0.0	0.0	**0.0**
7414.20	tr	0.0	tr	0.0	0.0	0.0	0.0	0.4	0.0	0.0	0.0	0.0	0.0	0.0	0.0	0.0	0.0	0.0	0.0	0.0	0.0	**0.5**	1.2	0.0	7.6	0.0	0.0	**8.8**	0.0	0.0	0.0	0.0	0.0	90.0	0.0	0.8	0.0	0.0	**90.8**	0.0	0.0	0.0	0.0	0.0	0.0	0.0	0.0	**0.0**
7416.15	17.2	0.0	3.6	0.0	0.0	0.0	0.0	1.6	0.0	0.0	0.4	0.0	0.0	0.0	0.8	10.0	0.0	0.0	0.0	0.0	0.0	**34.0**	0.0	0.0	59.6	0.0	0.0	**59.6**	0.0	0.0	0.0	0.0	1.2	1.6	0.0	3.6	0.0	0.0	**6.4**	0.0	0.0	0.0	0.0	0.0	0.0	0.0	0.0	**0.0**
7419.15	33.6	0.0	7.2	0.0	0.0	0.0	3.6	16.8	0.0	0.0	0.4	tr	0.0	0.0	2.0	0.0	0.0	0.0	0.0	1.6	0.0	**66.0**	0.0	0.0	26.4	1.2	0.0	**27.6**	0.0	0.4	0.0	0.4	1.2	0.0	0.0	4.4	0.0	0.0	**8.4**	0.0	0.0	0.0	0.0	0.0	0.0	0.0	0.0	**0.0**
7421.40	24.0	0.0	6.4	0.0	0.0	0.0	3.6	10.4	0.0	0.0	tr	0.0	0.0	0.0	4.4	0.0	0.0	0.0	0.0	1.2	0.0	**50.8**	0.0	0.0	34.4	10.4	0.0	**44.8**	0.0	0.0	0.0	0.0	0.0	0.0	0.0	4.0	0.0	0.4	**4.4**	0.0	0.0	0.0	0.0	0.0	0.0	0.0	0.0	**0.0**
7424.85	37.2	0.0	4.8	0.0	0.0	0.0	6.0	9.2	0.4	0.0	1.2	0.0	0.0	0.0	0.8	0.0	2.4	0.0	0.0	1.2	0.0	**63.2**	0.0	0.0	1.6	5.2	0.0	**6.8**	0.0	6.0	0.0	12.0	6.8	0.0	0.0	3.6	0.4	1.2	**30.0**	0.0	0.0	tr	0.0	0.0	0.0	0.0	0.0	**0.0**
7426.00	41.2	0.0	6.8	1.6	0.0	0.0	1.6	13.2	0.0	0.0	1.2	0.0	0.0	0.0	0.4	0.0	0.0	tr	0.0	2.4	0.0	**68.4**	0.0	0.0	7.6	4.8	0.0	**12.4**	0.0	2.8	0.0	5.6	7.6	0.0	0.0	2.8	0.4	tr	**19.2**	0.0	0.0	tr	0.0	0.0	0.0	0.0	0.0	**0.0**
7427.10	50.8	0.0	7.6	0.4	tr	0.0	1.6	7.6	0.4	0.0	2.4	0.0	0.0	0.0	0.0	0.0	0.0	0.0	0.0	2.0	0.0	**72.8**	0.0	0.0	2.4	9.6	0.0	**12.0**	tr	2.4	0.4	5.6	3.6	0.0	0.0	2.4	0.4	0.0	**14.8**	0.4	0.0	0.0	0.0	0.0	0.0	0.0	0.0	**0.4**

TABLE 2

THIN SECTION POINT-COUNT PETROGRAPHIC DATA

Fidelity E & P, Cane Creek 26-3 Well, Grand Co., Utah

	Framework Grains																									Matrix						Authigenic Minerals											Porosity							
Depth (ft)	Monocrystalline quartz	Polycrystalline quartz	Potassium feldspar	Plagioclase	Volcanic rock fragment	Metamorphic rock fragments	Limestone rock fragments	Dolomite rock fragments	Argillaceous rock fragments	Chert rock fragments	Micas	Heavy minerals, undif.	Oxid-dolomite	Peloid-calcite	Plant fragments	Peloid-dolomite	Rip-up/intraclast	Glauconite	Dolomite replaced grains	Calcite replaced grains	Pyrite replaced grains	Total Framework Constituents	Detrital clay matrix	Micrite matrix	Dolomitic matrix	Clay and carbonate matrix	Organic matrix	Total detrital matrix	Authigenic clay	Quartz overgrowths/replacement	Potassium feldspar overgrowths	Dolomite	Calcite	Anhydrite	Celestine	Pyrite	Titanium oxides	Halite	Total authigenic minerals	Intergranular	Intercrystalline	Intragranular	Intracrystalline	Moldic	Fracture	Fenestral	Total visible porosity
7429.10	52.8	0.0	8.8	1.2	0.0	0.0	2.8	6.0	0.4	0.0	0.8	0.4	0.0	0.0	0.0	0.0	0.0	0.0	0.0	3.6	0.0	**77.2**	0.0	0.0	3.6	5.6	0.0	**9.2**	0.4	2.8	0.4	3.6	3.6	0.0	0.0	2.4	0.4	0.0	**13.6**	tr	0.0	tr	0.0	0.0	0.0	0.0	**0.0**
7431.25	50.8	0.0	10.4	0.4	0.0	0.0	3.2	6.4	0.4	0.0	2.0	0.0	0.0	0.0	0.4	0.0	0.0	0.0	0.0	1.6	0.0	**76.8**	0.0	0.0	4.8	6.0	0.0	**10.8**	0.8	4.0	0.0	2.8	2.4	0.0	tr	1.6	0.0	0.4	**12.0**	tr	0.0	tr	0.0	0.0	0.4	0.0	**0.4**
7433.10	45.2	0.0	7.6	0.0	0.0	0.0	2.4	12.8	0.0	0.0	2.0	tr	0.0	0.0	0.8	0.0	0.0	0.0	0.0	1.6	0.0	**73.6**	0.0	0.0	4.8	4.4	0.0	**9.2**	0.8	5.6	0.4	6.0	1.6	1.2	0.4	0.8	0.0	0.4	**17.2**	0.0	0.0	0.0	0.0	0.0	0.0	0.0	**0.0**
7435.15	54.4	0.0	8.8	1.2	0.0	0.0	3.6	3.6	0.0	0.0	2.4	0.4	0.0	0.0	0.0	0.0	0.0	0.0	0.0	0.8	0.0	**75.6**	0.0	0.0	3.2	4.8	0.0	**8.0**	2.0	6.0	tr	2.8	2.0	0.0	0.0	2.0	0.0	1.2	**16.0**	0.4	0.0	0.4	0.0	0.0	0.0	0.0	**0.8**
7437.10	38.8	0.0	8.4	0.8	0.0	0.0	4.0	7.6	0.4	0.0	4.4	tr	0.0	0.0	1.2	0.0	tr	tr	0.0	1.2	0.0	**66.9**	0.0	0.0	7.2	6.8	0.0	**14.0**	2.8	6.8	0.0	3.6	2.0	0.0	0.0	1.6	0.8	1.6	**19.2**	0.0	0.0	0.0	0.0	0.0	0.0	0.0	**0.0**
7439.25	44.8	0.4	5.2	0.0	0.0	0.0	2.8	9.6	1.2	0.0	0.4	tr	0.0	0.0	2.0	0.0	0.0	0.0	0.0	2.4	0.0	**69.6**	0.0	0.0	4.0	4.0	0.0	**8.0**	2.8	8.0	tr	2.8	3.2	0.0	0.0	4.4	0.4	0.8	**22.4**	0.0	0.0	0.0	0.0	0.0	0.0	0.0	**0.0**
7441.20	42.4	0.0	4.4	0.0	0.0	0.0	10.8	8.8	2.0	0.0	4.8	0.0	0.0	0.0	0.0	0.0	0.0	0.0	0.0	3.6	0.0	**77.2**	0.0	0.0	1.2	2.0	0.0	**3.2**	3.2	6.0	0.4	2.4	4.0	0.0	0.0	3.2	0.0	0.0	**19.2**	0.4	0.0	0.0	0.0	tr	0.0	0.0	**0.4**
7443.00	56.0	0.0	6.0	tr	0.0	0.0	4.4	1.6	3.6	0.0	1.6	0.8	0.0	0.0	0.4	0.0	0.8	0.0	0.0	2.8	0.0	**78.8**	1.6	0.0	0.4	0.0	0.0	**2.0**	1.2	7.6	tr	0.8	4.4	0.4	0.0	2.0	tr	0.4	**16.9**	2.4	0.0	0.0	0.0	0.0	0.0	0.0	**2.4**
7446.15	40.8	0.4	6.8	0.0	0.0	0.4	2.8	16.0	0.4	0.0	0.8	tr	0.0	0.0	2.0	0.0	0.0	0.0	0.0	3.6	0.0	**74.8**	0.0	0.0	6.0	9.6	0.0	**15.6**	0.4	0.8	tr	2.0	2.8	0.4	0.0	3.2	0.0	0.0	**9.6**	0.0	0.0	0.0	0.0	0.0	0.0	0.0	**0.0**
7448.15	0.8	0.0	0.4	0.0	0.0	0.0	0.0	0.0	0.0	0.0	tr	0.0	0.0	0.0	tr	0.0	0.0	0.0	0.0	0.0	0.0	**1.3**	0.0	1.2	0.0	0.0	0.0	**1.2**	0.0	0.0	0.0	0.4	0.0	96.8	0.0	0.4	0.0	0.0	**97.6**	0.0	0.0	0.0	0.0	0.0	0.0	0.0	**0.0**
7450.10	1.6	0.0	0.4	0.0	0.0	0.0	0.0	0.8	0.0	0.0	tr	0.0	0.0	0.0	tr	0.0	0.0	0.0	0.0	0.0	0.0	**2.9**	0.0	2.8	0.0	0.0	0.0	**2.8**	0.0	0.0	0.0	1.6	tr	92.8	0.0	tr	0.0	0.0	**94.5**	0.0	0.0	0.0	0.0	0.0	0.0	0.0	**0.0**
7452.20	30.8	0.4	2.4	0.0	0.0	0.0	0.0	17.6	0.0	0.0	1.6	0.0	0.0	0.0	2.4	0.0	2.4	tr	0.0	0.0	0.4	**58.0**	0.0	0.0	34.8	0.0	0.0	**34.8**	0.0	0.8	0.0	4.4	0.0	0.0	0.0	1.6	0.0	0.0	**6.8**	0.0	0.0	0.4	0.0	0.0	0.0	0.0	**0.4**
7454.00	42.0	0.0	6.8	0.0	0.0	0.0	0.0	17.6	0.0	0.0	0.8	0.8	0.0	0.0	0.4	0.0	1.2	0.0	0.0	0.0	0.0	**70.8**	1.2	0.0	17.2	0.0	0.0	**18.4**	0.0	4.0	0.0	3.2	0.0	0.0	0.0	2.8	0.8	0.0	**10.8**	0.0	0.0	0.0	0.0	0.0	0.0	0.0	**0.0**
7456.10	54.0	0.0	8.8	0.0	0.0	0.0	0.4	6.8	0.8	0.0	3.6	0.0	0.0	0.0	0.4	0.0	0.0	0.0	0.0	2.4	0.0	**80.0**	4.0	0.0	0.8	0.0	0.0	**4.8**	0.4	6.4	1.2	0.4	0.8	1.2	0.0	2.0	0.4	2.0	**14.8**	0.0	0.0	0.4	0.0	0.0	0.0	0.0	**0.4**
7458.25	7.6	0.0	0.8	0.0	0.0	0.0	0.0	0.0	0.0	0.0	0.4	0.0	0.0	0.0	0.0	0.0	0.0	0.0	0.0	0.0	0.0	**8.8**	0.0	0.0	27.6	0.0	61.2	**88.8**	0.0	0.0	0.0	0.0	0.0	0.0	0.0	2.4	0.0	0.0	**2.4**	0.0	0.0	0.0	0.0	0.0	0.0	0.0	**0.0**
7460.15	2.0	0.0	0.4	0.0	0.0	0.0	0.0	0.0	0.0	0.0	0.0	0.0	0.0	0.0	0.0	0.0	0.0	0.0	0.0	0.0	0.0	**2.4**	0.0	0.0	10.8	0.0	0.0	**10.8**	0.0	0.0	0.0	0.0	0.0	84.8	2.0	0.0	0.0	0.0	**86.8**	0.0	0.0	0.0	0.0	0.0	0.0	0.0	**0.0**
7461.15	tr	0.0	tr	0.0	0.0	0.0	0.0	0.0	0.0	0.0	0.0	0.0	0.0	0.0	tr	0.0	0.0	0.0	0.0	0.0	0.0	**0.1**	0.0	0.0	0.0	0.0	0.0	**0.0**	0.0	0.0	0.0	tr	0.0	100.0	0.0	tr	0.0	0.0	**100.1**	0.0	0.0	0.0	0.0	0.0	0.0	0.0	**0.0**
7463.10	2.0	0.0	0.4	0.0	0.0	0.0	0.0	0.4	0.0	0.0	0.0	0.0	0.0	0.0	1.2	0.0	0.0	0.0	0.0	0.0	0.0	**4.0**	0.0	0.0	24.4	1.6	0.0	**26.0**	0.0	0.0	0.0	4.4	0.0	64.8	0.4	0.4	0.0	0.0	**70.0**	0.0	0.0	0.0	0.0	0.0	0.0	0.0	**0.0**
7469.10	39.2	0.0	5.6	0.0	0.0	0.0	0.0	16.0	0.8	0.0	0.4	0.0	0.0	0.0	4.4	0.0	0.0	0.0	0.0	0.0	0.0	**66.4**	5.6	0.0	13.2	0.0	0.0	**18.8**	0.0	5.2	0.8	2.8	0.0	0.0	0.0	5.6	0.0	0.4	**14.8**	tr	0.0	tr	0.0	tr	0.0	0.0	**0.1**
7471.20	2.8	0.0	0.4	0.0	0.0	0.0	0.0	2.0	0.0	0.0	0.4	0.0	0.0	0.0	0.0	0.0	0.0	0.0	0.0	0.0	0.0	**5.6**	0.0	0.0	22.8	0.0	0.0	**22.8**	0.0	0.0	0.0	0.0	0.0	71.2	0.0	0.4	0.0	0.0	**71.6**	0.0	0.0	0.0	0.0	0.0	0.0	0.0	**0.0**
7473.10	1.2	0.0	0.4	0.0	0.0	0.0	0.0	1.6	0.0	0.0	0.0	0.0	0.0	0.0	0.0	0.0	0.0	0.0	0.0	0.0	0.0	**3.2**	0.0	0.0	16.8	0.0	0.0	**16.8**	0.0	0.0	0.0	0.0	0.0	79.2	0.0	0.8	0.0	0.0	**80.0**	0.0	0.0	0.0	0.0	0.0	0.0	0.0	**0.0**
untreated "C"	44.6	0.0	8.4	0.0	0.0	0.0	1.2	2.8	1.2	0.0	1.6	0.0	0.0	0.0	1.2	0.0	0.0	0.0	0.0	1.2	0.8	**64.4**	0.0	0.0	5.6	14.0	0.0	**19.6**	0.0	7.6	0.0	1.6	2.8	0.0	0.0	3.6	0.4	0.0	**16.0**	0.0	0.0	0.0	0.0	0.0	0.0	0.0	**0.0**
7438-KCl "A"	45.6	0.0	7.6	0.0	0.0	0.0	2.8	6.4	0.4	0.0	2.0	0.0	0.0	0.0	0.6	0.0	0.0	0.0	0.0	2.0	0.0	**68.4**	0.0	0.0	6.4	10.8	0.0	**17.2**	0.4	3.2	0.0	3.6	4.0	0.0	0.0	2.8	0.0	0.4	**14.4**	0.0	0.0	0.0	0.0	0.0	0.0	0.0	**0.0**

TABLE 3

MINERALOGY DETERMINED BY X-RAY DIFFRACTION

Fidelity E & P, Cane Creek 26-3 Well, Grand Co., Utah

Depth (ft):	Whole Rock Mineralogy (Weight %)												Clay Abundance (Weight %)				
	Quartz	K-Feldspar	Plagioclase	Calcite	Dolomite	Anhydrite	Celestine	Halite	Sylvite	Pyrite	Fluor-apatite	Total Clay	Corrensite	Illite / Smectite	Illite & Mica	Kaolinite	Chlorite
7388.15	23.5	0.0	0.0	6.5	5.3	0.0	0.0	46.8	0.0	3.9	0.0	14.0	0.0	2.6	9.7	0.0	1.7
7389.15	4.1	0.0	0.0	0.0	77.5	1.9	0.0	16.1	0.0	0.5	0.0	0.0	0.0	0.0	0.0	0.0	0.0
7390.00	0.8	0.0	0.0	0.0	0.9	98.3	0.0	0.0	0.0	0.0	0.0	0.0	0.0	0.0	0.0	0.0	0.0
7391.15	0.0	0.0	0.0	0.0	0.1	99.7	0.0	0.0	0.0	0.2	0.0	0.0	0.0	0.0	0.0	0.0	0.0
7392.15	1.0	0.0	0.0	0.0	3.9	94.8	0.0	0.0	0.0	0.0	0.0	0.3	0.0	0.0	0.3	0.0	0.0
7393.00	32.2	3.6	0.0	27.8	16.2	0.0	0.0	0.0	0.0	1.8	0.0	18.4	0.0	2.5	13.9	0.9	1.1
7394.10	29.1	4.7	0.0	36.9	14.4	5.2	0.0	0.0	0.0	0.7	0.0	8.9	0.0	1.3	6.5	0.1	1.0
7395.25	42.2	5.2	0.0	19.4	8.6	0.0	0.0	0.6	0.0	2.9	0.0	21.1	0.0	2.5	16.3	0.2	2.1
7396.15	0.6	0.0	0.0	0.4	0.8	98.0	0.0	0.0	0.0	0.0	0.0	0.2	0.0	0.0	0.2	0.0	0.0
7397.15	10.5	0.0	0.0	2.5	0.0	85.8	0.0	0.6	0.0	0.0	0.0	0.6	0.0	0.0	0.6	0.0	0.0
7398.00	1.1	0.0	0.0	0.1	0.3	98.2	0.0	0.0	0.0	0.0	0.0	0.2	0.0	0.0	0.2	0.0	0.0
7399.15	38.2	4.1	0.0	18.8	25.4	0.0	0.0	1.2	0.0	1.6	0.0	10.8	0.0	1.6	8.2	0.0	1.0
7400.15	51.5	6.7	0.0	11.9	4.9	1.1	0.0	1.3	0.0	3.0	0.0	19.7	0.0	2.5	15.8	0.0	1.4
7401.40	4.7	0.8	0.0	0.0	60.5	26.4	4.0	1.0	0.0	0.0	0.0	2.6	0.0	0.3	2.1	0.0	0.2
7402.10	2.8	0.0	0.0	0.0	17.9	77.3	0.9	0.0	0.0	0.0	0.0	1.1	0.0	0.2	0.9	0.0	0.0
7403.15	4.6	0.7	0.0	0.0	24.9	66.1	0.0	0.0	0.0	0.4	0.0	3.2	0.0	0.4	2.5	0.0	0.3
7404.00	8.8	0.6	0.0	0.0	45.4	39.2	0.0	0.0	0.0	0.4	0.0	5.5	0.0	1.0	4.2	0.0	0.3
7405.15	12.8	0.5	0.0	0.5	42.2	35.2	0.0	0.0	0.0	0.9	0.0	7.9	0.0	0.8	6.5	0.0	0.6
7406.00	10.1	0.0	0.0	77.6	1.2	5.4	0.0	0.0	0.0	1.5	0.0	4.2	0.0	0.0	4.2	0.0	0.0
7407.65	4.2	0.0	0.0	0.0	12.7	81.0	0.6	0.6	0.0	0.4	0.0	0.4	0.0	0.0	0.4	0.0	0.0
7408.10	2.5	0.0	0.0	0.0	37.4	57.6	1.0	1.2	0.0	0.0	0.0	0.4	0.0	0.0	0.4	0.0	0.0
7409.00	11.7	1.3	0.0	2.1	69.4	0.0	0.0	1.0	0.0	2.1	0.0	12.4	0.0	2.1	8.9	0.0	1.4
7410.00	53.3	9.0	0.0	10.1	7.6	1.0	0.0	0.2	0.0	1.9	0.0	17.0	0.0	2.2	13.6	0.0	1.2
7411.20	12.2	1.1	0.0	3.9	64.0	0.0	0.0	0.0	0.0	2.1	0.0	16.7	0.0	2.2	12.6	0.0	1.9
7412.15	31.2	3.8	0.0	12.4	29.5	0.6	0.0	0.7	0.0	7.5	0.0	14.3	0.0	1.6	10.8	0.0	1.9
7413.25	2.0	0.7	0.0	90.2	1.7	3.1	0.0	0.0	0.0	0.3	0.0	1.9	0.0	0.0	1.9	0.0	0.0
7414.20	0.5	0.0	0.0	0.4	1.3	97.4	0.0	0.0	0.0	0.0	0.0	0.4	0.0	0.0	0.4	0.0	0.0
7415.10	12.0	0.7	0.0	30.3	6.3	45.4	0.0	0.0	0.0	0.8	0.0	4.4	0.0	0.6	3.3	0.0	0.5
7416.15	16.9	2.2	0.0	1.7	68.6	4.2	0.0	0.8	0.0	0.4	0.0	5.2	0.0	0.8	3.8	0.0	0.6
7417.15	12.5	2.0	0.0	9.1	56.1	0.0	0.0	1.0	0.0	2.6	0.0	16.8	0.0	2.3	12.2	0.5	1.8
7418.10	18.9	4.7	0.0	11.0	33.3	0.0	0.0	1.2	0.0	3.2	0.0	27.8	0.0	4.3	20.6	0.5	2.4
7419.15	29.4	5.2	0.0	13.7	40.9	0.0	0.0	0.4	0.0	1.6	0.0	8.8	0.0	0.9	6.0	0.5	1.4

TABLE 3

MINERALOGY DETERMINED BY X-RAY DIFFRACTION

Fidelity E & P, Cane Creek 26-3 Well, Grand Co., Utah

Depth (ft):	Whole Rock Mineralogy (Weight %)												Clay Abundance (Weight %)				
	Quartz	K-Feldspar	Plagioclase	Calcite	Dolomite	Anhydrite	Celestine	Halite	Sylvite	Pyrite	Fluor-apatite	Total Clay	Corrensite	Illite / Smectite	Illite & Mica	Kaolinite	Chlorite
7420.30	41.3	6.1	0.0	16.7	23.5	0.0	0.0	0.7	0.0	1.6	0.0	10.1	0.0	1.4	7.6	0.2	0.9
7421.40	23.7	3.2	0.0	21.8	31.1	0.0	0.0	0.8	0.0	2.7	0.0	16.7	0.0	2.2	12.1	0.5	1.9
7422.00	19.8	4.7	1.1	17.9	15.1	0.0	0.0	2.0	0.0	8.4	3.5	27.6	0.0	4.3	20.1	0.7	2.5
7423.15	37.9	5.0	0.5	13.6	24.2	0.0	0.0	1.3	0.0	2.1	0.0	15.4	0.0	1.6	11.8	0.3	1.7
7424.85	46.1	4.2	0.0	21.4	13.1	0.0	0.0	7.4	0.0	1.1	0.0	6.6	0.0	0.8	4.6	0.2	1.0
7425.45	51.2	6.3	0.0	10.0	18.7	0.0	0.0	1.0	0.0	1.4	0.0	11.5	0.0	1.6	8.3	0.0	1.6
7426.00	50.2	5.2	0.7	11.1	20.0	0.0	0.0	0.8	0.0	1.8	0.0	10.2	0.0	1.4	7.3	0.0	1.5
7427.10	60.8	7.2	0.0	11.9	5.6	0.9	0.0	1.9	0.0	1.7	0.0	9.9	0.0	0.9	7.5	0.0	1.5
7428.25	56.2	8.5	0.8	9.5	7.9	1.4	0.0	1.3	0.0	3.0	0.0	11.5	0.0	1.2	8.5	0.0	1.8
7429.10	62.1	6.6	0.7	10.2	6.7	0.0	0.0	0.9	0.0	1.6	0.0	11.0	0.0	1.3	8.0	0.0	1.7
7430.15	51.3	7.1	0.8	12.3	12.8	0.0	0.0	0.0	0.0	1.5	0.0	14.2	0.0	1.9	9.2	0.3	2.8
7431.25	51.9	8.8	0.7	13.5	10.0	0.0	0.0	0.8	0.0	1.8	0.0	12.3	0.0	1.9	8.5	0.3	1.6
7432.20	50.4	6.1	0.0	25.6	5.4	0.0	0.0	0.7	0.0	1.9	0.0	9.8	0.0	1.2	7.0	0.1	1.5
7433.10	55.3	4.8	0.0	13.3	15.9	0.0	0.0	0.0	0.0	1.3	0.0	9.4	0.0	1.2	5.9	0.2	2.1
7434.30	61.4	5.9	0.7	10.8	9.0	0.0	0.0	2.3	0.0	1.5	0.0	8.3	0.0	1.1	5.3	0.2	1.7
7435.15	62.6	7.5	0.6	9.0	7.4	0.0	0.0	1.3	0.0	1.8	0.0	9.9	0.0	1.4	7.2	0.1	1.2
7436.15	57.1	10.2	1.2	10.3	7.9	0.0	0.0	2.4	0.0	1.6	0.0	9.2	0.0	1.3	6.7	0.0	1.2
7437.10	53.3	7.0	0.8	11.8	8.5	0.0	0.0	2.0	0.0	1.0	0.0	15.7	0.0	2.7	9.9	0.2	2.9
7438.50	56.8	4.8	0.0	13.2	13.7	0.0	0.0	0.4	0.0	1.4	0.0	9.7	0.0	1.4	6.7	0.0	1.6
7439.25	55.7	5.4	0.0	12.8	15.1	0.0	0.0	1.4	0.0	1.8	0.0	7.9	0.0	1.1	5.6	0.0	1.2
7440.00	57.2	6.4	0.0	12.0	9.2	0.0	0.0	8.3	0.0	0.7	0.0	6.2	0.0	1.0	4.2	0.0	1.0
7441.20	50.2	6.3	0.0	13.5	14.3	0.0	0.0	0.0	0.0	1.0	0.0	14.8	0.0	2.0	9.9	0.4	2.5
7442.50	60.3	10.1	0.0	8.1	5.9	0.0	0.0	4.2	0.0	0.0	0.0	11.3	0.0	1.2	8.0	0.2	1.9
7443.00	59.0	6.1	0.0	22.5	3.0	0.0	0.0	1.5	0.0	1.6	0.0	6.4	0.0	0.8	4.3	0.0	1.3
7444.10	54.7	7.1	0.0	10.1	7.3	0.0	0.0	4.3	0.0	2.1	0.0	14.4	0.0	1.5	10.3	0.0	2.6
7445.15	52.9	6.0	0.8	8.9	11.2	0.0	0.0	4.0	0.0	2.8	0.0	13.5	0.0	1.8	8.5	0.2	3.0
7446.15	41.6	5.3	0.0	22.2	19.9	0.0	0.0	0.0	0.0	1.1	0.0	10.0	0.0	1.4	6.6	0.0	2.0
7447.15	3.0	0.0	0.0	4.0	9.4	80.4	1.0	0.0	0.0	0.0	0.0	2.2	0.0	0.2	1.5	0.0	0.5
7448.15	2.5	0.0	0.0	1.8	1.5	91.7	0.7	0.0	0.0	0.0	0.0	1.7	0.0	0.2	1.0	0.0	0.5
7449.10	4.9	1.0	0.0	1.6	2.8	87.4	0.6	0.0	0.0	0.0	0.0	1.7	0.0	0.3	1.1	0.0	0.3
7450.10	5.6	0.7	0.0	12.9	0.5	77.0	0.0	0.0	0.0	0.4	0.0	2.8	0.0	0.5	1.9	0.0	0.4
7451.15	46.0	7.2	0.5	14.5	12.9	4.5	0.0	0.0	0.0	0.8	0.0	13.5	0.0	1.3	9.9	0.0	2.3

TABLE 3

MINERALOGY DETERMINED BY X-RAY DIFFRACTION

Fidelity E & P, Cane Creek 26-3 Well, Grand Co., Utah

Depth (ft):	Whole Rock Mineralogy (Weight %)												Clay Abundance (Weight %)				
	Quartz	K-Feldspar	Plagioclase	Calcite	Dolomite	Anhydrite	Celestine	Halite	Sylvite	Pyrite	Fluor-apatite	Total Clay	Corrensite	Illite / Smectite	Illite & Mica	Kaolinite	Chlorite
7452.20	33.3	3.5	0.0	0.0	53.3	2.6	0.0	0.7	0.0	0.9	0.0	5.7	0.0	0.5	3.5	0.0	1.7
7453.40	42.2	5.0	0.0	0.0	38.6	2.2	0.0	0.7	0.0	1.6	0.0	9.8	0.0	1.4	6.6	0.2	1.6
7454.00	47.1	6.9	0.9	0.0	33.8	0.0	0.0	0.5	0.0	1.7	0.0	9.1	0.0	1.3	6.1	0.0	1.7
7456.10	57.3	9.0	0.0	7.3	4.6	1.8	0.0	1.2	0.0	0.9	0.0	17.8	0.0	2.0	12.9	0.2	2.7
7457.85	0.7	0.0	0.0	0.0	5.6	92.0	0.4	0.0	0.0	0.0	0.0	1.3	0.0	0.2	0.8	0.0	0.3
7458.25	11.1	2.1	0.3	3.5	63.5	0.0	0.0	1.3	0.0	3.6	0.0	14.7	0.0	1.9	10.0	0.0	2.8
7459.10	6.7	0.4	0.0	20.5	60.3	7.2	0.0	0.0	0.0	2.2	0.0	2.6	0.0	0.4	1.6	0.0	0.6
7460.15	2.4	0.0	0.0	0.0	10.8	83.8	1.2	0.0	0.0	0.0	0.0	1.8	0.0	0.3	1.2	0.0	0.3
7461.15	0.4	0.0	0.0	0.0	0.0	99.6	0.0	0.0	0.0	0.0	0.0	0.0	0.0	0.0	0.0	0.0	0.0
7462.15	0.8	0.0	0.0	0.2	0.7	98.1	0.0	0.0	0.0	0.0	0.0	0.2	0.0	0.0	0.2	0.0	0.0
7463.10	1.3	0.3	0.0	2.7	9.3	84.3	0.7	0.0	0.0	0.0	0.0	1.5	0.3	0.2	0.7	0.0	0.3
7464.15	5.8	0.0	0.0	15.5	3.7	69.3	0.0	0.0	0.0	1.6	0.0	4.1	1.5	0.3	1.7	0.0	0.6
7465.20	2.0	0.0	0.0	4.4	86.7	6.9	0.0	0.0	0.0	0.0	0.0	0.0	0.0	0.0	0.0	0.0	0.0
7466.15	0.6	0.0	0.0	0.0	0.7	98.7	0.0	0.0	0.0	0.0	0.0	0.0	0.0	0.0	0.0	0.0	0.0
7467.20	2.3	0.0	0.0	0.0	7.3	88.8	0.0	0.0	0.0	0.0	0.0	1.6	0.4	0.2	0.8	0.0	0.2
7468.10	17.8	0.7	0.0	0.0	25.4	1.2	0.0	47.9	0.0	1.3	0.0	5.6	1.1	0.5	3.5	0.0	0.5
7469.10	41.7	6.3	0.7	0.0	30.5	0.0	0.0	7.4	0.0	2.6	0.0	10.8	2.1	1.4	6.0	0.0	1.3
7470.15	9.8	0.0	0.0	0.0	70.5	0.0	0.0	11.4	0.0	1.5	0.0	6.8	1.2	0.6	4.3	0.0	0.7
7471.20	2.8	0.0	0.0	0.0	3.4	93.1	0.0	0.0	0.0	0.0	0.0	0.7	0.0	0.0	0.7	0.0	0.0
7472.15	0.3	0.0	0.0	0.0	2.1	97.6	0.0	0.0	0.0	0.0	0.0	0.0	0.0	0.0	0.0	0.0	0.0
7473.10	0.6	0.0	0.0	0.0	2.5	96.8	0.0	0.0	0.0	0.0	0.0	0.0	0.0	0.0	0.0	0.0	0.0
7473.95	0.3	0.0	0.0	0.0	0.2	99.5	0.0	0.0	0.0	0.0	0.0	0.0	0.0	0.0	0.0	0.0	0.0
7428-untreated "C"	50.7	6.2	0.0	11.3	15.9	0.0	0.0	0.0	0.0	2.2	0.0	13.7	0.0	2.1	9.5	0.0	2.1
7428-KCl "A"	53.8	7.0	0.0	10.9	12.2	0.0	0.0	0.7	2.0	1.7	0.0	11.7	0.0	1.8	8.2	0.0	1.7

Notes: *mixed-layer chlorite/smectite contains 50-60% smectite layers*
mixed-layer illite/smectite contains 15-25% smectite layers

TABLE 4

PARAGENETIC SEQUENCE

Fidelity E & P, Cane Creek 26-3 Well, Grand Co., Utah

Dark green = Apparent relative timing of most occurrences
Light green = Relative timing is unclear or periodic over long intervals of time
Vertical bars = Relative timing is unknown

Note: This paragenetic sequence is proposed for an ideal sample where all the events have occurred. In most cases, some events are missing, abbreviated, or more periodic than shown.
Overlap does not imply simultaneous precipitation.

FIGURE 1

Ternary Diagram - Sandstone Classification (Modified from Folk, 1980)

Fidelity E & P, Cane Creek 26-3 Well, Grand Co., Utah

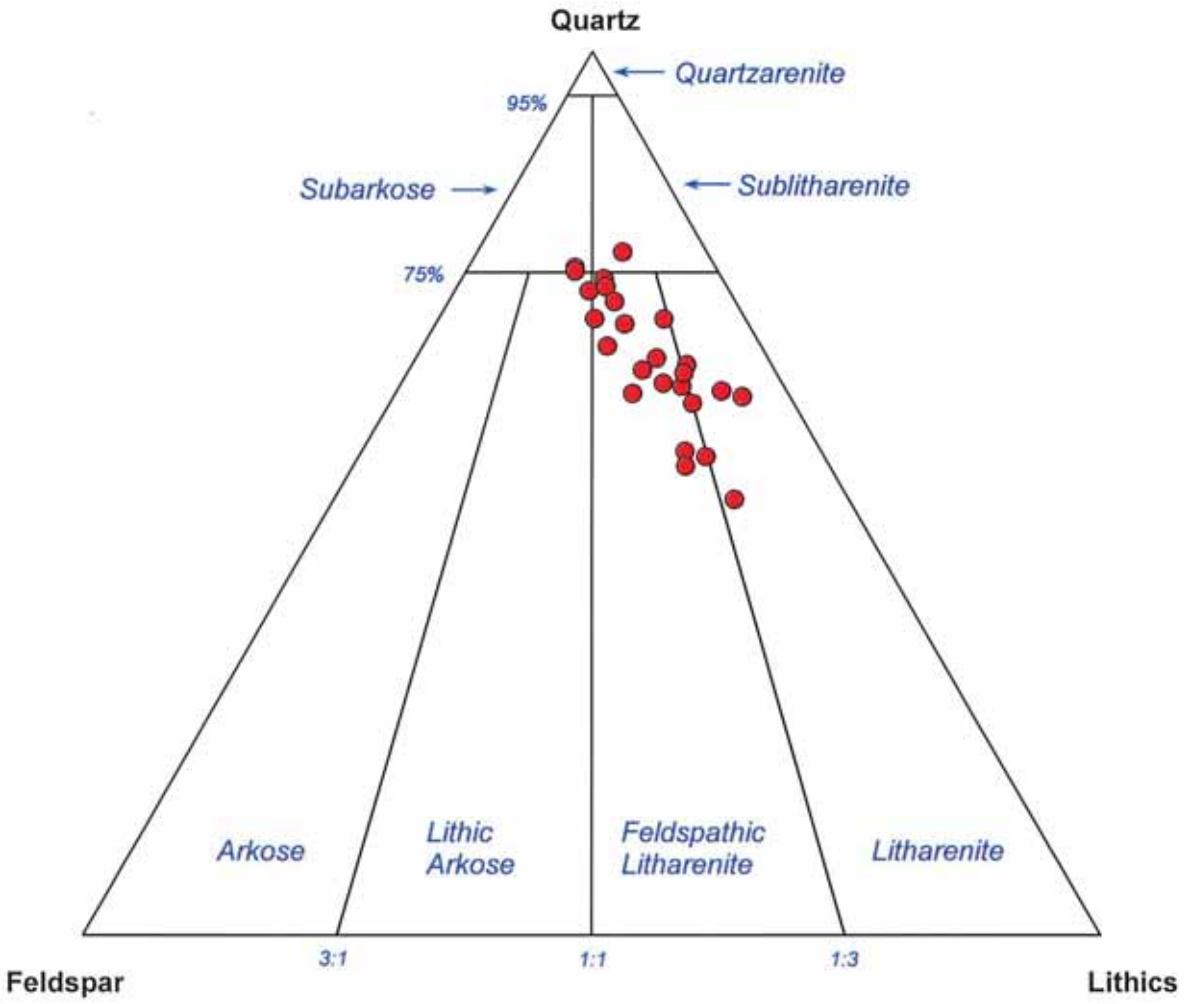

PLATE 1

Thin Section Petrography

Company:	**Fidelity E & P**
Well:	**Cane Creek 26-3**
Location:	**Grand Co., Utah**
Depth (ft):	**7389.15**
Unit:	**A**
Dep. Env.:	**Shallow Marine/Subaqueous**

A

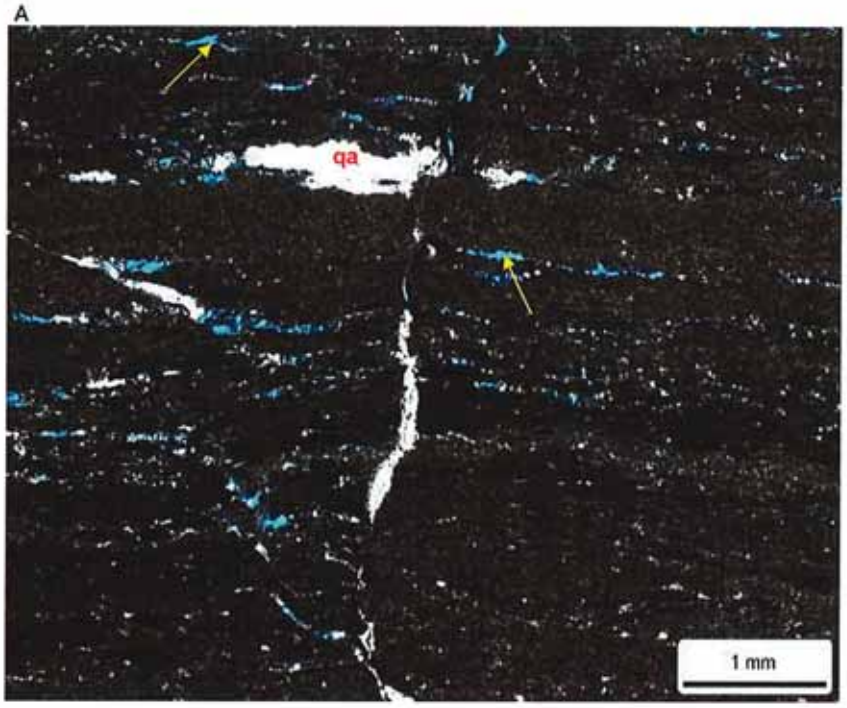

B

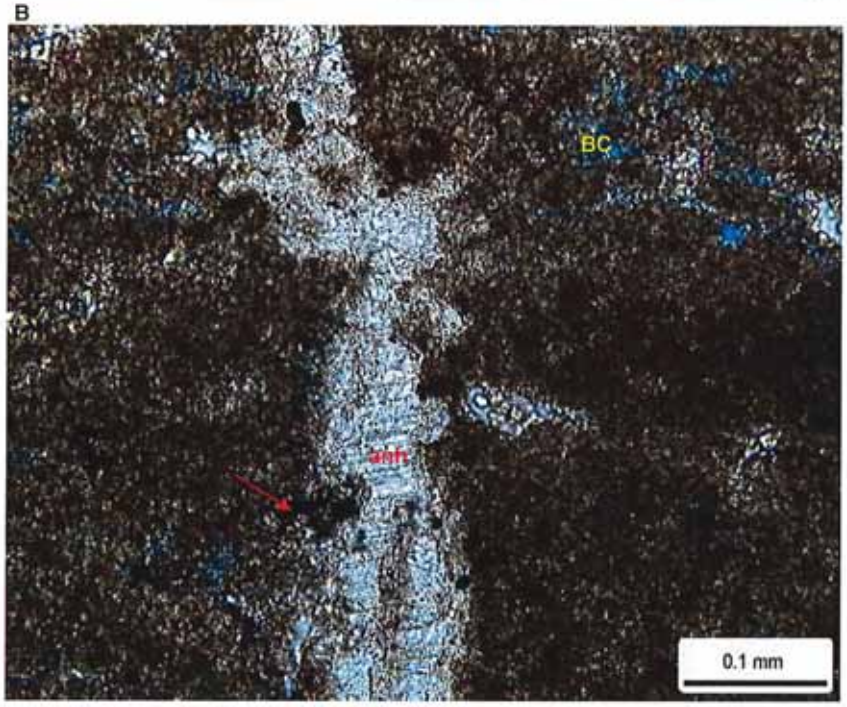

LITHOLOGY AND TEXTURE

Lithology:	Dolostone
Classific. (Dunham, 1962):	Doloboundstone
Grain Size (mm):	n/a
Sorting:	n/a
Structures:	thin parallel to wavy laminae; microfractures

Rock Composition (Point-Count)

Framework Grains:

Mono quartz:	0.0	Argillaceous RF:	0.0
Poly quartz:	0.0	Chert RF:	0.0
K-Feldspar:	0.0	Micas:	0.0
Plagioclase:	0.0	Heavy minerals:	0.0
Volcanic RF:	0.0	Plant fragments:	1.6
Metamorphic RF:	0.0	Glauconite:	0.0
Peloid-dolomite:	3.2	Rip-up/intraclasts:	0.0

Replaced Grains:

Dolomite RG:	0.0	Pyrite RG:	0.0
Calcite RG:	0.0	Kaolinite RG:	0.0

Detrital Matrix:

Detrital clay:	0.0	Micrite matrix:	0.0
Organic matrix:	0.0	Dolomitic matrix:	84.0

Pore-filling Authigenic Minerals:

Authigenic clay:	0.0	Dolomite:	0.0
Quartz OG/QA:	1.2	Calcite:	0.0
Kspar OG:	0.0	Anhydrite:	1.6
Pyrite:	1.2	Celestine:	0.0
Titanium oxides:	0.0	Halite:	1.6

Pore Types:

Intergranular:	0.0	Intercrystal:	3.6
Fracture:	0.4	Fenestral:	1.6

XRD-Whole Rock Mineralogy (Weight %)

Quartz	4.1	Anhydrite	1.9
K-Feldspar	0.0	Celestine	0.0
Plagioclase	0.0	Halite	16.1
Calcite	0.0	Pyrite	0.5
Dolomite	77.5	Total Clay	0.0

Clay Abundance (Weight %)

Corrensite	0.0	Kaolinite	0.0
Illite / Smectite	0.0	Chlorite	0.0
Illite & Mica	0.0		

Petrographic Description

This dolostone contains thin planar to wavy laminae and has an algal boundstone texture. Numerous microfractures are observed, and displacement is evident along some of the microfractures. Authigenic quartz (qa), anhydrite (anh), and halite partially fill some microfractures and other pores. Pore types include intercrystal pores (BC) between dolomite rhombs and larger fenestral-type pores (yellow arrows). Pyrite (red arrow) and organic matter are minor in abundance.

Core Lab
RESERVOIR OPTIMIZATION

Relative Abundances:

Trace	<1%
Minor	1-5%
Moderate	5-10%
Common	10-20%
Abundant	>20%

Core Analysis Data:

Porosity (%):	2.09
Permeability (md):	0.0263
Gr. Density (g/cc):	2.718
Oil Saturation (%):	16.4
Water Saturation	39.7

PLATE 2

Thin Section Petrography

Company:	**Fidelity E & P**
Well:	**Cane Creek 26-3**
Location:	**Grand Co., Utah**
Depth (ft):	**7391.15**
Unit:	**A**
Dep. Env.:	**Shallow Shelf Salina/Sabkha**

A

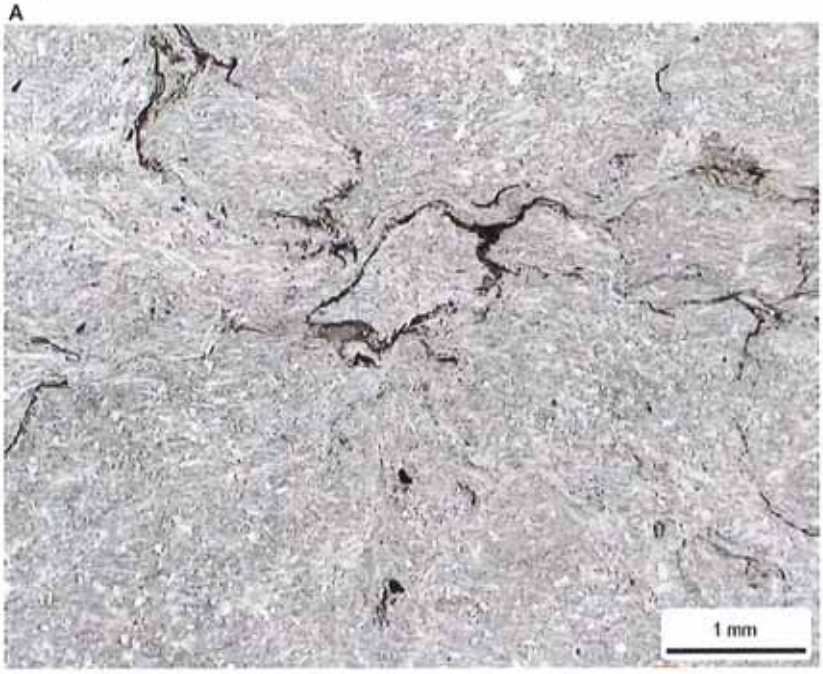

B

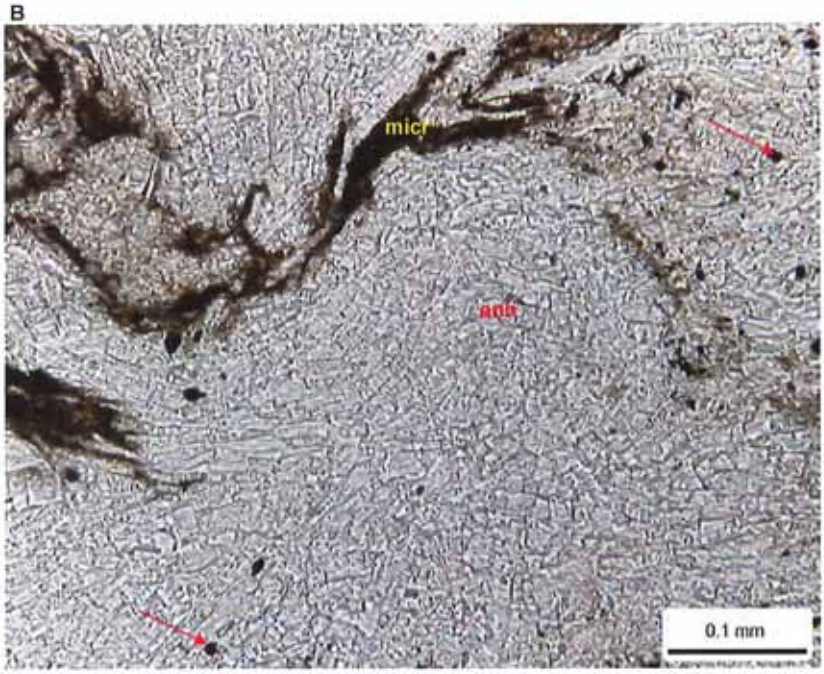

LITHOLOGY AND TEXTURE

Lithology:	Anhydrite
Classific. (Folk, 1980):	n/a
Grain Size (mm):	n/a
Sorting:	n/a
Structures:	faint nodular texture

Rock Composition (Point-Count)

Framework Grains:			
Mono quartz:	0.0	Argillaceous RF:	0.0
Poly quartz:	0.0	Chert RF:	0.0
K-Feldspar:	0.0	Micas:	0.0
Plagioclase:	0.0	Heavy minerals:	0.0
Volcanic RF:	0.0	Plant fragments:	0.8
Metamorphic RF:	0.0	Glauconite:	0.0
Limestone RF:	0.0	Rip-up/intraclasts:	0.0
Replaced Grains:			
Dolomite RG:	0.0	Pyrite RG:	0.0
Calcite RG:	0.0	Kaolinite RG:	0.0
Detrital Matrix:			
Detrital clay:	0.0	Micrite matrix:	1.2
Organic matrix:	0.0	Dolomitic matrix:	0.4
Pore-filling Authigenic Minerals:			
Authigenic clay:	0.0	Dolomite:	0.0
Quartz OG/QA:	0.0	Calcite:	0.0
Kspar OG:	0.0	Anhydrite:	96.8
Pyrite:	0.8	Celestine:	0.0
Titanium oxides:	0.0	Halite:	0.0
Pore Types:			
Intergranular:	0.0	Intragranular:	0.0
Fracture:	0.0	Moldic:	0.0

XRD-Whole Rock Mineralogy (Weight %)

Quartz	0.0	Anhydrite	99.7
K-Feldspar	0.0	Celestine	0.0
Plagioclase	0.0	Halite	0.0
Calcite	0.0	Pyrite	0.2
Dolomite	0.1	Total Clay	0.0
Clay Abundance (Weight %)			
Corrensite	0.0	Kaolinite	0.0
Illite / Smectite	0.0	Chlorite	0.0
Illite & Mica	0.0		

Petrographic Description

This sample is almost entirely anhydrite (anh). A faint nodular texture is defined by thin zones of micrite (micr) and organic matter. Scattered pyrite nodules (red arrows) are rare.

Relative Abundances:	
Trace	<1%
Minor	1-5%
Moderate	5-10%
Common	10-20%
Abundant	>20%

Core Analysis Data:	
Porosity (%):	0.49
Permeability (md):	0.0015
Gr. Density (g/cc):	2.962
Oil Saturation (%):	0.0
Water Saturation	40.2

PLATE 3

Thin Section Petrography

Company:	**Fidelity E & P**
Well:	**Cane Creek 26-3**
Location:	**Grand Co., Utah**
Depth (ft):	**7392.15**
Unit:	**A**
Dep. Env.:	**Shallow Shelf Salina/Sabkha**

A

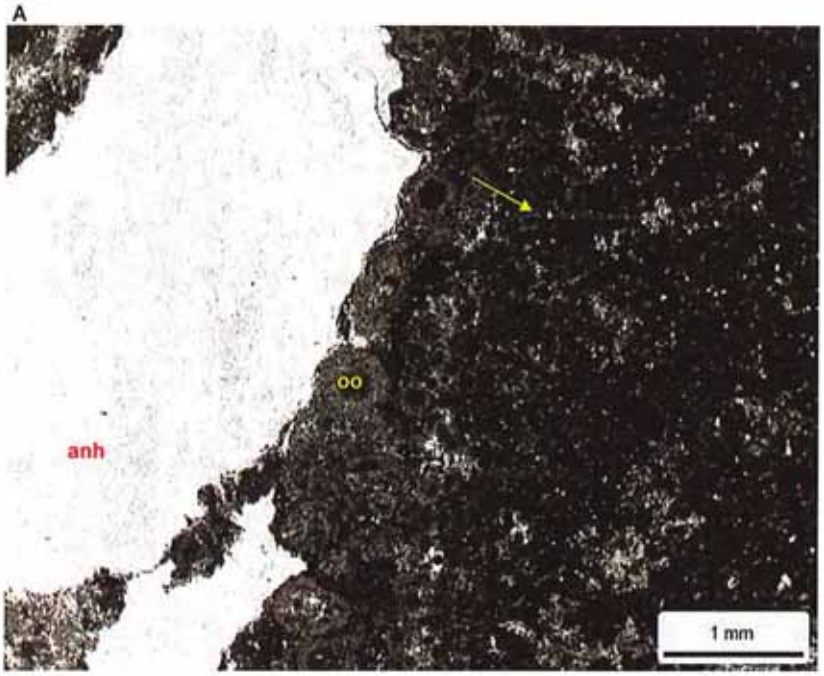

B

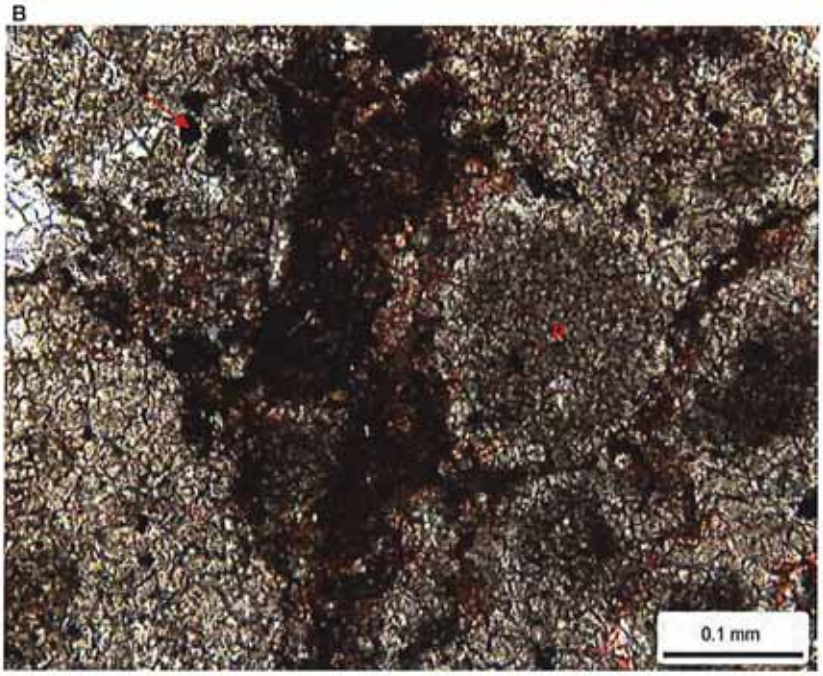

LITHOLOGY AND TEXTURE

Lithology:	Anhydrite / Dolostone
Classific. (Dunham, 1962):	Peloidal Lime Packstone
Grain Size (mm):	n/a
Sorting:	moderate
Structures:	nodular texture; anhydrite and calcite filled microfractures

Rock Composition (Point-Count)

Framework Grains:

Mono quartz:	0.0	Argillaceous RF:	0.0
Poly quartz:	0.0	Chert RF:	0.0
K-Feldspar:	0.0	Micas:	0.0
Plagioclase:	0.0	Heavy minerals:	0.0
Ooid-dolomite:	3.6	Plant fragments:	2.0
Peloid-calcite:	8.0	Glauconite:	0.0
Peloid-dolomite:	0.8	Rip-up/intraclasts:	0.8

Replaced Grains:

Dolomite RG:	0.0	Pyrite RG:	0.0
Calcite RG:	0.0	Kaolinite RG:	0.0

Detrital Matrix:

Detrital clay:	0.0	Micrite matrix:	0.0
Organic matrix:	0.0	Dolomitic matrix:	26.0

Pore-filling Authigenic Minerals:

Authigenic clay:	0.0	Dolomite:	0.0
Quartz OG/QA:	0.0	Calcite:	1.6
Kspar OG:	0.0	Anhydrite:	56.0
Pyrite:	1.2	Celestine:	0.0
Titanium oxides:	0.0	Halite:	0.0

Pore Types:

Intergranular:	0.0	Intercrystal:	tr
Fracture:	0.0	Moldic:	0.0

XRD-Whole Rock Mineralogy (Weight %)

Quartz	1.0	Anhydrite	94.8
K-Feldspar	0.0	Celestine	0.0
Plagioclase	0.0	Halite	0.0
Calcite	0.0	Pyrite	0.0
Dolomite	3.9	Total Clay	0.3

Clay Abundance (Weight %)

Corrensite	0.0	Kaolinite	0.0
Illite / Smectite	0.0	Chlorite	0.0
Illite & Mica	0.3		

Petrographic Description

This sample is comprised mostly of anhydrite and dolomite. XRD and point-count percentages differ because of sample heterogeneity, but core analysis grain density (2.89 g/cc) suggests more dolomite (2.86 g/cc) than anhydrite (2.98 g/cc) in the sample. Large patches of anhydrite (anh) are noted, as well as anhydrite-filled microfractures in the dolostone. The dolostone has a packstone texture. Peloids (p) are the most common allochem, and ooids (oo) are also observed in minor amounts. Plant fragments are dispersed throughout the dolomitic matrix. Pyrite framboids (red arrow) are concentrated in the dolostone, and occasionally replace plant fragments. A microfracture (yellow arrow) is noted in Photo A.

Core Lab
RESERVOIR OPTIMIZATION

Relative Abundances:

Trace	**<1%**
Minor	**1-5%**
Moderate	**5-10%**
Common	**10-20%**
Abundant	**>20%**

Core Analysis Data:

Porosity (%):	0.91
Permeability (md):	0.0009
Gr. Density (g/cc):	2.890
Oil Saturation (%):	13.6
Water Saturation	32.4

PLATE 4

Thin Section Petrography

Company:	**Fidelity E & P**
Well:	**Cane Creek 26-3**
Location:	**Grand Co., Utah**
Depth (ft):	**7394.10**
Unit:	**A**
Dep. Env.:	**Restricted Anoxic Shallow Marine/Subaqueous**

A

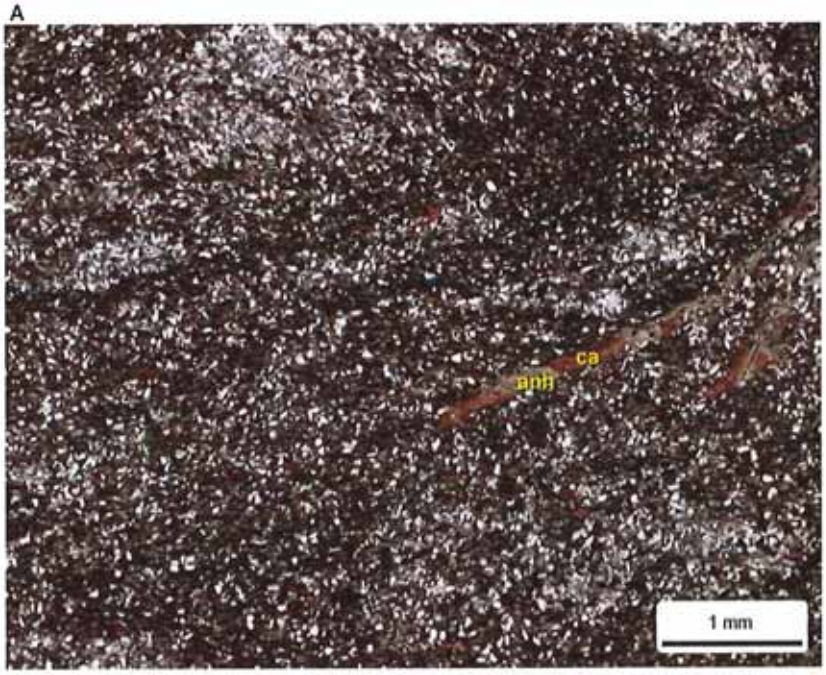

B

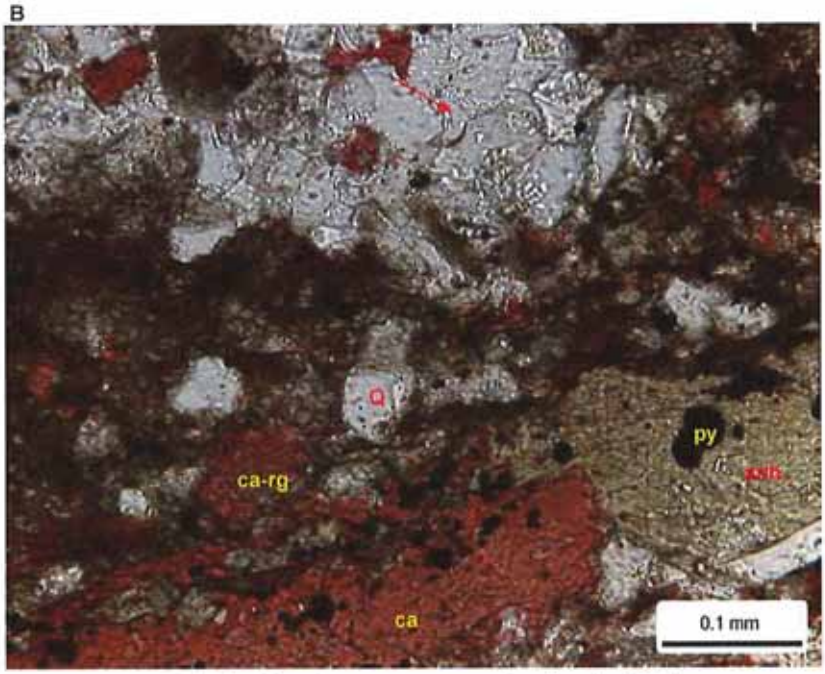

Relative Abundances:

Trace	<1%
Minor	1-5%
Moderate	5-10%
Common	10-20%
Abundant	>20%

Core Analysis Data:

Porosity (%):	6.22
Permeability (md):	0.0183
Gr. Density (g/cc):	2.716
Oil Saturation (%):	27.3
Water Saturation	57.8

LITHOLOGY AND TEXTURE

Lithology:	Argillaceous Calcareous Sandst
Classific. (Folk, 1980):	Feldspathic Litharenite
Grain Size (mm):	0.064 (L. very fine sand)
Sorting:	well
Structures:	bioturbated/burrowed; open microfractures; anhydrite and calcite cemented fracture

Rock Composition (Point-Count)

Framework Grains:

Mono quartz:	32.0	Argillaceous RF:	0.4
Poly quartz:	0.0	Dolomite RF:	8.4
K-Feldspar:	6.0	Micas:	0.4
Plagioclase:	0.0	Heavy minerals:	0.0
Volcanic RF:	2.0	Plant fragments:	2.0
Metamorphic RF:	0.0	Glauconite:	0.0
Limestone RF:	2.4	Rip-up/intraclasts:	0.0

Replaced Grains:

Dolomite RG:	0.0	Pyrite RG:	0.0
Calcite RG:	1.6	Kaolinite RG:	0.0

Detrital Matrix:

Detrital clay:	0.0	Mixed clay/carbonate:	22.0
Organic matrix:	0.0	Dolomitic matrix:	9.2

Pore-filling Authigenic Minerals:

Authigenic clay:	0.0	Dolomite:	1.6
Quartz OG/QA:	2.0	Calcite:	6.0
Kspar OG:	tr	Anhydrite:	1.2
Pyrite:	2.4	Celestine:	0.4
Titanium oxides:	tr	Halite:	0.0

Pore Types:

Intergranular:	0.0	Intragranular:	tr
Fracture:	tr	Moldic:	0.0

XRD-Whole Rock Mineralogy (Weight %)

Quartz	29.1	Anhydrite	5.2
K-Feldspar	4.7	Celestine	0.0
Plagioclase	0.0	Halite	0.0
Calcite	36.9	Pyrite	0.7
Dolomite	14.4	Total Clay	8.9

Clay Abundance (Weight %)

Corrensite	0.0	Kaolinite	0.1
Illite / Smectite	1.3	Chlorite	1.0
Illite & Mica	6.5		

mixed-layer illite/smectite contains 15-25% smectite layers

Petrographic Description

This sample is a very fine-grained argillaceous calcareous sandstone. Framework grains are mostly quartz (Q), with less common potassium feldspar, dolomite rock fragments, limestone rock fragments, and volcanic rock fragments. Some grains have been partially to completely replaced by calcite (ca-rg). Dolomite partially replaces the clay and micrite-rich matrix. Anhydrite (anh) and calcite (ca) cements fill microfractures. Discontinuous open microfractures a also observed in thin section, but it is unclear if they are natural or induced. Other minor cements include quartz overgrowths (red arrow) and pyrite (py).

PLATE 4

Scanning Electron Microscopy

Company:	**Fidelity E & P**
Well:	**Cane Creek 26-3**
Location:	**Grand Co., Utah**
Depth (ft):	**7394.10**
Unit:	**A**
Dep. Env.:	**Shallow Marine/Subaqueous**

LITHOLOGY

Argillaceous Calcareous Sandstone

C

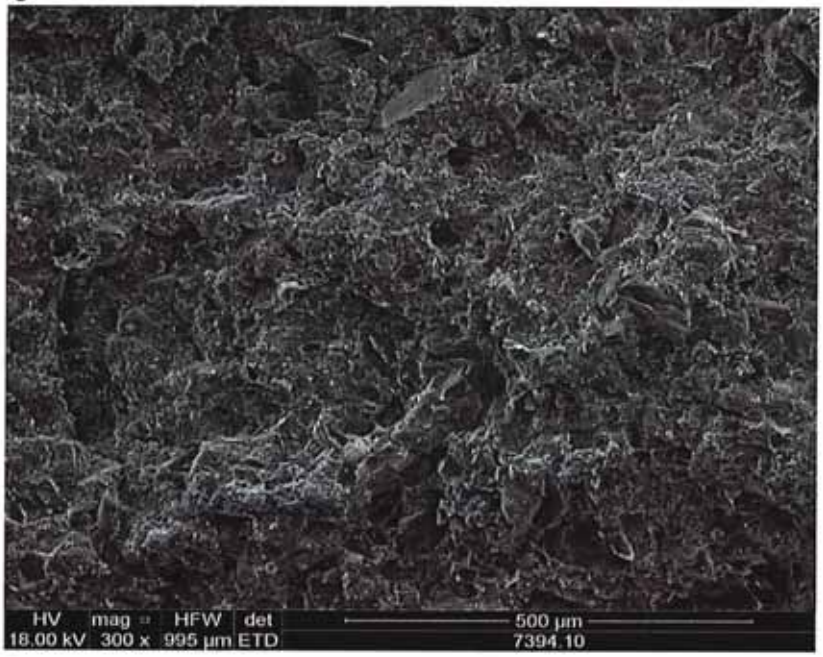

D

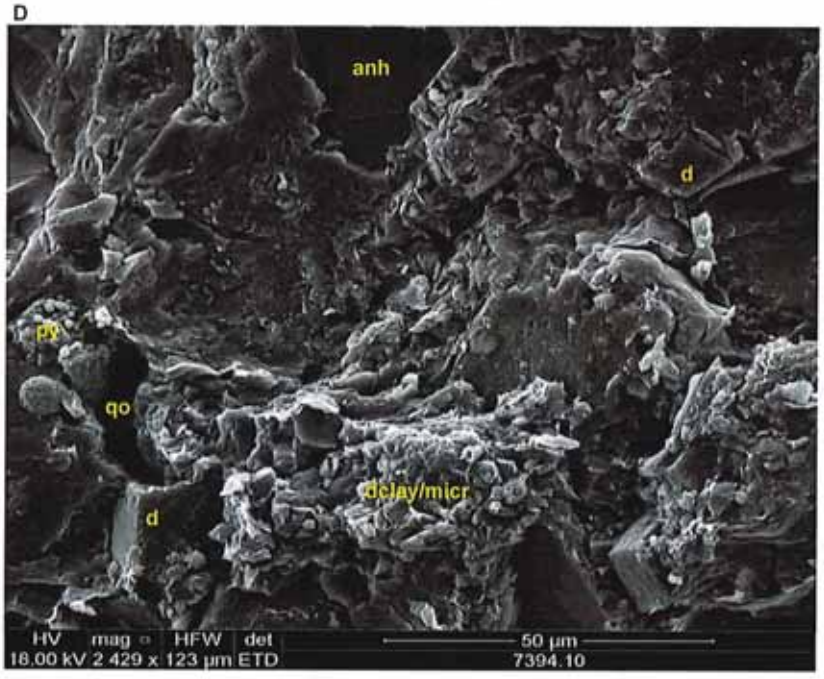

Mineralogy Determined by X-Ray Diffraction

(Weight %)

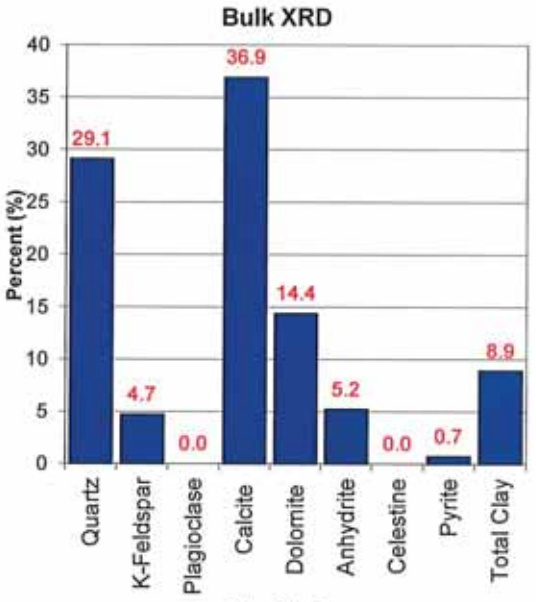

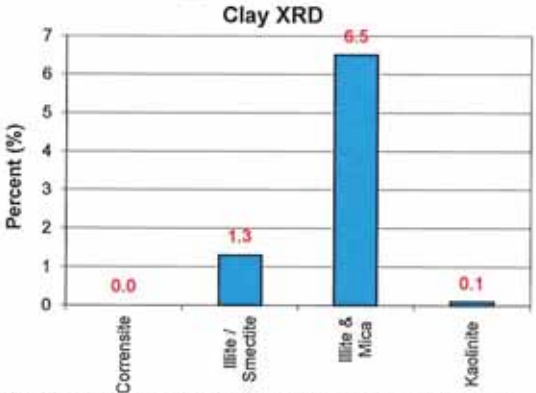

mixed-layer chlorite/smectite contains 50-60% smectite layers

SEM Description

These SEM images highlight the matrix of this argillaceous calcareous sandstone, which is made up of detrital clay and micrite (dclay/micr). Dolomite rhombs (d) partially replace matrix. Other authigenic constituents include anhydrite (anh), pyrite (py), and quartz overgrowths (qo). Most of the porosity comes from micropores associated with the matrix.

Core Lab
RESERVOIR OPTIMIZATION

Relative Abundances:	
Trace	<1%
Minor	1-5%
Moderate	5-10%
Common	10-20%
Abundant	>20%

Core Analysis Data:	
Porosity (%):	6.22
Permeability (md):	0.0183
Gr. Density (g/cc):	2.716
Oil Saturation (%):	27.3
Water Saturation	57.8

PLATE 5

Thin Section Petrography

Company:	**Fidelity E & P**
Well:	**Cane Creek 26-3**
Location:	**Grand Co., Utah**
Depth (ft):	**7395.25**
Unit:	**A**
Dep. Env.:	**Restricted Anoxic Shallow Marine/Subaqueous**

A

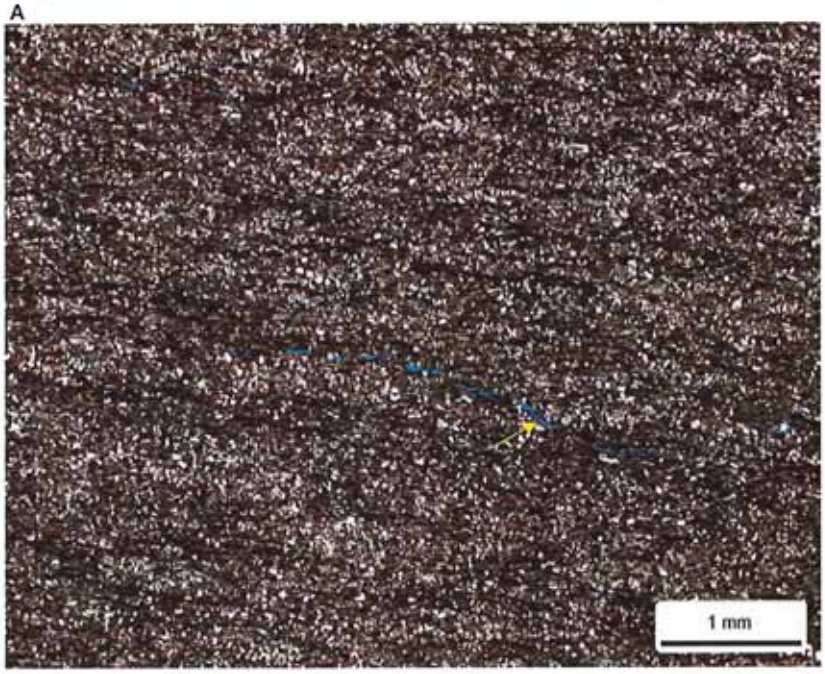

B

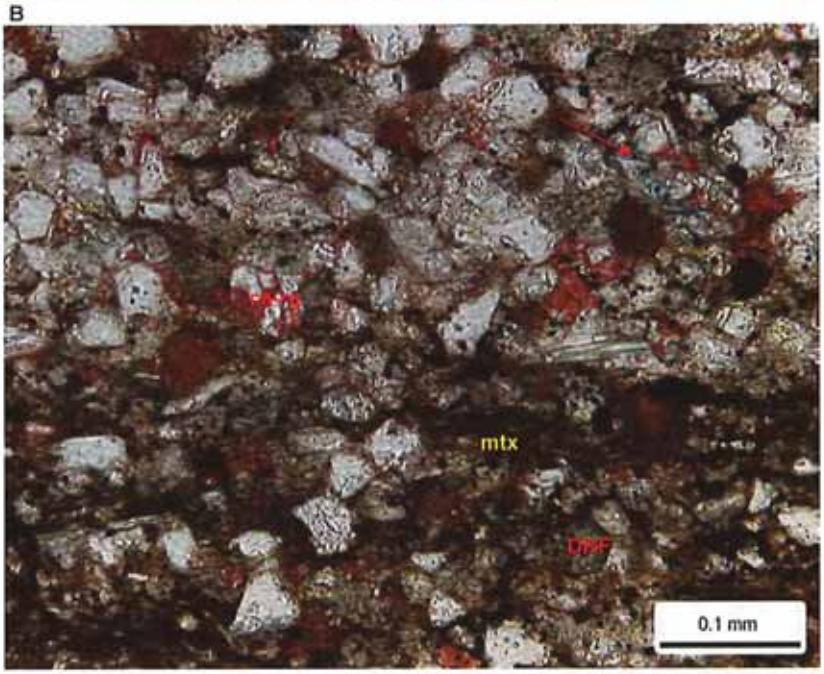

LITHOLOGY AND TEXTURE

Lithology:	Argillaceous Siltstone
Classific. (Folk, 1980):	Feldspathic Litharenite
Grain Size (mm):	0.059 (coarse silt)
Sorting:	well
Structures:	wavy laminated; open microfractures approximately parallel to bedding

Rock Composition (Point-Count)

Framework Grains:

Mono quartz:	34.4	Argillaceous RF:	2.0
Poly quartz:	0.0	Dolomite RF:	8.8
K-Feldspar:	8.0	Micas:	1.2
Plagioclase:	0.4	Heavy minerals:	0.4
Volcanic RF:	1.2	Plant fragments:	4.4
Metamorphic RF:	0.0	Glauconite:	0.0
Limestone RF:	7.6	Rip-up/intraclasts:	0.0

Replaced Grains:

Dolomite RG:	0.0	Pyrite RG:	0.0
Calcite RG:	1.2	Kaolinite RG:	0.0

Detrital Matrix:

Detrital clay:	0.0	Mixed clay/carbonate:	15.2
Organic matrix:	0.0	Dolomitic matrix:	2.8

Pore-filling Authigenic Minerals:

Authigenic clay:	0.8	Dolomite:	0.4
Quartz OG/QA:	2.4	Calcite:	3.2
Kspar OG:	0.0	Anhydrite:	tr
Pyrite:	4.8	Celestine:	0.0
Titanium oxides:	0.0	Halite:	0.0

Pore Types:

Intergranular:	tr	Intragranular:	tr
Fracture:	0.4	Moldic:	0.0

XRD-Whole Rock Mineralogy (Weight %)

Quartz	42.2	Anhydrite	0.0
K-Feldspar	5.2	Celestine	0.0
Plagioclase	0.0	Halite	0.6
Calcite	19.4	Pyrite	2.9
Dolomite	8.6	Total Clay	21.1

Clay Abundance (Weight %)

Corrensite	0.0	Kaolinite	0.2
Illite / Smectite	2.5	Chlorite	2.1
Illite & Mica	16.3		

mixed-layer illite/smectite contains 15-25% smectite layers

Petrographic Description

This argillaceous siltstone contains fine, wavy laminations characterized by variations in grain and matrix concentration. Quartz grains are abundant. Other less common grains include potassium feldspar, limestone rock fragments, dolomite rock fragments (DRF), and calcite replaced grains (ca-rg). The clay and micrite rich matrix (mtx) has been partially replaced by dolomite. Pyrite is associated with the matrix and organic matter. Calcite cement fills some intergranula areas. Intergranular pores and intragranular pores (red arrow) are rare. Open microfractures (yellow arrow) are approximately parallel to bedding

Core Lab

Relative Abundances:

Trace	<1%
Minor	1-5%
Moderate	5-10%
Common	10-20%
Abundant	>20%

Core Analysis Data:

Porosity (%):	11.11
Permeability (md):	0.2205
Gr. Density (g/cc):	2.717
Oil Saturation (%):	25.4
Water Saturation	60.5

PLATE 6

Thin Section Petrography

Company:	**Fidelity E & P**
Well:	**Cane Creek 26-3**
Location:	**Grand Co., Utah**
Depth (ft):	**7397.15**
Unit:	**A**
Dep. Env.:	**Shallow Shelf Salina/Sabkha**

A

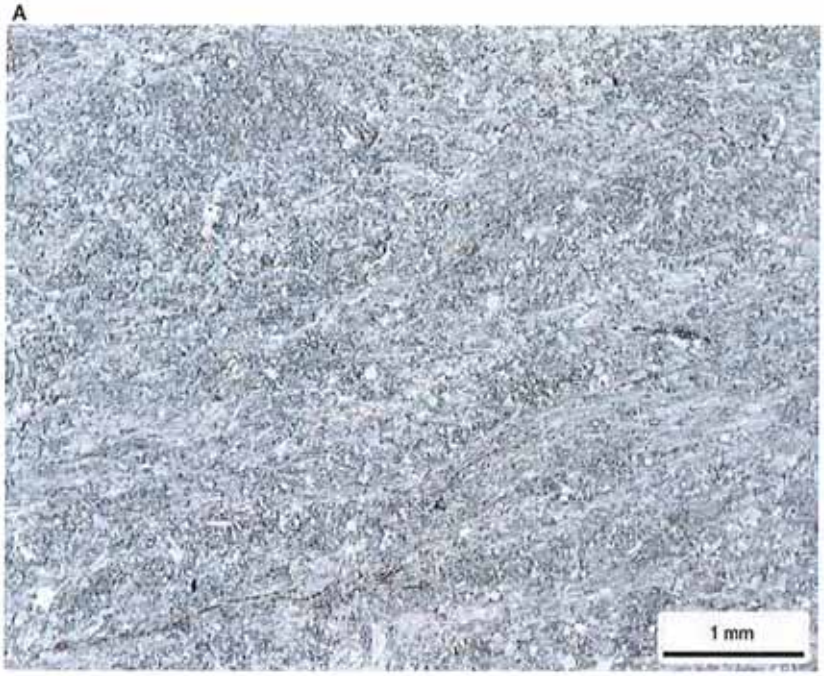

B

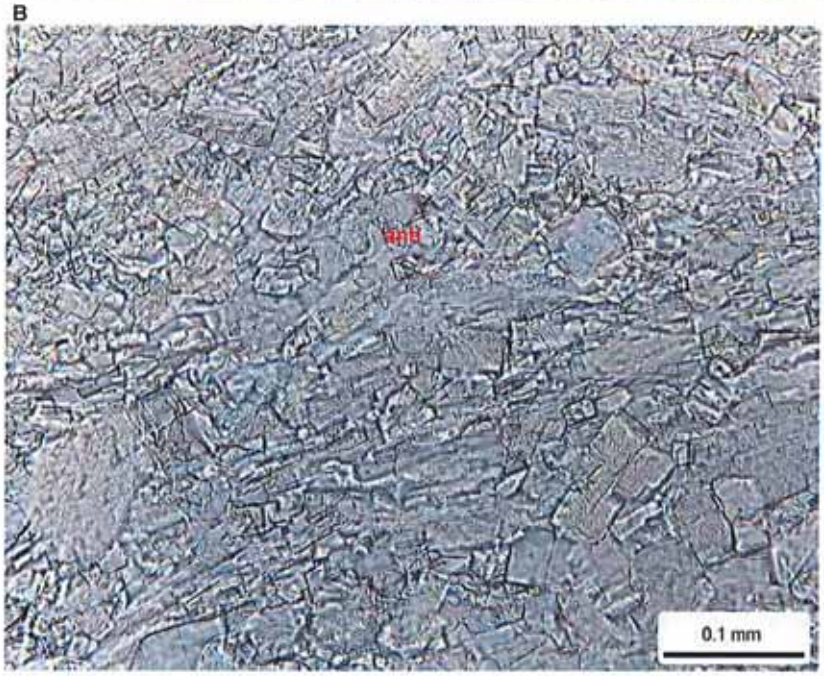

LITHOLOGY AND TEXTURE

Lithology:	Anhydrite
Classific. (Folk, 1980):	n/a
Grain Size (mm):	n/a
Sorting:	n/a
Structures:	none evident

Rock Composition (Point-Count)

Framework Grains:			
Mono quartz:	0.0	Argillaceous RF:	0.0
Poly quartz:	0.0	Chert RF:	0.0
K-Feldspar:	0.0	Micas:	0.0
Plagioclase:	0.0	Heavy minerals:	0.0
Volcanic RF:	0.0	Plant fragments:	0.4
Metamorphic RF:	0.0	Glauconite:	0.0
Limestone RF:	0.0	Rip-up/intraclasts:	0.0
Replaced Grains:			
Dolomite RG:	0.0	Pyrite RG:	0.0
Calcite RG:	0.0	Kaolinite RG:	0.0
Detrital Matrix:			
Detrital clay:	0.0	Micrite matrix:	0.0
Organic matrix:	0.0	Dolomitic matrix:	0.0
Pore-filling Authigenic Minerals:			
Authigenic clay:	0.0	Dolomite:	0.4
Quartz OG/QA:	0.4	Calcite:	0.0
Kspar OG:	0.0	Anhydrite:	98.8
Pyrite:	0.0	Celestine:	0.0
Titanium oxides:	0.0	Halite:	0.0
Pore Types:			
Intergranular:	0.0	Intragranular:	0.0
Fracture:	0.0	Moldic:	0.0

XRD-Whole Rock Mineralogy (Weight %)

Quartz	10.5	Anhydrite	85.8
K-Feldspar	0.0	Celestine	0.0
Plagioclase	0.0	Halite	0.6
Calcite	2.5	Pyrite	0.0
Dolomite	0.0	Total Clay	0.6
Clay Abundance (Weight %)			
Corrensite	0.0	Kaolinite	0.0
Illite / Smectite	0.0	Chlorite	0.0
Illite & Mica	0.6		

Petrographic Description

This sample is made up almost entirely of tightly interlocking, tabular crystals of anhydrite (anh). Traces of micrite remain. Other features (not pictured) include rare patches that have been partially replaced by authigenic quartz, as well as very rare dolomite crystals.

Relative Abundances:

Trace	<1%
Minor	1-5%
Moderate	5-10%
Common	10-20%
Abundant	>20%

Core Analysis Data:

Porosity (%):	0.09
Permeability (md):	0.0007
Gr. Density (g/cc):	2.931
Oil Saturation (%):	6.7
Water Saturation	14.8

Core Lab
RESERVOIR OPTIMIZATION

PLATE 7

Thin Section Petrography

Company:	**Fidelity E & P**
Well:	**Cane Creek 26-3**
Location:	**Grand Co., Utah**
Depth (ft):	**7398.00**
Unit:	**A**
Dep. Env.:	**Shallow Shelf Salina/Sabkha**

A

B

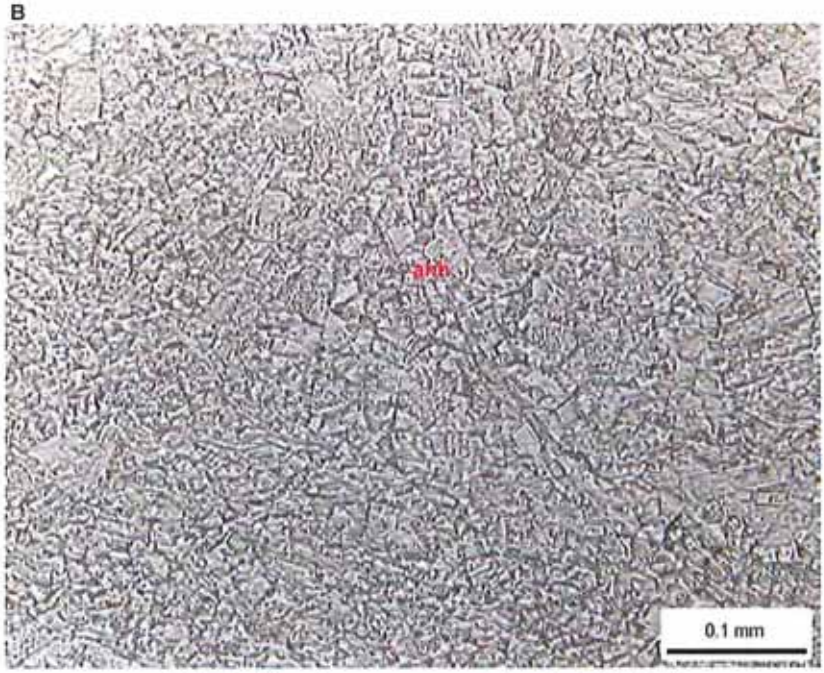

LITHOLOGY AND TEXTURE

Lithology:	Anhydrite
Classific. (Folk, 1980):	n/a
Grain Size (mm):	n/a
Sorting:	n/a
Structures:	none evident

Rock Composition (Point-Count)

Framework Grains:

Mono quartz:	0.0	Argillaceous RF:	0.0
Poly quartz:	0.0	Chert RF:	0.0
K-Feldspar:	0.0	Micas:	0.0
Plagioclase:	0.0	Heavy minerals:	0.0
Volcanic RF:	0.0	Plant fragments:	0.0
Metamorphic RF:	0.0	Glauconite:	0.0
Limestone RF:	0.0	Rip-up/intraclasts:	0.0

Replaced Grains:

Dolomite RG:	0.0	Pyrite RG:	0.0
Calcite RG:	0.0	Kaolinite RG:	0.0

Detrital Matrix:

Detrital clay:	0.0	Micrite matrix:	0.0
Organic matrix:	0.0	Dolomitic matrix:	0.0

Pore-filling Authigenic Minerals:

Authigenic clay:	0.0	Dolomite:	0.0
Quartz OG/QA:	0.0	Calcite:	0.0
Kspar OG:	0.0	Anhydrite:	100.0
Pyrite:	0.0	Celestine:	0.0
Titanium oxides:	0.0	Halite:	0.0

Pore Types:

Intergranular:	0.0	Intragranular:	0.0
Fracture:	0.0	Moldic:	0.0

XRD-Whole Rock Mineralogy (Weight %)

Quartz	1.1	Anhydrite	98.2
K-Feldspar	0.0	Celestine	0.0
Plagioclase	0.0	Halite	0.0
Calcite	0.1	Pyrite	0.0
Dolomite	0.3	Total Clay	0.2

Clay Abundance (Weight %)

Corrensite	0.0	Kaolinite	0.0
Illite / Smectite	0.0	Chlorite	0.0
Illite & Mica	0.2		

Petrographic Description

This entire thin section is made up of interlocking crystals of anhydrite (anh). Traces of quartz, calcite, dolomite, and clay were detected in XRD, but the thin section is essentially pure anhydrite.

Core Lab

Relative Abundances:

Trace	<1%
Minor	1-5%
Moderate	5-10%
Common	10-20%
Abundant	>20%

Core Analysis Data:

Porosity (%):	0.78
Permeability (md):	0.0014
Gr. Density (g/cc):	2.937
Oil Saturation (%):	8.4
Water Saturation	24.8

PLATE 8

Thin Section Petrography

Company:	**Fidelity E & P**
Well:	**Cane Creek 26-3**
Location:	**Grand Co., Utah**
Depth (ft):	**7400.15**
Unit:	**A**
Dep. Env.:	**Restricted Anoxic Shallow Marine/Subaqueous**

A

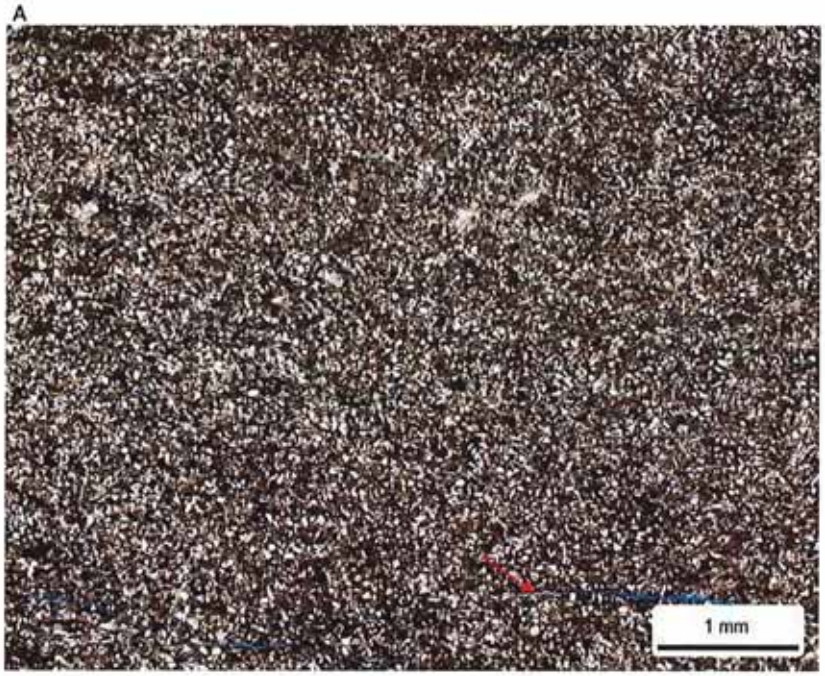

B

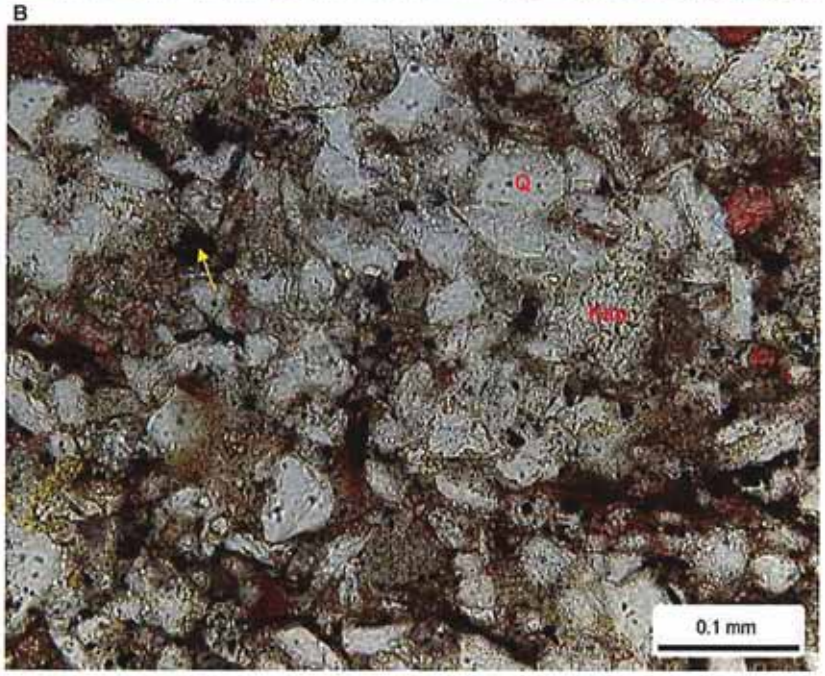

LITHOLOGY AND TEXTURE

Lithology:	Argillaceous Sandstone
Classific. (Folk, 1980):	Feldspathic Litharenite
Grain Size (mm):	0.070 (L. very fine sand)
Sorting:	well
Structures:	discontinuous wavy laminae; bioturbated; open microfractures

Rock Composition (Point-Count)

Framework Grains:			
Mono quartz:	44.0	Argillaceous RF:	1.6
Poly quartz:	0.0	Dolomite RF:	5.2
K-Feldspar:	10.0	Micas:	1.6
Plagioclase:	0.0	Heavy minerals:	tr
Volcanic RF:	1.6	Plant fragments:	1.6
Metamorphic RF:	0.0	Glauconite:	0.0
Limestone RF:	3.6	Rip-up/intraclasts:	0.0
Replaced Grains:			
Dolomite RG:	0.0	Pyrite RG:	0.0
Calcite RG:	0.4	Kaolinite RG:	0.0
Detrital Matrix:			
Detrital clay:	0.0	Mixed clay/carbonate:	16.8
Organic matrix:	0.0	Dolomitic matrix:	1.6
Pore-filling Authigenic Minerals:			
Authigenic clay:	1.2	Dolomite:	1.2
Quartz OG/QA:	2.4	Calcite:	1.2
Kspar OG:	0.8	Anhydrite:	0.0
Pyrite:	5.2	Celestine:	0.0
Titanium oxides:	0.0	Halite:	tr
Pore Types:			
Intergranular:	tr	Intragranular:	0.0
Fracture:	0.0	Moldic:	0.0

XRD-Whole Rock Mineralogy (Weight %)

Quartz	51.5	Anhydrite	1.1
K-Feldspar	6.7	Celestine	0.0
Plagioclase	0.0	Halite	1.3
Calcite	11.9	Pyrite	3.0
Dolomite	4.9	Total Clay	19.7
Clay Abundance (Weight %)			
Corrensite	0.0	Kaolinite	0.0
Illite / Smectite	2.5	Chlorite	1.4
Illite & Mica	15.8		

mixed-layer illite/smectite contains 15-25% smectite layers

Petrographic Description

This very fine-grained argillaceous sandstone contains discontinuous wavy laminae that have been disrupted by bioturbation. Open microfractures are oriented roughly parallel to bedding, and some are partially filled with halite (red arrow). Quartz (Q) and potassium feldspar (Ksp, stained yellow) are the most abundant framework grains. The detrital clay matrix has been partially replaced by dolomite. Quartz overgrowths are noted around some detrital quartz grains and pyrite (yellow arrow) is associated with the matrix. Intergranular pores are rare.

Core Lab
RESERVOIR OPTIMIZATION

Relative Abundances:	
Trace	<1%
Minor	1-5%
Moderate	5-10%
Common	10-20%
Abundant	>20%

Core Analysis Data:	
Porosity (%):	13.58
Permeability (md):	13.0125
Gr. Density (g/cc):	2.704
Oil Saturation (%):	29.1
Water Saturation	59.5

PLATE 9

Thin Section Petrography

Company:	**Fidelity E & P**
Well:	**Cane Creek 26-3**
Location:	**Grand Co., Utah**
Depth (ft):	**7401.40**
Unit:	**A**
Dep. Env.:	**Shallow Marine/Subaqueous**

A

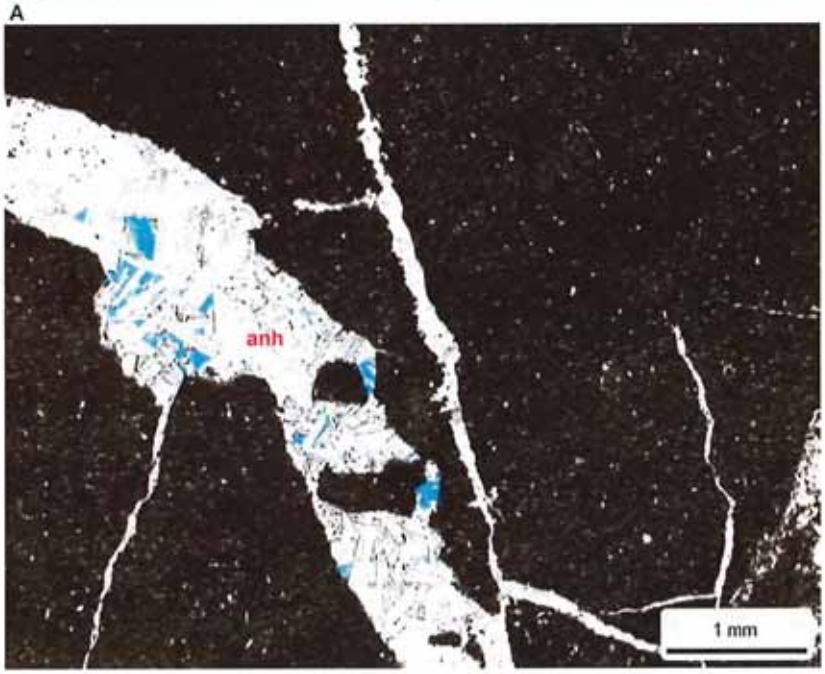

B

LITHOLOGY AND TEXTURE

Lithology:	Anhydritic Dolostone
Classific. (Dunham, 1962):	Dolomudstone
Grain Size (mm):	n/a
Sorting:	n/a
Structures:	anhydrite-filled microfractures; burrowed

Rock Composition (Point-Count)

Framework Grains:

Mono quartz:	2.8	Argillaceous RF:	0.0
Poly quartz:	0.0	Chert RF:	0.0
K-Feldspar:	0.4	Micas:	0.4
Plagioclase:	0.0	Heavy minerals:	0.0
Volcanic RF:	0.0	Plant fragments:	1.2
Metamorphic RF:	0.0	Glauconite:	0.0
Peloid-dolomite:	2.4	Rip-up/intraclasts:	2.0

Replaced Grains:

Dolomite RG:	0.0	Pyrite RG:	0.0
Calcite RG:	0.0	Kaolinite RG:	0.0

Detrital Matrix:

Detrital clay:	0.0	Micrite matrix:	0.0
Organic matrix:	0.0	Dolomitic matrix:	63.2

Pore-filling Authigenic Minerals:

Authigenic clay:	0.0	Dolomite:	0.0
Quartz OG/QA:	0.0	Calcite:	0.0
Kspar OG:	0.0	Anhydrite:	24.4
Pyrite:	2.4	Celestine:	0.0
Titanium oxides:	0.0	Halite:	0.0

Pore Types:

Intergranular:	0.0	Intracrystal:	0.8
Fracture:	0.0	Moldic:	0.0

XRD-Whole Rock Mineralogy (Weight %)

Quartz	4.7	Anhydrite	26.4
K-Feldspar	0.8	Celestine	4.0
Plagioclase	0.0	Halite	1.0
Calcite	0.0	Pyrite	0.0
Dolomite	60.5	Total Clay	2.6

Clay Abundance (Weight %)

Corrensite	0.0	Kaolinite	0.0
Illite / Smectite	0.3	Chlorite	0.2
Illite & Mica	2.1		

mixed-layer illite/smectite contains 15-25% smectite layers

Petrographic Description

This dolostone is burrowed, and contains anhydrite-filled microfractures (anh) that cross-cut the sample. Peloids and silt-size quartz are scattered throughout the dolomitic matrix. Pyrite framboids (py) are minor in abundance. Secondary intracrystal pores (swc) have formed within partially dissolved anhydrite.

Core Lab
RESERVOIR OPTIMIZATION

Relative Abundances:

Trace	<1%
Minor	1-5%
Moderate	5-10%
Common	10-20%
Abundant	>20%

Core Analysis Data:

Porosity (%):	1.21
Permeability (md):	0.0011
Gr. Density (g/cc):	2.925
Oil Saturation (%):	35.1
Water Saturation	21.0

PLATE 10

Thin Section Petrography

Company:	**Fidelity E & P**
Well:	**Cane Creek 26-3**
Location:	**Grand Co., Utah**
Depth (ft):	**7403.15**
Unit:	**A**
Dep. Env.:	**Shallow Shelf/Salina/Sabkha-proximal**

A

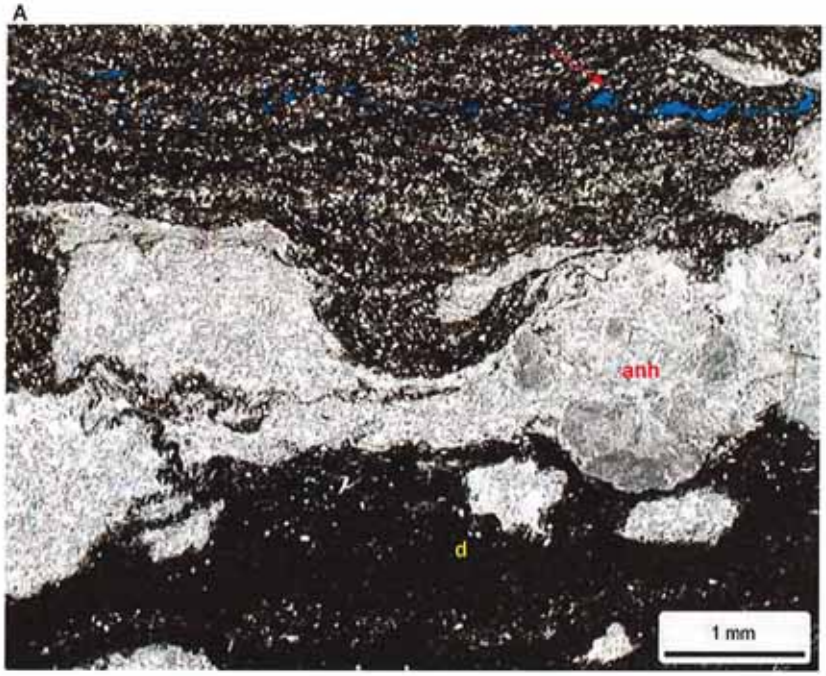

B

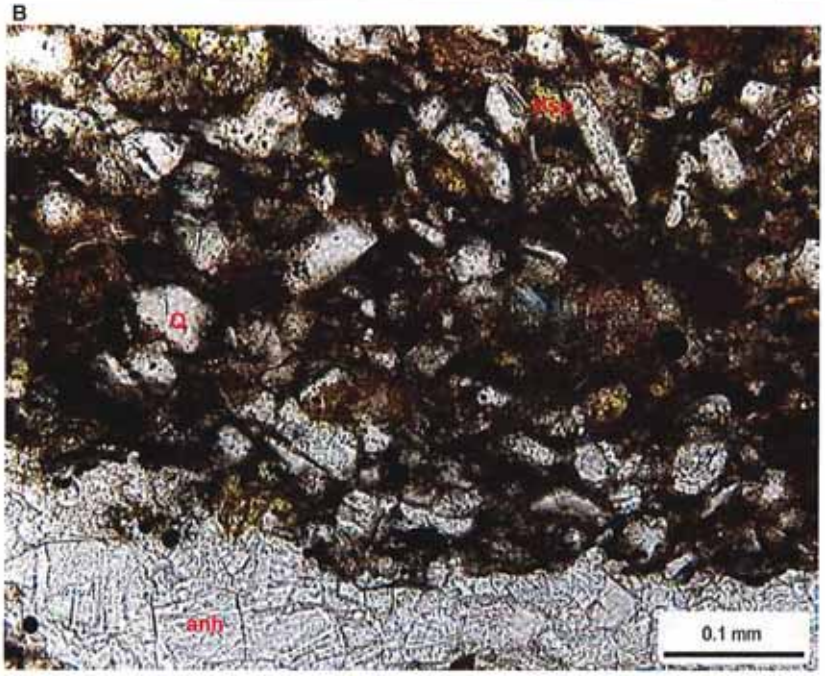

Relative Abundances:

Trace	<1%
Minor	1-5%
Moderate	5-10%
Common	10-20%
Abundant	>20%

Core Analysis Data:

Porosity (%):	3.64
Permeability (md):	0.0214
Gr. Density (g/cc):	2.884
Oil Saturation (%):	60.4
Water Saturation	22.2

LITHOLOGY AND TEXTURE

Lithology:	Anhydritic Silty Dolostone
Classific. (Folk, 1980):	n/a
Grain Size (mm):	n/a
Sorting:	n/a
Structures:	wavy silty laminae; anhydrite nodules; anhydrite-filled microfractures

Rock Composition (Point-Count)

Framework Grains:

Mono quartz:	13.6	Argillaceous RF:	0.8
Poly quartz:	0.0	Dolomite RF:	1.2
K-Feldspar:	4.4	Micas:	0.4
Plagioclase:	0.0	Heavy minerals:	0.0
Volcanic RF:	0.0	Plant fragments:	2.4
Metamorphic RF:	0.0	Glauconite:	0.0
Peloid-dolomite:	0.8	Rip-up/intraclasts:	0.0

Replaced Grains:

Dolomite RG:	0.0	Pyrite RG:	0.0
Calcite RG:	0.0	Kaolinite RG:	0.0

Detrital Matrix:

Detrital clay:	4.4	Micrite matrix:	0.0
Organic matrix:	0.0	Dolomitic matrix:	47.2

Pore-filling Authigenic Minerals:

Authigenic clay:	0.0	Dolomite:	0.0
Quartz OG/QA:	0.0	Calcite:	0.0
Kspar OG:	0.0	Anhydrite:	21.6
Pyrite:	2.8	Celestine:	0.0
Titanium oxides:	0.0	Halite:	0.0

Pore Types:

Intergranular:	0.0	Intracrystal:	0.4
Fracture:	0.0	Moldic:	0.0

XRD-Whole Rock Mineralogy (Weight %)

Quartz	4.6	Anhydrite	66.1
K-Feldspar	0.7	Celestine	0.0
Plagioclase	0.0	Halite	0.0
Calcite	0.0	Pyrite	0.4
Dolomite	24.9	Total Clay	3.2

Clay Abundance (Weight %)

Corrensite	0.0	Kaolinite	0.0
Illite / Smectite	0.4	Chlorite	0.3
Illite & Mica	2.5		

mixed-layer illite/smectite contains 15-25% smectite layers

Petrographic Description

There is a lot of variation within this thin section of an anhydritic silty dolostone. Anhydrite nodules (anh) are concentrated within laminae. Silt to very fine sand-size grains are locally abundant (upper portion of Photo A) and sparse in other areas (lower part of Photo A). Grains include abundant quartz (Q) and minor potassium feldspar (Ksp, stained yellow). Organic matter and detrital clay are concentrated in the silty zones. Other zones are extensively replaced by dolomite (d). Rare discontinuous anhydrite-filled microfractures (not pictured) are oriented perpendicular to bedding. It is unclear if the microfracture in Photo A (red arrow) is natural or induced.

PLATE 11

Thin Section Petrography

Company:	Fidelity E & P
Well:	Cane Creek 26-3
Location:	Grand Co., Utah
Depth (ft):	7404.00
Unit:	A
Dep. Env.:	Shallow Shelf/Salina/Sabkha-proximal

A

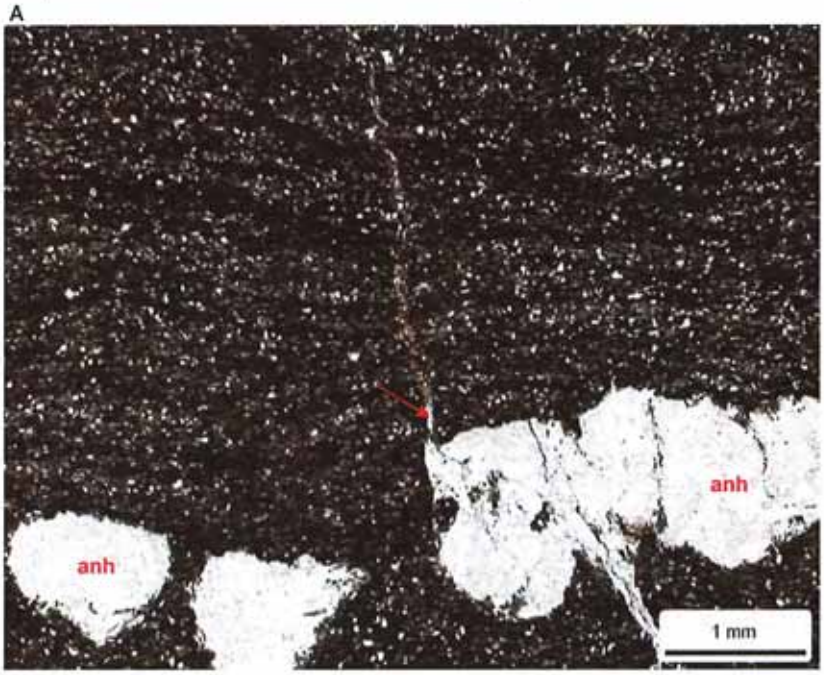

B

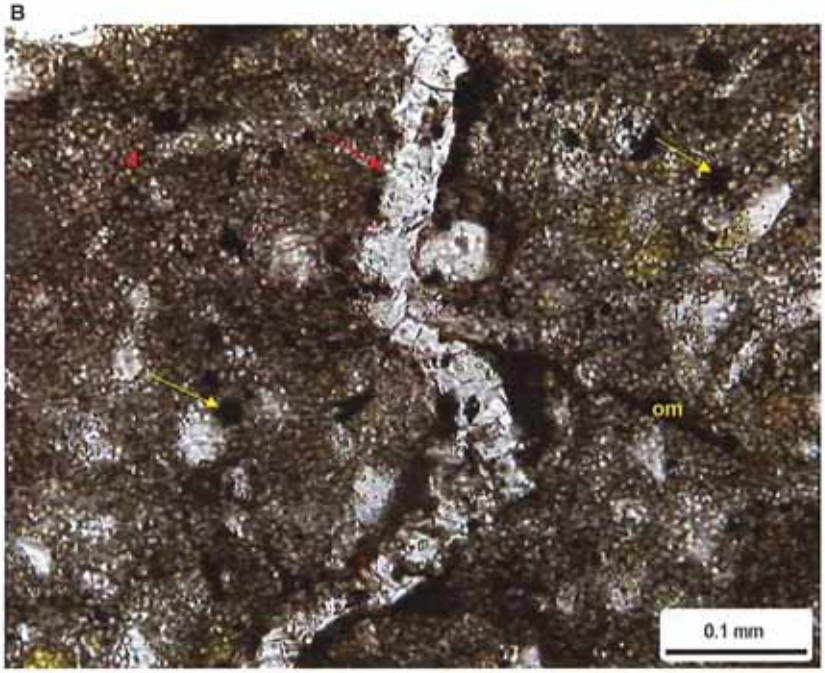

LITHOLOGY AND TEXTURE

Lithology:	Anhydritic Silty Dolostone
Classific. (Folk, 1980):	n/a
Grain Size (mm):	n/a
Sorting:	n/a
Structures:	wavy laminae; anhydrite-filled microfractures and nodules

Rock Composition (Point-Count)

Framework Grains:

Mono quartz:	12.0	Argillaceous RF:	0.0
Poly quartz:	0.0	Dolomite RF:	6.0
K-Feldspar:	1.6	Micas:	1.2
Plagioclase:	0.0	Heavy minerals:	0.0
Volcanic RF:	0.0	Plant fragments:	1.6
Metamorphic RF:	0.0	Glauconite:	0.0
Peloid-dolomite:	2.8	Rip-up/intraclasts:	0.0

Replaced Grains:

Dolomite RG:	0.0	Pyrite RG:	0.0
Calcite RG:	0.0	Kaolinite RG:	0.0

Detrital Matrix:

Detrital clay:	0.0	Micrite matrix:	0.0
Organic matrix:	0.0	Dolomitic matrix:	53.6

Pore-filling Authigenic Minerals:

Authigenic clay:	0.0	Dolomite:	0.0
Quartz OG/QA:	0.0	Calcite:	0.0
Kspar OG:	0.0	Anhydrite:	16.8
Pyrite:	4.4	Celestine:	0.0
Titanium oxides:	0.0	Halite:	0.0

Pore Types:

Intergranular:	0.0	Intragranular:	0.0
Fracture:	0.0	Moldic:	0.0

XRD-Whole Rock Mineralogy (Weight %)

Quartz	8.8	Anhydrite	39.2
K-Feldspar	0.6	Celestine	0.0
Plagioclase	0.0	Halite	0.0
Calcite	0.0	Pyrite	0.4
Dolomite	45.4	Total Clay	5.5

Clay Abundance (Weight %)

Corrensite	0.0	Kaolinite	0.0
Illite / Smectite	1.0	Chlorite	0.3
Illite & Mica	4.2		

mixed-layer illite/smectite contains 15-25% smectite layers

Petrographic Description

This silty dolostone contains anhydrite nodules (anh) and anhydrite cemented microfractures (red arrows). Silt-size detrital grains include common quartz and minor potassium feldspar and muscovite. Dolomitic peloids and elongate fragments of organic matter (om) are also observed in minor amounts. Very finely crystalline dolomite (d) replaces matrix. Pyrite framboids (yellow arrows) are dispersed throughout the matrix.

Core Lab

Relative Abundances:

Trace	<1%
Minor	1-5%
Moderate	5-10%
Common	10-20%
Abundant	>20%

Core Analysis Data:

Porosity (%):	4.40
Permeability (md):	0.0799
Gr. Density (g/cc):	2.859
Oil Saturation (%):	39.1
Water Saturation	44.4

PLATE 12

Thin Section Petrography

Company:	**Fidelity E & P**
Well:	**Cane Creek 26-3**
Location:	**Grand Co., Utah**
Depth (ft):	**7406.00**
Unit:	**A**
Dep. Env.:	**Restricted Anoxic Shallow Marine/Subaqueous**

A

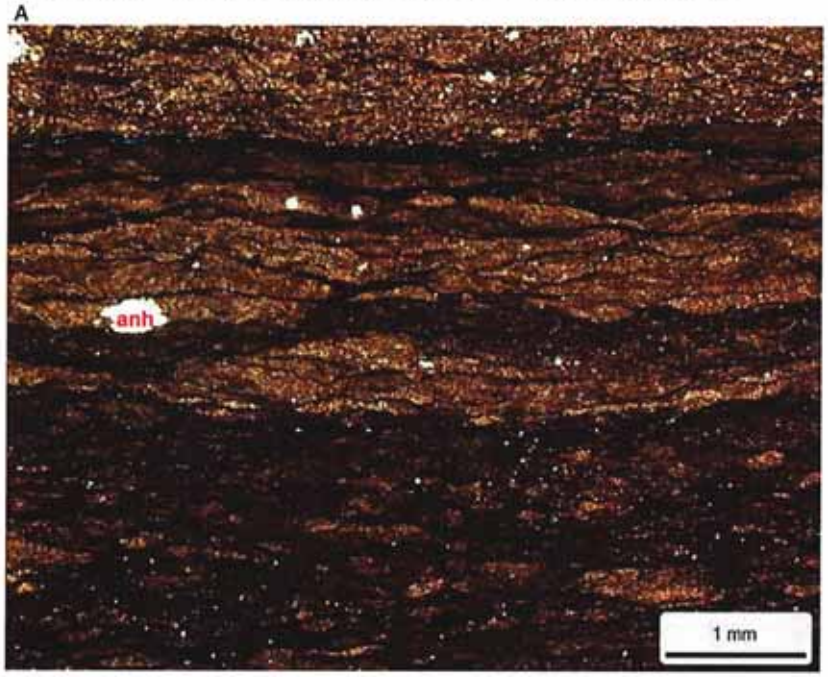

B

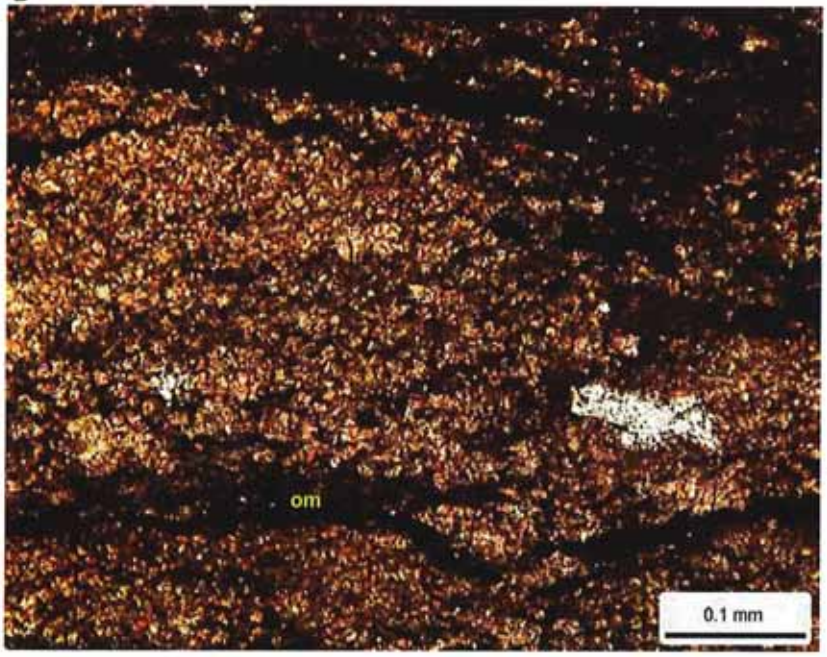

LITHOLOGY AND TEXTURE

Lithology:	Organic-Rich Limestone
Classific. (Dunham, 1962):	Lime Mudstone
Grain Size (mm):	n/a
Sorting:	n/a
Structures:	microstylolites; open microfractures

Rock Composition (Point-Count)

Framework Grains:

Mono quartz:	0.8	Argillaceous RF:	0.0
Poly quartz:	0.0	Chert RF:	0.0
K-Feldspar:	0.0	Micas:	0.0
Plagioclase:	0.0	Heavy minerals:	0.0
Volcanic RF:	0.0	Plant fragments:	0.0
Metamorphic RF:	0.0	Glauconite:	0.0
Limestone RF:	0.0	Rip-up/intraclasts:	0.0

Replaced Grains:

Dolomite RG:	0.0	Pyrite RG:	0.0
Calcite RG:	0.0	Kaolinite RG:	0.0

Detrital Matrix:

Detrital clay:	0.0	Micrite matrix:	72.0
Organic matrix:	23.2	Dolomitic matrix:	0.0

Pore-filling Authigenic Minerals:

Authigenic clay:	0.0	Dolomite:	0.0
Quartz OG/QA:	0.0	Calcite:	0.0
Kspar OG:	0.0	Anhydrite:	1.2
Pyrite:	2.8	Celestine:	0.0
Titanium oxides:	0.0	Halite:	0.0

Pore Types:

Intergranular:	0.0	Intragranular:	0.0
Fracture:	0.0	Moldic:	0.0

XRD-Whole Rock Mineralogy (Weight %)

Quartz	10.1	Anhydrite	5.4
K-Feldspar	0.0	Celestine	0.0
Plagioclase	0.0	Halite	0.0
Calcite	77.6	Pyrite	1.5
Dolomite	1.2	Total Clay	4.2

Clay Abundance (Weight %)

Corrensite	0.0	Kaolinite	0.0
Illite / Smectite	0.0	Chlorite	0.0
Illite & Mica	4.2		

Petrographic Description

This lime mudstone contains numerous microstylolites which gives the sample a nodular texture. Organic matter (om) is concentrated along the microstylolites and within some parts of the matrix. Most of the matrix consists of micrite, which has neomorphosed to microspar. Scattered quartz grains and patches of anhydrite cement (anh) are rare.

Core Lab
RESERVOIR OPTIMIZATION

Relative Abundances:

Trace	<1%
Minor	1-5%
Moderate	5-10%
Common	10-20%
Abundant	>20%

Core Analysis Data:

Porosity (%):	5.46
Permeability (md):	0.4015
Gr. Density (g/cc):	2.628
Oil Saturation (%):	41.4
Water Saturation	25.9

PLATE 13

Thin Section Petrography

Company:	**Fidelity E & P**
Well:	**Cane Creek 26-3**
Location:	**Grand Co., Utah**
Depth (ft):	**7407.65**
Unit:	**A**
Dep. Env.:	**Shallow Shelf Salina/Sabkha**

A

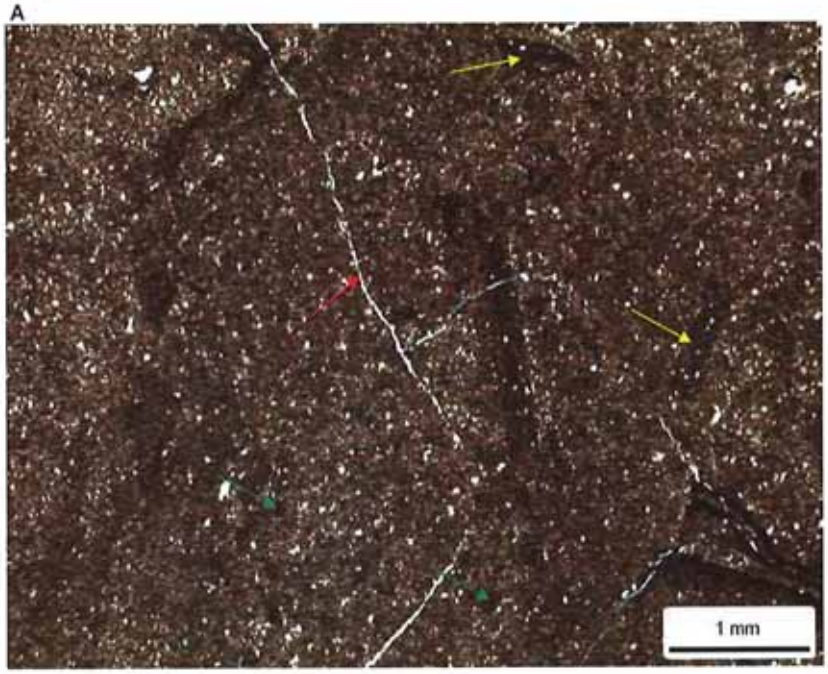

B

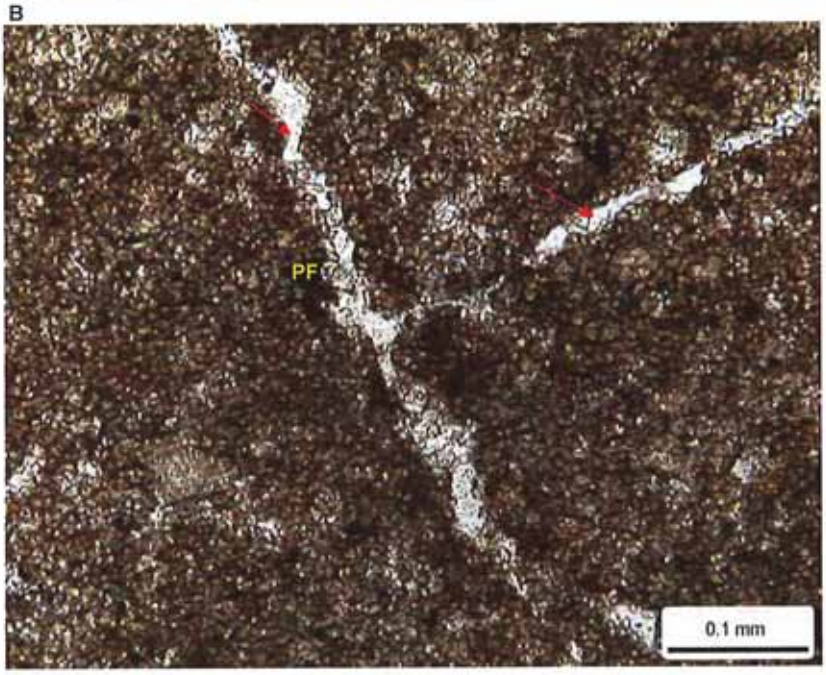

LITHOLOGY AND TEXTURE

Lithology:	Dolostone
Classific. (Dunham, 1962):	Intraclast Dolowackestone
Grain Size (mm):	n/a
Sorting:	n/a
Structures:	halite and dolomite cemented microfractures; microstylolites; bioturbated

Rock Composition (Point-Count)

Framework Grains:

Mono quartz:	1.6	Argillaceous RF:	0.0
Poly quartz:	0.0	Dolomite RF:	0.4
K-Feldspar:	tr	Micas:	0.0
Plagioclase:	0.0	Heavy minerals:	0.0
Volcanic RF:	0.0	Plant fragments:	2.4
Metamorphic RF:	0.0	Glauconite:	0.0
Peloid-dolomite:	6.8	Rip-up/intraclasts:	15.2

Replaced Grains:

Dolomite RG:	0.0	Pyrite RG:	0.0
Calcite RG:	0.0	Kaolinite RG:	0.0

Detrital Matrix:

Detrital clay:	0.0	Micrite matrix:	0.0
Organic matrix:	0.0	Dolomitic matrix:	65.2

Pore-filling Authigenic Minerals:

Authigenic clay:	0.0	Dolomite:	0.0
Quartz OG/QA:	0.0	Calcite:	0.0
Kspar OG:	0.0	Anhydrite:	4.4
Pyrite:	1.2	Celestine:	0.0
Titanium oxides:	0.0	Halite:	2.8

Pore Types:

Intergranular:	0.0	Intragranular:	tr
Fracture:	0.0	Intercrystal:	tr

XRD-Whole Rock Mineralogy (Weight %)

Quartz	4.2	Anhydrite	81.0
K-Feldspar	0.0	Celestine	0.6
Plagioclase	0.0	Halite	0.6
Calcite	0.0	Pyrite	0.4
Dolomite	12.7	Total Clay	0.4

Clay Abundance (Weight %)

Corrensite	0.0	Kaolinite	0.0
Illite / Smectite	0.0	Chlorite	0.0
Illite & Mica	0.4		

Petrographic Description

Numerous microfractures cross-cut this dolostone. A few of the microfractures remain open, but most are filled with halite (red arrows) and rarely dolomite. Intraclasts (yellow arrows) are common in this dolowackestone, and have random orientations. Peloids (green arrows) are moderate in abundance. Plant fragments (PF) are dispersed throughout the dolomitic matrix. Intercrystal micropores (faint blue, Photo B) are noted between dolomite rhombs. XRD and thin section point-count percentages of anhydrite an dolomite differ due to sample heterogeneity. Core analysis grain density is between that of pure dolomite (2.86 g/cc) and pure anhydrite (2.89 g/cc), suggesting both minerals are present in significant quantities.

Core Lab

Relative Abundances:

Trace	<1%
Minor	1-5%
Moderate	5-10%
Common	10-20%
Abundant	>20%

Core Analysis Data:

Porosity (%):	3.06
Permeability (md):	0.0075
Gr. Density (g/cc):	2.909
Oil Saturation (%):	37.7
Water Saturation	12.3

PLATE 14

Thin Section Petrography

Company:	**Fidelity E & P**
Well:	**Cane Creek 26-3**
Location:	**Grand Co., Utah**
Depth (ft):	**7410.00**
Unit:	**A**
Dep. Env.:	**Shallow Marine/Subaqueous**

A

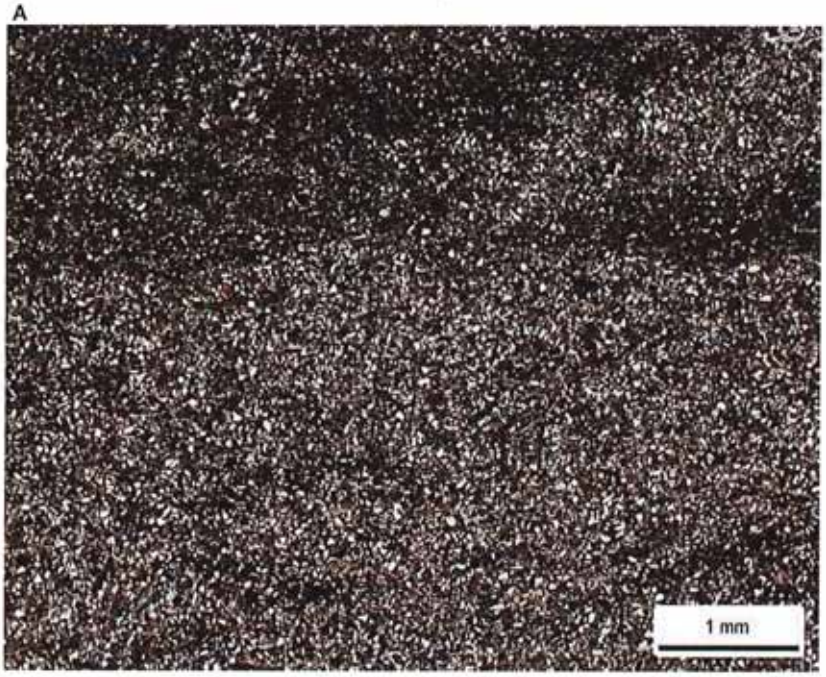

B

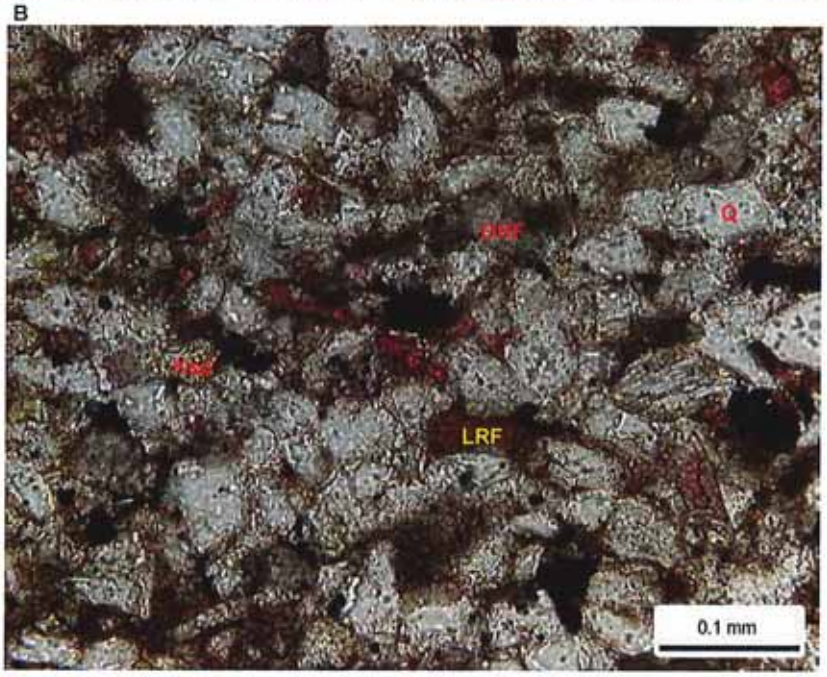

LITHOLOGY AND TEXTURE

Lithology:	Argillaceous Sandstone
Classific. (Folk, 1980):	Feldspathic Litharenite
Grain Size (mm):	0.074 (L. very fine sand)
Sorting:	well
Structures:	bioturbated; open microfractures

Rock Composition (Point-Count)

Framework Grains:

Mono quartz:	47.6	Argillaceous RF:	0.4
Poly quartz:	0.0	Dolomite RF:	5.6
K-Feldspar:	8.0	Micas:	0.8
Plagioclase:	0.4	Heavy minerals:	tr
Volcanic RF:	1.6	Plant fragments:	0.8
Metamorphic RF:	0.0	Glauconite:	0.0
Limestone RF:	5.2	Rip-up/intraclasts:	0.0

Replaced Grains:

Dolomite RG:	0.0	Pyrite RG:	0.0
Calcite RG:	0.4	Kaolinite RG:	0.0

Detrital Matrix:

Detrital clay:	0.0	Mixed clay/carbonate:	14.8
Organic matrix:	0.0	Dolomitic matrix:	1.6

Pore-filling Authigenic Minerals:

Authigenic clay:	0.4	Dolomite:	1.2
Quartz OG/QA:	3.2	Calcite:	1.2
Kspar OG:	0.4	Anhydrite:	0.8
Pyrite:	5.6	Celestine:	0.0
Titanium oxides:	tr	Halite:	tr

Pore Types:

Intergranular:	0.0	Intragranular:	0.0
Fracture:	0.0	Moldic:	0.0

XRD-Whole Rock Mineralogy (Weight %)

Quartz	53.3	Anhydrite	1.0
K-Feldspar	9.0	Celestine	0.0
Plagioclase	0.0	Halite	0.2
Calcite	10.1	Pyrite	1.9
Dolomite	7.6	Total Clay	17.0

Clay Abundance (Weight %)

Corrensite	0.0	Kaolinite	0.0
Illite / Smectite	2.2	Chlorite	1.2
Illite & Mica	13.6		

mixed-layer illite/smectite contains 15-25% smectite layers

Petrographic Description

This very fine-grained, well sorted argillaceous sandstone is bioturbated. Framework grains are mostly quartz (Q). Potassium feldspar (Ksp), dolomite rock fragments (DRF), and limestone rock fragments (LRF) are moderate in abundance. A minor amount of the detrital clay matrix has been replaced by dolomite. Pyrite is associated with the matrix. Quartz overgrowths rim some detrital quartz grains.

Core Lab
RESERVOIR OPTIMIZATION

Relative Abundances:

Trace	<1%
Minor	1-5%
Moderate	5-10%
Common	10-20%
Abundant	>20%

Core Analysis Data:

Porosity (%):	n/a
Permeability (md):	n/a
Gr. Density (g/cc):	n/a
Oil Saturation (%):	n/a
Water Saturation	n/a

PLATE 14

Scanning Electron Microscopy

Company: Fidelity E & P
Well: Cane Creek 26-3
Location: Grand Co., Utah
Depth (ft): 7410.00
Unit: A
Dep. Env.: Shallow Marine/Subaqueous

LITHOLOGY
Argillaceous Sandstone

C

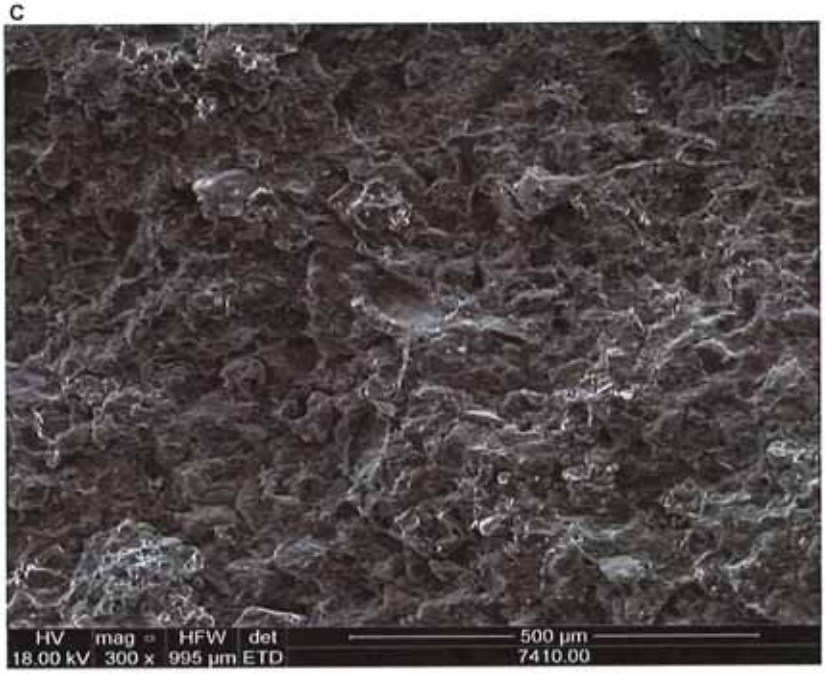

D

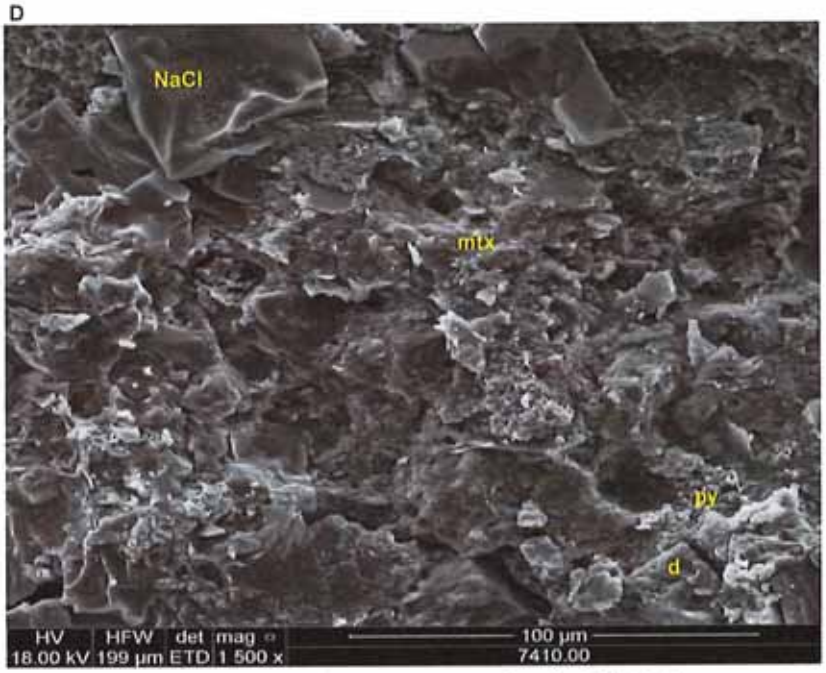

Mineralogy Determined by X-Ray Diffraction
(Weight %)

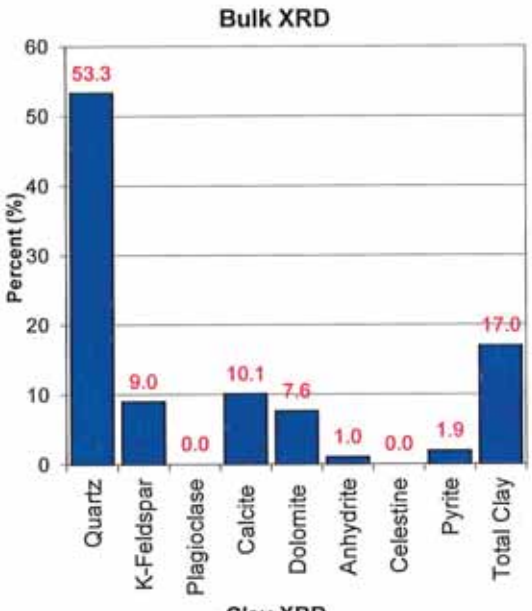

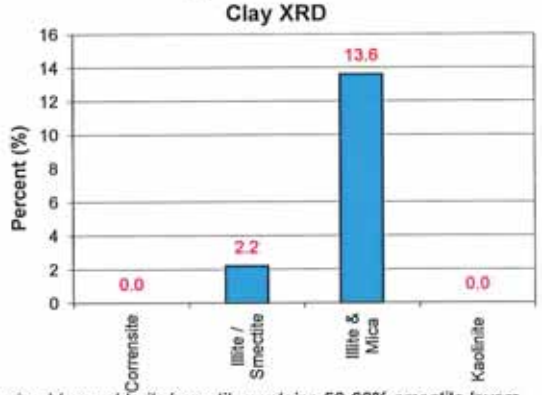

mixed-layer chlorite/smectite contains 50-60% smectite layers

SEM Description

Salt crystals (NaCl) are observed in the SEM piece of this argillaceous sandstone. The matrix (mtx) is rich in detrital clay and micrite. Dolomite (d) and pyrite (py) are also observed.

Core Lab

Relative Abundances:

Trace	<1%
Minor	1-5%
Moderate	5-10%
Common	10-20%
Abundant	>20%

Core Analysis Data:

Porosity (%):	n/a
Permeability (md):	n/a
Gr. Density (g/cc):	n/a
Oil Saturation (%):	n/a
Water Saturation	n/a

PLATE 15

Thin Section Petrography

Company:	**Fidelity E & P**
Well:	**Cane Creek 26-3**
Location:	**Grand Co., Utah**
Depth (ft):	**7412.15**
Unit:	**A**
Dep. Env.:	**Shallow Marine/Subaqueous**

A

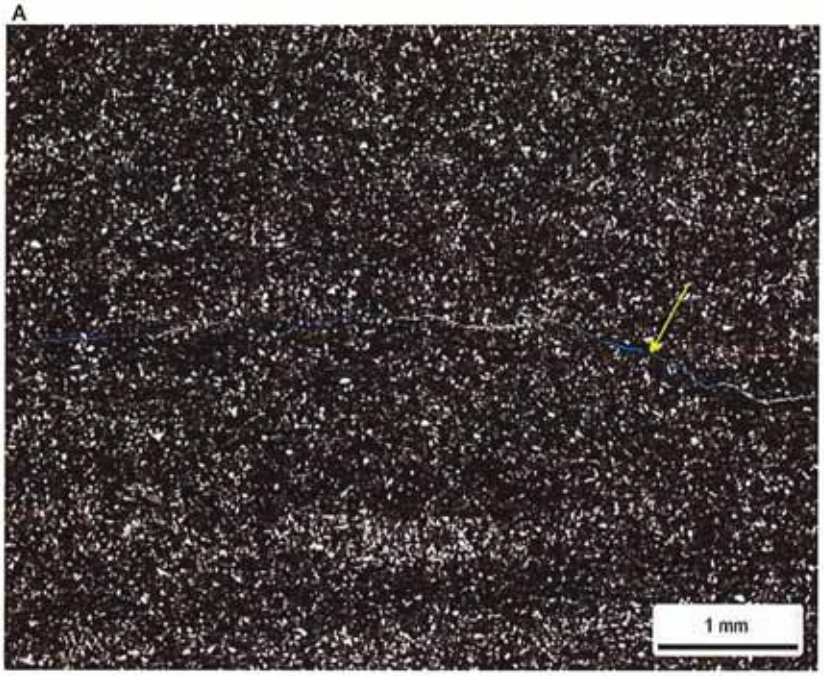

B

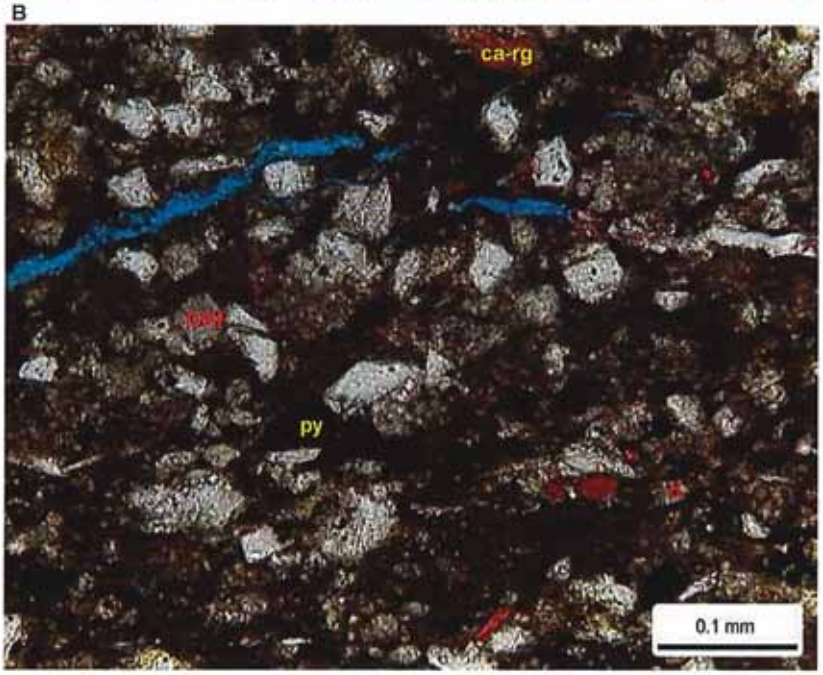

LITHOLOGY AND TEXTURE

Lithology:	Dolomitic Argill. Siltstone
Classific. (Folk, 1980):	Litharenite
Grain Size (mm):	0.060 (coarse silt)
Sorting:	well
Structures:	bioturbated; open microfractures

Rock Composition (Point-Count)

Framework Grains:			
Mono quartz:	28.0	Argillaceous RF:	0.8
Poly quartz:	tr	Dolomite RF:	18.4
K-Feldspar:	6.4	Micas:	1.2
Plagioclase:	0.0	Heavy minerals:	0.0
Volcanic RF:	1.2	Plant fragments:	2.0
Metamorphic RF:	0.0	Glauconite:	0.0
Limestone RF:	2.0	Rip-up/intraclasts:	0.0
Replaced Grains:			
Dolomite RG:	0.0	Pyrite RG:	0.0
Calcite RG:	1.2	Kaolinite RG:	0.0
Detrital Matrix:			
Detrital clay:	0.0	Mixed clay/carbonate:	7.6
Organic matrix:	5.2	Dolomitic matrix:	17.6
Pore-filling Authigenic Minerals:			
Authigenic clay:	0.0	Dolomite:	0.4
Quartz OG/QA:	0.4	Calcite:	1.2
Kspar OG:	tr	Anhydrite:	0.0
Pyrite:	6.0	Celestine:	0.0
Titanium oxides:	tr	Halite:	0.4
Pore Types:			
Intergranular:	0.0	Intragranular:	0.0
Fracture:	tr	Moldic:	0.0

XRD-Whole Rock Mineralogy (Weight %)

Quartz	31.2	Anhydrite	0.6
K-Feldspar	3.8	Celestine	0.0
Plagioclase	0.0	Halite	0.7
Calcite	12.4	Pyrite	7.5
Dolomite	29.5	Total Clay	14.3
Clay Abundance (Weight %)			
Corrensite	0.0	Kaolinite	0.0
Illite / Smectite	1.6	Chlorite	1.9
Illite & Mica	10.8		

mixed-layer illite/smectite contains 15-25% smectite layers

Petrographic Description

This dolomitic argillaceous siltstone is bioturbated. Quartz grains are abundant, dolomite rock fragments (DRF) are common, and potassium feldspar, volcanic rock fragments, limestone rock fragments, and mica are observed in minor to moderate amounts. Dolomite (d) commonly replaces matrix. Some grains have also been replaced by calcite (ca-rg). Pyrite (py) is moderate in abundance; other authigenic minerals are rare. Microfractures (yellow arrow) are oriented subparallel to bedding.

Core Lab

Relative Abundances:	
Trace	<1%
Minor	1-5%
Moderate	5-10%
Common	10-20%
Abundant	>20%

Core Analysis Data:	
Porosity (%):	10.34
Permeability (md):	0.0265
Gr. Density (g/cc):	2.782
Oil Saturation (%):	33.0
Water Saturation	50.1

PLATE 16

Thin Section Petrography

Company:	**Fidelity E & P**
Well:	**Cane Creek 26-3**
Location:	**Grand Co., Utah**
Depth (ft):	**7414.20**
Unit:	**A**
Dep. Env.:	**Shallow Shelf Salina/Sabkha**

A

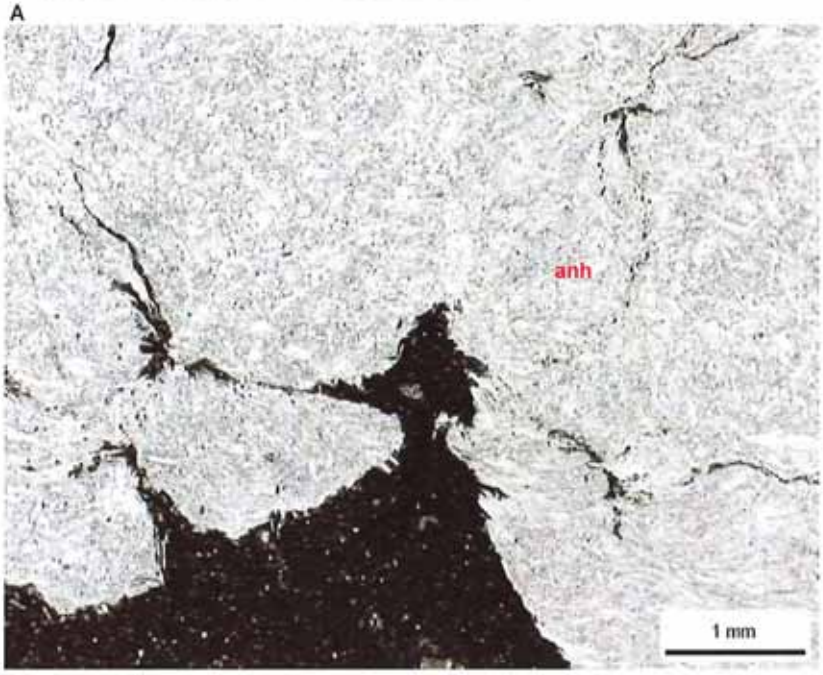

B

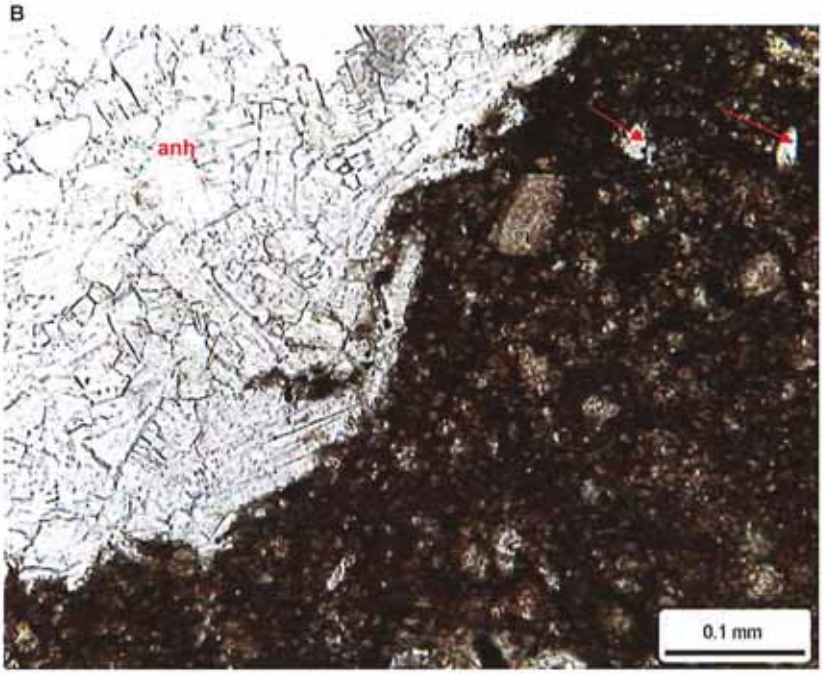

LITHOLOGY AND TEXTURE

Lithology:	Anhydrite
Classific. (Folk, 1980):	n/a
Grain Size (mm):	n/a
Sorting:	n/a
Structures:	nodular texture

Rock Composition (Point-Count)

Framework Grains:			
Mono quartz:	tr	Argillaceous RF:	0.0
Poly quartz:	0.0	Dolomite RF:	0.4
K-Feldspar:	tr	Micas:	0.0
Plagioclase:	0.0	Heavy minerals:	0.0
Volcanic RF:	0.0	Plant fragments:	0.0
Metamorphic RF:	0.0	Glauconite:	0.0
Limestone RF:	0.0	Rip-up/intraclasts:	0.0
Replaced Grains:			
Dolomite RG:	0.0	Pyrite RG:	0.0
Calcite RG:	0.0	Kaolinite RG:	0.0
Detrital Matrix:			
Detrital clay:	1.2	Micrite matrix:	0.0
Organic matrix:	0.0	Dolomitic matrix:	7.6
Pore-filling Authigenic Minerals:			
Authigenic clay:	0.0	Dolomite:	0.0
Quartz OG/QA:	0.0	Calcite:	0.0
Kspar OG:	0.0	Anhydrite:	90.0
Pyrite:	0.8	Celestine:	0.0
Titanium oxides:	0.0	Halite:	0.0
Pore Types:			
Intergranular:	0.0	Intragranular:	0.0
Fracture:	0.0	Moldic:	0.0

XRD-Whole Rock Mineralogy (Weight %)

Quartz	0.5	Anhydrite	97.4
K-Feldspar	0.0	Celestine	0.0
Plagioclase	0.0	Halite	0.0
Calcite	0.4	Pyrite	0.0
Dolomite	1.3	Total Clay	0.4
Clay Abundance (Weight %)			
Corrensite	0.0	Kaolinite	0.0
Illite / Smectite	0.0	Chlorite	0.0
Illite & Mica	0.4		

Petrographic Description

This sample is predominantly anhydrite (anh), but a moderate amount of dolomitized matrix (lower right, Photo B) remains. Quartz (red arrows), potassium feldspar, and dolomite rock fragments are scattered throughout the matrix, as well as rare pyrite framboids. No open pores are found in thin section.

Core Lab

Relative Abundances:	
Trace	<1%
Minor	1-5%
Moderate	5-10%
Common	10-20%
Abundant	>20%

Core Analysis Data:	
Porosity (%):	0.73
Permeability (md):	-
Gr. Density (g/cc):	2.957
Oil Saturation (%):	1.3
Water Saturation	11.0

PLATE 17

Thin Section Petrography

Company:	**Fidelity E & P**
Well:	**Cane Creek 26-3**
Location:	**Grand Co., Utah**
Depth (ft):	**7416.15**
Unit:	**B**
Dep. Env.:	**Restricted Anoxic Shallow Marine/Subaqueous**

A

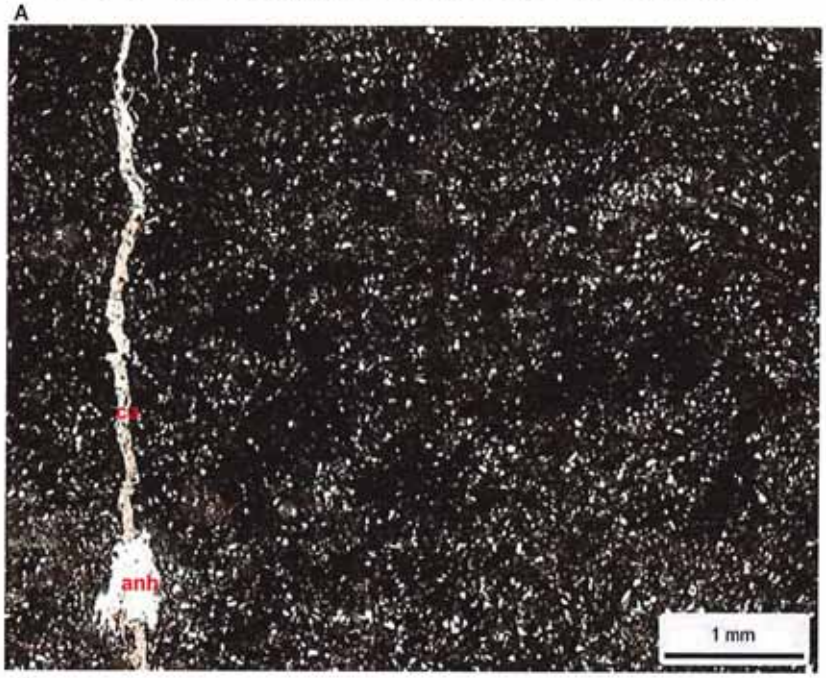

B

LITHOLOGY AND TEXTURE

Lithology:	Silty Dolostone
Classific. (Dunham, 1962):	Silty Peloidal Dolowackestone
Grain Size (mm):	0.055 (coarse silt)
Sorting:	well
Structures:	burrowed; calcite-cemented microfractures

Rock Composition (Point-Count)

Framework Grains:

Mono quartz:	17.2	Argillaceous RF:	0.0
Poly quartz:	0.0	Dolomite RF:	1.6
K-Feldspar:	3.6	Micas:	0.4
Plagioclase:	0.0	Heavy minerals:	0.0
Volcanic RF:	0.4	Plant fragments:	0.8
Metamorphic RF:	0.0	Glauconite:	0.0
Peloid-dolomite:	10.0	Rip-up/intraclasts:	0.0

Replaced Grains:

Dolomite RG:	0.0	Pyrite RG:	0.0
Calcite RG:	0.0	Kaolinite RG:	0.0

Detrital Matrix:

Detrital clay:	0.0	Micrite matrix:	0.0
Organic matrix:	0.0	Dolomitic matrix:	59.6

Pore-filling Authigenic Minerals:

Authigenic clay:	0.0	Dolomite:	0.0
Quartz OG/QA:	0.0	Calcite:	1.2
Kspar OG:	0.0	Anhydrite:	1.6
Pyrite:	3.6	Celestine:	0.0
Titanium oxides:	0.0	Halite:	0.0

Pore Types:

Intergranular:	0.0	Intragranular:	0.0
Fracture:	0.0	Moldic:	0.0

XRD-Whole Rock Mineralogy (Weight %)

Quartz	16.9	Anhydrite	4.2
K-Feldspar	2.2	Celestine	0.0
Plagioclase	0.0	Halite	0.8
Calcite	1.7	Pyrite	0.4
Dolomite	68.6	Total Clay	5.2

Clay Abundance (Weight %)

Corrensite	0.0	Kaolinite	0.0
Illite / Smectite	0.8	Chlorite	0.6
Illite & Mica	3.8		

mixed-layer illite/smectite contains 15-25% smectite layers

Petrographic Description

This sample is a burrowed silty dolostone. Microfractures are cemented by calcite (ca) and occasionally by anhydrite (anh). Grains include common quartz and dolomitic peloids (p), and minor potassium feldspar. The minor to moderate amount clay detected by XRD is associated with the dolomitized matrix. Pyrite framboids are dispersed throughout the matrix and occasionally replace organic matter. Visible pores are absent.

Core Lab
RESERVOIR OPTIMIZATION

Relative Abundances:

Trace	<1%
Minor	1-5%
Moderate	5-10%
Common	10-20%
Abundant	>20%

Core Analysis Data:

Porosity (%):	7.28
Permeability (md):	0.0041
Gr. Density (g/cc):	2.809
Oil Saturation (%):	25.1
Water Saturation	50.9

PLATE 18

Thin Section Petrography

Company:	**Fidelity E & P**
Well:	**Cane Creek 26-3**
Location:	**Grand Co., Utah**
Depth (ft):	**7419.15**
Unit:	**B**
Dep. Env.:	**Restricted Anoxic Shallow Marine/Subaqueous**

A

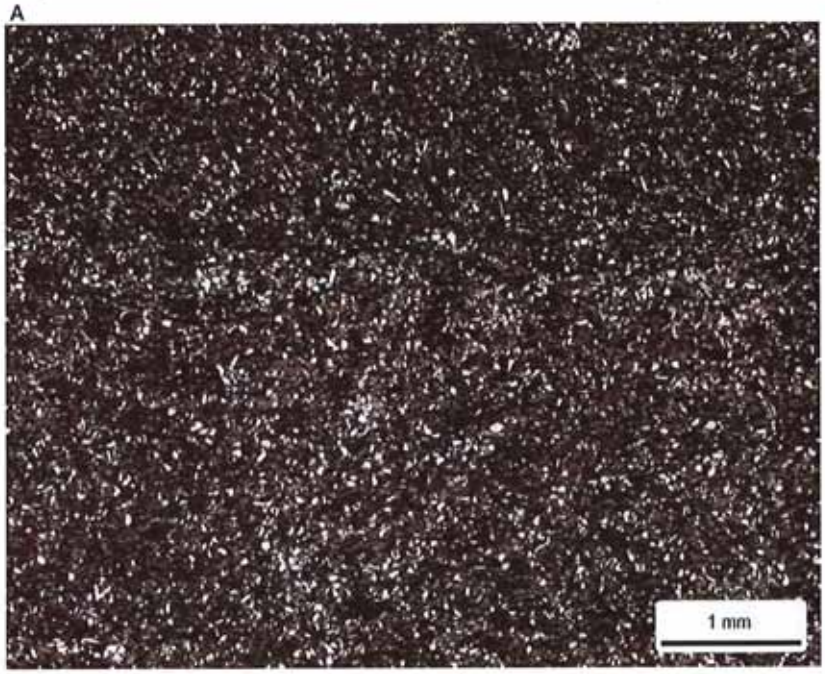

B

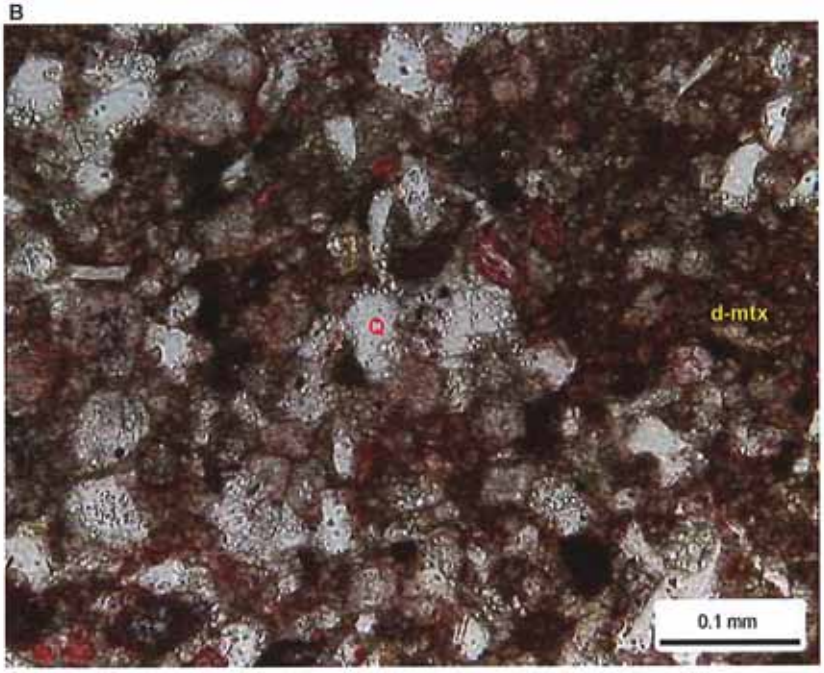

Relative Abundances:

Trace	<1%
Minor	1-5%
Moderate	5-10%
Common	10-20%
Abundant	>20%

Core Analysis Data:

Porosity (%):	4.94
Permeability (md):	0.0018
Gr. Density (g/cc):	2.752
Oil Saturation (%):	34.4
Water Saturation	59.3

LITHOLOGY AND TEXTURE

Lithology:	Dolomitic Argill. Siltstone
Classific. (Folk, 1980):	Feldspathic Litharenite
Grain Size (mm):	0.054 (coarse silt)
Sorting:	well
Structures:	bioturbated

Rock Composition (Point-Count)

Framework Grains:

Mono quartz:	33.6	Argillaceous RF:	0.0
Poly quartz:	0.0	Dolomite RF:	16.8
K-Feldspar:	7.2	Micas:	0.4
Plagioclase:	0.0	Heavy minerals:	tr
Volcanic RF:	0.8	Plant fragments:	2.0
Metamorphic RF:	0.0	Glauconite:	0.0
Limestone RF:	3.6	Rip-up/intraclasts:	0.0

Replaced Grains:

Dolomite RG:	0.0	Pyrite RG:	0.0
Calcite RG:	1.6	Kaolinite RG:	0.0

Detrital Matrix:

Detrital clay:	0.0	Mixed clay/carbonate:	1.2
Organic matrix:	0.0	Dolomitic matrix:	26.4

Pore-filling Authigenic Minerals:

Authigenic clay:	0.0	Dolomite:	0.4
Quartz OG/QA:	0.4	Calcite:	1.2
Kspar OG:	0.0	Anhydrite:	0.0
Pyrite:	4.4	Celestine:	0.0
Titanium oxides:	0.0	Halite:	0.0

Pore Types:

Intergranular:	0.0	Intragranular:	0.0
Fracture:	0.0	Moldic:	0.0

XRD-Whole Rock Mineralogy (Weight %)

Quartz	29.4	Anhydrite	0.0
K-Feldspar	5.2	Celestine	0.0
Plagioclase	0.0	Halite	0.4
Calcite	13.7	Pyrite	1.6
Dolomite	40.9	Total Clay	8.8

Clay Abundance (Weight %)

Corrensite	0.0	Kaolinite	0.5
Illite / Smectite	0.9	Chlorite	1.4
Illite & Mica	6.0		

mixed-layer illite/smectite contains 15-25% smectite layers

Petrographic Description

This dolomitic argillaceous siltstone is bioturbated. Most of the framework grains are quartz (Q), but other grains, including potassium feldspar, dolomite rock fragments, limestone rock fragments, and plant fragments are also observed in minor to moderate amounts. Most of the matrix (d-mtx) has been replaced by dolomite. Pyrite is minor in abundance, and concentrated in the matrix. Other minor to rare authigenic minerals include calcite and quartz overgrowths. No open pores are identified i thin section.

PLATE 19

Thin Section Petrography

Company: Fidelity E & P
Well: Cane Creek 26-3
Location: Grand Co., Utah
Depth (ft): 7421.40
Unit: B
Dep. Env.: Restricted Anoxic Shallow Marine/Subaqueous

A

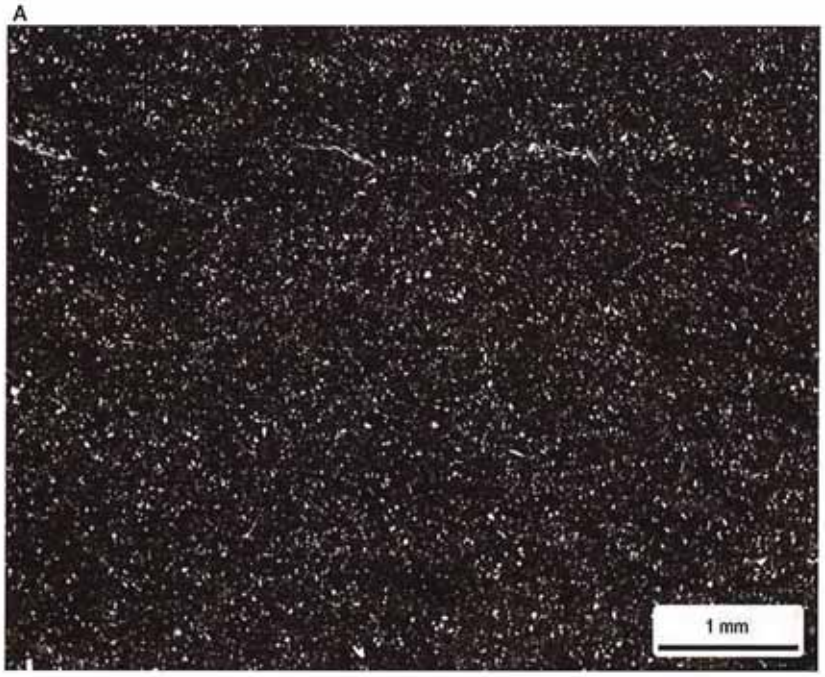

B

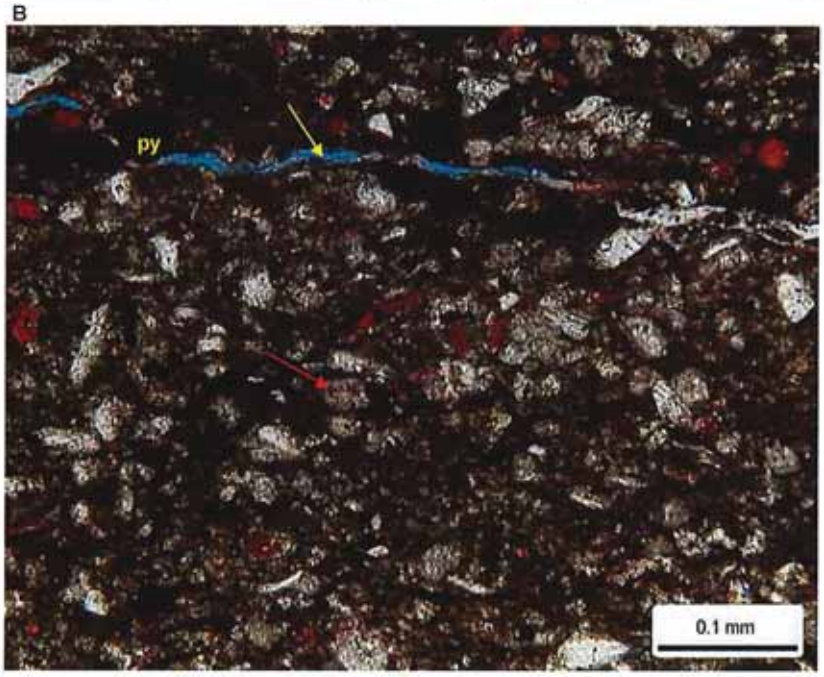

LITHOLOGY AND TEXTURE

Lithology:	Dolomitic Argill. Siltstone
Classific. (Folk, 1980):	Feldspathic Litharenite
Grain Size (mm):	0.051 (coarse silt)
Sorting:	well
Structures:	bioturbated; discontinuous open microfractures

Rock Composition (Point-Count)

Framework Grains:

Mono quartz:	24.0	Argillaceous RF:	0.0
Poly quartz:	0.0	Dolomite RF:	10.4
K-Feldspar:	6.4	Micas:	tr
Plagioclase:	0.0	Heavy minerals:	0.0
Volcanic RF:	0.8	Plant fragments:	4.4
Metamorphic RF:	0.0	Glauconite:	0.0
Limestone RF:	3.6	Rip-up/intraclasts:	0.0

Replaced Grains:

Dolomite RG:	0.0	Pyrite RG:	0.0
Calcite RG:	1.2	Kaolinite RG:	0.0

Detrital Matrix:

Detrital clay:	0.0	Mixed clay/carbonate:	10.4
Organic matrix:	0.0	Dolomitic matrix:	34.4

Pore-filling Authigenic Minerals:

Authigenic clay:	0.0	Dolomite:	0.0
Quartz OG/QA:	0.0	Calcite:	0.0
Kspar OG:	0.0	Anhydrite:	0.0
Pyrite:	4.0	Celestine:	0.0
Titanium oxides:	0.0	Halite:	0.4

Pore Types:

Intergranular:	0.0	Intragranular:	0.0
Fracture:	0.0	Moldic:	0.0

XRD-Whole Rock Mineralogy (Weight %)

Quartz	23.7	Anhydrite	0.0
K-Feldspar	3.2	Celestine	0.0
Plagioclase	0.0	Halite	0.8
Calcite	21.8	Pyrite	2.7
Dolomite	31.1	Total Clay	16.7

Clay Abundance (Weight %)

Corrensite	0.0	Kaolinite	0.5
Illite / Smectite	2.2	Chlorite	1.9
Illite & Mica	12.1		

mixed-layer illite/smectite contains 15-25% smectite layers

Petrographic Description

This dolomitic argillaceous siltstone is bioturbated. Quartz grains are abundant. Potassium feldspar, dolomite rock fragments, limestone rock fragments, and elongate plant fragments are observed in minor to moderate amounts. The matrix has been partially replaced by dolomite. Some of the larger dolomite rhombs are partially replaced by calcite (dedolomitized, red arrow). Pyrite framboids (py) are associated with the matrix. Microfractures (yellow arrow) are oriented subparallel to bedding and are partially filled with halite.

Core Lab
RESERVOIR OPTIMIZATION

Relative Abundances:

Trace	<1%
Minor	1-5%
Moderate	5-10%
Common	10-20%
Abundant	>20%

Core Analysis Data:

Porosity (%):	10.53
Permeability (md):	35.65
Gr. Density (g/cc):	2.749
Oil Saturation (%):	27.7
Water Saturation	63.7

PLATE 19

Scanning Electron Microscopy

Company:	**Fidelity E & P**
Well:	**Cane Creek 26-3**
Location:	**Grand Co., Utah**
Depth (ft):	**7421.40**
Unit:	**A**
Dep. Env.:	**Shallow Marine/Subaqueous**

LITHOLOGY

Dolomitic Argill. Siltstone

C

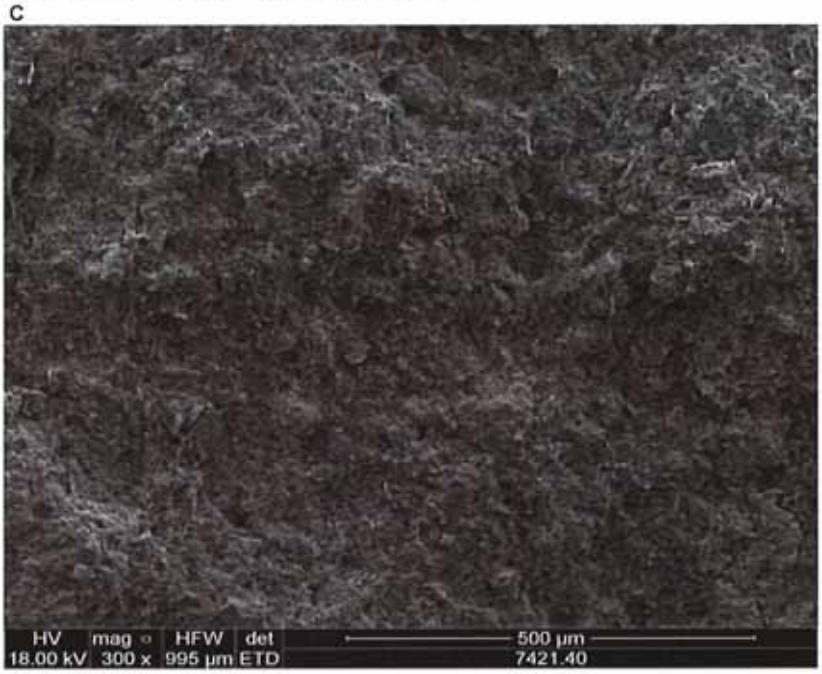

D

Mineralogy Determined by X-Ray Diffraction

(Weight %)

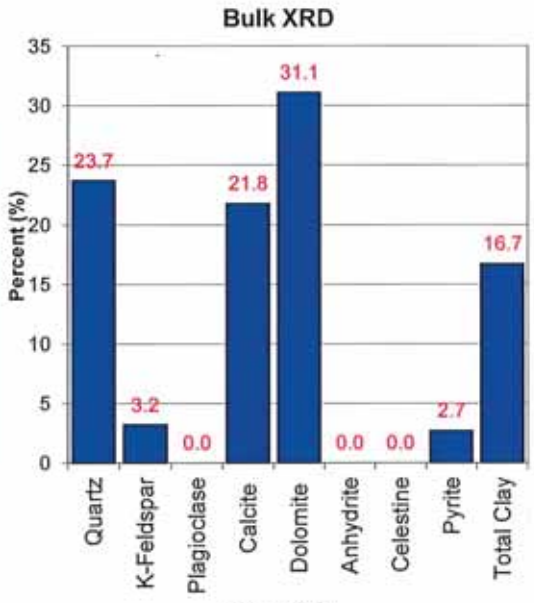

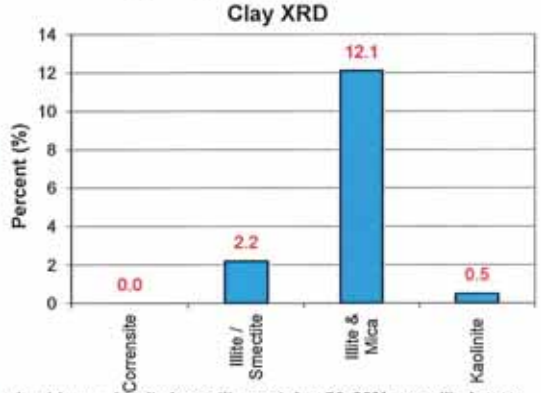

mixed-layer chlorite/smectite contains 50-60% smectite layers

SEM Description

The matrix of this dolomitic argillaceous siltstone is rich in detrital clay and micrite (dclay/micr). Dolomite cement/replacement (d) is common. Secondary intragranular pores (ip) have formed within partially dissolved plagioclase grains (P). Calcite cement (ca) is noted in the larger intragranular pore in the center of Photo D and calcite (ca-rg) appears to be replacing the plagioclase grain on the right side of the same image.

Core Lab
RESERVOIR OPTIMIZATION

Relative Abundances:

Trace	<1%
Minor	1-5%
Moderate	5-10%
Common	10-20%
Abundant	>20%

Core Analysis Data:

Porosity (%):	10.53
Permeability (md):	35.65
Gr. Density (g/cc):	2.749
Oil Saturation (%):	27.7
Water Saturation	63.7

PLATE 20

Thin Section Petrography

Company: Fidelity E & P
Well: Cane Creek 26-3
Location: Grand Co., Utah
Depth (ft): 7424.85
Unit: B
Dep. Env.: Restricted Shallow Marine Shoreface

A

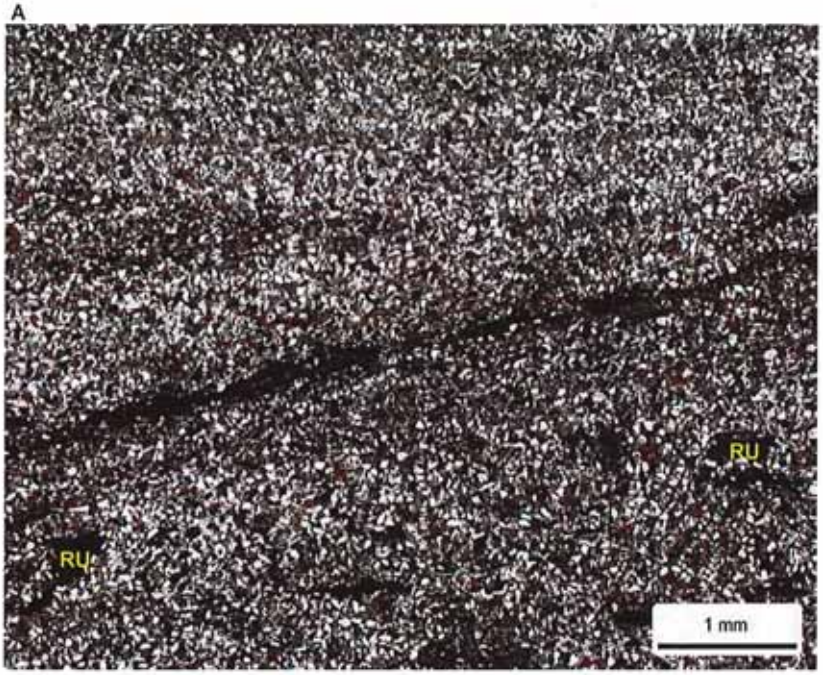

B

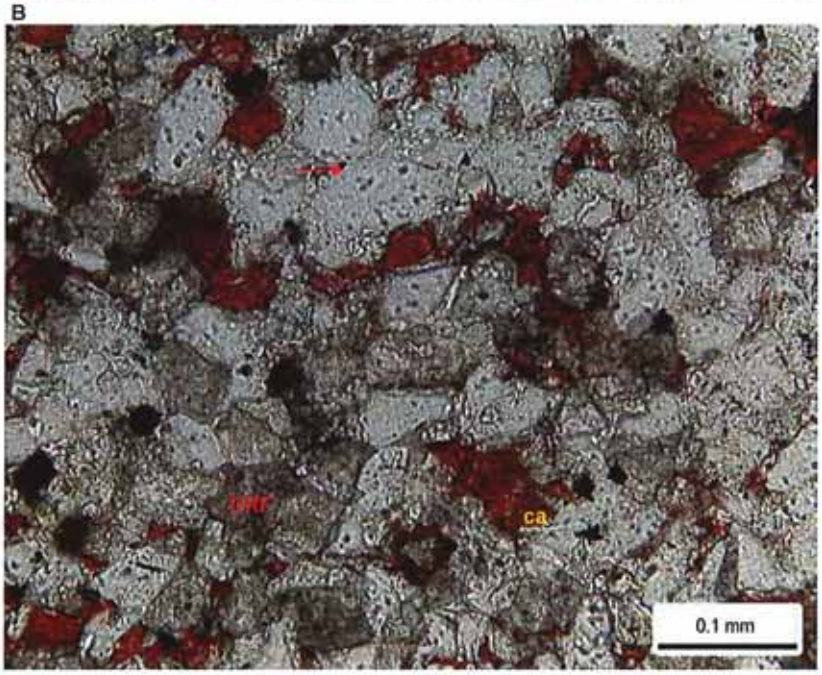

LITHOLOGY AND TEXTURE

Lithology:	Argillaceous Sandstone
Classific. (Folk, 1980):	Litharenite
Grain Size (mm):	0.083 (L. very fine sand)
Sorting:	well
Structures:	cross-laminated; open microfracture

Rock Composition (Point-Count)

Framework Grains:

Mono quartz:	37.2	Argillaceous RF:	0.4
Poly quartz:	0.0	Dolomite RF:	9.2
K-Feldspar:	4.8	Micas:	1.2
Plagioclase:	0.0	Heavy minerals:	0.0
Volcanic RF:	0.0	Plant fragments:	0.8
Metamorphic RF:	0.0	Glauconite:	0.0
Limestone RF:	6.0	Rip-up/intraclasts:	2.4

Replaced Grains:

Dolomite RG:	0.0	Pyrite RG:	0.0
Calcite RG:	1.2	Kaolinite RG:	0.0

Detrital Matrix:

Detrital clay:	0.0	Mixed clay/carbonate:	5.2
Organic matrix:	0.0	Dolomitic matrix:	1.6

Pore-filling Authigenic Minerals:

Authigenic clay:	0.0	Dolomite:	12.0
Quartz OG/QA:	6.0	Calcite:	6.8
Kspar OG:	0.0	Anhydrite:	0.0
Pyrite:	3.6	Celestine:	0.0
Titanium oxides:	0.4	Halite:	1.2

Pore Types:

Intergranular:	0.0	Intragranular:	tr
Fracture:	0.0	Moldic:	0.0

XRD-Whole Rock Mineralogy (Weight %)

Quartz	46.1	Anhydrite	0.0
K-Feldspar	4.2	Celestine	0.0
Plagioclase	0.0	Halite	7.4
Calcite	21.4	Pyrite	1.1
Dolomite	13.1	Total Clay	6.6

Clay Abundance (Weight %)

Corrensite	0.0	Kaolinite	0.2
Illite / Smectite	0.8	Chlorite	1.0
Illite & Mica	4.6		

mixed-layer illite/smectite contains 15-25% smectite layers

Petrographic Description

This sample is a cross-laminated, very fine-grained argillaceous sandstone. Quartz is, by far, the most abundant framework grain. Other less common grains include potassium feldspar, dolomite rock fragments (DRF), limestone rock fragments, mica, and dolomitic rip-up clasts (RU). Grains are occasionally replaced by by calcite. Detrital clay and carbonate-rich matrix is moderate in abundance and concentrated in laminae. Primary intergranular pore space is lost to dolomite and calcite (ca) cements, as well as quartz overgrowths. Secondary intragranular pores are rarely found within partially dissolved, less stable feldspar grains and lithic fragments (not pictured).

Core Lab
RESERVOIR OPTIMIZATION

Relative Abundances:

Trace	<1%
Minor	1-5%
Moderate	5-10%
Common	10-20%
Abundant	>20%

Core Analysis Data:

Porosity (%):	6.01
Permeability (md):	0.0043
Gr. Density (g/cc):	2.704
Oil Saturation (%):	32.8
Water Saturation	59.3

PLATE 21

Thin Section Petrography

Company:	**Fidelity E & P**
Well:	**Cane Creek 26-3**
Location:	**Grand Co., Utah**
Depth (ft):	**7426.00**
Unit:	**B**
Dep. Env.:	**Restricted Shallow Marine Shoreface**

A

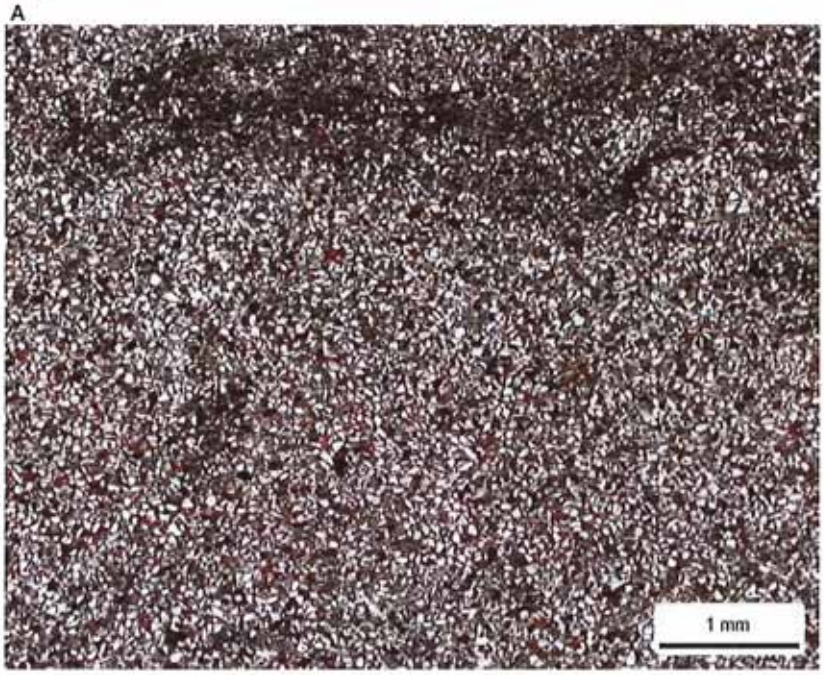

B

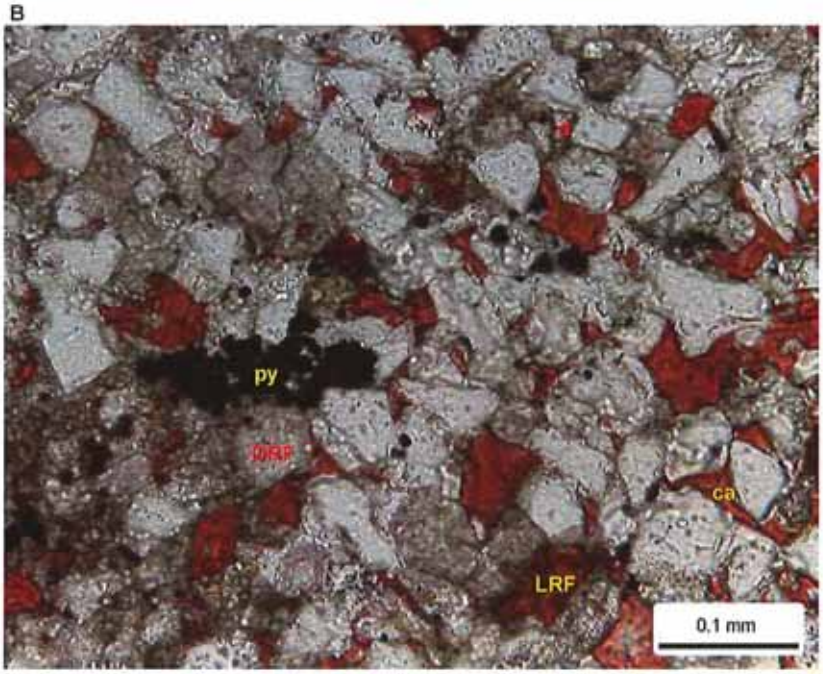

LITHOLOGY AND TEXTURE

Lithology:	Argillaceous Sandstone
Classific. (Folk, 1980):	Feldspathic Litharenite
Grain Size (mm):	0.072 (L. very fine sand)
Sorting:	well
Structures:	bioturbated; open and halite filled microfractures subparallel to bedding

Rock Composition (Point-Count)

Framework Grains:

Mono quartz:	41.2	Argillaceous RF:	0.0
Poly quartz:	0.0	Dolomite RF:	13.2
K-Feldspar:	6.8	Micas:	1.2
Plagioclase:	1.6	Heavy minerals:	0.0
Volcanic RF:	0.0	Plant fragments:	0.4
Metamorphic RF:	0.0	Glauconite:	tr
Limestone RF:	1.6	Rip-up/intraclasts:	0.0

Replaced Grains:

Dolomite RG:	0.0	Pyrite RG:	0.0
Calcite RG:	2.4	Kaolinite RG:	0.0

Detrital Matrix:

Detrital clay:	0.0	Mixed clay/carbonate:	4.8
Organic matrix:	0.0	Dolomitic matrix:	7.6

Pore-filling Authigenic Minerals:

Authigenic clay:	0.0	Dolomite:	5.6
Quartz OG/QA:	2.8	Calcite:	7.6
Kspar OG:	0.0	Anhydrite:	0.0
Pyrite:	2.8	Celestine:	0.0
Titanium oxides:	0.4	Halite:	tr

Pore Types:

Intergranular:	0.0	Intragranular:	tr
Fracture:	0.0	Moldic:	0.0

XRD-Whole Rock Mineralogy (Weight %)

Quartz	50.2	Anhydrite	0.0
K-Feldspar	5.2	Celestine	0.0
Plagioclase	0.7	Halite	0.8
Calcite	11.1	Pyrite	1.8
Dolomite	20.0	Total Clay	10.2

Clay Abundance (Weight %)

Corrensite	0.0	Kaolinite	0.0
Illite / Smectite	1.4	Chlorite	1.5
Illite & Mica	7.3		

mixed-layer illite/smectite contains 15-25% smectite layers

Petrographic Description

This very fine-grained, well sorted argillaceous sandstone is bioturbated. Quartz grains are abundant and dolomite rock fragments (DRF) are common. Other grains found in minor to moderate amounts include potassium feldspar, plagioclase, limestone rock fragments (LRF), calcite replaced grains, and mica. Matrix is common overall, and is a mixture of detrital clay and micrite that has been partially replaced by dolomite. Calcite (ca) and dolomite cements (d) are moderate in abundance, and fill intergranular pores. Other minor cements include quartz overgrowths and pyrite (py).

Core Lab
RESERVOIR OPTIMIZATION

Relative Abundances:

Trace	<1%
Minor	1-5%
Moderate	5-10%
Common	10-20%
Abundant	>20%

Core Analysis Data:

Porosity (%):	8.94
Permeability (md):	3.2788
Gr. Density (g/cc):	2.722
Oil Saturation (%):	24.7
Water Saturation	67.7

PLATE 21

Scanning Electron Microscopy

Company:	**Fidelity E & P**
Well:	**Cane Creek 26-3**
Location:	**Grand Co., Utah**
Depth (ft):	**7426.00**
Unit:	**A**
Dep. Env.:	**Shallow Marine/Subaqueous**

LITHOLOGY

Argillaceous Sandstone

C

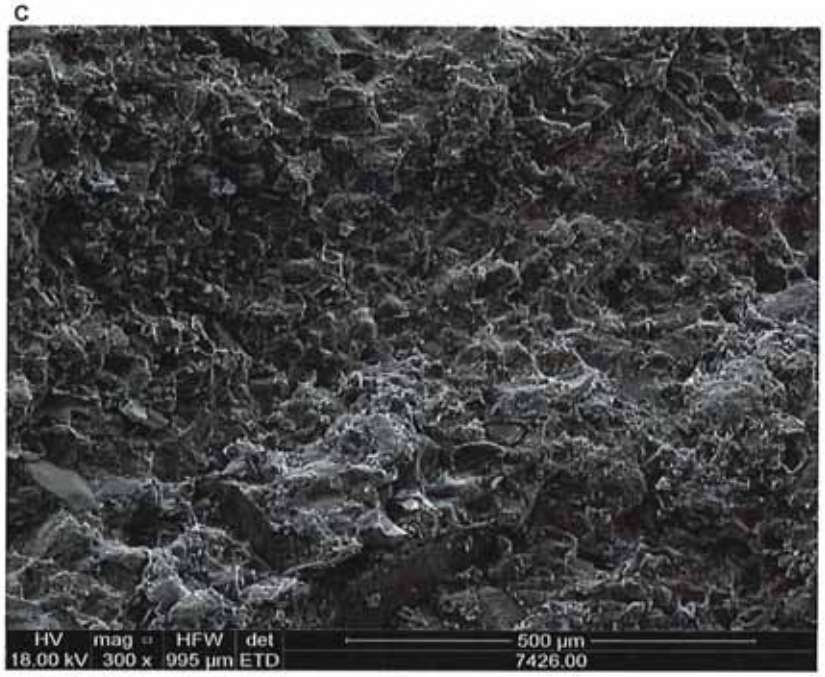

D

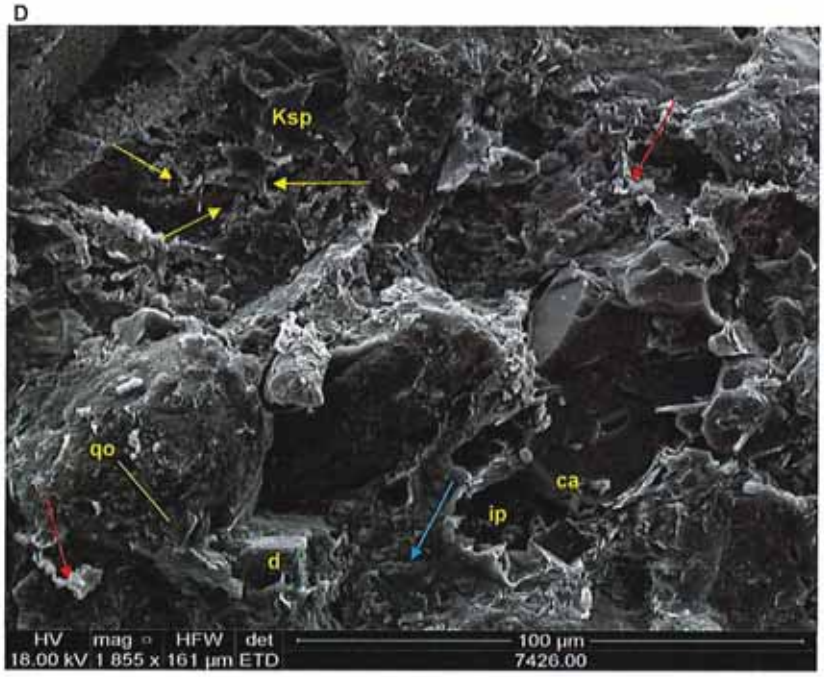

Mineralogy Determined by X-Ray Diffraction

(Weight %)

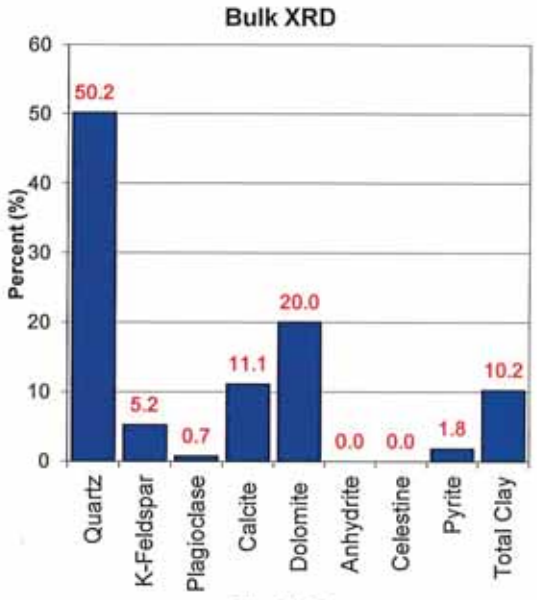

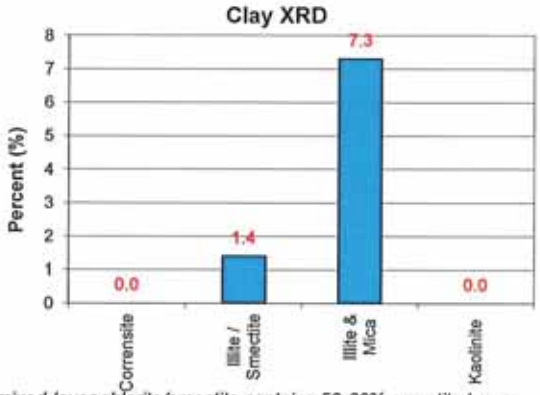

mixed-layer chlorite/smectite contains 50-60% smectite layers

SEM Description

Secondary intragranular pores (yellow arrows) have formed within a partially dissolved potassium feldspar grain (Ksp). Another intragranular pore (ip) is noted in the lower part of Photo D, in a grain that appears to have been replaced by calcite (ca). The matrix (red arrows) consists of detrital clay, often intermixed with micrite. Authigenic dolomite (d) occurs as a cement and partially replaces matrix. Quartz overgrowths (qo) are identified on some detrital quartz grains. Salt crystals (blue arrow) are noted on the surface of a grain.

Core Lab

RESERVOIR OPTIMIZATION

Relative Abundances:	
Trace	<1%
Minor	1-5%
Moderate	5-10%
Common	10-20%
Abundant	>20%

Core Analysis Data:	
Porosity (%):	8.94
Permeability (md):	3.2788
Gr. Density (g/cc):	2.722
Oil Saturation (%):	24.7
Water Saturation	67.7

PLATE 22

Thin Section Petrography

Company:	**Fidelity E & P**
Well:	**Cane Creek 26-3**
Location:	**Grand Co., Utah**
Depth (ft):	**7427.10**
Unit:	**B**
Dep. Env.:	**Restricted Shallow Marine Shoreface**

A

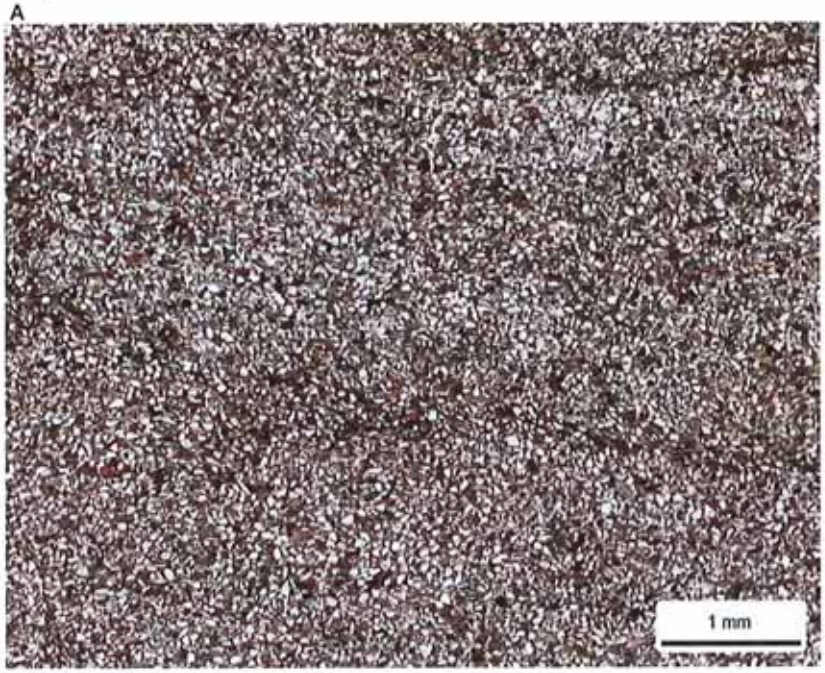

B

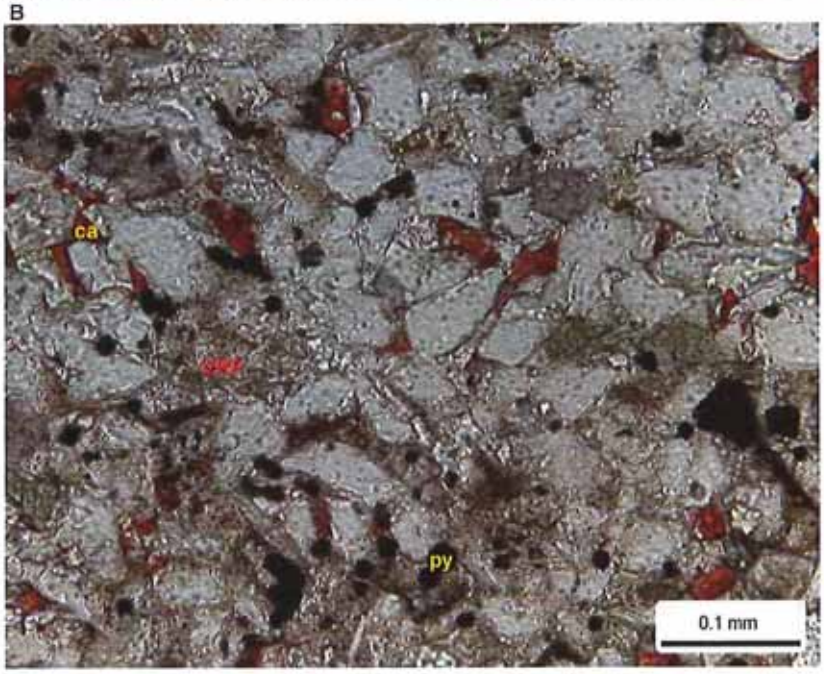

LITHOLOGY AND TEXTURE

Lithology:	Argillaceous Sandstone
Classific. (Folk, 1980):	Feldspathic Litharenite
Grain Size (mm):	0.077 (L. very fine sand)
Sorting:	well
Structures:	bioturbated; discontinuous open microfractures

Rock Composition (Point-Count)

Framework Grains:

Mono quartz:	50.8	Argillaceous RF:	0.4
Poly quartz:	0.0	Dolomite RF:	7.6
K-Feldspar:	7.6	Micas:	2.4
Plagioclase:	0.4	Heavy minerals:	0.0
Volcanic RF:	0.0	Plant fragments:	0.0
Metamorphic RF:	0.0	Glauconite:	0.0
Limestone RF:	1.6	Rip-up/intraclasts:	0.0

Replaced Grains:

Dolomite RG:	0.0	Pyrite RG:	0.0
Calcite RG:	2.0	Kaolinite RG:	0.0

Detrital Matrix:

Detrital clay:	0.0	Mixed clay/carbonate:	9.6
Organic matrix:	0.0	Dolomitic matrix:	2.4

Pore-filling Authigenic Minerals:

Authigenic clay:	tr	Dolomite:	5.6
Quartz OG/QA:	2.4	Calcite:	3.6
Kspar OG:	0.4	Anhydrite:	0.0
Pyrite:	2.4	Celestine:	0.0
Titanium oxides:	0.4	Halite:	0.0

Pore Types:

Intergranular:	0.4	Intragranular:	0.0
Fracture:	0.0	Moldic:	0.0

XRD-Whole Rock Mineralogy (Weight %)

Quartz	60.8	Anhydrite	0.9
K-Feldspar	7.2	Celestine	0.0
Plagioclase	0.0	Halite	1.9
Calcite	11.9	Pyrite	1.7
Dolomite	5.6	Total Clay	9.9

Clay Abundance (Weight %)

Corrensite	0.0	Kaolinite	0.0
Illite / Smectite	0.9	Chlorite	1.5
Illite & Mica	7.5		

mixed-layer illite/smectite contains 15-25% smectite layers

Petrographic Description

This very fine grained, well sorted argillaceous sandstone is bioturbated. Framework grains are mostly quartz, but a minor to moderate amount of potassium feldspar, dolomite rock fragments, limestone rock fragments, and mica along with rare volcanic rock fragments (VRF) are also observed. Dolomite occurs as intergranular cement and replaces matrix. Calcite cement (ca) and replaced grains are also found in minor amounts. Quartz overgrowths surround some detrital quartz grains. Pyrite (py) is associated with the matrix.

Core Lab

Relative Abundances:

Trace	<1%
Minor	1-5%
Moderate	5-10%
Common	10-20%
Abundant	>20%

Core Analysis Data:

Porosity (%):	9.68
Permeability (md):	0.0098
Gr. Density (g/cc):	2.687
Oil Saturation (%):	38.4
Water Saturation	58.9

PLATE 23

Thin Section Petrography

Company:	**Fidelity E & P**
Well:	**Cane Creek 26-3**
Location:	**Grand Co., Utah**
Depth (ft):	**7429.10**
Unit:	**B**
Dep. Env.:	**Restricted Shallow Marine Shoreface**

A

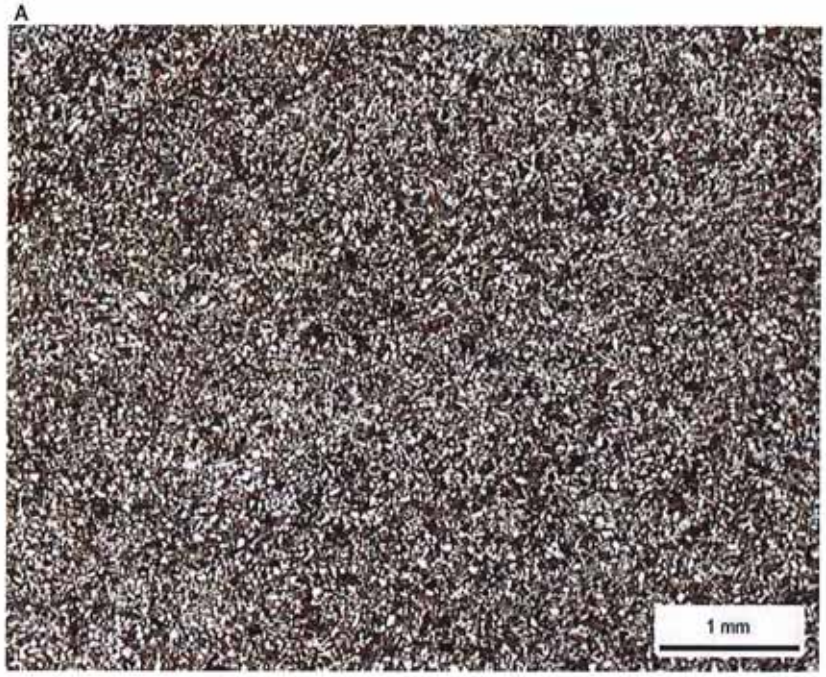

B

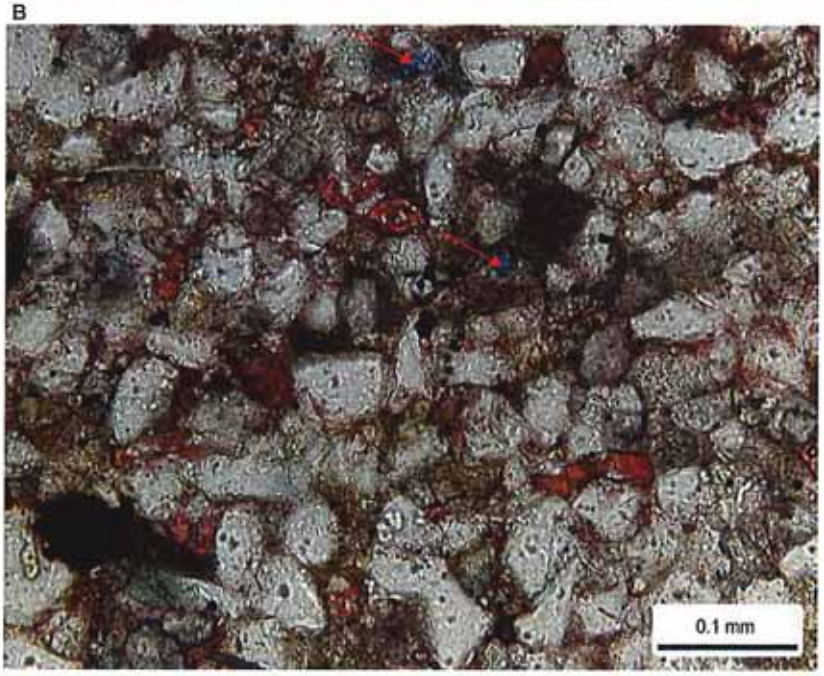

LITHOLOGY AND TEXTURE

Lithology:	Argillaceous Sandstone
Classific. (Folk, 1980):	Lithic Arkose
Grain Size (mm):	0.079 (L. very fine sand)
Sorting:	well
Structures:	bioturbated; discontinuous open microfractures

Rock Composition (Point-Count)

Framework Grains:

Mono quartz:	52.8	Argillaceous RF:	0.4
Poly quartz:	0.0	Dolomite RF:	6.0
K-Feldspar:	8.8	Micas:	0.8
Plagioclase:	1.2	Heavy minerals:	0.4
Volcanic RF:	0.4	Plant fragments:	0.0
Metamorphic RF:	0.0	Glauconite:	0.0
Limestone RF:	2.8	Rip-up/intraclasts:	0.0

Replaced Grains:

Dolomite RG:	0.0	Pyrite RG:	0.0
Calcite RG:	3.6	Kaolinite RG:	0.0

Detrital Matrix:

Detrital clay:	0.0	Mixed clay/carbonate:	5.6
Organic matrix:	0.0	Dolomitic matrix:	3.6

Pore-filling Authigenic Minerals:

Authigenic clay:	0.4	Dolomite:	3.6
Quartz OG/QA:	2.8	Calcite:	3.6
Kspar OG:	0.4	Anhydrite:	0.0
Pyrite:	2.4	Celestine:	0.0
Titanium oxides:	0.4	Halite:	0.0

Pore Types:

Intergranular:	tr	Intragranular:	tr
Fracture:	0.0	Moldic:	0.0

XRD-Whole Rock Mineralogy (Weight %)

Quartz	62.1	Anhydrite	0.0
K-Feldspar	6.6	Celestine	0.0
Plagioclase	0.7	Halite	0.9
Calcite	10.2	Pyrite	1.6
Dolomite	6.7	Total Clay	11.0

Clay Abundance (Weight %)

Corrensite	0.0	Kaolinite	0.0
Illite / Smectite	1.3	Chlorite	1.7
Illite & Mica	8.0		

mixed-layer illite/smectite contains 15-25% smectite layers

Petrographic Description

This very fine grained, well sorted argillaceous sandstone is bioturbated. Framework grains include abundant quartz and moderate potassium feldspar and dolomite rock fragments. Plagioclase and limestone rock fragments are also observed in minor amounts. Authigenic dolomite occurs as a replacement of matrix and fills some intergranular pores. Calcite cement is also observed in minor amounts, filling intergranular pores and partially replacing some grains. Other cements found in minor amounts include quartz overgrowths and pyrite. Intergranular pores and secondary intragranular pores (red arrows) are rare.

Core Lab
RESERVOIR OPTIMIZATION

Relative Abundances:	
Trace	<1%
Minor	1-5%
Moderate	5-10%
Common	10-20%
Abundant	>20%

Core Analysis Data:	
Porosity (%):	12.43
Permeability (md):	0.1123
Gr. Density (g/cc):	2.685
Oil Saturation (%):	27.9
Water Saturation	59.1

PLATE 23

Scanning Electron Microscopy

Company: Fidelity E & P
Well: Cane Creek 26-3
Location: Grand Co., Utah
Depth (ft): 7429.10
Unit: A
Dep. Env.: Shallow Marine/Subaqueous

LITHOLOGY
Argillaceous Sandstone

C

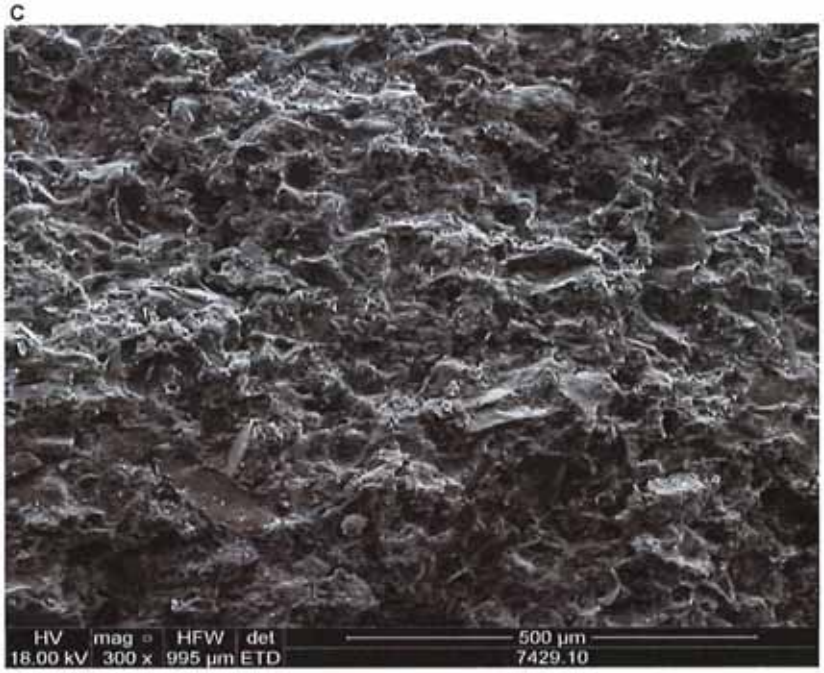

D

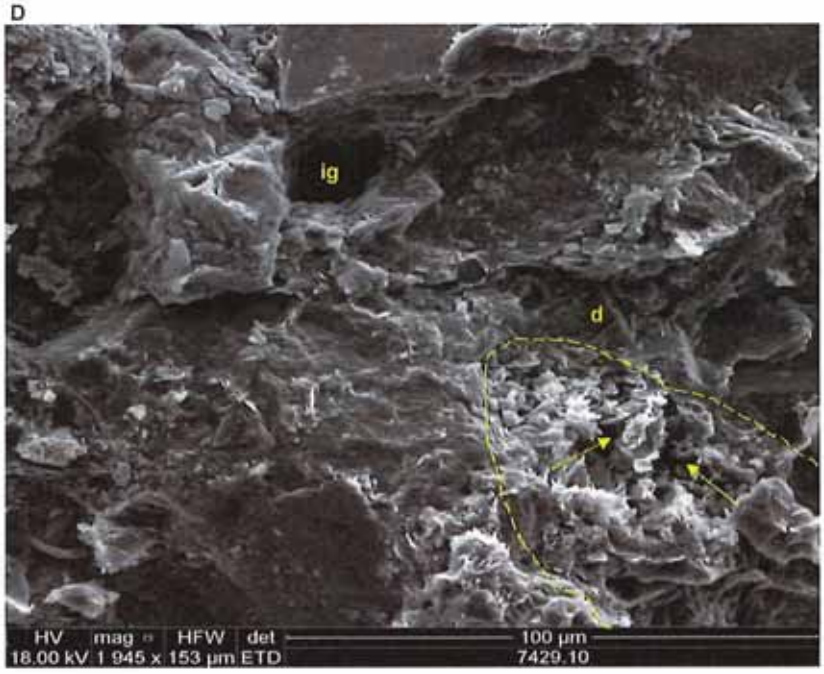

Mineralogy Determined by X-Ray Diffraction
(Weight %)

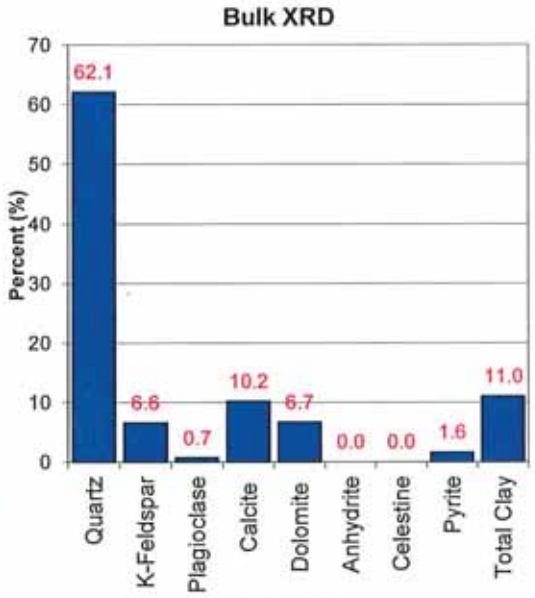

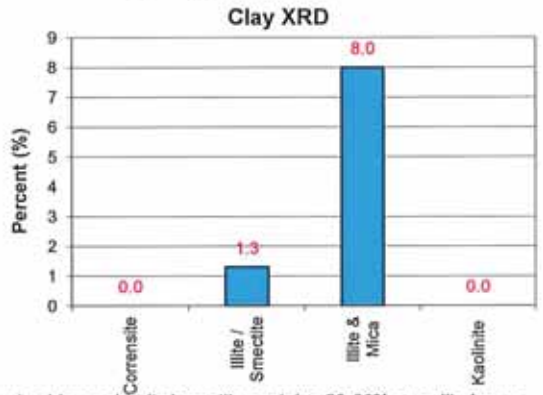

mixed-layer chlorite/smectite contains 50-60% smectite layers

SEM Description

Small intergranular pores (ig) are observed, scattered throughout the SEM sample. Secondary intragranular pores (yellow arrows) have formed within a partially dissolved and altered grain. Dolomite (d) is a dominant cement/replacement mineral at this depth.

Relative Abundances:

Trace	<1%
Minor	1-5%
Moderate	5-10%
Common	10-20%
Abundant	>20%

Core Analysis Data:

Porosity (%):	12.43
Permeability (md):	0.1123
Gr. Density (g/cc):	2.685
Oil Saturation (%):	27.9
Water Saturation	59.1

PLATE 24

Thin Section Petrography

Company:	**Fidelity E & P**
Well:	**Cane Creek 26-3**
Location:	**Grand Co., Utah**
Depth (ft):	**7431.25**
Unit:	**B**
Dep. Env.:	**Restricted Shallow Marine Shoreface**

A

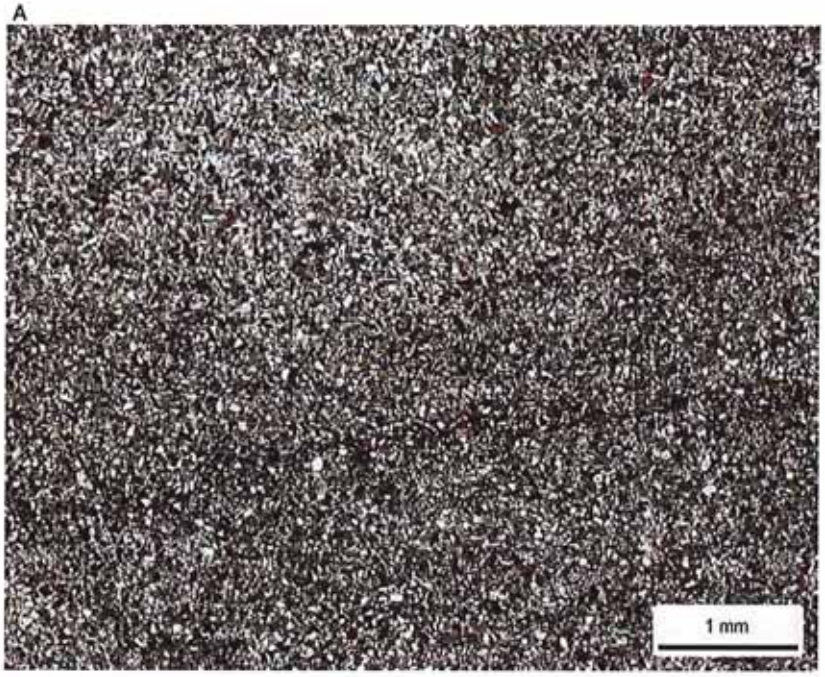

B

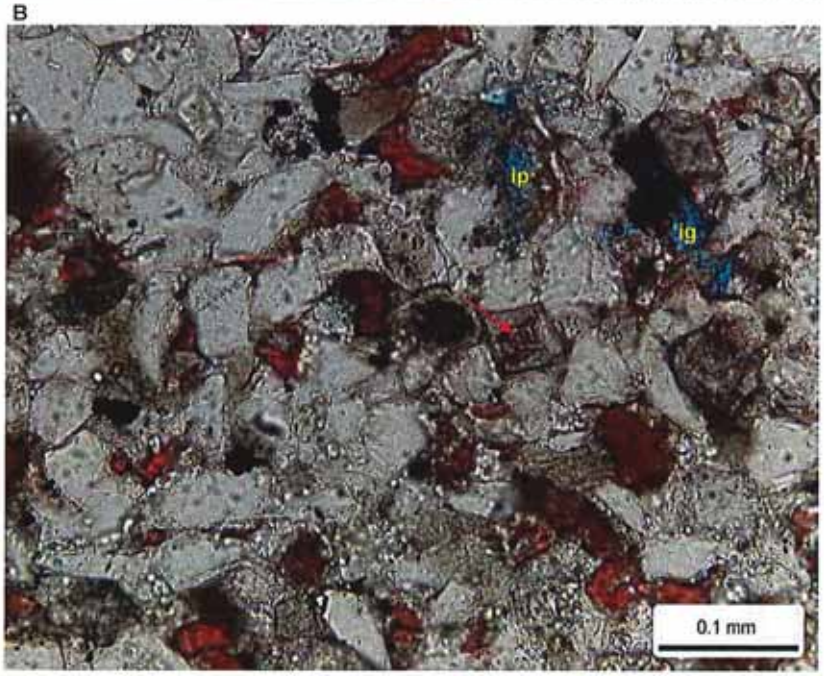

LITHOLOGY AND TEXTURE

Lithology:	Argillaceous Sandstone
Classific. (Folk, 1980):	Feldspathic Litharenite
Grain Size (mm):	0.071 (L. very fine sand)
Sorting:	well
Structures:	burrowed; discontinuous open microfractures

Rock Composition (Point-Count)

Framework Grains:			
Mono quartz:	50.8	Argillaceous RF:	0.4
Poly quartz:	0.0	Dolomite RF:	6.4
K-Feldspar:	10.4	Micas:	2.0
Plagioclase:	0.4	Heavy minerals:	0.0
Volcanic RF:	1.2	Plant fragments:	0.4
Metamorphic RF:	0.0	Glauconite:	0.0
Limestone RF:	3.2	Rip-up/intraclasts:	0.0
Replaced Grains:			
Dolomite RG:	0.0	Pyrite RG:	0.0
Calcite RG:	1.6	Kaolinite RG:	0.0
Detrital Matrix:			
Detrital clay:	0.0	Mixed clay/carbonate:	6.0
Organic matrix:	0.0	Dolomitic matrix:	4.8
Pore-filling Authigenic Minerals:			
Authigenic clay:	0.8	Dolomite:	2.8
Quartz OG/QA:	4.0	Calcite:	2.4
Kspar OG:	0.0	Anhydrite:	0.0
Pyrite:	1.6	Celestine:	tr
Titanium oxides:	0.0	Halite:	0.4
Pore Types:			
Intergranular:	tr	Intragranular:	tr
Fracture:	0.4	Moldic:	0.0

XRD-Whole Rock Mineralogy (Weight %)

Quartz	51.9	Anhydrite	0.0
K-Feldspar	8.8	Celestine	0.0
Plagioclase	0.7	Halite	0.8
Calcite	13.5	Pyrite	1.8
Dolomite	10.0	Total Clay	12.3
Clay Abundance (Weight %)			
Corrensite	0.0	Kaolinite	0.3
Illite / Smectite	1.9	Chlorite	1.6
Illite & Mica	8.5		

mixed-layer illite/smectite contains 15-25% smectite layers

Petrographic Description

This sample is a bioturbated argillaceous sandstone. Framework grains include abundant quartz, moderate potassium feldspar and dolomite rock fragments, and minor volcanic rock fragments, limestone rock fragments, and mica. Dolomite partially replaces matrix and fills some intergranular pores. Some of the dolomite has been replaced by calcite (dedolomitized; red arrow). A minor amount of calcite (stained pink) also occurs as intergranular cement and grain replacement. Other minor cements include quartz overgrowths and pyrite. Scattered intergranular pores (ig) and intragranular pores (ip) are rare.

Core Lab
RESERVOIR OPTIMIZATION

Relative Abundances:	
Trace	<1%
Minor	1-5%
Moderate	5-10%
Common	10-20%
Abundant	>20%

Core Analysis Data:	
Porosity (%):	11.45
Permeability (md):	0.1368
Gr. Density (g/cc):	2.699
Oil Saturation (%):	30.2
Water Saturation	68.4

PLATE 25

Thin Section Petrography

Company:	**Fidelity E & P**
Well:	**Cane Creek 26-3**
Location:	**Grand Co., Utah**
Depth (ft):	**7433.10**
Unit:	**B**
Dep. Env.:	**Restricted Shallow Marine Shoreface**

A

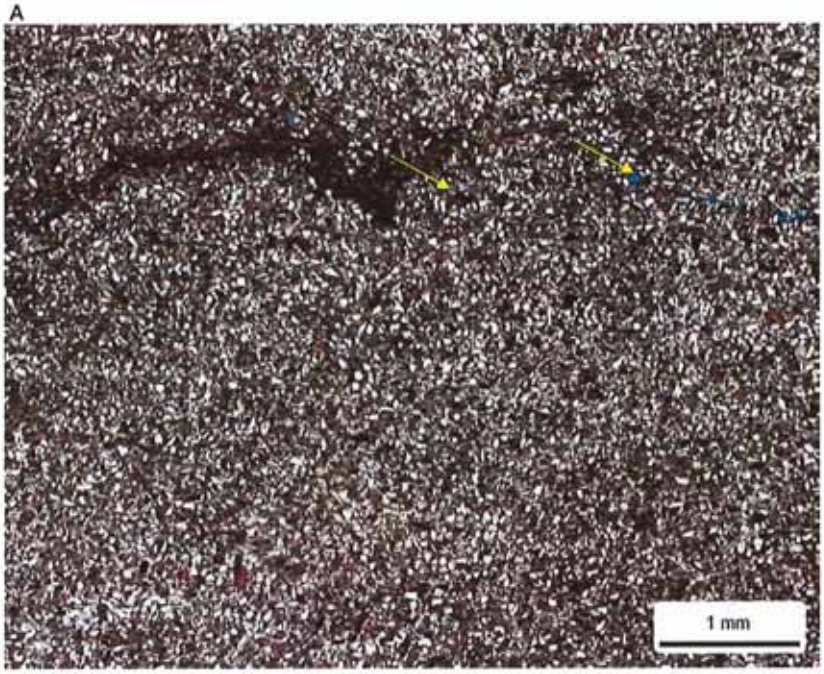

B

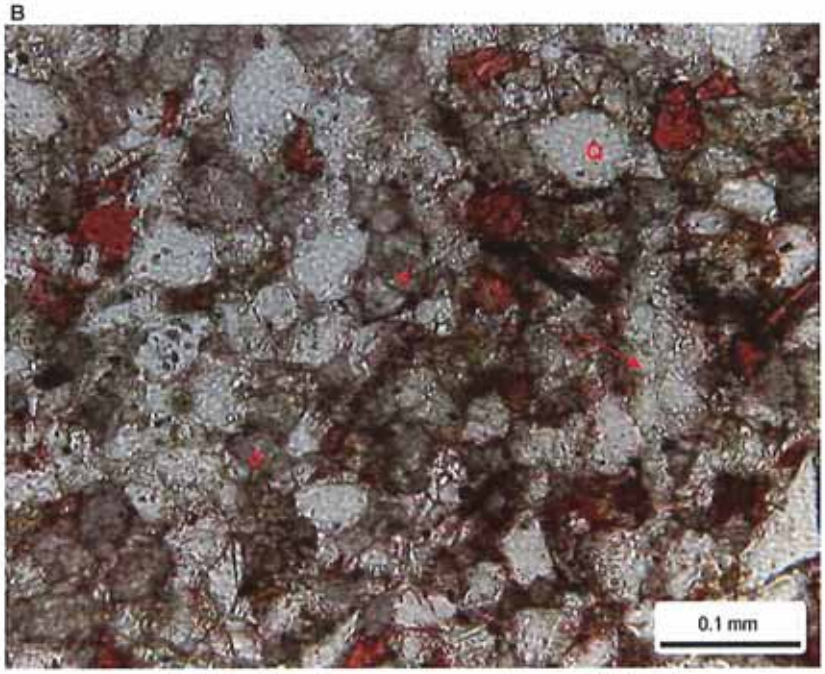

Relative Abundances:

Trace	<1%
Minor	1-5%
Moderate	5-10%
Common	10-20%
Abundant	>20%

Core Analysis Data:

Porosity (%):	9.85
Permeability (md):	0.0469
Gr. Density (g/cc):	2.704
Oil Saturation (%):	22.7
Water Saturation	66.3

LITHOLOGY AND TEXTURE

Lithology:	Argillaceous Sandstone
Classific. (Folk, 1980):	Feldspathic Litharenite
Grain Size (mm):	0.080 (L. very fine sand)
Sorting:	well
Structures:	bioturbated; discontinuous open microfractures

Rock Composition (Point-Count)

Framework Grains:

Mono quartz:	45.2	Argillaceous RF:	0.0
Poly quartz:	0.0	Dolomite RF:	12.8
K-Feldspar:	7.6	Micas:	2.0
Plagioclase:	0.0	Heavy minerals:	tr
Volcanic RF:	1.2	Plant fragments:	0.8
Metamorphic RF:	0.0	Glauconite:	0.0
Limestone RF:	2.4	Rip-up/intraclasts:	0.0

Replaced Grains:

Dolomite RG:	0.0	Pyrite RG:	0.0
Calcite RG:	1.6	Kaolinite RG:	0.0

Detrital Matrix:

Detrital clay:	0.0	Mixed clay/carbonate:	4.4
Organic matrix:	0.0	Dolomitic matrix:	4.8

Pore-filling Authigenic Minerals:

Authigenic clay:	0.8	Dolomite:	6.0
Quartz OG/QA:	5.6	Calcite:	1.6
Kspar OG:	0.4	Anhydrite:	1.2
Pyrite:	0.8	Celestine:	0.4
Titanium oxides:	0.0	Halite:	0.4

Pore Types:

Intergranular:	0.0	Intragranular:	0.0
Fracture:	0.0	Moldic:	0.0

XRD-Whole Rock Mineralogy (Weight %)

Quartz	55.3	Anhydrite	0.0
K-Feldspar	4.8	Celestine	0.0
Plagioclase	0.0	Halite	0.0
Calcite	13.3	Pyrite	1.3
Dolomite	15.9	Total Clay	9.4

Clay Abundance (Weight %)

Corrensite	0.0	Kaolinite	0.2
Illite / Smectite	1.2	Chlorite	2.1
Illite & Mica	5.9		

mixed-layer illite/smectite contains 15-25% smectite layers

Petrographic Description

This very fine grained, well sorted argillaceous sandstone is bioturbated. Quartz grains (Q) are abundant, dolomite rock fragments are common, and potassium feldspar is observed in moderate amounts. Other minor grains include volcanic rock fragments, limestone rock fragments, and mica. Authigenic dolomite replaces matrix and occurs as intergranular cement (overgrowths on dolomite rock fragments). A minor amount of calcite fills intergranular pores and replaces grains. Quartz overgrowths (red arrow) are well developed, and moderate in abundance. The larger areas of blue epoxy (yellow arrows) in Photo A are a result of sample plucking, and not natural pores.

PLATE 26

Thin Section Petrography

Company:	**Fidelity E & P**
Well:	**Cane Creek 26-3**
Location:	**Grand Co., Utah**
Depth (ft):	**7435.15**
Unit:	**B**
Dep. Env.:	**Restricted Shallow Marine Shoreface**

A

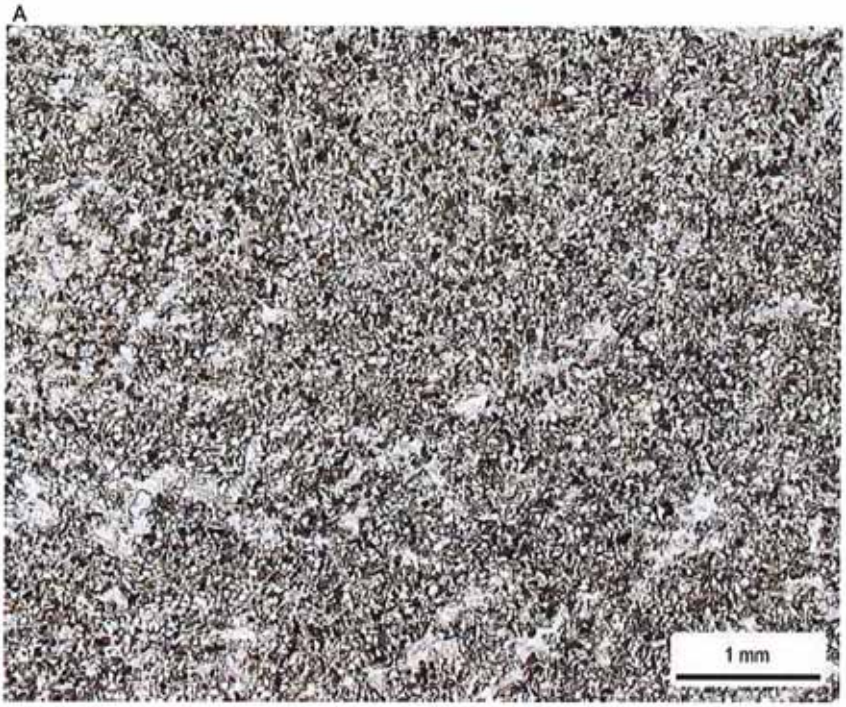

B

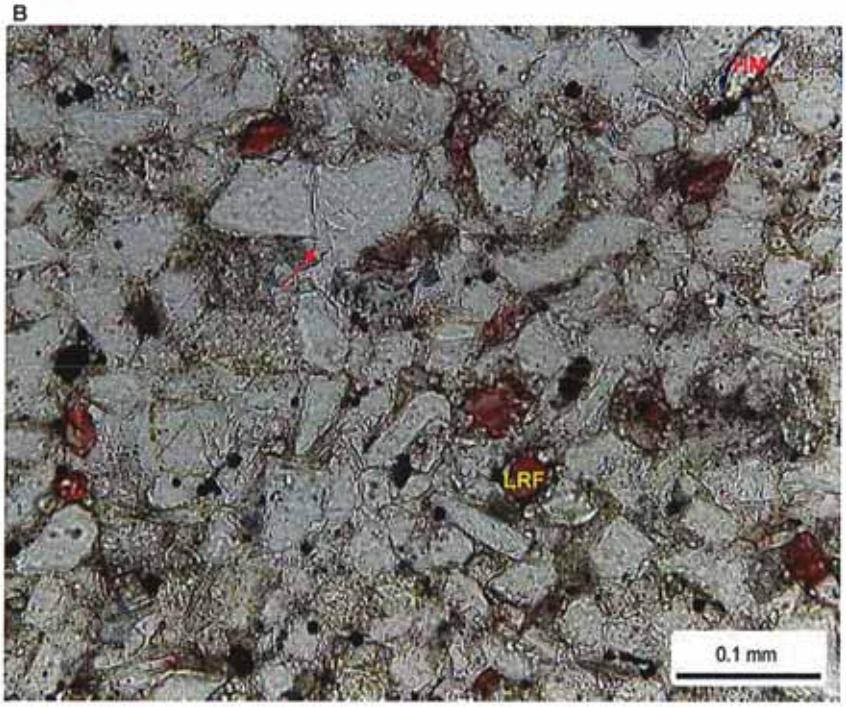

LITHOLOGY AND TEXTURE

Lithology:	Argillaceous Sandstone
Classific. (Folk, 1980):	Subarkose
Grain Size (mm):	0.074 (L. very fine sand)
Sorting:	well
Structures:	none evident

Rock Composition (Point-Count)

Framework Grains:

Mono quartz:	54.4	Argillaceous RF:	0.0
Poly quartz:	0.0	Dolomite RF:	3.6
K-Feldspar:	8.8	Micas:	2.4
Plagioclase:	1.2	Heavy minerals:	0.4
Volcanic RF:	0.4	Plant fragments:	0.0
Metamorphic RF:	0.0	Glauconite:	0.0
Limestone RF:	3.6	Rip-up/intraclasts:	0.0

Replaced Grains:

Dol RG:	0.0	Pyrite RG:	0.0
Cal RG:	0.8	Kaolinite RG:	0.0

Detrital Matrix:

Detrital clay:	0.0	Mixed clay/carbonate:	4.8
Organic matrix:	0.0	Dolomitic matrix:	3.2

Pore-filling Authigenic Minerals:

Authigenic clay:	2.0	Dolomite:	2.8
Quartz OG/QA:	6.0	Calcite:	2.0
Kspar OG:	tr	Anhydrite:	0.0
Pyrite:	2.0	Celestine:	0.0
Titanium oxides:	0.0	Halite:	1.2

Pore Types:

Intergranular:	0.4	Intragranular:	0.4
Frac SP:	0.0	Moldic:	0.0

XRD-Whole Rock Mineralogy (Weight %)

Quartz	62.6	Anhydrite	0.0
K-Feldspar	7.5	Celestine	0.0
Plagioclase	0.6	Halite	1.3
Calcite	9.0	Pyrite	1.8
Dolomite	7.4	Total Clay	9.9

Clay Abundance (Weight %)

Corrensite	0.0	Kaolinite	0.1
Illite / Smectite	1.4	Chlorite	1.2
Illite & Mica	7.2		

mixed-layer illite/smectite contains 15-25% smectite layers

Petrographic Description

This sample is a very fine grained, well sorted argillaceous sandstone. Framework grains include abundant quartz, moderate potassium feldspar, and minor to rare plagioclase, dolomite rock fragments, limestone rock fragments (LRF), volcanic rock fragments, mica, and heavy minerals (HM). The detrital clay matrix has been partially replaced by dolomite. Quartz overgrowths (red arrow) are the dominant intergranular cement. Pore-filling calcite and dolomite are also observed in minor amounts. Pyrite framboids are scattered throughout the sample. Rare intragranular pores (not pictured) have formed within partially dissolved feldspar grains.

Core Lab
RESERVOIR OPTIMIZATION

Relative Abundances:

Trace	<1%
Minor	1-5%
Moderate	5-10%
Common	10-20%
Abundant	>20%

Core Analysis Data:

Porosity (%):	10.38
Permeability (md):	0.0069
Gr. Density (g/cc):	2.684
Oil Saturation (%):	25.5
Water Saturation	67.2

PLATE 26

Scanning Electron Microscopy

Company:	**Fidelity E & P**
Well:	**Cane Creek 26-3**
Location:	**Grand Co., Utah**
Depth (ft):	**7435.15**
Unit:	**B**
Dep. Env.:	**Restricted Shallow Marine Shoreface**

LITHOLOGY

Argillaceous Sandstone

C

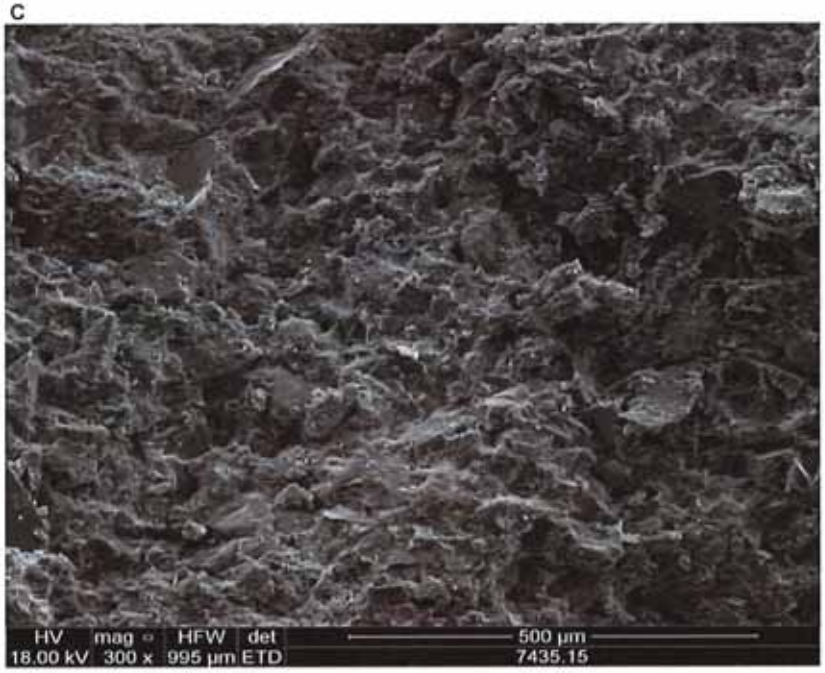

D

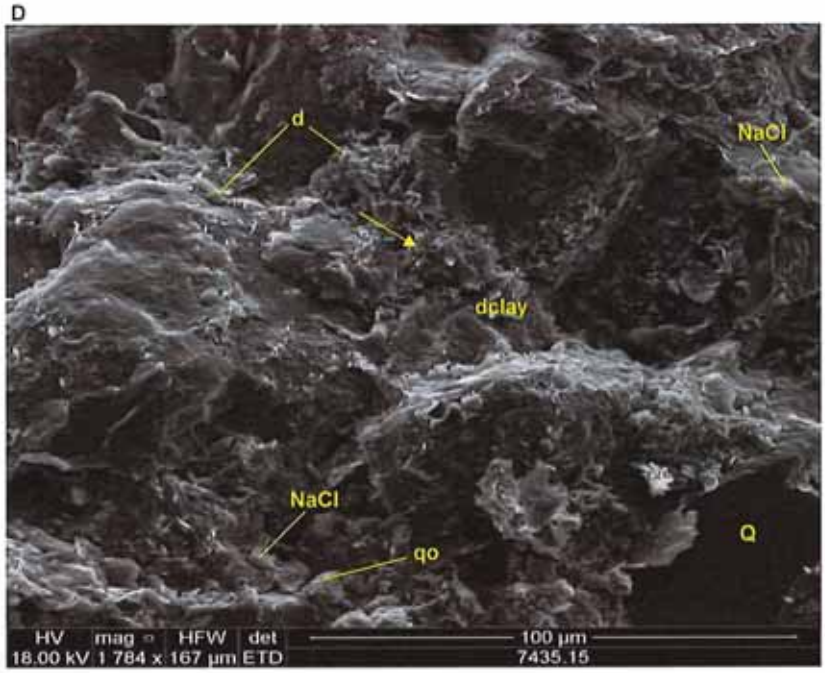

Mineralogy Determined by X-Ray Diffraction

(Weight %)

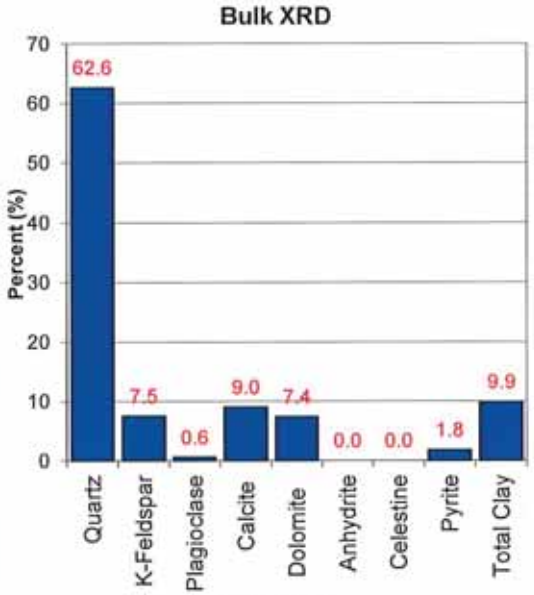

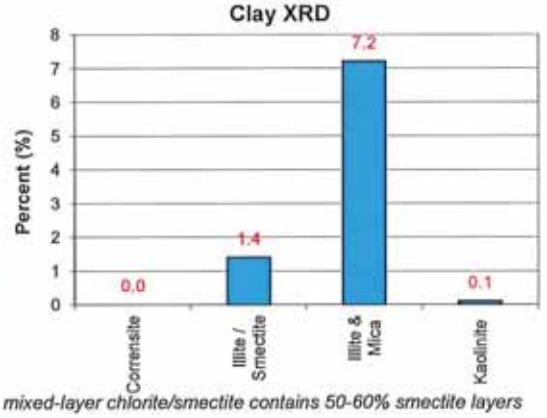

mixed-layer chlorite/smectite contains 50-60% smectite layers

SEM Description

Both authigenic (yellow arrow) and detrital clay (dclay) are observed in these SEM images. Small crystals of halite (NaCl) and dolomite (d) are noted throughout the SEM, typically associated with the clay. Composition was confirmed by EDX. Most of the framework grains are quartz. Quartz overgrowths (qo) are also noted.

Core Lab
RESERVOIR OPTIMIZATION

Relative Abundances:

Trace	<1%
Minor	1-5%
Moderate	5-10%
Common	10-20%
Abundant	>20%

Core Analysis Data:

Porosity (%):	10.38
Permeability (md):	0.0069
Gr. Density (g/cc):	2.684
Oil Saturation (%):	25.5
Water Saturation	67.2

PLATE 27

Thin Section Petrography

Company:	**Fidelity E & P**
Well:	**Cane Creek 26-3**
Location:	**Grand Co., Utah**
Depth (ft):	**7437.10**
Unit:	**B**
Dep. Env.:	**Restricted Shallow Marine Shoreface**

A

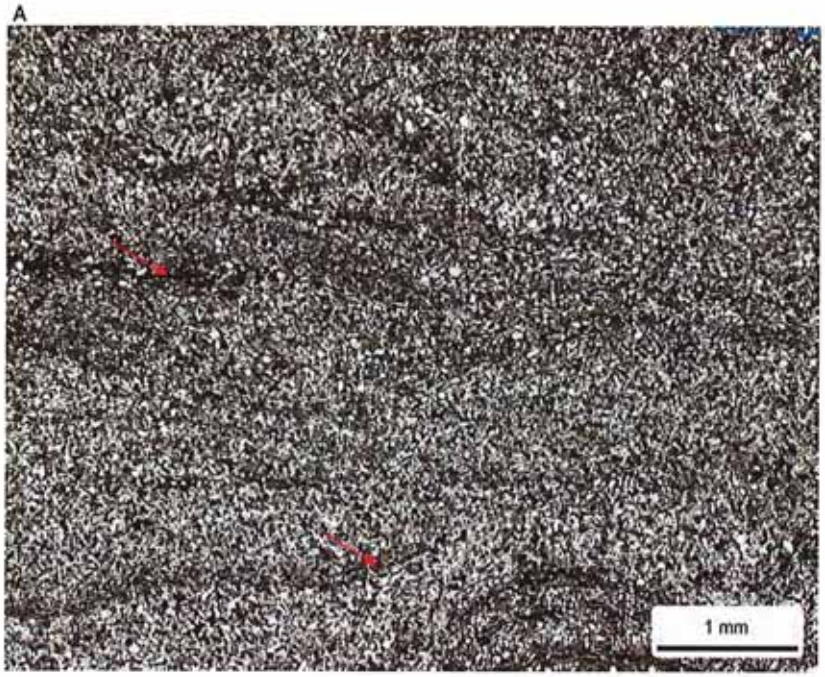

B

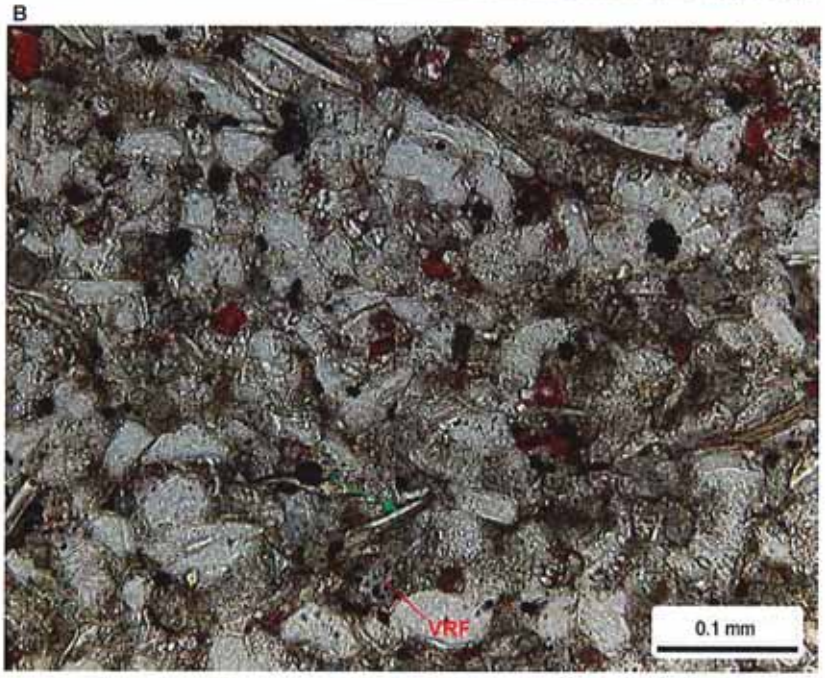

LITHOLOGY AND TEXTURE

Lithology:	Argillaceous Sandstone
Classific. (Folk, 1980):	Feldspathic Litharenite
Grain Size (mm):	0.068 (L. very fine sand)
Sorting:	well
Structures:	wavy laminae; open microfractures

Rock Composition (Point-Count)

Framework Grains:

Mono quartz:	36.8	Argillaceous RF:	0.4
Poly quartz:	0.0	Dolomite RF:	7.6
K-Feldspar:	8.4	Micas:	4.4
Plagioclase:	0.8	Heavy minerals:	tr
Volcanic RF:	2.0	Plant fragments:	1.2
Metamorphic RF:	0.0	Glauconite:	tr
Limestone RF:	4.0	Rip-up/intraclasts:	tr

Replaced Grains:

Dol RG:	0.0	Pyrite RG:	0.0
Cal RG:	1.2	Kaolinite RG:	0.0

Detrital Matrix:

Detrital clay:	0.0	Mixed clay/carbonate:	6.8
Organic matrix:	0.0	Dolomitic matrix:	7.2

Pore-filling Authigenic Minerals:

Authigenic clay:	2.8	Dolomite:	3.6
Quartz OG/QA:	6.8	Calcite:	2.0
Kspar OG:	0.0	Anhydrite:	0.0
Pyrite:	1.6	Celestine:	0.0
Titanium oxides:	0.8	Halite:	1.6

Pore Types:

Intergranular:	0.0	Intragranular:	0.0
Frac SP:	0.0	Moldic:	0.0

XRD-Whole Rock Mineralogy (Weight %)

Quartz	53.3	Anhydrite	0.0
K-Feldspar	7.0	Celestine	0.0
Plagioclase	0.8	Halite	2.0
Calcite	11.8	Pyrite	1.0
Dolomite	8.5	Total Clay	15.7

Clay Abundance (Weight %)

Corrensite	0.0	Kaolinite	0.2
Illite / Smectite	2.7	Chlorite	2.9
Illite & Mica	9.9		

mixed-layer illite/smectite contains 15-25% smectite layers

Petrographic Description

Detrital clay is concentrated into wavy laminae (red arrows) in this very fine grained argillaceous sandstone. Most of the framework grains are quartz; potassium feldspar, mica (green arrow), dolomite rock fragments, limestone rock fragments, and volcanic rock fragments (VRF) are also observed in minor to moderate amounts. The matrix has been replaced by dolomite. Calcite is less commonly found as a grain replacement and intergranular cement. Quartz overgrowths are the dominant pore-filling cement.

Core Lab
RESERVOIR OPTIMIZATION

Relative Abundances:

Trace	<1%
Minor	1-5%
Moderate	5-10%
Common	10-20%
Abundant	>20%

Core Analysis Data:

Porosity (%):	10.83
Permeability (md):	0.0314
Gr. Density (g/cc):	2.683
Oil Saturation (%):	22.5
Water Saturation	64.9

PLATE 28

Thin Section Petrography

Company:	**Fidelity E & P**
Well:	**Cane Creek 26-3**
Location:	**Grand Co., Utah**
Depth (ft):	**7439.25**
Unit:	**B**
Dep. Env.:	**Restricted Shallow Marine Shoreface**

A

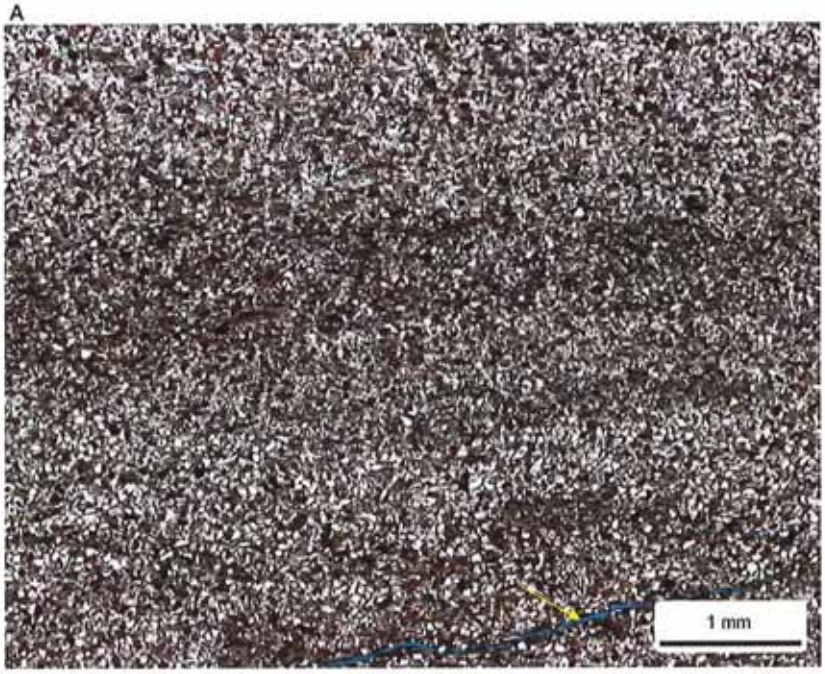

B

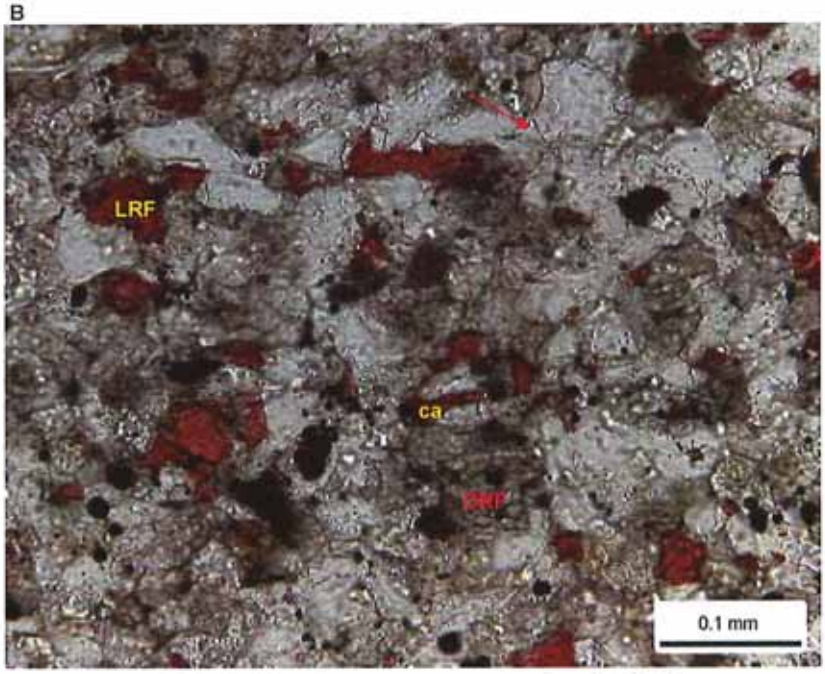

LITHOLOGY AND TEXTURE

Lithology:	Argillaceous Sandstone
Classific. (Folk, 1980):	Feldspathic Litharenite
Grain Size (mm):	0.075 (L. very fine sand)
Sorting:	well
Structures:	uneven laminae; burrowed

Rock Composition (Point-Count)

Framework Grains:

Mono quartz:	44.8	Argillaceous RF:	1.2
Poly quartz:	0.4	Dolomite RF:	9.6
K-Feldspar:	5.2	Micas:	0.4
Plagioclase:	0.0	Heavy minerals:	tr
Volcanic RF:	0.8	Plant fragments:	2.0
Metamorphic RF:	0.0	Glauconite:	0.0
Limestone RF:	2.8	Rip-up/intraclasts:	0.0

Replaced Grains:

Dol RG:	0.0	Pyrite RG:	0.0
Cal RG:	2.4	Kaolinite RG:	0.0

Detrital Matrix:

Detrital clay:	0.0	Mixed clay/carbonate:	4.0
Organic matrix:	0.0	Dolomitic matrix:	4.0

Pore-filling Authigenic Minerals:

Authigenic clay:	2.8	Dolomite:	2.8
Quartz OG/QA:	8.0	Calcite:	3.2
Kspar OG:	tr	Anhydrite:	0.0
Pyrite:	4.4	Celestine:	0.0
Titanium oxides:	0.4	Halite:	0.8

Pore Types:

Intergranular:	0.0	Intragranular:	0.0
Frac SP:	0.0	Moldic:	0.0

XRD-Whole Rock Mineralogy (Weight %)

Quartz	55.7	Anhydrite	0.0
K-Feldspar	5.4	Celestine	0.0
Plagioclase	0.0	Halite	1.4
Calcite	12.8	Pyrite	1.8
Dolomite	15.1	Total Clay	7.9

Clay Abundance (Weight %)

Corrensite	0.0	Kaolinite	0.0
Illite / Smectite	1.1	Chlorite	1.2
Illite & Mica	5.6		

mixed-layer illite/smectite contains 15-25% smectite layers

Petrographic Description

This very fine grained argillaceous sandstone contains uneven clay-rich laminae as well as "clean" sand-filled burrows. Framework grains are well sorted and predominantly quartz. Dolomite rock fragments (DRF) are moderate to common and potassium feldspar, argillaceous rock fragments, limestone rock fragments (LRF), calcite replaced grains, and plant fragments are observed in minor amounts. Quartz overgrowths (red arrow) are moderate in abundance. Dolomite, calcite (ca), and pyrite cements are minor in abundance. It is unclear if the microfracture (yellow arrow) in Photo A is natural or induced.

Core Lab

Relative Abundances:

Trace	<1%
Minor	1-5%
Moderate	5-10%
Common	10-20%
Abundant	>20%

Core Analysis Data:

Porosity (%):	9.07
Permeability (md):	0.0534
Gr. Density (g/cc):	2.707
Oil Saturation (%):	19.9
Water Saturation	68.5

PLATE 29

Thin Section Petrography

Company:	**Fidelity E & P**
Well:	**Cane Creek 26-3**
Location:	**Grand Co., Utah**
Depth (ft):	**7441.20**
Unit:	**B**
Dep. Env.:	**Restricted Shallow Marine Shoreface**

A

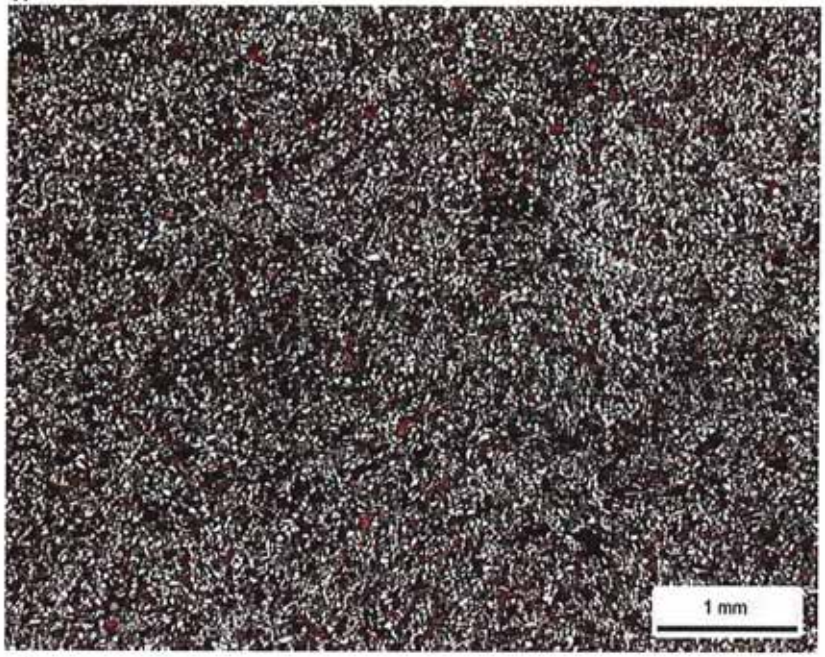

B

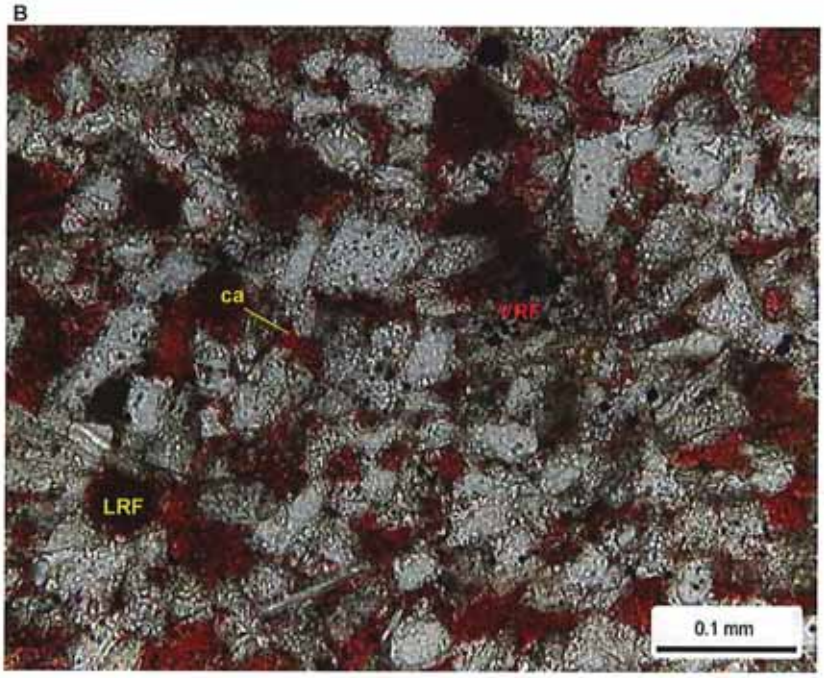

LITHOLOGY AND TEXTURE

Lithology:	Sandstone
Classific. (Folk, 1980):	Litharenite
Grain Size (mm):	0.067 (L. very fine sand)
Sorting:	well
Structures:	bioturbated

Rock Composition (Point-Count)

Framework Grains:			
Mono quartz:	42.4	Argillaceous RF:	2.0
Poly quartz:	0.0	Dolomite RF:	8.8
K-Feldspar:	4.4	Micas:	4.8
Plagioclase:	0.0	Heavy minerals:	0.0
Volcanic RF:	0.4	Plant fragments:	0.0
Metamorphic RF:	0.0	Glauconite:	0.0
Limestone RF:	10.8	Rip-up/intraclasts:	0.0
Replaced Grains:			
Dol RG:	0.0	Pyrite RG:	0.0
Cal RG:	3.6	Kaolinite RG:	0.0
Detrital Matrix:			
Detrital clay:	0.0	Mixed clay/carbonate:	2.0
Organic matrix:	0.0	Dolomitic matrix:	1.2
Pore-filling Authigenic Minerals:			
Authigenic clay:	3.2	Dolomite:	2.4
Quartz OG/QA:	6.0	Calcite:	4.0
Kspar OG:	0.4	Anhydrite:	0.0
Pyrite:	3.2	Celestine:	0.0
Titanium oxides:	0.0	Halite:	0.0
Pore Types:			
Intergranular:	0.4	Intragranular:	0.0
Frac SP:	0.0	Moldic:	tr

XRD-Whole Rock Mineralogy (Weight %)

Quartz	50.2	Anhydrite	0.0
K-Feldspar	6.3	Celestine	0.0
Plagioclase	0.0	Halite	0.0
Calcite	13.5	Pyrite	1.0
Dolomite	14.3	Total Clay	14.8
Clay Abundance (Weight %)			
Corrensite	0.0	Kaolinite	0.4
Illite / Smectite	2.0	Chlorite	2.5
Illite & Mica	9.9		

mixed-layer illite/smectite contains 15-25% smectite layers

Petrographic Description

This very fine grained, well sorted sandstone is bioturbated. Quartz grains are abundant, limestone rock fragments (LRF) and dolomite rock fragments are moderate to common, and potassium feldspar, mica, argillaceous rock fragments, volcanic rock fragments (VRF) and calcite replaced grains are minor to rare. Detrital clay matrix is minor in abundance, and partially replaced by dolomite. Intergranular pores (not pictured) are rare; most are cemented by well developed quartz overgrowths, calcite (ca), and dolomite cements. Secondary intragranular and moldic pores are rare.

Core Lab
RESERVOIR OPTIMIZATION

Relative Abundances:	
Trace	<1%
Minor	1-5%
Moderate	5-10%
Common	10-20%
Abundant	>20%

Core Analysis Data:	
Porosity (%):	11.74
Permeability (md):	0.0670
Gr. Density (g/cc):	2.686
Oil Saturation (%):	33.4
Water Saturation	48.5

PLATE 29

Scanning Electron Microscopy

Company:	**Fidelity E & P**
Well:	**Cane Creek 26-3**
Location:	**Grand Co., Utah**
Depth (ft):	**7441.20**
Unit:	**B**
Dep. Env.:	**Restricted Shallow Marine Shoreface**

LITHOLOGY

Sandstone

C

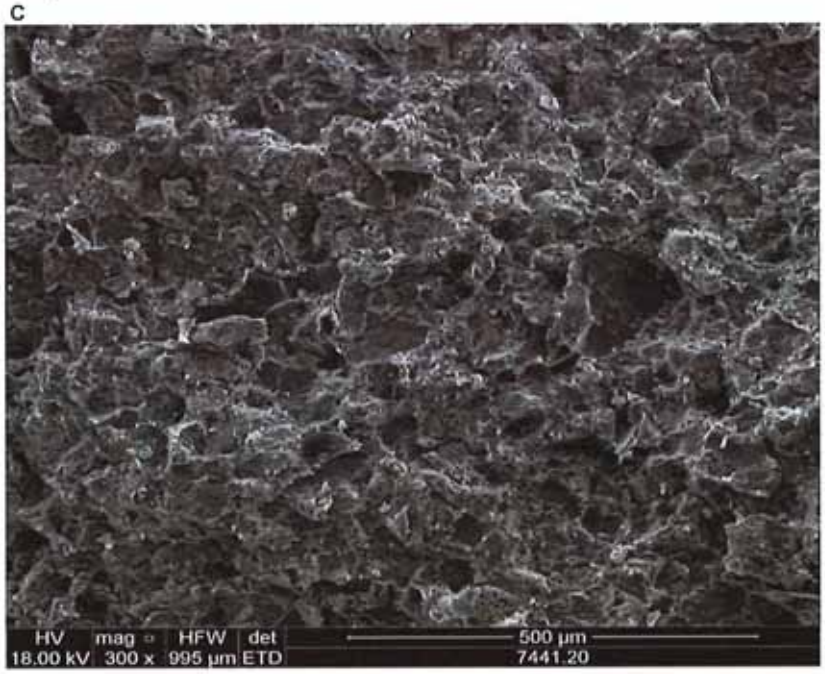

D

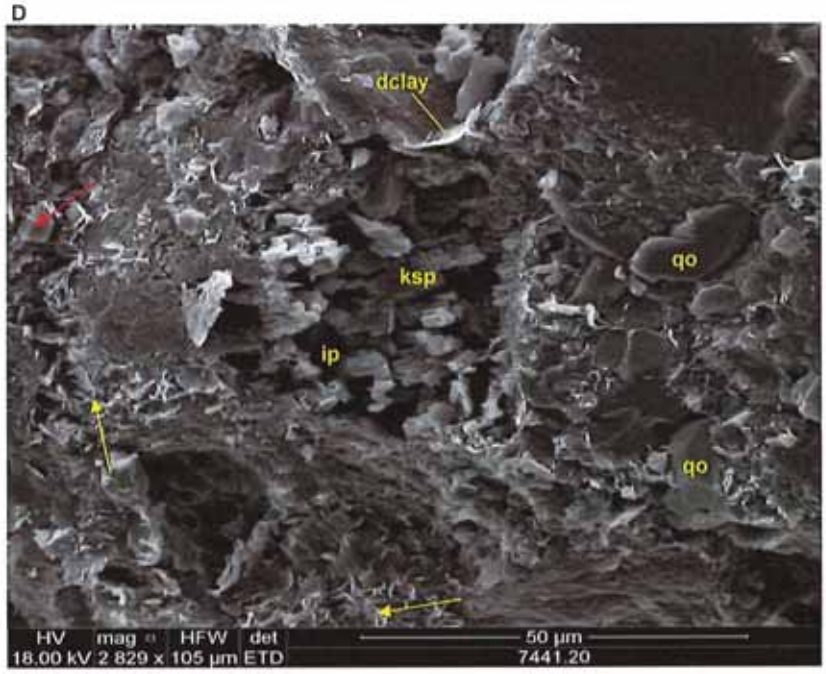

Mineralogy Determined by X-Ray Diffraction

(Weight %)

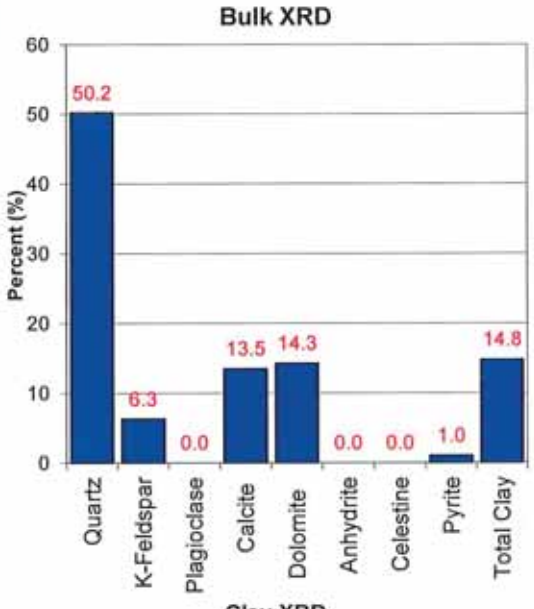

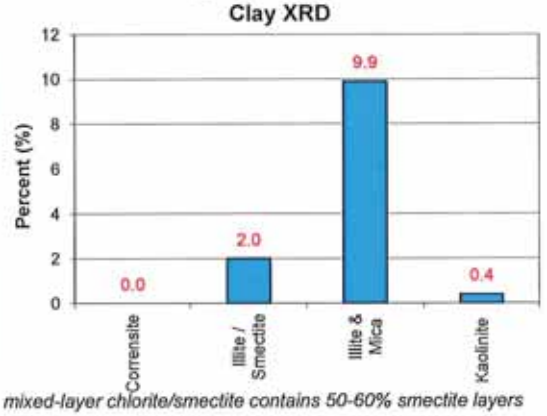

mixed-layer chlorite/smectite contains 50-60% smectite layers

SEM Description

Both grain coating authigenic mixed-layer illite/smectite (yellow arrows) and detrital clay (dclay) are observed in SEM. Other cements include quartz overgrowths (qo) and finely crystalline, euhedral dolomite (red arrow). A secondary intragranular pore (ip) has formed within a partially dissolved potassium feldspar grain (ksp).

Core Lab

Relative Abundances:

Trace	<1%
Minor	1-5%
Moderate	5-10%
Common	10-20%
Abundant	>20%

Core Analysis Data:

Porosity (%):	11.74
Permeability (md):	0.0670
Gr. Density (g/cc):	2.686
Oil Saturation (%):	33.4
Water Saturation	48.5

PLATE 30

Thin Section Petrography

Company:	**Fidelity E & P**
Well:	**Cane Creek 26-3**
Location:	**Grand Co., Utah**
Depth (ft):	**7443.00**
Unit:	**B**
Dep. Env.:	**Restricted Shallow Marine Shoreface**

A

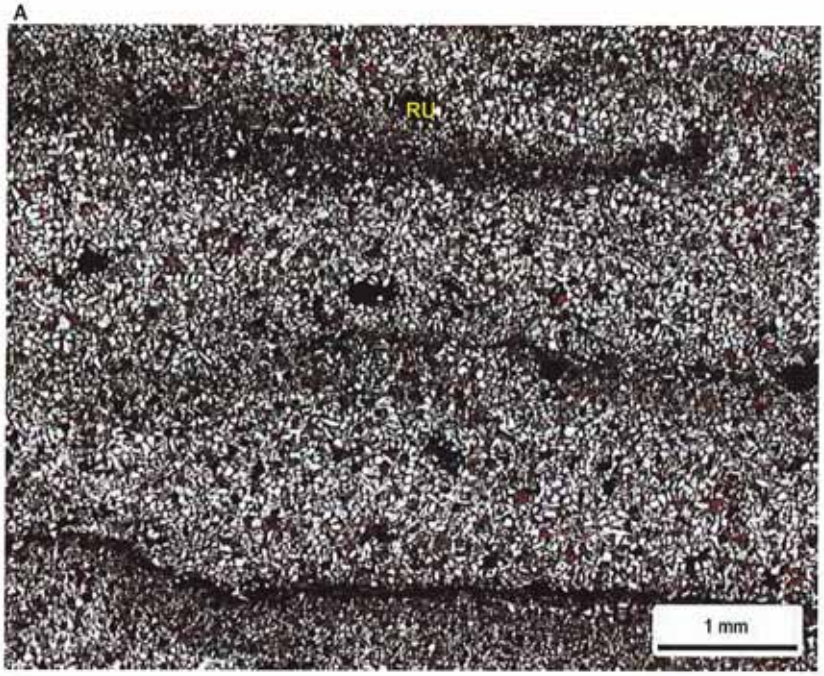

B

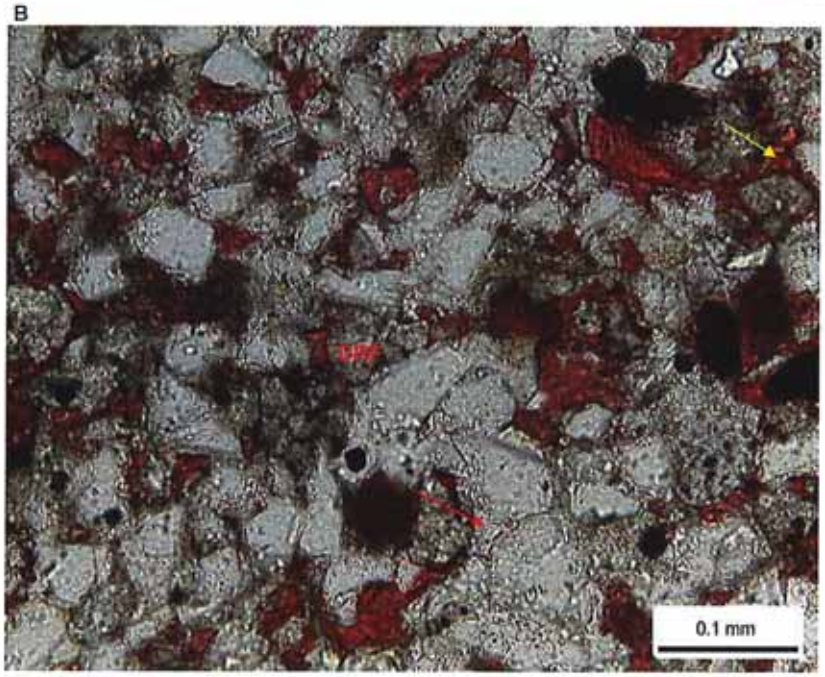

LITHOLOGY AND TEXTURE

Lithology:	Sandstone
Classific. (Folk, 1980):	Sublitharenite
Grain Size (mm):	0.075 (L. very fine sand)
Sorting:	well
Structures:	discontinuous laminae

Rock Composition (Point-Count)

Framework Grains:

Mono quartz:	56.0	Argillaceous RF:	3.6
Poly quartz:	0.0	Dolomite RF:	1.6
K-Feldspar:	6.0	Micas:	1.6
Plagioclase:	tr	Heavy minerals:	0.8
Volcanic RF:	0.8	Plant fragments:	0.4
Metamorphic RF:	0.0	Glauconite:	0.0
Limestone RF:	4.4	Rip-up/intraclasts:	0.8

Replaced Grains:

Dol RG:	0.0	Pyrite RG:	0.0
Cal RG:	2.8	Kaolinite RG:	0.0

Detrital Matrix:

Detrital clay:	1.6	Mixed clay/carbonate:	0.0
Organic matrix:	0.0	Dolomitic matrix:	0.4

Pore-filling Authigenic Minerals:

Authigenic clay:	1.2	Dolomite:	0.8
Quartz OG/QA:	7.6	Calcite:	4.4
Kspar OG:	tr	Anhydrite:	0.4
Pyrite:	2.0	Celestine:	0.0
Titanium oxides:	tr	Halite:	0.4

Pore Types:

Intergranular:	2.4	Intragranular:	0.0
Frac SP:	0.0	Moldic:	0.0

XRD-Whole Rock Mineralogy (Weight %)

Quartz	59.0	Anhydrite	0.0
K-Feldspar	6.1	Celestine	0.0
Plagioclase	0.0	Halite	1.5
Calcite	22.5	Pyrite	1.6
Dolomite	3.0	Total Clay	6.4

Clay Abundance (Weight %)

Corrensite	0.0	Kaolinite	0.0
Illite / Smectite	0.8	Chlorite	1.3
Illite & Mica	4.3		

mixed-layer illite/smectite contains 15-25% smectite layers

Petrographic Description

Discontinuous clay-rich laminae are observed in this very fine grained sandstone. Framework grains are well sorted and have mostly subangular to subrounded shapes. Quartz is the most abundant grain. Other grains found in minor to moderate amounts include potassium feldspar, dolomite rock fragments (DRF), limestone rock fragments, argillaceous rock fragments, mica, and calcite replaced grains. Localized dolomitic rip-up clasts (RU) are noted. Quartz overgrowths (red arrow) are well developed around some grains. Other pore-filling cements include calcite (yellow arrow) and pyrite. Intergranular pores (not pictured) are minor in abundance, and unevenly distributed.

Core Lab
RESERVOIR OPTIMIZATION

Relative Abundances:

Trace	<1%
Minor	1-5%
Moderate	5-10%
Common	10-20%
Abundant	>20%

Core Analysis Data:

Porosity (%):	6.90
Permeability (md):	0.0077
Gr. Density (g/cc):	2.679
Oil Saturation (%):	22.7
Water Saturation	53.6

PLATE 30

Scanning Electron Microscopy

Company: Fidelity E & P
Well: Cane Creek 26-3
Location: Grand Co., Utah
Depth (ft): 7443.00
Unit: B
Dep. Env.: Restricted Shallow Marine Shoreface

LITHOLOGY
Sandstone

C

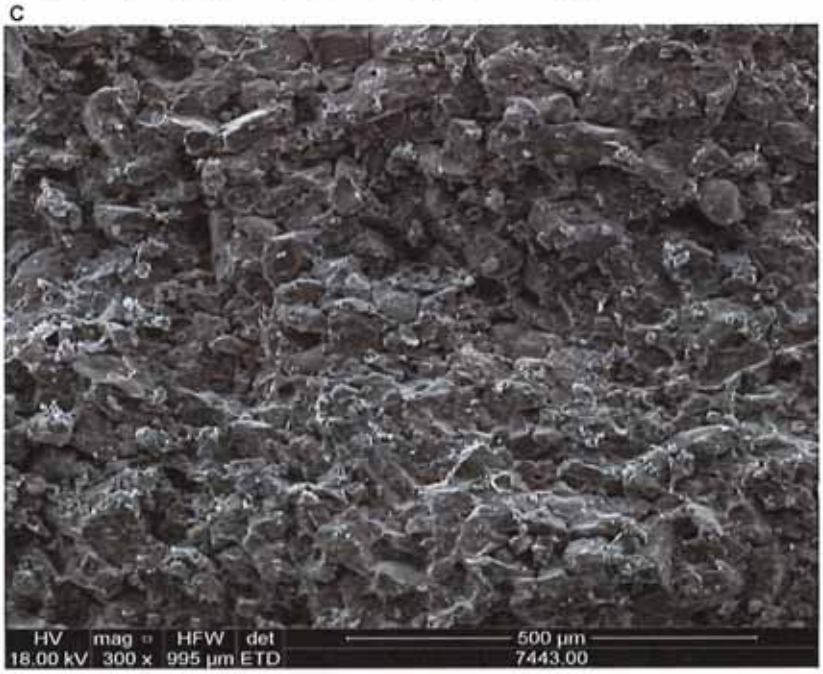

D

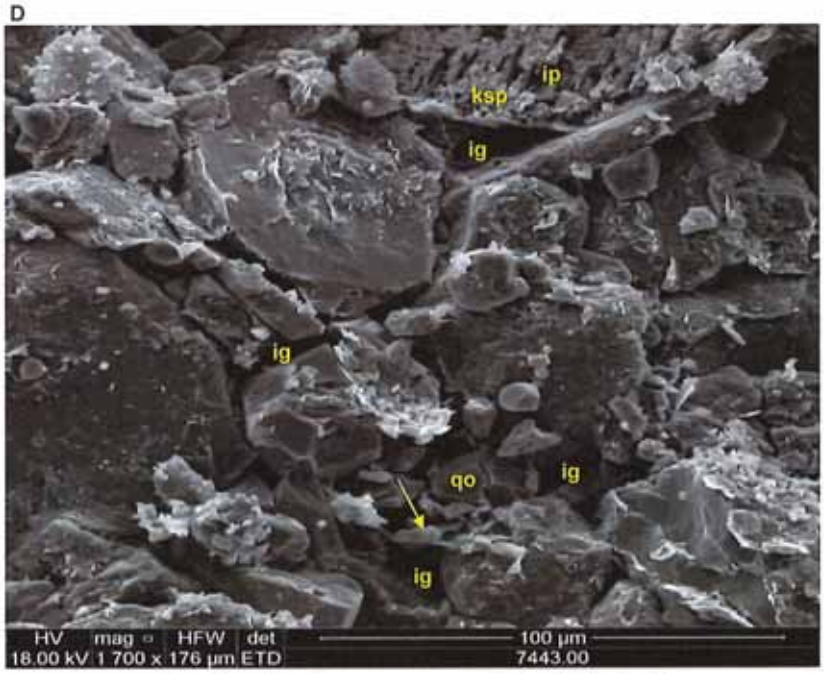

Mineralogy Determined by X-Ray Diffraction
(Weight %)

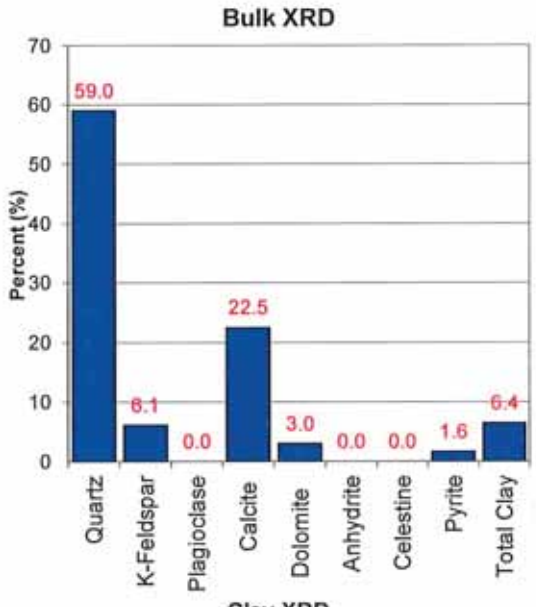

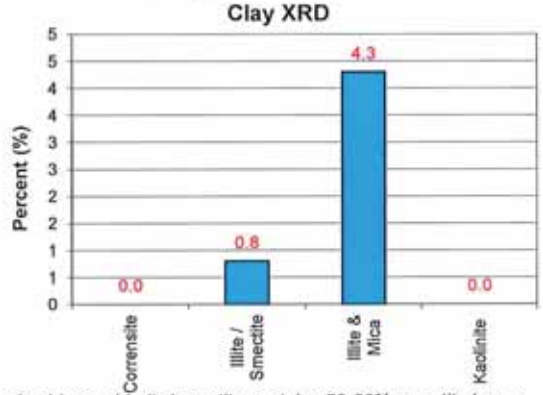

mixed-layer chlorite/smectite contains 50-60% smectite layers

SEM Description

Several small intergranular pores (ig) are noted in the high magnification SEM image (Photo D). Rare secondary intragranular pores (ip) are also observed within a partially dissolved potassium feldspar grain (ksp). Detrital clay flakes yellow arrow) are also identified.

Core Lab
RESERVOIR OPTIMIZATION

Relative Abundances:

Trace	<1%
Minor	1-5%
Moderate	5-10%
Common	10-20%
Abundant	>20%

Core Analysis Data:

Porosity (%):	6.90
Permeability (md):	0.0077
Gr. Density (g/cc):	2.679
Oil Saturation (%):	22.7
Water Saturation	53.6

PLATE 31

Thin Section Petrography

Company:	**Fidelity E & P**
Well:	**Cane Creek 26-3**
Location:	**Grand Co., Utah**
Depth (ft):	**7446.15**
Unit:	**C**
Dep. Env.:	**Restricted Shallow Marine Shoreface**

A

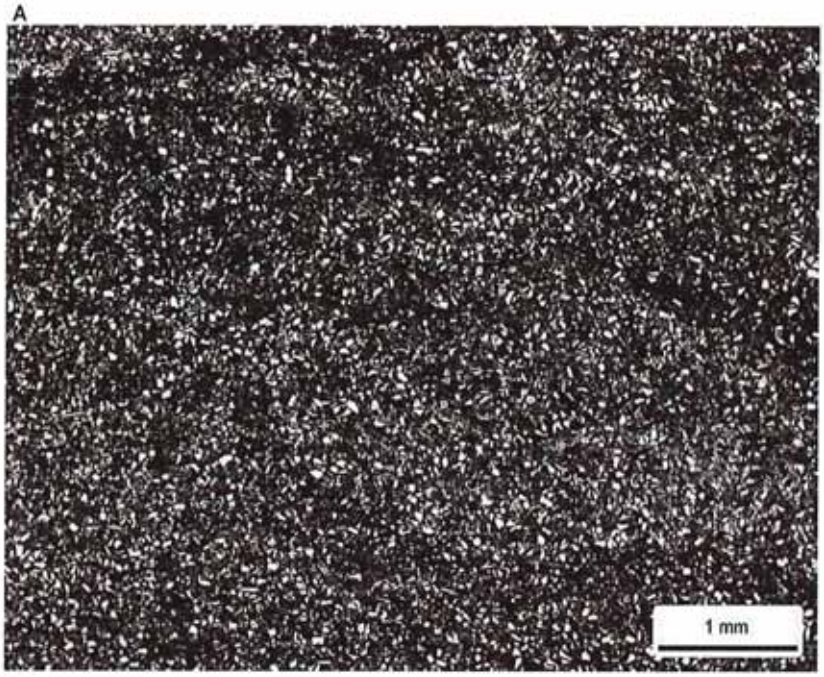

B

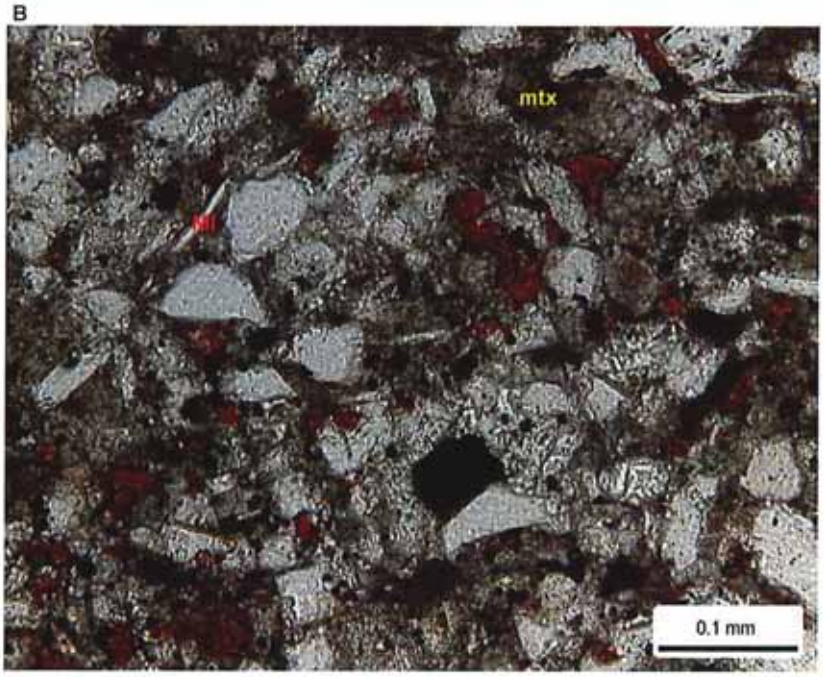

LITHOLOGY AND TEXTURE

Lithology:	Dolomitic Argill. Sandstone
Classific. (Folk, 1980):	Feldspathic Litharenite
Grain Size (mm):	0.066 (L. very fine sand)
Sorting:	moderately well
Structures:	faint laminae disrupted by bioturbation

Rock Composition (Point-Count)

Framework Grains:

Mono quartz:	40.8	Argillaceous RF:	0.4
Poly quartz:	0.4	Dolomite RF:	16.0
K-Feldspar:	6.8	Micas:	0.8
Plagioclase:	0.0	Heavy minerals:	tr
Volcanic RF:	0.8	Plant fragments:	2.0
Metamorphic RF:	0.4	Glauconite:	0.0
Limestone RF:	2.8	Rip-up/intraclasts:	0.0

Replaced Grains:

Dol RG:	0.0	Pyrite RG:	0.0
Cal RG:	3.6	Kaolinite RG:	0.0

Detrital Matrix:

Detrital clay:	0.0	Mixed clay/carbonate:	9.6
Organic matrix:	0.0	Dolomitic matrix:	6.0

Pore-filling Authigenic Minerals:

Authigenic clay:	0.4	Dolomite:	2.0
Quartz OG/QA:	0.8	Calcite:	2.8
Kspar OG:	tr	Anhydrite:	0.4
Pyrite:	3.2	Celestine:	0.0
Titanium oxides:	0.0	Halite:	0.0

Pore Types:

Intergranular:	0.0	Intragranular:	0.0
Frac SP:	0.0	Moldic:	0.0

XRD-Whole Rock Mineralogy (Weight %)

Quartz	41.6	Anhydrite	0.0
K-Feldspar	5.3	Celestine	0.0
Plagioclase	0.0	Halite	0.0
Calcite	22.2	Pyrite	1.1
Dolomite	19.9	Total Clay	10.0

Clay Abundance (Weight %)

Corrensite	0.0	Kaolinite	0.0
Illite / Smectite	1.4	Chlorite	2.0
Illite & Mica	6.6		

mixed-layer illite/smectite contains 15-25% smectite layers

Petrographic Description

This sample is a very fine grained, moderately well sorted dolomitic argillaceous sandstone. Faint laminations are disrupted by bioturbation. Quartz grains are abundant and dolomite rock fragments are common. Other less common grains include potassium feldspar, limestone rock fragments, plant fragments, mica (Mi) and calcite replaced grains. The matrix (mtx) is rich in calcite and detrital clay, and has been partially replaced by dolomite. Pore-filling cements include calcite, dolomite, and pyrite. No open pores are identified in thin section.

Core Lab
RESERVOIR OPTIMIZATION

Relative Abundances:

Trace	<1%
Minor	1-5%
Moderate	5-10%
Common	10-20%
Abundant	>20%

Core Analysis Data:

Porosity (%):	3.95
Permeability (md):	0.0015
Gr. Density (g/cc):	2.710
Oil Saturation (%):	31.2
Water Saturation	63.0

PLATE 32

Thin Section Petrography

Company:	**Fidelity E & P**
Well:	**Cane Creek 26-3**
Location:	**Grand Co., Utah**
Depth (ft):	**7448.15**
Unit:	**C**
Dep. Env.:	**Shallow Shelf Salina/Sabkha**

A

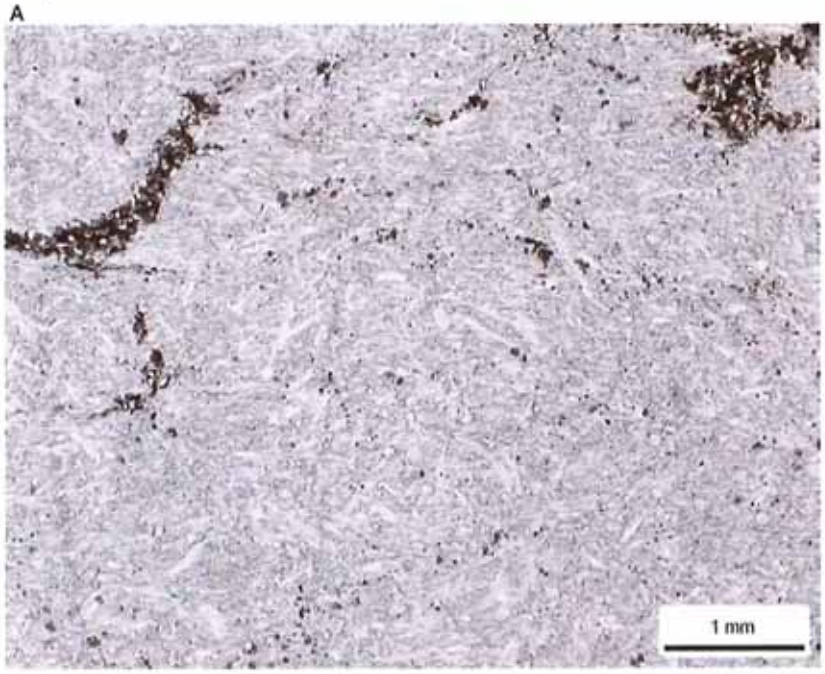

B

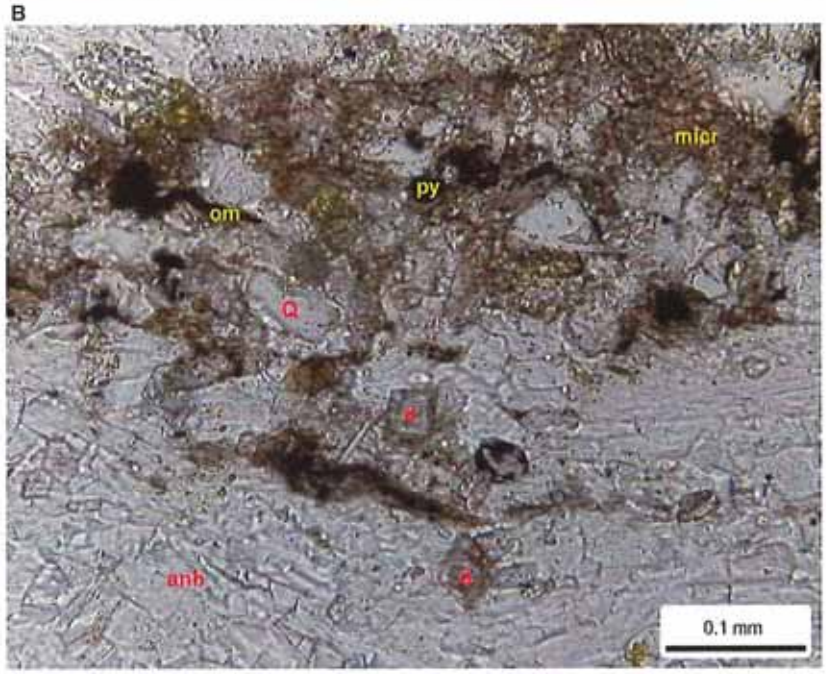

LITHOLOGY AND TEXTURE

Lithology:	Anhydrite
Classific. (Folk, 1980):	n/a
Grain Size (mm):	n/a
Sorting:	n/a
Structures:	none evident

Rock Composition (Point-Count)

Framework Grains:

Mono quartz:	0.8	Argillaceous RF:	0.0
Poly quartz:	0.0	Chert RF:	0.0
K-Feldspar:	0.4	Micas:	tr
Plagioclase:	0.0	Heavy minerals:	0.0
Volcanic RF:	0.0	Plant fragments:	tr
Metamorphic RF:	0.0	Glauconite:	0.0
Limestone RF:	0.0	Rip-up/intraclasts:	0.0

Replaced Grains:

Dol RG:	0.0	Pyrite RG:	0.0
Cal RG:	0.0	Kaolinite RG:	0.0

Detrital Matrix:

Detrital clay:	0.0	Micrite matrix:	1.2
Organic matrix:	0.0	Dolomitic matrix:	0.0

Pore-filling Authigenic Minerals:

Authigenic clay:	0.0	Dolomite:	0.4
Quartz OG/QA:	0.0	Calcite:	0.0
Kspar OG:	0.0	Anhydrite:	96.8
Pyrite:	0.4	Celestine:	0.0
Titanium oxides:	0.0	Halite:	0.0

Pore Types:

Intergranular:	0.0	Intragranular:	0.0
Frac SP:	0.0	Moldic:	0.0

XRD-Whole Rock Mineralogy (Weight %)

Quartz	2.5	Anhydrite	91.7
K-Feldspar	0.0	Celestine	0.7
Plagioclase	0.0	Halite	0.0
Calcite	1.8	Pyrite	0.0
Dolomite	1.5	Total Clay	1.7

Clay Abundance (Weight %)

Corrensite	0.0	Kaolinite	0.0
Illite / Smectite	0.2	Chlorite	0.5
Illite & Mica	1.0		

mixed-layer illite/smectite contains 15-25% smectite layers

Petrographic Description

This sample is made up almost entirely of anhydrite (anh). A minor amount of micrite matrix (micr) remains. Quartz (Q), potassium feldspar, muscovite, and organic matter (om) are concentrated in the micrite matrix. Pyrite (py) and dolomite cements (d) are rare.

Relative Abundances:

Trace	<1%
Minor	1-5%
Moderate	5-10%
Common	10-20%
Abundant	>20%

Core Analysis Data:

Porosity (%):	0.54
Permeability (md):	-
Gr. Density (g/cc):	2.943
Oil Saturation (%):	12.4
Water Saturation	15.2

Core Lab
RESERVOIR OPTIMIZATION

PLATE 33

Thin Section Petrography

Company:	**Fidelity E & P**
Well:	**Cane Creek 26-3**
Location:	**Grand Co., Utah**
Depth (ft):	**7450.10**
Unit:	**C**
Dep. Env.:	**Shallow Shelf Salina/Sabkha**

A

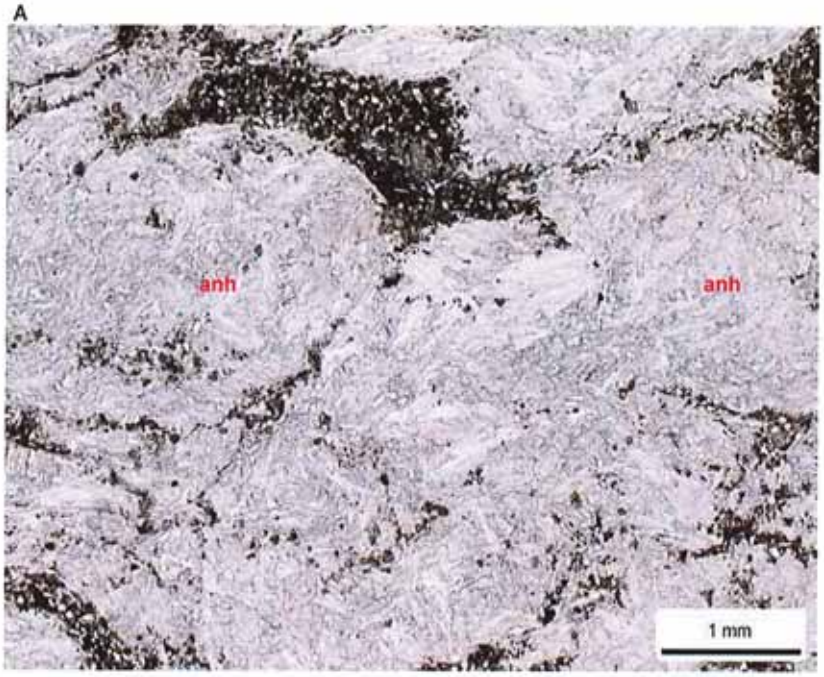

B

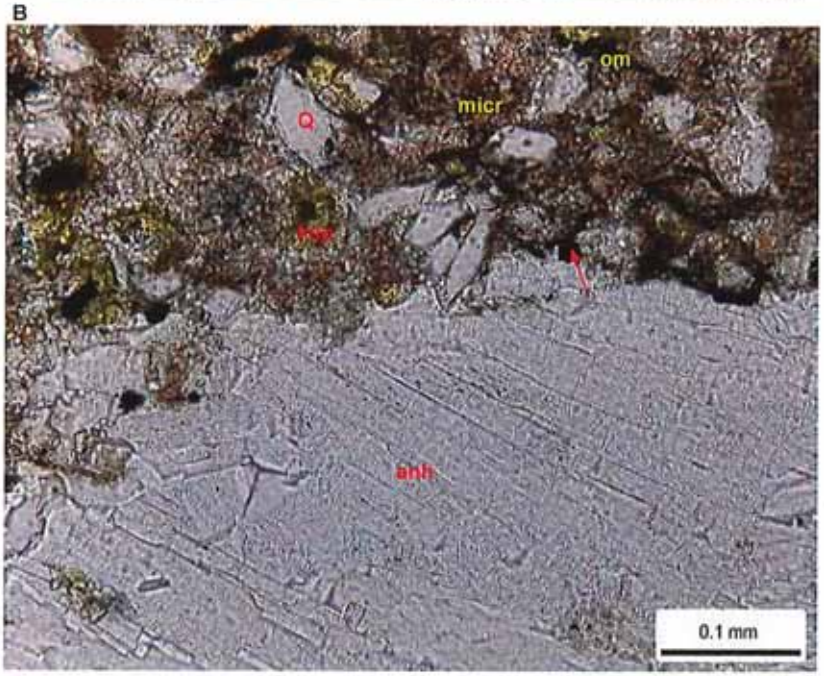

LITHOLOGY AND TEXTURE

Lithology:	Anhydrite
Classific. (Folk, 1980):	n/a
Grain Size (mm):	n/a
Sorting:	n/a
Structures:	nodular texture

Rock Composition (Point-Count)

Framework Grains:

Mono quartz:	1.6	Argillaceous RF:	0.0
Poly quartz:	0.0	Dolomite RF:	0.8
K-Feldspar:	0.4	Micas:	tr
Plagioclase:	0.0	Heavy minerals:	0.0
Volcanic RF:	0.0	Plant fragments:	tr
Metamorphic RF:	0.0	Glauconite:	0.0
Limestone RF:	0.0	Rip-up/intraclasts:	0.0

Replaced Grains:

Dol RG:	0.0	Pyrite RG:	0.0
Cal RG:	0.0	Kaolinite RG:	0.0

Detrital Matrix:

Detrital clay:	0.0	Micrite matrix:	2.8
Organic matrix:	0.0	Dolomitic matrix:	0.0

Pore-filling Authigenic Minerals:

Authigenic clay:	0.0	Dolomite:	1.6
Quartz OG/QA:	0.0	Calcite:	tr
Kspar OG:	0.0	Anhydrite:	92.8
Pyrite:	tr	Celestine:	0.0
Titanium oxides:	0.0	Halite:	0.0

Pore Types:

Intergranular:	0.0	Intragranular:	0.0
Frac SP:	0.0	Moldic:	0.0

XRD-Whole Rock Mineralogy (Weight %)

Quartz	5.6	Anhydrite	77.0
K-Feldspar	0.7	Celestine	0.0
Plagioclase	0.0	Halite	0.0
Calcite	12.9	Pyrite	0.4
Dolomite	0.5	Total Clay	2.8

Clay Abundance (Weight %)

Corrensite	0.0	Kaolinite	0.0
Illite / Smectite	0.5	Chlorite	0.4
Illite & Mica	1.9		

mixed-layer illite/smectite contains 15-25% smectite layers

Petrographic Description

This anhydrite sample has a nodular texture. The thin zones between the anhydrite nodules (anh) consist of quartz (Q) and potassium feldspar (ksp) in a micrite matrix (micr). Elongate fragments of organic matter (om) and muscovite are also observed. Dolomite, calcite, and pyrite (red arrow) cements are rare.

Core Lab
RESERVOIR OPTIMIZATION

Relative Abundances:

Trace	<1%
Minor	1-5%
Moderate	5-10%
Common	10-20%
Abundant	>20%

Core Analysis Data:

Porosity (%):	0.94
Permeability (md):	-
Gr. Density (g/cc):	2.896
Oil Saturation (%):	35.4
Water Saturation	26.0

PLATE 34

Thin Section Petrography

Company:	Fidelity E & P
Well:	Cane Creek 26-3
Location:	Grand Co., Utah
Depth (ft):	7452.20
Unit:	C
Dep. Env.:	Restricted Shallow Marine Shoreface

A

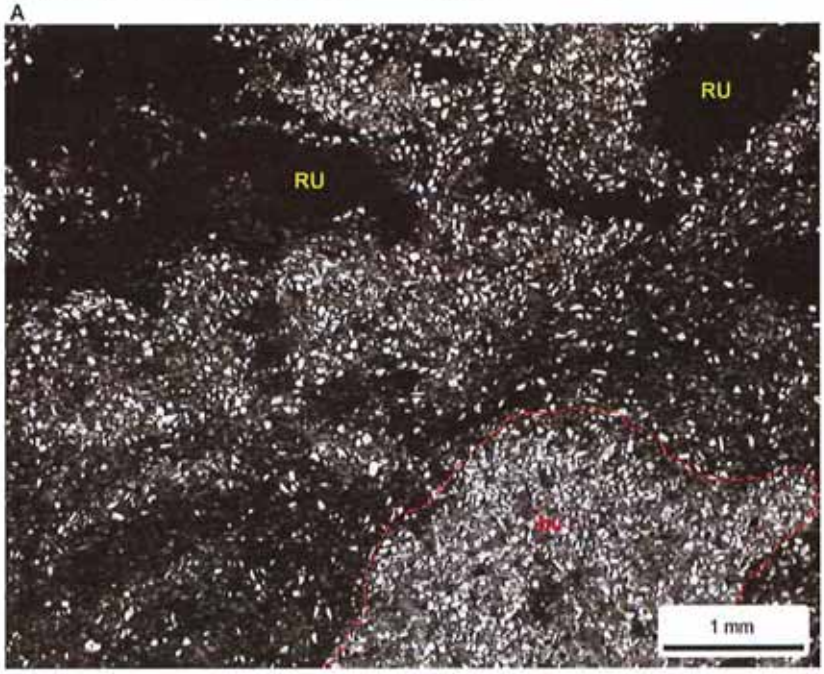

B

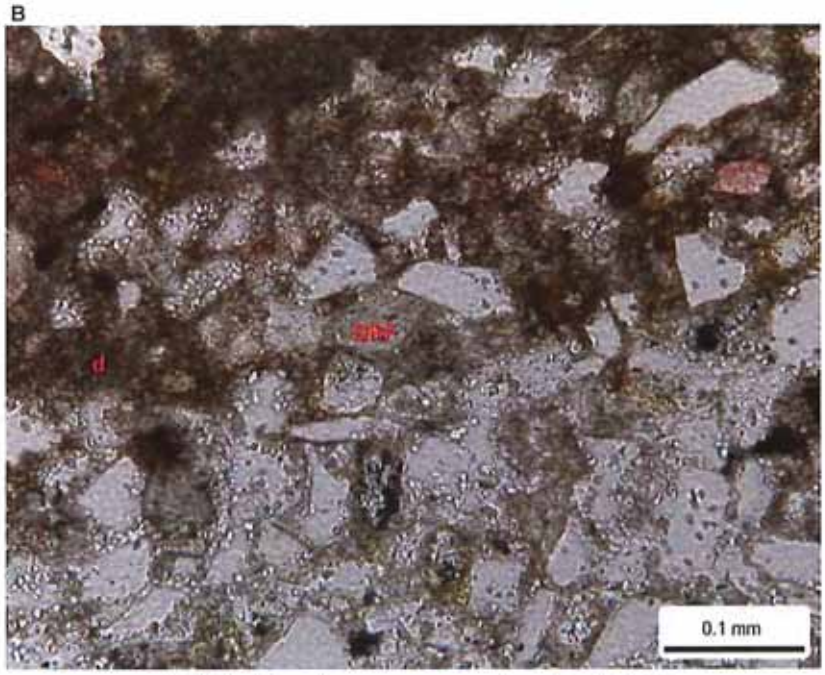

LITHOLOGY AND TEXTURE

Lithology:	Dolomitic Argill. Sandstone
Classific. (Folk, 1980):	Litharenite
Grain Size (mm):	0.078 (L. very fine sand)
Sorting:	moderately well
Structures:	bioturbated; discontinuous open microfractures

Rock Composition (Point-Count)

Framework Grains:

Mono quartz:	30.8	Argillaceous RF:	0.0
Poly quartz:	0.4	Dolomite RF:	17.6
K-Feldspar:	2.4	Micas:	1.6
Plagioclase:	0.0	Heavy minerals:	0.0
Volcanic RF:	0.0	Plant fragments:	2.4
Metamorphic RF:	0.0	Glauconite:	tr
Peloid-dolomite:	0.0	Rip-up/intraclasts:	2.4

Replaced Grains:

Dol RG:	0.0	Pyrite RG:	0.4
Cal RG:	0.0	Kaolinite RG:	0.0

Detrital Matrix:

Detrital clay:	0.0	Micrite matrix:	0.0
Organic matrix:	0.0	Dolomitic matrix:	34.8

Pore-filling Authigenic Minerals:

Authigenic clay:	0.0	Dolomite:	4.4
Quartz OG/QA:	0.8	Calcite:	0.0
Kspar OG:	0.0	Anhydrite:	0.0
Pyrite:	1.6	Celestine:	0.0
Titanium oxides:	0.0	Halite:	0.0

Pore Types:

Intergranular:	0.0	Intragranular:	0.4
Frac SP:	0.0	Moldic:	0.0

XRD-Whole Rock Mineralogy (Weight %)

Quartz	33.3	Anhydrite	2.6
K-Feldspar	3.5	Celestine	0.0
Plagioclase	0.0	Halite	0.7
Calcite	0.0	Pyrite	0.9
Dolomite	53.3	Total Clay	5.7

Clay Abundance (Weight %)

Corrensite	0.0	Kaolinite	0.0
Illite / Smectite	0.5	Chlorite	1.7
Illite & Mica	3.5		

mixed-layer illite/smectite contains 15-25% smectite layers

Petrographic Description

This very fine-grained dolomitic argillaceous sandstone is burrowed (bu). Most of the framework grains are quartz but dolomite rock fragments (DRF), potassium feldspar, muscovite, and organic matter are also observed in minor amounts. Dolomite has replaced rip-up clasts (RU). Most of the matrix has also been replaced by dolomite (d), although some detrital clay remains. Other minor to rare cements include quartz overgrowths and pyrite. Isolated intragranular pore within partially dissolved grains are the only pore type observed in thin section.

Core Lab

Relative Abundances:

Trace	<1%
Minor	1-5%
Moderate	5-10%
Common	10-20%
Abundant	>20%

Core Analysis Data:

Porosity (%):	9.24
Permeability (md):	0.0089
Gr. Density (g/cc):	2.754
Oil Saturation (%):	40.9
Water Saturation	36.1

PLATE 35

Thin Section Petrography

Company:	**Fidelity E & P**
Well:	**Cane Creek 26-3**
Location:	**Grand Co., Utah**
Depth (ft):	**7454.00**
Unit:	**C**
Dep. Env.:	**Restricted Shallow Marine Shoreface**

A

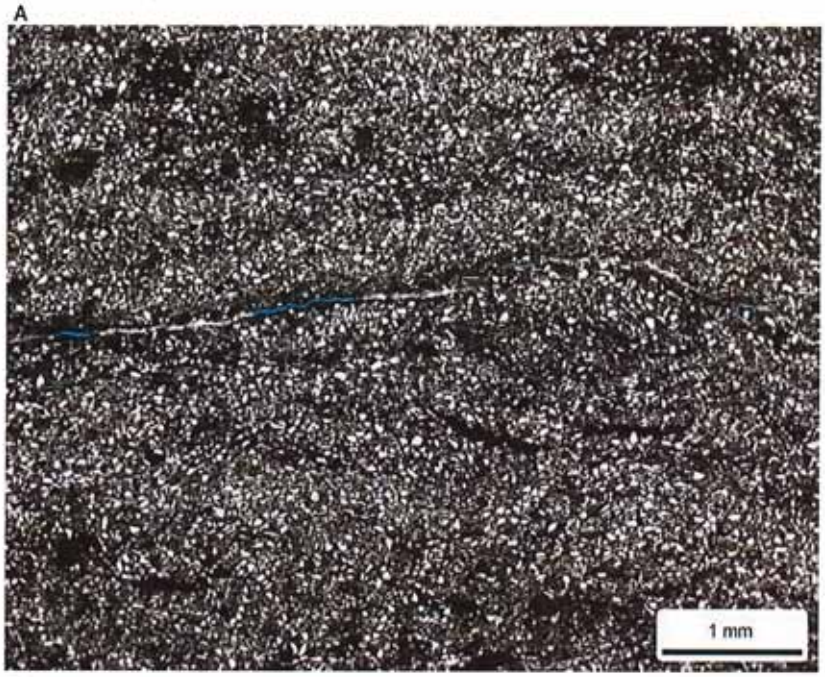

B

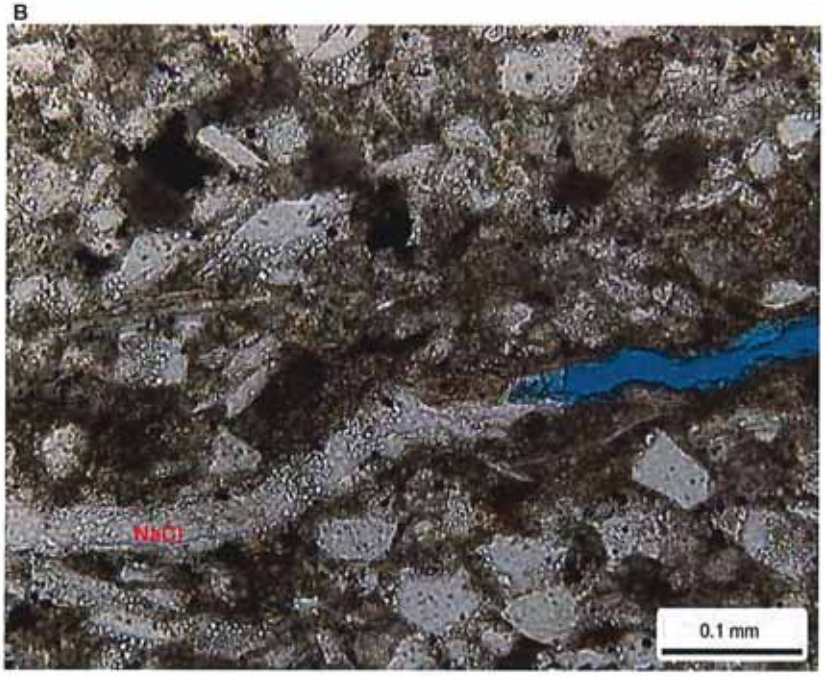

LITHOLOGY AND TEXTURE

Lithology:	Dolomitic Argill. Sandstone
Classific. (Folk, 1980):	Feldspathic Litharenite
Grain Size (mm):	0.064 (L. very fine sand)
Sorting:	well
Structures:	bioturbated; microfractures

Rock Composition (Point-Count)

Framework Grains:

Mono quartz:	42.0	Argillaceous RF:	0.0
Poly quartz:	0.0	Dolomite RF:	17.6
K-Feldspar:	6.8	Micas:	0.8
Plagioclase:	0.0	Heavy minerals:	0.8
Volcanic RF:	1.2	Plant fragments:	0.4
Metamorphic RF:	0.0	Glauconite:	0.0
Peloid-dolomite:	0.0	Rip-up/intraclasts:	1.2

Replaced Grains:

Dol RG:	0.0	Pyrite RG:	0.0
Cal RG:	0.0	Kaolinite RG:	0.0

Detrital Matrix:

Detrital clay:	1.2	Micrite matrix:	0.0
Organic matrix:	0.0	Dolomitic matrix:	17.2

Pore-filling Authigenic Minerals:

Authigenic clay:	0.0	Dolomite:	3.2
Quartz OG/QA:	4.0	Calcite:	0.0
Kspar OG:	0.0	Anhydrite:	0.0
Pyrite:	2.8	Celestine:	0.0
Titanium oxides:	0.8	Halite:	0.0

Pore Types:

Intergranular:	0.0	Intragranular:	0.0
Frac SP:	0.0	Moldic:	0.0

XRD-Whole Rock Mineralogy (Weight %)

Quartz	47.1	Anhydrite	0.0
K-Feldspar	6.9	Celestine	0.0
Plagioclase	0.9	Halite	0.5
Calcite	0.0	Pyrite	1.7
Dolomite	33.8	Total Clay	9.1

Clay Abundance (Weight %)

Corrensite	0.0	Kaolinite	0.0
Illite / Smectite	1.3	Chlorite	1.7
Illite & Mica	6.1		

mixed-layer illite/smectite contains 15-25% smectite layers

Petrographic Description

This very fine grained dolomitic argillaceous sandstone is bioturbated. Quartz is abundant and dolomite rock fragments are common. Other grains found in minor to moderate amounts include potassium feldspar, volcanic rock fragments, and dolomitic rip-up clasts. Much of the detrital clay matrix has been replaced by dolomite. Quartz overgrowths, pyrite, and dolomite cements fill intergranular pores in some of the "cleaner" areas of the sandstone. Horizontal microfractures are partially filled with halite (NaCl).

Core Lab
RESERVOIR OPTIMIZATION

Relative Abundances:

Trace	<1%
Minor	1-5%
Moderate	5-10%
Common	10-20%
Abundant	>20%

Core Analysis Data:

Porosity (%):	n/a
Permeability (md):	n/a
Gr. Density (g/cc):	n/a
Oil Saturation (%):	n/a
Water Saturation	n/a

PLATE 36

Thin Section Petrography

Company:	**Fidelity E & P**
Well:	**Cane Creek 26-3**
Location:	**Grand Co., Utah**
Depth (ft):	**7456.10**
Unit:	**C**
Dep. Env.:	**Restricted Shallow Marine Shoreface**

A

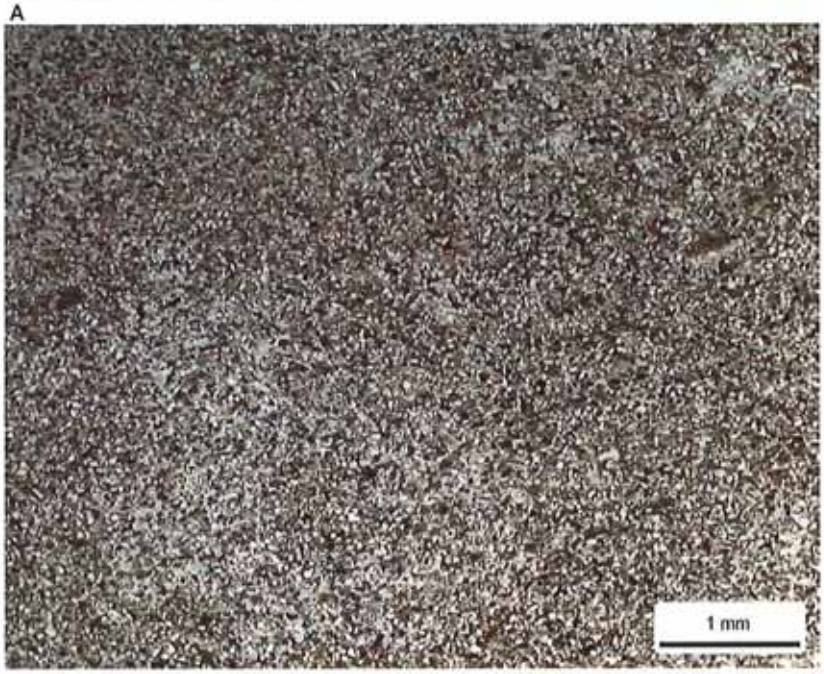

B

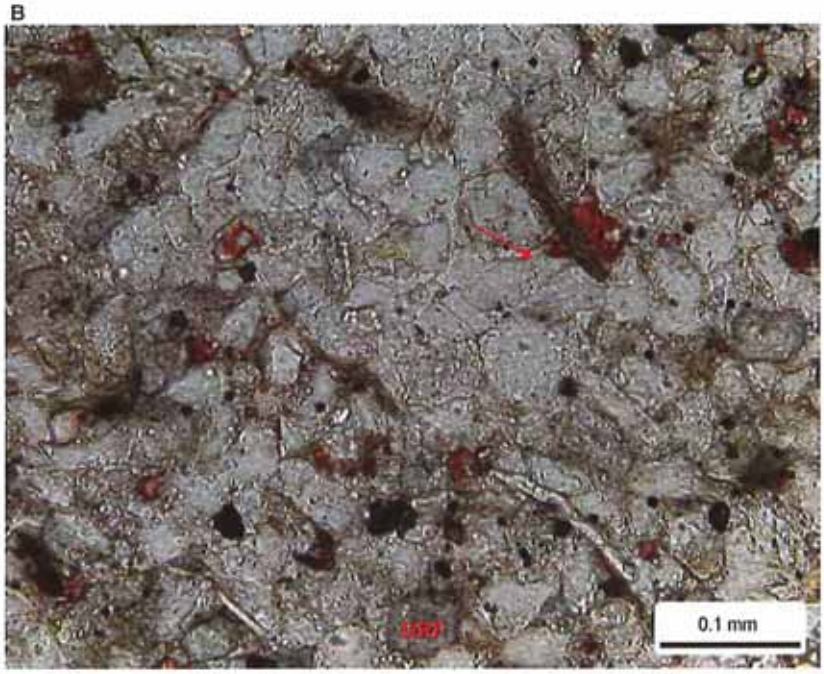

Relative Abundances:

Trace	<1%
Minor	1-5%
Moderate	5-10%
Common	10-20%
Abundant	>20%

Core Analysis Data:

Porosity (%):	11.12
Permeability (md):	0.0078
Gr. Density (g/cc):	2.682
Oil Saturation (%):	30.6
Water Saturation	61.8

LITHOLOGY AND TEXTURE

Lithology:	Argillaceous Siltstone
Classific. (Folk, 1980):	Feldspathic Litharenite
Grain Size (mm):	0.059 (coarse silt)
Sorting:	well
Structures:	bioturbated

Rock Composition (Point-Count)

Framework Grains:

Mono quartz:	54.0	Argillaceous RF:	0.8
Poly quartz:	0.0	Dolomite RF:	6.8
K-Feldspar:	8.8	Micas:	3.6
Plagioclase:	0.0	Heavy minerals:	0.0
Volcanic RF:	2.8	Plant fragments:	0.4
Metamorphic RF:	0.0	Glauconite:	0.0
Peloid-dolomite:	0.0	Rip-up/intraclasts:	0.0

Replaced Grains:

Dol RG:	0.0	Pyrite RG:	0.0
Cal RG:	2.4	Kaolinite RG:	0.0

Detrital Matrix:

Detrital clay:	4.0	Micrite matrix:	0.0
Organic matrix:	0.0	Dolomitic matrix:	0.8

Pore-filling Authigenic Minerals:

Authigenic clay:	0.4	Dolomite:	0.4
Quartz OG/QA:	6.4	Calcite:	0.8
Kspar OG:	1.2	Anhydrite:	1.2
Pyrite:	2.0	Celestine:	0.0
Titanium oxides:	0.4	Halite:	2.0

Pore Types:

Intergranular:	0.0	Intragranular:	0.4
Frac SP:	0.0	Moldic:	0.0

XRD-Whole Rock Mineralogy (Weight %)

Quartz	57.3	Anhydrite	1.8
K-Feldspar	9.0	Celestine	0.0
Plagioclase	0.0	Halite	1.2
Calcite	7.3	Pyrite	0.9
Dolomite	4.6	Total Clay	17.8

Clay Abundance (Weight %)

Corrensite	0.0	Kaolinite	0.2
Illite / Smectite	2.0	Chlorite	2.7
Illite & Mica	12.9		

mixed-layer illite/smectite contains 15-25% smectite layers

Petrographic Description

This argillaceous siltstone is bioturbated. Framework grains are mostly quartz. Potassium feldspar and dolomite rock fragments (DRF) are moderate in abundance and volcanic rock fragments, mica, and calcite replaced grains are observed in minor amounts. The detrital clay matrix has been partially replaced by dolomite. Quartz overgrowths (red arrow) are locally well developed. Potassium feldspar overgrowths occasionally surround feldspar grains. Small pyrite framboids are scattered throughout the thin section. Patches of anhydrite and halite cements are also observed. Secondary intragranular pores have formed within some partially dissolved feldspar grains.

PLATE 36

Scanning Electron Microscopy

Company:	**Fidelity E & P**
Well:	**Cane Creek 26-3**
Location:	**Grand Co., Utah**
Depth (ft):	**7456.10**
Unit:	**C**
Dep. Env.:	**Restricted Shallow Marine Shoreface**

LITHOLOGY

Argillaceous Siltstone

C

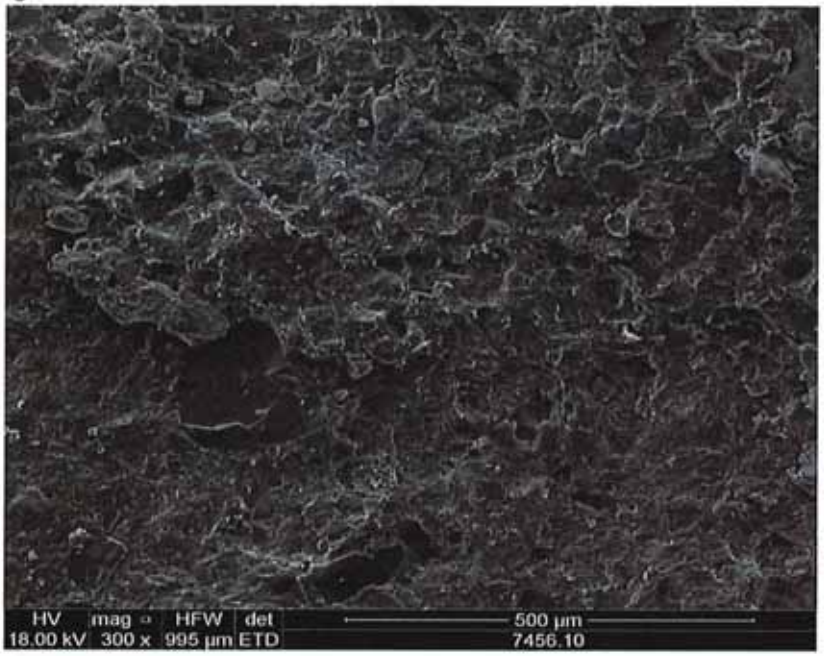

D

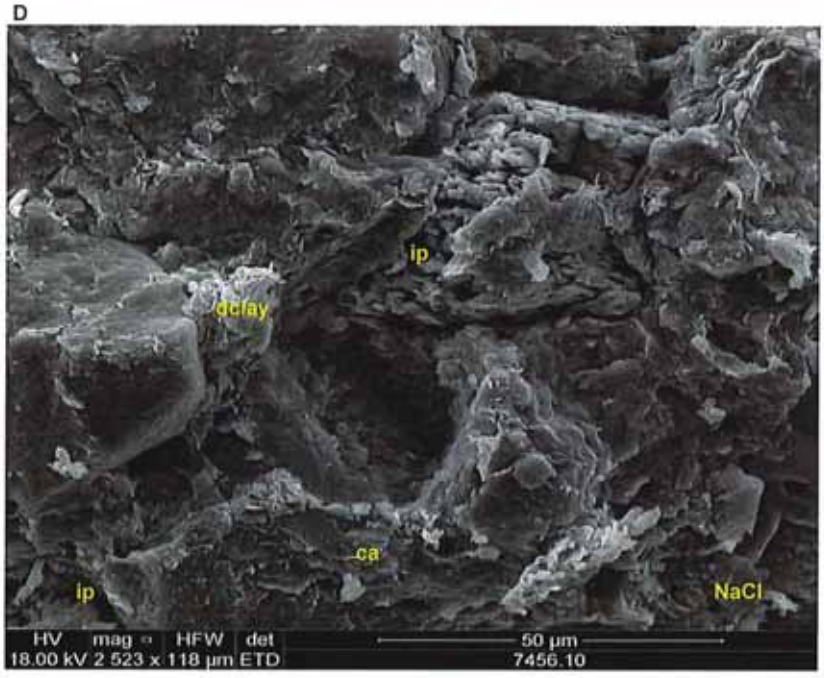

Mineralogy Determined by X-Ray Diffraction

(Weight %)

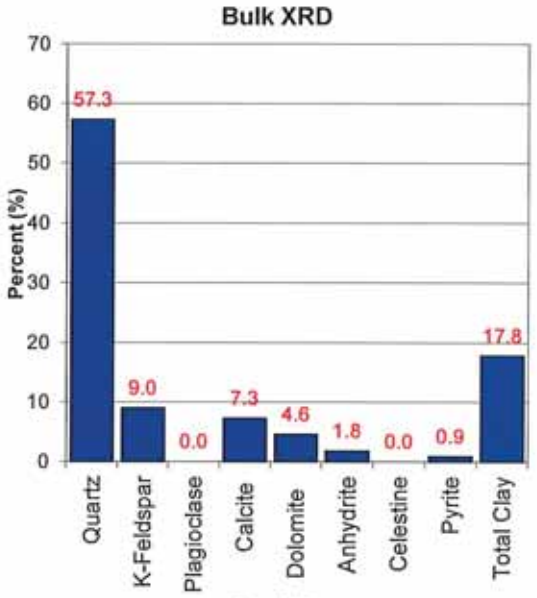

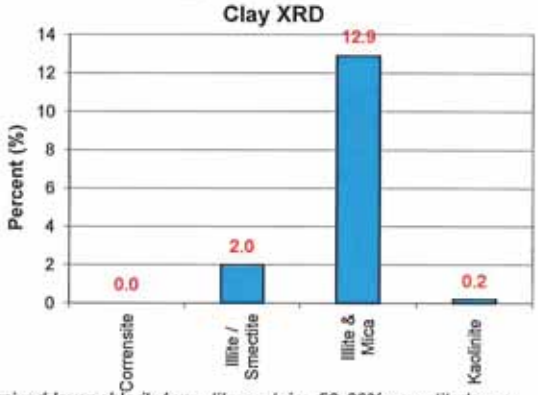

mixed-layer chlorite/smectite contains 50-60% smectite layers

SEM Description

The distribution of detrital clay matrix (dclay) is highlighted in these SEM images. Most of the clay is illitic (based on XRD and confirmed by EDX). Calcite (ca) is often associated with the matrix. Halite (NaCl) was observed in both thin section and SEM. Secondary intragranular pores (ip) have formed in several partially dissolved feldspar grains.

Core Lab

RESERVOIR OPTIMIZATION

Relative Abundances:	
Trace	<1%
Minor	1-5%
Moderate	5-10%
Common	10-20%
Abundant	>20%

Core Analysis Data:	
Porosity (%):	11.12
Permeability (md):	0.0078
Gr. Density (g/cc):	2.682
Oil Saturation (%):	30.6
Water Saturation	61.8

PLATE 37

Thin Section Petrography

Company:	**Fidelity E & P**
Well:	**Cane Creek 26-3**
Location:	**Grand Co., Utah**
Depth (ft):	**7458.25**
Unit:	**C**
Dep. Env.:	**Restricted Anoxic Shallow Marine/Subaqueous**

A

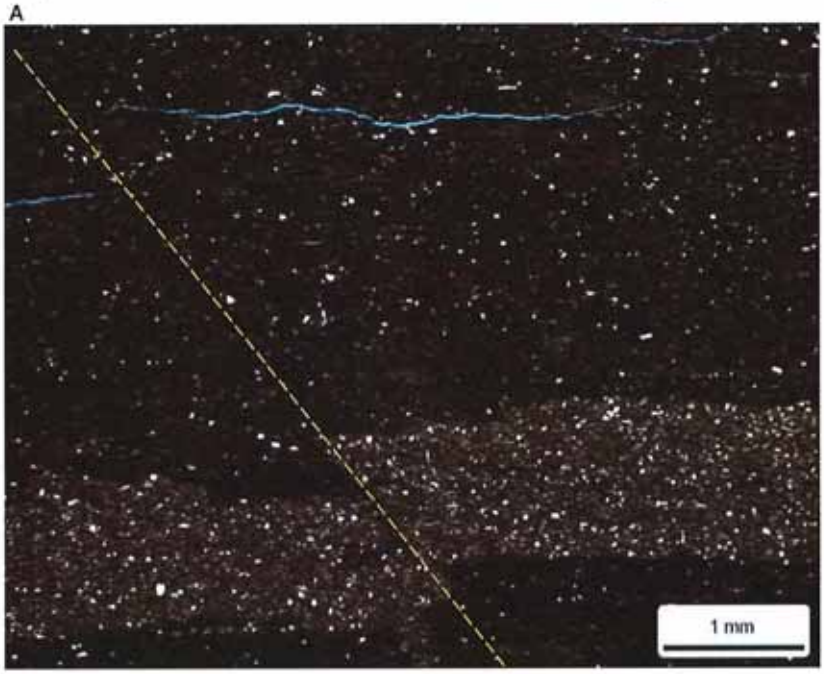

B

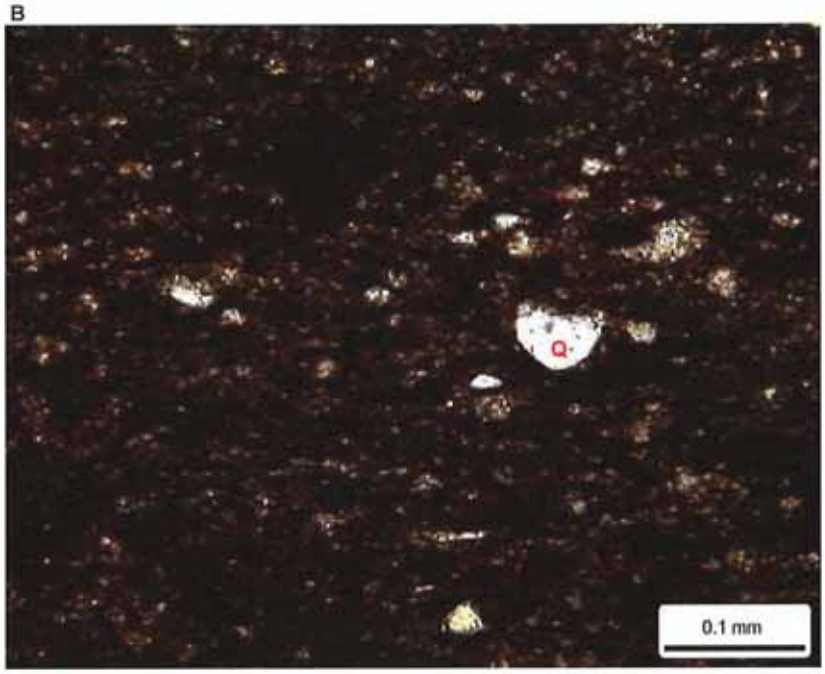

Relative Abundances:

Trace	<1%
Minor	1-5%
Moderate	5-10%
Common	10-20%
Abundant	>20%

Core Analysis Data:

Porosity (%):	13.20
Permeability (md):	0.0500
Gr. Density (g/cc):	2.658
Oil Saturation (%):	28.9
Water Saturation	37.5

LITHOLOGY AND TEXTURE

Lithology:	Organic-Rich Dolostone
Classific. (Dunham, 1962):	Dolomudstone
Grain Size (mm):	n/a
Sorting:	n/a
Structures:	silty laminae; microfaults; microfractures; silt-filled burrows

Rock Composition (Point-Count)

Framework Grains:

Mono quartz:	7.6	Argillaceous RF:	0.0
Poly quartz:	0.0	Chert RF:	0.0
K-Feldspar:	0.8	Micas:	0.4
Plagioclase:	0.0	Heavy minerals:	0.0
Volcanic RF:	0.0	Plant fragments:	0.0
Metamorphic RF:	0.0	Glauconite:	0.0
Limestone RF:	0.0	Rip-up/intraclasts:	0.0

Replaced Grains:

Dol RG:	0.0	Pyrite RG:	0.0
Cal RG:	0.0	Kaolinite RG:	0.0

Detrital Matrix:

Detrital clay:	0.0	Micrite matrix:	0.0
Organic matrix:	61.2	Dolomitic matrix:	27.6

Pore-filling Authigenic Minerals:

Authigenic clay:	0.0	Dolomite:	0.0
Quartz OG/QA:	0.0	Calcite:	0.0
Kspar OG:	0.0	Anhydrite:	0.0
Pyrite:	2.4	Celestine:	0.0
Titanium oxides:	0.0	Halite:	0.0

Pore Types:

Intergranular:	0.0	Intragranular:	0.0
Frac SP:	0.0	Moldic:	0.0

XRD-Whole Rock Mineralogy (Weight %)

Quartz	11.1	Anhydrite	0.0
K-Feldspar	2.1	Celestine	0.0
Plagioclase	0.3	Halite	1.3
Calcite	3.5	Pyrite	3.6
Dolomite	63.5	Total Clay	14.7

Clay Abundance (Weight %)

Corrensite	0.0	Kaolinite	0.0
Illite / Smectite	1.9	Chlorite	2.8
Illite & Mica	10.0		

mixed-layer illite/smectite contains 15-25% smectite layers

Petrographic Description

This organic-rich dolostone contains silt-filled burrows and silty laminae. The silty lamina in the lower part of Photo A, as well as the microfracture in the upper part of Photo A are displaced by a microfault (dashed yellow line). Most of the silt grains are quartz (Q); potassium feldspar and mica are rare. The dolomitic matrix is also rich in detrital clay and organic matter. A minor amount of pyrite is associated with the matrix.

PLATE 38

Thin Section Petrography

Company:	**Fidelity E & P**
Well:	**Cane Creek 26-3**
Location:	**Grand Co., Utah**
Depth (ft):	**7460.15**
Unit:	**C**
Dep. Env.:	**Shallow Shelf Salina/Sabkha**

A

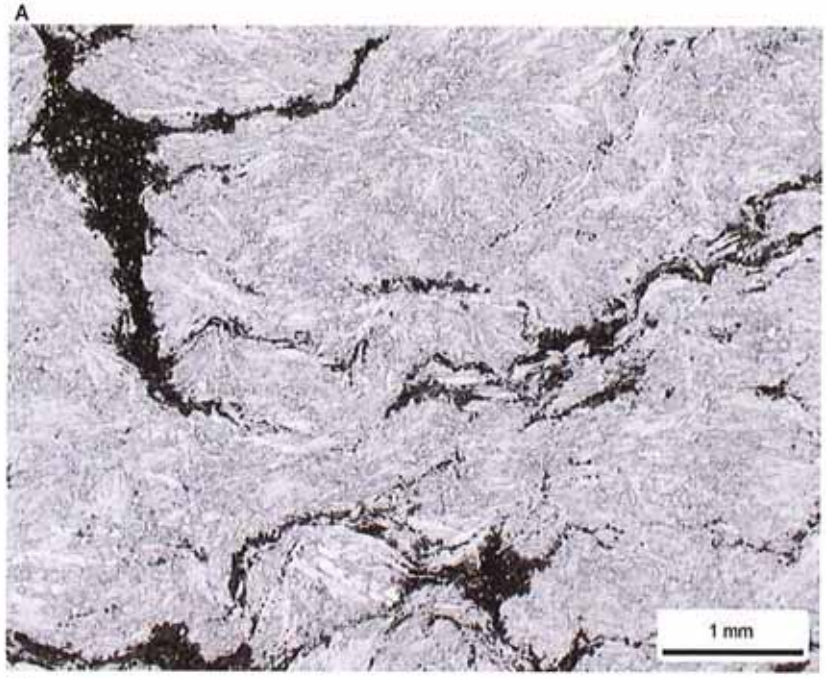

B

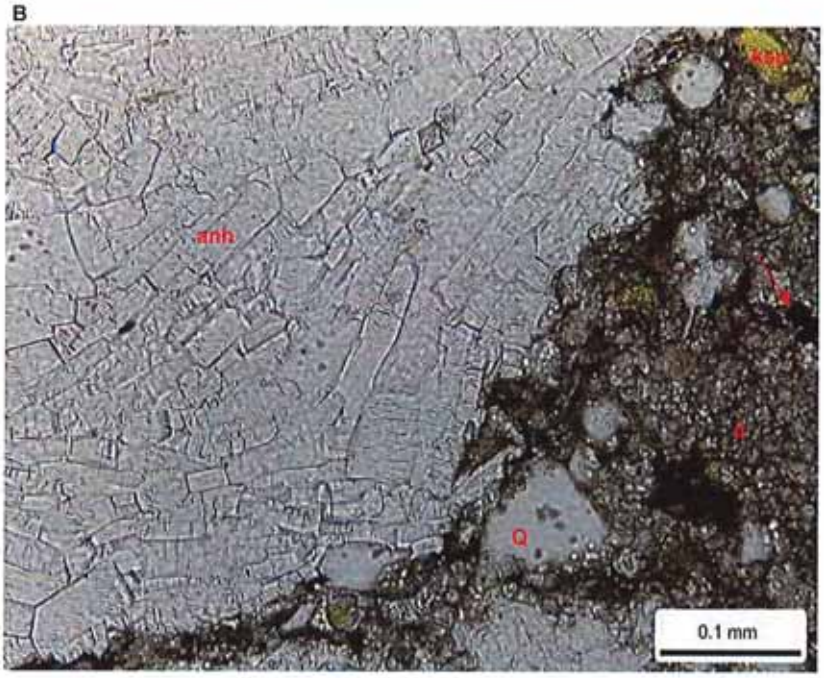

LITHOLOGY AND TEXTURE

Lithology:	Dolomitic Anhydrite
Classific. (Folk, 1980):	n/a
Grain Size (mm):	n/a
Sorting:	n/a
Structures:	nodular texture

Rock Composition (Point-Count)

Framework Grains:

Mono quartz:	2.0	Argillaceous RF:	0.0
Poly quartz:	0.0	Chert RF:	0.0
K-Feldspar:	0.4	Micas:	0.0
Plagioclase:	0.0	Heavy minerals:	0.0
Volcanic RF:	0.0	Plant fragments:	0.0
Metamorphic RF:	0.0	Glauconite:	0.0
Peloid-dolomite:	0.0	Rip-up/intraclasts:	0.0

Replaced Grains:

Dol RG:	0.0	Pyrite RG:	0.0
Cal RG:	0.0	Kaolinite RG:	0.0

Detrital Matrix:

Detrital clay:	0.0	Micrite matrix:	0.0
Organic matrix:	0.0	Dolomitic matrix:	10.8

Pore-filling Authigenic Minerals:

Authigenic clay:	0.0	Dolomite:	0.0
Quartz OG/QA:	0.0	Calcite:	0.0
Kspar OG:	0.0	Anhydrite:	84.8
Pyrite:	0.0	Celestine:	2.0
Titanium oxides:	0.0	Halite:	0.0

Pore Types:

Intergranular:	0.0	Intragranular:	0.0
Frac SP:	0.0	Moldic:	0.0

XRD-Whole Rock Mineralogy (Weight %)

Quartz	2.4	Anhydrite	83.8
K-Feldspar	0.0	Celestine	1.2
Plagioclase	0.0	Halite	0.0
Calcite	0.0	Pyrite	0.0
Dolomite	10.8	Total Clay	1.8

Clay Abundance (Weight %)

Corrensite	0.0	Kaolinite	0.0
Illite / Smectite	0.3	Chlorite	0.3
Illite & Mica	1.2		

mixed-layer illite/smectite contains 15-25% smectite layers

Petrographic Description

This anhydrite sample has a nodular texture. Dolomitic zones (d) separate the anhydrite nodules (anh) and contain quartz (Q) and potassium feldspar (ksp) grains, as well as organic matter. No open macropores are observed in thin section.

Core Lab

Relative Abundances:

Trace	<1%
Minor	1-5%
Moderate	5-10%
Common	10-20%
Abundant	>20%

Core Analysis Data:

Porosity (%):	0.63
Permeability (md):	0.0010
Gr. Density (g/cc):	2.950
Oil Saturation (%):	8.7
Water Saturation	37.1

PLATE 39

Thin Section Petrography

Company:	**Fidelity E & P**
Well:	**Cane Creek 26-3**
Location:	**Grand Co., Utah**
Depth (ft):	**7461.15**
Unit:	**C**
Dep. Env.:	**Shallow Shelf Salina/Sabkha**

A

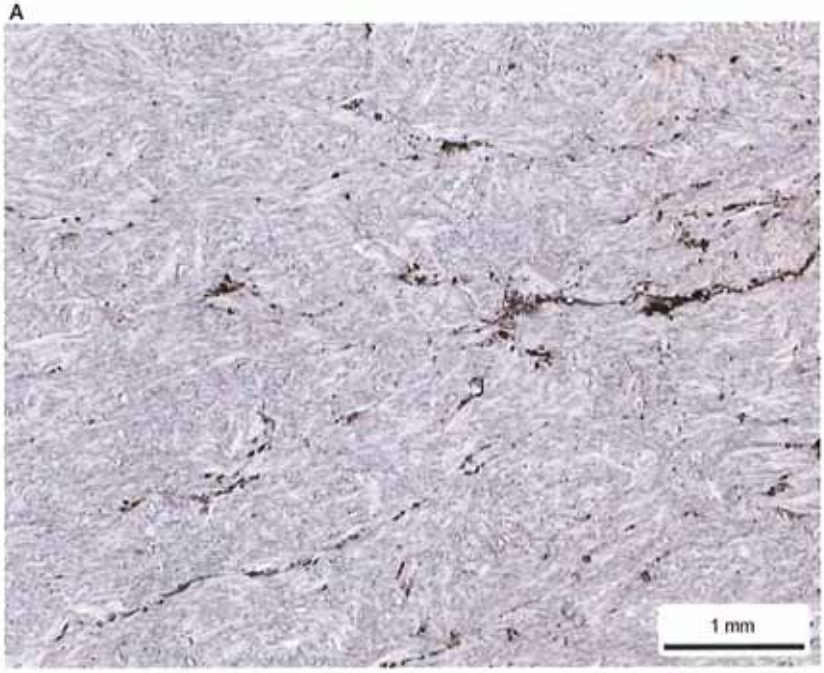

B

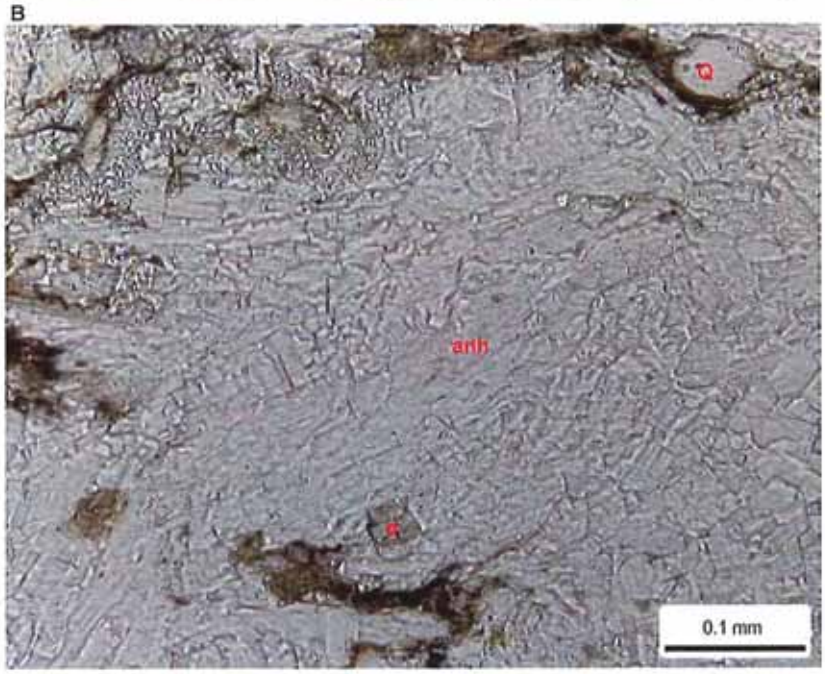

LITHOLOGY AND TEXTURE

Lithology:	Anhydrite
Classific. (Folk, 1980):	n/a
Grain Size (mm):	n/a
Sorting:	n/a
Structures:	none evident

Rock Composition (Point-Count)

Framework Grains:

Mono quartz:	tr	Argillaceous RF:	0.0
Poly quartz:	0.0	Chert RF:	0.0
K-Feldspar:	tr	Micas:	0.0
Plagioclase:	0.0	Heavy minerals:	0.0
Volcanic RF:	0.0	Plant fragments:	tr
Metamorphic RF:	0.0	Glauconite:	0.0
Limestone RF:	0.0	Rip-up/intraclasts:	0.0

Replaced Grains:

Dol RG:	0.0	Pyrite RG:	0.0
Cal RG:	0.0	Kaolinite RG:	0.0

Detrital Matrix:

Detrital clay:	0.0	Micrite matrix:	0.0
Organic matrix:	0.0	Dolomitic matrix:	0.0

Pore-filling Authigenic Minerals:

Authigenic clay:	0.0	Dolomite:	tr
Quartz OG/QA:	0.0	Calcite:	0.0
Kspar OG:	0.0	Anhydrite:	100.0
Pyrite:	tr	Celestine:	0.0
Titanium oxides:	0.0	Halite:	0.0

Pore Types:

Intergranular:	0.0	Intragranular:	0.0
Frac SP:	0.0	Moldic:	0.0

XRD-Whole Rock Mineralogy (Weight %)

Quartz	0.4	Anhydrite	99.6
K-Feldspar	0.0	Celestine	0.0
Plagioclase	0.0	Halite	0.0
Calcite	0.0	Pyrite	0.0
Dolomite	0.0	Total Clay	0.0

Clay Abundance (Weight %)

Corrensite	0.0	Kaolinite	0.0
Illite / Smectite	0.0	Chlorite	0.0
Illite & Mica	0.0		

mixed-layer illite/smectite contains 15-25% smectite layers

Petrographic Description

This sample is made up almost entirely of tightly interlocking, tabular crystals of anhydrite (anh). Thin zones of organic-rich matrix remain, and contain rare quartz (Q) and potassium feldspar grains. Dolomite (d) is also found in trace amounts.

Core Lab

Relative Abundances:

Trace	<1%
Minor	1-5%
Moderate	5-10%
Common	10-20%
Abundant	>20%

Core Analysis Data:

Porosity (%):	0.39
Permeability (md):	-
Gr. Density (g/cc):	2.959
Oil Saturation (%):	2.4
Water Saturation	20.7

PLATE 40

Thin Section Petrography

Company:	**Fidelity E & P**
Well:	**Cane Creek 26-3**
Location:	**Grand Co., Utah**
Depth (ft):	**7463.10**
Unit:	**C**
Dep. Env.:	**Shallow Shelf Salina/Sabkha**

A

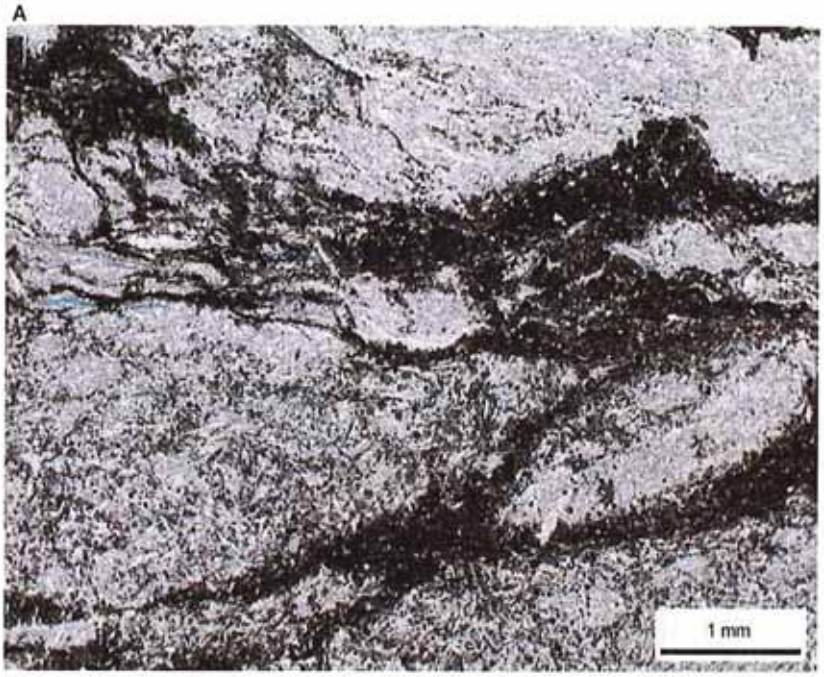

B

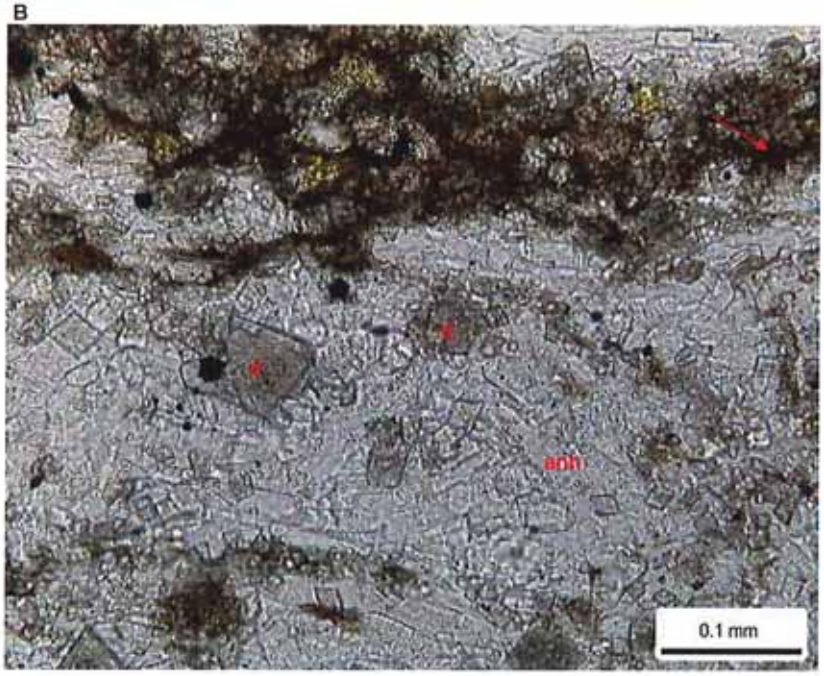

LITHOLOGY AND TEXTURE

Lithology:	Dolomitic Anhydrite
Classific. (Folk, 1980):	n/a
Grain Size (mm):	n/a
Sorting:	n/a
Structures:	nodular texture

Rock Composition (Point-Count)

Framework Grains:

Mono quartz:	2.0	Argillaceous RF:	0.0
Poly quartz:	0.0	Dolomite RF:	0.4
K-Feldspar:	0.4	Micas:	0.0
Plagioclase:	0.0	Heavy minerals:	0.0
Volcanic RF:	0.0	Plant fragments:	1.2
Metamorphic RF:	0.0	Glauconite:	0.0
Limestone RF:	0.0	Rip-up/intraclasts:	0.0

Replaced Grains:

Dol RG:	0.0	Pyrite RG:	0.0
Cal RG:	0.0	Kaolinite RG:	0.0

Detrital Matrix:

Detrital clay:	0.0	Mixed clay/carbonate:	1.6
Organic matrix:	0.0	Dolomitic matrix:	24.4

Pore-filling Authigenic Minerals:

Authigenic clay:	0.0	Dolomite:	4.4
Quartz OG/QA:	0.0	Calcite:	0.0
Kspar OG:	0.0	Anhydrite:	64.8
Pyrite:	0.4	Celestine:	0.4
Titanium oxides:	0.0	Halite:	0.0

Pore Types:

Intergranular:	0.0	Intragranular:	0.0
Frac SP:	0.0	Moldic:	0.0

XRD-Whole Rock Mineralogy (Weight %)

Quartz	1.3	Anhydrite	84.3
K-Feldspar	0.3	Celestine	0.7
Plagioclase	0.0	Halite	0.0
Calcite	2.7	Pyrite	0.0
Dolomite	9.3	Total Clay	1.5

Clay Abundance (Weight %)

Corrensite	0.3	Kaolinite	0.0
Illite / Smectite	0.2	Chlorite	0.3
Illite & Mica	0.7		

mixed-layer illite/smectite contains 15-25% smectite layers
mixed-layer chlorite/smectite contains 50-60% smectite layers

Petrographic Description

Most of this sample has been replaced / displaced by anhydrite (anh). Thin zones of silty dolostone remain, and are rich in organic matter (red arrow). Isolated rhombs of euhedral dolomite (d) are also found in the anydrite. Pyrite and celestine cements are rare.

Core Lab
RESERVOIR OPTIMIZATION

Relative Abundances:

Trace	<1%
Minor	1-5%
Moderate	5-10%
Common	10-20%
Abundant	>20%

Core Analysis Data:

Porosity (%):	0.91
Permeability (md):	-
Gr. Density (g/cc):	2.937
Oil Saturation (%):	13.6
Water Saturation	44.7

PLATE 41

Thin Section Petrography

Company:	Fidelity E & P
Well:	Cane Creek 26-3
Location:	Grand Co., Utah
Depth (ft):	7469.10
Unit:	C
Dep. Env.:	Restricted Shallow Marine Shoreface

A

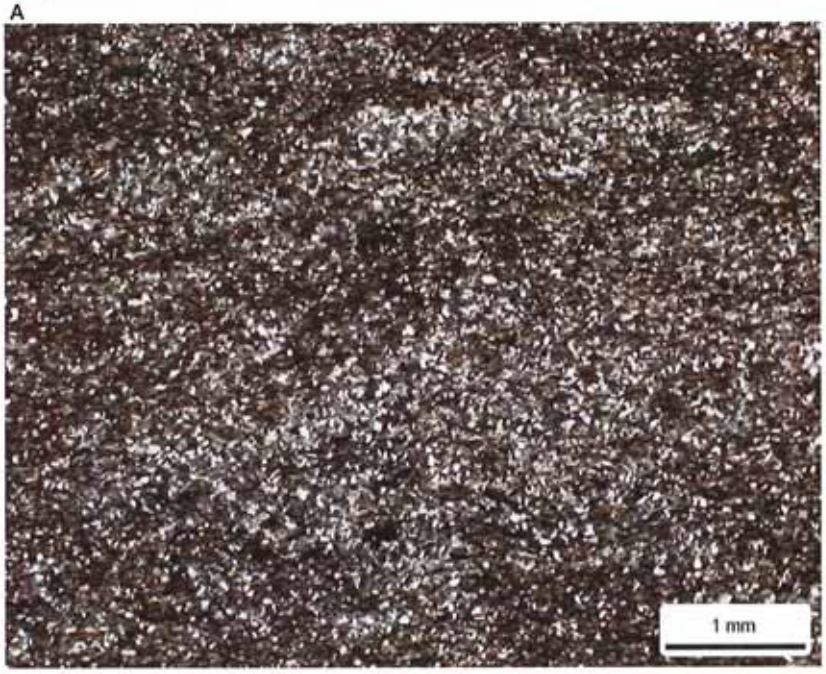

B

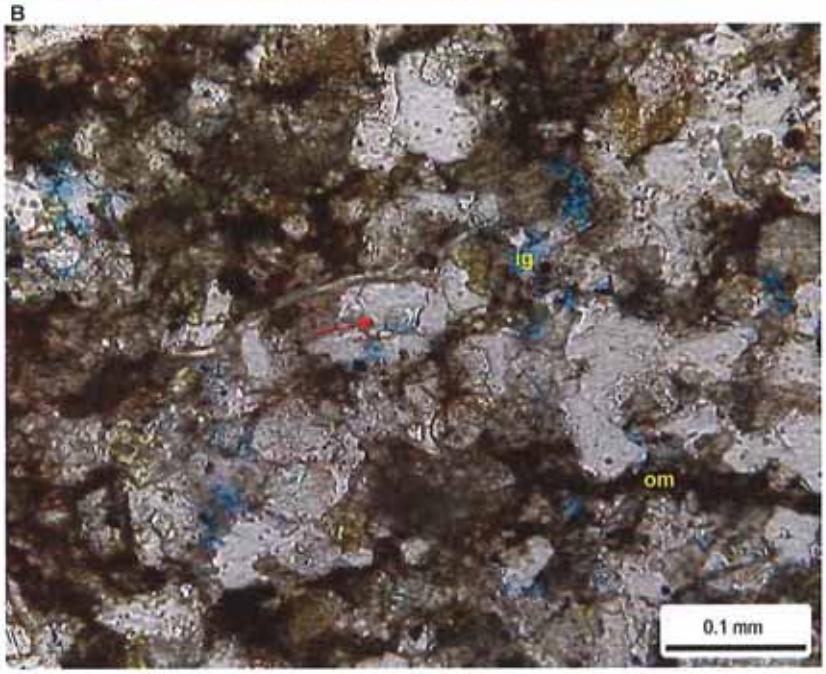

LITHOLOGY AND TEXTURE

Lithology:	Dolomitic Argill. Siltstone
Classific. (Folk, 1980):	Feldspathic Litharenite
Grain Size (mm):	0.057 (coarse silt)
Sorting:	well
Structures:	bioturbated

Rock Composition (Point-Count)

Framework Grains:

Mono quartz:	39.2	Argillaceous RF:	0.8
Poly quartz:	0.0	Dolomite RF:	16.0
K-Feldspar:	5.6	Micas:	0.4
Plagioclase:	0.0	Heavy minerals:	0.0
Volcanic RF:	0.0	Plant fragments:	4.4
Metamorphic RF:	0.0	Glauconite:	0.0
Limestone RF:	0.0	Rip-up/intraclasts:	0.0

Replaced Grains:

Dol RG:	0.0	Pyrite RG:	0.0
Cal RG:	0.0	Kaolinite RG:	0.0

Detrital Matrix:

Detrital clay:	5.6	Micrite matrix:	0.0
Organic matrix:	0.0	Dolomitic matrix:	13.2

Pore-filling Authigenic Minerals:

Authigenic clay:	0.0	Dolomite:	2.8
Quartz OG/QA:	5.2	Calcite:	0.0
Kspar OG:	0.8	Anhydrite:	0.0
Pyrite:	5.6	Celestine:	0.0
Titanium oxides:	0.0	Halite:	0.4

Pore Types:

Intergranular:	tr	Intragranular:	tr
Frac SP:	0.0	Moldic:	tr

XRD-Whole Rock Mineralogy (Weight %)

Quartz	41.7	Anhydrite	0.0
K-Feldspar	6.3	Celestine	0.0
Plagioclase	0.7	Halite	7.4
Calcite	0.0	Pyrite	2.6
Dolomite	30.5	Total Clay	10.8

Clay Abundance (Weight %)

Corrensite	2.1	Kaolinite	0.0
Illite / Smectite	1.4	Chlorite	1.3
Illite & Mica	6.0		

mixed-layer illite/smectite contains 15-25% smectite layers
mixed-layer chlorite/smectite contains 50-60% smectite layers

Petrographic Description

This sample is a bioturbated dolomitic argillaceous siltstone. Framework grains include abundant quartz, common dolomite rock fragments, and minor to rare potassium feldspar, argillaceous rock fragments, and muscovite. Detrital clay matrix is moderate in abundance, and has been replaced by dolomite. The sample is rich in organic matter (om); some of which has been replaced by pyrite. Quartz overgrowths (red arrow) and dolomite overgrowths fill intergranular pores A few intergranular pores (ig) and secondary intragranular and moldic pores remain. The intergranular pores are concentrated in the "cleaner" (matrix-free) parts of the thin section.

Core Lab
RESERVOIR OPTIMIZATION

Relative Abundances:

Trace	<1%
Minor	1-5%
Moderate	5-10%
Common	10-20%
Abundant	>20%

Core Analysis Data:

Porosity (%):	7.45
Permeability (md):	0.0071
Gr. Density (g/cc):	2.688
Oil Saturation (%):	37.2
Water Saturation	43.7

PLATE 41

Scanning Electron Microscopy

Company:	**Fidelity E & P**
Well:	**Cane Creek 26-3**
Location:	**Grand Co., Utah**
Depth (ft):	**7469.10**
Unit:	**C**
Dep. Env.:	**Restricted Shallow Marine Shoreface**

LITHOLOGY

Dolomitic Argill. Siltstone

C

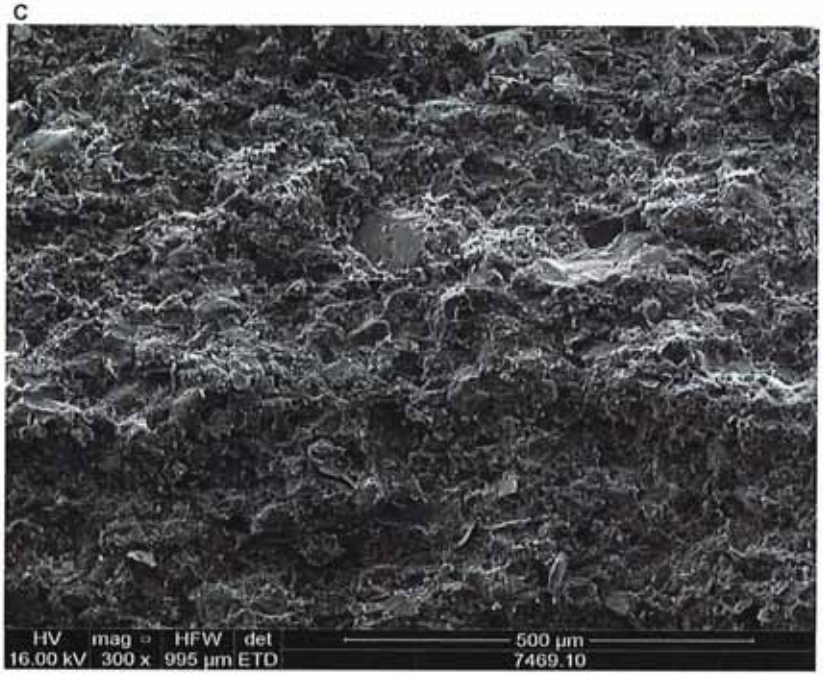

D

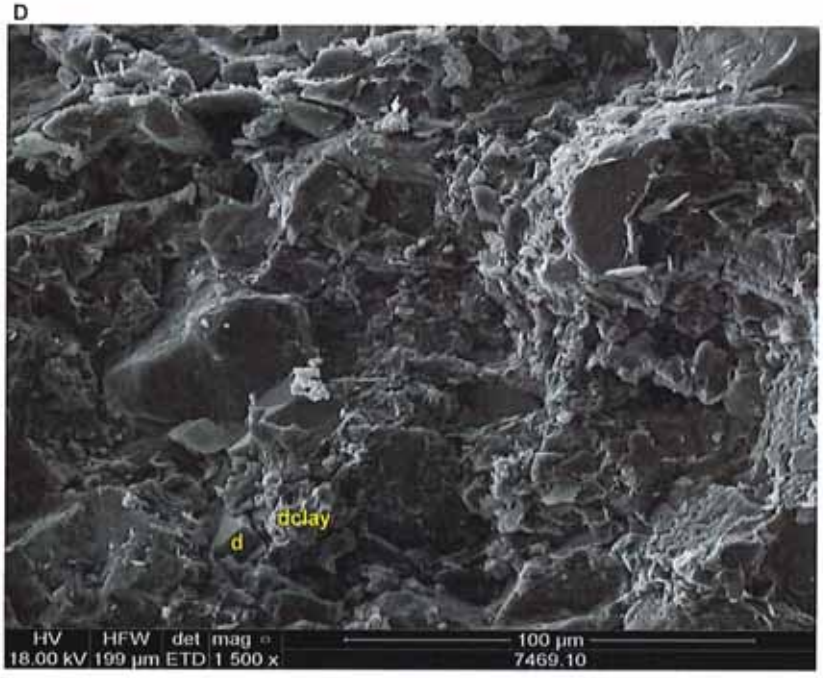

Mineralogy Determined by X-Ray Diffraction

(Weight %)

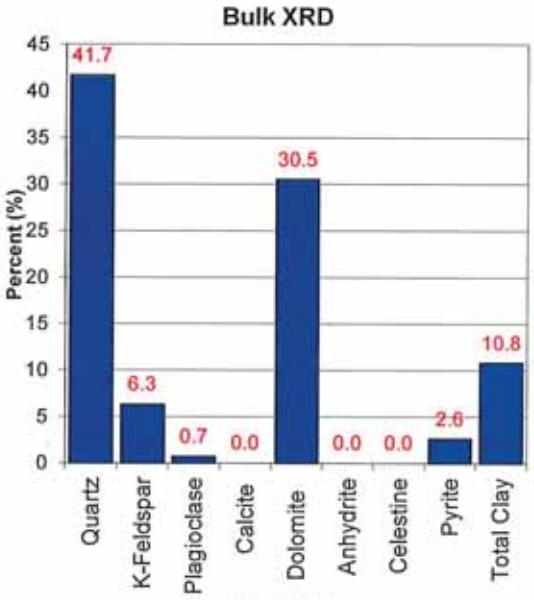

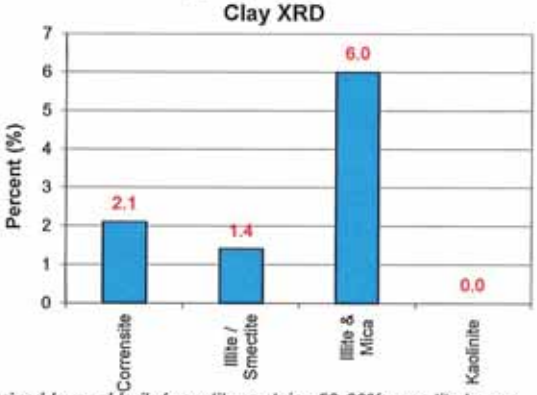

mixed-layer chlorite/smectite contains 50-60% smectite layers

0

SEM Description

These SEM images highlight the detrital clay matrix (dclay). The matrix has been partially replaced by dolomite (d). No open pores were observed in SEM.

Relative Abundances:	
Trace	<1%
Minor	1-5%
Moderate	5-10%
Common	10-20%
Abundant	>20%

Core Analysis Data:	
Porosity (%):	7.45
Permeability (md):	0.0071
Gr. Density (g/cc):	2.688
Oil Saturation (%):	37.2
Water Saturation	43.7

PLATE 42

Thin Section Petrography

Company:	Fidelity E & P
Well:	Cane Creek 26-3
Location:	Grand Co., Utah
Depth (ft):	7471.20
Unit:	C
Dep. Env.:	Shallow Shelf Salina/Sabkha

A

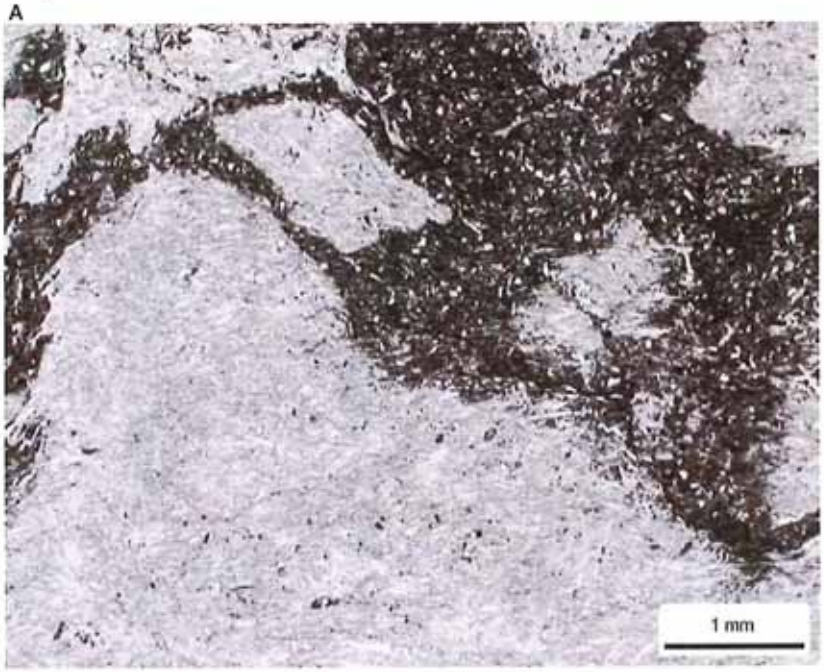

B

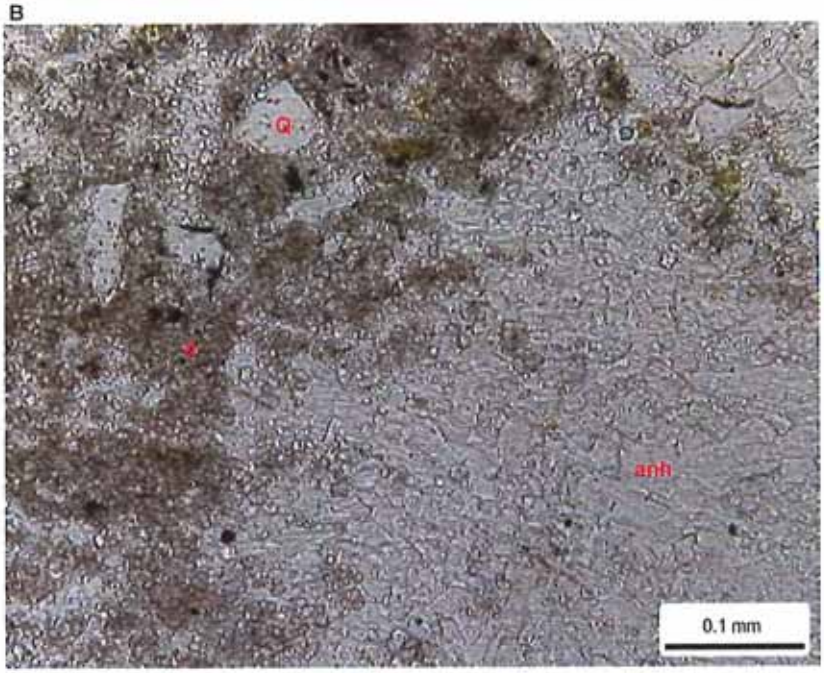

LITHOLOGY AND TEXTURE

Lithology:	Dolomitic Anhydrite
Classific. (Folk, 1980):	n/a
Grain Size (mm):	n/a
Sorting:	n/a
Structures:	nodular texture

Rock Composition (Point-Count)

Framework Grains:

Mono quartz:	2.8	Argillaceous RF:	0.0
Poly quartz:	0.0	Dolomite RF:	2.0
K-Feldspar:	0.4	Micas:	0.4
Plagioclase:	0.0	Heavy minerals:	0.0
Volcanic RF:	0.0	Plant fragments:	0.0
Metamorphic RF:	0.0	Glauconite:	0.0
Peloid-dolomite:	0.0	Rip-up/intraclasts:	0.0

Replaced Grains:

Dol RG:	0.0	Pyrite RG:	0.0
Cal RG:	0.0	Kaolinite RG:	0.0

Detrital Matrix:

Detrital clay:	0.0	Micrite matrix:	0.0
Organic matrix:	0.0	Dolomitic matrix:	22.8

Pore-filling Authigenic Minerals:

Authigenic clay:	0.0	Dolomite:	0.0
Quartz OG/QA:	0.0	Calcite:	0.0
Kspar OG:	0.0	Anhydrite:	71.2
Pyrite:	0.4	Celestine:	0.0
Titanium oxides:	0.0	Halite:	0.0

Pore Types:

Intergranular:	0.0	Intragranular:	0.0
Frac SP:	0.0	Moldic:	0.0

XRD-Whole Rock Mineralogy (Weight %)

Quartz	2.8	Anhydrite	93.1
K-Feldspar	0.0	Celestine	0.0
Plagioclase	0.0	Halite	0.0
Calcite	0.0	Pyrite	0.0
Dolomite	3.4	Total Clay	0.7

Clay Abundance (Weight %)

Corrensite	0.0	Kaolinite	0.0
Illite / Smectite	0.0	Chlorite	0.0
Illite & Mica	0.7		

Petrographic Description

This dolomitic anhydrite has a nodular texture. Both anhydrite (anh) and dolomite (d) are abundant. Quartz grains (Q) are concentrated in the dolomitic zones. Pyrite (black specks) are rare.

Core Lab
RESERVOIR OPTIMIZATION

Relative Abundances:

Trace	<1%
Minor	1-5%
Moderate	5-10%
Common	10-20%
Abundant	>20%

Core Analysis Data:

Porosity (%):	0.97
Permeability (md):	-
Gr. Density (g/cc):	2.933
Oil Saturation (%):	0.0
Water Saturation	64.8

PLATE 43

Thin Section Petrography

Company:	**Fidelity E & P**
Well:	**Cane Creek 26-3**
Location:	**Grand Co., Utah**
Depth (ft):	**7473.10**
Unit:	**C**
Dep. Env.:	**Shallow Shelf Salina/Sabkha**

A

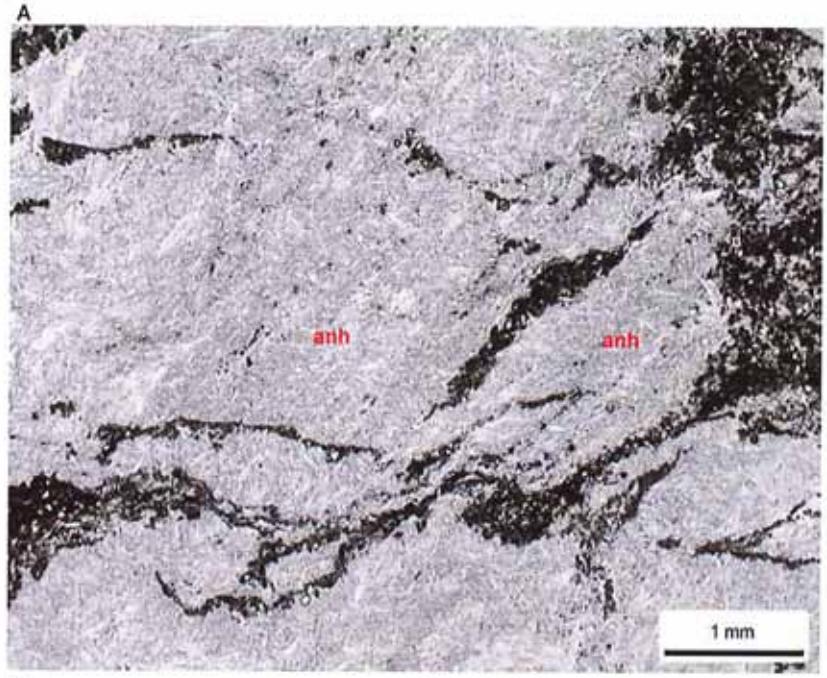

B

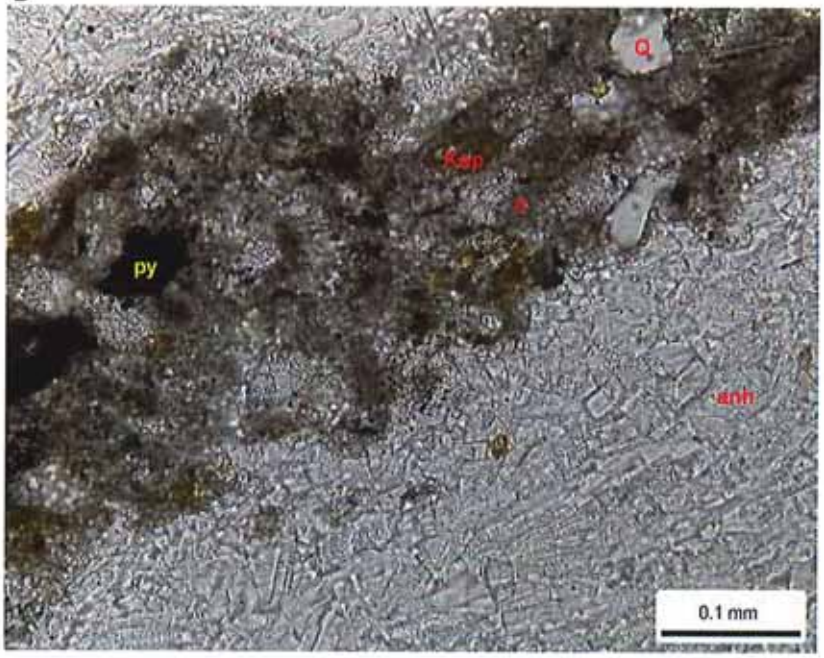

LITHOLOGY AND TEXTURE

Lithology:	Dolomitic Anhydrite
Classific. (Folk, 1980):	n/a
Grain Size (mm):	n/a
Sorting:	n/a
Structures:	nodular texture

Rock Composition (Point-Count)

Framework Grains:

Mono quartz:	1.2	Argillaceous RF:	0.0
Poly quartz:	0.0	Dolomite RF:	1.6
K-Feldspar:	0.4	Micas:	0.0
Plagioclase:	0.0	Heavy minerals:	0.0
Volcanic RF:	0.0	Plant fragments:	0.0
Metamorphic RF:	0.0	Glauconite:	0.0
Limestone RF:	0.0	Rip-up/intraclasts:	0.0

Replaced Grains:

Dol RG:	0.0	Pyrite RG:	0.0
Cal RG:	0.0	Kaolinite RG:	0.0

Detrital Matrix:

Detrital clay:	0.0	Micrite matrix:	0.0
Organic matrix:	0.0	Dolomitic matrix:	16.8

Pore-filling Authigenic Minerals:

Authigenic clay:	0.0	Dolomite:	0.0
Quartz OG/QA:	0.0	Calcite:	0.0
Kspar OG:	0.0	Anhydrite:	79.2
Pyrite:	0.8	Celestine:	0.0
Titanium oxides:	0.0	Halite:	0.0

Pore Types:

Intergranular:	0.0	Intragranular:	0.0
Frac SP:	0.0	Moldic:	0.0

XRD-Whole Rock Mineralogy (Weight %)

Quartz	0.6	Anhydrite	96.8
K-Feldspar	0.0	Celestine	0.0
Plagioclase	0.0	Halite	0.0
Calcite	0.0	Pyrite	0.0
Dolomite	2.5	Total Clay	0.0

Clay Abundance (Weight %)

Corrensite	0.0	Kaolinite	0.0
Illite / Smectite	0.0	Chlorite	0.0
Illite & Mica	0.0		

Petrographic Description

Thin zones of dolomite (d) separate anhydrite nodules (anh) in this sample. Quartz (Q) and potassium feldspar grains (Ksp) are concentrated in the dolomitic zones. Pyrite (py) is rare.

Relative Abundances:

Trace	<1%
Minor	1-5%
Moderate	5-10%
Common	10-20%
Abundant	>20%

Core Analysis Data:

Porosity (%):	0.46
Permeability (md):	-
Gr. Density (g/cc):	2.953
Oil Saturation (%):	0.0
Water Saturation	45.2

Core Lab
RESERVOIR OPTIMIZATION

PLATE 44

Supplemental Thin Section Petrography

Company:	Fidelity E & P
Well:	Cane Creek 26-3
Location:	Grand Co., Utah
Depth (ft):	7438-untreated "C"
Unit:	n/a
Dep. Env.:	n/a

A

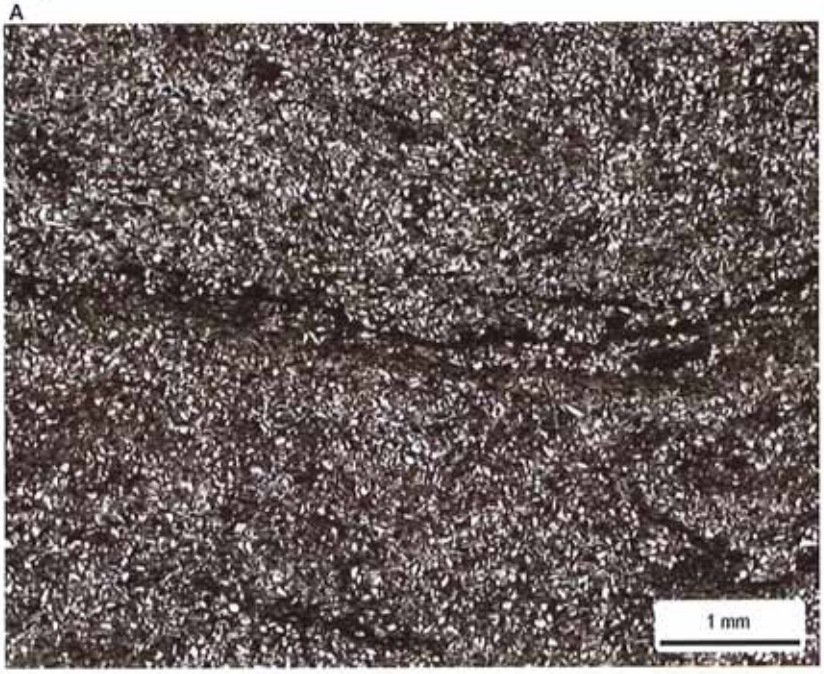

B

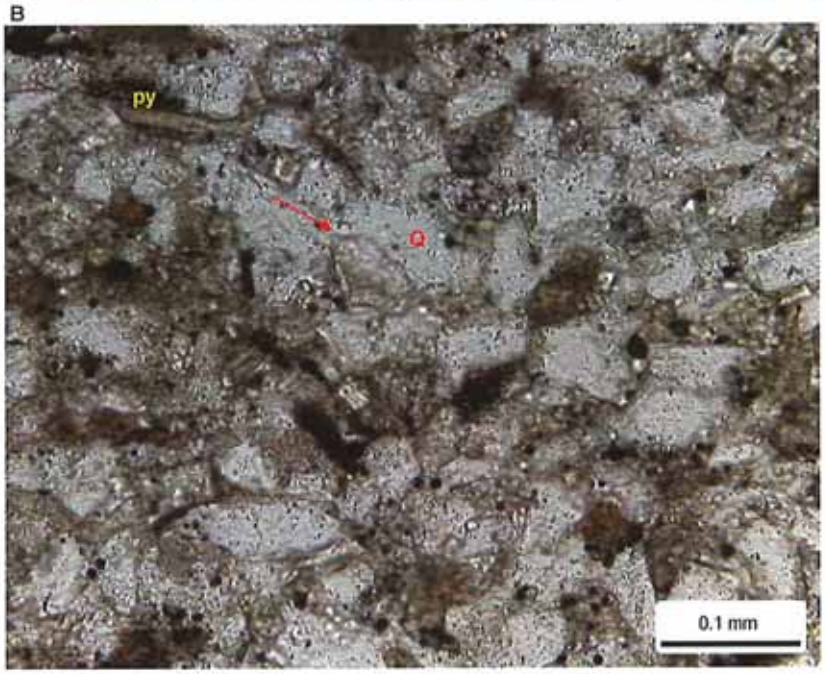

LITHOLOGY AND TEXTURE

Lithology:	Argillaceous Sandstone
Classific. (Folk, 1980):	Subarkose
Grain Size (mm):	0.068 (L. very fine sand)
Sorting:	well
Structures:	discontinuous wavy laminae; bioturbated

Rock Composition (Point-Count)

Framework Grains:			
Mono quartz:	44.8	Argillaceous RF:	1.2
Poly quartz:	0.0	Dolomite RF:	2.8
K-Feldspar:	8.4	Micas:	1.6
Plagioclase:	0.0	Heavy minerals:	0.0
Volcanic RF:	1.2	Plant fragments:	1.2
Metamorphic RF:	0.0	Glauconite:	0.0
Limestone RF:	1.2	Rip-up/intraclasts:	0.0
Replaced Grains:			
Dol RG:	0.0	Pyrite RG:	0.8
Cal RG:	1.2	Kaolinite RG:	0.0
Detrital Matrix:			
Detrital clay:	0.0	Mixed clay/carbonate:	14.0
Organic matrix:	0.0	Dolomitic matrix:	5.6
Pore-filling Authigenic Minerals:			
Authigenic clay:	0.0	Dolomite:	1.6
Quartz OG/QA:	7.6	Calcite:	2.8
Kspar OG:	0.0	Anhydrite:	0.0
Pyrite:	3.6	Celestine:	0.0
Titanium oxides:	0.4	Halite:	0.0
Pore Types:			
Intergranular:	0.0	Intragranular:	0.0
Frac SP:	0.0	Moldic:	0.0

XRD-Whole Rock Mineralogy (Weight %)

Quartz	50.7	Anhydrite	0.0
K-Feldspar	6.2	Celestine	0.0
Plagioclase	0.0	Halite	0.0
Calcite	11.3	Pyrite	2.2
Dolomite	15.9	Total Clay	13.7
Clay Abundance (Weight %)			
Corrensite	0.0	Kaolinite	0.0
Illite / Smectite	2.1	Chlorite	2.1
Illite & Mica	9.5		

mixed-layer illite/smectite contains 15-25% smectite layers

Petrographic Description

This thin section is of a sample not treated with KCl. The sample is a very fine grained, well sorted argillaceous sandstone. Quartz grains (Q) are abundant and potassium feldspar is observed in moderate amounts. Detrital matrix is common, and concentrated in discontinuous, wavy laminae. Quartz overgrowths (red arrow) are well developed in the "clean" parts of the sample. Calcite and dolomite fill intergranular pores and replace some grains. Dolomite also partially replace the matrix. Pyrite (py) is minor in abundance. No pores are visible in thin section.

Core Lab

Relative Abundances:	
Trace	<1%
Minor	1-5%
Moderate	5-10%
Common	10-20%
Abundant	>20%

Core Analysis Data:	
Porosity (%):	-
Permeability (md):	-
Gr. Density (g/cc):	-
Oil Saturation (%):	-
Water Saturation	-

PLATE 44

Supplemental Scanning Electron Microscopy

Company:	**Fidelity E & P**
Well:	**Cane Creek 26-3**
Location:	**Grand Co., Utah**
Depth (ft):	**7438-untreated "C"**
Unit:	**n/a**
Dep. Env.:	**n/a**

LITHOLOGY

Argillaceous Sandstone

C

D

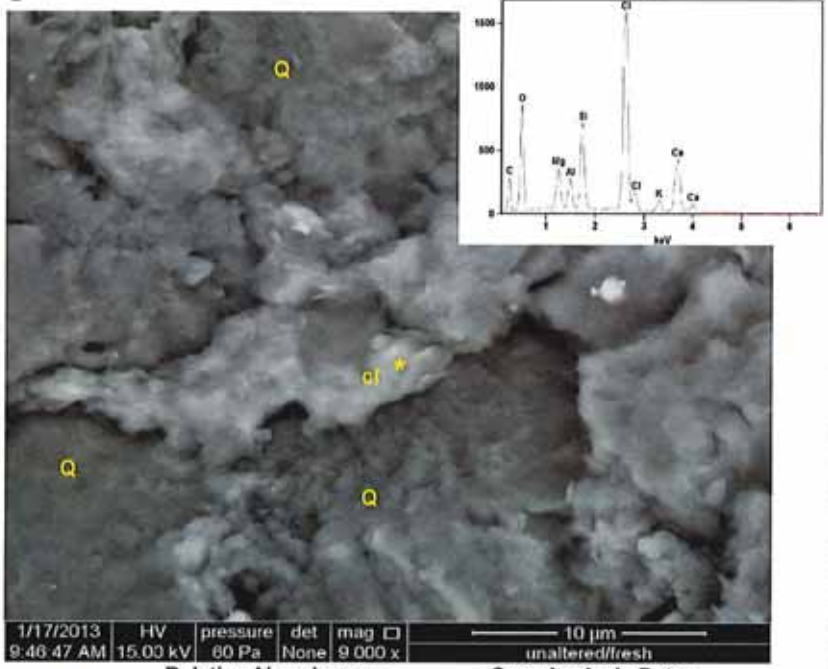

Mineralogy Determined by X-Ray Diffraction

(Weight %)

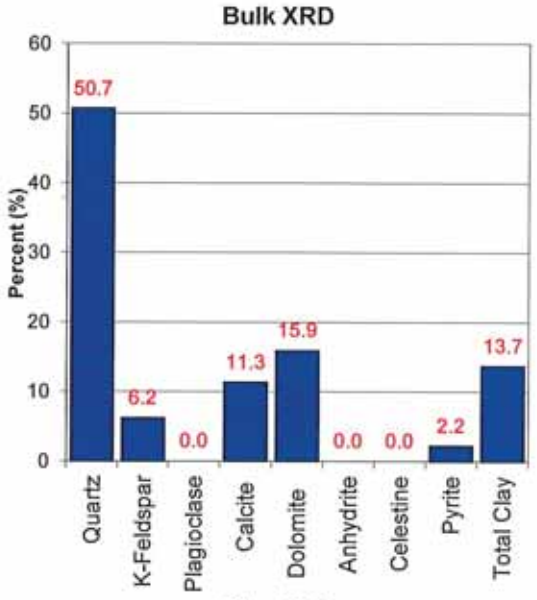

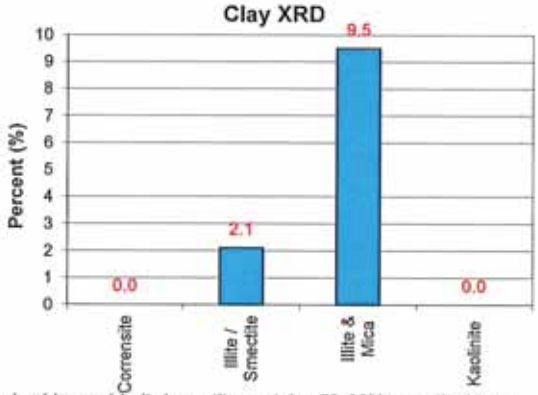

mixed-layer chlorite/smectite contains 50-60% smectite layers

SEM Description

These SEM images are from the sample not treated with KCl. Detrital grains include quartz (Q) and less common potassium feldspar (Ksp). Intergranular areas are filled with detrital clay, as well as occasional dolomite and calcite cements. The EDX spectrum of the clay showed Mg, Al, Si, and K peaks, indicating it is an illitic clay. A chlorine peak was also consistently detected in the clay-rich parts of the sample (cl*). No corresponding Na peak was detected in these areas to suggest the clay is coated with halite. The potassium peak would be much larger if sylvite coated the clay. A calcium peak was sometimes identified along with the chlorine.

Core Lab
RESERVOIR OPTIMIZATION

Relative Abundances:

Trace	<1%
Minor	1-5%
Moderate	5-10%
Common	10-20%
Abundant	>20%

Core Analysis Data:

Porosity (%):	-
Permeability (md):	-
Gr. Density (g/cc):	-
Oil Saturation (%):	-
Water Saturation	-

PLATE 44

Supplemental Scanning Electron Microscopy

Company:	**Fidelity E & P**
Well:	**Cane Creek 26-3**
Location:	**Grand Co., Utah**
Depth (ft):	**7438-untreated "C"**
Unit:	**n/a**
Dep. Env.:	**n/a**

E

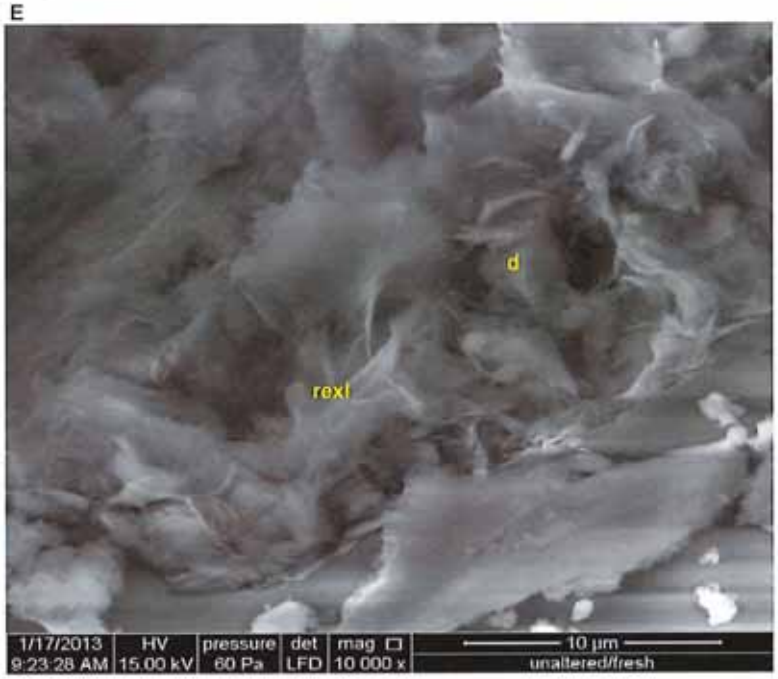

LITHOLOGY

Argillaceous Sandstone

Mineralogy Determined by X-Ray Diffraction

(Weight %)

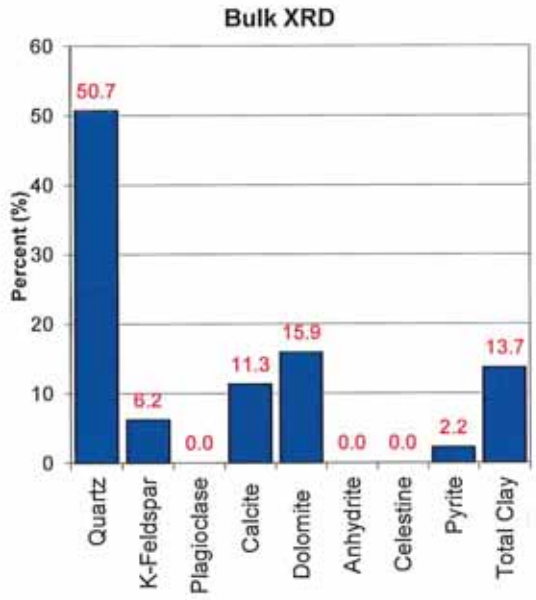

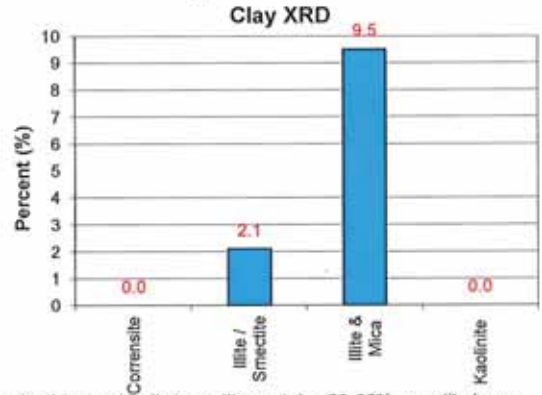

mixed-layer chlorite/smectite contains 50-60% smectite layers

SEM Description

This SEM image is also from the sample not treated with KCl. Most of the clay observed in SEM is detrital, but occasional patches of more crystalline clay platelets are observed, and are interpreted to be recrystallized detrital clay (rexl). Similar to the clay shown in images C and D, the recrystallized detrital clay shown in image E also showed a chlorine peak with no corresponding Na or K peak in the EDX spectrum. A euhedral dolomite rhomb (d) is also noted in this image.

Core Lab
RESERVOIR OPTIMIZATION

Relative Abundances:

Trace	<1%
Minor	1-5%
Moderate	5-10%
Common	10-20%
Abundant	>20%

Core Analysis Data:

Porosity (%):	-
Permeability (md):	-
Gr. Density (g/cc):	-
Oil Saturation (%):	-
Water Saturation	-

PLATE 45

Supplemental Thin Section Petrography

Company:	**Fidelity E & P**
Well:	**Cane Creek 26-3**
Location:	**Grand Co., Utah**
Depth (ft):	**7438-KCl "A"**
Unit:	**n/a**
Dep. Env.:	**n/a**

A

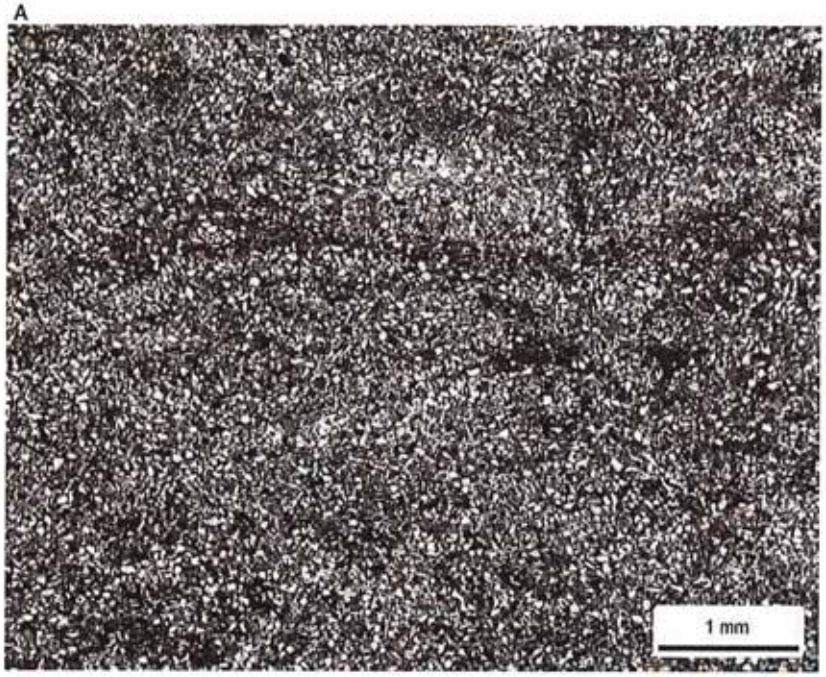

B

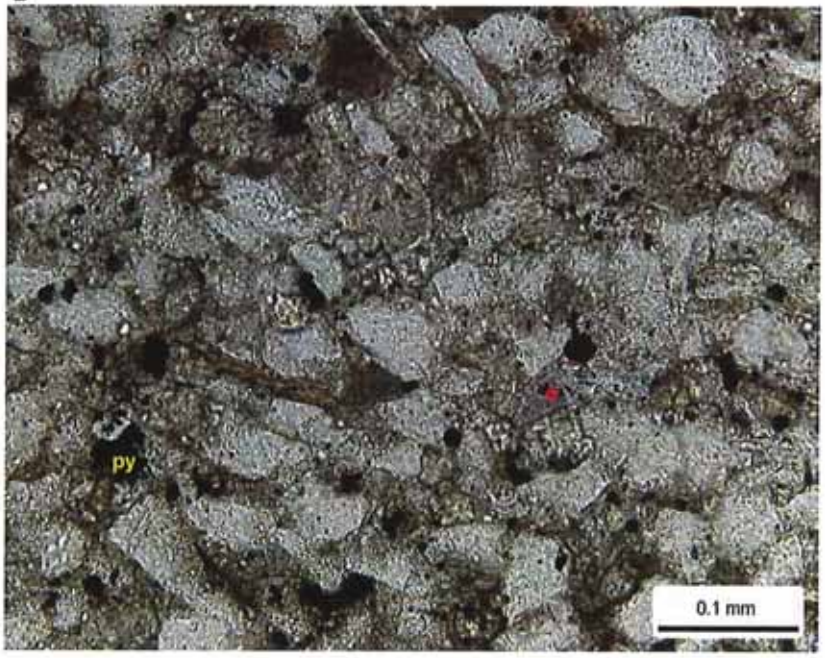

LITHOLOGY AND TEXTURE

Lithology:	Argillaceous Sandstone
Classific. (Folk, 1980):	Feldspathic Litharenite
Grain Size (mm):	0.070 (L. very fine sand)
Sorting:	well
Structures:	bioturbated; open microfracture

Rock Composition (Point-Count)

Framework Grains:

Mono quartz:	45.6	Argillaceous RF:	0.4
Poly quartz:	0.0	Dolomite RF:	6.4
K-Feldspar:	7.6	Micas:	2.0
Plagioclase:	0.0	Heavy minerals:	0.0
Volcanic RF:	0.8	Plant fragments:	0.8
Metamorphic RF:	0.0	Glauconite:	0.0
Limestone RF:	2.8	Rip-up/intraclasts:	0.0

Replaced Grains:

Dol RG:	0.0	Pyrite RG:	0.0
Cal RG:	2.0	Kaolinite RG:	0.0

Detrital Matrix:

Detrital clay:	0.0	Mixed clay/carbonate:	10.8
Organic matrix:	0.0	Dolomitic matrix:	6.4

Pore-filling Authigenic Minerals:

Authigenic clay:	0.4	Dolomite:	3.6
Quartz OG/QA:	3.2	Calcite:	4.0
Kspar OG:	0.0	Anhydrite:	0.0
Pyrite:	2.8	Celestine:	0.0
Titanium oxides:	0.0	Halite:	0.4

Pore Types:

Intergranular:	0.0	Intragranular:	0.0
Frac SP:	0.0	Moldic:	0.0

XRD-Whole Rock Mineralogy (Weight %)

Quartz	53.8	Anhydrite	0.0
K-Feldspar	7.0	Celestine	0.0
Plagioclase	0.0	Halite	0.7
Calcite	10.9	Pyrite	1.7
Dolomite	12.2	Total Clay	11.7

Clay Abundance (Weight %)

Corrensite	0.0.	Kaolinite	0.0.
Illite / Smectite	1.8	Chlorite	1.7
Illite & Mica	8.2		

mixed-layer illite/smectite contains 15-25% smectite layers

Petrographic Description

This sample is from the same depth as the previous sample, but was soaked overnight in 7% KCl. The two thin sections are very similar to each other. This very fine grained argillaceous sandstone is also comprised of abundant quartz grains and moderate potassium feldspar and dolomite rock fragments. The sample is bioturbated, and detrital matrix has been partially replaced by dolomite. Both dolomite (d) and calcite occur as intergranular cement and calcite replaces some grains. Other minor cements include quartz overgrowths and pyrite (py). Halite is rare. No visible pores are found in thin section.

Core Lab

Relative Abundances:

Trace	<1%
Minor	1-5%
Moderate	5-10%
Common	10-20%
Abundant	>20%

Core Analysis Data:

Porosity (%):	-
Permeability (md):	-
Gr. Density (g/cc):	-
Oil Saturation (%):	-
Water Saturation	-

PLATE 45

Supplemental Scanning Electron Microscopy

Company:	Fidelity E & P
Well:	Cane Creek 26-3
Location:	Grand Co., Utah
Depth (ft):	7438-KCl "A"
Unit:	n/a
Dep. Env.:	n/a

LITHOLOGY

Argillaceous Sandstone

C

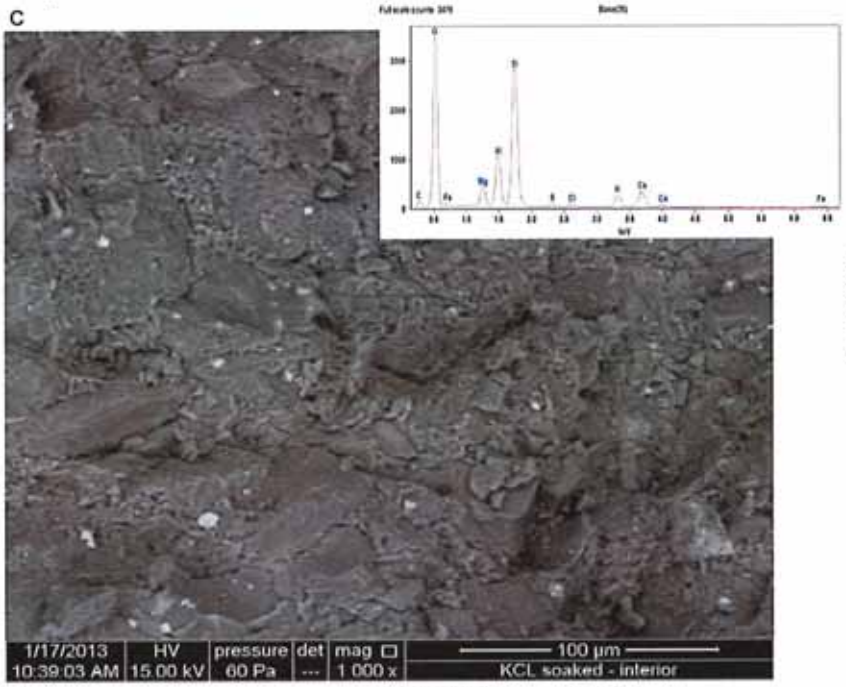

D

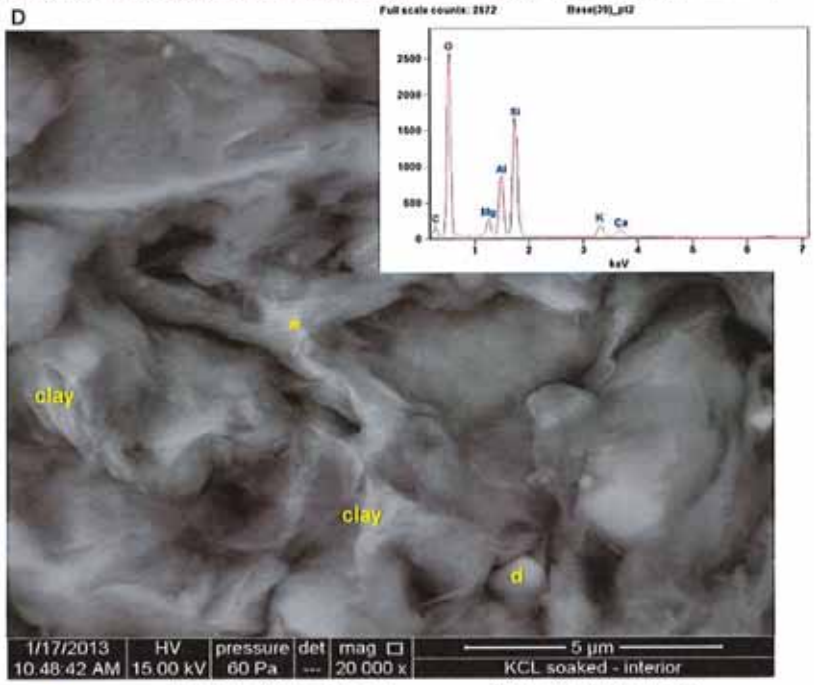

Mineralogy Determined by X-Ray Diffraction

(Weight %)

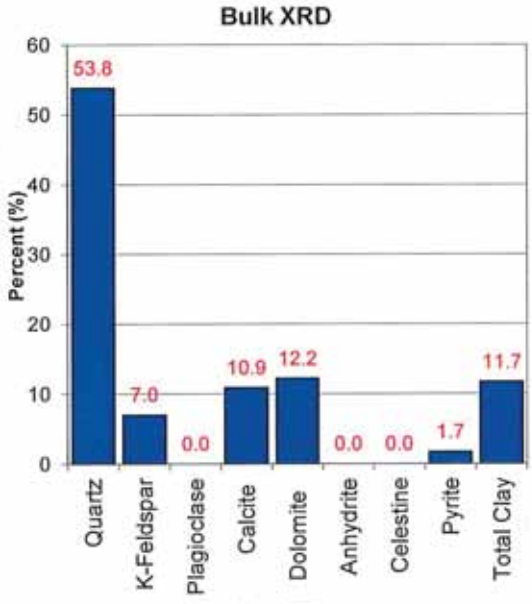

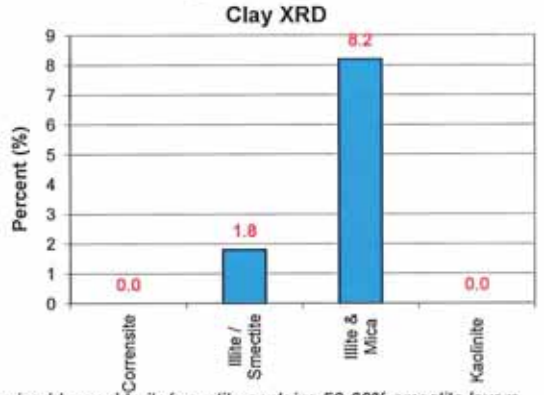

mixed-layer chlorite/smectite contains 50-60% smectite layers

SEM Description

These SEM images were taken from a freshly broken surface from the sample that was soaked overnight in 7% KCl. Most of the framework grains are quartz and feldspar. Intergranular areas are filled with detrital clay (clay), dolomite (d), and calcite (not pictured). The upper EDX spectrum was collected from the field of view shown in Photo C. The lower EDX spectrum is from the point on the detrital clay marked in Photo D (*). Unlike previous samples, there was no chlorine peak associated with the clay, and only a very small chlorine peak evident in the full raster low magnification SEM photo. This suggests there is little to no salt (or chlorine) in the interior of the KCl soaked sample.

Core Lab
RESERVOIR OPTIMIZATION

Relative Abundances:

Trace	<1%
Minor	1-5%
Moderate	5-10%
Common	10-20%
Abundant	>20%

Core Analysis Data:

Porosity (%):	-
Permeability (md):	-
Gr. Density (g/cc):	-
Oil Saturation (%):	-
Water Saturation	-

PLATE 45

Supplemental Scanning Electron Microscopy

Company:	**Fidelity E & P**
Well:	**Cane Creek 26-3**
Location:	**Grand Co., Utah**
Depth (ft):	**7438-KCl "A"**
Unit:	**n/a**
Dep. Env.:	**n/a**

LITHOLOGY

Argillaceous Sandstone

E

Mineralogy Determined by X-Ray Diffraction

(Weight %)

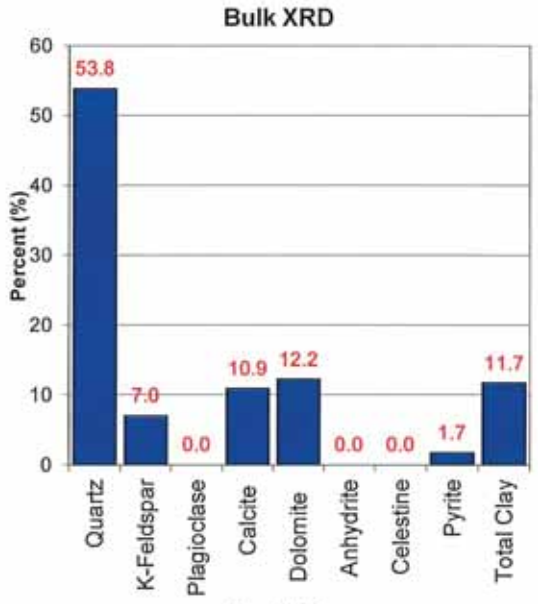

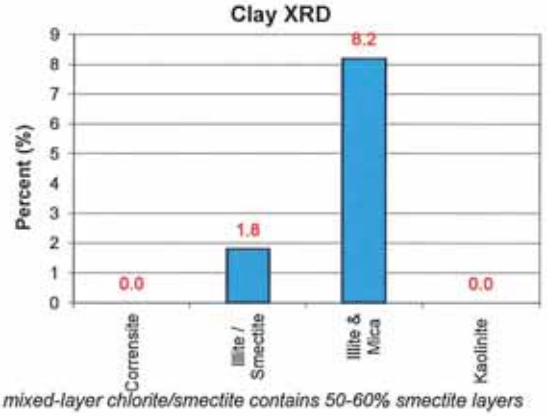

mixed-layer chlorite/smectite contains 50-60% smectite layers

SEM Description

A surface piece of the KCl soaked sample was also prepped for SEM analysis, to compare to the freshly broken surface of the same sample. As expected, an abundance of KCl is found along the surface. The lighter gray areas are comprised of KCl. The darker areas are mostly quartz and feldspar grains.

Relative Abundances:	
Trace	<1%
Minor	1-5%
Moderate	5-10%
Common	10-20%
Abundant	>20%

Core Analysis Data:	
Porosity (%):	-
Permeability (md):	-
Gr. Density (g/cc):	-
Oil Saturation (%):	-
Water Saturation	-

CMS-300 CONVENTIONAL PLUG ANALYSIS

Fidelity Exploration & Production Co.

Cane Creek Unit #26-3
Grand County, Utah

CL File Number: DEN-120128

Date: 02/04/2013

Fidelity Exploration & Production Co.
Cane Creek Unit #26-3
Grand County, Utah

CL File No.: DEN-120128
Date: 02/04/2013
Analyst(s): KF, JC

Permeability vs. Porosity at Various NCS

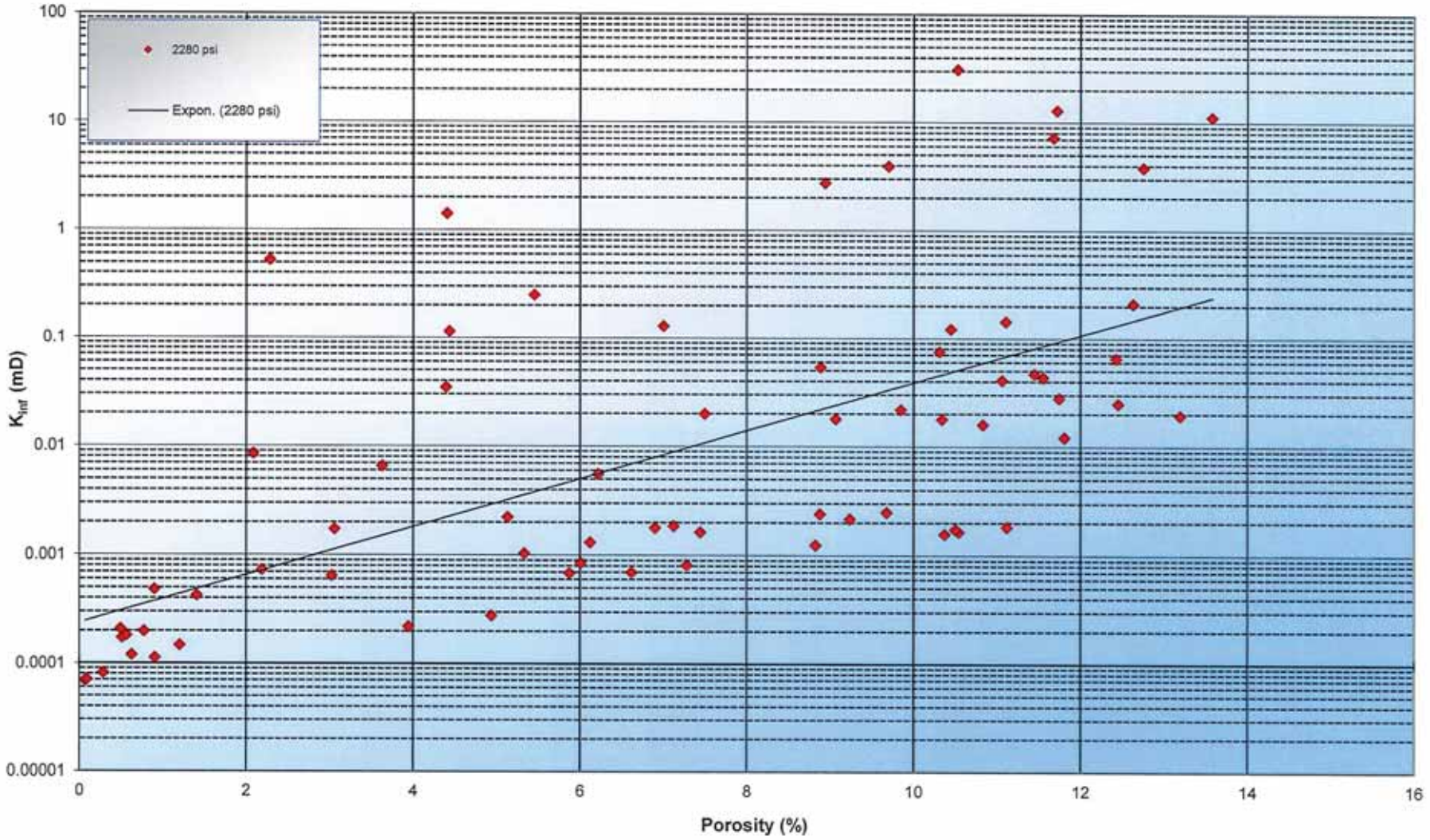

Figure 1

FRACTURE EVALUATION OF CONVENTIONAL CORE FROM THE FIDELITY EXPLORATION AND PRODUCTION CANE CREEK UNIT 26-3 WELL GRAND COUNTY, UTAH

Prepared

for

Fidelity Exploration & Production Inc.

Job # 121467G

CONFIDENTIAL

TABLE OF CONTENTS

SUMMARY

A fracture orientation study was performed on 87 feet of conventional core between 7388 and 7475 feet, from the Cane Creek Unit 26-3 Well located in Grand County, Utah. The core is predominantly very dolomitic siltstone to silty dolostones and silty shale beds separated by thick anhydrite beds. Occasional silty limestone beds occur near the top of the unit. It is assumed that this unit is part of the Pennsylvanian Age Paradox Formation in the Paradox Basin.

- Correlation of the core gamma depths to the electric log depths show that core depths minus 4.0 feet equals the electric log depths. Correlation of core depths to OBMI depth indicates that the core depths from 7388 to 7411 feet is core depth minus 2.5 feet equals OBMI depths and from core depths 7411 to 7475 feet is core depth minus 3.0 feet equals OBMI depth.

- The core is unoriented so a dashed yellow line was drawn on the down-dip bedding trend and all fractures were originally oriented to that yellow line. Later correlation of core to the imaging OBMI log indicates the down dip bedding trend is to the northeast at about 37 degree azimuth. All data was then rotated to a true north orientation and then rotated to a true down hole orientation because the well bore deviated 2 degree to the west southwest (257 azimuth).

- Bedding dips tends to be more scattered towards the bottom of the core.

- The fractures are mostly cemented with halite and commonly cemented with calcite/dolomite and anhydrite. The most productive open fracture is a brecciated zone at 7425 to 7426 feet that is coated with pyrobitumen and partially cemented with halite

- Most of the anhydrite cemented fractures are adjacent to large anhydrite beds that separate the dolomitic siltstones and shales. The massive, competent dolomitic siltstone beds have the best developed fractures. Fractures in the anhydrite beds are always healed and were hard to detect on the whole core because everything is coated with oil-based drilling mud.

- Drilling induced petal fractures have a fairly uniform orientation and strike in a northeast southwest orientation and dip to the southwest at about 234 degrees azimuth. This agrees with a set of what are termed “shear induced fractures” noted in the OBMI imaging log from 7430 to 7434 feet that also dip to the southwest at about 225 degrees azimuth but are not present in the core. This author would term the set of “shear induced fractures” fractures noted in the OBMI imaging log as break out fractures that are associated with the petal fractures.

- Most of the fractures that have slickenside surfaces on them are low angle and have both a down-dip azimuth direction (44 degrees azimuth) along with a somewhat similar down-dip movement direction noted on the striations measured on the slip surface that average 73 degrees azimuth.

- The following chart averages the strike azimuth, dip plunge, fracture thickness and confidence interval of different types of fractures.

Fracture Types	Strike Average (azimuth)	Dip Average (degrees)	Width Ave. (mm)	Confide. Interval	n
Halite Cemented	323°	71°	1.2	42°	31
Calcite/Halite Cemented	316°	76°	0.77	122°	13
Anhydrite Cemented	318°	79°	3.5	154°	5
Fract. with Slickenside	314°	13°	0.02	18°	19
Open Fractures	333°	75°	0.60	110°	6
Artificial Petal	324°	74°	0.01	21°	7

- The calcite cemented fractures tend to be more common at the top of the core and tend to be also cemented with halite.

Thank you for choosing Core Laboratories. If you have any questions about this report please call (713-328-2536) or write (Paul.Grover@corelab.com). All data, interpretations, and other matters related to this study are considered confidential and the sole property of Fidelity Exploration and Production.

Sincerely,

Paul W Grover, Ph.D.
Senior Geologist
Core Laboratories
Ph. 713-328-2536
Email: Paul.Grover@corelab.com

FRACTURE STUDY
OF CONVENTIONAL CORE FROM THE
CANE CREK UNIT 26-3 WELL
GRAND COUNTY, UTAH

INTRODUCTION

A fracture orientation study was performed on 87 feet of conventional core between 7388 and 7475 feet, from the Cane Creek Unit 26-3 Well located in Grand County, Utah. The core is predominantly composed of tan colored very dolomitic siltstone and dark gray silty shales from the Pennsylvanian Age, Cane Creek subinterval of the Paradox Formation. The objectives of this study are: 1) orient the core to the image log, 2) describe and measure the fractures and 3) evaluate the composition and reservoir characteristics of the core. Fracture orientations are listed in Table 1 and Figures 1-13. The fracture description panel is enclosed at the end of the report.

FRACTURE ANALYSIS

Fracture Orientation:

The core is unoriented so a dashed yellow north line was drawn down the down dip bedding plain that averages about 11 degrees. All fractures were measured using a 360 degree measurement system with the yellow dashed line being the zero point. Later correlation of core to the imaging OBMI log indicates the down dip bedding trend is to the northeast at about 37 degree azimuth. All data was then rotated to a true north orientation. There is no north line drawn on the core but further core fracture measurements can still be made if one assumes the dashed yellow line is at the 37 degree azimuth position. The core data is also rotated into a true down-hole orientation because the well bore has a slight deviation inclination of 2 degrees to the west southwest (257 azimuths). It appears the bit is climbing updip. The core is divided into "segments" which are parts of the core that fit together. Spin surfaces or non-fitting breaks divide the segments. Fractures within each segment have a true special relationship with each other. Within each segment a straight dashed yellow colored line was drawn down the length of the core along the best fit average of the down-dip bedding plains. Each segment has its own averaged bedding dip azimuth which was measured from the imaging OBMI log. Bedding dip directions tends to be more scattered towards the bottom of the core. The core gamma ray logs of the sleeved core shows that core depths minus 4.0 feet equals the electric log depths. Correlation of core depths to OBMI depth indicates that the core depths from 7388 to 7411 feet is core depth minus 2.5 feet equals OBMI depths and from core depths 7411 to 7475 feet is core depth minus 3.0 feet equals OBMI depth. The change in core to OBMI depth correction is due to much space given to a rubbly zone at 7411 to 7413 feet. Field notes also indicate there might be too much space given to the core from 7406 to 7407 feet. It should be noted that much of the core was tightly

wedged into the core barrels so keeping the core together and intact was extremely difficult and time consuming. For future reference a tightly wedged core like this might be a good candidate for CAT scan analysis before extraction. The bolded fracture data in Table 1 is oriented to true north and also includes fracture type, fracture cement, fracture width and length, fracture morphology, if it is open or closed, and lithology type.

Fracture can be cemented by a combination of halite, calcite, anhydrite, dolomite and lesser amounts of pyrite and pyrobitumen (dead carbon). The following chart shows the average strike azimuth, dip plunge, fracture thickness and confidence interval of different types of fractures.

Fracture Types	Strike Average (azimuth)	Dip Average (degrees)	Width Ave. (mm)	Confide. Interval	n
Halite Cemented	323°	71°	1.2	42°	31
Calcite/Halite Cemented	316°	76°	0.77	122°	13
Anhydrite Cemented	318°	79°	3.5	154°	5
Fract. with Slickenside	314°	13°	0.02	18°	19
Open Fractures	333°	75°	0.60	110°	6
Artificial Petal	324°	74°	0.01	21°	7

The most common fractures are cemented with halite (Figure 1) and are fairly high angle and tend to dip to the southwest. The most productive open fracture is a brecciated zone at 7425 to 7426 feet that is coated with pyrobitumen and partially cemented with halite. Most of the anhydrite cemented fractures are adjacent to large anhydrite beds that separate the dolomitic siltstones and shales. The massive, competent dolomitic siltstone beds have the best developed fractures. Fractures in the anhydrite beds are always healed and were hard to detect on the whole core that is coated with oil-based drilling mud. Along with most other fractures the anhydrite-cemented fractures show a conjugate set of high angle fractures that have an east northeast and west, southwest strike direction (Figure 2). Calcite/dolomite cemented fractures generally have halite associated with it and are more common at the top of the core (Figure 3). The partially open fractures tend to have a more random distribution with two conjugate sets of strike directions. Three fractures are annotated that have the best possibility of caring hydrocarbons (Figure 4) and are bolded in the fracture Table 1. The fractures that have slickenside surfaces on them are low angle and have a down-dip azimuth direction (44 degrees azimuth) that correlates to a somewhat similar down-dip movement direction noted on the striations measured on the slip surface that average 73 degrees azimuth (Figure 5 and 6).

Artificial fractures are commonly noted in the core and are divided into two categories; 1) curved, non-cemented petal fractures that are discontinuous and tend to curve outward toward the edges of the core from a center point position

and 2) straight to slightly irregular non-cemented fractures that have a natural look to them. Petal fractures are commonly paired but in this core petal fractures have a uniform dip azimuth direction to the southwest (average of 234 degrees) (Figure 7). This agrees with a set of what are termed "shear induced fractures" noted in the OBMI imaging log from 7430 to 7434 feet that also dip to the southwest at about 225 degrees azimuth but are not present in the core. This author would term this set of "shear induced fractures" fractures noted in the OBMI imaging log as break out fractures that are associated with the petal fractures. The tilted nature of the break out fractures (shear induced fractures) in the OBMI and the one-sided dip of the petal fractures may indicate horizontal compressive forces that are slightly tilted (Figure 13). Petal fractures can also occur in a core where the core barrel is bending or aggressively wanting to climb up dip combined with excessive and bouncing weight on bit. The petal fractures here do not look like bending or torquing petal fractures. There is not much difference between fractures that have a larger width (Figures 8 and 9) to fractures in the upper part of the core with small apertures (Figure 10). However, in the lower part of the core in segment 16 the small fractures tend to have a more northeast/southwest strike direction (Figure 11). An upper hemisphere pole plot of all cemented fractures (not including slickensides and petal fractures) show the general southwest dip direction and high angled tendency of the fractures (Figure 12).

Fractures are drawn on the core panel as if the yellow dashed line is in the up position. Irregular artificial fractures are not drawn in on the core panel. The longer fractures are more common in very well indurated dolomitic siltstone beds in the middle part of the core. Most fracture that show displacement seem to have normal slip movement.

Reservoir Potential:

The portion of the core that show the best reservoir potential are in the central part of the core at the margins of the dolomitic siltstone, shale margin zones that tend to form open fractures. The siltstone at the top of the core appears to be slightly coarser grained and may have more storage potential. In general the lighter colored beds in the OBMI log will develop better fractures.

Horizontal drilling would be most effective in a northeastern direction to possible north direction if you wanted to hit the less dominant second set of fractures.

Study Methods:

A detailed fracture description was made of the whole core at a vertical scale of 1:24 (one inch = two feet). Digitized wireline logs and OBMI logs are included alongside the lithology column. Correlation of the core to the electric logs show the following depth correction:
Core depth – 4feet = Log depth.
Core depths 7388 to 7411feet, Core Depths – 2.5 feet = Log Depth
Core depths 7411 to 7475 feet, Core Depths – 3.0 feet = Log Depth

The core panel is included in the back of this report.

TABLE 1

Fracture Orientation Data from Core

Fidelity CCU 26-3

Seg.	Beg. Depth	End Depth	Frac Dip Azimuth to Yellow Line	Fracture dip Azimuth Rotated to	Fracture Dip in Core	TRUE Down-Hole Dip Azimuth to	TRUE Downhole Dip	TRUE Fracture Strike	Liniation Striat. To Yellow line	TRUE Striation Liniation	Fracture Type	Fracture Cement	Fracture Condition	Comments	Fracture Width	Fracture Displacement	Lithology	Orientation yellow-dotted line, down-dip Azimuth	FMI down-dip bedding Azimuth	Well Bore Dip Inclination	Well Bore Dip Azimuth
	(Feet)	(Feet)	(degrees)	North (Az)	(degrees)	North	(degrees)	(Azimuth)	Azimuth on Slick						(mm)	(mm)					
1	7388.00	7389.20	245	280	80	280	78	190			Str	halite	closed	Cuts Slick	6.4	4.6R	SS /LS?	35	37	2	257
1	7388.30	7388.40	353	28	10	35	11	125	330	5	slick	clay	closed	Bedding	0.01	S	SS	35	37	2	257
1	7388.30	7388.70	222	257	79	257	77	167			str	halite	closed	start @ slick	3.0	1.3	SS	35	37	2	257
1	7388.50	7388.58	20	55	9	59	11	149			slick	clay	closed str	cuts fract	0.01	7.6	SS	35	24	2	257
1	7391.90	7392.00	221	256	75	256	73	166			disc	anh	closed		0.9	small	SS / Anhy	35	41	2	257
1	7392.70	7393.10	230	265	83	265	81	175			curv	halite	closed	disc	2.1	small	LS	35	50	2	257
1	7393.70	7393.90	220	255	85	255	83	165			str	hal/cal	closed	disc	0.2	small	LS	35	47	2	257
1	7393.70	7393.90	185	220	86	220	84	130			str (Tension?	no	art? Open	disc (Petal?)	0.01	small	LS	35	47	2	257
1	7394.60	7395.50	155	190	75	189	74	99			irr	cal?	closed	cont	0.4	small	LS	35	51	2	257
1	7394.65	7395.20	26	61	68	61	70	151			str	open?	open? (80%?)	natural Disc	0.5	small	LS	35	51	2	257
1	7395.30	9395.50	15	50	88	50	90	140			str	cal?	closed	disc	0.2	v small	LS	35	51	2	257
1	7396.00	7396.15	203	238	73	238	71	148			str	anh	closed	disc short	10.3	small	sh	35	41	2	257
1	7398.15	7398.60	210	245	84	245	82	155			irr	anh & hal	closed	disc	5.2	small	sltst	35	35	2	257
1	7398.15	7398.60	193	228	79	228	77	138			irr	hal	closed	disc	1.7	small	sltst	35	35	2	257
1	7399.80	7400.40	144	179	85	179	85	89			irr	hal?	closed	disc	0.2	v small	ss	35	44	2	257
1	7400.10	7400.50	292	327	83	327	82	237			irr	hal?	closed	disc	0.3	v small	ss	35	27	2	257
1	7400.15	7400.50	223	258	78	258	76	168			irr	hal?	closed disc	main set	0.2	small	ss	35	27	2	257
1	7400.55	7401.00	200	235	75	235	73	145			irr set	hal?	closed	disc	0.2	small	ss/sh	35	17	2	257
1	7400.50	7400.60	3	38	10	44	12	134	25	60	slick	clay	closed	str	0.01	small	sh	35	17	2	257
1	7400.90	7401.00	0	35	11	41	13	131	30	65	slick	clay	closed	curv	0.01	mod	sh	35	15	2	257
1	7405.50	7405.60	358	33	9	40	11	130	355	30	slick	clay	closed str	str	0.01	small	sh	35	38	2	257
1	7406.30	7406.35	345	20	10	28	11	118	0		slick	clay	closed str	str	0.01	small	sh	35	30	2	257
1	7406.40	7406.85	96	131	79	131	80	41			str	cal & hal	closed disc	stepped/slick	1.1	small	sh	35	30	2	257
1	7406.45	7406.85	124	159	62	158	62	68			str	cal & hal	closed disc	stepped/slick	0.97	small	sh	35	30	2	257
1	7406.55	7406.85?	110	145	74	144	75	54			str	al & cal & py	closed disc	disc	1.5	small	sh	35	30	2	257
1	7406.85	7406.89	351	26	12	33	13	123	95	130	slick	clay	closed str	frac termination	0.01	small	sh	35	37	2	257
1	7406.85	7406.90	350	25	11	32	12	122	45	80	slick	clay	closed str	frac termination	0.01	mod	ss	35	37	2	257
2	7406.85	7407.20	207	244	73	244	71	154			irr	hal	closed	disc	2.6	small	sh	37	37	2	257
2	7406.89	7407.40	220	257	75	257	73	167			irr	hal	closed	disc	1.3	small	sh	37	37	2	257
3	7409.10	7410.60	203	233	77	233	75	143			str	hal & cal	closed?	cont	1.8	small	sltst	30	37	2	257
3	7410.60	7410.65	351	21	10	29	11	119	?		slick	clay	closed	cont	0.01	small / mod	sltst	30	21	2	257
R4	7410.60	7411.30	200	221	80	221	78	131			Str	hal	closed	disc	0.5	small	sltst	21	21	2	257
R4	7410.5	7411.3	198	219	79	219	77	129			Str	hal	closed	disc	0.4	small	sltst	21	21	2	257
R4	7411.25	7411.3	165	186	11	176	11	86	150	171	slick	clay	closed	cont str	0.01	small	sltst	21	20	2	257
5	7412.9	7414	175	200	70	199	69	109			str	hal	closed	cont	2.0	small	sh	25	25	2	257
6	7415.9	7417.15	230	254	78	254	76	164			str-irr	hal	closed	cont	2.4	small	sltst	24	24	2	257
6	7416.48	7416.5	22	59	4	65	6	155			irr	hal	closed	cont	1.8	small	sltst	37	29	2	257
6	7417.30	7418.90	198	235	73	235	71	145			str	no? open?	closed?	disc	0.3	small	sltst	37	25	2	257
6	7418.50	7418.80	283	320	28	323	27	233			str	?	closed	disc (Artif?)	0.1	small	sltst	37	53	2	257
6	7418.80	7419.40	210	247	89	247	87	157			petal?	no	closed	disc	0.01	--	sltst	37	53	2	257
6	7419.60	7419.70	350	27	13	32	14	122	350	27	slick	clay	closed	cont	0.01	small	sltst	37	42	2	257
7	7420.30	7422.30	168	211	70	210	69	120			strait/curv	hal	closed	cont	4.3	small	sltst	43	41	2	257
7	7421.00	7421.50	120	163	58	162	58	72			Str set	hal	closed	cont	0.4	small	stst	43	46	2	257
7	7421.70	7422.80	193	236	76	236	74	146			irr	hal	closed	cont?	1.2	small	sltst	43	46	2	257
R8	7423.20	7424.50	185	222	52	221	50	131			irr	?	closed?	cont (Petal?)	1.0	no	sh	37	30	2	257
R8	7423.70	7424.30	40	77	67	77	69	167			irr	no?	open?	disc	0.5	small	sh	37	30	2	257
R8	7424.70	7425.3?	215	252	68	252	66	162			irr	no	closed?	disc (Petal)	1.5	?	sh	37	51	2	257
9	7425.10	7426.15	90	135	69	135	70	45			breccia	salt & bit	open (20%)	cont	1.5-12.0	large	sh	45	49	2	257
9	7428.25	7429.20	163	208	90	208	89	118			curved	cal & salt	closed	cont	1.1	?	sltst	45	49	2	257
9	7430.90	7431.55	187	232	82	232	80	142			petal?	--	closed	disc	0.01	--	sltst	45	43	2	257
9	7431.60	7431.65	356	41	11	46	13	136	14	59	slick	clay	closed	cont	0.01	large	sh	45	44	2	257
9	7431.65	7432.70	187	232	84	232	82	142			sl curv - str	cal	closed	disc	0.3	no	sltst	45	44	2	257
9	7432.70	7432.75	10	55	11	58	13	148	15	60	slick	clay	closed	cont	0.01	small	sh	45	42	2	257
9	7432.70	7432.95	174	219	74	219	72	129			petal?	--	closed	disc	0.0	--	sltst	45	42	2	257
9	7437.70	7438.75	203	248	85	248	83	158			str	hal & cal	closed?	disc	0.4	small	sltst	45	43	2	257
9	7438.75	7438.80	44	89	11	87	13	177	85	130	slick	clay	closed	cont	0.01	mod	sh	45	46	2	257
9	7438.80	7439.00	200	245	83	245	81	155			irr	hal?	closed	slick?	0.01	small	sh	45	46	2	257
9	7439.74	7441.60	218	263	78	263	76	173			str	cal & hal	closed	cont	1.6	v small	sltst	45	49	2	257

TABLE 1

Fracture Orientation Data from Core

Fidelity CCU 26-3

Seg.	Beg. Depth	End Depth	Frac Dip Azimuth to Yellow Line	Fracture dip Azimuth Rotated to	Fracture Dip in Core	TRUE Down-Hole Dip Azimuth to	TRUE Downhole Dip	TRUE Fracture Strike	Liniation Striat. To Yellow line	TRUE Striation Liniation	Fracture Type	Fracture Cement	Fracture Condition	Comments	Fracture Width	Fracture Displacement	Lithology	Orientation yellow-dotted line, down-dip	FMI down-dip bedding	Well Bore Dip	Well Bore Dip
	(Feet)	(Feet)	(degrees)	North (Az)	(degrees)	North	(degrees)	(Azimuth)	Azimuth on Slick						(mm)	(mm)		Azimuth	Azimuth	Inclination	Azimuth
11	7441.85	7441.90	50	87	10	85	12	175	22	59	slick	clay	closed	cont	0.1	small	sltst	37	35	2	257
11	7442.70	7443.50	145	182	68	181	67	91			str & curv	minor hal	closed	cont	0.1	small	sltst	37	40	2	257
14	7446.40	7446.45	45	80	5	79	7	169	35 & 155	70 & 190	slick	clay	osed cont almo	curved	0.01	small	sh	35	35	2	257
14	7446.50	7447.40	298	333	86	333	85	243			curves	anh	open (10%)	disc	1.1	small	sltst	35	35	2	257
14	7446.50	7446.80	160	195	37	193	36	103			sl irr	cal	closed	disc	0.2	s-o	sh	35	35	2	257
15	7451.70	7452.50	190	225	58	224	56	134			str	hal	closed	cont	0.3	small	sltst	35	34	2	257
15	7452.90	7452.95	355	30	10	37	11	127	11	46	slick	clay	closed	cont	0.01	v small	sh	35	70	2	257
16	7453.25	7453.40	190	225	39	224	37	134			str	?hal	closed	disc	0.1	v small	sltst	35	76	2	257
16	7453.25	7453.85	270	305	87	305	86	215			irr	hal	closed	disc	0.3	small	sltst	35	76	2	257
16	7453.25	7453.92	185	220	89	220	87	130			str	hal	open (20%?)	lateral slip	.7-9.2	mod >5	sltst	35	76	2	257
16	7453.85	7454.40	350	25	54	26	55	116			Str	hal	closed	cont	0.1	mod	sltst	35	76	2	257
16	7455.80	7457.50	277	312	88	312	87	222			str	hal cal?	closed	cont	0.3	small	sltst	35	53	2	257
16	7456.20	7458.50	280	315	89	315	88	225			st & cur	hal	closed	disc	0.3	small	sltst	35	7	2	257
16	7457.60	7459.00	268	303	84	303	83	213			curve	hal	closed	cont	0.2	small	sltst	35	17	2	257
17	7462.50	7464.00	124	175	85	175	85	85			str	? Anh	closed	cont	0.01	small	anhy	51	51	2	257
19	7466.35	7466.45	356	38	32	40	34	130	350	42	slick	clay	closed	cont	0.1	small	sltst	42	40	2	257
19	7468.4	7469.9	170	212	79	212	78	122			irr	hal	closed	cont	3.5	?	sltst	42	49	2	257
19	7468.7	7469.3	150	192	82	192	81	102			irr	hal	closed disc	disc joins cont	0.2	small	sltst	42	49	2	257
19	7469.7	7470.4	96	138	83	138	84	48			str	hal	closed	cont	0.3	small	sltst	42	16	2	257
19	7470.2	7470.6	210	252	78	252	76	162			petal?	--	closed	disc	0.01	--	sltst	42	5	2	257
20	7471	7471.1	15	45	16	48	18	138	50	80	slick	clay	closed	cont	0.1	small	slt/sh	30	30	2	257
20	7471.10	7471.50	243	273	81	273	79	183			curve	hal	closed	cont	1.6	small	sltst	30	30	2	257
Core Depth -4.0 feet = Log Depth																					

FIGURE 1

Rose & Fracture Plane Schmidt Plot (Lower Hemisphere)

Halite Cemented Fractures

Fidelity CCU 26-3 Core

Grand County, Utah

Fracture Plane Schmidt Plot

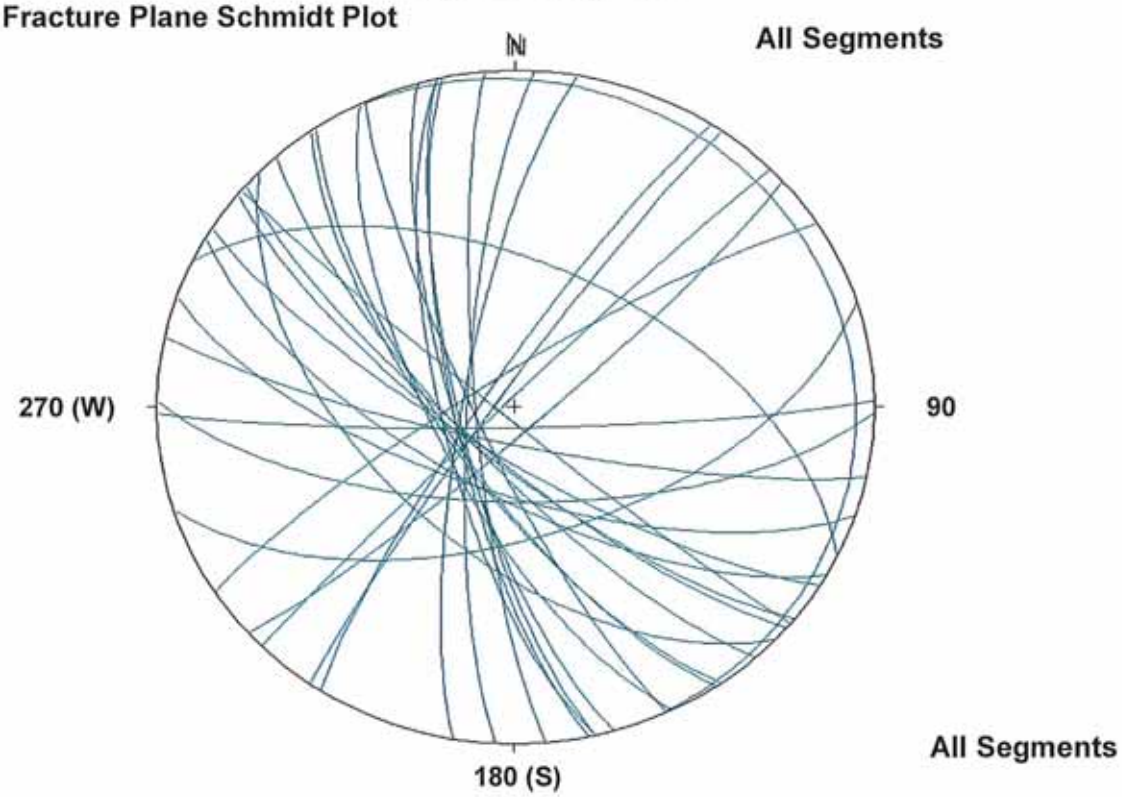

Strike Azimuth Rose Diagram

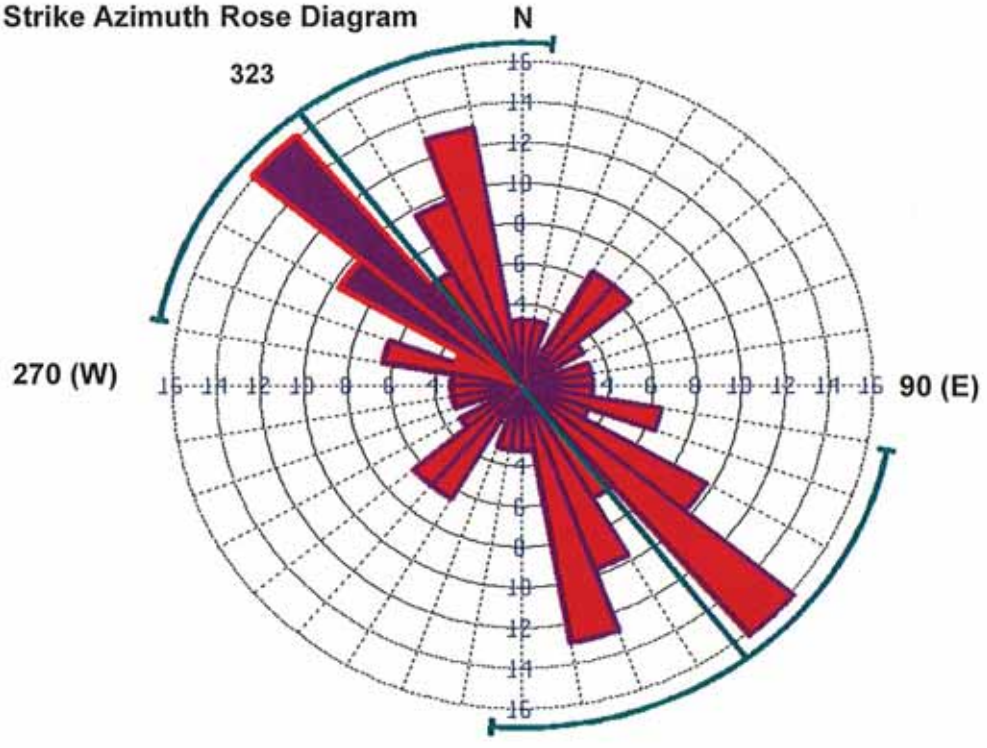

FIGURE 2

Rose & Fracture Plane Schmidt Plot (Lower Hemisphere)
Anhydrite Cemented Fractures
Fidelity CCU 26-3 Core
Grand County, Utah

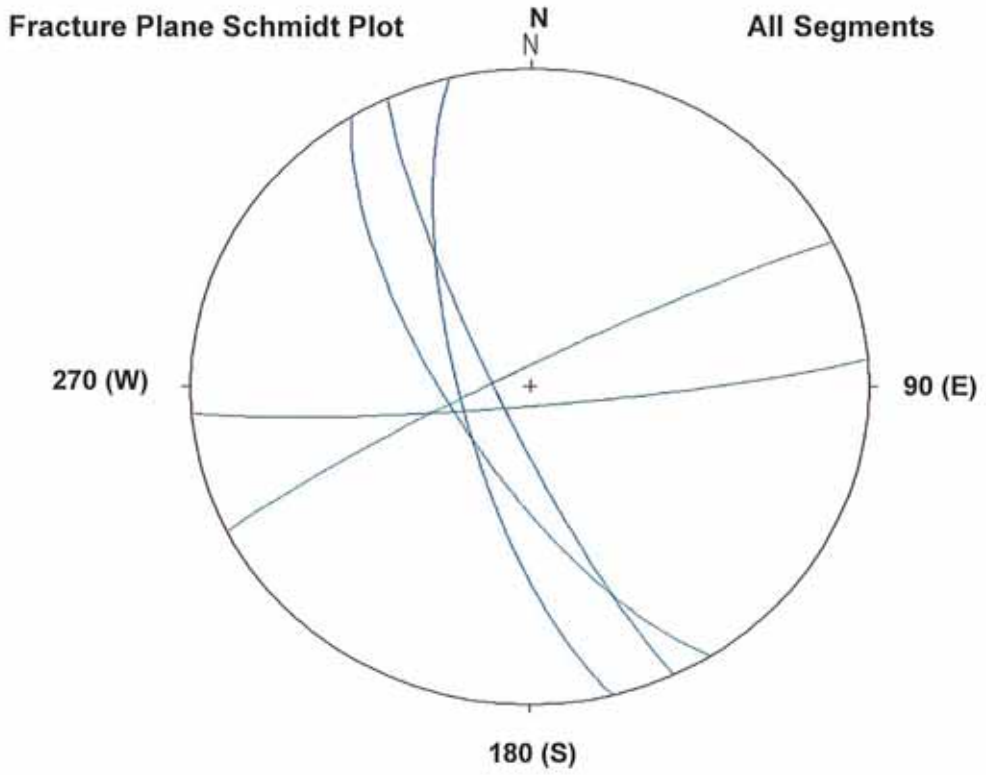

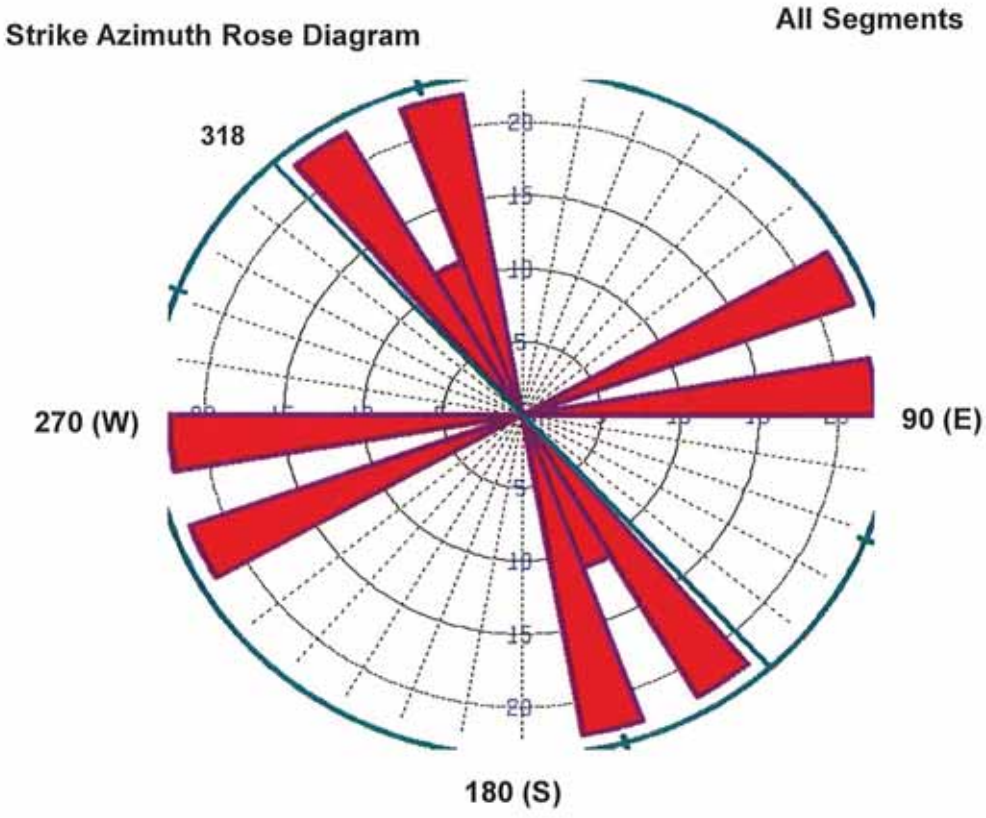

FIGURE 3

Rose & Fracture Plane Schmidt Plot (Lower Hemisphere)
Fractures Partially Cemented by Calcite
Fidelity CCU 26-3 Core
Grand County, Utah

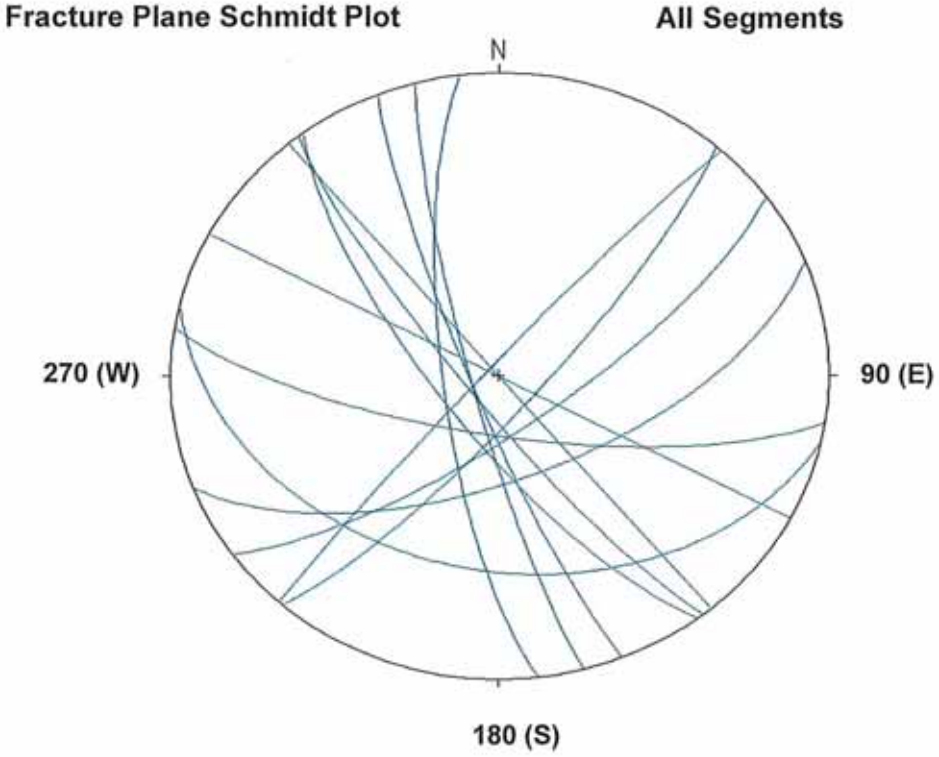

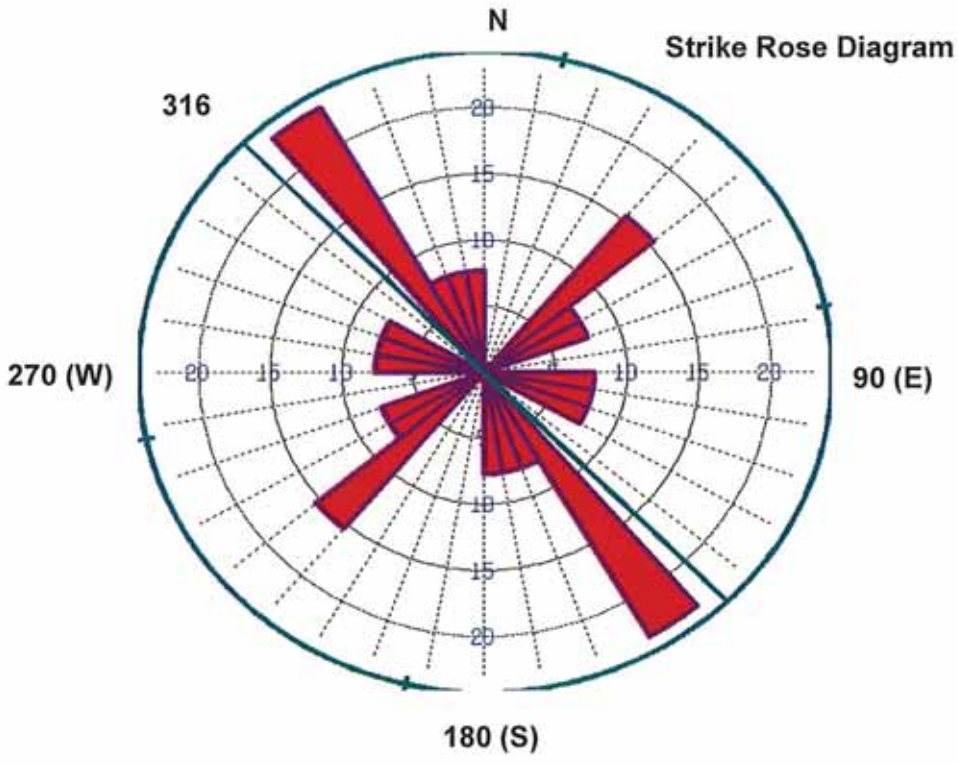

FIGURE 4

Rose & Fracture Plane Schmidt Plot (Lower Hemisphere)
ırtially Open and Non-Cemented Fractures (Artificiı
Fidelity CCU 26-3 Core
Grand County, Utah

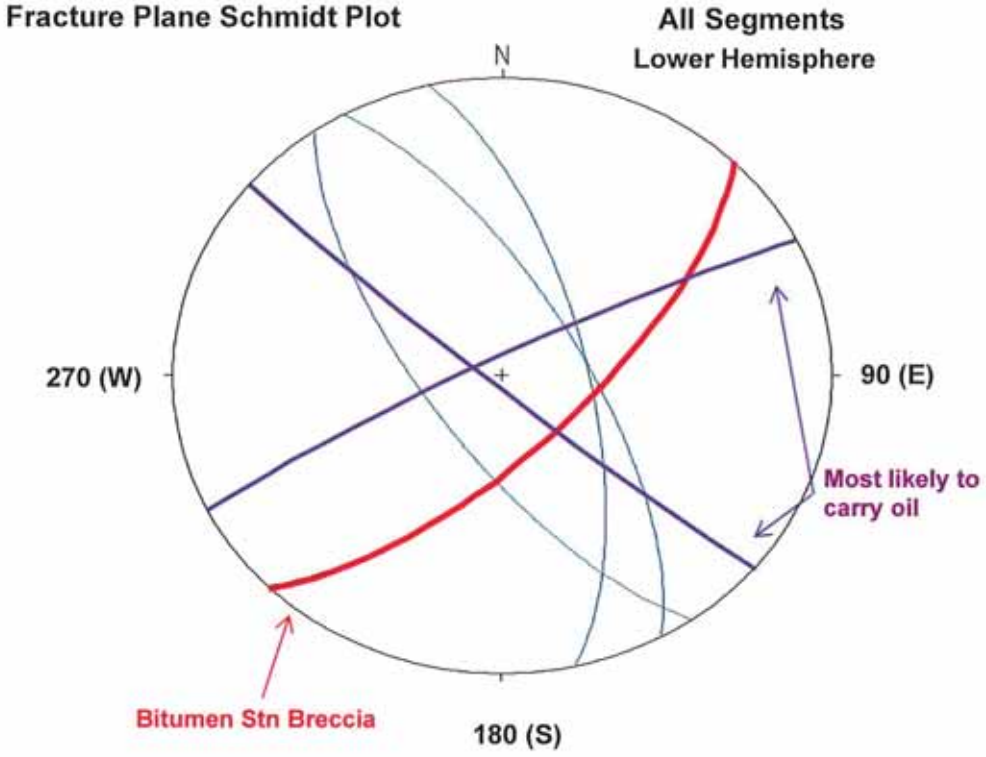

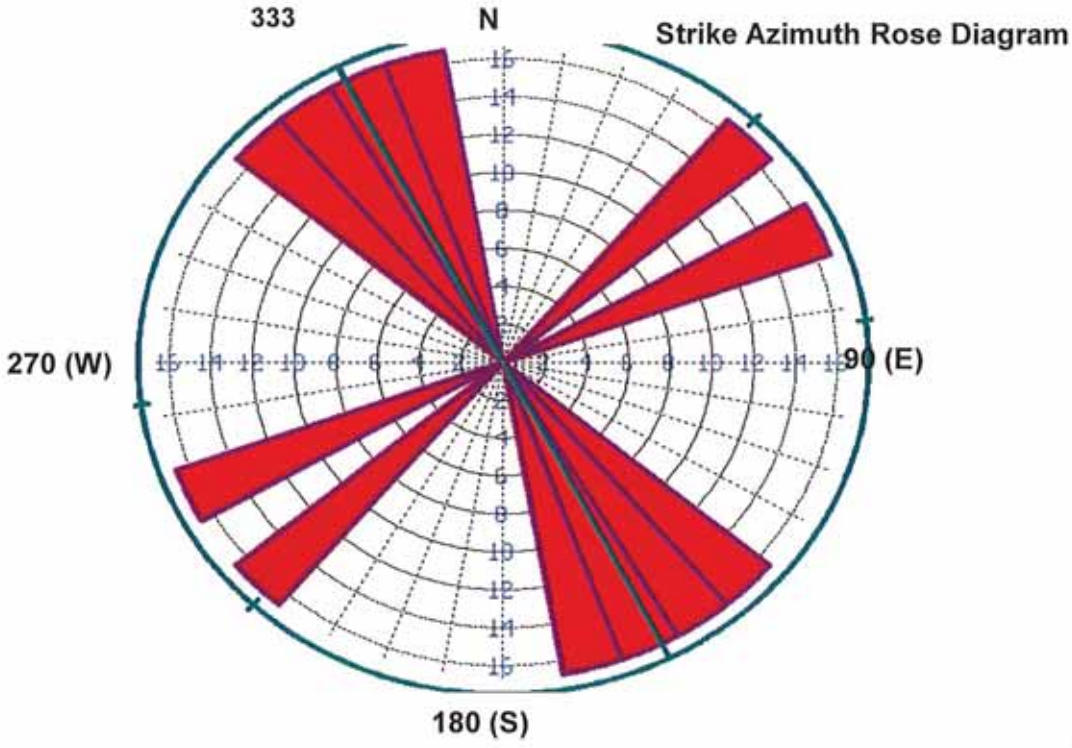

FIGURE 5

Rose & Fracture Plane Schmidt Plot (Lower Hemisphere)
Fractures with Slickenside Surfaces
Fidelity CCU 26-3 Core
Grand County, Utah

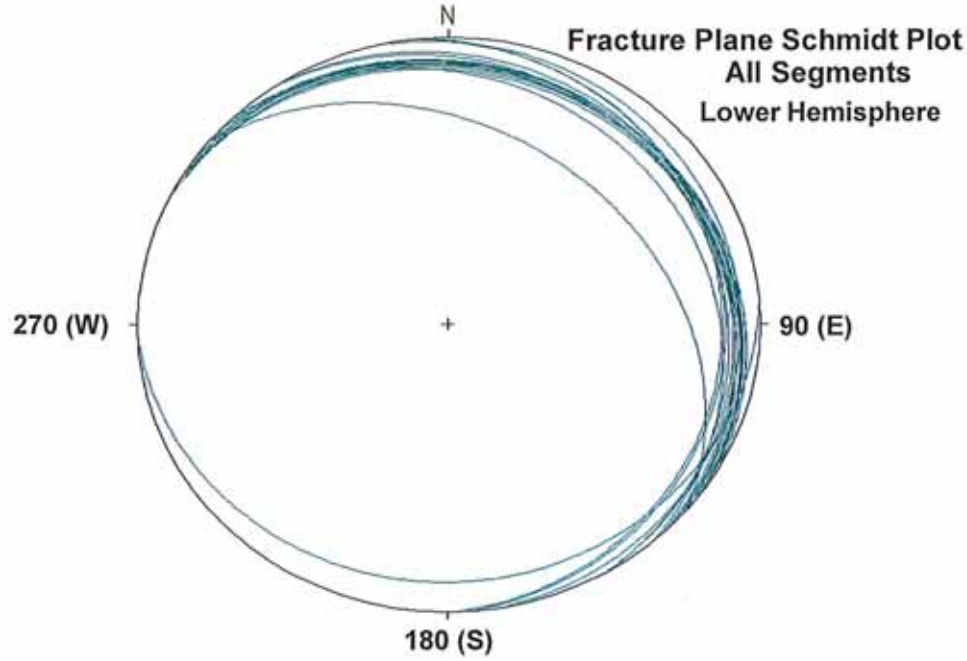

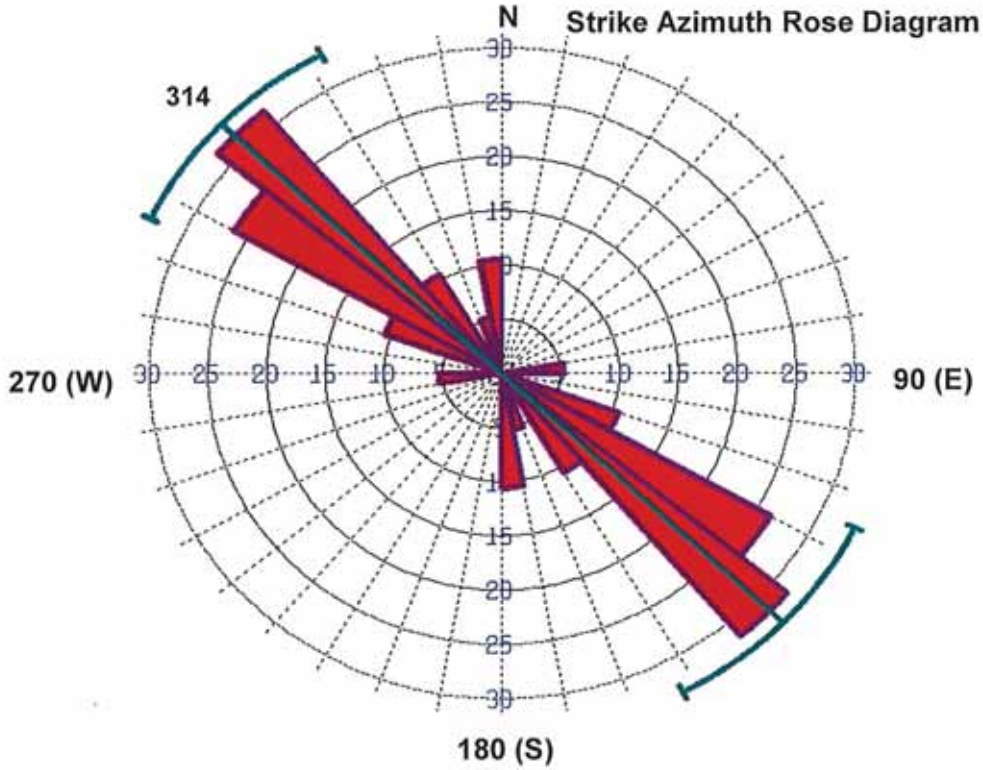

FIGURE 6

Unidirection Rose Diagrams
Direction of Bedding Dip and Slip on Slickensides
Fidelity CCU 26-3 Core
Grand County, Utah

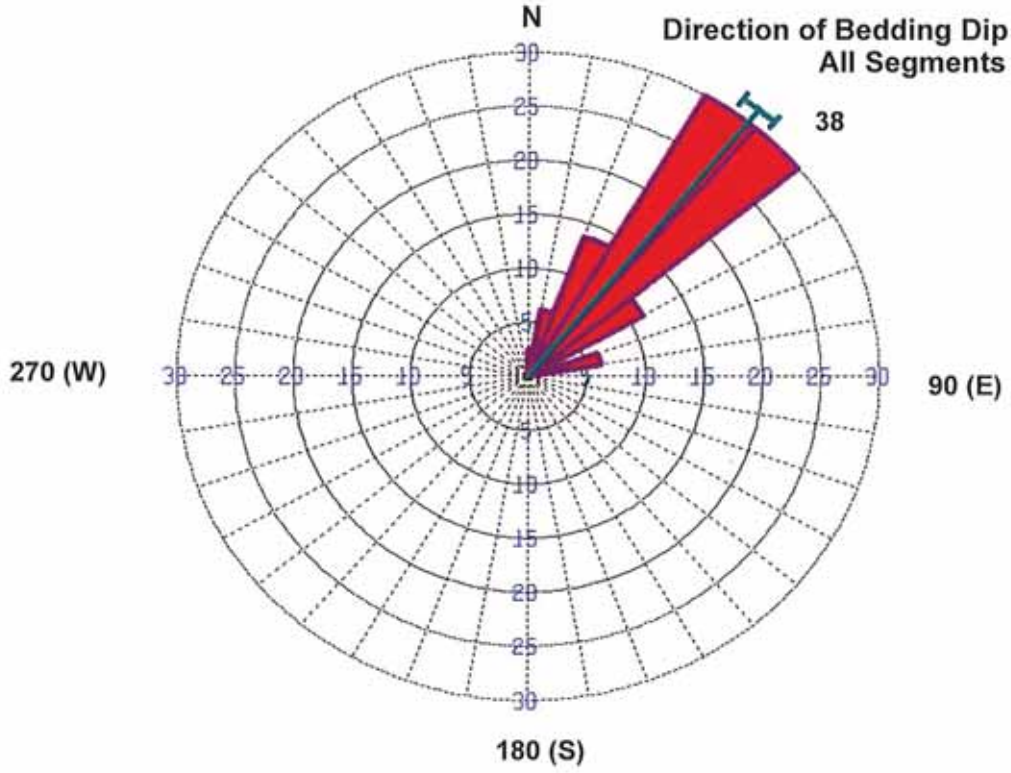

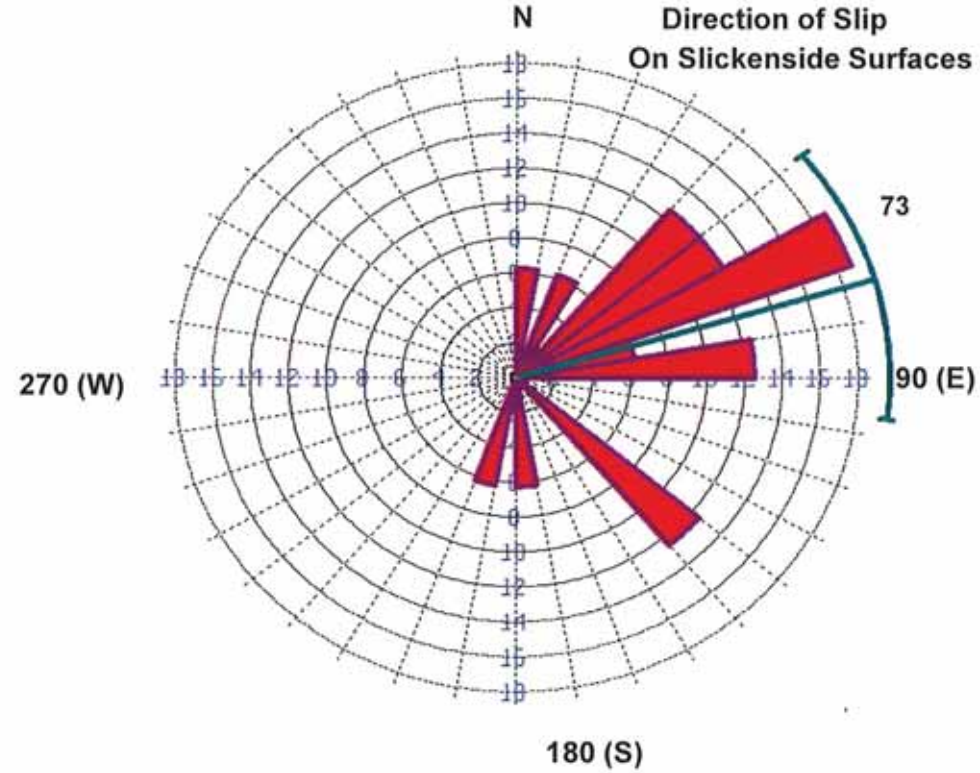

FIGURE 7

Rose & Fracture Plane Schmidt Plot (Lower Hemisphere)
Artificial Petal Fractures Fractures
Fidelity CCU 26-3 Core
Grand County, Utah

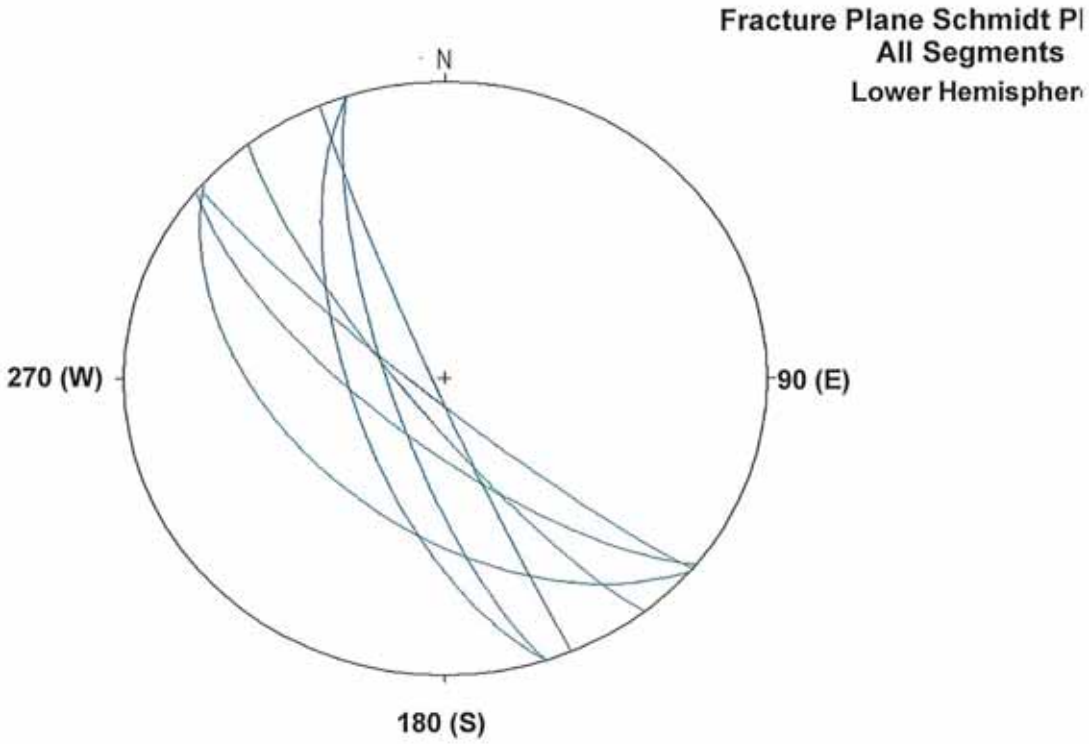

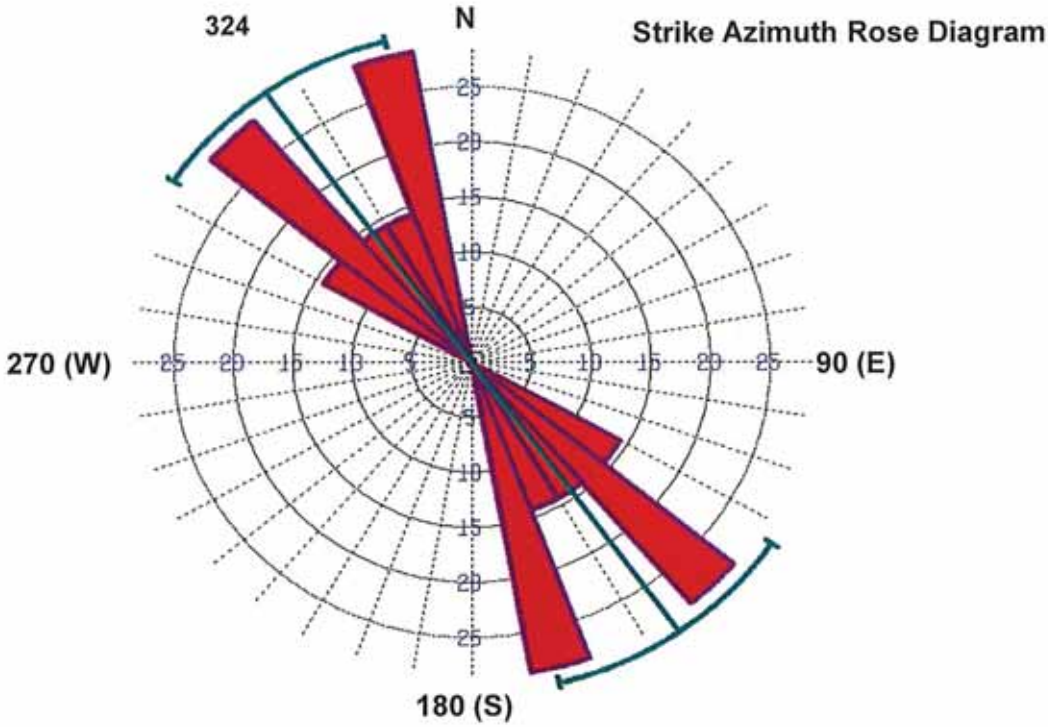

FIGURE 8

Rose & Fracture Plane Schmidt Plot (Lower Hemisphere)
Large Cemented Fractures > 3mm
Fidelity CCU 26-3 Core
Grand County, Utah

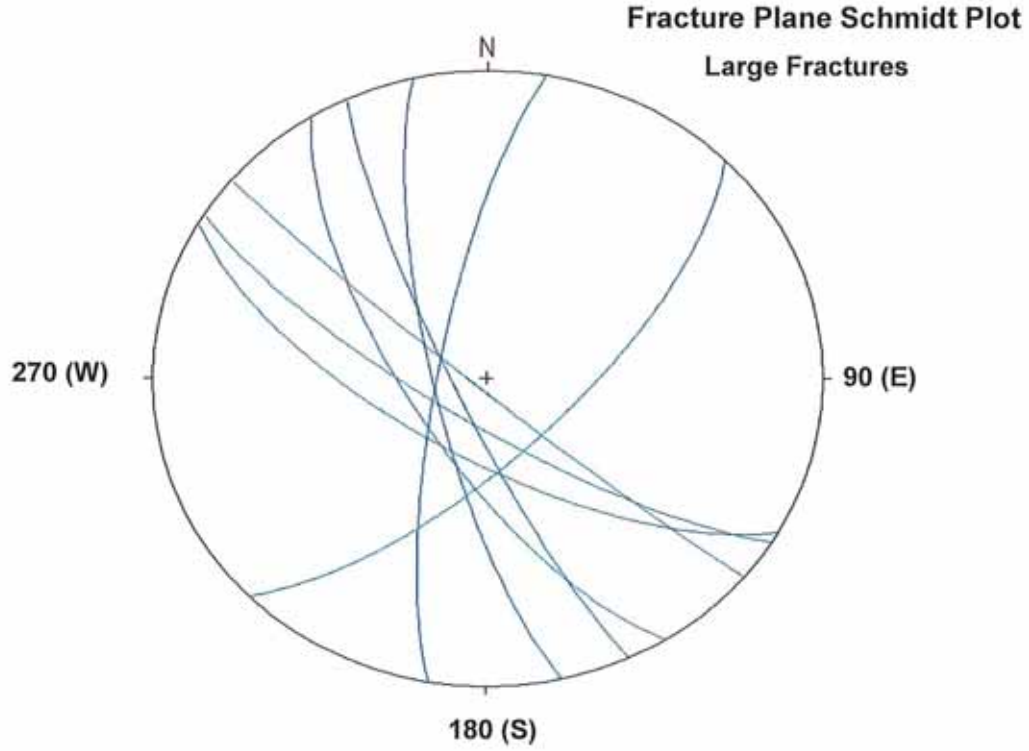

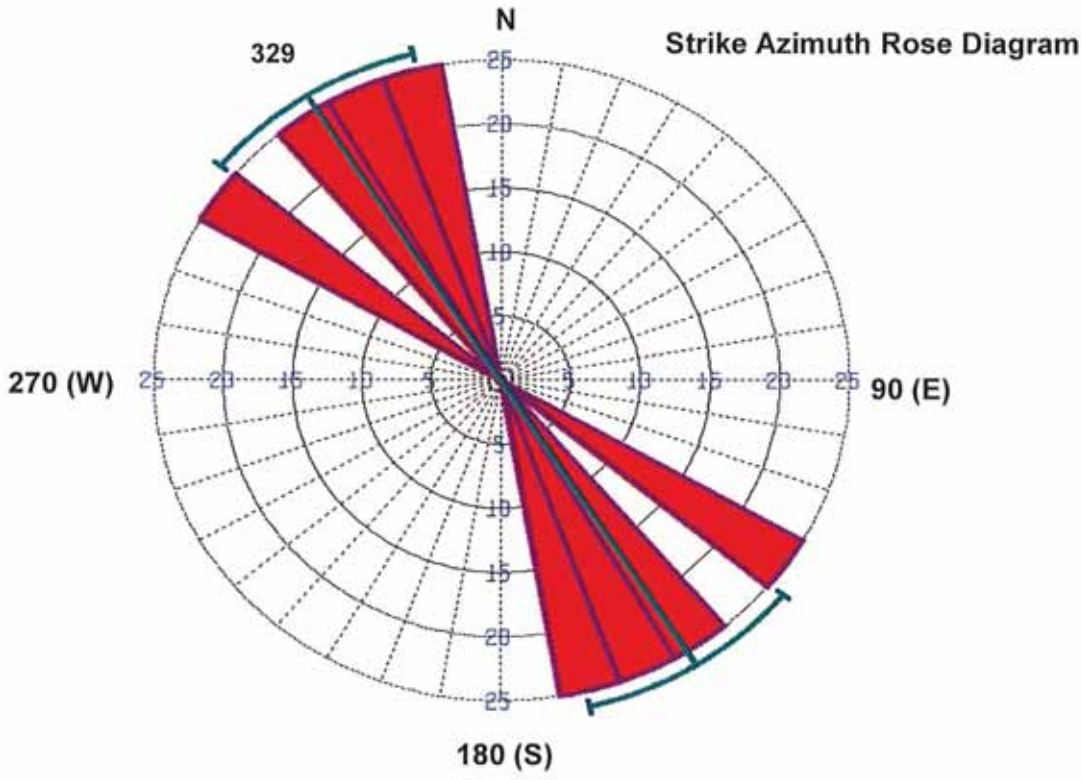

FIGURE 9

Rose & Fracture Plane Schmidt Plot (Lower Hemisphere)
Medium Cemented Fractures between 0.9 to 1.5 mm
Fidelity CCU 26-3 Core
Grand County, Utah

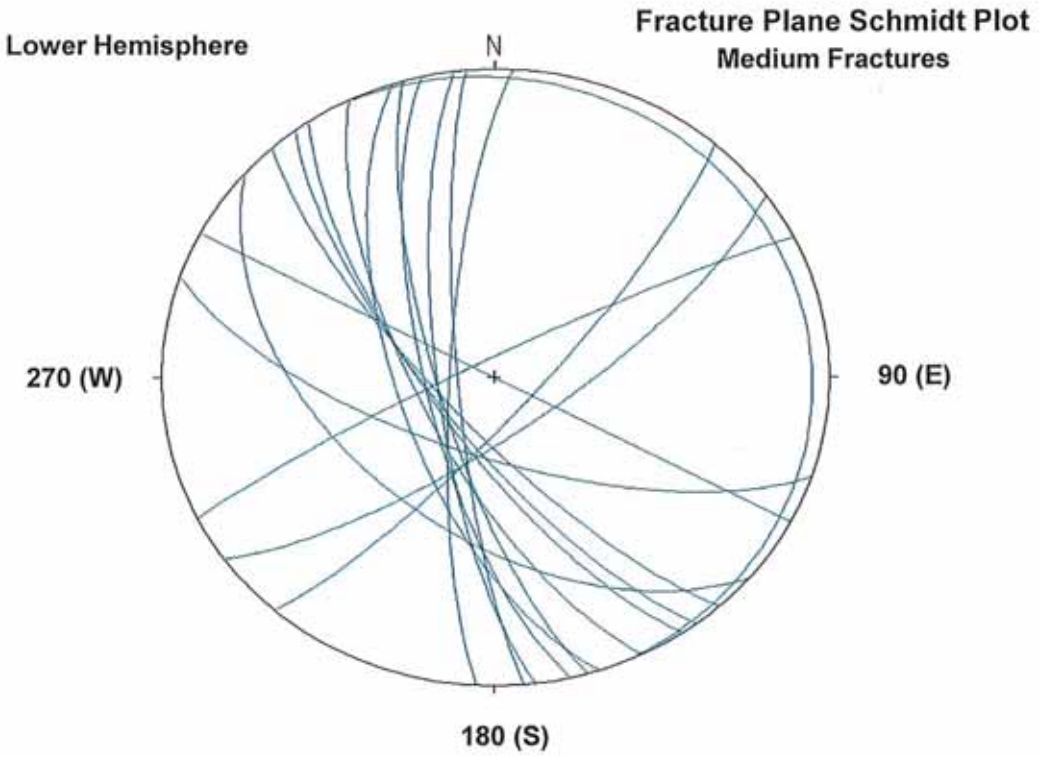

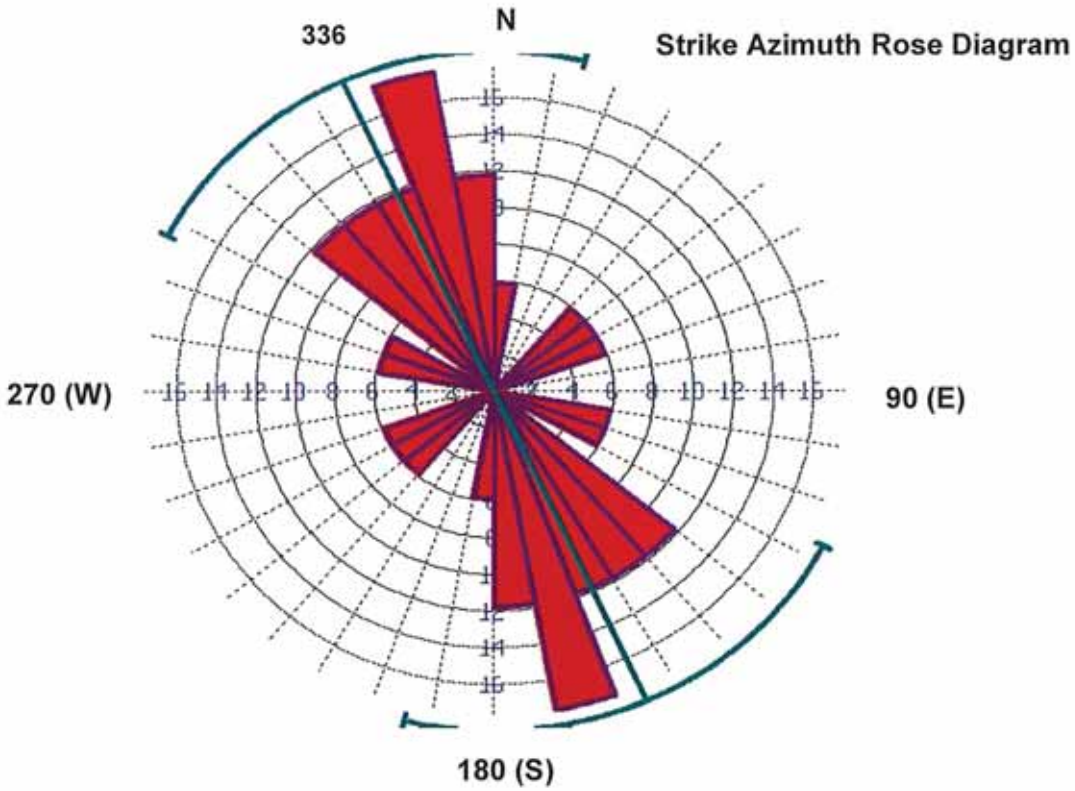

FIGURE 10

Rose & Fracture Plane Schmidt Plot (Lower Hemisphere)
Cemented Fractures Smaller than 0.3 mm
Fidelity CCU 26-3 Upper Core
Grand County, Utah

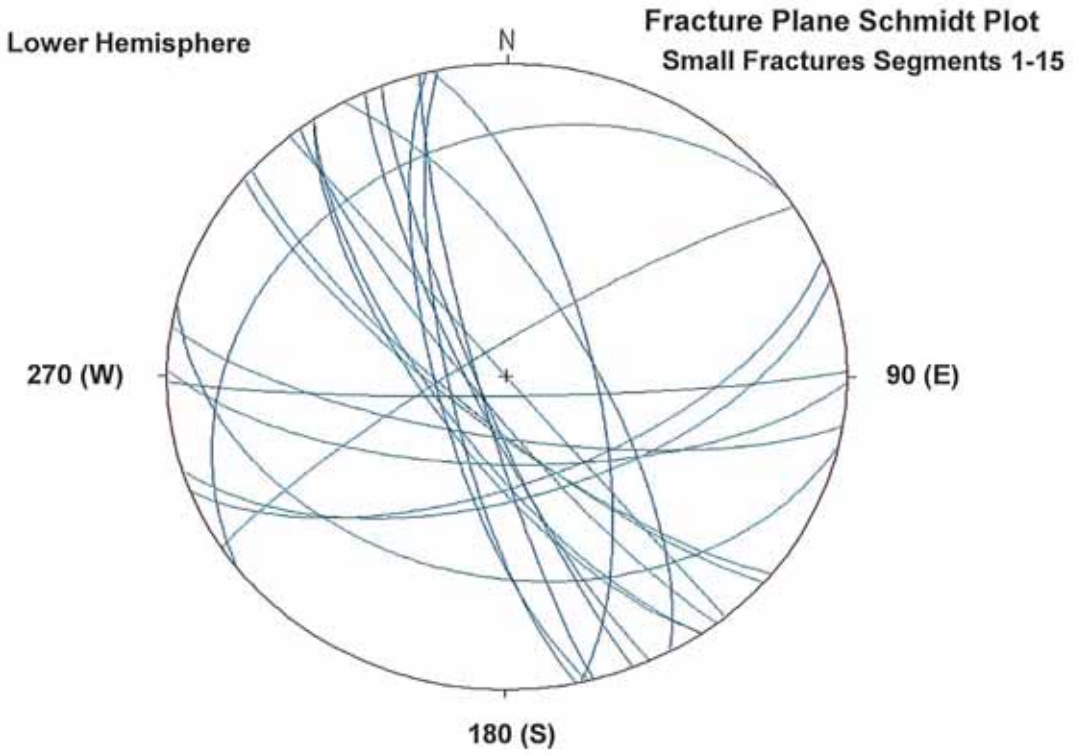

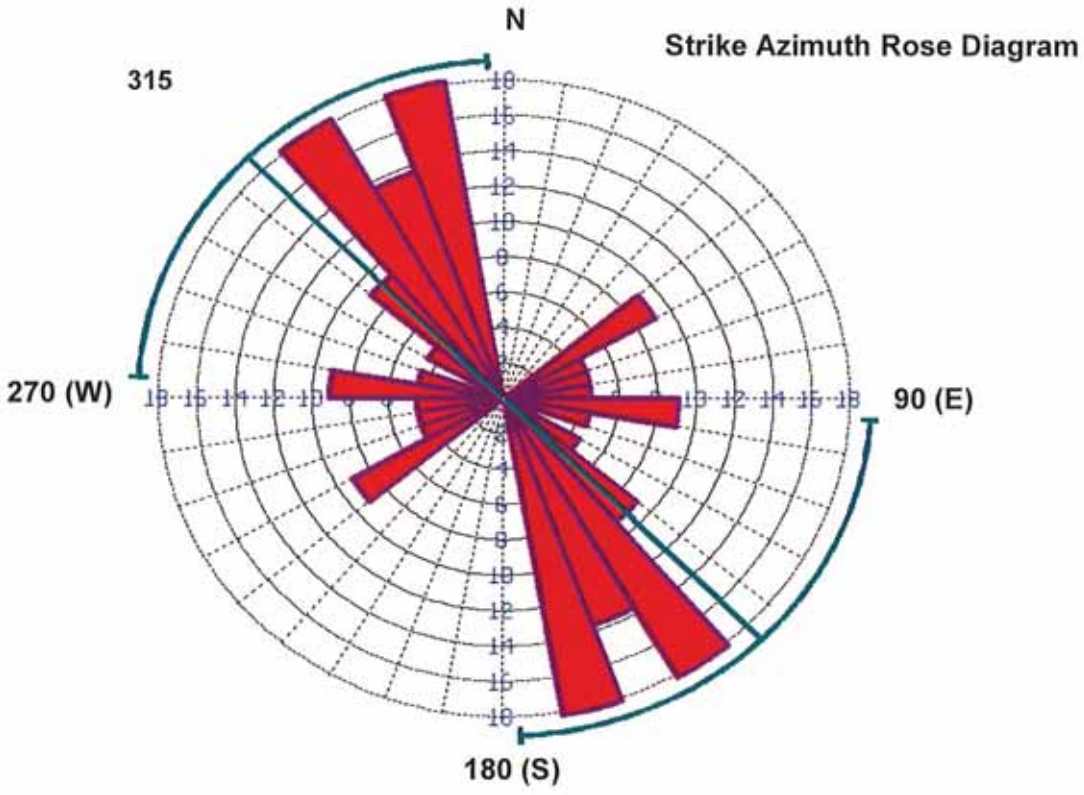

FIGURE 11

Rose & Fracture Plane Schmidt Plot (Lower Hemisphere)
Cemented Fractures Smaller than 0.3 mm
Fidelity CCU 26-3 Bottom Core
Grand County, Utah

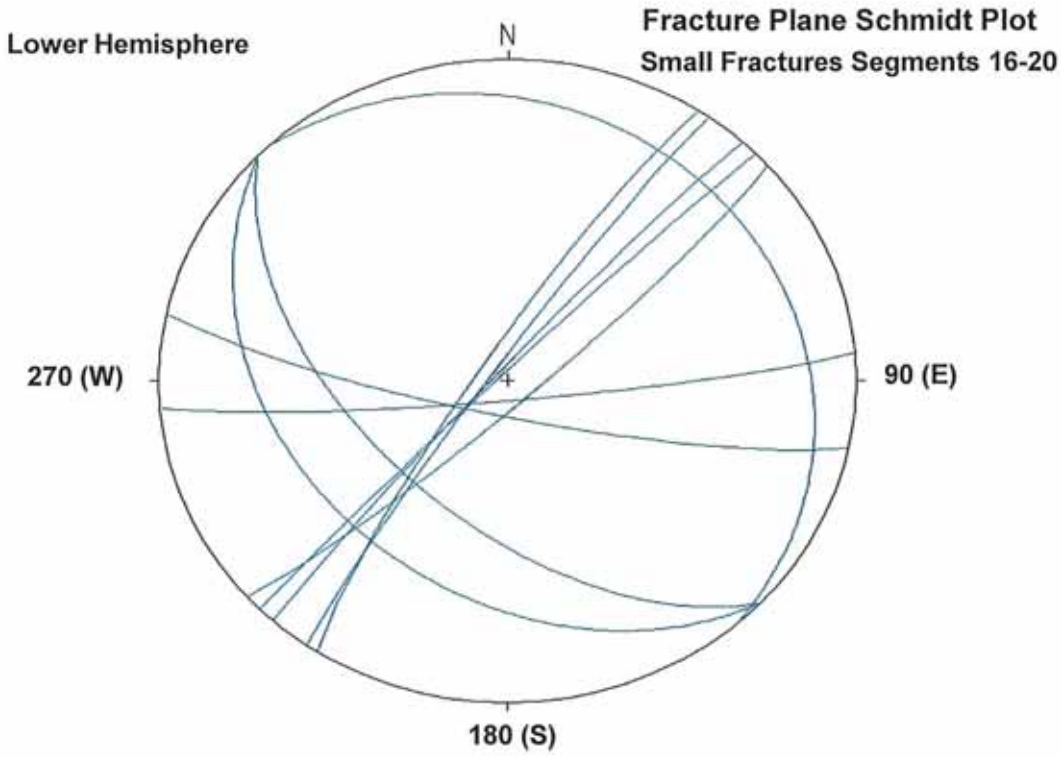

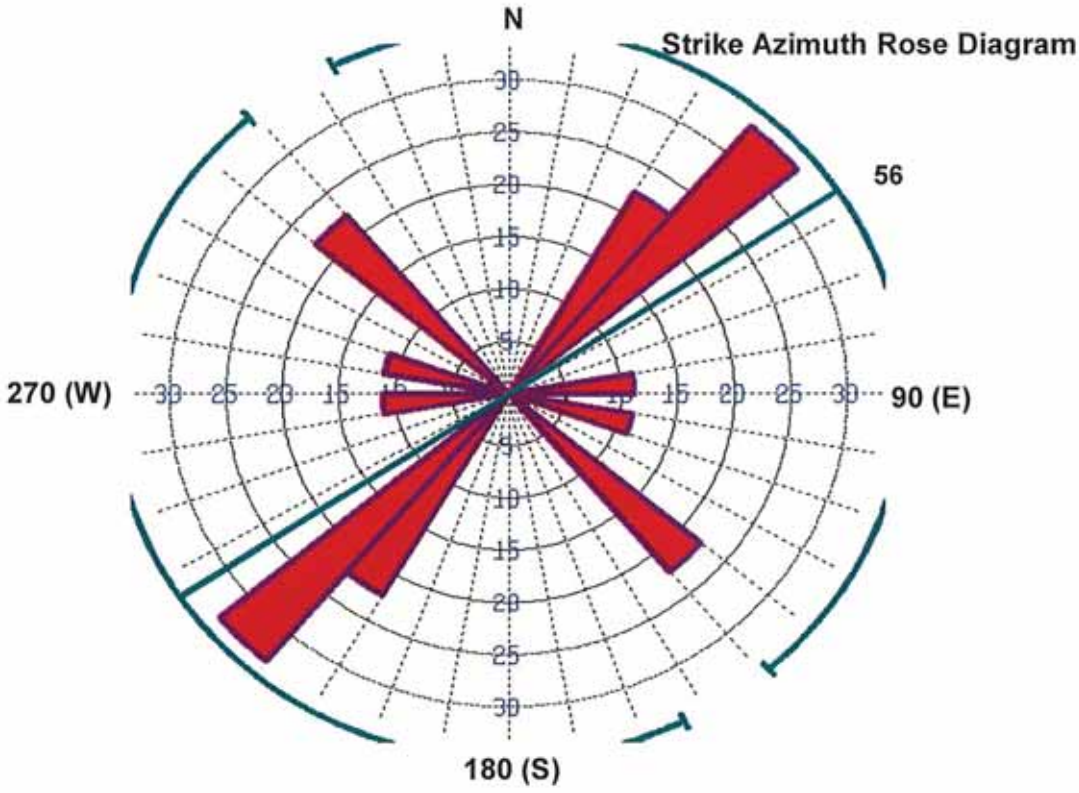

FIGURE 12
Pole Plot (Upper Hemisphere)
All Cemented Fractures (No Slickensides)
Fidelity CCU 26-3 Core
Grand County, Utah

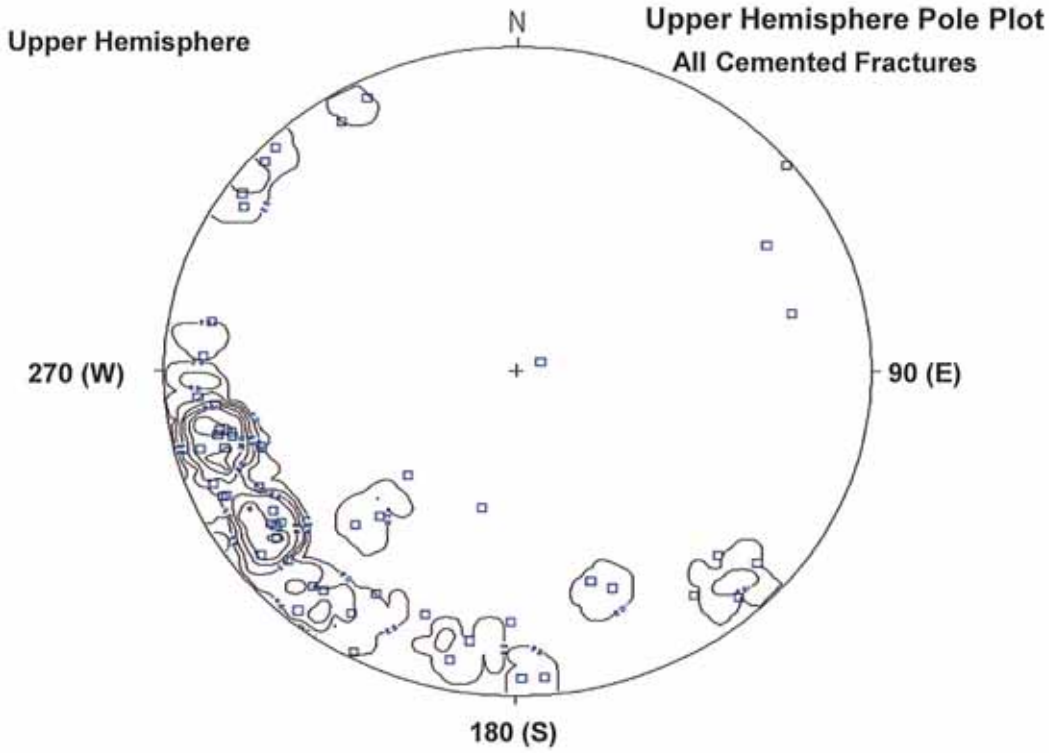

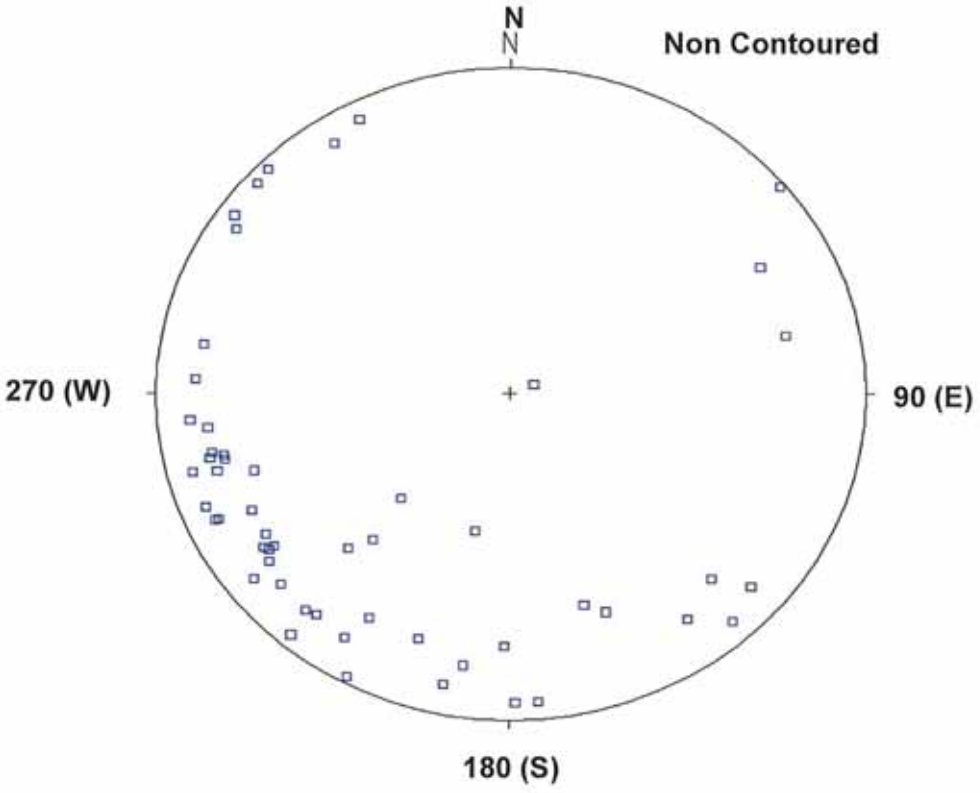

newmanenergyresearch

2 Rose Street
Christchurch
New Zealand 8025
phone 64 3 3381 887
fax 64 3 3381 033
email j.newman@newmanenergyresearch.com

Preliminary results of VIRF analysis on samples from Cane Creek Unit #26-3
28 January 2013

Summary

Six cuttings samples and three core chip composites (Units A to C in Table 1) were provided for VIRF analysis. Provisional results have been provided in two interim reports on 4 January and 22 January 2013. Samples were prepared non-aqueously, which has revealed a complex relationship between shale lithologies and salt/anhydrite, including evidence of hydrothermal microfabrics. Salt contains common relatively large and abundant oil inclusions within the Cane Creek Unit. Smaller oil inclusions occur in secondary carbonate within the Cane Creek Unit and in both salt and carbonate in the overlying succession.

VIRF analysis measures both reflectance and fluorescence intensity of each individual subject in a sample, which results in a bivariate chart on which compositionally distinct populations are differentiated. In contrast to standard vitrinite reflectance, VIRF chart classification is independant of subject morphology. This is particularly important for dark shales of Paleozoic age. (Appendix 1 & 2).

Most CCU #26-3 VIRF charts are complex due to the presence of multiple populations. Subjects which occupy the normal vitrinite compositional field have ambiguous morphology or resemble inertinite. Subjects with vitrinite morphology are interpreted as Population H "false" vitrinites (Appendix 2) based on their relative chart position. Ro (normal) ranges from 0.97% at 4790ft to 1.07% at 7460ft (Unit C), and Population H averages 0.50% lower reflectance than Ro (normal). The normal vitrinite population at 7000ft is inferred to exhibit bias towards the high reflectance end of the normal range, resulting in Ro (normal) 1.11% (Figure 1).

Organic assemblages in Units A and B (Table 1) exhibit considerable scatter on the VIRF chart indicating the occurrence of chemically altered organic matter and/or mixed maturity populations. In this situation VIRF analysis aims to define a Ro (normal) value for the least altered, highest maturity population present, whereas geochemical testing will characterise all of the organic matter in the sample. Consequently, parameters such as Rock-Eval Tmax are unlikely to exhibit a close relationship with VIRF Ro (normal) due to the complex nature of organic assemblages present, which include considerable amorphous organic matter.

VIRF analysis suggests that Unit B has highest maturity in the current sample set, with Ro (normal) 1.37%. However, salt at 7388ft, which could not be analysed due to an absence of shale, features areas with deep reddish orange fluorescence colours suggesting the presence of thermally altered hydrocarbon residues on fracture surfaces. Nevertheless, salt at both 7388ft and in Unit B features common inclusions of strongly fluorescing oil which is not thermally altered. The complex microstructure of this sample set and partitioning of oil, mainly within salt, suggests that the origin and characteristics of the oil may not relate well to the geological history and maturity of the host shales.

Introduction

VIRF analysis combines reflectance with quantitative fluorescence, to provide compositional information for both dispersed organic matter and coals (Appendix 1). This allows indigenous vitrinite of normal (orthohydrous) chemistry, which provides reliable reflectance data, to be distinguished from suppressed, altered and reworked vitrinite, inertinite, lower maturity cavings, or other sources of contamination. Ro (normal) is the average of measurements obtained from the orthohydrous vitrinite population in a sample.

One reason standard VR produces highly misleading results for many rock samples is that visual identification of vitrinite is morphology based and subjective. The original classification of vitrinite and inertinite was developed for coals and problems arise when vitrinite and inertinite occur as dispersed organic matter in sediments, where they often have ambiguous physical appearance. VIRF uses the relationship between reflectance and fluorescence as an analogue for the chemistry of organic matter, and consequently defines vitrinite and inertinite in chemical as opposed to morphological terms.

Dark shales of any age, and both light and dark shales older than Carboniferous, sometimes contain material which has vitrinite morphology but not vitrinite chemistry, based on reflectance and fluorescence relationships. This "false vitrinite" usually has reflectance between 0.20% and 0.40% lower than true vitrinite of normal chemistry. The low fluorescence of this population distinguishes it from true vitrinite with perhydrous chemistry, which is sometimes present in the same sample and has high fluorescence unless chemically altered. "False vitrinite" is referred to as Population G/H, because there are both granular and homogenous forms, and it is inferred to be derived from a primitive plant source because it first appears in samples of Ordovician to Devonian age (Appendix 2). Population H is present in the samples from Cane Creek Unit #26-3, and has an average reflectance 0.50% lower than Ro (normal).

Preparation

A solvent cleaning process has been undertaken by Weatherford Laboratories because the well was drilled with a synthetic mud. Both raw and cleaned cuttings samples were requested from Weatherford so that comparative VIRF analysis could be undertaken. The objective was to assess whether the solvent cleaning process depresses the fluorescence of VIRF measurement subjects because this could complicate interpretation of the analytical data. Previous work has already shown that synthetic drilling muds themselves do not cause problems for either VR or VIRF analysis.

Raw cuttings of the sample at 4790ft were 'washed' in hot water during which the bulk of the drilling fluid was removed from the cuttings. After drying, this sample was mounted in epoxy resin, which usually cures successfully even when residual hydrocarbons are present in a sample. Cuttings of the same sample which had been cleaned at Weatherford Laboratories were also mounted in epoxy. VIRF analyses undertaken on the raw and solvent cleaned fractions of sample 4790ft are very similar, which indicates that Weatherford's solvent cleaning process has not affected either fluorescence or reflectance of the organic matter. Consequently, the remaining samples were all prepared using solvent cleaned cuttings mounted in epoxy.

All of the samples responded very poorly to aqueous polishing methods even when multiple impregnations were used to stabilise the pellet surface at the fine grinding and polishing stages. Consequently, the samples were ground and polished in kerosene using non aqueous polishing media. Multiple impregnations of the pellet surface during the polishing cycle were required. An adequate polish was achieved. One reason for the poor response to aqueous methods is undoubtedly the presence of salt and anhydrite (Figures 2 to 4), which are present in varying amounts in all samples. However, even the organic rich shales, which do not contain salt, eroded rapidly during polishing. This sometimes results from the presence of swelling clays, but no swelling clays were observed in these samples.

Table 1. Sample ID's, character and depth intervals.

		Cuttings		Core composites	
Formation	Sample ID	Top (ft)	Base (ft)	Top (ft)	Base (ft)
Shale 2	4790ft	4760	4790		
Shale 7	5640ft	5600	5640		
Shale 8	5820ft	5780	5820		
Shale 10	6080ft		6080		
Shale 19	7000ft	6970	7000		
Cane Creek Shale	7388ft		7388		
A unit	7406ft				7400.1
				7406.0	7406.9
				7411.0	7411.9
B unit	7424ft				7416.9
				7418.0	7418.9
				7421.0	4121.9
					7424.0
				7430.5	7431.9
C unit	7460ft				7452.0
					7458.0
					7469.8

Table 2. VIRF data for samples from Cane Creek Unit #26-3. Samples above 7400ft are cuttings and samples below 7400ft are core chip composites (Table 1). Ro (normal) values are calculated from actual measurements on indigenous vitrinite subjects of normal chemistry when these are present in the sample. All data appear as VIRF charts in the file *Cane Creek Unit #26-3 VIRF data.xlsx*. The criteria for confidence ratings are coded blue for positive features and red for negative. Samples at 5640ft, 5820ft, and 6080ft have been analysed separately, and the data have then been interpreted on a composite VIRF chart.

Depth (ft)		Ro (normal) %	s.d.	Range	Confidence	Criteria
4790		0.97 (n=16)	0.097	0.81 – 1.10	Good	One dominant vitrinite population
5640		1.00 (n=25)	0.111	0.79 – 1.17	Good	Multiple populations; support from inertinite
5820						
6080						
7000		1.11 (n=7)[1]	0.065	1.01 – 1.18	Good	Multiple populations; support from inertinite and perhydrous vitrinite
7388		n.d. - salt with oil inclusions				
7406		1.22 (n=3)	0.094	1.11 – 1.30	Poor	Multiple populations, alteration
7424		1.37 (n=9)[1]	0.098	1.19 – 1.47	Poor plus	Multiple populations, alteration; good graphical distinction of populations
7460		1.07 (n=7)	0.076	0.97 – 1.17	Good	Multiple populations; good graphical definition of popns, support from inertinite

[1] biased towards the high reflectance end of the normal vitrinite compositional range

Results

Results are provided in Table 2 and a maturity profile appears in Figure 1. Sample descriptions appear in the following section. When the VIRF charts for closely adjacent samples exhibit a similar graphical distribution, it is sometimes useful to determine Ro (normal) from a composite chart, and this has been done for samples at 5640ft, 5820ft and 6080ft. This approach is particularly useful for complex distributions when Population H is present, and normal vitrinite subjects are relatively sparse and/or some samples exhibit bias towards the high or low reflectance end of the normal vitrinite compositional range.

VIRF analysis has not been undertaken on the sample at 7388ft because it consists entirely of salt. However, this sample is described in the following section because it features oil inclusions. In the sample descriptions, salt and anhydrite are collectively referred to as 'salt'.

Units A, B, and C are represented by core. Individual core samples represent a very restricted stratigraphic interval, which may contain a limited range of organic constituents, resulting in poor representation of normal vitrinite on the VIRF chart. Consequently, each VIRF sample is ideally made up as a composite comprising core chips from several stratigraphic positions (Table 1), which increases the chance that a useful organic assemblage will be encountered.

Fluorescence colour and intensity can vary between microscope systems. Comments on the fluorescence colour of hydrocarbons described in the following section relate to observations made with a specific UV filter set. They are internally consistent for all work undertaken on Newman Energy Research Ltd microscopes.

Background to discussion of evidence for hydrothermal activity is provided in Appendix 3.

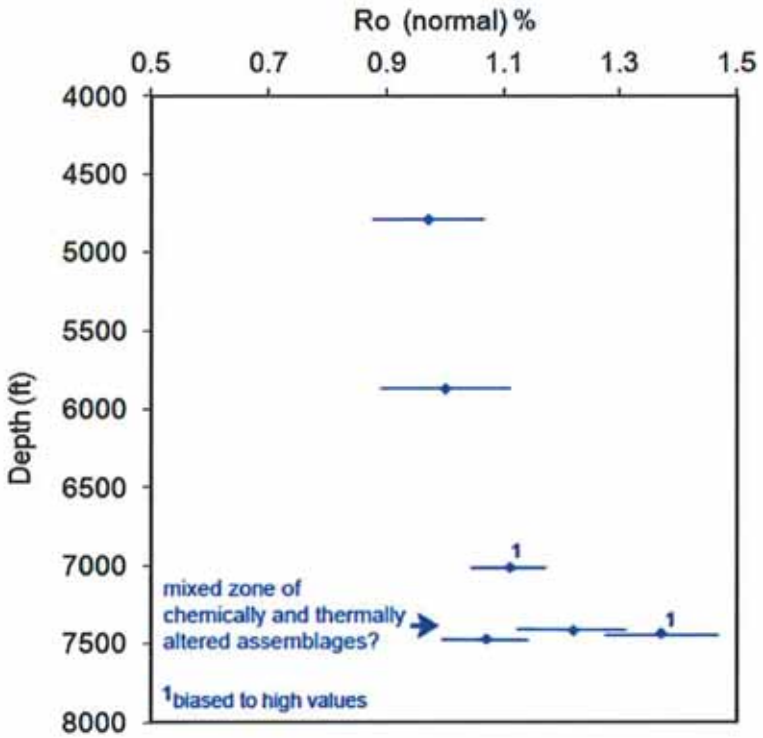

Figure 1 Ro (normal) profile for Cane Creek Unit #26-3. Bars represent 2 standard deviations of Ro (normal).

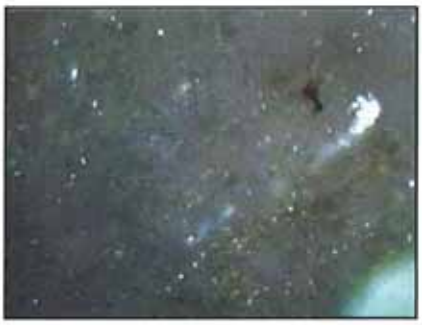

Figure 2a Translucent fine grained lithology viewed in incident light, oil immersion. Sample 5640ft, 160 microns.

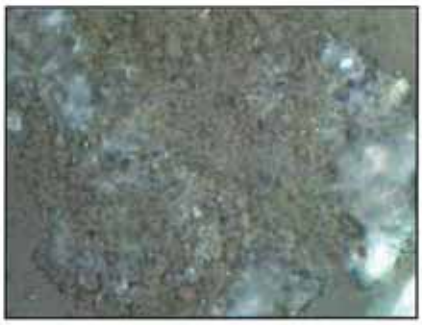

Figure 2b The subject in Figure 1a viewed with a dry objective. The polished surface has not been exposed to water during polishing.

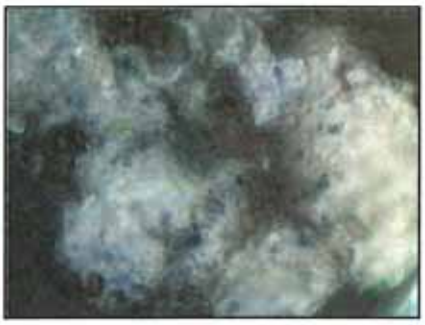

Figure 2c The subject in Figures 2a and b after exposure to water. The white crystalline material is inferred to be gypsum, produced by reaction of anhydrite with water.

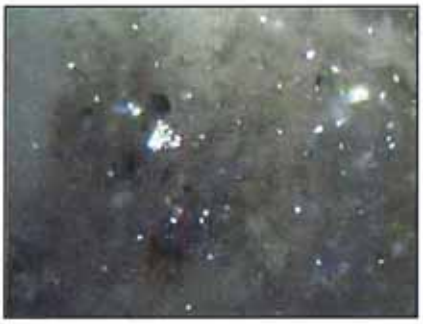

Figure 3a Translucent medium grained lithology viewed in incident light, oil immersion. Sample 5640ft, 160 microns.

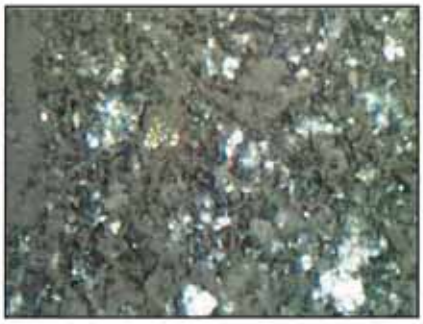

Figure 3b The subject in Figure 2a viewed with a dry objective. The polished surface has not been exposed to water during polishing.

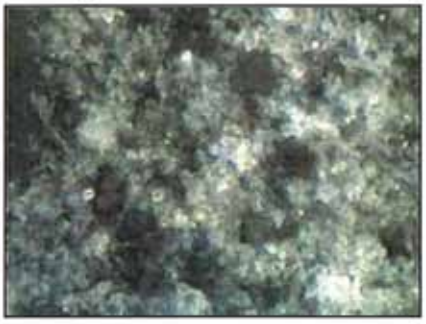

Figure 3c The subject in Figures 3a and b after exposure to water. The white crystalline material is inferred to be gypsum, produced by reaction of anhydrite with water.

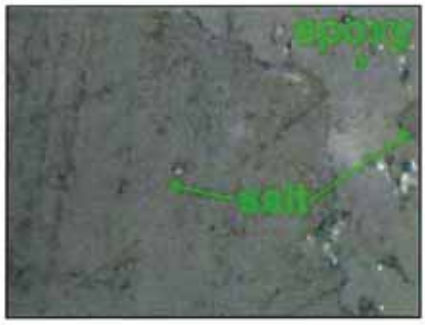

Figure 4a Large salt crystal surrounded by epoxy resin. The sample has not been exposed to water during polishing. Sample 5640ft, incident light, dry objective, 160 microns.

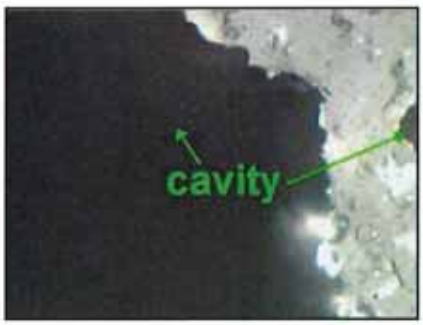

Figure 4b The subject in Figure 4a after exposure to water. The salt has completely dissolved.

Figure 4c. Network inferred to be gypsum resulting from exposure of anhydrite to water. Salt within the net has been completely dissolved. Sample 5640ft, incident light, dry objective, 160 microns.

Sample descriptions

4790ft (cuttings)

This sample comprises shale, some isolated blocks of salt, and significant amounts of Microfacies VS (Appendix 4), which is a subaqueous extrusive or shallow intrusive igneous lithology (Figure 5). Some translucent mineral grains in the shale, which are probably secondary carbonate, contain very small fluorescent oil inclusions. A mobile yellow fluorescing oil is expelled from fractures during UV illumination with a dry objective and nitrogen feed (Figure 6). In oil immersion, most shale cuttings emit a diffuse strongly fluorescent hydrocarbon, which suggests an amorphous solid hydrocarbon is present in the rock matrix. Under the hottest UV beam, in oil immersion, there is bubbling caused by vapourisation of a hydrocarbon. Traces of fluorescent oil are present in open fractures in salt. Liptinite has traces of residual orange florescence, which is very difficult to detect. This is consistent with the Ro (normal) value of 0.97% (Figure 7).

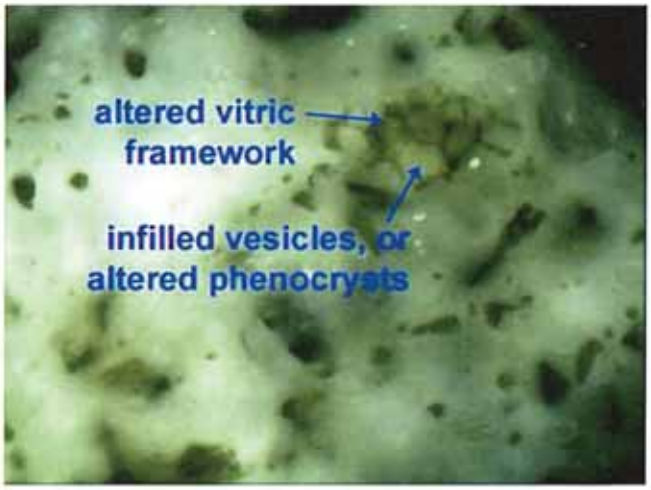

Figure 5 Altered subaqueous vitric tuff, or shallow igneous intrusive, in the sample at 4790ft. Incident light, oil immersion, 160 microns.

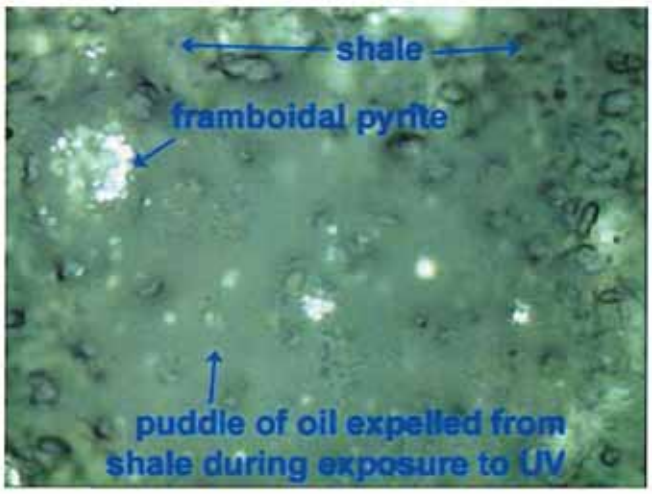

Figure 6 . Liquid hydrocarbon pooled on the polished surface of the sample at 4790ft. This oil disperses too rapidly for a photomicrograph showing fluorescence to be obtained. Incident white light, dry objective, 160 microns.

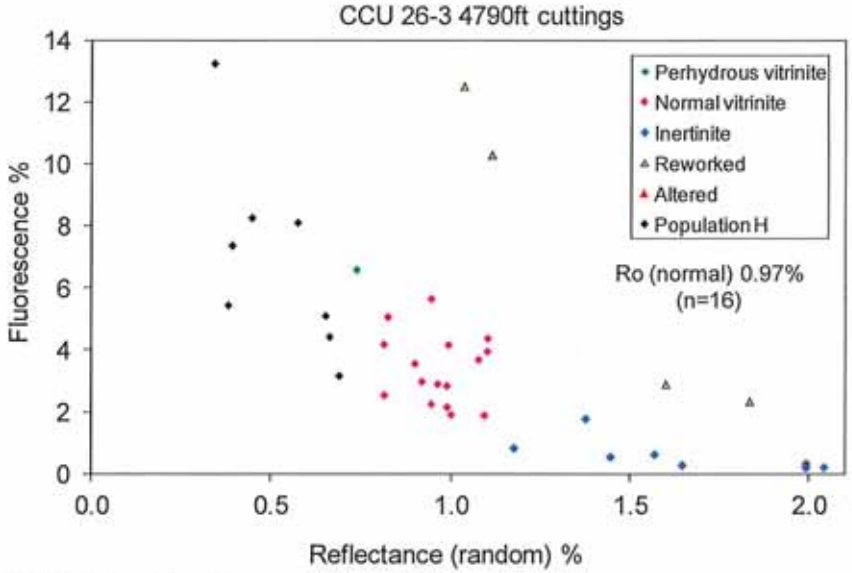

Figure 7 VIRF chart for the sample at 4790ft.

5640ft (cuttings)

There is considerable salt in this sample (Figures 2 to 4), in addition to shale, which includes some relatively coarse siltstone. Salt sometimes occurs attached to shale. All lithologies sometimes exhibit hydrothermal fabric (Figures 8 to 10), shattering of grains, and microveins of orange coloured fluidised sediment occur in this context. Sparse, very small (c. 1 micron) yellow fluorescing hydrocarbon inclusions are present in salt. No mobile hydrocarbon was observed in UV with a dry objective. The dark shale emits a diffuse fluorescent hydrocarbon when exposed to UV in oil immersion, but no bubbling (vapourising) of hydrocarbons was observed. VIRF data for samples in the interval 5640ft to 6080ft have been composited into a single chart for improved definition of populations. (Figure 11). This results in a well defined VIRF profile with Ro (normal) 1.00%. Scatter beneath the profile and low reflectance subjects are classified as chemically altered vitrinite and Population H (Appendix 2). Inertinite and subjects with normal vitrinite composition lack well defined morphology in these samples and chart classification is based solely on VIRF criteria. Ro (normal) 1.00% is supported by the very weak to absent fluorescence of liptinite constituents.

5820ft (cuttings)

Dark shale is rare in this sample and could be caved. The light coloured shale which is present exhibits shattered quartz grains and hydrothermal microfabrics with milky mineralisation, sometimes with orange coloured fluidised zones. No hydrocarbon emissions were observed. Oil inclusions are very rare.

6080ft (cuttings)

This sample contains light coloured shale and considerable salt. These lithologies usually occur in isolation from each other. Iron oxide bodies have the appearance of hydrothermal void infillings, but are typically very fragmentary. No hydrocarbon emissions were observed. Oil inclusions are very rare.

.

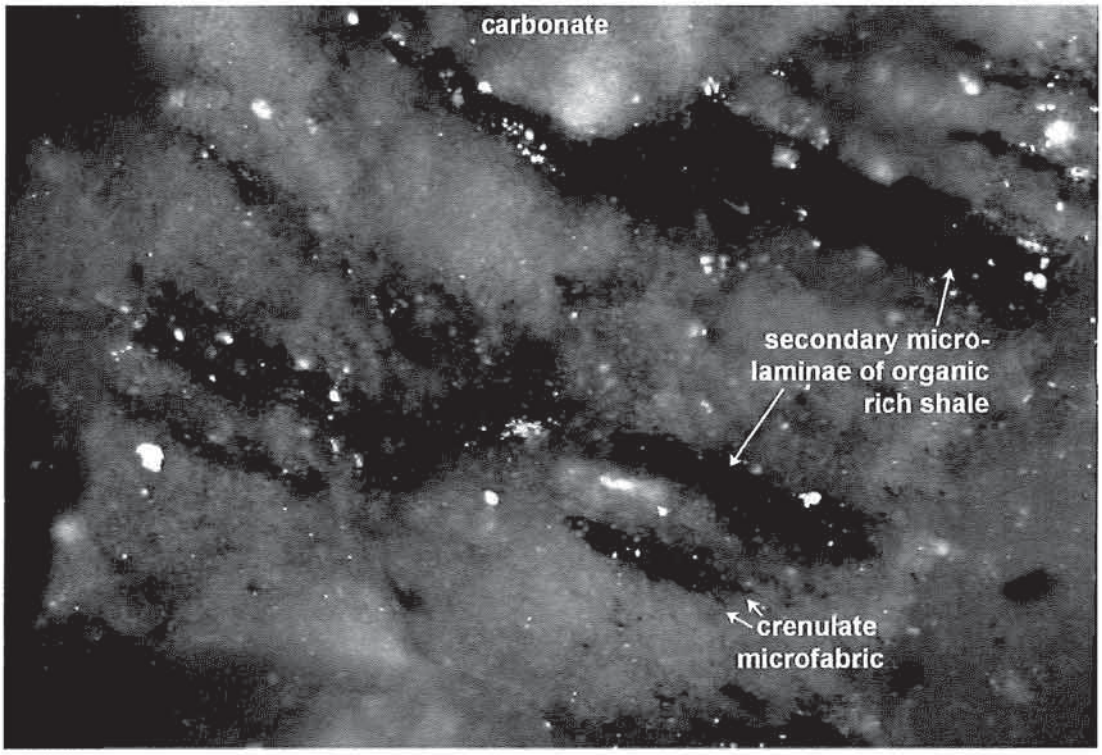

Figure 8 Dominant linear microfabric, with additional crenulated features, in hydrothermally deformed carbonate and shale. Sample at 5640ft, incident light, oil immersion, 400 microns.

7000ft cuttings

Both dark organic rich shale and light shale with little organic matter are present. Salt occurs as isolated blocks and also as angular fragments in the shale matrix. No hydrocarbon emissions were observed in UV light with a dry objective, but in oil immersion there are abundant greenish yellow fluorescing point source and diffuse emissions especially from the organic rich shale and also some bubbling caused by vapourising of hydrocarbons. There are hydrothermal microfabrics, shattered quartz grains, and carbonate mineralisation. Normal vitrinite is clustered towards the high reflectance end of the normal vitrinite compositional range, and Ro (normal) 1.11% is consequently considered to have a high bias. Population H is present. Differentiation of the normal vitrinite population is supported by the inertinite section of the VIRF profile (Figure 12).

7388ft cuttings

This sample consists entirely of salt and VIRF analysis was not attempted. However, the sample was mounted and polished in order to look for hydrocarbons. Mobile hydrocarbons were not observed but intensely yellow fluoresceing oil inclusions are common, occupying the spaces between salt crystals (Figures 13 & 14). At some locations, the fluorescence colour deepens to reddish orange, and liquid oil has disappeared, which suggests the presence of thermally altered hydrocarbon residues (Figures 15 & 16).

7406ft (A unit, core chip composite 7400.1ft to 7411.9ft)

This sample is an organic rich dark shale with rare laminae of medium silt sized quartz. Very small yellow fluorescing oil inclusions are common in fine grained secondary carbonate. Mobile hydrocarbons are restricted to minor diffuse emissions from the organic rich matrix

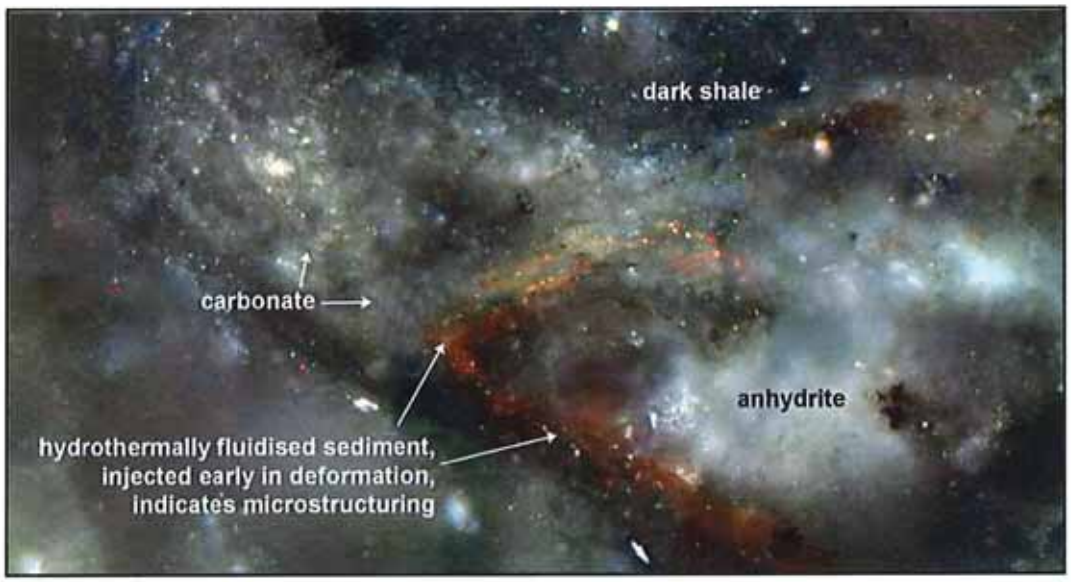

Figure 9 Crenulate and rotational hydrothermal microfabrics displayed by shale, carbonate, anhydrite and fluidised sediments. Sample at 5640ft, Incident light, oil immersion, 400 microns.

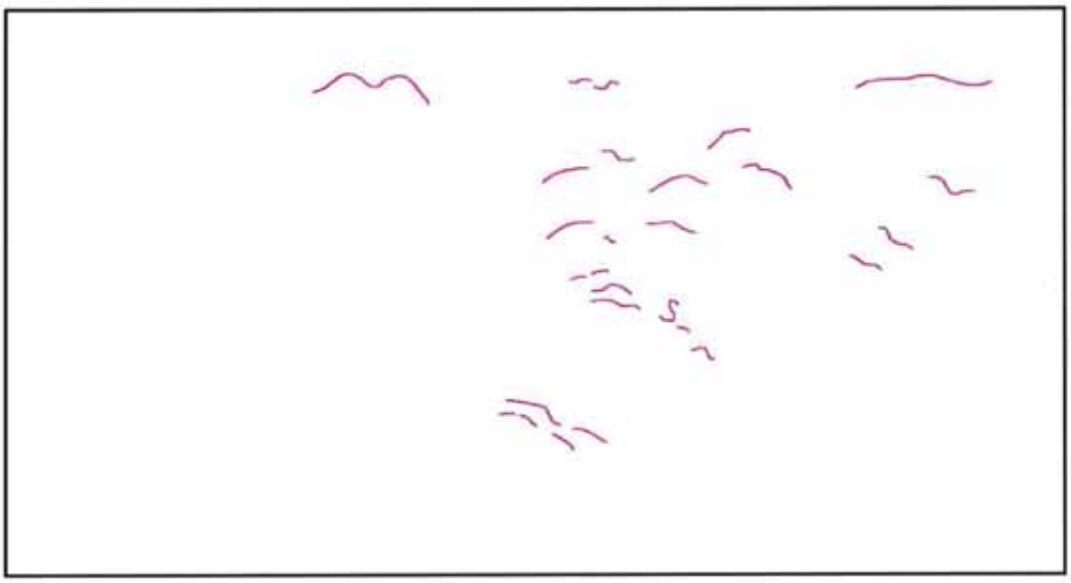

Figure 10 Guide to microfabric markers visible in Figure 9.

when viewed in oil immersion. The VIRF chart for this sample cannot be classified with confidence, due to scatter in the vitrinite field (Figure 17). The inertinite section of the VIRF profile is also poorly defined. There may be mixing of different maturity populations in this sample or some of the organic matter may be chemically altered. Alteration can occur when parts of a succession are affected by chemically aggressive fluids, which can result from igneous activity within the basin (Appendix 3). Ro (normal) 1.22% has been arrived at by utilising subjects located at the high fluorescence edge of the vitrinite envelope. Some support for a relatively high Ro (normal) value is provided by the high reflectance of Population H in this sample. Nevertheless, confidence in Ro (normal) 1.22% is poor (Table 2).

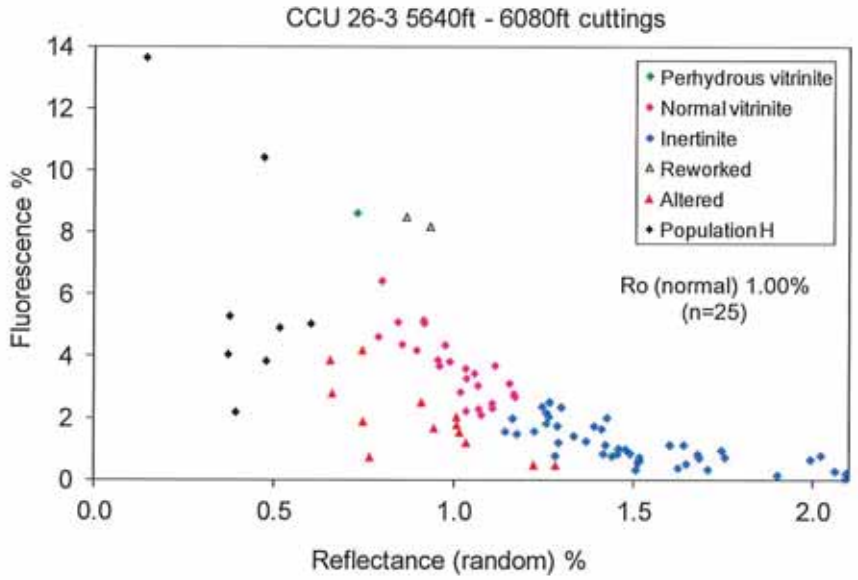

Figure 11 Composite VIRF chart showing data for samples at 5640ft, 5820ft and 6080ft.

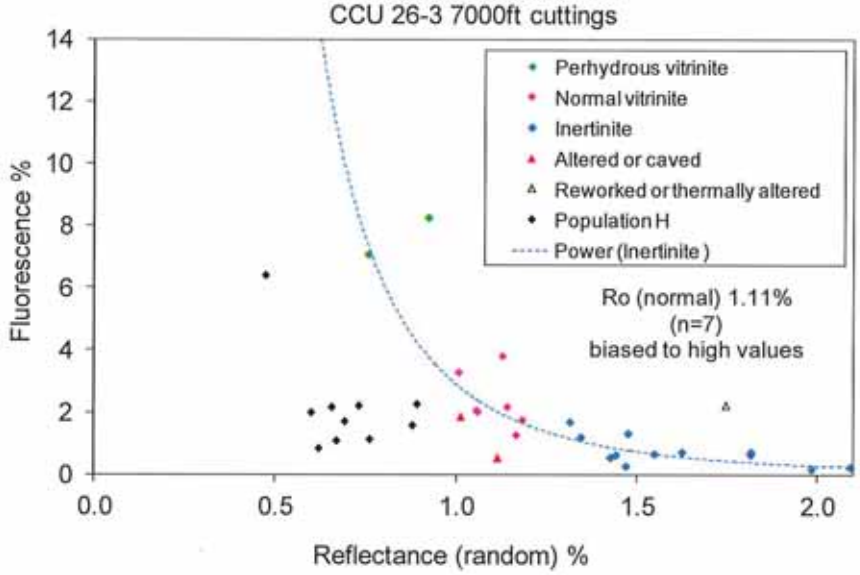

Figure 12 VIRF chart for the sample at 7000ft. The good fit of normal vitrinite to the inertinite trendline increases confidence in Ro (normal).

7424ft (B unit, core chip composite 7416.9m to 7431.9m)

This sample comprises dark and light shale, which are sometimes interlaminated. Some of the shale appears to be extremely rich in organic matter, and there is evidence of deformation and hydrothermal microfabrics. A significant amount of salt is also present, and this contains common oil inclusions (Figures 18 & 19). The sample apparently features organic bodies with complex margins, minimal fluorescence and approximately 0.70% reflectance (Figure 20 & 21). This material polishes poorly. Also present are bodies with a similarly complex margin containing a very low reflectance substance which in some cases appears to have been partly removed during polishing (Figure 22). The morphology of the bodies illustrated in Figures 20 to 22 is somewhat suggestive of a Botryococcus type of alginite. Figures 23 and 24 show examples of this type of alginite, exhibiting the typical low reflectance and intense fluorescence of alginite at relatively low maturity. If the examples in CCU #26-3 are alginite,

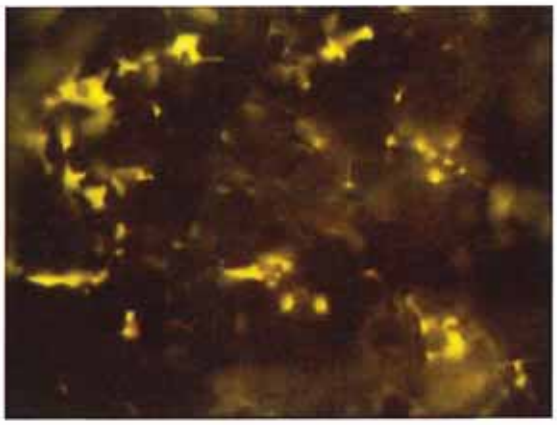

Figure 13 Salt with yellow fluorescing oil between crystals. Sample at 7388ft, incident UV light, dry objective, 160 microns.

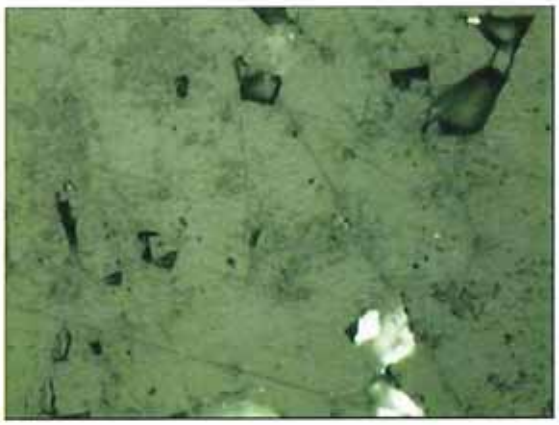

Figure 14 The subject in Figure 13 viewed in white light. Some oil staining is visible on the surface of the salt.

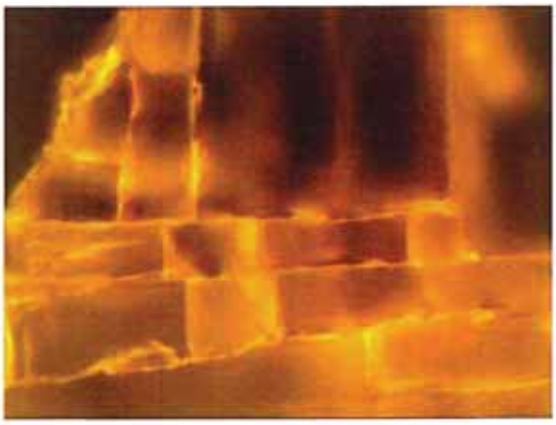

Figure 15 Reddish orange fluorescence of hydrocarbon residues on fracture planes in salt. Sample at 7388ft, incident UV light, dry objective, 160 microns.

Figure 16 The subject in Figure 15 viewed in white light.

they are inferred to have been thermally and possibly also chemically altered. Investigation of stratigraphically equivalent but lower maturity samples might provide useful insights into the true origin of the constituents illustrated in Figures 20 to 22. These constituents often occur as microbrecciated fragments scattered through shale which exhibits shear deformation and microbrecciation (Figures 25). Fragments of shale and the dark organic material also occur in a salt matrix (Figure 26).

The VIRF chart for this sample features more than one population in the vitrinite field. There is a relatively well defined population of subjects at the high fluorescence edge of the vitrinite envelope, and this population is supported by the inertinite section of the VIRF profile (Figure 27). Ro (normal) is 1.37% based on this chart classification, and the subjects which

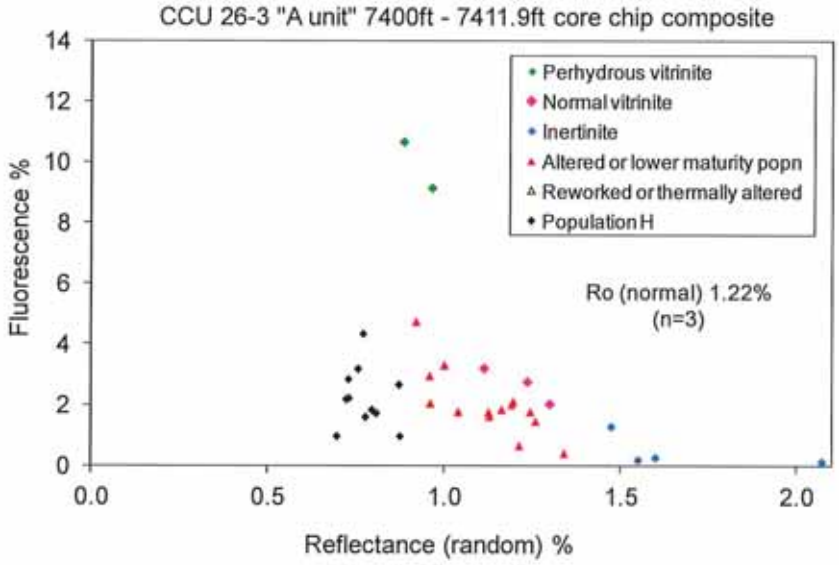

Figure 17 VIRF chart for Unit A core chip composite.

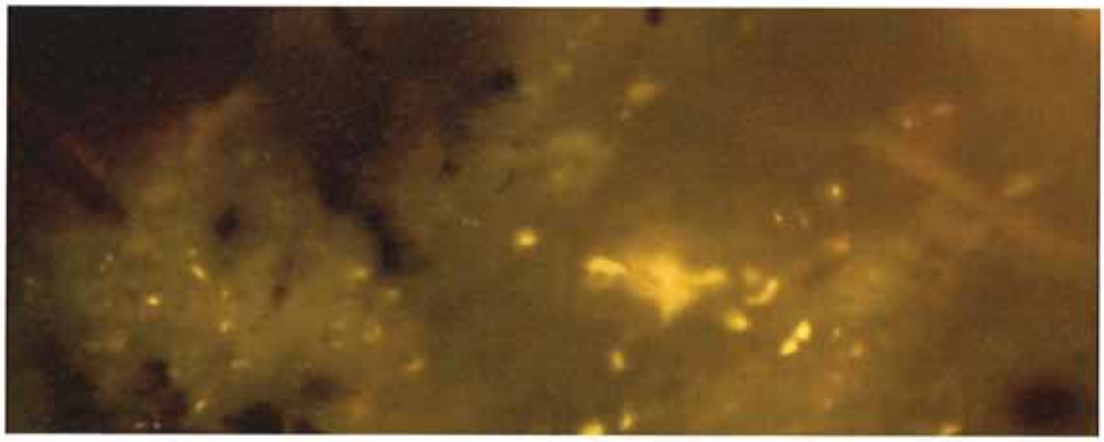

Figure 18 Yellow fluorescing oil inclusions in salt. Unit B core chip composite, incident UV light, oil immersion,

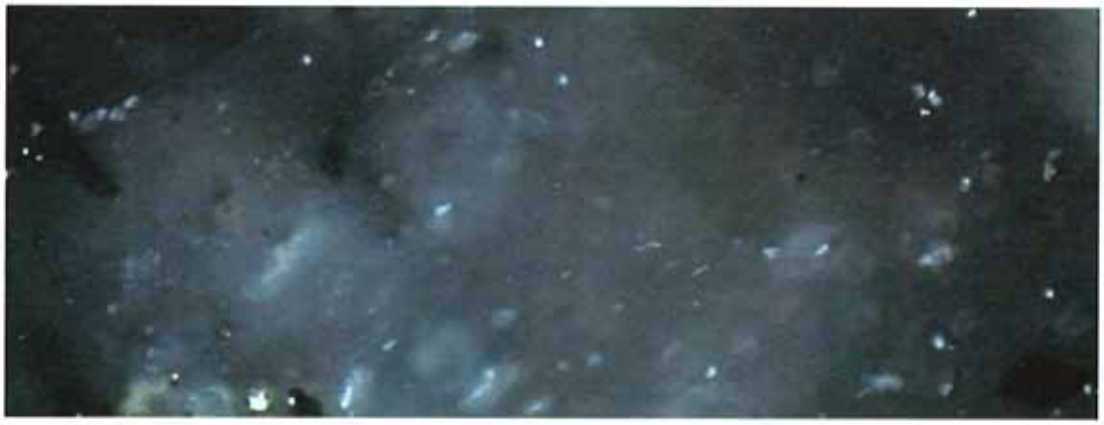

Figure 19 The subject in Figure 18, viewed in white light.

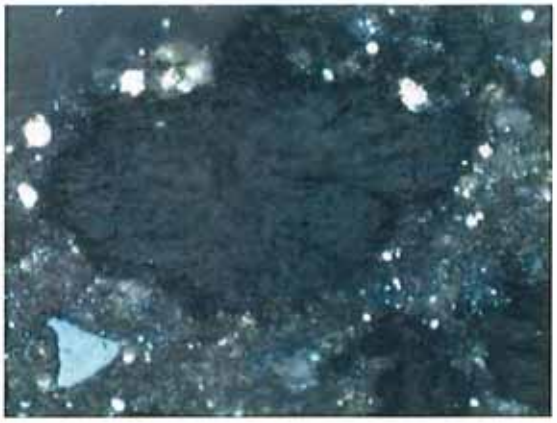

Figure 20 Common but unidentified organic material in shale of Unit B core chip composite. Incident light, oil immersion, 160 microns.

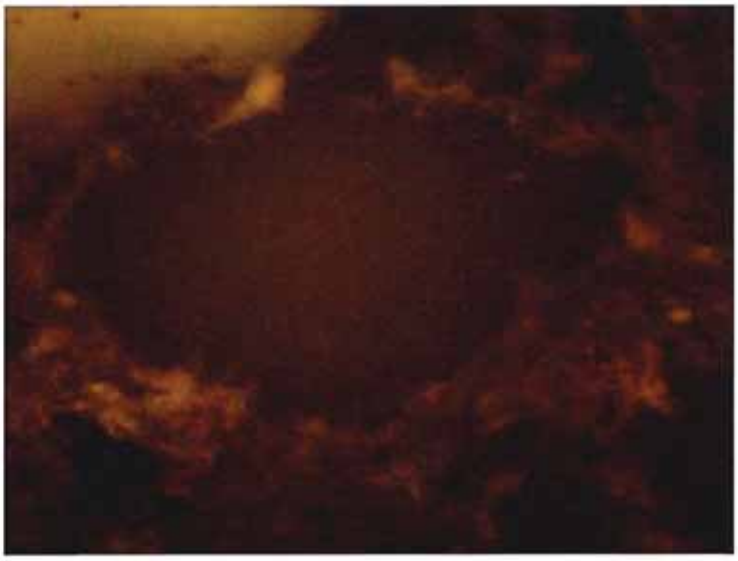

Figure 21 The subject in Figure 20 viewed in UV light. The complex margin of the structure is more evident in this image. The diffuse yellow fluorescence over this body results from weak hydrocarbon emissions.

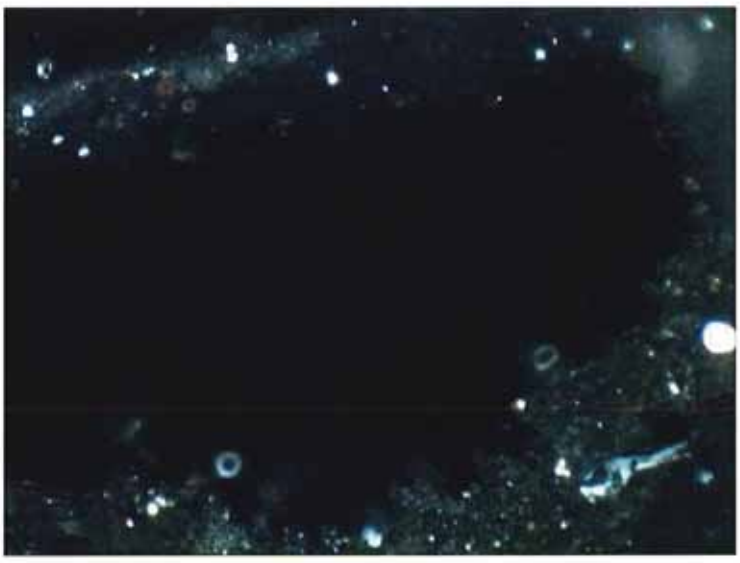

Figure 22 A distinctive dark structure with recessed centre and complex margin, in shale of Unit B core chip composite. Incident light, oil immersion, 160 microns.

Figure 23 This is image is included for comparison with CCU #26-3 subjects illustrated in Figures 20 to 22. The figure shows Botryococcus alginite, from a South African (Permian) "Torbanite" or boghead coal. This is Plate 28 in Falcon & Snyman, 1986. Incident UV light, dry objective, horizontal field 250 microns.

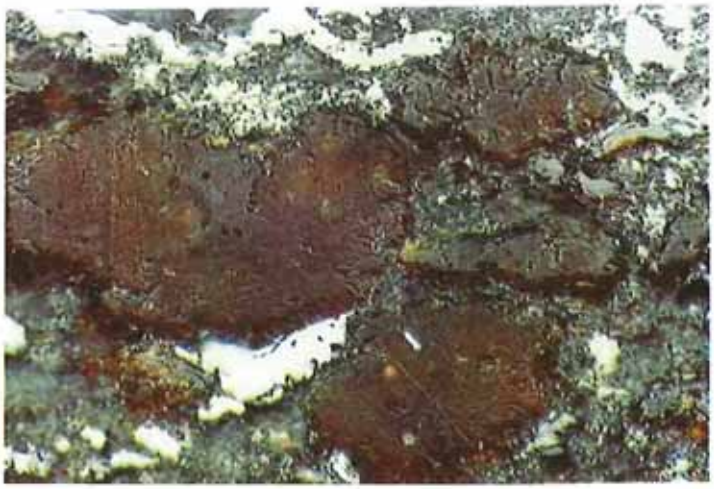

Figure 24 The subject in Figure 23 viewed in white light.

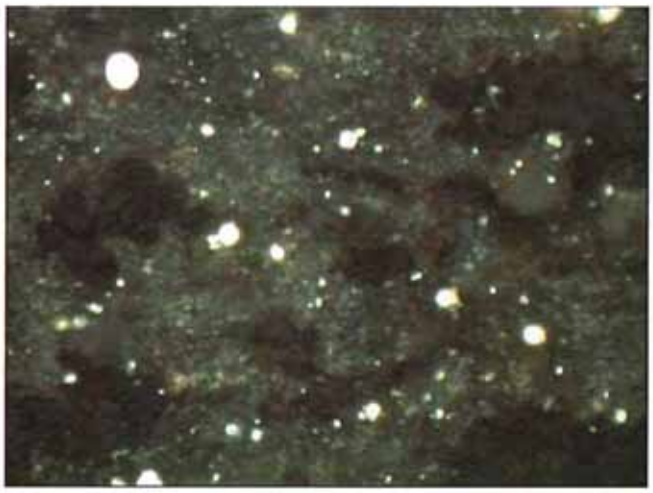

Figure 25 Microbrecciated dark organic material in shale exhibiting shear deformation. Unit B, incident light, oil immersion, 160 microns.

Figure 26 Fragments of microbrecciated shale and dark organic matter in salt. Unit B, incident light, oil immersion, 160 microns.

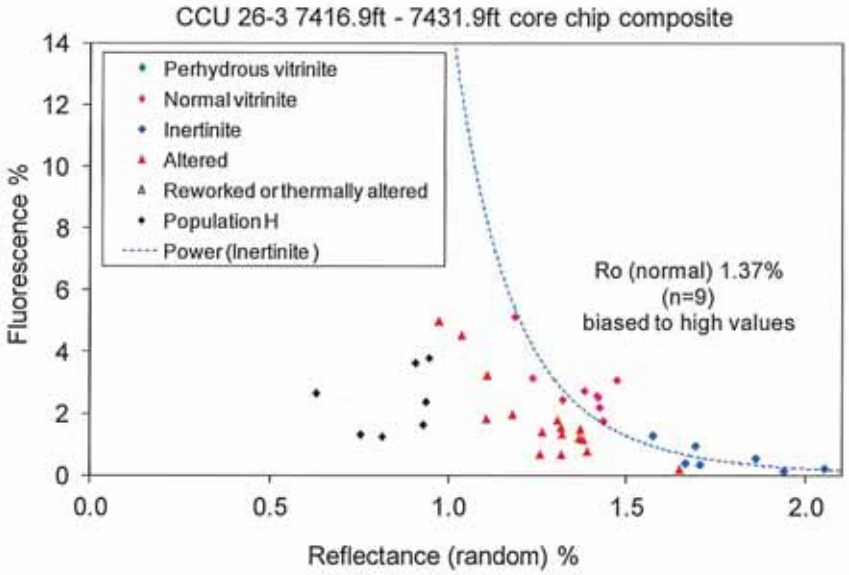

Figure 27 VIRF chart for "B unit" The good fit of normal vitrinite to the inertinite trendline increases confidence in Ro (normal).

fall below the VIRF profile are interpreted to be altered. Confidence in this result is rated as "Poor plus", which acknowledges the negative factor of chart complexity, offset by the fact that individual populations are relatively well defined. The adopted normal vitrinite population is clustered towards the high reflectance end of the normal vitrinite compositional range, resulting in a high bias (Table 2).

7460ft (C unit, core chip composite 7452.0m to 7469.8m)

Dominantly dark shale, with some lighter coloured shale. There are common horizons of finely crystalline carbonate, which contain tiny oil inclusions. These inclusions sometimes occur as clusters in individual carbonate crystals and also widely scattered in larger fields of carbonate. Some of the inclusions fluoresce green and others yellow, suggesting there has been some compositional differentiation and more than one phase of oil entrapment. Salt is relatively rare in this sample. When viewed in UV, the shale exhibits well defined strongly and weakly fluorescent layers, and in white light it is apparent that fluorescence intensity correlates with abundance of amorphous organic matter. No hydrocarbon emissions are observed in UV observation with a dry objective. There are probable diffuse emissions in oil

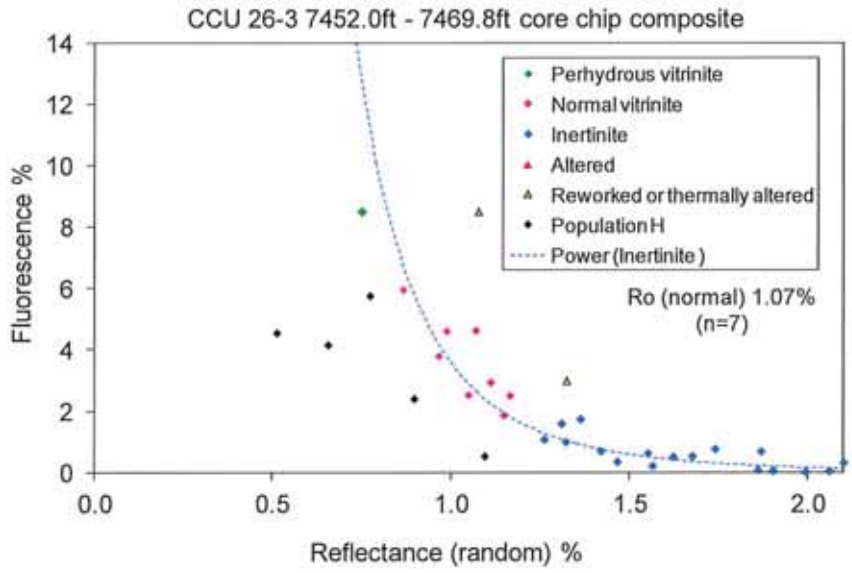

Figure 28 VIRF chart for "C unit" The good fit of normal vitrinite to the inertinite trendline increases confidence in Ro (normal).

Immersion, but the background fluorescence of the shale matrix makes it difficult to detect weak emissions with confidence.

This sample has a well defined VIRF profile and Ro (normal) is 1.07% (Figure 28). This value is well supported by the inertinite section of the profile.

Discussion and recommendations

Characterisation of the Cane Creek Unit #26-3 samples has been challenging due to the occurrence of salt. Even using non-aqueous preparation methods it is difficult to achieve an acceptable polish, and it was necessary to stabilise the samples using multiple impregnations during the grinding stages. A key finding has been that organic subjects with vitrinite morphology in all of the samples are Population H, which has an average reflectance 0.50% lower than material identified as normal vitrinite based on VIRF criteria. Another important finding is that oil is commonly hosted by salt in these samples.

VIRF analysis of CCU #26-3 indicates that even the shallowest sample (4790ft) has high maturity. Also, several samples provide microstructural evidence for hydrothermal activity and microbrecciation of salt and shale. Small amounts of fluorescent oil occupy fracture porosity at 4790ft and 6080ft. This oil is mobile at low observation temperatures and vapourises during exposure to a hot UV beam in oil immersion. Relatively common large inclusions of fluorescent oil are present in salt at both 7388ft and in core chip Unit B (7424ft), but no free oil was observed in the associated shales at these depths, which only contain small amounts of oil trapped as tiny inclusions in carbonate.

The sample at 4790ft features occasional altered remains of subaqueous volcanic extrusives or, potentially, shallow intrusive igneous material (Microfacies VS, Appendix 4). This lithology commonly occurs in successions which have experienced hydrothermal activity and is suggestive of an early igneous influence which may have recurred later in burial history.

Reddish orange fluorescence colours suggest there may be thermally altered hydrocarbon residues on fracture surfaces in the salt at 7388ft, and VIRF analysis of Unit B (7424ft) suggests this interval may have higher maturity than the underlying succession. However, much of the salt at 7388ft and in Unit B features a bright yellow fluorescing oil which is not thermally altered. The microstructure of Cane Creek Unit #26-3 samples indicates that there has been folding, shearing and consequent mixing of salt and shale lithologies. Given this context, and the partitioning of oil mainly in the salt, the origin, current distribution and character of the oil may not relate well to the geological history and maturity of the host shales.

VIRF analysis of the core chip composite Units A and B suggests that each of these intervals contains mixed maturity assemblages and/or organic matter which have been chemically altered by hydrothermal fluids. In this situation, VIRF analysis aims to define a Ro (normal) value for the least altered, highest maturity assemblage present, whereas geochemical testing will characterise all of the organic matter which is present in the sample. Consequently parameters such as Rock-Eval Tmax are unlikely to exhibit a close relationship with VIRF Ro (normal), due to the complex nature of organic assemblages present, which include significant amounts of amorphous organic matter.

The high maturity and microstructural modification of Cane Creek Unit samples in CCU #26-3 has made it difficult to observe liptinite and alginite, which cannot be distinguished from amorphous kerogen due to their very weak or absent fluorescence. Analysis of equivalent samples with lower maturity would provide more information on the organic assemblage and might clarify the tentative identification of large alginite bodies in Unit B.

APPENDIX 1

VIRF METHOD

Introduction

VIRF (Vitrinite-Inertinite Reflectance and Fluorescence, or VRF®) analysis combines reflectance with quantitative fluorescence, to provide compositional information for both dispersed organic matter and coals. This allows indigenous vitrinite of normal (orthohydrous) chemistry, which provides reliable reflectance data, to be distinguished from suppressed, altered and reworked vitrinite, inertinite, lower maturity cavings, or other sources of contamination. Due to the unreliability of standard VR, many existing wells require re-evaluation and revised interpretation of thermal history. In such cases, VIRF can be applied successfully to material which has been stored for long periods of time.

One reason VR produces highly misleading results for many rock samples is that visual identification of vitrinite is morphology based and subjective. The original classification of vitrinite and inertinite was developed for coals and problems arise when vitrinite and inertinite occur as dispersed organic matter in sediments, when they often have ambiguous physical appearance. VIRF uses the relationship between reflectance and fluorescence as an analogue for the chemistry of organic matter, and consequently defines vitrinite and inertinite in chemical as opposed to morphological terms.

The application of VIRF to both coals and sediments has made it clear that some subjects with the physical appearance of vitrinite can have inertinite chemistry. Also, some subjects with the appearance of inertinite can have vitrinite chemistry, particularly in the case of sapropelic (hydrogen rich) samples. The vitrinite population that is defined on a VIRF chart can have either orthohydrous ("normal") or perhydrous chemistry, which is assessed based on fluorescence intensity. Ro (normal) is the average of measurements obtained from the orthohydrous population in a sample.

Dark shales are particularly problematic for standard VR because they commonly lack true vitrinite derived from higher plant sources, although inertinite is sometimes present. These shales sometimes contain material which has vitrinite morphology but not vitrinite chemistry, based on reflectance and fluorescence relationships. This material has reflectance between 0.20% and 0.40% lower than true vitrinite, and the low fluorescence of this population distinguishes it from true vitrinite with perhydrous chemistry, which is sometimes present in the same sample. This "false vitrinite" is referred to as Population G/H, because there are both granular and homogenous forms, and it is inferred to be derived from a primitive plant source because it first appears in samples of Ordovician to Devonian age. Population G/H has been found in shales up to Cretaceous age.

Method

The VIRF method is outlined in Newman (1997a & b) and Newman et al. (2000). Reflectance and fluorescence intensity are measured for individual vitrinite and inertinite particles, and plotted as an x-y chart (Figure 1).

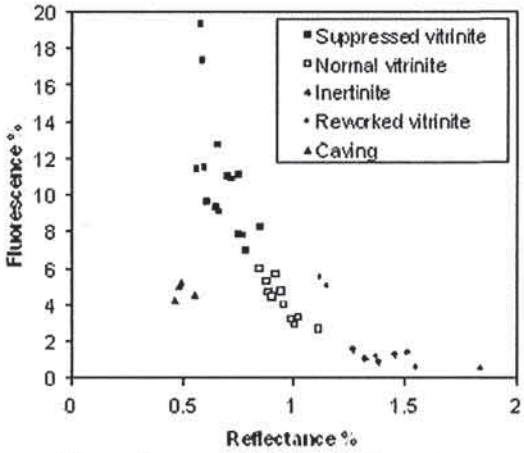

Figure 1 An example of a VIRF chart, illustrating the relative positions of different organic constituents.

Interpretation of VIRF charts is achieved with reference to a set of standard samples, including coals, in which vitrinite and inertinite can be reliably distinguished. The fluorescence range for vitrinite of normal chemistry is defined as approximately 2% - 6%, relative to a standard, based on analysis of materials with known thermal history. However, a different range applies at low and high maturities, and for freshly sampled coals and high TOC sediments.

VIRF charts routinely have standardised axial ranges, for ease of interpretation and comparison. However, in the presence of suppressed vitrinite with very high fluorescence, or high reflectance vitrinite, the plot has an extended y or x axis as appropriate. Charts and data are provided in Excel hence scale etc can be edited by clients as desired.

With increasing maturity, VIRF profiles move progressively upward and to the right (Figure 2). Cavings and hydrothermally altered vitrinite can therefore be identified because they plot below the trend defined by indigenous material in a sample. (Figure 1). Internal checks validate cavings identification, by ensuring that organic particles designated "caved" and "indigenous" never occur together in the same rock fragment. For this reason, during VIRF analysis of cuttings, each rock fragment is represented by

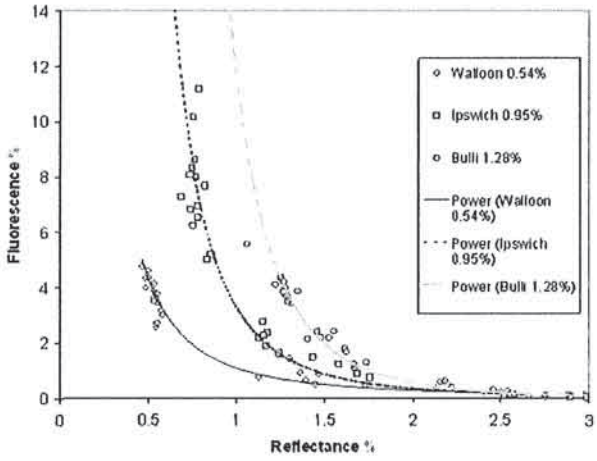

Figure 2 With increasing maturity, VIRF profiles move upward and to the right.

measurements on at least two organic particles, where possible. In the case of sidewall cores, which are taken after the well has reached target depth, contamination can come from both higher and lower than the designated position of the core. Some sidewall cores contain considerable drilling mud, with associated contamination. It is important to note that VIRF charts provide a qualitative rather than quantitative indication of the proportion of cavings or other contamination in a sample. The amount of contamination detected depends on the relative amounts of terrestrial organic matter in contaminating versus indigenous lithologies.

Reflectance can be measured either in polarised or unpolarised light. Vitrinite is significantly deformable under pressure and anisotropy consequently increases with increasing maturity. Anisotropic vitrinite exhibits systematic variations in reflectance when observed in polarised light. For each subject two maxima and two minima will be encountered during one 360°C stage rotation. "Ro max" represents these maxima and is utilized primarily by the coal industry for prediction of coking behavior. However, measurement of reflectance as Ro max at high maturities can result in vitrinite reflectance approaching and sometimes significantly overtaking the reflectance of inertinite, which generally exhibits less anisotropy. VIRF analysis now avoids the data distortions which can result from Ro max measurement by measuring reflectance in unpolarised light - Ro (random) - even on relatively high maturity samples. An exception is made in the case of extremely high maturity samples which have no fluorescence. For these samples a modified approach creates bivariate charts on axes of Ro max and Ro min (minimum), instead of reflectance and fluorescence.

Reporting

Where possible, Ro (normal) is calculated directly on measurements collected from vitrinite of normal chemistry. However, where normal vitrinite is sparse, absent, or significantly biased, Ro (normal) is sometimes inferred by comparing the overall VIRF profile of the sample – defined by all indigenous vitrinite and/or inertinite measurements – with profiles for reference samples which contain abundant normal vitrinite. A well-defined inertinite population is sometimes sufficient for delineation of this overall VIRF profile, and an inferred Ro (normal), when a sample lacks any indigenous vitrinite.

Data tables provide results in up to 3 categories. One column shows **Ro (normal)**, which is the average value calculated from all direct measurements on indigenous vitrinite of normal chemistry. Also shown is the number of measurements on which the average is based, the standard deviation, and the range, which is also indicated by the VIRF chart for each sample, provided in appendices. Another column in the results table may provide the **inferred** Ro (normal) value, described above. Where VR data are available for comparison, a final column may show **Ro (perhydrous, caved & altered)**, which provides an indication of the potential for depressed VR results. VR can be lower or higher than VIRF Ro (normal) in cases where VR analysts have been highly selective in their choice of measurement subjects, or have misidentified inertinite as vitrinite, or vice versa. Typical reasons for differences between VR and VIRF Ro (normal) when performed on the same samples are outlined in Table 1.1. In addition, poor sample preparation can sometimes be shown to have resulted in unreliable VR values.

Table 1. Typical reasons for differences (or similarities) between VIRF Ro (normal) and traditional VR.

Difference between VIRF and VR		Typical reasons
VIRF Ro (normal) higher than VR	Class A	VR includes perhydrous, caved or altered vitrinite, or Pop G/H
		VR analyst attributed normal vitrinite to the inertinite group
		Some inertinite has normal vitrinite chemistry
VIRF Ro (normal) the same as VR	Class B	Indicates well defined indigenous normal vitrinite population, or VR analyst has measured selectively
VIRF Ro (normal) lower than VR	Class C	VR includes reworked vitrinite
		VR analyst has measured some inertinite as vitrinite

References

Newman, J. 1997a. New approaches to detection and correction of suppressed vitrinite reflectance. APPEA Journal 1997, pp. 524 – 535.

Newman, J. 1997b. VRF™; Combined vitrinite reflectance and fluorescence. Coal Research Conference, Wellington, New Zealand.

Newman, J., Eckersley, K.M., Francis, D.A., & Moore, N.A., 2000. Application of vitrinite-inertinite reflectance and fluorescence to maturity assessment in the East Coast and Canterbury Basins of New Zealand. 2000 New Zealand Petroleum Conference Proceedings, pp. 314-333.

APPENDIX 2

Population G/H

Anomalous 'vitinites' in the Woodford Shale (and younger samples)

VRF analysis of the Devonian age Woodford Shale has identified a vitinite-like constituent, referred to here as 'Population G', which has reflectance >0.40% lower than 'normal' vitrinite in the same sample. When Population G is the dominant constituent, conventional VR reports a strongly suppressed result, with consequent underestimation of maturity. Population G features in DOM of samples as young as Mesozoic, hence recognition of this material is potentially important in many successions.

'Population G' often has a distinctive granular texture caused by inclusions of a liptinite-like constituent. However, some Population G material is internaly homogenous and easily confused with normal vitinite, although it can be distinguished on a VRF chart. A common floral source for the granular and homogeneous constituents of Population G can be demonstrated (below). A distinctive feature of some Population G subjects is an intimate association with euhedral carbonate (and sometimes quartz?) crystals, formed by replacement of the organic material.

Fluorescence of Population G is high at low to moderate maturity (up to Ro (normal) c. 0.70%), causing most Population G subjects to plot above the range of a standard VRF chart (14%). However, fluorescence rapidly declines above Ro (normal) 0.70%. The reflectance of Population G increases with increasing maturity, but more slowly than normal vitrinite, indicating different kinetic parameters.

Preserved plant parts are occasionally encountered in the Woodford samples. Figure B.1 exhibits a cross-section through an elongate body 13 microns wide and 200 microns long. The size and structure of this body are suggestive of, in broad terms, a root hair. One end which is unbroken, and may be a growth point, is heavily impregnated with liptinite-like material, with a homogeneous vitrinite-like core. Behind this tip the structure has the variably granular texture which is typical of Population G. Also present is a euhedral carbonate crystal which either displaces or replaces the plant tissue. Figure B2, provides an oblique cross-section through a plant part dominated by granular Population G, with a small homogeneous core.

These specific plant parts were measured at a total of 5 sites during VRF analysis. These sites are labeled in the photomicrographs and also on the relevant VRF charts. It is clear from this and other evidence that both the granular and homogenous elements which characterise Population G are, at least sometimes, derived from the same plant. There are a number of primitive plant groups which could be sourcing Population G.

Samples were provided by Doug Waples, who is gratefully acknowledged. Doug is currently interpreting organic geochemistry maturity parameters on the same sample set.

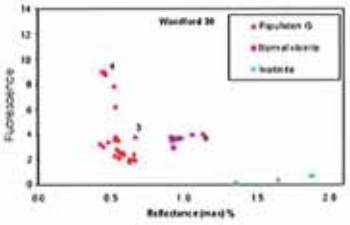

B1

B2

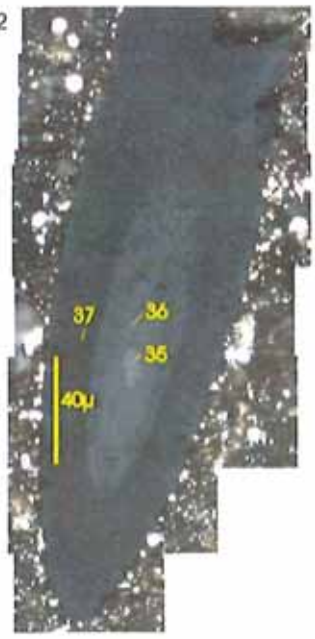

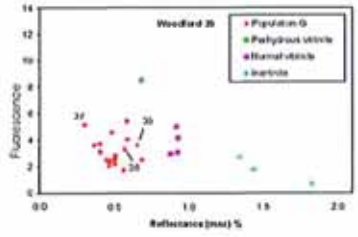

B

APPENDIX 3

Evidence for igneous and hydrothermal activity; background notes

Background information on igneous and hydrothermal activity in petroleum basins

VIRF analysis has clarified the burial history of sedimentary basins in many areas, including Australasia, Asia, the North Sea, Africa and North and South America. Ro (normal) provides more precise data than VR for maturity assessment, and geologically significant complexities in reflectance profiles can be sensitively delineated. This information is combined with systematic observation of additional petrographic features, including evidence for hydrothermal and igneous activity. Case studies comprising dozens of wells and hundreds of samples have provided considerable insight into the detailed burial history information that is potentially available from petrographic analysis.

Vitrinites and semi-inertinites in some intruded sequences exhibit locally developed coke microtextures. The anisotropic mesophase which characterises coked vitrinite indicates temperatures higher than 400°C (Stach et al. 1982). However, these extreme temperatures are experienced only at the time of intrusion and are ephemeral in geological terms. Coke textures are produced by more or less direct heating close to the intrusion and by exposure to superheated gases at greater distances. Coke textures are often only erratically observed in rock units which are distant from intrusions, suggesting that hot gases travel certain paths and leave a heterogeneous pattern of effect. Coke fragments are also commonly transported away from intrusions in hydrothermal fluidised flow. In some circumstances hydrocarbons and/or carbonaceous material are vapourised at the time of intrusion, resulting in precipitation of pyrolytic carbon when the gas stream moderates sufficiently.

Only vitrinites (and some semi-inertinites) with reflectance above c. 0.60% have the potential to form a coke, due to the requirement for organic matter to liquefy during rapid heating and then resolidify as coke. When lower maturity organic matter is rapidly heated it merely shrinks and evolves gases without transforming into coke.

Careful observation of complex microstructural features in many basins has revealed a chronology of mineralisation events which are believed to be initiated by igneous intrusion. Magnetite microveins are disrupted by multiple deformation and mineralisation events, hence are inferred to be an early-formed very high temperature phase. Later mineralisation is usually dominated by precipitation of hematite (or other iron oxides) in void and fissure spaces, or carbonate mineralisation in the case of successions which are intruded early, when sediments are relatively unconsolidated and have high pore moisture. Previous work has demonstrated that hydrothermal microbreccias and mineral complexes sometimes provide migration pathways and accommodation spaces for hydrocarbons.

Successions which provide evidence of igneous activity sometimes exhibit complex VIRF charts resulting from an abundance of chemically altered ("chemically damaged") organic matter, which loses the ability to mature normally and plots below the VIRF profile defined by unaltered indigenous organic matter. Altered material often occurs at considerable distances from the inferred intrusion, and is attributed to reaction with igneous fluids and gases which may have dissipated much of their heat but remain chemically active. Coals and coally sediments demonstrate alteration most dramatically, and are typically cracked, bleached and corroded. However some successions affected by hydrothermal activity do not exhibit alteration of organic matter. It is possible that the chemistry of the igneous intrusion may directly influence the nature and degree of chemical damage.

Mineralogical and microstructural evidence of hydrothermal activity is sometimes apparent in only part of a cuttings sample, and is rare in core samples, suggesting that activity is localised to particular pathways through the succession. In contrast, the hydrothermal effects following intrusion appear to be more pervasive, because they typically cause elevation of maturity in all unaltered material. A complex history is therefore indicated. Probably there is an initial episode of violent activity involving the escape of chemically aggressive igneous exhalations, and this is followed by a more pervasive, prolonged and genuinely hydrothermal episode whereby formation water (present in the sediments prior to intrusion) transfers igneous heat through the succession. Metasomatic alteration of sediments and organic matter could potentially occur during this phase.

Chemical damage of organic matter appears to be primarily an oxidising process and the resulting depression of fluorescence corresponds to a loss of hydrogen. These changes have affected Rock-Eval HI, kerogen kinetics and other organic geochemical analyses in some successions.

Solid (waxy and asphaltic) hydrocarbons with various melting points are commonly associated with the hydrothermal microbrecciation and mineralisation observed in wells. Petroleum produced in the Guaymas Basin (Gulf of California), in a ridge-crest hydrothermal system, also includes solid hydrocarbons (Simoneit, 1985). Simoneit states:

"In the case of the Guaymas Basin hydrothermal system, the petroleum products have migrated and are actively moving by advection, diffusion, distillation, and hydrothermal fluid circulation away from the heat sources. This appears to occur as bulk phase, cosolute fluid, and aqueous solution migration upward to the seabed. There the petroleum condenses and collects according to the ambient temperatures in the conduits and vugs of the hydrothermal mineral mounds. PAH and sulfur condense in the hot vents; waxes crystallise in intermediate temperature regions (20-80°C); and the volatile petroleum partially collects in cold areas (3°C) and emanates into the ambient seawater ....."

Hydrothermally mediated heat flow is controlled by rock permeability, hence lithological and microstructural variations can result in maturity profiles which are more complex than those predicted by conventional burial history models. In the Cerro Prieto geothermal field the succession exhibits (Barker & Elders 1981; Figure B.1 this report)
"moderate temperature gradients and low to moderate rank gradients at shallow depth in relatively unmetamorphosed mudrock..... These characteristics correspond to conductive heat transfer in the relatively impermeable caprock. The moderate temperature gradient at shallow depths tends to increase rapidly at a distinct depth ..... (which) correlates in boreholes M-84, M-94, and M-105 with a zone of authigenic illite and chlorite (Hoagland and Elders, 1978), which is taken to mark the onset of hydrothermal alteration in the Cerro Prieto system. The onset of hydrothermal alteration also correlates with the appearance of significant sandstone bodies in these boreholes. Boreholes M-84, M-94, and M-105 also show a (mutually similar) decrease in rank and temperature gradients at 1050m, 1300m, and 650m, respectively. This second inflection point correlates with the intersection of these boreholes with the geothermal reservoir, as indicated by temperatures of 200°C, low temperature gradients and common sandstone (permeable) zones (Elders et al., 1977)."

The Cerro Prieto system may not be a good temperature analogue for hydrothermal activity in most petroleum basins but it has the advantage of being currently active and accessible to investigation. A comparable maturity profile, with reflectances almost as high as the Cerro

Prieto system, is exhibited by Clipper-1 in the Canterbury Basin of New Zealand (Newman et al. 2000). This example provides convincing evidence that the heat source was a large igneous intrusion close to target depth, probably of Paleocene age. Present day temperatures in this succession are substantially lower than those experienced during the hydrothermal episode, and hydrocarbons are inferred to be relict from the early Tertiary.

Permeable sand units have been observed to correspond with intervals of uniform maturity in a number of basins examined by VIRF, including successions with Ro (normal) below 1.0%. Also, VIRF studies in the Northwest Shelf area of Australia and elsewhere have encountered successions in which permeability has been secondarily generated by microbrecciation of strata at the time of inferred igneous intrusion. This has resulted in some hundreds of vertical metres of succession in which a network of open fractures has allowed unrestricted hydrothermal circulation, resulting in uniform maturity from top to bottom of the affected interval.

Relatively recent and current projects suggest that hydrothermal activity in relatively poorly indurated successions can result in hydrothermal heat transfer via a silt-rich fluidised slurry, which can transport fragments of igneous material, coke, hydrothermal minerals and chemically altered organic matter over considerable stratigraphic distances, sometimes in association with mobile hydrocarbons. This fluidised material is typically tinted orange, presumably due to the presence of iron oxides.

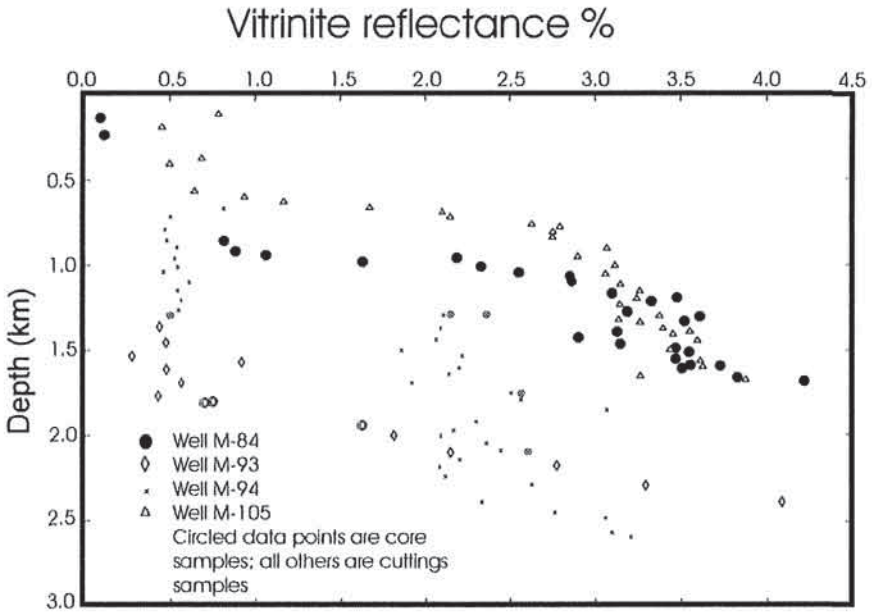

Figure 0-1 Reflectance profiles in boreholes at Cerro Prieto geothermal field. Adapted from Figure 2 of Barker & Elders (1981).

References

Barker, C.E. & Elders, W.A. 1981. Vitrinite reflectance geothermometry and apparent heating duration in the Cerro Prieto geothermal field. Geothermics, Vol. 10, pp. 207-223.

Newman, J. 1997a. New approaches to detection and correction of suppressed vitrinite reflectance. APPEA Journal 1997, pp. 524 – 535.

Newman, J. 1997b. VRF™; Combined vitrinite reflectance and fluorescence. Coal Research Conference, Wellington, New Zealand.

Newman, J., Eckersley, K.M., Francis, D.A., & Moore, N.A., 2000. Application of vitrinite-inertinite reflectance and fluorescence to maturity assessment in the East Coast and Canterbury Basins of New Zealand. 2000 New Zealand Petroleum Conference Proceedings, pp. 314-333.

Simoneit, B.R. 1985. Hydrothermal petroleum: genesis, migration, and deposition in Guaymas Basin, gulf of California. Canadian J of Earth Sciences, v22 pp 1919-1929.

APPENDIX 4

Microfacies VS

Microfacies VS

This microfacies is an altered vitric, vesicular lava or shallow intrusive rock. The framework has been partially replaced by an iron oxide mineral, and also by illite, which infills the structure (Figure 1).

Figure 1
Microfacies VS from an Australian well.

Microfacies VS is a highly distinctive lithology which occurs in many basins. One representative case (from a North Sea well) has been expertly examined in thin section and polished section (not by Newman Energy Research, but commissioned by them) with the following findings.

"Altered, oxidised, vitric, vesicular microphyric and fragmental mafic volcanic rock. Microphenocrysts of ghosted feldspar and pyroxenes are contained with formerly vitric and vesicular groundmasses. Ghosted intergranular to hyalopilitic textures are evident in some fragments (including ghosted vesicles in glass). Ghosted Fe/Ti-oxides are present in the vitric groundmasses. Xenoliths of ghosted vesicular fragments (shards) are present in some examples. Poorly sorted populations of ghosted, silt to less than silt sized vesicular, vitric fragments define former fragmental textures. Abundant, ultra fine-grained hematite and hydrated Fe-oxides have formed after mafic minerals and glass. Variably crystalline illitic clay has formed after most phenocrysts and groundmass/matrix material."

"Extrusion of the mafic melt into an aqueous or sub-aqueous environment would account for the highly vitric, vesicular and microphyric nature of the lithology. Furthermore, the rapid chilling/quenching and explosive fragmentation of a mafic melt upon extrusion into an aqueous or subaqueous environment would account for the fragmental or hyaloclastic textures evident in some drill chips. Some of the mafic volcanic textures/fabrics may be achieved equally well by (hot level) intrusion of the mafic melt into a wet, unconsolidated sediment..."

Cane Creek Unit #26-3

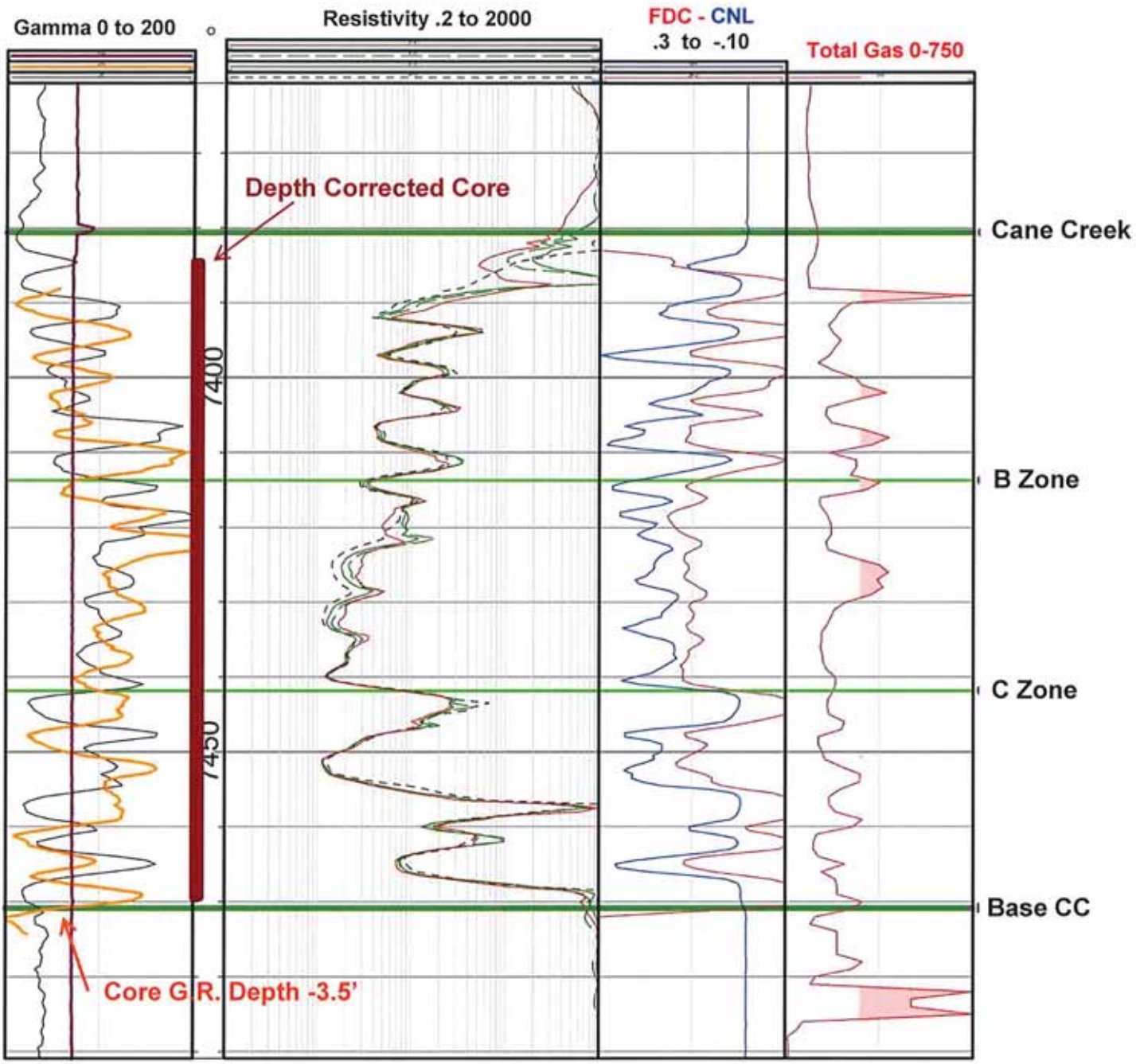

WELL: FIDELTY OIL & GAS CANE CREEK UNIT 26-3

FORMATION: Cane Creek Member

LOCATION:NESW Sec 26 - T25S - R19E

CORE DEPTH: 7388 - 7474

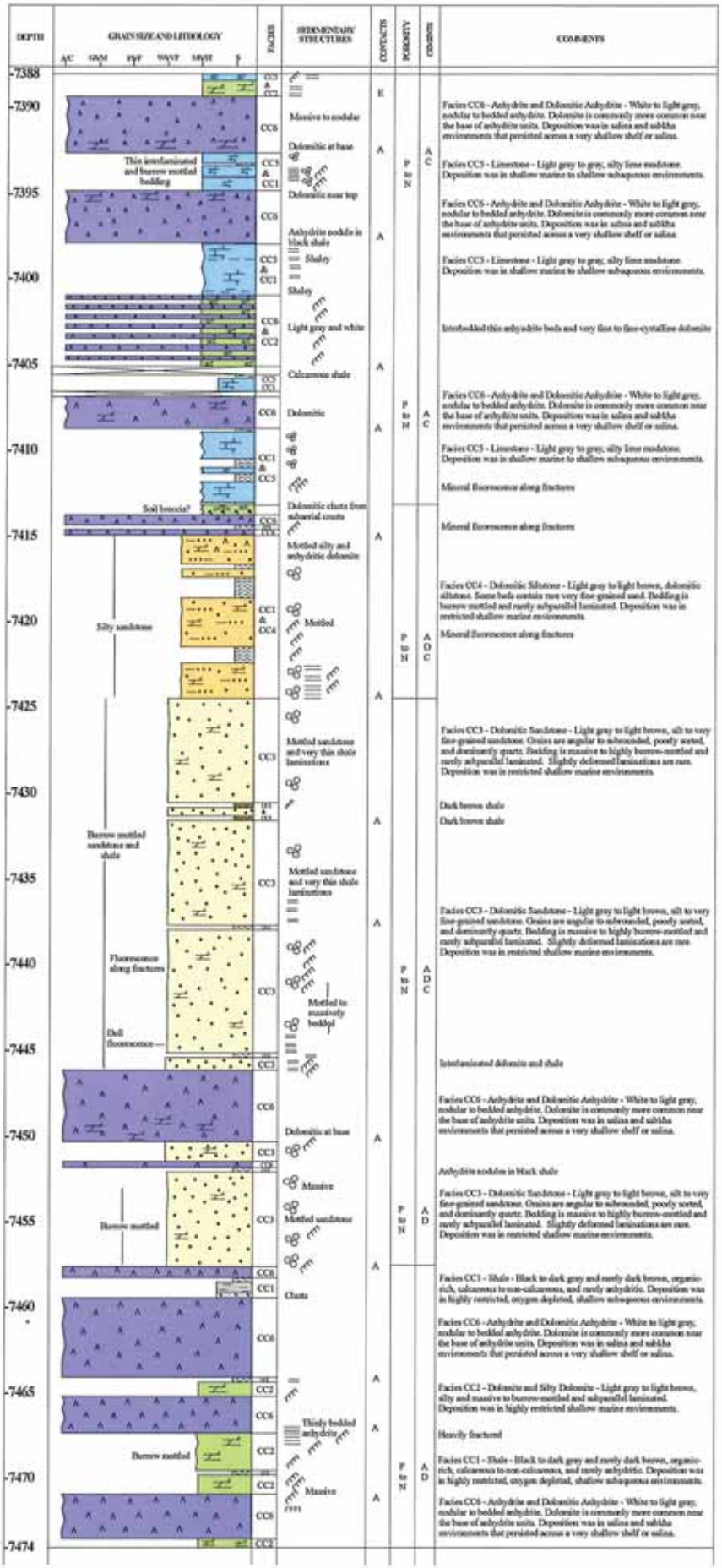

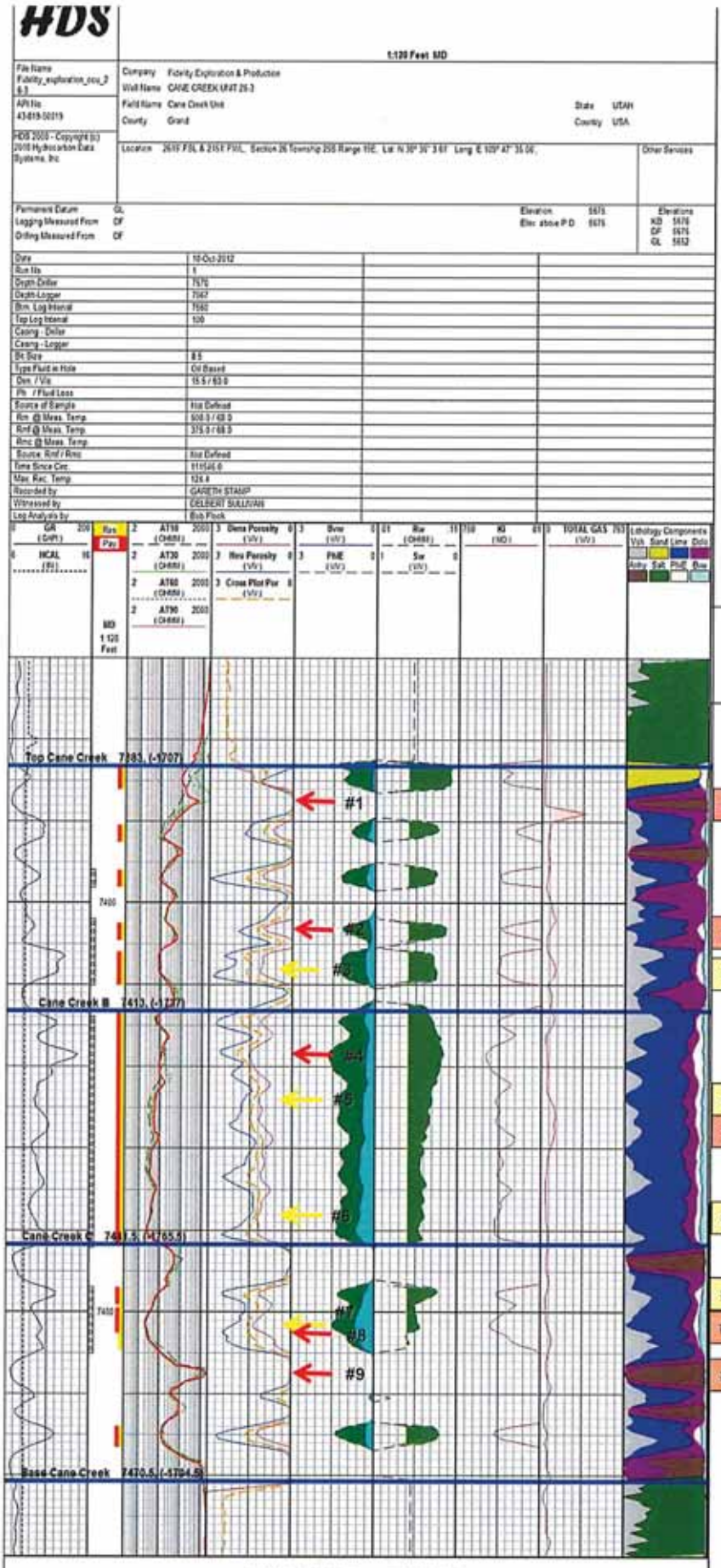

Note: Core is 3.5' Deep to Logs (add 3.5' to log for core depth)

#1 7390.5' Core

#2 7406' Core

#3 7410' – 7410.5 Core

#5 7426' – 7426.5' Core

#4 7426 – 7427' Core

#6 7439' – 7441' Core

#7 7454.5' – 7455.5' Core

#8 7455.5' – 7455.9' Core

#9 7461' – 7461.4 Core

← Rock Mech.

← Return Perm. & Wettability

Core Lab
RESERVOIR OPTIMIZATION

Fidelity Exploration & Production Co.
CCU #26-3
Grand Co., UT
Spectral Core Gamma
Scale 5" = 100'

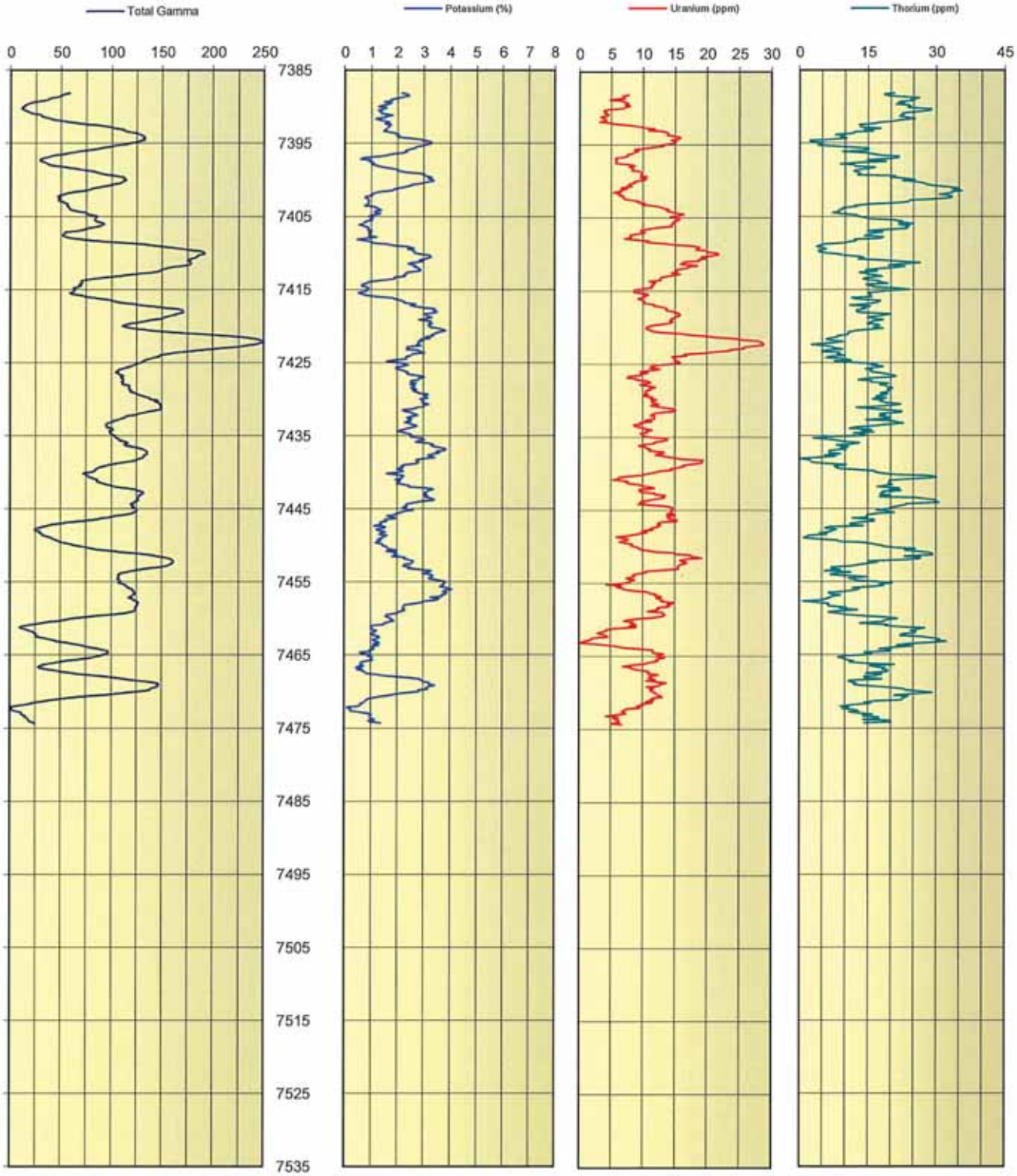

Appendix D:

Remington 21-1H

Thin Section Report by

Eby Petrography and Consulting, Inc.

UPRC REMINGTON #21-1H
THIN SECTION REPORT: 7435 ft.
(probably sampled at 7435.5 ft.)

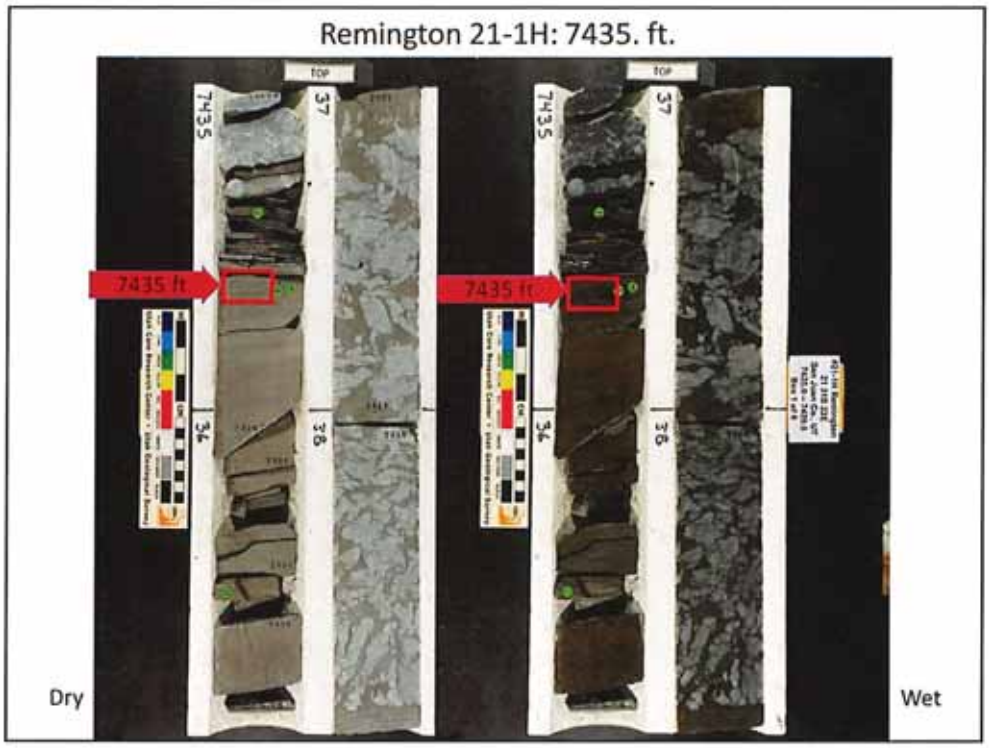

Fig. 1. Pair of core photos over the same depth interval, with a dry view on the left and a wet view on the right. The location of the 7435 ft. sample (actually sampled at 7435.5 ft.) is indicated by the red arrow adjacent to each core photo. Note the thin-bedded appearance of the brownish silty dolomite unit. The shale immediately above the sample has a measured TOC of 2.19%.

.

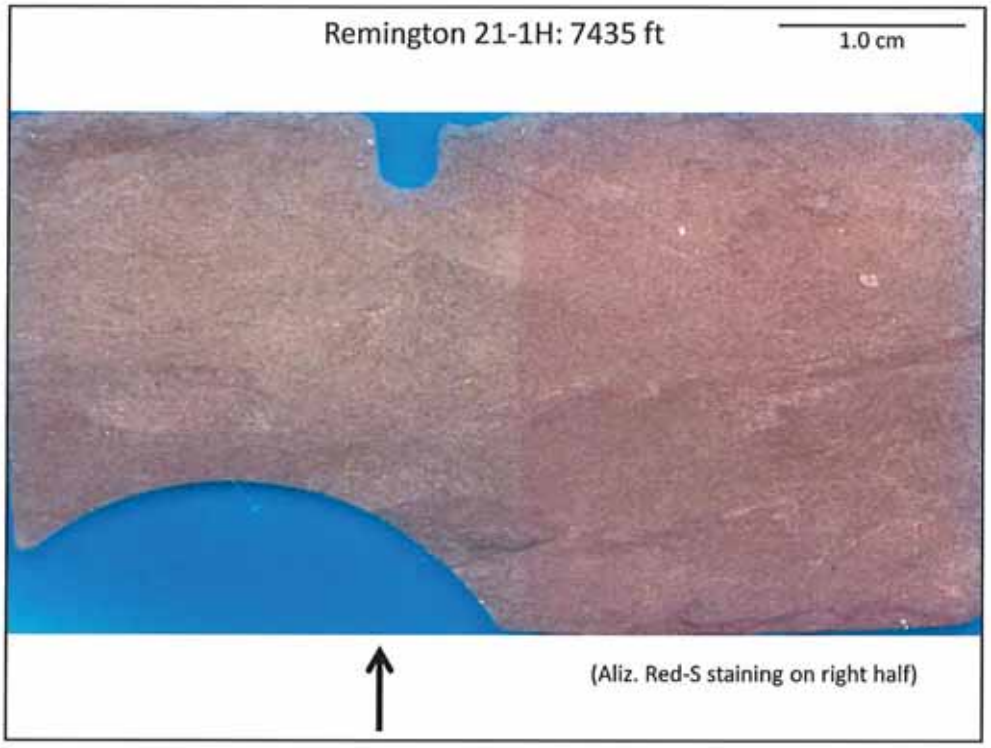

Fig. 2. Low magnification view of the entire 1" x 2" thin section. The rounded blue area at the base shows where a "perm" plug" had been removed from the conventional core. This finely crystalline dolomite displays a vague dark gray swirled fabric with no visible matrix porosity. The swirled pattern may be the result of either bioturbation or evaporate haloturbation. The right half of this image displays a pink cast due to Alizarin Red-S staining.

Fig. 3. Pair of images of the same area at the same magnification, with a plane light (PL) view in the upper left and a cross-polarized (XN) view in the lower right. Note that the matrix is composed of grain-supported fine peloids, with a mottled to swirled matrix.

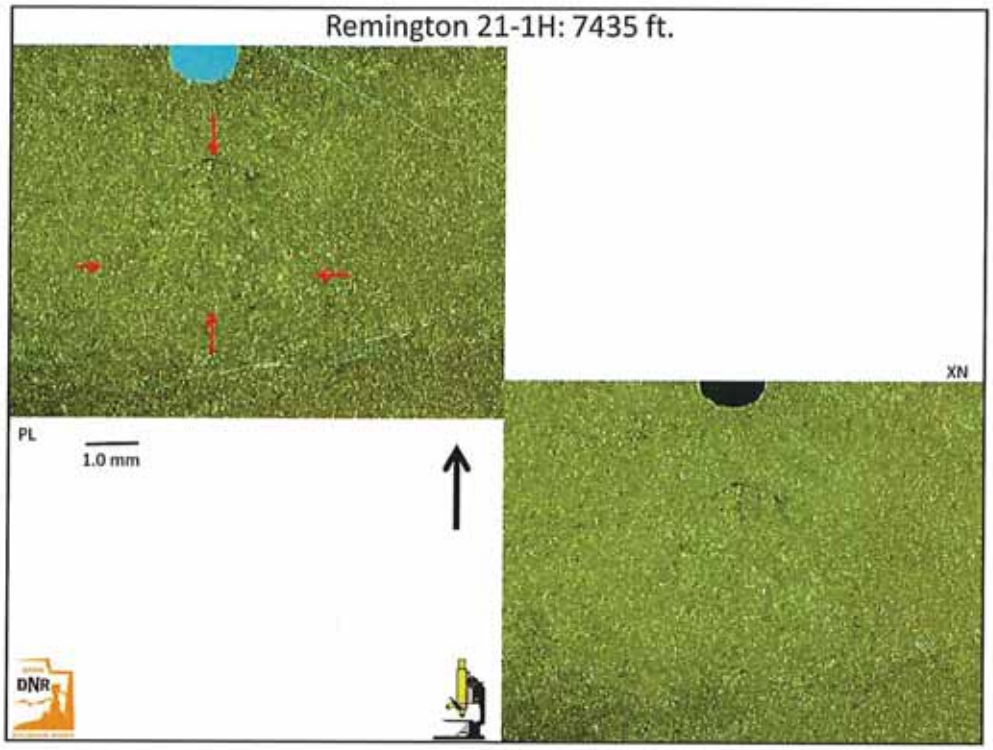

Fig. 4. Another pair of images from a different representative area than shown in Fig. 3. The plane light (PL) view is shown in the upper left and a cross-polarized (XN) view in the lower right. There is a distinct circular area (within the red arrows in the upper left view) that that displays a distinctive swirled pattern, perhaps the result of a burrow infilling.

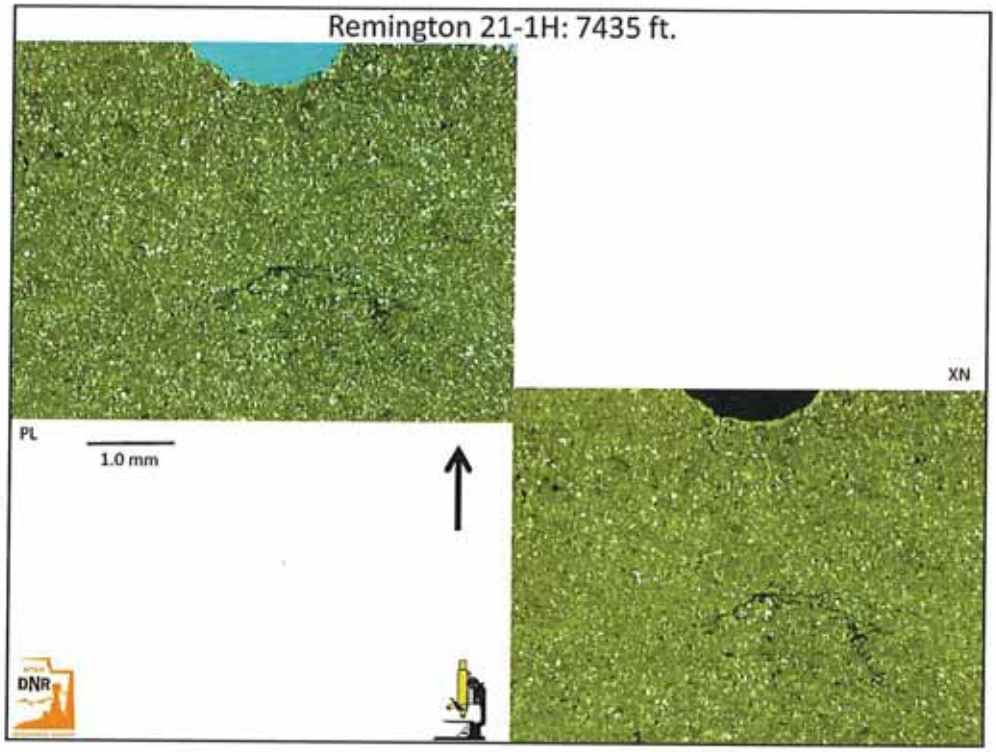

Fig. 5. A third pair of images from yet a different representative area than shown in Figs. 3 & 4. The plane light (PL) view is shown in the upper left and a cross-polarized (XN) view in the lower right. The matrix composition of the area appears to contain small peloids and elongate intraclasts. Note the wispy black seams near the middle of the image. These may be organic remnants.

Fig. 6. This plane light (PL) view shows a significant content of silt grains (as white specks) mixed in with peloidal dolomite. Note the absence of any significant porosity (i.e. no blue areas). Traces of microfractures (see red arrows) are present within this finely crystalline dolomite, possibly along thin organic seams. Note the swirled and mottled character of this silty peloidal dolomite.

Fig. 7. A representative cross-polarized and reflected light (XN + Refl) image at higher magnification (than Fig. 6) illustrates the disseminated quartz-rich silt grains (in white, gray and black). Note that some of these silts have rounded outlines, consistent with a possible aeolian delivery system. Note the crinkly black organic or carbonaceous seam (between the red arrows).

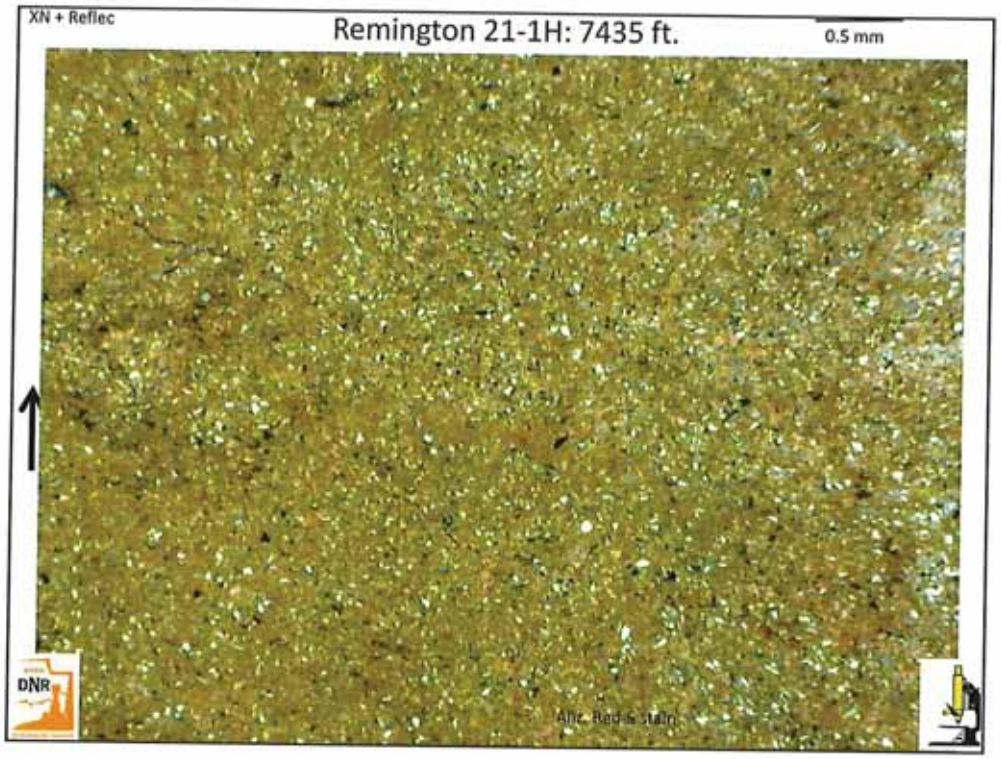

Fig. 8. A representative cross-polarized and reflected light (XN + Refl) image of a portion of the sample that has been stained with Alizaren Red-S solution. Note the small but abundant patches of red to pink staining, indicating some calcite that has not been dolomitized. These remnant limestones include portions of grains (mostly peloids) and interparticle cements. In addition to the quartz-rich silt grains, not the black (opaque) areas which are composed of diagenetic pyrite.

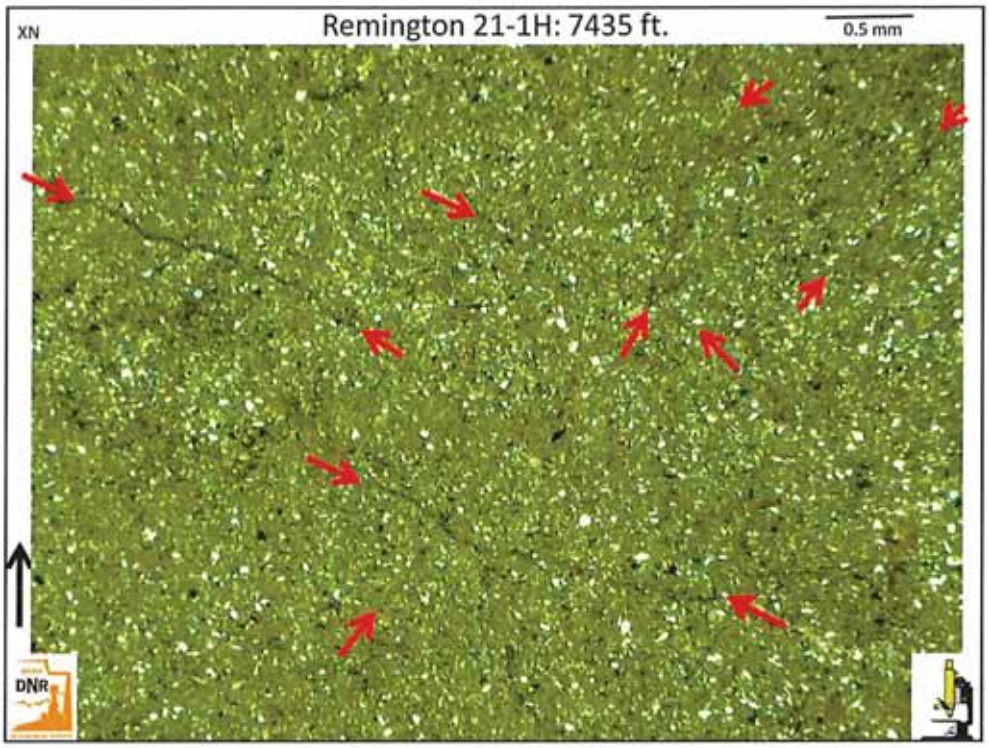

Fig. 9. Same field of view as imaged in Fig. 8, but shown in crossed polarized (XN) light only. Note the intersecting conjugate set of microfractures (see red arrows). These microfractures appear to be open.

UPRC REMINGTON #21-1H
THIN SECTION REPORT: 7,437.3 ft.

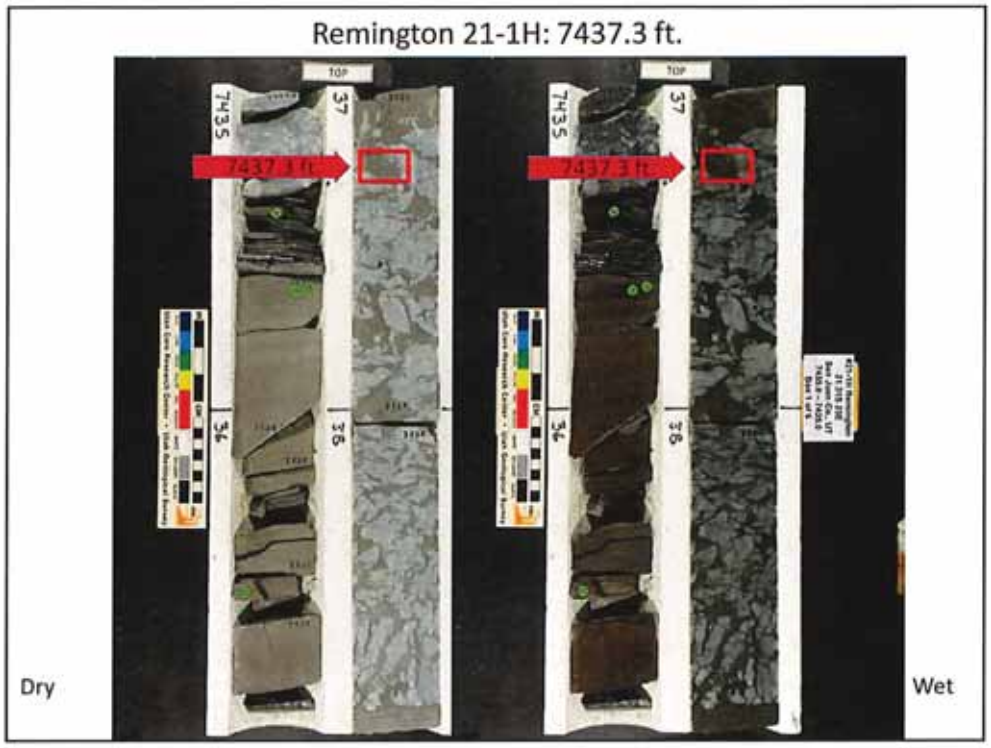

Fig. 1. A pair of core photos shows the same depth interval, with a dry view on the left and a wet view on the right. The location of the 7437.3 ft. sample is indicated by the red arrow adjacent to each core photo. Note the elongate, "palmate" anhydrite structures within a matrix of brown, very finely crystalline dolomite above and below the location of the 2"x3" (oversized) thin section prepared from this interval.

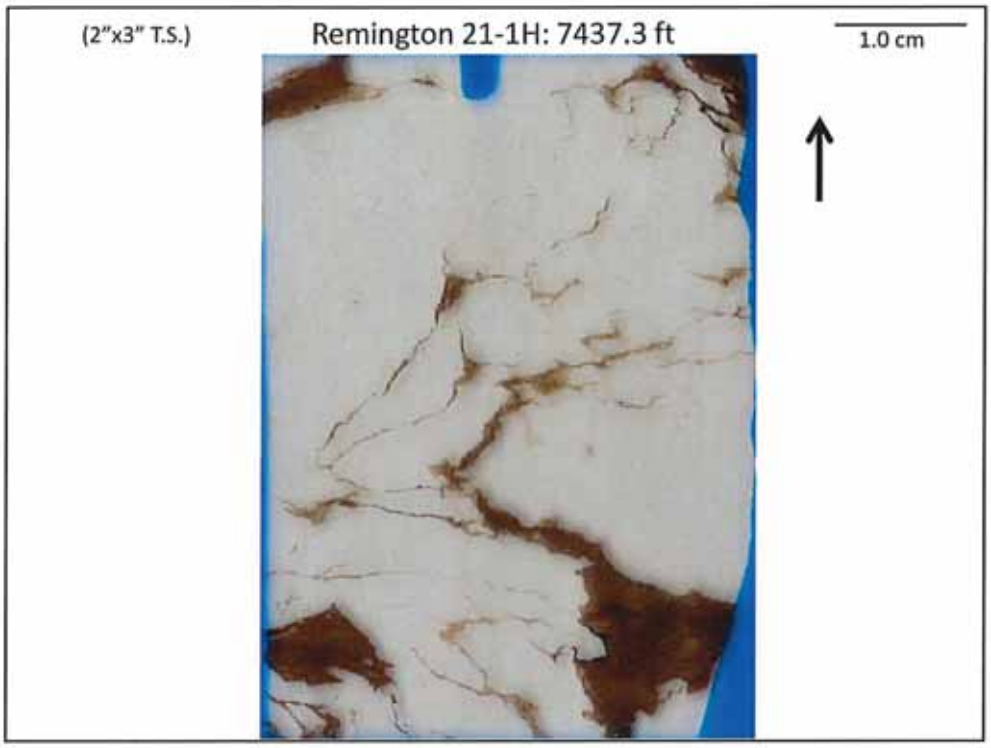

Fig. 2. Low magnification overview of the entire 2" x 3" thin section. The white areas of the sample are composed of anhydrite which occur within distinct palmate structures, indicative of subaqueous sulfate mineral growth. The dark brown areas are composed of dolomite which was displaced during palmate evaporite growth. The blue notch at the top indicates the stratigraphic "UP" direction.

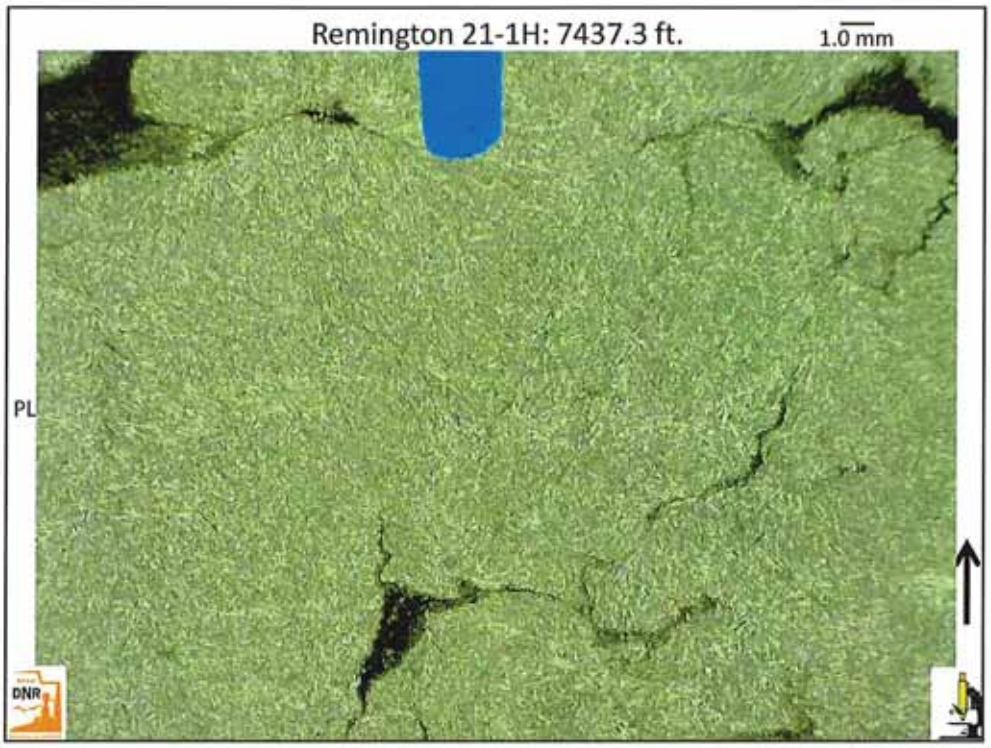

Fig. 3. A closer view of the white anhydrite shown in Fig. 2 shows a fine "felted" fabric in the plane light (PL) view. Note the islands of dark-colored dolomitic mudstone surrounded by anhydrite. The blue notch at the top indicates the stratigraphic "UP" direction.

Fig. 4. The same field of view as Fig. 3, but under cross-polarized (XN) lighting shows the high-brirefringence pastel colors of the "felted" anhydrite ground mass within the palmate nodules.

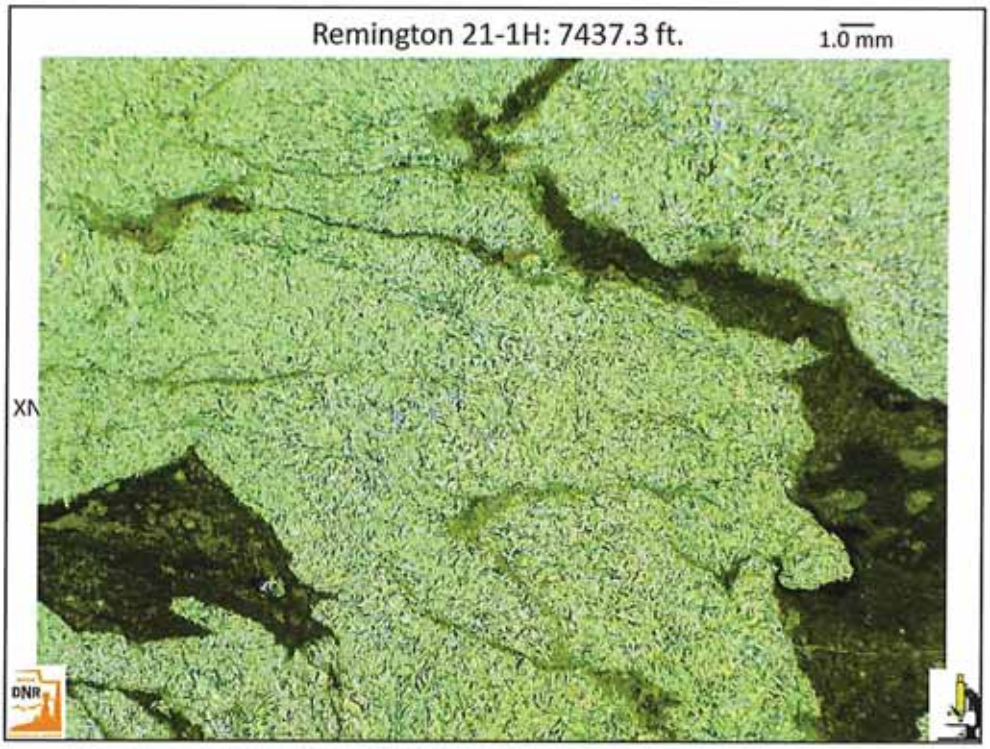

Fig. 5. Another representative cross-polarized (XN) image of the "felted" anhydrite microfabric displays the sealing capacity of this type of evaporate deposit. Note the islands and wispy seams composed of dark-colored, organic-rich dolomite that are incorporated into this anhydrite.

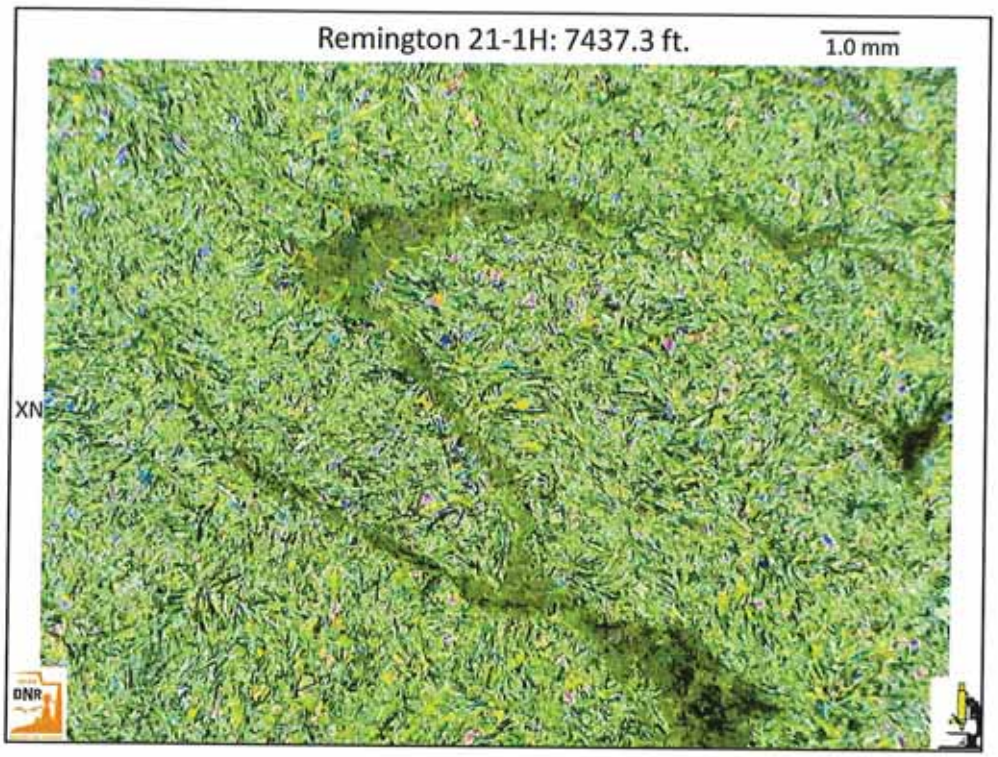

Fig. 6. This cross-polarized (XN) light view shows the non-porous "felted" fabric of the anhydritic palmate laths within this core interval. Anhydrite subcrystals can be seen within the pastel birefringent pattern. Note the thin remnants of brown dolomite matrix that was displaced during early evaporite (gypsum) growth.

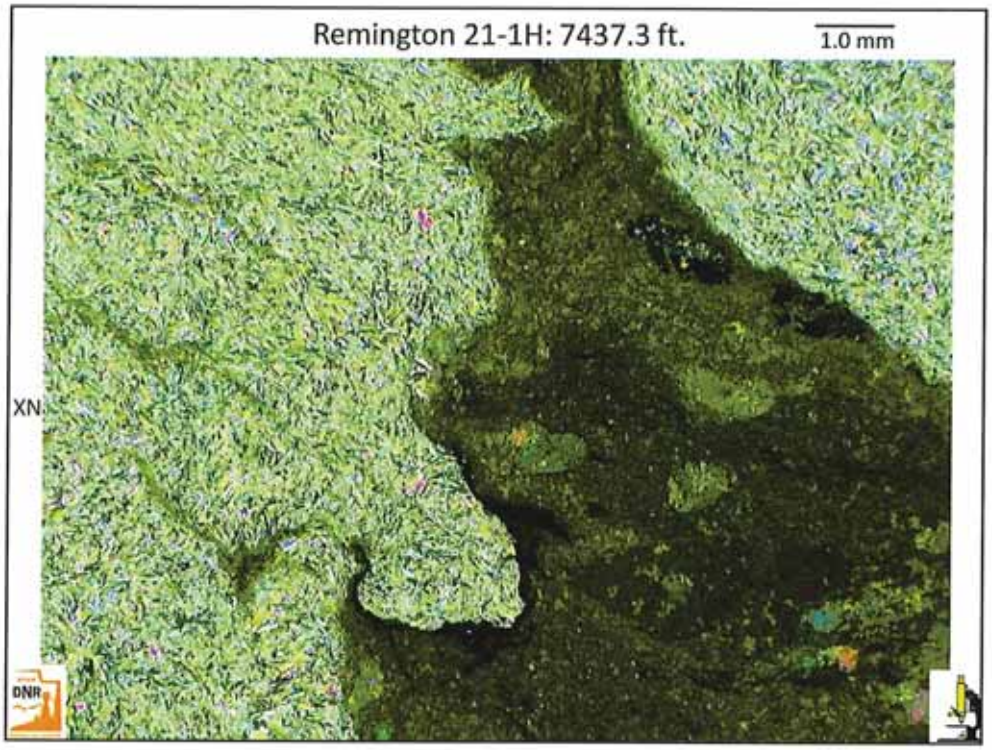

Fig. 7. Mottled brown dolomite between two displacive anhydrite masses displaying a tight "felted" fabric under cross-polarized (XN) light. The mottling within the dolomite may be the result of either bioturbation or haloturbation within a hypersaline evaporitic setting.

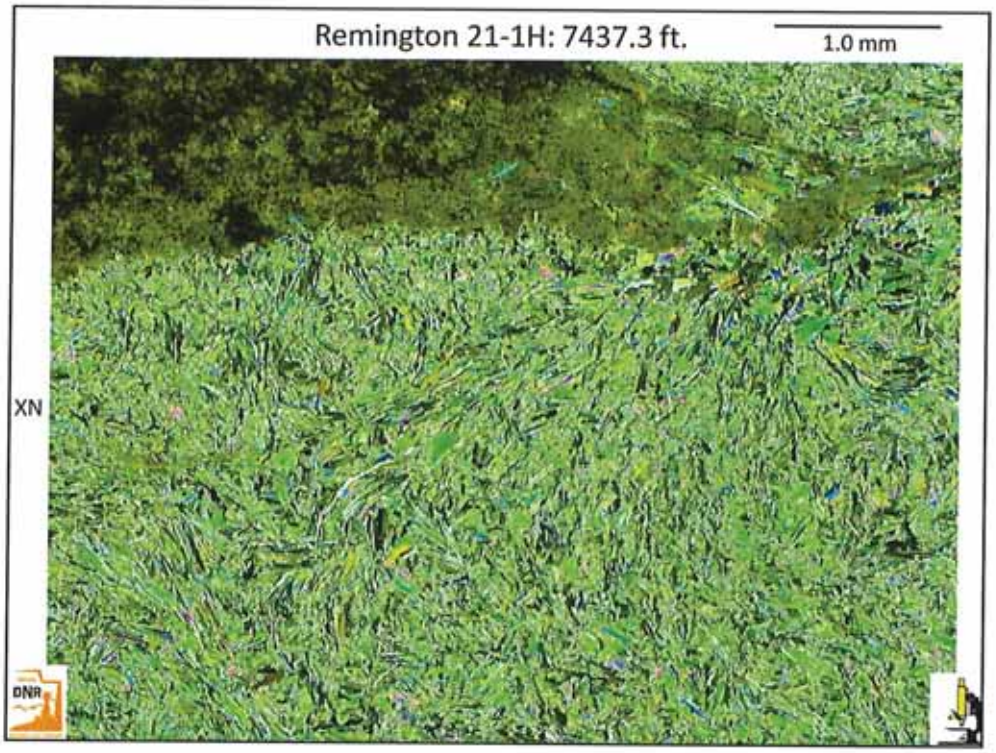

Fig. 8. "Feathery" microfabric within an anhydrite palmate nodule under cross-colorarized (XN) light. Note the patch of peloidal dolomite at the top. This dolomitic grainstone/packstone occurs between displacive anhydrite nodules.

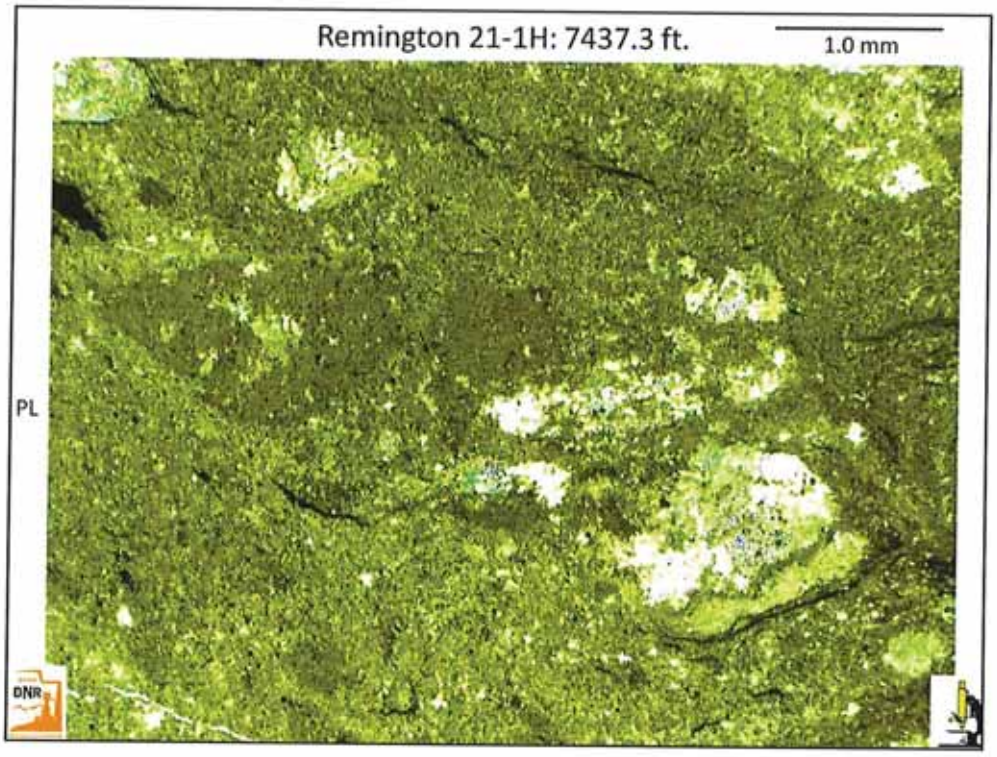

Fig. 9. Mottled or "swirled" dolomitic matrix with small patches of white anhydrite. This plane light (PL) view also shows relicts of peloids, small intraclasts, and black organic matter. The mottled pattern is the result wither of bioturbation or haloturbation.

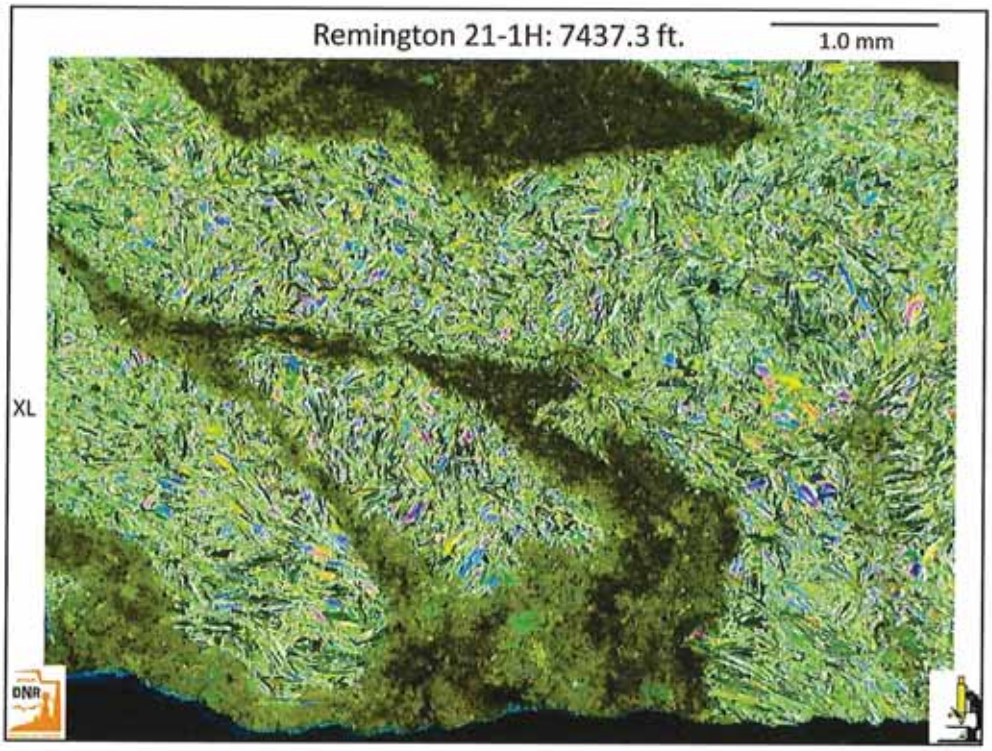

Fig. 11. A portion of an anhydrite nodule with scalloped margins is illustrated here under cross-polarized (XN) light. Needle-shaped anhydrite subcrystals make up this tight felted groundmass. Mottled peloidal dolomite (in dark brown) is present around the margins of this anhydrite nodule. Note the anhydrite-filled microfracture between the red arrows.

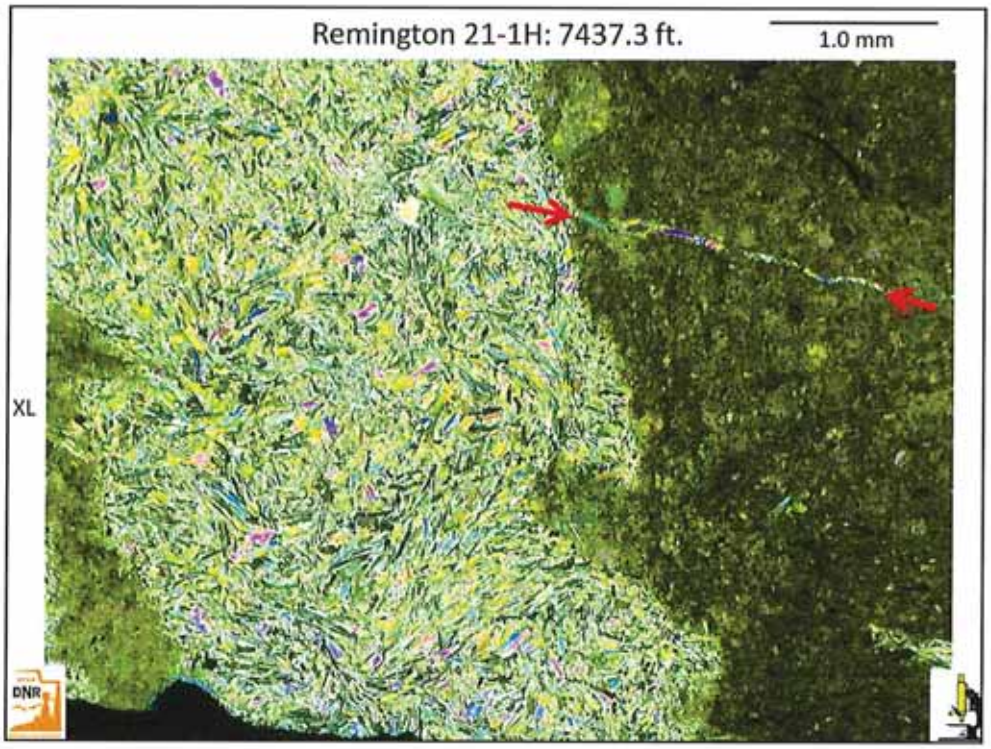

Fig. 11. A portion of an anhydrite nodule with scalloped margins is illustrated here under cross-polarized (XN) light. Needle-shaped anhydrite subcrystals make up the the tight felted groundmass. Mottled peloidal dolomite (in dark brown) is present around the margins of this anhydrite nodule. Note the anhydrite-filled microfracture between the red arrows.

UPRC REMINGTON #21-1H
THIN SECTION REPORT: 7,445.6 ft.

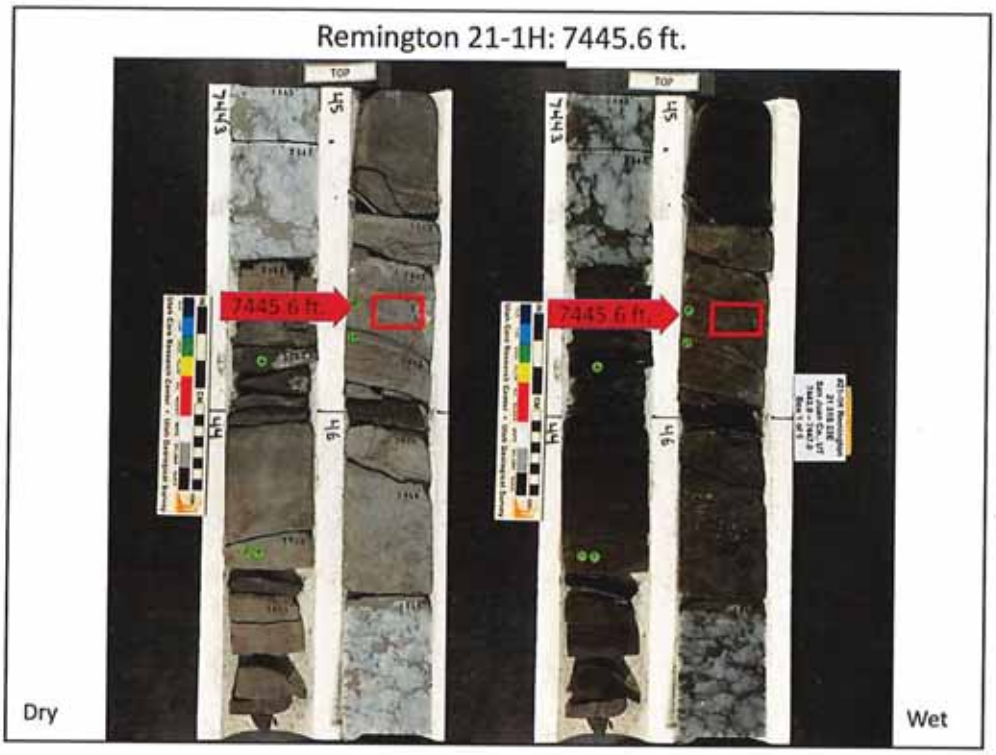

Fig. 1. A pair of core photos shows the same depth interval, with a dry view on the left and a wet view on the right. The location of the 7445.6 ft. sample is indicated by the red arrow adjacent to each core photo. Note the brown dolomite at the location of the 1"x2" thin section prepared from this interval. This dolomite appears to be a laminated stromatolite with some synoptic relief.

.

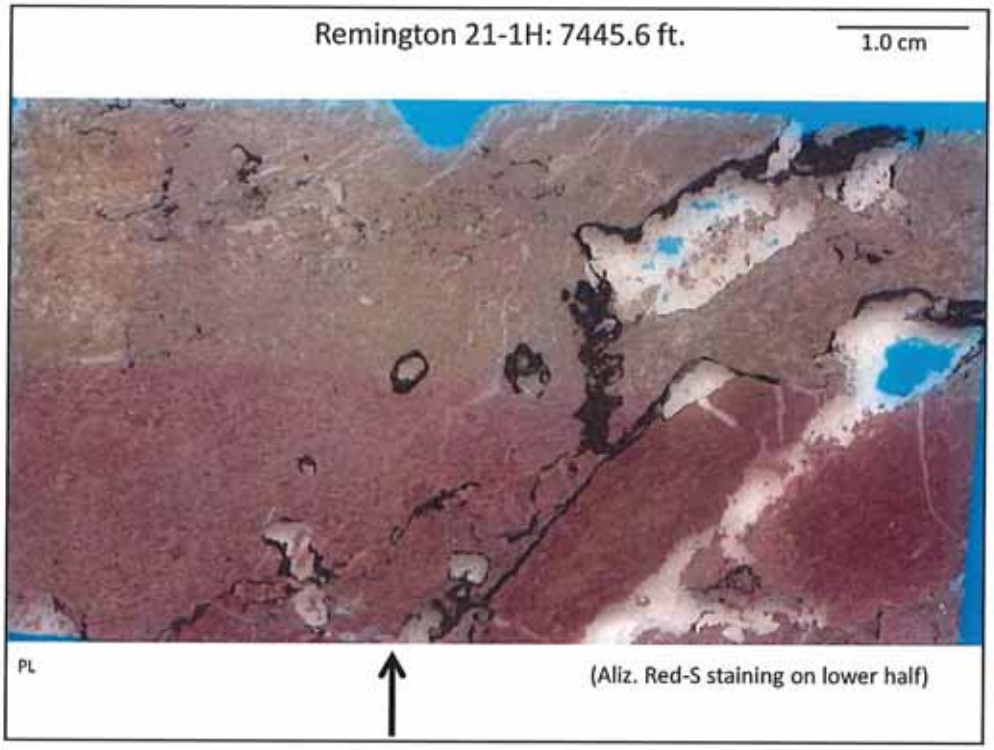

Fig. 2. Low magnification overview of the entire 1" x 2" thin section. The lower half of the thin section has been stained with Alizarin Red-S stain. The left portion of the slide displays a "clotted" to vaguely laminated fabric that may be microbial in origin. The right portion shows vugs and large pores, some of which are partially filled with white anhydrite. The thin back areas are composed of insoluble residues concentrated along stylolites of pressure-solution origin. The blue notch at the top indicates the stratigraphic "UP" direction.

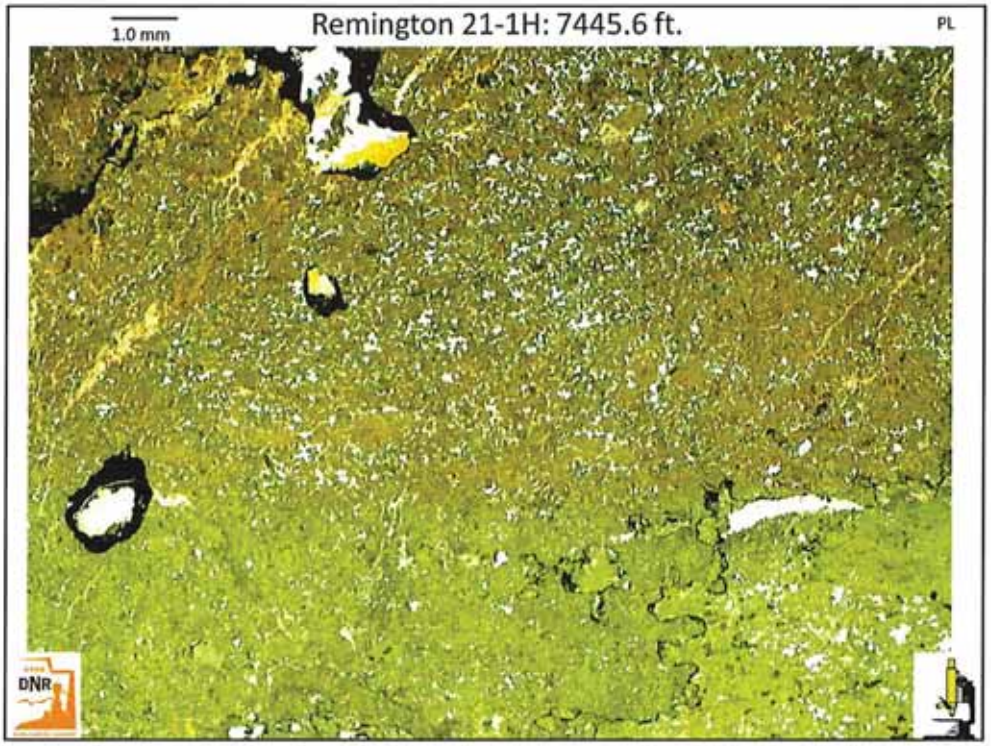

Fig. 3. This low-magnification view shows more details of the interesting "clotted" to vaguely laminated fabric of probable microbial origin shown under plane light (PL). Note the white-filled "fenestral" or "birdseye" structures within this dolomitic matrix. All of the fillings are composed of anhydrite cements. There are also oversized pores or vugs lined with black bitumen and internal anhydrite fillings. Scattered stylolites are also visible. The pink coloring covering part of this field of view is due to Alizarin Red-S staining for mineralogy.

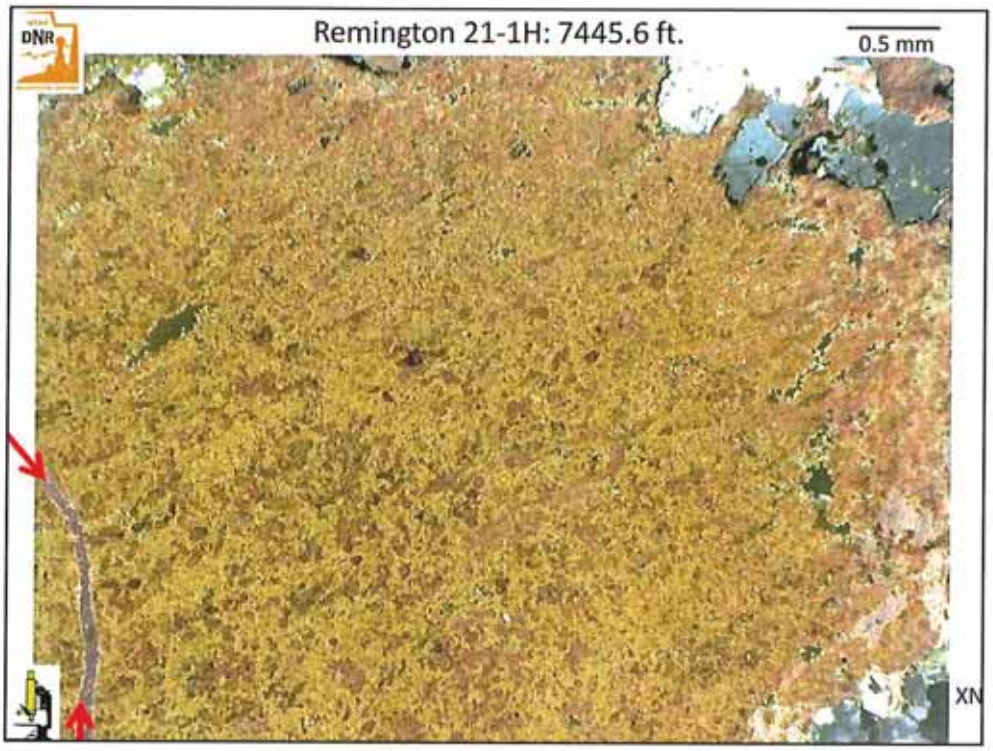

Fig. 4. This cross-polarized (XN) image from an area of the slide stained with Alizarin Red-S illustrates remnants of calcite (in deep red colors) surrounded by unstained (brown) early replacement dolomite. Note the small patches of anhydrite (in the white and gray colors of this thick section). Between the red arrows is a filled with ferroan calcite (stained purple).

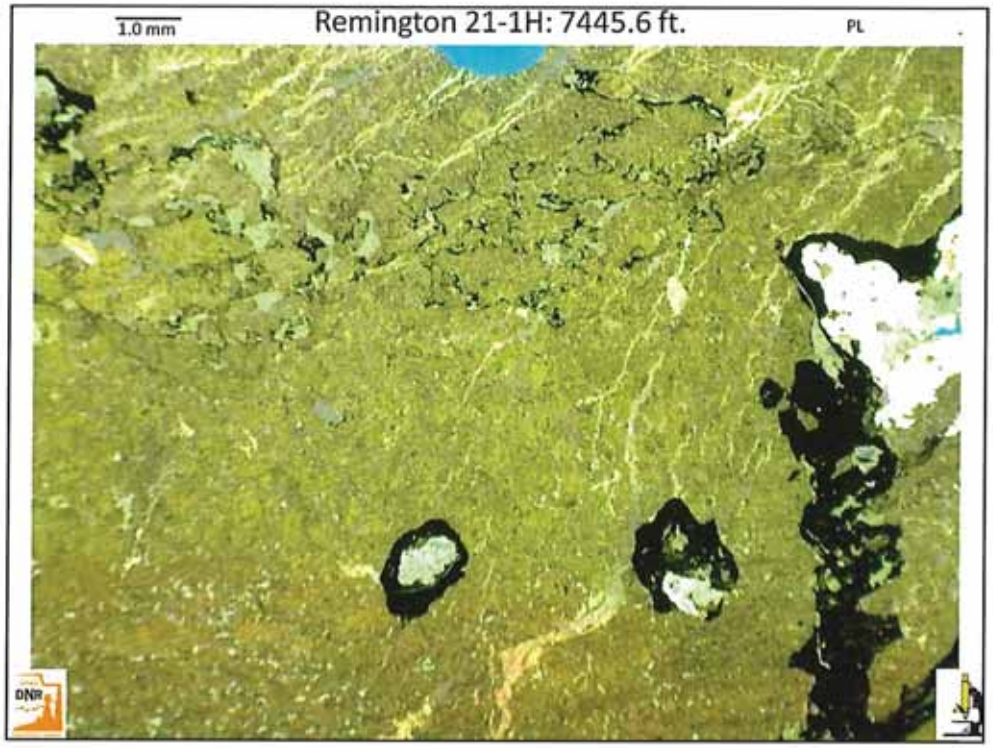

Fig. 5. This representative plane light (PL) image shows the "clotted" fabric of this slightly limy dolomite. Note the abundant closely spaced, high-angle fractures that dominated the upper third of this file of view. All are filled with calcite and some anhydrite. Cross cutting the fractures are abundant stylolites lined with black insoluble residues. The pink coloring across the bottom of this field of view is due to Alizarin Red-S staining for mineralogy.

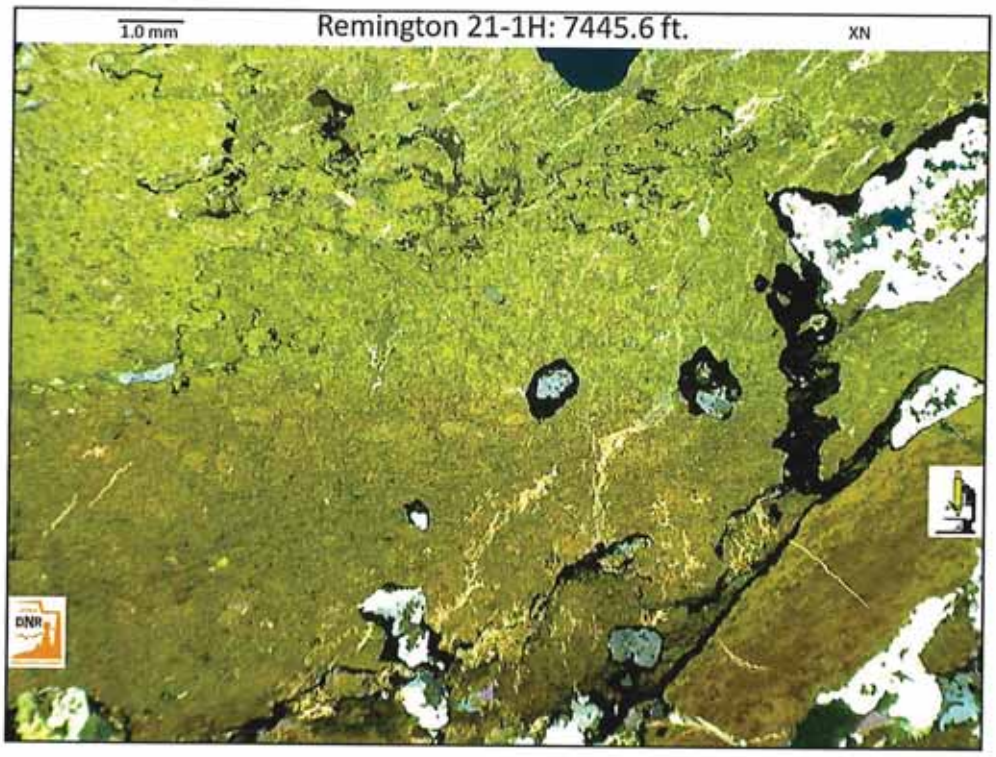

Fig. 6. This cross-polarized (XN) light view shows a portion of the same area imaged in Fig. 5, but at lower magnification. The pink coloring in the lower half of this field of view is due to Alizarin Red-S staining for mineralogy. Note the abundance of stylolites (lined with black insoluble residues) that crosscut the "clotted" fabric of probable microbial origin. Tensional fractures filled with calcite are also visible.

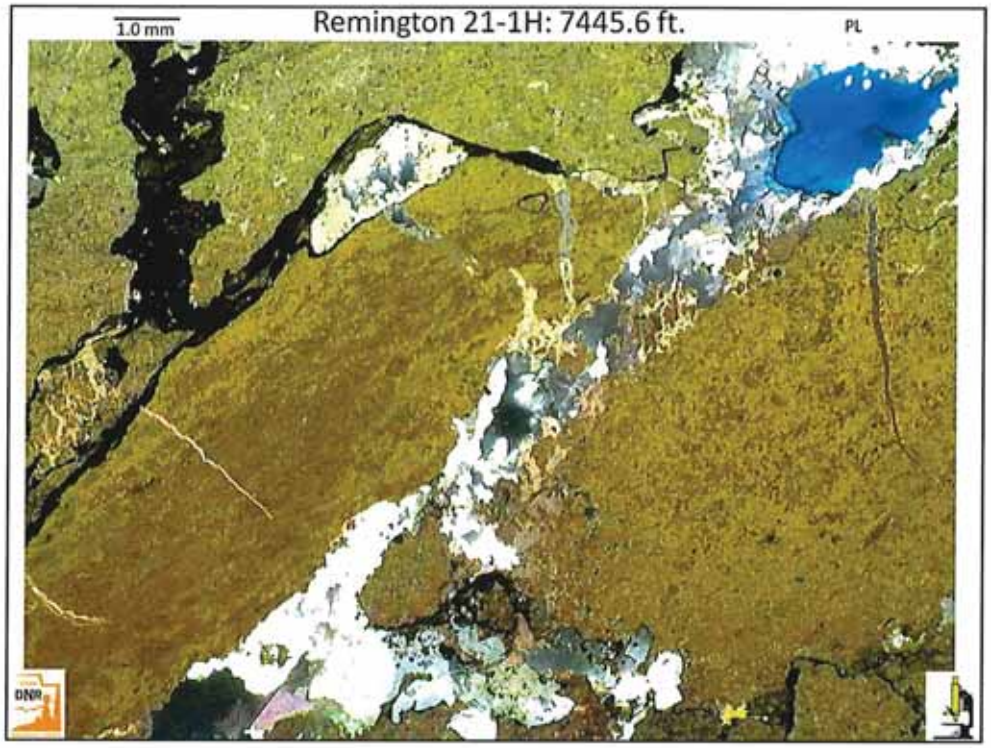

Fig. 7. A plane light (PL) close up of a detached or brecciated microbialite composed of a "clotted" dolomite matrix as well as some calcite (in deep red) remnants as identified by the artificial Alizarin Red-S staining of this portion of the thin section. Some of the megascopic pore spaces between these "clasts" are partially filled with anhydrite (mostly white and gray in this image). Small tension gash fractures are filled with calcite and ferroan calcite (stained purple). The black areas consist of insoluble residues along stylolites.

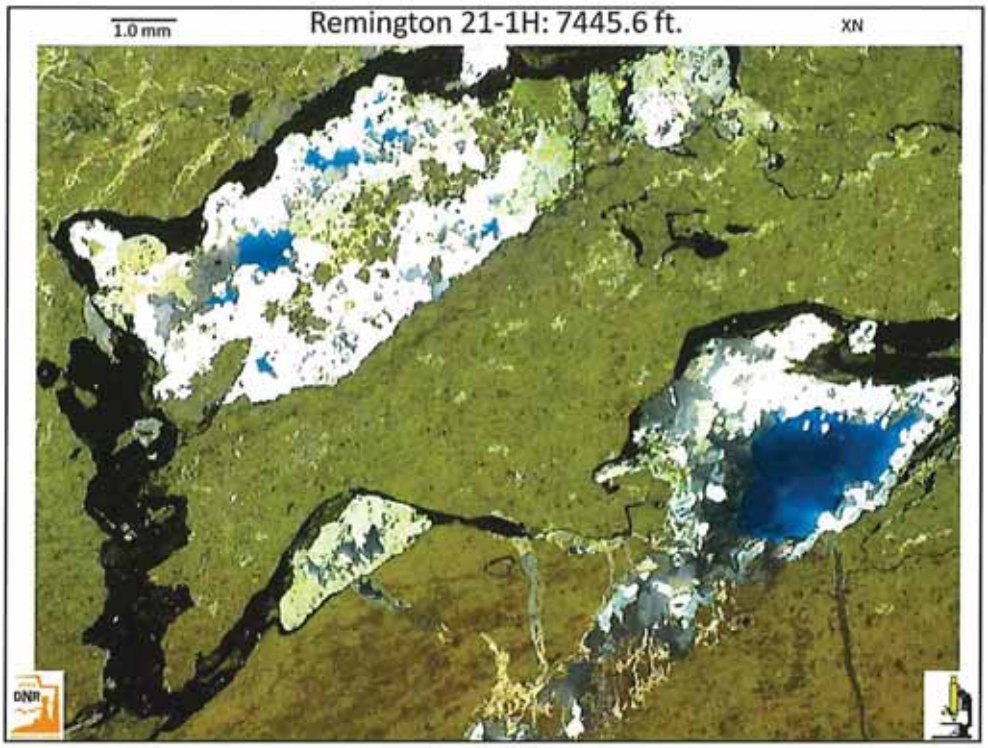

Fig. 8. Another representative close-up image (within an unstained portion of the thin section) shows vugs of various cross-sectional shapes that are partially filled with white, yellow and gray anhydrite. The blue and black areas are the open or unfilled portions of the vugs. This cross-polarized (XN) view also shows the fractured microbal(?) dolomite matrix as well as the thick black insoluble residues along stylolites.

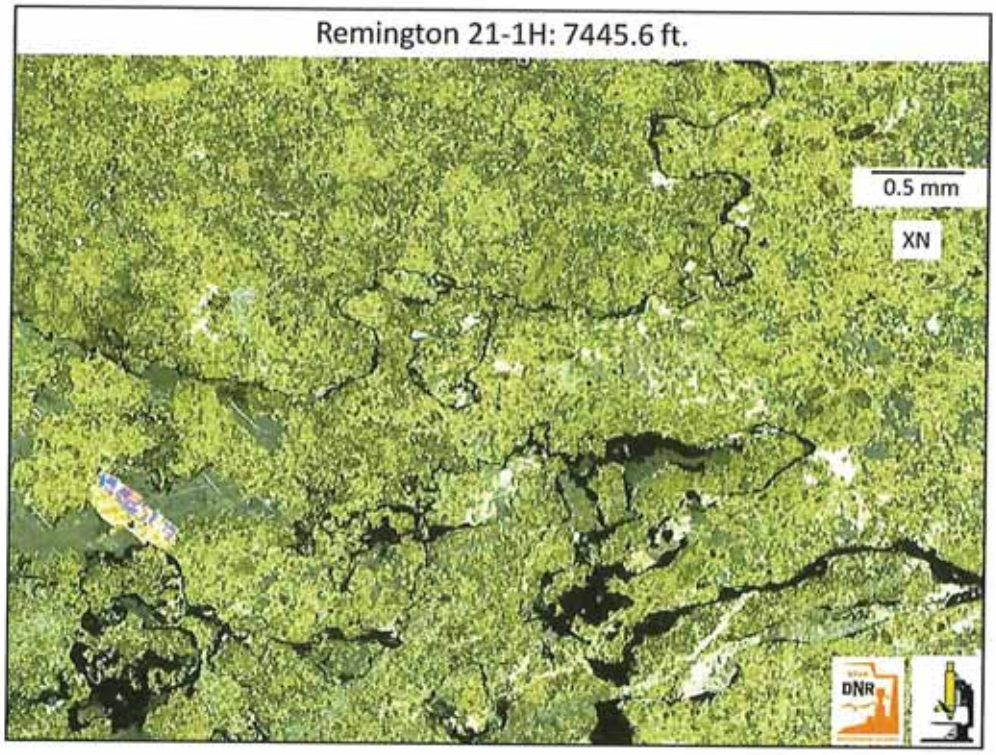

Fig. 9. This cross-polarized (XN) representative view shows some of the features of the "clotted" microstructures in this probable microbial dolomite. Some of the white and gray areas are fractures and paleopores filled with calcite and anhydrite. Stylolites lined with back insoluble residues snake through this dolomite in all directions.

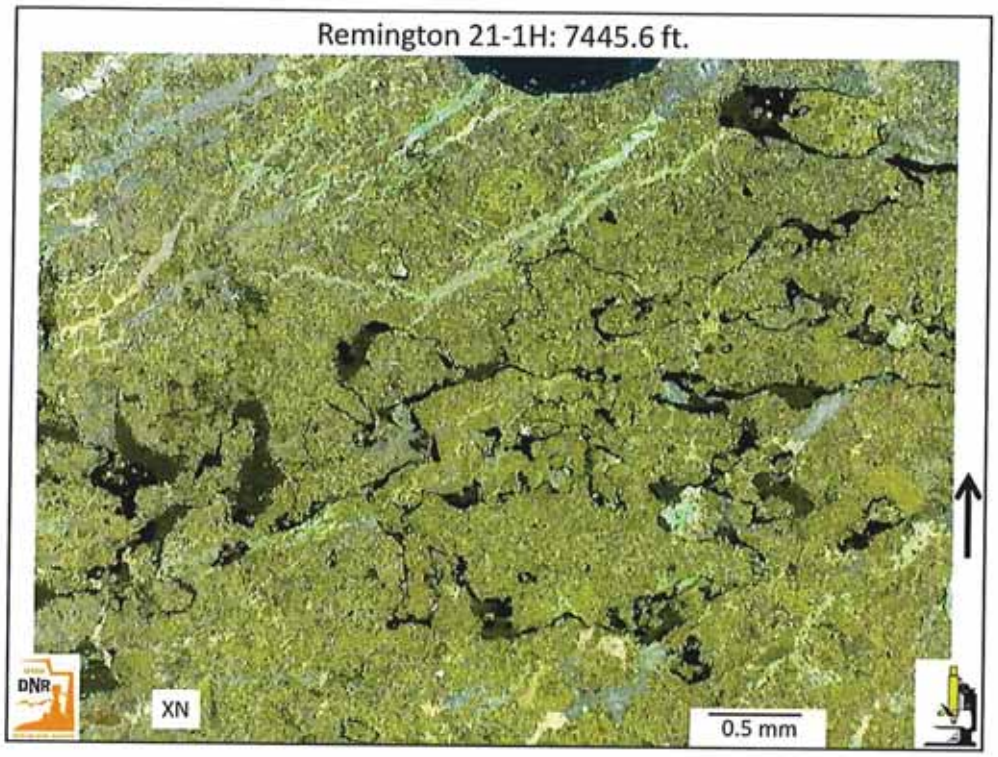

Fig. 10. An additional cross-polarized (XN) image of intricate pressure-solution seams and stylolites that are outlined by black insoluble residues. Between the stylolite traces are remnants or the "clotted" dolomites with probable microbial construction. Note the abundant fractures filled with calcite and some anhydrite

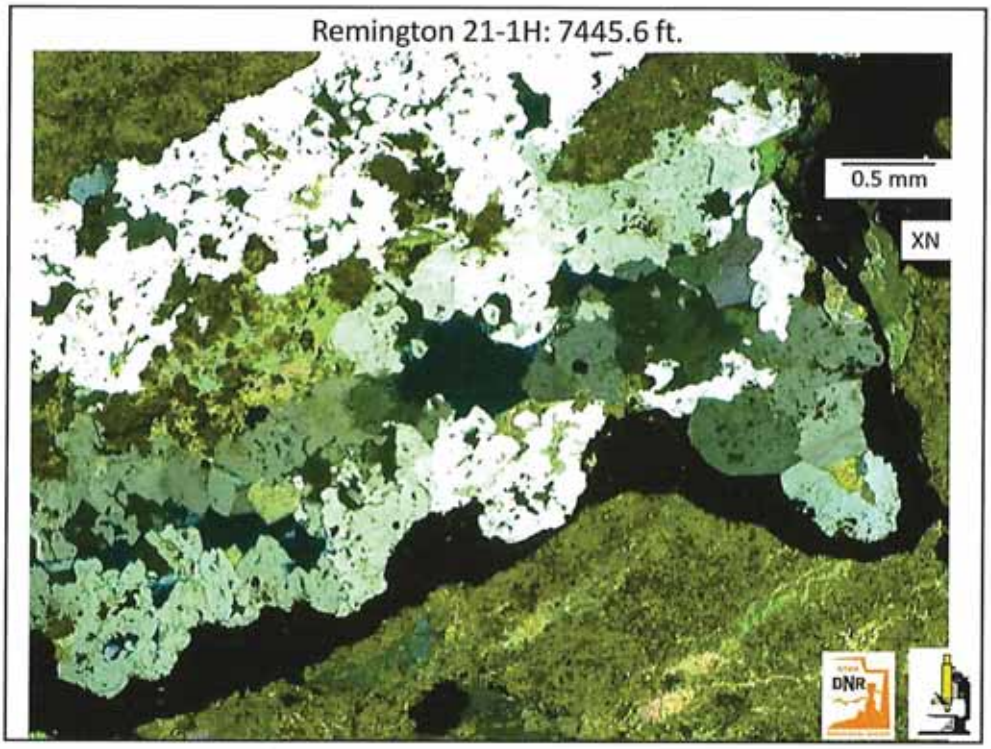

Fig. 11. A highly magnified view shows abundant anhydrite replacement (the white through dark gray areas in this thick thin section) of a "structured" dolomite matrix. Note the thick black concentration of insoluble residues along a pressure-solution seam.

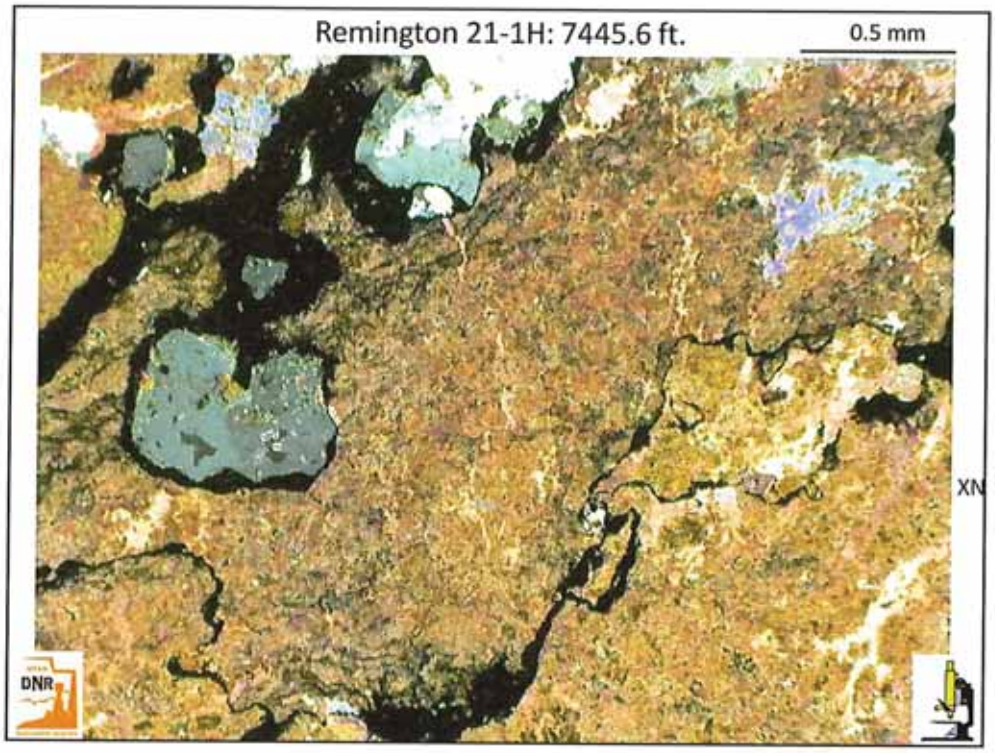

Fig. 12. Another high-magnification image under cross-polarized (XN) of portion of the sample stained with Alizarin Red-S solution. The dark red patches are calcite (limy) remnants within an otherwise dolomitized matrix. The other colored areas (gray, white and pastels) are replacements and fractures filled dominated by anhydrite. Note the black insoluble residues along the jagged traces of stylolites.

UPRC REMINGTON #21-1H
THIN SECTION REPORT: 7,446.7 ft.

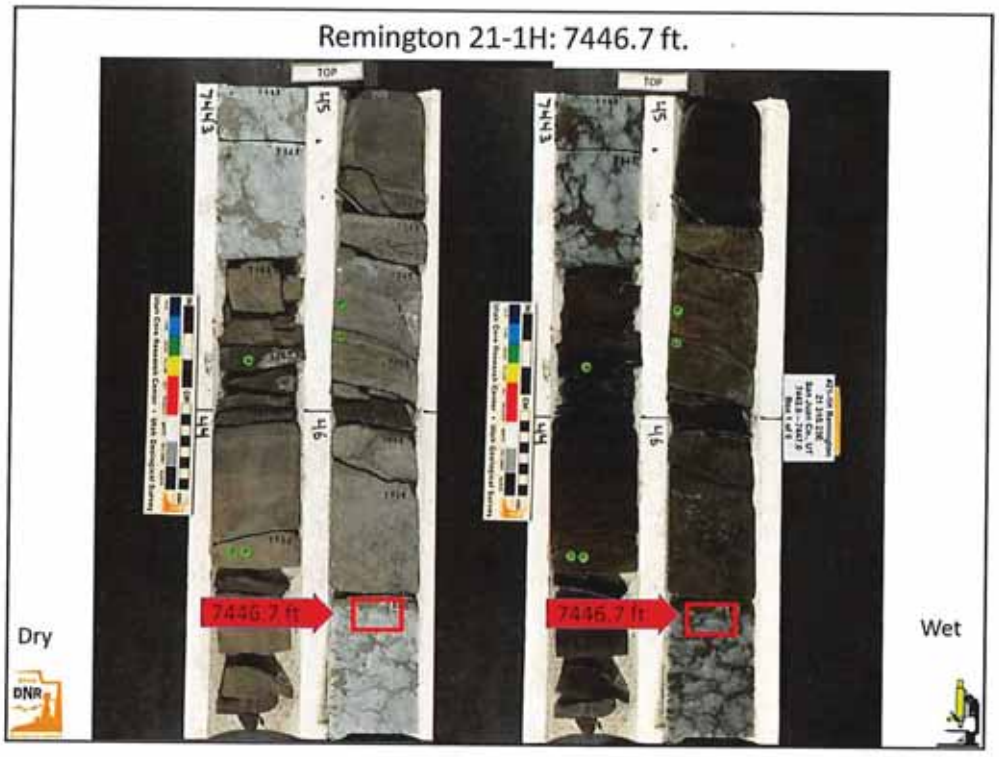

Fig. 1. A pair of core photos shows the same depth interval, with a dry view on the left and a wet view on the right. The location of the 7446.7 ft. sample is indicated by the red arrow adjacent to each core photo. Note the nodular mosaic pattern of anhydrite in a dolomite matrix. This mosaic resembles "chicken wire" textures in hypersaline sabka settings.

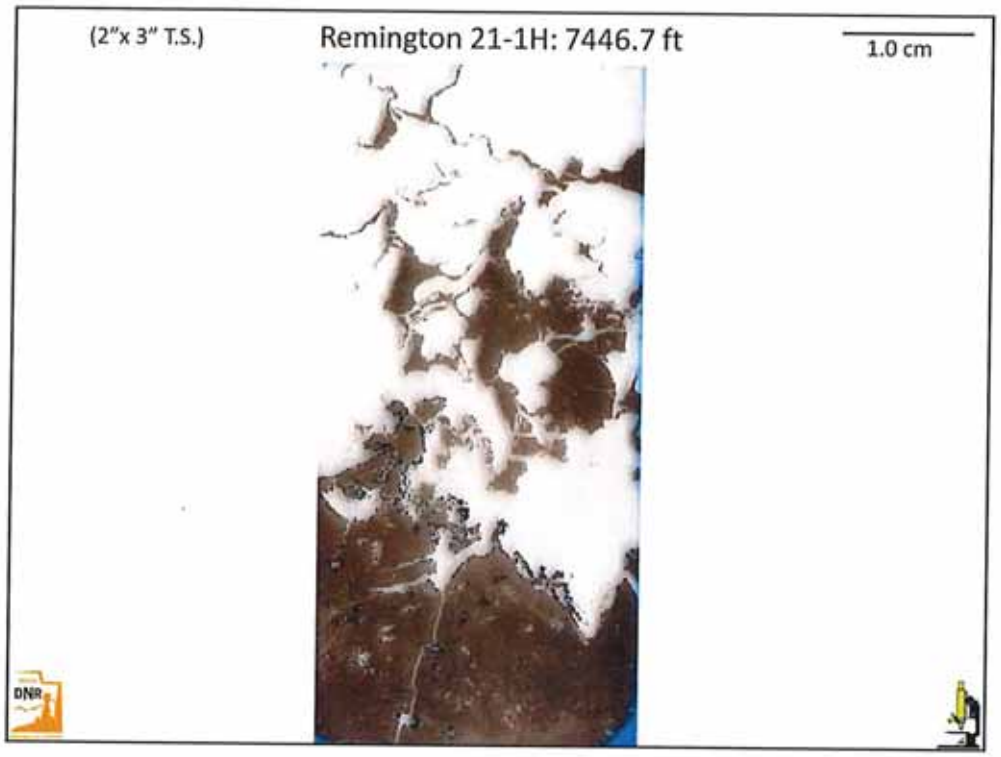

Fig. 2. Low magnification overview of the entire 2" x 3" thin section. Note the dark brown muddy dolomite matrix that has been disrupted and displaced by nodular white anhydrite.

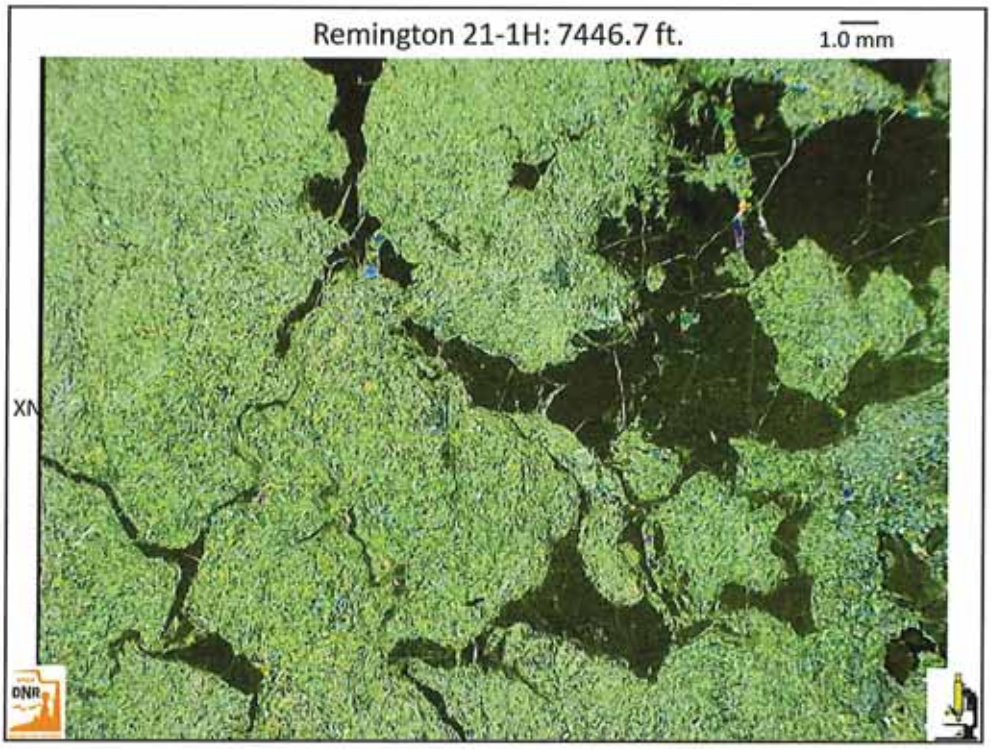

Fig. 3. Low magnification (under cross-polarized [XN] lighting) shows the "felted" texture of the anhydrite nodules that have displaced the massive brown dolomite matrix. Note the numerous cracks between nodular patches that have filled with coarser crystals of anhydrite.

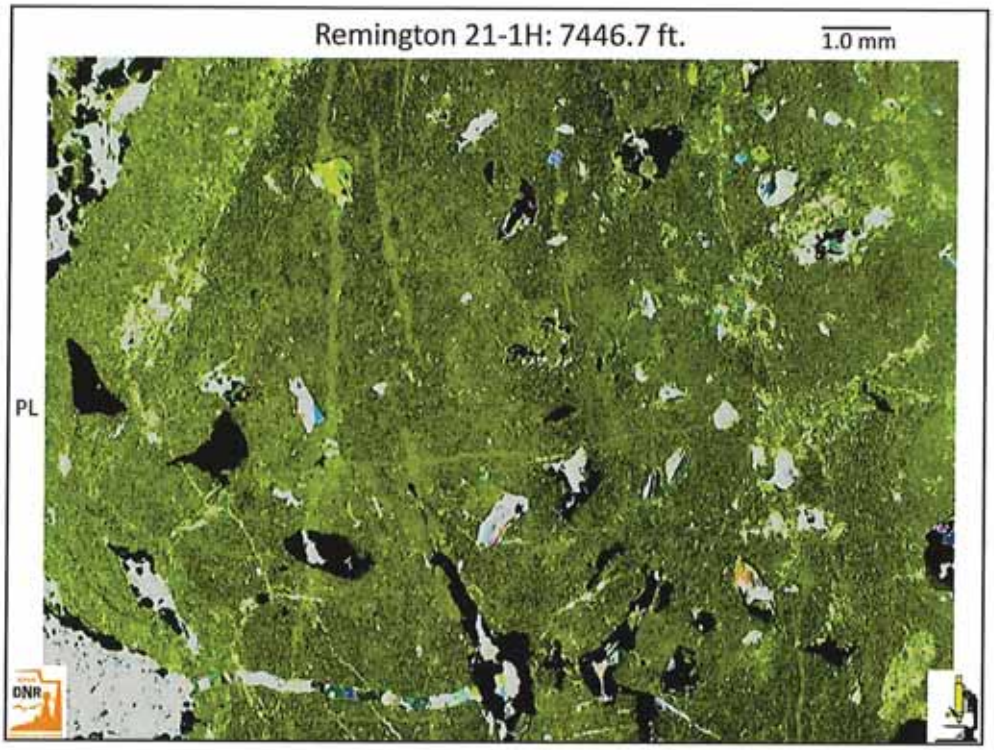

Fig. 5. This close-up view of nodular anhydrite surrounded by thin dark dolomite partings is shown here under cross-polarized (XN) light. Note the pastel colors of the birefringent "felted" anhydrite subcrystals.

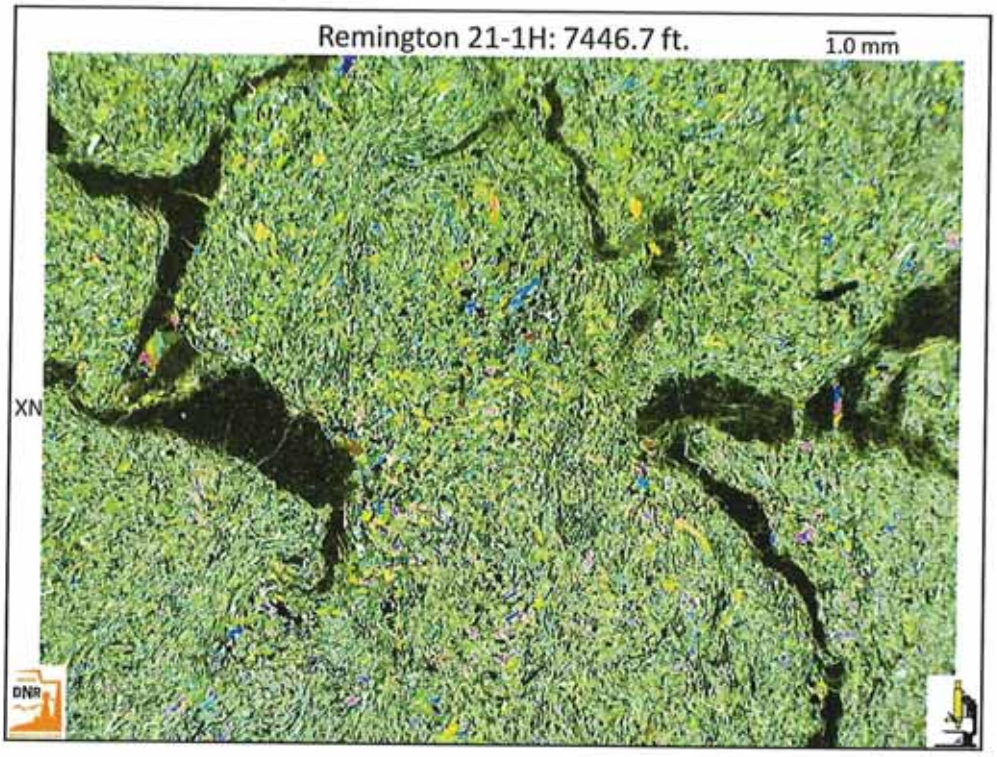

Fig. 4. Plane light (PL) image of highly fractured dolomite mudstone with abundant anhydrite-filled vugs and replacement blebs. Note the black patches of bitumen and opaque sulfide mineral replacements.

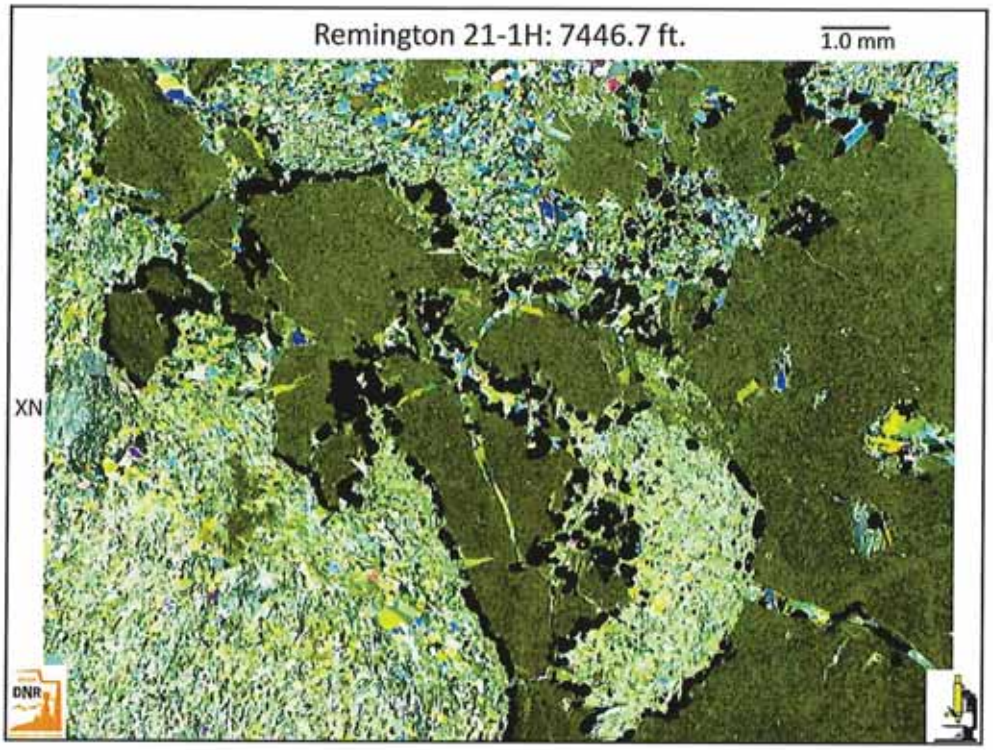

Fig. 6. Another representative cross-polarized (XN) image of nodular anhydrite with massive dolomitic mud between the nodules also shows black (opaque) crystals concentrated at many dolomite/anhydrite contacts and within fractures.. These crystals are probably Fe-sulfides.

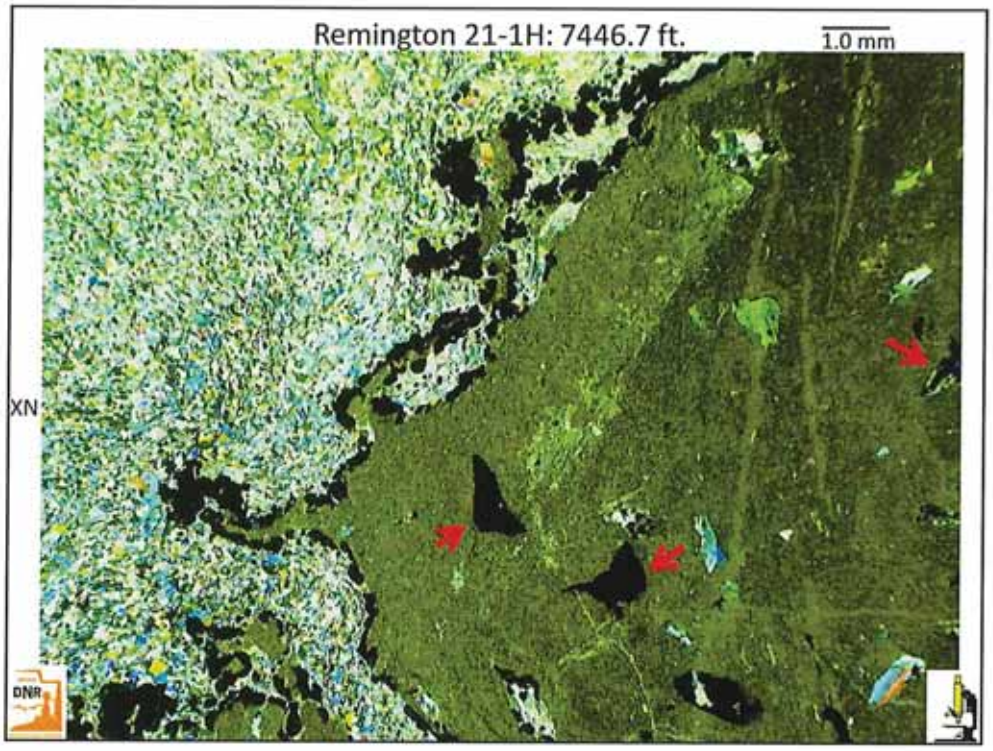

Fig. 7. Angular opaque sulfide crystals line most of the contacts between "felted" anhydrite within nodules and massive dolomitic mudstones. This cross-polarized (XN) light view also show black bitumen (see red arrows) within the dolomitic matrix.

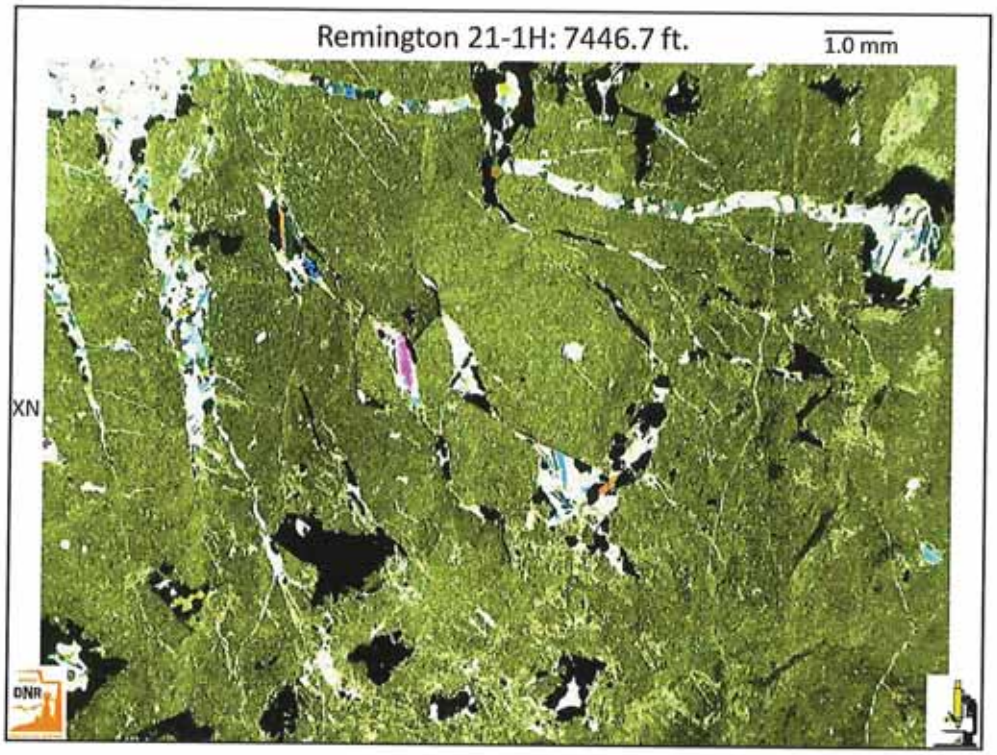

Fig. 8. This overview under cross-polarized (XN) lighting appears to show both (opaque) crystalline Fe-sulfides as well as black bitumen lining vugs and within anhydrite-healed fractures. Note in particular the highly fractured nature of this dolomitic mudstone.

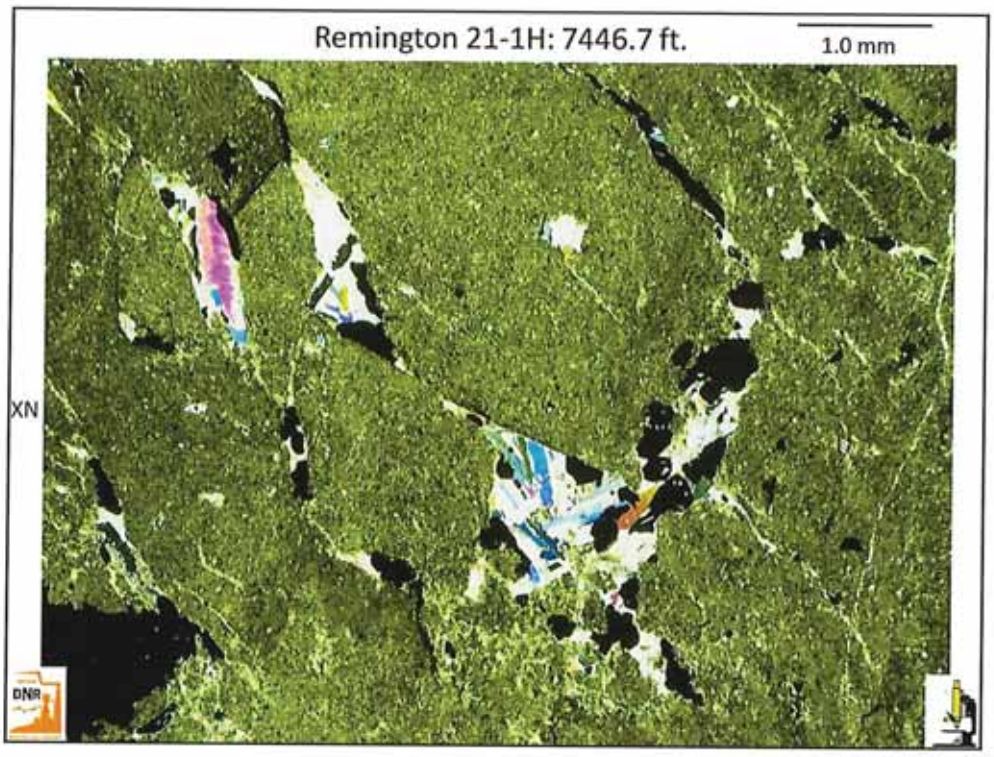

Fig. 9. A closer view of the fractured dolomitic mudstone displays coarse, birefringent anhydrite (in the pastel colors) filling fractures cutting the dolomitic mudstone matrix. Note also the crystalline outlines of opaque Fe-sulfides.

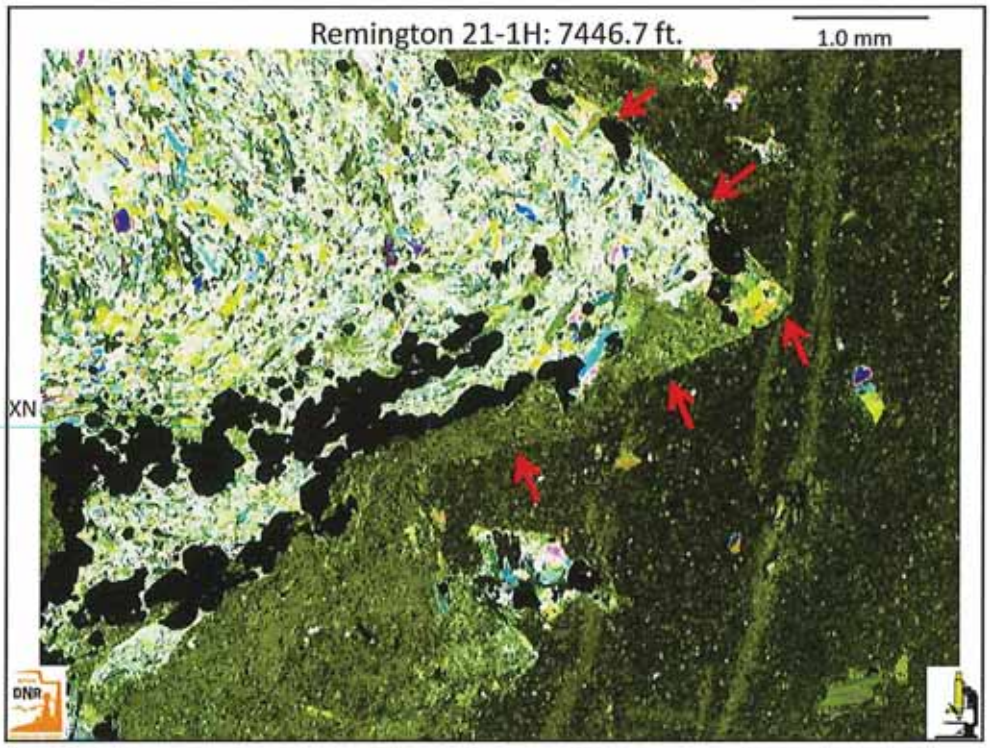

Fig. 10. The termination of a lozenge-shaped crystal filled with anhydrite and an edge of disrupted dolomitic sediment (see the lower red arrows) is illustrated here under cross-polarized (XN) light. Note also the concentrations of opaque Fe-sulfide crystals replacing parts of the anhydrite crystal.

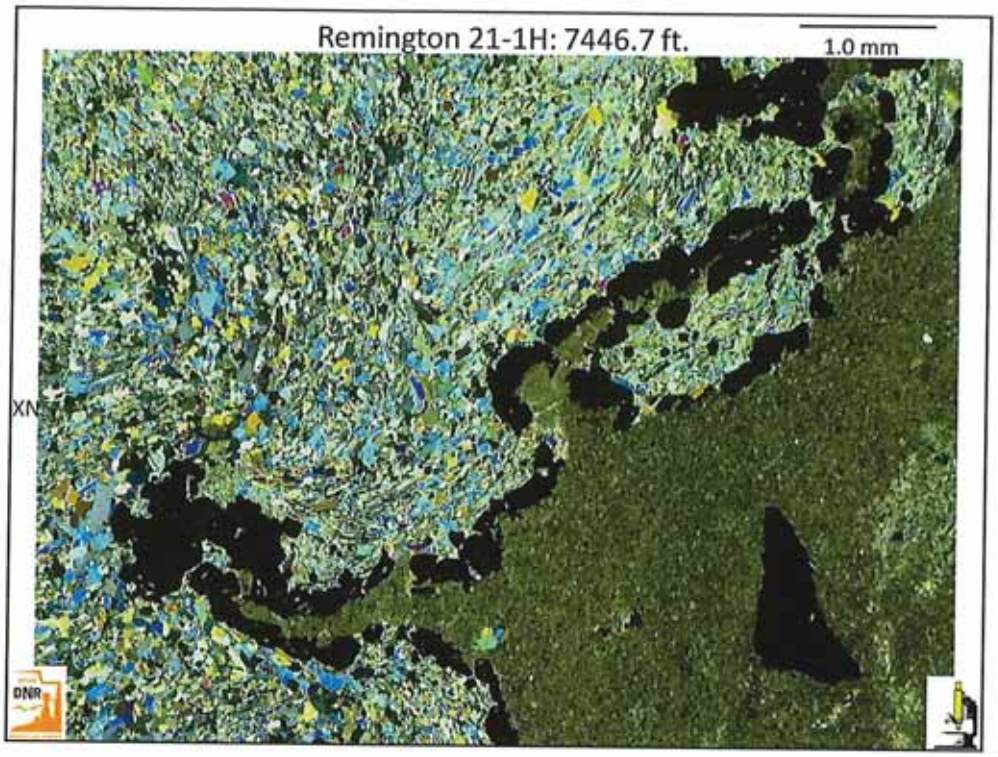

Fig. 11. Opaque (black) crystal trains of probable sulfide minerals line the contacts between a "felted" anhydrite nodule and a dolomitic mudstone matrix. This image is illustrated here under cross-polarized (XN) light.

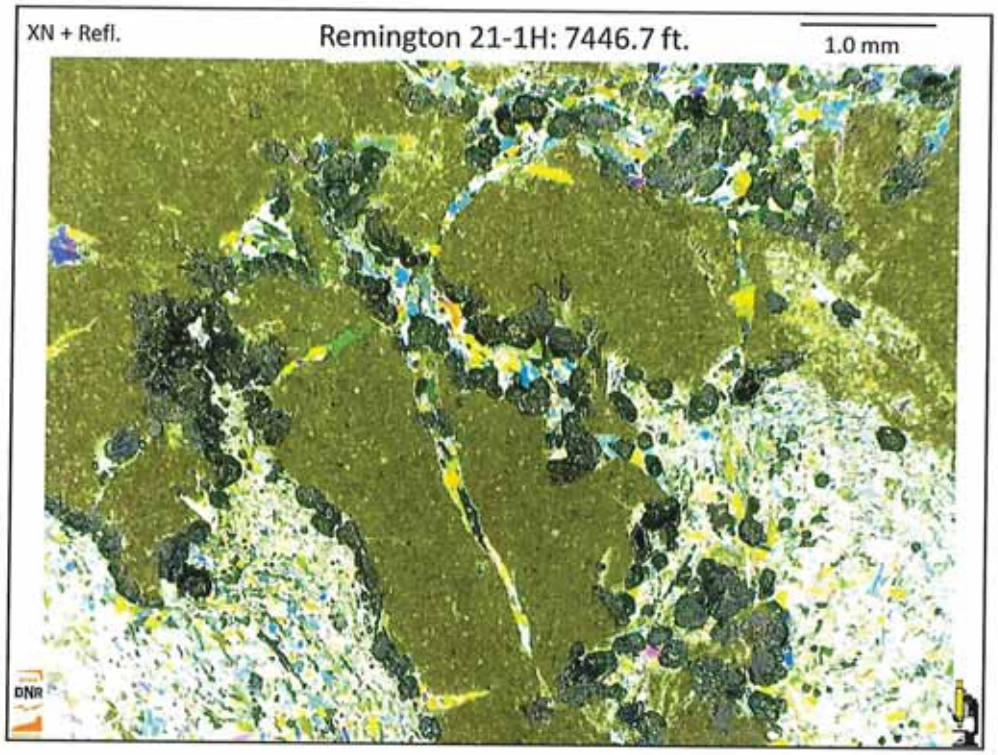

Fig. 12. Combining cross-polarized (XN) and reflected (Refl.) light, it is possible to see the "reflective" or brassy nature of the polygonal sulfide crystals lining the contacts between the dolomitic mudstone matrix and the nodular anhydrite.

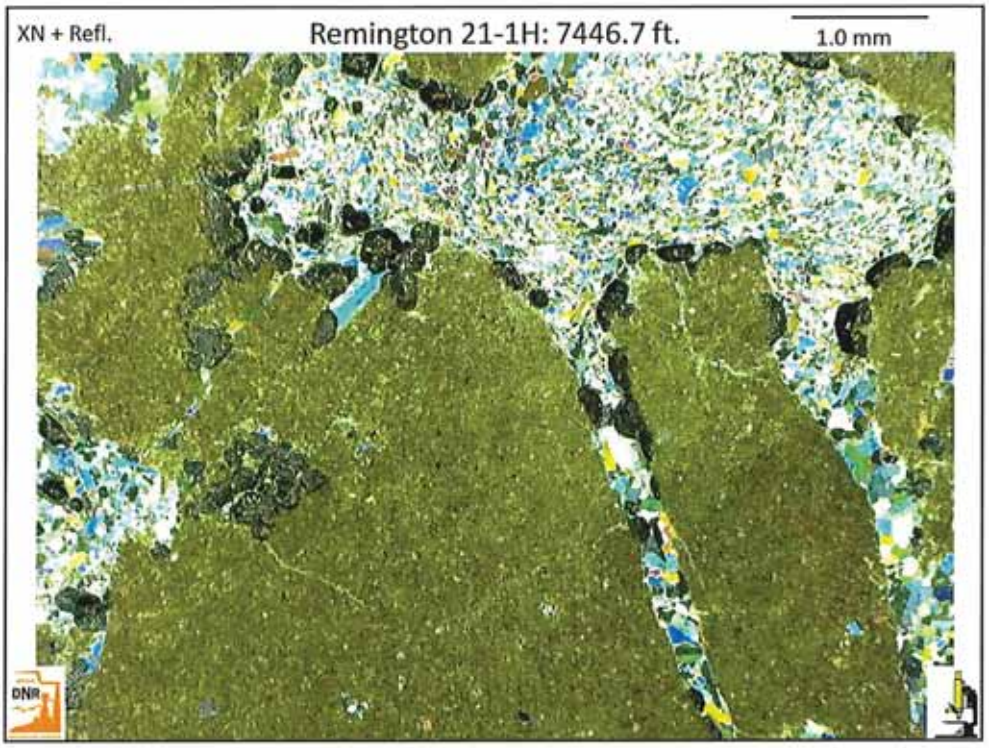

Fig. 13. Another representative view using combined cross-polarized (XN) and reflected (Refl.) light shows brassy or "reflective" crystals composed of probable iron sulfide minerals. These replacement metallic minerals seemingly line anhydrite-filled fractures as well as the contacts between anhydrite nodules and dolomite matrix.

UPRC REMINGTON #21-1H
THIN SECTION REPORT: 7,448.0 ft.

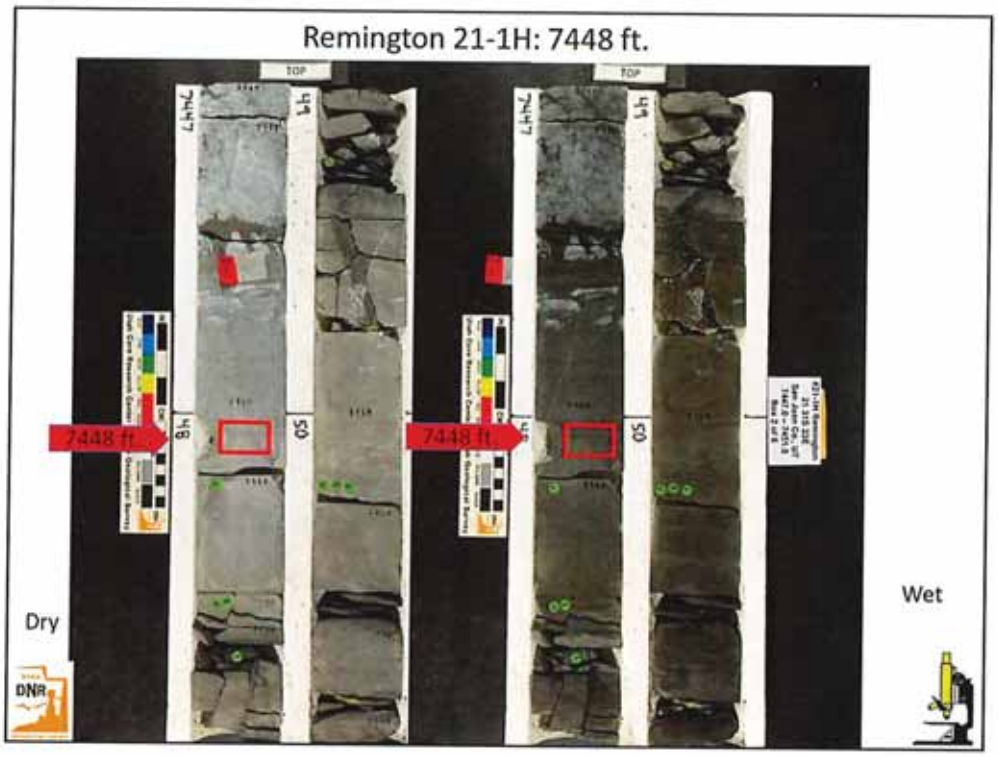

Fig. 1. A pair of core photos shows the same depth interval, with a dry view on the left and a wet view on the right. The location of the 7448 ft. (7448.0'?) sample is indicated by the red arrow adjacent to each core photo. Note the brown dolomite at the location of the 1"x2" thin section prepared from this interval. This anhydritic dolomite appears to be a laminated with some microbial influence on its deposition.

.

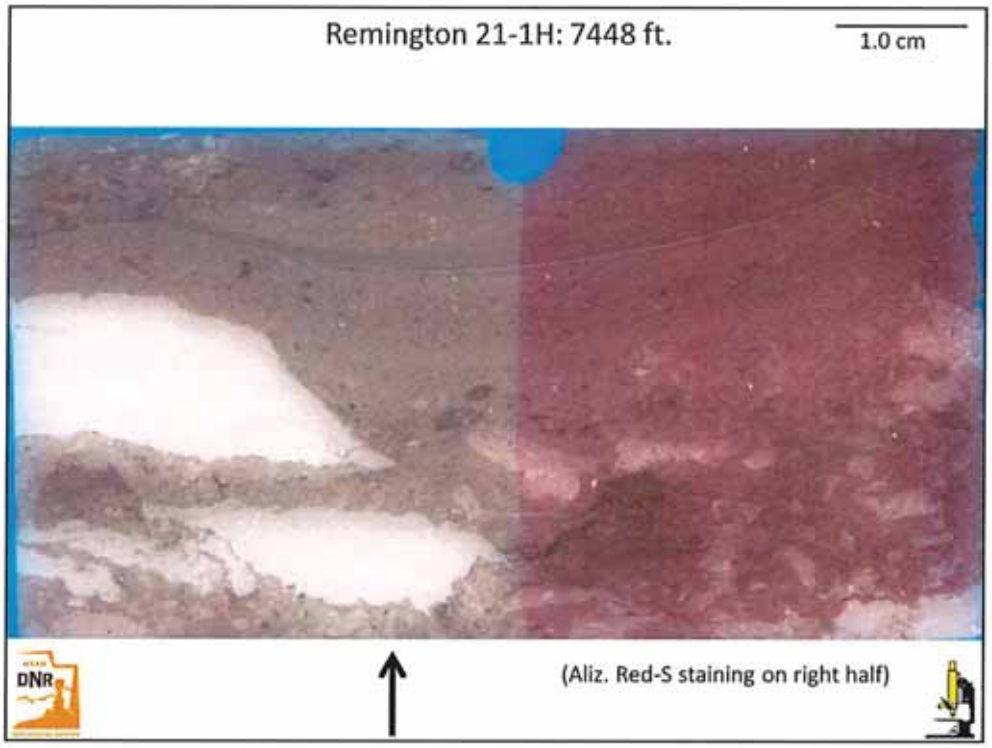

Fig. 2. Low magnification overview of the entire 1" x 2" thin section. The right half of the thin section has been stained with Alizarin Red-S stain. Note the laminate defined by compositional and grain size differences across this thin section. The white areas are anhydrite replacements. The blue notch in the upper center is a stratigraphic "UP" indicator.

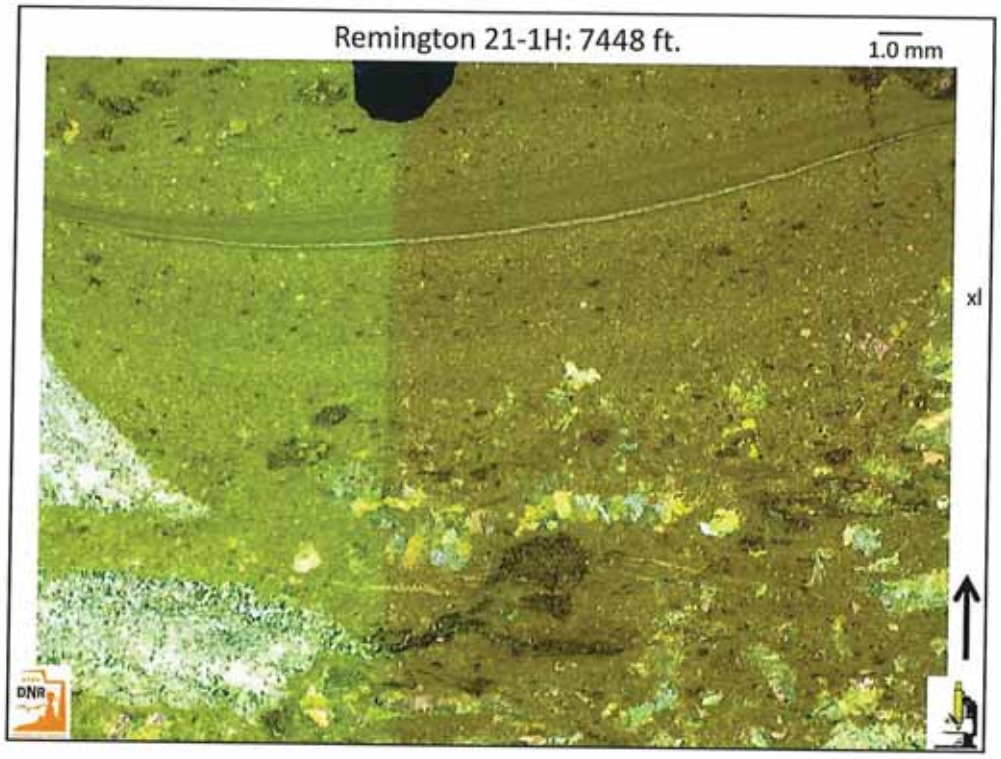

Fig. 3. A low-magnification, cross-polarized (XN) image of a well-laminated dolomite composed of alternating mud-rich and grain-rich laminae. These laminae may be part of a stromatolitic microbialite. The white, gray and multicolored patches are composed of replacement anhydrites.

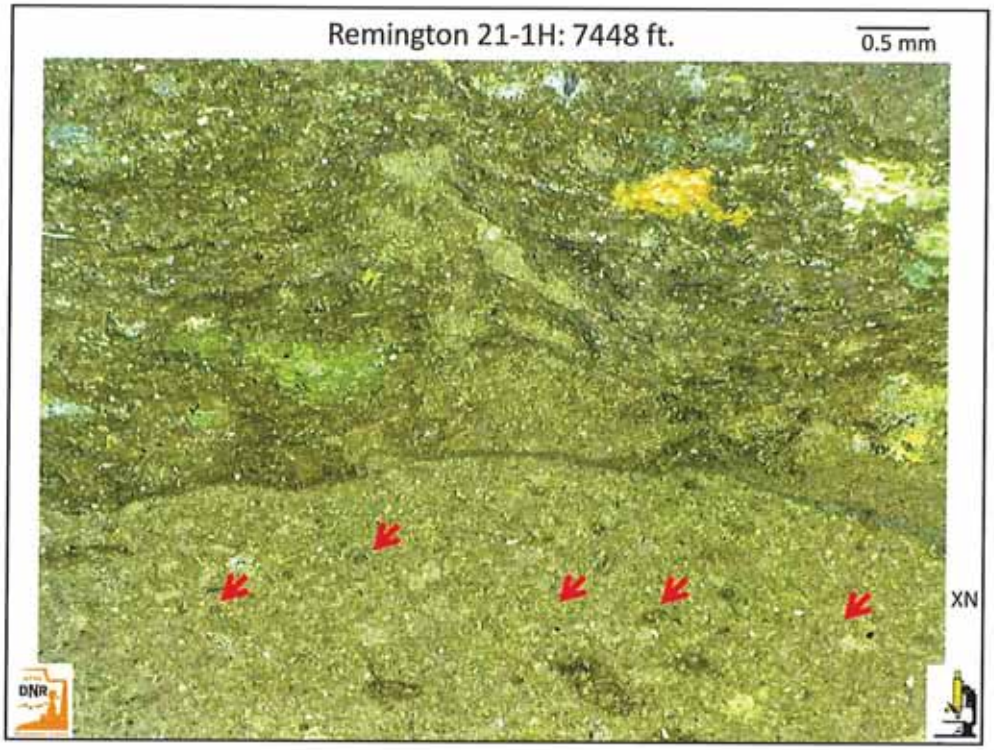

Fig. 4. A higher magnification cross-polarized (XN) view of a representative area of this sample shows a lower grain-supported layer overlain with a vaguely laminated interval composed of probable microbial microstructures. The pastel-colored patches are composed of replacement anhydrites. The grains in the lower half of this field of view are composed mostly of dolomitized coated grains (see red arrows) and peloids.

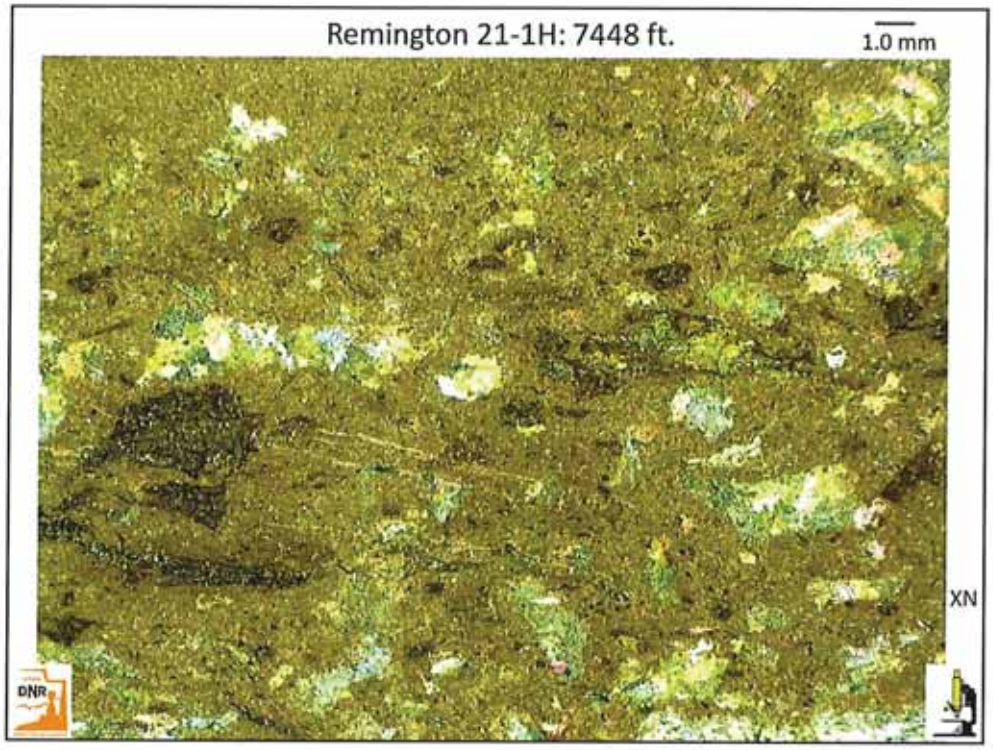

Fig. 5. Scattered anhydrite replacement of dolomitic grains and mud can be seen in the light pastel-colored areas under cross-polarized (XN) light. Remnants of original grains, including peloids and possible thin-shelled skeletal fragments can be seen.

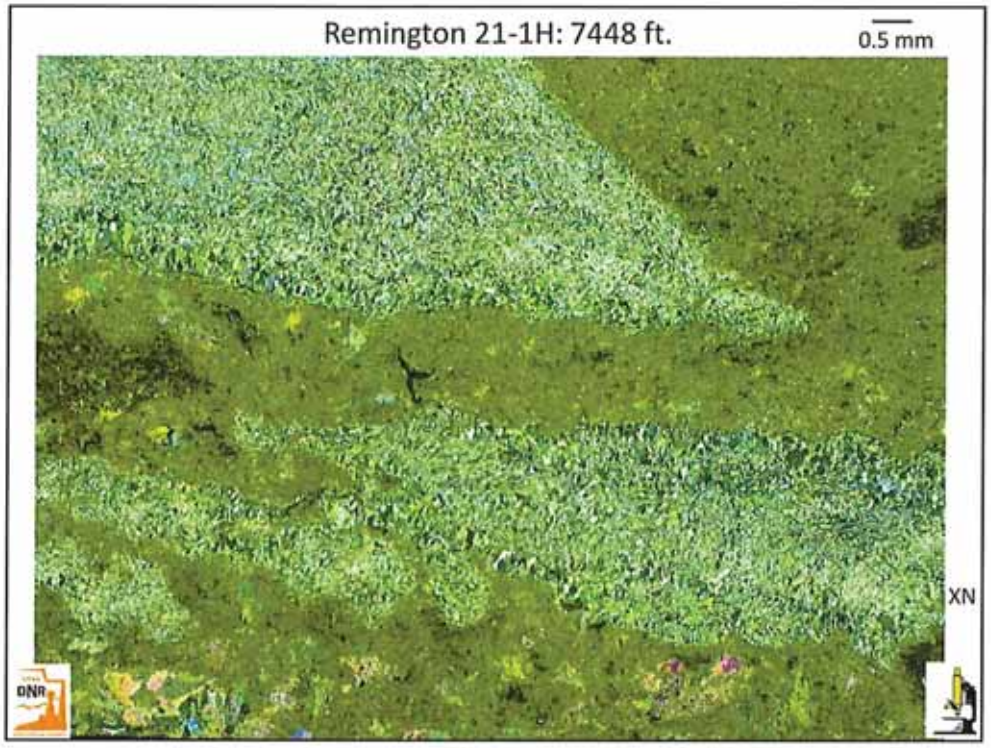

Fig. 6. Sharp-edged, ax-head shapes of anhydrite probably originated as gypsum crystals within a soft carbonate sediment "mush". These "ax head anhydrites" now display a "felted" fabric of subcrystals under cross-polarized (XN) lighting. The surrounding dolomitic sediment contains abundant pelleted mud.

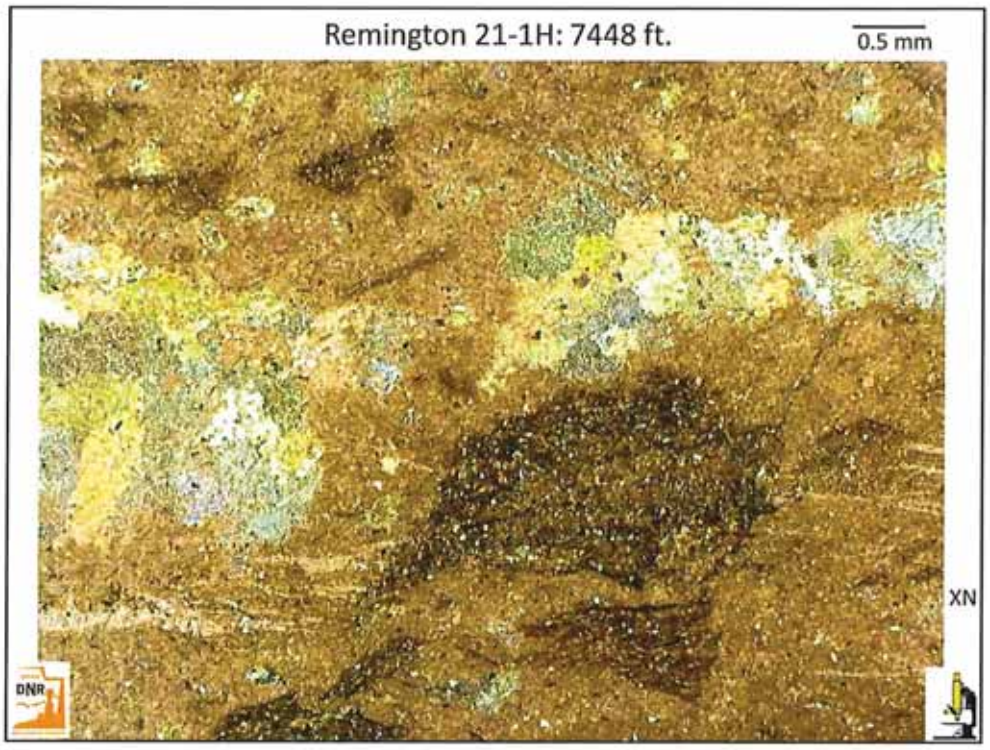

Fig. 7. The reddish cast of this cross-polarized (XN) is due to the artificial staining by Alizarin Red-S solution over this portion of the thin section. Remnants of precursor calcite are present within the peloidal dolomite in this field of view. Note the small patches of replacement anhydrite that display tabular habit across the central portion of this image. The dark-colored to black patches are probably small amounts of bitumen that impregnated microporous areas with grains and microbrial structures.

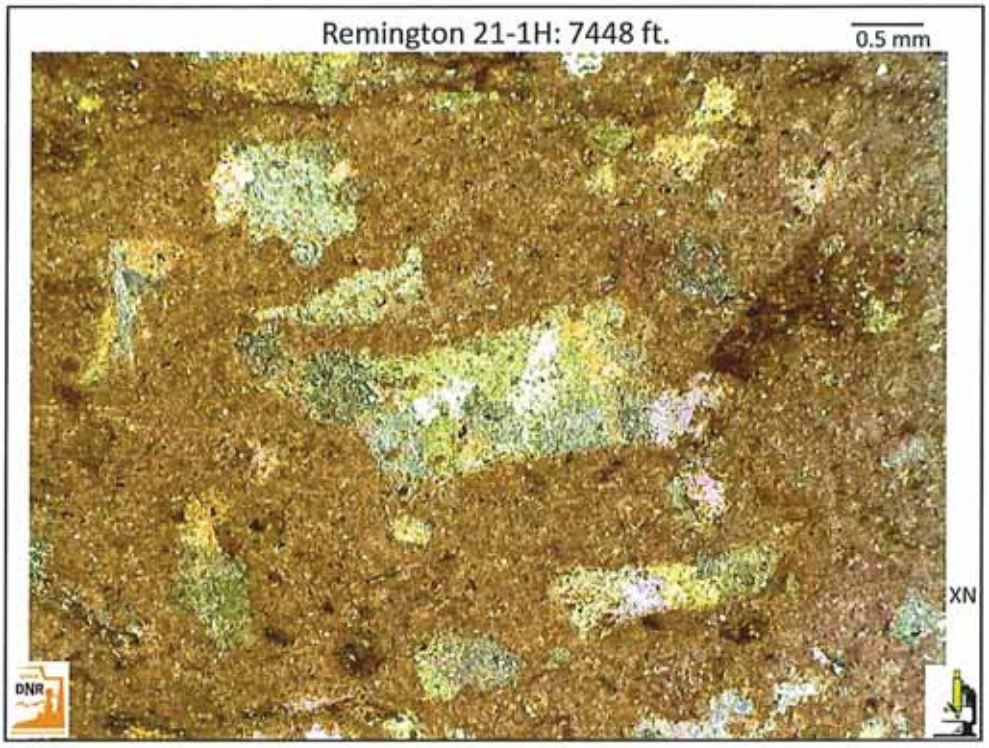

Fig. 8. Another representative view of a portion of the thin section stained with Alizarin Red-S stain. Note that the finely crystalline dolomite matrix is slightly calcareous as shown by the reddish background color, reflecting some remnant calcite taking the stain. The pastel-colored subcrystals are composed of anhydrite that has replaced the dolomitic muds.

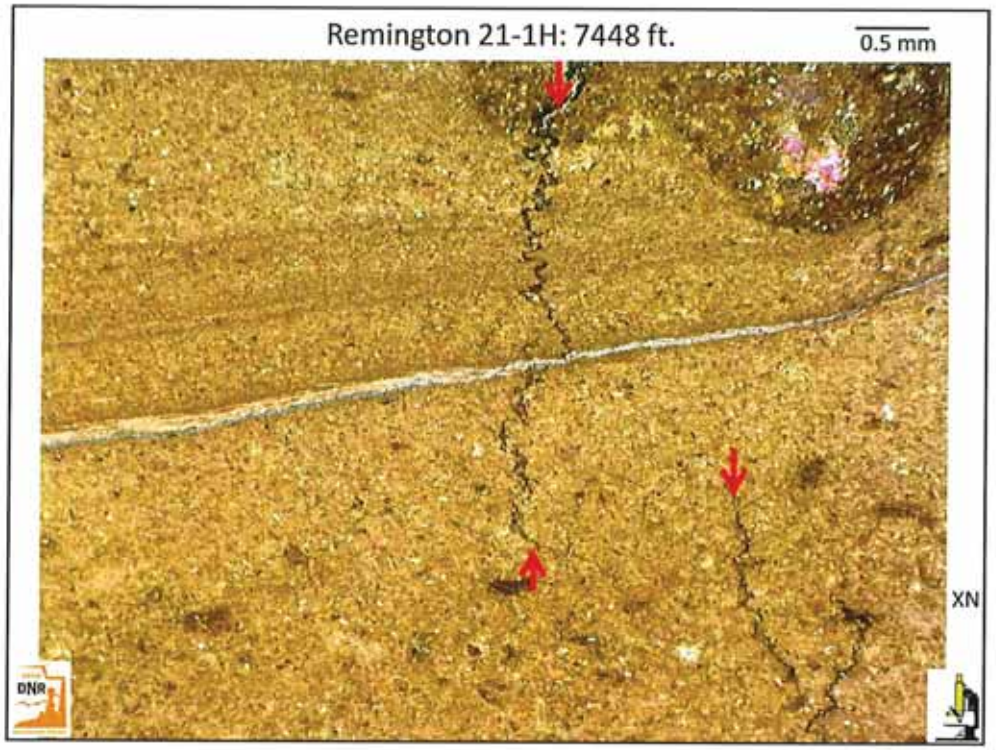

Fig. 9. Laminated dolomitic muds are shown here under cross-polarized (XN) light. These laminae appear to be stromatolitic and display disrupted areas (see the upper right corner) that are probably the result of either haloturation or bioturbation. Note also the low-amplitude vertical (bed-normal) stylolites (see red arrows) that are indicative of tectonic compression of this rock matrix.

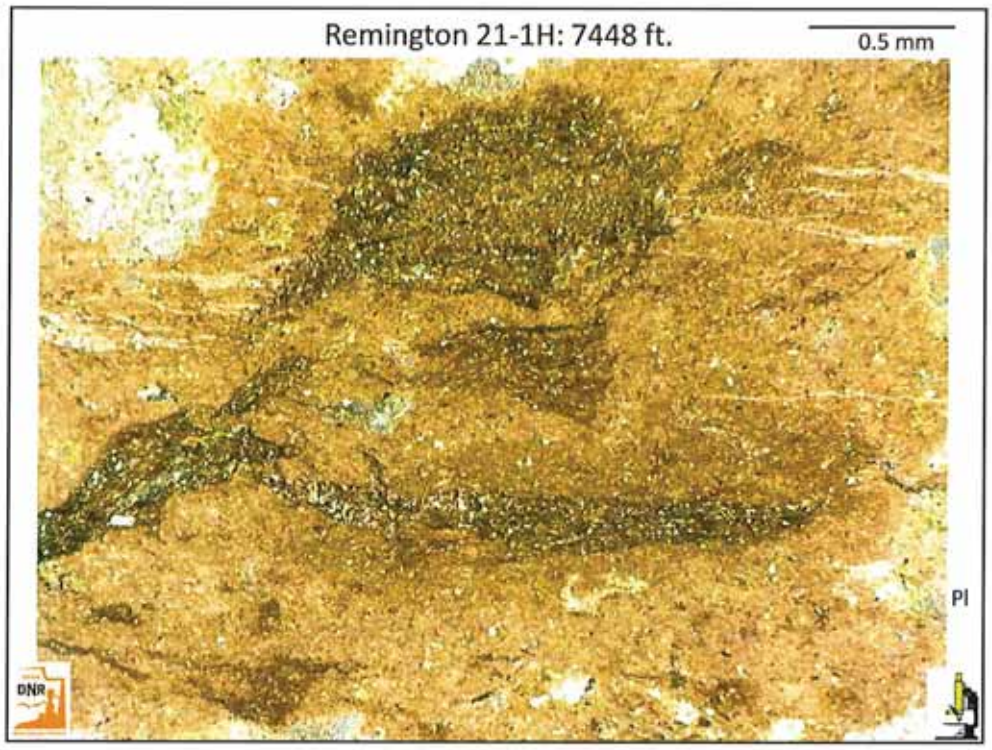

Fig. 10. Shown in the plane light (PL) view are several argillaceous patches that appear to contain more clay minerals and perhaps more silt grains than the surrounding muddy matrix. These disruptions may be the result of either haloturbation or bioturbation. The black material within these patches of disruption may be bitumen impregnation of former microporosity.

UPRC REMINGTON #21-1H
THIN SECTION REPORT: 7,450.0 ft.

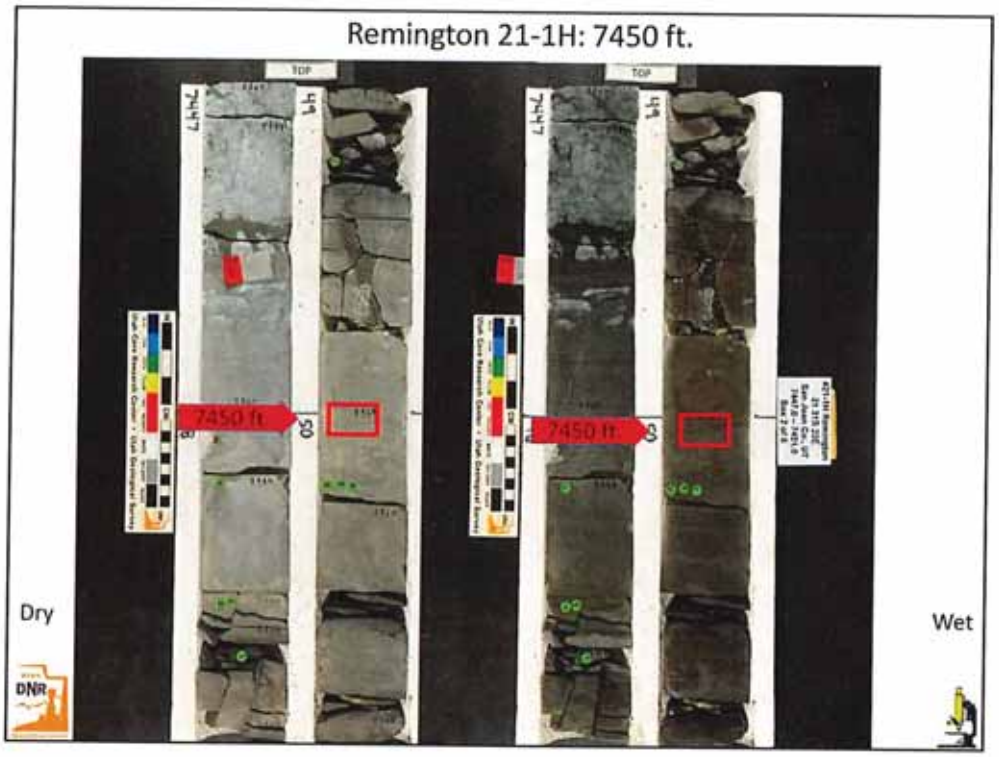

Fig. 1. A pair of core photos shows the same depth interval, with a dry view on the left and a wet view on the right. The location of the 7450 ft. (7450.0'?) sample is indicated by the red arrow adjacent to each core photo. Note the brownish dolomite at the location of the 1"x2" thin section prepared from this interval. This dolomitic interval appears to be massive to mottled.

.

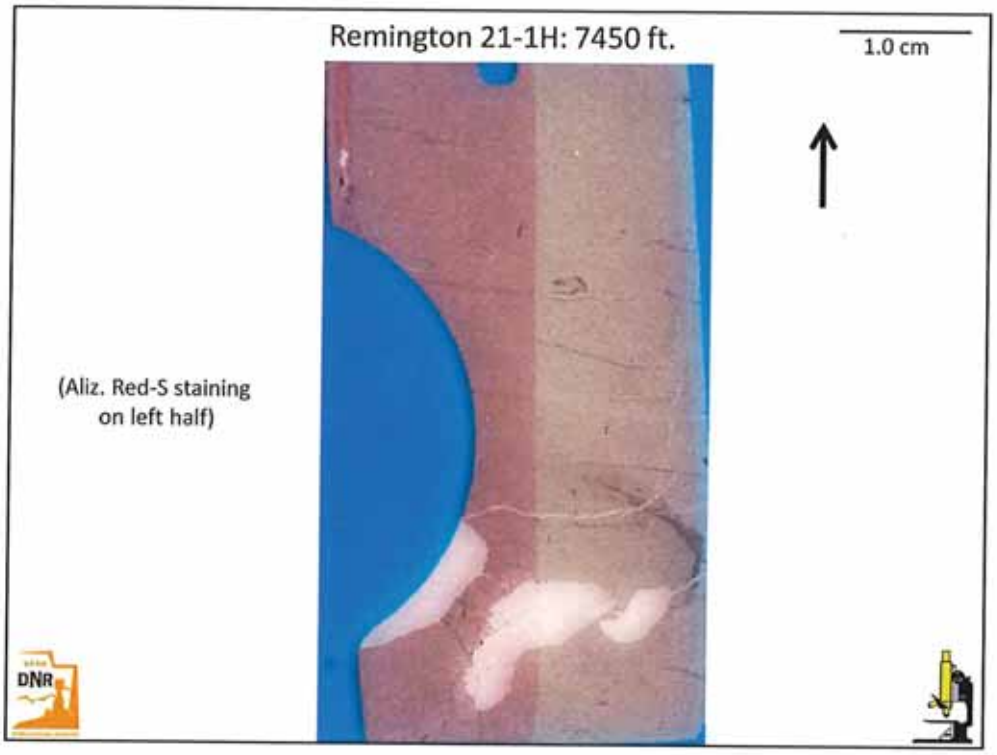

Fig. 2. Low magnification overview of the entire 1" x 2" thin section. The left half of the thin section has been stained with Alizarin Red-S stain. Note the generally massive matrix of the dolomite as well as some white patches of replacement anhydrite. The blue notch in the upper center is a stratigraphic "UP" indicator.

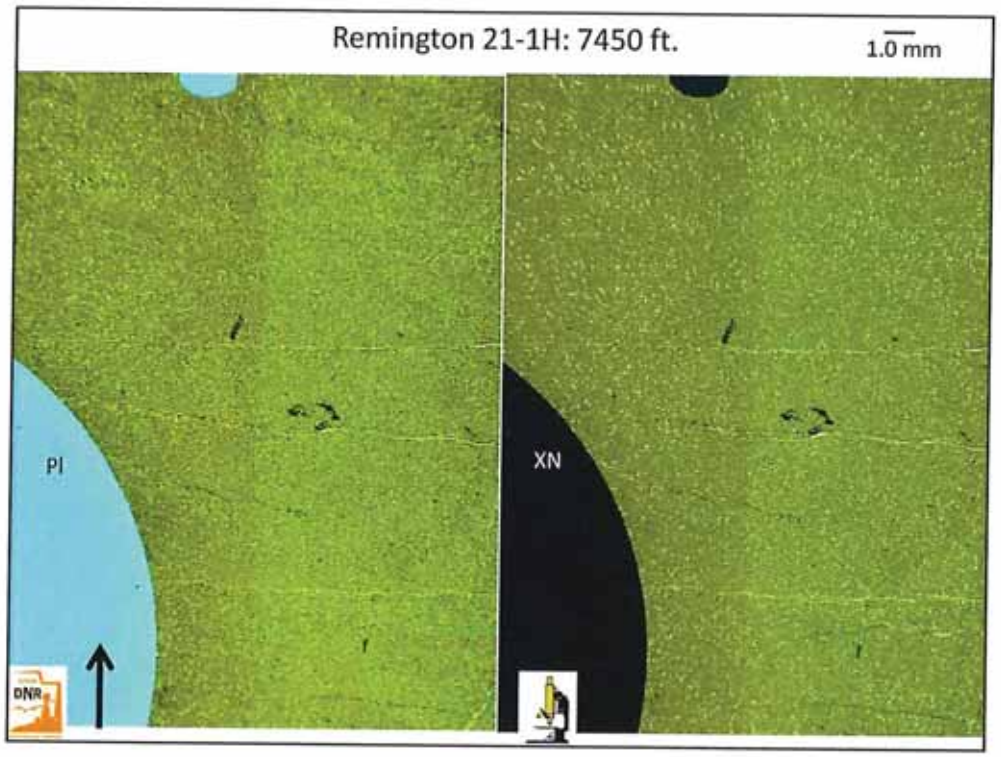

Fig. 3. A pair of low-magnification images shows the same field of view at the same magnification. A plane light (PL) view is on the left, and a cross-polarized (XN) view is on the right. The darkened area on the right of each view reflects artificial staining with Alizarin Red-S solution. Most of the white "specks" in each view are detrital quartz silt grains. Note the parallel horizontal microfractures that are healed with carbonate cements.

.

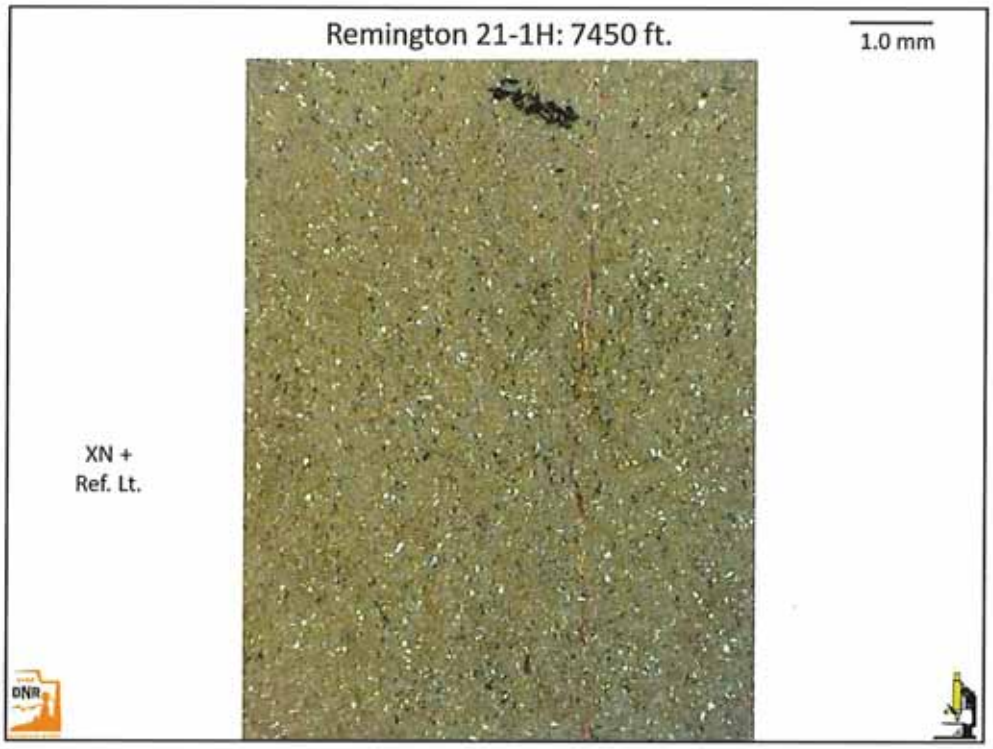

Fig. 4. This view, which is oriented "UP", shows detrital silt grains in white and gray as well as a patch of black bitumen (in the uppermost center). Note the red stained vertical fracture filling of calcite. In addition, artificial Alizarin red-S staining shows reddish patches of relict calcite within the dolomitized matrix. This slide is illuminated under a combination of cross-polarized (XN) and reflected lighting (Ref. Lt.).

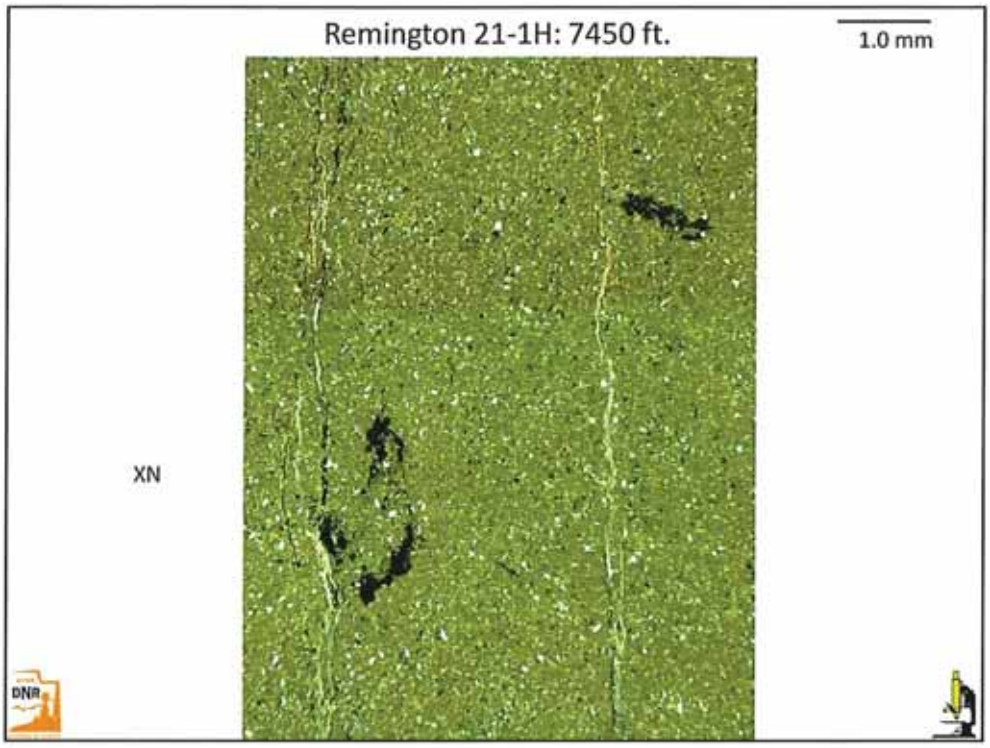

Fig. 5. Another "UP" oriented view field view shown under cross-polarized (XN) light displays a silty dolomite with patches of black bitumen. Note the parallel vertical fractures that are healed with calcite.

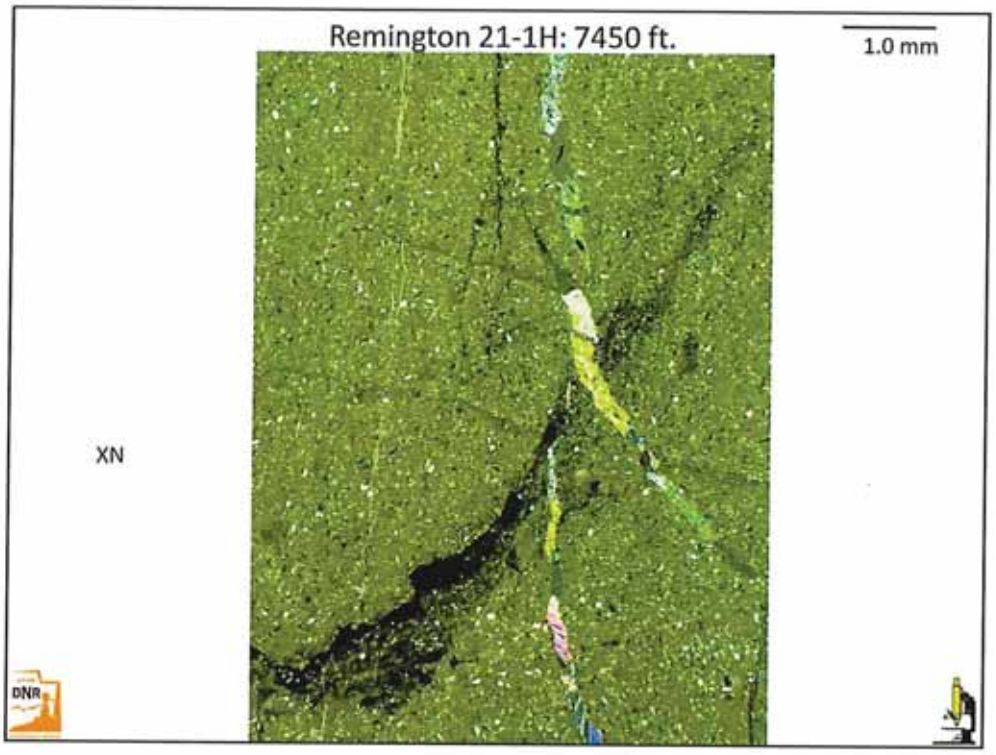

Fig. 6. An oriented view shows a highly fractured massive matrix with calcite and anhydrite (in pastel colors) and black bitumen under cross-polarized (XN) illumination. The disseminated white and gray specks within the dolomitic matrix are silt-sized detrital grains.

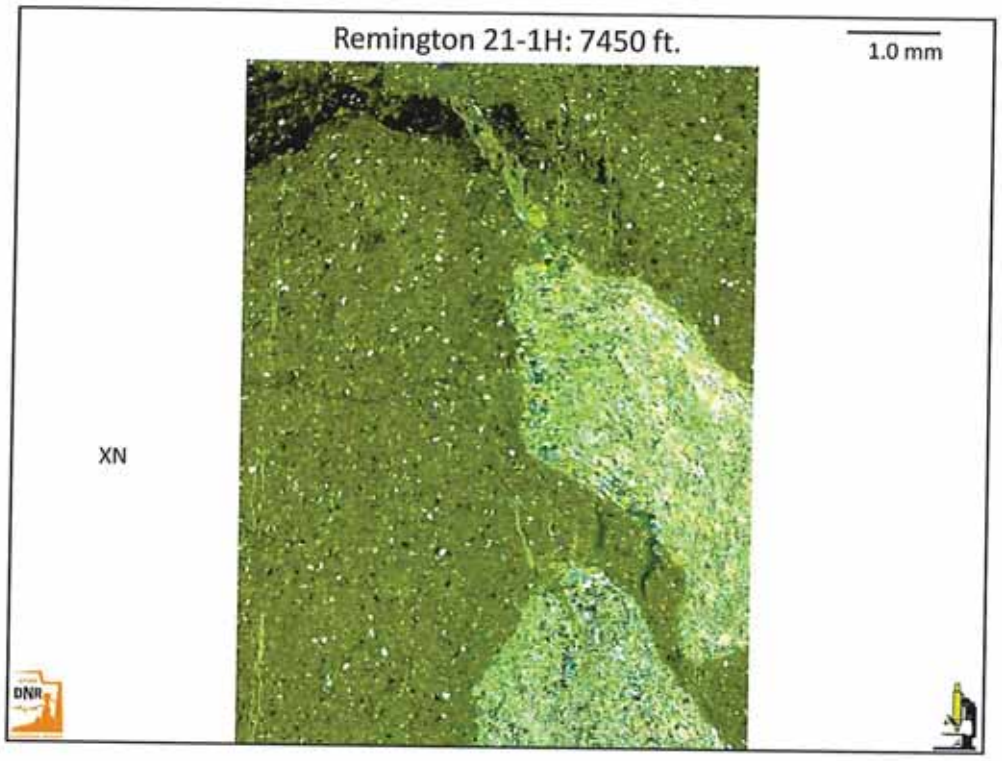

Fig. 7. Patches of nodular anhydrite with internal "felted" subcrystals have grown displacively within the massive silty dolomite sediment. The cross-polarized (XN) view also shows fractures and tension gashes healed with anhydrite as well as a patch of black bitumen.

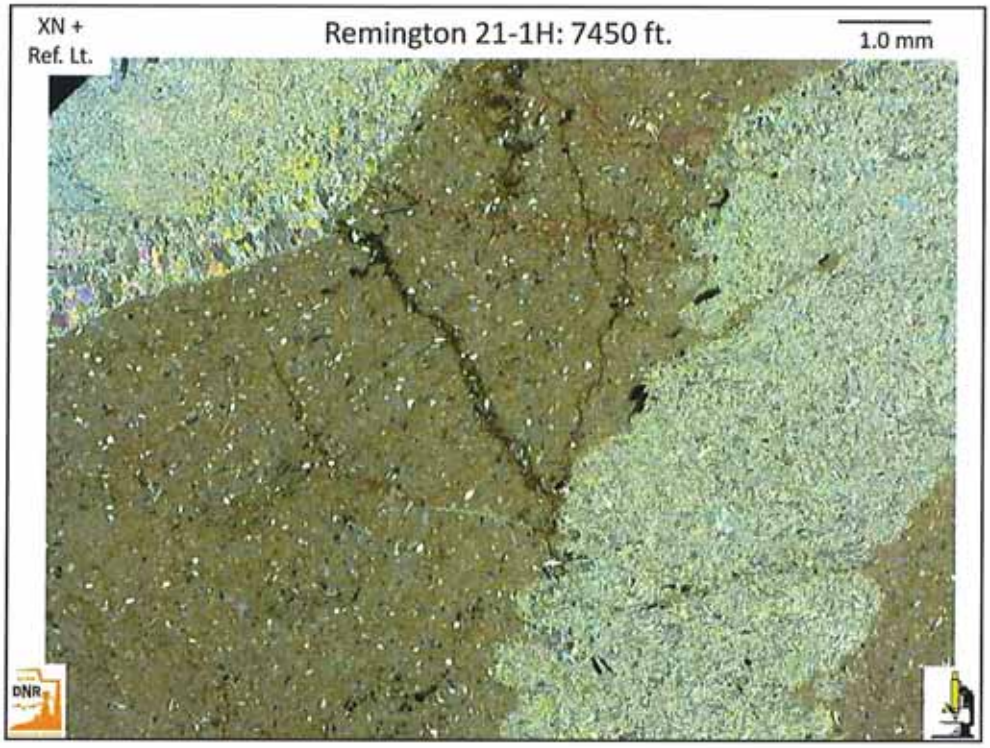

Fig. 8. Two contorted masses of "felted" anhydrite nodules are surrounded by a massive silty dolomite groundmass in this image shown under cross-polarized (XN) and reflected light (Ref. Lt.). Fractures are partially lined with black bitumen.

Fig. 9. Another representative image illuminated under a combination of cross-polarized (XN) and reflected light (Ref. Lt.) comes from an area artificially stained with Alizarin Red-S solution. Note the remnants of calcite (in red patches) within the dolomitized matrix. Along the left side is a fracture healed by a combination of coarse anhydrite (in pastel colors) and calcite (stained red).

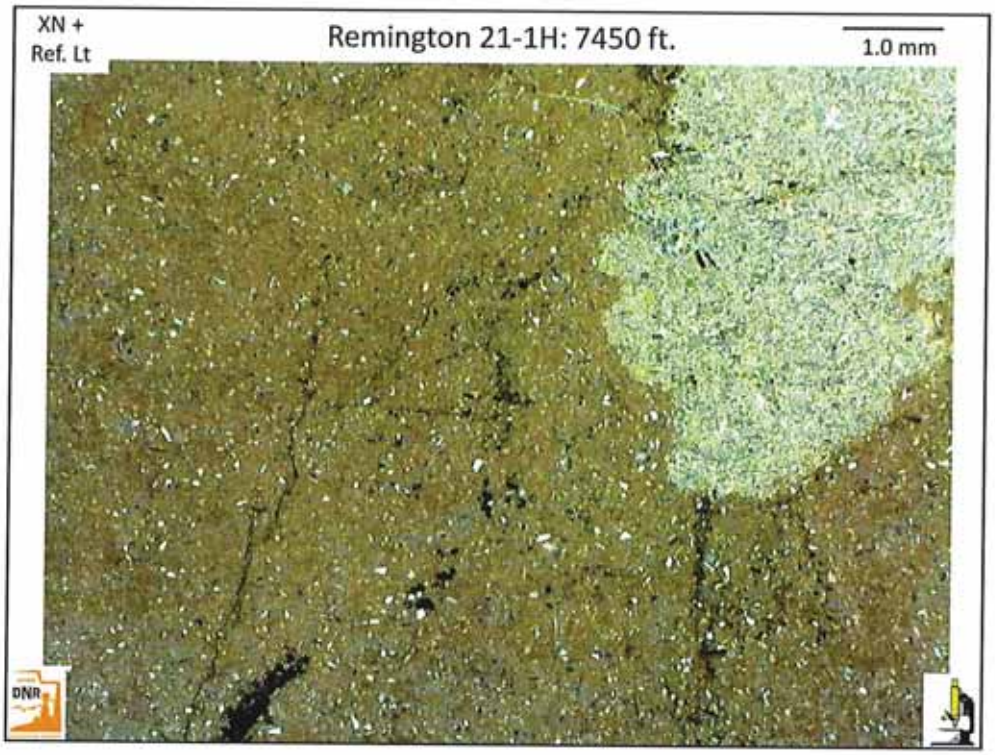

Fig. 10. Microfractures lined with black bitumen can be easily seen in this image shown under cross-polarized (XN) and reflected light (Ref. Lt.). Note the abundance of white detrital silt grains within the slightly calcareous (note the red patches stained with Alizarin Red-S) dolomite matrix. Small disseminated pyrite crystals (opaque and black) are also present in the matrix.

UPRC REMINGTON #21-1H
THIN SECTION REPORT: 7,450.7 ft.

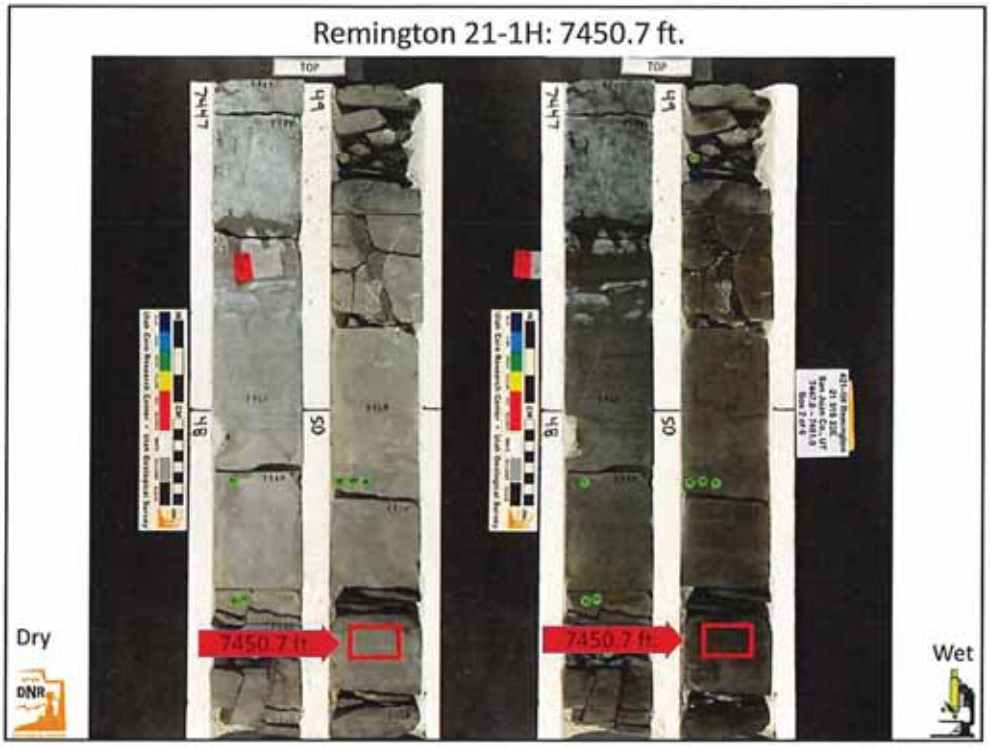

Fig. 1. A pair of core photos shows the same depth interval, with a dry view on the left and a wet view on the right. The location of the 7450.7 ft. sample is indicated by the red arrow adjacent to each core photo. Note the brownish dolomite at the location of the 1"x2" thin section prepared from this interval. This dolomitic interval appears to be vaguely laminated with some mottling.

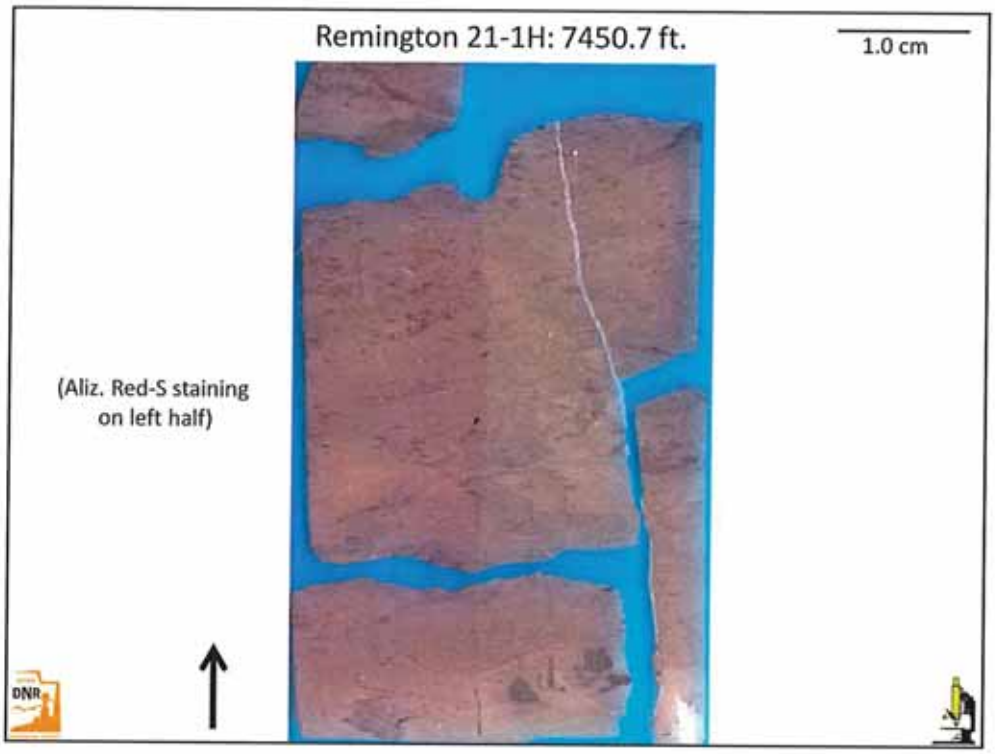

Fig. 2. Low magnification overview of the entire 1" x 2" thin section. The left half of the thin section has been artificially stained with Alizarin Red-S solution. Note the generally mottled overprint on laminated dolomite. The blue notch in the upper center is a stratigraphic "UP" indicator.

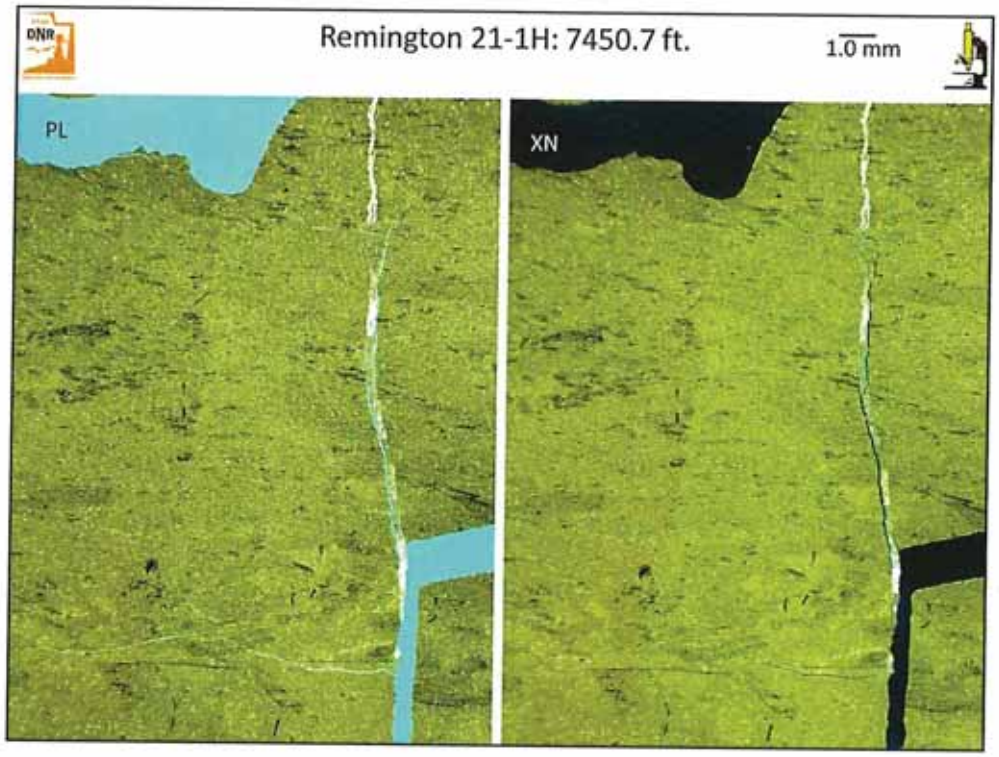

Fig. 3. This pair of micrographs shows the same field of view at the same magnification. The left view is under plane-polarized light (PL) while the right view is under cross-polarized (XN) light. Note the relict laminae with an overprint of either haloturbation or bioturbation. There is a partially healed vertical fracture along the right center portion of the thin section.

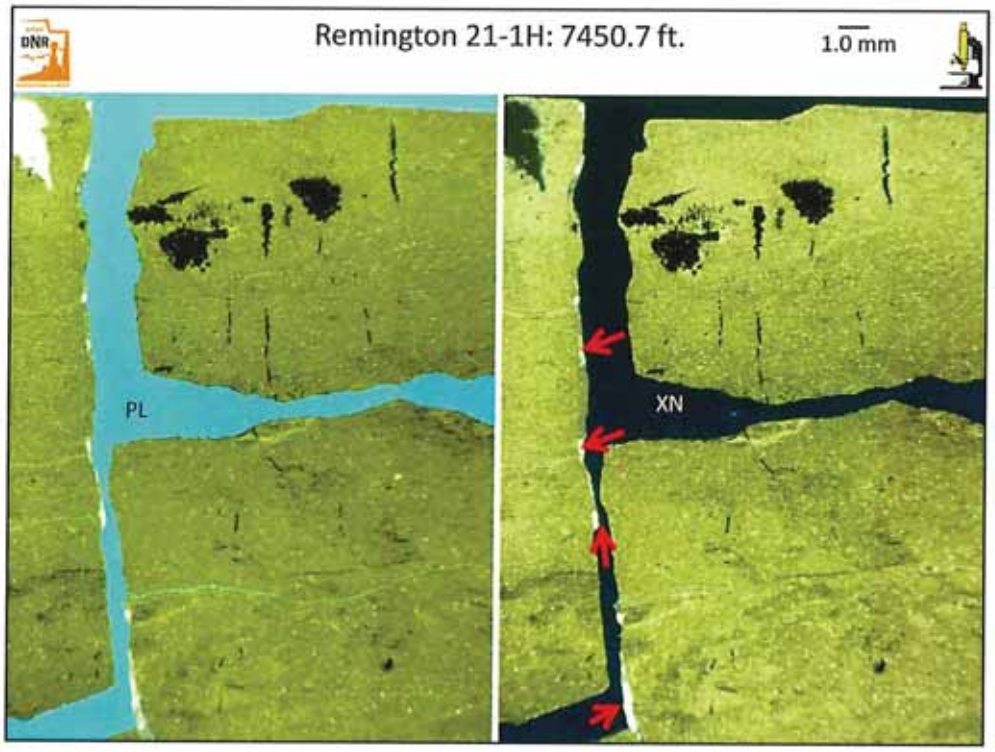

Fig. 4. Another pair of micrographs shows conventional core fragments at the same field of view at the same magnification. The left view is under plane-polarized light (PL) while the right view is under cross-polarized (XN) light. The angular fragments were broken along fractures. Partial fracture linings are indicated by the red arrows on the XN view. Note the disrupted dolomitic mud matrix and the black (opaque) fillings within former anhydritic patches and microfracture linings. These black areas are mostly iron sulfide (pyritic) mineral replacements and fillings.

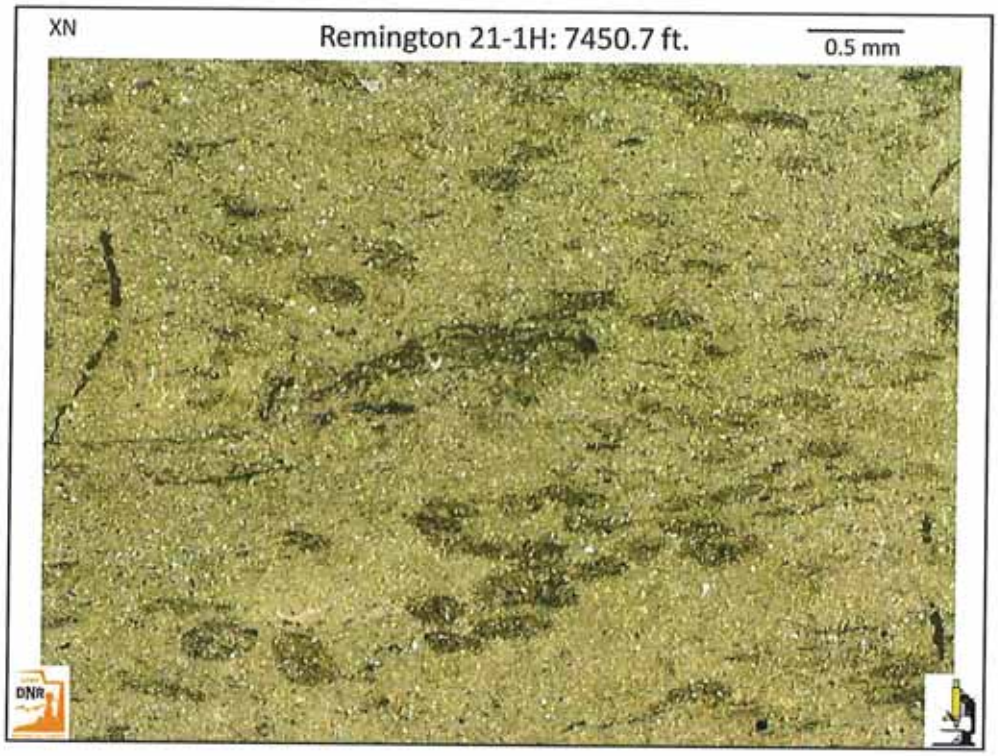

Fig. 5. This representative image under cross-polarized (XN) light shows numerous black pyrite and possibly bitumen-bearing disrupted patches that were the result of sediment mottling due to either bioturbation or haloturbation. The matrix of this dolomite consists of a silty mudstone. Short tension gashes and microfractures are also lined with the dark (opaque) materials.

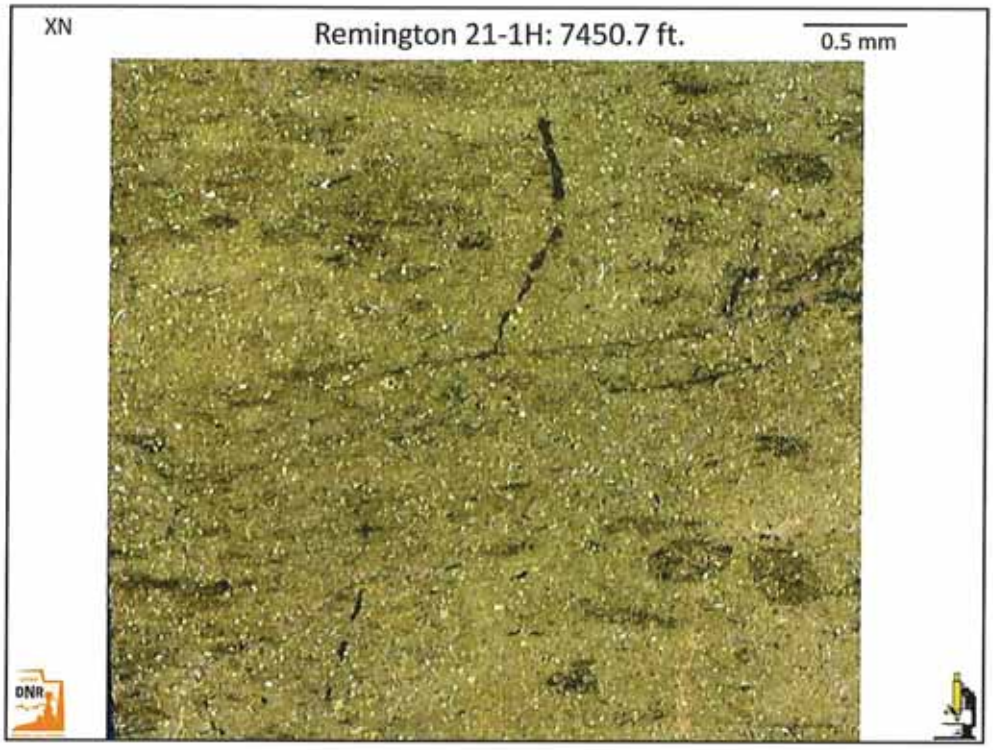

Fig. 6. Relict sub-horizontal laminae can be seen within this silty dolomite matrix despite the abundant mottled disruptions and vertical microfractures outlined with black pyrite and/or bitumen. This view is also under cross-polarized (XN) lighting.

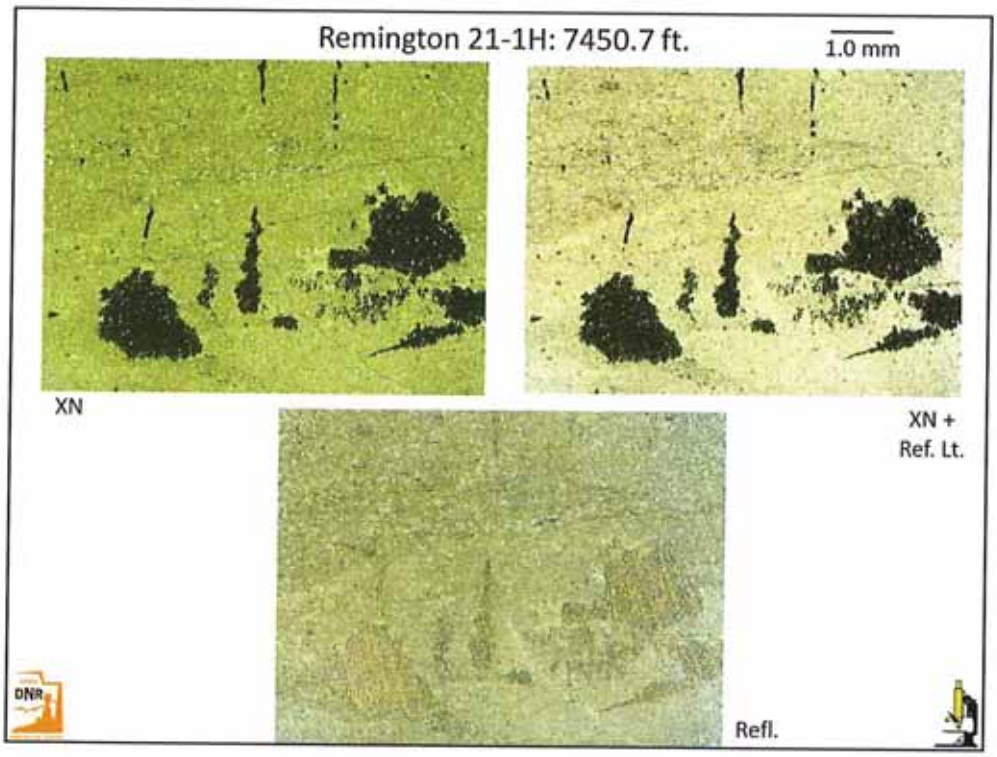

Fig. 7. These three images show the same field of view at the same magnification. The upper left is illuminated under cross-polarized (XN) light, the upper right combines XN with reflected (Ref. Lt.) and the lower image is under reflected (Refl.) light only. Note that the black (opaque) patches and microfracture fillings is reflective and "brassy" in the lower photo. This material is likely pyrite

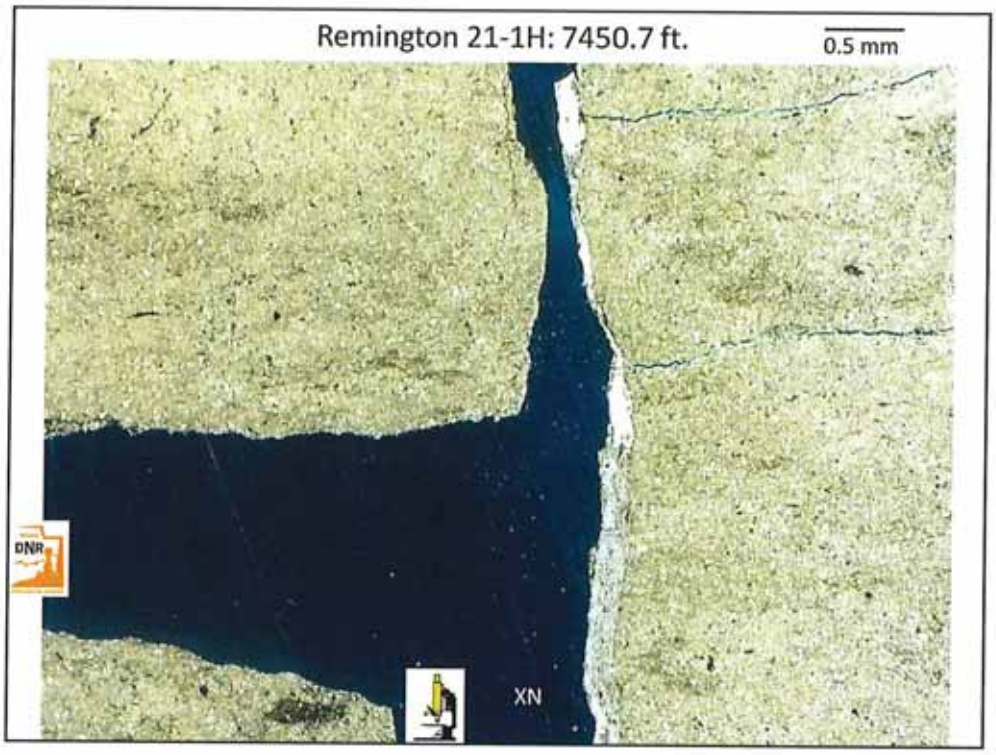

Fig. 8. These broken core fragments fit together along a vertical fracture surface. In this cross-polarized (XN) view, note the calcite fracture filling (in white and pastel colors) that acted to heal this fracture within a dolomitic mudstone matrix.

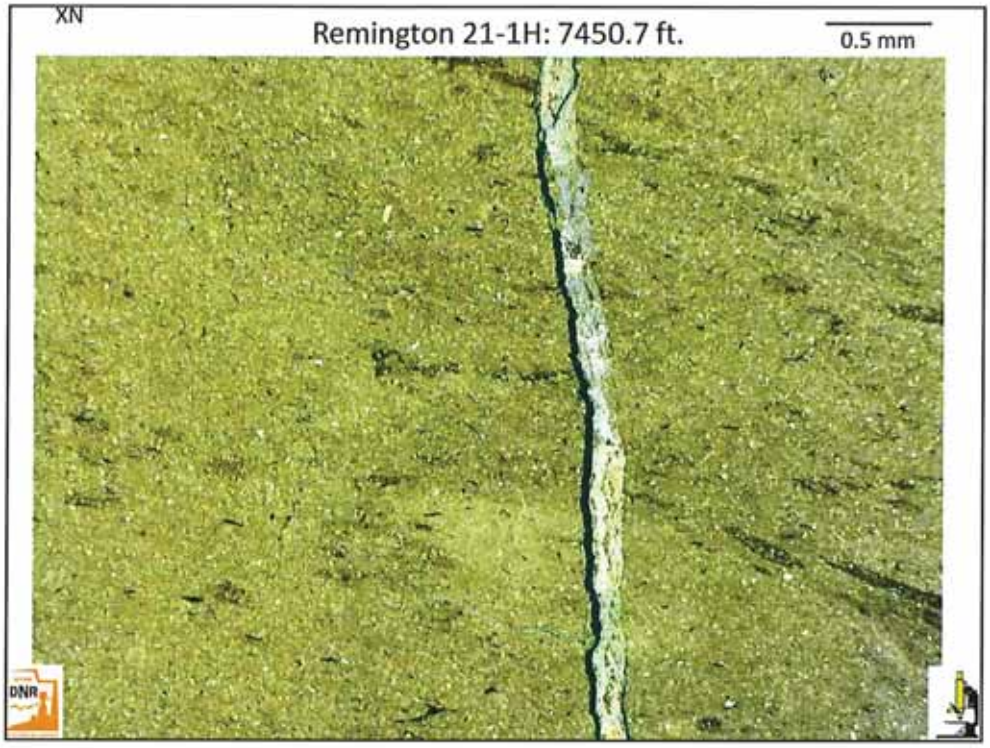

Fig. 9. A cross-polarized (XN) overview shows the mottled or disrupted dolomitic mudstone cut by a vertical fracture that has been healed with coarse calcite spar.

Appendix E:

Remington 21-1H

Core Analysis Report by TerraTek

a Schlumberger Company

CORE ANALYSIS PROGRAM

Remington 21-1H Well
San Juan County, Utah

Prepared for:

Union Pacific Resources Company
801 Cherry Street
Fort Worth, Texas 76101

Attn: Joe Svoboda

Prepared by:

TerraTek, Inc.
University Research Park
420 Wakara Way
Salt Lake City, Utah 84108

TR95-5848
April 1995

1 PROJECT SUMMARY

1.1 WELL SUMMARY

Company:	Union Pacific Resources Co.	State:	Utah
Well Name:	Remington 21-1H	County:	San Juan
Field:	Lisbon Valley	Location:	Sec.21, T31S, R23W
Drilling Fluid:	Oil Base	Elevation:	6395' KB

1.2 CORE SUMMARY

Diamond coring equipment and oil base drilling mud were used in the UPRC Remington 21-1H well, located in San Juan County, Utah, to obtain a four-inch diameter core. The interval and formation cored are listed below in Table 1-1.

Table 1-1. Core Interval Summary

Core Number	Depth Interval	Formation
1	7435.0' - 7495.0'	Cane Creek Shale

A representative of TerraTek, Inc. was at well site to retrieve the core and prepare it for transport to the TerraTek laboratory in Salt Lake City, Utah for analysis. The core was retrieved in an aluminum inner-barrel liner, which was cut to approximate five-foot lengths. Residual core fluids were preserved by sealing the cut ends with rubber end caps and hose clamps.

1.3 SUMMARY OF ANALYSES

A variety of core analysis testing procedures were performed on the core material obtained from the UPRC Remington 21-1H well. Analytical procedures and test results are provided in separate sections of this report for the following types of testing: routine core analysis, petrographic analysis, fracture analysis, electrical resistivity, capillary suction time (CST) testing, liquid permeability testing, geochemical analysis, rock mechanics, and color photographs under natural light of the whole core and slabs.

1.4 DISTRIBUTION OF FINAL REPORTS

Copies of this core analysis report were distributed as outlined in Table 1-2.

Table 1-2. Distribution of Final Reports

Number of Copies	Company Name	Recipient
2	Union Pacific Resources Company 801 Cherry Street Mail Station 3903 Ft. Worth, Texas 76101	Joe Svoboda
2	Sinclair Oil Corporation 550 East South Temple Street Salt Lake City, Utah 84102	Don Harris
2	Marathon Oil Company 1501 Stampede Avenue Cody, Wyoming 82414	Bill Zogg

2 ROUTINE CORE ANALYSIS

2.1 INTRODUCTION

Routine core analysis testing was performed on core material obtained from the UPRC Remington 21-1H well. A total core gamma log was recorded for the entire cored interval. Routine core analysis tests were performed on full diameter samples obtained from the interval 7448' to 7473'. One sample was prepared from each foot of core in that interval, for a total of 25 samples. The following measurements were performed on each sample as requested: fluid saturations using the Dean-Stark solvent extraction technique, porosity and grain density using expanding helium at ambient conditions, and permeability to nitrogen gas in two horizontal directions and in the vertical direction.

2.2 PROCEDURES

Upon arrival in the laboratory, the core was laid out on a core rack, the preservation material was removed, the core pieces were properly fitted together, and a total core gamma log was recorded. Photographs were taken of the whole core under natural light (photographs appear in the final section of this report). Full diameter samples were cut from the designated interval using a diamond edge saw blade and fresh water as blade coolant.

Fluid saturations were determined by means of the solvent distillation extraction (Dean-Stark) technique using toluene as the extracting solvent. Oil remaining in the core samples following the initial extraction phase was removed by cleaning in a pressurized CO_2/toluene core cleaner. The samples were dried in a convection oven at 110°C prior to performing porosity and permeability measurements.

Porosity was determined by measuring grain volumes and bulk volumes. Grain volumes were measured in a helium expansion porosimeter using Boyle's law. Bulk volumes were measured by submerged weight in water using Archimedes' principle of buoyancy. Grain volume and dry weight values were utilized to determine grain density for each sample.

Permeability was measured in a pressurized Hassler sleeve core holder. Nominal sleeve pressure of 400 psi was applied to prevent gas from leaking around the outside of the sample being tested. Steady-state downstream flow rate was monitored using a calibrated orifice-equipped pressure transducer. A form of Darcy's equation was employed to calculate absolute gas permeability values. Each sample was tested in three directions: parallel to the direction of maximum horizontal flow, perpendicular to the direction of maximum horizontal flow, and in the vertical direction.

Following completion of the requested testing, the core was double slabbed using fresh water as blade coolant. Natural light photographs were taken of one set of the slabs (photographs appear in the final section of this report). The butt section of the core was shipped to the UPRC core storage facility in Ft. Worth, Texas, one set of slabs was sent to Marathon Oil in Cody, Wyoming, and the other set of slabs was sent to Sinclair Oil in Salt Lake City, Utah.

2.3 RESULTS

Results of the tests described above are presented in graphical and tabular form on the following pages. A plot of the total gamma ray activity appears on the Teklog™, along with plots of grain density, permeability, porosity, and fluid saturations. Table 2-1 summarizes results of permeability, porosity, fluid saturation, and grain density measurements, and includes a brief lithological description of each sample. A key to the lithological abbreviations is included. A porosity versus permeability crossplot, including statistical information, appears at the end of this report section.

TERRA TEK GEOSCIENCE SERVICES

360 Wakara Way, SLC Utah 84108 (801) 584-2480

UNION PACIFIC RESOURCES CO.
Remington 21-1H Well

TEKLOG

January 13, 1995
TerraTek No. 5848

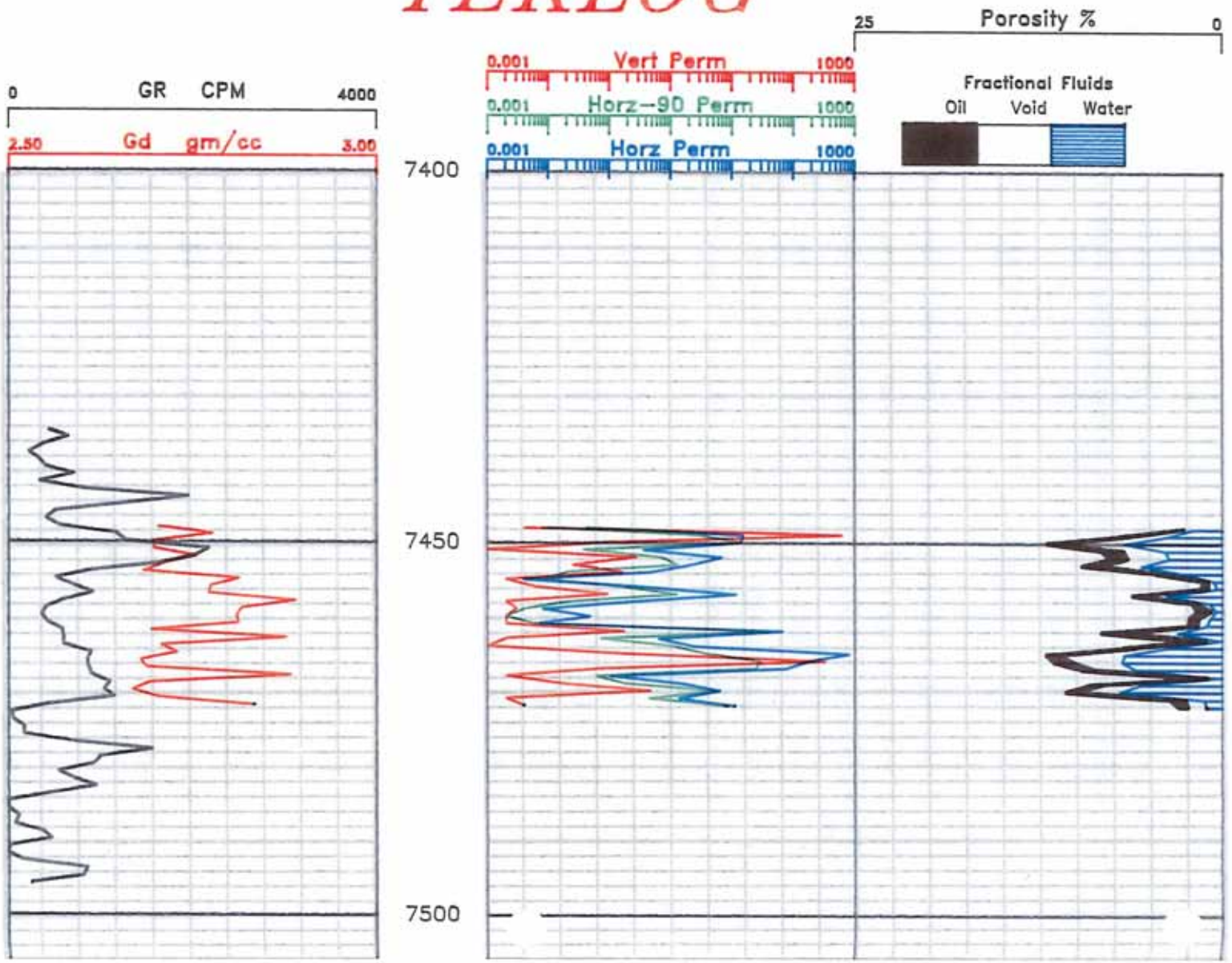

Table 2-1. Full Diameter Dean-Stark Analysis Results

Cane Creek Shale

Sample Number	Depth (feet)	Permeability			Porosity (%)	Saturation		Grain Density (gm/cm^3)	Lithology
		Kh-max (md)	Kh-90° (md)	Kv (md)		Oil (%)	H_2O (%)		
1	7448.0 - 7449.0	0.04	<0.01	<0.01	2.7	1.5	75.3	2.70	Ls,mgy,vfxl,cff
2	7449.0 - 7450.0	VF 15.	VF 2.6	VF 614.	7.0	10.9	54.1	2.78	Ls,m-ltgy,vfxl,anhy,cff,of
3	7450.0 - 7451.0	+ 14.	+ 14.	0.10	12.0	8.9	55.3	2.69	Ls,mgy,vfxl,cff,if
4	7451.0 - 7452.0	0.35	0.04	<0.01	8.2	18.6	47.7	2.70	Ls,dkgy,vfxl,cff
5	7452.0 - 7453.0	+ 6.8	+ 0.71	VF 0.27	7.7	16.7	47.6	2.76	Ls,mgy,vfxl,cff,anhy,pof
6	7453.0 - 7454.0	+ 2.1	+ 1.3	0.03	9.6	15.0	57.6	2.71	Ls,m-ltgy,vfxl,cff,pof
7	7454.0 - 7455.0	0.47	0.02	0.16	4.6	12.0	59.2	2.68	Ls,m-ltgy,vfxl,cff,if
8	7455.0 - 7456.0	<0.01	<0.01	<0.01	1.4	32.8	44.0	2.81	Ls,m-ltgy w/ wh anhy,vfxl
9	7456.0 - 7457.0	0.34	0.16	<0.01	1.5	37.3	24.4	2.77	Ls,m-ltgy w/ wh anhy,vfxl,sa frac,cff
10	7457.0 - 7458.0	+ 12.	+ 1.2	0.09	6.2	8.5	61.8	2.77	Ls,m-ltgy w/ wh anhy,vfxl,sa frac,cff
11	7458.0 - 7459.0	0.23	0.02	<0.01	2.1	20.8	43.1	2.89	Anhy,wh w/ gy ls,vfxl,cff
12	7459.0 - 7460.0	<0.01	<0.01	<0.01	1.8	59.8	24.5	2.82	Ls,mgy w/ wh anhy,vfxl,cff
13	7460.0 - 7461.0	0.05	<0.01	<0.01	2.3	28.5	37.4	2.81	Ls,mgy w/ wh anhy,vfxl,cff
14	7461.0 - 7462.0	<0.01	<0.01	<0.01	2.4	30.3	46.5	2.81	Ls,mgy w/ wh anhy,vfxl,cff
15	7462.0 - 7463.0	+ 65.	+ 40.	0.17	8.3	23.1	37.3	2.69	Ls,dkgy-blk,vfxl,anhy,sa frac,of,if
16	7463.0 - 7464.0	0.63	0.07	<0.01	2.6	59.5	7.9	2.88	Anhy,wh w/ dkgy ls,vfxl,sa frac
17	7464.0 - 7465.0	+ 2.3	+ 1.1	<0.01	6.8	13.0	56.5	2.71	Ls,dkgy,vfxl,cff,pof
18	7465.0 - 7466.0	+ 804.	+ 3.6	0.16	12.0	8.8	56.0	2.73	Ls,lt-mgy,vfxl,pof,of

Sample Number	Depth (feet)	Permeability			Porosity (%)	Saturation		Grain Density (gm/cm^3)	Lithology
		Kh-max (md)	Kh-90° (md)	Kv (md)		Oil (%)	H_2O (%)		
19	7466.0 - 7467.0	+ 167.	+ 29.	VF 326.	11.5	11.2	60.0	2.68	Ls,lt-mgy,vfxl,pof,of
20	7467.0 - 7468.0	+ 74.	+ 24.	0.08	9.6	9.3	61.5	2.69	Ls,lt-mgy,vfxl,pof,of
21	7468.0 - 7469.0	0.10	0.06	<0.01	1.6	40.9	22.2	2.88	Anhy,wh w/ dkgy ls,vfxl,cff
22	7469.0 - 7470.0	1.5	0.17	0.02	9.1	9.7	62.3	2.69	Ls,lt-mgy,vfxl,cff
23	7470.0 - 7471.0	+ 6.2	+ 6.2	0.47	10.7	6.9	65.5	2.67	Ls,lt-mgy,vfxl,cff,pof
24	7471.0 - 7472.0	1.3	0.44	<0.01	3.5	29.7	35.3	2.70	Ls,m-dkgy,vfxl,cff,pof
25	7472.0 - 7473.0	+ 11.	+ 8.1	<0.01	3.0	22.5	36.7	2.83	Ls,m-dkgy w/ wh anhy,vfxl,pof

VF - Vertical fracture affecting permeability

+ - Dehydration crack affecting permeability

TerraTek
University Research Park
420 Wakara Way • Salt Lake City, Utah 84108
Telephone (801) 584-2480
FAX (801) -2432

Description Scheme for Carbonate Sedimentary Rocks:
Rock Type, Color, Grain Size/Crystal Size, Porosity Type, Accessories

Description Scheme for Clastic Sedimentary Rocks:
Rock Type, Color, Grain Size, Cement, Structures and Accessories

Key to Abbreviations:

aff	- anhydrite filled fracture	fos	- fossil(iferous)	pel	- peloids
alt	- altered	frac	- fracture	pff	- pyrite filled fracture
anhy	- anhydrite(ic)	fri	- friable	pis	- pisolitic
arg	- argillaceous	gff	- gouge filled fracture	pk	- pink
bdd	- bedded	glauc	- glauconitic	pof	- partially open fracture
bent	- bentonite	gn	- green	ppvgs	- pinpoint vugs
bf	- buff	gr	- grain(ed)	ptg	- parting(s)
biot	- bioturbated	grnl	- granule	purp	- purple
bit	- bitumen	gy	- gray	pyr	- pyrite(ic)
bl	- blue(ish)	gyp	- gypsum(iferous)	qff	- quartz filled fracture
blk	- black	hem	- hematite(ic)	qtz	- quartz
bnd	- banded	if	- incipient fracture	red	- red
brec	- breccia(ted)	incl	- inclusion	sa	- salty
brn	- brown	intprt	- interparticle	sdy	- sandy
bur	- burrowed	intrprt	- intraparticle	sh	- shale
c	- coarse	intxl	- intercrystalline	shy	- shaley
calc	- calcite(areous)	lam	- laminated	sid	- siderite
carb	- carbonaceous	lav	- lavender	sil	- silica(eous)
cff	- calcite filled fracture	lig	- lignite(ic)	sl/	- slightly
cgl	- conglomerate	ls	- limestone	sltst	- siltstone
chky	- chalky	lt	- light	slty	- silty
chlor	- chlorite	m	- medium	ss	- sandstone
cht	- chert	mar	- maroon	stn	- stain(ed)(ing)
chty	- cherty	mas	- massive	str	- streak
clst	- clast	mdy	- muddy	styl	- stylolite
cly	- clay(ey)	mic	- micro	suc	- sucrosic
clyst	- claystone	mica	- micaceous	tan	- tan
cob	- cobble	mol	- moldic	v/	- very
dism	- disseminated	ms	- mudstone	vc	- very coarse
dk	- dark	mtx	- matrix	vf	- very fine
dff	- dolomite filled fracture	nod	- nodule(s)	vgy	- vuggy
dol	- dolomite(ic)	o	- oil	wh	- white
f	- fine	of	- open fracture	wthrd	- weathered
fen	- fenestral	ool	- oolitic	yel	- yellow
fis	- fissile	org	- organic	xl	- crystalline
		orng	- orange		
		pbl	- pebble		

TerraTek
University Research Park
420 Wakara Way • Salt Lake City, Utah 84108
Telephone (801) 584-2480
FAX (801) 584-2432

Terra Tek Geoscience Services®

University Research Park – 360 Wakara Way – Salt Lake City, Utah 84108 – (801) 584-2480 – FAX 801-584-2408

HORIZONTAL PERMEABILITY VS POROSITY

UNION PACIFIC RESOURCES CO.
REMINGTON 21-1H Well
Lisbon Valley Field
San Juan County, Utah
January 13, 1995

Depth Interval: 7448.0 to 7473.0 Feet
TerraTek File# 5848

Porosity (phi), %

Min	Max	Average
1.366	12.027	5.919

Permeability (Kh), md

Min	Max	Geo. Ave
0.002	39.620	0.327

Equation of the Line

log Kh = α phi + β

log Kh = 0.2662 phi −2.0617

Correlation Coefficient : 0.749

Cane Creek Formation

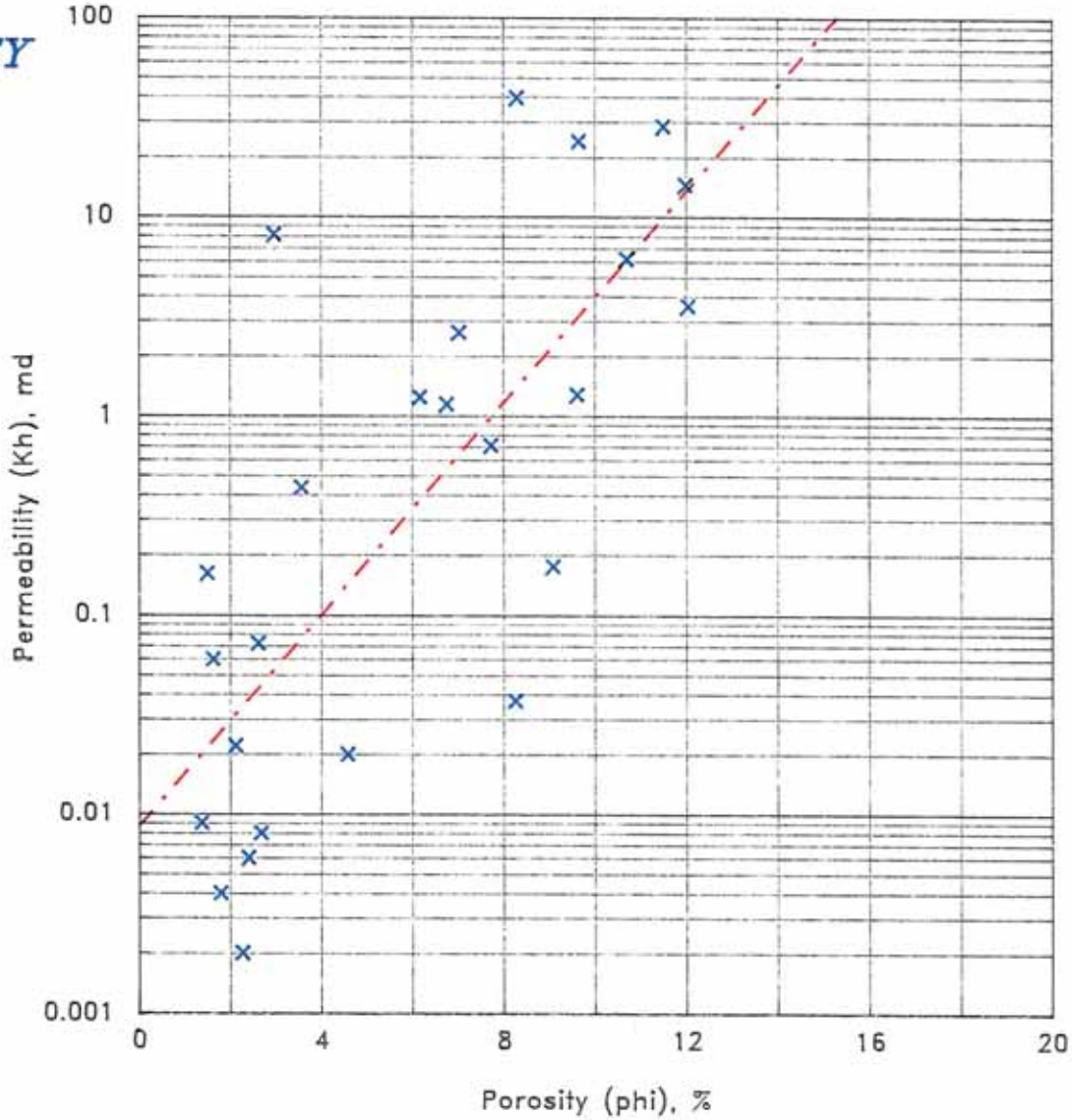

3 PETROGRAPHIC ANALYSIS

3.1 INTRODUCTION

Petrographic analysis was conducted on core material representing the Cane Creek shale member of the Pennsylvanian Paradox Formation, obtained from Union Pacific Resources Company well Remington 21-1H, Paradox Basin, San Juan County, Utah. Analysis consisted of thin-section petrography (two samples) and X-ray diffraction (XRD) analysis (three samples). Sample depths and analyses are listed in Table 3-1 below.

Table 3-1. Petrographic Samples

Sample Depth (ft)	Thin Section	XRD†	Plate No.
7451.5		X	
7456.2	X		1, 2
7459.9		X	
7463.1	X		2, 3
7468		X	

† XRD samples correspond to Special Core Analysis samples.

3.2 ANALYTICAL PROCEDURES

3.2.1 Thin-Section Analysis

Rectangular rock slabs were cut from the full diameter core (parallel to bedding), and were impregnated with fluorescent red-dye epoxy resin under high vacuum to access intercrystalline, moldic, and fracture porosity in the sample fabric. Samples were surfaced, mounted to oversized thin-section slides (2 in x 3 in), and ground to a thickness of approximately 30 microns. Thin

sections were stained with a mixture of potassium ferricyanide and Alizarin Red "S" to aid in identification of carbonate minerals. Samples were examined and photographed at 20×, 40×, 100×, and 200× magnification, under plane-polarized, cross-polarized, and reflected ultraviolet light to determine rock classification and composition, cement types, porosity types, and nature and orientation of veins and fractures.

3.2.2 X-Ray Diffraction (XRD) Analysis

Bulk Analysis- A representative split of the crushed sample was ground in acetone in an agate mortar to <325 mesh (<45 microns). The ground rock material was spread on a glass slide and scanned 2° 2 theta per minute from 2° to 65° 2 theta. Diagnostic peaks of minerals identified on the resulting diffractogram were rescanned on duplicate samples. Approximate weight percentages of mineral phases were determined by comparing diagnostic peak intensities with those generated by pure standard phases mixed in various known proportions. Data presented in this report are the average of three scanning runs.

Clay Analysis- Bulk samples were sonically disaggregated in deionized water, allowed to settle sufficiently to yield the desired particle size fraction (generally <2 microns or <5 microns), decanted, and centrifuged. The resulting slurries were smeared on glass slides, air dried, and X-rayed. If smectite was present, samples were vapor glycolated at 60°C, heated to 250°C, rescanned, heated to 550°C, and scanned a final time. Approximate weight percentages of clay minerals were determined by comparison with diagnostic peak intensities generated by pure reference clays in appropriate mixtures.

3.3 PETROGRAPHIC DESCRIPTION

3.3.1 Composition and Texture

Thin-section sample 7456.2 (ft) is classified as an intraclastic, silty, dolomitic mudstone. Subangular grains of terrigenous silt (mostly quartz, feldspar, and mica), mud-rich intraclasts, peloids, and disseminated pyrite are supported by a finely crystalline-to-microcrystalline matrix

of carbonate mud and clay. Close examination of stained portion of the sample reveals that carbonate mud matrix is partially dolomitized, containing both calcitic and dolomitic "micrite." Also distributed throughout the sample fabric are variably sized nodules of finely crystalline, authigenic anhydrite, some of which exhibit a "ghost" mudstone texture within the nodule interior. Orientation of thin section does not allow for determination of sedimentary structure, however, a finely laminated (cryptalgal?) fabric is recognized within muddy intraclasts. Structural features at this depth include at least two sets of calcite- or calcite/anhydrite-filled veins and stylolites that cross-cut veins (see Fractures and Veins Section below).

Sample depth 7463.1 ft is also a silty, dolomitic mudstone, however, in this case, dolomitization of matrix appears complete. Mud-supported grains include abundant terrigenous silt (with somewhat patchy distribution), dolomitized peloids, calcitic grains of unknown affinity, pyrite, and rare glauconite, phosphate, and chert. Skeletal grains are not recognizable in either thin-section sample. Nodules composed of finely crystalline laths and blocks of anhydrite can be found throughout the fabric at this depth; in addition, anhydrite partially fills veins and intercrystalline voids. Trace amounts of finely crystalline ferroan dolomite (ankerite) cement are admixed with nonferroan dolomite and clays in the matrix. As in the shallower sample, several cross-cutting veins and fractures are observed; vein fillings include ferroan calcite, anhydrite, halite, possible fluorite, and minor ferroan dolomite.

3.3.2 Porosity

Small amounts of porosity visible under reflected ultraviolet light are distributed among open or partially mineralized fractures/veins, matrix intercrystalline voids, and dissolution pores. Porosity development overall is fair to poor. In sample 7456.2 (ft), matrix porosity is limited to sparse patches of intercrystalline or microintercrystalline porosity present in zones of more loosely packed silt and mud. Discontinuous fracture porosity at this depth is associated with reopened veins and stylolites, however, density and interconnectivity of fractures is limited, and fractures do not appear to effectively connect isolated patches of intercrystalline porosity.

At depth 7463.1 ft, intercrystalline matrix porosity is somewhat better developed than above, but also exhibits a patchy distribution. Selective leaching of silt grains has created a few isolated dissolution pores, but these represent a very minor component of overall porosity. Fracture porosity found in nonmineralized microfractures and refractured veins is moderately developed and somewhat better interconnected than above. In both samples, open fracture porosity likely enhances vertical permeability and communication between mudstone beds; matrix pores appear to contribute minimally to reservoir porosity and permeability.

3.3.3 Fractures and Veins

Structural features such as veins, fractures, and stylolites cross-cut sedimentary textures in both thin-section samples. In sample 7456.2 (ft), at least two sets of thin, calcite-filled veins are recognized: an older set with approximate orientation of N-N20°W is cross-cut by a younger set with predominant orientation of N30-60°E. In addition, some veins exhibit a definite en échelon arrangement, as shown in Plate 1. Part of a larger calcite + anhydrite vein is also visible, but timing of vein formation with respect to thinner calcite-filled veins is unknown. Stylolites typically cross-cut, and, are therefore younger than most veins. Vein-filling calcite is coarsely crystalline and granular (though slightly fibrous in larger vein), and anhydrite is acicular and blocky in form. In larger calcite-filled veins, sets of wall-parallel inclusion bands record multiple reopening and remineralization (crack-seal) episodes.

Variably sized veins and fractures characterize sample 7463.1 (ft). Two notably larger veins (several mm to several cm in width) are filled with either 1) ferroan calcite + anhydrite + halite(?) + ankerite *or* 2) halite + fluorite(?) + ferroan calcite + anhydrite; with the exception of ankerite, vein fillings are coarsely crystalline and granular. One of these larger viens is approximately oriented N04°W, and smaller calcite-and/or halite-filled veinlets are oriented N60-70°E. Several open microfractures are also observed, though cross-cuttings relationships between vein sets and fractures are not well established. Table 3-2 below summarizes vein/fracture orientation data for both thin-section samples.

Table 3-2. Fracture/Vein Orientation Data

Sample	Feature	Orientation
7456.2 ft	calcite vein	N61°E
	calcite vein	N54°E
	calcite veinlet	N45°E
	calcite veinlet	N11°W
	calcite vein	N12°W
	calcite veinlet	N18°W
	en échelon calcite veins	N31°E
	calcite veinlet	N41°E
	calcite veinlet	N59°E
	calcite veinlet	N55°E
	calcite veinlet	N00°E
	en échelon calcite veins	N45°E
	microstylolite	N59°W
	microstylolite	N68°W
	stylolite	N09°E (approx)
7463.1 ft	wall of large halite vein	N14°W (approx.)
	calcite veinlet	N35°W
	calcite veinlet	N68°E
	calcite veinlet	N61°E
	calcite + anhydrite vein	N04°W

3.3.4 X-Ray Diffraction Results

Whole-rock abundances, relative clay abundances, and size fractions were determined for three samples using X-ray diffraction (XRD) techniques. Tables 3-3 and 3-4 below summarize XRD data.

Table 3-3. X-Ray Diffraction Data (Whole Rock and Relative Clay Abundances), Cane Creek Shale

Mineral	Sample Depth (ft)					
	7451.5		7459.9		7468	
	Bulk	Clay	Bulk	Clay	Bulk	Clay
Quartz	21		12		41	
Potassium Feldspar	1		1		5	
Plagioclase	1		trace		2	
Calcite	1		12		8	
Ankerite	1		-		-	
Dolomite	61		7		12	
Siderite	trace		trace		trace	
Pyrite	2		trace		2	
Gypsum	-		1		-	
Anhydrite	-		58		1	
Illite-smectite†	3	26	3	35	8	26
Illite-Mica	7	60	4	51	17	58
Kaolinite	trace	2	trace	2	1	5
Chlorite	1	12	1	12	3	11
TOTAL	100	100	100	100	100	100

†Contains 20 percent expandable interlayers.

Table 3-4. X-Ray Diffraction Data (Size Fraction), Cane Creek Shale

	Sample Depth (ft)		
Minerals < 4 Microns	**7451.5**	**7459.9**	**7468**
Total Weight Percent	13	12	27
Illite-smectite	17	19	24
Illite	42	27	50
Kaolinite	2	2	2
Chlorite	2	3	7
Quartz	7	4	8
Potassium Feldspar	-	-	-
Plagioclase	1	trace	-
Calcite	trace	8	3
Ankerite	trace	-	-
Dolomite	26	4	3
Siderite	1	trace	1
Pyrite	1	1	1
Anhydrite	-	31	1
Total	100	100	100
Minerals > 4 Microns			
Total Weight Percent	87	88	73
Quartz	23	13	53
Potassium Feldspar	1	1	7
Plagioclase	1	trace	2
Calcite	1	13	10
Ankerite	2	-	-
Dolomite	66	8	15
Siderite	trace	-	-
Pyrite	2	trace	2
Gypsum	-	2	-
Anhydrite	-	61	1
Illite-smectite	1	trace	2
Illite-mica	2	1	5
Kaolinite	-	-	1
Chlorite	1	1	2
Total	100	100	100

3.4 RESERVOIR QUALITY / SENSITIVITY

As illustrated in both thin-section samples, the effectiveness of the reservoir depends on the distribution and interconnectivity of open natural fractures and reopened veins, and, to a lesser extent, on the relationship between fractures and matrix porosity. Development of intercrystalline matrix porosity or microporosity is generally fair or poor, leaving fractures as the primary permeability pathways. If these thin sections are representative of the reservoir, density, continuity, and interconnectivity of fractures is only moderate. Isolated dissolution pores also contribute little to both porosity and permeability.

The presence of significant amounts of anhydrite could affect reservoir quality under the influence of water-based fluids. The conversion of anhydrite to gypsum in the presence of fresh water results in a net volume increase, which may subsequently reduce reservoir porosity and restrict or clog fluid pathways. X-ray diffraction analysis also reveals the presence of variable amounts of mixed-layer illite-smectite (20 percent expandable interlayers), which will also swell to some degree in the presence of fresh water. Minor amounts of chlorite could form porosity-reducing hydroxide gels if in contact with HCl. Fines migration caused by dispersal of clays is also a potential sensitivity hazard.

PHOTOMICROGRAPHS

TerraTek
University Research Park
420 Wakara Way • Salt Lake City, Utah 84108
Telephone (801) 584-2480
FAX (801) 584-2432

PLATE 1

Sample Depth: 7456.2 ft

A. Low-magnification overview of silty, carbonate mudstone illustrating a set of calcite-filled, en échelon veins cross-cutting sedimentary texture. At least two sets of small calcite-filled veins characterize this sample, in addition to a larger calcite + anhydrite vein (which is cross-cut by a stylolite). White grains dispersed throughout matrix are composed of terrigenous silt, mostly quartz and mica. Plane-polarized light. (20×)

B. General view of texture showing variably sized anhydrite nodules and anhydritic intraclasts, common features at this depth. Nodule at center is cross-cut by a thin vein filled with calcite and anhydrite. Calcareous/dolomitic matrix contains both terrigenous silt and disseminated pyrite. Faint pink color in matrix reflects stained calcitic mud rather than epoxy-filled microporosity, which is rare in this sample. Plane-polarized light. (40×)

C. Detailed view of stained portion of sample. Subangular silt grains are supported by a finely crystalline-to-micritic matrix of dolomite and calcite: calcite is stained pink, and dolomite appears brownish gray. This carbonate texture likely signifies incomplete dolomitization of calcareous mudstone matrix. Also note disseminated pyrite (black) and pyritic/organic stringer in upper right. Plane-polarized light. (100×)

D. Another general view highlighting porosity types and distribution. Porosity is generally poor at this depth, and what limited porosity is present is distributed among partially mineralized microfractures (**arrow**) and rare patches of microporosity in the micritic matrix (**m**). Fracture porosity likely enhances permeability in this reservoir, however, fracture density and interconnectivity at this depth are not well developed. Reflected ultraviolet light with rhodamine filter. (40×)

A

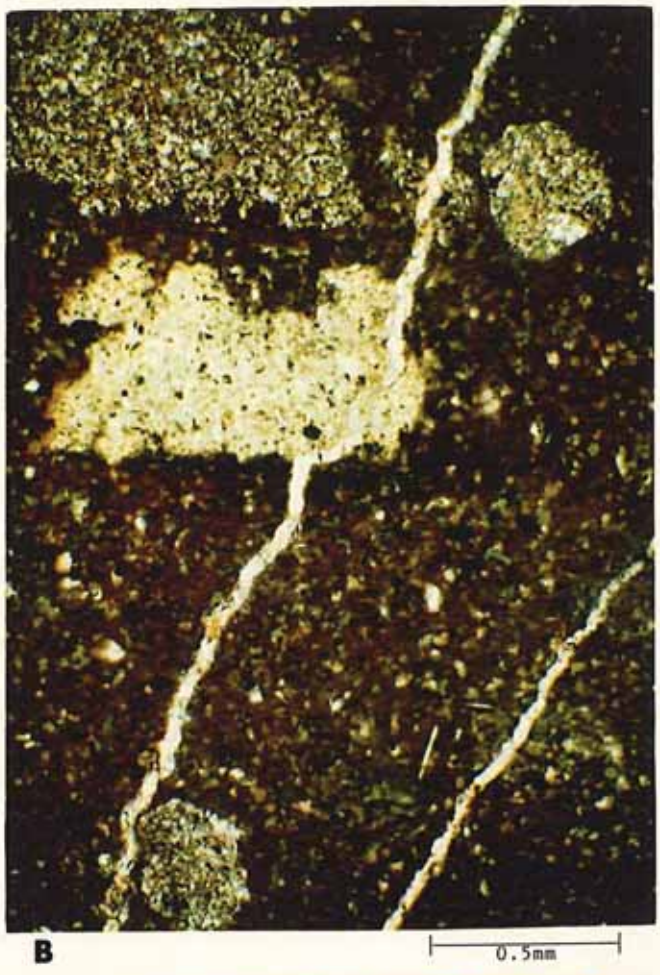

B

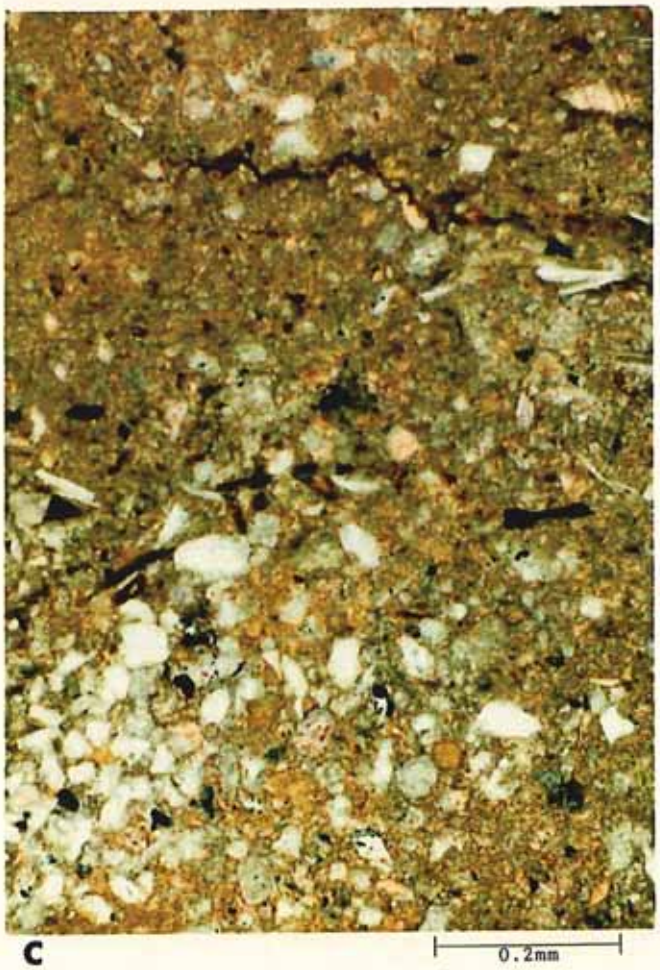

C

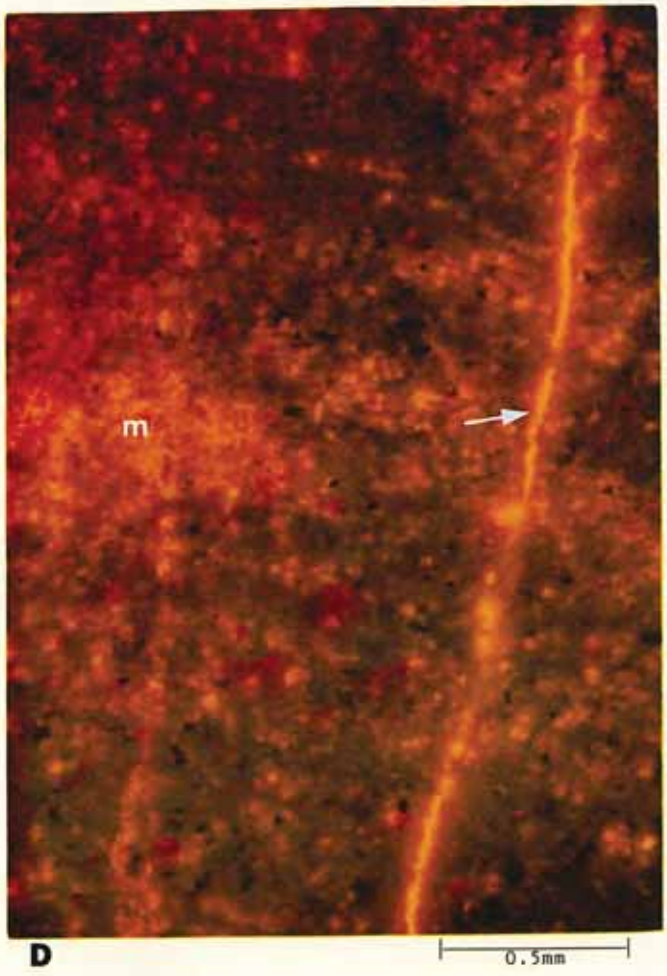

D

PLATE 2

Sample Depth: 7456.2 ft

A. Overview of intersecting calcite-filled fractures in the relatively tight matrix. The cross-cutting relationship here suggests that the fracture oriented from top to bottom post dates the thicker fracture which is oriented left to right. Plane-polarized light. (40×)

B. Same view as the previous photomicrograph showing evidence of reactivation and porosity development along the vertically oriented fracture. Minor vuggy porosity may also be present along the other fracture. Very little porosity is visible in the matrix. Partially mineralized and partially open fractures provide essential permeability to the Cane Creek reservoir. Reflected ultraviolet light with blue-violet filter. (40×)

Sample Depth: 7463.1 ft

C. Overview of several fractures in the silty, dolomitic matrix. The fracture at the top of view is lined by anhydrite (**a**) and filled by halite (**h**). This fracture is relatively wide (5 to 10 mm) and oriented vertically in the core. Open fractures parallel the halite-filled fracture; one is visible in the lower portion of the view and the other along the edge of the mineral filling. The fracture adjacent to the halite-filled fracture may have opened in response to stress relief and may not be present in the reservoir. Plane-polarized light. (40×)

D. Same view as the previous photomicrograph showing open fractures. Two open fractures parallel the halite-filled fracture at the top of the view. A narrower fracture connects the longer open fractures. Minor amounts of ''leak-off'' porosity are visible in the matrix adjacent to open fractures. Such porosity may represent dissolution of the matrix adjacent to fractures. Reflected ultraviolet light with blue-violet filter. (40×)

A

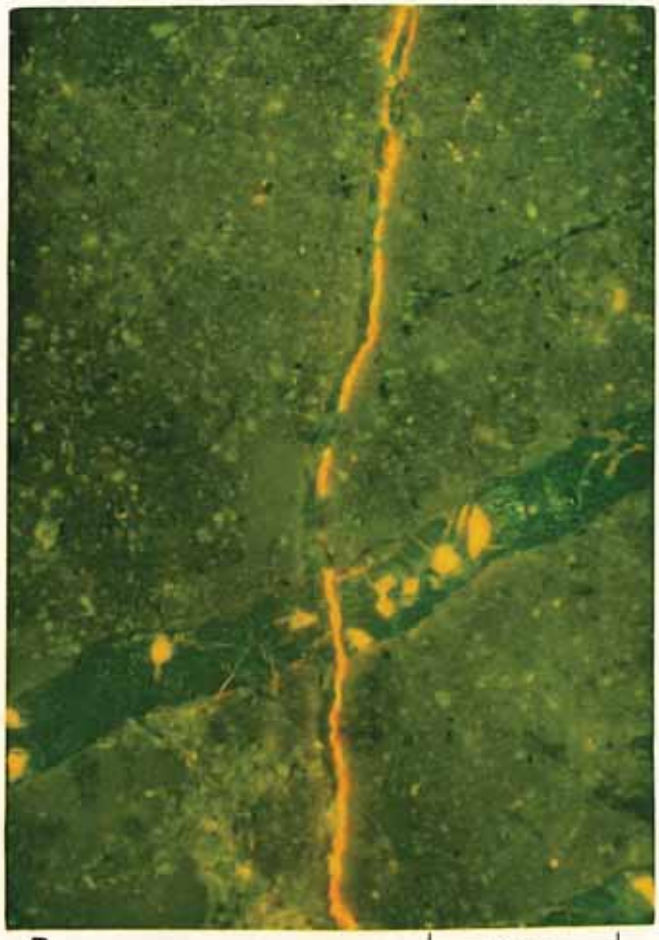

B

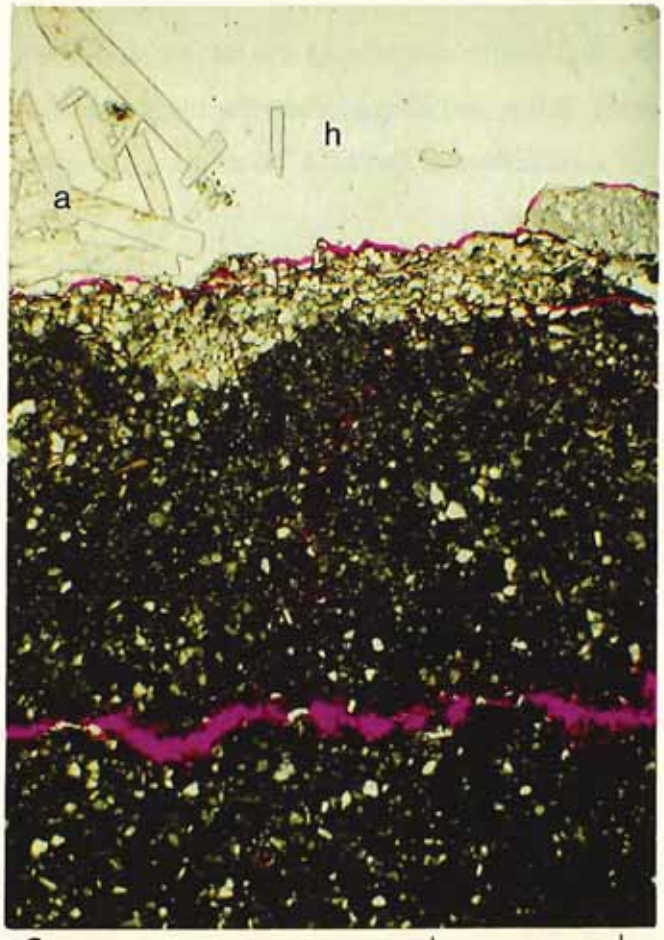

C

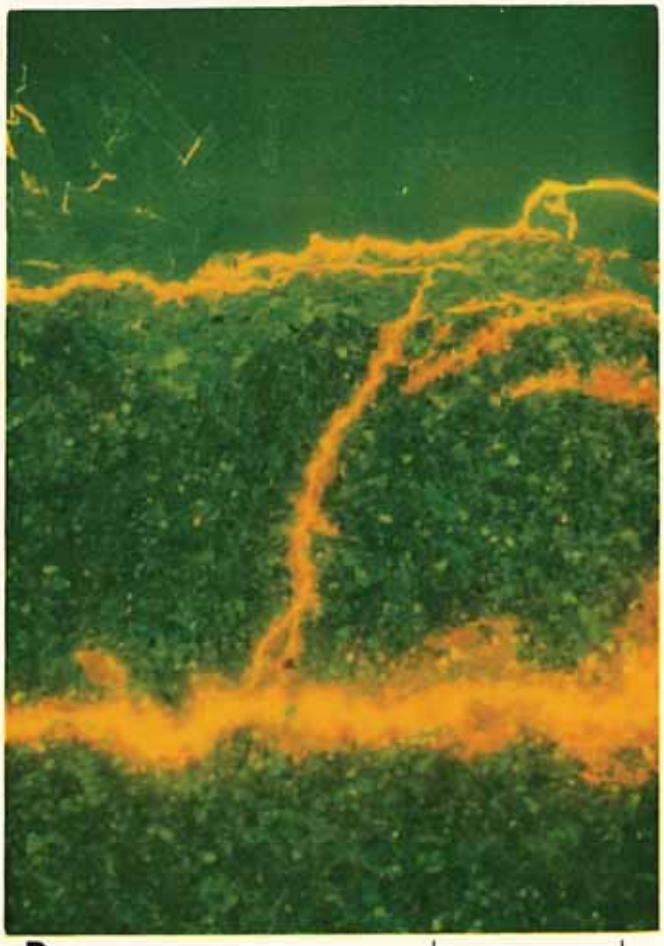

D

PLATE 3

Sample Depth: 7463.1 ft

A. General overview of silty, dolomitic mudstone. As in sample 7456.2, finely crystalline anhydrite is present as vein fillings and nodules (**a**) throughout the sample. Terrigenous silt composed of quartz, feldspar, and mica comprise the most abundant grain type overall, though peloids, small ooids, other calcitic grains of unknown affinity, phosphate, pyrite, and glauconite are also present. Note lack of any visible porosity. Plane-polarized light. (40×)

B. Several large veins cross-cut sedimentary fabric at this depth; the vein shown in this low-magnification overview is filled with a combination of coarse (ferroan) calcite (**c**) and granular anhydrite (vibrant interference colors), as well as lesser amounts of ferroan dolomite (not visible) and an isotropic mineral of low relief (**arrow**, likely halite). Crossed nicols. (20×)

C. In addition to large veins, several smaller veinlets also characterize this sample, as shown in this general view. Calcite (shown here), halite, and anhydrite are the most common veinlet fillings. Matrix fabric contains silt, dolomitic mud, peloids (darker grains), pyrite, and pore-filling anhydrite. Crossed nicols. (40×)

D. High-magnification view of grains and matrix showing that matrix and carbonate grains have been completely dolomitized, unlike the previous sample. Pink epoxy at **arrow** highlights small and generally sparse patches of intercrystalline microporosity. Other pore types include rare dissolution pores (leached silt or carbonate grains) and fracture porosity. Overall porosity development at this depth is fair at best. Plane-polarized light. (100×)

A

B

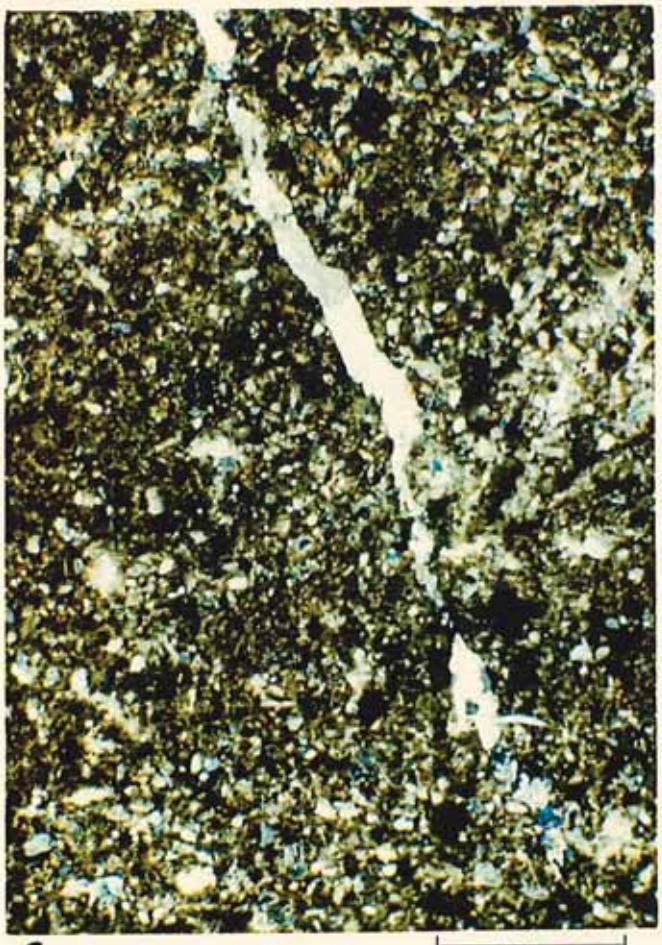

C

D

TOTAL ORGANIC CARBON

TerraTek
University Research Park
420 Wakara Way • Salt Lake City, Utah 84108
Telephone (801) 584-2480
FAX (801) 584-2432

3.5 TOTAL ORGANIC CARBON

Table 3-5. Total Organic Carbon and Rock-Eval Pyrolysis Data, Cane Creek Shale

Sample Number	Depth (ft)	TOC wt%	S1 mg/g	S2 mg/g	S3 mg/g	Tmax °C	S1/ TOC	HI	OI	S2/ S3	PI
1	7445	18.28	16.51	40.51	0.42	442	90	222	2	96.45	0.29
2	7451	3.67									
3	7457	13.47									
4	7468	16.70	12.64	43.26	0.64	441	76	259	4	67.59	0.23
5	7479	5.11									

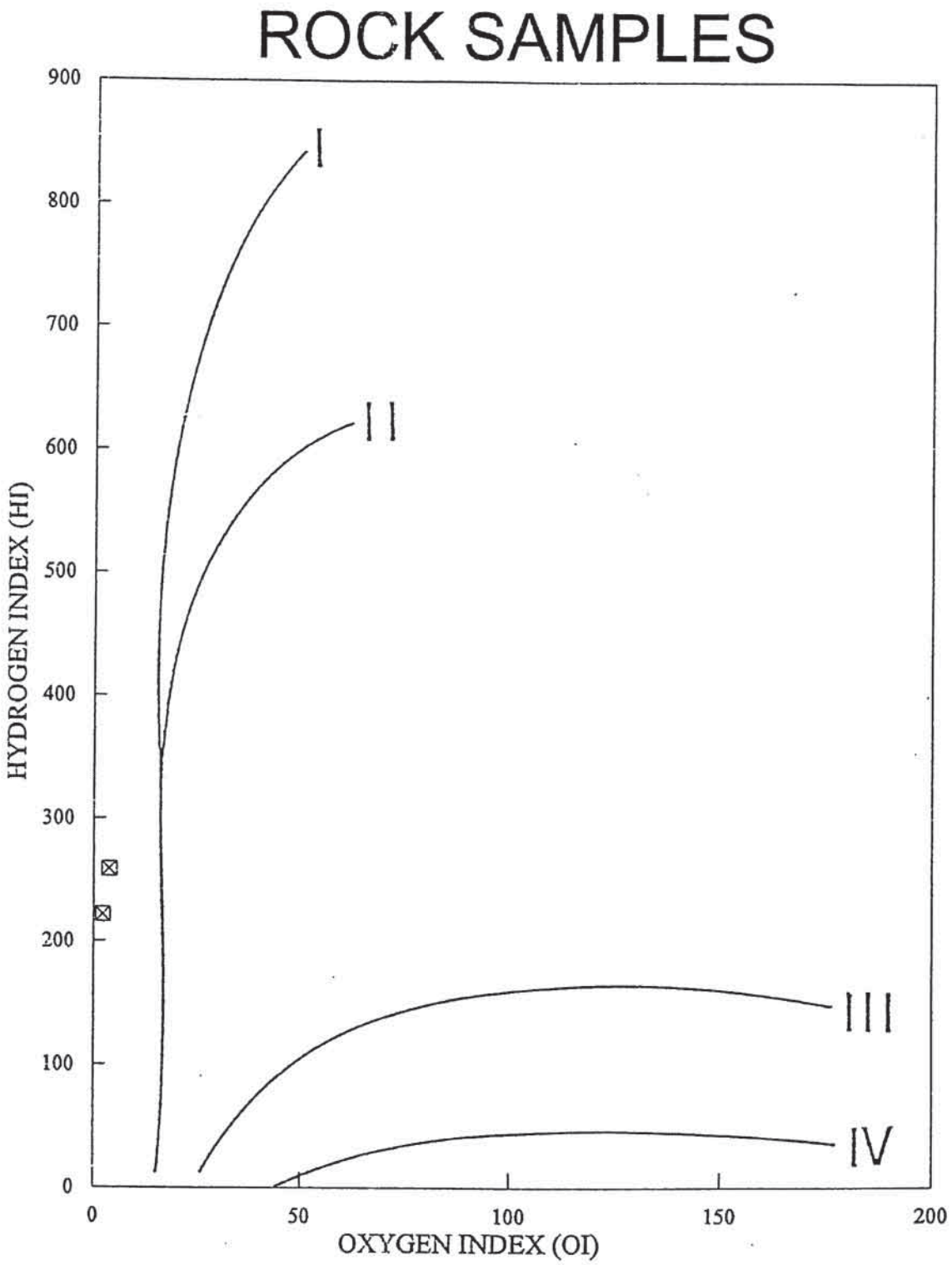

FIGURE 1 - Kerogen type determination from TOC and Rock-Eval pyrolysis data. Types I and II will generate oil, type III gas, and type IV little or no hydrocarbons.

4 FRACTURE ANALYSIS

4.1 INTRODUCTION

Fracture analysis was performed on 61 feet of core belonging to the Cane Creek Shale, recovered from Union Pacific Resources Company's Remington #21-1H well in San Juan County, Utah. Fractures were described and orientation measurements performed for the cored interval from 7435.0' to 7496.0'.

4.2 SUMMARY

The intervals studied consist of moderately to well-fractured silty argillaceous dolomite, interbedded with poorly fractured anhydrite and anhydritic dolomite. Figure 1 illustrates the distribution of open and partially open fractures (including partially mineralized fractures), and completely filled (mineralized) fractures, as a function of depth. Total fracture intensity is highest in zones where silty dolomite and anhydrite are closely interlaminated. Completely mineralized fractures predominate in anhydrite and anhydritic dolomite zones, whereas partially open and partially mineralized fractures are slightly more abundant in silty dolomite intervals. In shale zones, low-angle totally open fractures and filled fractures are most abundant. Figure 2 summarizes the relationship between fracture frequency, fracture type and lithology. The average parameters for the different fracture types present are listed in Table 4-1.

Table 4-1. Average Fracture Parameters

Fracture Type	Avg Length (cm)	Avg Fill Width (mm)	Avg Aperture (mm)	Avg Spacing (mm)	Total Fracture (# fracs)	Avg Intensity (fracs/ft)
Totally Open	10.4			47.6	51	0.8
Partially Open Penetrative	11.0		0.05	*	3	0.05
Partially Open Non-penetrative	5.9		0.05	16.8	32	0.5
Partially Mineralized	9.9	1.45	0.07	25.9	95	1.6
Completely Mineralized	7.1	0.61		16.2	341	5.6

* - Fractures occur singly in 1 - ft interval

Figure 1. Depth versus Frequency
UPRC Remington #21-1H Well

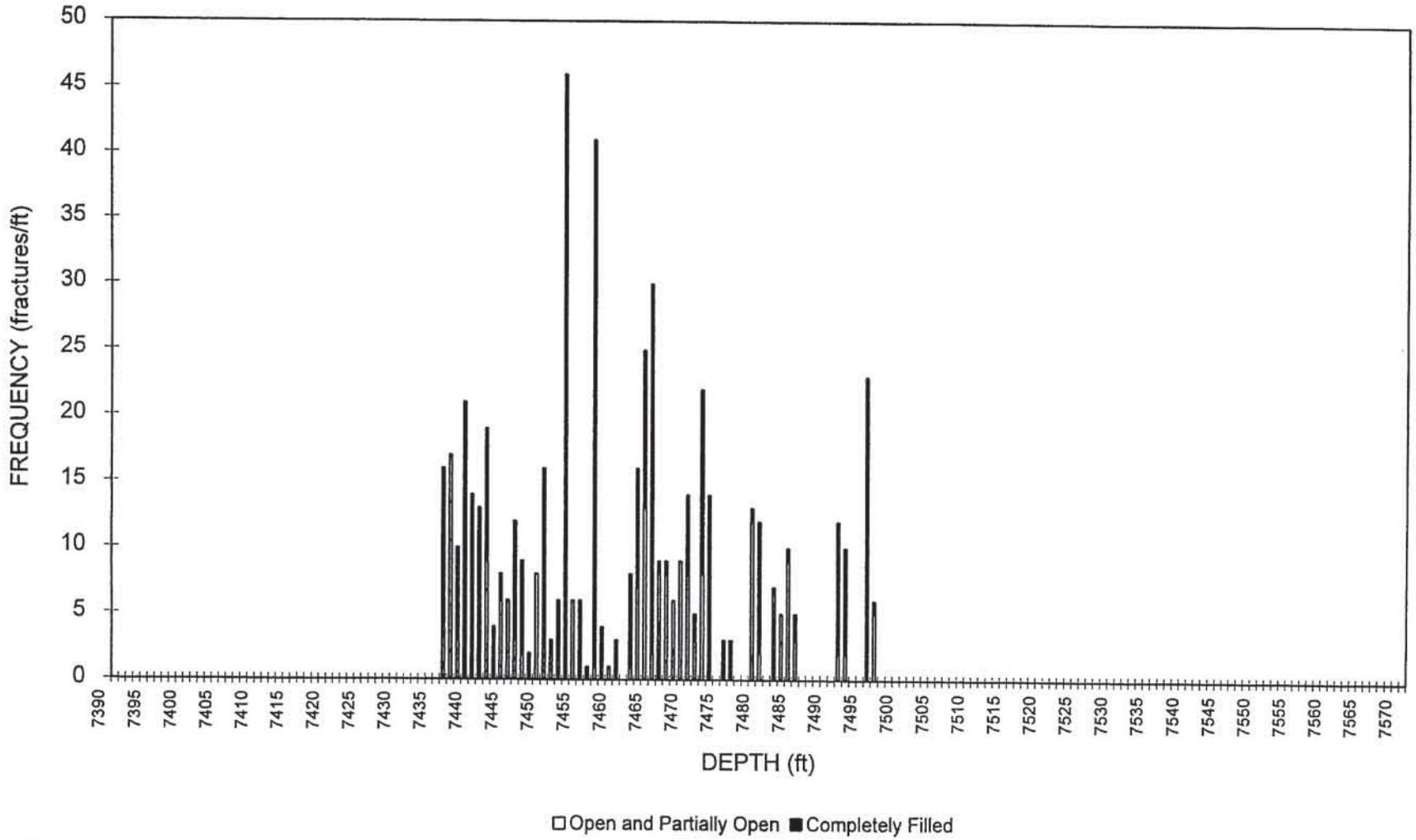

TerraTek
University Research Park
420 Wakara Way • Salt Lake City, Utah 84108
Telephone (801) 584-2480
FAX (801) 584-2432

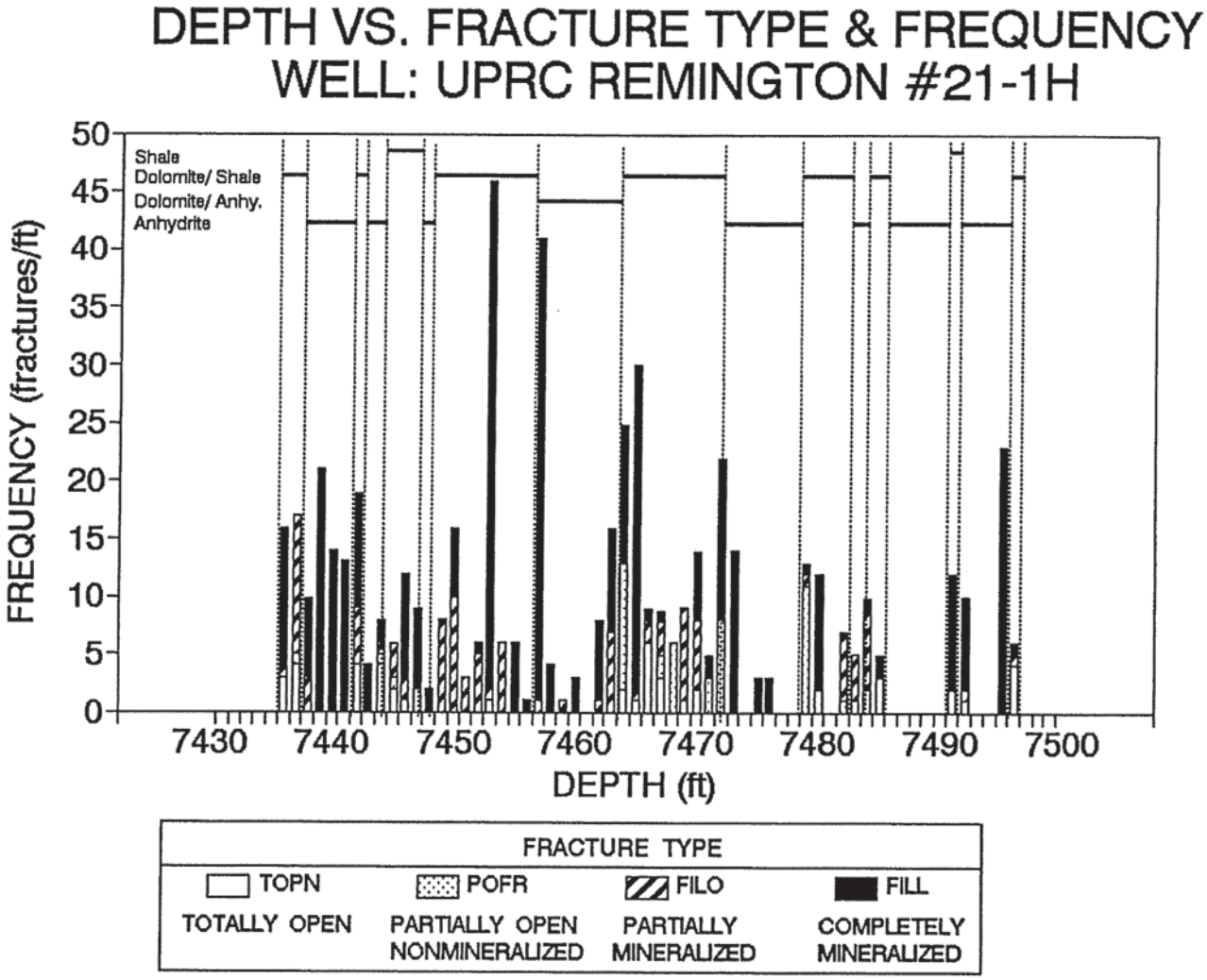

Figure 2. Depth versus Fracture Type and Frequency

TerraTek
University Research Park
420 Wakara Way • Salt Lake City, Utah 84108
Telephone (801) 584-2480
FAX (801) 584-2432

Completely mineralized fractures are the most abundant fracture type throughout the core (except in the anhydrite between 7485.0' to 7490.8'). Short anhydrite filled fractures measuring less than 10cm long and less than 1mm wide are most abundant. Penetrative halite filled fractures measuring up to several millimeters wide are less abundant. Fractures filled with gouge/anhydrite in the interval 7445.0' to 7471.0' show evidence of displacement along the fracture plane. Several fracture terminations at bedding contacts were observed.

Partially mineralized fractures containing natural porosity are second in abundance, especially in argillaceous silty dolomite zones. Anhydrite, halite, calcite, and gouge are common fracture-lining minerals. Most of these fractures contain narrow apertures less than 0.1 mm wide. Several fractures measuring up to several millimeters wide, containing euhedral crystals and vuggy apertures 0.2mm to 0.5mm wide, are also present. Many partially mineralized fractures are broken open. Evidence of movement along fracture planes, such as gouge filling, slickensides, or bedding displacement, was observed throughout the interval.

Non-mineralized fracture types are much less abundant than mineralized fractures. Totally open fractures dipping at angles less than 30 degrees are present in shale zones throughout the cored interval. Many totally open fractures are parallel to bedding, and nearly all bedding-parallel fractures display slickensides on exposed fracture surfaces. Partially open non-mineralized fractures are rare except in the silty dolomite interval from 7463.0' to 7471.5'. Fractures dip at moderate to high angles, but appear relatively narrow and nonpenetrative. At least one fracture (7457'), which is broken open to reveal slickensides, appears to be of natural origin. One set of face cleats, possibly containing traces of halite, was observed in carbonaceous beds at 7463.4'.

Fracture orientations in this interval are varied, due in part to variability in the bedding orientation (see Table 4-2, Average Dip Azimuth of Bedding). Fracture and bedding orientations are summarized in Table 4-3.

Table 4-2. Average Dip Azimuth of Bedding

Depth (ft)	Average Dip Azimuth (0 = North)					
	330-005	006-045	046-100	101-180	220-255	256-329
7435-7436					241	
7436-7437					229	
7437-7438						
7438-7439						279
7439-7440					238	
7440-7441						282
7441-7442						262
7442-7443						
7443-7444				118		
7444-7445	347		079			
7445-7446				120		
7446-7447				113		
7447-7448						
7448-7449				137		258
7449-7450		015				
7450-7451		038	070			
7451-7452			080			
7452-7453		018				
7453-7454						
7454-7455						
7455-7456		022				
7456-7457	356					
7457-7458	357					
7458-7459	337			128		
7459-7460			069			
7460-7461			082			
7461-7462			070			
7462-7463			069			
7463-7464			054			

Depth (ft)	Average Dip Azimuth (0 = North)					
	330-005	006-045	046-100	101-180	220-255	256-329
7464-7465			051			
7465-7466	005	035				
7466-7467		036				
7467-7468		032				
7468-7469		030				
7469-7470						287
7470-7471					252	298
7471-7472						261
7472-7473	353					
7473-7474				122		
7474-7475				125		
7475-7476				149		
7476-7477		039				
7477-7478		021				
7478-7479		038				
7479-7480			061			
7480-7481		044				
7481-7482		042				
7482-7483				118		
7483-7484		022				
7484-7485			060			
7485-7486			060			
7486-7487						
7487-7488	341					
7488-7489	333					
7489-7490	357					312
7490-7491	334					312
7491-7492						
7489-7490				156		270
7490-7491				165		285
7491-7492						275

Depth (ft)	Average Dip Azimuth (0 = North)					
	330-005	006-045	046-100	101-180	220-255	256-329
7492-7493				163		
7493-7494			096			
7494-7495			089			
7495-7496				110		

Table 4-3. Average Fracture Orientations

Fracture Type	Principal Dip Azimuth	Secondary Dip Azimuth	Tertiary Dip Azimuth	Quaternary Dip Azimuth	Quint Dip Azimuth
Totally Open	040	075			
Partially Open	150, 330	250			
Partially Mineralized	030, 210	070, 250	120		
Completely Mineralized	250	080	185	135	
Bedding Planes	065	030	120	285	345

This summary indicates that most natural fractures in the core strike northwest-southeast, parallel to the two most commonly observed bedding orientations. Other fractures strike northeast-southwest, parallel to the less predominant bedding orientation.

Offsetting and terminating fracture relationships indicate that fractures striking north northwest-south southeast, strike parallel to the most common bedding orientation, formed relatively early. Fractures striking northwest-southeast found somewhat later, and fractures striking northeast-southwest appeared most recently. Wide halite-filled fractures generally strike northwest-southeast and may have formed relatively early. Observation of anhydrite-filled fractures which have been subsequently opened and filled with secondary halite, indicates that anhydrite-filled fractures oriented northwest-southeast may have formed earlier than fractures filled only with halite.

Fracture permeability is probably relatively high in argillaceous silty dolomite zones containing partially open or partially mineralized fractures (7442.1' to 7446.6', 7448.0' to 7454.0', 7463.0' to 7471.5', 7482.0' to 7485.0'). Partially mineralized fractures are more abundant and penetrative than non-mineralized fracture types and probably provide localized permeability through these dolomite zones. Anhydrite zones which are relatively unfractured or contain completely filled fractures, appear relatively impermeable (7437.1' to 7440.9', 7456.6' to 7463.0', 7472.0' to 7478.2', and 7485.0' to 7490.8').

TerraTek
University Research Park
420 Wakara Way • Salt Lake City, Utah 84108
Telephone (801) 584-2480
FAX (801) 584-2432

Figure 3

Axial CT image, 7450.8', shows the intersection of two low-angle partially mineralized fractures in argillaceous silty dolomite. Linear traces represent fractures, with mineralized fractures represented as red traces. Partially open portions of fractures are traces in yellow, green, or blue, with blue representing the least dense (most open) apertures. The larger fracture in this image (#48) measures 1.10mm wide and contains an aperture 0.08mm wide. The smaller fracture (#47) is more typical of fractures in this interval, measuring 0.27mm wide with an aperture 0.02mm wide. The smaller fracture, which strikes northwest-southeast, probably formed more recently than the larger fracture striking west northwest-east southeast. The larger fracture is divided into several filled (red) and partially open (green) layers near the bottom of this view, indicating that the original fracture may have been episodically reopened and subsequently filled again. Green matrix area near the top of the view probably represents either a less-dense shale bed, or locally higher porosity adjacent to the open portion of the fracture.

FIGURE 3

AXIAL CT IMAGE
WELL : UPRC REMINGTON 21-1H
DEPTH : 7450.8'

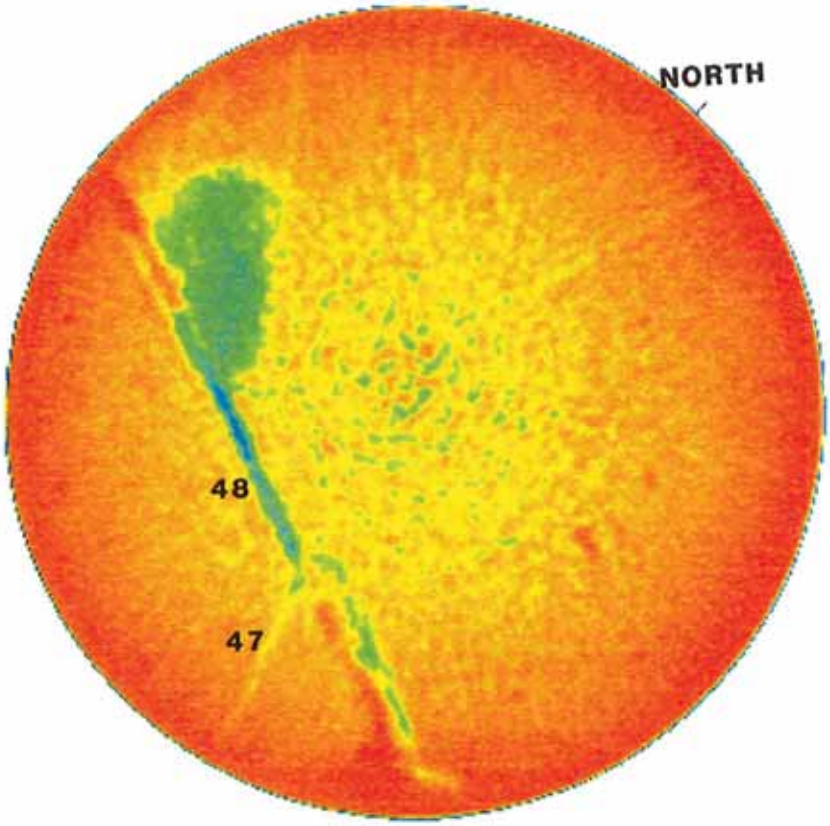

uprc5848/dry/R002.vff
TerraTek CORESCAN (c)1993 KV:130 MA:250 FOV:160 ID:(4)UPRC5848

Figure 4

Axial CT image, 7452.5', shows the intersection of two orthogonal fracture sets completely filled with halite. Fracture set striking northwest-southeast (#51) terminates at contact between shale and dolomite, below this view. Fracture set striking northeast-southwest (#52) penetrates both shale and dolomite. Fractures are relatively closely spaced, between 15mm and 18mm apart. Relatively wide fracture (#54) striking northeast-southwest dips to the southeast, offsetting a fracture set also striking northeast-southwest but dipping to the northwest (#50, not visible in this view). Fractures striking northeast-southwest appear to have formed more recently than fractures in other orientations.

Small indentation at the top of the image (and all other axial images) is the principal orientation scribe. Approximate position of true north has been measured using orientation survey data provided by Scientific Drilling International.

FIGURE 4

AXIAL CT IMAGE
WELL : UPRC REMINGTON 21-1H
DEPTH : 7452.5'

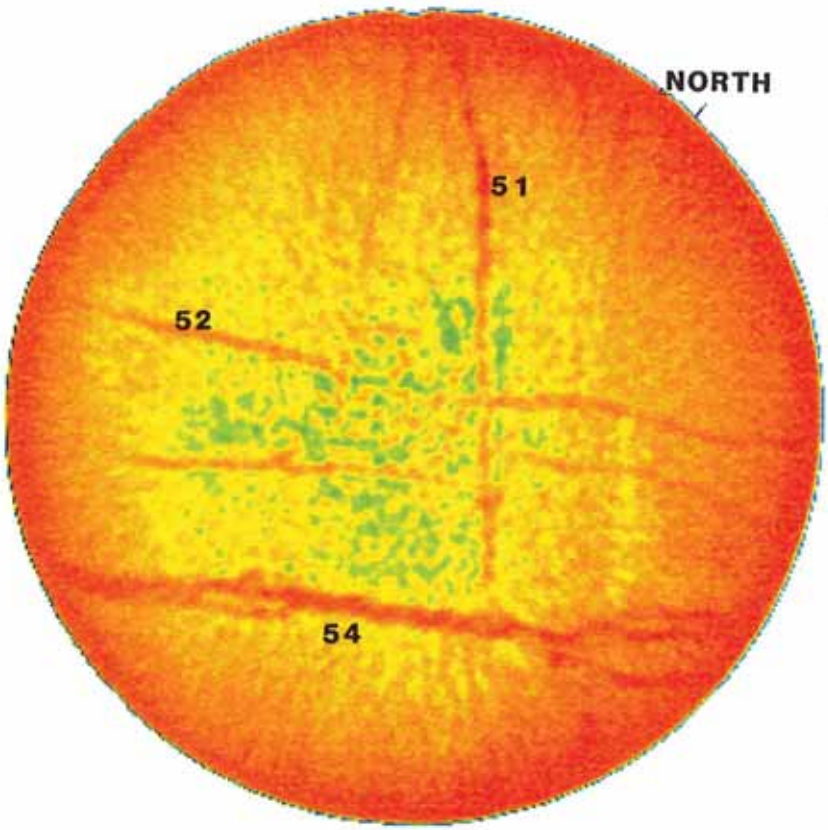

uprc5848c/dry/R003.vff
TerraTek CORESCAN (c)1993 KV:130 MA:250 FOV:160 ID:(4)UPRC5848C

Figure 5

Axial CT image, 7456.4', shows intersecting fractures at contact between shale (green) and silty dolomite (red). Strike of bedding is north northwest-south southeast, the dominant bedding orientation in this interval. Shale zones typically contain completely mineralized fractures (red to yellow linear traces #0, #62a and #64) and totally open fractures (not visible in this view). Dolomite intervals are more likely to contain partially mineralized fractures (green and red linear trace #62c) and non-mineralized fractures (green trace #63) as well as completely filled fractures (red trace #62b). Porosity along one partially mineralized fracture (#62c) was not apparent in core examination. Non-mineralized fracture (#63) was broken open during coring/handling to reveal slickensides on exposed fracture surface; such evidence of fracture movement was observed in fractures throughout the core. Gouge appears to be present along fracture #0 (which was evident in thin section and CT images but not in core examination).

Crosscutting and terminating relationships indicate that fracture sets originated in the following order, from oldest to most recent: #0, #61 (not visible), #63, #64 and #62. Fractures striking northwest-southeast may have formed relatively early, followed by fractures striking northeast-southwest. Filled fractures striking north northwest-south southeast are more abundant than filled fractures in other orientations (see Table 4-3).

FIGURE 5

AXIAL CT IMAGE
WELL : UPRC REMINGTON 21-1H
DEPTH : 7456.4'

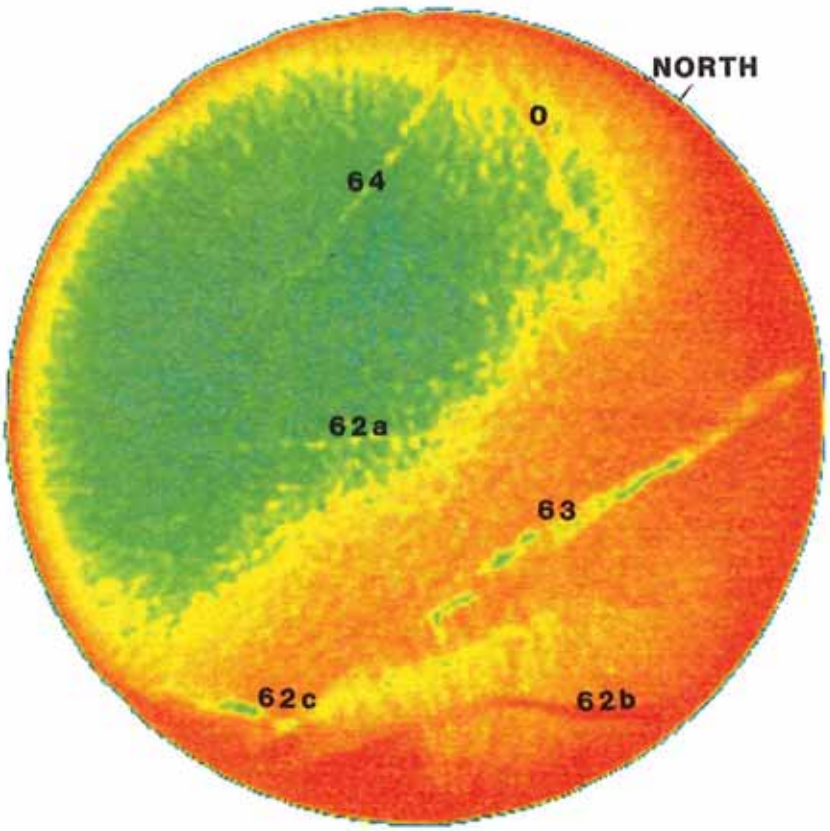

uprc5848d/density/R014.vff
TerraTek CORESCAN (c)1993 KV:130 MA:250 FOV:160 ID:(8)UPRC5848D

Figure 6

Axial CT image, 7463.4', shows the intersection of completely mineralized fractures (red linear traces) and one non-mineralized fracture (yellow-green trace) in shaley dolomite. Network of parallel filled fractures (#71) combine to form a single fracture approximately 8mm wide and containing an aperture 0.2mm wide, seen in Figure 7. The entire fracture is approximately 34cm long. Other filled fractures in this view are more typical of filled fractures in the core, averaging about 7cm long and measuring less than 1mm wide. The fracture(s) striking north-south (#71) appears to have formed earliest, followed by fractures striking northeast-southwest (#78, #79). Partially open fracture (#00) was not visible in core examination and is probably relatively narrow and discontinuous; partially open fractures are much less abundant than completely filled fractures in shale zones.

FIGURE 6

AXIAL CT IMAGE
WELL : UPRC REMINGTON 21-1H
DEPTH : 7463.4'

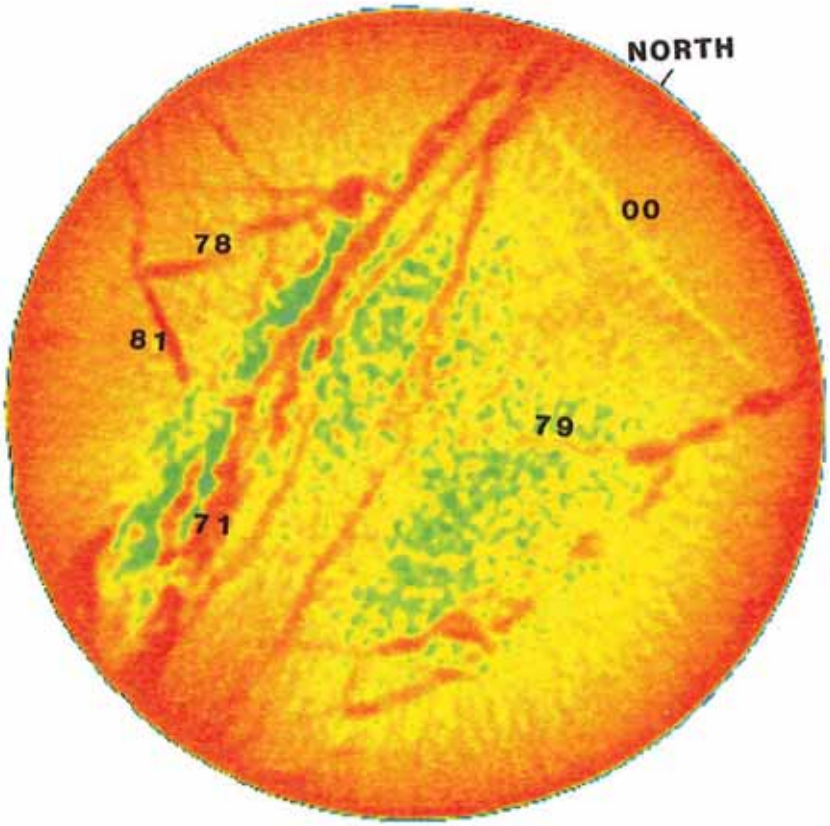

uprc5848c/dry/R002.vff
TerraTek CORESCAN (c)1993 KV:130 MA:250 FOV:160 ID:(4)UPRC5848C

4.3 FRACTURE ANALYSIS METHODOLOGY

Fractures are described using the format developed by TerraTek. The fracture description scheme delineates the various fracture types present, their morphologic characteristics, and intensity on a foot-by-foot basis. Each fracture (or set of similar parallel fractures within a foot is assigned a unique fracture identification number, which is recorded with the depth on the fracture printout. The depth listed for each fracture set is the bottom depth of the one-foot interval in which the fractures originate. The printout documents ten characteristics for the fracture set, including fracture type, qualifier (fracture origin), apparent fracture dip, length, width of fracture mineralization, aperture, filling (mineralization), fracture porosity type, fracture spacing, and the number of fractures per set. Percent fracture porosity is estimated for mineralized fractures containing vugs. This information is followed by a column for comments concerning each set of fractures.

The fracture dip recorded in the description database is visual estimate that in not corrected for deviation of the wellbore from vertical. Fracture width (for filled fractures) is the width of fracture mineralization. Fracture aperture is the measured aperture width for partially open and partially mineralized fractures. Fracture length is measured along the long dimension of the fracture. For fractures that penetrate the core, length is a direct function of fracture dip. Fracture porosity is classified as follows: Open or partially open, closed, vuggy, or partially open with vugs.

Fracture data are presented with fracture types in order, progressing from most open to least open. The following paragraphs provide a brief description of each of these fracture types. **Totally open fractures** split the core into two pieces. Only open fractures which are definitely or possibly natural in origin are classified as totally open (open fractures which are definitely induced are classified as induced). The qualifier code indicates whether a fracture is definitely natural, possibly natural, or probably induced. Totally open fractures which are definitely natural are given a qualifier of "0". These fractures are commonly planar and may exhibit striations,

slickensides, or incipient mineralization of fracture surfaces. Open fractures which are possibly natural are given a qualifier of ''1''. These fractures are planar, but lacking the slickensides or incipient mineralization which characterize fractures which are definitely natural. Open fractures give a qualifier of ''2'' are of very questionable origin, probably induced. These fractures lack the slickensides or traces of mineralization typically present in natural open fractures, and fracture surfaces may be slightly curved or exhibiting a fresher appearance than fractures which are known to be natural.

Partially open fractures (non-mineralized) are divided into two groups based on size and penetrativeness. Partially open penetrative fractures are partially open fractures that can be traced around the circumference of the core. Partially open non-penetrative fractures are short, discontinuous fractures that commonly terminate within the core or are confined to a single bed. These fractures are assigned qualifiers of ''0'', ''1'', or ''2'' (natural, possibly natural, or probably induced). Partially open fractures with a qualifier of ''0'' might exhibit vuggy porosity, or slickensides on exposed fracture surfaces, indicating a fracture of natural origin. Fractures with a qualifier of ''1'' lack these indications of origin, but may possibly be natural. A qualifier of ''2'' indicates a fracture which may have been induced during coring or handling. These fractures may exhibit slightly sinusoidal traces or incipient petal morphology (steepening dip angle as the fracture penetrates the core).

Face cleats in coal or carbonaceous material, are the most penetrative and thoroughgoing cleat set. Where only are set of cleats is present, they are automatically designated face cleats. **Filled fractures** contain some type of mineral or gouge filling. Filled fractures containing natural porosity are classified separately from completely mineralized (closed) fractures.

Fractures are described in their least disrupted state. For example, a partially open penetrative fracture that is totally open along part of its trace is described as partially open because that is probably its natural state in the reservoir.

4.4 TABLES AND CALCULATIONS

The average fracture parameters listed in Table 4-1, are calculated from values listed in the fracture description printout. Average fracture length, width, aperture, and spacing, are calculated by dividing the sum of measurements (one per fracture set) by the number of fracture sets for the given fracture type. No correction is made for the number of fractures in each set. Average fracture intensity is the total number of fractures of the given type, divided by the total vertical core footage (61 feet). Fracture intensity values in Figures 1 and 2 have been adjusted to reflect the actual number of fractures in each foot of core, although the fractures may originate above the foot listed. Dip azimuth values in Table 4-2 are calculated by averaging representative bedding plane orientation measurements for each foot of core. More than one dip azimuth value may be listed for a foot of core in which the bedding orientation changes. Average fracture orientations in Table 4-3 are approximations (±5°) of the predominant dip azimuth values for each fracture type; no correction is made for the number of fractures in each set.

4.5 FRACTURE ORIENTATIONS

Initially, continuous sections of core were pieced together and any breaks or spins were noted. The principal reference scribe was used to obtain a bench orientation measurement for each fracture set and for representative bedding planes, using TerraTek's computerized goniometer. One measurement was performed for each fracture set. These bench data were correlated with orientation survey data provided by Scientific Drilling International. The resulting in-situ orientations are tabulated by depth and by fracture type. Fracture description and orientation data can be correlated using the fracture numbers listed under ''Fracture Number'' in the description table, and after the asterisk under ''Sample'' in the orientation table.

4.6 FRACTURE PLOTS

In-situ orientations for each fracture type, and for bedding planes, are represented by a suite of three color diagrams (strike rose diagram, dip azimuth rose diagram, dip histogram). Partially open penetrative fractures and partially open non-penetrative fracture have been plotted together under the heading "Partially Open Non-mineralized Fractures." Each measurement on the fracture plots represents one set of fractures, rather than individual fractures.

4.7 FRACTURE DESCRIPTION DATA FORMAT

Lines read from left to right according to the following key:

Column

1 Depth (bottom depth of the one foot interval)
2 Fracture Number
3 Sample Number
4 Fracture Type
- 1 - Partially open penetrative fracture
- 2 - Totally open penetrative fracture
- 3 - Partially open non-penetrative fracture
- 4 - Filled fracture, no natural porosity
- 5 - Filled fracture with some natural porosity
- 6 - Coring or handling induced fracture
- 7 - Face Cleat

5 Fracture Qualifier
- 0 - Natural in origin
- 1 - Possibly natural in origin
- 2 - Probably coring or handling induced

6 Fracture Dip Angle (visual estimate in degrees)
7 Fracture Length
8 Fracture Fill Width (mm.)
9 Fracture Aperture (mm.)
10 Fracture Filling Code
- 0 - No filling
- 6 - Other (Halite)
- 7 - Gypsum/Anhydrite
- 9 - Gouge

11 Fracture Porosity Type
- 0 - Closed
- 1 - Vugs
- 2 - Open or partially open
- 3 - Open or partially open with vugs

12 Percent porosity (est. for partially filled fractures)
13 Fracture Spacing (mm.)
14 Fracture Intensity (fractures/set)
15 Comments (see Fracture Comments for legend)

4.8 FRACTURE COMMENTS

1. Induced
2. Probably induced
3. Induced open
4. Possibly induced
5. May be induced open
6. Part of fracture induced open
7. Induced by hammer
8. Induced, fracture surface curved
9. Induced by scribe
10. Fractures within cherty bed (or chert nodule)
11. Extends into next foot
12. Extends into next two feet
13. Extends into next three feet
14. Extends into next four feet
15. Extends into next five feet
16. Interval rubblized
17. Part of interval rubblized
18. Interval rubblized, natural fractures present
19. No natural fractures
20. No other natural fractures
21. No preferred orientation
22. Fill material discontinuous
23. Stylolite open or partially open
24. Stylolite acts as barrier to oil
25. Fracture offset by stylolite
26. Fracture truncated by stylolite
27. Staining spotty
28. Parallel to bedding
29. Fracture width variable
30. Slickensides
31. Not orientable
32. Bedding displaced by fracture
33. Fractures confined by bedding
34. Slickensided surfaces in rubble
35. Thin highly fractured beds
36. Part of fracture totally open
37. Fractures in rubble
38. Subparallel to bedding
39. Normal shear displacement along fracture
40. Reverse shear displacement along fracture

FRACTURE DESCRIPTION DATABASE
UNION PACIFIC RESOURCES COMPANY
WELL: REMINGTON #21-1H

Depth (ft)	Fracture Number	Sample Number	Fracture Type	Qualifier	Dip Angle	Fracture Length (cm)	Fracture Width (mm)	Fracture Aperture (mm)	Fracture Fill	Porosity Type	Percent Porosity	Fracture Spacing (mm)	Fracture Intensity (fracs/set)	Comments
7436	1	1	2	0	15	10			0	2		78	3	28,30
7436	2	1	4	0	85	5	0.22		6	0		5	4	
7436	4	1	4	0	90	4	0.11		6	0		20	6	Terminates at fracture set #2
7436	3	1	4	0	90	5	0.08		6	0		37	2	Terminates at fracture set #2
7436	5	1	5	0	20	10	0.63	0.02	6,9	2			1	6,30
7437	9	2	2	0	15	10			0	2		18	4	28,30
7437	6	2	3	1	50	6		0.03	0	2			1	
7437	7	2	5	0	85	9	0.13	0.04	6	2		9	9	6
7437	8	2	5	0	90	6	0.22	0.02	6	2		47	3	11,6
7438	11	3	4	0	50	6	0.22		7	0		5	4	
7438	10	3	4	0	70	6	0.27		7	0		13	3	
7439	13	4	4	0	70	2	0.35		7	0		7	8	
7439	12	4	4	0	90	6	0.61		7	0		7	13	11, Braided w/fractures in set #13
7440	14	5	4	0	85	4	0.27		7	0			1	
7441	15	6	4	0	90	4	0.63		6	0		8	10	
7441	16	6	4	0	85	1	0.28		6	0		21	3	
7442	17	7	2	0	15	10			0	2		34	4	28,36
7442	20	7	4	0	80	6	0.33		7	0		20	3	
7442	19	7	4	0	90	4	0.41		6	0		9	7	6
7442	18	7	5	0	90	11	0.96	0.07	6,9	2		35	5	6,30
7443	21	8	4	0	50	8	0.57		7	0		10	4	
7444	24	9	1	1	75	12		0.06	0	2			1	
7444	22	9	2	0	10	10			0	2		96	3	28,30
7444	23	9	2	0	20	11			0	2			1	30
7444	26	9	4	0	80	6	1.40		7	0		53	2	
7444	25	9	5	0	75	9	0.65	0.03	6	2			1	
7445	31	10	1	1	75	11		0.04	0	2			1	
7445	29	10	2	0	10	10			0	2		11	2	28,30
7445	28	10	5	0	90	9	0.11	0.01	6	2			1	6
7445	27	10	5	0	85	8	0.18	0.02	6	2		90	2	6
7446	30	11	2	0	30	12			0	2			1	30
7446	34	11	4	0	45	9	0.55		6	0		15	5	
7446	33	11	4	0	30	10	0.87		6,9	0		15	2	6
7446	35	11	4	0	90	5	1.38		6	0			1	
7446	36	11	4	0	10	10	2.05		6	0			1	
7446	32	11	5	0	40	11	2.06	0.48	6,9	3	15	12	2	6,30, Fracture contains euhedral crystals
7447	38	12	2	0	20	11			0	2			1	30
7447	37	12	2	0	10	10			0	2			1	30

Depth (ft)	Fracture Number	Sample Number	Fracture Type	Qualifier	Dip Angle	Fracture Length (cm)	Fracture Width (mm)	Fracture Aperture (mm)	Fracture Fill	Porosity Type	Percent Porosity	Fracture Spacing (mm)	Fracture Intensity (fracs/set)	Comments
7447	39	12	4	0	85	10	0.42		7	0		17	7	
7448	40	13	4	0	80	7	0.55		7	0		10	2	
7449	41	14	5	0	85	10	0.48	0.06	6	2		15	8	6
7450	46	15	4	0	10	7	0.19		7	0		6	2	
7450	45	15	4	0	80	10	0.28		7	0		18	4	
7450	42	15	5	0	90	4	0.17	0.02	7,6	2		4	5	
7450	44	15	5	0	20	10	1.82	0.03	7,6	2			1	
7450	43	15	5	0	90	7	0.17	0.01	7,6	2		10	4	
7451	48	16	5	0	30	13	1.10	0.08	7,6	2			1	
7451	47	16	5	0	15	10	0.27	0.02	7,6	2		120	2	
7452	50	17	4	0	80	20	1.45		6	0			1	11
7452	49	17	5	0	85	6	0.30	0.04	7,6	2		9	5	6
7453	57	18	2	0	5	10			0	2			1	30
7453	55	18	4	0	10	10	0.83		6,9	0		96	2	
7453	53	18	4	0	70	9	0.31		7,6	0		23	7	
7453	51	18	4	0	85	5	0.28		7,6	0		12	15	Terminates at lower shale contact
7453	54	18	4	0	80	13	0.52		9	0			1	Offsets fracture in set #50
7453	52	18	4	0	90	3	0.25		7,6	0		10	18	
7453	56	18	5	0	65	15	0.43	0.11	6,9	2			1	11,32
7454	58	19	5	0	15	10	0.29	0.07	6	2		21	5	
7455	59	20	4	0	85	7	0.16		7	0		4	6	Closely spaced fractures arranged en echelon
7456	60	21	4	0	85	8	0.44		7	0			1	
7457	63	22	3	0	65	9		0.04	0	2			1	6,30
7457	62	22	4	0	90	6	0.15		6	0		12	30	Terminates at upper shale contact
7457	61	22	4	0	80	5	0.22		6	0		31	3	Terminates at upper shale contact
7457	64	22	4	0	75	10	0.14		7	0		14	7	
7458	65	23	4	0	50	10	0.46		7,9	0		38	2	Fracture sl. stylolitic
7458	67	23	4	0	80	14	4.50		7	0			1	
7458	66	23	4	0	85	10	0.31		7,9	0			1	
7459	68	24	5	0	85	4	0.46	0.02	7	2			1	6
7460	69	25	4	0	75	17	0.33		7	0		6	3	
7461	70	26												19
7462	72	27	4	0	85	2	0.13		7	0		25	7	33
7462	71	27	5	0	90	34	8.00	0.20	7,6	3	20		1	12,28, Oil staining in fracture
7463	76	28	4	0	90	13	6.00		7	0			1	11, Merges w/fracture in set #71
7463	73	28	4	0	85	2	0.21		7	0		31	6	33
7463	75	28	4	0	85	6	0.13		6	0		8	2	
7463	74	28	5	0	75	5	0.29	0.03	6	2		11	7	Terminates at fracture set #71
7464	80	29	2	0	10	10			0	2		107	2	28,30
7464	79	29	4	0	85	7	0.28		6	0		5	9	
7464	78	29	4	0	90	3	1.00		6	0			1	
7464	81	29	4	0	60	7	0.05		9	0			1	11

Depth (ft)	Fracture Number	Sample Number	Fracture Type	Qualifier	Dip Angle	Fracture Length (cm)	Fracture Width (mm)	Fracture Aperture (mm)	Fracture Fill	Porosity Type	Percent Porosity	Fracture Spacing (mm)	Fracture Intensity (fracs/set)	Comments
7464	77	29	7	0	90	1		0.01	0	2		4	11	Cleats in coal beds at 7463.4', may contain tr. halite
7465	82	30	2	0	15	10			0	2			1	30
7465	84	30	4	0	80	5	0.44		7,9	0		10	9	Terminates at fracture set #83
7465	87	30	4	0	85	2	0.23		6	0		2	5	Terminates at fracture set #86
7465	83	30	4	0	15	10	0.80		7,9	0			1	
7465	86	30	4	0	90	5	0.21		6	0		6	12	
7465	85	30	5	0	90	10	0.84	0.15	6	2			1	
7466	88	31	2	0	10	10			0	2		32	3	30
7466	90	31	2	0	30	12			0	2			1	30
7466	89	31	2	0	20	11			0	2			1	30
7466	94	31	2	0	25	11			0	2			1	11,30
7466	92	31	4	0	90	8	0.13		9	0			1	
7466	91	31	5	0	70	12	0.32	0.04	6,9	2			1	
7466	93	31	5	0	90	2	0.11	0.01	6	2			1	6
7467	97	32	2	0	30	11			0	2			1	30
7467	96	32	2	0	50	13			0	2			1	30
7467	95	32	2	0	25	11			0	2			1	30
7467	102	32	3	1	40	6.0		0.05	0	2		31	2	
7467	100	32	4	0	90	8	0.31		6	0			1	
7467	98	32	5	0	25	8	1.88	0.06	6,9	2			1	
7467	101	32	5	0	65	10	0.35	0.13	6	2			1	
7467	99	32	5	0	75	10	0.47	0.04	6	2			1	6
7468	103	33	3	1	40	8.0		0.10	0	2		27	5	
7468	104	33	3	1	70	7.0		0.03	0	2			1	
7469	105	34	2	0	5	10			0	2			1	30
7469	106	34	5	0	90	2	0.56	0.02	7,6	2		7	5	33,11, Terminates at fracture set #107
7469	108	34	5	0	90	2	0.11	0.02	7,6	2		9	2	
7469	107	34	5	0	90	3	0.37	0.08	7,6	2			1	33,11
7470	109	35	2	0	10	10			0	2		59	2	28,30
7470	111	35	4	0	90	5	0.46		7	0		22	2	
7470	110	35	4	0	90	6	0.28		7	0		24	4	33
7471	113	36	3	1	90	2		0.02	0	2		16	3	6
7471	112	36	4	0	30	8	0.15		9	0			2	32
7472	114	37	3	1	90	5		0.02	0	2		5	8	
7472	115	37	4	0	90	6	0.17		7	0		5	14	
7473	117	38	4	0	85	6	0.18		7	0		8	8	
7473	116	38	4	0	85	8	0.14		7	0		9	6	
7474	118	39												19, Anhydrite
7475	119	40	4	0	90	5	0.17		7	0		23	3	11
7476	120	41												20, Anhydrite
7477	121	42												19, Anhydrite
7478	122	43												19, Anhydrite

Depth (ft)	Fracture Number	Sample Number	Fracture Type	Qualifier	Dip Angle	Fracture Length (cm)	Fracture Width (mm)	Fracture Aperture (mm)	Fracture Fill	Porosity Type	Percent Porosity	Fracture Spacing (mm)	Fracture Intensity (frac/set)	Comments
7479	124	44	1	0	20	10		0.04	0	2			1	6,30
7479	125	44	3	1	90	1		0.01	0	2		5	10	
7479	123	44	4	0	90	9	0.15		7	0			1	
7479	126	44	5	0	30	11	0.23	0.04	6,9	2			1	32
7480	127	45	2	0	5	10			0	2			1	30
7480	128	45	2	0	10	10			0	2			1	30
7480	129	45	4	0	85	3	0.41		6	0			1	
7480	131	45	4	0	15	10	0.83		7	0			1	
7480	131	45	4	0	15	10	0.83		7	0			1	
7480	130	45	4	0	90	3	0.11		6	0		4	7	6,30
7481	132	46												19
7482	135	47	3	1	70	9		0.11	0	2			1	
7482	137	47	5	0	90	4	0.11	0.02	6	2		6	3	11,6
7482	133	47	5	0	75	36	3.00	0.18	6	2			1	11,6
7482	134	47	5	0	20	11	0.12	0.02	6	2		29	2	
7483	136	48	2	0	10	10			0	2			1	30
7484	139	49	2	0	15	10			0	2		32	2	28,30
7484	140	49	4	0	15	10	2.50		7	0			1	11
7484	138	49	5	0	80	6	0.13	0.02	6	2		7	7	6
7485	142	50	2	0	15	10			0	2			1	28,30
7485	143	50	2	0	10	10			0	2		21	2	30
7485	141	50	4	0	85	15	0.11		7	0			1	Terminates at upper shale contact
7486	144	51												19, Anhydrite
7487	145	52												19, Anhydrite
7488	146	53												19, Anhydrite
7489	147	54												19, Anhydrite
7490	148	55												19, Anhydrite
7491	149	56	2	0	5	10			0	2		60	2	28,30
7491	151	56	4	0	90	4	0.10		7	0		15	9	
7491	150	56	4	0	20	10	3.50		7	0			1	11,6
7492	155	57	2	0	10	10			0	2			1	28,30
7492	153	57	4	0	90	5	0.16		7	0		7	6	
7492	154	57	4	0	90	3	0.09		7	0			1	
7492	152	57	5	0	90	20	17.00	0.20	7,6	3	15		1	6, Fracture contains euhedral crystals
7493	156	58												19, Anhydrite
7494	157	59												19, Anhydrite
7495	158	60	4	0	90	4	0.38		7	0		8	13	33
7495	159	60	4	0	90	2	0.22		7	0		6	10	33
7496	163	62												17, Rubble contains shale fragments w/slickensides
7496	161	61	2	0	10	10			0	2		23	4	28,30
7496	160	61	4	0	90	12	0.25		7	0			1	
7496	162	61	5	0	90	9	8.00	0.12	7,6	3	20		1	6, Fracture contains euhedral crystals

FRACTURE ORIENTATIONS

TerraTek
University Research Park
420 Wakara Way • Salt Lake City, Utah 84108
Telephone (801) 584-2480
FAX (801) 584-2432

FRACTURE ORIENTATION DATA BASE
UNION PACIFIC RESOURCES COMPANY
WELL: REMINGTON 21-1H

```
**************************************************************
*                                                            *
*                          LEGEND                            *
*                                                            *
* TOPN = TOTALLY OPEN FRACTURE                               *
* POPN = PARTIALLY OPEN PENETRATIVE FRACTURE                 *
* PONP = PARTIALLY OPEN NON-PENETRATIVE FRACTURE             *
* FACE = FACE CLEAT                                          *
* FILO = PARTIALLY MINERALIZED FRACTURE WITH NATURAL POROSITY *
* FILL = COMPLETELY MINERALIZED FRACTURE, NO NATURAL POROSITY *
* BDDG = BEDDING PLANE                                       *
*                                                            *
**************************************************************
```

DEPTH	SAMPLE	TOPN	POPN	PONP	FACE	FILO	FILL	BDDG
7436	1							N29W12S
7436	1*5					N19W51S		
7436	1*4						N68E84N	
7436	1*3						N86W90	
7436	1*2						N 1W80N	
7436	1							N29W12S
7436	1*1	N49W19S						
7436	1							N28W 9S
7437	2*6			N23W60S				
7437	2*9	N32W12S						
7437	2							N50W13S
7437	2*8					N21W85N		
7437	2*7					N57E86S		
7437	2							N38W11S
7437	2							N34W 8S
7438	3*10						N11W78S	
7438	3*11						N63E41N	
7439	4*13						N37W71S	
7439	4*14						N87E83S	
7439	4							N 9E12N
7439	4*12						N10E90	
7440	5							N40W 7S
7440	5							N24W 1S
7440	5							N30W 3S
7440	5*16						N40E85S	
7440	5*15						N14W79N	
7441	6							N34E18N
7441	6							N 1E14N
7441	6							N 1E 6N
7442	7							N 9W12S
7442	7*19						N87E83S	
7442	7*18					N 9E83S		
7442	7							N 4W 9S
7442	7*17	N 6E12N						
7442	7*20						N 2E83S	
7442	7							N12W 2S
7443	8*21						N76E54N	
7444	9*26						N 8E62S	
7444	9*24		N31E76S					

DEPTH	SAMPLE	TOPN	POPN	PONP	FACE	FILO	FILL	BDDG
7444	9*23	N10E19S						
7444	9*25					N31E79S		
7444	9							N28E11S
7444	9*22	N66W 8S						
7445	10*27					N26E79S		
7445	10							N77E10N
7445	10*28					N67W85S		
7445	10*29	N25W14N						
7445	10							N 6W17N
7445	10							N15W14N
7445	10*31		N11W69S					
7446	11							N40E18S
7446	11*30	N54W42N						
7446	11							N39E10S
7446	11							N10E 6S
7446	11*34						N17W60N	
7446	11*36						N78E 7S	
7446	11*33						N87W38S	
7446	11*35						N 5W83N	
7446	11*32					N82W43N		
7447	12							N 5E 5S
7447	12*37	N36E15S						
7447	12*39						N29E79S	
7447	12*38	N11W20N						
7447	12							N46E13S
7447	12							N18E 4S
7448	13*40						N13W79S	
7449	14							N47E 3N
7449	14							N 3W 6S
7449	14*41					N20W80S		
7449	14							N21W 7S
7450	15*44					N79E16S		
7450	15*42					N56E90		
7450	15*43					N38W86S		
7450	15							N80W10N
7450	15							N76W13N
7450	15*46						N71W 8N	
7450	15*45						N68W86S	
7450	15							N69W13N
7451	16*48					N65W40N		
7451	16							N52W18N
7451	16*47					N44W24N		
7451	16							N14W17N
7451	16							N26W 8N
7451	16							N20W13N
7452	17							N11W10N
7452	17							N 0E 3E
7452	17*49					N19E83N		
7452	17*50						N57E85N	
7452	17							N18W 9N
7453	18*56					N60W53S		
7453	18							N68W16N
7453	18							N76W14N
7453	18*57	N 9W 4N						
7453	18*51						N46W87N	
7453	18							N73W13N
7453	18*55						N 8W18S	

DEPTH	SAMPLE	TOPN	POPN	PONP	FACE	FILO	FILL	BDDG
7453	18*54						N58E80S	
7453	18*53						N 9W55S	
7453	18*52						N52E83N	
7454	19*58					N38W24N		
7455	20*59						N13E83N	
7456	21							N66W26N
7456	21							N67W26N
7456	21*60						N33W86S	
7456	21							N71W26N
7457	22*64						N39W71S	
7457	22							N87E18N
7457	22*61						N21E77N	
7457	22*62						N40E87S	
7457	22							N90E16N
7457	22*63			N13E53S				
7457	22							N81E18N
7458	23							N76E17N
7458	23							N83W21N
7458	23							N89E19N
7458	23*67						N12E87N	
7458	23*66						N 4E84N	
7458	23*65						N61W58N	
7459	24							N37E14S
7459	24							N67E 7N
7459	24							N40E13S
7459	24							N65E 9N
7459	24							N70E 9N
7459	24*68					N42W87S		
7459	24							N37E18S
7460	25							N23W15N
7460	25							N25W13N
7460	25							N16W14N
7460	25*69						N28W80S	
7461	26							N14W 9N
7461	26							N 5W23N
7461	26							N 4W17N
7462	27							N21W21N
7462	27							N23W12N
7462	27							N16W12N
7462	27*72						N 2W79S	
7462	27*71					N15W88N		
7463	28							N 9W18N
7463	28*75						N34E75N	
7463	28*74					N52W64S		
7463	28*73						N 1W74S	
7463	28							N32W20N
7463	28							N22W22N
7463	28*76						N18E75N	
7464	29*79						N42E89S	
7464	29							N51W11N
7464	29							N30W13N
7464	29							N25W12N
7464	29*78						N 9E86S	
7464	29*81						N79E56S	
7464	29*77				N20W88S			
7464	29*80	N28E10S						
7465	30*86						N 4W80N	

DEPTH	SAMPLE	TOPN	POPN	PONP	FACE	FILO	FILL	BDDG
7465	30*82	N59W23N						
7465	30							N39W17N
7465	30							N41W15N
7465	30*84						N24W80N	
7465	30*83						N33W38S	
7465	30*85					N 3E81S		
7465	30							N37W 9N
7465	30*87						N90E89S	
7466	31*89	N18W28N						
7466	31							N59W10N
7466	31*93					N65W86N		
7466	31							N89E20N
7466	31*92						N78W86S	
7466	31							N81W17N
7466	31							N82W22N
7466	31*91					N30E69N		
7466	31							N52W15N
7466	31*94	N83W19N						
7466	31*88	N43W17N						
7466	31*90	N 2W28S						
7466	31							N51W19N
7467	32*98					N61W27N		
7467	32*101					N60W43N		
7467	32*102			N85E52N				
7467	32*95	N71W33N						
7467	32*99					N20E60S		
7467	32							N53W23N
7467	32							N51W14N
7467	32							N61W20N
7467	32*96	N28E44N						
7467	32*97	N66W27S						
7467	32*100						N18W87S	
7468	33*104			N37E66S				
7468	33							N52W18N
7468	33							N63W10N
7468	33*103			N64E37N				
7468	33							N58W14N
7469	34							N67W12N
7469	34*107					N13E85N		
7469	34							N40W16N
7469	34*105	N84W 1S						
7469	34*108					N55E88N		
7469	34							N73W10N
7469	34*106					N53W90		
7470	35*111						N66W82N	
7470	35*109	N30W12S						
7470	35							N16E13N
7470	35							N15E 4N
7470	35*110						N16E77S	
7470	35							N21E10N
7471	36							N28E 5N
7471	36*113			N64E89N				
7471	36							N26W 7S
7471	36							N10W 8S
7471	36*112						N26W52N	
7471	36							N17W10S
7472	37							N25W 9S

DEPTH	SAMPLE	TOPN	POPN	PONP	FACE	FILO	FILL	BDDG
7472	37							
7472	37*115							N 0W11W
7472	37*114						N79W87S	
7472	37			N66E88S				
7473	38							N 2W 9S
7473	38							N87W20N
7473	38*116							N74E23N
7473	38						N30W79S	
7473	38*117							N82E12N
7474	39						N51E82S	
7474	39							N34E 8S
7474	39							N30E18S
7475	40							N31E14S
7475	40*119							N34E20S
7475	40						N55W88N	
7475	40							N29E18S
7476	41							N41E 6S
7476	41							N64E20S
7476	41							N55E12S
7477	42							N59E19S
7477	42							N44W10N
7477	42							N51W16N
7478	43							N59W14N
7478	43							N73W 5N
7478	43							N66W 9N
7479	44*124		N68W15S					N69W 7N
7479	44							N60W11N
7479	44*125			N56W74S				
7479	44*126					N67W36N		
7479	44							N44W14N
7479	44*123						N60W84S	
7480	44							N52W10N
7480	45*127	N35W10N						
7480	45							N29W13N
7480	45*130						N44E81S	
7480	45							N18W14N
7480	45*129						N41W89N	
7480	45*128	N71W14N						
7480	45							N40W17N
7480	45*131						N42W10S	
7481	46							N43W16N
7481	46							N52W20N
7481	46							N42W19N
7482	47*133					N26W69S		
7482	47							N37W21N
7482	47*134					N48E19S		
7482	47*137					N10W82S		
7482	47							N53W19N
7482	47							N55W13N
7482	47*135			N55E54S				
7483	48*136	N16W17N						
7483	48							N29E 8S
7483	48							N35E 3S
7483	48							N21E12S
7484	49*138					N52W80S		
7484	49*139	N41W13N						
7484	49							N73W15N

DEPTH	SAMPLE	TOPN	POPN	PONP	FACE	FILO	FILL	BDDG
7484	49							N68W15N
7484	49*140						N34W42N	
7484	49							N62W13N
7485	50*141						N47E74S	
7485	50							N36W17N
7485	50*143	N41W10N						
7485	50*142	N54W14N						
7485	50							N31W14N
7485	50							N22W15N
7486	51							N27W12N
7486	51							N32W13N
7487	52							N45E24N
7487	52							N34E20N
7487	52							N46E17N
7488	53							N45E20N
7488	53							N38E 8N
7488	53							N71E11N
7489	54							N61E17N
7489	54							N66E25N
7489	54							N63E26N
7490	55							N66E15S
7490	55							N87E25N
7490	55							N 0W 5W
7491	56*150						N22W38S	
7491	56							N15E 7N
7491	56							N75E 9S
7491	56							N55E 9N
7491	56							N74E14N
7491	56							N64E13N
7491	56*149	N79E 3N						
7491	56*151						N38W85S	
7492	57							N29E10N
7492	57							N29W10S
7492	57*154						N48E82N	
7492	57*155	N 8E14N						
7492	57							N14E13N
7492	57*153						N59W83N	
7492	57*152					N20W86N		
7493	58							N85E15S
7493	58							N72E18S
7493	58							N63E16S
7494	59							N23E11S
7494	59							N29W 6N
7494	59							N24E12S
7495	60*158						N26W86S	
7495	60							N 4W11N
7495	60							N15E17S
7495	60							N14W 9N
7495	60*159						N63W89S	
7496	61*160						N30E86S	
7496	61							N14E 8S
7496	61							N25E 9S
7496	61							N20E10S

FRACTURE PLOTS

TerraTek
University Research Park
420 Wakara Way • Salt Lake City, Utah 84108
Telephone (801) 584-2480
FAX (801) 584-2432

STRIKE ORIENTATION ROSE DIAGRAM

TOTALLY OPEN FRACTURES

UPRC

WELL: REMINGTON 21-1H

7435 - 7496 feet; n = 29

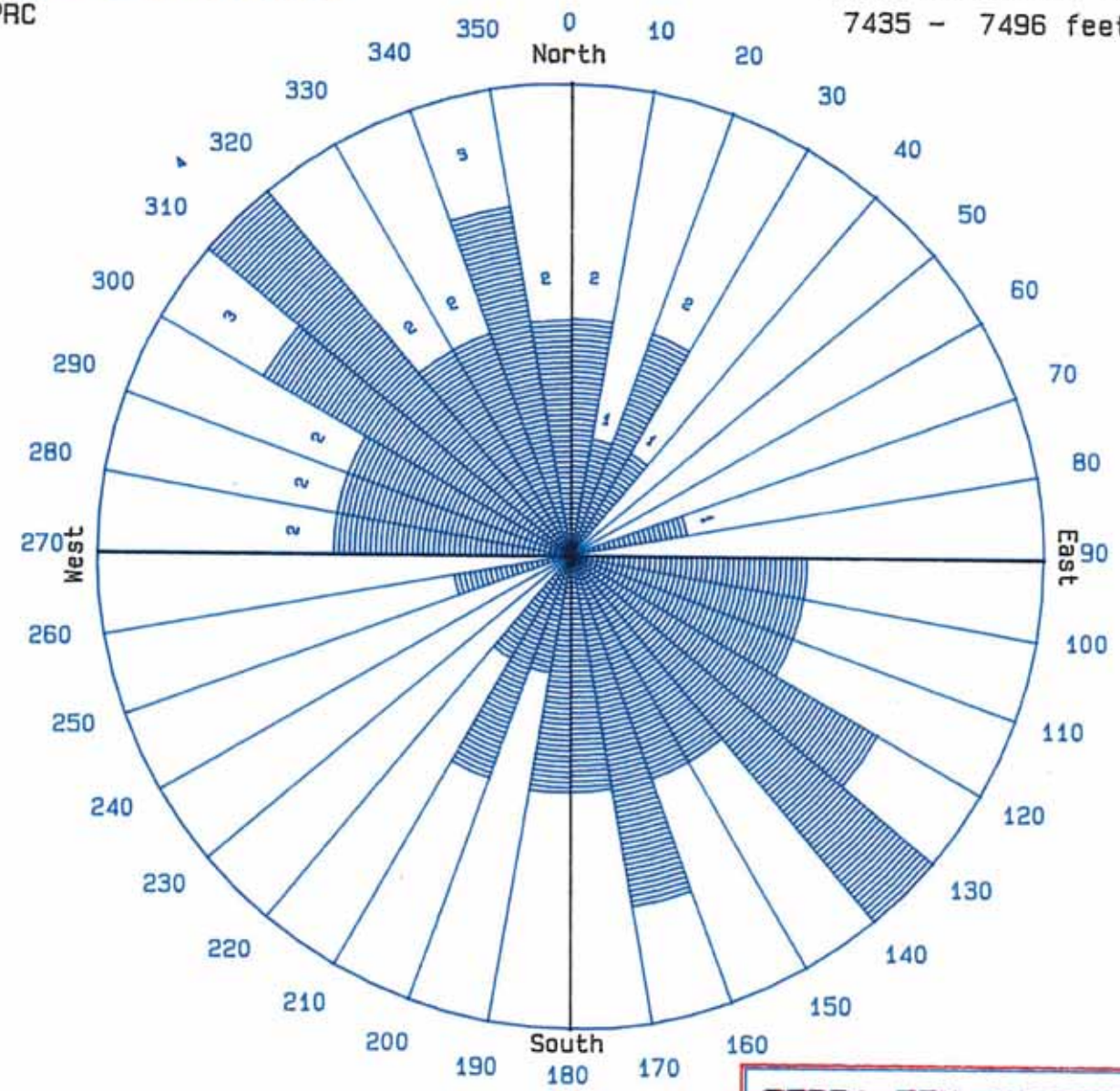

TERRA TEK GEOSCIENCE SERVICES

Ph: 1-800-FracLab

DIP AZIMUTH ROSE DIAGRAM

TOTALLY OPEN FRACTURES

UPRC

WELL: REMINGTON 21-1H

7435 - 7496 feet; n = 29

No vertical fractures present

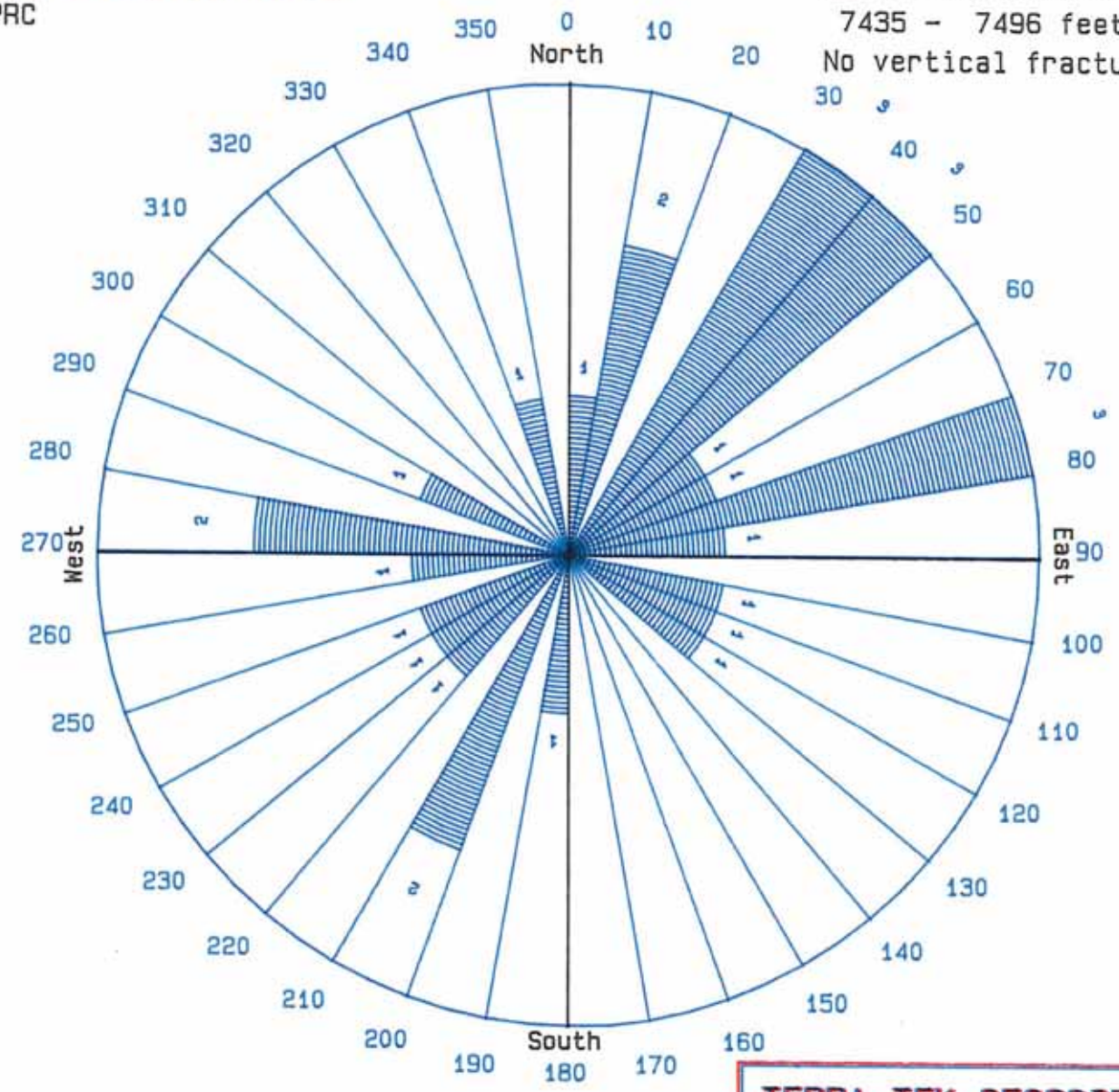

TERRA TEK GEOSCIENCE SERVICES

Ph: 1-800-FracLab

TERRA TEK GEOSCIENCE SERVICES

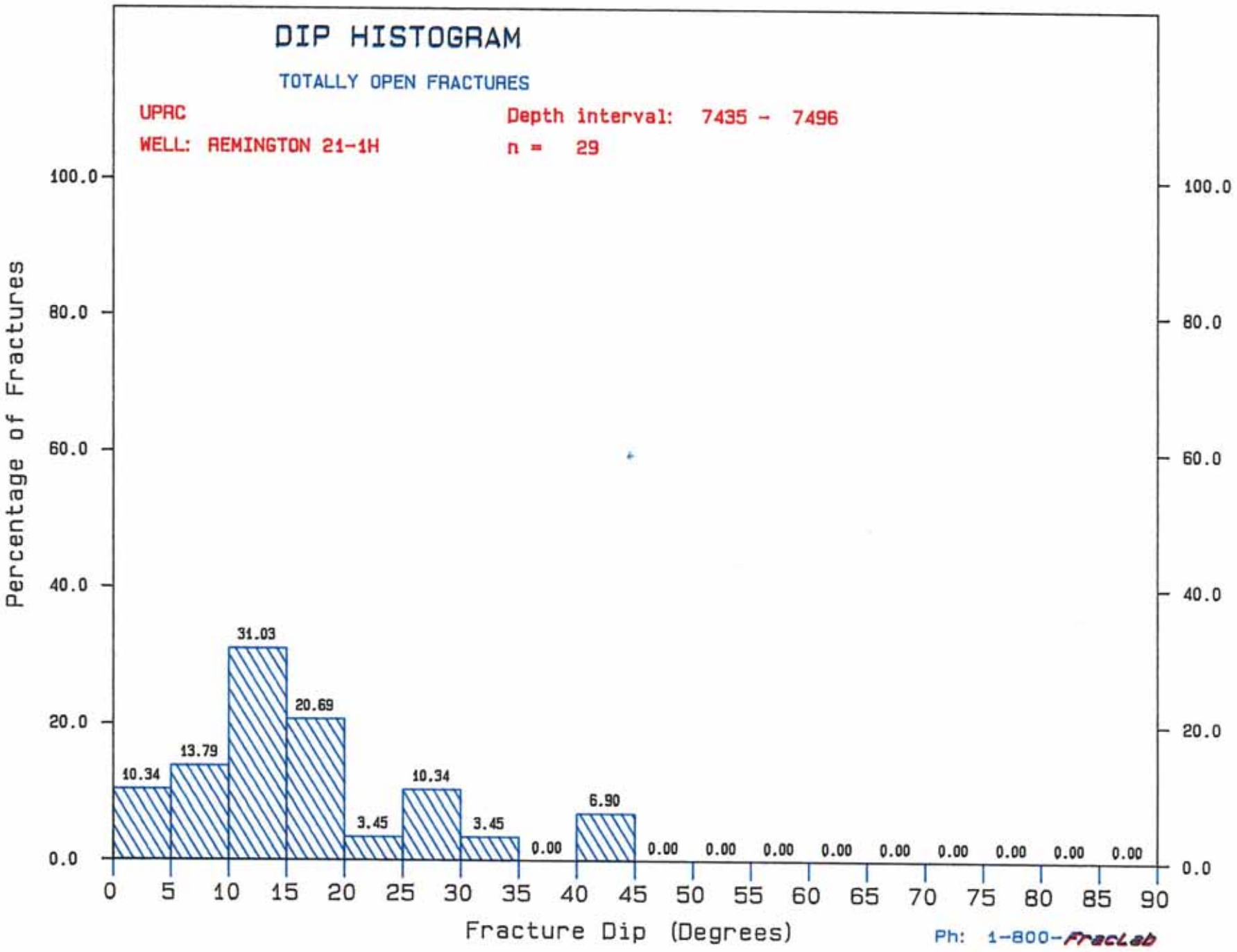

STRIKE ORIENTATION ROSE DIAGRAM

PART. OPEN NON-MINERALIZED FRACTURES
UPRC

WELL: REMINGTON 21-1H
7435 - 7496 feet; n = 13

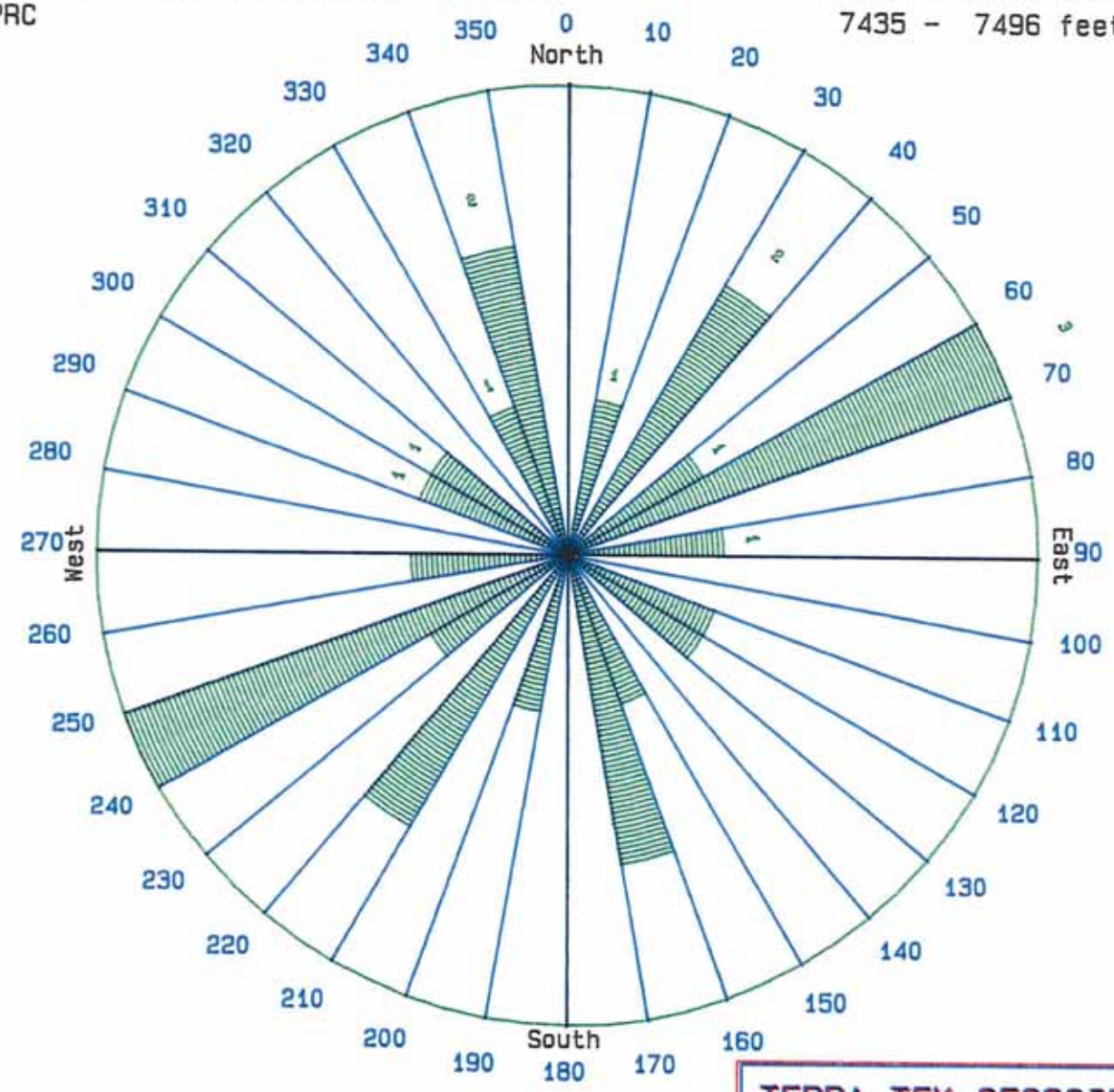

TERRA TEK GEOSCIENCE SERVICES
Ph: 1-800-FracLab

DIP AZIMUTH ROSE DIAGRAM

PART. OPEN NON-MINERALIZED FRACTURES
UPRC

WELL: REMINGTON 21-1H
7435 - 7496 feet; n = 13
No vertical fractures present

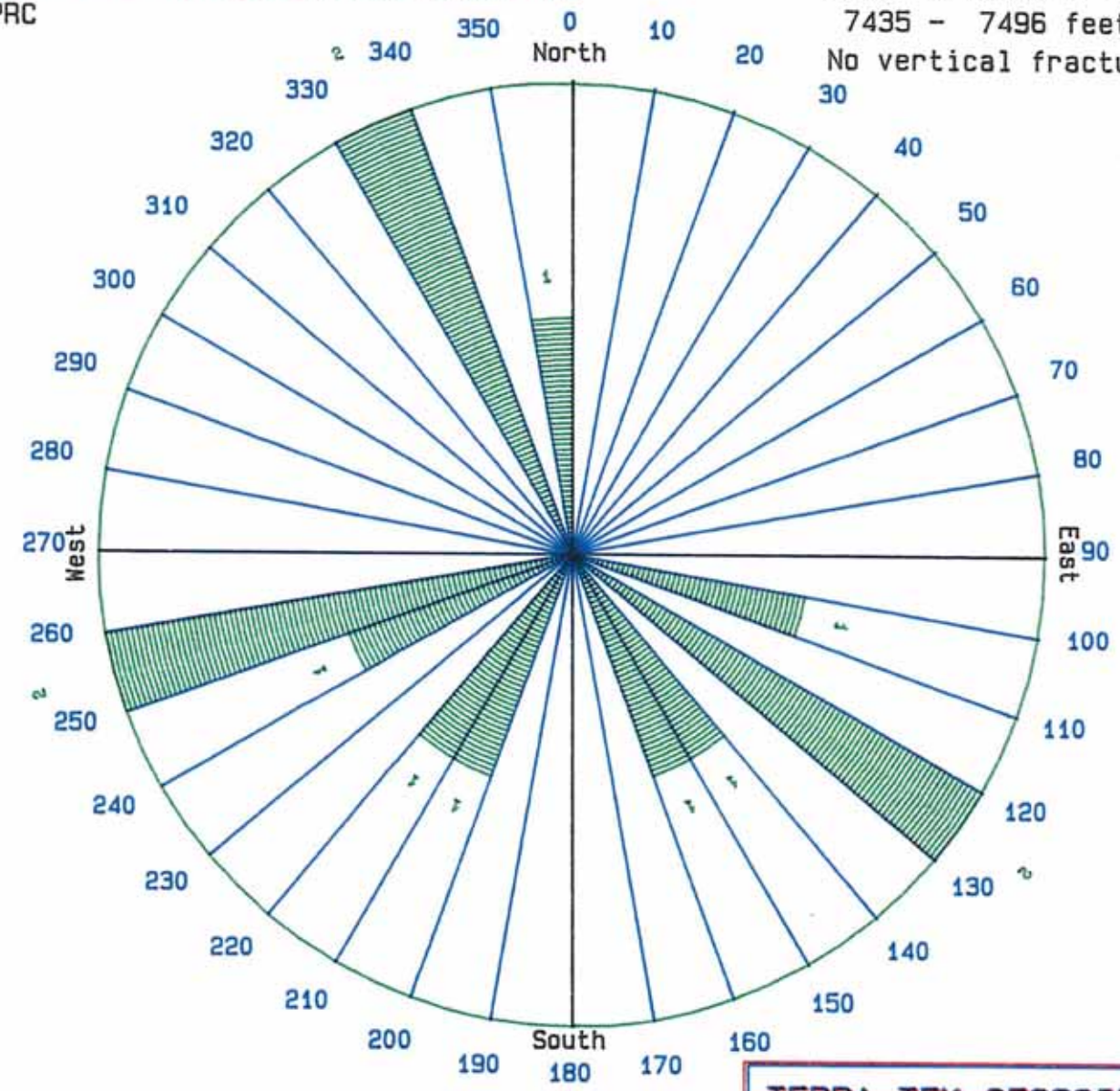

TERRA TEK GEOSCIENCE SERVICES
Ph: 1-800-FracLab

TERRA TEK GEOSCIENCE SERVICES

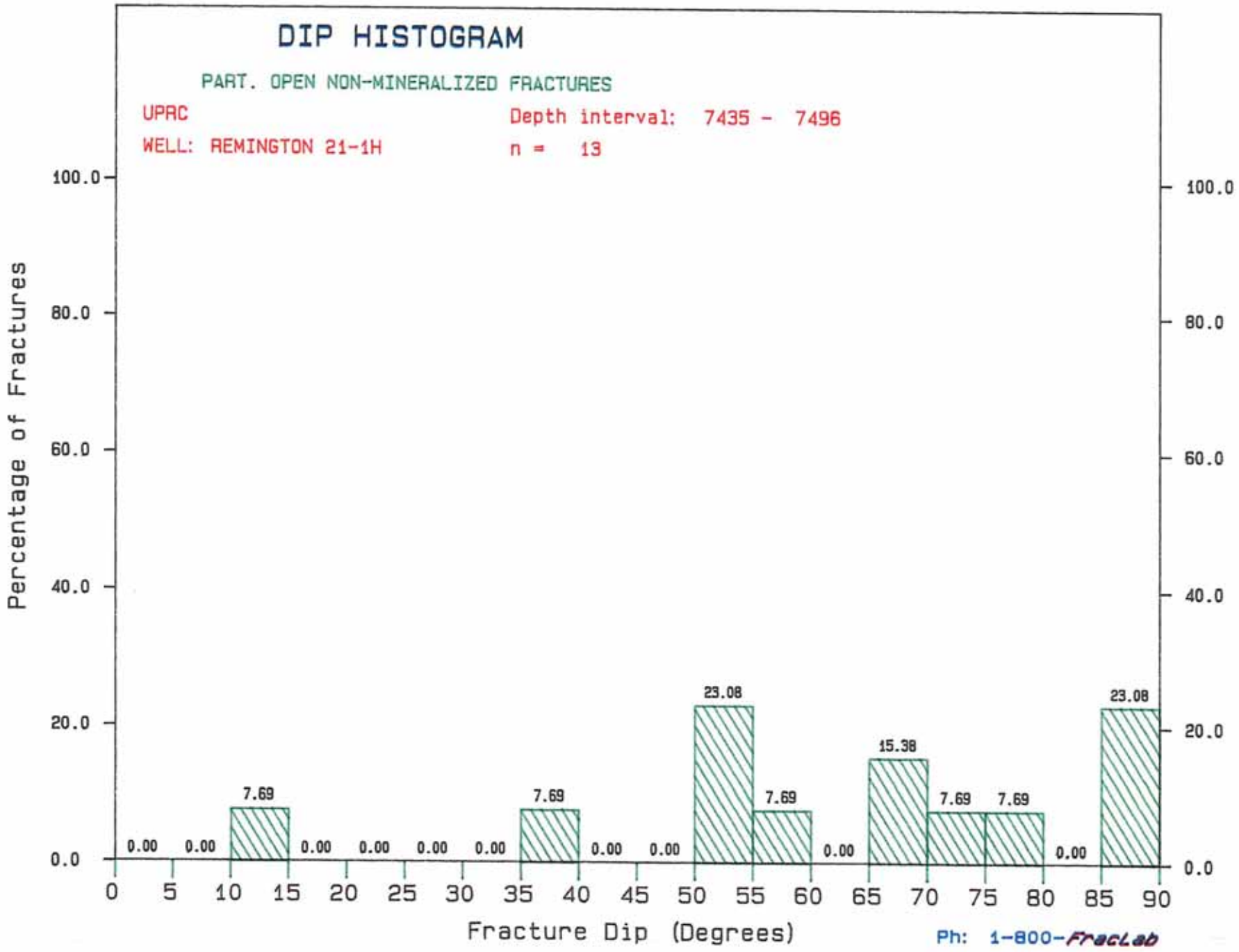

STRIKE ORIENTATION ROSE DIAGRAM

MINERALIZED FRACTURES W/POROSITY

UPRC

WELL: REMINGTON 21-1H

7435 - 7496 feet; n = 35

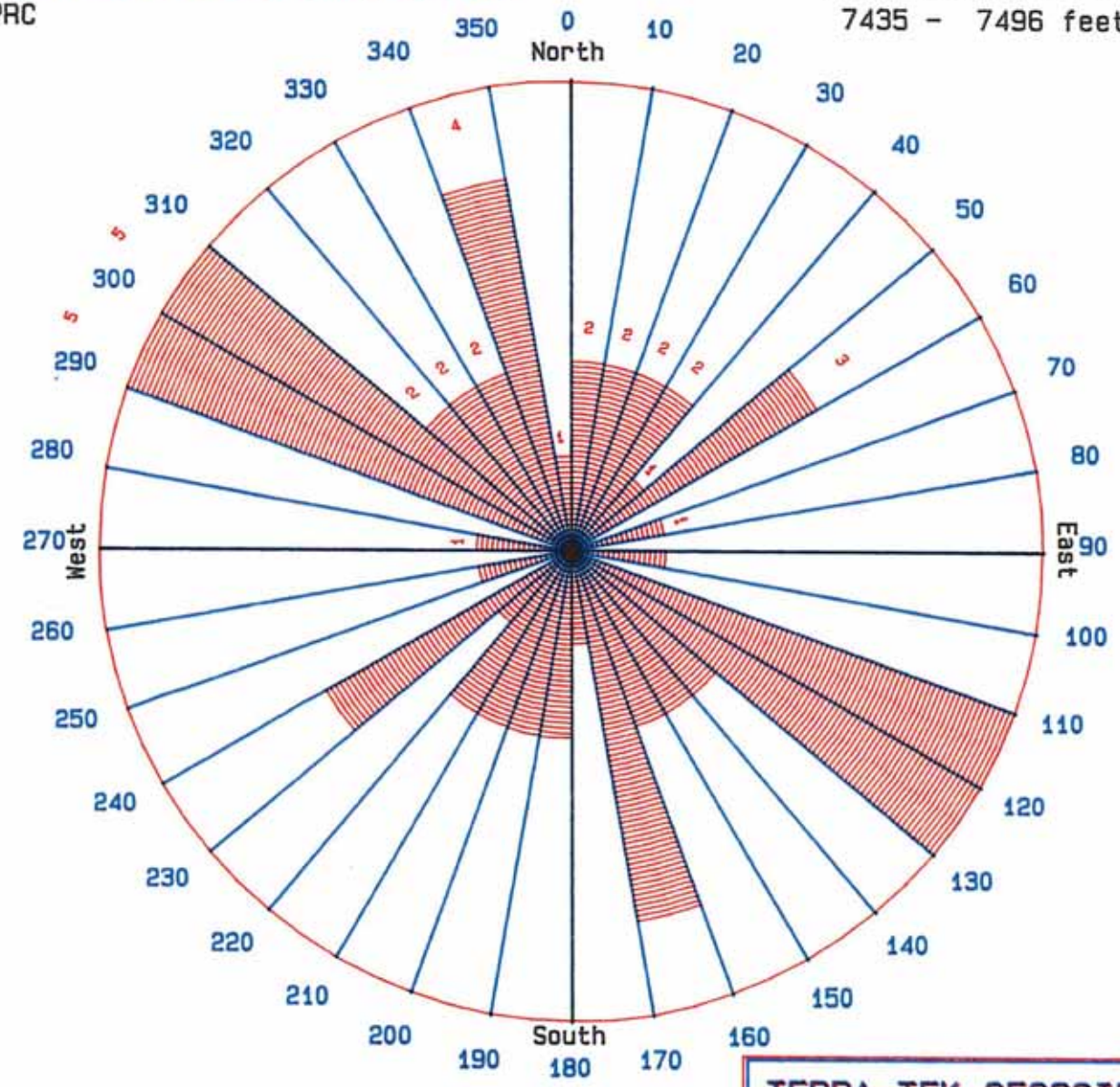

TERRA TEK GEOSCIENCE SERVICES

Ph: 1-800-FracLab

DIP AZIMUTH ROSE DIAGRAM

MINERALIZED FRACTURES W/POROSITY

UPRC

WELL: REMINGTON 21-1H

7435 - 7496 feet; n = 33

2 vertical feature(s) not plotted

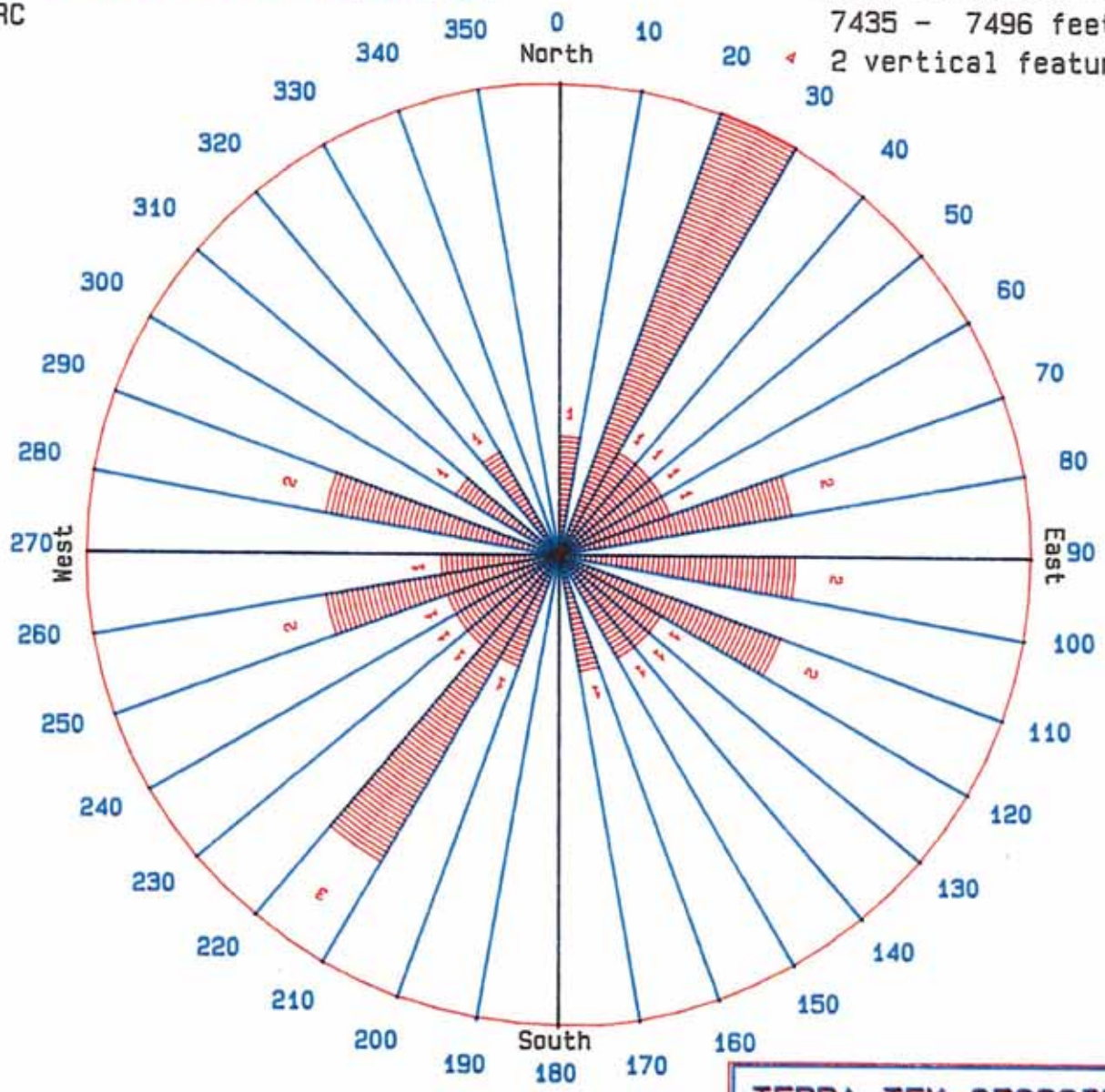

TERRA TEK GEOSCIENCE SERVICES

Ph: 1-800-FracLab

TERRA TEK GEOSCIENCE SERVICES

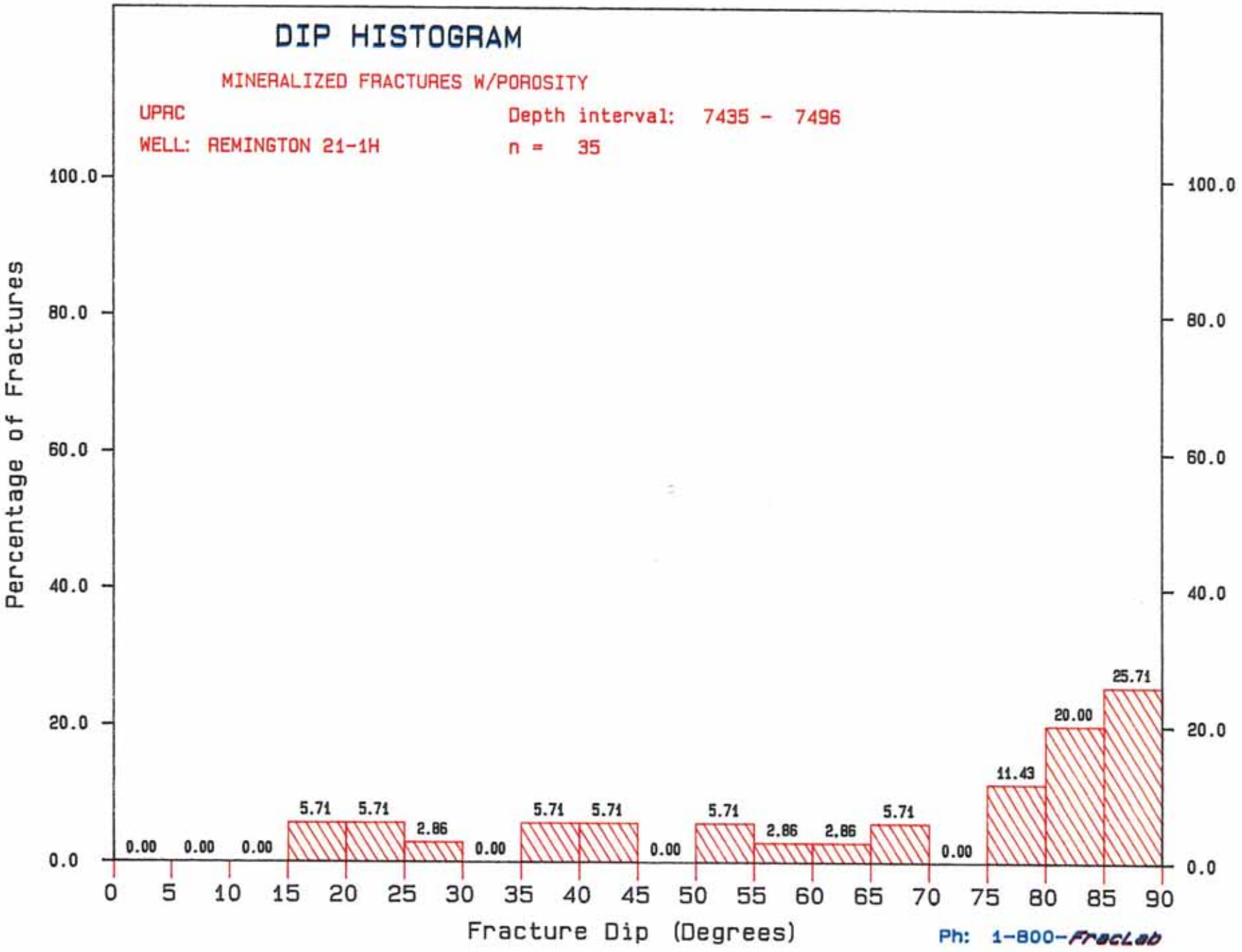

STRIKE ORIENTATION ROSE DIAGRAM

MINERALIZED FRACTURES, NO POROSITY

UPRC

WELL: REMINGTON 21-1H

7435 - 7496 feet; n = 70

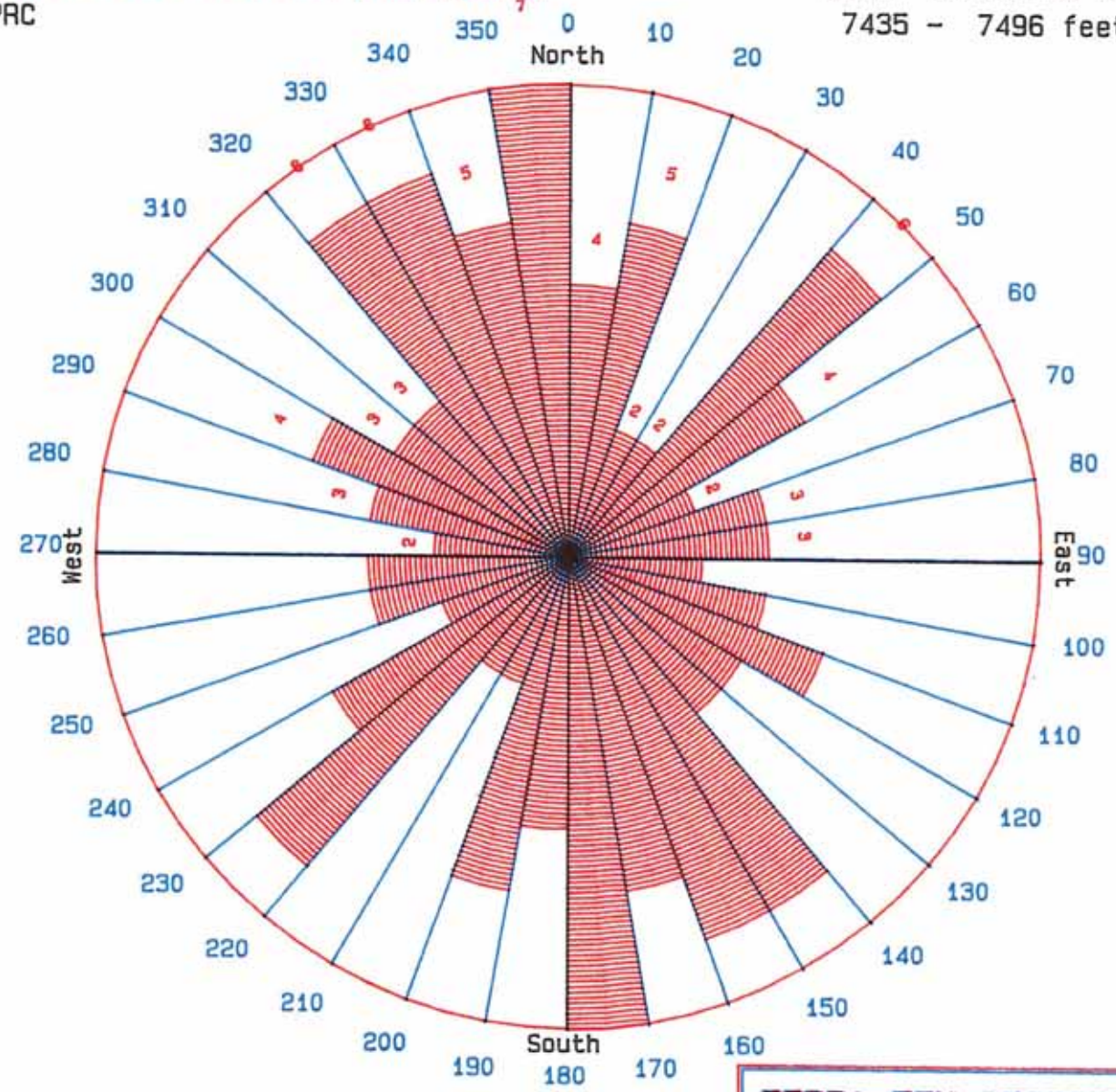

TERRA TEK GEOSCIENCE SERVICES

Ph: 1-800-Fractab

DIP AZIMUTH ROSE DIAGRAM

MINERALIZED FRACTURES, NO POROSITY

UPRC

WELL: REMINGTON 21-1H
7435 - 7496 feet; n = 68
2 vertical feature(s) not plotted

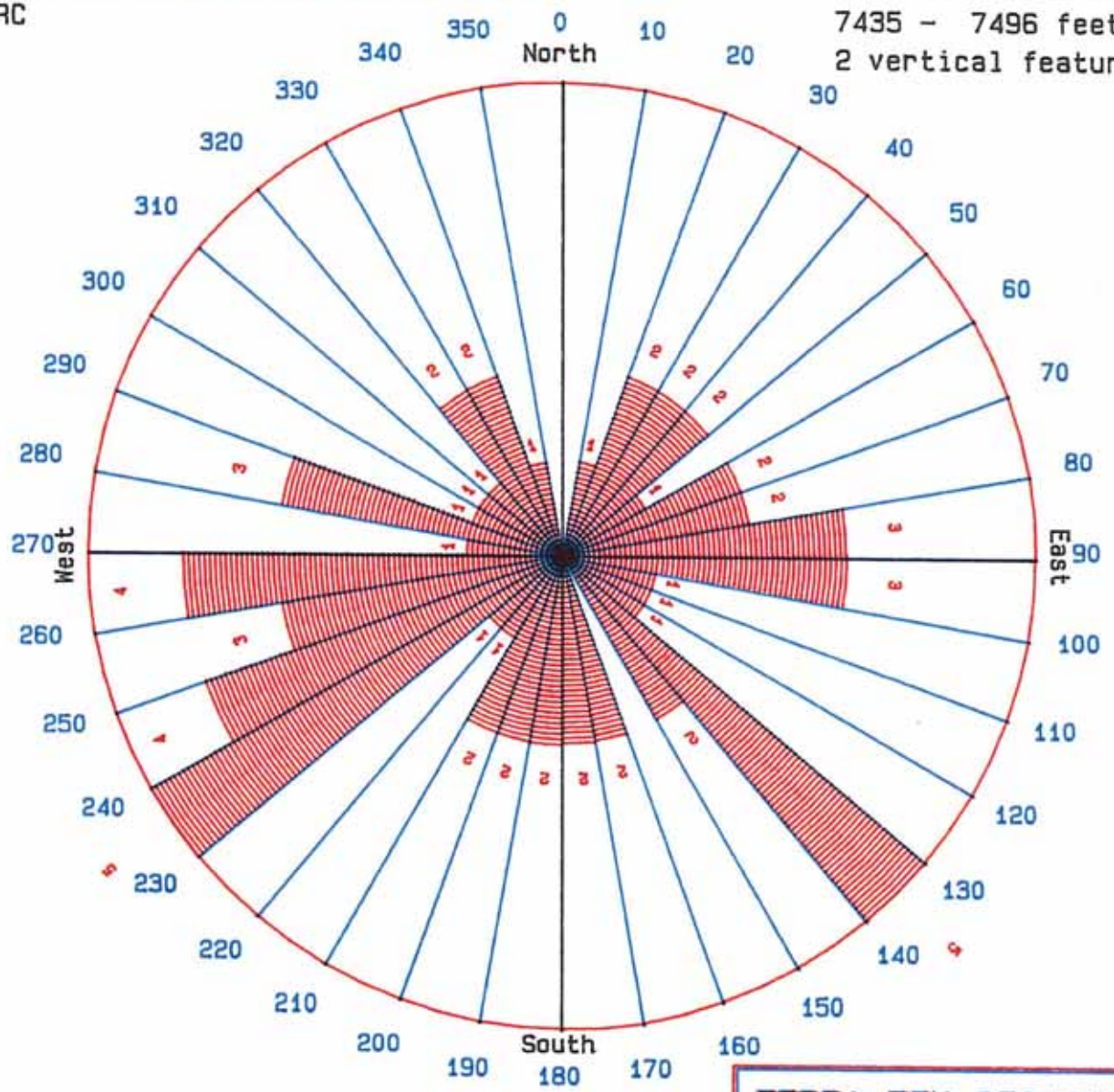

TERRA TEK GEOSCIENCE SERVICES
Ph: 1-800-FracLab

TERRA TEK GEOSCIENCE SERVICES

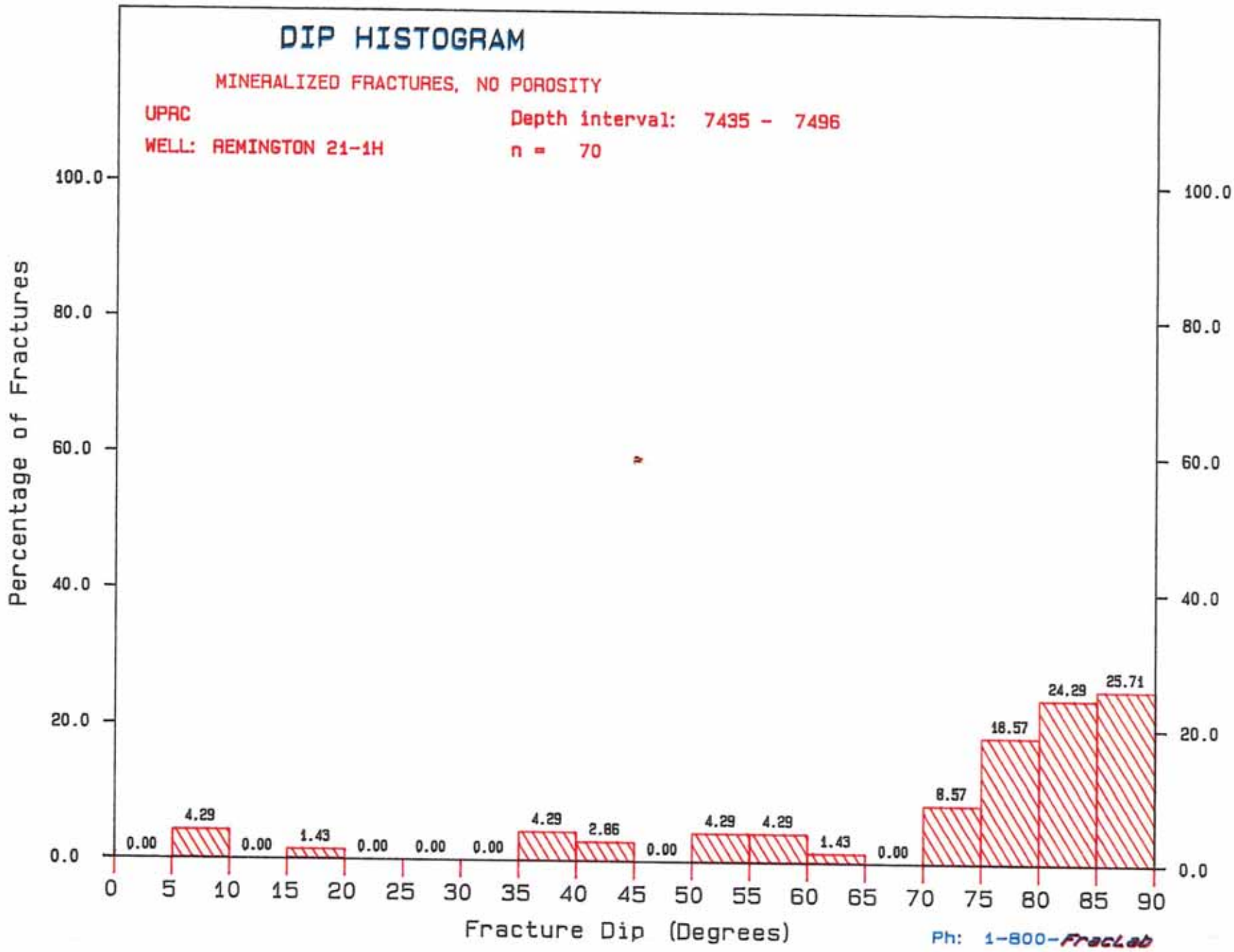

STRIKE ORIENTATION ROSE DIAGRAM

BEDDING PLANES
UPRC

WELL: REMINGTON 21-1H
7435 - 7496 feet; n = 173

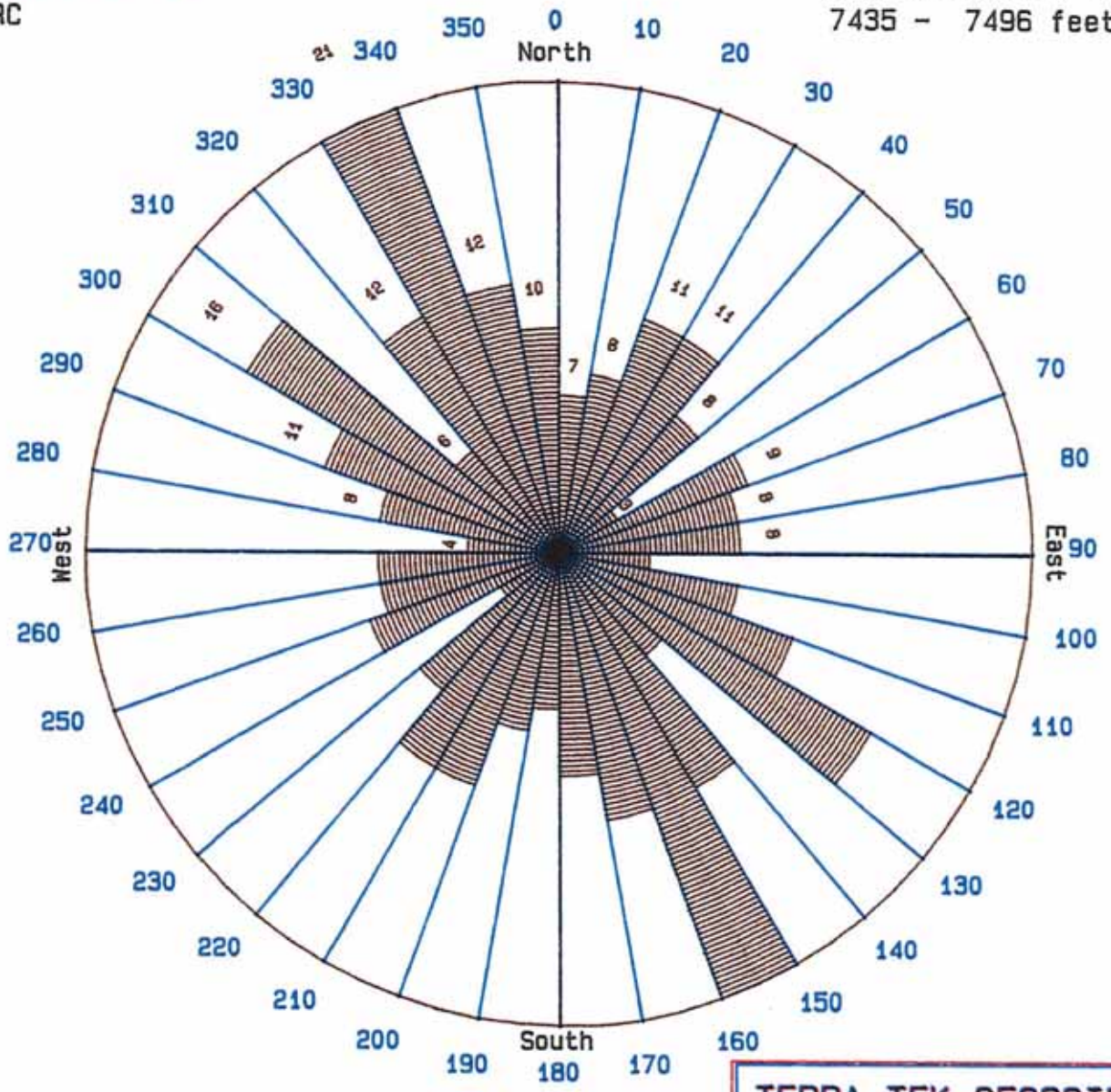

TERRA TEK GEOSCIENCE SERVICES
Ph: 1-800-Fractal

DIP AZIMUTH ROSE DIAGRAM

BEDDING PLANES
UPRC

WELL: REMINGTON 21-1H
7435 - 7496 feet; n = 173
No vertical fractures present

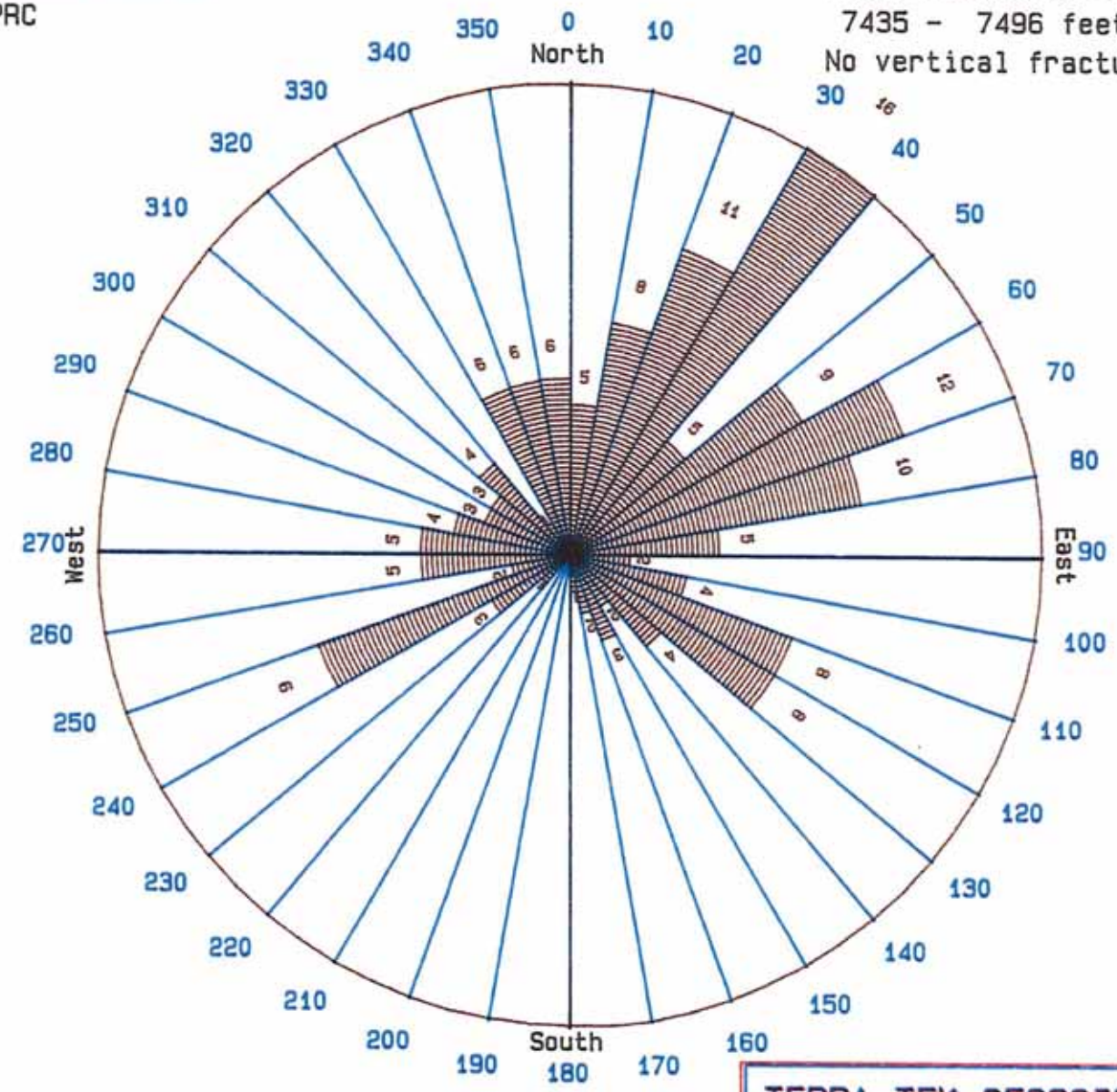

TERRA TEK GEOSCIENCE SERVICES
Ph: 1-800-FracLab

TERRA TEK GEOSCIENCE SERVICES

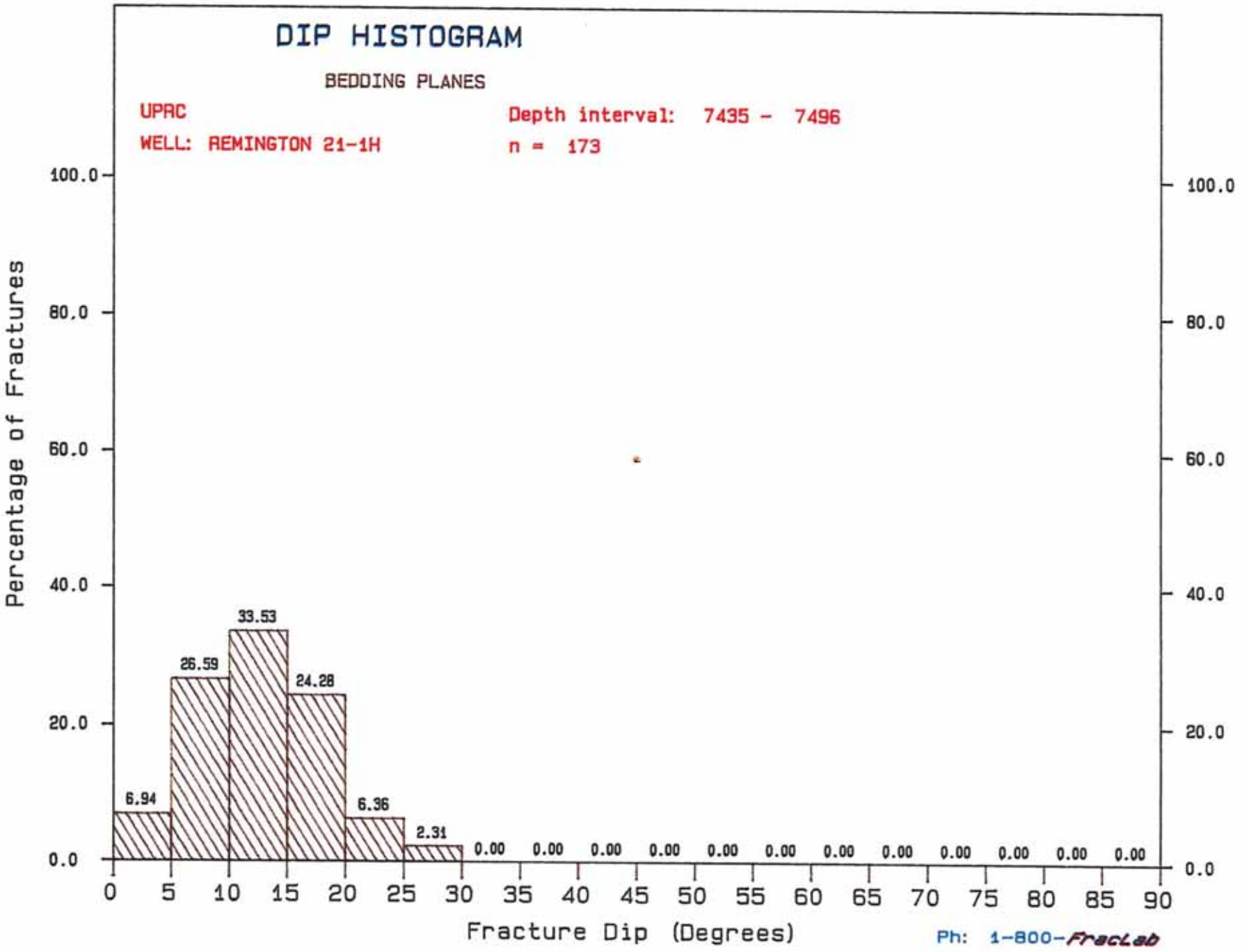

5 RETURN PERMEABILITY TESTING

5.1 Introduction

In December of 1994, Joe Svoboda of Union Pacific Resources Corporation, authorized TerraTek to perform return permeability testing and Capillary Suction Time (CST). The samples were cut from core recovered from the Remington 21-1H well, located in San Juan County, Utah. Table 5-1 summarizes the samples taken, whether they were naturally fractured and what testing was performed.

Table 5-1. Summary of Samples and Depths

Sample Number	Depth (ft)	Lithology	Capillary Suction Time	Return Permeability	Natural Fracture?
1	7442	Siltstone	X	-	No
2	7448	Siltstone	X	-	No
3	7452	Siltstone	X	3	Yes
4	7456	Siltstone	X	-	No
5	7460	Siltstone	X	5a	No
6	7464	Siltstone	X	-	No
7	7468	Siltstone	X	7a, 7b	Yes
8	7472	Siltstone	X	8	Yes

5.2 Sample Preparation

Right circular cylindrical plug samples, 1.5 inches in diameter by 3.0 inches long, were cut from the received core using odorless mineral spirits as the bit coolant. Samples 3, 7, and 8 were cut so that a natural fracture transected the full length of the vertical axis of the sample. The other five samples had no fractures. Samples 5 and 7 were cut in half and designated 5a, 5b, 7a, and

7b. The plug dimensions were measured by caliper. The trimmed end pieces were identified and used as the formation material for the CST tests.

5.3 Testing Procedures

Capillary Suction Time (CST) testing was performed on all eight samples using three fluids: deionized water, 3% KCl and Moab Brine. Moab Brine is a proposed brine for use as a drilling fluid. It is designated "Moab Brine" to differentiate it from formation brine. Tests were attempted using a fourth fluid, mud filtrate, but CST testing is not reliable when using an oil base fluid. Results of these tests are presented in the CST section (Section 6) of this report.

Return permeability testing was performed to study the change in permeability following the injection of various drilling and clean-up fluids, as outlined in Table 5-2.

Table 5-2. Samples and Fluids Used for Return Permeability Testing

Sample Number	Depth (ft)	Fluids Tested
3	7452	Moab Brine, mud filtrate, diesel, methanol
5a	7460	Moab Brine, diesel
7a	7468	Moab Brine, Moab Brine followed by 10% HCl: 3% Morflo II[1], diesel, methanol
7b	7468	Mud filtrate, mud filtrate followed by 10% HCl: Morflo II,[1] xylene
8	7472	Moab Brine

All return permeability testing was performed at a temperature of 75°F and a confining pressure of 500 psig. Permeability to nitrogen gas was measured on each sample in the "as-received" condition. In order to establish a baseline permeability on a wet sample, each sample, except

[1] Product of the Western Company

Sample 7b, was injected with Moab Brine, blown down with nitrogen gas for sixteen hours and permeability was measured again. This same procedure was used for each fluid to assess the effect of the various fluids. Sample 7b had mud filtrate injected as the first fluid.

5.4 Return Permeability Test Results

Return permeability testing was performed on five samples designated as Samples 3 (7452 ft.), 5a (7460 ft.), 7a (7468 ft.), 7b (7468 ft.) and 8 (7472 ft.).

The original test program entailed performing an initial permeability measurement to nitrogen gas on the ''as-received'' sample, followed by a liquid permeability, monitoring the change in permeability to determine whether or not there was an interaction between the fluid and the matrix of the formation. After testing Samples 3, and 5, it was apparent that there was a fluid compatability problem but that more meaningful information would be obtained by reverse flowing nitrogen gas through the sample for sixteen hours and measuring the nitrogen gas permeability of the wet sample and comparing this with the initial nitrogen gas permeability. All subsequent tests were performed by comparing the as- received gas permeability with the ''wet'' sample gas permeability.

5.4.1 Sample 3 (7452 ft.)

Sample 3 was tested to evaluate the compatability with Moab Brine. The permeability to gas in the ''as-received'' condition was 13.2 md. The permeability to Moab Brine started at 2.1 md and dropped to 1.6 md, after flowing approximately five pore volumes of fluid through the sample. This demonstrated that the Moab Brine caused a significant decrease in permeability and no further testing was performed at this time. Results of this test are presented in Table 5-3 and Figure 5-1. The sample was placed in a desiccator and air-dried at ambient conditions for seven days.

Table 5-3. Liquid Permeability versus Throughput

Sample Number	Sample Depth	Flow Rate (cc/s)	ΔP (atm)	Cumulative Throughput (cc)	Liquid Permeability (md)	Normalized Permeability (ratio)
3 Moab Brine	7452	0.0083	0.821	5	2.119	1.000
		0.0083	1.055	10	1.650	0.779
		0.0083	1.117	5	1.559	0.736
7a Moab Brine	7468	0.0167	1.380	5	4.066	1.000
		0.0167	2.307	10	2.432	0.598
		0.0167	3.510	20	1.598	0.393
		0.0167	4.486	30	1.251	0.308
		0.0167	5.677	45	0.988	0.243
		0.0167	6.294	55	0.891	0.219
		0.0167	6.877	75	0.816	0.201
		0.0167	7.081	80	0.792	0.195
7b Mud Filtrate	7468	0.0333	0.375	5	33.387	1.000
		0.0333	0.414	10	30.229	0.905
		0.0333	0.472	20	26.534	0.795
		0.0333	0.519	30	24.137	0.723
		0.0333	0.533	40	23.520	0.704
		0.0333	0.552	50	22.683	0.679
		0.0333	0.601	65	20.853	0.625
		0.0333	0.649	80	19.297	0.578

Figure 5-1. Normalized Liquid Permeability versus Throughput

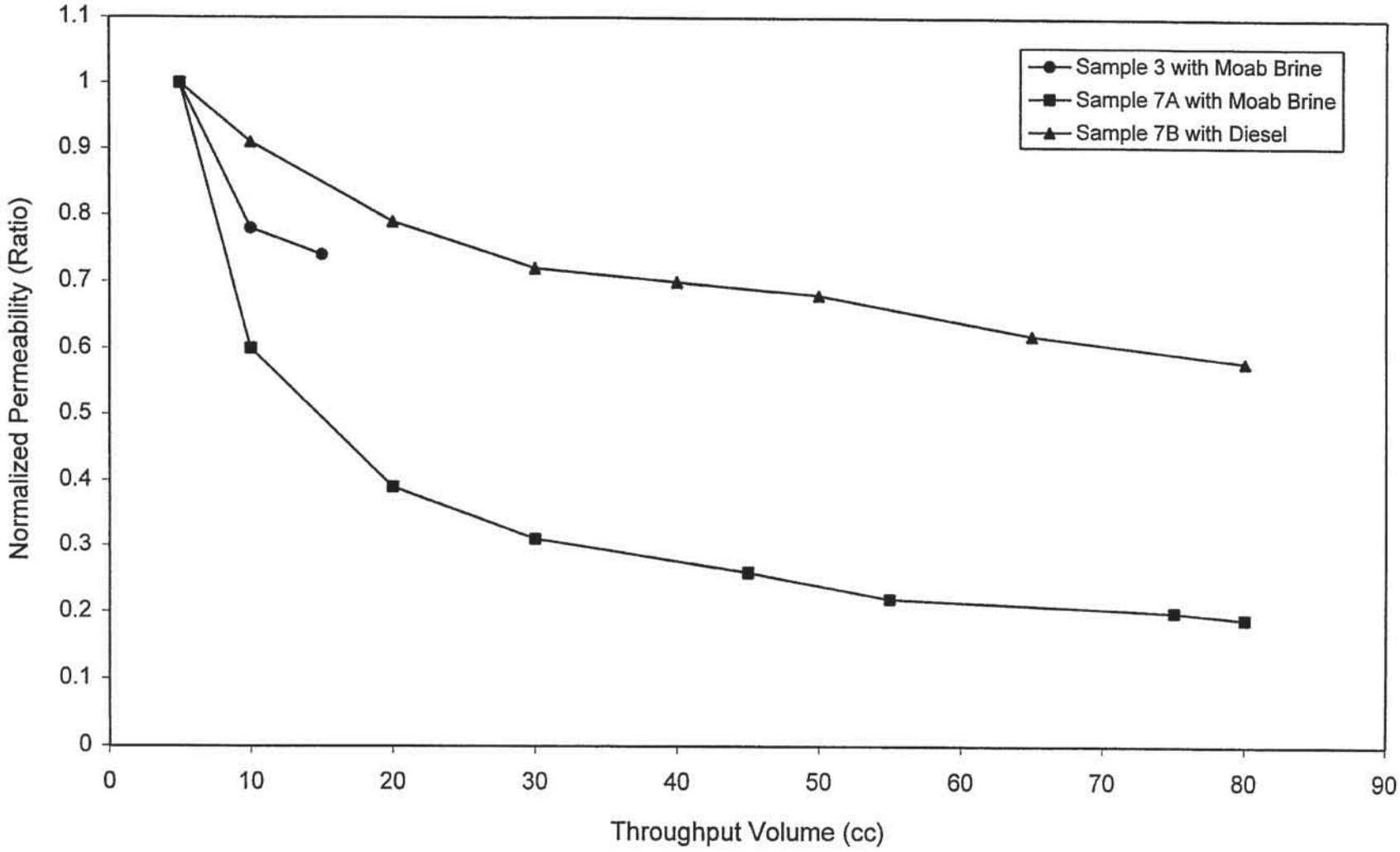

After seven days, return permeability tests were performed on this sample to evaluate the change in permeability to gas before and after exposure to Moab Brine, mud filtrate, diesel and methanol. The procedures, sequence of fluids and test results are presented in Table 5-4 and Figure 5-2.

5.4.2 Sample 5a (7460 ft.)

Sample 5a was tested to evaluate the compatability with Moab Brine. The permeability to gas in the ''as-received'' condition was 0.077 md. The permeability to Moab Brine was less than 0.0002 md. No attempt was made to measure permeability to gas immediately after the Moab Brine injection. The sample was placed in a desiccator and allowed to air dry at ambient conditions for 28 days.

After 28 days, a return permeability test was performed to evaluate the change in permeability to gas before and after the injection of diesel. The procedures, sequence of fluids and test results are presented in Table 5-5 and Figure 5-3. The permeability of this sample after the final test was so low that no further testing was attempted.

5.4.3 Sample 7a (7468 ft.)

Sample 7a was tested to evaluate its compatability with five fluids: Moab Brine, 10% HCl:3% Morflo II, diesel, and methanol.

As a basis for the return permeability following Moab Brine injection, the permeability to gas in the ''as-received'' condition was 20.3 md. The permeability to Moab Brine started at 4.07 md. and dropped to 0.79 md after flowing approximately 20 pore volumes of fluid through the sample. Results of the permeability to Moab Brine are presented in Table 5-3 and shown graphically in Figure 5-1. Immediately following the flow of Moab Brine, the sample was injected with nitrogen gas for sixteen hours, in the opposite direction of liquid flow, to simulate blow-down in a well. Return permeability to gas at residual water was 0.024 md. This demonstrated that Moab Brine caused a significant decrease in permeability to gas. The sample

Table 5-4. Return Permeability History for Sample 3, 7452 feet, when Flowed with Various Fluids

Procedure	Fluid Type	Volume of Fluid Injected (cc)	Injection Pressure (psig)	Elapsed Fluid Injection Time (hr)	Elapsed Nitrogen Drive Time (hr)	Permeability During Fluid Drive (md)	Stage	Permeability During Nitrogen Drive (md)
Permeability to nitrogen measured		--	--	--	--	--	1	13.2
Permeability to brine measured	Moab Brine	15.0	16.4	0.50	--	1.60	2	--
Dry sample at ambient conditions for approximately seven days		--	--	--	--	--	3	--
Permeability to nitrogen measured		--	--	--	--	--	4	17.5
Permeability to brine measured	Moab Brine	54.0	9.18	3.60	--	1.40	5	--
Backflow with nitrogen gas and permeability to nitrogen measured		0.00	20.0	--	48.0	--	6	0.06
Dry sample at ambient conditions for approximately four days		--	--	--	--	--	7	--
Permeability to nitrogen measured		--	--	--	--	--	8	10.9
Permeability to oil measured	Mud Filtrate	60.0	84.0	1.00	--	0.73	9	--
Backflow with nitrogen gas and permeability to nitrogen measured		--	50.0	--	4.0	--	10	0.90
Dry sample at ambient conditions for approximately seventeen days		--	--	--	--	--	11	--
Permeability to nitrogen measured		--	--	--	--	--	12	3.96
Permeability to oil measured	Diesel	100	57.8	1.67	--	1.31	13	--
Backflow with nitrogen gas and permeability to nitrogen measured		--	50.0	--	15	--	14	2.38
Dry sample at ambient conditions for approximately five days		--	--	--	--	--	15	--
Permeability to nitrogen measured		--	--	--	--	--	16	13.9
Permeability to solvent measured	Methanol	165	13.4	2.75	--	2.28	17	--
Backflow with nitrogen gas and permeability to nitrogen measured		0.00	100	--	16	--	18	1.81

Note: Confining Pressure = 500 psi Flow Test Temperature = 23°C

Figure 5-2. Return permeability history for Sample 3, 7452 feet, when flowed with various fluids.

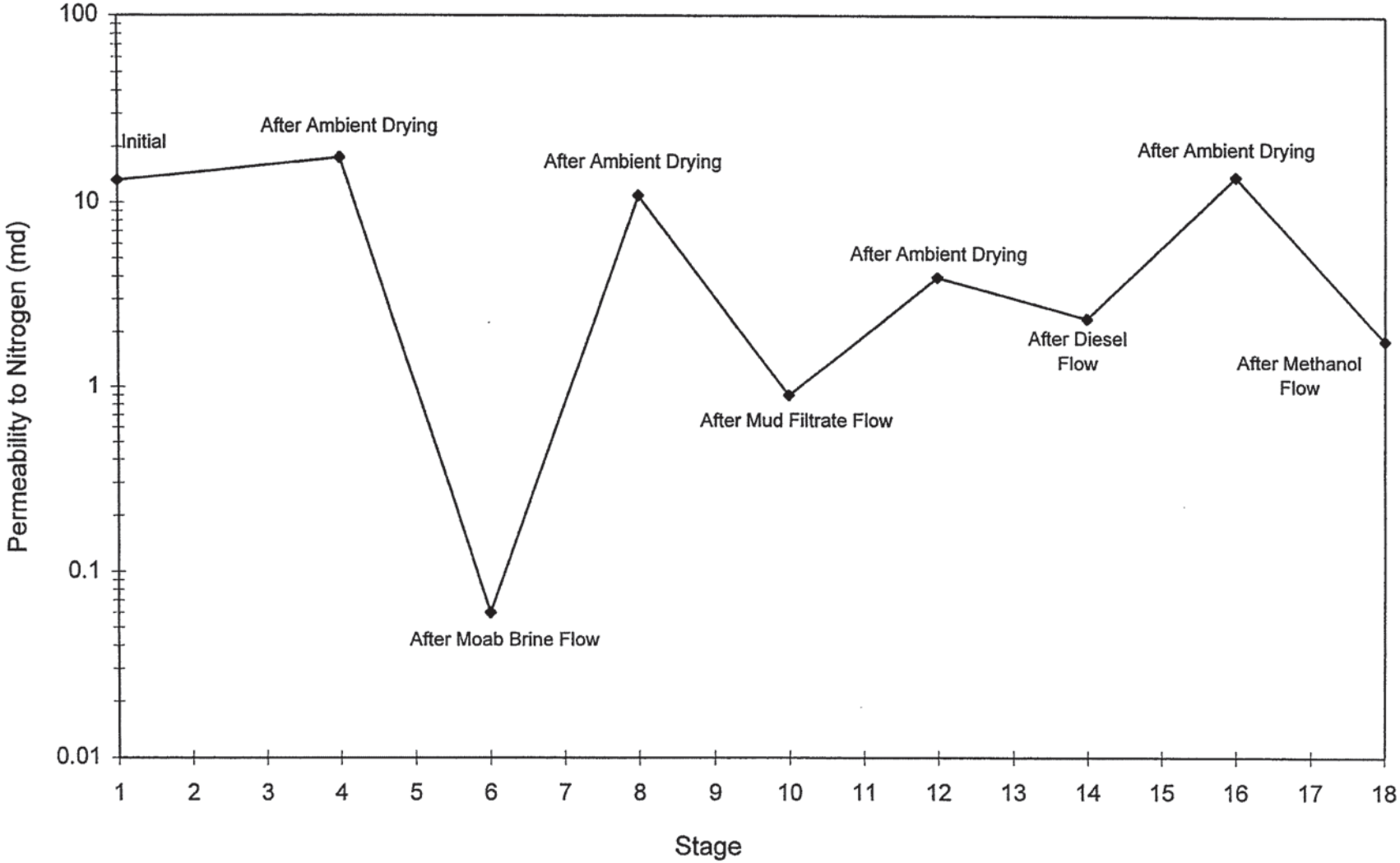

Table 5-5. Return Permeability History for Sample 5a, 7460 feet, when Flowed with Various Fluids

Procedure	Fluid Type	Volume of Fluid Injected (cc)	Injection Pressure (psig)	Elapsed Fluid Injection Time (hr)	Elapsed Nitrogen Drive Time (hr)	Permeability During Fluid Drive (md)	Stage	Permeability During Nitrogen Drive (md)
Permeability to nitrogen measured		--	--	--	--	--	1	7.7×10^{-2}
Permeability to brine	Moab Brine	0.50	127	16.5	--	$< 0.2 \times 10^{-3}$	2	--
Dry sample at ambient conditions for approximately 28 days		--	--	--	--	--	3	--
Permeability to nitrogen measured		--	--	--	--	--	4	1.0×10^{-3}
Permeability to oil measured	Diesel	0.50	450	8.0	--	$< 0.2 \times 10^{-3}$	5	--
Backflow with nitrogen gas and permeability to nitrogen measured		--	300	--	15	--	6	5.0×10^{-4}

Note: Confining Pressure = 500 psi
Flow Test Temperature = 23°C

Figure 5-3. Return permeability history for Sample 5a, 7460 feet, when flowed with various fluids.

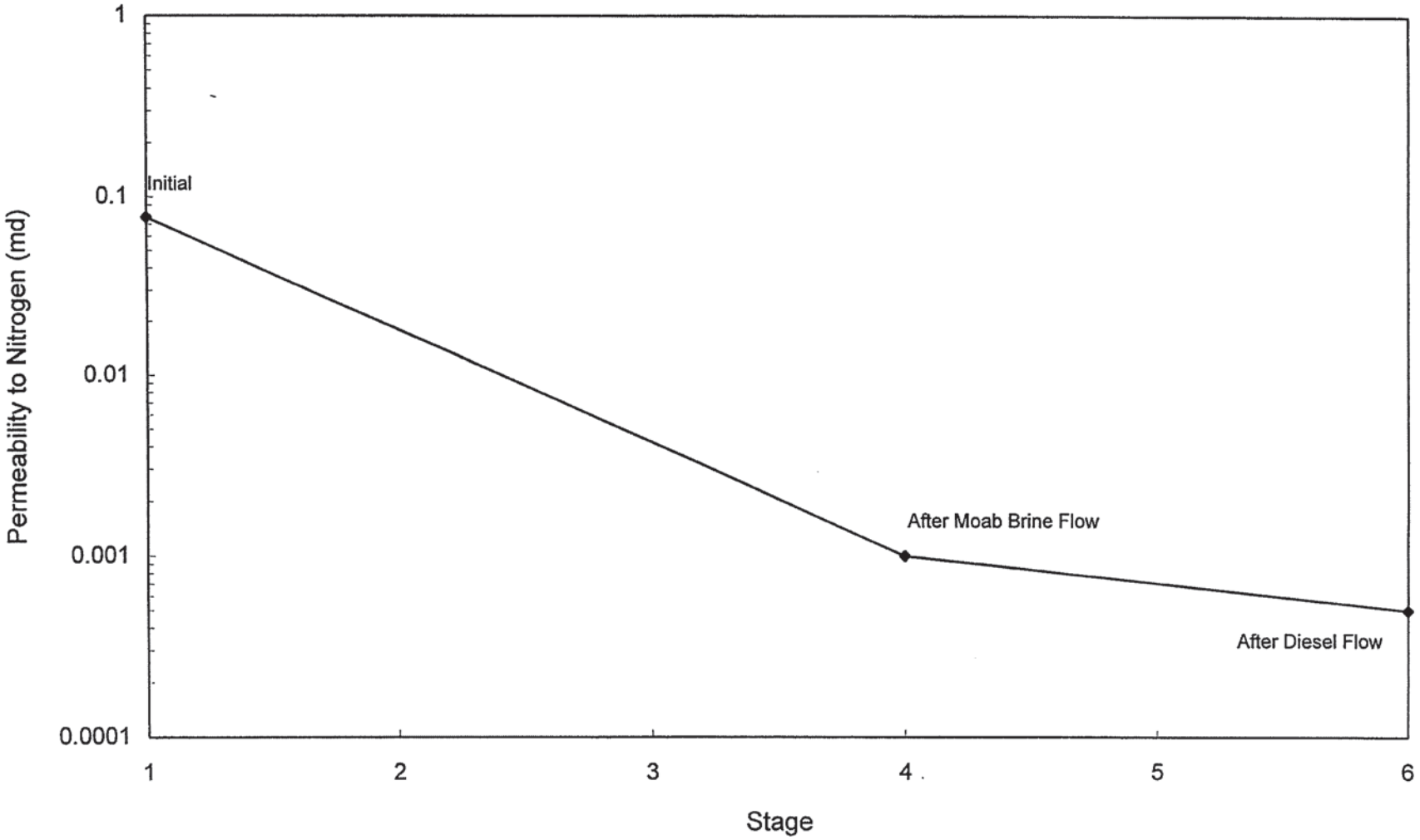

was placed in a desiccator and allowed to dry at ambient conditions for approximately ten days.

After 10 days, the sample fracture was brushed clean and a new permeability to gas was measured (21.9 md). Immediately following the gas permeability test, the sample was injected with Moab Brine and the permeability to Moab Brine was measured (0.02 md). Following brine injection, the sample was blown down with nitrogen gas in the reverse direction and permeability to gas was measured (0.02 md). An acid supplied by the Western Company of North America (10% HCl:3 % Morflo II), was injected to determine if the permeability could be enhanced with an acid treatment. Immediately following the acid treatment the sample was injected with nitrogen gas for sixteen hours and the return permeability to gas was 0.06 md. The sample was removed from the test fixture, placed in a desiccator and dried at an ambient temperature for approximately 20 days.

After 20 days the sample fracture was brushed clean and a new permeability to gas was measured (21.9 md). Diesel fuel was flowed through the sample and permeability to diesel was measured (7.82 md). Immediately following the diesel flow period, nitrogen gas was flowed through the sample, in a reverse direction, for sixteen hours. The return permeability to gas at residual oil was 12.6 md. The sample was placed back in the desiccator and air-dried for five days.

After five days the sample fracture was brushed clean and a new gas permeability was measured (17.9 md). Methanol was flowed through the sample and permeability to methanol was measured (0.72 md). Immediately following the flow of methanol, nitrogen gas was flowed through the sample, in a reverse direction, for sixteen hours. The return permeability to gas at residual methanol was 1.59 md.

A condensed version of these procedures is outlined in Table 5-6 and the results are presented graghically in Figure 5-4.

Table 5-6. Return Permeability History for Sample 7a, 7468 feet, when Flowed with Various Fluids

Procedure	Fluid Type	Volume of Fluid Injected (cc)	Injection Pressure (psig)	Elapsed Fluid Injection Time (hr)	Elapsed Nitrogen Drive Time (hr)	Permeability During Fluid Drive (md)	Stage	Permeability During Nitrogen Drive (md)
Permeability to nitrogen measured		--	--	--	--	--	1	20.3
Permeability to brine measured	Moab Brine	80.0	104	1.33	--	0.79	2	--
Backflow with nitrogen gas and permeability to nitrogen measured		--	15.0	--	40.0	--	3	0.02
Dry sample at ambient conditions for approximately ten days		--	--	--	--	--	4	--
Permeability to nitrogen measured		--	--	--	--	--	5	10.0
Permeability to brine measured	Moab Brine	50.0	137	1.67	--	0.30	6	--
Backflow with nitrogen gas and permeability to nitrogen measured		--	50.0	--	20.0	--	7	0.02
Inject acid into sample	10% HCL:3% Morflo II	10.0	50.0	16.0	--	--	8	--
Backflow with nitrogen gas and permeability to nitrogen measured		--	100	--	3.0	--	9	0.06
Dry sample at ambient conditions for approximately twenty days		--	--	--	--	--	10	--
Permeability to nitrogen measured		--	--	--	--	--	11	21.9
Permeability to oil measured	Diesel	90.0	15.6	1.50	--	7.82	12	--
Backflow with nitrogen gas and permeability to nitrogen measured		0.00	100	--	15.0	--	13	12.6
Dry sample at ambient conditions for approximately five days		--	--	--	--	--	14	--
Permeability to nitrogen measured		--	--	--	--	--	15	17.9
Permeability to solvent measured	Methanol	120	68.6	2.00	--	0.72	16	--
Backflow with nitrogen gas and permeability to nitrogen measured		--	100	--	15.0	--	17	1.59

Note: Confining Pressure = 500 psi Flow Test Temperature = 23°C

Figure 5-4. Return permeability history for Sample 7a, 7468 feet, when flowed with various fluids.

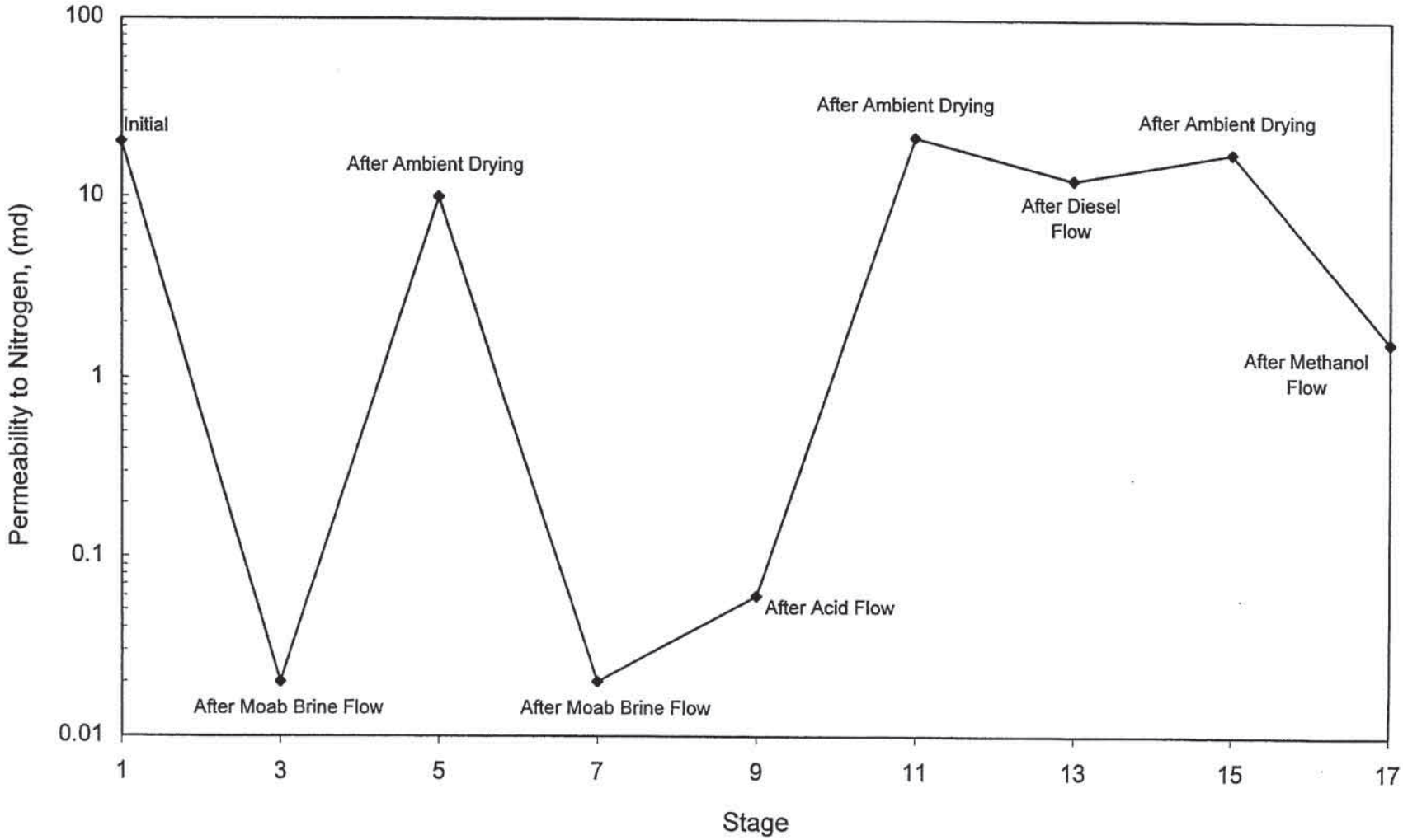

5.4.4 Sample 7b (7468 ft.)

Sample 7b was tested in a similar manner to Sample 7a, with the exception that it was initially injected with an oil-based fluid. This test was designed to evaluate the effects of injecting mud filtrate only, mud filtrate followed by an acid treatment using 10% HCl:3% Morflo II and a third test using xylene. Results of permeability versus throughput while injecting the mud filtrate are included in Table 5-3 and Figure 5-1. A summary of procedures, sequence of fluids and test results are presented in Table 5-7 and Figure 5-5.

5.4.5 Sample 8 (7472 ft.)

Sample 8 was tested to evaluate the effects of Moab Brine. Results of this test are presented in Table 5-8 and Figure 5-6.

Table 5-7. Return Permeability History for Sample 7b, 7468 feet, when Flowed with Various Fluids

Procedure	Fluid Type	Volume of Fluid Injected (cc)	Injection Pressure (psig)	Elapsed Fluid Injection Time (hr)	Elapsed Nitrogen Drive Time (hr)	Permeability During Fluid Drive (md)	Stage	Permeability During Nitrogen Drive (md)
Permeability to nitrogen measured		--	--	--	--	--	1	24.4
Permeability to oil measured	Mud Filtrate	80.0	9.54	0.67	--	19.3	2	--
Backflow with nitrogen gas and permeability to nitrogen measured		--	50.0	--	20.0	--	3	14.2
Dry sample at ambient conditions for approximately ten days		--	--	--	--	--	4	--
Permeability to nitrogen measured		--	--	--	--	--	5	30.1
Permeability to oil measured	Mud Filtrate	80.0	20.0	1.33	--	4.9	6	--
Backflow with nitrogen gas and permeability to nitrogen measured		--	100	--	4.0	--	7	11.0
Inject acid into sample	10% HCL:3% Morflo II	5.0	50.0	3.0	--	--	8	--
Backflow with nitrogen gas and permeability to nitrogen measured		--	50.0	--	15.0	--	9	2.59
Dry sample at ambient conditions for approximately twenty days		--	--	--	--	--	10	--
Permeability to nitrogen measured		--	--	--	--	--	11	4.41
Inject solvent into sample	Xylene	50.0	200	0.25	--	--	12	--
Backflow with nitrogen gas and permeability to nitrogen measured		--	100	--	64.0	--	13	1.65

Note: Confining Pressure = 500 psi
Flow Test Temperature = 23°C

Figure 5-5. Return permeability history for Sample 7b, 7468 feet, when flowed with various fluids.

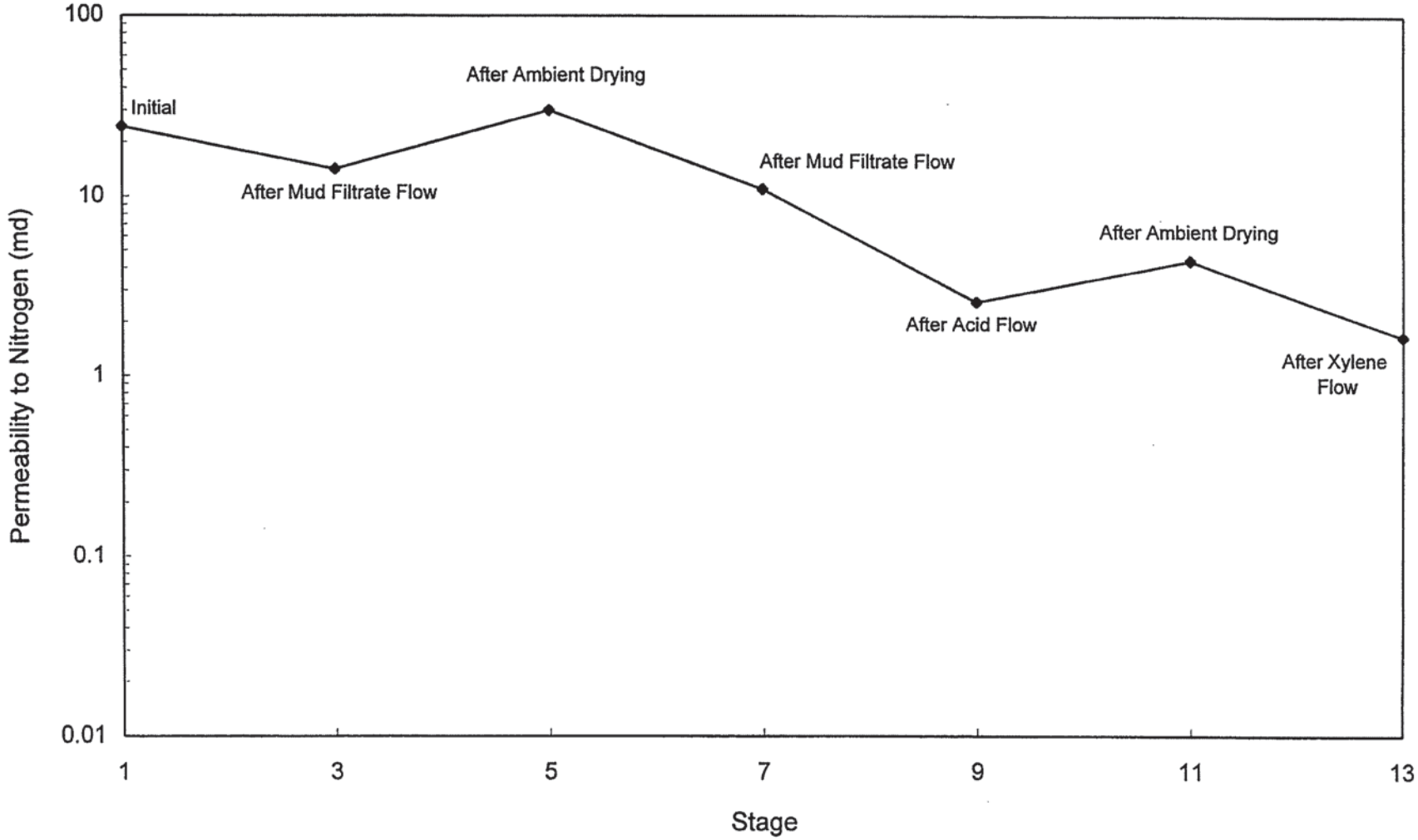

Table 5-8. Return Permeability History for Sample 8, 7472 feet, when Flowed with Various Fluids

Procedure	Fluid Type	Volume of Fluid Injected (cc)	Injection Pressure (psig)	Elapsed Fluid Injection Time (hr)	Elapsed Nitrogen Drive Time (hr)	Permeability During Fluid Drive (md)	Stage	Permeability During Nitrogen Drive (md)
Permeability to nitrogen measured		--	--	--	--	--	1	166
Permeability to brine measured	Moab Brine	120.0	2.2	2.0	--	40.0	2	--
Backflow with nitrogen gas and permeability to nitrogen measured		--	5.0	--	16.0	--	3	4.3

Note: Confining Pressure = 500 psi
Flow Test Temperature = 23°C

Figure 5-6. Return permeability history for Sample 8, 7472 feet, when flowed with various fluids.

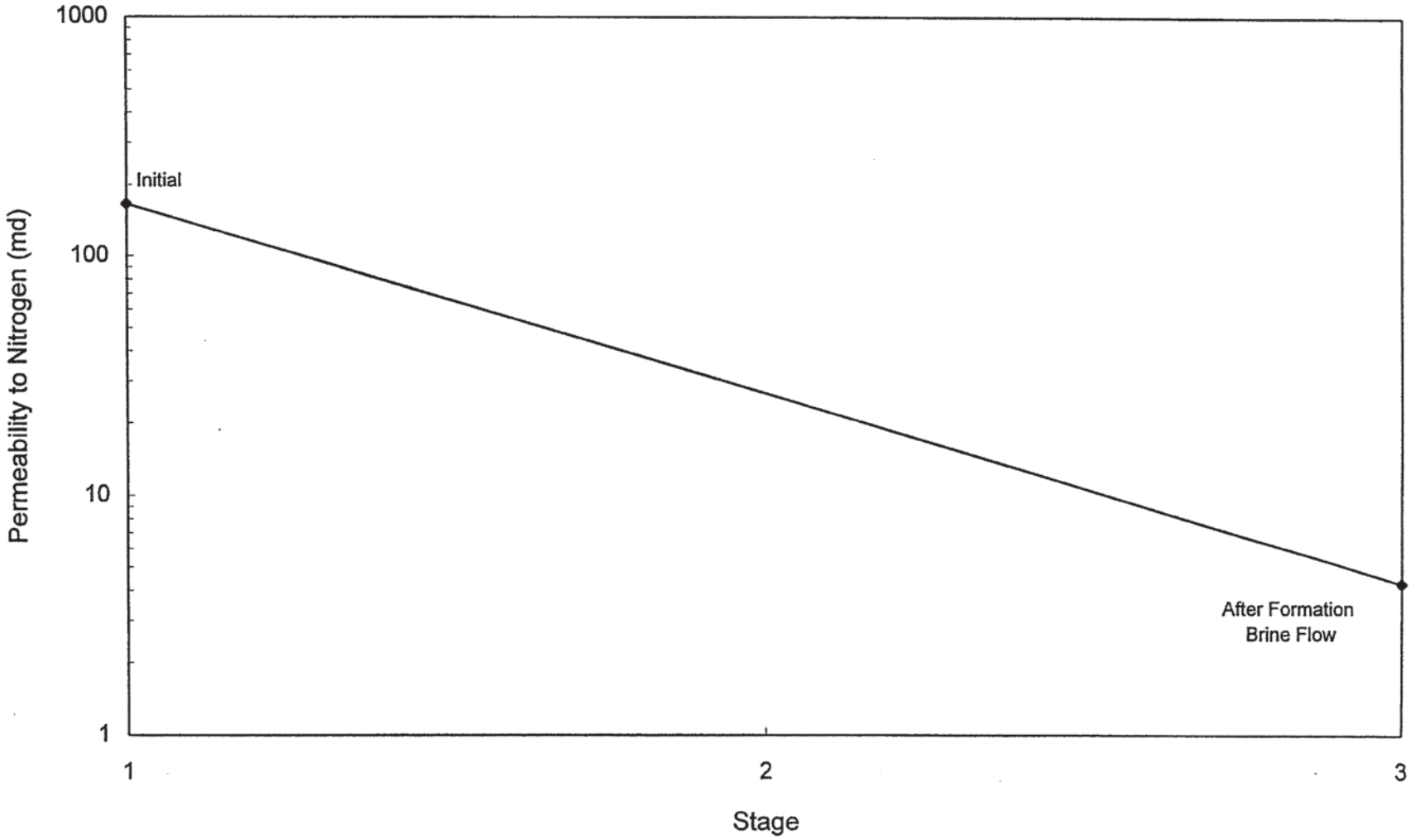

6 CST TESTING

6.1 Introduction

Capillary Suction Time testing (CST) was performed on eight siltstone samples from the Remington 21-1H well, located in San Juan County, Utah. Table 6-1 summarizes the samples taken. The purpose of this testing was to determine the relative ''sensitivity'' of these samples to de-ionized water, 3% KCl, Moab Brine and mud filtrate.

Table 6-1. Summary of Samples and Depths

Sample Number	Depth (ft)
1	7442
2	7448
3	7452
4	7456
5	7462
6	7464
7	7468
8	7472

6.2 Testing Procedures

The samples were allowed to dry for two days at 105°C. The samples were then crushed and divided to obtain representative splits. Each of the splits was then ground so that the entire split passed through a 100 mesh screen.

Capillary Suction Time (CST) measurements were conducted on slurry samples made by blending

1 gram of sample in 20 ml of fluid for 15 minutes. A uniform slurry was withdrawn, placed in the CST device and its CST value was measured. The procedure was repeated three or more times for each sample to ensure repeatability.

6.3 Results

The testing results are indicated in Table 6-2 and presented graphically in Figures 6-1 and 6-2. These results include the fluid type, the average CST values for the fluid only (Fluid Calibration), the average CST value for fluid with sample, and the ratio of the average values of the fluid with sample versus fluid only.

Table 6-2. Capillary Suction Times

Sample Number	Depth (ft)	Seconds /Ratio	Average Capillary Suction Time (seconds/ratio)			
			DI Water	3% KCl	Mud Filtrate	Moab Brine
Fluid Only		Seconds Normalized	7.9 1.0	8.0 1.0	36.9 1.0	11.2 1.0
1	7442	Seconds Normalized	14.2 1.8	13.8 1.7		21.4 1.9
2	7448	Seconds Normalized	14.2 1.8	20.5 2.6		30.1 2.7
3	7452	Seconds Normalized	21.2 2.7	18.9 2.4		31.5 2.8
4	7456	Seconds Normalized	14.5 1.8	16.5 2.1		37.3 3.3
5	7460	Seconds Normalized	18.7 2.4	16.3 2.0	58.6 1.6	33.5 3.0
6	7464	Seconds Normalized	13.1 1.7	13.2 1.7		26.8 2.4
7	7468	Seconds Normalized	31.8 4.0	32.1 4.0		36.0 3.2
8	7472	Seconds Normalized	17.6 2.2	15.8 2.0		21.9 2.0

Figure 6-1. Capillary Suction Time Analysis

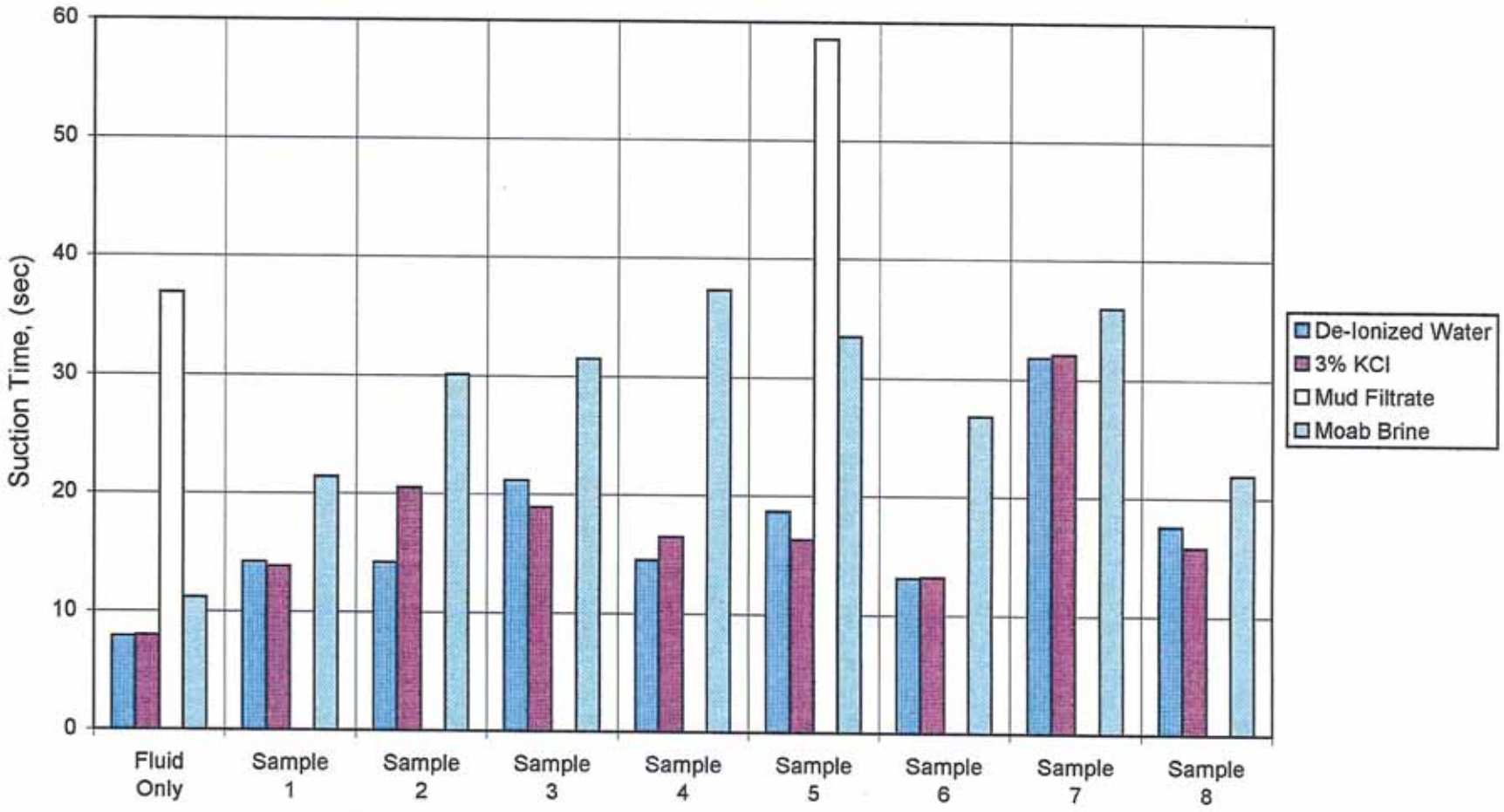

Figure 6-2. Normalized Capillary Suction Time Analysis

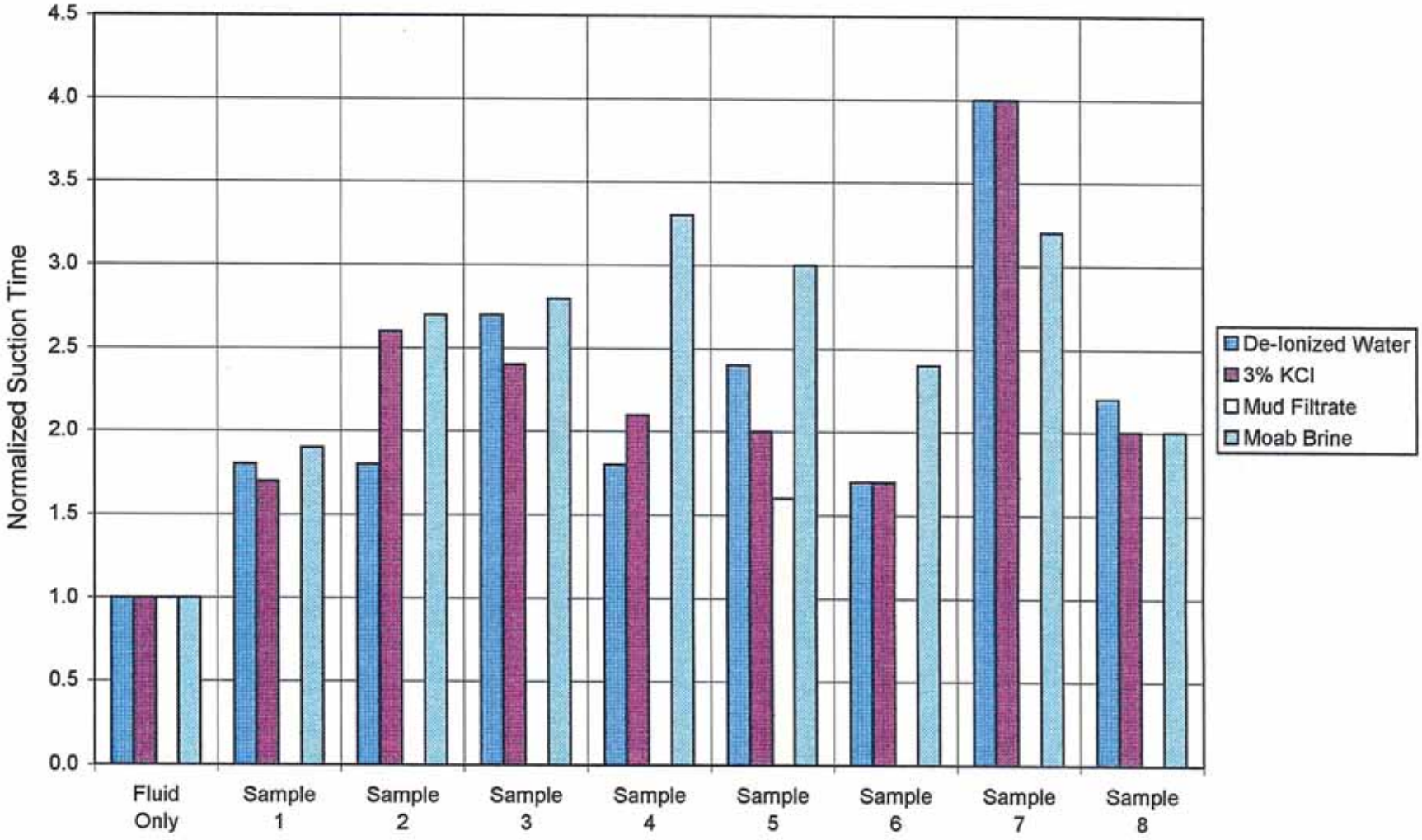

6.4 Discussion

The capillary suction time device measures the time for a free amount of fluid in a slurry to travel radially between two electrodes on a thick porous filter paper. Short filtration times are indicative of particle aggregation, where particle attraction is high and fluid particle interaction is weak. Long filtration times are indicative of particle dispersion, where particle attraction is weak and fluid particle interaction is high.

For the various fluids tested, each one had a different CST value for the fluid alone. To infer the various degrees of fluid/formation interaction between the different fluids, it is necessary to compare the ratio of the CST values of the fluid plus sample with the values for the specific fluid alone. This ratio becomes the indcator of the fluid/formation interaction. Large ratios (>2) are a consequence of longer filtration rates and hence higher fluid/formation interaction. Small ratios are a consequence of shorter filtration rates and hence low fluid/formation interaction.

Hence, for the fluids in the testing matrix used:

- The mud filtrate measurements performed on restricted number of samples, shows the least interaction with the formation.
- The performance of the mud filtrate is consistant with formation damage evaluations which indicated less damage for oil based, as opposed to aqueous, fluid systems.
- However, CST measurements are inherently less accurate for non-aqueous systems. Of the aqueous systems evaluated, there does not appear to be any clear cut preferential fluid. On an overall basis, 3% KCl appears to be the best aqueous fluid, although it is not substantially better than de-ionized water. The performance of the Moab brine is sporadic, in some cases better and in some cases worse than its counterparts, sometimes substantially worse. On this basis alone, 3% KCl may be slightly preferable to Moab Brine, strictly from a performance point-of-view.

7 FLUID ANALYSIS

7.1 Brine Analysis

Three water samples were submitted for analysis. Two samples were formation brine designated as Day #1, Run #4 and Day #2, Run #3. A third sample, which was to be used as a drilling fluid, was designated as Moab Brine. Results of these analyses are presented in the Brine Analysis in Tables 7-2, 7-3, and 7-4.

7.2 Oil Analysis

Two oil samples from Day #2, Run #8, were submitted were submitted for analysis. One sample was decanted from the top of the fluid in the bottle and the second sample was taken from the sludge in the bottom of the bottle. The oil samples were designated ''Top'' and ''Bottom''. Results of the oil analyses are included in Appendix A at the end of this section.

Tests were also performed to examine the effect of exposing the oil to CO_2. The density and viscosity were measured on the ''as received'' oil to establish baseline values. CO_2 was bubbled through a sample of oil for 72 hours and density and viscosoty were measured every 24 hours. Results of this experiment are presented in Table 7-1.

A second 25 ml oil sample was placed in a vessel with CO_2 and pressurized to 3000 psig at 140°F for 72 hours. The oil was returned to ambient pressure and temperature and the density and viscosity were measured. Results of this test are also included in Table 7-1.

API gravity of the oil is 38.8° API @ 60°F.

Table 7-1. Oil Properties

Exposure Time to CO_2	Density (gm/cc)	Viscosity (cP)
As Received	0.827	3.186
24 Hrs.	0.829	3.62
48 Hrs.	0.831	3.66
72 Hrs.	0.833	3.79
After 72 Hrs @ 3000 psi and 140°F	0.828	3.27

Table 7-2. Brine Analysis

Sample: Moab Brine

Analysis	Method	Result
Bicarbonate	SM17 2320B	0 mg/l
Calcium	EPA 200.7	1,810 mg/l
Carbonate	SM17 2320B	0 mg/l
Chloride	EPA 325.3	181,000 mg/l
Iron	EPA 200.7	0.0 mg/l
Magnesium	EPA 200.7	132 mg/l
Potassium	EPA 200.7	988 mg/l
Sodium	EPA 200.7	117,000 mg/l
Sulfate	EPA 375.4	4,090 mg/l
TDS	EPA 160.1	313,000
Specific Gravity	ASTM D-891	1,201

Table 7-3. Brine Analysis

Sample: Day #1 Run #4

Analysis	Method	Result
Bicarbonate	SM17 2320B	787 mg/l
Calcium	EPA 200.7	76,700 mg/l
Carbonate	SM17 2320B	0 mg/l
Chloride	EPA 325.3	219,000 mg/l
Iron	EPA 200.7	2.4 mg/l
Magnesium	EPA 200.7	5,490 mg/l
Potassium	EPA 200.7	4,660 mg/l
Sodium	EPA 200.7	52,100 mg/l
Sulfate	EPA 375.4	104 mg/l
TDS	EPA 160.1	402,000 mg/l
Specific Gravity	ASTM D-891	1.269

Table 7-4. Brine Analysis

Sample: Day #2 Run #3

Analysis	Method	Result
Bicarbonate	SM17 2320B	863 mg/l
Calcium	EPA 200.7	74,400 mg/l
Carbonate	SM17 2320B	0 mg/l
Chloride	EPA 325.3	218,000 mg/l
Iron	EPA 200.7	0.0 mg/l
Magnesium	EPA 200.7	5,130 mg/l
Potassium	EPA 200.7	5,420 mg/l
Sodium	EPA 200.7	53,100 mg/l
Sulfate	EPA 375.4	136 mg/l
TDS	EPA 160.1	402,000 mg/l
Specific Gravity	ASTM D-891	1.258

APPENDIX A

Whole Oil Gas Chromatography of Two Oils

TerraTek
University Research Park
420 Wakara Way • Salt Lake City, Utah 84108
Telephone (801) 584-2400
FAX (801) 584-2432

WHOLE OIL GAS CHROMATOGRAPHY OF TWO OILS

Prepared for:

Terratek, Inc.
University Research Park
400 Wakara Way
Salt Lake City, Utah 84108

Prepared by:

Wallace G. Dow
DGSI Project: 95/3210
February 22, 1995

DGSI
Total Quality Geochemistry

DGSI • 8701 NEW TRAILS DRIVE • THE WOODLANDS, TX 77381 • (713) 363-2176 • FAX (713) 292-3528 • TELEX 881137 DGSI

DISCUSSION

Two oil samples identified only as "top" and "bottom" were analyzed with whole oil gas chromatography. The samples are nearly identical and will be described together as if they were one.

On the basis of lower molecular weight compounds, the samples appear to be a very mature crude oil (Figure 1). Pristane/nC_{17} and phytane/nC_{18} ratios suggest a moderate maturity and a source rock containing mostly algal plus bacterial organic matter, possibly with minor terrigenous material. This also is supported by pr/ph ratios and carbon preference indices (CPI). Isoprenoid distributions in the C_{13} to C_{20} carbon number range are nearly identical and suggest minor terrigenous material in the source rock (iC_{16} and iC_{19} predominance)

Whole oil gas chromatograms show a range of n-alkanes from nC_5 to nC_{30} with a concentration in the nC_{10} to nC_{20} range. The rapid diminution of compounds above nC_{20} i consistent with a mature crude oil but the loss of lower molecular weight compounds (especially less than nC_{10}) is unusual. This could be explained by any of several causes such as early biodegradation, partial gas stripping, and mixture of a mature crude oil with an additive such as light lubricating (diesel) oil.

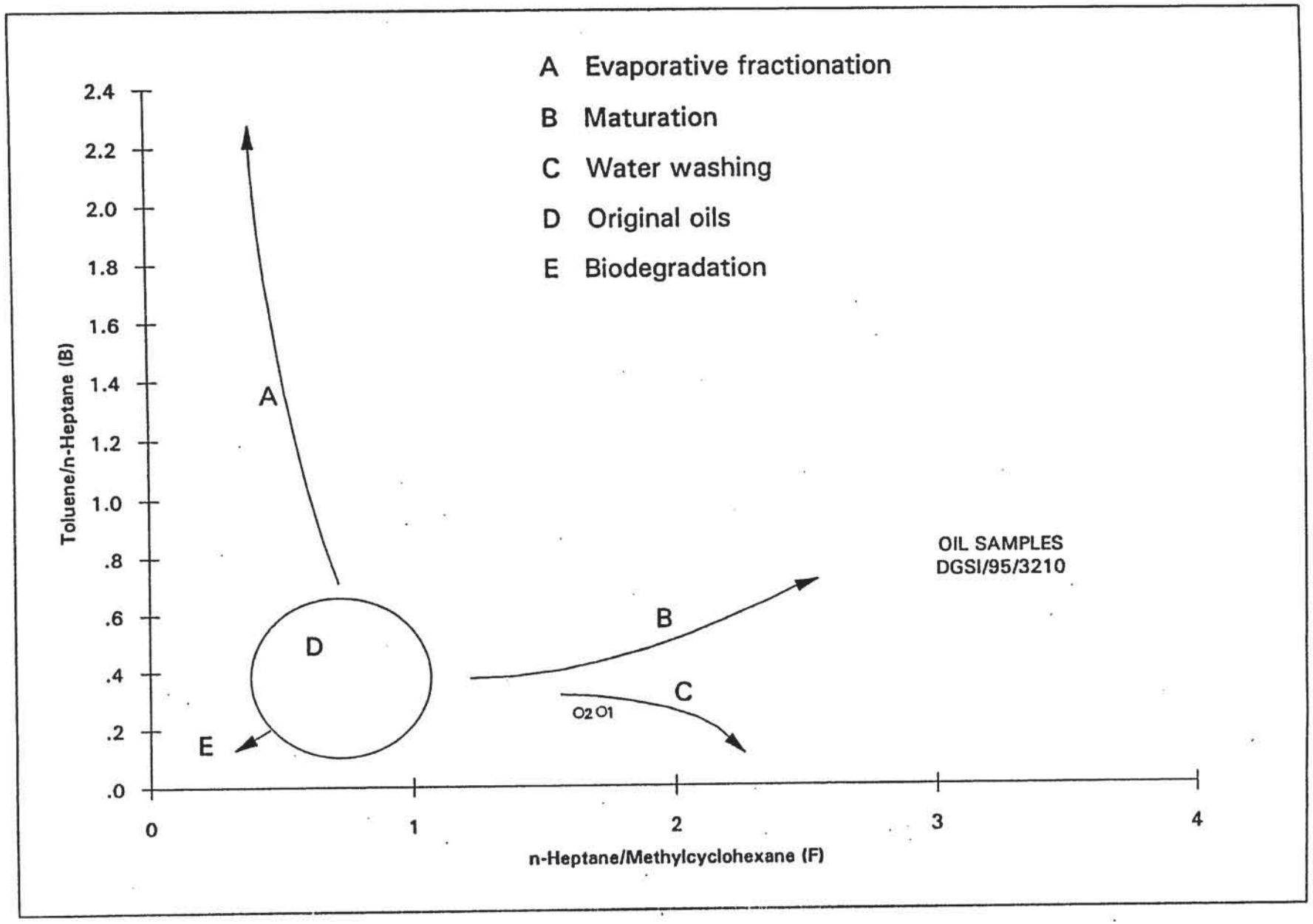

FIGURE 1 - Thompsons alteration vectors from light hydrocarbon data.

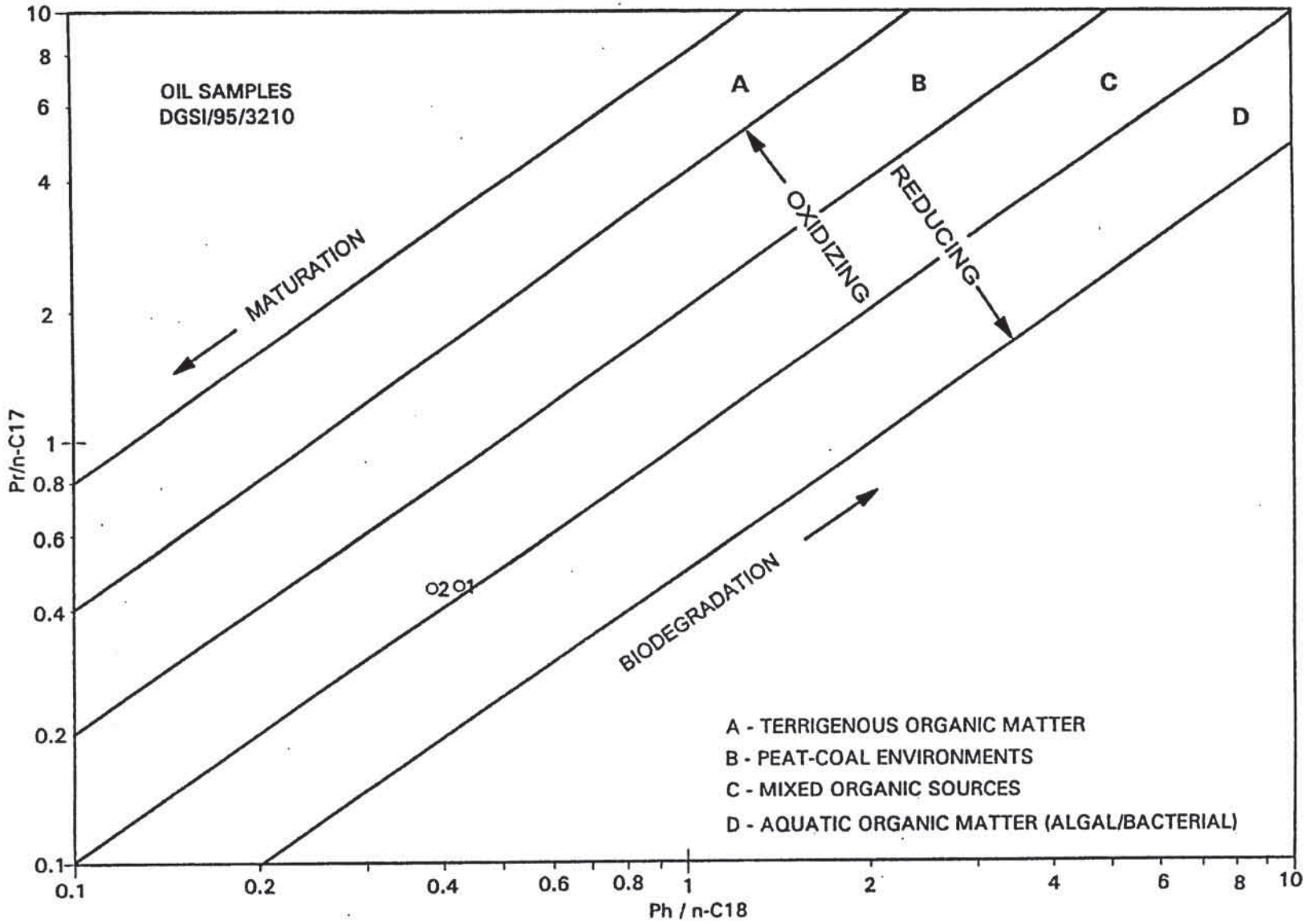

FIGURE 2 - Plot from chromatography data showing organic matter type, source rock depositional environment, and thermal maturity.

WHOLE OIL GAS CHROMATOGRAPHY

A sample of whole oil is injected directly into a Varian model 3400 gas chromatograph fitted with a Quadrex 50 meter fused silica capillary column. The GC is programmed from 40° to 350° C at 9° C/minute with a 2 minute hold at 40° and a 20 minute hold at 340° C. Analytical data are processed with a Nelson Analytical model 3000 chromatograph data system and IBM computer hardware. This software system facilitates data processing and graphic display as well as electronic data transmittal. All standard calculations are made including pristane/phytane ratio, carbon preference index, and other key parameters (Tables 1, and 2). Two gas chromatograms are provided, one showing all compounds between nC_2 and nC_{40} (Figure 1A) and the other a computer enhanced version of the chromatogram between nC_2 and nC_{10} (Figure 1B). Compounds as low as ethane can be detected if present. In addition, the concentration of C_{13} to C_{20} isoprenoids are determined and plotted.

OIL LIGHT ENDS: COMPOUND IDENTIFICATION

No.	Abbreviation	Name
1.	n-C_2	ETHANE
2.	n-C_3	PROPANE
3.	i-C_4	ISOBUTANE
4.	n-C_4	n-BUTANE
5.	i-C_5	ISOPENTANE
6.	n-C_5	n-PENTANE
7.	22DMB	2,2-DIMETHYLBUTANE
8.	2MP	2-METHYLPENTANE
9.	3MP	3-METHYLPENTANE
*10.	n-C_6	n-HEXANE
11.	24DMP+MCP+22DMP	2,2 & 2,4 DIMETHYLPENTANE + METHYLCYCLOPENTANE
12	BZ	BENZENE
13.	CH	CYCLOHEXANE
14.	2MH	2-METHYLHEXANE
15.	23DMP	2,3-DIMETHYLPENTANE
16.	11DMCP	1,1 DIMETHYLCYCLOPENTANE
17.	3MH	3-METHYLHEXANE
18.	1C3DMCP	1-c-3-DIMETHYLCYCLOPENTANE
19.	1T2DMCP+3EP	1-t-2-DIMETHYLCYCLOPENTANE + 3-ETHYLPENTANE
20.	1T3DMCP	1-t-3-DIMETHYLCYCLOPENTANE
*21.	n-C_7	n-HEPTANE
*22.	MCH	METHYLCYCLOHEXANE
*23.	TOL	TOLUENE
*24.	n-C_8	n-OCTANE
*25.	n-C_9	n-NONANE
*26.	n-C_{10}	n-DECANE

* These compounds are identified on the chromatograms.

LIGHT ENDS GAS CHROMATOGRAPHY

OIL SAMPLES

DGSI/95/3210

GAS CHROMATOGRAPHY RATIOS

Property Index	Formula Ref.	TOP	BOTTOM
Heptane Value	H	39.79	39.62
Paraffinicity	F	1.72	1.63
Aromaticity	B	0.25	0.25
Isoheptane Value	I	5.92	5.79
Aromaticity	A	0.06	0.07
Paraffin Branching	R	3.79	4.16

AREA DATA

Compound	Formula Ref.	TOP	BOTTOM
n-HEXANE	a	34891	19148
BENZENE	b	2243	1332
CYCLOHEXANE	c	9488	5737
2-METHYLHEXANE	d	10496	6136
2,3-DIMETHYLPENTANE	e	1282	1150
1,1-DMCP	f	683	581
3-METHYLHEXANE	g	9654	6424
1-cis,3-DMCP	h	1447	859
1-trans,3-DMCP + 3-EP	i	1954	1311
1-trans,2-DMCP	j	2036	1074
n-HEPTANE	k	39803	25554
METHYLCYCLOHEXANE	l	23183	15675
TOLUENE	m	10088	6399

FORMULAS

$H = (k/\text{sum of c thru l}) * 100$

$F = k/l$

$B = m/k$

$I = (d+g)/(h+i)$

$A = b/a$

$R = k/d$

WHOLE OIL GAS CHROMATOGRAPHY

OIL SAMPLES

DGSI/95/3210

GAS CHROMATOGRAPHY RATIOS

DGSI No.	Sample Identification	Pr/Ph	Pr/C17	Ph/C18	CPI
1	TOP	1.4	0.45	0.42	1.01
2	BOTTOM	1.5	0.45	0.38	1.03

AREA DATA

DGSI No.	C17	Pr	C18	Ph	C28	C29	C30
1	168369	76396	132211	56153	6107	4941	3698
2	132722	59446	105261	40385	4135	3790	3191

NORMALIZED ISOPRENOID PERCENT

DGSI No.	iC13	iC14	iC15	iC16	iC18	iC19	iC20
1	13.7	9.5	17.1	19.7	11.7	16.3	12.0
2	13.1	9.6	17.6	20.1	12.4	16.2	11.0

AREA DATA

DGSI No.	iC13	iC14	iC15	iC16	iC18	iC19	iC20
1	64397	44494	80355	92167	54892	76396	56153
2	47818	35076	64622	73595	45454	59446	40385

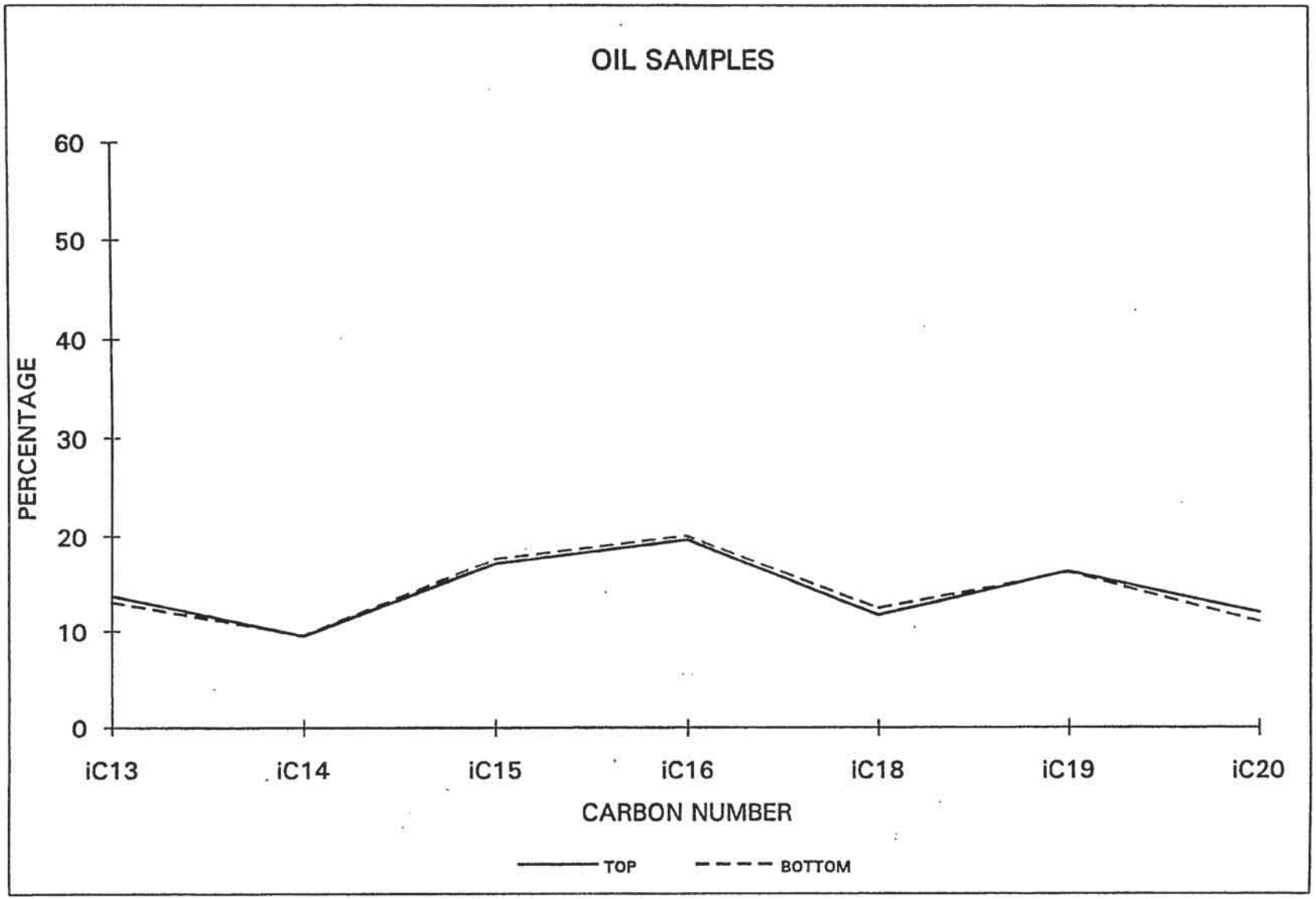
OIL SAMPLES
60
50
40
30
20
10
0
PERCENTAGE
iC13
iC14
iC15
iC16
iC18
iC19
iC20
CARBON NUMBER
TOP
BOTTOM

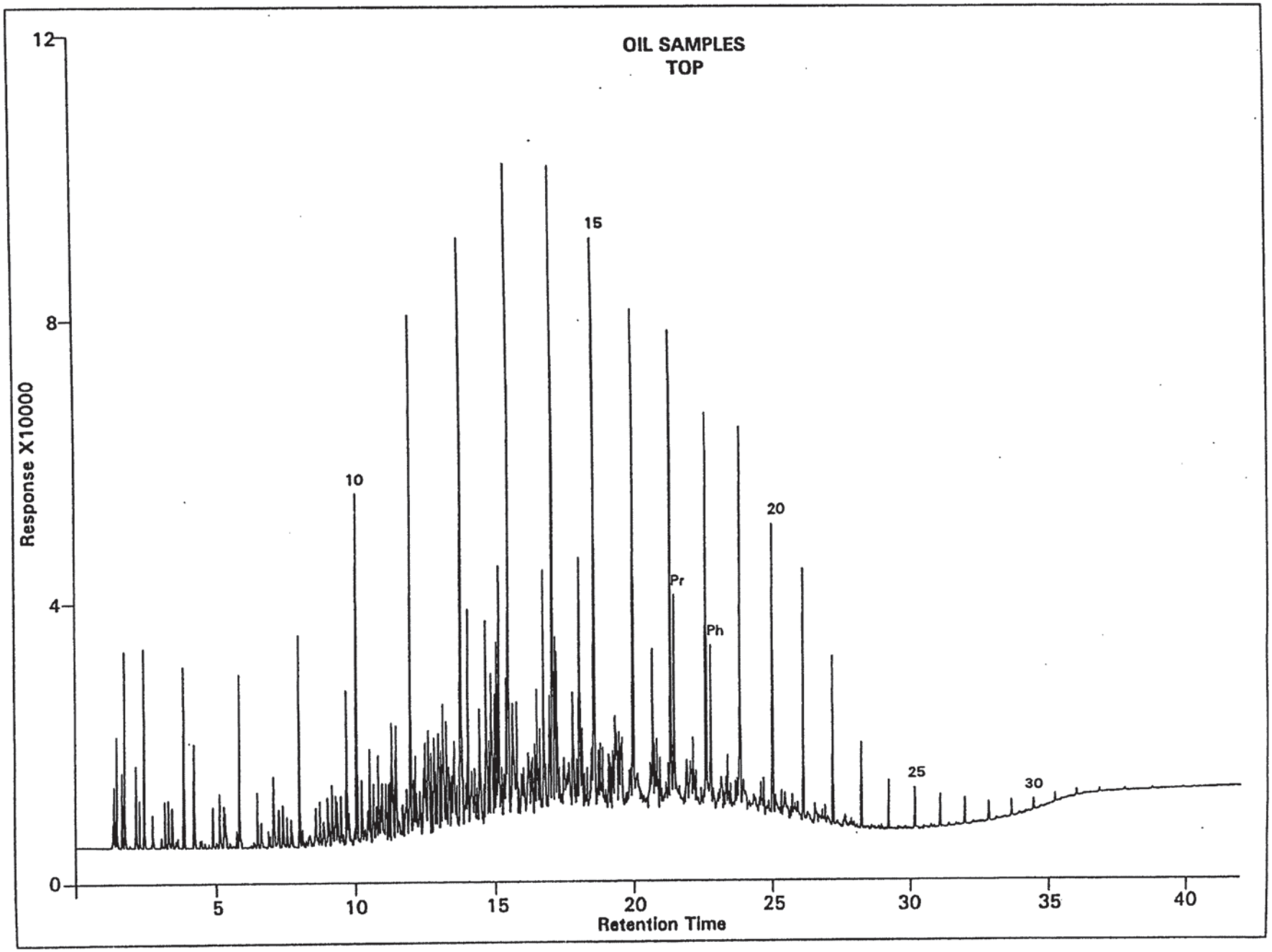
OIL SAMPLES
TOP
Response X10000
12
8
4
0
10
15
20
Pr
Ph
25
30
5
10
15
20
25
30
35
40
Retention Time

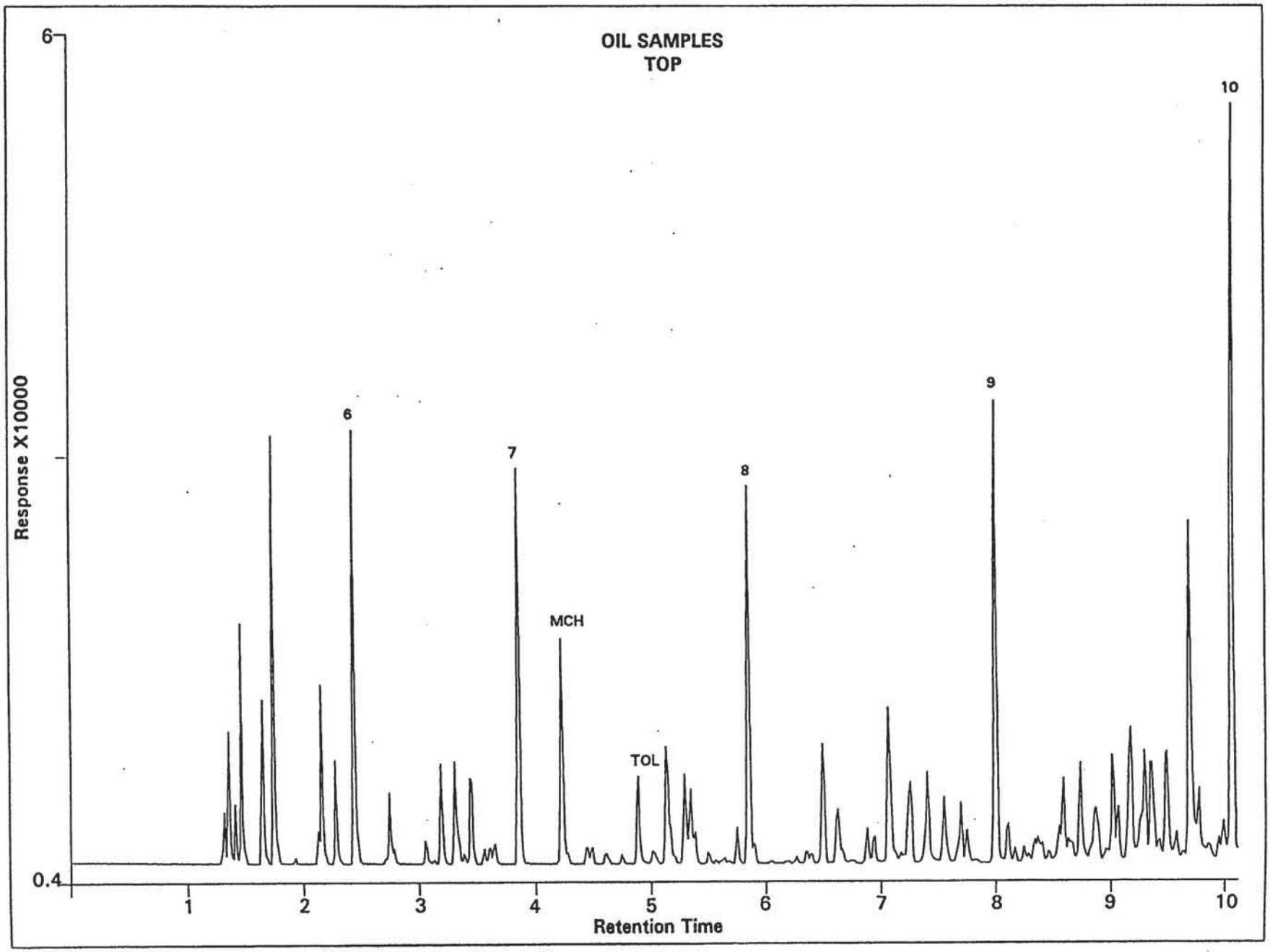
OIL SAMPLES
TOP
Response X10000
6
0.4
6
7
MCH
TOL
8
9
10
1
2
3
4
5
6
7
8
9
10
Retention Time

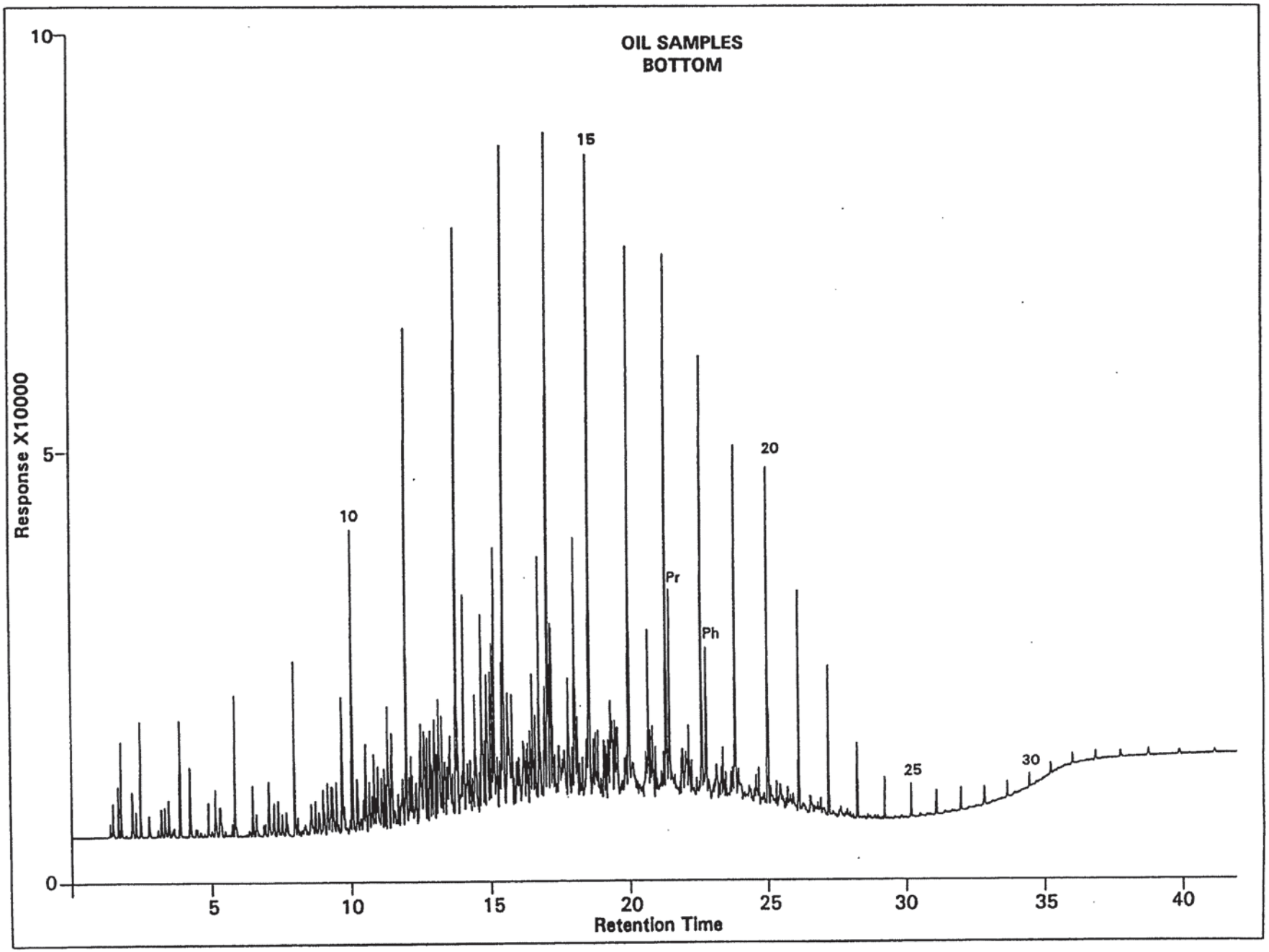
OIL SAMPLES
BOTTOM
Response X10000
10
5
0
15
10
20
Pr
Ph
25
30
5
10
15
20
25
30
35
40
Retention Time

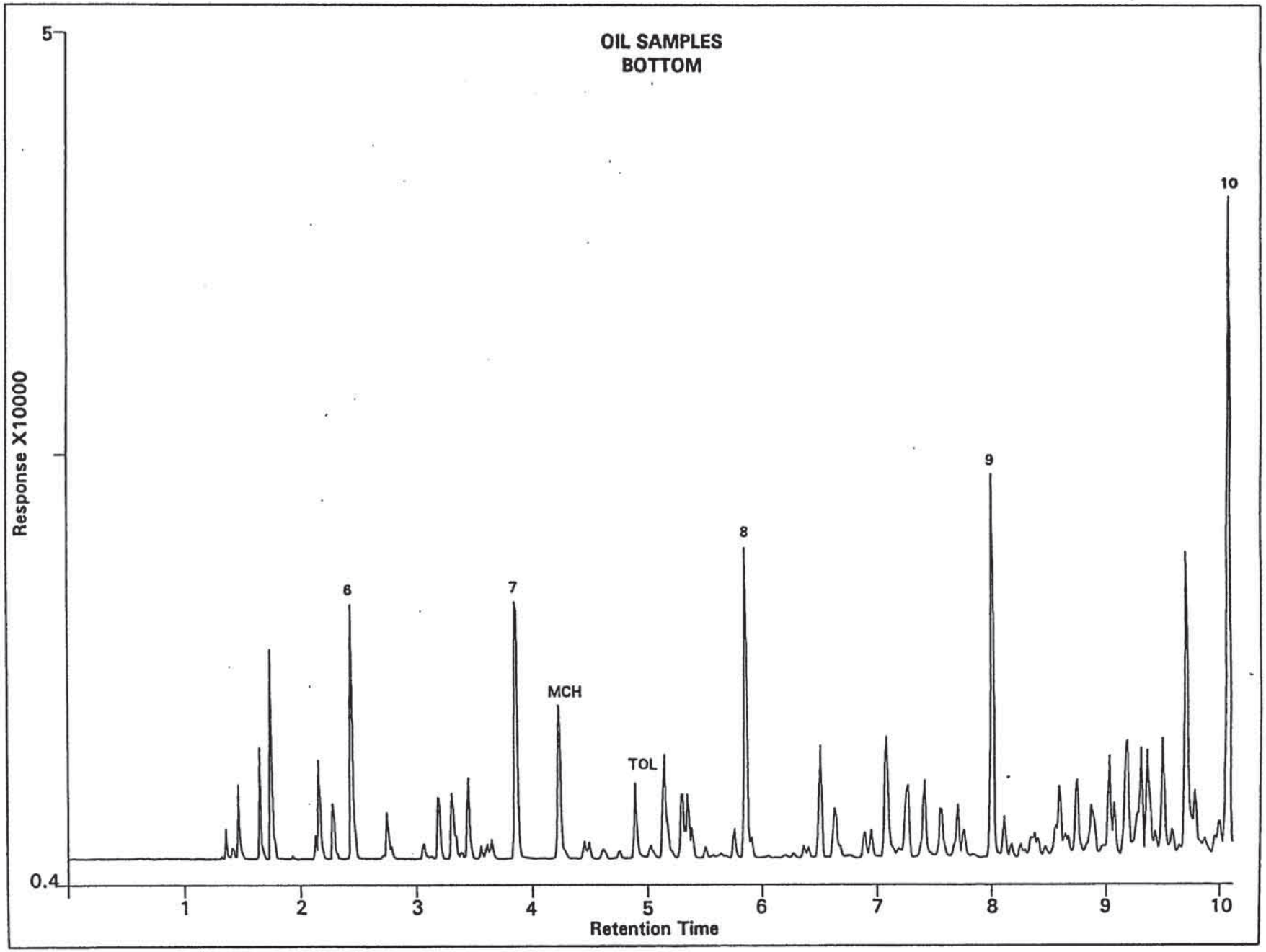
OIL SAMPLES
BOTTOM
5
0.4
Response X10000
6
7
MCH
TOL
8
9
10
1
2
3
4
5
6
7
8
9
10
Retention Time

8 TRIAXIAL COMPRESSION TESTING

8.1 BACKGROUND

Triaxial compression tests were performed on six selected core samples from the Remington 21-1H well. Vertical cylindrical test specimens were drilled from each of the six cores for determination of compressive strength, Young's modulus and Poisson's ratio. Each test sample had nominal dimensions of 1 inch in diameter by 2 inches in length, with the ends being end-ground flat and parallel to within ±0.001 inch per inch length of sample (as per ASTM and ISRM standards). The coring was performed using water and the surface grinding was performed dry (no fluid lubrication or coolant). Pre-test bulk density was determined from the sample's mass and calipered volume. The samples were tested under a simulated net-effective stress. In this case, the pore pressure gradient was subtracted from the horizontal stress gradient (i.e., 0.75 psi/ft - 0.43 psi/ft = 0.32 psi/ft). The net-effective stress gradient (0.32 psi/ft) was multiplied by each sample's vertical depth to obtain the appropriate confining stress for testing. The confining pressure target was held constant while maintaining zero pore pressure during triaxial compression. While maintaining the confining pressure constant, the axial stress was increased using an axial strain rate of $1 \times 10^{-5} s^{-1}$ until failure occurred. The static moduli (Young's, Bulk, and Shear) and Poisson's ratio were determined between 10% and 50% of the maximum axial stress difference[1]. Each test specimen was tested in its "as-received" dry condition.

8.2 RESULTS

The test results are summarized in Table 8-1. Included in this summary table are values of the maximum axial stress difference, compressive strength, pre-test bulk density, Poisson's ratio, and

[1]Axial stress difference is the stress above the confining pressure. Confining pressure acts on all sides of the sample, including the ends. To fail a material, an additional stress, known as the axial stress difference, must be applied along the axis of the core. The effective compressive strength of a sample is the maximum axial stress difference plus the effective confining pressure.

the static moduli determined for each sample. The stress-strain plots are provided in Appendix A. The compressive strengths (i.e., the sum of the maximum axial stress difference and the effective confining pressure) ranged from 19,980 to 28,100 psi. The lower strengths were determined for samples from a depth of 7463 and 7467 feet, which were lithologically different (finer-grained carbonates). Test samples from 7447 and 7475 feet were composed dominantly of anhydrite, as indicated by their high bulk density and exceptionally high moduli. The test sample from 7455 feet. contained some anhydrite clasts in a carbonate matrix. This particular sample had the highest compressive strength, 28,100 psi, and a high value of Young's modulus, 5.35×10^6 psi. The test sample from a depth of 7451 feet appeared to be a fine to medium-grained massive limestone, which had an average compressive strength of 26,840 psi and a Young's modulus of 2.63×10^6 psi. Poisson's ratios were very consistent for the anhydrite samples (0.39) and fairly consistent for the carbonates with values ranging from 0.24 to 0.29.

Table 8-1. Summary of Quasi-Static Mechanical Properties

Sample Depth (ft)	Pre-Test Bulk Density (gm/cm^3)	Confining Pressure (psi)	Maximum Axial Stress Difference (psi)	Compressive Strength (psi)	Poisson's Ratio	Young's Modulus (10^6 psi)	Bulk Modulus (10^6 psi)	Shear Modulus (10^6 psi)
7447	2.94	2380	24,200	26,580	0.39	9.25	14.41	3.32
7451	2.59	2380	24,460	26,840	0.29	2.63	2.10	1.02
7455	2.70	2390	25,710	28,100	0.25	5.35	3.57	2.14
7463	2.44	2390	21,530	23,920	0.24	3.31	2.12	1.33
7467	2.52	2390	17,590	19,980	0.26	2.28	1.56	0.91
7475	2.94	2390	25,390	27,780	0.39	9.32	14.29	3.35

APPENDIX A

STRESS-STRAIN CURVES

TerraTek
University Research Park
420 Wakara Way • Salt Lake City, Utah 84108
Telephone (801) 584-2480
FAX (801) 584-2432

UPRC
7447 ft.

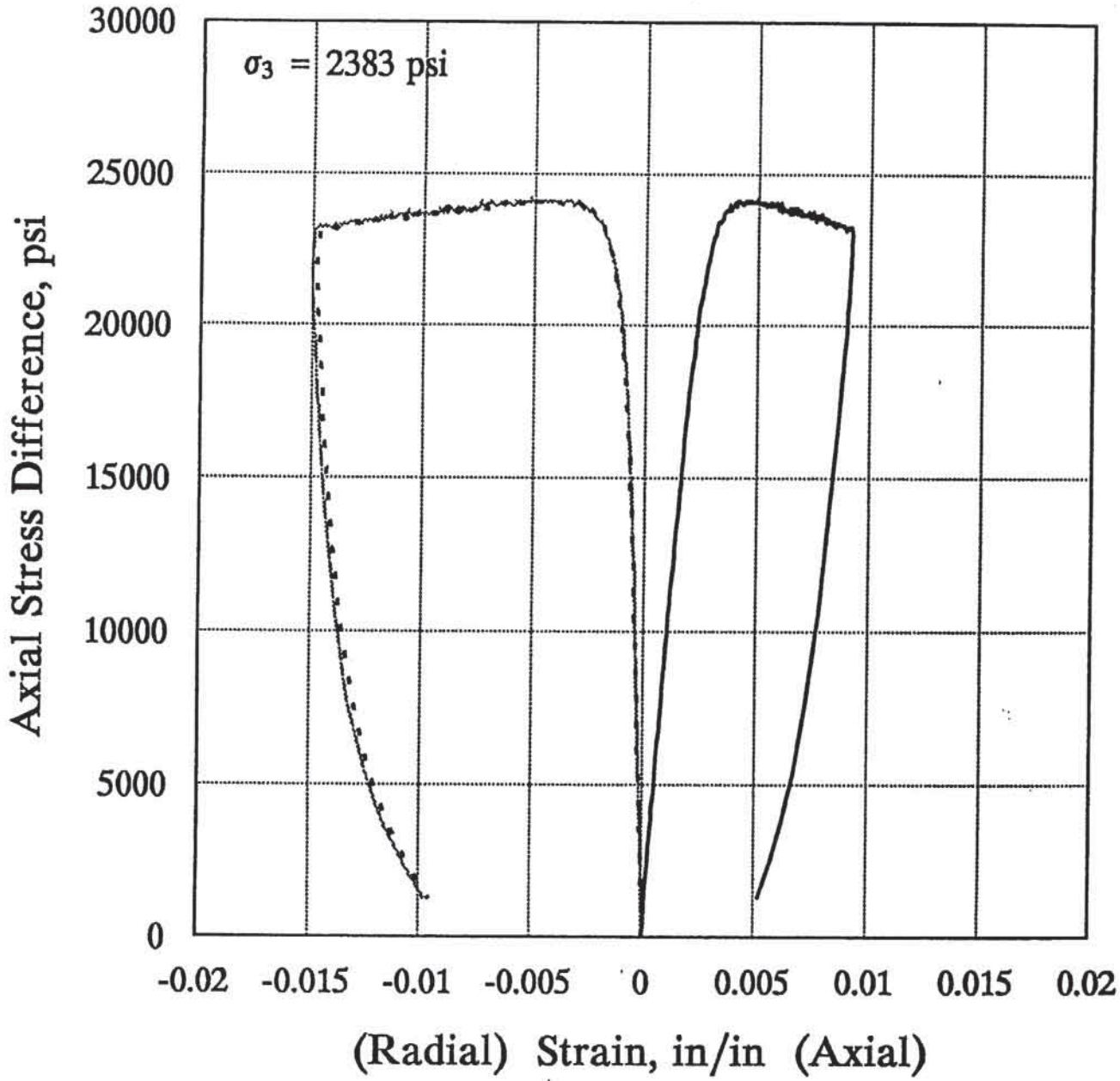

TerraTek
University Research Park
420 Wakara Way • Salt Lake City, Utah 84108
Telephone (801) 584-2480
FAX (801) 584-2432

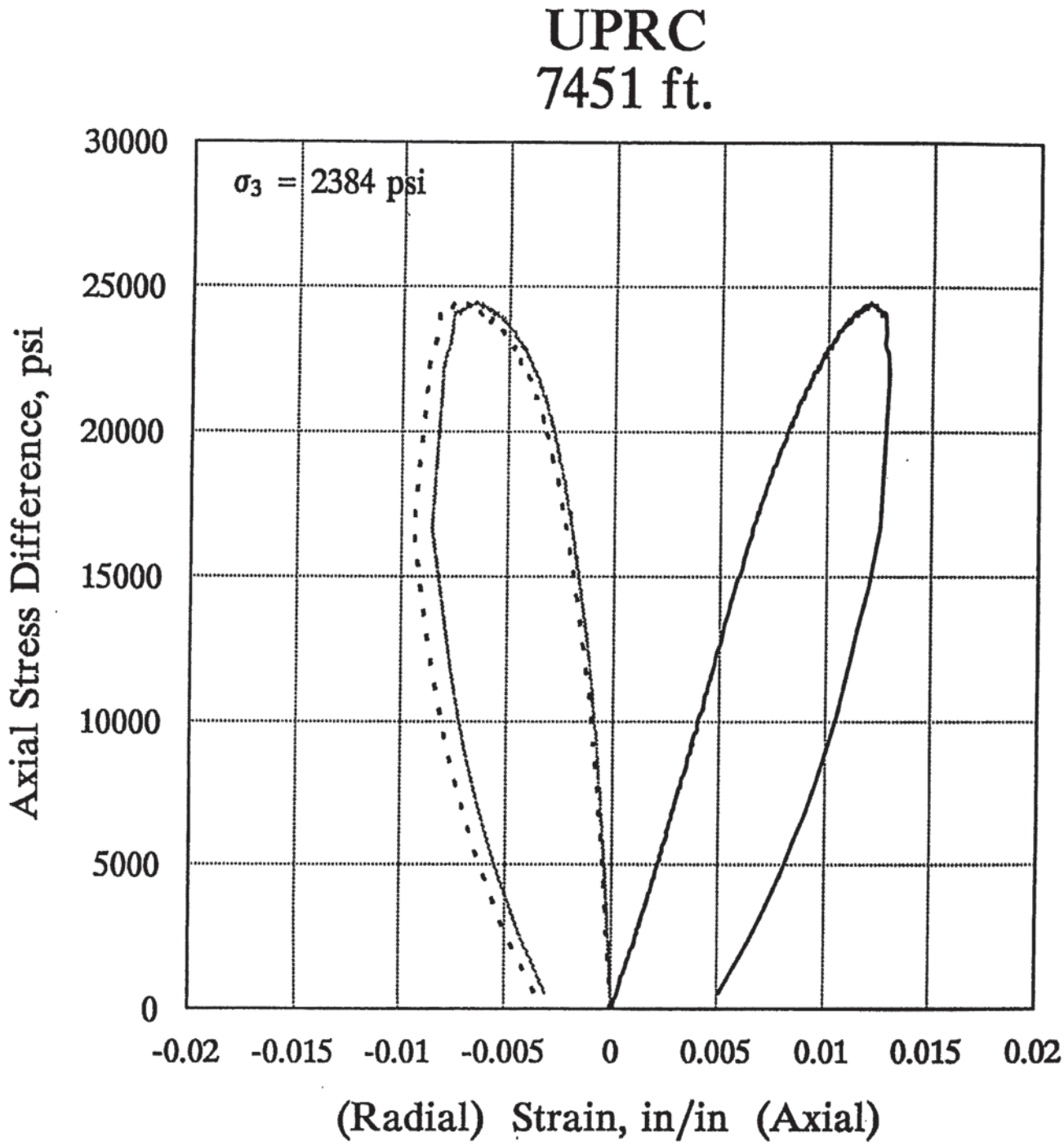

TerraTek
University Research Park
420 Wakara Way • Salt Lake City, Utah 84108
Telephone (801) 584-2480
FAX (801) 584-2432

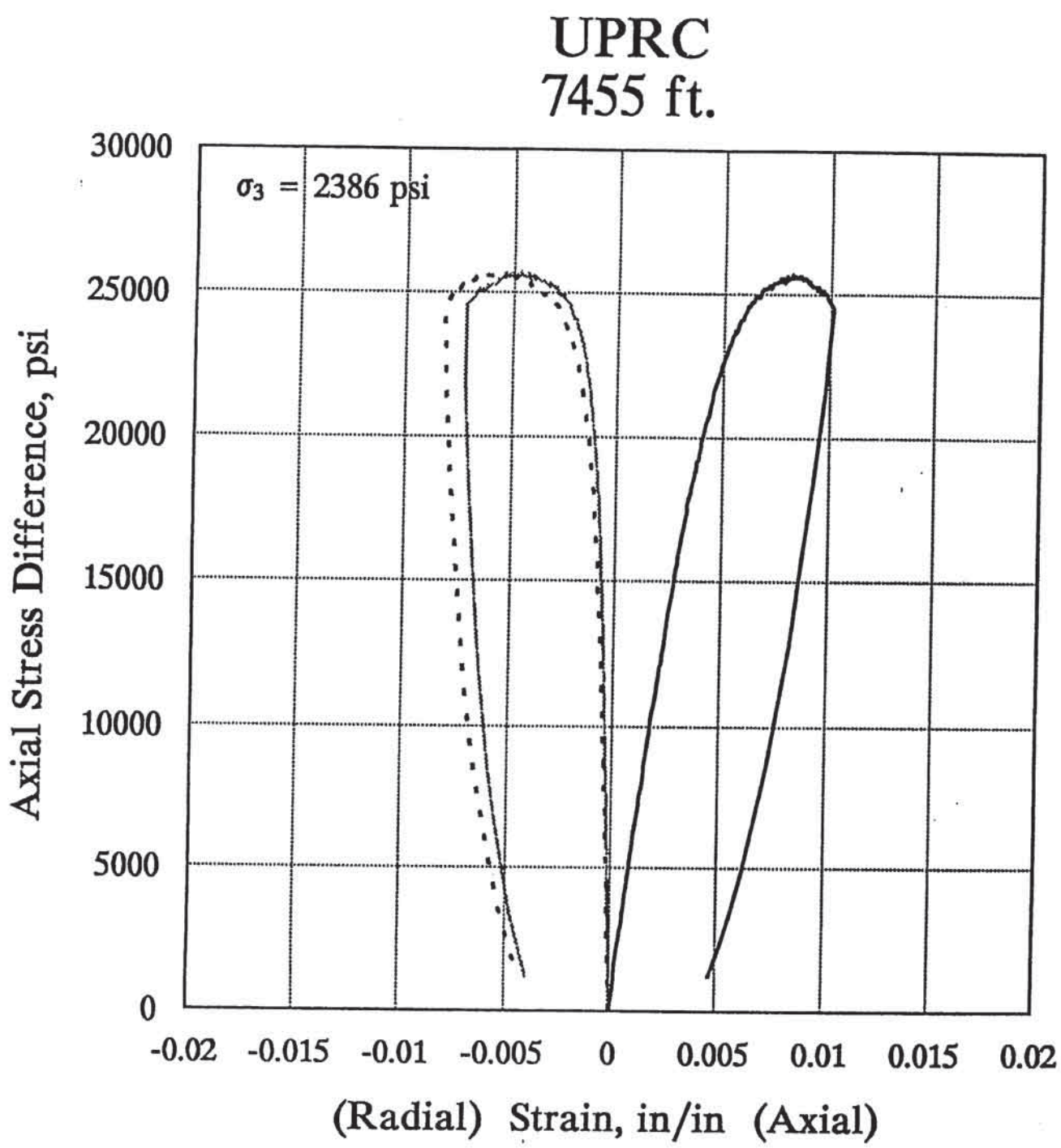

TerraTek
University Research Park
420 Wakara Way • Salt Lake City, Utah 84108
Telephone (801) 584-2480
FAX (801) 584-2432

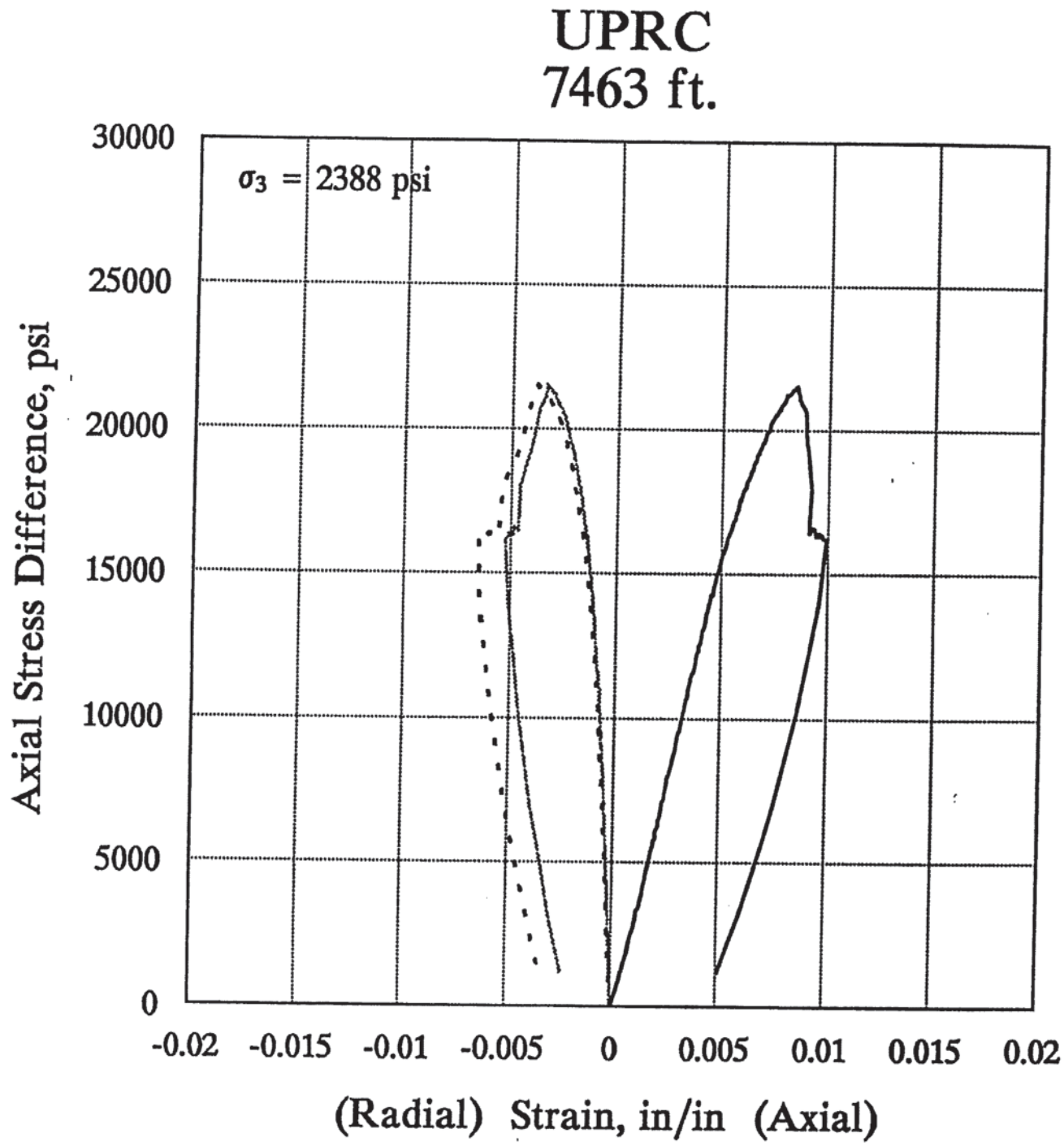

TerraTek
University Research Park
420 Wakara Way • Salt Lake City, Utah 84108
Telephone (801) 584-2480
FAX (801) 584-2432

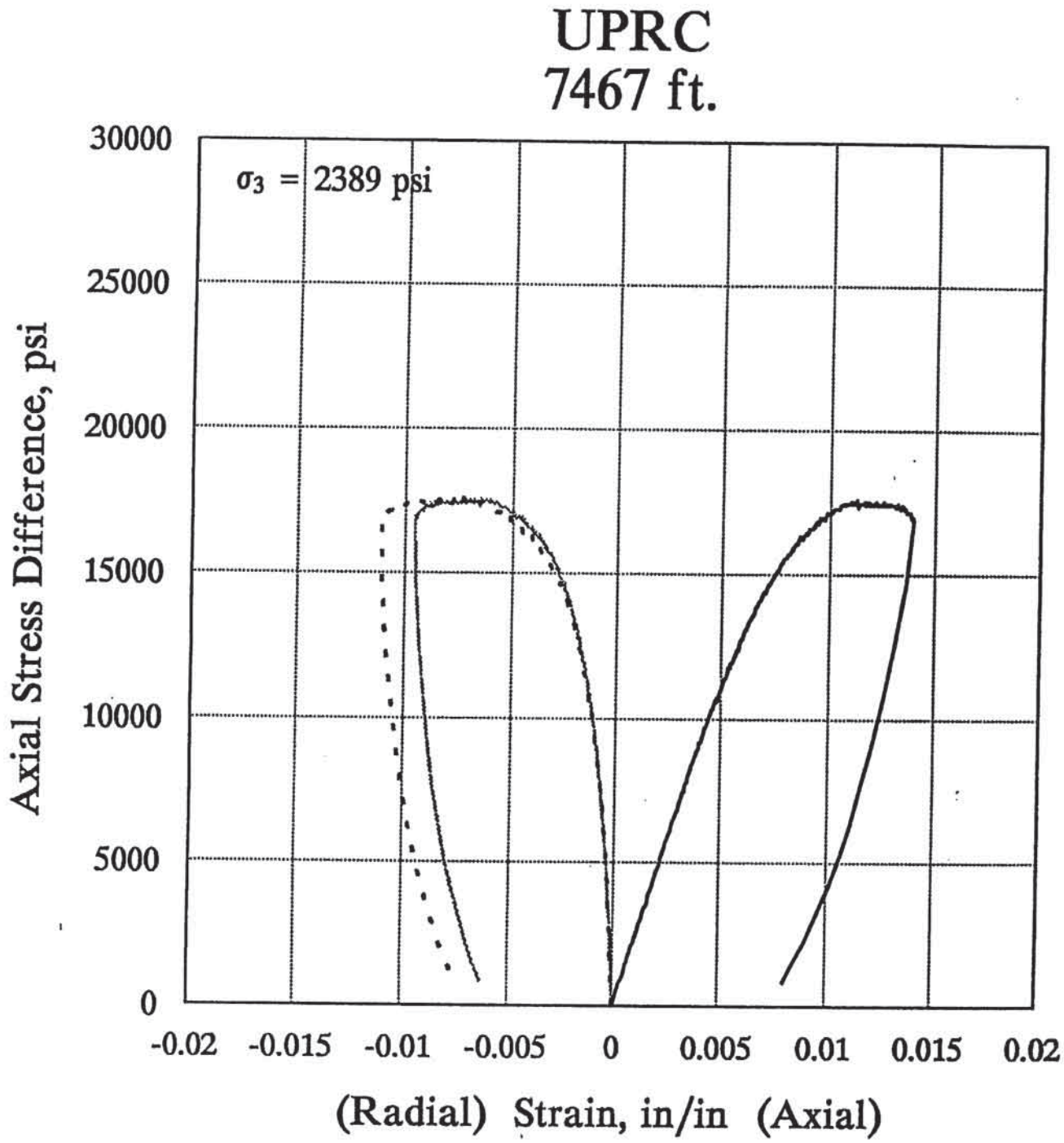

TerraTek
University Research Park
420 Wakara Way • Salt Lake City, Utah 84108
Telephone (801) 584-2480
FAX (801) 584-2432

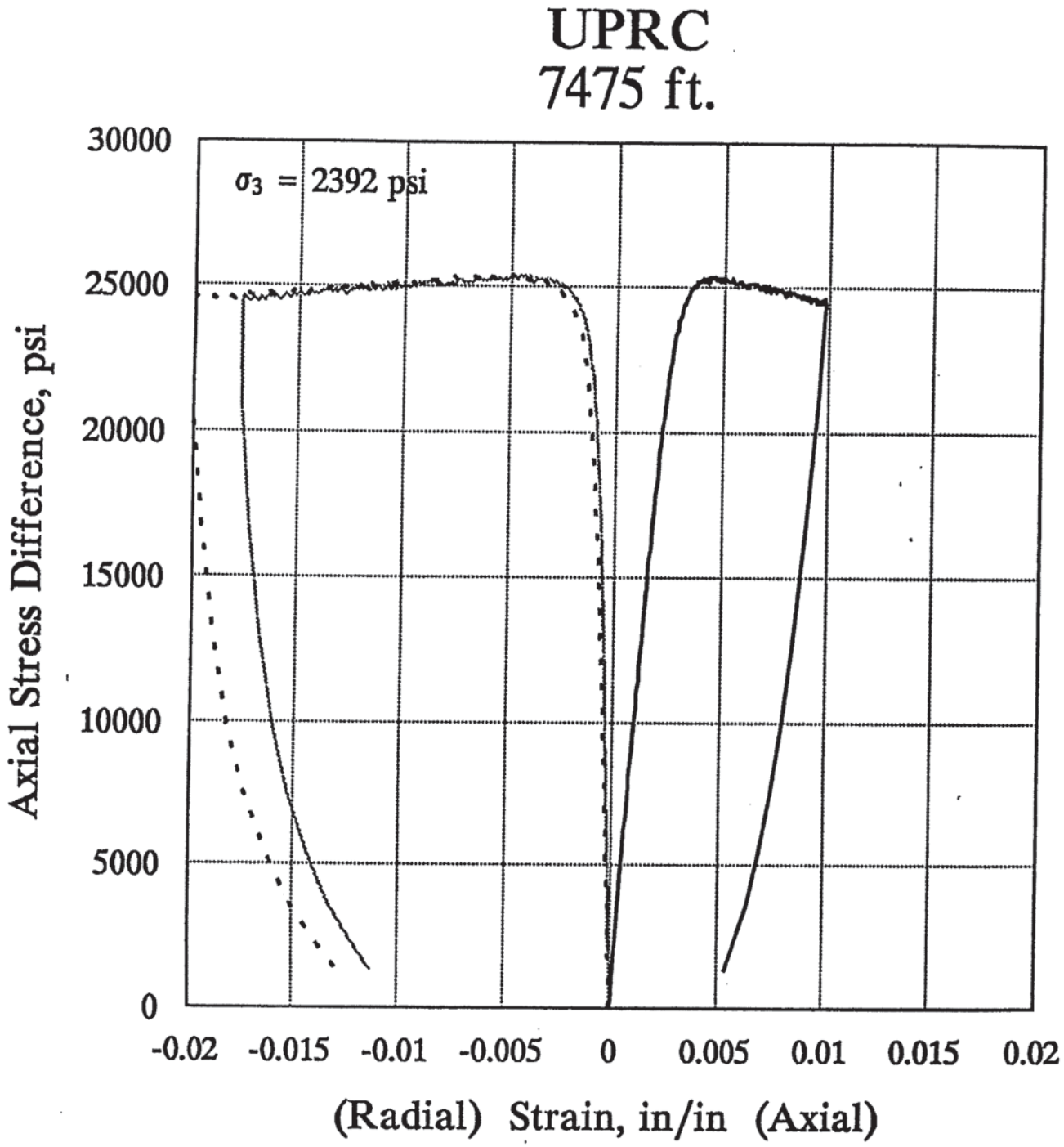

TerraTek
University Research Park
420 Wakara Way • Salt Lake City, Utah 84108
Telephone (801) 584-2480
FAX (801) 584-2432

Appendix: F:

Cisco State 36-13

Core Analysis Report by Core Laboratories, Inc.

CMS-300 CONVENTIONAL PLUG ANALYSIS

Patara Oil & Gas

Cane Creek 042711
Cane Creek
Grand Co., UT

CL File Number: DEN-110039

Date: 8.31.2011

Patara Oil & Gas
Cane Creek 042711
Cane Creek
Grand Co., UT

CL File No.: DEN-110039
Date: 8.31.2011
Analyst(s): KF

CMS-300 CONVENTIONAL PLUG ANALYSIS

Sample Number	Depth (ft)	Net Confining Stress (psig)	Porosity (%)	Permeability Klinkenberg (md)	Permeability Kair (md)	b(air) psi	Beta ft(-1)	Alpha (microns)	Saturation Oil % Pore Volume	Saturation Water % Pore Volume	Grain Density (g/cm3)	Footnote
1	7588.00	2310	7.75	.004	.0155	82.35	5.28E+14	7.17E+03	0.0	91.8	2.729	
2	7589.00	2310	10.25	.0158	.0338	32.83	1.05E+13	5.26E+02	0.0	64.5	2.715	
3	7590.00	2310	0.41	.001	.003	71.12	1.13E+15	4.13E+03	0.0	72.9	2.935	(4)
4	7591.00	2310	0.07	.0001	.0009	303.31	6.16E+17	2.06E+05	0.0	98.1	2.958	(4)
5	7592.80	2310	12.29	.0185	.0375	29.24	4.33E+13	2.56E+03	0.0	66.2	2.701	
6	7593.00	2310	17.68	.389	.592	12.11	2.70E+11	3.37E+02	0.0	74.9	2.692	
7	7594.00	2310	0.64	.0002	.001	251.64	2.29E+17	1.27E+05	0.0	88.2	2.895	(4)
8	7595.00	2310	0.21	.00009	.0008	307.91	6.53E+17	2.10E+05	0.0	99.7	2.918	(4)
9	7596.20	2310	0.49	.0001	.001	281.13	4.08E+17	1.67E+05	0.0	99.8	2.920	(4)
10	7597.00	2310	0.81	.0002	.001	237.18	1.68E+17	1.10E+05	0.0	97.4	2.885	(4)
11	7598.30	2310	2.92	.003	.0105	97.25	1.26E+15	1.08E+04	0.0	30.8	2.777	
12	7599.00	2310	0.27	.0001	.0009	297.37	5.46E+17	1.92E+05	0.0	94.5	2.936	(4)
13	7600.55	2310	12.96	.512	.553	1.83	4.84E+12	8.01E+03	0.0	96.6	2.780	(1)
14	7601.90	2310	14.61	2.09	2.42	3.27	1.31E+11	8.86E+02	0.0	77.8	2.760	(1)
15	7602.90	2310	1.15	.0001	.001	306.39	6.42E+17	2.07E+05	0.0	54.4	2.884	(4)
16	7603.10	2310	0.26	.0001	.001	273.99	3.57E+17	1.57E+05	0.0	92.0	2.943	(4)
17	7604.10	Ambient	1.76	***	***	***	***	***	0.0	13.5	2.956	(2)(4)
18	7605.10	2310	5.74	.002	.004	46.54	2.59E+15	1.44E+04	0.0	83.8	2.814	
19	7606.10	2310	10.98	.087	.129	12.52	2.28E+12	6.51E+02	0.0	97.6	2.793	
20	7607.90	2310	11.65	.0182	.0467	44.43	3.08E+13	1.82E+03	0.0	98.9	2.721	
21	7608.80	2310	13.16	.0302	.0546	22.21	6.19E+12	6.15E+02	0.0	99.9	2.765	
22	7609.10	2310	10.25	3.49	4.06	3.30	1.15E+11	1.30E+03	0.0	80.5	2.768	(1)
23	761.50	Ambient	12.66	***	***	***	***	***	0.0	62.7	2.700	(5)
24	7611.50	2310	8.77	.0344	.0545	15.98	3.61E+12	4.07E+02	0.0	99.7	2.728	
25	7612.90	2310	2.15	.0116	.0245	32.91	7.07E+13	2.78E+03	0.0	87.9	2.929	(4)
26	7613.10	2310	1.94	.0004	.002	178.99	3.61E+16	5.29E+04	0.0	85.8	2.941	(4)
27	7614.10	Ambient	1.89	***	***	***	***	***	0.0	24.1	2.960	(5)(4)
28	7615.10	2310	9.14	.001	.006	117.70	3.57E+15	1.77E+04	0.0	96.4	2.761	
29	7616.10	2310	10.13	.0422	.0937	32.96	8.30E+12	1.14E+03	0.0	99.5	2.756	
30	7617.00	2310	9.59	.0275	.0504	23.03	1.76E+13	1.64E+03	0.0	99.3	2.767	
31	7618.30	2310	8.48	.866	.971	2.67	1.31E+12	3.71E+03	0.0	54.9	2.843	(1)
32	7619.10	2310	9.13	.003	.0111	92.57	9.73E+14	9.55E+03	0.0	98.8	2.735	
33	7620.10	2310	10.73	.0242	.0595	40.88	5.61E+13	4.54E+03	0.0	97.7	2.721	
34	7621.40	2310	2.14	.0931	.113	5.44	2.88E+13	8.88E+03	0.0	96.6	2.909	(4)
35	7622.10	2310	8.51	.0274	.0630	36.10	1.32E+13	1.16E+03	0.0	72.6	2.723	
36	7623.90	2310	15.42	***	***	***	***	***	0.0	72.8	2.706	(5)
37	7624.30	2310	8.79	.007	.0198	50.78	8.09E+13	1.99E+03	0.0	88.0	2.847	(1)(4)
38	7631.10	2310	9.11	.143	.223	13.99	8.70E+11	4.03E+02	0.0	99.1	2.742	
39	7632.10	2310	9.74	.004	.008	26.64	2.09E+12	2.99E+01	0.0	93.4	2.736	(1)
40	7633.20	2310	7.20	.008	.0254	64.80	1.56E+14	4.02E+03	0.0	99.3	2.682	
41	7634.10	2310	12.40	.119	.218	20.77	1.64E+12	6.38E+02	0.0	98.8	2.721	(1)
42	7635.10	2310	2.79	***	***	***	***	***	0.0	21.2	2.926	(5)(4)
43	7636.30	2310	10.43	.0224	.0360	17.23	1.75E+12	1.27E+02	0.0	66.3	2.752	
44	7637.10	2310	1.80	***	***	***	***	***	0.0	13.2	2.958	(2)(4)
45	7648.10	2310	2.01	***	***	***	***	***	0.0	21.8	2.946	(2)(4)
46	7650.10	2310	0.91	.0001	.0009	308.57	6.58E+17	2.10E+05	0.0	98.9	2.743	

Footnotes :

(1) : Denotes fractured or chipped sample. Permeability and/or porosity may be optimistic.

(2) : Sample permeability below the measurement range of CMS-300 equipment at indicated net confining stress (NCS). Porosity determined using Archimedes bulk volume at ambient condit

Patara Oil & Gas
Cane Creek 042711
Cane Creek
Grand Co., UT

CL File No.: DEN-110039
Date: 8.31.2011
Analyst(s): KF

CMS-300 CONVENTIONAL PLUG ANALYSIS

Sample Number	Depth (ft)	Net Confining Stress (psig)	Porosity (%)	Permeability		b(air) psi	Beta ft(-1)	Alpha (microns)	Saturation		Grain Density (g/cm3)	Footnote
				Klinkenberg (md)	Kair (md)				Oil % Pore Volume	Water		

(3) : Denotes very short sample, porosity may be optimistic due to lack of conformation of boot material to plug surface.

(4) : Sample contains anhydrite.

(5) : Denotes sample unsuitable for measurement at stress. Porosity determined using Archimedes bulk volume at ambient conditions.

Permeability greater than 0.1 mD measured using helium gas. Permeability less than 0.1 mD measured using nitrogen gas. All b values converted to b (air)

Patara Oil & Gas
Cane Creek 042711
Cane Creek
Grand Co., UT

CL File No.: DEN-110039
Date: 8.31.2011
Analyst(s): KF

Figures: Porosity (%) vs Permeability (md) at various NCS (psi)

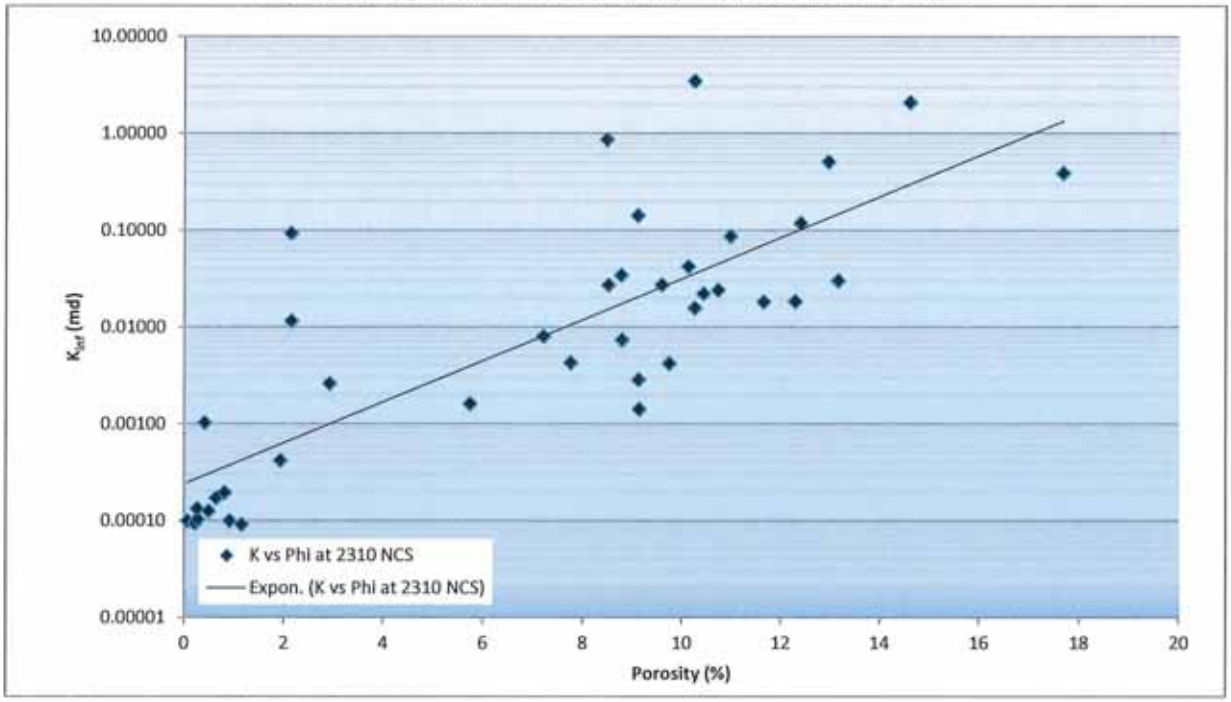

APPENDIX A: EXPLANATION OF CMS-300 TERMS "b", "Beta, and "Alpha"

K_∞	=	Equivalent non-reactive liquid permeability, corrected for gas slippage, mD
K_{air}	=	Permeability to Air, calculated using K_∞ and b, mD
b	=	Klinkenberg slip factor, psi
β (Beta)	=	Forcheimer inertial resistance factor, ft^{-1}
α (Alpha)	=	A factor equal to the product of Beta and K_∞. This factor is employed in determining the pore level heterogeneity index, H_I.
H_I	=	$\log_{10}(\alpha\phi/RQI)$ α, microns = $3.238E^{-9}\ \beta K_\infty$
Ø	=	Porosity, fraction
RQI	=	Reservoir Quality Index, microns
RQI	=	$0.0314(K/\phi)^{0.5}$

For further information please refer to:

Jones, S.C.: "Two-Point Determination of Permeability and PV vs. Net Confining Stress" SPE Formation Evaluation (March 1988) 235-241.

Jones S.C.: "A Rapid Accurate Unsteady-State Klinkenberg Permeameter," Soc. Pet. Eng. J. (Oct. 1972) 383-397.

Jones, S.C.: "Using the Inertial Coefficient, β, To Characterize Heterogeneity in Reservoir Rock: SPE 16949 (September 1987).

Amaefule, J.O.; Kersey, D.G.; Marschall, D.M.; Powell, J.D.; Valencia, L.E.; Keelan, D.K.: "Reservoir Description: A Practical Synergistic Engineering and Geological Approach Based on Analysis of Core Data,: SPE Technical Conference (Oct. 1988) SPE 18167.

Patara Oil & Gas
Cane Creek 042711
Cane Creek
Grand Co., UT

CL File No.: DEN-110039
Date: 8.31.2011
Analyst(s): KF

CMS-300 CONVENTIONAL PLUG ANALYSIS PROTOCOL

Sample Preparation
1.0" diameter plugs were drilled with liquid nitrogen and trimmed into right cylinders with a diamond-blade trim saw.
All sample trims were archived.

Core Extraction
Plugs selected for routine core analysis were placed in Dean Stark equipment using toluene, followed by Soxhlet extraction using a chloroform / methanol (87:13) azeotrope.

Sample Drying
Samples were oven dried at 240° F to weight equilibrium (+/- 0.001 g).

Porosity
Porosity was determined using Boyle's Law technique by measuring grain volume at ambient conditions & pore volume at indicated net confining stresses (NCS)

Grain Density
Grain density values were calculated by direct measurement of grain volume and weight on dried plug samples.
Grain volume was measured by Boyle's Law technique.

Permeability
Permeability to air was measured on each sample using unsteady-state method at indicated NCS.

Fluid Saturations
Fluid saturations were determined by the Dean Stark technique using the following fluid properties:

Brine	1.032 g/cc (50000 ppm TDS)
Oil	0.845 g/cc (36° API)

Core Laboratories XRD
Whole-Rock and Clay Fraction Analytical Procedures

Sample Preparation

Samples submitted for whole-rock and clay-fraction XRD mineral analyses are first cleaned of obvious drilling contaminants and then disaggregated in a mortar and pestle. Approximately five grams of each sample are transferred to reagent grade isopropyl alcohol and ground using a McCrone micronizing mill with a five minute grind time. The resultant powders are dried, disaggregated, and back-loaded into aluminum sample holders to produce random whole-rock mounts. A separate split of each sample is dispersed in a dilute sodium phosphate solution using a sonic probe. The suspensions are then centrifugally size-fractionated to isolate clay-size (<4 micron ESD) materials for a separate clay-fraction mount. The suspensions are then vacuum-deposited on silver membrane filters to produce oriented clay mineral aggregates. Membrane mounts are attached to stainless steel slugs and exposed to ethylene glycol vapor for a minimum of 24 hours.

Analytical Procedures

XRD analyses of the samples are performed utilizing a Scintag or Philips automated powder diffractometer equipped with a copper source (40kV, 40mA) and a solid state or scintillation detector. The whole rock samples are analyzed over an angular range of 2-60 degrees 2-theta at a scan rate of one degree/minute. The glycol-solvated clay-fraction mounts are analyzed over an angular range of 2-50 degrees 2-theta at a rate of 1.5 degrees/minute.

Semi-quantitative determinations of whole-rock and phyllosilicate mineral amounts are done utilizing integrated peak areas (derived from peak-decomposition / profile-fitting methods) and empirical reference intensity ratio (RIR) factors determined specifically for the diffractometer used in data collection. The total clay mineral (including mica) abundance of each sample is determined from the whole-rock XRD patterns using combined {00l} and {hkl} clay mineral reflections and suitable empirical RIR factors.

XRD patterns from glycol-solvated clay-fraction samples are analyzed using techniques similar to those described above. Determinations of mixed-layer clay ordering and expandability are done by comparing experimental diffraction data from the glycol-solvated clay mineral aggregates with simulated one dimensional diffraction profiles generated using the program NEWMOD written by R.C. Reynolds.

Patara Oil & Gas
Cane Creek 042711

Composition Determined by XRD and TOC

File: 110920G

Depth	7601.90	7609.10	7612.90	7620.10	7622.10	7632.10
TOC	1.54	1.02	n/a	n/a	n/a	0.12
Weight % Mineralogy (Without TOC)						
Quartz	28.0	28.2	3.0	55.5	58.6	42.4
Anhydrite	0.0	0.0	91.3	0.6	0.7	0.4
K-Feldspar	3.4	4.1	0.5	6.5	4.4	5.7
Plagioclase	0.9	0.8	0.0	1.0	0.7	0.6
Calcite	1.2	15.7	1.6	11.8	5.9	0.0
Dolomite	39.2	38.3	1.4	8.1	20.6	34.4
Halite	0.3	0.4	0.0	1.0	0.1	3.1
Pyrite	5.9	2.8	0.4	0.0	1.7	2.0
Total Clay	21.1	9.7	1.9	15.4	7.4	11.5
Relative Clay %						
Illite & Mica	92.1	86.6	86.0	87.1	89.8	87.6
Kaolinite	0.0	2.3	6.3	2.3	2.6	3.1
Chlorite	7.9	11.1	7.8	10.6	7.6	9.3
Sum Bulk	100.0	100.0	100.1	99.9	100.1	100.1
Sum Clay	100.0	100.0	100.1	100.0	100.0	100.0
Volume % Composition (Includes TOC as Kerogen)						
Quartz	28.6	28.7	3.4	56.0	60.1	43.4
Anhydrite	0.0	0.0	90.7	0.5	0.6	0.3
K-Feldspar	3.5	4.3	0.5	6.7	4.6	5.9
Plagioclase	1.0	0.9	0.0	1.0	0.7	0.6
Calcite	1.2	15.7	1.7	11.7	5.9	0.0
Dolomite	37.3	36.4	1.4	7.6	19.6	32.8
Halite	0.3	0.6	0.0	1.2	0.1	3.9
Pyrite	3.2	1.5	0.2	0.0	0.9	1.1
Illite & Mica	19.7	8.5	1.8	13.4	6.7	10.2
Kaolinite	0.0	0.2	0.1	0.4	0.2	0.4
Chlorite	1.5	1.0	0.1	1.5	0.5	1.0
Kerogen	3.6	2.4	0.0	0.0	0.0	0.3
Total	99.9	100.2	99.9	100.0	99.9	99.9
Vclay	21.2	9.7	2.0	15.3	7.4	11.6
Calc. G.D. (g/cc)	2.757	2.735	2.950	2.671	2.716	2.721

Core Lab

Reservoir Geology
Core Lab

Core Lab
RESERVOIR OPTIMIZATION

ADVANCED CORE ANALYSIS STUDY

Patara Oil & Gas LLC.

Cane Creek 042711

Paradox Basin

Grand County, Utah

Rock Mechanics:
Triaxial Compressive Strength
Data Report

CL File Number: HOU-110920

Date: 29-Aug-2011

Performed by:
Core Laboratories
Petroleum Services Division
6316 Windfern
Houston, Texas 77040

Phone: (713) 328-CORE

Core Lab
RESERVOIR OPTIMIZATION

TRIAXIAL COMPRESSIVE STRENGTH TESTING
Static and Dynamic Elastic Properties

PETROLEUM SERVICES

Sample Preparation

1" diameter samples trimmed to right cylinders were tested with the saturation condition "as received". Sample dimension and mass were measured and recorded.

Triaxial Testing

Each sample was inserted into a heat-shrink jacket and a radial Linear Variable Displacement Transducer (LVDT) calibrated to an accuracy of 0.0002 inch was placed around the lateral surface of the sample. Two sets of internal linear LVDTs was also placed within a pressure vessel to measure axial deformation.

The jacketed sample was mounted between pistons and the entire assembly was mounted in the pressure vessel that allows application of confining pressure and axial stress. The upper piston extends through the top of the pressure vessel enabling the application of axial load.

The pressure vessel was then placed into a computer-controlled load frame where another linear LVDT was attached to monitor piston displacement, and filled with hydraulic oil. Confining pressure was increased to the desired hydrostatic testing pressure.

Compression (P)- and Shear (S)-wave sonic velocities were measured at the initial hydrostatic condition.

The LVDT responses were recorded as the axial load was increased at a constant incremental rate, while holding the confining pressure constant.

P- and S-wave sonic velocities were measured during the triaxial testing.

The test was terminated upon attaining the desired level of axial stress or after sample failure.

Calculated data

Results of the triaxial compression tests are presented by stress-strain curves. Differential stresses are plotted as a function of both axial strain ε_L (= $\Delta L/L_o$ where L is the sample length) and radial strain ε_R (= $\Delta D/D_o$ where D is the sample diameter). Differential stress (σ_d) is defined as the difference between the total axial stress and the confining pressure. Since all tests were conducted under compressive stresses, compressive stress and contraction (shortening) are considered positive. Accordingly, positive axial strain indicates sample shortening and negative radial strain indicates increase in sample diameter during deformation.

When the sample is deformed to failure, the maximum stress achieved during the deformation is taken as the triaxial compressive strength of the sample. The static values of elastic constants are determined from the slope of the stress-strain curves. The static Young's modulus is determined by taking the average slope of linear elastic portion of the stress-axial strain curve. The static Poisson's ratio (= $-\Delta\varepsilon_R/\Delta\varepsilon_L$) is determined in a similar way by taking the ratio of the slope of axial curve to the slope of radial curve.

Dynamic elastic parameters (bulk modulus, Young's modulus, shear modulus, and Poisson's ratio) were calculated using compressional-wave and shear-wave velocities (Vp and Vs, respectively) and the bulk density of the sample, based on the linear elastic theory. Sonic velocities testing techniques are consistent with ASTM Standard D2845–1995: "Method for Laboratory Measurement of Pulsed Sonic Velocities and Ultrasonic Elastic Constants of Rock." The equipment is calibrated to 1% accuracy by using aluminum cylinders as a standard.

TRIAXIAL COMPRESSIVE TEST RESULTS

Company:	**Patara Oil & Gas LLC**	Date:	**August 2011**
Well:	**Cane Creek 042711**	File:	**HOU-110920**
Field:	**Paradox Basin**	Saturation Fluid:	**As Received**
Location:	**Grand County, Utah**	Rock Type:	**Shale**

Triaxial Static Young's Modulus, Poisson's Ratio and Compressive Strength

Sample Number	Depth (ft)	Confining Pressure (psi)	Bulk Density (g/cm^3)	Compressive Strength (psi)	Young's Modulus (10^6 psi)	Poisson's Ratio
22	7609.50	1000	2.51	8885	1.46	0.25
25	7612.90	1000	2.52	6113	1.18	0.25
33	7620.65	1000	2.48	7934	1.35	0.23
35	7622.10	1000	2.46	5419	1.33	0.24

Core Laboratories

Core Lab

ACOUSTIC VELOCITIES AND DYNAMIC ELASTIC PARAMETERS

Company:	**Patara Oil & Gas LLC**	Date:	**August 2011**
Well:	**Cane Creek 042711**	File:	**HOU-110920**
Field:	**Paradox Basin**	Saturation Fluid:	**As Received**
Location:	**Grand County, Utah**	Rock Type:	**Shale**

Acoustic Velocities and Dynamic Moduli at Triaxial Stress Conditions

Sample Number	Depth (ft)	Confining Pressure (psi)	Axial Pressure (psi)	Bulk Density (g/cm^3)	Acoustic Velocity				Dynamic Elastic Parameters			
					Compressional		Shear		Bulk Modulus ($x10^6$ psi)	Young's Modulus ($x10^6$ psi)	Shear Modulus ($x10^6$ psi)	Poisson's Ratio
					ft/sec	µs/ft	ft/sec	µs/ft				
22	7609.50	1000	1000	2.51	12968	77.11	6862	145.74	3.57	4.16	1.59	0.31
		1000	5500	2.51	14198	70.43	7274	137.48	4.43	4.73	1.79	0.32
25	7612.90	1000	1000	2.52	12514	79.91	6944	144.00	3.14	4.19	1.64	0.28
		1000	2000	2.52	13407	74.59	7291	137.16	3.70	4.67	1.81	0.29
33	7620.65	1000	1000	2.48	11700	85.47	6878	145.38	2.47	3.92	1.58	0.24
		1000	5000	2.48	13880	72.05	7487	133.57	3.95	4.86	1.88	0.29
35	7622.10	1000	1000	2.46	12376	80.80	7142	140.03	2.83	4.24	1.69	0.25
		1000	2000	2.46	12957	77.18	7370	135.68	3.17	4.55	1.80	0.26

Results of Triaxial Test

Company:	**Patara Oil & Gas LLC**	Date:	**August 2011**
Well:	**Cane Creek 042711**	File:	**HOU-110920**
Field:	**Paradox Basin**	Saturation Fluid:	**As Received**
Location:	**Grand County, Utah**	Rock Type:	**Shale**

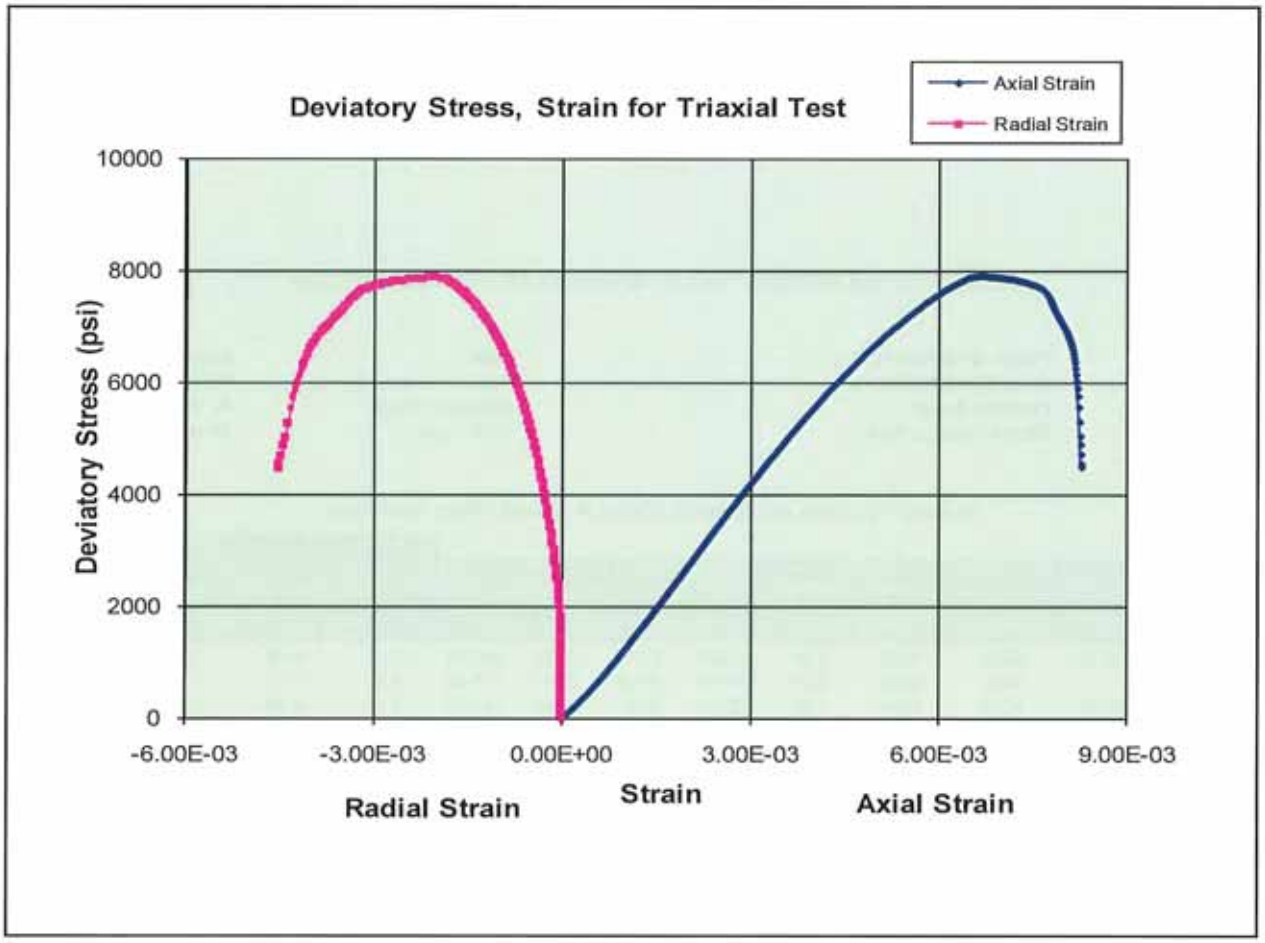

Sample	22
Depth (ft)	7609.50
Diameter (in)	0.9598
Length (in)	1.5266
Mass (g)	45.43
Saturation Fluid	As Received
Bulk Density (g/cm^3)	2.51
Confining Pressure (psi)	1000
Pore Pressure (psi)	0
Static Young's Modulus (X10^6 psi)	1.46
Static Poisson's Ratio	0.25
Compressive Strength (psi)	8885

Core Laboratories

Results of Triaxial Test

Company:	**Patara Oil & Gas LLC**	Date:	**August 2011**
Well:	**Cane Creek 042711**	File:	**HOU-110920**
Field:	**Paradox Basin**	Saturation Fluid:	**As Received**
Location:	**Grand County, Utah**	Rock Type:	**Shale**

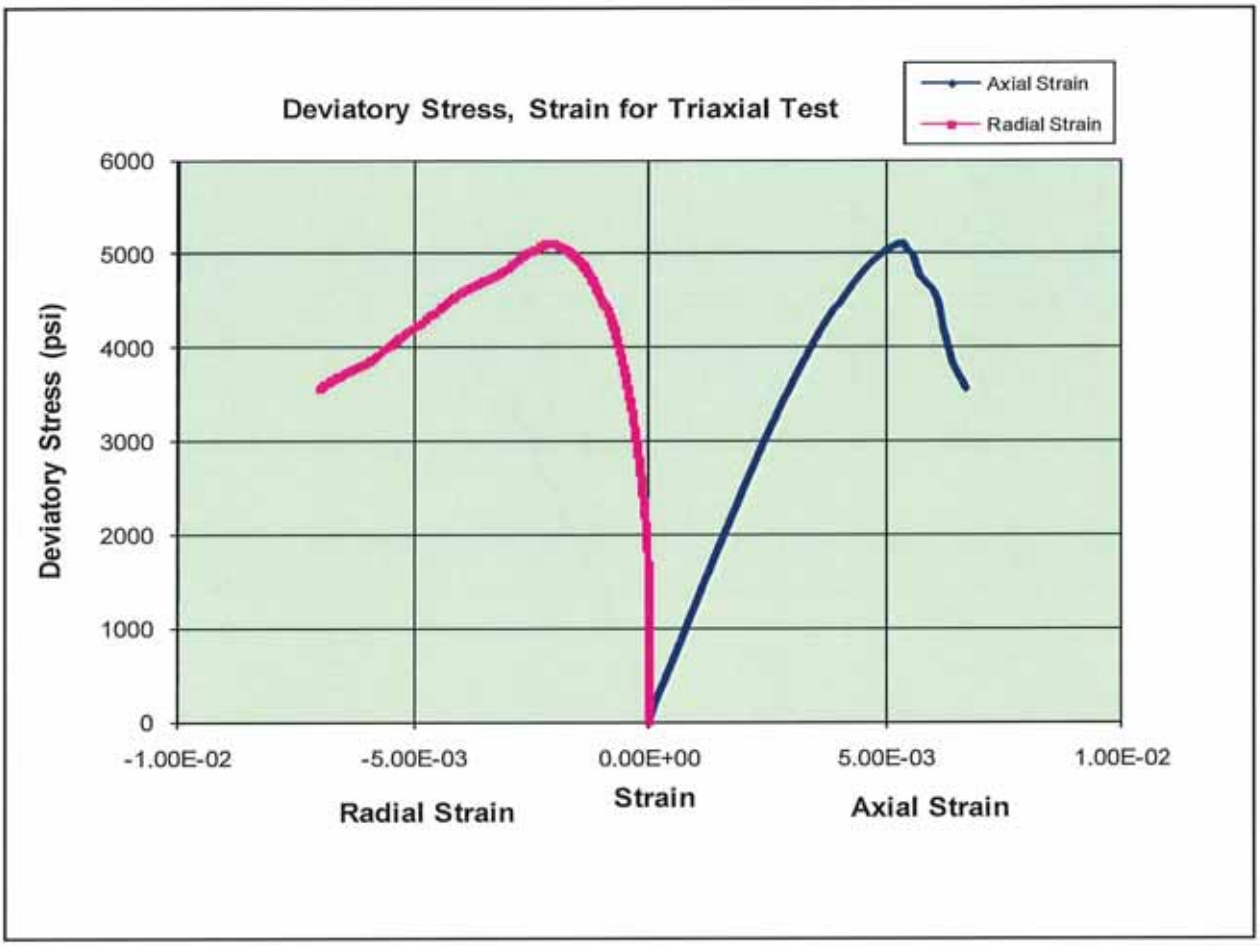

Sample	25
Depth (ft)	7612.90
Diameter (in)	0.9598
Length (in)	1.5783
Mass (g)	47.22
Saturation Fluid	As Received
Bulk Density (g/cm^3)	2.52
Confining Pressure (psi)	1000
Pore Pressure (psi)	0
Static Young's Modulus (X10^6 psi)	1.18
Static Poisson's Ratio	0.25
Compressive Strength (psi)	6113

Core Laboratories

Results of Triaxial Test

Company:	**Patara Oil & Gas LLC**	Date:	**August 2011**
Well:	**Cane Creek 042711**	File:	**HOU-110920**
Field:	**Paradox Basin**	Saturation Fluid:	**As Received**
Location:	**Grand County, Utah**	Rock Type:	**Shale**

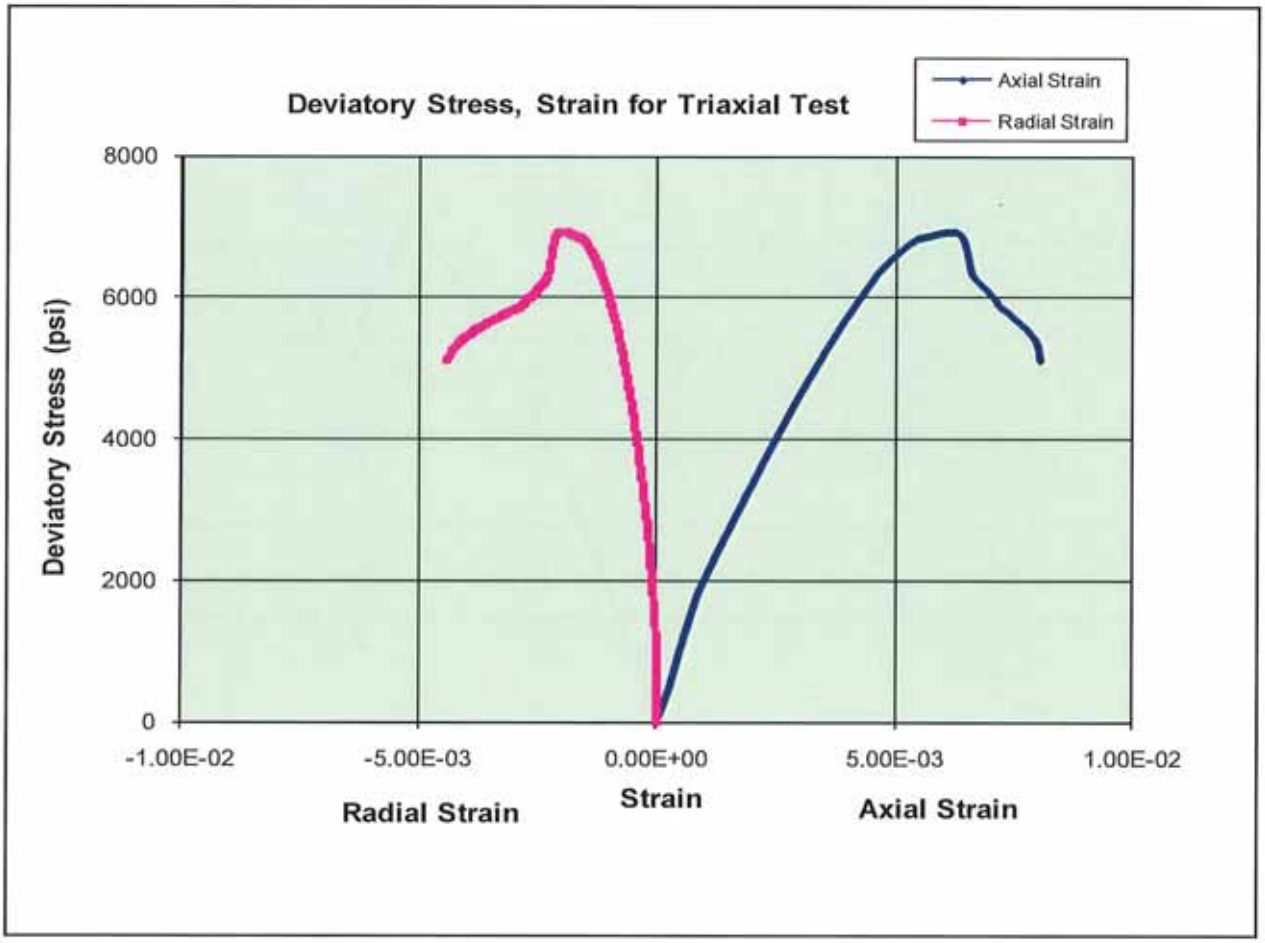

Sample	33
Depth (ft)	7620.65
Diameter (in)	0.9625
Length (in)	1.1176
Mass (g)	33.11
Saturation Fluid	As Received
Bulk Density (g/cm^3)	2.48
Confining Pressure (psi)	1000
Pore Pressure (psi)	0
Static Young's Modulus (X10^6 psi)	1.35
Static Poisson's Ratio	0.23
Compressive Strength (psi)	7934

Core Laboratories

Results of Triaxial Test

Company:	**Patara Oil & Gas LLC**	Date:	**August 2011**
Well:	**Cane Creek 042711**	File:	**HOU-110920**
Field:	**Paradox Basin**	Saturation Fluid:	**As Received**
Location:	**Grand County, Utah**	Rock Type:	**Shale**

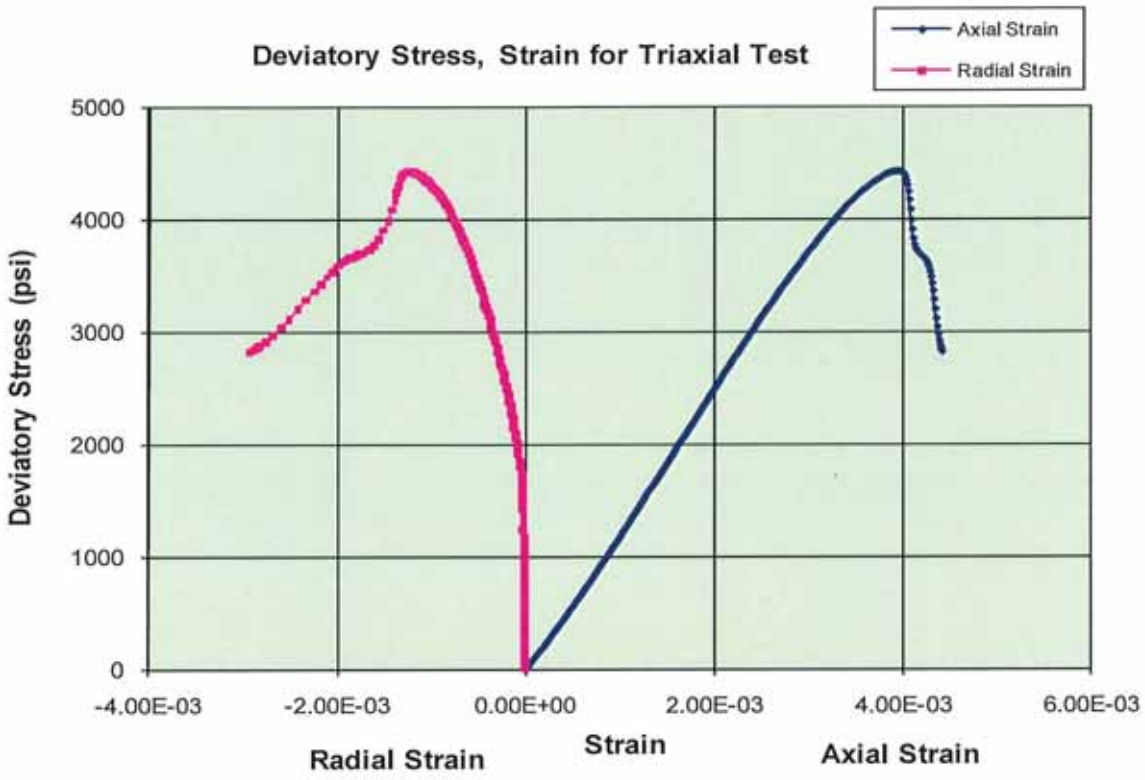

Sample	35
Depth (ft)	7622.10
Diameter (in)	0.9665
Length (in)	1.6574
Mass (g)	49.10
Saturation Fluid	As Received
Bulk Density (g/cm^3)	2.46
Confining Pressure (psi)	1000
Pore Pressure (psi)	0
Static Young's Modulus (X10^6 psi)	1.33
Static Poisson's Ratio	0.24
Compressive Strength (psi)	5419

Core Laboratories

Core Lab
RESERVOIR OPTIMIZATION

ADVANCED CORE ANALYSIS STUDY

Patara Oil & Gas LLC

Cane Creek 042711

Paradox Basin

Grand County, Utah

High-Pressure Mercury Injection Data Report

CL File Number: HOU-110920

Date: 8-Aug-2011

Performed by:
Core Laboratories
Petroleum Services Division
6316 Windfern
Houston, Texas 77040

Phone: (713) 328-CORE

HIGH-PRESSURE MERCURY INJECTION

PETROLEUM SERVICES

Sample Cleaning
Core plug trim samples were cleaned by soxhlet extraction using toluene followed by methanol.

Sample Drying
Trim samples were oven dried at 240° F to weight equilibrium (+/- 0.001 g).

Porosity
Porosity for the trims was determined by measuring grain volume at ambient conditions using Boyle's Law technique and bulk volume by mercury immersion and Archimedes' Principle. Pore volume was also determined by toluene saturation.

High-Pressure Mercury Injection
High-pressure mercury injection data were acquired using a Micromeritics AutoPore instrument, an automated, high-pressure mercury injection device. During the mercury injection test, each clean dry sample was immersed in mercury in a pressure-sealed chamber attached to a capillary stem with a cylindrical coaxial capacitor. The pressure of the surrounding mercury was gradually increased from 0 psia up to 55,000 psia. The increasing pressure gradually forced the mercury to intrude into the sample pore spaces, and time was allowed for saturation equilibrium to be established at each pressure. The volume of mercury injected at each pressure was determined by the change in capacitance of the capillary stem. Mercury saturation was calculated as a fraction of pore volume. The relationship of injection pressure to mercury saturation was used to calculate several parameters, including pore throat size distribution, capillary pressure for various fluid systems, and Swanson[1] permeability.

Calculated data
Pore throat radius: Calculated using the injection pressure, interfacial tension and contact angle of the air-mercury system. Pore throat size distribution data are typically used for pore geometry characterizations and comparisons.
The following classification is utilized in this data set for pore throat radii:
<0.50microns = Micro; 0.5microns to 2.5microns = Meso; >2.5microns = Macro

J-Function and system conversions: Some of the additional data which are presented on the tabular pages are the "J - Function" and conversions of mercury injection data to (laboratory) gas-water, gas-oil, and oil-water systems. Conversions of air-mercury pressures to other fluid systems can be refined by applying measured values in place of the "typical" parameters which are used here.

Height above free water: The mercury injection laboratory-condition data are converted to equivalent reservoir oil-water or gas-water values using "typical" fluid density gradients and should be considered as estimates only. Measured reservoir parameter values should be input into the conversion equation whenever possible.

Maximum Sb/Pc: Bulk saturation term used in the calculation of the Swanson permeability.

R35: Reservoir quality indicator. The pore throat radius at 35% mercury saturation.

R50: Median pore throat radius.

[1]Swanson, B.F. ("A Simple Correlation Between Permeabilities and Mercury Capillary Pressures" Journal of Petroleum Technology, December 1981

Core Lab
RESERVOIR OPTIMIZATION

CALCULATIONS

PETROLEUM SERVICES

1. Pore entry radius:

$$Ri = \frac{2T * \cos\theta * C}{Pc}$$

2. J-Function

$$\text{J-Function} = \frac{0.2166 * Pc * (K/\varphi)^{1/2}}{(T*\cos\theta)}$$

3. Conversion of pressure from one fluid system to another:

$$Pc_{(g\text{-}w)} = Pc_{(meas.)} * \frac{(T * \cos\theta)_{(g\text{-}w)}}{(T * \cos\theta)_{(meas)}}$$

4. Height above free water:

$$Pc_R = Pc_L * (T*\cos\theta)_R \div (T*\cos\theta)_L$$

$$\text{Height} = Pc_R \div (\rho_w - \rho_h)$$

where:

Ri = Pore entry radius, microns
T = Interfacial tension,dynes/cm
C = Unit conversion constant (to microns) = 0.145
θ = Contact angle, degrees
Pc = Mercury injection pressure, psia
$Pc_{(g\text{-}w)}$ = Capillary pressure in a gas-water system, psi
$Pc_{(meas)}$ = Capillary pressure of the measured fluid system, psi
Pc_L = Laboratory measured capillary pressure, psi
K = Permeability to air (or Klinkenberg), millidarcys
φ = Porosity, fraction
$T*\cos\theta_R$ = Interfacial tension * cosine of contact angle (reservoir)
$T*\cos\theta_L$ = Interfacial tension * cosine of contact angle (laboratory)
ρ_w = Reservoir density gradient, water, g/cm3
ρ_h = Reservoir density gradient, hydrocarbon, g/cm3

Core Lab
RESERVOIR OPTIMIZATION

SUMMARY OF CALCULATION PARAMETERS

PETROLEUM SERVICES

	Fluid System	Contact Angle (θ)	Cosine Contact Angle	Interfacial Tension (T)	T Cosine θ
Laboratory	Gas-water	0	1.00	72.	72.
	Oil-water	30	0.866	48.	41.6
	Gas-oil	0	1.00	24.	24.
	Air-mercury	140	0.765	485.	372.
Reservoir[1]	Oil-water	30	0.866	30.	26.
	Gas-water	0	1.00	50.	50.

Density Gradients (g/cm^3)

water	=	0.433
oil	=	0.346
gas	=	0.100

[1] Reservoir IFT values can vary widely but are typically between 20 and 35 dynes/cm in an oil/water system. Reservoir oil/water theta values are highly variable, with strongly water being an angle of 0° and strongly oil wet being an angle of 120°.

Listed reservoir gas/water values are fairly typical to a depth of approximately 5000 feet. IFT will decrease with increasing depth (increasing temperature and pressure).

Company:	Patara Oil & Gas LLC
Well:	Cane Creek 042711
Field:	Paradox Basin
Formation:	Cane Creek
Location:	Grand County, Utah
File:	HOU:110920

Sample:	35m	un-	Host Plug	
Depth, feet:	7622.10	stressed	2310psi	na
Klinkenberg Permeability, md:		n/a	0.0274	-
Permeability to Air, md:		n/a	0.630	-
Swanson Permeability, md:		0.0127	-	-
Porosity, fraction:		0.090	0.085	-
maximum Sb/Pc, fraction:		0.002		
R35, microns:		0.0602		
R50 (median pore throat radius):		0.0323		

MERCURY INJECTION

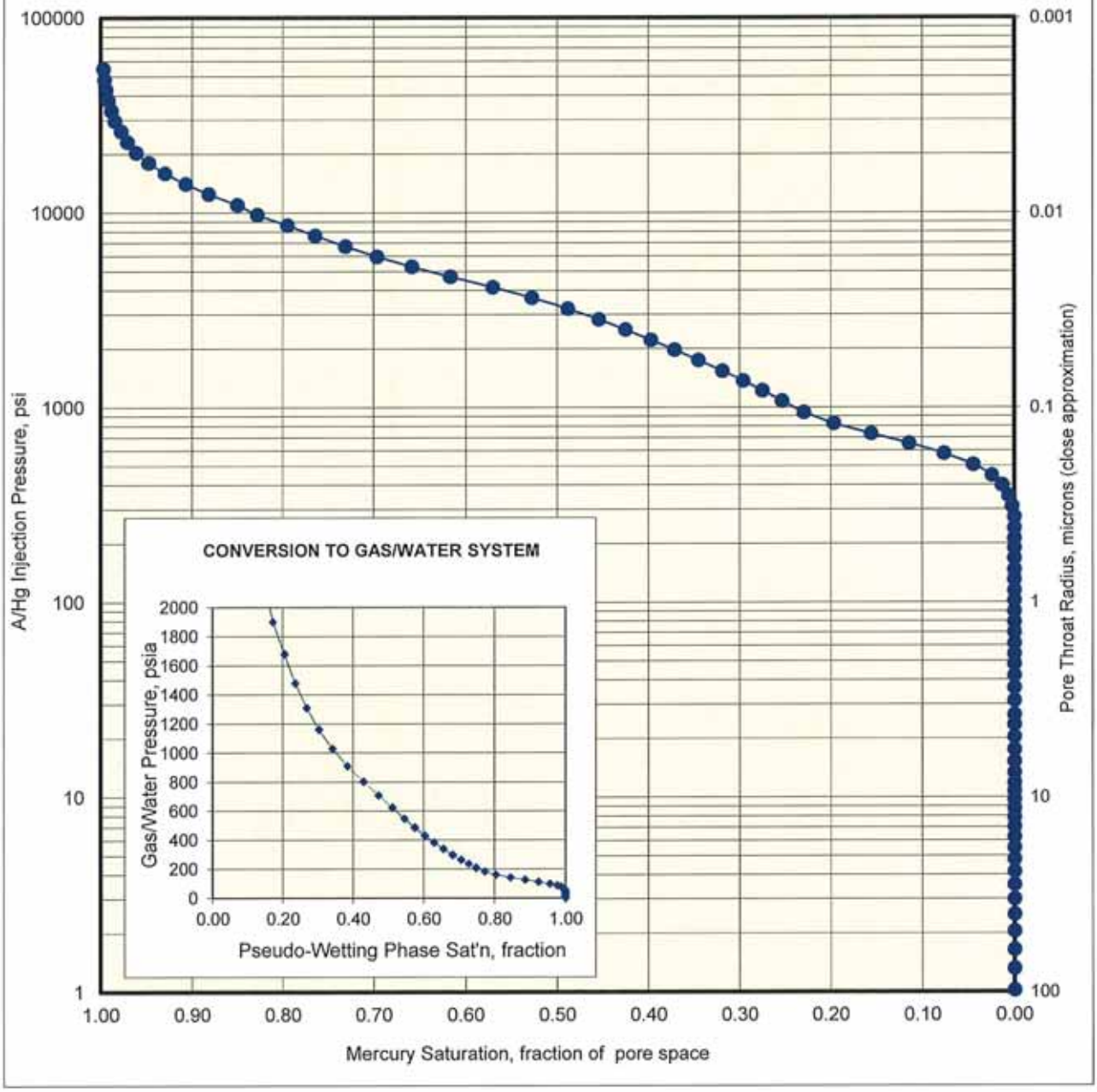

Core Laboratories

Company:	Patara Oil & Gas LLC
Well:	Cane Creek 042711
Field:	Paradox Basin
Formation:	Cane Creek
Location:	Grand County, Utah
File:	HOU:110920

Sample:	35m	un-	Host Plug	
Depth, feet:	7622.10	stressed	2310psi	na
Klinkenberg Permeability, md:		n/a	0.0274	-
Permeability to Air, md:		n/a	0.630	-
Swanson Permeability, md:		0.0127	-	-
Porosity, fraction:		0.090	0.085	-
maximum Sb/Pc, fraction:		0.002		
R35, microns:		0.0602		
R50 (median pore throat radius):		0.0323		

PORE THROAT RADIUS DISTRIBUTION

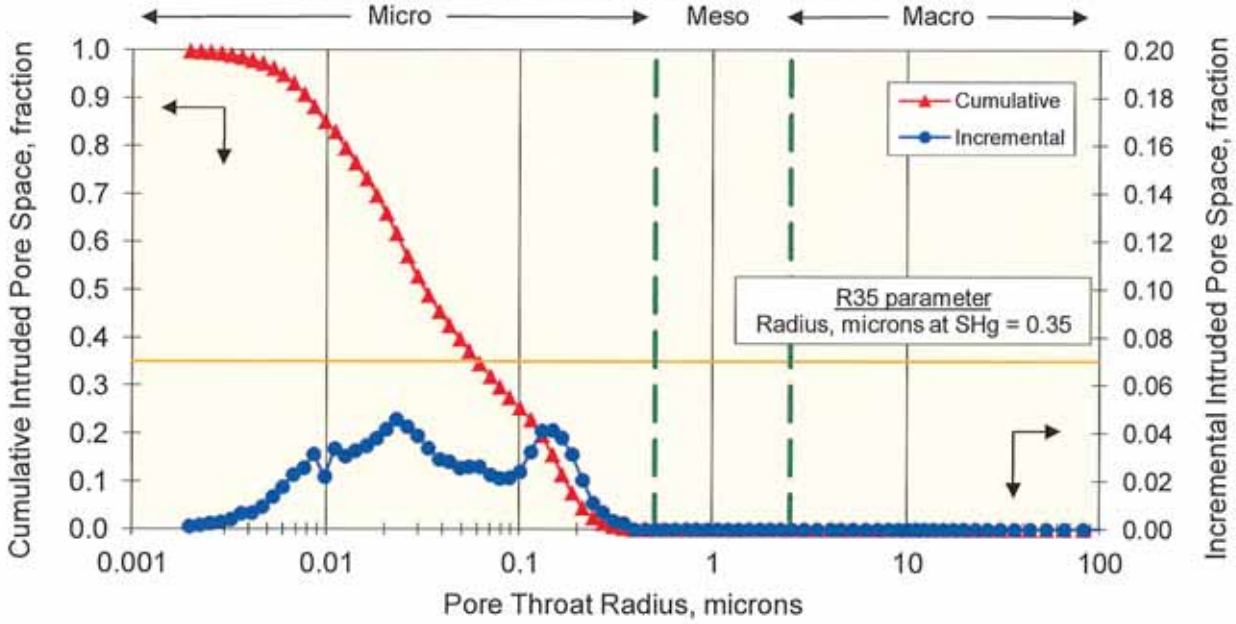

PERMEABILITY DISTRIBUTION

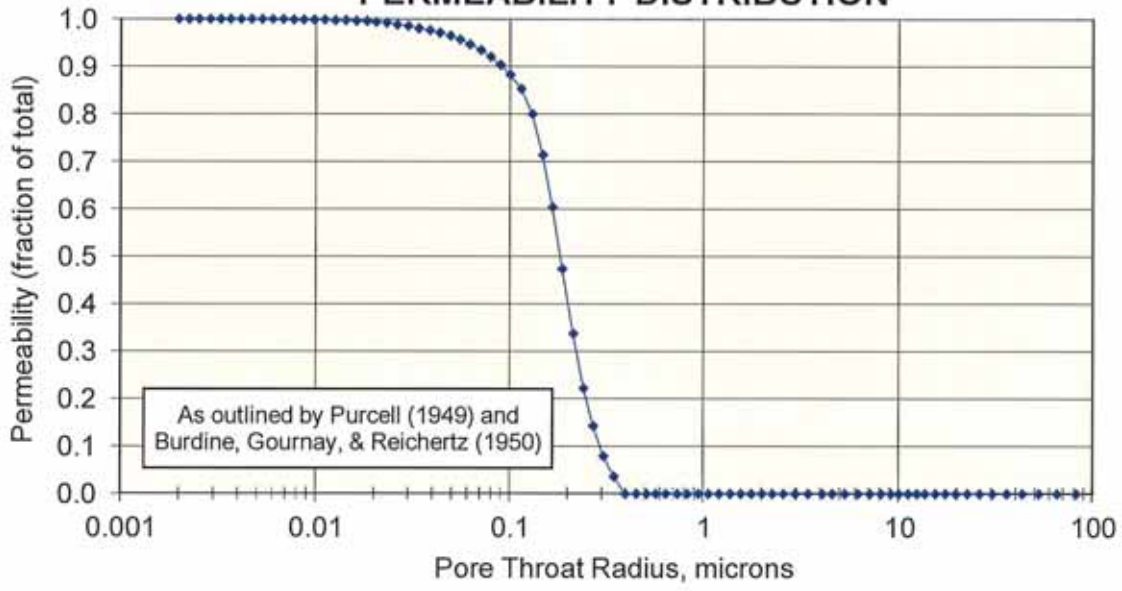

Core Laboratories

Company:	Patara Oil & Gas LLC
Well:	Cane Creek 042711
Field:	Paradox Basin
Formation:	Cane Creek
Location:	Grand County, Utah
File:	HOU:110920

Sample:	**35m**	un-	Host Plug	
Depth, feet:	7622.10	stressed	2310psi	na
Klinkenberg Permeability, md:		n/a	0.0274	-
Permeability to Air, md:		n/a	0.630	-
Swanson Permeability, md:		0.0127	-	-
Porosity, fraction:		0.090	0.085	-
maximum Sb/Pc, fraction:		0.002		
R35, microns:		0.0602		
R50 (median pore throat radius):		0.0323		

PORE THROAT SIZE HISTOGRAM

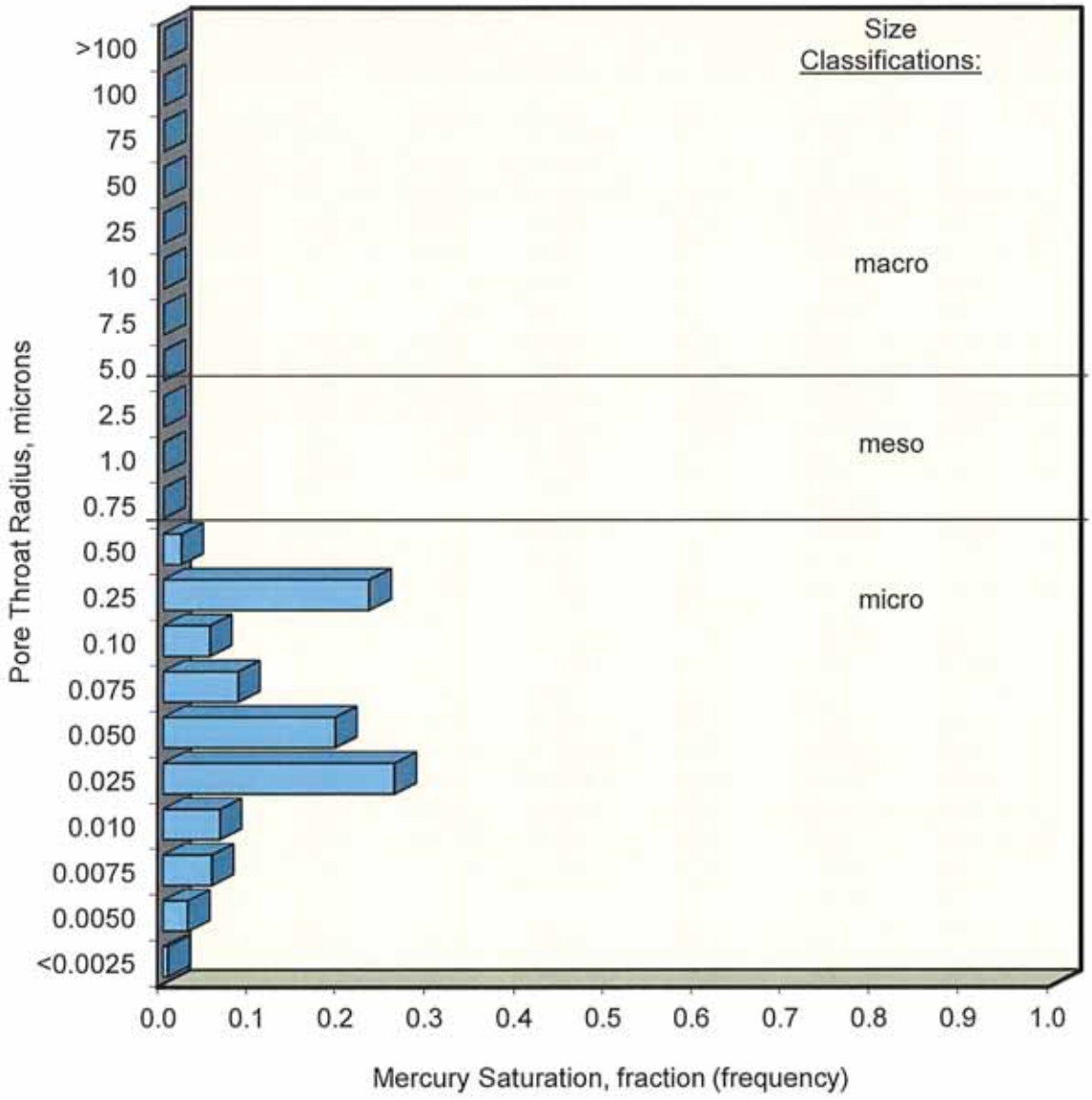

Core Laboratories

MERCURY INJECTION DATA SUMMARY

Company:	Patara Oil & Gas LLC
Well:	Cane Creek 042711
Field:	Paradox Basin
Formation:	Cane Creek
Location:	Grand County, Utah
File:	HOU:110920

Sample:	**35m**	un-	Host Plug	
Depth, feet:	7622.10	stressed	2310psi	na
Klinkenberg Permeability, md:		n/a	0.0274	-
Permeability to Air, md:		n/a	0.630	-
Swanson Permeability, md:		0.0127	-	-
Porosity, fraction:		0.090	0.085	-
maximum Sb/Pc, fraction:		0.002		
R35, microns:		0.0602		
R50 (median pore throat radius):		0.0323		

Injection Pressure, psia	Mercury Saturation, fraction	Pseudo-Wetting Saturation, fraction	Pore Throat Radius, microns	J Values	Conversion to other Laboratory Fluid Systems, psia			Estimated Height Above Free Water, feet	
					G-W	G-O	O-W	G-W	O-W
0.77	0.000	1.000	140	0.000168	0.149	0.0497	0.0862	0.311	0.619
1.02	0.000	1.000	106	0.000223	0.198	0.0659	0.114	0.412	0.820
1.32	0.000	1.000	81.6	0.000288	0.256	0.0853	0.148	0.533	1.06
1.65	0.000	1.000	65.3	0.000361	0.320	0.107	0.185	0.667	1.33
2.05	0.000	1.000	52.6	0.000448	0.397	0.132	0.229	0.828	1.65
2.50	0.000	1.000	43.1	0.000546	0.484	0.161	0.280	1.01	2.01
3.00	0.000	1.000	35.9	0.000655	0.581	0.194	0.336	1.21	2.41
3.55	0.000	1.000	30.4	0.000776	0.688	0.229	0.397	1.43	2.85
4.15	0.000	1.000	26.0	0.000907	0.804	0.268	0.464	1.68	3.34
4.80	0.000	1.000	22.4	0.00105	0.930	0.310	0.537	1.94	3.86
5.50	0.000	1.000	19.6	0.00120	1.07	0.355	0.615	2.22	4.42
6.25	0.000	1.000	17.2	0.00137	1.21	0.404	0.699	2.53	5.02
7.05	0.000	1.000	15.3	0.00154	1.37	0.455	0.789	2.85	5.67
7.90	0.000	1.000	13.6	0.00173	1.53	0.510	0.884	3.19	6.35
8.79	0.000	1.000	12.3	0.00192	1.70	0.568	0.983	3.55	7.07
9.74	0.000	1.000	11.1	0.00213	1.89	0.629	1.09	3.94	7.83
10.8	0.000	1.000	9.99	0.00236	2.09	0.697	1.21	4.36	8.68
11.9	0.000	1.000	9.06	0.00260	2.30	0.768	1.33	4.81	9.56
13.4	0.000	1.000	8.06	0.00292	2.59	0.864	1.50	5.42	10.8
15.3	0.000	1.000	7.06	0.00334	2.96	0.986	1.71	6.18	12.3
17.6	0.000	1.000	6.14	0.00383	3.40	1.13	1.96	7.11	14.1
20.4	0.000	1.000	5.29	0.00445	3.95	1.32	2.28	8.24	16.4
23.6	0.000	1.000	4.57	0.00516	4.57	1.52	2.64	9.54	19.0
26.5	0.000	1.000	4.06	0.00580	5.14	1.71	2.97	10.7	21.3
31.3	0.000	1.000	3.44	0.00685	6.07	2.02	3.51	12.6	25.2
36.5	0.000	1.000	2.95	0.00798	7.08	2.36	4.08	14.8	29.3
42.1	0.000	1.000	2.56	0.0092	8.16	2.72	4.71	17.0	33.8
48.2	0.000	1.000	2.24	0.0105	9.33	3.11	5.39	19.5	38.7
54.5	0.000	1.000	1.98	0.0119	10.6	3.52	6.10	22.0	43.8
61.7	0.000	1.000	1.75	0.0135	11.9	3.98	6.90	24.9	49.6
70.2	0.000	1.000	1.54	0.0153	13.6	4.53	7.85	28.4	56.4
79.3	0.000	1.000	1.36	0.0173	15.4	5.12	8.87	32.0	63.7
89.9	0.000	1.000	1.20	0.0196	17.4	5.81	10.1	36.3	72.3

MERCURY INJECTION DATA SUMMARY

Company:	Patara Oil & Gas LLC
Well:	Cane Creek 042711
Field:	Paradox Basin
Formation:	Cane Creek
Location:	Grand County, Utah
File:	HOU:110920

Sample:	**35m**	un-	Host Plug	
Depth, feet:	7622.10	stressed	2310psi	na
Klinkenberg Permeability, md:		n/a	0.0274	-
Permeability to Air, md:		n/a	0.630	-
Swanson Permeability, md:		0.0127	-	-
Porosity, fraction:		0.090	0.085	-
maximum Sb/Pc, fraction:		0.002		
R35, microns:		0.0602		
R50 (median pore throat radius):		0.0323		

Injection Pressure, psia	Mercury Saturation, fraction	Pseudo-Wetting Saturation, fraction	Pore Throat Radius, microns	J Values	Conversion to other Laboratory Fluid Systems, psia			Estimated Height Above Free Water, feet	
					G-W	G-O	O-W	G-W	O-W
102	0.000	1.000	1.06	0.0223	19.7	6.58	11.4	41.2	82.0
115	0.000	1.000	0.940	0.0251	22.2	7.41	12.8	46.5	92.4
131	0.000	1.000	0.824	0.0286	25.3	8.44	14.6	52.9	105
147	0.000	1.000	0.734	0.0321	28.5	9.49	16.4	59.4	118
168	0.000	1.000	0.640	0.0368	32.6	10.9	18.8	67.9	135
190	0.000	1.000	0.568	0.0414	36.7	12.2	21.2	76.8	153
213	0.000	1.000	0.507	0.0465	41.2	13.7	23.8	86.1	171
241	0.000	1.000	0.448	0.0526	46.6	15.5	26.9	97.4	194
274	0.000	1.000	0.393	0.0600	53.2	17.7	30.7	111	220
311	0.002	0.998	0.346	0.0681	60.4	20.1	34.8	126	250
352	0.006	0.994	0.306	0.0770	68.3	22.8	39.4	142	283
399	0.013	0.987	0.270	0.0873	77.4	25.8	44.7	161	321
448	0.024	0.976	0.240	0.0979	86.9	29.0	50.2	181	360
508	0.045	0.955	0.212	0.111	98.5	32.8	56.8	205	408
580	0.076	0.924	0.186	0.127	112	37.4	64.8	234	466
653	0.114	0.886	0.165	0.143	127	42.2	73.1	264	525
734	0.156	0.844	0.147	0.160	142	47.4	82.2	297	590
829	0.197	0.803	0.130	0.181	161	53.5	92.7	335	666
944	0.229	0.771	0.114	0.206	183	61.0	106	382	759
1080	0.253	0.747	0.0999	0.236	209	69.7	121	436	868
1220	0.275	0.725	0.0884	0.266	236	78.7	136	493	981
1370	0.296	0.704	0.0787	0.299	265	88.4	153	554	1100
1540	0.319	0.681	0.0701	0.336	298	99.4	172	622	1240
1750	0.345	0.655	0.0616	0.382	339	113	196	707	1410
1980	0.371	0.629	0.0545	0.432	383	128	221	800	1590
2220	0.397	0.603	0.0486	0.485	430	143	248	897	1780
2510	0.425	0.575	0.0430	0.548	486	162	281	1010	2020
2830	0.455	0.545	0.0381	0.618	548	183	316	1140	2270
3220	0.488	0.512	0.0335	0.703	624	208	360	1300	2590
3660	0.528	0.472	0.0295	0.799	709	236	409	1480	2940
4150	0.571	0.429	0.0260	0.906	804	268	464	1680	3340
4700	0.617	0.383	0.0229	1.03	910	303	525	1900	3780
5300	0.658	0.342	0.0203	1.16	1030	342	593	2140	4260
5960	0.696	0.304	0.0181	1.30	1160	385	667	2410	4790

MERCURY INJECTION DATA SUMMARY

Company:	Patara Oil & Gas LLC
Well:	Cane Creek 042711
Field:	Paradox Basin
Formation:	Cane Creek
Location:	Grand County, Utah
File:	HOU:110920

Sample:	**35m**	un-	Host Plug	
Depth, feet:	7622.10	stressed	2310psi	na
Klinkenberg Permeability, md:		n/a	0.0274	-
Permeability to Air, md:		n/a	0.630	-
Swanson Permeability, md:		0.0127	-	-
Porosity, fraction:		0.090	0.085	-
maximum Sb/Pc, fraction:		0.002		
R35, microns:		0.0602		
R50 (median pore throat radius):		0.0323		

Injection Pressure, psia	Mercury Saturation, fraction	Pseudo-Wetting Saturation, fraction	Pore Throat Radius, microns	J Values	Conversion to other Laboratory Fluid Systems, psia			Estimated Height Above Free Water, feet	
					G-W	G-O	O-W	G-W	O-W
6750	0.731	0.269	0.0160	1.47	1310	436	755	2730	5430
7650	0.764	0.236	0.0141	1.67	1480	494	855	3090	6150
8640	0.795	0.205	0.0125	1.89	1680	558	967	3490	6940
9790	0.828	0.172	0.0110	2.14	1900	632	1090	3960	7870
11000	0.850	0.150	0.00977	2.41	2140	713	1230	4450	8840
12500	0.882	0.118	0.00862	2.73	2420	807	1400	5050	10000
14100	0.907	0.093	0.00763	3.09	2740	912	1580	5700	11300
16000	0.930	0.070	0.00674	3.49	3100	1030	1790	6470	12900
18100	0.948	0.052	0.00596	3.95	3500	1170	2020	7310	14500
20400	0.962	0.038	0.00527	4.46	3960	1320	2290	8240	16400
23100	0.971	0.029	0.00466	5.05	4480	1490	2590	9340	18600
26200	0.978	0.022	0.00412	5.72	5070	1690	2930	10600	21100
29600	0.984	0.016	0.00364	6.46	5730	1910	3310	12000	23800
33500	0.989	0.011	0.00322	7.32	6490	2160	3750	13500	26900
37800	0.992	0.008	0.00285	8.27	7330	2440	4230	15300	30400
43000	0.994	0.006	0.00250	9.40	8340	2780	4810	17400	34600
48400	0.996	0.004	0.00223	10.6	9380	3130	5410	19600	38900
55000	0.997	0.003	0.00196	12.0	10700	3550	6150	22200	44200

Company:	Patara Oil & Gas LLC	**Sample:**	**25m**	un-	Host Plug	
Well:	Cane Creek 042711	Depth, feet:	7612.90	stressed	2310psi	na
Field:	Paradox Basin	Klinkenberg Permeability, md:		n/a	0.0116	-
Formation:	Cane Creek	Permeability to Air, md:		n/a	0.0245	-
Location:	Grand County, Utah	Swanson Permeability, md:		0.00127	-	-
File:	HOU:110920	Porosity, fraction:		0.101	0.022	-
		maximum Sb/Pc, fraction:		0.001		
		R35, microns:		0.0166		
		R50 (median pore throat radius):		0.0120		

MERCURY INJECTION

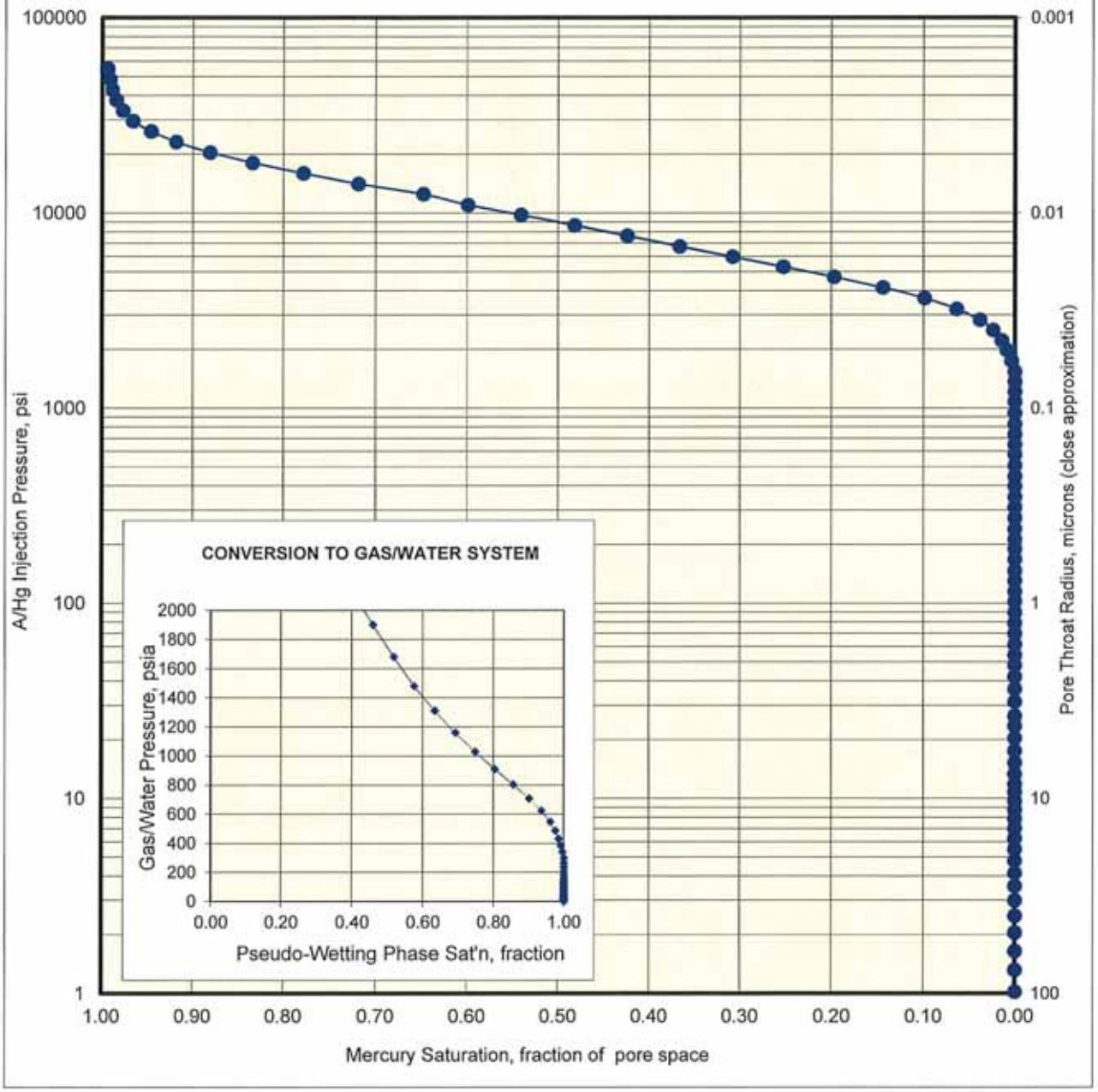

Core Laboratories

Company:	Patara Oil & Gas LLC
Well:	Cane Creek 042711
Field:	Paradox Basin
Formation:	Cane Creek
Location:	Grand County, Utah
File:	HOU:110920

Sample:	**25m**	un-	Host Plug	
Depth, feet:	7612.90	stressed	2310psi	na
Klinkenberg Permeability, md:		n/a	0.0116	-
Permeability to Air, md:		n/a	0.0245	-
Swanson Permeability, md:		0.00127	-	-
Porosity, fraction:		0.101	0.022	-
maximum Sb/Pc, fraction:		0.001		
R35, microns:		0.0166		
R50 (median pore throat radius):		0.0120		

PORE THROAT RADIUS DISTRIBUTION

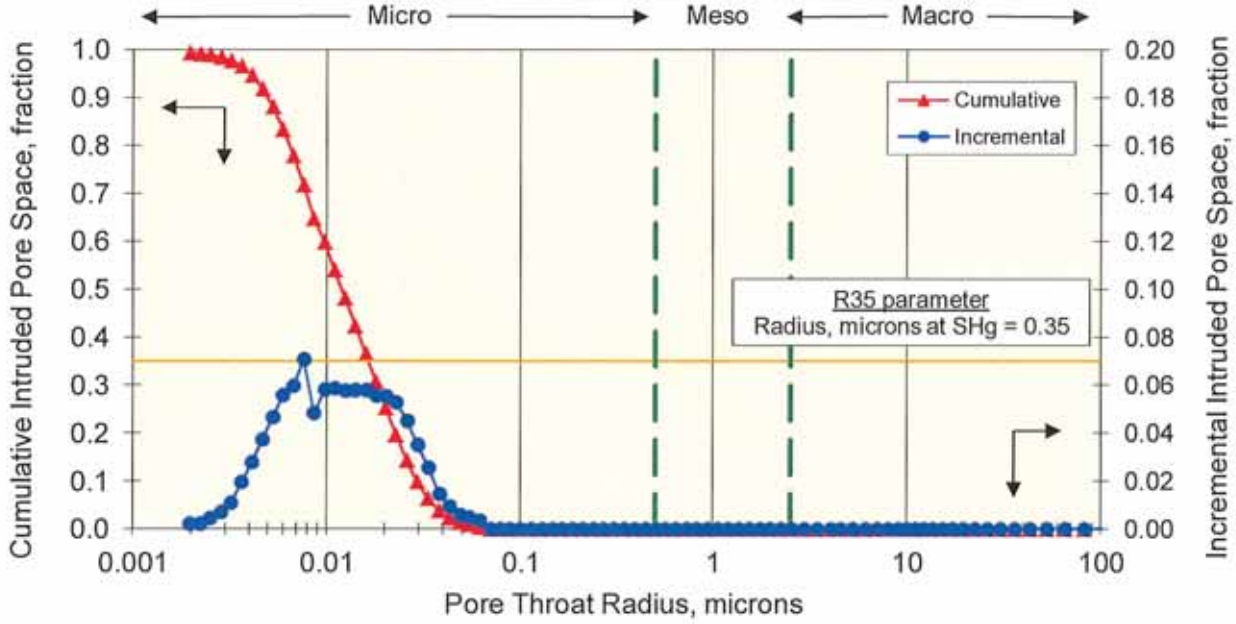

PERMEABILITY DISTRIBUTION

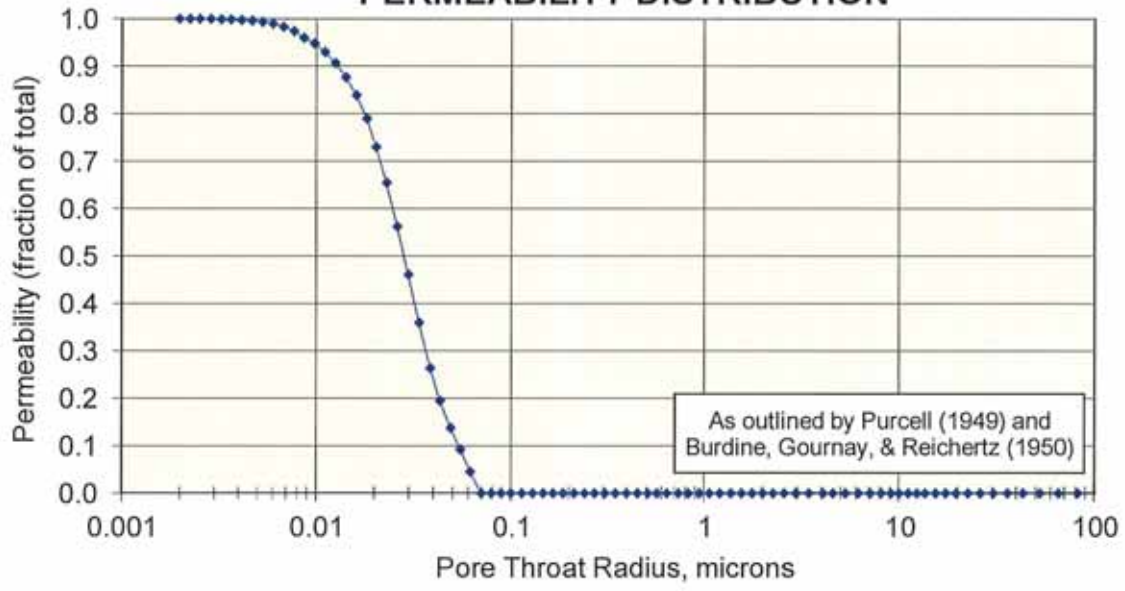

Core Laboratories

Company:	Patara Oil & Gas LLC
Well:	Cane Creek 042711
Field:	Paradox Basin
Formation:	Cane Creek
Location:	Grand County, Utah
File:	HOU:110920

Sample:	**25m**	un-	Host Plug	
Depth, feet:	7612.90	stressed	2310psi	na
Klinkenberg Permeability, md:		n/a	0.0116	-
Permeability to Air, md:		n/a	0.0245	-
Swanson Permeability, md:		0.00127	-	-
Porosity, fraction:		0.101	0.022	-
maximum Sb/Pc, fraction:		0.001		
R35, microns:		0.0166		
R50 (median pore throat radius):		0.0120		

PORE THROAT SIZE HISTOGRAM

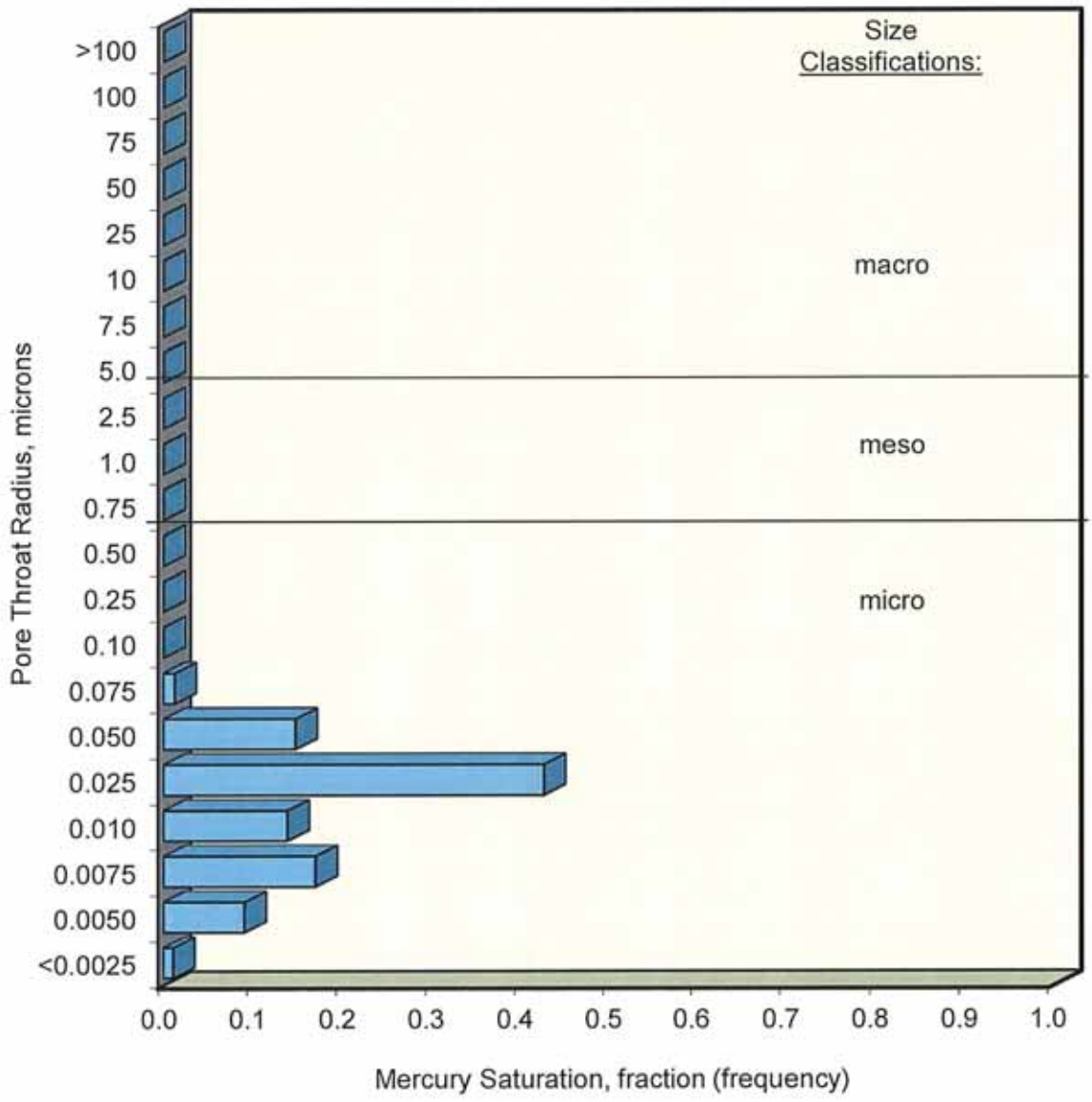

Core Laboratories

MERCURY INJECTION DATA SUMMARY

Company:	Patara Oil & Gas LLC
Well:	Cane Creek 042711
Field:	Paradox Basin
Formation:	Cane Creek
Location:	Grand County, Utah
File:	HOU:110920

Sample:	**25m**	un-	Host Plug	
Depth, feet:	7612.90	stressed	2310psi	na
Klinkenberg Permeability, md:		n/a	0.0116	-
Permeability to Air, md:		n/a	0.0245	-
Swanson Permeability, md:		0.00127	-	-
Porosity, fraction:		0.101	0.022	-
maximum Sb/Pc, fraction:		0.001		
R35, microns:		0.0166		
R50 (median pore throat radius):		0.0120		

Injection Pressure, psia	Mercury Saturation, fraction	Pseudo-Wetting Saturation, fraction	Pore Throat Radius, microns	J Values	Conversion to other Laboratory Fluid Systems, psia			Estimated Height Above Free Water, feet	
					G-W	G-O	O-W	G-W	O-W
0.77	0.000	1.000	140	0.000050	0.149	0.0497	0.0862	0.311	0.619
1.02	0.000	1.000	106	0.000067	0.198	0.0659	0.114	0.412	0.820
1.32	0.000	1.000	81.6	0.000086	0.256	0.0853	0.148	0.533	1.06
1.65	0.000	1.000	65.3	0.000108	0.320	0.107	0.185	0.667	1.33
2.05	0.000	1.000	52.6	0.000134	0.397	0.132	0.229	0.828	1.65
2.50	0.000	1.000	43.1	0.000164	0.484	0.161	0.280	1.01	2.01
3.00	0.000	1.000	35.9	0.000196	0.581	0.194	0.336	1.21	2.41
3.55	0.000	1.000	30.4	0.000232	0.688	0.229	0.397	1.43	2.85
4.15	0.000	1.000	26.0	0.000272	0.804	0.268	0.464	1.68	3.34
4.80	0.000	1.000	22.4	0.000314	0.930	0.310	0.537	1.94	3.86
5.50	0.000	1.000	19.6	0.000360	1.07	0.355	0.615	2.22	4.42
6.25	0.000	1.000	17.2	0.000409	1.21	0.404	0.699	2.53	5.02
7.05	0.000	1.000	15.3	0.000462	1.37	0.455	0.789	2.85	5.67
7.90	0.000	1.000	13.6	0.000517	1.53	0.510	0.884	3.19	6.35
8.79	0.000	1.000	12.3	0.000576	1.70	0.568	0.983	3.55	7.07
9.74	0.000	1.000	11.1	0.000638	1.89	0.629	1.09	3.94	7.83
10.8	0.000	1.000	9.99	0.000707	2.09	0.697	1.21	4.36	8.68
11.9	0.000	1.000	9.06	0.000779	2.30	0.768	1.33	4.81	9.56
13.4	0.000	1.000	8.06	0.000876	2.59	0.864	1.50	5.42	10.8
15.3	0.000	1.000	7.06	0.00100	2.96	0.986	1.71	6.18	12.3
17.6	0.000	1.000	6.14	0.00115	3.40	1.13	1.96	7.11	14.1
20.4	0.000	1.000	5.29	0.00133	3.95	1.32	2.28	8.24	16.4
23.6	0.000	1.000	4.57	0.00155	4.57	1.52	2.64	9.54	19.0
26.5	0.000	1.000	4.06	0.00174	5.14	1.71	2.97	10.7	21.3
31.3	0.000	1.000	3.44	0.00205	6.07	2.02	3.51	12.6	25.2
36.5	0.000	1.000	2.95	0.00239	7.08	2.36	4.08	14.8	29.3
42.1	0.000	1.000	2.56	0.00276	8.16	2.72	4.71	17.0	33.8
48.2	0.000	1.000	2.24	0.00315	9.33	3.11	5.39	19.5	38.7
54.5	0.000	1.000	1.98	0.00357	10.6	3.52	6.10	22.0	43.8
61.7	0.000	1.000	1.75	0.00404	11.9	3.98	6.90	24.9	49.6
70.2	0.000	1.000	1.54	0.00460	13.6	4.53	7.85	28.4	56.4
79.3	0.000	1.000	1.36	0.00519	15.4	5.12	8.87	32.0	63.7
89.9	0.000	1.000	1.20	0.00589	17.4	5.81	10.1	36.3	72.3

MERCURY INJECTION DATA SUMMARY

Company:	Patara Oil & Gas LLC
Well:	Cane Creek 042711
Field:	Paradox Basin
Formation:	Cane Creek
Location:	Grand County, Utah
File:	HOU:110920

Sample:	**25m**	un-	Host Plug	
Depth, feet:	7612.90	stressed	2310psi	na
Klinkenberg Permeability, md:		n/a	0.0116	-
Permeability to Air, md:		n/a	0.0245	-
Swanson Permeability, md:		0.00127	-	-
Porosity, fraction:		0.101	0.022	-
maximum Sb/Pc, fraction:		0.001		
R35, microns:		0.0166		
R50 (median pore throat radius):		0.0120		

Injection Pressure, psia	Mercury Saturation, fraction	Pseudo-Wetting Saturation, fraction	Pore Throat Radius, microns	J Values	Conversion to other Laboratory Fluid Systems, psia			Estimated Height Above Free Water, feet	
					G-W	G-O	O-W	G-W	O-W
102	0.000	1.000	1.06	0.00667	19.7	6.58	11.4	41.2	82.0
115	0.000	1.000	0.940	0.00751	22.2	7.41	12.8	46.5	92.4
131	0.000	1.000	0.824	0.00856	25.3	8.44	14.6	52.9	105
147	0.000	1.000	0.734	0.00962	28.5	9.49	16.4	59.4	118
168	0.000	1.000	0.640	0.0110	32.6	10.9	18.8	67.9	135
190	0.000	1.000	0.568	0.0124	36.7	12.2	21.2	76.8	153
213	0.000	1.000	0.507	0.0139	41.2	13.7	23.8	86.1	171
241	0.000	1.000	0.448	0.0158	46.6	15.5	26.9	97.4	194
274	0.000	1.000	0.393	0.0180	53.2	17.7	30.7	111	220
311	0.000	1.000	0.346	0.0204	60.4	20.1	34.8	126	250
352	0.000	1.000	0.306	0.0231	68.3	22.8	39.4	142	283
399	0.000	1.000	0.270	0.0262	77.4	25.8	44.7	161	321
448	0.000	1.000	0.240	0.0294	86.9	29.0	50.2	181	360
508	0.000	1.000	0.212	0.0333	98.5	32.8	56.9	205	408
580	0.000	1.000	0.186	0.0380	112	37.4	64.9	234	466
653	0.000	1.000	0.165	0.0428	127	42.2	73.1	264	525
735	0.000	1.000	0.147	0.0481	142	47.5	82.2	297	591
829	0.000	1.000	0.130	0.0543	161	53.5	92.7	335	666
945	0.000	1.000	0.114	0.0619	183	61.0	106	382	760
1080	0.000	1.000	0.0999	0.0707	209	69.7	121	436	868
1220	0.000	1.000	0.0884	0.0798	236	78.7	136	493	981
1370	0.000	1.000	0.0787	0.0896	265	88.4	153	554	1100
1540	0.000	1.000	0.0700	0.101	298	99.4	172	622	1240
1750	0.004	0.996	0.0616	0.115	339	113	196	707	1410
1980	0.008	0.992	0.0545	0.130	383	128	221	800	1590
2220	0.014	0.986	0.0486	0.145	430	143	248	897	1780
2510	0.024	0.976	0.0429	0.164	486	162	281	1010	2020
2830	0.038	0.962	0.0381	0.185	548	183	316	1140	2270
3220	0.064	0.936	0.0335	0.211	624	208	360	1300	2590
3660	0.099	0.901	0.0295	0.240	709	236	409	1480	2940
4150	0.144	0.856	0.0260	0.272	804	268	464	1680	3340
4700	0.197	0.803	0.0229	0.308	910	303	526	1900	3780
5300	0.252	0.748	0.0203	0.347	1030	342	593	2140	4260
5970	0.308	0.692	0.0181	0.391	1160	385	667	2410	4800

MERCURY INJECTION DATA SUMMARY

Company:	Patara Oil & Gas LLC
Well:	Cane Creek 042711
Field:	Paradox Basin
Formation:	Cane Creek
Location:	Grand County, Utah
File:	HOU:110920

Sample:	**25m**	un-	Host Plug	
Depth, feet:	7612.90	stressed	2310psi	na
Klinkenberg Permeability, md:		n/a	0.0116	-
Permeability to Air, md:		n/a	0.0245	-
Swanson Permeability, md:		0.00127	-	-
Porosity, fraction:		0.101	0.022	-
maximum Sb/Pc, fraction:		0.001		
R35, microns:		0.0166		
R50 (median pore throat radius):		0.0120		

Injection Pressure, psia	Mercury Saturation, fraction	Pseudo-Wetting Saturation, fraction	Pore Throat Radius, microns	J Values	Conversion to other Laboratory Fluid Systems, psia			Estimated Height Above Free Water, feet	
					G-W	G-O	O-W	G-W	O-W
6750	0.366	0.634	0.0160	0.442	1310	436	755	2730	5430
7650	0.424	0.576	0.0141	0.501	1480	494	855	3090	6150
8650	0.482	0.518	0.0125	0.566	1680	558	967	3500	6950
9790	0.541	0.459	0.0110	0.641	1900	632	1090	3960	7870
11000	0.599	0.401	0.00977	0.723	2140	713	1230	4450	8840
12500	0.648	0.352	0.00862	0.818	2420	807	1400	5050	10000
14100	0.719	0.281	0.00763	0.925	2740	912	1580	5700	11300
16000	0.778	0.222	0.00674	1.05	3100	1030	1790	6470	12900
18100	0.834	0.166	0.00596	1.18	3500	1170	2020	7310	14500
20400	0.881	0.119	0.00527	1.34	3960	1320	2290	8240	16400
23100	0.918	0.082	0.00466	1.51	4480	1490	2590	9340	18600
26200	0.946	0.054	0.00412	1.71	5070	1690	2930	10600	21100
29600	0.966	0.034	0.00364	1.94	5730	1910	3310	12000	23800
33500	0.977	0.023	0.00322	2.19	6490	2160	3750	13500	26900
37800	0.984	0.016	0.00285	2.48	7330	2440	4230	15300	30400
43000	0.989	0.011	0.00250	2.82	8340	2780	4810	17400	34600
48400	0.991	0.009	0.00223	3.17	9380	3130	5410	19600	38900
55000	0.994	0.006	0.00196	3.60	10700	3550	6150	22200	44200

Source Rock Analyses

TOC, Rock-Eval and Maturity Testing

Job # 110920G
Grand County, Utah

Core Laboratories

August 30, 2011

Core Laboratories - Thomas Dunkirk — Job # 110000S, Grand County, Utah

Sample ID										Source Rock Analysis														
Project / Sample ID	Rock ID	Well Name	Sampling Date	Sampling Time	Formation Name	Upper Depth (ft)	Lower Depth (ft)	Median Depth (ft)	Sample Type	Percent Kerogen (calculated) (wt%)	Loss TOC (wt%)	Rock-Eval S1 (mg HC/g)	Rock-Eval S2 (mg HC/g)	Rock-Eval S3 (mg CO2/g)	Tmax (C)	Measured %Ro (Vitrinite Refl.)	PyGAS® "S" Maturity (wt%)	Hydrogen Index (standard/TOC)	Oxygen Index (standard/TOC)	S2/S3 (Lmc. (mg HC/mg CO2))	S1/TOC Maturity Index (Leckie)	Pre-Asphalt Index (pi) (standard)	Environmental Assessment
R110K-FSR00-001	1	110000S				7,540.00		7,540.00			1.00	0.09	0.50	0.50	548			50	10	0	250	0.50	Low Temp S1 Shoulder
R110K-FSR00-002	2	110000S				7,541.00		7,541.00			1.04	0.22	0.84	0.51	460			81	37	0	315	0.47	Low Temp S1 Shoulder
R110K-FSR00-003	3	110000S				7,542.10		7,542.10			1.05	0.13	1.04	0.50	545			101	18	0	443	0.70	Low Temp S1 Shoulder
R110K-FSR00-004	4	110000S				7,543.10		7,543.10			0.97	0.04	0.43	0.46	470			111	74	0	143	0.63	Low Temp S1 Peak
R110K-FSR00-005	5	110000S				7,544.10		7,544.10			0.10	0.28	0.15	0.35	420			150	127	0	233	0.62	Low Temp S1 Peak
R110K-FSR00-006	6A	110000S				7,547.10		7,547.10			0.08	0.02	0.01	0.15	0			25	188	0	50	0.67	
R110K-FSR00-007	7A	110000S				7,554.10		7,554.10			0.08	0.04	0.08	0.27	414			78	34	1	164	0.75	Low Temp S1 Shoulder

Interpretation by Current Research Lab

Client: Core Laboratories
Field / Well: Job # 1109200
Contact: Thomas Gentzis

Core Laboratories - Thomas Gentzis | **Job # 1109200, Grand County, Utah**

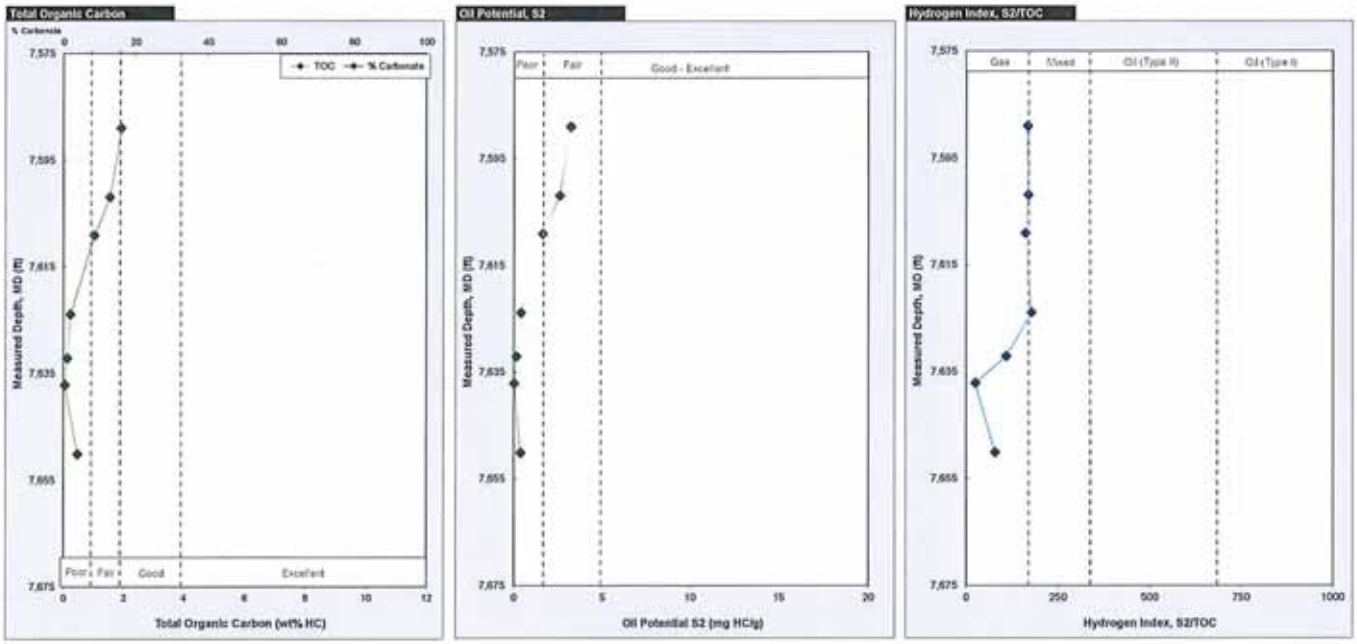

GeoMark Source Rock Services
218 Higgins Street
Humble, TX 77338

(832) 644-1184
info@geomarkresearch.com
August 30, 2011

Core Laboratories - Thomas Gentzis | Job # 110920G, Grand County, Utah

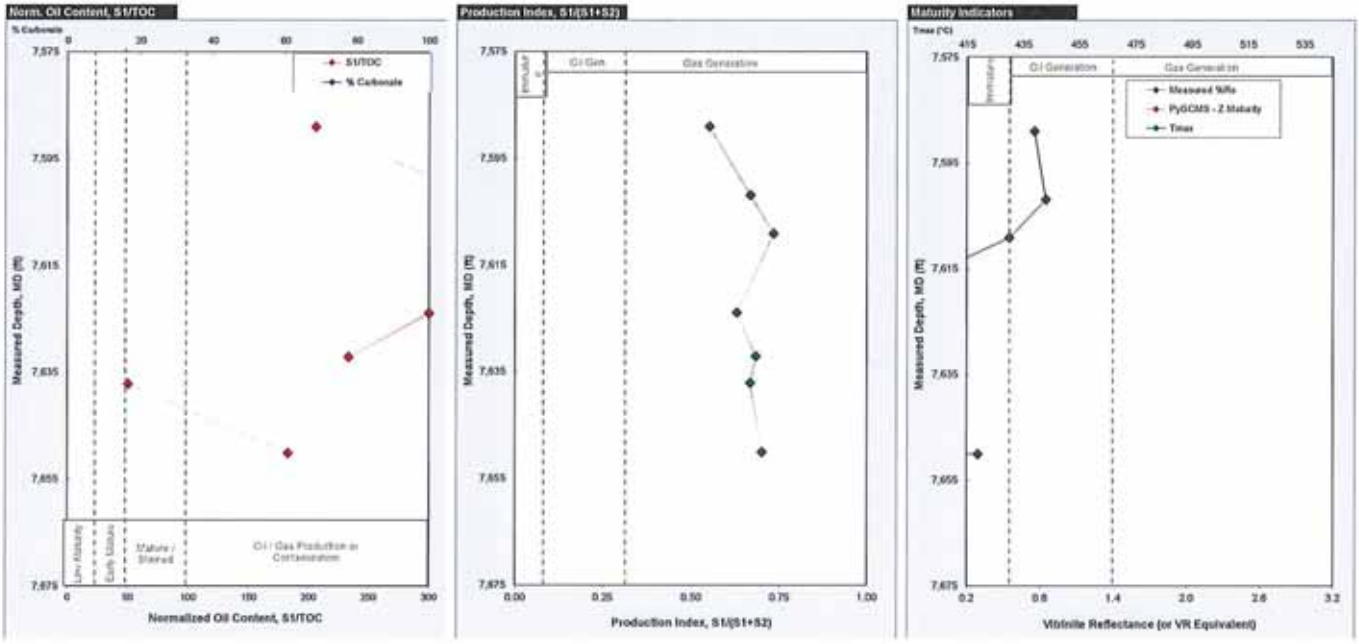

Core Laboratories - Thomas Gentzis | Job # 110920G, Grand County, Utah

Kerogen Quality Plot

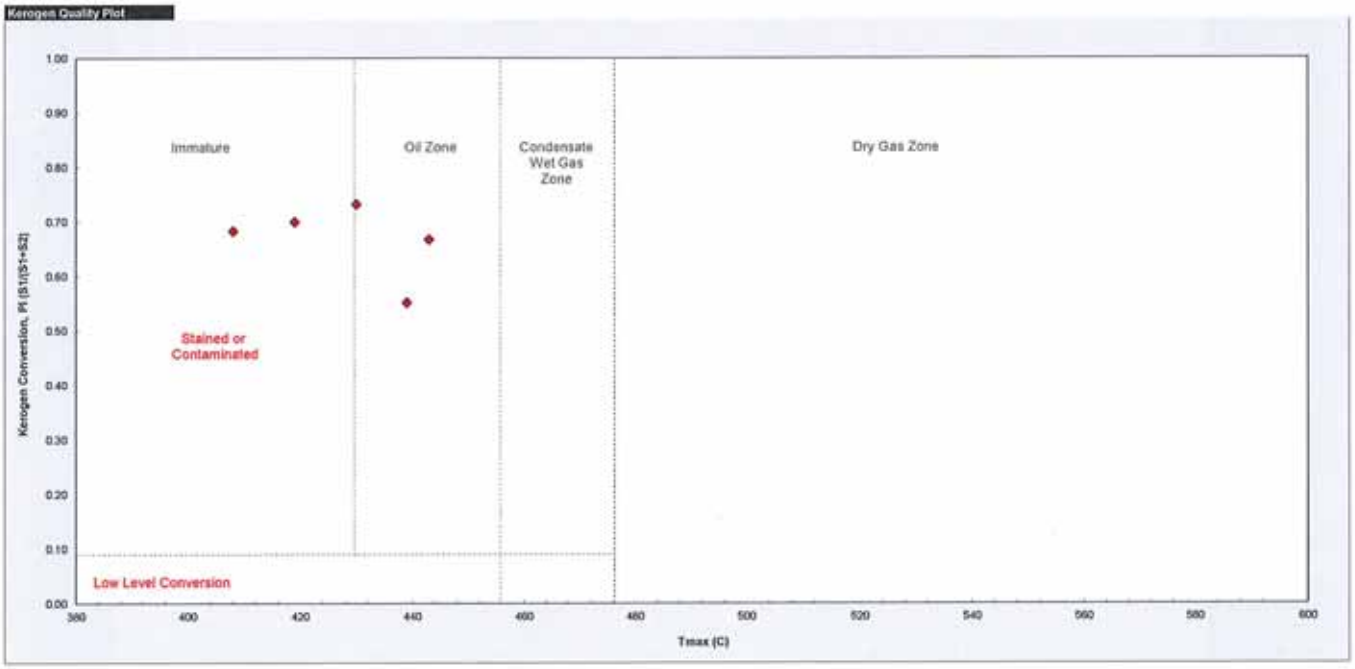

Core Laboratories - Thomas Gentzis | **Job # 110920G, Grand County, Utah**

Kerogen Type and Maturity

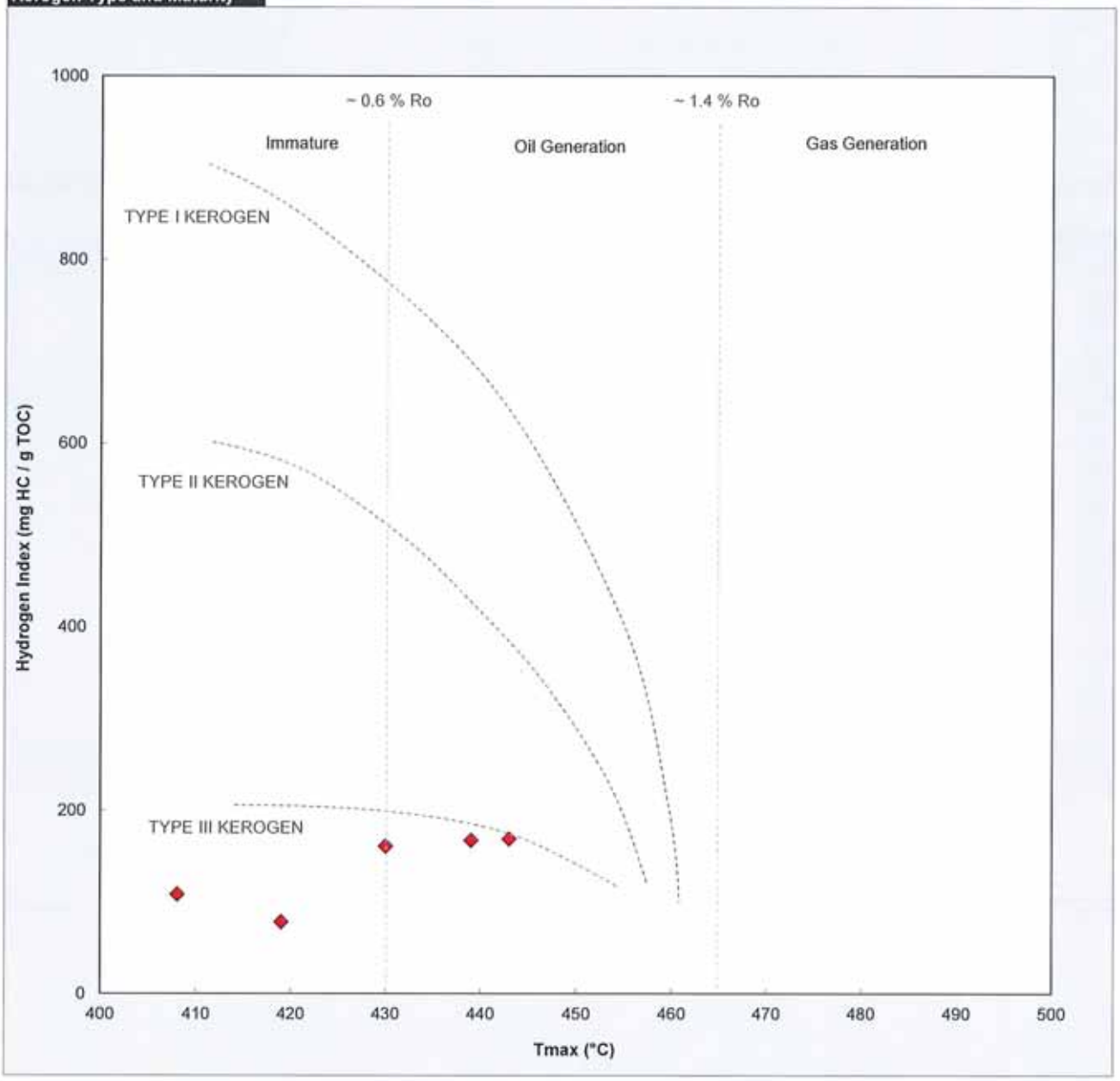

Core Laboratories - Thomas Gentzis | **Job # 110920G, Grand County, Utah**

Kerogen Quality Plot

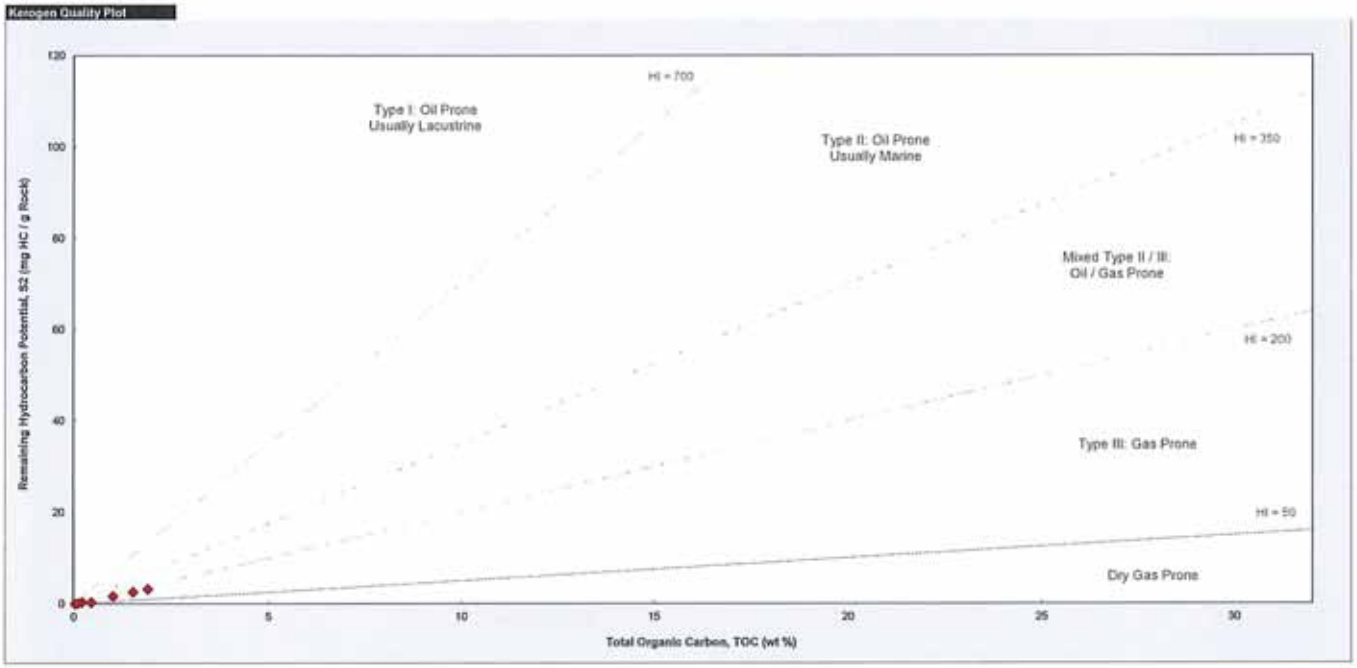

Core Laboratories - Thomas Gentzis | **Job # 110920G, Grand County, Utah**

Pseudo Van Krevelen Plot

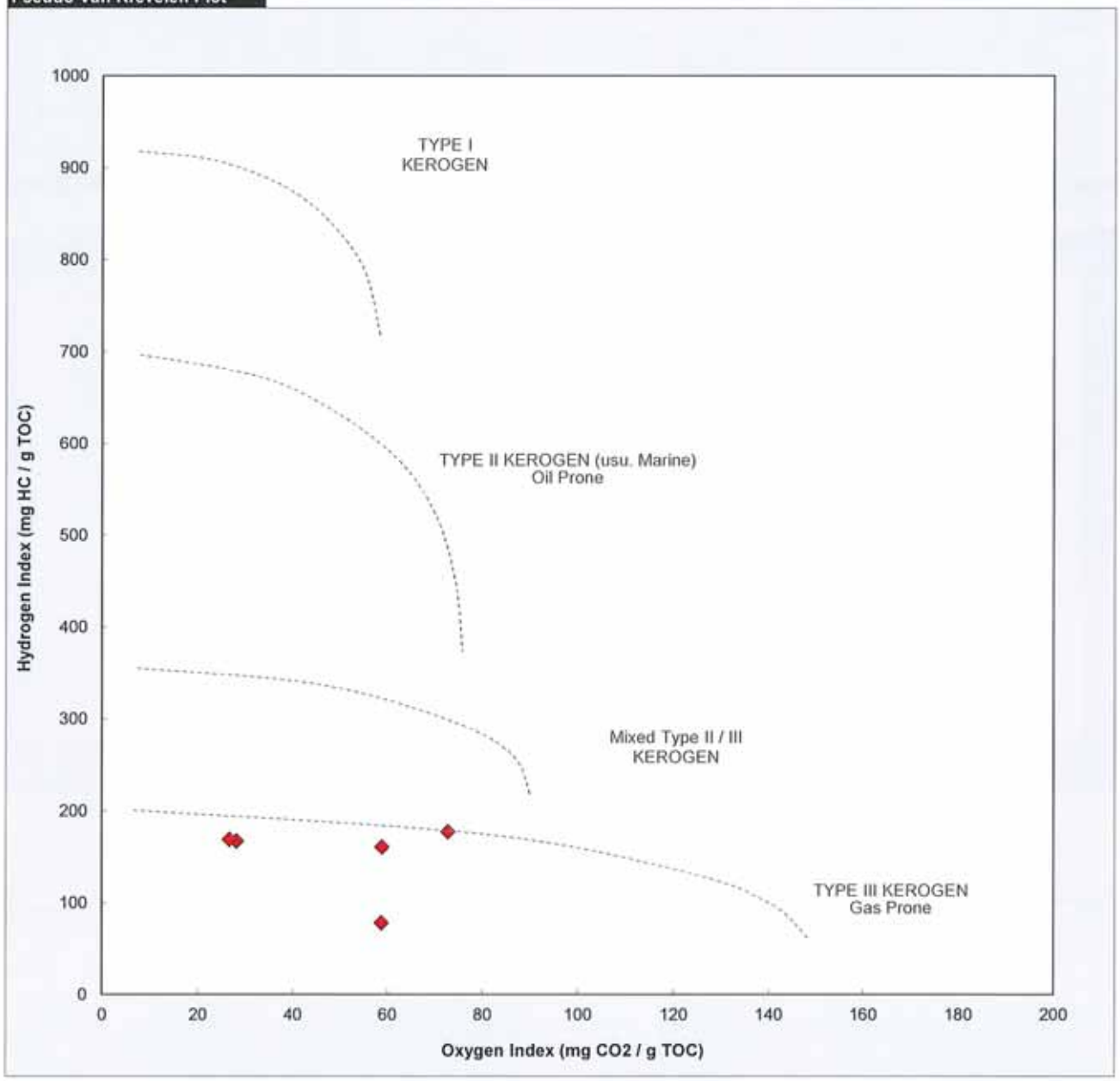

Core Lab
RESERVOIR OPTIMIZATION

Patara Oil & Gas
Cane Creek 042711
Grand Co., UT
Spectral Core Gamma
Scale 5" = 100'

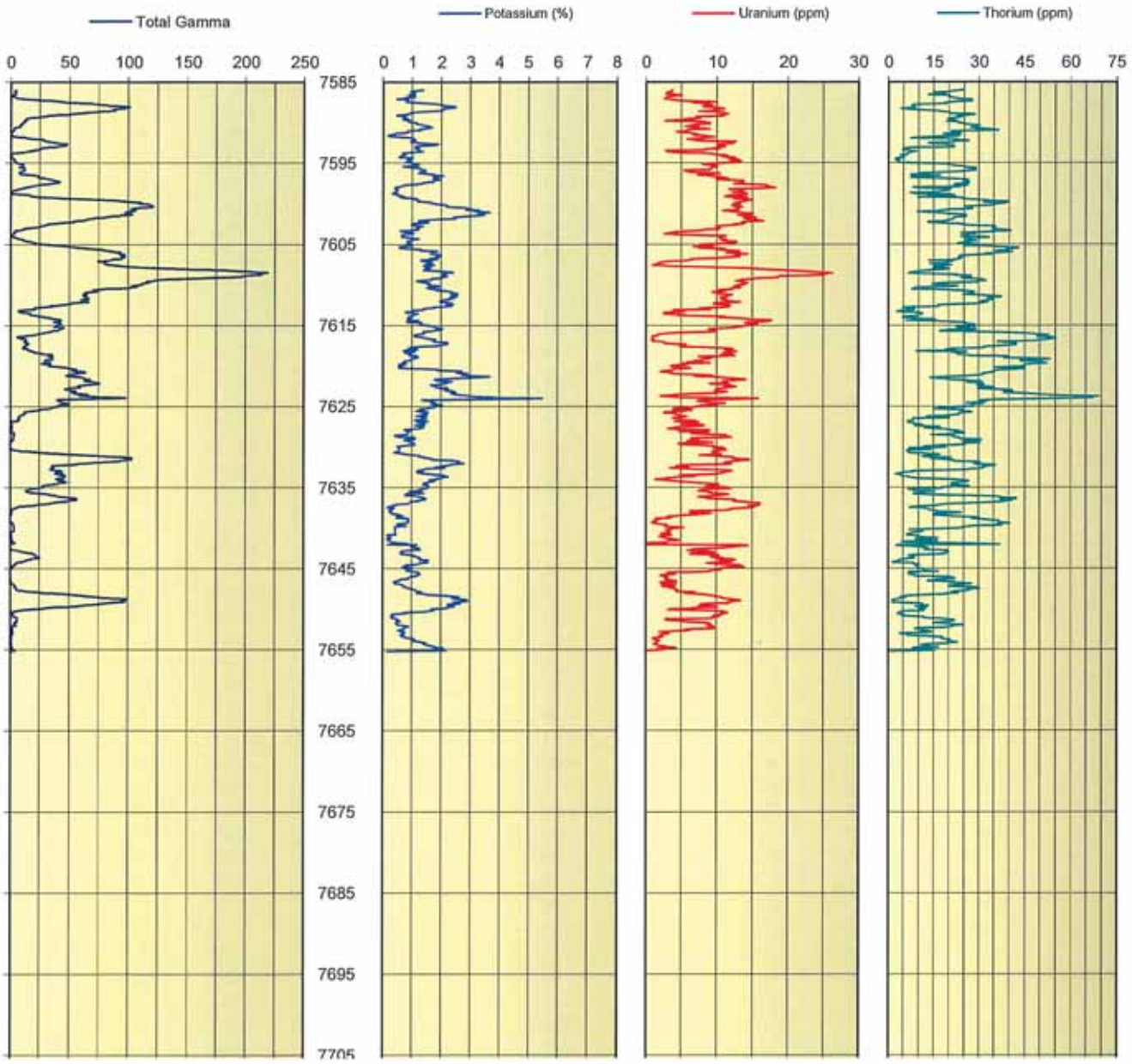

Patara Oil & Gas

Cane Creek 042711
Grand Co., UT
July 3, 2011
CL File No.: DEN-110039

Spectral Core Gamma

Core 1

Depth (feet)	Gamma (API)	Th (ppm)	U (ppm)	K (%)
7586.02	4.97	24.83	3.77	1.38
7586.1	3.42	21.04	3.47	1.05
7586.18	3.42	20.98	3.59	0.96
7586.27	4.38	18.98	2.96	1.01
7586.35	4.38	14.83	2.95	1.11
7586.43	4.38	14.98	2.83	1.09
7586.52	3.5	18.94	3.96	1.03
7586.6	1.86	13.31	5.02	0.88
7586.68	2.41	20.02	4.6	1.00
7586.77	1.66	20.47	3.09	1.11
7586.85	3.99	20.47	2.86	1.11
7586.93	5.28	20.47	3.01	0.75
7587.02	5.94	23.26	2.67	0.71
7587.1	12.61	22.85	3.44	0.47
7587.18	19.71	27.6	3.44	0.88
7587.27	28.03	27.6	5.23	0.85
7587.35	36.55	27.59	7	0.85
7587.43	42.91	23.06	9.97	0.80
7587.52	46.31	20.32	6.54	0.94
7587.6	59.7	18.49	9.02	1.52
7587.68	69.7	19.28	8.21	1.77
7587.77	73.08	12.05	8.17	1.91
7587.85	81.63	7.89	9.46	2.05
7587.93	83.7	7.89	9.02	2.10
7588.02	95.32	8.55	8.12	2.43
7588.1	101.02	8.99	8.64	2.50
7588.18	95.04	8.99	9.95	2.44
7588.27	96.49	4.19	10.98	2.09
7588.35	88.99	5.71	9.59	2.10
7588.43	86.59	7.94	10.09	2.06
7588.52	88.29	14.02	9.28	1.99
7588.6	81.69	17.26	7.5	1.66
7588.68	73.35	17.26	10.49	1.30
7588.77	67.5	20.28	11.04	1.08
7588.85	61.43	20.22	10.98	0.91
7588.93	52.88	20.95	11.59	0.90
7589.02	49.89	28.47	10.31	0.81
7589.1	37.22	25.59	10.97	0.47
7589.18	31.51	22.74	10.05	0.73
7589.27	28.29	24.3	7.07	0.80
7589.35	24.02	23.9	7.22	0.80
7589.43	16.89	21.5	7.68	0.75
7589.52	14.06	19.68	5.56	0.68
7589.6	12.81	20.17	6.8	0.90
7589.68	12.54	20.86	4.89	0.73
7589.77	13.54	22.32	2.75	0.92
7589.85	11.54	19.44	8.13	0.91
7589.93	11.86	23.1	8.2	0.88

Core 2

Depth (feet)	Gamma (API)	Th (ppm)	U (ppm)	K (%)
7624.17	40.02	32.65	7.54	1.35
7624.25	42.99	30.4	8.99	1.51
7624.33	41.66	32.45	7.27	1.66
7624.42	42.47	32.45	8.23	1.64
7624.5	43.65	29.82	9.29	1.77
7624.58	46.1	25.8	11.14	1.79
7624.67	49.8	31.37	9.91	1.85
7624.75	49.46	27.95	10.21	1.69
7624.83	41.81	28.12	7.77	2.05
7624.92	40.48	27.06	9.73	1.8
7625	41.07	28.04	7.28	1.85
7625.08	36.43	19.74	6.54	1.7
7625.17	35.19	16.62	4.27	1.62
7625.25	34.87	21.96	3.93	1.54
7625.33	28.15	15.12	4.82	1.28
7625.42	25.38	24.59	6.53	1.33
7625.5	22.33	24.59	3.87	1.44
7625.58	16.47	24.12	5.54	1.18
7625.67	12.39	27.58	2.64	1.55
7625.75	11.66	24.38	2.63	1.54
7625.83	12.22	23.35	3.96	1.36
7625.92	12.22	23.35	4.08	1.52
7626	10.73	23.35	4.59	1.52
7626.08	9.01	19.8	4.86	1.42
7626.17	8.02	19.8	5.35	1.18
7626.25	7.53	12.9	5.85	1.29
7626.33	7.53	20.27	4.3	1.51
7626.42	7.53	20.27	3.87	1.47
7626.5	7.72	8.21	5.01	1.32
7626.58	7.72	8.21	5.01	1.43
7626.67	5.86	8.25	4.92	1.11
7626.75	6.7	8.23	7.09	1.38
7626.83	1.17	6.55	4.15	1.54
7626.92	1.17	6.55	7.6	1.19
7627	1.16	6.6	5.94	1.37
7627.08	1.16	8.55	5.68	1.45
7627.17	1.16	8.55	5.15	1.45
7627.25	1.16	11.24	8.01	1.34
7627.33	1.16	10.93	8.25	1.12
7627.42	1.71	8.95	7.66	1.23
7627.5	1.53	17.06	5.27	1.41
7627.58	1.53	17.06	3.97	1.36
7627.67	1.53	12.02	4.6	1.29
7627.75	0.69	13.65	3.16	1.29
7627.83	0.69	20.47	4.97	0.77
7627.92	1.1	20.47	9.05	0.76
7628	1.1	21.07	4.92	0.98
7628.08	1.1	23.76	4.71	0.87

7590.02	10.16	23.12	9.07	1.16	7628.17	1.1	21.86	8.82	0.85
7590.1	10.16	25.1	9.06	1.16	7628.25	3.31	25.08	8.82	0.85
7590.18	10.16	25.1	7.14	1.20	7628.33	3.31	23.05	6.46	0.89
7590.27	8.39	25.68	6.94	1.29	7628.42	3.31	20.83	9.06	0.85
7590.35	8.38	30.25	6.06	1.43	7628.5	2.76	14.34	11.37	0.61
7590.43	8.38	29.45	5.54	1.58	7628.58	2.76	21.27	11.37	0.42
7590.52	8.38	29.45	7.44	1.58	7628.67	2.76	21.27	11.06	0.49
7590.6	5.72	27.2	6.53	1.67	7628.75	2.75	21.68	12.02	0.58
7590.68	3.1	30.02	7.19	1.44	7628.83	2.86	23.04	10.61	1.1
7590.77	3.09	28.56	8.96	1.44	7628.92	2.46	23.61	6.43	1.12
7590.85	2.64	33.22	5.93	1.26	7629	2.46	24.2	7.45	1.11
7590.93	2.64	36.41	5.74	1.26	7629.08	2.47	30.65	7.45	0.82
7591.02	2.32	32.02	5.74	0.87	7629.17	2.47	29.77	6.7	0.77
7591.1	0.69	20.71	4.37	0.87	7629.25	0.26	26.72	5.9	0.95
7591.18	0.69	20.71	4.61	0.89	7629.33	0.26	24.55	8.56	0.91
7591.27	0.76	21.93	6.44	0.76	7629.42	0.26	30.39	9.48	1.01
7591.35	0.76	23.83	6.44	0.42	7629.5	0.25	29.96	6.24	1.07
7591.43	0.76	18.25	7.35	0.42	7629.58	0.26	25.03	4.68	1.07
7591.52	0.76	23.35	6.76	0.27	7629.67	0.26	25.27	5.16	1.1
7591.6	1.58	23.35	8.53	0.19	7629.75	0.26	23.98	7.39	1.01
7591.68	1.58	22.23	8.12	0.19	7629.83	0.15	17.82	8.97	0.79
7591.77	5.49	16.86	9.68	0.44	7629.92	0.15	11.87	9.88	0.5
7591.85	13.48	9.38	8.36	0.88	7630	0.15	19.12	10.08	0.57
7591.93	13.48	7.45	7.96	1.02	7630.08	0.15	15.2	10.98	0.57
7592.02	19.91	18.53	5.88	0.99	7630.17	0.15	6.99	9.7	0.58
7592.1	27.31	22.81	6.62	1.10	7630.25	1.03	6.99	11.07	0.57
7592.18	27.31	22.81	7.11	1.10	7630.33	2.44	14.09	11.37	0.57
7592.27	29.67	26.46	9.08	1.09	7630.42	6.54	6.27	10.57	0.57
7592.35	30.89	21.22	12.63	0.96	7630.5	9.54	6.27	9.69	0.57
7592.43	35.4	21.22	12.52	1.20	7630.58	18.52	6.83	9.45	0.5
7592.52	39.31	13.25	12.2	1.20	7630.67	24	7.32	10.13	0.4
7592.6	40.6	14.59	11.37	1.47	7630.75	32.32	7.09	9.97	0.52
7592.68	48.01	19.77	10.08	1.90	7630.83	43.41	14.05	10.6	0.79
7592.77	44.66	19.77	10.3	1.76	7630.92	53.96	16.96	9.66	0.84
7592.85	46.64	21.08	10.66	1.45	7631	65.94	15.88	7.63	1.07
7592.93	40.1	21.62	11.18	1.12	7631.08	74.66	12.92	9.2	1.26
7593.02	39.51	21.39	10.12	1.12	7631.17	83.1	11.33	11.08	1.25
7593.1	30.2	6.79	9.72	1.23	7631.25	93.84	13.01	12.42	1.42
7593.18	26.66	6.33	10.46	1.11	7631.33	102.51	20.78	12.2	1.42
7593.27	25	4.98	8.36	1.24	7631.42	102.63	14.27	12.61	1.7
7593.35	23.68	4.98	8.37	1.24	7631.5	102.99	17.64	14.65	1.7
7593.43	20.25	7	2.82	1.21	7631.58	97.98	19.95	14.65	1.75
7593.52	15.45	7.15	4.1	1.20	7631.67	94.58	21.37	13.29	2.35
7593.6	14.6	9.26	3.08	1.38	7631.75	91.11	22.55	12.16	2.62
7593.68	10.34	7.13	4.37	0.88	7631.83	81.91	29.91	11.4	2.55
7593.77	4.53	6.34	9.15	0.68	7631.92	71.35	30.34	11.17	2.58
7593.85	0.56	6.34	9.2	0.75	7632	63.31	30.34	11.15	2.78
7593.93	0.56	6.12	10.13	0.78	7632.08	57.15	28.49	12.07	2.49
7594.02	0.16	4.07	11.44	0.71	7632.17	55.23	30.74	9.13	2.31
7594.1	0.16	5.25	11.42	0.63	7632.25	42.61	35.59	5.03	2.31
7594.18	0.16	5.25	10.74	0.61	7632.33	35.69	33.45	4.39	2.02
7594.27	0.45	5.25	12.59	0.56	7632.42	37.47	31.08	4.34	2.04
7594.35	1.55	3.77	11.54	1.03	7632.5	35.44	31.66	6.05	1.81
7594.43	1.55	2.55	12.28	0.82	7632.58	36.43	31.66	3.45	2.13
7594.52	3.36	3.65	13.09	0.89	7632.67	36.31	30.08	6.19	1.46
7594.6	3.36	2.39	11.89	0.98	7632.75	34	26.37	7.05	1.47
7594.68	3.36	3.38	13.19	0.88	7632.83	37.21	26.37	10.6	1.38
7594.77	3.36	3.38	13.37	0.88	7632.92	42.4	11.41	12.18	1.19
7594.85	4.21	3.38	12.73	0.80	7633	43.98	7.73	11.46	1.37

7594.93	4.87	3.68	11.19	1.00	7633.08	42.63	7.85	11.22	1.26
7595.02	6.91	8.56	9.41	1.00	7633.17	38.57	5.14	10.91	1.22
7595.1	10.35	18.97	8.02	1.12	7633.25	38.54	3.72	10.23	1.39
7595.18	10.35	20.1	8.71	1.24	7633.33	45.49	2.71	9.43	1.68
7595.27	10.6	21.6	9.44	1.16	7633.42	41.55	4.62	8.23	1.75
7595.35	10.6	21.67	10.12	1.16	7633.5	44.92	4.62	4.8	2.04
7595.43	9.5	25.22	10.04	0.69	7633.58	47.1	4.24	7.07	2.18
7595.52	7.69	25.28	9.25	0.95	7633.67	45.53	7.08	5.29	2.25
7595.6	12.04	28.93	9.25	1.26	7633.75	45.77	6.97	4.17	2.04
7595.68	12.04	28.93	9.19	1.26	7633.83	43	9.27	2.82	1.95
7595.77	12.04	26.82	8.91	1.29	7633.92	39.17	13.12	2.61	1.81
7595.85	11.22	29.01	5.44	1.44	7634	44.38	20.1	1.48	1.86
7595.93	11.73	27.58	5.59	1.47	7634.08	40.46	23.11	2.44	1.62
7596.02	9.65	23.68	6.53	1.42	7634.17	45.94	26.59	4.18	1.77
7596.1	7.87	20.05	6.13	1.42	7634.25	45.34	26.59	5.21	1.6
7596.18	7.98	15.1	9.59	1.24	7634.33	47.87	24.54	5.65	1.59
7596.27	7.98	10.13	10.52	1.27	7634.42	41.9	21.18	8.19	1.43
7596.35	8.87	11.71	7.33	1.66	7634.5	40.87	21.18	9.34	1.54
7596.43	13.39	7.61	7.36	1.80	7634.58	38.13	23.04	10.31	1.41
7596.52	20.35	17.06	9.13	1.74	7634.67	32.92	20.78	9.7	1.39
7596.6	23.5	13.77	9.22	2.09	7634.75	28.85	25.85	9.25	1.58
7596.68	23.93	7.52	10.69	1.74	7634.83	27.38	26.67	8.58	1.58
7596.77	24.19	7.54	10.69	1.86	7634.92	27.67	22.08	9.74	1.58
7596.85	29.06	14.12	11.53	1.75	7635	25.86	17.74	11.41	1.55
7596.93	30.06	18.87	9.99	1.84	7635.08	21.88	17.65	12	1.43
7597.02	34.53	26.28	10.29	1.95	7635.17	18.18	11.22	9.4	1.43
7597.1	36.2	26.24	13.29	1.79	7635.25	15.41	6.72	7.85	1.27
7597.18	37.76	24.87	13.76	1.74	7635.33	13.89	8.94	8.43	1.32
7597.27	40.62	24.99	13.39	1.74	7635.42	13.63	8.81	7.48	1.21
7597.35	41.93	26.65	13.79	1.49	7635.5	14.62	15.46	8.82	0.92
7597.43	39.37	25.62	13.27	1.36	7635.58	15.91	11.8	9.32	1.03
7597.52	34.75	26.31	12.45	1.36	7635.67	21.29	10.96	9.08	1.41
7597.6	30.44	21.88	15.62	1.09	7635.75	28.6	8.44	10.78	0.92
7597.68	23.7	25.99	17.16	0.75	7635.83	32.9	9.77	11.67	0.79
7597.77	22.25	25.98	16.8	0.75	7635.92	34.66	19.68	10.3	0.79
7597.85	17.36	21.51	17.52	0.58	7636	39.53	26.23	9.87	1.03
7597.93	16.99	23.57	17.53	0.56	7636.08	39.63	33.35	8.25	1.18
7598.02	12.47	8.27	18.34	0.41	7636.17	44.89	36.79	7.42	1.29
7598.1	11.37	10.72	16.7	0.41	7636.25	50.48	37.32	9.14	1.42
7598.18	7.85	20.59	11.76	0.51	7636.33	55.92	42.41	8.8	1.47
7598.27	5.75	20.49	13.37	0.51	7636.42	54.68	41.93	10.66	1.49
7598.35	2.9	18.8	13.16	0.51	7636.5	56.06	37.09	12.66	1.44
7598.43	1.39	18.95	13.69	0.44	7636.58	50.33	40.76	12.67	1.2
7598.52	1.39	16.4	13.84	0.44	7636.67	48.73	38.59	12.34	1.23
7598.6	1.39	16.45	12.18	0.47	7636.75	43.81	38.59	13.88	0.96
7598.68	1.38	7.34	14.26	0.34	7636.83	38.81	36.06	14.16	0.94
7598.77	1.38	9.21	14.31	0.34	7636.92	33.91	28.06	16.23	0.9
7598.85	7.33	20.65	13.85	0.44	7637	33.04	22.01	16.16	0.9
7598.93	15.1	13.28	13.44	0.57	7637.08	24.7	18.88	16.12	0.5
7599.02	17.34	21.79	11.7	0.49	7637.17	22.04	16.24	16.12	0.39
7599.1	18.19	19.89	11.16	0.74	7637.25	17.15	16.04	14.54	0.39
7599.18	25.16	9.73	14.33	0.62	7637.33	7.12	10.62	15.58	0.27
7599.27	34.02	24.04	12.73	0.68	7637.42	5.7	7.26	14.86	0.16
7599.35	45.11	24.78	12.45	1.16	7637.5	5.67	12.31	14.07	0.38
7599.43	59.22	25.47	14.53	1.05	7637.58	2.89	12.31	12.35	0.38
7599.52	74.28	28.28	15.08	1.23	7637.67	1.98	13.4	11.9	0.34
7599.6	87.96	32.01	14.28	1.23	7637.75	1.84	13.4	11.95	0.24
7599.68	93.31	34.46	13.77	1.20	7637.83	1.44	15.88	9.07	0.24
7599.77	100.43	39.86	13.21	1.38	7637.92	1.04	15.88	6.31	0.23

7599.85	110.31	31.51	13.07	1.66	7638	1.04	15.88	6.35	0.24
7599.93	108.84	39.02	12.54	1.64	7638.08	1.03	23.9	6.36	0.33
7600.02	112.15	36.53	13.36	1.82	7638.17	1.03	21.2	9.23	0.33
7600.1	118.13	34.93	13.26	2.06	7638.25	1.03	15.04	8.62	0.33
7600.18	119.26	34.93	12.11	2.16	7638.33	0.15	15.04	7.47	0.51
7600.27	119.71	29.49	12.71	2.23	7638.42	0.15	15.04	5.12	0.6
7600.35	121.12	25.4	13.6	2.19	7638.5	0.15	20.77	4.64	0.71
7600.43	120.01	27.83	13.08	2.36	7638.58	0.14	21.34	3.12	0.49
7600.52	109.56	27.14	12.81	2.72	7638.67	0.14	29.97	3.64	0.49
7600.6	104.12	27.83	12.76	2.95	7638.75	0.14	28.8	3.31	0.49
7600.68	102.62	26.01	12.7	3.04	7638.83	0.14	27.66	1.55	0.86
7600.77	104.49	19	13.2	2.86	7638.92	0.14	29.83	2.03	0.91
7600.85	105.99	18.79	10.87	3.32	7639	0.14	33.72	1.39	0.9
7600.93	100.42	15.25	12.39	3.14	7639.08	0.15	36.61	1.48	0.87
7601.02	99.4	9.64	12.37	3.44	7639.17	0.15	36.61	1.55	0.91
7601.1	97.25	11.99	13.36	3.67	7639.25	0.15	37.18	1	0.91
7601.18	101.97	19.07	15.21	3.36	7639.33	2.12	38.06	1.13	0.79
7601.27	100.08	19.07	14.78	3.26	7639.42	2.11	40.25	1.44	0.73
7601.35	102.94	23.39	14.46	3.39	7639.5	2.7	36.04	1.77	0.53
7601.43	93.79	25.57	13.05	3.48	7639.58	2.7	36.83	3	0.53
7601.52	91.77	25.57	14.84	2.98	7639.67	2.7	37.64	2.73	0.51
7601.6	82.68	25.57	13.77	2.76	7639.75	2.7	28.36	2.68	0.81
7601.68	81.2	21.92	15.48	2.45	7639.83	2.7	26.45	2.89	0.44
7601.77	71.52	21.34	13.91	2.49	7639.92	3.14	24.27	5.33	0.44
7601.85	69.87	21.34	14.67	2.49	7640	3.13	24.27	3.92	0.43
7601.93	65.41	21.34	15.79	1.82	7640.08	3.24	20.07	3.92	0.43
7602.02	64.36	20.43	14.45	1.62	7640.17	3.24	7.11	2.85	0.43
7602.1	60.9	18.87	16.63	1.23	7640.25	3.34	11.75	3.05	0.44
7602.18	53.42	18.87	14.52	1.31	7640.33	3.33	11.75	3.39	0.44
7602.27	53.98	13.2	13.52	1.47	7640.42	1.37	11.58	3.17	0.44
7602.35	45.89	13.2	13.94	1.56	7640.5	1.08	9.37	3.45	0.44
7602.43	39.37	19.4	13.87	1.07	7640.58	0.79	7.64	3.35	0.44
7602.52	31.92	24.49	12.4	1.02	7640.67	0.79	7.64	2.27	0.45
7602.6	30.49	24.49	12.82	1.00	7640.75	0.79	6.37	3.36	0.45
7602.68	28.62	27.26	10.61	1.12	7640.83	0.78	6.37	3.62	0.16
7602.77	25.97	34.74	9.9	1.38	7640.92	1.1	8.01	2.83	0.16
7602.85	24.42	35.65	9.93	1.25	7641	1.1	9.79	1.96	0.26
7602.93	22.12	35.65	10.49	1.25	7641.08	1.18	10.6	2.33	0.24
7603.02	16.34	34.75	10.15	1.16	7641.17	1.16	12.95	2.85	0.27
7603.1	11.16	34.75	10.24	1.12	7641.25	1.27	16.42	2.81	0.3
7603.18	11.16	34.75	8.23	1.23	7641.33	1.25	9.06	3.49	0.16
7603.27	7.78	40.47	7.69	0.99	7641.42	1.4	9.74	4.21	0.19
7603.35	4.01	40.5	5.75	0.60	7641.5	1.59	10.91	4.86	0.22
7603.43	3.86	34.27	4.97	0.78	7641.58	1.85	16.23	3.16	0.25
7603.52	3.87	33.85	4.14	0.87	7641.67	2.23	4.53	3.05	0.29
7603.6	3.87	24.16	3.04	1.06	7641.75	2.82	6.57	2.89	0.37
7603.68	2.54	27.09	2.65	1.06	7641.83	3.9	12.2	0.27	0.52
7603.77	1.32	28.85	3.93	0.68	7641.92	0.14	26.29	0.19	0.87
7603.85	1.33	25.68	5.11	0.68	7642	0.13	36.93	0.18	0.18
7603.93	1.4	25.11	11.28	0.68	7642.08	0.15	4.15	13.34	1.18
7604.02	2.27	24.11	10.9	0.70	7642.17	0.14	2.87	14.42	0.97
7604.1	2.27	25.36	10.41	0.65	7642.25	0.15	7.01	13.28	0.97
7604.18	4.7	33.39	10.38	0.85	7642.33	0.15	10.94	11.82	1.06
7604.27	5.55	25.58	10.47	1.05	7642.42	0.15	13.13	11.14	1.13
7604.35	8.21	27.32	10.46	1.23	7642.5	0.15	12.15	9.51	1.27
7604.43	10.79	26.17	11.38	1.05	7642.58	0.15	12.15	6.44	1.25
7604.52	10.79	26.03	10.82	1.01	7642.67	2.73	12.15	7.56	1.28
7604.6	12.56	29.07	11.25	0.85	7642.75	5.27	19.77	5.93	0.91
7604.68	16.88	25.36	12.77	0.85	7642.83	8.45	19.77	8.47	0.75

7604.77	18.43	27.01	11.54	0.85	7642.92	9.93	19.97	9.21	0.64
7604.85	20.39	24.19	12.58	0.85	7643	13.15	19.97	9.77	0.62
7604.93	22.54	23.13	11.05	0.97	7643.08	18.04	18.77	6.54	0.61
7605.02	29.26	28.44	7.7	0.97	7643.17	19.59	18.72	6.33	0.67
7605.1	37.04	30.8	7.7	1.02	7643.25	20.72	14.47	9.42	0.91
7605.18	41.6	25.02	9.54	0.77	7643.33	22.01	8.08	10.36	1.01
7605.27	48.11	35.01	6.78	0.74	7643.42	22.01	6.79	9.91	1.07
7605.35	53.73	35.73	7.55	0.58	7643.5	22.44	7.6	9.32	1.16
7605.43	57.44	42.86	7.51	0.58	7643.58	24.77	8.63	9.32	1.22
7605.52	63.73	42.32	10.47	0.74	7643.67	24.77	8.63	10.93	1.26
7605.6	71.79	39.27	11.15	1.01	7643.75	19.65	8.63	9.91	1.31
7605.68	77.97	40.03	10.36	1.30	7643.83	18.54	4.9	12.37	1.26
7605.77	79.78	38.41	12.57	1.30	7643.92	14.99	3.69	12.67	1.31
7605.85	84.56	35.57	13.22	1.86	7644	13.4	3.69	10.41	1.57
7605.93	87.42	40.95	12.41	1.74	7644.08	12.05	3.69	11.35	1.46
7606.02	93.72	38.58	11.31	1.74	7644.17	8.52	1.63	12.11	1.45
7606.1	91.47	35.49	12.97	1.73	7644.25	5.86	1.64	10.65	1.54
7606.18	92.14	32.07	14.37	1.65	7644.33	4.55	8.33	8.71	1.28
7606.27	96.46	34.78	13.3	1.87	7644.42	4.55	8.33	10.23	1.25
7606.35	94.05	27.57	12.46	2.00	7644.5	4.11	10.39	11.91	1.13
7606.43	94.07	23.71	13.22	1.86	7644.58	4.12	9.13	13.43	0.83
7606.52	96.83	23.37	13.23	1.94	7644.67	1.79	9.83	12.8	0.78
7606.6	95.78	23.37	11	1.78	7644.75	1.79	9.83	13.85	0.7
7606.68	94.12	24.19	9.95	1.80	7644.83	1.79	9.83	11.4	0.7
7606.77	94.44	23.43	7.47	1.61	7644.92	1.79	9.83	10.98	1.04
7606.85	86.77	23.46	6.2	1.88	7645	0.16	11.26	10.16	0.92
7606.93	86.14	21.01	6.26	1.33	7645.08	0.16	12.06	9.91	0.92
7607.02	82.11	13.41	5.29	1.33	7645.17	0.16	12.06	10.65	0.81
7607.1	74.56	21.3	3.13	1.40	7645.25	0.16	12.06	9.12	0.81
7607.18	79.1	19.83	2.59	1.69	7645.33	0.16	16.59	9.13	1
7607.27	80.73	19.53	1.99	1.66	7645.42	0.16	6.77	7.73	1.12
7607.35	79.7	19.39	1.67	1.50	7645.5	0.16	9.59	3.11	1.25
7607.43	81.25	13.98	1.84	1.50	7645.58	0.15	6.88	3.22	1.23
7607.52	83.28	20.79	0.98	1.75	7645.67	0.15	6.91	4.17	1.28
7607.6	89.92	15.54	3.02	1.42	7645.75	0.25	7.51	2.64	1.21
7607.68	92.81	15.2	3.02	1.53	7645.83	0.25	8.86	2.14	1.21
7607.77	99.32	18.65	5.77	1.66	7645.92	0.26	8.86	2.8	1.08
7607.85	109.67	18.65	11.67	1.47	7646	0.25	20.53	2.79	0.98
7607.93	122.24	14.94	13.92	1.47	7646.08	0.25	20.53	3.22	0.91
7608.02	137.96	20.06	15.17	1.61	7646.17	0.25	21.96	2.7	0.91
7608.1	153.02	18.41	17.52	1.54	7646.25	0.25	21.96	2.74	0.91
7608.18	175.26	13.85	20.01	1.41	7646.33	0.57	15.65	2.99	0.63
7608.27	188.42	12.46	20.87	1.78	7646.42	0.81	18.88	3.19	0.59
7608.35	200.41	10.31	22.92	2.01	7646.5	0.8	13.19	4.37	0.54
7608.43	210.81	7.86	24.43	2.41	7646.58	0.81	19.25	4.36	0.4
7608.52	219.26	7.07	26.29	2.08	7646.67	0.81	21.84	2.15	0.46
7608.6	210.54	6.61	24.8	2.17	7646.75	0.81	20.66	3.41	0.41
7608.68	210.59	13.05	25.4	2.08	7646.83	0.71	27.35	2.3	0.42
7608.77	213.26	22.88	25.08	2.04	7646.92	3.08	26.13	4.32	0.56
7608.85	202.57	21.74	22.69	2.03	7647	3.08	24.35	3.37	0.68
7608.93	197.74	27.15	18.98	2.20	7647.08	3.19	21.98	2.41	0.7
7609.02	195.48	27.15	18.53	2.09	7647.17	3.78	20.07	2.41	0.73
7609.1	180.13	24.24	18.5	1.95	7647.25	4.88	22.49	4.17	0.73
7609.18	164	24.24	15.95	1.97	7647.33	4.88	28.95	3.23	0.86
7609.27	146.98	27.28	15.37	1.68	7647.42	4.88	30.22	4.17	0.89
7609.35	130.31	31.62	13.36	1.69	7647.5	5.2	27.14	4.17	1.03
7609.43	123.41	31.62	13.36	1.44	7647.58	5.64	26.06	4.26	1.03
7609.52	121.33	32.34	12.74	1.25	7647.67	6.54	27.46	4.62	1.15
7609.6	115.75	29.53	13.76	1.17	7647.75	12.34	24.87	4.46	1.18

7609.68	117.96	29.53	13.49	1.40	7647.83	15.41	21.17	4.45	1.27
7609.77	115.13	21.19	14.39	1.61	7647.92	24.82	23.07	6.96	1.33
7609.85	112.02	16.95	13.91	1.52	7648	27.51	23.07	5.48	1.2
7609.93	111.21	14.53	13.91	1.57	7648.08	40.61	19.18	6.57	1.39
7610.02	109.88	18.72	12.87	1.62	7648.17	48.51	19.18	7.85	1.48
7610.1	103.41	18.72	13.08	1.69	7648.25	55.12	14.07	8.68	1.53
7610.18	107.54	22.79	12.46	1.96	7648.33	62.22	5.73	9.74	2.25
7610.27	104.68	14.18	13.07	1.76	7648.42	66.85	5.72	9.88	2.37
7610.35	101.18	8.68	13.41	1.53	7648.5	75.86	4.1	10.61	2.63
7610.43	96.71	8.68	11.88	1.54	7648.58	76.08	5.79	10.62	2.52
7610.52	79.3	7.87	12.17	1.76	7648.67	87.07	3.71	11.09	2.4
7610.6	74.58	19.73	10.29	1.97	7648.75	98.87	3.71	11.7	2.58
7610.68	70.36	20.86	11.37	1.85	7648.83	98.37	2.36	12.4	2.78
7610.77	74.24	25.02	10.27	2.15	7648.92	94.41	1.47	13.37	2.91
7610.85	70.92	28.22	9.42	2.36	7649	96.71	1.47	11.87	2.91
7610.93	64.26	28.22	10.82	2.34	7649.08	97.16	1.47	12.32	2.63
7611.02	62.99	27.17	10.3	2.42	7649.17	88.24	1.47	11.65	2.45
7611.1	63.31	26.7	10.03	2.56	7649.25	81.4	8.46	11.63	2.45
7611.18	65.01	24.71	12.18	2.57	7649.33	76.1	11.3	7.97	2.67
7611.27	61.75	28.92	11.79	2.35	7649.42	70.84	11.3	9.3	2.24
7611.35	64.85	31.46	11.58	2.55	7649.5	63.77	11.3	7.87	2.24
7611.43	62.66	37.44	11.26	2.47	7649.58	59.87	13.35	7.58	2.34
7611.52	64.71	37.44	10.47	2.48	7649.67	54.68	9.09	8.93	2.47
7611.6	65.14	32.77	10.76	2.30	7649.75	38.22	10.59	10.08	2.31
7611.68	66.62	34.49	11.28	2.40	7649.83	30.67	12.59	6.69	2.21
7611.77	63.91	34.56	10.73	2.24	7649.92	27.48	10.3	6.78	2.02
7611.85	60.11	34.56	11.05	2.10	7650	19.61	11.87	3.46	1.69
7611.93	62.26	32.19	11.46	1.99	7650.08	12.86	11.87	3.21	1.76
7612.02	62.69	30.62	12.41	1.97	7650.17	7.44	11.87	9.25	1.76
7612.1	66.25	33.04	13.36	2.07	7650.25	3.66	4.69	10.89	1.53
7612.18	59.84	31.76	10.99	2.21	7650.33	1.55	4.58	11.07	1.53
7612.27	51.85	31.61	9.65	2.30	7650.42	0.15	3.59	11.51	0.75
7612.35	50.87	27.75	9.73	2.40	7650.5	0.15	3.59	10.67	0.83
7612.43	45.81	20.24	11.41	2.20	7650.58	2.57	3.2	10.9	0.57
7612.52	41.59	16.42	11.93	2.18	7650.67	2.57	5.19	10.82	0.32
7612.6	34.33	16.83	10.86	2.38	7650.75	2.57	5.19	9.56	0.32
7612.68	35.56	16.21	11.65	2.07	7650.83	2.57	4.52	10.43	0.32
7612.77	25.95	4.92	11.12	1.72	7650.92	2.57	9.44	10.2	0.3
7612.85	20.79	4.92	8.35	1.78	7651	5.9	11.95	9.45	0.39
7612.93	21.53	8.76	7.47	1.46	7651.08	5.9	11.95	9.61	0.33
7613.02	20.08	8.66	9.14	1.38	7651.17	5.9	18.38	8.88	0.44
7613.1	12.28	8.48	3.88	1.38	7651.25	5.9	18.38	2.79	0.51
7613.18	7.48	4.67	3.92	1.05	7651.33	5.9	21.81	3.18	0.51
7613.27	7.48	3.05	5.42	1.04	7651.42	5.91	21.29	5.29	0.51
7613.35	8.48	5.73	3.53	0.80	7651.5	5.9	20.63	5.29	0.59
7613.43	13.41	9.72	2.59	0.84	7651.58	4.67	20.12	5.66	0.47
7613.52	17.37	11.39	2.6	1.22	7651.67	3.49	15.27	8.92	0.47
7613.6	17.51	11.19	3.19	1.16	7651.75	3.49	18.96	8.56	0.47
7613.68	16.96	9.84	5.62	1.04	7651.83	4	18.96	9.2	0.5
7613.77	20.88	9.84	4.51	1.04	7651.92	4	24.73	9.2	0.5
7613.85	23.76	9.84	10.3	1.03	7652	5.33	22.37	9.2	0.72
7613.93	26.77	4.93	11.33	0.89	7652.08	1.99	21.2	8.85	0.8
7614.02	30.84	4.93	10.34	0.89	7652.17	2	21.13	9.66	0.91
7614.1	33.77	6.43	12.79	0.89	7652.25	1.99	18.26	9.56	0.77
7614.18	36.32	10.51	14.54	1.00	7652.33	2	10.06	9.72	0.73
7614.27	41.26	15.53	14.5	0.86	7652.42	1.99	8.89	8.9	0.73
7614.35	42.97	15.53	17.7	0.86	7652.5	2	11.44	5.6	0.73
7614.43	42.33	5.89	17.7	1.24	7652.58	2	11.3	6.26	0.54
7614.52	38.63	18.78	16.98	0.88	7652.67	1.99	13.58	5.19	0.62

7614.6	37.27	21.03	15.64	0.86	7652.75	2	10.73	3.59	0.62
7614.68	42.32	25.44	14.03	1.32	7652.83	2.47	14.43	2	0.76
7614.77	41.65	25.44	15.69	1.28	7652.92	2.47	12.8	2.85	0.76
7614.85	43.11	26.49	15	1.33	7653	2.47	3.96	3.32	0.65
7614.93	40.82	28.65	14.41	1.33	7653.08	1.15	5.14	2.87	0.74
7615.02	38.9	28.65	14.44	1.53	7653.17	1.15	6.91	2.07	0.72
7615.1	39.96	28.65	13.39	1.75	7653.25	1.15	6.74	2.45	0.61
7615.18	38.09	22.57	12.61	1.79	7653.33	1.15	11.98	2.45	0.7
7615.27	45.21	22.83	12.81	1.80	7653.42	1.15	18.01	2.14	0.73
7615.35	44.39	25.14	9.98	2.05	7653.5	1.15	18.01	1.64	0.82
7615.43	42.64	28.95	8.89	1.92	7653.58	1.15	17.71	1.1	0.91
7615.52	41.57	28.44	9.29	2.02	7653.67	1.15	17.71	1.18	1.09
7615.6	40.92	20.1	9.88	1.84	7653.75	1.15	20.42	1.27	1.01
7615.68	35.57	17.11	9.98	1.69	7653.83	0.16	19.96	1.95	1.07
7615.77	34.91	27.57	9.25	1.39	7653.92	0.16	20.78	1.63	1.04
7615.85	30.08	31.39	6.18	1.39	7654	0.15	19.67	1.68	1.17
7615.93	28.57	40.25	3.85	1.42	7654.08	0.92	22.89	1.59	1.37
7616.02	25.71	47.13	2.34	1.42	7654.17	0.92	19.9	1.57	1.49
7616.1	22.29	48.16	1.72	1.21	7654.25	0.92	19.37	1.21	1.4
7616.18	20.69	52.75	1.75	1.11	7654.33	0.99	13.55	1.4	1.42
7616.27	13.7	51.81	1.39	1.09	7654.42	1.06	10.64	1.66	1.55
7616.35	11.32	49	0.91	1.11	7654.5	1.16	13.28	2.01	1.55
7616.43	6	49.28	0.99	1.26	7654.58	1.28	12.17	2.55	1.68
7616.52	8.15	55.01	0.98	1.38	7654.67	1.43	16.61	3.03	1.83
7616.6	8.85	55.06	1.04	1.55	7654.75	1.63	9.57	4.27	1.76
7616.68	13.01	53.26	1.12	1.64	7654.83	1.9	8.27	1.71	2.08
7616.77	13.52	52.3	0.96	1.81	7654.92	2.29	12.32	2.58	1.97
7616.85	13.52	49.24	0.96	1.81	7655	2.9	15.54	1.71	2.07
7616.93	12.53	47.22	1.49	1.74	7655.08	4	13.91	0.19	2.17
7617.02	11.76	36.28	2.67	1.78	7655.2	0.17	0.2	0.12	0.16
7617.1	14.04	37.61	2.67	2.20					
7617.18	13.49	41.88	2.64	2.10					
7617.27	15.75	42.19	3.76	2.22					
7617.35	14.23	42.19	5.68	2.15					
7617.43	13.5	42.19	4.73	1.94					
7617.52	13.5	36.89	4.95	1.84					
7617.6	11.52	33.27	4.95	1.30					
7617.68	11.44	31.39	7.31	1.08					
7617.77	11.33	31.37	11.28	0.89					
7617.85	10.82	22.42	12.28	0.89					
7617.93	14.96	20.49	11.05	1.19					
7618.02	15.07	19.09	12.14	1.15					
7618.1	16.38	22.43	11.25	0.73					
7618.18	18.57	9.21	12.77	0.95					
7618.27	19.81	25.77	11.32	1.10					
7618.35	21.7	20.88	11.87	0.77					
7618.43	26.38	23.5	10.82	0.91					
7618.52	26.37	23.19	12.2	0.99					
7618.6	35.14	22.9	12.42	0.93					
7618.68	36.01	26.85	12.56	0.93					
7618.77	33.89	26.85	11.34	1.16					
7618.85	32.54	39.76	7.51	1.17					
7618.93	35.79	38.51	9.61	1.21					
7619.02	35.68	38.51	9.02	1.08					
7619.1	36.23	48.98	9.02	1.05					
7619.18	35.44	53.16	7.93	0.97					
7619.27	29.95	45.87	7.93	0.98					
7619.35	29.71	43.55	6.79	0.83					
7619.43	29.43	43.55	7.57	0.75					

7619.52	29.9	50.9	5.92	0.74
7619.6	34.08	50.9	9.05	0.67
7619.68	26.88	52.07	5.11	0.79
7619.77	30.14	48.17	5.94	0.81
7619.85	33.98	45.78	5.76	0.56
7619.93	32.57	44.66	3.6	0.56
7620.02	33.25	44.66	3.67	0.54
7620.1	41.4	44.3	3.65	0.71
7620.18	45.16	35.22	6.34	0.71
7620.27	49.5	42.62	6.34	0.56
7620.35	53.11	44.99	4	1.27
7620.43	56.15	43.77	3.99	1.91
7620.52	54.94	36.37	3.7	1.91
7620.6	52.58	35.54	2.61	2.39
7620.68	59.28	35.09	2.13	2.72
7620.77	63.91	34.14	3.36	2.55
7620.85	59.71	32.32	3.68	2.59
7620.93	56.12	31.27	3.68	2.90
7621.02	52.91	31.98	5.17	2.76
7621.1	49.65	30.41	9.4	2.73
7621.18	47.63	27.93	9.28	2.96
7621.27	52.4	26.14	6.98	3.17
7621.35	57.86	20.85	9.98	3.68
7621.43	61.54	13.97	11.11	2.95
7621.52	62.4	15.27	12.12	2.51
7621.6	62.73	20.01	13.21	2.18
7621.68	67.52	18.99	14.13	1.80
7621.77	63.93	26.25	12.22	1.92
7621.85	63.36	26.35	10.89	1.92
7621.93	70.14	30.65	10.95	2.38
7622.02	71.32	25.92	11.48	2.19
7622.1	75.54	30.19	11.61	2.20
7622.18	75.76	31.22	9.1	2.10
7622.27	68.92	31.53	11.59	1.88
7622.35	64.07	29.48	12.05	1.67
7622.43	57.76	29.48	11.05	1.81
7622.52	58.58	30.33	12.76	1.79
7622.6	59.55	35.06	11.7	1.84
7622.68	52.57	30.16	11.27	2.22
7622.77	48.73	32.77	10.59	1.98
7622.85	46.75	29.67	9.93	2.15
7622.93	50.37	38.36	10.13	2.24
7623.02	51.74	40.98	9.83	2.16
7623.1	55.79	40.98	10.45	2.36
7623.18	51.82	38.9	11.48	2.44
7623.27	54.26	38.4	9.93	2.51
7623.35	53.72	41.32	9.3	2.36
7623.43	60.03	46.18	6.66	2.43
7623.52	65.61	50.92	4.03	2.52
7623.6	58.64	53.77	3.18	2.79
7623.68	60.96	57.33	2.15	2.94
7623.77	69.86	69.22	2.74	2.99
7623.85	74.99	65.06	5.02	3.84
7623.93	97.73	67.05	10.3	3.28
7624.02	74.93	59.57	15.88	5.47

Appendix G:

Gibson Dome 1 Rock Eval Data

Weatherford LABORATORIES

TOTAL ORGANIC CARBON, PROGRAMMED PYROLYSIS DATA

UTAH GEOLOGICAL SURVEY

Well Name : Gibson Dome No. 1 | **Operator :** BS/AR | **SRA ID :** Fletch Junior | **State :** UT | **County :** Grand | **Weatherford Labs Project** CO-75804

Weatherford Labs ID	Median Depth (feet)	Formation	Sample Type	Sample Prep	*	TOC	S1	S2	S3	Tmax (°C)	**	Meas. % Ro	HI	OI	S2/S3	S1/TOC *100	PI	Notes Checks	Notes Pyrogram	Lab ID
1	5224.1	Cane Creek Shale	Core Chip	NOPR		10.30	8.55	32.45	0.96	438			315	9	34	83	0.21	TOC	ltS2sh	75804-1.RAW
2	5241.1	Cane Creek Shale	Core Chip	NOPR		9.81	3.50	16.16	0.77	442			165	8	21	36	0.18		ltS2sh	75804-2.RAW
3	5257.6	Cane Creek Shale	Core Chip	NOPR		20.80	8.52	101.91	0.63	444			490	3	162	41	0.08		n	75804-3.RAW
4	5286.7	Cane Creek Shale	Core Chip	NOPR		2.72	3.09	9.47	0.70	437			348	26	14	114	0.25		ltS2sh	75804-4.RAW
5	5293.0	Cane Creek Shale	Core Chip	NOPR		5.59	3.86	16.16	0.56	443			289	10	29	69	0.19	SRA	ltS2sh	75804-5.RAW

Notes:

"-1" – not measured or invalid value for T_{max}
TOC - Total Organic Carbon, wt. %
S1 - volatile hydrocarbon (HC) content, mg HC/ g rock
S2 - remaining HC generative potential, mg HC/ g rock
S3 - carbon dioxide content, mg CO_2/ g rock

* - comments regarding contamination
** - low S2, Tmax is unreliable
Meas. %Ro - measured vitrinite reflectance
HI - Hydrogen Index = S2 x 100 / TOC, mg HC/ g TOC
OI - Oxygen Index = S3 x 100 / TOC, mg CO_2/ g TOC
PI - Production Index = S1 / (S1+S2)

Pyrogram:
f - flat S2 peak
n - normal
ltS2sh - low temperature S2 shoulder
ltS2p - low temperature S2 peak
htS2p - high temperature S2 peak

RE - Programmed pyrolysis on Rock-Eval instrument
EXT - Extracted Rock
NOPR - Normal Preparation

Weatherford LABORATORIES

KEROGEN CONVERSION AND MATURITY (Tmax) - Gibson Dome No. 1

Company: UTAH GEOLOGICAL SURVEY

Project #: CO-75804

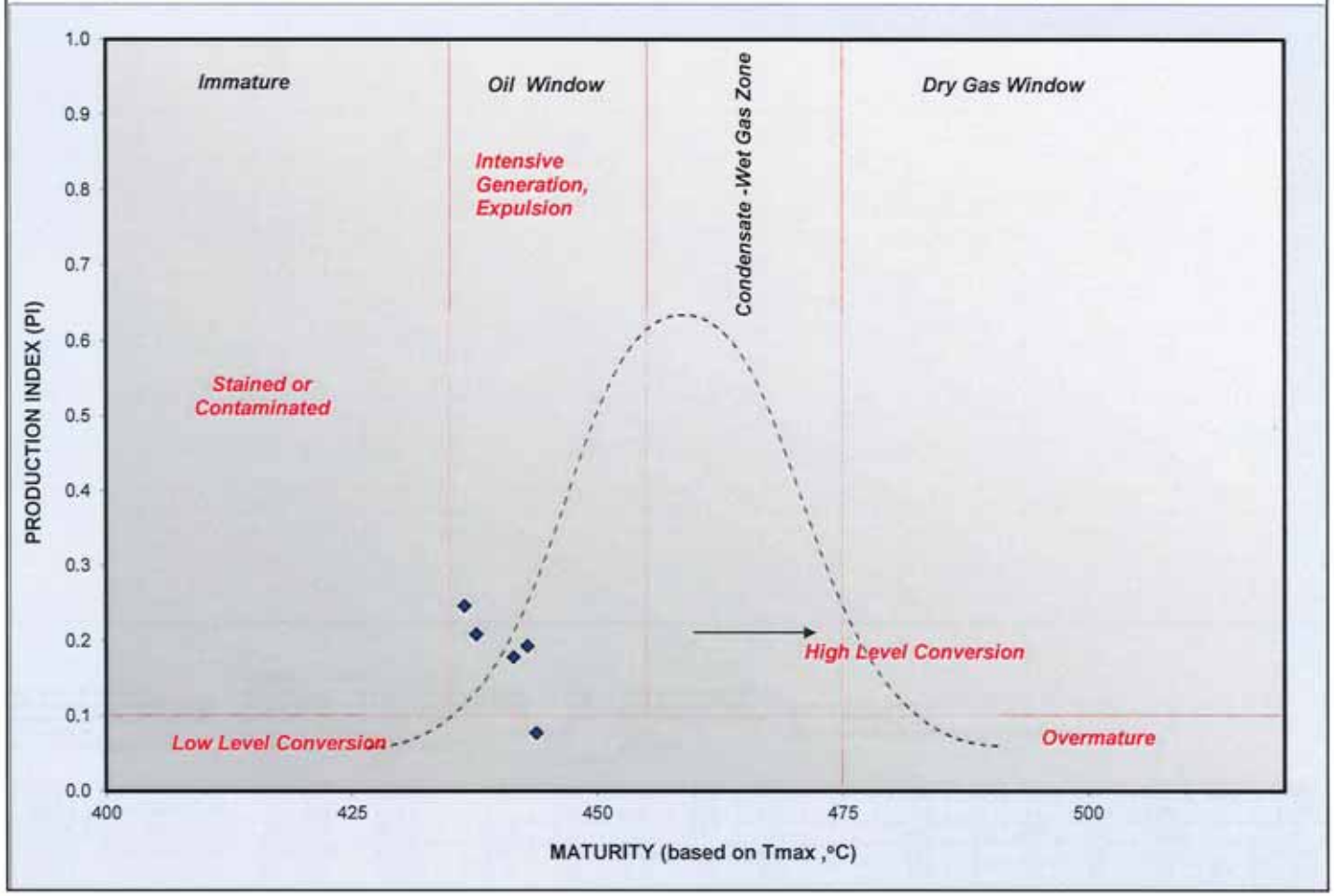

Weatherford labs, 16161 Table Mountain Parkway, Golden, CO 80403 • Phone: 720-898-8200 • Fax: 720-898-8222

Weatherford
LABORATORIES

KERogen TYPE AND MATURITY (Tmax) - Gibson Dome No. 1

Company: UTAH GEOLOGICAL SURVEY Project #: CO-75804

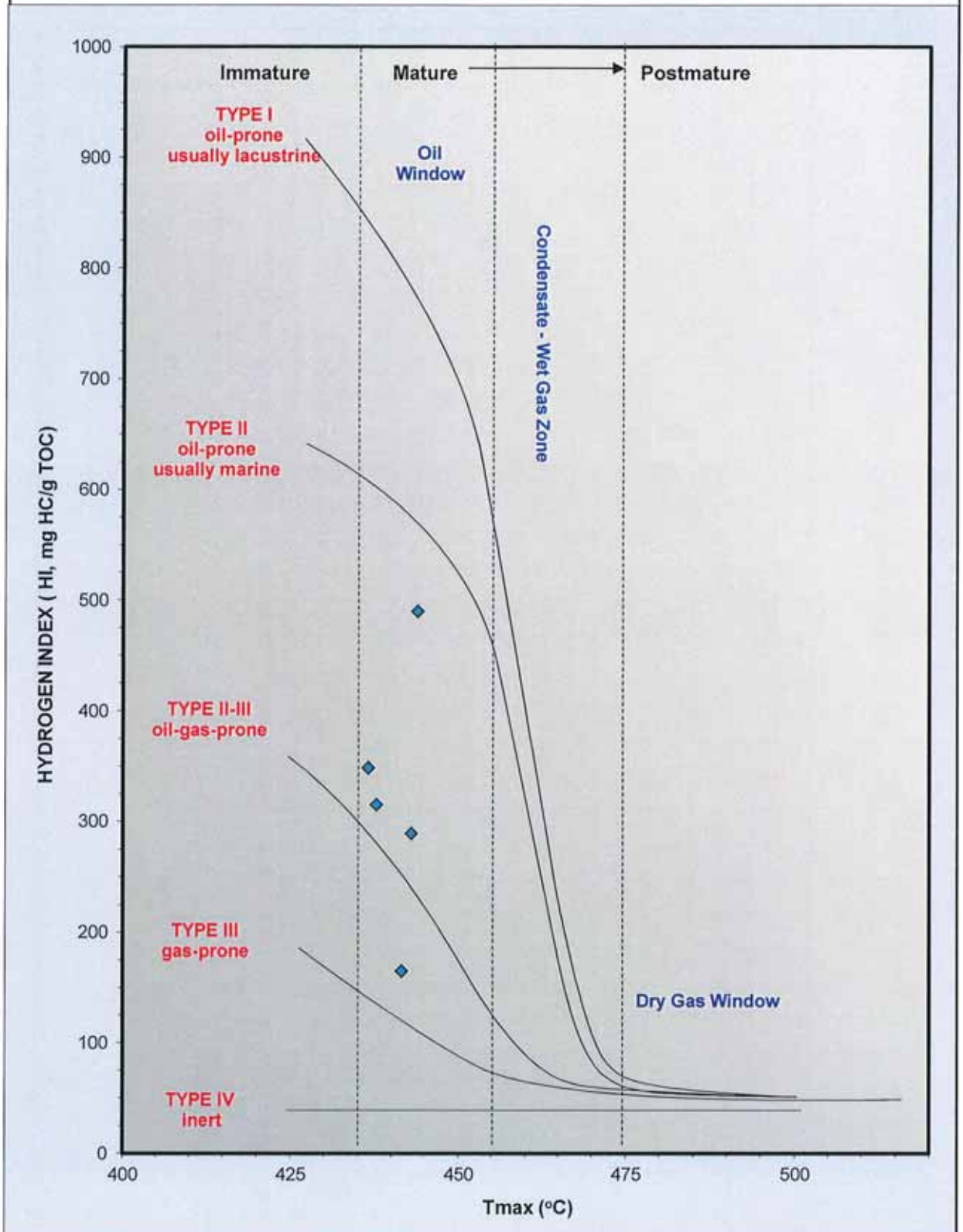

Weatherford Labs, 16161 Table Mountain Parkway, Golden, CO 80403 • Phone: 720-898-8200 • Fax: 720-898-8222

Weatherford LABORATORIES

KEROGEN TYPE - Gibson Dome No. 1

Company: UTAH GEOLOGICAL SURVEY **Project #: CO-75804**

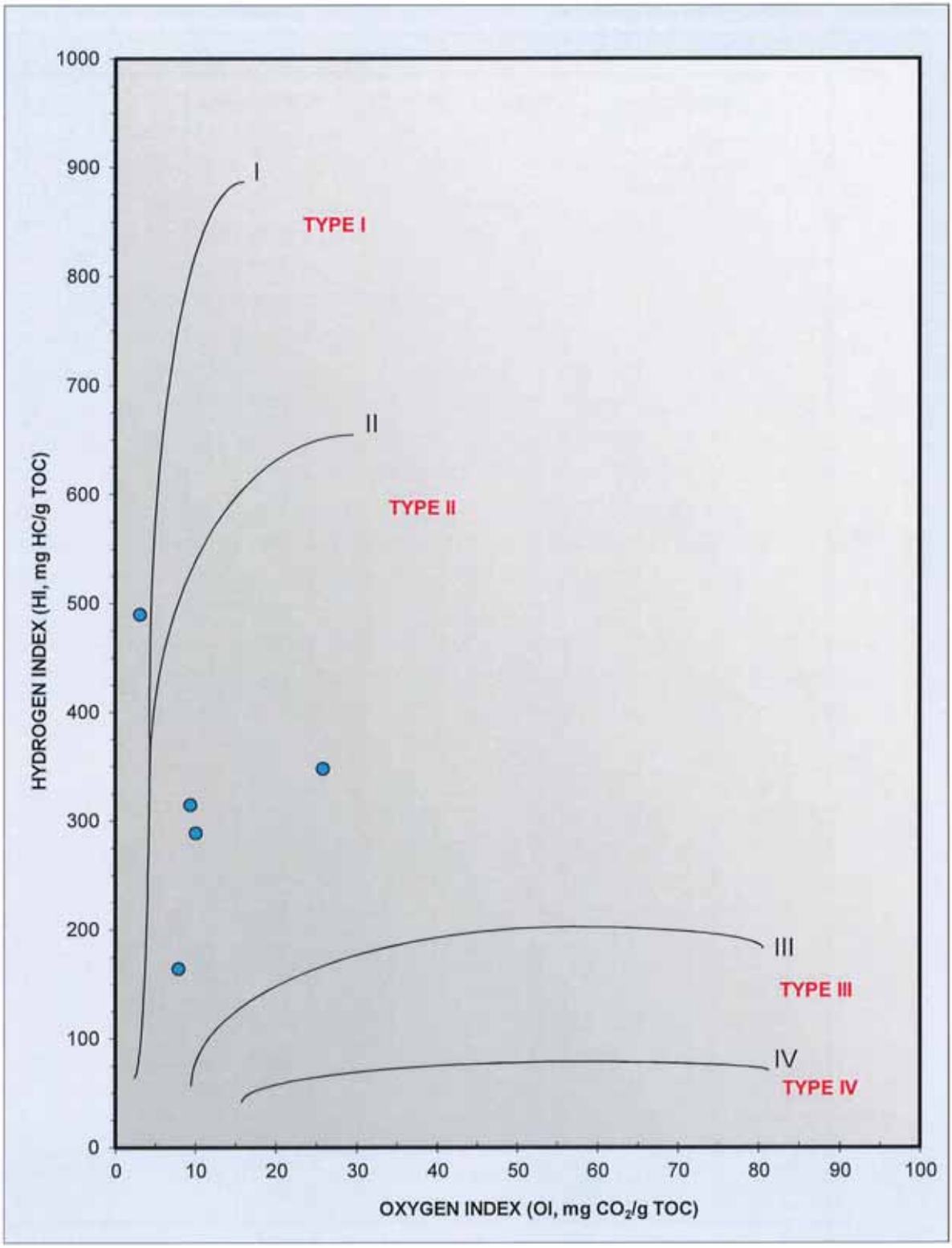

Weatherford Labs, 16161 Table Mountain Parkway, Golden, CO 80403 • Phone: 720-898-8200 • Fax: 720-898-8222

Weatherford LABORATORIES

KEROGEN QUALITY PLOT - Gibson Dome No. 1

Company: UTAH GEOLOGICAL SURVEY **Project #: CO-75804**

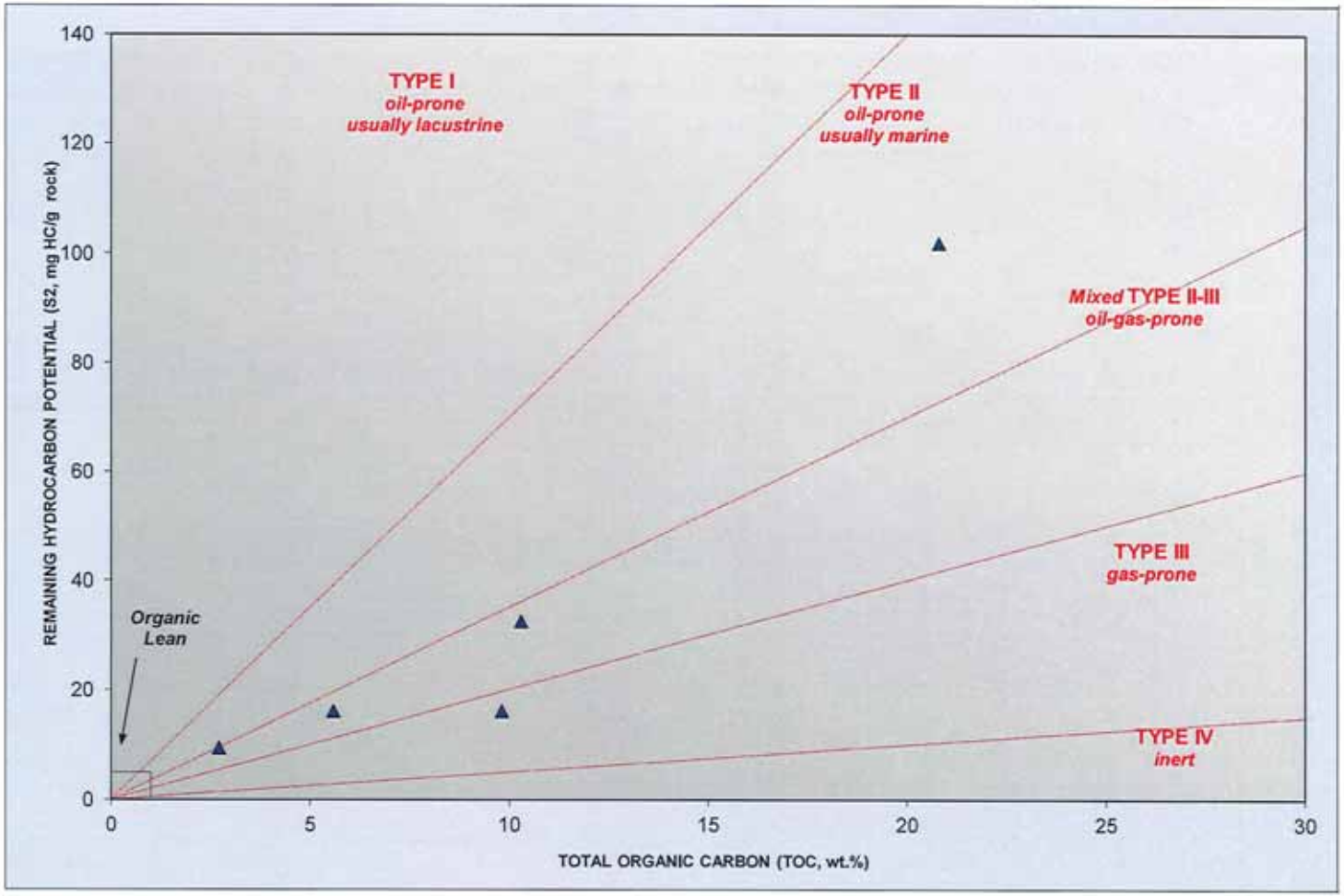

Weatherford Labs, 16161 Table Mountain Parkway, Golden, CO 80403 • Phone: 720-898-8200 • Fax: 720-898-8222

Weatherford LABORATORIES

KEROGEN QUALITY PLOT - Gibson Dome No. 1

Company: UTAH GEOLOGICAL SURVEY **Project #: CO-75804**

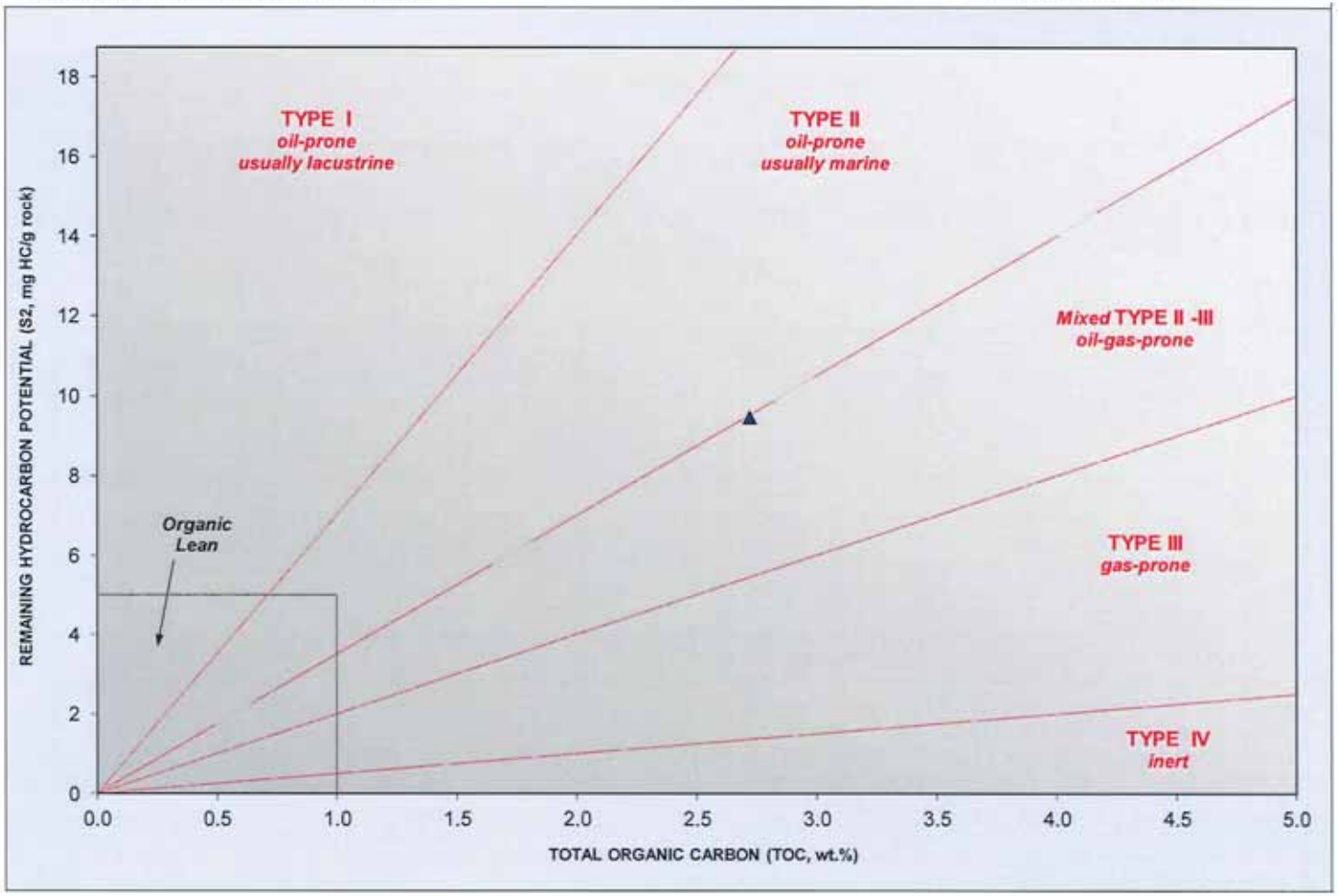

Weatherford Labs, 16161 Table Mountain Parkway, Golden, CO 80403 • Phone: 720-898-8200 • Fax: 720-898-8222

Weatherford LABORATORIES

KEROGEN QUALITY PLOT - Gibson Dome No. 1

Company: UTAH GEOLOGICAL SURVEY **Project #: CO-75804 / CO-75804**

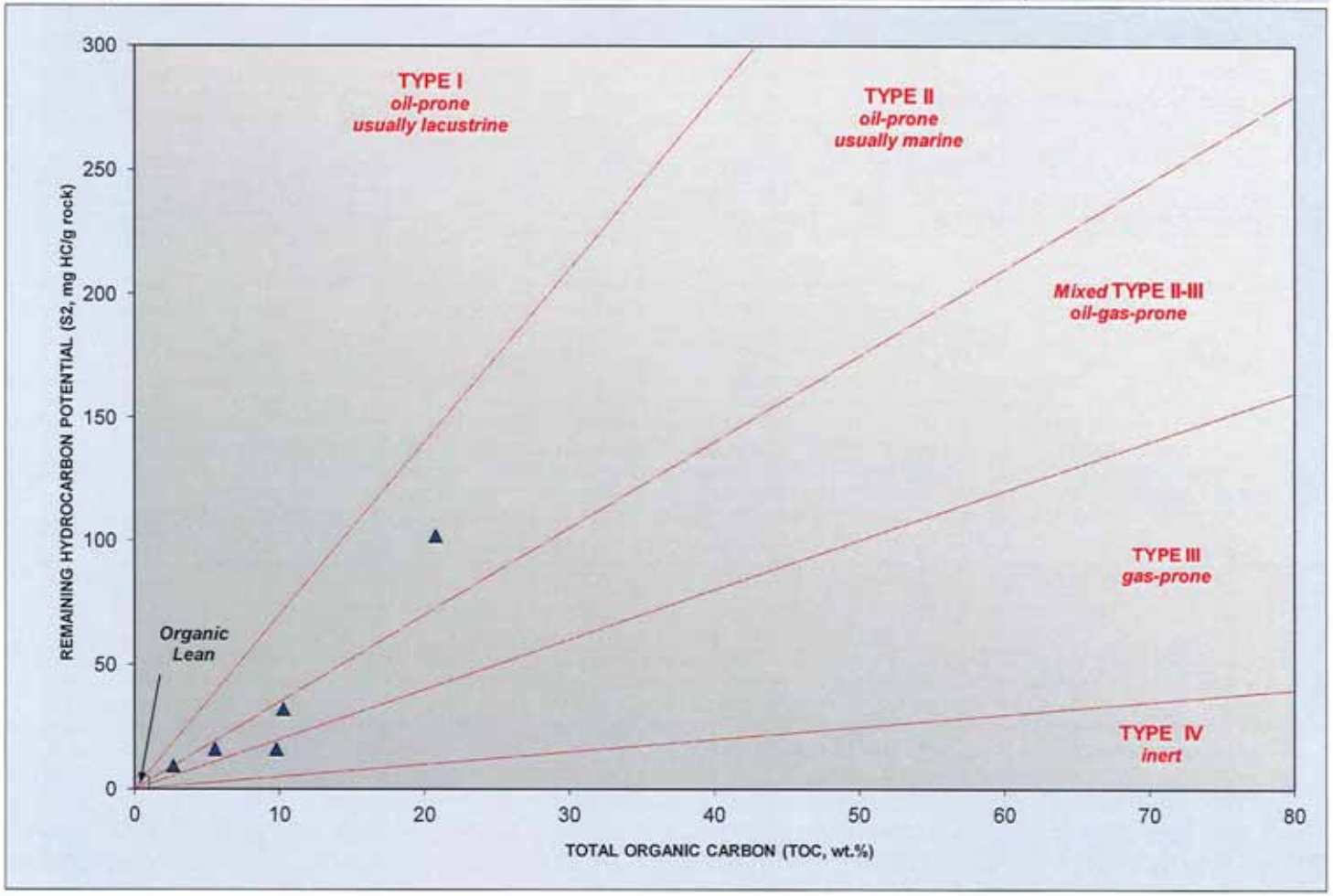

Weatherford Labs, 16161 Table Mountain Parkway, Golden, CO 80403 • Phone: 720-898-8200 • Fax: 720-898-8222

Weatherford
LABORATORIES

GEOCHEMICAL LOGS - Gibson Dome No. 1

Company: UTAH GEOLOGICAL SURVEY

Project #: CO-75804

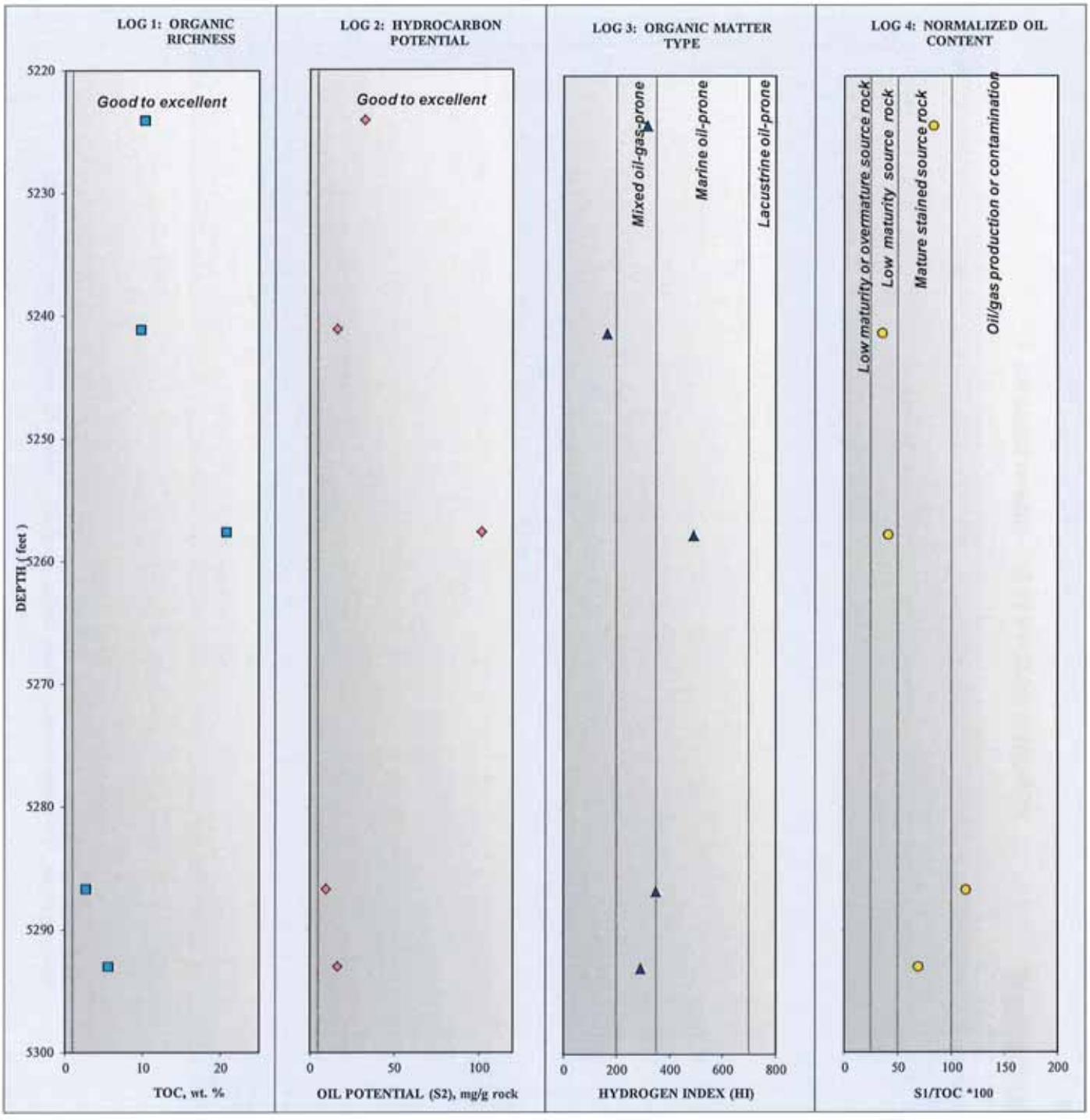

Weatherford Labs, 16161 Table Mountain Parkway, Golden, CO 80403 • **720-898-8200** • Fax: 720-898-8222

Apepndix H:

Fluid Inclusion Report by Joseph Moore, EGI

A FLUID INCLUSION INVESTIGATION OF SELECTED SAMPLES FROM THE CANE CREEK OIL FIELD, UTAH

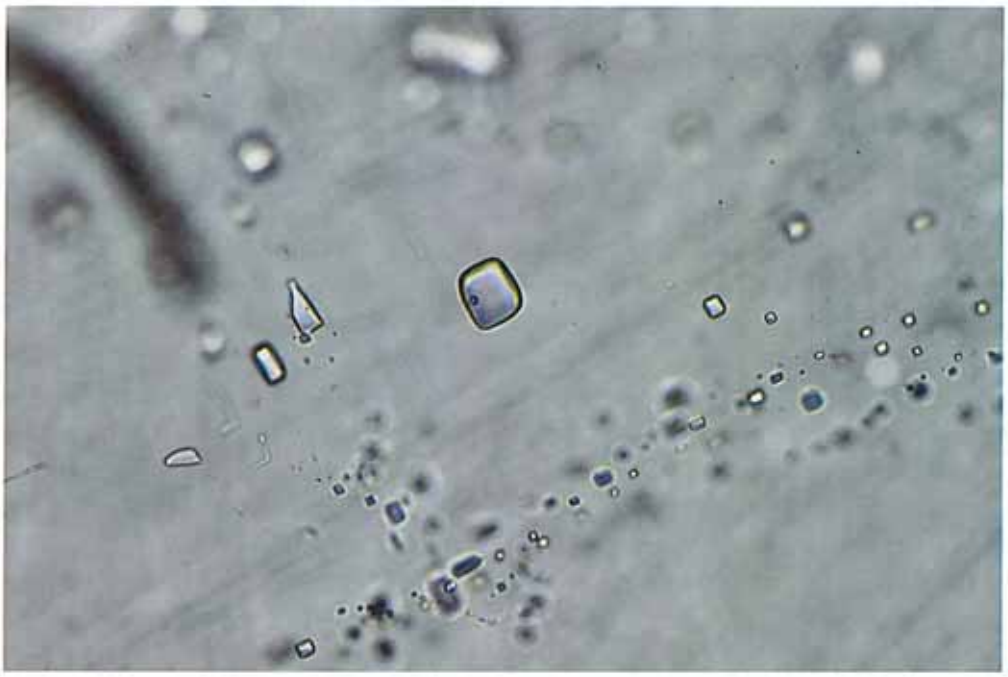

Prepared for:
Utah Geological Survey
Salt Lake City, Utah

By
Dr. Joseph Moore
3685 S. Stream Side Ct.
Salt Lake City, UT 84109 USA.

March 17, 2015

Introduction

Fluid inclusion and petrographic studies were conducted on samples from three wells: CCU-26-3, CS-36-13 and REM-211H (Table 1). These samples were selected because they contain veins and pore fillings of anhydrite, dolomite and halite. The primary objectives of this work were to: 1) characterize the temperatures and salinities of the fluids responsible for mineral deposition; and 2) determine the relative timing of oil migration with respect to the deposition of the vein filling minerals. Both oil and aqueous inclusions were observed in the samples. .

Methodology

Doubly polished 2" x 3" sections of the vein samples were prepared for study. The samples were examined petrographically to identify the minerals present in the sample and characterize the fluid inclusion assemblages in terms of their host mineral, the fluid they contained (oil, aqueous liquid, gas and/or vapor) and their relative ages and origins (e.g. primary or secondary). The sections were examined under both transmitted and ultraviolet light. Although aqueous and oil inclusions can appear similar under transmitted light, oil inclusions fluoresce under ultraviolet light whereas aqueous inclusions do not. Furthermore the fluorescent color is a useful indicator of the oil's ^{o}API gravity (Burrus, 1991). Although fluid inclusions are common, relatively few two-phase aqueous inclusions of a suitable size (> ~3 micrometers) and clarity sufficient to identify phase changes during the microthermometic measurements. Few of the inclusions that were studied exceeded 8 micrometers in length.

The fluid inclusion measurements were made on a Linkam THSMG 600 heating and freezing stage equipped with a 100x objective and calibrated with synthetic fluid inclusions. The precision of the measurements is estimated to be $\pm$ 0.1°C at 0.0°C and $\pm$ 3°C at 374°C. Homogenization, ice-melting and halite dissolution temperatures were obtained on two-and three phase liquid-rich aqueous inclusions; no measurements were made on the oil or gas-rich inclusions. Upon heating, all of the aqueous inclusions homogenized to the liquid phase. With two exceptions, the inclusions yielded ice-melting temperatures <-21.2°C. Liquid was observed between -40 and -50°C. These low eutectic temperatures suggest the presence of divalent cations in the fluid, most likely Ca and Mg, in addition to Na. Salinities of these inclusions were approximated from relationships in the system H_2O-NaCl-$CaCl_2$ (Oakes and others, 1990). Salinities of inclusions with ice-melting temperatures >-21.2°C were calculated using the equation presented by Bodnar (1993). The salinity of the fluid inclusion from CCU-26-3-7420-FL that contained halite was estimated from the solubility curve presented by Shepard and others (1985). Although the dissolution temperature of halite from CS-36-13-7630.9 FL was not measured, its presence at room temperature implies a salinity >26 wt% NaCl, the saturation of halite at 20°C. The results of the temperature and salinity measurements are shown in Table 2.

Results and Discussion

All of the samples are characterized by similar mineral and fluid inclusion relationships. The veins consist of various proportions of anhydrite, dolomite and halite (Figs. 1-2). Where

halite is present, it is invariably the last mineral to have been deposited, filling the remaining open space in the veins.

Heating and freezing measurements were conducted on fluid inclusions trapped in dolomite and anhydrite and studied petrographically in halite. Both primary and secondary oil and aqueous inclusions were observed. Primary inclusions form at the time of mineral deposition. They frequently define growth zones within the crystal interiors (Fig. 3). Secondary fluid inclusion mark the locations of healed fractures. Thus they provide evidence of fluid movement after mineral deposition and vein filling (Fig. 4).

Aqueous inclusions dominate the fluid inclusion assemblages. They occur as one-phase liquid-rich inclusions, two-phase inclusions containing liquid and a small vapor bubble, and rarely three-phase inclusions containing liquid, a vapor-bubble and halite (Figs. 5-10). Homogenization temperatures of the liquid-rich inclusions ranged from 83.5° to 120°C whereas the ice melting temperatures ranged from -0.4° to -27.5°C, which correspond to salinities of 0.7 to ~30 wt% $NaCl+CaCl_2$ equivalent (Figs. 11 and 12 respectively). The halite dissolution temperature (132°C) of the inclusion from CCU-26-3-7420-FL (refer to Fig. 10) indicates an NaCl content of 29 wt%.

Oil-bearing inclusions range from light to dark brown in color and typically consist of oil and a gas bubble, although one-phase liquid oil, three-phase inclusions containing oil, gas and an aqueous liquid and gas-rich inclusions are also present (Figs. 13-14). Although it was not possible to conduct microthermometric measurements on the gas phase, measurements on gas-bearing inclusions in petroleum systems typically demonstrates that they are enriched in methane (Goldstein and Reynolds. 1994). Contemporaneous migration of water and oil is indicated by the presence of both aqueous and oil inclusions within the same growth zones, healed fractures and rarely the same fluid inclusions (Fig. 15-17). Under ultraviolet light, the oil inclusions fluoresce bright green, indicating an °API gravity of approximately 35 (Figs. 18-19).

The presence of one- and two phase aqueous inclusions with small vapor bubbles is significant. These inclusions are found in all of the vein minerals and in both primary and secondary fluid inclusion assemblages. As discussed by Goldstein and Reynolds (1994), one-phase liquid inclusions are metastable and indicative of trapping temperatures <50°C. In contrast, assemblages of two-phase inclusions imply temperatures >50°C. Figure 9 provides a good example of coexisting one- and two-phase inclusions in halite. In this sample, one-phase inclusions dominate. Although assemblages of single-phase inclusions are common, fluid inclusion assemblages consisting of two-phase liquid-rich inclusions with generally similar liquid- to vapor ratios are also found. Thus, the inclusion assemblages appear to present contradictory temperature indicators. Two common low-temperature environments can lead to the formation of fluid inclusion populations containing one- and two-phase inclusions. Inclusions formed in the vadose zone will typically contain only liquid or liquid and vapor with variable liquid to vapor ratios. However, oil migration and vein formation is unlikely in this environment and highly variable liquid to vapor ratios are commonly not observed in the same fluid inclusion assemblage. Alternatively, the fluid inclusions could have formed at low temperatures and thermally reequilibrated as the rocks were progressively buried (Bodnar, 2003). As the fluid inclusions are heated, the pressure within the inclusions will also increase. The effects of this pressure increase can range from a slight increase in the volume of the inclusion to decrepitation. The shape and size of the inclusion and the host mineral will influence the degree of reequilibration that occurs, but it is not possible to predict which inclusions will reequilibrate. In general, however, it has been observed that more of the larger inclusions will reequilibrate than

the smaller ones. Thermal reequilibration thus provides a simple explanation for the occurrence of one-and two-phase inclusions in the same assemblage. Although the measured homogenization temperatures of the fluid inclusions will not be representative of the actual conditions of trapping, the salinities of the inclusions still provide a reliable estimate of the fluid's composition.

Conclusions

1. Fluid inclusions were trapped in fracture filling dolomite, anhydrite and halite. Anhydrite and dolomite were precipitated before halite.
2. Oil migration occurred during and after vein formation. During vein formation, aqueous and oil inclusions were trapped contemporaneously in dolomite and halite. Healed fractures in dolomite containing oil inclusions suggest oil migration continued after vein formation.
3. The presence of aqueous inclusions containing only liquid suggests that mineral deposition and later fracturing occurred at temperatures of <50°C. The inclusions were subsequently thermally reequilibrated as the rocks were progressively buried and heated.
4. Oil migration and vein formation must have occurred at relatively shallow depths. Low- to moderate-thermal gradients (<~25°C/km) would imply that mineral deposition occurred at depths of less than approximately 2 km.
5. The majority of the aqueous inclusions contain liquid with a salinity of approximately 30 wt% NaCl + $CaCl_2$ equivalent. These high salinities suggest interactions with evaporites.
6. Fluorescence colors of the oil inclusions indicate they have a moderate °API gravity of approximately 35.

References

Bodnar, R.J., 2003, Reequilibration of fluid inclusions *in* Fluid Inclusions Analysis and Interpretation (eds. Samson, I., Anderson, A., and Marshall, D.,): Mineralogical Association of Canada, Short Course Series Volume 32, p. 213-231.

Burrus, R.C., 1991, Practical aspects of fluorescence microscopy of petroleum fluid inclusions *in* Luminescence microscopy: Qualitative and quantitative applications: Short Course 25 (eds. Barker, C.E., and Kopp, O), p. 1-7 SEPM (Society for Sedimentary Geology).

Goldstein, R.H., and Reynolds, T.J., 1994, Systematics of Fluid Inclusions in Diagenetic Minerals: Short Course 31, SEPM (Society for Sedimentary Geology), 199 p.

Oakes, C.S., Bodnar R.J., and Simonson, J.M., 1990, The system NaCl-CaCl2-H2O. 1. The ice liquidus at 1 atm total pressure: Geochimica Cosmochimica Acta, v. 54, p. 603-610.

Shepard, T., Rankin, A.H., and Alderton, D.H.M., 1985, A Practical Guide to Fluid Inclusion Studies: Blackie & Son Ltd. Bishopbriggs, Glasgow G64 2NZ, 239 p.

Table 1. List of samples studied. Y = yes

Well	FI Measurements	Oil Inclusions	Halite-bearing inclusions
CCU-26-3-7412.3 FL	Y		
CCU-26-3-7420-FL	Y		
CCU-26-3-7420-FL		Y	
CCU-26-3-7420-FL1			Y
CCU-26-3-7439.3-FL			
CCU-26-3-7446.6-FL		Y	
CCU-26-3-7467.7 FL			
CS-36-13-7605.4 FL	Y		
CS-36-13-7614.6 FL	Y		
CS-36-13-7630.9 FL		Y	Y
REM-211H-7437.3 FL			
REM-211H-7446.7 FL			
REM-211H-7447.78 FL	Y		
REM-211H-7456.8 FL		Y	
REM-211H-7491.3 FL	Y		

Table 2. Microthermometric data. Abbreviations: Th(°C) = homogenization temperature; Tmice (°C) ice melting temperature; wt % NaCl + $CaCl_2$ eq = salinity as weight percent NaCl + $CaCl_2$ equivalent: T (°C) halite = halite dissolution temperature; wt% NaCl = weight percent NaCl based on halite dissolution temperature; p/s primary or secondary inclusion; mineral = dol (dolomite), anhy (anhydrite).

Well	Th (°C)	Tmice (°C)	wt % NaCl + $CaCl_2$ eq	T (°C) halite	wt% NaCl	p/s	Mineral
CCU-26-3-7412.3 FL	77.5					s	dol
CCU-26-3-7412.3 FL	87.5					s	dol
CCU-26-3-7412.3 FL	72.5					s	dol
CCU-26-3-7412.3 FL	82.5					s	dol
CCU-26-3-7412.3 FL	102.5					s	dol
CCU-26-3-7412.3 FL	92.5					s	dol
CCU-26-3-7412.3 FL		-27.5	~30			s	dol
CCU-26-3-7412.3 FL		-12.5	16.4			s	dol
CCU-26-3-7412.3 FL		-22.5	27.0			s	dol
CCU-26-3-7412.3 FL		-27.5	~30			s	dol
CCU-26-3-7412.3 FL		-27.5	~30			s	dol
CCU-26-3-7420-FL		-12.5	16.4			s	dol
CCU-26-3-7420-FL		-12.5	16.4			s	dol
CCU-26-3-7420-FL		-27.5	~30			s	dol
CCU-26-3-7420-FL		-27.5	~30			s	dol
CCU-26-3-7420-FL	120.0			132.0	29	s	dol
CS-36-13-7605.4 FL	92.5					s	dol

CS-36-13-7605.4 FL	92.5					s	dol
CS-36-13-7605.4 FL	92.5					s	dol
CS-36-13-7605.4 FL	92.5					s	dol
CS-36-13-7605.4 FL	92.5					s	dol
CS-36-13-7605.4 FL	92.5					s	dol
CS-36-13-7605.4 FL	92.5					s	dol
CS-36-13-7605.4 FL	92.5					s	dol
CS-36-13-7605.4 FL	92.5					s	dol
CS-36-13-7605.4 FL	87.5					s	dol
CS-36-13-7614.6 FL	112.5	-27.5	~30			p	dol
CS-36-13-7614.6 FL	92.5	-27.5	~30			s	dol
CS-36-13-7614.6 FL	92.5	-27.5	~30			s	dol
CS-36-13-7614.6 FL	92.5	-27.5	~30			s	dol
CS-36-13-7614.6 FL	92.5	-27.5	~30			s	dol
CS-36-13-7614.6 FL	92.5	-27.5	~30			s	dol
CS-36-13-7614.6 FL	92.5	-27.5	~30			s	dol
CS-36-13-7614.6 FL	92.5	-27.5	~30			s	dol
CS-36-13-7614.6 FL	92.5	-27.5	~30			s	dol
CS-36-13-7614.6 FL		-4	6.4			s	dol
CS-36-13-7614.6 FL	97.5	-27.5	~30			s	dol
CS-36-13-7614.6 FL	87.5	-27.5	~30			s	dol
CS-36-13-7614.6 FL	83.5					s	dol
REM-211H-7447.78 FL		-22.5	27.0			p	anhy

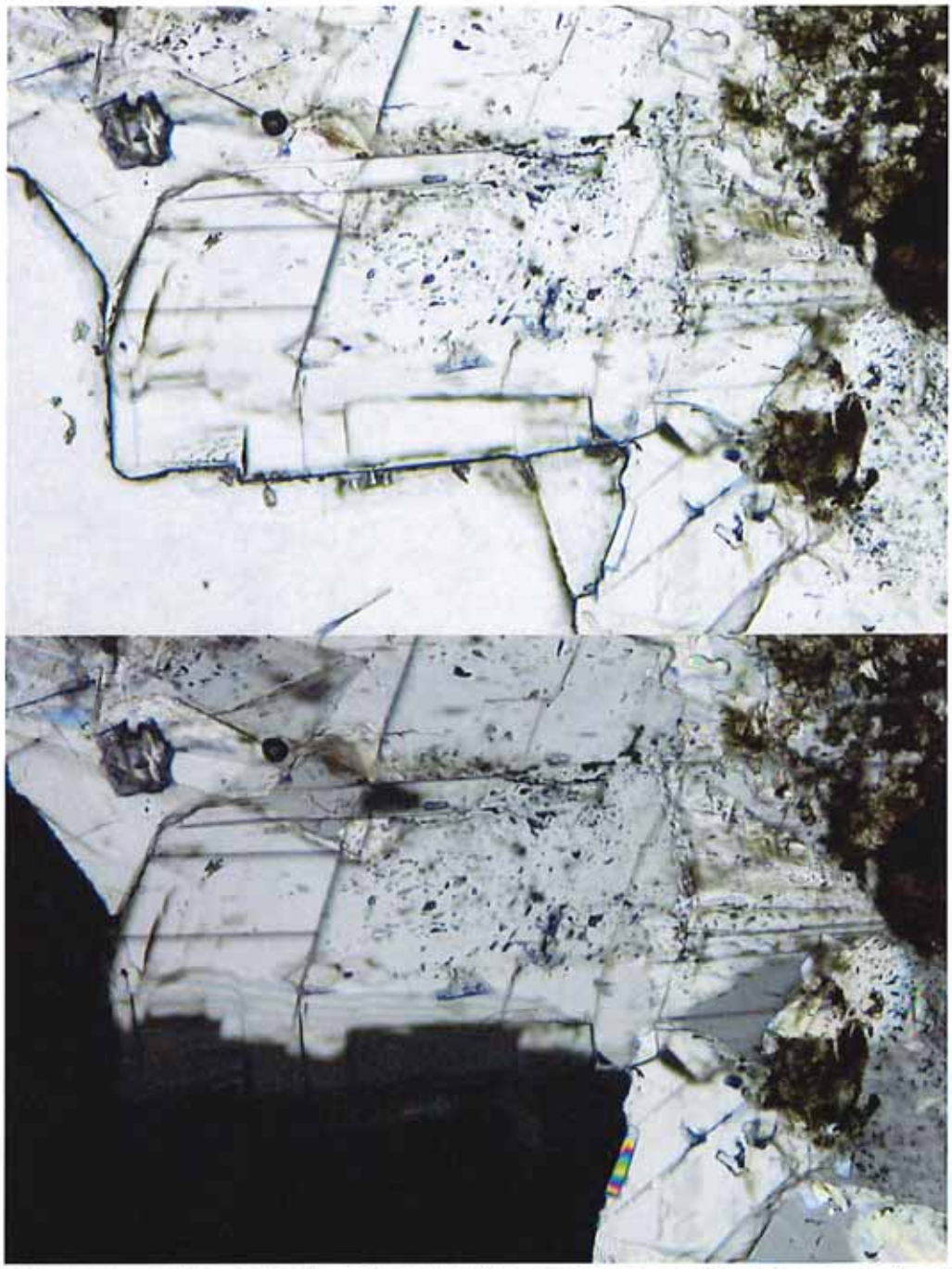

Fig. 1. Halite encapsulating dolomite. The upper image was taken under plane polarized light; the lower image under crossed nicols. The white mineral in the lower image is dolomite. The halite is black. The interiors of the dolomite crystals contain numerous small primary fluid inclusions. From CS-36-13-7630.9 FL. The field of view is 1 mm.

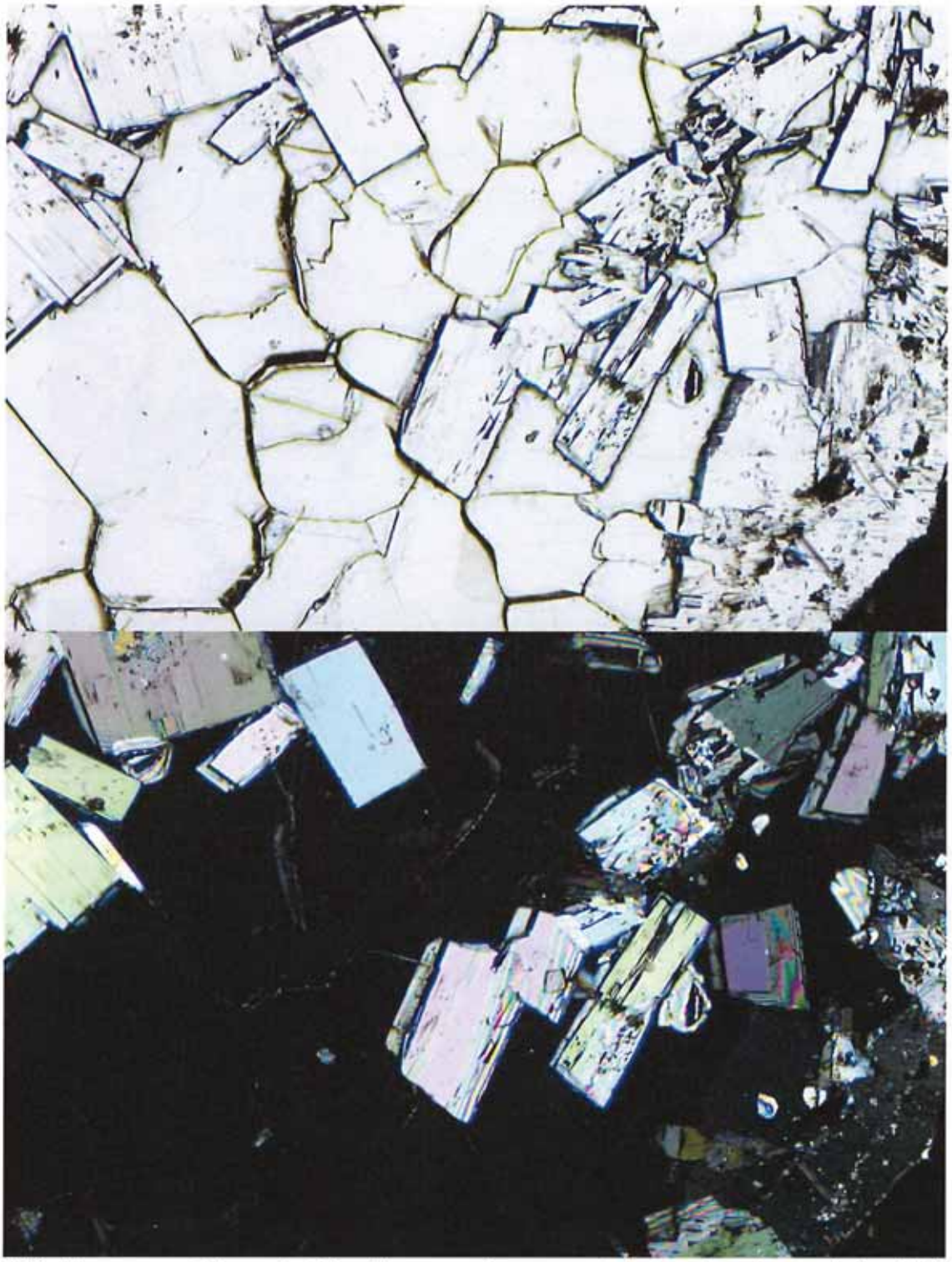

Fig. 2. Halite encapsulating anhydrite. The upper image was taken under plane polarized light; the lower image under crossed nicols. The brightly colored mineral in the lower image is anhydrite. The halite is black. From CCU-26-3-7467.7 FL. The field of view is 3 mm.

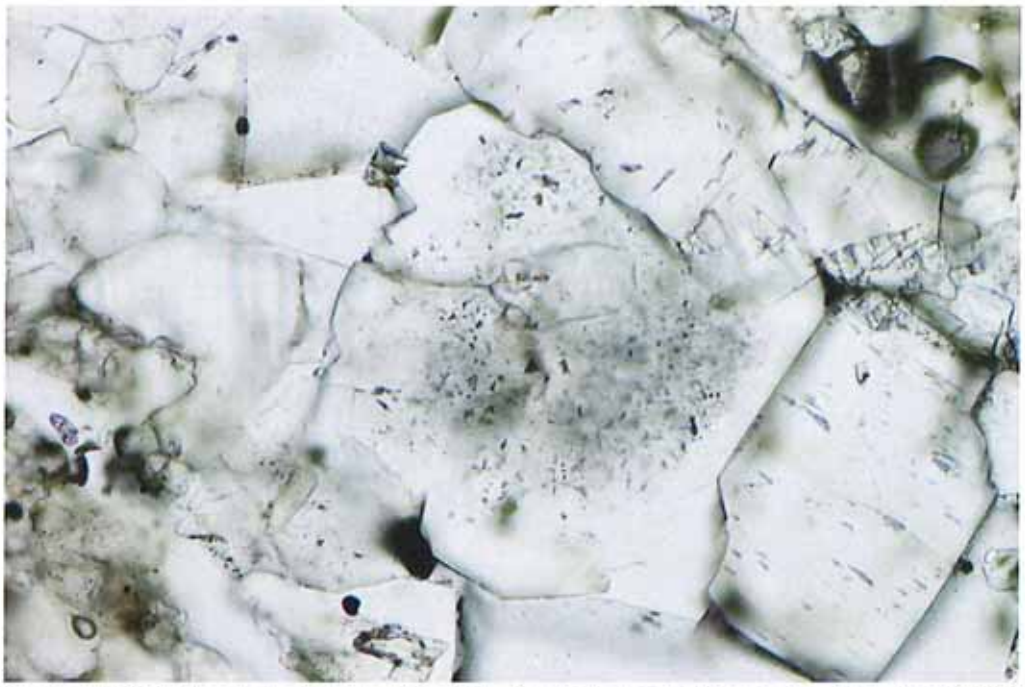

Fig. 3. Primary fluid inclusions in dolomite. The inclusions define a growth zone within the interior of the crystal. The image was taken under plane polarized light. From CCU-26-3-7439.3 FL. The field of view is 1 mm.

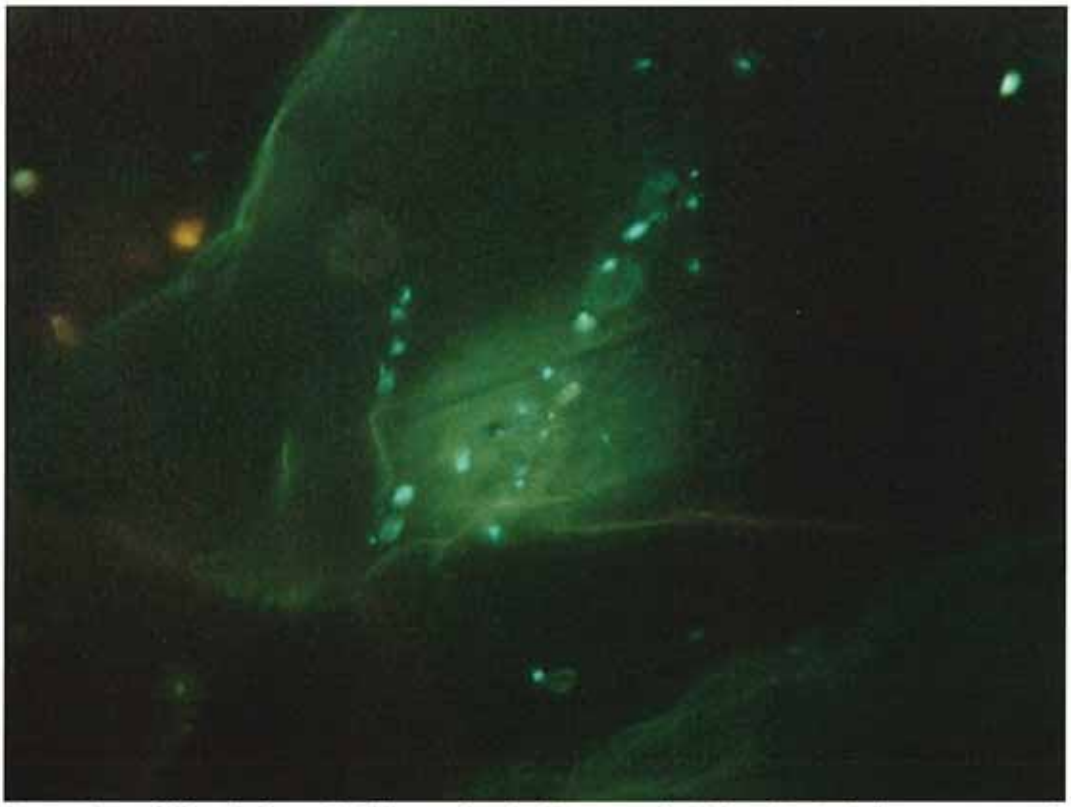

Fig. 4. Secondary oil inclusions defining a healed fracture in dolomite. The image was taken under ultraviolet light. From REM 21-1H 7491.3 FL. The field of view is 0.3 mm.

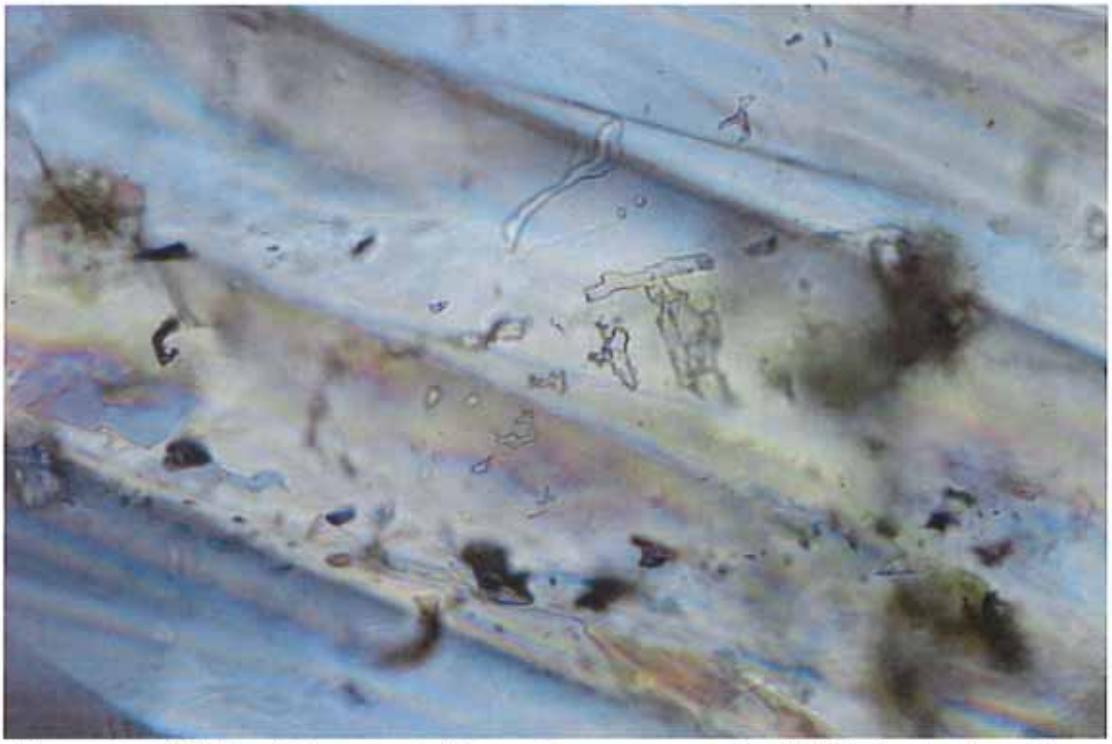

Fig. 5. Secondary fluid inclusions containing only an aqueous liquid. The host mineral is dolomite. The image were taken under crossed nicols. From CS-36-13-7630.9 FL. The field of view is 0.3 mm.

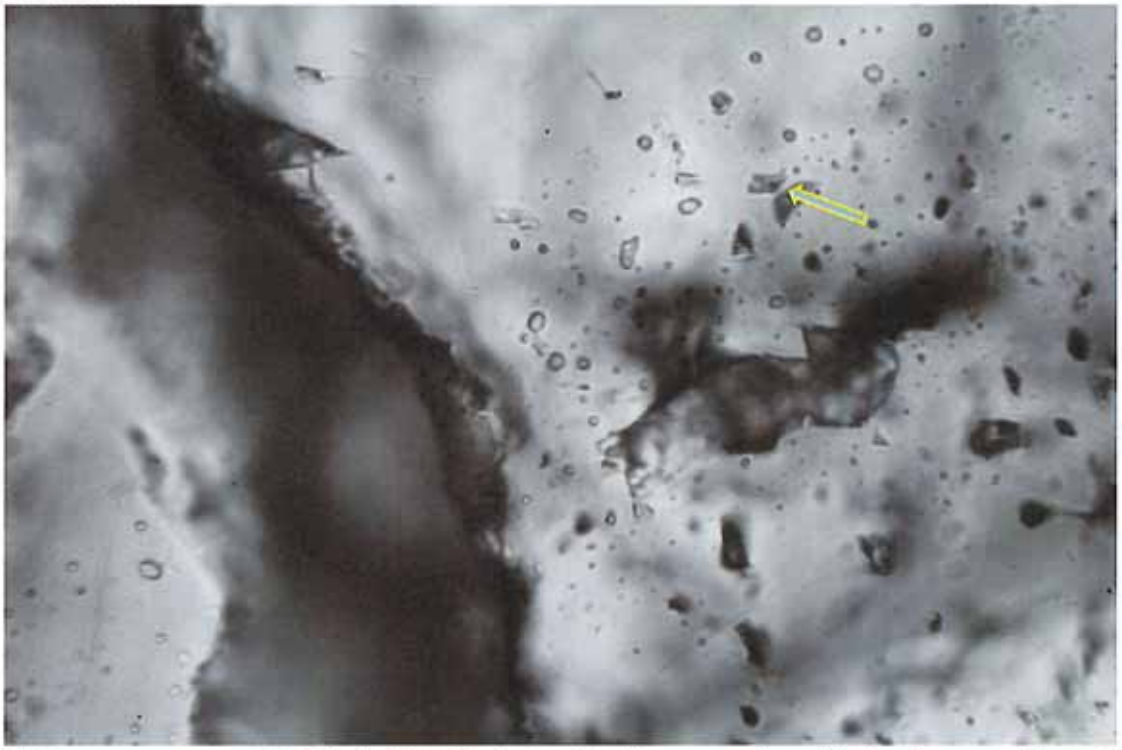

Fig. 6. Primary aqueous fluid inclusions in dolomite. The majority of inclusions contain only liquid. The arrow points to a two-phase inclusion. The image were taken under plane polarized light. From CS-36-13-7630.9 FL. The field of view is 0.3 mm.

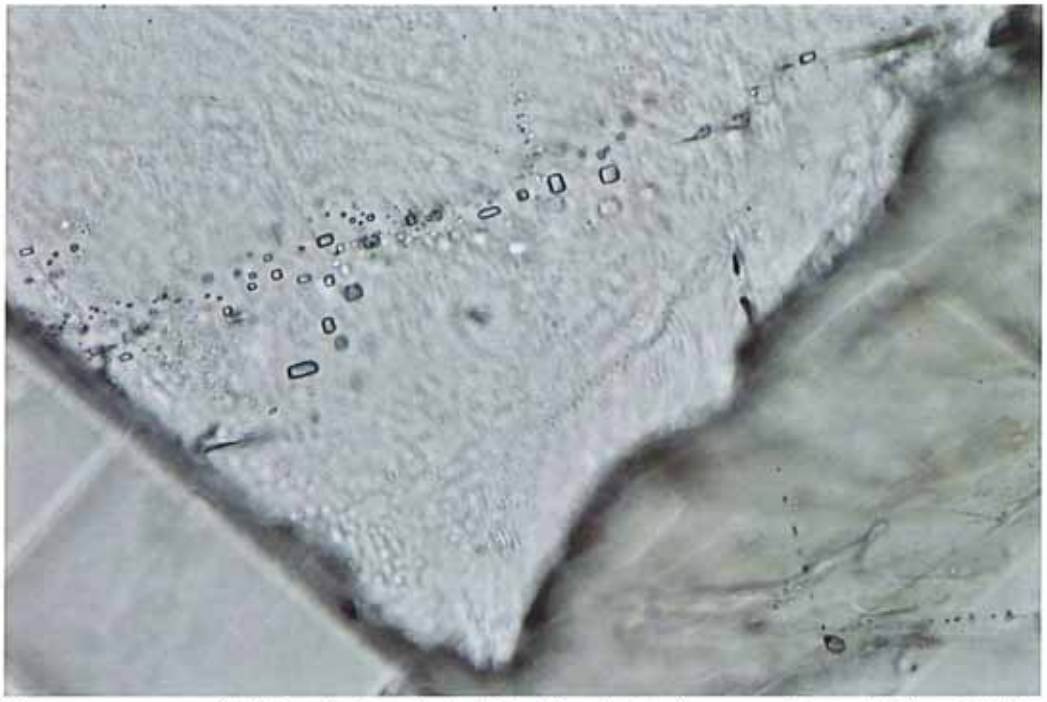

Fig. 7. Primary aqueous fluid inclusions in halite. The inclusions contain only liquid. The image was taken under plane polarized light. From CS-36-13-7630.9 FL. The field of view is 1 mm.

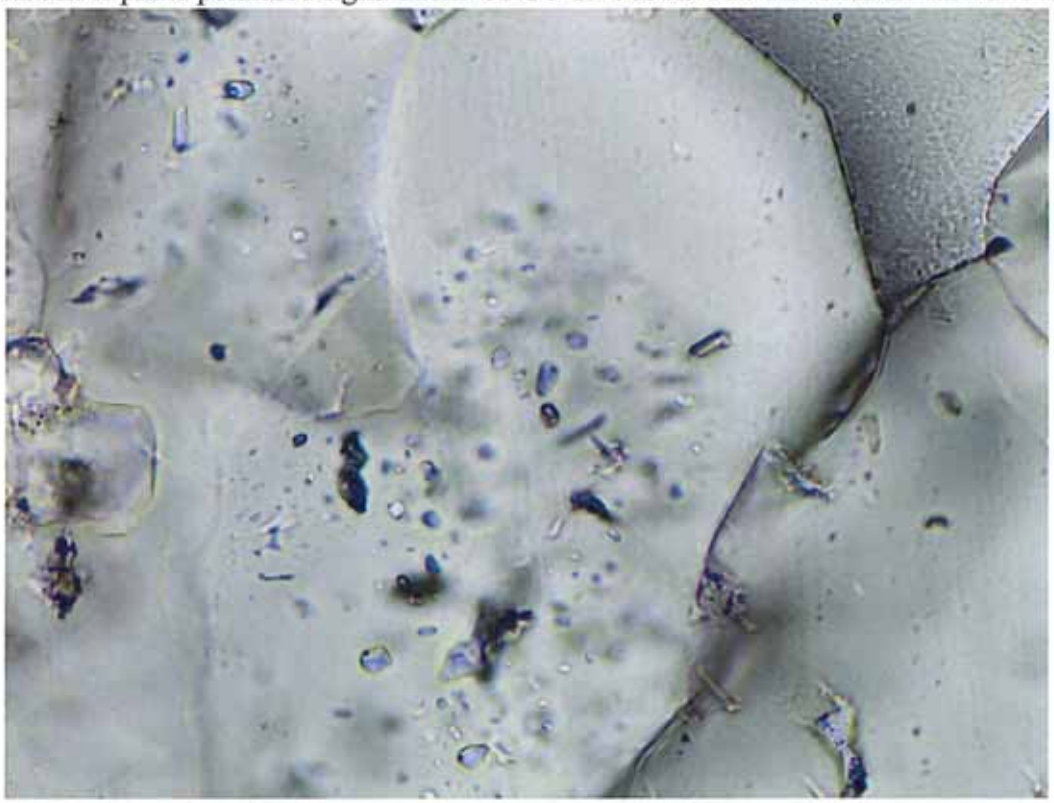

Fig. 8. One- and two-phase primary aqueous fluid inclusions in dolomite. The one-phase inclusions contain only liquid. The two-phase inclusions have small vapor bubbles and generally consistent liquid to vapor ratios. From CCU-26-3-7439.3 FL. The image was taken under plane polarized light. The field of view is 0.4 mm.

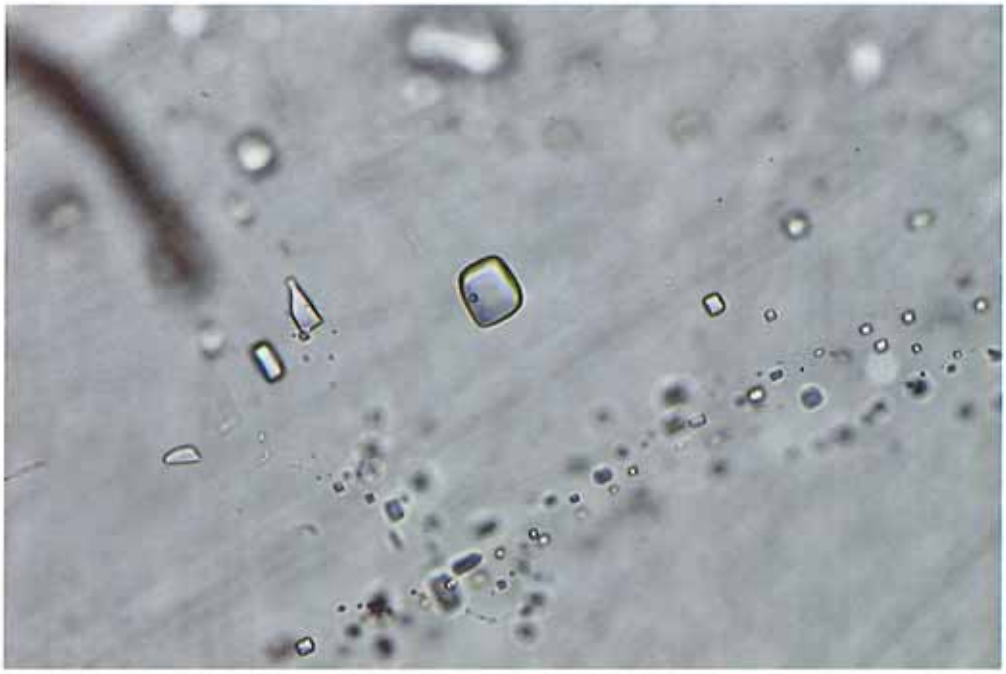

Fig. 9. One- and two-phase aqueous fluid inclusions in halite. The large central inclusion contains a small vapor bubble; the other inclusions contain only liquid. The image was taken under plane polarized light. From CS-36-13-7630.9 FL. The field of view is 1 mm.

Fig. 10. Three-phase aqueous fluid inclusion containing liquid, a vapor bubble and a halite crystal (at point of arrow). This exceptionally large inclusion is 61 micrometers long. The dissolution temperature of the halite indicates an NaCl content of 29 wt%.

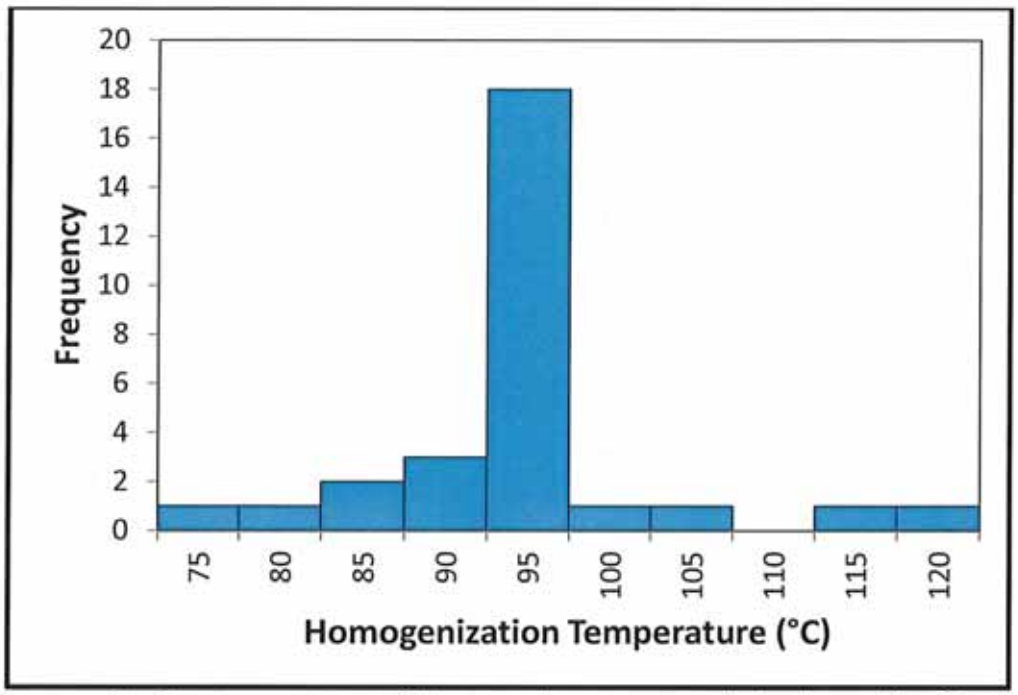

Fig. 11. Homogenization temperatures of the two-phase aqueous inclusions. All of the inclusions homogenized to the liquid phase.

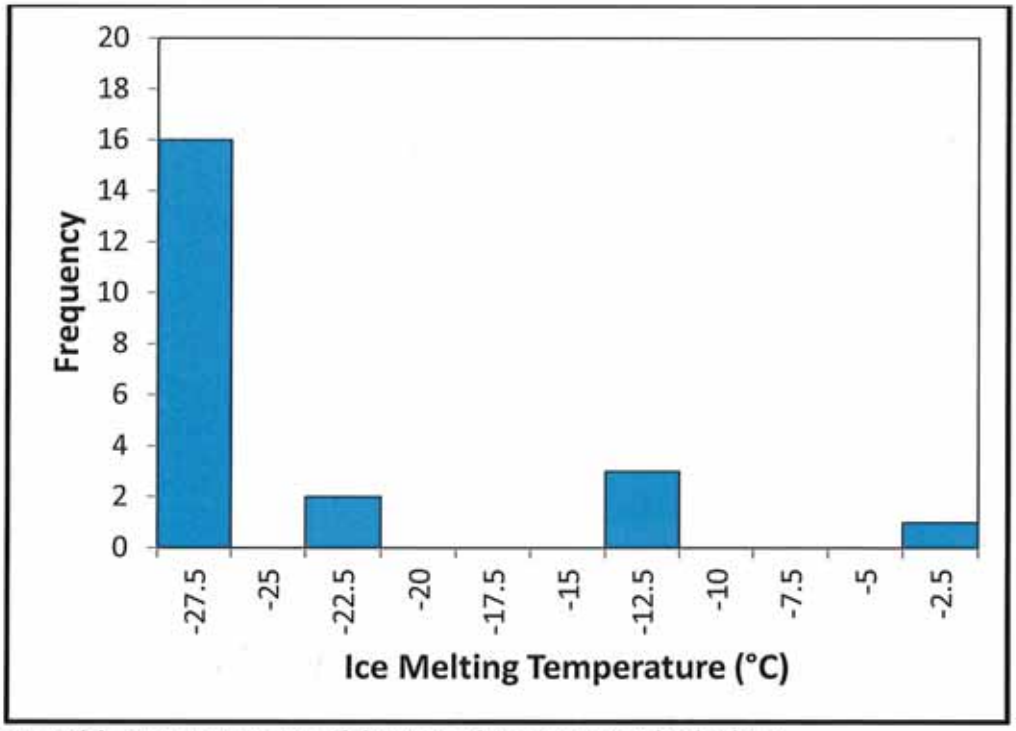

Fig. 12. Ice-melting temperatures of the two-phase aqueous inclusions.

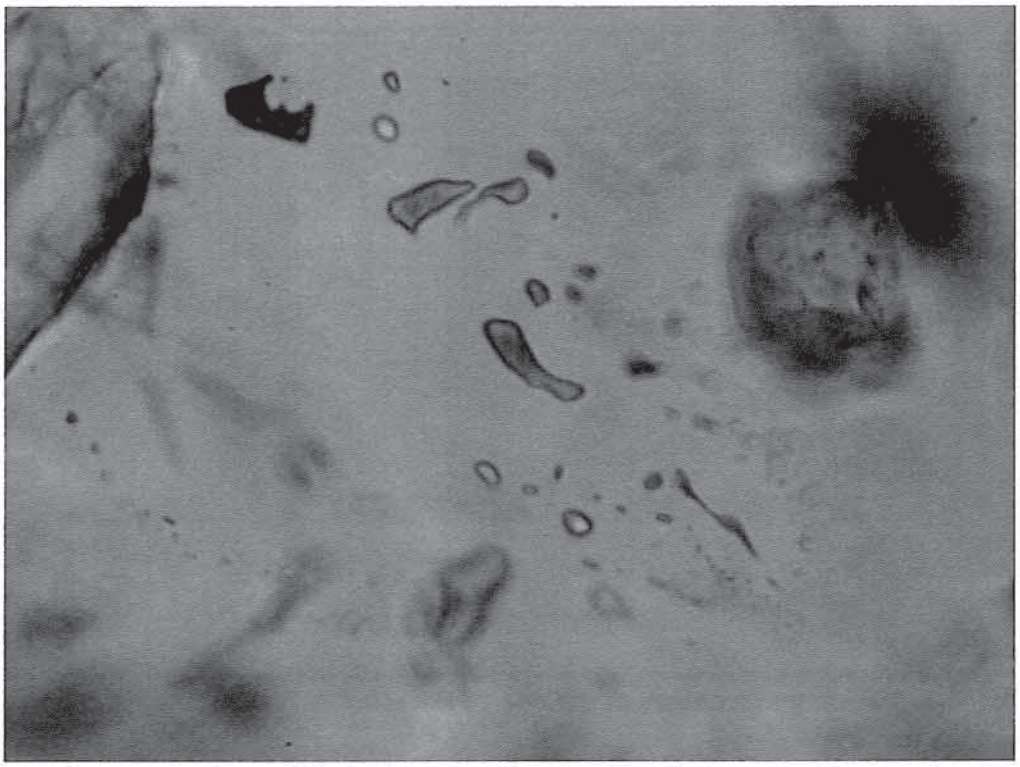

Fig 13. One-phase secondary oil inclusions in dolomite. The image was taken under plane polarized light. From CS-36-13-7630.9 FL. The field of view is 0.3 mm.

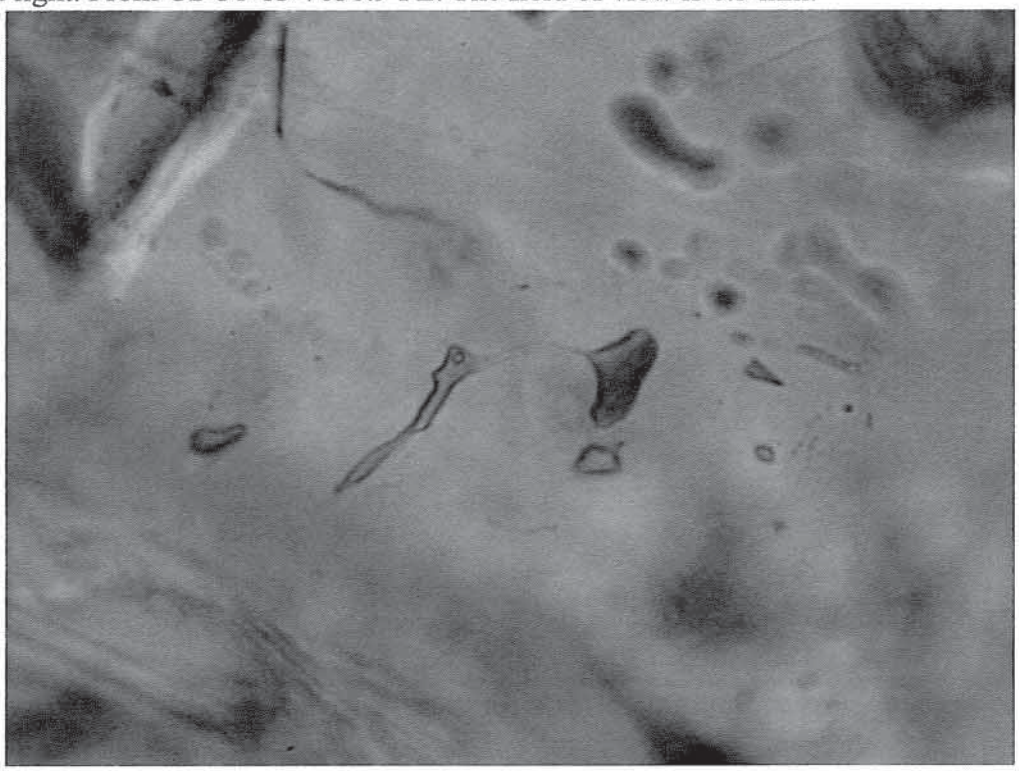

Fig 14. One-and two-phase secondary oil inclusions in dolomite. The central inclusion contains a small vapor bubble. The image was taken under plane polarized light. From CS-36-13-7630.9 FL. The field of view is 0.3 mm.

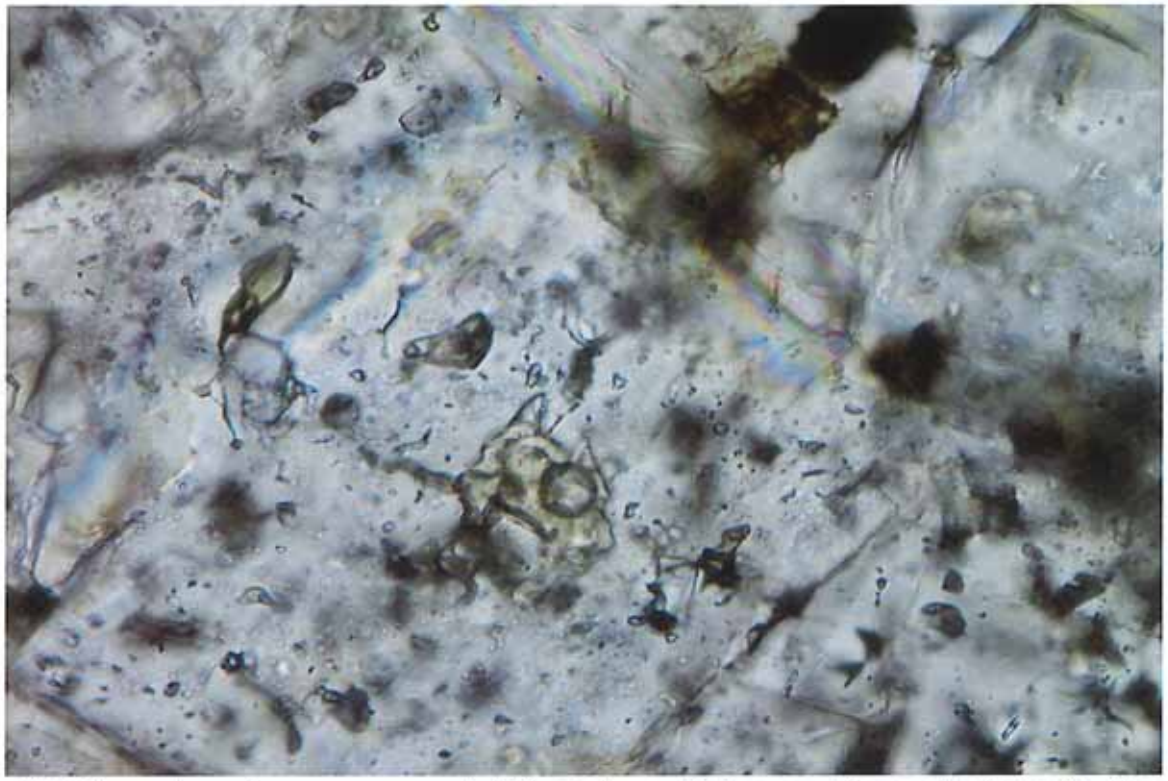

Fig. 15. Primary two-phase aqueous and oil inclusions within a growth zone in dolomite. The image was taken under plane polarized light. CS-36-13-7630.9 FL. The field of view is 0.3 mm.

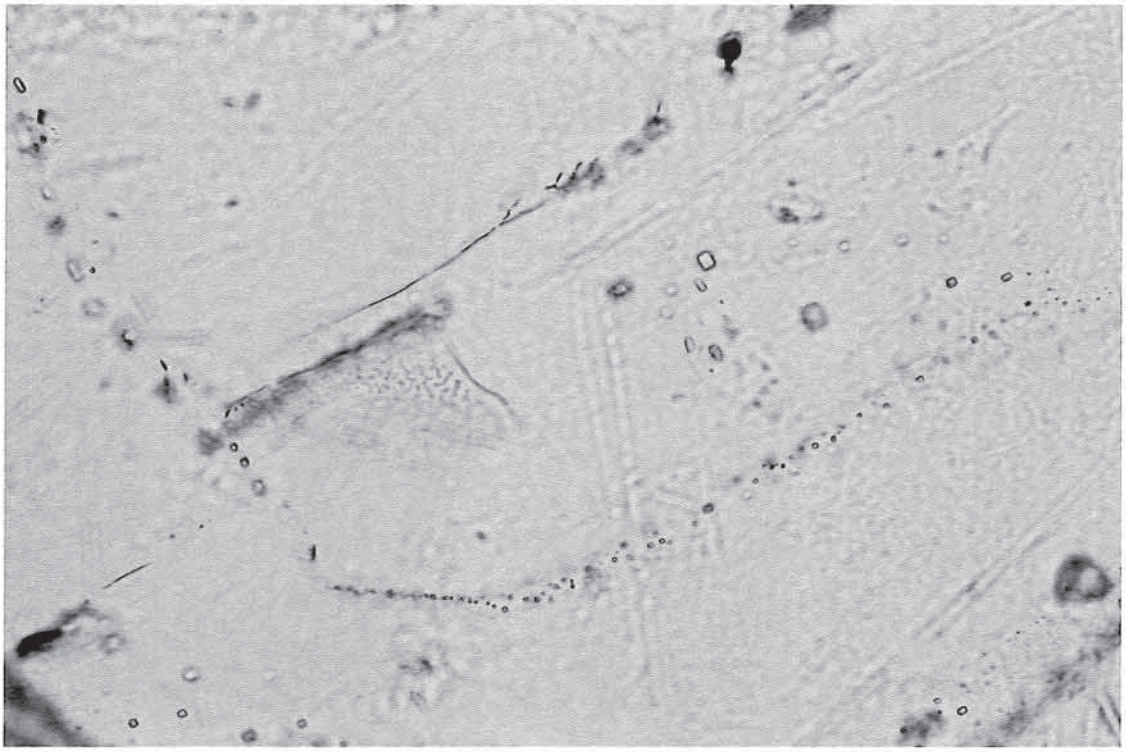

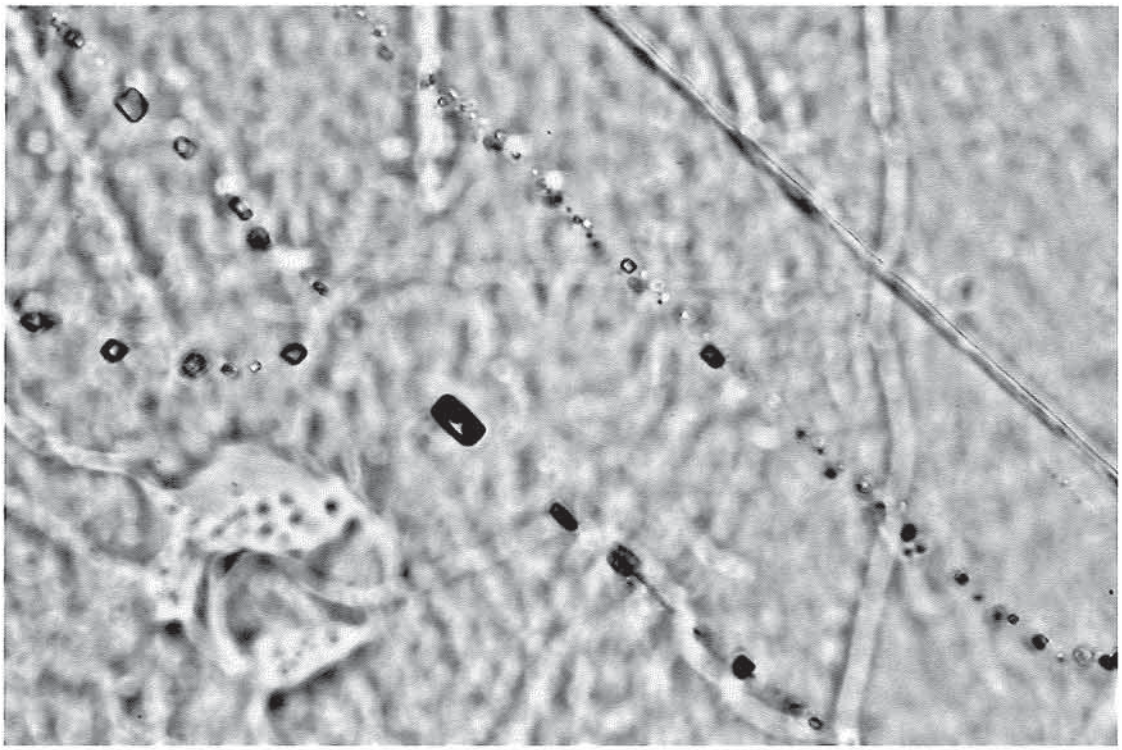

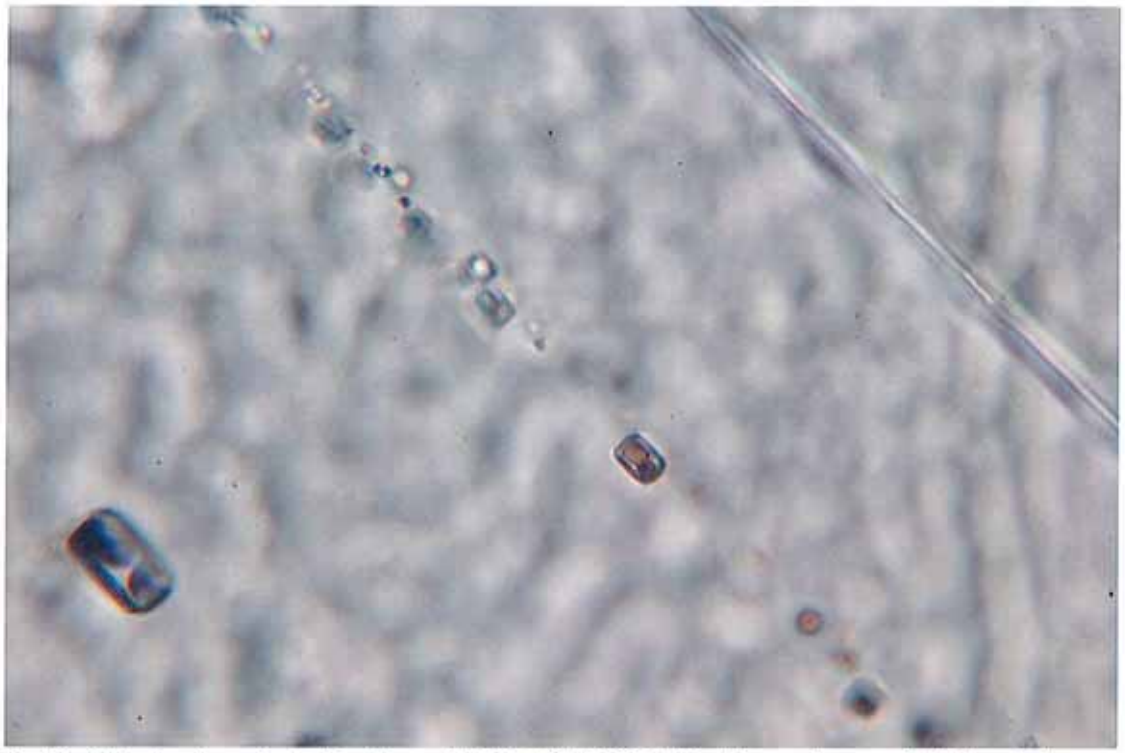

Fig. 16. Fluid inclusions in halite from CS-36-13-7630.9 FL. Top: primary fluid inclusions trapped along a growth zone. The large primary inclusions right of center contain only aqueous liquid. Field of view is 0.4 mm. Middle: Inclusions within the growth zone. The brown inclusions contain oil. The large one-phase clear inclusions in the upper left contain only aqueous liquid. Field of view is 0.4 mm. Bottom: Close-up of fluid inclusions in the central part of the middle image. The inclusions in the center and left side of the image contain aqueous liquid (clear fluid), oil and gas. The field of view is 0.3 mm. All images taken under plane polarized light.

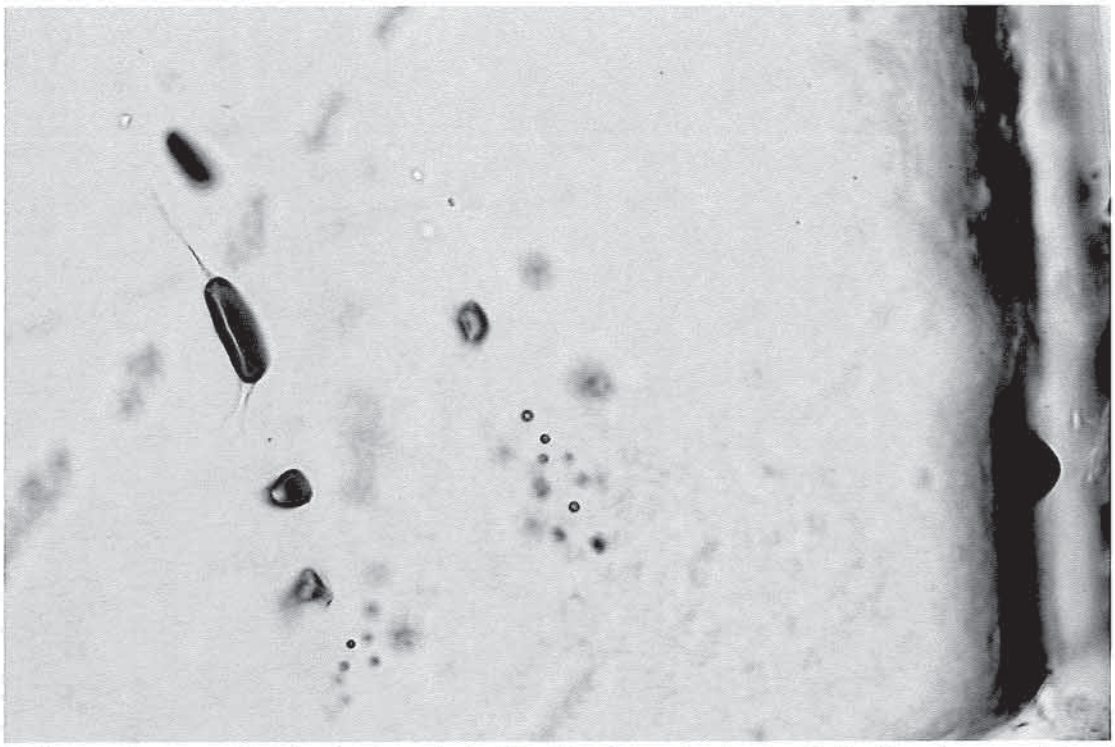

Fig. 17. Secondary gas-rich inclusions in halite. The large inclusion left of center consists of a dark bubble and a clear liquid. The dark bubble is interpreted to consist of a gas phase, possibly rich in methane. From CCU-26-3-7439.3 FL. The image was taken under plane polarized light. The field of view is 0.4 mm.

Fig. 18. Large, two-phase oil-bearing inclusion in dolomite. Top: plane polarized light. Bottom: ultraviolet light. From CS-36-13-7630.9 FL. The field of view is 0.3 mm.

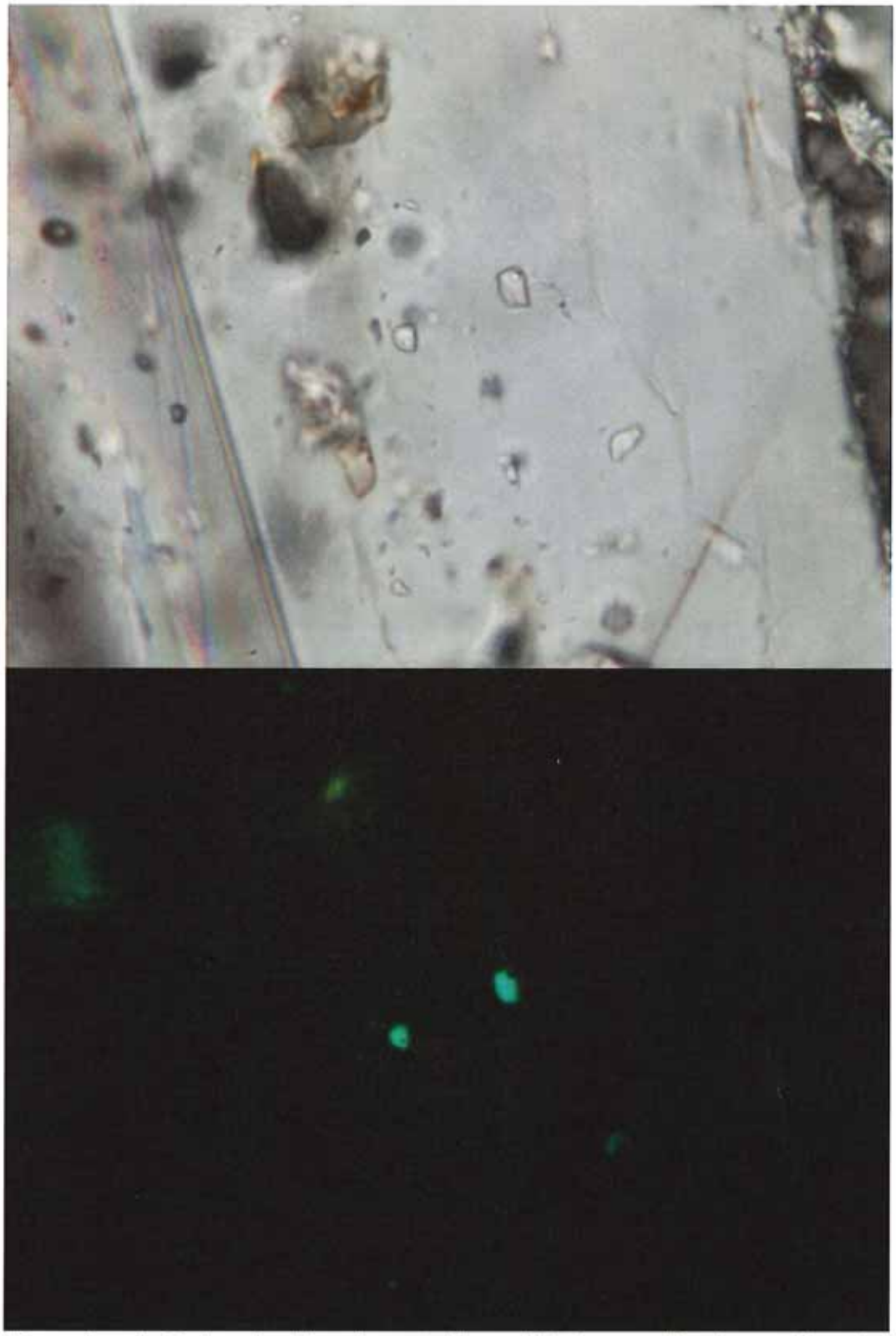

Fig. 19. Two-phase inclusions in dolomite containing a light brown oil and a small gas bubble. Top: plane polarized light. Bottom: ultraviolet light. From CS-36-13-7630.9 FL. The field of view is 0.3 mm.

Appendix VIII

Potential Oil-Prone Areas in the Cane Creek Shale Play, Paradox Basin, Utah, Identified by Epifluorescence Microscopy Techniques

Thomas C. Chidsey, Jr.[1] and David E. Eby[2]

[1]Utah Geological Survey, Salt Lake City, UT
[2]Eby Petrography & Consulting, Inc., Denver, CO

Utah Geological Survey Special Study 160

POTENTIAL OIL-PRONE AREAS IN THE CANE CREEK SHALE PLAY, PARADOX BASIN, UTAH, IDENTIFIED BY EPIFLUORESCENCE MICROSCOPE TECHNIQUES

by Thomas C. Chidsey, Jr., and David E. Eby

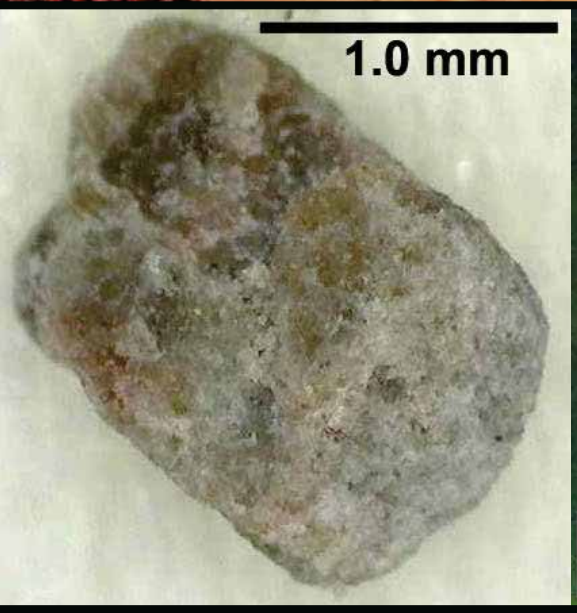

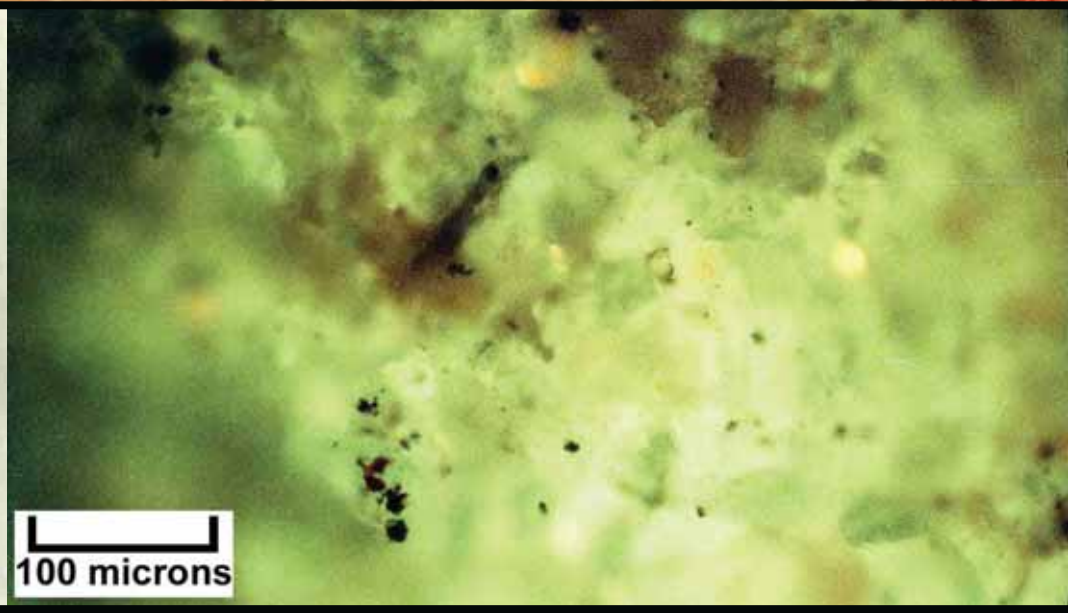

SPECIAL STUDY 160
UTAH GEOLOGICAL SURVEY
a division of
UTAH DEPARTMENT OF NATURAL RESOURCES
2017

*Blank pages are intentional for printing purpose**s.***

POTENTIAL OIL-PRONE AREAS IN THE CANE CREEK SHALE PLAY, PARADOX BASIN, UTAH, IDENTIFIED BY EPIFLUORESCENCE MICROSCOPE TECHNIQUES

by
Thomas C. Chidsey, Jr.
Utah Geological Survey, Salt Lake City, Utah
and
David E. Eby
Eby Petrography & Consulting, Inc., Denver, Colorado

Cover photo: *Top photo: Panorama of the Cane Creek anticline (middle ground); view east from Dead Horse Point State Point overlook. Bottom left photo: Microscope image of a single cutting from the Long Canyon No. 1 well, Long Canyon field, Grand County, Utah, showing light gray to medium brown, medium crystalline dolomite containing intercrystalline porosity, from the productive B interval of the Cane Creek shale, Pennsylvanian Paradox Formation, Paradox Basin, southeastern Utah. Bottom right photo: Photomicrograph of the same sample showing patchy, bright epifluorescence indicating a very good potential for movable oil and the capability of production. The vertical Long Canyon No. 1 well has produced over 1 million barrels of oil since its discovery in 1962.*

ISBN: 978-1-55791-937-3

SPECIAL STUDY 160
UTAH GEOLOGICAL SURVEY
a division of
UTAH DEPARTMENT OF NATURAL RESOURCES
2017

STATE OF UTAH
Gary R. Herbert, Governor

DEPARTMENT OF NATURAL RESOURCES
Michael Styler, Executive Director

UTAH GEOLOGICAL SURVEY
Richard G. Allis, Director

PUBLICATIONS
contact
Natural Resources Map & Bookstore
1594 W. North Temple
Salt Lake City, UT 84116
telephone: 801-537-3320
toll-free: 1-888-UTAH MAP
website: mapstore.utah.gov
email: geostore@utah.gov

UTAH GEOLOGICAL SURVEY
contact
1594 W. North Temple, Suite 3110
Salt Lake City, UT 84116
telephone: 801-537-3300
website: geology.utah.gov

CONTENTS

FIGURES

TABLES

POTENTIAL OIL-PRONE AREAS IN THE CANE CREEK SHALE PLAY, PARADOX BASIN, UTAH, IDENTIFIED BY EPIFLUORESCENCE MICROSCOPE TECHNIQUES

by Thomas C. Chidsey, Jr., and David E. Eby

ABSTRACT

The Cane Creek shale of the Pennsylvanian Paradox Formation has produced over 7.8 million barrels of oil and about 7.9 billion cubic feet of gas from 18 fields in the Paradox Basin of southeastern Utah. Potential oil-prone areas in the Cane Creek play area were identified in the northern part of the basin based on hydrocarbon shows recognized using nondestructive epifluorescence (EF) microscope techniques on cuttings, core chips, and uncovered thin sections. Approximately 2650 individual cuttings samples and core chips were evaluated from 31 wells penetrating the Cane Creek shale throughout the region. The wells include seven producers, one having cumulative production of >1 million barrels of oil from the Cane Creek since its completion in 1962.

The Cane Creek shale is divided into three intervals, based on wireline geophysical well-log characteristics and lithology, referred to as the A, B, and C intervals; the B interval is the primary oil producer. Finely crystalline dolomites and sandstones in the B interval have been the main targets of horizontal drilling. The dolomites in these intervals display intercrystalline porosity and microbial constructional pores whereas sandstones exhibit intergranular porosity; both rock types contain microporosity and fracture porosity. A new, qualitative visual EF rating was developed and applied to the group of samples from each cuttings sample interval in each well. The highest, average highest, highest average, and average of the sample averages of the EF ratings from each well were plotted and mapped for the entire Cane Creek as well as the A, B, and C intervals.

As expected, productive wells (fields) are distinguished by their generally higher EF ratings. However, an area of moderate to good fluorescence (indicating probable capacity of some oil production if there is adequate porosity and permeability) is indicated within a northwest- to southeast-oriented curvilinear fairway in the Cane Creek shale of the Paradox fold and fault belt. In contrast, the northeastern area shows a regional trend of low EF. This implies that hydrocarbon migration in Cane Creek dolomite, sandstone, and other porous lithologies was along regional northwest-trending folds, faults, and fracture zones, and created a potential oil-prone area that to date is relatively untested.

INTRODUCTION

The Cane Creek shale of the Pennsylvanian (Desmoinesian) Paradox Formation has produced over 7.8 million barrels of oil (MMBO) and about 7.9 billion cubic feet of gas (BCFG) from 18 fields in the Paradox Basin of southeastern Utah (figures 1 and 2) (Utah Division of Oil, Gas and Mining, 2016). The Cane Creek consists of naturally fractured and overpressured, thin dolomitic sandstone/siltstone and dolomite interbedded with anhydrite and organic-rich marine shale (Smith, 1978; Morgan, 1992; Grove and others, 1993). Petroleum is usually trapped in fractured dolomites and sandstones, on subtle subsidiary structural noses along major southeast-northwest-trending salt-cored regional anticlines, or on the crests of other smaller anticlinal closures. Since the early 1990s, horizontal drilling has been used to successfully develop the Cane Creek "tight" oil play. However, large areas in the Paradox Basin remain untested and possibly contain Cane Creek oil.

In environmentally sensitive areas of the Paradox Basin, prospect definition in the Cane Creek play often requires expensive, three-dimensional seismic acquisition. For this study, potential oil-prone areas in the play were identified based on mapping of hydrocarbon shows recognized using innovative, comparably low cost, noninvasive and nondestructive epifluorescence (EF) microscope techniques on cuttings, core chips, and thin sections. The dolomites in Cane Creek well cuttings and cores display intercrystalline porosity, and microbial constructional pores whereas sandstones exhibit intergranular porosity; both rock types contain microporosity and fracture porosity. EF microscope techniques enable better imaging of poorly preserved textures and grains in carbonate rocks, particularly dolomites. In addition, EF provides information on diagenesis, pore types, and organic matter (including "live" hydrocarbons) within sedimentary rocks. It is a rapid procedure that uses a petrographic microscope equipped with reflected-light capabilities, an Hg-vapor lamp, and appropriate filtering. The resulting EF show maps provide an assessment of the northern Paradox Basin that can be used to high-grade areas for (1) more detailed Cane Creek evaluations (such as seismic surveys), (2) lease acquisition, and (3) exploratory drilling.

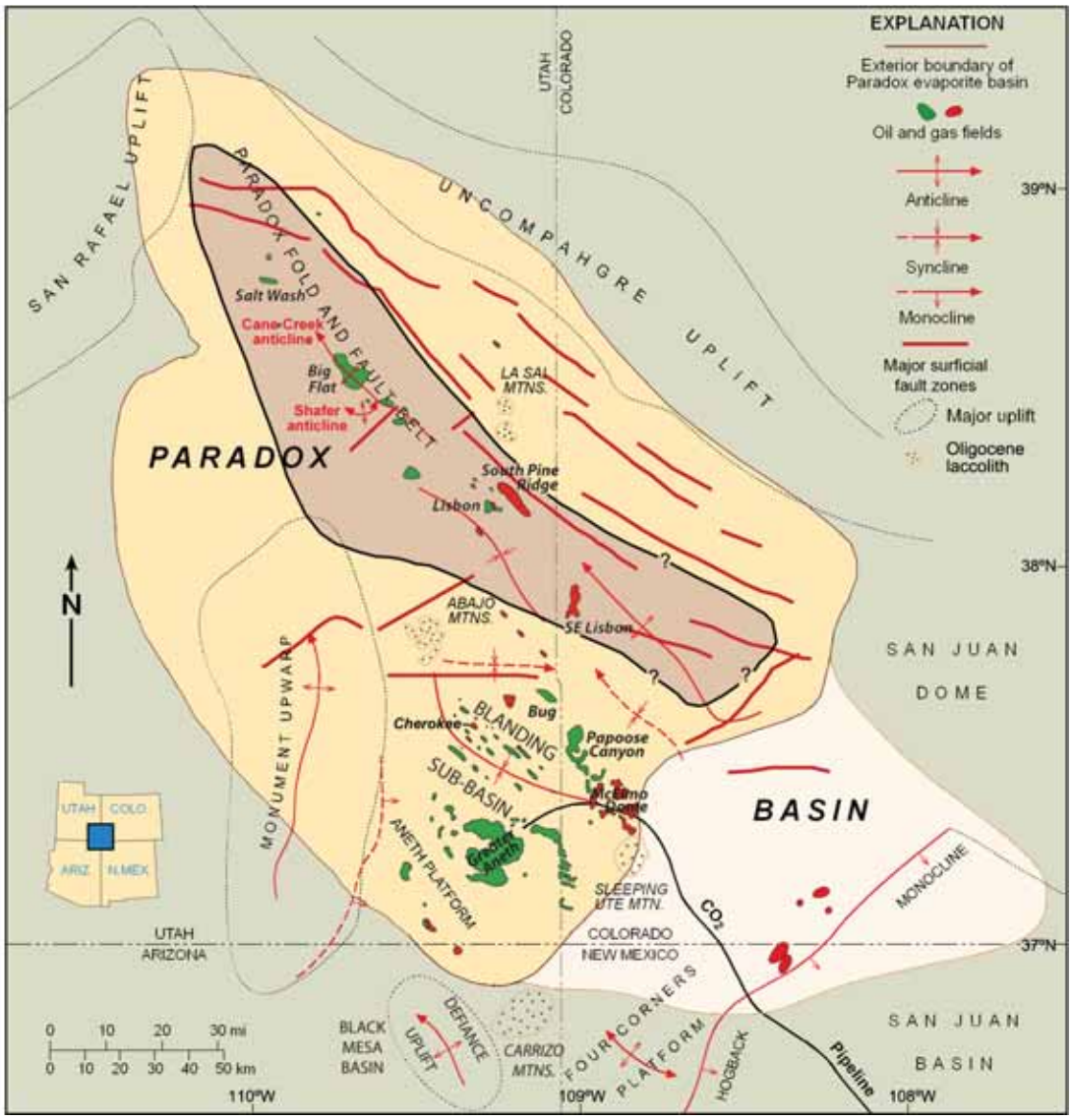

Figure 1. *Oil and gas fields in the Paradox Basin of Utah, Colorado, Arizona, and New Mexico. Modified from Harr (1996). The extent of Pennsylvanian Paradox Formation is shown in light orange; the Cane Creek shale play area within is light brown.*

GEOLOGIC OVERVIEW OF THE CANE CREEK SHALE

Paradox Basin

The Paradox Basin is located principally in southeastern Utah and southwestern Colorado and has small portions in northeastern Arizona and the northwestern corner of New Mexico (figure 1). The Paradox Basin is an elongate, northwest-southeast-trending, evaporite-rich basin that developed predominately during the Pennsylvanian, about 330 to 310 million years ago. The dominant structural features in the basin are surface anticlines that extend for miles in the northwesterly trending fold and fault belt (figure 1). During Cambrian through Mississippian time, this region, as well as most of eastern Utah, was the site of typical marine deposition represented by a relatively thin stratigraphic section on a craton with thicker deposits in a miogeocline to the west (Hintze and Kowallis, 2009). However, major changes began in the Pennsylvanian when a pattern of basins and fault-bounded uplifts developed from Utah to Oklahoma. One result of this tectonism was the uplift of the Ancestral Rockies in the western United States, including the Uncompahgre Highlands (uplift) in eastern Utah and western Colorado.

The Uncompahgre Highlands are bounded along their southwestern flank by a stack of large basement-involved, high-angle, reverse faults identified from seismic surveys and exploration drilling (Frahme and Vaughn, 1983; Kluth and DuChene, 2009). As the highlands rose, an accompanying depression, or foreland basin, formed to the southwest—the Paradox Basin. Rapid basin subsidence, particularly during the Pennsylvanian and continuing into the Permian, accom-

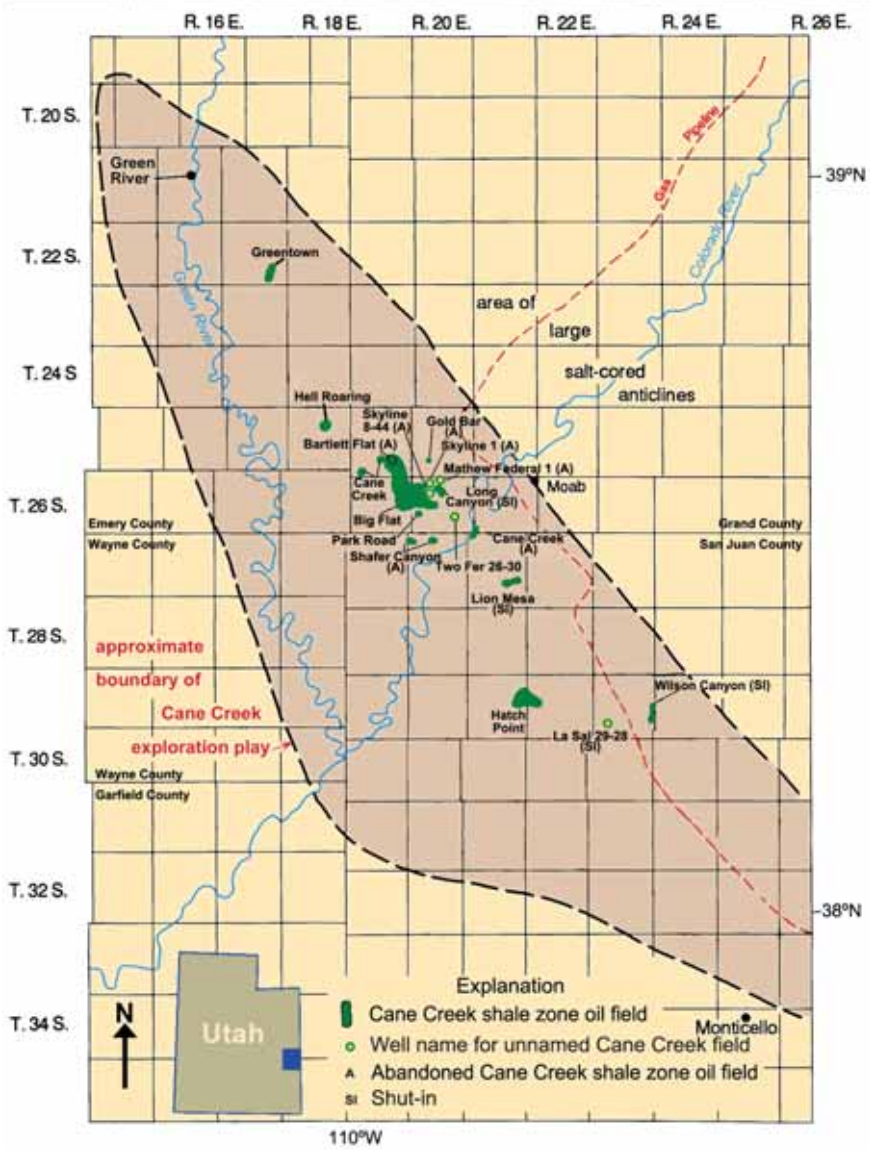

Figure 2. *Location of fields that produce from the Cane Creek shale and play area (light brown) within the Paradox Basin of southeastern Utah.*

modated large volumes of evaporitic and marine sediments that intertongue with non-marine arkosic material shed from the highland area to the northeast (Hintze and Kowallis, 2009). Deposition in the basin produced the thick cyclical sequence of carbonates, evaporites, and organic-rich shale that comprise the Paradox Formation.

The Paradox Basin can generally be divided into three areas: the Paradox fold and fault belt in the north, the Blanding subbasin in the south-southwest, and the Aneth platform in the southernmost part in Utah (figure 1). The area now occupied by the Paradox fold and fault belt was also the site of greatest Pennsylvanian/Permian subsidence and salt deposition. The area was created during the Late Cretaceous through Quaternary by a combination of (1) reactivation of basement normal faults, (2) additional salt flowage followed by dissolution and collapse, and (3) regional uplift (Doelling, 2003; Trudgill and Paz, 2009).

Stratigraphy and Thickness

The Paradox Formation is part of the Pennsylvanian Hermosa Group (figure 3). The 500- to 5000-foot-thick (150–1500 m) Paradox Formation is overlain by the Honaker Trail Formation and underlain by the Pinkerton Trail Formation. Hite (1960), Hite and Cater (1972), and Hite and Buckner (1981) divided the saline section of the Paradox Formation in the evaporite basin into 29 salt cycles that onlap onto the basin shelf to the west and southwest (figure 3); Rasmussen (2010) recognizes as many as 35 cycles. Each cycle consists of a clastic-carbonate interval/salt couplet. The clastic-carbonate intervals are typically interbedded dolomite, dolomitic siltstone, silty limestone, black organic-rich shale, and anhydrite. Within the interior of the basin, a typical cycle consists of a clastic-carbonate interval or zone overlain almost entirely by halite (Morgan, 1992). The Cane Creek shale is

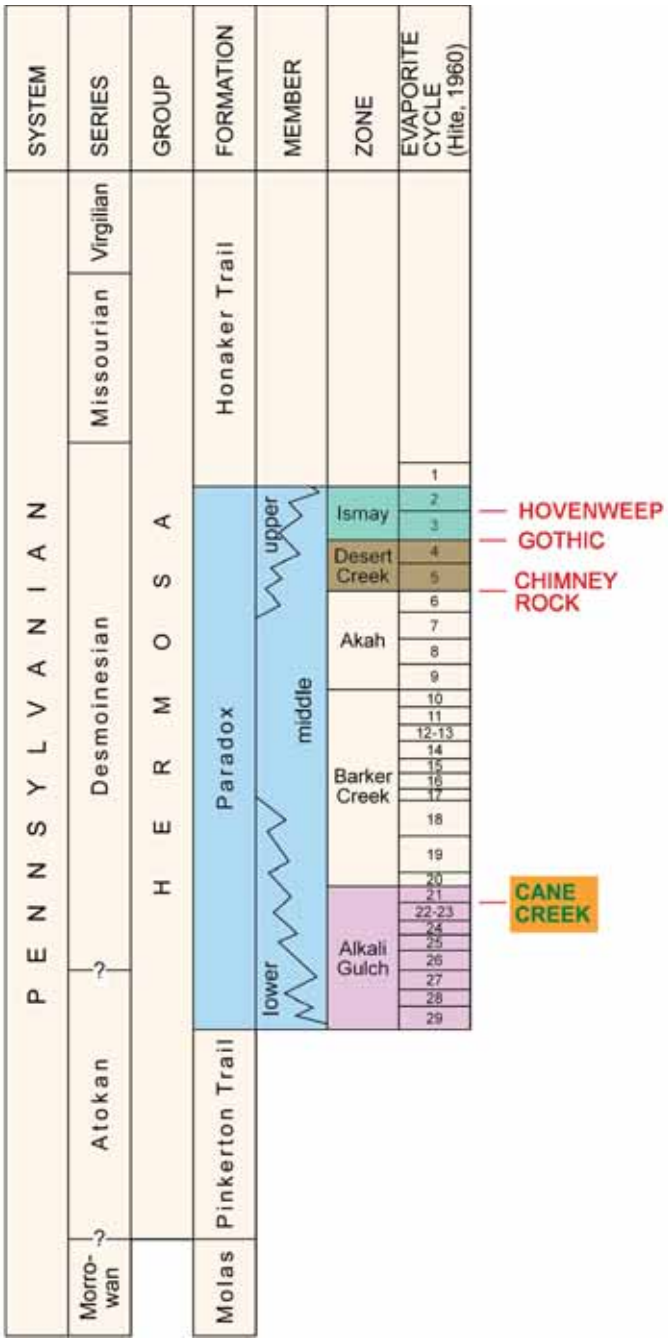

Figure 3. *Stratigraphic column of a portion of the Pennsylvanian section determined from subsurface well data in the Paradox fold and fault belt in Utah. Note the position of the Cane Creek shale, which occurs below the other potential resource play shales in the Paradox Basin (the Hovenweep, Gothic, and Chimney Rock shales). Modified from Hite (1960), Hite and Cater (1972), Reid and Berghorn (1981).*

the clastic-carbonate interval representing the basal part of cycle 21 (figure 3) and has a wide regional extent.

The Cane Creek shale generally ranges from 0 to about 200 feet (0–60 m) thick in the region. Within the main Cane Creek play "fairway" (figures 1, 2, and 4), the thickness is 60 to 170+ feet (18–52+ m). The depositional strike of the Cane Creek is north-northwest to east-southeast with a thinner section through the central part of the trend that thickens to the northeast and southwest (figure 4). However, farther to the southwest it thins where it laps onto the lower Paradox member or the Pinkerton Trail Formation (Carney and others, 2014; Morgan and others, 2014). Thickness variations are the results of diapiric salt movement, depositional thickening on the downthrown side of faults, or depositional thinning on the upthrown side of faults or over subtle, early structural highs (Morgan, 1992).

Depositional Environment

Throughout the Pennsylvanian, the Paradox Basin had subtropical, dry climatic conditions. During transgressions, open-marine waters flowed across a shallow cratonic shelf into the basin through up to four postulated marine access ways (Fetzner, 1960; Ohlen and McIntyre, 1965; Hite, 1970). Periodic decreased water circulation resulted in deposition of thick salts (halite with sporadic thinner beds of potash and magnesium salts) and anhydrite in the north and northeast part of the basin.

Cyclicity during Paradox Basin deposition was primarily controlled by glacio-eustatic sea-level fluctuations. These sea-level cycles were also influenced by (1) regional tectonic activity and basin subsidence (Baars, 1966; Baars and Stevenson, 1982), (2) proximity to basin margin (Hite, 1960; Hite and Buckner, 1981), (3) climatic variation and episodic blockage of open marine-water access ways, and (4) fluctuations in water depth and water energy (Peterson and Ohlen, 1963; Peterson, 1966; Hite and Buckner, 1981; Heckel, 1983).

The Cane Creek shale generally records a low-energy environment varying between aerobic to dysaerobic and occasionally anoxic conditions (for thin, organic-rich black shale intervals). Water depths were probably variable, ranging from below fair-weather and storm wave base for organic shales to relatively shallow to near exposure for the siltstones, sandstones, limestones, finely crystalline primary or very early diagenetic dolomites, and nodular anhydrites and other evaporites.

Petroleum Geology

Structure and Trapping Mechanisms

Structurally the Cane Creek shale is deepest in the north part of the play area, -2400 to -4000 feet (-730 to -1200 m) subsea (figure 5). The Cane Creek shallows near the southwestern edge/shelf of the basin. Oil is trapped on the crests of anticlines and along structural noses (figures 6). Salt movement along zones of weakness or areas of low confining pressure formed large folds such as the Cane Creek and Shafer anticlines (figure 7). Second-order folds caused by salt flowage are aligned directly over local bulges or pillows of Paradox salt and the overlying rocks are fractured (Lorenz and Cooper, 2009). Fracture data from oriented cores in the Cane Creek show regional, north-

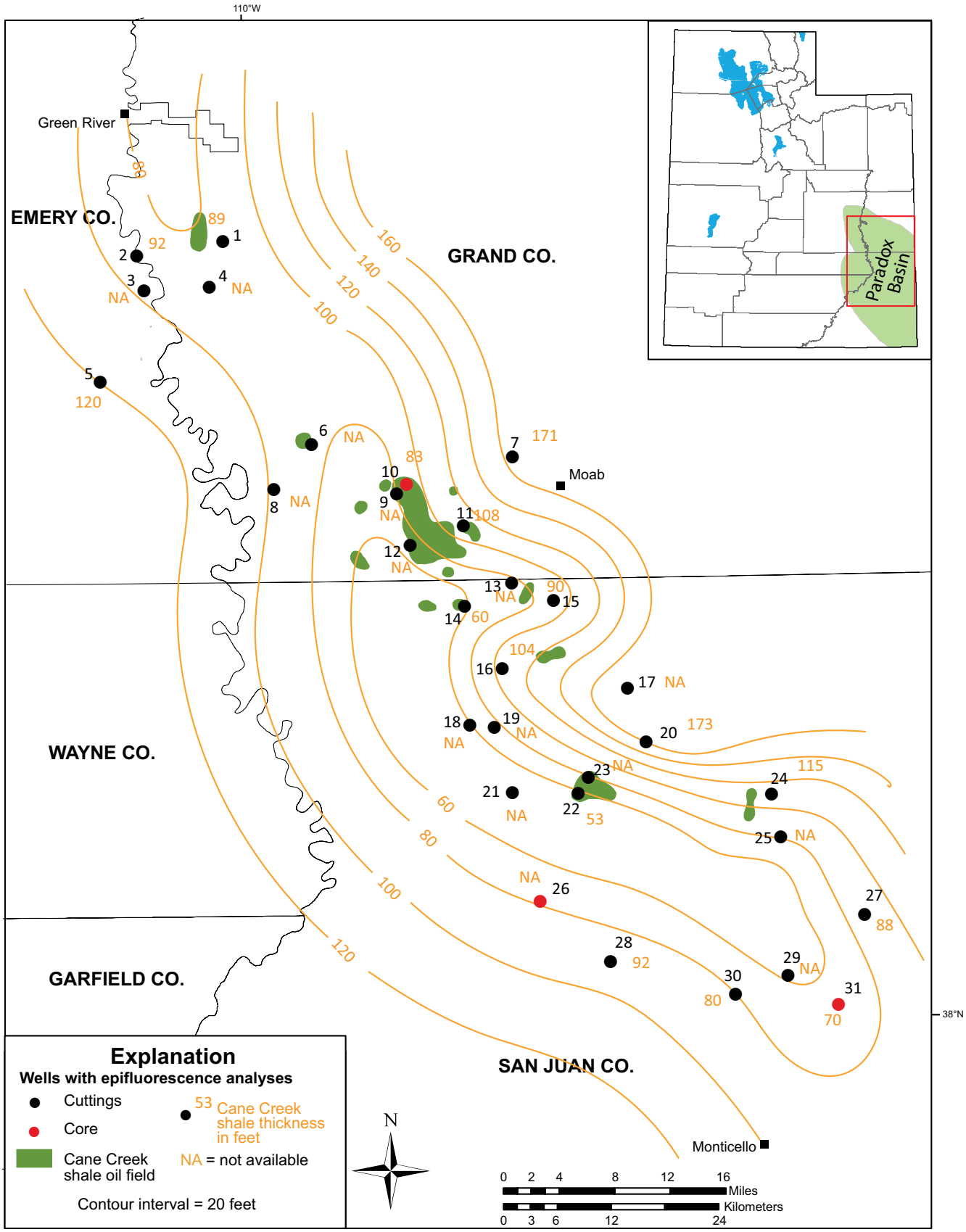

Figure 4. *General thickness of the Cane Creek shale using only wells with EF analysis. Other wells not included are scattered throughout the region or concentrated in the producing oil fields would likely result in a map showing additional thick and thin areas related to salt flowage, faulting, or depositional thinning over minor early structural highs. See table 3 for list of wells corresponding to the numbers by the black or red dots.*

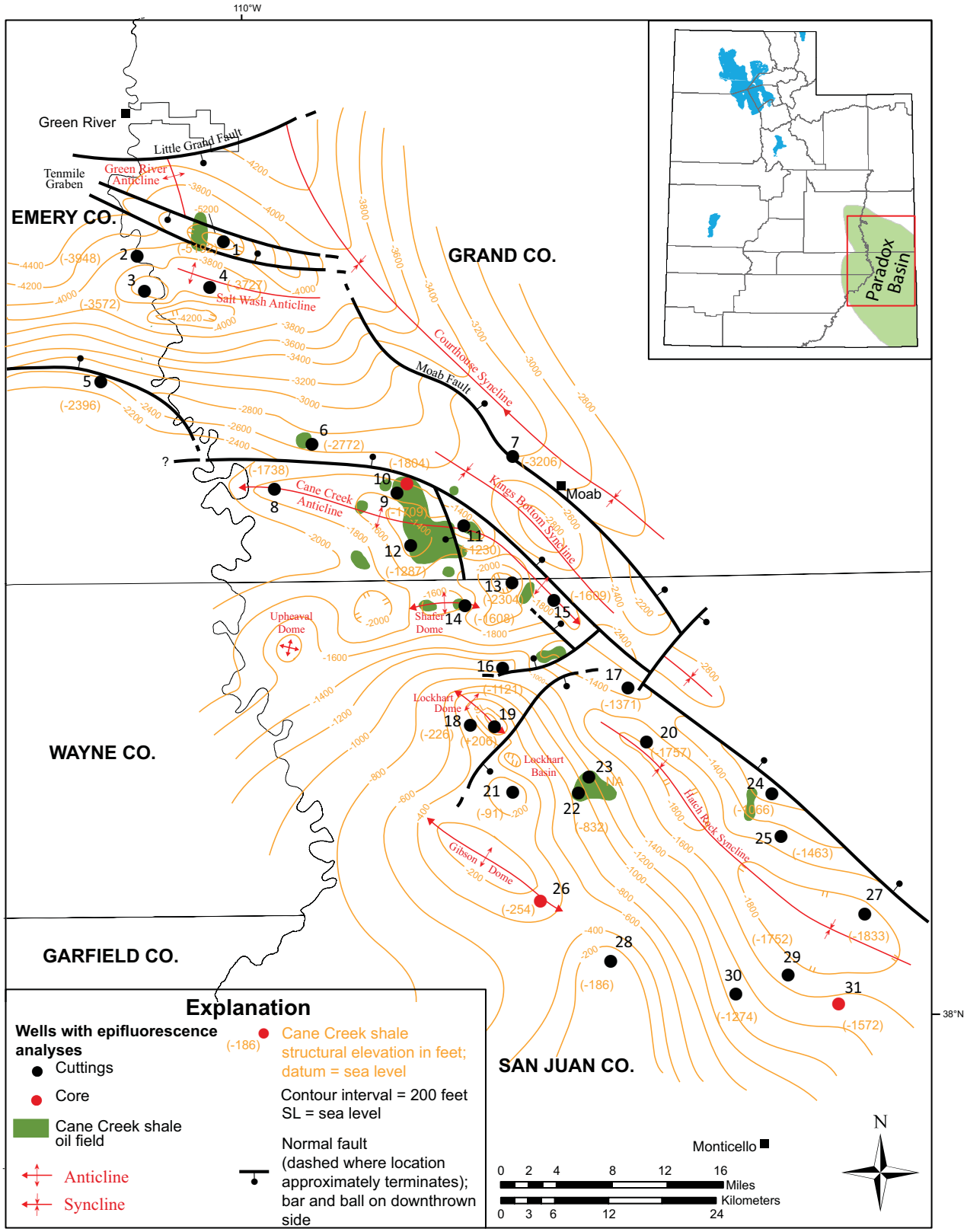

Figure 5. *Generalized structural map on top of the Cane Creek shale using only wells with EF analysis. Other wells not included are scattered throughout the region or concentrated in the producing oil fields and would likely result in a map with greater structural complexity. Additional faults and folds are present but are not shown given the small scale of the map. The map was created by combining published oil field reservoir maps (Peterson, 1973; Quigley, 1983; Grove and others, 1993; Morgan, 1994), and regional geologic maps and cross sections (Doelling, 2001, 2004) without the benefit of seismic data. Major folds and faults projected from surface expressions may die out in Paradox salt zones above the Cane Creek, whereas basement-involved structures may be present at the Cane Creek level where they can best be detected by seismic. See table 3 for list of wells corresponding to the numbers by the black or red dots.*

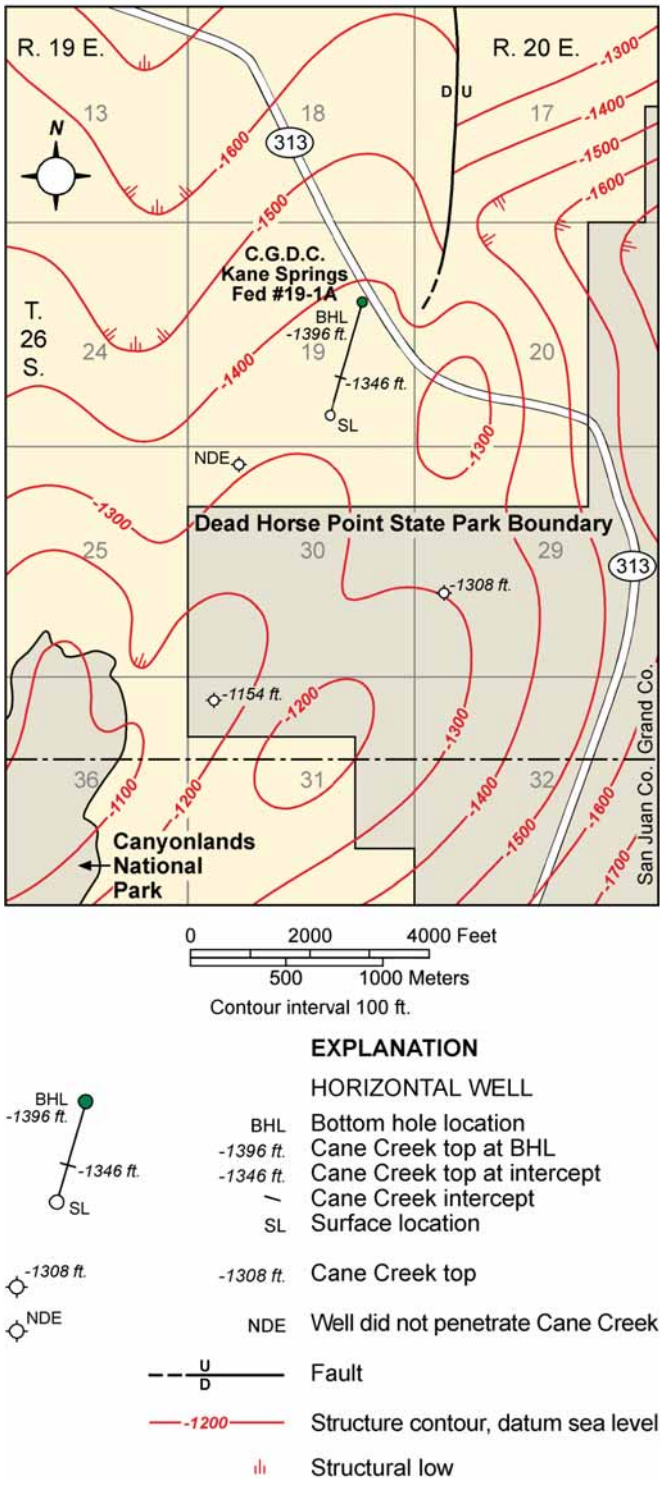

Figure 6. *Cane Creek shale structure map, Park Road oil field, Grand County, Utah. Surface location, direction, and length of horizontal well shown. After Grove and others (1993). See figure 2 for location of Park Road field.*

west to southeast and northeast to southwest, near-vertical, open, extensional fracture systems that are not significantly affected by orientations of localized folds (Grove and Rawlins, 1997; Morgan and others, 2014). Hydrocarbon production from the Cane Creek is not limited to the crests of anticlines but also from structurally high positions on upthrown fault blocks and on the downthrown side of faults. Plunging noses without apparent four-way closure produce from the Cane Creek as well as where extensive fracturing exists.

Hydrocarbon Source and Seals

Hydrocarbons in Paradox Formation reservoirs were generated from source rocks within the formation itself. Organic-rich sapropelic shale in the Cane Creek and other organic-rich shales are well-established source rocks for hydrocarbon production in the Paradox Basin (Hite and others, 1984; Nuccio and Condon, 1996). The average total organic content of the black shale in the Cane Creek is 15% with some samples containing up to 28% (Grummon, 1993; Morgan and others, 2014). Kerogens are oil-prone types I and II; maturity (based on T_{max}) and production indices from three cores studied as part of this project place the Cane Creek in the oil window (Morgan and others, 2014). The Cane Creek shale began to generate hydrocarbons within the Paradox fold and fault belt from 270 to 239 Ma (Middle Permian–Middle Triassic) (Rasmussen and Rasmussen, 2009). Expulsed hydrocarbons migrated in through dolomite, sandstone, and other porous lithologies along regional northwest-trending folds, faults, and fracture zones.

The upper and lower seals for the reservoir units in the Cane Creek shale are provided by anhydrite and halite beds. Lateral seals are permeability barriers in unfractured rock. Thus, the Cane Creek serves as the source and seal, as well as the oil reservoir rock.

Reservoir and Hydrocarbon Properties

The Cane Creek shale in the Big Flat field area (figure 2) exhibits a net-pay thickness of 25 to 30 feet (7–9 m). Dolomites and sandstones have been the main targets of horizontal drilling. Productive zones have porosity (matrix and fractures) up to 15% (Grove and others, 1993; Morgan and others, 2014). Pore types in dolomite beds are predominantly intercrystalline and microbial constructional pores, microporosity, and minor interparticle porosity. Sandstones and siltstones exhibit intergranular porosity. These lithologies can also contain significant microporosity and fracture porosity. Microfractures resulted from internal hydrocarbon generation (Fritz, 1991). Matrix permeability from Horner plots is less the 0.1 millidarcies (mD), but ranges from 39 to 400 mD with fractures (Grove and others, 1993). The larger tectonic fractures may account for most of the permeability, but the microfractures probably provide most of the fracture porosity in the reservoir. Core analysis from the productive interval in the Cane Creek No. 26-3 well (section 26, T. 25 S., R. 19 E., Salt Lake Base Line and Meridian [SLBL&M]) in Big Flat field (figure 2), Grand County, Utah, showed sandstones, argillaceous sandstones, and dolomitic argillaceous siltstones contain 5% to 12% porosity, and permeability ranging from 0.002 to 36 mD; porosity and permeability in silty dolomite was 7% and 0.004 mD, respectively (Core Laboratories, Inc., 2013).

Figure 7. *Panorama of the Cane Creek anticline (middle ground); view east from Dead Horse Point State Point overlook. Note solar evaporation ponds in front of the fold and the jointed Jurassic Navajo outcrops of the Behind the Rocks area in front of the La Sal Mountains in the distance.*

Initial water saturations are estimated at 10% for the fractured Cane Creek shale. The Cane Creek is highly overpressured which is probably the result of hydrocarbon generation between very impermeable upper and lower anhydrite and halite seals. Fluid gradients exceed 0.85 to 0.94 pounds per square inch (psi)/foot (19.23–21.27 kPa/m); the initial reservoir pressures average 6650 psi (45,850 kPa) (Grove and others, 1993; C.D. Morgan, Utah Geological Survey, written communication, 2015). The reservoir temperatures range from 119° to 132°F (48°–56°C) and the reservoir drive mechanism is solution gas (Grove and others, 1993).

The produced Cane Creek oils are sweet, paraffinic crudes, and amber in color. The API gravity of the oil ranges from 36° to 43°; the gas-to-oil ratio ranges from 745 to 850 cubic feet/barrel. The pour point of the crude oil ranges from 25° to 55°F (-4°–13°C) and the viscosity ranges from 7.7 to 13.3 centistokes at 104°F (40°C). The associated gas composition is 67% to 81% methane; 18% to 29% ethane, propane, and butane; 1% to 3% N_2; a trace of CO_2; and no H_2S. The gas heating value ranges from 1205 to 1471 British thermal units per cubic feet; the specific gravity ranges from 0.692 to 0.860 (Stowe, 1972; Grove and others, 1993; unpublished analyses of field oils stored at the Utah Core Research Center [UCRC]).

Drilling History, Production, and Resource Potential

The Cane Creek shale has been a target for tight-oil exploration on and off since the late 1950s. Many vertical wells have been completed in the Cane Creek, but only the Long Canyon No. 1 well (section 8, T. 26 S., R. 20 E., SLBL&M) in Long Canyon field (figure 2), Grand County, Utah, has been an economic success. Drilled in 1962, the well has produced more than 1 MMBO. The Cane Creek generated much interest in the early 1990s with the successful use of horizontal drilling. All wells drilled and completed in the Cane Creek since 1991 have used horizontal drilling techniques, with the exception of one vertical well in Greentown field, completed in 2008 (figure 2). Initial production rates generally range from 250 to 900 barrels of oil per day and around 300,000 cubic feet of gas per day.

Eighteen fields have produced over 7.8 MMBO and associated gas of about 7.9 BCF from the Cane Creek shale as of January 1, 2016 (figure 2; tables 1 and 2); associated water production is over 1.4 million barrels (Stowe, 1972; Utah Division of Oil, Gas and Mining, 2016). Between 1959 and 1982, 10 Cane Creek discoveries were made in the Paradox Basin. Cumulative production from these fields is about 1.4 MMBO and over 3.3 BCFG, all from vertical wells. However, seven of these fields are now abandoned and three are shut-in (table 1). Currently, eight active fields produce from the Cane Creek, seven have horizontal wells. Cumulative oil production as of January 1, 2016, from the horizontal wells is over 6.3 MMBO and 4.3 BCFG; 30 active horizontal wells exist in these fields (table 2) (Utah Division of Oil, Gas and Mining, 2016). The majority of production is from Big Flat field and the surrounding area (figure 2).

Estimated recovery for successful Cane Creek horizontal wells is 250,000 to 1 MMBO per well (IHS Inc., 2013). The U.S. Geological Survey (2012), Whidden and others (2014), and Anna and others (2014) re-assessed the undiscovered oil resource in the Cane Creek at 103 MMBO at a 95% confidence level and 198 MMBO at a 50% confidence level.

EPIFLUORESCENCE

Epifluorescence microscopy is a technique that has been used successfully in recent years to provide additional information on grain and textural recognition, diagenesis, pore shapes and sizes, fracture recognition, and organic matter (including "live" hydrocarbons) within sedimentary rocks. It is a rapid, non-destructive procedure that requires a high-quality petro-

Table 1. *Cumulative oil and gas production from fields having vertical wells completed in the Cane Creek shale. Data from Stowe (1972) and the Utah Division of Oil, Gas and Mining as of January 1, 2016. See figure 2 for field locations; all well locations are SLBL&M.*

Field Name and/or Well Name and Location	Completion Date	Current Status	Cumulative Production Oil* Gas†
Greentown Federal 28-11 Section 28, T. 22 S., R. 17 E.	2008	Producing‡	71,535 BO 0.27 BCFG
Bartlett Flat	1961	Abandoned 1965	39,393 BO 0.02 BCFG
Gold Bar Gold Bar 1 Section 29, T. 25 S., R. 20 E.	1982	Abandoned 1984	13,393 BO 0.01 BCFG
Unnamed Mathew Federal 1 Section 4, T. 26 S., R. 20 E.	1981	Abandoned 1982	1343 BO 0 BCFG
Unnamed Skyline 1 Section 5, T. 26 S., R. 20 E.	1982	Abandoned 1982	675 BO 0.001 BCFG
Unnamed Skyline 8-44 Section 8, T. 26 S., R. 20 E.	1976	Abandoned 1976	507 BO 0 BCFG
Long Canyon	1962	Shut-in	1,152,150 BO 1.2 BCFG
Kane Creek	1959	Abandoned 1969	1887 BO 0.03 BCFG
Shafer Canyon	1962	Abandoned 1967	67,556 BO 0.06 BCFG
Lion Mesa	1980	Shut-in	1904 BO 0 BCFG
Wilson Canyon	1968	Shut-in	126,918 BO 2.0 BCFG
TOTAL			1,477,261 BO 3.6 BCFG

* BO = barrels of oil
† BCFG = billion cubic feet of gas
‡ comingled with cycle 19 in the Paradox Formation

graphic (polarizing) microscope equipped with reflected light capabilities as well as an Hg-vapor light source and appropriate filters. The basic principles and equipment for EF were largely developed in the 1960s and 1970s for applications in coal petrology and palynology (van Gijzel, 1967; Teichmuller and Wolf, 1977). All applications depend upon the emission of light (by a material capable of producing fluorescence) that continues only during absorption of the excitation-generating light beam (Rost, 1992; Scholle and Ulmer-Scholle, 2003).

Epifluorescence techniques have been used within industry and research for three objectives. Firstly, EF microscopy has been used extensively for enhancing petrographic observations, including the recognition of depositional and diagenetic fabrics within recrystallized limestone and massive dolomite (Dravis and Yurewicz, 1985; Cercone and Pedone, 1987; Dravis, 1991; LaFlamme, 1992). Secondly, the study of pore structures, microfractures, and microporosity within both carbonates and sandstones has been greatly facilitated by impregnating these voids with epoxy spiked with fluorescing dyes (Yanguas and Dravis, 1985; Gies, 1987; Cather and others, 1989a, 1989b; Soeder, 1990; and Dravis, 1991). Thirdly, the evaluation of "oil shows" (Eby and Hager, 1986; Kirby and Tinker, 1992) and determination of the gravity or type cements and minerals has been facilitated by EF microscopy (Burruss, 1981, 1991; Burruss and others, 1986; Guihaumou and others, 1990; LaVoie and others, 2001). The third objective, i.e., "oil show" analysis, is the principal goal of this study.

Previous Work

We know of no published use of EF microscope techniques on the Cane Creek shale of the Paradox Basin. However, applications to carbonate reservoirs include Eby and Hager (1986) who studied a Permian Basin carbonate field in West Texas;

Table 2. *Cumulative oil and gas production from fields having horizontal wells completed in the Cane Creek shale. Data from the Utah Division of Oil, Gas and Mining as of January 1, 2016. See figure 2 for field locations; all well locations are SLBL&M.*

Field Name or Well Name and Location	Completion Date	Active Horizontal Wells	Current Status	Cumulative Production Oil* Gas†
Big Flat	1991	21	Producing	5,034,861 BO 3.4 BCFG
Park Road	1991	2	Producing	489,564 BO 0.2 BCFG
Hell Roaring Field	1992	1	Producing	659,883 BO 0.6 BCFG
Hatch Point	2009	2	Producing	71,836 BO 0.04 BCFG
Unnamed Two Fer 26-30 Section 26, T. 26 S., R. 20 E.	2009	1	Producing	11,028 BO 0 BCFG
Unnamed La Sal 29-28 Section 29, T. 29 S., R. 23 E.	2011	1	Shut-in	5458 BO 0.01 BCFG
Cane Creek	2014	2	Producing	57,582 BO 0.03 BCFG
TOTAL		30		6,330,212 BO 4.3 BCFG

* BO = barrels of oil
† BCFG = billion cubic feet of gas

case studies documented by Dravis (1988, 1992) on the Upper Jurassic Haynesville limestones, East Texas and Devonian Upper Elk Point dolomites, western Canada; a regional "oil show" analysis within the Devonian Keg River/Winnipegosis petroleum system in Alberta (Kirby and Tinker, 1992); and more recently an evaluation of the Mississippian Leadville Limestone in the Paradox Basin by Eby and others (2008). These studies provided justifications to apply EF petrography to the Cane Creek shale reservoir rocks.

Methods

Epifluorescence petrography for this project used incident (reflected) blue-light fluorescence microscopy employing the general procedures outlined by Dravis and Yurewicz (1985). Ultraviolet (UV) fluorescence did not effectively add any textural or pore structure information that could not otherwise be seen under blue-light excitation, even though some researchers use UV fluorescence for evaluating fluid inclusions and compositional zoning within dolomite crystals (Scholle and Ulmer-Scholle, 2003). Fluorescence data and observations collected for this study used a Jena (now part of Carl Zeiss) research-grade combination polarizing-reflected light microscope equipped with a high-pressure mercury vapor lamp for EF excitation, a Zeiss IIIRS epifluorescence nosepiece, and a film imaging system (figure 8). Magnification ranges for examination and image-documentation were between about 130 and 320X. The EF optical configuration used is similar to that shown in figure 9.

The light pathways and mechanics of the EF used in this study have been generally outlined by Soeder (1990). As described by Burruss (1991):

> These excitation wavelengths are reflected to the microscope objective and sample by a dichroic beamsplitter which has a dielectric coating that reflects a specific short wavelength range. Fluorescence emission and reflected short wavelength excitation light is collected by the objective. The dichroic beamsplitter transmits the long wavelength fluorescence emission, but reflects the short wavelengths back toward the light source. The fluorescence emission passes through a barrier filter that removes any remaining short wavelength excitation light.

Blue light (about 420 to 490 nanometer [nm] exciter filter/520 nm barrier filter) was used to excite the cuttings and core-chip samples, and uncovered thin sections. Broadband, blue-light EF was found to be the most helpful in observational work on dolomites, although some workers report applications using UV light (330 to 380 nm exciter filter/420 nm barrier filter) or narrow-band, blue-violet light (400 to 440 nm exciter filter/480 nm barrier filter). Finally, the greater depth of investigation into a sample by the reflected fluorescence technique than by transmitted polarized light or other forms of reflected light makes it possible to better evaluate "live oil shows" in the samples as well as resolve grain boundary and compositional features that are normally not appreciated in cutting or thin-section petrography.

Figure 8. *Microscope equipment used for this study.*

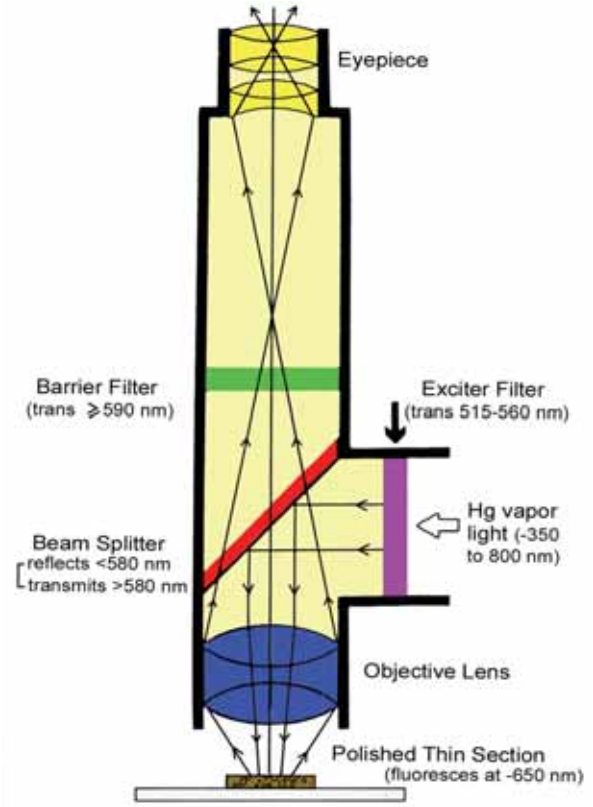

Figure 9. *Generalized optical configuration of a microscope for observing fluorescence under incident light (nm = nanometer). Modified from Soeder, 1990. AAPG© 1990, reprinted by permission of the American Association of Petroleum Geologists whose permission is required for further use.*

Sampling, Examination, and Evaluation

Cuttings or cores (as well as a few selected thin sections) from wells penetrating the Cane Creek shale were obtained from the collection at the UCRC and the Texas Bureau of Economic Geology core repository (one well – Gibson Dome) (table 3). Cuttings were examined under a binocular microscope and representative samples of dolomites, limestones, sandstones, siltstones, and shales were selected from various intervals over the Cane Creek section (see figure 10, table 3, and appendices A and B): usually 10 samples (in a few wells, less than 10 good quality samples were available) per cuttings sample interval, typically every 10 feet (3 m), from each well. The cuttings or core chips were placed on Petrologs™, small plastic, self-adhesive compartmentalized cuttings storage units, for EF examination (figure 11). Thus, sample collection and preparation is relatively inexpensive; however, it can be time consuming depending on the quality and number of samples.

Examination of each sample (cutting or core chip) often included the use of image-photography and a petrographic description under EF (see appendix C). Photomicrography of any "live oil" fluorescence attributes used high-speed film (ISO 800 and 1600). Since the image brightness is directly proportional to magnification, we obtained the best images at relatively high magnifications (such as greater than 100X). Image brightness can be affected by how the samples are stored, under what conditions, etc. Thus, fluorescence can decrease its intensity through time and environment of stor-

Table 3. *Wells containing cuttings or core chips in the Cane Creek shale evaluated using epifluorescence techniques. See figure 10 for well number locations.*

Well #	Well Name	Location			County	Well Type	Interval (ft)	Wellbore	N
		Section	Township	Range					
1	Salt Wash Unit 22-34	34	22S	17E	Grand	Dry hole	9420−9500	V	80
2	Jakey's Ridge 12-3	3	23S	16E	Emery	Dry hole	7990−8090	V	97
3	Jakey's Ridge 34-15	15	23S	16E	Emery	Dry hole	7640−7740	V	100
4	Salt Wash 1-16	16	23S	17E	Grand	Dry hole	8250−8330	V	71
5	Gruvers Mesa 1	19	24S	16E	Emery	Dry hole	7185−7290	V	100
6	Kane Springs Fed 10-1	10	25S	18E	Grand	Producing oil well	8890−8940	V	49
7	Utah 2	18	25S	21E	Grand	Dry hole	7580−7730	V	108
8	Fed Bowknot 1	30	25S	18E	Grand	Dry hole	6940−7020	V	71
9	Kane Springs Fed 25-19-34-1	34	25S	19E	Grand	Producing oil well	7550−7770	H	149
10	Cane Creek Unit 26-3	26	25S	19E	Grand	Producing oil well	7389−7470	V	197
11	Long Canyon 1	9	26S	20E	Grand	Producing oil well	7020−7135	V	39
12	Mineral Canyon U 1-14	14	26S	19E	Grand	PA oil well	7330−7420	V	65
13	Federal 1-X	36	26S	20E	San Juan	Dry hole	6520−6685	V	43
14	Featherstone-Federal 9-1	9	27S	20E	San Juan	Dry hole	5790−5895	V	100
15	West Bridger Jack U 3	3	27S	21E	San Juan	Dry hole	5900−5970	V	68
16	Cane Creek State 1-36	36	27S	20E	San Juan	Dry hole	7000−7100	V	90
17	Red Rock Unit 1	9	28S	22E	San Juan	Dry hole	6790−6910	V	104
18	Lockhart-Fed 1	22	28S	20E	San Juan	Dry hole	4765−4820	V	94
19	USA Lockhart 1	23	28S	20E	San Juan	Dry hole	4380−4430	V	46
20	Government B-1	34	28S	22E	San Juan	Dry hole	7535−7720	V	156
21	Horsehead Unit 1	18	29S	21E	San Juan	Dry hole	6290−6390	V	100
22	Hatch Point 1	14	29S	21E	San Juan	Producing oil well	7220−7270	V	38
23	Threemile 12-7	12	29S	21E	San Juan	Producing oil well	7530−7690	H	38
24	La Sal USA 1	19	29S	24E	San Juan	Dry hole	7580−7700	V	106
25	Lisbon D232	32	29.5S	24E	San Juan	Dry hole	7820−7870	V	60
26	Gibson Dome	21	30S	21E	San Juan	Dry hole	5220−5310	V	89
27	Little Valley 2	29	30S	25E	San Juan	Dry hole	8370−8410	V	35
28	Hart Point Fed 1	8	31S	22E	San Juan	Dry hole	6740−6830	V	77
29	Winchester 21-1H	21	31S	24E	San Juan	Dry hole	7740−7840	H	90
30	Church Rock Unit 1	26	31S	23E	San Juan	Dry hole	7460−7510	V	48
31	Cisco State 36-13	36	31S	24E	San Juan	Dry hole	7589−7649	V	133

N = number of samples
V = vertical
H = horizontal

age. However, we choose not to rate these factors. Low-power fluorescence is often too dim to effectively record on film. These techniques are applicable to clean or broken cuttings surfaces as well as uncovered thin sections from both core and core chips. Samples of well cuttings or core chips selected for image-documentation under EF were also photographed using a binocular microscope (appendix C).

Approximately 2650 cuttings samples and core chips were evaluated from 31 wells penetrating the Cane Creek shale throughout the region (figure 10 and table 3; see appendices A and B for EF evaluation and detailed descriptions). Samples from three cores (a producer and two dry holes) provided a template for selection of the drill cuttings and calibration of EF shows. The 31 study wells include 7 producers, including the Long Canyon No. 1 well discussed previously. The binocular microscope study of the samples accompanied the EF work. We described carbonate fabrics according to Dunham's (1962) and Embry and Klovan's (1971) classification schemes. We defined pore types and pore systems using Choquette and Pray's (1970) classification.

Epifluorescence petrography makes it possible to clearly identify hydrocarbon shows in Cane Creek cuttings and core chips. A note of caution that "newer" cores can have higher fluorescence than "older" cores, especially in the first

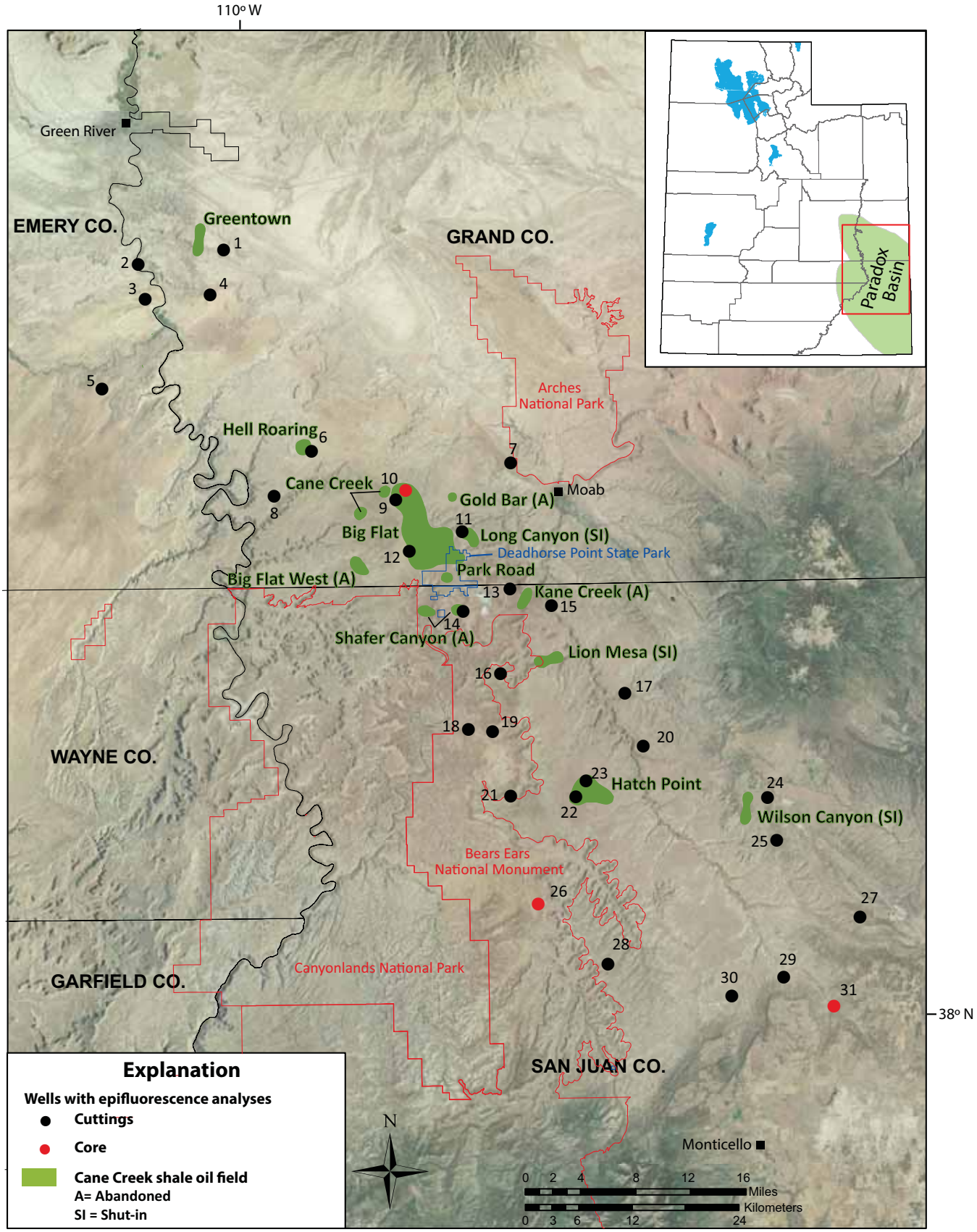

Figure 10. *Wells containing cuttings or core chips in the Cane Creek shale evaluated using epifluorescence techniques. See table 3 for list of wells corresponding to the numbers by the black or red dots.*

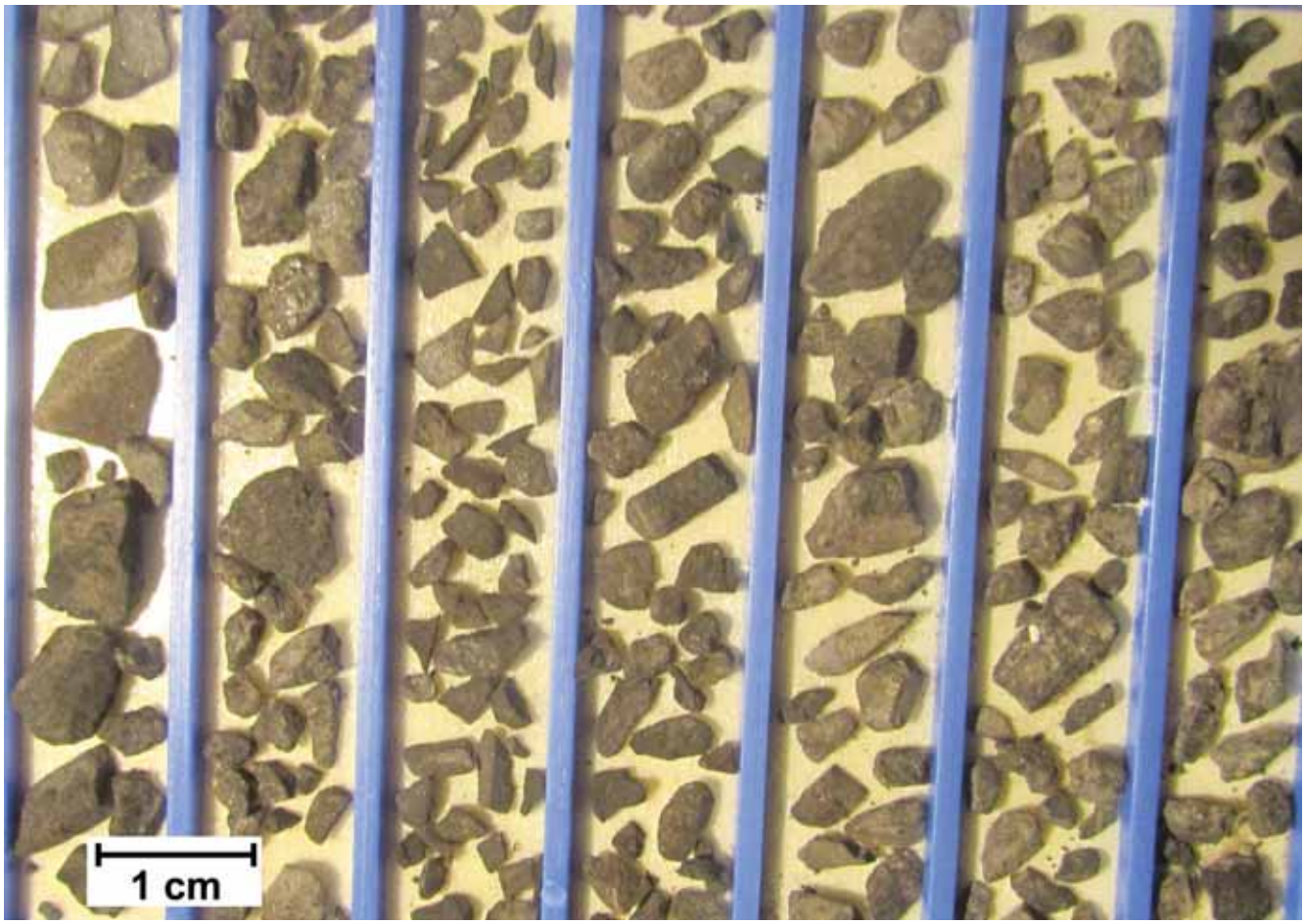

Figure 11. *Example of handpicked Cane Creek shale cuttings samples selected from various depths from 7770 to 7870 feet, Lisbon No. D232 well (well #25 on figure 10; NE1/4NE1/4 section 32, T. 29.5 S., R. 24 E., SLBL&M, Grand County, Utah, placed on Petrologs™ for epifluorescence examination.*

few months after coring. We developed and applied a new qualitative visual rating scale (a range and average) based on EF visual evaluation, but not quantitative measurements with samples of equal quality, to the group of cuttings or core chips (when available as well as a few uncovered thin sections) from each depth in each well (figure 12, table 4, and appendices A and B). The photomicrographs of EF images shown on figure 12 can be matched to the EF rating scale and general interpretation listed in table 4. Using the qualitative visual rating scale, a variety of EF readings from each well were plotted and mapped to aid in the identification of hydrocarbon "sweet spots" in the Cane Creek shale.

CHARACTERISTICS OF CANE CREEK INTERVALS

The Cane Creek shale is overlain and generally underlain by anhydrite and halite. It is divided into three intervals in descending order: A, B, and C (figure 13). Each interval has a fairly distinct wireline well log characteristic, especially the gamma-ray profile, which allows good correlations through the region.

When cores are available, like those at the UCRC, the data on wireline logs can be matched directly to the cored lithologies from the well. These logs then become templates to identify Cane Creek lithology, reservoir properties, and other core-derived information for the A, B, and C interval in wells that have no cores (figure 14). However, good quality Cane Creek cuttings also provide a wealth of data as demonstrated by this study. These data can be tied to wireline logs as well. Finally, the cuttings and core chips from the Cane Creek provide means to characterize the lithology and pore types found in the A, B, and C intervals, and determine oil shows through EF as described in the sections that follow.

Core-Based Lithology, Porosity Types, and Fracturing

In the Cane Creek shale (figure 14), the A interval is generally composed of alternating thin beds (1 to 4 feet [0.3–1.2 m] thick) of silty to shaly carbonates (both limestone and dolomite); anhydritic dolomites; interbedded, gray to black organic-rich shale; and laminated, mottled, or nodular anhydrite. Other lithologies include dolomitic siltstone and mudstone. Sedimentary features include thin, horizontal laminations

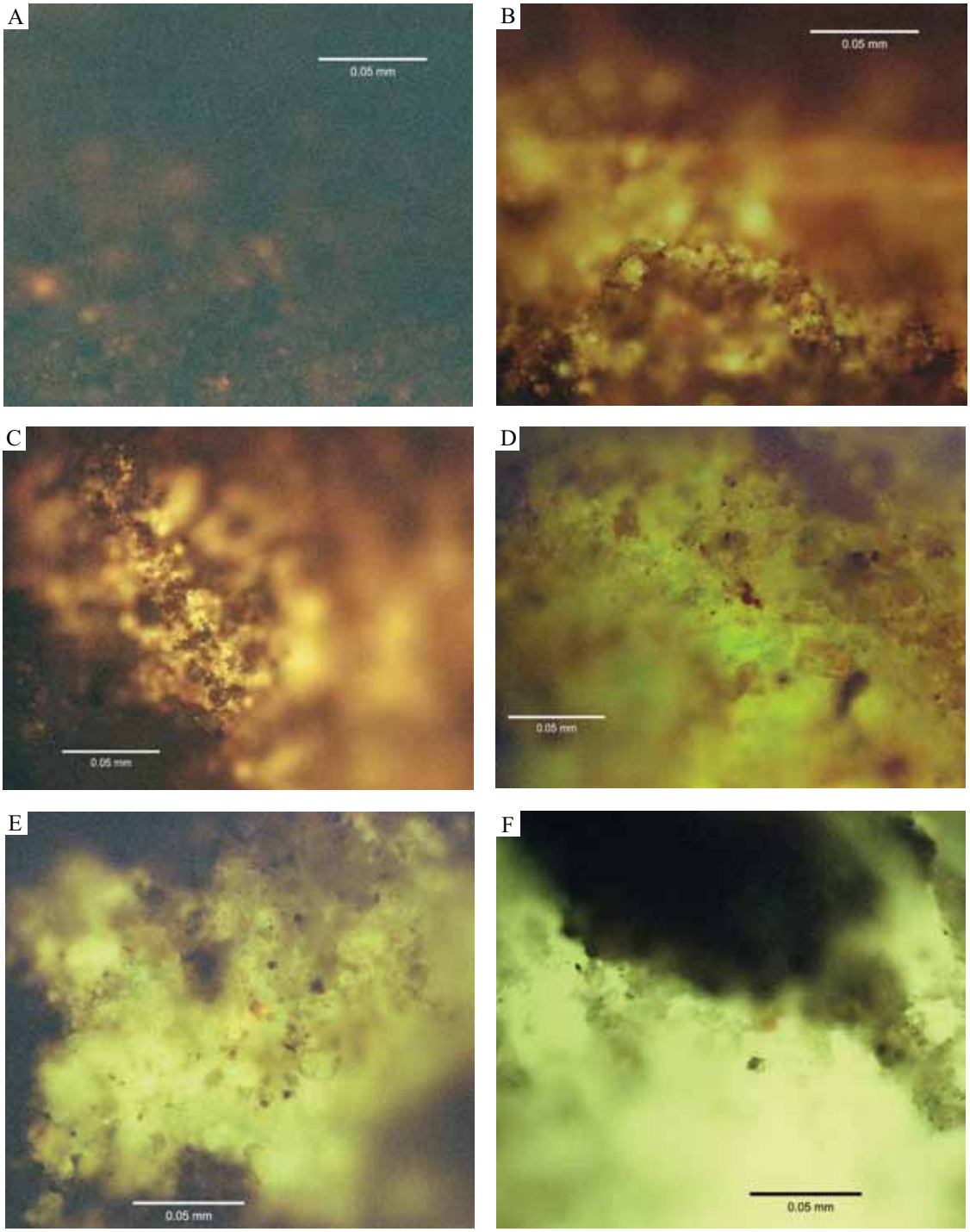

Figure 12. *Photomicrographs showing examples of visually rated epifluorescence in the Cane Creek shale play; these images can be matched to the qualitative visual epifluorescence rating scale and general interpretation listed on table 4.* ***A.*** *Almost no fluorescence (rated at 0.7) in a silty to dolomitic shale from the 6290–6300 foot sample in the Horsehead Unit No. 1 well (well #21; NW1/4SW1/4 section 18, T. 29 S., R. 21 E., SLBL&M, San Juan County).* ***B.*** *Very weak fluorescence (rated at 1.3) in a microcrystalline dolomitic mudstone from the 6290–6300 foot sample from the Horsehead Unit No. 1 well. Note the crinkly lamina that could be microbial in origin.* ***C.*** *Weak and spotty fluorescence (rated at 1.5) in a microcrystalline and microporous dolomitic mudstone from the 7380–90 foot sample in the Mineral Canyon No. 1-14 well (well #12; SW1/4SE1/4 section 14, T. 26 S., R. 19 E., SLBL&M, Grand County).* ***D.*** *Moderate and continuous fluorescence (rated at 2.4) in rhombic clusters of crystalline dolomite within a peloidal(?) grainstone from the 7260–70 foot sample in the Hatch Point No. 1 well (well #23; NE1/4SE1/4 section 14, T. 29 S., R. 21 E., SLBL&M, San Juan County).* ***E.*** *Moderately bright fluorescence (rated at 2.5) in a microcrystalline dolomite with possible organic or microbial structures from the 4800–10 foot sample in the Lockhart Federal No. 1 well (well #18; SW1/4SW1/4 section 22, T. 28 S., R. 20 E., SLBL&M, San Juan County).* ***F.*** *Moderately bright fluorescence (rated at 3.0) in a microlaminated (microbial?), medium crystalline dolomite from the 7600–10 foot sample in the Kane Springs Federal No. 25-19-34-1 well (well #9; NW1/4SE1/4 section 34, T. 25 S., R. 19 E., SLBL&M, Grand County).*

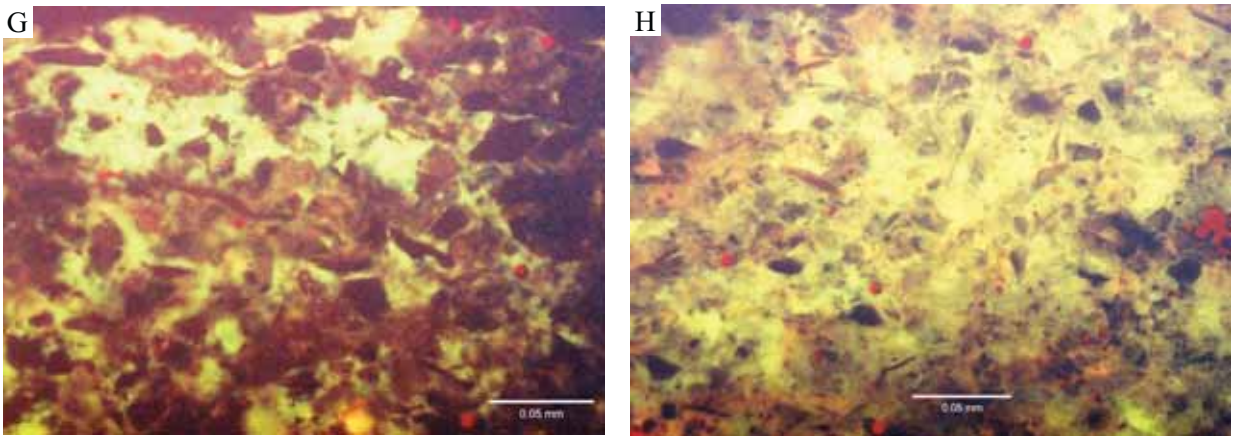

Figure 12 continued. G. *Moderately bright fluorescence (rated at 3.0) in a silty and dolomitic peloidal grainstone/packstone imaged in a polished uncovered thin section from conventional core at 7439 feet from the Cane Creek Unit No. 26-3 well (well #10; NE1/4SW1/4 section 26, T. 25 S., R. 19 E., SLBL&M, Grand County). Note the connected bands of bright yellow oil fluorescence. The rare reddish spots are iron-rich, and probably micro-pyrite.* ***H.*** *Very bright and continuous fluorescence (rated at 3.6) in a very silty microcrystalline dolomite mudstone imaged in a polished uncovered thin section from conventional core at 7430.9 feet from the Cane Creek Unit No. 26-3 well. The reddish spots are iron-rich, and probably micro-pyrite. See figure 10 for well number locations.*

Table 4. *Key to epifluorescence qualitative visual rating scale. See photomicrographs shown on figure 12 for examples of epifluorescence at the various visual ratings listed in the table below.*

Rating	Generalized Interpretation
0–1.0	No Fluorescence: not capable of oil production. May be wet, if not a gas-bearing interval. See figure 12A.
1.0–1.5	Very Weak Fluorescence: an "oil" show. Indicative of minor oil in the system, but not capable of production. Some dull or weak fluorescence may exist in a wet zone (especially if there is "speckled" fluorescence) or in a mixed oil/water zone. See figure 12B.
1.5–2.0	Weak/Spotty Fluorescence: a good "oil" show. Indicative of oil in the system, but probably not capable of production. See figure 12C.
2.0–2.5	Moderate Fluorescence: a good indication of oil within this interval. Probably capable of some oil production if there is adequate porosity and permeability/fracturing. See figure 12D.
2.5–3.0	Moderately Bright Fluorescence: a good to very good indication of movable oil within this interval. May be capable of some oil production if there is adequate porosity and permeability/fracturing. See figure 12E.
3.0–3.5	Bright Fluorescence: a very good to excellent indication of oil within this interval. Should be capable of oil production if there is adequate porosity and permeability. See figures 12F and 12G.
3.5–4.0	Very Bright, Intense Fluorescence: also an excellent to the best indication of oil within this interval. However, some very bright fluorescence may indicate very tight oil-bearing rocks or mature oil-generating source rocks. See figure 12H.

(possibly microbial) and evidence of bioturbation or haloturbation; some rip-up clasts are found near the base of the interval. The A interval, with its abundant anhydrite, represents the main seal for the reservoir rocks in the B interval below.

The B interval, the primary oil reservoir unit, is composed of interbedded thin gray and black organic-rich shale, shaly, muddy, silty or sandy dolomite, finely crystalline dolomite, dolomitic mudstone, limestone, thin dolomitic siltstone, and dolomitic sandstone (figures 14 and 15). Some dolomite beds contain peloids and minor mottled anhydrite. Sandstone is very fine grained consisting of quartz and feldspar cemented with calcite or dolomite. Sedimentary features include thin, horizontal to wavy laminations or zones of bioturbation or haloturbation. Rip-up clasts are found near the base of a few sandstones or at the top of dolomites. Typically the B interval is naturally fractured.

The C interval is composed of interbedded shaly to silty dolomite; dolomite containing mottled anhydrite; dolomitic sandstone to siltstone; anhydrite; and a few thin, black, organic-rich shale beds. The sandstones are very fine grained, showing massive to some horizontal bedding. Other lithologies show thin bedding, fine lamination, or possible wavy beds; anhydrite is bedded to massive. Several units show bioturbation or haloturbation. The C interval represents the lower seal for the reservoir rocks in the B interval above. The anhydrite and low-permeability dolomite helps prevent fracture communication with underlying halite beds (Morgan and others, 2014).

The dolomites in Cane Creek A, B, and C intervals all display well-developed intercrystalline porosity, microporosity, and microbial constructional (tubular) pores. Clusters of micro-rhombic dolomites typically contain intercrystalline pores. A few vugs or molds and minor interparticle porosity are

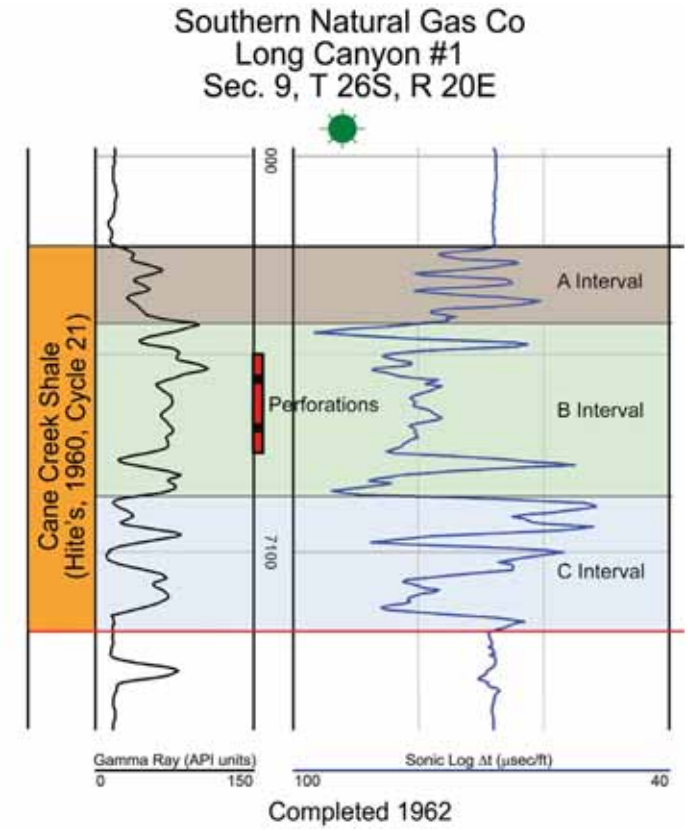

Figure 13. *Typical gamma-ray–sonic log of the Cane Creek shale, Long Canyon field, Grand County, Utah, showing the division of the Cane Creek shale into "A," "B," and "C" intervals. Cumulative production from a vertical borehole in this well (to January 1, 2016) = 1,125,446 barrels of oil, 1.16 BCFG, and 571,991 barrels of water (Utah Division of Oil, Gas and Mining, 2016). See figure 2 for location of Long Canyon field.*

preserved. Pores may be lined with secondary calcite or dolomite crystals, or plugged with anhydrite. Brittle sandstone and siltstone beds typically contain fracture porosity. They also exhibit intergranular porosity as well as microporosity.

Both vertical and subvertical fractures are common; some can be classified as microfractures and microstylolites. Horizontal to subhorizontal fractures are sparse. Zones of brecciation (including autobrecciation) are commonly present, especially near the base of the intervals or above anhydrite beds; a few slickensides are also present. Fractures are typically sealed with halite, anhydrite, clay, and calcite whereas some fractures remain open (Morgan and others, 2014); bitumen-lined fractures also occur. Microfractures contain dolomite fill and sulfide minerals. Fractures trend northeast-southwest (Morgan and others, 2014).

Principal Rock Types for Epifluorescence Evaluation of Cuttings and Cores

The principal rock types used for our epifluorescence evaluation in cuttings and core chips collected from the A, B, and C intervals in the Cane Creek shale are (1) dolomitic sandstone and siltstone, (2) microcrystalline dolomite mudstone, (3) dolomitized peloidal grainstone, (4) dolomitized peloidal/coated grain grainstone/packstone, (5) dolomitized microbialites, (6) dolomitized oncolitic/pisolitic rudstone, and (7) dolomitic to silty shale (figure 16; see appendices B and C for complete petrographic descriptions; however, diagenesis and depositional environments were not part of this study). Some of these rock types are more prevalent in one or two of the Cane Creek intervals. For example, dolomitic sandstone and siltstone, peloidal grainstone/packstone, and dolomitized microbialites are most common in the B interval. Finely crystalline dolomites, limestones, siltstones, and sandstones are the best samples for qualitative EF analysis (most of our samples were finely crystalline dolomites), especially if they are porous, whereas black shales are generally "dead" or lack visible EF.

A Interval

Cuttings and core chip samples from the A interval consist of (1) microcrystalline and fine to medium crystalline dolomite, (2) silty to argillaceous dolomite, (3) dolomitic mudstone (figures 12B and 16A), (4) black organic-rich shale, silty shale, silty dolomitic shale (figure 16A), and dolomitic shale, (5) siltstone, dolomitic siltstone, and argillaceous siltstone, and (6) anhydrite and salt. These lithologies can include patches of anhydrite and argillaceous material or clusters of dolomite crystals in the matrix. Dolomitized carbonate fabrics range from grainstones to mudstones, and include some framestones and boundstones as well. Packstones and grainstones are sporadically fossiliferous containing bryozoans or other fossil remains. Interbedding of various lithologies or carbonate fabrics is common. Laminations in boundstones may be microbial in origin with tubular structures. Siltstone is typically poorly sorted.

B Interval

Cuttings and core chip samples from the productive B interval consist of (1) microcrystalline (figure 12C) and silty microcrystalline dolomite (figure 12H), (2) fine- to medium-crystalline dolomite, (3) silty to black argillaceous dolomite, (4) black organic-rich shale, silty shale, silty dolomitic shale, and dolomitic shale, (5) siltstone and dolomitic siltstone, (6) dolomitic sandstone (figure 16A), (7) silty limestone, and (8) anhydrite and salt. Some dolomite cuttings appear to be organic rich. Patches of coarse-grained dolomite display rhombic crystals. Carbonate fabrics, most of which are dolomitized, range from grainstones to mudstones. Skeletal grainstones contain bryozoans and possible ostracods; some packstones and wackestones are also fossiliferous. Carbonate textural components include peloids (figure 12G), ooids, and coated grains. Well-developed microbialites (figure 12F) are relatively common displaying microbial laminations, tubular microstructures with possible construction pores, and other diagnostic textures. Microbial constructional pores, where present and well developed, likely enhance reservoir quality

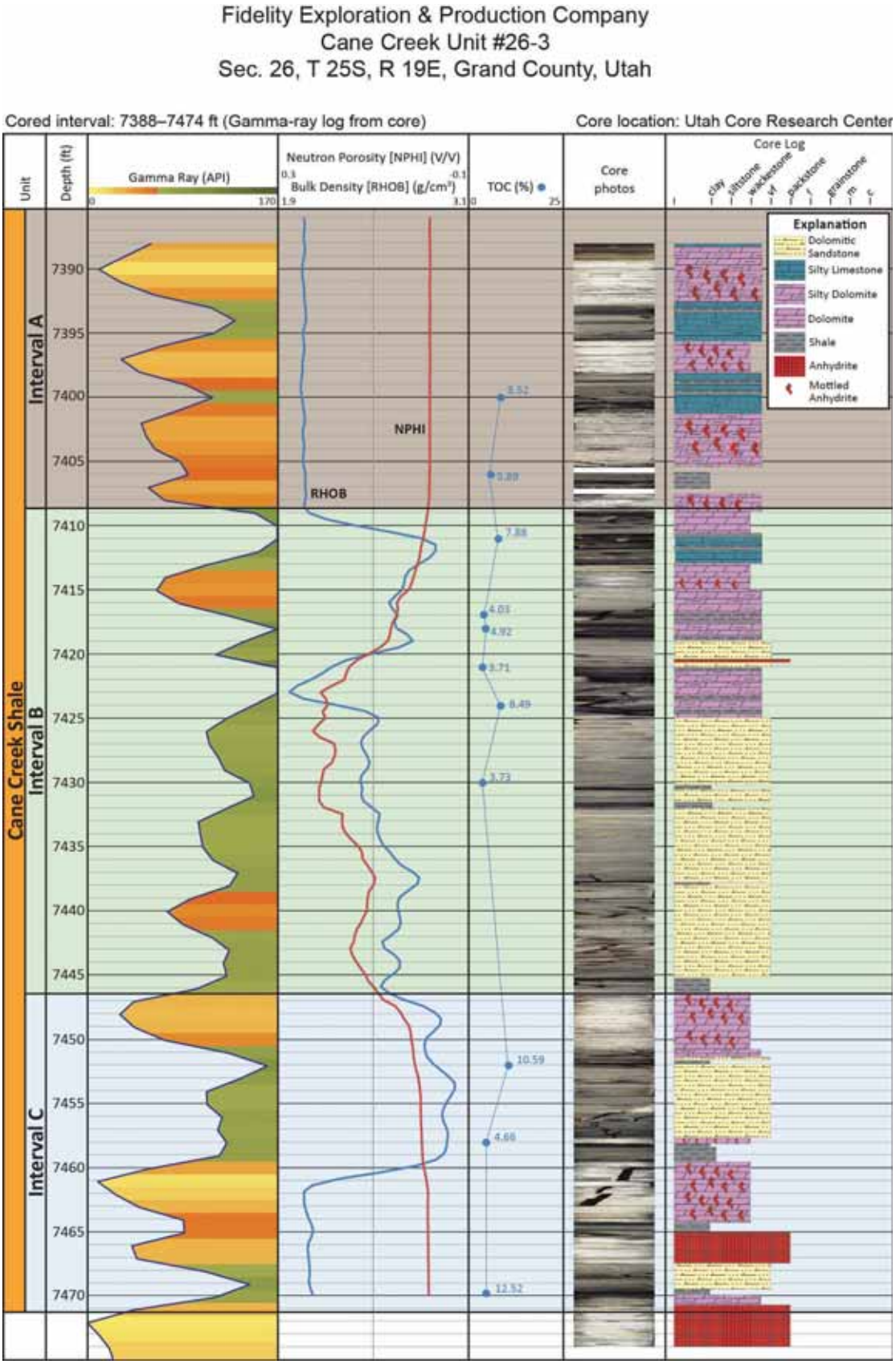

Figure 14. *Gamma-ray–neutron porosity–bulk density log profiles as well as total organic carbon (TOC), tied to lithology data from a recent Cane Creek shale core in Big Flat field, Grand County, Utah. Note the variations between the log and lithologic characteristics of the A, B, and C intervals. Cumulative production from a horizontal borehole in this well (to January, 1, 2016) = 370,515 barrels of oil, 0.21 BCFG, and 6172 barrels of water (Utah Division of Oil, Gas and Mining, 2016). See figure 2 for location of Big Flat field.*

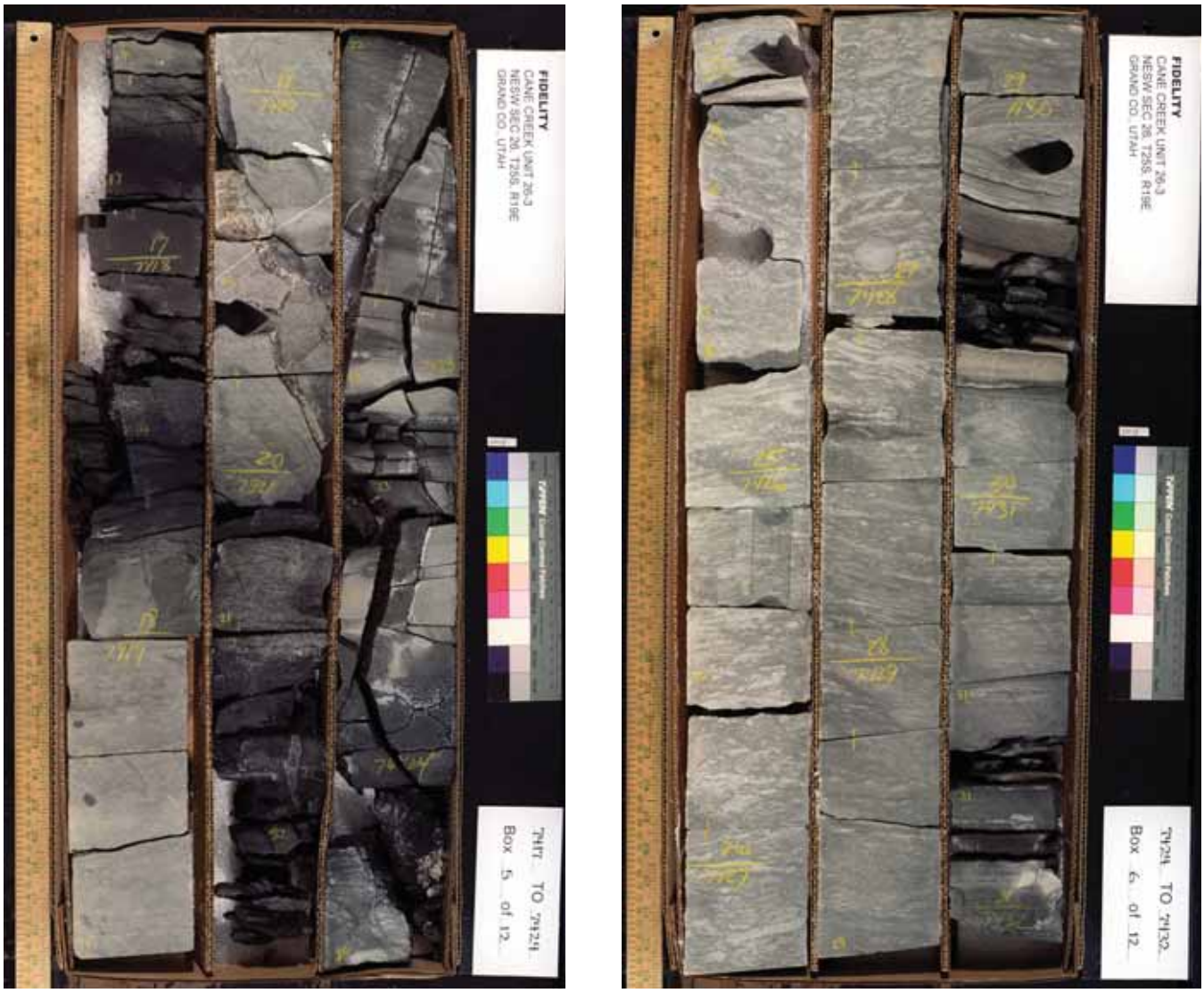

Figure 15. *Typical fractured, silty to muddy dolomite (finely crystalline) with thin siltstone and black organic-rich shale beds of the B interval in the Cane Creek shale; Cane Creek Unit No. 26-3 well (well #10 on figure 10; section 26, T. 25 S., R. 19 E., SLBL&M), Big Flat field, San Juan County, Utah, slabbed core from 7418 to 7432 feet. Core photography by Triple O Slabbing, Denver, Colorado, provided courtesy of Fidelity Exploration & Production Company.*

and production. Similar to the overlying A interval, interbedding of various lithologies and carbonate fabrics exists within some B interval cuttings.

C Interval

Cuttings and core chip samples from the C interval consist of (1) microcrystalline dolomite, (2) fine- to coarsely crystalline dolomite, (3) anhydritic dolomite, silty dolomite, argillaceous silty dolomite, and shaly dolomite (4) black organic-rich shale, silty shale, and dolomitic shale, (5) dolomitic limestone, and (6) siltstone and argillaceous siltstone. Black, finely crystalline dolomite cuttings are likely organic rich. These lithologies can include patches of argillaceous dolomite or clusters of anhydrite in the matrix; well-preserved coarse rhombic dolomite crystals are also present in a few cuttings. Carbonate fabrics, most which are also dolomitized, range from grainstones to mudstones (the most common). Bryozoans (possibly colonial) are recognized in fossiliferous grainstones, packstone, and wackestones. Carbonate textural components include peloids in dolomitized grainstones to wackestones, oncolites, pisolites, and coated grains (figures 12D, 16C, 16D, and 16F). Possible microbialites are represented by dolomitized microlaminations (figure 16E), and lumpy or tubular structures.

MAPPING OF CANE CREEK EPIFLUORESCENCE

Four sets of maps were created for the entire Cane Creek shale, and the A, B, and C intervals based on EF readings: (1) the highest EF, (2) the average of the highest EF, (3) the high-

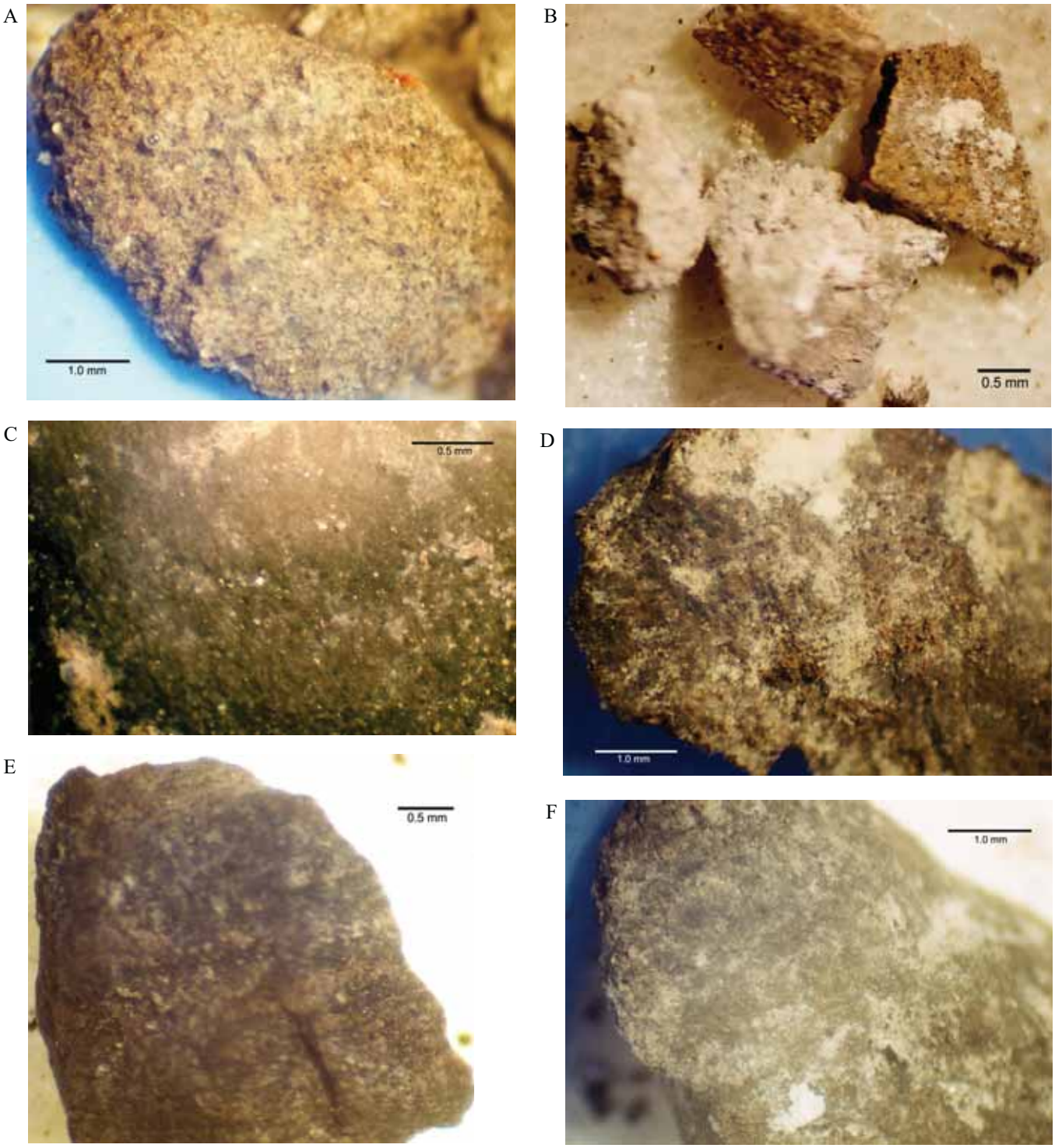

Figure 16. *Principal rock types for epifluorescence work in Cane Creek shale cuttings observed with a binocular microscope.* ***A.*** *Dolomitic sandstone cutting composed of quartz grains surrounded by dolomitic mud and/or cement from the 7380–90 foot sample in the Mineral Canyon No. 1-14 well (well #12; SW1/4SE1/4 section 14, T. 26 S., R. 19 E., SLBL&M, Grand County).* ***B.*** *Microcrystalline dolomite mudstone cutting displaying microporosity from the 6290–6300 foot sample in the Horsehead Unit No. 1 well (well #21; NW1/4SW1/4 section 18, T. 29 S., R. 21 E., SLBL&M, San Juan County).* ***C.*** *Dolomitized peloidal grainstone with minor amounts of quartz sand grains from the 6350–60 foot sample in the Horsehead Unit No. 1 well (well #21; NW1/4SW1/4 section 18, T. 29 S., R. 21 E., SLBL&M, San Juan County).* ***D.*** *Dolomitized peloidal/coated grain grainstone/packstone displaying good visible porosity from the 6360–70 foot sample in the Horsehead Unit No. 1 well (well #21; NW1/4SW1/4 section 18, T. 29 S., R. 21 E., SLBL&M, San Juan County).* ***E.*** *Dolomitized microbial laminite ("stromatolitic bindstone") displaying alternating light and dark crinkly laminations from the 5940–50 foot sample in the West Bridger Jack Unit No. 3 well (well #15; SE1/4SW1/4 section 3, T. 27 S., R. 21 E., SLBL&M, San Juan County).* ***F.*** *Dolomitized oncolitic/pisolitic rudstone from the 5960–70 foot sample in the West Bridger Jack Unit No. 3 well (well #15; SE1/4SW1/4 section 3, T. 27 S., R. 21 E., SLBL&M, San Juan County). See figure 10 for well number locations.*

est average EF, and (4) the average of the EF sample averages (appendix A). The intent of these maps was to use various EF data and combinations of EF averages to identify potential hydrocarbon "sweet spots." As shown on the maps and described in the following sections, some maps indicate the same fairways of hydrocarbon potential whereas other maps suggest possible areas to explore not identified on the others.

The highest EF maps show the highest EF value determined from all cuttings samples in each well from the entire Cane Creek and within each interval. The values for average of the highest EF maps were determined by averaging the highest EF from each cuttings sample interval in each well for the entire Cane Creek and the A, B, and C intervals. The values for the highest average EF maps represent the highest average EF out of all cuttings sample intervals in each well within the entire Cane Creek and the A, B, and C. Finally, the values for the average of the EF sample averages maps were determined by averaging the average of each cuttings sample interval in each well for the entire Cane Creek and the A, B, and C intervals.

Entire Cane Creek Shale

The map of the highest EF based on visual rating of well cuttings and core chips for the entire Cane Creek shale in each well (combining the results of the A, B, and C intervals) is shown on figure 17. In this map, and those that follow, mapped ratings that are considered highly prospective for oil are shown in dark purple (rating of 2.0–2.5) and green (rating higher than 2.5). A pronounced curvilinear fairway of very high (in green) ratings trends from northwest to southeast through the Paradox fold and fault belt. Note the lobes of high ratings that occur both northwest and southeast of the largest Cane Creek field—Big Flat (figures 2 and 10). The regions within these oil prospective lobes are sparsely explored. Areas to the northeast and southwest of the fairway defined in the map are characterized by relatively low EF ratings (in orange), and thus have lower potential for finding new oil reserves.

Figure 18 shows the average highest EF in each well based on visual rating for the entire Cane Creek shale. The same curvilinear fairway seen on figure 17 is shown with the average highest rating (in purple) trending from northwest to southeast. A large, elongate lobe present in Big Flat field continues to the northwest in light green (rating of 2.0–2.5). This lobe represents a relatively large, untested area of the Cane Creek play. It includes the small Hell Roaring field (figures 2 and 10) that has the same average highest EF rating (2.8) as a well in Big Flat field (well #10). A small north-northeast to south-southwest-trending ovate lobe, also with an average highest EF rating of 2.5 or higher just southeast of Big Flat, corresponds to a similar lobe at the same locale as observed on figure 17. A boot-shaped area, which includes Hatch Point field (figures 2 and 10), and a very small lobe at the end of the fairway have average highest EF ratings of 2.0 (in dark purple), and thus may also represent additional exploration potential providing there is adequate porosity and permeability.

Figure 19 shows the highest average EF in each well based on visual rating for the entire Cane Creek shale. Again, a pronounced curvilinear fairway of anomalous fluorescence ratings exists that follows the same northwest to southeast trend seen in the highest EF map (figure 17). The anomalous trend displays lower average ratings (displayed in both green and purple) than highest EF ratings shown on figure 17. The lobes of highest average ratings that occur both northwest and southeast of the Big Flat field are not as pronounced nor are they as large and continuous as those suggested by the highest EF map (figure 17). Some of the smaller fields containing productive Cane Creek wells display highest average ratings that are less than the area around and possibly to the northwest of Big Flat field.

Figure 20 shows the average of the EF sample averages in each well based on visual rating of the Cane Creek shale. The curvilinear pattern remains with three distinct lobes of high EF ratings. Once again, the area of greatest potential is the large lobe with an EF rating of 2.0 (in dark purple) northeast of Big Flat field.

A Interval

The map of the highest EF in each well based on visual rating of the A interval, the uppermost stratigraphic portion of the Cane Creek shale, is shown on figure 21. A constricted fairway of very highest (in green) ratings for the A interval follows the same general trend as the total Cane Creek thickness highest ratings. Very prospective A interval sections appear to exist in large lobes to the northwest and southeast of Big Flat field. The northern and western portions of Big Flat field seem to have lower highest ratings than the southeastern and eastern productive areas. High-risk areas that have low ratings (in orange) within the A interval occur at the northwest end of the highest fairway as well as to the northeast and southwest of the overall favorable ratings fairway.

Figure 22 shows the average highest EF in each well based on visual rating of the A interval. The overall curvilinear Cane Creek fairway is shown where two distinct, narrow lobes have an average highest EF of 3.0 (in dark green) northwest and southeast of Big Flat field that lies in a saddle in between. A dry hole, the Cane Creek State No. 1-16 (section 36, T. 27 S., R. 20 E., SLBL&M, Grand County, well #16, figure 10 and table 3) has high ER ratings (3.0 and 3.1) in the A interval, creating the small lobe shown on figure 21 and the thickness maps by Morgan and others (2014) and Carney and others (2014). Thus, the B interval in this well and the immediate surrounding area, deserves closer examination for oil potential. A larger, somewhat round lobe is mapped towards the southeast end of the fairway and has an EF rating of 2.5 (in light green). This area includes Hatch Point field along the northwestern edge of the lobe and a large, sparsely drilled area of the Cane Creek shale play to the southeast.

Figure 23 shows the highest average EF in each well based on visual rating of the A interval. The anomalous trend on this

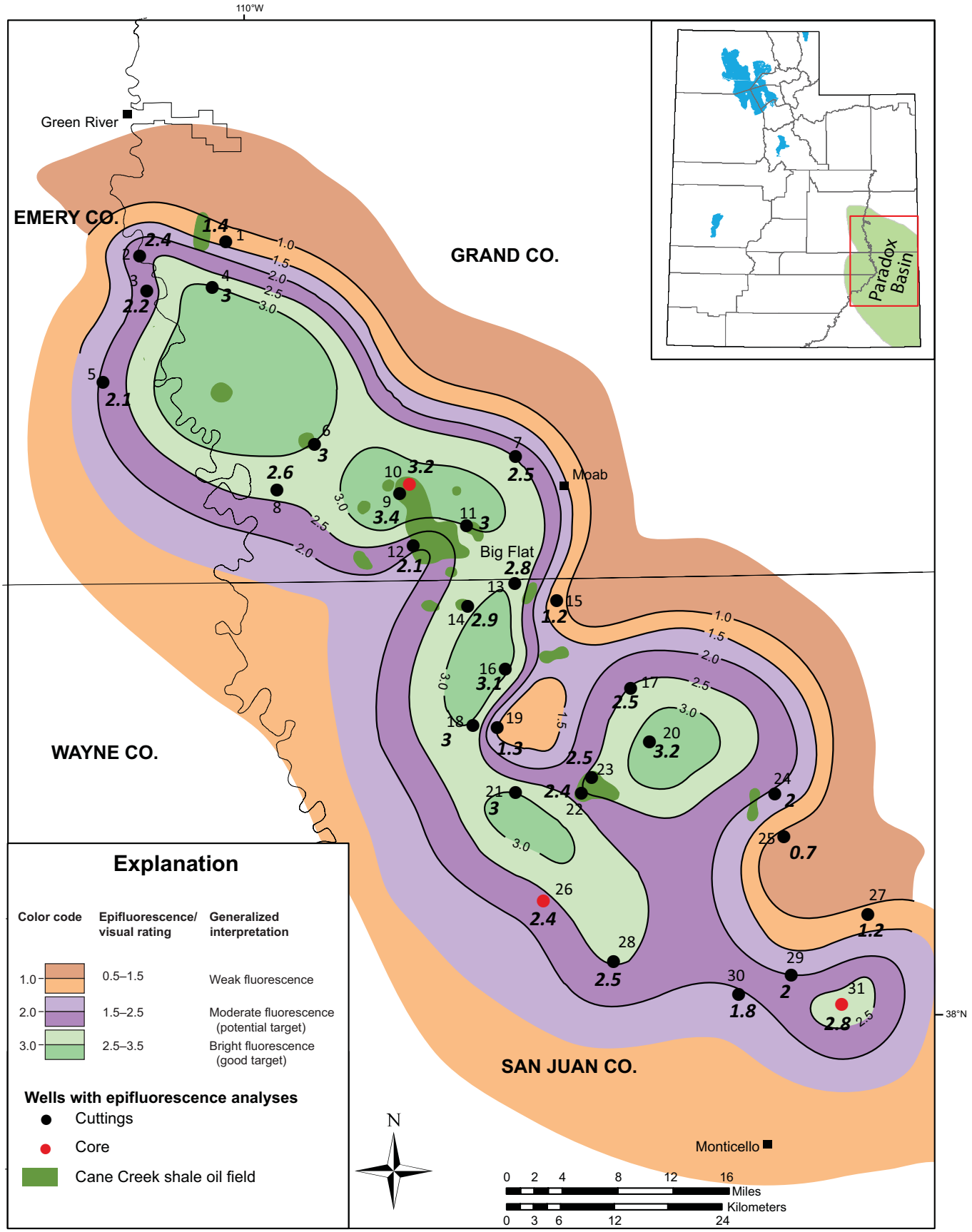

Figure 17. *The highest epifluorescence based on visual rating of Cane Creek well cuttings and core chips. See table 3 for list of wells corresponding to the numbers by the black or red dots.*

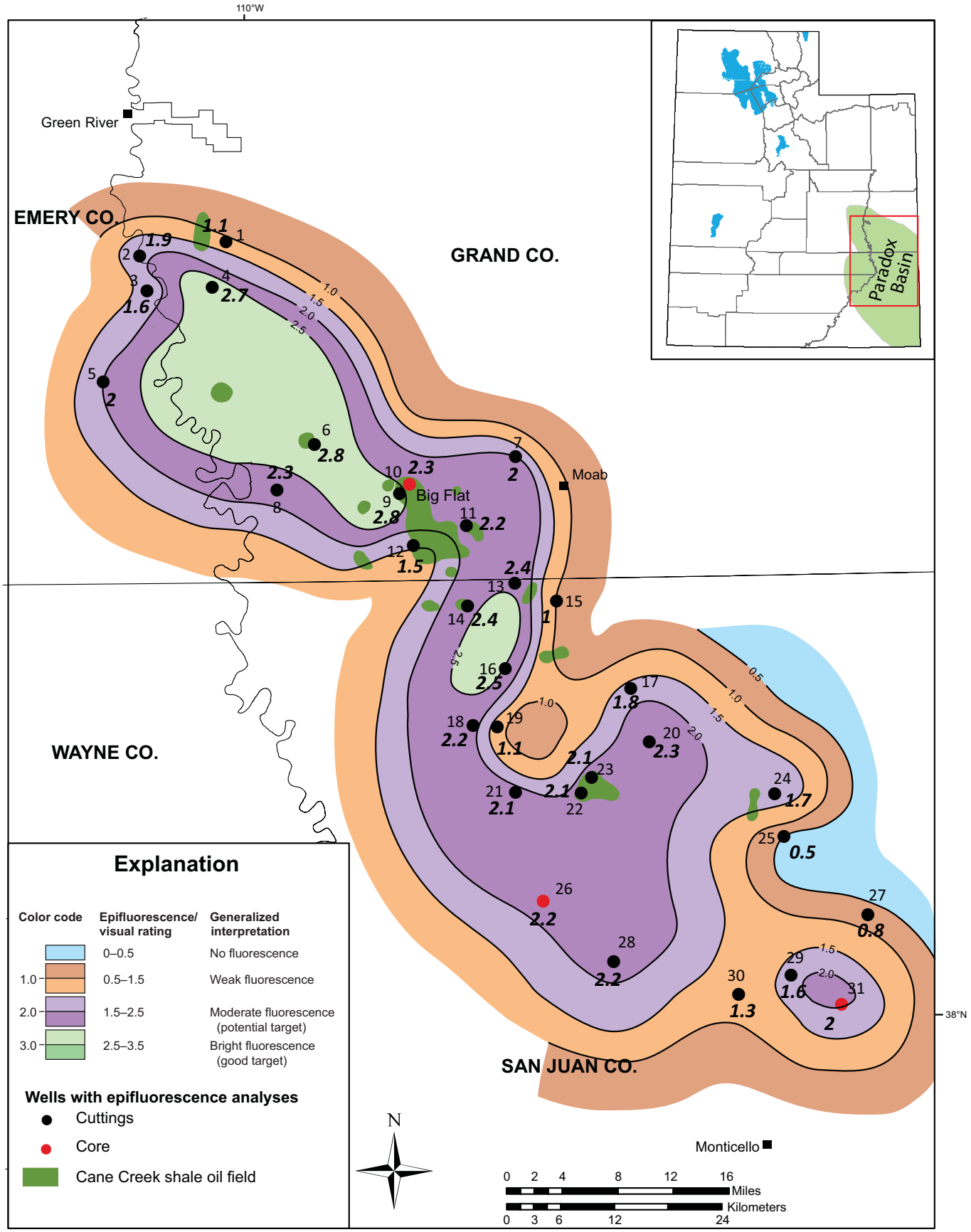

Figure 18. *The average highest epifluorescence based on visual rating of Cane Creek well cuttings and core chips. See table 3 for list of wells corresponding to the numbers by the black or red dots.*

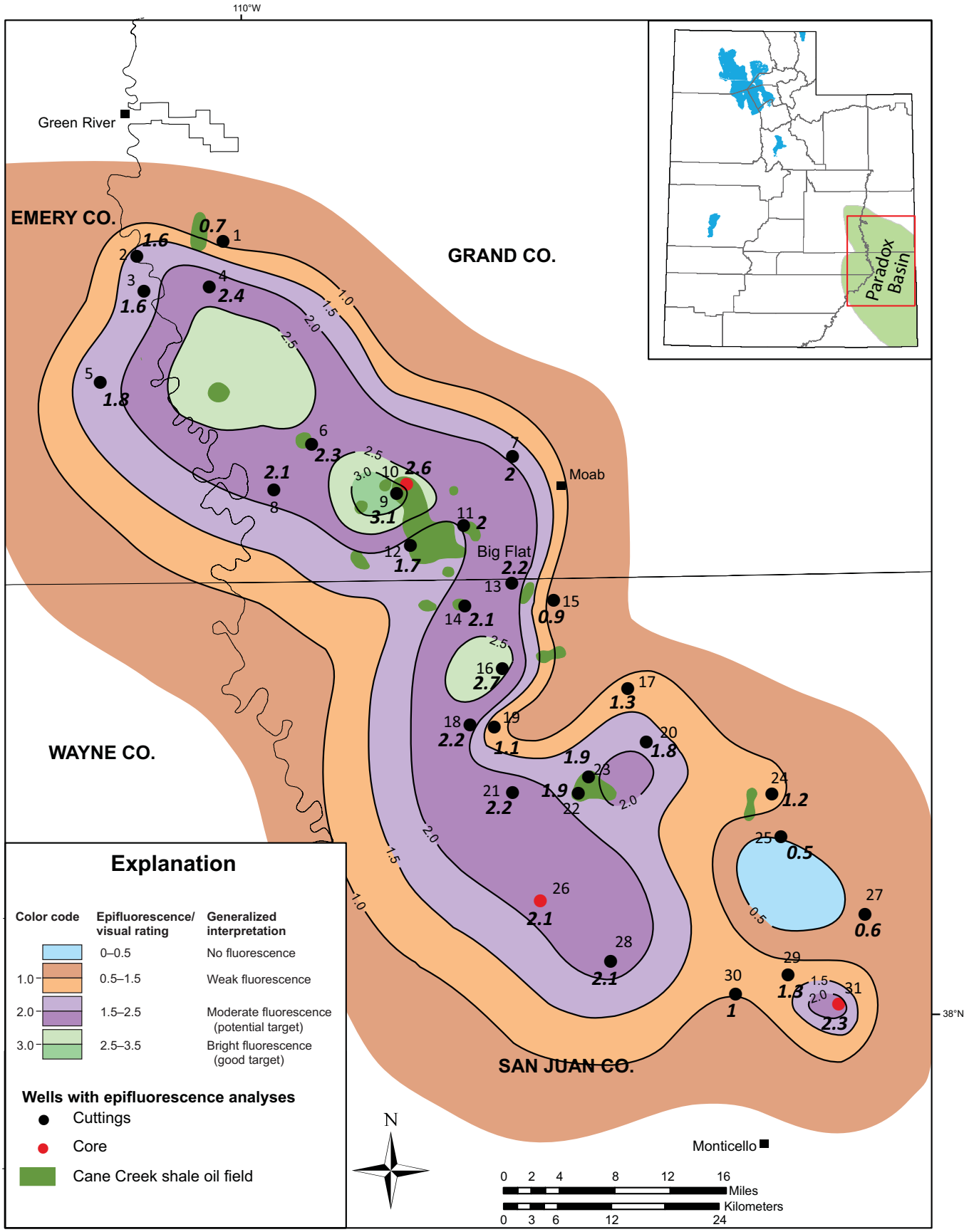

Figure 19. *The highest average epifluorescence based on visual rating of Cane Creek well cuttings and core chips. See table 3 for list of wells corresponding to the numbers by the black or red dots.*

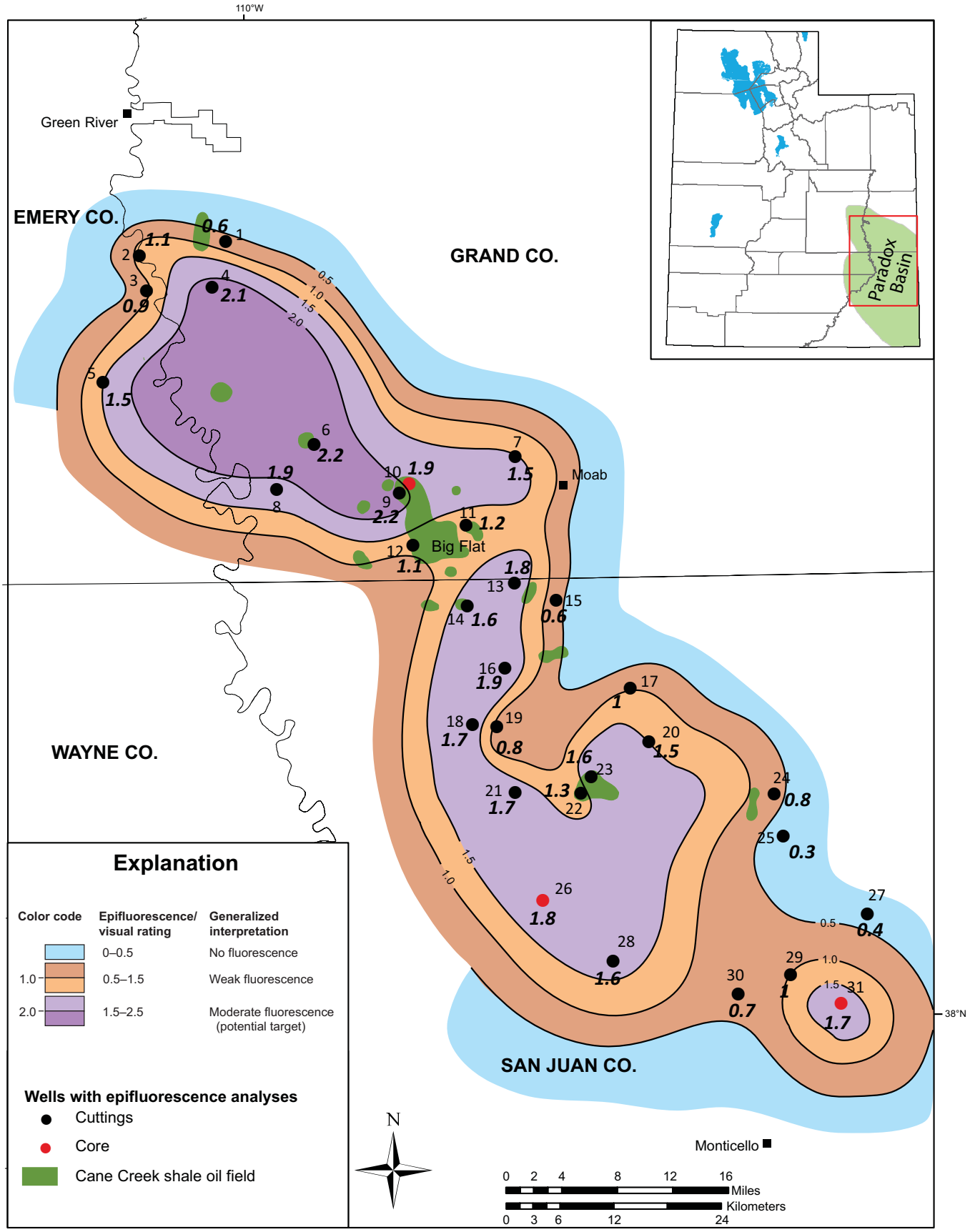

Figure 20. *The average of the epifluorescence sample averages based on visual rating of Cane Creek well cuttings and core chips. See table 3 for list of wells corresponding to the numbers by the black or red dots.*

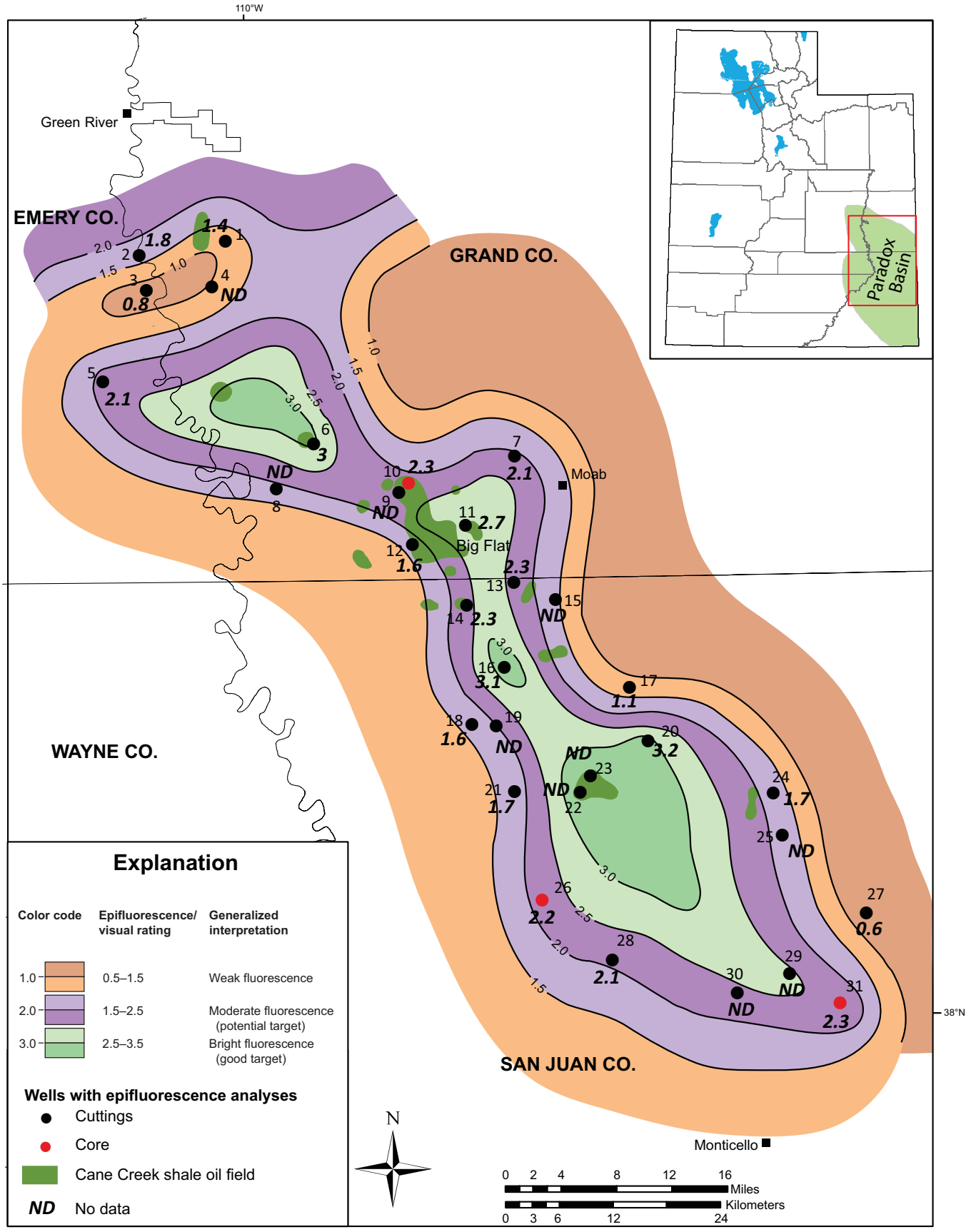

Figure 21. *The highest epifluorescence based on visual rating of Cane Creek well cuttings and core chips, A interval. See table 3 for list of wells corresponding to the numbers by the black or red dots.*

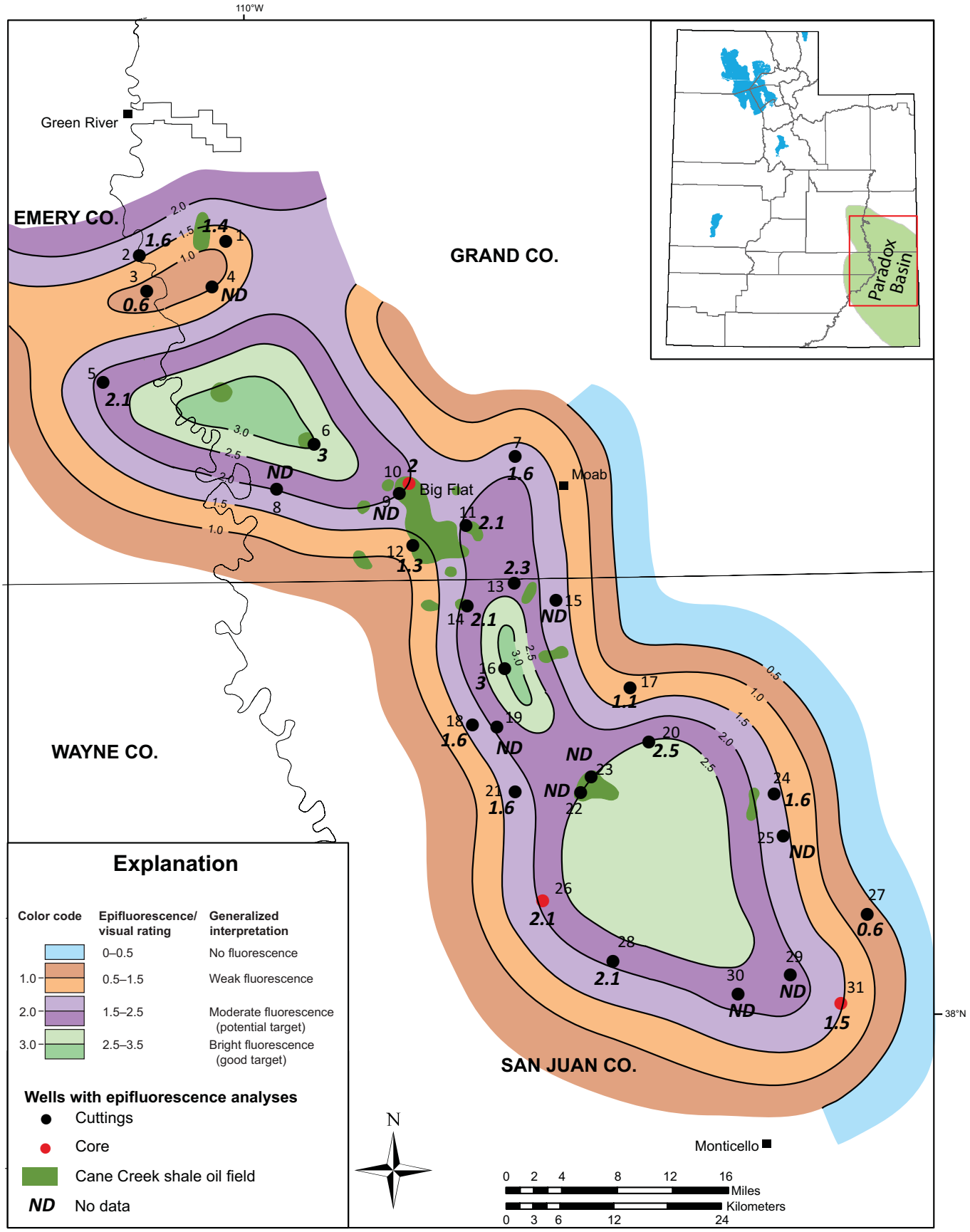

Figure 22. *The average highest epifluorescence based on visual rating of Cane Creek well cuttings and core chips, A interval. See table 3 for list of wells corresponding to the numbers by the black or red dots.*

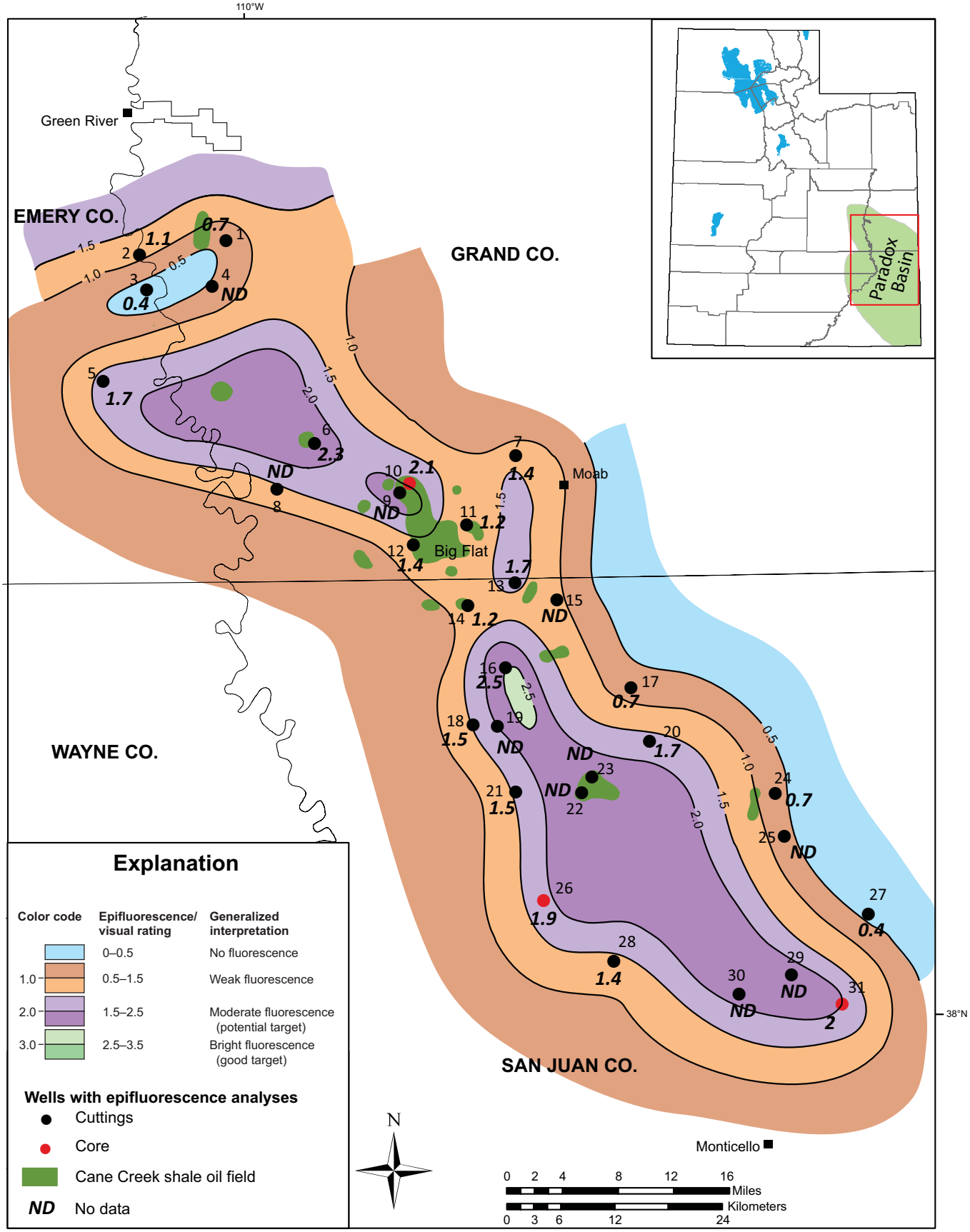

Figure 23. *The highest average epifluorescence based on visual rating of Cane Creek well cuttings and core chips, A interval. See table 3 for list of wells corresponding to the numbers by the black or red dots.*

map displays lower average ratings (shown in both green and dark purple) than highest EF ratings for the A interval shown on figure 21. Fragmented or isolated pods of highest average ratings (shown in green and dark purple) suggest that the A interval does not have uniform prospectivity or productivity along the favorable Cane Creek shale fairway. The southern portions of Big Flat field do not rate very well for the A interval using the highest average ratings, suggesting that the A interval may not be highly productive through the entire area of the field. Very prospective A interval sections appear to exist in discrete lobes to the northwest and southeast of Big Flat field as determined by the high average ratings (in green and dark purple). High-risk areas that have low ratings (in orange and blue) within the A interval occur at the northwest end of the highest average fairway as well as to the northeast and southwest of the overall favorable ratings fairway.

Figure 24 shows the average of the EF sample averages in each well based on visual rating of the A interval. The overall Cane Creek shale fairway appears very similar to that shown on figure 23, but narrower. However, only the west-northwest- to east-southeast-trending lobe just west of Big Flat field has an EF rating high enough (2.0) to suggest the potential for moderate oil productivity in the A interval. Another very small lobe of the same EF rating is associated with the Cane Creek State No. 1-36 well (well #16).

B Interval

The map of the highest EF in each well based on visual rating of the B interval, the primary reservoir and the middle stratigraphic portion of the Cane Creek shale zone, is shown on figure 25. A well-defined fairway of very highest (in green and dark purple) ratings for the B interval follows the same general trend as the total Cane Creek shale thickness highest ratings. All of the Cane Creek oil fields to date have the B interval highest ratings that are rated very high (in green and purple). Based on EF ratings, the B interval appears to be the best and most widespread Cane Creek shale interval for oil production and prospectivity. Very prospective B interval sections appear to exist in lobes to the northwest and southeast of Big Flat field. High-risk areas that have low ratings (in orange) within the B interval occur only to the northeast and southwest of the overall favorable ratings fairway.

Figure 26 shows the average highest epifluorescence in each well based on visual rating of the B interval. It shows the same well-defined curvilinear Cane Creek fairway that is mapped for highest EF on figure 25. However, there are fewer lobes of high EF and surprisingly a significant part of Big Flat field lies in the relatively low 1.5–2.0 EF rating range (in light purple). A pear-shaped, west-northwest- to east-southeast-trending lobe, including the northern part of Big Flat field and Hell Roaring field, has an EF rating 2.5 (in light green) indicating movable oil potential in the B interval. The southern part of the fairway shows a large area with a rating 2.0 and higher—a good indication of potential and now confirmed with the recent discovery of Cane Creek production in the La Sal No. 29-28 well (section 29, T. 29 S., R. 23 E., SLBL&M, San Juan County; see figure 2 and table 2). This area lies in between Hatch Point and Wilson Canyon fields, each with lower EF ratings in the B interval (1.5–2.0).

Figure 27 shows the highest average EF in each well based on visual rating of the B interval. The anomalous trend displays lower average ratings (shown in both green and purple) than highest EF ratings for the B interval shown on figure 25. Discontinuous or patchy areas of highest average ratings (shown in green and dark purple) suggest that the B interval may not have uniform prospectivity or productivity along the favorable Cane Creek shale fairway. Relatively large undrilled areas exist in which the B interval appears to be prospective for oil accumulations.

Figure 28 shows the average of the EF sample averages in each well based on visual rating of the B interval. The Cane Creek fairway appears very similar to that shown on figure 25 displaying multiple lobes of higher EF ratings. Again the pear-shaped, west-northwest- to east-southeast-trending lobe is present, including the northern part of Big Flat field and Hell Roaring field. It has an EF rating 2.0–2.5 suggesting oil is present in the B interval and may be capable of production where there is good porosity and permeability. Smaller lobes to the south and southeast of Big Flat have EF ratings of 2.0.

C Interval

The map of the highest EF in each well based on visual rating of the C interval, the lowest stratigraphic portion of the Cane Creek shale zone, is shown on figure 29. A well-defined fairway of very highest ratings (in green and dark purple) for the C interval is smaller in area than the fairways defined on the other rating maps. The most prospective areas for the C interval may occur in a continuous, curvilinear fairway to the northwest, south, and southeast of Big Flat field. Some of the wells are labeled "ND" (No Data) because the C interval is either absent or very thin in those wells. High-risk areas that have low ratings (in orange) within the C interval occur only to the northeast and southwest of the overall favorable ratings fairway.

Figure 30 shows the average highest EF in each well based on visual rating of the C interval. As expected the EF ratings show relatively low potential in the Cane Creek fairway including Big Flat field. There is a large west-northwest- to east-southeast-trending lobe that curves around Big Flat field and extends to the west with EF ratings of 2.5 (in light green). This lobe includes Long Canyon field (figures 2 and 10 [well #11]); however, caution must be applied to this interpretation as the data are limited. An additional small, north- to south-trending lobe is shown on the center of the Cane Creek fairway whereas the remaining areas show very limited potential with EF ratings less than 2.5.

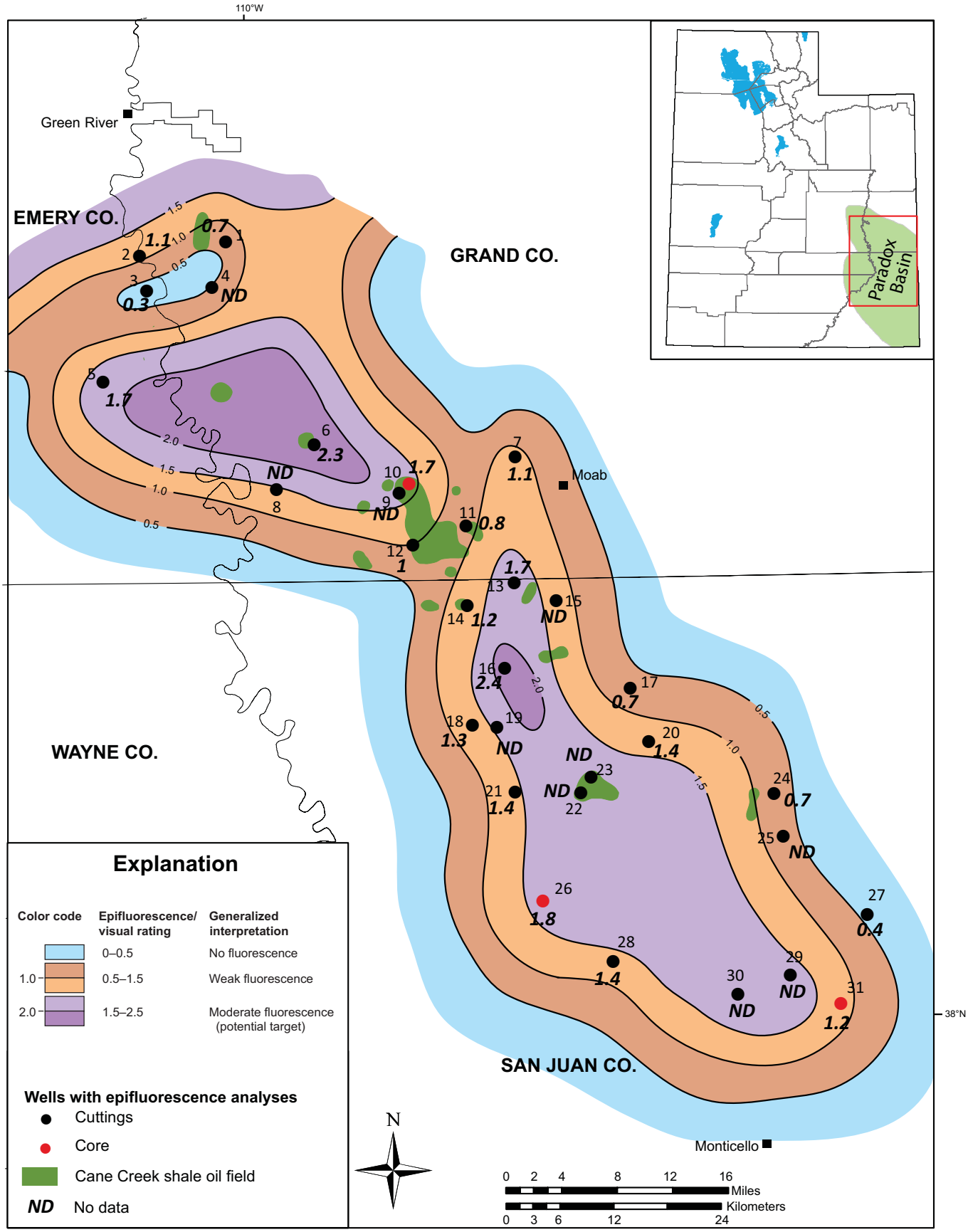

Figure 24. *The average of the epifluorescence sample averages based on visual rating of Cane Creek well cuttings and core chips, A interval. See table 3 for list of wells corresponding to the numbers by the black or red dots.*

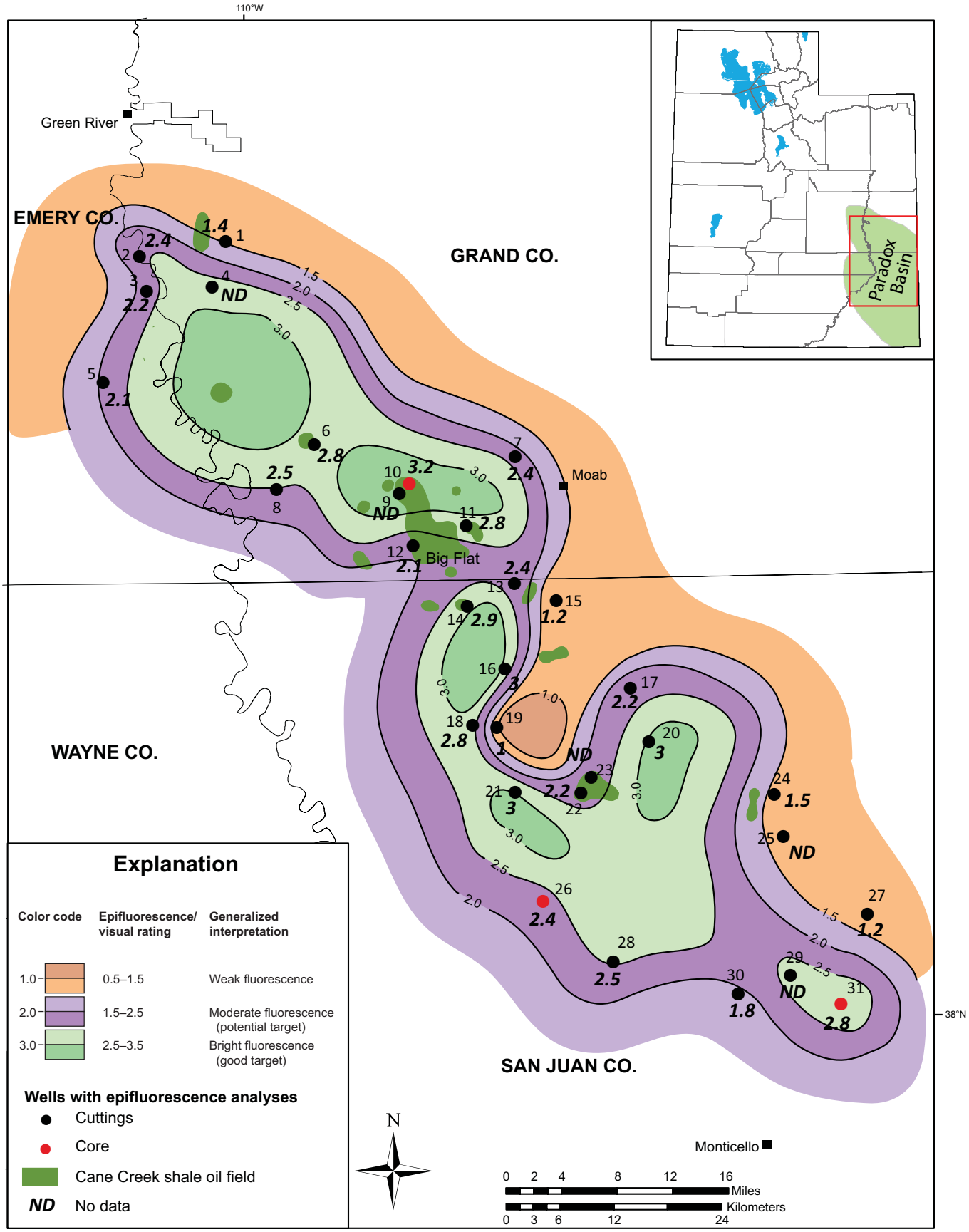

Figure 25. *The highest epifluorescence based on visual rating of Cane Creek well cuttings and core chips, B interval. See table 3 for list of wells corresponding to the numbers by the black or red dots.*

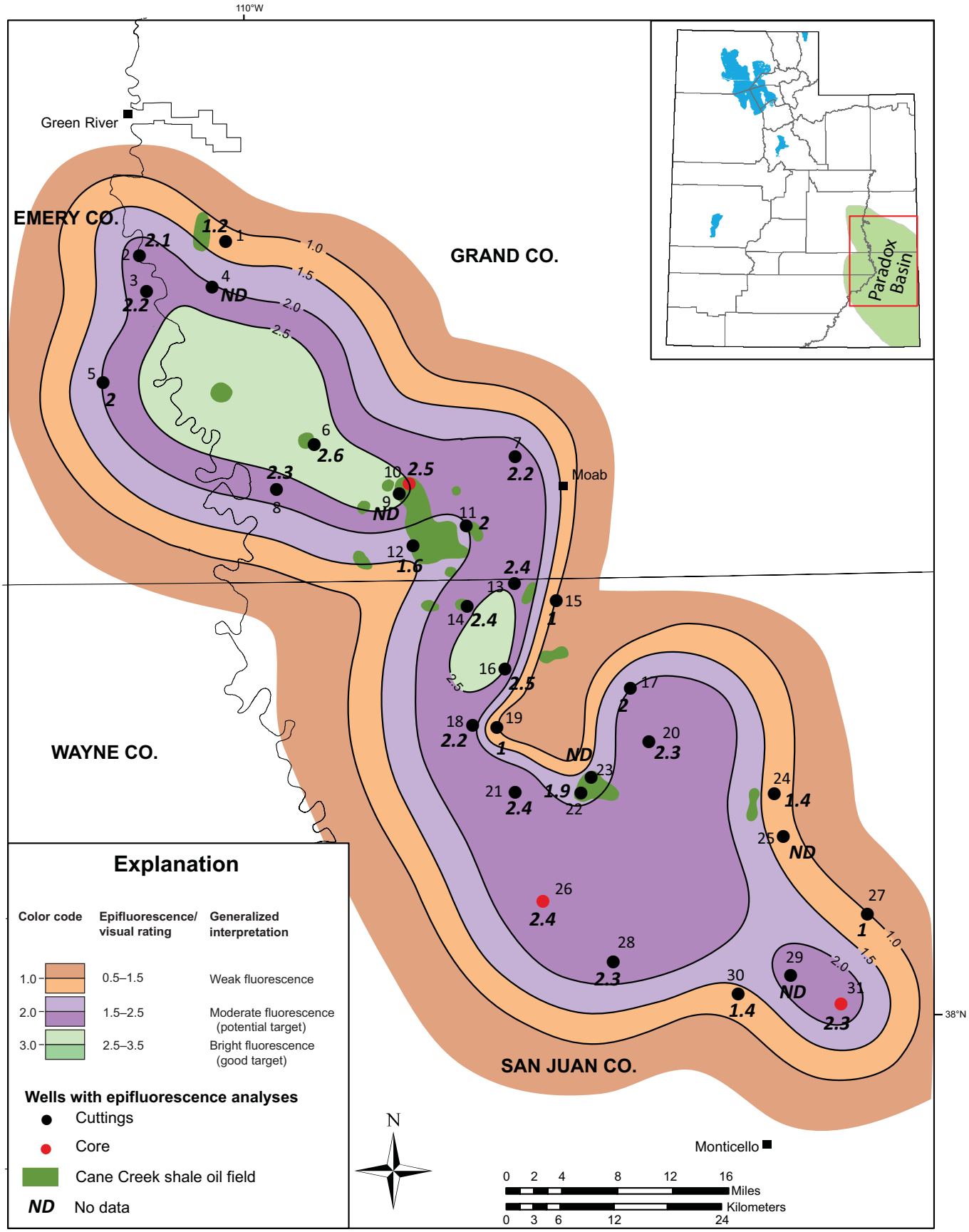

Figure 26. *The average highest epifluorescence based on visual rating of Cane Creek well cuttings and core chips, B interval. See table 3 for list of wells corresponding to the numbers by the black or red dots.*

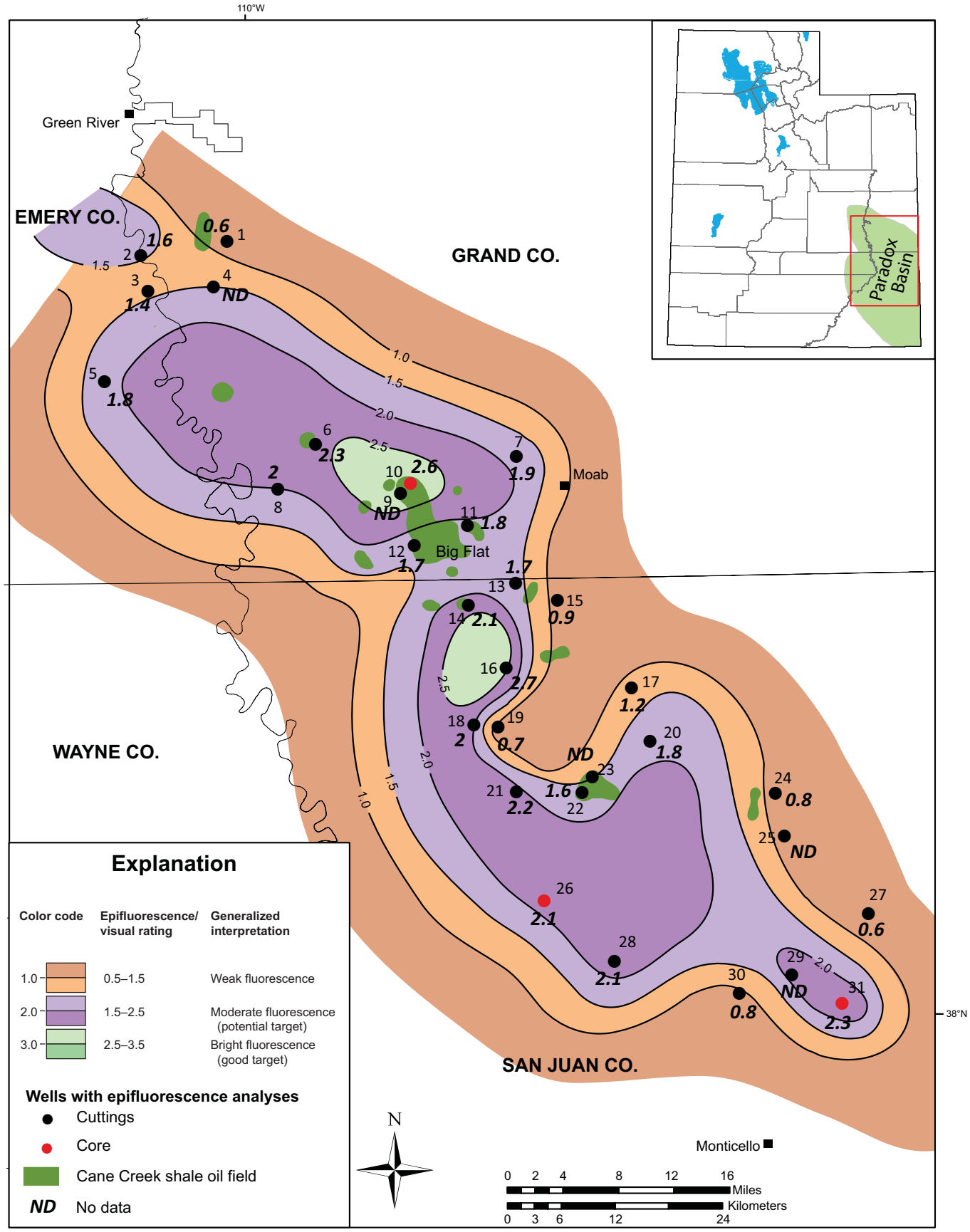

Figure 27. *The highest average epifluorescence based on visual rating of Cane Creek well cuttings and core chips, B interval. See table 3 for list of wells corresponding to the numbers by the black or red dots.*

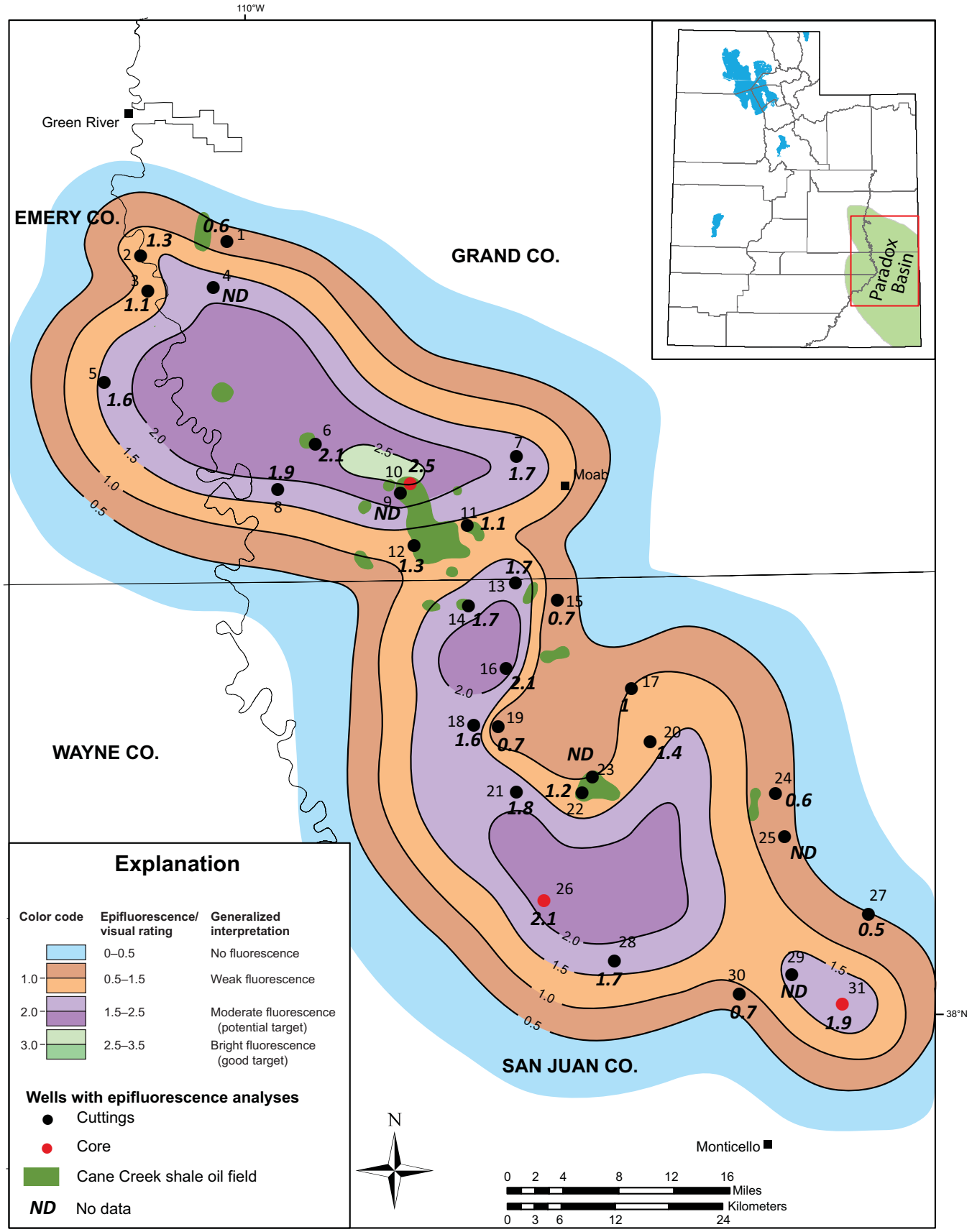

Figure 28. *The average of the epifluorescence sample averages based on visual rating of Cane Creek well cuttings and core chips, B interval. See table 3 for list of wells corresponding to the numbers by the black or red dots.*

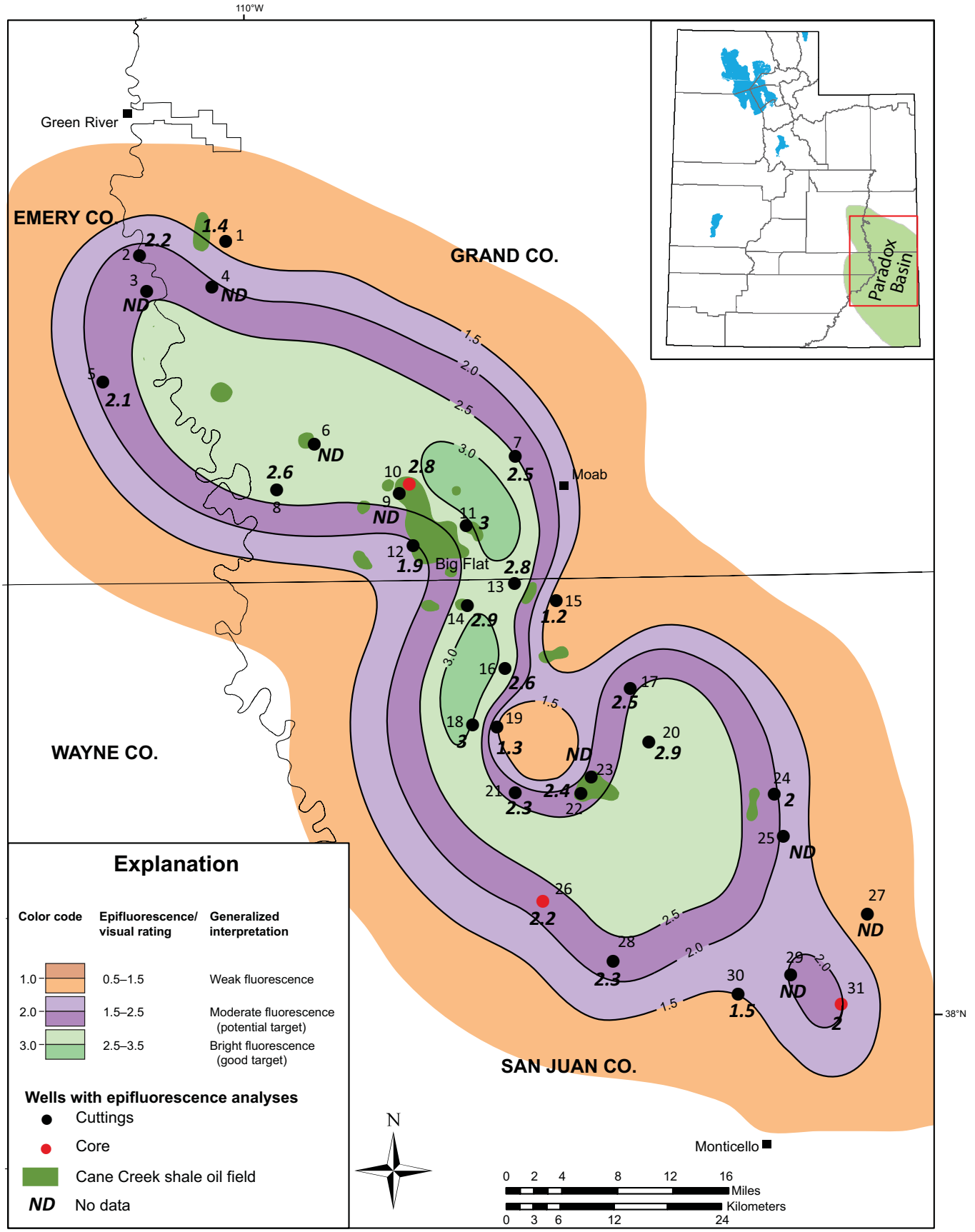

Figure 29. *The highest epifluorescence based on visual rating of Cane Creek well cuttings and core chips, C interval. See table 3 for list of wells corresponding to the numbers by the black or red dots.*

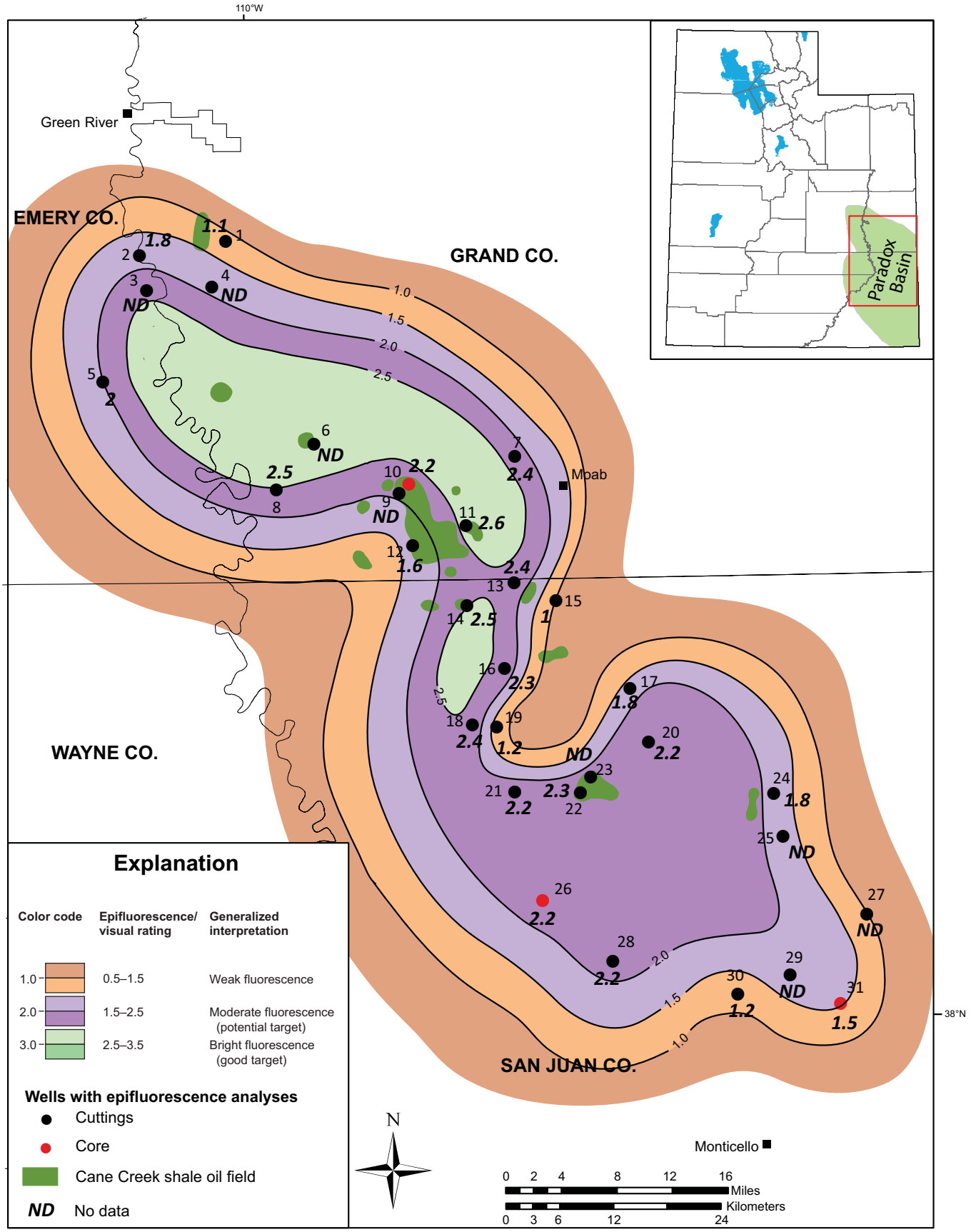

Figure 30. *The average highest epifluorescence based on visual rating of Cane Creek well cuttings and core chips, C interval. See table 3 for list of wells corresponding to the numbers by the black or red dots.*

Figure 31 shows the highest average EF in each well based on visual rating of Cane Creek well cuttings and core chips, C interval. The anomalous trend displays lower average ratings (shown only in purple) than highest EF ratings for the C interval shown on figure 29. A favorable Cane Creek shale fairway for the C interval based on highest average ratings is somewhat narrowed and smaller than the fairway defined on the previous map using highest EF ratings. Relatively large areas exist that may have high exploration risk associated with them (the orange map areas) for oil accumulations within the C interval based on highest average ratings.

Figure 32 shows the average of the EF sample averages in each well based on visual rating of the C interval. In this map the Cane Creek fairway is very narrow, showing limited potential; most of it has EF ratings of less than 2.0. A relatively large, west-northwest- to east-trending lobe is mapped in the northern part of the fairway. However, this lobe is based on only two data points. Therefore, the map of the average of the EF sample averages confirms that the C interval is the lower seal (and a probable source) for the oil in the overlying B interval and should not be a drilling target.

STATISTICAL ANALYSIS

The EF data collected were analyzed to determine basic statistical values—the arithmetic mean (or average), mode, median, and standard deviation. About 2650 EF rating measurements from well cuttings and core chips were compiled from 256 samples from 31 wells (see section on Methods, and figure 10, table 3, and appendix B). Each sample covers 10 feet of Cane Creek section (with a few exceptions) and usually represents 10 measurements per sample, unless not enough good quality cuttings were available. For this statistical analysis, the average EF value recorded for each sample was averaged for the A, B, and C intervals rating (see appendix A and EF rating maps – figures 20, 24, 28, and 32). Histograms showing the distribution of these EF averages by Cane Creek interval are shown on figure 33. Note that not all three of these intervals were encountered in all 31 wells. As shown on figure 33, the A interval was sampled in 21 of the wells, the B interval in 26 wells, and the C interval in 23 wells, and thus no one dataset was significantly higher or lower than the others. Figure 33 also shows that the mean, median, and standard deviation (std.) of the average of the EF sample averages for these stratigraphic intervals are similar. However, the distributions do show some differences. These differences may be useful to evaluate the potential of the A and C intervals when compared to the productive B interval. The distributions may also assist interpretation of the various EF maps (figures 17 through 32).

The statistical mode is the EF average that appears most often in each dataset and represents the value most likely to be sampled. The EF distribution shown for interval A is dominated by a single peak, which includes the mean value of 1.25. Thus, the dataset is unimodal. The EF distribution for interval B is bimodal with EF peaks near 0.75 and 1.65 that bracket, but do not include the mean value of 1.41. The distribution for interval C is likewise bimodal with a broad peak near EF value 0.9, and another peak near EF value 1.65; neither of these peaks include the EF mean value of 1.39.

The median is the EF value that separates the higher half from the lower half or the middle EF value of each dataset. The medians for the EF sample averages from the A, B, and C intervals are 1.2, 1.5, and 1.5, respectively. In this case, the medians for the B and C intervals are the same, like the means for these same intervals. However, unlike the means, the medians are not skewed by large or small EF values. Such values can affect the means and thus the median may represent a more common value. For example, the B interval contains both high and low EF sample averages that lead to a mean of 1.41 whereas the median is 1.5 and therefore more typical. It is important to note that the means and medians for the three intervals are, in reality, quite close, indicating that the data have not been skewed to a large extent.

The standard deviation quantifies the amount of variation or spread of the EF sample average data. The standard deviations for the EF sample averages from the A, B, and C intervals are 0.56, 0.56, and 0.46, respectively. All three intervals show similar ranges of variation. For example, the A and B intervals have the same standard deviation (0.56). Perhaps surprisingly, the potentially multimodal C interval shows a slightly smaller range of variation (standard deviation = 0.46).

The statistical analysis of the datasets from the average of the epifluorescence sample averages for the A, B, and C intervals shows relatively minor differences between most of the basic statistical values generated from each dataset. Recall that only the B interval is currently productive in the Cane Creek shale. Thus, this analysis supports the additional and untested potential for the A and C intervals identified by the EF maps.

SUMMARY AND CONCLUSIONS

The Cane Creek shale play in the Pennsylvanian Paradox Formation, Paradox fold and fault belt of the Paradox Basin, southeastern Utah, contains potential oil-prone exploration areas identified from oil shows recognized using EF microscope techniques on cuttings, core chips, and uncovered thin sections. EF is a noninvasive and nondestructive procedure that can be done using a petrographic microscope equipped with reflected light capabilities, mercury-vapor light, and appropriate filtering. Sample preparation is relatively inexpensive. EF allows one to observe the presence or absence of oil shows, especially in the dolomites, limestones (including microbialites), siltstones, and sandstones of the Cane Creek. Samples displaying significant fluorescence help define areas where hydrocarbons may have migrated or accumulated. If no fluorescence

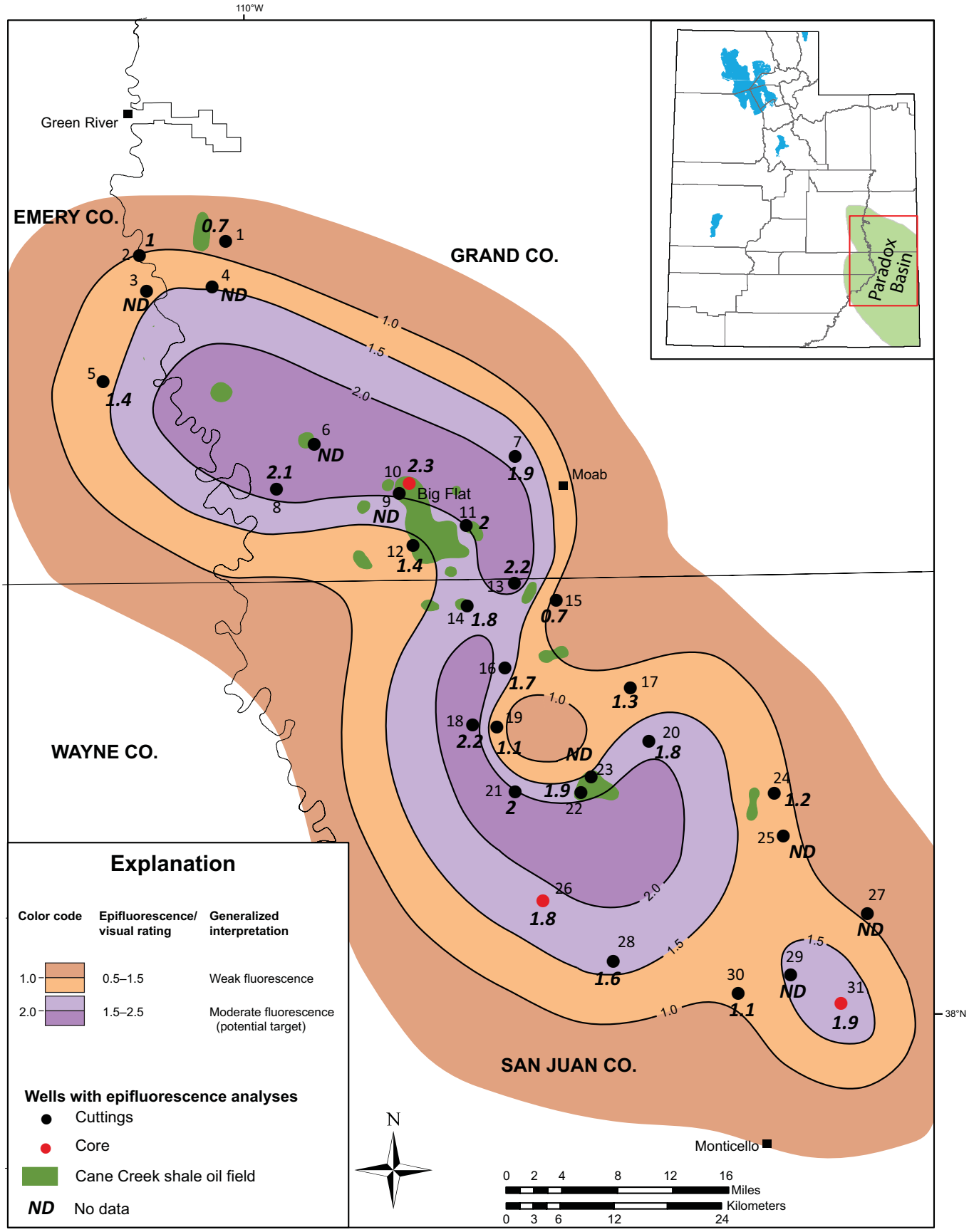

Figure 31. *The highest average epifluorescence based on visual rating of Cane Creek well cuttings and core chips, C interval. See table 3 for list of wells corresponding to the numbers by the black or red dots.*

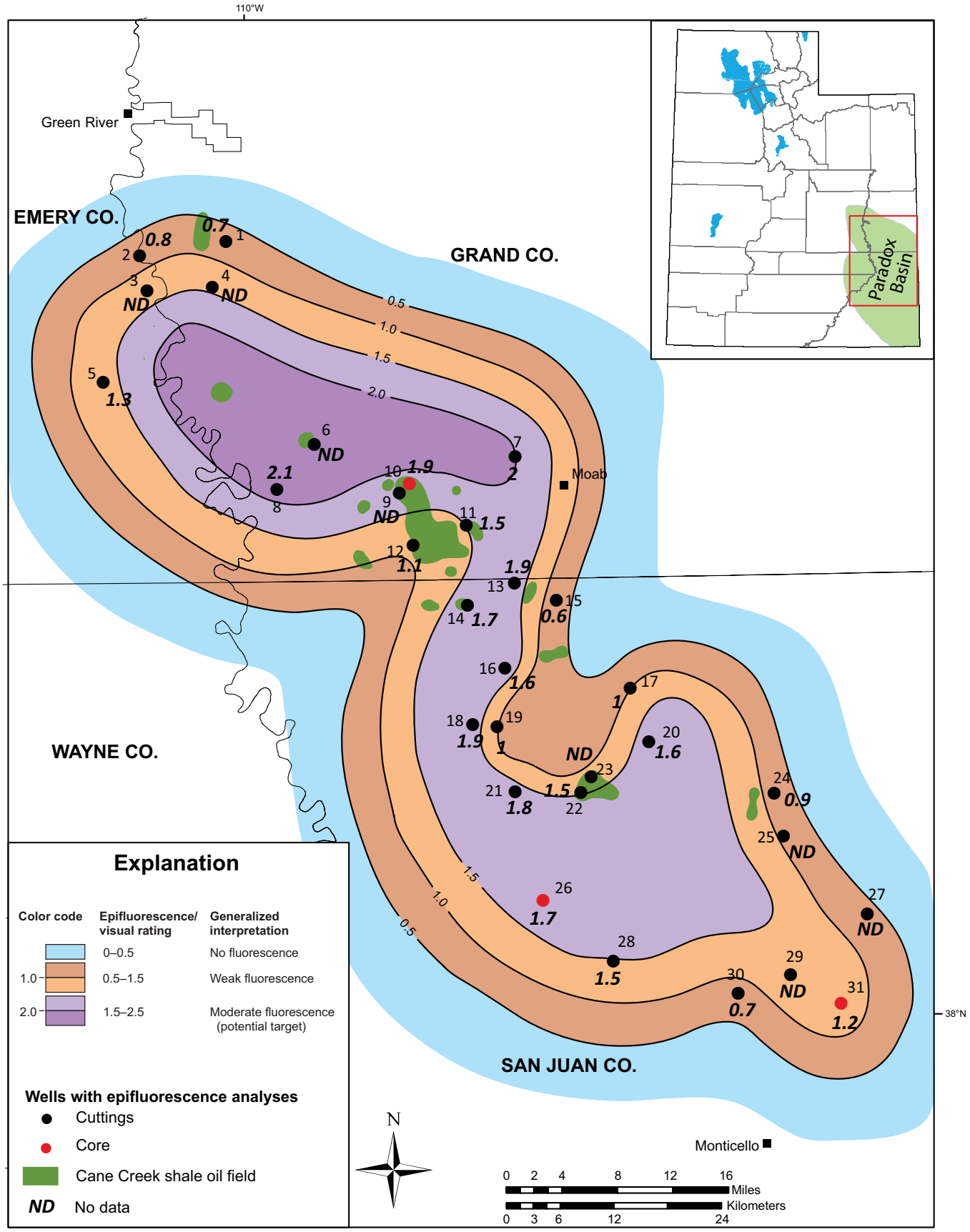

Figure 32. *The average of the epifluorescence sample averages based on visual rating of Cane Creek well cuttings and core chips, C interval. See table 3 for list of wells corresponding to the numbers by the black or red dots.*

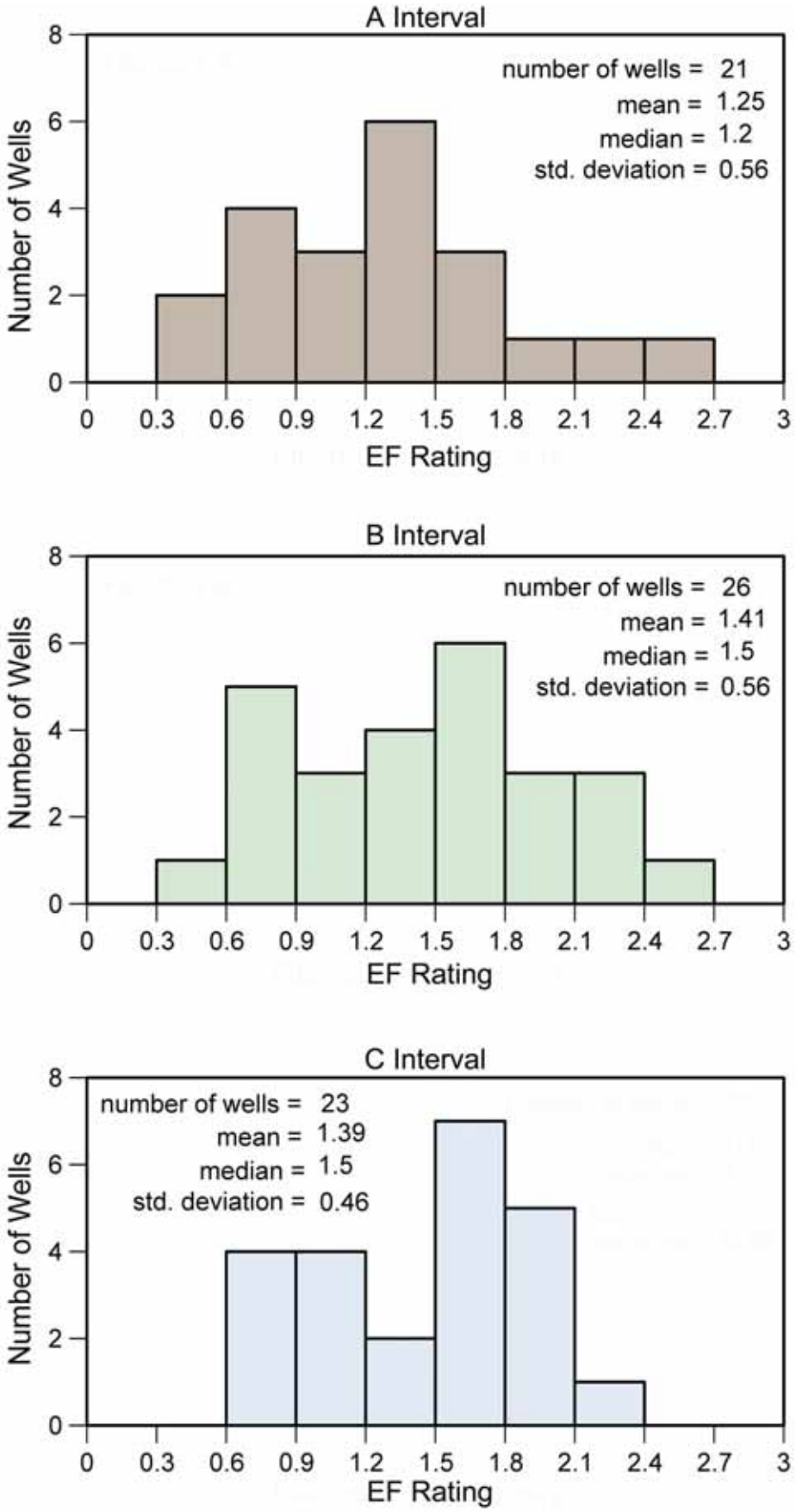

Figure 33. *Histograms for the A, B, and C intervals plotting the average of the epifluorescence sample averages versus number of wells. The statistical mean, median, and standard (std.) deviation from each dataset are also provided.*

is observed in porous dolomites for example, the samples are also good representatives of areas where liquid hydrocarbons are not currently stored/trapped in the subsurface.

Cuttings and core chips from 31 productive and dry exploratory wells penetrating the Cane Creek shale in the Utah portion of the Paradox fold and fault belt were examined under a binocular microscope. Over 2650 representative samples of porous dolomite, siltstone, sandstones, limestones, and some shales were selected from various intervals over the Cane Creek section for EF evaluation. A qualitative visual "rating" scale (a range and average) based on EF evaluation was applied to the group of handpicked cuttings (or core chips) from each depth in each well. The highest, average highest, highest average, and average of the averages of EF ratings from each well were plotted and mapped for the entire Cane Creek shale as well as for three recognized intervals (A, B, and C) within the Cane Creek.

The EF analysis and mapping indicate there is a narrow, distinct, curvilinear, northwest- to southeast-trending fairway and isolated lobes of moderate to good fluorescence (indicating probable capacity of some oil production if there is adequate porosity and permeability) that are most perspective for future exploration and development in the Cane Creek shale within the Utah portion of the Paradox fold and fault belt. Productive wells (fields), as expected, are distinguished by their generally higher EF ratings. The northeastern portion of the play area shows a regional trend of low EF. Not surprisingly, the EF rating maps show the productive B interval has the greatest potential in areas where several, sparely drilled, large lobes have high EF ratings.

Oil shows can exist within carbonate reservoir seal rocks, although they may not represent mobile hydrocarbons. One common situation for such oil shows in sealing would be associated with organic facies of good source-rock potential. In the A and C intervals, we encountered good EF shows in certain wells within the study area. The EF maps of the A interval show similar lobes those of the B interval that suggest overlooked potential whereas the EF maps of the C interval confirm its standing as a seal with a few possible areas that warrant further investigation. Statistical analysis supports the additional potential identified by the A, B, and C interval EF maps.

Hydrocarbons likely migrated in Cane Creek dolomite, sandstone, and other porous lithologies along regional northwest-trending folds, faults, and fracture zones. This event created the potential oil-prone fairway in the Cane Creek shale that to date is relatively untested.

ACKNOWLEDGMENTS

This research was conducted as part of a project titled "Liquid-Rich Shale Potential of Utah's Uinta and Paradox Basins: Reservoir Characterization and Development Optimization" funded by the U.S. Department of Energy, National Energy Technology Laboratory, contract number DE-FE0010667. Support was also provided by the Utah Geological Survey (UGS) and Eby Petrography & Consulting, Inc., Denver, Colorado. Drill cuttings and core samples were collected by William Hurlbut, Stephanie Carney, Taylor Boden, Rebekah Stimpson, and Michael D. Vanden Berg of the UGS. Jeff Quick (UGS) conducted the statistical analysis of the EF dataset. Core photography was conducted by Rebekah Stimpson (UGS) and Triple O Slabbing, Denver, Colorado; Jay Hill, Cheryl Gustin, and John Good of the UGS drafted figures.

This study was carefully reviewed by David Bowen, Montana State University, and Michael D. Vanden Berg, Craig D. Morgan, Mike Hylland, and Richard G. Allis, UGS. Their suggestions and constructive criticism greatly improved the manuscript. Finally, we thank Vicky Clarke, John Good, and the UGS editorial production team for producing a very high-quality publication.

REFERENCES

Anna, L.O., Whidden, K.J., Lillis, P.G., and Pearson, K.M., 2014, Assessment of continuous oil and gas reservoirs, Paradox Basin, Utah, Colorado, New Mexico, and Arizona: The Mountain Geologist, v. 51, no. 2, p. 139–160.

Baars, D.L., 1966, Pre-Pennsylvanian paleotectonics—key to basin evolution and petroleum occurrences in the Paradox Basin, Utah and Colorado: American Association of Petroleum Geologists Bulletin, v. 50, no. 10, p. 2082–2111.

Baars, D.L., and Stevenson, G.M., 1982, Subtle stratigraphic traps in Paleozoic rocks of Paradox Basin, *in* Halbouty, M.T., editor, The deliberate search for the subtle trap: American Association of Petroleum Geologists Memoir 32, p. 131–158.

Burruss, R.C., 1981, Hydrocarbon fluid inclusions in studies of sedimentary diagenesis, *in* Hollister, L.S., and Crawford, M.L., editors, Fluid inclusions—applications in petrology: Mineralogical Association of Canada Short Course Notes, v. 6, p. 138–156.

Burruss, R.C., 1991, Practical aspects of fluorescent microscopy of petroleum fluid inclusions, *in* Barker, C.E., and Kopp, O.C., editors, Luminescence microscopy—quantitative and qualitative aspects: Society for Sedimentary Geology (SEPM) Short Course 25 Notes, p. 1–7.

Burruss, R.C., Cercone, K.R., and Harris, P.M., 1986, Timing of hydrocarbon migration—evidenced from fluid inclusions in calcite cements, tectonics and burial history, *in* Schneidermann, N., and Harris, P.M., editors, Carbonate cements: Society for Sedimentary Geology (SEPM) Special Publication 36, p. 277–289.

Carney, S.M., Nielsen, P., and Vanden Berg, M.D., 2014, Geological evaluation of the Cane Creek shale, Pennsyl-

vanian Paradox Formation, Paradox Basin, southeastern Utah [abs.]: American Association of Petroleum Geologists, Annual Convention and Exhibition, (1838157).

Cather, M.E., Morrow, N.R., Brower, K.R., and Buckley, J.S., 1989a, Uses of epi-fluorescent microscopy in evaluation of Mesaverde tight gas sands [abs.]: American Association of Petroleum Geologists Bulletin, v. 73, p. 1150–1151.

Cather, M.E., Morrow, N.R., and Klich, I., 1989b, Applications of fluorescent dye staining techniques to reservoir studies of tight gas sands, Mesaverde Group, southwestern Colorado [abs.]: American Association of Petroleum Geologists Bulletin, v. 73, p. 342.

Cercone, K.R., and Pedone, V.A., 1987, Fluorescence (photoluminescence) of carbonate rocks—instrumental and analytical sources of observational error: Journal of Sedimentary Petrology, v. 57, p. 780–782.

Choquette, P.W., and Pray, L.C., 1970, Geologic nomenclature and classification of porosity in sedimentary carbonates: American Association of Petroleum Geologists Bulletin, v. 54, no. 2, p. 207–250.

Core Laboratories, Inc., 2013, Petrographic analysis of conventional core samples, Cane Creek 26-3 well, Grand County, Utah: Unpublished consultant's report for Fidelity Exploration, 10 p., 1 appendix.

Doelling, H.H., 2001, Geologic map of the Moab and eastern part of the San Rafael Desert 30′ x 60′ quadrangles, Grand and Emery Counties, Utah, and Mesa County, Colorado: Utah Geological Survey Map 180, scale 1:100,000, 3 plates.

Doelling, H.H., 2003, Geology of Arches National Park, Grand County, Utah, *in* Sprinkel, D.A., Chidsey, T.C., Jr., and Anderson, P.B., editors, Geology of Utah's parks and monuments: Utah Geological Association Publication 28, p. 11–36.

Doelling, H.H., 2004, Geologic map of the La Sal 30′ x 60′ quadrangle, San Juan, Wayne, and Garfield Counties, Utah, and Montrose and San Miguel Counties, Colorado: Utah Geological Survey Map 205, scale 1:100,000, 2 plates.

Dravis, J.J., 1988, Deep-burial microporosity in Upper Jurassic Haynesville oolitic grainstones, East Texas: Sedimentary Geology, v. 63, p. 325–341.

Dravis, J.J., 1991, Carbonate petrography—update on new techniques and applications: Journal of Sedimentary Petrology, v. 61, p. 626–628.

Dravis, J.J. 1992. Burial dissolution in limestones and dolomites—criteria for recognition and discussion of controls: a case study approach (part 1: Upper Jurassic Haynesville limestones, East Texas; part 2: Devonian Upper Elk Point dolomites, western Canada): Calgary, Canada, American Association of Petroleum Geologists/Canadian Society of Petroleum Geologists Short Course on Subsurface Dissolution Porosity in Carbonates, 171 p.

Dravis, J.J., and Yurewicz, D.A., 1985, Enhanced carbonate petrography using fluorescence microscopy: Journal of Sedimentary Petrology, v. 55, p. 795–804.

Dunham, R.J., 1962, Classification of carbonate rocks according to depositional texture, *in* Ham, W.E., editor, Classification of carbonate rocks: American Association of Petroleum Geologists Memoir 1, p. 108–121.

Eby, D.E., Chidsey, T.C., Jr., and Morgan, C.D., 2008, The use of epifluorescence techniques to determine potential oil-prone areas in the Mississippian Leadville Limestone, northern Paradox Basin, Utah [abs.]: Rocky Mountain Natural Gas Geology and Resource Conference, Rocky Mountain Section of the American Association of Petroleum Geologists and Colorado Oil & Gas Association Official Program with Abstracts, p. 88–89.

Eby, D.E., and Hager, R.C., 1986, Fluorescence petrology of San Andres dolomites—H.O. Mahoney lease, Wasson field, Yoakum County, Texas: Permian Basin Section, Society for Sedimentary Geology (SEPM) Publication 86-26, p. 37–38.

Embry, A.R., and Klovan, J.E., 1971, A Late Devonian reef tract on northeastern Banks Island, Northwest Territories: Canadian Petroleum Geologists Bulletin, v. 19, p. 730–781.

Fetzner, R.W., 1960, Pennsylvanian paleotectonics of the Colorado Plateau: American Association of Petroleum Geologists Bulletin, v. 44, no. 8, p. 1371–1413.

Frahme, C.W., and Vaughn, E.B., 1983, Paleozoic geology and seismic stratigraphy of the northern Uncompahgre front, Grand County, Utah, *in* Lowell, J.D., editor, Rocky Mountain foreland basins and uplifts: Rocky Mountain Association of Geologists Guidebook, p. 201–211.

Fritz, M., 1991, Horizontal drilling comes full circle—seismic, technology triumphs in Utah find: American Association of Petroleum Geologists Explorer, v. 12, p. 1 and 18.

Gies, R.M., 1987, An improved method for viewing micropore systems in rocks with the polarizing microscope: Society of Petroleum Engineers Formation Evaluation, v. 2, p. 209–214.

Grove, K.W., Horgan, C.C., Flores, F.E., and Bayne, R.C., 1993, Bartlett Flat Big Flat (Kane Springs unit), *in* Hill, B.G., and Bereskin, S.R., editors, Oil and gas fields of Utah: Utah Geological Association Publication 22, nonpaginated.

Grove, K.W., and Rawlins, D.M., 1997, Horizontal exploration of oil and gas-bearing natural fracture systems in the Cane Creek clastic interval of the Pennsylvanian Paradox Formation, Grand and San Juan Counties, Utah, *in* Close, J., and Casey, T., editors, Natural fracture systems in the southern Rockies: Four Corners Geological Society Guidebook, p. 133–134.

Grummon, M.L., 1993, Exploiting the self-sourced Cane Creek zone of the Paradox Formation with horizontal

well bores [abs.]: American Association of Petroleum Geologists Bulletin, v. 77, no. 8, p. 1449–1450.

Guihaumou, N., Szydlowskii, N., and Padier, B., 1990, Characterization of hydrocarbon fluid inclusions by infrared and fluorescence microspectrometry: Mineralogical Magazine, v. 54, p. 311–324.

Harr, C.L., 1996, Paradox oil and gas potential of the Ute Mountain Ute Indian Reservation, *in* Huffman, A.C., Jr., Lund, W.R., and Godwin, L.H., editors, Geology and resources of the Paradox Basin: Utah Geological Association Publication 25, p. 13–28.

Heckel, P.H., 1983, Diagenetic model for carbonate rocks in midcontinent Pennsylvanian eustatic cyclothems: Journal of Sedimentary Petrology, v. 53, p. 733–759.

Hintze, L.F., and Kowallis, B.J., 2009, Geologic history of Utah: Brigham Young University Geology Studies Special Publication 9, 225 p.

Hite, R.J., 1960, Stratigraphy of the saline facies of the Paradox Member of the Hermosa Formation of southeastern Utah and southwestern Colorado, *in* Smith, K.G., editor, Geology of the Paradox Basin fold and fault belt: Four Corners Geological Society, Third Field Conference Guidebook, p. 86–89.

Hite, R.J., 1970, Shelf carbonate sedimentation controlled by salinity in the Paradox Basin, southeast Utah, *in* Ran, J.L., and Dellwig, L.F., editors, Third symposium on salt: Northern Ohio Geological Society, v. 1, p. 48–66.

Hite, R.J., Anders, D.E., and Ging, T.G., 1984, Organic-rich source rocks of Pennsylvanian age in the Paradox Basin of Utah and Colorado, *in* Woodward, J., Meissner, F.F, and Clayton, J.L., editors, Hydrocarbon source rocks of the greater Rocky Mountain region: Rocky Mountain Association of Geologists Guidebook, p. 255–274.

Hite, R.J., and Buckner, D.H., 1981, Stratigraphic correlation, facies concepts and cyclicity in Pennsylvanian rocks of the Paradox Basin, *in* Wiegand, D.L., editor, Geology of the Paradox Basin: Rocky Mountain Association of Geologists 1981 Field Conference, p. 147–159.

Hite, R.J., and Cater, F.W., 1972, Pennsylvanian rocks and salt anticlines, Paradox Basin, Utah and Colorado, *in* Mallory, W.W., editor, Geologic atlas of the Rocky Mountain region: Rocky Mountain Association of Geologists Guidebook, p. 133–138.

IHS Inc., 2013, Rocky Mountain regional report, August 14, 2013, non-paginated.

Kirby, K.C., and Tinker, S.W., 1992, The Keg River/Winnipegosis petroleum system in northeast Alberta [abs.]: American Association of Petroleum Geologists Annual Convention, Official Program with Abstracts, v. 1, p. A66.

Kluth, C.F., and DuChene, H.R., 2009, Late Pennsylvanian and Early Permian Structural Geology and Tectonic History of the Paradox Basin and Uncompahgre Uplift, Colorado and Utah, *in* Houston, W.S., Wray, L.L., and Moreland, P.G., editors, The Paradox Basin revisited—new developments in petroleum systems and basin analysis: Rocky Mountain Association of Geologists Special Publication, p. 178–197.

LaFlamme, A.K., 1992, Replacement dolomitization in the Upper Devonian Leduc and Swan Hills Formations, Caroline area, Alberta, Canada [abs.]: American Association of Petroleum Geologists Annual Convention, Official Program with Abstracts, v. 1, p. A70.

LaVoie, D., Chi G., and Fowler, M.G., 2001, The Lower Devonian Upper Gaspe Limestones in eastern Gaspe—carbonate diagenesis and reservoir potential: Bulletin of Canadian Petroleum Geology, v. 49, p. 346–365.

Lorenz, J.C., and Cooper, S.P., 2009, Extension–fracture patterns in sandstones above mobile salt—the Salt Valley anticline, Arches National Park, Utah, *in* Houston, W.S., Wray, L.L., and Moreland, P.G., editors, The Paradox Basin revisited—new developments in petroleum systems and basin analysis: Rocky Mountain Association of Geologists Special Publication, p. 198–220.

Morgan, C.D., 1992, Horizontal drilling potential of the Cane Creek shale, Paradox Formation, Utah, *in* Schmoker, J.W., Coalson, E.B., and Brown, C.A., editors, Geologic studies relevant to horizontal drilling—examples from western North America: Rocky Mountain Association of Geologists Guidebook, p. 257–265.

Morgan, C.D., 1994, Exploring for new oil in old fields, Salt Wash field—a case study: Utah Geological Survey Open-File Report 307, 41 p., 2 plates.

Morgan, C.D., Carney, S.M., Nielsen, P.J., Vanden Berg, M.D., and Wood, R.E., 2014, Play analysis of the Cane Creek shale, Pennsylvanian Paradox Formation, Paradox Basin, southeast Utah [abs.]: American Association of Petroleum Geologists, Rocky Mountain Section Meeting Official Program with Abstracts, p. 36.

Nuccio, V.F., and Condon, S.M., 1996, Burial and thermal history of the Paradox Basin, Utah and Colorado, and petroleum potential of the Middle Pennsylvanian Paradox Formation, *in* Huffman, A.C., Jr., Lund, W.R., and Godwin, L.H., editors, Geology of the Paradox Basin: Utah Geological Association Publication 25, p. 57–76.

Ohlen, H.R., and McIntyre, L.B., 1965, Stratigraphy and tectonic features of Paradox Basin, Four Corners area: American Association of Petroleum Geologists Bulletin, v. 49, no. 11, p. 2020–2040.

Peterson, J.A., 1966, Stratigraphic vs. structural controls on carbonate-mound accumulation, Aneth area, Paradox Basin: American Association of Petroleum Geologists Bulletin, v. 50, no. 10, p. 2068–2081.

Peterson, J.A., and Ohlen, H.R., 1963, Pennsylvanian shelf carbonates, Paradox Basin, *in* Bass, R.O., editor, Shelf carbonates of the Paradox basin: Four Corners, Geological Society Symposium, 4th Field Conference, p. 65–79.

Peterson, P.R., 1973, Salt Wash field: Utah Geological and Mineralogical Survey Oil and Gas Field Studies No. 4, 3 p., 1 plate.

Quigley, W.D., 1983, Lion Mesa, San Juan County, Utah, *in* Fassett, J.E., editor, Oil and gas fields of the Four Corners area: Four Corners Geological Society, v. III, p. 1089–1091.

Rasmussen, D.L., 2010, Halokinesis features related to flowage and dissolution of Pennsylvanian Hermosa salt in the Paradox Basin, Colorado and Utah [abs.]: American Association of Petroleum Geologists, Rocky Mountain Section Meeting Program with Abstracts, p. 59.

Rasmussen, L., and Rasmussen, D.L., 2009, Burial history analysis of the Pennsylvanian petroleum system in the deep Paradox Basin fold and fault belt, Colorado and Utah, *in* Houston, W.S., Wray, L.L., and Moreland, P.G., editors, The Paradox Basin revisited—new developments in petroleum systems and basin analysis: Rocky Mountain Association of Geologists Special Publication, p. 24–94.

Reid, F.S., and Berghorn, C.E., 1981, Facies recognition and hydrocarbon potential of the Pennsylvanian Paradox Formation, *in* Wiegand, D.L., editor, Geology of the Paradox Basin: Rocky Mountain Association of Geologists Guidebook, p. 111–117.

Rost, F.W.D., 1992, Fluorescence microscopy, v. 1: New York, Cambridge University Press, 253 p.

Scholle, P.A., and Ulmer-Scholle, D.S., 2003, A color guide to the petrography of carbonate rocks: American Association of Petroleum Geologists Bulletin Memoir 77, p. 427–440.

Smith, K.T., 1978, Bartlett Flat, *in* Fassett, J.E., editor, Oil and gas fields of the Four Corners area: Four Corners Geological Society, v. 2, p. 1061–1063.

Soeder, D.J., 1990, Applications of fluorescent microscopy to study of pores in tight rocks: American Association of Petroleum Geologists Bulletin, v. 74, p. 30–40.

Stowe, C., 1972, Oil and gas production in Utah to 1970: Utah Geological and Mineralogical Survey Bulletin 94, 179 p.

Teichmuller, M., and Wolf, M., 1977, Application of fluorescence microscopy in coal petrology and oil exploration: Journal of Microscopy, v. 109, p. 49–73.

Trudgill, B.D., and Paz, M., 2009, Restoration of Mountain Front and Salt Structures in the northern Paradox Basin, SE Utah, *in* Houston, W.S., Wray, L.L., and Moreland, P.G., editors, The Paradox Basin revisited—new developments in petroleum systems and basin analysis: Rocky Mountain Association of Geologists Special Publication, p. 132–177.

U.S. Geological Survey, 2012, Assessment of undiscovered oil and gas resources in the Paradox Basin province, Utah, Colorado, New Mexico, and Arizona, 2011: U.S. Geological Survey Fact Sheet 2012-3021, March 2012, 4 p.: Online, http://pubs.usgs.gov/fs/2012/3031/FS12-3031.pdf, accessed July 2012.

Utah Division of Oil, Gas and Mining, 2016, Oil and gas summary production report by field, December 2015: Online, https://oilgas.ogm.utah.gov/pub/Publications/Reports/Prod/Field/Fld_Dec_2015.pdf, accessed March 2016.

van Gijzel, P., 1967, Palynology and fluorescence microscopy: Reviews of Paleobotany and Palynology, v. 1, p. 49–79.

Whidden, K.J., Lillis, P.G., Anna, L.O., Pearson, K.M., and Dubiel, R.F., 2014, Geology and total petroleum systems of the Paradox Basin, Utah, Colorado, New Mexico, and Arizona: The Mountain Geologist, v. 51, no. 2, p. 119–138.

Yanguas, J.E., and Dravis, J.J., 1985, Blue fluorescent dye technique for recognition of microporosity in sedimentary rocks: Journal of Sedimentary Petrology, v. 55, p. 600–602.

APPENDICES

APPENDIX A

CANE CREEK SHALE EPIFLUORESCENCE VALUES USED FOR MAPPING EPIFLUORESCENCE TRENDS

Appendix A – Cane Creek Shale Epifluorescence Values Used for Mapping Epifluorescence Trends

Well #	Well Name	Location			Well Type	N	Visual Epifluorescence Rating															
		Section	Township	Range			Cane Creek Highest Value	Cane Creek Average Highest Value	Cane Creek Highest Average Value	Cane Creek Average of Sample Averages	A Interval Highest Value	A Interval Average Highest Value	A Interval Highest Average Value	A Interval Average of Sample Averages	B Interval Highest Value	B Interval Average Highest Value	B Interval Highest Average Value	B Interval Average of Sample Averages	C Interval Highest Value	C Interval Average Highest Value	C Interval Highest Average Value	C Interval Average of Sample Averages
1	Salt Wash Unit 22-34	34	22S	17E	Dry hole	80	1.4	1.1	0.7	0.6	1.4	1.4	0.7	0.7	1.4	1.2	0.6	0.6	1.4	1.1	0.7	0.7
2	Jakey's Ridge 12-3	3	23S	16E	Dry hole	97	2.4	1.9	1.6	1.1	1.8	1.6	1.1	1.1	2.4	2.1	1.6	1.3	2.2	1.8	1.0	0.8
3	Jakey's Ridge 34-15	15	23S	16E	Dry hole	100	2.2	1.6	1.6	0.9	0.8	0.6	0.4	0.3	2.2	2.2	1.4	1.1	ND	ND	ND	ND
4	Salt Wash 1-16	16	23S	17E	Dry hole	71	3.0	2.7	2.4	2.1	NA	NA	NA	NA	NA	NA	NA	NA	NA	NA	NA	NA
5	Gruvers Mesa 1	19	24S	16E	Dry hole	100	2.1	2.0	1.8	1.5	2.1	2.1	1.7	1.7	2.1	2.0	1.8	1.6	2.1	2.0	1.4	1.3
6	Kane Springs Fed 10-1	10	25S	18E	Producing oil well	49	3.0	2.8	2.3	2.2	3.0	3.0	2.3	2.3	2.8	2.6	2.3	2.1	ND	ND	ND	ND
7	Utah 2	18	25S	21E	Dry hole	108	2.5	2.0	2.0	1.5	2.1	1.6	1.4	1.1	2.4	2.2	1.9	1.7	2.5	2.4	1.9	2.0
8	Fed Bowknot 1	30	25S	18E	Dry hole	71	2.6	2.3	2.1	1.9	ND	ND	ND	ND	2.5	2.3	2.0	1.9	2.6	2.5	2.1	2.1
9	Kane Springs Fed 25-19-34-1	34	25S	19E	Producing oil well	149	3.4	2.8	3.1	2.2	H	H	H	H	H	H	H	H	H	H	H	H
10	Cane Creek Unit 26-3	26	25S	19E	Producing oil well	197	3.2	2.3	2.6	1.9	2.3	2.0	2.1	1.7	3.2	2.5	2.6	2.5	2.8	2.2	2.3	1.9
11	Long Canyon 1	9	26S	20E	Producing oil well	39	3.0	2.2	2.0	1.2	2.7	2.1	1.2	0.8	2.8	2.0	1.8	1.1	3.0	2.6	2.0	1.5
12	Mineral Canyon U 1-14	14	26S	19E	PA oil well	65	2.1	1.5	1.7	1.1	1.6	1.3	1.4	1.0	2.1	1.6	1.7	1.3	1.9	1.6	1.4	1.1
13	Federal 1-X	36	26S	20E	Dry hole	43	2.8	2.4	2.2	1.8	2.3	2.3	1.7	1.7	2.4	2.4	1.7	1.7	2.8	2.4	2.2	1.9
14	Featherstone-Federal 9-1	9	27S	20E	Dry hole	100	2.9	2.4	2.1	1.6	2.3	2.1	1.2	1.2	2.9	2.4	2.1	1.7	2.9	2.5	1.8	1.7
15	West Bridger Jack U 3	3	27S	21E	Dry hole	68	1.2	1.0	0.9	0.6	ND	ND	ND	ND	1.2	1.0	0.9	0.7	1.2	1.0	0.7	0.6
16	Cane Creek State 1-36	36	27S	20E	Dry hole	90	3.1	2.5	2.7	1.9	3.1	3.0	2.5	2.4	3.0	2.5	2.7	2.1	2.6	2.3	1.7	1.6
17	Red Rock Unit 1	9	28S	22E	Dry hole	104	2.5	1.8	1.3	1.0	1.1	1.1	0.7	0.7	2.2	2.0	1.2	1.0	2.5	1.8	1.3	1.0
18	Lockhart-Fed 1	22	28S	20E	Dry hole	94	3.0	2.2	2.2	1.7	1.6	1.6	1.5	1.3	2.8	2.2	2.0	1.6	3.0	2.4	2.2	1.9
19	USA Lockhart 1	23	28S	20E	Dry hole	46	1.3	1.1	1.1	0.8	ND	ND	ND	ND	1.0	1.0	0.7	0.7	1.3	1.2	1.1	1.0
20	Government B-1	34	28S	22E	Dry hole	156	3.2	2.3	1.8	1.5	3.2	2.5	1.7	1.4	3.0	2.3	1.8	1.4	2.9	2.2	1.8	1.6
21	Horsehead Unit 1	18	29S	21E	Dry hole	100	3.0	2.1	2.2	1.7	1.7	1.6	1.5	1.4	3.0	2.4	2.2	1.8	2.3	2.2	2.0	1.8
22	Hatch Point 1	14	29S	21E	Producing oil well	38	2.4	2.1	1.9	1.3	ND	ND	ND	ND	2.2	1.9	1.6	1.2	2.4	2.3	1.9	1.5
23	Threemile 12-7	12	29S	21E	Producing oil well	38	2.5	2.1	1.9	1.6	H	H	H	H	H	H	H	H	H	H	H	H
24	La Sal USA 1	19	29S	24E	Dry hole	106	2.0	1.7	1.2	0.8	1.7	1.6	0.7	0.7	1.5	1.4	0.8	0.6	2.0	1.8	1.2	0.9
25	Lisbon D232	32	29.5S	24E	Dry hole	60	0.7	0.5	0.5	0.3	NA	NA	NA	NA	NA	NA	NA	NA	NA	NA	NA	NA
26	Gibson Dome	21	30S	21E	Dry hole	89	2.4	2.2	2.1	1.8	2.2	2.1	1.9	1.8	2.4	2.4	2.1	2.1	2.2	2.2	1.8	1.7
27	Little Valley 2	29	30S	25E	Dry hole	35	1.2	0.8	0.6	0.4	0.6	0.6	0.4	0.4	1.2	1.0	0.6	0.5	ND	ND	ND	ND
28	Hart Point Fed 1	8	31S	22E	Dry hole	77	2.5	2.2	2.1	1.6	2.1	2.1	1.4	1.4	2.5	2.3	2.1	1.7	2.3	2.2	1.6	1.5
29	Winchester 21-1H	21	31S	24E	Dry hole	90	2.0	1.6	1.3	1.0	H	H	H	H	H	H	H	H	H	H	H	H
30	Church Rock Unit 1	26	31S	23E	Dry hole	48	1.8	1.3	1.0	0.7	ND	ND	ND	ND	1.8	1.4	0.8	0.7	1.5	1.2	1.1	0.7
31	Cisco State 36-13	36	31S	24E	Dry hole	133	2.8	2.0	2.3	1.7	2.3	1.5	2.0	1.2	2.8	2.3	2.3	1.9	2.0	1.5	1.9	1.2

Note: See figure 10 for well number locations.

N = number of samples
NA = interval tops not available
ND = no data (no cuttings or cores)
H = horizontal wellbore

APPENDIX B

EPIFLUORESCENCE ANALYSES AND DESCRIPTIONS OF WELL CUTTINGS AND CORES FROM THE CANE CREEK SHALE, PENNSYLVANIAN PARADOX FORMATION, PARADOX FOLD AND FAULT BELT AREA, UTAH

Appendix B – Epifluorescence Analyses and Descriptions of Well Cuttings and Cores from the Cane Creek Shale, Pennsylvanian Paradox Formation, Paradox Fold and Fault Belt Area, Utah

Well #	Well Name	Location	County	Interval (ft)	N	Rating*		Sample Type	Comments**	Epifluorescence Photomicrograph Image (see appendix C)	Binocular or Digital Microscope Image† (see appendix C)
		Section, Township, Range				Range	Ave.				
1	Salt Wash 22-34	SENW 34 22S 17E	Grand	9420–30	10	0.0–1.4	0.6	cuttings	A interval – patchy fine to medium crystalline dolomite, often in a black shaly matrix.		
1	Salt Wash 22-34	SENW 34 22S 17E	Grand	9430–40	10	0.4–1.3	0.7	cuttings	A interval – patchy fine to medium crystalline dolomite, often in a black shaly matrix; one sample of bryozoan packstone to framestone fabric.		
1	Salt Wash 22-34	SENW 34 22S 17E	Grand	9440–50	10	0.4–1.0	0.6	cuttings	B interval – fine to medium crystalline dolomitic mudstone/wackestone fabric, somewhat silty.		
1	Salt Wash 22-34	SENW 34 22S 17E	Grand	9450–60	10	0.3–0.7	0.5	cuttings	B interval – peloidal packstone/grainstone fabric, and dolomitic and limey bryozoan grainstone/framestone fabric containing minor dolomitic shale.		
1	Salt Wash 22-34	SENW 34 22S 17E	Grand	9460–70	10	0.2–1.4	0.7	cuttings	C interval – finely crystalline dolomitic mudstone and a fragmental grainstone/framestone fabric, slightly dolomitic.		
1	Salt Wash 22-34	SENW 34 22S 17E	Grand	9470–80	10	0.3–1.1	0.7	cuttings	C interval – microcrystalline dolomitic mudstone and silty medium crystalline dolomitic mudstone/wackestone fabric.		
1	Salt Wash 22-34	SENW 34 22S 17E	Grand	9480–90	10	0.3–0.9	0.6	cuttings	C interval – silty, fossiliferous dolomitic wackestone to packstone fabric containing slightly dolomitic bryozoan.		
1	Salt Wash 22-34	SENW 34 22S 17E	Grand	9490–9500	10	0.3–1.0	0.6	cuttings	C interval – microcrystalline dolomitic mudstone and fossiliferous medium crystalline dolomitic wackestone fabric.		
2	Jakey's Ridge 12-3	SWNW 3 23S 16E	Emery	7990–8000	7	0.4–1.3	1	cuttings	A interval – patchy, fine to medium crystalline dolomite in a black shale matrix.		
2	Jakey's Ridge 12-3	SWNW 3 23S 16E	Emery	8000–10	10	0.4–1.8	1.1	cuttings	A interval – silty dolomitic mudstone and slightly dolomite fossiliferous packstone to grainstone fabrics containing possible bryozoans.		
2	Jakey's Ridge 12-3	SWNW 3 23S 16E	Emery	8010–20	10	0.4–1.5	0.9	cuttings	B interval – silty dolomitic mudstone and a slightly dolomitic fossiliferous packstone/wackestone fabric.		
2	Jakey's Ridge 12-3	SWNW 3 23S 16E	Emery	8020–30	10	0.4–2.0	1.1	cuttings	B interval – slightly silty, finely crystalline dolomitic mudstone and medium crystalline dolomitic packstone to wackestone fabrics containing possible fossil fragments.		

Well #	Well Name	Location	County	Interval (ft)	N	Rating*		Sample Type	Comments**	Epifluorescence Photomicrograph Image (see appendix C)	Binocular or Digital Microscope Image† (see appendix C)
		Section, Township, Range				Range	Ave.				
2	Jakey's Ridge 12-3	SWNW 3 23S 16E	Emery	8030–40	10	0.4–2.4	1.4	cuttings	B interval – mixed lithologies of slightly silty shale and dolomitized skeletal grainestone/packstone fabric containing small possible molds, and dolomitized microbialite.	X	X
2	Jakey's Ridge 12-3	SWNW 3 23S 16E	Emery	8040–50	10	0.9–2.2	1.6	cuttings	B interval – silty dolomitic mudstone to wackestone fabrics; possible carbonate or fossil fragments.	X	X
2	Jakey's Ridge 12-3	SWNW 3 23S 16E	Emery	8050–60	10	0.5–2.4	1.4	cuttings	B interval – slightly to very silty dolomitic mudstone; no fossil fragments.	X	X
2	Jakey's Ridge 12-3	SWNW 3 23S 16E	Emery	8060–70	10	0.3–2.2	1	cuttings	C interval – silty dolomitic mudstone and medium crystalline dolomitic wackestone/packstone fabric.		
2	Jakey's Ridge 12-3	SWNW 3 23S 16E	Emery	8070–80	10	0.3–1.8	0.8	cuttings	C interval – silty, finely crystalline dolomitic mudstone and shaley mudstone.		
2	Jakey's Ridge 12-3	SWNW 3 23S 16E	Emery	8080–90	10	0.2–1.3	0.7	cuttings	C interval – slightly silty black shale and argillaceous silty dolomitic mudstone.		
3	Jakey's Ridge 34-15	SWSE 15 23S 16E	Emery	7640–50	10	0.1–0.5	0.2	cuttings	A interval – black, highly organic shale; no visible dolomite or silt.		
3	Jakey's Ridge 34-15	SWSE 15 23S 16E	Emery	7650–60	10	0.1–0.6	0.4	cuttings	A interval – black organic-rich shale including rare patches of very finely crystalline dolomite.		
3	Jakey's Ridge 34-15	SWSE 15 23S 16E	Emery	7660–70	10	0.1–0.8	0.4	cuttings	A interval – black organic-rich shale including rare patches of very finely crystalline dolomite.		
3	Jakey's Ridge 34-15	SWSE 15 23S 16E	Emery	7670–80	10	0.2–1.6	0.8	cuttings	B interval – fine to medium crystalline dolomite, slightly silty; wackestone/mudstone fabric showing no visible porosity and very dim fluorescence.		
3	Jakey's Ridge 34-15	SWSE 15 23S 16E	Emery	7680–90	10	0.3–2.1	1.1	cuttings	B interval – interbedded, fine to medium crystalline dolomite; grainstone/packstone fabric and good fluorescence. Occasionally silty and organic-rich, finely crystalline dolomite showing dim fluorescence.	X	X
3	Jakey's Ridge 34-15	SWSE 15 23S 16E	Emery	7690–7700	10	0.3–2.1	1	cuttings	B interval – interbedded finely crystalline dolomite; grainstone/packstone fabric showing moderate fluorescence and argillaceous silty finely crystalline dolomite showing very dim fluorescence.	X	X
3	Jakey's Ridge 34-15	SWSE 15 23S 16E	Emery	7700–10	10	0.2–2.2	1.4	cuttings	B interval – silty microcrystalline dolomite; mudstone/wackestone fabric showing fair fluorescence, and interbedded with argillaceous finely crystalline dolomite showing dim fluorescence.		
3	Jakey's Ridge 34-15	SWSE 15 23S 16E	Emery	7710–20	10	0.3.–2.2	1.3	cuttings	B interval – very silty dolomite to dolomitic siltstone, patchy and highly variable fluorescence; no visible porosity.		

Well #	Well Name	Location	County	Interval (ft)	N	Rating*		Sample Type	Comments**	Epifluorescence Photomicrograph Image (see appendix C)	Binocular or Digital Microscope Image† (see appendix C)
		Section, Township, Range				Range	Ave.				
3	Jakey's Ridge 34-15	SWSE 15 23S 16E	Emery	7720–30	10	0.5–1.9	1.1	cuttings	B interval – dolomitic siltstone consisting of low visible porosity and dim to moderate fluorescence and argillaceous, slightly dolomitic siltstone consisting of very low fluorescence.		
3	Jakey's Ridge 34-15	SWSE 15 23S 16E	Emery	7730–40	10	0.6–2.0	1.6	cuttings	B interval – slightly dolomitic siltstone to highly silty dolomite; variable visible porosity and fluorescence.		
4	Salt Wash 1-16	NESW 16 23S 17E	Grand	8250–60	10	1.8–3.0	2.1	cuttings	Interval tops not available – medium crystalline dolomite throughout microbial grainstone fabric showing visible porosity throughout; fair to very good oil fluorescence.	X	X
4	Salt Wash 1-16	NESW 16 23S 17E	Grand	8260–70	10	1.8–2.6	2.1	cuttings	Interval tops not available – medium crystalline dolomite; grainstone/packstone fabric showing good uniform fluorescence throughout, some microfractures displaying fluorescence.	X	X
4	Salt Wash 1-16	NESW 16 23S 17E	Grand	8270–80	8	1.9–2.9	2.1	cuttings	Interval tops not available – fine to medium crystalline dolomite showing variable fluorescence and porosity; microbial and wackestone/packstone fabric.	X	X
4	Salt Wash 1-16	NESW 16 23S 17E	Grand	8280–90	10	2.0–2.8	2.3	cuttings	Interval tops not available – medium crystalline dolomite and grainstone microbial fabrics; good oil fluorescence.	X	X
4	Salt Wash 1-16	NESW 16 23S 17E	Grand	8290–8300	8	1.5–2.4	2	cuttings	Interval tops not available – fine to medium dolomite composed of wackestone/packstone and possible microbial fabrics; low visible porosity.		
4	Salt Wash 1-16	NESW 16 23S 17E	Grand	8300–10	7	1.5–2.3	1.9	cuttings	Interval tops not available – medium crystalline dolomite; microbial fabric showing patches of interlocking anhydrite crystals and argillaceous matrix.		
4	Salt Wash 1-16	NESW 16 23S 17E	Grand	8310–20	9	1.5–2.2	1.9	cuttings	Interval tops not available – fine to medium crystalline dolomite showing patches of argillaceous matrix, low visible porosity, and patchy fluorescence.		
4	Salt Wash 1-16	NESW 16 23S 17E	Grand	8320–30	9	1.3–3.0	2.4	cuttings	Interval tops not available – silty, fine to medium crystalline dolomite; grainstone/packstone/wackestone fabric showing variable anhydrite plugging and moderate to bright oil fluorescence.	X	X
5	Gruvers Mesa 1	SENW 19 24S 16E	Emery	7185–95	10	1.1–2.0	1.7	cuttings	A interval – fine to medium crystalline dolomite with terrigenous silt, generally low visible porosity; mudstone/wackestone fabric.		

Well #	Well Name	Location	County	Interval (ft)	N	Rating*		Sample Type	Comments**	Epifluorescence Photomicrograph Image (see appendix C)	Binocular or Digital Microscope Image† (see appendix C)
		Section, Township, Range				Range	Ave.				
5	Gruvers Mesa 1	SENW 19 24S 16E	Emery	7195–7205	10	1.0–2.1	1.6	cuttings	A interval – finely crystalline dolomite, occasionally silty to argillaceous showing no visible porosity; mudstone fabric having generally dim fluorescence.		
5	Gruvers Mesa 1	SENW 19 24S 16E	Emery	7205–15	10	1.0–2.1	1.5	cuttings	B interval – silty, finely crystalline dolomite consisting of variable argillaceous content interbedded with fine to medium crystalline dolomite; intercrystalline porosity.		
5	Gruvers Mesa 1	SENW 19 24S 16E	Emery	7215–25	10	1.1–2.1	1.6	cuttings	B interval – finely crystalline dolomite, slightly silty; packstone/wackestone fabric showing very low visible porosity and some disseminated pyrite.		
5	Gruvers Mesa 1	SENW 19 24S 16E	Emery	7225–35	10	1.5–2.1	1.8	cuttings	B interval – fine to medium crystalline dolomite with low visible porosity; occasional silty argillaceous interbeds.		
5	Gruvers Mesa 1	SENW 19 24S 16E	Emery	7235–45	10	0.5–1.8	1.3	cuttings	B interval – silty to argillaceous dolomite, finely crystalline showing no visible porosity; mudstone.		
5	Gruvers Mesa 1	SENW 19 24S 16E	Emery	7245–55	10	0.5–2.0	1.3	cuttings	C interval – fine to medium crystalline dolomite showing no visible porosity, dim fluorescence, and occasionally argillaceous.		
5	Gruvers Mesa 1	SENW 19 24S 16E	Emery	7255–65	10	0.8–2.0	1.4	cuttings	C interval – fine to medium crystalline dolomite containing some visible intercrystalline porosity and occasionally silty to argillaceous; mudstone.		
5	Gruvers Mesa 1	SENW 19 24S 16E	Emery	7265–75	10	0.8–2.1	1.4	cuttings	C interval – fine to medium crystalline dolomite consisting of some visible intercrystalline porosity and occasionally silty to argillaceous; mudstone.		
5	Gruvers Mesa 1	SENW 19 24S 16E	Emery	7275–90	10	0.9–1.8	1.2	cuttings	C interval – silty to argillaceous dolomite and fine crystalline dolomite, mudstone fabric, and no visible porosity.		
6	Kane Springs Federal 10-1	NWSE 10 25S 18E	Grand	8890–8900	10	1.9–3.0	2.3	cuttings	A interval – silty dolomite to clean, fine crystalline dolomite showing patchy but very bright fluorescence; grainstone/packstone fabric(?).		
6	Kane Springs Federal 10-1	NWSE 10 25S 18E	Grand	8900–10	10	2.0–2.9	2.3	cuttings	A interval – fine to medium crystalline dolomite, generally laminated containing frequent tubular microbial textures, good visible pores within the microbialites, and some interbedded silty and anhydrite intervals; good bright fluorescence throughout.	X	X

Well #	Well Name	Location	County	Interval (ft)	N	Rating*		Sample Type	Comments**	Epifluorescence Photomicrograph Image (see appendix C)	Binocular or Digital Microscope Image† (see appendix C)
		Section, Township, Range				Range	Ave.				
6	Kane Springs Federal 10-1	NWSE 10 25S 18E	Grand	8910–20	10	1.8–2.5	2.1	cuttings	B interval – slightly silty, fine to medium crystalline dolomite showing possible microbialite structures; lower visible porosity than previous samples.	X	X
6	Kane Springs Federal 10-1	NWSE 10 25S 18E	Grand	8920–30	9	1.8–2.8	2.3	cuttings	B interval – fine to medium crystalline dolomite, slightly silty displaying occasional laminated microbial textures; some interbedded anhydrite.		
6	Kane Springs Federal 10-1	NWSE 10 25S 18E	Grand	8930–40	10	0.6–2.6	1.8	cuttings	B interval – interbedded, fine to medium dolomite, silty wackestone/packstone fabric and argillaceous, organic, fine dolomite showing very dim fluorescence.		
7	Utah 2	NWSW 36 31S 24E	Grand	7580–90	10	0.5–1.9	1.3	cuttings	A interval – silty shale with little to no dolomite; very low porosity showing patchy fluorescence.		
7	Utah 2	NWSW 36 31S 24E	Grand	7590–7600	10	0.9–2.1	1.4	cuttings	A interval – siltstone consisting of variable amounts of fine to medium dolomite clusters exhibiting patchy fluorescence.	X	X
7	Utah 2	NWSW 36 31S 24E	Grand	7600–10	8	0.5–1.2	0.8	cuttings	A interval – silty shale having very little dolomite, no visible porosity, and generally dim fluorescence.		
7	Utah 2	NWSW 36 31S 24E	Grand	7610–20	10	0.5–1.2	0.9	cuttings	A interval – black shale containing small patches of fine dolomite and silty dolomite; no visible porosity.		
7	Utah 2	NWSW 36 31S 24E	Grand	7620–30	7	0.7–2.1	1.4	cuttings	B interval – patches of fine to medium dolomite interbedded with silty shale; highly variable fluorescence.		
7	Utah 2	NWSW 36 31S 24E	Grand	7630–40	9	0.9–2.1	1.4	cuttings	B interval – fine to medium crystalline dolomite showing fair to good fluorescence; packstone/wackestone fabric interbedded with slightly dolomitic shale.		
7	Utah 2	NWSW 36 31S 24E	Grand	7640–50	10	1.1–2.0	1.7	cuttings	B interval – fine to medium crystalline dolomite showing fair to good fluorescence; packstone/wackestone fabric interbedded with slightly dolomitic shale.		
7	Utah 2	NWSW 36 31S 24E	Grand	7650–60	10	1.0–2.1	1.7	cuttings	B interval – fine to medium crystalline dolomite surrounded by patches of argillaceous and organic matrix; no visible porosity and patchy fluorescence.		
7	Utah 2	NWSW 36 31S 24E	Grand	7660–90					No cuttings.		
7	Utah 2	NWSW 36 31S 24E	Grand	7690–7700	8	1.0–2.4	1.9	cuttings	B interval – fine to medium crystalline dolomite showing very good fluorescence and some visible intercrystalline pores interbedded with silty shale.	X	X

Well #	Well Name	Location	County	Interval (ft)	N	Rating*		Sample Type	Comments**	Epifluorescence Photomicrograph Image (see appendix C)	Binocular or Digital Microscope Image† (see appendix C)
		Section, Township, Range				Range	Ave.				
7	Utah 2	NWSW 36 31S 24E	Grand	7700–10	7	1.5–2.3	1.9	cuttings	B interval – fine to medium crystalline dolomite consisting of variable intercrystalline porosity and good fluorescence, interbedded with silty shale.	X	X
7	Utah 2	NWSW 36 31S 24E	Grand	7710–20	10	1.0–2.3	1.9	cuttings	C interval – fine to medium crystalline dolomite showing of variable intercrystalline porosity and good fluorescence, interbedded with silty shale.		
7	Utah 2	NWSW 36 31S 24E	Grand	7720–30	9	1.0–2.5	2	cuttings	C interval – mostly finely crystalline dolomite showing variable fluorescence; mudstone/wackestone fabric containing scattered silt grains.		
8	Federal Bowknot 1	NESE 30 25S 18E	Grand	6940–50	10	1.0–2.2	1.6	cuttings	B interval – dolomite and dolomitic shale; dolomite crystal aggregates also present.	X	X
8	Federal Bowknot 1	NESE 30 25S 18E	Grand	6950–60	10	1.5–2.0	1.8	cuttings	B interval – dolomite and dolomitic shale.		
8	Federal Bowknot 1	NESE 30 25S 18E	Grand	6960–70	9	0.7–2.5	2	cuttings	B interval – mostly dolomite and some slightly silty dolomitic shale. Rhombic dolomite clusters and dolomite contain visible intercrystalline porosity.	X	X
8	Federal Bowknot 1	NESE 30 25S 18E	Grand	6970–75	7	1.7–2.4	2	cuttings	B interval – silty dolomite and complete dolomite.	X	X
8	Federal Bowknot 1	NESE 30 25S 18E	Grand	6975–80	7	1.3–2.2	2	cuttings	B interval – mostly dolomite and dolomitic shale.		
8	Federal Bowknot 1	NESE 30 25S 18E	Grand	6980–88	10	1.5–2.2	2	cuttings	B interval – dolomitic shale (missing cuttings from 6988–7000').		
8	Federal Bowknot 1	NESE 30 25S 18E	Grand	7000–10	9	1.6–2.4	2	cuttings	C interval – microcrystalline dolomite.	X	X
8	Federal Bowknot 1	NESE 30 25S 18E	Grand	7015–20	9	1.5–2.6	2.1	cuttings	C interval – mostly dolomitic shale (missing cuttings from 7010–7015').		
9	Kane Springs 25-19-34-1	NWSE 34 25S 19E	Grand	7550–60	6	2.4–3.0	2.7	cuttings	Horizontal well – dolomitic shale to silty dolomite.		
9	Kane Springs 25-19-34-1	NWSE 34 25S 19E	Grand	7560–70	7	2.8–3.2	2.9	cuttings	Horizontal well – dolomite and silty dolomite.	X	X
9	Kane Springs 25-19-34-1	NWSE 34 25S 19E	Grand	7570–80	9	2.9–3.4	2.9	cuttings	Horizontal well – microcrystalline dolomite and anhydritic dolomite; oil films.	X	X
9	Kane Springs 25-19-34-1	NWSE 34 25S 19E	Grand	7580–90	6	1.8–3.2	2.6	cuttings	Horizontal well – honeycomb remnants of microbial filaments(?).	X	X
9	Kane Springs 25-19-34-1	NWSE 34 25S 19E	Grand	7590–7600	5	1.5–2.6	2	cuttings	Horizontal well – slightly silty shale and very minor dolomite.		
9	Kane Springs 25-19-34-1	NWSE 34 25S 19E	Grand	7600–10	10	1.5–3.0	2.3	cuttings	Horizontal well – silty dolomite and microlaminated microbial dolomite.	X (see figure 11F)	X
9	Kane Springs 25-19-34-1	NWSE 34 25S 19E	Grand	7610–20	9	1.6–2.4	1.9	cuttings	Horizontal well – shale to silty shale.		

Well #	Well Name	Location	County	Interval (ft)	N	Rating*		Sample Type	Comments**	Epifluorescence Photomicrograph Image (see appendix C)	Binocular or Digital Microscope Image† (see appendix C)
		Section, Township, Range				Range	Ave.				
9	Kane Springs 25-19-34-1	NWSE 34 25S 19E	Grand	7620–30	10	0.8–3.0	2	cuttings	Horizontal well – dolomitic shale, shale, and microbial dolomite.		
9	Kane Springs 25-19-34-1	NWSE 34 25S 19E	Grand	7630–40	6	1.8–2.3	2.1	cuttings	Horizontal well – silty and slightly dolomitic shale.		
9	Kane Springs 25-19-34-1	NWSE 34 25S 19E	Grand	7640–50	7	1.5–2.4	1.9	cuttings	Horizontal well – slightly dolomitic shale.		
9	Kane Springs 25-19-34-1	NWSE 34 25S 19E	Grand	7650–60	7	2.0–2.9	2.4	cuttings	Horizontal well – dolomite to dolomitic shale.		
9	Kane Springs 25-19-34-1	NWSE 34 25S 19E	Grand	7660–70	6	1.5–3.0	2.2	cuttings	Horizontal well – microcrystalline dolomite and dolomitic shale.		
9	Kane Springs 25-19-34-1	NWSE 34 25S 19E	Grand	7670–80	5	2.0–3.3	2.5	cuttings	Horizontal well – dolomite and silty shale.		
9	Kane Springs 25-19-34-1	NWSE 34 25S 19E	Grand	7680–90	7	1.8–2.5	2.1	cuttings	Horizontal well – silty shale to dolomitic silty shale.		
9	Kane Springs 25-19-34-1	NWSE 34 25S 19E	Grand	7690–7700	5	0.5–2.8	1.9	cuttings	Horizontal well – mostly silty shale to slightly dolomitic shale.		
9	Kane Springs 25-19-34-1	NWSE 34 25S 19E	Grand	7700–10	10	1.5–2.6	2	cuttings	Horizontal well – slightly dolomitic shale.		
9	Kane Springs 25-19-34-1	NWSE 34 25S 19E	Grand	7710–20	9	1.8–3.0	2.3	cuttings	Horizontal well – silty dolomitic shale.		
9	Kane Springs 25-19-34-1	NWSE 34 25S 19E	Grand	7720–30	6	2.8–3.3	3.1	cuttings	Horizontal well – mostly dolomite and silty shale.		
9	Kane Springs 25-19-34-1	NWSE 34 25S 19E	Grand	7730–40	5	1.2–2.6	1.6	cuttings	Horizontal well – patchy fluorescence in dolomitic mudstone; somewhat shaly/argillaceous matrix.	X	X
9	Kane Springs 25-19-34-1	NWSE 34 25S 19E	Grand	7740–50	6	2.3–2.9	2.7	cuttings	Horizontal well – patchy dolomitic mudstone and argillaceous partings.	X	X
9	Kane Springs 25-19-34-1	NWSE 34 25S 19E	Grand	7750–60	5	0.3–2.5	1.4	cuttings	Horizontal well – interbedded black shale and patchy fluorescent dolomite.		
9	Kane Springs 25-19-34-1	NWSE 34 25S 19E	Grand	7760–70	3	1.0–1.5	1.2	cuttings	Horizontal well – mostly shale with small patches of dolomite crystalline clusters.		
10	Cane Creek Unit 26-3	NESW 26 25S 19E	Grand	7388.9	9	1.3–2.1	1.8	core	A interval – medium crystalline dolomite containing rare floating silt grains and low visible porosity; mudstone/wackestone fabric.		
10	Cane Creek Unit 26-3	NESW 26 25S 19E	Grand	7394.5	10	1.7–2.2	2	core	A interval – finely crystalline dolomite, wackestone/mudstone fabric, and very low visible porosity partially due to calcite between the dolomite crystals.		
10	Cane Creek Unit 26-3	NESW 26 25S 19E	Grand	7398.4	10	0.3–1.3	0.7	core	A interval – black, organic finely crystalline dolomite; mudstone fabric containing argillaceous patches, and rare floating silt grains.		
10	Cane Creek Unit 26-3	NESW 26 25S 19E	Grand	7403.1	10	1.3–2.1	1.8	core	A interval – slightly silty, finely crystalline dolomite; mudstone fabric having no visible of porosity but patches of anhydrite.		

Well #	Well Name	Location	County	Interval (ft)	N	Rating*		Sample Type	Comments**	Epifluorescence Photomicrograph Image (see appendix C)	Binocular or Digital Microscope Image† (see appendix C)
		Section, Township, Range				Range	Ave.				
10	Cane Creek Unit 26-3	NESW 26 25S 19E	Grand	7408.9	10	1.9–2.3	2.1	core	A interval – fine to medium crystalline dolomite, slightly silty, showing probable microbial structures; fair visible porosity and fluorescence.		
10	Cane Creek Unit 26-3	NESW 26 25S 19E	Grand	7410.4	10	2.1–2.6	2.2	core	B interval – silt to silty dolomite and a medium crystalline grainstone fabric or microbialite consisting of good intercrystalline porosity.	X	X
10	Cane Creek Unit 26-3	NESW 26 25S 19E	Grand	7413.2	10	0.5–1.7	1.1	core	B interval – black organic-rich, finely crystalline dolomite; mudstone showing very low visible porosity and dim fluorescence.		
10	Cane Creek Unit 26-3	NESW 26 25S 19E	Grand	7416.2	10	1.3–2.2	1.7	core	B interval – fine to medium crystalline dolomite, packstone/grainstone fabric, and poor visible porosity; some anhydrite plugging.		
10	Cane Creek Unit 26-3	NESW 26 25S 19E	Grand	7419.5	10	1.8–2.1	2	core	B interval – fine to medium crystalline dolomite, mudstone/wackestone fabric showing poor visible porosity and patchy fluorescence.		
10	Cane Creek Unit 26-3	NESW 26 25S 19E	Grand	7428.1	10	2.2–3.2	2.6	core	B interval – medium crystalline and silty dolomite having a probable microbialite texture; excellent intercrystallline porosity and bright fluorescence.	X	X
10	Cane Creek Unit 26-3	NESW 26 25S 19E	Grand	7429.8	10	2.0–2.8	2.3	core	B interval – fine to medium crystalline dolomite, mudstone/wackestone fabric showing poor visible porosity and patchy fluorescence.		
10	Cane Creek Unit 26-3	NESW 26 25S 19E	Grand	7433.3	10	0.7–2.1	1.4	core	B interval – slightly silty limestone, mudstone showing no visible porosity and patchy poor fluorescence.		
10	Cane Creek Unit 26-3	NESW 26 25S 19E	Grand	7437.5	10	2.2–3.0	2.6	core	B interval – slightly silty fine to medium crystalline dolomite displaying probable microbialite textures; good visible porosity and fluorescence.	X	X
10	Cane Creek Unit 26-3	NESW 26 25S 19E	Grand	7440.5	10	2.0–2.6	2.2	core	B interval, fine to medium crystalline dolomite, wackestone/packstone, microbial with variable but frequently good porosity, occasional silt grains and silty dolomite	X	X
10	Cane Creek Unit 26-3	NESW 26 25S 19E	Grand	7445.1	10	2.0–3.0	2.3	core	B interval – medium crystalline dolomite, microbial grainstone/packstone fabric showing rare floating silt grains and good intercrystalline and interparticle pores.	X	X
10	Cane Creek Unit 26-3	NESW 26 25S 19E	Grand	7453.5	10	2.0–2.6	2.3	core	C interval – fine to medium crystalline dolomite, wackestone/mudstone fabric, some black organic-rich shale, and generally low visible porosity but good bright fluorescence; no silt grain observed.		

Well #	Well Name	Location	County	Interval (ft)	N	Rating*		Sample Type	Comments**	Epifluorescence Photomicrograph Image (see appendix C)	Binocular or Digital Microscope Image† (see appendix C)
		Section, Township, Range				Range	Ave.				
10	Cane Creek Unit 26-3	NESW 26 25S 19E	Grand	7456	10	2.1–2.8	2.3	core	C interval – medium crystalline to silty dolomite showing excellent visible intercrystalline porosity; probable microbial textures throughout.	X	X
10	Cane Creek Unit 26-3	NESW 26 25S 19E	Grand	7464.8	8	0.3–0.9	0.6	core	C interval –black, organic finely crystalline dolomite to dolomitic shale, no visible porosity, and rare scattered silt grains.		
10	Cane Creek Unit 26-3	NESW 26 25S 19E	Grand	7469.2	10	1.9–2.5	2.1	core	C interval – medium crystalline to silty/argillaceous dolomite showing microlaminated microbialite structures and good visible intercrystalline porosity.	X	X
10	Cane Creek Unit 26-3	NESW 26 25S 19E	Grand	7470.4	10	1.8–2.2	2	core	C interval – calcareous dolomite to dolomitic limestone consisting of highly variable visible porosity and fluorescence, some microbial textures as well as mudstone/wackestone fabric; possible baffle but with fair to good fluorescence.		
11	Long Canyon 1	SENW 9 25S 20E	Grand	7020–30	4	0.0–1.5	0.4	cuttings	A interval – all samples are anhydrite; white to clear.		
11	Long Canyon 1	SENW 9 25S 20E	Grand	7030–40	4	0.5–2.7	1.2	cuttings	A interval – weakly fluorescing shale and one medium crystalline dolomite; wackestone to packstone(?) fabric.	X	X
11	Long Canyon 1	SENW 9 25S 20E	Grand	7040–50	5	0.0–0.3	0.2	cuttings	B interval – black shale, no fluorescence.		
11	Long Canyon 1	SENW 9 25S 20E	Grand	7050–60	5	0.3–2.4	1.1	cuttings	B interval – black shale containing no fluorescence, and medium crystalline dolomite that is slightly anhydritic.		
11	Long Canyon 1	SENW 9 25S 20E	Grand	7060–70	4	0.2–2.8	1.3	cuttings	B interval – black shale and medium crystalline dolomite showing apparent intercrystalline porosity.	X	X
11	Long Canyon 1	SENW 9 25S 20E	Grand	7070–80	4	0.7–2.4	1.8	cuttings	B interval – slightly dolomitized skeletal grainstone fabric containing possible ostracods.	X	X
11	Long Canyon 1	SENW 9 25S 20E	Grand	7080–95					No cuttings		
11	Long Canyon 1	SENW 9 25S 20E	Grand	7095–7100	5	1.3–2.8	2	cuttings	C interval – micro colonial fossil, possible bryozoan.	X	X
11	Long Canyon 1	SENW 9 25S 20E	Grand	7100–10					No cuttings		
11	Long Canyon 1	SENW 9 25S 20E	Grand	7110–15	4	0.5–3.0	1.4	cuttings	C interval – skeletal grainstone fabric composed of colonial bryozoan fragments.	X	
11	Long Canyon 1	SENW 9 25S 20E	Grand	7115–35	4	0.1–2.0	1	cuttings	C interval – black shale and medium to coarsely crystalline dolomite.		
12	Mineral Canyon 1-14	SWSE 14 26S 19E	Grand	7330–40	5	1.1–1.6	1.4	cuttings	A interval – dolomitic mudstone to wackestone fabrics, clean, and dull uniform fluorescence.		

Well #	Well Name	Location	County	Interval (ft)	N	Rating*		Sample Type	Comments**	Epifluorescence Photomicrograph Image (see appendix C)	Binocular or Digital Microscope Image† (see appendix C)
		Section, Township, Range				Range	Ave.				
12	Mineral Canyon 1-14	SWSE 14 26S 19E	Grand	7340–50	10	0.3–1.0	0.6	cuttings	A interval – very small samples.		
12	Mineral Canyon 1-14	SWSE 14 26S 19E	Grand	7350–60	9	0.3–0.8	0.6	cuttings	B interval – slightly argillaceous dolomitic wackestone to packstone fabrics; fine to medium crystal size.		
12	Mineral Canyon 1-14	SWSE 14 26S 19E	Grand	7360–70	7	1.1–1.8	1.5	cuttings	B interval – medium crystalline dolomite showing intercrystalline porosity; dull fluorescence exhibits some nonfluorescent argillaceous patches.	X	X
12	Mineral Canyon 1-14	SWSE 14 26S 19E	Grand	7370–80					No samples		
12	Mineral Canyon 1-14	SWSE 14 26S 19E	Grand	7380–90	10	1.2–2.1	1.7	cuttings	B interval – highly dolomitic shale consisting of well-developed dolomite crystals and microporosity.	X (see figure 11C)	X (see figure 19A)
12	Mineral Canyon 1-14	SWSE 14 26S 19E	Grand	7390–7400	7	0.1–1.8	1	cuttings	C interval – mostly finely crystalline dolomitic mudstone, moderately argillaceous.		
12	Mineral Canyon 1-14	SWSE 14 26S 19E	Grand	7400–10	7	1.1–1.9	1.4	cuttings	C interval – patchy, microcrystalline dolomitic mudstone.		
12	Mineral Canyon 1-14	SWSE 14 26S 19E	Grand	7410–20	10	0.5–1.2	0.8	cuttings	C interval – very small samples.		
13	Federal 1-X	NESE 36 26S 20E	San Juan	6520–30	9	0.5–2.3	1.7	cuttings	A interval – shale containing isolated clusters of dolomite.		
13	Federal 1-X	NESE 36 26S 20E	San Juan	6530–40	6	0.5–2.4	1.7	cuttings	B interval – microfractured dolomitic shale (no cuttings, 6540–6580'; all halite, 6580–6590'; no cuttings, 6590–6610').	X	X
13	Federal 1-X	NESE 36 26S 20E	San Juan	6610–20	10	1.5–2.3	1.9	cuttings	C interval – mostly shale, slightly dolomitic.		
13	Federal 1-X	NESE 36 26S 20E	San Juan	6620–30	8	1.0–2.1	1.7	cuttings	C interval – silty and slightly dolomitic shale containing aggregates of rhombic dolomite.	X	X
13	Federal 1-X	NESE 36 26S 20E	San Juan	6630–40	10	1.8–2.8	2.2	cuttings	C interval – highly dolomitic shale, anhydritic dolomite, and crystalline dolomite containing anhydrite clusters (no cuttings, 6640–6685').	X	X
14	Featherstone 9-1	NENE 9 27S 20E	San Juan	5790–5800	10	0.3–1.8	1.1	cuttings	A interval – black shale containing clusters of fine to medium dolomite crystals and dolomitic siltstone.		
14	Featherstone 9-1	NENE 9 27S 20E	San Juan	5800–10	10	0.5–2.3	1.2	cuttings	A interval – dolomitic siltstone and fine to medium crystalline mudstone, occasionally argillaceous.	X	X
14	Featherstone 9-1	NENE 9 27S 20E	San Juan	5810–20	10	1.1–2.3	1.8	cuttings	B interval – dolomitic siltstone and fossiliferous dolomitic packstone/wackestone fabric; fine to medium crystalline.	X	X
14	Featherstone 9-1	NENE 9 27S 20E	San Juan	5820–30	10	0.7–1.5	1	cuttings	B interval – dolomitic siltstone and fine to medium crystalline dolomitic wackestone/packstone fabric.		

Well #	Well Name	Location	County	Interval (ft)	N	Rating*		Sample Type	Comments**	Epifluorescence Photomicrograph Image (see appendix C)	Binocular or Digital Microscope Image† (see appendix C)
		Section, Township, Range				Range	Ave.				
14	Featherstone 9-1	NENE 9 27S 20E	San Juan	5830–40	10	1.7–2.8	2.1	cuttings	B interval – dolomitic siltstone to silty dolomite, some of which have clusters of medium crystalline dolomite; no fossils observed.	X	X
14	Featherstone 9-1	NENE 9 27S 20E	San Juan	5840–50	10	1.5–2.9	1.9	cuttings	B interval – medium crystalline interlocking dolomite containing modest intercrystalline porosity; some variable argillaceous dolomite.	X	X
14	Featherstone 9-1	NENE 9 27S 20E	San Juan	5850–60	10	1.1–2.7	1.8	cuttings	C interval – fine to medium crystalline dolomite, mudstone to wackestone fabric, and argillaceous dolomite containing medium crystalline dolomite clusters.	X	X
14	Featherstone 9-1	NENE 9 27S 20E	San Juan	5860–70	10	0.9–2.9	1.7	cuttings	C interval – medium crystalline dolomite, wackestone/packstone fabric, and shale containing silt and clusters of medium crystalline dolomite.	X	X
14	Featherstone 9-1	NENE 9 27S 20E	San Juan	5870–80	10	0.6–2.3	1.6	cuttings	C interval – shaly and silty dolomite showing occasional cleaner fossiliferous wackestone to packstone fabrics, and fine to medium crystalline dolomite.	X	X
14	Featherstone 9-1	NENE 9 27S 20E	San Juan	5880–95	10	1.3–2.0	1.7	cuttings	C interval – mostly shale and silty shale containing fine to medium dolomite crystal clusters.		
15	West Bridger Jack U 3	SESW 3 27S 21E	San Juan	5900–10	10	0.6–1.1	0.9	cuttings	B interval – finely dolomitic shale.		
15	West Bridger Jack U 3	SESW 3 27S 21E	San Juan	5910–20	10	0.3–0.8	0.6	cuttings	B interval – dolomitic shale; medium size cuttings.		
15	West Bridger Jack U 3	SESW 3 27S 21E	San Juan	5920–30	10	0.2–1.2	0.5	cuttings	B interval – dolomitic shale.	X	X
15	West Bridger Jack U 3	SESW 3 27S 21E	San Juan	5930–40	10	0.1–0.5	0.4	cuttings	C interval – slightly silty shale.		
15	West Bridger Jack U 3	SESW 3 27S 21E	San Juan	5940–50	10	0.3–1.1	0.7	cuttings	C interval – finely crystalline dolomitic shale.		X (see figure 19E)
15	West Bridger Jack U 3	SESW 3 27S 21E	San Juan	5950–60	8	0.1–1.2	0.4	cuttings	C interval – mostly black shale, minor dolomite.		
15	West Bridger Jack U 3	SESW 3 27S 21E	San Juan	5960–70	10	0.1–1.1	0.7	cuttings	C interval – mostly black shale.		X (see figure 19F)
16	Cane Creek State 1-36	NWSE 36 27S 20E	San Juan	7000–10	6	1.8–2.8	2.2	cuttings	A interval – microbial dolomite, containing good intercrystalline porosity, and occasional argillaceous intervals.	X	X
16	Cane Creek State 1-36	NWSE 36 27S 20E	San Juan	7010–20	9	2.0–3.1	2.5	cuttings	A interval – porous fine to medium crystalline dolomitic microbial boundstone fabric to silty dolomite; variable amounts of anhydrite and bitumen present.	X	X
16	Cane Creek State 1-36	NWSE 36 27S 20E	San Juan	7020–30	7	1.5–3.0	2.2	cuttings	B interval – silty dolomite, fine to medium crystal size, dolomitic mudstone; microbialite(?).		

Well #	Well Name	Location	County	Interval (ft)	N	Rating*		Sample Type	Comments**	Epifluorescence Photomicrograph Image (see appendix C)	Binocular or Digital Microscope Image† (see appendix C)
		Section, Township, Range				Range	Ave.				
16	Cane Creek State 1-36	NWSE 36 27S 20E	San Juan	7030–40	10	2.0–2.9	2.7	cuttings	B interval – very silty dolomitic mudstone to wackestone fabric showing micro-stylolites and probable micro fractures.		
16	Cane Creek State 1-36	NWSE 36 27S 20E	San Juan	7040–50	9	1.0–2.2	1.8	cuttings	B interval – black argillaceous dolomite having a generally non fluorescence matrix except where fine to medium crystalline dolomite crystal occur; mudstone/wackestone fabric.		
16	Cane Creek State 1-36	NWSE 36 27S 20E	San Juan	7050–60	10	1.3–1.9	1.6	cuttings	B interval – laminated dolomitic shale showing fluorescence only in some finely crystalline dolomite layers; shale, possibly silty in some laminae.		
16	Cane Creek State 1-36	NWSE 36 27S 20E	San Juan	7060–70	9	1.1–2.3	1.7	cuttings	C interval – fine to medium crystalline dolomite, some intercrystal pores, and occasionally argillaceous; maybe peloidal packstone/wackestone fabric, bitumen present.	X	X
16	Cane Creek State 1-36	NWSE 36 27S 20E	San Juan	7070–80	10	0.9–2.1	1.4	cuttings	C interval – fine to medium crystalline dolomite, occasionally argillaceous, and hints of microporous microbialite textures; bitumen present.	X	X
16	Cane Creek State 1-36	NWSE 36 27S 20E	San Juan	7080–90	10	0.6–2.6	1.4	cuttings	C interval – interbedded non-fluorescing shale and fine to medium crystalline dolomite showing porosity and fluorescence; bitumen present.	X	X
16	Cane Creek State 1-36	NWSE 36 27S 20E	San Juan	7090–7100	10	1.1–2.0	1.7	cuttings	C interval – silty, peloidal packstone/grainstone fabric showing variable fluorescence as well as dolomitic shale showing only low fluorescence.		
17	Red Rock Unit 1	NWNE 9 28S 22E	San Juan	6790–6800	9	0.3–1.1	0.7	cuttings	A interval – black organic shale showing silty and dolomitic patches; no visible porosity or microbial structure.		
17	Red Rock Unit 1	NWNE 9 28S 22E	San Juan	6800–10	8	0.3–1.9	1	cuttings	B interval – finely crystalline dolomite, packstone/grainstone fabric consisting of small hard peloids and possibly coated grains; low visible porosity.		
17	Red Rock Unit 1	NWNE 9 28S 22E	San Juan	6810–20	8	0.3–2.0	1.2	cuttings	B interval – medium crystalline dolomite, often with good rhombic crystal shape; patches of argillaceous matrix have no visible porosity.		
17	Red Rock Unit 1	NWNE 9 28S 22E	San Juan	6820–30	9	0.3–2.2	0.7	cuttings	B interval – fine to medium dolomite having an occasional microbial fabric interbedded with slightly dolomitic shale; microbial dolomite shows some visible porosity.		

Well #	Well Name	Location	County	Interval (ft)	N	Rating*		Sample Type	Comments**	Epifluorescence Photomicrograph Image (see appendix C)	Binocular or Digital Microscope Image† (see appendix C)
		Section, Township, Range				Range	Ave.				
17	Red Rock Unit 1	NWNE 9 28S 22E	San Juan	6830–40	10	0.3–1.3	0.7	cuttings	C interval – fine to medium crystalline dolomite, wackestone/packstone fabric, and no visible porosity, interbedded with slightly dolomitic black shale.		
17	Red Rock Unit 1	NWNE 9 28S 22E	San Juan	6840–50	8	0.5–1.5	1	cuttings	C interval – fine to medium crystalline dolomitic showing probable good microbialite structures and patches of argillaceous dolomite.		
17	Red Rock Unit 1	NWNE 9 28S 22E	San Juan	6850–60	9	0.7–2.2	1.3	cuttings	C interval – fine to medium crystalline dolomite, traces of anhydrite, and packstone/grainstone fabric interbedded with slightly dolomitic argillaceous intervals; some bitumen.	X	X
17	Red Rock Unit 1	NWNE 9 28S 22E	San Juan	6860–70	7	0.3–2.4	1.1	cuttings	C interval – slightly silty and argillaceous microcrystalline dolomite including some tight limestone, generally low visible porosity; packstone/wackestone fabric. Anhydrite cement and bitumen are present.	X	X
17	Red Rock Unit 1	NWNE 9 28S 22E	San Juan	6870–80	10	0.4–1.7	1.1	cuttings	C interval – fine to medium dolomite showing possible microbial fabric and patches of argillaceous material.		
17	Red Rock Unit 1	NWNE 9 28S 22E	San Juan	6880–90	8	0.3–2.5	1.1	cuttings	C interval – fine to medium dolomite, packstone/grainstone/mudstone fabric, and occasional argillaceous patches.	X	
17	Red Rock Unit 1	NWNE 9 28S 22E	San Juan	6890–6900	10	0.3–2.1	1.2	cuttings	C interval – fine to medium dolomite consisting of lumpy microbial structures and grainstone/packstone fabric interbedded with dolomitic shale.		
17	Red Rock Unit 1	NWNE 9 28S 22E	San Juan	6900–10	8	0.3–0.8	0.5	cuttings	C interval – black organic-rich shale containing little to no dolomite; possible microfractures with minor fluorescence.		
18	Gulf-Aztec-Lockhart-Fed 1	SWSW 22 28S 20E	San Juan	4765–70	8	0.2–1.5	1	cuttings	A interval – dolomite crystal aggregate or grainstone/packstone fabric.	X	X
18	Gulf-Aztec-Lockhart-Fed 1	SWSW 22 28S 20E	San Juan	4770–75	8	1.4–1.6	1.5	cuttings	A interval – dolomite and dolomitic shale.		
18	Gulf-Aztec-Lockhart-Fed 1	SWSW 22 28S 20E	San Juan	4775–80	10	0.8–1.5	1.1	cuttings	B interval – micro rhombic dolomite; possible ooids or peloids.		
18	Gulf-Aztec-Lockhart-Fed 1	SWSW 22 28S 20E	San Juan	4780–85	10	0.6–2.2	1.8	cuttings	B interval – crystalline dolomite to skeletal grainstone fabric showing good epifluorescence and microcrystalline dolomite aggregates; some anhydrite lathes and rhombic dolomite.	X	X
18	Gulf-Aztec-Lockhart-Fed 1	SWSW 22 28S 20E	San Juan	4785–90	10	1.2–2.8	2	cuttings	B interval – anhydritic dolomite showing live oil films; anhydrite lathes, organic (microbial?) structures, and bitumen present.	X	X

Well #	Well Name	Location	County	Interval (ft)	N	Rating*		Sample Type	Comments**	Epifluorescence Photomicrograph Image (see appendix C)	Binocular or Digital Microscope Image† (see appendix C)
		Section, Township, Range				Range	Ave.				
18	Gulf-Aztec-Lockhart-Fed 1	SWSW 22 28S 20E	San Juan	4790–95	9	0.8–2.2	1.6	cuttings	C interval – dolomitic shale.		
18	Gulf-Aztec-Lockhart-Fed 1	SWSW 22 28S 20E	San Juan	4795–4800	10	1.7–2.2	1.9	cuttings	C interval – silty and dolomitic shale.		
18	Gulf-Aztec-Lockhart-Fed 1	SWSW 22 28S 20E	San Juan	4800–10	10	1.6–2.5	2	cuttings	C interval – completely oil saturated dolomite to silty dolomite, crystalline dolomite and dolomitic aggregates, and some possible laminations; bitumen present.	X (see figure 11E)	X
18	Gulf-Aztec-Lockhart-Fed 1	SWSW 22 28S 20E	San Juan	4810–15	9	1.5–2.4	1.9	cuttings	C interval – silty dolomites.		
18	Gulf-Aztec-Lockhart-Fed 1	SWSW 22 28S 20E	San Juan	4815–20	10	1.8–3.0	2.2	cuttings	C interval – fractured dolomite showing live oil films; anhydritic dolomite and rhombic crystalline dolomite.	X	X
19	USA Lockhart 1	SESE 23 28S 20E	San Juan	4380–90	10	0.3–1.0	0.6	cuttings	B interval – slightly dolomitic shale; medium size cuttings.		
19	USA Lockhart 1	SESE 23 28S 20E	San Juan	4390–4400	7	0.4–1.0	0.7	cuttings	B interval – dolomitized shale; large size cuttings.		
19	USA Lockhart 1	SESE 23 28S 20E	San Juan	4400–10	10	0.7–1.1	0.9	cuttings	C interval – slightly to highly dolomitic shale; medium-large cuttings.		
19	USA Lockhart 1	SESE 23 28S 20E	San Juan	4410–20	9	0.9–1.3	1.1	cuttings	C interval –dolomitic shale; medium-large cuttings.		
19	USA Lockhart 1	SESE 23 28S 20E	San Juan	4420–30	10	0.7–1.2	0.9	cuttings	C interval – slightly to moderate dolomitic shale; medium-large cuttings.		
20	Government B-1	NENE 34 28S 22E	San Juan	7535–45	9	1.4–2.1	1.7	cuttings	A interval – medium crystalline dolomite, silty, wackestone/packstone fabric, and highly variable fluorescent.		
20	Government B-1	NENE 34 28S 22E	San Juan	7545–55					No samples		
20	Government B-1	NENE 34 28S 22E	San Juan	7555–65	9	0.6–1.8	1.3	cuttings	A interval – fine to medium crystalline dolomite, occasionally silty, mudstone/wackestone fabric containing patches of argillaceous matrix; no visible porosity.		
20	Government B-1	NENE 34 28S 22E	San Juan	7565–75	10	0.5–3.2	1.6	cuttings	A interval – fine to medium crystalline dolomite, silty, and mudstone/wackestone fabric showing variable dim to bright fluorescence.	X	X
20	Government B-1	NENE 34 28S 22E	San Juan	7575–85	10	0.5–3.1	1.2	cuttings	A interval – finely crystalline dolomite containing silty and argillaceous mixtures; highly variable fluorescence and no visible porosity.	X	X
20	Government B-1	NENE 34 28S 22E	San Juan	7585–95	10	0.7–2.1	1.4	cuttings	A interval – fine to medium crystalline dolomite consisting of a silty and argillaceous matrix; mudstone/wackestone fabric, no visible porosity, and generally dim fluorescence.		

Well #	Well Name	Location	County	Interval (ft)	N	Rating*		Sample Type	Comments**	Epifluorescence Photomicrograph Image (see appendix C)	Binocular or Digital Microscope Image† (see appendix C)
		Section, Township, Range				Range	Ave.				
20	Government B-1	NENE 34 28S 22E	San Juan	7595–7600	10	0.5–2.5	1	cuttings	B interval – fine to medium crystalline dolomite consisting of a silty and argillaceous matrix; mudstone/wackestone fabric, no visible porosity, and generally dim fluorescence.		
20	Government B-1	NENE 34 28S 22E	San Juan	7600–10	10	0.6–1.9	1.4	cuttings	B interval – medium crystalline dolomite, mudstone/wackestone fabric showing argillaceous patches, no visible porosity, and generally dim fluorescence.		
20	Government B-1	NENE 34 28S 22E	San Juan	7610–20	9	0.8–3.0	1.7	cuttings	B interval – fine to medium crystalline dolomite, wackestone/packstone fabric, occasionally silty and argillaceous showing no visible porosity and highly variable fluorescence.	X	X
20	Government B-1	NENE 34 28S 22E	San Juan	7620–30	10	0.5–2.1	1.4	cuttings	B interval – silty dolomite, fine to medium crystalline, mudstone/wackestone fabric showing no visible porosity and variable fluorescence.		
20	Government B-1	NENE 34 28S 22E	San Juan	7630–40	7	0.8–1.9	1.3	cuttings	B interval – medium crystalline dolomite showing a patchy argillaceous matrix, slightly silty, mudstone/wackestone fabric, no visible porosity, and generally dim fluorescence.		
20	Government B-1	NENE 34 28S 22E	San Juan	7640–50	9	0.9–2.9	1.8	cuttings	B interval – fine to medium crystalline dolomite, occasional silty packstone/wackestone fabric showing argillaceous patches, no visible porosity, and highly variable fluorescence.	X	X
20	Government B-1	NENE 34 28S 22E	San Juan	7650–60	7	0.6–1.5	1	cuttings	B interval – fine to medium crystalline dolomite, mudstone/wackestone fabric having argillaceous patches, no visible porosity, and very dim fluorescence.		
20	Government B-1	NENE 34 28S 22E	San Juan	7660–70					No samples.		
20	Government B-1	NENE 34 28S 22E	San Juan	7670–80	9	0.5–2.7	1.6	cuttings	C interval – fine to medium crystalline dolomite, wackestone/packstone/grainstone fabric, occasional argillaceous patches, low to moderate visible porosity, and highly variable fluorescence.	X	X
20	Government B-1	NENE 34 28S 22E	San Juan	7680–90	8	1.3–2.0	1.8	cuttings	C interval – fine to medium crystalline dolomite, mudstone/wackestone fabric, very poor visible porosity, and highly variable fluorescence.		
20	Government B-1	NENE 34 28S 22E	San Juan	7690–7700	10	0.5–1.9	1.4	cuttings	C interval – fine to medium crystalline dolomite, mudstone/wackestone fabric, occasional argillaceous patches, no visible porosity, and generally dim fluorescence.		

Well #	Well Name	Location	County	Interval (ft)	N	Rating*		Sample Type	Comments**	Epifluorescence Photomicrograph Image (see appendix C)	Binocular or Digital Microscope Image† (see appendix C)
		Section, Township, Range				Range	Ave.				
20	Government B-1	NENE 34 28S 22E	San Juan	7700–10	9	1.2–1.7	1.5	cuttings	C interval – medium crystalline dolomite, wackestone/packstone fabric, occasional argillaceous patches, no visible porosity, and generally dim fluorescence.		
20	Government B-1	NENE 34 28S 22E	San Juan	7710–20	10	1.4–2.9	1.7	cuttings	C interval – fine to medium crystalline dolomite, wackestone/packstone/grainstone fabric, generally low visible porosity, some possible anhydrite and argillaceous patches, and highly variable fluorescence; bitumen present.	X	X
21	Horsehead Unit 1	NWSW 18 29S 21E	San Juan	6290–6300	10	0.7–1.5	1.3	cuttings	A interval – microcrystalline, argillaceous dolomite, disseminated sulfides, and dolomitic shale to silty dolomitic shale. Note: cutting are half shale and half halite.	X (see figures 11A and 11B)	X (see figure 19B)
21	Horsehead Unit 1	NWSW 18 29S 21E	San Juan	6300–10	10	1.3–1.7	1.5	cuttings	A interval – mostly black to dark gray shale and minor amount of dark brown microcrystalline dolomite; dolomitic shale, slightly silty.	X	X
21	Horsehead Unit 1	NWSW 18 29S 21E	San Juan	6310–20	10	1.0–1.7	1.4	cuttings	B interval – mostly dark gray dolomitic shale to silt and minor amounts of dolomite.	X	X
21	Horsehead Unit 1	NWSW 18 29S 21E	San Juan	6320–30	10	1.4–2.2	1.8	cuttings	B interval – microcrystalline dolomite showing microporosity and probable oil saturation; saline minerals (anhydrite or halite) also present.	X	X
21	Horsehead Unit 1	NWSW 18 29S 21E	San Juan	6330–40	10	1.8–3.0	2.2	cuttings	B interval – dolomitic shale containing significant halite and/or anhydrite; 50% microcrystalline dolomite either highly organic or oil saturated, 50% slightly dolomitic shale.	X	X
21	Horsehead Unit 1	NWSW 18 29S 21E	San Juan	6340–50	10	1.5–2.5	1.9	cuttings	B interval – mostly highly organic black to dark gray, highly dolomitic shale showing small nodes of incipient dolomite formation; minor evaporites.	X	X
21	Horsehead Unit 1	NWSW 18 29S 21E	San Juan	6350–60	10	1.8–2.2	2	cuttings	C interval – peloidal black organic shale (non-laminated) and dolomitic shale.		X (see figure 19C)
21	Horsehead Unit 1	NWSW 18 29S 21E	San Juan	6360–70	10	1.3–2.0	1.6	cuttings	C interval – peloidal, partially dolomitized organic shale and slightly dolomitic shale.	X	X (see figure 19D)
21	Horsehead Unit 1	NWSW 18 29S 21E	San Juan	6370–80	10	1.1–2.3	1.7	cuttings	C interval – dark gray to black peloidal shale and dolomitic shale; partially dolomitized and medium to dark brown peloidal dolomite.	X	X
21	Horsehead Unit 1	NWSW 18 29S 21E	San Juan	6380–90	10	1.1–2.1	1.7	cuttings	C interval – mostly non-laminated peloidal organic shale, black to dark gray and much less brown dolomite; some shale and dolomitic shale. White dolomite-filled microfractures contain abundant sulfide minerals in fractures fill.	X	X

Well #	Well Name	Location	County	Interval (ft)	N	Rating*		Sample Type	Comments**	Epifluorescence Photomicrograph Image (see appendix C)	Binocular or Digital Microscope Image† (see appendix C)
		Section, Township, Range				Range	Ave.				
22	Hatch Point 1	NESE 14 29S 21E	San Juan	7220–30	10	1.2–2.2	1.6	cuttings	B interval – dolomitic shale and rhombic dolomite clasts within black shale; bitumen present in intercrystalline pores (all halite from 7230–7240').	X	X
22	Hatch Point 1	NESE 14 29S 21E	San Juan	7240–50	10	0.0–1.5	0.7	cuttings	B interval – mostly black shale, no epifluorescence.		
22	Hatch Point 1	NESE 14 29S 21E	San Juan	7250–60	10	0.3–2.2	1.1	cuttings	C interval – silty and slightly dolomitic shale.		
22	Hatch Point 1	NESE 14 29S 21E	San Juan	7260–70	8	1.2–2.4	1.9	cuttings	C interval – dolomitic shale, anhydritic dolomite, and dolomite aggregates within shale; bitumen present.	X (see figure 11D)	X
23	Threemile 12-7	NWSE 12 29S 21E	San Juan	7530–60	8	1.5–2.3	1.9	cuttings	Horizontal well – dolomitic shale, dolomite, and silty shale(?) (all halite from 7560–7650').		
23	Threemile 12-7	NWSE 12 29S 21E	San Juan	7650–70	10	1.0–2.5	1.9	cuttings	Horizontal well – dolomitic shale and anhydritic dolomite.	X	X
23	Threemile 12-7	NWSE 12 29S 21E	San Juan	7670–78	10	1.0–2.2	1.6	cuttings	Horizontal well – silty slightly dolomitic shale.		
23	Threemile 12-7	NWSE 12 29S 21E	San Juan	7678–90	10	0.3–1.5	0.8	cuttings	Horizontal well – silty shale.		
24	La Sal USA 1	NWNE 19 29S 24E	San Juan	7580–90	10	0.3–1.5	0.7	cuttings	A interval –black organic shale, occasional patches of finely crystalline dolomite, and no visible porosity.		
24	La Sal USA 1	NWNE 19 29S 24E	San Juan	7590–7600	9	0.3–1.7	0.7	cuttings	A interval – black organic shale, occasional patches of finely crystalline dolomite consisting of greater amounts of microcrystalline dolomite showing no visible porosity and very dim fluorescence.		
24	La Sal USA 1	NWNE 19 29S 24E	San Juan	7600–10	9	0.3–1.5	0.6	cuttings	B interval – organic-rich black shale showing very little dolomite or silt grains.		
24	La Sal USA 1	NWNE 19 29S 24E	San Juan	7610–20	9	0.3–1.3	0.5	cuttings	B interval – organic-rich black shale showing very little dolomite or silt grains.		
24	La Sal USA 1	NWNE 19 29S 24E	San Juan	7620–30	9	0.3–1.5	0.8	cuttings	B interval – silty dolomite, occasionally argillaceous, and showing visible intercrystalline pores.		
24	La Sal USA 1	NWNE 19 29S 24E	San Juan	7630–40	8	0.3–2.0	0.7	cuttings	C interval – black, argillaceous dolomite, traces of halite; possible microbialite fabric in finely crystalline dolomite.		
24	La Sal USA 1	NWNE 19 29S 24E	San Juan	7640–50	6	0.3–1.1	0.9	cuttings	C interval – black, argillaceous dolomite showing possible microbialite fabric in finely crystalline dolomite.		
24	La Sal USA 1	NWNE 19 29S 24E	San Juan	7650–60	10	0.5–1.7	0.9	cuttings	C interval – black, argillaceous dolomite (slightly more than the 7640–50' zone); possible microbialite fabric in finely crystalline dolomite.		

Well #	Well Name	Location	County	Interval (ft)	N	Rating*		Sample Type	Comments**	Epifluorescence Photomicrograph Image (see appendix C)	Binocular or Digital Microscope Image† (see appendix C)
		Section, Township, Range				Range	Ave.				
24	La Sal USA 1	NWNE 19 29S 24E	San Juan	7660–70	10	0.7–2.0	1.2	cuttings	C interval – highly dolomitic matrix with occasional argillaceous patches, fine to medium crystalline dolomite; possibly microbial showing some visible porosity.		
24	La Sal USA 1	NWNE 19 29S 24E	San Juan	7670–80	8	0.3–1.8	0.9	cuttings	C interval – black, organic shale interbedded with slightly argillaceous dolomite and fine to medium crystalline dolomite; mudstone/wackestone fabric.		
24	La Sal USA 1	NWNE 19 29S 24E	San Juan	7680–90	10	0.5–2.0	1.1	cuttings	C interval – fine to medium crystalline dolomite showing some possible tubular microbial structures and patches of argillaceous and/or organic matrix.		
24	La Sal USA 1	NWNE 19 29S 24E	San Juan	7690–7700	8	0.3–1.7	0.8	cuttings	C interval – black organic-rich shale, minor small patches of finely crystalline dolomite, and no visible porosity.		
25	Lisbon D232	NENE 32 29.5S 24E	San Juan	7770–7820	10	0	0	cuttings	Interval tops not available – large fresh samples dominated by sections of black shale.		
25	Lisbon D232	NENE 32 29.5S 24E	San Juan	7820–30	10	0–0.6	0.4	cuttings	Interval tops not available – silty shale.		
25	Lisbon D232	NENE 32 29.5S 24E	San Juan	7830–40	10	0–0.4	0.1	cuttings	Interval tops not available – silty shale.		
25	Lisbon D232	NENE 32 29.5S 24E	San Juan	7840–50	10	0.2–0.7	0.5	cuttings	Interval tops not available – silty shale.		
25	Lisbon D232	NENE 32 29.5S 24E	San Juan	7850–60	10	0.0–0.5	0.2	cuttings	Interval tops not available – silty and dolomitic shale.		
25	Lisbon D232	NENE 32 29.5S 24E	San Juan	7860–70	10	0.1–0.4	0.2	cuttings	Interval tops not available – dolomitic shale.		
26	Gibson Dome	21 30S 21E	San Juan	5220–30	10	0.7–2.1	1.6	core	A interval – dolomitic siltstone to silty dolomite showing fine to medium dolomite rhombs and some intercrystalline porosity; moderately good fluorescence.		
26	Gibson Dome	21 30S 21E	San Juan	5230–40	10	1.1–2.2	1.8	core	A interval – fine to medium crystalline or anhydritic dolomite showing patchy variable fluorescence; also organic slightly silty black shale.	X	X
26	Gibson Dome	21 30S 21E	San Juan	5240–50	10	1.3–2.1	1.9	core	A interval – siltstone with some intercrystalline porosity and occasional patches of finely crystalline dolomite.		
26	Gibson Dome	21 30S 21E	San Juan	5250–60	10	2.0–2.4	2.1	core	B interval – well sorted siltstone showing some intercrystalline porosity, occasional patches of medium crystalline to silty dolomite, and thin beds of silty shale.	X	X
26	Gibson Dome	21 30S 21E	San Juan	5260–70	9	2.0–2.3	2.1	core	B interval – dolomitic siltstone and purer siltstone showing variable amounts of visible pore space; fair to good fluorescence.	X	X

Well #	Well Name	Location	County	Interval (ft)	N	Rating*		Sample Type	Comments**	Epifluorescence Photomicrograph Image (see appendix C)	Binocular or Digital Microscope Image† (see appendix C)
		Section, Township, Range				Range	Ave.				
26	Gibson Dome	21 30S 21E	San Juan	5270–80	10	0.7–2.2	1.3	core	C interval – silty shale to argillaceous siltstone, with very low visible porosity, possible interbeds of pure siltstone with fair fluorescence.		
26	Gibson Dome	21 30S 21E	San Juan	5280–90	10	1.5–2.1	1.8	core	C interval, silty shale to argillaceous siltstone very low visible porosity, and possible interbeds of pure siltstone showing fair fluorescence.		
26	Gibson Dome	21 30S 21E	San Juan	5290–5300	10	0.5–2.2	1.8	core	C interval – well sorted siltstone and dolomitic siltstone as well as dolomite grainstone fabric; fair to good visible intercrystalline porosity.	X	X
26	Gibson Dome	21 30S 21E	San Juan	5300–10	10	1.0–2.1	1.8	core	C interval – dolomitic siltstone and pure siltstone showing variable visible intercrystalline porosity; some possible microbial dolomite.	X	X
27	Little Valley 2	SESE 29 30S 25E	San Juan	8370–80	5	0.3–0.5	0.3	cuttings	A interval – soft organic black shale and very minor patches of finely crystalline dolomite; note strong sampling bias to black shale.		
27	Little Valley 2	SESE 29 30S 25E	San Juan	8380–90	10	0.3–0.6	0.4	cuttings	A interval – soft organic black shale containing very minor patches of finely crystalline dolomite; note strong sampling bias to black shale.		
27	Little Valley 2	SESE 29 30S 25E	San Juan	8390–8400	10	0.3–0.8	0.4	cuttings	B interval – black organic shale and larger isolated patches of fine to medium crystalline dolomite.		
27	Little Valley 2	SESE 29 30S 25E	San Juan	8400–10	10	0.3–1.2	0.6	cuttings	B interval – good sample of fine to medium crystalline dolomite showing intercrystalline porosity and possible microbial fabric; variable amounts of organic black argillaceous matrix.		
28	Hart Point Unit #1	SENW 8 31S 22E	San Juan	6740–50	8	0.7–2.1	1.4	cuttings	A interval – black silty organic-rich shale, very little to no dolomite; patchy fluorescence.		
28	Hart Point Unit #1	SENW 8 31S 22E	San Juan	6750–60	10	0.5–2.0	1.4	cuttings	A interval – black dolomitic and silty shale, small clusters of finely crystalline dolomite, and anhydrite patchy fluorescence.		
28	Hart Point Unit #1	SENW 8 31S 22E	San Juan	6760–70	10	0.7–1.8	1.2	cuttings	B interval – black dolomitic and silty shale, small clusters of finely crystalline dolomite, and anhydrite patchy fluorescence; slightly more silty than 6750–60'.		
28	Hart Point Unit #1	SENW 8 31S 22E	San Juan	6770–80	9	0.8–2.5	1.9	cuttings	B interval – fine to medium crystalline dolomite and siltstone, some visible pore space; possible microbial structure in the dolomite.		

Well #	Well Name	Location	County	Interval (ft)	N	Rating*		Sample Type	Comments**	Epifluorescence Photomicrograph Image (see appendix C)	Binocular or Digital Microscope Image† (see appendix C)
		Section, Township, Range				Range	Ave.				
28	Hart Point Unit #1	SENW 8 31S 22E	San Juan	6780–90	10	1.7–2.5	2.1	cuttings	B interval – patches of fine to medium crystalline dolomite surrounded by silty argillaceous matrix and visible intercrystalline pores within dolomite patches; bitumen present.	X	X
28	Hart Point Unit #1	SENW 8 31S 22E	San Juan	6790–6800					No cuttings.		
28	Hart Point Unit #1	SENW 8 31S 22E	San Juan	6800–10	10	0.8–2.1	1.5	cuttings	C interval – argillaceous siltstone showing possible anhydrite patches.		
28	Hart Point Unit #1	SENW 8 31S 22E	San Juan	6810–20	10	0.7–2.3	1.6	cuttings	C interval – argillaceous siltstone and clusters of fine to medium crystalline dolomite, and anhydritic; highly variable and patchy fluorescence.	X	X
28	Hart Point Unit #1	SENW 8 31S 22E	San Juan	6820–30	10	0.7–2.3	1.5	cuttings	C interval – fine to medium crystalline dolomite showing microbial tubular structures interbedded with silty shale.		
29	Winchester 21-1H	NWNW 21 31S 24E	San Juan	7750–60	10	0.4–1.5	0.9	cuttings	Horizontal well – silty black shale and slightly dolomitic shale.		
29	Winchester 21-1H	NWNW 21 31S 24E	San Juan	7760–70	10	0.5–1.3	1	cuttings	Horizontal well – fine to medium crystalline dolomite mudstone and black shale containing dolomite crystal clusters.		
29	Winchester 21-1H	NWNW 21 31S 24E	San Juan	7770–80	10	0.4–1.5	0.8	cuttings	Horizontal well – silty and finely crystalline shale plus argillaceous dolomite mudstone.		
29	Winchester 21-1H	NWNW 21 31S 24E	San Juan	7780–90	10	0.3–1.2	0.8	cuttings	Horizontal well – black shale, clusters of fine to medium crystalline dolomite, and argillaceous dolomitic mudstone.		
29	Winchester 21-1H	NWNW 21 31S 24E	San Juan	7790–7800	10	0.5–1.3	0.9	cuttings	Horizontal well – finely crystalline dolomitic siltstone and shale containing finely crystalline dolomite clusters.		
29	Winchester 21-1H	NWNW 21 31S 24E	San Juan	7800–10	10	0.5–1.8	1	cuttings	Horizontal well – finely crystalline dolomitic siltstone and shale containing finely crystalline dolomite clusters.		
29	Winchester 21-1H	NWNW 21 31S 24E	San Juan	7810–20	10	0.5–1.6	1.1	cuttings	Horizontal well – silty, slightly dolomitic shale.		
29	Winchester 21-1H	NWNW 21 31S 24E	San Juan	7820–30	10	0.9–2.0	1.3	cuttings	Horizontal well – silty, slightly dolomitic shale and finely crystalline dolomitic mudstone.		
29	Winchester 21-1H	NWNW 21 31S 24E	San Juan	7830–40	10	0.5–1.8	0.9	cuttings	Horizontal well – silty, slightly dolomitic shale and finely crystalline dolomitic mudstone.		
30	Church Rock Unit 1	SENW 26 31S 23E	San Juan	7460–70	10	0.1–1.0	0.6	cuttings	B interval – shale and slightly silty shale.		
30	Church Rock Unit 1	SENW 26 31S 23E	San Juan	7470–80	10	0.3–1.8	0.8	cuttings	B interval – silty shale with occasional traces of dolomite.		
30	Church Rock Unit 1	SENW 26 31S 23E	San Juan	7480–90	9	0.5–1.5	1.1	cuttings	C interval – dolomite, dolomitic shale, and silty dolomite.		

Well #	Well Name	Location	County	Interval (ft)	N	Rating*		Sample Type	Comments**	Epifluorescence Photomicrograph Image (see appendix C)	Binocular or Digital Microscope Image† (see appendix C)
		Section, Township, Range				Range	Ave.				
30	Church Rock Unit 1	SENW 26 31S 23E	San Juan	7490–7500	10	0.1–1.2	0.5	cuttings	C interval – slightly dolomitic shale.		
30	Church Rock Unit 1	SENW 26 31S 23E	San Juan	7500–10	9	0.3–0.8	0.5	cuttings	C interval – silty shale and dolomitic shale.		
31	Cisco State 36-13	NWNE 36 31S 24E	San Juan	7589.3	6	0.3–0.5	0.3	core	A interval – organic black shale; no visible silt or dolomite.		
31	Cisco State 36-13	NWNE 36 31S 24E	San Juan	7592.5	10	1.7–2.3	2	core	A interval – light colored siltstone, occasional dolomite crystals and cement, generally poorly sorted, and low visible porosity.		
31	Cisco State 36-13	NWNE 36 31S 24E	San Juan	7595.5	7	1.0–1.6	1.2	core	A interval – argillaceous, poorly sorted siltstone showing low visible porosity and no evidence of dolomite.		
31	Cisco State 36-13	NWNE 36 31S 24E	San Juan	7600	10	1.0–1.8	1.3	core	B interval – silty dolomite, wackestone/packstone fabric; very low visible porosity.		
31	Cisco State 36-13	NWNE 36 31S 24E	San Juan	7602.1	10	0.5–1.9	1.4	core	B interval – silty dolomite, wackestone/packstone fabric; very low visible porosity.		
31	Cisco State 36-13	NWNE 36 31S 24E	San Juan	7604.7	10	1.5–2.3	1.9	core	B interval – medium crystalline dolomite, slightly silty showing poor to fair visible porosity; wackestone/packstone fabric.		
31	Cisco State 36-13	NWNE 36 31S 24E	San Juan	7607.7	10	1.8–2.1	2	core	B interval – silty dolomite showing fine to medium dolomite crystals, patchy visible porosity, and fluorescence; wackestone/packstone fabric.		
31	Cisco State 36-13	NWNE 36 31S 24E	San Juan	7611.3	10	1.9–2.5	2.2	core	B interval – slightly silty medium crystalline dolomite, packstone/grainstone and possible microbial fabrics; fairly good visible intercrystalline pores.	X	X
31	Cisco State 36-13	NWNE 36 31S 24E	San Juan	7615.8	10	2.0–2.6	2.2	core	B interval – medium crystalline to silty dolomite, packstone/grainstone fabric showing good visible intercrystalline and interparticle porosity.	X	X
31	Cisco State 36-13	NWNE 36 31S 24E	San Juan	7617.2	10	1.8–2.2	2	core	B interval – dolomitic siltstone, moderately well sorted showing patches of intercrystalline porosity and fluorescence.		
31	Cisco State 36-13	NWNE 36 31S 24E	San Juan	7619.3	10	2.0–2.3	2.2	core	B interval – medium crystalline dolomite, packstone/grainstone fabric containing very minor silt; good visible intercrystalline porosity.	X	X
31	Cisco State 36-13	NWNE 36 31S 24E	San Juan	7623.1	10	2.0–2.8	2.3	core	B interval – moderately well sorted siltstone, slightly dolomitic showing good visible intercrystalline porosity and fluorescence.	X	X

Well #	Well Name	Location	County	Interval (ft)	N	Rating*		Sample Type	Comments**	Epifluorescence Photomicrograph Image (see appendix C)	Binocular or Digital Microscope Image† (see appendix C)
		Section, Township, Range				Range	Ave.				
31	Cisco State 36-13	NWNE 36 31S 24E	San Juan	7632.5	10	1.3–2.0	1.9	core	C interval – silty dolomite showing very low visible porosity and dim fluorescence; generally finely crystalline dolomite and silty wackestone/mudstone fabric.		
31	Cisco State 36-13	NWNE 36 31S 24E	San Juan	7648.8	10	0.1–0.9	0.4	core	C interval – black organic shale containing occasional isolated silt grains.		

*Notes:

- See figure 10 for well number location.
- Samples evaluated at 100X.
- Yellow highlighted epifluorescence rating represents the highest maximum value for the well.

N = number of samples

**Horizontal well – no Cane Creek shale intervals could be determined.

†Core samples are shown by high-resolution, close-up photographs of slabbed cores.

APPENDIX C

EPIFLUORESCENCE PHOTOMICROGRAPHS AND BINOCULAR/DIGITAL MICROSCOPE IMAGES

Note: Figure 10 shows the well number locations. Also, the quality of the cuttings images is variable. Most images were taken with a binocular microscope and are usually good quality, whereas some of the images taken with a digital microscope system resulted in quality that tended to be mixed. The poor-quality images of slabbed core from the Gibson Dome #1 well were the only ones available from the Texas Bureau of Economic Geology where the core is stored.

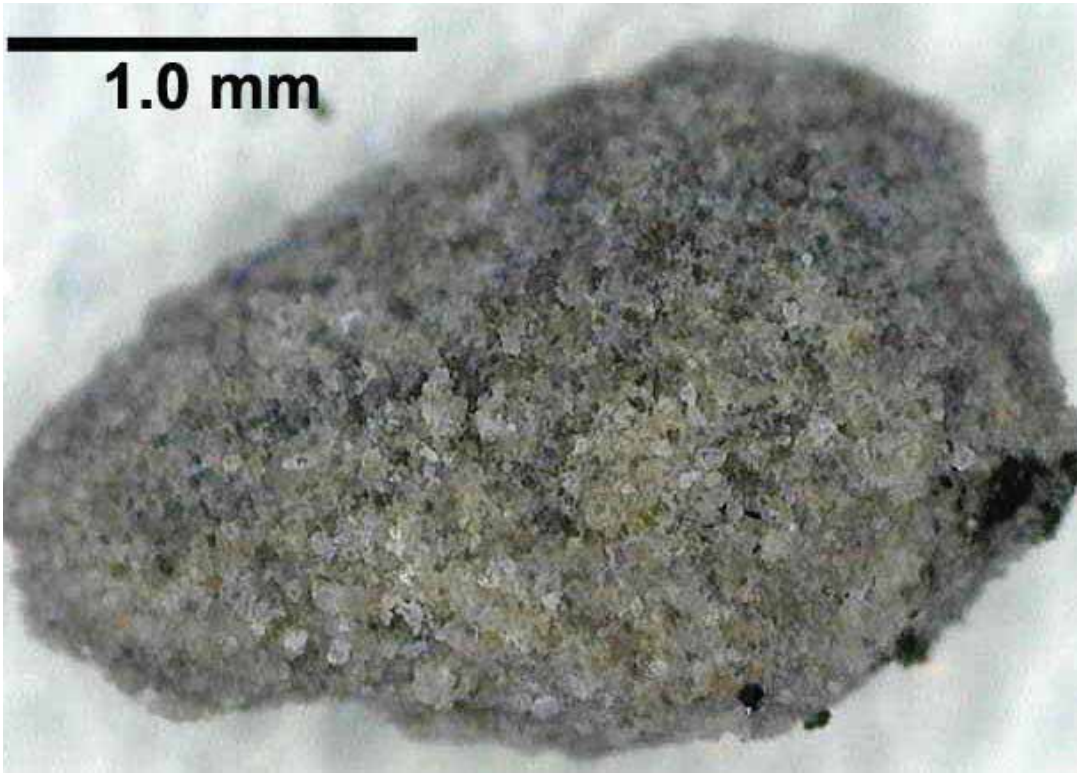

Digital microscope image (dry) – Jakey's Ridge #12-3 (Map #2), 8030-40 feet, B interval, dolomite, medium crystalline with patchy intercrystalline porosity and black particulate organic matter and micro-pyrite.

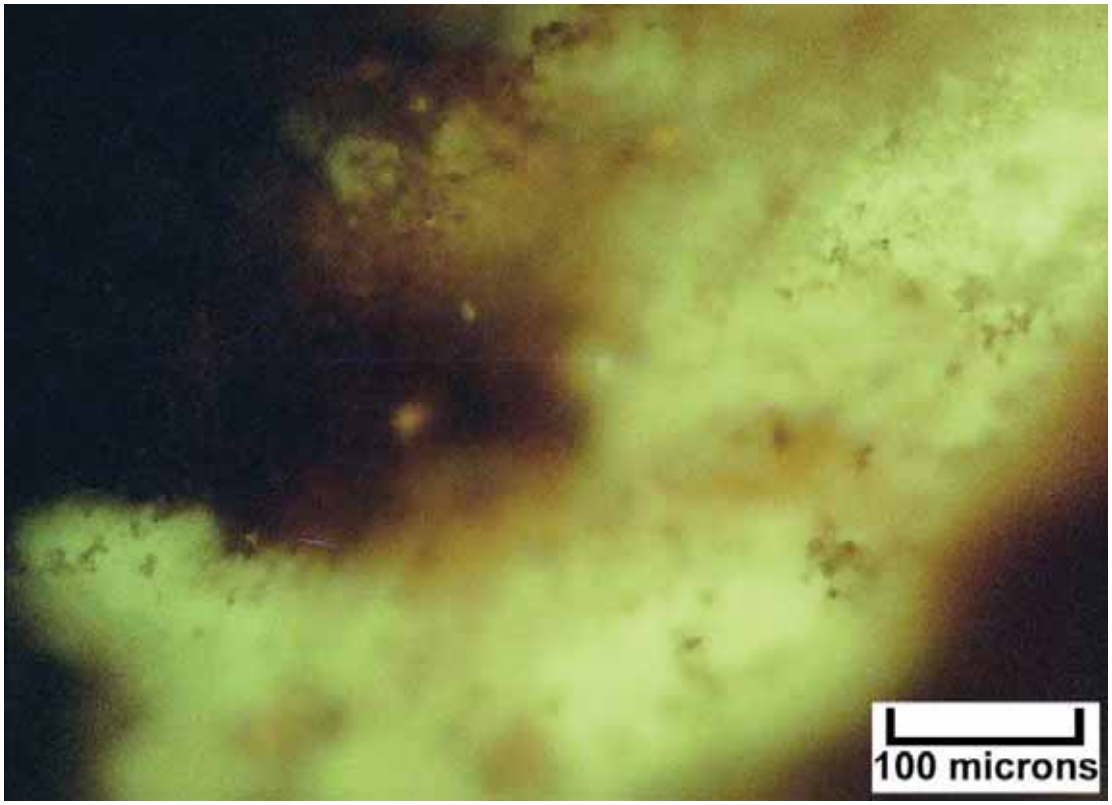

EF photomicrograph – Jakey's Ridge #12-3 (Map #2), 8030-40 feet, B interval, 2.4 visual epifluorescence rating in grain moldic dolomite.

Digital microscope image (dry) – Jakey's Ridge #12-3 (Map #2), 8040-50 feet, B interval, medium to dark gray, organic-rich dolomite, fine to medium crystalline with patchy moldic and intercrystalline porosity. Possible bitumen within some pores.

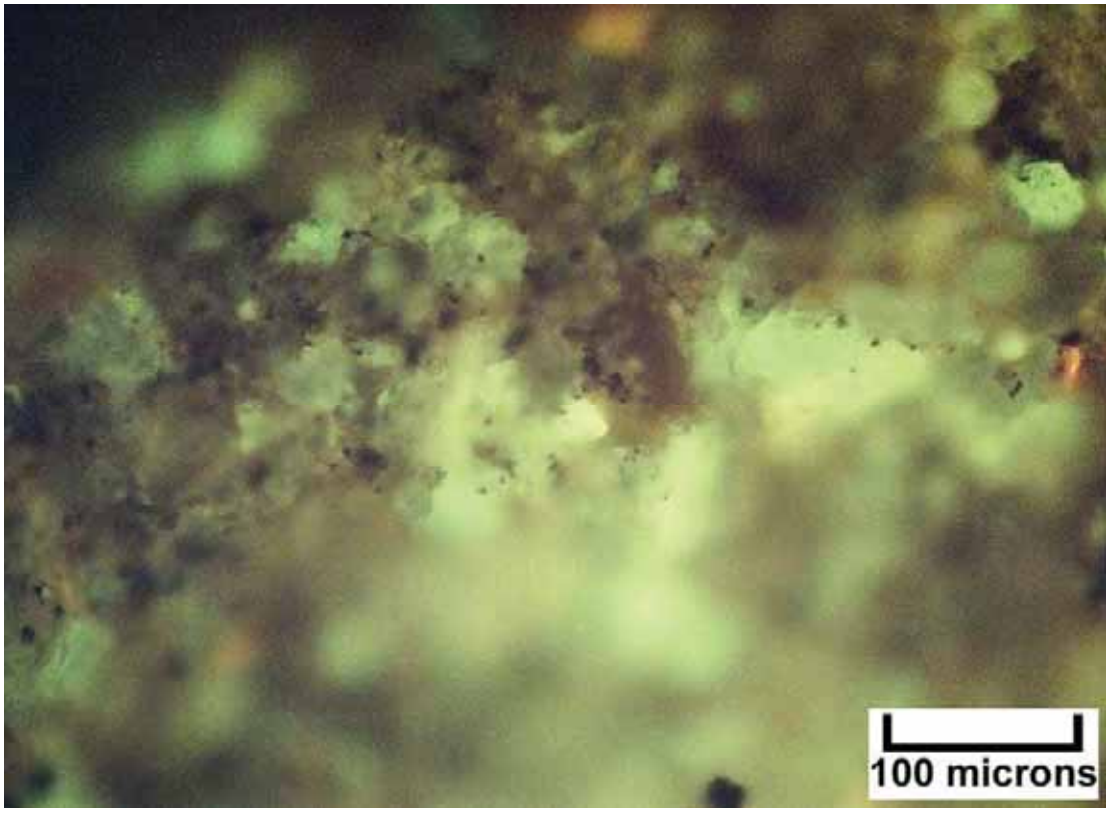

EF photomicrograph – Jakey's Ridge #12-3 (Map #2), 8040-50 feet, B interval, 2.2 visual epifluorescence rating in dolomitic skeletal wackestone/packstone with possible bitumen lining pores.

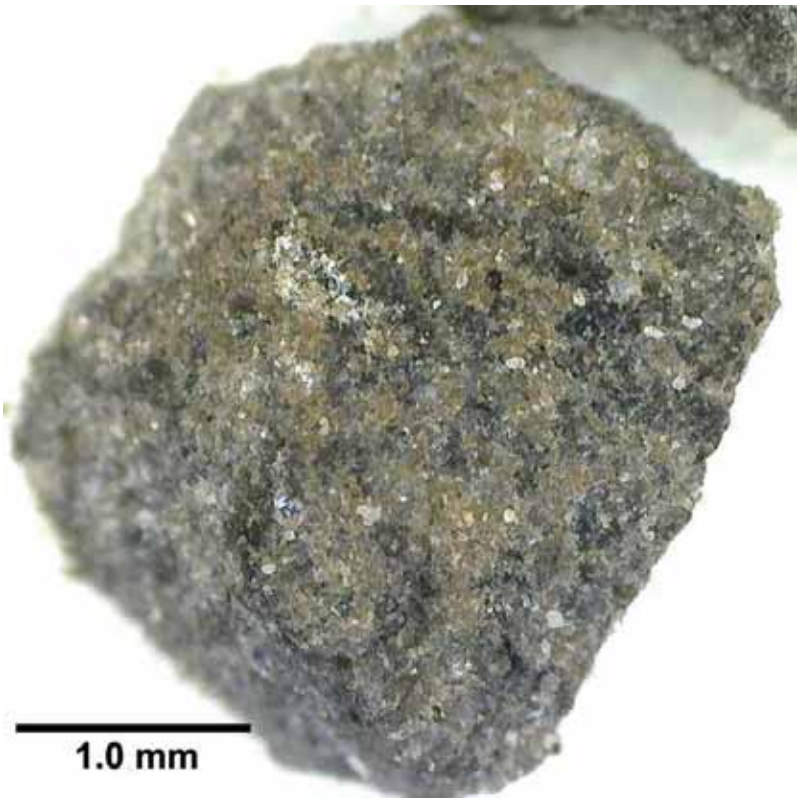

Digital microscope image (dry) – Jakey's Ridge #12-3 (Map #2), 8050-60 feet, B interval, medium to dark gray, medium crystalline dolomite, slightly silty with large patches of brownish oil staining around intercrystalline pore space.

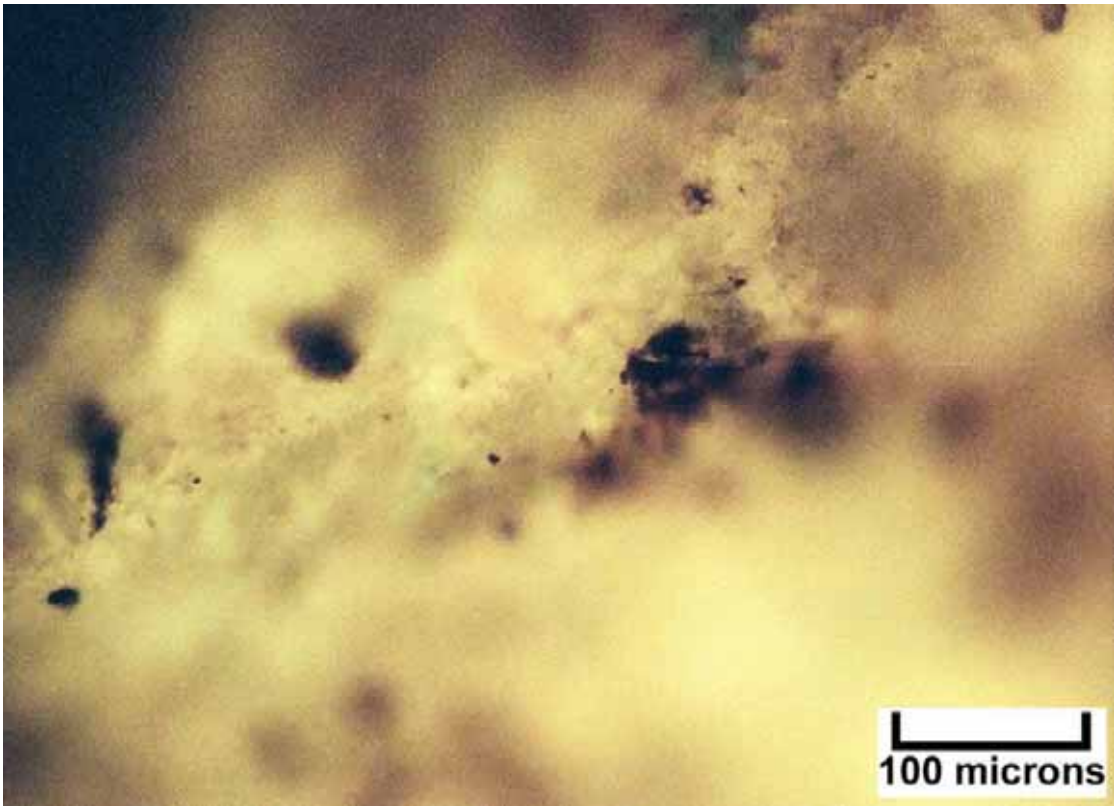

EF photomicrograph – Jakey's Ridge #12-3 (Map #2), 8050-60 feet, B interval, 2.4 visual epifluorescence rating in silty medium crystalline dolomitic wackestone/mudstone.

Digital microscope image (dry) – Jakey's Ridge #34-15 (Map #3), 7680-90 feet, B interval, two lithologies shown – left consists of slightly silty dolomitic black shale; right shows light gray, medium crystalline dolomite, possibly a grainstone/packstone.

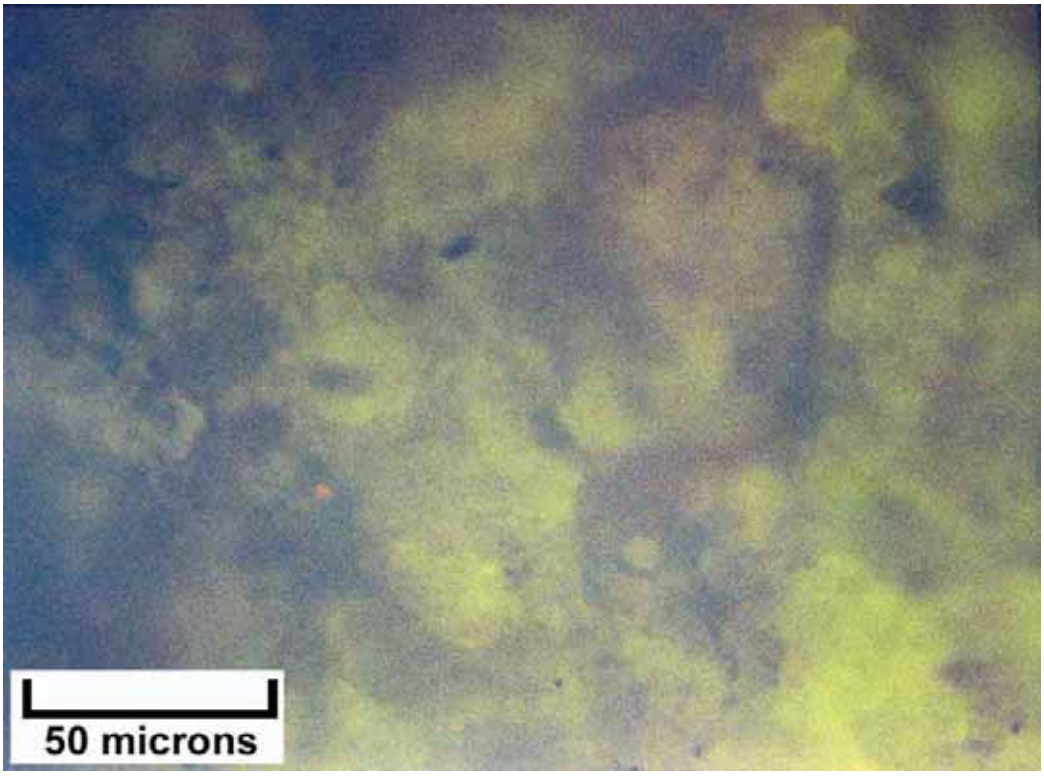

EF photomicrograph – Jakey's Ridge #34-15 (Map #3), 7680-90 feet, B interval, 2.1 visual epifluorescence rating in fine to medium crystalline dolomitic grainstone composed of micropeloids or coated grains, moderately bright fluorescence.

Digital microscope image (wet) – Jakey's Ridge #34-15 (Map #3), 7690-7700 feet, B interval, light gray to white, medium crystalline dolomite, grainstone/packstone with black argillaceous patches.

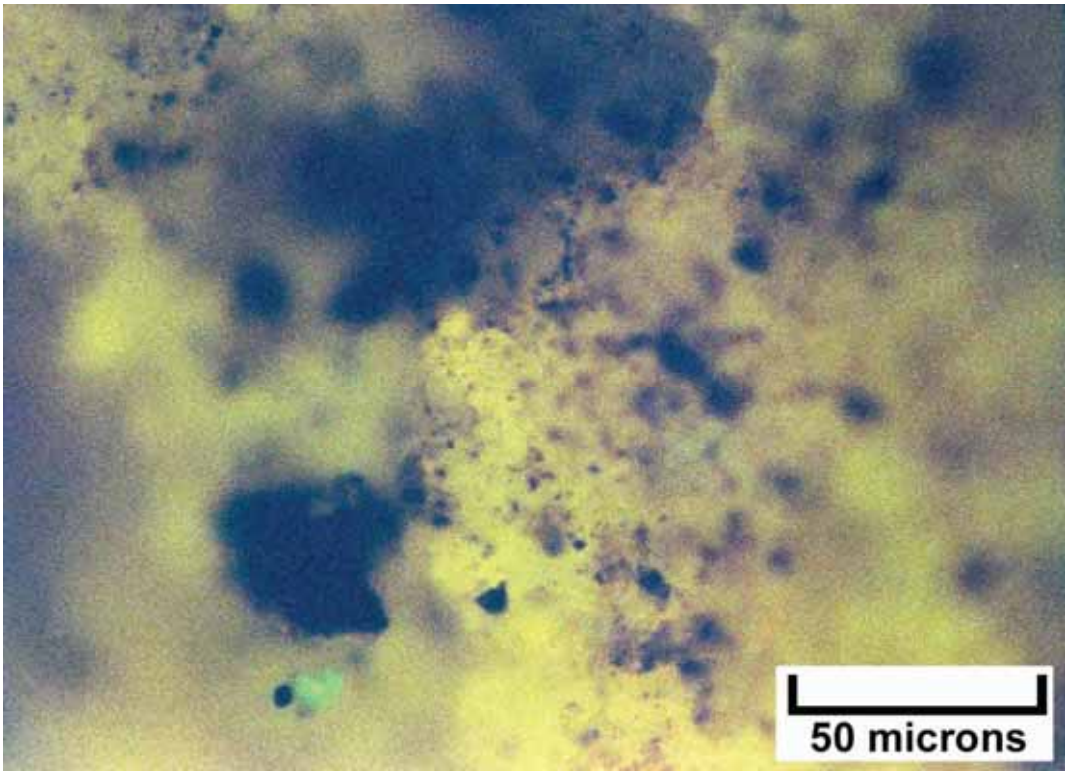

EF photomicrograph – Jakey's Ridge #34-15 (Map #3), 7690-7700 feet, B interval, 2.1 visual epifluorescence rating in finely crystalline dolomite, grainstone/packstone with small visible interparticle pores and moderate fluorescence.

Digital microscope image (dry) – Salt Wash #1-16 (Map #4), 8250-60 feet (interval tops not available), light to medium gray, medium crystalline dolomite, grainstone/packstone with moderate intercrystalline pore space and patches of white anhydrite.

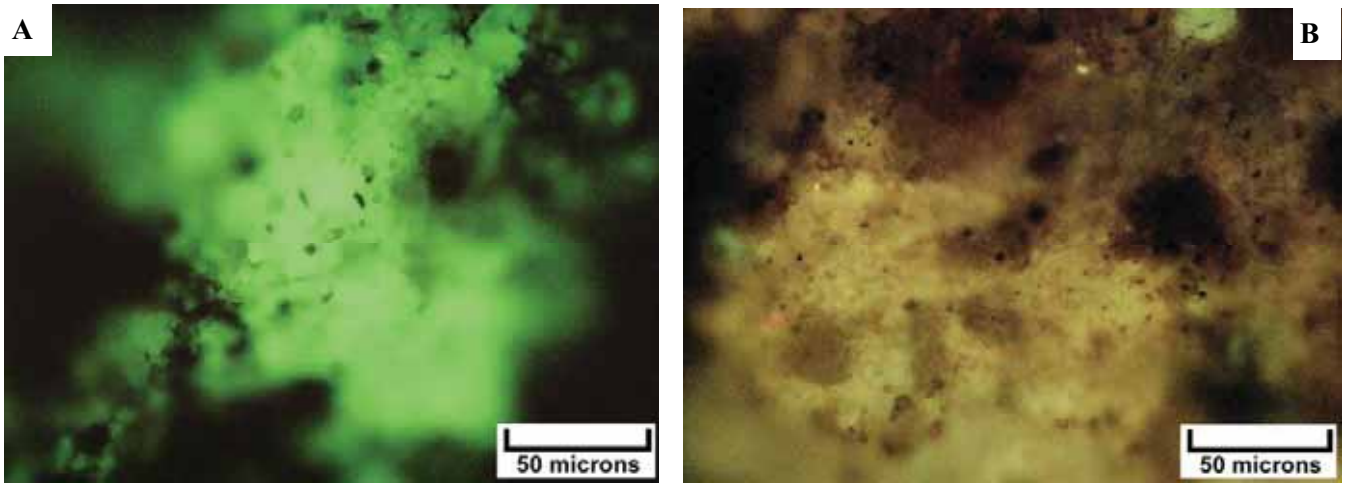

EF photomicrographs – Salt Wash #1-16 (Map #4), 8250-60 feet (interval tops not available). A: 3.0 visual epifluorescence rating in finely crystalline patchy dolomite within a black organic, non-fluorescing organic argillaceous matrix. B: 2.3 visual epifluorescence rating in fine to medium dolomite, porous tubular microbial fabric.

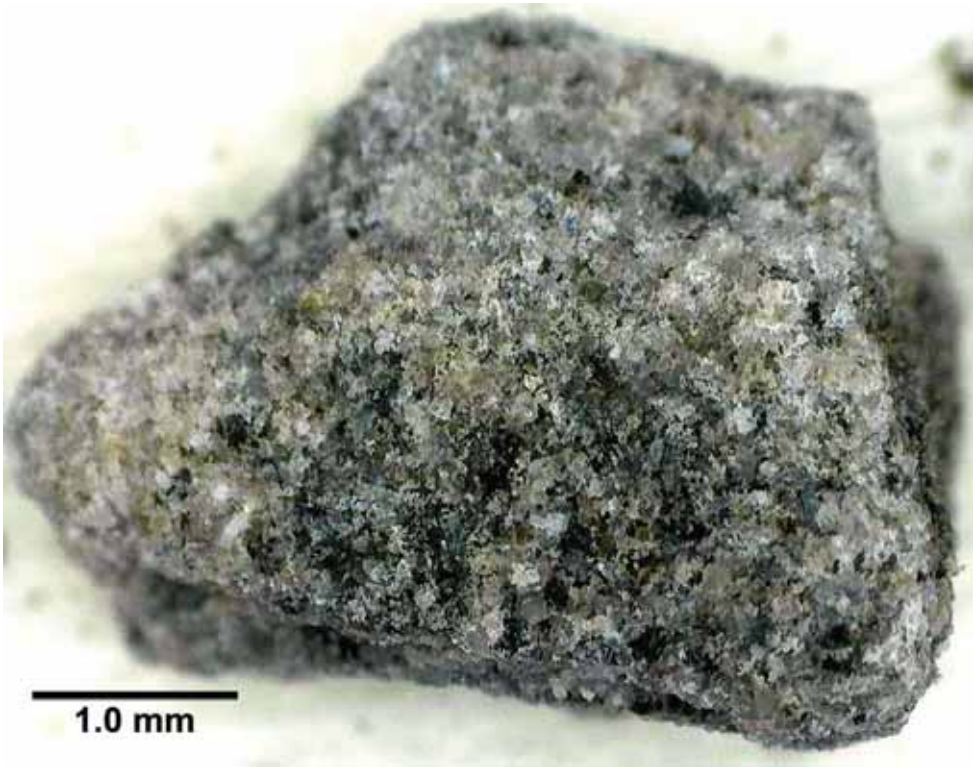

Digital microscope image (dry) – Salt Wash #1-16 (Map #4), 8260-70 feet (interval tops not available), medium to dark gray, medium crystalline dolomite, packstone/wackestone with some intercrystalline pore space.

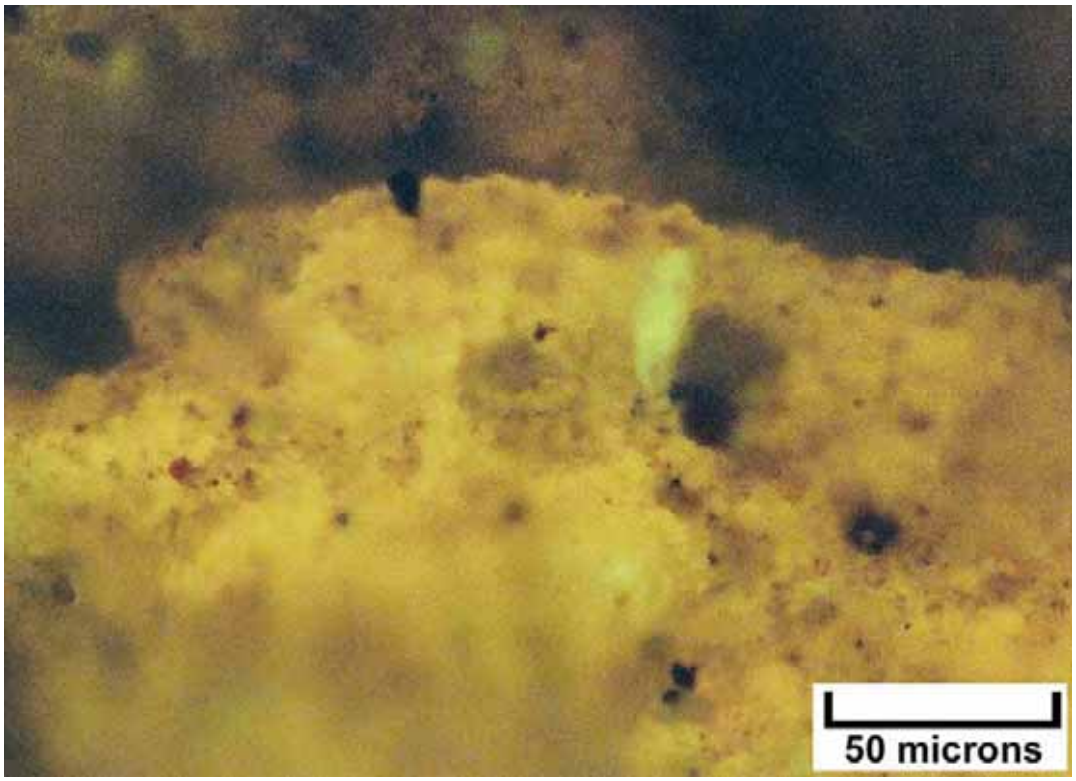

EF photomicrograph – Salt Wash #1-16 (Map #4), 8260-70 feet (interval tops not available), 2.6 visual epifluorescence rating in fine to medium crystalline dolomite, grainstone/ microbialite with good oil saturation.

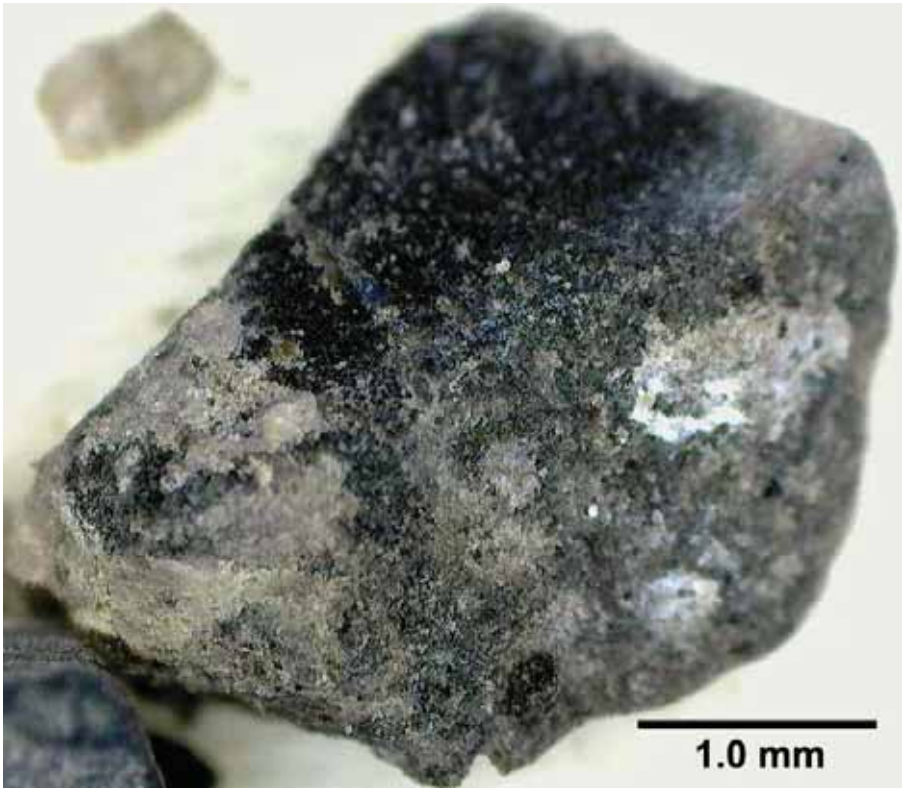

Digital microscope image (dry) – Salt Wash #1-16 (Map #4), 8270-80 feet (interval tops not available), medium to dark gray dolomite with pustular to lumpy microbial fabric, very limited visible intercrystalline porosity.

EF photomicrograph – Salt Wash #1-16 (Map #4), 8270-80 feet (interval tops not available), visual epifluorescence rating 2.9 in very fluorescent dolomite with microbialite texture.

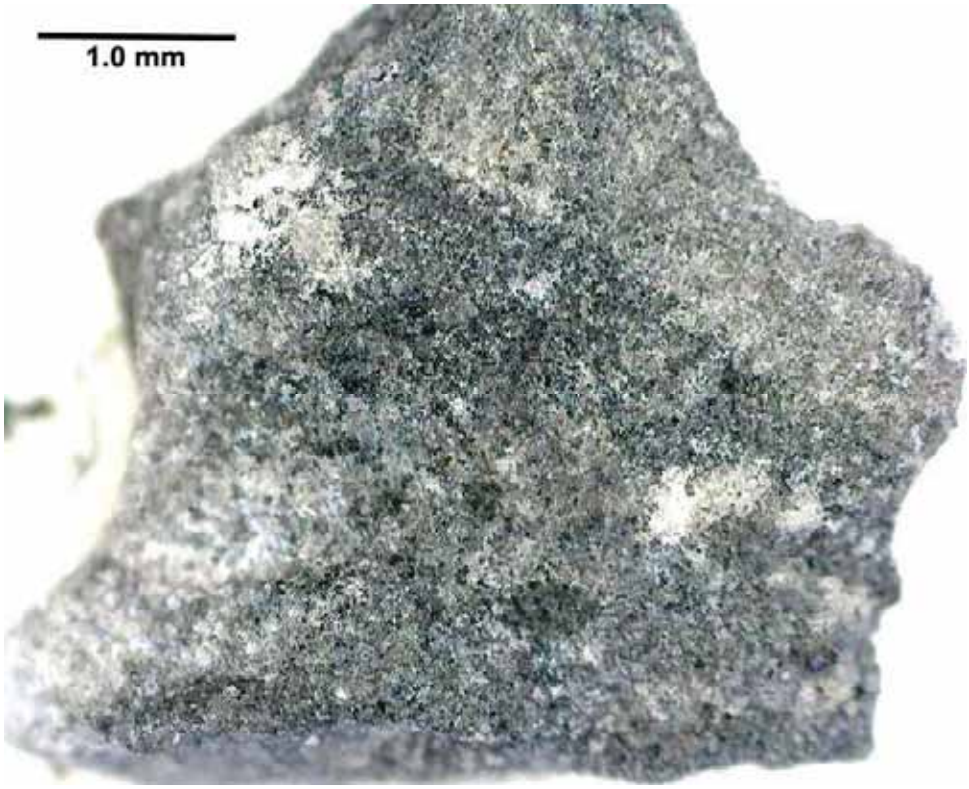

Digital microscope image (dry) – Salt Wash #1-16 (Map #4), 8280-90 feet (interval tops not available), medium to dark gray, fine to medium crystalline dolomite with wavy to horizontal lamination, possible microbial wackestone. Possible bitumen lining pores.

EF photomicrograph – Salt Wash #1-16 (Map #4), 8280-90 feet (interval tops not available), 2.8 visual epifluorescence rating in dolomitic tubular microbial fabric with visible porosity.

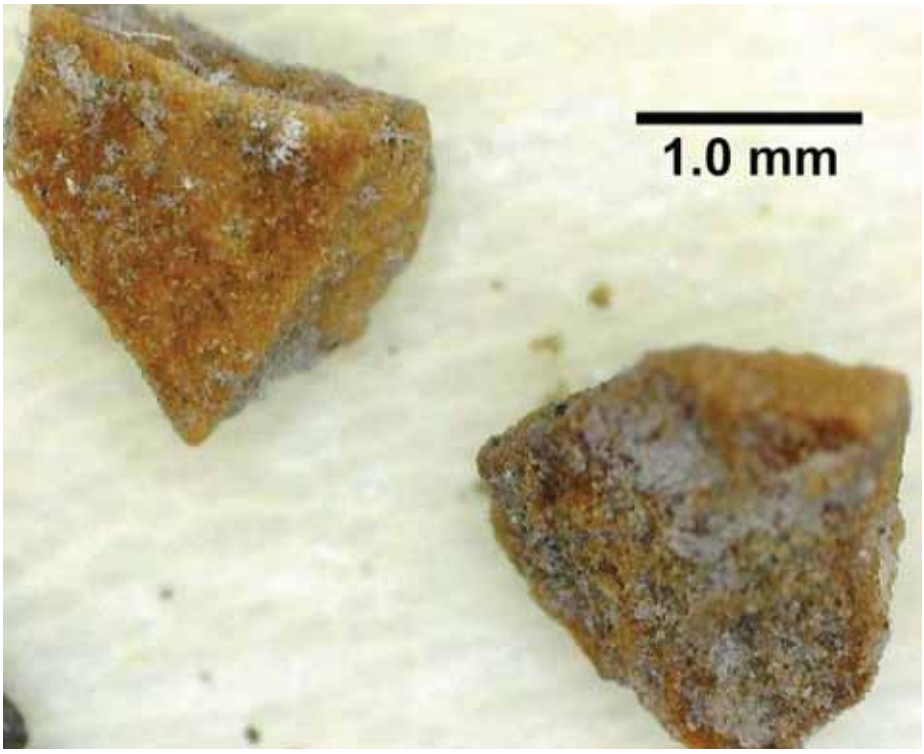

Digital microscope image (dry) – Salt Wash #1-16 (Map #4), 8320-30 feet (interval tops not available), light gray to gold, silty dolomite with apparent heavy oil staining.

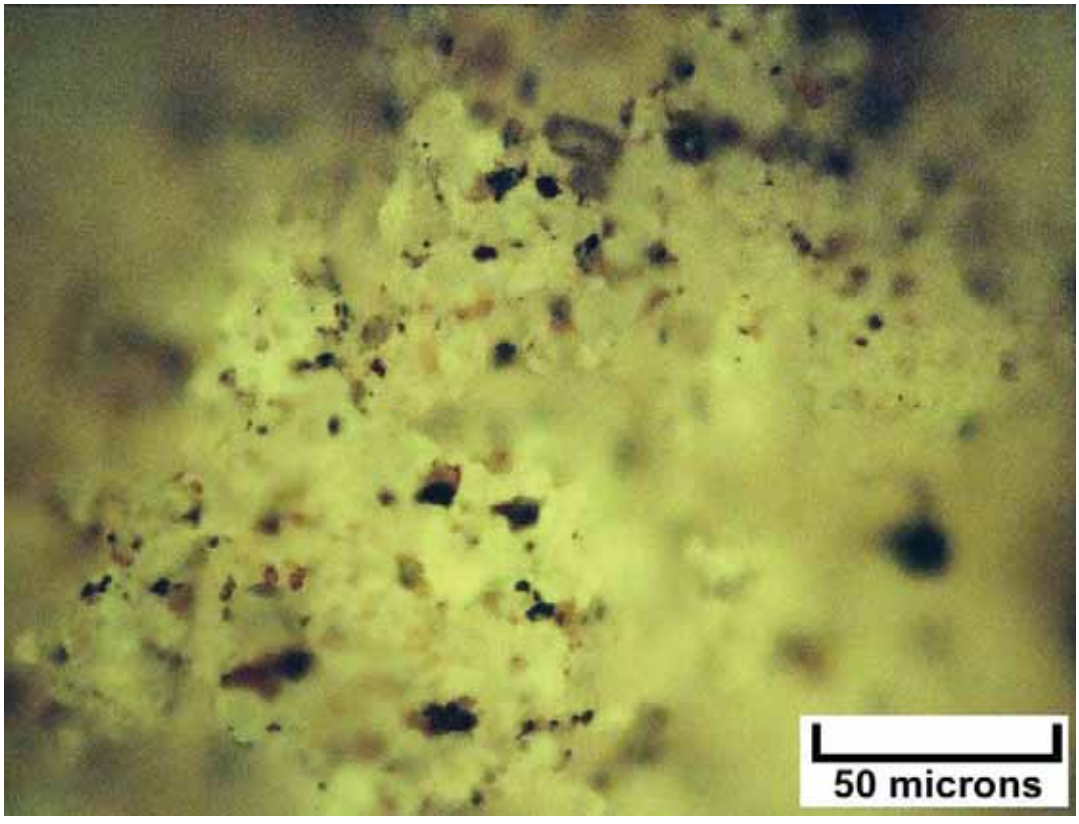

EF photomicrograph – Salt Wash #1-16 (Map #4), 8320-30 feet (interval tops not available), 3.0 visual epifluorescence rating in silty fine to medium crystalline dolomite, packstone/ wackestone with visible intercrystalline pores, bright oil fluorescence.

Digital microscope image (dry) – Kane Springs Federal #10-1 (Map #6), 8900-10 feet, A interval, light to medium gray, fine crystalline dolomite with microlaminations and sub-vertical filamentous microbial structures

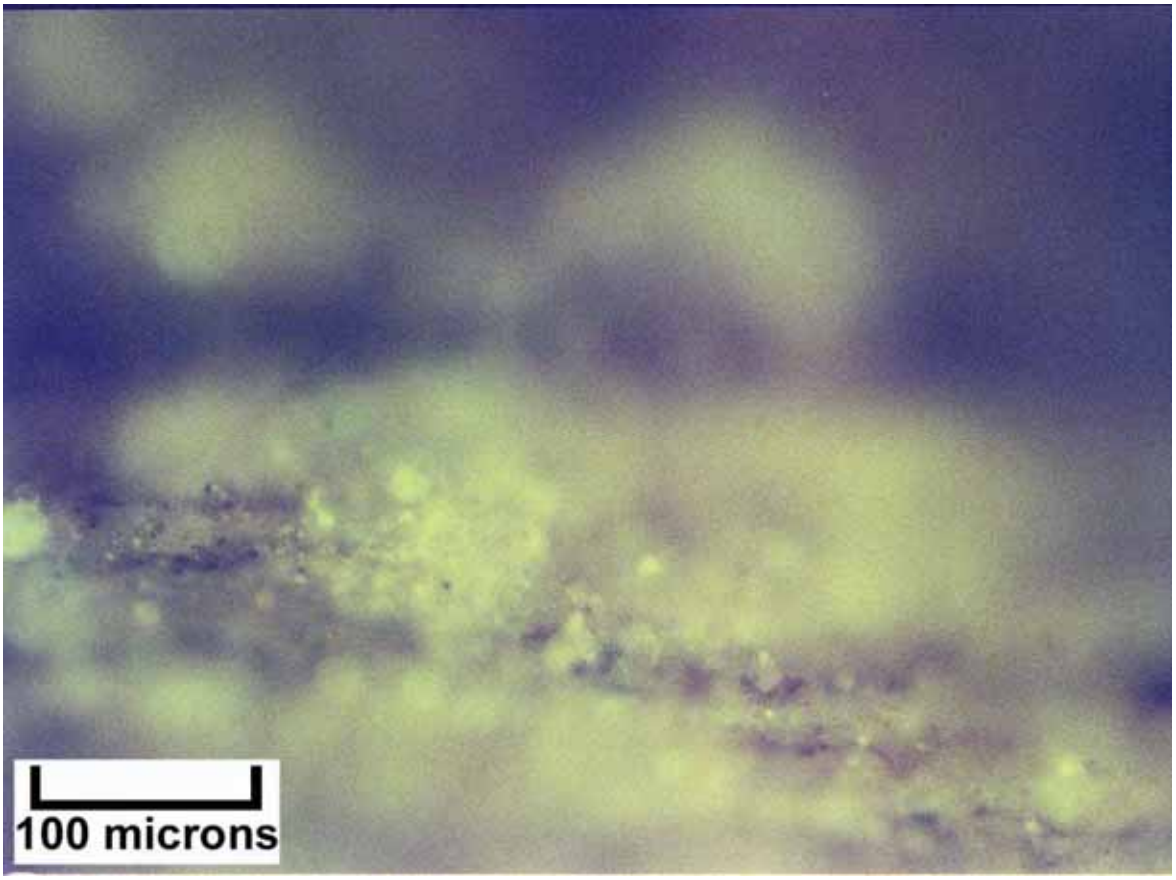

EF photomicrograph – Kane Springs Federal #10-1 (Map #6), 8900-10 feet, A interval, 2.0 visual epifluorescence rating in microlaminated microbialite with visible pores and possible patchy anhydrite.

Digital microscope image (dry) – Kane Springs Federal #10-1 (Map #6), 8910-20 feet, B interval, light gray and black, organic-rich medium crystalline dolomite with vague hints of filamentous microbial structures, no visible porosity. Possible bitumen within some pores.

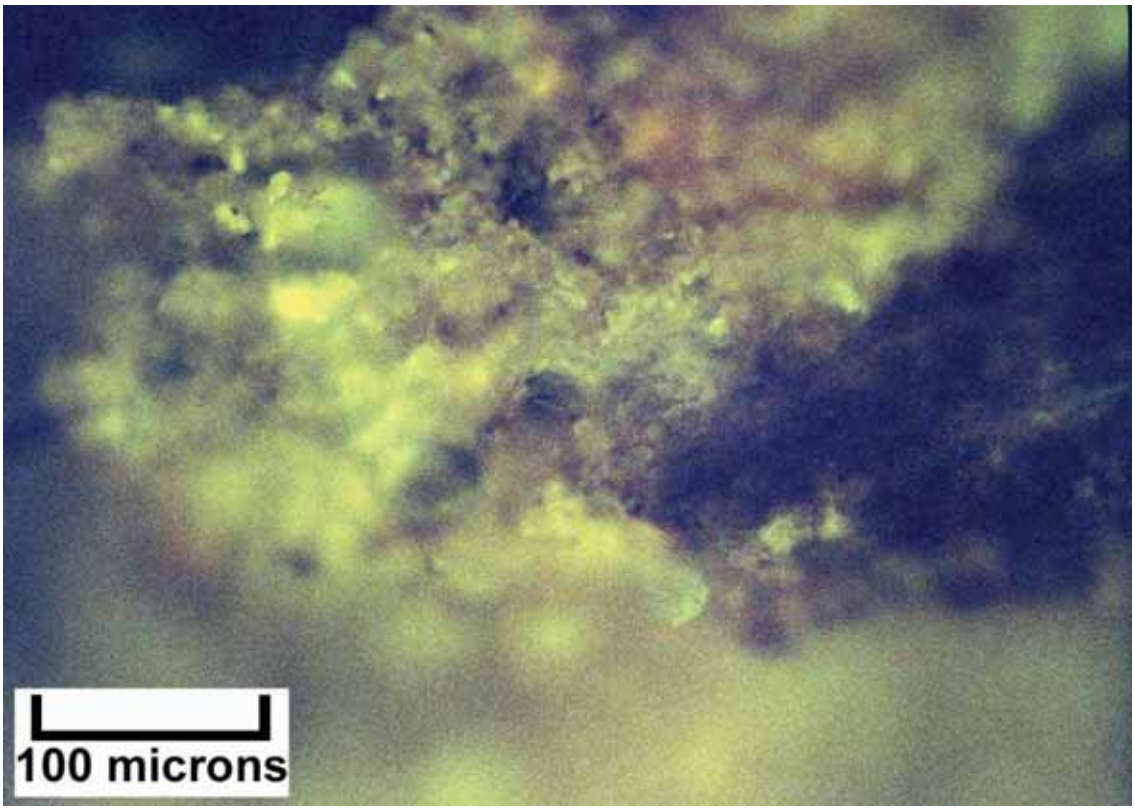

EF photomicrograph – Kane Springs Federal #10-1 (Map #6), 8910-20 feet, B interval, 2.5 visual epifluorescence rating microbial dolomite with bright fluorescence and visible pores, possible anhydrite.

Digital microscope image (dry) – Utah #2 (Map #7), 7590-7600 feet, B interval, fine to medium crystalline dolomite, grainstone/packstone with possible fossil fragment, some visible intercrystalline pore space.

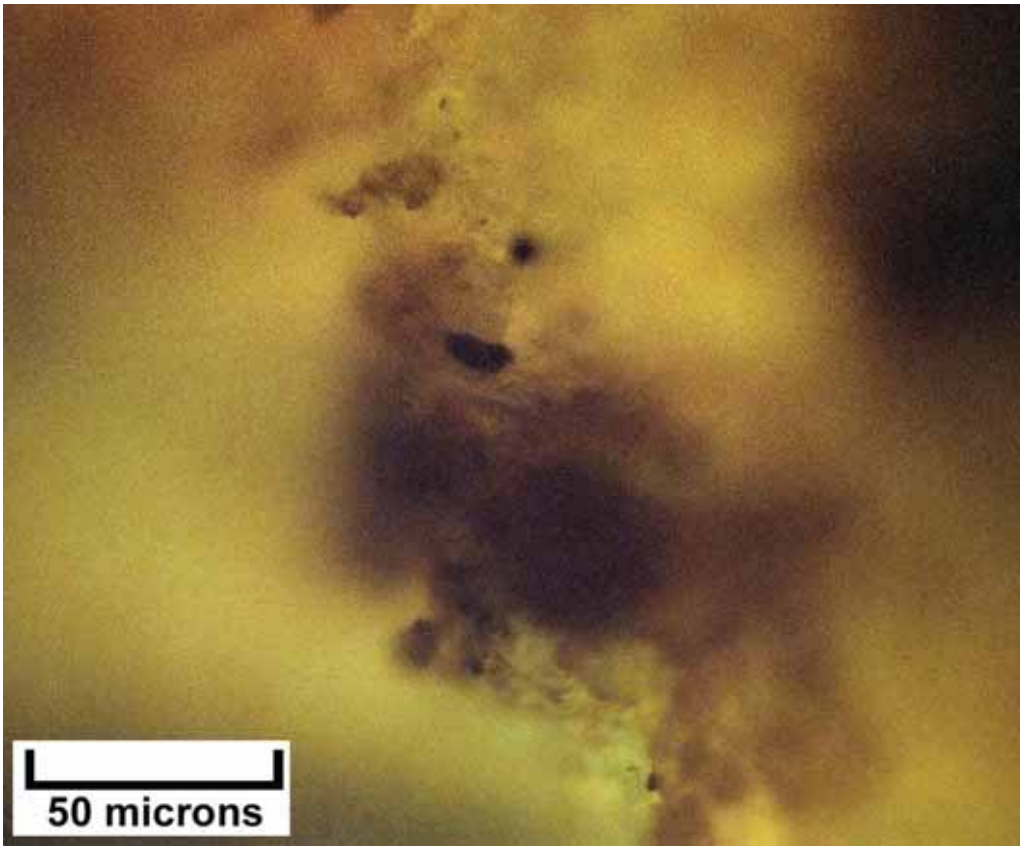

EF photomicrograph – Utah #2 (Map #7), 7590-7600 feet, A interval, 2.1 visual epifluorescence rating in medium crystalline dolomite patch within a slightly argillaceous siltstone.

Digital microscope image (wet) – Utah #2 (Map #7), 7690-7700 feet, B interval, three cuttings samples showing dolomitic and argillaceous siltstone with variable dolomite crystal sizes.

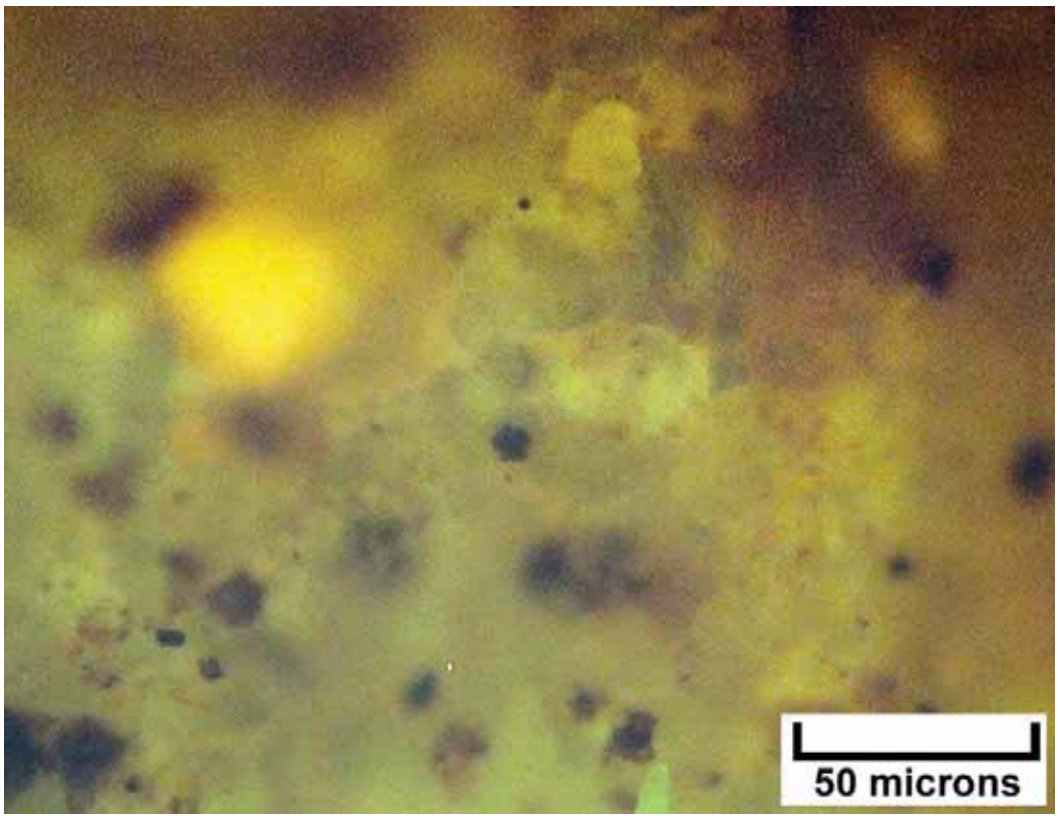

EF photomicrograph – Utah #2 (Map #7), 7690-7700 feet, B interval, 2.2 visual epifluorescence rating in finely crystalline dolomite, mudstone/wackestone with scattered silt grains. Note the small pyrite crystal clusters.

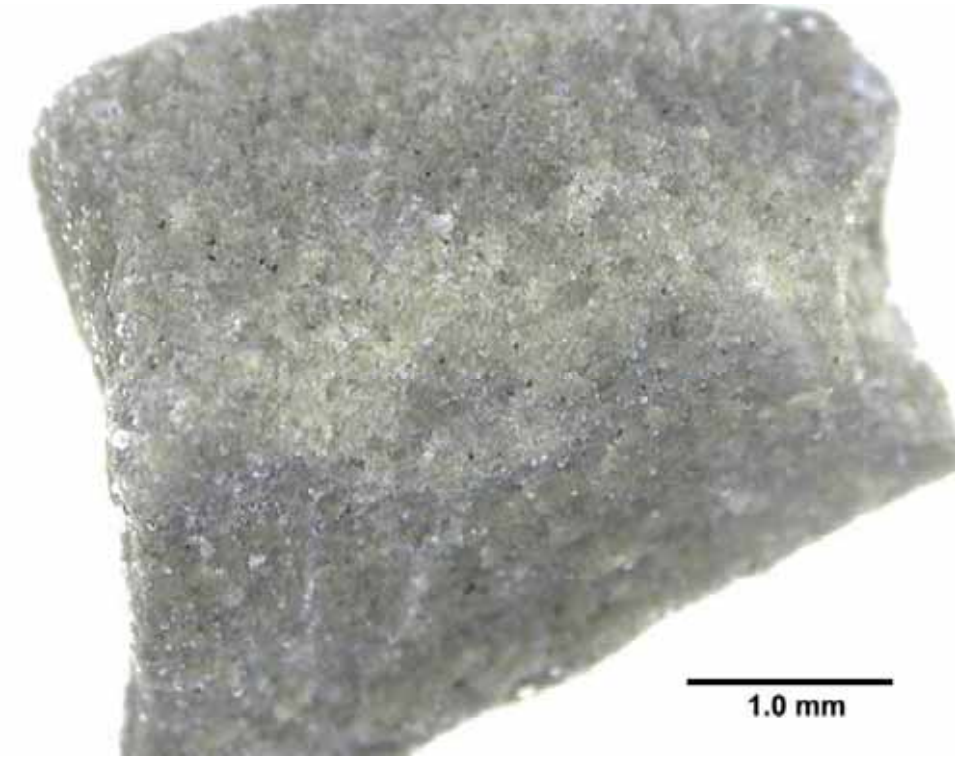

Digital microscope image (wet) – Utah #2 (Map #7), 7700-10 feet, B interval, light to medium gray, dolomitic siltstone with small patches containing visible porosity and oil staining.

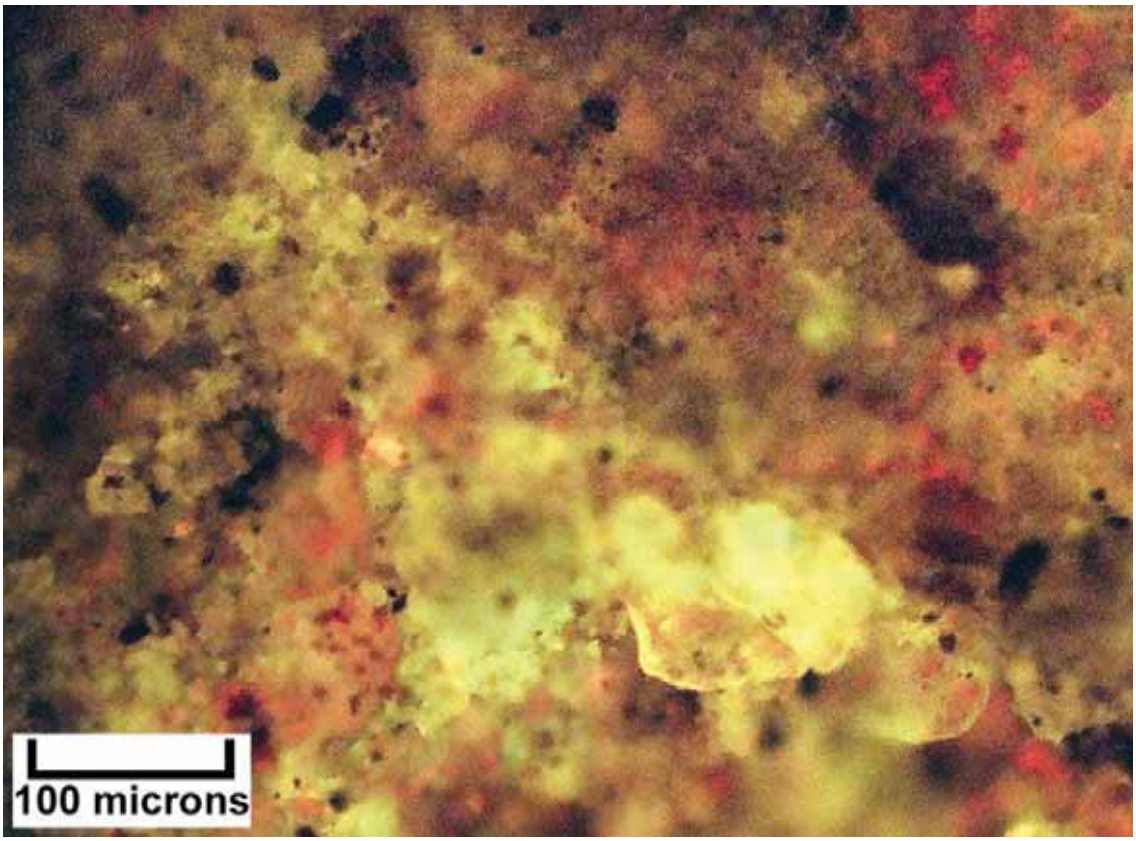

EF photomicrograph – Utah #2 (Map #7), 7700-10 feet, B interval, 2.3 visual epifluorescence rating in medium crystalline dolomite with good interparticle pores, packstone/grainstone. The reddish patches may be iron-rich.

Digital microscope image (dry) – Federal Bowknot #1 (Map #8), 6940-50 feet, B interval, light to medium gray, fine to medium crystalline dolomite with patches or layers of black argillaceous material and possible bitumen.

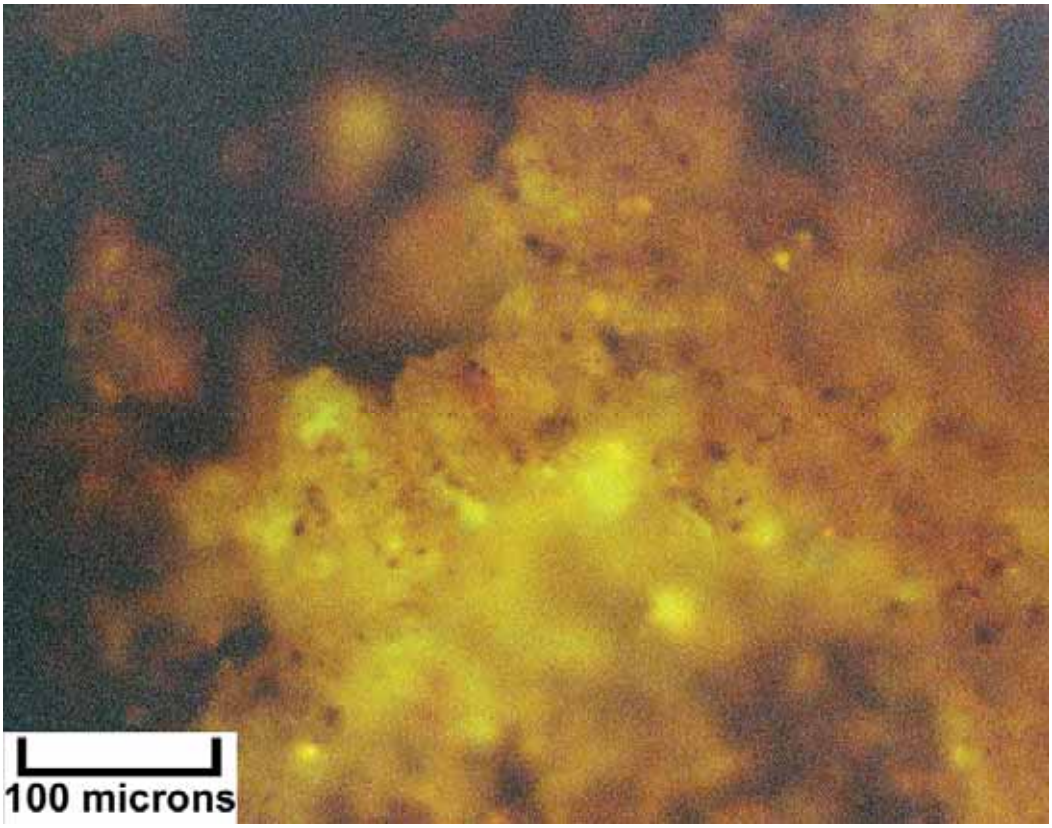

EF photomicrograph – Federal Bowknot #1 (Map #8), 6940-50 feet, B interval, 2.2 visual epifluorescence rating in medium crystalline dolomite crystal matrix.

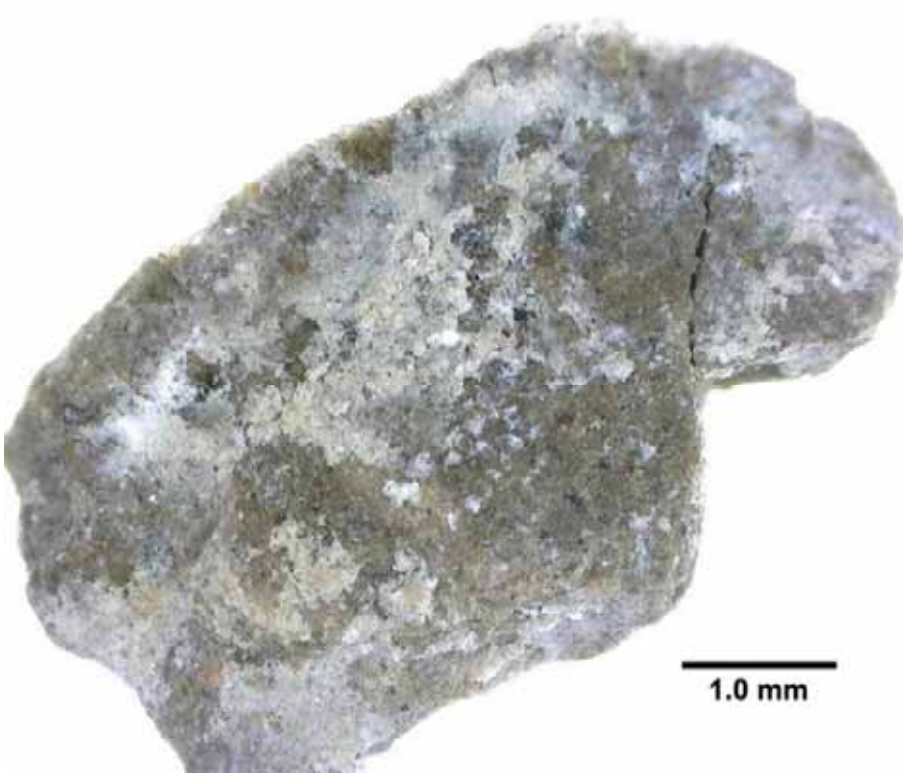

Digital microscope image (dry) – Federal Bowknot #1 (Map #8), 6960-70 feet, B interval, light to medium gray, finely crystalline silty dolomite with no visible porosity.

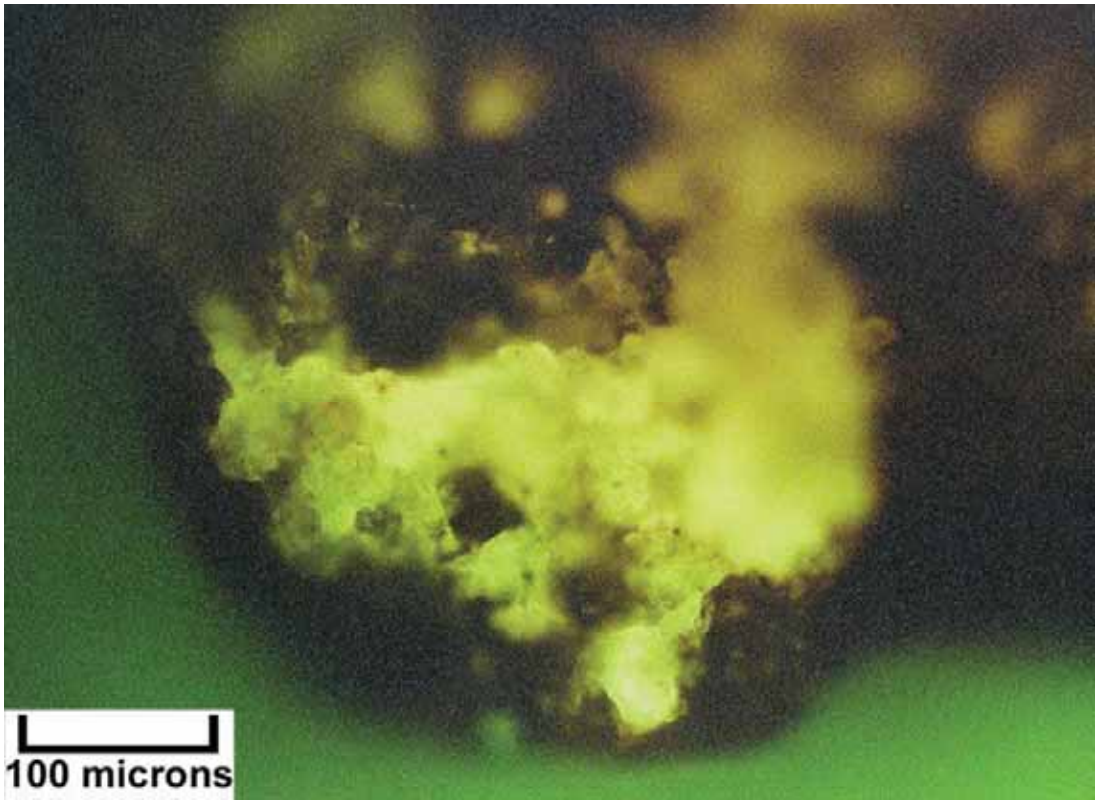

EF photomicrograph – Federal Bowknot #1 (Map #8), 6960-70 feet, B interval, 2.5 visual epifluorescence rating in dolomite with visible intercrystalline pores and live oil films.

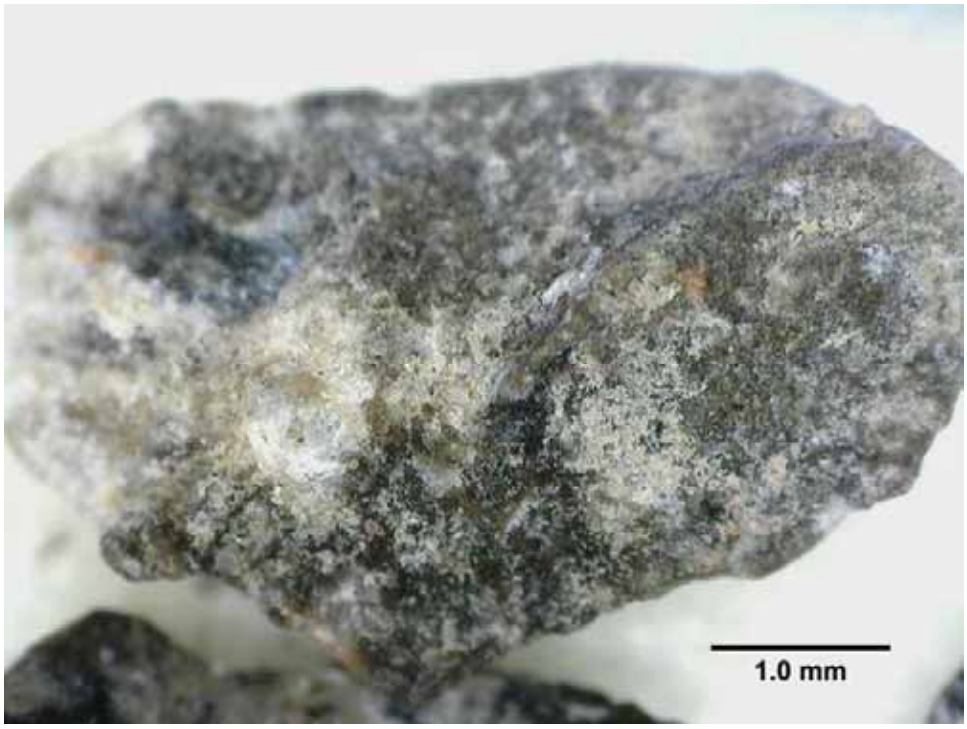

Digital microscope image (dry) – Federal Bowknot #1 (Map #8), 6970-75 feet, B interval, medium to dark gray, silty, argillaceous and anhydritic dolomite with wispy seam stylolites.

EF photomicrograph – Federal Bowknot #1 (Map #8), 6970-75 feet, B interval, 2.4 visual epifluorescence rating in silty dolomite with stylolites.

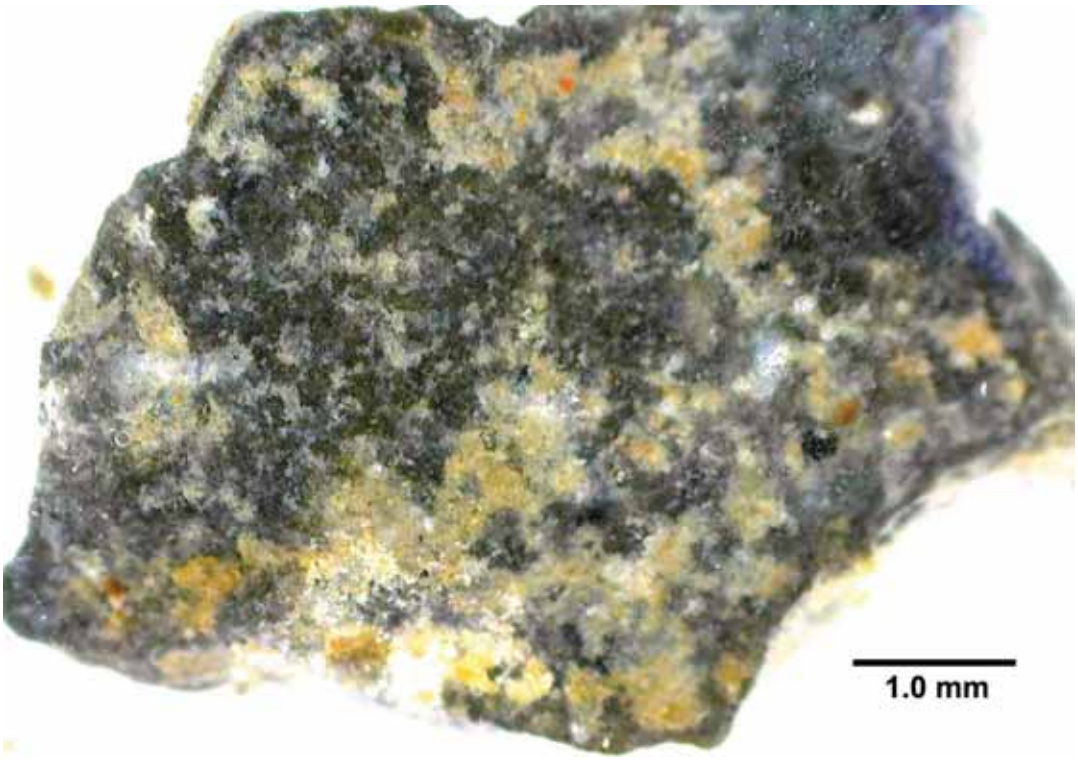

Digital microscope image (wet) – Federal Bowknot #1 (Map #8), 7000-10 feet, C interval, medium to dark gray, microcrystalline dolomite with lumpy patches of possible thrombolitic texture.

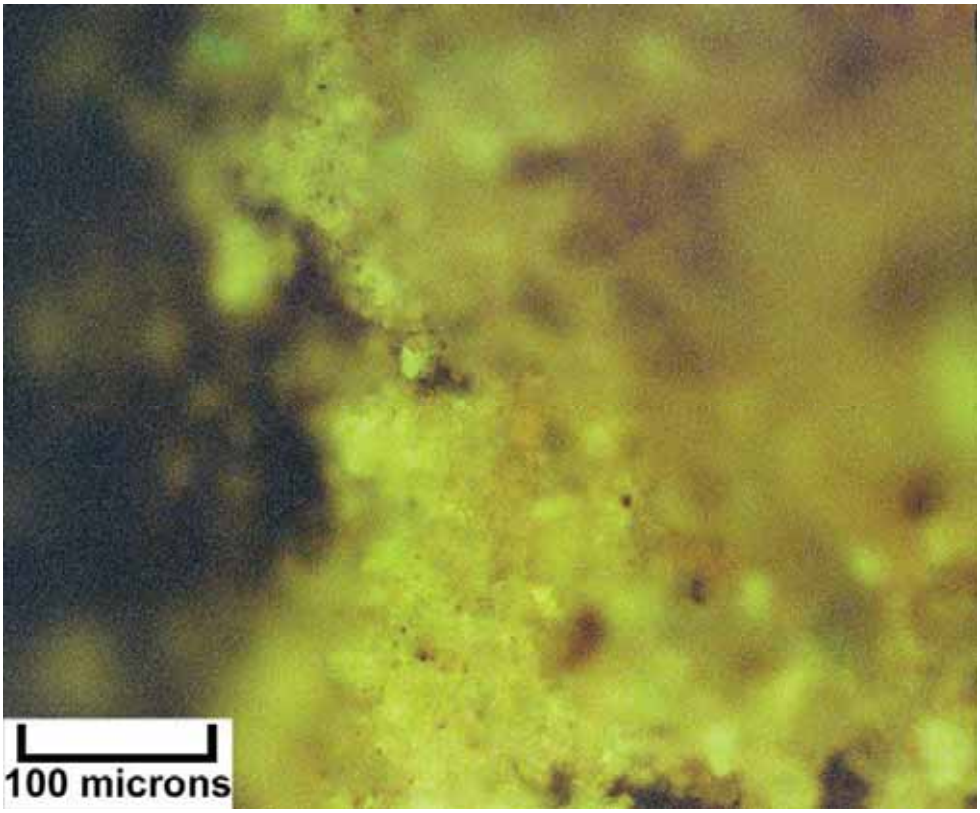

EF photomicrograph – Federal Bowknot #1 (Map #8), 7000-10 feet, C interval, 2.4 visual epifluorescence rating in microcrystalline microbial dolomite.

Digital microscope image (dry) – Kane Springs #25-19-34-1 (Map #9), 7560-70 feet (horizontal well), medium to dark gray, finely crystalline silty dolomite with ax-head crystals of anhydrite.

EF photomicrograph – Kane Springs Federal #25-19-34-1 (Map #9), 7560-70 feet (horizontal well), 3.0 visual epifluorescence rating in cluster of dolomite crystals.

Digital microscope image (dry) – Kane Springs #25-19-34-1 (Map #9), 7570-80 feet (horizontal well), two cuttings, the upper consists of dark gray to black microcrystalline dolomite, commonly massive; lower sample is medium dark gray, medium crystalline dolomitic wackestone/ packstone. Some of the back material in both samples may be bitumen.

EF photomicrograph – Kane Springs Federal #25-19-34-1 (Map #9), 7570-80 feet (horizontal well), 3.4 visual epifluorescence rating in microcrystalline dolomite with bright fluorescing oil films and halos.

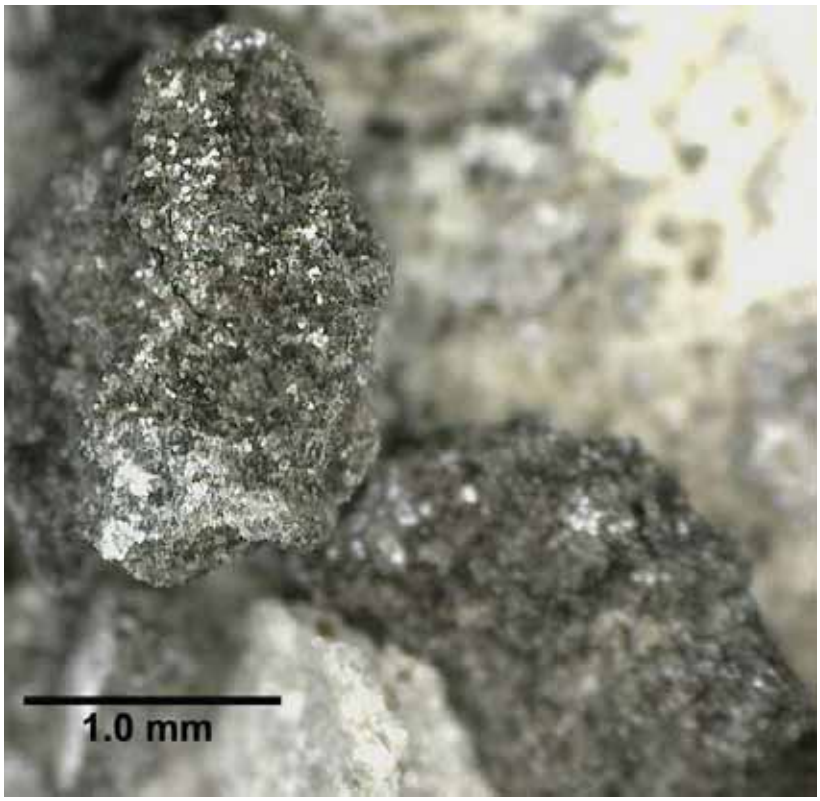

Digital microscope image (dry) – Kane Springs #25-19-34-1 (Map #9), 7580-90 feet (horizontal well), medium to dark gray, organic-rich dolomite with probable microbial boxwork and linear filaments.

EF photomicrograph – Kane Springs Federal #25-19-34-1 (Map #9), 7580-90 feet (horizontal well), 3.0 visual epifluorescence rating in honeycomb remnants of microbial filaments.

Digital microscope image (dry) – Kane Springs #25-19-34-1 (Map #9), 7600-10 feet (horizontal well), two cuttings in this image show a clean micro- to medium crystalline dolomite with packstone/ grainstone fabric on the left and a dark argillaceous microcrystalline dolomite with a wackestone or possible microbial fabric.

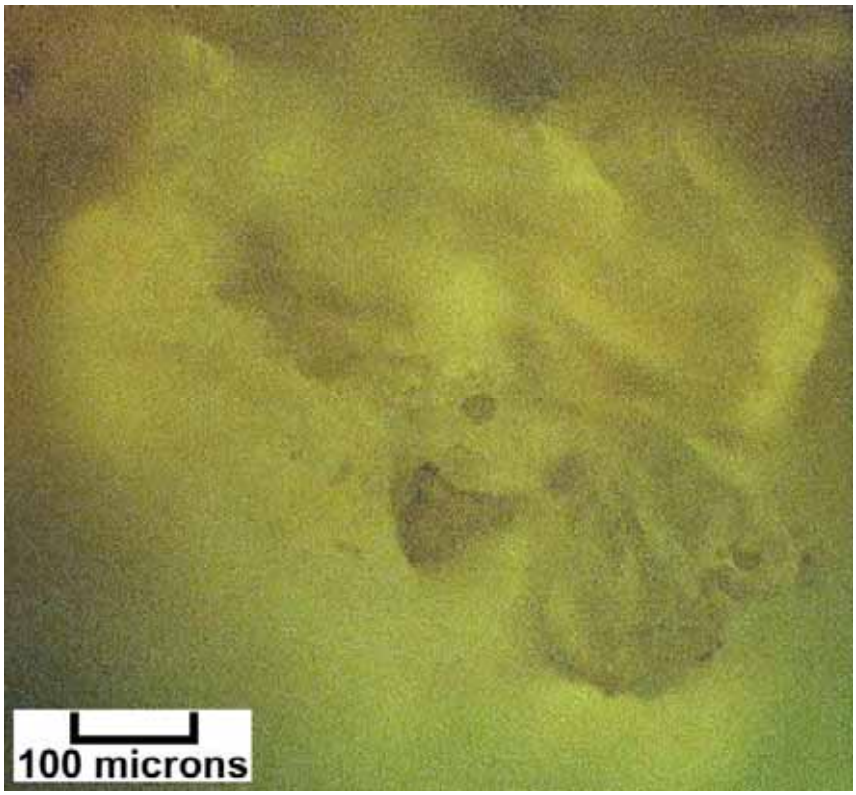

EF photomicrograph – Kane Springs Federal #25-19-34-1 (Map #9), 7600-10 feet (horizontal well), 3.0 visual epifluorescence rating in microlaminated microbial(?) texture; note alternating epifluorescence and microlamination.

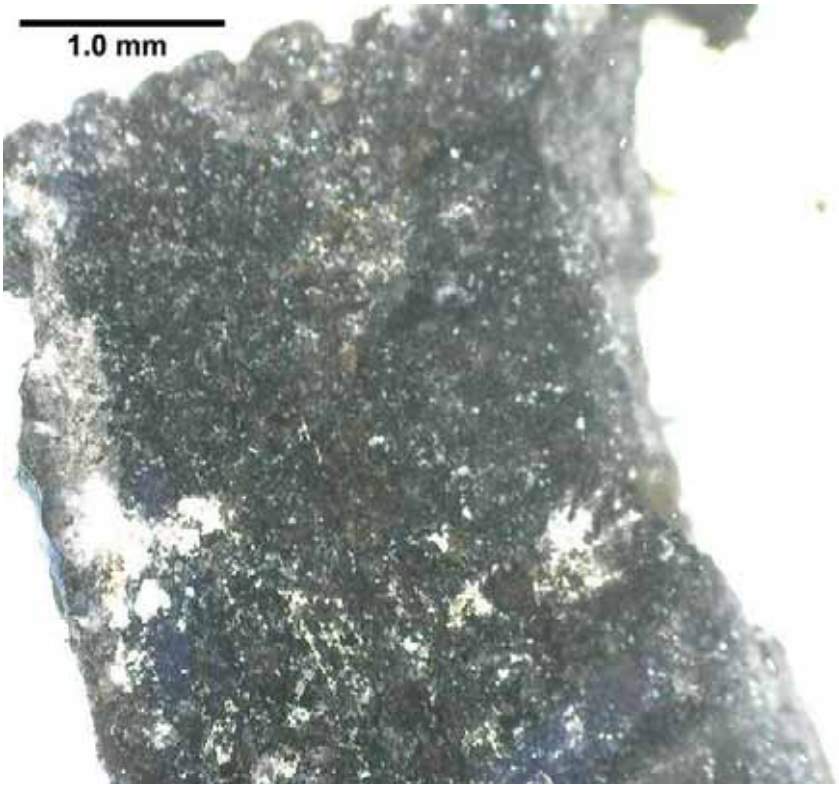

Digital microscope image (wet) – Kane Springs #25-19-34-1 (Map #9), 7730-40 feet (horizontal well), dark gray, organic-rich to argillaceous dolomite with a possible lumpy microbial or pisolitic texture.

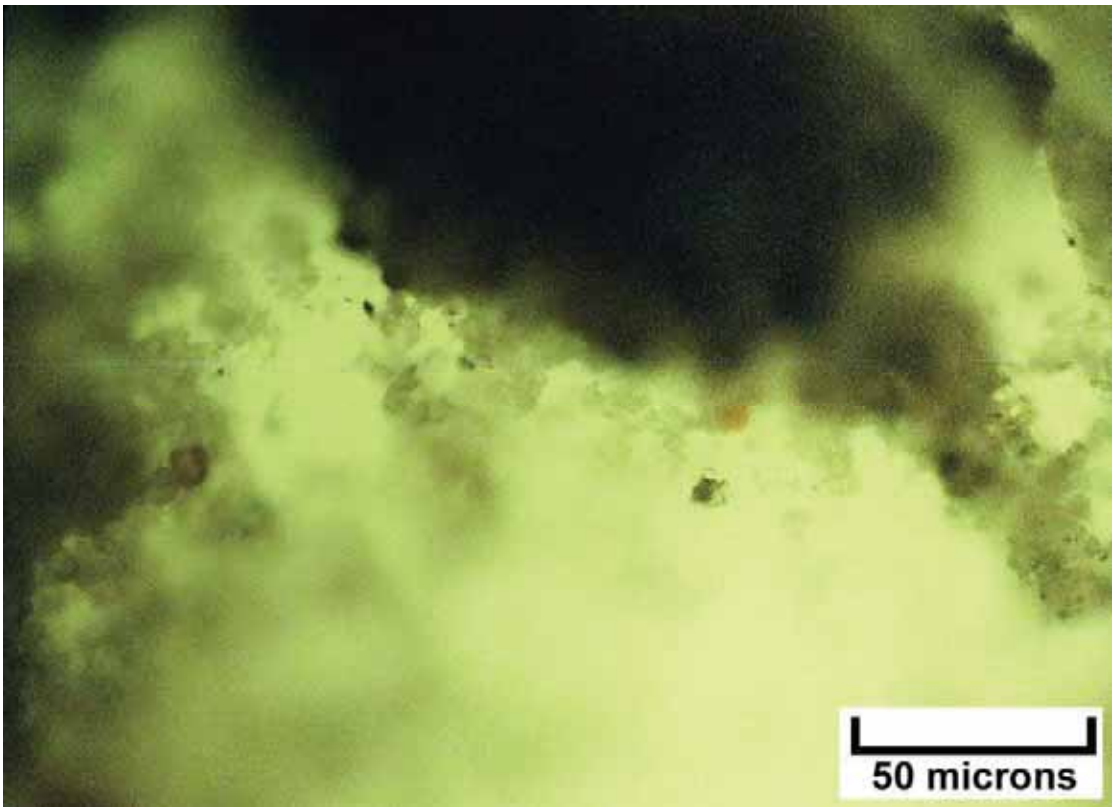

EF photomicrograph – Kane Spring #25-19-34-1 (Map #9), 7730-40 feet (horizontal well), 2.6 visual epifluorescence rating in patch of crystalline dolomite displaying a bright yellow fluorescing oil film.

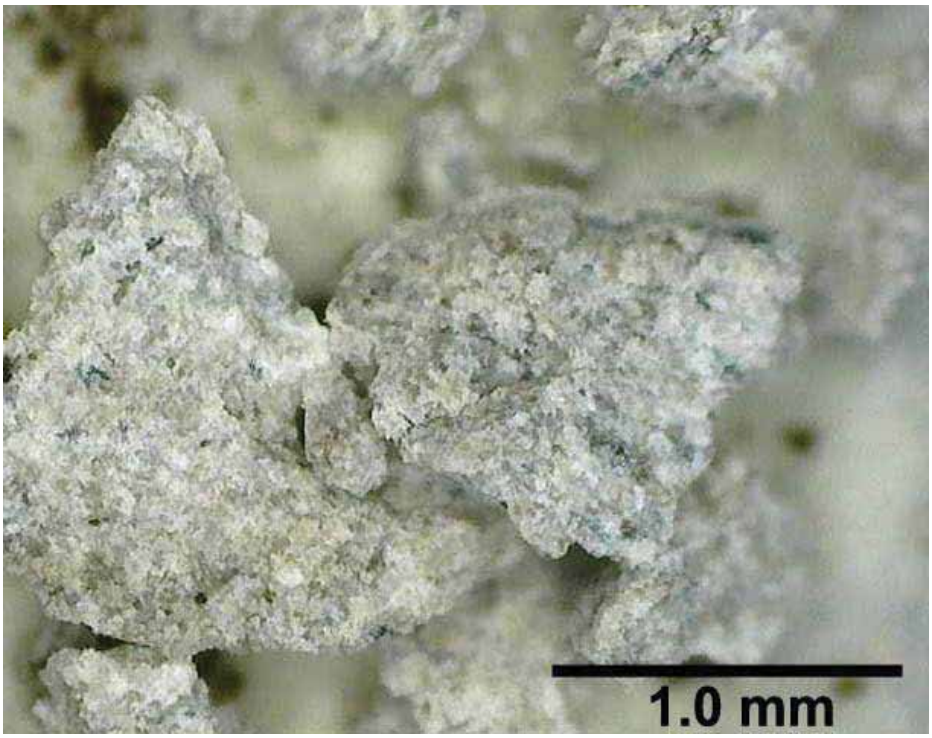

Digital microscope image (dry) – Kane Springs #25-19-34-1 (Map #9), 7740-50 feet (horizontal well), two cuttings showing light gray, fine to medium crystalline dolomite, probable packstone/wackestone fabric with possible microbial boxwork.

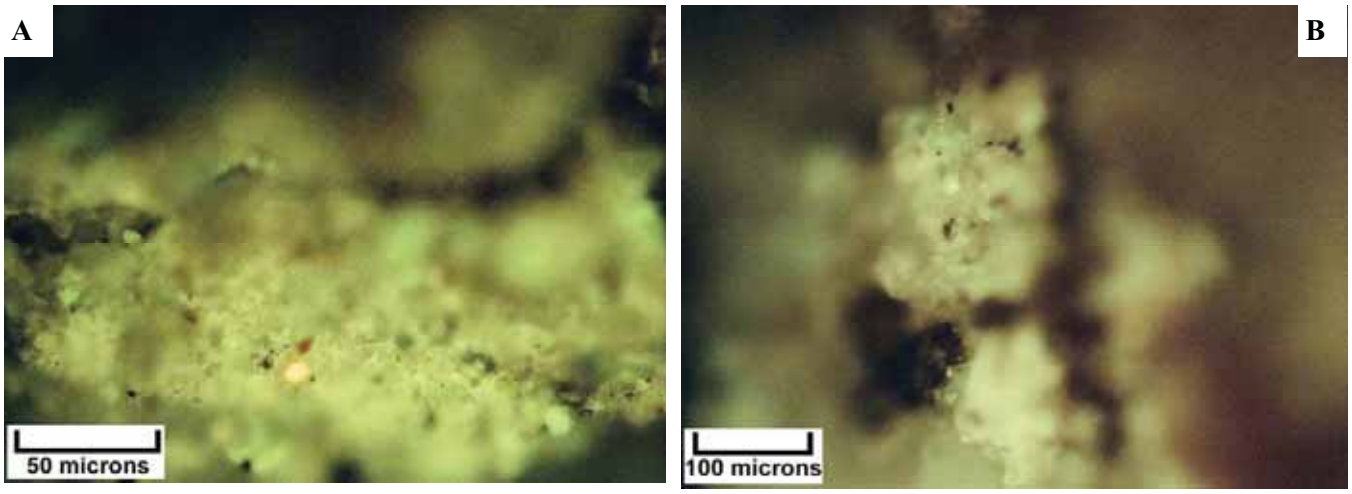

EF photomicrographs – Kane Spring #25-19-34-1 (Map #9), 7740-50 feet (horizontal well). A: 2.8 visual epifluorescence rating in fluorescent dolomitic patch. B: 2.3 visual epifluorescence rating in dolomitic patch containing "dead" argillaceous matrix.

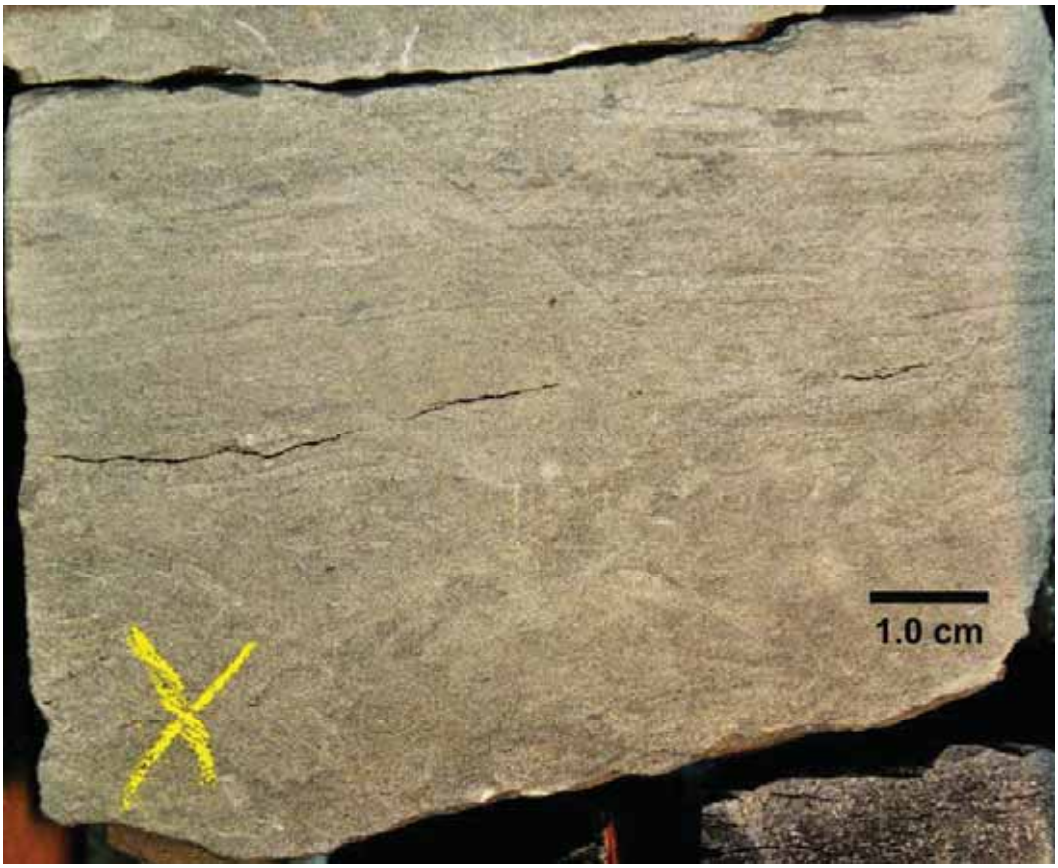

Close-up image (dry) of slabbed core – Cane Creek Unit #26-3 (Map 10), 7410.4 feet, B interval, silty dolomite with light brown oil staining. Note the bed of oncolites and other grains at the base overlain by laminae of possible microbial origin.

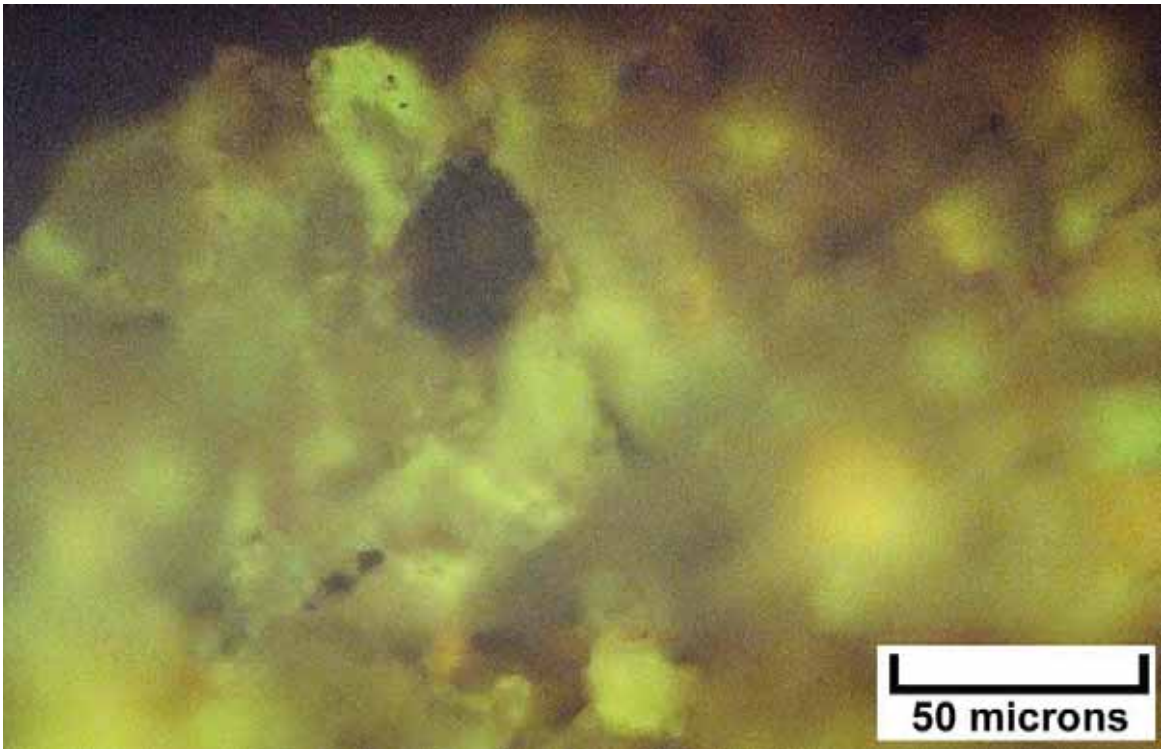

EF photomicrograph – Cane Creek Unit #26-3 (Map #10), 7410.4 feet, B interval, 2.6 visual epifluorescence rating in silty dolomite, medium crystalline with good visible porosity.

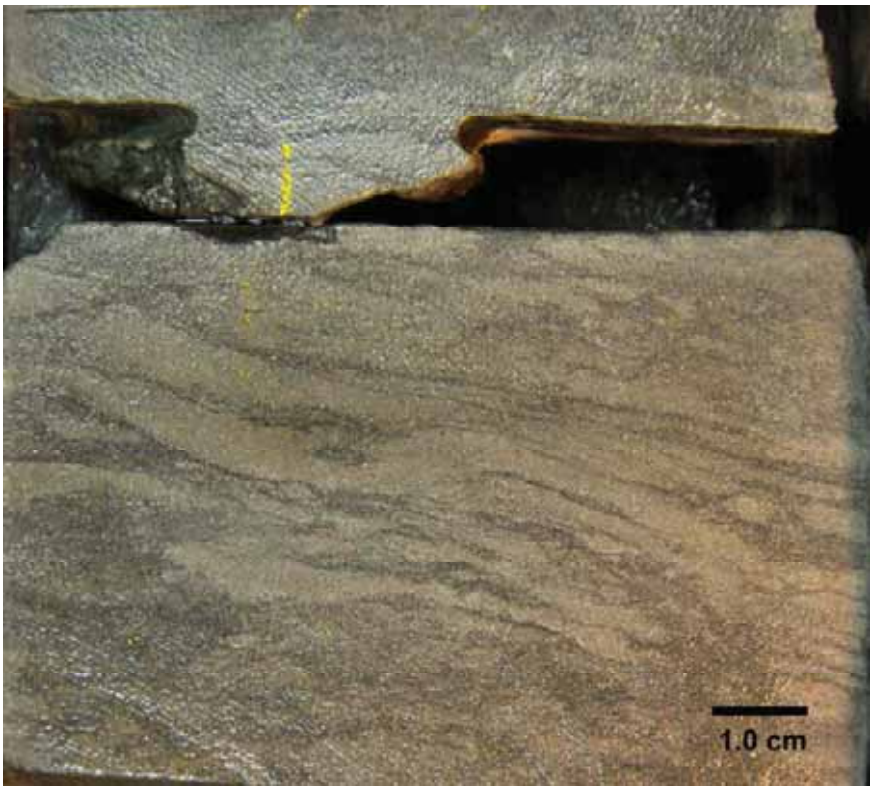

Close-up image (wet) of slabbed core – Cane Creek Unit #26-3 (Map 10), 7428.1 feet, B interval, silty dolomite with light brown oil staining. Relict laminae with bioturbation in this segment. Note the dark gray areas which consist of bitumen within the intercrystalline pores of the dolomite.

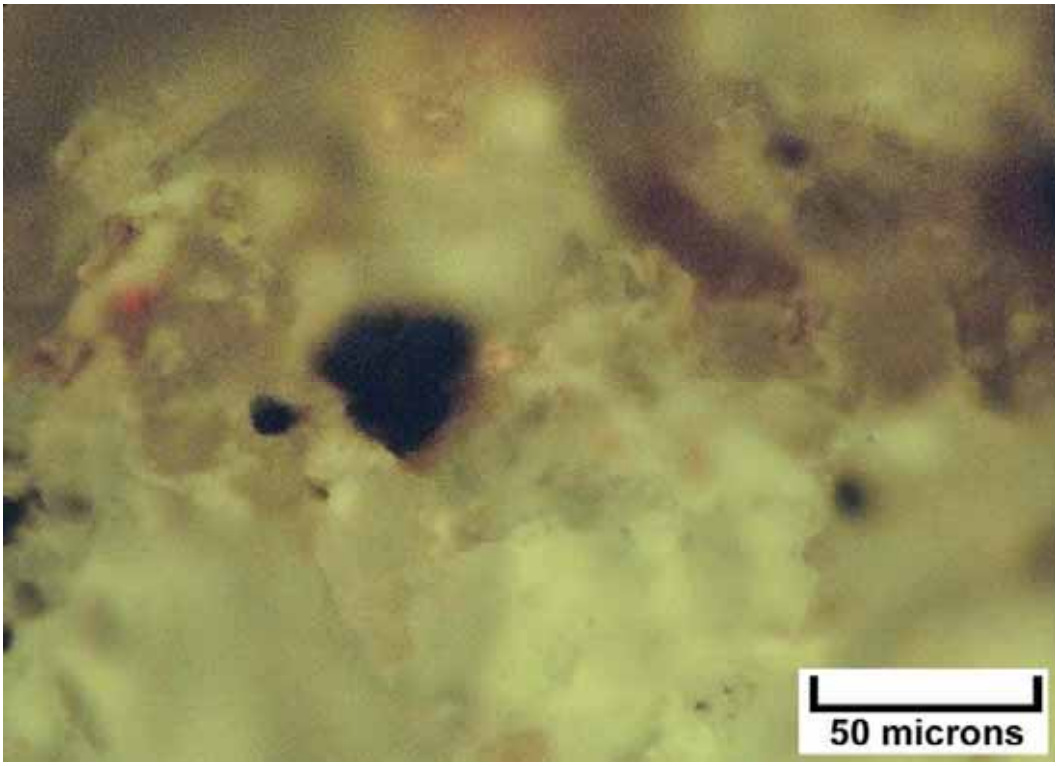

EF photomicrograph – Cane Creek Unit #26-3 (Map #10), 7428.1 feet, B interval, 2.6 visual epifluorescence rating in medium crystalline dolomite with visible pore space, possible microbialite structure containing disseminated pyrite.

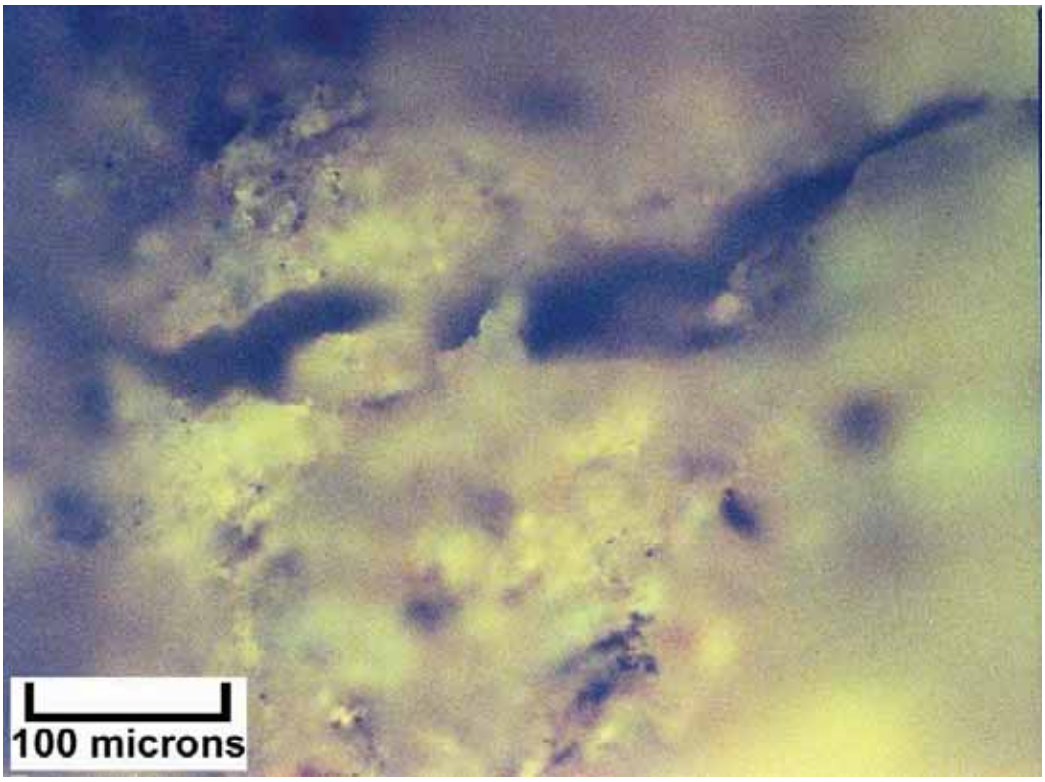

EF photomicrograph of uncovered thin section – Cane Creek Unit #26-3 (Map #10), 7430.9 feet, B interval, 3.5 visual epifluorescence rating, silty dolomite with ostracod shells and anhydrite-filled fractures.

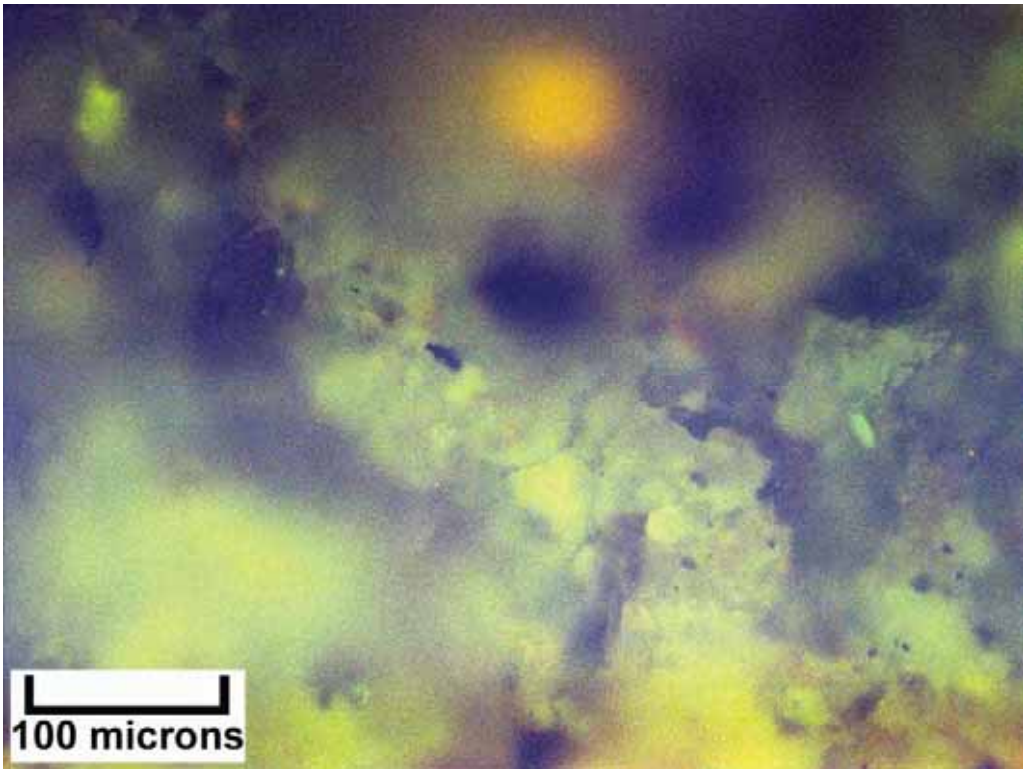

EF photomicrograph of uncovered thin section – Cane Creek Unit #26-3 (Map #10), 7439 feet, B interval, 3.3 visual epifluorescence rating, silty dolomite with ostracod shells.

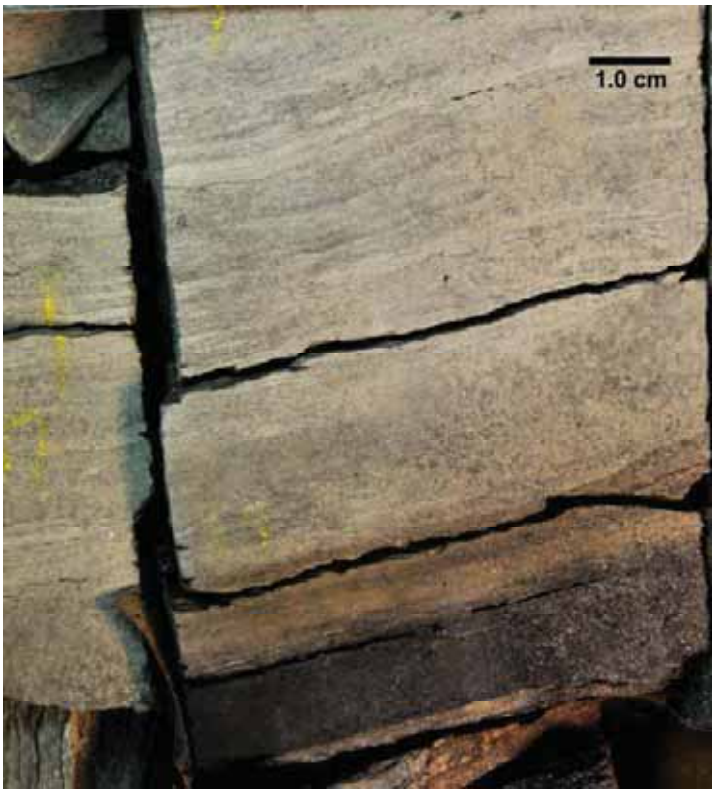

Close-up image (dry) of slabbed core – Cane Creek Unit #26-3 (Map 10), 7437.5 feet, B interval, dolomite with light brown oil staining that overlies a thin, organic black shale bed. Note the wavy microbially induced laminations, partially outlined with dark bitumen-lined pores.

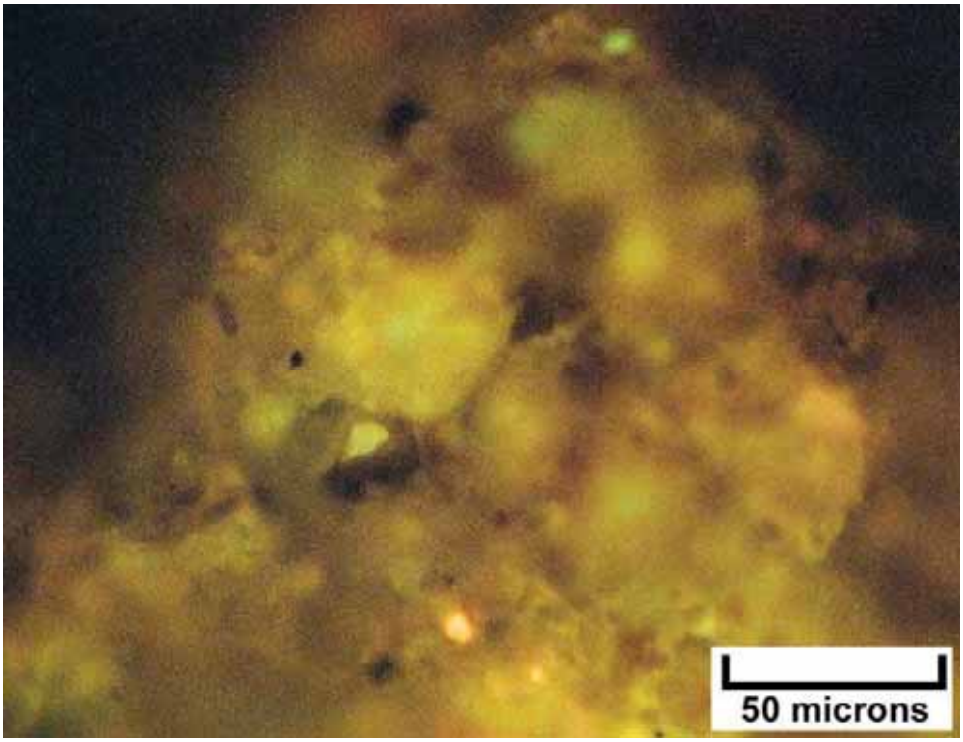

EF photomicrograph – Cane Creek Unit #26-3 (Map #10), 7437.5 feet, B interval, 2.8 visual epifluorescence rating in medium crystalline microbial dolomite with intercrystalline porosity and fluorescence.

Close-up image (wet) of slabbed core – Cane Creek Unit #26-3 (Map 10), 7440.5 feet, B interval, dolomitic siltstone with light and variable oil staining. Note the ripple-laminated thin beds that display bioturbated tops. Oil staining seems to be best developed in the burrowed bed caps. The vertical fractures are partially lined with anhydrite.

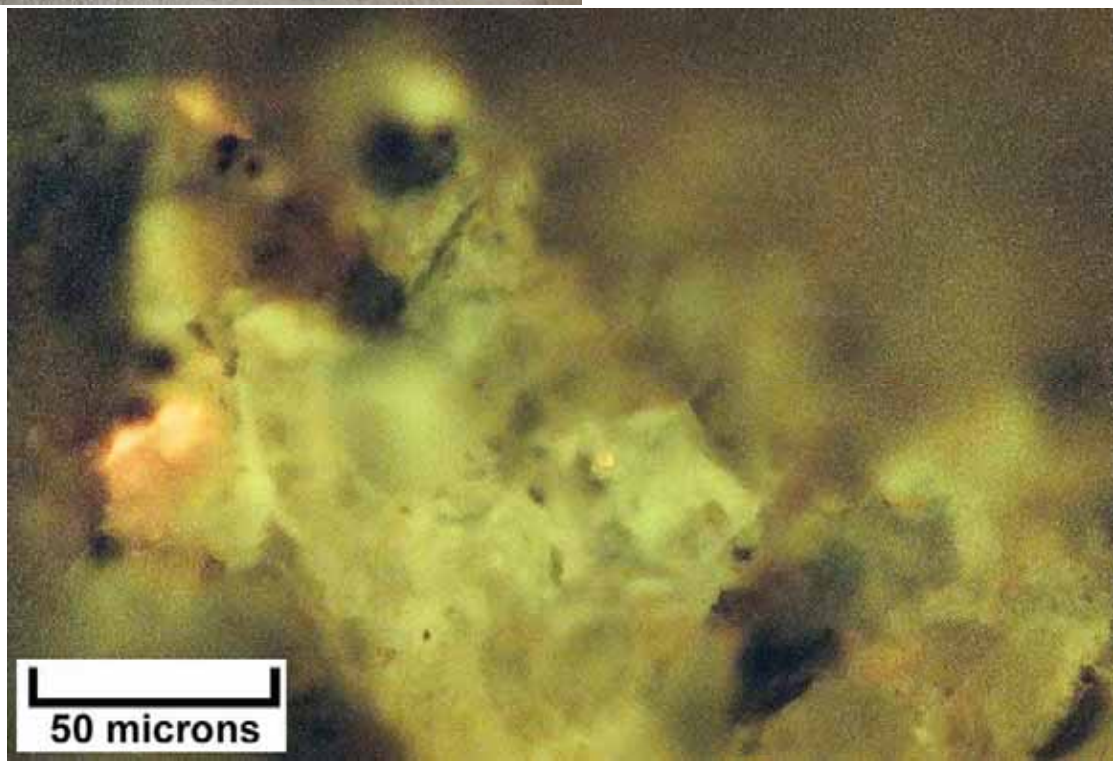

EF photomicrograph – Cane Creek Unit #26-3 (Map #10), 7440.5 feet, B interval, 2.6 visual epifluorescence rating in medium crystalline dolomite, probable microbial textures with good visible open pores.

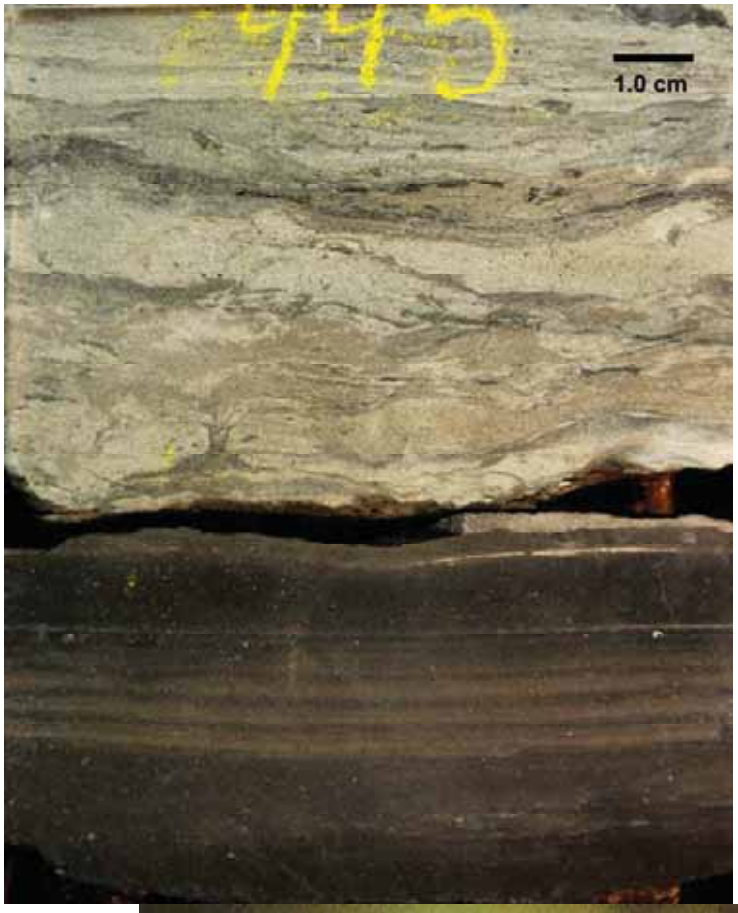

Close-up image (dry) of slabbed core – Cane Creek Unit #26-3 (Map 10), 7445.1 feet, B interval, black organic-rich shale with brown dolomitic laminae overlain by light-colored silty dolomite with patchy oil staining. Small microbial stromatolites, separated by desiccation cracks.

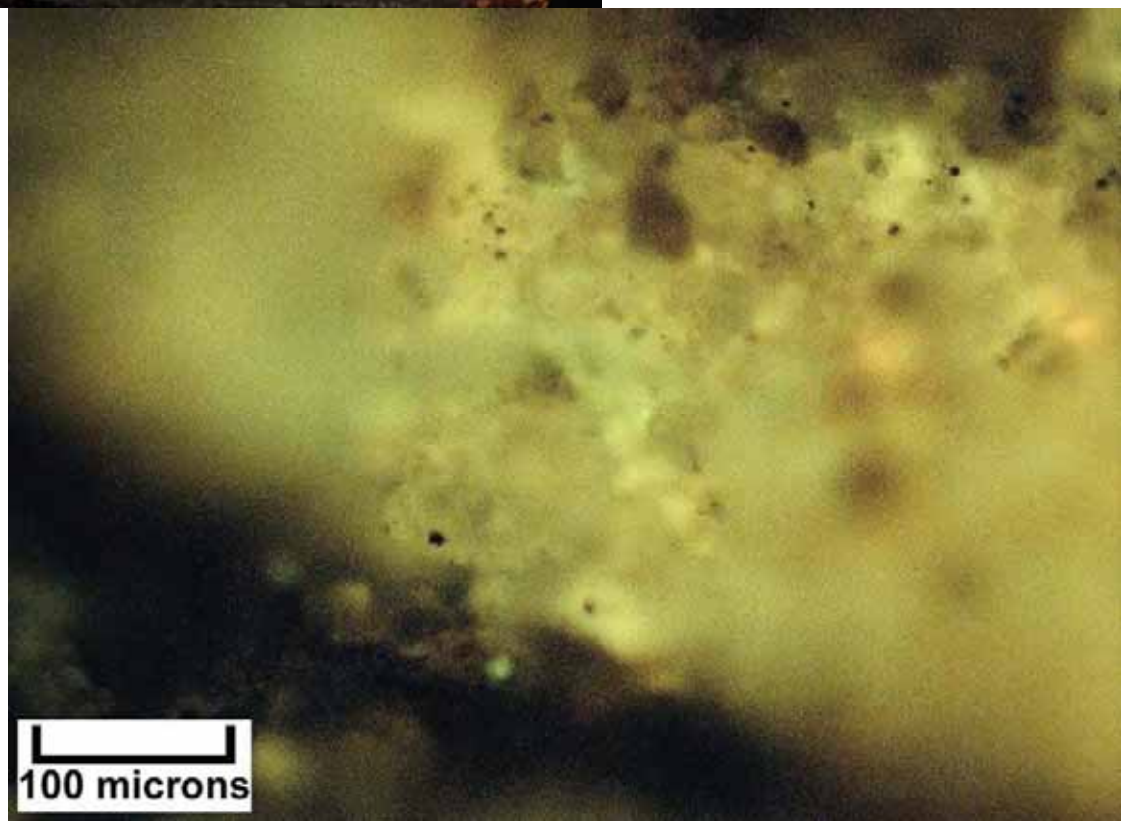

EF photomicrograph – Cane Creek Unit #26-3 (Map #10), 7445.1 feet, B interval, 3.0 visual epifluorescence rating in medium crystalline dolomite with probable microbial structures, rare floating silt grains and very bright fluorescence.

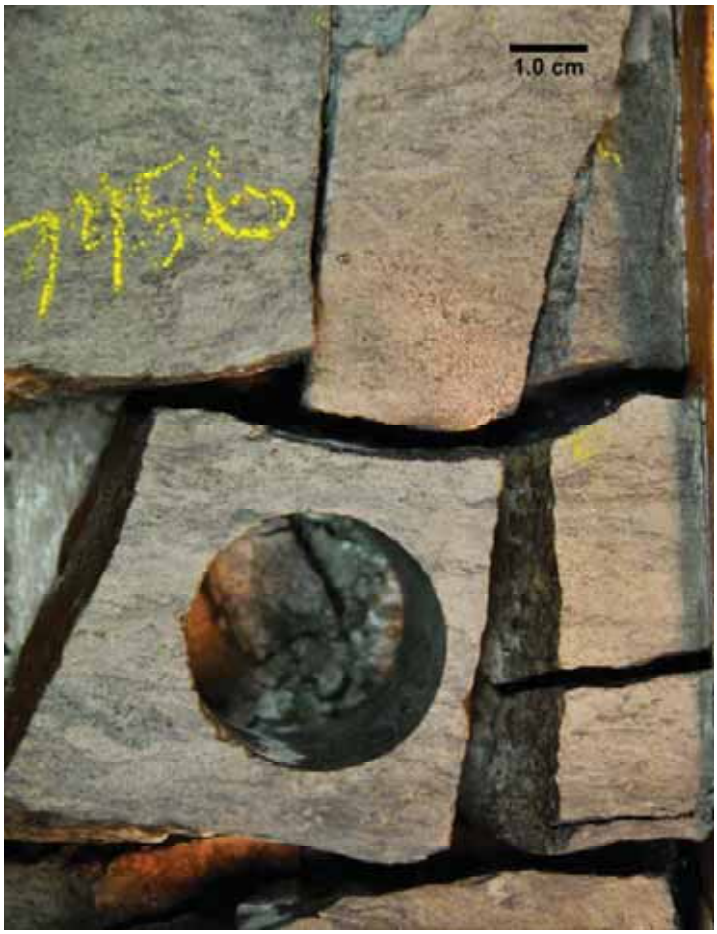

Close-up image (wet) of slabbed core – Cane Creek Unit #26-3 (Map 10), 7456.0 feet, B interval, silty dolomite with probable microbial structures that range from small wavy stromatolites (laminated) to thrombolites (clotted). Some of the dark gray concentrations are the result of bitumen within matrix pore spaces. The broken nature of this core interval may indicate the presence of vertical fracture sets.

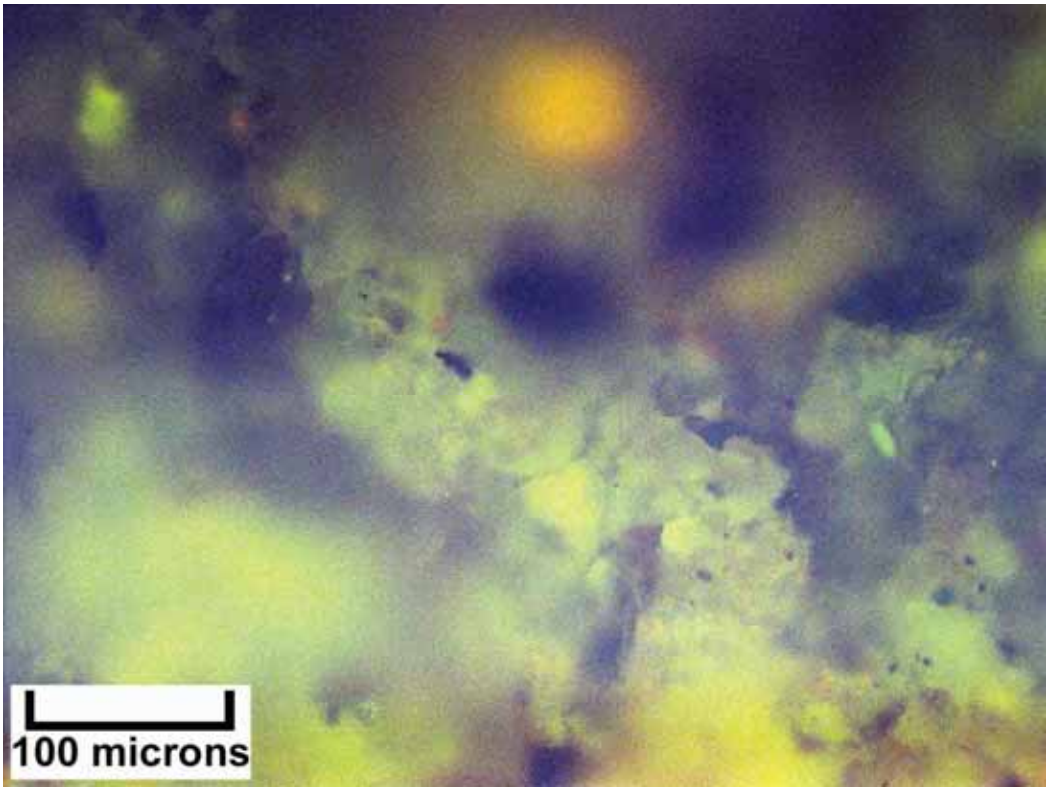

EF photomicrograph – Cane Creek Unit #26-3 (Map #10), 7456 feet, C interval, 2.1 visual epifluorescence rating in medium crystalline dolomite, possible microbial texture with excellent visible porosity.

Close-up image (dry) of slabbed core – Cane Creek Unit #26-3 (Map 10), 7469.2 feet, C interval, silty to argillaceous dolomite with patchy light brown oil staining. The lower portion of this segment consists of wavy laminations (stromatolitic)which are overlain by a distinctive clotted (thrombolitic) fabric. Note the vertical fracture on the left side of the segment that is lined with anhydrite.

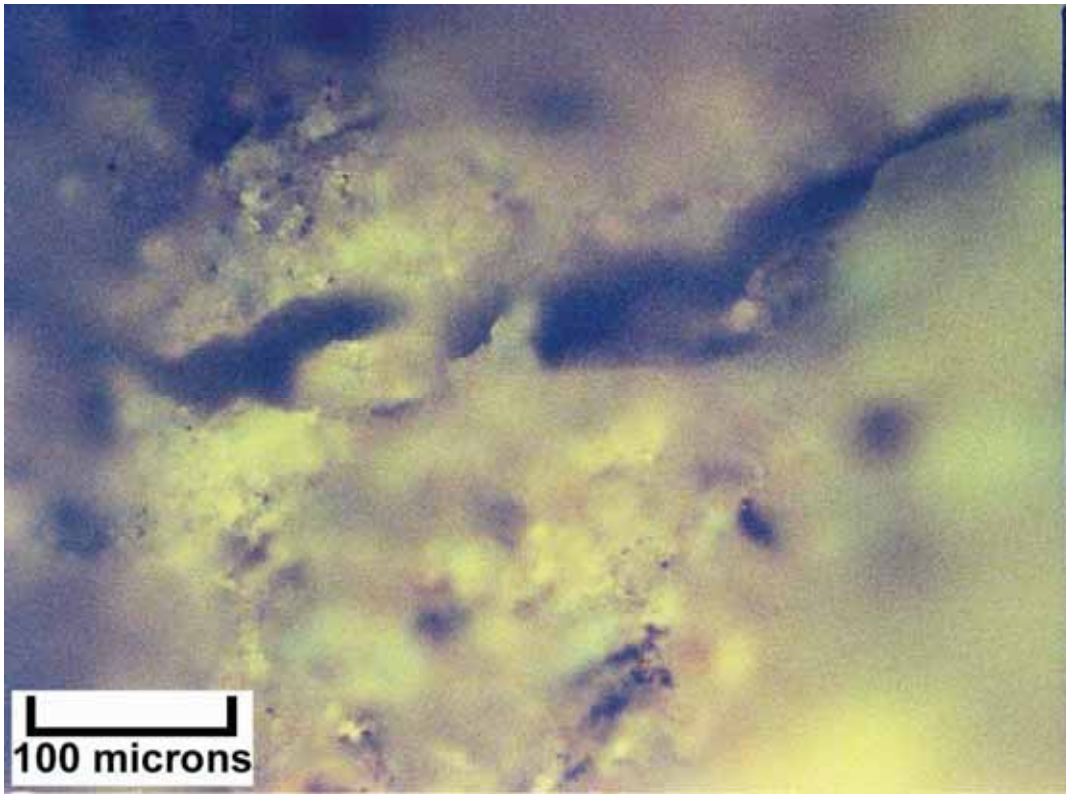

EF photomicrograph – Cane Creek Unit #26-3 (Map #10), 7469.2 feet, C interval, 2.2 visual epifluorescence rating in anastomosing linear pore network associated with the microbial texture.

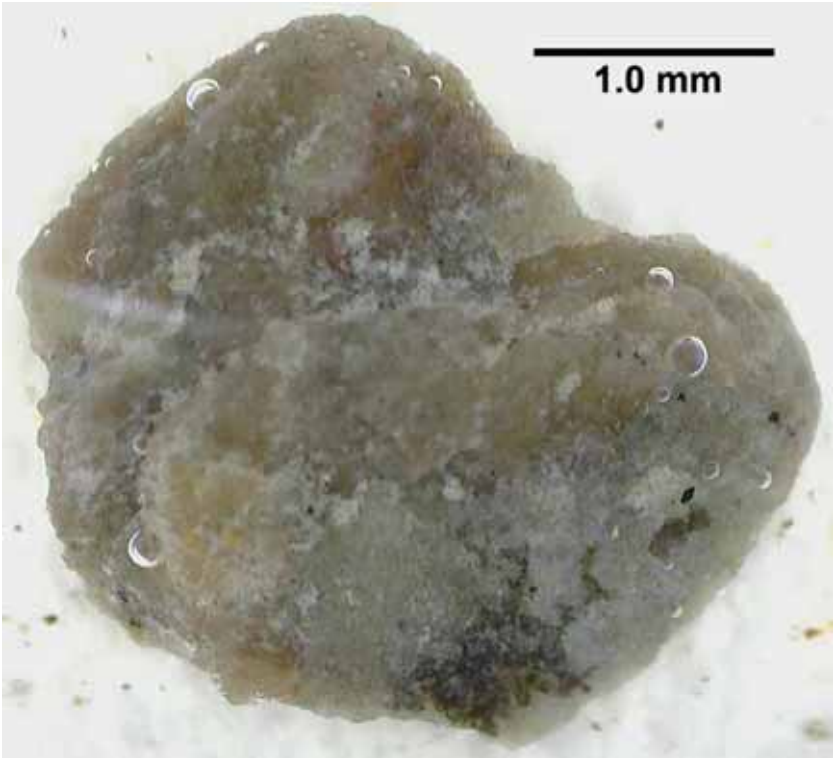

Digital microscope image (wet) – Long Canyon #1 (Map #11), 7030-40 feet, A interval, light gray, microcrystalline dolomite, ostracodal and peloidal grainstone/packstone with modest intercrystalline porosity.

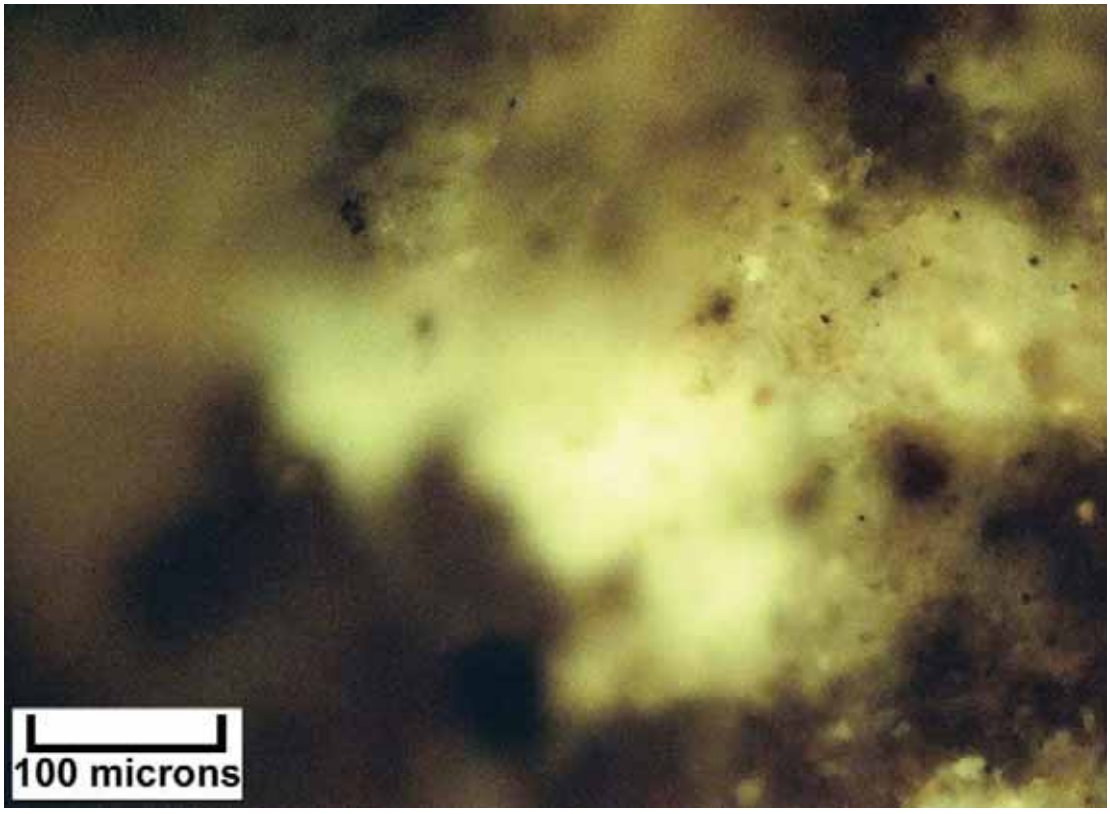

EF photomicrograph – Long Canyon #1 (Map #11), 7030-40 feet, A interval, 2.7 visual epifluorescence rating in medium to coarsely crystalline dolomite with patchy bright fluorescence.

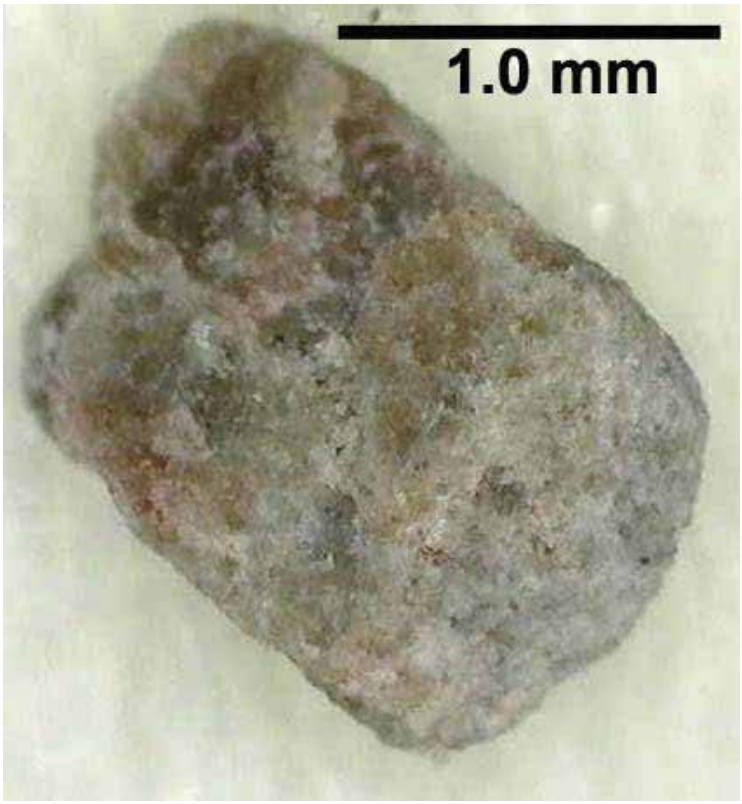

Digital microscope image (dry) – Long Canyon #1 (Map #11), 7060-70 feet, B interval, light gray to medium brown, medium crystalline dolomite composed of ostracods and coated skeletal grains to form a grainstone/packstone, modest intercrystalline porosity present.

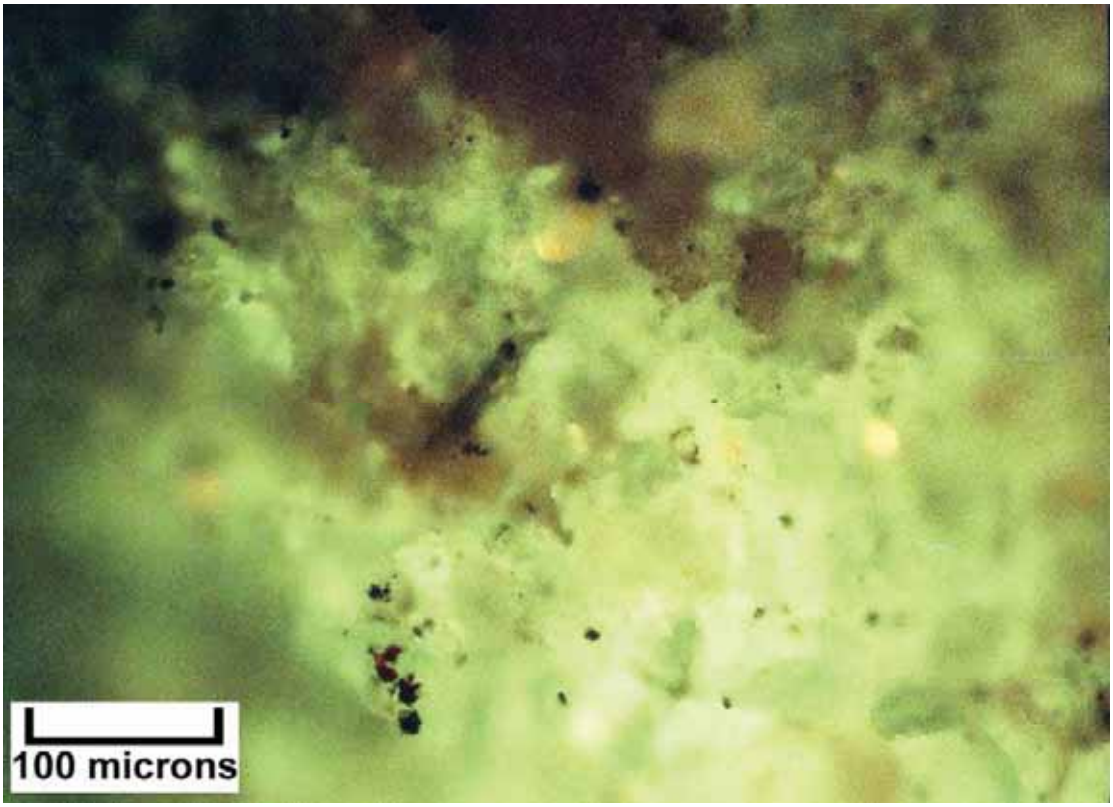

EF photomicrograph – Long Canyon #1 (Map #11), 7060-70 feet, B interval, 2.8 visual epifluorescence rating in medium crystalline dolomite with patchy bright fluorescence.

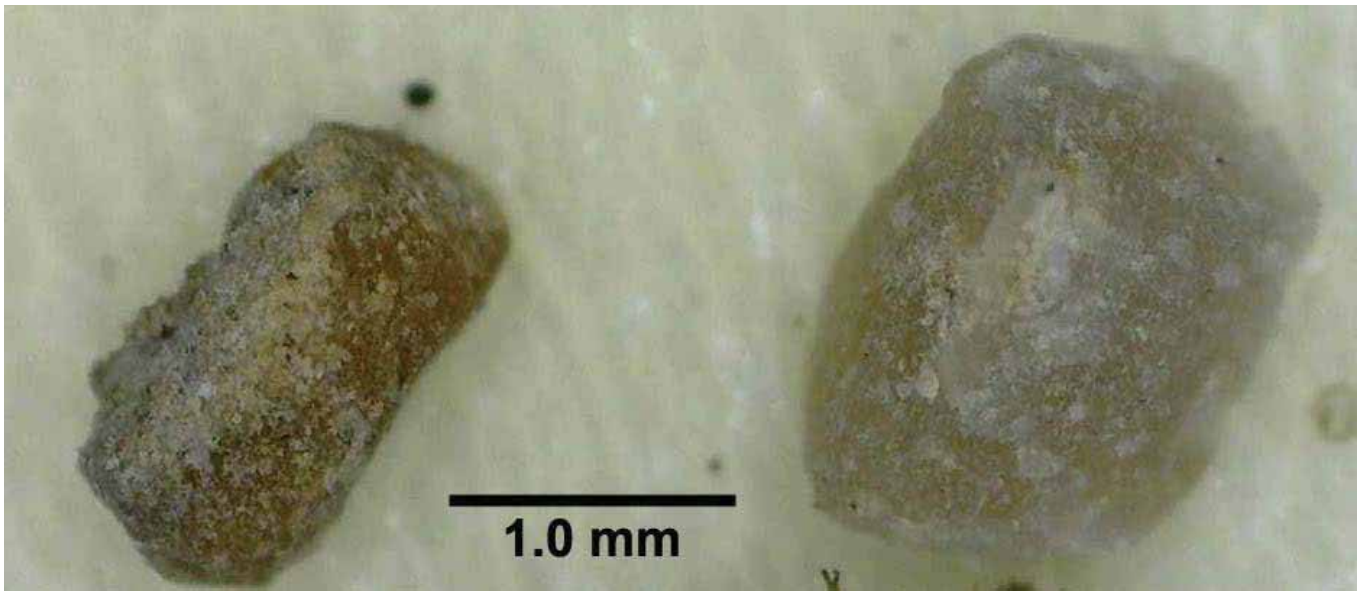

Digital microscope image (dry) – Long Canyon #1 (Map #11), 7070-80 feet, B interval, two cuttings consisting of light gray microcrystalline dolomite, ostracod-rich grainstone.

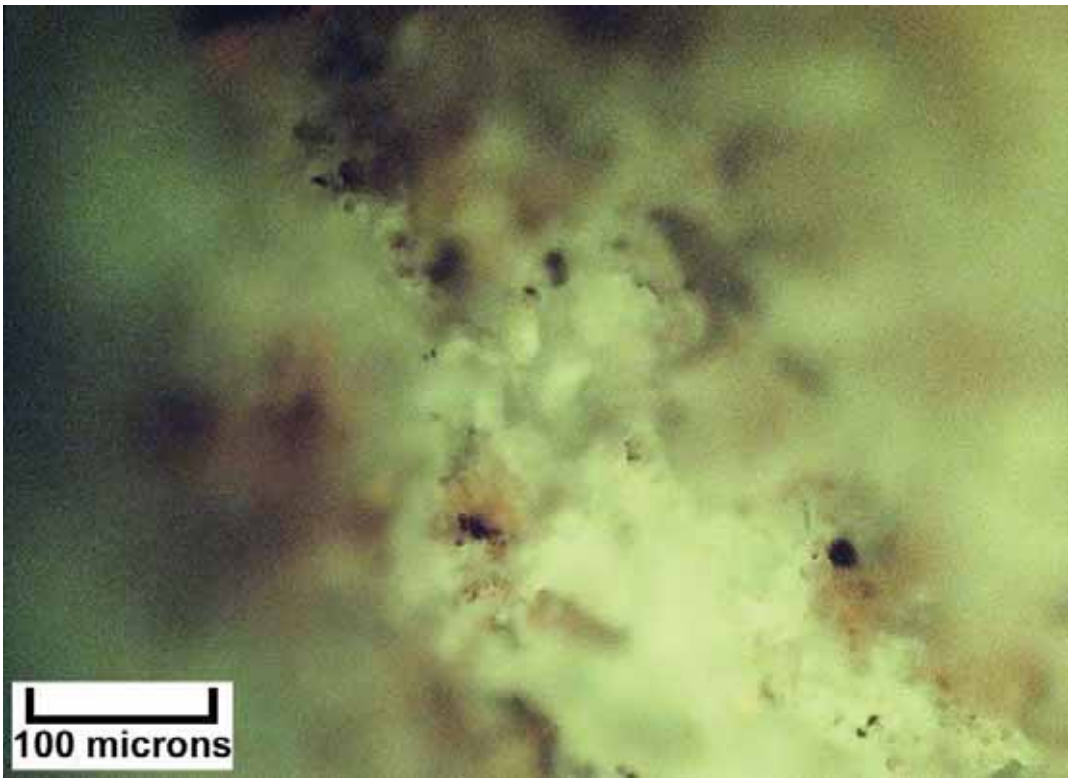

EF photomicrograph – Long Canyon #1 (Map #11), 7070-80 feet, B interval, 2.4 visual epifluorescence rating in skeletal grainstone containing possible ostracods.

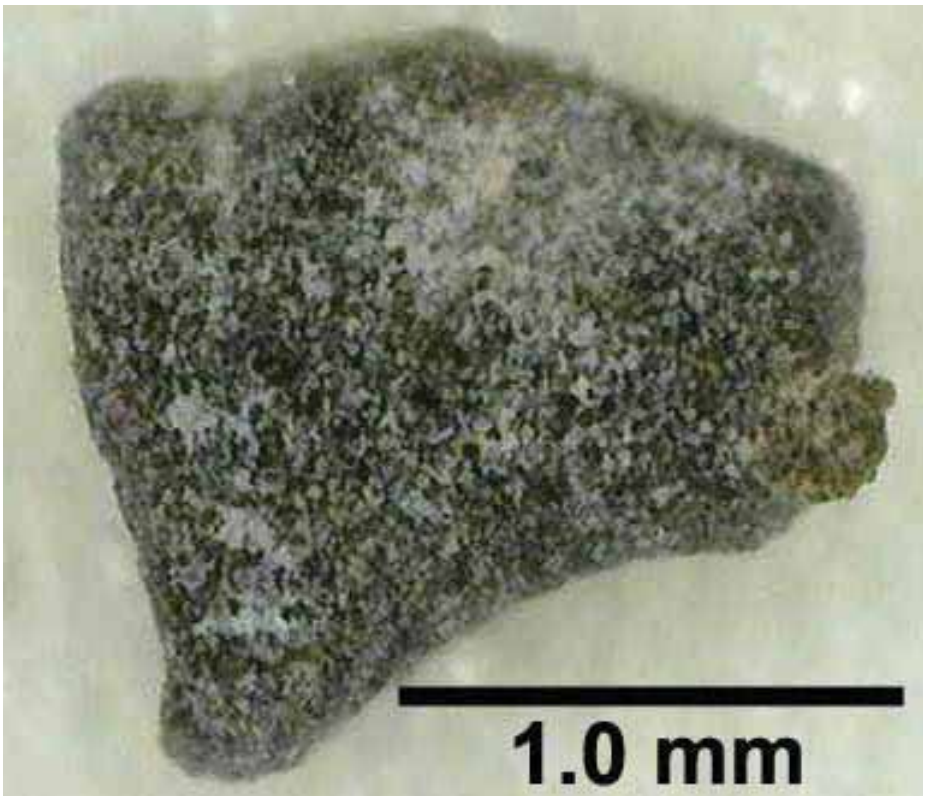

Digital microscope image (dry) – Long Canyon #1 (Map #11), 7095-7100 feet, C interval, dark gray, microcrystalline dolomite consisting of a poorly sorted skeletal grainstone with probable small fenestrate bryozoan fragments.

EF photomicrograph – Long Canyon #1 (Map #11), 7095-7100 feet, C interval, 2.8 visual epifluorescence rating of colonial bryozoan(?); longitudinal view.

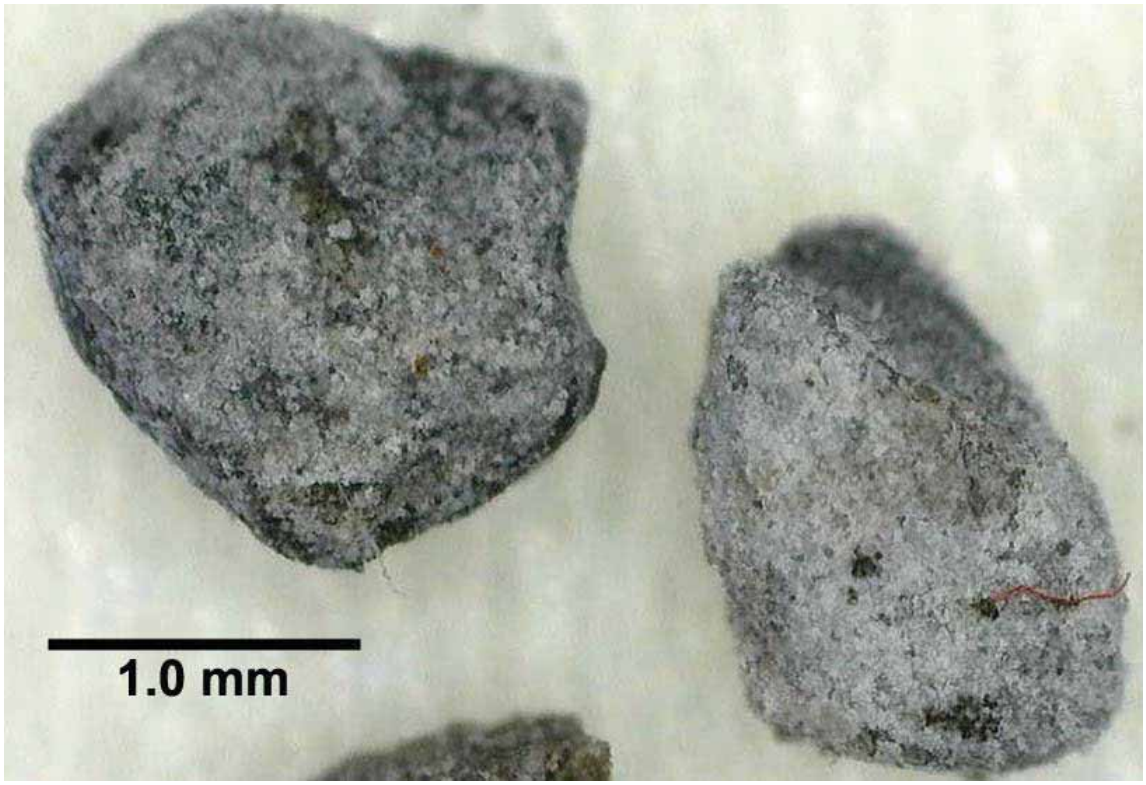

Digital microscope image (dry) – Mineral Canyon #1-14 (Map #12), 7360-70 feet, B interval, two samples showing a light to medium gray, medium crystalline dolomite displaying fair to good intercrystalline porosity partially lined with bitumen; probably composed of skeletal grainstone/packstone containing some ostracods.

EF photomicrograph – Mineral Canyon #1-14 (Map #12), 7360-70 feet, B interval, 1.7 visual epifluorescence rating in medium crystalline dolomite with modest fluorescence.

Binocular microscope image (wet) – Mineral Canyon #1-14 (Map #12), 7380-90 feet, B interval, hand-picked cuttings showing peloidal dolomite with porosity.

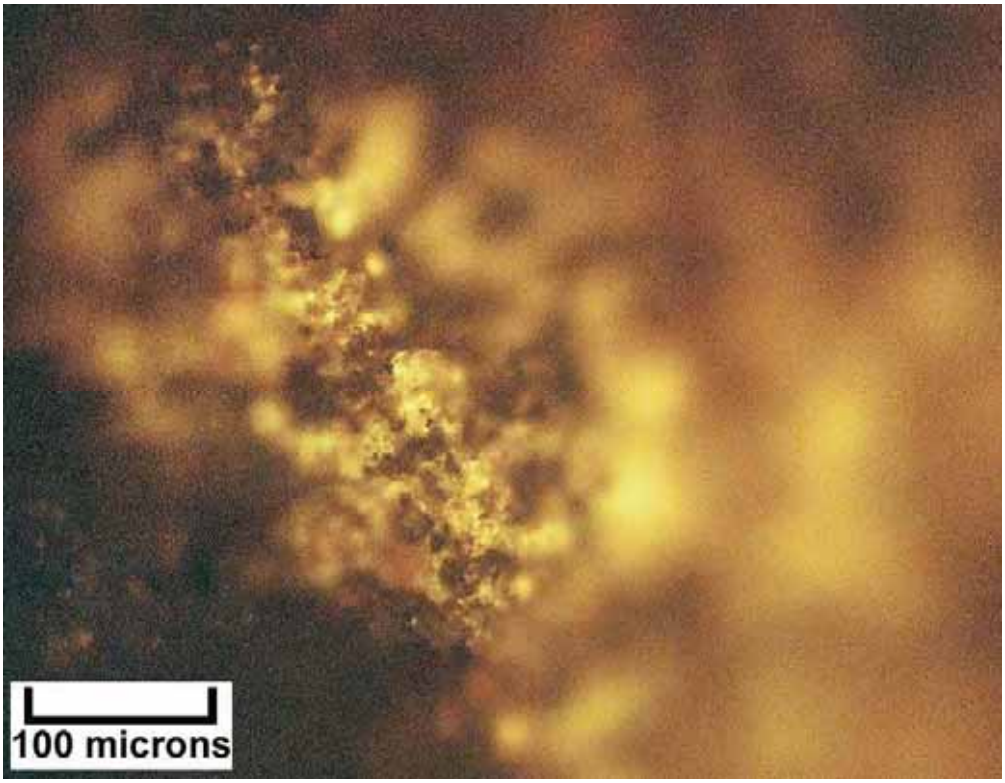

EF photomicrograph – Mineral Canyon #1-14 (Map #12), 7380-90 feet, B interval, 1.5 visual epifluorescence rating in very small samples, highly dolomitic shale with well developed dolomite crystals and microporosity.

Digital microscope image (dry) – Federal #1-X (Map #13), 6530-40 feet, B interval, medium to dark gray, argillaceous or organic-rich microcrystalline dolomite, possible lumpy microbial structure and anhydrite-filled microstructures.

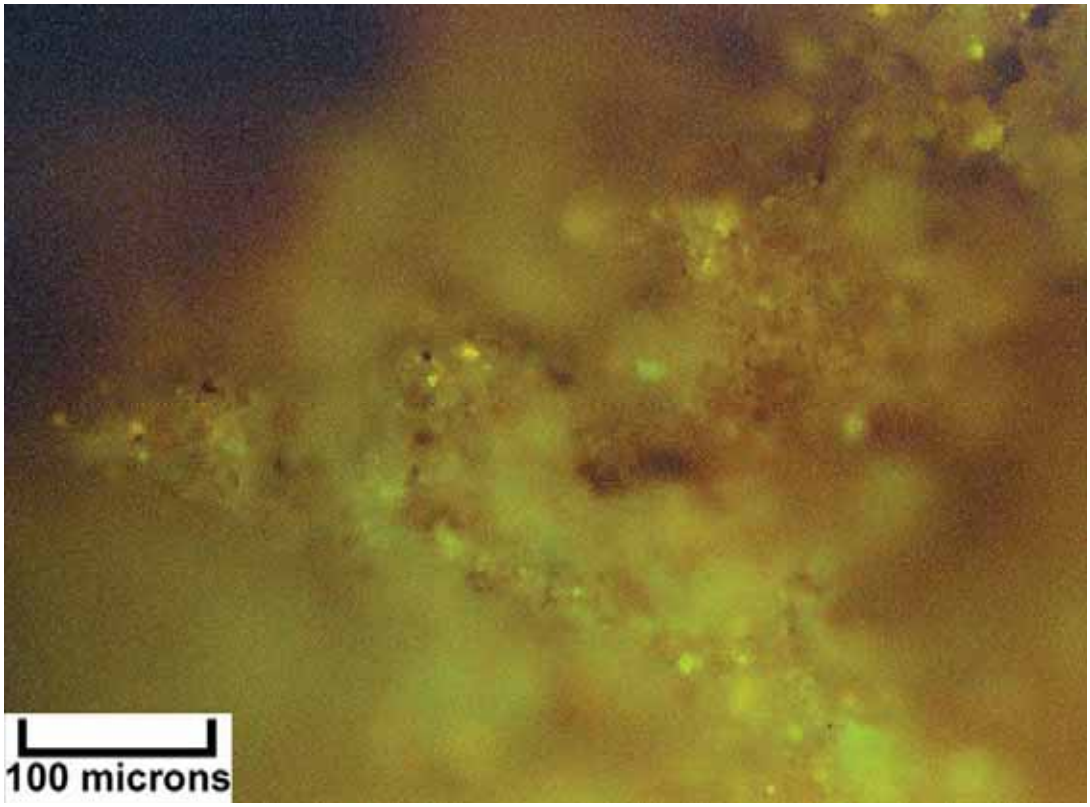

EF photomicrograph – Federal #1-X (Map #13), 6530-40 feet, B interval, 2.1 visual epifluorescence rating in microfractured dolomitic shale.

Digital microscope image (dry) – Federal #1-X (Map #13), 6620-30 feet, C interval, dark gray laminated dolomitic shale with patches of white dolomite rhombs, no visible porosity.

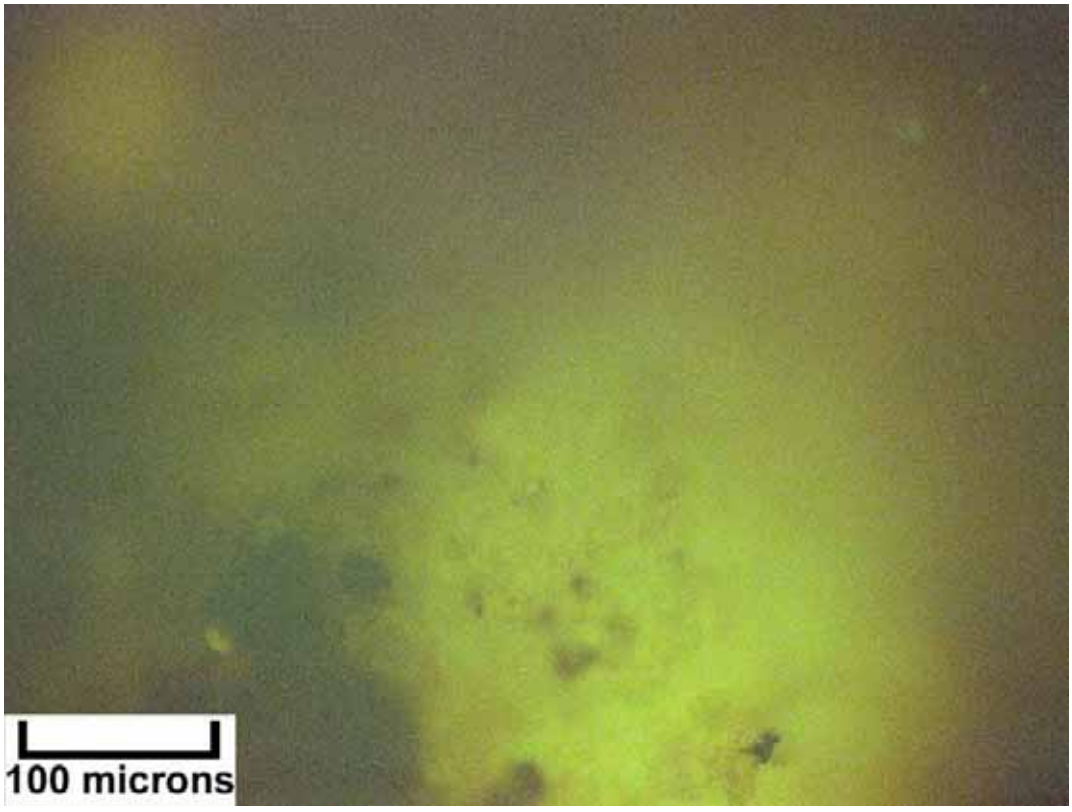

EF photomicrograph – Federal #1-X (Map #13), 6620-30 feet, C interval, 2.1 visual epifluorescence rating in aggregates of rhombic dolomite in silty and slightly dolomitic shale.

Digital microscope image (dry) – Federal #1-X (Map #13), 6630-40 feet, C interval, light to dark gray, finely crystalline argillaceous dolomite with isolated patches of light gray, medium crystalline dolomite.

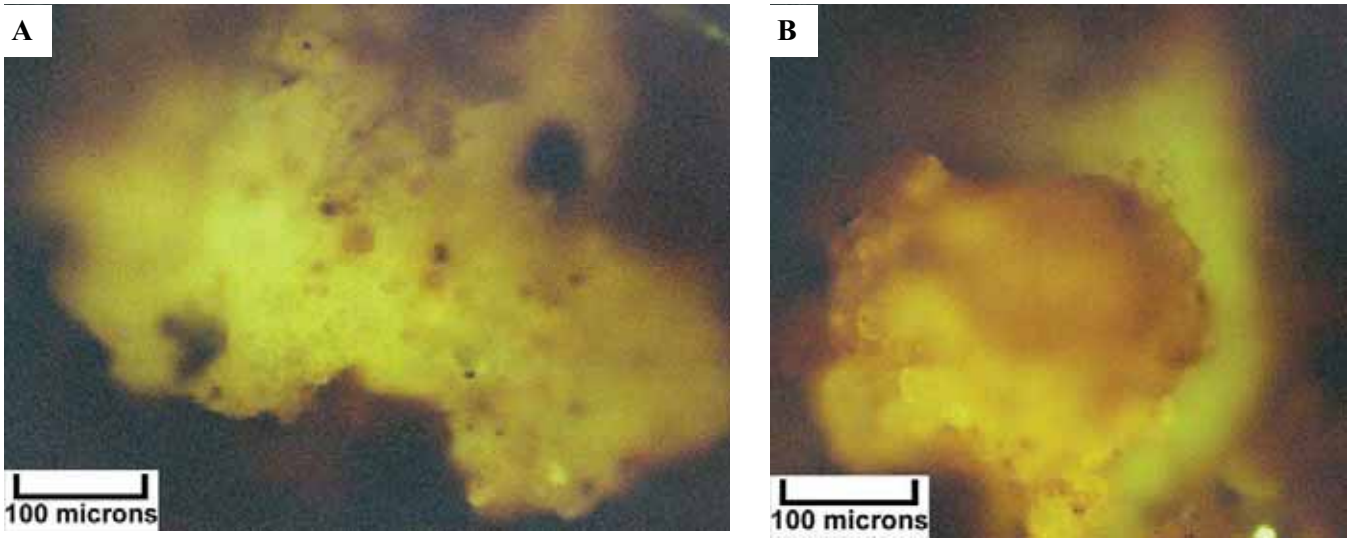

EF photomicrographs – Federal #1-X (Map #13), 6630-40 feet, C interval. A: 2.0 visual epifluorescence rating in highly dolomitic shale with possible anhydrite clusters. B: 2.8 visual epifluorescence rating in anhydritic dolomite.

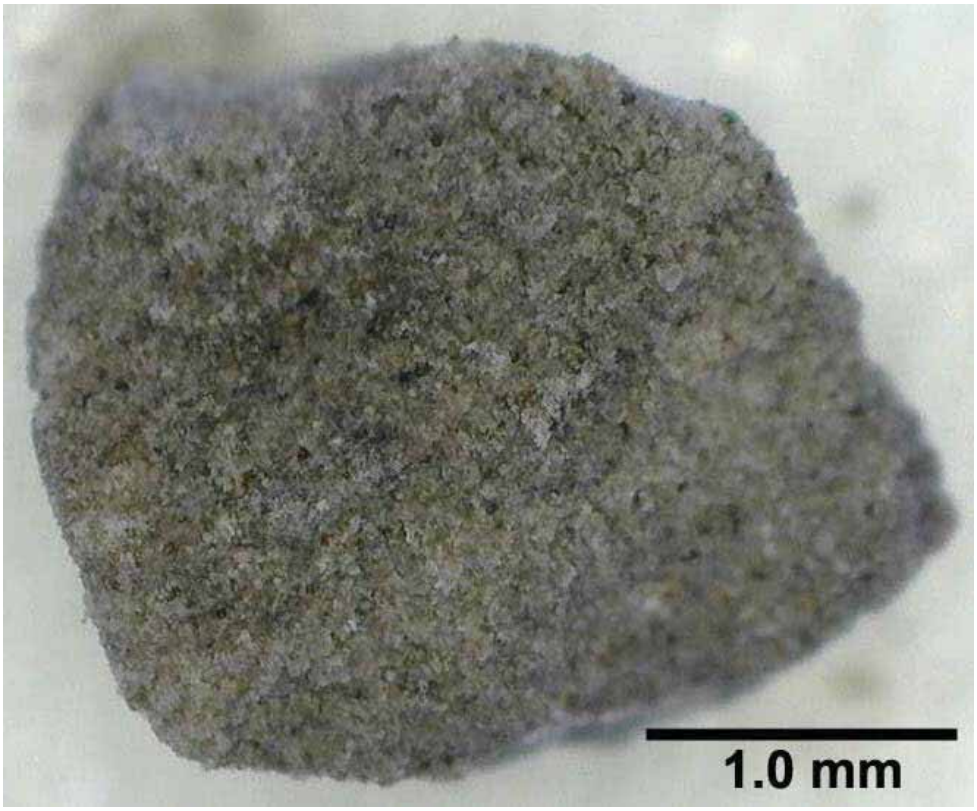

Digital microscope image (dry) – Featherstone #9-1 (Map #14), 5800-10 feet, A interval, medium gray, silty to slightly argillaceous dolomite, fine to medium crystalline with modest intercrystalline porosity.

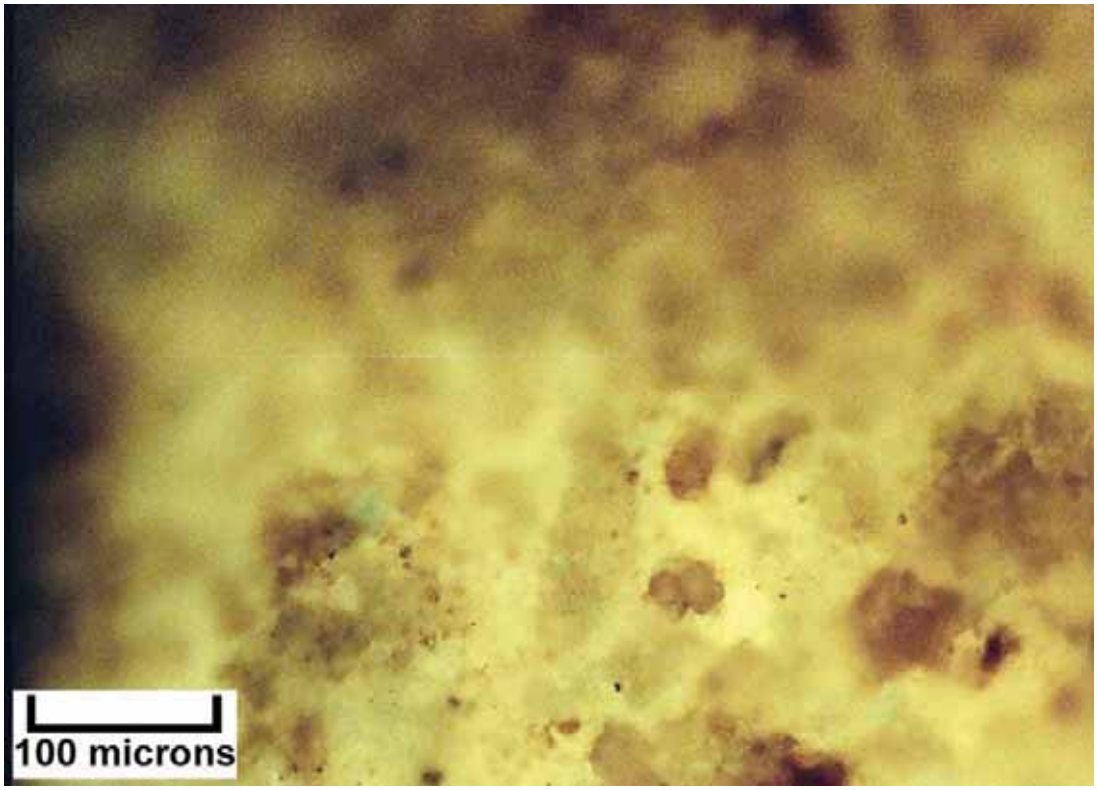

EF photomicrograph – Featherstone #9-1 (Map #14), 5800-10 feet, A interval, 2.3 visual epifluorescence rating in porous dolomitic siltstone.

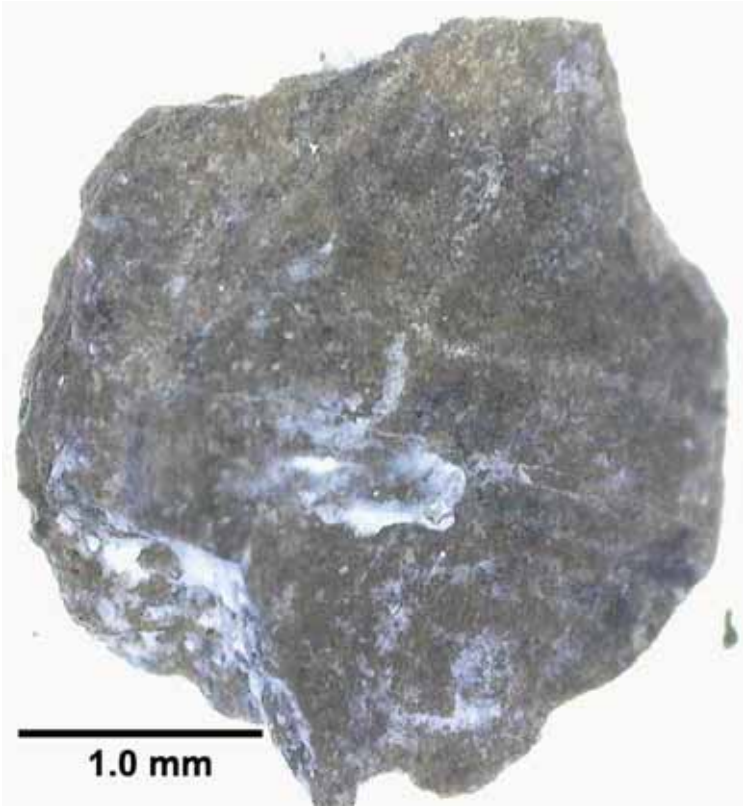

Digital microscope image (wet) – Featherstone #9-1 (Map #14), 5810-20 feet, B interval, medium brown-gray microcrystalline dolomite, thin bedded with a mixed skeletal and microbial composition, possibly packstone or bindstone fabric; no visible porosity.

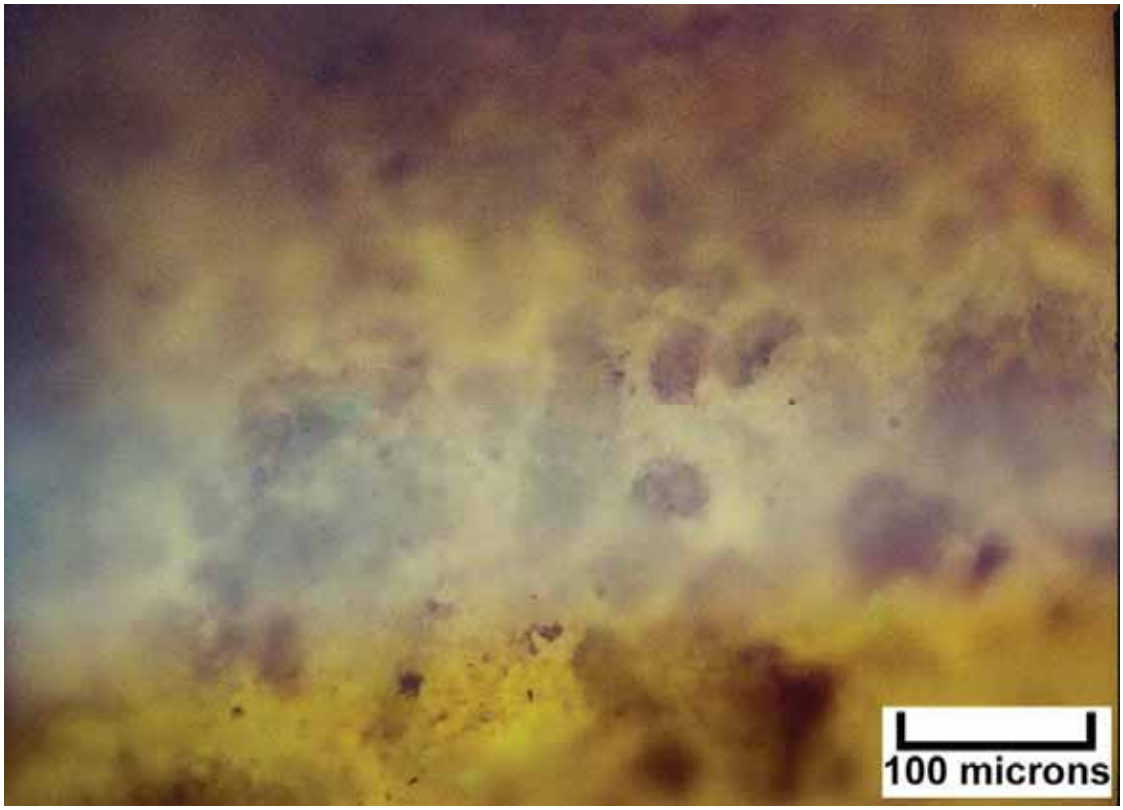

EF photomicrograph – Featherstone #9-1 (Map #14), 5810-20 feet, B interval, 2.3 visual epifluorescence rating in partially dolomitized fossiliferous siltstone, possibly bryozoan.

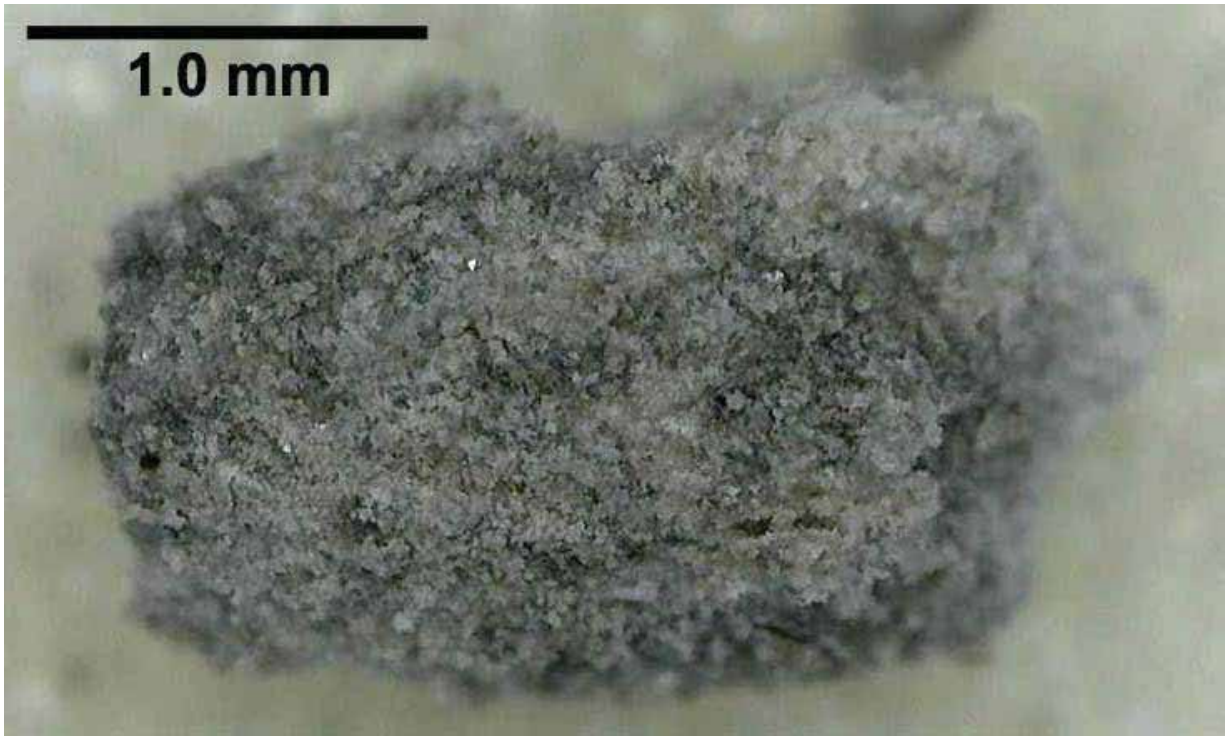

Digital microscope image (dry) – Featherstone #9-1 (Map #14), 5830-40 feet, B interval, white to medium gray dolomite, fine to medium crystalline with visible intercrystalline pore spaces, probable skeletal-peloidal packstone/wackestone.

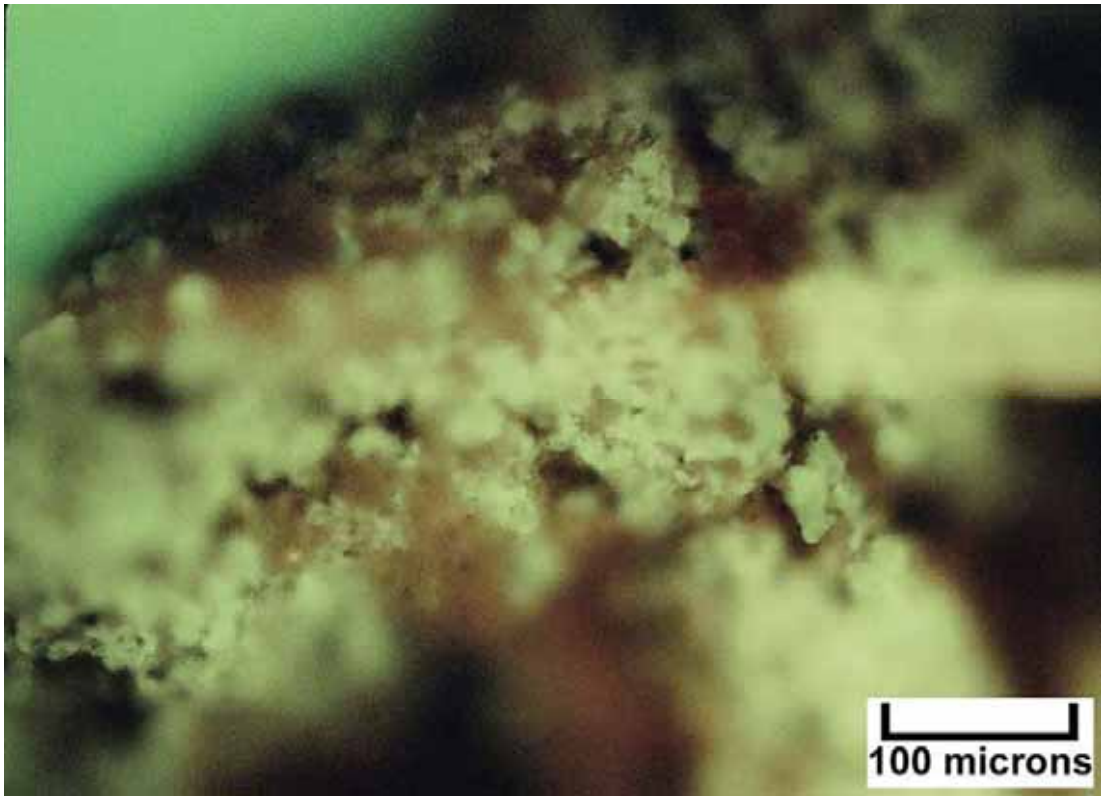

EF photomicrograph – Featherstone #9-1 (Map #14), 5830-40 feet, B interval, 2.5 visual epifluorescence rating in very silty dolomite with fine to medium dolomite crystal aggregates.

Digital microscope image (dry) – Featherstone #9-1 (Map #14), 5840-50 feet, B interval, medium gray to black, slightly dolomitic shale to argillaceous dolomite, occasional isolated patches of medium crystalline dolomite.

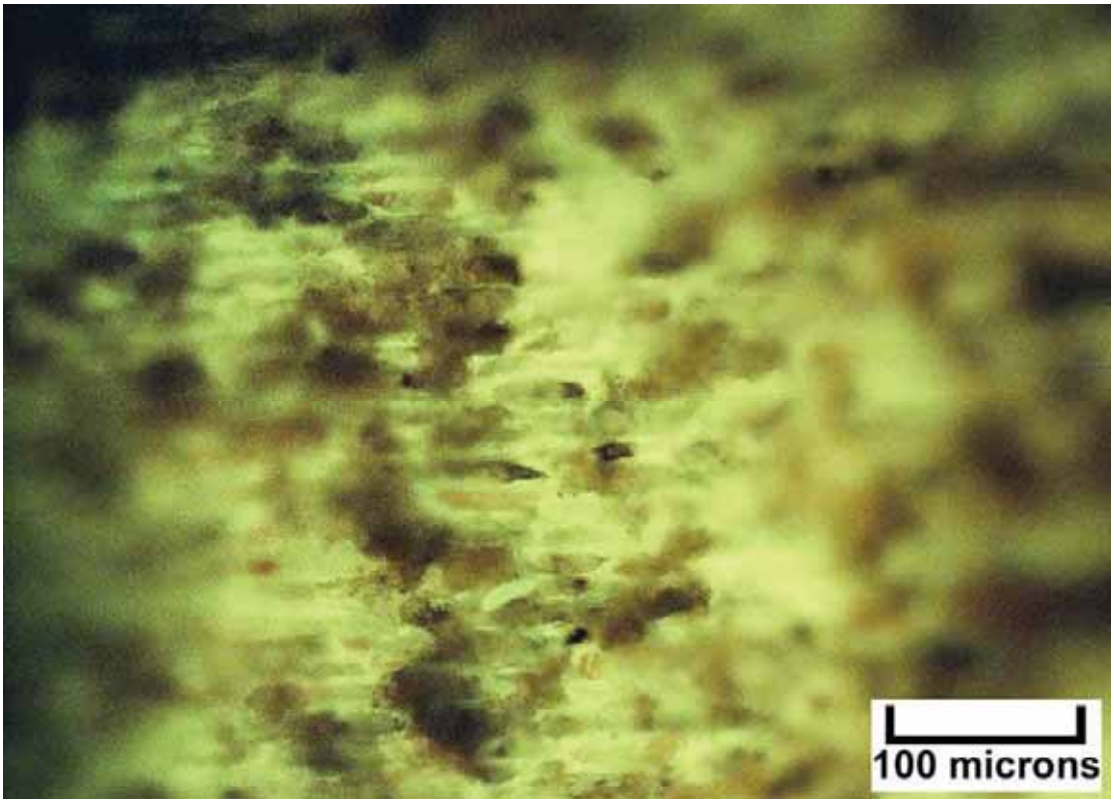

EF photomicrograph – Featherstone #9-1 (Map #14), 5840-50 feet, B interval, 2.9 visual epifluorescence rating in dolomitic tubular microbialite matrix with modest intercrystalline and within-tubule porosity.

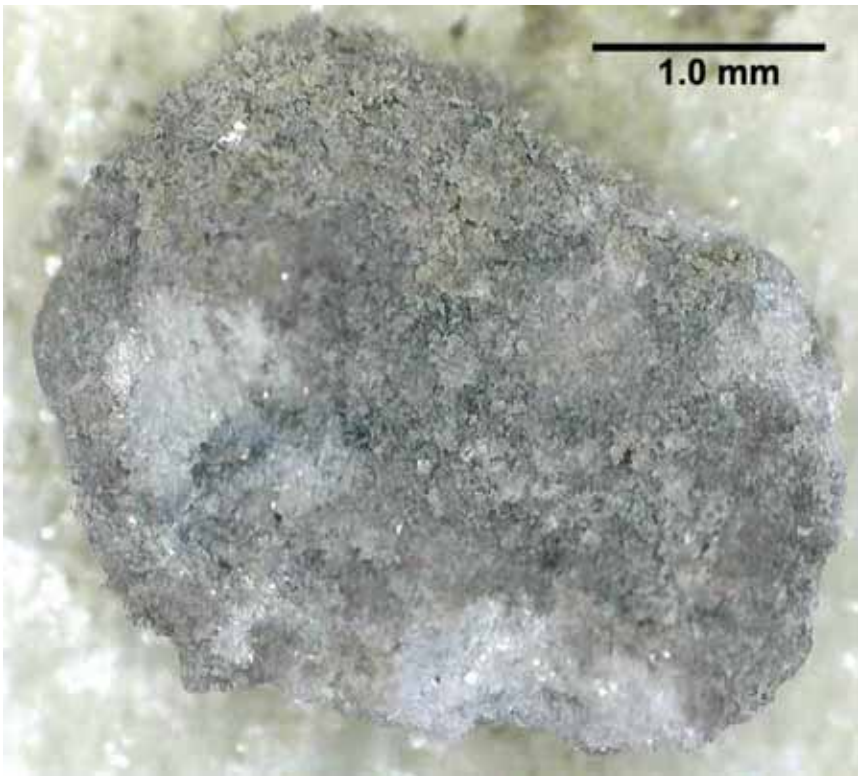

Digital microscope image (dry) – Featherstone #9-1 (Map #14), 5850-60 feet, B interval, light to medium gray dolomite, fine to medium crystalline, skeletal wackestone/packstone; fair to good intercrystalline porosity despite patches of anhydrite replacement.

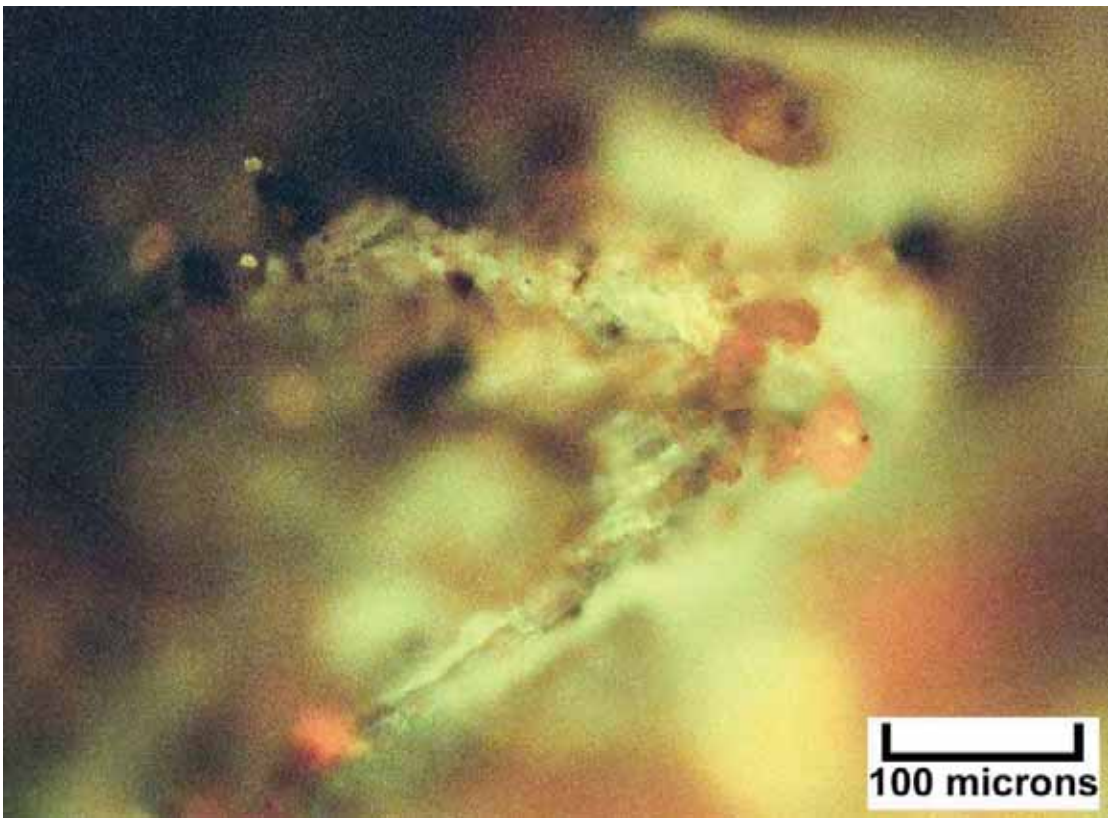

EF photomicrograph – Featherstone #9-1 (Map #14), 5850-60 feet, C interval, 2.7 visual epifluorescence rating in cluster of dolomite near a styolite seam or microfracture.

Digital microscope image (dry) – Featherstone #9-1 (Map #14), 5860-70 feet, B interval, light to medium gray, fine to medium crystalline dolomite, slightly argillaceous, fine-grained skeletal wackestone/ packstone with modest intercrystalline pore space.

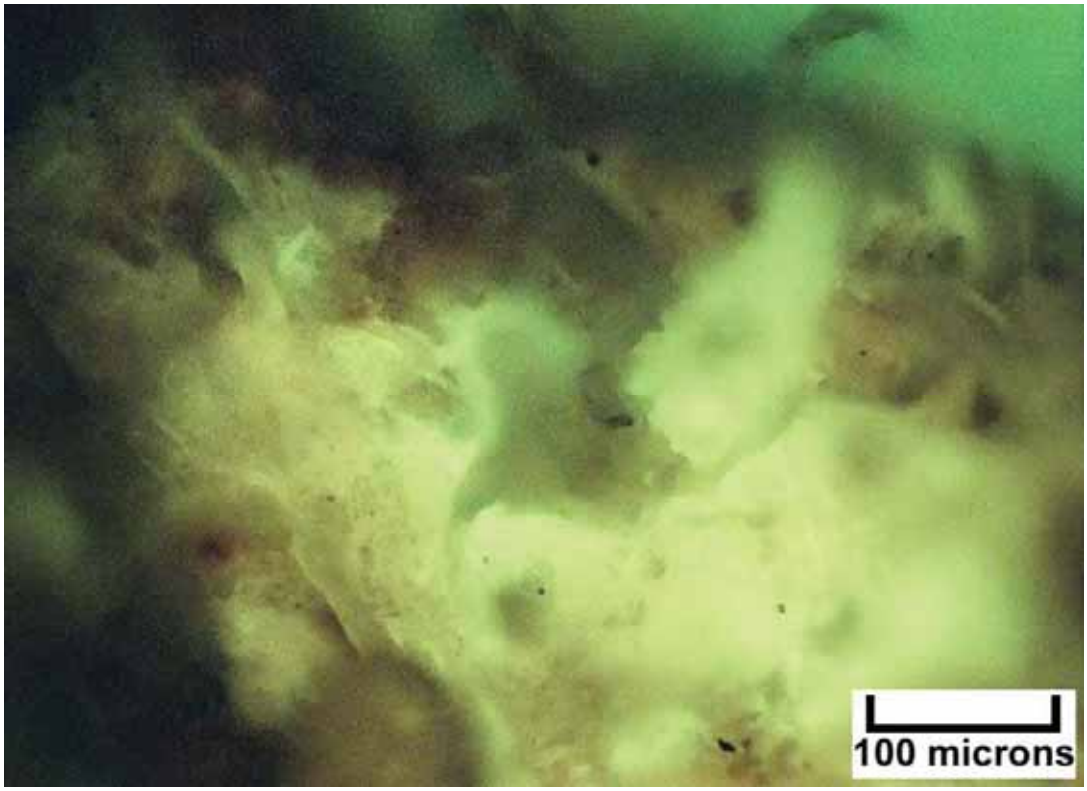

EF photomicrograph – Featherstone #9-1 (Map #14), 5860-70 feet, B interval, 2.9 visual epifluorescence rating in medium to coarse crystalline dolomite with possible fossil debris and visible pore spaces.

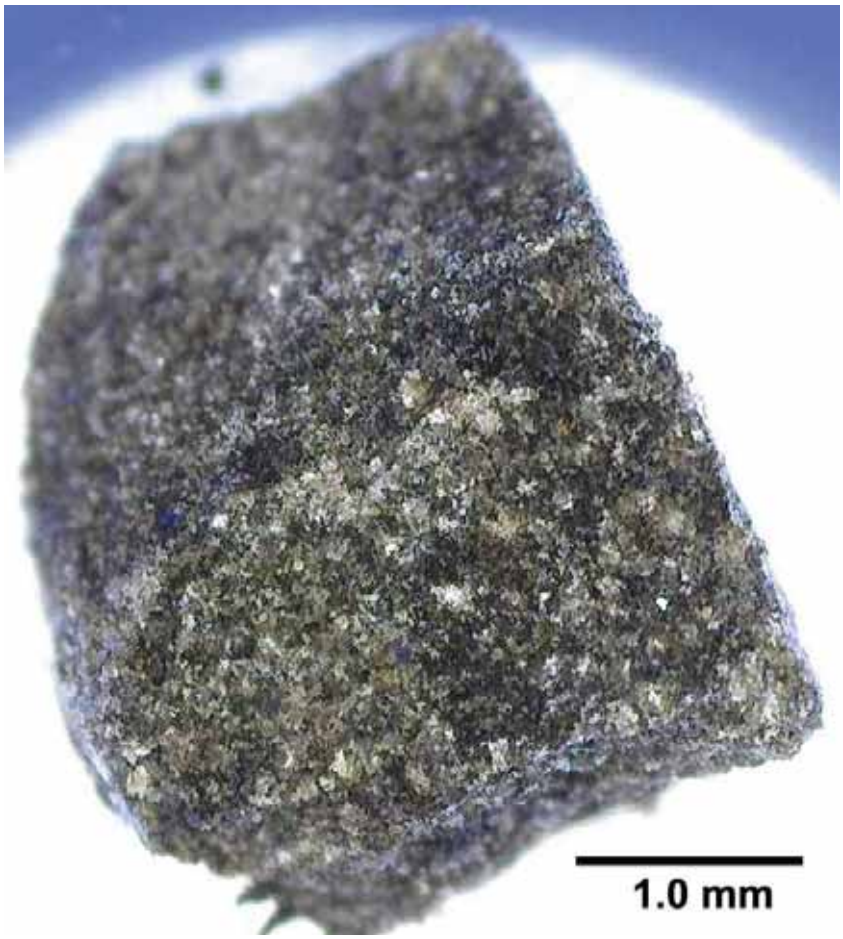

Digital microscope image (dry) – Featherstone #9-1 (Map #14), 5870-80 feet, B interval, medium to dark gray, argillaceous dolomite with fine to medium crystal size, peloidal-skeletal wackestone; no visible porosity.

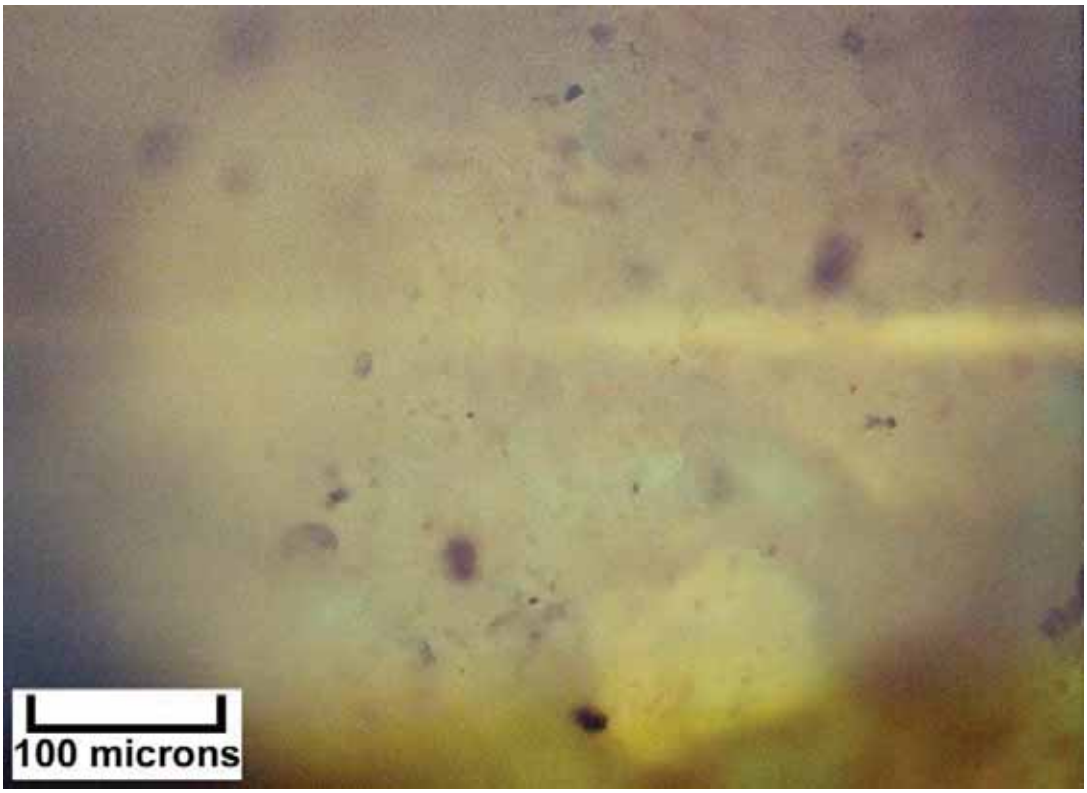

EF photomicrograph – Featherstone #9-1 (Map #14), 5870-80 feet, B interval, 2.3 visual epifluorescence rating in silty dolomitic wackestone.

Binocular microscope image (wet and etched) – Bridger Jack U #3 (Map #15), 5920-30 feet, B interval, dark gray peloidal dolomite with pyrite.

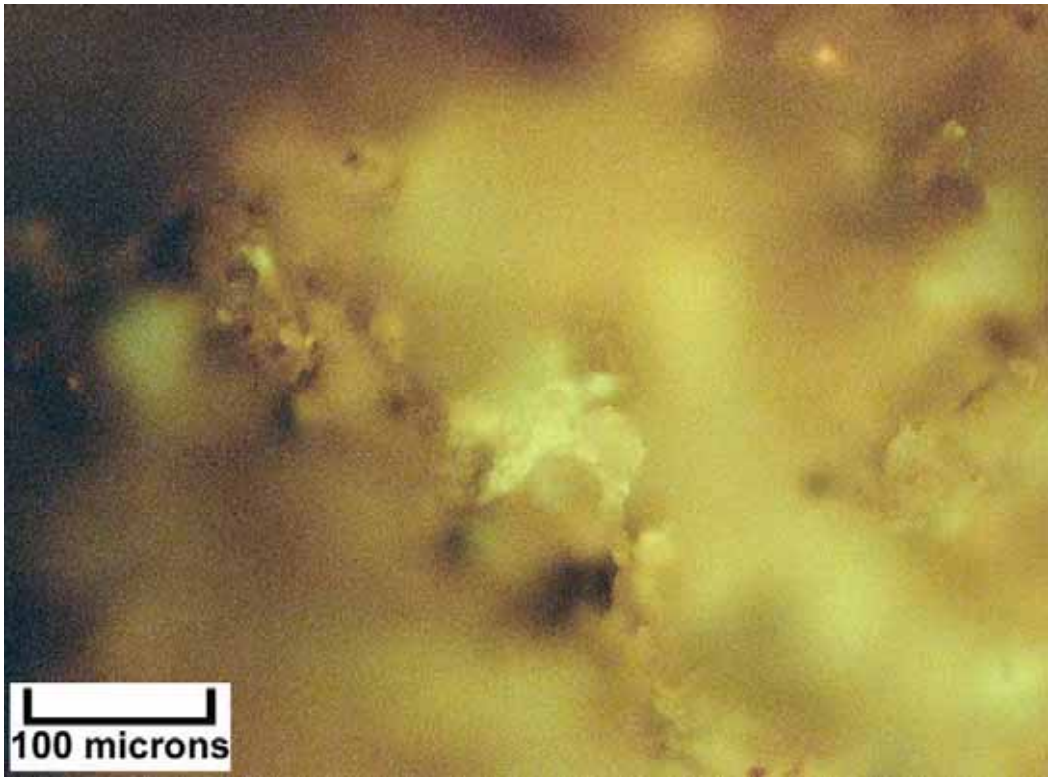

EF photomicrograph – West Bridger Jack U #3 (Map #15), 5920-30 feet, B interval, 1.2 visual epifluorescence rating in dolomitic shale.

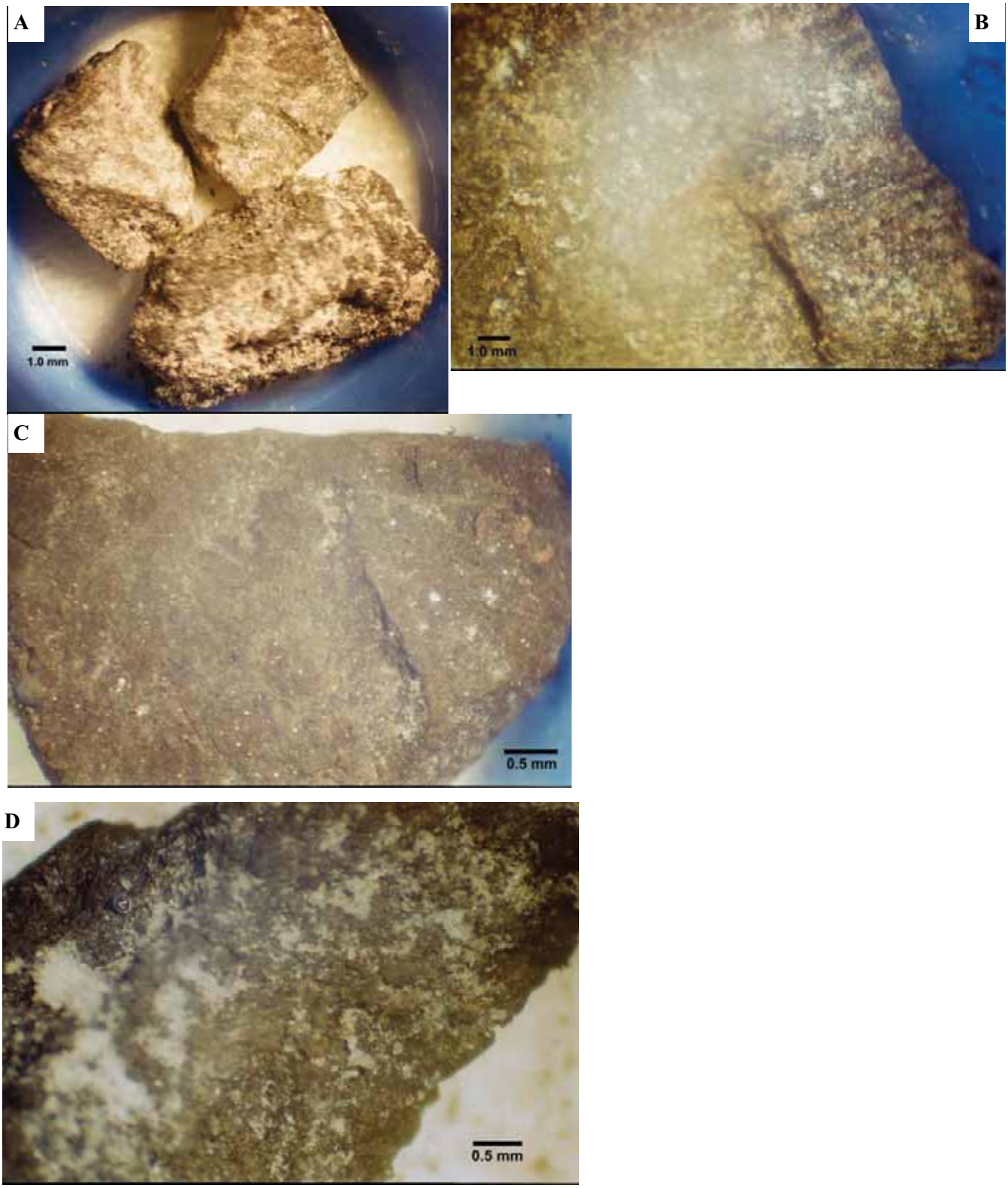

Binocular microscope images – Bridger Jack U #3 (Map #15), 5940-50 feet, C interval. A: (dry) three representative cuttings. B: (wet) close up of microporous microbialite showing stromatolitic microlaminae. C: (wet) peloidal dolomite with hints of parallel microfractures. D: (wet) peloidal black shale with white dolomite and anhydrite.

Binocular microscope image (wet) – Bridger Jack U #3 (Map #15), 5960-70 feet, C interval, representative dolomitic sample showing oncolites/pisolites(?).

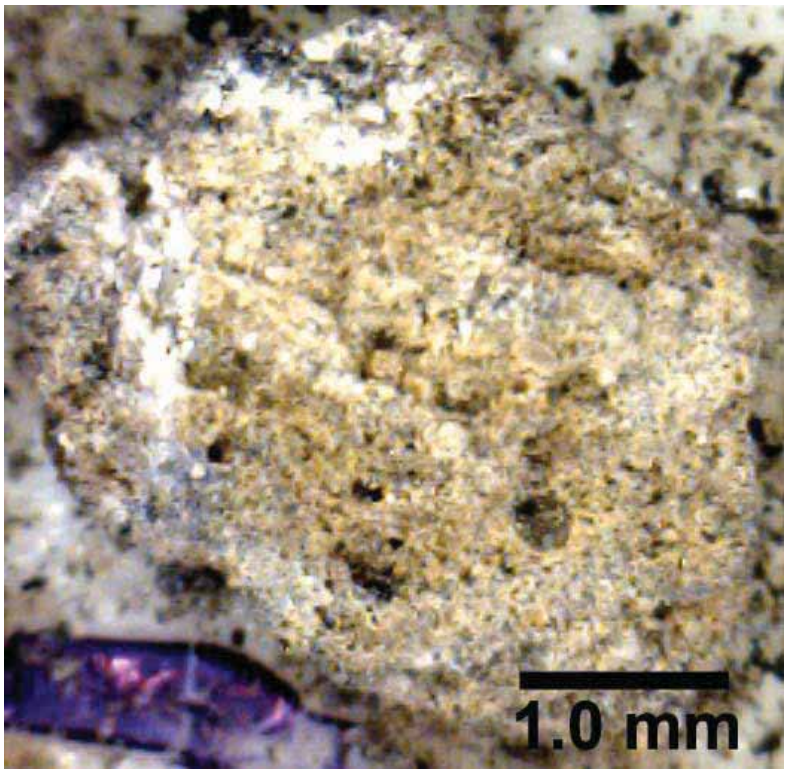

Digital microscope image (dry) – Cane Creek State #1-36 (Map #16), 7000-10 feet, A interval, very porous microbial dolomite. Note the visible pores between the constructional microbialite fabric network as well as the light brown oil staining.

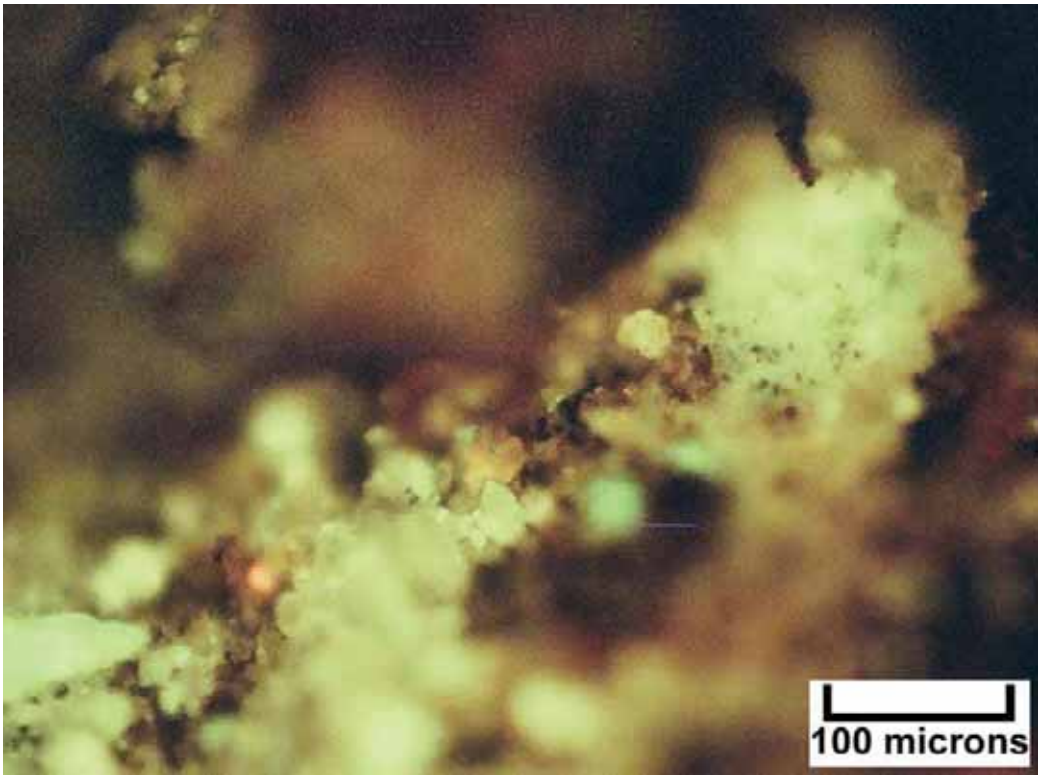

EF photomicrograph – Cane Creek State #1-36 (Map #16), 7000-10 feet, A interval, 2.8 visual epifluorescence rating in dolomitized microbialite with fluorescence in pore space surrounding dolomite crystals and microbial filaments.

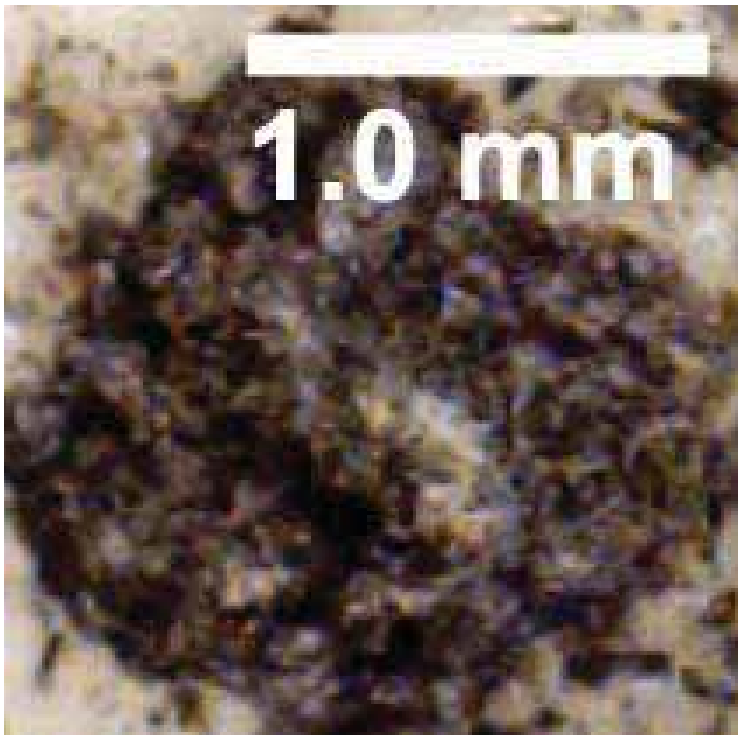

Digital microscope image (dry) – Cane Creek State #1-36 (Map #16), 7010-20 feet, A interval, silty dolomite with visible pores between the dolomite crystals. Black bitumen lines some of the pores.

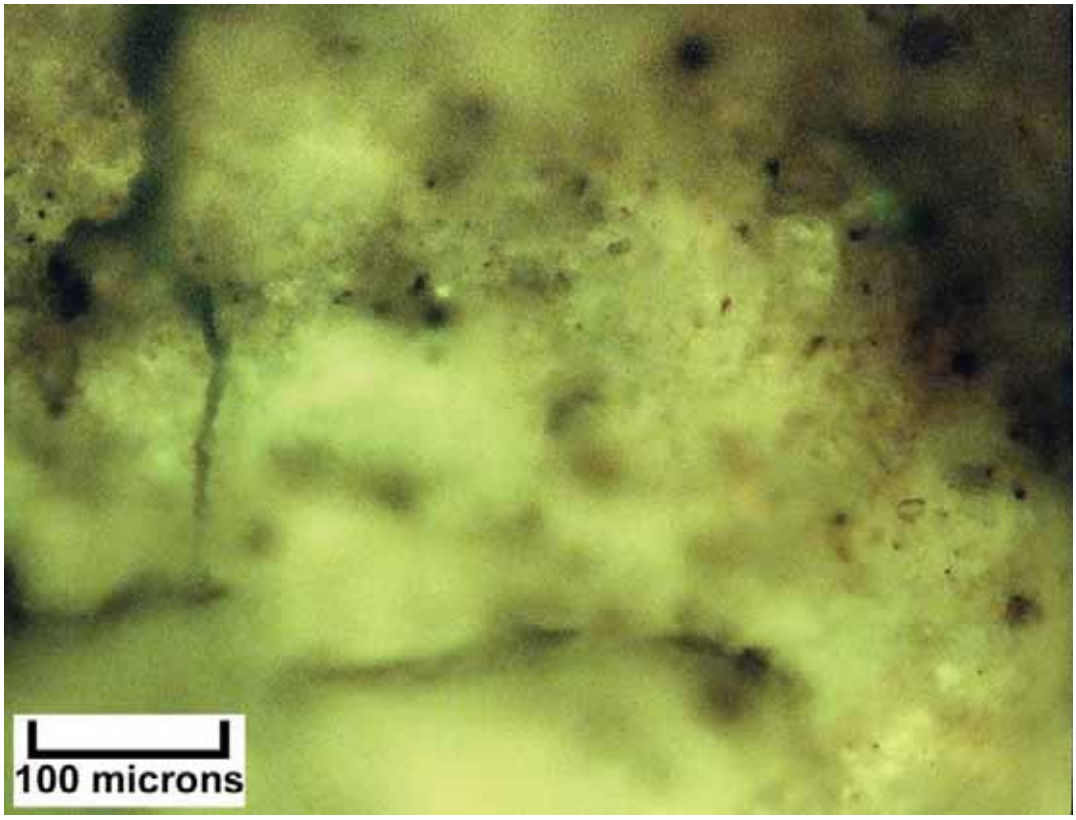

EF photomicrograph – Cane Creek State #1-36 (Map #16), 7010-20 feet, A interval, 2.9 visual epifluorescence rating in slightly dolomitic siltstone with excellent fluorescence between detrital silt grains and dolomite crystals.

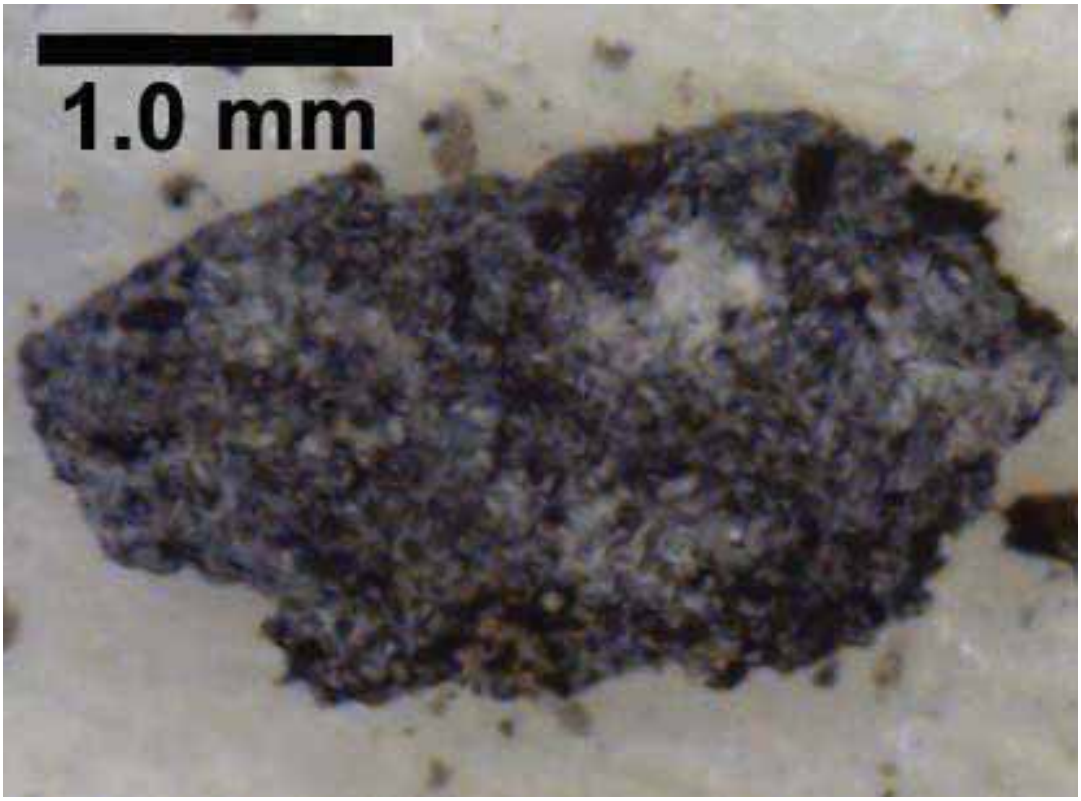

Digital microscope image (dry) – Cane Creek State #1-36 (Map #16), 7060-70 feet, C interval, dolomitic wackestone to packstone in which black bitumen appears to be present within the intercrystalline pores between dolomite crystals.

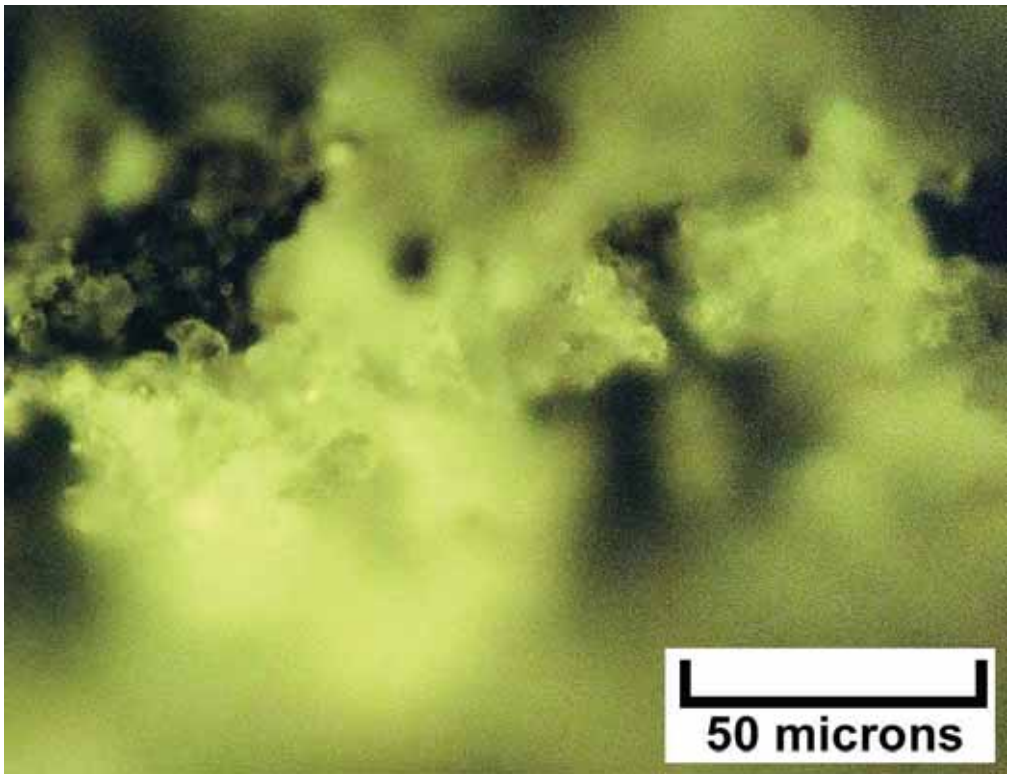

EF photomicrograph – Cane Creek State #1-36 (Map #16), 7060-70 feet, C interval, 2.3 visual epifluorescence rating in fine to medium dolomite with intercrystalline porosity, wackestone/packstone.

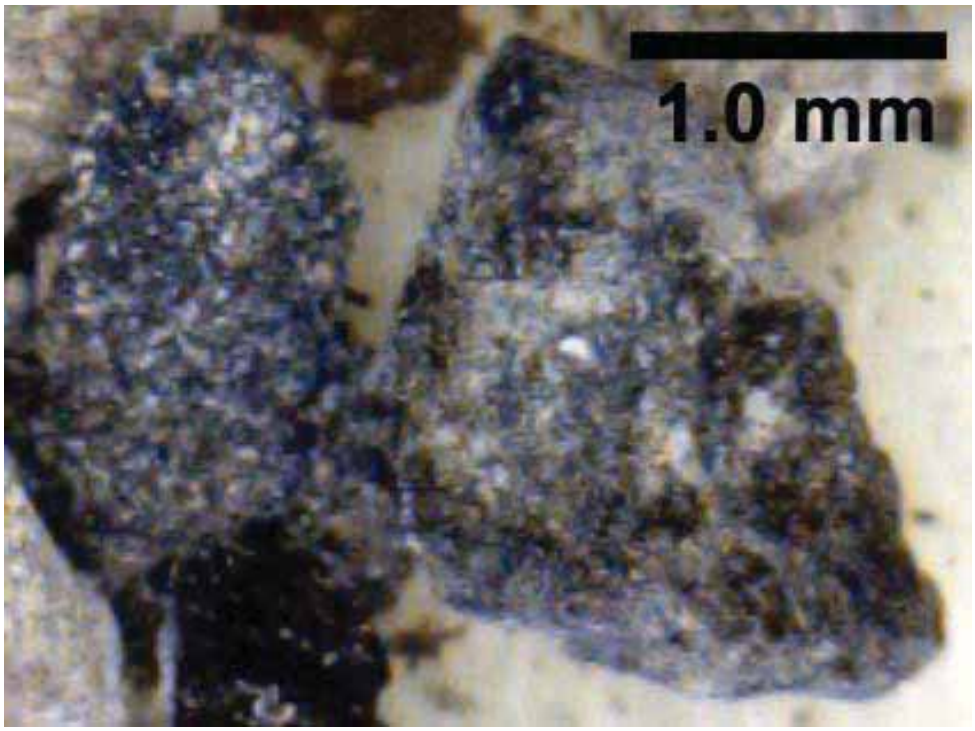

Digital microscope image (dry) – Cane Creek State #1-36 (Map #16), 7070-80 feet, C interval, pair of dark-colored dolomite cuttings from a porous microbialite interval. Note the abundant black bitumen that is present within the pore spaces of the microbial framework.

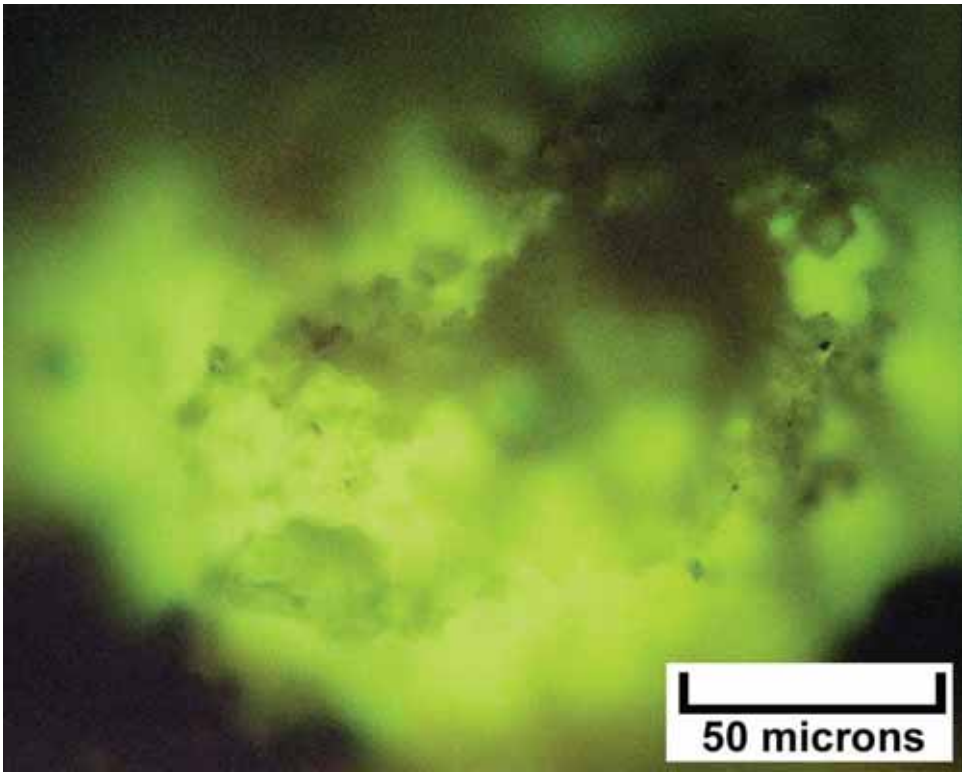

EF photomicrograph – Cane Creek State #1-36, (Map #16), 7070-80 feet, C interval, 2.1 visual epifluorescence rating in porous microcrystalline dolomite with excellent fluorescence in a possible microbial fabric.

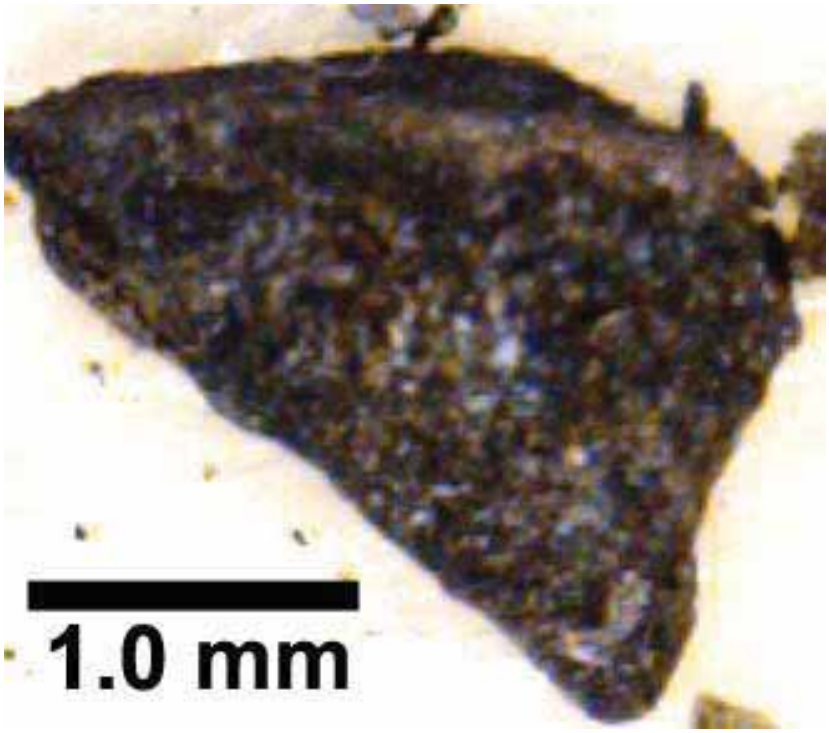

Digital microscope image (dry) – Cane Creek State #1-36 (Map 16), 7080-90 feet, C interval, dark-colored dolomite sample with hint of brown oil staining. Some of the black color is due to the presence of bitumen within the intercrystalline pore spaces.

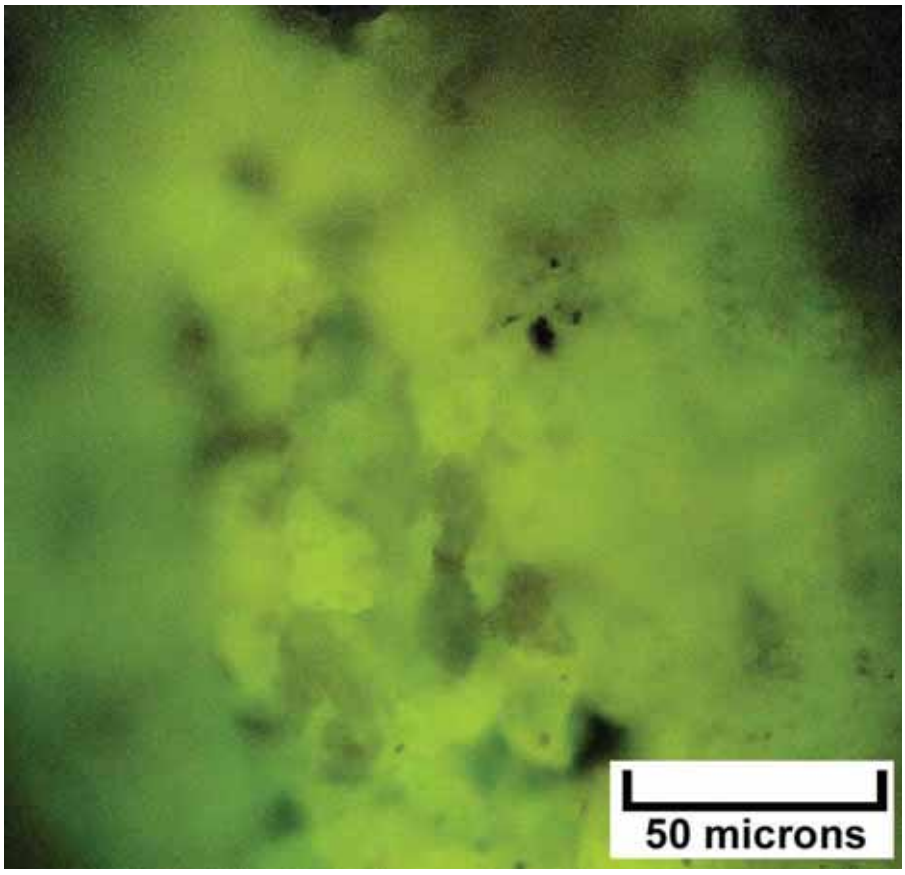

EF photomicrograph – Cane Creek State #1-36 (Map #16), 7080-90 feet, C interval, 2.6 visual epifluorescence rating in slightly silty dolomite with fine to medium crystals, good intercrystalline and moldic pore space, bright fluorescence.

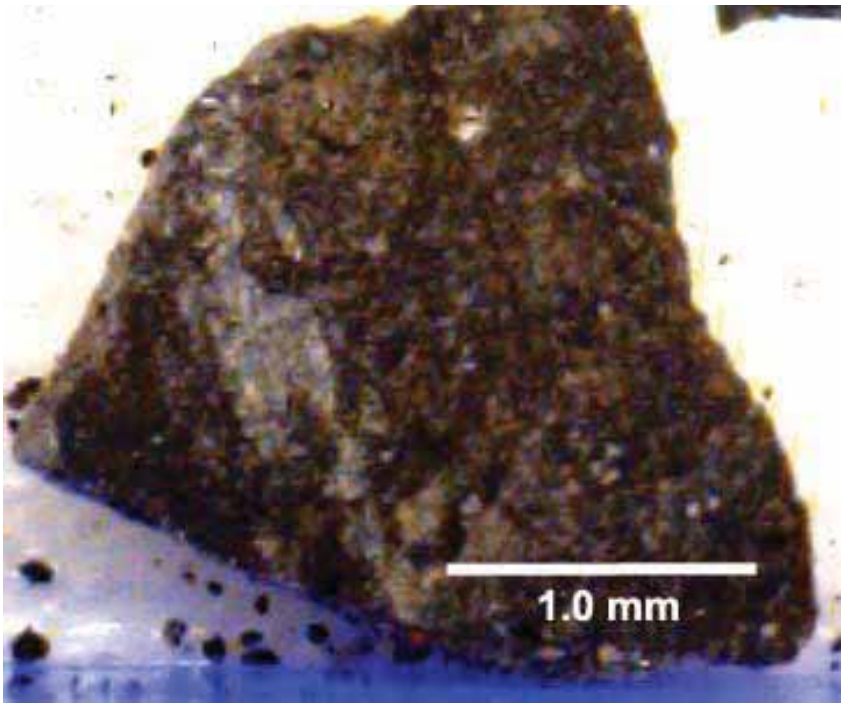

Digital microscope image (dry) – Red Rock Unit #1 (Map #17), 6850-60 feet, C interval, dolomite with medium to dark brown oil staining. A fine crystalline dolomite matrix does not contain silt grains. There appears to be some bitumen with the fine intercrystalline porosity along with the oil staining. An elongate white patch of probable anhydrite is present in the left center of this view.

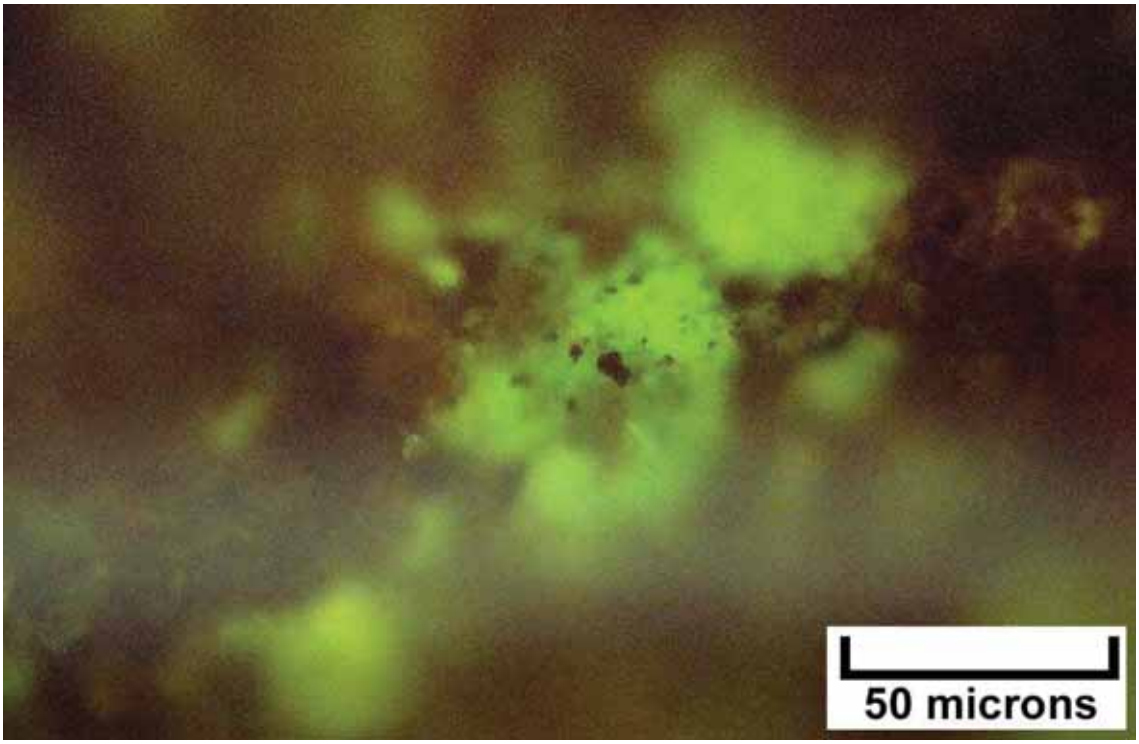

EF photomicrograph – Red Rock Unit #1 (Map #17), 6850-60 feet, C interval, 2.2 visual epifluorescence rating in medium crystalline dolomite with some interparticle porosity, possible packstone/grainstone.

Digital microscope image (dry) – Red Rock Unit #1 (Map #17), 6860-70 feet, C interval, two samples of silty dolomite are shown here. The upper sample is a light gray silty sample with probable anydritic cement as well as a patch of black bitumen. The lower sample appears to contain abundant black bitumen patches in the silty dolomite matrix.

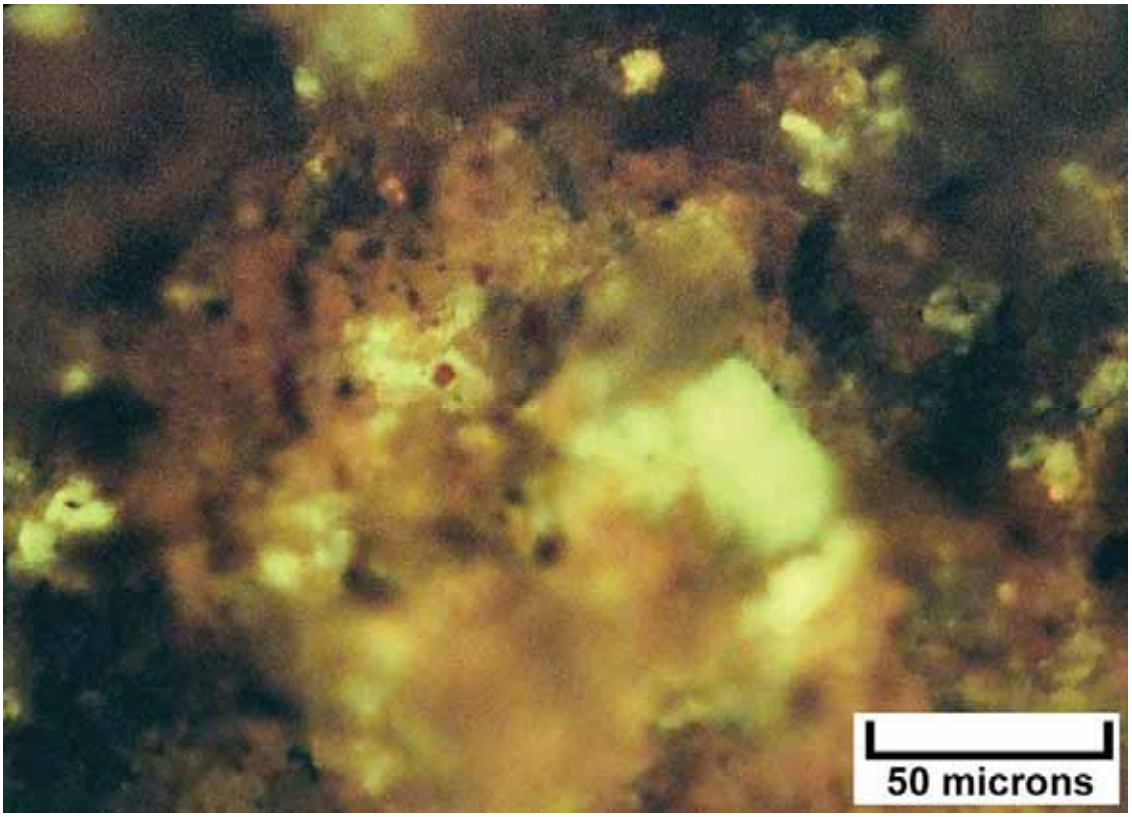

EF photomicrograph – Red Rock Unit #1 (Map #17), 6860-70 feet, C interval, 2.4 visual epifluorescence rating in dolomite with visible porosity associated with microbial fabric.

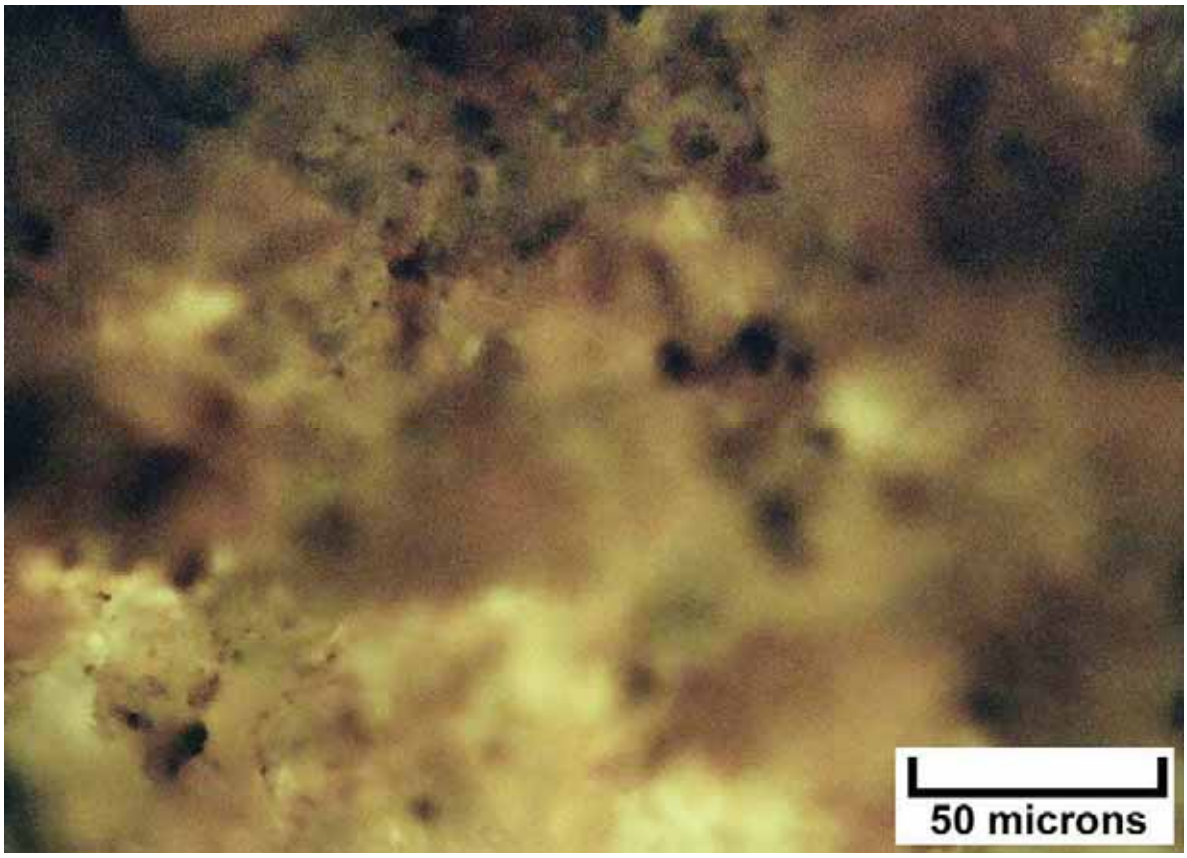

EF photomicrograph – Red Rock Unit #1 (Map #17), 6880-90 feet, C interval, 2.5 visual epifluorescence rating in dolomitic packstone/grainstone, fine to medium crystalline with possible visible porosity and opaque disseminated pyrite.

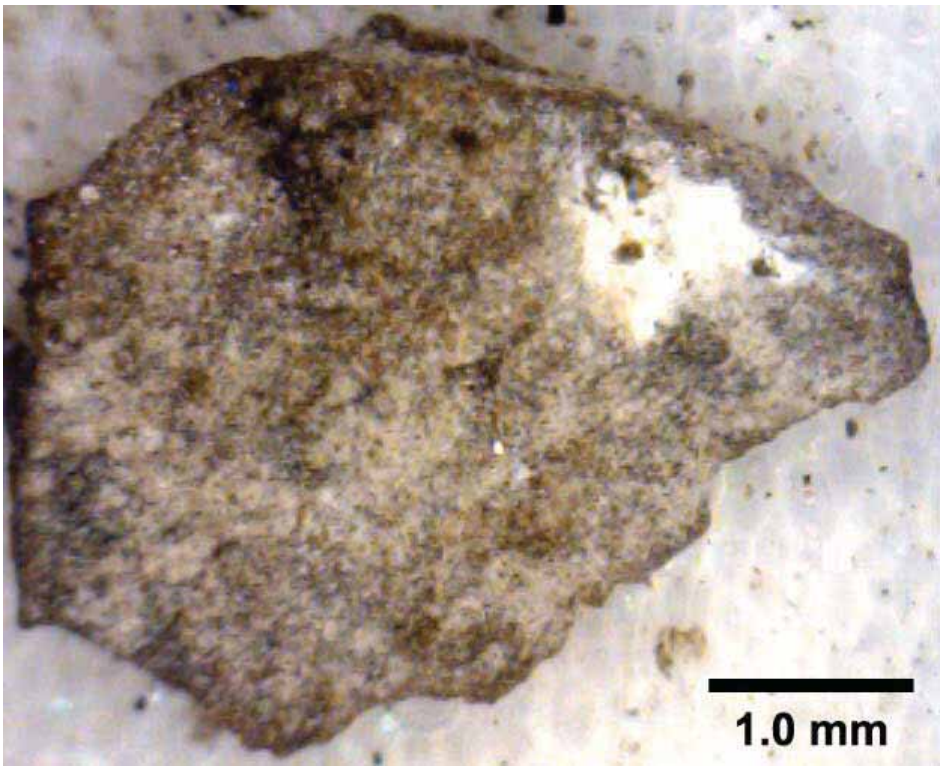

Digital microscope image (dry) – Lockhart Federal #1 (Map #18), 4765-70 feet, A interval, dolomite displaying light brown oil staining. Small, well-sorted grains (some skeletal and some coated grains) are visible within this porous dolomitized grainstone to packstone.

EF photomicrograph – Lockhart Federal #1 (Map #18), 4765-70 feet, A interval, 1.5 visual epifluorescence rating in dolomite crystal aggregate.

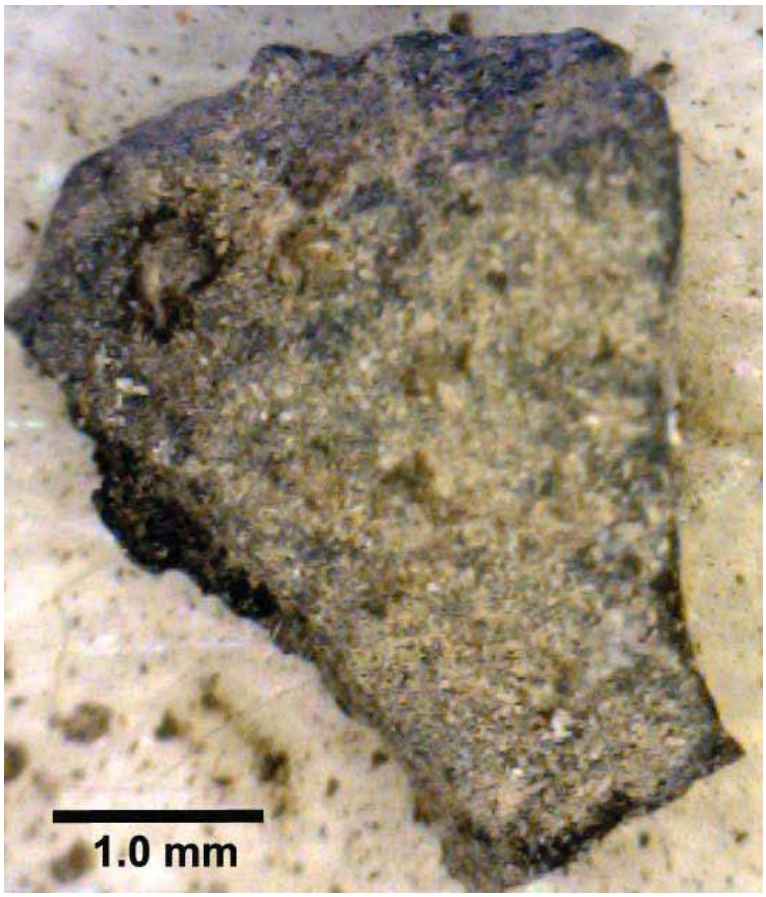

Digital microscope image (dry) – Lockhart Federal #1 (Map #18), 4780-85 feet, B interval, dolomite displaying patchy light brown oil staining. Grain outlines can be easily seen in this skeletal grainstone.

EF photomicrograph – Lockhart Federal #1 (Map #18), 4780-85 feet, B interval, 2.2 visual epifluorescence rating in crystalline dolomite with patchy good epifluorescence.

Digital microscope image (dry) – Lockhart Federal #1 (Map 18), 4785-90 feet, B interval, dolomite with patchy black bitumen concentrations as well as light brown oil staining within the matrix porosity. Possible organic (microbial?) structures or clots surrounded by carbonate grains can be seen in this sample.

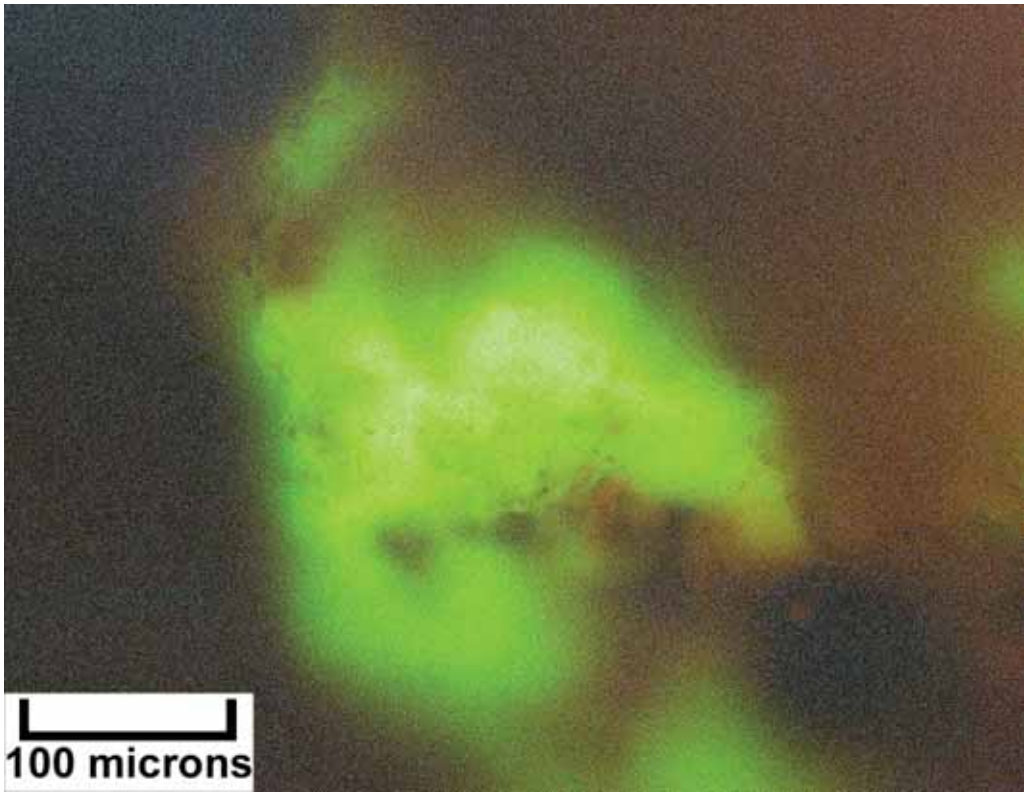

EF photomicrograph – Lockhart Federal #1 (Map #18), 4785-90 feet, B interval, 2.5 visual epifluorescence rating in anhydrite lathes and organic structures.

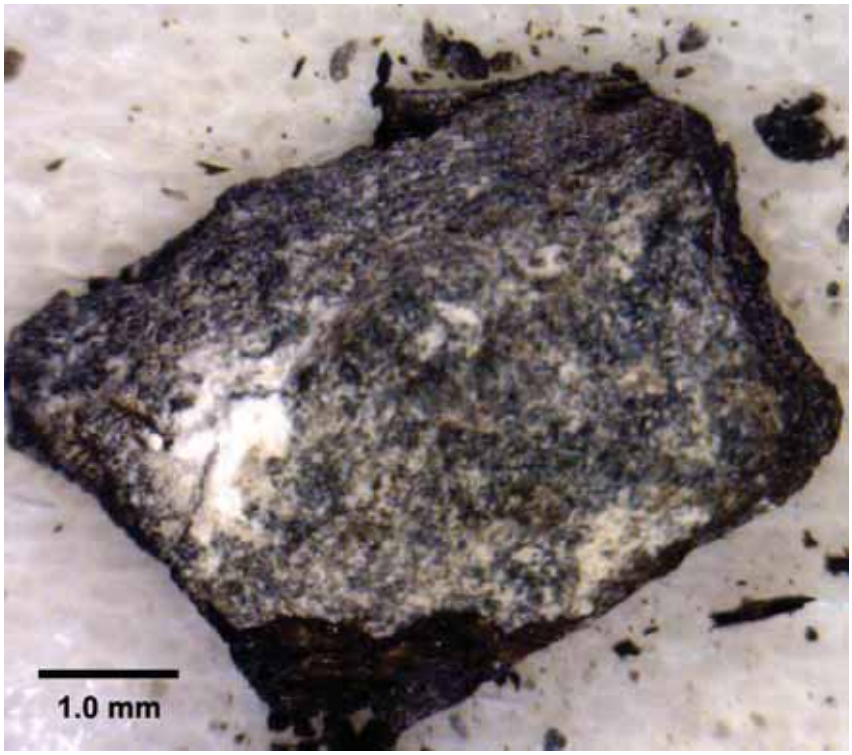

Digital microscope image (dry) – Lockhart Federal #1 (Map #18), 4800-10 feet, C interval, dolomite to silty dolomite with layered and possibly laminated microstructures. Note the black (bitumen-bearing) matrix with patchy dark brown oil staining. The white materials may be artifacts of anhydrite within the rock section.

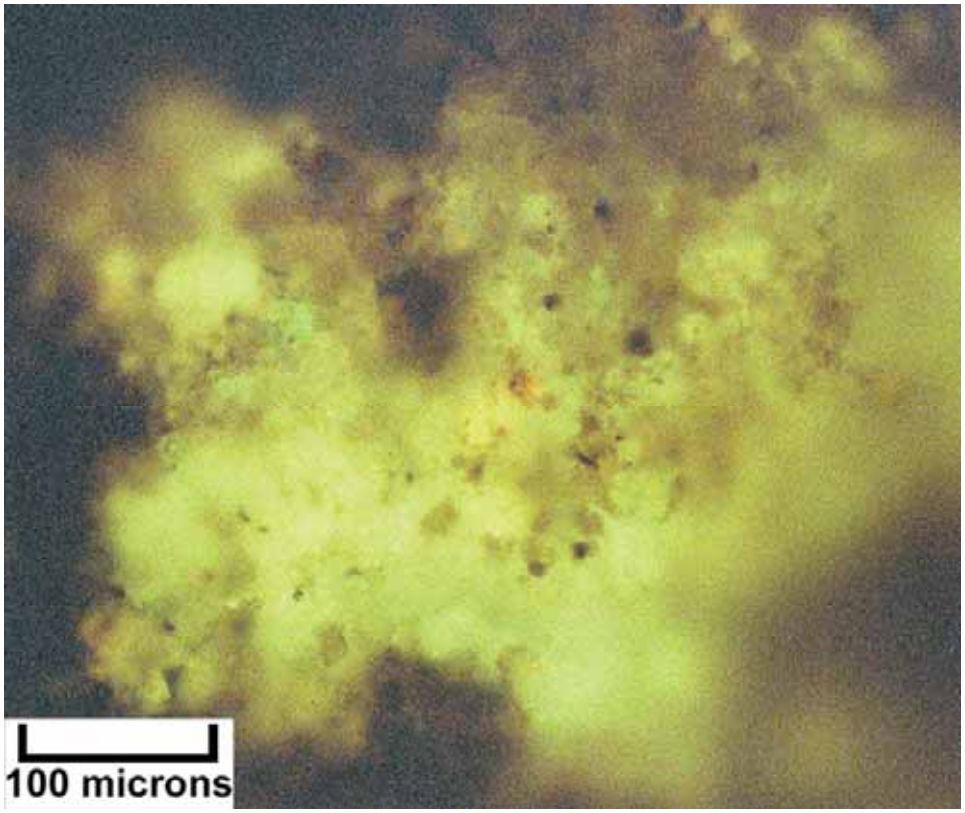

EF photomicrograph – Lockhart Federal #1 (Map #18), 4800-10 feet, C interval, 2.4 visual epifluorescence rating in fluorescing oil saturated dolomite.

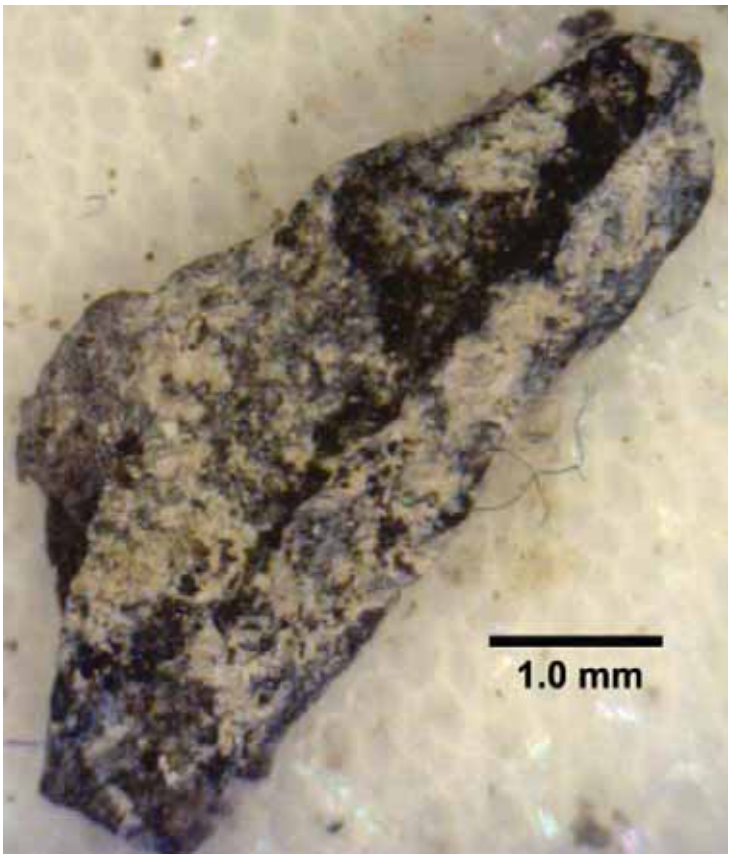

Digital microscope image (dry) – Lockhart Federal #1 (Map #18), 4815-20 feet, C interval, elongate sample composed of a dolomite to limy dolomite matrix. The linear nature of this cutting sample as well as the alignment of the black material (possibly bitumen) is probably indicative of a naturally fractured rock interval.

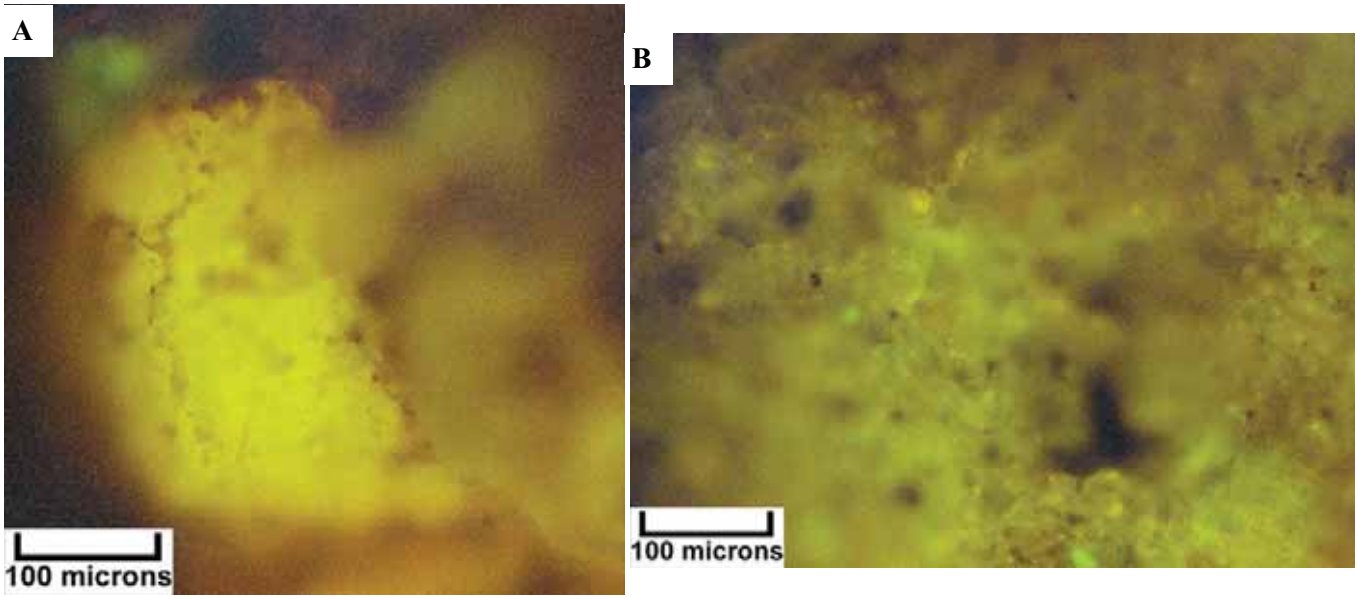

EF photomicrographs – Lockhart Federal #1 (Map #18), 4815-20 feet, C interval. A: 3.0 visual epifluorescence rating in fractured dolomite with live oil films. B: 3.0 visual epifluorescence rating in fractured dolomite with live oil films (same sample, different area on sample).

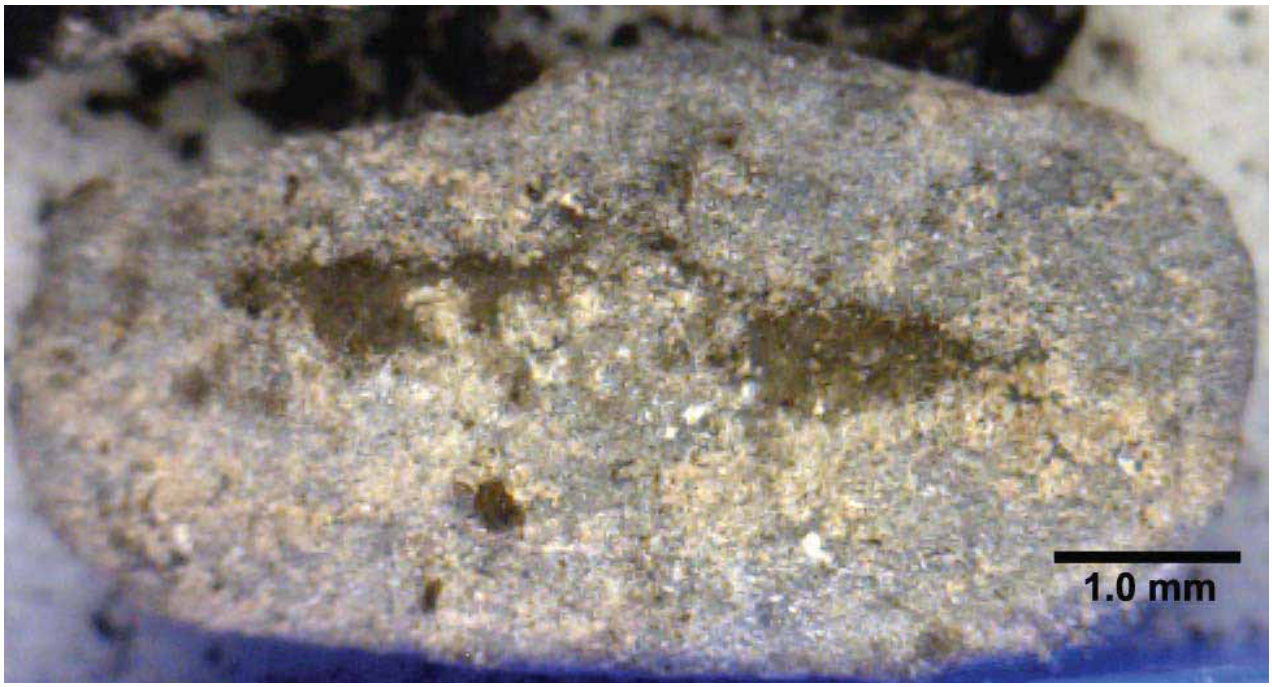

Digital microscope image (dry) – Government #B-1 (Map #20), 7565-75 feet, A interval, limy and silty dolomite with very small patches of possible light brown oil staining. Note the intersecting pair of linear fracture traces.

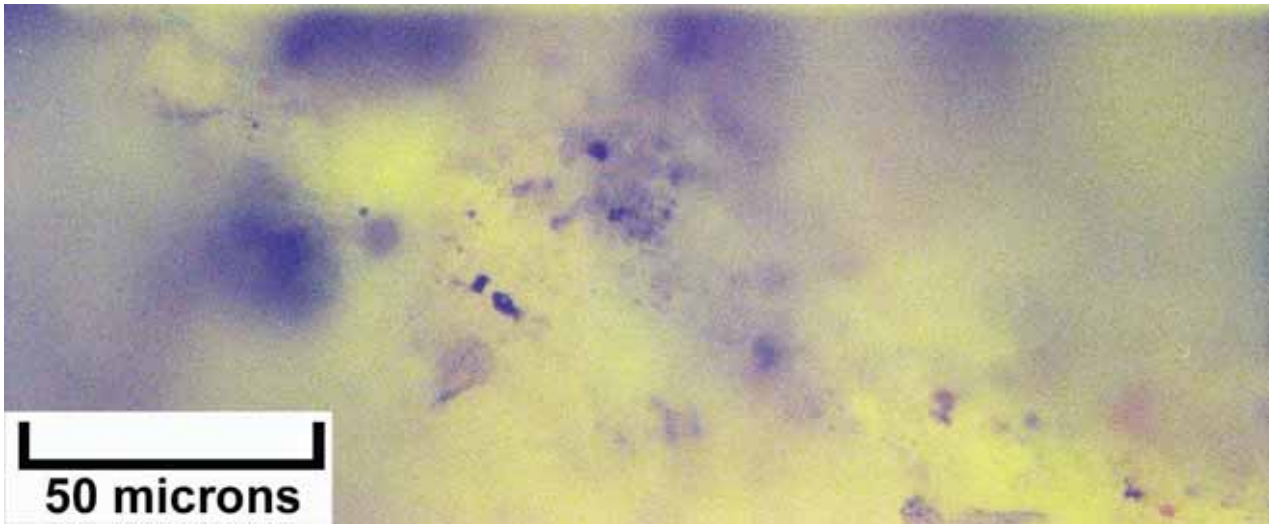

EF photomicrograph – Government #B-1 (Map #20), 7565-75 feet, A interval, 3.2 visual epifluorescence rating in microcrystalline dolomite, floating silt grains, very bright oil fluorescence.

Digital microscope image (dry) – Government #B-1 (Map #20), 7575-85 feet, A interval, portions of two cuttings samples of light-colored silty dolomite. Possible carbonate grains can also be seen among the silty matrix. Note the very light brown oil staining.

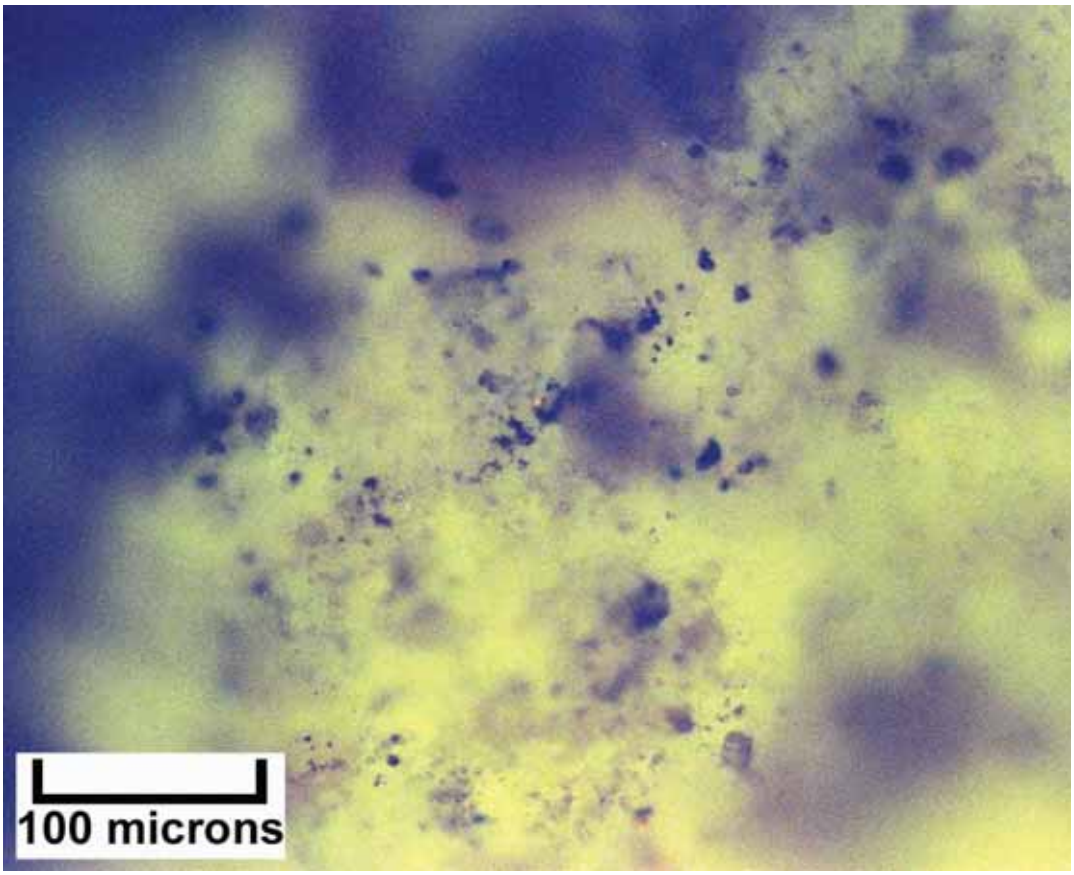

EF photomicrograph – Government #B-1 (Map #20), 7575-85 feet, A interval, 3.1 visual epifluorescence rating in finely crystalline dolomite, grainstone/packstone with occasional silt grains and disseminated pyrite, low visible porosity.

Digital microscope image (dry) – Government #B-1 (Map #20), 7610-20 feet, B interval, silty dolomite displaying a packstone texture as well as patchy light brown oil staining. Note the white concentration of probable salt (halite) and anhydrite. In addition, there are some small replacement pyrite crystals.

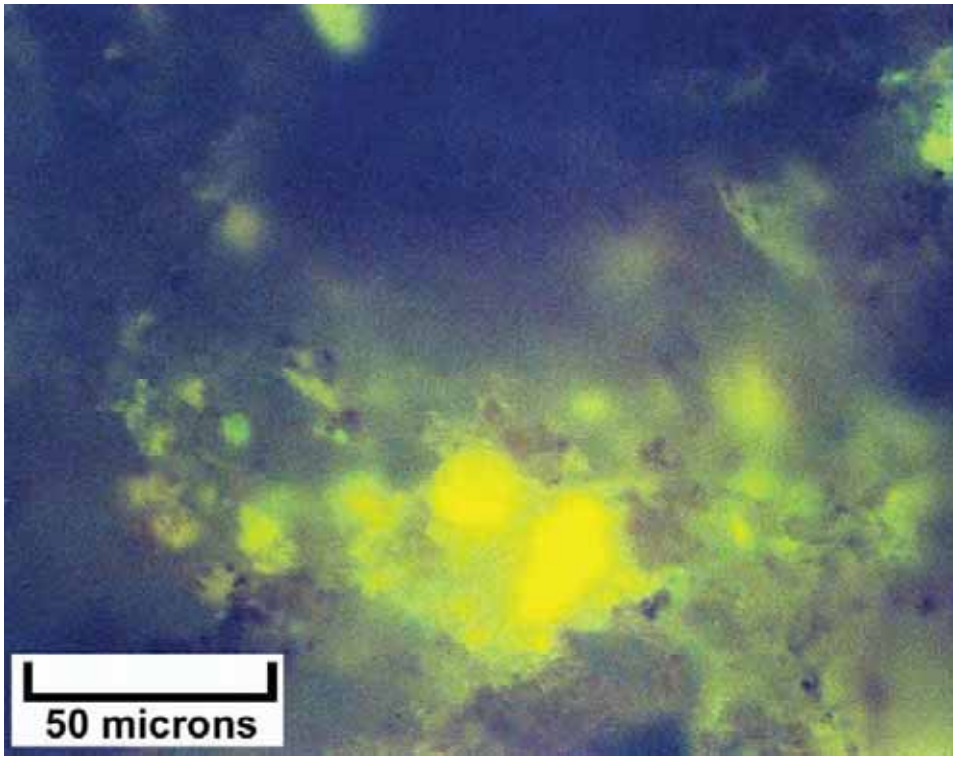

EF photomicrograph – Government #B-1 (Map #20), 7610-20 feet, B interval, 2.3 visual epifluorescence rating in medium crystalline dolomite, silty wackestone/ packstone with some possible salt plugging.

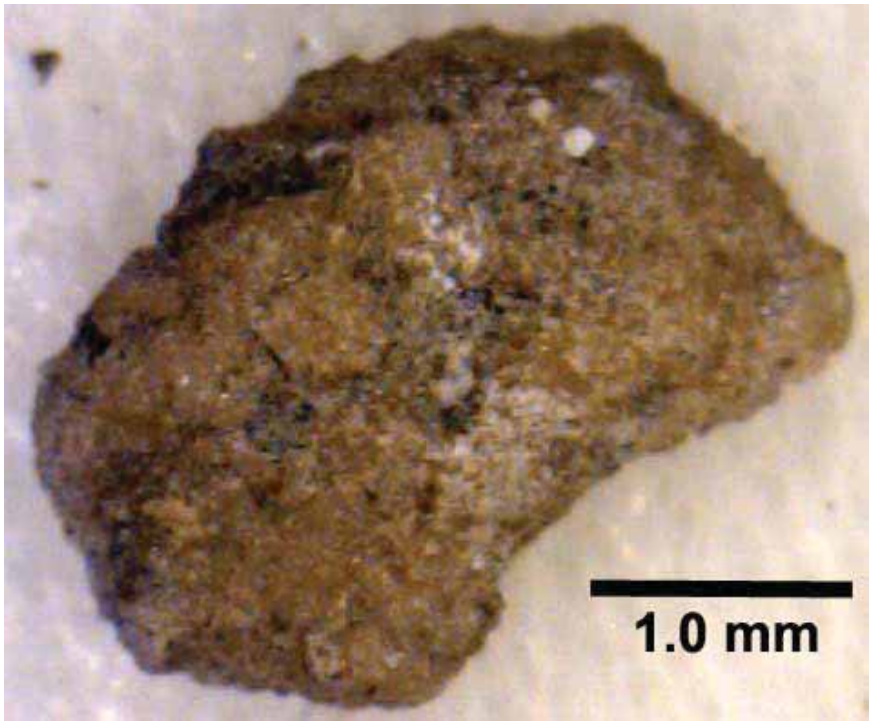

Digital microscope image (dry) – Government #B-1 (Map #20), 7640-50 feet, B interval, silty dolomite with medium brown oil staining. This packstone to wackestone contains "floating" carbonate grains in a muddy matrix as well as some pyrite.

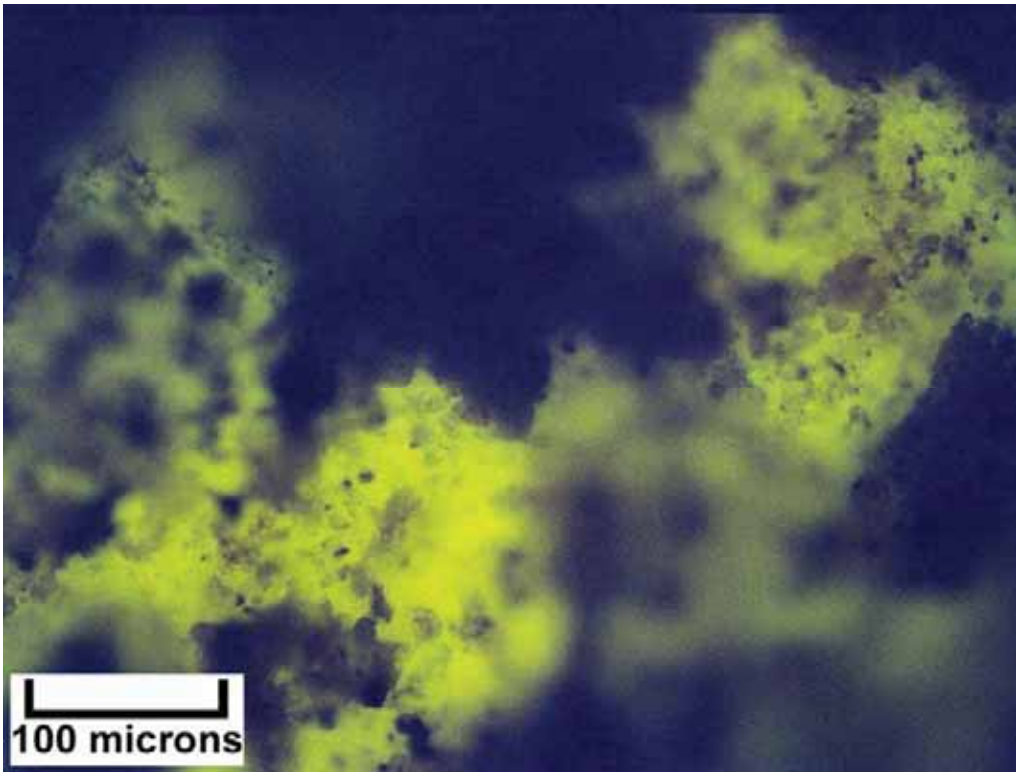

EF photomicrograph – Government #B-1 (Map #20), 7640-50 feet, B interval, 2.9 visual epifluorescence rating in silty microcrystalline dolomite, wackestone/packstone with bright fluorescence, possible anhydrite.

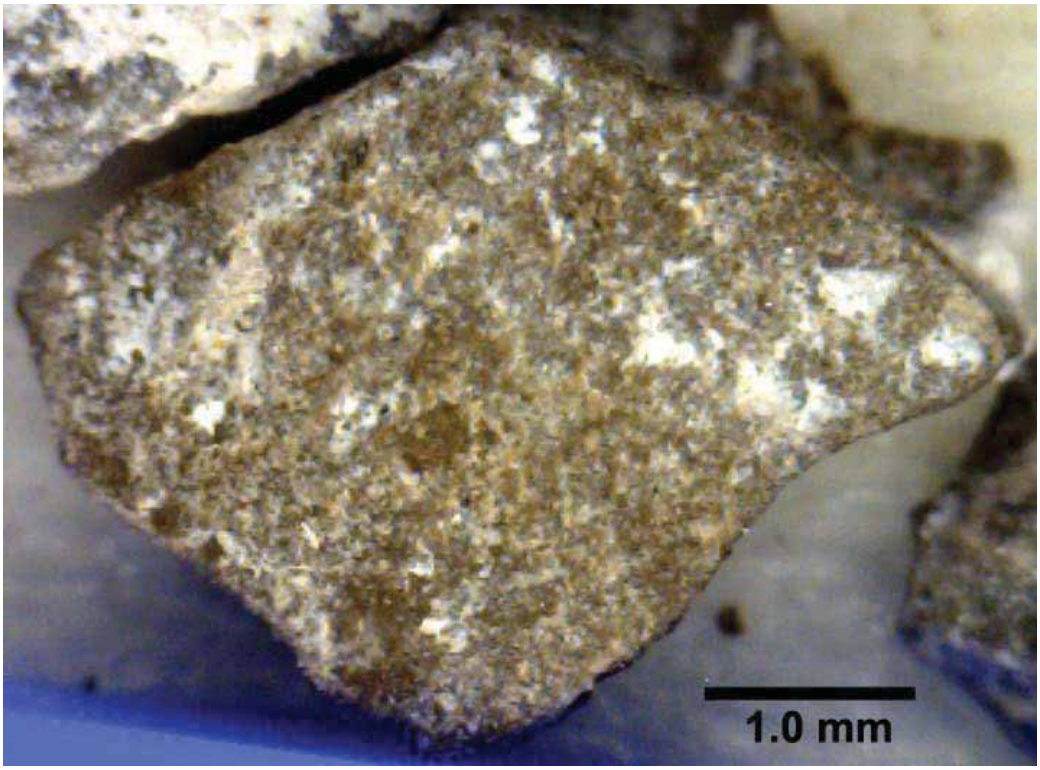

Digital microscope image (dry) – Government #B-1 (Map #20), 7670-80 feet, C interval, dolomite with patches of medium brown oil staining. This grainstone to packstone contains both small skeletal and non-skeletal grains.

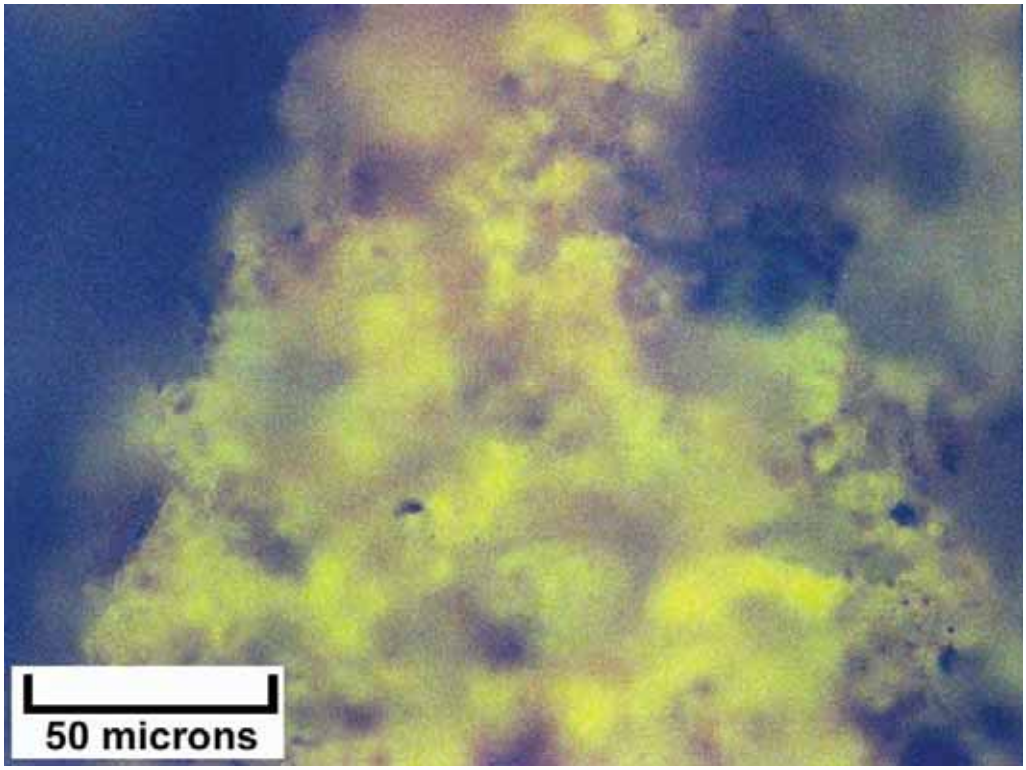

EF photomicrograph – Government #B-1 (Map #20), 7670-80 feet, C interval, 2.7 visual epifluorescence rating in silty medium crystalline dolomite with modest visible porosity, grainstone/packstone with bright fluorescence.

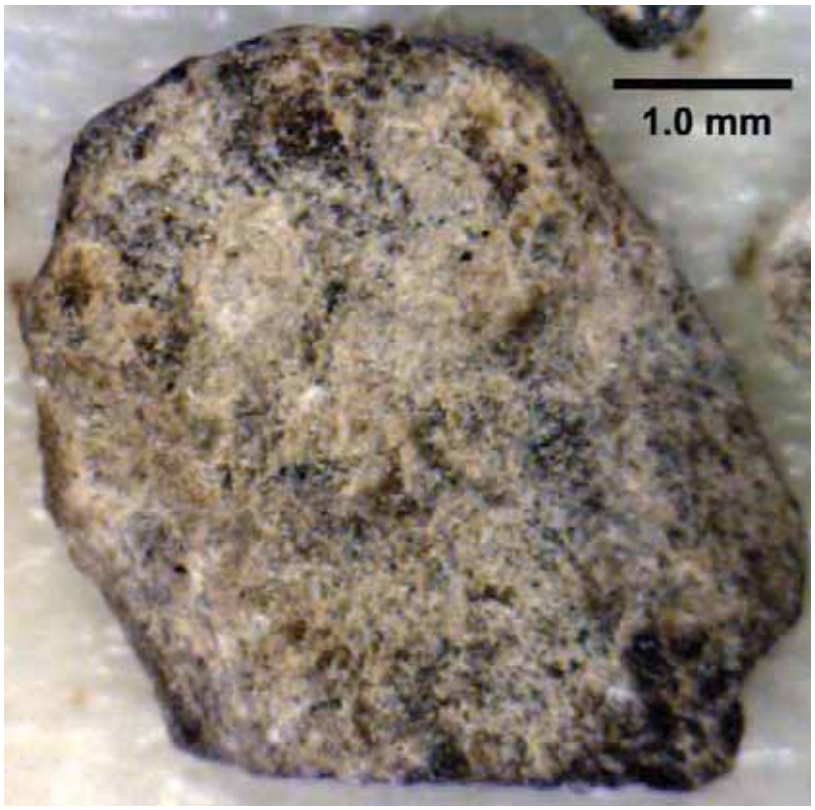

Digital microscope image (dry) – Government #B-1 (Map #20), 7710-20 feet, C interval, dolomite with porosity partially filled with black bitumen.

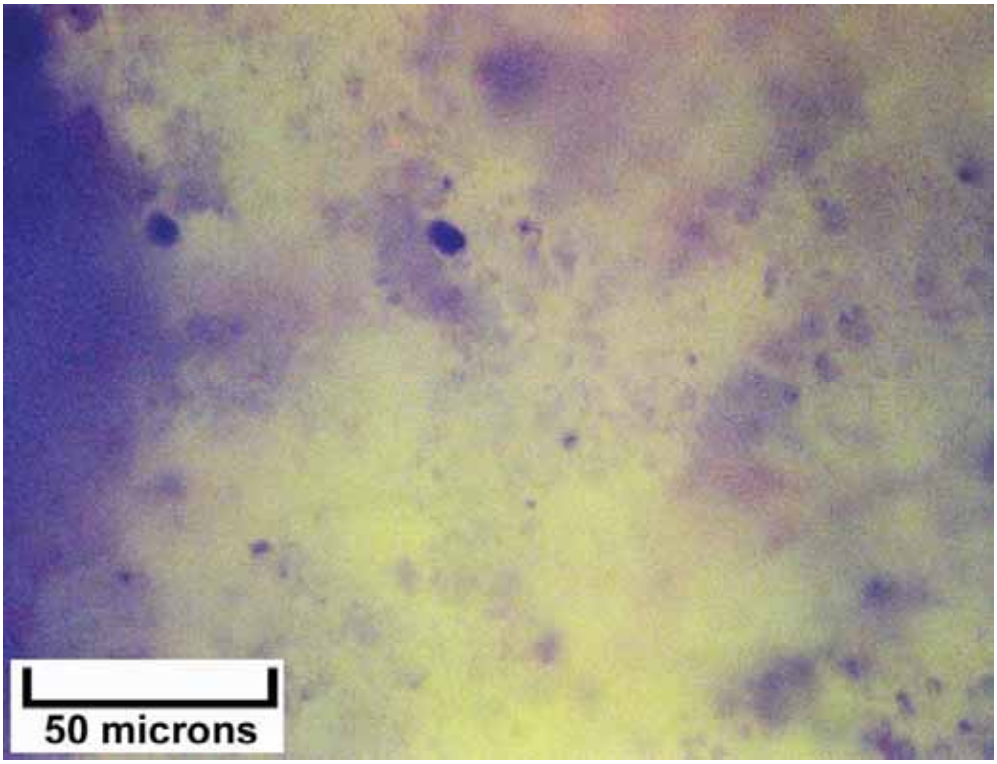

EF photomicrograph – Government #B-1 (Map #20), 7710-20 feet, C interval, 2.9 visual epifluorescence rating in fine to medium crystalline dolomite, packstone/grainstone, low visible porosity, probable microporosity, with very bright fluorescence.

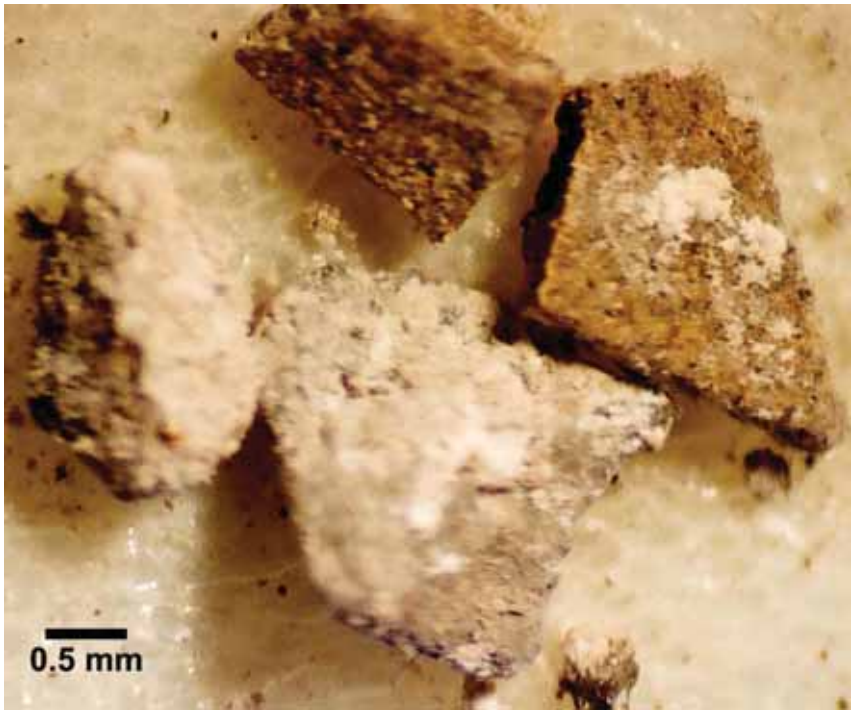

Binocular microscope image (wet) – Horsehead Unit #1 (Map #21), 6290-6300 feet, A interval, slightly dolomitic shale with abundant sulfides.

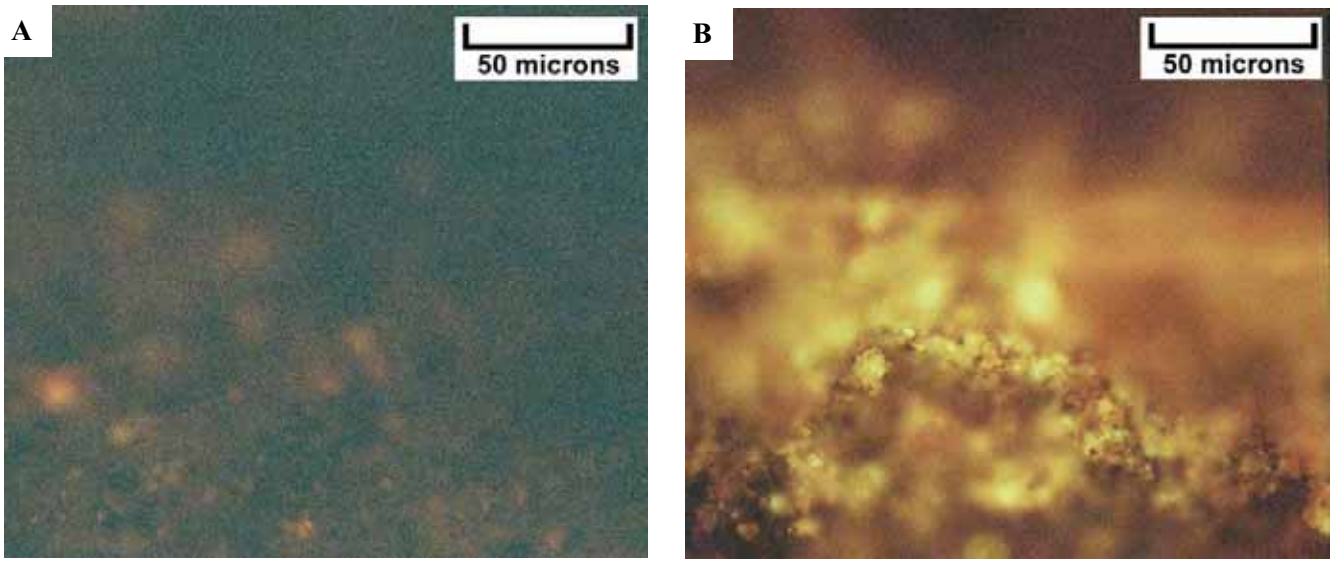

EF photomicrographs – Horsehead Unit #1 (Map #21), 6290-6300 feet, A interval, 0.7 visual epifluorescence rating (A) and 1.3 visual epifluorescence rating (B) in dolomitic shale to silty dolomitic shale.

Binocular microscope image (dry) – Horsehead Unit #1 (Map #21), 6300-10 feet, A interval, mostly dark brown to dark gray shale with minor amount of dark brown microcrystalline dolomite.

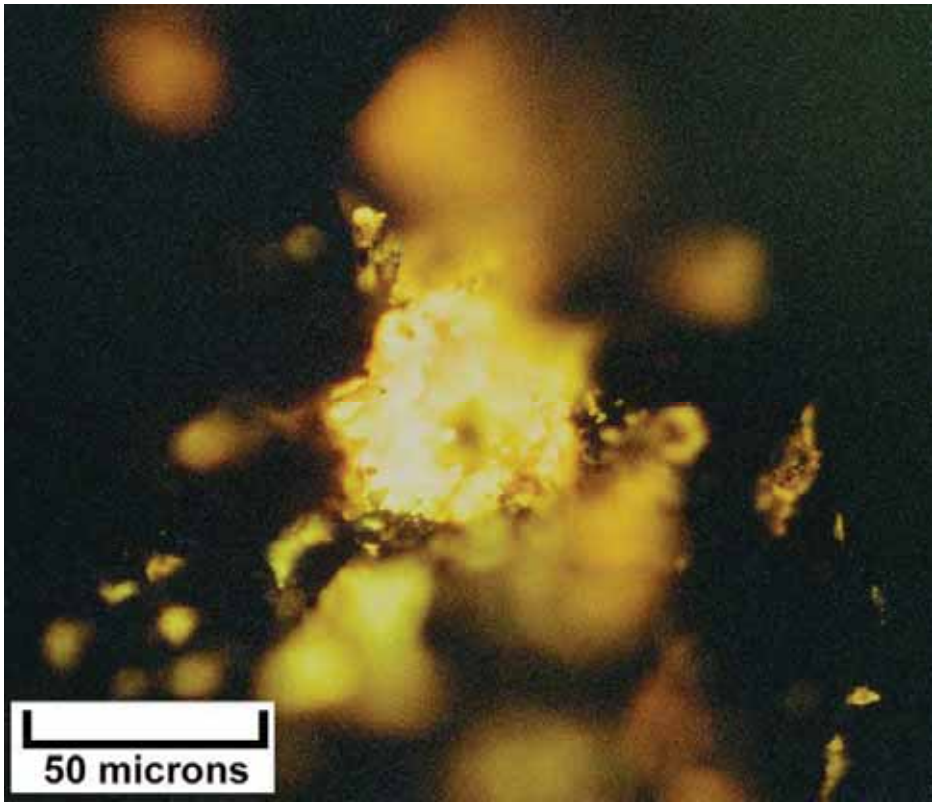

EF photomicrograph – Horsehead Unit #1 (Map #21), 6300-10 feet, A interval, 1.7 visual epifluorescence rating in dolomitic shale, slightly silty.

Binocular microscope image (dry) – Horsehead Unit #1 (Map #21), 6310-20 feet, B interval, mostly dark gray shale with minor amount of microcrystalline dolomite.

EF photomicrograph – Horsehead Unit #1 (Map #21), 6310-20 feet, B interval, 1.7 visual epifluorescence rating in dolomitic shale to silty shale.

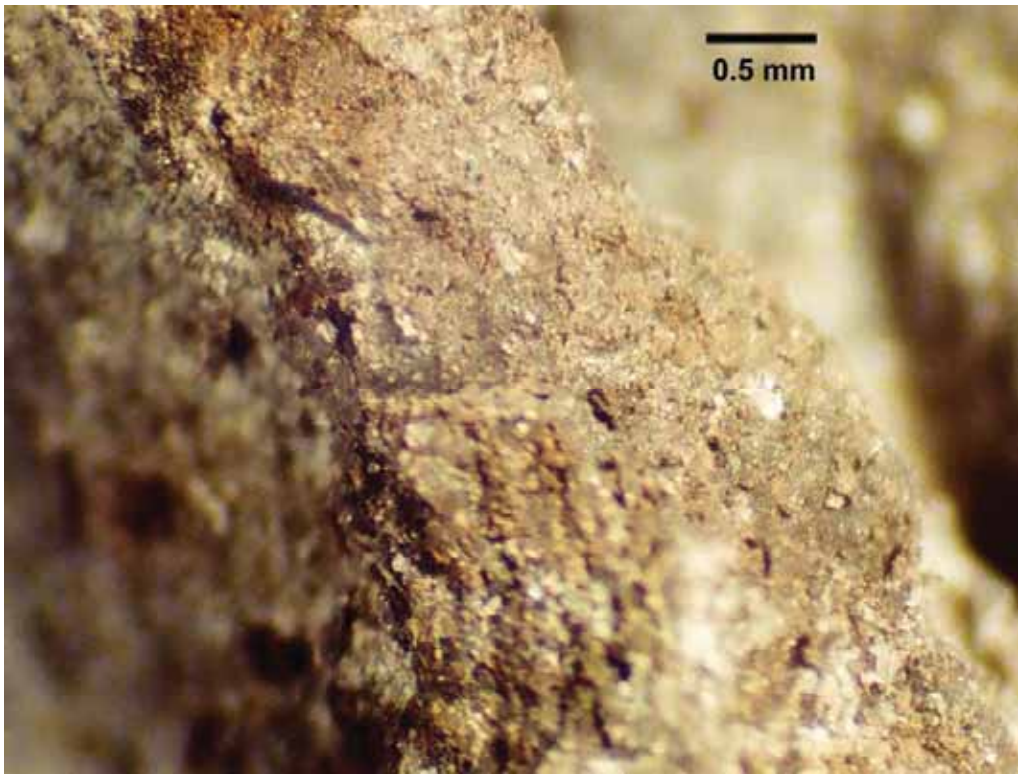

Binocular microscope image (dry) – Horsehead Unit #1 (Map #21), 6320-30 feet, B interval, microcrystalline dolomite with microporosity and light brown oil staining.

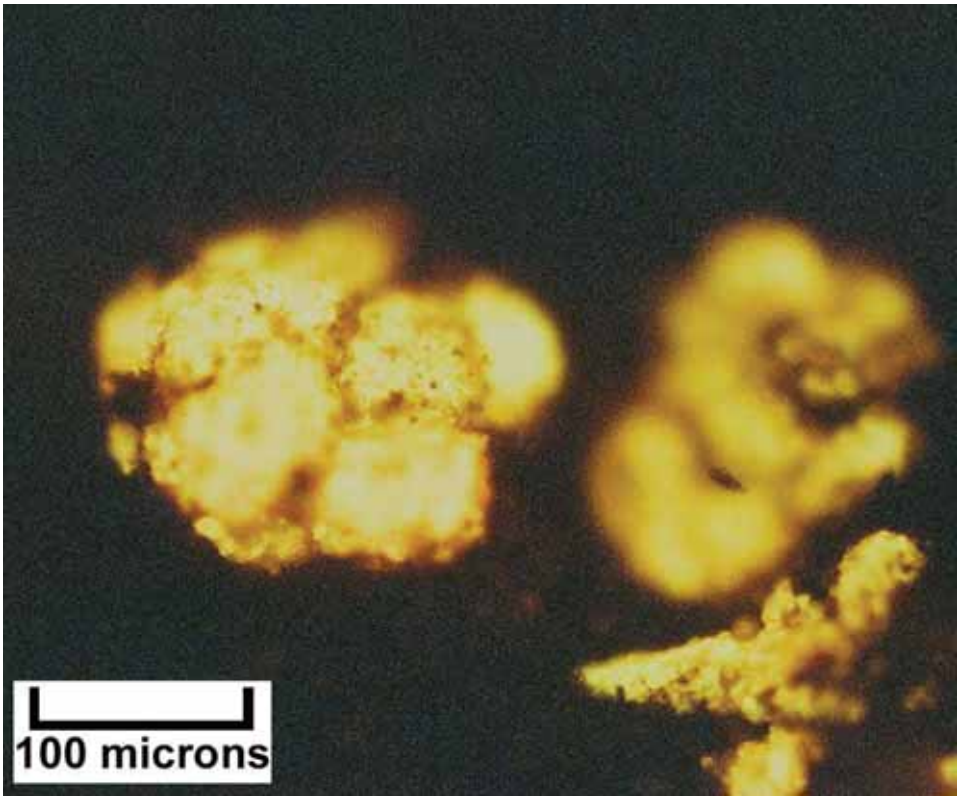

EF photomicrograph – Horsehead Unit #1 (Map #21), 6320-30 feet, B interval, 2.2 visual epifluorescence rating in microcrystalline dolomite with microporosity and probable oil saturation plus saline minerals (anhydrite or halite).

Binocular microscope image (wet) – Horsehead Unit #1 (Map #21), 6330-40 feet, B interval, 50% microcrystalline dolomite, bioturbated, either highly organic or oil saturated, 50% slightly dolomitic shale.

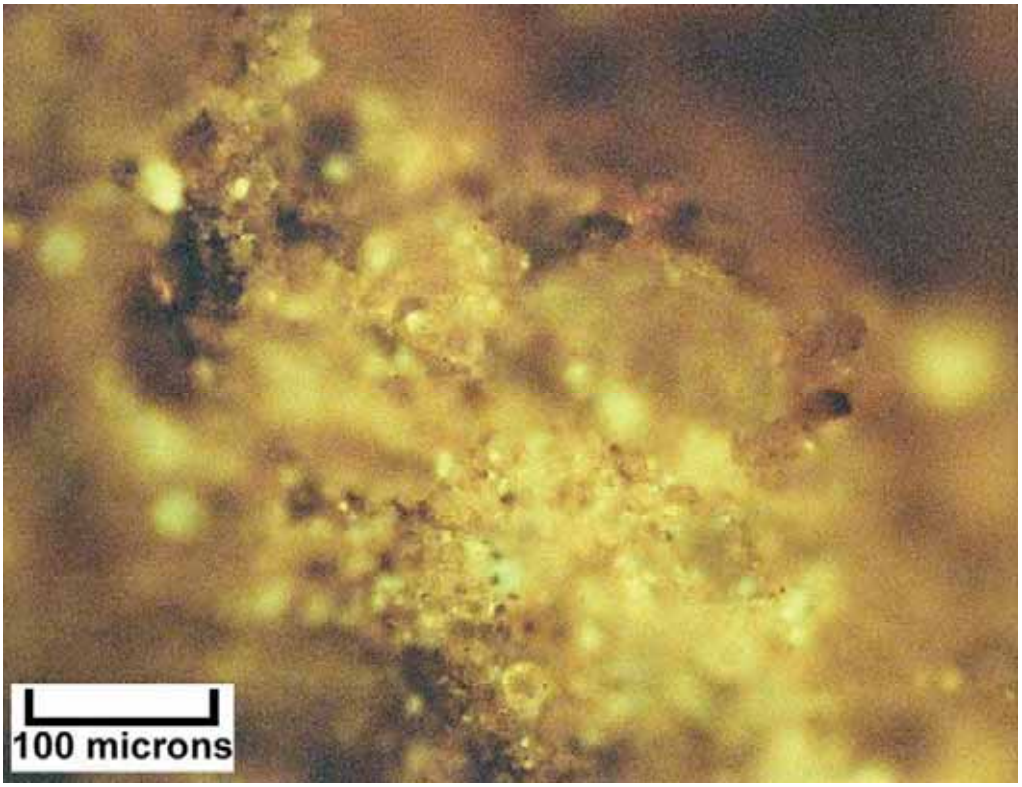

EF photomicrograph – Horsehead Unit #1 (Map #21), 6330-40 feet, B interval, 3.0 visual epifluorescence rating in dolomite and dolomitic shale.

Binocular microscope image (dry) – Horsehead Unit #1 (Map #21), 6340-50 feet, B interval, mostly highly organic black to dark gray shale with isolated patches or small nodes of incipient dolomite forming as replacement of phosphatic pellets.

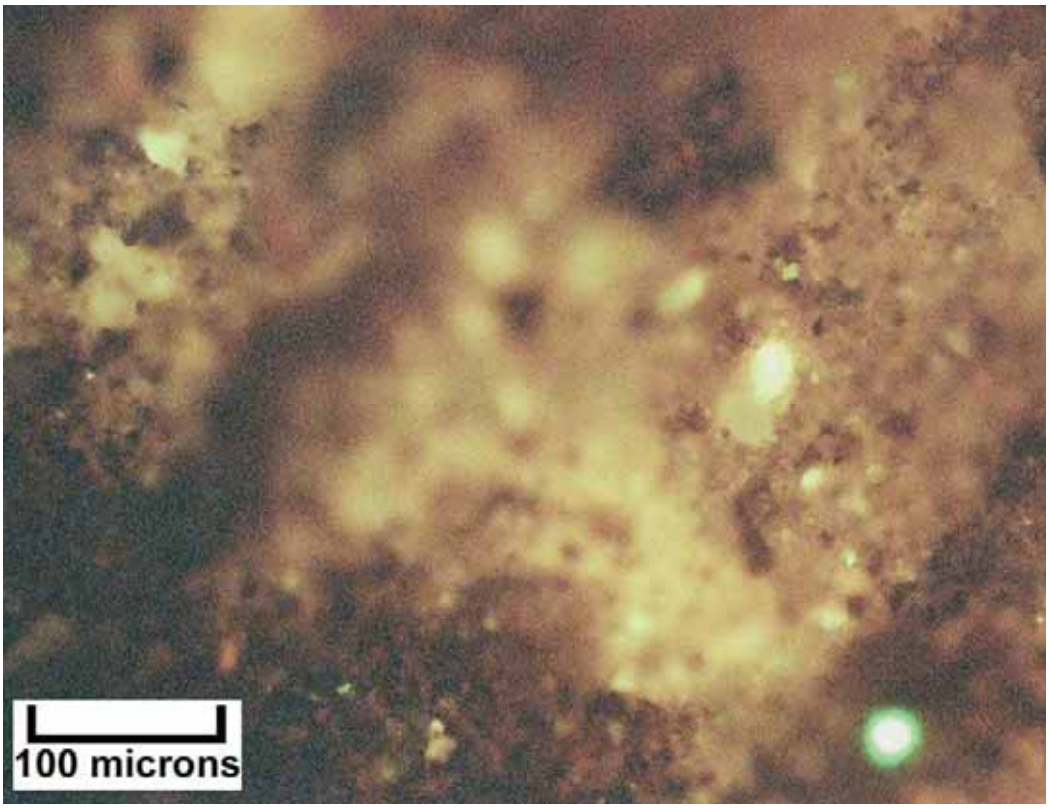

EF photomicrograph – Horsehead Unit #1 (Map #21), 6340-50 feet, B interval, 1.8 visual epifluorescence rating in shale and highly dolomitic shale.

A

B

Binocular microscope images (A: dry, B: wet) – Horsehead Unit #1 (Map #21), 6350-60 feet, C interval, representative peloidal black organic shale, non-laminated.

Binocular microscope image (wet) – Horsehead Unit #1 (Map #21), 6360-70 feet, C interval, peloidal, partially dolomitized organic shale.

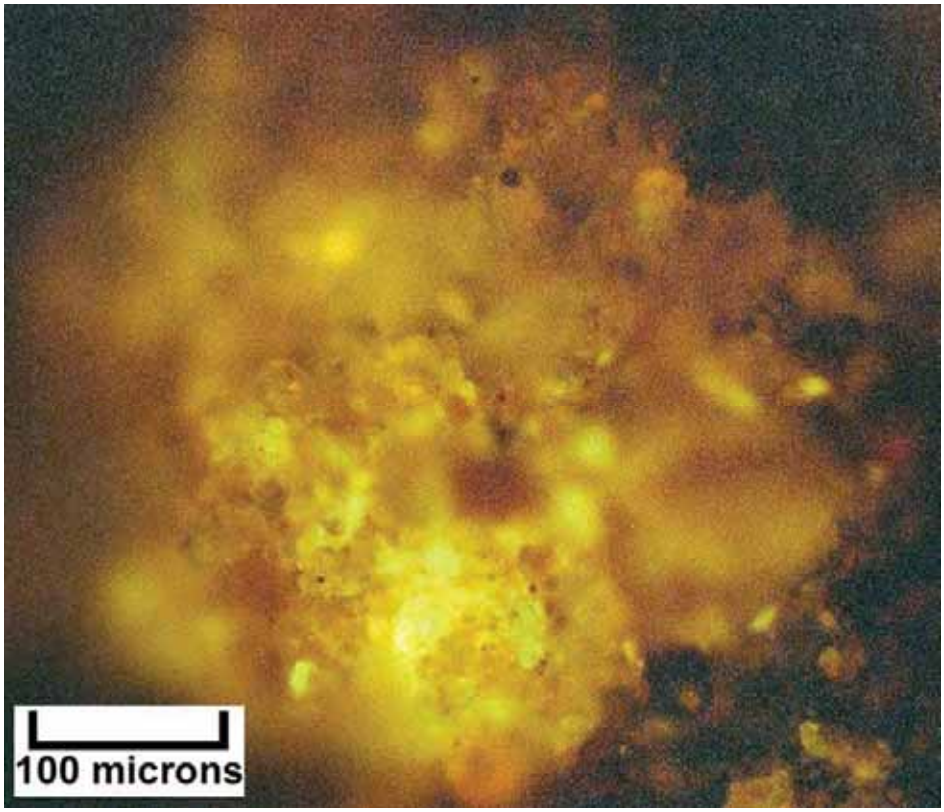

EF photomicrograph – Horsehead Unit #1 (Map #21), 6360-70 feet, C interval, 2.0 visual epifluorescence rating in mostly organic shale, slightly dolomitic.

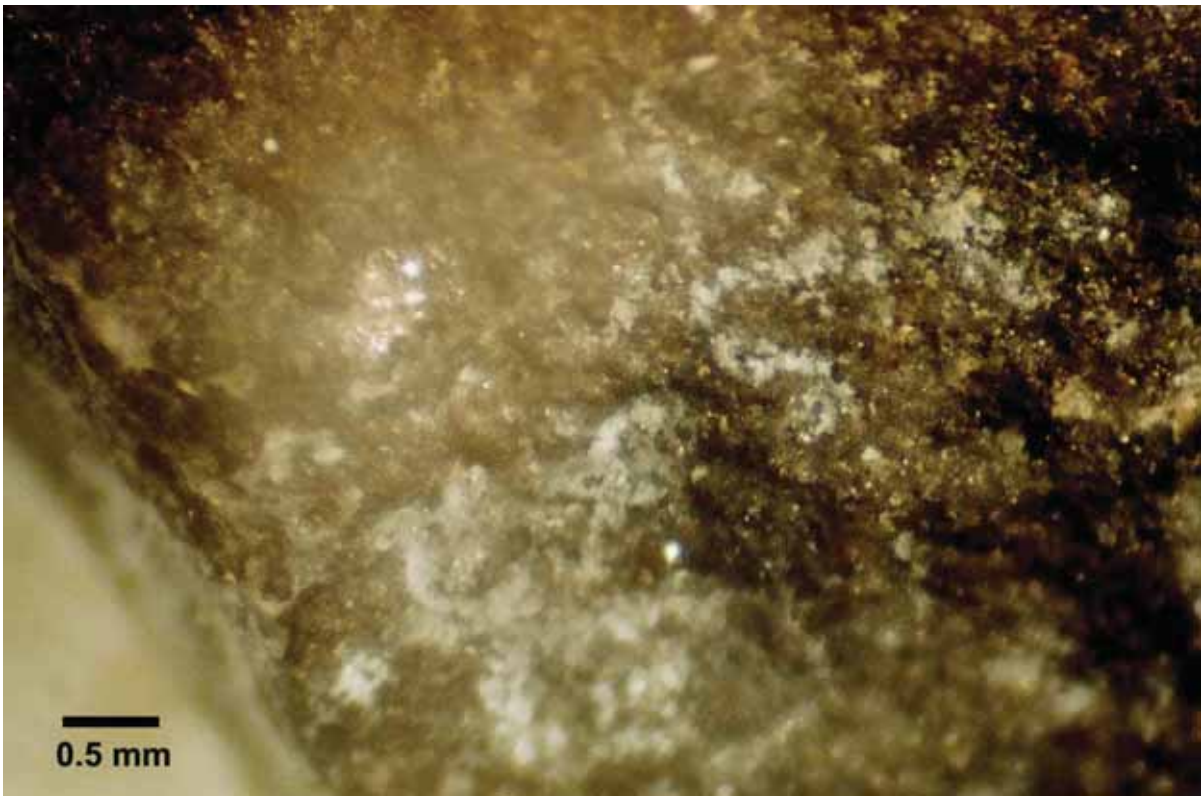

Binocular microscope image (wet and etched) – Horsehead Unit #1 (Map #21), 6370-80 feet, C interval, microcrystalline brown dolomite with micropeloidal fabric.

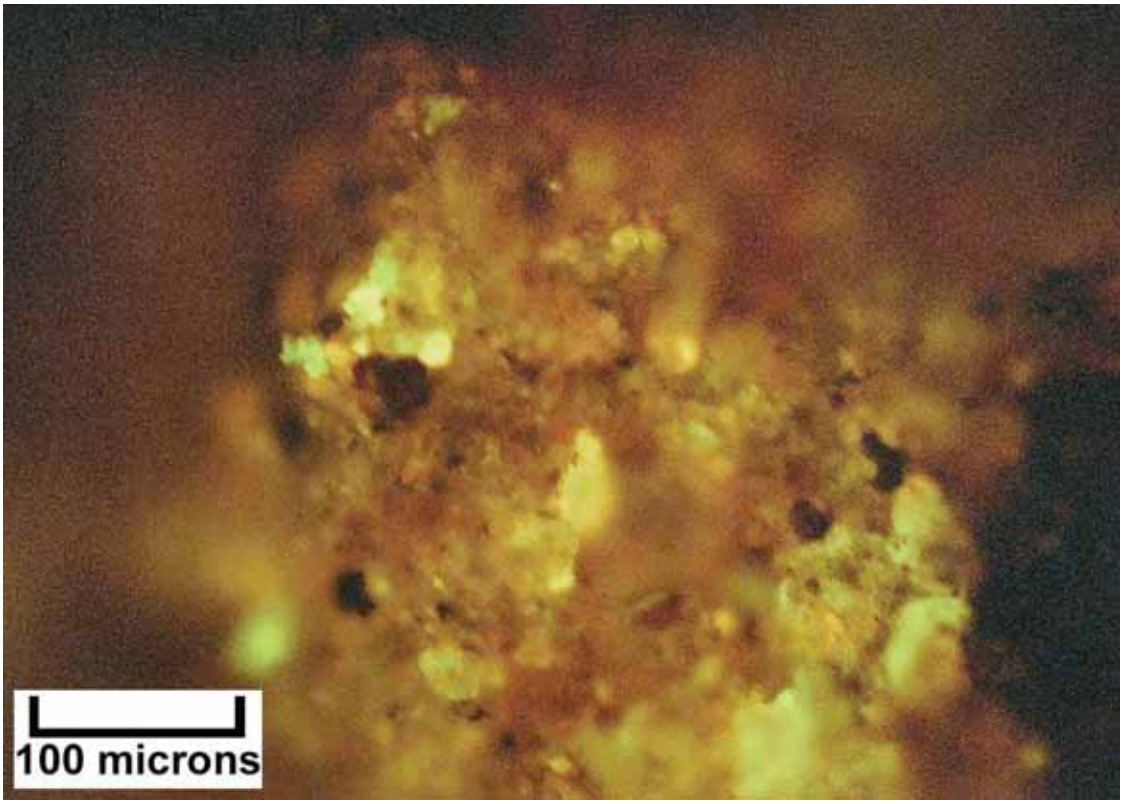

EF photomicrograph – Horsehead Unit #1 (Map #21), 6370-80 feet, C interval, 2.0 visual epifluorescence rating in shale and dolomitic shale.

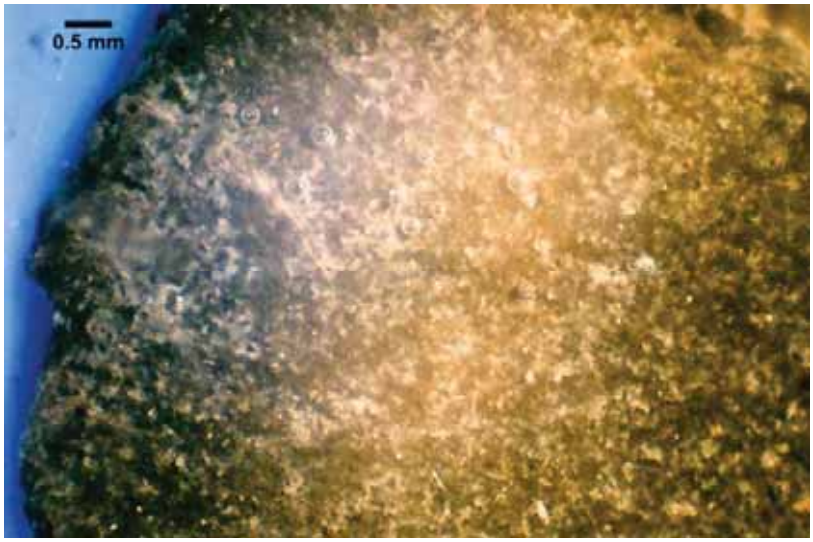

A

B

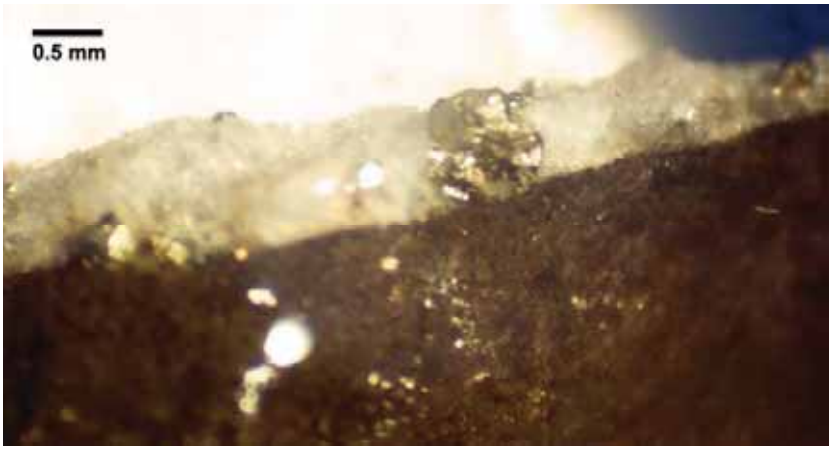

Binocular microscope images (A: dry, B: wet and etched) – Horsehead Unit #1 (Map #21), 6380-90 feet, C interval. A: overview of dolomitic shale matrix. B: close up of mineralized fracture.

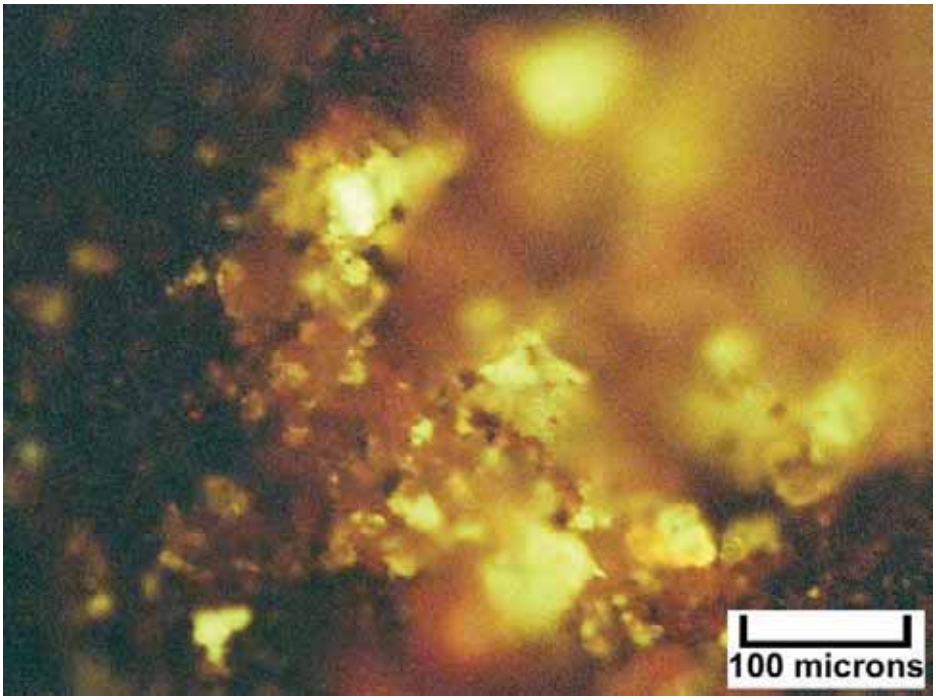

EF photomicrograph – Horsehead Unit #1 (Map #21), 6380-90 feet, C interval, 1.9 visual epifluorescence rating in shale and dolomitic shale.

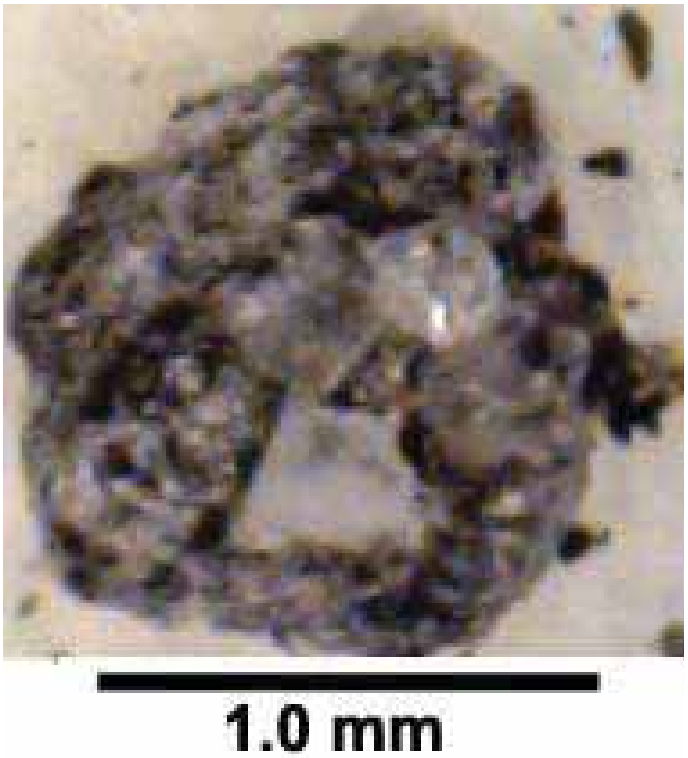

Digital microscope image (dry) – Hatch Point #1 (Map #22), 7220-30 feet, C interval, dolomite with black bitumen. Medium-sized euhedral crystals of dolomite (and possibly halite) are visible within a small representative cutting. The black bitumen is present within intercystalline pore spaces.

EF photomicrograph – Hatch Point #1 (Map #22), 7220-30 feet, C interval, 2.2 visual epifluorescence rating in rhombic dolomite clusters within black shale.

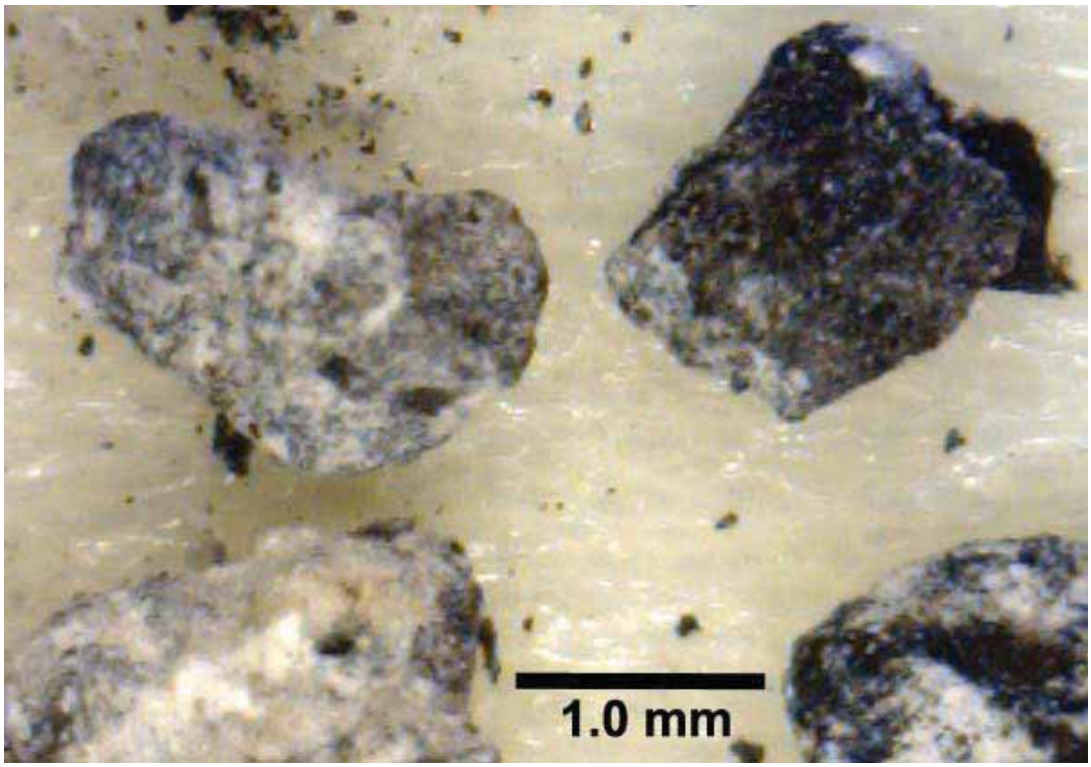

Digital microscope image (dry) – Hatch Point #1 (Map #22), 7260-70 feet, C interval, portions of four small cuttings that are composed of anhydritic dolomites with variable amounts of pore-filling black bitumen and some black argillaeous materials. Note the patches and hints of light to medium brown oil staining.

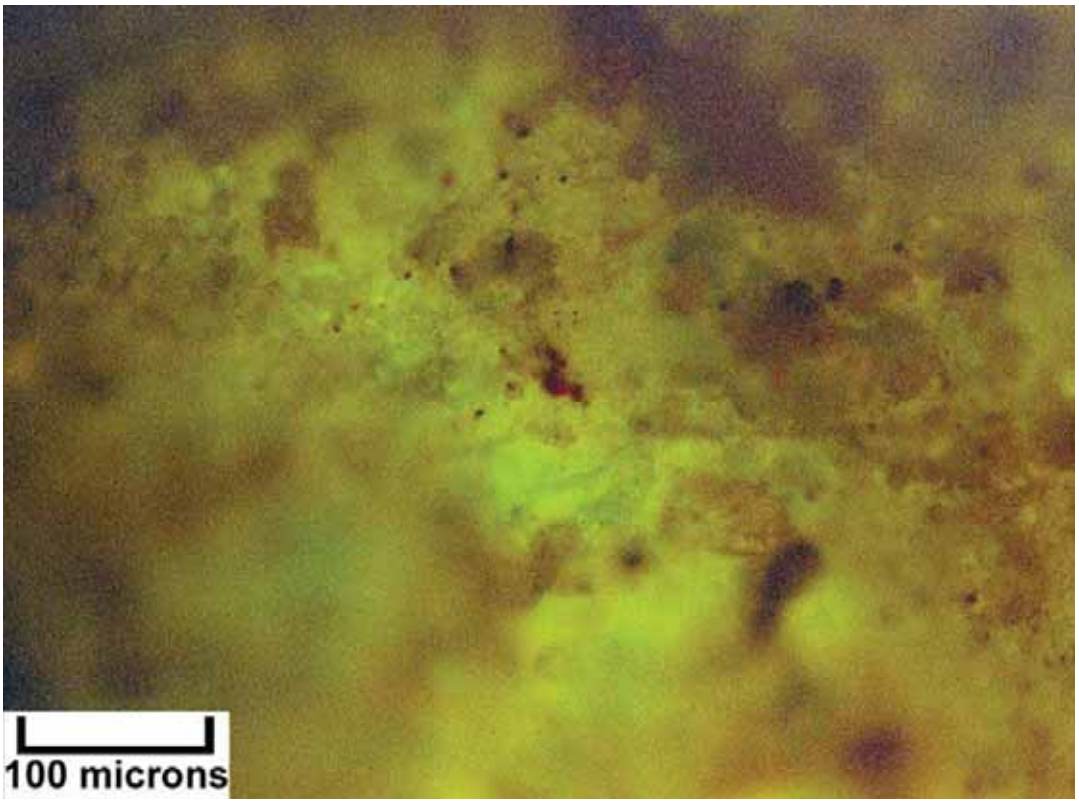

EF photomicrograph – Hatch Point #1 (Map #22), 7260-70 feet, C interval, 2.4 visual epifluorescence rating in microcrystalline dolomite in shale.

Digital microscope image (dry) – Threemile #12-7 (Map #23), 7650-70 feet (horizontal well), anhyditic dolomite. Generally low-porosity, finely crystalline dolomite with minor black bitumen within the limited intercrystalline pores.

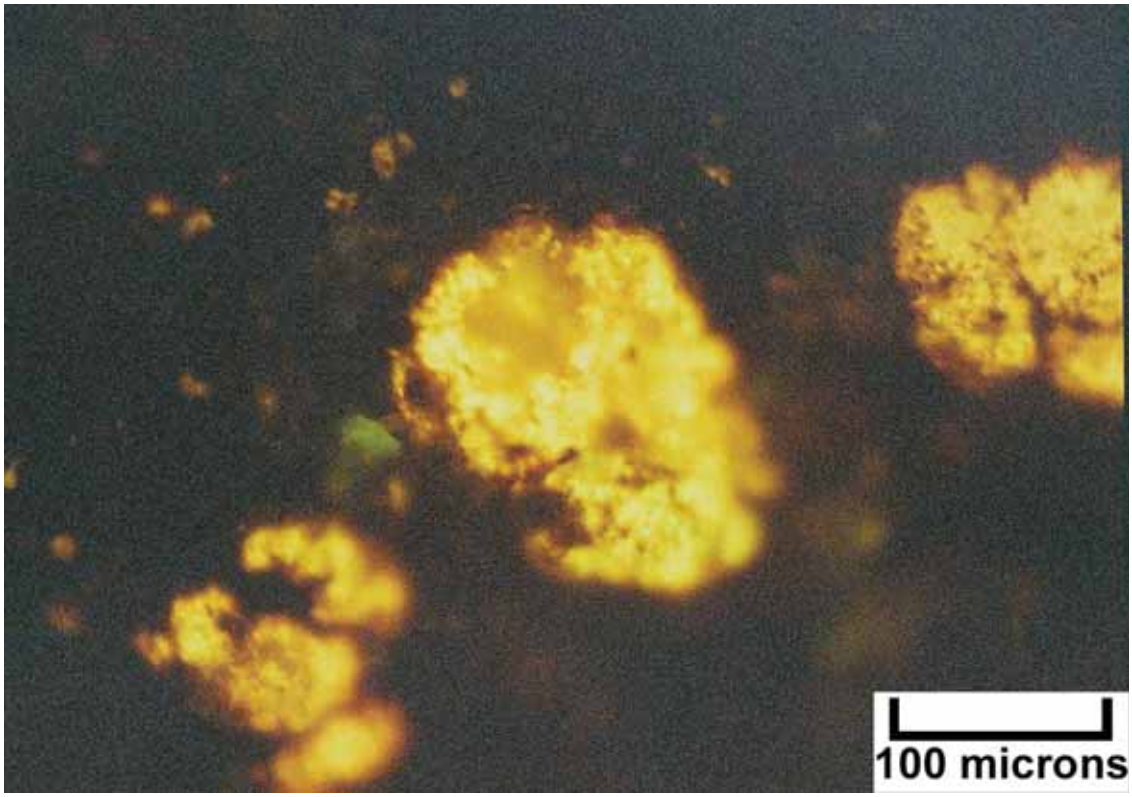

EF photomicrograph – Threemile #12-7 (Map #23), 7650-70 feet (horizontal well), 2.5 visual epifluorescence rating in very finely crystalline anhydritic dolomite.

Close-up image (dry) of slabbed core – Gibson Dome #1 (Map 26), 5235-36 feet, A interval, anhydritic dolomite with light brown oil staining. Massive to laminated dolomite contains displacive nodules of white to light gray anhydrite. Small microbial "domes" or "biscuits" are present near the top of this core segment.

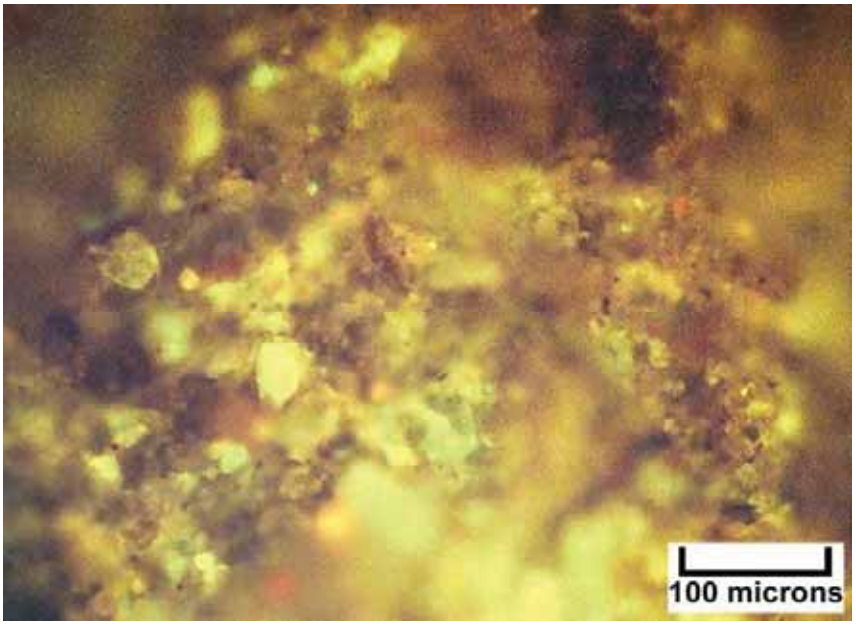

EF photomicrograph – Gibson Dome (Map #26), 5230-40 feet, A interval, 2.2 visual epifluorescence rating in fine to medium crystalline dolomite, packstone/grainstone with visible intercrystalline pores.

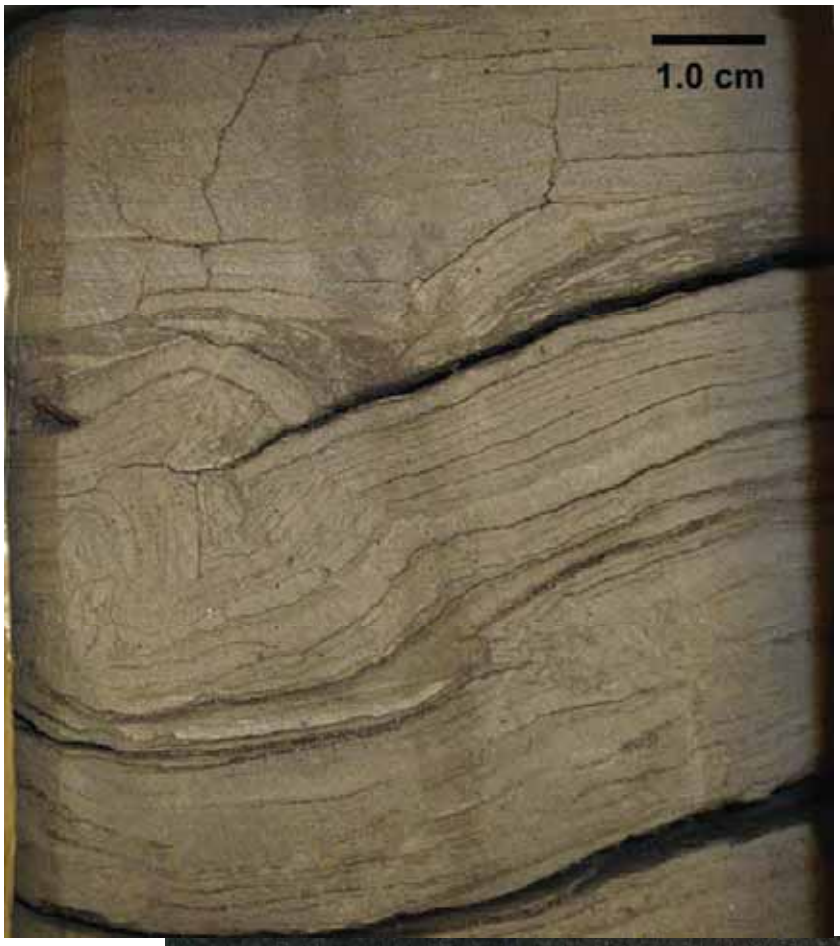

Close-up image (dry) of slabbed core – Gibson Dome #1 (Map #26), 5257.8 feet, B interval, silty dolomite with light brown oil staining. Laminated dolomites organized into undulatory thin beds which display early deformation or contortions. These laminites may be microbial in origin, and may be part of larger stromatolitic structures. Note the thin, angular rip-ups present in one dark brown, oil-stained layer within the laminites.

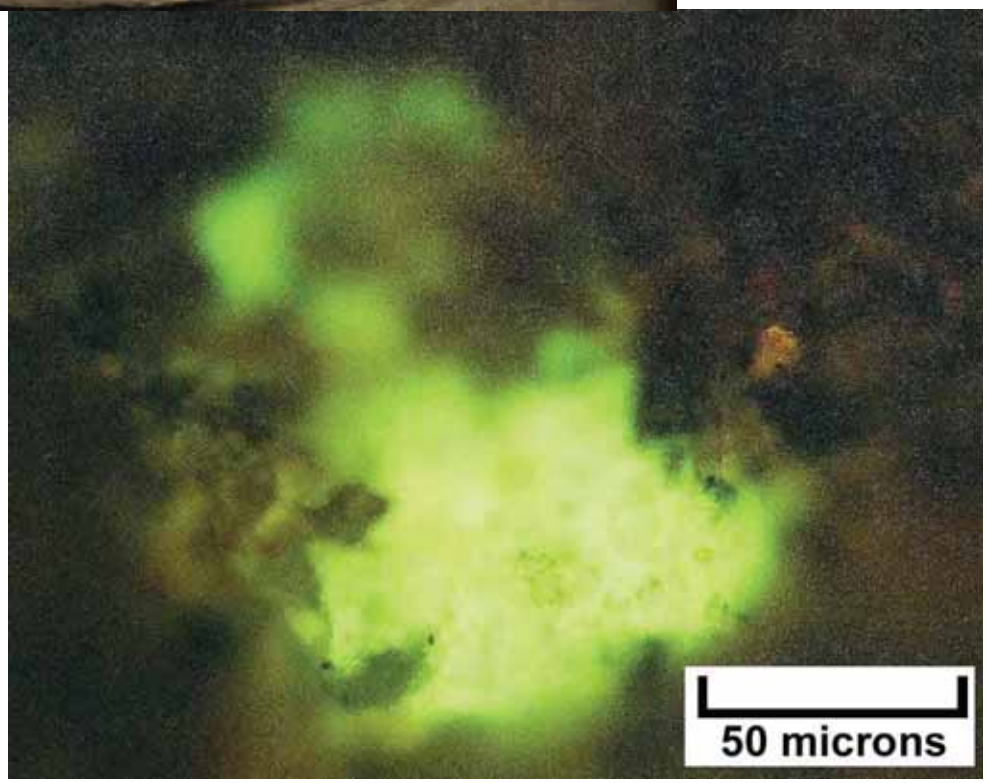

EF photomicrograph – Gibson Dome (Map #26), 5250-60 feet, B interval, 2.1 visual epifluorescence rating in well sorted siltstone with interparticle porosity and a few patches of dolomite.

Close-up image (wet) of slabbed core – Gibson Dome #1 (Map #26), 5260-61 feet, B interval, silty to argillaceous dolomites with light brown oil staining. Laminated silty dolomites with black clay-rich drapes are interbedded with thin black to dark gray organic-rich shales. Note the desiccation cracks and shallow burrows that interrupt the laminated dolomites.

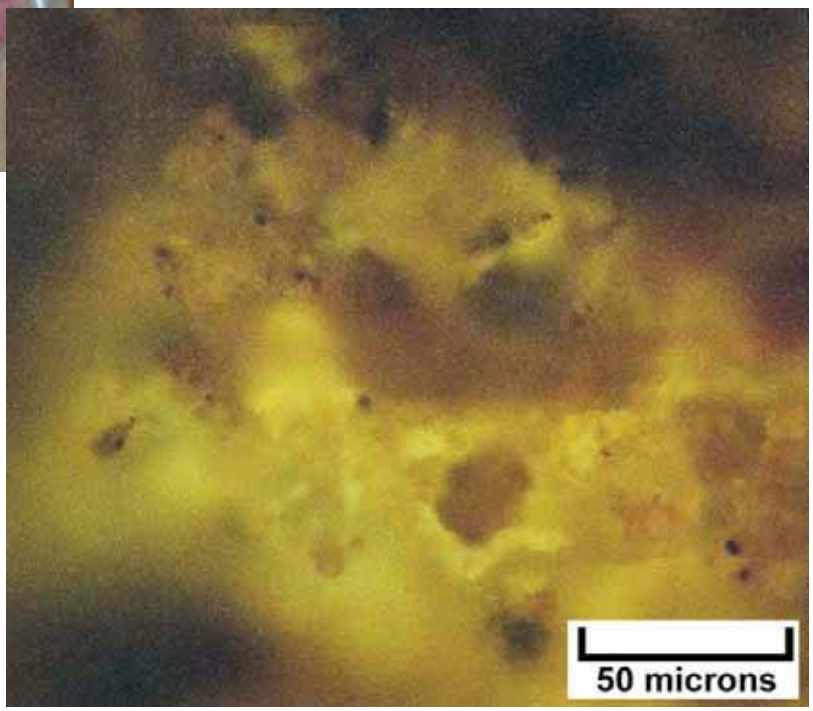

EF photomicrograph – Gibson Dome (Map #26), 5260-70 feet, B interval, 2.3 visual epifluorescence rating in partially cemented siltstone with remnant interparticle porosity and good fluorescence.

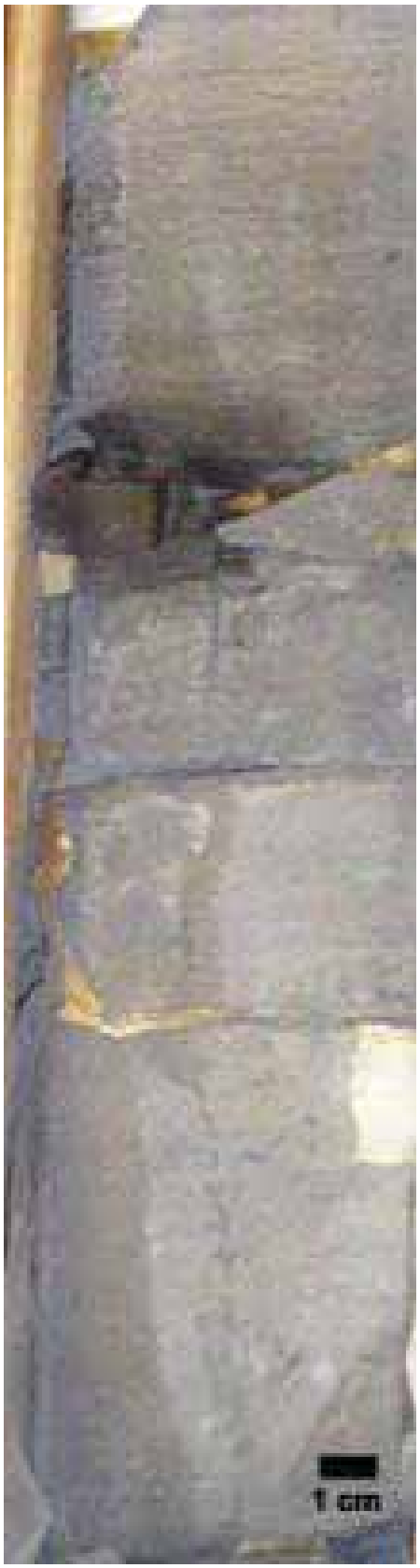

Close-up image (dry) of slabbed core – Gibson Dome #1 (Map #26), 5292-93 feet. C interval, calcareous dolomites with minor light brown oil staining. Generally massive to reworked grains and rip-up clasts alternate with well-laminated (microbial) beds.

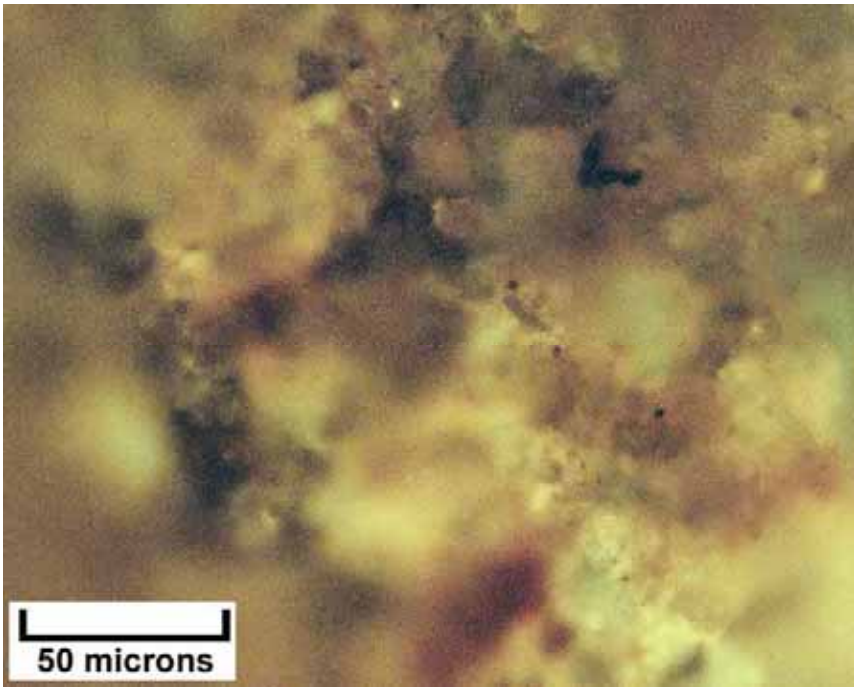

EF photomicrograph – Gibson Dome (Map #26), 5290-5300 feet, C interval, 2.0 visual epifluorescence rating in dolomitic grainstone, fine to very fine dolomite crystals, visible interparticle porosity.

Close-up image (wet) of slabbed core – Gibson Dome #1 (Map #26), 5302-03 feet, C interval, dolomite with light to medium brown oil staining throughout alternating with very thin, organic black shale beds. The dolomites exhibit wavy laminated beds, consistent with a microbial origin.

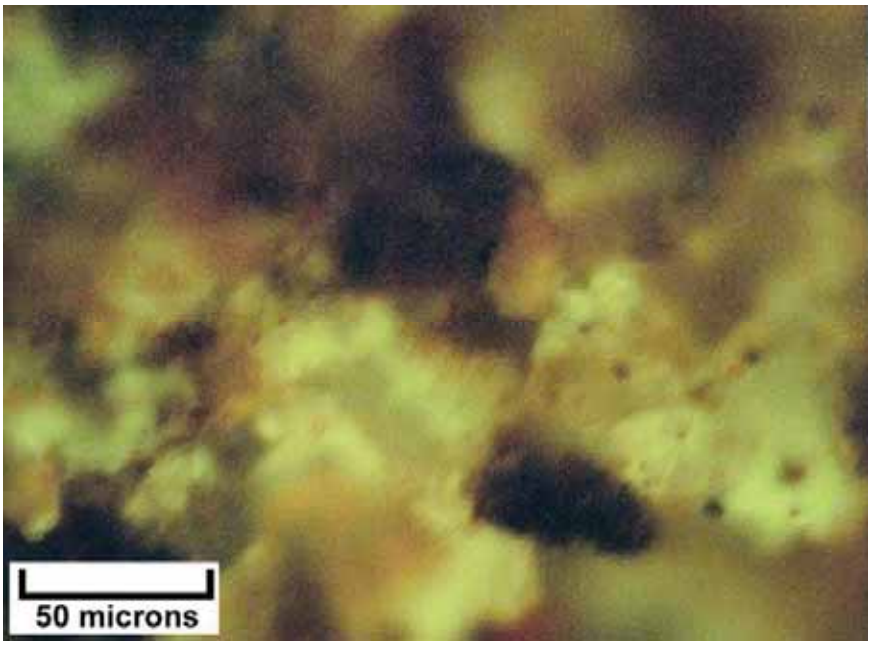

EF photomicrograph – Gibson Dome (Map #26), 5300-10 feet, C interval, 2.1 visual epifluorescence rating in dolomitic siltstone containing possible dolomitic grains and interparticle porosity.

Digital microscope image (dry) – Hart Point Unit #1 (Map #28), 6780-90 feet, B interval, very silty dolomite with medium brown oil staining. Fine crystalline dolomite matrix with abundant silt grains. Note the numerous patches of black bitumen.

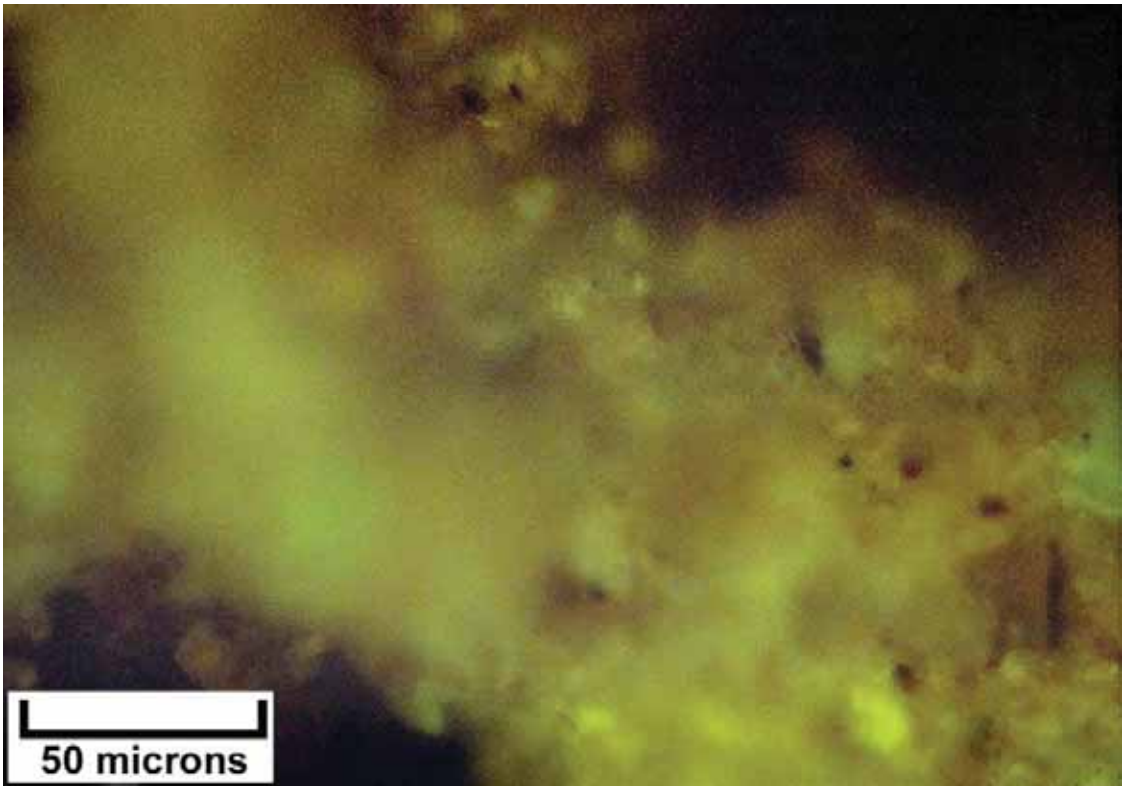

EF photomicrograph – Hart Point Federal #1 (Map #28), 6780-90 feet, B interval, 2.5 visual epifluorescence rating in patchy medium crystalline dolomite associated with small microbialite structures; good uniform fluorescence.

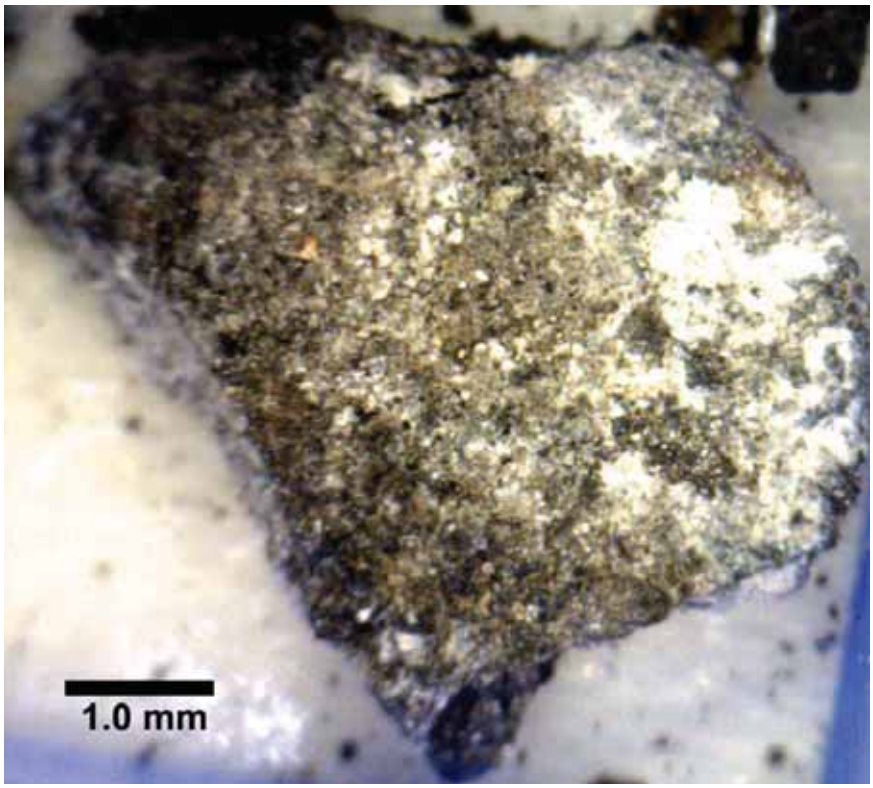

Digital microscope image (dry) – Hart Point Unit #1 (Map #28), 6810-20 feet, C interval, anhydritic (in white) and silty dolomite with only a hint of very light brown oil staining. Detrital silt-sized grains are visible within the dolomite matrix, while the anhydrite occurs in isolated white patches.

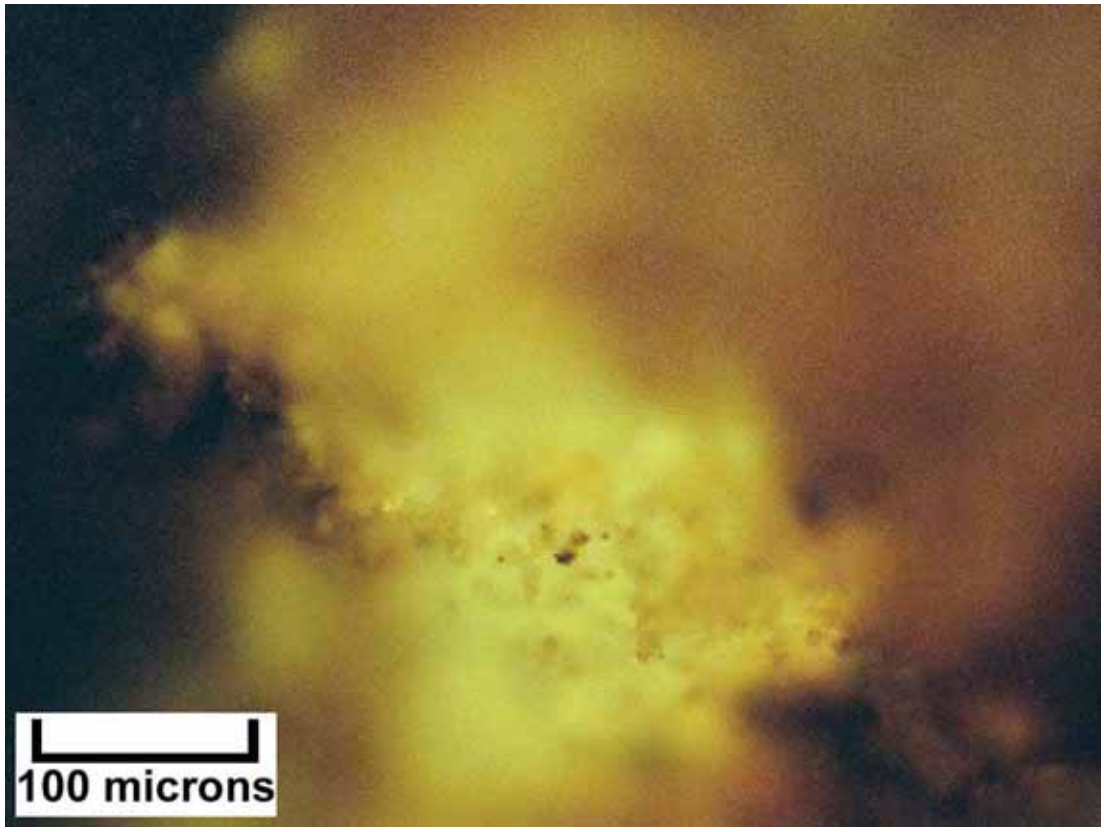

EF photomicrograph – Hart Point Federal #1 (Map #28), 6810-20 feet, C interval, 2.3 visual epifluorescence rating in patch of medium crystalline dolomite within tight, argillaceous matrix.

Close-up image (wet) of slabbed core – Cisco State #36-13 (Map #31), 7611.3 feet, B interval, dolomite with light brown oil staining. Rip-up clasts composed of laminated (stromatolitic?) microbialites with black bitumen lining intercrystalline pores within the dolomite matrix.

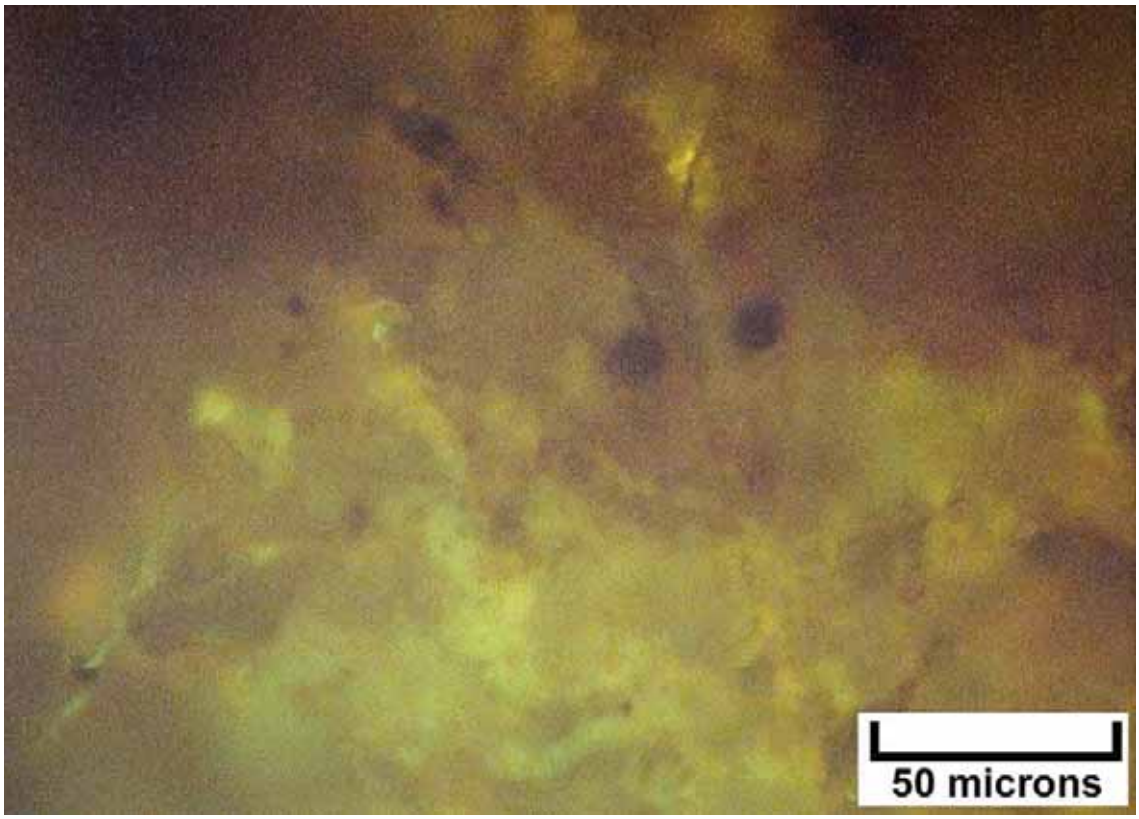

EF photomicrograph – Cisco State #36-13 (Map #31), 7611.3 feet, B interval, 2.5 visual epifluorescence rating in slightly silty medium crystalline dolomite with intercrystalline porosity, possible grainstone/packstone.

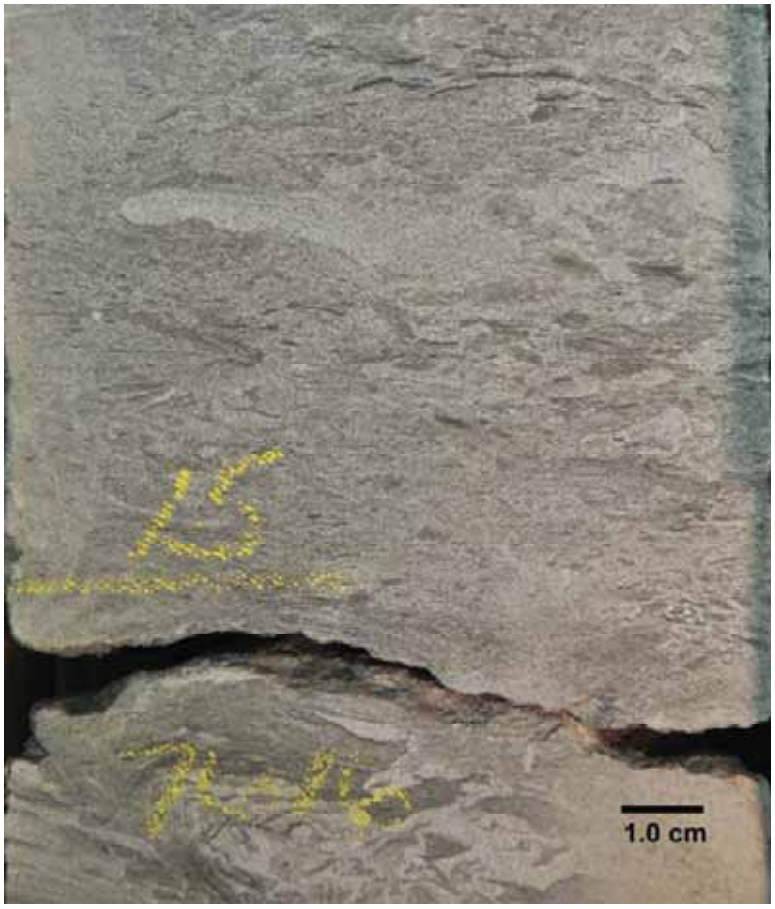

Close-up image (dry) of slabbed core – Cisco State #36-13 (Map #31), 7615.8 feet, B interval, silty dolomite consisting of rip-up clasts composed of laminated (stromatolitic?) microbialites with black bitumen lining intercrystalline pores within the dolomite matrix. Sediment-filled burrows are also present.

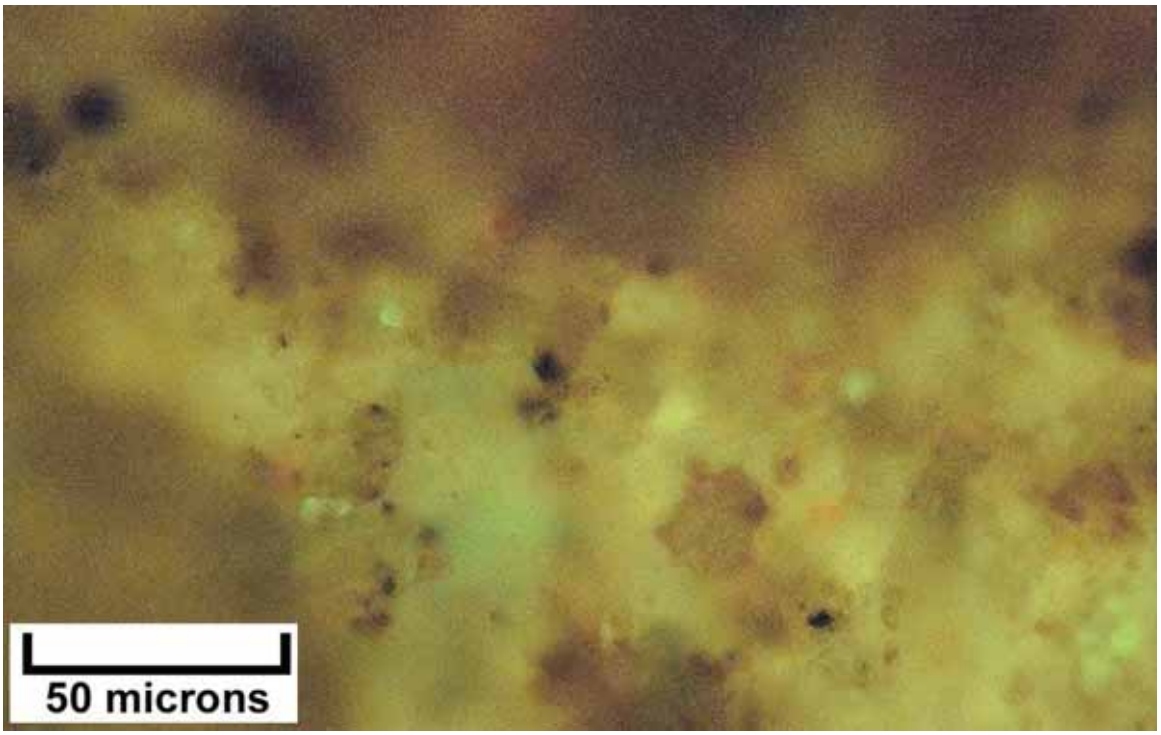

EF photomicrograph – Cisco State #36-13 (Map #31), 7615.8 feet, B interval, 2.6 visual epifluorescence rating in fine to medium crystalline dolomite with patchy good fluorescence and visible pores, packstone/grainstone(?).

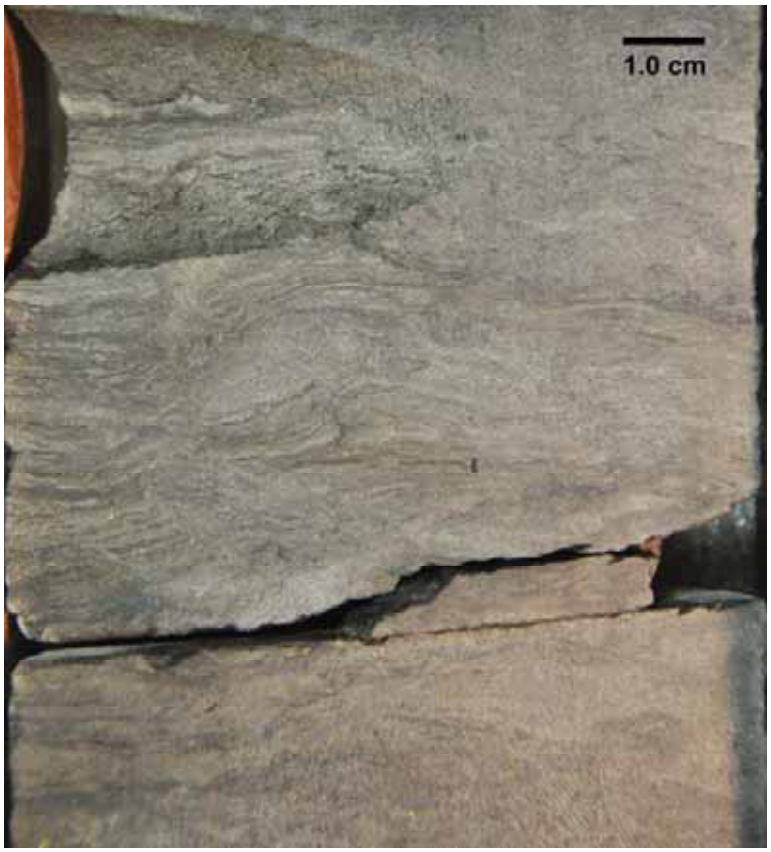

Close-up image (wet) of slabbed core – Cisco State #36-13 (Map #31), 7619.3 feet, B interval, dolomite with patchy light brown oil staining. Wavy stromatolitic laminae are occasionally draped with argillaceous layers. Black bitumen is present within some of the intercrystalline pores.

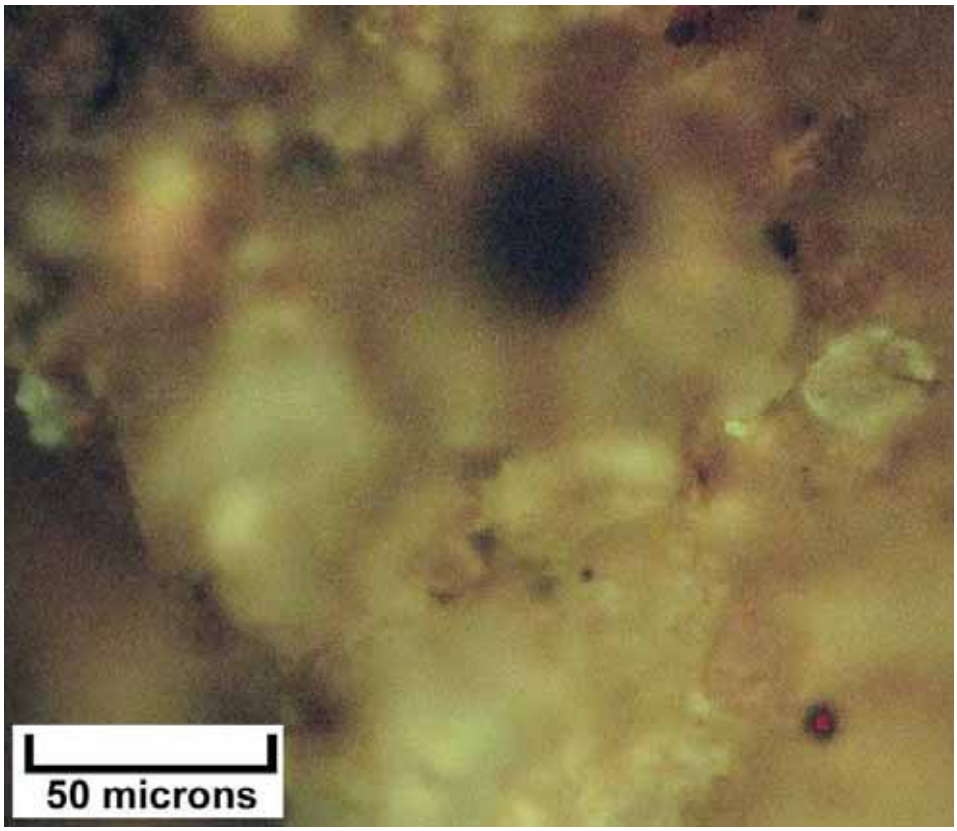

EF photomicrograph – Cisco State #36-13 (Map #31), 7619.3 feet, B interval, 2.3 visual epifluorescence rating in slightly silty dolomite, packstone/grainstone with fair to good intercrystalline porosity.

Close-up image (wet) of slabbed core – Cisco State #36-13 (Map #31), 7623.1 feet, B interval, silty to slightly argillceous dolomite composed of an interval of wavy laminae (stromatolitic?) overlain by dolomitized skeletal and non-skeletal coated grains. Note the black patches of bitumen that are concentrated within matrix porosity.

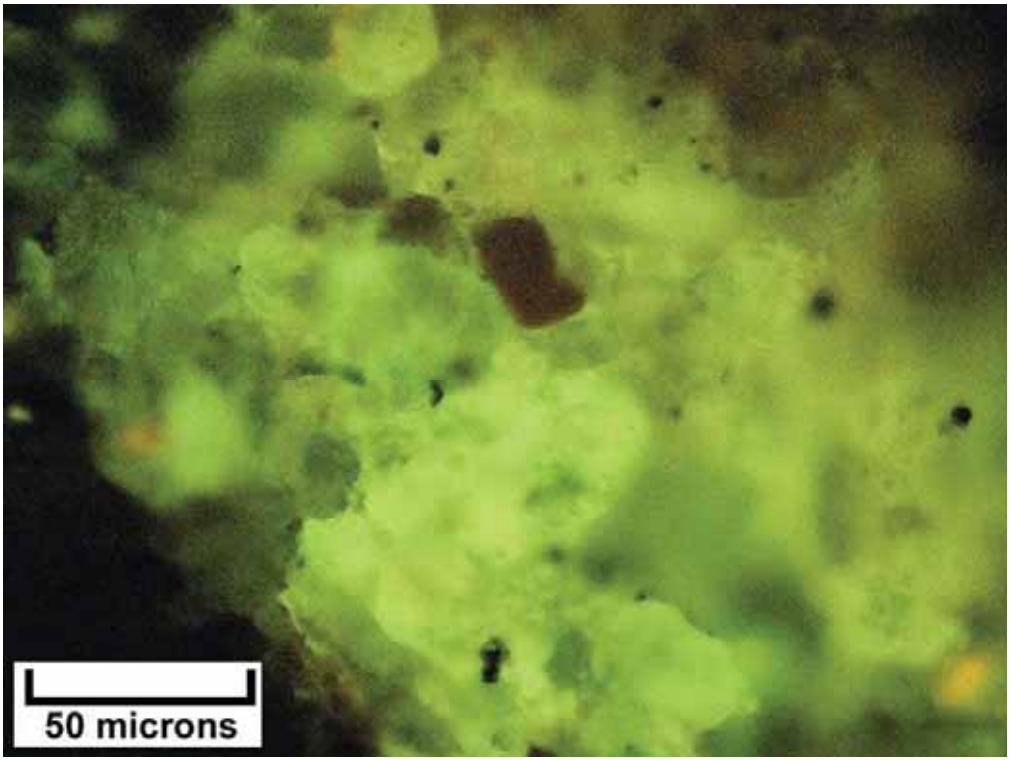

EF photomicrograph – Cisco State #36-13 (Map #31), 7623.1 feet, B interval, 2.8 visual epifluorescence rating in slightly dolomitic siltstone, moderately well sorted with bright fluorescence in interparticle porosity.

Appendix IX

Geomechanical Characterization of the Uteland Butte and Cane Creek Tight Oil Plays

John McLennan and Josh Zannoni

Energy and Geoscience Institute, University of Utah, Salt Lake City, UT

Appendix

Geomechanical Considerations

Executive Summary

The Opportunity

One aim has been to explore methodologies for predicting brittle rock behavior and considering the consequences during well stimulation. By comprehending a reservoir's characteristics, a second goal has been to use hydraulic fracturing simulations to suggest potentially appropriate treatment methods for application in the Cane Creek and Uteland Butte plays. The rocks encountered in these two plays are relatively brittle and industry has become casually comfortable with terms such as brittleness and fracability. While inferences on brittleness and fracability can be useful for selecting landing zones and qualitatively assessing barriers, incorporating them into numerical simulations is still challenging. In fact, one might still ask "What is fracability?" The answer might be that fracability is a colloquial slang that suggests that tensile fracturing may dominate, and that expended energy on failure goes to creation of open, extensive, conductive fractures (although maintenance of conductivity is not guaranteed). There is confusion as to whether this implies a dominant single discontinuity or a complex network of fractures. There is confusion as to whether this implies a contained or vertically extensive fracture. Presume that those (complexity and containment) are separate criteria that need to be dealt with in order for a stimulation to be effective. Presume further that brittleness can help in the determination of fracability.

Brittleness and Fracability

Conventional methods for determining brittleness were summarized. One problem with the concept of brittleness is that most definitions do not take into account the plastic deformation that takes place. Plastic deformation is non-recoverable. It occurs after the regime in which elastic properties such as Young's modulus and Poisson's ratio - commonly used in brittleness assessments - are determined. In fact, **by its very nature, brittleness must imply consideration of behavior after yield of a material has initiated - well after conditions where elastic moduli are determinant.** By ignoring non-recoverable (plastic) deformation, the energy that needs to continue being put into more plastic rocks versus more brittle ones is completely ignored. How can we improve?

1. As several authors have pointed out, large scale geological controls - in particular stress conditions and major geologic structural defects - need to be explicitly considered. In most cases, little effort is made to determine what these stress conditions are. **Brittle-ductile behavior is governed by in-situ stresses. It should be a priority to measure stresses or infer from them logs at the least.**
2. For core-based measurements of brittleness, newer interpretation methods should be considered. Several techniques for assessing brittleness have been evaluated in this report, with particular emphasis on considering how a rock fails,

and how it deforms after it starts to yield. This is the implicit discriminator between brittle and ductile behavior. Several new techniques are suggested. **Consider post-peak behavior in brittleness predictions.**

3. Most brittleness predictions cannot readily be put into hydraulic fracturing simulators. How is mechanical stratigraphy (fracture frequency and mechanical and hydraulic character, in particular) used to predict fracture growth? How do we represent brittleness in standard models? Some possibilities are simulations that take into account post-peak behavior (strain softening or hardening). **Continue to improve models for propagation along/through weaknesses.**
4. As is evident, all of these effects are overshadowed by what role natural discontinuities play in fracture propagation. The industry has come a long way in terms of developing models that incorporate these discontinuities - their detection and mechanical characterization - is still challenging. **Use these discontinuities in simulations.** Figure i illustrates these challenges.

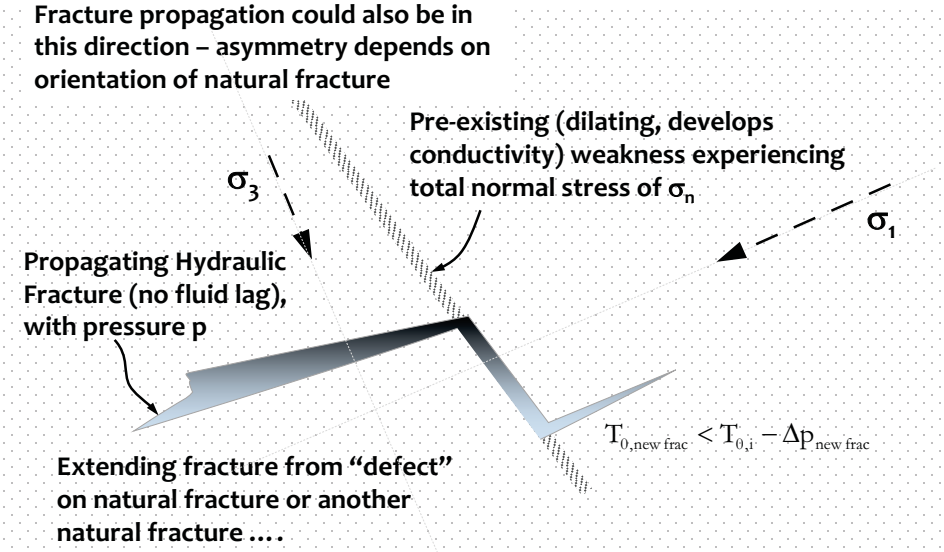

Figure i. A hydraulic fracture propagates from a weak point along the opposite face of a natural fracture offset. We have a semi-quantitative appreciations of fracture propagation under conditions such as these. The challenges are designation of the discontinuities in-situ and inference of their mechanical and hydraulic resistances. Even more complicated for researchers will be to struggle with the recognition that process zones, loading rates, and non-elastic fracture mechanics may invalidate instinctual appreciations, such as the one shown here.

The move towards incorporating brittleness is exciting because it recognizes lithologic, structural, and stress-related control of fracture propagation. To improve assessment of brittleness, several new calculation methods have been tried on the wells available for this project. In all cases, the governing premise is that an energy balance is relevant. For example, a certain amount of energy is consumed by quasi-static deformation of a particular formation. This consumption may be more for a ductile material. Alternatively, a certain amount of energy is released after a rock starts to lose its ability to absorb the energy input into it (this input is from geologic events, hydraulic fracturing, production …). The magnitude and the rate at which this extraneous energy is ultimately released can be taken to indicate brittle versus ductile behavior. The premise then is to consider energy stored, energy released, and the rate/magnitude of energy release during a "failure". Five new methods were proposed and have been tested in a preliminary fashion. These are:

- ***Zone 1: Ratio of secant modulus to Young's modulus:*** The premise here is that an appropriately picked secant modulus incorporates non-recoverable deformation and Young's modulus manifests elastic, recoverable deformation. The premise is that the lower the ratio of the secant modulus to Young's modulus, the more ductile the failure will be because energy has been consumed/expended even before strain softening. This might be called a Deformation Index.
- ***Zone 2: Ductility Index - Amount of plasticity or strain hardening:*** This index quantifies the amount of perfect plasticity or strain hardening in advance of stronger localization and reduction in load bearing capacity.
- ***Zone 3a: Tang and Kaiser (axial)*** Tang and Kaiser (1998) provided a very insightful relationship for failure of coal pillars. One measure of this is the amount of energy released when failure occurs. This can be approximated as follows, as modified by Bereskin and McLennan (2008).

$$E_f = \frac{1}{2E}(\Delta\sigma_f)^2 V_f \qquad \text{(i)}$$

$$V_f = \underbrace{\varepsilon_a(1-2\nu)}_{\substack{\text{Volumetric Strain}\\ \text{Based on Axial strain}}} \underbrace{\frac{\pi}{4}D^2L}_{\substack{\text{Sample}\\ \text{Volume}}} \qquad \text{(ii)}$$

(27)

where:

E_f ..... energy released by failure
E ..... Young's modulus
$\Delta\sigma_f$ ..... stress drop after brittle failure
V_f ..... failed volume (reported here for triaxial testing)
ε_a ..... axial strain occurring during strain softening (energy release)
ν ..... Poisson's ratio

D .....sample diameter
L..... sample length

- ***Zone 3b: Tang and Kaiser (volumetric):*** This is similar to the technique described above with the exception that the bulk modulus is used instead of Young's modulus and the volume is based on the measured volumetric strain (rather than the axial strain and Poisson's ratio).
- ***Zone 4: Peak to Residual Strength Ratio:*** This is the ratio of the peak to residual stresses and provides an indication of the energy released with catastrophic failure.
- ***Zone 5: Ratio of Stored to Expended Energy:*** This method involves integration under a stress-strain curve. This ratio of energies can provide indications of brittleness versus ductility.

Field Assessments

In conjunction with these evaluations of brittleness, data from six wells were processed. Three of these wells targeted the Uteland Butte formation. These wells are: Bill Barrett 14-1-46, Bill Barrett 14-3-45, and Newfield Cesspooch 15-21-3-3W. The other three wells accessed the Cane Creek formation. These wells are Cane Creek 26-3, Cisco State 36-13, and Cane Creek 7-1. All of these wells have well logs available except Cane Creek 7-1. Core was available for all six of the wells for triaxial testing but the Cane Creek 7-1 well was not available for other core testing. Other than the Cane Creek 7-1 well, the other five cores provided measurements of porosity, permeability, TOC, oil maturity, and fracture toughness. Representative sections were created for fracture modelling.

Comparative fracture modeling was carried out to determine what additional treatment optimization may be relevant. Recognizing the absence of well-specific data, generic surrogate wells were assessed in some instances, especially for representing horizontal wells. For the horizontal wells evaluated, logging data, mechanical properties and the limited stress data were incorporated into representative type sections penetrated by the horizontal drilling. For these type wells, various appropriate stimulation were. Fracture modeling was carried out with commercial stimulation software.

Vertical completions were evaluated first since the legacy wells were mostly straight hole. Planar 3D hydraulic fracturing treatment simulations were carried out using E-StimPlan™. The two wells simulated were Bill Barrett well 14-3-45 in the Uteland Butte and the Cisco State 36-13 well in the Cane Creek. In each case, vertical height growth was problematic. In the Cane Creek wells, the problem related to penetration into adjacent salts. Alternatively, for Uteland Butte scenarios, predicted vertical growth and unrealistic perforating scenarios limited production. Figure ii suggests that the predictions were reasonable. This figure also emphasizes why vertical completions will not be economic.

The production history (real and simulated), and current industry practice endorsed changing from a vertical drilling trajectory in both of these plays. This was already starting to happen when this study was initiated. Horizontal type wells were developed for this study. After compiling the laboratory and logging data for the two generic locations, type reservoirs were developed, by amalgamating the various sources of information. In either scenario - Uteland Butte or Cane Creek, the key issue was containment of the fracture in a discrete pay zone/intervals.

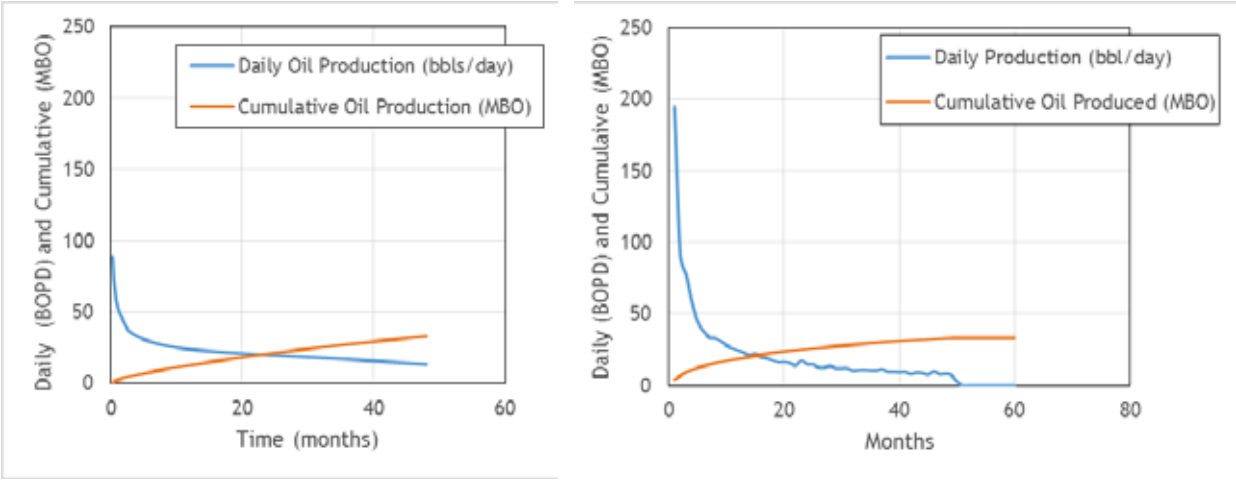

Figure ii. This is predicted (left panel) versus actual (right panel) oil production for Bill Barrett 14-3-45. Large length perforated - counterproductive. Significant upward growth was also an issue. These forecasts were based on the simulated fracture geometries.

In the case of the Cane Creek play, salt immediately adjacent to the pay is particularly challenging. Penetration of a water-based treatment fluid into saline zones will result in subsequent salt precipitation and loss of productive capacity. In the case of the Uteland Butte, upward growth out of pay jeopardizes the effectiveness of the stimulation by limiting in-zone surface area.

Horizontal Completions in Cane Creek

Legacy wells completed in the Cane Creek (vertical or horizontal) were marginally productive. There was some evidence and inference that fracturing treatments used in these wells were penetrating into the over- and underlying salt zones and causing salt to block fractures and perforations, thereby reducing the productivity of the well, if not killing it. This would be even more exaggerated for situations where the well wandered out of the pay. Regardless, it was decided to prioritize horizontal wells in the treatment simulations. Generically, the fluids considered were as follows.

Oil-Based Fluid: To their credit, a previous operator treated the formation with mineral oil. Lease crude would have been another possibility but the synthetic oil is likely more biodegradable and easier to justify with regulators and the public. The benefit of this fluid genre is the limited reaction with the adjacent salt formations. A viscosity of nominally 2 cP was used for the oil - relatively low and this inhibits proppant carrying.

Gelled Oil: This is another possible fluid that would minimize interaction with adjacent salt. The drawback is perceived to be out-of-zone growth with the higher viscosity. However, the treating fluids themselves will not interact with the salt. Other issues could be environmental and safety.

Water Based Fluid: Both slickwater and a 50 lb pptg (per thousand gallons) borate crosslinked fluid were evaluated. The slickwater was assumed to have a viscosity of nominally 0.64 cP at reservoir temperature. The properties of the crosslinked were taken from the simulator database. Two extreme fluid scenarios were assessed to comprehend height growth. An intermediate situation might be a low loading linear gel (a viscoelastic surfactant was also evaluated). Obviously there are pros and cons for all of the viscosified fluids including expense, failure to break, and residual polymer damage. The purpose was to assess the role of rate and rheology and presume that good treatment design (proper breaker systems and loading, customized for the play) could overcome residual damage. The disadvantages of the slickwater relate to proppant carrying capacity.

Composite: One of the observations with the crosslinked fluid was screenout when proppant (other than 80/100 mesh) reached the perforations - particularly when rate was reduced to avoid upwards growth. At the other extreme, proppant from the low viscosity treatments would settle. Cyclic injection was evaluated to consider the possibility of fracture placement with proppant acting as an in-fracture diverter and inhibiting height growth. This concept is not new. Diversion treatments for height containment were described in the 1980s. One relevant publication is Greener, 1994. Cyclic injection would seem to offer some possibilities.

The basis for the composite/cyclic treatments was low viscosity fluid pumped in small stage volumes with sand concentrations of 0.5 followed by 1.0 ppg. This was followed by displacement with higher viscosity fluid to push the proppant to the top and the bottom of the pay and to nominally extend the fracture. This was followed by a final cycle of low viscosity fluid with the same low proppant concentrations. The same concept could be applied by fingering the low viscosity fluid through a proppant carrying more viscous fluid or simply running cycled proppant concentrations. Figure iii is an example. **More clusters and smaller alternating/cyclic fluids seemed to be desirable. Oil based fluids were most appropriate. Of course, smaller fracture treatments implies more stages are required and wells will need to be drilled closer together. Economic optimization will be necessary.**

Horizontal Completions in the Uteland Butte

Until less than a decade ago, wells in the Uteland Butte member of the Green River formation were vertical wells that completed the Uteland Butte section as a secondary target. Recently, operators have targeted the Uteland Butte member specifically, with varying success - much more success with horizontal completions. As with the Cane Creek, horizontal wells were simulated, using Schlumberger's Kinetix Stimulation Software suite.

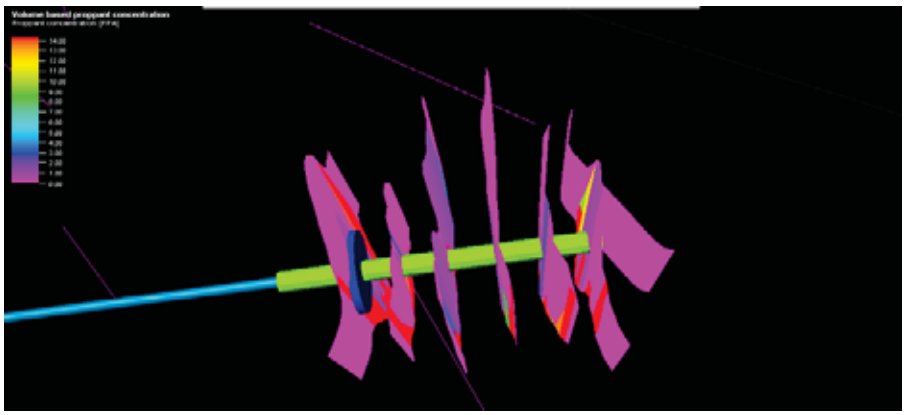

Figure iii. This is an EOJ view of the extent of six fracture systems (one from each perforation cluster) with cycled water based fluids having different viscosities. The contours are for proppant concentration from 0 to 14 ppa. Proppant coverage is poor but there appears to be moderate containment.

As with the Cane Creek, vertical containment is important. Options that merit further consideration include reduced rate, low viscosity treatments, cyclic injection (could be favorable), and dramatically reduced tactical treatments similar to fracpacks. The latter were simulated to be effective but may not be practical because of the consequence of screenout. **Smaller treatments mandate closer well spacing.**

In either case (Cane Creek or Uteland Butte) the recommendations might seem to be contrary to industry practice. The philosophy is that significant volumes of fluid and proppant are wasted at best for noncontributing pay. At worst, as for salt precipitation in the Cane Creek, larger treatments can be catastrophic.

In either situation, simulations at least support more clusters (or more stages), smaller fluid volumes, aggressive sand schedules where feasible and smaller well spacing (economic justification and optimization of spacing is beyond the scope of this project). Cyclic fluid injection merits consideration.

Subtask 6.1 Fracability

I. Objectives

Summarize methodologies for predicting brittle rock behavior and the consequences during well stimulation, including methods that are based on fundamental energy relationships, mineralogy, and multivariate calculations, as well as simpler routines based on combinations of Young's modulus and Poisson's ratio before failure.

II. Introduction

At the most fundamental level fracture mechanics is an energy balance that looks at the energy of new surfaces that are created as well as the energy that was originally holding them together. In the early part of the twentieth century, Griffith (1921) articulated basic fracture mechanics concepts mathematically. To summarize, in a material such as rock, molecules have rearranged within the structure of the rock to minimize repulsive forces such as those due to electrostatic, or van der Waal's forces. This results in a lower overall energy of the structure. When the rock is fractured the new surfaces no longer have molecules adjacent to the surface to stabilize the molecules on the surface of the fracture. As a result, these surfaces have a higher energy than before the fracture was formed. In addition to this there are also cohesive forces between molecules due to the molecular forces mentioned above. This force must be overcome in order to separate the molecules far enough to create a fracture. As a result, the energy required to fracture a brittle rock - with no plastic deformation (non-recoverable deformation) - is the combination of the additional surface energy created on the newly formed surfaces as well as the cohesive force between molecules before the fracture formed. With rock that deforms plastically (non-recoverable deformation of a nominal continuum, some of this energy is also necessarily transformed into heat or acoustic energy. This is additional energy that is not required for brittle rock in order to form a fracture. As a result, fracturing "non-brittle" formations requires more energy; in a hydraulic fracturing scenario, this means that more hydraulic pressure would be required. The more pressure that is required to fracture a well, the more expensive the well construction will be; from casing and cement design all the way to the pump trucks required to fracture the formation. The premise then is that it is desirable to treat formations at lower energy expenditure (the product of rate and pressure) to create a more extensive and conductive fracture network. Those zones might colloquially be considered to be more "fracable". Ideally, portions of a reservoir with good reservoir quality such as porosity, permeability, and total organic content and good completion quality (rocks that are more "fracable") would be chosen for stimulation. Researchers have pursued numerous ways to develop relative values that relate the "fracability" of rocks to a combination of properties that can be obtained by logging or laboratory measurements.

What is brittleness? Brittleness characterizes a material that FAILS with little plastic deformation prior to and/or during failure. Failure is a more complicated term from an engineering perspective, but will be interpreted here to imply that temporally unstable fracture propagation is occurring.

What is fracability? As was evident above, this is a sloppy term that suggests that tensile fracturing may dominate, that expended energy on failure goes to creation of open, extensive, conductive fractures (although maintenance of conductivity is not guaranteed). There is confusion as to whether this implies a dominant single discontinuity or a complex network of fractures. There is confusion as to whether this implies a contained or vertically extensive fracture. Presume that those (complexity and containment) are separate criteria that need to be dealt with in order for a stimulation to be effective.

III. Fracability

In the past, the main indicator of a "fracability" parameter has been some form of brittleness index (BI). We will continue with that assumption and presume that brittle behavior can be correlated to fracability. Brittleness indices were derived in hopes of finding a reliable parameter that would lead to better control of fracture geometry and containment. The anticipation was that this could then translate into better production in addition to lower well construction costs. Presently, one main problem with using a brittleness index is that there is no consensus within the fracturing community about what the definition of a brittleness index should be. As a result, three categories of brittleness indices have been developed with dozens of definitions. These three categories of brittleness indices are based on mineralogy, combinations of moduli, and combinations of strength parameters.

Brittleness indices that are based on mineralogy typically use a definition that prescribes the brittleness according to the relative volume fraction of characteristically brittle minerals forming the rock. Originally, Jarvie et al. (2007) defined the brittle component as quartz, as shown in equation 1. This was later expanded by Wang and Gale (2009) and others to include other brittle and ductile minerals, as is shown in equation 2. The definitions developed by these two groups are representative but do not encompass all of the definitions of brittleness in this category.

$$BI = \frac{V_{Quartz}}{V_{Quartz} + V_{Calcite} + V_{Clay}} \quad (1)$$

$$BI = \frac{V_{Quartz} + V_{Dolomite}}{V_{Quartz} + V_{Calcite} + V_{Clay} + V_{Dolomite} + V_{TOC}} \quad (2)$$

where:

V_{Quartz} ..... Volume of quartz,
$V_{Calcite}$ ..... Volume of calcite
V_{clay} ..... Volume of clay
$V_{Dolomite}$ ..... Volume of dolomite, and,
V_{TOC} ..... .Volume of organic material

While intuitively appealing, this definition may downplay the significant role of a small volume of cementitious material, for example.

The second category of brittleness indices includes those that use a combination of elastic moduli.[1] One of the more prolifically used BIs was initially developed by Rickman et al. (2008). Rickman used a combination of Young's Modulus, E, and Poisson's Ratio, ν, with a high Young's Modulus and a low Poisson's Ratio indicating a brittle rock. This index could be any combination of different moduli such as Lamé's parameters, λ and μ, as used by Goodman et al. (2010). An equivalent index could be built using logging parameters; the acoustic compressional wave velocity, v_p, the acoustic shear wave velocity, v_s, and the bulk density, ρ_B. Young's modulus, E, is the slope of the linear portion of a stress vs strain plot from a triaxial compression test. Poisson's ratio is the negative ratio of radial to axial strain in a similar testing scenario. Rickman's BI is given in Equations 3 through 5.

$$E_{Brit} = \frac{E_{Composite} - 1}{8 - 1} \times 100 \quad (3)$$

$$o_{Brit} = \frac{\mu_{Composite} - 0.4}{0.15 - 0.4} \times 100 \quad (4)$$

$$BI = \frac{E_{Brit} + \nu_{Brit}}{2} \quad (5)$$

where:

$E_{Composite}$ ..... Young's Modulus of rock (10^6 psi),
$\nu_{Composite}$ ..... Poisson's ratio of rock,
E_{Brit} ..... normalized brittle contribution from Young's modulus,
ν_{Brit} ..... normalized brittle contribution from Poisson's ratio.

[1] Parameters such as Young's modulus, shear modulus and Poisson's ratio that describe elastic deformation of a material.

One problem with this type of definition is that it does not take into account the plastic deformation that takes place after the elastic portion of the compression test in which elastic properties are determined. In fact, **by its very nature, brittleness must imply consideration of behavior after yield has occurred.** By ignoring non-recoverable (plastic) deformation, the energy that needs to continue being put into more plastic rocks versus more brittle ones is completely ignored. This definition is also essentially a lithology indicator like the first index above.

A third category of BIs uses combinations of strength parameters. The BI developed by Altindag (2003) is an example. That definition is given below.

$$\mathrm{BI} = \frac{\text{Compressive Strength}}{\text{Tensile Strength}} \tag{6}$$

If this definition is considered in terms of a linear Mohr-Coulomb failure envelope[2] it can be seen that if tensile strength is held constant the steeper the gradient of the failure envelope the more brittle the rock. The slope of the failure envelope, μ, is related to the coefficient of internal friction, ϕ, by a monotonously increasing function, given below.

$$\mu = \tan\phi' \tag{7}$$

where:

ϕ' ..... effective angle of internal friction (°)

This relation shows that a large frictional coefficient, μ, is indicative of a large angle of internal friction. A review of literature on the angle of internal friction for rocks with high concentrations of a given mineral (Plumb, 1994, Vernik et al., 1993, and Crawford et al. 2010) shows that rocks dominated by more brittle minerals (such as quartz) have higher angles of internal friction than those with more ductile minerals such as clays. As a result, rocks dominated by more brittle minerals could display a high brittleness index with this index type just as with the other two types above. In a sense, this makes all three of these generic index types more of a lithology index than a brittleness index. These and other brittleness index have been summarized by Jin et al. (2014) and some are shown in Table 1.

The features of the three index types described above were summarized by Herwanger et al. (2015). Those authors proposed that these are not useful indices for consistently

[2] A failure envelope is a locus of points defining failure on a plot of shear stress versus effective normal stress. A Coulomb criterion is a linear relationship defining this locus.

comparing the brittleness of rocks since they essentially indicate lithology. They argued that the factors dictating where and in which mode stimulated fractures occur is governed by the stress state and strength of the material and can occur in rock with both a traditionally high or low BI. The stress state is the combination of the vertical stress, minimum and maximum horizontal stresses (presuming that one of the principal stress axes is vertical) and the pore pressure. As well as explicitly representing the in-situ stresses, in any consideration of fracture propagation potential, the rock strength should be represented by the failure of intact rock in shear and tension. In reality, this index (where possible) should be upscaled to involve the imprint of the strength of preexisting planes of weakness such as natural fractures and flaws, and weak bed boundaries.

A simple demonstration that the stress magnitude is important comes from the appreciation that the strength and Young's modulus of a rock are affected by the confining pressure in the laboratory (or the effective mean stress in situ). Holt et al. (2011) showed that the static Young's Modulus increases with increasing confining pressure. **For this reason, confining pressure and therefore the complete stress tensor must be considered when trying to determine the "fracability" of the rock.**

Due to advances in computational geomechanics, fracture initiation modeling can be simulated for situations with complex stress states and loading parameters. Application of more complicated constitutive laws and fracture propagation algorithms has been demonstrated by Safari et al. (2013, 2014) and Busetti et al. (2012a, 2012b), for example. **These models have been used to show that the stress state, loading rate, and many other parameters can combine to make a ductile rock act brittle and vice versa.** Mojtaba et al (2015) suggested using these dependencies to optimize hydraulic fracturing treatments for a given reservoir. The goal is to amalgamate basic properties into a dimensionless equation that would take into account the more significant parameters affecting fracturing potential of a particular formation. Figure 1 is from Mojtaba et al. (2015). It shows the ranking and reliability of various parameters that may affect fracturing potential.

Table 1. Selected Expressions of Brittleness Jin et al. (2014)

Formula	Nomenclature	Test Method	Reference
$B_1 = (H_m \times H)/K$	H and H_m are macro- and microhardnesses, K is the bulk modulus	Hardness measurement	Honda and Sanada, 1956
$B_2 = q\sigma_c$	q is the percent of debris with a diameter <0.6 mm. σ_c is compressive strength	Indentation test	Protodyaknov, 1962
$B_3 = \varepsilon_{ux} \times 100\%$	ε_{ux} is unrecoverable elastic strain	Axial loading or some form of loading with measurement of stress and strain	Andreev, 1995
$B_4 = (\varepsilon_p - \varepsilon_r)/\varepsilon_p$	ε_p is peak strain and ε_r is residual strain		Hajiabdolmajid and Kaiser, 2003
$B_5 = (\tau_p - \tau_r)/\tau_p$	τ_p is peak shear stress and τ_r is residual shear stress		Bishop, 1967
$B_6 = \varepsilon_r/\varepsilon_t$	ε_r is recoverable strain and ε_t is total strain		Hucka and Das, 1974
$B_7 = W_r/W_t$	W_r is recoverable and W_t is total strain energy		
$B_8 = \sigma_c/\sigma_t$	σ_c and σ_t are the unconfined compressive and tensile strengths, respectively	Uniaxial compressive strength and Brazilian (or equivalent)	
$B_9 = (\sigma_c - \sigma_t)/(\sigma_c + \sigma_t)$			
$B_{10} = (\sigma_c\sigma_t)/2$			Altindag, 2003
$B_{11} = \sqrt{\sigma_c\sigma_t}/2$			
$B_{12} = H/K_{IC}$	H is hardness and K_{IC} is mode I fracture toughness		Lavin and Marshall, 1979
$B_{13} = c/d$	C is crack length and dis the indent size from a Vickers' indentation test at a specified load, empirically related to H/K_{IC}.	Indentation testing	Sehgal et al., 2003
$B_{14} = P_{inc}/P_{dec}$	P indicates force; "inc" and "dec" indicate increment and decrement, respectively.		Copur et al., 2003
$B_{15} = F_{max}/P$	F is maximum applied force and P is penetration.		Yagiz, 2009
$B_{16} = HE/K_{IC}^2$	H is hardness, E is Young's modulus and K_{IC} is mode I fracture toughness.	Hardness, stress-strain and fracture toughness	Quinn and Quinn, 1997
$B_{17} = \pi/4 + \phi/2$	ϕ is the angle of internal friction	Mohr-Coulomb failure envelope	Hucka and Das, 1974
$B_{18} = \sin\phi$			
$B_{19} = (E_n + \nu_n)/2$	Normalized Young's modulus and Poisson's ratio	Logging or laboratory triaxial measurements	Rickman et al., 2008
$B_{20} = V_{quartz}/V_{total}$	Volume fraction quartz	Logging or XRD	Jarvie et al., 2007

Formula	Nomenclature	Test Method	Reference
$B_{21} = (V_{quartz} + V_{dolomite}) // V_{total}$	Volume fraction of quartz and dolomite		Wang and Gale, 2009
$B_{21} = (V_{QFM} + V_{carbonate} +) // V_{total}$	Volume fraction of quartz, feldspar, mica and carbonates		Jin et al., 2014

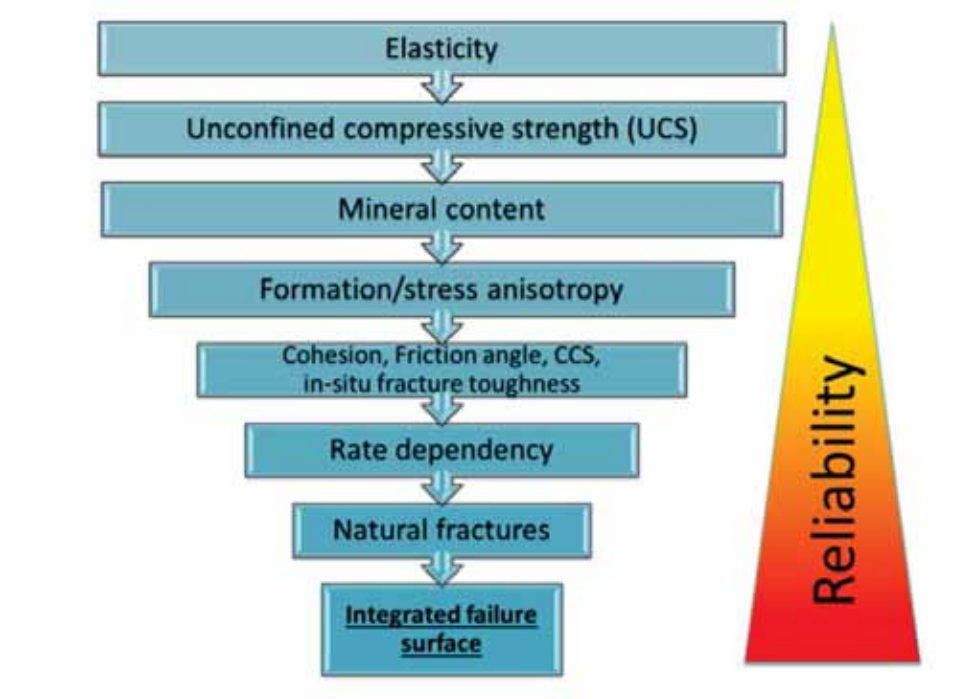

Figure 1. Ranking of parameters by importance in determining how a hydraulic fracture will propagate, as perceived by Mojtaba et al. (2015).

After evaluating the many available techniques and considering data that are readably available for many wells it was determined that using triaxial compressive strength measurements offered a pragmatic method for attempting to create a new "fracability" index. Above all, it was felt that any realistic index should be based on the energy required to fracture. Rate of energy expenditure was also considered to be relevant. Section 6.3 summarizes this method. It is based on acquiring data from triaxial compressive strength testing (at a representative confining pressure). Relative brittleness has been determined based on the stress versus strain curve of these triaxial tests, considering the peak strength, the residual strength, and plastic deformation before significant strain softening. Before describing this physically rationale method for comparing fracturing in different lithologies, it is necessary to consider the influence of pre-existing natural discontinuities and weaknesses. These structural defects will need to be used to modify any core based measurement.

IV. Mechanical Stratigraphy

In the unconventional world, we often hear discussion of "fracability." As indicated previously, it is uncertain as to what this may mean. It is certain that stimulation is required in low and ultralow permeability reservoirs. It is also certain that effective stimulation requires creation or reactivation of fracture systems that reduce the distance that gas or oil needs to travel before it reaches highly conductive networks. It further implies that fabric and stratigraphy are relevant to effective stimulation. The implication is that pre-existing fractures (open or healed), latent fractures (metastable environments) and heterogeneities are relevant. These fractures/weaknesses need to be considered, in conjunction with their encompassing formations being **brittle enough** to favor these fractures in the first place.

How do we infer these brittle characteristics? Are their petrophysical methods for inferring the brittleness of a formation? Can straightforward logging interpretation (predominantly velocity data) be used to infer relative brittleness? Energy-based calculations can be carried out that acknowledge mechanical properties and in-situ stress conditions, as well as geometric lithologic constraints and mineralogy – for the purpose of presuming where natural fracturing may be preferred. This relates to a new approach that can be labeled as "mechanical stratigraphy" rather than "fracability." This incorporates predicting the ability of a formation to carry applied stresses and how it will deform. It implicitly accounts for transversely isotropic, orthotropic or fully anisotropic behavior associated with bedding planes, grain orientation, fractures, and other discontinuities. It also designates how the facies or unit will respond after it has yielded – this means how it will deform, fracture, maintain or lose load-bearing capacity after it has yielded – essentially will it respond in a ductile or brittle manner – in tension or in compression. If fracturing occurs, how is it regulated by lithologic boundaries, pre-existing fractures, and the stress tensor?

Structural geologists have long implicitly considered these topics. Optimizing completion targets and procedures has brought it into the realm of hydraulic of hydraulic fracturing. Early work in the 1980s was summarized by Roegiers et al. who considered the morphology of fractures approaching a discontinuity such as a fault or a bedding plane interface. Even differences in moduli can impact fracture branching. Figure 2 is a schematic example.

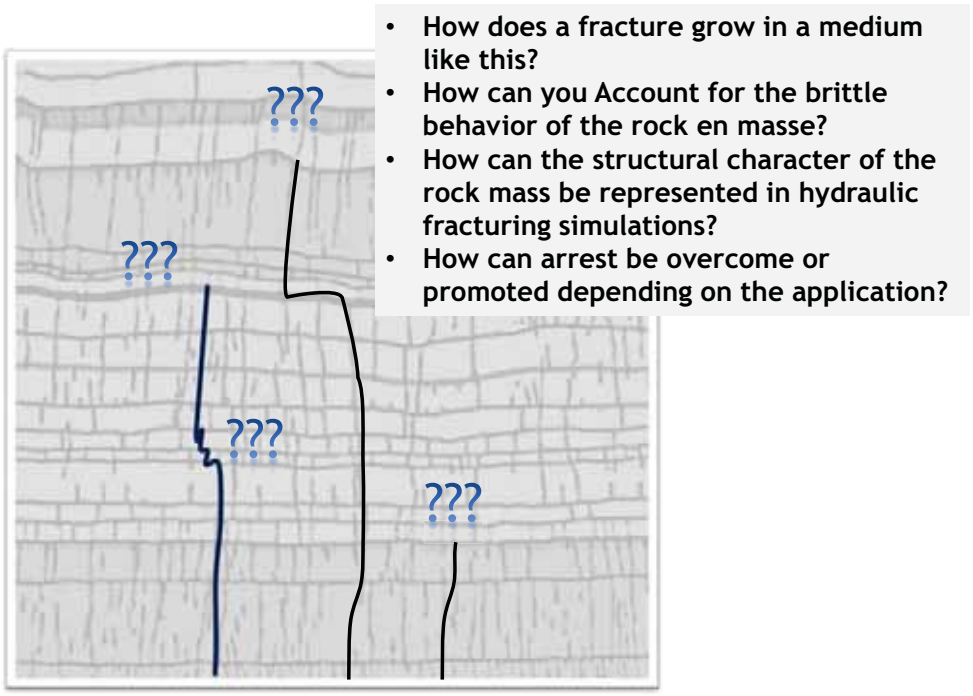

Figure 2. Schematic representation of a hydraulic fracture approaching a preexisting discontinuity. A premise is that the behavior is scalable; i.e., if brittleness is evident on a nominally representative portion of the matrix, that brittleness is reflected at a larger scale. This is an area where additional work is required. In structural geology the relationships between fracture frequency and continuity can be related to layer thickness. In civil engineering, brittle behavior takes into account the size of the structure (for example, the dimensions of a concrete beam). The amalgamation of brittleness from small scale laboratory or near-well logging inferences with structural integrity at a larger scale remains to be reliably dealt with.

"Several authors (Cook and Erdogan, 1972; Erdogan and Biricikoglu, 1973; Ashbaugh, 1978; Hanson and Shaffer, 1980…) have considered the case of constant far-field stress across a bonded interface. The assumptions made in most of the published analyses were that the hydraulic fracture was perpendicular to the interface and that the entire

fracture was uniformly pressurized. … that the stress intensity factor decreases to zero when the fracture approaches a stiffer material and increases to infinity when the fracture approaches a less stiff material."

"Although it would be expected that a fracture would arrest at the interface with a stiffer material, in-situ and laboratory experiments have disproved this expectation. In these experiments, fractures have consistently propagated into stiffer materials. Among the reasons cited by Hanson et al., 1978, and Warpinski et al., 1978, was the reversal of stress intensity trends after interface penetration. For example, for a fracture in a higher modulus material growing towards a lower modulus material, as the interface is penetrated the stress intensity factor decreases."

"Furthermore, stress intensity formulations were derived under the assumptions of medium homogeneity. Near an interface, stresses do not necessarily exhibit a square root singularity at the crack tip (Goree and Venezia, 1977); i.e., the interface starts to exert an influence in advance of the fracture reaching it."

There have been numerous assessments of mechanisms for generation of natural factures in shales (for example, Aydin, 2000; Bai and Pollard, 2000; Gale and Holder, 2008; and many more). Nelson et al. (2000), Eichhubl et al. (2001), Dewhurst et al. (2002), Ross (2004), and Ross and Bustin (2008), have started the dialog about correlations between natural fractures, sedimentology and potential for effective hydraulic fracturing. Kennedy, 2011, described predicting fracture potential in the Mancos formation in Utah.

Subtask 6.2 Discontinuities

I. Objectives

This section summarizes methodologies for fracture growth towards and in the presence of discontinuities. Raw brittleness predictions from core or logging measurements will need to be qualified based on the frequency and character of natural weaknesses and discontinuities.

II. Heterogeneity (Natural Fractures)

During simulations and planning for drilling and stimulating a well, the target formation is often assumed to be homogeneous; in reality, this is almost always not the case. Variations in grain size, laminations, saturation, local diagenetic alterations, natural fractures, as well as other flaws create local stress and strength differences. Due to this inherent complexity of strengths and stresses, hydraulic fractures do not typically propagate in the ideal double wing symmetrical shape that is frequently assumed during simulation. For this reason, methods for accounting for how different flaws impact hydraulic fracturing are being explored by dozens of authors to improve predictions of fracture geometry. While there are many flaws within formations, natural fractures and formation layering may most significantly affect hydraulic fracture propagation. One recent summary of the influence of natural fractures is Jing et al. (2017). The classic reference is Renshaw and Pollard (1995) and the textbook "Hydraulic Fracturing Mechanics," by Yew and Weng (2015) provides a comprehensive and cogent discussion.

II.1 Natural Fractures and Bedding Discontinuities

Natural fractures complicate forecasting hydraulic fracture propagation and have significant consequences for drilling and production. For example, during drilling, natural fractures can cause lost circulation, stuck drill pipe and wellbore instability. During fracturing, fluid can be diverted from a propagating fracture into a natural fracture. If a hydraulic fracture intersects a natural fracture that communicates with an undesirable zone such as a large salt zone, water zone, or through the seal above or below the reservoir, ineffective production can ensue. This suggests that one extreme is that natural fractures can capture hydraulic fractures and cause extension into nonproductive domains. At the other extreme, arrest of a hydraulic fracture by a natural fracture or ductile formation impedes accessing vertically remote pay, as in the case of the Vaca Muerta Formation in Argentina (Sidney Green, personal communication, 2015). As an intermediate scenario, offset of a hydraulic fracture (along a natural fracture) can increase local tortuosity and make proppant transport into that fracture difficult or impossible. That being said, intersecting natural fractures can also increase production by increasing the number of highly permeable conduits

communicating from the reservoir to the wellbore. With these factors to consider, the goal of stimulation design might be to intersect appropriately oriented natural fractures while avoiding increases in tortuosity. It is also preferable to avoid excessive fluid loss that results in the pressure dropping below the pressure required to propagate the hydraulic fracture. Ideally, proppant will be placed in secondary fractures opened in the reservoir although this is often an unfulfilled scenario.

II.2 Will the Fracture Cross a Discontinuity?

The first condition to be considered is: for a hydraulic fracture approaching a natural fracture, under what conditions does the fracture arrest, cross, or offset. One of the first researchers to look at this was Daneshy (1974). Daneshy (1974) considered small flaws, on the scale of several inches and intuitively argued that these do not significantly affect the direction of hydraulic fracture propagation. For medium flaws on the scale of several feet, Daneshy hypothesized that the direction of hydraulic fracture propagation could be impacted, usually only on a local level. If a medium sized flaw is open, the fracture can take 3 different paths as shown by paths A, B, and C in Figure 3 (see also Figure 2 to comprehend the role of natural fracture extent).

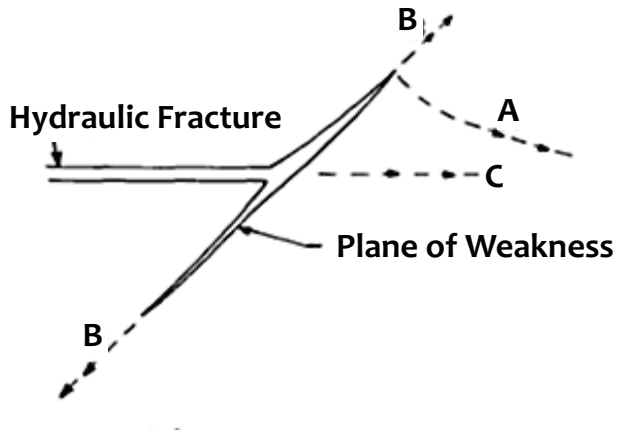

Figure 3. Possible propagation paths of a hydraulic fracturing intersecting a medium-sized flaw (plane of weakness); after Daneshy (1974)

Referring to Figure 3, if the fracture takes path A, the pressure required for a secondary fracture to break out from the end of the flaw and then reorient will be higher than the pressure originally required to propagate the hydraulic fracture. The pressure will then nominally return to the original propagation pressure once the fracture is reoriented to its original propagation plane. That being said, the pressure may be higher if this deviation significantly increases tortuosity and this can also make proppant placement more difficult. The fracture is more likely to take this path if there is a secondary defect near the end of the flaw.

For the fracture to propagate along path B (Figure 3), the pressure will have to increase to above the stress acting normal to the plane of the flaw. This is unlikely since the original fracture plane was perpendicular to the minimum principal stress. As a result, the stress perpendicular to the flaw will be higher than that of the original fracture plane. This impedes the fracture from propagating in this direction; as long as the stress state is fairly uniform through the portion of the formation that the fracture is propagating in and there are no nearby weaknesses. This emphasizes why it is important to know the stress state of the formation and any local variations that may occur. Ideally, local reorientation of hydraulic fractures might be anticipated.

For path C (Figure 3), the hydraulic fracture encompasses the flaw and continues along its original plane with negligible change in propagation pressure. This can be possible in certain stress fields when medium sized flaws are smaller than the dimension of the hydraulic fracture itself. This analysis also holds true for closed, medium-sized flaws. Notice that path A becomes even more unlikely since additional pressure is required to open the flaw and this was not required for an already open flaw. For this reason, Daneshy argued that an unaltered propagation path, path C, is the most likely consequence for a medium-sized closed flaw. For all medium sized flaws, significant orientation change is unlikely, whether the flaw is open or closed. The exception to this is if the concentration of these medium sized flaws is high enough that the area of influence around one flaw overlaps with that of another medium-sized flaw. Under these circumstances, multiple medium-sized flaws can connect and encourage the fracture to reorient as long as there are medium sized flaws close enough together to keep influencing the fracture propagation.

The last type of flaw that Daneshy discussed was a "large-sized" flaw - a fracture or other weakness that is so large that the hydraulic fracture cannot encompass it. If such a significant flaw is closed, the hydraulic fracture is likely to intersect it and cross it maintaining the original propagation plane as long as the treatment pressure remains below that which is required to open the natural fracture/bedding plane discontinuity. If the natural discontinuity is open or partially healed and somewhat conductive, the fracture is not likely to cross this flaw. Instead, it will reorient itself to be parallel to the plane of the flaw and continue in this direction.

Regardless of the flaw size, Daneshy argued that most of them are closed in situ – maybe healed or infilled. Regardless, they are likely to have a higher permeability than the country rock and their tensile strength will be similarly impaired, as demonstrated by Gale et al. (2007). Consequently, fluid leakoff may be a greater concern when intersecting a natural fracture. This is especially true in formations with low matrix permeability. This enhanced leakoff, in combination with the possibility of enhanced tortuosity, increases the likelihood of a premature screenout when higher proppant concentrations are used. In slickwater treatments, this diversion may only locally

change the morphology of the hydraulically stimulated network. Remember that Daneshy was writing this in 1974 when natural fractures were considered a disadvantage rather than a potential mechanism for increasing productive surface area if they can be inflated and propped.

Beyond flaw size, major factors that dictate if a hydraulic fracture arrests at a natural discontinuity, crosses it, or diverts into and propagates along it are the angle of intersection between the natural fracture and the hydraulic fracture and the horizontal stress ratio (the ratio of the maximum and minimum total principal stresses).

Blanton (1982) first investigated this experimentally and concluded that high angles of intersection, greater than ~60°,[3] and high horizontal stress differences would cause a hydraulic fracture to be more likely to cross a natural fracture and not arrest or divert into it.

As indicated previously, Renshaw and Pollard (1995) created a mathematical criterion for when a hydraulic fracture would cross an orthogonal natural fracture. They determined that crossing would occur when:

- the stress zone at the tip of the hydraulic fracture extended across the natural fracture and
- this local stress became high enough to reinitiate the hydraulic fracture on the opposite face but,
- this stress was low enough to not overcome the friction between the faces of the natural fracture and cause shear slippage of the natural fracture.

Blanton mathematically characterized how the angle of intersection and the differential far-field stresses[4] determine whether a natural fracture will open or if the hydraulic fracture will cross this natural fracture. Blanton used insights from his laboratory measurements to extrapolate to field scenarios. As a hydraulic fracture approaches a natural fracture and presuming that it intersects the natural fracture, Blanton argued that the tip of the hydraulic fracture is blunted and the hydraulic fracture is arrested, at least momentarily. In fact, still today, **it is uncertain as to whether and how a process zone (preceding a hydraulic fracture) intersecting the latent natural fracture is relevant.** According to Blanton the natural fracture will open if the pressure at the intersection exceeds the normal stress acting on the natural

[3] This is the angle between the plane of propagation of the natural fracture and the plane of the weakness or discontinuity.
[4] where differential stress is the difference between the maximum and minimum horizontal stresses, although other scenarios are analogous.

fracture and the hydraulic fracture will cross if the pressure required for re-initiation of the hydraulic fracture is below the opening pressure for the natural fracture. Mathematically this is shown in Equations (8) and (9).

For a hydraulic fracture crossing a natural fracture with no dilation (Figure 4):

$$\sigma_n > p > \sigma_t + T_0 \quad (8)$$

For a hydraulic fracture opening a natural fracture and being arrested (Figure 5):

$$\sigma_t + T_0 > p > \sigma_n \quad (9)$$

where:

p ..... pressure inside the fracture,
σ_t ..... total stress acting parallel to the natural fracture,
T_0 ..... tensile strength of the rock, and,
σ_n .....total normal stress acting on the plane of the natural fracture.

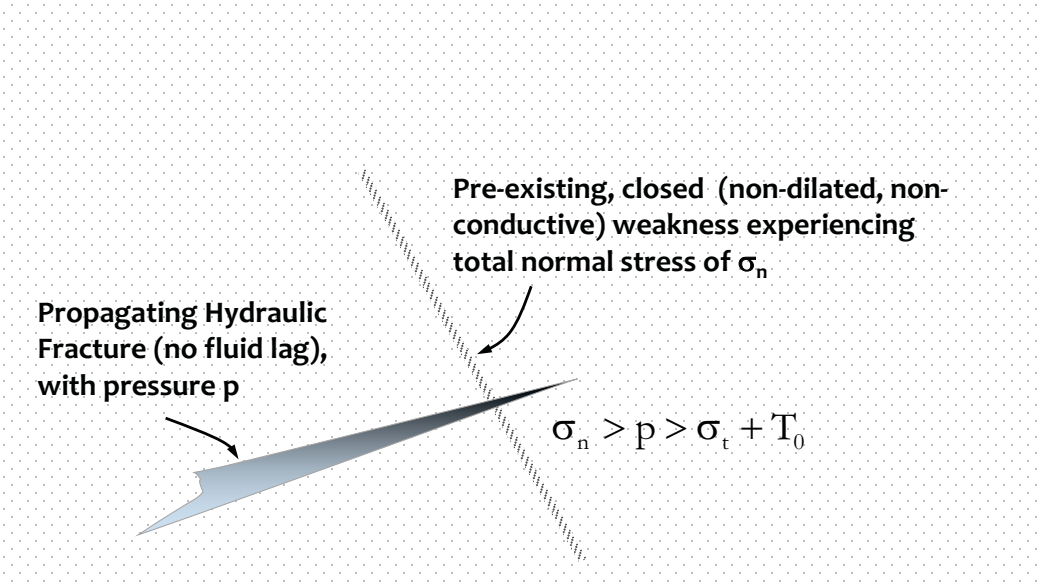

Figure 4. Hydraulic fracture crossing closed natural fracture.

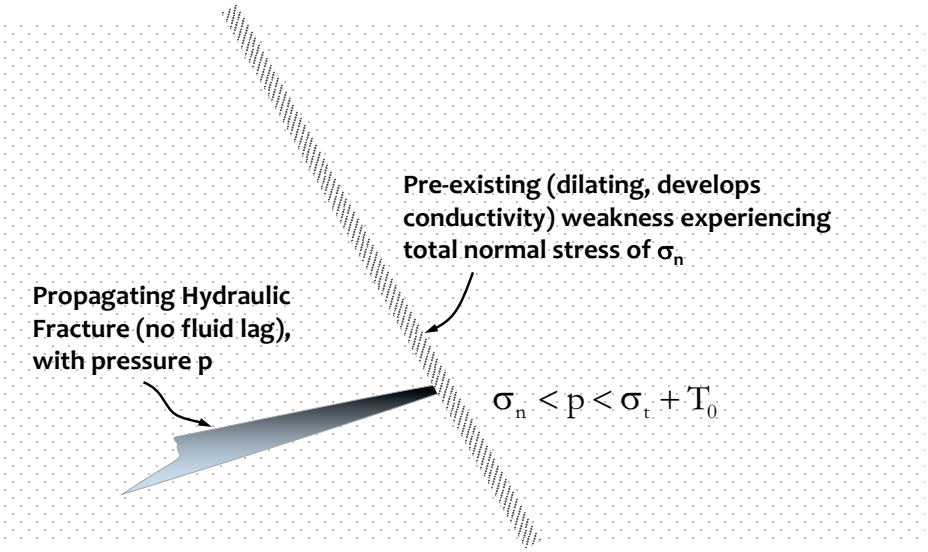

Figure 5. Hydraulic Fracture dilating and arresting at the hydraulic fracture.

According to Blanton, σ_t depends on the far field stresses, pressure in the fracture, frictional slippage along the natural fracture, and the geometry of the interaction zone. Considering these factors Blanton's equation for crossing become (refer to Figures 6 and 7 for geometric definitions):

$$\frac{\sigma_1 - \sigma_3}{T_0} > \frac{1}{\cos 2\theta - b \sin 2\theta} \tag{10}$$

$$b = \frac{1}{2a}\left(v(x_0) - \frac{x_0 - 1}{\mu} \right) \tag{11}$$

$$v(x_0) = \frac{1}{\pi}\left\{ (x_0 + \ell)\ln\left(\frac{x_0 + \ell + a}{x_0 + \ell} \right)^2 + (x_0 - \ell)\ln\left(\frac{x_0 - \ell - a}{x_0 - \ell} \right)^2 + a\ln\left(\frac{x_0 + \ell + a}{x_0 - \ell - a} \right)^2 \right\} \tag{12}$$

$$x_0 = \sqrt{\frac{(1+a)^2 + e^{\pi/2\mu}}{1 + e^{\pi/2\mu}}} \tag{13}$$

where (refer to Figures 6 and 7):

σ_1 ..... maximum principal stress,
σ_2 ..... minimum principal stress,
θ ..... angle of interaction,
a ..... length of the shear slippage zone for the natural fracture,

-l to +l ..... length of the open natural fracture,
μ ..... coefficient of friction,
(l+a) ..... distance past the open section of the natural fracture
.....where the shear stress equals the far field stress, and,
x_0 ..... point of re-initiation of the hydraulic fracture.
Δp_1 ..... pressure drop from the intersection point and the breakout point

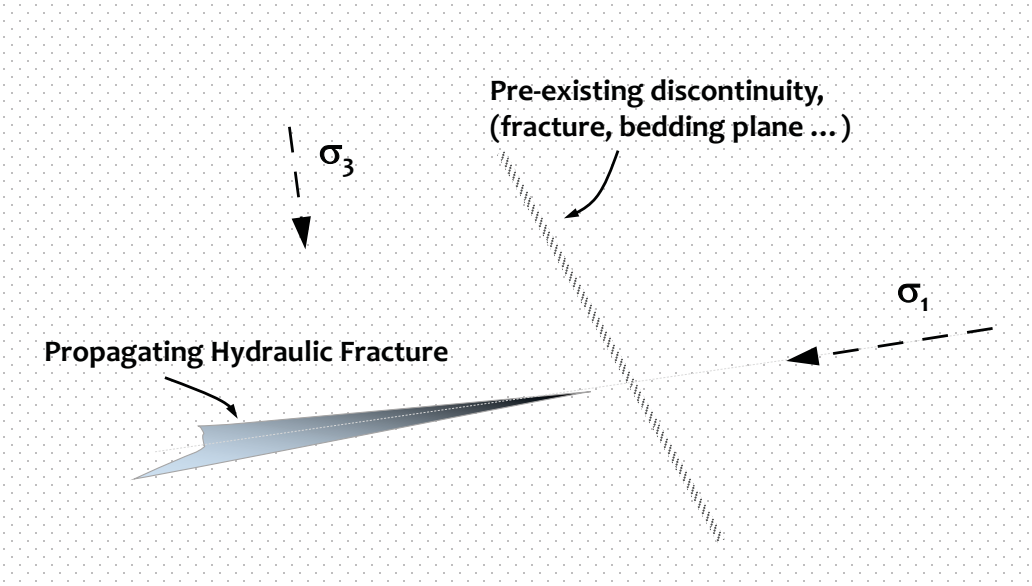

Figure 6. Hydraulic fracture intersecting a natural fracture (modified after Potluri et al. 2005).

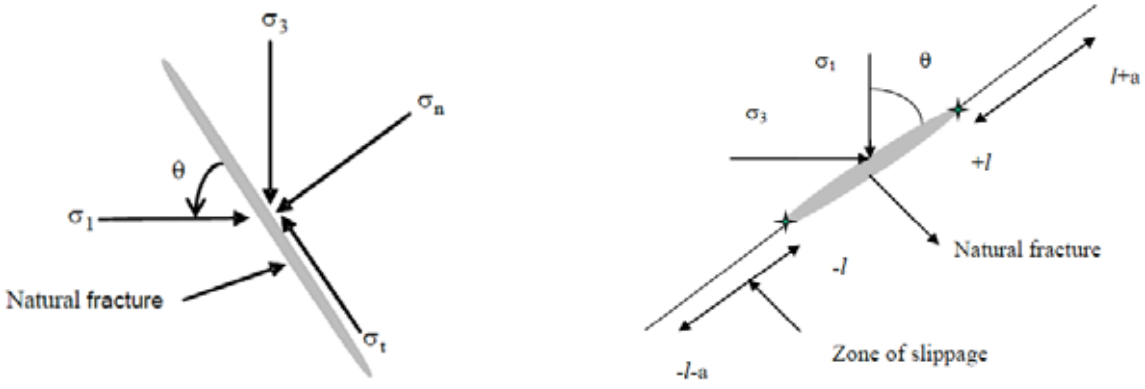

Figure 7. Stress resolution on the natural fracture plane (left panel) and zone of slippage for natural facture (after Potluri et al. 2005).

Once a natural fracture has been intersected by (and possibly even before then) and has dilated, the hydraulic fracture will arrest, at least momentarily. When this happens, there are several possible outcomes, according to Potluri, 2005.

1. The treatment pressure may never exceed $T_{0,I} + \sigma_t$ at any point along the natural fracture. In this situation, shown in Figure 8, the hydraulic fracture does not propagate beyond the intersection with the natural fracture.
2. If the treatment pressure does exceed $T_{0,I} + \sigma_t$ somewhere along the natural fracture, the hydraulic fracture will propagate. This will occur wherever - along the face of the natural facture - the pressure in the dilated fracture is higher than $T_{0,I} + \sigma_t$. This is usually caused by a flaw on the opposite face of the natural fracture that creates a stress concentration that lowers the energy barrier to the propagation of the hydraulic fracture. This can occur directly across from where the hydraulic fracture intersected the natural fracture, at one or both of the tips of the natural fracture, or anywhere along the face between the point of intersection and the tips of the natural fracture. Crossing directly across from the point of intersection is likely since this is the location in the natural fracture that will have the highest pressure. While this is true, the fracture will not propagate in this manner if a flaw elsewhere in the natural fracture creates a lower barrier to propagation (Figure 9).
3. Other situations are shown in Figures 10 and 11.

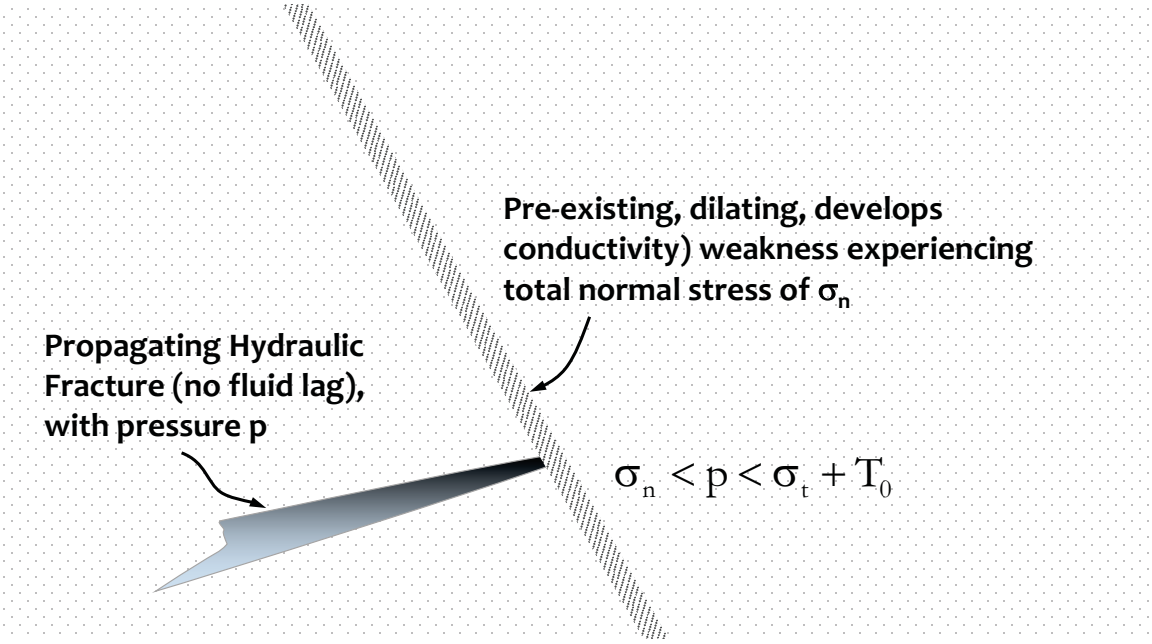

Figure 8. Hydraulic Fracture dilating and arresting at the hydraulic fracture.

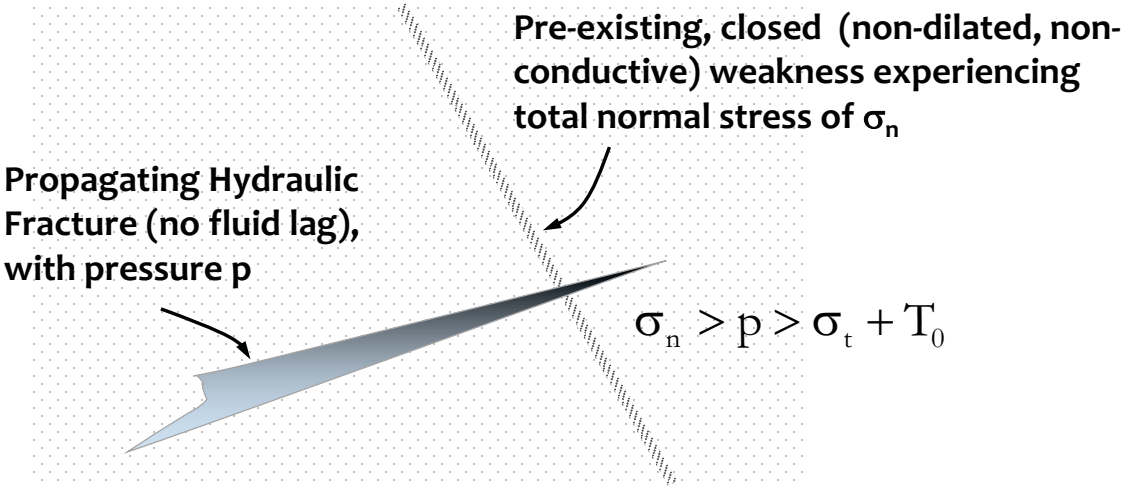

Figure 9. Hydraulic fracture crossing closed natural fracture.

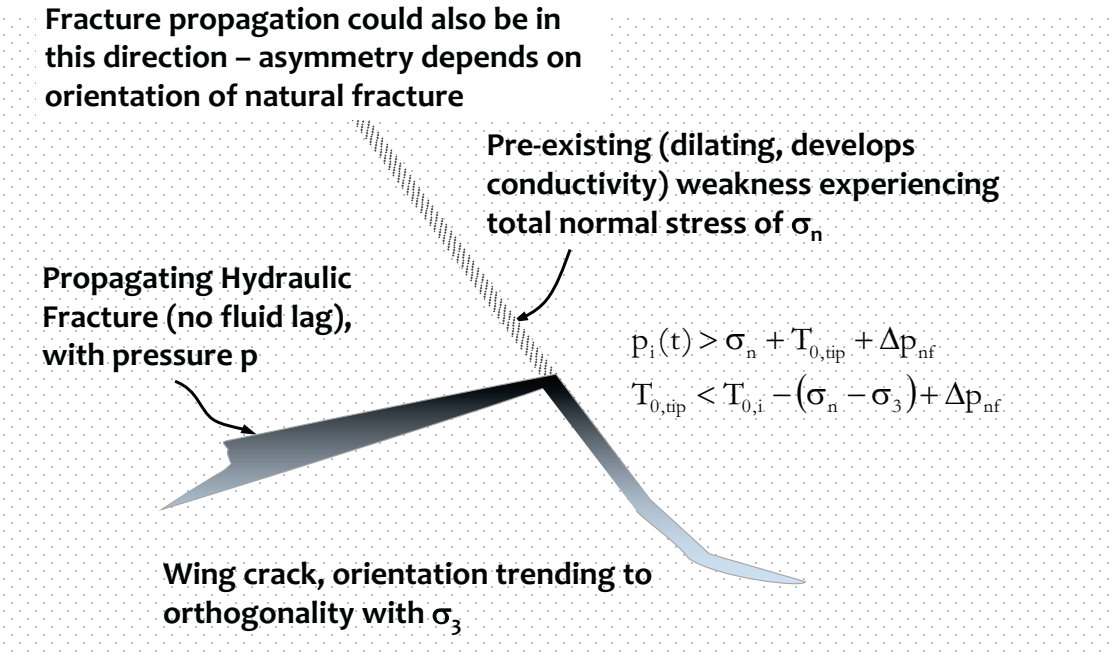

Figure 10. Hydraulic fracture propagates from natural fracture tip (Potluri et al. 2005). Δp_{nf} is the pressure drop from the point of intersection to the fracture tip. Subscript "i" indicates position on the natural fracture.

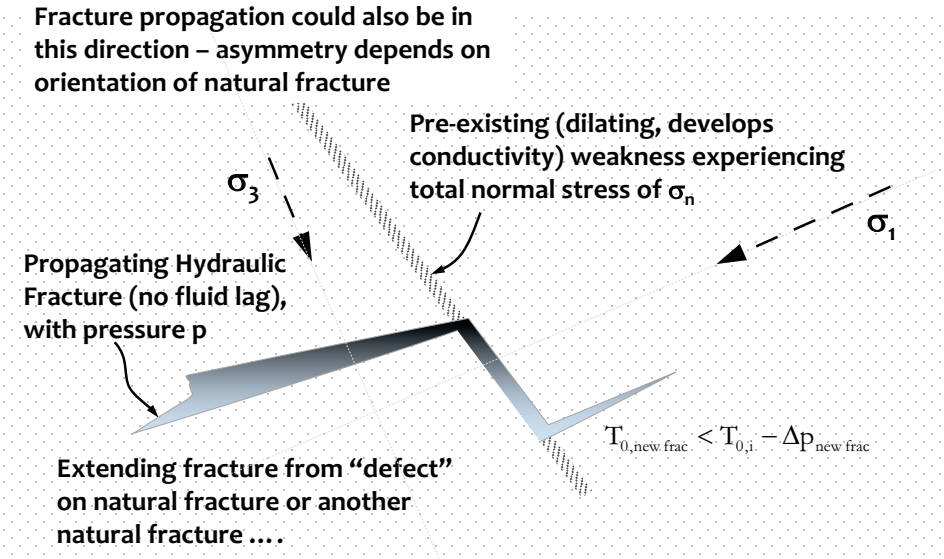

Figure 11. Hydraulic fracture propagates from weak point along the opposite face of the natural fracture offset (Potluri et al. 2005) or another natural fracture is extended. Δp_e is the pressure drop from the point of intersection to the breakout point where the "new" fracture propagates.

Using these mathematical concepts and experimental data obtained from naturally fractured as well as manufactured samples, Blanton was able to forecast that hydraulic fractures tend to cross natural fractures under high differential stress and high angles of approach, otherwise the hydraulic fracture would arrest or divert into the natural fracture.

After Blanton, Warpinski and Teufel (1987) took into account the mechanism of arrest of the hydraulic fracture as it approaches a natural fracture. They attributed arrest to shear slippage along the faces of the natural fracture and/or the dilating of the natural fracture causing leakoff. To a large extent, this view persists today. Using a linear friction law the relationship between the shear stress and the normal stress acting on the natural fracture plane is given by:

$$|\tau| = \tau_0 + (\sigma'_n = \sigma_n - \alpha p)\tan\phi' \qquad (14)$$

where:

τ ..... shear stress,
τ_0 ..... inherent shear strength of the natural fracture plane,
ϕ' ..... effective angle of internal friction,
α..... Biot's poroelastic parameter, and,

$\sigma'_n = \sigma_n - \alpha p$ ..... effective normal stress acting on the fracture plane.

Shear slippage occurs if the shear stress exceeds the resistance associated with cohesion and friction; simply, presuming (for a Terzaghi effective stress definition with $\alpha = 1$):

$$|\tau| > \tau_0 + (\sigma_n - p)\tan\phi' \quad (15)$$

With slippage, the shear stress (τ), normal stress (σ_n), and the pressure at the intersection (of a hydraulic fracture and a natural fracture) are given by:

$$\tau = \frac{\sigma_1 - \sigma_3}{2}\sin 2\left(\frac{\pi}{2} - \theta\right) \quad (16)$$

$$\sigma_n = \frac{\sigma_1 + \sigma_3}{2} + \frac{\sigma_1 - \sigma_3}{2}\cos 2\left(\frac{\pi}{2} - \theta\right) \quad (17)$$

$$p = \sigma_3 + p_{net} \quad (18)$$

where:

p_σ .. excess pressure (in excess of the total minimum stress) causing propagation, and,
θ ..... angle between σ_1 and natural fracture (Figure 12).

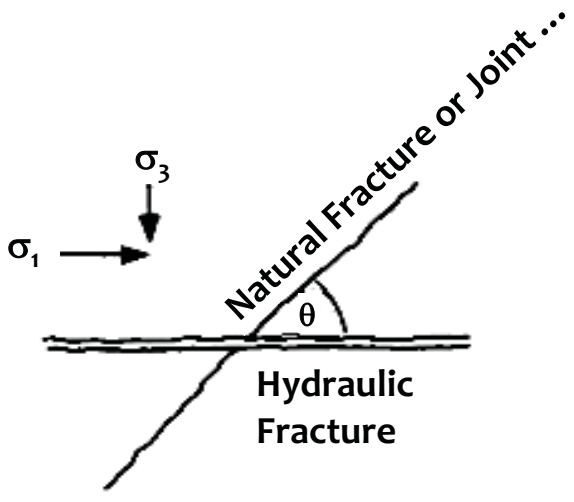

Figure 12. Warpinski and Teufel stress and angle orientation (Warpinski and Teufel, 1987).

Substituting Equations (16) and (17) into Equation (15), the expression for imminent shear slippage on a pre-existing natural fracture can be written as:

$$\sigma_1 - \sigma_3 > \frac{2\tau_0 - 2\mu p_{net}}{\sin 2\theta + \tan\phi'(\cos 2\theta - 1)} \quad (19)$$

If the pressure in the hydraulic fracture exceeds the total normal stress acting on the natural fracture, i.e. $p > \sigma_n$, substituting Equations (17) and (18) into Equation (20) gives a criterion for natural fracture dilation (neglecting any tensile strength):

$$p_{net} = \frac{\sigma_1 - \sigma_3}{2}(1 - \cos 2\theta) \quad (20)$$

The scenario of a hydraulic fracture approaching a discontinuity is complicated because of the alteration of the stress field in advance of the propagating fracture. In its simplest form, linear elastic fracture mechanics would allocate an elevated stress field ahead of the fracture tip. In reality, modelers represent a process zone or a cohesive zone in this domain where partial to complete loss of cohesion (or alternatively plastic deformation) would change the interaction with the natural fracture. Following, LEFM concepts, Renshaw and Pollard (1995) examined the mathematical criteria for a hydraulic fracture crossing a natural fracture orthogonally ($\theta = 90^\circ$) and where the natural fracture does not dilate. They argued that the hydraulic fracture could only cross the natural fracture if the magnitude of the compressional stress acting perpendicular to the faces of the natural fracture is high enough to prevent slip along the faces at the moment when the stress ahead of the fracture tip is sufficient to initiate a fracture on the opposite face. Mathematically this is represented by:

$$-\frac{\sigma_3}{T_0 - \sigma_1} > \frac{0.35(1 + 1/\tan\phi')}{1.06} \quad (21)$$

While these equations provide a mathematical representation of how a fracture can propagate, they do not help significantly with the design of a treatment since the varying fracture toughness in-situ is not known and often there is not significant information about the underlying natural fractures. The Renshaw and Pollard formulations was later extended by Gu and Weng (2010) for natural fractures that were not orthogonal to the original direction of hydraulic fracture propagation. They also formalized the shearing resistance relationship for the natural fractures/bedding plane discontinuities to have friction between the faces as well as some amount of cohesion. Their mathematical algorithm, while not an explicit equation, is easily incorporated into hydraulic fracturing simulators to determine what will happen when a hydraulic

fracture intersects a natural fracture. They make effective use of available reconnaissance for faults (seismic information), local geologic structures, image data at a wellbore scale and stresses to infer natural fractures and determine their orientation and mechanical properties.

II.3 Controlling Complexity

The factors described above are set by the geologic provenance and history and can be optimized through well placement and orientation. On the other hand, treating fluid viscosity and pump rate can be controlled during the treatment process. Manipulating these engineering parameters can help to dictate if the hydraulic fracture will arrest at the natural fracture, cross it, or dilate and propagate along it. For example:

- Low injection rate and low viscosity fracturing fluid can encourage leakoff into a natural fracture causing pressure to build in the natural fracture. If the pressure exceeds the closure pressure of the natural fracture, the natural fracture will dilate (as described above). If pressure continues to build in the natural fracture due to leakoff, the natural fracture can ultimately propagate from either a discontinuity somewhere along its face, from either end of the fracture, or both. This was first described by Nolte in 1979, and he provided equations for estimating when reopening of intersected secondary fractures would occur.[5]
- A higher pump rate and a higher viscosity reduces leakoff which could otherwise be responsible for a pressure drop at the intersection of a hydraulic fracture and a natural fracture. Under these conditions pressure builds more rapidly at the intersection and more easily reaches a level that will propagate the hydraulic fracture on the opposite face of the natural fracture before enough leakoff can occur and dilate the natural fracture Chunfang et al. (2011). That is, viscous losses into the natural fracture afford preferential propagation of the main fracture. One school of thought is that hybrid or reverse hybrid treatments can access multiple secondary fractures. Higher viscosity will favor most hydraulic fractures crossing natural fractures with an occasional natural fracture dilating and causing branching. This branching can increase the surface area of the fracture.

II.4 Near-Wellbore Effects

If the flow path for fluids is complicated by interaction with natural fractures, pressure losses can occur. Near-wellbore tortuosity has been recognized for decades. This type of tortuosity and reduced widths are different than when the hydraulic fracture has been established away from the wellbore. The first consideration for minimizing near

[5] It was assumed that the hydraulic fracture path was unaltered and the fracture propagated through the weakness, initially without opening. Nolte predicted when opening would occur after this time.

wellbore tortuosity is correct perforation orientation. An initiated fracture will preferentially propagate perpendicular to the minimum principal secondary principal stress – away from the wellbore this will be the far-field total principal stress. Therefore, a rule of thumb when initiating the fracture near the wellbore is to have the perforations oriented within 10° of this preferred fracture plane. Otherwise, the fracture may not initiate from the perforation (Behrman et al (1991)). This may result in a much narrower fracture near the wellbore than in the main body of the fracture, It is well known that this will increase the pumping pressure required to propagate the fracture or could lead to a screenout (Romero et al (1995)). Pumping slugs of 100 mesh or similar sand or other proppant has been shown to reduce these losses by erosion.

In addition to perforation orientation Fallahzadeh et al. (2015) proposed manipulating a parameter termed as "fracturing power". This is an insightful parameter regardless of whether the obstruction to fracture growth is near to the wellbore or is a distant discontinuity. Fallahzadeh et al. defined pumping power as the pumping rate times the viscosity divided by the time from the beginning of pressurization until breakdown and propagation – for understanding near-wellbore restrictions.[6] One can imagine a similar term for determining the complexity of a propagating fracture. *They found that values of fracture power between 0.5 and 2.0 resulted in planar fracture geometry, where values above this resulted in curved fractures and values below this resulted in multiple fracture branches from the point of initiation.* For a fracturing treatment, this suggests that:

- The pump rate should start out low keeping the fracture power low enough to start a planar fracture and reduce tortuosity.
- Once the fracture has moved away from the wellbore, the pump rate should be increased to increase the fracture power in order to facilitate crossing natural fractures. With some geostatistical appreciation of in-situ discontinuities it should be possible to tune a treatment to either follow or ignore natural weaknesses; i.e., in and ideal world, to predict when the hydraulic fracture will cross "promising" natural fractures and to reduce pump rate at these intersections to dilate these natural fractures and cause branching. Since, actual fracture location will rarely be known, cyclic injection could be a serious possibility that has not been significantly explored by the industry. Alternatively, viscosity variation is possible.

III. Heterogeneity (Layering, Bedding Plane Discontinuities ….)

In many ways, layering influences hydraulic fracture propagation similarly to the interaction of hydraulic fractures with natural fractures. There are two main differences.

[6] Power is energy per unit time (lbf-ft/s).

1. The first difference is that the interface between layers may often have a great deal more cohesion than between a closed but unhealed fracture. This often helps prevent delamination of layers and allows the hydraulic fracture to cross from one layer to the next. That being said, the multiplicity of interfaces can gradually impede and arrest a propagating fracture.
2. The second main difference is that the material on the "other side" of the layering interface can have significantly different mechanical properties when compared to the material the hydraulic fracture is propagating from. If the material on the other side of the interface has a higher tensile strength (or fracture toughness), the hydraulic fracture will have a harder time propagating across the interface and into the new material. Similarly, for modulus and local stress variations (see Clifton et al., 1978). As a result, one or many interfaces between the layers is/are more likely to delaminate and have the hydraulic fracture propagate along it/them. Thinking about this in a slightly different way, a large change in material properties means that the two layers cannot deform equally. If the stress due to deformation of one layer is enough to overcome the bonding strength or cohesion between the two layers then the fracture will be encouraged to propagate along the interface (at least for some distance).

Other than these complexities, the same type of rules for crossing a natural fracture can apply to crossing an interface between two layers. High differential stress, high approach angle, and high friction between layers will cause the fracture to cross the interface. For approach angles higher the 70°, coefficients of frictions greater than 0.5, moderate horizontal stress differentials of 400 psi or more, hydraulic fractures are much more likely to cross an interface (Dong et al., 2015). Ranking these factors qualitatively, based on established research, from most important to crossing to least important to crossing are: differential stress, approach angle, friction/cohesion at the interface, and then strength contrast across the interface.

IV. Summary

This section demonstrated that at a small scale, some index of brittle behavior could be considered in deciding on the extent of fracture propagation and possibly how complex that fracture geometry might be. Beyond a simple brittleness index, the geologic context is essential (stress magnitudes and contrast, frequency and character of discontinuities and layering). Finally, treatment parameters can be considered in a fashion similar to a brittleness index, by considering energy expenditure over time (power).

Subtask 6.3 Brittleness

I. Objectives

Recognizing the role of brittleness, it is relevant to identify potential analytical algorithms that can be applied to available well-scale data (logs, cuttings, core, etc.) to illuminate brittle characteristics. The two Utah shale plays will be used to demonstrate the procedure.

II. Introduction

How and when a rock fails is an important factor in well construction and stimulation – as well as in a wide range of other industries - from constructing tunnels, bridges and large buildings to mining. Brittleness is a concept used in many of these disciplines. Mining engineers are interested in the integrity of pillars and avoiding rock bursts. Civil engineers will characterize the brittleness of reinforced concrete structural components. The petroleum industry also often characterizes performance of a hydraulic fracture by terms such as brittleness. Unfortunately, the petroleum industry often determines brittleness from pre-failure elastic properties. Most industries do consider brittleness but recognize it as explicitly characterizing the rate of energy release and/or loss of load bearing capacity after peak load or yield. While at first "brittleness" may seem like good terminology for describing rock failure, there is a significant problem with the terminology. Alternative definitions will improve comprehension of hydraulic fracture propagation and containment.

III. Why is Brittleness Important?

Brittleness has been a term used for the describing the failure mechanism of materials since the 1950s when Honda and Sanada (1956) developed one of the first brittleness indicators using bulk modulus along with micro- and macro hardness (Table 1). Since then, dozens of brittleness indicators have been developed, each with some moderate success in describing how and when materials will fail relative to each other. Many of these indices have been correlated to well logging parameters with fairly good success. Yet, many definitions of brittleness can often be more of a lithology or mineral composition indicator rather than a true indication of suitability for efficient hydraulic fracturing and optimal production. For that reason, the rock mechanics community has been moving toward a more comprehensive approach for evaluating the suitability of a location to complete. This approach has led to the development of several indices that have been termed "Fracability Indices", FI (for example, Mullen et al. 2012, Jin et al. 2015). Brittleness Indices, BIs, have not been abandoned in favor of the development of FIs. Instead, some definitions of FIs have incorporated a BI in conjunction with one or more of the following: fracture toughness measurements, an energy term such as

strain energy release rate, G_{IC}, the strike and dip angle of natural fractures, the difference between the minimum and maximum horizontal stresses, and the ratio of shear to normal stress acting on natural fractures (Jin et al. 2014, Fuxiang et al. 2015, Alzahabi et al. 2015). As an example, Mullen et al. (2012) used the parameters in Table 2 to determine a complex fracturing index (CFI) for a reservoir that contains three types of faults. Table 3 shows what type of fracture network is created based on the type of fault, the dip angle, and the strike angle. Table 3 is particularly important because it enfranchises large scale geologic structures. The table shows a so-called Stress Fracture Index that bases the complexity of the hydraulic fracture on the nature of the in-situ stresses, the dominant local Andersonian faulting regime and the orientation of weaknesses relative to the nominal direction of fracture propagation. The levels of fracture complexity defined were:

Thief ..... Natural fracture that causes excessive leakoff,
Complex..... Natural fracture causes some branching of the fracture network,
Very Complex ..... Natural fracture causes extensive fracturing, and,
Inconsequential ..... Natural fracture remains closed and does not cause branching.

Using these parameters in conjunction with a BI to develop an FI provides a more comprehensive view on how hydraulic fractures would propagate and how they might interact with discontinuities such as bedding planes and natural fractures.

Table 2. CFI method (Mullen et al. 2012) - Contributing Data

Composition and Storage Properties	Elastic Properties	Strength and Failure Properties
Porosity	Young's Modulus	Fracture Toughness
Water Saturation	Poisson's Ratio	Unconfined Compressive Strength
Clay Volume	Dry Brinell Hardness	Tensile Strength
Mineralogy	Brittleness Index	Cohesion
		Angle of Internal Friction
		Coefficient of Sliding Friction

Table 3. Qualitative Guidelines for Stress Fracture Index: The Effect of the Orientation of Preexisting Planes of Weakness (Mullen et al. 2012)

	Thief	Complex Geometry	Very Complex Geometry	Inconsequential
Normal Fault				
Fault Strike†	±15°	±15°	-30-50° 0° 30-50°	Does Not Meet Other Criteria
Fault Dip	50-70°	30-50° or 50-70°	30-90°	
Stress Fracture Index	1	2	3	0
Strike Slip Fault				
Fault Strike†	±15°	±15°	-20-40° 0° 20-40°	Does Not Meet Other Criteria
Fault Dip			30-90°	
Stress Fracture Index	1	2	3	0
Reverse Fault				
Fault Strike†	-105-75° 0° 75-105°		Any orientation other than Thief	Does Not Meet Other Criteria
Fault Dip	15-45°		0-45°	
Stress Fracture Index	1		3	0

† Relative to the azimuth of the maximum horizontal stress.

IV. Currently Suggested Brittleness Indicators

Numerous definitions for brittleness have been developed (Table 1), with no consensus about which definition is most appropriate for describing the brittle characteristics accompanying failure. A good reference is Jin et al. (2014). In reality, many of the developed terms for brittle behavior may be inappropriate for predicting rock failure behavior since many of them are based on parameters that are **not** determined under representative in-situ conditions - or do not characterize post-yield behavior.

The premise of this section is that incorporating fracture mechanics concepts into assessment of "brittleness", could be useful. At its most fundamental level, this implies considering an energy balance. If a formation does not deform plastically,[7] the energy required to hydraulically fracture that formation incorporates the pressure required to overcome the minimum principal stress and the cohesive forces among the grains forming the matrix of the rock.[8] If the rock deforms plastically, additional energy is required to overcome the energy dissipated by this plastic deformation. Currently, few brittleness indices directly rely on an energy approach. An alternative method is suggested that explicitly considers the energy associated with fracture generation. First, however, conventional brittleness indicators are summarized.[9] In general there are three major categories of brittleness indices; characterizing the rock by its elastic properties, petrophysical properties, or strength properties. These three categories were reviewed and discussed by Herwanger et al. (2015).

IV.1 Indices Based on the Elastic Properties

The first category contains the most commonly used index, which was developed by Rickman et al. (2008). This index uses Young's Modulus and Poisson's Ratio to describe the brittleness of the rock. When using this protocol, rocks with a high Young's Modulus and a low Poisson's Ratio are classified as being brittle. An example of a Rickman-type brittleness index is shown in Equation (22):

$$\mathrm{BI} = 0.5\left\{\left(\frac{\mathrm{E}-1}{7}\right)\times 100 - \left(\frac{\nu - 0.4}{0.25}\right)\times 100\right\} \qquad (22)$$

where:

BI ..... Brittleness Indicator nominally varying from 0 to 1. The lower the value, the greater the perceived ductility.

[7] Deformation is entirely elastic (recoverable).
[8] For a propagating hydraulic fracture, it is also necessary to consider viscous losses due to fluid flow in the fracture. Energy will also be expended as fluid leaks off into the formation.
[9] See also Section 6.1

E ..... Young's Modulus (x 10^6 psi)
ν ..... Poisson's ratio (dimensionless)

Other brittleness indices that fall into this category use related parameters such as acoustic logging shear and compressional wave velocities, bulk density, and/or other combinations of Lamé's parameters.

IV.2 Indices Based on Mineralogy

The second category of indices uses the mineralogy of the rock to indicate if it should be described as being brittle. With these indices, the logic is that a larger proportion of more rigid minerals, i.e. higher bulk and Young's moduli, indicates a more brittle rock and vice versa. An example of this type of index, developed by Wang and Gale (2009), is shown Equation (23):

$$BI = \frac{V_{Quartz} + V_{Dolomite}}{V_{Quartz} + V_{Calcite} + V_{Clay} + V_{Dolomite} + V_{TOC}} \quad (23)$$

where:

BI ..... Brittleness Indicator nominally varying from 0 to 1.
V_{Quartz} ..... Volume fraction of quartz
$V_{Dolomite}$ ..... Volume fraction of dolomite
$V_{Calcite}$ ..... Volume fraction of calcite
V_{Clay} ..... Volume fraction of clay
V_{roc} ..... Volume fraction of rock fragments

IV.3 Indices Based on Strength

The third category uses nondimensionalization of strength parameters such as the unconfined compressive strength and the tensile strength to determine if the rock is brittle or not. An example of such an index is that developed by Altindag (2003), as shown in Equation (24).

$$BI = \frac{\sigma_c}{\sigma_t} \quad (24)$$

where:
BI ..... Brittleness Indicator nominally greater than 0.
σ_c ..... Unconfined compressive strength (psi, MPa)
σ_t ..... Tensile strength -absolute value (psi, MPa)

As Herwanger et al. pointed out, this type of BI suggests that the steeper gradient of the Mohr-Coulomb failure envelope the more brittle the material. As they put it, when "assuming a linear Mohr-Coulomb failure envelope, by this definition a high brittleness index implies, at a constant tensile strength, a steeper gradient of the failure envelope (**measured by the coefficient of internal friction, ϕ**) than a low brittleness index."

IV.4 Critique

Herwanger et al. go on to argue that all of these brittleness indices are essentially equivalent to lithology indicators and may not actually indicate brittleness. In fact, these indices preferentially result in a high BI for a quartz-rich rock and a low BI indicates a clay-rich rock. Qualitatively this may be realistic but relative comparisons are inaccurate.

V. A Comprehensive (Compromise) Brittleness Indicator

Taking into account the definitions above, a dimensionless brittleness index is proposed that is based on the energy required for failure and the energy expended after the initiation of-nonrecoverable deformation. The testing platform selected was a triaxial compression test. This was selected because the confining pressure in such a test is an analog to the stresses acting in situ which have a first order control on energy expenditure - either by localized deformation (brittle) or expenditure of energy by plastic deformation without reduced load bearing capacity. What does this indicator need to do?

1. Acknowledge that brittleness is a reflection of how a rock behaves after peak or yield strength. This implies that the second item (below) is true. Brittle or elastic behavior cannot be exclusively forecast from elastic properties.
2. Cannot be exclusively described by elastic properties.
3. Should have some correlation with facies and lithology.
4. Considers the rate at which energy is expended after peak or yield strength (in addition to the amount of energy stored before peak/yield (partially accounted for by item 2)).

There is some precedent. Energy based reservoir evaluations were published by Bereskin and McLennan (2008). The foundation for their analysis was a criterion for rock bursting of coal mine pillars, presented by Tang and Kaiser (1998). Kennedy (2011) built on these relationships and developed correlations of brittleness with various Mancos formation lithofacies.

It was proposed that the methodology should represent energy (units of force multiplied by displacement) and that laboratory triaxial testing could provide baseline data. Five example triaxial tests are shown in Figures 13 through 18 for six different wells where core was available. These are indicated in Table 4.

Table 4. Wells Evaluated

Well	Target Formation
Bill Barrett 14-1-46	Uteland Butte member of the Green River formation
Bill Barret 14-3-45	Uteland Butte member of the Green River formation
Cesspooch 15-21-3-3W	Uteland Butte member of the Green River formation
Cane Creek 7-1	Cane Creek member of the Paradox formation
Cane Creek 26-3	Cane Creek member of the Paradox formation
Cisco State 36-13	Cane Creek member of the Paradox formation

Three of the wells, Bill Barrett 14-1-46, Bill Barret 14-3-45 and Cesspooch 15-21-3-3W, are located in the Uteland Butte member of the Green River formation in the Uinta basin in eastern Utah, south of the Uintah Mountains. The other three wells, Cane Creek 26-3, Cisco State 36-13, and Cane Creek 7-1, exploit the Cane Creek member of the Paradox formation in the Paradox basin in southeastern Utah. An example triaxial test from each well is shown in Figures 13 through 18. Additional laboratory data are included in Appendix A.

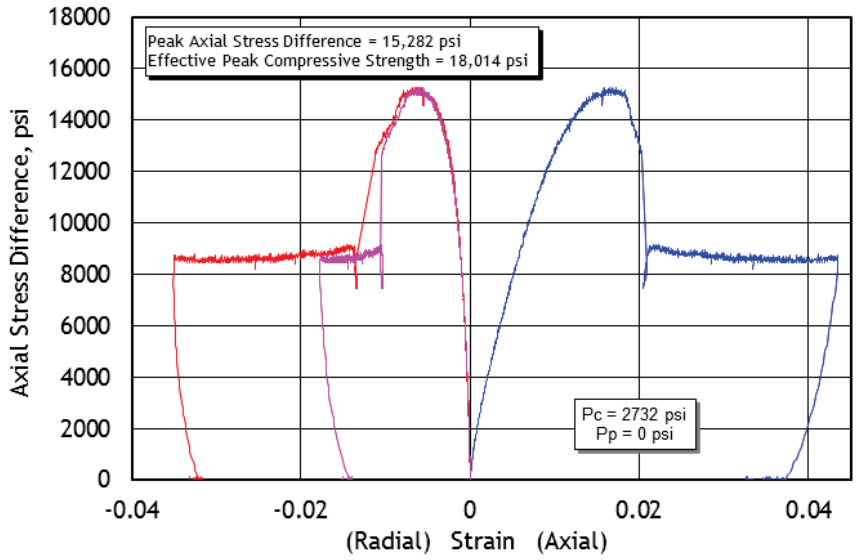

Figure 13. Example triaxial test for Cisco State 36-13 well. The confining pressure was 2732 psi and no pore pressure was applied. This sample was plugged vertically from a depth of 7,588.80 ft MD. The effective compressive strength at this confining pressure is 18,000 psi. The peak axial stress difference is 15,282 psi.

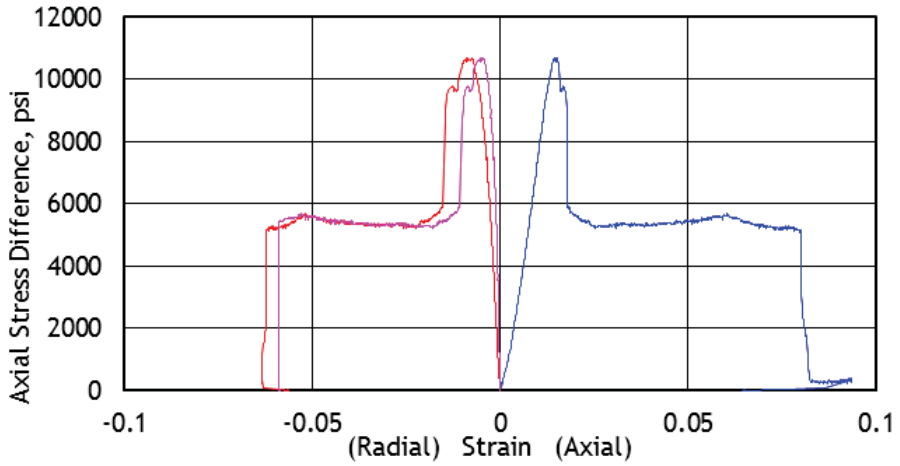

Figure 14. Example triaxial test for Cesspooch 15-21-3-3W. The confining pressure was 1813 psi and no pore pressure was applied. This sample was plugged vertically from a depth of 8497.05 ft MD. The effective compressive strength at this confining pressure is 12,500 psi. The peak axial deviatoric stress was 10,685 psi. Notice the similarities and differences with Figure 13. After failure, stress drops rapidly in both cases. More strain is accommodated by ductility in the sample shown in Figure 13 (i.e., after the yield point is reached in Figure 13, there is more strain before catastrophic loss in load-bearing ability).

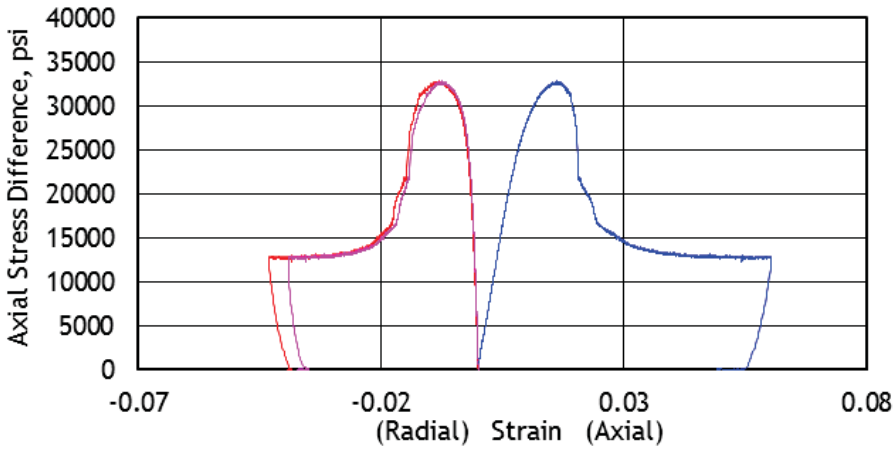

Figure 15. Example triaxial test for well Cane Creek 26-3. The confining pressure was 3882 psi and no pore pressure was applied. This sample was plugged vertically from a depth of 7464.5 ft MD. The effective compressive strength at this confining pressure is 36,700 psi. The peak axial deviatoric stress was 32,820 psi. While the morphology of the stress-strain curve at failure is similar to Figure 13, the stresses experienced are much higher because the confining pressure is higher.

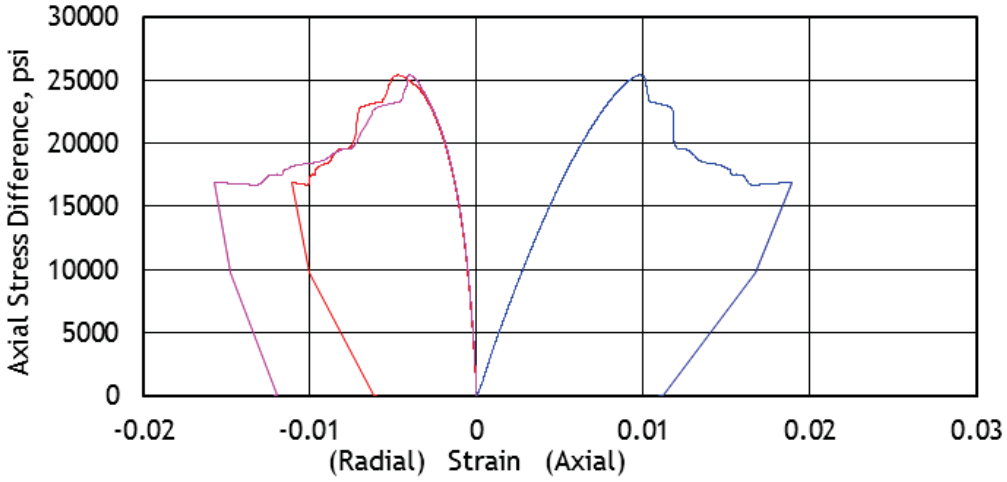

Figure 16. Example triaxial test for well Cane Creek 7-1. The confining pressure was 3348 psi and no pore pressure was applied. This sample was plugged vertically from a depth of 7609.35 ft MD. The effective compressive strength at this confining pressure is 28,760 psi. The peak axial deviatoric stress was 25,407 psi. The morphology of the stress-strain curve at failure is very different from the samples shown in the previous figures. A much more ductile failure process is indicated in the sample shown in this figure.

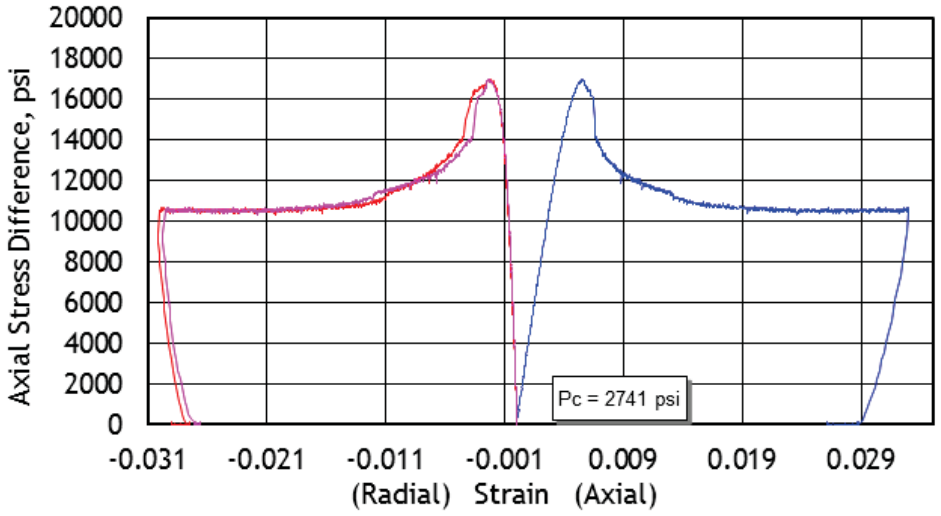

Figure 17. Example triaxial test for well Bill Barrett 14-1-46. The confining pressure was 2741 psi and no pore pressure was applied. This sample was plugged parallel to bedding (nominally horizontal) from a depth of 6684.70 ft MD. The effective compressive strength at this confining pressure is 19,740 psi. The peak axial deviatoric stress was 16,995 psi.

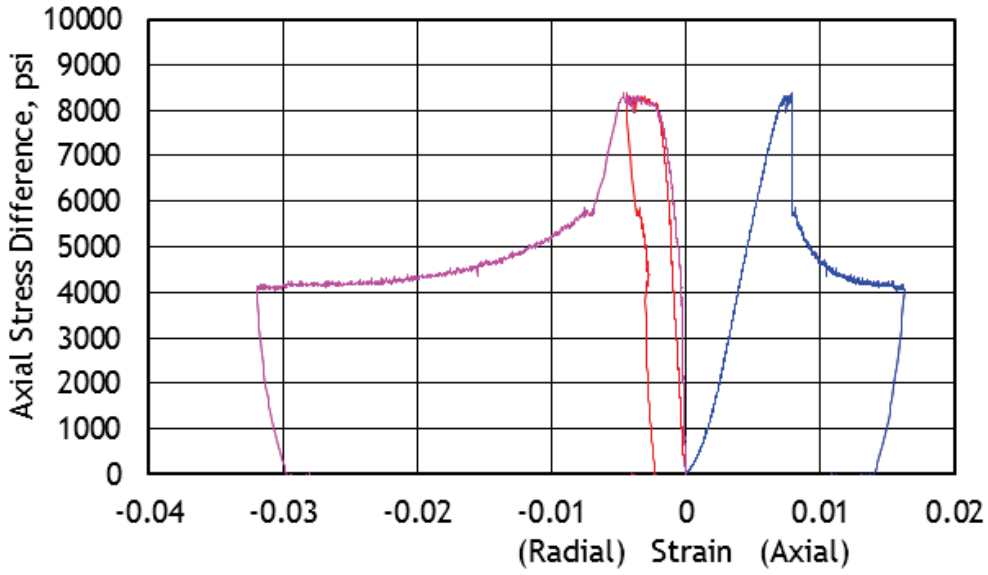

Figure 18. Example triaxial test for well Bill Barrett 14-3-45. The confining pressure was 1325 psi and no pore pressure was applied. This sample was plugged perpendicular to bedding (nominally vertical) from a depth of 7358.35 ft MD. The effective compressive strength at this confining pressure is 9,700 psi. The peak axial deviatoric stress was 8378 psi. This sample again appears to be quite brittle. In fact, this may correlate with the lower confining pressure - increased brittleness.

Multiple techniques were evaluated to infer comparative brittleness. The methods explored were as follows.

- ***Zone 1: Ratio of secant modulus to Young's modulus:*** The premise here is that the secant modulus (from the start of the application of deviatoric stress to the peak stress) incorporates non-recoverable deformation. The premise is that the lower this number, the more ductile the failure will be because energy has been expended before strain softening. Figure 19 shows an example. This might be called a Deformation Index.
- ***Zone 2: Ductility Index - Amount of plasticity or strain hardening:*** Figure 20 shows a second segment of a stress strain curve which may or may not exist. This is perfect plasticity or strain hardening in advance of stronger localization and reduction in load bearing capacity.
- ***Zone 3a: Tang and Kaiser (axial)*** Tang and Kaiser provided a very insightful relationship for failure of coal pillars. One measure of this is the amount of energy released when failure occurs. This can be approximated as follows, using the methodology of Bereskin and McLennan (2008).

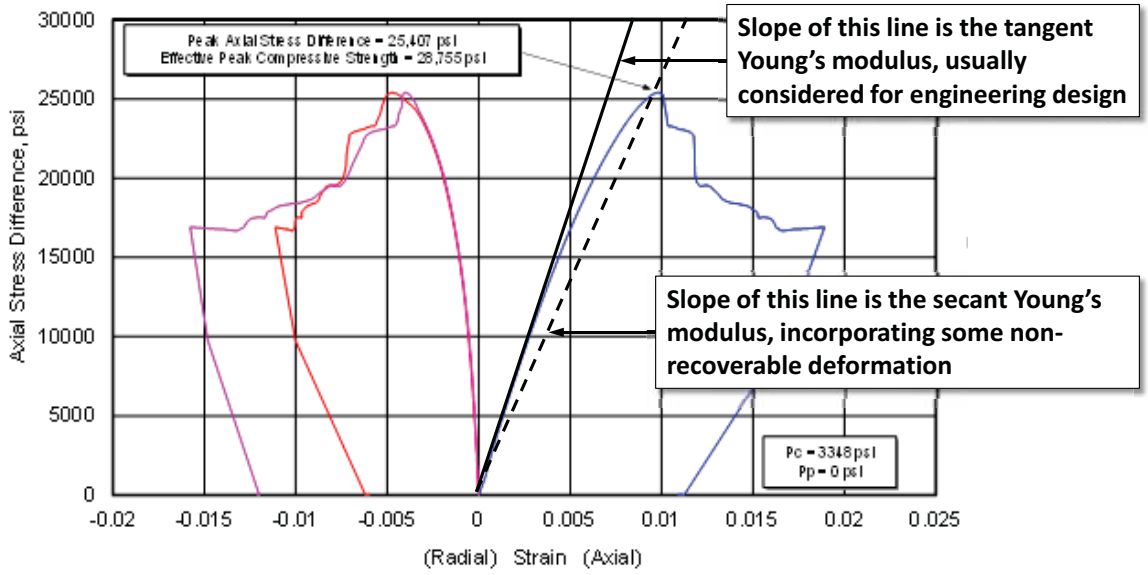

Figure 19. The ratio of the secant to the tangent Young's modulus is an indication of how much plastic deformation is experienced before failure. Presumably, if energy is dissipated before a localized fracture results, the overall behavior can be considered to be more brittle. It was called Zone 1 because it included elastic behavior experienced early in the loading process.

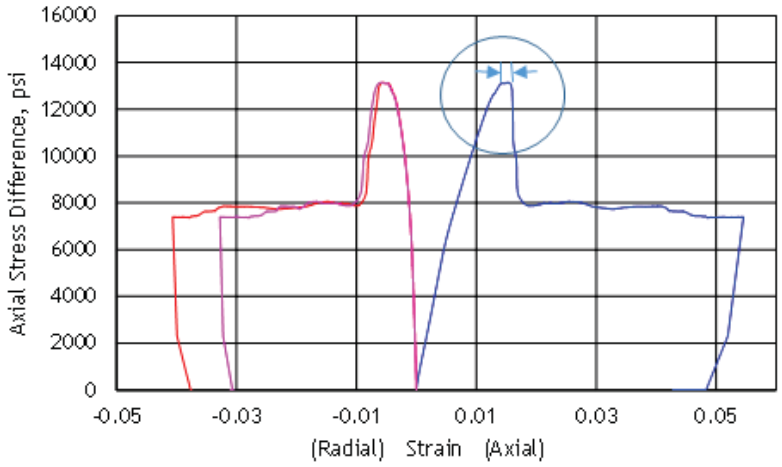

Figure 20. Plastic strain (strain hardening or perfectly plastic behavior) is another indication of dissipation of energy before failure. Albeit in this sample, the stress drop occurring after this period is substantial and still indicates brittle behavior. Picking start and end points for this index adds further complexity. It could be extended to consider volumetric behavior.

Continuing with Zone 3a:

1. Approximate the stress drop on failure as the difference between the peak and the residual triaxial strengths. Calibrate this with laboratory testing and logging data.
2. Grossly approximate the energy released (alternatively view this as energy stored with potential for fracturing) as follows ("C" denotes the triaxial compressive strength, either peak or residual):

$$\text{Energy} \equiv 0.5\frac{C_{peak}}{E}\left(C_{peak} - C_{residual}\right)(1-2\nu) \qquad (25)$$

This energy analog is plotted in Figure 21 for a well in the Paradox Basin. The speculation is that the greatest fracture potential is where the released energy is highest and where it occurs most rapidly. This and a similar calculation described below can delineate an energy-based zone where brittle fracturing is favored. More recently, Birgenheier and her students at the University of Utah (personal communication) have developed these concepts further, evaluating energy release associated with triaxial compression testing. Figure 22 shows a schematic diagram of how this can be applied for evaluating triaxial compression data. By integrating under the stress-strain curve (Figure 22), an estimate of stored energy is derived. If this is used in conjunction with the rapidity and magnitude of post-peak strain softening, an energy release indicator is developed that is favorable for forecasting the potential for fracturing. Birgenheier and her students have calculated an energy index using mining industry protocols (after Tang and Kaiser, 1998), as shown in Equation 26. This can be reported in energy units (Joules) or specific energy (energy per unit mass, J/kg).

$$E_f = \frac{1}{2E}(\Delta\sigma_f)^2 V_f \qquad (26)$$

where:

E_f ..... energy released by failure
E ..... Young's modulus
$\Delta\sigma_f$ ..... stress drop after brittle failure
V_f ..... failed volume

The failed volume was approximated as:

$$V_f = \underbrace{\varepsilon_a(1-2\nu)}_{\substack{\text{Volumetric Strain} \\ \text{Based on Axial strain}}} \underbrace{\frac{\pi}{4}D^2L}_{\substack{\text{Sample} \\ \text{Volume}}} \qquad (27)$$

where:

ε_a ..... axial strain occurring during strain softening (energy release)
ν ..... Poison's ratio
D ..... sample diameter
L ..... sample length

Multivariate regression using (grain size, bioturbation and lamination indices, calcite content, and Poisson's ratio) gave a remarkably high coefficient of determination ($R^2 = 0.71$) for samples from the Mancos formation. This suggests the total combined geologic variability accounts for approximately 70% of the variability in E_f for those Mancos formation samples.

- ***Zone 3b: Tang and Kaiser (volumetric)*** Tang and Kaiser provided a very insightful relationship for failure of coal pillars. This is similar to the technique described above with the exception that the bulk modulus is used instead of Young's modulus and the volume is based on the measured volumetric strain (rather than the axial strain and Poisson's ratio).

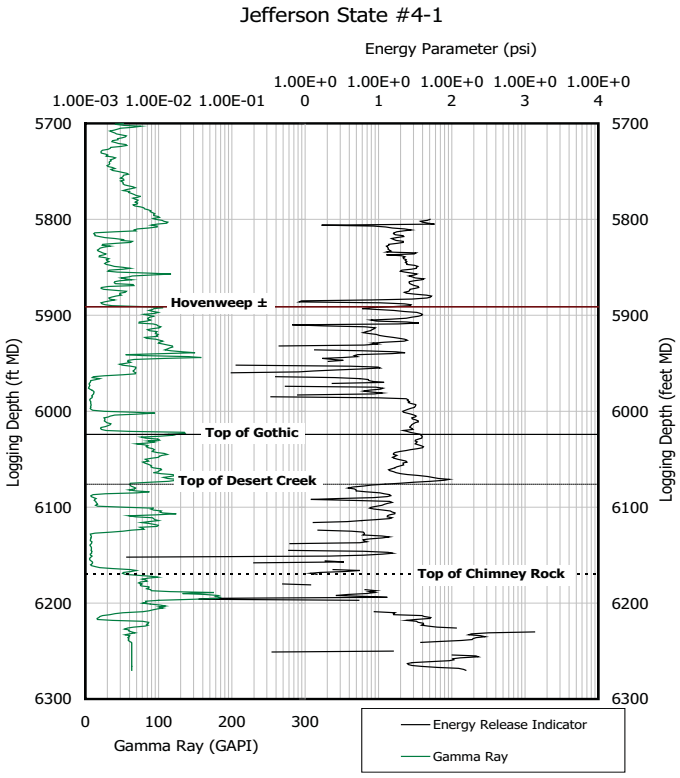

Figure 21. Logging inference of brittleness – based on estimates of stored energy. It is hypothesized that the higher this released energy, the greater the potential for fracturing, shear, extensional or flexural during previous history.

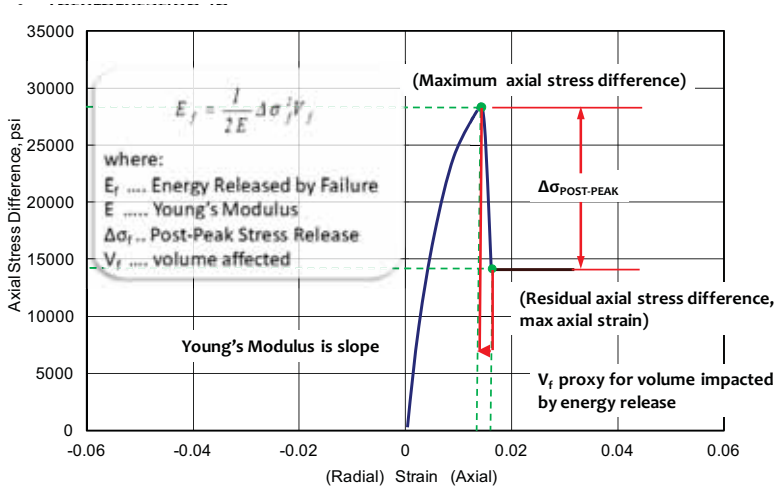

See Tang and Kaiser (1998)

Figure 22. Application of the Tang and Kaiser method for axial deformation during a triaxial compression test.

- ***Zone 4: Peak to Residual Strength Ratio:*** The mechanics of this technique are demonstrated in Figure 23.

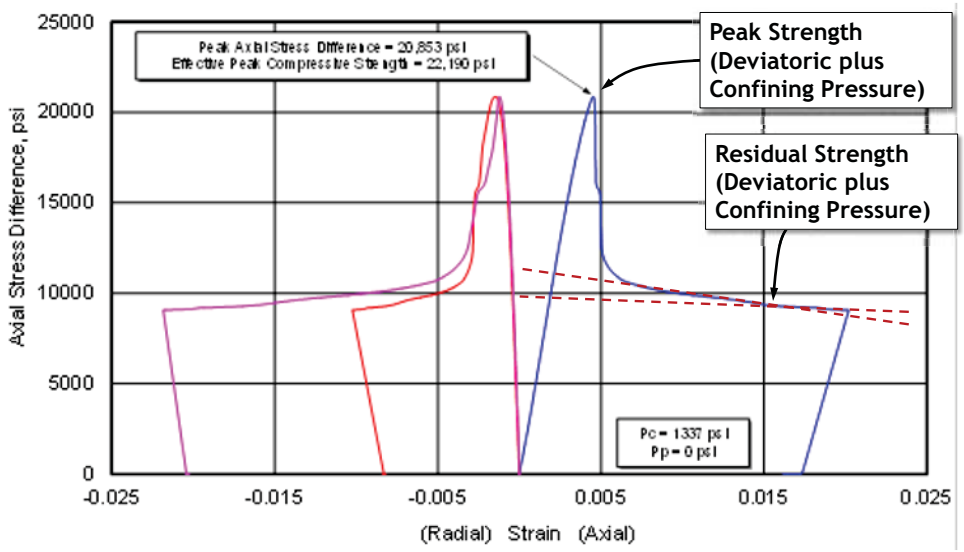

Figure 23. Another method of inferring the brittleness is the ratio of the peak to residual strengths. This can be done using deviatoric stresses but is probably more appropriately done with the deviatoric stress plus the confining pressure. There is difficulty frequently in picking an appropriate value for the residual stress. Some agreed upon criterion for picking that stress is appropriate.

Examples are shown in Figures 24 through 29.

Lithology	Sample ID	Depth (ft)	Orientation	As Received Bulk Density (g/cm^3)	Confining Pressure (psi)	Peak Effective Compressive Strength (psi)	Effective Residual Compressive Strength (psi)	Young's Modulus (10^6 psi)	Poisson's Ratio
Fidelity Cane Creek CCU7-1									
silty dolomite	CCU1-1	7609.35	Vertical	2.624	3348	28,755	20,162	3.447	0.23
	CCU1-3	7609.15	Horizontal	2.599	3881	44,946	24,935	5.507	0.30

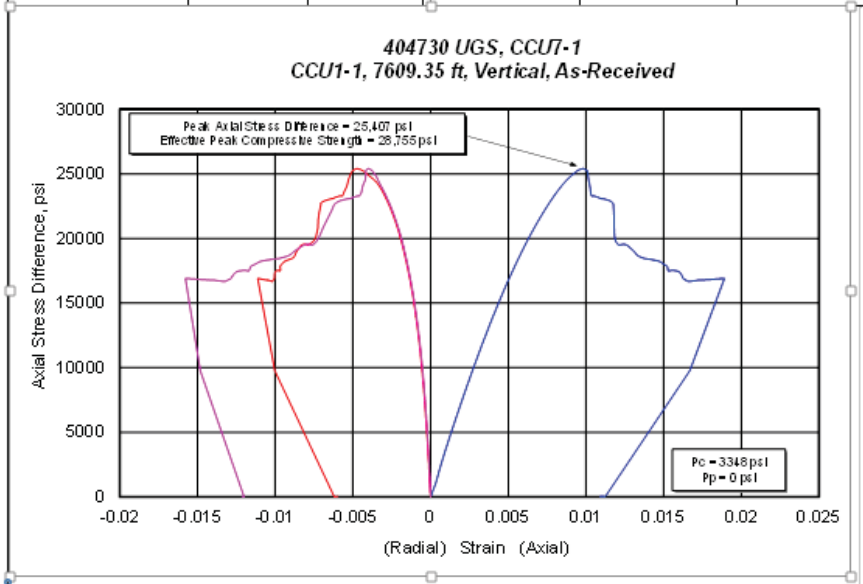

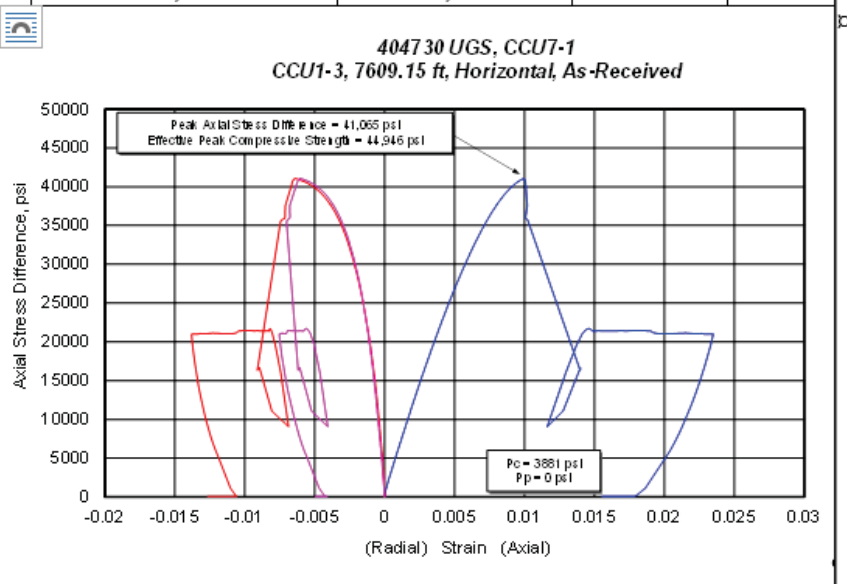

Zone 1 Deformation Index: Ratio of Secant E at Peak to E: 1.36	Zone 1 Deformation Index: Ratio of Secant E at Peak to E: 1.34
Zone 2 Ductility Index: Amount of Plastic or Strain Hardening Strain: 0.006	Zone 2 Ductility Index: Amount of Plastic or Strain Hardening Strain: 0
Zone 3a: Tang and Kaiser Index (Axial): 1.85 J/g	Zone 3a: Tang and Kaiser Index (Axial): 6.54
Zone 3b: Tang and Kaiser Index (Volumetric): 2.42 J/g	Zone 3b: Tang and Kaiser Index (Volumetric): N/A
Zone 4: Peak to Residual Strength Ratio: 1.51	Zone 4: Peak to Residual Strength Ratio: 1.90

Figure 24. A comparison of behavior between a vertical and horizontal sample from approximately 7609 ft MD in the Cane Creek CCU7-1 well. In this case, the vertical sample somewhat more ductile in that it releases energy more slowly after peak strength has been exceeded. Five methods (denoted as zones) were shown to reflect how failure occurred.

Bill Barrett 14-1-46

Lithology	Sample ID	Depth (ft)	Orientation	As-Received Bulk Density (g/cm^3)	Confining Pressure (psi)	Peak Effective Compressive Strength (psi)	Effective Residual Compressive Strength (psi)	Young's Modulus (10^6 psi)	Poisson's Ratio
tan dolomite	BTR1-1	6684.40	Vertical	2.282	1337	19420	9580		
	BTR1-6	6684.40	Vertical	2.348	1337	22190	10410	5.390	0.22
	BTR1-2	6684.780	Horizontal	2.140	2741	19740	13240	3.829	0.27

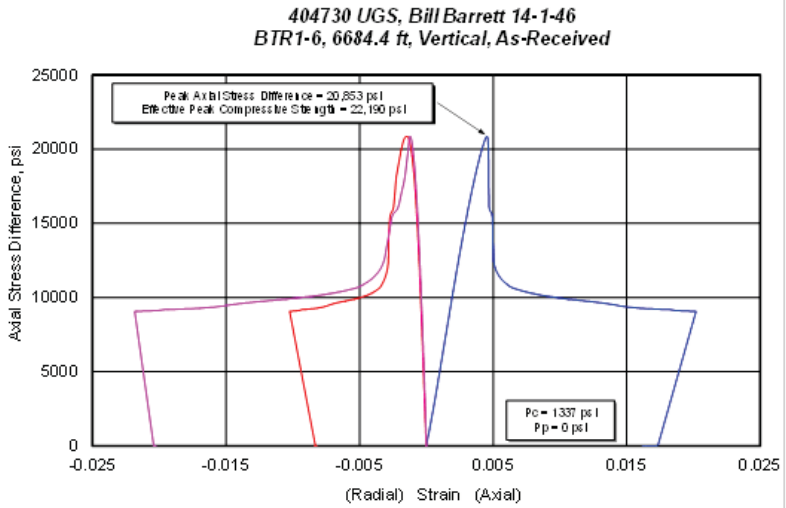

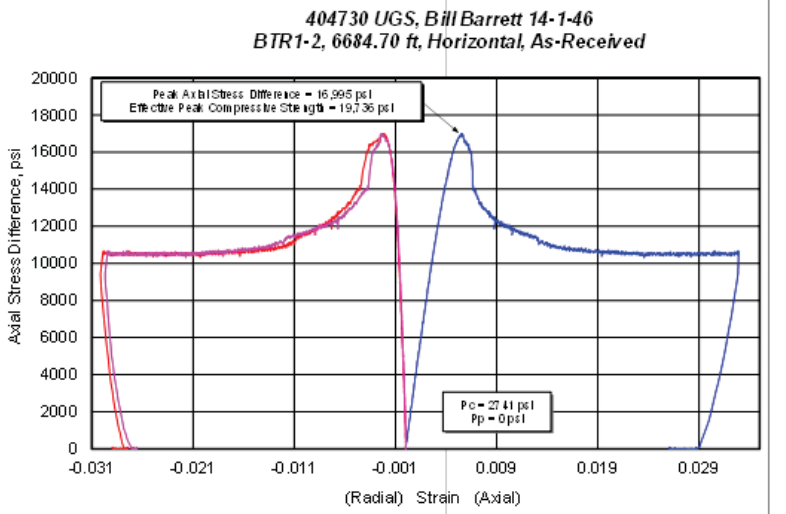

Zone 1 Deformation Index: Ratio of Secant E at Peak to E: 1.16	Zone 1 Deformation Index: Ratio of Secant E at Peak to E: 1.23
Zone 2 Ductility Index: Amount of Plastic or Strain Hardening Strain: 0.01	Zone 2 Ductility Index: Amount of Plastic or Strain Hardening Strain: 0.05
Zone 3a: Tang and Kaiser Index (Axial): 3.21	Zone 3a: Tang and Kaiser Index (Axial): 3.095
Zone 3b: Tang and Kaiser Index (Volumetric): 3.83	Zone 3b: Tang and Kaiser Index (Volumetric): 3.137
Zone 4: Peak to Residual Strength Ratio: 2.18	Zone 4: Peak to Residual Strength Ratio: 1.61

Figure 25. A comparison of behavior between a vertical and horizontal sample from approximately 6684 ft MD in the Bill Barrett 14-1-46 well. In this case, the vertical sample failed in a brittle manner in that it released energy rapidly after peak strength has been exceeded and there was little non-linearity before loss in load bearing capability. Five methods (denoted as zones) were shown to reflect how failure occurred.

Bill Barrett 14-1-46

Lithology	Sample ID	Depth (ft)	Orientation	As Received Bulk Density (g/cm^3)	Confining Pressure (psi)	Peak Effective Compressive Strength (psi)	Effective Residual Compressive Strength (psi)	Young's Modulus (10^6 psi)	Poisson's Ratio
dolomite	BTR2-1	6693.70	Vertical	2.428	1399	29110	9470	4.861	0.29
	BTR2-2	6693.45	Horizontal	2.544	2744	49930	20490	7.011	0.29
	BTR2-5	6693.45	Horizontal	2.433	2744			4.796	0.31

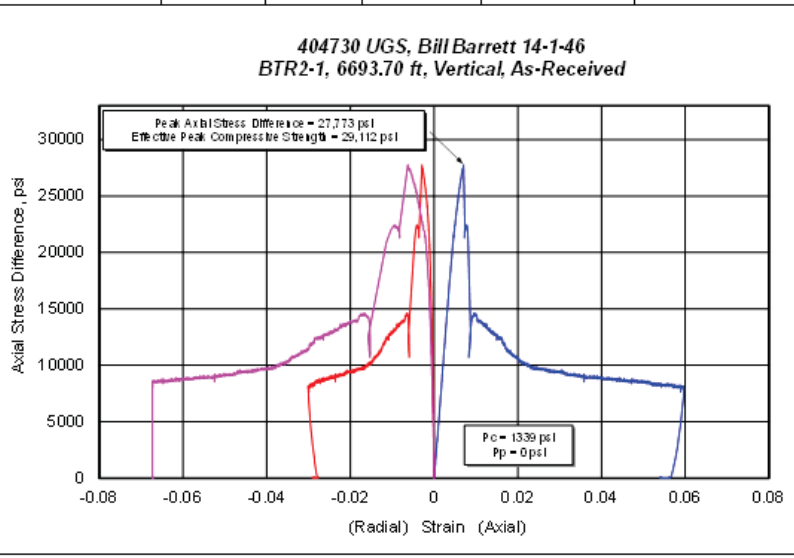

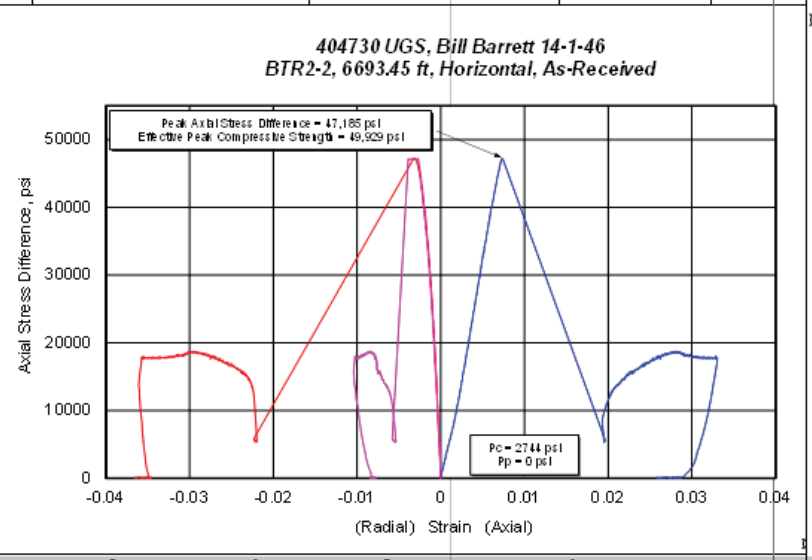

Zone 1 Deformation Index: Ratio of Secant E at Peak to E: 1.22
Zone 2 Ductility Index: Amount of Plastic or Strain Hardening Strain: 0
Zone 3a: Tang and Kaiser Index (Axial): 16.3
Zone 3b: Tang and Kaiser Index (Volumetric): 23.0
Zone 4: Peak to Residual Strength Ratio: 2.80

Zone 1 Deformation Index: Ratio of Secant E at Peak to E: 0.98
Zone 2 Ductility Index: Amount of Plastic or Strain Hardening Strain: N/A
Zone 3a: Tang and Kaiser Index (Axial): N/A
Zone 3b: Tang and Kaiser Index (Volumetric): N/A
Zone 4: Peak to Residual Strength Ratio: N/A

Figure 26. A comparison of behavior between a vertical and horizontal sample from approximately 663 ft MD in the Bill Barrett 14-1-46 well. In this case, the vertical and horizontal samples failed in a brittle manner in that they released energy rapidly after peak strength has been exceeded and there was little non-linearity before loss in load bearing capability. Five methods (denoted as zones) were shown to reflect how failure occurred. The horizontal sample failed with a large motion on its macroscopic failure plane.

Bill Barrett 14-1-46

Lithology	Sample ID	Depth (ft)	Orientation	As Received Bulk Density (g/cm^3)	Confining Pressure (psi)	Peak Effective Compressive Strength (psi)	Effective Residual Compressive Strength (psi)	Young's Modulus (10^6 psi)	Poisson's Ratio
gray limestone	BTR3-1	6698.25	Vertical	2.586	1340	23980	13700	4.038	0.14
	BTR3-2	6699.00	Horizontal	2.614	2747	52680	19850	8.657	0.32

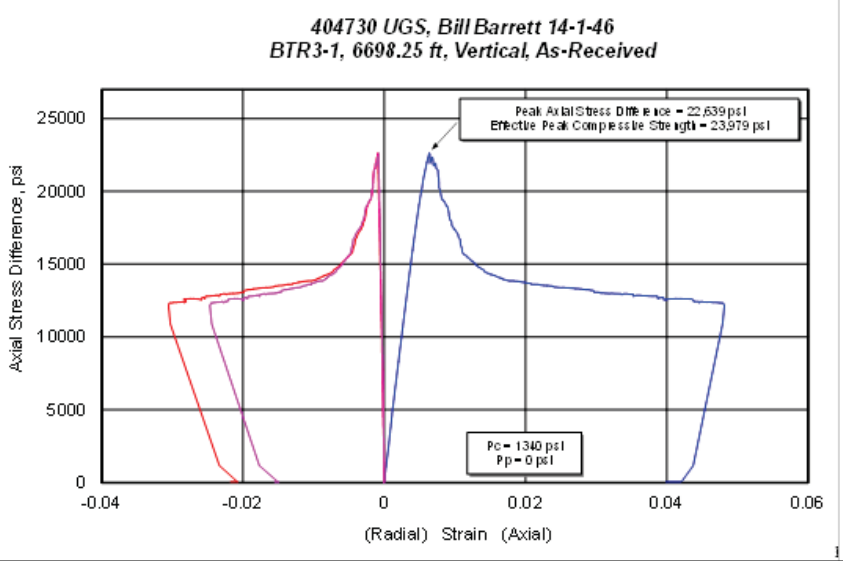

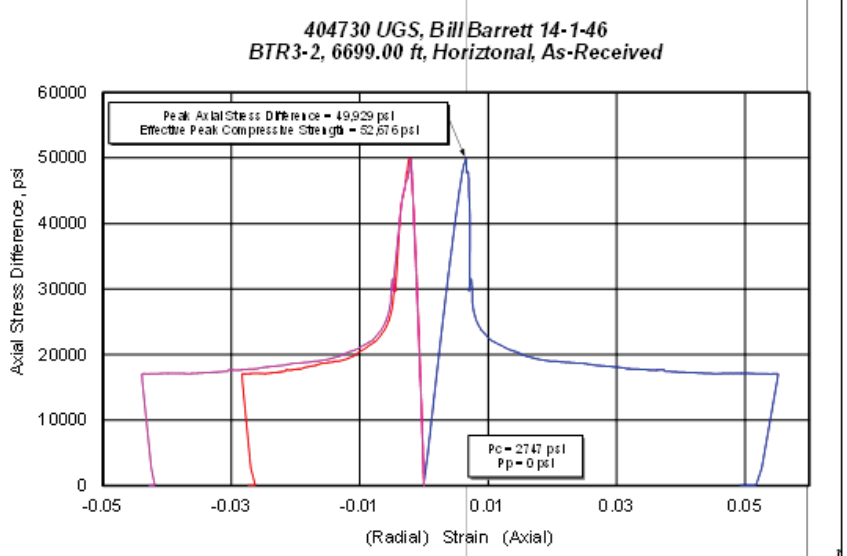

Zone 1 Deformation Index: Ratio of Secant E at Peak to E: 1.12
Zone 2 Ductility Index: Amount of Plastic or Strain Hardening Strain: 0.12
Zone 3a: Tang and Kaiser Index (Axial): 1.99
Zone 3b: Tang and Kaiser Index (Volumetric): 1.19
Zone 4: Peak to Residual Strength Ratio: 1.60

Zone 1 Deformation Index: Ratio of Secant E at Peak to E: 1.12
Zone 2 Ductility Index: Amount of Plastic or Strain Hardening Strain: 0.02
Zone 3a: Tang and Kaiser Index (Axial): 51.0
Zone 3b: Tang and Kaiser Index (Volumetric): 18.5
Zone 4: Peak to Residual Strength Ratio: 1.79

Figure 27. A comparison of behavior between a vertical and horizontal sample from approximately 6698 ft MD in the Bill Barrett 14-1-46 well. In this case, both samples failed in a somewhat brittle manner in that they released energy rapidly after peak strength has been exceeded and there was little non-linearity before loss in load bearing capability. Five methods (denoted as zones) were shown to reflect how failure occurred.

Bill Barrett 14-1-46

Lithology	Sample ID	Depth (ft)	Orientation	As Received Bulk Density (g/cm^3)	Confining Pressure (psi)	Peak Effective Compressive Strength (psi)	Effective Residual Compressive Strength (psi)	Young's Modulus (10^6 psi)	Poisson's Ratio
tan dolomite	BTR4-4	6703.10	Vertical	2.543	1341	23340	14290	6.422	0.28
	BTR4-2	3702.90	Horizontal	2.473	2748	26760	11050	6.223	0.26

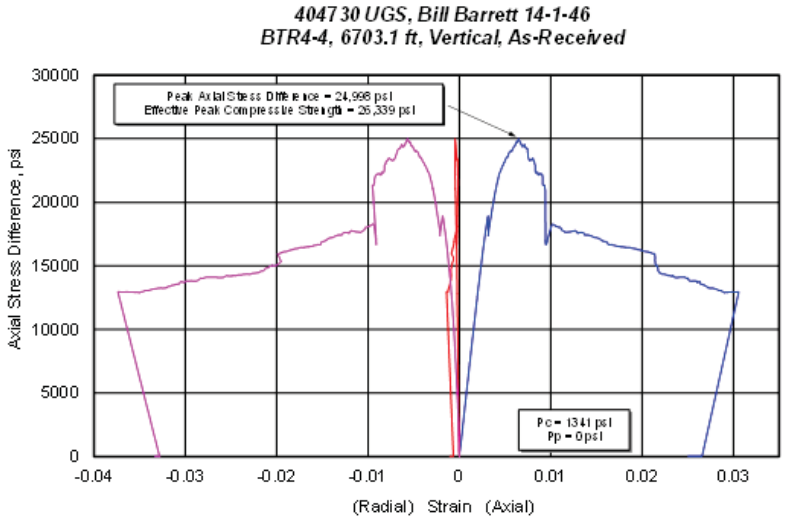

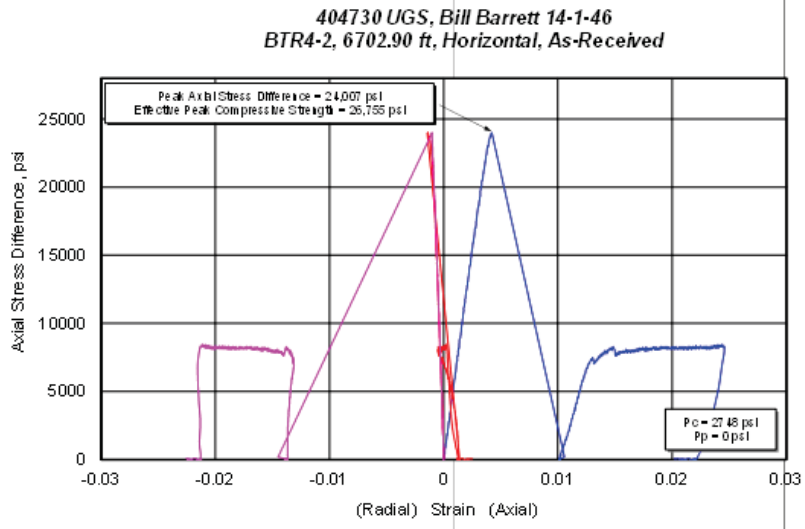

Zone 1 Deformation Index: Ratio of Secant E at Peak to E: 1.62
Zone 2 Ductility Index: Amount of Plastic or Strain Hardening Strain: 0.67
Zone 3a: Tang and Kaiser Index (Axial): 0.12
Zone 3b: Tang and Kaiser Index (Volumetric): 1.20?
Zone 4: Peak to Residual Strength Ratio: 1.36

Zone 1 Deformation Index: Ratio of Secant E at Peak to E: 1.09
Zone 2 Ductility Index: Amount of Plastic or Strain Hardening Strain: N/A
Zone 3a: Tang and Kaiser Index (Axial): N/A
Zone 3b: Tang and Kaiser Index (Volumetric): N/A
Zone 4: Peak to Residual Strength Ratio: 2.89

Figure 28. A comparison of behavior between a vertical and horizontal sample from approximately 6703 ft MD in the Bill Barrett 14-1-46 well. In this case, the vertical sample failed in a brittle manner in that it released energy rapidly after peak strength has been exceeded and there was little non-linearity before loss in load bearing capability. Five methods (denoted as zones) were shown to reflect how failure occurred. The horizontal sample failed with a large motion on its macroscopic failure plane.

Bill Barrett 14-1-46

Lithology	Sample ID	Depth (ft)	Orientation	As-Received Bulk Density (g/cm^3)	Confining Pressure (psi)	Peak Effective Compressive Strength (psi)	Effective Residual Compressive Strength (psi)	Young's Modulus (10^6 psi)	Poisson's Ratio
shale	BTR5-4	6706.50	Vertical	2.487	1341	14450	9190	1.295	0.18
	BTR5-2	6706.65	Horizontal	2.502	2750	17250	13270	3.797	0.26

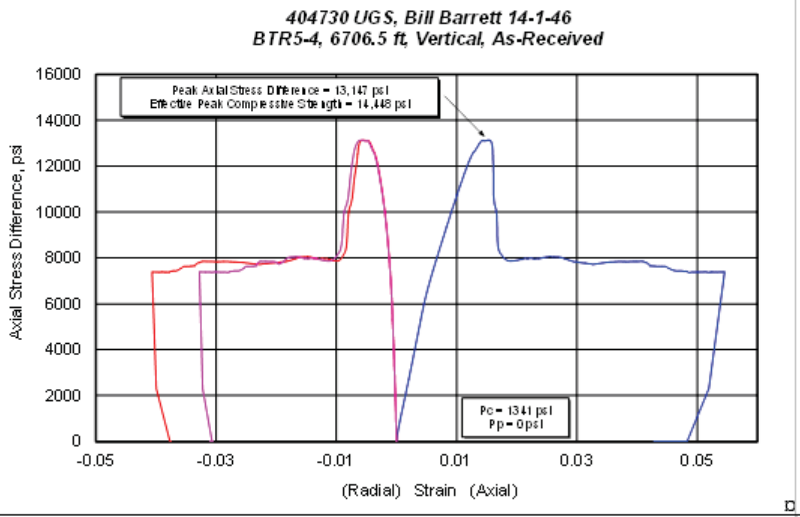

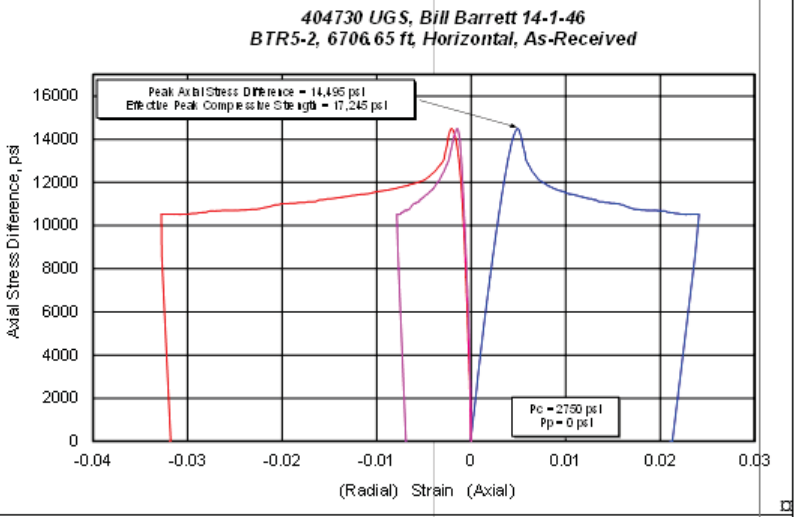

Zone 1 Deformation Index: Ratio of Secant E at Peak to E: 1.37
Zone 2 Ductility Index: Amount of Plastic or Strain Hardening Strain: 0.35
Zone 3a: Tang and Kaiser Index (Axial): 0.842
Zone 3b: Tang and Kaiser Index (Volumetric): 2.044
Zone 4: Peak to Residual Strength Ratio: 1.64

Zone 1 Deformation Index: Ratio of Secant E at Peak to E: 1.24
Zone 2 Ductility Index: Amount of Plastic or Strain Hardening Strain: 0.03
Zone 3a: Tang and Kaiser Index (Axial): 0.594
Zone 3b: Tang and Kaiser Index (Volumetric): 0.613
Zone 4: Peak to Residual Strength Ratio: 1.33

Figure 29. A comparison of behavior between a vertical and horizontal sample from approximately 6706-7 ft MD in the Bill Barrett 14-1-46 well. In this case, the vertical sample failed in a moderately brittle manner in that it released energy rapidly after peak strength has been exceeded although there was some pre-failure nonlinearity before loss in load bearing capability. Five methods (denoted as zones) were shown to reflect how failure occurred.

A fifth method (called Zone 5 for consistency) for determining a BI can be considered. This entails integrating under the triaxial stress-strain curve behavior of a laboratory sample (this is an energy/volume). This method is described below:

1. The area under the stress strain curve will indicate an energy per unit volume. While the portion of the curve with hydrostatic application of confining pressure could be useful, the procedure described only applies after the start of applying deviatoric stress (when the piston is actually brought in contact with the sample). The integration starts at the beginning of loading. Figures 13 through 18 showed sample raw triaxial data. All of the plots are included in Appendix A.
2. Smooth the data with a moving average to reduce noise and to remove outliers judged to be inappropriate. Use anywhere from 20-50 points for the moving average. Start with 20 points and use the fewest points possible. Figures 30 through 35 are the moving average smoothed data corresponding to Figures 13 through 18. All of the plots are included in Appendix B.
3. Calculate the slope "instantaneously for all of the averaged data - before and after peak strength. Average this slope over 20-60 points using the lowest number of points possible. The number of moving average points has been determined from qualitative experience in processing the data.
4. Using the averaged instantaneous slope, identify segments of the stress-strain curve where the slope changes by more than 2%. These inflections will be relevant for identifying segments of the curves to process. If the segment where the curve "rolls over" at the peak is especially broad this parameter (2% change) may need to be reduced. Do not reduce this parameter to less than 0.5%.
5. Identify a strain where residual behavior is inferred to initiate. This is done by evaluating slope changes post-peak (after the maximum stress). In particular, this occurs when the slope of the stress vs. strain curve becomes negative. Locate where the slope of the curve is closest to zero and the percent change of the slope is closest to zero. Call this the residual stress. This should be located after any visible, but minor drops in the load-bearing capacity that could indicate smaller fractures forming or non-catastrophic slip along a localization. This is the end point of integration under the stress-strain curve. Some exceptions to this parameter have been developed, again based on experience with these data. For example:
    a. If the sample catastrophically fractures and the deviatoric stress drops very rapidly to a value which is less than or equal to 20% of the peak deviatoric stress value then the end point for the integration is the termination of this drop in deviatoric stress. This is shown in Figure 36.

b. If the sample only stain hardens or has a drop in deviatoric stress that plateaus at 80% or more of the peak strength, then take the area under this whole area until the end of the test. This is shown in Figure 37.

   i. The end of the test is indicated when the stress sharply drops to zero post peak

   ii. For comparing these types of results between one another a ratio of the stress at the end of the test to the peak stress should be taken. The closer to one the ratio is the less brittle the rock is in comparison to rocks that fail similarly.

6. Take the integral from the beginning of the curve to where the curve has a slope percent change greater than determined in step 5. This will be the numerator of the BI.
7. Take the integral from the beginning of the curve to the end point described in step 6. This will be the denominator of the curve.
8. Divide 6 by 7 and this is the BI.

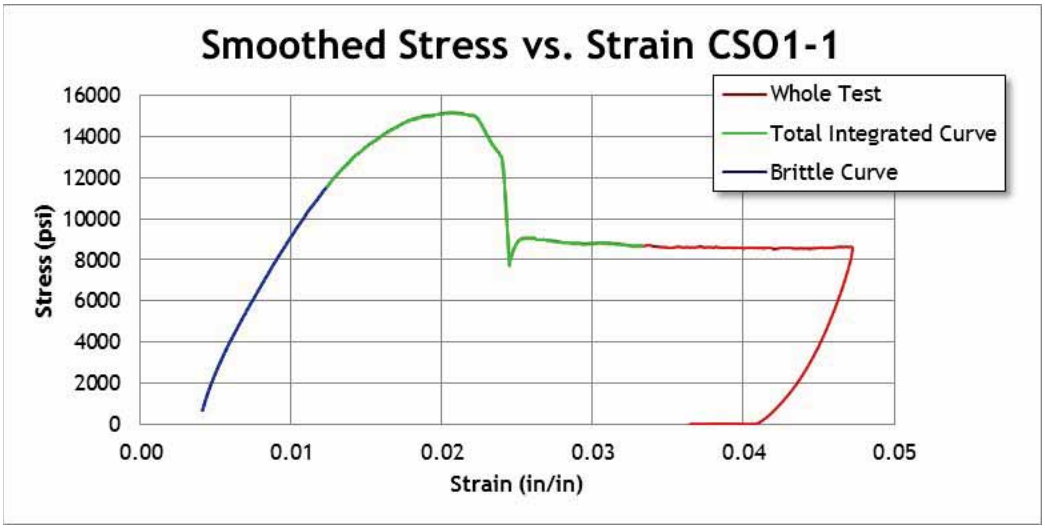

Figure 30. Smoothed deviatoric stress vs. axial strain curve for the Cisco State 36-13 well. The confining pressure was 2732 psi and no pore pressure was applied. This sample was plugged vertically from a depth of 7,588.80 ft MD. The effective compressive strength at this confining pressure is 18,000 psi. The peak axial stress difference is 15,282 psi.

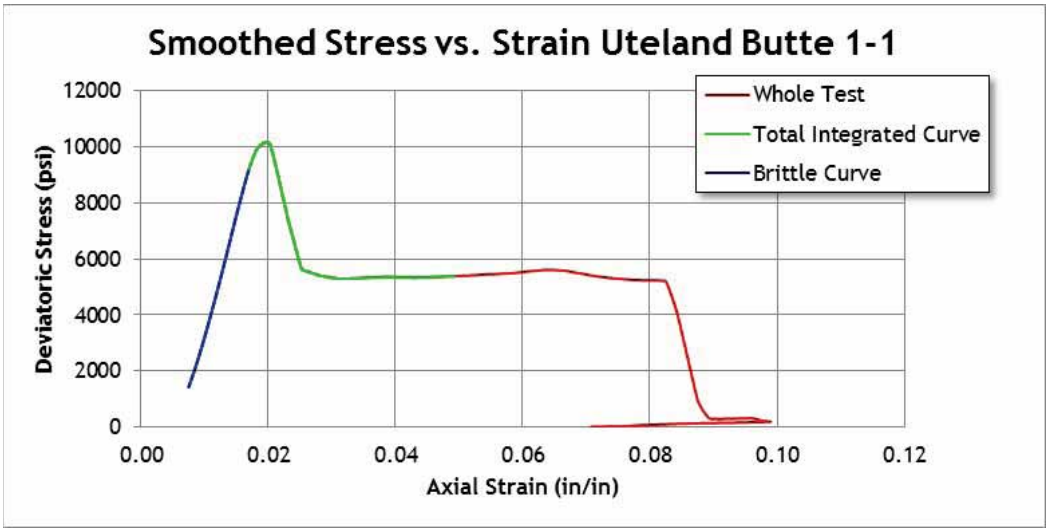

Figure 31. Smoothed stress vs. strain curve Uteland Butte well. The confining pressure was 1813 psi and no pore pressure was applied. This sample was plugged vertically from a depth of 8497.05 ft MD. The effective compressive strength at this confining pressure is 12,500 psi. The peak axial deviatoric stress was 10,685 psi.

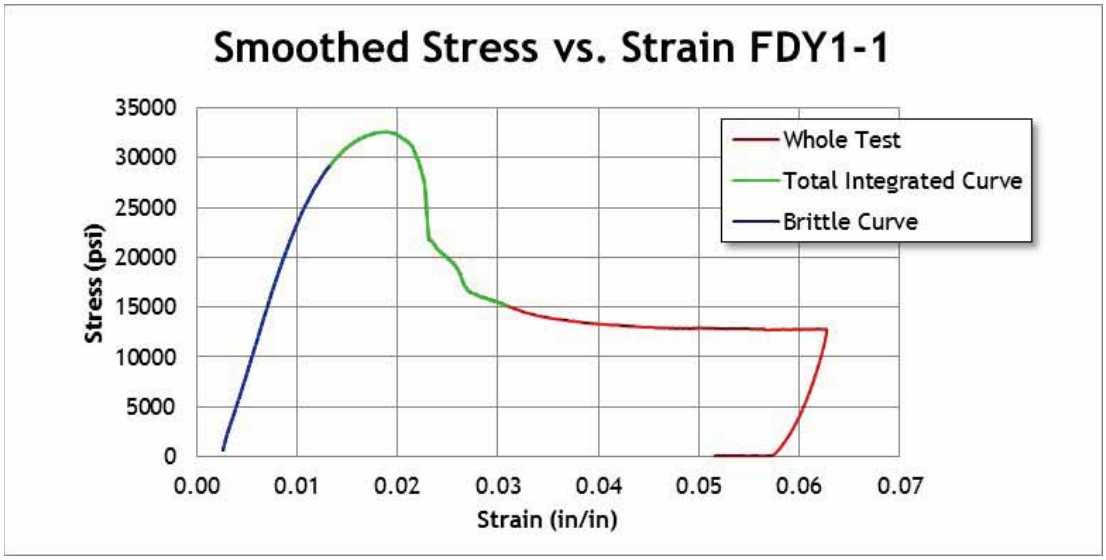

Figure 32. Smoothed stress vs. strain curve for Cane Creek 26-3. The confining pressure was 3882 psi and no pore pressure was applied. This sample was plugged vertically from a depth of 7464.5 ft MD. The effective compressive strength at this confining pressure is 36,700 psi. The peak axial deviatoric stress was 32,820 psi.

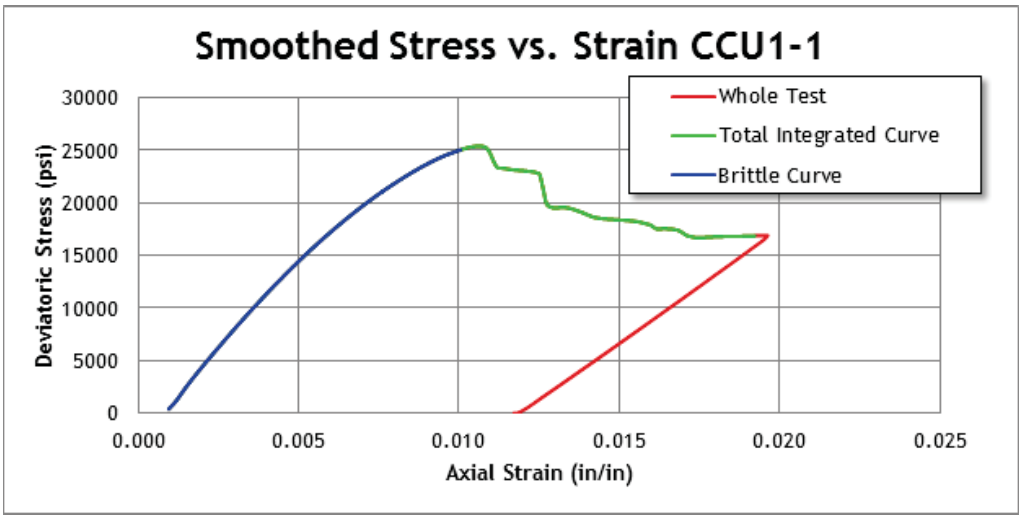

Figure 33. Smoothed stress vs. strain curve for well Cane Creek 7-1. The confining pressure was 3348 psi and no pore pressure was applied. This sample was plugged vertically from a depth of 7609.35 ft MD. The effective compressive strength at this confining pressure is 28,760 psi. The peak axial deviatoric stress was 25,407 psi.

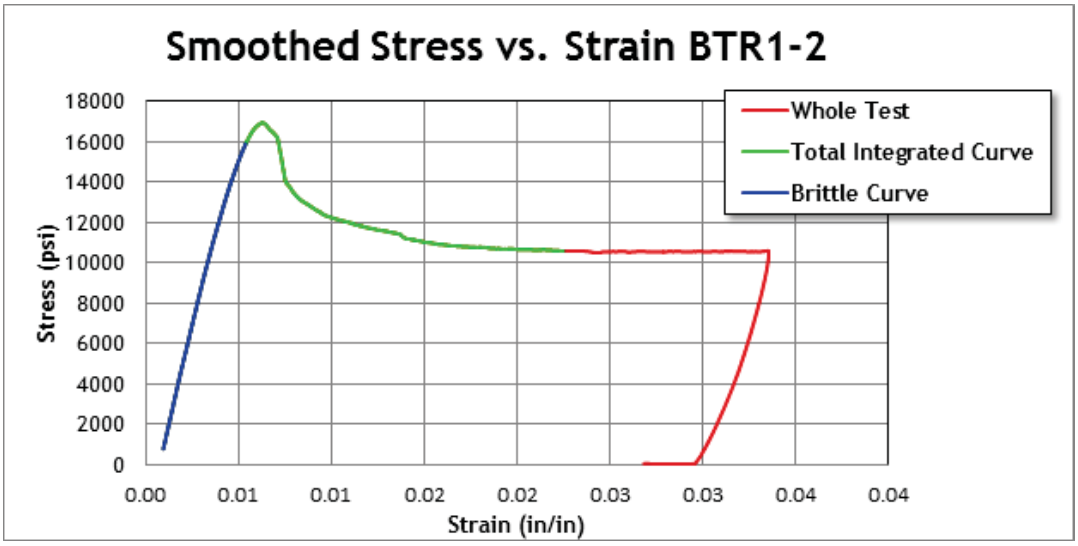

Figure 34. Smoothed stress vs. strain curve for well Bill Barrett 14-1-46. The confining pressure was 2741 psi and no pore pressure was applied. This sample was plugged parallel to bedding (nominally horizontal) from a depth of 6684.70 ft MD. The effective compressive strength at this confining pressure is 19,740 psi. The peak axial deviatoric stress was 16,995 psi.

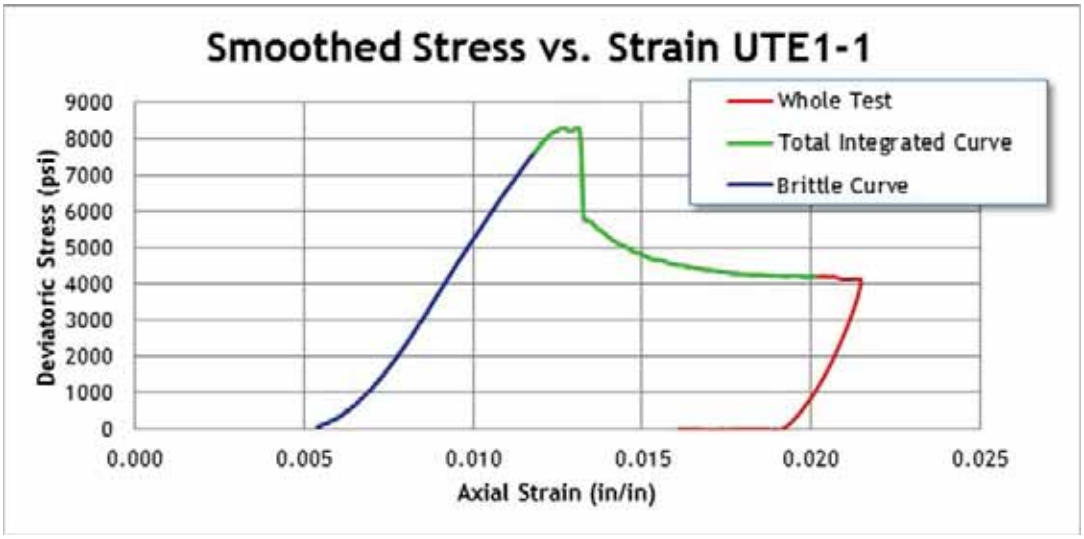

Figure 35. Smoothed stress vs. strain curve for Bill Barrett 14-3-45. The confining pressure was 1325 psi and no pore pressure was applied. This sample was plugged perpendicular to bedding (nominally vertical) from a depth of 7358.35 ft MD. The effective compressive strength at this confining pressure is 9,700 psi. The peak axial deviatoric stress was 8378 psi.

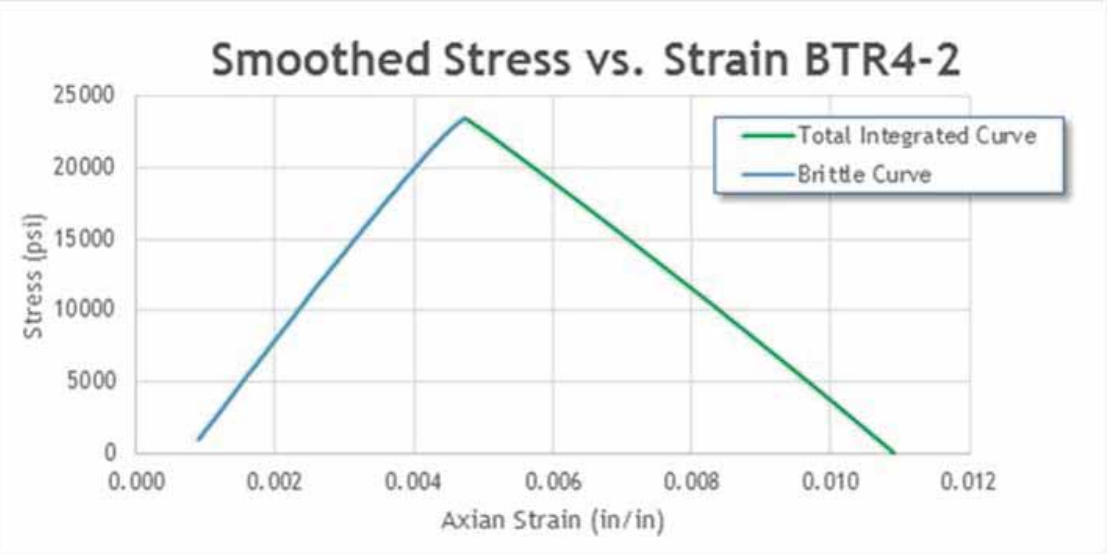

Figure 36. Example of procedure for special case discussed in step 6a above.

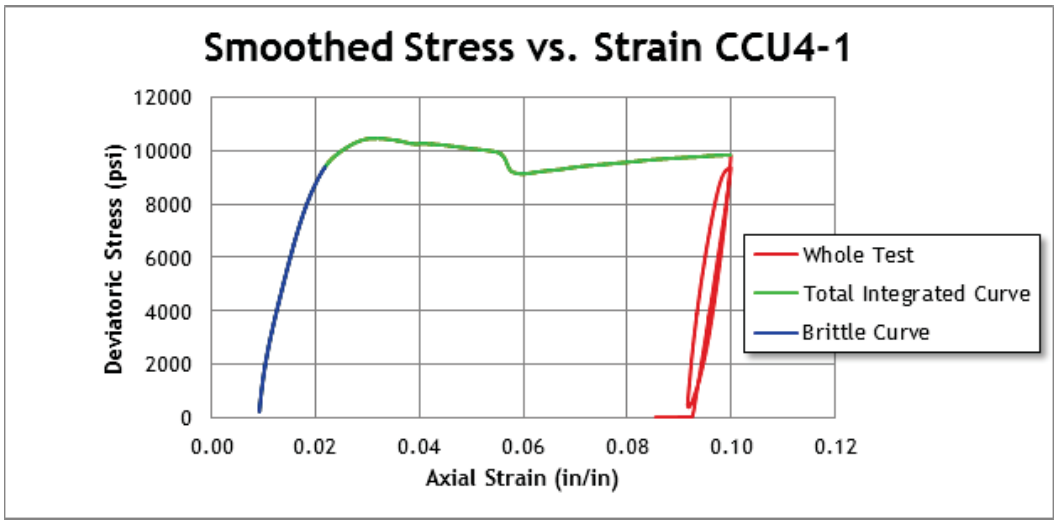

Figure 37. Example of procedure for special case discussed in step 6b above.

The integral taken for the numerator of the BI is the area under blue portion of the smoothed curves. If the rock is perfectly brittle the stress strain curve would linearly increase and then - at failure – the stress (load bearing capacity) would fall vertically from the peak stress to zero forming a right triangle. The *numerator* of the newly developed BI gives the energy per unit volume that would have been expended if the rock had not experienced significant plastic deformation and failed immediately and catastrophically.

The *denominator* of the BI is the area under the entire stress-strain curve, the area under the blue curve plus the area under the green curve in the smoothed deviatoric stress vs axial strain curves, which is the total energy actually input and expended while fracturing the rock. The BI is then the ratio of these two areas. Table 5 shows this brittleness index for the samples whose smoothed curves are shown in Figures 30 through 35. Brittleness indices for all samples are tabulated in Appendix C.

Table 5. Selected Brittleness Index Results

Sample	BI	Stress-Strain Curve
CSO1-1	0.19	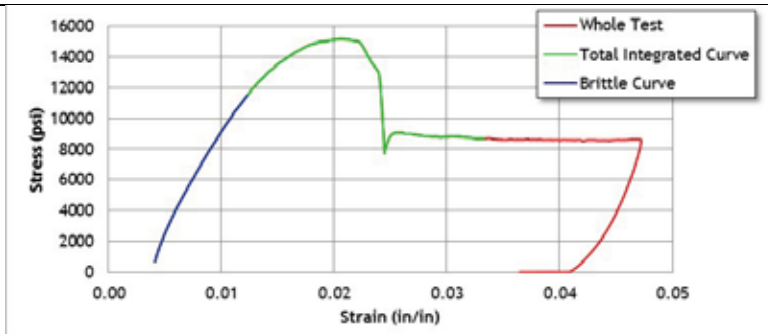
Uteland Butte 1-1	0.21	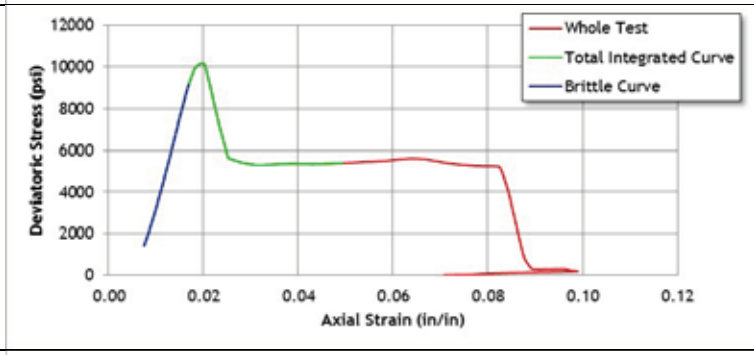
FDY1-1	0.29	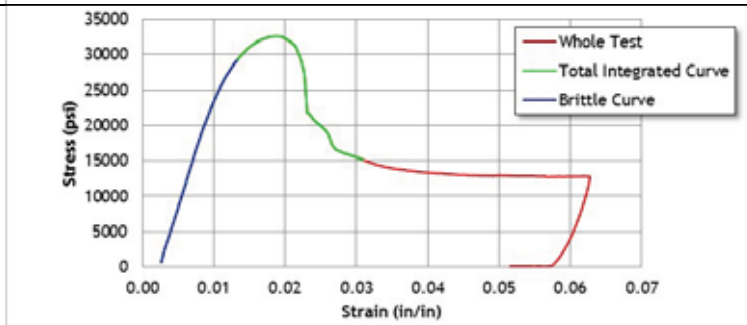
CCU1-1	0.43	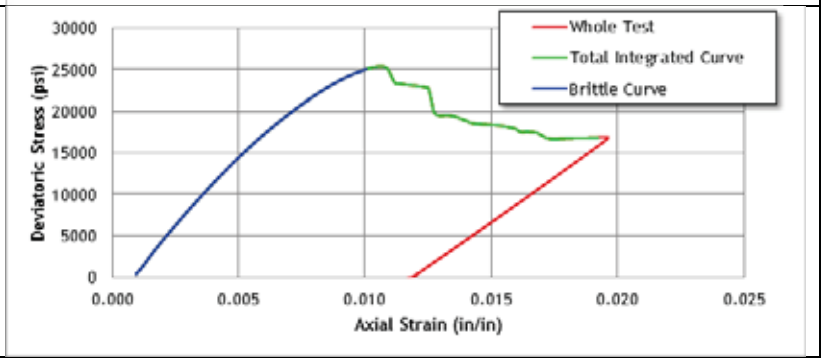

Sample	BI	Stress-Strain Curve
BTR1-2	0.17	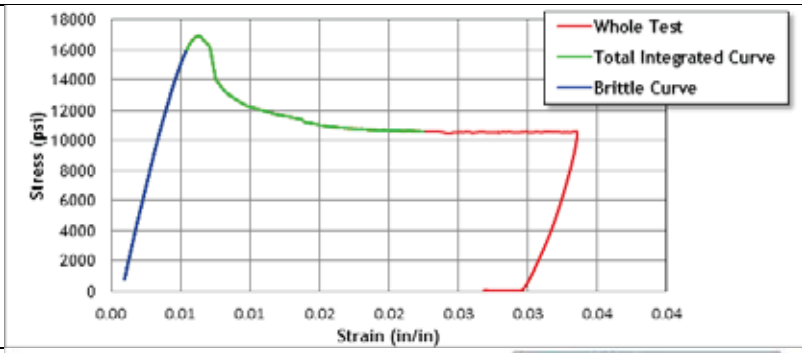
UTE1-1	0.33	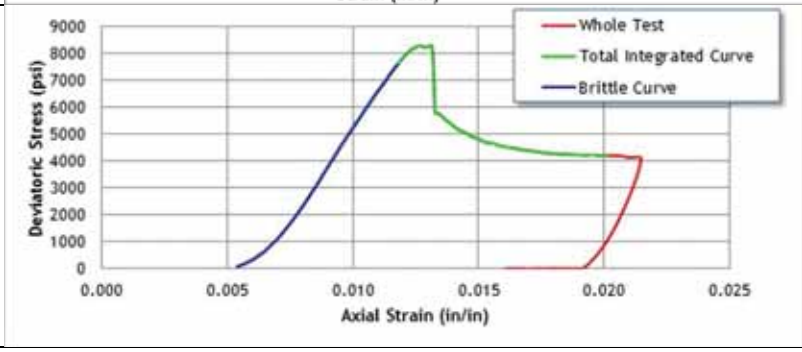

One of the problems with many of the brittleness indices that have been developed is that they require core. The index proposed is no different. Ideally a correlation between tests on core and readily available logging and other field data would allow brittleness and fracability to be calculated without needing core. This has been done by He et al., date, for other brittleness indices that are defined by strength parameters with a broad range of formations. The five indices examined by He et al. are as follows:

$$B_1 = \frac{\sigma_c}{\sigma_t} \text{ or } B_2 = \frac{\sigma_c - \sigma_t}{\sigma_c + \sigma_t} \text{ or } B_3 = 0.5\sqrt{\sigma_c - \sigma_t} \text{ or } B_4 = \sigma_c \qquad (28)$$

where:

σ_c ..... unconfined compressive strength,
σ_t ..... unconfined tensile strength,

He et al., correlated these indices with different parameters; dynamic Young's Modulus, Static Young's Modulus, compressional wave velocity, porosity, and shale volumes. Both Young's Modulus correlations, dynamic and static, were reasonable with all BI's with R^2 values between 0.7272 and 0.8671. The dynamic Young's Modulus provided a better correlation than the static one. The correlation equations were power law form - the correlations were poor.

After evaluating these and other published correlations, it became apparent that a dipole sonic log (or equivalent) in combination with porosity and/or gamma ray would most likely provide the best correlation with the newly developed index. Of the wells being examined, Cisco State 36-13 was the only well with an available dipole sonic log. This well also had 13 triaxial compression tests done on core from which the brittleness index could be calculated. Correlations were attempted for individual and combinations of porosity, GR value, Young's Modulus, Poisson's Ratio, compressional wave velocity, fast shear wave velocity, and slow shear wave velocity. The best correlation was with a combination of slow shear wave velocity, compressional wave velocity and the gamma ray values. Porosity values from logs, whether density, sonic, or neutron porosity always made the correlation worse. The adjusted R^2 value for the best correlation was found to be 0.89:

$$\ln(\mathrm{BI}) = 6.9772\times10^{-2}\,\mathrm{DTSM}_{\mathrm{slow}} + 1.22806\times10^{-1}\,\mathrm{DTCO} - 4.267\times10^{-2}\,\mathrm{GR} - 16.2711 \qquad (29)$$

In an ideal world, triaxial extension testing might be the preferred methodology. Triaxial extension is significantly harder to perform and would only be valuable if the tests have a significantly stronger correlation with logging parameters than the triaxial compression tests.

VI. Landing Zones or Selecting Completion Zones

Brittleness logging tracks, in combination with resistivity logs that allow for a determination of TOC and density or sonic logs and porosity logs can be used to determine the premium reservoir quality (porosity, TOC) and reservoir quality (brittleness for completion).

Ortega et al. (2014) examined drill cuttings and devised a way to quantitatively use them to help locate optimum completion positions within the formation based on permeability, porosity and brittleness as defined by Rickman et al. (2008). Another metric obtained can be a "frac value" that is indicative of natural fracturing that can be detected in cuttings. This was devised by Hews, 2011, and is found by the inspection of cuttings under a binocular microscope.

While this is appropriate for locating natural fractures that will provide increased permeability it will likely miss larger fractures that cannot be captured by the cuttings and fractures whose permeability was destroyed during drilling. The use of these cuttings for porosity confirmation, permeability estimates, and natural fracture identification used in conjunction with an appropriate BI derived from a logging correlation, provides a good combination of metrics for determining where to complete a well without having to take core and run more tests.

Subtasks 6.4-6.7 Brittleness and Completion Characteristics

I. Objective

As discussed previously, six well were considered. Three of these wells targeted the Uteland Butte formation. These wells are: Bill Barrett 14-1-46, Bill Barrett 14-3-45, and Cesspooch 15-21-3-3W. The other three wells accessed the Cane Creek formation. These wells are: Cane Creek 26-3, Cisco State 36-13, and Cane Creek 7-1. All of these wells have well logs available except Cane Creek 7-1. Core was available for all six of the wells for triaxial testing but the Cane Creek 7-1 well was not available for other core testing. Other than the Cane Creek 7-1 well, the other five well cores were tested for porosity, permeability, TOC, oil maturity, and fracture toughness.

The logs examined were neutron porosity, density porosity, gamma ray, shallow resistivity, and deep resistivity. Each log was examined individually and locations for potential completion were provided based on optimal log readings regardless of depth. Optimal locations from each log for a given well were compared and depths were chosen where these logs overlap. This process was then again repeated with the core testing data. Then the core data and log data were compared and the geology was considered to choose the final suggested completion locations.

II. Stimulation Protocols

There is some stimulation information available in the public domain. Assessment of these stimulation protocols was being undertaken in the Uintah and Paradox basins. Comparative fracture modeling is being carried out to determine if additional optimization may be relevant. Recognizing the absence of well-specific data, generic surrogate wells are being assessed. Logging and mechanical properties and stress data are being incorporated into representative type wells. For these type wells, various appropriate stimulation and cleanup protocols are being implemented and production is being predicted to assess if there are preferable techniques. Fracture modeling is being carried out with commercial stimulation software. Production is being assessed using commercial and in-house tools.

III. Treatment Design

Production from vertical wells in the Uteland Butte was disappointing. Fracture treatments were simulated using commercial planar hydraulic fracturing codes for a vertical well with multiple perforations. StimPlan™ was used. Vertical wells are probably not appropriate in the Cane Creek play. Stimulation history matching and production matching for **** in the Uteland Butte play is described below.

IV. Vertical Wells

A planar 3D hydraulic fracturing treatment simulation was carried out using the program E-StimPlan for wells in the Uteland Butte and Cane Creek plays. The two wells simulated were Bill Barrett well 14-3-45 in the Uteland Butte and the Cisco State 36-13 well in the Cane Creek. The inputs for these simulations were obtained from fracture toughness and triaxial compression testing. This supplemented basic well file information such as drilled diameter, casing schedule, perforation programs, pump schedules, etc. The planned DFIT for the Cisco State well was used in the simulation. A second, alternative pump schedule was also used to represent a full scale stimulation scenario. For the Bill Barrett well (Uteland Butte) the actual pump schedule was approximated from the well file and used in that the simulation.

Cane Creek: Cisco State 36-13

The simplified lithologic properties are shown in Table 6.

Table 6. Simulated Lithologic Properties for Cisco State 36-13

Depth (ft TVD)			Stress (psi)		Gradient (psi/ft)	E (10^6 psi)	ν	K_{IC} (psi·√in)	Fluid Loss (ft/√min)
Top	Bottom	Thickness	Top	Bottom					
6000	7285	1285	5400	6556.5	0.9	5.18	0.27	550	0.0001
7285	7585	300	6556.5	6826.5	0.9	5.01	0.27	550	0.0001
7585	7600	15	6826.5	6840	0.9	7.33	0.26	1525	0.001
7600	7626	26	6840	6863.4	0.9	4.46	0.26	837	0.001
7626	7655	29	6863.4	6889.5	0.9	7.61	0.26	1048	0.001
7655	7735	80	6889.5	6961.5	0.9	4.78	0.28	550	0.0001
7735	7900	165	6961.5	7110	0.9	5.48	0.28	550	0.0001

A limited entry perforation schedule was planned. This is shown in Table 7. The zones were perforated at 4 spf, with an entry diameter of 0.34 inches and a prescribed efficiency of 100% (all perforations contributing).

Table 7. Perforation Schedule Cisco State 36-13

Top of Perforations (ft MD)	Bottom of Perforations (ft MD)	Perforated Height (ft)
6850	6851	1[10]
7588	7590	2
7600	7603	3
7606	7613	7
7621	7626	5

[10] The top perforation was shot and then squeezed closed.

Table 8 shows a planned DFIT and a generic treatment that was simulated. The proppant concentration in the treatment is high to encourage diversion.

Table 8. DFIT and Generic Treatment

DFIT									
Stage	Slurry Volume (gallons)	Proppant Concentration (ppg)		Rate (bpm)	Proppant (lb)	Pump Time (min)	Cumulative Time (min)	Fluid	Proppant
		Start	End						
1	500	0	0	2	0	5.95	6.0	20 pptg linear gel	20/40 sand
2	150	0	0	2	0	1.79	7.7	20 pptg linear gel	20/40 sand
3	420	0	0	4	0	2.5	10.2	20 pptg linear gel	20/40 sand
Generic Treatment									
Stage	Slurry Volume (gallons)	Proppant Concentration (ppg)		Rate (bpm)	Proppant (lb)	Pump Time (min)	Cumulative Time (min)	Fluid	Proppant
		Start	End						
1	20,000	0	0	30	0	15.87	15.9	20 pptg linear gel	20/40 sand
2	26,666	1	2	30	37,500	21.16	37.0	20 pptg linear gel	20/40 sand
3	26,666	2.5	3	30	65,200	21.16	58.2	20 pptg linear gel	20/40 sand
4	26,666	3.5	4	30	85,500	21.16	79.4	20 pptg linear gel	20/40 sand

Table 9 shows the predictions from the main simulated treatment. The DFIT was predicted to create a 500 ft unpropped fracture half-length.

Table 9. Cisco State 36-13 Simulated Treatment after Closure

Perforation Depth (ft MD)	Average Width (in)	Half-Length (ft)	Propped Half-Length (ft)	Maximum Fracture Height (ft)	Average Conductivity (md·ft)
7588-7590	0.22	1060.6	271	651.2	114.2
7600-7603	0.17	61	61	6.5	303.1
7606-7613	0.12	73.8	61	13	400.3
7621-7626	0.07	65.1	61	126.6	380.5

The treatment is wasteful. A slickwater treatment with lower sand concentrations would have been equally effective and led to much less out-of-zone growth. Regardless,

this treatment should be superseded by treatments in horizontal wells, as will be described subsequently.

Uteland Butte: Bill Barrett 14-3-45

The simplified lithologic properties are shown in Table 10.

Table 10. Simulated Lithologic Properties for Bill Barrett 14-3-45

Depth (ft TVD)			Stress (psi)		Gradient (psi/ft)	E (10^6 psi)	ν	K_{IC} (psi·√in)	Fluid Loss (ft/√min)
Top	Bottom	Thickness	Top	Bottom					
6000	6400	400	3780	4032	0.63	5.71	0.25	1161	0.00084
6400	6510	110	3968	4036.2	0.62	5.4	0.25	1390	0.00074
6510	6560	50	4036.2	4067.2	0.62	5.61	0.25	1302	0.00076
6560	6650	90	4067.2	4123	0.62	5.52	0.25	1429	0.00073
6650	6850	200	4123	4247	0.62	5.42	0.25	1561	0.0007
6850	6950	100	4247	4309	0.62	5.52	0.25	1420	0.00073
6950	7125	175	4309	4417.5	0.62	5.59	0.25	1327	0.00077
7125	7225	100	4702.5	4768.5	0.66	5.8	0.25	1040	0.00087
7225	7275	50	4768.5	4801.5	0.66	5.7	0.25	1075	0.00086
7275	7350	75	4801.5	4851	0.66	5.7	0.25	1129	0.00083
7350	7540	190	4851	4976.4	0.66	5.7	0.25	1078	0.00086
7540	7600	60	4976.4	5016	0.66	5.65	0.25	1249	0.0008
7600	7710	110	5016	5088.6	0.66	5.48	0.25	1472	0.00074
7710	7935	225	5165.7	0	0.67	5.59	0.25	1327	0.00076
7935	8060	125	5395.8	5480.8	0.68	5.53	0.25	1405	0.00074
8060	8150	90	5480.8	5542	0.68	5.61	0.25	1305	0.00077
8150	8225	75	5542	5593	0.68	5.55	0.25	1383	0.00074
8225	8300	75	5675.25	5727	0.69	5.71	0.25	1171	0.00081

Due to the condition of the core, limited fracture toughness testing was possible. Only 3 values for fracture toughness were determined experimentally. To be able to evaluate the formation with this simulation and include the other rock mechanics properties where data were plentiful (triaxial testing) the fracture toughness was linearly with Young's modulus. Although there is likely not a strong linear correlation between modulus and fracture toughness, this was the best way to have reasonable fracture toughness values for layers where data were not available.

The perforation schedule is shown in Table 11.

Table 11. Vertical Hole - Bill Barrett 14-3-45 - Perforation Schedule

Top of Perforations (ft MD)	Bottom of Perforations (ft MD)	Perforated Height (ft)	Shots (-)/Spacing (spf)
6871	7100	220	46/0.20
7125	7271	146	39/0.27
7295	7515	220	44/0.20
7536	7702	166	45/0.27
7717	7904	187	41/0.22
7936	8117	181	45/0.25
8145	8344	199	42/0.21
8369	8560	281	53/0.19

The treatment pumped on this well (per the well report) is shown in Table 12. Although the rate is moderately large and it is a moderately viscous fluid, effectively stimulating such a large zone is challenging.

Table 12. Bill Barrett 14-3-45 - Treatment Schedule

Stage	Slurry Volume (gallons)	Proppant Concentration (ppg)		Rate (bpm)	Proppant (lb)	Pump Time (min)	Cumulative Time (min)	Fluid	Proppant
		Start	End						
1	26,000	0	0	70.6	0	8.77	8.8	40 pptg linear HPG	20/40 sand
2	27,000	2	2	70.6	49,700	9.11	17.9	40 pptg linear HPG	20/40 sand
3	27,000	2.5	2.5	70.6	60,900	9.11	27.0	40 pptg linear HPG	20/40 sand
4	26,999	3	3	70.6	71,600	9.11	36.1	40 pptg linear HPG	20/40 sand
5	26,999	3.5	3.5	70.6	82,000	9.11	45.2	40 pptg linear HPG	20/40 sand
6	27,000	4	4	70.6	91,900	9.11	54.3	40 pptg linear HPG	20/40 sand

Predictions are summarized in Table 13. As expected, limited entry was not particularly successful and the fractures were only effective for the first one or two perforation zones. At greater depths, the propped lengths and conductivities are low. This is reflected in the well's production

Table 13. Vertical Hole - Bill Barrett 14-3-45 - Simulation Results

Perforation (ft MD)	Average Width at EOJ (in)	Propped Half-Length (ft)	Maximum Fracture Height (ft)	Average Conductivity (md·ft)
6871-7100	0.43	444.2	750.8	566.3
7125-7271	0.11	47	150	364.9
7295-7515	0.01	46	241.3	6.1
7536-7702	0	46	193.7	2.9
7717-7904	0	23	196.9	0.7
7936-8117	0	46	191.5	0.5
8145-8344	0	46	230.4	0.5
8369-8560	0	46	292.1	0.3

V. Production Estimates

Production was estimated after these conventional fracturing treatment simulations were carried out. The reservoir was assumed to be at the initial bottomhole pressure and had not flowed yet. During production, the bottomhole flowing pressure was assumed to be 500 psi for the Cisco state well and 250 psi for the Bill Barrett well. The drainage radius was assumed to be 80 acres for the Cisco State well and 160 acres for the Bill Barrett well. The pay height was assumed to be 100 feet, approximately the thickness of all three Cane Creek units combined, for the Cisco state well. The pay height was assumed to be 40 feet for the Bill Barrett well which is the maximum thickness expected for the producing sections within this well. The rest of the input parameters were taken from the well file or estimated by calculations within E-StimPlan™. The fluid and reservoir properties are shown in Tables 14 through 16.

Table 14. Reservoir Properties for Production Estimation

Property	Bill Barrett 14-3-45 Uteland Butte	Cisco State 36-13 Cane Creek
Wellbore radius (ft)	0.35	0.35
Drainage radius (acres)	160	80
Initial reservoir pressure (psi)	4593	3420
Bottomhole flowing pressure (psi)		
Bottomhole temperature (°F)	200	196
Porosity (%)	10	5
Permeability (md)	0.10	0.01
Nominal net pay (ft)	14	78
Formation compressibility (10^{-6} psi^{-1})	5.3	0.3
Water compressibility (10^{-6} psi^{-1})	6.7	2.7
Closure pressure (psi)	3500	6830
Effective stress on proppant (psi)	3250	6330
Pre-frac skin (-)	0	0

Property	Bill Barrett 14-3-45 Uteland Butte	Cisco State 36-13 Cane Creek
SG gas at separator (-)	0.7	0.8
GOR (scf/bbl)	100	100
Pressure at separator (psi)	100	100
Temperature at separator (°F)	100	100
API gravity of stock tank oil	38	38
Gas viscosity (cP)	1.006	0.033
Gas compressibility (10^{-6} psi^{-1})	10.08	0.03
Formation volume factor (rb/stb)	1.15	0.033

Predicted and actual production for Bill Barrett 14-3-45 are shown in Figure 38. The actual well produced its last oil in month 50 with a total cumulative production of 33.455 MBO. The simulation projected that the well would produce for 48 months and have a cumulative oil production of 33 MBO. This shows good correspondence with the actual well and was achieved by indicating a pay height of only 14 feet. This is consistent with the simulated fracture generation only covering the upper part of the play.

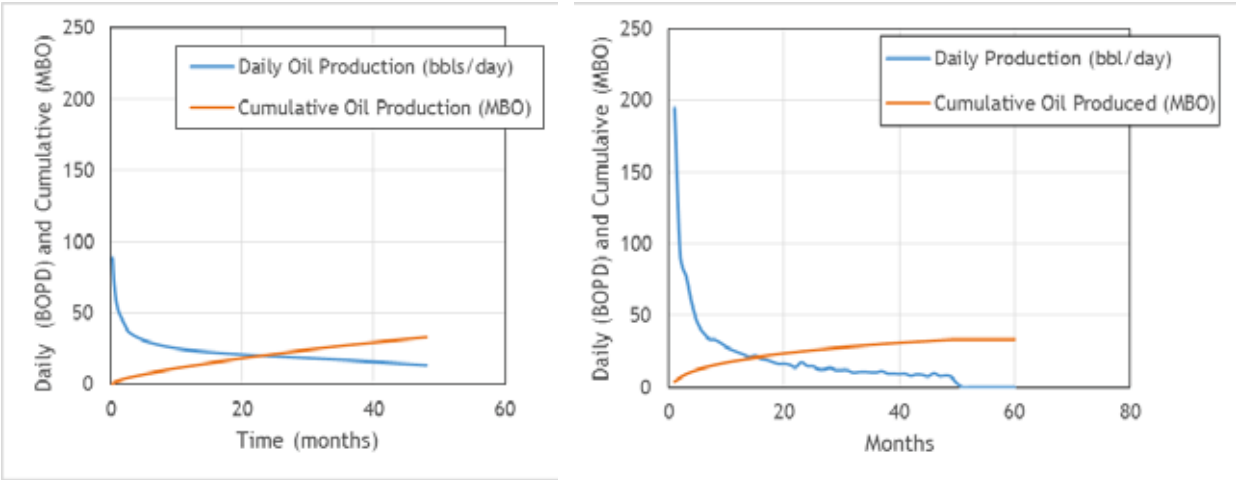

Figure 38. This is predicted (left panel) versus actual (right panel) oil production for Bill Barrett 14-3-45.

Production forecasts are shown in Figure 39. These are optimistic because they presume no salt precipitation problems. There is no production data. In either case, the cumulative production is probably not enough to pay off the well.

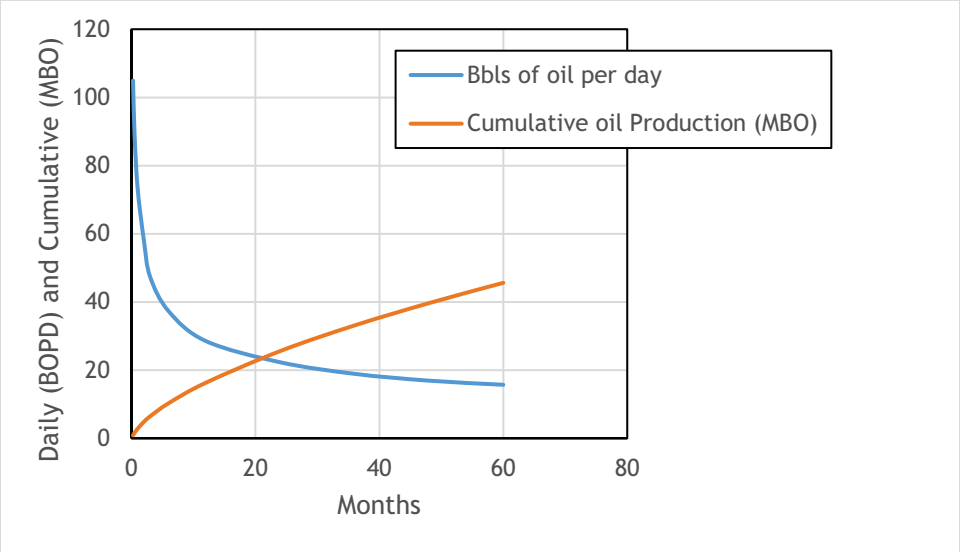

Figure 39. Simulated production profile for a typical vertical penetration in the Cane Creek formation (Cisco State 36-13).

VI. Horizontal Wells

The production history, and current industry practice endorse changing the drilling trajectory in both of these plays. This was already starting to happen when this study was initiated. Horizontal type wells were developed for this study. After compiling the laboratory and logging data for the two generic locations, type reservoirs were developed, by amalgamating the various sources of information. In either scenario - Uteland Butte or Cane Creek, the key issue was containment of the fracture in a discrete pay zone.

In the case of the Cane Creek play, salt immediately adjacent to the pay is particularly challenging. Penetration of a water-based treatment fluid into saline zones will result in subsequent salt precipitation and loss of productive capacity. In the case of the Uteland Butte, upward growth out of pay jeopardizes the effectiveness of the stimulation by limiting in-zone surface area.

VI.1 Cane Creek Shale - Horizontal Well Fracturing Simulations

Legacy wells completed in the Cane Creek (vertical or horizontal) were marginally productive. There was some evidence and inference that fracturing treatments used in these wells are penetrating into the over- and underlying salt zones and causing salt to block fractures and perforations, thereby reducing the productivity of the well, if not killing it. This would be even more exaggerated for situations where the well wandered

out of the pay. Regardless, it was decided to prioritize horizontal wells in the treatment simulations.

In these simulations, core data, rock mechanics measurements, and logging data from the Cisco State 36-13 well were used to build properties for the lithologic zones considered to be relevant. The number of zones and their thicknesses were based on a combination of GR data and core examination for the depth and thickness of the Cane Creek A, B, and C intervals as well as overlying layers. The natural fracture orientation was inferred using a rose plot from the sonic scanner data from the CS 36-13 well. The spacing and length of these natural fractures were estimated and distributed stochastically (Table 15). That table infers the major fractures only and their specification is intuitive and speculative. The lithology and stress data were determined as follows.

Pore Pressure Gradient ..Mud weight from drilling reports to subdue reservoir pressure
Porosity..... Core data for Cane Creek and literature for over and underlying salt
Young's Modulus ..... Calculated from sonic log
Poisson's Ratio ..... Calculated from sonic log
Rock Compressibility ..... Calculated from sonic log
Vertical Stress .....Integration of density log
Fracture Gradient (σ_{HMIN}) .....Planned DFIT from drilling reports
Maximum Horizontal Stress (σ_{HMAX}).... Assumed equal to the minimum horizontal stress
Tensile Strength. Core data for Cane Creek and literature for over- and underlying salt
Permeability .....From rock type

Table 15. Orientation of Fractures

Fracture Set	Property	Length (ft)	Orientation (°)	Spacing (ft)
1	Average	200	30	344
	Standard Deviation	100	15	240
2	Average	66	330	344
	Standard Deviation	33	15	240

Once the zones and fractures were specified, the well was created as a horizontal well with the lateral trajectory perpendicular to the major fracture set. The azimuth was set at 330° based on data from the sonic scanner. The lateral was set to a length of 4,300 feet in the pay, which is approximately the length of the lateral of the Cane Creek well CCU26-3. In reality, current drilling technology might allow this to be extended, depending on leasing restrictions. The horizontal leg of this well was landed at 7612 ft TVD. The trajectory and zone properties are in Table 16. Figure 40 shows the zones adopted in the simulations.

Table 16. Cane Creek Petrel Simulation Geologic Zones

Parameter	Zone 1	Zone 2	Zone 3	Zone 4	Zone 5
Top TVD (ft)	7285	7585	7600	7626	7655
Gross height (ft)	300	15	26	29	80
Rock type	Salt	Dolomite[11]	Dolomite	Dolomite	Salt
Pay zone	No	No	Yes	No	No
Pore pressure gradient (psi/ft)	0.82	0.82	0.82	0.82	0.82
Reservoir pressure (psi)	6097	6226	6243	6265	6310
Fracture gradient (psi/ft)	1.0	0.9	0.9	0.9	1.0
Minimum horizontal stress (psi)	7435	6833	6852	6876	7695
Maximum horizontal stress (psi)	7435	6833	6852	6876	7695
Porosity (%)	0.01	5.1	8.2	5.5	0.01
Young's modulus (10^6 psi)	6.17	7.96	7.96	7.96	4.49
Poisson's ratio	0.27	0.28	0.31	0.32	0.27
Rock compressibility (1/psi)	1×10^{-6}	1×10^{-6}	1×10^{-6}	1×10^{-6}	1×10^{-6}
Overburden stress (psi)	7936	8055	8095	8155	8289
Coefficient of friction	0.6	0.6	0.6	0.6	0.6
Tensile strength (psi)	650	864	1090	1043	650
Intrinsic permeability (mD)	1×10^{-4}	0.16	0.04	0.05	1×10^{-6}

[11] While labelled dolomite for convenience, Figure 40 indicates that these are interbedded dolomitic siltstones, anhydrites and some organic rich shales.

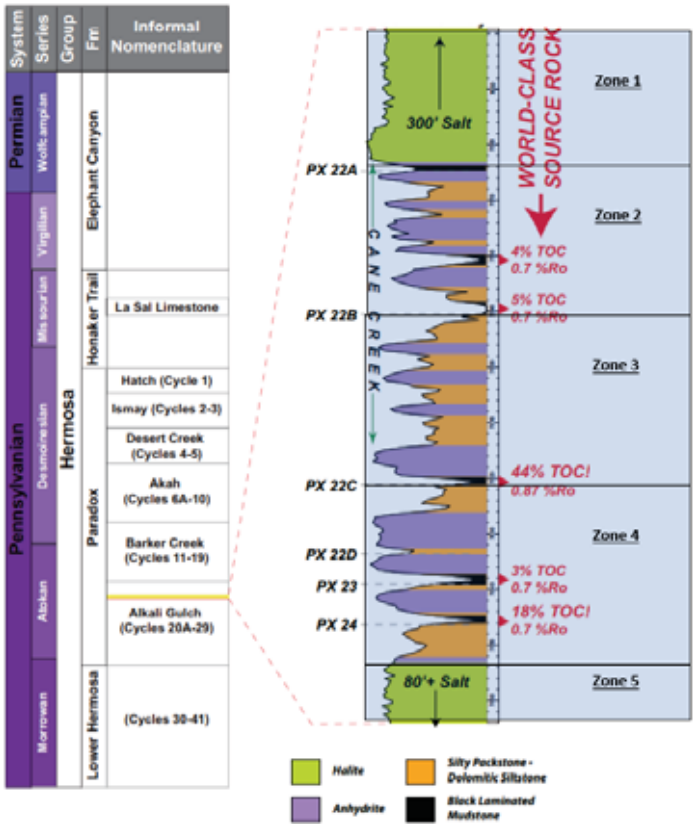

Figure 40. Zones adopted in the simulations.

Simulations were carried out using Schlumberger's Kinetix Stimulation Software Suite. This simulation package enables the user to study hydraulic fracture interaction with vertical natural fractures. The hydraulic fracturing is represented by pseudo-three-dimensional fracture growth mechanisms. The treatment and completion options are described in the following section.

VI.2 Treatment Fluid

Various treatments were attempted to look for a preferred stimulation method (to avoid growth into the salt). The fluids considered in the simulations are summarized in Table 17 and described individually in the text following the table. Proppant was usually 80/100 sand although some stages with 20/40 sand were also considered.

Table 17. Treating Fluids Considered (160°F)

Fluid	Abbreviation	Specific Gravity	n	K ($lb\text{-}s^n/ft^2$)	Apparent Viscosity at 170 s^{-1} (cP)
Slickwater	SW	1.01	1	1.35×10^{-5}	0.64
Mineral Oil-1	MO1	.85	1	4.17×10^{-5}	2
Mineral Oil-2[12]	MO2	1.01	1	1.35×10^{-5}	0.64
50 pptg[13] Crosslinked Borat	XL	1	0.49	0.02	586
Gelled Oil I	GO	1	0.23	0.02	157
Viscoelastic Surfactant	VES	1	0.51	0.01	44

Generically, the fluids considered were as follows.

Oil-Based Fluid: To their credit, a previous operator treated the formation with mineral oil. Lease crude would have been another possibility but the synthetic oil is likely more biodegradable. The benefit of this fluid genre is the limited reaction with the adjacent salt formations. A viscosity of nominally 2 cP was used for the oil - relatively low and this inhibits proppant carrying.

Gelled Oil: This is another possible fluid that would minimize interaction with adjacent salt. The drawback is perceived to be out-of-zone growth with the higher viscosity. However, the treating fluids themselves will not interact with the salt. The issues could be environmental and safety.

Water Based Fluid: Both slickwater, at 20 bpm, and a 50 lb per thousand-gallon borate crosslinked fluid were evaluated. The slickwater was assumed to have a viscosity of nominally 0,64 cP at reservoir temperature. The properties of the crosslinked fluid were taken from the simulator database. Two extreme fluid scenarios were assessed to comprehend height growth. An intermediate situation might be a low loading linear gel.

Composite: One of the observations with the crosslinked fluid is screenout when proppant (other than 80/100 mesh) reached the perforations. At the other extreme, proppant from the low viscosity treatments would settle. Cyclic injection was evaluated to consider the possibility of fracture placement with proppant acting as an in-fracture diverter and inhibiting height growth. This concept is not new. Diversion treatments for height containment were described in the 1980s. One relevant publication is Greener, 1994.

[12] Artificially implemented to have the same properties as slickwater but can be pumped with gelled oil without forming an emulsion.
[13] pptg indicates pounds per thousand gallons of base fluid.

The basis for the composite/cyclic treatments was low viscosity fluid pumped in small stage volumes with sand concentrations of 0.5 followed by 1.0 ppg. This was followed by displacement with higher viscosity fluid to push the proppant to the top and the bottom of the pay and to nominally extend the fracture. This was followed by a final cycle of low viscosity fluid with the same low proppant concentrations. The same concept could be applied by fingering the low viscosity fluid through a proppant carrying more viscous fluid or simply running cycled proppant concentrations.

VI.3 Completions

As indicated, a surrogate horizontal well was compiled for each basin. This was based on logging and completion information from various vertical wells and inferences of natural fracture geometry. A generic stage was considered in order to compare performance. This stage was 300 ft long. Three cluster options were considered. These were one (A), three (B) and six (C) clusters per stage, each 10 feet long, perforated at 6 spf and 60° phasing. The clusters were evenly and symmetrically spaced through the stage. The stage was nominally at the toe of the surrogate well, from 11,589 to 11,889 ft MD.

VI.4 Treatments

An array of treatments was carried out with the specific intent to assess the potential to create contained fractures. The baseline slickwater frac schedule is summarized in Table 18. Results are shown in Figures 41 and 42.

Table 18. Summary of Baseline Slickwater Treatment

Pump Schedule 1 (SW1)								
Step	Pump Rate (bbl/min)	Fluid	Fluid Volume (gal)	Proppant	Proppant Concentration (ppa)	Proppant Mass (lbm)	Slurry Volume (bbl)	Pump Time (min)
Pad	20	SW	10000	None	0	0	238.1	11.9
0.5 ppa	20	SW	15500	80/100	0.50	7750	377.42	18.87
1 ppa	20	SW	15500	80/100	1.00	15500	385.8	19.29
Total			41000			23250	1001.32	50.06

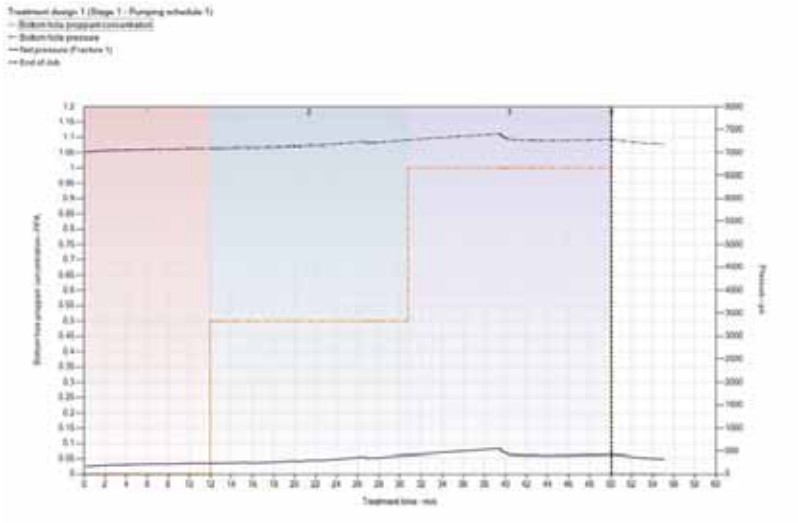

Figure 41. This is a chronology of the bottomhole treating pressure, the net pressure and the downhole proppant concentration. The net pressure is elevated, although not extreme. It suggests that out-of-zone growth is possible and that the rate should be reduced. The consequence would be further/earlier proppant settlement.

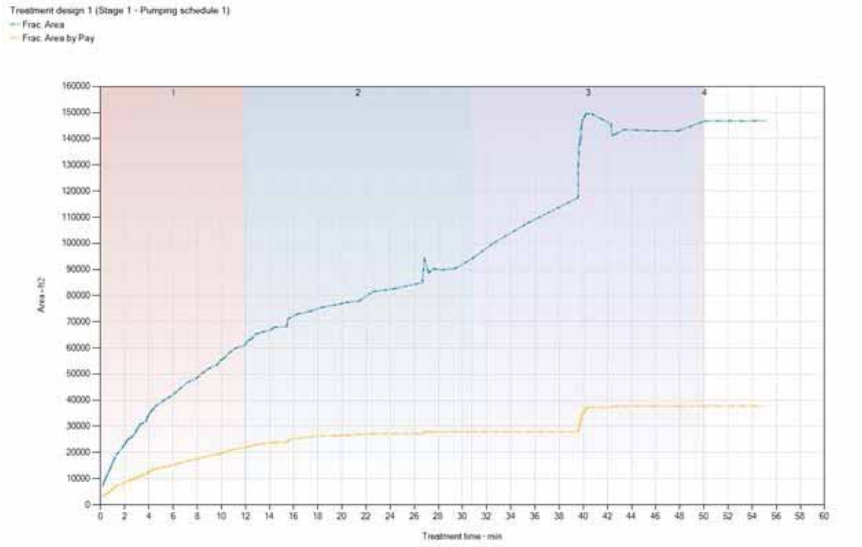

Figure 42. This is an EOJ[14] view of the total and propped area. As with most slickwater jobs we see a tremendous difference between the total created surface area and the functional area that is propped. The maximum total height is approximately 110 feet and the average total height is approximately 100 feet. The dominant fracture is approximately 960 feet long.

[14] EOJ is end of job, implying geometry at shutdown.

The maximum distance the fracture can grow upwards without growing into the salt zone is 28 feet and the maximum distance the fracture can grow downward without growing into the salt zone is 42 feet. This gives a maximum allowable fracture height for a water-based fracturing system of 70 ft. It is clear that for this perforation arrangement and pump schedule the well would likely experience salt-induced production problems. This is also true for this pump schedule and all other perforation arrangements, with three clusters (B) having the smallest maximum fracture height of 98 feet. To try and control fracture height growth and maximize fracture area in the pay the approach was to reduce the rate and increase the fluid viscosity.

What would happen if the fluid viscosity was increased? One's initial instinct dictates that the greater frictional losses in the fracture would insure out of zone growth unless the rates were drastically increased. Three water-based fracturing systems were investigated that had increased viscosities. Two of these systems alternated viscous and non-viscous fluids.

The pump schedule for a cross-linked treatment is shown in Table 19. 80/100 proppant would be consistent with industry practice. To try to keep the viscous fluid from breaking into the salt, the rate is dramatically reduced after the slickwater pad.

Table 19. Summary of Viscosified Water-Based Treatments

Pump Schedule 9 (XL2) 50 pptg Borate Crosslinked Gel								
Step	Pump Rate (bbl/min)	Fluid	Fluid Volume (gal)	Proppant	Proppant Concentration (ppa)	Proppant Mass (lbm)	Slurry Volume (bbl)	Pump Time (min)
Pad	20	SW	10000	None	0	0	238.1	11.9
0.5 PPA	4	XL	2000	80/100	0.50	1000	48.7	12.17
1 PPA	4	XL	2000	80/100	1.00	2000	49.78	12.45
1.5 PPA	4	XL	4000	80/100	1.50	6000	101.72	25.43
2 PPA	4	XL	4000	80/100	2.00	8000	103.88	25.97
2.5 PPA	4	XL	3500	80/100	2.50	8750	92.79	23.2
3 PPA	4	XL	3500	80/100	3.00	10500	94.68	23.67
3.5 PPA	4	XL	3000	80/100	3.50	10500	82.78	20.69
4 PPA	4	XL	3000	80/100	4.00	12000	84.4	21.1
4.5 PPA	4	XL	3000	80/100	4.50	13500	86.02	21.5
5 PPA	4	XL	3000	80/100	5.00	15000	87.64	21.91

Tables 20 and 21 show treatments where there is cyclic alteration between proppant laden viscosified fluids and slickwater, where it is hoped to use the proppant as a diverting agent to impede upwards and downwards vertical growth.

Table 20. Summary of Cyclic Water Based Treatment (Slickwater and Viscoelastic Surfactant)

Pump Schedule 9 (VES-SW-1) Alternating Slickwater and Viscoelastic Surfactant								
Step	Pump Rate (bbl/min)	Fluid	Fluid Volume (gal)	Proppant	Proppant Concentration (ppa)	Proppant Mass (lbm)	Slurry Volume (bbl)	Pump Time (min)
Pad	8	SW	10000	None	0	0	238.1	29.76
0.25 PPA	4	VES	800	80/100 Sand	0.25	200	19.26	4.82
0.75 PPA	4	VES	800	80/100 Sand	0.75	600	19.7	4.92
Pad	8	SW	4300	None	0	0	102.38	12.8
0.25 PPA	4	VES	800	80/100 Sand	0.25	200	19.26	4.82
0.75 PPA	4	VES	800	80/100 Sand	0.75	600	19.7	4.92
Pad	8	SW	4300	None	0	0	102.38	12.8
0.25 PPA	4	VES	800	80/100 Sand	0.25	200	19.26	4.82
0.75 PPA	4	VES	800	80/100 Sand	0.75	600	19.7	4.92
Pad	8	SW	7300	None	0	0	173.81	21.73
0.25 PPA	4	VES	800	80/100 Sand	0.25	200	19.26	4.82
0.75 PPA	4	VES	800	80/100 Sand	0.75	600	19.7	4.92
Pad	8	SW	4300	None	0	0	102.38	12.8
0.25 PPA	4	VES	800	80/100 Sand	0.25	200	19.26	4.82
0.75 PPA	4	VES	800	80/100 Sand	0.75	600	19.7	4.92
Pad	8	SW	4200	None	0	0	100	12.5
0.25 PPA	4	VES	800	80/100 Sand	0.25	200	19.26	4.82
0.75 PPA	4	VES	800	80/100 Sand	0.75	600	19.7	4.92

Table 21. Summary of Cyclic Water Based Treatment (Slickwater and Crosslinked Gel)

Pump Schedule 13 (XL-SW-1) Alternating Slickwater and Crosslinked Gel								
Step	Pump Rate (bbl/min)	Fluid	Fluid Volume (gal)	Proppant	Proppant Concentration (ppa)	Proppant Mass (lbm)	Slurry Volume (bbl)	Pump Time (min)
Pad	8	SW	10000	None	0	0	238.1	29.76
0.5 PPA	4	XL	800	80/100 Sand	0.50	400	19.48	4.87
0.75 PPA	4	XL	800	80/100 Sand	0.75	600	19.7	4.92
Pad	8	SW	4300	None	0	0	102.38	12.8
0.5 PPA	4	XL	800	80/100 Sand	0.50	400	19.48	4.87
0.75 PPA	4	XL	800	80/100 Sand	0.75	600	19.7	4.92
Pad	8	SW	4300	None	0	0	102.38	12.8
0.5 PPA	4	XL	800	80/100 Sand	0.50	400	19.48	4.87
0.75 PPA	4	XL	800	80/100 Sand	0.75	600	19.7	4.92
Pad	8	SW	4300	None	0	0	173.81	21.73

Pump Schedule 13 (XL-SW-1) Alternating Slickwater and Crosslinked Gel								
Step	Pump Rate (bbl/min)	Fluid	Fluid Volume (gal)	Proppant	Proppant Concentration (ppa)	Proppant Mass (lbm)	Slurry Volume (bbl)	Pump Time (min)
0.5 PPA	4	XL	800	80/100 Sand	0.50	400	19.48	4.87
0.75 PPA	4	XL	800	80/100 Sand	0.75	600	19.7	4.92
Pad	8	SW	4300	None	0	0	102.38	12.8
0.5 PPA	4	XL	800	80/100 Sand	0.50	400	19.48	4.87
0.75 PPA	4	XL	800	80/100 Sand	0.75	600	19.7	4.92
Pad	8	SW	4200	None	0	0	100	12.5
0.5 PPA	4	XL	800	80/100 Sand	0.50	400	19.48	4.87
0.75 PPA	4	XL	800	80/100 Sand	0.75	600	19.7	4.92

None of these water-based systems, when tested with any of the perforation arrangements, was able to keep the maximum height growth below 70 feet. It is not surprising based on the viscosity of the viscosified fluids - lower gel loading could be the key with cycling. Of the four water based systems: the slickwater (SW1), the high viscosity (XL), the medium viscosity alternating/cyclic (VES-SW-1), and the high viscosity alternating/cyclic (XL-SW-1), the system and perforation combination that was most successful at containing the fracture was the medium viscosity alternating/cyclic fluid design with perforation arrangement C which had six perforation clusters. This was the alternating slickwater-viscoelastic surfactant.

The code cannot discriminate fluid properties other than rheology. Hence, any lower viscosity fluid used in the cyclic system would be desirable. The maximum height for that treatment (Table 19) was 77 feet. The best way to reduce the maximum height of this system would be to reduce the volume of fluid used but this would be a detriment to maximizing proppant volume. The difficulty in placing large volumes of proppant in combination with the proximity to salt suggests using an oil-based system. The results for a cyclic medium-viscosity/slickwater treatment are shown in Figures 43 through 45.

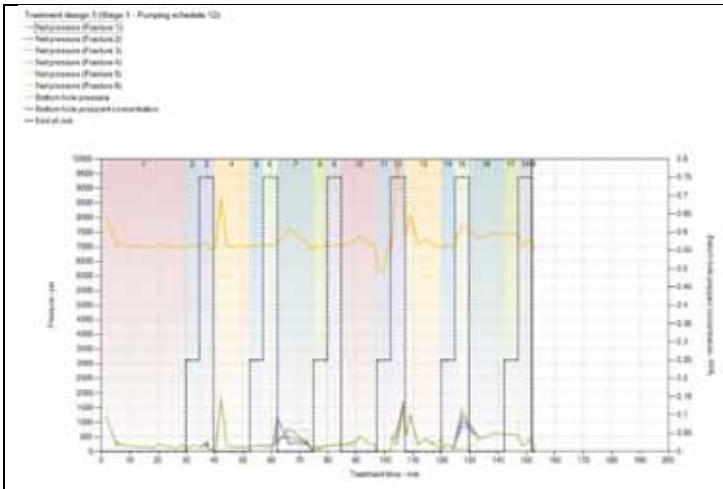

Figure 43. This is a chronology of the bottomhole treating pressure, the net pressure and the downhole proppant concentration for Pump Schedule 12, where a VES was alternated with slickwater. The net pressure is periodically elevated when proppant reaches a cluster. This could cause near-wellbore horizontal fracturing and potential casing distress. It suggests that out-of-zone growth could occur and could be ameliorated by lower rates or viscosity. Even smaller diameter proppant could be considered.

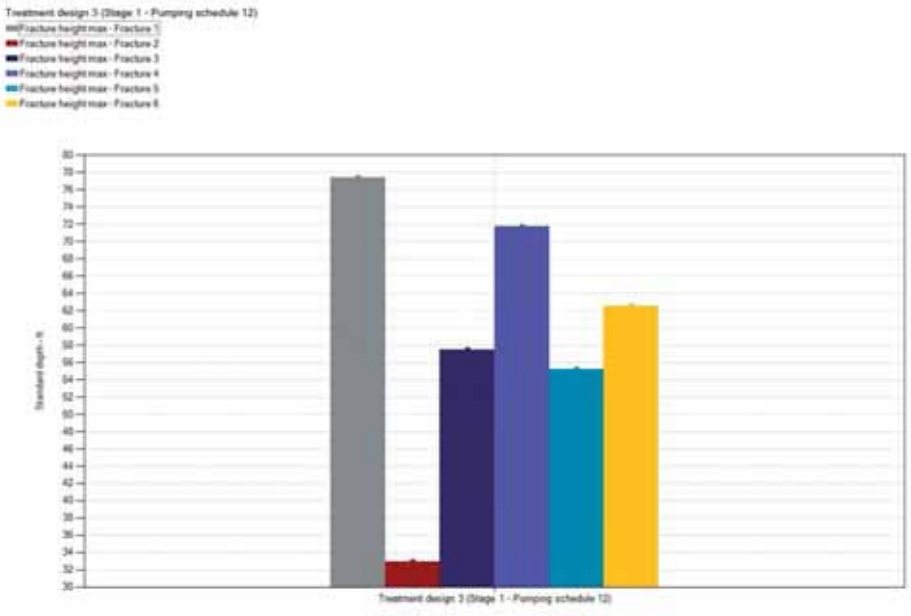

Figure 44. This is an EOJ view of the vertical extent of six fracture systems (one from each perforation cluster) for Pump Schedule 12, where a VES was alternated with slickwater. The most upstream cluster is shown to penetrate into the salt. Minor modifications might reduce the penetration.

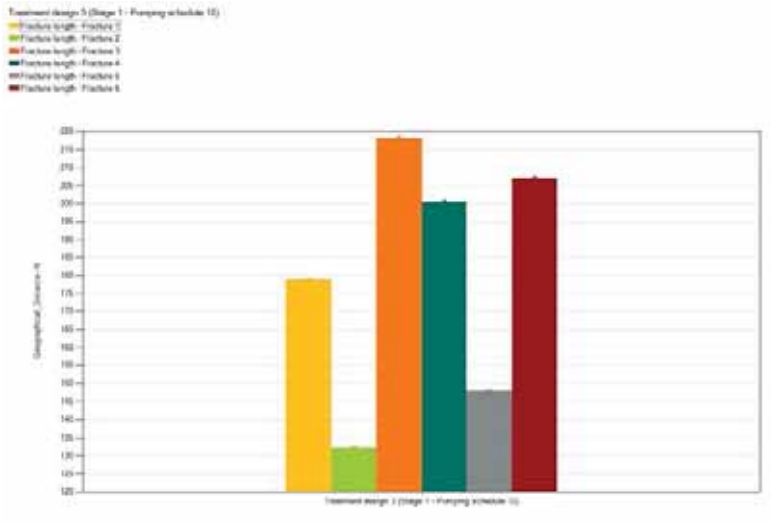

Figure 45. This is an EOJ view of the "lateral" extent of six fracture systems (one from each perforation cluster) for Pump Schedule 12, where a VES was alternated with slickwater. The most upstream cluster is shown to penetrate into the salt. Minor modifications might reduce the penetration. The variation may relate to natural fractures.

Figure 46 provides an EOJ perspective of the fracture growth from the six perforation clusters.

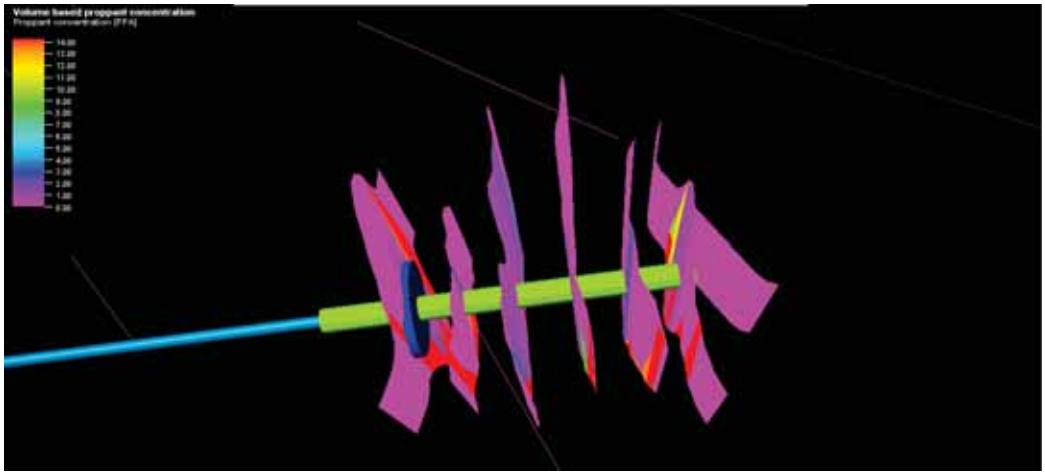

Figure 46. This is an EOJ view of the extent of six fracture systems (one from each perforation cluster) for Pump Schedule 12, where a VES was alternated with slickwater. The contours are for proppant concentration from 0 to 14 ppa. Proppant coverage is poor but there appears to be moderate containment.

There are occurrences during the treatment where the total propped area approaches the area propped within the pay zone. This occurs for most of the treatments that alternate between viscous and non-viscous fluids with and without proppant. This is the only treatment where this occurs in non-sequential sweeps. This indicates that proppant is falling down through the fracture as the low viscosity fluid is pumped and back into the pay zone causing a higher concentration of proppant within the pay zone during these sweeps.

The oil-based fracturing systems were treated differently than the water-based ones. These treatments were not judged based on containment alone but on the surface area of the pay zone that was propped. The highest in-pay ratio or propped surface area, 0.97, occurred for pump schedule a gelled oil frac, with perforation arrangement A. The pump schedule for one gelled oil frac design is shown in Table 20.

Table 20. Summary of Gelled Oil Treatment

Pump Schedule 10 (GO-1) Gelled Oil								
Step	Pump Rate (bbl/min)	Fluid	Fluid Volume (gal)	Proppant	Proppant Concentration (ppa)	Proppant Mass (lbm)	Slurry Volume (bbl)	Pump Time (min)
Pad	20	GO	10000	None	0	0	238.1	11.9
0.5 PPA	20	MO-2	9500	80/100 Sand	0.50	4750	231.32	11.57
1 PPA	20	GO	4800	80/100 Sand	1.00	4800	119.47	5.97
Pad	2	GO	2400	None	0	0	57.14	28.57
0.5 PPA	20	MO-2	9500	80/100 Sand	0.50	4750	231.32	11.57
1 PPA	20	MO-2	4800	80/100 Sand	1.00	4800	119.47	5.97

In this gelled oil treatment (Pump Schedule 10), only one of the proppant carrying stages ran and the fracture width of the stage ends with a value of zero. This indicates that after the first proppant stage and the subsequent sweep the fractures were unable to be reopened and the job terminated. While initially this treatment plan looked promising upon further inspection it is seen that this is not the case. With this in mind, pump schedule GO-2 with perforation arrangement B may be the best completion method, with a ratio in-pay to out-of-pay propping of 0.79. That pump schedule used alternating between proppant-laden lower viscosity fluids with more viscous low rate sweep stages.

As with the water-based fluids, alternating viscosity stages. Table 21 shows one example schedule, even trying to pump some larger diameter proppant.

Table 21. Summary of Gelled Oil Treatment - Cyclic

Pump Schedule 11 (GO-MO-2-1) Gelled Oil-Mineral Oil Cycles								
Step	Pump Rate (bbl/min)	Fluid	Fluid Volume (gal)	Proppant	Proppant Concentration (ppa)	Proppant Mass (lbm)	Slurry Volume (bbl)	Pump Time (min)
Pad	20	MO-2	10000	None	0	0	238.1	11.9
0.5 PPA	20	MO-2	6000	80/100 Sand	0.50	3000	146.1	7.3
1 PPA	20	MO-2	3000	80/100 Sand	1.00	3000	74.67	3.73
Pad	2	GO	2000	None	0	0	47.62	2.38
0.5 PPA	20	MO-2	6000	80/100 Sand	0.50	3000	146.1	7.3
1 PPA	20	MO-2	3000	80/100 Sand	1.00	3000	74.67	3.73
Pad	2	GO	2000	None	0	0	47.62	2.38
0.5 PPA	20	MO-2	6000	80/100 Sand	0.50	3000	146.1	7.3
1 PPA	20	MO-2	3000	80/100 Sand	1.00	3000	74.67	3.73

The results for the treatment shown in Table 21, with perforation arrangement B, are shown in Figures 47 through 49. It is readily apparent that the sweeps allow the closing of fractured area outside the pay zone by letting proppant fall back down into the pay zone and increasing the proppant concentration in this zone. Treatment schedule **GO-MO-2-1** with perforation arrangement B is a possibility for completing the Cane Creek.

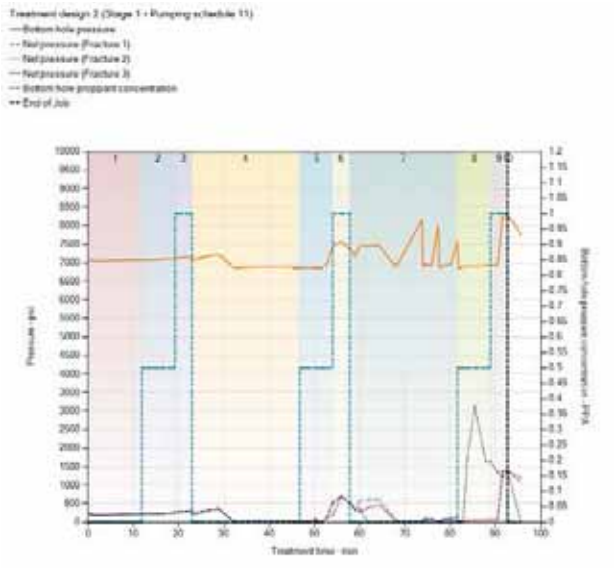

Figure 47. This is a chronology of the bottomhole treating pressure, the net pressure and the downhole proppant concentration where a gelled oil and mineral oil were cycled. The net pressure is periodically elevated when proppant reaches a cluster, particularly for the third cluster from the heel.

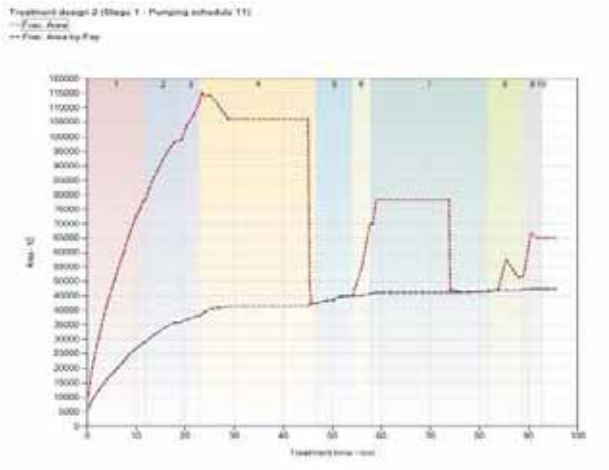

Figure 48. This is the area (propped and unpropped) where a gelled oil and mineral oil were cycled. The distribution because of the cycling merits additional study.

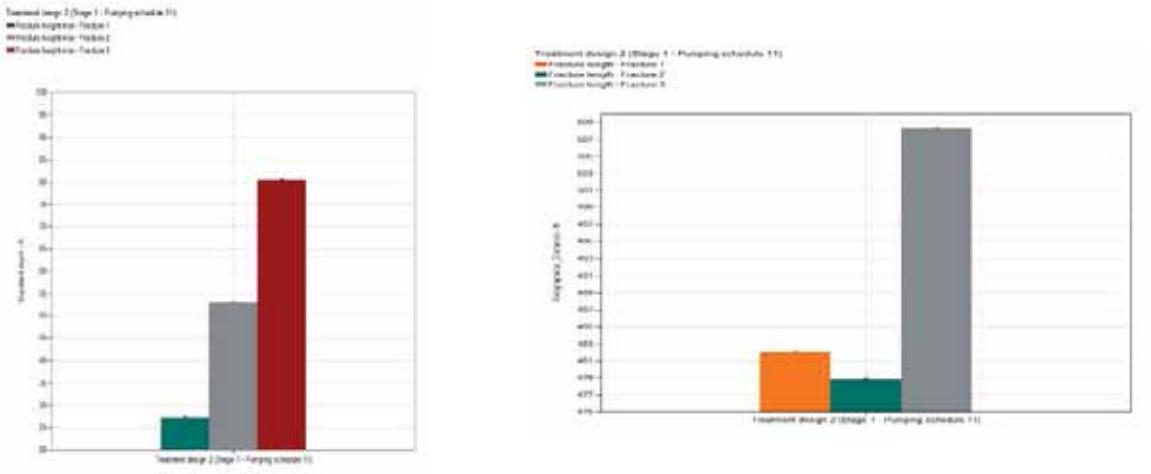

Figure 49. At left is the height growth for fractures from each cluster. At right is the dominant length growth for the distil stage. Why the farthest stage dominates is uncertain.

The proppant concentration at the EOJ is shown for one alternating gelled oil-mineral oil treatment with a single perforation cluster (Figure 50). Figure 51 shows a similar treatment with three clusters.

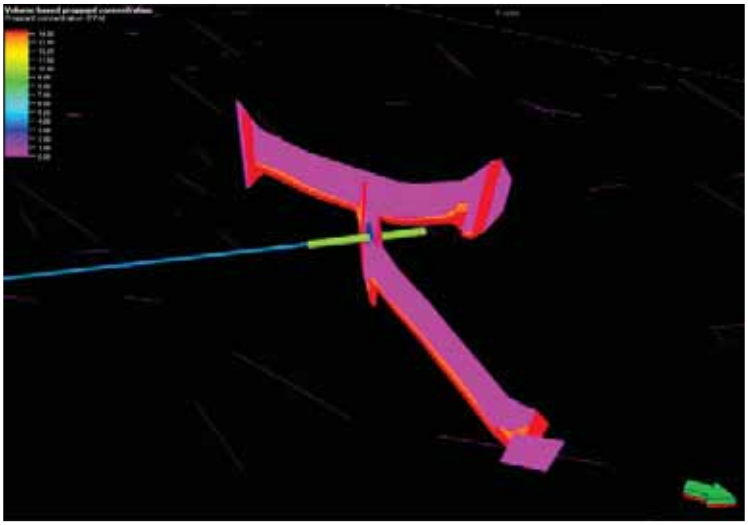

Figure 50. Geometry of an alternating mineral oil-gelled oil treatment with one perforation cluster. The contours are proppant concentration in ppa. The role of pre-existing fractures is particularly evident as is setting of the proppant. An equivalent treatment, but with three clusters, is shown in Figure 51.

Figure 51. Geometry of an alternating mineral oil-gelled oil treatment with three perforation clusters. The contours are proppant concentration in ppa. The role of pre-existing fractures is particularly evident as is setting of the proppant. An equivalent treatment, but with one cluster, is shown in Figure 50.

VII. Uteland Butte - Horizontal Well Fracturing Simulations

Until less than a decade ago, wells in the Uteland Butte member of the Green River formation were vertical wells that completed the Uteland Butte section as a secondary target after other productive intervals within the well. Recently, operators have begun to try and target the Uteland Butte member specifically, with varying success. For this reason, it is desirable to develop a completion plan that will result in consistent fracture geometry ensuring consistent productivity. This is the purpose of the simulations that are described here.

Core data, rock mechanics, and logging data from well BTR 14-3-45 were used to build properties for the layers that were represented in the simulations. The number of zones and their location were based on a combination of GR data and core examination for the depth and thickness of the target dolomites, PZ-1 and PZ-1', as well as the over- and underlying limestones. The natural fracture orientation was also found from a Newfield report and the fracture frequency was found from a Search and Discovery article by Anderson and Roesink, 2013, evaluating the reservoir characteristics of the Uteland Butte formation. The formation properties and how the layer properties were obtained are summarized below.

Pore Pressure Gradient ..... Mud weight from Drilling Reports and bottomhole pressures
Fracture Gradient..... Fracturing report
Porosity.....BTR 14-3-45 core data correlated with Young's modulus
Young's Modulus ..... Core testing
Poisson's Ratio ..... Core testing correlated with GR for missing intervals
Rock Compressibility ..... Correlated with gamma ray[15]
Vertical Stress .....Integration of density log
Tensile Strength..... Core testing and correlated linearly with porosity
Permeability..... Core testing and linearly correlated with density porosity using core data permeability-porosity crossplot

The fracture network data are summarized in Table 22. They were represented as subvertical to vertical for simulation purposes.

[15] The lower bound of the gamma ray corresponding to the grain compressibility for kaolinite and the upper bound corresponding to the grain compressibility of quartz.

Table 22. Uteland Butte Fracture Set Data

Fracture Set	Property	Length (ft)	Strike (°)	Spacing (ft)	Upper Bound	Lower Bound
1	Average	100	112	200	Zone 1[16]	Zone 8
	Standard Deviation	50	15	64		
2	Average	100	112	24	Zone 9	Zone 10
	Standard Deviation	50	15	8		
3	Average	100	112	100	Zone 11	Zone 11
	Standard Deviation	50	15	30		
4	Average	100	112	24	Zone 12	Zone 12
	Standard Deviation	50	15	8		
5	Average	100	112	100	Zone 13	Zone 13
	Standard Deviation	50	15	30		
6	Average	100	112	24	Zone 14	Zone 14
	Standard Deviation	50	15	8		
7	Average	100	112	200	Zone 15	Zone 23
	Standard Deviation	50	15	64		

The well was created as a horizontal well with the lateral perpendicular to the major fracture set. The lateral was set to 4,500 feet, which is the average lateral length of the available Bill Barrett horizontal well. It is recognized that laterals are now much longer than this but stimulation design may not be significantly impacted. The well was landed between two target dolomites at a typical depth of 7368 feet TVD. The azimuth of the well 202°.

[16] The zones that are referred to in Table 22 are summarized in Table 23.

Table 23. Zones in the Fracture Simulations

Zone	1	2	3	4	5	6	7	8	9	10	11	12
Top (ft TVD)	6400	6510	6560	6650	6850	6950	7125	7225	7275	7350	7362	7367
Gross height (ft)	110	50	90	200	100	175	100	50	75	12	5	4
Fracture gradient (psi/ft)	0.69	0.68	0.68	0.68	0.68	0.68	0.68	0.74	0.74	0.75	0.75	0.75
Max horizontal stress (psi)	4454	4444	4491	4590	4692	4786	4879	5365	5411	5517	5523	5527
Min horizontal stress (psi)	4454	4444	4491	4590	4692	4786	4879	5365	5411	5517	5523	5527
Overburden stress gradient (psi/ft)	1.17	1.17	1.17	1.17	1.17	1.17	1.17	1.17	1.17	1.17	1.17	1.17
Poisson's ratio	0.26	0.27	0.27	0.28	0.28	0.28	0.27	0.25	0.26	0.26	0.26	0.26
Pore pressure gradient (psi/ft)	0.54	0.54	0.54	0.53	0.54	0.53	0.54	0.54	0.54	0.54	0.54	0.54
Porosity (%)	8.04	4.66	3.87	4.1	6.38	6.74	7.78	5.83	6.65	9.48	9.48	9.48
Rock compressibility (1/psi)	10^{-6}	10^{-6}	10^{-6}	10^{-6}	10^{-6}	10^{-6}	10^{-6}	10^{-6}	10^{-6}	10^{-6}	10^{-6}	10^{-6}
Rock type	Shale	Shale	Shale	Shale	Shale	Shale	Shale	Shale	Limestone	Limestone	Dolomite	Limestone
Temperature (°F)	134	136	137	140	143	146	149	150	152	153	153	153
Tensile strength (psi)	995	1493	1609	1575	1239	1186	1033	1320	1219	783	783	783
Top TVD (ft)	6400	6510	6560	6650	6850	6950	7125	7225	7275	7350	7362	7367
Young's modulus (10^6 psi)	5.47	5.77	5.70	5.80	5.90	5.79	5.67	5.33	5.40	5.51	5.51	5.51
Pay zone	No	No	No	No	No	No	No	No	No	No	Yes	No
Coefficient of friction	0.6	0.6	0.6	0.6	0.6	0.6	0.6	0.6	0.6	0.6	0.6	0.6
Overburden stress (psi)	7552	7646	7728	7898	8073	8234	8395	8482	8556	8607	8616	8622
Reservoir pressure (psi)	3486	3529	3567	3578	3726	3730	3875	3915	3949	3972	3977	3979
Intrinsic permeability (mD)	0.0005	0.0002	1.00E-04	0.0002	0.0003	0.0003	0.0005	0.0003	0.0003	0.0008	0.0008	0.0008

Zone	13	14	15	16	17	18	19	20	21	22	23	
Top (ft TVD)	7371	7375	7540	7600	7710	7935	8060	8150	8225	8300	8724	
Gross height (ft)	4	165	60	110	225	125	90	75	75	424	76	
Fracture gradient (psi/ft)	0.75	0.75	0.75	0.76	0.76	0.78	0.8	0.8	0.81	0.8	0.78	
Max horizontal stress (psi)	5530	5593	5678	5818	5945	6238	6484	6550	6693	6810	6834	
Min horizontal stress (psi)	5530	5593	5678	5818	5945	6238	6484	6550	6693	6810	6834	
Overburden stress gradient (psi/ft)	1.17	1.17	1.17	1.17	1.17	1.17	1.17	1.17	1.17	1.17	1.17	
Poisson's ratio	0.26	0.26	0.25	0.27	0.27	0.27	0.27	0.27	0.27	0.27	0.27	
Pore pressure gradient (psi/ft)	0.54	0.53	0.54	0.54	0.53	0.54	0.54	0.54	0.54	0.53	0.54	
Porosity (%)	9.48	9.48	5.48	2.99	3.63	6	3.19	3.41	3.68	1.37	1.66	
Rock compressibility (1/psi)	10^{-6}	10^{-6}	10^{-6}	10^{-6}	10^{-6}	10^{-6}	10^{-6}	10^{-6}	10^{-6}	10^{-6}	10^{-6}	
Rock type	Dolomite	Limestone	Shale	Shale	Shale	Shale	Shale	Shale	Shale	Shale	Shale	
Temperature (°F)	153	155	157	159	162	166	168	170	171	177	182	
Tensile strength (psi)	783	783	1372	1738	1643	1295	1708	1676	1637	1976	1933	
Top TVD (ft)	7371	7375	7540	7600	7710	7935	8060	8150	8225	8300	8724	
Young's modulus (10^6 psi)	5.51	5.51	5.35	5.58	5.77	5.70	5.75	5.68	5.77	5.54	5.74	
Pay zone	Yes	No	No	No	No	No	No	No	No	No	No	
Coefficient of friction	0.6	0.6	0.6	0.6	0.6	0.6	0.6	0.6	0.6	0.6	0.6	
Overburden stress (psi)	8626	8725	8857	8956	9152	9357	9483	9579	9667	9959	10252	
Reservoir pressure (psi)	3981	3952	4088	4134	4146	4319	4377	4421	4462	4511	4731	
Intrinsic permeability (mD)	0.0008	0.0008	0.0002	0.0001	0.0001	0.0003	1.00E-04	1.00E-04	1.00E-04	6.00E-05	7.00E-05	

Various treatments were considered to infer the best completion strategy - placing sand and maintaining restricted height growth. The approach was to contain the fracture within the fractured limestone above and below the target dolomite. This was attempted by varying treating volumes, rates, and the viscosity of the treating fluid. The viscosities and specific gravities of these fluids are shown in Table 24.

Table 24. Fluids Used in Simulations (at 160°F)

Fluid	Designation	Specific Gravity	n'	K' ($lb_f.s^n/ft^2$)	Apparent Viscosity[17] (cP)
Slickwater	SW	1.01	1	0.00001	0.6365
20 pptg[18] borate crosslinked gel	XL	1	0.58	0.003	160.0537
0.04 pptg viscoelastic surfactant		1	0.39	0.004	8.5905

Four different perforations strategies were assessed (Tables 25 through 28). Simulations for done (in all cases) for the stage at the toe of the well.

- Perforation arrangement A used a single ten-foot cluster of 60 shots,
- Perforation arrangement B used three ten-foot clusters of 60 shots each separated by 70 feet,
- Perforation arrangement C used three ten-foot clusters of 60 shots each separated by 35 feet, and,
- Perforation arrangement D was four perforation clusters at uneven intervals.

Table 25. Perforation Arrangement A

Perforation name	Perforation 3
Perforation top MD (ft)	11778
Perforation bottom MD (ft)	11788
Cluster length (ft)	10
Number of shots	60
Cluster spacing (ft)	N/A
Perf diameter (in)	0.44
Tunnel length (in)	8
Phasing (°)	60

[17] At 170 s^{-1}.
[18] pptg is pounds per thousand gallons of base fluid

Table 26. Perforation Arrangement B

Perforation name	Perforation 5	Perforation 3	Perforation 1
Perforation top MD (ft)	11698	11778	11858
Perforation bottom MD (ft)	11708	11788	11868
Cluster length (ft)	10	10	10
Number of shots	60	60	60
Perforation spacing (ft)	80	80	-
Perforation diameter (in)	0.44	0.44	0.44
Tunnel length (in)	8	8	8
Phasing (°)	60	60	60

Table 27. Perforation Arrangement C

Perforation name	6	5	4	3	2	1
Perforation top MD (ft)	11658	11698	11738	11778	11818	11858
Perforation bottom MD (ft)	11668	11708	11748	11788	11828	11868
Cluster length (ft)	10	10	10	10	10	10
Number of shots	60	60	60	60	60	60
Perforation spacing (ft)	40	40	40	40	40	-
Perforation diameter (in)	0.44	0.44	0.44	0.44	0.44	0.44
Tunnel length (in)	8	8	8	8	8	8
Phasing (°)	60	60	60	60	60	60

Table 28. Perforation Arrangement D

Perforation name	6	4	3	1
Perforation top MD (ft)	11658	11738	11778	11858
Perforation bottom MD (ft)	11668	11748	11788	11868
Cluster length (ft)	10	10	10	10
Number of shots	60	60	60	60
Perforation spacing (ft)	80	40	80	-
Perforation diameter (in)	0.44	0.44	0.44	0.44
Tunnel length (in)	8	8	8	8
Phasing (°)	60	60	60	60

The last step in developing simulator input was to generate pump schedules.

The first case run was an actual pump schedule that was estimated from the well file of a horizontal Bill Barrett well. This schedule was run for perforation arrangements A and B but not C and D. Most schedules were not run for D.

To remain inside the fractured limestone the fracture could grow to a maximum height of 265 feet. But, in reality the fractures grew down very little and grew mostly upward. This limited the maximum fracture height to around 100 feet. All three treatment schedules for the pump schedule from the horizontal Bill Barrett well grew significantly out of zone. The pump schedule and results for this pump schedule (pump schedule 1) are shown in Table 29.

Table 29. Treatment Schedule 1

Step	Pump Rate (bbl/min)	Fluid	Fluid Volume (gal)	Proppant	Proppant Concentration (ppa)	Proppant Mass (lb)	Slurry Volume (bbl)	Pump Time (min)
Pad	44	SW	15500	None	0	0	369.05	8.39
0.5 ppa	44	XL	30000	80/100 Sand	0.50	15000	730.5	16.6
1 ppa	44	XL	15000	80/100 Sand	1.00	15000	373.35	8.49
1.5 ppa	44	XL	25000	20/40 Sand	1.5	37500	635.76	14.45
2 ppa	44	XL	20000	20/40 Sand	2	40000	519.42	11.8
2.5 ppa	44	XL	16000	20/40 Sand	2.5	40000	424.18	9.64
3 ppa	44	XL	11000	20/40 Sand	3	33000	297.57	6.76

Figures 52 through 55 show the simulated results for the treatment described in Table 29.

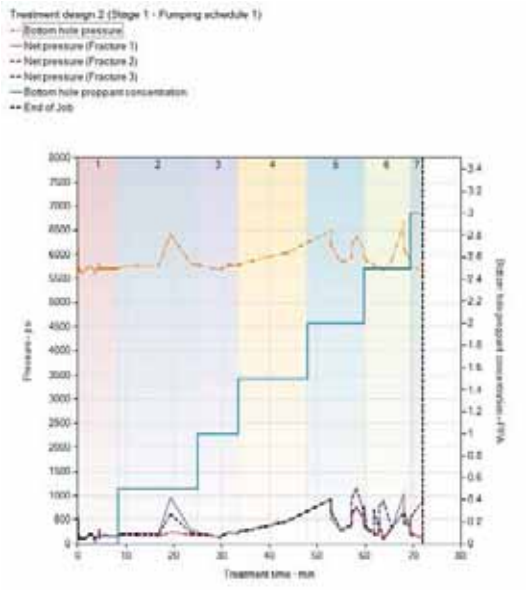

Figure 52. This is the chronology of bottomhole pressure, downhole proppant concentration and net pressure at each of three perforations clusters. The treatment schedule is 20 pptg borate crosslinked gel, shown in Table 29. Notice the sporadic variations in treating pressure due to individual fracture propagation events, presumably. Treatment reports are not available.

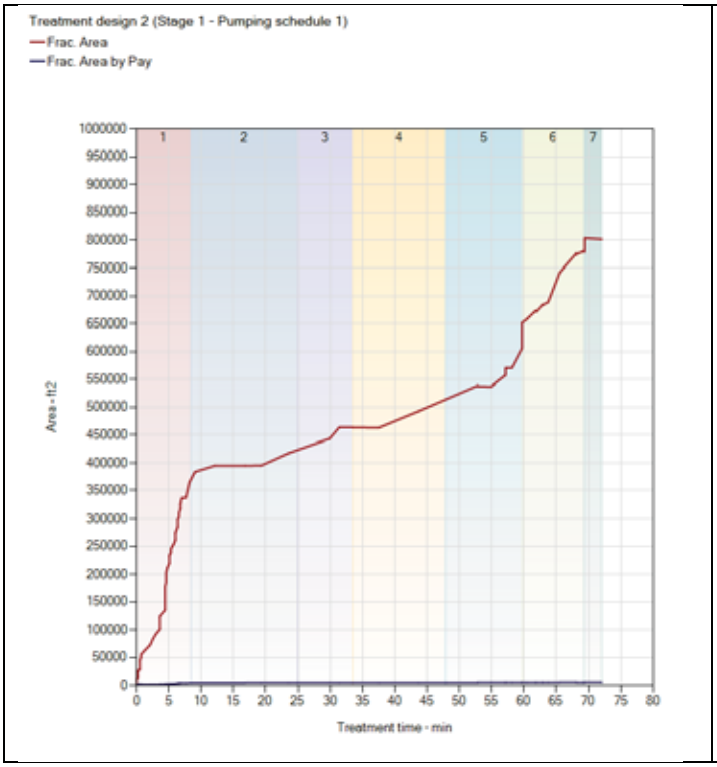

Figure 53. This is the created fracture surface area in pay. The treatment schedule is 20 pptg borate crosslinked gel, shown in Table 29. The increase in slope correlates with starting 20/40 sand.

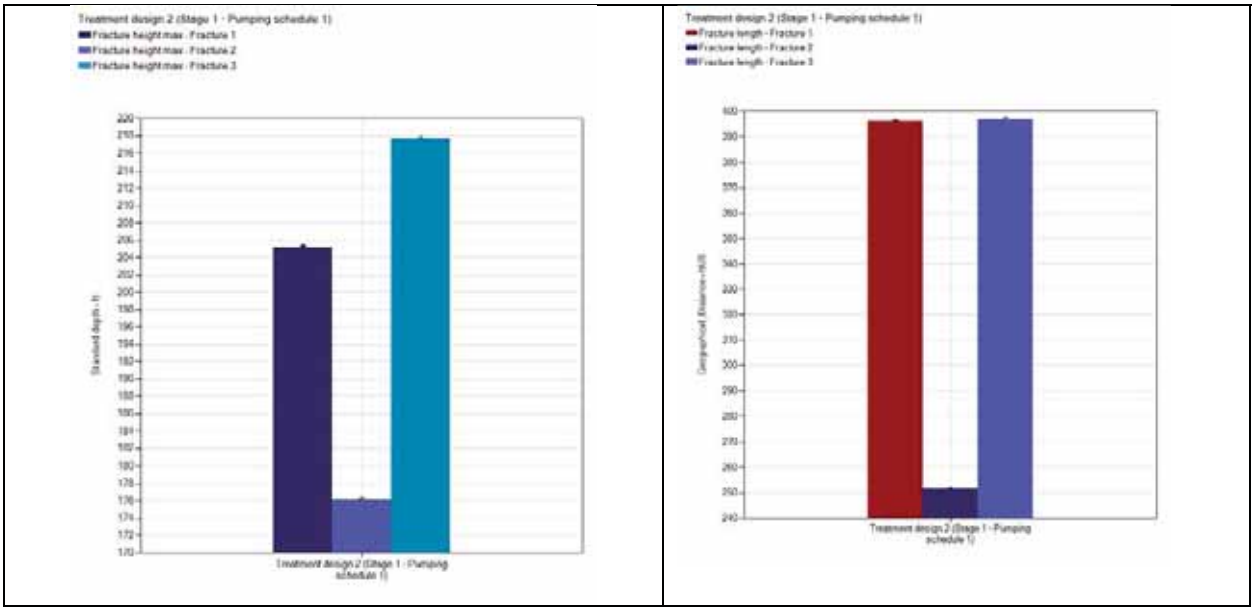

Figure 54. These are the created fracture geometries. The treatment schedule is 20 pptg borate crosslinked gel, shown in Table 29. The left-hand panel shows the total height for each of the three clusters. Based on the stress field used in the simulations, there is significant upward growth in the external clusters (the middle cluster is pinched and length extension is restricted. The right-hand panel shows lateral extent for fractures from each cluster.

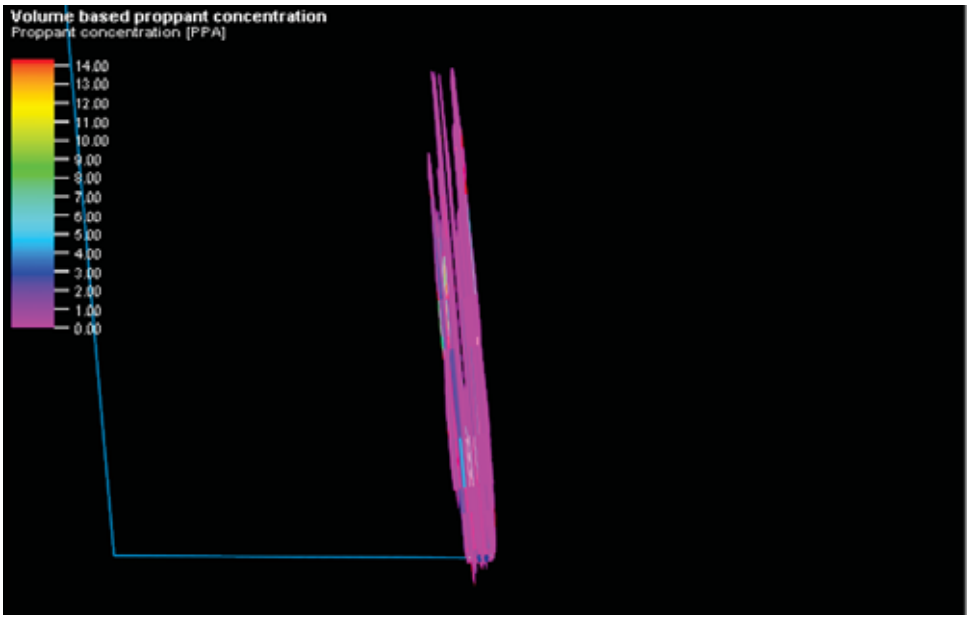

Figure 55. The vertical and horizontal scales are not equal. The maximum vertical growth (Figure 54) was approximately 220 feet - well out-of-zone.

After recognizing the potential for excessive vertical growth, the pumping rate was reduced in the next set of simulations. Pump schedule 2 (Table 30) reduced the volume of pump schedule 1. The pumping rate was reduced for pump schedules 3 through 5 (Tables 31 through 33). Pump schedule 2 with perforation arrangement C provided some height control. However, for pump schedule 2, the pressure plots indicate that sand settles and that almost all proppant placement is restricted to near the wellbore. This schedule did not actually reduce the rate just the volume.

Table 30. Pump Schedule 2 (Reduced Volume)

Step	Pump Rate (bbl/min)	Fluid	Fluid Volume (gal)	Proppant	Proppant Concentration (ppa)	Proppant Mass (lb)	Slurry Volume (bbl)	Pump Time (min)
Pad	44	SW	10000	None	0	0	238.1	5.41
0.5 ppa	44	XL	10000	80/100 Sand	0.50	5000	243.5	5.53
1 ppa	44	XL	10000	80/100 Sand	1.00	10000	248.9	5.66
1.5 ppa	44	XL	5000	20/40 Sand	1.5	7500	127.15	2.89
2 ppa	44	XL	2500	20/40 Sand	2	5000	64.93	1.48
2.5 ppa	44	XL	2500	20/40 Sand	2.5	6250	66.28	1.51
3 ppa	44	XL	2500	20/40 Sand	3	7500	67.63	1.54

Table 31. Pump Schedule 3 - Reduced Rate

Step	Pump Rate (bbl/min)	Fluid	Fluid Volume (gal)	Proppant	Proppant Concentration (ppa)	Proppant Mass (lb)	Slurry Volume (bbl)	Pump Time (min)
Pad	44	SW	10000	None	0	0	238.1	5.41
0.5 PPA	22	XL	10000	80/100 Sand	0.50	5000	243.5	11.07
1 PPA	22	XL	10000	80/100 Sand	1.00	10000	248.9	11.31
1.5 PPA	22	XL	5000	20/40 Sand	1.5	7500	127.15	5.78
2 PPA	22	XL	2500	20/40 Sand	2	5000	64.93	2.95
2.5 PPA	22	XL	2500	20/40 Sand	2.5	6250	66.28	3.01
3 PPA	22	XL	2500	20/40 Sand	3	7500	67.63	3.07

Table 32. Pump Schedule 4 - Further Reduced Rate

Step	Pump Rate (bbl/min)	Fluid	Fluid Volume (gal)	Proppant	Proppant Concentration (ppa)	Proppant Mass (lb)	Slurry Volume (bbl)	Pump Time (min)
Pad	44	SW	10000	None	0	0	238.1	5.41
0.5 PPA	11	XL	10000	80/100 Sand	0.50	5000	243.5	22.14
1 PPA	11	XL	10000	80/100 Sand	1.00	10000	248.9	22.63
1.5 PPA	11	XL	5000	20/40 Sand	1.5	7500	127.15	11.56
2 PPA	11	XL	2500	20/40 Sand	2	5000	64.93	5.9
2.5 PPA	11	XL	2500	20/40 Sand	2.5	6250	66.28	6.03
3 PPA	11	XL	2500	20/40 Sand	3	7500	67.63	6.15

Table 33 Pump Schedule 5 - Further Reduced Rate (reduced pad rate)

Step	Pump Rate (bbl/min)	Fluid	Fluid Volume (gal)	Proppant	Proppant Concentration (ppa)	Proppant Mass (lb)	Slurry Volume (bbl)	Pump Time (min)
Pad	11	SW	10000	None	0	0	238.1	21.65
0.5 PPA	11	XL	10000	80/100 Sand	0.50	5000	243.5	22.14
1 PPA	11	XL	10000	80/100 Sand	1.00	10000	248.9	22.63
1.5 PPA	11	XL	5000	20/40 Sand	1.5	7500	127.15	11.56
2 PPA	11	XL	2500	20/40 Sand	2	5000	64.93	5.9

Step	Pump Rate (bbl/min)	Fluid	Fluid Volume (gal)	Proppant	Proppant Concentration (ppa)	Proppant Mass (lb)	Slurry Volume (bbl)	Pump Time (min)
2.5 PPA	11	XL	2500	20/40 Sand	2.5	6250	66.28	6.03
3 PPA	11	XL	2500	20/40 Sand	3	7500	67.63	6.15

The progressive reduction in rate and stage volume. Pumping schedule 5 with six regularly spaced perforation clusters (perforation arrangement C) was one of the more contained treatment options. The results are shown in Figures 56 through 59.

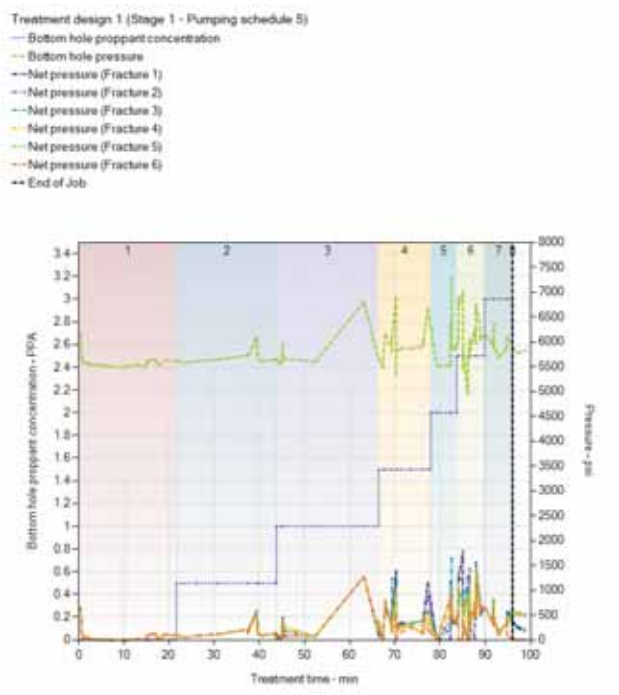

Figure 56. This is the chronology of bottomhole pressure, downhole proppant concentration and net pressure at each of six perforations clusters. The treatment schedule is 20 pptg borate crosslinked gel, shown in Table 33. Notice the sporadic variations in treating pressure due to individual fracture propagation events, presumably. Treatment reports are not available. This would argue for reduced proppant concentration and avoiding/minimizing the use of 20/40 which is a widely adopted practice.

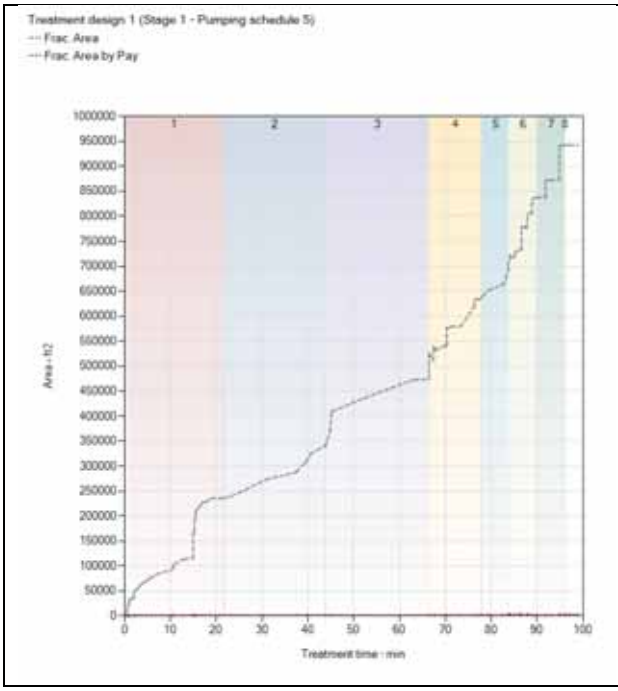

Figure 57. This is the created fracture surface area in pay. The treatment schedule is 20 pptg borate crosslinked gel, shown in Table 33. The increase in slope correlates with starting 20/40 sand.

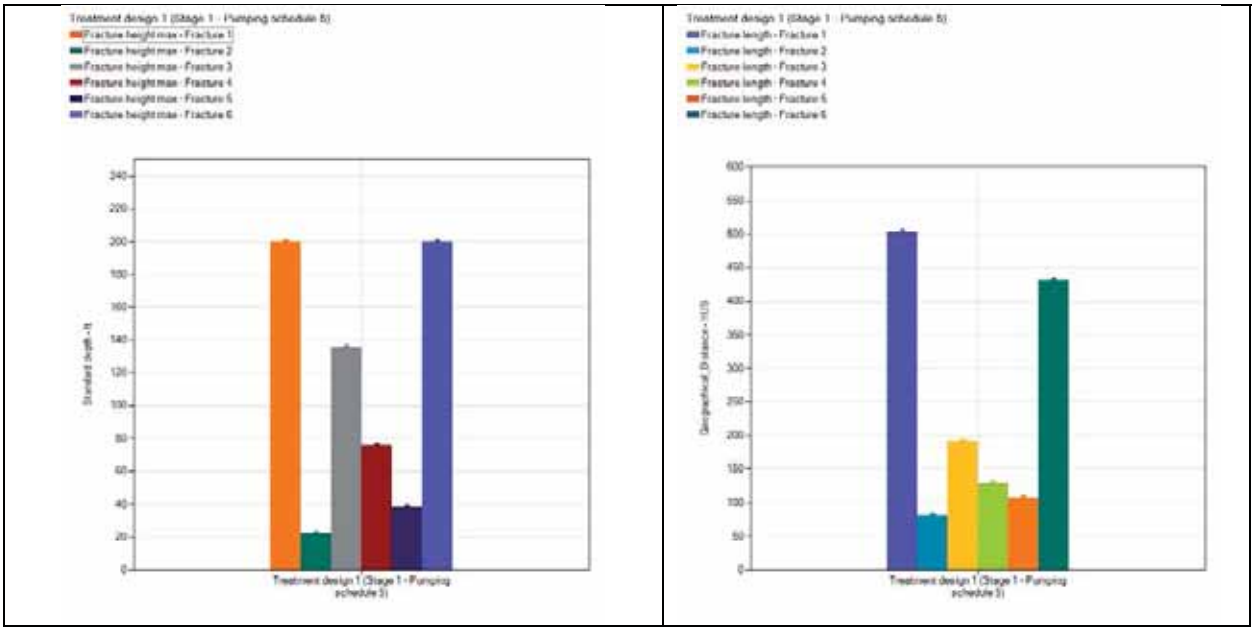

Figure 58. These are the created fracture geometries. The treatment schedule is 20 pptg borate crosslinked gel, shown in Table 33. The left-hand panel shows the total height for each of the six clusters. Based on the stress field used in the simulations, there is still significant upward growth in the external clusters (the middle clusters are pinched and length extension is restricted. The right-hand panel shows lateral extent for fractures from each cluster. Additional diversion could be useful in reducing the upwards growth.

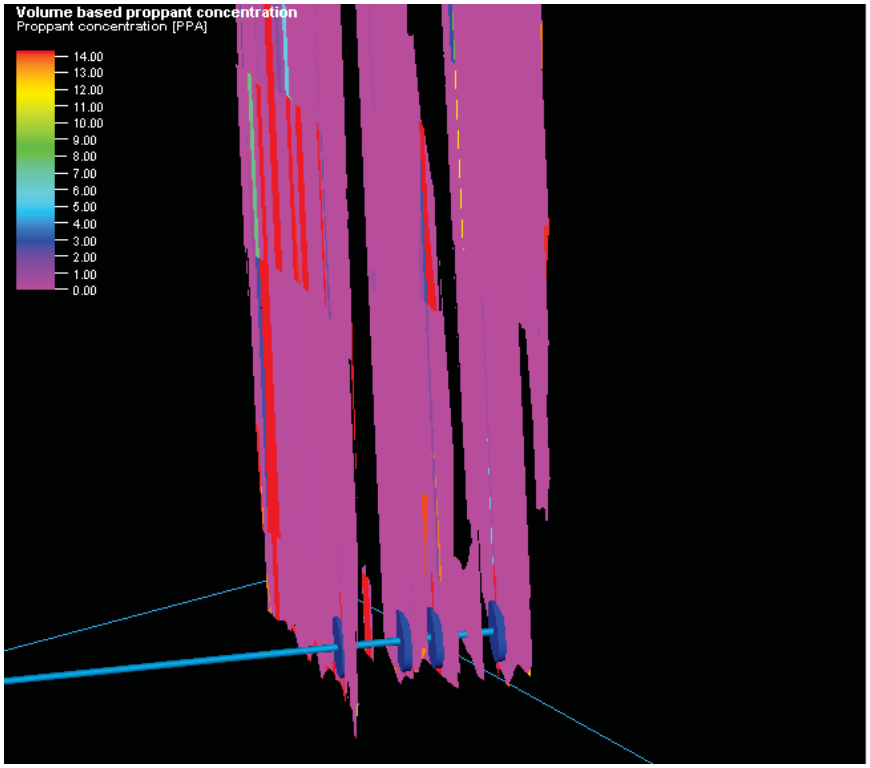

Figure 59. The vertical and horizontal scales are not equal. The maximum vertical growth (Figure 58) was approximately 220 feet - still well out-of-zone. The inner clusters are "guarded" and upwards growth is less. The two outside clusters might be considered as sacrificial. This is shown more dramatically in Figure 58.

The next tactic was to reduce the viscosity of the carrying fluid to promote leakoff into the natural fracture network and reduce upward growth.

- Pump schedule 8 (Table 34), which exclusively uses slickwater, still grows quite substantially upwards.
- Pump schedule 6 (Table 35) used a fluid that was less viscous than previous treatments but more viscous than slickwater. It was able to carry the same concentration of proppant as before.
- Pump schedule 7 (Table 36) is just a modification of pump schedule 6 - using the same clean pumped volume but pumping more sand by increasing the volumes pumped of the higher concentrations of sand.

Pump schedule 6 with perforation arrangement B (three clusters) was the most effective of these treatment schedules was. This yielded the lowest height. However, large portions of the fractures still remain unpropped.

Table 34. Pump Schedule 8 - Reduced Viscosity (Slickwater)

Step	Pump Rate (bbl/min)	Fluid	Fluid Volume (gal)	Proppant	Proppant Concentration (ppa)	Proppant Mass (lb)	Slurry Volume (bbl)	Pump Time (min)
pad	11	SW	10000	None	0	0	238.1	21.65
0.5 ppa	11	SW	10000	80/100 Sand	0.50	5000	243.5	22.14
1 ppa	11	SW	10000	80/100 Sand	1.00	10000	248.9	22.63
1.5 ppa	11	SW	10000	80/100 Sand	1.50	15000	254.31	23.12
2 ppa	11	SW	10000	80/100 Sand	2.00	20000	259.71	23.61

Table 35. Pump Schedule 6 - Reduced Viscosity (Viscoelastic Surfactant)

Step	Pump Rate (bbl/min)	Fluid	Fluid Volume (gal)	Proppant	Proppant Concentration (ppa)	Proppant Mass (lb)	Slurry Volume (bbl)	Pump Time (min)
Pad	11	SW	10000	None	0	0	238.1	21.65
0.5 PPA	11	VES	10000	80/100 Sand	0.50	5000	243.5	22.14
1 PPA	11	VES	10000	-80/100 Sand	1.00	10000	248.9	22.63
1.5 ppa	11	VES	5000	20/40 Sand	1.5	7500	127.15	11.56
2 PPA	11	VES	2500	20/40 Sand	2	5000	64.93	5.9
2.5 PPA	11	VES	2500	20/40 Sand	2.5	6250	66.28	6.03
3 PPA	11	VES	2500	20/40 Sand	3	7500	67.63	6.15

Table 36. Pump Schedule 7 - Reduced Viscosity and Volume (Viscoelastic Surfactant)

Step	Pump Rate (bbl/min)	Fluid	Fluid Volume (gal)	Proppant	Proppant Concentration (ppa)	Proppant Mass (lb)	Slurry Volume (bbl)	Pump Time (min)
pad	11	SW	10000	None	0	0	238.1	21.65
0.5 ppa	11	VES	2000	80/100 Sand	0.50	1000	48.7	4.43
1 ppa	11	VES	3000	80/100 Sand	1.00	3000	74.67	6.79
1.5 ppa	11	VES	5000	80/100 Sand	1.5	7500	127.15	11.56
2 ppa	11	VES	5000	80/100 Sand	2	10000	129.85	11.8
2.5 ppa	11	VES	10000	80/100 Sand	2.5	25000	265.11	24.1
3 ppa	11	VES	10000	80/100 Sand	3	30000	270.52	24.59

Typical results for the reduced viscosity scenarios are shown in Figures 60 through 63.

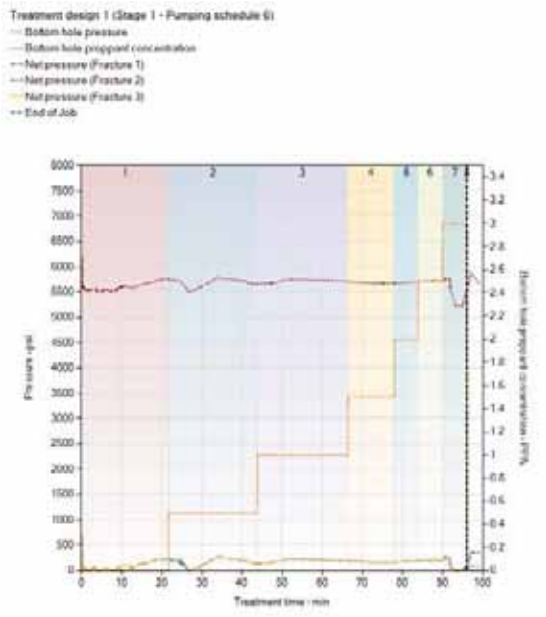

Figure 60. This is the chronology of bottomhole pressure, downhole proppant concentration and net pressure at each of three perforations clusters. The treatment schedule uses a reduced viscosity fluid (VES was selected but the calculations are agnostic to the chemistry behind the rheology), shown in Table 36 Notice the lower and more consistent values of the net pressure - suggesting improved containment.

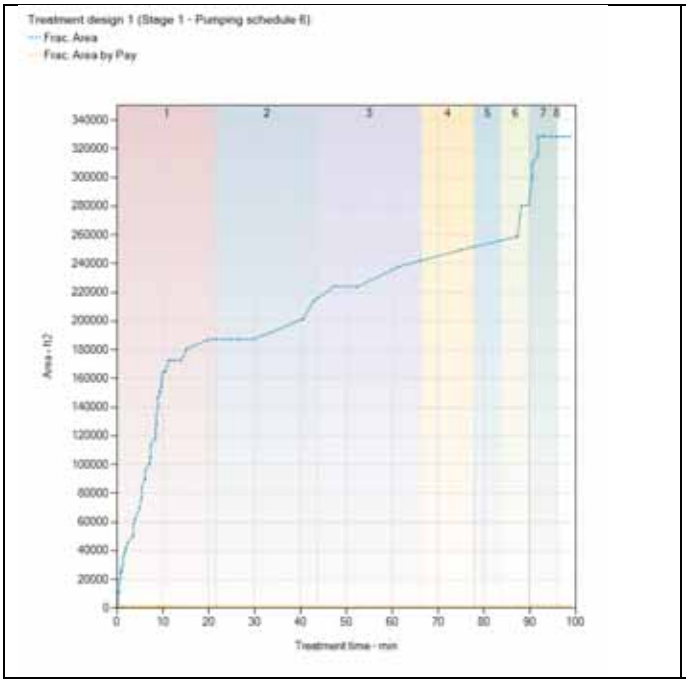

Figure 61. This is the created fracture surface area in pay. The treatment schedule is an intermediate viscosity fluid, shown in Table 36. The increase in slope correlates with starting 20/40 sand.

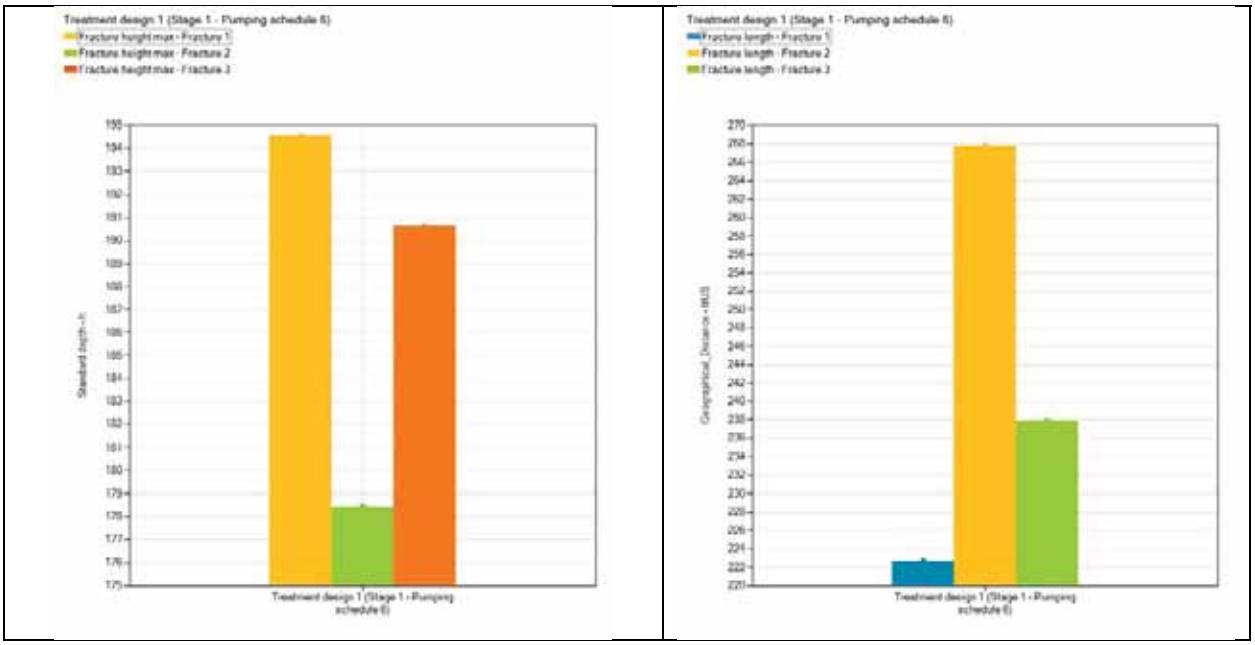

Figure 62. These are the created fracture geometries. The treatment schedule is for a viscoelastic surfactant (mid-range viscosity), shown in Table 36. The left-hand panel shows the total height for each of the three clusters. Based on the stress field used in the simulations, there is still significant upward growth in the external clusters (the middle cluster is pinched and length extension is restricted. The right-hand panel shows lateral extent for fractures from each cluster. Additional diversion could be useful in balancing the growth.

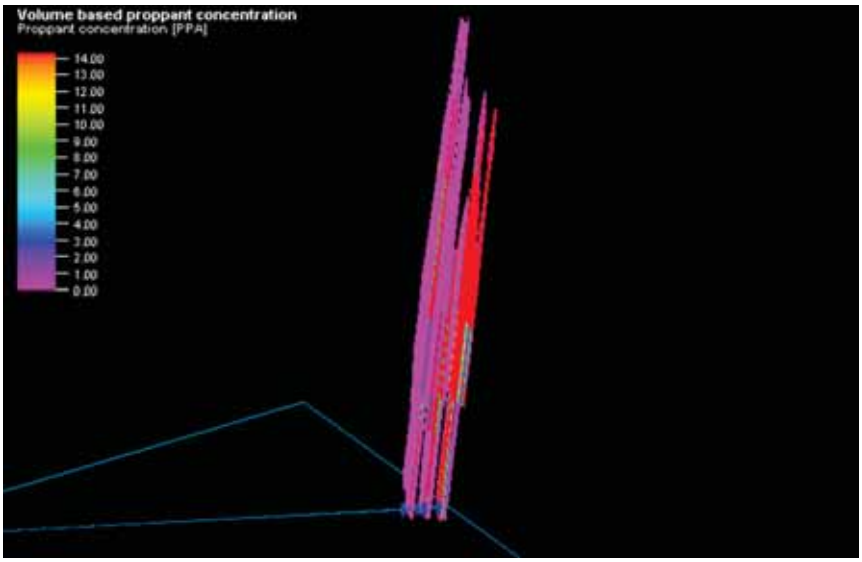

Figure 63. The vertical and horizontal scales are not equal. The maximum vertical growth (Figure 62) was approximately 220 feet - still well out-of-zone. The inner clusters are "guarded" and upwards growth is less. The two outside clusters might be considered as sacrificial. This is shown more dramatically in Figure 62. There is improved proppant coverage.

The previous figure suggests that the most remote fracture (initiating from the furthest cluster) is well propped. Statistics indicate a correlation between proppant mass and production. This led to a modification of the pump schedule to include a higher concentration of proppant in each stage and to change the perforation arrangement to try and create even length and uniformly propped fractures. This is where perforation arrangement E was developed and the best treatment schedule, pumping schedule 12, evolved. The maximum length of the fracture was predicted to be 97 ft. with all four fractures having lengths greater than 90 ft. When volumetric proppant concentrations are examined there is evidence of good concentration in all four fractures and through their entire length (this is the goal of fracturing design).

This treatment takes the job very close to screenout. The challenge with this job is the small volumes pumped and the large concentrations of sand. The pump time without the flush is just over 10 minutes (very strategic injection). The flush stage is not slickwater as was used in all of the other pump schedules, but it uses the same fluid as the treating fluid. The flush time for all treatments is 24.63 minutes. These small jobs would require a blender with a very small tub, sometimes called a "tubless'" blender, so that concentrations could be changed quickly and the small treatment could be run correctly. This is a treatment method that may merit consideration for wells drilled in the Uteland Butte play. Naturally this is an extreme simulation. Ultimate proppant

concentrations would likely be much less. The pump schedule and results are shown in Table 16. **Smaller treatments mandate closer well spacing.**

Table 37. Low Volume Strategic - High Proppant Concentration (Pumping Schedule 12)

Step	Pump Rate (bbl/min)	Fluid	Fluid Volume (gal)	Proppant	Proppant Concentration (ppa)	Proppant Mass (lb)	Slurry Volume (bbl)	Pump Time (min)
pad	11	SW	500	None	0	0	11.9	1.08
1 ppa	11	XL	500	80/100 Sand	1.00	500	12.45	1.13
2 ppa	11	XL	500	80/100 Sand	2.00	1000	12.99	1.18
3 ppa	11	XL	500	80/100 Sand	3.00	1500	13.53	1.23
4 ppa	11	XL	500	20/40 Sand	4	2000	14.07	1.28
5 ppa	11	XL	500	20/40 Sand	5	2500	14.61	1.33
6 ppa	11	XL	500	20/40 Sand	6	3000	15.15	1.38
7 ppa	11	XL	250	20/40 Sand	7	1750	7.84	0.71
8 ppa	11	XL	250	20/40 Sand	8	2000	8.11	0.74

Typical results for the reduced viscosity scenarios are shown in Figures 64 through 67.

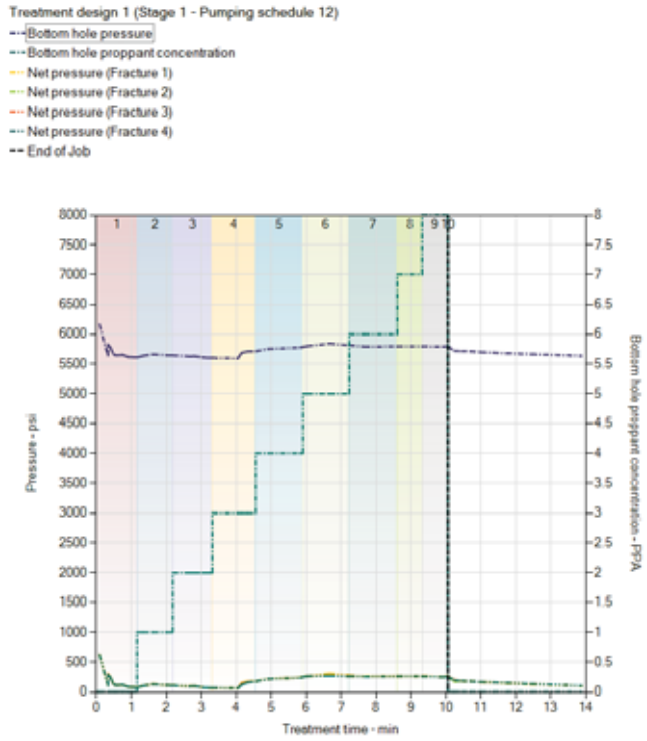

Figure 64. This is the chronology of bottomhole pressure, downhole proppant concentration and net pressure at each of four perforations clusters. The treatment schedule uses a smaller volume of increased viscosity fluid with increased proppant concentration, as shown in Table 37. Surprisingly the net pressure is relatively low.

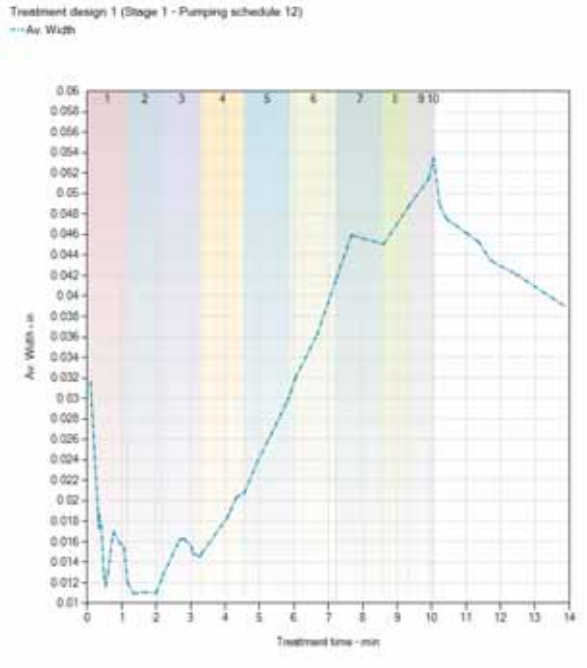

Figure 65. This is the created fracture surface area in pay. The treatment schedule is low guar loading crosslinked fluid, shown in Table 37. Small strategic fracs would seem to stay in zone. The consequence is that additional drilling is required and wells will need to be closer together.

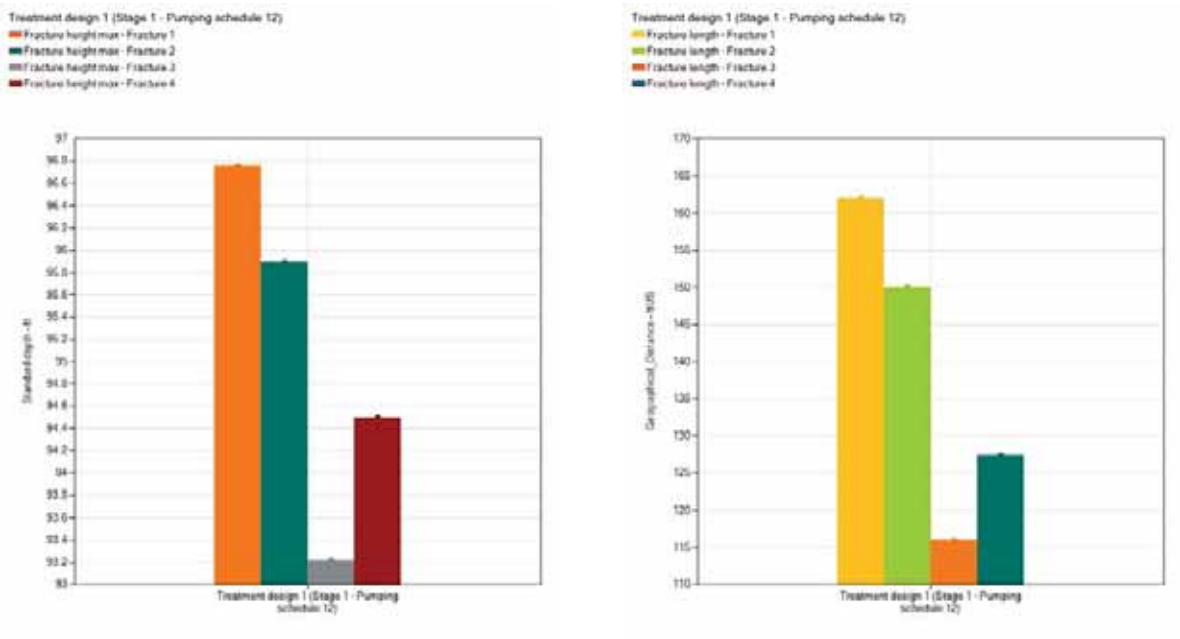

Figure 66. These are the created fracture geometries. The treatment schedule is for a strategic injection of small volumes of viscosified fluid and going to high concentrations rapidly, as shown in Table 37. The obvious risk is screenout with proppant in the tubulars. The left-hand panel shows the total height for each of the clusters (extremely consistent - suggesting the clusters were far apart so that there was not significant interaction of the fractures). The right-hand panel shows lateral extent for fractures from each cluster.

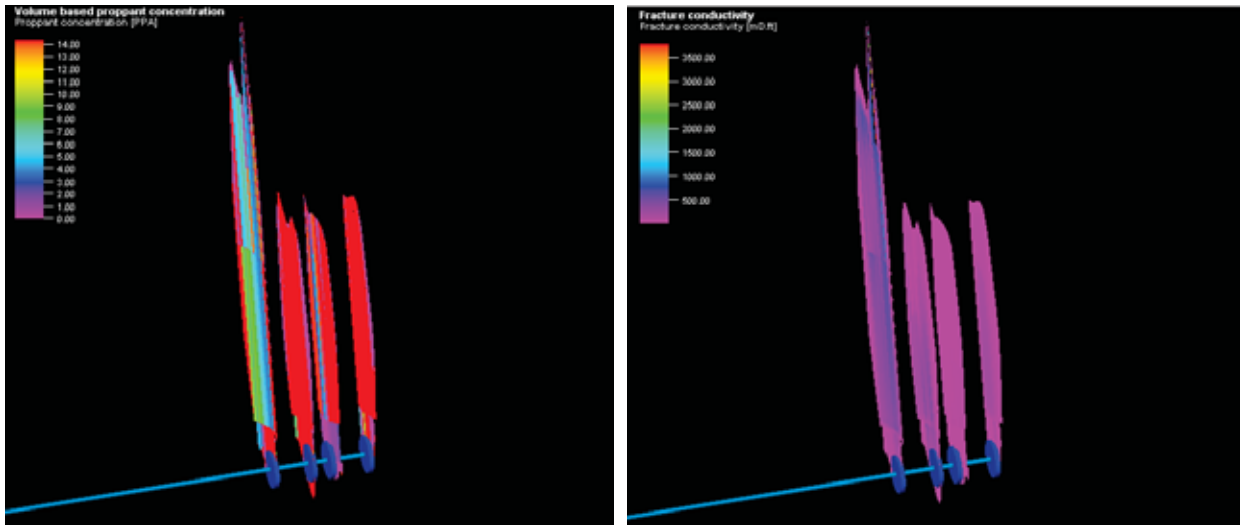

Figure 67. The vertical and horizontal scales are not equal. The maximum vertical growth (Figure 15) was approximately 90 feet which is desirable. There is improved proppant coverage. The casualty of any higher viscosity will be conductivity damage and ineffective break - and additional expense because of the viscosifying agents.

References

1. Altindag, R. Correlation of specific energy with rock brittleness concepts on rock cutting. The J. of the South African Inst. of Min. and Metall., Apr. 2003, pp. 163–171.
2. Alzahabi, A., AlQahtani, G., Soliman, M. Y., Bateman, R. M., Asquith, G., & Vadapalli, R. (2015, June 4). Fracturability Index is a Mineralogical Index: A New Approach for Fracturing Decision. Society of Petroleum Engineers. doi:10.2118/178033-MS
3. Behrmann, L. A., & Elbel, J. L. (1991). Effect of perforations on fracture initiation. Journal of Petroleum Technology, 43(05), 608-615.Romero et al (1995)
4. Blanton, T.L. (1982), "An Experimental Study of Interaction Between Hydraulically Induced and Pre-Existing Fractures," SPE Unconventional Gas Recovery Symposium, Pittsburgh, Pennsylvania, SPE of AIME
5. Busetti, S., K. Mish, and Z. Reches (2012a), Damage and plastic deformation of reservoir rocks: Part 1. Damage fracturing, AAPG Bull., 96(9), 1687–1709.
6. Busetti, S., K. Mish, P. Hennings, and Z. Reches (2012b), Damage and plastic deformation of reservoir rocks: Part 2. Propagation of a hydraulic fracture, AAPG Bull., 96(9), 1711–1732.
7. Crawford, B.R., Gaillot, P.J., and Alramahi., B., 2010, Petrophysical methodology for predicting compressive strength in siliciclastic "sandstone-to-shale" rocks, ARMA 10-196, presented at the 44th US Rock Mechanics Symposium, Salt Lake City, UT 27-30 June 2010
8. Daneshy, A. A. (1974, January 1). Hydraulic Fracture Propagation in the Presence of Planes of Weakness. Society of Petroleum Engineers. doi:10.2118/4852-MS
9. Fallahzadeh, S. H., Rasouli, V., and Sarmadivaleh, M. (2015). An investigation of hydraulic fracturing initiation and near-wellbore propagation from perforated boreholes in tight formations. Rock Mechanics and Rock Engineering, 48(2), 573.Clifton et al., 1978
10. Gale, J. F. W., & Holder, J. (2008, January 1). Natural fractures in the Barnett Shale: constraints on spatial organization and tensile strength with implications for hydraulic fracture treatment in shale-gas reservoirs. American Rock Mechanics Association
11. Goodway, B. Perez, M., Varsek, J., and Abaco, C., 2010, Seismic petrophysics and isotropic-anisotropic AVO methods for unconventional gas exploration, The Leading Edge, 1500-1508.

12. Greener, M.R., 1994, Evaluation of Height Growth Controlled with Placement of Artificial Barriers, SPE 29186-MS, SPE Eastern Regional Meeting, Charleston, West Virginia, 8-10 November.

13. Griffith, A. A. (1921), "The phenomena of rupture and flow in solids" (PDF), Philosophical Transactions of the Royal Society of London, A, 221: 163–198, Bibcode:1921RSPTA.221..163G, doi:10.1098/rsta.1921.0006

14. Gu, H., & Weng, X. (2010, January 1). Criterion for Fractures Crossing Frictional Interfaces At Non-orthogonal Angles. American Rock Mechanics Association.

15. He, J., Chen, Y., Zhengchun, L., and Samuel, R. (2016, August 22). Global Correlation of Rock Brittleness Indices with Petrophysical and Geomechanical Properties and its Application to the Prediction of Rate of Penetration (ROP). Society of Petroleum Engineers. doi:10.2118/180518-MS

16. Herwanger, J. V., Bottrill, A. D., and Mildren, S. D. (2015, July 20). Uses and Abuses of the Brittleness Index with Applications to Hydraulic Stimulation. Unconventional Resources Technology Conference. doi:10.15530/URTEC-2015-2172545

17. Hews, P. 2011. Structural Features That Can Be Identified From Drill Cuttings. Geological Workshop Material, Calgary, Canada: Hara Consulting Ltd.

18. Holt, R. M., Fjaer, E., Nes, O. M., and Alassi, H. T. (2011, January 1). A Shaly Look At Brittleness. American Rock Mechanics Association

19. Honda, H., and Y. Sanada (1956), Hardness of coal, Fuel, 35, 451-461

20. Jarvie, D. M., R. J. Hill, T. E. Ruble, and R. M. Pollastro, 2007, Unconventional shale-gas systems: The Mississippian Barnett Shale of North-Central Texas as one model for thermogenic shale-gas assessment: AAPG Bulletin, 91, 475–499, doi: 10.1306/12190606068.

21. Jin, X., Shah, S. N., Roegiers, J.-C., & Zhang, B. (2014, February 4). Fracability Evaluation in Shale Reservoirs - An Integrated Petrophysics and Geomechanics Approach. Society of Petroleum Engineers. doi:10.2118/168589-MS

22. Jin, X., Shah, S. N., Roegiers, J.-C., & Zhang, B. (2015, June 1). An Integrated Petrophysics and Geomechanics Approach for Fracability Evaluation in Shale Reservoirs. Society of Petroleum Engineers. doi:10.2118/168589-PA

23. Kangxing, D., He, L., Suling, W., and Minzheng, J. (2015, October 20). Experiment and Simulation Research on Hydraulic Fracture Propagation Characteristic under Interface Layer Influence. Society of Petroleum Engineers. DOI: 10.2118/176130-MS.

24. Kennedy, A.D., 2011, Geological Predictors of the Hydrocarbon Extraction Potential of the Mancos Shale, Master of Science Thesis, University of Utah, Salt Lake City, Utah.

25. Mullen, M. J., & Enderlin, M. B. (2012, January 1). Fracability Index - More Than Rock Properties. Society of Petroleum Engineers. doi:10.2118/159755-M

26. Nolte, K. G. (1979, January 1). Determination of Fracture Parameters from Fracturing Pressure Decline. Society of Petroleum Engineers. doi:10.2118/8341-MSChunfang et al. (2011)

27. Ortega, C., & Aguilera, R. (2014, August 1). A Complete Petrophysical-Evaluation Method for Tight Formations from Drill Cuttings Only in the Absence of Well Logs. Society of Petroleum Engineers. doi:10.2118/161875-PA

28. Plumb, R.A., 1994. Influence of composition and texture on the failure properties of clastic rocks. Eurock 94, Rock Mechanics in Petroleum Engineering conference, Delft, Netherlands, pp. 13–20

29. Potluri, N.K., Zhu, D. (2005), "The Effect of Natural Fractures on Hydraulic Fracture Propagation," SPE European Formation Damage Conference, Sheveningen, The Netherlands, SPE.

30. Rasmussen, L., Smith, T., Canter, L., Sonnenfeld, M., and Forster, J., 2016, Analysis of a Long Cane Creek Horizontal: New Insight into an Unconventional Tight Oil Reservoir Play, Paradox Basin, Utah, Search and Discovery Article #10873 (2016), Posted October 31, 2016, adapted from AAPG Rocky Mountain Session poster, Fort Lewis College, Durango, CO, June 13-16, 2010.

31. Renshaw, C.E. and Pollard, D.D. (1995) "An Experimentally Verified Criterion for Propagations across Unbounded Frictional Interfaces in Brittle, Linear Elastic Materials", Int. J. Rock Mech. Min. Sci. & Geomech. Abstr., 32, 237-249.

32. Rickman, R., M. Mullen, E. Petre, B. Grieser, and Kundert, D., 2008, A practical use of shale petrophysics for stimulation design optimization: All shale plays are not clones of the Barnett Shale: Presented at SPE Annual Technical Conference and Exhibition.

33. Roegiers, J-C., McLennan, J.D., and Murphy, D.L. 1982, Influence of Preexisting Discontinuities on the Hydraulic Fracturing Propagation Process, in Hydraulic Fracturing and Geothermal Energy, Nemat-Nasser, S., Abé, H. and Hirakawa, S. (ed.), Proc. First Japan-United States Joint Seminar on Hydraulic Fracturing and Geothermal Energy, Tokyo, Japan, November 2-5.

34. Roesink, J. and Anderson, J., 2013, Wasatch – Green River Resource Play, Uinta Basin, Utah, Search and Discovery Article #110167 (2013)

35. Safari, M. R., Gandikota, R., Mutlu, U., Ji, M., Glanville, J., & Abass, H. (2013, August 12). Pulsed Fracturing in Shale Reservoirs: Geomechanical Aspects, Ductile-Brittle Transition and Field Implications. Unconventional Resources Technology Conference.

36. Safari, R., Huang, J., Mutlu, U., & Glanville, J. (2014, August 18). 3D Analysis and Engineering Design of Pulsed Fracturing in Shale Gas Reservoirs. American Rock Mechanics Association

37. Shahri, M. P., Chok, H., Safari, R., Huang, J., Amorocho, C., Mejia, C., & Mutlu, U. (2015, July 20). Automated Hydraulic Fracturing Stage Design Based on Integrated Fracture Potential. Unconventional Resources Technology Conference. doi:10.15530/URTEC-2015-2153591

38. Tang, C.A. and Kaiser, P.K., 1998. Numerical Simulation of Cumulative and Seismic Energy Release During Brittle Rock Failure – Part I: Fundamentals. Int. J. Rock Mech. Min. Sci. Vol 35, No.2, pp. 113 121.

39. Vernik, L., Bruno, M., Bovberg, C., 1993. Empirical relations between compressive strength and porosity of siliciclastic rocks. Int. J. Rock Mech. Min. Sci. Geomech. Abstr. 30, 677–680.

40. Vernik, L., Bruno, M., Bovberg, C., 1993. Empirical relations between compressive strength and porosity of siliciclastic rocks. Int. J. Rock Mech. Min. Sci. Geomech. Abstr. 30, 677–680.

41. Wang, F. P., and J. F. W. Gale, 2009, Screening criteria for shale-gas systems: Gulf Coast Association of Geological Societies Transactions, 59, 779–793.

42. Wang, J., Luo, H., Liu, H., Cao, F., Li, Z., & Sepehrnoori, K. (2017, February 1). An Integrative Model To Simulate Gas Transport and Production Coupled With Gas Adsorption, Non-Darcy Flow, Surface Diffusion, and Stress Dependence in Organic-Shale Reservoirs. Society of Petroleum Engineers. doi:10.2118/174996-PA

43. Warpinski, N.R. and Teufel, L.W. (1987). "Influence of Geologic Discontinuities on Hydraulic Fracture Propagation," (includes associated papers 17011 and 17074) SPE Journal of Petroleum Technology 39(2), 209-220.

44. Yew, C., and Xiaowei Weng. (2015) Hydraulic Fracturing Mechanics Second Edition. Waltam, MA: Elsevier.

45. Zhang, F., Zhang, H., Yuan, F., Wang, Z., Chen, S., Li, C., & Han, X. (2015, November 9). Geomechanical Mechanism of Hydraulic Fracturing and Fracability Evaluation of Natural Fractured Tight Sandstone Reservoir in Keshen Gasfield in Tarim Basin. Society of Petroleum Engineers. doi:10.2118/177457-MS

Appendix A

Laboratory Rock Mechanics Data

Introduction

Wells within this program were: Fidelity Cane Creek CCU 7-1; Cane Creek 26-3; Cisco State 36-13 along with Bill Barrett Corporation wells 14-1-46 and 14-3-45. Formations were Cane Creek & Uteland Butte shale, from the Paradox and Uintah basins of Utah. The testing program consisted of:

- Indirect tensile strength testing (Brazilian method) on samples loaded perpendicular to bedding;
- Triaxial compression testing with concurrent ultrasonic velocity measurements on vertically and horizontally oriented, as-received samples at room temperature to determine compressive strength and elastic properties (all samples were tested using a standard loading axial strain rate of 1×10^{-5} in/in/s);
- TRA - Pressure Decay Permeability - Conducted on crushed sample material in as- received saturation conditions, along with measurements of Bulk Density (including fracture volume), Grain Density, Gas-Filled Porosity determination, Fluid Saturation (oil, water and clay-bound water saturation) and effective total interconnected porosity; and
- Continuous surface, thermal conductivity profiling of approximately 70 feet of client selected core intervals from 4 out of 5 wells;
- FTIR (Fourier transform infrared spectroscopy) of five samples from Bill Barrett well 14-1-46; and
- Shale fluid extractions with GC analysis on ten samples from wells Fidelity Cane Creek CCU 7-1 and Bill Barrett 14-1-46.

For this test program, the UGS provided core from five wells, as part of the Utah Tight Oil Plays project, and is listed in the Material Received (Table A - 3). All depths indicated within this summary are measured depths taken directly from the received material. From these available core sections, TerraTek prepared samples from 32 depths of interest.

Table A-1. Uteland Butte Sample Selection:
Bill Barrett Corporation 14-1-46 and 14-3-45

Zone	Lithology	Well	Depth (ft MD core)	Depth (ft MD log)	Sample	Triaxial (vertical)	Triaxial (horizontal)
D-Shale	Shale	14-1-46	6706-6707.5	6698.5+	1	x	x
PZ-2	Dolomite	14-1-46	6702-6703.5	6694.5-96	2	x	x
Above PZ-2	Limestone	14-1-46	6698.7	6691.2	3	x	x
PZ-1 (prime)	Dolomite	14-1-46	6693-4	6685.5-6	4	x	x
PZ-1 (cherty)	Dolomite and Chert	14-1-46	6684—4.5?	6676.5-6	5	x	x
C-Shale	Shale	14-3-35	7358-59.5	7347.8-8.7	6	x	x
	Laminated Dolomite and Shale	14-3-35	7332.8, 7333	7322.6, 7322.8	7	x	x
Top Uteland Butte Carbonate		14-3-35	7327.3	7317.1	8	x	x

Table A 2. Stress Gradients

Well ID 1,2,3,4,5	Pore Pressure Gradient (psi/ft) (guess)	Minimum Horizontal Stress Gradient (psi/ft)	Maximum Horizontal Stress Gradient (psi/ft)	Estimated Vertical Stress Gradient (psi/ft)	Confining Pressure Gradient for Vertical Plug (psi/ft) (no pore pressure)	Confining Pressure Gradient for Horizontal Plug (psi/ft) (no pore pressure)
Fidelity Cane Creek CCU 7-1	0.45	0.89	Same as Minimum	1.03	0.44	0.510
Fidelity Cane Creek 26-3	0.45	0.97	Same as Minimum	1.02	0.52	0.545
Fidelity Cisco State 36-13	0.45	0.81	Same as Minimum	1.04	0.36	0.475
Bill Barrett14-3-35	0.45	0.63	Same as Minimum	1.07	0.18	0.400
Bill Barrett 14-1-46	0.45	0.65	Same as Minimum	1.07	0.20	0.410

[1] All stresses/gradients (and additional footnotes) provided by EGI (working in partnership with the UGS)

[2] The overburden stress was calculated by integrating the bulk density log to the sample depth and multiplying it by the acceleration due to gravity. The wells are nearly vertical except for the Cane Creek 26-3 well. For this well a gradient was calculated before the kickoff point and used for the remaining vertical drop. If the log did not go to the surface a gradient of 1.0 psi/ft was assumed from zero to the start of the log.

[3] The horizontal stress was calculated using either the fracture gradient the company found from the ISIP for the first zone fractured, the mud weight used to drill that section, or an average of the two. Using the mud weight only will result in a slightly lower horizontal stress.

[4] For a vertical plug, the effective confining pressure was found by taking the horizontal stress and subtracting the pore pressure. The pore pressure was assumed to have a gradient of 0.45 psi/ft. For a horizontal plug the effective confining pressure was estimated by averaging the minimum horizontal and vertical total stresses and subtracting the pore pressure.

[5] The Fidelity CCU 7-1 well is an average of the two other Cane Creek well parameters since little data for this well were available.

Table A-3. Material Received

Pallet #	Well ID	Box #	Top Depth (ft)	Bottom Depth (ft)	Approx. Length (ft)	Approx. Diameter (in)	Comments
1	Fidelity Cane Creek CCU7-1	1	~ 1 ft length cores, #'s 1, 2, and 3 contained in box				10 preserved, slabbed core sections. Majority were previously plugged. CT shows numerous fractures.
		2	~ 1 ft length cores, #'s 4 and 5 contained in box				
		3	~ 1 ft length cores, #'s 6 and 7 contained in box				
		4	~ 1 ft length cores, #'s 8, 9, and 10 contained in box				
	Fidelity Cane Creek CC 26-3	1	7388.00	7390.90	2.90	4	Unpreserved slabbed core sections. Previously plugged and highly damaged. Note, core boxes are marked with 'Core 1'
		2	7390.90	7393.90	3.00	4	
		3	7393.90	7396.90	3.00	4	
		4	7396.90	7399.90	3.00	4	
		5	7399.90	7403.00	3.10	4	
		6	7403.00	7406.00	3.00	4	
		7	7406.00	7409.00	3.00	4	
		8	7409.00	7411.80	2.80	4	
		9	7411.80	7414.95	3.15	4	
		10	7414.95	7416.85	1.90	4	
		11	7416.85	7419.55	2.70	4	
		12	7419.55	7422.00	2.45	4	
		13	7422.00	7425.00	3.00	4	
		14	7425.00	7428.00	3.00	4	
		15	7428.00	7431.00	3.00	4	
		16	7431.00	7434.00	3.00	4	
		17	7434.00	7437.00	3.00	4	
		18	7437.00	7440.00	3.00	4	
		19	7440.00	7443.00	3.00	4	
		20	7443.00	7446.00	3.00	4	
		21	7446.00	7449.00	3.00	4	
		22	7449.00	7452.00	3.00	4	
		23	7452.00	7455.20	3.20	4	
		24	7455.70	7458.25	2.55	4	
		25	7458.25	7461.00	2.75	4	
		26	7461.00	7464.00	3.00	4	
		27	7464.00	7467.00	3.00	4	
		28	7467.00	7470.00	3.00	4	
		29	7470.00	7473.00	3.00	4	
		30	7473.00	7474.05	1.05	4	

Pallet #	Well ID	Box #	Top Depth (ft)	Bottom Depth (ft)	Approx. Length (ft)	Approx. Diameter (in)	Comments
2	Fidelity Cisco St 36-13	1	7586.00	7589.00	3.00	4	Unpreserved slabbed core sections. Previously plugged and highly damaged. Note, core boxes are marked with 'Core 1' & Patara Oil & Gas
		2	7589.00	7592.00	3.00	4	
		3	7592.00	7595.00	3.00	4	
		4	7595.00	7598.00	3.00	4	
		5	7598.00	7601.00	3.00	4	
		6	7601.00	7604.00	3.00	4	
		7	7604.00	7607.00	3.00	4	
		8	7607.00	7610.00	3.00	4	
		9	7610.00	7613.00	3.00	4	
		10	7613.00	7616.00	3.00	4	
		11	7616.00	7619.00	3.00	4	
		12	7619.00	7622.00	3.00	4	
		13	7622.00	7625.00	3.00	4	
		14	7625.00	7628.00	3.00	4	
		15	7628.00	7631.00	3.00	4	Unpreserved slabbed core sections. Previously plugged and highly damaged. Note, core boxes are marked with 'Core 2' & Patara Oil & Gas
		16	7631.00	7634.00	3.00	4	
		17	7634.00	7637.00	3.00	4	
		18	7637.00	7640.00	3.00	4	
		19	7640.00	7643.00	3.00	4	
		20	7643.00	7646.00	3.00	4	
		21	7646.00	7649.00	3.00	4	
		22	7649.00	7652.00	3.00	4	
		23	7652.00	7654.80	2.80	4	
3	Bill Barrett 14-3-45	1	7324.00	7327.00	3.00	4	Unpreserved slabbed core sections. Previously plugged and highly damaged. Note, core boxes are marked with 'Core 1'
		2	7327.00	7330.00	3.00	4	
		3	7330.00	7333.20	3.20	4	
		4	7333.20	7336.00	2.80	4	
		5	7336.00	7339.00	3.00	4	
		6	7339.00	7342.00	3.00	4	
		7	7342.00	7344.70	2.70	4	
		8	7344.70	7347.60	2.90	4	
		9	7347.60	7350.65	3.05	4	
		10	7350.65	7353.65	3.00	4	
		11	7353.65	7356.70	3.05	4	
		12	7356.70	7359.50	2.80	4	

Pallet #	Well ID	Box #	Top Depth (ft)	Bottom Depth (ft)	Approx. Length (ft)	Approx. Diameter (in)	Comments
		13	7359.50	7362.50	3.00	4	
		14	7362.50	7365.50	3.00	4	
3	Bill Barrett 14-3-45	15	7365.50	7368.45	2.95	4	Unpreserved slabbed core sections. Previously plugged and highly damaged. Note, core boxes are marked with 'Core 1'
		16	7368.45	7371.50	3.05	4	
		17	7371.50	7374.50	3.00	4	
		18	7374.50	7377.25	2.75	4	
		19	7377.25	7380.20	2.95	4	
		20	7380.20	7383.20	3.00	4	
		21	7383.20	7386.00	2.80	4	
4	Bill Barrett 14-1-46	1	6647.00	6650.00	3.00	4	Unpreserved slabbed core sections. Previously plugged and highly damaged. Note, core boxes are marked with 'Core 1'
		2	6650.00	6653.00	3.00	4	
		3	6653.00	6656.00	3.00	4	
		4	6656.00	6659.00	3.00	4	
		5	6659.00	6662.00	3.00	4	
		6	6662.00	6665.00	3.00	4	
		7	6665.00	6668.00	3.00	4	
		8	6668.00	6669.70	1.70	4	
		1	6672.00	6675.00	3.00	4	Unpreserved slabbed core sections. Previously plugged and highly damaged. Note, core boxes are marked with 'Core 2'
		2	6675.00	6678.00	3.00	4	
		3	6678.00	6680.70	2.70	4	
		4	6680.70	6683.50	2.80	4	
		5	6683.50	6686.45	2.95	4	
		6	6686.45	6689.90	3.45	4	
		7	6689.90	6691.90	2.00	4	
		8	6691.90	6695.00	3.10	4	
		9	6695.00	6697.80	2.80	4	
		10	6697.80	6700.90	3.10	4	
		11	6700.90	6703.70	2.80	4	
		12	6703.70	6706.80	3.10	4	
		13	6706.80	6707.05	0.25	4	

Table A-4. Testing Matrix

Well ID	Core Depth Range (ft)	Brazil[1]	TXC w/UV	TRA	TC (range in feet)	FTIR	SFE
Fidelity Cane Creek CCU7-1	7609.05 – 7609.45	CCU1_2A, CCU1_2B	CCU1-1, CCU1-3	CCU1-4	-	-	CCU1-5
	7614.00 – 7614.65	CCU2_2A, CCU2_2B	CCU2-1, CCU2-3	CCU2-4	-	-	-
	7619.00 – 7619.90	CCU3_2A, CCU3_2B	CCU3-1, CCU3-5	CCU3-4	7619.00 – 7620.90	-	CCU3-6
	7620.30 – 7620.90	CCU4_2A, CCU4_2B	CCU4-1, CCU4-5	CCU4-4		-	CCU4-6
	7624.50 – 7624.90	CCU5_2A, CCU5_2B	CCU5-1, CCU5-3	CCU5-4	7624.10 – 7624.98	-	CCU5-5
	7630.25 – 7630.85	CCU6_2A, CCU6_2B	CCU6-1, CCU6-3	CCU6-4	7630.08 – 7630.97	-	CCU6-5
	7638.20 – 7638.45	CCU7_2A, CCU7_2B	CCU7-1	CCU7-4	7638.00 – 7638.50	-	CCU7-5
	7645.30 – 7645.75	CCU8_2A, CCU8_2B	CCU8-1, CCU8-3	CCU8-4	-	-	-
	7651.10 – 7651.60	CCU9_2A, CCU9_2B	CCU9-1, CCU9-3	CCU9-4	-	-	CCU9-5
	7657.40 – 7657.80	CCU10_2A, CCU10_2B	CCU10-1, CCU10-5	CCU10-4	7657.40 – 7658.00	-	CCU10-6
Well Specific Totals:		**20**	**19**	**10**	**~ 5 (ft)[2]**	**0**	**8**

Well ID	Core Depth Range (ft)	Brazil	TXC w/UV	TRA	TC (range in feet)	FTIR	SFE
Fidelity Cane Creek 26-3	7413.00 – 7413.05	FDY3_3A, FDY3_3C	FDY3-1, FDY3-2	-	-	-	-
	7417.70 – 7417.85	FDY2_3A, FDY2_3B	FDY2-1, FDY2-2	-	-	-	-
	7431.00 – 7446.00	-	-	-	7431.00 – 7446.00[3]	-	-
	7464.30 – 7464.50	FDY1_3A, FDY1_3B	**FDY1-2[4]**, FDY1-1, FDY1-4	-	-	-	-
Well Specific Totals:		**6**	**6**	**0**	**~ 15 (ft)**	**0**	**0**

Well ID	Core Depth Range (ft)	Brazil	TXC w/UV	TRA	TC (range in feet)	FTIR	SFE
Fidelity Cisco State 36-13	7588.80 – 7589.40	CSO1_3A, CSO1_3B	CSO1-1, CSO1-2	-	-	-	-
	7592.90 – 7593.00	CSO2_3A, CSO2_3B	CSO2-1, CSO2-2	-	-	-	-
	7599.75 – 7599.85	CSO3_3B, CSO3_3C	CSO3-1, CSO3-2	-	-	-	-
	7600.00 – 7620.00	-	-	-	7600.00 – 7620.00[5]	-	-
	7605.30 – 7605.65	CSO4_3A, CSO4_3B	CSO4-4, CSO4-2	-	-	-	-
	7615.25 – 7615.40	CSO5_3A, CSO5_3B	CSO5-1, CSO5-2	-	-	-	-
	7627.10 – 7627.30	CSO6_3A, CSO6_3B	CSO6-1, CSO6-2	-	-	-	-

[1] **Brazil** = indirect tensile strength test (Brazilian method); **TXC w/UV** = triaxial compression test with concurrent ultrasonic velocity measurements; **TRA** = tight rock analysis including pressure decay permeability; **TC** continuous surficial thermal conductivity measurements; **FTIR** = Fourier transform infrared spectroscopy; **SFE** = shale fluid extractions with GC analysis.

[2] TC depth range - attempted the full 5 ft interval for TC analysis, however, there were several rubbly zones, and sections missing core (due to prior sampling outside TerraTek) that could not be analyzed.

[3] TC depth range - attempted the full 15 ft interval for TC analysis, however, there were several rubbly zones, and sections missing core (due to prior sampling outside TerraTek) that could not be analyzed.

[4] FDY1-2 was the wrong target lithology (shale). Sample FDY1-1 and FDY1-4 are duplicates, and as such, only one will be invoiced. There is no additional material to pull a horizontally oriented sample to match either samples FDY1-1 or FDY1-4.

[5] TC depth range - attempted the full 20 ft interval for TC analysis, however, there were several rubbly zones, and sections missing core (due to prior sampling outside TerraTek) that could not be analyzed.

Well ID	Core Depth Range (ft)	Brazil[1]	TXC w/UV	TRA	TC (range in feet)	FTIR	SFE
Well Specific Totals:		**12**	**12**	**0**	**~ 20 (ft)**	**0**	**0**
Bill Barrett 14-3-35	7327.30 – 7327.40	UTE3_3A, UTE3_3B	UTE3-1, UTE3-2	-	-	-	-
	7332.70 – 7333.10	UTE2_3A, UTE2_3B	UTE2-1, UTE2-2	-	-	-	-
	7358.15 – 7358.35	UTE1_3A, UTE1_3B	UTE1-1, UTE1-2	-	-	-	-
Well Specific Totals:		**6**	**6**	**0**	**0**	**0**	**0**

Well ID	Core Depth Range (ft)	Brazil	TXC w/UV	TRA	TC (range in feet)	FTIR	SFE
Bill Barrett 14-1-46	6676.00 – 6706.00	-	-	-	6676.00 – 6706.00[6]	-	-
	6684.30 – 6684.70	BTR1_3A, BTR1_3B	**BTR1-1**[7] BTR1-6 BTR1-2	-	-	BTR1-5	BTR1-4
	6693.40 – 6693.70	BTR2_3A, BTR2_3B	BTR2-1, BTR2-2 **BTR2-5**[8]	-	-	BTR2-4	-
	6698.25 – 6699.00	BTR3_4A, BTR3_4B	BTR3-1, BTR3-2	-	-	-	-
	6702.55 – 6703.30	BTR4_7A, BTR4_7B	BTR4-4, BTR4-2	-	-	BTR4-6	BTR4-5
	6706.50 – 6706.65	BTR5_3A, BTR5_3B	BTR5-4, BTR5-2	-	-	-	-
	6683.50	-	-	-	-	BTR6-1	-
	6689.50	-	-	-	-	BTR7-1	-
Well Specific Totals:		**10**	**10**	**0**	**~ 30 (ft)**	**5**	**2**
Overall Totals (All 5 Wells):		**54**	**53**	**10**	**~ 70 (ft)**	**5**	**10**

[6] TC depth range - attempted the full 30 ft interval for TC analysis, however, there were several rubbly zones, and sections missing core (due to prior sampling outside TerraTek) that could not be analyzed.

[7] BTR1-1 – Unknown error regarding axial strain gauges resulting in erroneous values for Young's Modulus and Poisson's ratio. Replacement sample (BTR1-6) has a higher bulk density than its horizontal counterpart, however, no additional material remains. Not invoicing for sample BTR1-1

[8] Bulk density out of spec for sample BTR2-2. BTR2-5 pulled as replacement, however, only Young's modulus and Poisson's ratio were collected due to error in test setup. Not invoicing.

Table A5. Summary of Indirect Tensile Strength Tests (Brazilian Method) - Horizontal Samples

Well ID	Lithology	Sample	Depth (ft)	Orientation	Average Length (in)	Average Diameter (in)	Mass (g)	Dry Bulk Density (g/cm3)	Maximum Load (lbf)	Tensile Strength (psi)
Fidelity Cane Creek CCU7	silty dolomite	CCU1_2A	7609.45	Perpendicular	0.509	0.996	17.067	2.628	979	1230
		CCU1_2B	7609.45	Parallel	0.538	0.994	17.779	2.602	372	443
	anhydrite	CCU2_2A	7614.30	Perpendicular	0.767	1.496	64.652	2.924	1160	643
		CCU2_2B	7614.30	Parallel	0.759	1.497	63.941	2.922	1740	975
	silty dolomite-shale	CCU3_2A	7619.30	Perpendicular	0.508	0.995	16.033	2.478	275	346
		CCU3_2B	7619.30	Parallel	0.524	0.996	16.704	2.499	288	351
	shale	CCU4_2A	7620.90	Perpendicular	0.507	0.996	16.315	2.525	479	605
		CCU4_2B	7620.90	Parallel	0.500	0.996	16.119	2.529	549	703
	silty dolomite	CCU5_2A	7624.55	Parallel	0.754	1.497	56.298	2.590	952	537
		CCU5_2B	7624.55	Perpendicular	0.763	1.497	57.012	2.592	1410	786
	silty dolomite	CCU6_2A	7630.85	Perpendicular	0.756	1.498	54.812	2.512	1080	608
		CCU6_2B	7630.85	Parallel	0.767	1.498	55.701	2.514	596	330
	shale	CCU7_2A	7638.45	Perpendicular	0.511	0.993	14.571	2.244	479	600
		CCU7_2B	7638.45	Parallel	0.519	0.995	15.218	2.302	253	312
	anhydrite	CCU8_2A	7645.60	Perpendicular	0.772	1.496	65.086	2.926	1940	1069
		CCU8_2B	7645.60	Parallel	0.763	1.496	64.356	2.927	1480	825
	silty dolomite	CCU9_2A	7651.50	Perpendicular	0.775	1.497	58.112	2.599	2160	1185
		CCU9_2B	7651.50	Parallel	0.765	1.497	57.450	2.606	1550	862
	Fractured silty dolomite	CCU10_2A	7657.60	Perpendicular	0.523	0.996	18.033	2.703	1040	1272
		CCU10_2B	7657.60	Parallel	0.518	0.996	18.039	2.730	1410	1740
Fidelity Cane Creek 26-3	shale	FDY3_3A	7413.05	Perpendicular	0.524	0.992	13.659	2.060	260	319
		FDY3_3C	7413.05	Parallel	0.513	0.994	13.420	2.056	186	232
	shale	FDY2_3A	7417.70	Perpendicular	0.772	1.497	50.882	2.287	1550	854
		FDY2_3B	7417.70	Parallel	0.742	1.496	49.184	2.301	893	512
	shale	FDY1_3A	7464.40	Perpendicular	0.523	0.994	15.916	2.395	501	614
		FDY1_3B	7464.40	Parallel	0.545	0.995	16.556	2.388	384	451

Well ID	Lithology	Sample	Depth (ft)	Orientation	Average Length (in)	Average Diameter (in)	Mass (g)	Dry Bulk Density (g/cm3)	Maximum Load (lbf)	Tensile Strength (psi)
Fidelity Cisco State 36-13	dolomite	CSO1_3A	7589.40	Perpendicular	0.494	0.996	16.520	2.619	1550	2005
		CSO1_3B	7589.40	Parallel	0.505	0.996	17.089	2.655	1190	1508
	shale	CSO2_3A	7592.90	Perpendicular	0.514	0.992	15.526	2.388	312	390
		CSO2_3B	7592.90	Parallel	0.517	0.994	15.701	2.385	300	371
	shale	CSO3_3B	7599.85	Perpendicular	0.534	0.995	17.633	2.594	453	543
		CSO3_3C	7599.85	Parallel	0.519	0.995	17.064	2.583	298	368
	silty dolomite	CSO4_3A	7605.30	Perpendicular	0.516	0.996	17.424	2.645	1390	1721
		CSO4_3B	7605.30	Parallel	0.512	0.996	17.224	2.639	1430	1787
	silty dolomite	CSO5_3A	7615.25	Perpendicular	0.526	0.995	16.828	2.513	249	303
		CSO5_3B	7615.25	Parallel	0.523	0.995	16.839	2.532	449	550
	anhydrite	CSO6_3A	7627.10	Perpendicular	0.517	0.959	17.925	2.933	921	1184
		CSO6_3B	7627.10	Parallel	0.471	0.959	16.376	2.939	640	902
Bill Barrett 14-3-35	dolomite	UTE3_3A	7327.40	Perpendicular	0.482	0.996	16.048	2.609	1490	1976
		UTE3_3B	7327.40	Parallel	0.480	0.996	16.278	2.658	858	1144
	shale -finely laminated	UTE2_3A	7333.10	Perpendicular	0.760	1.498	52.915	2.412	2190	1225
		UTE2_3B	7333.10	Parallel	0.737	1.498	51.447	2.420	920	531
	shale	UTE1_3A	7358.15	Perpendicular	0.497	0.995	16.256	2.566	860	1107
		UTE1_3B	7358.15	Parallel	0.543	0.994	17.772	2.572	389	459
Bill Barret 14-1-46	tan dolomite	BTR1_3A	6684.30	Perpendicular	0.749	1.496	46.207	2.143	1274	724
		BTR1_3B	6684.30	Parallel	0.725	1.495	45.204	2.169	1060	623
	dolomite	BTR2_3A	6693.55	Perpendicular	0.753	1.497	54.631	2.515	1963	1108
		BTR2_3B	6693.55	Parallel	0.766	1.497	55.327	2.505	3150	1749
	grey limestone	BTR3_3A 23	6698.90	Perpendicular	0.491	0.998	16.293	2.591	2118	2753
		BTR3_4A	6698.50	Perpendicular	0.511	0.996	16.614	2.548	2207	2761
		BTR3_4B	6698.50	Parallel	0.535	0.996	17.685	2.591	730	873

Well ID	Lithology	Sample	Depth (ft)	Orientation	Average Length (in)	Average Diameter (in)	Mass (g)	Dry Bulk Density (g/cm3)	Maximum Load (lbf)	Tensile Strength (psi)
	tan dolomite	BTR4_7A	6702.55	Perpendicular	0.523	0.997	16.576	2.477	643	785
		BTR4_7B	6702.55	Parallel	0.515	0.997	16.249	2.467	1020	1265
	shale	BTR5_3A	6706.65	Perpendicular	0.496	0.996	15.834	2.502	735	948
		BTR5_3B	6706.65	Parallel	0.506	0.995	16.151	2.507	474	600

Table A-6. Summary of Triaxial Compression Tests (for all tests, pore pressure drained to atmosphere)

Well ID	Lithology	Sample ID	Depth (ft)	Orientation	As Received Bulk Density (g/cm^3)	Confining Pressure (psi)	Peak Effective Compressive Strength (psi)	Effective Residual Compressive Strength (psi)	Young's Modulus (10^6 psi)	Poisson's Ratio
Fidelity Cane Creek CCU7-1	silty dolomite	CCU1-1	7609.35	Vertical	2.624	3348	28,755	20,162	3.447	0.23
		CCU1-3	7609.15	Horizontal	2.599	3881	44,946	24,935	5.507	0.30
	anhydrite	CCU2-1	7614.00	Vertical	2.886	3350	31,827	19,750	7.383	0.34
		CCU2-3	7614.65	Horizontal	2.954	3883	33,347	21,675	8.060	0.33
	silty dolomite -shale	CCU3-1	7619.00	Vertical	2.509	3352	18,220	-	1.686	0.28
		CCU3-5	7619.20	Horizontal	2.500	3886	21,688	16,561	2.054	0.24
	shale	CCU4-1	7620.80	Vertical	2.487	3353	13,814	-	0.820	0.15
		CCU4-5	7620.30	Horizontal	2.514	3886	18,825	14,071	1.118	0.24
	silty dolomite	CCU5-1	7624.65	Vertical	2.597	3355	20,803	11,732	2.696	0.13
		CCU5-3	7624.90	Horizontal	2.591	3886	33,942	20,104	4.517	0.25
	silty dolomite	CCU6-1	7630.25	Vertical	2.504	3357	15,416	-	1.5060	0.24
		CCU6-3	7630.60	Horizontal	2.530	3892	20,564	17,198	2.774	0.15
	shale	CCU7-1[9]	7638.30	Vertical	2.458	3361	14,945	14,459	0.972	0.18
	anhydrite	CCU8-1	7645.30	Vertical	2.940	3364	28,267	-	7.233	0.35
		CCU8-3	7645.75	Horizontal	2.931	3899	30,497	-	7.603	0.35
	silty dolomite	CCU9-1	7651.60	Vertical	2.577	3367	21,372	14,963	3.891	0.17
		CCU9-3	7651.25	Horizontal	2.582	3902	29,687	16,128	3,891,000	0.24
	fractured silty	CCU10-1	7657.50	Vertical	2.678	3369	29,259	-	4.290	0.18

[9] CCU7-1 – Not enough material available to obtain additional samples, thus, no horizontally oriented sample was tested

Well ID	Lithology	Sample ID	Depth (ft)	Orientation	As Received Bulk Density (g/cm^3)	Confining Pressure (psi)	Peak Effective Compressive Strength (psi)	Effective Residual Compressive Strength (psi)	Young's Modulus (10^6 psi)	Poisson's Ratio
	dolomite	CCU10-5	7657.65	Horizontal	2.696	3905	39,972	20,882	6.534	0.33
Fidelity Cane Creek 26-3	shale	FDY3-1	7413.00	Vertical	2.041	3855	11,586 (Y)	-	0.706	0.23
		FDY3-2	7413.05	Horizontal	2.009	4040	11,716 (Y)[10] 14,254	-	1.128	0.25
	shale	FDY2-1	7417.75	Vertical	2.407	3857	18,534	14,557	1.119	0.24
		FDY2-2	7417.85	Horizontal	2.406	4043	20,699	15,143	2.074	0.30
	shale	FDY1-2 [11]	7464.30	Horizontal	2.310	4068	17,700	14,498	1.571	0.22
	silty dolomite	FDY1-1 [12]	7464.50	Vertical	2.617	3882	36,702	16,682	3.276	0.23
		FDY1-4	7464.50	Vertical	2.611	3881	35,955	16,935	3.620	0.18
Fidelity Cisco State 36-13	dolomite	CSO1-1	7588.80	Vertical	2.512	2732	18,014	11,332	1.338	0.19
		CSO1-2	7588.90	Horizontal	2.503	3605	19,081	14,105	1.782	0.25
	shale	CSO2-1	7593.00	Vertical	2.327	2733	12,833	11,298	1.356	0.22
		CSO2-2	7592.90	Horizontal	2.364	3607	15,912	14,647	1.763	0.24
	shale	CSO3-1	7599.75	Vertical	2.582	2736	19,880	14,736	1.104	0.17
		CSO3-2	7599.85	Horizontal	2.537	3610	23,329	19,880	2.037	0.27
	silty dolomite	CSO4-4	7605.65	Vertical	2.564	2738	19,646	13,002	1.282	0.18
		CSO4-2	7605.65	Horizontal	2.534	3613	22,643	17,113	1.985	0.25
	silty dolomite	CSO5-1	7615.40	Vertical	2.464	2742	14,412	12,942	1.094	0.27
		CSO5-2	7615.25	Horizontal	2.511	3617	19,097	17,017	1.755	0.23
	anhydrite	CSO6-1	7627.30	Vertical	2.944	2746	23,662	16,346	8.081	0.34
		CSO6-2	7627.10	Horizontal	2.937	3623	28,796	19,423	8.780	0.33
Bill Barrett 14-3-35	dolomite	UTE3-1	7327.30	Vertical	2.645	1319	27330	12200	3.196	0.18
		UTE3-2	7327.40	Horizontal	2.655	2931	52280	19630	8.166	0.30
	shale-finely laminated	UTE2-1	7332.70	Vertical	2.382	1320	15350	5400	1.411	0.21
		UTE2-2	7332.85	Horizontal	2.342	2933	21240	12430	3.962	0.27
	shale	UTE1-1[13]	7358.35	Vertical	2.439	1325	9700	5510	1.428	0.21

[10] (Y) denotes axial yield
[11] FDY1-2 – No additional shale material remains for a matching horizontal sample, from this backup shale depth interval.
[12] FDY1-1 – No additional silty dolomite material for a matching horizontal sample. Sample FDY1-4 tested as accident, originally marked with an incorrect depth.
[13] Note density difference between UTE 1-1 and UTE 1-2. No additional material available.

Well ID	Lithology	Sample ID	Depth (ft)	Orientation	As Received Bulk Density (g/cm^3)	Confining Pressure (psi)	Peak Effective Compressive Strength (psi)	Effective Residual Compressive Strength (psi)	Young's Modulus (10^6 psi)	Poisson's Ratio
		UTE1-2	7358.15	Horizontal	2.584	2943	22040	14640	3.963	0.26
Bill Barrett 14-1-46	tan dolomite	BTR1-1	6684.40	Vertical	2.282	1337	19420	9580		
		BTR1-6	6684.40	Vertical	2.348	1337	22190	10410	5.390	0.22
		BTR1-2	6684.780	Horizontal	2.140	2741	19740	13240	3.829	0.27
	dolomite	BTR2-1	6693.70	Vertical	2.428	1399	29110	9470	4.861	0.29
		BTR2-2	6693.45	Horizontal	2.544	2744	49930	20490	7.011	0.29
		BTR2-5	6693.45	Horizontal	2.433	2744			4.796	0.31
	gray limestone	BTR3-1	6698.25	Vertical	2.586	1340	23980	13700	4.038	0.14
		BTR3-2	6699.00	Horizontal	2.614	2747	52680	19850	8.657	0.32
	tan dolomite	BTR4-4	6703.10	Vertical	2.543	1341	23340	14290	6.422	0.28
		BTR4-2	3702.90	Horizontal	2.473	2748	26760	11050	6.223	0.26
	shale	BTR5-4	6706.50	Vertical	2.487	1341	14450	9190	1.295	0.18
		BTR5-2	6706.65	Horizontal	2.502	2750	17250	13270	3.797	0.26

Table A-7. Dynamic Mechanical Properties Determined During Triaxial Compression Testing

Well ID	Lithology	Sample ID Depth (ft) Orientation	Axial Stress Difference (psi)	Effective Confining Pressure[14] (psi)	Effective Mean Stress (psi)	As Received Bulk Density (g/cm^3)	P-Wave Velocity (ft/s)	S-Wave Velocity (ft/s)	Poisson's Ratio	Young's Modulus (10^6 psi)	Bulk Modulus (10^6 psi)	Shear Modulus (10^6 psi)
Fidelity Cane Creek CCU7-1	silty dolomite	CCU1-1 7609.35 Vertical	0	3348	3348	2.631	15,966	9032	0.26	7.313	5.180	2.891
			3343	3348	4462	2.632	16,028	9039	0.27	7.341	5.248	2.898
			6979	3348	5674	2.634	16,056	9029	0.27	7.342	5.291	2.893
			18,990	3348	9678	2.637	16,127	8874	0.28	7.179	5.511	2.798
			25,385	3348	11,810	2.633	15,985	8618	0.30	6.826	5.553	2.635
			16,887	3348	8977	2.610	15,581	8266	0.30	6.267	5.334	2.403
		CCU1-3 7609.15 Horizontal	0	3882	3882	2.606	16,982	9970	0.24	8.635	5.473	3.490
			2297	3881	4647	2.606	17,001	9983	0.24	8.659	5.483	3.500
			13,511	3882	8386	2.609	17,159	9916	0.25	8.636	5.742	3.456
			28,095	3883	13,248	2.610	17,156	9782	0.26	8.474	5.865	3.365
			40,321	3881	17,321	2.603	16,991	9355	0.28	7.874	6.032	3.070
			21,053	3881	10,899	2.611	16,553	9217	0.28	7.624	5.656	2.989
	anhydrite	CCU2-1 7614.00 Vertical	0	3350	3350	2.894	19,697	10,556	0.30	11.284	9.336	4.345
			6370	3350	5473	2.895	20,024	10,603	0.31	11.448	9.794	4.386
			13,690	3350	7913	2.896	19,876	10,571	0.30	11.361	9.601	4.360
			24,651	3350	11,567	2.895	19,547	10,365	0.30	10.934	9.317	4.191
			28,467	3350	12,839	2.878	18,496	9556	0.32	9.335	8.546	3.542
			16,409	3350	8820	2.822	17,642	8990	0.32	8.143	7.737	3.074
		CCU2-3 7614.65 Horizontal	0	3882	3882	2.960	19,812	10,808	0.29	12.002	9.442	4.659
			5520	3882	5722	2.962	19,799	10,822	0.29	12.029	9.411	4.674
			13,444	3882	8363	2.963	19,827	10,825	0.29	12.047	9.455	4.678
			20,828	3882	10,825	2.963	19,807	10,815	0.29	12.025	9.437	4.669
			29,462	3882	13,703	2.933	18,615	9642	0.32	9.674	8.795	3.674

[14] All tests drained to atmosphere

Well ID	Lithology	Sample ID Depth (ft) Orientation	Axial Stress Difference (psi)	Effective Confining Pressure[14] (psi)	Effective Mean Stress (psi)	As Received Bulk Density (g/cm^3)	P-Wave Velocity (ft/s)	S-Wave Velocity (ft/s)	Poisson's Ratio	Young's Modulus (10^6 psi)	Bulk Modulus (10^6 psi)	Shear Modulus (10^6 psi)
			17,912	3882	9853	2.863	17,847	9107	0.32	8.473	8.022	3.200
Fidelity Cane Creek CCU7-1	silty dolomite - shale	CCU3-1 7619.00 Vertical	0	3352	3352	2.525	13,185	7793	0.23	5.090	3.160	2.066
			1974	3352	4010	2.526	13,267	7813	0.23	5.131	3.221	2.078
			5631	3352	5229	2.529	13,472	7867	0.24	5.235	3.373	2.109
			10,632	3352	6896	2.531	13,666	7889	0.25	5.307	3.539	2.123
			14,866	3352	8307	2.519	13,645	7627	0.27	5.026	3.687	1.974
			14,833	3352	8296	2.516	13,617	7591	0.27	4.979	3.681	1.953
		CCU3-5 7619.20 Horizontal	0	3886	3886	2.522	14,362	8335	0.25	5.883	3.861	2.361
			3407	3885	5021	2.524	14,443	8364	0.25	5.936	3.922	2.379
			7465	3885	6373	2.526	14,738	8392	0.26	6.041	4.197	2.397
			13,372	3887	8344	2.530	14,766	8313	0.27	5.974	4.291	2.356
			17,763	3884	9805	2.514	14,228	7791	0.29	5.287	4.115	2.056
			12,641	3886	8100	2.460	13,630	7308	0.30	4.596	3.797	1.770
	shale	CCU4-1 7620.80 Vertical	0	3354	3354	2.517	11,741	7048	0.22	4.104	2.429	1.684
			2026	3354	4029	2.519	12,126	7164	0.23	4.291	2.668	1.742
			3859	3354	4640	2.522	12,390	7264	0.24	4.440	2.827	1.793
			8015	3354	6026	2.532	13,001	7337	0.27	4.652	3.319	1.837
			10,459	3354	6840	2.559	12,979	7180	0.28	4.548	3.439	1.777
			9207	3354	6423	2.576	12,599	6965	0.28	4.310	3.264	1.683
		CCU4-5 7620.30 Horizontal	0	3885	3885	2.541	13,890	7897	0.26	5.386	3.759	2.135
			3411	3886	5023	2.543	13,999	7913	0.27	5.429	3.855	2.145
			6781	3886	6146	2.546	14,183	7912	0.27	5.472	4.037	2.147
			11,108	3886	7589	2.550	14,242	7922	0.28	5.502	4.094	2.156
			14,905	3884	8852	2.539	14,108	7568	0.30	5.086	4.197	1.959
			10,194	3885	7283	2.511	13,618	7397	0.29	4.779	3.806	1.851
Fidelity Cane Creek CCU7-1	silty dolomite	CCU5-1 7624.65	0	3355	3355	2.606	15,834	9277	0.24	7.486	4.774	3.022
			3191	3354	4418	2.608	15,940	9302	0.24	7.552	4.874	3.041

Well ID	Lithology	Sample ID Depth (ft) Orientation	Axial Stress Difference (psi)	Effective Confining Pressure[14] (psi)	Effective Mean Stress (psi)	As Received Bulk Density (g/cm^3)	P-Wave Velocity (ft/s)	S-Wave Velocity (ft/s)	Poisson's Ratio	Young's Modulus (10^6 psi)	Bulk Modulus (10^6 psi)	Shear Modulus (10^6 psi)
		Vertical	6099	3354	5387	2.610	16,019	9309	0.25	7.590	4.961	3.048
			10,787	3354	6950	2.614	16,057	9280	0.25	7.578	5.036	3.033
			15,368	3355	8478	2.619	16,060	9190	0.26	7.489	5.128	2.980
			17,301	3354	9121	2.622	16,005	9054	0.26	7.327	5.190	2.897
		CCU5-3 7624.90 Horizontal	0	3887	3887	2.599	17,006	9489	0.27	8.034	5.923	3.153
			7397	3886	6352	2.601	17,147	9540	0.28	8.139	6.052	3.190
			11,924	3886	7861	2.602	17,268	9523	0.28	8.150	6.216	3.180
			20,747	3885	10,801	2.604	17,573	9539	0.29	8.246	6.580	3.193
			30,020	3887	13,894	2.604	17,235	9303	0.29	7.862	6.375	3.037
			16,214	3886	9291	2.566	16,460	8862	0.30	7.036	5.746	2.715
	silty dolomite	CCU6-1 7630.25 Vertical	0	3356	3356	2.519	13,685	7932	0.25	5.327	3.509	2.136
			1696	3357	3922	2.521	13,740	7950	0.25	5.359	3.550	2.147
			3370	3357	4480	2.522	13,802	7970	0.25	5.396	3.595	2.158
			4809	3357	4960	2.523	13,850	7978	0.25	5.417	3.636	2.164
			9010	3357	6360	2.525	13,909	7954	0.26	5.411	3.712	2.152
			12,037	3357	7369	2.499	13,731	7552	0.28	4.929	3.788	1.921
		CCU6-3 7630.60 Horizontal	0	3891	3891	2.544	16,895	9652	0.26	8.032	5.526	3.193
			1990	3891	4554	2.545	16,813	9657	0.25	8.019	5.429	3.198
			4925	3891	5533	2.547	16,882	9662	0.26	8.050	5.509	3.204
			11,711	3891	7795	2.552	16,963	9650	0.26	8.073	5.624	3.201
			16,671	3891	9448	2.552	16,890	9482	0.27	7.851	5.687	3.091
			13,309	3891	8327	2.518	16,683	9409	0.27	7.611	5.439	3.004
Fidelity Cane Creek CCU7-1	shale	CCU7-1 7638.30 Vertical	0	3361	3361	2.478	12,505	7188	0.25	4.325	2.921	1.726
			2196	3361	4093	2.480	12,619	7251	0.25	4.405	2.979	1.757
			4311	3361	4798	2.484	12,912	7299	0.27	4.511	3.203	1.783
			8944	3362	6343	2.496	13,242	7265	0.28	4.561	3.530	1.775
			11,580	3361	7221	2.514	13,201	7013	0.30	4.342	3.682	1.666

Well ID	Lithology	Sample ID Depth (ft) Orientation	Axial Stress Difference (psi)	Effective Confining Pressure[14] (psi)	Effective Mean Stress (psi)	As Received Bulk Density (g/cm^3)	P-Wave Velocity (ft/s)	S-Wave Velocity (ft/s)	Poisson's Ratio	Young's Modulus (10^6 psi)	Bulk Modulus (10^6 psi)	Shear Modulus (10^6 psi)
			11,058	3361	7047	2.523	12,891	6864	0.30	4.171	3.513	1.601
	anhydrite	CCU8-1 7645.30 Vertical	0	3364	3364	2.945	19,759	10,694	0.29	11.735	9.442	4.538
			5541	3364	5211	2.946	19,782	10,748	0.29	11.837	9.422	4.586
			12,679	3364	7590	2.947	19,831	10,693	0.30	11.761	9.564	4.541
			22,430	3364	10,841	2.947	19,656	10,355	0.31	11.137	9.664	4.258
			24,892	3364	11,661	2.922	18,474	9348	0.33	9.139	8.851	3.441
			24,886	3364	11,659	2.914	18,319	9209	0.33	8.864	8.737	3.330
		CCU8-3 7645.75 Horizontal	561	3898	4085	2.942	19,704	10,857	0.28	11.982	9.161	4.673
			8011	3898	6568	2.943	19,732	10,903	0.28	12.071	9.155	4.714
			15,460	3898	9051	2.944	19,760	10,849	0.28	11.991	9.264	4.669
			21,405	3898	11,033	2.944	19,673	10,718	0.29	11.746	9.275	4.556
			26,589	3898	12,761	2.887	17,851	9127	0.32	8.575	8.076	3.241
			25,796	3898	12,497	2.837	17,295	8567	0.34	7.505	7.694	2.806
Fidelity Cane Creek CCU7-1	silty dolomite	CCU9-1 7651.60 Vertical	585	3366	3561	2.589	14,919	8701	0.24	6.561	4.243	2.641
			5464	3367	5188	2.592	14,991	8725	0.24	6.616	4.304	2.659
			9637	3366	6578	2.595	15,003	8693	0.25	6.592	4.349	2.643
			15,466	3367	8522	2.599	14,987	8508	0.26	6.399	4.486	2.535
			18,005	3367	9369	2.596	14,872	8270	0.28	6.105	4.546	2.392
			11,566	3367	7222	2.517	14,367	7835	0.29	5.365	4.225	2.082
		CCU9-3 7651.25 Horizontal	4589	3901	5431	2.600	16,271	9705	0.22	8.077	4.876	3.300
			8684	3901	6796	2.602	16,319	9723	0.22	8.118	4.917	3.314
			12,451	3901	8051	2.603	16,396	9684	0.23	8.106	5.043	3.289
			18,914	3901	10,206	2.604	16,396	9615	0.24	8.033	5.108	3.244
			25,313	3901	12,339	2.602	16,354	9496	0.25	7.877	5.162	3.162
			12,294	3901	7999	2.556	16,130	9374	0.24	7.537	4.926	3.027
	fractured silty	CCU10-1 7657.50	707	3368	3604	2.688	17,548	9925	0.26	9.026	6.396	3.568
			4750	3368	4951	2.690	17,806	10,007	0.27	9.213	6.652	3.630

Well ID	Lithology	Sample ID Depth (ft) Orientation	Axial Stress Difference (psi)	Effective Confining Pressure[14] (psi)	Effective Mean Stress (psi)	As Received Bulk Density (g/cm^3)	P-Wave Velocity (ft/s)	S-Wave Velocity (ft/s)	Poisson's Ratio	Young's Modulus (10^6 psi)	Bulk Modulus (10^6 psi)	Shear Modulus (10^6 psi)
	dolomite	Vertical	8984	3368	6363	2.692	17,867	10,014	0.27	9.246	6.729	3.637
			13,183	3368	7762	2.693	18,036	10,024	0.28	9.309	6.943	3.646
			17,047	3368	9050	2.695	18,018	10,020	0.28	9.305	6.927	3.646
			25,515	3368	11,873	2.698	18,147	9865	0.29	9.131	7.256	3.538
		CCU10-5 7657.65 Horizontal	200	3904	3971	2.708	19,333	10,786	0.27	10.817	7.979	4.245
			9962	3904	7225	2.710	19,924	10,808	0.29	11.018	8.807	4.266
			16,556	3904	9423	2.711	20,194	10,756	0.30	11.004	9.262	4.226
			22,666	3904	11,459	2.711	20,141	10,713	0.30	10.925	9.230	4.193
			35,905	3903	15,871	2.709	19,741	10,385	0.31	10.304	8.976	3.937
			16826	3904	9513	2.687	18,995	10,119	0.30	9.652	8.121	3.707
Fidelity Cane Creek 26-3	shale	FDY3-1 7413.00 Vertical	691	3854	4084	2.091	8,770	5124	0.24	1.836	1.181	0.740
			2745	3854	4769	2.095	8,889	5183	0.24	1.885	1.219	0.759
			4642	3854	5401	2.103	9,201	5250	0.26	1.967	1.358	0.781
			6630	3854	6064	2.111	9,502	5321	0.27	2.048	1.494	0.805
			8515	3854	6692	2.103	9,873	5389	0.29	2.120	1.665	0.823
			9640	3854	7067	2.040	10,041	5335	0.30	2.040	1.728	0.783
		FDY3-2 7413.05 Horizontal	0	4040	4040	2.049	10,482	6238	0.23	2.634	1.601	1.074
			2898	4040	5006	2.053	10,572	6259	0.23	2.666	1.647	1.084
			4183	4038	5432	2.058	10,721	6285	0.24	2.713	1.727	1.095
			6470	4038	6195	2.073	10,912	6347	0.24	2.800	1.826	1.125
			9267	4040	7129	2.097	11,269	6419	0.26	2.934	2.036	1.164
			10,203	4039	7440	2.102	11,387	6375	0.27	2.927	2.138	1.151
	shale	FDY2-1 7417.75 Vertical	0	3862	3862	2.423	11,780	6982	0.23	3.912	2.408	1.591
			4078	3862	5221	2.426	11,971	7025	0.24	3.992	2.534	1.613
			5182	3862	5589	2.427	12,039	7038	0.24	4.019	2.580	1.620
			8234	3847	6592	2.431	12,209	7069	0.25	4.085	2.700	1.637
			13,008	3862	8198	2.434	12,411	7050	0.26	4.113	2.878	1.630

Well ID	Lithology	Sample ID Depth (ft) Orientation	Axial Stress Difference (psi)	Effective Confining Pressure[14] (psi)	Effective Mean Stress (psi)	As Received Bulk Density (g/cm^3)	P-Wave Velocity (ft/s)	S-Wave Velocity (ft/s)	Poisson's Ratio	Young's Modulus (10^6 psi)	Bulk Modulus (10^6 psi)	Shear Modulus (10^6 psi)
			10,670	3847	7404	2.389	12,079	6732	0.27	3.720	2.752	1.459
		FDY2-2 7417.85 Horizontal	0	4057	4057	2.421	14,201	8476	0.22	5.734	3.454	2.343
			2153	4042	4760	2.422	14,253	8484	0.23	5.758	3.498	2.349
			7004	4042	6377	2.424	14,382	8505	0.23	5.817	3.605	2.363
			8653	4042	6926	2.425	14,420	8510	0.23	5.833	3.639	2.366
			15,931	4042	9352	2.423	14,514	8392	0.25	5.743	3.813	2.299
			11,047	4042	7724	2.389	14,191	8207	0.25	5.416	3.592	2.169
Fidelity Cane Creek 26-3	shale	FDY1-2 [15] 7464.30 Horizontal	0	4069	4069	2.357	12,681	7682	0.21	4.536	2.608	1.874
			3337	4069	5181	2.359	12,661	7677	0.21	4.531	2.597	1.873
			4730	4069	5646	2.360	12,823	7675	0.22	4.574	2.732	1.873
			6914	4068	6373	2.363	12,845	7697	0.22	4.603	2.738	1.886
			13,628	4069	8612	2.374	13,103	7550	0.25	4.564	3.062	1.824
			10,435	4069	7547	2.356	12,813	7536	0.24	4.456	2.808	1.803
	silty dolomite	FDY1-1 7464.50 Vertical	0	3877	3877	2.628	14,638	9062	0.19	6.916	3.709	2.908
			8686	3877	6772	2.632	16,242	9389	0.25	7.810	5.187	3.126
			11,985	3877	7872	2.634	16,419	9440	0.25	7.925	5.351	3.162
			15,155	3877	8929	2.635	16,615	9473	0.26	8.024	5.554	3.186
			27,348	3877	12,993	2.639	16,919	9461	0.27	8.100	5.935	3.182
			12,826	3877	8152	2.573	16,041	8789	0.29	6.886	5.351	2.678
		FDY1-4[16] 7464.50 Vertical	0	3881	3881	2.622	15,000	9068	0.21	7.042	4.076	2.905
			1631	3881	4425	2.623	15,296	9141	0.22	7.218	4.331	2.953
			9057	3881	6900	2.626	16,367	9405	0.25	7.847	5.305	3.130
			15,880	3881	9174	2.629	16,918	9514	0.27	8.137	5.865	3.207
			32,027	3881	14557	2.632	16,963	9294	0.29	7.876	6.121	3.064

[15] Note – sample ended up being shale lithology. Also there is not additional material to pull a vertically oriented sister sample.
[16] FDY1-4 and FDY1-1 are the same lithology. It was originally hoped one of the two would be a match to shale sample FDY1-2. No additional material remains from this depth section to prepare a horizontal sister sample.

Well ID	Lithology	Sample ID Depth (ft) Orientation	Axial Stress Difference (psi)	Effective Confining Pressure[14] (psi)	Effective Mean Stress (psi)	As Received Bulk Density (g/cm^3)	P-Wave Velocity (ft/s)	S-Wave Velocity (ft/s)	Poisson's Ratio	Young's Modulus (10^6 psi)	Bulk Modulus (10^6 psi)	Shear Modulus (10^6 psi)
			13,041	3881	8228	2.601	14,975	8758	0.24	6.667	4.275	2.688
Fidelity Cisco State 36-13	dolomite	CSO1-1 7588.80 Vertical	0	2739	2739	2.529	12,668	7929	0.18	5.048	2.612	2.143
			1477	2724	3216	2.530	12,818	7952	0.19	5.119	2.728	2.156
			4837	2739	4351	2.534	13,196	8040	0.20	5.318	3.003	2.207
			7389	2739	5202	2.537	13,404	8087	0.21	5.427	3.161	2.235
			15,144	2724	7772	2.538	13,595	7830	0.25	5.249	3.526	2.097
			8520	2724	5564	2.511	13,206	7698	0.24	4.983	3.228	2.005
		CSO1-2 7588.90 Horizontal	0	3622	3622	2.525	14,167	8502	0.22	5.993	3.550	2.459
			2217	3607	4346	2.526	14,241	8511	0.22	6.027	3.616	2.465
			4317	3607	5046	2.527	14,347	8534	0.23	6.083	3.703	2.480
			10,456	3593	7078	2.532	14,566	8536	0.24	6.156	3.924	2.485
			15,302	3607	8708	2.530	14,540	8349	0.25	5.959	4.039	2.376
			9680	3607	6834	2.457	14,107	8153	0.25	5.498	3.655	2.200
	shale	CSO2-1 7593.00 Vertical	0	2732	2732	2.349	11,368	7074	0.18	3.750	1.978	1.584
			665	2732	2954	2.349	11,480	7075	0.19	3.783	2.059	1.585
			2030	2732	3409	2.351	11,607	7119	0.20	3.847	2.127	1.605
			6833	2732	5010	2.357	11,901	7240	0.21	4.017	2.278	1.665
			10,088	2732	6095	2.352	11,833	7026	0.23	3.841	2.351	1.564
			8567	2733	5589	2.227	11,282	6629	0.24	3.261	2.062	1.319
		CSO2-2 7592.90 Horizontal	0	3606	3606	2.393	12,039	7481	0.19	4.279	2.268	1.805
			4579	3609	5135	2.397	12,340	7483	0.21	4.374	2.507	1.809
			7522	3610	6117	2.400	12,582	7564	0.22	4.504	2.653	1.851
			10,619	3608	7148	2.401	12,843	7588	0.23	4.590	2.852	1.863
			12,286	3607	7702	2.346	12,529	7330	0.24	4.211	2.698	1.698
			11,047	3608	7290	2.253	12,234	7151	0.24	3.852	2.473	1.552
Fidelity Cisco State	shale	CSO3-1 7599.75	329	2735	2845	2.596	12,105	7782	0.15	4.863	2.302	2.118
			4321	2736	4176	2.602	12,935	7927	0.20	5.284	2.928	2.203

Well ID	Lithology	Sample ID Depth (ft) Orientation	Axial Stress Difference (psi)	Effective Confining Pressure[14] (psi)	Effective Mean Stress (psi)	As Received Bulk Density (g/cm^3)	P-Wave Velocity (ft/s)	S-Wave Velocity (ft/s)	Poisson's Ratio	Young's Modulus (10^6 psi)	Bulk Modulus (10^6 psi)	Shear Modulus (10^6 psi)
36-13		Vertical	6528	2736	4912	2.605	13,239	7986	0.21	5.436	3.167	2.239
			11,592	2736	6600	2.610	13,836	8031	0.25	5.652	3.709	2.268
			17,139	2736	8449	2.583	13,845	7566	0.29	5.128	4.014	1.992
			12,049	2736	6752	2.540	13,228	7205	0.29	4.580	3.619	1.777
		CSO3-2 7599.85 Horizontal	677	3609	3835	2.563	14,119	8541	0.21	6.105	3.525	2.520
			7680	3610	6170	2.567	14,587	8580	0.24	6.293	3.966	2.547
			9519	3610	6783	2.568	14,688	8598	0.24	6.341	4.055	2.558
			14,038	3610	8289	2.570	14,814	8537	0.25	6.316	4.235	2.524
			19,614	3610	10,148	2.555	14,577	8208	0.27	5.883	4.224	2.320
			16,324	3610	9051	2.504	14,304	7945	0.28	5.440	4.065	2.130
	silty dolomite	CSO4-4 7605.65 Vertical	0	2739	2739	2.579	14,604	8236	0.27	5.971	4.268	2.357
			3284	2738	3833	2.582	16,244	8371	0.32	6.431	5.929	2.437
			5896	2738	4703	2.585	16,251	8455	0.31	6.546	5.878	2.490
			10,596	2738	6270	2.590	16,595	8542	0.32	6.721	6.217	2.546
			16,911	2738	8375	2.586	16,697	8267	0.34	6.371	6.540	2.382
			10,289	2738	6168	2.549	15,498	7961	0.32	5.750	5.348	2.177
		CSO4-2 7605.65 Horizontal	0	3613	3613	2.556	14,386	8690	0.21	6.309	3.660	2.601
			8932	3613	6590	2.562	14,479	8705	0.22	6.367	3.750	2.616
			14,897	3613	8579	2.565	14,835	8710	0.24	6.487	4.110	2.622
			18,218	3613	9686	2.565	14,918	8676	0.24	6.474	4.222	2.601
			13,733	3611	8189	2.560	14,874	8260	0.28	6.011	4.494	2.353
			13,377	3613	8072	2.574	14,526	8300	0.26	6.011	4.133	2.390
Fidelity Cisco State 36-13	silty dolomite	CSO5-1 7615.40 Vertical	0	2742	2742	2.490	11,355	7264	0.15	4.085	1.965	1.771
			1834	2743	3354	2.492	11,575	7322	0.17	4.200	2.099	1.800
			4066	2744	4099	2.494	11,782	7350	0.18	4.290	2.245	1.815
			8643	2742	5623	2.497	12,332	7371	0.22	4.469	2.680	1.828
			11,653	2744	6628	2.446	12,060	6922	0.25	3.962	2.688	1.579

Well ID	Lithology	Sample ID Depth (ft) Orientation	Axial Stress Difference (psi)	Effective Confining Pressure[14] (psi)	Effective Mean Stress (psi)	As Received Bulk Density (g/cm^3)	P-Wave Velocity (ft/s)	S-Wave Velocity (ft/s)	Poisson's Ratio	Young's Modulus (10^6 psi)	Bulk Modulus (10^6 psi)	Shear Modulus (10^6 psi)
			10,185	2742	6137	2.291	11,574	6544	0.27	3.345	2.373	1.322
		CSO5-2 7615.25 Horizontal	0	3617	3617	2.528	13,648	8201	0.22	5.577	3.290	2.290
			2835	3617	4562	2.529	13,831	8261	0.22	5.687	3.418	2.326
			6442	3616	5763	2.532	14,196	8281	0.24	5.812	3.756	2.339
			11,427	3616	7425	2.536	14,335	8175	0.26	5.751	3.977	2.284
			15,461	3615	8769	2.533	13,980	7820	0.27	5.312	3.888	2.088
			13,334	3618	8063	2.498	14,002	7694	0.28	5.116	3.943	1.993
	anhydrite	CSO6-1 7627.30 Vertical	0	2739	2739	2.974	19,782	10,536	0.30	11.584	9.752	4.449
			6414	2739	4877	2.975	19,951	10,592	0.30	11.728	9.962	4.498
			14,225	2739	7481	2.976	19,982	10,570	0.31	11.699	10.038	4.480
			19,454	2754	9239	2.975	19,721	10,386	0.31	11.312	9.824	4.324
			20,745	2739	9654	2.962	18,925	9852	0.31	10.182	9.129	3.874
			13,450	2739	7222	2.780	16,405	9922	0.21	8.936	5.164	3.688
		CSO6-2 7627.10 Horizontal	0	3637	3637	2.947	19,700	10,732	0.29	11.789	9.312	4.573
			6044	3622	5637	2.948	19,881	10,804	0.29	11.965	9.518	4.636
			14,644	3622	8503	2.949	19,937	10,811	0.29	11.996	9.600	4.644
			21,330	3622	10,732	2.949	19,829	10,737	0.29	11.842	9.515	4.581
			25,090	3622	11,985	2.934	18,802	10,040	0.30	10.365	8.663	3.985
			15,968	3622	8945	2.844	17,621	8937	0.33	8.121	7.818	3.060
Bill Barrett 14-3-45	dolomite	UTE3-1 7327.30 Vertical	2618	1317	2190	2.654	17,172	9670	0.27	8.478	6.084	3.344
			8127	1317	4026	2.658	17,847	9974	0.27	9.070	6.656	3.563
			11,492	1317	5148	2.659	18,055	10,057	0.28	9.242	6.848	3.624
			19,096	1317	7682	2.663	18,371	10,137	0.28	9.446	7.192	3.687
			25,561	1317	9837	2.665	18,675	10,180	0.29	9.592	7.562	3.722
			10,222	1317	4724	2.709	17,356	9591	0.28	8.596	6.517	3.357
		UTE3-2 7327.40	0	2934	2934	2.657	18,632	10,948	0.24	10.613	6.707	4.292
			4412	2934	4405	2.658	18,705	10,927	0.24	10.615	6.831	4.277

Well ID	Lithology	Sample ID Depth (ft) Orientation	Axial Stress Difference (psi)	Effective Confining Pressure[14] (psi)	Effective Mean Stress (psi)	As Received Bulk Density (g/cm^3)	P-Wave Velocity (ft/s)	S-Wave Velocity (ft/s)	Poisson's Ratio	Young's Modulus (10^6 psi)	Bulk Modulus (10^6 psi)	Shear Modulus (10^6 psi)
		Horizontal	12,739	2934	7180	2.660	18,815	10,915	0.25	10.643	6.994	4.270
			28,943	2934	12582	2.662	18,973	10,915	0.25	10.705	7.214	4.273
			47,632	2934	18811	2.662	19,049	10,831	0.26	10.613	7.404	4.208
			17,355	2919	8704	2.591	18,392	10,552	0.25	9.753	6.625	3.887
	shale - finely laminated	UTE2-1 7332.70 Vertical	0	1317	1317	2.390	10,070	5967	0.23	2.820	1.737	1.147
			3028	1317	2326	2.394	10,307	6029	0.24	2.907	1.863	1.173
			4443	1317	2798	2.395	10,465	6056	0.25	2.955	1.956	1.184
			7088	1317	3680	2.398	10,665	6108	0.26	3.028	2.067	1.205
			13,895	1317	5949	2.402	11,124	6201	0.27	3.173	2.345	1.245
			4022	1317	2658	2.369	10,458	5989	0.26	2.876	1.964	1.145
		UTE2-2 7332.85 Horizontal	0	2934	2934	2.352	14,889	9113	0.20	6.320	3.517	2.632
			2590	2919	3782	2.353	14,921	9108	0.20	6.328	3.552	2.630
			6475	2934	5092	2.354	14,933	9104	0.20	6.332	3.568	2.629
			9965	2934	6256	2.355	14,957	9099	0.21	6.339	3.596	2.627
			17,076	2934	8626	2.357	15,035	9072	0.21	6.344	3.693	2.614
			9438	2934	6080	2.335	14,883	8998	0.21	6.174	3.572	2.547
Bill Barrett 14-3-45	shale	UTE1-1 7358.35 Vertical	2589	1332	2195	2.473	10,715	5710	0.30	2.829	2.377	1.087
			3378	1332	2458	2.474	10,911	5846	0.30	2.959	2.450	1.139
			4265	1332	2754	2.475	11,099	5959	0.30	3.073	2.529	1.184
			6565	1332	3520	2.476	11,424	6168	0.29	3.286	2.662	1.269
			8191	1332	4062	2.465	11,800	6256	0.30	3.392	2.892	1.300
			4199	1317	2717	2.423	11,532	6153	0.30	3.216	2.693	1.236
		UTE1-2 7358.15 Horizontal	0	2949	2949	2.602	14,804	8894	0.22	6.755	3.986	2.774
			814	2934	3205	2.603	14,828	8898	0.22	6.767	4.009	2.776
			5564	2949	4804	2.604	14,893	8916	0.22	6.810	4.063	2.789
			12,542	2949	7130	2.606	14,999	8939	0.22	6.873	4.159	2.806
			18,512	2934	9105	2.605	15,261	8951	0.24	6.962	4.426	2.812

Well ID	Lithology	Sample ID Depth (ft) Orientation	Axial Stress Difference (psi)	Effective Confining Pressure[14] (psi)	Effective Mean Stress (psi)	As Received Bulk Density (g/cm^3)	P-Wave Velocity (ft/s)	S-Wave Velocity (ft/s)	Poisson's Ratio	Young's Modulus (10^6 psi)	Bulk Modulus (10^6 psi)	Shear Modulus (10^6 psi)
			11,634	2934	6812	2.579	14,801	8740	0.23	6.542	4.073	2.654
Bill Barrett 14-1-46	tan dolomite	BTR1-6 6684.40 Vertical	0	1337	1337	2.352	15,625	8935	0.26	6.362	4.365	2.531
			4584	1337	2865	2.354	15,909	9038	0.26	6.537	4.572	2.591
			7822	1337	3944	2.355	16,046	9060	0.27	6.594	4.697	2.604
			15,495	1337	6502	2.356	16,094	9051	0.27	6.600	4.756	2.601
			20,876	1337	8296	2.357	15,974	8948	0.27	6.466	4.713	2.543
			9096	1337	4369	2.325	15,455	9079	0.24	6.386	4.040	2.582
		BTR1-2 6684.70 Horizontal	0	2739	2739	2.146	13,625	8066	0.23	4.629	2.859	1.881
			1380	2739	3199	2.147	13,712	8079	0.23	4.660	2.921	1.888
			5418	2739	4545	2.148	13,801	8102	0.24	4.701	2.979	1.900
			12,494	2739	6904	2.150	13,824	8079	0.24	4.691	3.014	1.890
			16,856	2739	8358	2.149	13,736	7958	0.25	4.574	3.017	1.834
			10,523	2739	6247	2.091	13,360	7798	0.24	4.255	2.745	1.713
Bill Barrett 14-1-46	dolomite	BTR2-1 6693.70 Vertical	0	1332	1332	2.446	15,857	9319	0.24	7.077	4.470	2.862
			8032	1332	4009	2.448	16,121	9457	0.24	7.303	4.640	2.950
			13,056	1332	5684	2.449	16,230	9487	0.24	7.369	4.733	2.970
			21,871	1347	8637	2.449	16,294	9464	0.25	7.362	4.820	2.956
			27,380	1332	10,459	2.442	16,194	9321	0.25	7.160	4.817	2.859
			8130	1347	4057	2.352	15,251	8720	0.26	6.060	4.158	2.410
		BTR2-2 6693.45 Horizontal	0	2739	2739	2.553	17,474	10,031	0.25	8.683	5.889	3.462
			8611	2739	5609	2.556	18,166	10,270	0.27	9.190	6.522	3.632
			15,481	2739	7899	2.557	18,430	10,378	0.27	9.410	6.755	3.711
			22,254	2739	10,157	2.558	18,597	10,425	0.27	9.521	6.925	3.746
			37,097	2739	15,105	2.559	18,683	10,418	0.27	9.537	7.045	3.742
			17,750	2739	8656	2.521	18,162	10,214	0.27	8.991	6.480	3.543
	grey limestone	BTR3-1 6698.25	0	1340	1340	2.592	15,786	9242	0.24	7.394	4.727	2.983
			1933	1340	1984	2.593	15,867	9280	0.24	7.463	4.785	3.009

Well ID	Lithology	Sample ID Depth (ft) Orientation	Axial Stress Difference (psi)	Effective Confining Pressure[14] (psi)	Effective Mean Stress (psi)	As Received Bulk Density (g/cm^3)	P-Wave Velocity (ft/s)	S-Wave Velocity (ft/s)	Poisson's Ratio	Young's Modulus (10^6 psi)	Bulk Modulus (10^6 psi)	Shear Modulus (10^6 psi)
		Vertical	6172	1341	3398	2.595	16,130	9310	0.25	7.579	5.057	3.031
			13,944	1341	5989	2.599	16,537	9403	0.26	7.809	5.447	3.096
			22,010	1341	8678	2.604	16,914	9446	0.27	7.974	5.864	3.131
			12,361	1341	5461	2.575	16,838	8922	0.30	7.206	6.154	2.761
		BTR3-2 6699.00 Horizontal	0	2746	2746	2.616	18,728	10,269	0.29	9.553	7.408	3.717
			3177	2746	3805	2.617	18,945	10,337	0.29	9.706	7.631	3.768
			11,607	2746	6615	2.618	18,815	10,360	0.28	9.710	7.439	3.786
			28,593	2746	12,277	2.620	19,014	10,333	0.29	9.727	7.736	3.769
			49,311	2745	19182	2.622	18,938	10,259	0.29	9.612	7.714	3.719
			17,053	2746	8430	2.572	17,772	9743	0.29	8.456	6.560	3.290
Bill Barrett 14-1-46	tan dolomite	BTR4-4 6703.10 Vertical	0	1341	1341	2.550	17,752	10,785	0.21	9.653	5.500	3.997
			4337	1341	2787	2.551	17,791	10,711	0.22	9.590	5.622	3.944
			10,751	1341	4925	2.552	17,853	10,715	0.22	9.622	5.698	3.948
			16,682	1341	6902	2.553	17,869	10,706	0.22	9.619	5.726	3.942
			24,355	1341	9459	2.551	17,952	10,901	0.21	9.869	5.632	4.085
			12,948	1341	5657	2.530	17,446	10,451	0.22	9.085	5.410	3.723
		BTR4-2 6702.90 Horizontal	0	1347	1347	2.480	17,100	9889	0.25	8.162	5.413	3.268
			2827	1332	2274	2.481	17,229	9923	0.25	8.240	5.534	3.291
			9167	1332	4388	2.482	17,336	9965	0.25	8.324	5.622	3.321
			15,506	1347	6516	2.483	17,412	9981	0.26	8.369	5.699	3.333
			21,267	1347	8436	2.484	17,412	9973	0.26	8.362	5.709	3.329
			8105	1332	4034	2.487	16,801	9611	0.26	7.779	5.331	3.095
	shale	BTR5-4 6706.50 Vertical	1932	1341	1985	2.500	10,778	7192	0.10	3.828	1.590	1.742
			4496	1341	2840	2.503	11,797	7576	0.15	4.449	2.113	1.936
			5787	1340	3269	2.505	12,211	7724	0.17	4.698	2.347	2.014
			9432	1341	4485	2.510	13,286	8058	0.21	5.310	3.042	2.196
			13,145	1341	5723	2.507	14,493	8157	0.27	5.700	4.099	2.247

Well ID	Lithology	Sample ID Depth (ft) Orientation	Axial Stress Difference (psi)	Effective Confining Pressure[14] (psi)	Effective Mean Stress (psi)	As Received Bulk Density (g/cm^3)	P-Wave Velocity (ft/s)	S-Wave Velocity (ft/s)	Poisson's Ratio	Young's Modulus (10^6 psi)	Bulk Modulus (10^6 psi)	Shear Modulus (10^6 psi)
			7385	1340	3802	2.451	13,530	7798	0.25	5.027	3.369	2.009
		BTR5-2 6706.65 Horizontal	661	2749	2969	2.523	15,940	9572	0.22	7.587	4.485	3.115
			4521	2749	4256	2.524	16,283	9606	0.23	7.740	4.833	3.138
			7964	2749	5404	2.525	16,314	9634	0.23	7.783	4.846	3.158
			11,015	2749	6421	2.526	16,443	9652	0.24	7.847	4.975	3.171
			14,374	2749	7540	2.526	16,508	9655	0.24	7.868	5.044	3.173
			10,529	2749	6259	2.482	16,214	9603	0.23	7.586	4.680	3.084

Table A-8. Dynamic and Quasi-Static Mechanical Properties Determined During Triaxial Compression Testing

Well ID	Lithology	Sample ID	Depth (ft)	Orientation	Effective Confining Pressure (psi)	Static Poisson's Ratio	Dynamic Poisson's Ratio	Static Young's Modulus (psi)	Dynamic Young's Modulus (psi)	Dynamic/ Static Young's Modulus	Dynamic/ Static Poisson's Ratio
Fidelity Cane Creek CCU7-1	silty dolomite	CCU1-1	7609.35	Vertical	3348	0.23	0.27	3,447,000	7,342,000	2.13	1.17
		CCU1-3	7609.15	Horizontal	3881	0.30	0.25	5,507,000	8,636,000	1.57	0.83
	anhydrite	CCU2-1	7614.00	Vertical	3350	0.34	0.31	7,383,000	11,448,000	1.55	0.91
		CCU2-3	7614.65	Horizontal	3883	0.33	0.29	8,060,000	12,047,000	1.49	0.88
	silty dolomite - shale	CCU3-1	7619.00	Vertical	3352	0.28	0.24	1,686,000	5,235,000	3.10	0.86
		CCU3-5	7619.20	Horizontal	3886	0.24	0.26	2,054,000	6,041,000	2.94	1.08
	shale	CCU4-1	7620.80	Vertical	3353	0.15	0.24	819,700	4,440,000	5.42	1.60
		CCU4-5	7620.30	Horizontal	3886	0.24	0.27	1,778,000	5,429,000	3.05	1.13
	silty dolomite	CCU5-1	7624.65	Vertical	3355	0.13	0.25	2,696,000	7,590,000	2.82	1.92
		CCU5-3	7624.90	Horizontal	3886	0.25	0.28	4,517,000	8,150,000	1.80	1.12
	silty dolomite	CCU6-1	7630.25	Vertical	3357	0.24	0.25	1,506,000	5,396,000	3.58	1.04
		CCU6-3	7630.60	Horizontal	3892	0.15	0.26	2,774,000	8,050,000	2.90	1.73
	shale	CCU7-1	7638.30	Vertical	3361	0.18	0.27	972,400	4,511,000	4.64	1.50
	anhydrite	CCU8-1	7645.30	Vertical	3364	0.35	0.29	7,233,000	11,837,000	1.64	0.83
		CCU8-3	7645.75	Horizontal	3899	0.35	0.28	7,603,000	12,071,000	1.59	0.80
	silty dolomite	CCU9-1	7651.60	Vertical	3367	0.17	0.24	2,262,000	6,616,000	2.92	1.41
		CCU9-3	7651.25	Horizontal	3902	0.24	0.22	3,891,000	8,118,000	2.09	0.92
	fractured silty dolomite	CCU10-1	7657.50	Vertical	3369	0.18	0.27	4,290,000	9,246,000	2.16	1.50
		CCU10-5	7657.65	Horizontal	3905	0.33	0.30	6,534,000	11,004,000	1.68	0.91
									Average:	**2.58**	**1.17**

Well ID	Lithology	Sample ID	Depth (ft)	Orientation	Effective Confining Pressure (psi)	Static Poisson's Ratio	Dynamic Poisson's Ratio	Static Young's Modulus (psi)	Dynamic Young's Modulus (psi)	Dynamic/ Static Young's Modulus	Dynamic/ Static Poisson's Ratio
Fidelity Cane Creek 26-3	shale	FDY3-1	7413.00	Vertical	3855	0.23	0.24	706,400	1,836,000	2.60	1.04
		FDY3-2	7413.05	Horizontal	4040	0.25	0.23	1,128,000	2,634,000	2.34	0.92
	shale	FDY2-1	7417.75	Vertical	3857	0.24	0.24	1,119,000	4,019,000	3.59	1.00
		FDY2-2	7417.85	Horizontal	4043	0.30	0.23	2,074,000	5,817,000	2.80	0.77
	shale	FDY1-2	7464.30	Horizontal	4068	0.22	0.21	1,571,000	4,531,000	2.88	0.95
	silty dolomite	FDY1-1	7464.50	Vertical	3882	0.23	0.25	3,276,000	7,925,000	2.42	1.09
		FDY1-4	7464.50	Vertical	3881	0.18	0.25	3,620,000	7,847,000	2.17	1.39
									Average:	**2.69**	**1.02**
Fidelity Cisco St 36-13	dolomite	CSO1-1	7588.80	Vertical	2732	0.19	0.20	1,338,000	5,318,000	3.97	1.05
		CSO1-2	7588.90	Horizontal	3605	0.25	0.23	1,782,000	6,083,000	3.41	0.92
	shale	CSO2-1	7593.00	Vertical	2733	0.22	0.20	1,356,000	3,847,000	2.84	0.91
		CSO2-2	7592.90	Horizontal	3607	0.24	0.21	1,763,000	4,374,000	2.48	0.88
	shale	CSO3-1	7599.75	Vertical	2736	0.17	0.21	1,104,000	5,436,000	4.92	1.24
		CSO3-2	7599.85	Horizontal	3610	0.27	0.24	2,037,000	6,293,000	3.09	0.89
	silty dolomite	CSO4-4	7605.65	Vertical	2738	0.18	0.31	1,282,000	6,546,000	5.11	1.72
		CSO4-2	7605.65	Horizontal	3613	0.25	0.22	1,985,000	6,367,000	3.21	0.88
	silty dolomite	CSO5-1	7615.40	Vertical	2742	0.27	0.18	1,094,000	4,290,000	3.92	0.67
		CSO5-2	7615.25	Horizontal	3617	0.23	0.24	1,755,000	5,812,000	3.31	1.04
	anhydrite	CSO6-1	7627.30	Vertical	2746	0.34	0.30	8,081,000	11,728,000	1.45	0.88
		CSO6-2	7627.10	Horizontal	3623	0.33	0.29	8,780,000	11,965,000	1.36	0.88
									Average:	**3.26**	**1.00**
Bill Barrett 14-3-45	dolomite	UTE3-1	7327.30	Vertical	1319	0.18	0.27	3,196,000	9,070,000	2.84	1.50
		UTE3-2	7327.40	Horizontal	2931	0.30	0.25	8,166,000	10,643,000	1.30	0.83

Well ID	Lithology	Sample ID	Depth (ft)	Orientation	Effective Confining Pressure (psi)	Static Poisson's Ratio	Dynamic Poisson's Ratio	Static Young's Modulus (psi)	Dynamic Young's Modulus (psi)	Dynamic/ Static Young's Modulus	Dynamic/ Static Poisson's Ratio
	shale - finely laminated	UTE2-1	7332.70	Vertical	1320	0.21	0.25	1,411,000	2,955,000	2.09	1.19
		UTE2-2	7332.85	Horizontal	2933	0.27	0.20	3,962,000	6,332,000	1.60	0.74
	shale	UTE1-1	7358.35	Vertical	1325	0.21	0.30	1,428,000	2,959,000	2.07	1.43
		UTE1-2	7358.15	Horizontal	2943	0.26	0.22	3,963,000	6,810,000	1.72	0.85
									Average:	**1.94**	**1.09**
Bill Barrett 14-1-46	tan dolomite	BTR1-6	6684.40	Vertical	1337	0.22	0.27	5,390,000	6,594,000	1.22	1.23
		BTR1-2	6684.70	Horizontal	2741	0.27	0.24	3,829,000	4,701,000	1.23	0.89
	dolomite	BTR2-1	6693.70	Vertical	1339	0.29	0.24	4,861,000	7,303,000	1.50	0.83
		BTR2-2	6693.45	Horizontal	2744	0.29	0.27	7,011,000	9,410,000	1.34	0.93
	grey limestone	BTR3-1	6698.25	Vertical	1340	0.14	0.25	4,038,000	7,579,000	1.88	1.79
		BTR3-2	6699.00	Horizontal	2747	0.32	0.28	8,657,000	9,710,000	1.12	0.88
	tan dolomite	BTR4-4	6703.10	Vertical	1341	0.28	0.22	6,422,000	9,622,000	1.50	0.79
		BTR4-2	6702.90	Horizontal	2748	0.26	0.25	6,223,000	8,324,000	1.34	0.96
	shale	BTR5-4	6706.50	Vertical	1341	0.18	0.15	1,295,000	4,449,000	3.44	0.83
		BTR5-2	6706.65	Horizontal	2750	0.26	0.23	3,797,000	7,740,000	2.04	0.88
									Average:	**1.66**	**1.00**

Triaxial Compression Test Plots – Fidelity Cane Creek CCU7-1

Fidelity Cane Creek CCU7-1									
Lithology	Sample ID	Depth (ft)	Orientation	As Received Bulk Density (g/cm^3)	Confining Pressure (psi)	Peak Effective Compressive Strength (psi)	Effective Residual Compressive Strength (psi)	Young's Modulus (10^6 psi)	Poisson's Ratio
silty dolomite	CCU1-1	7609.35	Vertical	2.624	3348	28,755	20,162	3.447	0.23
	CCU1-3	7609.15	Horizontal	2.599	3881	44,946	24,935	5.507	0.30

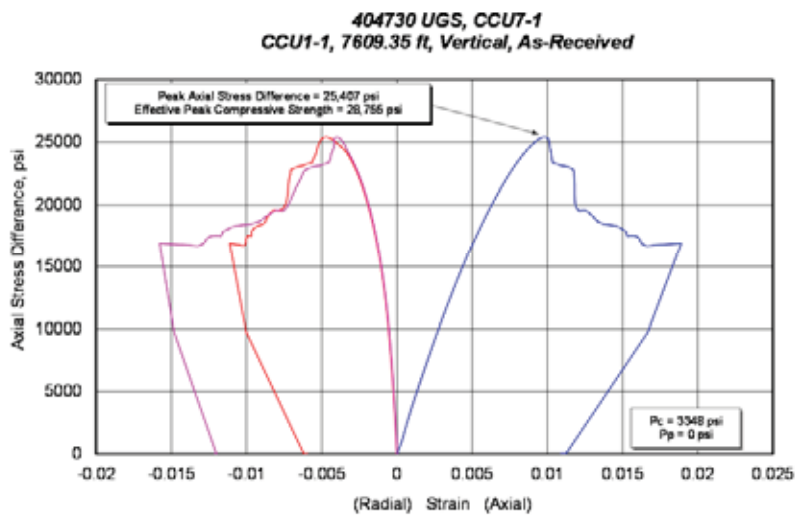

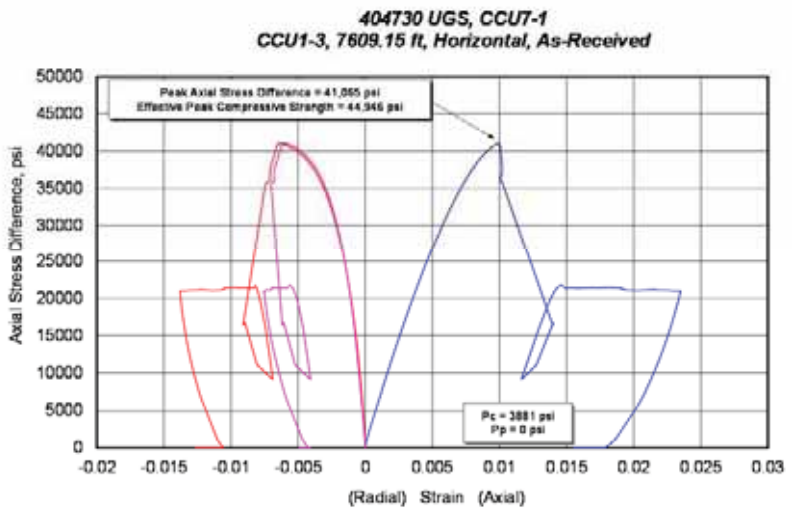

Zone 1 Deformation Index: Ratio of Secant E at Peak to E: 1.36	Zone 1 Deformation Index: Ratio of Secant E at Peak to E: 1.34
Zone 2 Ductility Index: Amount of Plastic or Strain Hardening Strain: 0.006	Zone 2 Ductility Index: Amount of Plastic or Strain Hardening Strain: 0
Zone 3a: Tang and Kaiser Index (Axial): 1.85 J/g	Zone 3a: Tang and Kaiser Index (Axial): 6.54
Zone 3b: Tang and Kaiser Index (Volumetric): 2.42 J/g	Zone 3b: Tang and Kaiser Index (Volumetric): N/A
Zone 4: Peak to Residual Strength Ratio: 1.51	Zone 4: Peak to Residual Strength Ratio: 1.90

Fidelity Cane Creek CCU7-1

Lithology	Sample ID	Depth (ft)	Orientation	As Received Bulk Density (g/cm^3)	Confining Pressure (psi)	Peak Effective Compressive Strength (psi)	Effective Residual Compressive Strength (psi)	Young's Modulus (10^6 psi)	Poisson's Ratio
anhydrite	CCU2-1	7614.00	Vertical	2.886	3350	31,827	19,750	7.383	0.34
	CCU2-3	7614.65	Horizontal	2.954	3883	33,347	21,675	8.060	0.33

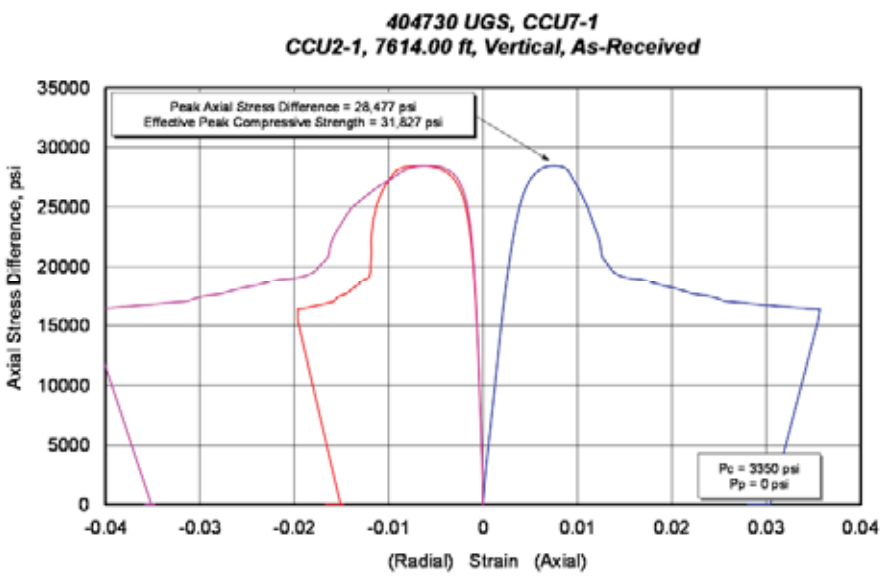

Zone 1 Deformation Index: Ratio of Secant E at Peak to E:
Zone 2 Ductility Index: Amount of Plastic or Strain Hardening Strain:
Zone 3a: Tang and Kaiser Index (Axial):
Zone 3b: Tang and Kaiser Index (Volumetric):
Zone 4: Peak to Residual Strength Ratio:

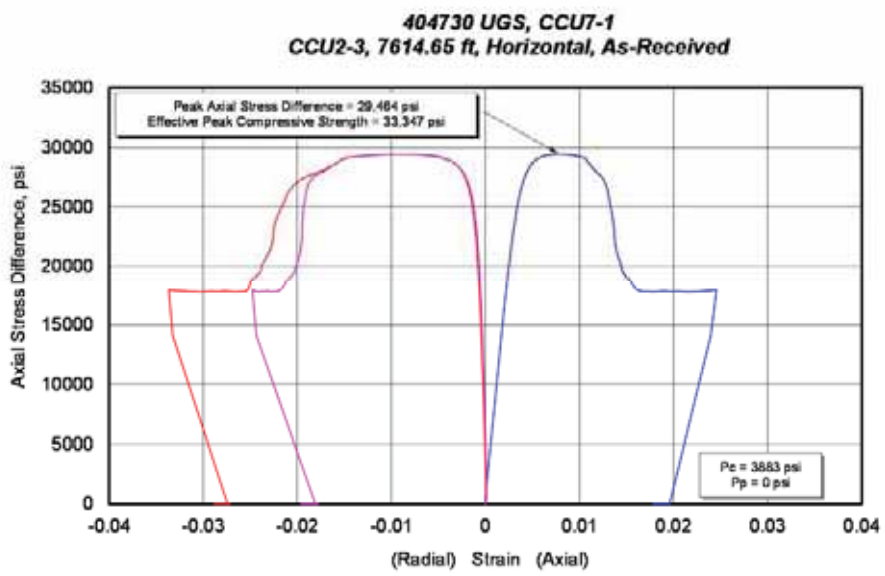

Zone 1 Deformation Index: Ratio of Secant E at Peak to E:
Zone 2 Ductility Index: Amount of Plastic or Strain Hardening Strain:
Zone 3a: Tang and Kaiser Index (Axial):
Zone 3b: Tang and Kaiser Index (Volumetric):
Zone 4: Peak to Residual Strength Ratio:

Fidelity Cane Creek CCU7-1									
Lithology	Sample ID	Depth (ft)	Orientation	As Received Bulk Density (g/cm^3)	Confining Pressure (psi)	Peak Effective Compressive Strength (psi)	Effective Residual Compressive Strength (psi)	Young's Modulus (10^6 psi)	Poisson's Ratio
silty dolomite - shale	CCU3-1	7619.00	Vertical	2.509	3352	18,220	-	1.686	0.28
	CCU3-5	7619.20	Horizontal	2.500	3886	21,688	16,561	2.054	0.24

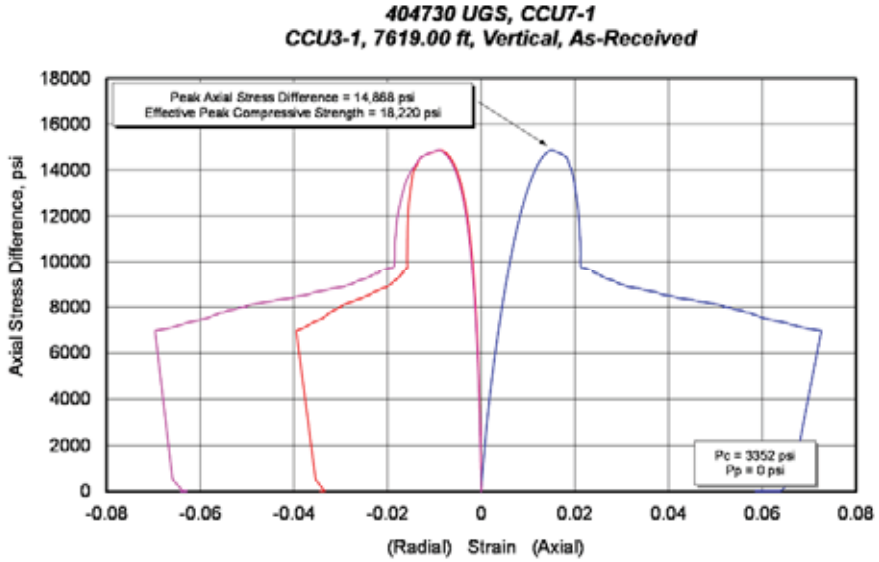

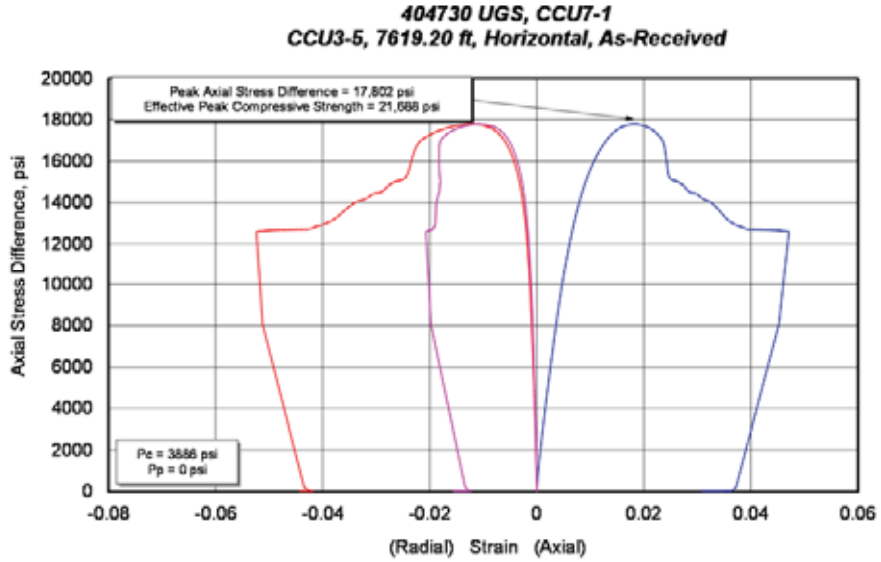

Fidelity Cane Creek CCU7-1

Lithology	Sample ID	Depth (ft)	Orientation	As Received Bulk Density (g/cm^3)	Confining Pressure (psi)	Peak Effective Compressive Strength (psi)	Effective Residual Compressive Strength (psi)	Young's Modulus (10^6 psi)	Poisson's Ratio
shale	CCU4-1	7620.80	Vertical	2.487	3353	13,814	-	0.820	0.15
	CCU4-5	7620.30	Horizontal	2.514	3886	18,825	14,071	1.118	0.24

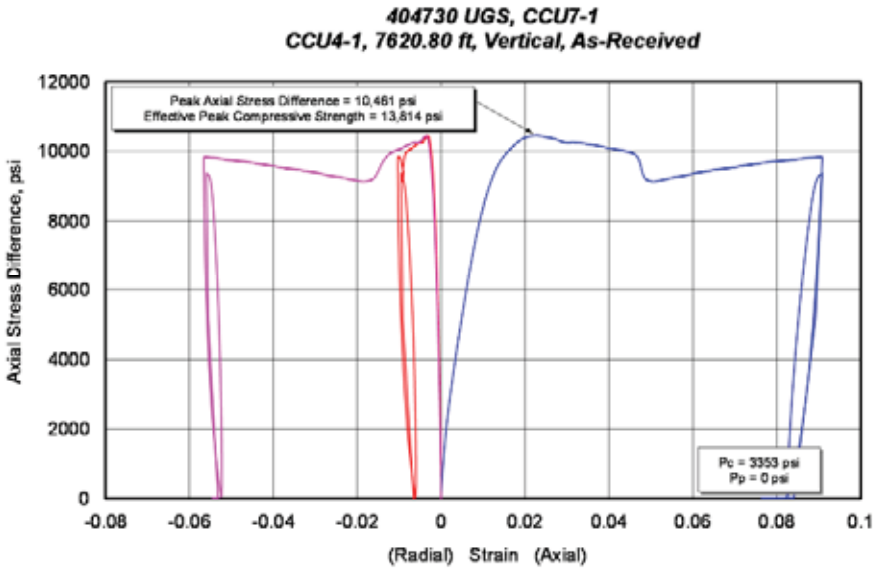

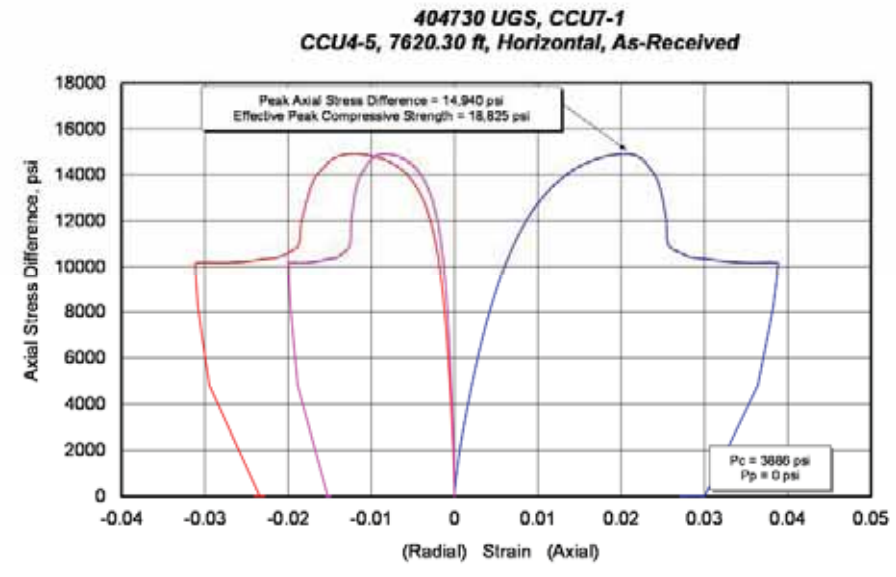

Fidelity Cane Creek CCU7-1

Lithology	Sample ID	Depth (ft)	Orientation	As Received Bulk Density (g/cm^3)	Confining Pressure (psi)	Peak Effective Compressive Strength (psi)	Effective Residual Compressive Strength (psi)	Young's Modulus (10^6 psi)	Poisson's Ratio
silty dolomite	CCU5-1	7624.65	Vertical	2.597	3355	20,803	11,732	2.696	0.13
	CCU5-3	7624.90	Horizontal	2.591	3886	33,942	20,104	4.517	0.25

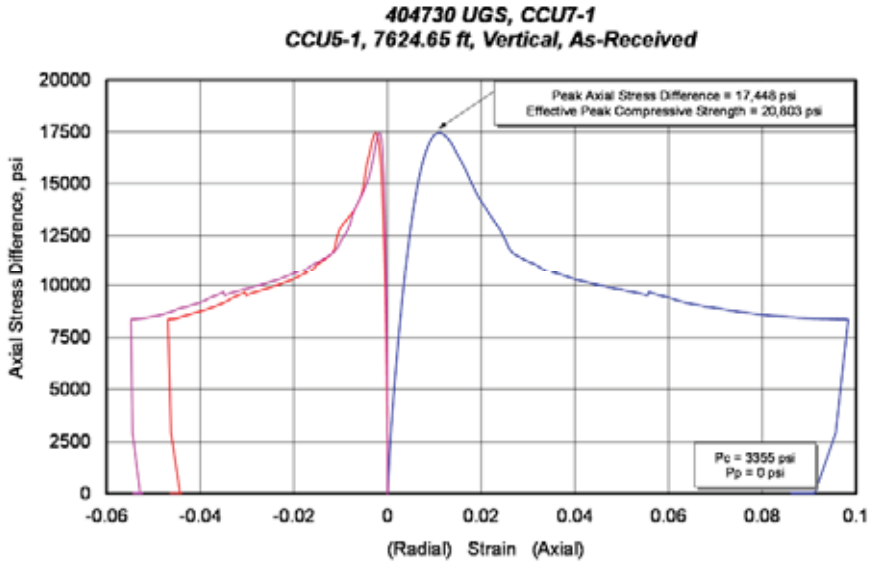

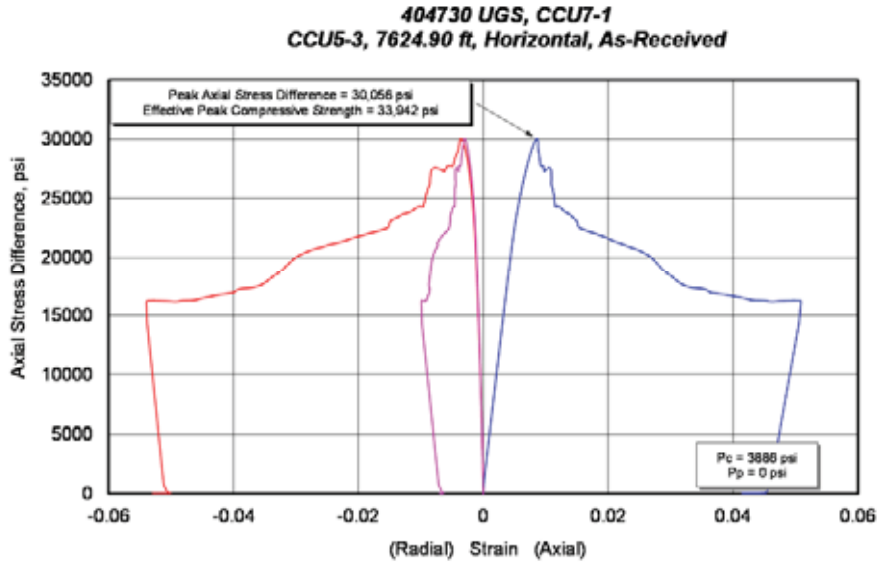

Fidelity Cane Creek CCU7-1

Lithology	Sample ID	Depth (ft)	Orientation	As Received Bulk Density (g/cm^3)	Confining Pressure (psi)	Peak Effective Compressive Strength (psi)	Effective Residual Compressive Strength (psi)	Young's Modulus (10^6 psi)	Poisson's Ratio
silty dolomite	CCU6-1	7630.25	Vertical	2.504	3357	15,416	-	1.5060	0.24
	CCU6-3	7630.60	Horizontal	2.530	3892	20,564	17,198	2.774	0.15

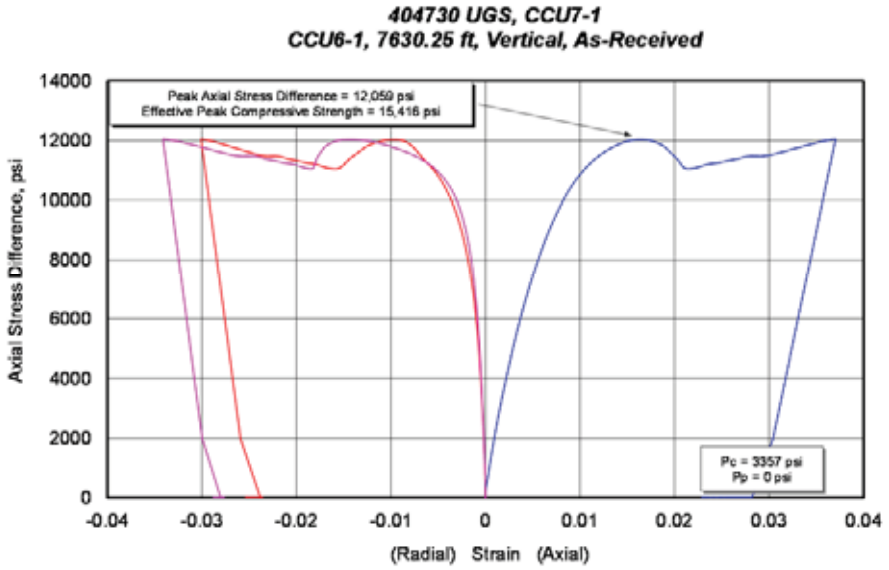

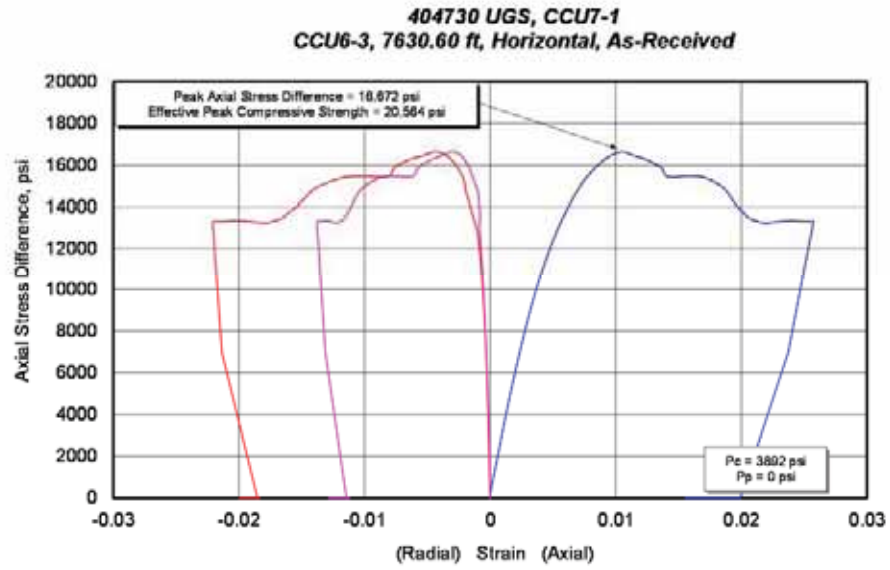

Fidelity Cane Creek CCU7-1									
Lithology	Sample ID	Depth (ft)	Orientation	As Received Bulk Density (g/cm^3)	Confining Pressure (psi)	Peak Effective Compressive Strength (psi)	Effective Residual Compressive Strength (psi)	Young's Modulus (10^6 psi)	Poisson's Ratio
shale	CCU7-1[17]	7638.30	Vertical	2.458	3361	14,945	14,459	0.972	0.18

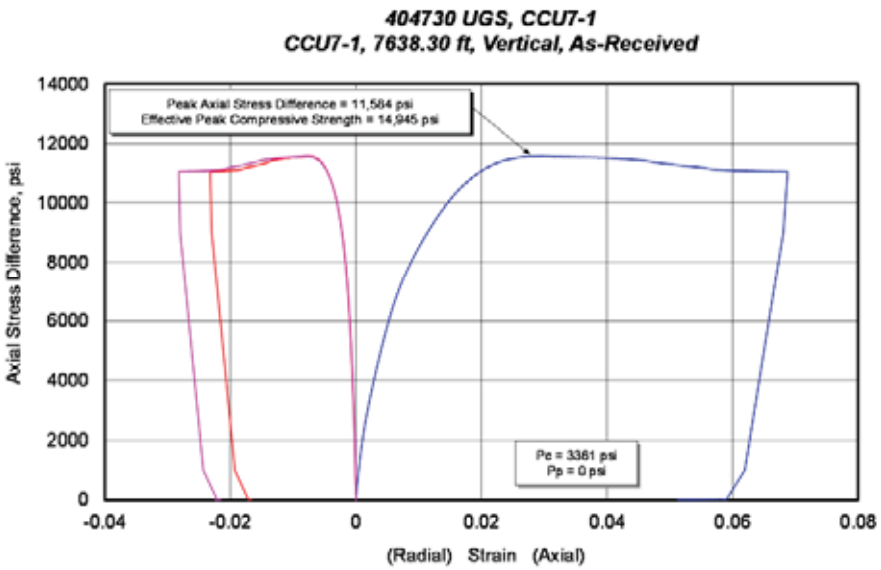

[17] CCU7-1 – Not enough material available to obtain additional samples, thus, no horizontally oriented sample was tested

Fidelity Cane Creek CCU7-1									
Lithology	Sample ID	Depth (ft)	Orientation	As Received Bulk Density (g/cm^3)	Confining Pressure (psi)	Peak Effective Compressive Strength (psi)	Effective Residual Compressive Strength (psi)	Young's Modulus (10^6 psi)	Poisson's Ratio
anhydrite	CCU8-1	7645.30	Vertical	2.940	3364	28,267	-	7.233	0.35
	CCU8-3	7645.75	Horizontal	2.931	3899	30,497	-	7.603	0.35

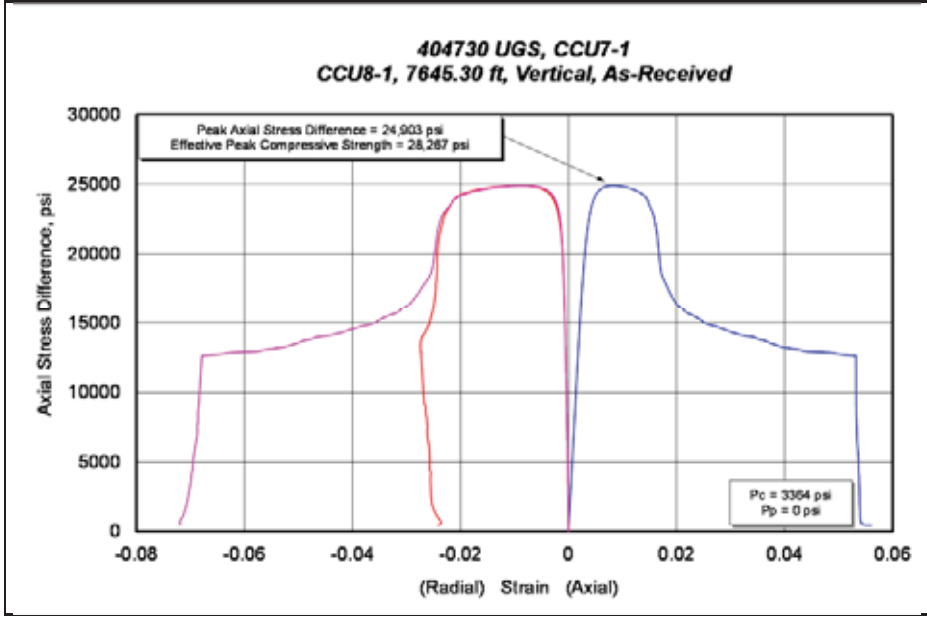

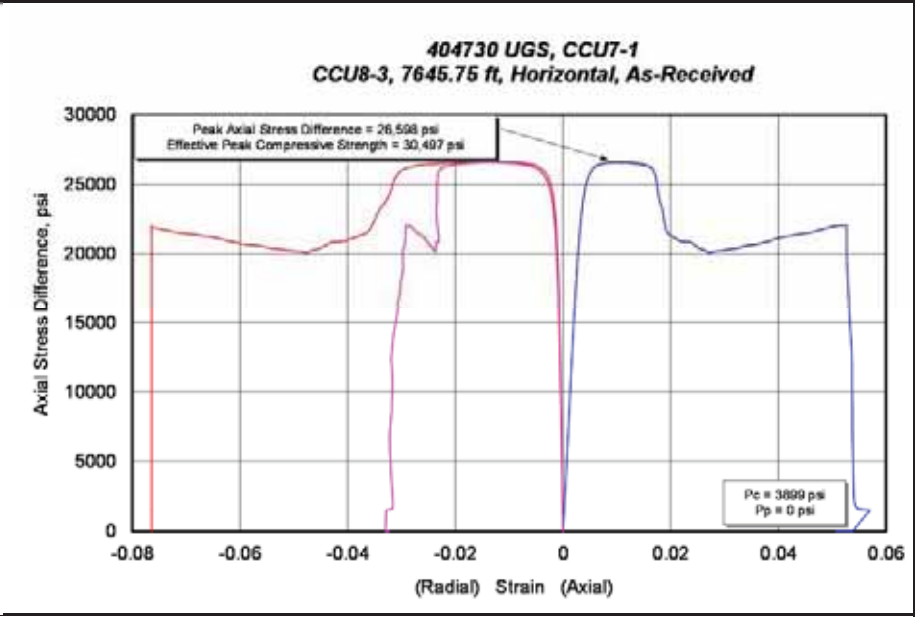

Fidelity Cane Creek CCU7-1									
Lithology	Sample ID	Depth (ft)	Orientation	As Received Bulk Density (g/cm^3)	Confining Pressure (psi)	Peak Effective Compressive Strength (psi)	Effective Residual Compressive Strength (psi)	Young's Modulus (10^6 psi)	Poisson's Ratio
silty dolomite	CCU9-1	7651.60	Vertical	2.577	3367	21,372	14,963	3.891	0.17
	CCU9-3	7651.25	Horizontal	2.582	3902	29,687	16,128	3,891,000	0.24

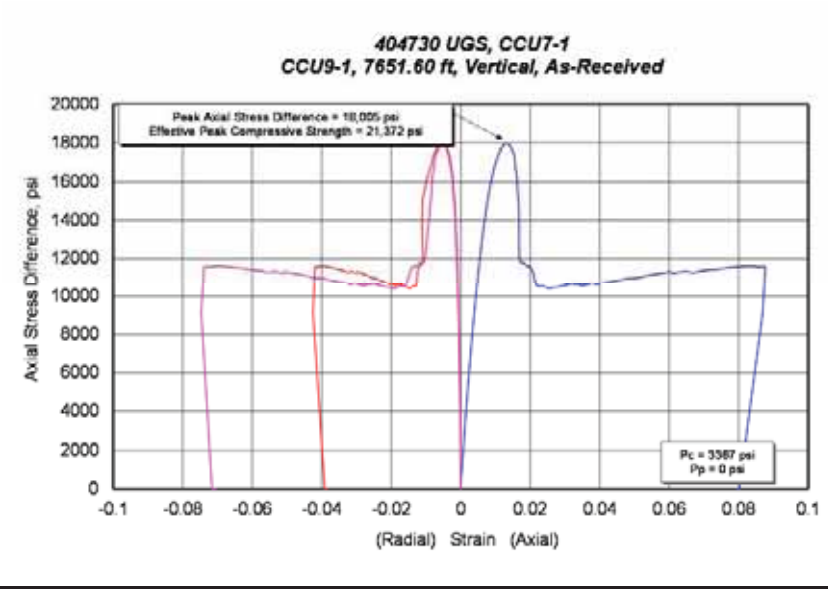

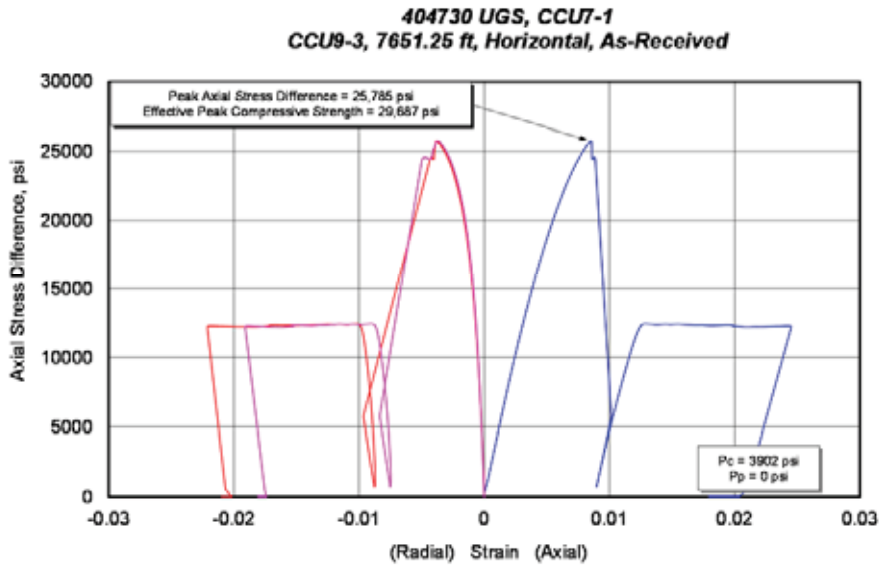

Fidelity Cane Creek CCU7-1

Lithology	Sample ID	Depth (ft)	Orientation	As Received Bulk Density (g/cm^3)	Confining Pressure (psi)	Peak Effective Compressive Strength (psi)	Effective Residual Compressive Strength (psi)	Young's Modulus (10^6 psi)	Poisson's Ratio
fractured silty dolomite	CCU10-1	7657.50	Vertical	2.678	3369	29,259	-	4.290	0.18
	CCU10-5	7657.65	Horizontal	2.696	3905	39,972	20,882	6.534	0.33

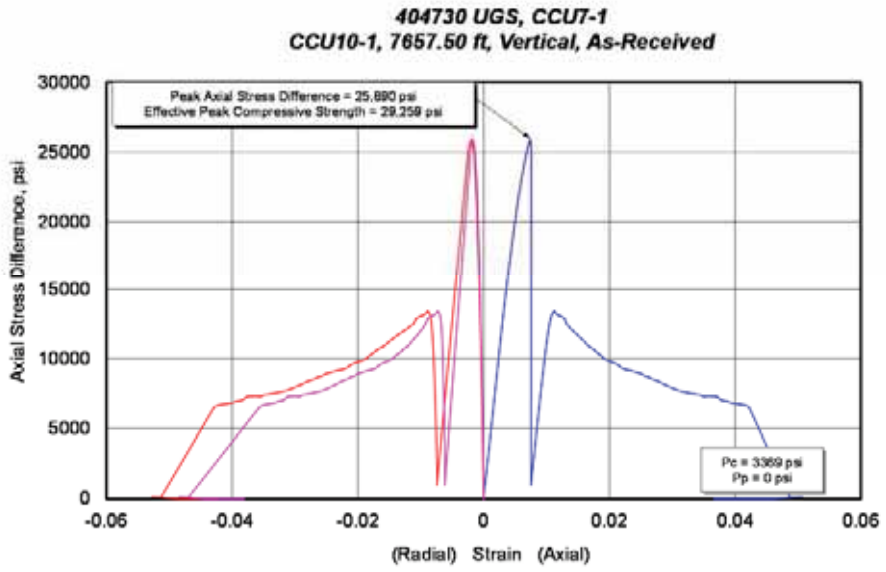

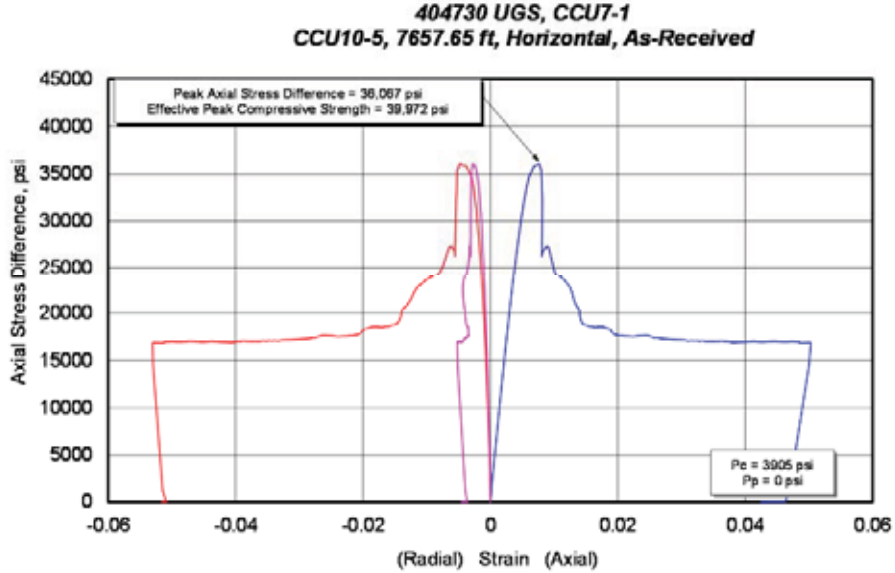

Fidelity Cane Creek 26-31									
Lithology	Sample ID	Depth (ft)	Orientation	As Received Bulk Density (g/cm^3)	Confining Pressure (psi)	Peak Effective Compressive Strength (psi)	Effective Residual Compressive Strength (psi)	Young's Modulus (10^6 psi)	Poisson's Ratio
shale	FDY3-1	7413.00	Vertical	2.041	3855	11,586 (Y)	-	0.706	0.23
	FDY3-2	7413.05	Horizontal	2.009	4040	11,716 (Y)[18] 14,254	-	1.128	0.25

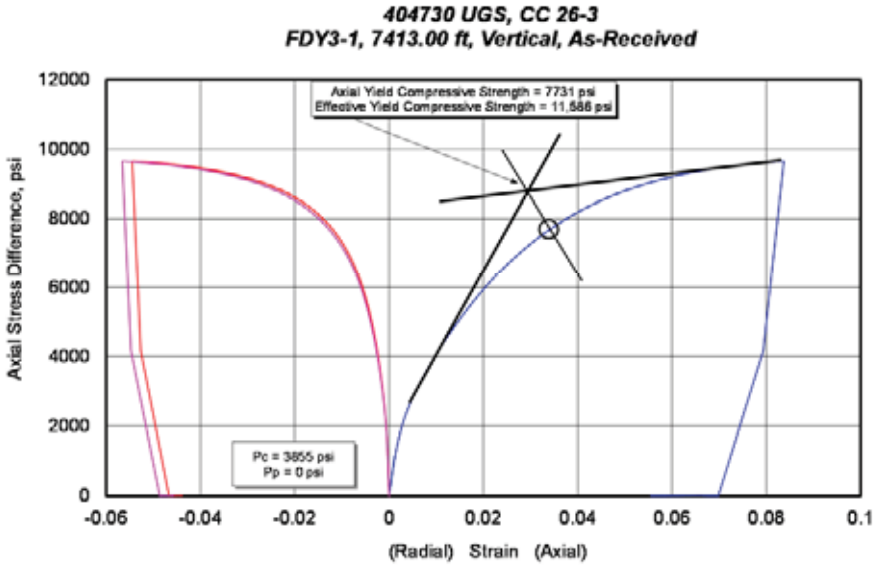

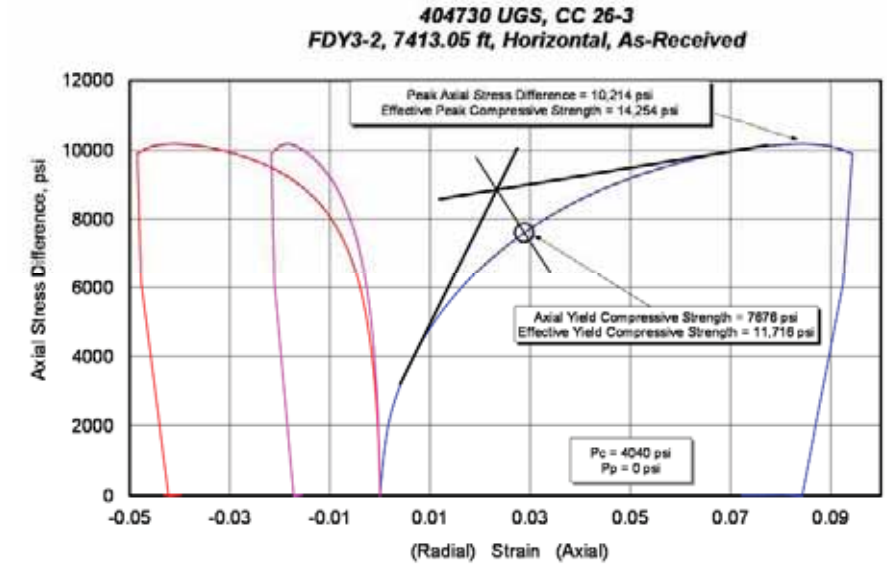

[18] (Y) denotes axial yield

Fidelity Cane Creek 26-31

Lithology	Sample ID	Depth (ft)	Orientation	As Received Bulk Density (g/cm^3)	Confining Pressure (psi)	Peak Effective Compressive Strength (psi)	Effective Residual Compressive Strength (psi)	Young's Modulus (10^6 psi)	Poisson's Ratio
shale	FDY2-1	7417.75	Vertical	2.407	3857	18,534	14,557	1.119	0.24
	FDY2-2	7417.85	Horizontal	2.406	4043	20,699	15,143	2.074	0.30

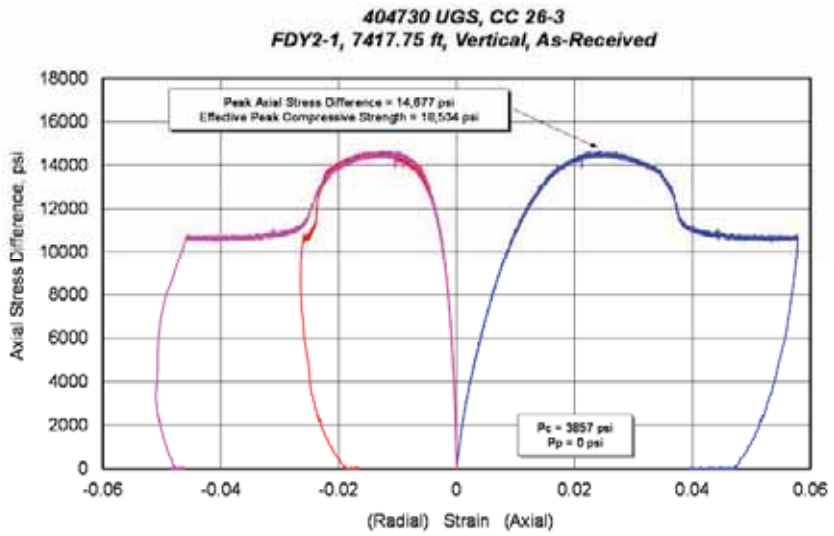

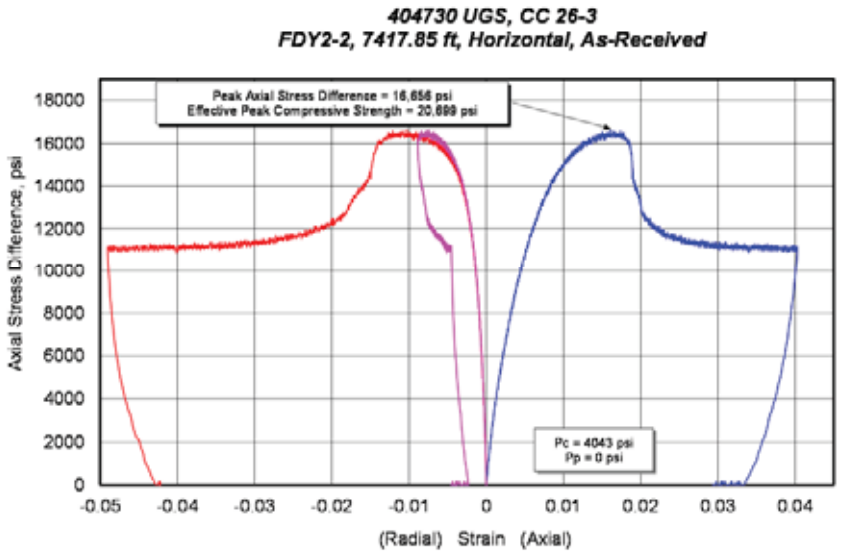

Fidelity Cane Creek 26-31									
Lithology	Sample ID	Depth (ft)	Orientation	As Received Bulk Density (g/cm^3)	Confining Pressure (psi)	Peak Effective Compressive Strength (psi)	Effective Residual Compressive Strength (psi)	Young's Modulus (10^6 psi)	Poisson's Ratio
shale	FDY1-2 [19]	7464.30	Horizontal	2.310	4068	17,700	14,498	1.571	0.22

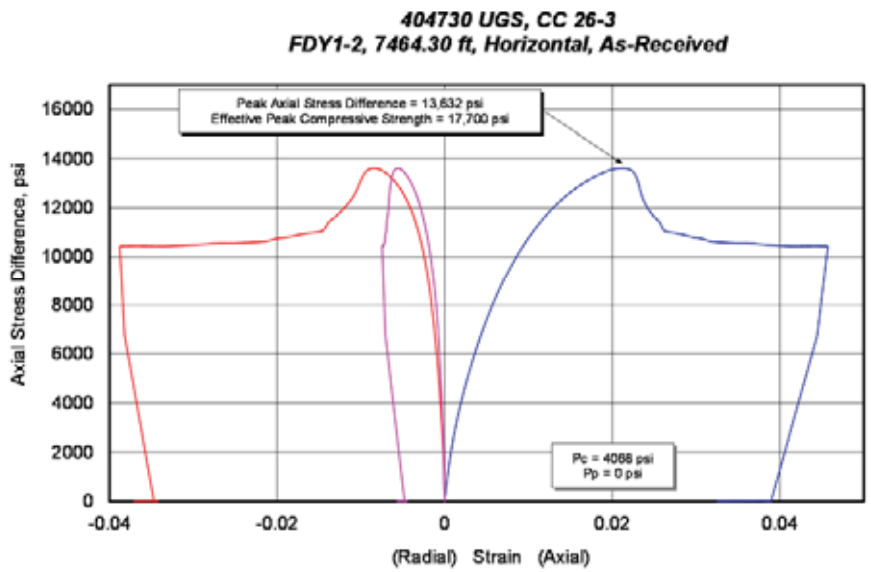

[19] FDY1-2 – No additional shale material remains for a matching horizontal sample, from this backup shale depth interval.

Fidelity Cane Creek 26-31									
Lithology	Sample ID	Depth (ft)	Orientation	As Received Bulk Density (g/cm^3)	Confining Pressure (psi)	Peak Effective Compressive Strength (psi)	Effective Residual Compressive Strength (psi)	Young's Modulus (10^6 psi)	Poisson's Ratio
silty dolomite	FDY1-1 [20]	7464.50	Vertical	2.617	3882	36,702	16,682	3.276	0.23
	FDY1-4	7464.50	Vertical	2.611	3881	35,955	16,935	3.620	0.18

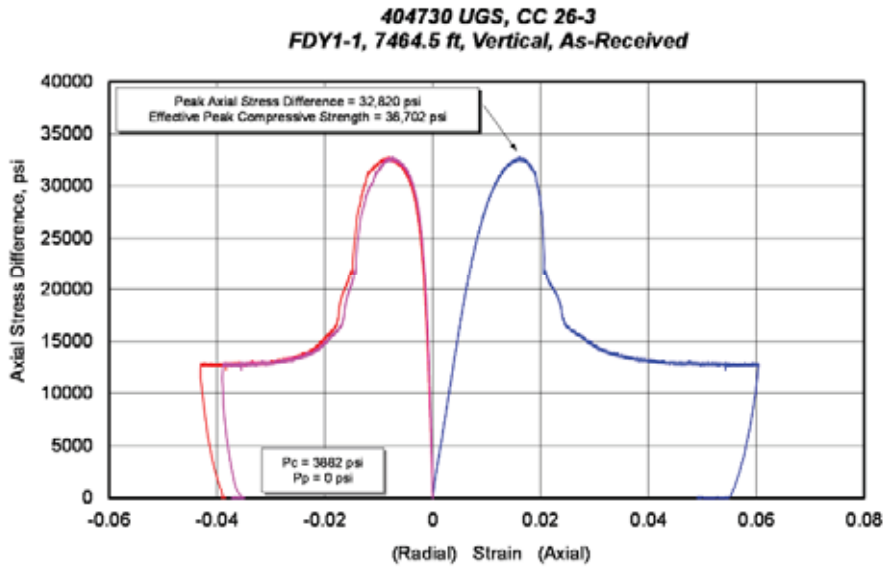

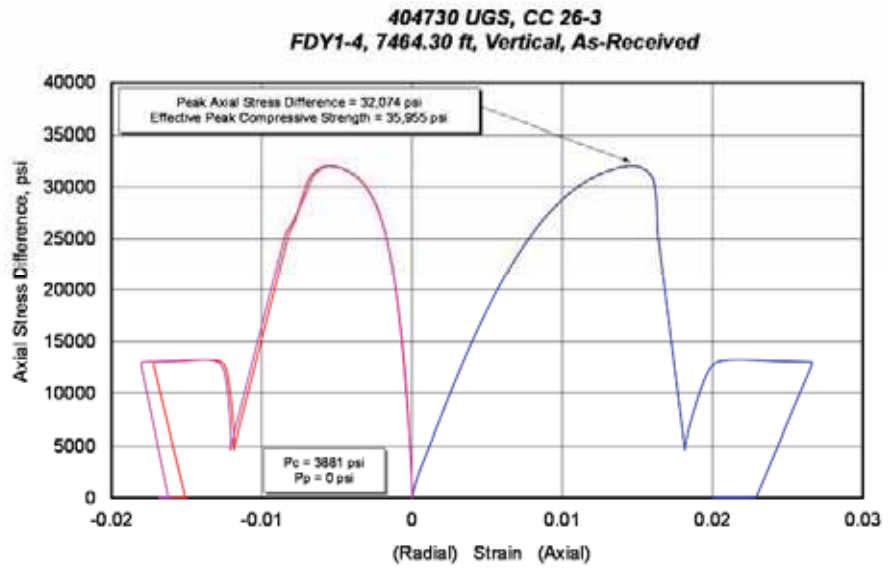

[20] FDY1-1 – No additional silty dolomite material for a matching horizontal sample. Sample FDY1-4 tested as accident, originally marked with an incorrect depth.

Fidelity Cisco State 36-13

Lithology	Sample ID	Depth (ft)	Orientation	As Received Bulk Density (g/cm^3)	Confining Pressure (psi)	Peak Effective Compressive Strength (psi)	Effective Residual Compressive Strength (psi)	Young's Modulus (10^6 psi)	Poisson's Ratio
dolomite	CSO1-1	7588.80	Vertical	2.512	2732	18,014	11,332	1.338	0.19
	CSO1-2	7588.90	Horizontal	2.503	3605	19,081	14,105	1.782	0.25

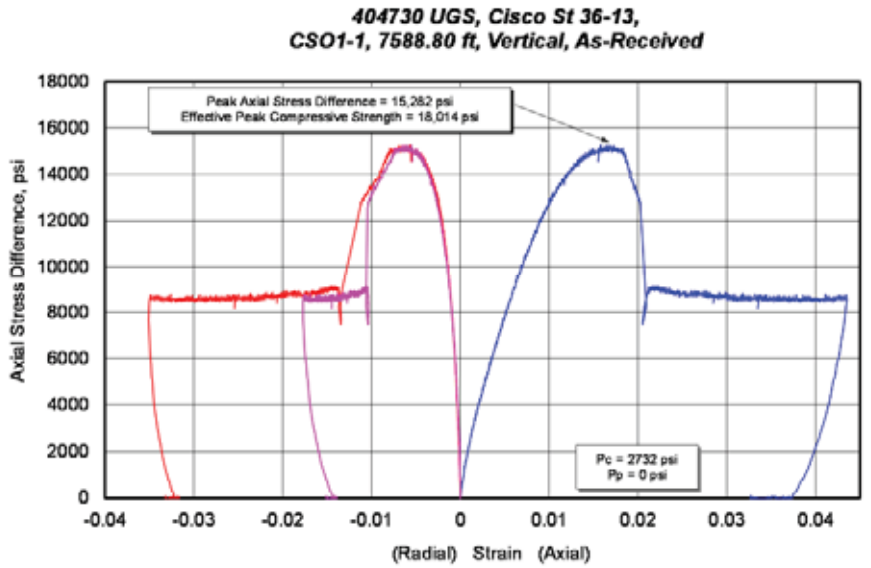

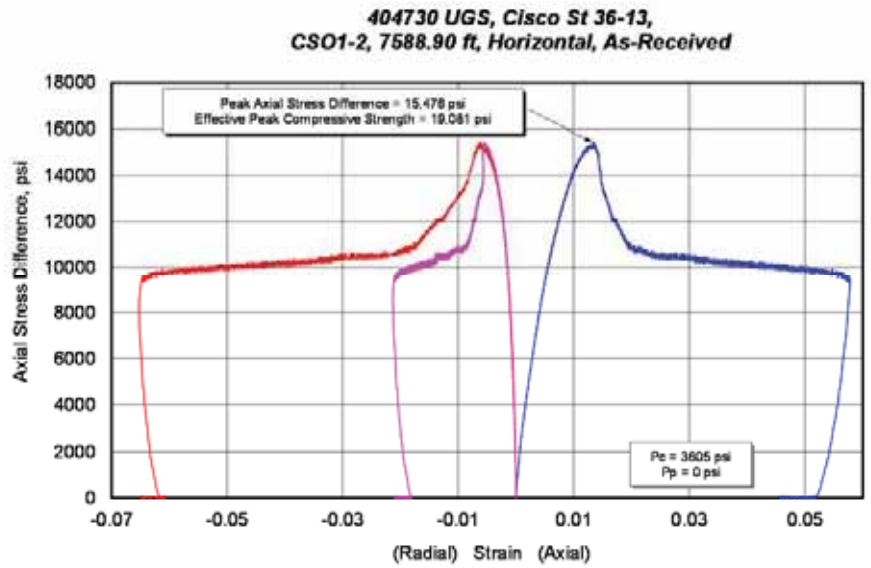

Fidelity Cisco State 36-13

Lithology	Sample ID	Depth (ft)	Orientation	As Received Bulk Density (g/cm^3)	Confining Pressure (psi)	Peak Effective Compressive Strength (psi)	Effective Residual Compressive Strength (psi)	Young's Modulus (10^6 psi)	Poisson's Ratio
shale	CSO2-1	7593.00	Vertical	2.327	2733	12,833	11,298	1.356	0.22
	CSO2-2	7592.90	Horizontal	2.364	3607	15,912	14,647	1.763	0.24

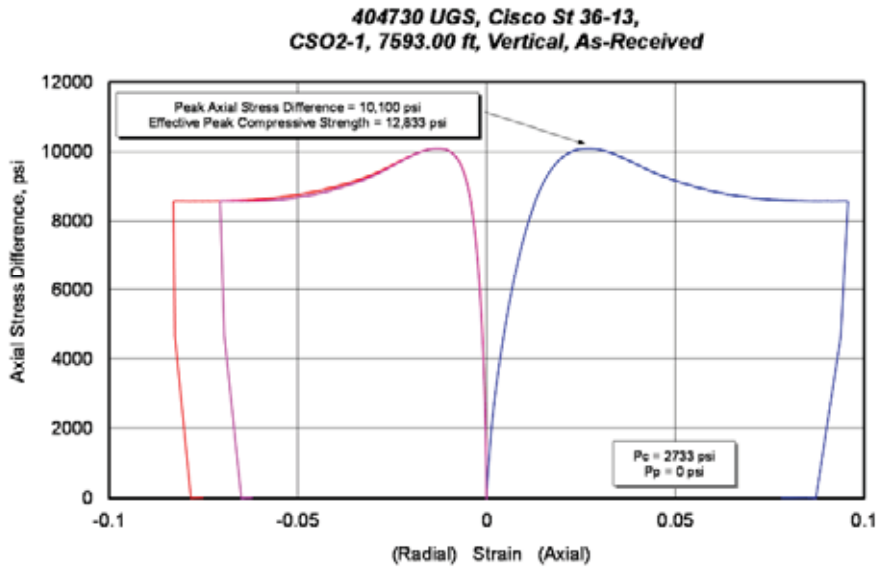

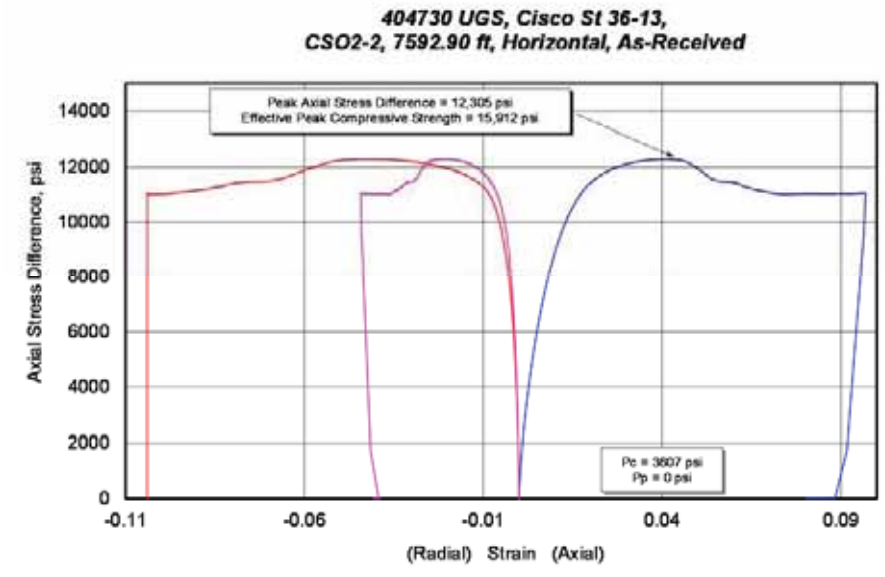

Fidelity Cisco State 36-13

Lithology	Sample ID	Depth (ft)	Orientation	As Received Bulk Density (g/cm^3)	Confining Pressure (psi)	Peak Effective Compressive Strength (psi)	Effective Residual Compressive Strength (psi)	Young's Modulus (10^6 psi)	Poisson's Ratio
shale	CSO3-1	7599.75	Vertical	2.582	2736	19,880	14,736	1.104	0.17
	CSO3-2	7599.85	Horizontal	2.537	3610	23,329	19,880	2.037	0.27

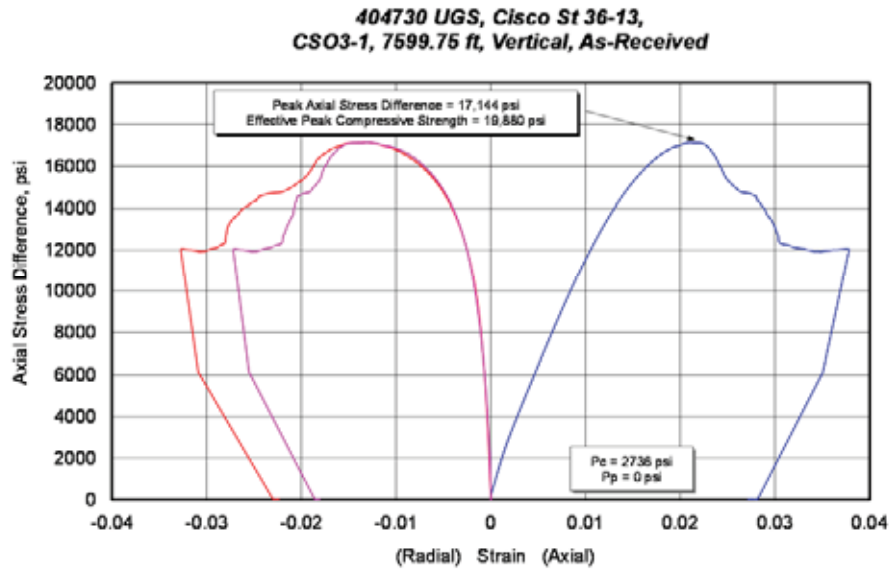

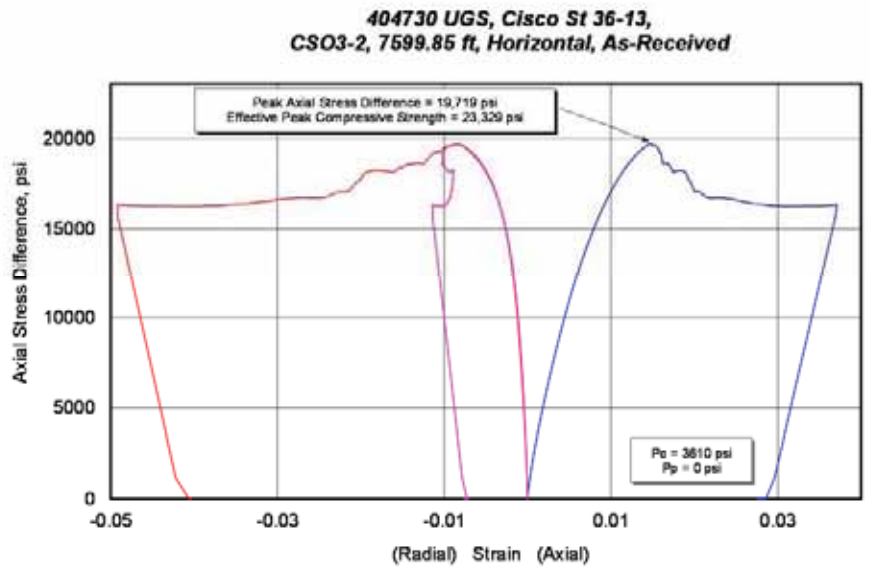

Fidelity Cisco State 36-13

Lithology	Sample ID	Depth (ft)	Orientation	As Received Bulk Density (g/cm^3)	Confining Pressure (psi)	Peak Effective Compressive Strength (psi)	Effective Residual Compressive Strength (psi)	Young's Modulus (10^6 psi)	Poisson's Ratio
silty dolomite	CSO4-1	7605.35	Vertical	2.636	2738	35340	20120	5.071	
	CSO4-4	7605.65	Vertical	2.564	2738	19,646	13,002	1.282	0.18
	CSO4-2	7605.65	Horizontal	2.534	3613	22,643	17,113	1.985	0.25

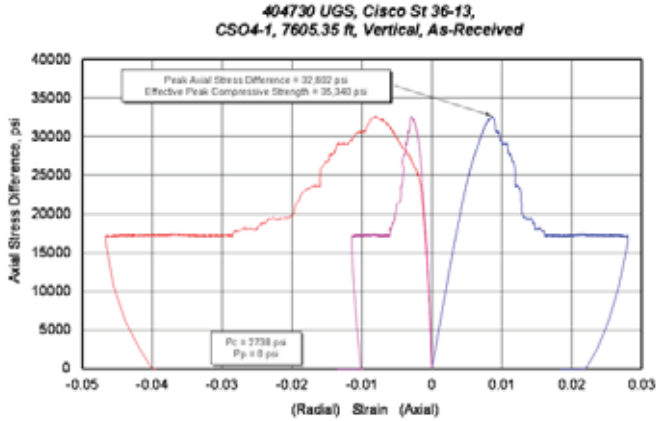

Not reported

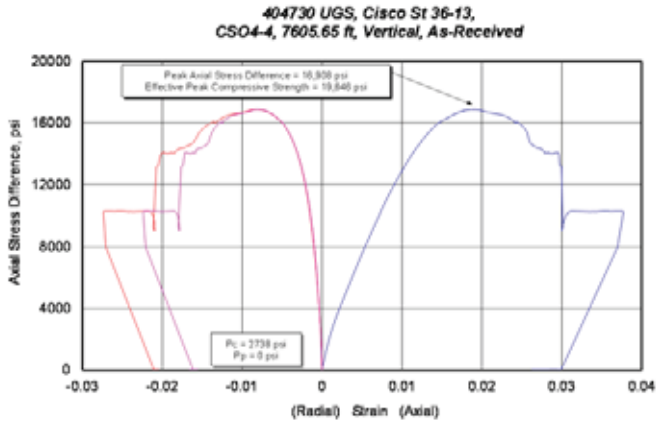

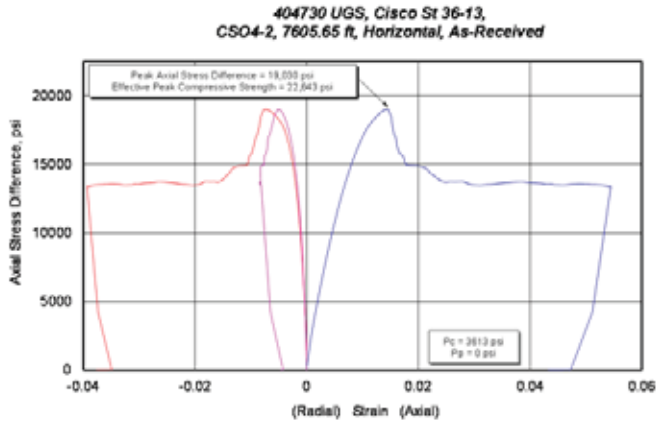

Fidelity Cisco State 36-13

Lithology	Sample ID	Depth (ft)	Orientation	As Received Bulk Density (g/cm^3)	Confining Pressure (psi)	Peak Effective Compressive Strength (psi)	Effective Residual Compressive Strength (psi)	Young's Modulus (10^6 psi)	Poisson's Ratio
silty dolomite	CSO5-1	7615.40	Vertical	2.464	2742	14,412	12,942	1.094	0.27
	CSO5-2	7615.25	Horizontal	2.511	3617	19,097	17,017	1.755	0.23

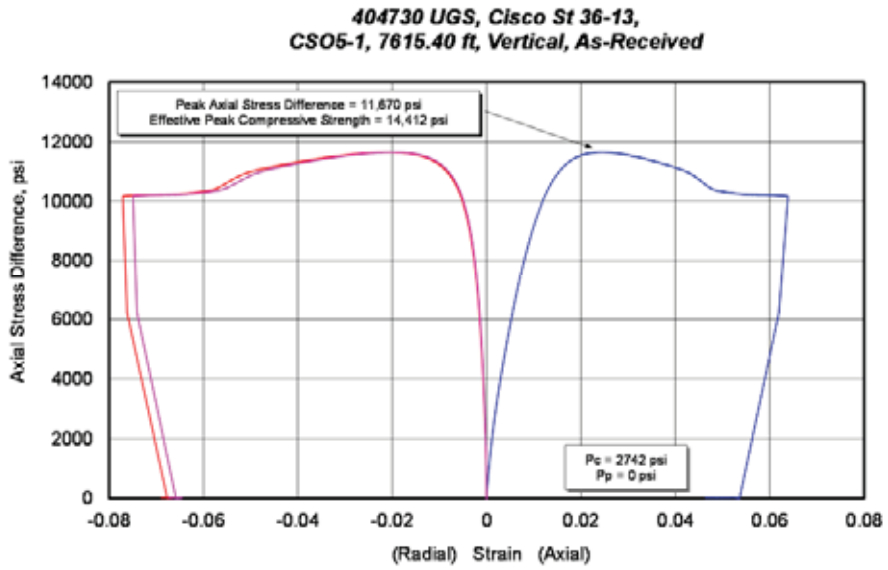

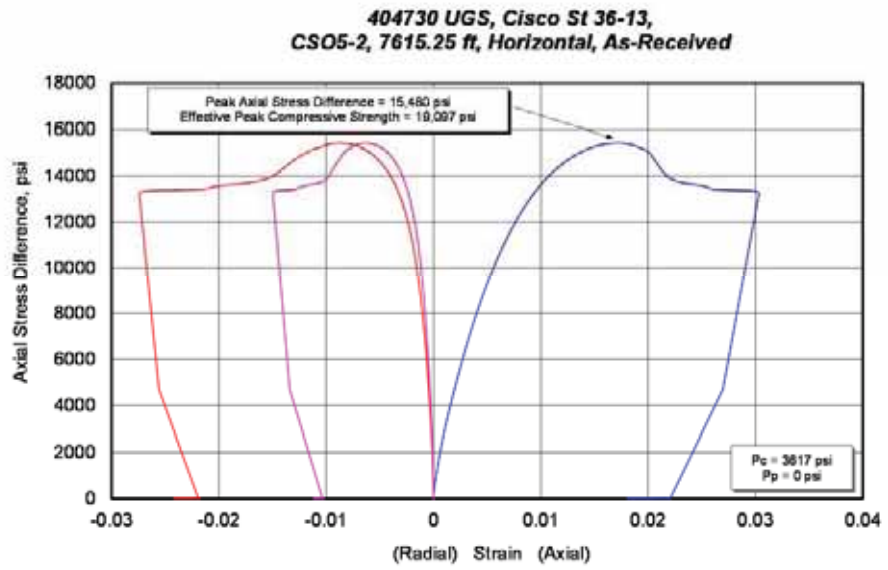

Fidelity Cisco State 36-13

Lithology	Sample ID	Depth (ft)	Orientation	As Received Bulk Density (g/cm^3)	Confining Pressure (psi)	Peak Effective Compressive Strength (psi)	Effective Residual Compressive Strength (psi)	Young's Modulus (10^6 psi)	Poisson's Ratio
anhydrite	CSO6-1	7627.30	Vertical	2.944	2746	23,662	16,346	8.081	0.34
	CSO6-2	7627.10	Horizontal	2.937	3623	28,796	19,423	8.780	0.33

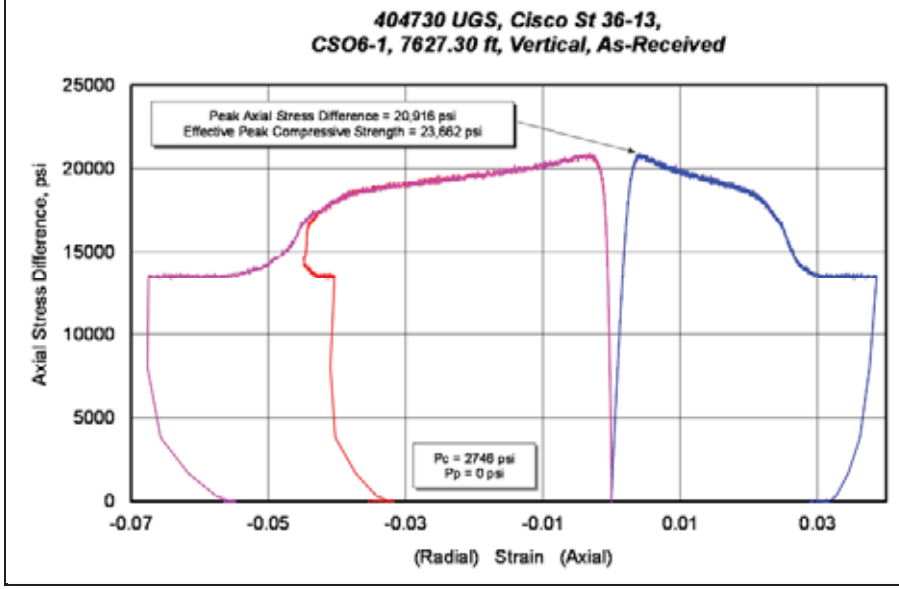

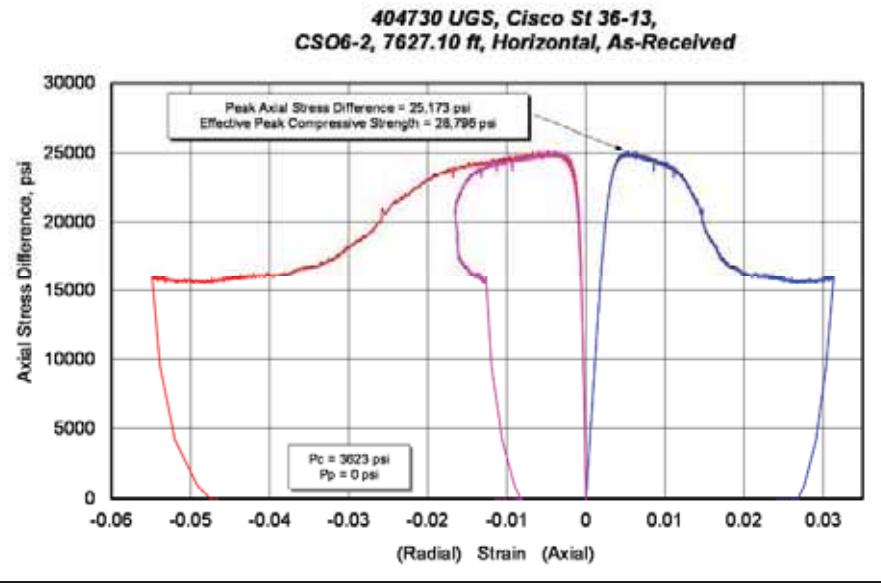

Bill Barrett 14-3-35

Lithology	Sample ID	Depth (ft)	Orientation	As Received Bulk Density (g/cm^3)	Confining Pressure (psi)	Peak Effective Compressive Strength (psi)	Effective Residual Compressive Strength (psi)	Young's Modulus (10^6 psi)	Poisson's Ratio
dolomite	UTE3-1	7327.30	Vertical	2.645	1319	27330	12200	3.196	0.18
	UTE3-2	7327.40	Horizontal	2.655	2931	52280	19630	8.166	0.30

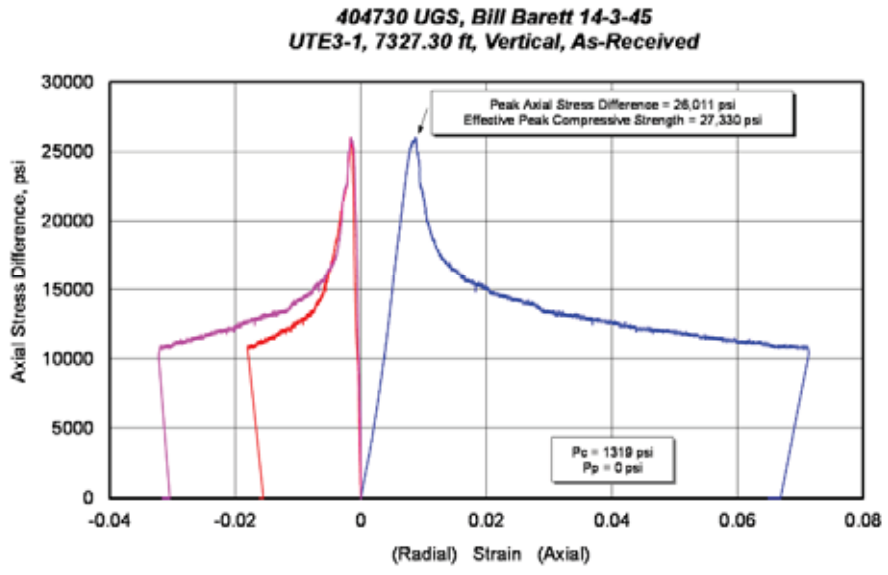

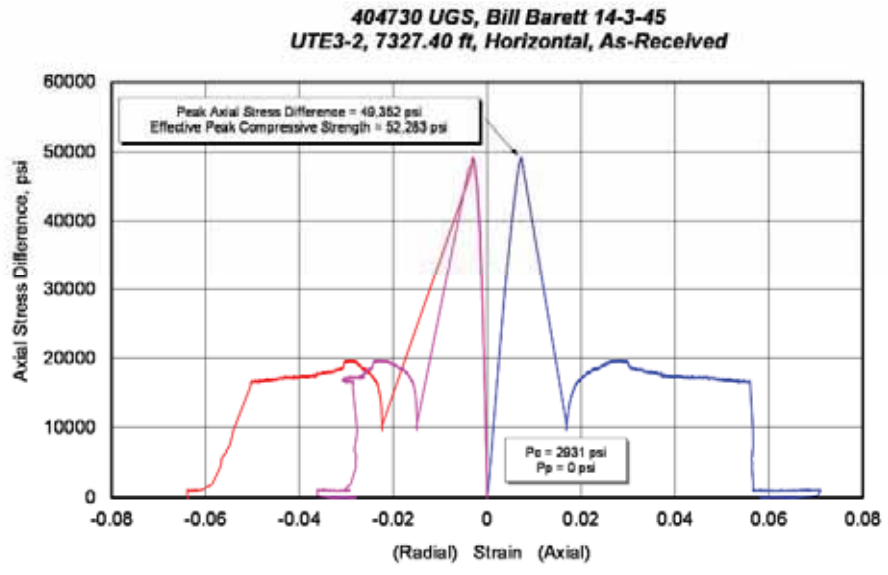

Bill Barrett 14-3-35

Lithology	Sample ID	Depth (ft)	Orientation	As Received Bulk Density (g/cm^3)	Confining Pressure (psi)	Peak Effective Compressive Strength (psi)	Effective Residual Compressive Strength (psi)	Young's Modulus (10^6 psi)	Poisson's Ratio
shale-finely laminated	UTE2-1	7332.70	Vertical	2.382	1320	15350	5400	1.411	0.21
	UTE2-2	7332.85	Horizontal	2.342	2933	21240	12430	3.962	0.27

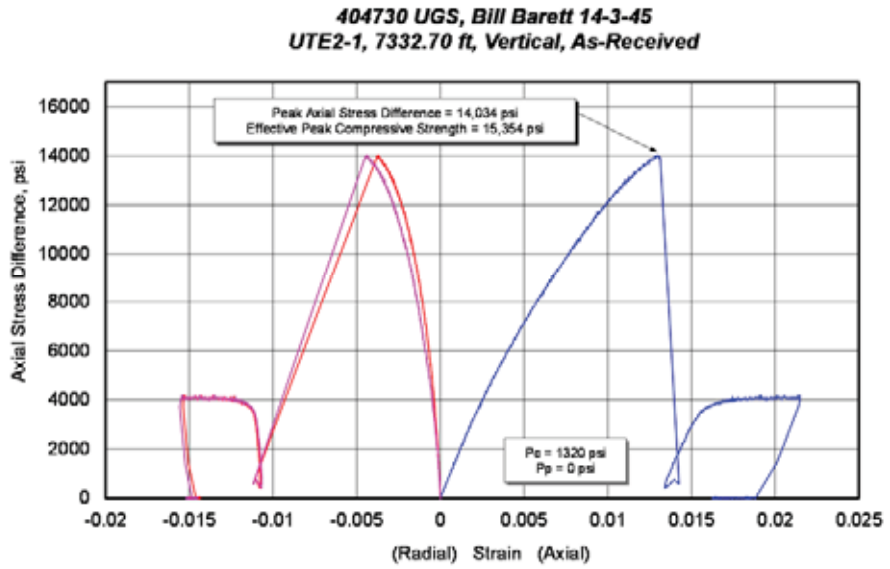

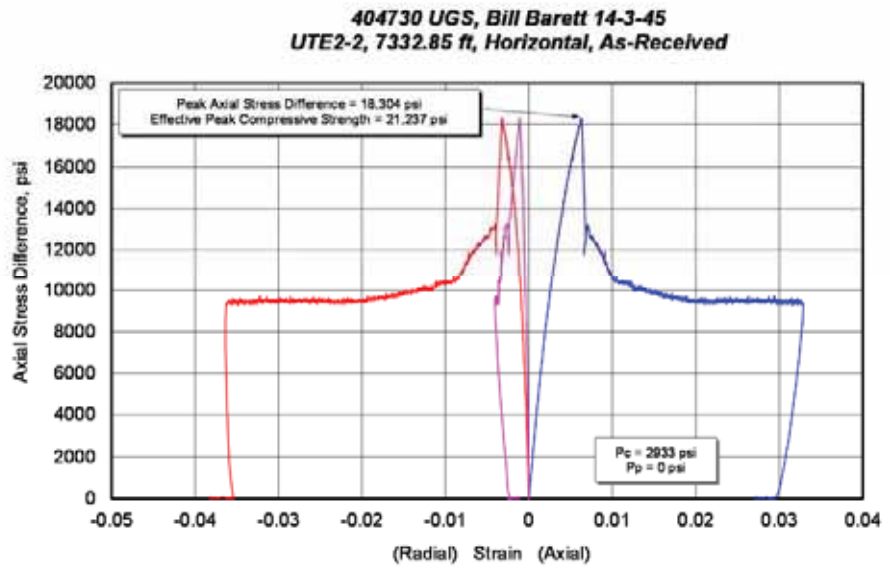

Bill Barrett 14-3-35									
Lithology	Sample ID	Depth (ft)	Orientation	As Received Bulk Density (g/cm^3)	Confining Pressure (psi)	Peak Effective Compressive Strength (psi)	Effective Residual Compressive Strength (psi)	Young's Modulus (10^6 psi)	Poisson's Ratio
shale	UTE1-1[21]	7358.35	Vertical	2.439	1325	9700	5510	1.428	0.21
	UTE1-2	7358.15	Horizontal	2.584	2943	22040	14640	3.963	0.26

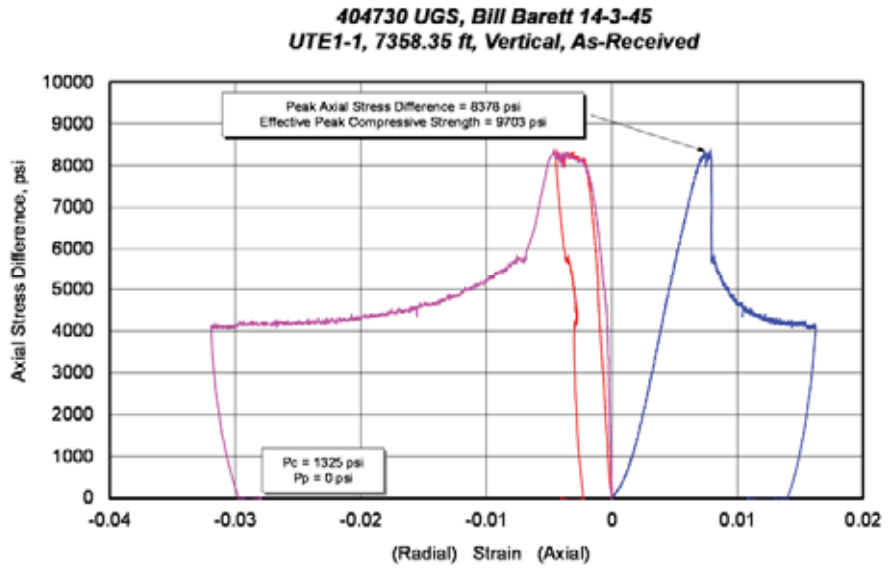

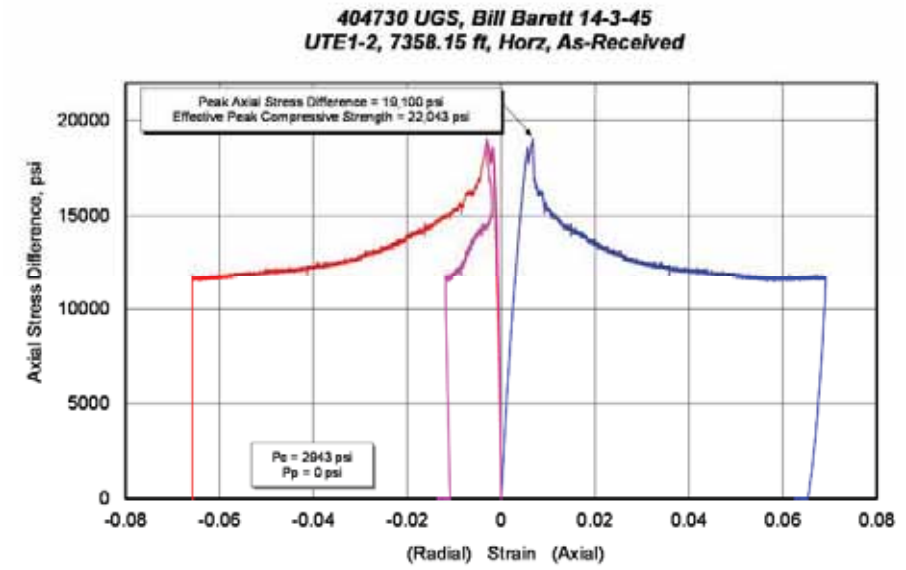

[21] Note density difference between UTE 1-1 and UTE 1-2. No additional material available.

Bill Barrett 14-1-46

Lithology	Sample ID	Depth (ft)	Orientation	As Received Bulk Density (g/cm^3)	Confining Pressure (psi)	Peak Effective Compressive Strength (psi)	Effective Residual Compressive Strength (psi)	Young's Modulus (10^6 psi)	Poisson's Ratio
tan dolomite	BTR1-1	6684.40	Vertical	2.282	1337	19420	9580		
	BTR1-6	6684.40	Vertical	2.348	1337	22190	10410	5.390	0.22
	BTR1-2	6684.780	Horizontal	2.140	2741	19740	13240	3.829	0.27

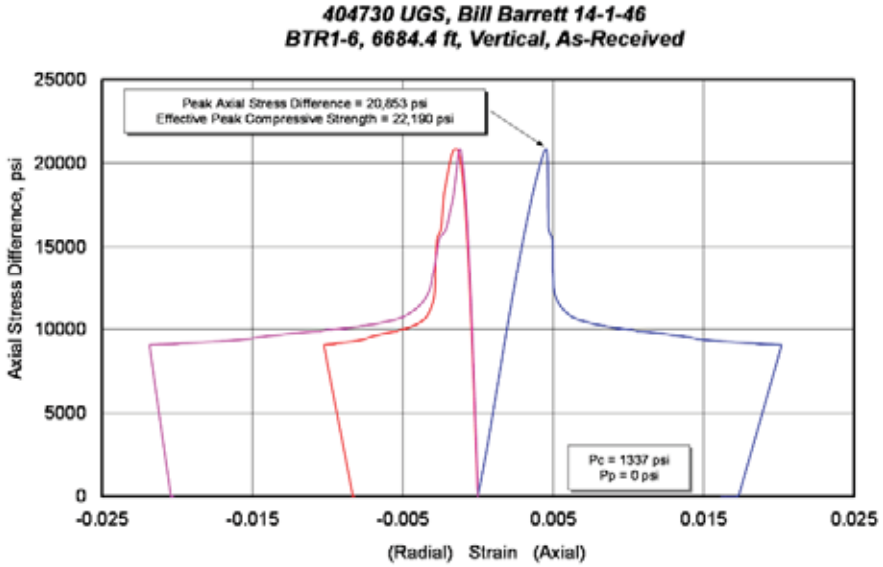

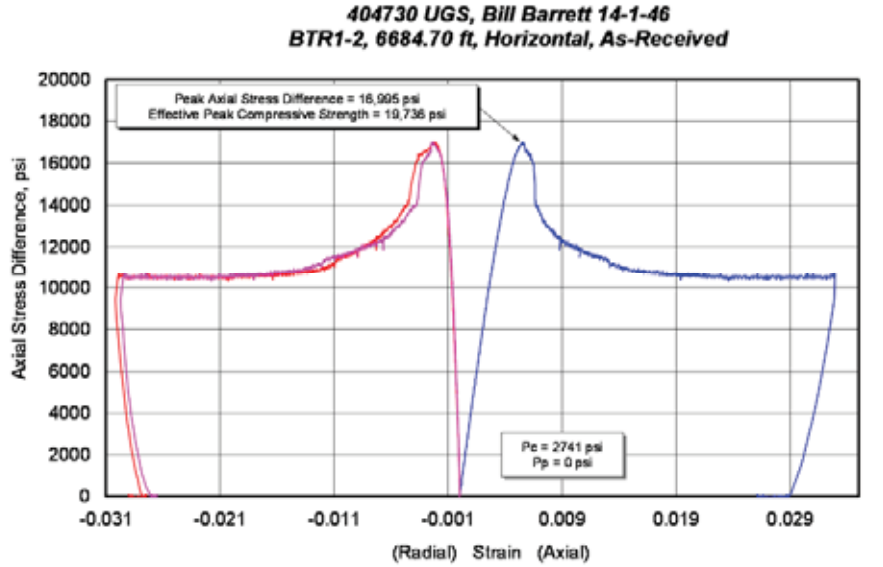

Zone 1 Deformation Index: Ratio of Secant E at Peak to E: 1.16
Zone 2 Ductility Index: Amount of Plastic or Strain Hardening Strain: 0.01
Zone 3a: Tang and Kaiser Index (Axial): 3.21
Zone 3b: Tang and Kaiser Index (Volumetric): 3.83
Zone 4: Peak to Residual Strength Ratio: 2.18

Zone 1 Deformation Index: Ratio of Secant E at Peak to E: 1.23
Zone 2 Ductility Index: Amount of Plastic or Strain Hardening Strain: 0.05
Zone 3a: Tang and Kaiser Index (Axial): 3.095
Zone 3b: Tang and Kaiser Index (Volumetric): 3.137
Zone 4: Peak to Residual Strength Ratio: 1.61

Bill Barrett 14-1-46

Lithology	Sample ID	Depth (ft)	Orientation	As Received Bulk Density (g/cm^3)	Confining Pressure (psi)	Peak Effective Compressive Strength (psi)	Effective Residual Compressive Strength (psi)	Young's Modulus (10^6 psi)	Poisson's Ratio
dolomite	BTR2-1	6693.70	Vertical	2.428	1399	29110	9470	4.861	0.29
	BTR2-2	6693.45	Horizontal	2.544	2744	49930	20490	7.011	0.29
	BTR2-5	6693.45	Horizontal	2.433	2744			4.796	0.31

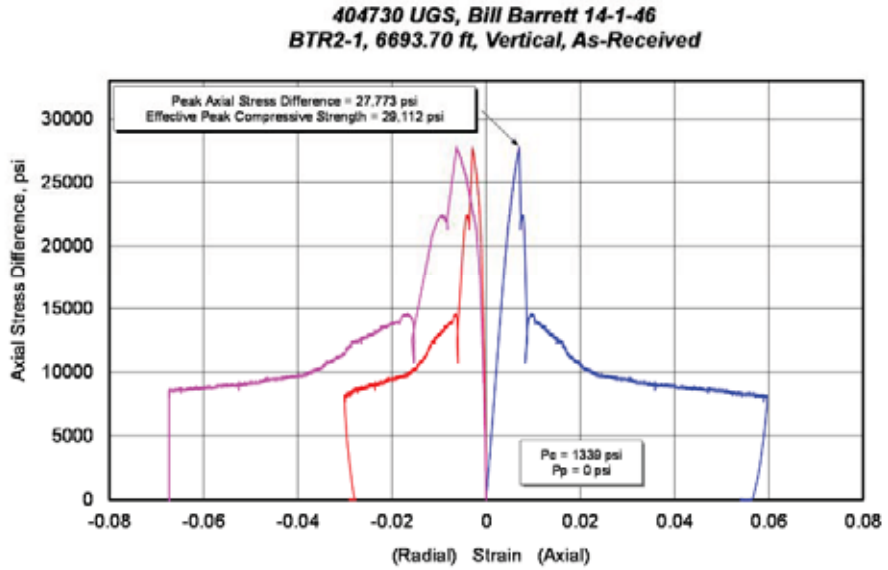

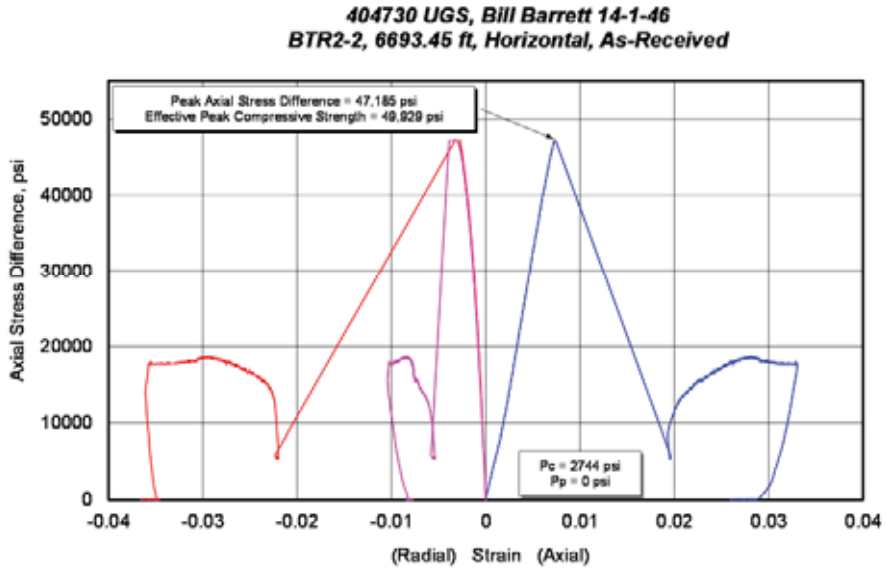

Zone 1 Deformation Index: Ratio of Secant E at Peak to E: 1.22
Zone 2 Ductility Index: Amount of Plastic or Strain Hardening Strain: 0
Zone 3a: Tang and Kaiser Index (Axial): 16.3
Zone 3b: Tang and Kaiser Index (Volumetric): 23.0
Zone 4: Peak to Residual Strength Ratio: 2.80

Zone 1 Deformation Index: Ratio of Secant E at Peak to E: 0.98
Zone 2 Ductility Index: Amount of Plastic or Strain Hardening Strain: N/A
Zone 3a: Tang and Kaiser Index (Axial): N/A
Zone 3b: Tang and Kaiser Index (Volumetric): N/A
Zone 4: Peak to Residual Strength Ratio: N/A

Bill Barrett 14-1-46

Lithology	Sample ID	Depth (ft)	Orientation	As Received Bulk Density (g/cm^3)	Confining Pressure (psi)	Peak Effective Compressive Strength (psi)	Effective Residual Compressive Strength (psi)	Young's Modulus (10^6 psi)	Poisson's Ratio
gray limestone	BTR3-1	6698.25	Vertical	2.586	1340	23980	13700	4.038	0.14
	BTR3-2	6699.00	Horizontal	2.614	2747	52680	19850	8.657	0.32

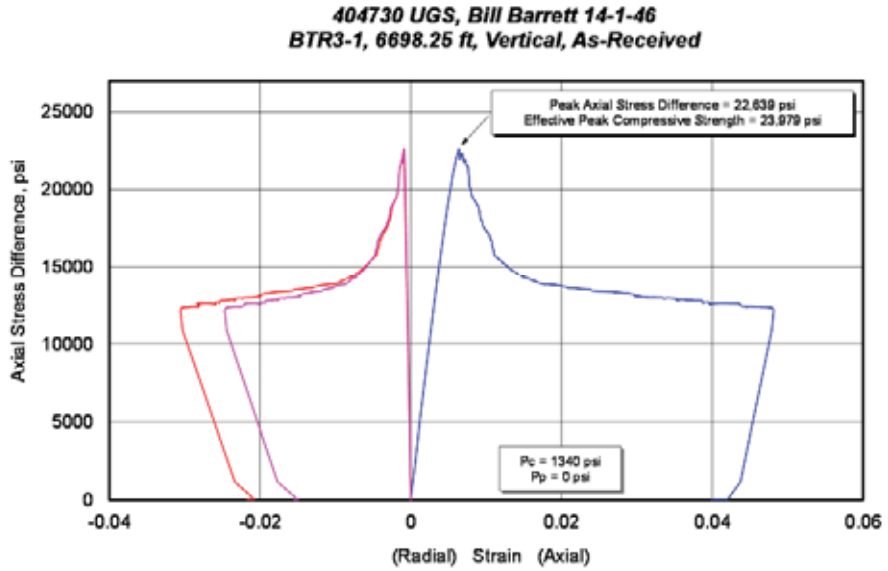

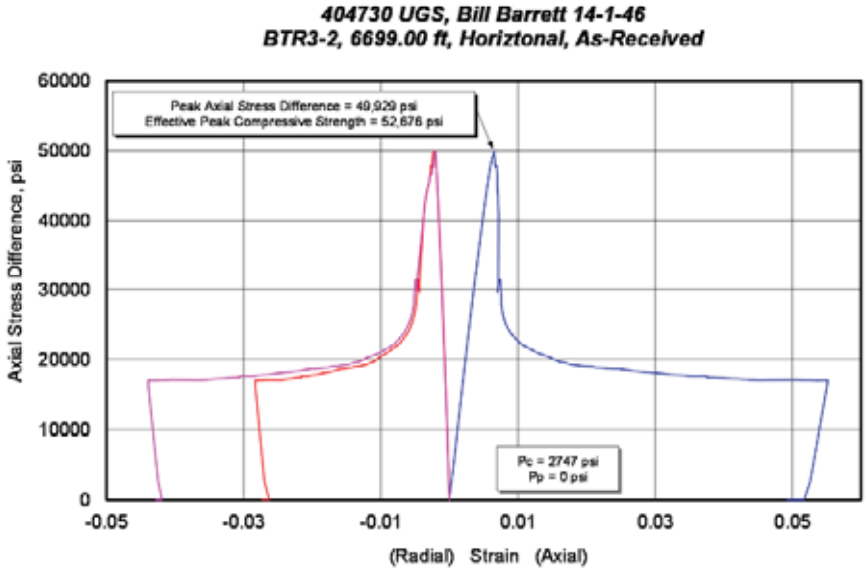

Zone 1 Deformation Index: Ratio of Secant E at Peak to E: 1.12
Zone 2 Ductility Index: Amount of Plastic or Strain Hardening Strain: 0.12
Zone 3a: Tang and Kaiser Index (Axial): 1.99
Zone 3b: Tang and Kaiser Index (Volumetric): 1.19
Zone 4: Peak to Residual Strength Ratio: 1.60

Zone 1 Deformation Index: Ratio of Secant E at Peak to E: 1.12
Zone 2 Ductility Index: Amount of Plastic or Strain Hardening Strain: 0.02
Zone 3a: Tang and Kaiser Index (Axial): 51.0
Zone 3b: Tang and Kaiser Index (Volumetric): 18.5
Zone 4: Peak to Residual Strength Ratio: 1.79

Bill Barrett 14-1-46

Lithology	Sample ID	Depth (ft)	Orientation	As Received Bulk Density (g/cm^3)	Confining Pressure (psi)	Peak Effective Compressive Strength (psi)	Effective Residual Compressive Strength (psi)	Young's Modulus (10^6 psi)	Poisson's Ratio
tan dolomite	BTR4-4	6703.10	Vertical	2.543	1341	23340	14290	6.422	0.28
	BTR4-2	3702.90	Horizontal	2.473	2748	26760	11050	6.223	0.26

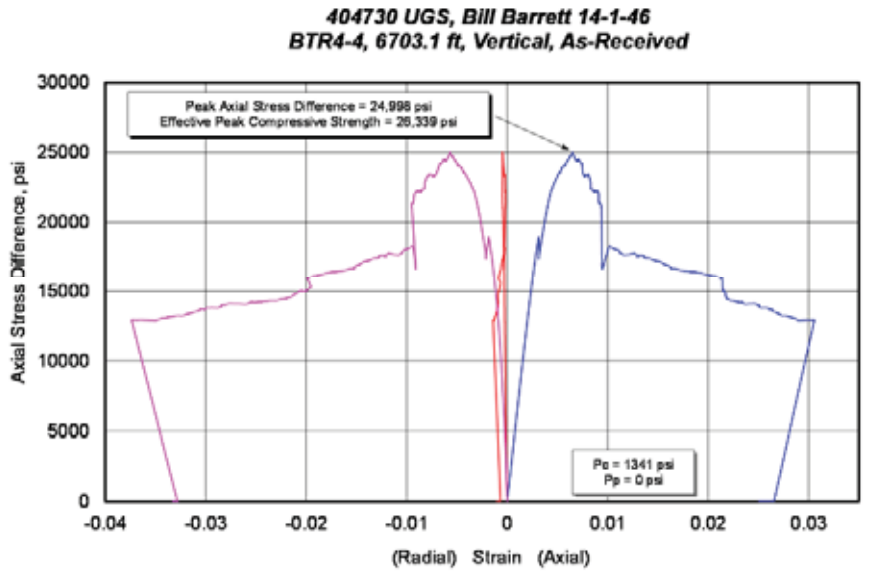

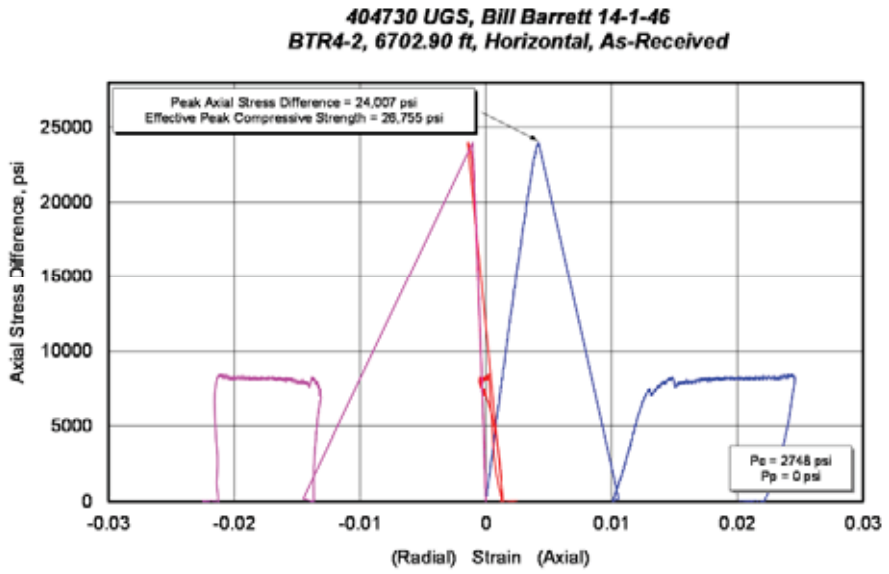

Zone 1 Deformation Index: Ratio of Secant E at Peak to E: 1.62
Zone 2 Ductility Index: Amount of Plastic or Strain Hardening Strain: 0.67
Zone 3a: Tang and Kaiser Index (Axial): 0.12
Zone 3b: Tang and Kaiser Index (Volumetric): 1.20?
Zone 4: Peak to Residual Strength Ratio: 1.36

Zone 1 Deformation Index: Ratio of Secant E at Peak to E: 1.09
Zone 2 Ductility Index: Amount of Plastic or Strain Hardening Strain: N/A
Zone 3a: Tang and Kaiser Index (Axial): N/A
Zone 3b: Tang and Kaiser Index (Volumetric): N/A
Zone 4: Peak to Residual Strength Ratio: 2.89

Bill Barrett 14-1-46

Lithology	Sample ID	Depth (ft)	Orientation	As Received Bulk Density (g/cm^3)	Confining Pressure (psi)	Peak Effective Compressive Strength (psi)	Effective Residual Compressive Strength (psi)	Young's Modulus (10^6 psi)	Poisson's Ratio
shale	BTR5-4	6706.50	Vertical	2.487	1341	14450	9190	1.295	0.18
	BTR5-2	6706.65	Horizontal	2.502	2750	17250	13270	3.797	0.26

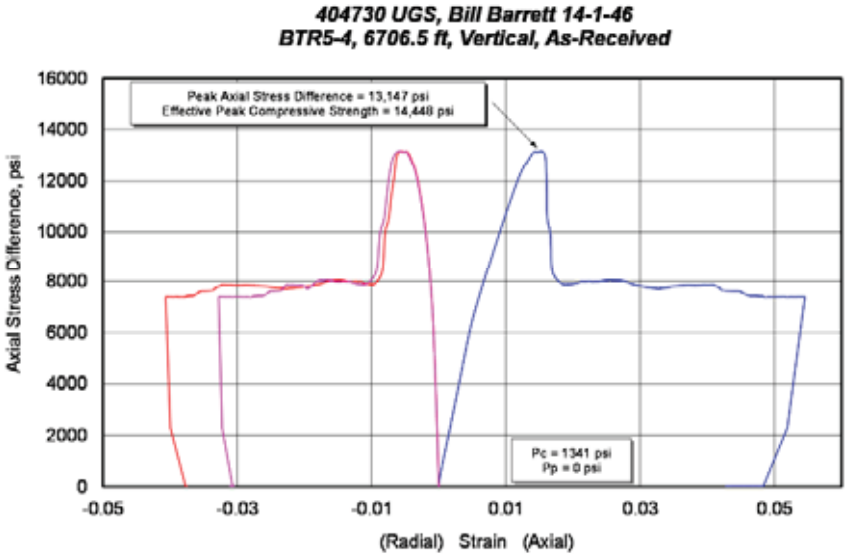

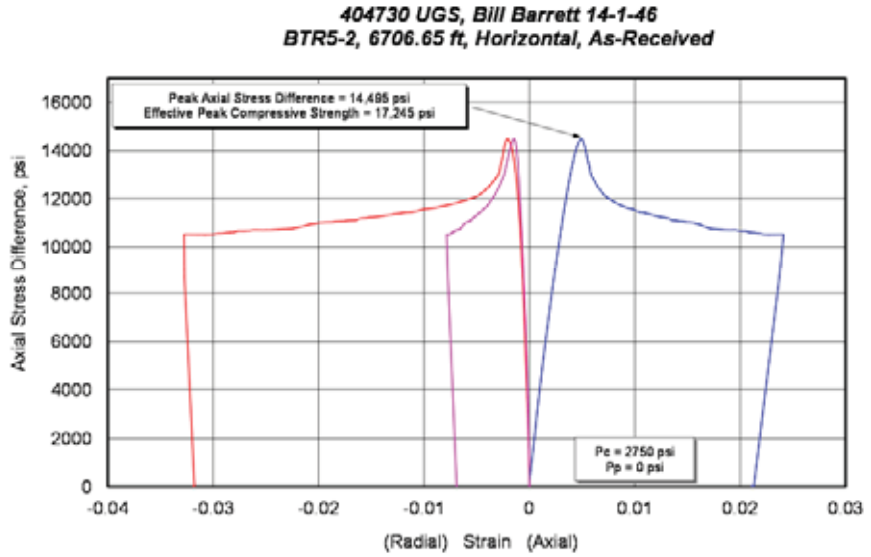

Zone 1 Deformation Index: Ratio of Secant E at Peak to E: 1.37
Zone 2 Ductility Index: Amount of Plastic or Strain Hardening Strain: 0.35
Zone 3a: Tang and Kaiser Index (Axial): 0.842
Zone 3b: Tang and Kaiser Index (Volumetric): 2.044
Zone 4: Peak to Residual Strength Ratio: 1.64

Zone 1 Deformation Index: Ratio of Secant E at Peak to E: 1.24
Zone 2 Ductility Index: Amount of Plastic or Strain Hardening Strain: 0.03
Zone 3a: Tang and Kaiser Index (Axial): 0.594
Zone 3b: Tang and Kaiser Index (Volumetric): 0.613
Zone 4: Peak to Residual Strength Ratio: 1.33

TIGHT ROCK ANALYSIS (TRA)

Tight rock analysis (TRA), also referred to as pressure decay permeability, was measured on 10 samples from Fidelity well Cane Creek CCU7-1, at 'as-received' saturation conditions (measured prior to additional processing). A specific weight fraction of crushed, sieved sample material was loaded into a matrix cup for gas expansion. Data derived from the gas expansion measurement were used to calculate permeability to gas. Since the samples were crushed, the permeability measurement was not conducted at net overburden conditions; however, a correlation for net overburden data has been developed and is routinely used for specific shale types. The following tables report the effective and total porosity for each sample.

Table A-9. Summary of Effective Porosity Measured During Tight Rock Analysis – Fidelity Well Cane Creek CCU7-1

Sample ID	Lithology	Core Depth (ft)	As Received Bulk Density (g/cm^3)	As Received Grain Density (g/cm^3)	Effective Dry Grain Density (g/cm^3)	Gas Filled Porosity (% of BV)	Hydrocarbon Filled Porosity (% of BV)	Effective Porosity (% of BV)	Effective Water Saturation (% of PV)	Effective Gas Saturation (% of PV)
CCU1-4	silty dolomite	7609.05	2.618	2.692	2.736	2.74	2.79	5.20	46.27	52.80
CCU2-4	anhydrite	7614.55	2.914	2.921	2.922	0.25	0.26	0.27	3.95	92.10
CCU3-4	silty/dolomite/shale	7619.90	2.567	2.610	2.666	1.63	1.73	4.94	65.05	33.03
CCU4-4	shale	7620.40	2.452	2.515	2.604	2.48	2.75	7.87	65.11	31.46
CCU5-4	silty dolomite	7624.90	2.586	2.624	2.654	1.42	1.51	3.22	53.06	43.99
CCU6-4	silty dolomite	7630.50	2.518	2.549	2.614	1.21	1.30	5.19	74.94	23.27
CCU7-4	shale	7638.20	2.565	2.634	2.649	2.63	3.01	3.48	13.52	75.66
CCU8-4	anhydrite	7645.75	2.930	2.939	2.940	0.33	0.34	0.35	3.08	93.84
CCU9-4	silty dolomite	7651.10	2.602	2.643	2.694	1.53	1.58	4.52	65.04	33.91
CCU10-4	fractured/silty/dolomite	7657.40	2.528	2.629	2.680	3.81	4.94	6.62	25.44	57.60

Sample ID -	Effective Oil Saturation (% of PV)	Bound Hydrocarbon (% of BV)	Clay Bound Water (% of BV)	Structural Water (% of BV)	Pressure- Decay Permeability (mD)
CCU1-4	0.93	0.00	3.08	0.77	7.1×10^{-5}
CCU2-4	3.95	0.10	0.00	0.20	3.4
CCU3-4	1.91	0.19	3.87	1.98	6.4
CCU4-4	3.43	0.45	5.22	3.33	7.9
CCU5-4	2.95	0.00	2.09	1.42	3.5
CCU6-4	1.78	0.00	3.89	2.22	3.9
CCU7-4	10.82	0.66	0.94	1.22	4.9
CCU8-4	3.08	0.01	0.00	0.10	3.3
CCU9-4	1.05	0.00	2.75	1.23	5.1
CCU10-4	16.96	2.25	1.31	0.56	5.2

Table A-10. Summary of Total Porosity Measured During Tight Rock Analysis – Fidelity Well Cane Creek CCU7-1

Sample ID	Lithology	Core Depth (ft)	As Received Bulk Density (g/cm^3)	As Received Grain Density (g/cm^3)	Total Dry Grain Density (g/cm^3)	Total Porosity (% of BV)	Total Water Saturation (% of PV)	Total Gas Saturation (% of PV)	Total Oil Saturation (% of PV)
CCU1-4	silty dolomite	7609.05	2.618	2.692	2.794	8.28	66.26	33.16	0.58
CCU2-4	anhydrite	7614.55	2.914	2.921	2.922	0.27	3.95	92.10	3.95
CCU3-4	silty/dolomite/shale	7619.90	2.567	2.610	2.737	8.81	80.42	18.51	1.07
CCU4-4	shale	7620.40	2.452	2.515	2.700	13.09	79.02	18.92	2.06
CCU5-4	silty dolomite	7624.90	2.586	2.624	2.691	5.30	71.53	26.69	1.79
CCU6-4	silty dolomite	7630.50	2.518	2.549	2.683	9.08	85.68	13.30	1.02
CCU7-4	shale	7638.20	2.565	2.634	2.665	4.42	31.93	59.55	8.52
CCU8-4	anhydrite	7645.75	2.930	2.939	2.940	0.35	3.08	93.84	3.08
CCU9-4	silty dolomite	7651.10	2.602	2.643	2.744	7.26	78.27	21.08	0.65
CCU10-4	fractured/silty/dolomite	7657.40	2.528	2.629	2.704	7.93	37.76	48.08	14.16

Continuous Surface Thermal Conductivity Profiling

Thermal conductivity was evaluated by obtaining a continuous surface thermal conductivity profile of approximately 70 feet of requested intervals from four out of the five wells of interest in the Utah Tight Oil Plays project. The cores selected for thermal profiling and conductivity measurements were placed into a core holder and tightened down. After that the cores were lightly ground to provide the same height of upper surfaces of all cores placed in a holder. Grinding created a grove providing a constant distance (Z) between the down edges of both of the cold and hot IR sensors in the vertical direction relative to ground surfaces of the cores. After grinding, the core surface is coated along the ground groove with a black paint with width of 8-12 mm. Procedure of coating provides an approximately equal thickness for both test samples and standards. Cores are then placed with their painted surface directed upward and far from heat sources (sun light, heating radiators, heating convectors, electrical lamps, etc.).

Table A-11. Summary of Continuous Surface Thermal Conductivity Values

Well ID	Core Depth Range (ft)	Low W/K	High W/K	Average W/K
Fidelity Cane Creek CCU7-1	7619.00 - 7620.90	1.30	2.92	2.20
	7624.10 - 7624.98	2.50	3.70	3.05
	7630.08 - 7630.97	2.25	3.60	2.80
	7638.00 - 7638.50	1.20	2.70	1.85
	7657.40 - 7658.00	2.55	3.30	2.80
Fidelity Cane Creek 26-3	7431.00 - 7434.05	1.80	2.90	2.40
	7434.15 - 7437.15	2.15	3.30	2.60
	7437.15 - 7440.00	1.65	3.20	2.45
	7440.60 - 7442.12	2.35	3.49	2.85
	7444.15 - 7445.75	1.60	3.00	2.30
Fidelity Cisco State 36-13	7602.60 - 7605.24	1.90	4.70	3.60
	7605.83 - 7608.97	1.00	2.70	1.70
	7611.70 - 7614.54	2.00	4.40	3.30
	7614.70 - 7617.65	1.70	4.30	2.75
	7617.65 - 7620.08	1.70	4.75	2.75
Bill Barrett 14-1-46	6676.00 - 6678.00	1.42	2.67	1.80
	6678.00 - 6680.70	1.40	2.34	1.77
	6680.70 - 6683.40	1.63	2.41	1.97
	6684.12 - 6686.31	1.18	2.37	1.45
	6686.45 - 6688.80	1.33	2.48	1.75

Well ID	Core Depth Range (ft)	Low W/K	High W/K	Average W/K
	6688.93 – 6691.90	1.79	2.37	1.98
	6692.00 – 6695.00	1.58	2.35	1.95
	6695.70 – 6696.73	1.59	2.44	2.05
	6697.82 – 6698.45	1.73	2.12	1.88
	6701.57 – 6703.56	1.56	2.20	1.92
	6703.80 – 6706.02	1.55	2.72	2.00

Thermal Conductivity Plots

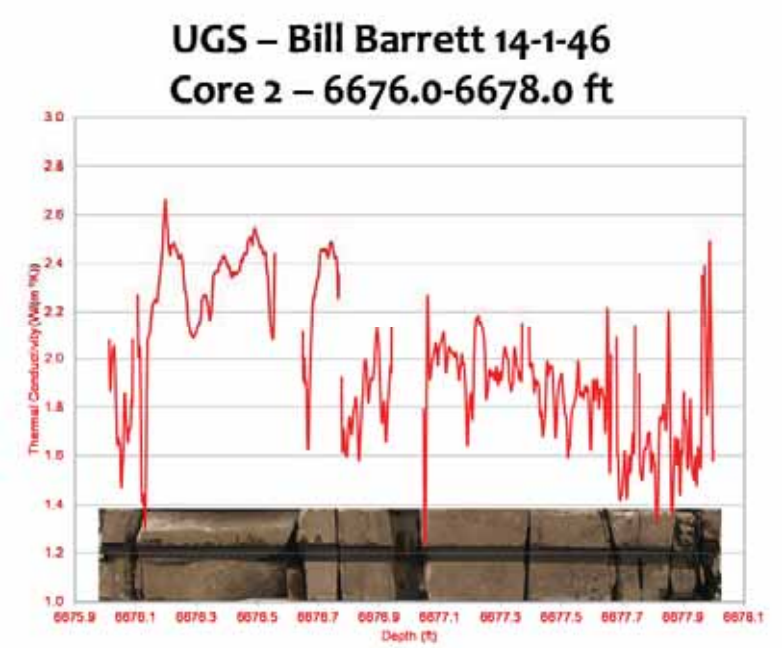

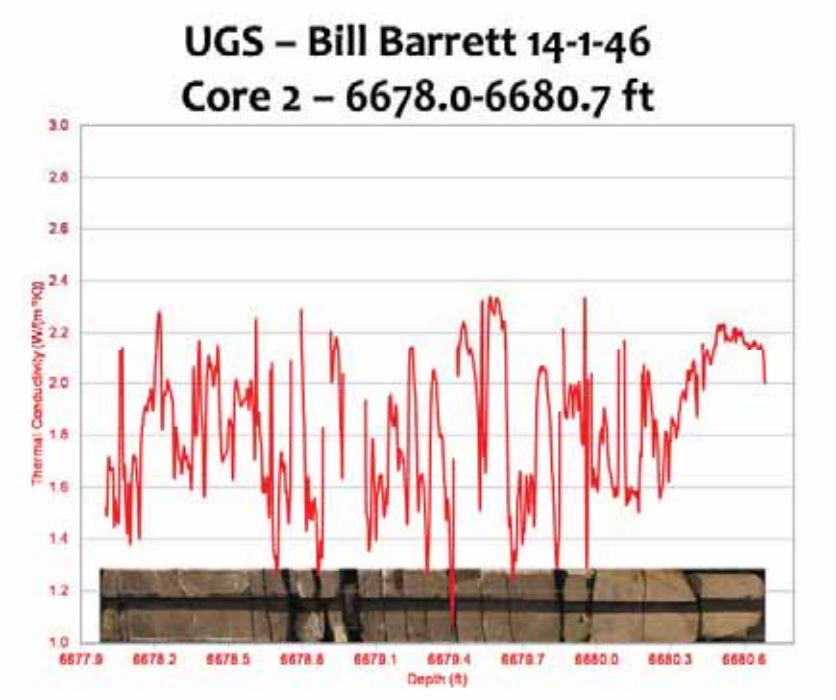
UGS – Bill Barrett 14-1-46
Core 2 – 6678.0-6680.7 ft
Thermal Conductivity (W/(m*K))
3.0
2.8
2.6
2.4
2.2
2.0
1.8
1.6
1.4
1.2
1.0
6677.9
6678.2
6678.5
6678.8
6679.1
6679.4
6679.7
6680.0
6680.3
6680.6
Depth (ft)

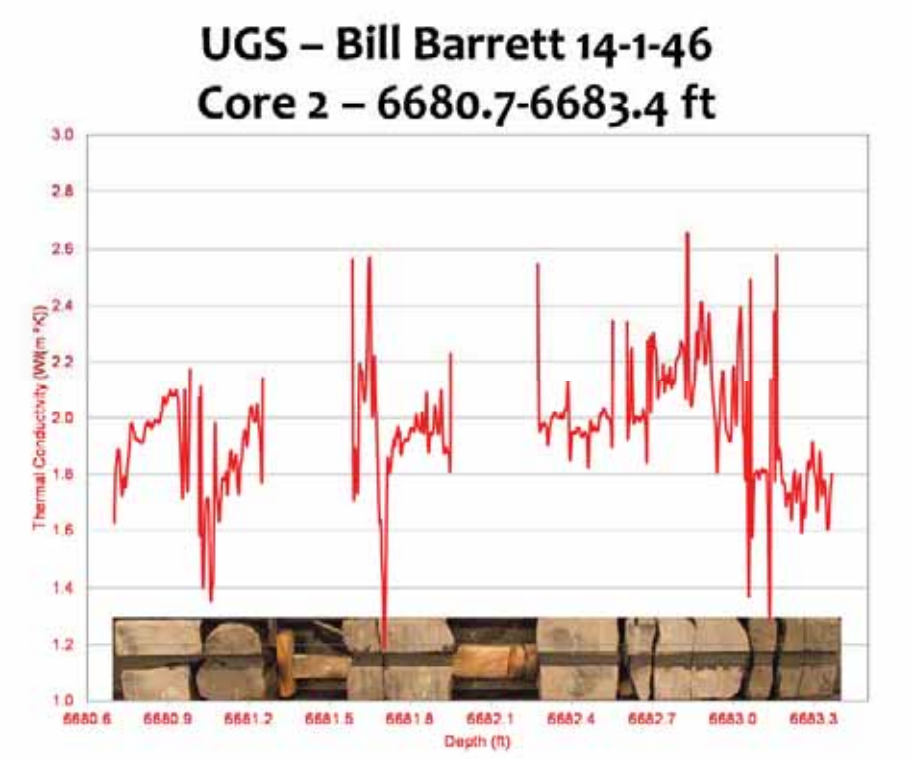
UGS – Bill Barrett 14-1-46
Core 2 – 6680.7-6683.4 ft
Thermal Conductivity (W/(m*K))
3.0
2.8
2.6
2.4
2.2
2.0
1.8
1.6
1.4
1.2
1.0
6680.6
6680.9
6681.2
6681.5
6681.8
6682.1
6682.4
6682.7
6683.0
6683.3
Depth (ft)

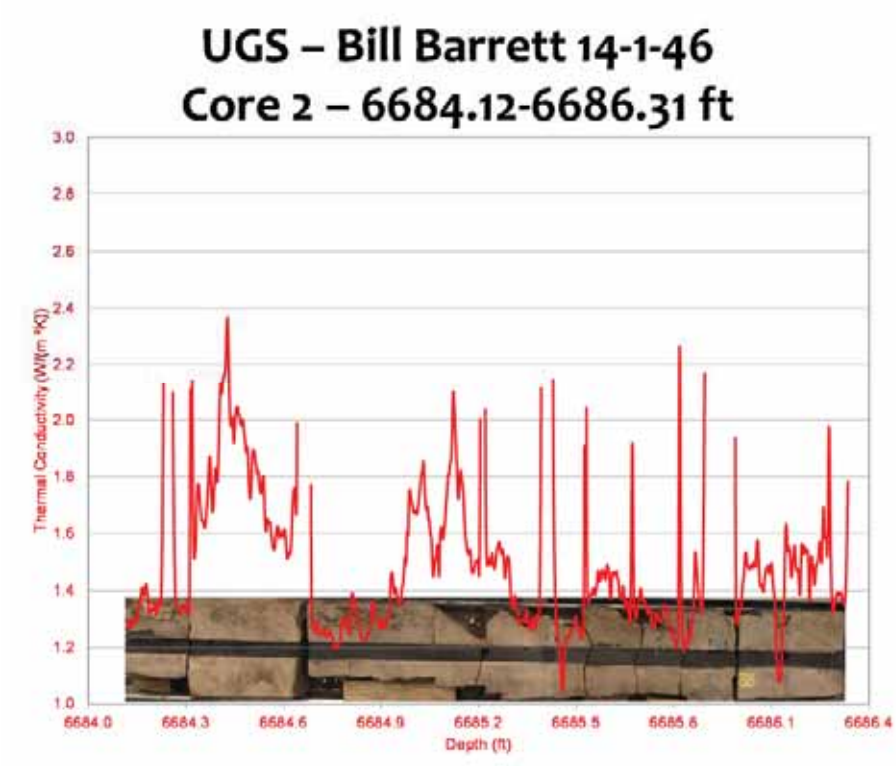
UGS – Bill Barrett 14-1-46
Core 2 – 6684.12-6686.31 ft
Thermal Conductivity (W/(m *K))
3.0
2.8
2.6
2.4
2.2
2.0
1.8
1.6
1.4
1.2
1.0
6684.0
6684.3
6684.6
6684.9
6685.2
6685.5
6685.8
6686.1
6686.4
Depth (ft)

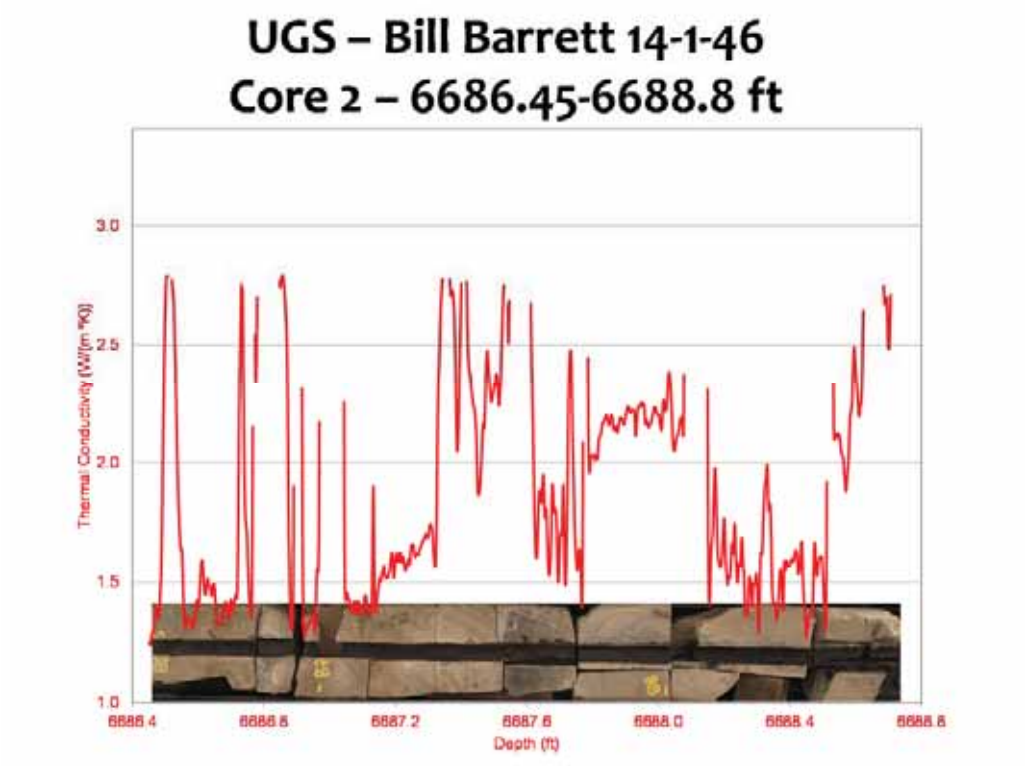
UGS – Bill Barrett 14-1-46
Core 2 – 6686.45-6688.8 ft
Thermal Conductivity (W/(m *K))
3.0
2.5
2.0
1.5
1.0
6686.4
6686.8
6687.2
6687.6
6688.0
6688.4
6688.8
Depth (ft)

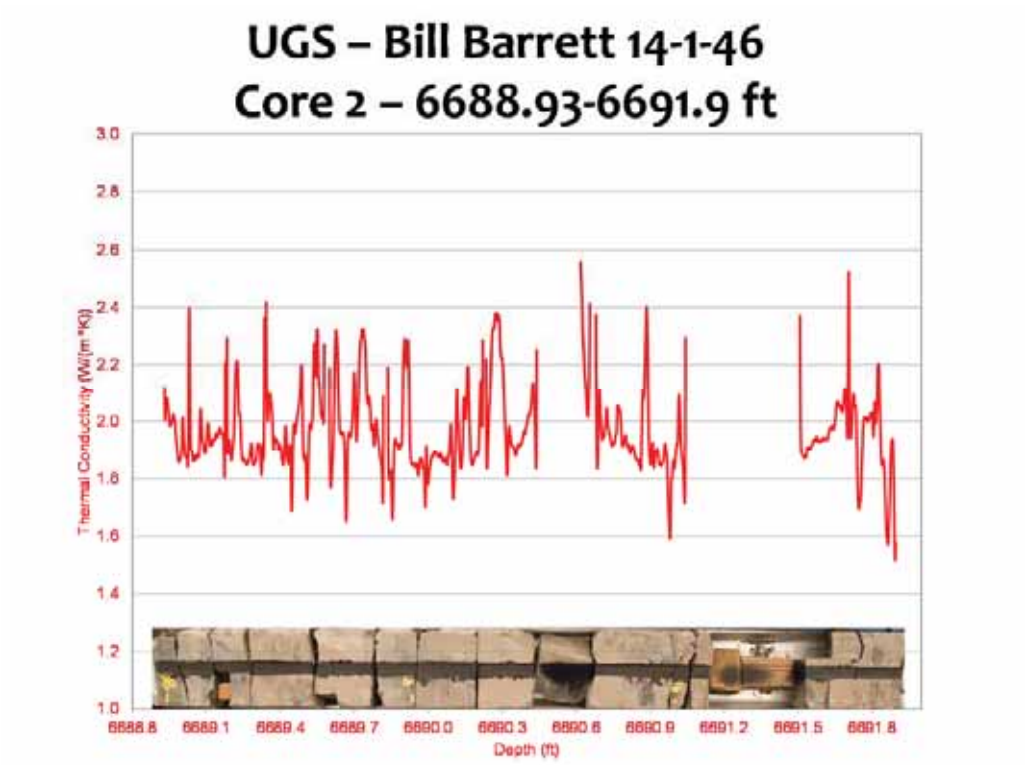
UGS – Bill Barrett 14-1-46
Core 2 – 6688.93-6691.9 ft
Thermal Conductivity (W/(m*K))
3.0
2.8
2.6
2.4
2.2
2.0
1.8
1.6
1.4
1.2
1.0
6688.8
6689.1
6689.4
6689.7
6690.0
6690.3
6690.6
6690.9
6691.2
6691.5
6691.8
Depth (ft)

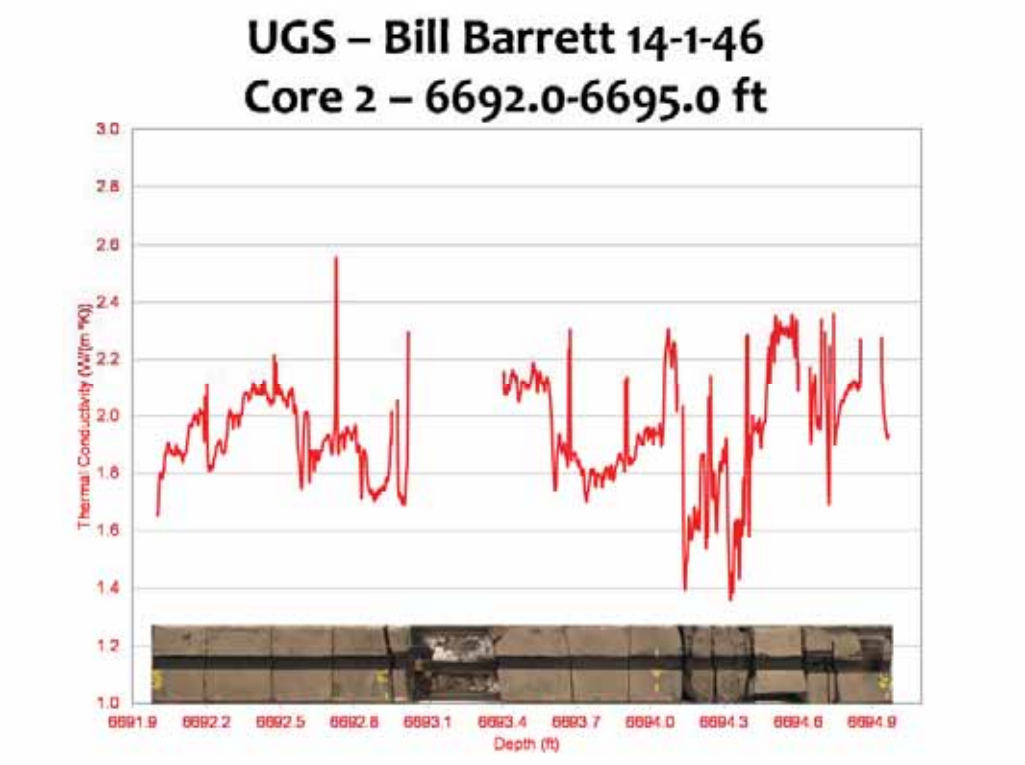
UGS – Bill Barrett 14-1-46
Core 2 – 6692.0-6695.0 ft
Thermal Conductivity (W/(m*K))
3.0
2.8
2.6
2.4
2.2
2.0
1.8
1.6
1.4
1.2
1.0
6691.9
6692.2
6692.5
6692.8
6693.1
6693.4
6693.7
6694.0
6694.3
6694.6
6694.9
Depth (ft)

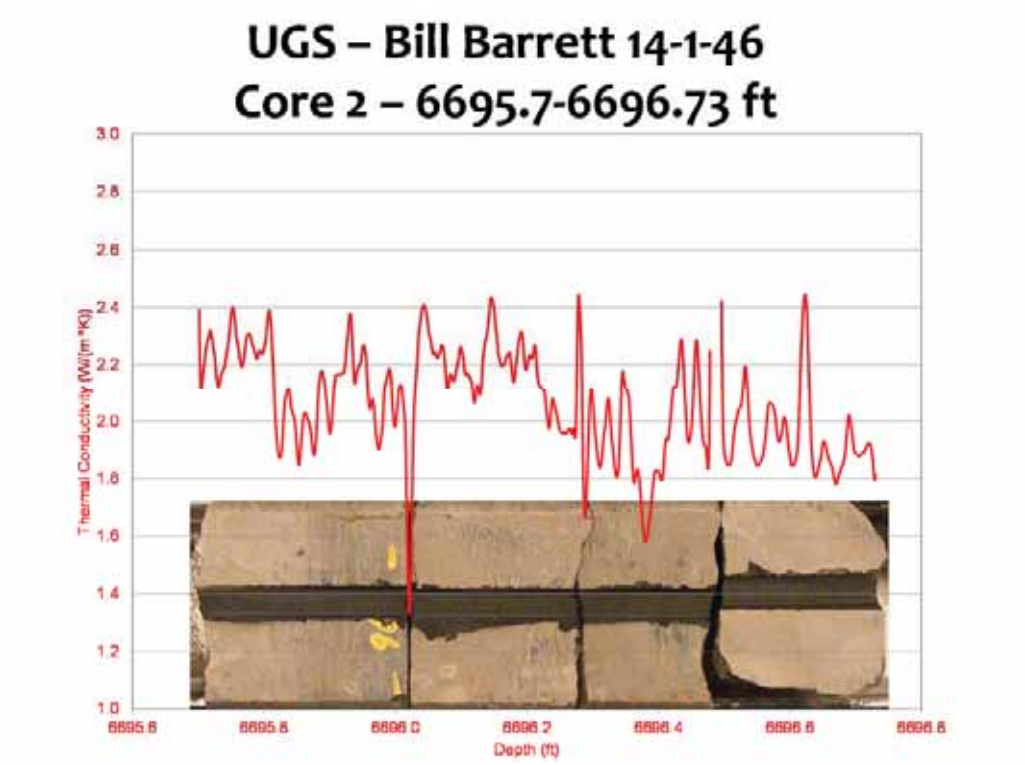
UGS – Bill Barrett 14-1-46
Core 2 – 6695.7-6696.73 ft
Thermal Conductivity (W/(m*K))
3.0
2.8
2.6
2.4
2.2
2.0
1.8
1.6
1.4
1.2
1.0
6695.6
6695.8
6696.0
6696.2
6696.4
6696.6
6696.8
Depth (ft)

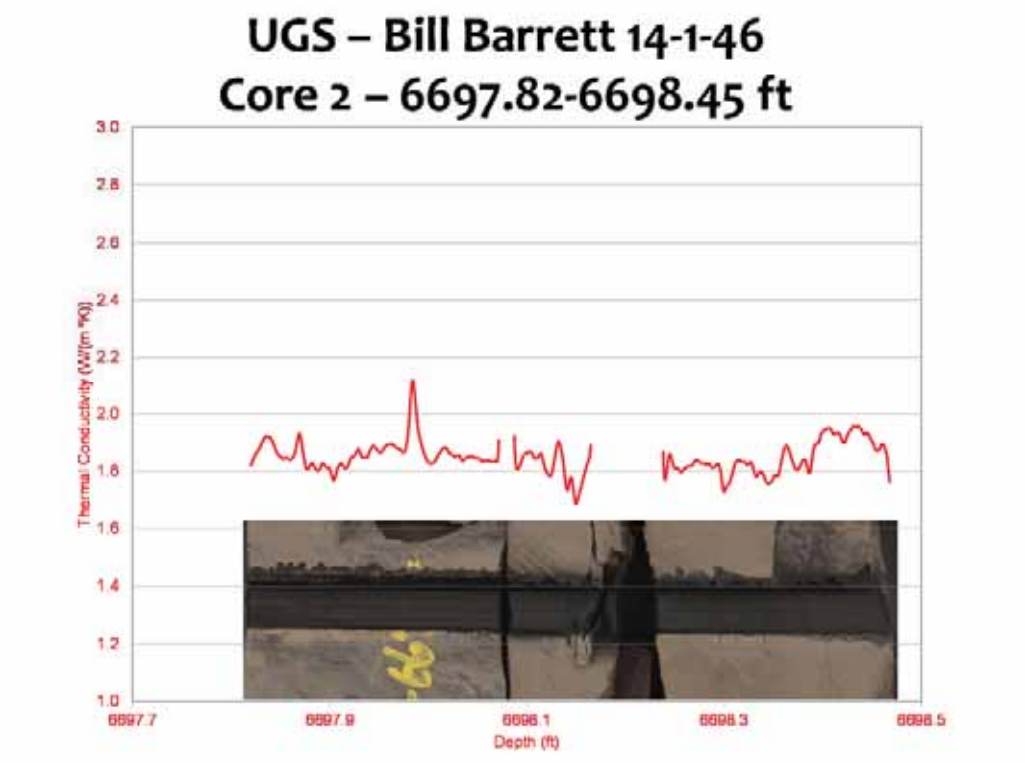
UGS – Bill Barrett 14-1-46
Core 2 – 6697.82-6698.45 ft
Thermal Conductivity (W/(m*K))
3.0
2.8
2.6
2.4
2.2
2.0
1.8
1.6
1.4
1.2
1.0
6697.7
6697.9
6698.1
6698.3
6698.5
Depth (ft)

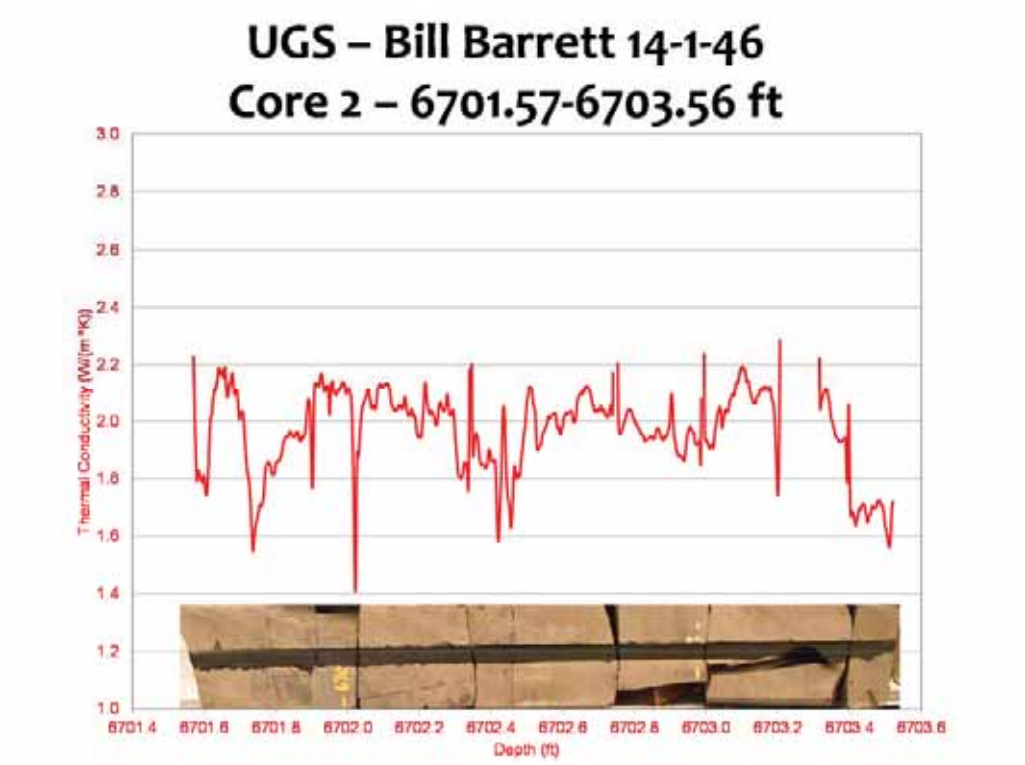
UGS – Bill Barrett 14-1-46
Core 2 – 6701.57-6703.56 ft
Thermal Conductivity (W/(m*K))
3.0
2.8
2.6
2.4
2.2
2.0
1.8
1.6
1.4
1.2
1.0
6701.4
6701.6
6701.8
6702.0
6702.2
6702.4
6702.6
6702.8
6703.0
6703.2
6703.4
6703.6
Depth (ft)

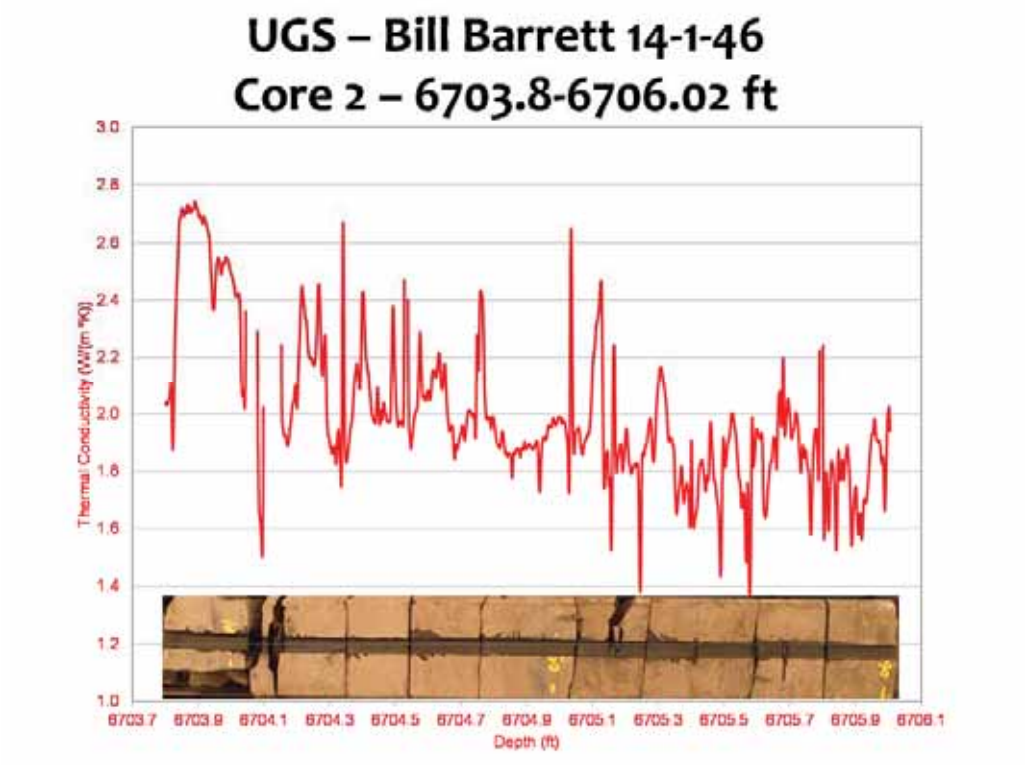
UGS – Bill Barrett 14-1-46
Core 2 – 6703.8-6706.02 ft
Thermal Conductivity (W/(m*K))
3.0
2.8
2.6
2.4
2.2
2.0
1.8
1.6
1.4
1.2
1.0
6703.7
6703.9
6704.1
6704.3
6704.5
6704.7
6704.9
6705.1
6705.3
6705.5
6705.7
6705.9
6706.1
Depth (ft)

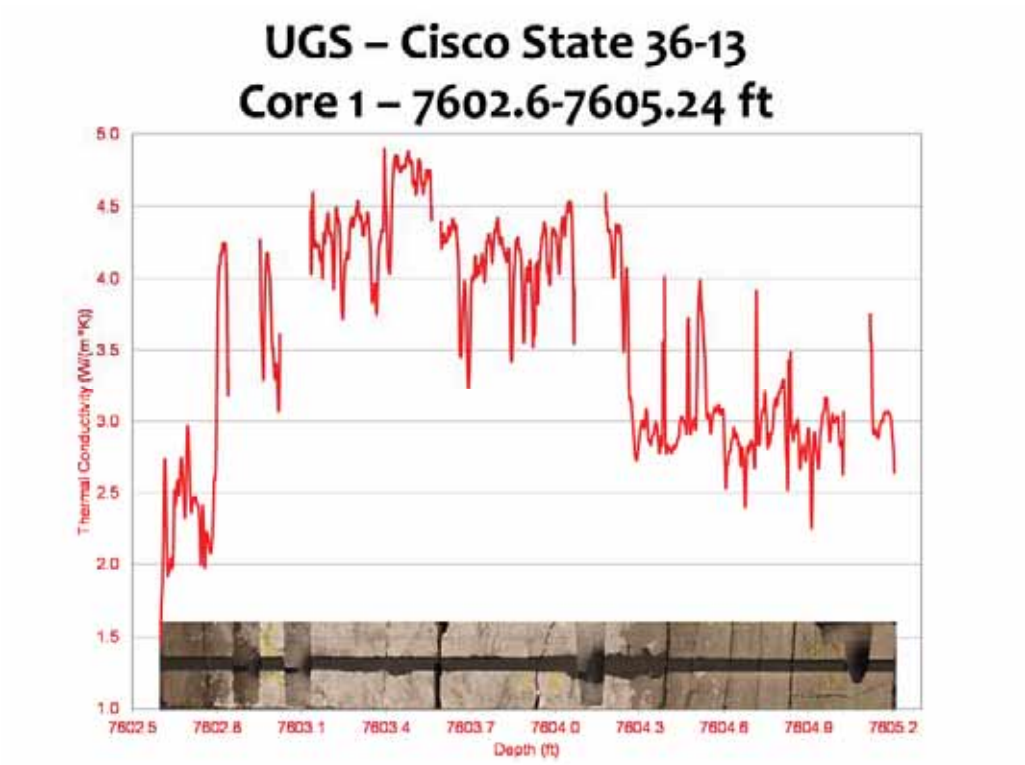
UGS – Cisco State 36-13
Core 1 – 7602.6-7605.24 ft
Thermal Conductivity (W/(m*K))
5.0
4.5
4.0
3.5
3.0
2.5
2.0
1.5
1.0
7602.5
7602.8
7603.1
7603.4
7603.7
7604.0
7604.3
7604.6
7604.9
7605.2
Depth (ft)

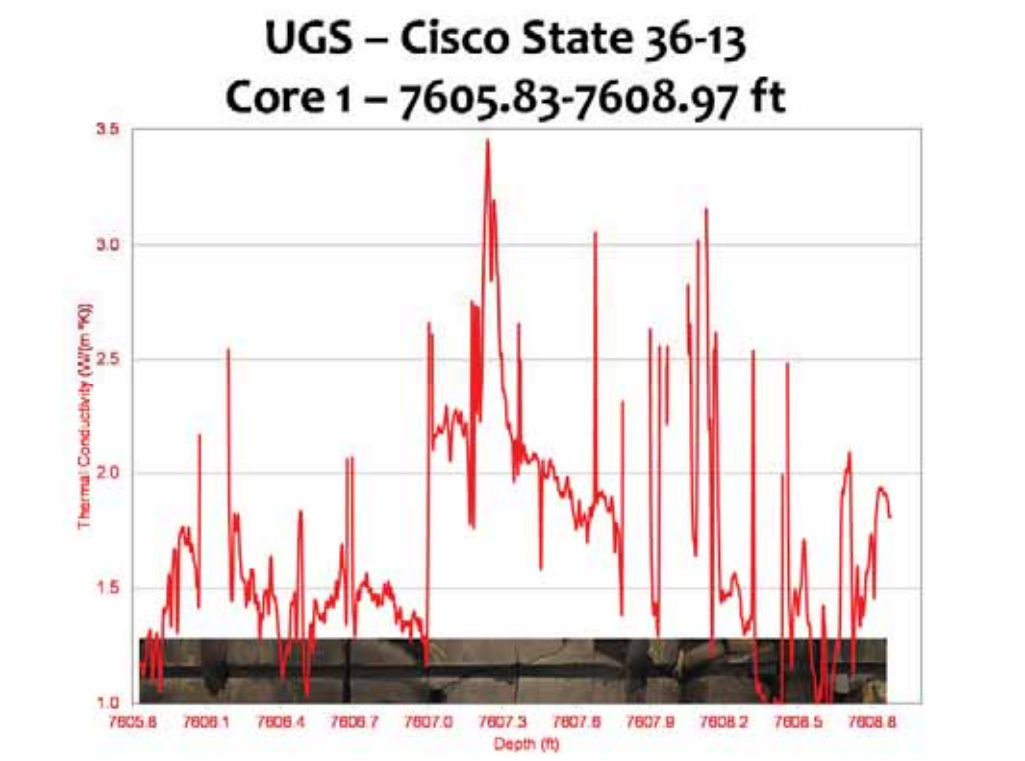
UGS – Cisco State 36-13
Core 1 – 7605.83-7608.97 ft
Thermal Conductivity (W/(m*K))
3.5
3.0
2.5
2.0
1.5
1.0
7605.8
7606.1
7606.4
7606.7
7607.0
7607.3
7607.6
7607.9
7608.2
7608.5
7608.8
Depth (ft)

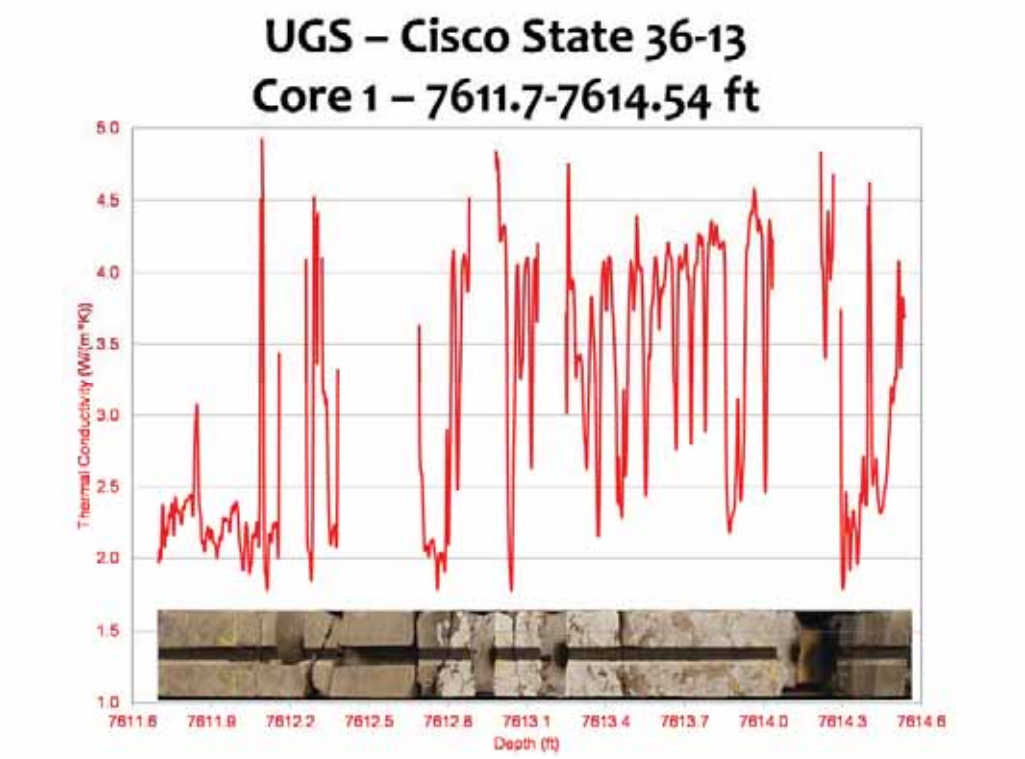
UGS – Cisco State 36-13
Core 1 – 7611.7-7614.54 ft
Thermal Conductivity (W/(m*K))
5.0
4.5
4.0
3.5
3.0
2.5
2.0
1.5
1.0
7611.6
7611.9
7612.2
7612.5
7612.8
7613.1
7613.4
7613.7
7614.0
7614.3
7614.6
Depth (ft)

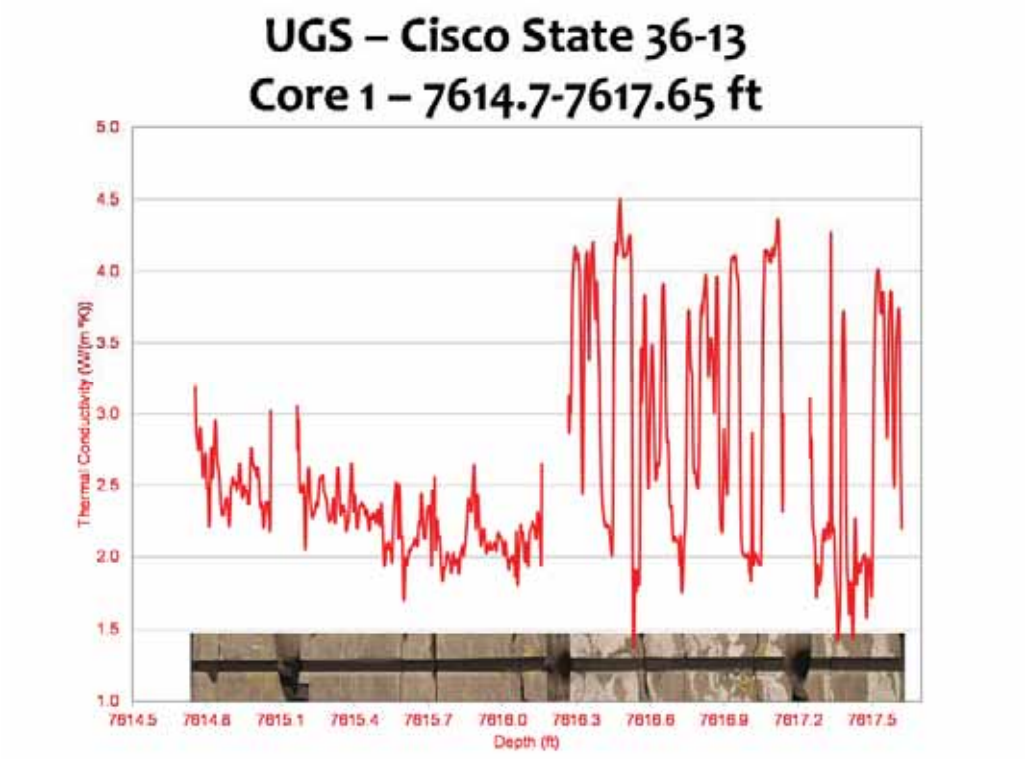
UGS – Cisco State 36-13
Core 1 – 7614.7-7617.65 ft
Thermal Conductivity (W/(m*K))
5.0
4.5
4.0
3.5
3.0
2.5
2.0
1.5
1.0
7614.5
7614.8
7615.1
7615.4
7615.7
7616.0
7616.3
7616.6
7616.9
7617.2
7617.5
Depth (ft)

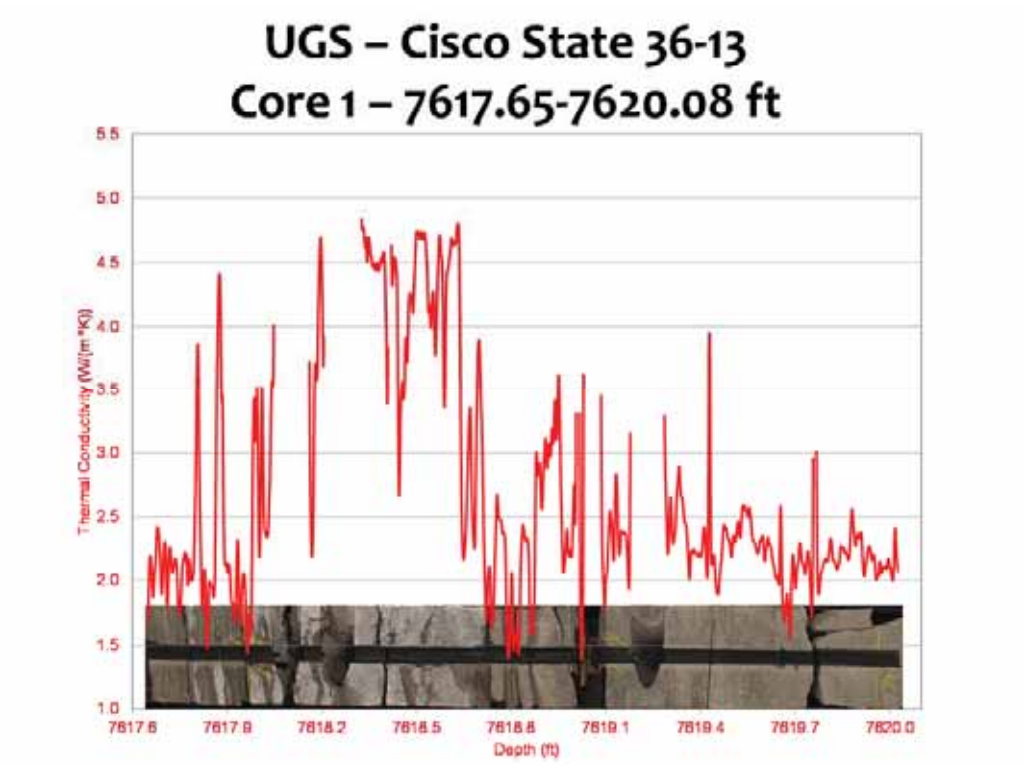
UGS – Cisco State 36-13
Core 1 – 7617.65-7620.08 ft
Thermal Conductivity (W/(m*K))
5.5
5.0
4.5
4.0
3.5
3.0
2.5
2.0
1.5
1.0
7617.6
7617.9
7618.2
7618.5
7618.8
7619.1
7619.4
7619.7
7620.0
Depth (ft)

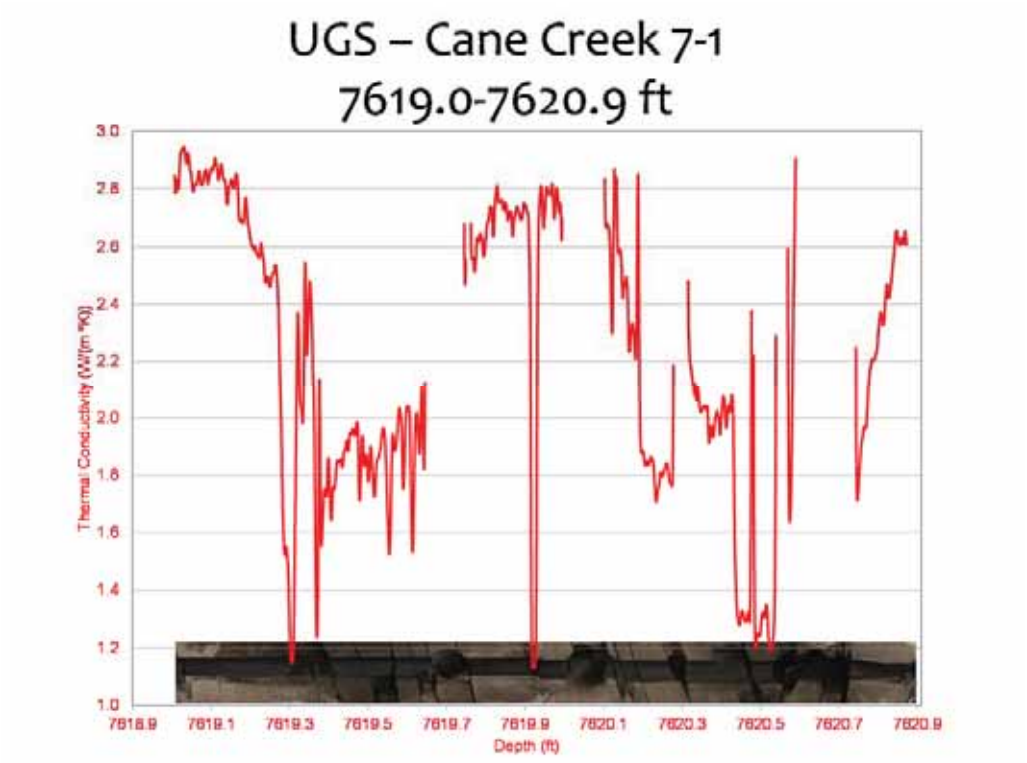
UGS – Cane Creek 7-1
7619.0-7620.9 ft
Thermal Conductivity (W/(m*K))
3.0
2.8
2.6
2.4
2.2
2.0
1.8
1.6
1.4
1.2
1.0
7618.9
7619.1
7619.3
7619.5
7619.7
7619.9
7620.1
7620.3
7620.5
7620.7
7620.9
Depth (ft)

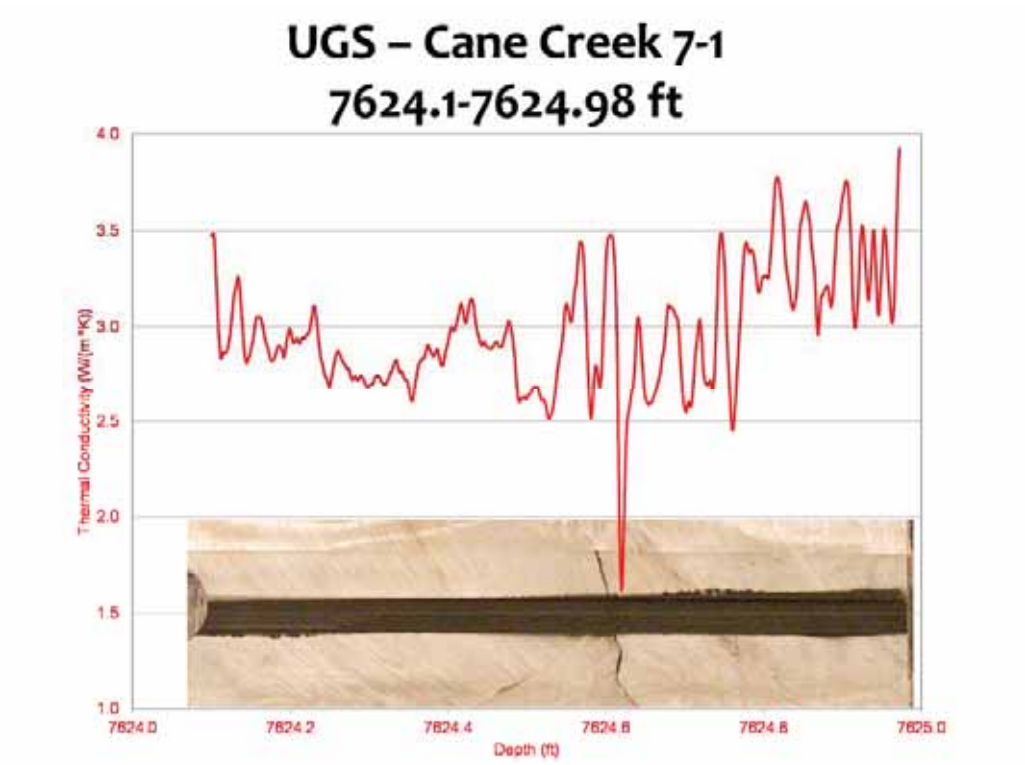
UGS – Cane Creek 7-1
7624.1-7624.98 ft
Thermal Conductivity (W/(m*K))
4.0
3.5
3.0
2.5
2.0
1.5
1.0
7624.0
7624.2
7624.4
7624.6
7624.8
7625.0
Depth (ft)

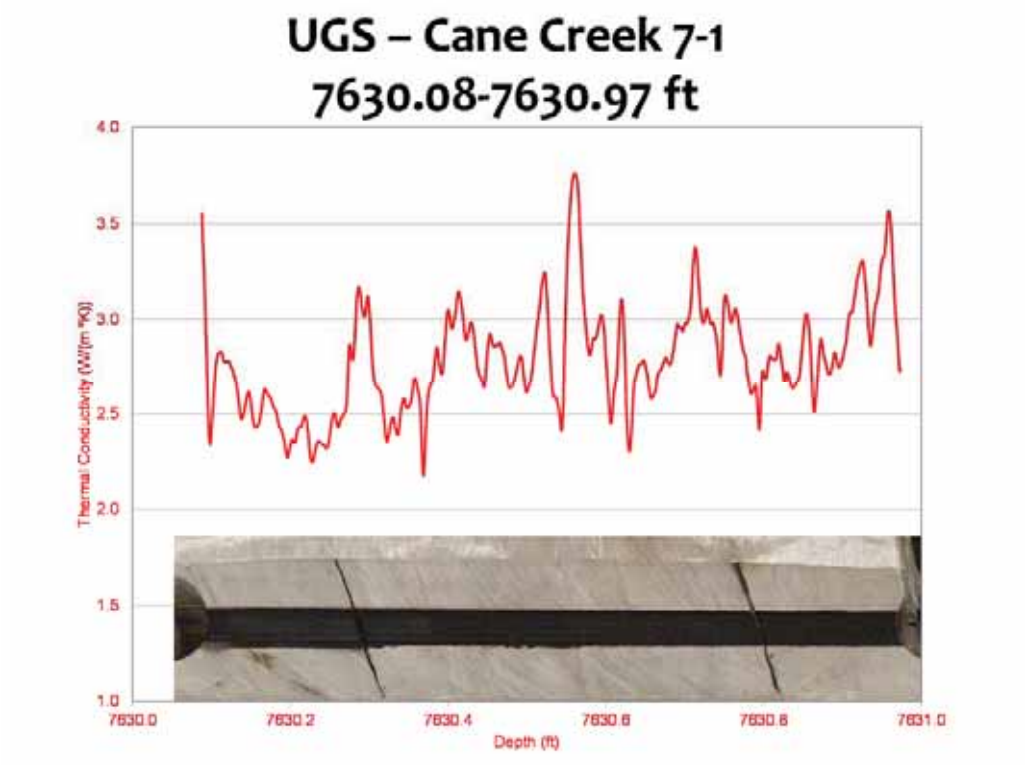
UGS – Cane Creek 7-1
7630.08-7630.97 ft
Thermal Conductivity (W/(m*K))
4.0
3.5
3.0
2.5
2.0
1.5
1.0
7630.0
7630.2
7630.4
7630.6
7630.8
7631.0
Depth (ft)

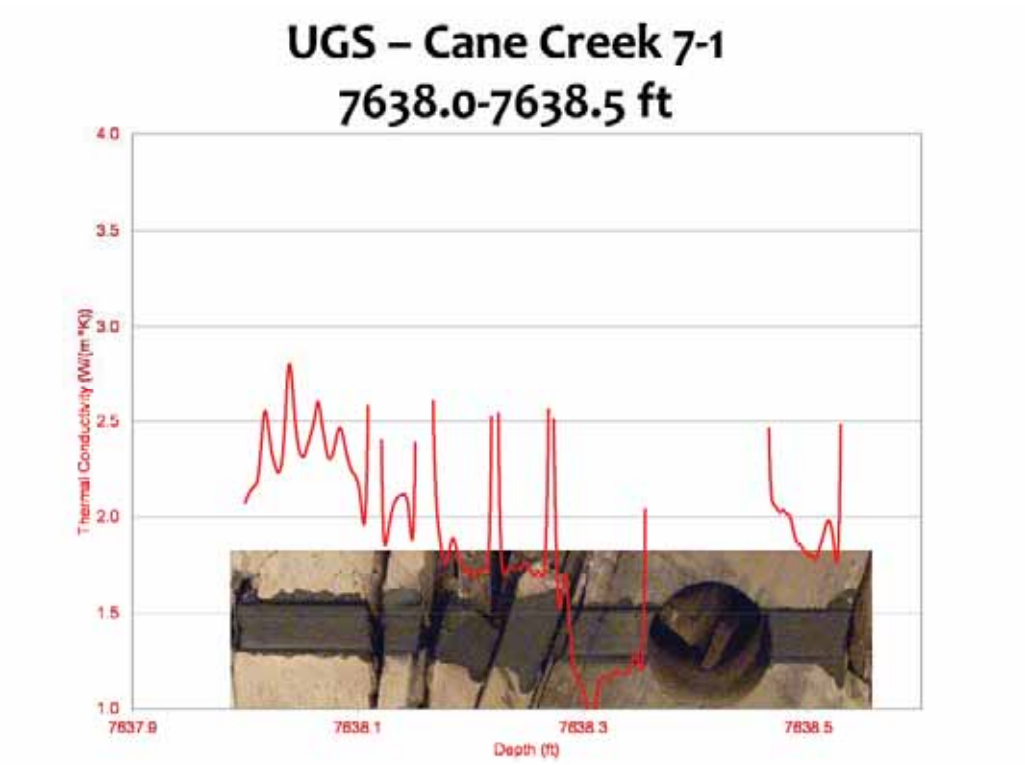
UGS – Cane Creek 7-1
7638.0-7638.5 ft
Thermal Conductivity (W/(m*K))
4.0
3.5
3.0
2.5
2.0
1.5
1.0
7637.9
7638.1
7638.3
7638.5
Depth (ft)

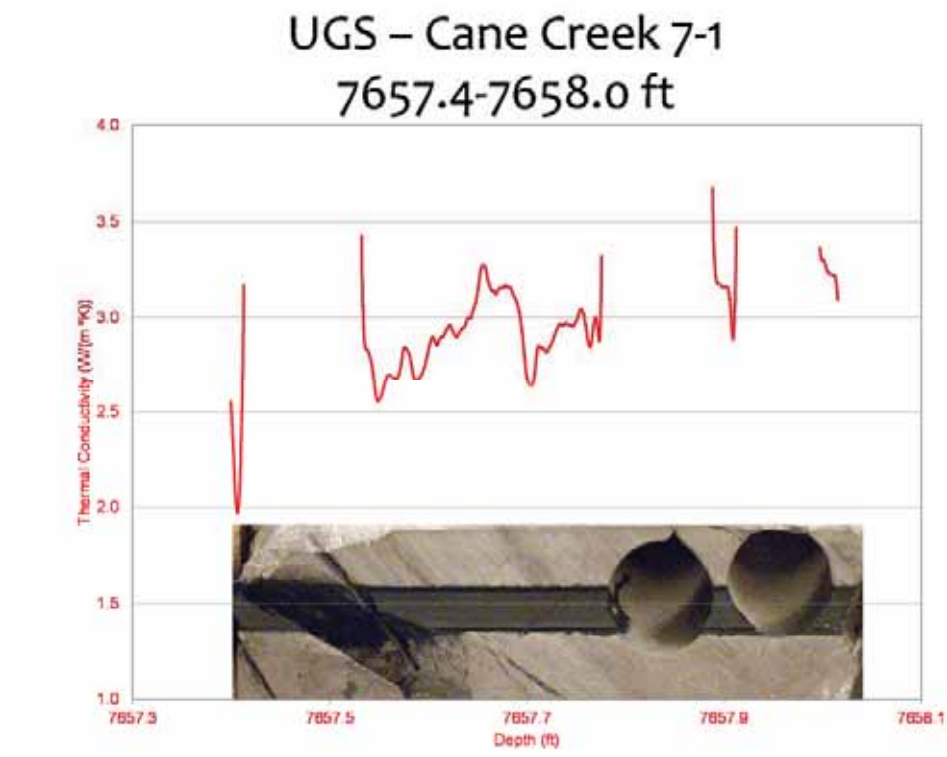
UGS – Cane Creek 7-1
7657.4-7658.0 ft
Thermal Conductivity (W/(m*K))
4.0
3.5
3.0
2.5
2.0
1.5
1.0
7657.3
7657.5
7657.7
7657.9
7658.1
Depth (ft)

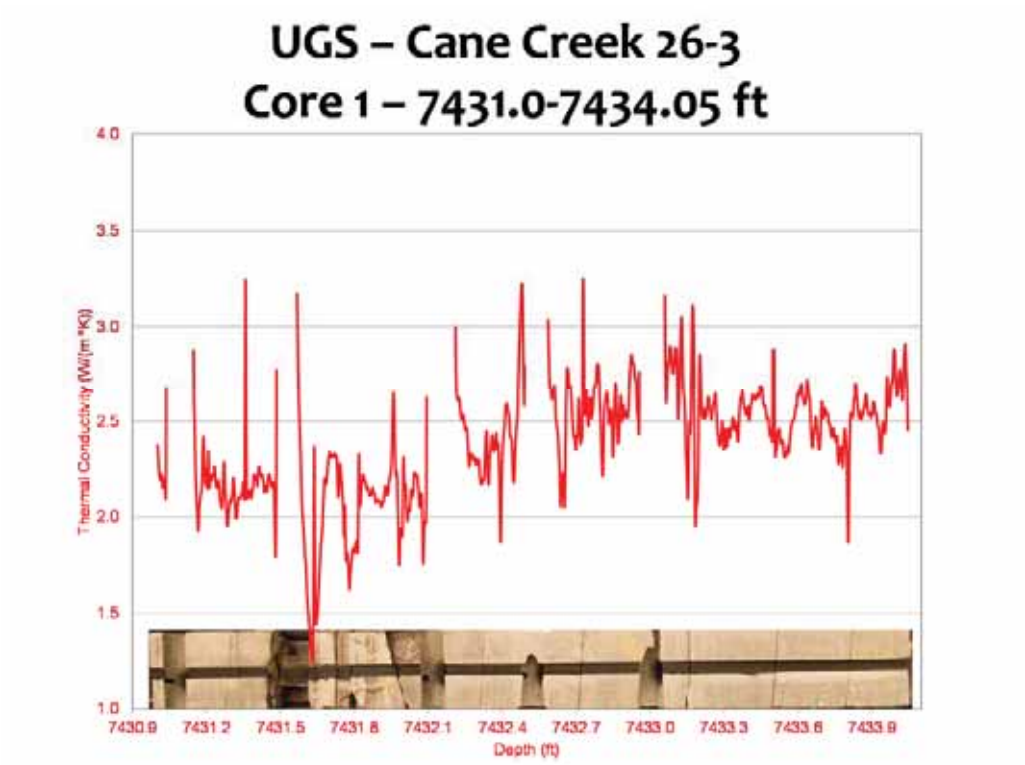
UGS – Cane Creek 26-3
Core 1 – 7431.0-7434.05 ft
Thermal Conductivity (W/(m*K))
4.0
3.5
3.0
2.5
2.0
1.5
1.0
7430.9
7431.2
7431.5
7431.8
7432.1
7432.4
7432.7
7433.0
7433.3
7433.6
7433.9
Depth (ft)

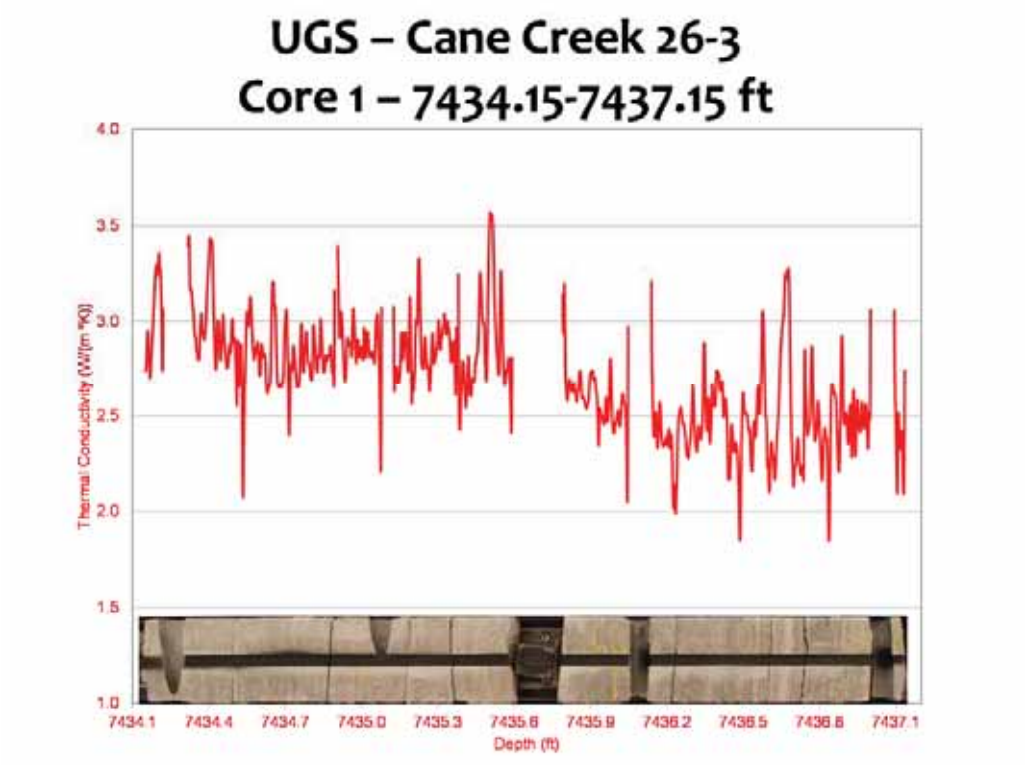
UGS – Cane Creek 26-3
Core 1 – 7434.15-7437.15 ft
Thermal Conductivity (W/(m*K))
4.0
3.5
3.0
2.5
2.0
1.5
1.0
7434.1
7434.4
7434.7
7435.0
7435.3
7435.6
7435.9
7436.2
7436.5
7436.8
7437.1
Depth (ft)

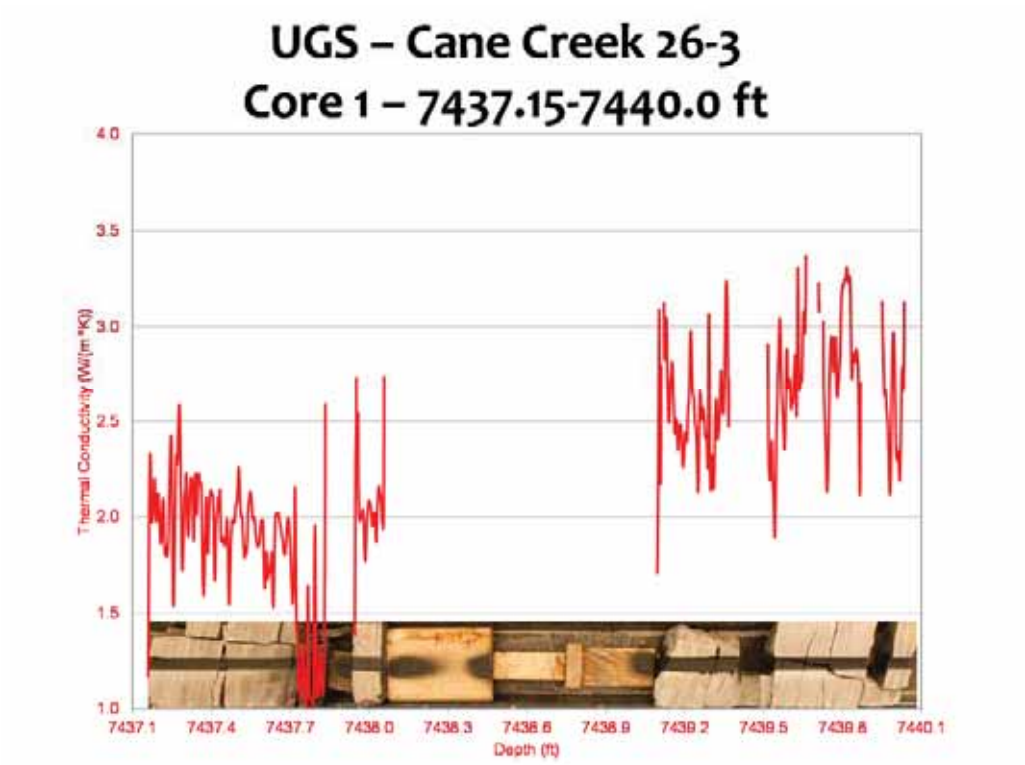
UGS – Cane Creek 26-3
Core 1 – 7437.15-7440.0 ft
Thermal Conductivity (W/(m*K))
4.0
3.5
3.0
2.5
2.0
1.5
1.0
7437.1
7437.4
7437.7
7438.0
7438.3
7438.6
7438.9
7439.2
7439.5
7439.8
7440.1
Depth (ft)

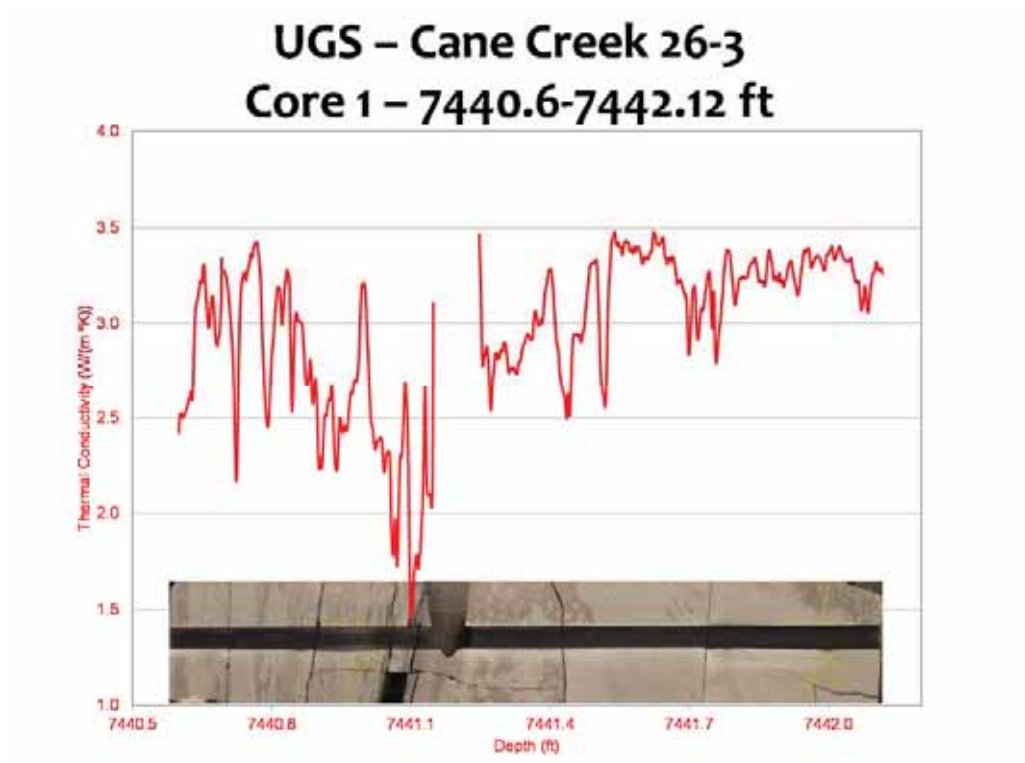
UGS – Cane Creek 26-3
Core 1 – 7440.6-7442.12 ft
Thermal Conductivity (W/(m*K))
4.0
3.5
3.0
2.5
2.0
1.5
1.0
7440.5
7440.8
7441.1
7441.4
7441.7
7442.0
Depth (ft)

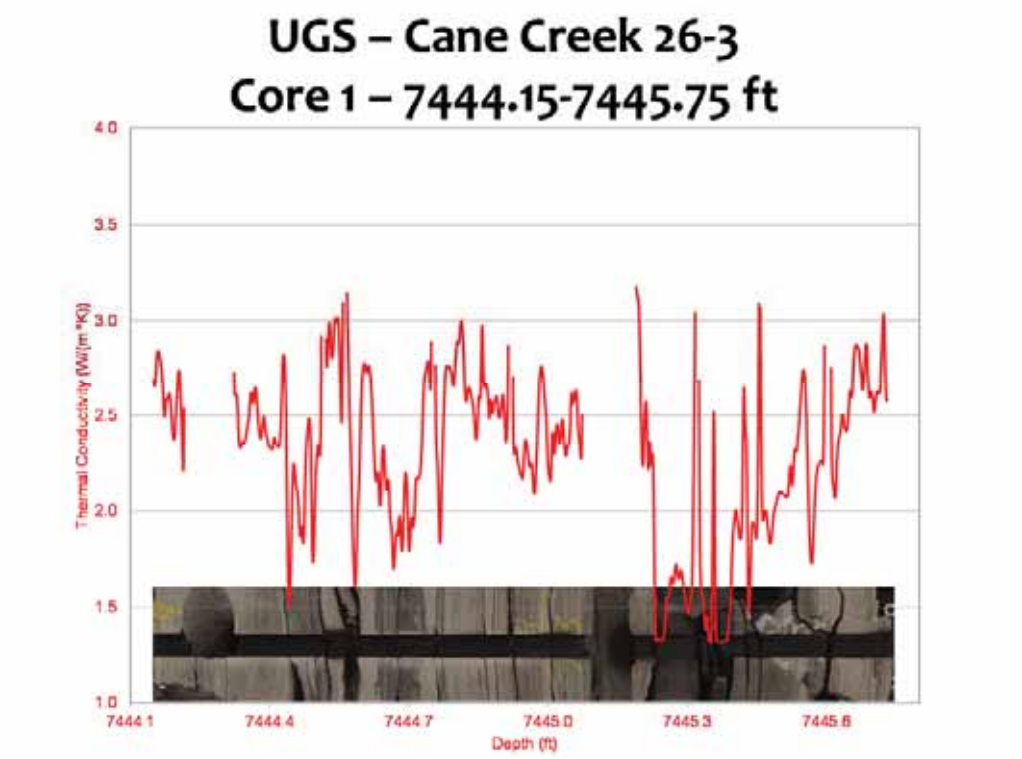
UGS – Cane Creek 26-3
Core 1 – 7444.15-7445.75 ft
Thermal Conductivity (W/(m*K))
4.0
3.5
3.0
2.5
2.0
1.5
1.0
7444.1
7444.4
7444.7
7445.0
7445.3
7445.6
Depth (ft)

CT Scans – Fidelity Cane Creek CCU7-1

Designation	Scan
7609.00_L	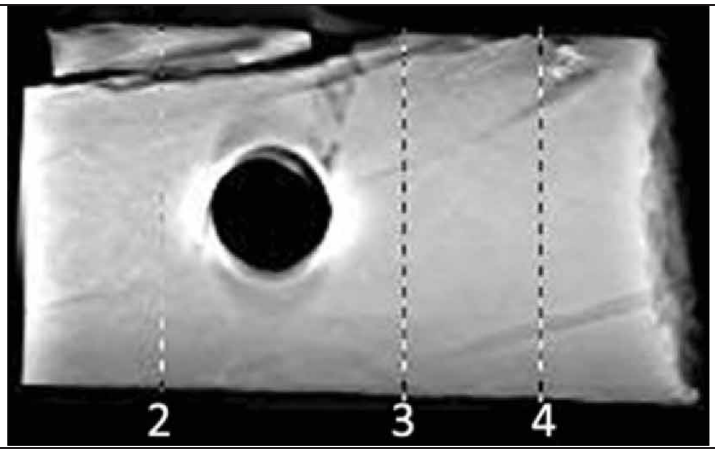
7609.0_X1	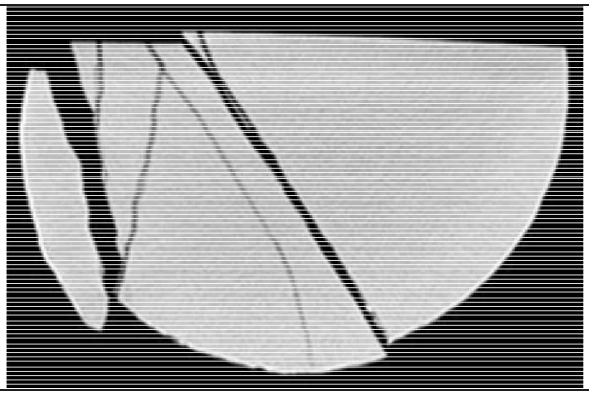
7609.0_x2	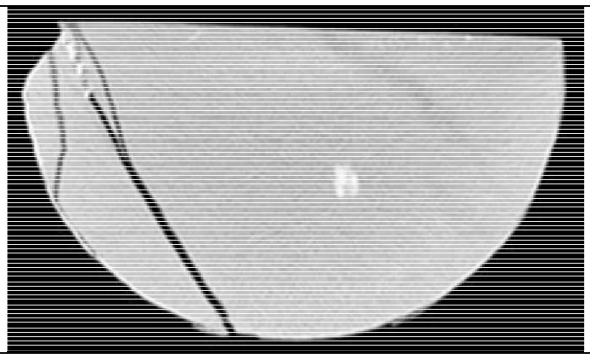

7609.0_x3	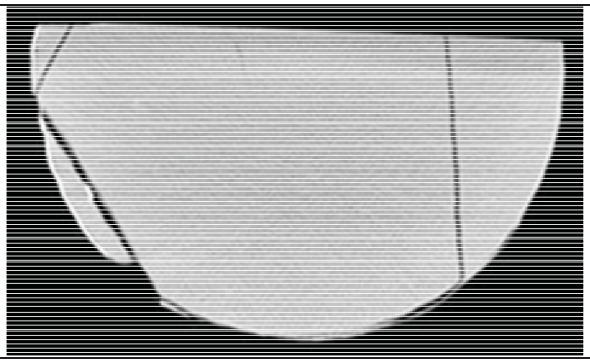
7614.0_L	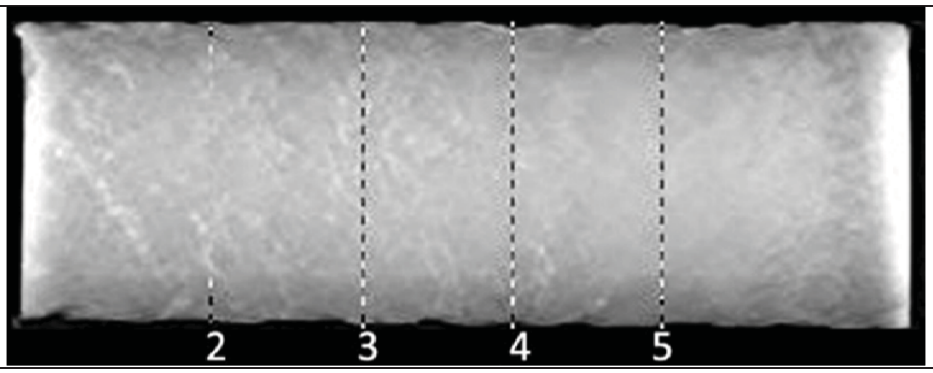
7614.0_X1	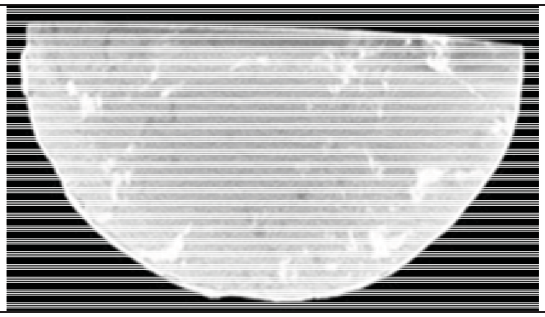
7614.0_x2	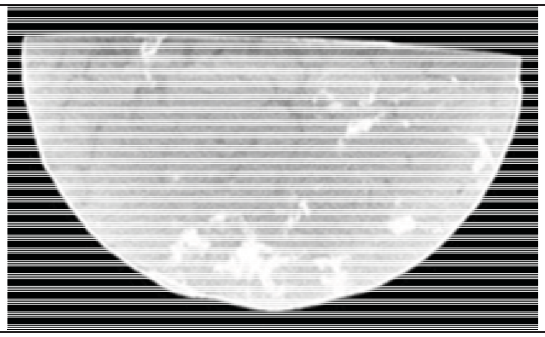

7614.0_x3	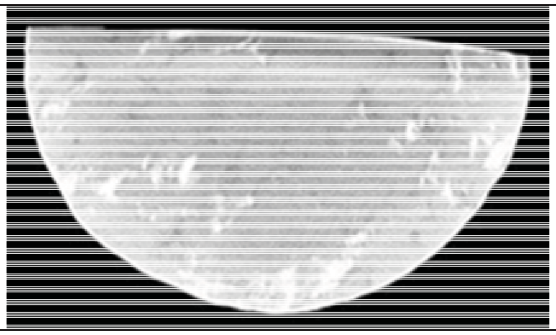
7614.0_x4	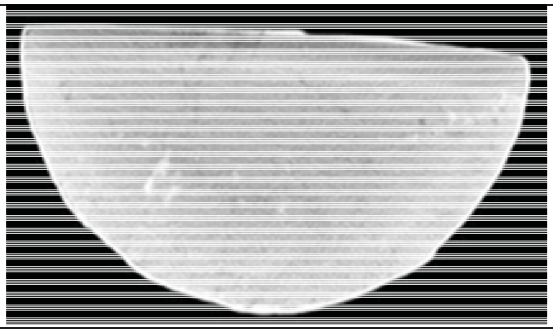
7619.0_L	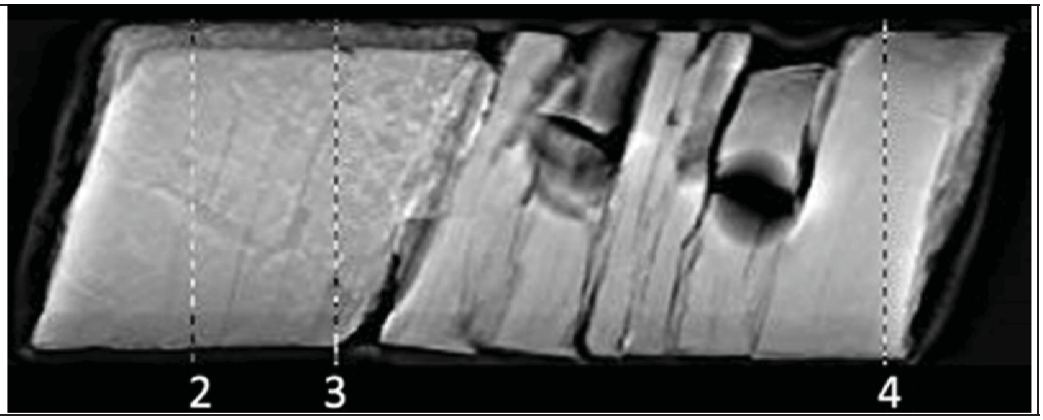
7619.0_X1	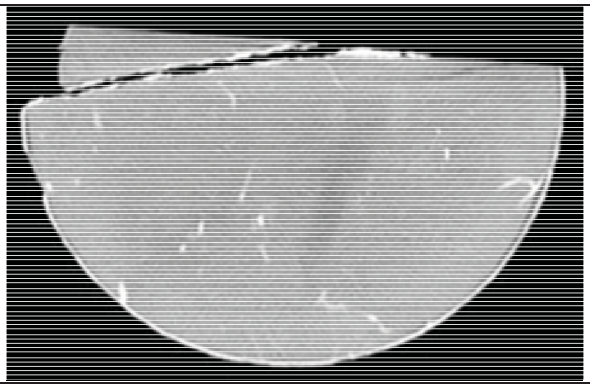

7619.0_x2	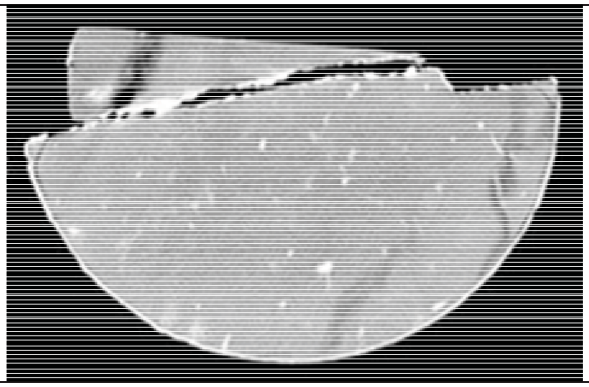
7619.0_x3	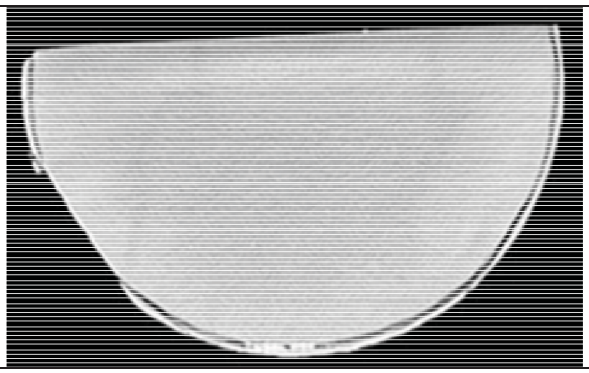
7620.0_L	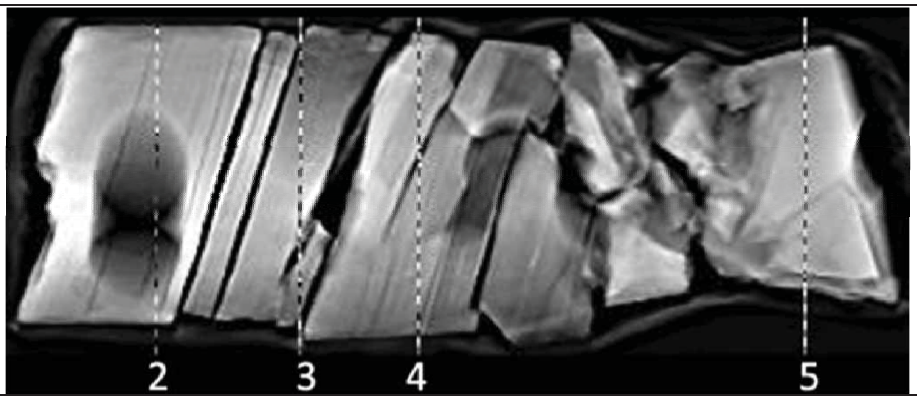
7620.0_X1	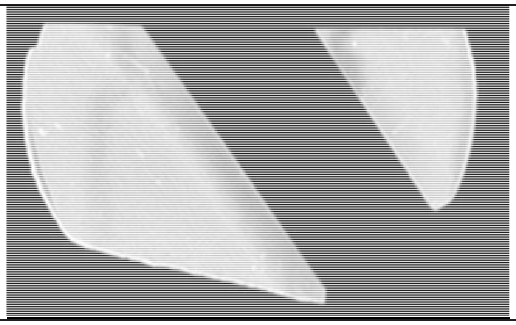

7620.0_x2	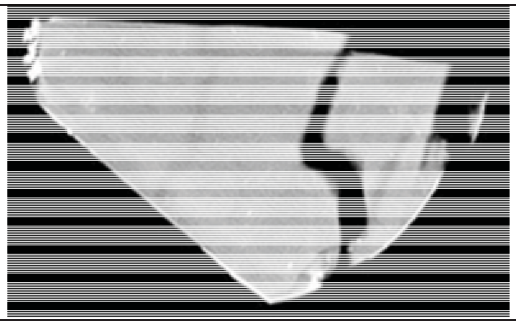
7620.0_x3	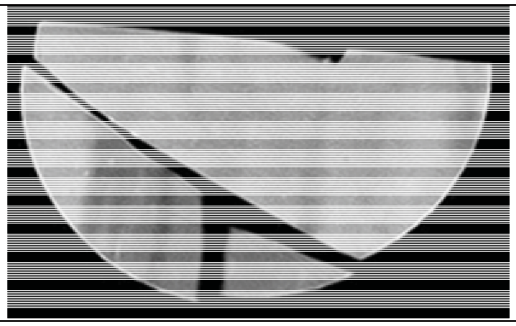
7620.0_x4	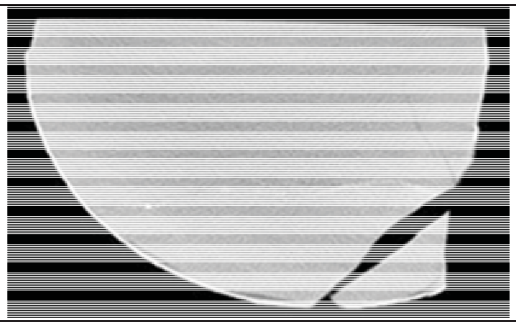
7624.0_L	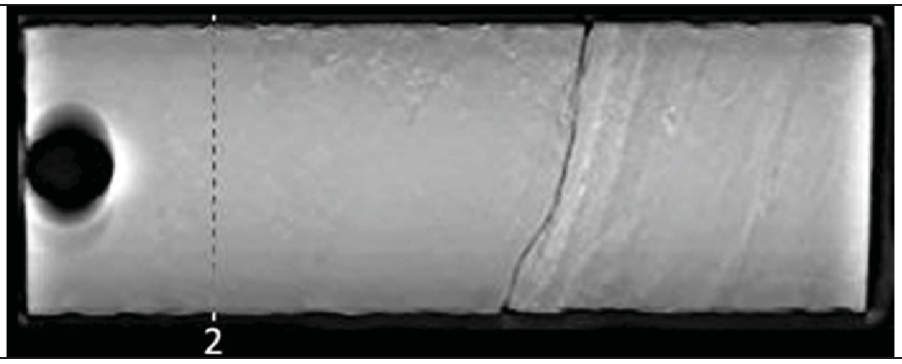
7624.0_X1	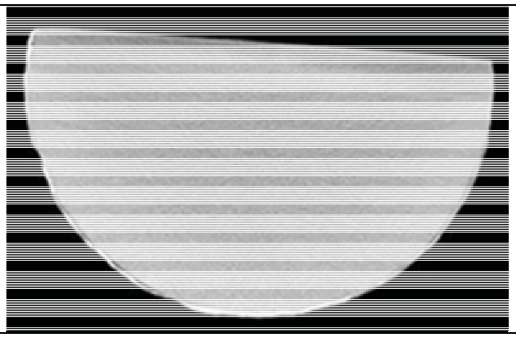

7624.0_x2	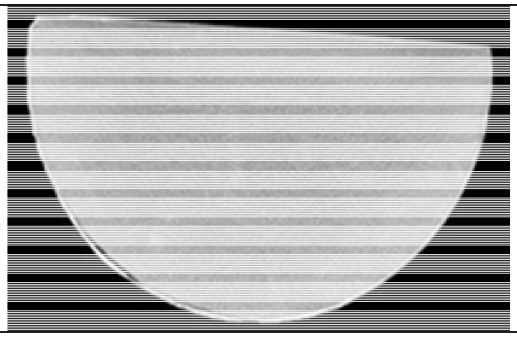
7624.0_x3	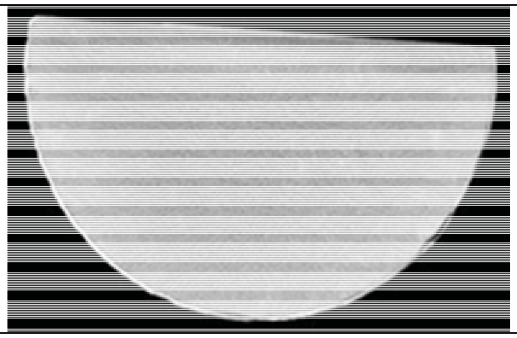
7624.0_x4	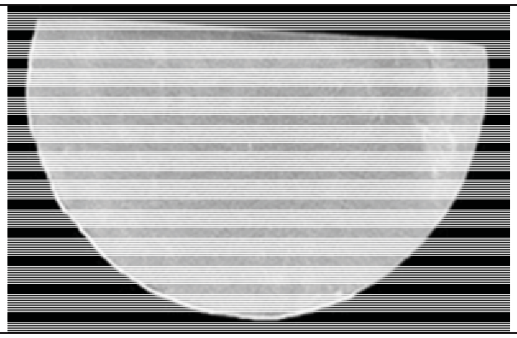
7630.0_L	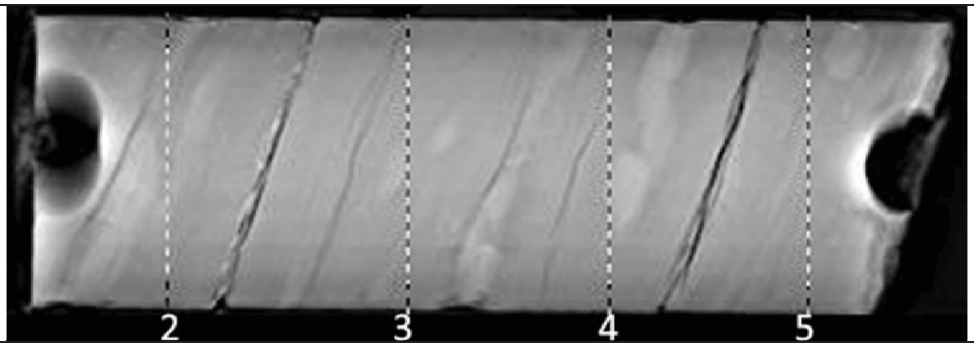

7630.0_X1	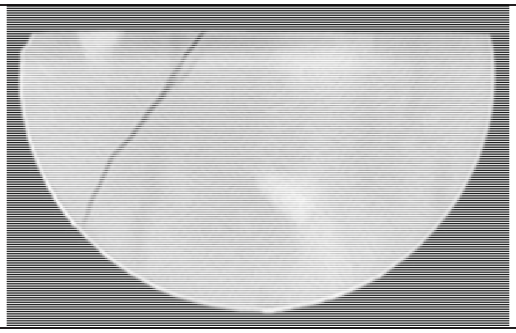	
7630.0_x2	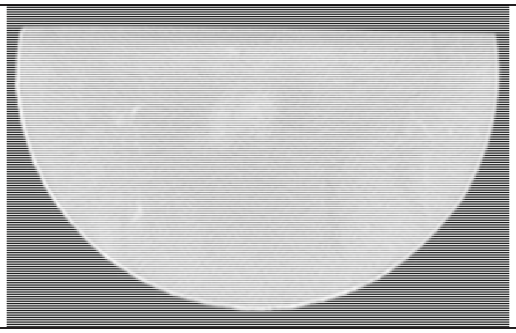	
7630.0_x3	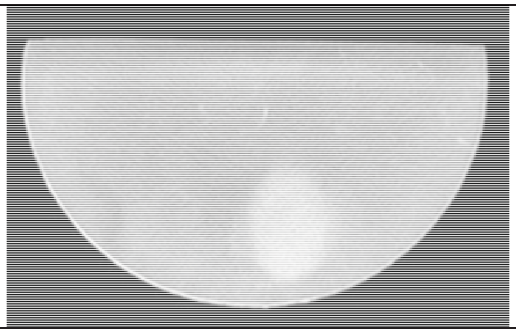	
7630.0_x4	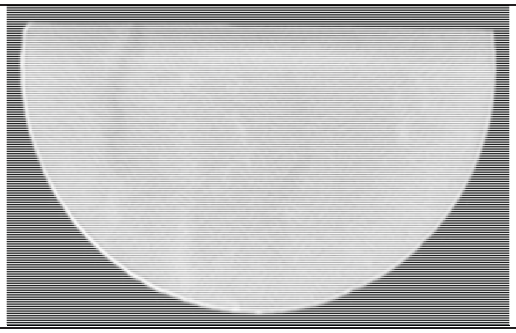	

7638.0_L	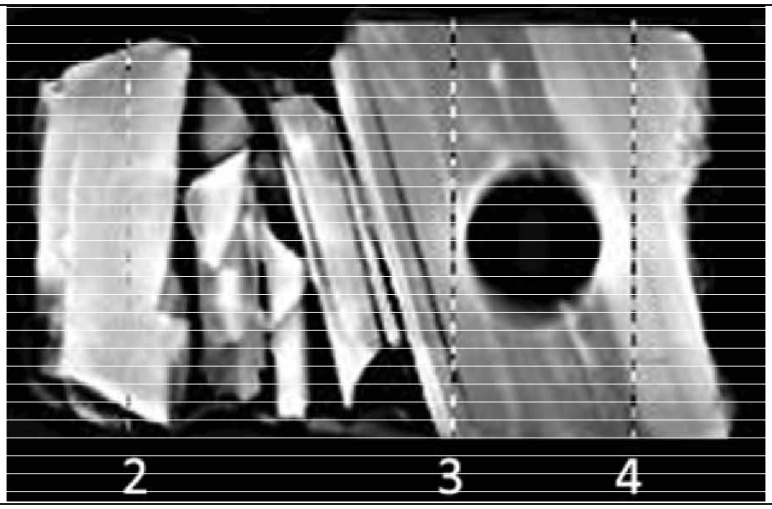
7638.0_X1	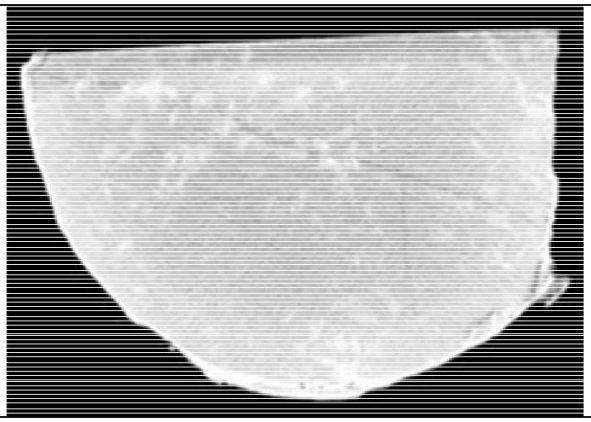
7638.0_x2	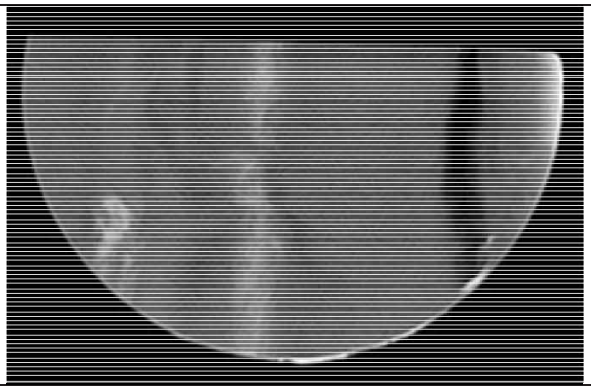

7638.0_x3	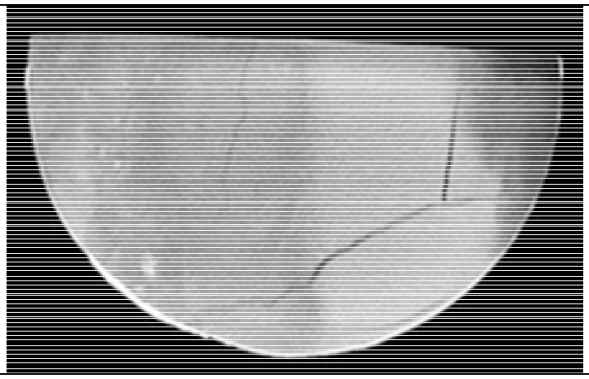	
7645.3_L	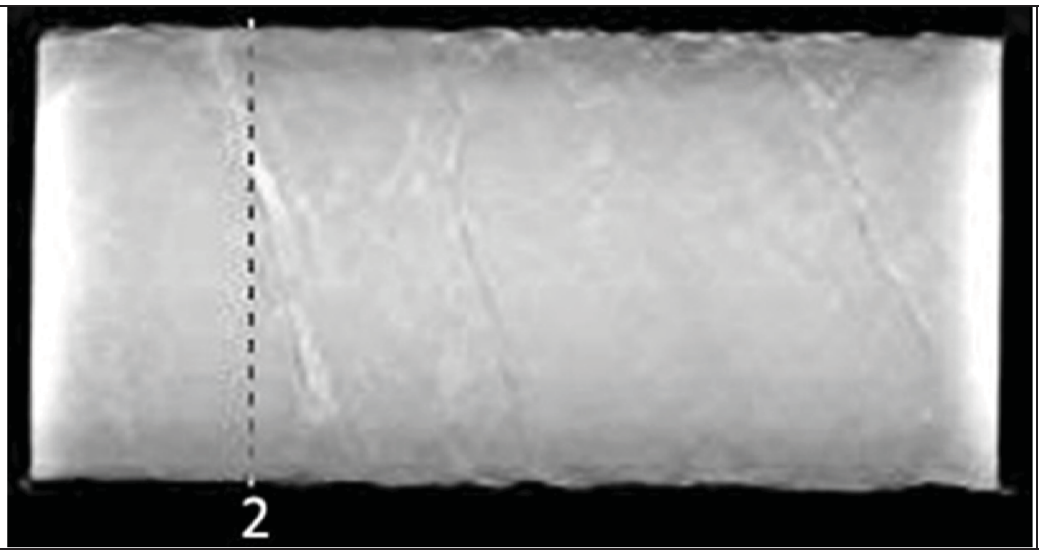	
7645.3_X1	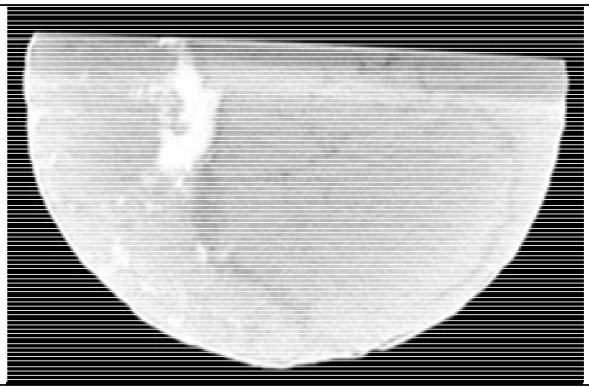	

7645.3_x2	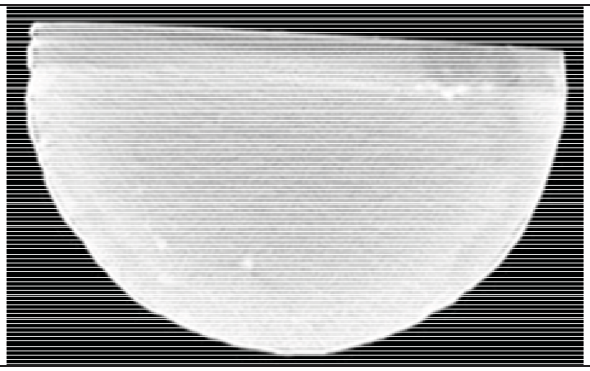
7645.3_x3	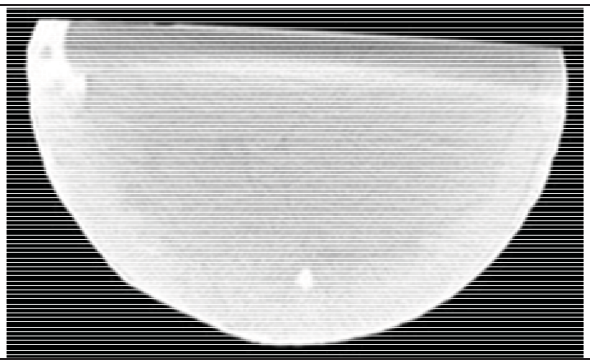
7651.3_L	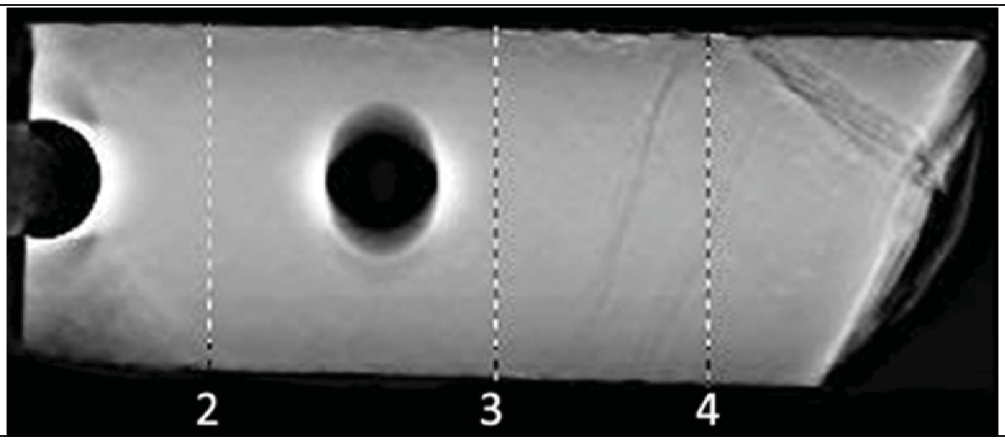
7651.0_X1	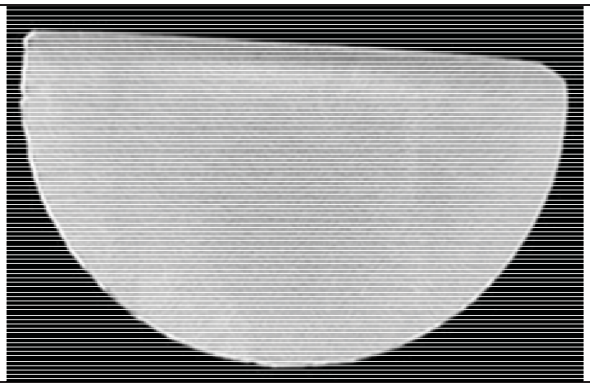

7651.0_x2	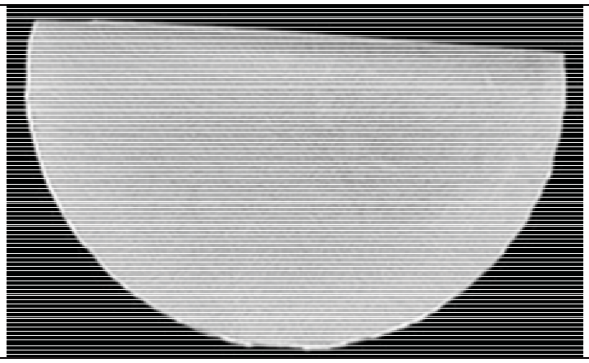	
7651.0_x3	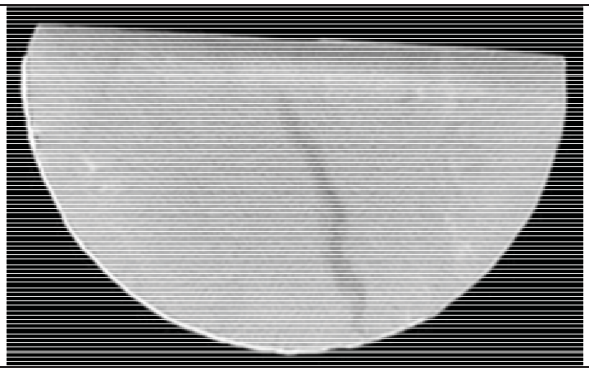	
7657.4_L	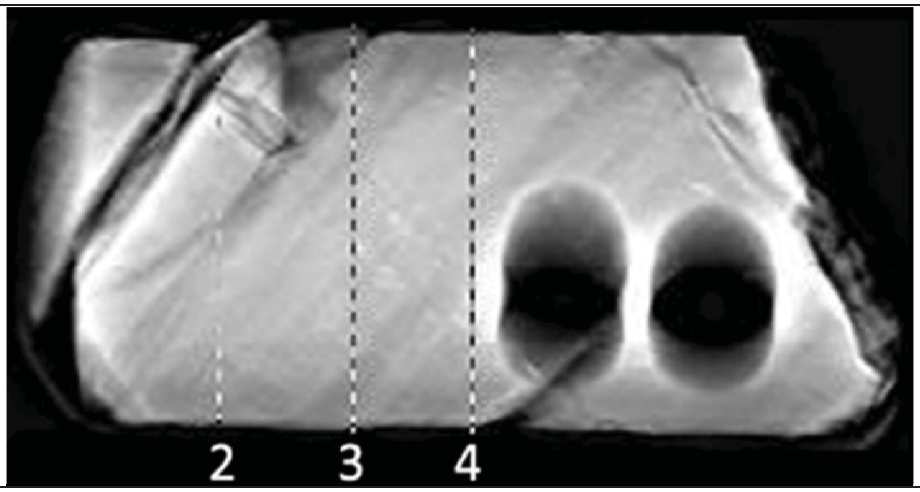	

7657.4_X1	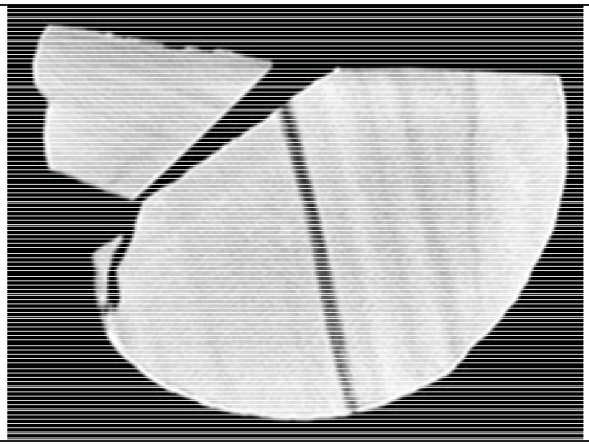	
7657.4_x2	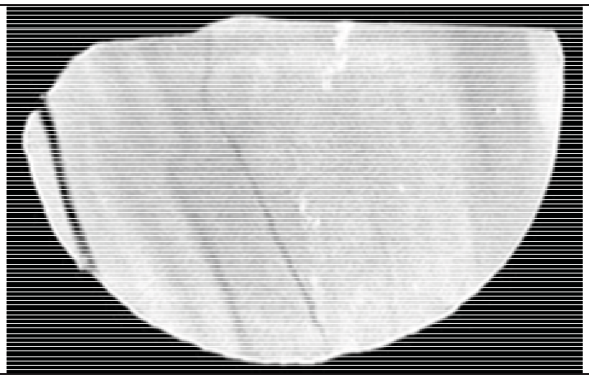	
7657.4_x3	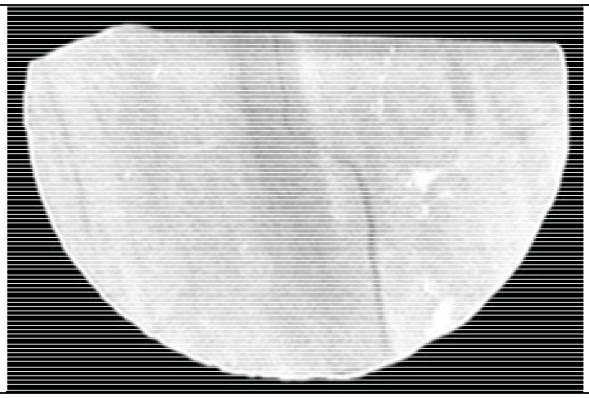	

Whole Core 1	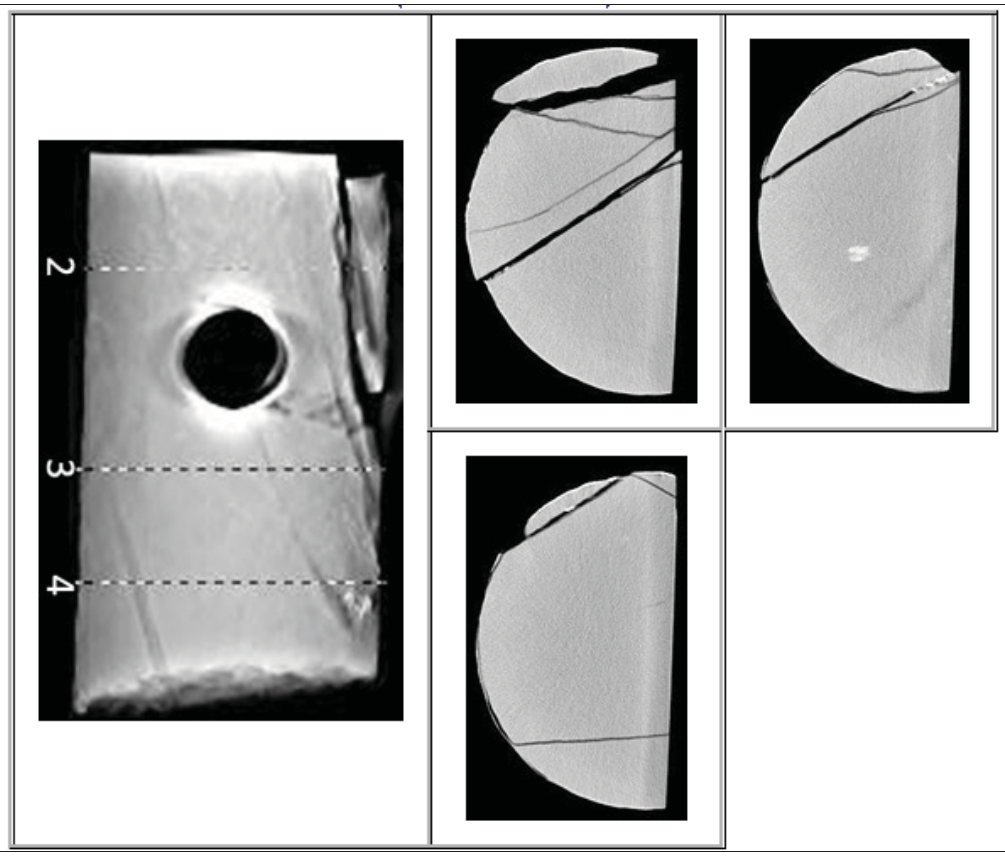

Whole Core 2

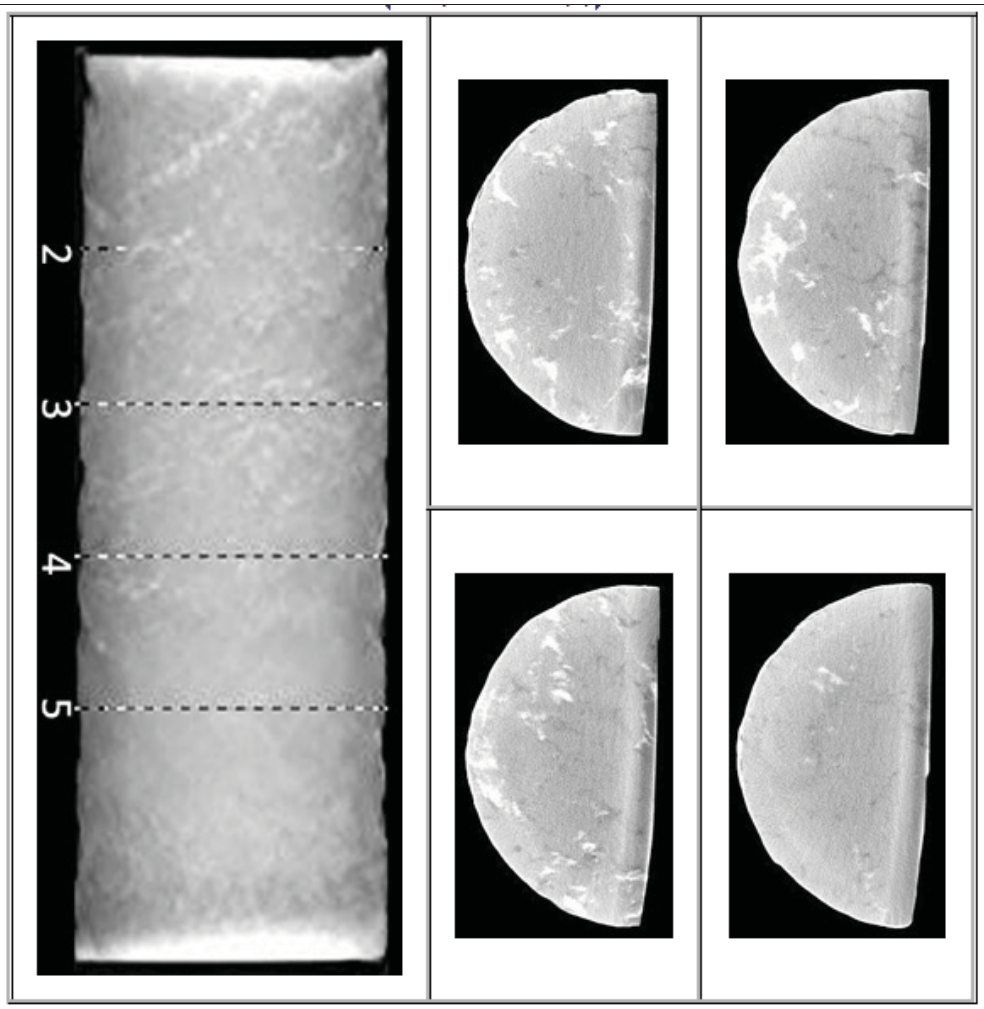

Whole Core 3	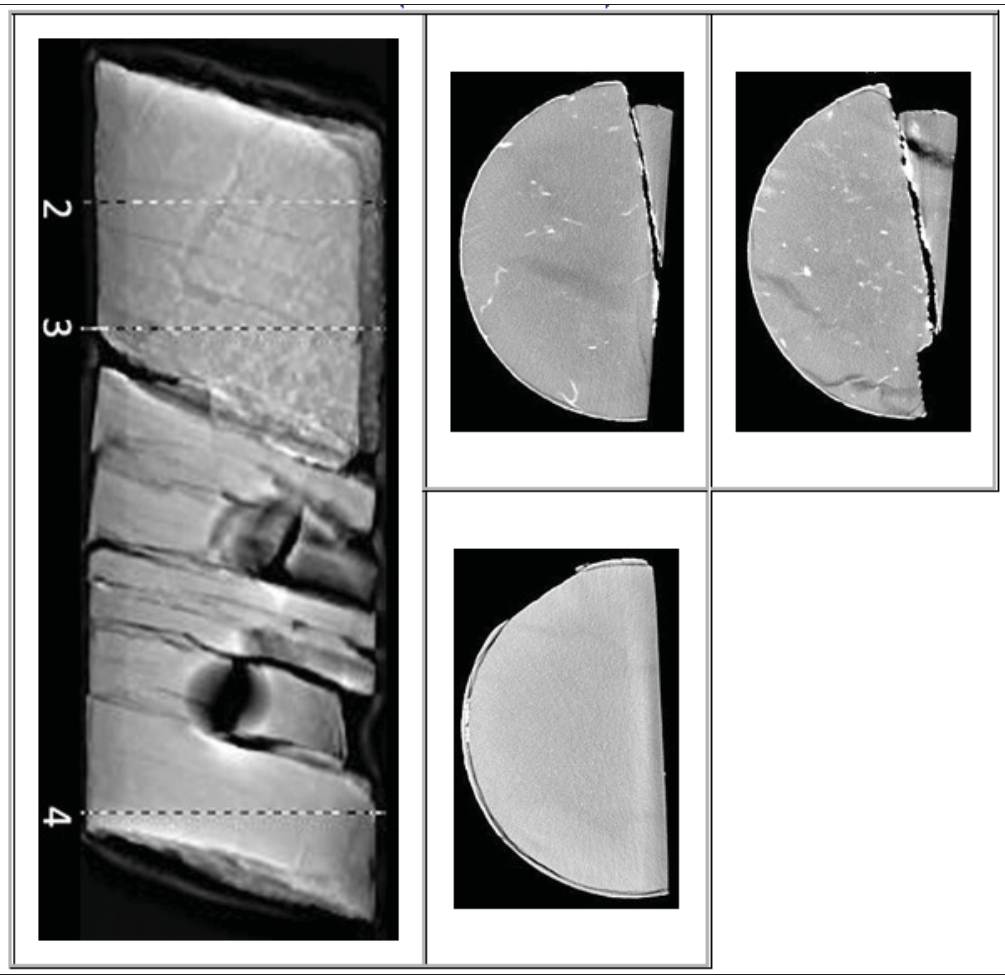

Whole Core 4	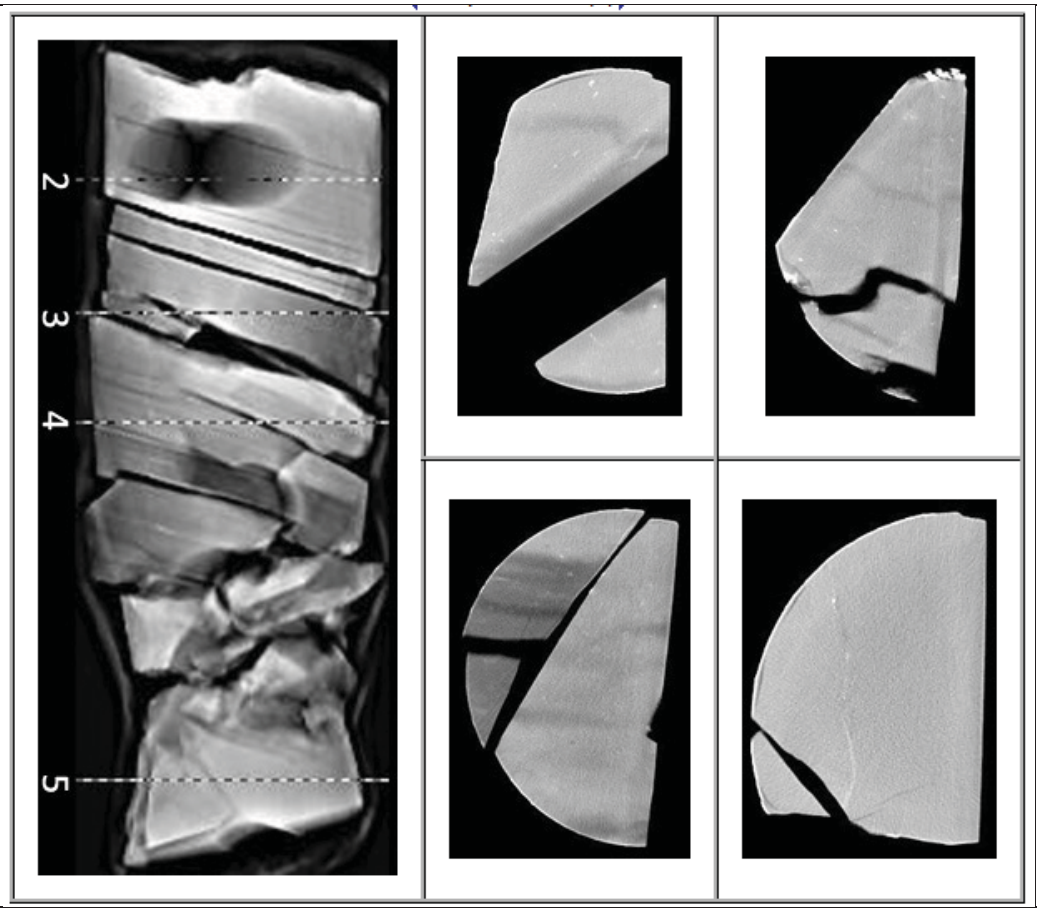

Whole Core 5	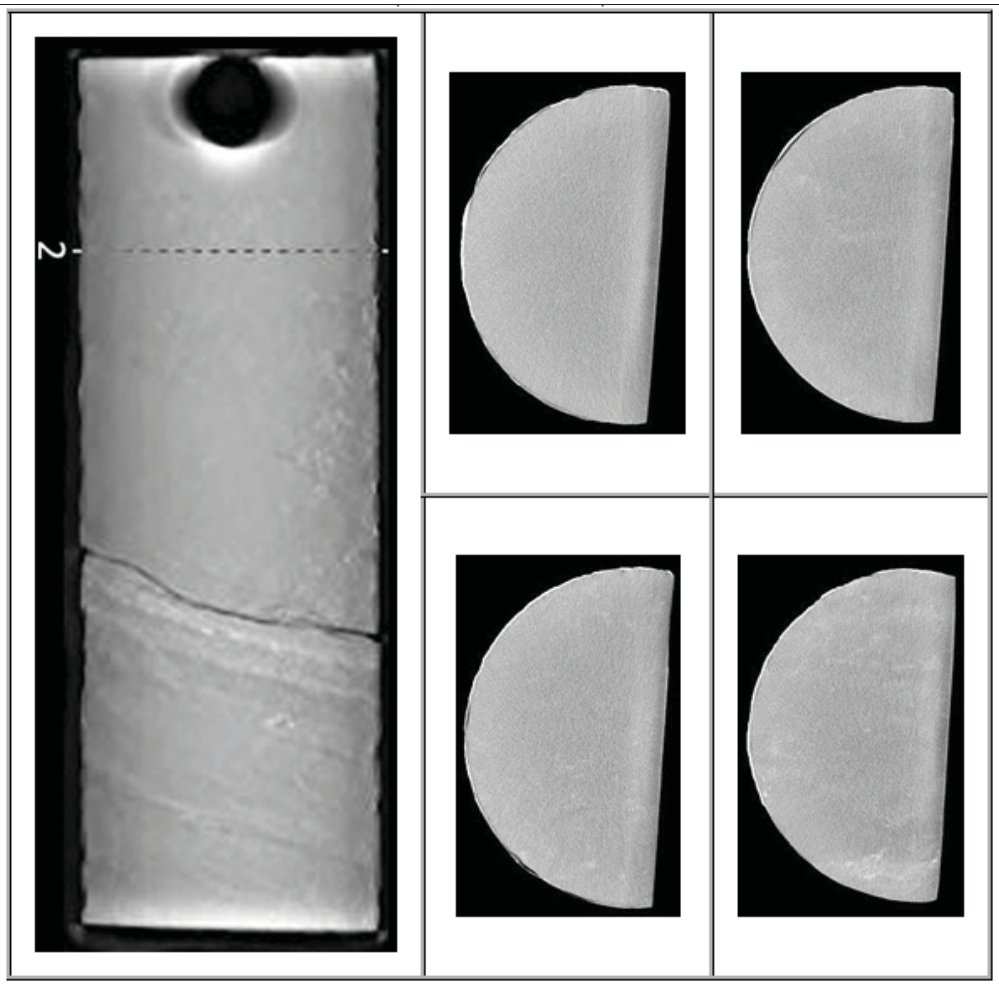

Whole Core 6	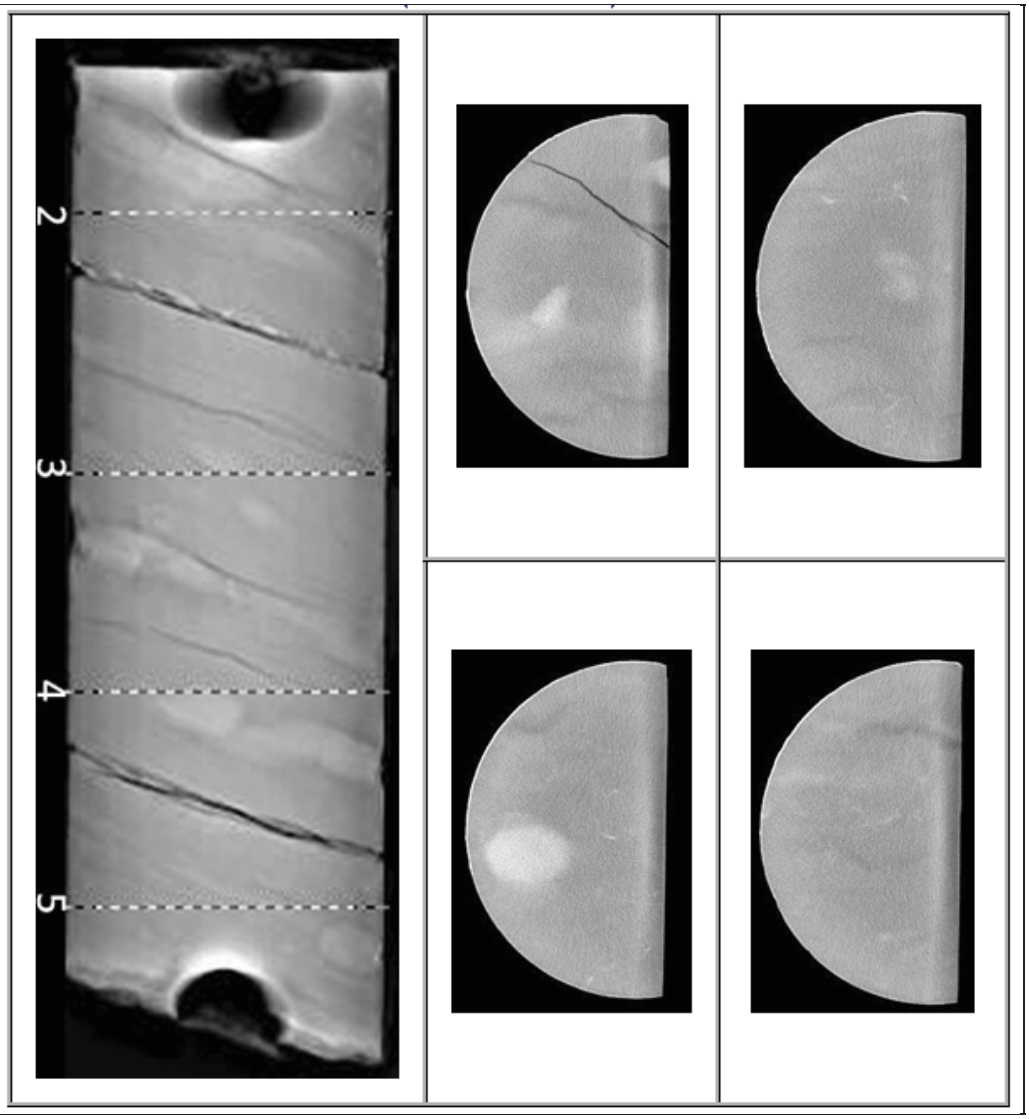

Whole Core 7	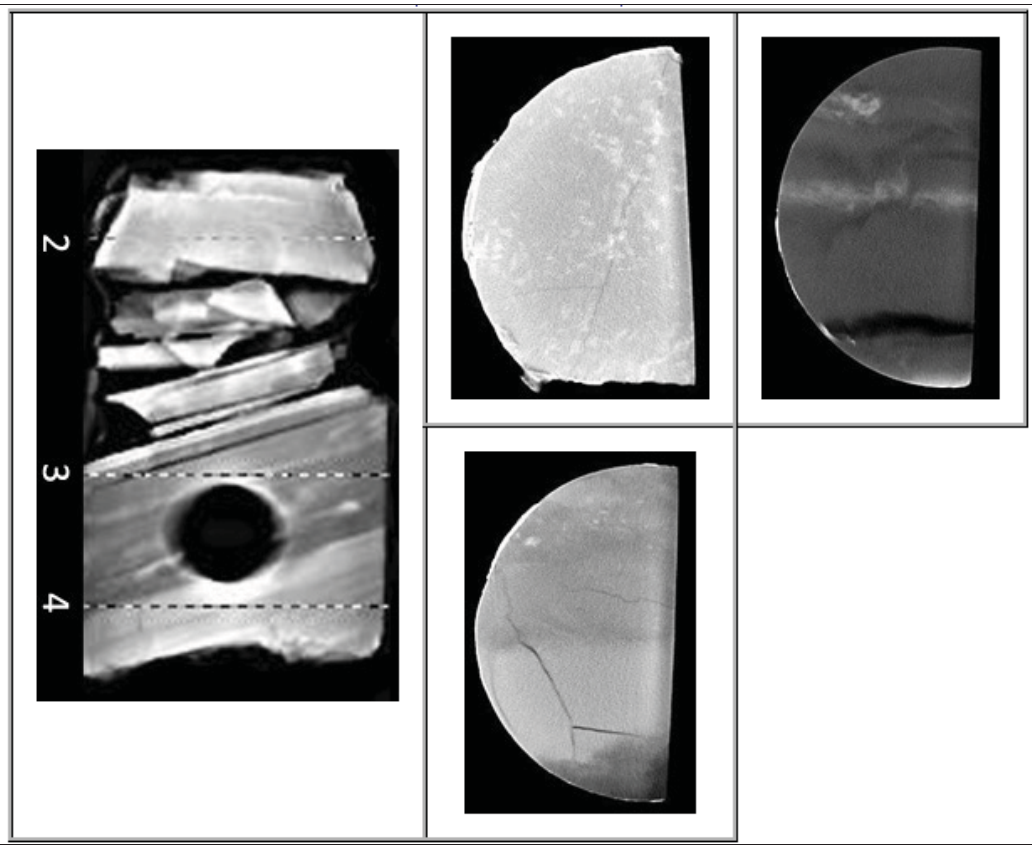

Whole Core 8	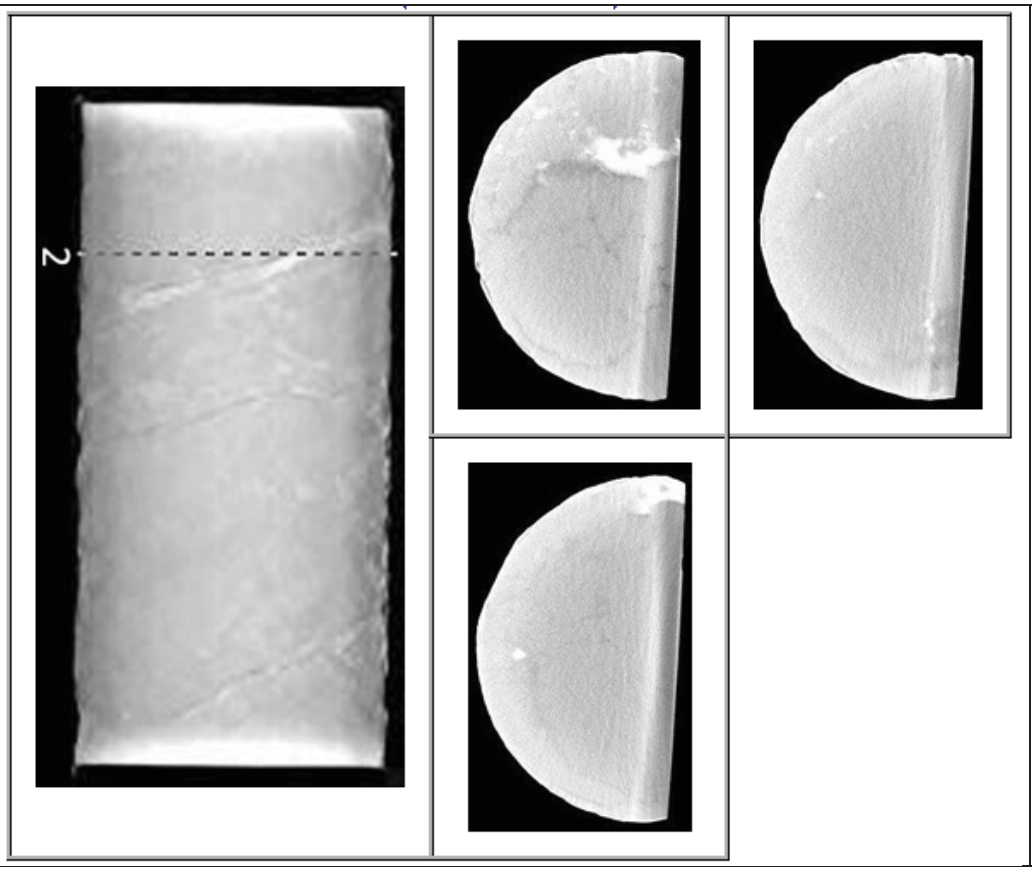

Whole Core 9	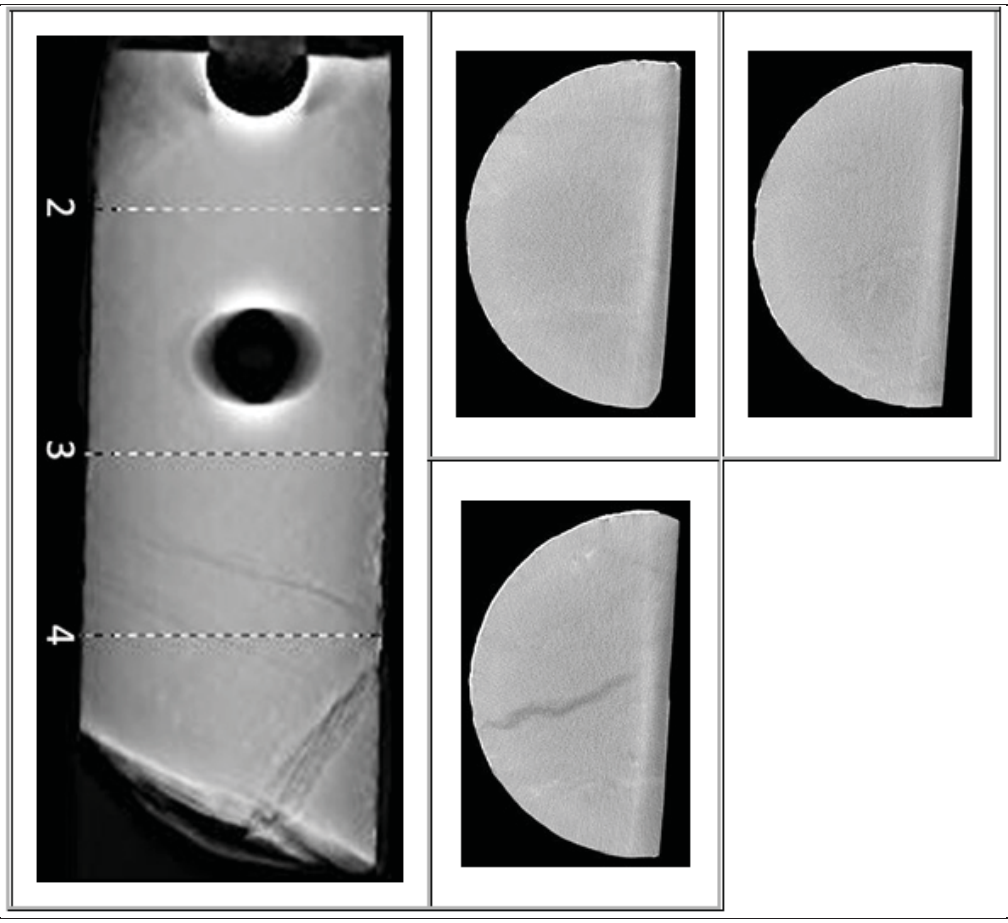

Whole Core 10	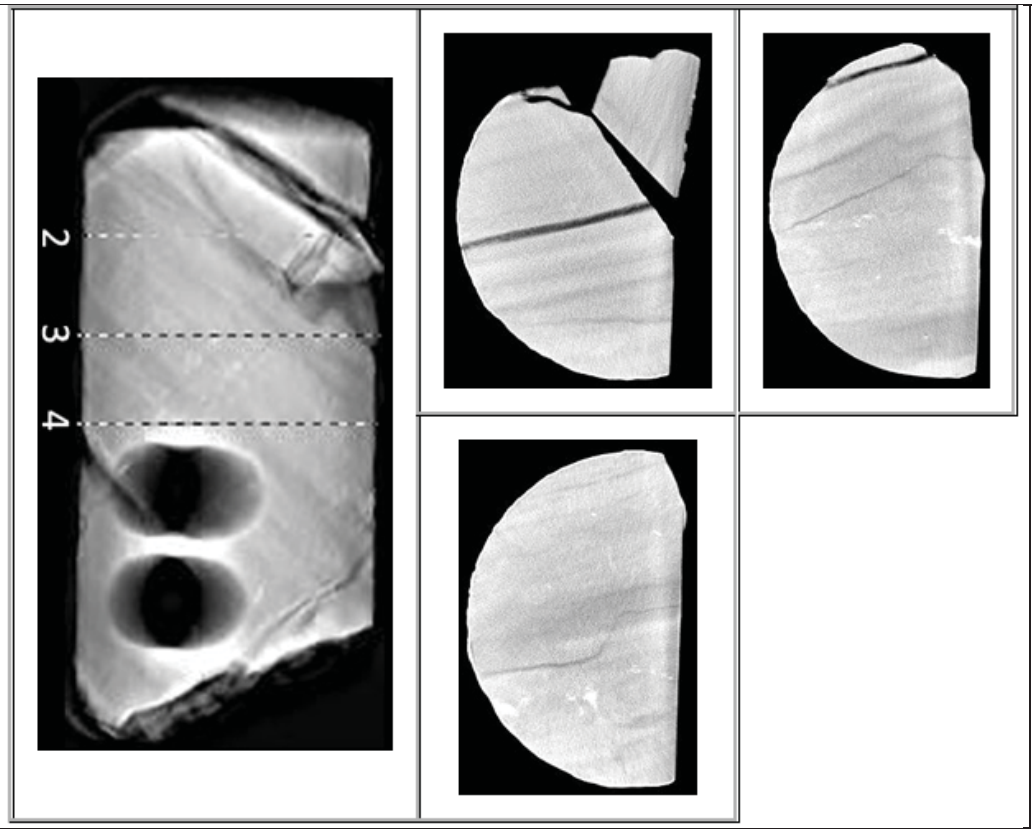

FTIR

TerraTek received 5 samples for FTIR and elemental analyses. Samples were crushed, split, and milled to <2 microns, mixed with KBr to create a homogeneous mixture, and then pressed to create a high-quality pellet to be run on the Bruker Vertex 70 machine. The resulting spectrum from the dual-range FTIR spectrometer was processed by a software program that reconstructs the spectrum based on standards in a reference mineral library and the quantitative mineralogic composition of the sample (as relative weight percent) is determined based on least-squares fitting.

Mineralogy

The FTIR results indicate the samples represent dolostone, limestone, and argillaceous mudstone. The dolostones are composed of 76-85% dolomite, 8-16% calcite, 2-3% siderite, 2-5% quartz, and 3-6% clay + mica. BTR6-1 (6683.50 ft) represents an argillaceous mudstone with 50% clay, 16% quartz, 20% total carbonate (10% calcite and 10% dolomite), and 4% K-feldspar. Sample BTR7-1 (6689.50 ft) represents a limestone, composed of 90% total carbonate (84% calcite, 1% dolomite, and 5% ankerite), 3% quartz, and 5% clay + mica. Trace to minor amounts of pyrite (1-10%) are also present in some samples.

Table A-12. FTIR Results - Mineralogy in Relative Wt %

Sample ID	BTR1-5	BTR2-4	BTR4-6	BTR6-1	BTR7-1
Depth (ft)	6684.70	6693.40	6703.30	6683.50	6689.50
Quartz	3	2	5	16	3
K-feldspar	0	0	0	4	0
Na-feldspar	0	0	0	0	0
Ca-feldspar	0	0	0	0	0
Total Feldspar	0	0	0	4	0
Calcite	10	8	16	10	84
Dolomite	85	80	76	10	1
Ankerite	0	0	0	0	5
Siderite	2	3	0	0	0
Total Carbonate	97	91	92	20	90
Illite	0	4	2	50	4
Smectite	0	1	0	0	1
Kaolinite	0	1	0	0	0
Chlorite	0	0	0	0	1
Muscovite	0	0	0	0	0
Total Clay + Mica	0	6	3	50	5
Pyrite	0	2	0	10	1
Total	100	100	100	100	100

ANALYTE		WtKg	H2OP	C	S	CO3_C	ORG_C	LOI	SiO2	Al2O3	Fe2O3	MgO	CaO	K2O	Na2O	TiO2	MnO
METHOD		G_WGH 79	G_PHY 09B	GE_CS A06V	GE_CS A06V	GE_CS B03V	GE_CS B03V	GO_XR F76V	GO_XR F76V	GO_XR F76V	GO_XR F76V	GO_XR F76V	GO_XR F76V	GO_XR F76V	GO_XR F76V	GO_XR F76V	GO_X RF76V
DETECTION		0.001	0.1	0.01	0.01	0.01	0.05	-10	0.01	0.01	0.01	0.01	0.01	0.01	0.01	0.01	0.01
UNITS		kg	%	%	%	%	%	%	%	%	%	%	%	%	%	%	%
Sample ID	Depth (ft)																
BTR1-5	6684.70	N.A.	3.10	13.70	<0.01	12.00	1.97	45.90	4.26	0.23	0.14	17.10	30.80	0.04	0.10	<0.01	0.03
BTR2-4	6693.40	N.A.	3.00	13.20	0.35	12.00	1.47	43.50	5.51	1.55	0.95	15.50	30.10	0.29	0.13	0.04	0.09
BTR4-6	6703.30	N.A.	3.60	13.70	0.04	10.50	3.50	45.10	6.60	0.68	0.33	16.90	28.50	0.12	0.13	0.02	0.07
BTR6-1	6683.50	N.A.	4.80	3.97	7.43	3.24	0.76	17.00	42.20	12.10	9.44	4.13	7.94	2.73	0.72	0.48	0.05
BTR7-1	6689.50	N.A.	1.40	11.50	0.23	10.80	0.90	40.50	6.28	1.14	0.49	1.21	48.70	0.23	0.12	0.04	0.14
BTR1-5	6684.70	N.A.	0.06	<0.01	<0.01	98.70	0.13	320.00	<5	20.40	<10	<10	0.08	<0.1	20.00	10.30	210.00
BTR2-4	6693.40	N.A.	0.06	<0.01	<0.01	97.80	0.86	350.00	<5	19.90	<10	<10	0.63	0.30	20.00	9.43	690.00
BTR4-6	6703.30	N.A.	0.08	<0.01	<0.01	98.60	0.38	520.00	<5	18.90	<10	<10	0.21	0.10	30.00	10.10	450.00
BTR6-1	6683.50	N.A.	0.17	0.01	0.03	97.00	6.65	190.00	<5	5.20	60.00	40.00	6.42	2.60	100.00	2.33	360.00
BTR7-1	6689.50	N.A.	0.20	<0.01	<0.01	99.10	0.61	590.00	<5	>25	<10	<10	0.32	0.30	10.00	0.74	1020.00
BTR1-5	6684.70	N.A.	<5	0.02	<5	1040.00	<0.01	<5	<5	<1	<5	<0.1	<0.2	0.80	0.70	0.10	0.14
BTR2-4	6693.40	N.A.	<5	0.02	<5	580.00	0.03	18.00	18.00	<1	<5	<0.1	<0.2	9.00	1.80	0.80	0.74
BTR4-6	6703.30	N.A.	<5	0.03	<5	660.00	0.01	11.00	12.00	<1	<5	<0.1	<0.2	3.30	0.90	0.30	0.31
BTR6-1	6683.50	N.A.	36.00	0.07	10.00	240.00	0.28	113.00	106.00	<1	41.00	0.30	0.80	53.10	13.80	8.50	3.18
BTR7-1	6689.50	N.A.	<5	0.09	<5	950.00	0.02	9.00	17.00	<1	8.00	<0.1	<0.2	5.60	2.50	0.70	0.38
BTR1-5	6684.70	N.A.	0.06	<0.05	<1	0.12	<1	<1	<0.05	<0.2	0.40	<0.05	<2	<1	0.50	<5	0.12

ANALYTE		WtKg	H2OP	C	S	CO3_C	ORG_C	LOI	SiO2	Al2O3	Fe2O3	MgO	CaO	K2O	Na2O	TiO2	MnO
METHOD		G_WGH 79	G_PHY 09B	GE_CS A06V	GE_CS A06V	GE_CS B03V	GE_CS B03V	GO_XR F76V	GO_XR F76V	GO_XR F76V	GO_XR F76V	GO_XR F76V	GO_XR F76V	GO_XR F76V	GO_XR F76V	GO_XR F76V	GO_X RF76V
DETECTION		0.001	0.1	0.01	0.01	0.01	0.05	-10	0.01	0.01	0.01	0.01	0.01	0.01	0.01	0.01	0.01
UNITS		kg	%	%	%	%	%	%	%	%	%	%	%	%	%	%	%
Sample ID	Depth (ft)																
BTR2-4	6693.40	N.A.	0.46	0.21	2.00	0.84	<1	<1	0.15	<0.2	4.90	0.06	3.00	1.00	4.40	<5	1.12
BTR4-6	6703.30	N.A.	0.21	0.06	<1	0.34	<1	<1	0.06	<0.2	1.70	<0.05	3.00	<1	1.80	<5	0.46
BTR6-1	6683.50	N.A.	2.04	0.76	19.00	3.43	1.00	3.00	0.65	<0.2	28.50	0.32	15.00	11.00	23.50	17.00	6.53
BTR7-1	6689.50	N.A.	0.21	0.11	2.00	0.39	<1	<1	0.07	<0.2	3.00	<0.05	4.00	1.00	2.70	<5	0.68
BTR1-5	6684.70	N.A.	2.20	<0.1	0.10	1.00	<0.5	<0.05	<0.1	<0.5	<0.05	0.26	<1	1.10	<0.1	12.20	
BTR2-4	6693.40	N.A.	14.90	0.10	0.80	1.00	<0.5	0.13	1.00	<0.5	0.05	1.12	<1	4.90	0.30	22.60	
BTR4-6	6703.30	N.A.	5.80	<0.1	0.40	2.00	<0.5	0.06	0.30	<0.5	<0.05	0.41	<1	2.10	0.20	10.10	
BTR6-1	6683.50	N.A.	123.00	2.60	4.10	3.00	0.70	0.51	8.30	0.70	0.32	4.37	1.00	20.30	2.00	113.00	
BTR7-1	6689.50	N.A.	12.50	<0.1	0.50	<1	<0.5	0.06	0.80	<0.5	<0.05	0.65	<1	2.50	0.20	17.90	

Appendix B:

Available Brittleness Indices

Available Indices for Brittleness:

People will argue that Rickman's index accounts for geomechanical characteristics of brittleness. While this index can have merit from the perspective of convenience it is patently not a representation of brittleness or ductility because it only incorporates elastic properties. We are comparing various mechanical properties of rocks to develop energy release indices to assess if there is a preferred calculation. The indices used are as follows.

- For comparative purposes, we are assessing mineralogically-based indices (Figure B-1).

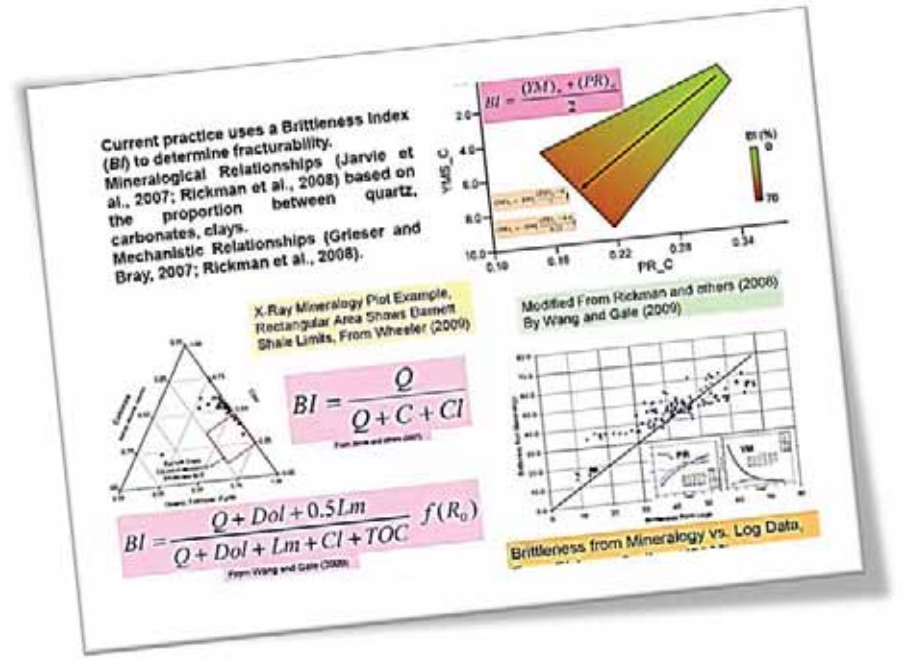

Figure B-1. Various mineralogic indices for so-called brittleness prediction.

The two indices include:

$$BI = \frac{Quartz}{Quartz + Calcite + Clay} \qquad BI = \frac{Quartz + Dolomite + 0.5Limestone}{Quartz + Dolomite + Limestone + Clay + TOC} f(Ro)$$

- For comparative purposes, we report the Rickman-type brittleness index. This is:

$$BRIT = 0.5\left\{\left(\frac{E-1}{8-1}\right)\times 100 + \left(\frac{\nu - 0.4}{0.15 - 0.40}\right)\times 100\right\}$$

- We then have developed descriptive indices for understanding potential energy release on failure. The first – denoted as Index 1 – qualitatively suggests energy lost up to the peak load. This is:

$$ER1 = \frac{Tangent\ Modulus}{Secant\ Modulus}$$

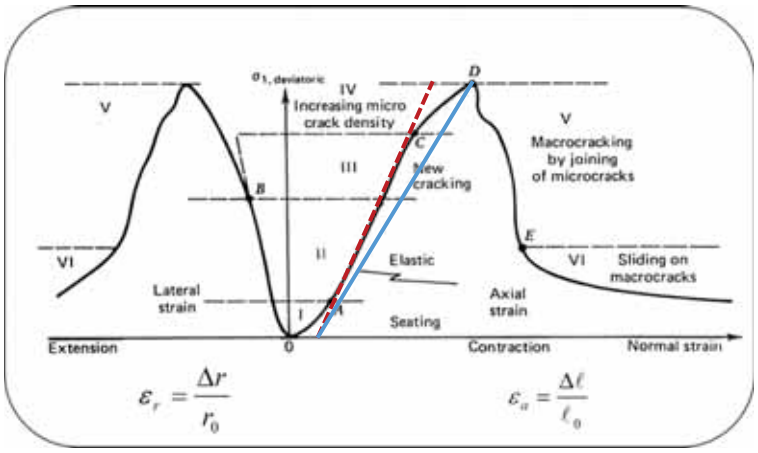

Figure B-2. The slope of the red dashed line indicates a tangent, elastic Young's modulus. The slope of the solid blue line is a secant. Notice that these do not need to pass through the origin if there is "seating" and/or microcrack closing.

The larger is this ratio, we speculate that more energy is released before ultimate failure and there will be less extreme release of energy on failure.

- The second Energy Release Index (ER2) is based on the relative amount of axial deformation after the peak strain

$$ER2 = \frac{\varepsilon_b - \varepsilon_a}{\varepsilon_r - \varepsilon_a}$$

- ε_b is the strain when rapid, unstable load capacity degradation is first experienced.
- ε_a is the strain at or near peak loading (post-yield, initiation of strain hardening or perfect plasticity.
- ε_r Onset of residual load-bearing capacity (notice the backwards trending tangent).

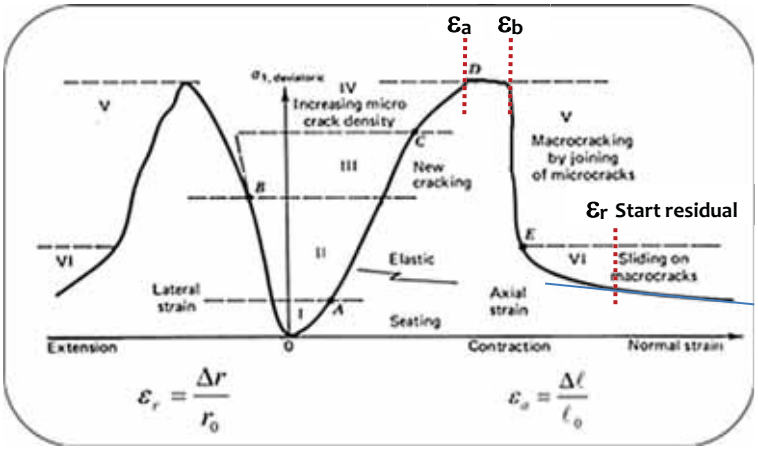

Figure B-3. Ratio of Stable Plastic Strain to Strain at Residual (axial).

a) If this ratio is small and the onset of residual strain is small, behavior is brittle.
b) If this ratio is small and residual is large, behavior is ductile.
c) If this ratio is about 1, the ductility is indeterminate.

- The third Energy Release Index (ER3a) is based on the relative amount of energy released after the peak strain, using only axial stress and strain.

$$ER3 = \frac{V_f}{2mE_t}\left[(\sigma_1 - \sigma_3)\big|_2 - (\sigma_1 - \sigma_3)\big|_3\right]$$

$$V_f = \pi\frac{D^2}{4}(\varepsilon_b - \varepsilon_r)(1 - 2\nu)$$

- ε_b is the strain when rapid, unstable load capacity degradation is first experienced.
- ε_r is the onset of residual load-bearing capacity (notice the backwards trending tangent) for axial strain.

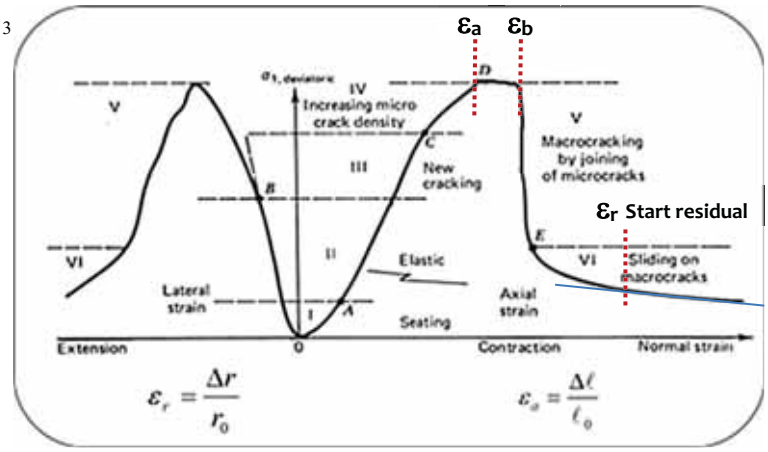

Figure B-4. Ratio of Stable Plastic Strain to Strain at Residual (axial).

- σ_1 is the peak axial stress (Pa)
- σ_3 is the total hydrostatic confining pressure (Pa)
- $\sigma_1 - \sigma_3$ is the peak axial differential stress (Pa)
- m is the mass of the sample (kg)
- E_t is the tangent Young's modulus (Pa)
- V_f is a proxy for the volume impacted (-)
- D is the sample diameter (m)
- V_f is the axial strain drop from b to residual plus an approximation for two radial strains in the same load space. The approximation uses a proxy for radial strain (Poisson's ratio) but uses the elastic value.
- ν is Poisson's ratio

The larger is this ratio, the more energy is released during post-peak deformation and load bearing capacity degradation. This was modified from Tang and Kaiser's work.

- A corollary Energy Release Index (ER3b) is based on the relative amount of energy released after the peak strain, using volumetric strain. It is analogous to ER3 with the exception that volumetric deformation is considered.

$$ER3 = \frac{V_f}{2mK}\left[(\sigma_1 - \sigma_3)\big|_{a-b} - (\sigma_1 - \sigma_3)\big|_{a-r}\right]^2$$

$$V_f = \pi \frac{D^2}{4}\left\{(\varepsilon_{a-b} - \varepsilon_{a-r}) + \sum_{i=1,2}(\varepsilon_{r-bi} - \varepsilon_{r-ri})\right\}$$

- $\varepsilon_{a\text{-}b}$ is the strain when rapid, unstable load capacity degradation is first experienced.
- $\varepsilon_{a\text{-}r}$ is the axial strain at the onset of residual load-bearing capacity (notice backwards trending tangent).

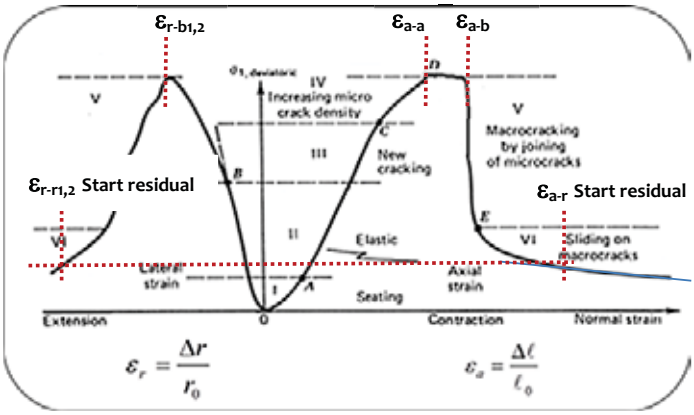

Figure B-5. Ratio of Stable Plastic Strain to Strain at Residual (axial).

- σ_1 is the peak axial stress (Pa)
- σ_3 is the total hydrostatic confining pressure (Pa)
- $\sigma_1 - \sigma_3$ is the peak axial differential stress (Pa)
- m is the mass of the sample (kg)
- K is the elastic, isotropic bulk modulus (Pa)
- V_f is a proxy for the volume impacted (-)
- D is the sample diameter (m)
- V_f is the volumetric strain drop from b to r (residual).

The larger is this ratio, the more energy is released during post-peak deformation and load bearing capacity degradation. This was modified from Tang and Kaiser's work.

- The fourth Energy Release Index (ER4) is based on the ratio of the peak and the residual axial differential stresses at in-situ conditions.

$$ER4 = \frac{(\sigma_1 - \sigma_3)\big|_a}{(\sigma_1 - \sigma_3)\big|_r}$$

- σ_1 is the total axial stress (Pa)
- σ_3 is the total hydrostatic confining pressure (Pa)
- $\sigma_1 - \sigma_3$ is the axial differential stress (Pa)
- Subscript "a" is for peak and "r" is for residual in the accompanying plot.

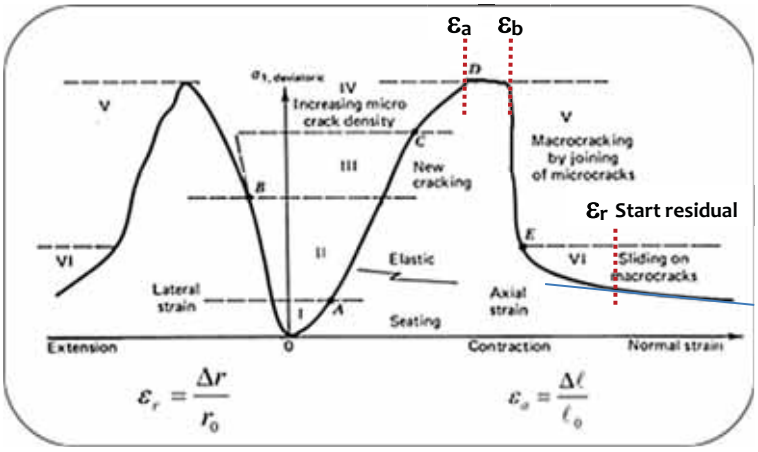

Figure B-6. Ratio of Stable Plastic Strain to Strain at Residual (axial).

If this ratio is large, substantial energy release can be anticipated. It is not an absolute identifier because absolute magnitudes of the numerator and denominator are important as well.

These calculations are documented in Appendix B-1. Appendix B-2 shows the indices plotted against logging parameters for Bill Barrett 1-14-46. The data for the other wells is being similarly evaluated.

Appendix B-1

Processed Triaxial Stress Data

Fidelity Cane Creek CCU7-1

Lithology	Sample ID	Depth (ft)	Orientation	As Received Bulk Density (g/cm^3)	Confining Pressure (psi)	Peak Effective Compressive Strength (psi)	Effective Residual Compressive Strength (psi)	Young's Modulus (10^6 psi)	Poisson's Ratio
silty dolomite	CCU1-1	7609.35	Vertical	2.624	3348	28,755	20,162	3.447	0.23
	CCU1-3	7609.15	Horizontal	2.599	3881	44,946	24,935	5.507	0.30

404730 UGS, CCU7-1
CCU1-1, 7609.35 ft, Vertical, As-Received

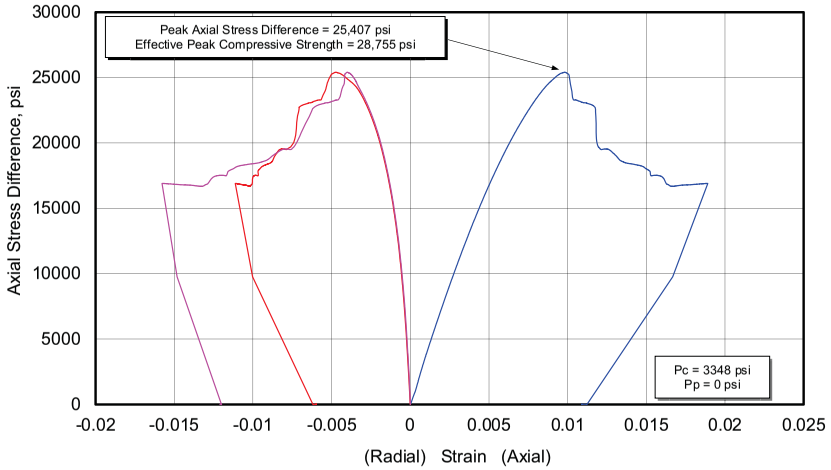

404730 UGS, CCU7-1
CCU1-3, 7609.15 ft, Horizontal, As-Received

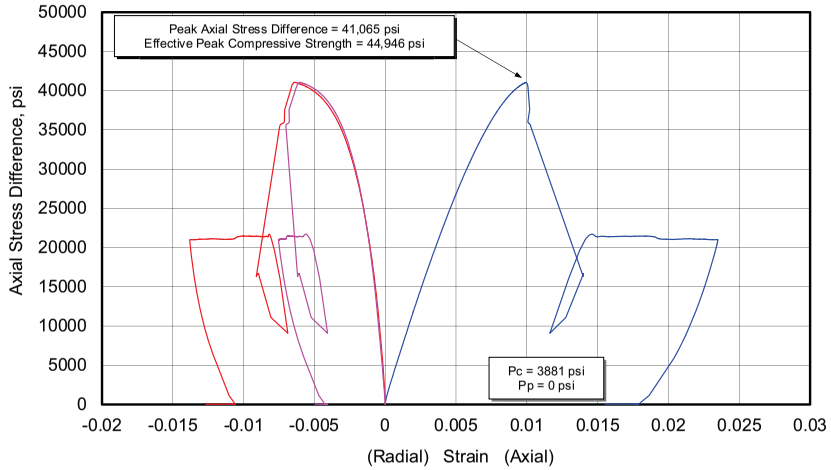

Zone 1 Deformation Index: Ratio of Secant E at Peak to E: 1.36
Zone 2 Ductility Index: Amount of Plastic or Strain Hardening Strain: 0.006
Zone 3a: Tang and Kaiser Index (Axial): 0.68 J/tonne
Zone 3b: Tang and Kaiser Index (Volumetric): 2.48 J/tonne
Zone 4: Peak to Residual Strength Ratio: 1.51

Zone 1 Deformation Index: Ratio of Secant E at Peak to E: 1.35
Zone 2 Ductility Index: Amount of Plastic or Strain Hardening Strain: 0
Zone 3a: Tang and Kaiser Index (Axial): 1.615
Zone 3b: Tang and Kaiser Index (Volumetric): N/A
Zone 4: Peak to Residual Strength Ratio: 1.88

Fidelity Cane Creek CCU7-1

Lithology	Sample ID	Depth (ft)	Orientation	As Received Bulk Density (g/cm^3)	Confining Pressure (psi)	Peak Effective Compressive Strength (psi)	Effective Residual Compressive Strength (psi)	Young's Modulus (10^6 psi)	Poisson's Ratio
anhydrite	CCU2-1	7614.00	Vertical	2.886	3350	31,827	19,750	7.383	0.34
	CCU2-3	7614.65	Horizontal	2.954	3883	33,347	21,675	8.060	0.33

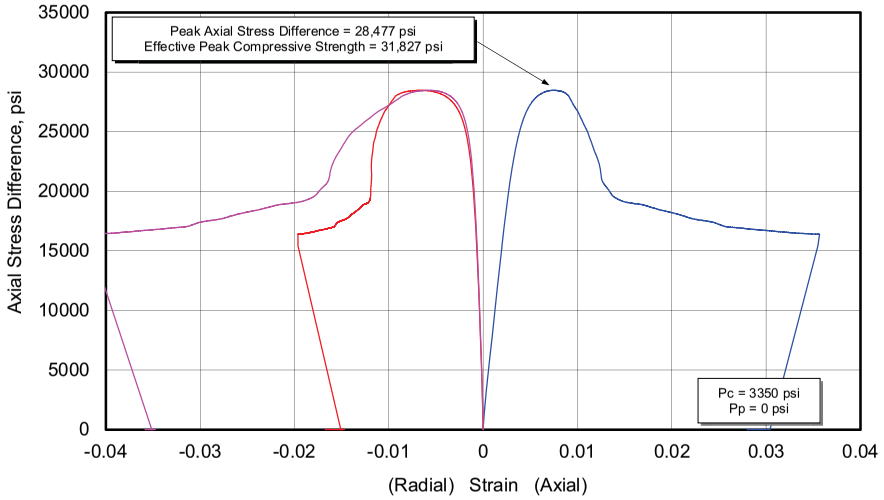

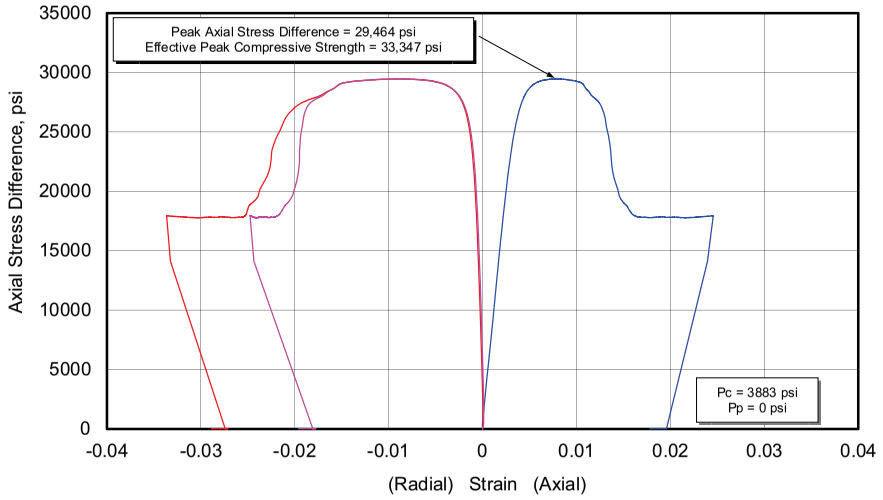

Zone 1 Deformation Index: Ratio of Secant E at Peak to E: 1.94
Zone 2 Ductility Index: Amount of Plastic or Strain Hardening Strain: 0.186
Zone 3a: Tang and Kaiser Index (Axial): 0.186 J/tonne
Zone 3b: Tang and Kaiser Index (Volumetric): 0.733 J/tonne
Zone 4: Peak to Residual Strength Ratio: 1.48

Zone 1 Deformation Index: Ratio of Secant E at Peak to E: 1.90
Zone 2 Ductility Index: Amount of Plastic or Strain Hardening Strain: 0.293
Zone 3a: Tang and Kaiser Index (Axial): 0.379 J/tonne
Zone 3b: Tang and Kaiser Index (Volumetric): 0.2.45 J/tonne
Zone 4: Peak to Residual Strength Ratio:1.64

Fidelity Cane Creek CCU7-1

Lithology	Sample ID	Depth (ft)	Orientation	As Received Bulk Density (g/cm^3)	Confining Pressure (psi)	Peak Effective Compressive Strength (psi)	Effective Residual Compressive Strength (psi)	Young's Modulus (10^6 psi)	Poisson's Ratio
silty dolomite - shale	CCU3-1	7619.00	Vertical	2.509	3352	18,220	-	1.686	0.28
	CCU3-5	7619.20	Horizontal	2.500	3886	21,688	16,561	2.054	0.24

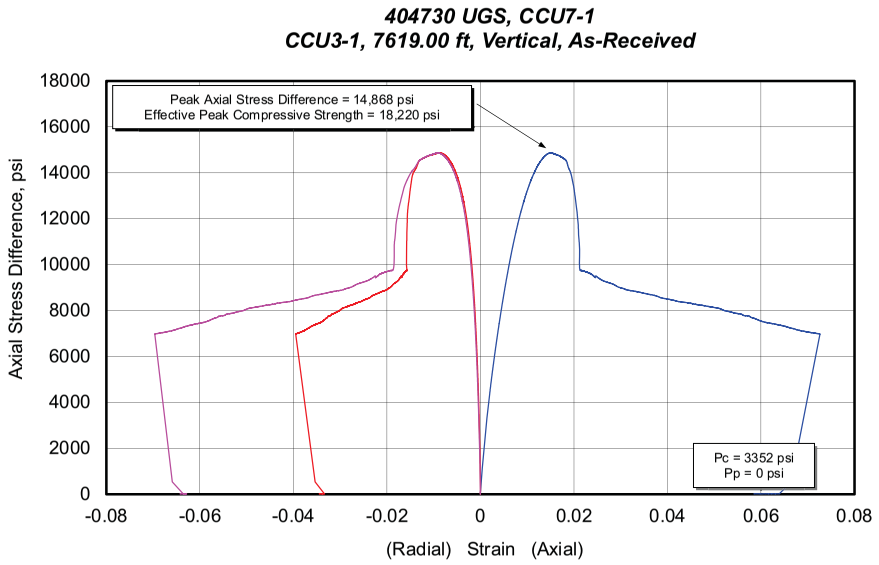

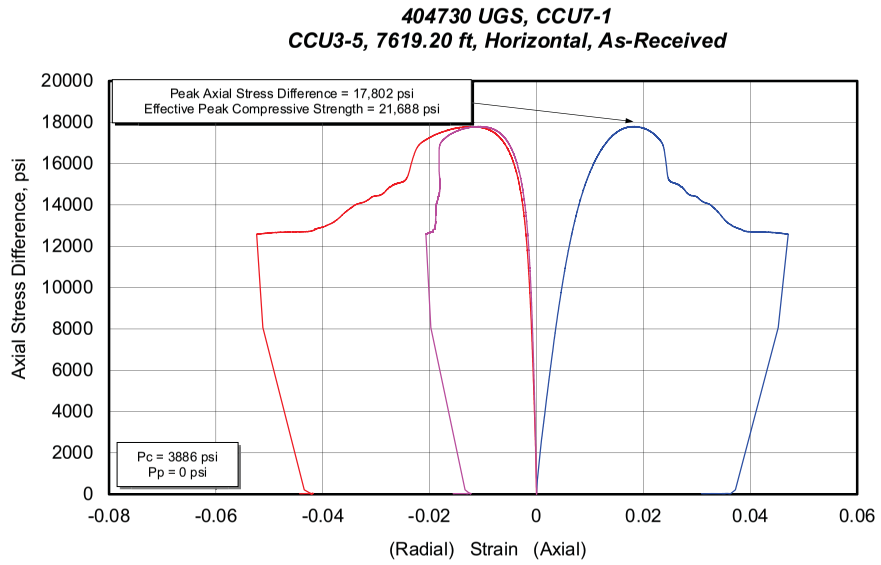

Zone 1 Deformation Index: Ratio of Secant E at Peak to E: 1.73
Zone 2 Ductility Index: Amount of Plastic or Strain Hardening Strain: 0.482
Zone 3a: Tang and Kaiser Index (Axial): 0.171 /tonne
Zone 3b: Tang and Kaiser Index (Volumetric): 0.971 J/tonne
Zone 4: Peak to Residual Strength Ratio: 1.51

Zone 1 Deformation Index: Ratio of Secant E at Peak to E: 1.90
Zone 2 Ductility Index: Amount of Plastic or Strain Hardening Strain: 0.309
Zone 3a: Tang and Kaiser Index (Axial): .889 J/tonne
Zone 3b: Tang and Kaiser Index (Volumetric): 3.97 J/Tonne
Zone 4: Peak to Residual Strength Ratio:1.39

Fidelity Cane Creek CCU7-1

Lithology	Sample ID	Depth (ft)	Orientation	As Received Bulk Density (g/cm^3)	Confining Pressure (psi)	Peak Effective Compressive Strength (psi)	Effective Residual Compressive Strength (psi)	Young's Modulus (10^6 psi)	Poisson's Ratio
shale	CCU4-1	7620.80	Vertical	2.487	3353	13,814	-	0.820	0.15
	CCU4-5	7620.30	Horizontal	2.514	3886	18,825	14,071	1.118	0.24

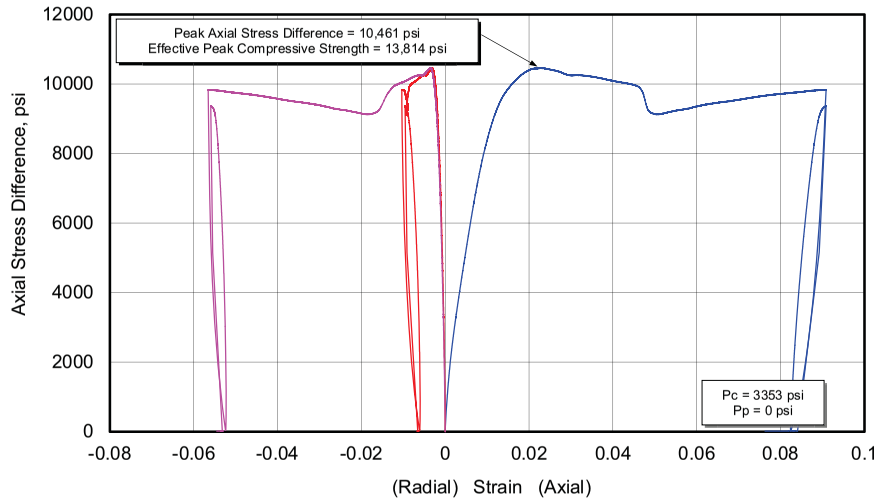

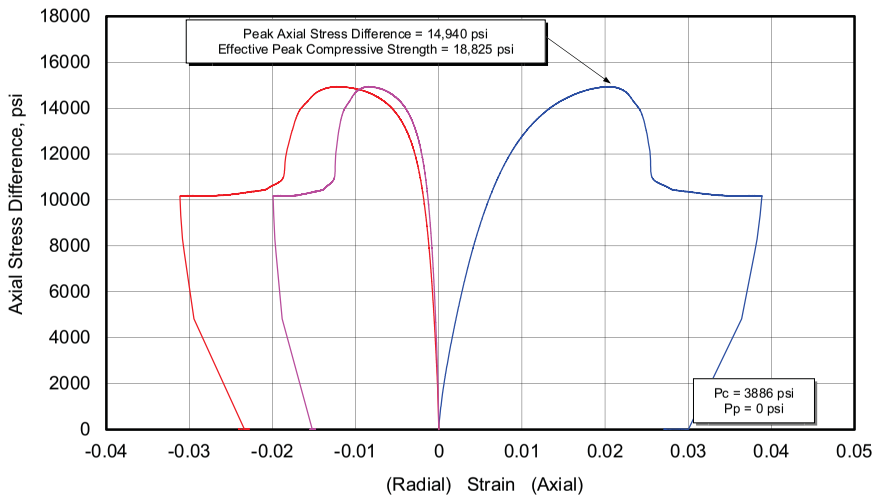

Zone 1 Deformation Index: Ratio of Secant E at Peak to E: 1.67
Zone 2 Ductility Index: Amount of Plastic or Strain Hardening Strain: 0.92
Zone 3a: Tang and Kaiser Index (Axial): .0045
Zone 3b: Tang and Kaiser Index (Volumetric): .047
Zone 4: Peak to Residual Strength Ratio: 1.05

Zone 1 Deformation Index: Ratio of Secant E at Peak to E: 2.24
Zone 2 Ductility Index: Amount of Plastic or Strain Hardening Strain: 0.33
Zone 3a: Tang and Kaiser Index (Axial): .031 J/tonne
Zone 3b: Tang and Kaiser Index (Volumetric): 0.88 J/tonne
Zone 4: Peak to Residual Strength Ratio:1.41

Fidelity Cane Creek CCU7-1

Lithology	Sample ID	Depth (ft)	Orientation	As Received Bulk Density (g/cm^3)	Confining Pressure (psi)	Peak Effective Compressive Strength (psi)	Effective Residual Compressive Strength (psi)	Young's Modulus (10^6 psi)	Poisson's Ratio
silty dolomite	CCU5-1	7624.65	Vertical	2.597	3355	20,803	11,732	2.696	0.13
	CCU5-3	7624.90	Horizontal	2.591	3886	33,942	20,104	4.517	0.25

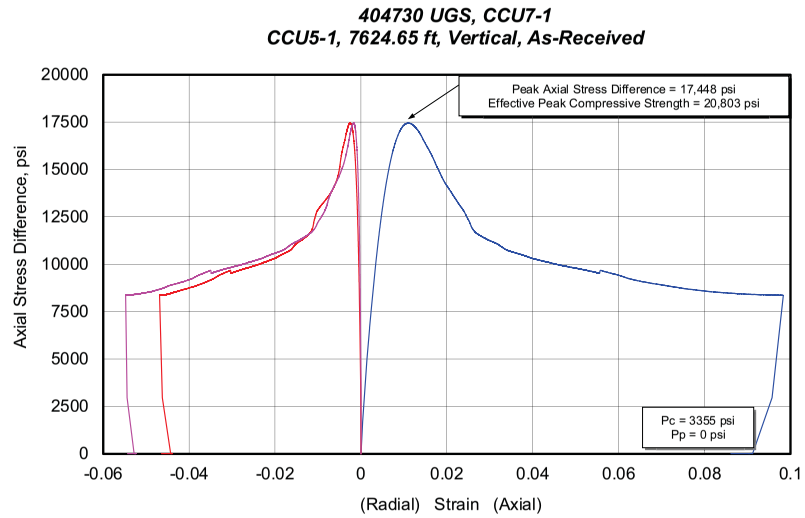

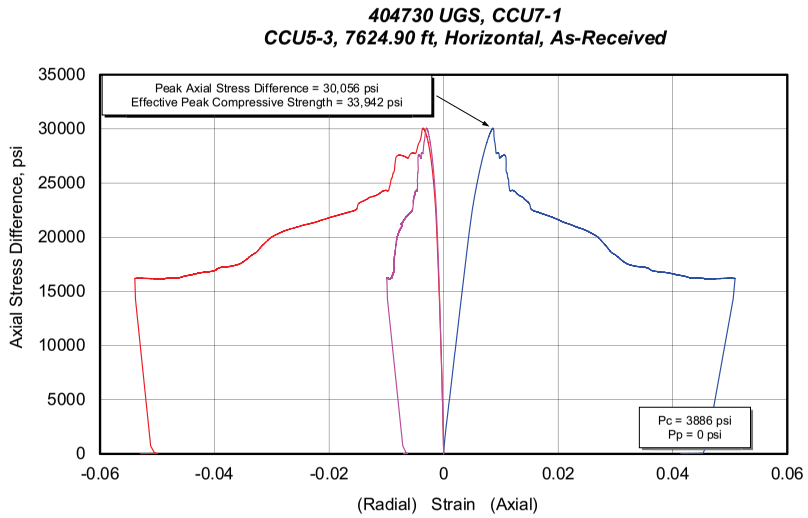

Zone 1 Deformation Index: Ratio of Secant E at Peak to E: 1.68
Zone 2 Ductility Index: Amount of Plastic or Strain Hardening Strain: 0.017
Zone 3a: Tang and Kaiser Index (Axial): 1.7 J/tonne
Zone 3b: Tang and Kaiser Index (Volumetric): 24.1 J/tonne
Zone 4: Peak to Residual Strength Ratio: 1.62

Zone 1 Deformation Index: Ratio of Secant E at Peak to E: 1.28
Zone 2 Ductility Index: Amount of Plastic or Strain Hardening Strain: 0.096
Zone 3a: Tang and Kaiser Index (Axial): 3.37 J/tonne
Zone 3b: Tang and Kaiser Index (Volumetric): 9.99 J/tonne
Zone 4: Peak to Residual Strength Ratio:1.71

Fidelity Cane Creek CCU7-1

Lithology	Sample ID	Depth (ft)	Orientation	As Received Bulk Density (g/cm^3)	Confining Pressure (psi)	Peak Effective Compressive Strength (psi)	Effective Residual Compressive Strength (psi)	Young's Modulus (10^6 psi)	Poisson's Ratio
silty dolomite	CCU6-1	7630.25	Vertical	2.504	3357	15,416	-	1.5060	0.24
	CCU6-3	7630.60	Horizontal	2.530	3892	20,564	17,198	2.774	0.15

404730 UGS, CCU7-1
CCU6-1, 7630.25 ft, Vertical, As-Received

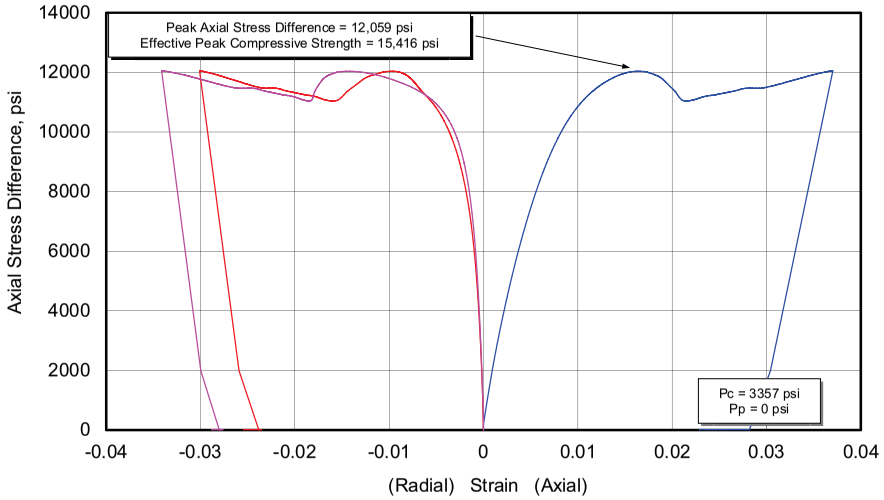

404730 UGS, CCU7-1
CCU6-3, 7630.60 ft, Horizontal, As-Received

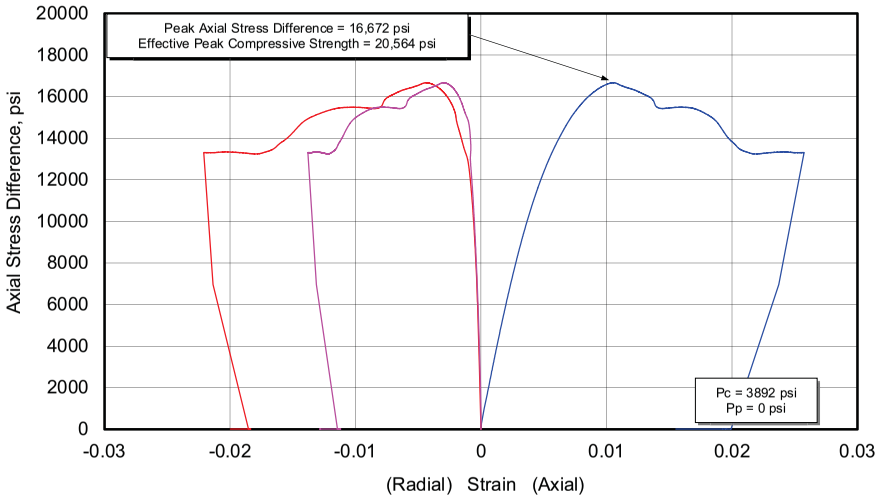

Zone 1 Deformation Index: Ratio of Secant E at Peak to E: 1.88
Zone 2 Ductility Index: Amount of Plastic or Strain Hardening Strain: 0.459
Zone 3a: Tang and Kaiser Index (Axial): 0.0855
Zone 3b: Tang and Kaiser Index (Volumetric): .0257 J/tonne
Zone 4: Peak to Residual Strength Ratio: 1.08

Zone 1 Deformation Index: Ratio of Secant E at Peak to E: 1.74
Zone 2 Ductility Index: Amount of Plastic or Strain Hardening Strain: 0.749
Zone 3a: Tang and Kaiser Index (Axial): 0.01597 J/tonne
Zone 3b: Tang and Kaiser Index (Volumetric): 0.0421 J/tonne
Zone 4: Peak to Residual Strength Ratio: 1.26

Fidelity Cane Creek CCU7-1

Lithology	Sample ID	Depth (ft)	Orientation	As Received Bulk Density (g/cm^3)	Confining Pressure (psi)	Peak Effective Compressive Strength (psi)	Effective Residual Compressive Strength (psi)	Young's Modulus (10^6 psi)	Poisson's Ratio
shale	CCU7-1[1]	7638.30	Vertical	2.458	3361	14,945	14,459	0.972	0.18

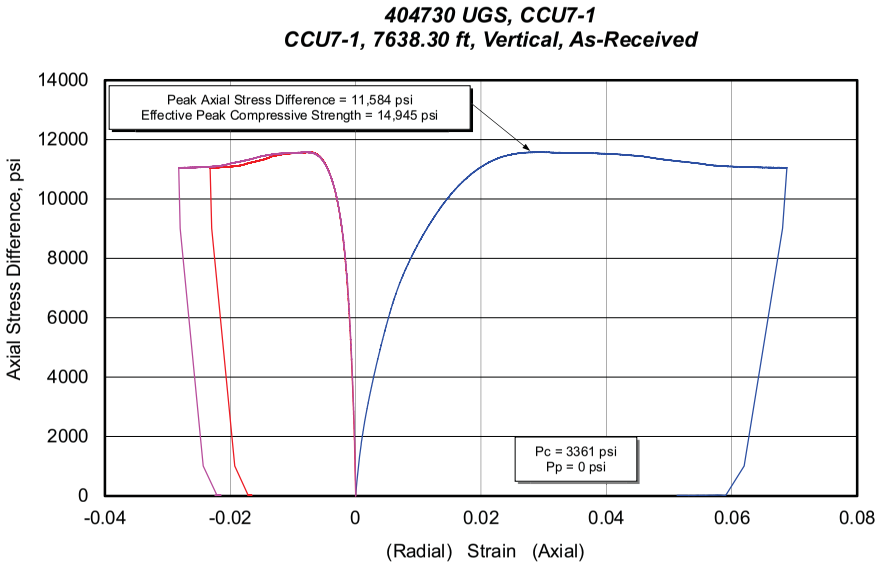

Zone 1 Deformation Index: Ratio of Secant E at Peak to E: 2.17
Zone 2 Ductility Index: Amount of Plastic or Strain Hardening Strain: 0.605
Zone 3a: Tang and Kaiser Index (Axial): 0.0089 J/tonne
Zone 3b: Tang and Kaiser Index (Volumetric): 0.01 J/tonne
Zone 4: Peak to Residual Strength Ratio: 1.04

[1] CCU7-1 – Not enough material available to obtain additional samples, thus, no horizontally oriented sample was tested

Fidelity Cane Creek CCU7-1

Lithology	Sample ID	Depth (ft)	Orientation	As Received Bulk Density (g/cm^3)	Confining Pressure (psi)	Peak Effective Compressive Strength (psi)	Effective Residual Compressive Strength (psi)	Young's Modulus (10^6 psi)	Poisson's Ratio
anhydrite	CCU8-1	7645.30	Vertical	2.940	3364	28,267	-	7.233	0.35
	CCU8-3	7645.75	Horizontal	2.931	3899	30,497	-	7.603	0.35

404730 UGS, CCU7-1
CCU8-1, 7645.30 ft, Vertical, As-Received

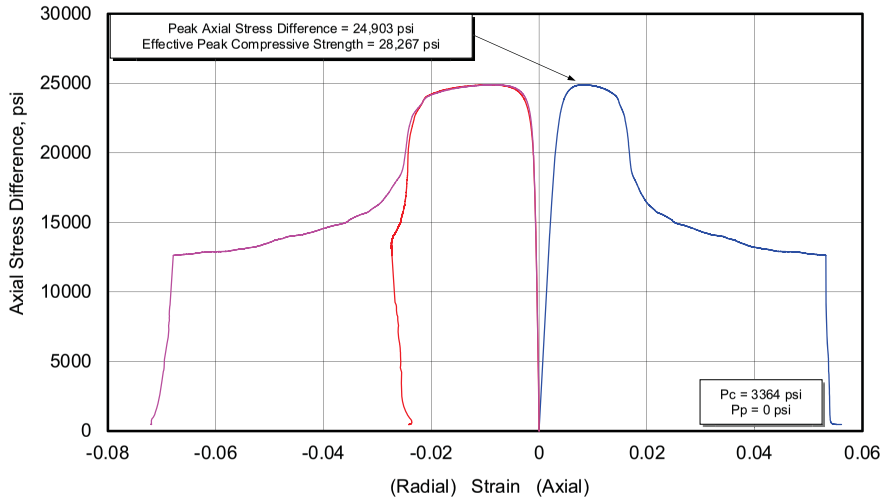

404730 UGS, CCU7-1
CCU8-3, 7645.75 ft, Horizontal, As-Received

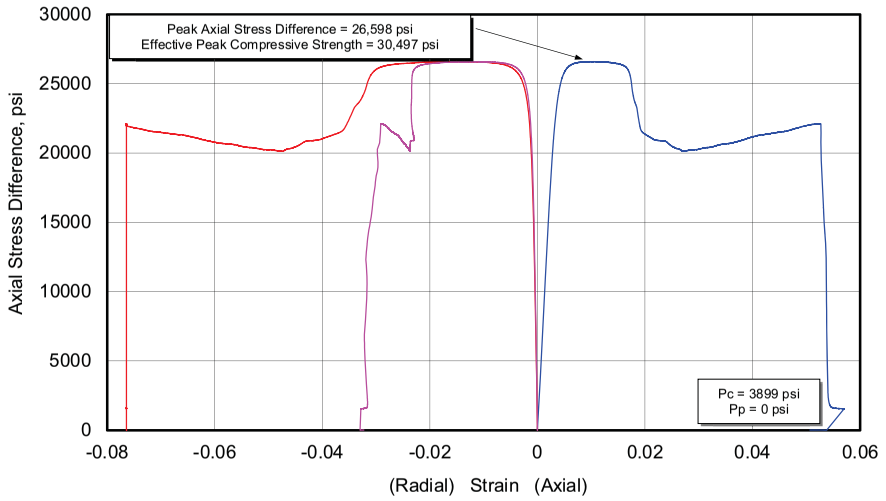

Zone 1 Deformation Index: Ratio of Secant E at Peak to E: 1.68
Zone 2 Ductility Index: Amount of Plastic or Strain Hardening Strain: 0.244
Zone 3a: Tang and Kaiser Index (Axial): 1.05 J/tonne
Zone 3b: Tang and Kaiser Index (Volumetric): 1.72 J/tonne
Zone 4: Peak to Residual Strength Ratio: 1.86

Zone 1 Deformation Index: Ratio of Secant E at Peak to E: 1.71
Zone 2 Ductility Index: Amount of Plastic or Strain Hardening Strain: 0.542
Zone 3a: Tang and Kaiser Index (Axial): 0.108 J/tonne
Zone 3b: Tang and Kaiser Index (Volumetric): 0.251 J/tonne
Zone 4: Peak to Residual Strength Ratio:1.30

Fidelity Cane Creek CCU7-1

Lithology	Sample ID	Depth (ft)	Orientation	As Received Bulk Density (g/cm^3)	Confining Pressure (psi)	Peak Effective Compressive Strength (psi)	Effective Residual Compressive Strength (psi)	Young's Modulus (10^6 psi)	Poisson's Ratio
silty dolomite	CCU9-1	7651.60	Vertical	2.577	3367	21,372	14,963	3.891	0.17
	CCU9-3	7651.25	Horizontal	2.582	3902	29,687	16,128	3,891,000	0.24

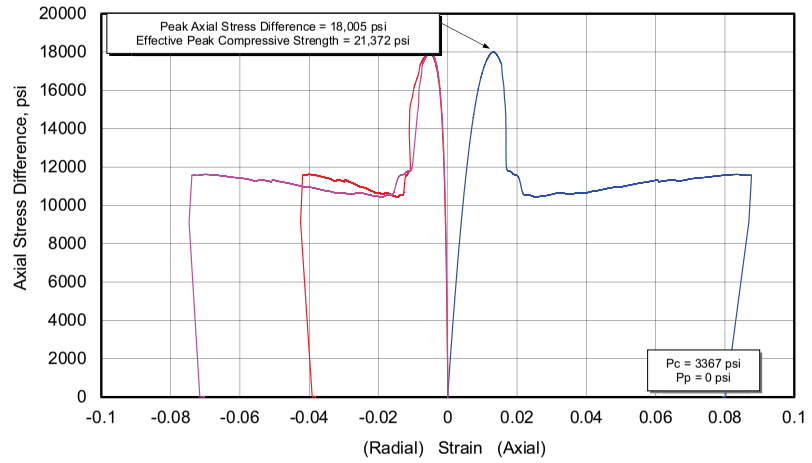

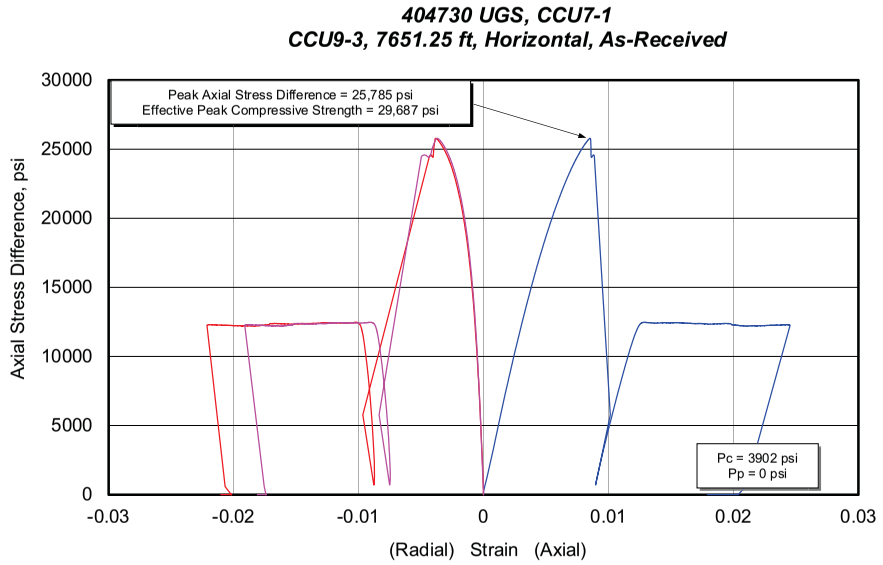

Zone 1 Deformation Index: Ratio of Secant E at Peak to E: 1.64
Zone 2 Ductility Index: Amount of Plastic or Strain Hardening Strain: 0.232
Zone 3a: Tang and Kaiser Index (Axial): 0.899 J/tonne
Zone 3b: Tang and Kaiser Index (Volumetric): 3.09 J/tonne
Zone 4: Peak to Residual Strength Ratio: 1.70

Zone 1 Deformation Index: Ratio of Secant E at Peak to E: 1.29
Zone 2 Ductility Index: Amount of Plastic or Strain Hardening Strain: 0
Zone 3a: Tang and Kaiser Index (Axial): 0.901 J/tonne
Zone 3b: Tang and Kaiser Index (Volumetric): 3.09 J/tonne
Zone 4: Peak to Residual Strength Ratio: 1.70

Fidelity Cane Creek CCU7-1

Lithology	Sample ID	Depth (ft)	Orientation	As Received Bulk Density (g/cm^3)	Confining Pressure (psi)	Peak Effective Compressive Strength (psi)	Effective Residual Compressive Strength (psi)	Young's Modulus (10^6 psi)	Poisson's Ratio
fractured silty dolomite	CCU10-1	7657.50	Vertical	2.678	3369	29,259	-	4.290	0.18
	CCU10-5	7657.65	Horizontal	2.696	3905	39,972	20,882	6.534	0.33

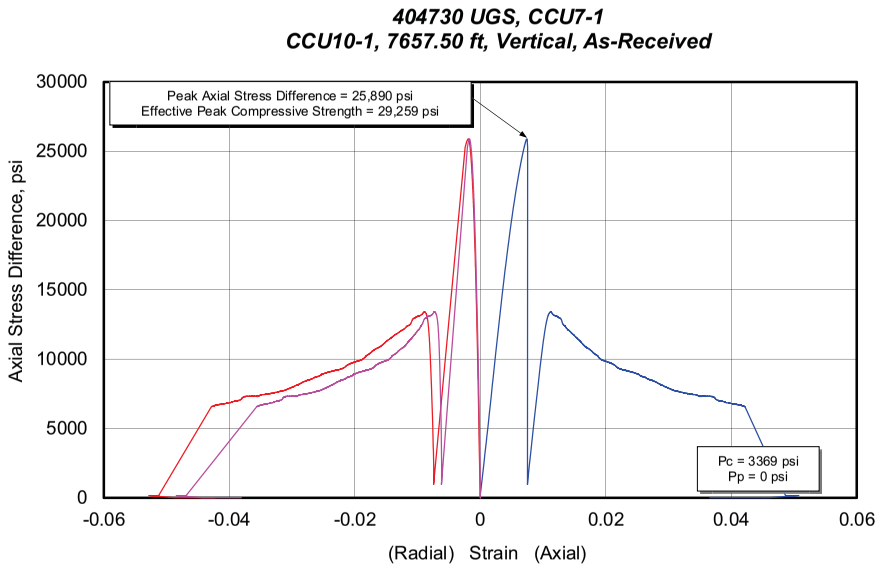

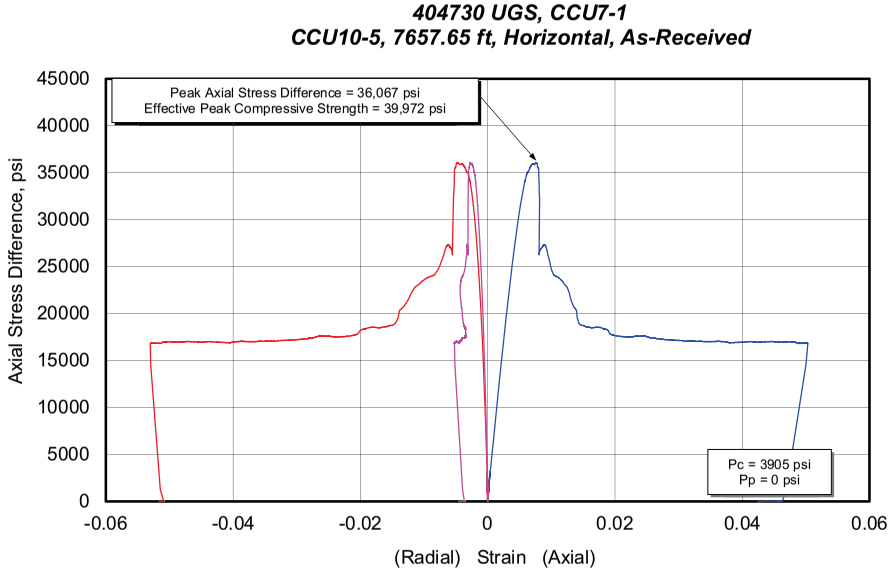

Zone 1 Deformation Index: Ratio of Secant E at Peak to E: 1.22
Zone 2 Ductility Index: Amount of Plastic or Strain Hardening Strain: 0
Zone 3a: Tang and Kaiser Index (Axial): 0.765 J/tonne
Zone 3b: Tang and Kaiser Index (Volumetric): 5.43 J/tonne
Zone 4: Peak to Residual Strength Ratio: 1.94

Zone 1 Deformation Index: Ratio of Secant E at Peak to E: 1.23
Zone 2 Ductility Index: Amount of Plastic or Strain Hardening Strain: 0.15
Zone 3a: Tang and Kaiser Index (Axial): 0.785 J/tonne
Zone 3b: Tang and Kaiser Index (Volumetric): 4.77 J/tonne
Zone 4: Peak to Residual Strength Ratio:1.84

Fidelity Cane Creek 26-3

Lithology	Sample ID	Depth (ft)	Orientation	As Received Bulk Density (g/cm^3)	Confining Pressure (psi)	Peak Effective Compressive Strength (psi)	Effective Residual Compressive Strength (psi)	Young's Modulus (10^6 psi)	Poisson's Ratio
shale	FDY3-1	7413.00	Vertical	2.041	3855	11,586 (Y)	-	0.706	0.23
	FDY3-2	7413.05	Horizontal	2.009	4040	11,716 (Y)[2] 14,254	-	1.128	0.25

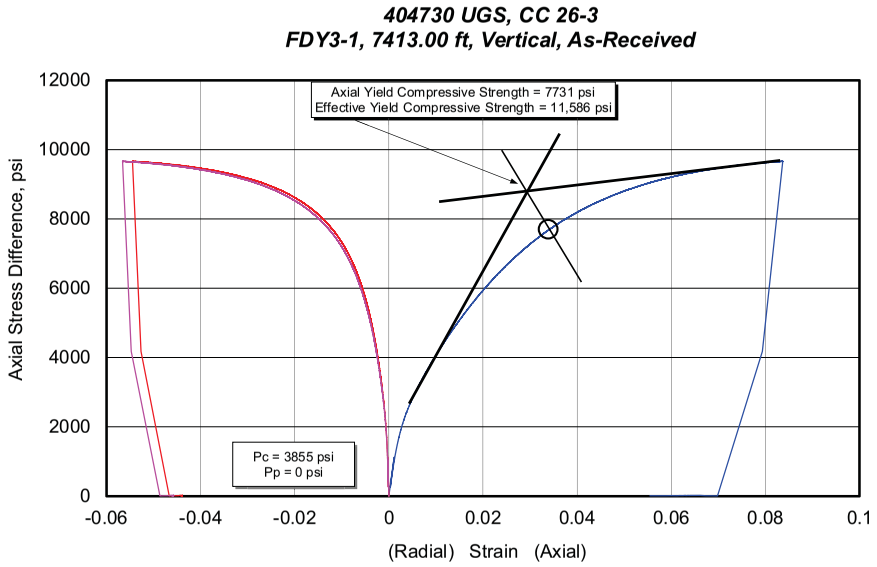

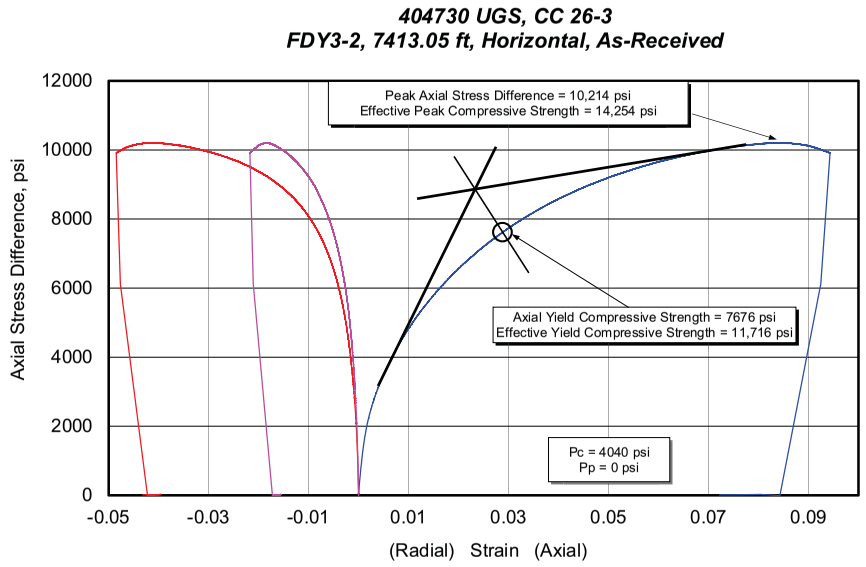

Zone 1 Deformation Index: Ratio of Secant E at Peak to E: 5.05
Zone 2 Ductility Index: Amount of Plastic or Strain Hardening Strain: 0.994
Zone 3a: Tang and Kaiser Index (Axial): 5.08×10^{-8}
Zone 3b: Tang and Kaiser Index (Volumetric): 1.88×10^{-4}
Zone 4: Peak to Residual Strength Ratio: 1.00

Zone 1 Deformation Index: Ratio of Secant E at Peak to E: 8.98
Zone 2 Ductility Index: Amount of Plastic or Strain Hardening Strain: 1
Zone 3a: Tang and Kaiser Index (Axial): 0
Zone 3b: Tang and Kaiser Index (Volumetric): 0.0077
Zone 4: Peak to Residual Strength Ratio:1.02

[2] (Y) denotes axial yield

Fidelity Cane Creek 26-3

Lithology	Sample ID	Depth (ft)	Orientation	As Received Bulk Density (g/cm^3)	Confining Pressure (psi)	Peak Effective Compressive Strength (psi)	Effective Residual Compressive Strength (psi)	Young's Modulus (10^6 psi)	Poisson's Ratio
shale	FDY2-1	7417.75	Vertical	2.407	3857	18,534	14,557	1.119	0.24
	FDY2-2	7417.85	Horizontal	2.406	4043	20,699	15,143	2.074	0.30

404730 UGS, CC 26-3
FDY2-1, 7417.75 ft, Vertical, As-Received

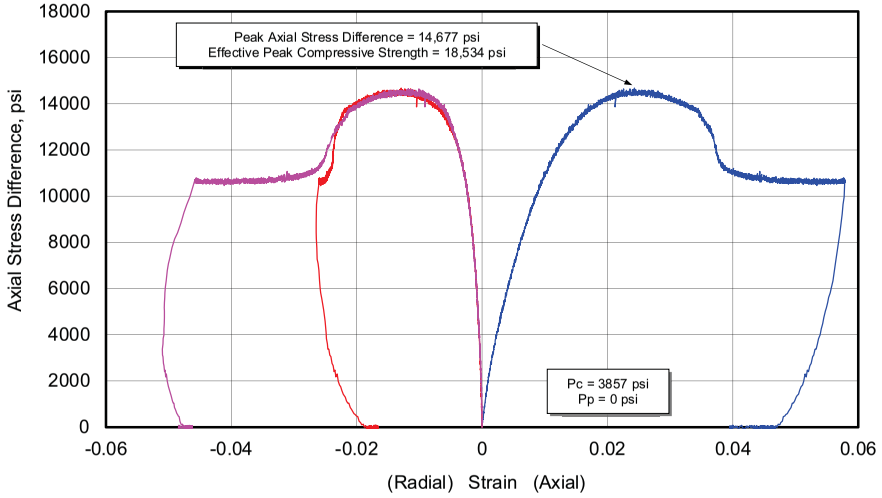

404730 UGS, CC 26-3
FDY2-2, 7417.85 ft, Horizontal, As-Received

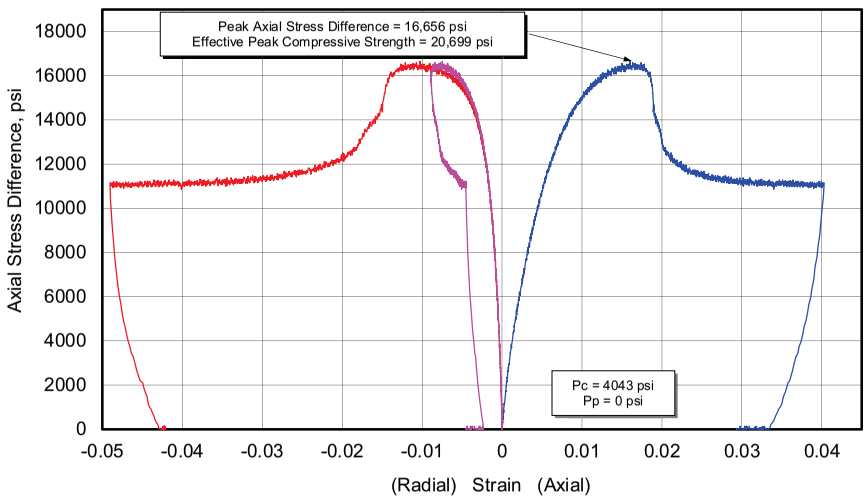

Zone 1 Deformation Index: Ratio of Secant E at Peak to E: 1.82
Zone 2 Ductility Index: Amount of Plastic or Strain Hardening Strain: 0.737
Zone 3a: Tang and Kaiser Index (Axial): 0.427 J/tonne
Zone 3b: Tang and Kaiser Index (Volumetric): 1.42 J/tonne
Zone 4: Peak to Residual Strength Ratio: 1.34

Zone 1 Deformation Index: Ratio of Secant E at Peak to E: 1.77
Zone 2 Ductility Index: Amount of Plastic or Strain Hardening Strain: 0.198
Zone 3a: Tang and Kaiser Index (Axial): 0.518
Zone 3b: Tang and Kaiser Index (Volumetric): 0.812
Zone 4: Peak to Residual Strength Ratio:1.46

Fidelity Cane Creek 26-3

Lithology	Sample ID	Depth (ft)	Orientation	As Received Bulk Density (g/cm^3)	Confining Pressure (psi)	Peak Effective Compressive Strength (psi)	Effective Residual Compressive Strength (psi)	Young's Modulus (10^6 psi)	Poisson's Ratio
shale	FDY1-2 [3]	7464.30	Horizontal	2.310	4068	17,700	14,498	1.571	0.22

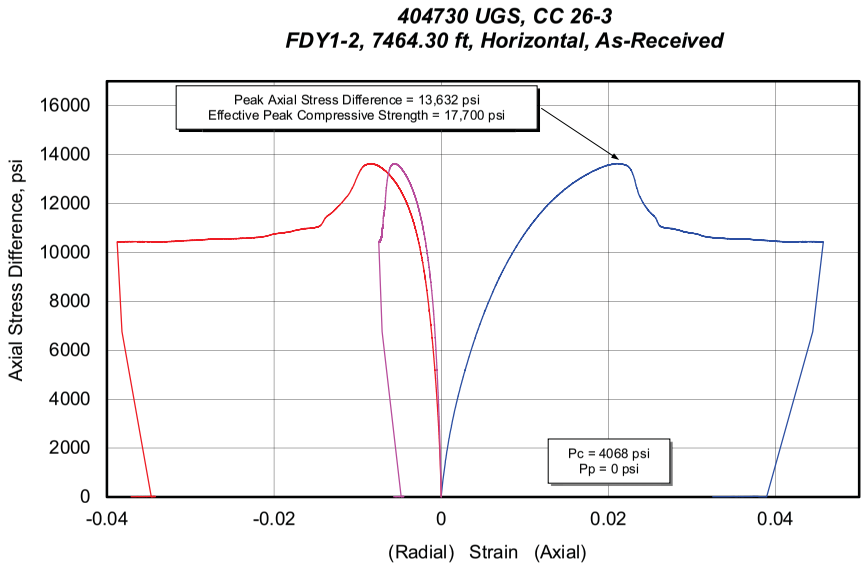

Zone 1 Deformation Index: Ratio of Secant E at Peak to E: 2.32
Zone 2 Ductility Index: Amount of Plastic or Strain Hardening Strain: 0.403
Zone 3a: Tang and Kaiser Index (Axial): 0.0078 J/tonne
Zone 3b: Tang and Kaiser Index (Volumetric): 0.152 J/tonne
Zone 4: Peak to Residual Strength Ratio: 1.23

[3] FDY1-2 – No additional shale material remains for a matching horizontal sample, from this backup shale depth interval.

Fidelity Cane Creek 26-3

Lithology	Sample ID	Depth (ft)	Orientation	As Received Bulk Density (g/cm^3)	Confining Pressure (psi)	Peak Effective Compressive Strength (psi)	Effective Residual Compressive Strength (psi)	Young's Modulus (10^6 psi)	Poisson's Ratio
silty dolomite	FDY1-1 [4]	7464.50	Vertical	2.617	3882	36,702	16,682	3.276	0.23
	FDY1-4	746.30	Vertical	2.611	3881	35,955	16,935	3.620	0.18

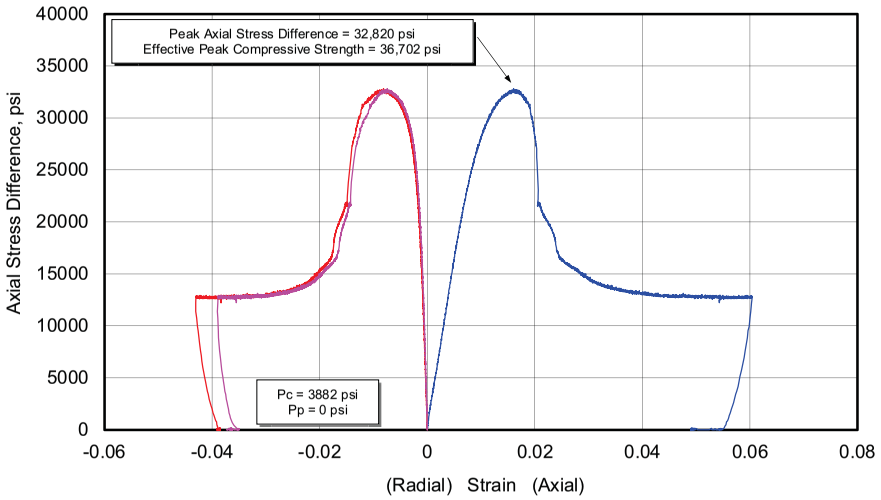

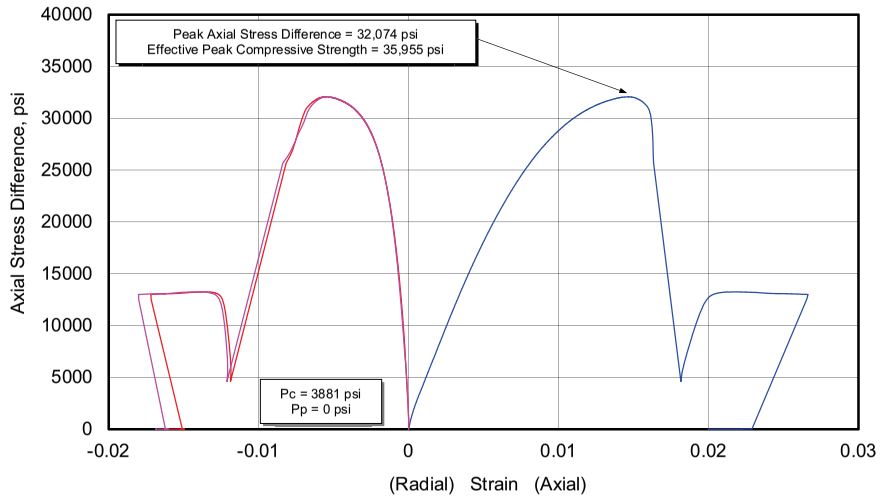

Zone 1 Deformation Index: Ratio of Secant E at Peak to E: 1.58
Zone 2 Ductility Index: Amount of Plastic or Strain Hardening Strain: 0.133
Zone 3a: Tang and Kaiser Index (Axial): 8.49 J/tonne
Zone 3b: Tang and Kaiser Index (Volumetric): 14.58 J/tonne
Zone 4: Peak to Residual Strength Ratio: 2.38

Zone 1 Deformation Index: Ratio of Secant E at Peak to E: 1.66
Zone 2 Ductility Index: Amount of Plastic or Strain Hardening Strain: 0.385
Zone 3a: Tang and Kaiser Index (Axial): 1.798
Zone 3b: Tang and Kaiser Index (Volumetric): 66.1
Zone 4: Peak to Residual Strength Ratio:2.46

[4] FDY1-1 – No additional silty dolomite material for a matching horizontal sample. Sample FDY1-4 tested as accident, originally marked with an incorrect depth.

Fidelity Cisco State 36-13

Lithology	Sample ID	Depth (ft)	Orientation	As Received Bulk Density (g/cm^3)	Confining Pressure (psi)	Peak Effective Compressive Strength (psi)	Effective Residual Compressive Strength (psi)	Young's Modulus (10^6 psi)	Poisson's Ratio
dolomite	CSO1-1	7588.80	Vertical	2.512	2732	18,014	11,332	1.338	0.19
	CSO1-2	7588.90	Horizontal	2.503	3605	19,081	14,105	1.782	0.25

404730 UGS, Cisco St 36-13, CSO1-1, 7588.80 ft, Vertical, As-Received

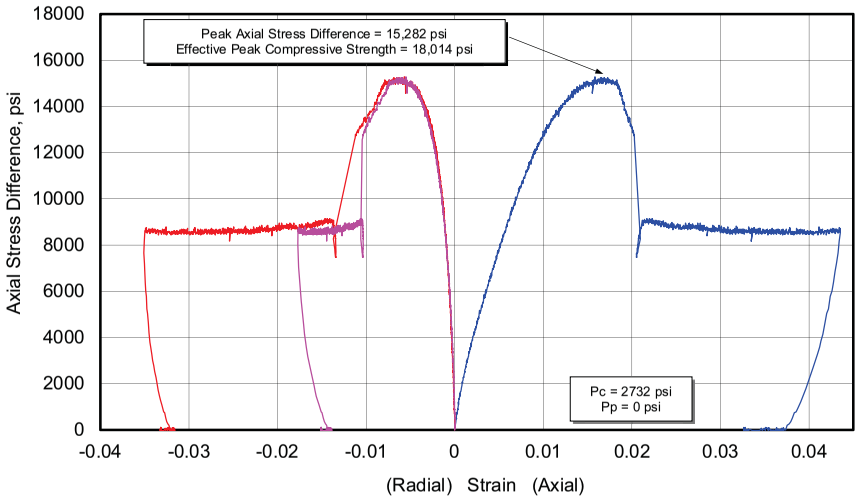

404730 UGS, Cisco St 36-13, CSO1-2, 7588.90 ft, Horizontal, As-Received

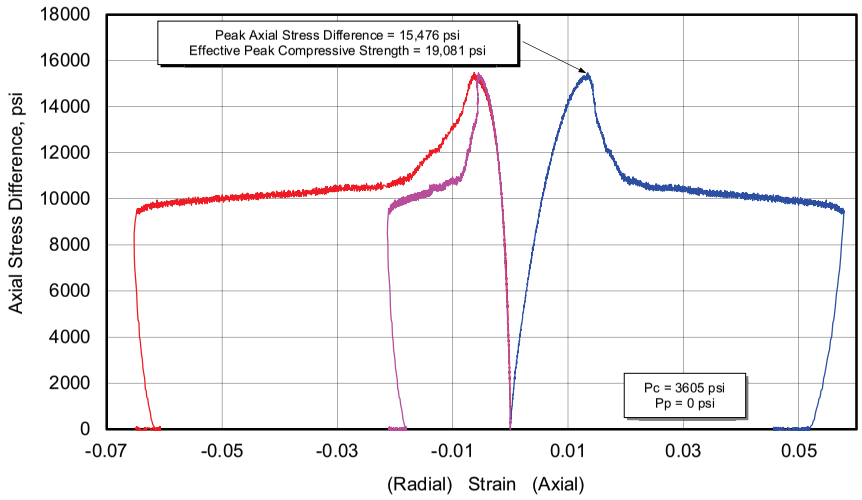

Zone 1 Deformation Index: Ratio of Secant E at Peak to E: 1.28
Zone 2 Ductility Index: Amount of Plastic or Strain Hardening Strain: 0.566
Zone 3a: Tang and Kaiser Index (Axial): 0.497 J/tonne
Zone 3b: Tang and Kaiser Index (Volumetric): 3.97 J/tonne
Zone 4: Peak to Residual Strength Ratio: 1.65

Zone 1 Deformation Index: Ratio of Secant E at Peak to E: 1.40
Zone 2 Ductility Index: Amount of Plastic or Strain Hardening Strain: 0.227
Zone 3a: Tang and Kaiser Index (Axial): 0.269 J/tonne
Zone 3b: Tang and Kaiser Index (Volumetric): 1.122 J/tonne
Zone 4: Peak to Residual Strength Ratio: 1.37

Fidelity Cisco State 36-13

Lithology	Sample ID	Depth (ft)	Orientation	As Received Bulk Density (g/cm^3)	Confining Pressure (psi)	Peak Effective Compressive Strength (psi)	Effective Residual Compressive Strength (psi)	Young's Modulus (10^6 psi)	Poisson's Ratio
shale	CSO2-1	7593.00	Vertical	2.327	2733	12,833	11,298	1.356	0.22
	CSO2-2	7592.90	Horizontal	2.364	3607	15,912	14,647	1.763	0.24

404730 UGS, Cisco St 36-13, CSO2-1, 7593.00 ft, Vertical, As-Received

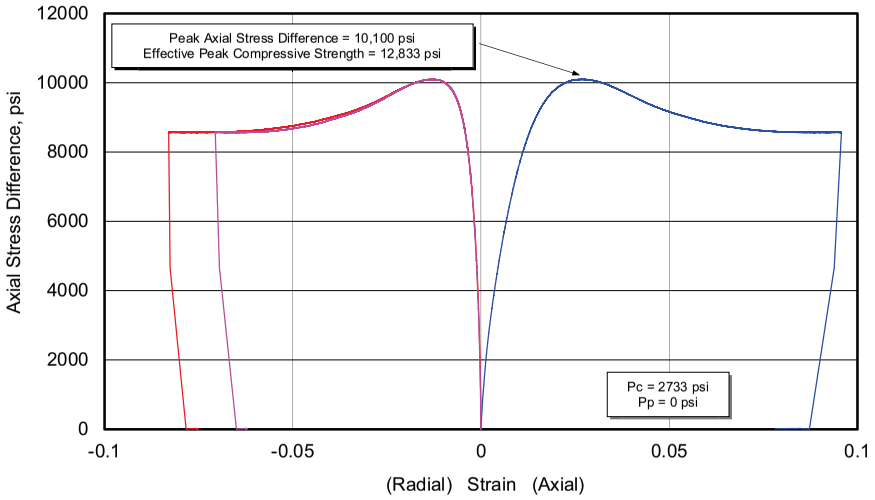

404730 UGS, Cisco St 36-13, CSO2-2, 7592.90 ft, Horizontal, As-Received

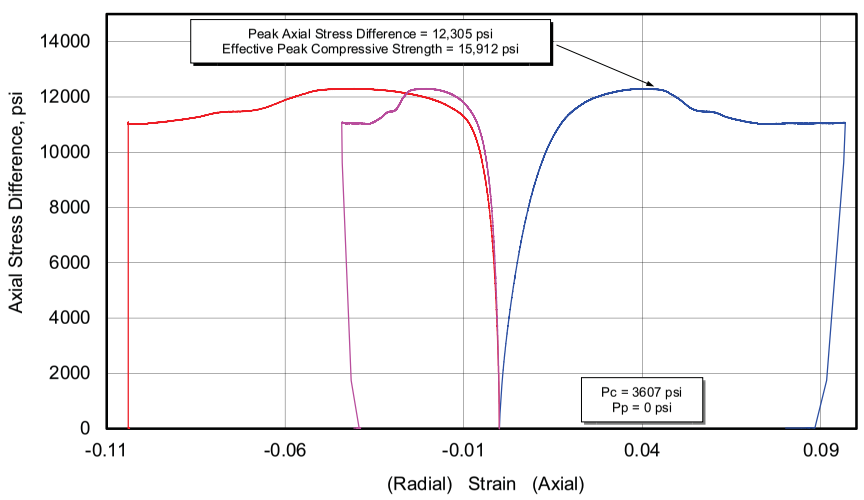

Zone 1 Deformation Index: Ratio of Secant E at Peak to E: 3.2
Zone 2 Ductility Index: Amount of Plastic or Strain Hardening Strain: 0.166
Zone 3a: Tang and Kaiser Index (Axial): 0.286 J/tonne
Zone 3b: Tang and Kaiser Index (Volumetric): 0.839 J/tonne
Zone 4: Peak to Residual Strength Ratio: 1.16

Zone 1 Deformation Index: Ratio of Secant E at Peak to E: 4.81
Zone 2 Ductility Index: Amount of Plastic or Strain Hardening Strain: 0.601
Zone 3a: Tang and Kaiser Index (Axial): 0.0107 J/tonne
Zone 3b: Tang and Kaiser Index (Volumetric): 0.111 J/tonne
Zone 4: Peak to Residual Strength Ratio:1.06

Fidelity Cisco State 36-13

Lithology	Sample ID	Depth (ft)	Orientation	As Received Bulk Density (g/cm^3)	Confining Pressure (psi)	Peak Effective Compressive Strength (psi)	Effective Residual Compressive Strength (psi)	Young's Modulus (10^6 psi)	Poisson's Ratio
shale	CSO3-1	7599.75	Vertical	2.582	2736	19,880	14,736	1.104	0.17
	CSO3-2	7599.85	Horizontal	2.537	3610	23,329	19,880	2.037	0.27

404730 UGS, Cisco St 36-13, CSO3-1, 7599.75 ft, Vertical, As-Received

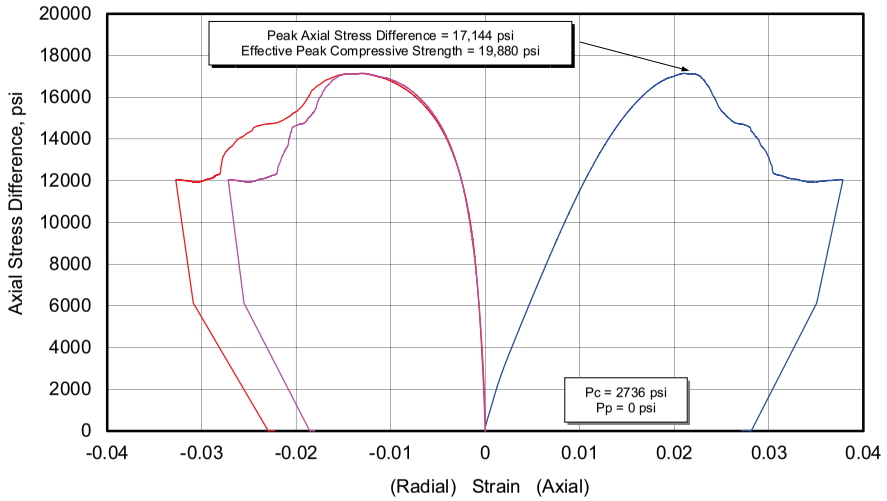

404730 UGS, Cisco St 36-13, CSO3-2, 7599.85 ft, Horizontal, As-Received

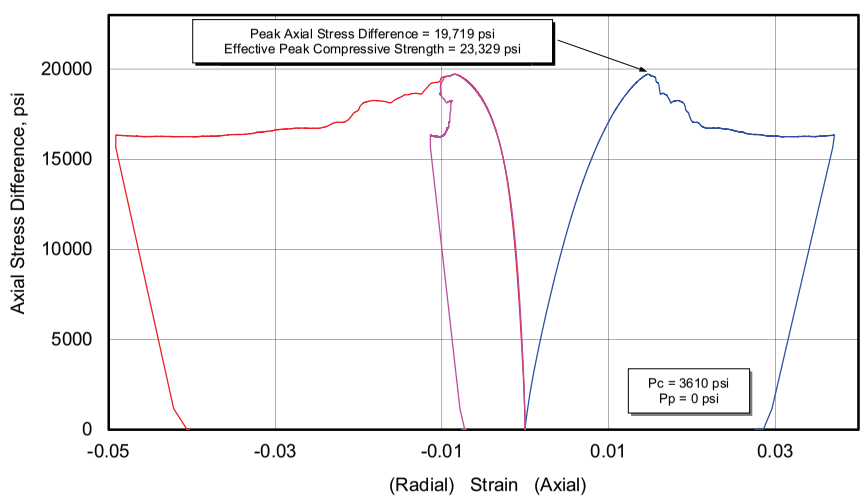

Zone 1 Deformation Index: Ratio of Secant E at Peak to E: 1.32
Zone 2 Ductility Index: Amount of Plastic or Strain Hardening Strain: 0.163
Zone 3a: Tang and Kaiser Index (Axial): 0.101 J/tonne
Zone 3b: Tang and Kaiser Index (Volumetric): 0.593 J/tonne
Zone 4: Peak to Residual Strength Ratio: 1.38

Zone 1 Deformation Index: Ratio of Secant E at Peak to E: 1.50
Zone 2 Ductility Index: Amount of Plastic or Strain Hardening Strain: 0.0045
Zone 3a: Tang and Kaiser Index (Axial): 0.0098 J/tonne
Zone 3b: Tang and Kaiser Index (Volumetric): 0.578 J/tonne
Zone 4: Peak to Residual Strength Ratio:1.17

Fidelity Cisco State 36-13

Lithology	Sample ID	Depth (ft)	Orientation	As Received Bulk Density (g/cm^3)	Confining Pressure (psi)	Peak Effective Compressive Strength (psi)	Effective Residual Compressive Strength (psi)	Young's Modulus (10^6 psi)	Poisson's Ratio
silty dolomite	CSO4-1	7605.35	Vertical	2.636	2738	35340	20120	5.071	
	CSO4-4	7605.65	Vertical	2.564	2738	19,646	13,002	1.282	0.18
	CSO4-2	7605.65	Horizontal	2.534	3613	22,643	17,113	1.985	0.25

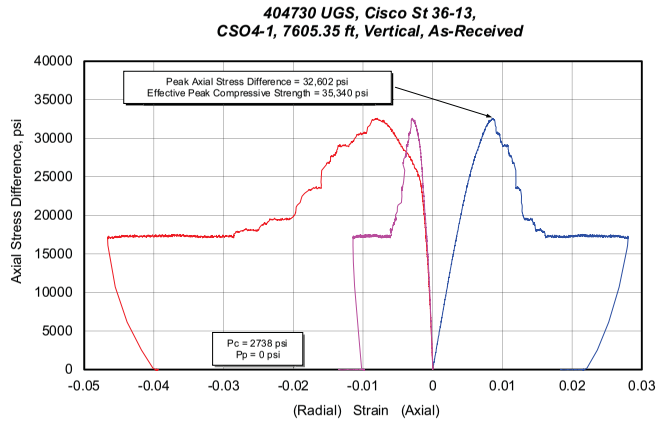

Not reported

Fidelity Cisco State 36-13

Lithology	Sample ID	Depth (ft)	Orientation	As Received Bulk Density (g/cm^3)	Confining Pressure (psi)	Peak Effective Compressive Strength (psi)	Effective Residual Compressive Strength (psi)	Young's Modulus (10^6 psi)	Poisson's Ratio

404730 UGS, Cisco St 36-13,
CSO4-4, 7605.65 ft, Vertical, As-Received

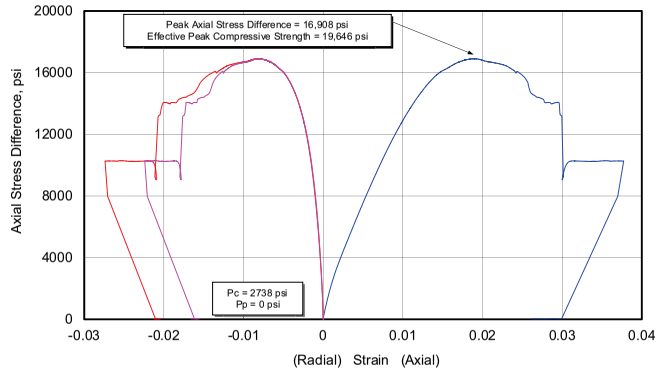

404730 UGS, Cisco St 36-13,
CSO4-2, 7605.65 ft, Horizontal, As-Received

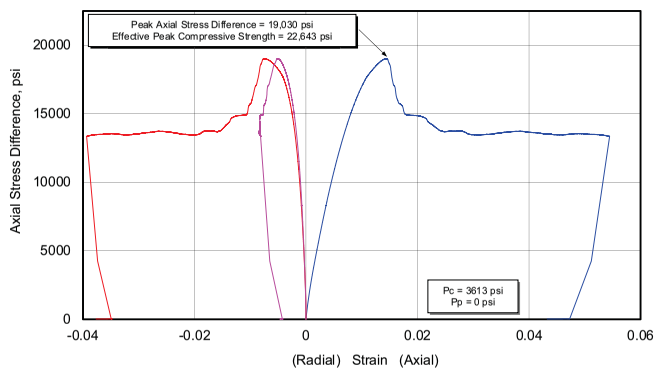

Zone 1 Deformation Index: Ratio of Secant E at Peak to E: 1.34
Zone 2 Ductility Index: Amount of Plastic or Strain Hardening Strain: 0
Zone 3a: Tang and Kaiser Index (Axial): 1.42 J/tonne
Zone 3b: Tang and Kaiser Index (Volumetric): 9.77 J/tonne
Zone 4: Peak to Residual Strength Ratio: 1.90

Zone 1 Deformation Index: Ratio of Secant E at Peak to E: 1.44
Zone 2 Ductility Index: Amount of Plastic or Strain Hardening Strain: 0.856
Zone 3a: Tang and Kaiser Index (Axial): 0.005 J/tonne
Zone 3b: Tang and Kaiser Index (Volumetric): 0.103 J/tonne
Zone 4: Peak to Residual Strength Ratio: 1.14

Zone 1 Deformation Index: Ratio of Secant E at Peak to E: 1.44
Zone 2 Ductility Index: Amount of Plastic or Strain Hardening Strain: 0.095
Zone 3a: Tang and Kaiser Index (Axial): 0.541 J/tonne
Zone 3b: Tang and Kaiser Index (Volumetric): 0.0098 J/tonne
Zone 4: Peak to Residual Strength Ratio: 1.36

Fidelity Cisco State 36-13

Lithology	Sample ID	Depth (ft)	Orientation	As Received Bulk Density (g/cm^3)	Confining Pressure (psi)	Peak Effective Compressive Strength (psi)	Effective Residual Compressive Strength (psi)	Young's Modulus (10^6 psi)	Poisson's Ratio
silty dolomite	CSO5-1	7615.40	Vertical	2.464	2742	14,412	12,942	1.094	0.27
	CSO5-2	7615.25	Horizontal	2.511	3617	19,097	17,017	1.755	0.23

404730 UGS, Cisco St 36-13, CSO5-1, 7615.40 ft, Vertical, As-Received

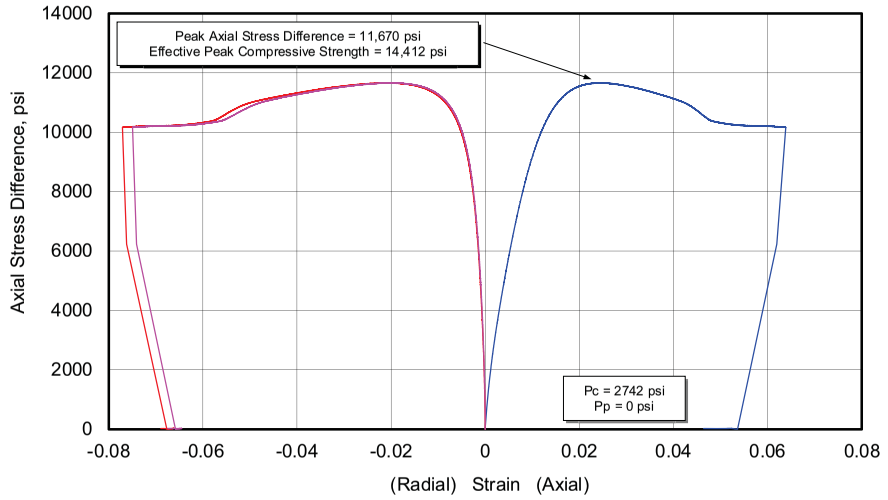

Zone 1 Deformation Index: Ratio of Secant E at Peak to E: 2.10
Zone 2 Ductility Index: Amount of Plastic or Strain Hardening Strain: 0
Zone 3a: Tang and Kaiser Index (Axial): 0.124
Zone 3b: Tang and Kaiser Index (Volumetric): 1.56
Zone 4: Peak to Residual Strength Ratio: 1.11

404730 UGS, Cisco St 36-13, CSO5-2, 7615.25 ft, Horizontal, As-Received

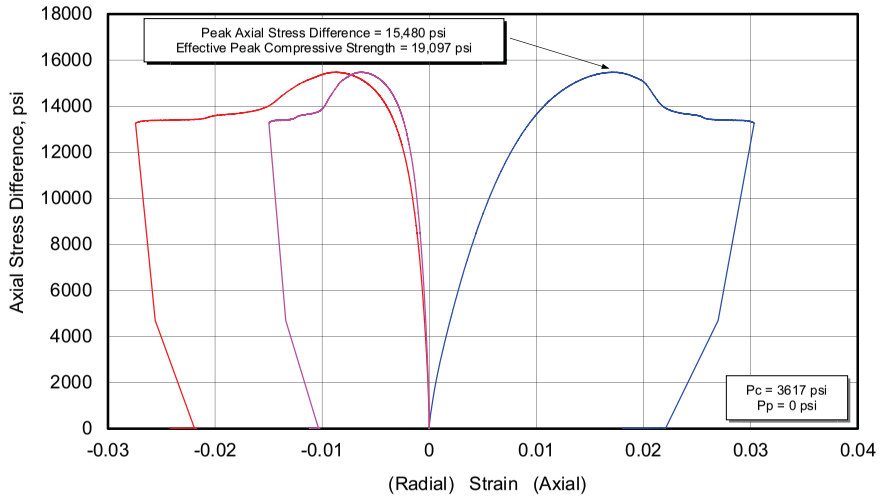

Zone 1 Deformation Index: Ratio of Secant E at Peak to E: 1.90
Zone 2 Ductility Index: Amount of Plastic or Strain Hardening Strain: 0.71
Zone 3a: Tang and Kaiser Index (Axial): 0.0034 J/tonne
Zone 3b: Tang and Kaiser Index (Volumetric): 0.234 J/tonne
Zone 4: Peak to Residual Strength Ratio:1.10

Fidelity Cisco State 36-13

Lithology	Sample ID	Depth (ft)	Orientation	As Received Bulk Density (g/cm^3)	Confining Pressure (psi)	Peak Effective Compressive Strength (psi)	Effective Residual Compressive Strength (psi)	Young's Modulus (10^6 psi)	Poisson's Ratio
anhydrite	CSO6-1	7627.30	Vertical	2.944	2746	23,662	16,346	8.081	0.34
	CSO6-2	7627.10	Horizontal	2.937	3623	28,796	19,423	8.780	0.33

404730 UGS, Cisco St 36-13, CSO6-1, 7627.30 ft, Vertical, As-Received

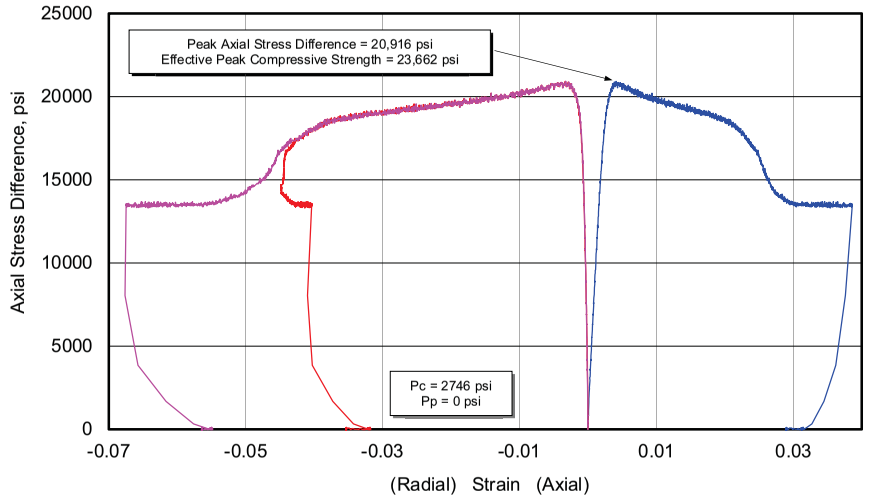

404730 UGS, Cisco St 36-13, CSO6-2, 7627.10 ft, Horizontal, As-Received

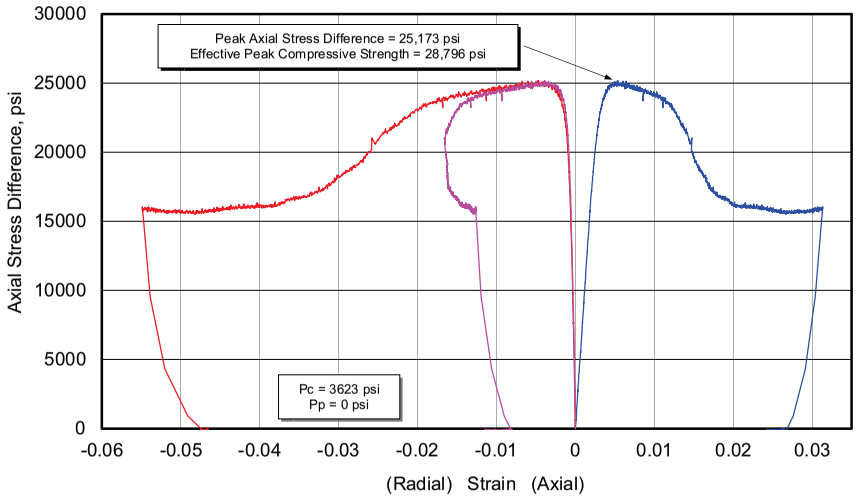

Zone 1 Deformation Index: Ratio of Secant E at Peak to E: 1.43
Zone 2 Ductility Index: Amount of Plastic or Strain Hardening Strain: 0.675
Zone 3a: Tang and Kaiser Index (Axial): .0062 J/tonne
Zone 3b: Tang and Kaiser Index (Volumetric): 1.45 J/tonne
Zone 4: Peak to Residual Strength Ratio: 1.52

Zone 1 Deformation Index: Ratio of Secant E at Peak to E: 1.76
Zone 2 Ductility Index: Amount of Plastic or Strain Hardening Strain: 0.443
Zone 3a: Tang and Kaiser Index (Axial): 0.139 J/tonne
Zone 3b: Tang and Kaiser Index (Volumetric): 1.47 J/tonne
Zone 4: Peak to Residual Strength Ratio: 1.53

Bill Barrett 14-3-35

Lithology	Sample ID	Depth (ft)	Orientation	As Received Bulk Density (g/cm^3)	Confining Pressure (psi)	Peak Effective Compressive Strength (psi)	Effective Residual Compressive Strength (psi)	Young's Modulus (10^6 psi)	Poisson's Ratio
dolomite	UTE3-1	7327.30	Vertical	2.645	1319	27330	12200	3.196	0.18
	UTE3-2	7327.40	Horizontal	2.655	2931	52280	19630	8.166	0.30

404730 UGS, Bill Barett 14-3-45
UTE3-1, 7327.30 ft, Vertical, As-Received

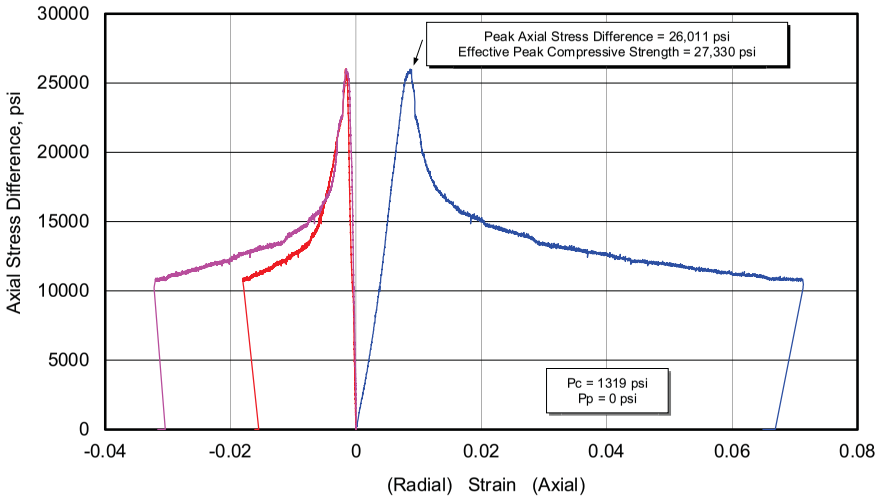

404730 UGS, Bill Barett 14-3-45
UTE3-2, 7327.40 ft, Horizontal, As-Received

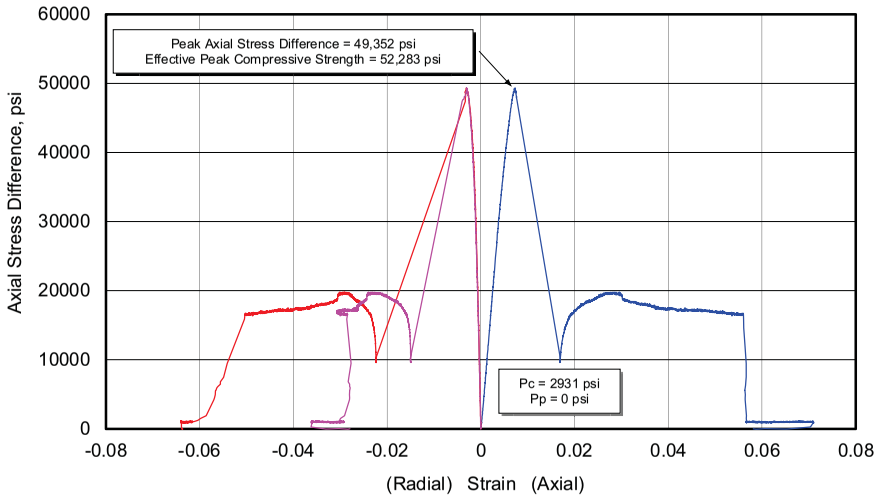

Zone 1 Deformation Index: Ratio of Secant E at Peak to E: 0.85
Zone 2 Ductility Index: Amount of Plastic or Strain Hardening Strain: 0
Zone 3a: Tang and Kaiser Index (Axial): 5.82
Zone 3b: Tang and Kaiser Index (Volumetric): 13.61
Zone 4: Peak to Residual Strength Ratio: 1.93

Zone 1 Deformation Index: Ratio of Secant E at Peak to E: 1.19
Zone 2 Ductility Index: Amount of Plastic or Strain Hardening Strain: 0
Zone 3a: Tang and Kaiser Index (Axial): 9.62 J/tonne
Zone 3b: Tang and Kaiser Index (Volumetric): 29.8 J/tonne
Zone 4: Peak to Residual Strength Ratio:2.63

Bill Barrett 14-3-35

Lithology	Sample ID	Depth (ft)	Orientation	As Received Bulk Density (g/cm^3)	Confining Pressure (psi)	Peak Effective Compressive Strength (psi)	Effective Residual Compressive Strength (psi)	Young's Modulus (10^6 psi)	Poisson's Ratio
shale-finely laminated	UTE2-1	7332.70	Vertical	2.382	1320	15350	5400	1.411	0.21
	UTE2-2	7332.85	Horizontal	2.342	2933	21240	12430	3.962	0.27

404730 UGS, Bill Barett 14-3-45
UTE2-1, 7332.70 ft, Vertical, As-Received

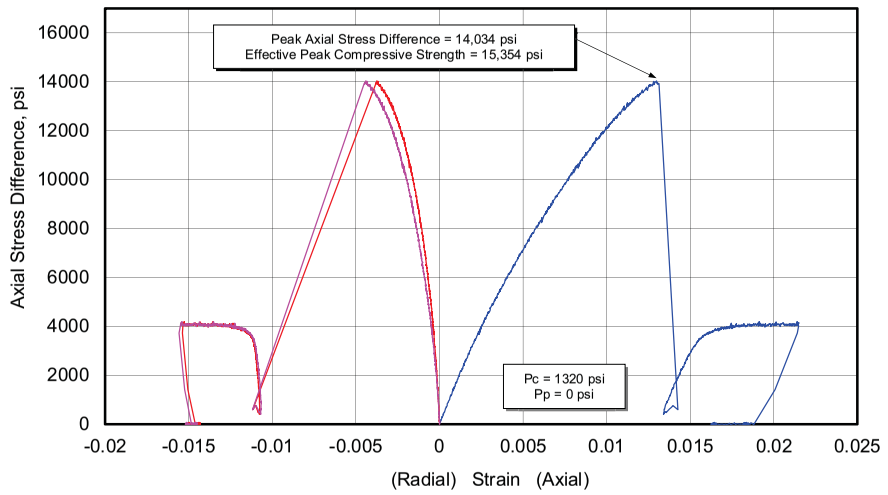

404730 UGS, Bill Barett 14-3-45
UTE2-2, 7332.85 ft, Horizontal, As-Received

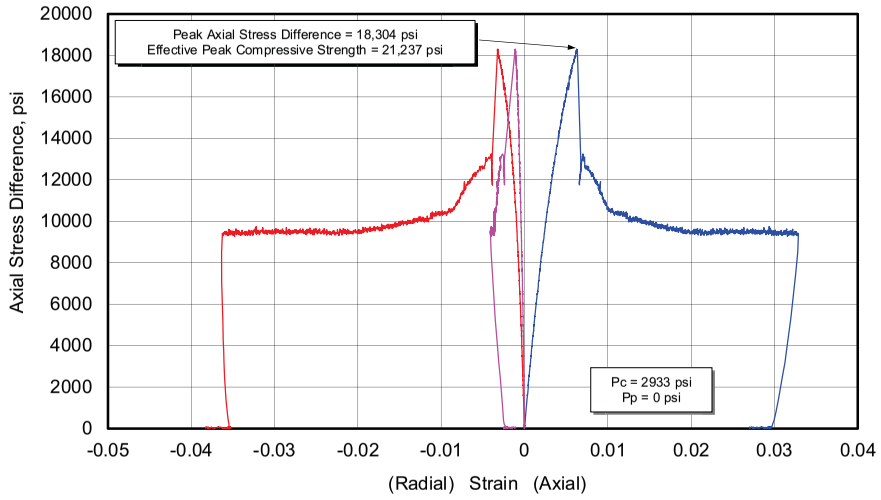

Zone 1 Deformation Index: Ratio of Secant E at Peak to E: 1.32
Zone 2 Ductility Index: Amount of Plastic or Strain Hardening Strain: 0
Zone 3a: Tang and Kaiser Index (Axial): 1.86 J/tonne
Zone 3b: Tang and Kaiser Index (Volumetric): 14.5 J/tonne
Zone 4: Peak to Residual Strength Ratio: 3.54

Zone 1 Deformation Index: Ratio of Secant E at Peak to E: 1.87
Zone 2 Ductility Index: Amount of Plastic or Strain Hardening Strain: 0
Zone 3a: Tang and Kaiser Index (Axial): 0.13 J/tonne
Zone 3b: Tang and Kaiser Index (Volumetric): 1.04 J/tonne
Zone 4: Peak to Residual Strength Ratio: 1.90

Bill Barrett 14-3-35

Lithology	Sample ID	Depth (ft)	Orientation	As Received Bulk Density (g/cm^3)	Confining Pressure (psi)	Peak Effective Compressive Strength (psi)	Effective Residual Compressive Strength (psi)	Young's Modulus (10^6 psi)	Poisson's Ratio
shale	UTE1-1[5]	7358.35	Vertical	2.439	1325	9700	5510	1.428	0.21
	UTE1-2	7358.15	Horizontal	2.584	2943	22040	14640	3.963	0.26

404730 UGS, Bill Barett 14-3-45
UTE1-1, 7358.35 ft, Vertical, As-Received

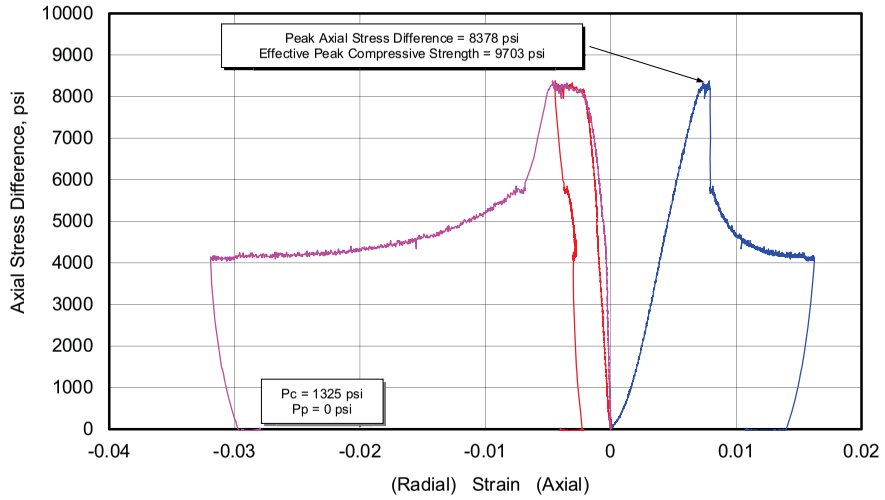

404730 UGS, Bill Barett 14-3-45
UTE1-2, 7358.15 ft, Horz, As-Received

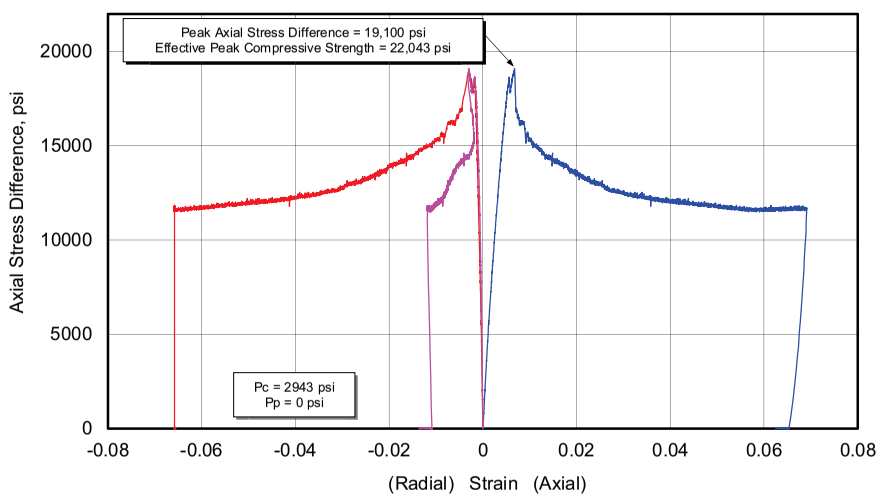

Zone 1 Deformation Index: Ratio of Secant E at Peak to E: 1.23
Zone 2 Ductility Index: Amount of Plastic or Strain Hardening Strain: 0.16
Zone 3a: Tang and Kaiser Index (Axial): 2.69x 10^{-4} J/tonne
Zone 3b: Tang and Kaiser Index (Volumetric): 1.89 x 10^{-4} J/tonne
Zone 4: Peak to Residual Strength Ratio: 1.91

Zone 1 Deformation Index: Ratio of Secant E at Peak to E: 1.19
Zone 2 Ductility Index: Amount of Plastic or Strain Hardening Strain: 0.052
Zone 3a: Tang and Kaiser Index (Axial): 0.785 J/tonne
Zone 3b: Tang and Kaiser Index (Volumetric): 1.45 J/tonne
Zone 4: Peak to Residual Strength Ratio:1.45

[5] Note density difference between UTE 1-1 and UTE 1-2. No additional material available.

Bill Barrett 14-1-46

Lithology	Sample ID	Depth (ft)	Orientation	As Received Bulk Density (g/cm^3)	Confining Pressure (psi)	Peak Effective Compressive Strength (psi)	Effective Residual Compressive Strength (psi)	Young's Modulus (10^6 psi)	Poisson's Ratio
tan dolomite	BTR1-1	6684.40	Vertical	2.282	1337	19420	9580		
	BTR1-6	6684.40	Vertical	2.348	1337	22190	10410	5.390	0.22
	BTR1-2	6684.780	Horizontal	2.140	2741	19740	13240	3.829	0.27

404730 UGS, Bill Barrett 14-1-46
BTR1-6, 6684.4 ft, Vertical, As-Received

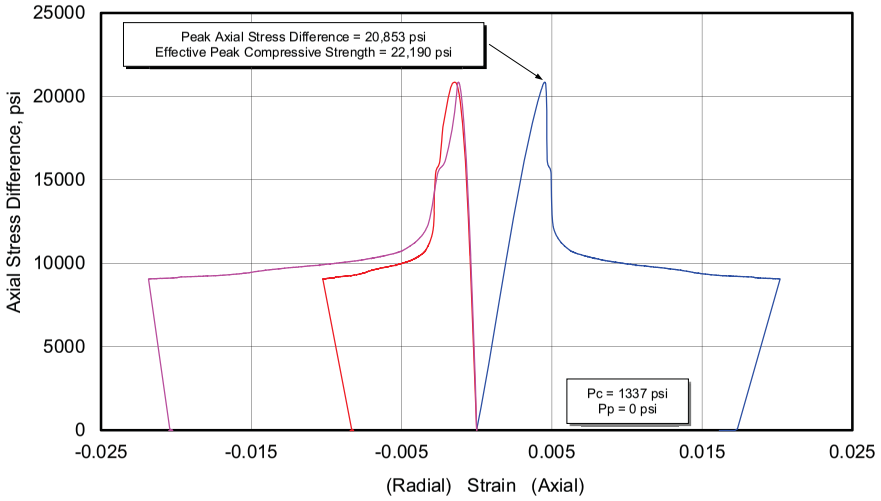

404730 UGS, Bill Barrett 14-1-46
BTR1-2, 6684.70 ft, Horizontal, As-Received

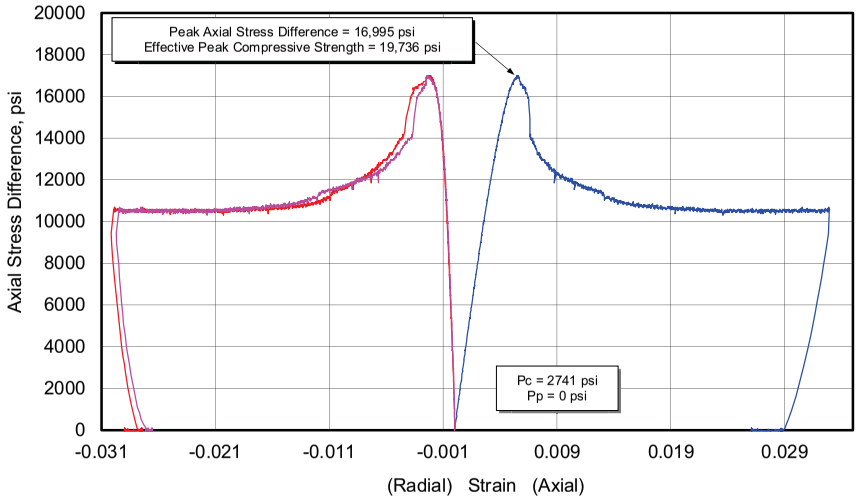

Zone 1 Deformation Index: Ratio of Secant E at Peak to E: 1.15
Zone 2 Ductility Index: Amount of Plastic or Strain Hardening Strain: 0.009
Zone 3a: Tang and Kaiser Index (Axial): 0.245 J/tonne
Zone 3b: Tang and Kaiser Index (Volumetric): 2.87 J/tonne
Zone 4: Peak to Residual Strength Ratio: 1.86

Zone 1 Deformation Index: Ratio of Secant E at Peak to E: 1.23
Zone 2 Ductility Index: Amount of Plastic or Strain Hardening Strain: 0.044
Zone 3a: Tang and Kaiser Index (Axial): 0.69 J/tonne
Zone 3b: Tang and Kaiser Index (Volumetric): 3.987 J/tonne
Zone 4: Peak to Residual Strength Ratio: 1.59

Bill Barrett 14-1-46

Lithology	Sample ID	Depth (ft)	Orientation	As Received Bulk Density (g/cm^3)	Confining Pressure (psi)	Peak Effective Compressive Strength (psi)	Effective Residual Compressive Strength (psi)	Young's Modulus (10^6 psi)	Poisson's Ratio
dolomite	BTR2-1	6693.70	Vertical	2.428	1399	29110	9470	4.861	0.29
	BTR2-2	6693.45	Horizontal	2.544	2744	49930	20490	7.011	0.29
	BTR2-5	6693.45	Horizontal	2.433	2744			4.796	0.31

404730 UGS, Bill Barrett 14-1-46
BTR2-1, 6693.70 ft, Vertical, As-Received

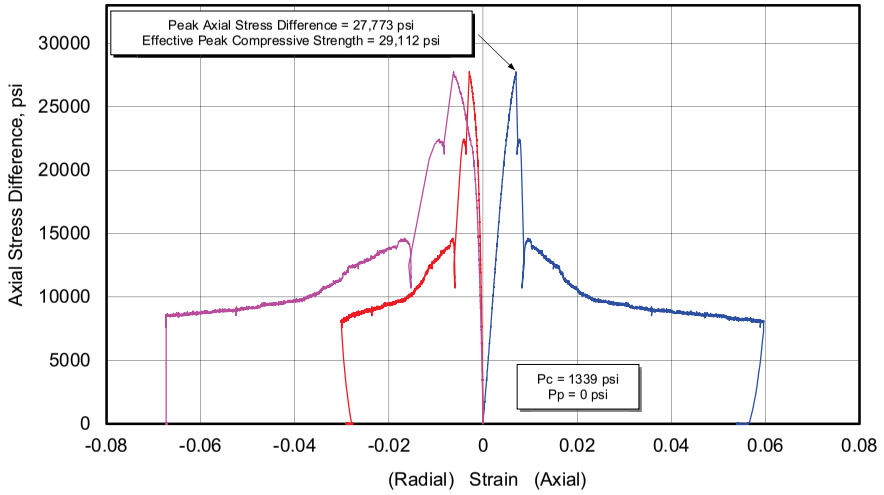

404730 UGS, Bill Barrett 14-1-46
BTR2-2, 6693.45 ft, Horizontal, As-Received

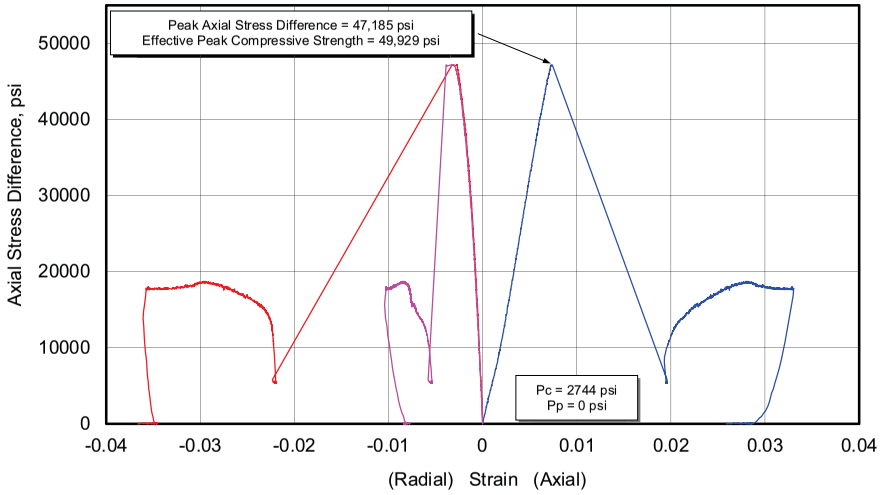

Zone 1 Deformation Index: Ratio of Secant E at Peak to E: 1.20
Zone 2 Ductility Index: Amount of Plastic or Strain Hardening Strain: 0
Zone 3a: Tang and Kaiser Index (Axial): 3.94 J/tonne
Zone 3b: Tang and Kaiser Index (Volumetric): 21.25 J/tonne
Zone 4: Peak to Residual Strength Ratio: 2.72

Zone 1 Deformation Index: Ratio of Secant E at Peak to E: 1.08
Zone 2 Ductility Index: Amount of Plastic or Strain Hardening Strain: N/A
Zone 3a: Tang and Kaiser Index (Axial): N/A
Zone 3b: Tang and Kaiser Index (Volumetric): N/A
Zone 4: Peak to Residual Strength Ratio: N/A

Bill Barrett 14-1-46

Lithology	Sample ID	Depth (ft)	Orientation	As Received Bulk Density (g/cm^3)	Confining Pressure (psi)	Peak Effective Compressive Strength (psi)	Effective Residual Compressive Strength (psi)	Young's Modulus (10^6 psi)	Poisson's Ratio
gray limestone	BTR3-1	6698.25	Vertical	2.586	1340	23980	13700	4.038	0.14
	BTR3-2	6699.00	Horizontal	2.614	2747	52680	19850	8.657	0.32

404730 UGS, Bill Barrett 14-1-46
BTR3-1, 6698.25 ft, Vertical, As-Received

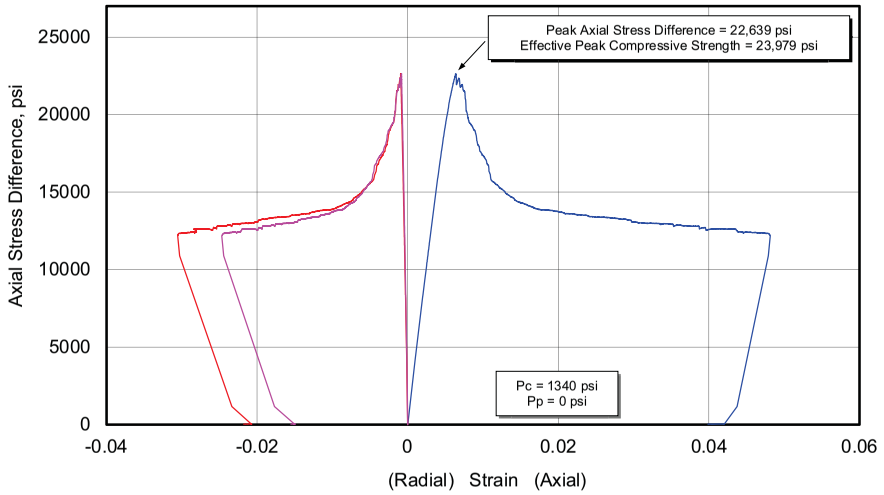

404730 UGS, Bill Barrett 14-1-46
BTR3-2, 6699.00 ft, Horiztonal, As-Received

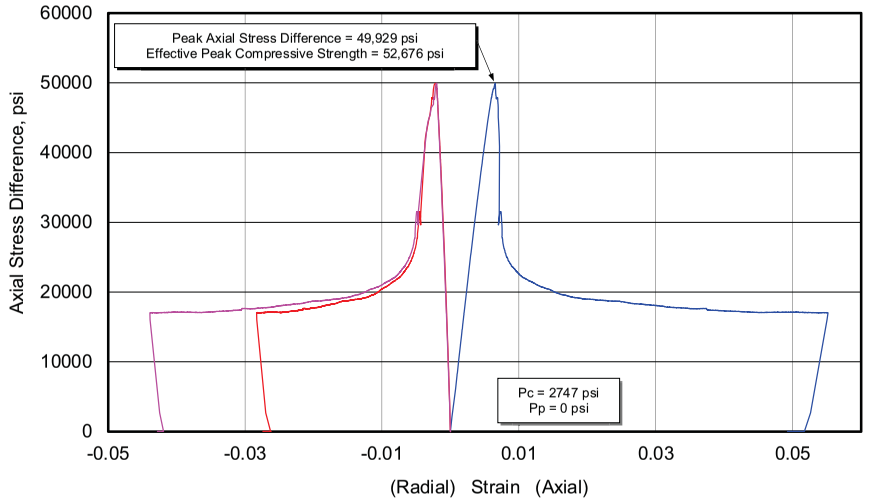

Zone 1 Deformation Index: Ratio of Secant E at Peak to E: 1.13
Zone 2 Ductility Index: Amount of Plastic or Strain Hardening Strain: 0.093
Zone 3a: Tang and Kaiser Index (Axial): 0.972 J/tonne
Zone 3b: Tang and Kaiser Index (Volumetric): 1.82 J/tonne
Zone 4: Peak to Residual Strength Ratio: 1.60

Zone 1 Deformation Index: Ratio of Secant E at Peak to E: 1.12
Zone 2 Ductility Index: Amount of Plastic or Strain Hardening Strain: 0
Zone 3a: Tang and Kaiser Index (Axial): 4.34
Zone 3b: Tang and Kaiser Index (Volumetric): 12.75
Zone 4: Peak to Residual Strength Ratio: 2.58

Bill Barrett 14-1-46

Lithology	Sample ID	Depth (ft)	Orientation	As Received Bulk Density (g/cm^3)	Confining Pressure (psi)	Peak Effective Compressive Strength (psi)	Effective Residual Compressive Strength (psi)	Young's Modulus (10^6 psi)	Poisson's Ratio
tan dolomite	BTR4-4	6703.10	Vertical	2.543	1341	23340	14290	6.422	0.28
	BTR4-2	6702.90	Horizontal	2.473	2748	26760	11050	6.223	0.26

404730 UGS, Bill Barrett 14-1-46
BTR4-4, 6703.1 ft, Vertical, As-Received

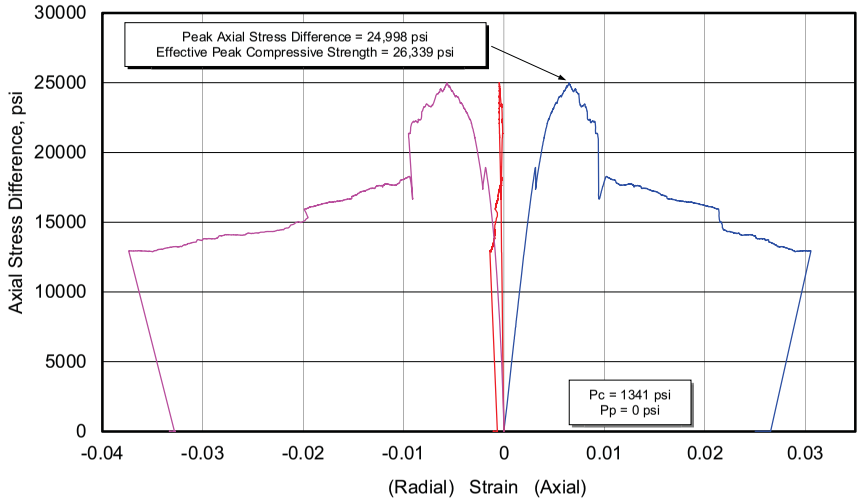

404730 UGS, Bill Barrett 14-1-46
BTR4-2, 6702.90 ft, Horizontal, As-Received

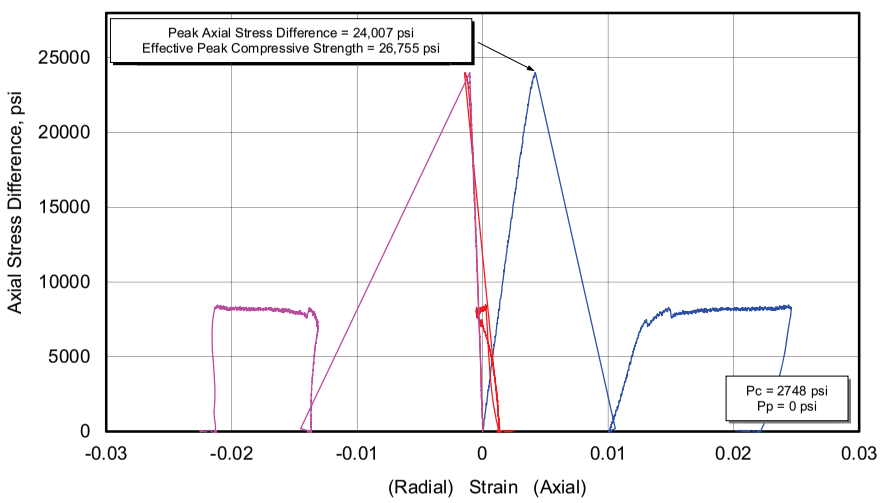

Zone 1 Deformation Index: Ratio of Secant E at Peak to E: 1.62
Zone 2 Ductility Index: Amount of Plastic or Strain Hardening Strain: 0.902
Zone 3a: Tang and Kaiser Index (Axial): 0.0039
Zone 3b: Tang and Kaiser Index (Volumetric): 0.0132
Zone 4: Peak to Residual Strength Ratio: 1.44

Zone 1 Deformation Index: Ratio of Secant E at Peak to E: 1.06
Zone 2 Ductility Index: Amount of Plastic or Strain Hardening Strain: N/A
Zone 3a: Tang and Kaiser Index (Axial): N/A
Zone 3b: Tang and Kaiser Index (Volumetric): N/A
Zone 4: Peak to Residual Strength Ratio: 3.17

Bill Barrett 14-1-46

Lithology	Sample ID	Depth (ft)	Orientation	As Received Bulk Density (g/cm^3)	Confining Pressure (psi)	Peak Effective Compressive Strength (psi)	Effective Residual Compressive Strength (psi)	Young's Modulus (10^6 psi)	Poisson's Ratio
shale	BTR5-4	6706.50	Vertical	2.487	1341	14450	9190	1.295	0.18
	BTR5-2	6706.65	Horizontal	2.502	2750	17250	13270	3.797	0.26

404730 UGS, Bill Barrett 14-1-46
BTR5-4, 6706.5 ft, Vertical, As-Received

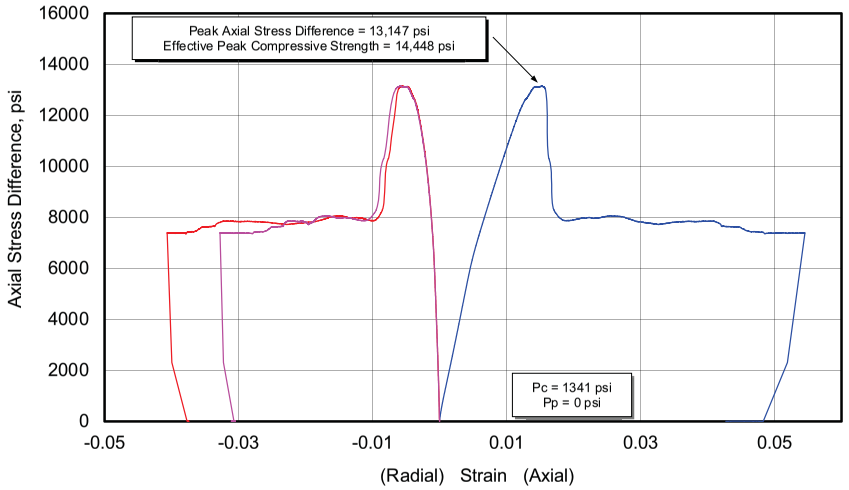

404730 UGS, Bill Barrett 14-1-46
BTR5-2, 6706.65 ft, Horizontal, As-Received

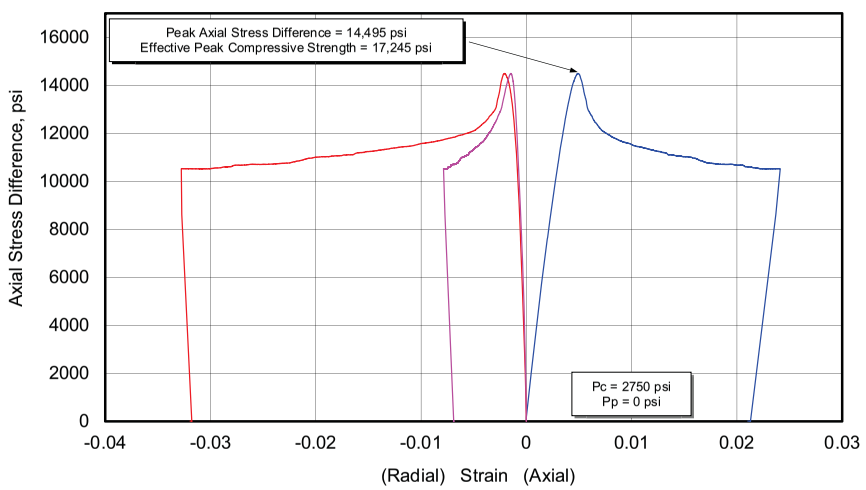

Zone 1 Deformation Index: Ratio of Secant E at Peak to E: 1.38
Zone 2 Ductility Index: Amount of Plastic or Strain Hardening Strain: 0.48
Zone 3a: Tang and Kaiser Index (Axial): 0.205 J/tonne
Zone 3b: Tang and Kaiser Index (Volumetric): 1.576 J/tonne
Zone 4: Peak to Residual Strength Ratio: 1.60

Zone 1 Deformation Index: Ratio of Secant E at Peak to E: 1.22
Zone 2 Ductility Index: Amount of Plastic or Strain Hardening Strain: 0.083
Zone 3a: Tang and Kaiser Index (Axial): 0.00527
Zone 3b: Tang and Kaiser Index (Volumetric): 0.196
Zone 4: Peak to Residual Strength Ratio: 1.24

Appendix B-2

Processed Energy Release Indices

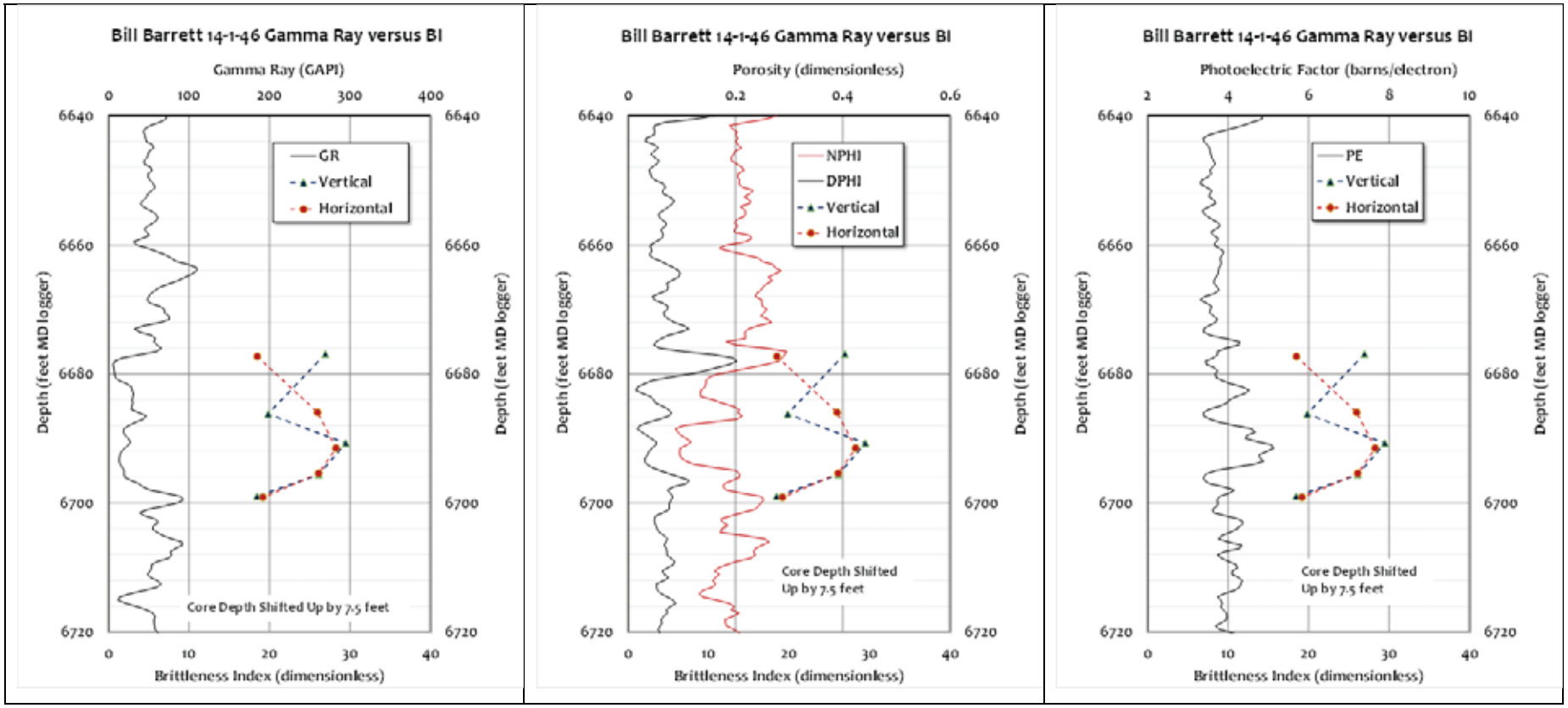
Bill Barrett 14-1-46 Gamma Ray versus BI
Gamma Ray (GAPI)
GR
Vertical
Horizontal
Core Depth Shifted Up by 7.5 feet
Depth (feet MD logger)
Brittleness Index (dimensionless)
Bill Barrett 14-1-46 Gamma Ray versus BI
Porosity (dimensionless)
NPHI
DPHI
Vertical
Horizontal
Core Depth Shifted Up by 7.5 feet
Depth (feet MD logger)
Brittleness Index (dimensionless)
Bill Barrett 14-1-46 Gamma Ray versus BI
Photoelectric Factor (barns/electron)
PE
Vertical
Horizontal
Core Depth Shifted Up by 7.5 feet
Depth (feet MD logger)
Brittleness Index (dimensionless)

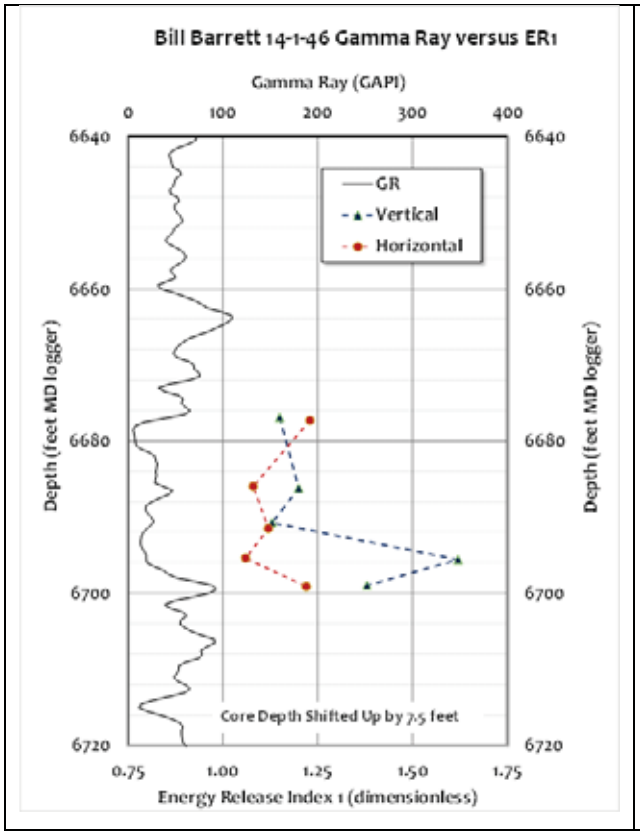
Bill Barrett 14-1-46 Gamma Ray versus ER1
Gamma Ray (GAPI)
0
100
200
300
400
GR
Vertical
Horizontal
Depth (feet MD logger)
6640
6660
6680
6700
6720
Core Depth Shifted Up by 7.5 feet
0.75
1.00
1.25
1.50
1.75
Energy Release Index 1 (dimensionless)

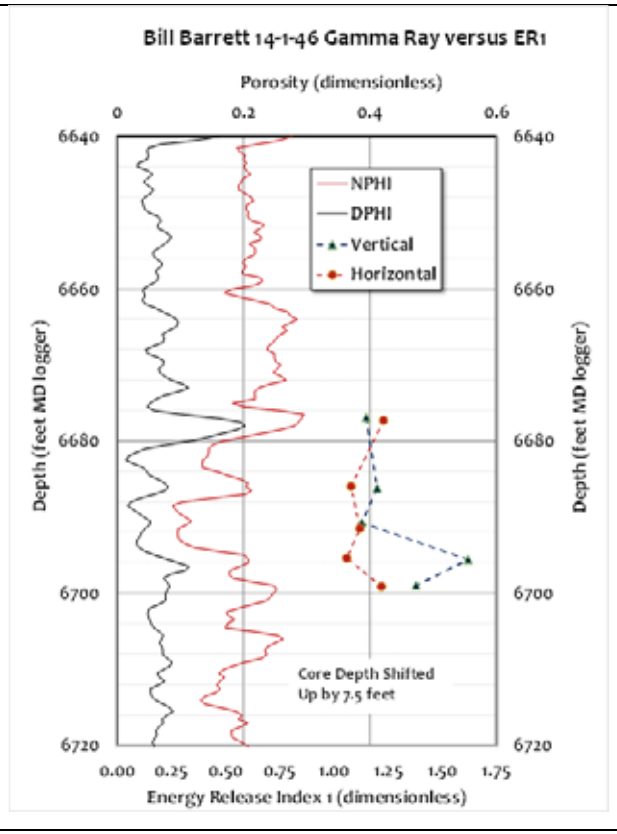
Bill Barrett 14-1-46 Gamma Ray versus ER1
Porosity (dimensionless)
0
0.2
0.4
0.6
NPHI
DPHI
Vertical
Horizontal
Depth (feet MD logger)
6640
6660
6680
6700
6720
Core Depth Shifted
Up by 7.5 feet
0.00
0.25
0.50
0.75
1.00
1.25
1.50
1.75
Energy Release Index 1 (dimensionless)

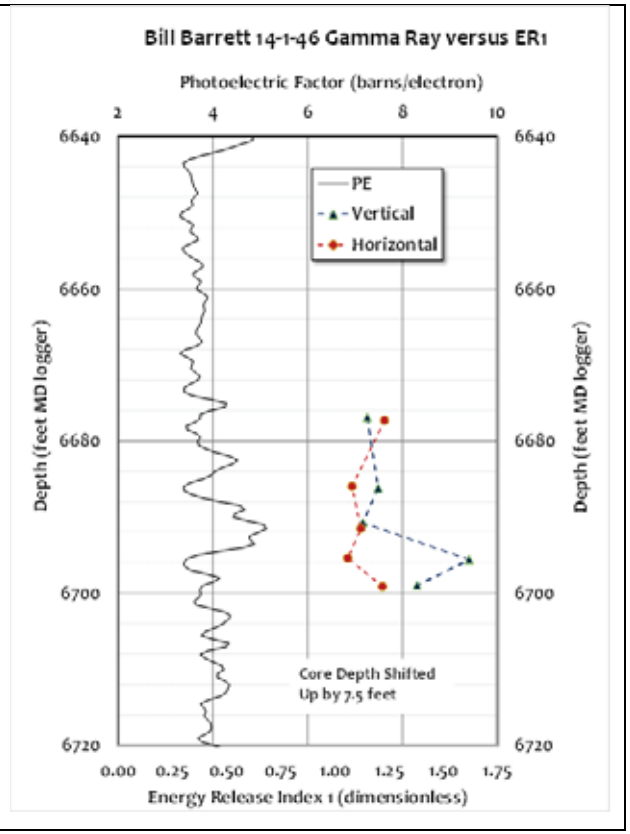
Bill Barrett 14-1-46 Gamma Ray versus ER1
Photoelectric Factor (barns/electron)
2
4
6
8
10
PE
Vertical
Horizontal
Depth (feet MD logger)
6640
6660
6680
6700
6720
Core Depth Shifted
Up by 7.5 feet
0.00
0.25
0.50
0.75
1.00
1.25
1.50
1.75
Energy Release Index 1 (dimensionless)

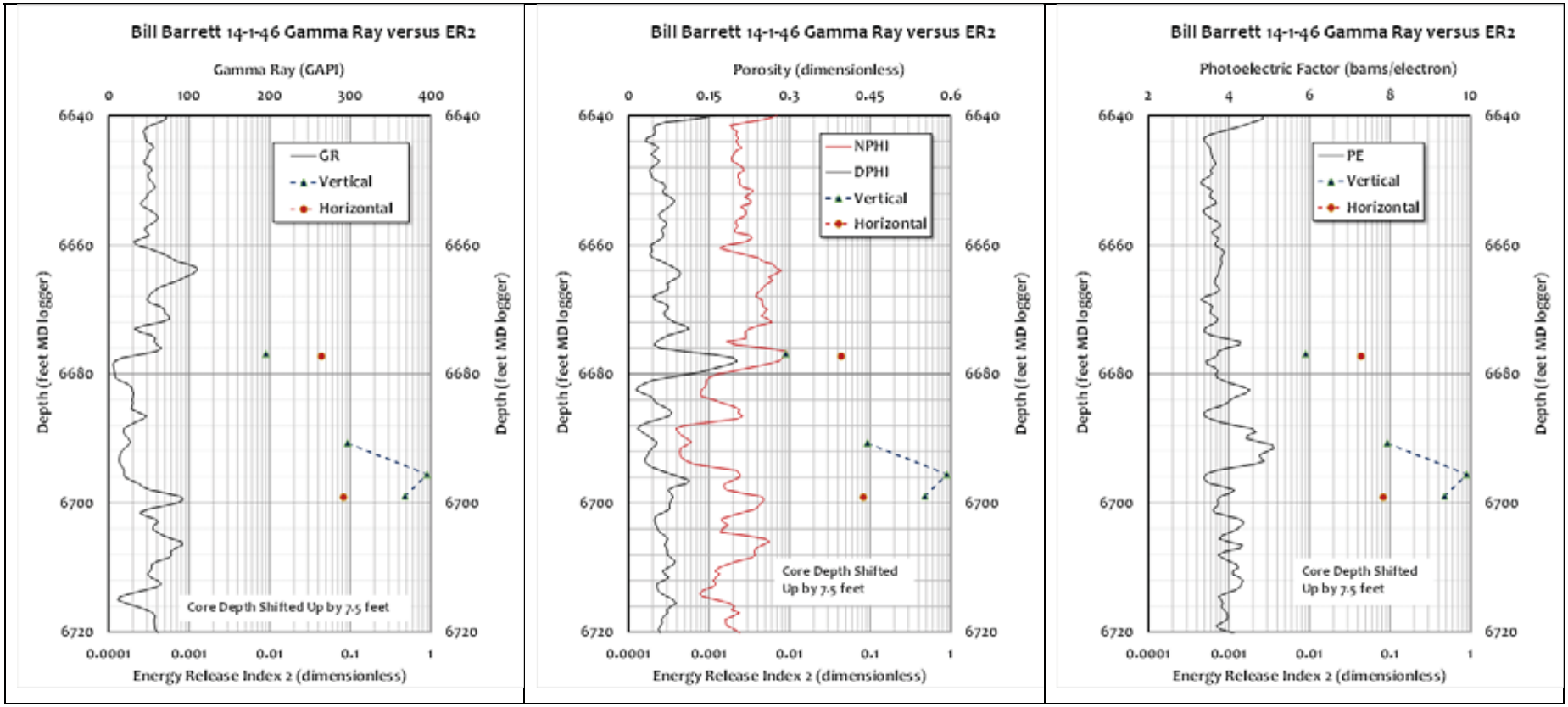
Bill Barrett 14-1-46 Gamma Ray versus ER2
Gamma Ray (GAPI)
0
100
200
300
400
GR
Vertical
Horizontal
Core Depth Shifted Up by 7.5 feet
Depth (feet MD logger)
6640
6660
6680
6700
6720
0.0001
0.001
0.01
0.1
1
Energy Release Index 2 (dimensionless)
Bill Barrett 14-1-46 Gamma Ray versus ER2
Porosity (dimensionless)
0
0.15
0.3
0.45
0.6
NPHI
DPHI
Vertical
Horizontal
Core Depth Shifted Up by 7.5 feet
Depth (feet MD logger)
Energy Release Index 2 (dimensionless)
Bill Barrett 14-1-46 Gamma Ray versus ER2
Photoelectric Factor (barns/electron)
2
4
6
8
10
PE
Vertical
Horizontal
Core Depth Shifted Up by 7.5 feet
Depth (feet MD logger)
Energy Release Index 2 (dimensionless)

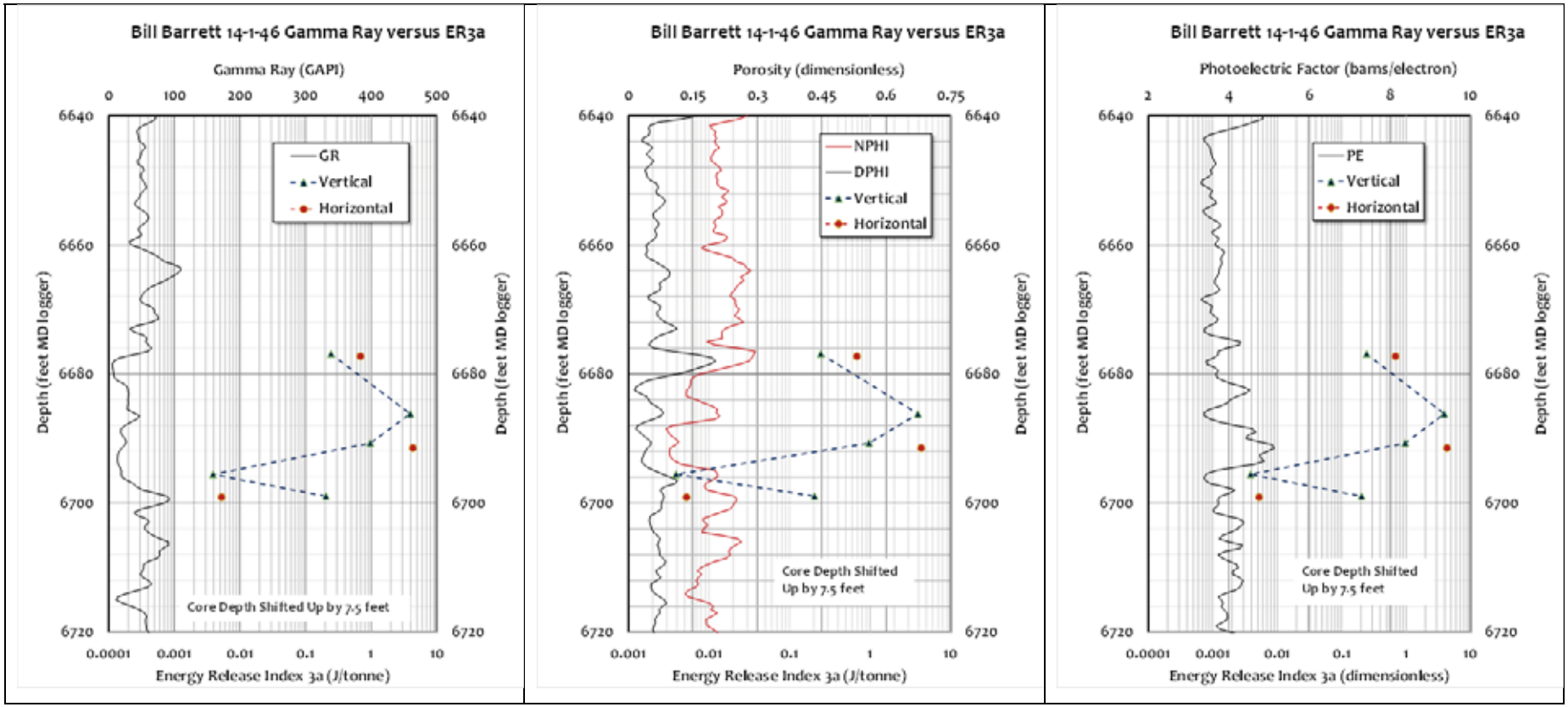
Bill Barrett 14-1-46 Gamma Ray versus ER3a
Gamma Ray (GAPI)
0 100 200 300 400 500
6640 6660 6680 6700 6720
GR
Vertical
Horizontal
Core Depth Shifted Up by 7.5 feet
Depth (feet MD logger)
0.0001 0.001 0.01 0.1 1 10
Energy Release Index 3a (J/tonne)
Bill Barrett 14-1-46 Gamma Ray versus ER3a
Porosity (dimensionless)
0 0.15 0.3 0.45 0.6 0.75
6640 6660 6680 6700 6720
NPHI
DPHI
Vertical
Horizontal
Core Depth Shifted Up by 7.5 feet
Depth (feet MD logger)
0.001 0.01 0.1 1 10
Energy Release Index 3a (J/tonne)
Bill Barrett 14-1-46 Gamma Ray versus ER3a
Photoelectric Factor (barns/electron)
2 4 6 8 10
6640 6660 6680 6700 6720
PE
Vertical
Horizontal
Core Depth Shifted Up by 7.5 feet
Depth (feet MD logger)
0.0001 0.001 0.01 0.1 1 10
Energy Release Index 3a (dimensionless)

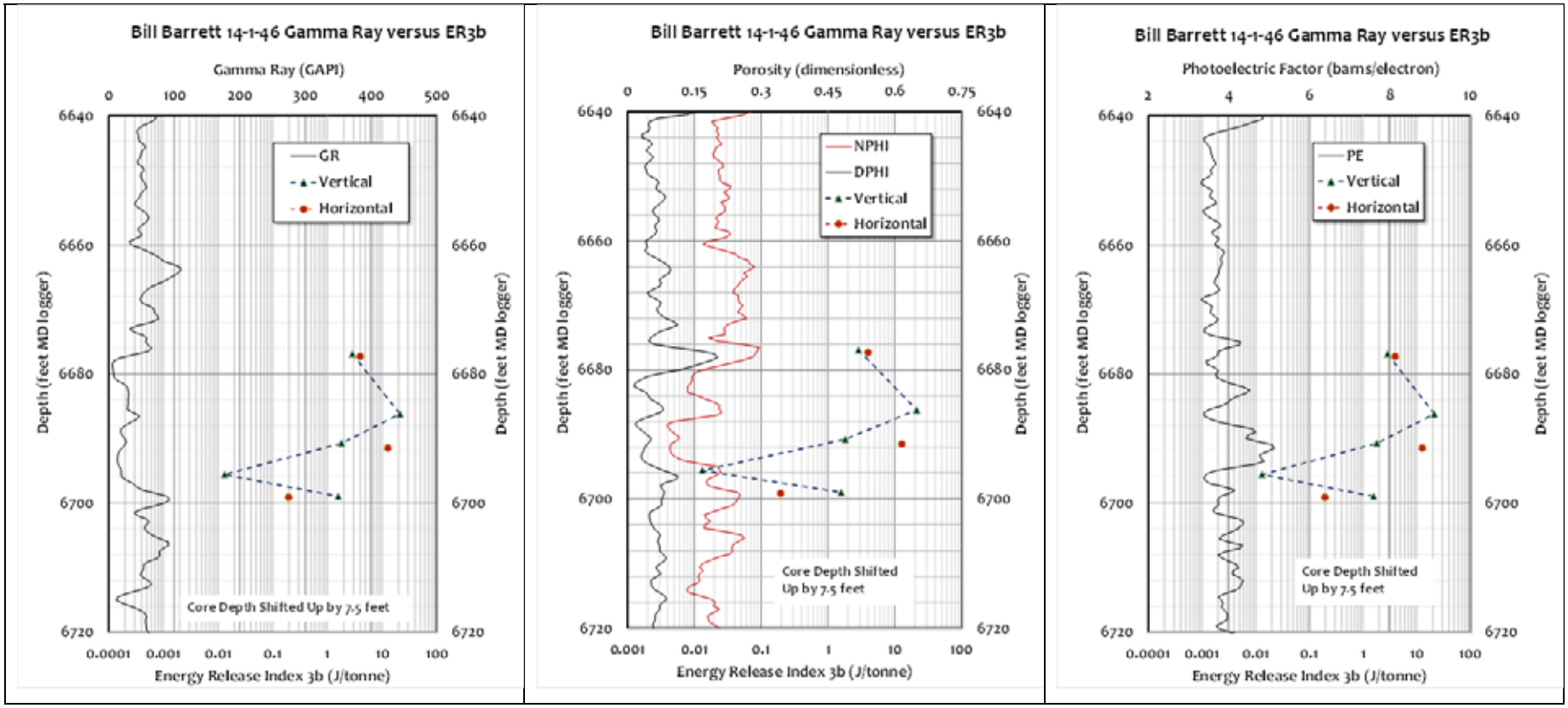
Bill Barrett 14-1-46 Gamma Ray versus ER3b
Gamma Ray (GAPI)
0 100 200 300 400 500
GR
Vertical
Horizontal
Core Depth Shifted Up by 7.5 feet
Depth (feet MD logger)
6640 6660 6680 6700 6720
0.0001 0.001 0.01 0.1 1 10 100
Energy Release Index 3b (J/tonne)
Bill Barrett 14-1-46 Gamma Ray versus ER3b
Porosity (dimensionless)
0 0.15 0.3 0.45 0.6 0.75
NPHI
DPHI
Vertical
Horizontal
Core Depth Shifted Up by 7.5 feet
Depth (feet MD logger)
6640 6660 6680 6700 6720
0.001 0.01 0.1 1 10 100
Energy Release Index 3b (J/tonne)
Bill Barrett 14-1-46 Gamma Ray versus ER3b
Photoelectric Factor (barns/electron)
2 4 6 8 10
PE
Vertical
Horizontal
Core Depth Shifted Up by 7.5 feet
Depth (feet MD logger)
6640 6660 6680 6700 6720
0.0001 0.001 0.01 0.1 1 10 100
Energy Release Index 3b (J/tonne)

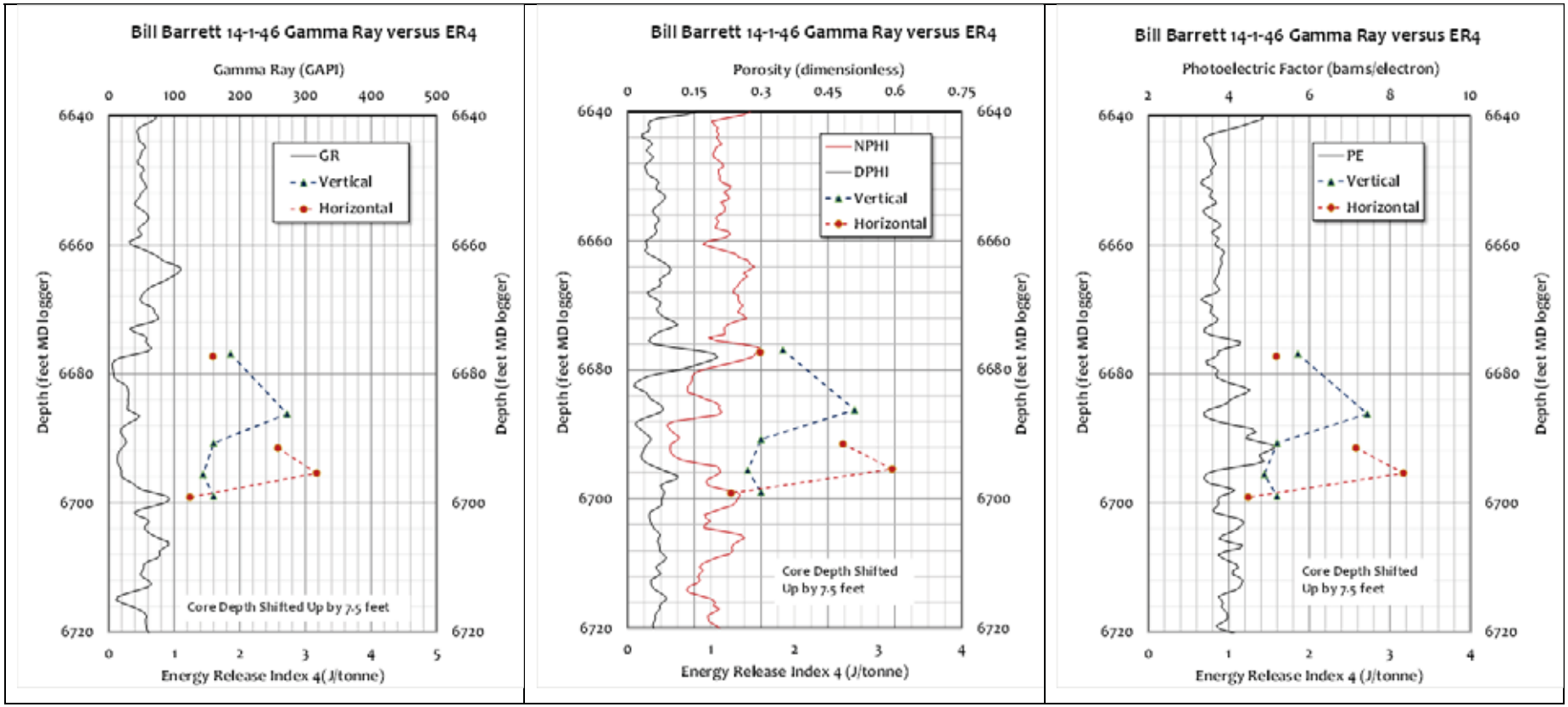
Bill Barrett 14-1-46 Gamma Ray versus ER4
Gamma Ray (GAPI)
GR
Vertical
Horizontal
Core Depth Shifted Up by 7.5 feet
Depth (feet MD logger)
Energy Release Index 4(J/tonne)
Bill Barrett 14-1-46 Gamma Ray versus ER4
Porosity (dimensionless)
NPHI
DPHI
Vertical
Horizontal
Core Depth Shifted Up by 7.5 feet
Depth (feet MD logger)
Energy Release Index 4 (J/tonne)
Bill Barrett 14-1-46 Gamma Ray versus ER4
Photoelectric Factor (barns/electron)
PE
Vertical
Horizontal
Core Depth Shifted Up by 7.5 feet
Depth (feet MD logger)
Energy Release Index 4 (J/tonne)

Appendix C

Well Descriptions

Bill Barrett 14-3-45

This was nominally straight hole. It was perforated with 3 spf, 120° phasing. It had a similar frac program to Bill Barrett 14-1-46. The perforations were overflushed by 15 bbl. This well flowed back sand. The operator attempted/ran a production log.

Some XRD and thin section observations are available and these are shown in Tables C-1 and C-2.

Table C-1. Sample Description – (Bill Barrett 14-3-45 Well)

Depth (ft)	Lithology	Classification (Dunham)
7330.75	*argillaceous dolostone*	
7338.45	*sandy dolostone*	
7346.50	*sandy dolostone*	
7354.70	*argillaceous limestone*	
7361.40	*limestone*	
7362.10	sandy dolostone	wackestone
7363.50	*sandy dolostone*	
7365.05	limestone	wackestone
7367.20	*dolostone*	
7368.70	limestone	shelly mudstone
7369.15	*slightly argillaceous limestone*	
7371.25	limestone	shelly wackestone
7373.65	*dolostone*	
7374.50	cherty dolomitic limestone	pel-skel packstone/cherty calcareous dolostone
7375.40	*calcareous dolostone*	
7377.10	limestone	ostracod mudstone
7379.90	*limestone*	
7380.00	limestone	ostracod mudstone
7381.90	*dolostone*	
7383.79	dolostone	peloidal wackestone-packstone

Table C-2. X-Ray Diffraction – (Bill Barrett 14-3-45 Well)

Whole Rock Mineralogy (Weight %)							Clay Mineralogy (Weight %)		
Depth (ft)	Quartz	K Feldspar	Plagioclase	Calcite	Dolomite and Fe-Dolomite	Pyrite	Total Clay	Illite / Smectite*	Illite and Mica
7,330.75	14.5	0.5	2.7	10.8	43.9	3.2	24.4	9.7	14.7
7,338.45	22.0	0.0	0.5	1.2	67.8	1.1	7.5	4.4	3.1
7,346.50	24.0	0.0	0.0	1.5	65.8	2.2	6.4	3.8	2.6
7,354.70	13.3	0.0	1.2	63.8	1.8	3.5	16.5	9.1	7.4
7,361.40	26.9	0.0	0.0	7.8	59.7	0.9	4.8	3.1	1.7
7,362.10	na	na	na	na	na	na	na	na	na
7,363.50	25.3	0.0	0.2	1.0	66.8	0.3	6.5	3.4	3.1
7,365.05	12.1	0.0	1.1	70.4	1.6	2.3	12.4	7.1	5.3
7,367.20	12.0	0.0	0.5	5.5	75.2	0.8	5.9	3.2	2.7
7,368.70	na	na	na	na	na	na	na	na	na
7,369.15	7.9	0.0	0.4	74.1	1.3	2.4	13.9	6.5	7.4
7,371.25	11.9	0.0	0.8	68.0	2.2	3.7	13.4	6.6	6.8
7,373.65	0.7	0.0	0.0	11.4	84.8	0.6	2.4	1.5	0.9
7,374.50	na	na	na	na	na	na	na	na	na
7,375.40	0.8	0.0	0.0	29.7	66.4	0.6	2.5	1.5	1.0
7,377.10	3.4	0.0	0.0	88.4	0.6	1.6	5.9	2.9	3.1
7,379.90	9.8	0.0	1.0	64.6	8.8	1.6	14.3	5.5	8.8
7,380.00	na	na	na	na	na	na	na	na	na
7,381.90	13.4	0.0	0.3	7.7	69.7	1.4	7.4	4.2	3.2
7,383.79	11.6	0.0	0.0	10.4	72.3	0.8	4.8	2.0	2.8

Laboratory routine core analysis data are shown in Table C-3 and Figure C-1.

The source rock data is summarized in Table C-4 and Figure C-2.

Table C-3. Routine Core Analysis Data – (Bill Barrett 14-3-45 Well)

Sample Number	Depth (ft)	Net Confining Pressure (psig)	Porosity (%)	Klinkenberg Permeability (md)	Air Permeability (md)	b (psi)	β (ft^{-1})	α (micron)	Oil Saturation (%PV)	Water Saturation (%PV)	Grain Density (g/cm^3)	Footnote
1	7324.85	1420	9.35	***	***	***	***	***	24.3	66.1	2.683	(5)
2	7326.20	1420	5.99	.0756	.0782	0.90	7.52E+12	1.84E+03	14.8	48.6	2.666	(1)
3	7328.20	1420	4.78	***	***	***	***	***	55.7	10.9	2.693	(5)
4	7330.75	1420	6.88	.804	.925	2.96	3.58E+12	9.41E+03	34.7	35.6	2.697	(1)
5	7332.15	1420	6.95	.0744	.0865	4.21	1.10E+13	2.65E+03	47.5	35.4	2.703	(1)
6	7335.00	1420	4.90	2.53	2.83	2.09	8.48E+09	6.99E+01	64.4	14.7	2.748	(1)
7	7336.00	1420	6.31	.00008	.0007	323.78	9.18E+17	2.57E+05	66.0	0.0	2.740	
8	7338.45	1420	3.52	.00004	.0004	406.80	2.73E+18	4.24E+05	75.9	0.0	2.745	
9	7340.15	1420	1.88	.00002	.0002	634.09	2.69E+19	1.42E+06	76.5	0.0	2.746	
10	7342.00	1420	8.19	***	***	***	***	***	23.3	48.5	2.696	(5)
11	7344.20	1420	7.24	.0001	.0009	288.52	4.92E+17	1.87E+05	62.1	0.0	2.739	
12	7346.50	1420	8.98	.006	.0208	70.47	2.37E+14	4.90E+03	61.2	0.0	2.793	
13	7348.40	1420	6.72	.0002	.001	252.39	2.43E+17	1.33E+05	64.6	0.0	2.767	
14	7350.20	1420	4.39	.239	.294	5.48	1.31E+13	1.02E+04	34.9	42.8	2.680	(1)
15A	7351.00	1420	4.78	.0666	.135	27.03	4.10E+12	8.85E+02	57.2	0.0	2.763	(1)
16	7354.70	1420	4.64	***	***	***	***	***	68.4	0.0	2.682	(5)
17	7356.00	1420	5.54	***	***	***	***	***	72.7	21.2	2.681	(5)
18	7358.00	1420	6.69	***	***	***	***	***	40.9	51.7	2.681	(5)
19	7360.45	1420	8.55	***	***	***	***	***	70.4	0.0	2.751	(5)
20	7361.40	1420	15.01	.0260	.0494	25.02	1.61E+13	1.37E+03	60.0	0.0	2.769	
21	7362.10	1420	6.67	***	***	***	***	***	78.7	0.0	2.759	(5)
22	7363.50	1420	9.18	.0007	.004	149.08	1.33E+16	3.32E+04	66.9	0.0	2.767	
23	7364.50	1420	2.89	.00006	.0006	348.21	1.29E+18	2.98E+05	75.3	0.0	2.750	

Sample Number	Depth (ft)	Net Confining Pressure (psig)	Porosity (%)	Klinkenberg Permeability (md)	Air Permeability (md)	b (psi)	β (ft^{-1})	α (micron)	Oil Saturation (%PV)	Water Saturation (%PV)	Grain Density (g/cm^3)	Footnote
24	7365.05	1420	3.55	2.87	3.13	1.62	9.82E+09	9.14E+01	69.3	12.5	2.666	(1)
27	7368.70	1420	3.89	***	***	***	***	***	70.4	0.0	2.677	(5)
28	7369.15	1420	3.20	1.83	1.92	0.89	2.31E+10	1.38E+02	71.4	0.0	2.665	(1)
29	7370.65	1420	2.44	.0001	.001	261.69	2.89E+17	1.44E+05	75.2	0.0	2.690	
30A	7371.25	1420	3.29	8.59	9.89	2.53	5.41E+11	1.50E+04	48.2	19.4	2.674	(1)
30B	7371.40	1420	3.01	.0009	.004	144.21	1.10E+16	3.02E+04	77.4	0.0	2.690	
32	7373.65	1420	26.52	.0770	.229	50.99	1.70E+12	4.29E+02	38.8	33.8	2.789	
33	7374.50	1420	5.15	***	***	***	***	***	77.2	0.0	2.700	(5)
34	7375.40	1420	20.07	***	***	***	***	***	62.1	28.9	2.775	(5)
35	7376.00	1420	14.25	***	***	***	***	***	76.4	0.0	2.750	(5)
36	7377.10	1420	0.98	.00002	.0003	504.70	8.26E+18	7.50E+05	75.5	0.0	2.683	
37	7378.10	1420	3.28	.0002	.001	227.33	1.39E+17	1.02E+05	71.4	0.0	2.681	
38	7379.90	1420	5.17	1.09	1.29	3.51	1.45E+12	5.13E+03	60.1	0.0	2.677	(1)
39	7380.00	1420	5.81	.0614	.0863	10.66	9.31E+13	1.83E+04	15.9	41.4	2.708	(1)
40	7381.90	1420	8.71	.0002	.001	225.38	1.32E+17	9.93E+04	79.8	0.0	2.764	
41	7382.55	1420	2.59	.0003	.002	195.46	5.89E+16	6.69E+04	75.3	0.0	2.761	
42A	7383.79	1420	8.56	***	***	***	***	***	72.3	0.0	2.695	(5)
42B	7383.79	1420	8.01	***	***	***	***	***	73.4	0.0	2.697	(5)

Footnotes:

(1) Denotes fractured or chipped sample. Permeability and/or porosity may be optimistic.

(2) Sample permeability below the measurement range of CMS-300 equipment at indicated net confining stress (NCS). Data unavailable.

(3) Denotes very short sample, porosity may be optimistic due to lack of conformation of boot material to plug surface.

(4) Sample contains bitumen or other solid hydrocarbon residue.

(5) Denotes sample unsuitable for measurement at stress. Porosity determined using Archimedes bulk volume at ambient conditions. Permeability >0.1 mD measured using helium gas. Permeability less than 0.1 mD measured using nitrogen gas. All b values converted to b (air)

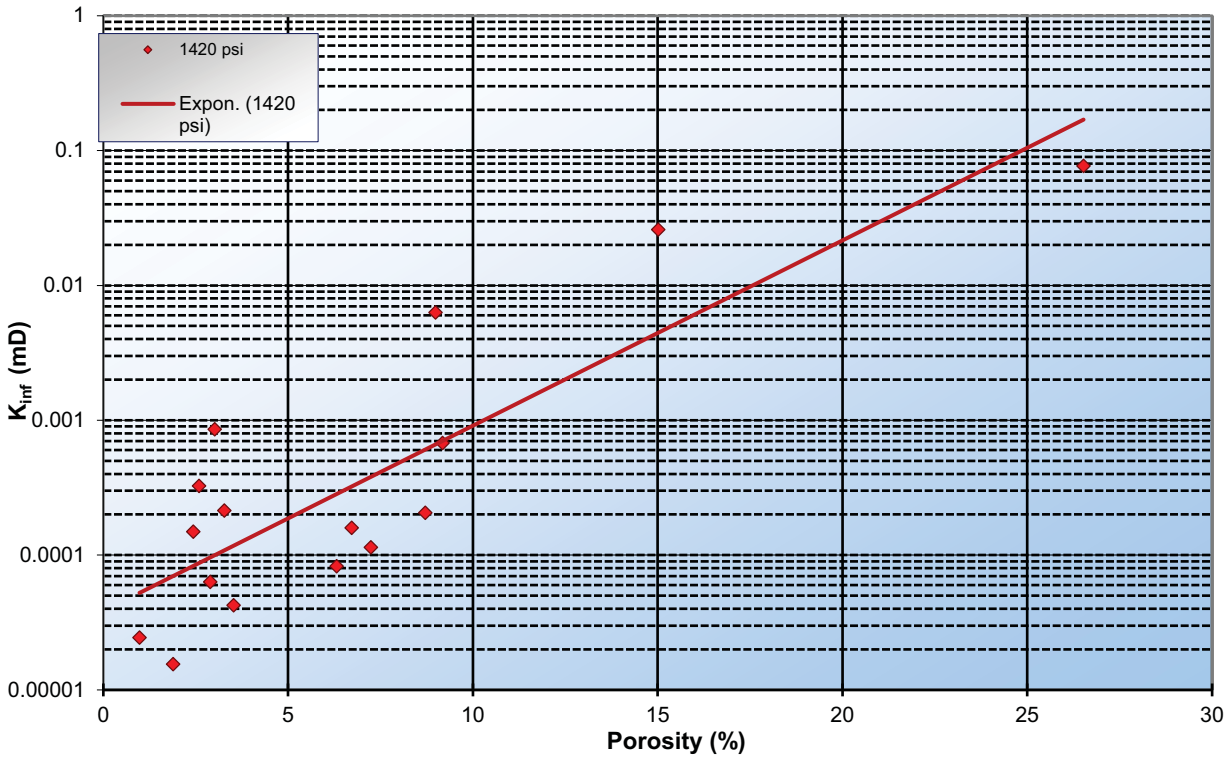

Figure C-1. Air permeability versus porosity on laboratory samples. Most samples are in the microdarcy regime.

Table C-4. Source Rock Data – (Bill Barrett 14-3-45 Well)

Depth (ft)	Percent Carbonate (wt %)	Leco TOC (wt% HC)	Rock-Eval S1 (mg HC/g)	Rock-Eval S2 (mg HC/g)	Rock-Eval S3 (mg CO2/g)	Tmax (°C)	Calculated %Ro (RE TMAX)	Hydrogen Index (S2x100/TOC)	Oxygen Index (S3x100/TOC)
7,325.75		5.16	4.88	9.88	0.32	457	1.07	191	6
7,333.25		2.10	8.69	8.99	0.28	444	0.83	428	13
7,333.45		2.61	3.37	6.29	0.27	449	0.92	241	10
7,340.50		1.12	3.82	3.44	0.30	440	0.76	307	27
7,347.50		2.39	3.39	5.91	0.37	450	0.94	247	15
7,359.20		4.02	4.38	8.88	0.39	454	1.01	221	10
7,367.55		2.14	6.06	6.33	0.39	446	0.87	296	18
7,367.95		2.99	3.31	5.81	0.36	455	1.03	194	12
7,373.75		2.20	17.35	10.57	0.55	440	0.76	480	25

Depth (ft)	S2/S3 Conc. (mg HC/mg CO2)	S1/TOC Norm. Oil Content	Production Index (S1/(S1+S2)	Experimental Notations
7,325.75	31	95	0.33	Low Temp S2 Shoulder
7,333.25	32	414	0.49	Low Temp S2 Shoulder
7,333.45	23	129	0.35	Low Temp S2 Shoulder
7,340.50	11	341	0.53	Low Temp S2 Shoulder
7,347.50	16	142	0.36	Low Temp S2 Shoulder
7,359.20	23	109	0.33	Low Temp S2 Shoulder
7,367.55	16	283	0.49	Low Temp S2 Shoulder
7,367.95	16	111	0.36	Low Temp S2 Shoulder
7,373.75	19	789	0.62	Low Temp S2 Shoulder

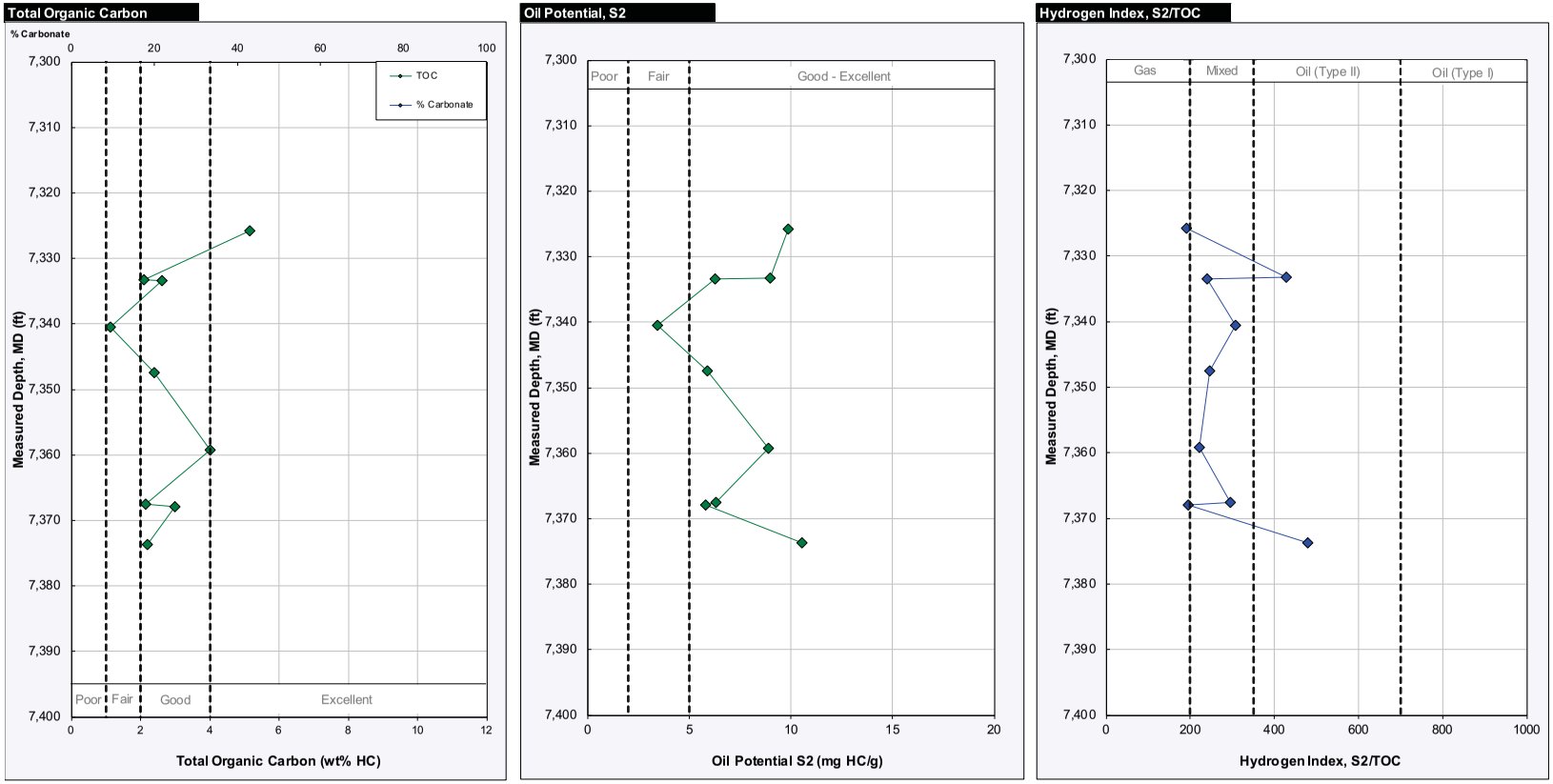

Figure C-2. Source rock potential - (Bill Barrett 14-3-45 Well).

The perforations were run with a 3.125 PJ Omega 3104 gun (0.36 inch perforation charges), 16 gm, and 0.44 inch diameter holes. They were run for Stage 1 CR-4A/CR-4 at depths of 8369-70 ft (probably logging depth?), 8381-82 ft, 8393-94 ft, 8403-04 ft, 8412-13 ft, 8427-38 ft, 8455-56 ft, 8476-77 ft, 8491-92 ft, 8513-14 ft, 8533-34 ft, 8539-40 ft, 8561-62 ft, 8583-84 ft, 8599-8600 ft, 8613-14 ft, 8637-38 ft, 8649-50 ft (54 shots).

Production data for this well are shown in Figure C-3.

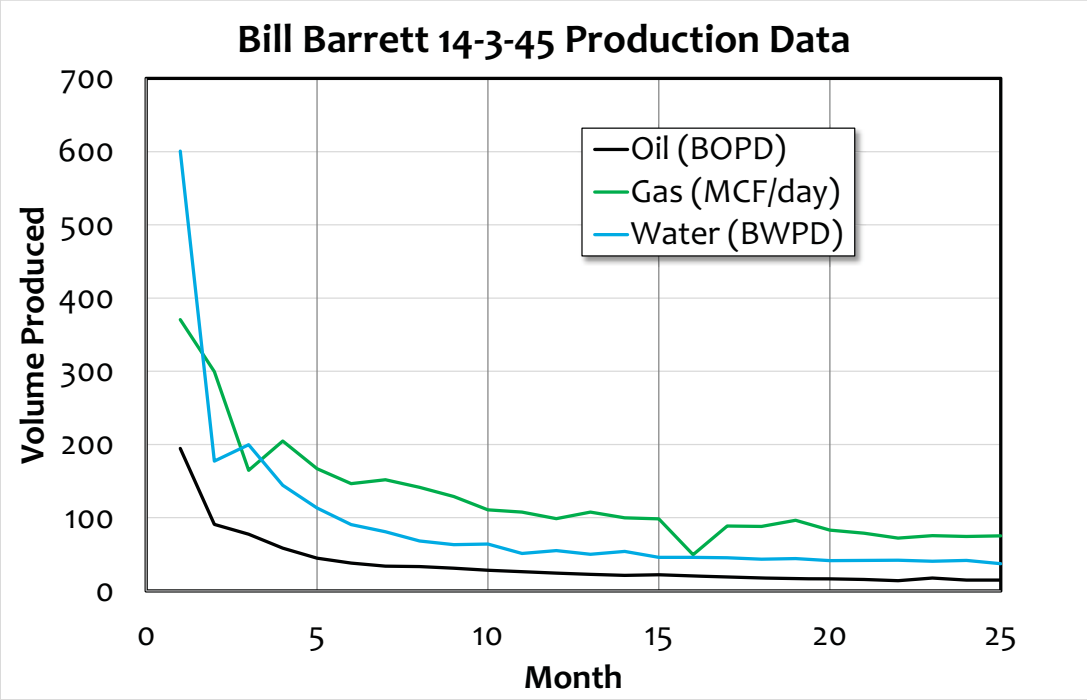

Figure C-3. Production data from Bill Barrett 14-3-45.

Mechanical properties for this well are shown in Table C-5. The confining pressure is not reported and these values may be inaccurate since the samples were apparently short.

Table C-5. Mechanical Properties – (Bill Barrett 14-3-45 Well)

Sample	30C	43	41A
Depth (ft)	7372	7349	7383
Static Young's Modulus (x 10^6 psi)	6.12	5.43	5.85
Static Poisson's Ratio	0.24	0.26	0.25
Compressive Strength (psi)	38,699	41,354	44,225

Table C-6. Material Received by TerraTek for Testing

Pallet #	Well ID	Box #	Top Core Depth (ft)	Bottom Core Depth (ft)	Approx. Length (ft)	Approx. Diameter (in)	Comments
3	Bill Barrett 14-3-45	1	7324	7327	3	4	Unpreserved slabbed core sections. Previously plugged and highly damaged. Note, core boxes are marked with 'Core 1'
		2	7327	7330	3	4	
		3	7330	7333.2	3.2	4	
		4	7333.2	7336	2.8	4	
		5	7336	7339	3	4	
		6	7339	7342	3	4	
		7	7342	7344.7	2.7	4	
		8	7344.7	7347.6	2.9	4	
		9	7347.6	7350.65	3.05	4	
		10	7350.65	7353.65	3	4	
		11	7353.65	7356.7	3.05	4	
		12	7356.7	7359.5	2.8	4	
		13	7359.5	7362.5	3	4	
		14	7362.5	7365.5	3	4	
		15	7365.5	7368.45	2.95	4	
		16	7368.45	7371.5	3.05	4	
		17	7371.5	7374.5	3	4	
		18	7374.5	7377.25	2.75	4	
		19	7377.25	7380.2	2.95	4	
		20	7380.2	7383.2	3	4	
		21	7383.2	7386	2.8	4	

Table C-7. Brittleness – (Bill Barrett 14-3-45 Well)

Sample	Orientation	Core Depth	Log Depth	BI1	BI2	BI3a	BI3b	BI4	BI5
UTE1-1	Vertical	7358.35	7348.15	0.74	0.65	2.75E-05	-3.60E-04	1.52	0.33
UTE1-2	Horizontal	7358.15	7347.95	0.28	0.22	3.71E-04	-7.72E-04	1.25	0.06
UTE2-1	Vertical	7332.7	7322.5	0.73	0.00	5.19E-04	-4.79E-02	33.73	0.79
UTE 2-2	Horizontal	7332.85	7322.65	0.27	0.00	9.88E-05	-1.40E-03	1.56	0.36
UTE3-1	Vertical	7327.3	7317.1	0.26	0.00	2.11E-03	-1.64E-03	1.50	0.093
UTE3-2	Horizontal	7327.4	7317.2	0.12	0.00	1.01E-01	-6.80E-01	5.07	0.33

Table C-8. Fracture Toughness – (Bill Barrett 14-3-45 Well)

Sample	Core Depth	Log Depth	Value Using Sample Height for R	FT Using Half Sample D for R	D (mm)	H (mm)	B (thickness) (mm)	B/D	Orientation	Testing Round	Machining Round
BTR14-3-45 Bag2 Sample A	7331.3	7321.1	935.2	831	36.9	17.1	12.5	0.34	No	1	1
BTR14-3-45 Bag3 Sample D	7356.8	7346.6	1356	1393	37.5	19.1	14.4	0.38	No	1	1

Table C-9. Dynamic Mechanical Properties Determined During Triaxial Compression Testing

Well ID	Lithology	Sample ID Core Depth (ft) Orientation	Axial Stress Difference (psi)	Effective Confining Pressure[1] (psi)	Effective Mean Stress (psi)	As Received Density (g/cm^3)	P-Wave Velocity (ft/s)	S-Wave Velocity (ft/s)	Poisson's Ratio	Young's Modulus (10^6 psi)	Bulk Modulus (10^6 psi)	Shear Modulus (10^6 psi)
Bill Barrett 14-3-45	dolomite	UTE3-1 7327.3 Vertical	2618	1317	2190	2.654	17,172	9670	0.27	8.478	6.084	3.344
			8127	1317	4026	2.658	17,847	9974	0.27	9.07	6.656	3.563
			11,492	1317	5148	2.659	18,055	10,057	0.28	9.242	6.848	3.624
			19,096	1317	7682	2.663	18,371	10,137	0.28	9.446	7.192	3.687
			25,561	1317	9837	2.665	18,675	10,180	0.29	9.592	7.562	3.722
			10,222	1317	4724	2.709	17,356	9591	0.28	8.596	6.517	3.357
		UTE3-2 7327.4 Horizontal	0	2934	2934	2.657	18,632	10,948	0.24	10.613	6.707	4.292
			4412	2934	4405	2.658	18,705	10,927	0.24	10.615	6.831	4.277
			12,739	2934	7180	2.66	18,815	10,915	0.25	10.643	6.994	4.27
			28,943	2934	12582	2.662	18,973	10,915	0.25	10.705	7.214	4.273
			47,632	2934	18811	2.662	19,049	10,831	0.26	10.613	7.404	4.208
			17,355	2919	8704	2.591	18,392	10,552	0.25	9.753	6.625	3.887
	shale - finely laminated	UTE2-1 7332.7 Vertical	0	1317	1317	2.39	10,070	5967	0.23	2.82	1.737	1.147
			3028	1317	2326	2.394	10,307	6029	0.24	2.907	1.863	1.173
			4443	1317	2798	2.395	10,465	6056	0.25	2.955	1.956	1.184
			7088	1317	3680	2.398	10,665	6108	0.26	3.028	2.067	1.205
			13,895	1317	5949	2.402	11,124	6201	0.27	3.173	2.345	1.245
			4022	1317	2658	2.369	10,458	5989	0.26	2.876	1.964	1.145

Well ID	Lithology	Sample ID Core Depth (ft) Orientation	Axial Stress Difference (psi)	Effective Confining Pressure[1] (psi)	Effective Mean Stress (psi)	As Received Density (g/cm^3)	P-Wave Velocity (ft/s)	S-Wave Velocity (ft/s)	Poisson's Ratio	Young's Modulus (10^6 psi)	Bulk Modulus (10^6 psi)	Shear Modulus (10^6 psi)
Bill Barrett 14-3-45	shale - finely laminated	UTE2-2 7332.85 Horizontal	0	2934	2934	2.352	14,889	9113	0.2	6.32	3.517	2.632
			2590	2919	3782	2.353	14,921	9108	0.2	6.328	3.552	2.63
			6475	2934	5092	2.354	14,933	9104	0.2	6.332	3.568	2.629
			9965	2934	6256	2.355	14,957	9099	0.21	6.339	3.596	2.627
			17,076	2934	8626	2.357	15,035	9072	0.21	6.344	3.693	2.614
			9438	2934	6080	2.335	14,883	8998	0.21	6.174	3.572	2.547
	shale	UTE1-1 7358.35 Vertical	2589	1332	2195	2.473	10,715	5710	0.3	2.829	2.377	1.087
			3378	1332	2458	2.474	10,911	5846	0.3	2.959	2.45	1.139
			4265	1332	2754	2.475	11,099	5959	0.3	3.073	2.529	1.184
			6565	1332	3520	2.476	11,424	6168	0.29	3.286	2.662	1.269
			8191	1332	4062	2.465	11,800	6256	0.3	3.392	2.892	1.3
			4199	1317	2717	2.423	11,532	6153	0.3	3.216	2.693	1.236
		UTE1-2 7358.15 Horizontal	0	2949	2949	2.602	14,804	8894	0.22	6.755	3.986	2.774
			814	2934	3205	2.603	14,828	8898	0.22	6.767	4.009	2.776
			5564	2949	4804	2.604	14,893	8916	0.22	6.81	4.063	2.789
			12,542	2949	7130	2.606	14,999	8939	0.22	6.873	4.159	2.806
			18,512	2934	9105	2.605	15,261	8951	0.24	6.962	4.426	2.812
			11,634	2934	6812	2.579	14,801	8740	0.23	6.542	4.073	2.654

[1]For all tests, pore pressure drained to atmosphere.

Table C-10. Summary of Indirect Tensile Strength Tests (Brazilian Method) - Horizontal Samples

Well ID	Lithology	Sample #	Core Depth (ft)	Orientation	Average Length (in)	Average Diameter (in)	Mass (g)	Dry Bulk Density (g/cm^3)	Maximum Load (lb_f)	Tensile Strength[1] (psi)
Bill Barret 14-3-35	dolomite	UTE3_3A	7327.4	Perpendicular	0.482	0.996	16.048	2.609	1490	1976
		UTE3_3B	7327.4	Parallel	0.48	0.996	16.278	2.658	858	1144
	shale - finely laminated	UTE2_3A	7333.1	Perpendicular	0.76	1.498	52.915	2.412	2190	1225
		UTE2_3B	7333.1	Parallel	0.737	1.498	51.447	2.42	920	531
	shale	UTE1_3A	7358.15	Perpendicular	0.497	0.995	16.256	2.566	860	1107
		UTE1_3B	7358.15	Parallel	0.543	0.994	17.772	2.572	389	459

Table C-11. Summary of Triaxial Compression Tests (for all tests, pore pressure drained to atmosphere)

Well ID	Lithology	Sample ID	Core Depth (ft)	Orientation	As Received Bulk Density (g/cm^3)	Confining Pressure (psi)	Peak Effective Compressive Strength (psi)	Effective Residual Compressive Strength (psi)	Young's Modulus (psi)	Poisson's Ratio
Bill Barrett 14-3-45	dolomite	UTE3-1	7327.3	Vertical	2.645	1319	27,330	12,199	3,196,000	0.18
		UTE3-2	7327.4	Horizontal	2.655	2931	52,283	19,631	8,166,000	0.3
	shale - finely laminated	UTE2-1	7332.7	Vertical	2.382	1320	15,354	5400	1,411,000	0.21
		UTE2-2	7332.85	Horizontal	2.342	2933	21,237	12,433	3,962,000	0.27
	shale	UTE1-1	7358.35	Vertical	2.439	1325	9703	5505	1,428,000	0.21
		UTE1-2 [1]	7358.15	Horizontal	2.584	2943	22,043	14,643	3,963,000	0.26

[1] UTE1-2 & UTE1-1 - Note difference in bulk density for these two samples. No additional material remains for replacement samples however.

Table C-12. Dynamic versus Quasi-Static Mechanical Properties Determined During Triaxial Compression Testing

Well ID	Lithology	Sample ID	Core Depth (ft)	Orientation	Effective Confining Pressure (psi)	Static Poisson's Ratio	Dynamic Poisson's Ratio	Static Young's Modulus (psi)	Dynamic Young's Modulus (psi)	Dynamic/ Static Young's Modulus	Dynamic/ Static/ Poisson's Ratio
Bill Barrett 14-3-45	dolomite	UTE3-1	7327.3	Vertical	1319	0.18	0.27	3,196,000	9,070,000	2.84	1.5
		UTE3-2	7327.4	Horizontal	2931	0.3	0.25	8,166,000	10,643,000	1.3	0.83
	shale - finely laminated	UTE2-1	7332.7	Vertical	1320	0.21	0.25	1,411,000	2,955,000	2.09	1.19
		UTE2-2	7332.85	Horizontal	2933	0.27	0.2	3,962,000	6,332,000	1.6	0.74
	shale	UTE1-1	7358.35	Vertical	1325	0.21	0.3	1,428,000	2,959,000	2.07	1.43
		UTE1-2	7358.15	Horizontal	2943	0.26	0.22	3,963,000	6,810,000	1.72	0.85
									Average:	1.94	1.09

Triaxial Compression Test Plots – Bill Barrett 14-3-35 these are to be replaced?

Bill Barrett 14-3-35

Lithology	Sample ID	Depth (ft)	Orientation	As Received Bulk Density (g/cm^3)	Confining Pressure (psi)	Peak Effective Compressive Strength (psi)	Effective Residual Compressive Strength (psi)	Young's Modulus (10^6 psi)	Poisson's Ratio
shale	UTE1-1[1]	7358.35	Vertical	2.439	1325	9700	5510	1.428	0.21
	UTE1-2	7358.15	Horizontal	2.584	2943	22040	14640	3.963	0.26

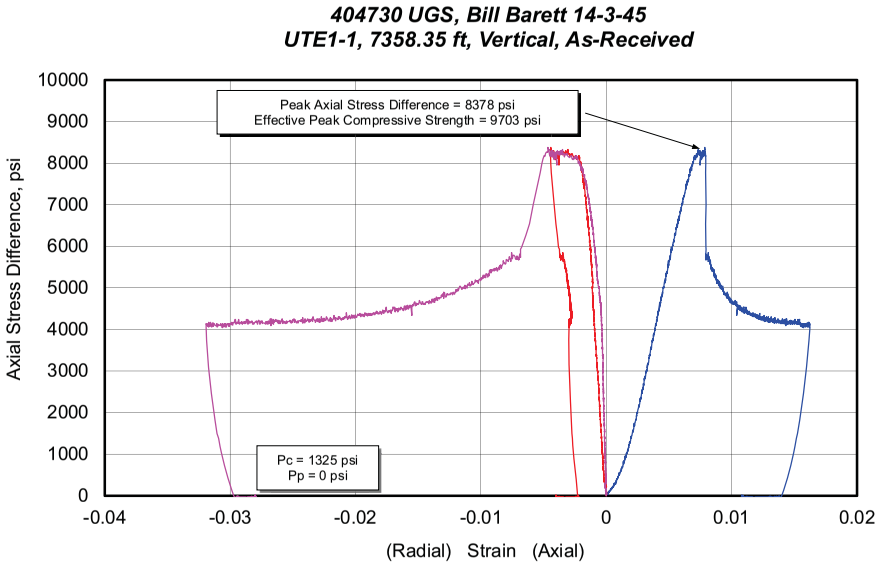

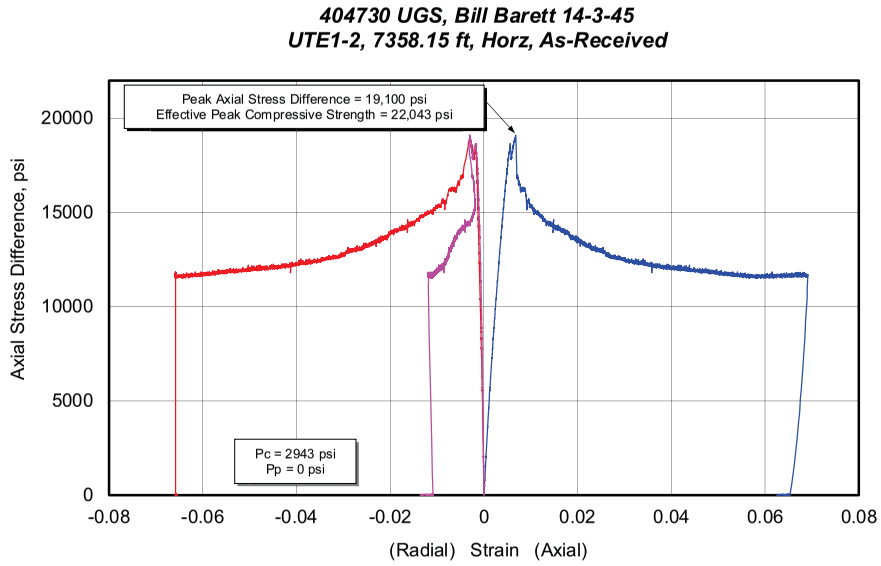

[1] Note density difference between UTE 1-1 and UTE 1-2. No additional material available.

Bill Barrett 14-3-35

Lithology	Sample ID	Depth (ft)	Orientation	As Received Bulk Density (g/cm^3)	Confining Pressure (psi)	Peak Effective Compressive Strength (psi)	Effective Residual Compressive Strength (psi)	Young's Modulus (10^6 psi)	Poisson's Ratio
shale-finely laminated	UTE2-1	7332.70	Vertical	2.382	1320	15350	5400	1.411	0.21
	UTE2-2	7332.85	Horizontal	2.342	2933	21240	12430	3.962	0.27

404730 UGS, Bill Barett 14-3-45
UTE2-1, 7332.70 ft, Vertical, As-Received

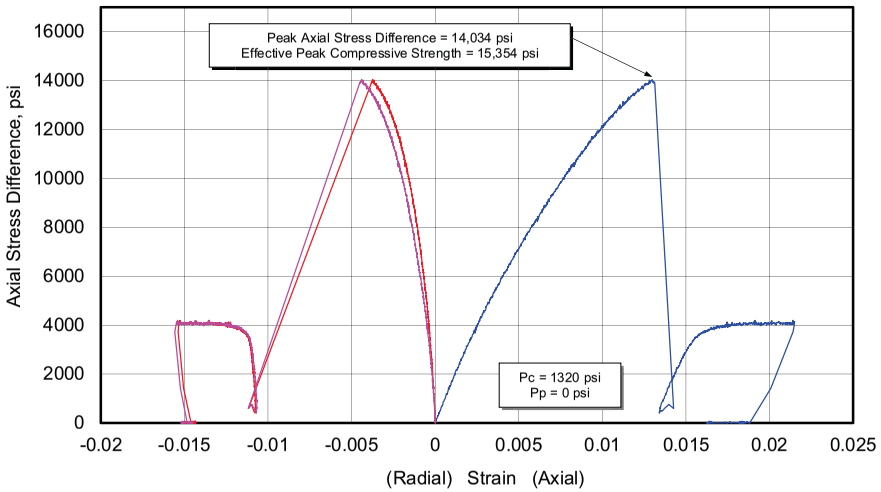

404730 UGS, Bill Barett 14-3-45
UTE2-2, 7332.85 ft, Horizontal, As-Received

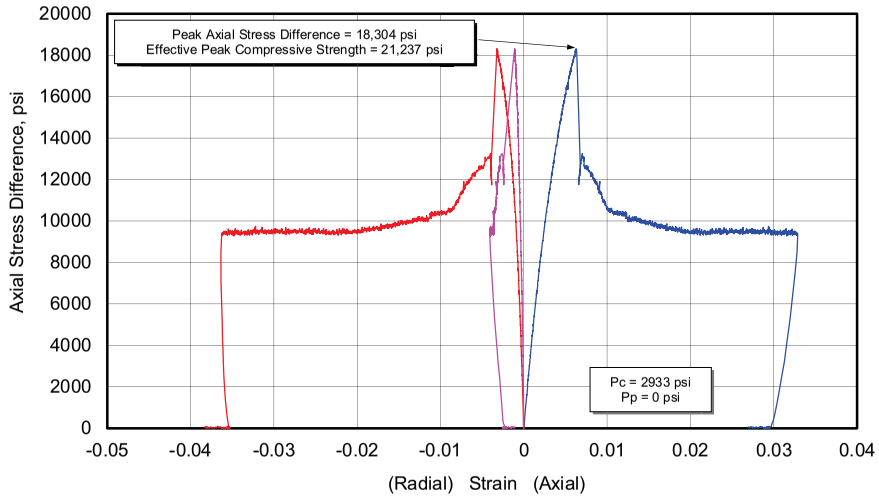

Bill Barrett 14-3-35

Lithology	Sample ID	Depth (ft)	Orientation	As Received Bulk Density (g/cm^3)	Confining Pressure (psi)	Peak Effective Compressive Strength (psi)	Effective Residual Compressive Strength (psi)	Young's Modulus (10^6 psi)	Poisson's Ratio
dolomite	UTE3-1	7327.30	Vertical	2.645	1319	27330	12200	3.196	0.18
	UTE3-2	7327.40	Horizontal	2.655	2931	52280	19630	8.166	0.30

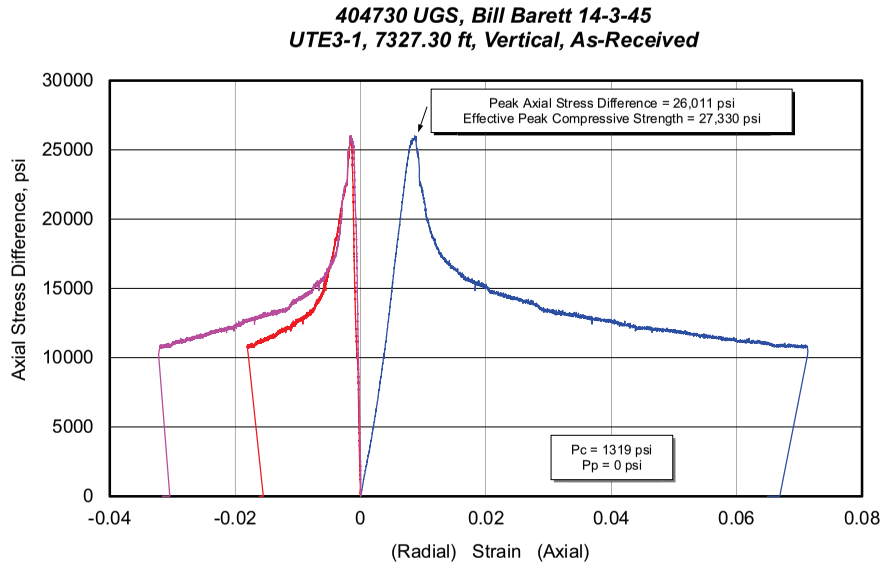

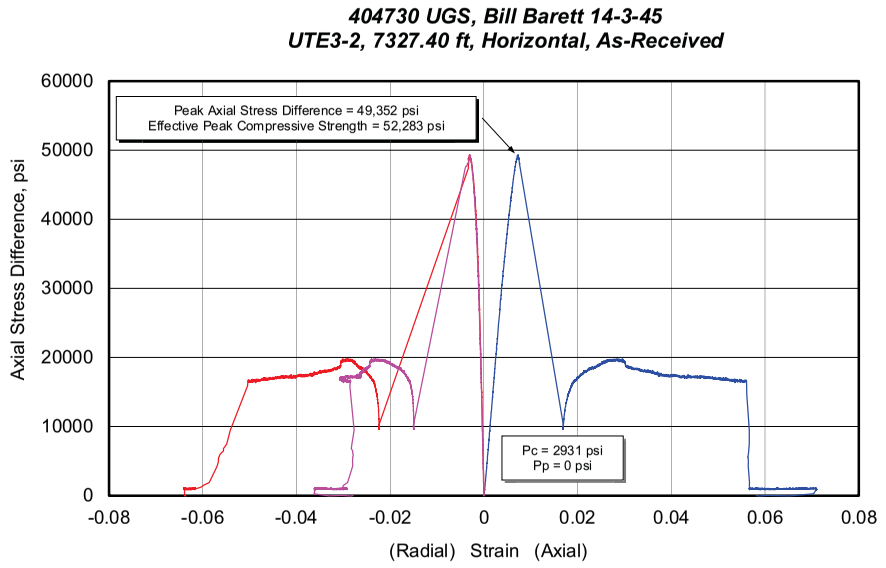

Bill Barret 14-1-46

The permeability for this well (from laboratory Klinkenberg permeabilities) is shown in Figure C-7.

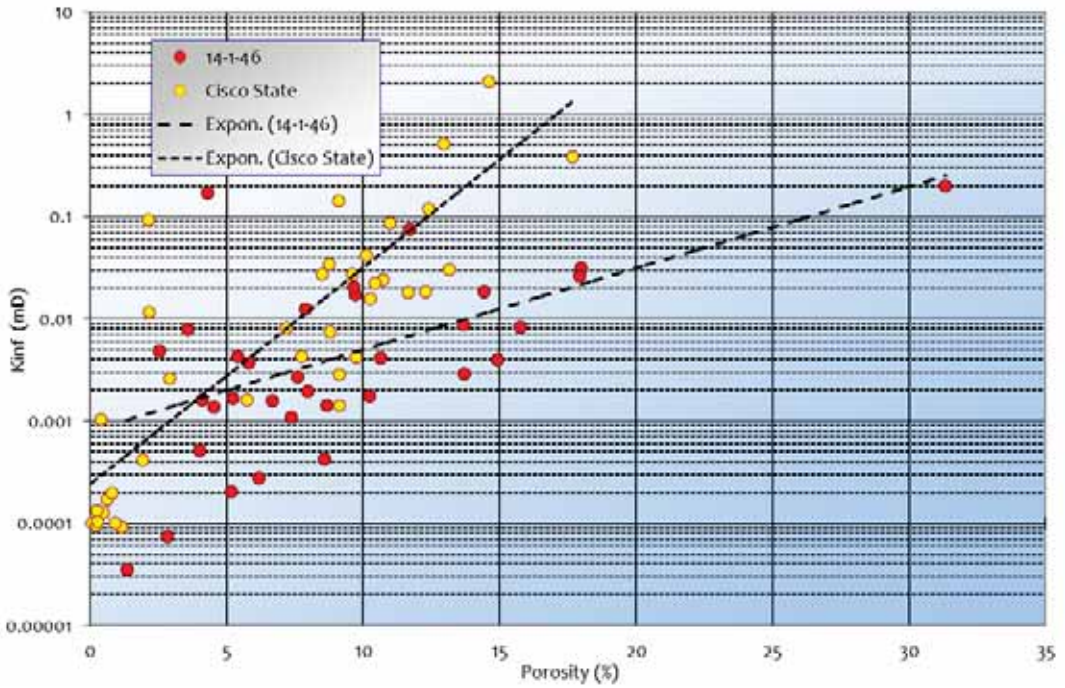

Figure C-4. Klinkenberg permeabilities for Bill Barrett 14-1-46 and Cisco State 36-13.

Triaxial compression data are shown in Table C-13. Notice that the value of Young's modulus (at approximately the same confining pressure) is approximately two times higher than for Cisco State 36-13. Composition is shown (based on S-Ray Diffraction) in Table C-14.

Source rock data are shown in Table C-15 and Figure C-5

Table C-13. Triaxial Compressive Strength Data (Bill Barrett 14-1-46)

Sample	Depth (ft MD)	Confining Pressure (psi)	Bulk Density (g/cm3)	Compressive Strength (psi)	E (106 psi)	ν
1	6659.25-6660.00	1290	2.557	13646	4.37	0.23
2	6682.10-6682.45	1290	2.637	13467	4.56	0.27
3	6695.15-6695.80	1290	2.616	27184	4.28	0.26

Table C-14. Mineralogy for 6647.10 to 6706.95 ft (Bill Barrett 14-1-46)

Whole Rock Mineralogy (Weight %)								Clay (Phyllosilicate) Mineralogy (Weight %)		
Depth	Quartz	K Feldspar	Plagioclase	Calcite	Dolomite and Fe Dolomite	Pyrite	Total Clay	Illite /Smectite	Illite & Mica	Chlorite
6647.10	12.8	0.5	1.0	11.2	57.0	1.7	15.7	7.8	7.9	0.0
6650.80	18.5	0.0	0.6	11.2	61.2	1.0	7.4	3.5	3.9	0.0
6655.05	20.0	1.1	2.9	31.0	5.9	5.3	33.8	13.9	18.9	1.0
6658.95	8.3	0.0	0.4	12.5	69.8	1.5	7.6	4.0	3.6	0.0
6663.35	23.2	0.0	0.0	1.7	69.0	0.9	5.3	2.8	2.5	0.0
6667.05	19.8	0.7	1.5	39.0	3.2	6.4	29.4	12.6	16.1	0.7
6672.40	19.9	0.4	5.9	17.5	23.6	5.9	26.9	12.1	14.0	0.8
6675.70	7.8	0.0	0.8	12.9	60.0	3.4	15.1	6.7	8.4	0.0
6679.00	21.2	0.0	1.0	7.8	47.6	4.7	17.7	8.4	9.3	0.0
6681.70	22.0	0.6	3.4	29.6	3.9	6.7	33.8	15.9	17.0	0.9
6684.00	8.8	0.0	0.4	9.9	76.6	0.4	3.9	1.6	2.3	0.0
6686.20	7.4	0.0	0.5	22.5	66.1	0.7	2.8	1.4	1.4	0.0
6688.20	11.6	0.0	0.0	43.4	44.4	0.6	0.0	0.0	0.0	0.0
6690.00	7.6	0.0	0.7	76.1	1.2	1.7	12.7	6.9	5.8	0.0
6692.25	10.6	0.0	0.3	9.0	68.0	1.9	10.2	5.6	4.6	0.0
6694.00	12.1	0.0	0.0	9.6	68.1	2.7	7.4	4.3	3.1	0.0
6696.00	6.1	0.0	0.0	84.9	0.6	1.3	7.2	3.8	3.4	0.0
6698.00	5.5	0.0	1.4	80.9	1.9	1.5	8.7	6.0	2.7	0.0

Whole Rock Mineralogy (Weight %)								Clay (Phyllosilicate) Mineralogy (Weight %)		
Depth	Quartz	K Feldspar	Plagioclase	Calcite	Dolomite and Fe Dolomite	Pyrite	Total Clay	Illite /Smectite	Illite & Mica	Chlorite
6699.45	9.4	0.0	0.5	71.8	2.8	1.1	14.4	7.0	7.4	0.0
6699.75	6.8	0.0	0.7	68.9	10.9	1.9	10.8	5.0	5.8	0.0
6702.95	14.6	0.0	0.0	0.0	75.9	1.1	8.4	4.2	4.2	0.0
6706.95	21.7	0.7	5.7	11.0	4.1	8.7	48.1	17.5	29.2	1.4

Table C-15. Source Rock Data (Bill Barrett 14-1-46)

Depth (ft)	Percent Carbonate (wt %)	Leco TOC (wt% HC)	Rock-Eval S1 (mg HC/g)	Rock-Eval S2 (mg HC/g)	Rock-Eval S3 (mg CO2/g)	Tmax (°C)	Calculated %Ro (RE TMAX)	Hydrogen Index (S2x100/TOC)	Oxygen Index (S3x100/TOC)
6650.05		2.160	9.070	5.970	0.340	442.000	0.796	276.389	15.741
6656.80		1.840	1.440	3.240	0.330	447.000	0.886	176.087	17.935
6665.45		1.800	11.050	5.100	0.370	435.000	0.670	283.333	20.556
6668.65		1.640	1.610	4.030	0.340	434.000	0.652	245.732	20.732
6681.65		3.340	1.970	8.830	0.150	446.000	0.868	264.371	4.491
6685.25		1.060	3.620	2.770	0.360	432.000	0.616	261.321	33.962
6689.15		0.903	0.520	1.220	0.250	448.000	0.904	135.105	27.685
6703.30		1.940	10.230	5.880	0.450	435.000	0.670	303.093	23.196
6706.35		2.930	1.590	6.990	0.350	448.000	0.904	238.567	11.945

Depth (ft)	S2/S3 Conc. mg HC/mg CO2)	S1/TOC Norm. Oil Content	Production Index (S1/(S1+S2)	Experimental Notations
6650.05	17.559	419.907	0.603	
6656.80	9.818	78.261	0.308	Low Temp S2 Shoulder
6665.45	13.784	613.889	0.684	Low Temp S2 Shoulder
6668.65	11.853	98.171	0.285	Low Temp S2 Shoulder
6681.65	58.867	58.982	0.182	Low Temp S2 Shoulder
6685.25	7.694	341.509	0.567	Low Temp S2 Shoulder
6689.15	4.880	57.586	0.299	
6703.30	13.067	527.320	0.635	Low Temp S2 Shoulder
6706.35	19.971	54.266	0.185	Low Temp S2 Shoulder

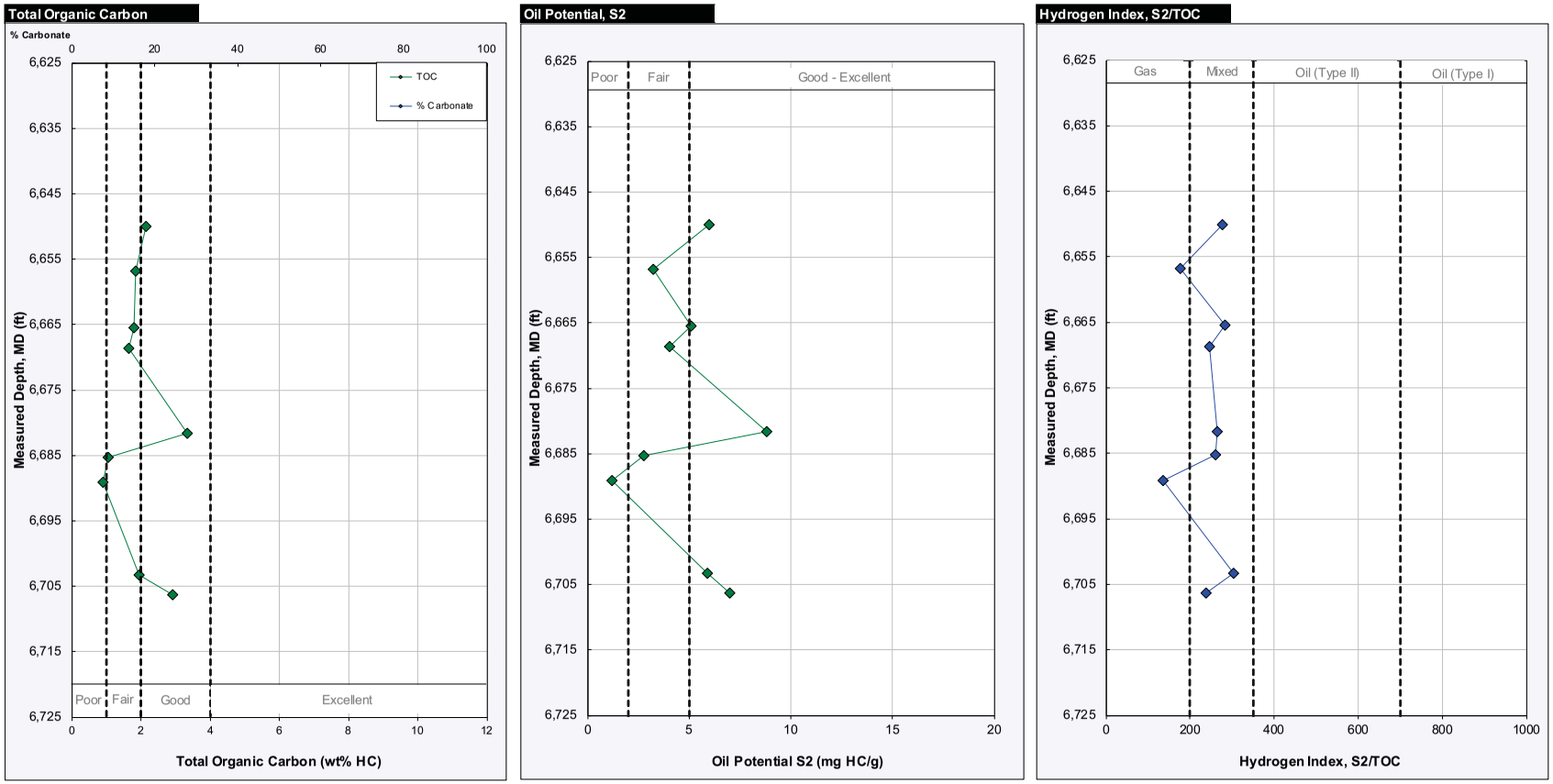

Figure C-5. Source rock data (Bill Barrett 14-1-46).

Stimulation procedures were as follows

Stage 1 (CR4 and CR4A):

1. The iron was pressure tested to 9100 psi.
2. The well was broken down at 8.8 bpm at a surface pressure of 2883 psi.
3. 94 bbl of 15% HCl were pumped along with bio balls for diversion.
4. 3% KCL slickwater pad was pumped at 70.6 bpm at 3168 psi (average?).
5. It appeared that 40 out of 48 perforations were open.
6. The ISIP was 1914. The frac gradient (probably based on the ISIP was reported as 0.65 psi/ft).
7. Started a crosslinked pad at 70.2 bpm (3139 psi)
8. Started 2 ppg 20/40 premium white sand at 70.5 bpm (3385 psi). Pressure was 3047 psi and rate 70.6 bpm when the 2 ppg stage reached the perforations.
9. Started 3 ppg 20/40 premium white sand at 70.5 bpm (2858 psi). Pressure was 2692 psi and rate 70.6 bpm when the 3 ppg stage reached the perforations.
10. Started 4 ppg 20/40 premium white sand at 70.5 bpm (2684 psi). Pressure was 2633 psi and rate 70.6 bpm when the 2 ppg stage reached the perforations.
11. On flush (72.3 bpm), the pressure was 2703. It was felt that all 48 perforations were open.
12. ISIP was 1784 psi, giving a frac gradient of 0.67 psi. 66,972 gallons of crosslinked fluid had been pumped, along with 64,541 gallons of produced water and 157,200 lb of sand.

Six stages were pumped in all. Table C-16 is a summary

Table C-16. Summary of Stimulation Procedures - (Bill Barrett 14-1-46)

Stage	Perforations		Breakdown		15% HCl	Slickwater			
	Depth (ft MD)	Density (spf)	Rate (bpm)	Pressure (psi)	Volume (bbl)	Rate (bpm)	Pressure (psi)	Volume (gal)[2]	ISIP (depth, gradient)
1	7811-7883, 7609-7800	48 holes	8.8	2883	94	70.6	3168	64,541	1914 psi, 0.65 psi/ft
2	7343-7584	45 holes	5.1	2428	94	70.5	3440	70,671	2014 psi, 0.75 psi/ft
3	7108-7295	39 holes	9.6	2750	74	70.5	3525	70,097	1994 psi, 0.70 psi/ft
4	6848-7082	45 holes	10.3	3231	97	70.4	3329	63,442	1723 psi, 0.69 psi/ft
5	6609-6824	45 holes	9.3	2125	93	69.9	2880	68,377	1575 psi, 0.68 psi/ft
6	6475-6578, 6291-6454	56 holes	9.3	1865	92	70.5	2794	83,001	1228 psi, 0.64 psi/ft

Stage	Perforations		Crosslinked Fluid					Flush			
	Depth (ft MD)	Density (spf)	Rate (bpm)	Pressure[3] (psi)	Proppant[4] (ppg)	Volume (gallons)	Weight of proppant (lb)	Rate (bpm)	Pressure (psi)	ISIP (pressure gradient)	Volume (gallons)
1	7811-7883, 7609-7800	48 holes	70.2	3139				72.3	2703	1784	0.67
			70.5, 70.6	3385, 3047	2						
			70.5, 70.6	2858,2800	3						
			70.5,70.6	2755,2692	3.5						
			70.5, 70.5	2684, 2633	4						
						66,972	157,200				
2	7343-7584	45 holes	70.5	3440				70.2	2690	1968	0.70
			70.5,70.5	3536, 3271	2						
			70.4, 70.5	3214, 3033	3						
			70.5, 70.5	2905, 2839	3.5						
			70.5, 70.4	2851, 2788	4						
						75,505	169,900				
3	7108-7295	39 holes	70.5	3525				69.8	2867	2184	0.74
			70.5, 70.4	3684, 3423	2						
			70.6, 70.5	3257, 3139	3						
			70.5, 70.5	3006, 2936	3.5						
			70.5, 70.4	2932, 2864	4						
						69,679	170,000				

[2] May contain flush volume
[3] Initial pressure and pressure when proppant reached perforations. Same designation for rate.
[4] 20/40 premium White sand

Stage	Perforations		Breakdown		15% HCl	Slickwater			
	Depth (ft MD)	Density (spf)	Rate (bpm)	Pressure (psi)	Volume (bbl)	Rate (bpm)	Pressure (psi)	Volume (gal)[5]	ISIP (depth, gradient)
1	7811-7883, 7609-7800	48 holes	8.8	2883	94	70.6	3168	64,541	1914 psi, 0.65 psi/ft
2	7343-7584	45 holes	5.1	2428	94	70.5	3440	70,671	2014 psi, 0.75 psi/ft
3	7108-7295	39 holes	9.6	2750	74	70.5	3525	70,097	1994 psi, 0.70 psi/ft
4	6848-7082	45 holes	10.3	3231	97	70.4	3329	63,442	1723 psi, 0.69 psi/ft
5	6609-6824	45 holes	9.3	2125	93	69.9	2880	68,377	1575 psi, 0.68 psi/ft
6	6475-6578, 6291-6454	56 holes	9.3	1865	92	70.5	2794	83,001	1228 psi, 0.64 psi/ft

Stage	Perforations		Crosslinked Fluid					Flush			
	Depth (ft MD)	Density (spf)	Rate (bpm)	Pressure[6] (psi)	Proppant[7] (ppg)	Volume (gallons)	Weight of proppant (lb)	Rate (bpm)	Pressure (psi)	ISIP (pressure)	ISIP (psi/ft)
4	6848-7082	45 holes	70.4	3487				71.2	3020	2118	0.74
			70.6, 70.6	3500, 3248	2						
			70.5, 70.6	3190, 3010	3						
			70.5, 70.5	3111, 3093	3.5						
			70.3, 70.5	3044, 3015	4						
						65,117	159,400				
5	6609-6824	45 holes	70.6	3032				72.7	2659	2131	0.76
			70.2, 70.2	2910, 2810	1[8]						
			70.2, 70.2	2854, 2800	2						
			70.5, 70.5	2783, 2684	3						
			70.5, 70.5	2650, 2631	3.5						
			70.5, 70.5	2632, 2640	4						
						84,781	21,200,[9] 176,200				

[5] May contain flush volume
[6] Initial pressure and pressure when proppant reached perforations. Same designation for rate.
[7] 20/40 premium White sand
[8] 100 mesh
[9] 100 mesh

Stage	Perforations		Breakdown		15% HCl	Slickwater			
	Depth (ft MD)	Density (spf)	Rate (bpm)	Pressure (psi)	Volume (bbl)	Rate (bpm)	Pressure (psi)	Volume (gal)[10]	ISIP (depth, gradient)
1	7811-7883, 7609-7800	48 holes	8.8	2883	94	70.6	3168	64,541	1914 psi, 0.65 psi/ft
2	7343-7584	45 holes	5.1	2428	94	70.5	3440	70,671	2014 psi, 0.75 psi/ft
3	7108-7295	39 holes	9.6	2750	74	70.5	3525	70,097	1994 psi, 0.70 psi/ft
4	6848-7082	45 holes	10.3	3231	97	70.4	3329	63,442	1723 psi, 0.69 psi/ft
5	6609-6824	45 holes	9.3	2125	93	69.9	2880	68,377	1575 psi, 0.68 psi/ft
6	6475-6578, 6291-6454	56 holes	9.3	1865	92	70.5	2794	83,001	1228 psi, 0.64 psi/ft

Stage	Perforations		Crosslinked Fluid					Flush			
	Depth (ft MD)	Density (spf)	Rate (bpm)	Pressure[11] (psi)	Proppant[12] (ppg)	Volume (gallons)	Weight of proppant (lb)	Rate (bpm)	Pressure (psi)	ISIP (pressure)	ISIP (psi/ft)
6	6475-6578 6291-6454	56 holes	70.4	2663				70.7	2200	1181	0.62
			70.4, 70.6	2466, 2270	1[13]						
			70.5, 70.4	2244, 2215	2						
			70.4, 70.4	2200, 2046	3						
			70.4, 70.4	2051, 2048	3.5						
			70.4, 70.4	2050, 2041	4						
						68,407	21,200, 175,900				

[10] May contain flush volume
[11] Initial pressure and pressure when proppant reached perforations. Same designation for rate.
[12] 20/40 premium White sand
[13] 100 mesh

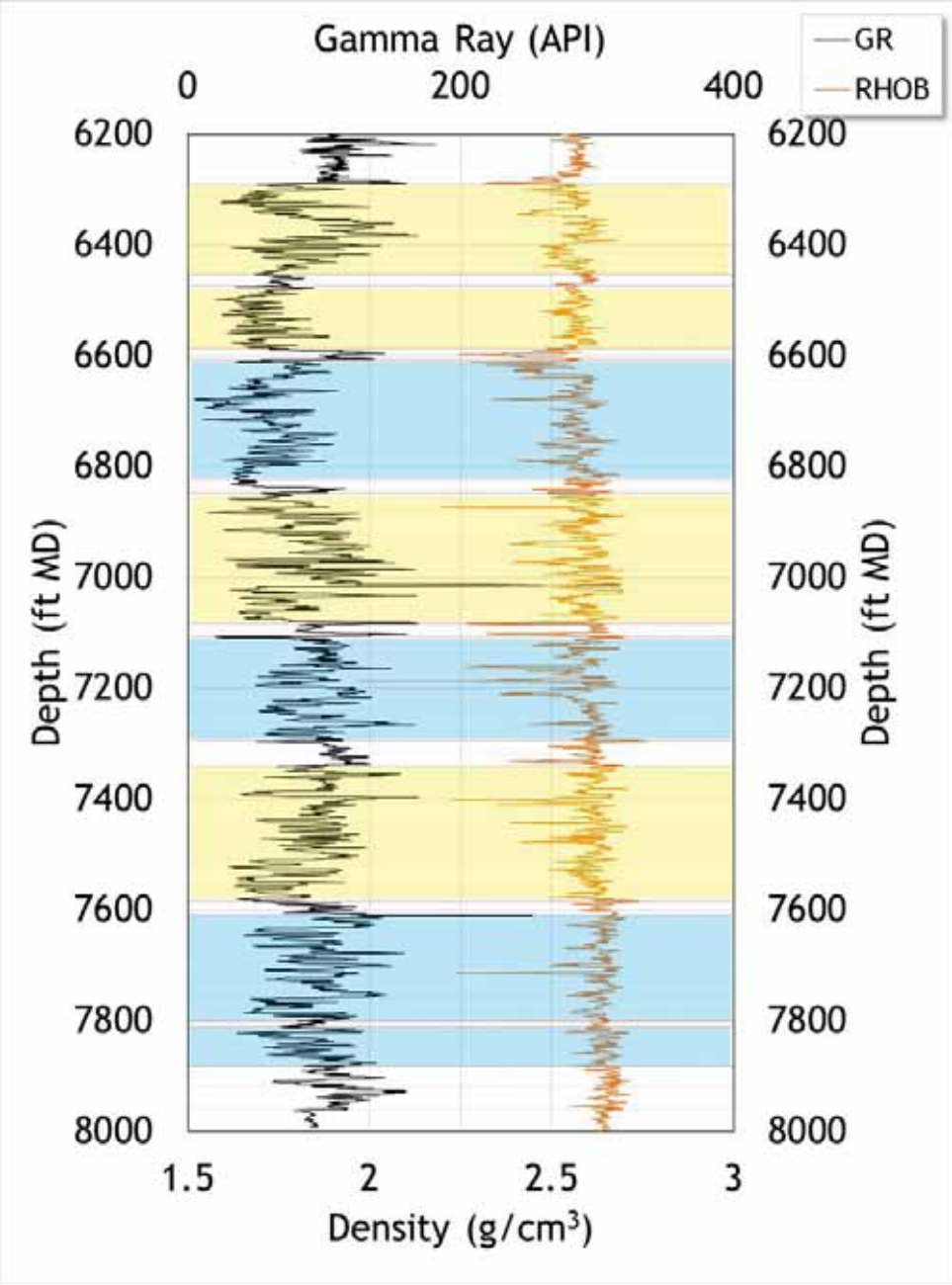

Figure C-6. Gamma ray and density tracks. The frac stages are shaded (refer to Table C-16).

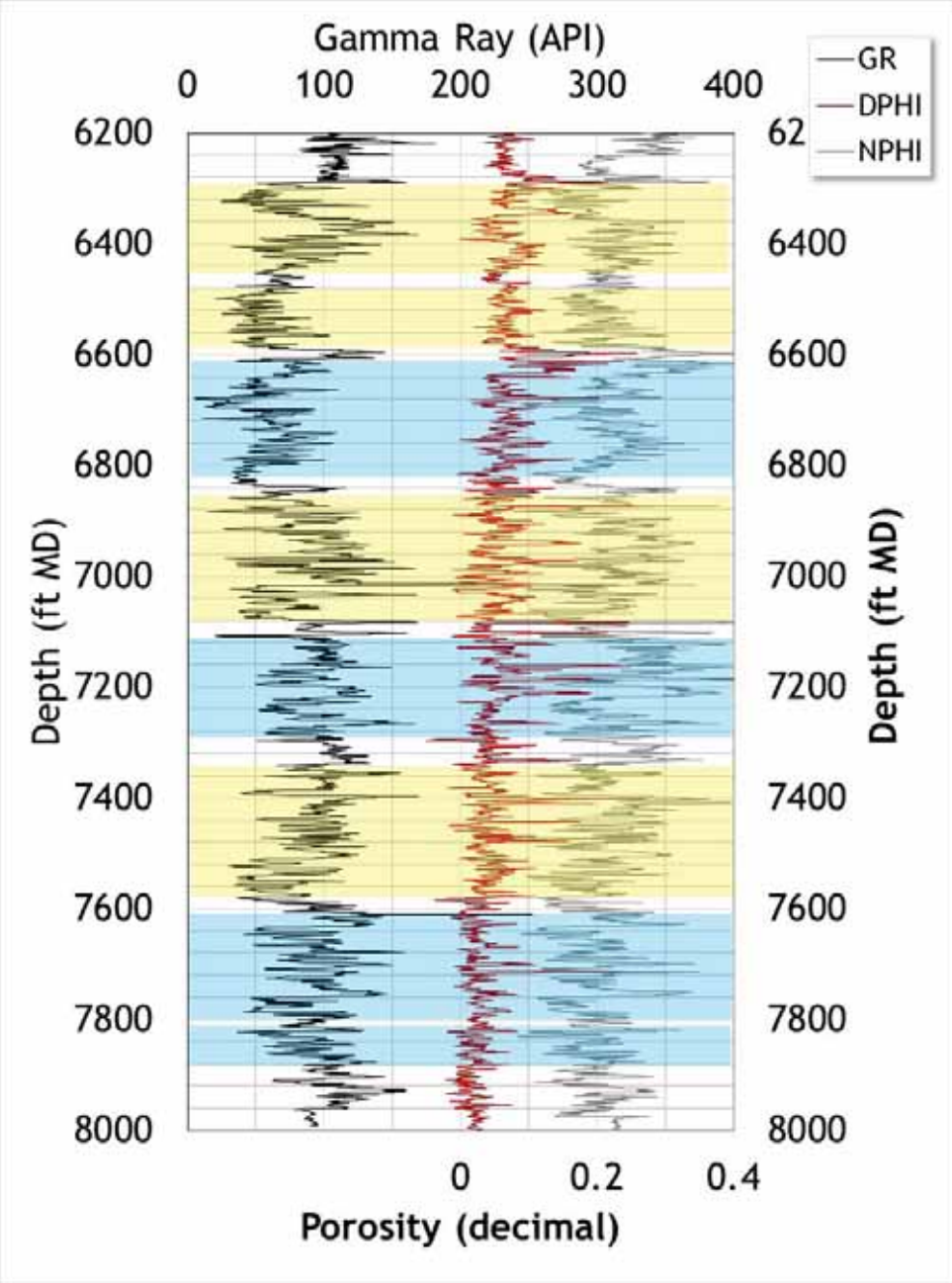

Figure C-7. Gamma ray and porosity tracks. The frac stages are shaded (refer to Table C-16).

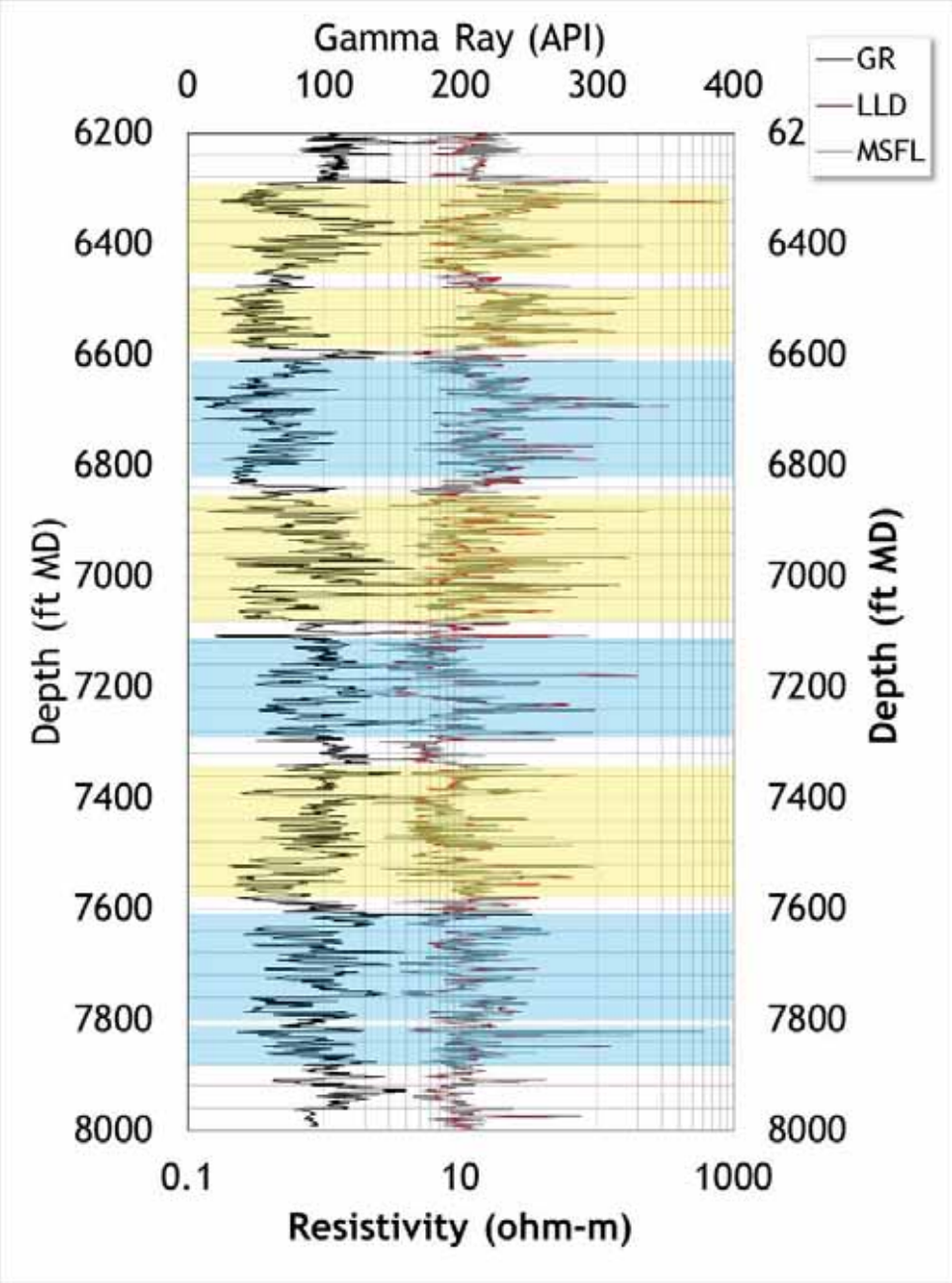

Figure C-8. Gamma ray and resistivity tracks. The frac stages are shaded (refer to Table C-16). No separation is evident.

Production history for this well is shown in Figure C-9.

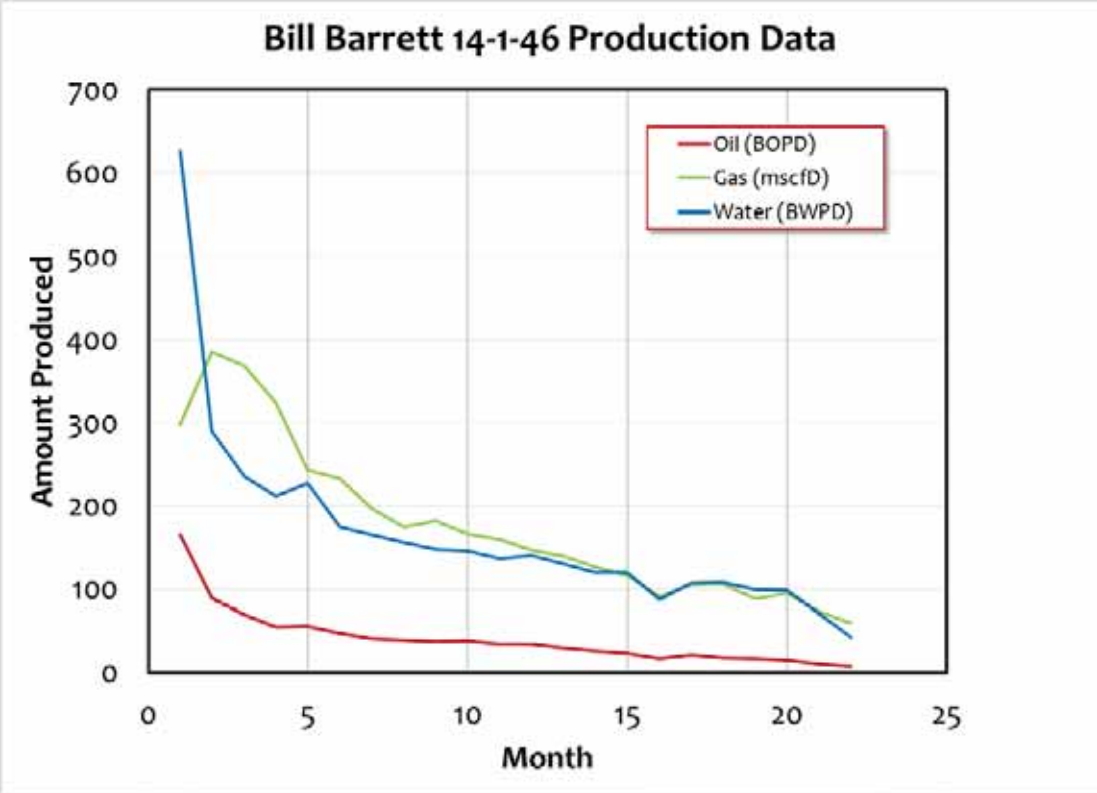

Figure C-9. Production history.

Table C-17. Material Received By TerraTek for Testing

Pallet #	Well ID	Box #	Top Core Depth (ft)	Bottom Core Depth (ft)	Approx. Length (ft)	Approx. Diameter (in)	Comments
4	Bill Barrett	1	6647	6650	3	4	Unpreserved slabbed core sections.
	14-1-46	2	6650	6653	3	4	Previously plugged and highly damaged.
		3	6653	6656	3	4	
		4	6656	6659	3	4	Note, core boxes are
		5	6659	6662	3	4	marked with 'Core 1'
		6	6662	6665	3	4	
		7	6665	6668	3	4	
		8	6668	6669.7	1.7	4	
		1	6672	6675	3	4	Unpreserved slabbed core sections.
		2	6675	6678	3	4	Previously plugged and highly damaged.
		3	6678	6680.7	2.7	4	
		4	6680.7	6683.5	2.8	4	Note, core boxes are
		5	6683.5	6686.45	2.95	4	marked with 'Core 2'
		6	6686.45	6689.9	3.45	4	
		7	6689.9	6691.9	2	4	
		8	6691.9	6695	3.1	4	
		9	6695	6697.8	2.8	4	
		10	6697.8	6700.9	3.1	4	
		11	6700.9	6703.7	2.8	4	
		12	6703.7	6706.8	3.1	4	
		13	6706.8	6707.05	0.25	4	

Table C-18. Brittleness (Bill Barrett 14-1-46).

Core Depth	Log Depth	BI1	BI2	BI3a (J/kg)	BI3b (J/kg)	BI4	BI5
6684.4	6676.9	0.25	0.46	9.80E-05	-8.20E-04	1.23	0.17
6684.4	6676.9	0.17	0.02	5.45E-04	-5.68E-03	1.82	0.31
6693.7	6686.2	0.20	0.00	2.48E-03	-6.24E-02	2.59	0.12
6693.45	6685.95	0.12	0.26	1.44E-01	-4.39E-01	8.79	0.39
6693.45	6685.95	0.09	-0.91	-4.88E-03	-3.00E-01	68069.74	0.72
6698.25	6690.75	0.22	0.16	2.04E-03	-4.54E-03	1.48	0.37
6699	6691.5	0.10	0.00	1.76E-02	-1.05E-01	2.21	0.38
6702.9	6695.4	0.14	0.00	2.27E-02	-4.44E-02	127.61	0.46
6703.1	6695.6	0.21	0.89	1.38E-03	-4.04E-03	1.50	0.06
6706.65	6699.15	0.27	0.17	9.38E-05	-3.25E-04	1.20	0.17
6706.5	6699	0.92	0.33	6.80E-04	-3.55E-03	1.67	0.27

Table C-19. Fracture Toughness (Bill Barrett 14-1-46)

Core Depth	Log Depth	Value Using Sample Height for R	FT Using Half Sample D for R	D (mm)	H (mm)	B (thickness) (mm)	B/D	Orientation	Testing Round	Machining Round
6692.5	6685	1653	1469	37	17.3	13.6	0.37	No	1	1

Table C-20. Dynamic Mechanical Properties Determined During Triaxial Compression Testing

Well ID	Lithology	Sample ID Core Depth (ft) Orientation	Axial Stress Difference (psi)	Effective Confining Pressure[1] (psi)	Effective Mean Stress (psi)	As Received Density (g/cm3)	P-Wave Velocity (ft/s)
Bill Barrett 14-1-46	tan dolomite	BTR1-6 6684.4 Vertical	0	1337	1337	2.352	15,625
			4584	1337	2865	2.354	15,909
			7822	1337	3944	2.355	16,046
			15,495	1337	6502	2.356	16,094
			20,876	1337	8296	2.357	15,974
			9096	1337	4369	2.325	15,455
		BTR1-2 6684.7 Horizontal	0	2739	2739	2.146	13,625
			1380	2739	3199	2.147	13,712
			5418	2739	4545	2.148	13,801
			12,494	2739	6904	2.15	13,824
			16,856	2739	8358	2.149	13,736
			10,523	2739	6247	2.091	13,360
	dolomite	BTR2-1	0	1332	1332	2.446	15,857
		6693.7	8032	1332	4009	2.448	16,121
		Vertical	13,056	1332	5684	2.449	16,230
			21,871	1347	8637	2.449	16,294
			27,380	1332	10,459	2.442	16,194
			8130	1347	4057	2.352	15,251

Well ID	Lithology	Sample ID Core Depth (ft) Orientation	Axial Stress Difference (psi)	Effective Confining Pressure[1] (psi)	Effective Mean Stress (psi)	As Received Density (g/cm3)	P-Wave Velocity (ft/s)
Bill Barrett 14-1-46	dolomite	BTR2-2 6693.45 Horizontal	0	2739	2739	2.553	17,474
			8611	2739	5609	2.556	18,166
			15,481	2739	7899	2.557	18,430
			22,254	2739	10,157	2.558	18,597
			37,097	2739	15,105	2.559	18,683
			17,750	2739	8656	2.521	18,162
	grey limestone	BTR3-1 6698.25 Vertical	0	1340	1340	2.592	15,786
			1933	1340	1984	2.593	15,867
			6172	1341	3398	2.595	16,130
			13,944	1341	5989	2.599	16,537
			22,010	1341	8678	2.604	16,914
			12,361	1341	5461	2.575	16,838
		BTR3-2 6699 Horizontal	0	2746	2746	2.616	18,728
			3177	2746	3805	2.617	18,945
			11,607	2746	6615	2.618	18,815
			28,593	2746	12,277	2.62	19,014
			49,311	2745	19182	2.622	18,938
			17,053	2746	8430	2.572	17,772

Well ID	Lithology	Sample ID Core Depth (ft) Orientation	Axial Stress Difference (psi)	Effective Confining Pressure1 (psi)	Effective Mean Stress (psi)	As Received Density (g/cm3)	P-Wave Velocity (ft/s)
Bill Barrett 14-1-46	tan dolomite	BTR4-4 6703.1 Vertical	0	1341	1341	2.55	17,752
			4337	1341	2787	2.551	17,791
			10,751	1341	4925	2.552	17,853
			16,682	1341	6902	2.553	17,869
			24,355	1341	9459	2.551	17,952
			12,948	1341	5657	2.53	17,446
		BTR4-2 6702.9 Horizontal	0	1347	1347	2.48	17,100
			2827	1332	2274	2.481	17,229
			9167	1332	4388	2.482	17,336
			15,506	1347	6516	2.483	17,412
			21,267	1347	8436	2.484	17,412
			8105	1332	4034	2.487	16,801
	shale	BTR5-4 6706.5 Vertical	1932	1341	1985	2.5	10,778
			4496	1341	2840	2.503	11,797
			5787	1340	3269	2.505	12,211
			9432	1341	4485	2.51	13,286
			13,145	1341	5723	2.507	14,493
			7385	1340	3802	2.451	13,530

Well ID	Lithology	Sample ID Core Depth (ft) Orientation	Axial Stress Difference (psi)	Effective Confining Confining Pressure1 (psi)	Effective Mean Stress (psi)	As Received Density (g/cm3)	P-Wave Velocity (ft/s)
	shale	BTR5-2 6706.65 Horizontal	661	2749	2969	2.523	15,940
			4521	2749	4256	2.524	16,283
			7964	2749	5404	2.525	16,314
			11,015	2749	6421	2.526	16,443
			14,374	2749	7540	2.526	16,508
			10,529	2749	6259	2.482	16,214

[1]For all tests, pore pressure drained to atmosphere.

Table C-21. Summary of Indirect Tensile Strength Tests (Brazilian Method) - Horizontal Samples

Well ID	Lithology	Sample #	Core Depth (ft)	Orientation	Average Length (in)	Average Diameter (in)	Mass (g)	Dry Bulk Density (g/cm^3)	Maximum Load (lb_f)	Tensile Strength[1] (psi)
Bill Barret 14-1-46	tan dolomite	BTR1_3A	6684.3	Perpendicular	0.749	1.496	46.207	2.143	1274	724
		BTR1_3B	6684.3	Parallel	0.725	1.495	45.204	2.169	1060	623
	dolomite	BTR2_3A	6693.55	Perpendicular	0.753	1.497	54.631	2.515	1963	1108
		BTR2_3B	6693.55	Parallel	0.766	1.497	55.327	2.505	3150	1749
	grey limestone	BTR3_3A [2]	6698.9	Perpendicular	0.491	0.998	16.293	2.591	2118	2753
		BTR3_4A	6698.5	Perpendicular	0.511	0.996	16.614	2.548	2207	2761
		BTR3_4B	6698.5	Parallel	0.535	0.996	17.685	2.591	730	873
	tan dolomite	BTR4_7A	6702.55	Perpendicular	0.523	0.997	16.576	2.477	643	785
		BTR4_7B	6702.55	Parallel	0.515	0.997	16.249	2.467	1020	1265
	shale	BTR5_3A	6706.65	Perpendicular	0.496	0.996	15.834	2.502	735	948
		BTR5_3B	6706.65	Parallel	0.506	0.995	16.151	2.507	474	600

[1] Equation for Tensile Strength in psi is: (2 * Load in lbf) / (pi * diameter in " * length in ")

[2] Sample BTR3_3A was replaced with sample BTR3_4A, due to difference in depth. No major difference in results were seen however.

Table C-22. Summary of Triaxial Compression Tests (for all tests, pore pressure drained to atmosphere)

Well ID	Lithology	Sample ID	Core Depth (ft)	Orientation	As Received Bulk Density (g/cm^3)	Confining Pressure (psi)	Peak Effective Compressive Strength (psi)	Effective Residual Compressive Strength (psi)	Young's Modulus (psi)	Poisson's Ratio
Bill Barrett 14-1-46	tan dolomite	BTR1-1 [2]	6684.4	Vertical	2.282	1337	19,416	9577	N.A.	
		BTR1-6	6684.4	Vertical	2.348	1337	22,190	10,407	5,390,000	0.22
		BTR1-2	6684.7	Horizontal	2.14	2741	19,736	13,241	3,829,000	0.27
	dolomite	BTR2-1	6693.7	Vertical	2.428	1339	29,112	9473	4,861,000	0.29
		BTR2-2 [3]	6693.45	Horizontal	2.544	2744	49,929	20,494	7,011,000	0.29
		BTR2-5	6693.45	Horizontal	2.433	2744	N.A.		4,796,000	0.31
	grey limestone	BTR3-1	6698.25	Vertical	2.586	1340	23,979	13,700	4,038,000	0.14
		BTR3-2	6699	Horizontal	2.614	2747	52,676	19,847	8,657,000	0.32
	tan dolomite	BTR4-4	6703.1	Vertical	2.543	1341	26,339	14,291	6,422,000	0.28
		BTR4-2	6702.9	Horizontal	2.473	2748	26,755	11,048	6,223,000	0.26
	shale	BTR5-4	6706.5	Vertical	2.487	1341	14,448	9191	1,295,000	0.18
		BTR5-2	6706.65	Horizontal	2.502	2750	17,245	13,270	3,797,000	0.26

[2] BTR1-1 – Unknown error regarding axial strain gauges resulting in erroneous values for Young's Modulus and Poisson's ratio. Replacement sample (BTR1-6) has a higher bulk density than its horizontal counterpart. No additional material remains.

[3] BTR2-2 – bulk density higher than vertical counterpart. Sample BTR2-5 is replacement sample, however, due to equipment failure (axial strain gauge) only Young's modulus and Poisson's ratio were measured. Peak and residual strengths for this sample are not available.

Table C-23. Dynamic versus Quasi-Static Mechanical Properties Determined During Triaxial Compression Testing

Well ID	Lithology	Sample ID	Core Depth (ft)	Orientation	Effective Confining Pressure (psi)	Static Poisson's Ratio	Dynamic Poisson's Ratio	Static Young's Modulus (psi)	Dynamic Young's Modulus (psi)	Dynamic / Static Young's Modulus	Dynamic / Static Poisson's Ratio
Bill Barrett 14-1-46	tan dolomite	BTR1-6	6684.4	Vertical	1337	0.22	0.27	5,390,000	6,594,000	1.22	1.23
		BTR1-2	6684.7	Horizontal	2741	0.27	0.24	3,829,000	4,701,000	1.23	0.89
	dolomite	BTR2-1	6693.7	Vertical	1339	0.29	0.24	4,861,000	7,303,000	1.5	0.83
		BTR2-2	6693.45	Horizontal	2744	0.29	0.27	7,011,000	9,410,000	1.34	0.93
	grey limestone	BTR3-1	6698.25	Vertical	1340	0.14	0.25	4,038,000	7,579,000	1.88	1.79
		BTR3-2	6699	Horizontal	2747	0.32	0.28	8,657,000	9,710,000	1.12	0.88
	tan dolomite	BTR4-4	6703.1	Vertical	1341	0.28	0.22	6,422,000	9,622,000	1.5	0.79
		BTR4-2	6702.9	Horizontal	2748	0.26	0.25	6,223,000	8,324,000	1.34	0.96
	shale	BTR5-4	6706.5	Vertical	1341	0.18	0.15	1,295,000	4,449,000	3.44	0.83
		BTR5-2	6706.65	Horizontal	2750	0.26	0.23	3,797,000	7,740,000	2.04	0.88
									Average:	1.66	1

Table C-24. Summary of Continuous Surface Thermal Conductivity Values

Well ID	Core Depth Range (ft)	Low W/m °K	High W/m °K	Average W/m °K
Bill Barrett 14-1-46	6676.00 - 6678.00	1.42	2.67	1.8
	6678.00 - 6680.70	1.4	2.34	1.77
	6680.70 - 6683.40	1.63	2.41	1.97
	6684.12 - 6686.31	1.18	2.37	1.45
	6686.45 - 6688.80	1.33	2.48	1.75
	6688.93 - 6691.90	1.79	2.37	1.98
	6692.00 - 6695.00	1.58	2.35	1.95
	6695.70 - 6696.73	1.59	2.44	2.05
	6697.82 - 6698.45	1.73	2.12	1.88
	6701.57 - 6703.56	1.56	2.2	1.92
	6703.80 - 6706.02	1.55	2.72	2

Table C-25. FTIR Results - Mineralogy in Relative Wt % - Bill Barrett Well 14-1-46

Sample ID Core Depth (ft)	BTR1-5 6684.7	BTR2-4 6693.4	BTR4-6 6703.3	BTR6-1 6683.5	BTR7-1 6689.5
Quartz:	3	2	5	16	3
K-feldspar	0	0	0	4	0
Na-feldspar	0	0	0	0	0
Ca-feldspar	0	0	0	0	0
Total Feldspar:	**0**	**0**	**0**	**4**	**0**
Calcite	10	8	16	10	84
Dolomite	85	80	76	10	1
Ankerite	0	0	0	0	5
Siderite	2	3	0	0	0
Total Carbonate:	**97**	**91**	**92**	**20**	**90**
Illite	0	4	2	50	4
Smectite	0	1	0	0	1
Kaolinite	0	1	0	0	0
Chlorite	0	0	0	0	1
Muscovite	0	0	0	0	0
Total Clay + Mica:	**0**	**6**	**3**	**50**	**5**
Pyrite:	**0**	**2**	**0**	**10**	**1**
Total:	**100**	**100**	**100**	**100**	**100**

Triaxial Compression Test Plots Bill Barrett 14-1-46

Bill Barrett 14-1-46

Lithology	Sample ID	Depth (ft)	Orientation	As Received Bulk Density (g/cm^3)	Confining Pressure (psi)	Peak Effective Compressive Strength (psi)	Effective Residual Compressive Strength (psi)	Young's Modulus (10^6 psi)	Poisson's Ratio
tan dolomite	BTR1-1	6684.40	Vertical	2.282	1337	19420	9580		
	BTR1-6	6684.40	Vertical	2.348	1337	22190	10410	5.390	0.22
	BTR1-2	6684.780	Horizontal	2.140	2741	19740	13240	3.829	0.27

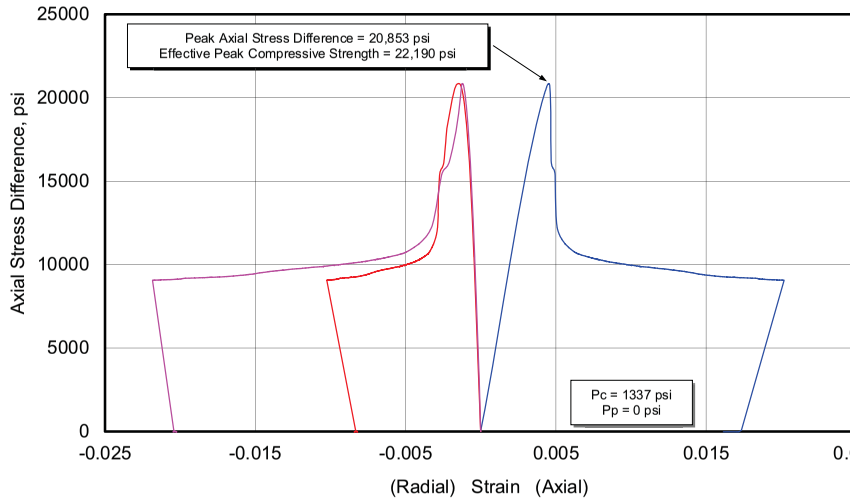

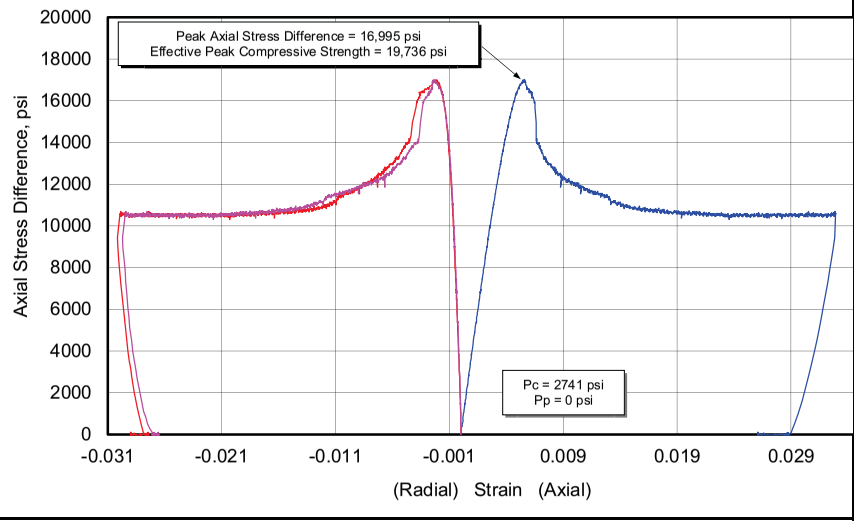

Bill Barrett 14-1-46

Lithology	Sample ID	Depth (ft)	Orientation	As Received Bulk Density (g/cm3)	Confining Pressure (psi)	Peak Effective Compressive Strength (psi)	Effective Residual Compressive Strength (psi)	Young's Modulus (106 psi)	Poisson's Ratio
dolomite	BTR2-1	6693.70	Vertical	2.428	1399	29110	9470	4.861	0.29
	BTR2-2	6693.45	Horizontal	2.544	2744	49930	20490	7.011	0.29
	BTR2-5	6693.45	Horizontal	2.433	2744			4.796	0.31

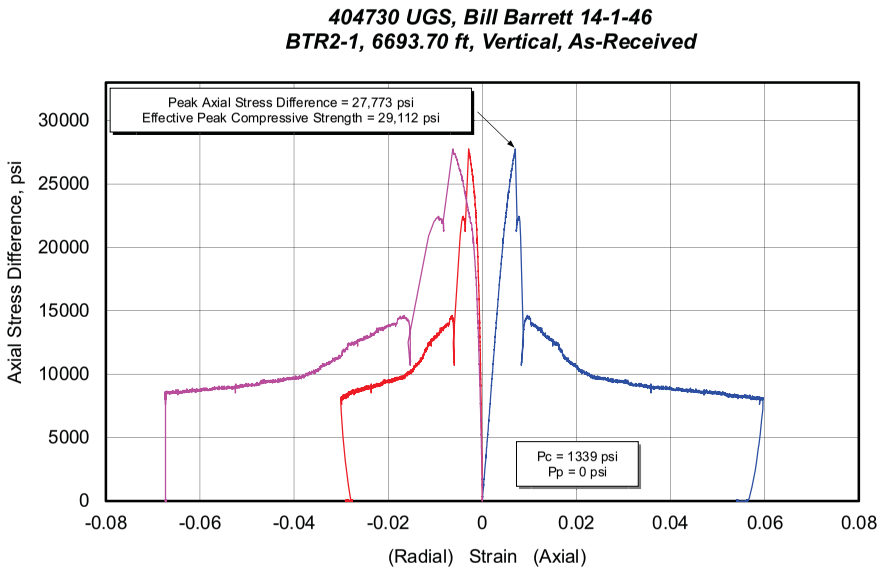

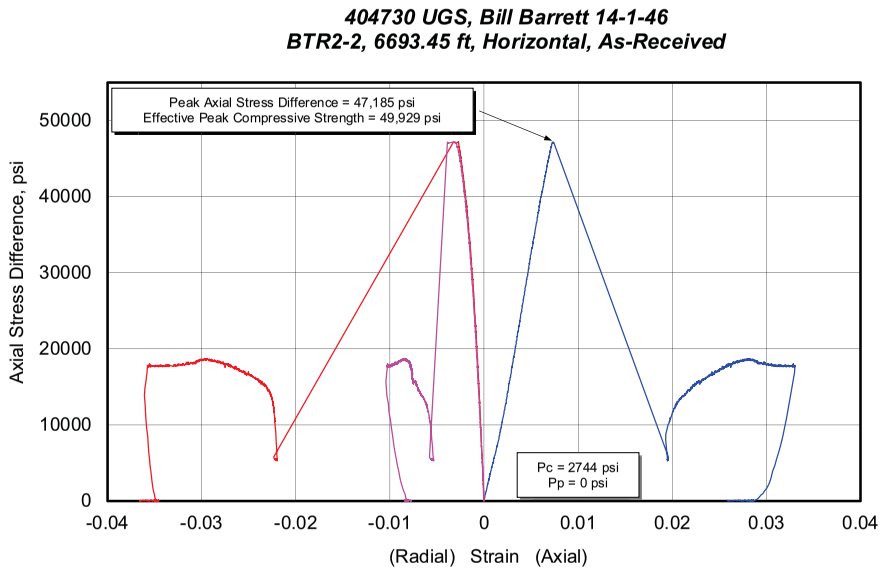

Bill Barrett 14-1-46

Lithology	Sample ID	Depth (ft)	Orientation	As Received Bulk Density (g/cm3)	Confining Pressure (psi)	Peak Effective Compressive Strength (psi)	Effective Residual Compressive Strength (psi)	Young's Modulus (106 psi)	Poisson's Ratio
tan dolomite	BTR4-4	6703.10	Vertical	2.543	1341	23340	14290	6.422	0.28
	BTR4-2	3702.90	Horizontal	2.473	2748	26760	11050	6.223	0.26

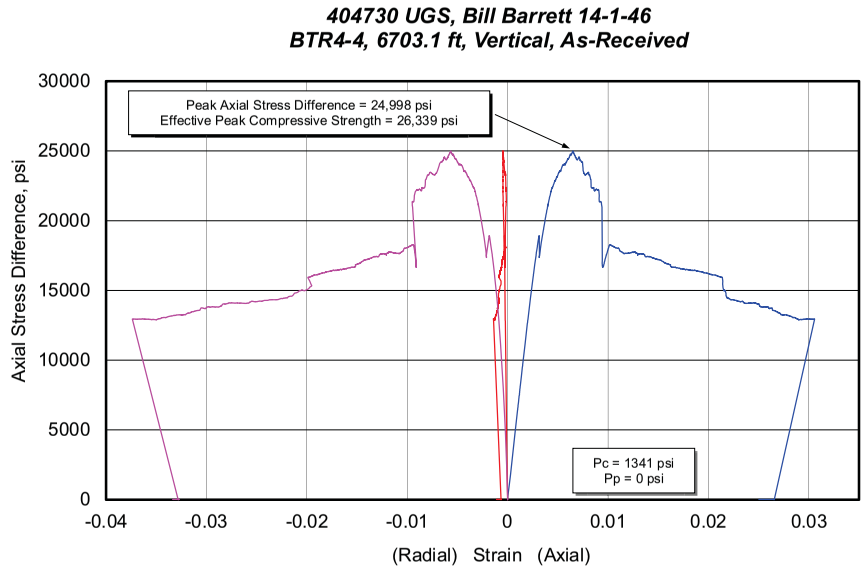

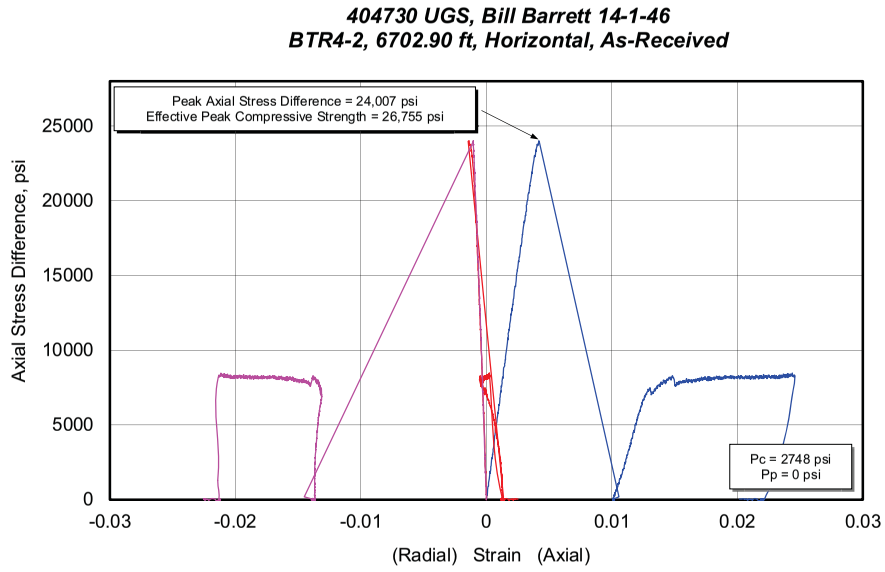

Bill Barrett 14-1-46

Lithology	Sample ID	Depth (ft)	Orientation	As Received Bulk Density (g/cm3)	Confining Pressure (psi)	Peak Effective Compressive Strength (psi)	Effective Residual Compressive Strength (psi)	Young's Modulus (106 psi)	Poisson's Ratio
shale	BTR5-4	6706.50	Vertical	2.487	1341	14450	9190	1.295	0.18
	BTR5-2	6706.65	Horizontal	2.502	2750	17250	13270	3.797	0.26

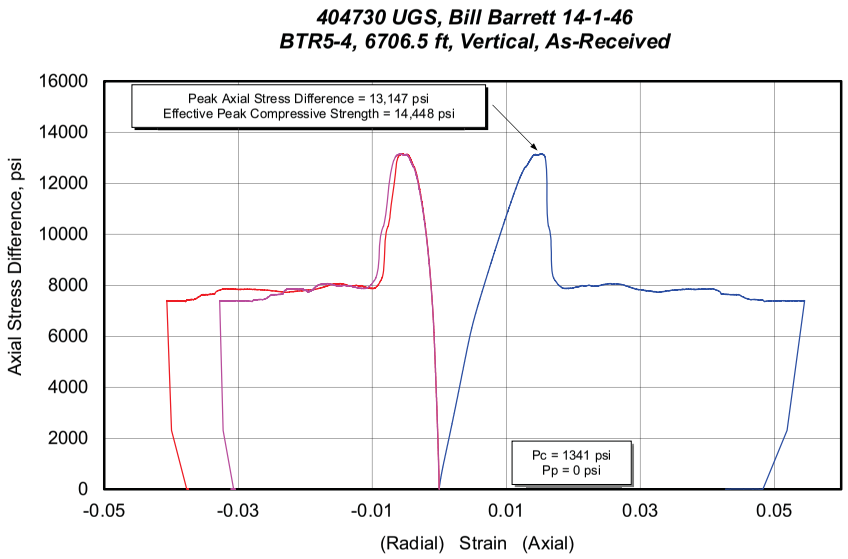

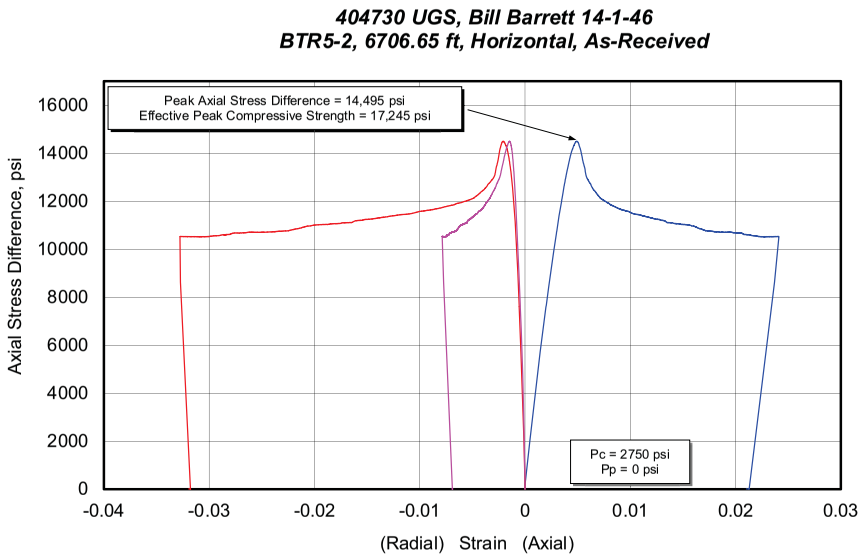

Fidelity Cisco State 36-13

This well is nominally straight hole (8-3/4-inch bit at TD). It has been plugged and abandoned. Core was taken from 7523 to 7586 feet (38 feet recovered), from 7586 to 7623 feet, from 7623 to 7658 ft MD and 7658 to 7688 ft MD.

7-inch P110 casing was run and cemented with 120 sacks of Class G (15.8 ppg) cement. The well was perforated and the Alkali Gulch and Cane Creek tested dry. A wellbore schematic is shown in Figure C-10.

Laboratory permeability and porosity data are shown in Table C-26 and in the crossplot (Figure C-11). X-Ray Diffraction mineralogical data are shown in Table C-27. The source rock potential for this zone is shown in Figure C-12 and Table C-28.

Some rudimentary triaxial compression data were available. These are shown in Table C-29.

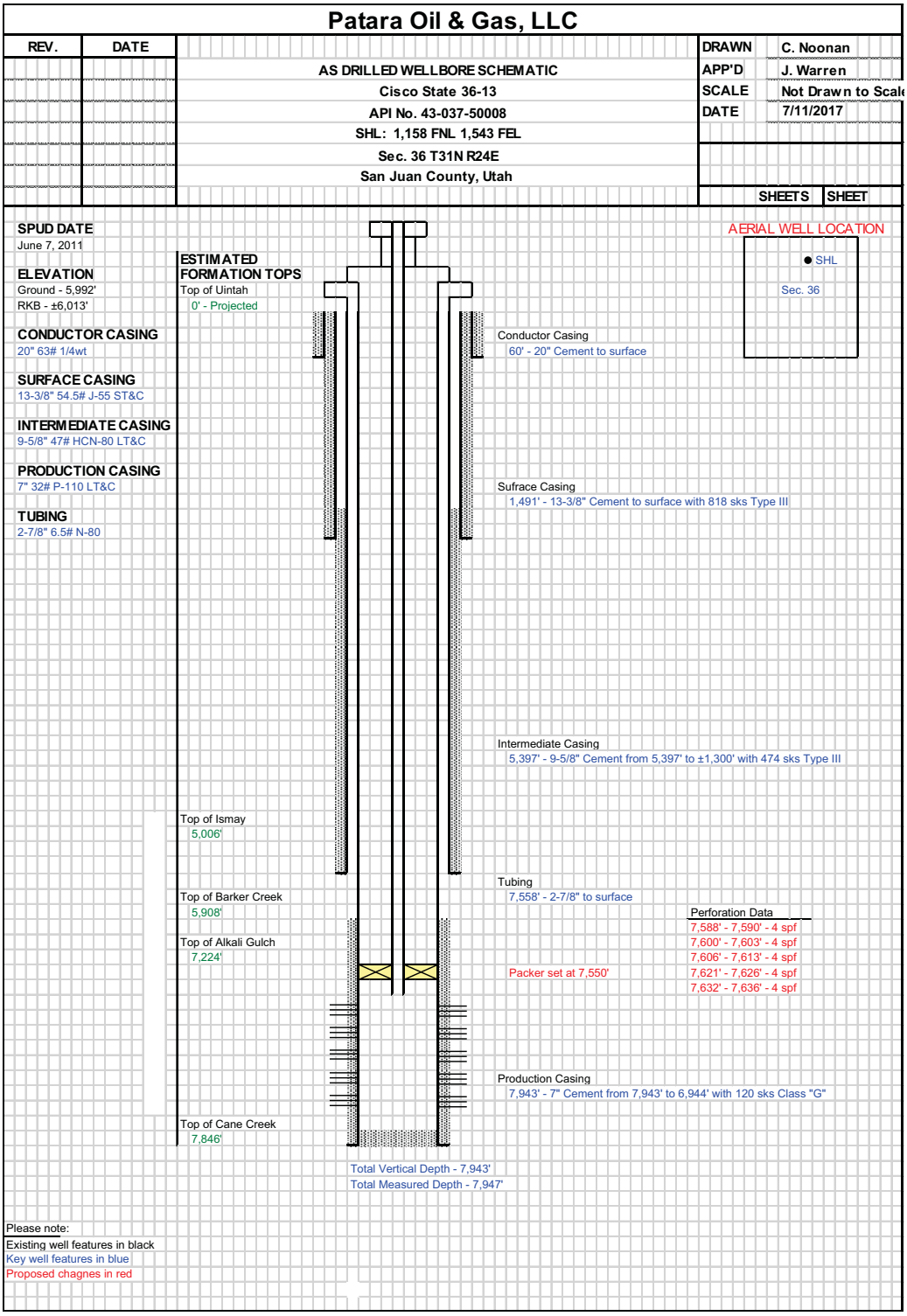

Figure C-10. Wellbore schematic for Cisco State 36-13.

Table C-26. Laboratory Permeability and Porosity - Cisco State 36-13.
The confining pressure was 2310 psi.

Depth (ft MD)	Lithology	Oil Potential	Hydrogen Index	Porosity (%)	k_{klink} (md)	k_{air} (md)	S_{oil} (%)	S_w (%)	Grain Density
7588.8	Shaley dolomite	N/A	N/A	9.7531	0.0135	0.0301	0.0000	69.9486	2.7180
7589	Dolomite from A	Fair	Mostly Gas (Maybe mixed)	10.2530	0.0158	0.0338	0.0000	64.4898	2.7152
7593	Shale from A??	N/A	N/A	17.6772	0.3891	0.5915	0.0000	74.9005	2.6919
7600	Mix of shale and dolomite	Fair	Mostly Gas (Maybe mixed)	8.5093	0.3306	0.3575	0.0000	114.2661	3.4089
7605.4	Silty dolomite - light gray	N/A	N/A	7.3146	0.0272	0.0415	0.0000	87.9372	2.8080
7615.3	Silty dolomite	N/A	N/A	9.3360	0.0096	0.0238	0.0000	97.0063	2.7597
7622	Dolomite			7.6031	0.0368	0.0702	0.0000	76.0053	2.7495
	Anhydrite	N/A	N/A	9.6775	0.0181	0.0293	0.0000	93.9385	2.7366
7632	Silty Dolomite	Poor	Gas	3.9562	0.0224	0.0360	0.0000	26.4780	2.9066
7636.9	Shaley dolomite	N/A	N/A	N/A	N/A	N/A	N/A	N/A	N/A
7647.8	Dolomite with some shale	N/A	N/A	N/A	N/A	N/A	N/A	N/A	N/A
7649.7	Shaley dolomite	Poor	Gas	N/A	N/A	N/A	N/A	N/A	N/A

Depth	Net Confining Stress (psi)	Porosity (%)	Klinkenberg Permeability (md)	Air Permeability (md)	b(air)	β	α	S_{oil} (%)	S_{water} (%)	Grain Density (g/cm^3)	Footnote
7588.00	2310	7.75	.004	.0155	82.35	5.28E+14	7174.304	0.0	91.8	2.729	
7589.00	2310	10.25	.0158	.0338	32.83	1.05E+13	526.0016	0.0	64.5	2.715	
7590.00	2310	0.41	.001	.003	71.12	1.13E+15	4.13E+03	0.0	72.9	2.935	(4)
7591.00	2310	0.07	.0001	.0009	303.31	6.16E+17	2.06E+05	0.0	98.1	2.958	(4)
7592.80	2310	12.29	.0185	.0375	29.24	4.33E+13	2.56E+03	0.0	66.2	2.701	
7593.00	2310	17.68	.389	.592	12.11	2.70E+11	3.37E+02	0.0	74.9	2.692	
7594.00	2310	0.64	.0002	.001	251.64	2.29E+17	1.27E+05	0.0	88.2	2.895	(4)
7595.00	2310	0.21	.00009	.0008	307.91	6.53E+17	2.10E+05	0.0	99.7	2.918	(4)
7596.20	2310	0.49	.0001	.001	281.13	4.08E+17	1.67E+05	0.0	99.8	2.920	(4)
7597.00	2310	0.81	.0002	.001	237.18	1.68E+17	1.10E+05	0.0	97.4	2.885	(4)
7598.30	2310	2.92	.003	.0105	97.25	1.26E+15	1.08E+04	0.0	30.8	2.777	
7599.00	2310	0.27	.0001	.0009	297.37	5.46E+17	1.92E+05	0.0	94.5	2.936	(4)
7600.55	2310	12.96	.512	.553	1.83	4.84E+12	8.01E+03	0.0	96.6	2.780	(1)
7601.90	2310	14.61	2.09	2.42	3.27	1.31E+11	8.86E+02	0.0	77.8	2.760	(1)
7602.90	2310	1.15	.0001	.001	306.39	6.42E+17	2.07E+05	0.0	54.4	2.884	(4)
7603.10	2310	0.26	.0001	.001	273.99	3.57E+17	1.57E+05	0.0	92.0	2.943	(4)
7605.10	2310	5.74	.002	.004	46.54	2.59E+15	1.44E+04	0.0	83.8	2.814	
7606.10	2310	10.98	.087	.129	12.52	2.28E+12	6.51E+02	0.0	97.6	2.793	
7607.90	2310	11.65	.0182	.0467	44.43	3.08E+13	1.82E+03	0.0	98.9	2.721	
7608.80	2310	13.16	.0302	.0546	22.21	6.19E+12	6.15E+02	0.0	99.9	2.765	
7609.10	2310	10.25	3.49	4.06	3.30	1.15E+11	1.30E+03	0.0	80.5	2.768	(1)
7611.50	2310	8.77	.0344	.0545	15.98	3.61E+12	4.07E+02	0.0	99.7	2.728	
7612.90	2310	2.15	.0116	.0245	32.91	7.07E+13	2.78E+03	0.0	87.9	2.929	(4)

Depth	Net Confining Stress (psi)	Porosity (%)	Klinkenberg Permeability (md)	Air Permeability (md)	b(air)	β	α	S_{oil} (%)	S_{water} (%)	Grain Density (g/cm^3)	Footnote
7613.10	2310	1.94	.0004	.002	178.99	3.61E+16	5.29E+04	0.0	85.8	2.941	(4)
7615.10	2310	9.14	.001	.006	117.70	3.57E+15	1.77E+04	0.0	96.4	2.761	
7616.10	2310	10.13	.0422	.0937	32.96	8.30E+12	1.14E+03	0.0	99.5	2.756	
7617.00	2310	9.59	.0275	.0504	23.03	1.76E+13	1.64E+03	0.0	99.3	2.767	
7618.30	2310	8.48	.866	.971	2.67	1.31E+12	3.71E+03	0.0	54.9	2.843	(1)
7619.10	2310	9.13	.003	.0111	92.57	9.73E+14	9.55E+03	0.0	98.8	2.735	
7620.10	2310	10.73	.0242	.0595	40.88	5.61E+13	4.54E+03	0.0	97.7	2.721	
7621.40	2310	2.14	.0931	.113	5.44	2.88E+13	8.88E+03	0.0	96.6	2.909	(4)
7622.10	2310	8.51	.0274	.0630	36.10	1.32E+13	1.16E+03	0.0	72.6	2.723	
7624.30	2310	8.79	.007	.0198	50.78	8.09E+13	1.99E+03	0.0	88.0	2.847	(1)(4)
7631.10	2310	9.11	.143	.223	13.99	8.70E+11	4.03E+02	0.0	99.1	2.742	
7632.10	2310	9.74	.004	.008	26.64	2.09E+12	2.99E+01	0.0	93.4	2.736	(1)
7633.20	2310	7.20	.008	.0254	64.80	1.56E+14	4.02E+03	0.0	99.3	2.682	
7634.10	2310	12.40	.119	.218	20.77	1.64E+12	6.38E+02	0.0	98.8	2.721	(1)
7636.30	2310	10.43	.0224	.0360	17.23	1.75E+12	1.27E+02	0.0	66.3	2.752	
7650.10	2310	0.91	.0001	.0009	308.57	6.58E+17	2.10E+05	0.0	98.9	2.743	

Footnotes:

(1) Denotes fractured or chipped sample. Permeability and/or porosity may be optimistic.

(2) Sample permeability below the measurement range of CMS-300 equipment at indicated net confining stress (NCS). Data unavailable.

(3) Denotes very short sample, porosity may be optimistic due to lack of conformation of boot material to plug surface.

(4) Sample contains bitumen or other solid hydrocarbon residue.

(5) Denotes sample unsuitable for measurement at stress. Porosity determined using Archimedes bulk volume at ambient conditions. Permeability >0.1 mD measured using helium gas. Permeability less than 0.1 mD measured using nitrogen gas. All b values converted to b (air)

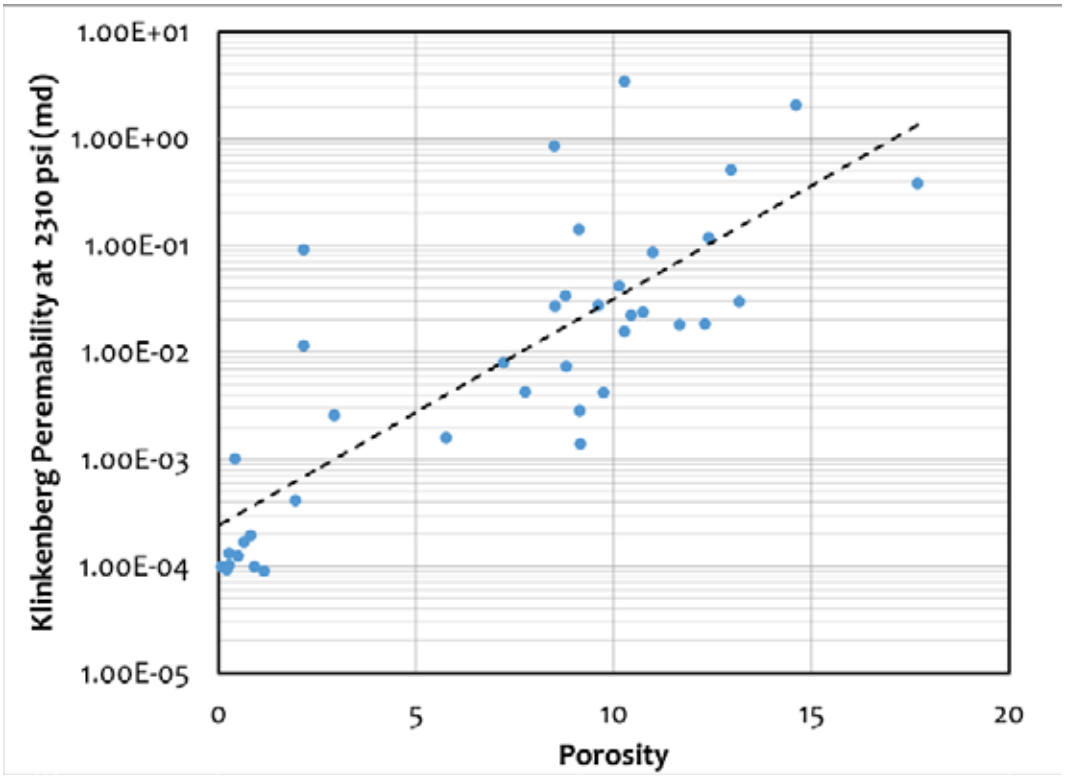

Figure C-11. Crossplot of porosity and permeability for Cisco State 36-13 with some higher porosity values - the credibility of the data is uncertain.

Table C-27. X-Ray Diffraction Mineralogy - Cisco State 36-13

Depth	7601.90	7609.10	7612.90	7620.10	7622.10	7632.10
TOC	1.54	1.02	n/a	n/a	n/a	0.12
Weight % Mineralogy (Without TOC)						
Quartz	28.0	28.2	3.0	55.5	58.6	42.4
Anhydrite	0.0	0.0	91.3	0.6	0.7	0.4
K-Feldspar	3.4	4.1	0.5	6.5	4.4	5.7
Plagioclase	0.9	0.8	0.0	1.0	0.7	0.6
Calcite	1.2	15.7	1.6	11.8	5.9	0.0
Dolomite	39.2	38.3	1.4	8.1	20.6	34.4
Halite	0.3	0.4	0.0	1.0	0.1	3.1
Pyrite	5.9	2.8	0.4	0.0	1.7	2.0
Total Clay	21.1	9.7	1.9	15.4	7.4	11.5
Relative Clay %						
Illite & Mica	92.1	86.6	86.0	87.1	89.8	87.6
Kaolinite	0.0	2.3	6.3	2.3	2.6	3.1
Chlorite	7.9	11.1	7.8	10.6	7.6	9.3
Sum Bulk	100.0	100.0	100.1	99.9	100.1	100.1
Sum Clay	100.0	100.0	100.1	100.0	100.0	100.0
Volume % Composition (Includes TOC as Kerogen)						
Quartz	28.6	28.7	3.4	56.0	60.1	43.4
Anhydrite	0.0	0.0	90.7	0.5	0.6	0.3
K-Feldspar	3.5	4.3	0.5	6.7	4.6	5.9
Plagioclase	1.0	0.9	0.0	1.0	0.7	0.6
Calcite	1.2	15.7	1.7	11.7	5.9	0.0
Dolomite	37.3	36.4	1.4	7.6	19.6	32.8
Halite	0.3	0.6	0.0	1.2	0.1	3.9
Pyrite	3.2	1.5	0.2	0.0	0.9	1.1
Illite and Mica	19.7	8.5	1.8	13.4	6.7	10.2
Kaolinite	0.0	0.2	0.1	0.4	0.2	0.4
Chlorite	1.5	1.0	0.1	1.5	0.5	1.0
Kerogen	3.6	2.4	0.0	0.0	0.0	0.3
Total	99.9	100.2	99.9	100.0	99.9	99.9
Vclay	21.2	9.7	2.0	15.3	7.4	11.6
Calc. Grain Density (g/cm^3)	2.757	2.735	2.950	2.671	2.716	2.721

Table C-28. TOC, S2, HI and other source rock data for well Cisco State 36-13.

Depth (ft)	Percent Carbonate (wt%)	Leco TOC (wt% HC)	Rock-Eval S1 (mg HC/g)	Rock-Eval S2 (mg HC/g)	Rock-Eval S3 (mg CO2/g)	Tmax (°C)	Calculated %Ro (RE TMAX)	Hydrogen Index (S2x100/TOC)	Oxygen Index (S3x100/TOC)
7,589.00		2.160	9.070	5.970	0.340	442.000	0.796	276.389	15.741
7,601.90		1.840	1.440	3.240	0.330	447.000	0.886	176.087	17.935
7,609.10		1.92	3.95	3.21	0.54	439		167	28
7,623.90		1.54	5.22	2.60	0.41	443		169	27
7,632.10		1.02	4.49	1.64	0.60	430		161	59
7,637.10		0.22	0.66	0.39	0.16	370		177	73
7,650.10		0.12	0.28	0.13	0.38	408		108	317

Depth (ft)	S2/S3 Conc. (mg HC/mg CO2)	S1/TOC Norm. Oil Content	Production Index (S1/(S1+S2)	Experimental Notations
6650.05	6	206	0.55	Low Temp S2 Shoulder
6656.80	6	339	0.67	Low Temp S2 Shoulder
6665.45	3	440	0.73	Low Temp S2 Shoulder
6668.65	2	300	0.63	Low Temp S2 Peak
6681.65	0	233	0.68	Low Temp S2 Peak
6685.25	0	50	0.67	
6689.15	1	183	0.70	Low Temp S2 Shoulder

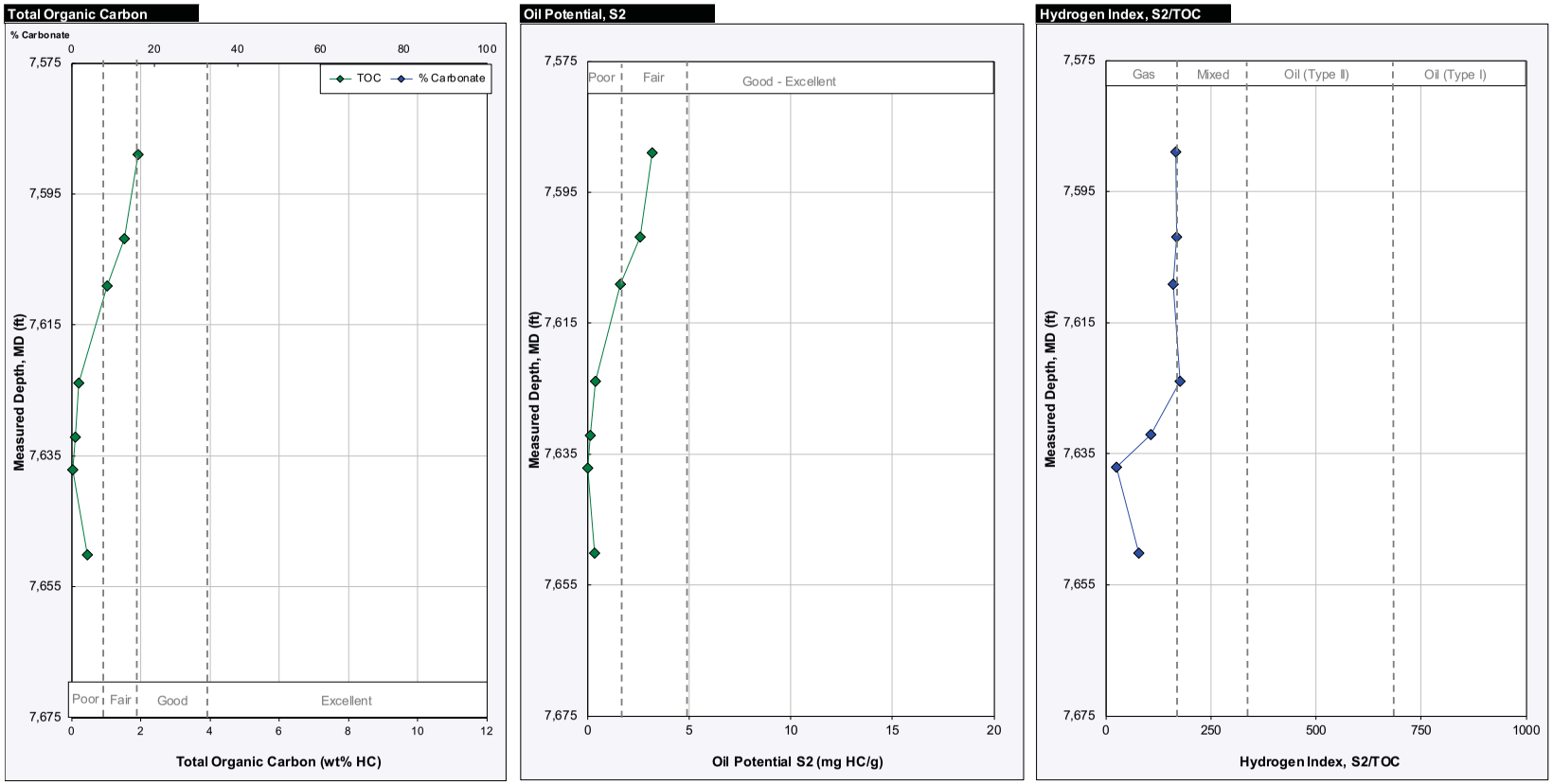

Figure C-12. Source rock potential. Is this true. Cane Creek?

Core Depth (ft)	8100
Bubblepoint Pressure (psig)	3500
Bottom-Hole Temperature (at core depth, °F)	125
Gas-Oil Ratio (scf/bbl)	1200
Mud Weight (lb / gal)	13.5
Core Barrel Length (ft)	90
Stand Length (ft)	90
Core Diameter (in)	4.00
Porosity (%)	7.50
Sw (%)	35.00
Absolute Permeability (mD)	4.00E-03

The azimuth of the fast shear wave is shown in Figure C-13. A sonic scanner logging survey was run (Figure C-14).

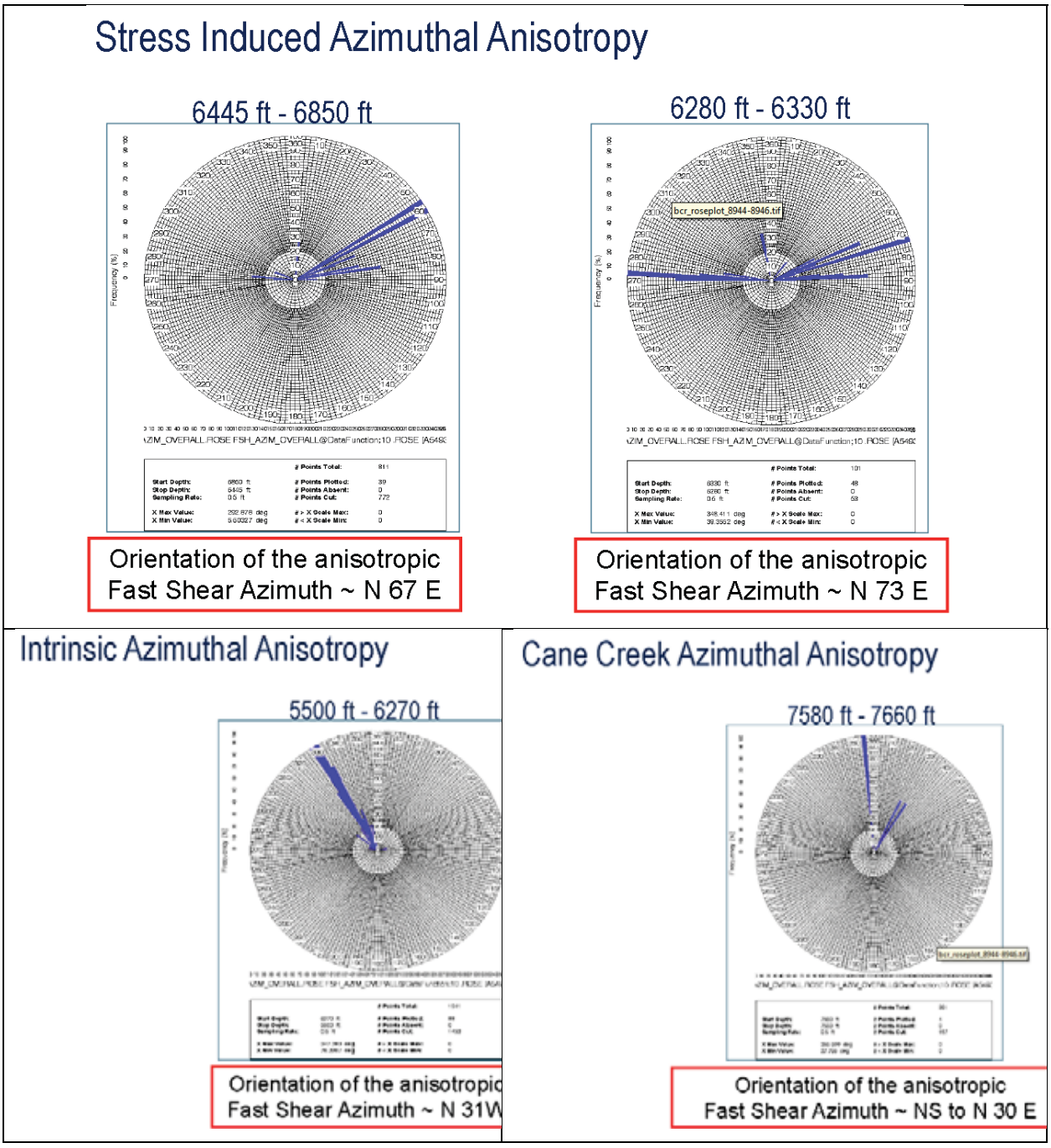

Figure C-13. Azimuth of the fast shear wave at 6445-6850 and 6280-6330 ft MD logging. Several portions of the well displayed azimuthal anisotropy which appears to be intrinsic anisotropy or stress induced anisotropy. The orientation of the fast shear for stress induced anisotropy was N67E. The orientation of the fast shear for intrinsic anisotropy was N31W. The Cane Creek anisotropy is caused by both intrinsic and stress induced anisotropy, and has an orientation of NS to N30E.

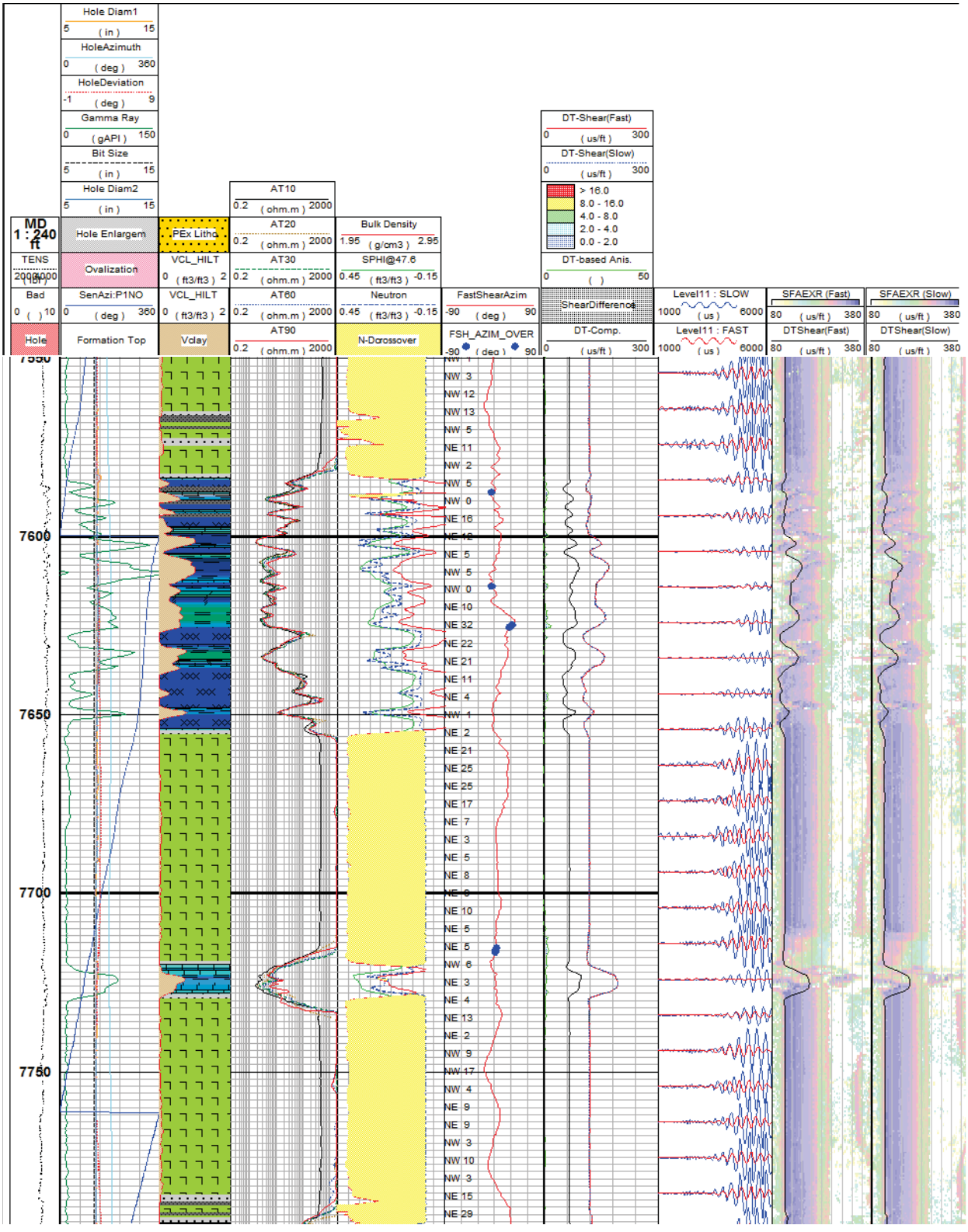

Figure C-14. Sonic scanner logging run Cisco State 36-13.

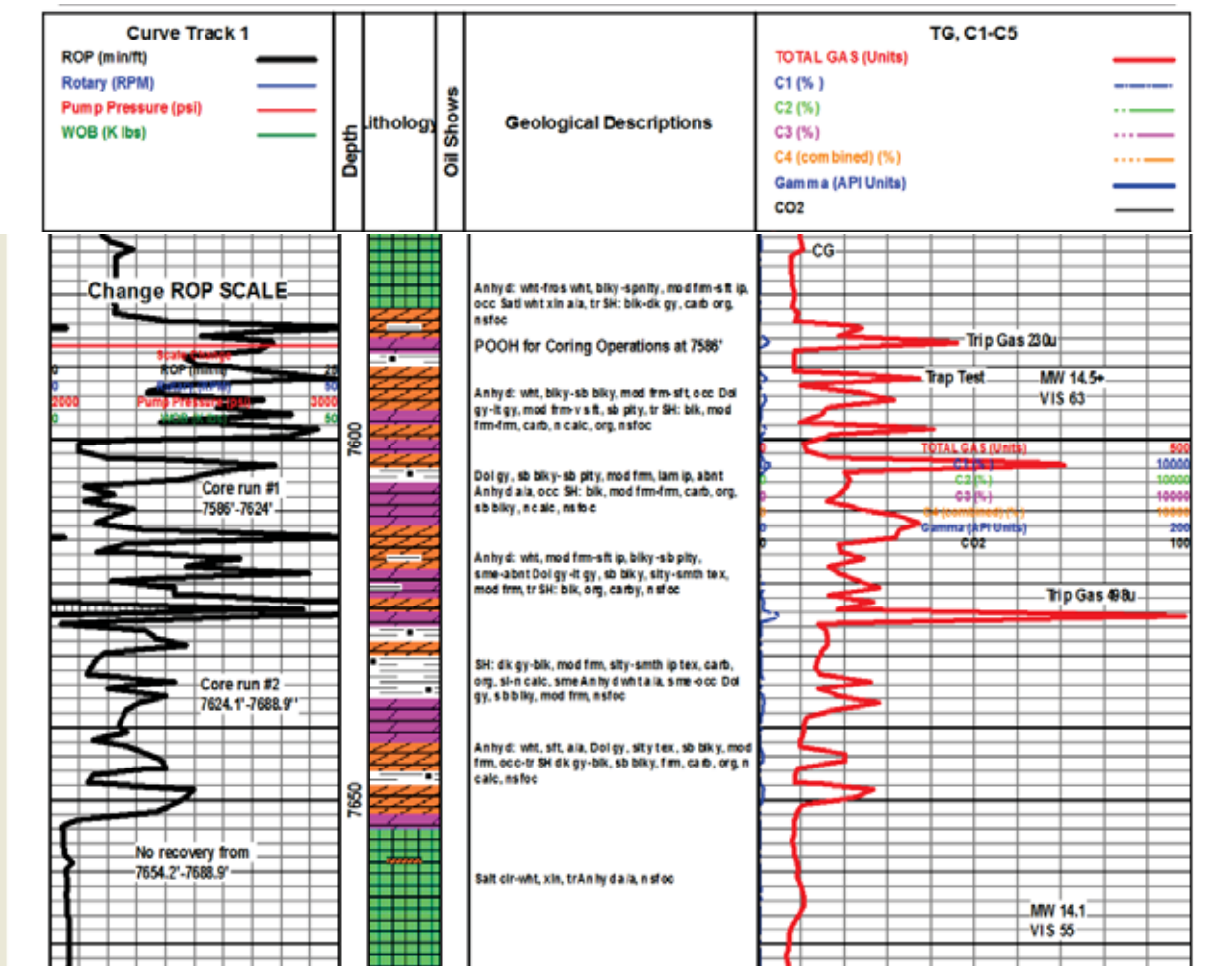

Figure C-14. Mud logging run Cisco State 36-13.

The slabbed core photographs of core from Cisco State 36-13 follow.

Slabbed photos – Cisco State 36-13

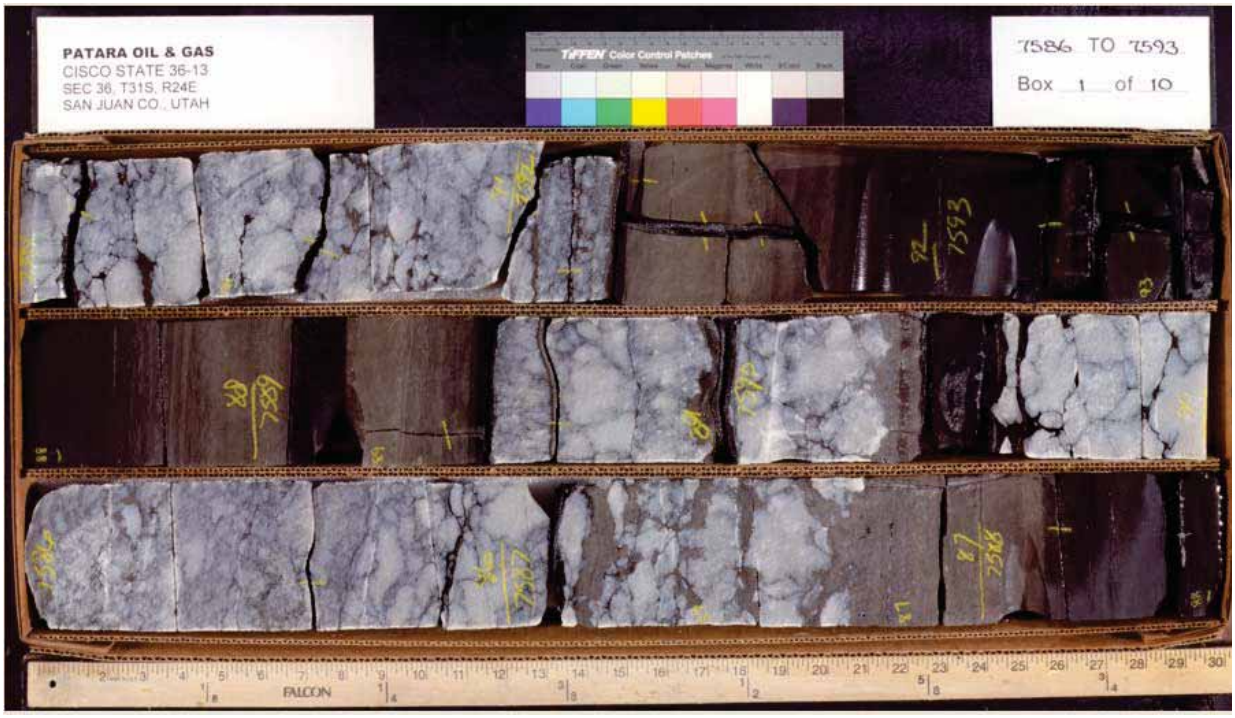

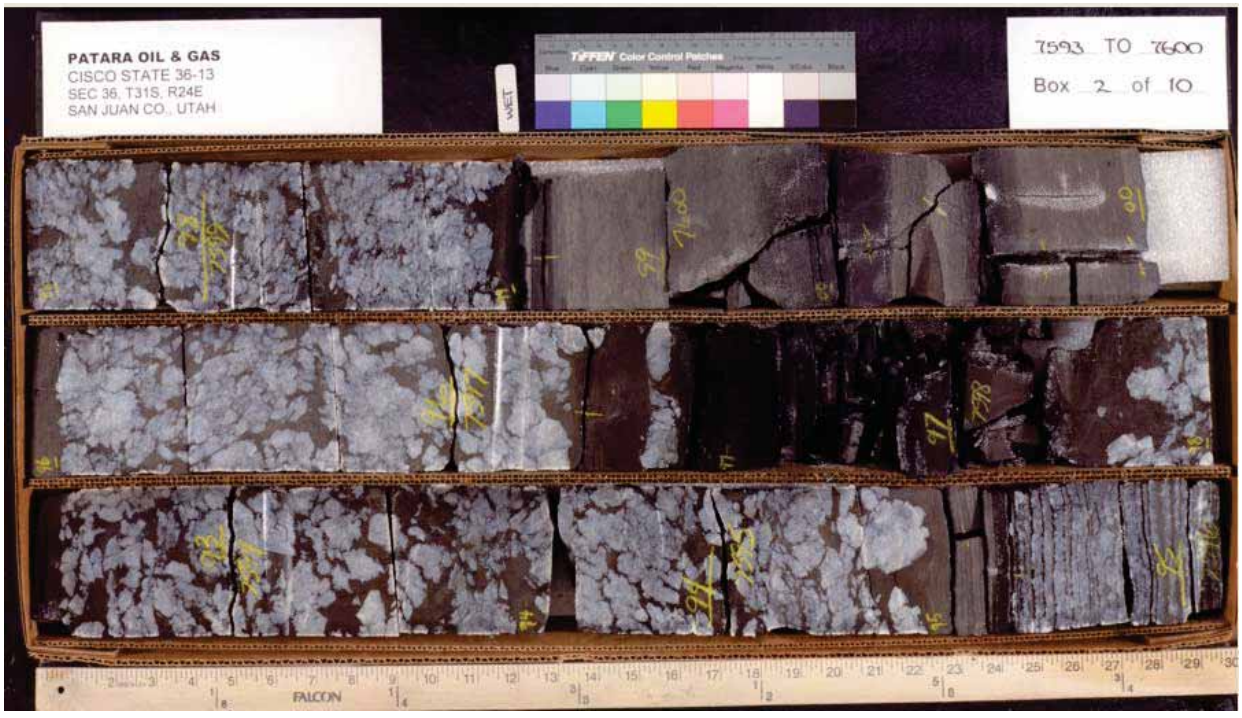


PATARA OIL & GAS
CISCO STATE 36-13
SEC 36, T31S, R24E
SAN JUAN CO., UTAH
WEST
7601 TO 7608
Box 3 of 10
FALCON

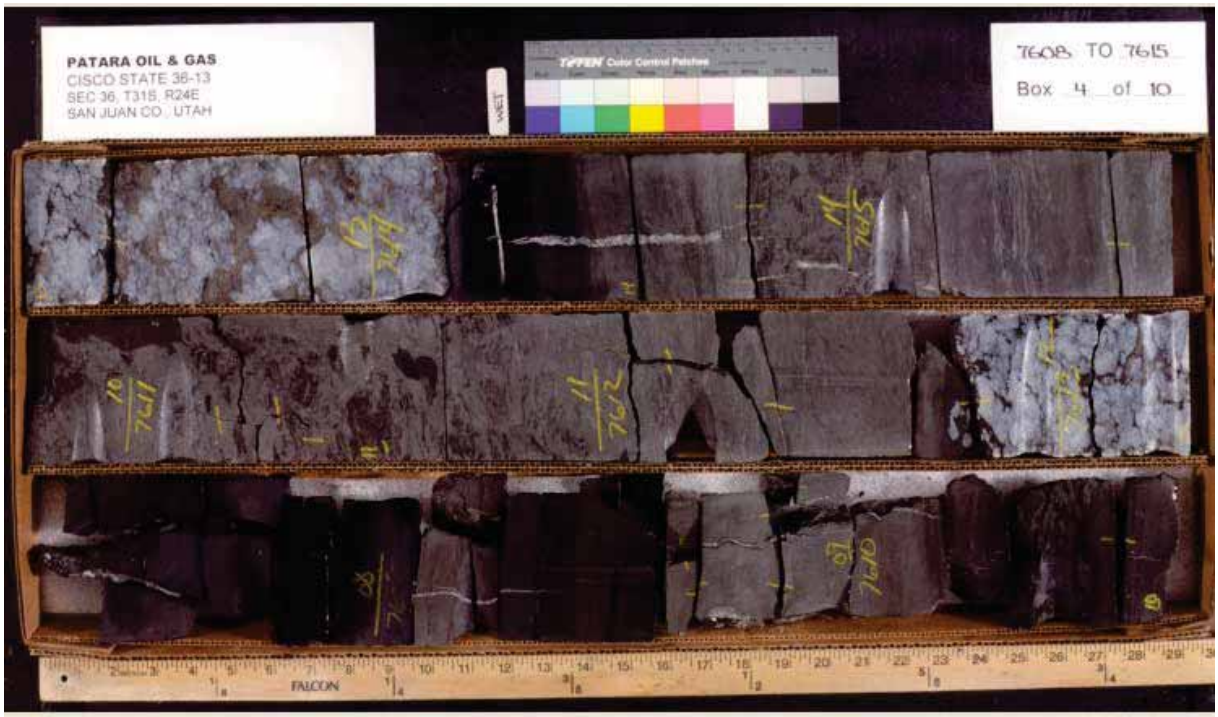
PATARA OIL & GAS
CISCO STATE 36-13
SEC 36, T31S, R24E
SAN JUAN CO., UTAH
WEST
7608 TO 7615
Box 4 of 10
FALCON


PATARA OIL & GAS
CISCO STATE 36-13
SEC 36, T31S, R24E
SAN JUAN CO., UTAH
7615 TO 7622
Box 5 of 10
FALCON

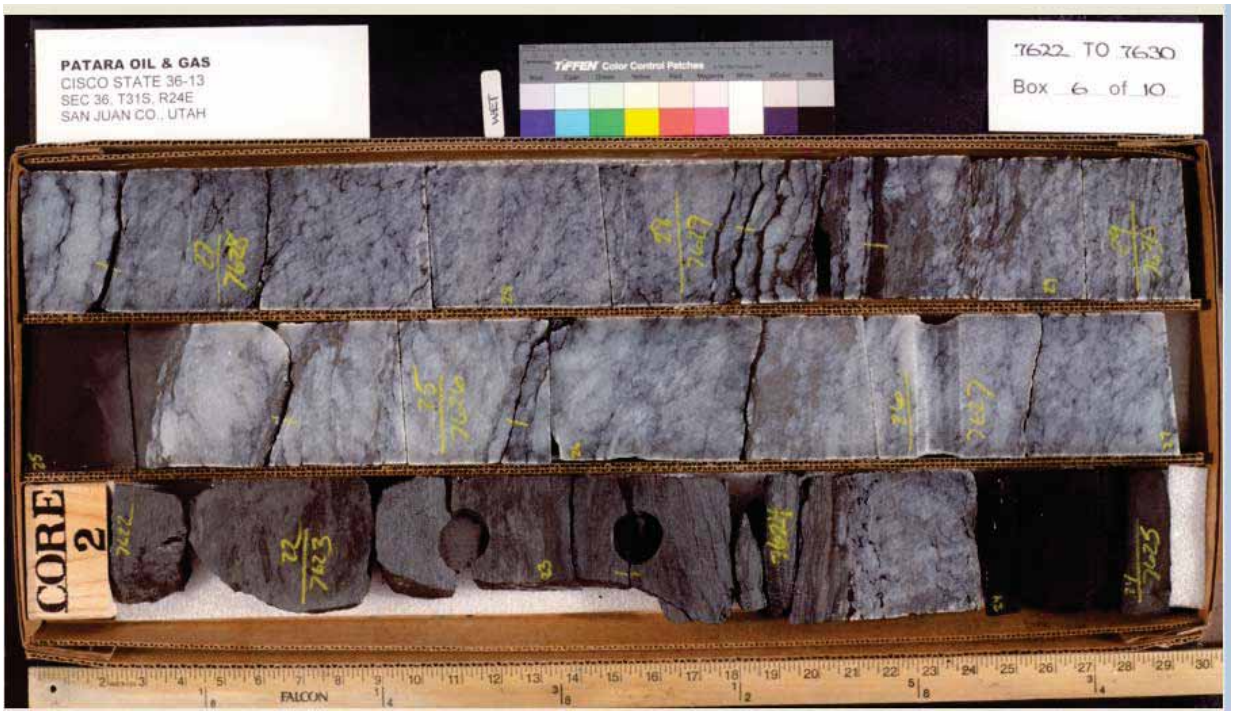
PATARA OIL & GAS
CISCO STATE 36-13
SEC 36, T31S, R24E
SAN JUAN CO., UTAH
7622 TO 7630
Box 6 of 10
CORE 2
FALCON

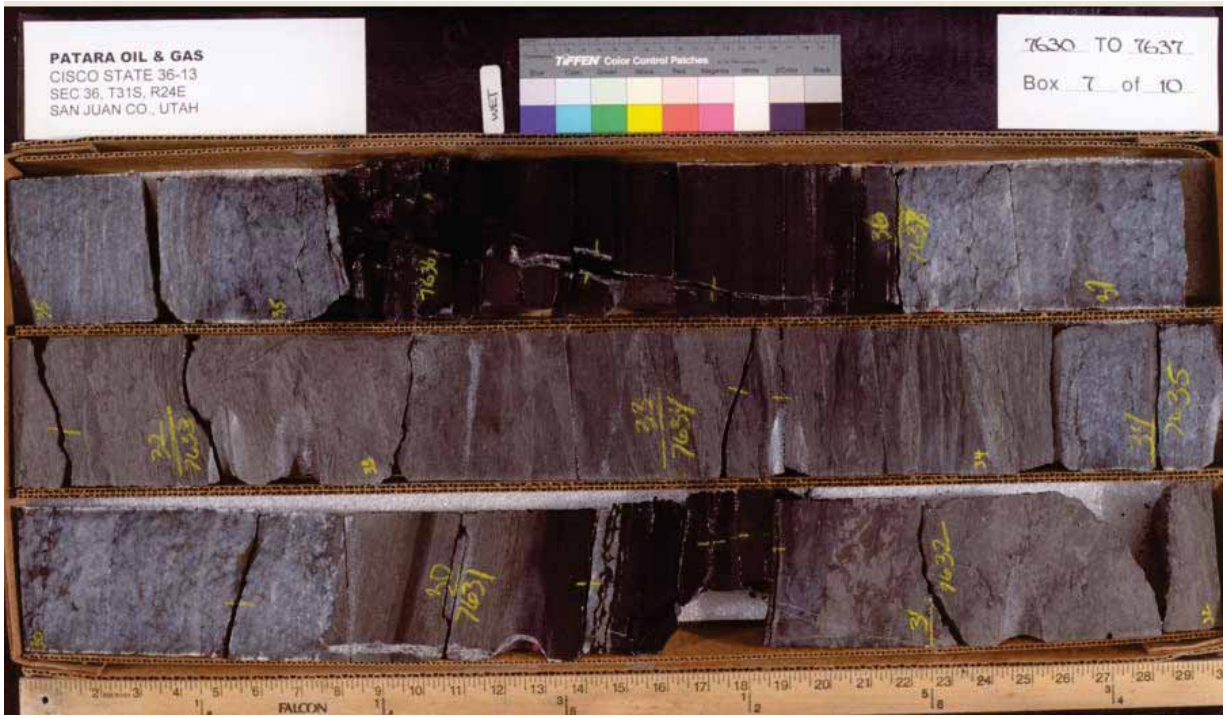
PATARA OIL & GAS
CISCO STATE 36-13
SEC 36, T31S, R24E
SAN JUAN CO., UTAH
TIFFEN Color Control Patches
WET
7630 TO 7637
Box 7 of 10
FALCON

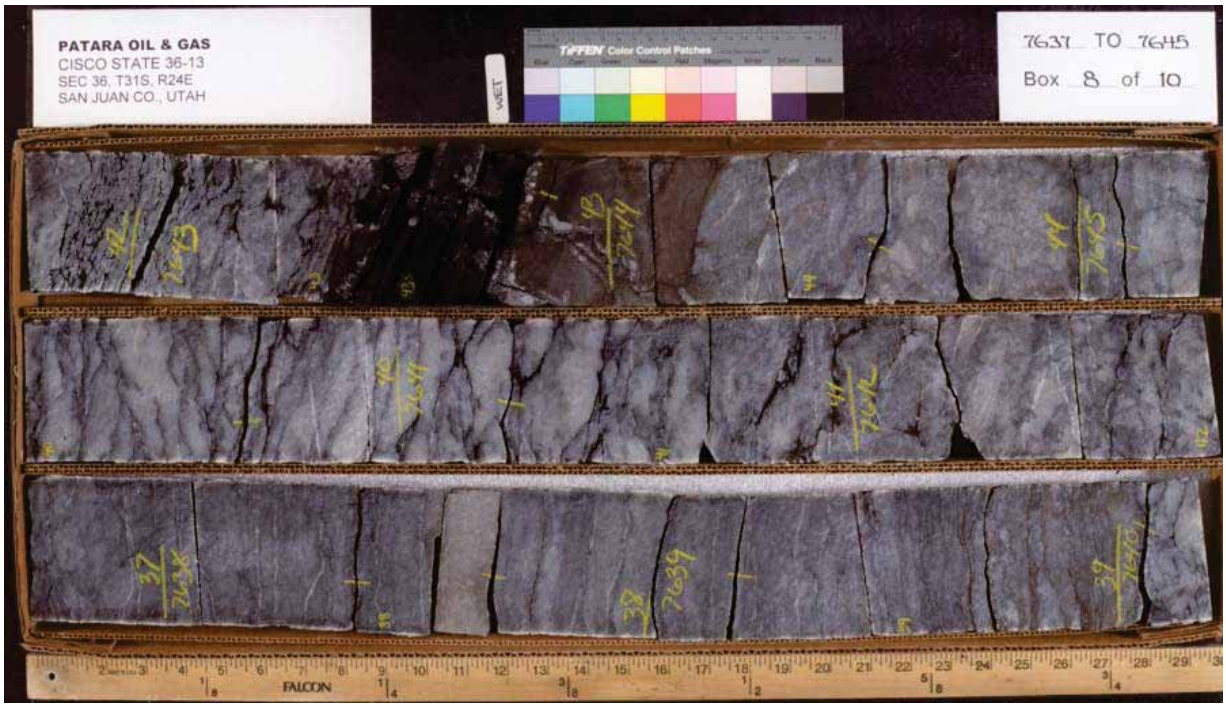
PATARA OIL & GAS
CISCO STATE 36-13
SEC 36, T31S, R24E
SAN JUAN CO., UTAH
TIFFEN Color Control Patches
WET
7637 TO 7645
Box 8 of 10
FALCON

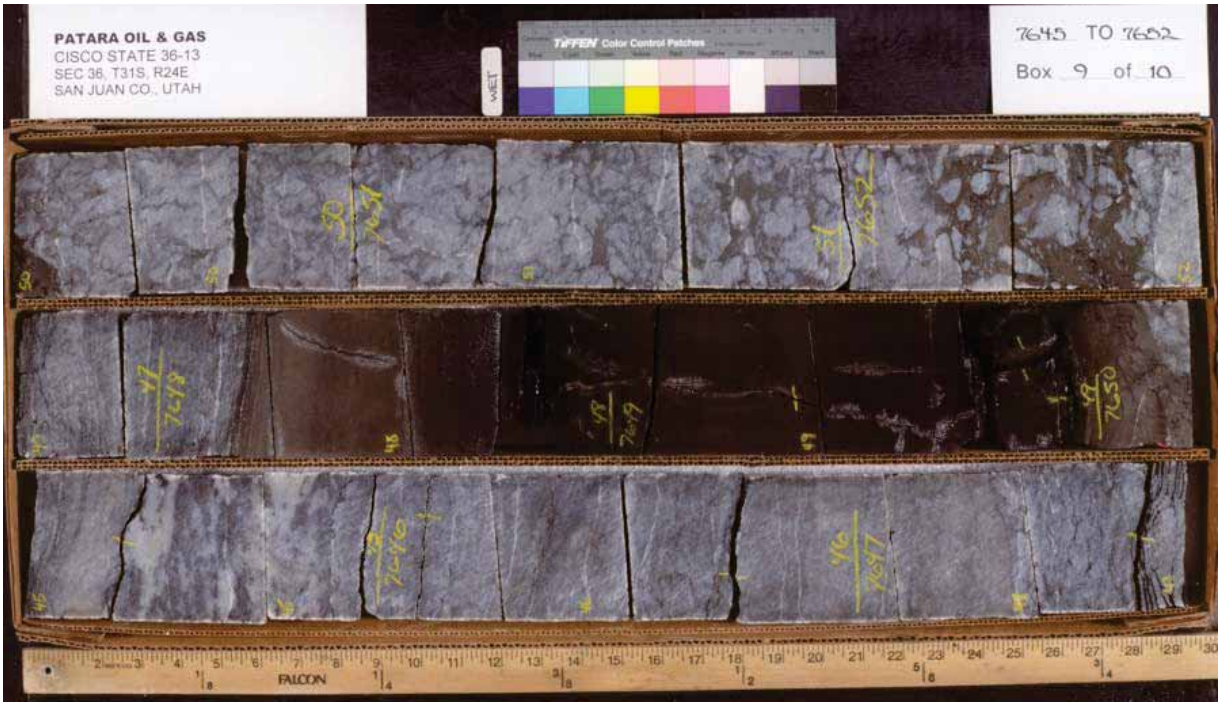
PATARA OIL & GAS
CISCO STATE 36-13
SEC 36, T31S, R24E
SAN JUAN CO., UTAH
WET
TIFFEN Color Control Patches
7645 TO 7652
Box 9 of 10
FALCON

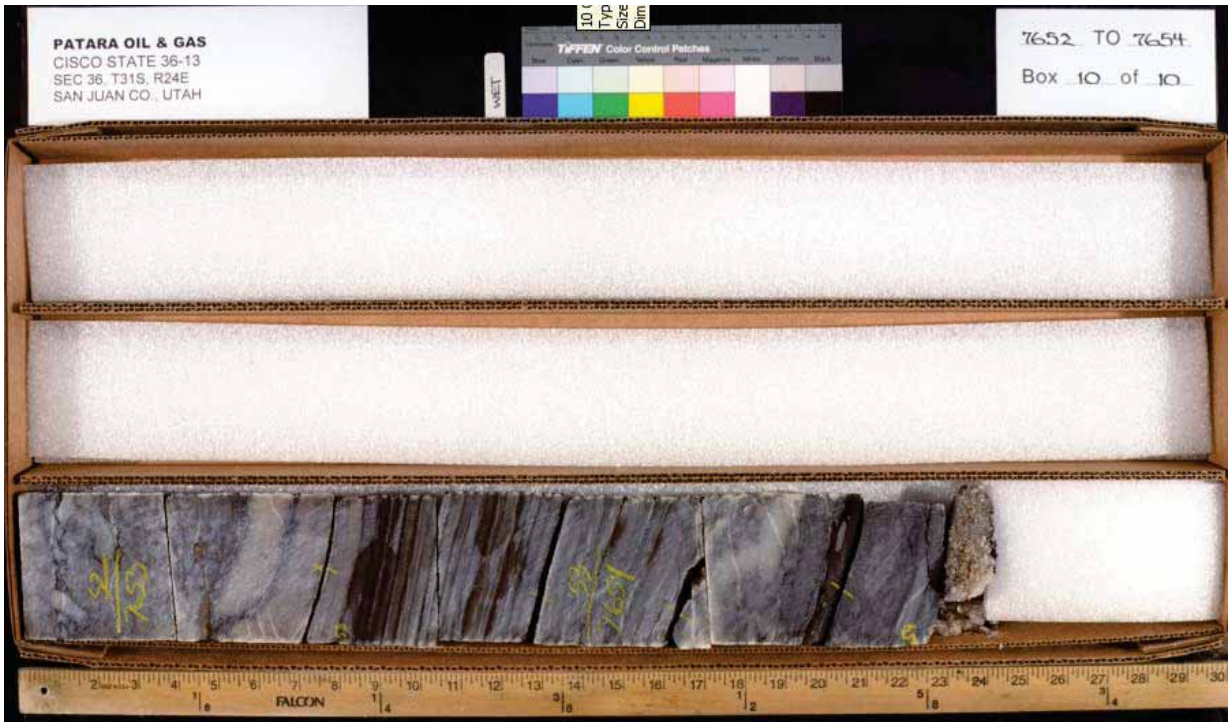
PATARA OIL & GAS
CISCO STATE 36-13
SEC 36, T31S, R24E
SAN JUAN CO., UTAH
WET
TIFFEN Color Control Patches
7652 TO 7654
Box 10 of 10
FALCON

Table C-29. Triaxial Compression Data - Cisco State 36-13.

Sample Number	Depth (ft)	Confining Pressure (psi)	Bulk Density (g/cm^3)	Compressive Strength (psi)	E (10^6 psi)	Poisson's Ratio
22	7609.50	1000	2.51	8885	1.46	0.25
25	7612.90	1000	2.52	6113	1.18	0.25
33	7620.65	1000	2.48	7934	1.35	0.23
35	7622.10	1000	2.46	5419	1.33	0.24

Zone 1				**Zone 3**		
Start	6850	ft		Start	7600	ft
End	6851	ft		End	7603	ft
Shots per foot	4			Shots per foot	4	
Total Shots	4			Total Shots	12	
Perforation Diameter	0.34	in		Perforation Diameter	0.34	in
Squeezed closed						
Zone 2				**Zone 4**		
Start	7588	ft		Start	7606	ft
End	7590	ft		End	7613	ft
Shots per foot	4			Shots per foot	4	
Total Shots	8			Total Shots	28	
Perforation Diameter	0.34	in		Perforation Diameter	0.34	in

CALCULATED RATES, PRESSURES & HHP REQUIREMENTS

	Maximum	Minimum	Average
Surface Treating Pressure (psi)	3,924	3,562	3,606
Slurry Rate (bpm)	4.0	0.0	0.6
Slurry Hydraulic Horsepower	385	1	56

PROCEDURE

Stage	Fluid		Diverting Agents				
	Type	Volume (gal)	Conc. (pda)	Type	Stage (volume)	Cum (lbs)	Cum (b.s.)
1	Treated Water	500		Load Hole			
2	Treated Water	150		Breakdown			
3	Treated Water	420		Diagnostic Injection			
4	Treated Water	13		Isip-Shut-In			
Total		1083					

TREATMENT SCHEDULE

Stage	Surface Treating Pressure (psi)	Rates			Volume				Stage Pump Time hh:mm:ss
		Slurry (bpm)	Clean Fluid (bpm)	Divertor Rate (lb/min)	Slurry		Fluid		
					Stage (bbls)	Cum. (bbls)	Stage (bbls)	Cum. (bbls)	
1	3681	2.0	2.0		11.9	11.9	11.9	11.9	00:05:57
2	3681	2.0	2.0		3.6	15.5	3.6	15.5	00:01:47
3	3923	4.0	4.0		10.0	25.5	10.0	25.5	00:02:30
4	3561	0.0	0.0		0.3	25.8	0.3	25.8	00:30:57
								Total Pump Time:	00:41:11

Figure C-15. This shows a planned DFIT for this well.

A DFIT was pumped on July 20, 2011. The maximum surface pressure was 3923 psi. 1083 gals of treated water (6% KCl?) were pumped at a nominal rate of 4 bpm. The planned treatment was for mid-perforations at 7624 ft (7621-6 ft MD) at an estimated gradient of 0.90 psi/ft. The treatment would be down 2-7/8-inch 6.5 lb/ft N80 tubing.

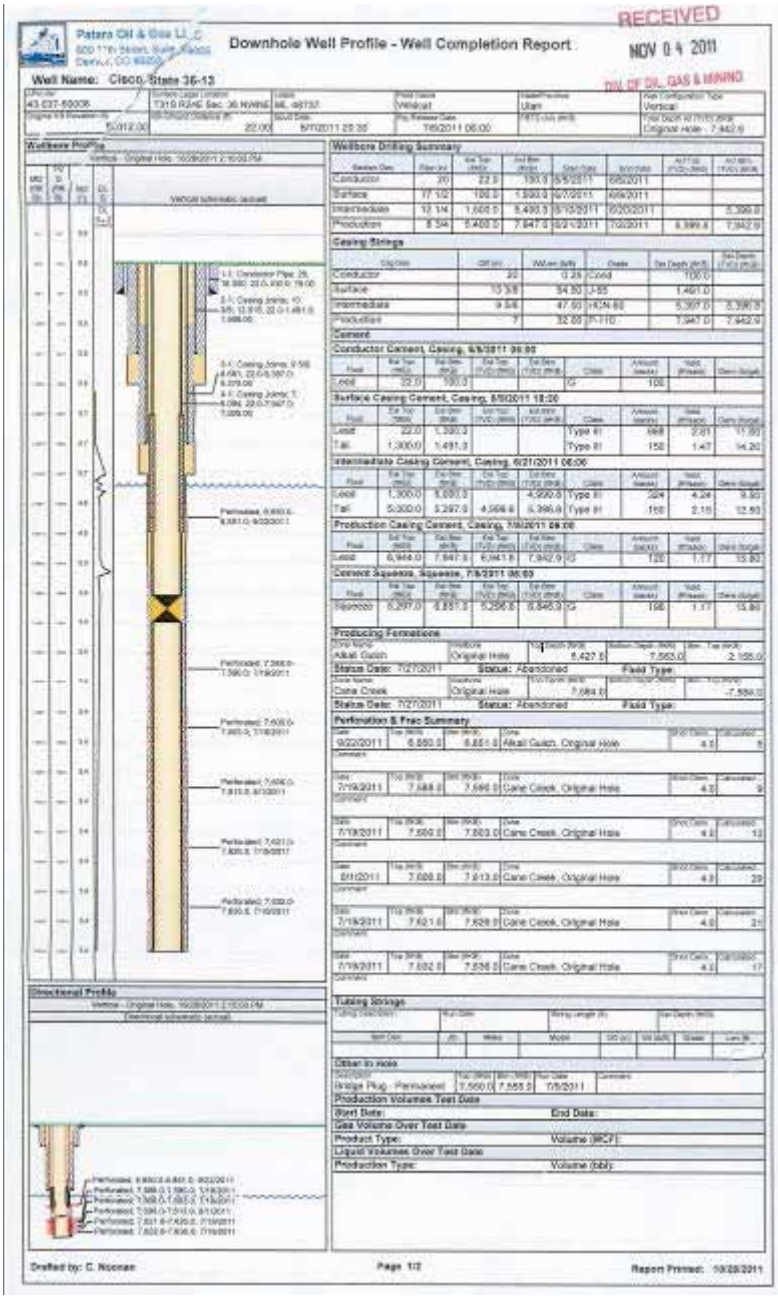

Figure C-16. Downhole well profile – Well Completion Report – Cisco State 36-13.

RESERVOIR DATA

Formation	Cane Creek
Depth to Middle Perforation	7,624 ft
Fracture Gradient	0.90 psi/ft
Bottom Hole Fracture Pressure	6,861 psi
Bottom Hole Static Temperature	196 ° F

PERFORATED INTERVAL

DEPTH(ft)		Shots per Foot	Perf Diameter (in)	Total Perfs
MEASURED	TRUE VERTICAL			
7,621 - 7,626	7,621 - 7,626	4	0.40	20

Total Number of Perforations	20
Total Feet Perforated	5 ft

TUBULAR GEOMETRY

				Top	Bottom
Casing	7" O.D.	(6.094" .I.D)	32 # J-55	0	7,912
Tubing	2 7/8" O.D.	(2.441" .I.D)	6.5 # N-80	0	7,600

End of Tubing	7,600 ft
Pump Via	Tubing

Figure C-17. Reservoir Data

The samples were depth shifted to logging depths using the laboratory and logging gamma ray tracks (Figure C-18). Table C-30 shows the brittleness indices calculated.

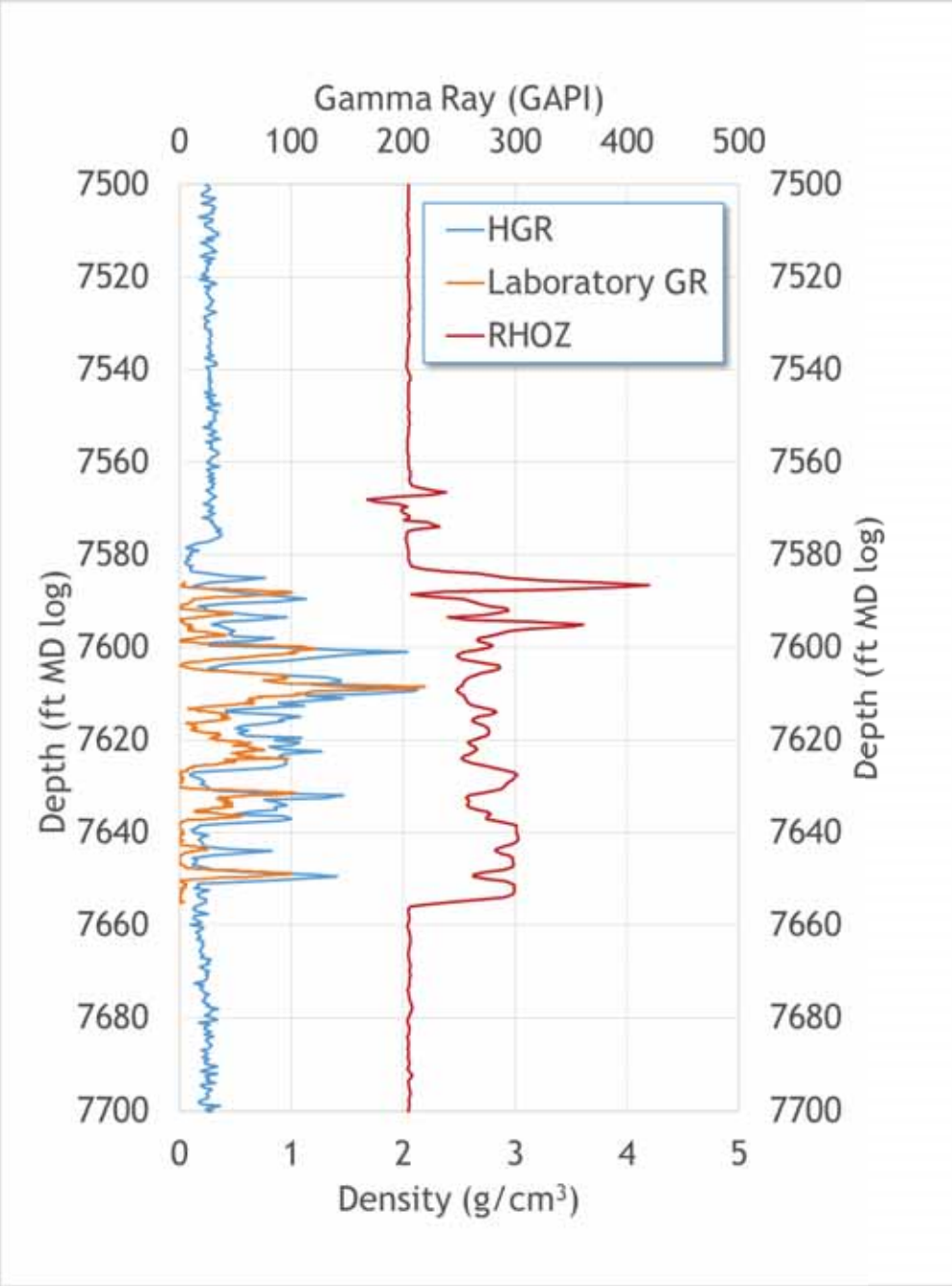

Figure C-18. Depth shifting was based on the gamma ray signals.

Table C-30. Brittleness Indices

Driller's Depth (ft MD)	Logging Depth (ft MD)	Orientation	I	II	IIIA	IIIB	IIIAV	IV	V
7588.9	7590.002	H	1.4	0.227	0.269	1.122	0.6955	1.37	0.12
7592.9	7593.941	H	4.81	0.601	0.0107	0.111	0.06085	1.06	0.086
7599.85	7600.799	H	1.5	0.045	0.0098	0.578	0.2939	1.17	0.33
7605.65	7606.536	H	1.44	0.095	0.541	0.0098	0.2754	1.36	0.44
7615.25	7616.053	H	1.9	0.71	0.0034	0.234	0.1187	1.1	0.29
7627.1	7627.831	H	1.76	0.433	0.139	1.47	0.8045	1.53	0.047
7588.8	7589.903	V	1.28	0.566	0.497	3.97	2.2335	1.65	0.19
7593	7594.039	V	3.2	0.166	0.286	0.839	0.5625	1.16	0.09
7599.75	7600.7	V	1.32	0.163	0.101	0.593	0.347	1.38	0.45
7605.35	7606.239	V	1.34	0	1.42	9.77	5.595	1.9	0.21
7605.65	7606.536	V	1.44	0.856	0.005	0.103	0.054	1.14	0.39
7615.4	7616.202	V	2.1	0	0.124	1.56	0.842	1.11	0.11
7627.3	7628.03	V	1.43	0.675	0.0062	1.45	0.7281	1.52	0.045

Table C-31. Brittleness

Sample	Orientation	Core Depth	Log Depth	BI1	BI2	BI3a	BI3b	BI4	BI5
CSO1-1	Vertical	7588.8	7589.3	0.82	0.63	1.92E-03	-1.27E-02	2.044475	0.19
CSO1-2	Horizontal	7588.9	7589.4	0.68	0.23	7.54E-04	-3.00E-03	1.402809	0.12
CSO2-1	Vertical	7593	7593.5	2.16	0.13	9.15E-04	-2.56E-03	1.178848	0.090
CSO2-2	Horizontal	7592.9	7593.4	2.58	0.32	3.60E-04	-1.56E-03	1.116449	0.086
CSO3-1	Vertical	7559.75	7560.25	0.97	0.16	1.45E-03	-7.31E-03	1.386088	0.45
CSO3-2	Horizontal	7559.85	7560.35	0.59	0.00	4.18E-04	-1.80E-03	1.178853	0.33
CSO4-1	Vertical	7605.35	7605.85	0.21	0.00	1.24E-02	-7.89E-02	1.913241	0.21
CSO4-2	Horizontal	7605.65	7606.15	0.60	0.21	4.35E-04	-9.19E-04	1.276026	0.44
CSO4-4	Vertical	7605.65	7606.15	0.89	0.54	4.58E-03	-2.17E-02	1.868195	0.39
CSO5-1	Vertical	7615.4	7615.9	1.63	0.00	3.80E-04	-2.20E-03	1.137364	0.11
CSO5-2	Horizontal	7615	7615.5	0.87	0.44	1.81E-04	-8.35E-04	1.136685	0.29
CSO6-1	Vertical	7627.3	7627.8	0.16	0.67	9.17E-03	-9.01E-02	1.541962	0.045
CSO6-2	Horizontal	7627.1	7627.6	0.17	0.41	8.82E-03	-6.06E-02	1.57193	0.047

Table C-32. Fracture Toughness

Sample	Core Depth	Log Depth	Value Using Sample Height for R	FT Using Half Sample D for R	D (mm)	H (mm)	B (thickness) (mm)	B/D	Orientation	Testing Round	Machining Round
CS36-13 Bag3SampleH	7617	7616.5	1023	884	37	16.9	13.10	0.35	No	1	1
CS36-13 Bag3SampleF	7617	7616.5	773	795	37.3	19	14.80	0.40	No	1	2
CS36-13 Bag3SampleE	7586.7	7586.2	1638	1442	37.28	17.24	20.17	0.54	Yes	2	2
CS36-13 Bag3SampleB	7586.7	7586.2	2473	2035	37.23	16.89	18.41	0.49	Yes	2	2
CS36-13 Bag5SampleA	7594.7	7594.2	1778	1414	36.95	16.44	12.63	0.34	Yes	2	2
CS36-13 Bag5SampleE	7594.7	7594.2	1364	1157	37.29	17.21	23.84	0.64	Yes	2	2
CS36-13 OldBag4SampleC	7612	7611.5	563	476	37.06	17.11	15.40	0.42	No	2	1
CS36-13 OldBag3SampleA	7617	7616.5	931	816	36.97	17.39	12.40	0.34	No	2	1
CS36-13 OldBag3SampleH	7617	7616.5	30287	23864	37	16.62	13.10	0.35	No	2	1
CS36-13 Bag2SampleA	7622.5	7622	616	461	36.7	15.62	24.96	0.68	Yes	2	2
CS36-13 Bag7SampleA	7629.6	7629.1	1193	1001	37.12	16.9	21.70	0.58	Yes	2	2
CS36-13 Bag7SampleC	7629.6	7629.1	1025	895	37.22	17.41	23.53	0.63	Yes	2	2
CS36-13 Bag1SampleB	7640.1	7639.6	1707	1600	37.18	18.05	22.73	0.61	Yes	2	2
CS36-13 Bag6SampleC	7647.4	7646.9	1145	892	36.9	15.72	21.05	0.57	Yes	2	2
CS36-13 Bag6SampleD	7647.4	7646.9	961	953	37.43	18.63	21.08	0.56	Yes	2	2
CS36-13 Bag4SampleF	7654.78	7654.28	1309	1166	37.28	17.7	21.09	0.57	Yes	2	2
CS36-13 Bag1SampleA	7640.1	7639.6	1709	1363	36.92	16.49	22.97	0.62	Yes	2	2
CS36-13	7628.8	7628.3	1584	1227	36.8	16.12	12.20	0.33	No	2	1

Sample	Core Depth	Log Depth	Value Using Sample Height for R	FT Using Half Sample D for R	D (mm)	H (mm)	B (thickness) (mm)	B/D	Orientation	Testing Round	Machining Round
OldBag6SampleA											
CS36-13 OldBag6SampleB	7628.8	7628.3	1650	1556	37.2	18.12	12.30	0.33	No	2	1
CS36-13 OldBag6SampleE	7628.8	7628.3	1684	1449	37.1	17.3	13.30	0.36	No	2	1
CS36-13 OldBag6SampleG	7628.8	7628.3	1772	1679	37.3	18.21	13.30	0.36	No	2	1
CS36-13 OldBag7SampleC	7633.8	7633.3	1229	1014	36.94	16.8	15.15	0.41	No	2	1

Table C-33. Material Received by TerraTek for Testing

Pallet #	Well ID	Box #	Top Core Depth (ft)	Bottom Core Depth (ft)	Approx. Length (ft)	Approx. Diameter (in)	Comments
2	Fidelity	1	7586	7589	3	4	Unpreserved slabbed core sections.
	Cisco	2	7589	7592	3	4	Previously plugged and highly damaged.
	St 36-13	3	7592	7595	3	4	
		4	7595	7598	3	4	Note, core boxes are
		5	7598	7601	3	4	marked with 'Core 1' &
		6	7601	7604	3	4	
		7	7604	7607	3	4	Patara Oil & Gas
		8	7607	7610	3	4	
		9	7610	7613	3	4	
		10	7613	7616	3	4	
		11	7616	7619	3	4	

Pallet #	Well ID	Box #	Top Core Depth (ft)	Bottom Core Depth (ft)	Approx. Length (ft)	Approx. Diameter (in)	Comments
		12	7619	7622	3	4	
		13	7622	7625	3	4	
		14	7625	7628	3	4	
		15	7628	7631	3	4	Unpreserved slabbed core sections.
		16	7631	7634	3	4	Previously plugged and highly damaged.
		17	7634	7637	3	4	
		18	7637	7640	3	4	Note, core boxes are marked with 'Core 2' &
		19	7640	7643	3	4	Patara Oil & Gas
		20	7643	7646	3	4	
		21	7646	7649	3	4	
		22	7649	7652	3	4	
		23	7652	7654.8	2.8	4	

Table C-34. Dynamic Mechanical Properties Determined During Triaxial Compression Testing

Well ID	Lithology	Sample ID Core Depth (ft) Orientation	Axial Stress Difference (psi)	Effective Confining Pressure[1] (psi)	Effective Mean Stress (psi)	As Received Density (g/cm^3)	P-Wave Velocity (ft/s)	S-Wave Velocity (ft/s)	Poisson's Ratio	Young's Modulus (10^6 psi)	Bulk Modulus (10^6 psi)	Shear Modulus (10^6 psi)
Fidelity Cisco State 36-13	dolomite	CSO1-1 7588.8 Vertical	0	2739	2739	2.529	12,668	7929	0.18	5.048	2.612	2.143
			1477	2724	3216	2.53	12,818	7952	0.19	5.119	2.728	2.156
			4837	2739	4351	2.534	13,196	8040	0.2	5.318	3.003	2.207
			7389	2739	5202	2.537	13,404	8087	0.21	5.427	3.161	2.235
			15,144	2724	7772	2.538	13,595	7830	0.25	5.249	3.526	2.097
			8520	2724	5564	2.511	13,206	7698	0.24	4.983	3.228	2.005
		CSO1-2 7588.9 Horizontal	0	3622	3622	2.525	14,167	8502	0.22	5.993	3.55	2.459
			2217	3607	4346	2.526	14,241	8511	0.22	6.027	3.616	2.465
			4317	3607	5046	2.527	14,347	8534	0.23	6.083	3.703	2.48
			10,456	3593	7078	2.532	14,566	8536	0.24	6.156	3.924	2.485
			15,302	3607	8708	2.53	14,540	8349	0.25	5.959	4.039	2.376
			9680	3607	6834	2.457	14,107	8153	0.25	5.498	3.655	2.2
	shale	CSO2-1 7593 Vertical	0	2732	2732	2.349	11,368	7074	0.18	3.75	1.978	1.584
			665	2732	2954	2.349	11,480	7075	0.19	3.783	2.059	1.585
			2030	2732	3409	2.351	11,607	7119	0.2	3.847	2.127	1.605
			6833	2732	5010	2.357	11,901	7240	0.21	4.017	2.278	1.665
			10,088	2732	6095	2.352	11,833	7026	0.23	3.841	2.351	1.564
			8567	2733	5589	2.227	11,282	6629	0.24	3.261	2.062	1.319
		CSO2-2 7592.9 Horizontal	0	3606	3606	2.393	12,039	7481	0.19	4.279	2.268	1.805
			4579	3609	5135	2.397	12,340	7483	0.21	4.374	2.507	1.809
			7522	3610	6117	2.4	12,582	7564	0.22	4.504	2.653	1.851
			10,619	3608	7148	2.401	12,843	7588	0.23	4.59	2.852	1.863
			12,286	3607	7702	2.346	12,529	7330	0.24	4.211	2.698	1.698
			11,047	3608	7290	2.253	12,234	7151	0.24	3.852	2.473	1.552

[1]For all tests, pore pressure drained to atmosphere.

Well ID	Lithology	Sample ID Core Depth (ft)	Axial Stress	Effective Confining	Effective Mean	As Received	P-Wave Velocity	S-Wave Velocity	Poisson's Ratio	Young's Modulus	Bulk Modulus	Shear Modulus

		Orientation	Difference (psi)	Pressure[1] (psi)	Stress (psi)	Density (g/cm^3)	(ft/s)	(ft/s)		(10^6 psi)	(10^6 psi)	(10^6 psi)
Fidelity Cisco State 36-13		CSO3-1 7599.75 Vertical	329	2735	2845	2.596	12,105	7782	0.15	4.863	2.302	2.118
			4321	2736	4176	2.602	12,935	7927	0.2	5.284	2.928	2.203
			6528	2736	4912	2.605	13,239	7986	0.21	5.436	3.167	2.239
			11,592	2736	6600	2.61	13,836	8031	0.25	5.652	3.709	2.268
			17,139	2736	8449	2.583	13,845	7566	0.29	5.128	4.014	1.992
			12,049	2736	6752	2.54	13,228	7205	0.29	4.58	3.619	1.777
		CSO3-2 7599.85 Horizontal	677	3609	3835	2.563	14,119	8541	0.21	6.105	3.525	2.52
			7680	3610	6170	2.567	14,587	8580	0.24	6.293	3.966	2.547
			9519	3610	6783	2.568	14,688	8598	0.24	6.341	4.055	2.558
			14,038	3610	8289	2.57	14,814	8537	0.25	6.316	4.235	2.524
			19,614	3610	10,148	2.555	14,577	8208	0.27	5.883	4.224	2.32
	shale		16,324	3610	9051	2.504	14,304	7945	0.28	5.44	4.065	2.13
	silty dolomite	CSO4-4 7605.65 Vertical	0	2739	2739	2.579	14,604	8236	0.27	5.971	4.268	2.357
			3284	2738	3833	2.582	16,244	8371	0.32	6.431	5.929	2.437
			5896	2738	4703	2.585	16,251	8455	0.31	6.546	5.878	2.49
			10,596	2738	6270	2.59	16,595	8542	0.32	6.721	6.217	2.546
			16,911	2738	8375	2.586	16,697	8267	0.34	6.371	6.54	2.382
			10,289	2738	6168	2.549	15,498	7961	0.32	5.75	5.348	2.177
		CSO4-2 7605.65 Horizontal	0	3613	3613	2.556	14,386	8690	0.21	6.309	3.66	2.601
			8932	3613	6590	2.562	14,479	8705	0.22	6.367	3.75	2.616
			14,897	3613	8579	2.565	14,835	8710	0.24	6.487	4.11	2.622
			18,218	3613	9686	2.565	14,918	8676	0.24	6.474	4.222	2.601
			13,733	3611	8189	2.56	14,874	8260	0.28	6.011	4.494	2.353
			13,377	3613	8072	2.574	14,526	8300	0.26	6.011	4.133	2.39

[1]For all tests, pore pressure drained to atmosphere

Well ID	Lithology	Sample ID Core Depth (ft) Orientation	Axial Stress Difference (psi)	Effective Confining Pressure1 (psi)	Effective Mean Stress (psi)	As Received Density (g/cm3)	P-Wave Velocity (ft/s)	S-Wave Velocity (ft/s)	Poisson's Ratio	Young's Modulus (10^6 psi)	Bulk Modulus (10^6 psi)	Shear Modulus (10^6 psi)
Fidelity Cisco State 36-13	silty dolomite	CSO5-1 7615.4 Vertical	0	2742	2742	2.49	11,355	7264	0.15	4.085	1.965	1.771
			1834	2743	3354	2.492	11,575	7322	0.17	4.2	2.099	1.8
			4066	2744	4099	2.494	11,782	7350	0.18	4.29	2.245	1.815
			8643	2742	5623	2.497	12,332	7371	0.22	4.469	2.68	1.828
			11,653	2744	6628	2.446	12,060	6922	0.25	3.962	2.688	1.579
			10,185	2742	6137	2.291	11,574	6544	0.27	3.345	2.373	1.322
		CSO5-2 7615.25 Horizontal	0	3617	3617	2.528	13,648	8201	0.22	5.577	3.29	2.29
			2835	3617	4562	2.529	13,831	8261	0.22	5.687	3.418	2.326
			6442	3616	5763	2.532	14,196	8281	0.24	5.812	3.756	2.339
			11,427	3616	7425	2.536	14,335	8175	0.26	5.751	3.977	2.284
			15,461	3615	8769	2.533	13,980	7820	0.27	5.312	3.888	2.088
			13,334	3618	8063	2.498	14,002	7694	0.28	5.116	3.943	1.993
		CSO6-1 7627.3 Vertical	0	2739	2739	2.974	19,782	10,536	0.3	11.584	9.752	4.449
			6414	2739	4877	2.975	19,951	10,592	0.3	11.728	9.962	4.498
			14,225	2739	7481	2.976	19,982	10,570	0.31	11.699	10.038	4.48
			19,454	2754	9239	2.975	19,721	10,386	0.31	11.312	9.824	4.324
			20,745	2739	9654	2.962	18,925	9852	0.31	10.182	9.129	3.874
			13,450	2739	7222	2.78	16,405	9922	0.21	8.936	5.164	3.688
		CSO6-2 7627.1 Horizontal	0	3637	3637	2.947	19,700	10,732	0.29	11.789	9.312	4.573
			6044	3622	5637	2.948	19,881	10,804	0.29	11.965	9.518	4.636
			14,644	3622	8503	2.949	19,937	10,811	0.29	11.996	9.6	4.644
			21,330	3622	10,732	2.949	19,829	10,737	0.29	11.842	9.515	4.581
			25,090	3622	11,985	2.934	18,802	10,040	0.3	10.365	8.663	3.985
	anhydrite		15,968	3622	8945	2.844	17,621	8937	0.33	8.121	7.818	3.06

[1]For all tests, pore pressure drained to atmosphere

Table C-35. Summary of Indirect Tensile Strength Tests (Brazilian Method) - Horizontal Samples

Well ID	Lithology	Sample #	Core Depth (ft)	Orientation	Average Length (in)	Average Diameter (in)	Mass (g)	Dry Bulk Density (g/cm^3)	Maximum Load (lb_f)	Tensile Strength[1] (psi)
Fidelity Cisco State 36-13	dolomite	CSO1_3A	7589.4	Perpendicular	0.494	0.996	16.52	2.619	1550	2005
		CSO1_3B	7589.4	Parallel	0.505	0.996	17.089	2.655	1190	1508
	shale	CSO2_3A	7592.9	Perpendicular	0.514	0.992	15.526	2.388	312	390
		CSO2_3B	7592.9	Parallel	0.517	0.994	15.701	2.385	300	371
	shale	CSO3_3B	7599.85	Perpendicular	0.534	0.995	17.633	2.594	453	543
		CSO3_3C	7599.85	Parallel	0.519	0.995	17.064	2.583	298	368
	silty dolomite	CSO4_3A	7605.3	Perpendicular	0.516	0.996	17.424	2.645	1390	1721
		CSO4_3B	7605.3	Parallel	0.512	0.996	17.224	2.639	1430	1787
	silty dolomite	CSO5_3A	7615.25	Perpendicular	0.526	0.995	16.828	2.513	249	303
		CSO5_3B	7615.25	Parallel	0.523	0.995	16.839	2.532	449	550
	anhydrite	CSO6_3A	7627.1	Perpendicular	0.517	0.959	17.925	2.933	921	1184
		CSO6_3B	7627.1	Parallel	0.471	0.959	16.376	2.939	640	902

[1] Equation for Tensile Strength in psi is: (2 * Load in lbf) / (pi * diameter in " * length in ")

Table C-36. Summary of Triaxial Compression Tests (for all tests, pore pressure drained to atmosphere)

Well ID	Lithology	Sample ID	Core Depth (ft)	Orientation	As Received Bulk Density (g/cm^3)	Confining Pressure (psi)	Peak Effective Compressive Strength[1] (psi)	Effective Residual Compressive Strength (psi)	Young's Modulus (psi)	Poisson's Ratio
Fidelity Cisco State 36-13	dolomite	CSO1-1	7588.8	Vertical	2.512	2732	18,014	11,332	1,338,000	0.19
		CSO1-2	7588.9	Horizontal	2.503	3605	19,081	14,105	1,782,000	0.25
	shale	CSO2-1	7593	Vertical	2.327	2733	12,833	11,298	1,356,000	0.22
		CSO2-2	7592.9	Horizontal	2.364	3607	15,912	14,647	1,763,000	0.24
	shale	CSO3-1	7599.75	Vertical	2.582	2736	19,880	14,736	1,104,000	0.17
		CSO3-2	7599.85	Horizontal	2.537	3610	23,329	19,880	2,037,000	0.27
	silty dolomite	CSO4-4	7605.65	Vertical	2.564	2738	19,646	13,002	1,282,000	0.18
		CSO4-2	7605.65	Horizontal	2.534	3613	22,643	17,113	1,985,000	0.25
	silty dolomite	CSO5-1	7615.4	Vertical	2.464	2742	14,412	12,942	1,094,000	0.27
		CSO5-2	7615.25	Horizontal	2.511	3617	19,097	17,017	1,755,000	0.23
	anhydrite	CSO6-1	7627.3	Vertical	2.944	2746	23,662	16,346	8,081,000	0.34
		CSO6-2	7627.1	Horizontal	2.937	3623	28,796	19,423	8,780,000	0.33

Table C-37. Dynamic versus Quasi-Static Mechanical Properties Determined During Triaxial Compression Testing

Well ID	Lithology	Sample ID	Core Depth (ft)	Orientation	Effective Confining Pressure (psi)	Static Poisson's Ratio	Dynamic Poisson's Ratio	Static Young's Modulus (psi)	Dynamic Young's Modulus (psi)	Dynamic / Static Young's Modulus	Dynamic / Static Poisson's Ratio
Fidelity Cane Creek 26-3	shale	FDY3-1	7413	Vertical	3855	0.23	0.24	706,400	1,836,000	2.6	1.04
		FDY3-2	7413.05	Horizontal	4040	0.25	0.23	1,128,000	2,634,000	2.34	0.92
	shale	FDY2-1	7417.75	Vertical	3857	0.24	0.24	1,119,000	4,019,000	3.59	1
	shale	FDY2-2	7417.85	Horizontal	4043	0.3	0.23	2,074,000	5,817,000	2.8	0.77
	shale	FDY1-2	7464.3	Horizontal	4068	0.22	0.21	1,571,000	4,531,000	2.88	0.95
	silty dolomite	FDY1-1	7464.5	Vertical	3882	0.23	0.25	3,276,000	7,925,000	2.42	1.09
		FDY1-4	7464.5	Vertical	3881	0.18	0.25	3,620,000	7,847,000	2.17	1.39
									Average:	2.69	1.02

Table C-38. Summary of Continuous Surface Thermal Conductivity Values

Well ID	Core Depth Range (ft)	Low W/m °K	High W/m °K	Average W/m °K
Fidelity Cisco State 36-13	7602.60 - 7605.24	1.9	4.7	3.6
	7605.83 - 7608.97	1	2.7	1.7
	7611.70 - 7614.54	2	4.4	3.3
	7614.70 - 7617.65	1.7	4.3	2.75
	7617.65 - 7620.08	1.7	4.75	2.75

Triaxial Compression Test Plots – Fidelity Cisco State 36-13

Fidelity Cisco State 36-13									
Lithology	Sample ID	Depth (ft)	Orientation	As Received Bulk Density (g/cm^3)	Confining Pressure (psi)	Peak Effective Compressive Strength (psi)	Effective Residual Compressive Strength (psi)	Young's Modulus (10^6 psi)	Poisson's Ratio
anhydrite	CSO6-1	7627.30	Vertical	2.944	2746	23,662	16,346	8.081	0.34
	CSO6-2	7627.10	Horizontal	2.937	3623	28,796	19,423	8.780	0.33

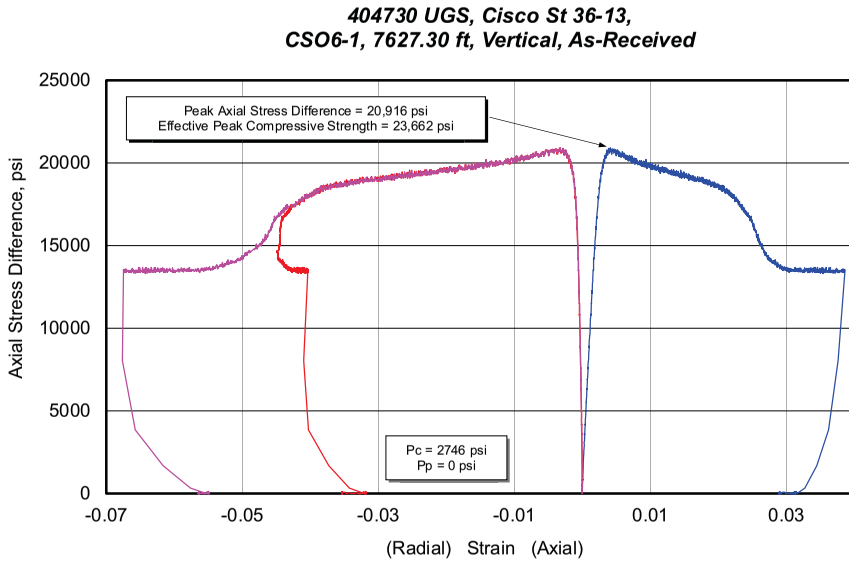

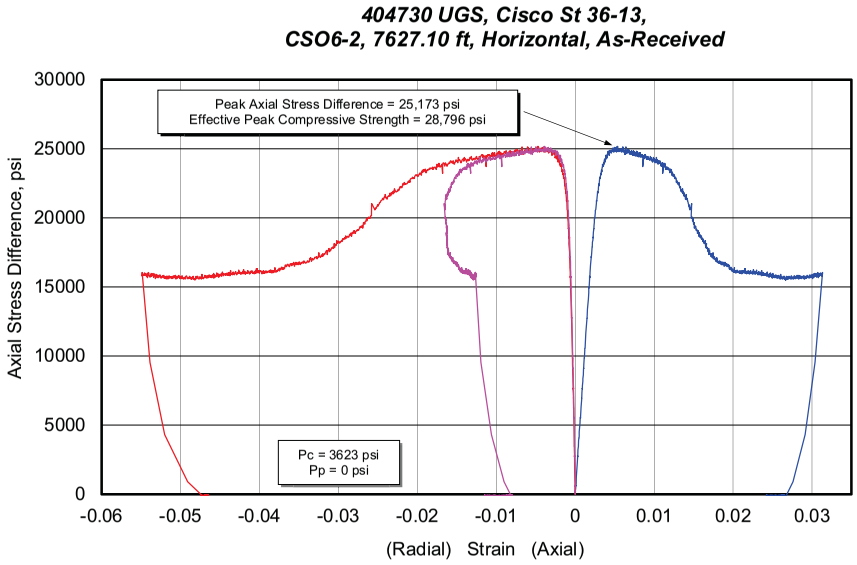

Fidelity Cisco State 36-13

Lithology	Sample ID	Depth (ft)	Orientation	As Received Bulk Density (g/cm^3)	Confining Pressure (psi)	Peak Effective Compressive Strength (psi)	Effective Residual Compressive Strength (psi)	Young's Modulus (10^6 psi)	Poisson's Ratio
silty dolomite	CSO5-1	7615.40	Vertical	2.464	2742	14,412	12,942	1.094	0.27
	CSO5-2	7615.25	Horizontal	2.511	3617	19,097	17,017	1.755	0.23

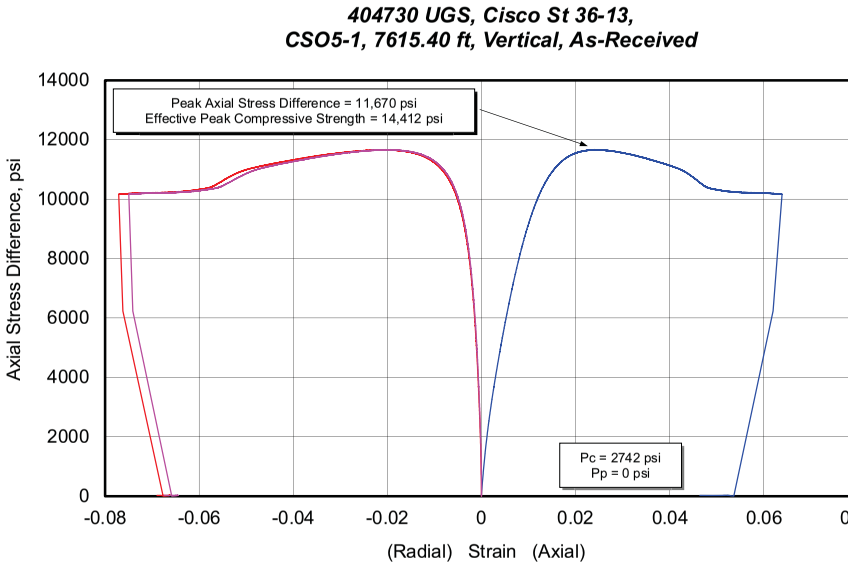

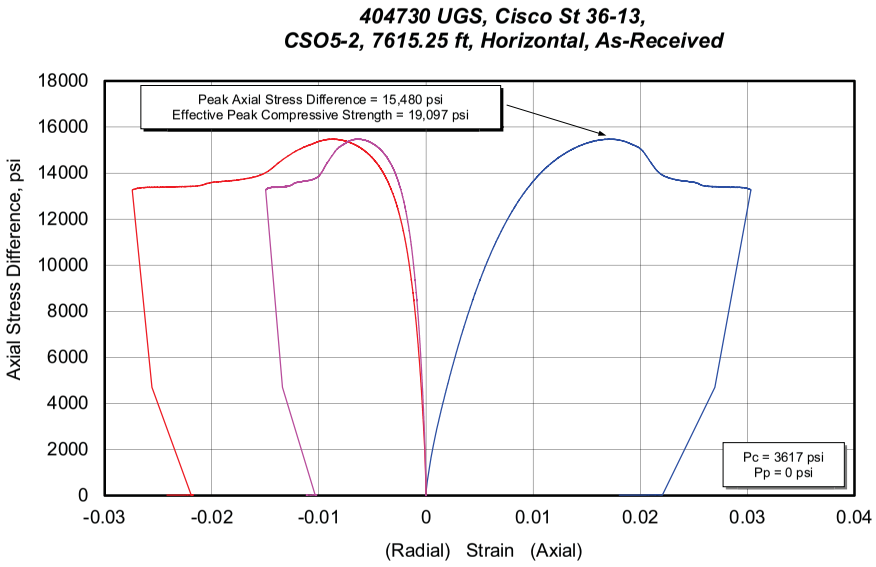

Fidelity Cisco State 36-13

Lithology	Sample ID	Depth (ft)	Orientation	As Received Bulk Density (g/cm^3)	Confining Pressure (psi)	Peak Effective Compressive Strength (psi)	Effective Residual Compressive Strength (psi)	Young's Modulus (10^6 psi)	Poisson's Ratio
silty dolomite	CSO4-1	7605.35	Vertical	2.636	2738	35340	20120	5.071	
	CSO4-4	7605.65	Vertical	2.564	2738	19,646	13,002	1.282	0.18
	CSO4-2	7605.65	Horizontal	2.534	3613	22,643	17,113	1.985	0.25

404730 UGS, Cisco St 36-13,
CSO4-1, 7605.35 ft, Vertical, As-Received

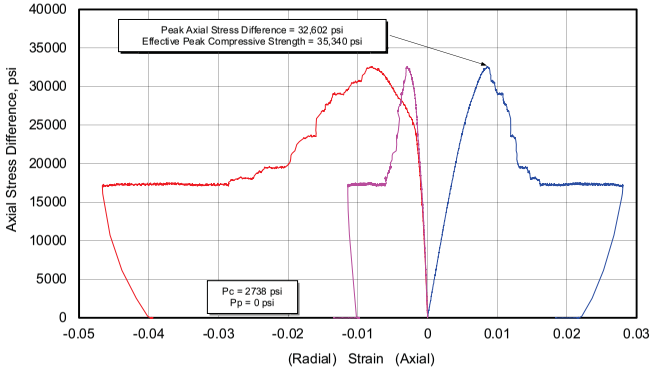

Not reported

404730 UGS, Cisco St 36-13,
CSO4-4, 7605.65 ft, Vertical, As-Received

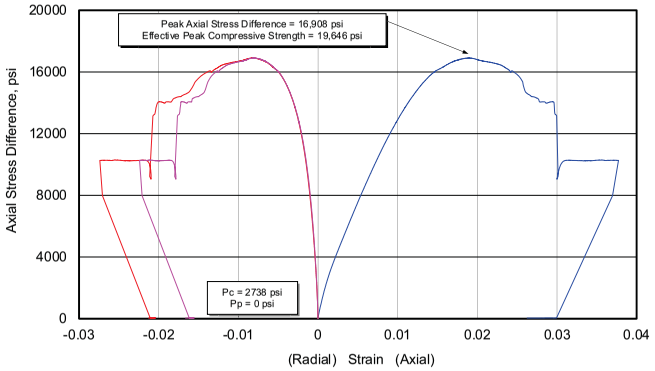

404730 UGS, Cisco St 36-13,
CSO4-2, 7605.65 ft, Horizontal, As-Received

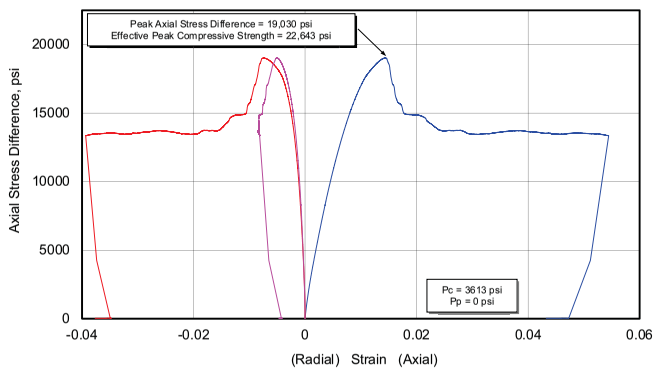

Fidelity Cisco State 36-13

Lithology	Sample ID	Depth (ft)	Orientation	As Received Bulk Density (g/cm^3)	Confining Pressure (psi)	Peak Effective Compressive Strength (psi)	Effective Residual Compressive Strength (psi)	Young's Modulus (10^6 psi)	Poisson's Ratio
shale	CSO3-1	7599.75	Vertical	2.582	2736	19,880	14,736	1.104	0.17
	CSO3-2	7599.85	Horizontal	2.537	3610	23,329	19,880	2.037	0.27

404730 UGS, Cisco St 36-13, CSO3-1, 7599.75 ft, Vertical, As-Received

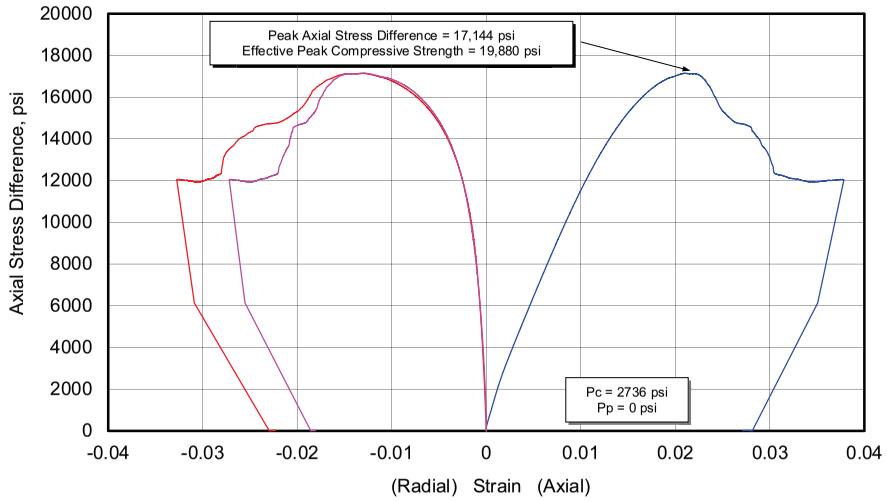

404730 UGS, Cisco St 36-13, CSO3-2, 7599.85 ft, Horizontal, As-Received

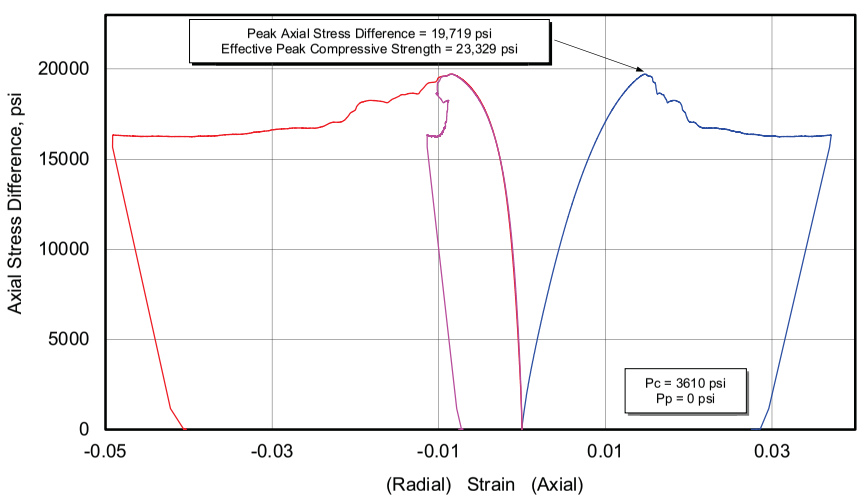

Fidelity Cisco State 36-13

Lithology	Sample ID	Depth (ft)	Orientation	As Received Bulk Density (g/cm^3)	Confining Pressure (psi)	Peak Effective Compressive Strength (psi)	Effective Residual Compressive Strength (psi)	Young's Modulus (10^6 psi)	Poisson's Ratio
shale	CSO2-1	7593.00	Vertical	2.327	2733	12,833	11,298	1.356	0.22
	CSO2-2	7592.90	Horizontal	2.364	3607	15,912	14,647	1.763	0.24

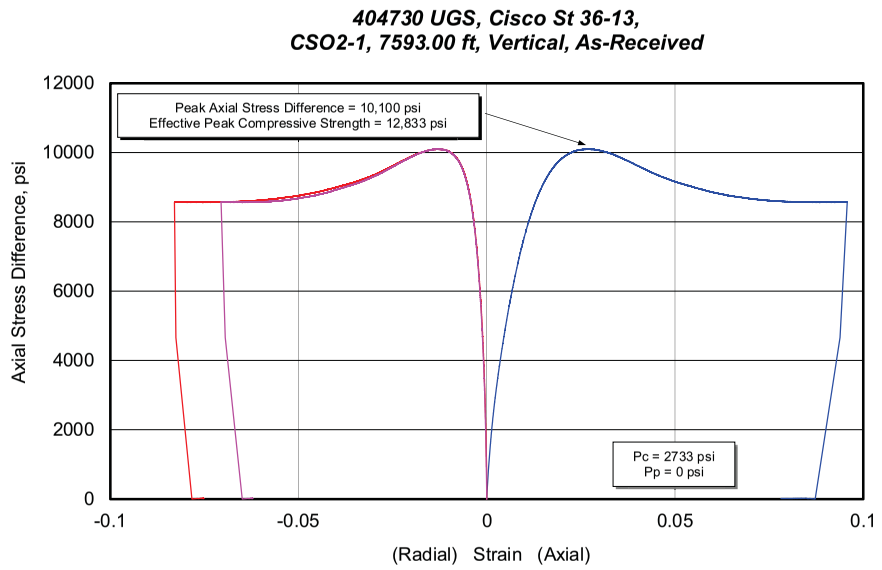

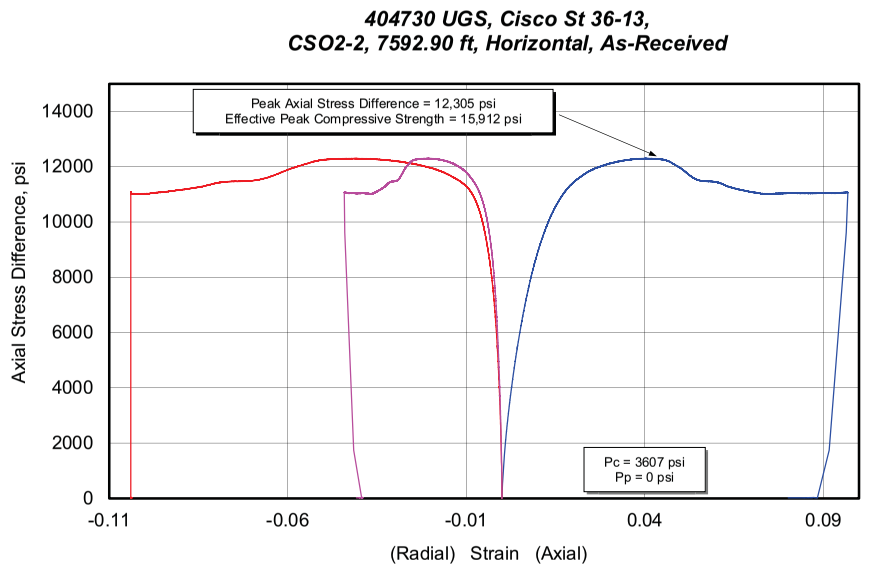

Fidelity Cisco State 36-13

Lithology	Sample ID	Depth (ft)	Orientation	As Received Bulk Density (g/cm^3)	Confining Pressure (psi)	Peak Effective Compressive Strength (psi)	Effective Residual Compressive Strength (psi)	Young's Modulus (10^6 psi)	Poisson's Ratio
dolomite	CSO1-1	7588.80	Vertical	2.512	2732	18,014	11,332	1.338	0.19
	CSO1-2	7588.90	Horizontal	2.503	3605	19,081	14,105	1.782	0.25

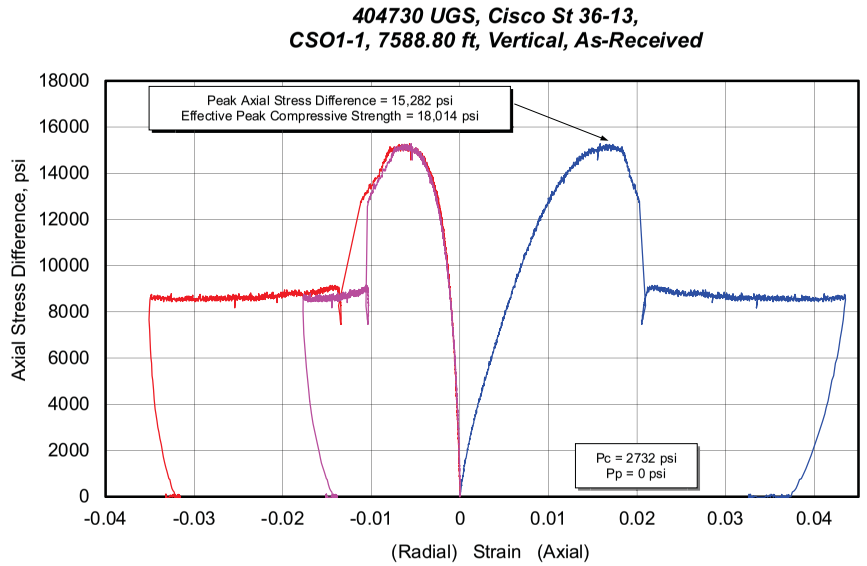

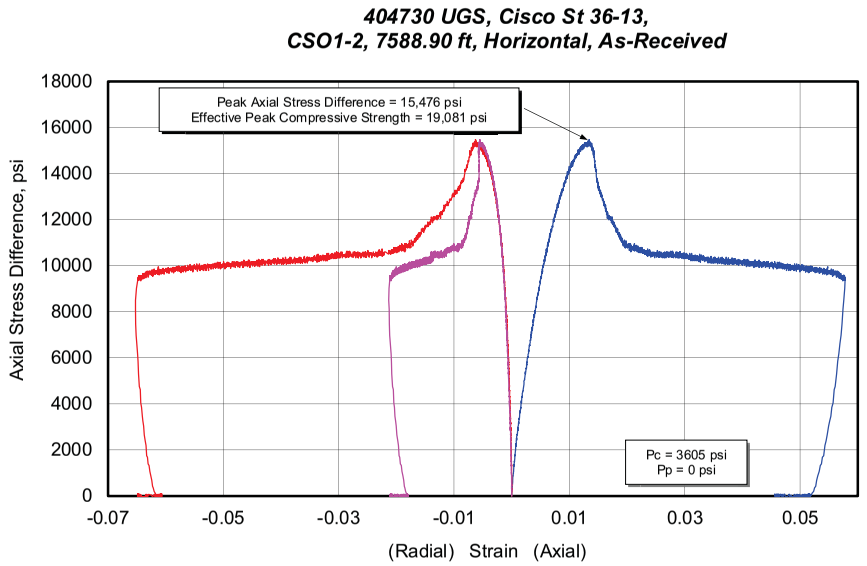

Fidelity Cane Creek 26-3

This well was drilled NE-SW, Section 26, T25S, R19E. TD was at 7570 feet. The target zone was reached with OBM. The well penetrated multiple black shales before entering Cane Creek Shale at 7388 ft±. Anhydrite predominates near top. Black shale and light to medium gray dolomite predominate in the middle Cane Creek with anhydrite and dolomite (some black shales) below. The mud weight was 15.5 lbm/gal throughout. If this was required strictly to subdue formation pressure that would correspond to 0.81 psi/ft. However, as shown in the daily drilling synopsis, Figure C-19, the rational for the OBM and the elevated mud weight are more likely to control the Paradox salt. During coring, the hole was taking mud 25 bbl in 4 hours to 50 bbl in 8 hours).

DAY	DATE 2012	DEPTH 06:00 HRS	24 HR FOOTAGE	BIT #	24 HR ACTIVITY	FORMATION
14	5-Oct	4831	400	6/7	Drill f/ 4,831' to 4,892' Circulate, build and pump slug. TOOH. Lay down Motor / bit. PU new bit / Motor. TIH Drill f/ 4,892' to 5,231'	Paradox Salt Section
15	6-Oct	5231	1531	7	Drill f/ 5,231' to 5,888' Rig service. Drill f/ 5,888' to 6762	Paradox Salt Section
16	7-Oct	6762	626	7	Drill f/ 6,762' to 7,388' Circulate, pump slug, TOOH, LD Directional tools. PU Core tools TIH w/ Core tools	Paradox Salt Section Cane Creek
17	8-Oct	7388	85	8	TIH w/ Core tools. Wash and ream to bottom. Circulate, Drop ball. Start to core Core # 1 7,388' to 7,473' Full recovery, Circulate, Pull 1 stand, 1/2Hr flow check, no flow, Circulate bottoms up, Pump slug, TOOH w/ Core # 1	Cane Creek
18	9-Oct	7473	0	RR7	TOOH w/ Core # 1. LD core, Full recovery. Slip and cut drilling line, Wait on welder, Weld on rig, Racking board, PU bit/ bit sub/float, TIH	Cane Creek
19	10-Oct	7473	97	RR7	TIH drill f/ 7,473' to 7,570' Circulate, TOOH for logs. PJSM w/ Schlumberger, Rig up loggers. run logs Run Triple combo.	Cane Creek
20	11-Oct	7570	0		Logging w/ Schlumberger Run Triple Combo, OBMI, CMR	Cane Creek
21	12-Oct	7570	0	RR7	Run CMR log, Pull tool to clean iron filings from magnetic tool. Run CMR, Safety shut down trapped pressure, Run CMR. Rig down Loggers, PU bit, TIH Circulate, Lay down 4 1/2" Drill pipe.	Cane Creek
22	13-Oct	7570	0		Lay down 4 1/2" Drill pipe, PJSM w/ Casers. Rig up casers. Run 7" HCP-110	Cane Creek
23	14-Oct	7570	0		Run 178 joints HCP-110 7" casing set at 7,568', PJSM w/ cementers, rig up cementers, test lines. Cement. Geologists released.	Cane Creek

Figure C-19. Summary of drilling events for Cane Creek Unit 26-3.

"The upper one third of the Cane Creek Shale is composed of alternating thin beds of anhydrite, black shale and dolomite. Anhydrite tends to predominate towards the top of the interval. Black, radioactive, carbonaceous, sooty shale and light to medium gray, argillaceous dolomite are the predominate lithology in the middle of the Cane Creek and this is the principal productive interval; in the shale. The lower one third of the Cane Creek is dominated by anhydrite and dolomite with some thin black shales.

The entire Cane Creek Shale was cored in this well with 100% recovery. Cuttings samples were taken every 10 feet while coring and a microscopic description is detailed on the mud log. Drilling mud weight was a consistent 15.5 lb/gal throughout. Background gas averaged 50 units while coring, with periodic increases peaking every 5 to 10 feet from 100 to 138 units in the interval. The hole was taking mud while coring with losses of 25 bbls in 4 hours to 50 bbls in 8 hours being recorded. The core was encapsulated in an aluminum core barrel and after being brought to the surface was cut into 3-foot lengths, with the ends capped to prevent any loss of contained fluid and to preserve the core for detailed laboratory analysis. While cutting the core into sections with a diamond saw, small chips and pieces were salvaged from the cut ends and are described in detail on Core Log #1.

After coring, the well was drilled to total depth of 7570' (driller) 7567' (e logger) in Salt #23. Electric logs were run prior to running and cementing 7-inch casing at TD. A completion attempt will be made in the Cane Creek Shale based on hydrocarbon shows in this hole as well as in the offsetting twin 26-2 well."

Figures 20 and 21 show the well trajectory.

The early production data are shown in Figure C-22 - disappointing. The next step was to mill a window in the 7-inch casing to drill a 6-inch SE trending horizontal lateral. The whipstock was set at 6474 ft into Paradox Formation Salt #12 and the build was 10°/100 feet. The hole bottomed in Clastic #22, below the Cane Creek Shale (encountered at 7884 ft md, 7251 TVD). Tops are shown in Figure C-23.

This sets the top shot @7396 ft.

- ROOH w/ wireline, RD &release. MI & NU all flowback equip & tanks.
- Set the packer @7256', the elements are @7259'. Release L-10 from packer.
- Drop the firing bar to fire the guns.
- The bar fired the guns in 4 min 42 sec.
- The well went on a strong vacuum immediately.
- Tubing on a pulsing vac.

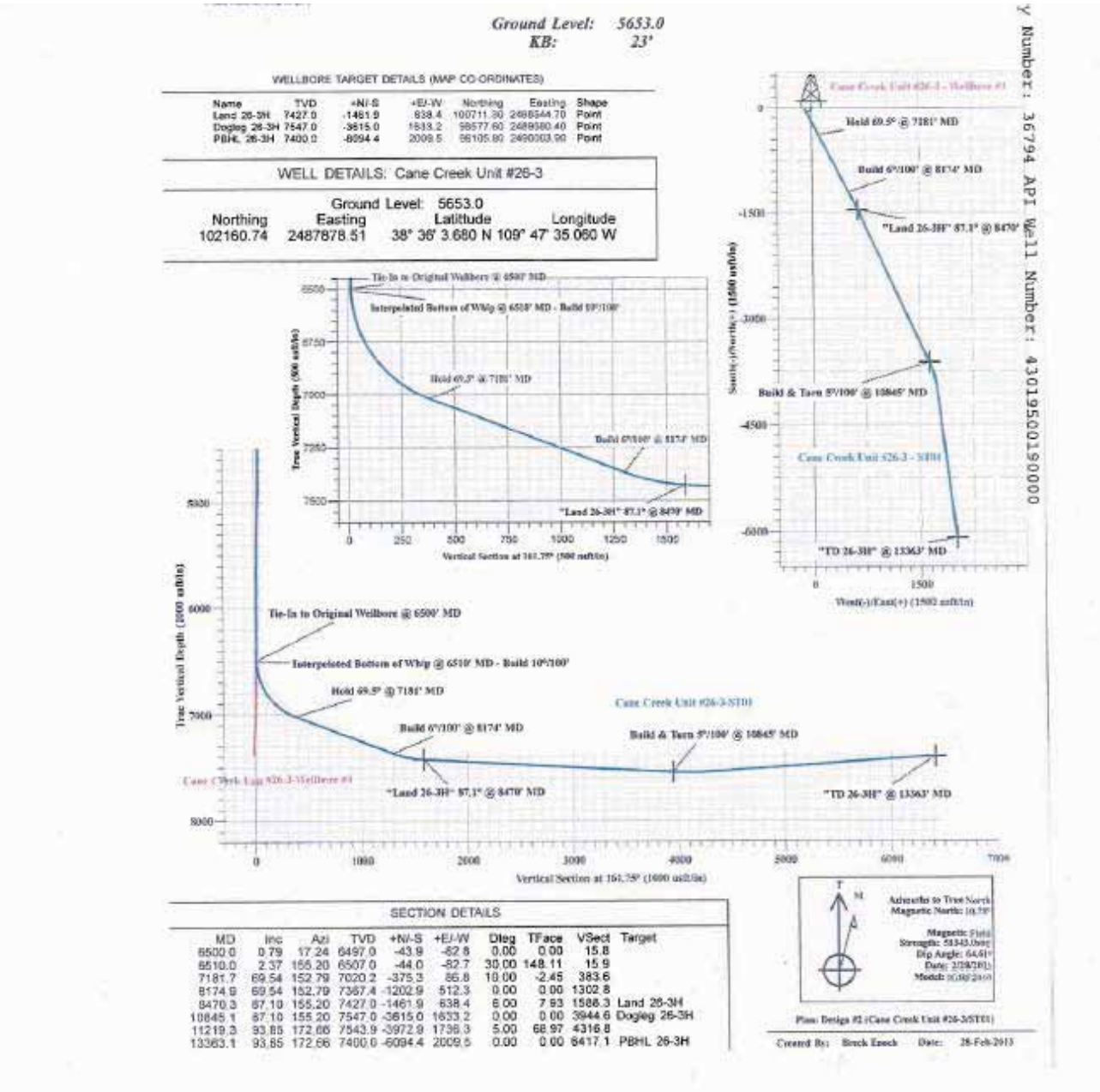

Figure C-20. Wellbore target details??

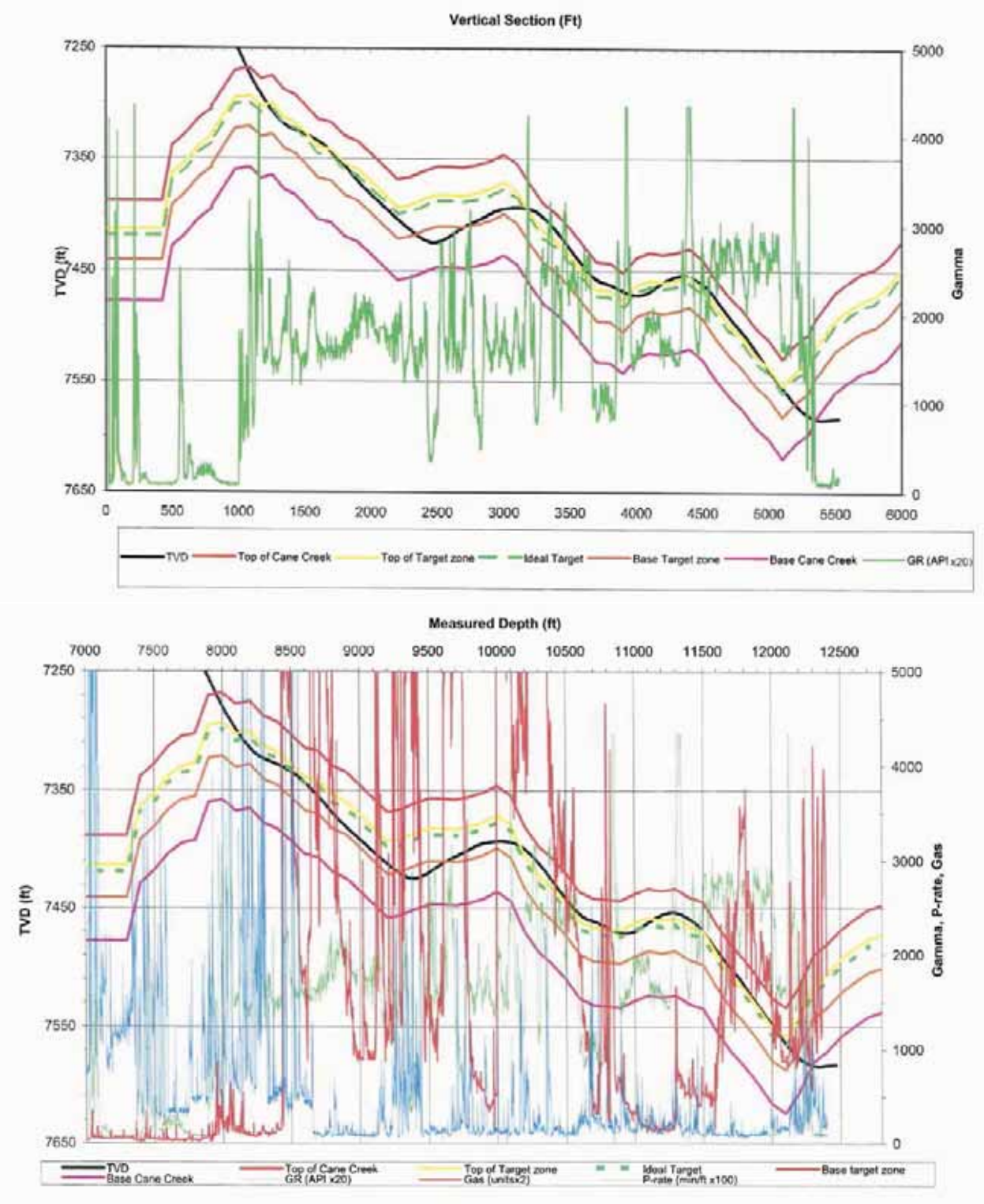

Figure C-21. Tops, target zones?

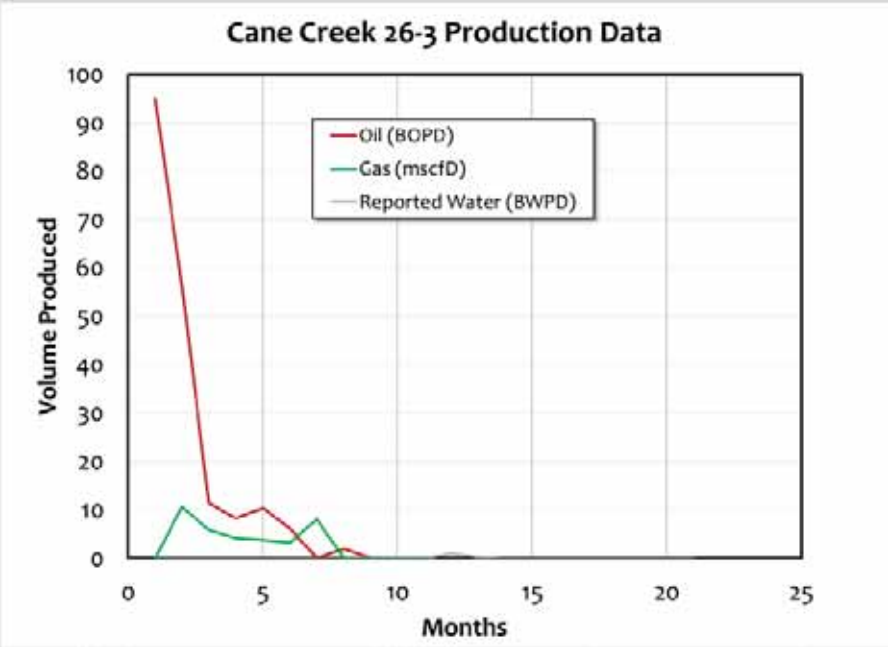

Figure C-22. Summary of early production for Cane Creek Unit 26-3.

SALT TOPS
FIDELITY EXPLORATION AND PRODUCTION
CANE CREEK UNIT 26-3H

FIDELITY E&P CANE CREEK 26-3H SALT TOPS
KB: 5,675'

	CCU 26-3 PILOT HOLE SALT TOPS		CCU 26-3H CURVE SALT TOPS		
	MD	SUB SEA	MD	TVD	SUB SEA
CLASTIC # 15	6,506'	-831'	6,506'	6,503'	-828'
SALT # 16	6,515'	-840'	6,516'	6,513'	-838'
CLASTIC # 16	6,544'	-869'	6,546'	6,543'	-868'
SALT # 17	6,568'	-893'	6,572'	6,568'	-893'
CLASTIC # 17	6,703'	-1,028'	6,708'	6,702'	-1,027'
SALT # 18	6,712'	-1,037'	6,715'	6,709'	-1,034'
CLASTIC # 18/19	6,974'	-1,299'	7,022'	6,969'	-1,294'
SALT # 20	7,022'	-1,347'	7,088'	7,012'	-1,337'
CLASTIC # 20	7,150'	-1,475	7,413'	7,144'	-1,469'
SALT # 21	7,160'	-1,485'	7,459'	7,155'	-1,480'
CANE CREEK TOP	7,382'	-1,707'	7,884'	7,251'	-1,576'
TARGET DOLOMITE	7,424'	-1,749'	8,194'	7,313'	-1,638'
BASE CANE CREEK	7,468'	-1,973'	12,293'	7,583'	-1,908'

DRILLED 4409' OF CANE CREEK IN THE LATERAL

Figure C-23. Summary of tops for Cane Creek Unit 26-3 (before whipstock)

Significant drilling events were as follows.

- While drilling from 7886-8136 ft MD there were gas increases with black shales in a (7970 ft) and B (8046 ft) zones with a mud weight of 14.4 ppg and an ECD of 16.4 ppg.
- The second target was a dolomite (8080 ft).
- Fractures were encountered at 8435 ft ("motor stalled – fractures – 25 bbl mud increase and wellhead pressure increased to 1770 psi. High gas units and 15 ft flare (at least 0.52 psi/ft). Mud weight was 14.5 to 14.7 ppg).
- There was fractured dolomite at 8560 feet and the mud weight was 15.4 ppg and the driller circulated out a kick (15.55 ppg, ECD 18 ppg).
- From 9070-9137 ft MD 111 bbl mud were lost –LCM sweeps – fractured B dolomite.
- From 9100-9450 ft and 9600-9810 ft there were numerous motor stalls and pressure spikes – indicating fracturing caused by changes in dip. The mud weight was generally 15.3 ppg (ECDs 17.8-17.9 ppg).
- AT 11350 ft MD, they drilled through the top of the B "hot" shale into dolomite. Gas was encountered at the top of the B zone, the mud weight was increased to 15.3 ppg and the ECD varied from 18.2 to 18.5.
- From 11297-11304 ft there was a gas increase, a motor stall and a pressure spike
- 10916 –11322 ft – lost 25 bbl mud (15.3 ppg, 18.1 ppg ECD)
- AT ~12,150 ft MD, the dip changed from 9° down to from 8 to 17° upward. The hole inclination was brought up from 81 to 88°to drill through the B zone, the C zone and out the Cane Creek shale into Salt 22 and Clastic 22 at 12,466 ft MD.
- Numerous motor stalls and pressure spikes were experienced from 12220 to 12280 ft MD while drilling the C zone
- The premise was to follow the southerly dipping Cane Creek shale to 12,286 ft MD where the underlying Salt #22 and Clastic #22 were encountered and TD was called at 12,466 ft MD, 7853 ft TVD.

After drilling, a 4-1/2 liner was cemented (20 bbl diesel spacer, 30 bbl tuned spacer, 20 bbl of lead slurry at 19.0 ppg, 90 bbl of tail slurry at 19.0 ppg. This was displaced with 152 bbl (88.5 bbl OBM at 16.5 ppg, 10 bbl of 18.7 ppg tuned spacer and 53.5 bbl of 16.5 ppg OBM. They held backpressure with MPD as needed (30 to 165 psi). The job was pumped at 1.5 to 2.5 bpm.

The sample selection for testing is shown in Table C-39.

Table C-39. Sample Selection for Testing

Top Core Depth (ft MD)	Comments
7406	Finely interbedded dolomite and shale
7418	
7445.2	Already attempted to take a core but did not work – but probably no good from butt but could get a sample from the slab
7469.8	Good sample
7458.1	Good sample
7464.5	Mixture of shale and dolomite but it is a good sample
7413	Organic shale – small chunks but might work
	14.4 ppg mud at 6474 ft. last found mud weight

The stimulation was not documented. Presumably it was just designed to provide a connection to the reservoir and NATURAL fracture cleanout at low rate and **Salt avoidance**. When first tested through 7/64-inch choke, the tubing pressure was 4113 psi and the casing pressure was 1173 psi. Presumably, beyond drilling, some of the geologic issues were the dip variations. Improved production was evident (Figure C-24).

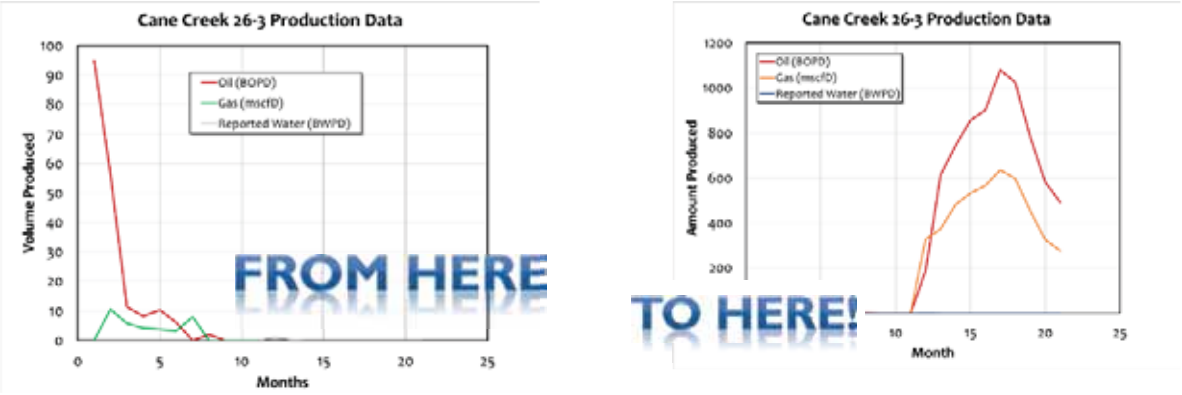

Figure C-24. The production after drilling and stimulating the horizontal well is shown in the right-hand panel.

"Oil is produced from the Cane Creek Shale interval of the Paradox Formation at six fields within the Paradox Basin. This interval is composed of highly fractured dolomitic siltstone and shale interbedded with halite and other evaporites (Morgan and Chidsey, 1991; Grove and Rawlins, 1997). Morgan and Chidsey (1991) indicate that fracture orientation is related to folding, with the more productive fractures occurring along the crest and flanks of anticlinal structures. Grove and Rawlins

(1997) note that these highly permeable fracture systems also have a complex history that is related to episodic movement of salt within the Paradox Formation. Thus the fractures within the Cane Creek Shale interval are probably similar in initiation and propagation history to those observed within the Entrada Formation at Arches National Park. That is, the fractures are formed during salt flowage and the formation of anticlines and synclines. As observed at Arches National Park these structures have a complex history. Therefore, the fracture patterns on the surface at Arches provide a direct model for the subsurface Cane Creek interval. This in turn may help determine the best orientation for horizontal drilling to intersect the maximum number of these fracture systems."[14]

Table C-40. Brittleness Indices – Cane Creek Unit 26-3

Sample	Orientation	Core Depth	Log Depth	BI1	BI2	BI3a	BI3b	BI4	BI5
FDY1-1	Vertical	7464.5	7459.5	0.39	0.31	1.49E-02	-6.78E-02	1.98	0.29
FDY1-2	Horizontal	7464.3	7459.3	1.22	0.39	2.42E-04	-5.46E-04	1.23	0.34
FDY1-4	Vertical	7464.3	7459.3	0.36	0.64	1.80E-02	-1.80E-01	6.98	0.52
FDY2-1	Vertical	7417.75	7412.75	1.30	0.69	1.33E-03	-5.69E-03	1.33	0.11
FDY2-2	Horizontal	7417.85	7412.85	0.76	0.15	3.38E-03	-6.79E-03	1.51	0.14
FDY3-1	Vertical	7413	7408	6.83	1.00	4.02E-10	-2.81E-09	1.00	8.90E-03
FDY3-2	Horizontal	7413.05	7408.05	6.53	1.12	2.35E-06	-8.50E-06	1.02	5.77E-03

[14] Lorenz, J.C. and Cooper S.P. 2001Interpreting Fracture Patterns in Sandstones Interbedded with Ductile Strata at the Salt Valley Anticline, Arches National Park, Utah, November 1, 2001, Utah State University.

Table C-41. Fracture Toughness - Cane Creek Unit 26-3

Sample	Core Depth	Log Depth	FT Using Sample Height for R	FT Using Half Sample D for R	D (mm)	H (mm)	B (thickness) (mm)	B/D	Orientation	Testing Round	Machining Round
CCU26-3 Bag2SampleA	7469.8	7464.8	1521	1267	37.3	16.7	13.8	0.37	No	1	1
CCU26-3 Bag2SampleC	7469.8	7464.8	795	772	37.3	18.3	14.1	0.38	No	1	1
CCU26-3 Bag3SampleA	7404.8	7399.8	1377	1357	37.4	18.5	15.9	0.43	No	1	1
CCU26-3 Bag3SampleG	7404.8	7399.8	1147	953	37.2	16.6	15.3	0.41	No	1	1
CCU26-3 Bag4SampleA	7469.6	7464.6	1280	1243	37.5	18.4	14.7	0.39	No	1	1
CCU26-3 Bag4SampleF	7469.6	7464.6	559	418	36.9	15.6	13.4	0.36	No	1	1
CCU26-3 Bag5SampleB	7392.6	7387.6	1741	1621	37.2	17.7	14.7	0.40	No	1	1
CCU26-3 Bag5SampleC	7392.6	7387.6	950	760	36.8	16.2	13.6	0.37	No	1	1
CCU26-3 Bag5SampleE	7392.6	7387.6	2033	1812	37.2	17.4	12.8	0.34	No	1	1
CCU26-3 Bag8SampleF	7402.5	7397.5	1410	1268	37.5	17.6	13.2	0.35	No	1	1
CCU26-3 Bag8SampleK	7402.5	7397.5	1870	1689	37.4	17.6	13	0.35	No	1	1
CCU26-3 Bag13SampleA	7389	7384	32	26	37.2	16.9	21.79	0.59	Yes	2	2
CCU26-3 Bag1SampleB	7397.6	7392.6	1597	1347	37.37	17.17	22.4	0.60	Yes	2	2
CCU26-3 Bag10SampleB	7399.1	7394.1	575	462	37.03	16.38	16.24	0.44	Yes	2	2
CCU26-3 OldBag10SampleB	7413.9	7408.9	1037	970	37.46	18.19	15.53	0.41	No	2	1

Sample	Core Depth	Log Depth	FT Using Sample Height for R	FT Using Half Sample D for R	D (mm)	H (mm)	B (thickness) (mm)	B/D	Orientation	Testing Round	Machining Round
CCU26-3 OldBag10SampleH	7413.9	7408.9	1885	1612	37.28	17.35	12.17	0.33	No	2	1
CCU26-3 Bag3SampleA	7433.6	7428.6	725	585	37.16	16.62	20.13	0.54	Yes	2	2
CCU26-3 Bag3SampleE	7433.6	7428.6	713	649	37.15	17.65	7.9	0.21	Yes	2	2
CCU26-3 Bag5SampleE	7465.8	7460.8	779	725	37.41	18.1	21.04	0.56	Yes	2	2
CCU26-3 Bag5SampleB	7465.8	7460.8	308	236	37.05	16.09	19.42	0.52	Yes	2	2

Table C-42. Material Received By TerraTek for Testing

Pallet #	Well ID	Box #	Top Core Depth (ft)	Bottom Core Depth (ft)	Approx. Length (ft)	Approx. Diameter (in)	Comments
1	Fidelity Cane Creek CC 26-3	1	7388	7390.9	2.9	4	Unpreserved slabbed core sections. Previously plugged and highly damaged. Note, core boxes are marked with 'Core 1'
		2	7390.9	7393.9	3	4	
		3	7393.9	7396.9	3	4	
		4	7396.9	7399.9	3	4	
		5	7399.9	7403	3.1	4	
		6	7403	7406	3	4	
		7	7406	7409	3	4	
		8	7409	7411.8	2.8	4	
		9	7411.8	7414.95	3.15	4	
		10	7414.95	7416.85	1.9	4	
		11	7416.85	7419.55	2.7	4	
		12	7419.55	7422	2.45	4	
		13	7422	7425	3	4	
		14	7425	7428	3	4	
		15	7428	7431	3	4	
		16	7431	7434	3	4	
		17	7434	7437	3	4	
		18	7437	7440	3	4	
		19	7440	7443	3	4	
		20	7443	7446	3	4	
		21	7446	7449	3	4	
		22	7449	7452	3	4	
		23	7452	7455.2	3.2	4	
		24	7455.7	7458.25	2.55	4	
		25	7458.25	7461	2.75	4	
		26	7461	7464	3	4	
		27	7464	7467	3	4	
		28	7467	7470	3	4	
		29	7470	7473	3	4	
		30	7473	7474.05	1.05	4	

Table C-43. Dynamic Mechanical Properties Determined During Triaxial Compression Testing

Well ID	Lithology	Sample ID Core Depth (ft) Orientation	Axial Stress Difference (psi)	Effective Confining Pressure[1] (psi)	Effective Mean Stress (psi)	As Received Density (g/cm^3)	P-Wave Velocity (ft/s)	S-Wave Velocity (ft/s)	Poisson's Ratio	Young's Modulus (10^6 psi)	Bulk Modulus (10^6 psi)	Shear Modulus (10^6 psi)
Fidelity Cane Creek 26-3	shale	FDY3-1 7413 Vertical	691	3854	4084	2.091	8,770	5124	0.24	1.836	1.181	0.74
			2745	3854	4769	2.095	8,889	5183	0.24	1.885	1.219	0.759
			4642	3854	5401	2.103	9,201	5250	0.26	1.967	1.358	0.781
			6630	3854	6064	2.111	9,502	5321	0.27	2.048	1.494	0.805
			8515	3854	6692	2.103	9,873	5389	0.29	2.12	1.665	0.823
			9640	3854	7067	2.04	10,041	5335	0.3	2.04	1.728	0.783
		FDY3-2 7413.05 Horizontal	0	4040	4040	2.049	10,482	6238	0.23	2.634	1.601	1.074
			2898	4040	5006	2.053	10,572	6259	0.23	2.666	1.647	1.084
			4183	4038	5432	2.058	10,721	6285	0.24	2.713	1.727	1.095
			6470	4038	6195	2.073	10,912	6347	0.24	2.8	1.826	1.125
			9267	4040	7129	2.097	11,269	6419	0.26	2.934	2.036	1.164
			10,203	4039	7440	2.102	11,387	6375	0.27	2.927	2.138	1.151
	shale	FDY2-1 7417.75 Vertical	0	3862	3862	2.423	11,780	6982	0.23	3.912	2.408	1.591
			4078	3862	5221	2.426	11,971	7025	0.24	3.992	2.534	1.613
			5182	3862	5589	2.427	12,039	7038	0.24	4.019	2.58	1.62
			8234	3847	6592	2.431	12,209	7069	0.25	4.085	2.7	1.637
			13,008	3862	8198	2.434	12,411	7050	0.26	4.113	2.878	1.63
			10,670	3847	7404	2.389	12,079	6732	0.27	3.72	2.752	1.459
		FDY2-2 7417.85 Horizontal	0	4057	4057	2.421	14,201	8476	0.22	5.734	3.454	2.343
			2153	4042	4760	2.422	14,253	8484	0.23	5.758	3.498	2.349
			7004	4042	6377	2.424	14,382	8505	0.23	5.817	3.605	2.363
			8653	4042	6926	2.425	14,420	8510	0.23	5.833	3.639	2.366
			15,931	4042	9352	2.423	14,514	8392	0.25	5.743	3.813	2.299
			11,047	4042	7724	2.389	14,191	8207	0.25	5.416	3.592	2.169

[1]For all tests, pore pressure drained to atmosphere.

Well ID	Lithology	Sample ID Core Depth (ft) Orientation	Axial Stress Difference (psi)	Effective Confining Pressure[1] (psi)	Effective Mean Stress (psi)	As Received Density (g/cm^3)	P-Wave Velocity (ft/s)	S-Wave Velocity (ft/s)	Poisson's Ratio	Young's Modulus (10^6 psi)	Bulk Modulus (10^6 psi)	Shear Modulus (10^6 psi)
Fidelity Cane Creek 26-3	shale	FDY1-2 [2] 7464.3 Horizontal	0	4069	4069	2.357	12,681	7682	0.21	4.536	2.608	1.874
			3337	4069	5181	2.359	12,661	7677	0.21	4.531	2.597	1.873
			4730	4069	5646	2.36	12,823	7675	0.22	4.574	2.732	1.873
			6914	4068	6373	2.363	12,845	7697	0.22	4.603	2.738	1.886
			13,628	4069	8612	2.374	13,103	7550	0.25	4.564	3.062	1.824
			10,435	4069	7547	2.356	12,813	7536	0.24	4.456	2.808	1.803
	silty dolomite	FDY1-1 7464.5 Vertical	0	3877	3877	2.628	14,638	9062	0.19	6.916	3.709	2.908
			8686	3877	6772	2.632	16,242	9389	0.25	7.81	5.187	3.126
			11,985	3877	7872	2.634	16,419	9440	0.25	7.925	5.351	3.162
			15,155	3877	8929	2.635	16,615	9473	0.26	8.024	5.554	3.186
			27,348	3877	12,993	2.639	16,919	9461	0.27	8.1	5.935	3.182
			12,826	3877	8152	2.573	16,041	8789	0.29	6.886	5.351	2.678
		FDY1-4 [3] 7464.5 Vertical	0	3881	3881	2.622	15,000	9068	0.21	7.042	4.076	2.905
			1631	3881	4425	2.623	15,296	9141	0.22	7.218	4.331	2.953
			9057	3881	6900	2.626	16,367	9405	0.25	7.847	5.305	3.13
			15,880	3881	9174	2.629	16,918	9514	0.27	8.137	5.865	3.207
			32,027	3881	14557	2.632	16,963	9294	0.29	7.876	6.121	3.064
			13,041	3881	8228	2.601	14,975	8758	0.24	6.667	4.275	2.688

[1]For all tests, pore pressure drained to atmosphere.
[2] Note – sample ended up being shale lithology (which was not of primary interest for client). Also there is not additional material to pull a vertically oriented sister sample.
[3]FDY1-4 and FDY1-1 are the same lithology. It was originally hoped one of the two would be a match to shale sample FDY1-2. No additional material remains from this depth section to prepare a horizontal sister sample.

Table C-44. Summary of Indirect Tensile Strength Tests (Brazilian Method) - Horizontal Samples

Well ID	Lithology	Sample #	Core Depth (ft)	Orientation	Average Length (in)	Average Diameter (in)	Mass (g)	Dry Bulk Density (g/cm^3)	Maximum Load (lb_f)	Tensile Strength[1] (psi)
Fidelity Cane Creek 26-3	shale	FDY3_3A	7413.05	Perpendicular	0.524	0.992	13.659	2.06	260	319
		FDY3_3C	7413.05	Parallel	0.513	0.994	13.42	2.056	186	232
	shale	FDY2_3A	7417.7	Perpendicular	0.772	1.497	50.882	2.287	1550	854
		FDY2_3B	7417.7	Parallel	0.742	1.496	49.184	2.301	893	512
	shale	FDY1_3A	7464.4	Perpendicular	0.523	0.994	15.916	2.395	501	614
		FDY1_3B	7464.4	Parallel	0.545	0.995	16.556	2.388	384	451

Table C-45. Summary of Triaxial Compression Tests (for all tests, pore pressure drained to atmosphere)

Well ID	Lithology	Sample ID	Core Depth (ft)	Orientation	As Received Bulk Density (g/cm^3)	Confining Pressure (psi)	Peak Effective Compressive Strength[1] (psi)	Effective Residual Compressive Strength (psi)	Young's Modulus (psi)	Poisson's Ratio
Fidelity Cane Creek 26-3	shale	FDY3-1	7413	Vertical	2.041	3855	11,586 (Y)	-	706,400	0.23
		FDY3-2	7413.05	Horizontal	2.009	4040	11,716 (Y) 14,254	-	1,128,000	0.25
	shale	FDY2-1	7417.75	Vertical	2.407	3857	18,534	14,557	1,119,000	0.24
		FDY2-2	7417.85	Horizontal	2.406	4043	20,699	15,143	2,074,000	0.3
	shale	FDY1-2 [2]	7464.3	Horizontal	2.31	4068	17,700	14,498	1,571,000	0.22
	silty dolomite	FDY1-1 [3]	7464.5	Vertical	2.617	3882	36,702	16,682	3,276,000	0.23
		FDY1-4	7464.5	Vertical	2.611	3881	35,955	16,935	3,620,000	0.18

[1] (Y) denotes axial yield
[2]FDY1-2 – No additional shale material remains for a matching horizontal sample, from this backup shale depth interval.
[3]FDY1-1 – No additional silty dolomite material for a matching horizontal sample. Sample FDY1-4 tested as accident, originally marked with an incorrect depth.

Table C-46. Dynamic versus Quasi-Static Mechanical Properties Determined During Triaxial Compression Testing

Well ID	Lithology	Sample ID	Core Depth (ft)	Orientation	Effective Confining Pressure (psi)	Static Poisson's Ratio	Dynamic Poisson's Ratio	Static Young's Modulus (psi)	Dynamic Young's Modulus (psi)	Dynamic / Static Young's Modulus	Dynamic / Static Poisson's Ratio
Fidelity Cane Creek 26-3	shale	FDY3-1	7413	Vertical	3855	0.23	0.24	706,400	1,836,000	2.6	1.04
		FDY3-2	7413.05	Horizontal	4040	0.25	0.23	1,128,000	2,634,000	2.34	0.92
	shale	FDY2-1	7417.75	Vertical	3857	0.24	0.24	1,119,000	4,019,000	3.59	1
	shale	FDY2-2	7417.85	Horizontal	4043	0.3	0.23	2,074,000	5,817,000	2.8	0.77
	shale	FDY1-2	7464.3	Horizontal	4068	0.22	0.21	1,571,000	4,531,000	2.88	0.95
	silty dolomite	FDY1-1	7464.5	Vertical	3882	0.23	0.25	3,276,000	7,925,000	2.42	1.09
		FDY1-4	7464.5	Vertical	3881	0.18	0.25	3,620,000	7,847,000	2.17	1.39
Average:										2.69	1.02

Table C-47. Summary of Continuous Surface Thermal Conductivity Values

Well ID	Core Depth Range (ft)	Low W/m °K	High W/m °K	Average W/m °K
Fidelity Cane Creek 26-3	7431.00 - 7434.05	1.8	2.9	2.4
	7434.15 - 7437.15	2.15	3.3	2.6
	7437.15 - 7440.00	1.65	3.2	2.45
	7440.60 - 7442.12	2.35	3.49	2.85
	7444.15 - 7445.75	1.6	3	2.3

Triaxial Compression Test Plots – Fidelity Cane Creek 26-3

Fidelity Cane Creek 26-3									
Lithology	Sample ID	Depth (ft)	Orientation	As Received Bulk Density (g/cm^3)	Confining Pressure (psi)	Peak Effective Compressive Strength (psi)	Effective Residual Compressive Strength (psi)	Young's Modulus (10^6 psi)	Poisson's Ratio
silty dolomite	FDY1-1 [15]	7464.50	Vertical	2.617	3882	36,702	16,682	3.276	0.23
	FDY1-4	7464.50	Vertical	2.611	3881	35,955	16,935	3.620	0.18

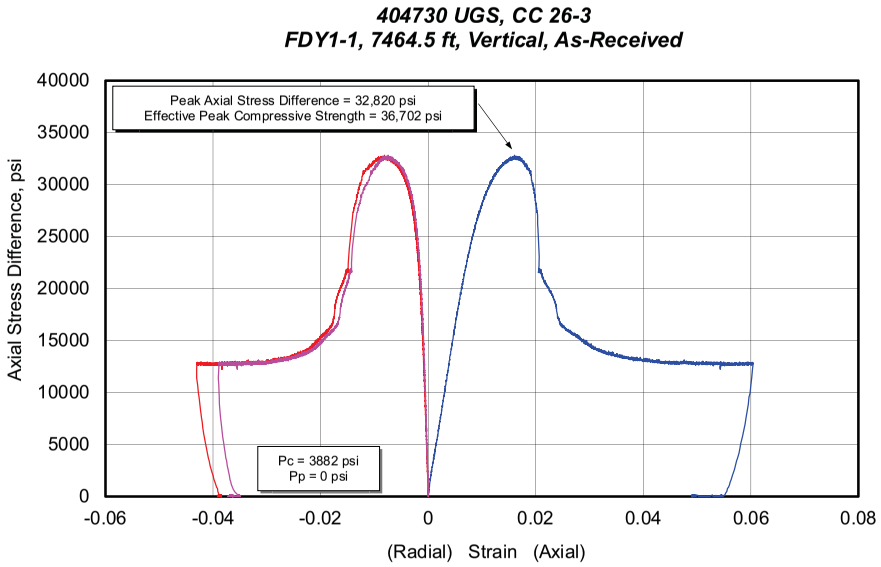

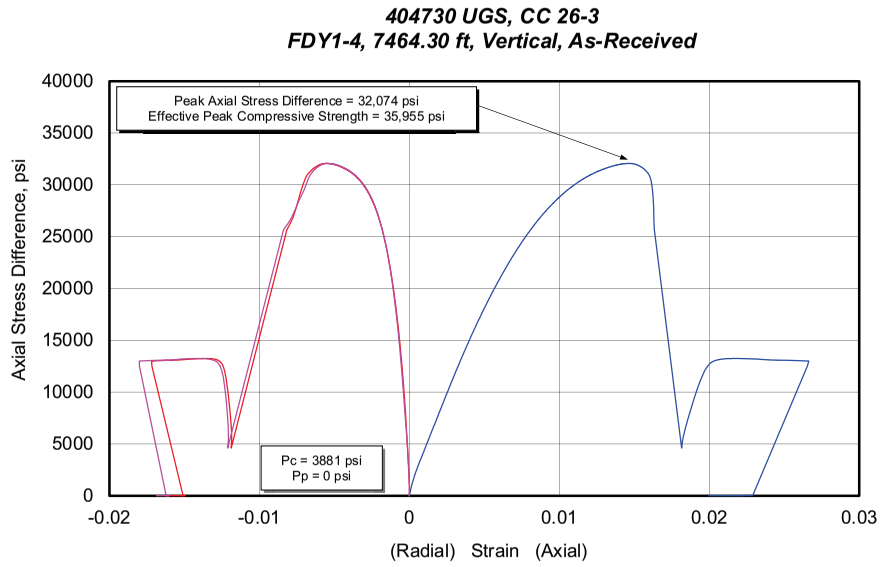

[15] FDY1-1 – No additional silty dolomite material for a matching horizontal sample. Sample FDY1-4 tested as accident, originally marked with an incorrect depth.

Fidelity Cane Creek 26-3

Lithology	Sample ID	Depth (ft)	Orientation	As Received Bulk Density (g/cm^3)	Confining Pressure (psi)	Peak Effective Compressive Strength (psi)	Effective Residual Compressive Strength (psi)	Young's Modulus (10^6 psi)	Poisson's Ratio
shale	FDY1-2 [16]	7464.30	Horizontal	2.310	4068	17,700	14,498	1.571	0.22

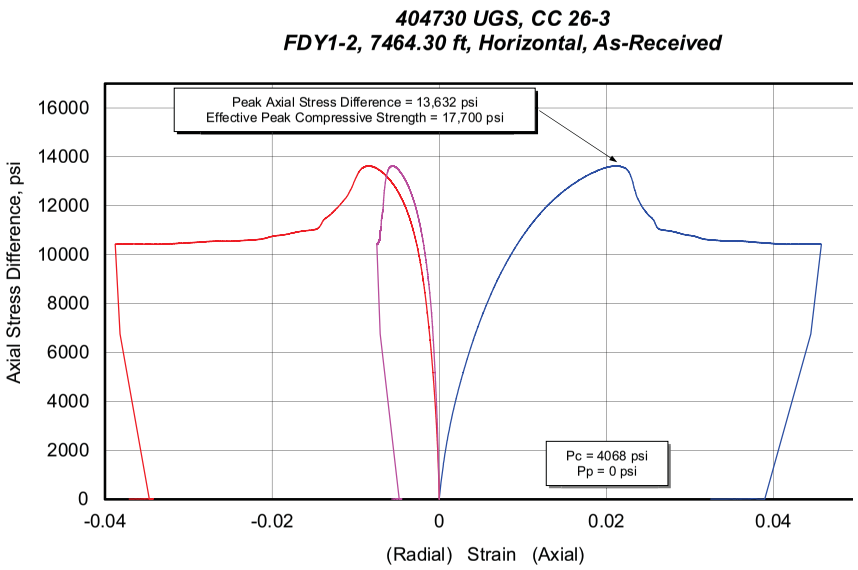

[16] FDY1-2 – No additional shale material remains for a matching horizontal sample, from this backup shale depth interval.

Fidelity Cane Creek 26-3

Lithology	Sample ID	Depth (ft)	Orientation	As Received Bulk Density (g/cm^3)	Confining Pressure (psi)	Peak Effective Compressive Strength (psi)	Effective Residual Compressive Strength (psi)	Young's Modulus (10^6 psi)	Poisson's Ratio
shale	FDY2-1	7417.75	Vertical	2.407	3857	18,534	14,557	1.119	0.24
	FDY2-2	7417.85	Horizontal	2.406	4043	20,699	15,143	2.074	0.30

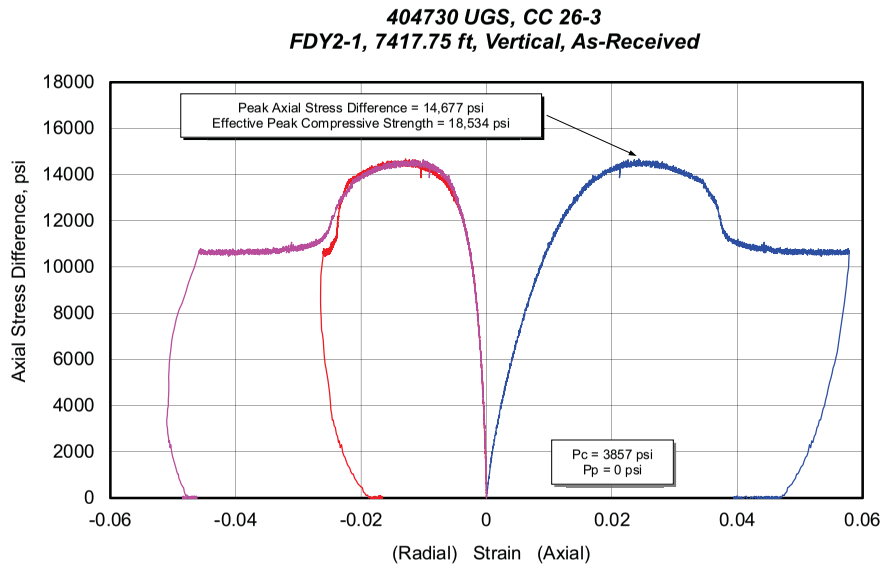

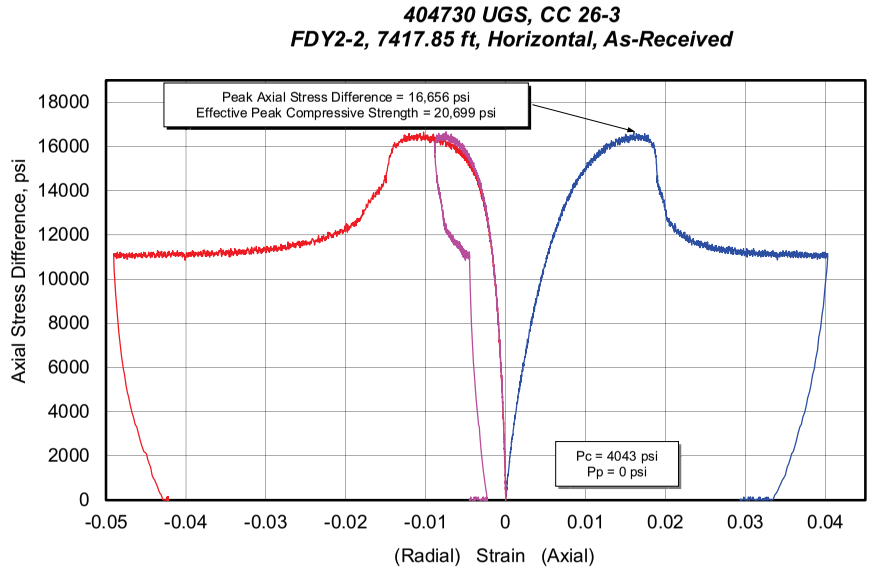

Fidelity Cane Creek 26-3

Lithology	Sample ID	Depth (ft)	Orientation	As Received Bulk Density (g/cm^3)	Confining Pressure (psi)	Peak Effective Compressive Strength (psi)	Effective Residual Compressive Strength (psi)	Young's Modulus (10^6 psi)	Poisson's Ratio
shale	FDY3-1	7413.00	Vertical	2.041	3855	11,586 (Y)	-	0.706	0.23
	FDY3-2	7413.05	Horizontal	2.009	4040	11,716 (Y)[17] 14,254	-	1.128	0.25

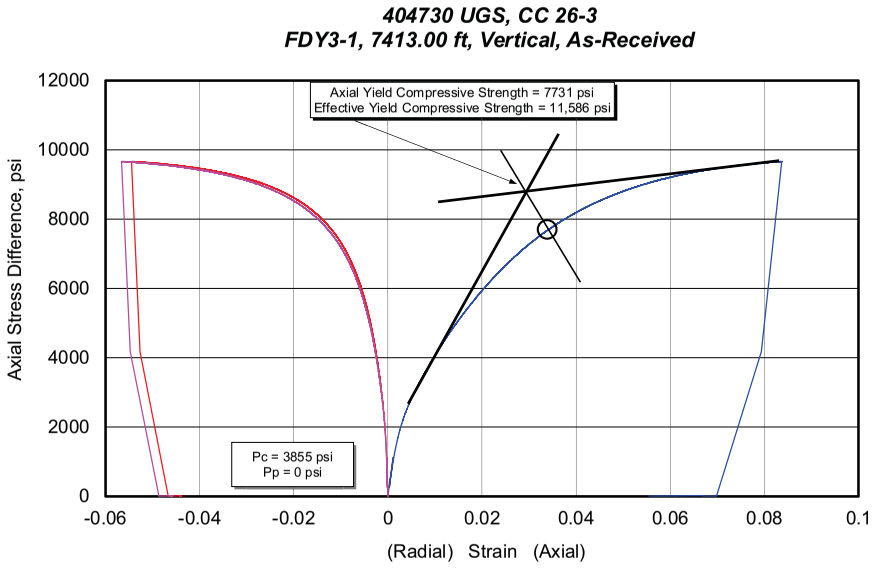

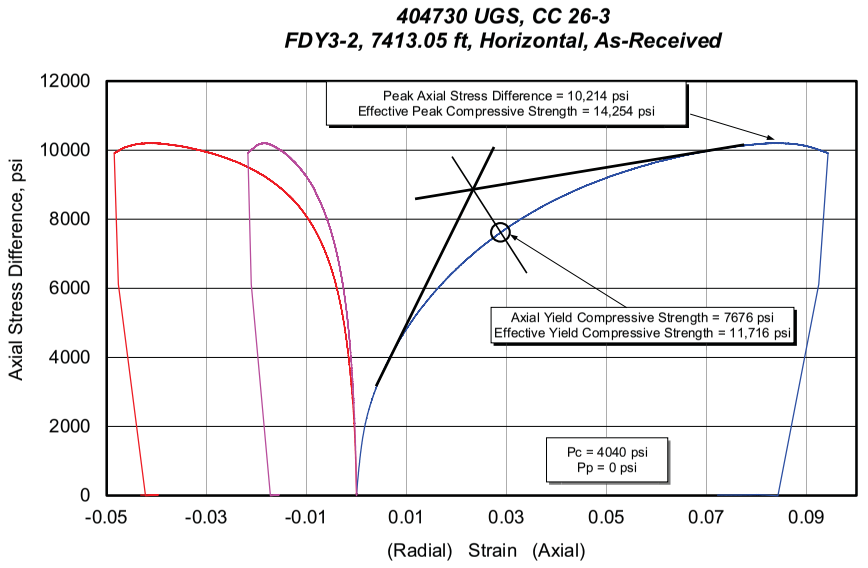

[17] (Y) denotes axial yield

Fidelity Cane Creek 7-1

"The Cane Creek is a fractured shale, with oil accumulating in the fractures. Wells that intercept these fractures tend to produce very well whereas wells that do not intercept fractures do not produce. Available information indicates that these fracture systems are not interconnected over large distance, and to date, each producing well is in its own isolated fracture system. The fractures tend to be nearly vertical …."[18]

Laboratory Tight Rock Analysis data are shown in Table C-48 and C-49. Material received and the samples selected for rock mechanics testing at TerraTek are shown in Table C-50. These samples were preserved with Seal Peal.

[18] United States Department of the Interior BLM, Feb 26, 1998, Proposed Action for EA # UT-062-98-054.

Table C-48. Summary of Effective Porosity Measured During Tight Rock Analysis – Fidelity Well Cane Creek CCU7-1

Sample ID	Lithology	Core Depth (ft)	As Received Bulk Density (g/cm^3)	As Received Grain Density (g/cm^3)	Effective Dry Grain Density (g/cm^3)	Gas Filled Porosity (% of BV)	Hydrocarbon Filled Porosity (% of BV)	Effective Porosity (% of BV)	Effective Water Saturation (% of PV)	Effective Gas Saturation (% of PV)
CCU1-4	silty dolomite	7609.05	2.618	2.692	2.736	2.74	2.79	5.20	46.27	52.80
CCU2-4	anhydrite	7614.55	2.914	2.921	2.922	0.25	0.26	0.27	3.95	92.10
CCU3-4	silty/dolomite/shale	7619.90	2.567	2.610	2.666	1.63	1.73	4.94	65.05	33.03
CCU4-4	shale	7620.40	2.452	2.515	2.604	2.48	2.75	7.87	65.11	31.46
CCU5-4	silty dolomite	7624.90	2.586	2.624	2.654	1.42	1.51	3.22	53.06	43.99
CCU6-4	silty dolomite	7630.50	2.518	2.549	2.614	1.21	1.30	5.19	74.94	23.27
CCU7-4	shale	7638.20	2.565	2.634	2.649	2.63	3.01	3.48	13.52	75.66
CCU8-4	anhydrite	7645.75	2.930	2.939	2.940	0.33	0.34	0.35	3.08	93.84
CCU9-4	silty dolomite	7651.10	2.602	2.643	2.694	1.53	1.58	4.52	65.04	33.91
CCU10-4	fractured/silty/dolomi	7657.40	2.528	2.629	2.680	3.81	4.94	6.62	25.44	57.60

Sample ID-	Effective Oil Saturation (% of PV)	Bound Hydrocarbon (% of BV)	Clay Bound Water (% of BV)	Structural Water (% of BV)	Pressure-Decay Permeability (mD)
CCU1-4	0.93	0.00	3.08	0.77	7.1×10^{-5}
CCU2-4	3.95	0.10	0.00	0.20	3.4
CCU3-4	1.91	0.19	3.87	1.98	6.4
CCU4-4	3.43	0.45	5.22	3.33	7.9
CCU5-4	2.95	0.00	2.09	1.42	3.5
CCU6-4	1.78	0.00	3.89	2.22	3.9
CCU7-4	10.82	0.66	0.94	1.22	4.9
CCU8-4	3.08	0.01	0.00	0.10	3.3
CCU9-4	1.05	0.00	2.75	1.23	5.1
CCU10-4	16.96	2.25	1.31	0.56	5.2

Table C-49. Summary of Total Porosity Measured During Tight Rock Analysis
Fidelity Well Cane Creek CCU7-1

Sample ID	Lithology	Core Depth (ft)	As Received Bulk Density (g/cm^3)	As Received Grain Density (g/cm^3)	Total Dry Grain Density (g/cm^3)	Total Porosity (% of BV)	Total Water Saturation (% of PV)	Total Gas Saturation (% of PV)	Total Oil Saturation (% of PV)
CCU1-4	silty dolomite	7609.05	2.618	2.692	2.794	8.28	66.26	33.16	0.58
CCU2-4	anhydrite	7614.55	2.914	2.921	2.922	0.27	3.95	92.10	3.95
CCU3-4	silty/dolomite/shale	7619.90	2.567	2.610	2.737	8.81	80.42	18.51	1.07
CCU4-4	shale	7620.40	2.452	2.515	2.700	13.09	79.02	18.92	2.06
CCU5-4	silty dolomite	7624.90	2.586	2.624	2.691	5.30	71.53	26.69	1.79
CCU6-4	silty dolomite	7630.50	2.518	2.549	2.683	9.08	85.68	13.30	1.02
CCU7-4	shale	7638.20	2.565	2.634	2.665	4.42	31.93	59.55	8.52
CCU8-4	anhydrite	7645.75	2.930	2.939	2.940	0.35	3.08	93.84	3.08
CCU9-4	silty dolomite	7651.10	2.602	2.643	2.744	7.26	78.27	21.08	0.65
CCU10-4	fractured/silty/dolomit	7657.40	2.528	2.629	2.704	7.93	37.76	48.08	14.16

Table C-50. Material Received by TerraTek for Testing

Pallet #	Well ID	Box #	Top Core Depth (ft)	Bottom Core Depth (ft)	Approx. Length (ft)	Approx. Diameter (in)	Comments
1	Fidelity	1	~ 1 ft length cores, #'s 1, 2, and 3 contained in box				10 preserved, slabbed core sections. Majority were previously plugged. CT shows numerous fractures.
	Cane	2	~ 1 ft length cores, #'s 4 and 5 contained in box				
	Creek	3	~ 1 ft length cores, #'s 6 and 7 contained in box				
	CCU7-1	4	~ 1 ft length cores, #'s 8, 9, and 10 contained in box				

Preserved Samples for Triaxial Testing

Sample	Top Depth (ft MD)	Bottom Depth (ft MD)	Triaxial (vertical)	Triaxial (horizontal)	Toughness	Fluid Sensitivity	Lithology
1	7609	7609.6	x	x	x	x	silty dolomite
2	7614	7615	x	x	x	x	anhydrite
3	7619	7620	x	x	x	x	silty dolomite - shale
4	7620	7621	x	x	x	x	shale
5	7624	7625	x	x	x	x	silty dolomite
6	7630	763f1	x	x	x	x	silty dolomite
7	7638	7638.5	x	x	x	x	shale
8	7645.3	7646	x	x	x	x	anhydrite
9	7651	7651.8	x	x	x	x	silty dolomite
10	7657.4	7658	x	x	x	x	fractured silty dolomite

Table C-51. Brittleness

Sample	Orientation	Core Depth	Log Depth	BI1	BI2	BI3a	BI3b	BI4	BI5
CCU1-3	Horizontal	7609.15	7604.15	0.305635193	0.206868667	0.0005271	-0.003253908	1.301057291	0.63
CCU2-3	Horizontal	7614.65	7609.65	0.191768457	0	0.0165475	0.013775248	2.513846873	0.12
CCU3-5	Horizontal	7619.2	7614.2	0.204484657	0.198127689	0.0036147	-0.021117571	1.462602102	0.12
CCU4-5	Horizontal	7620.3	7615.3	0.207734826	0.368443956	0.007453	-0.063536742	1.639916823	0.29
CCU5-3	Horizontal	7624.9	7619.9	0.797647997	0.314548847	0.0018426	-0.008822069	1.570422568	0.17
CCU6-3	Horizontal	7630.6	7625.6	0.802870808	0	0.0003663	-0.002029592	1.180042695	0.18
CCU8-3	Horizontal	7645.75	7640.75	1.740908365	0.823910889	0.0003349	-0.000582128	1.145484647	0.05
CCU9-3	Horizontal	7651.25	7646.25	1.088975745	0.406858076	0.0006258	-0.002297104	1.381838793	0.76
CCU10-5	Horizontal	7657.65	7652.65	0.504531929	0.010794436	0.0070399	-0.006872028	1.627216341	0.16
CCU1-1	Vertical	7609.35	7604.35	0.228116312	0.29431657	0.0029798	-0.01163733	1.343987457	0.43
CCU2-1	Vertical	7614	7609	2.428974418	0.433780322	-2.62E-10	1.69812E-09	1.000131802	0.11
CCU3-1	Vertical	7619	7614	0.499721066	0.802280634	0.0007361	-0.004101915	1.243249408	0.35
CCU4-1	Vertical	7620.8	7615.8	1.996208611	0.451308169	7.707E-05	-7.24781E-05	1.048967897	0.09
CCU5-1	Vertical	7624.65	7619.65	0.271182415	0.657268908	0.003611	-0.031734869	1.420931757	0.26
CCU6-1	Vertical	7630.25	7625.25	0.309486887	0.781734838	0.0017944	-0.016950794	1.246063394	0.18
CCU7-1	Vertical	7638.3	7633.3	0.579512608	0.190054425	0.0040095	-0.013914656	1.710999027	0.14
CCU8-1	Vertical	7645.3	7640.3	0.26180833	0	0.0018807	-0.105752926	36.85632972	0.07
CCU9-1	Vertical	7651.6	7646.6	0.226544869	0	0.000488	-0.122951803	26.76316815	0.16
CCU10-1	Vertical	7657.5	7652.5	0.167123842	0.143294635	0.013819	-0.026371383	1.915681089	0.78

Table C-52. Dynamic Mechanical Properties Determined During Triaxial Compression Testing

Well ID	Lithology	Sample ID Core Depth (ft) Orientation	Axial Stress Difference (psi)	Effective Confining Pressure[1] (psi)	Effective Mean Stress (psi)	As Received Density (g/cm^3)	P-Wave Velocity (ft/s)	S-Wave Velocity (ft/s)	Poisson's Ratio	Young's Modulus (10^6 psi)	Bulk Modulus (10^6 psi)	Shear Modulus (10^6 psi)
Fidelity Cane Creek CCU7-1	silty dolomite	CCU1-1 7609.35 Vertical	0	3348	3348	2.631	15,966	9032	0.26	7.313	5.18	2.891
			3343	3348	4462	2.632	16,028	9039	0.27	7.341	5.248	2.898
			6979	3348	5674	2.634	16,056	9029	0.27	7.342	5.291	2.893
			18,990	3348	9678	2.637	16,127	8874	0.28	7.179	5.511	2.798
			25,385	3348	11,810	2.633	15,985	8618	0.3	6.826	5.553	2.635
			16,887	3348	8977	2.61	15,581	8266	0.3	6.267	5.334	2.403
		CCU1-3 7609.15 Horizontal	0	3882	3882	2.606	16,982	9970	0.24	8.635	5.473	3.49
			2297	3881	4647	2.606	17,001	9983	0.24	8.659	5.483	3.5
			13,511	3882	8386	2.609	17,159	9916	0.25	8.636	5.742	3.456
			28,095	3883	13,248	2.61	17,156	9782	0.26	8.474	5.865	3.365
			40,321	3881	17,321	2.603	16,991	9355	0.28	7.874	6.032	3.07
			21,053	3881	10,899	2.611	16,553	9217	0.28	7.624	5.656	2.989
	anhydrite	CCU2-1 7614 Vertical	0	3350	3350	2.894	19,697	10,556	0.3	11.284	9.336	4.345
			6370	3350	5473	2.895	20,024	10,603	0.31	11.448	9.794	4.386
			13,690	3350	7913	2.896	19,876	10,571	0.3	11.361	9.601	4.36
			24,651	3350	11,567	2.895	19,547	10,365	0.3	10.934	9.317	4.191
			28,467	3350	12,839	2.878	18,496	9556	0.32	9.335	8.546	3.542
			16,409	3350	8820	2.822	17,642	8990	0.32	8.143	7.737	3.074
		CCU2-3 7614.65 Horizontal	0	3882	3882	2.96	19,812	10,808	0.29	12.002	9.442	4.659
			5520	3882	5722	2.962	19,799	10,822	0.29	12.029	9.411	4.674
			13,444	3882	8363	2.963	19,827	10,825	0.29	12.047	9.455	4.678
			20,828	3882	10,825	2.963	19,807	10,815	0.29	12.025	9.437	4.669
			29,462	3882	13,703	2.933	18,615	9642	0.32	9.674	8.795	3.674
			17,912	3882	9853	2.863	17,847	9107	0.32	8.473	8.022	3.2

Well ID	Lithology	Sample ID Core Depth (ft) Orientation	Axial Stress Difference (psi)	Effective Confining Pressure[1] (psi)	Effective Mean Stress (psi)	As Received Density (g/cm^3)	P-Wave Velocity (ft/s)	S-Wave Velocity (ft/s)	Poisson's Ratio	Young's Modulus (10^6 psi)	Bulk Modulus (10^6 psi)	Shear Modulus (10^6 psi)
Fidelity Cane Creek CCU7-1	silty dolomite - shale	CCU3-1 7619 Vertical	0	3352	3352	2.525	13,185	7793	0.23	5.09	3.16	2.066
			1974	3352	4010	2.526	13,267	7813	0.23	5.131	3.221	2.078
			5631	3352	5229	2.529	13,472	7867	0.24	5.235	3.373	2.109
			10,632	3352	6896	2.531	13,666	7889	0.25	5.307	3.539	2.123
			14,866	3352	8307	2.519	13,645	7627	0.27	5.026	3.687	1.974
			14,833	3352	8296	2.516	13,617	7591	0.27	4.979	3.681	1.953
		CCU3-5 7619.2 Horizontal	0	3886	3886	2.522	14,362	8335	0.25	5.883	3.861	2.361
			3407	3885	5021	2.524	14,443	8364	0.25	5.936	3.922	2.379
			7465	3885	6373	2.526	14,738	8392	0.26	6.041	4.197	2.397
			13,372	3887	8344	2.53	14,766	8313	0.27	5.974	4.291	2.356
			17,763	3884	9805	2.514	14,228	7791	0.29	5.287	4.115	2.056
			12,641	3886	8100	2.46	13,630	7308	0.3	4.596	3.797	1.77
	shale	CCU4-1 7620.8 Vertical	0	3354	3354	2.517	11,741	7048	0.22	4.104	2.429	1.684
			2026	3354	4029	2.519	12,126	7164	0.23	4.291	2.668	1.742
			3859	3354	4640	2.522	12,390	7264	0.24	4.44	2.827	1.793
			8015	3354	6026	2.532	13,001	7337	0.27	4.652	3.319	1.837
			10,459	3354	6840	2.559	12,979	7180	0.28	4.548	3.439	1.777
			9207	3354	6423	2.576	12,599	6965	0.28	4.31	3.264	1.683
		CCU4-5 7620.3 Horizontal	0	3885	3885	2.541	13,890	7897	0.26	5.386	3.759	2.135
			3411	3886	5023	2.543	13,999	7913	0.27	5.429	3.855	2.145
			6781	3886	6146	2.546	14,183	7912	0.27	5.472	4.037	2.147
			11,108	3886	7589	2.55	14,242	7922	0.28	5.502	4.094	2.156
			14,905	3884	8852	2.539	14,108	7568	0.3	5.086	4.197	1.959
			10,194	3885	7283	2.511	13,618	7397	0.29	4.779	3.806	1.851

Well ID	Lithology	Sample ID Core Depth (ft) Orientation	Axial Stress Difference (psi)	Effective Confining Pressure[1] (psi)	Effective Mean Stress (psi)	As Received Density (g/cm^3)	P-Wave Velocity (ft/s)	S-Wave Velocity (ft/s)	Poisson's Ratio	Young's Modulus (10^6 psi)	Bulk Modulus (10^6 psi)	Shear Modulus (10^6 psi)
Fidelity Cane Creek CCU7-1	silty dolomite	CCU5-1 7624.65 Vertical	0	3355	3355	2.606	15,834	9277	0.24	7.486	4.774	3.022
			3191	3354	4418	2.608	15,940	9302	0.24	7.552	4.874	3.041
			6099	3354	5387	2.61	16,019	9309	0.25	7.59	4.961	3.048
			10,787	3354	6950	2.614	16,057	9280	0.25	7.578	5.036	3.033
			15,368	3355	8478	2.619	16,060	9190	0.26	7.489	5.128	2.98
			17,301	3354	9121	2.622	16,005	9054	0.26	7.327	5.19	2.897
		CCU5-3 7624.9 Horizontal	0	3887	3887	2.599	17,006	9489	0.27	8.034	5.923	3.153
			7397	3886	6352	2.601	17,147	9540	0.28	8.139	6.052	3.19
			11,924	3886	7861	2.602	17,268	9523	0.28	8.15	6.216	3.18
			20,747	3885	10,801	2.604	17,573	9539	0.29	8.246	6.58	3.193
			30,020	3887	13,894	2.604	17,235	9303	0.29	7.862	6.375	3.037
			16,214	3886	9291	2.566	16,460	8862	0.3	7.036	5.746	2.715
	silty dolomite	CCU6-1 7630.25 Vertical	0	3356	3356	2.519	13,685	7932	0.25	5.327	3.509	2.136
			1696	3357	3922	2.521	13,740	7950	0.25	5.359	3.55	2.147
			3370	3357	4480	2.522	13,802	7970	0.25	5.396	3.595	2.158
			4809	3357	4960	2.523	13,850	7978	0.25	5.417	3.636	2.164
			9010	3357	6360	2.525	13,909	7954	0.26	5.411	3.712	2.152
			12,037	3357	7369	2.499	13,731	7552	0.28	4.929	3.788	1.921
		CCU6-3 7630.6 Horizontal	0	3891	3891	2.544	16,895	9652	0.26	8.032	5.526	3.193
			1990	3891	4554	2.545	16,813	9657	0.25	8.019	5.429	3.198
			4925	3891	5533	2.547	16,882	9662	0.26	8.05	5.509	3.204
			11,711	3891	7795	2.552	16,963	9650	0.26	8.073	5.624	3.201
			16,671	3891	9448	2.552	16,890	9482	0.27	7.851	5.687	3.091
			13,309	3891	8327	2.518	16,683	9409	0.27	7.611	5.439	3.004

Well ID	Lithology	Sample ID Core Depth (ft) Orientation	Axial Stress Difference (psi)	Effective Confining Pressure[1] (psi)	Effective Mean Stress (psi)	As Received Density (g/cm^3)	P-Wave Velocity (ft/s)	S-Wave Velocity (ft/s)	Poisson's Ratio	Young's Modulus (10^6 psi)	Bulk Modulus (10^6 psi)	Shear Modulus (10^6 psi)
Fidelity Cane Creek CCU7-1	shale	CCU7-1 7638.3 Vertical	0	3361	3361	2.478	12,505	7188	0.25	4.325	2.921	1.726
			2196	3361	4093	2.48	12,619	7251	0.25	4.405	2.979	1.757
			4311	3361	4798	2.484	12,912	7299	0.27	4.511	3.203	1.783
			8944	3362	6343	2.496	13,242	7265	0.28	4.561	3.53	1.775
			11,580	3361	7221	2.514	13,201	7013	0.3	4.342	3.682	1.666
			11,058	3361	7047	2.523	12,891	6864	0.3	4.171	3.513	1.601
	anhydrite	CCU8-1 7645.3 Vertical	0	3364	3364	2.945	19,759	10,694	0.29	11.735	9.442	4.538
			5541	3364	5211	2.946	19,782	10,748	0.29	11.837	9.422	4.586
			12,679	3364	7590	2.947	19,831	10,693	0.3	11.761	9.564	4.541
			22,430	3364	10,841	2.947	19,656	10,355	0.31	11.137	9.664	4.258
			24,892	3364	11,661	2.922	18,474	9348	0.33	9.139	8.851	3.441
			24,886	3364	11,659	2.914	18,319	9209	0.33	8.864	8.737	3.33
		CCU8-3 7645.75 Horizontal	561	3898	4085	2.942	19,704	10,857	0.28	11.982	9.161	4.673
			8011	3898	6568	2.943	19,732	10,903	0.28	12.071	9.155	4.714
			15,460	3898	9051	2.944	19,760	10,849	0.28	11.991	9.264	4.669
			21,405	3898	11,033	2.944	19,673	10,718	0.29	11.746	9.275	4.556
			26,589	3898	12,761	2.887	17,851	9127	0.32	8.575	8.076	3.241
			25,796	3898	12,497	2.837	17,295	8567	0.34	7.505	7.694	2.806
Fidelity Cane Creek CCU7-1	silty dolomite	CCU9-1 7651.6 Vertical	585	3366	3561	2.589	14,919	8701	0.24	6.561	4.243	2.641
			5464	3367	5188	2.592	14,991	8725	0.24	6.616	4.304	2.659
			9637	3366	6578	2.595	15,003	8693	0.25	6.592	4.349	2.643
			15,466	3367	8522	2.599	14,987	8508	0.26	6.399	4.486	2.535
			18,005	3367	9369	2.596	14,872	8270	0.28	6.105	4.546	2.392
			11,566	3367	7222	2.517	14,367	7835	0.29	5.365	4.225	2.082

Well ID	Lithology	Sample ID Core Depth (ft) Orientation	Axial Stress Difference (psi)	Effective Confining Pressure[1] (psi)	Effective Mean Stress (psi)	As Received Density (g/cm^3)	P-Wave Velocity (ft/s)	S-Wave Velocity (ft/s)	Poisson's Ratio	Young's Modulus (10^6 psi)	Bulk Modulus (10^6 psi)	Shear Modulus (10^6 psi)
		CCU9-3 7651.25 Horizontal	4589	3901	5431	2.6	16,271	9705	0.22	8.077	4.876	3.3
			8684	3901	6796	2.602	16,319	9723	0.22	8.118	4.917	3.314
			12,451	3901	8051	2.603	16,396	9684	0.23	8.106	5.043	3.289
			18,914	3901	10,206	2.604	16,396	9615	0.24	8.033	5.108	3.244
			25,313	3901	12,339	2.602	16,354	9496	0.25	7.877	5.162	3.162
			12,294	3901	7999	2.556	16,130	9374	0.24	7.537	4.926	3.027
	fractured silty dolomite	CCU10-1 7657.5 Vertical	707	3368	3604	2.688	17,548	9925	0.26	9.026	6.396	3.568
			4750	3368	4951	2.69	17,806	10,007	0.27	9.213	6.652	3.63
			8984	3368	6363	2.692	17,867	10,014	0.27	9.246	6.729	3.637
			13,183	3368	7762	2.693	18,036	10,024	0.28	9.309	6.943	3.646
			17,047	3368	9050	2.695	18,018	10,020	0.28	9.305	6.927	3.646
			25,515	3368	11,873	2.698	18,147	9865	0.29	9.131	7.256	3.538
		CCU10-5 7657.65 Horizontal	200	3904	3971	2.708	19,333	10,786	0.27	10.817	7.979	4.245
			9962	3904	7225	2.71	19,924	10,808	0.29	11.018	8.807	4.266
			16,556	3904	9423	2.711	20,194	10,756	0.3	11.004	9.262	4.226
			22,666	3904	11,459	2.711	20,141	10,713	0.3	10.925	9.23	4.193
			35,905	3903	15,871	2.709	19,741	10,385	0.31	10.304	8.976	3.937
			16826	3904	9513	2.687	18,995	10,119	0.3	9.652	8.121	3.707

[1]For all tests, pore pressure drained to atmosphere.

Table C-53. Summary of Indirect Tensile Strength Tests (Brazilian Method) - Horizontal Samples

Well ID	Lithology	Sample #	Core Depth (ft)	Orientation	Average Length (in)	Average Diameter (in)	Mass (g)	Dry Bulk Density (g/cm^3)	Maximum Load (lb_f)	Tensile Strength[1] (psi)
Fidelity Cane Creek CCU7-1	silty dolomite	CCU1_2A	7609.45	Perpendicular	0.509	0.996	17.067	2.628	979	1230
		CCU1_2B	7609.45	Parallel	0.538	0.994	17.779	2.602	372	443
	anhydrite	CCU2_2A	7614.3	Perpendicular	0.767	1.496	64.652	2.924	1160	643
		CCU2_2B	7614.3	Parallel	0.759	1.497	63.941	2.922	1740	975
	silty dolomite - shale	CCU3_2A	7619.3	Perpendicular	0.508	0.995	16.033	2.478	275	346
		CCU3_2B	7619.3	Parallel	0.524	0.996	16.704	2.499	288	351
	shale	CCU4_2A	7620.9	Perpendicular	0.507	0.996	16.315	2.525	479	605
		CCU4_2B	7620.9	Parallel	0.5	0.996	16.119	2.529	549	703
	silty dolomite	CCU5_2A	7624.55	Parallel	0.754	1.497	56.298	2.59	952	537
		CCU5_2B	7624.55	Perpendicular	0.763	1.497	57.012	2.592	1410	786
	silty dolomite	CCU6_2A	7630.85	Perpendicular	0.756	1.498	54.812	2.512	1080	608
		CCU6_2B	7630.85	Parallel	0.767	1.498	55.701	2.514	596	330
	shale	CCU7_2A	7638.45	Perpendicular	0.511	0.993	14.571	2.244	479	600
		CCU7_2B	7638.45	Parallel	0.519	0.995	15.218	2.302	253	312
	anhydrite	CCU8_2A	7645.6	Perpendicular	0.772	1.496	65.086	2.926	1940	1069
		CCU8_2B	7645.6	Parallel	0.763	1.496	64.356	2.927	1480	825
	silty dolomite	CCU9_2A	7651.5	Perpendicular	0.775	1.497	58.112	2.599	2160	1185
		CCU9_2B	7651.5	Parallel	0.765	1.497	57.45	2.606	1550	862
	fractured silty dolomite	CCU10_2A	7657.6	Perpendicular	0.523	0.996	18.033	2.703	1040	1272
		CCU10_2B	7657.6	Parallel	0.518	0.996	18.039	2.73	1410	1740

[1] Equation for Tensile Strength in psi is: (2 * Load in lbf) / (pi * diameter in " * length in ")

Table C-54. Summary of Triaxial Compression Tests (for all tests, pore pressure drained to atmosphere)

Well ID	Lithology	Sample ID	Core Depth (ft)	Orientation	As Received Bulk Density (g/cm^3)	Confining Pressure (psi)	Peak Effective Compressive Strength (psi)	Effective Residual Compressive Strength (psi)	Young's Modulus (psi)	Poisson's Ratio
Fidelity Cane Creek CCU7-1	silty dolomite	CCU1-1	7609.35	Vertical	2.624	3348	28,755	20,162	3,447,000	0.23
		CCU1-3	7609.15	Horizontal	2.599	3881	44,946	24,935	5,507,000	0.3
	anhydrite	CCU2-1	7614	Vertical	2.886	3350	31,827	19,750	7,383,000	0.34
		CCU2-3	7614.65	Horizontal	2.954	3883	33,347	21,675	8,060,000	0.33
	silty dolomite-shale	CCU3-1	7619	Vertical	2.509	3352	18,220	-	1,686,000	0.28
		CCU3-5	7619.2	Horizontal	2.5	3886	21,688	16,561	2,054,000	0.24
	shale	CCU4-1	7620.8	Vertical	2.487	3353	13,814	-	819,700	0.15
		CCU4-5	7620.3	Horizontal	2.514	3886	18,825	14,071	1,778,000	0.24
	silty dolomite	CCU5-1	7624.65	Vertical	2.597	3355	20,803	11,732	2,696,000	0.13
		CCU5-3	7624.9	Horizontal	2.591	3886	33,942	20,104	4,517,000	0.25
	silty dolomite	CCU6-1	7630.25	Vertical	2.504	3357	15,416	-	1,506,000	0.24
		CCU6-3	7630.6	Horizontal	2.53	3892	20,564	17,198	2,774,000	0.15
	shale	CCU7-1 [1]	7638.3	Vertical	2.458	3361	14,945	14,459	972,400	0.18
	anhydrite	CCU8-1	7645.3	Vertical	2.94	3364	28,267	-	7,233,000	0.35
		CCU8-3	7645.75	Horizontal	2.931	3899	30,497	-	7,603,000	0.35
	silty dolomite	CCU9-1	7651.6	Vertical	2.577	3367	21,372	14,963	2,262,000	0.17
		CCU9-3	7651.25	Horizontal	2.582	3902	29,687	16,128	3,891,000	0.24
	fractured silty dolomite	CCU10-1	7657.5	Vertical	2.678	3369	29,259	-	4,290,000	0.18
		CCU10-5	7657.65	Horizontal	2.696	3905	39,972	20,882	6,534,000	0.33

[1] CCU7-1 – Not enough material available to obtain additional samples, thus, no horizontally oriented sample was tested.

Table C-55. Dynamic versus Quasi-Static Mechanical Properties Determined During Triaxial Compression Testing

Well ID	Lithology	Sample ID	Core Depth (ft)	Orientation	Effective Confining Pressure (psi)	Static Poisson's Ratio	Dynamic Poisson's Ratio	Static Young's Modulus (psi)	Dynamic Young's Modulus (psi)	Dynamic / Static Young's Modulus	Dynamic / Static Poisson's Ratio
Fidelity Cane Creek CCU7-1	silty dolomite	CCU1-1	7609.35	Vertical	3348	0.23	0.27	3,447,000	7,342,000	2.13	1.17
		CCU1-3	7609.15	Horizontal	3881	0.3	0.25	5,507,000	8,636,000	1.57	0.83
	anhydrite	CCU2-1	7614	Vertical	3350	0.34	0.31	7,383,000	11,448,000	1.55	0.91
		CCU2-3	7614.65	Horizontal	3883	0.33	0.29	8,060,000	12,047,000	1.49	0.88
	silty dolomite - shale	CCU3-1	7619	Vertical	3352	0.28	0.24	1,686,000	5,235,000	3.1	0.86
		CCU3-5	7619.2	Horizontal	3886	0.24	0.26	2,054,000	6,041,000	2.94	1.08
	shale	CCU4-1	7620.8	Vertical	3353	0.15	0.24	819,700	4,440,000	5.42	1.6
		CCU4-5	7620.3	Horizontal	3886	0.24	0.27	1,778,000	5,429,000	3.05	1.13
	silty dolomite	CCU5-1	7624.65	Vertical	3355	0.13	0.25	2,696,000	7,590,000	2.82	1.92
		CCU5-3	7624.9	Horizontal	3886	0.25	0.28	4,517,000	8,150,000	1.8	1.12
	silty dolomite	CCU6-1	7630.25	Vertical	3357	0.24	0.25	1,506,000	5,396,000	3.58	1.04
		CCU6-3	7630.6	Horizontal	3892	0.15	0.26	2,774,000	8,050,000	2.9	1.73
	shale	CCU7-1	7638.3	Vertical	3361	0.18	0.27	972,400	4,511,000	4.64	1.5
	anhydrite	CCU8-1	7645.3	Vertical	3364	0.35	0.29	7,233,000	11,837,000	1.64	0.83
		CCU8-3	7645.75	Horizontal	3899	0.35	0.28	7,603,000	12,071,000	1.59	0.8
	silty dolomite	CCU9-1	7651.6	Vertical	3367	0.17	0.24	2,262,000	6,616,000	2.92	1.41
		CCU9-3	7651.25	Horizontal	3902	0.24	0.22	3,891,000	8,118,000	2.09	0.92
	fractured silty dolomite	CCU10-1	7657.5	Vertical	3369	0.18	0.27	4,290,000	9,246,000	2.16	1.5
		CCU10-5	7657.65	Horizontal	3905	0.33	0.3	6,534,000	11,004,000	1.68	0.91
									Average:	2.58	1.17

Table C-56. Summary of Continuous Surface Thermal Conductivity Values

Well ID	Core Depth Range (ft)	Low W/m °K	High W/m °K	Average W/m °K
Fidelity Cane Creek CCU7-1	7619.00 - 7620.90	1.3	2.92	2.2
	7624.10 - 7624.98	2.5	3.7	3.05
	7630.08 - 7630.97	2.25	3.6	2.8
	7638.00 - 7638.50	1.2	2.7	1.85
	7657.40 - 7658.00	2.55	3.3	2.8

CT Scans Whole Core Fidelity Cane Creek Unit 7-1

7609.0 L

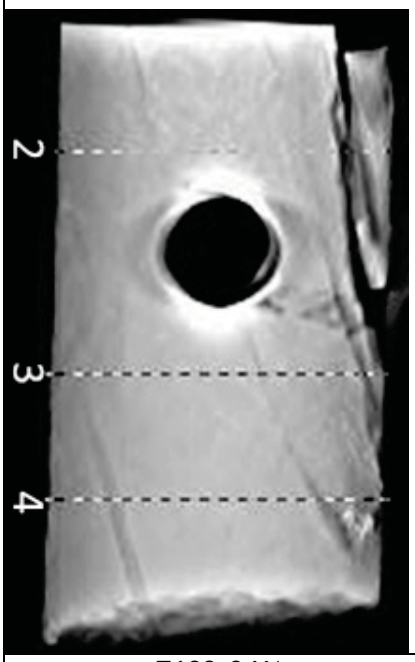

7609.0 X1

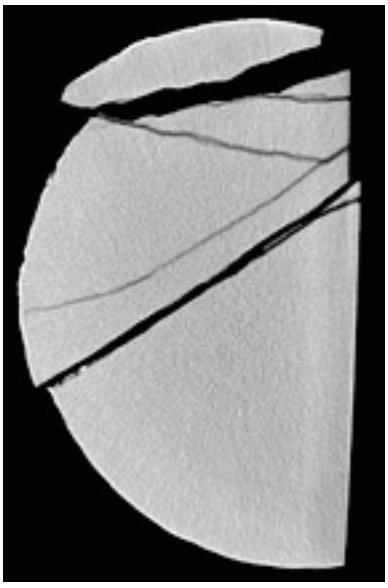

7609.0 X2

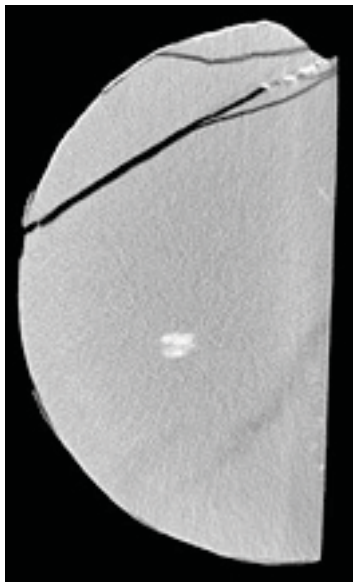

7609.0 X3

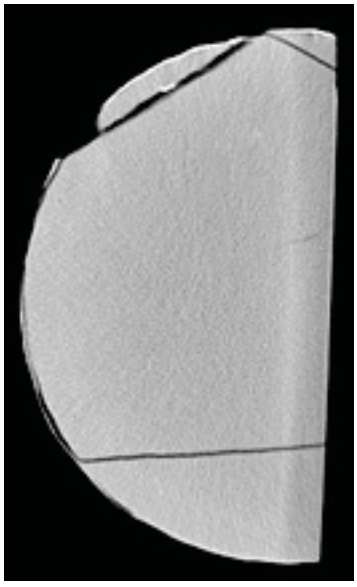

7614.0 L 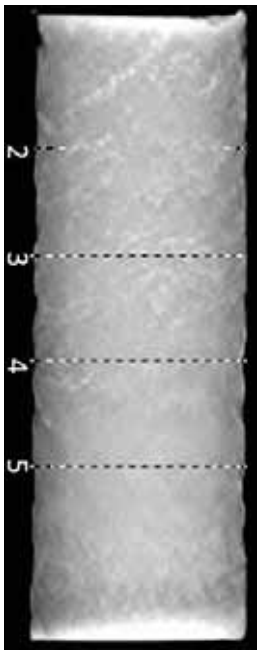 		7614.0 X1 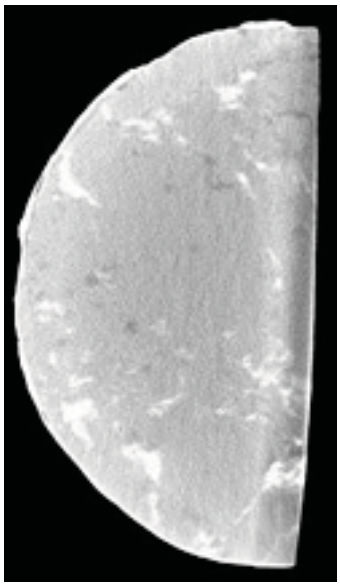
7614.0 X2 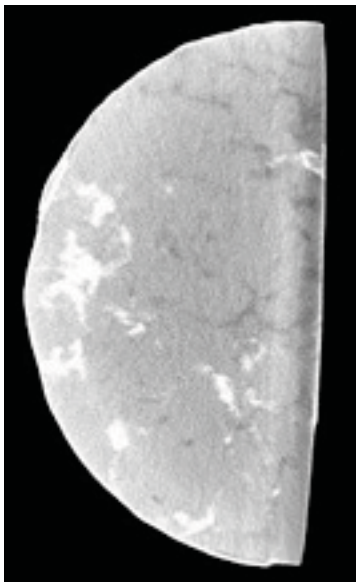	7614.0 X3 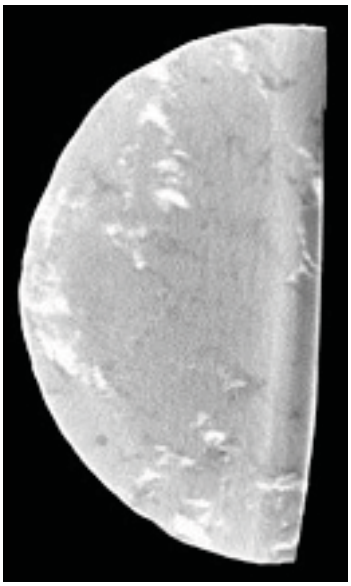	7614.0 X4 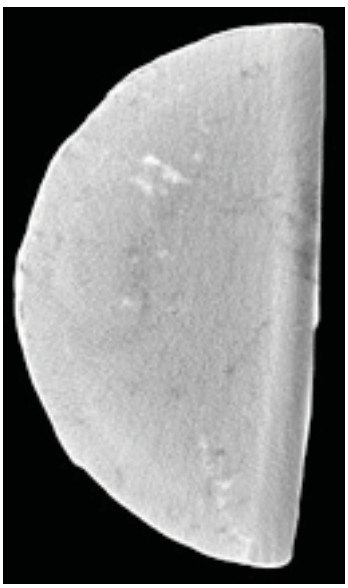

7619.0 L  		
7619.0 X1 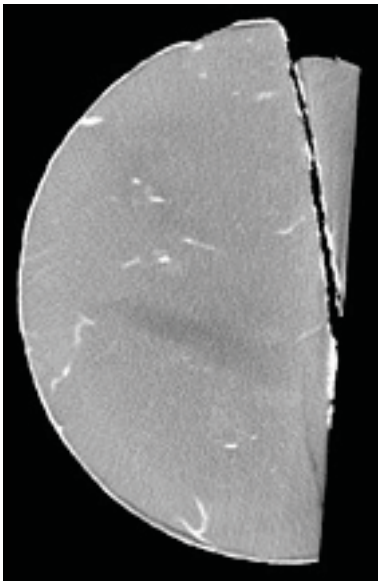	7619.0 X2 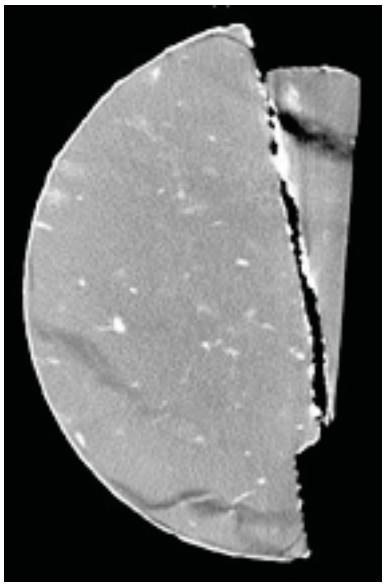	7619.0 X3 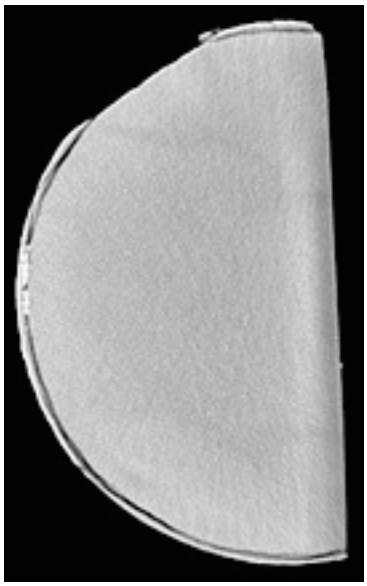

7620.0 L 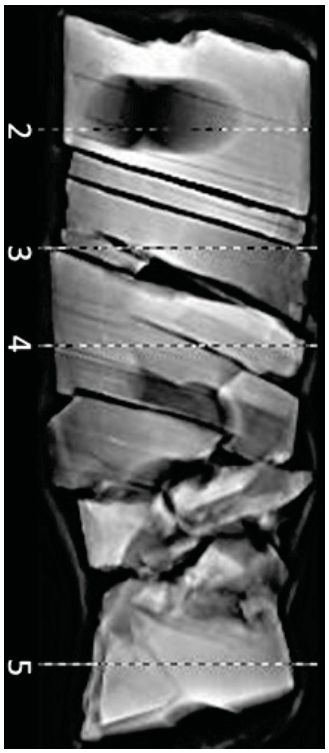 		7620.0 X1 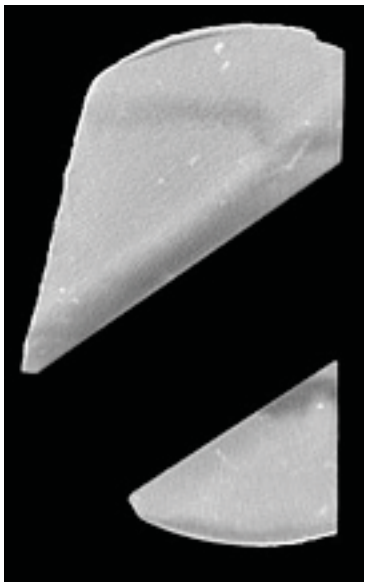
7620.0 X2 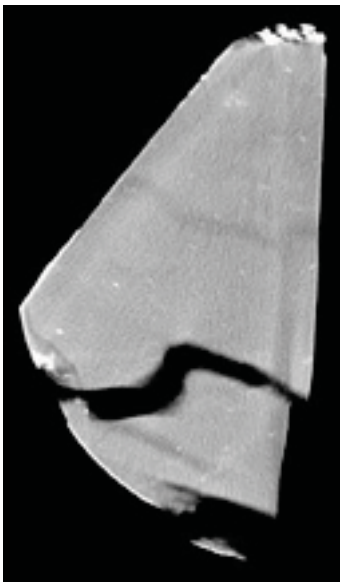	7620.0 X3 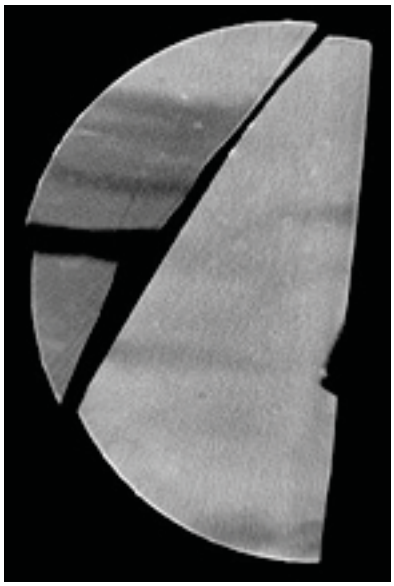	7620.0 X4 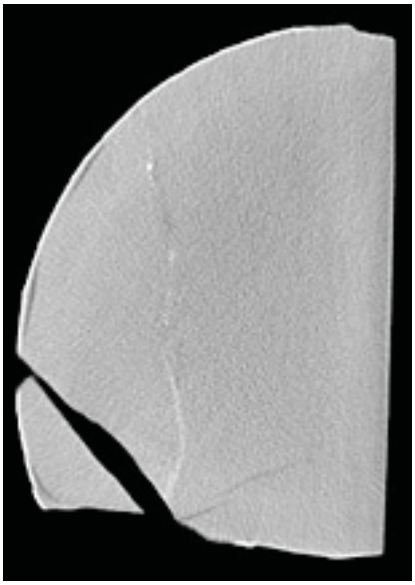

7624.0 L 		7624.0 X1 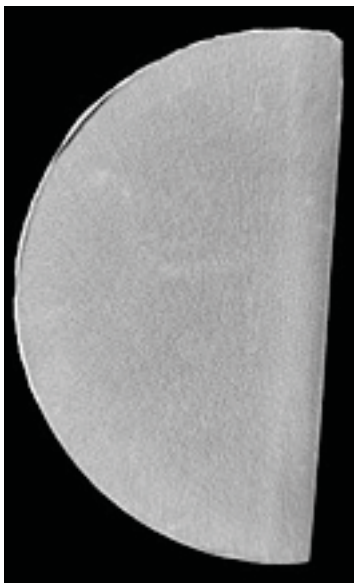
7624.0 X2 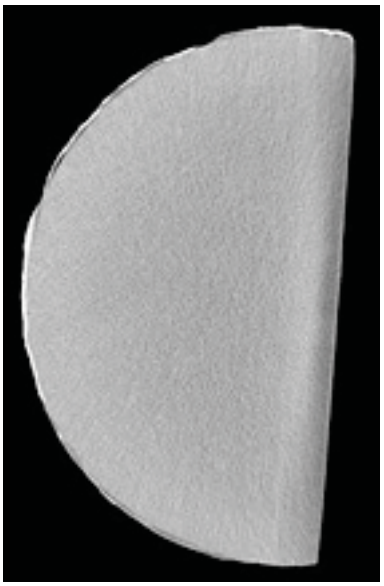	7624.0 X3 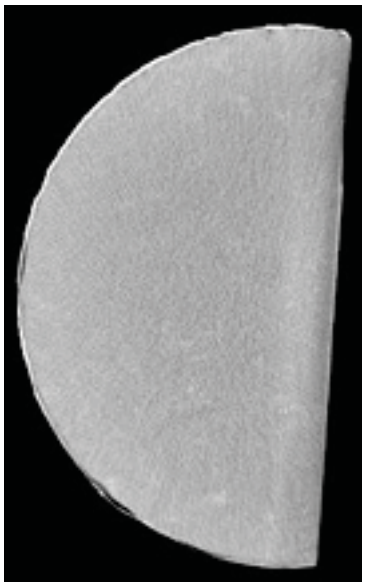	7624.0 X4 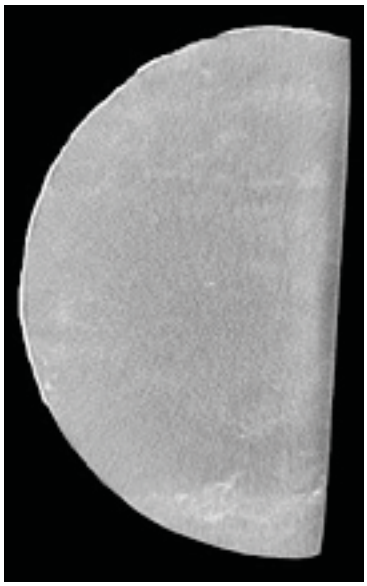

7630.0 L 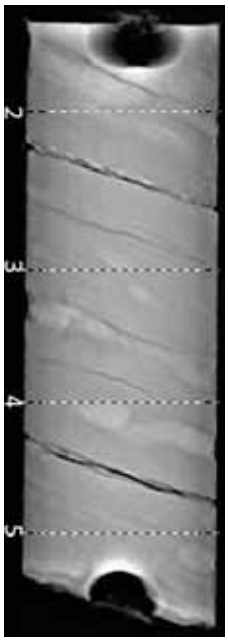		7630.0 X1 
7630.0 X2 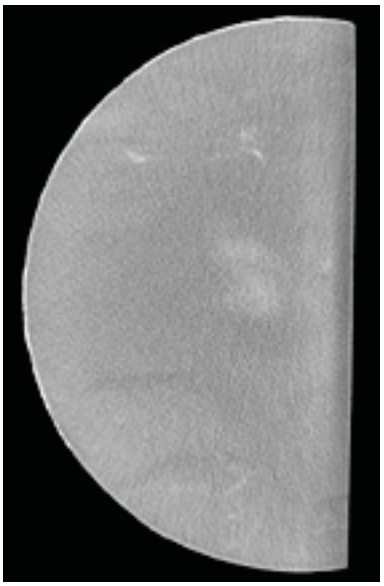	7630.0 X3 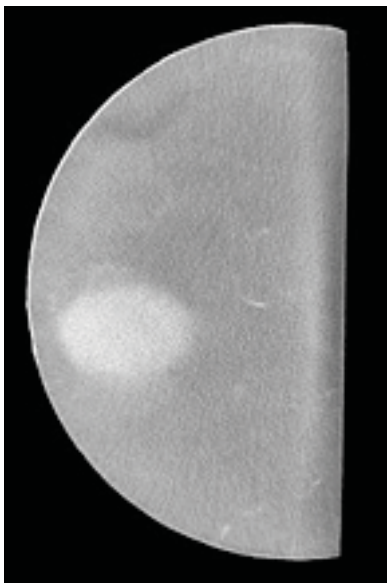	7630.0 X4 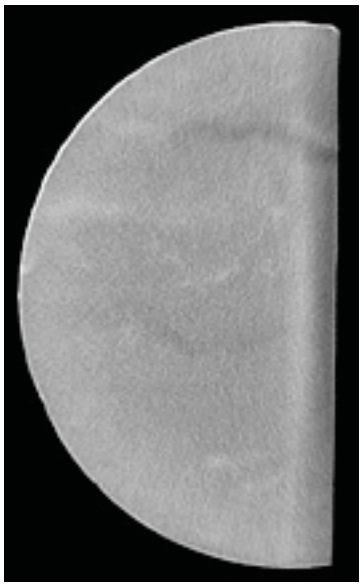

7638.0 L 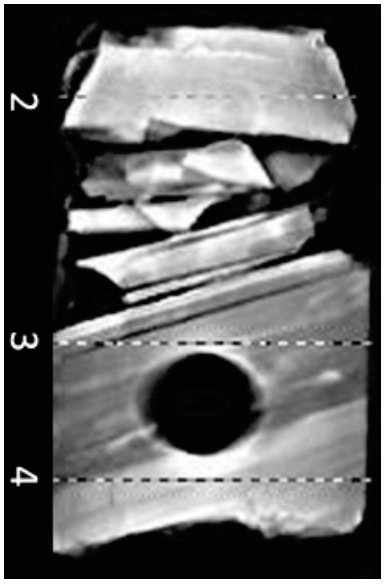		
7638.0 X1 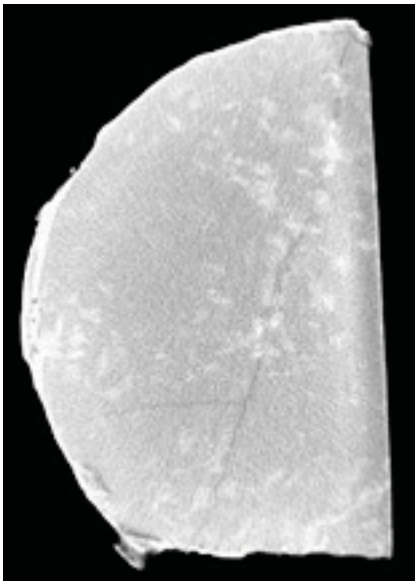	7638.0 X2 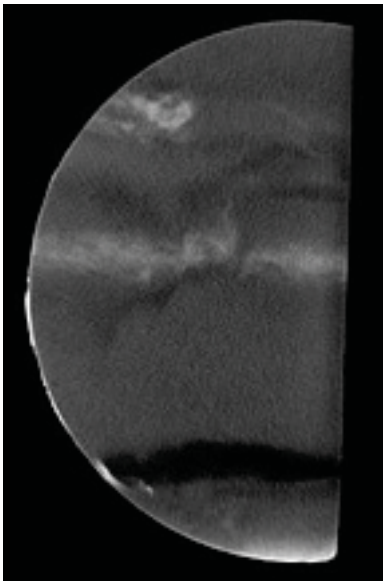	7638.0 X3 

7645.3 L 		
7645.3 X1 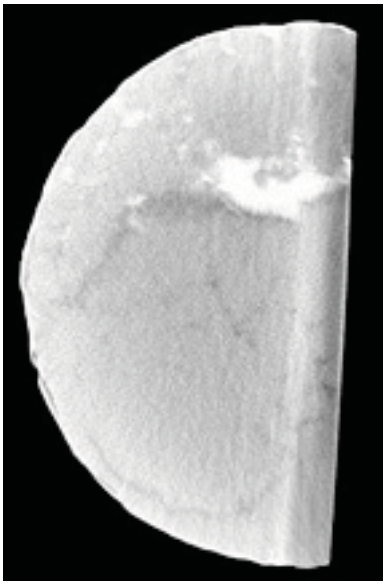	7645.3 X2 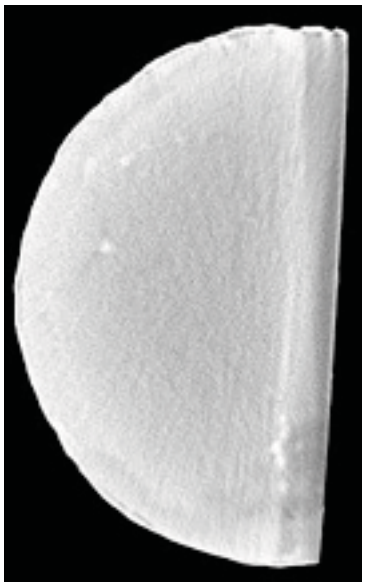	7645.3.0 X3 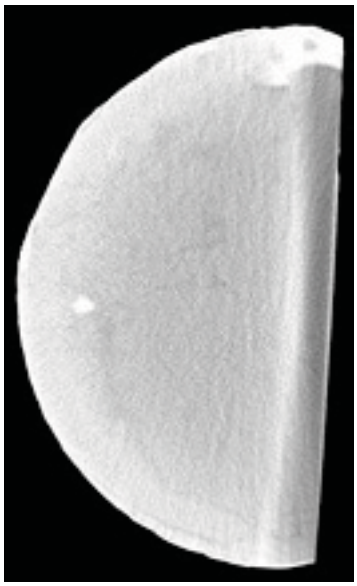

7651.0 L

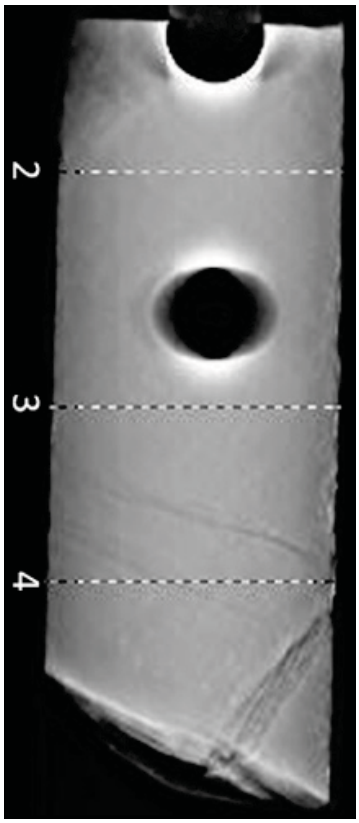

7651.0 X1

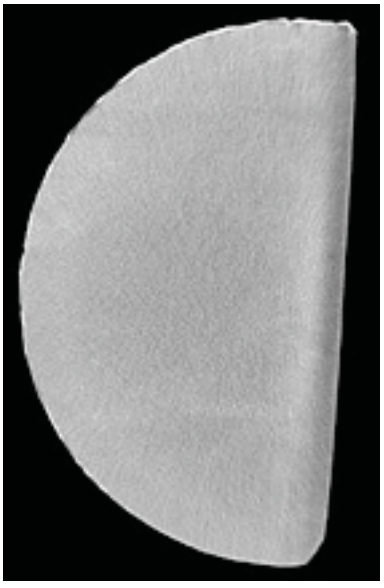

7651.0 X2

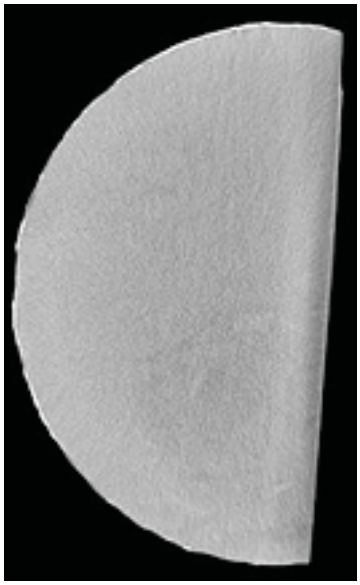

7651.0 X3

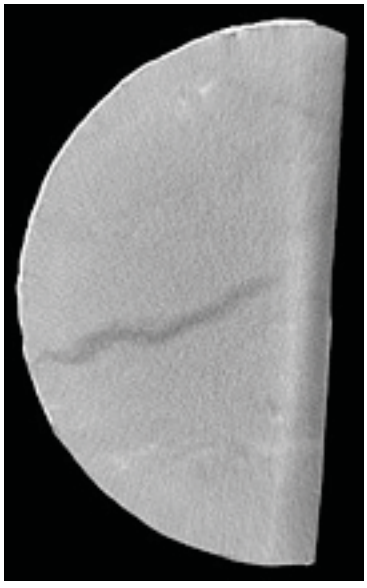

7657.4 L

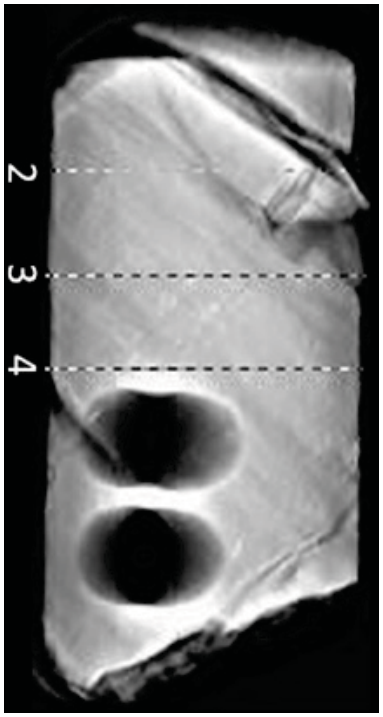

7657.4 X1

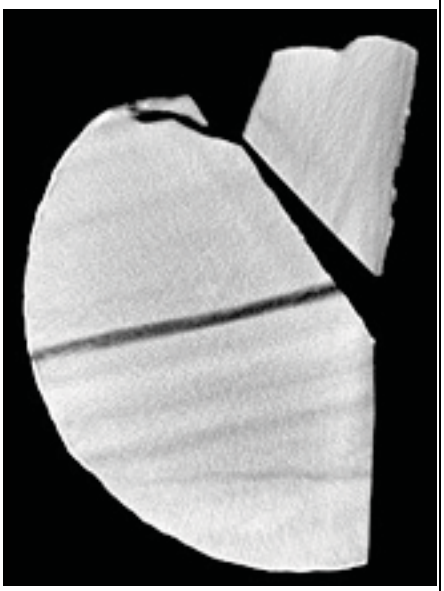

7657.4 X2

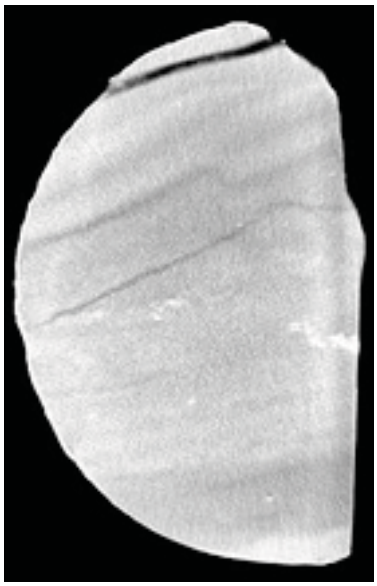

7657.4 X3

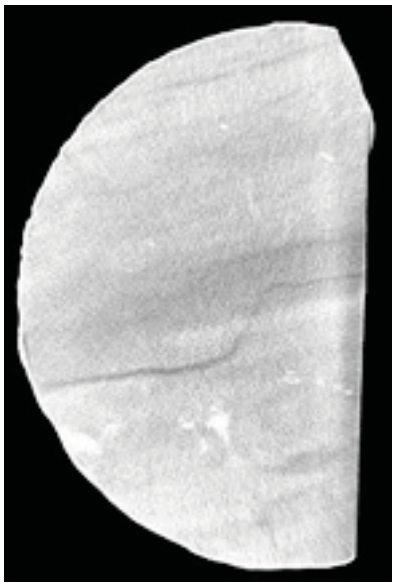

Triaxial Compression Test Plots – Fidelity Cane Creek 7-1

Fidelity Cane Creek CCU7-1									
Lithology	**Sample ID**	**Depth (ft)**	**Orientation**	**As Received Bulk Density (g/cm^3)**	**Confining Pressure (psi)**	**Peak Effective Compressive Strength (psi)**	**Effective Residual Compressive Strength (psi)**	**Young's Modulus (10^6 psi)**	**Poisson's Ratio**
fractured silty dolomite	CCU10-1	7657.50	Vertical	2.678	3369	29,259	-	4.290	0.18
	CCU10-5	7657.65	Horizontal	2.696	3905	39,972	20,882	6.534	0.33

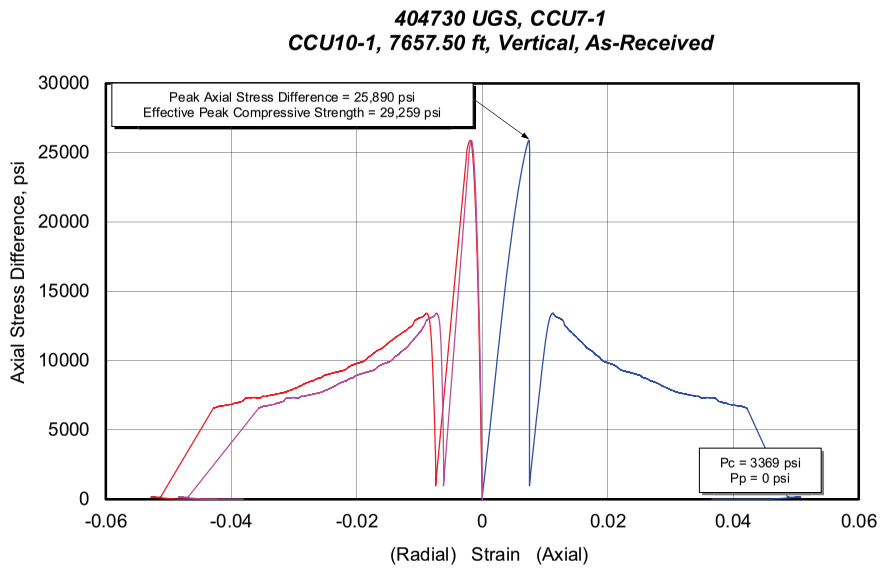

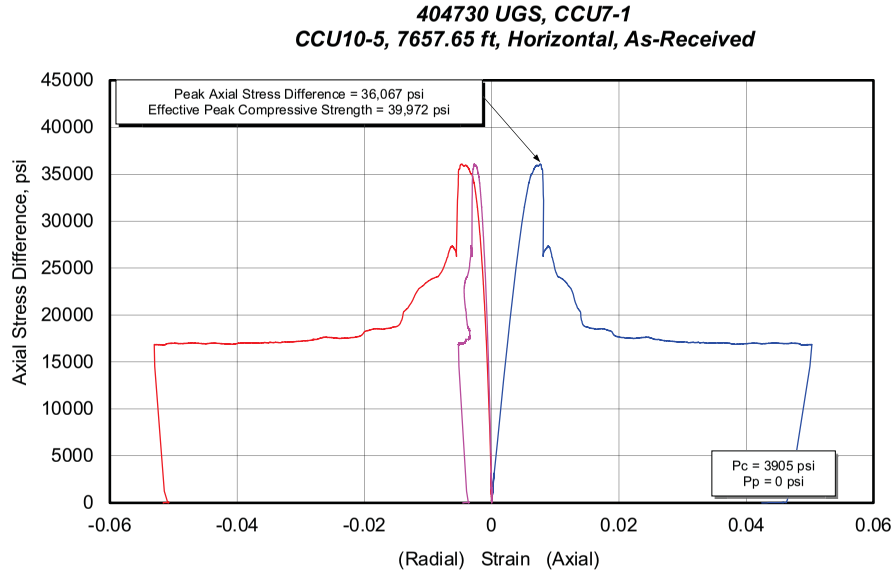

Fidelity Cane Creek CCU7-1

Lithology	Sample ID	Depth (ft)	Orientation	As Received Bulk Density (g/cm^3)	Confining Pressure (psi)	Peak Effective Compressive Strength (psi)	Effective Residual Compressive Strength (psi)	Young's Modulus (10^6 psi)	Poisson's Ratio
silty dolomite	CCU9-1	7651.60	Vertical	2.577	3367	21,372	14,963	3.891	0.17
	CCU9-3	7651.25	Horizontal	2.582	3902	29,687	16,128	3,891,000	0.24

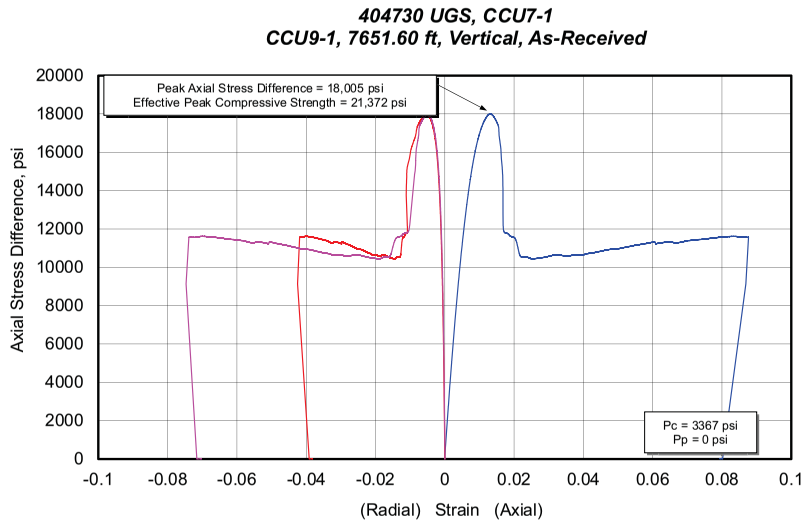

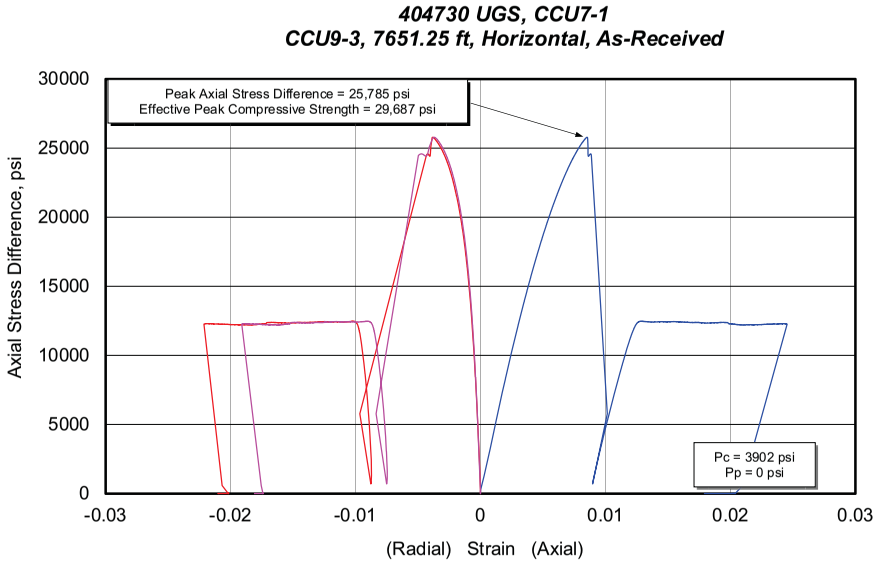

Fidelity Cane Creek CCU7-1

Lithology	Sample ID	Depth (ft)	Orientation	As Received Bulk Density (g/cm^3)	Confining Pressure (psi)	Peak Effective Compressive Strength (psi)	Effective Residual Compressive Strength (psi)	Young's Modulus (10^6 psi)	Poisson's Ratio
anhydrite	CCU8-1	7645.30	Vertical	2.940	3364	28,267	-	7.233	0.35
	CCU8-3	7645.75	Horizontal	2.931	3899	30,497	-	7.603	0.35

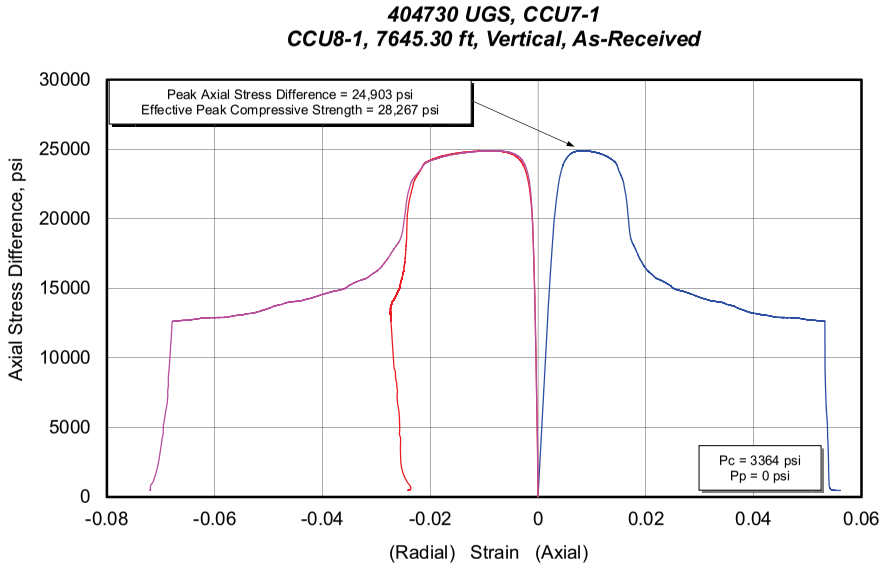

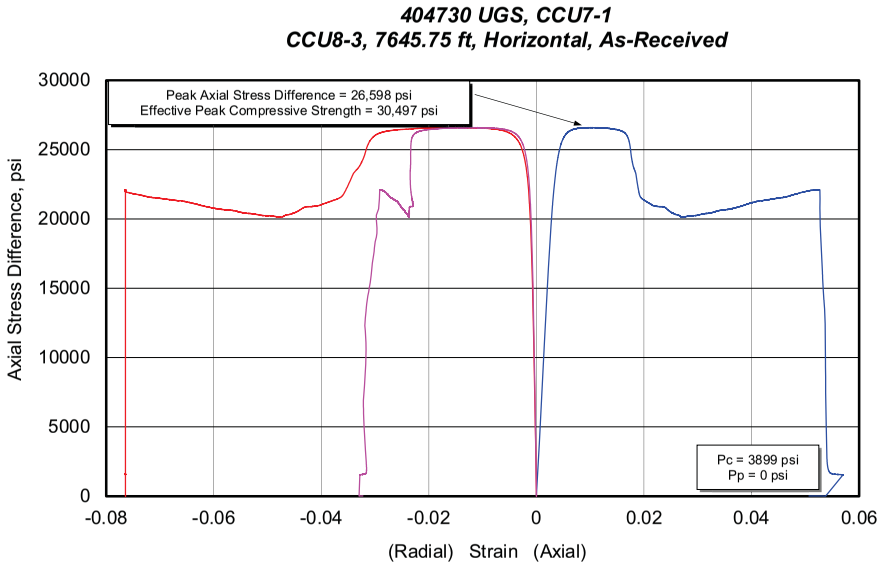

Fidelity Cane Creek CCU7-1

Lithology	Sample ID	Depth (ft)	Orientation	As Received Bulk Density (g/cm^3)	Confining Pressure (psi)	Peak Effective Compressive Strength (psi)	Effective Residual Compressive Strength (psi)	Young's Modulus (10^6 psi)	Poisson's Ratio
shale	CCU7-1[19]	7638.30	Vertical	2.458	3361	14,945	14,459	0.972	0.18

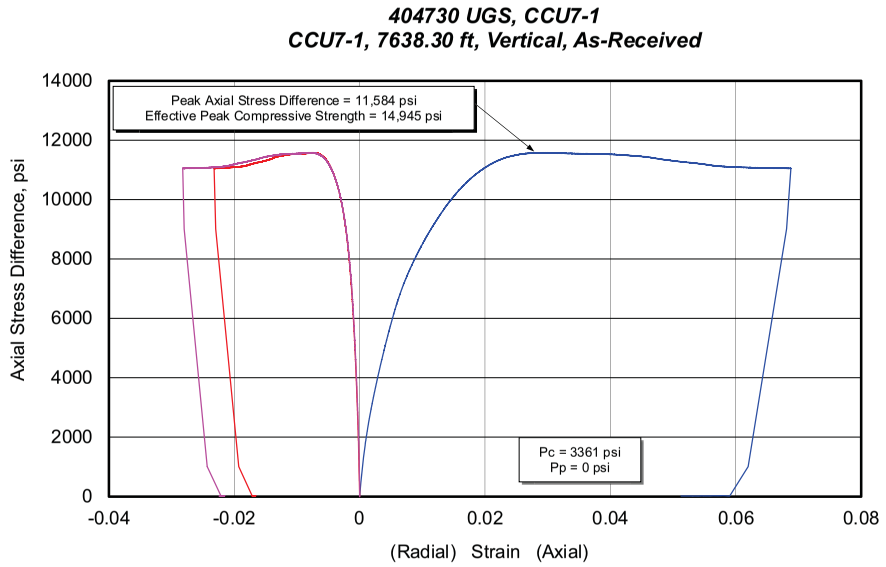

[19] CCU7-1 – Not enough material available to obtain additional samples, thus, no horizontally oriented sample was tested

Fidelity Cane Creek CCU7-1

Lithology	Sample ID	Depth (ft)	Orientation	As Received Bulk Density (g/cm^3)	Confining Pressure (psi)	Peak Effective Compressive Strength (psi)	Effective Residual Compressive Strength (psi)	Young's Modulus (10^6 psi)	Poisson's Ratio
silty dolomite	CCU6-1	7630.25	Vertical	2.504	3357	15,416	-	1.5060	0.24
	CCU6-3	7630.60	Horizontal	2.530	3892	20,564	17,198	2.774	0.15

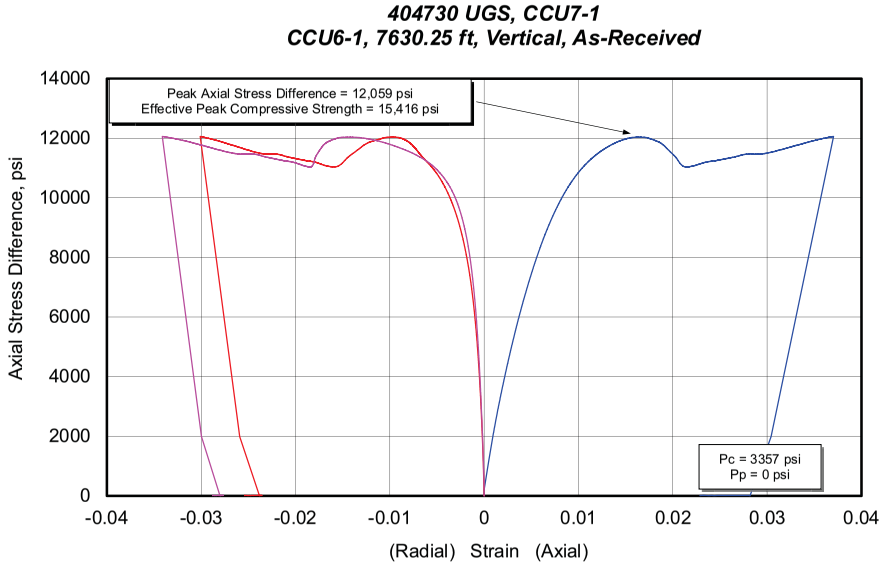

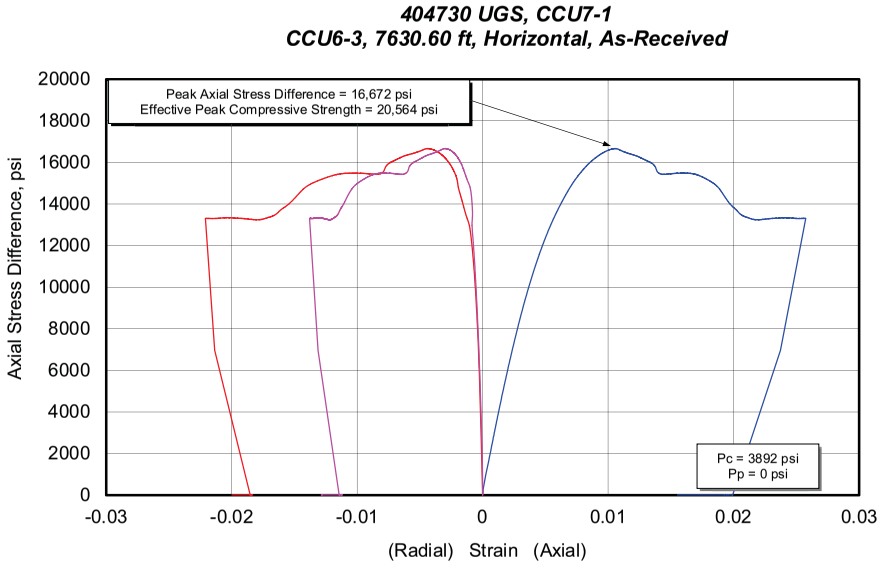

Fidelity Cane Creek CCU7-1

Lithology	Sample ID	Depth (ft)	Orientation	As Received Bulk Density (g/cm^3)	Confining Pressure (psi)	Peak Effective Compressive Strength (psi)	Effective Residual Compressive Strength (psi)	Young's Modulus (10^6 psi)	Poisson's Ratio
silty dolomite	CCU5-1	7624.65	Vertical	2.597	3355	20,803	11,732	2.696	0.13
	CCU5-3	7624.90	Horizontal	2.591	3886	33,942	20,104	4.517	0.25

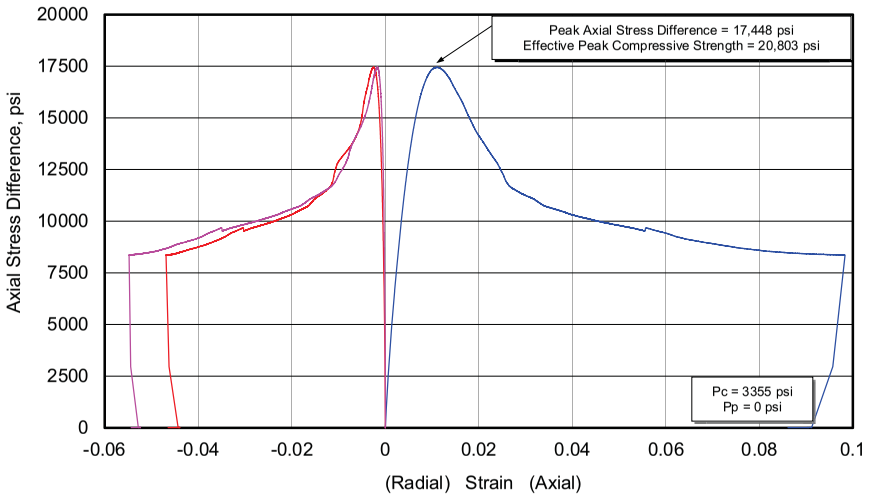

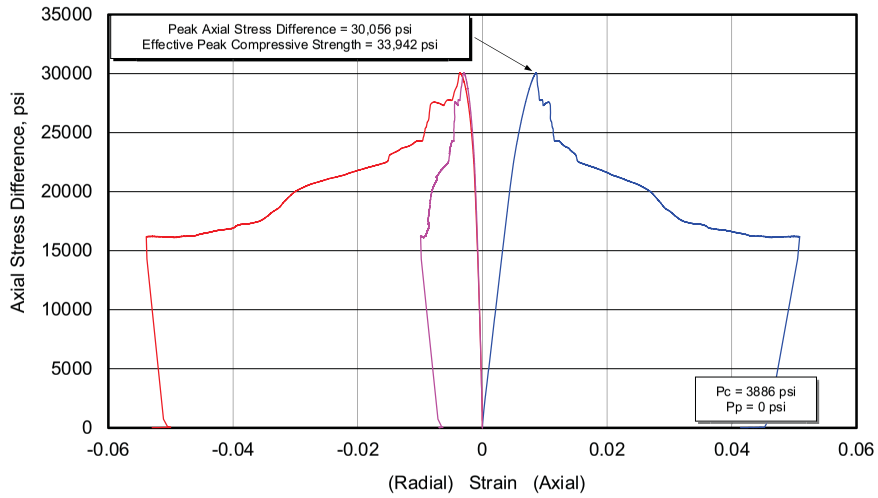

Fidelity Cane Creek CCU7-1

Lithology	Sample ID	Depth (ft)	Orientation	As Received Bulk Density (g/cm^3)	Confining Pressure (psi)	Peak Effective Compressive Strength (psi)	Effective Residual Compressive Strength (psi)	Young's Modulus (10^6 psi)	Poisson's Ratio
shale	CCU4-1	7620.80	Vertical	2.487	3353	13,814	-	0.820	0.15
	CCU4-5	7620.30	Horizontal	2.514	3886	18,825	14,071	1.118	0.24

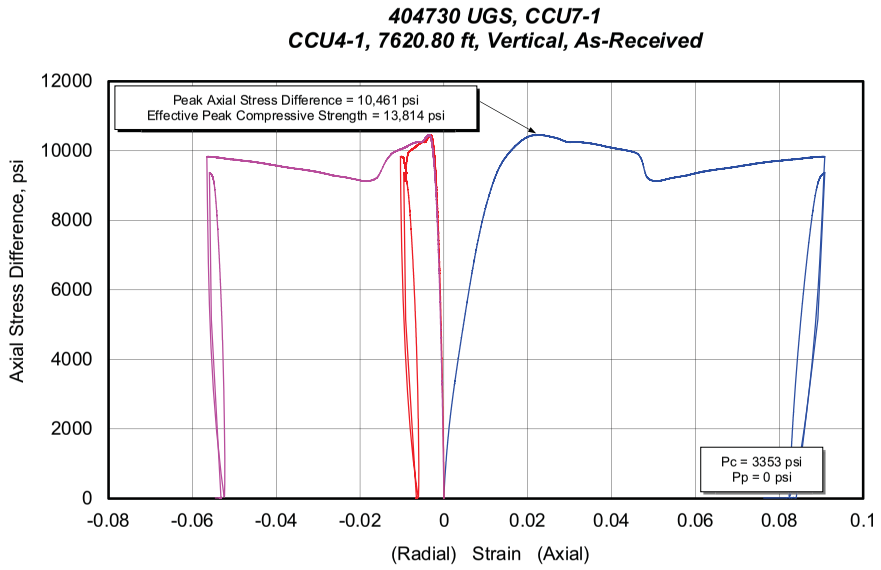

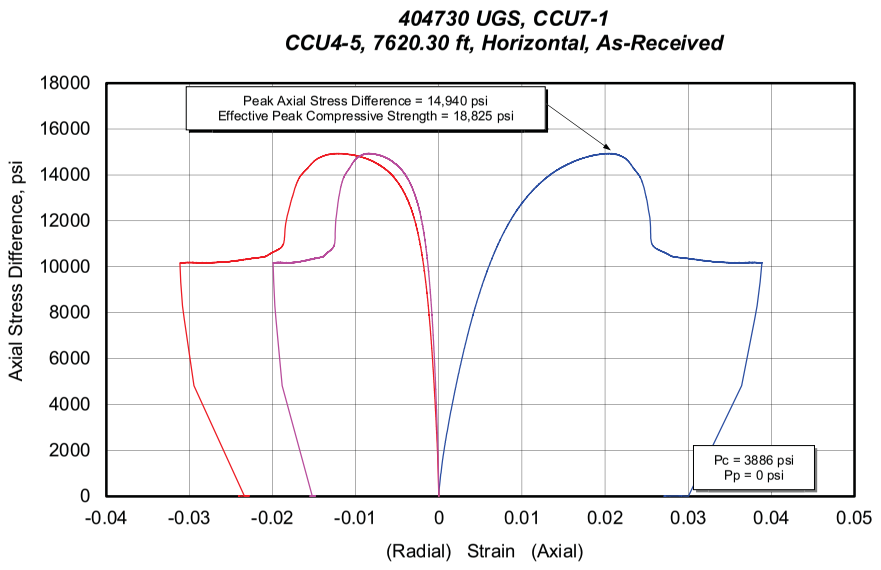

Fidelity Cane Creek CCU7-1

Lithology	Sample ID	Depth (ft)	Orientation	As Received Bulk Density (g/cm^3)	Confining Pressure (psi)	Peak Effective Compressive Strength (psi)	Effective Residual Compressive Strength (psi)	Young's Modulus (10^6 psi)	Poisson's Ratio
silty dolomite - shale	CCU3-1	7619.00	Vertical	2.509	3352	18,220	-	1.686	0.28
	CCU3-5	7619.20	Horizontal	2.500	3886	21,688	16,561	2.054	0.24

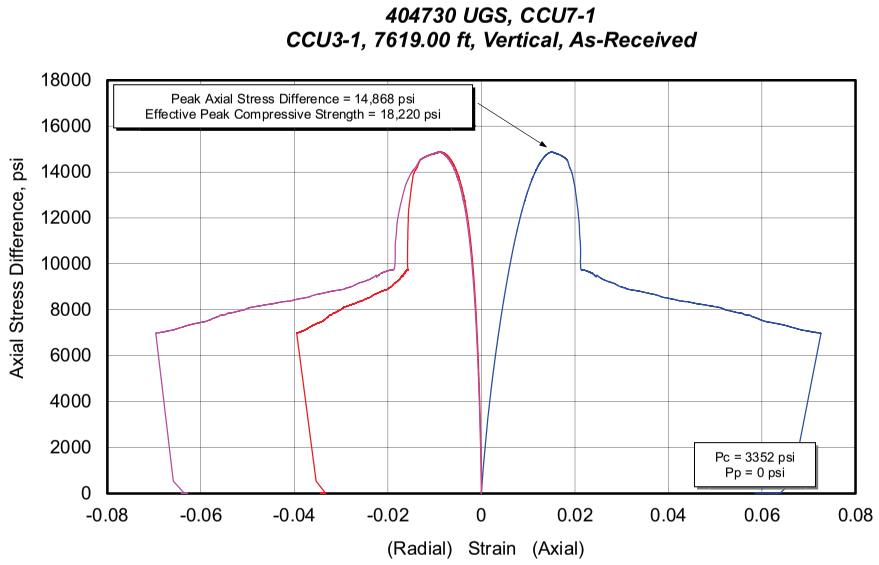

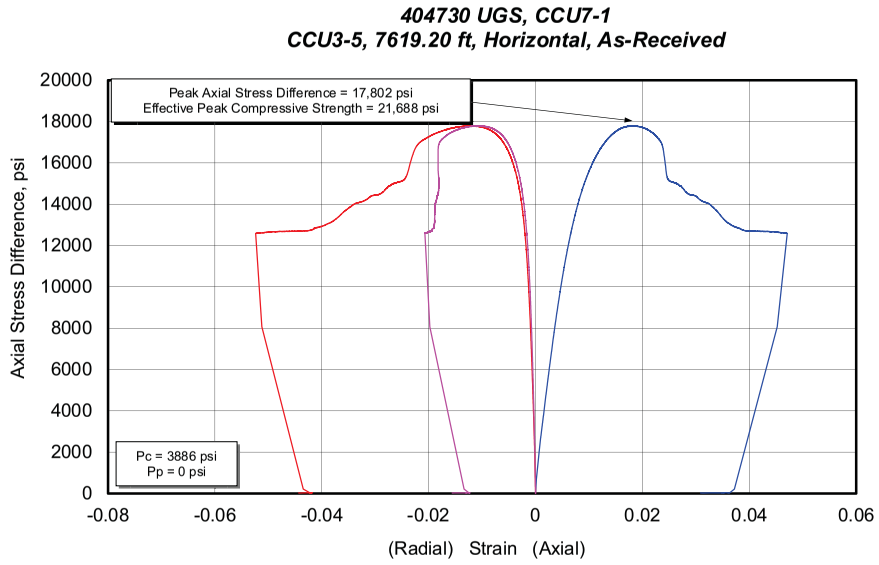

Fidelity Cane Creek CCU7-1

Lithology	Sample ID	Depth (ft)	Orientation	As Received Bulk Density (g/cm^3)	Confining Pressure (psi)	Peak Effective Compressive Strength (psi)	Effective Residual Compressive Strength (psi)	Young's Modulus (10^6 psi)	Poisson's Ratio
anhydrite	CCU2-1	7614.00	Vertical	2.886	3350	31,827	19,750	7.383	0.34
	CCU2-3	7614.65	Horizontal	2.954	3883	33,347	21,675	8.060	0.33

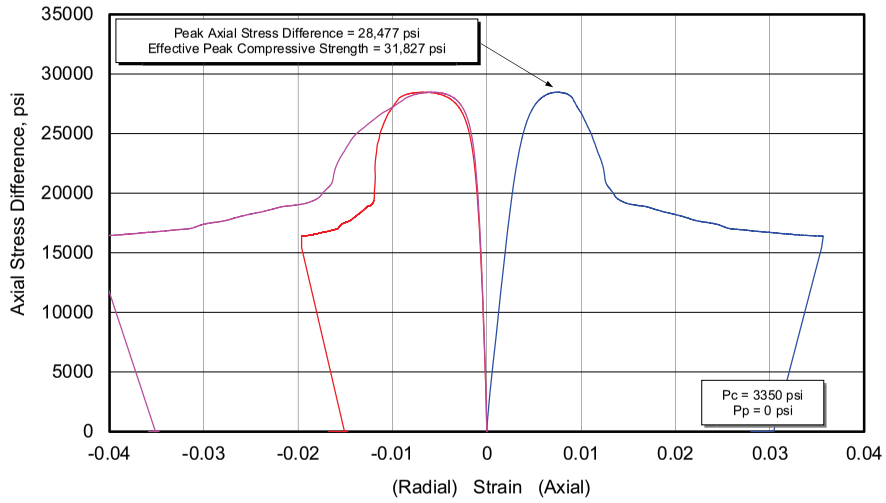

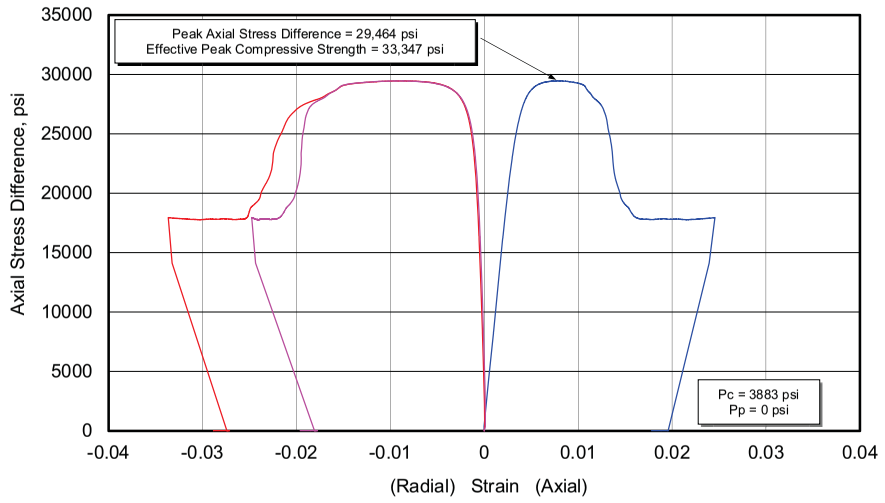

Fidelity Cane Creek CCU7-1

Lithology	Sample ID	Depth (ft)	Orientation	As Received Bulk Density (g/cm^3)	Confining Pressure (psi)	Peak Effective Compressive Strength (psi)	Effective Residual Compressive Strength (psi)	Young's Modulus (10^6 psi)	Poisson's Ratio
silty dolomite	CCU1-1	7609.35	Vertical	2.624	3348	28,755	20,162	3.447	0.23
	CCU1-3	7609.15	Horizontal	2.599	3881	44,946	24,935	5.507	0.30

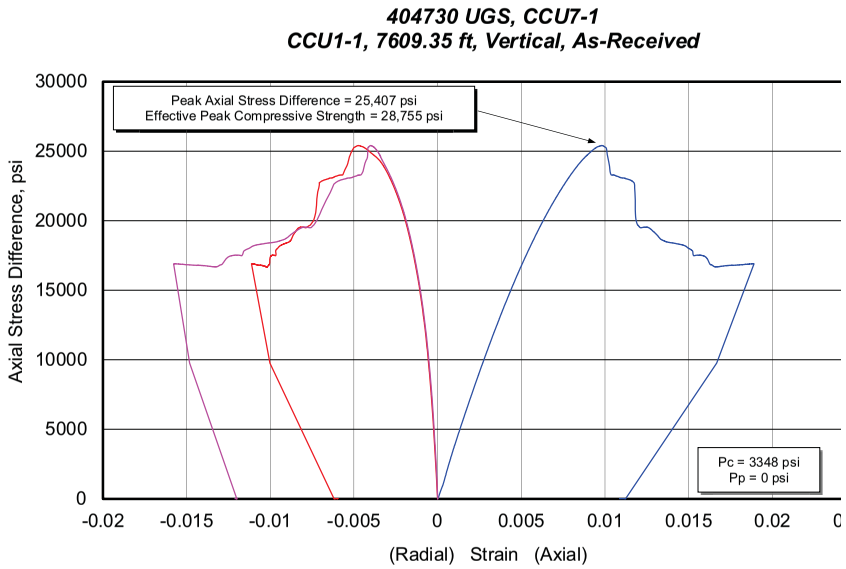

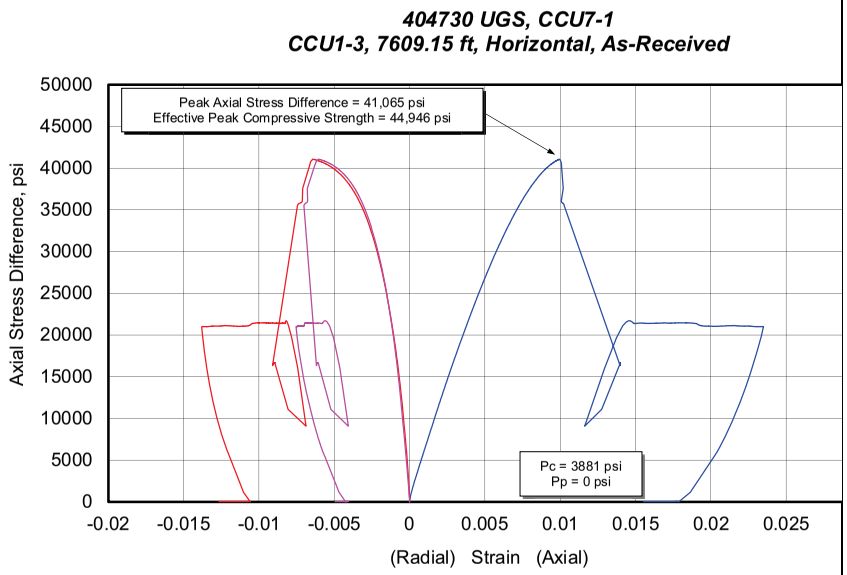

Newfield Cesspooch

ELEV_GR => 5,310 Active Only Read Only Save (*=Aliased) Default Sort Order

Fm Name	Src	MD	SSTVD	TVD	QUAL	Time(ms)	Rpt	Sym	HoleAngle	ChgDate	Remark	Description
GRNRVR *	DWS							0				GREEN RIVER
TRONA_TOP *	DWS							0				TRONA_TOP
MAHOGANY_BENCH_	DWS							0				MAHOGANY_BENCH_T
GG *	ZJG	6,041	-731	6,041				0	0.5	07/24/2013		Garden Gulch
GG1 *	ZJG	6,312	-1,001	6,311				0	0.7	07/24/2013		Garden Gulch 1
GG2 *	ZJG	6,461	-1,151	6,461				0	0.6	07/24/2013		Garden Gulch 2
DGCK *	ZJG	7,150	-1,839	7,149				0	0.6	07/26/2013		Douglas Creek
BLS *	DWS							0				BLS
LBLKSH *	LJF							0				Lower Black Shale Top
CPLS *	ZJG							0				Castle Peak
CP_LIMES *	ZJG							0				CP_LIMES
CP_LIMES_2 *	ZJG							0				CP_LIMES_2
BSCARB *	ZJG	8,435	-3,123	8,433				0	4.0	08/16/2013		BSCARB
BSCARB_A *	ZJG	8,452	-3,140	8,450				0	4.0	08/16/2013		BSCARB_A
BSCARB_B *	ZJG	8,467	-3,154	8,464				0	4.0	08/16/2013		BSCARB_B
BSCARB_C *	ZJG	8,499	-3,186	8,496				0	4.0	08/16/2013		BSCARB_C
BSCARB_C_PZ *	ZJG	8,512	-3,199	8,509				0	4.0	08/16/2013		BSCARB_C_PZ
BSCARB_C_BZ *	ZJG	8,517	-3,204	8,514				0	4.0	08/16/2013		BSCARB_C_BZ
BSCARB_C_PZ2	ZJG	8,532	-3,219	8,529				0	3.9	08/16/2013		BSCARB_C_PZ2
BSCARB_C_BZ2	ZJG	8,536	-3,223	8,533				0	3.9	08/16/2013		BSCARB_C_BZ2
BSCARB_D_PZ	ZJG	8,561	-3,248	8,558				0	3.9	08/16/2013		BSCARB_D_PZ
BSCARB_D_BZ	ZJG	8,566	-3,253	8,563				0	3.9	08/16/2013		BSCARB_D_BZ
BSCARB_D *	ZJG	8,539	-3,227	8,537				0	3.9	08/16/2013		BSCARB_D
WASATCH *	ZJG	8,590	-3,278	8,588				0	3.9	08/16/2013		WASATCH
TF10 *	BAC	8,766	-3,453	8,763				0	4.1	08/15/2013		TF10
TF15 *	BAC	9,004	-3,691	9,001				0	4.0	08/12/2013		Tertiary Flagstaff TF15
TF28 *	BAC	9,365	-4,051	9,361				0	3.3	08/12/2013		TF28
604PCRV	3							0				

Figure C-25. Formation Tops

Table C-57. Depth Shifting

LOGDEPTH	COREDEPTH
FEET	FEET
8457.2	8455
8477.5	8475.3
8482.2	8480
8487.5	8485.3
8493.05	8490.85
8498.170887	8496.041506
8502.421222	8500.394603
8506.159469	8504.223231
8511.280356	8509.467927
8515.530692	8513.821024
8520.088281	8518.488803
8524.64587	8523.156582
8529.766756	8528.401278
8532.890497	8531.600543
8536.98414	8535.497678
8540.571827	8538.798062

LOGDEPTH	COREDEPTH
FEET	FEET
8545.115889	8543.273364
8549.711589	8548.019534
8553.652207	8551.871616
8557.545912	8555.524856
8560.407551	8558.209766
8564.066696	8561.642931
8568.331944	8565.795348
8572.031918	8569.598072
8574.601344	8572.238853
8577.787433	8575.513421
8582.174316	8580.264958
8585.991474	8584.61442
8590.093495	8589.288468
8594.147485	8593.573155
8597.058042	8596.598634
8599.916625	8599.570087
8603.398898	8603.189857
8606.829198	8606.7556
8612.026621	8612.158241

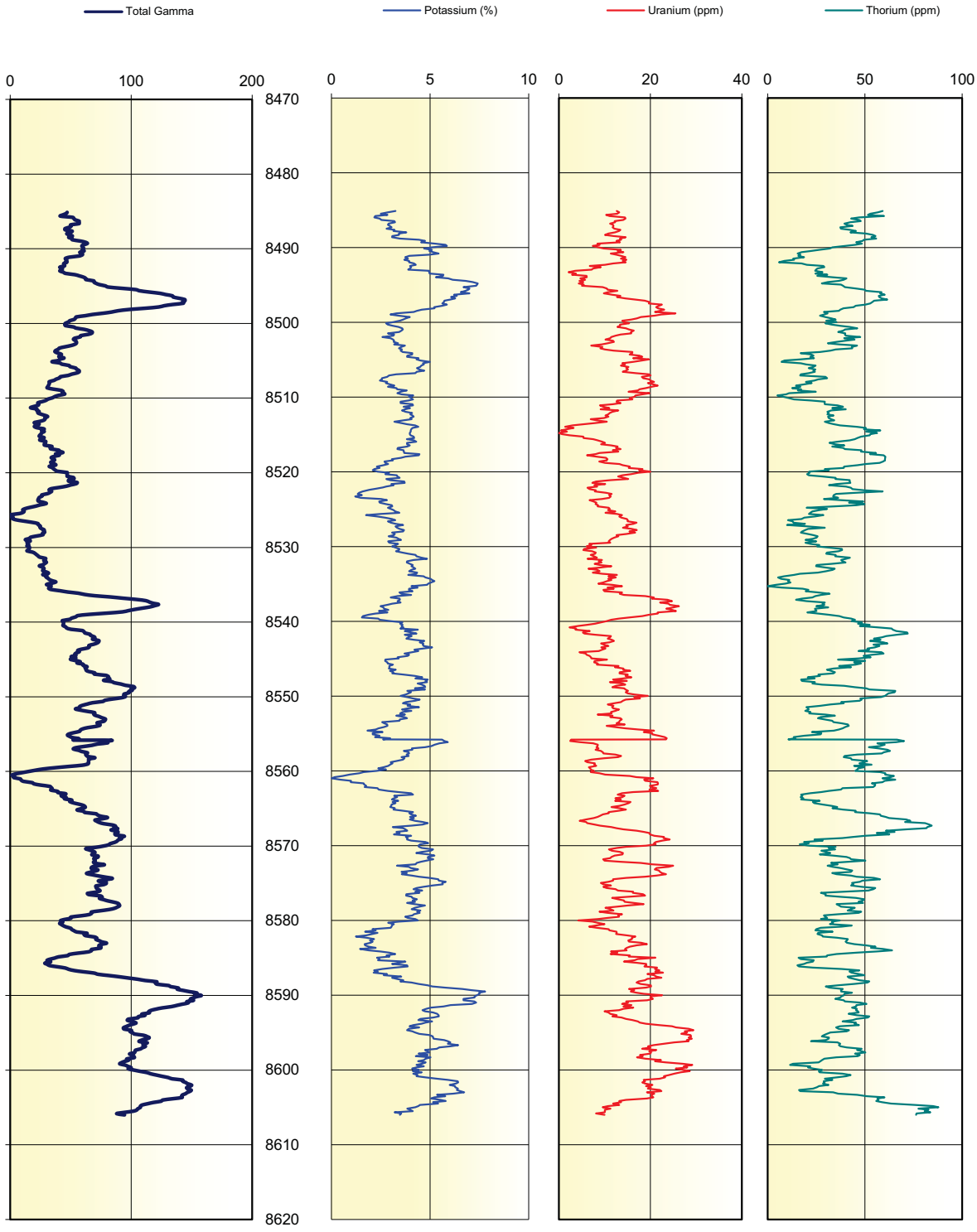

Figure C-26. Core Gamma – Newfield Cesspooch?

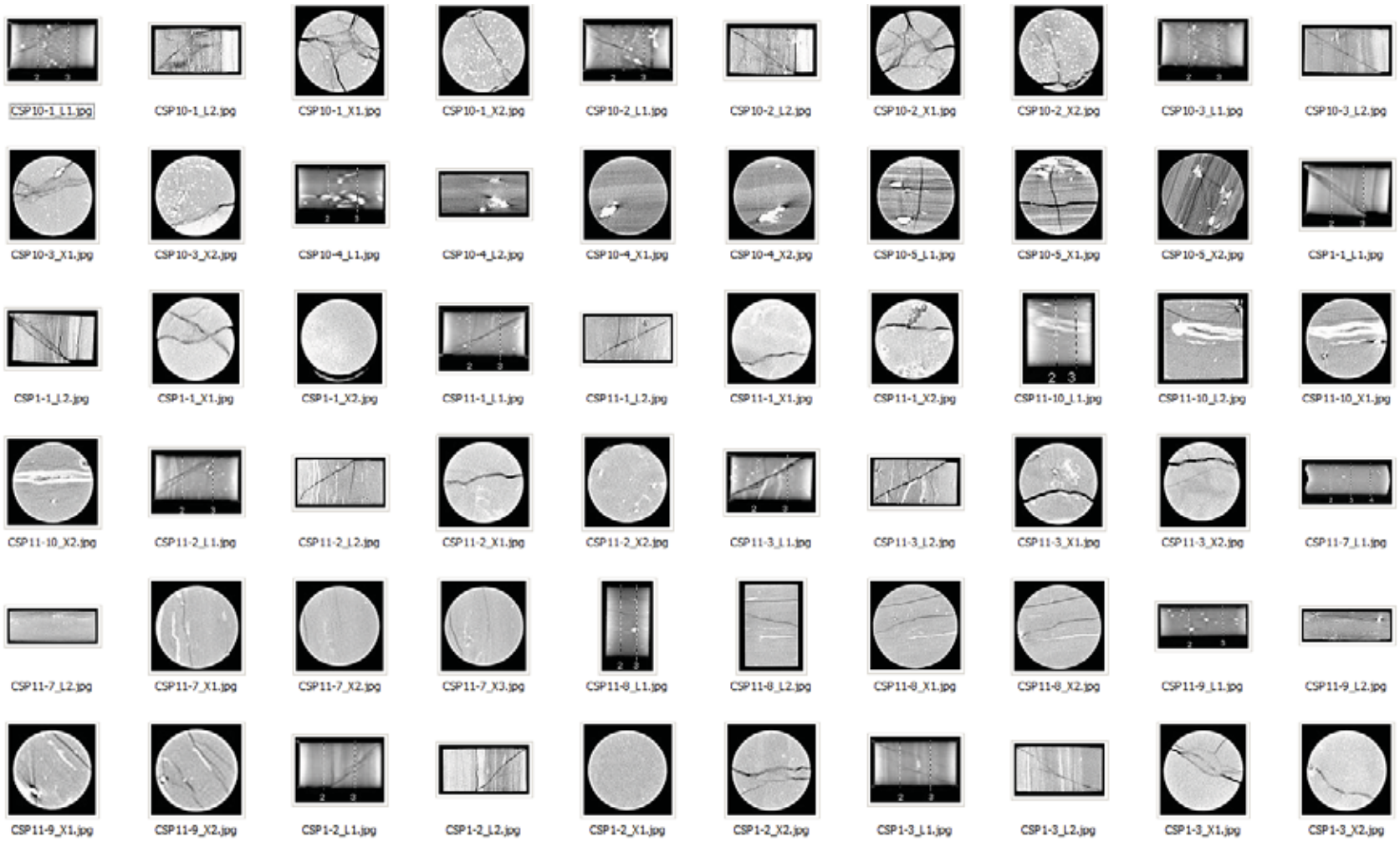

Figure C-27. CT scans - Newfield Cesspooch

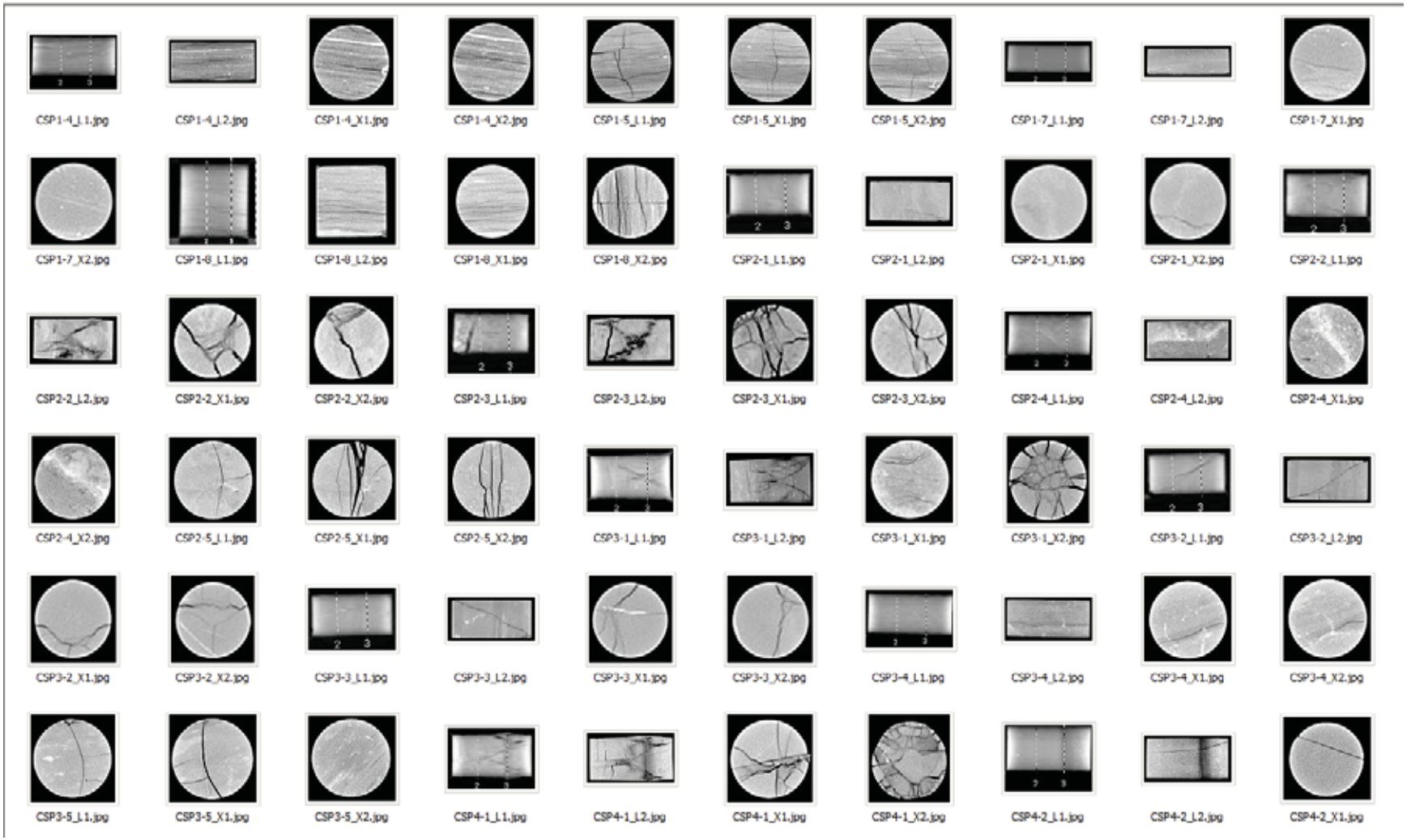

Figure C-27a. CT scans - Newfield Cesspooch

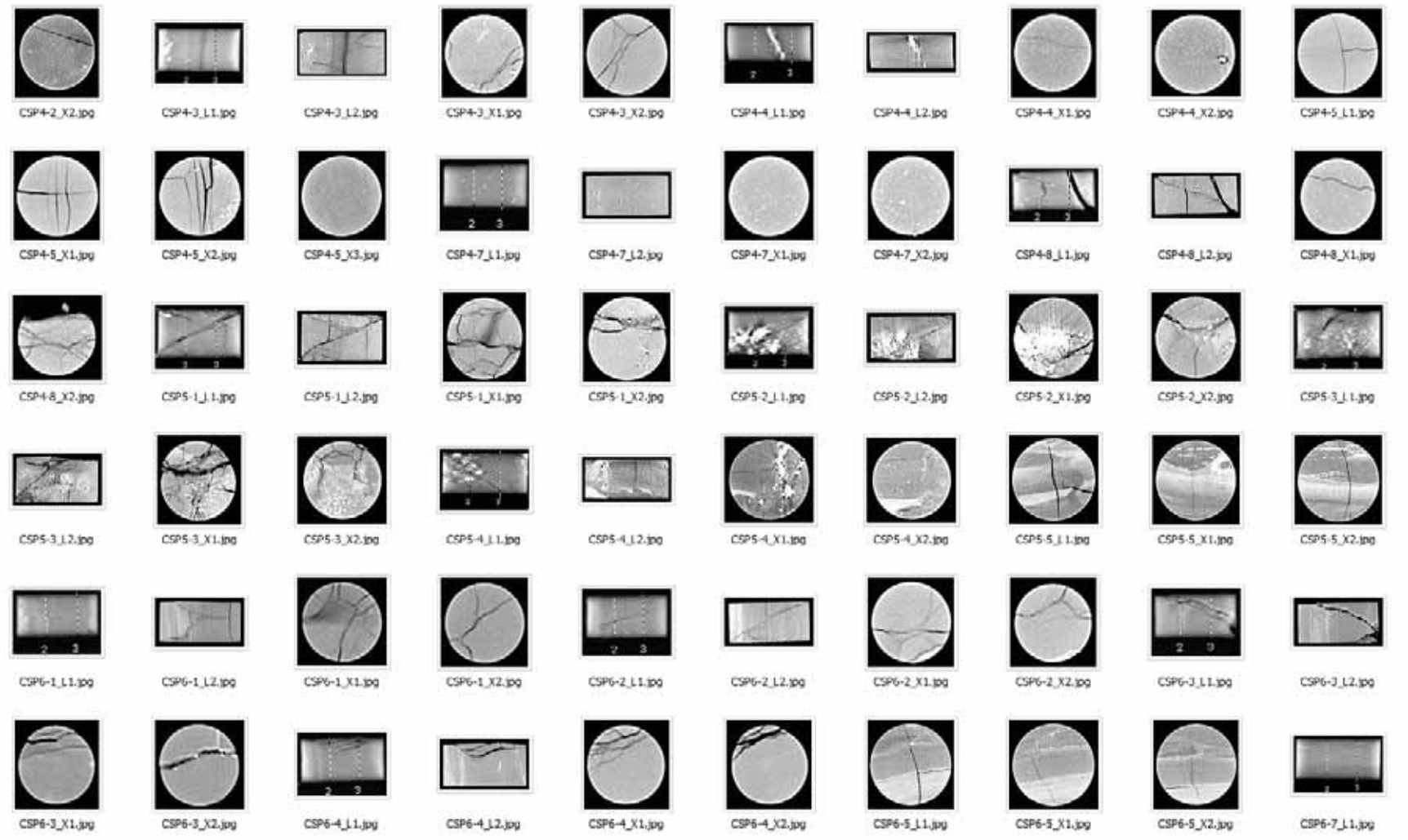

Figure C-27b. CT scans - Newfield Cesspooch

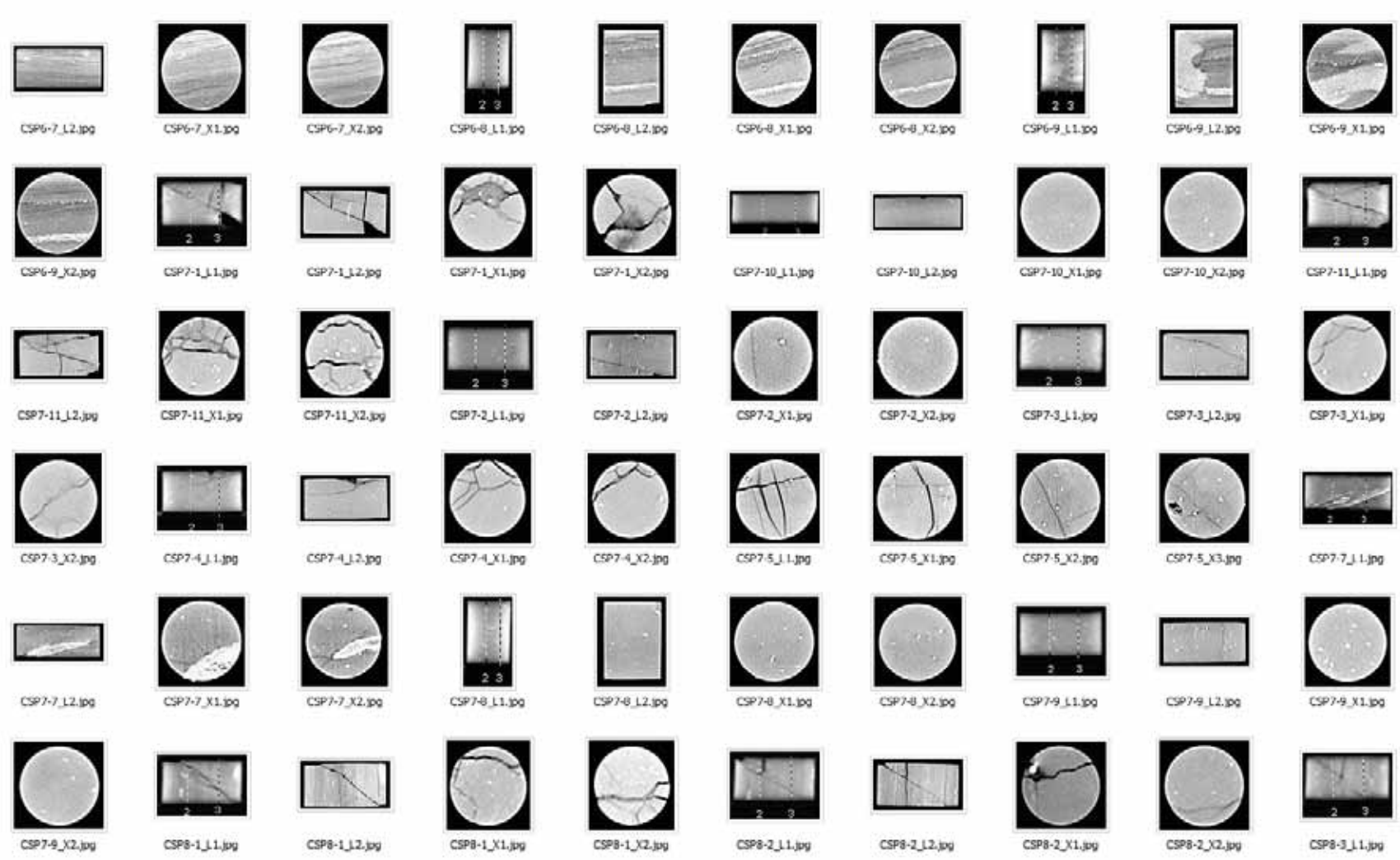

Figure C-27c. CT scans - Newfield Cesspooch

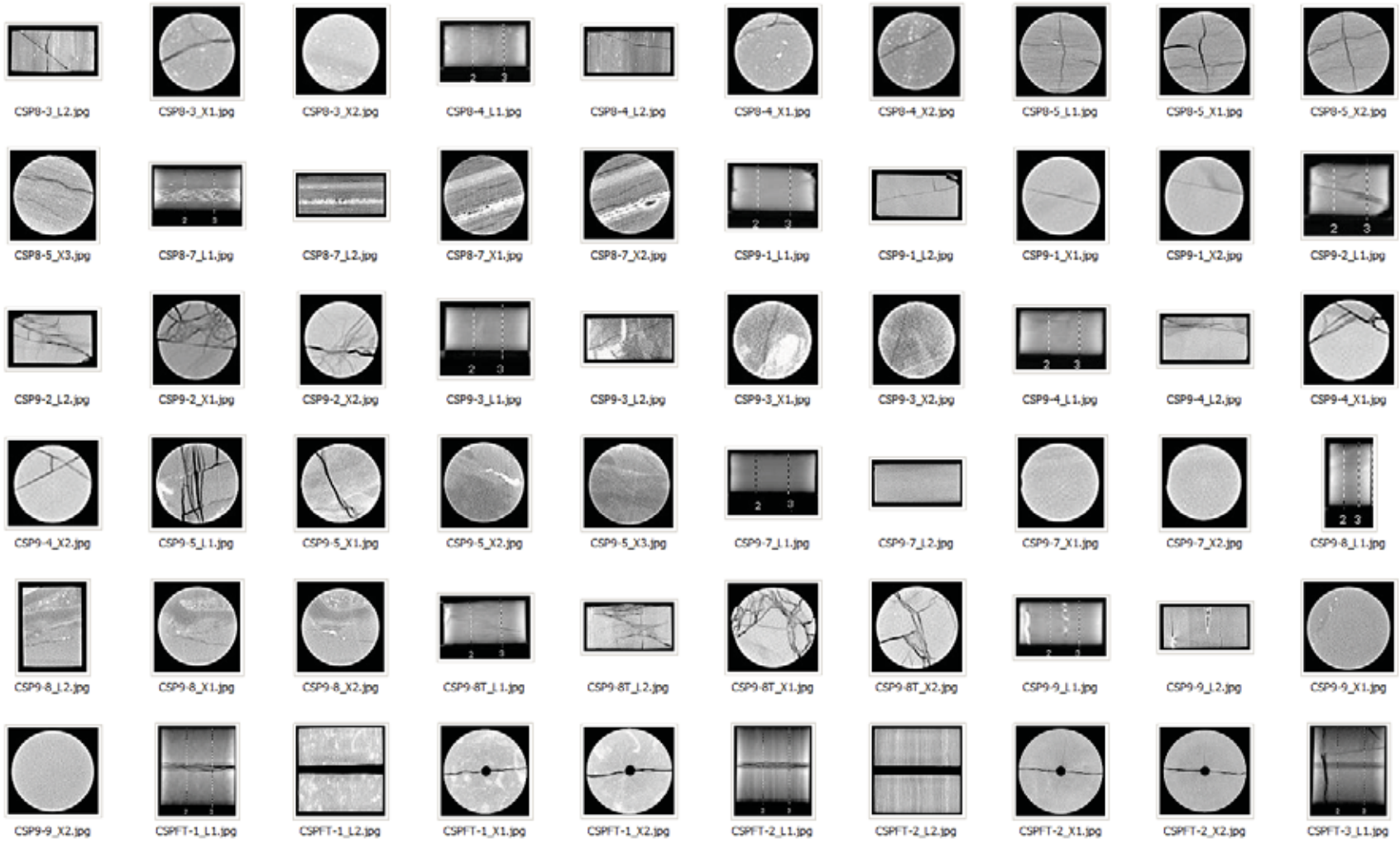

Figure C-27d. CT scans - Newfield Cesspooch

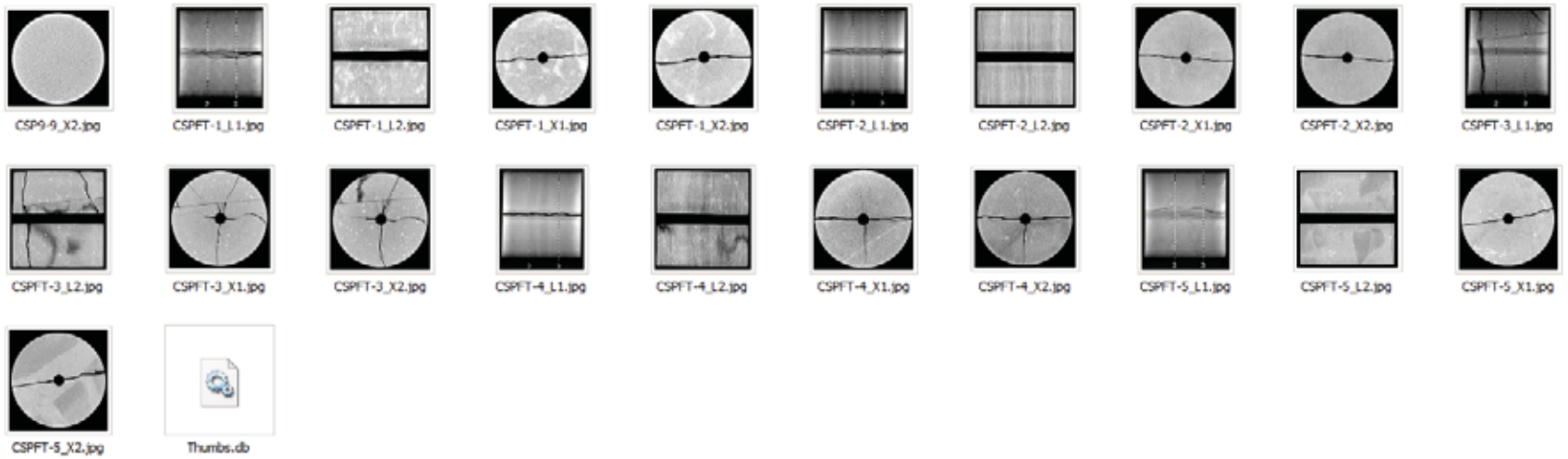

Figure C-27e. CT scans - Newfield Cesspooch

Table C-58. X-Ray Diffraction Data – Newfield Cesspooch

Sample	Depth Log (ft)	Depth Core (ft)	Offset	Illite	Interlayered illite/smectite	% illite in I/S	Quartz	Plagioclase	K-feldspar	Calcite	Dolomite	Pyrite	Scaled GR	Scaled LLD	Scaled DTC	Scaled DTS	Scaled PE	Scaled Nphi_LS	Scaled Nphi_SS	Scaled LLS
1	8487.99	8485.35	2.64	9	0		11	6	2	10	61	1	0.37	0.04	0.68	0.65	0.75	0.48	0.55	0.08
2	8490.41	8487.8	2.61	12	0		13	3	1	60	11	0	0.35	0.02	0.67	0.62	0.84	0.43	0.50	0.04
3	8493.08	8490.5	2.58	0	0		18	1	1	9	70	0	0.45	0.02	0.68	0.63	0.68	0.53	0.59	0.04
4	8495.26	8492.7	2.56	0	0		8	0	0	1	91	0	0.45	0.02	0.68	0.60	0.66	0.41	0.48	0.04
5	8497.04	8494.5	2.54	0	18	> 90%	12	2	1	60	8	0	0.57	0.02	0.75	0.69	0.71	0.54	0.60	0.04
6	8498.77	8496.25	2.52	0	38	> 90%	24	9	2	16	7	4	0.88	0.03	0.80	0.72	0.68	0.70	0.74	0.05
4-Jan	8500.1	8497.55	2.51	26.3	0		20	14.9	0	21.2	15.2	2.5	0.58	0.02	0.76	0.68	0.67	0.68	0.73	0.04
7	8501.39	8498.9	2.49	5	0		26	0	0	2	67	0	0.32	0.03	0.72	0.66	0.68	0.65	0.70	0.06
8	8503.62	8501.15	2.47	3	0		19	0	0	5	73	0	0.49	0.03	0.70	0.65	0.69	0.51	0.57	0.06
9	8508.07	8505.65	2.42	0	12	> 90%	13	0	0	64	10	1	0.34	0.03	0.63	0.58	0.83	0.33	0.41	0.06
10	8511.78	8509.4	2.38	24	0		19	8	2	40	6	2	0.31	0.04	0.58	0.51	0.65	0.51	0.57	0.07
43	8514.16	8511.8	2.36	0	0		29	0	0	0	70	0	0.13	0.03	0.59	0.50	0.71	0.59	0.64	0.05
NA	8514.26	8511.9	2.36	0	0		13	0	0	0	86	0	0.13	0.03	0.60	0.50	0.72	0.60	0.65	0.05
11	8514.85	8512.5	2.35	0	0		0	0	0	2	97	0	0.15	0.03	0.60	0.50	0.76	0.57	0.63	0.05
4-Feb	8515.4	8513.05	2.34	0	0		13.5	0	0	13.4	73.2	0	0.20	0.03	0.59	0.52	0.75	0.43	0.50	0.06
12	8516.19	8513.85	2.34	4	0		9	0	0	80	7	0	0.24	0.06	0.59	0.53	0.82	0.32	0.40	0.09
4-Mar	8516.8	8514.45	2.33	11.9	0		10.1	0	0	64.1	13.1	0.9	0.22	0.08	0.59	0.52	0.90	0.28	0.35	0.12
13	8519.8	8517.5	2.3	6	0		9	0	0	71	14	0	0.27	0.15	0.62	0.55	0.85	0.35	0.42	0.22
14	8525.63	8523.4	2.23	5	0		7	0	0	80	7	0	0.19	0.29	0.55	0.50	0.91	0.19	0.28	0.39
15	8528.6	8526.4	2.2	1	0		5	0	0	91	2	0	0.22	0.45	0.55	0.49	0.93	0.18	0.27	0.46
2-Apr	8530.9	8528.7	2.18	3.1	0		8.3	0	0	72.2	16.5	0	0.17	0.85	0.58	0.52	0.93	0.21	0.29	0.79

Sample	Depth Log (ft)	Depth Core (ft)	Offset	Illite	Interlayered illite/smectite	% illite in I/S	Quartz	Plagioclase	K-feldspar	Calcite	Dolomite	Pyrite	Scaled GR	Scaled LLD	Scaled DTC	Scaled DTS	Scaled PE	Scaled Nphi_LS	Scaled Nphi_SS	Scaled LLS
16	8532.12	8529.95	2.17	0	0		4	0	0	87	9	0	0.17	0.53	0.60	0.53	0.89	0.25	0.33	0.69
1V	8532.66	8530.5	2.16	3	0		8	2	0	69	18	0	0.18	0.15	0.61	0.54	0.84	0.36	0.43	0.20
44	8533.06	8530.9	2.16	5	0		8	2	0	63	21	0	0.21	0.11	0.62	0.55	0.77	0.48	0.54	0.15
4-May	8533.7	8531.6	2.15	0	0		9.1	0	0	2	88.9	0	0.24	0.07	0.62	0.55	0.66	0.61	0.66	0.11
17	8534.89	8532.75	2.14	7	0		6	0	0	5	83	0	0.25	0.06	0.63	0.56	0.66	0.52	0.58	0.10
18	8537.36	8535.25	2.11	10	0		7	0	0	78	4	2	0.31	0.07	0.70	0.64	0.85	0.32	0.40	0.15
19	8538.79	8536.7	2.09	20	0		14	9	2	43	12	2	0.64	0.02	0.74	0.66	0.79	0.83	0.86	0.04
7-Jun	8540.1	8538.05	2.08	6	0		8.8	3.2	0	14.8	66.1	1	0.69	0.03	0.69	0.60	0.72	0.74	0.78	0.06
3-Jun	8540.2	8538.1	2.08	11.7	0		10.8	6.3	0	23	46.9	1.3	0.68	0.03	0.69	0.60	0.72	0.73	0.77	0.06
20	8541.17	8539.1	2.07	4	0		13	0	0	2	81	0	0.47	0.06	0.67	0.60	0.70	0.63	0.68	0.12
21	8545.37	8543.35	2.02	0	25	> 90%	14	0	0	53	8	1	0.42	0.02	0.66	0.59	0.86	0.42	0.49	0.04
22	8548.19	8546.2	1.99	0	12	> 90%	8	0	0	50	29	1	0.35	0.07	0.71	0.63	0.79	0.48	0.55	0.13
23	8552.99	8551.05	1.94	0	14	> 90%	15	2	0	55	13	0	0.50	0.02	0.66	0.60	0.79	0.65	0.70	0.06
24	8557.15	8555.25	1.9	9	0		8	1	0	76	5	0	0.42	0.02	0.64	0.59	0.87	0.38	0.45	0.03
2-Jul	8559.8	8557.9	1.87	3.5	0		7.6	1.9	0	73.1	13.2	0.7	0.31	0.10	0.63	0.55	0.90	0.30	0.38	0.22
25	8560.56	8558.7	1.86	0	0		72	0	0	2	26	0	0.39	0.14	0.61	0.54	0.87	0.32	0.40	0.22
2V	8561.75	8559.9	1.85	2	0		1	2	0	2	93	0	0.36	0.20	0.58	0.50	0.71	0.46	0.52	0.39
26	8562.44	8560.6	1.84	0	0		20	0	0	2	78	0	0.23	0.52	0.58	0.49	0.70	0.48	0.55	0.68
7-Sep	8564	8562.15	1.82	11	0		12	4	0	51.6	20.5	1	0.10	0.54	0.64	0.55	0.65	0.51	0.57	0.68
NA	8564.42	8562.6	1.82	0	0		32	0	0	7	60	0	0.12	0.58	0.67	0.57	0.65	0.52	0.58	0.65
45	8564.42	8562.6	1.82	0	0		6	0	0	6	88	0	0.12	0.58	0.67	0.57	0.65	0.52	0.58	0.65
27	8564.57	8562.75	1.82	0	0		11	0	0	11	77	1	0.13	0.54	0.67	0.58	0.65	0.51	0.57	0.61

Sample	Depth Log (ft)	Depth Core (ft)	Offset	Illite	Interlayered illite/smectite	% illite in I/S	Quartz	Plagioclase	K-feldspar	Calcite	Dolomite	Pyrite	Scaled GR	Scaled LLD	Scaled DTC	Scaled DTS	Scaled PE	Scaled Nphi_LS	Scaled Nphi_SS	Scaled LLS
28	8565.56	8563.75	1.81	0	32	> 90%	15	0	0	27	9	17	0.24	0.07	0.72	0.63	0.72	0.46	0.52	0.12
29	8568.72	8566.95	1.77	0	21	> 90%	11	2	0	16	47	2	0.57	0.01	0.74	0.69	0.78	0.57	0.63	0.03
1-Aug	8571.4	8569.7	1.74	0	0		3.8	0	0	12.1	83.6	0	0.53	0.02	0.78	0.68	0.81	0.64	0.69	0.05
30	8571.69	8569.95	1.74	28	0		20	0	0	45	7	1	0.51	0.02	0.79	0.69	0.79	0.60	0.65	0.06
31	8574.81	8573.1	1.71	0	23	> 90%	14	2	0	52	9	1	0.54	0.01	0.78	0.70	0.76	0.63	0.68	0.02
32	8577.58	8575.9	1.68	8	0		11	8	0	16	56	1	0.48	0.02	0.76	0.67	0.86	0.53	0.59	0.05
33	8577.63	8575.95	1.68	8	0		11	7	0	15	57	1	0.48	0.02	0.76	0.67	0.87	0.53	0.59	0.05
34	8582.53	8580.9	1.63	4	0		7	4	0	73	11	0	0.32	0.20	0.73	0.66	0.93	0.76	0.79	0.38
35	8585.49	8583.9	1.59	0	0		13	0	0	5	82	0	0.33	0.04	0.76	0.66	0.74	0.52	0.58	0.09
36	8587.42	8585.85	1.57	7	0		11	3	0	73	6	0	0.28	0.10	0.84	0.75	0.94	0.53	0.59	0.24
4-Oct	8592	8590.45	1.52	29.8	0		21.2	5.8	9.3	0	34	0	0.83	0.01	0.79	0.68	0.75	0.73	0.77	0.02
37	8592.47	8590.95	1.52	0	29	> 90%	21	14	9	2	23	3	0.87	0.01	0.78	0.66	0.75	0.74	0.78	0.02
38	8595.68	8594.2	1.48	23	0		11	4	5	7	50	0	0.64	0.02	0.74	0.63	0.69	0.63	0.68	0.04
39	8598.36	8596.9	1.46	0	22	> 90%	15	11	6	10	36	0	0.71	0.03	0.73	0.61	0.68	0.63	0.68	0.05
40	8601.32	8599.9	1.42	6	0		17	7	3	7	62	0	0.67	0.02	0.86	0.73	0.62	0.70	0.74	0.04
41	8604.34	8602.95	1.39	0	32	> 90%	18	5	13	1	29	2	0.87	0.01	0.79	0.66	0.67	0.74	0.77	0.02
42	8606.86	8605.5	1.36	4	0		6	3	0	0	87	0	0.53	0.04	0.73	0.61	0.66	0.58	0.63	0.07

Table C 60. Brittleness – Newfield Cesspooch

Sample	Orientation	Core Depth	Log Depth	BI1	BI2	BI3a	BI3b	BI4	BI5
CSP1-1	Vertical	8497.05	8495.45	1.12	0.73	5.19E-04	-5.43E-03	1.83	0.21
CSP1-2	Vertical	8497.05	8495.45	0.90	0.83	1.75E-04	-8.79E-03	2.40	0.80
CSP1-3	Vertical	8497.3	8495.7	1.14	0.37	2.90E-03	-1.34E-02	1.79	0.45
CSP2-1	Vertical	8513.5	8511.9	1.10	0.45	8.89E-06	-4.68E-04	1.23	0.95
CSP2-2	Vertical	8513.5	8511.9	1.14	0.20	3.59E-03	-8.56E-02	5865.13	0.70
CSP2-3	Vertical	8513.5	8511.9	1.19	0.04	7.45E-03	-2.11E-02	2.67	0.20
CSP3-1	Vertical	8514.5	8512.9	1.25	0.15	1.43E-03	-1.43E-03	1.52	0.27
CSP3-2	Vertical	8514.35	8512.75	1.28	0.35	6.58E-04	-6.92E-03	1.94	0.65
CSP3-3	Vertical	8514.35	8512.75	1.18	0.97	4.01E-04	-1.08E-02	2.97	0.64
CSP4-1	Vertical	8528.7	8527.1	1.06	0.19	4.32E-04	-4.93E-03	1.55	0.42
CSP4-3	Vertical	8528.9	8527.3	1.53	0.39	8.16E-05	-1.44E-03	1.43	0.53
CSP4-8	Vertical	8528.75	8527.15	1.14	0.96	2.24E-04	-2.01E-03	1.52	0.36
CSP5-1	Vertical	8531.55	8529.95	1.26	0.03	4.19E-03	-1.71E-02	2.02	0.13
CSP5-2	Vertical	8531.55	8529.95	1.14	0.31	4.95E-04	-4.83E-03	1.96	0.29
CSP5-3	Vertical	8531.55	8529.95	1.09	0.11	1.67E-03	-4.93E-03	1.94	0.12
CSP6-1	Vertical	8538.1	8536.5	1.23	0.24	6.18E-04	-4.51E-03	1.65	0.49
CSP6-2	Vertical	8538.1	8536.5	1.40	0.32	9.72E-04	-1.91E-03	1.79	0.49
CSP6-3	Vertical	8538.1	8536.5	1.11	0.21	6.39E-04	-1.38E-03	1.85	0.16
CSP7-1	Vertical	8557.9	8556.3	1.19	0.05	4.91E-03	-2.15E-02	2.78	0.20
CSP7-3	Vertical	8557.9	8556.3	1.28	0.37	4.12E-04	-2.18E-03	1.49	0.30
CSP7-11	Vertical	8557.45	8555.85	1.26	0.76	3.50E-04	-9.66E-03	2.32	0.22
CSP8-1	Vertical	8569.7	8568.1	1.07	0.05	4.65E-03	-2.21E-02	2.42	0.27
CSP8-2	Vertical	8569.7	8568.1	1.16	0.69	4.77E-04	-7.59E-03	2.68	0.72
CSP8-3	Vertical	8569.7	8568.1	1.46	0.24	3.67E-04	-2.61E-03	1.37	0.49
CSP9-1	Vertical	8561.9	8560.3	1.29	0.78	1.93E-05	1.20E-04	1.34	0.40

Sample	Orientation	Core Depth	Log Depth	BI1	BI2	BI3a	BI3b	BI4	BI5
CSP9-2	Vertical	8561.9	8560.3	1.31	0.02	9.24E-04	-3.89E-03	2.08	0.25
CSP9-3	Vertical	8561.9	8560.3	1.63	0.05	7.77E-05	-3.55E-04	1.85	0.32
CSP9-8T	Vertical	8560.3	8558.7	1.22	0.12	3.58E-03	-1.79E-01	6969.14	0.67
CSP10-1	Vertical	8590.1	8588.5	1.12	0.21	8.51E-04	6.51E-02	8335.22	0.39
CSP10-2	Vertical	8590.1	8588.5	1.24	0.02	3.08E-03	-1.57E-02	2.22	0.31
CSP10-3	Vertical	8590.1	8588.5	1.23	0.21	3.67E+01	-1.67E-02	2.23	0.47
CSP11-1	Vertical	8549.3	8547.7	1.31	1.79	1.27E-04	-4.60E-03	2.11	0.64
CSP11-2	Vertical	8549.3	8547.7	1.21	0.90	1.10E-04	-2.29E-03	1.55	0.58
CSP11-3	Vertical	8549.3	8547.7	1.12	0.13	1.66E-04	-3.98E-03	2.28	0.30

Initials In-Situ Stress Estimates

The total vertical stress has been estimated by integrating the density logs. An initial estimate of the closure stress has been made for each of the wells using information from the daily reports. Similarly, daily reports are being evaluated to estimate closure stress, so that the minimum horizontal stress has been determined. These data have been used to specify effective confining pressure for the TerraTek triaxial testing. They will also be correlated with logging data so that we can have a profile of in-situ stress with depth for each of the wells. This is required for upcoming hydraulic fracturing simulations.

Fracture Toughness and Brittleness Index Correlations:

For each well, six different brittleness indices were calculated. These indices were then attempted to be correlated with the wells log data. First many correlations were carried out for BI5 and then some of the correlations with the highest values were chosen to be carried out for the other five brittleness indices. Then logging parameters that were common to all wells were chosen and correlations were carried out for those parameters using combined logging and brittleness data for the five wells. For this combined data, different resistivity and porosity data was available from well to well. Porosity data was chosen a sonic porosity as the preference, then neutron porosity and then density porosity. An exception to this was if a well had two porosity logs, say density and neutron porosity, then the log with the least negative values was chosen because of the compatibility with creating a liner natural log correlation. Below the notation for variables written as ln(var1-var2-var3- . . .) means that the natural log of each of the variables inside the parenthesis was taken along with the given brittleness index. These values were used to create a multiple linear regression with the natural log of the logging variables as the x values and the natural log of the brittleness index as the y value. If the regression uses more than one x variable then the adjusted R^2 value is more relevant although both values are reported. Table C-59 contain these values.

Table C-59. Brittleness Index Correlations by Well

BTR14-3-45

BI1							
Variables (X1,X2,X3,X4)	R^2	Adjusted R^2	X1 Coefficient	X2 Coefficient	X3 Coefficient	X4 Coefficient	Intercept
DRHO	0.26	0.08	-7.76				0.59
PE	0.10	-0.13	0.38				-0.99
DRHO-PE	0.37	-0.05	-7.91	0.40			-0.87
ln(NPHI-GR)	0.48	0.13	-9.08	-0.71			-11.34
ln(NPHI)	0.48	0.35	-9.73				-15.43
ln(NPHI-SP)	0.48	0.13	-9.32	-0.56			-12.35
ln(NPHI-GR-SP)	0.48	-0.21	-9.32	0.00	-0.56		-12.35
ln(NPHI-PE)	0.48	0.13	-9.72	0.03			-15.44
ln(LLD)	0.15	-0.07	-1.36				2.70
ln(PE-LLD-NPHI-GR)	0.48	-0.54	0.00	-0.01	-9.71	0.00	-15.37
ln(PE)	0.12	-0.10	4.19				-6.57
ln(SP)	0.47	0.34	-13.08				55.80
ln(SP-PE)	0.48	0.13	-13.71	-0.70			59.43
ln(GR-SP)	0.48	0.13	-27.26	21.22			26.64
BI2							
Variables (X1,X2,X3,X4)	R^2	Adjusted R^2	X1 Coefficient	X2 Coefficient	X3 Coefficient	X4 Coefficient	Intercept
DRHO	0.00	-0.25	0.25				0.14
PE	0.73	0.66	1.02				-3.61
DRHO-PE	0.73	0.55	-0.15	1.02			-3.61
ln(NPHI-GR)	0.68	0.47	-180.42	198.82			-1141.34
ln(NPHI)	0.18	-0.02	5.17				7.28
ln(NPHI-SP)	0.68	0.47	-112.47	158.85			-856.95
ln(NPHI-GR-SP)	0.68	0.13	-112.47	0.00	158.85		-856.95
ln(NPHI-PE)	0.68	0.47	0.15	-8.41			10.83
ln(LLD)	0.68	0.60	2.54				-7.43
ln(PE-LLD-NPHI-GR)	0.68	-0.20	0.00	2.60	-0.46	0.00	-8.28
ln(PE)	0.68	0.60	-8.47				10.70
ln(SP)	0.23	0.03	7.78				-34.19
ln(SP-PE)	0.68	0.47	0.20	-8.40			9.71
ln(GR-SP)	0.68	0.47	-329.10	421.78			-386.21

BI3a							
Variables (X1,X2,X3,X4)	R^2	Adjusted R^2	X1 Coefficient	X2 Coefficient	X3 Coefficient	X4 Coefficient	Intercept
DRHO	0.31	0.13	1.28				-0.01
PE	0.10	-0.12	-0.06				0.23
DRHO-PE	0.42	0.03	1.30	-0.06			0.21
ln(NPHI-GR)	0.70	0.50	-89.59	146.74			-785.34
ln(NPHI)	0.69	0.61	47.39				62.40
ln(NPHI-SP)	0.70	0.50	-39.44	117.24			-575.44
ln(NPHI-GR-SP)	0.70	0.17	-39.44	0.00	117.24		-575.44
ln(NPHI-PE)	0.70	0.50	43.68	-6.21			65.02
ln(LLD)	0.30	0.13	7.94				-29.51
ln(PE-LLD-NPHI-GR)	0.70	-0.17	0.00	1.92	43.23	0.00	50.92
ln(PE)	0.27	0.08	-24.92				25.14
ln(SP)	0.70	0.62	64.27				-286.93
ln(SP-PE)	0.70	0.50	61.61	-2.95			-271.53
ln(GR-SP)	0.70	0.50	-115.40	209.44			-410.37
BI3b							
Variables (X1,X2,X3,X4)	R^2	Adjusted R^2	X1 Coefficient	X2 Coefficient	X3 Coefficient	X4 Coefficient	Intercept
DRHO	0.26	0.07	-7.88				0.07
PE	0.11	-0.11	0.42				-1.66
DRHO-PE	0.38	-0.03	-8.05	0.44			-1.53
ln(NPHI-GR)	0.42	0.03	-490.73	556.99			-3180.10
ln(NPHI)	0.25	0.06	29.20				37.69
ln(NPHI-SP)	0.42	0.03	-300.37	445.01			-2383.38
ln(NPHI-GR-SP)	0.42	-0.30	-300.37	0.00	445.01		-2383.38
ln(NPHI-PE)	0.42	0.03	15.13	-23.56			47.64
ln(LLD)	0.38	0.23	9.16				-30.89
ln(PE-LLD-NPHI-GR)	0.42	-0.64	0.00	7.29	13.43	0.00	-5.91
ln(PE)	0.37	0.21	-30.04				33.83
ln(SP)	0.28	0.10	41.57				-186.15
ln(SP-PE)	0.42	0.03	21.34	-22.43			-68.91
ln(GR-SP)	0.42	0.03	-878.87	1147.18			-1126.26

BI4							
Variables (X1,X2,X3,X4)	R^2	Adjusted R^2	X1 Coefficient	X2 Coefficient	X3 Coefficient	X4 Coefficient	Intercept
DRHO	0.25	0.07	-367.81				16.63
PE	0.14	-0.08	-21.57				86.78
DRHO-PE	0.38	-0.04	-359.79	-20.67			92.48
ln(NPHI-GR)	0.34	-0.11	-323.54	345.40			-1995.93
ln(NPHI)	0.00	-0.25	-1.13				-0.56
ln(NPHI-SP)	0.34	-0.11	-205.50	275.95			-1501.88
ln(NPHI-GR-SP)	0.34	-0.44	-205.50	0.00	275.95		-1501.88
ln(NPHI-PE)	0.34	-0.11	-9.86	-14.61			5.62
ln(LLD)	0.21	0.01	3.00				-7.29
ln(PE-LLD-NPHI-GR)	0.34	-0.77	0.00	4.52	-10.91	0.00	-27.59
ln(PE)	0.23	0.03	-10.39				14.62
ln(SP)	0.00	-0.25	-0.06				1.38
ln(SP-PE)	0.34	-0.11	-13.91	-15.35			81.59
ln(GR-SP)	0.34	-0.11	-601.29	756.35			-641.81
BI5							
Variables (X1,X2,X3,X4)	R^2	Adjusted R^2	X1 Coefficient	X2 Coefficient	X3 Coefficient	X4 Coefficient	Intercept
DRHO	0.39	0.24	-9.23				0.56
PE	0.16	-0.05	-0.47				2.06
DRHO-PE	0.54	0.23	-9.05	-0.45			2.20
ln(NPHI-GR)	0.44	0.06	-270.03	284.78			-1652.84
ln(NPHI)	0.05	-0.19	-4.20				-7.63
ln(NPHI-SP)	0.44	0.06	-172.70	227.53			-1245.49
ln(NPHI-GR-SP)	0.44	-0.27	-172.70	0.00	227.53		-1245.49
ln(NPHI-PE)	0.44	0.06	-11.40	-12.05			-2.54
ln(LLD)	0.16	-0.04	2.02				-7.10
ln(PE-LLD-NPHI-GR)	0.44	-0.60	0.00	3.73	-12.27	0.00	-29.92
ln(PE)	0.19	-0.02	-7.16				7.86
ln(SP)	0.03	-0.21	-4.44				17.87
ln(SP-PE)	0.44	0.06	-16.08	-12.90			85.28
ln(GR-SP)	0.44	0.06	-505.33	631.26			-522.67

BTR 14-1-46

BI1							
Variables (X1,X2,X3,X4)	R^2	Adjusted R^2	X1 Coefficient	X2 Coefficient	X3 Coefficient	X4 Coefficient	Intercept
ln(Orientation)	0.19	0.09	0.72				-1.81
ln(PE-Orientation)	0.19	-0.04	-0.39	0.71			-1.28
ln(PE-LLD-NPHI-GR)	0.51	0.11	0.64	0.02	0.20	0.80	-5.02
ln(NPHI-PE)	0.24	0.03	1.43	2.72			-2.89
ln(NPHI-GR)	0.50	0.36	-0.05	0.83			-4.58
ln(NPHI)	0.13	0.02	0.62				-0.55
ln(SP-PE)	0.59	0.47	130.87	-0.22			-786.21
ln(NPHI-GR-SP)	0.62	0.43	0.45	-0.43	177.13		-1061.67
ln(NPHI-SP)	0.61	0.50	0.26	123.85			-743.93
ln(SP)	0.59	0.54	131.45				-789.96
ln(PE)	0.01	-0.11	-0.48				-0.91
ln(GR-SP)	0.59	0.47	0.06	123.41			-741.93
BI2							
Variables (X1,X2,X3,X4)	R^2	Adjusted R^2	X1 Coefficient	X2 Coefficient	X3 Coefficient	X4 Coefficient	Intercept
ln(Orientation)	0.07	-0.05	-0.87				-0.78
ln(PE-Orientation)	0.07	-0.20	-0.26	-0.87			-0.43
ln(PE-LLD-NPHI-GR)	0.56	0.21	-26.32	5.92	-5.33	8.16	-24.93
ln(NPHI-PE)	0.36	0.17	-3.57	-8.08			4.04
ln(NPHI-GR)	0.17	-0.06	-0.59	-0.69			0.39
ln(NPHI)	0.11	0.00	-1.14				-2.95
ln(SP-PE)	0.06	-0.21	-81.08	-0.32			485.63
ln(NPHI-GR-SP)	0.24	-0.14	0.17	-2.62	270.84		-1615.90
ln(NPHI-SP)	0.13	-0.12	-1.00	-51.17			304.23
ln(SP)	0.05	-0.06	-80.23				480.12
ln(PE)	0.00	-0.12	-0.15				-0.88
ln(GR-SP)	0.24	0.02	-2.43	250.68			-1495.92

BI3a							
Variables (X1,X2,X3,X4,X5,X6,X7)	R^2	Adjusted R^2	X1 Coefficient	X2 Coefficient	X3 Coefficient	X4 Coefficient	Intercept
ln(Orientation)	0.06	-0.06	-1.54				-5.65
ln(PE-Orientation)	0.06	-0.21	0.50	-1.53			-6.33
ln(PE-LLD-NPHI-GR)	0.60	0.29	-24.45	2.02	-8.97	2.44	-3.79
ln(NPHI-PE)	0.59	0.48	-8.91	-19.14			5.17
ln(NPHI-GR)	0.33	0.14	-1.80	-1.72			-2.98
ln(NPHI)	0.23	0.13	-3.18				-11.36
ln(SP-PE)	0.20	-0.03	-298.05	0.09			1781.28
ln(NPHI-GR-SP)	0.33	0.00	-2.09	-0.99	-103.12		612.40
ln(NPHI-SP)	0.33	0.14	-2.53	-224.57			1336.60
ln(SP)	0.20	0.10	-298.28				1782.82
ln(PE)	0.00	-0.12	0.68				-7.11
ln(GR-SP)	0.29	0.08	-3.25	144.03			-858.49
BI3b							
Variables (X1,X2,X3,X4)	R^2	Adjusted R^2	X1 Coefficient	X2 Coefficient	X3 Coefficient	X4 Coefficient	Intercept
ln(Orientation)	0.02	-0.10	-0.91				-4.27
ln(PE-Orientation)	0.02	-0.26	-0.55	-0.92			-3.52
ln(PE-LLD-NPHI-GR)	0.50	0.11	-20.37	1.07	-7.68	1.18	2.33
ln(NPHI-PE)	0.50	0.36	-7.82	-17.83			6.79
ln(NPHI-GR)	0.24	0.03	-1.22	-1.57			-1.00
ln(NPHI)	0.15	0.04	-2.48				-8.62
ln(SP-PE)	0.24	0.02	-312.38	-1.06			1870.42
ln(NPHI-GR-SP)	0.32	-0.01	-2.75	2.31	-542.78		3238.13
ln(NPHI-SP)	0.30	0.10	-1.72	-259.23			1547.37
ln(SP)	0.23	0.14	-309.53				1851.85
ln(PE)	0.00	-0.12	-0.44				-3.99
ln(GR-SP)	0.24	0.02	-0.68	-216.97			1299.15

BI4							
Variables (X1,X2,X3,X4)	R^2	Adjusted R^2	X1 Coefficient	X2 Coefficient	X3 Coefficient	X4 Coefficient	Intercept
ln(Orientation)	0.15	0.05	-1.54				1.64
ln(PE-Orientation)	0.26	0.05	-3.64	-1.60			6.58
ln(PE-LLD-NPHI-GR)	0.41	-0.07	-18.20	3.03	-3.03	3.43	-2.53
ln(NPHI-PE)	0.32	0.13	-3.31	-10.81			10.33
ln(NPHI-GR)	0.20	-0.03	1.09	-1.45			8.04
ln(NPHI)	0.00	-0.12	-0.07				0.99
ln(SP-PE)	0.21	-0.02	-134.04	-3.71			810.04
ln(NPHI-GR-SP)	0.29	-0.06	2.12	-4.06	366.63		-2179.89
ln(NPHI-SP)	0.10	-0.16	0.31	-133.25			800.83
ln(SP)	0.09	-0.02	-124.06				745.18
ln(PE)	0.10	-0.02	-3.45				5.76
ln(GR-SP)	0.16	-0.07	-1.76	114.91			-681.82
BI5							
Variables (X1,X2,X3,X4)	R^2	Adjusted R^2	X1 Coefficient	X2 Coefficient	X3 Coefficient	X4 Coefficient	Intercept
ln(Orientation)	0.12	0.01	-0.61				-1.25
ln(PE-Orientation)	0.26	0.05	1.88	-0.58			-3.81
ln(PE-LLD-NPHI-GR)	0.17	-0.50	4.52	-0.83	0.24	-1.13	-0.09
ln(NPHI-PE)	0.15	-0.09	0.02	1.99			-4.13
ln(NPHI-GR)	0.11	-0.14	-0.72	0.17			-3.25
ln(NPHI)	0.10	-0.01	-0.58				-2.41
ln(SP-PE)	0.15	-0.09	-4.67	1.94			23.93
ln(NPHI-GR-SP)	0.16	-0.27	-1.03	0.97	-111.42		661.70
ln(NPHI-SP)	0.10	-0.15	-0.60	7.65			-48.34
ln(SP)	0.00	-0.12	-9.89				57.88
ln(PE)	0.15	0.05	1.95				-4.11
ln(GR-SP)	0.01	-0.28	-0.15	10.88			-66.20

Newfield Cesspooch

BI1									
Variables (X1,X2,X3,X4,X5,X6)	R^2	Adjusted R^2	X1 Coefficient	X2 Coefficient	X3 Coefficient	X4 Coefficient	X5 Coefficient	X6 Coefficient	Intercept
ln(NPHI_LS-GR-SP)	0.01	-0.03	-0.02						0.14
ln(GR-SP)	0.05	-0.02	0.05	0.00					0.00
ln(SP-NPHI_LS)	0.01	-0.05	-0.12	-0.01					0.66
ln(PE-SP)	0.07	0.01	0.37	0.26					-1.44
ln(GR-PE-LLD-NPHI_LS)	0.06	-0.07	0.01	0.13	0.01	0.04			-0.03
ln(PE-NPHI_LS)	0.05	-0.01	0.20	0.00					-0.09
ln(GR-NPHI_LS)	0.05	-0.02	0.05	0.01					0.03
ln(NPHI_LS)	0.01	-0.03	-0.02						0.14
ln(SP)	0.01	-0.02	-0.13						0.74
ln(PE)	0.05	0.02	0.20						-0.09
ln(NPHI_LS-DTS-DTC-GR-LLD-PE)	0.21	0.04	0.19	-1.30	0.31	-0.02	-0.06	1.03	4.42
ln(NPHI_LS-DTS-DTC-GR-LLD)	0.08	-0.09	0.13	0.82	-1.10	0.06	0.01		0.92
ln(NPHI_LS-DTS-DTC-GR-PE)	0.17	0.02	0.22	-0.14	-0.53	-0.01	0.62		2.75
ln(NPHI_LS-DTS-DTC-LLD)	0.04	-0.09	0.09	0.59	-0.68	0.03			0.31
ln(NPHI_LS-DTS-DTC-GR)	0.08	-0.05	0.11	0.70	-1.00	0.07			1.03
ln(DTS-DTC-GR)	0.05	-0.04	-0.07	0.02	0.04				0.31
PE	0.05	0.02	0.06						0.98
SP	0.02	-0.02	0.00						1.38
LLD-SP	0.02	-0.05	0.00	0.00					1.41
LLD-PE	0.06	0.00	0.00	0.08					0.92
GR-PE-LLD	0.06	-0.03	0.00	0.06	0.00				0.95
GR-PE-NPHI_LS	0.05	-0.04	0.00	0.07	-0.29				0.99
GR-PE-LLD-NPHI_LS	0.10	-0.02	0.00	0.07	0.00	-1.06			1.05

BI2									
Variables (X1,X2,X3,X4,X5,X6)	R^2	Adjusted R^2	X1 Coefficient	X2 Coefficient	X3 Coefficient	X4 Coefficient	X5 Coefficient	X6 Coefficient	Intercept
ln(NPHI_LS-GR-SP)	0.00	-0.03	0.02						-1.46
ln(GR-SP)	0.01	-0.05	-0.20	0.40					-2.40
ln(SP-NPHI_LS)	0.01	-0.06	1.23	-0.13					-6.99
ln(PE-SP)	0.12	0.07	-5.63	-5.01					27.57
ln(GR-PE-LLD-NPHI_LS)	0.10	-0.02	0.49	-3.72	-0.21	-0.68			1.36
ln(PE-NPHI_LS)	0.08	0.02	-2.76	-0.35					1.64
ln(GR-NPHI_LS)	0.01	-0.05	-0.31	-0.18					-0.76
ln(NPHI_LS)	0.00	-0.03	0.02						-1.46
ln(SP)	0.01	-0.02	1.01						-5.73
ln(PE)	0.07	0.04	-2.38						1.88
ln(NPHI_LS-DTS-DTC-GR-LLD-PE)	0.19	0.01	-1.91	11.84	-3.57	0.80	0.43	-11.40	-36.47
ln(NPHI_LS-DTS-DTC-GR-LLD)	0.05	-0.12	-1.23	-11.61	12.13	-0.12	-0.37		2.33
ln(NPHI_LS-DTS-DTC-GR-PE)	0.17	0.03	-2.13	3.59	2.42	0.73	-8.52		-24.57
ln(NPHI_LS-DTS-DTC-LLD)	0.05	-0.08	-1.15	-11.17	11.33	-0.41			3.47
ln(NPHI_LS-DTS-DTC-GR)	0.02	-0.11	-0.58	-7.82	8.82	-0.39			-1.09
ln(DTS-DTC-GR)	0.02	-0.08	-3.69	3.40	-0.24				2.75
PE	0.04	0.01	-0.15						1.01
SP	0.01	-0.03	0.00						0.11
LLD-SP	0.01	-0.05	0.00	0.00					0.30
LLD-PE	0.04	-0.02	0.00	-0.14					0.99
GR-PE-LLD	0.10	0.01	0.01	-0.30	0.00				1.34
GR-PE-NPHI_LS	0.07	-0.02	0.00	-0.29	0.39				1.33
GR-PE-LLD-NPHI_LS	0.11	-0.01	0.01	-0.29	0.00	-1.48			1.47

BI3a									
Variables (X1,X2,X3,X4,X5,X6)	R^2	Adjusted R^2	X1 Coefficient	X2 Coefficient	X3 Coefficient	X4 Coefficient	X5 Coefficient	X6 Coefficient	Intercept
ln(NPHI_LS-GR-SP)	0.07	0.04	1.68						-3.38
ln(GR-SP)	0.01	-0.06	-0.21	-2.17					2.73
ln(SP-NPHI_LS)	0.11	0.05	-5.50	2.35					21.26
ln(PE-SP)	0.06	0.00	8.18	7.21					-49.05
ln(GR-PE-LLD-NPHI_LS)	0.18	0.06	-0.67	8.69	-0.28	1.71			-11.92
ln(PE-NPHI_LS)	0.16	0.11	6.28	2.51					-10.42
ln(GR-NPHI_LS)	0.09	0.03	0.72	2.15					-5.02
ln(NPHI_LS)	0.07	0.04	1.68						-3.38
ln(SP)	0.00	-0.03	-1.54						-0.70
ln(PE)	0.03	0.00	3.50						-12.13
ln(NPHI_LS-DTS-DTC-GR-LLD-PE)	0.18	0.00	2.52	16.86	-17.76	-0.41	-0.10	6.98	-15.40
ln(NPHI_LS-DTS-DTC-GR-LLD)	0.17	0.02	2.10	31.22	-27.37	0.16	0.39		-39.16
ln(NPHI_LS-DTS-DTC-GR-PE)	0.18	0.04	2.57	18.71	-19.10	-0.39	6.33		-18.07
ln(NPHI_LS-DTS-DTC-LLD)	0.17	0.06	2.00	30.64	-26.33	0.44			-40.66
ln(NPHI_LS-DTS-DTC-GR)	0.16	0.05	1.42	27.20	-23.87	0.44			-35.54
ln(DTS-DTC-GR)	0.15	0.07	17.08	-10.58	0.08				-44.95
PE	0.07	0.04	3.08						-11.76
SP	0.01	-0.02	-0.07						6.08
LLD-SP	0.03	-0.03	0.00	-0.14					10.97
LLD-PE	0.14	0.08	-0.01	5.08					-18.63
GR-PE-LLD	0.14	0.05	-0.01	5.34	-0.01				-19.23
GR-PE-NPHI_LS	0.25	0.18	-0.01	4.71	70.13				-25.86
GR-PE-LLD-NPHI_LS	0.26	0.15	-0.04	4.71	0.00	83.07			-26.85

BI3b									
Variables (X1,X2,X3,X4,X5,X6)	R^2	Adjusted R^2	X1 Coefficient	X2 Coefficient	X3 Coefficient	X4 Coefficient	X5 Coefficient	X6 Coefficient	Intercept
ln(NPHI_LS-GR-SP)	0.06	0.03	0.98						-2.99
ln(GR-SP)	0.01	-0.05	-0.11	1.32					-10.36
ln(SP-NPHI_LS)	0.06	0.00	-0.01	0.98					-2.96
ln(PE-SP)	0.03	-0.03	3.17	5.03					-30.84
ln(GR-PE-LLD-NPHI_LS)	0.14	0.02	0.10	2.14	-0.65	-0.27			-6.36
ln(PE-NPHI_LS)	0.07	0.01	1.15	1.13					-4.29
ln(GR-NPHI_LS)	0.06	0.00	0.09	1.04					-3.19
ln(NPHI_LS)	0.06	0.03	0.98						-2.99
ln(SP)	0.01	-0.02	1.65						-12.12
ln(PE)	0.00	-0.03	-0.10						-5.05
ln(NPHI_LS-DTS-DTC-GR-LLD-PE)	0.14	-0.05	-0.18	1.50	-1.67	0.12	-0.64	2.06	-6.30
ln(NPHI_LS-DTS-DTC-GR-LLD)	0.13	-0.02	-0.30	5.73	-4.50	0.29	-0.50		-13.30
ln(NPHI_LS-DTS-DTC-GR-PE)	0.11	-0.05	0.16	13.89	-10.67	0.23	-2.28		-24.20
ln(NPHI_LS-DTS-DTC-LLD)	0.13	0.01	-0.49	4.64	-2.55	-0.40			-16.10
ln(NPHI_LS-DTS-DTC-GR)	0.10	-0.02	0.57	10.84	-8.96	-0.07			-17.91
ln(DTS-DTC-GR)	0.10	0.01	6.75	-3.59	-0.22				-21.72
PE	0.02	-0.01	0.01						-0.05
SP	0.03	0.00	0.00						0.05
LLD-SP	0.03	-0.03	0.00	0.00					0.04
LLD-PE	0.02	-0.04	0.00	0.01					-0.04
GR-PE-LLD	0.02	-0.08	0.00	0.01	0.00				-0.05
GR-PE-NPHI_LS	0.06	-0.04	0.00	0.01	0.20				-0.07
GR-PE-LLD-NPHI_LS	0.11	-0.02	0.00	0.01	0.00	0.40			-0.09

BI4									
Variables (X1,X2,X3,X4,X5,X6)	R^2	Adjusted R^2	X1 Coefficient	X2 Coefficient	X3 Coefficient	X4 Coefficient	X5 Coefficient	X6 Coefficient	Intercept
ln(NPHI_LS-GR-SP)	0.04	0.01	1.23						4.14
ln(GR-SP)	0.02	-0.04	-0.11	3.27					-11.96
ln(SP-NPHI_LS)	0.04	-0.02	1.91	1.00					-4.39
ln(PE-SP)	0.10	0.04	8.93	13.14					-66.52
ln(GR-PE-LLD-NPHI_LS)	0.07	-0.06	-0.72	4.73	-0.33	0.57			0.11
ln(PE-NPHI_LS)	0.05	-0.01	2.06	1.50					1.83
ln(GR-NPHI_LS)	0.04	-0.02	-0.08	1.18					4.32
ln(NPHI_LS)	0.04	0.01	1.23						4.14
ln(SP)	0.02	-0.01	3.59						-13.71
ln(PE)	0.00	-0.03	0.40						0.81
ln(NPHI_LS-DTS-DTC-GR-LLD-PE)	0.20	0.03	0.84	-64.78	51.49	-1.96	-2.00	23.48	80.03
ln(NPHI_LS-DTS-DTC-GR-LLD)	0.05	-0.12	-0.56	-16.48	19.16	-0.07	-0.36		0.12
ln(NPHI_LS-DTS-DTC-GR-PE)	0.10	-0.06	1.88	-26.10	23.40	-1.64	9.95		24.19
ln(NPHI_LS-DTS-DTC-LLD)	0.05	-0.08	-0.52	-16.23	18.70	-0.38			0.78
ln(NPHI_LS-DTS-DTC-GR)	0.05	-0.09	0.07	-12.77	15.92	-0.33			-3.23
ln(DTS-DTC-GR)	0.05	-0.05	-13.27	16.58	-0.35				-3.69
PE	0.01	-0.02	344.44						-809.49
SP	0.01	-0.02	29.63						-1366.13
LLD-SP	0.03	-0.03	-1.31	11.01					100.80
LLD-PE	0.07	0.01	-2.58	940.57					-2866.56
GR-PE-LLD	0.07	-0.02	-4.19	1024.18	-2.34				-3053.14
GR-PE-NPHI_LS	0.08	-0.02	-12.72	963.20	11246.34				-4041.81
GR-PE-LLD-NPHI_LS	0.08	-0.05	-6.61	961.82	-1.09	8247.76			-3810.58

BI5									
Variables (X1,X2,X3,X4,X5,X6)	R^2	Adjusted R^2	X1 Coefficient	X2 Coefficient	X3 Coefficient	X4 Coefficient	X5 Coefficient	X6 Coefficient	Intercept
ln(NPHI_LS-GR-SP)	0.11	0.08	0.46						0.05
ln(GR-SP)	0.11	0.05	-0.01	1.70					-8.11
ln(SP-NPHI_LS)	0.15	0.09	1.19	0.32					-5.29
ln(PE-SP)	0.12	0.07	-0.92	0.75					-2.84
ln(GR-PE-LLD-NPHI_LS)	0.20	0.09	0.31	-1.76	-0.07	0.25			1.24
ln(PE-NPHI_LS)	0.16	0.11	-1.04	0.33					1.22
ln(GR-NPHI_LS)	0.11	0.05	-0.05	0.43					0.18
ln(NPHI_LS)	0.11	0.08	0.46						0.05
ln(SP)	0.11	0.08	1.73						-8.26
ln(PE)	0.12	0.09	-1.40						1.00
ln(NPHI_LS-DTS-DTC-GR-LLD-PE)	0.21	0.03	0.08	-4.63	4.62	0.23	-0.14	-1.10	3.22
ln(NPHI_LS-DTS-DTC-GR-LLD)	0.20	0.06	0.15	-6.89	6.13	0.14	-0.22		6.96
ln(NPHI_LS-DTS-DTC-GR-PE)	0.20	0.05	0.15	-1.93	2.66	0.25	-2.04		-0.67
ln(NPHI_LS-DTS-DTC-LLD)	0.19	0.08	0.05	-7.43	7.10	-0.17			5.58
ln(NPHI_LS-DTS-DTC-GR)	0.15	0.04	0.52	-4.67	4.20	-0.01			4.96
ln(DTS-DTC-GR)	0.13	0.04	-8.42	9.11	-0.15				1.48
PE	0.16	0.14	-0.16						1.09
SP	0.14	0.12	0.01						-0.33
LLD-SP	0.18	0.13	0.00	0.01					-0.10
LLD-PE	0.19	0.13	0.00	-0.12					0.96
GR-PE-LLD	0.25	0.17	0.00	-0.21	0.00				1.15
GR-PE-NPHI_LS	0.22	0.14	0.00	-0.21	1.37				1.04
GR-PE-LLD-NPHI_LS	0.25	0.15	0.00	-0.21	0.00	0.47			1.11

CCU26-3

BI1							
Variables (X1,X2,X3,X4)	R^2	Adjusted R^2	X1 Coefficient	X2 Coefficient	X3 Coefficient	X4 Coefficient	Intercept
ln(RHOB)	0.84	0.80	-7.20				7.16
ln(PE)	0.78	0.73	-4.69				10.81
ln(RHOB-PEF-90_2FT_R)	0.89	0.79	-8.57	1.94	-0.47		7.30
ln(RHOB-PE-GR)	0.89	0.79	-17.49	6.05	0.80		1.70
ln(GR)	0.18	0.01	-1.08				2.57
ln(PE-GR)	0.78	0.67	-4.85	0.15			10.85
ln(RHOB-PE-90_2ft_R-GR)	0.89	0.45	0.00	-2.00	-0.93	-0.76	12.68
ln(RHOB-GR)	0.86	0.79	-8.12	0.50			6.97
BI2							
Variables (X1,X2,X3,X4)	R^2	Adjusted R^2	X1 Coefficient	X2 Coefficient	X3 Coefficient	X4 Coefficient	Intercept
ln(RHOB)	0.45	0.34	-3.13				2.30
ln(PE)	0.29	0.15	-1.69				3.12
ln(RHOB-PEF-90_2FT_R)	0.91	0.82	-20.44	11.88	-0.01		-7.79
ln(RHOB-PE-GR)	0.91	0.82	-20.59	11.94	0.01		-7.89
ln(GR)	0.41	0.29	-0.97				1.37
ln(PE-GR)	0.46	0.20	-0.89	-0.75			2.89
ln(RHOB-PE-90_2ft_R-GR)	0.91	0.48	0.00	2.46	-1.09	-1.82	5.04
ln(RHOB-GR)	0.54	0.31	-2.10	-0.56			2.51
BI3a							
Variables (X1,X2,X3,X4)	R^2	Adjusted R^2	X1 Coefficient	X2 Coefficient	X3 Coefficient	X4 Coefficient	Intercept
ln(RHOB)	0.79	0.75	36.66				-44.01
ln(PE)	0.74	0.69	23.98				-62.89
ln(RHOB-PEF-90_2FT_R)	0.79	0.59	49.31	-9.43	0.36		-37.34
ln(RHOB-PE-GR)	0.79	0.59	56.11	-12.57	-0.61		-33.07
ln(GR)	0.28	0.14	7.16				-24.16
ln(PE-GR)	0.75	0.63	22.41	1.46			-62.44
ln(RHOB-PE-90_2ft_R-GR)	0.79	0.25	0.00	13.28	2.98	4.40	-68.29
ln(RHOB-GR)	0.79	0.68	36.66	0.00			-44.01

BI3b							
Variables (X1,X2,X3,X4)	R^2	Adjusted R^2	X1 Coefficient	X2 Coefficient	X3 Coefficient	X4 Coefficient	Intercept
ln(RHOB)	0.78	0.73	35.94				-41.90
ln(PE)	0.75	0.69	23.72				-60.88
ln(RHOB-PEF-90_2FT_R)	0.78	0.56	37.29	-2.19	0.60		-42.30
ln(RHOB-PE-GR)	0.78	0.56	48.53	-7.37	-1.00		-35.23
ln(GR)	0.24	0.09	6.61				-21.56
ln(PE-GR)	0.75	0.62	22.87	0.79			-60.64
ln(RHOB-PE-90_2ft_R-GR)	0.78	0.23	0.00	14.98	2.57	3.32	-65.70
ln(RHOB-GR)	0.78	0.67	37.12	-0.65			-41.65
BI4							
Variables (X1,X2,X3,X4)	R^2	Adjusted R^2	X1 Coefficient	X2 Coefficient	X3 Coefficient	X4 Coefficient	Intercept
ln(RHOB)	0.27	0.12	2.27				-1.66
ln(PE)	0.27	0.12	1.53				-2.93
ln(RHOB-PEF-90_2FT_R)	0.41	-0.17	-1.51	1.62	0.45		-4.77
ln(RHOB-PE-GR)	0.41	-0.17	7.03	-2.31	-0.76		0.60
ln(GR)	0.00	-0.20	0.02				0.46
ln(PE-GR)	0.35	0.03	2.07	-0.50			-3.08
ln(RHOB-PE-90_2ft_R-GR)	0.41	-0.51	0.00	0.93	0.37	-0.13	-3.82
ln(RHOB-GR)	0.40	0.10	3.45	-0.65			-1.41
BI5							
Variables (X1,X2,X3,X4)	R^2	Adjusted R^2	X1 Coefficient	X2 Coefficient	X3 Coefficient	X4 Coefficient	Intercept
ln(RHOB)	0.93	0.91	11.24				-13.16
ln(PE)	0.90	0.88	7.47				-19.21
ln(RHOB-PEF-90_2FT_R)	0.99	0.97	5.96	1.96	0.78		-17.78
ln(RHOB-PE-GR)	0.99	0.97	20.60	-4.78	-1.31		-8.59
ln(GR)	0.15	-0.01	1.50				-5.61
ln(PE-GR)	0.91	0.87	8.06	-0.54			-19.38
ln(RHOB-PE-90_2ft_R-GR)	0.99	0.64	0.00	4.71	1.09	0.53	-21.53
ln(RHOB-GR)	0.98	0.96	13.20	-1.08			-12.76

CS36-13

BI1										
Variables (X1,X2,X3,X4,X5,X6,X7)	R^2	Adjusted R^2	X1 Coefficient	X2 Coefficient	X3 Coefficient	X4 Coefficient	X5 Coefficient	X6 Coefficient	X7 Coefficient	Intercept
ln(SPHI-DTSM_SLOW-DTSM_FAST-DTCO-GR)	0.76	0.59	3.01	-46.34	39.26	-13.74	1.19			93.46
ln(SPHI-DTSM_SLOW-DTSM_FAST-DTCO-GR-AF90-PE)	0.77	0.45	1.66	-124.22	81.57	-33.28	13.25	1.32	-6.41	303.46
ln(SPHI-DTSM_SLOW-DTSM_FAST-DTCO-GR-AF90)	0.76	0.52	2.66	-56.95	48.54	-18.25	3.12	0.27		109.54
ln(SPHI-DTSM_SLOW-DTSM_FAST-DTCO-GR-PE)	0.76	0.53	3.15	-56.94	38.03	-12.74	2.27	-2.60		146.82
ln(SPHI-DTSM_SLOW-DTSM_FAST-DTCO-AF90)	0.71	0.56	1.42	-55.15	47.56	0.20				38.49
ln(DTSM_SLOW-DTCO-GR)	0.59	0.45	-8.05	7.62	0.29					5.18
ln(SPHI-GR-AF90-PE)	0.75	0.62	4.28	-5.40	-0.90	0.50				32.30
ln(PE-GR-AF90)	0.57	0.43	1.85	1.28	0.22					-9.42
ln(SPHI-PE)	0.63	0.56	0.86	1.61						-1.38
ln(SPHI-GR)	0.45	0.33	1.05	-0.37						3.25
ln(PE)	0.11	0.03	1.16							-2.36
ln(SPHI)	0.43	0.38	0.77							1.19
BI2										
Variables (X1,X2,X3,X4,X5,X6,X7)	R^2	Adjusted R^2	X1 Coefficient	X2 Coefficient	X3 Coefficient	X4 Coefficient	X5 Coefficient	X6 Coefficient	X7 Coefficient	Intercept
ln(SPHI-DTSM_SLOW-DTSM_FAST-DTCO-GR)	0.60	0.31	-2.03	7.40	-4.33	-5.58	3.38			-10.26
ln(SPHI-DTSM_SLOW-DTSM_FAST-DTCO-GR-AF90-PE)	0.79	0.50	9.53	479.11	-334.85	151.66	-75.63	-9.87	20.44	-1019.05
ln(SPHI-DTSM_SLOW-DTSM_FAST-DTCO-GR-AF90)	0.75	0.49	6.35	264.43	-229.46	103.69	-43.31	-6.53		-400.24
ln(SPHI-DTSM_SLOW-DTSM_FAST-DTCO-GR-PE)	0.61	0.22	-1.59	-25.65	-8.16	-2.46	6.73	-8.11		156.15
ln(SPHI-DTSM_SLOW-DTSM_FAST-DTCO-AF90)	0.43	0.15	-6.52	-17.51	19.14	33.84				-165.65
ln(DTSM_SLOW-DTCO-GR)	0.58	0.44	4.46	-20.24	4.02					46.65

BI2 continued										
Variables (X1,X2,X3,X4,X5,X6,X7)	R^2	Adjusted R^2	X1 Coefficient	X2 Coefficient	X3 Coefficient	X4 Coefficient	X5 Coefficient	X6 Coefficient	X7 Coefficient	Intercept
ln(SPHI-GR-AF90-PE)	0.61	0.42	-0.67	0.08	-0.56	-1.24				1.08
ln(PE-GR-AF90)	0.61	0.48	-1.45	-0.97	-0.74					7.64
ln(SPHI-PE)	0.04	-0.15	-0.20	-1.07						0.13
ln(SPHI-GR)	0.59	0.50	-2.71	3.36						-20.35
ln(PE)	0.03	-0.06	-0.96							0.36
ln(SPHI)	0.01	-0.08	-0.14							-1.57
BI3a										
Variables (X1,X2,X3,X4,X5,X6,X7)	R^2	Adjusted R^2	X1 Coefficient	X2 Coefficient	X3 Coefficient	X4 Coefficient	X5 Coefficient	X6 Coefficient	X7 Coefficient	Intercept
ln(SPHI-DTSM_SLOW-DTSM_FAST-DTCO-GR)	0.51	0.17	-8.20	-27.85	27.18	50.42	-2.53			-223.29
ln(SPHI-DTSM_SLOW-DTSM_FAST-DTCO-GR-AF90-PE)	0.67	0.22	2.29	396.10	-272.04	192.86	-73.71	-8.92	17.84	-1122.27
ln(SPHI-DTSM_SLOW-DTSM_FAST-DTCO-GR-AF90)	0.64	0.28	-0.49	208.77	-180.07	151.01	-45.51	-6.01		-582.31
ln(SPHI-DTSM_SLOW-DTSM_FAST-DTCO-GR-PE)	0.53	0.05	-7.77	-60.39	23.41	53.49	0.77	-7.98		-59.47
ln(SPHI-DTSM_SLOW-DTSM_FAST-DTCO-AF90)	0.42	0.13	-4.84	-9.20	9.61	20.89				-106.90
ln(DTSM_SLOW-DTCO-GR)	0.28	0.04	6.43	-9.22	0.12					0.83
ln(SPHI-GR-AF90-PE)	0.38	0.07	-3.87	4.36	0.65	-0.50				-33.44
ln(PE-GR-AF90)	0.32	0.10	-1.72	-1.68	-0.36					4.29
ln(SPHI-PE)	0.34	0.21	-1.06	-1.37						-6.44
ln(SPHI-GR)	0.31	0.17	-1.52	0.71						-12.61
ln(PE)	0.02	-0.07	-0.81							-5.23
ln(SPHI)	0.28	0.21	-0.98							-8.62

BI3b										
Variables (X1,X2,X3,X4,X5,X6,X7)	R^2	Adjusted R^2	X1 Coefficient	X2 Coefficient	X3 Coefficient	X4 Coefficient	X5 Coefficient	X6 Coefficient	X7 Coefficient	Intercept
ln(SPHI-DTSM_SLOW-DTSM_FAST-DTCO-GR)	0.52	0.18	-8.35	-2.69	3.63	48.26	-2.37			-221.35
ln(SPHI-DTSM_SLOW-DTSM_FAST-DTCO-GR-AF90-PE)	0.64	0.14	2.23	404.09	-294.69	190.81	-71.57	-8.85	14.34	-1044.14
ln(SPHI-DTSM_SLOW-DTSM_FAST-DTCO-GR-AF90)	0.63	0.25	0.01	253.49	-220.75	157.16	-48.91	-6.51		-610.02
ln(SPHI-DTSM_SLOW-DTSM_FAST-DTCO-GR-PE)	0.54	0.08	-7.74	-48.60	-1.70	52.60	2.28	-11.27		9.83
ln(SPHI-DTSM_SLOW-DTSM_FAST-DTCO-AF90)	0.46	0.20	-5.20	14.82	-12.86	20.56				-112.16
ln(DTSM_SLOW-DTCO-GR)	0.34	0.12	7.37	-12.20	0.29					9.78
ln(SPHI-GR-AF90-PE)	0.44	0.16	-4.93	5.51	0.84	-0.43				-39.43
ln(PE-GR-AF90)	0.37	0.17	-1.99	-2.18	-0.45					8.66
ln(SPHI-PE)	0.40	0.28	-1.38	-1.54						-5.23
ln(SPHI-GR)	0.37	0.24	-1.93	0.84						-12.34
ln(PE)	0.02	-0.07	-0.81							-3.66
ln(SPHI)	0.34	0.28	-1.29							-7.68
BI4										
Variables (X1,X2,X3,X4,X5,X6,X7)	R^2	Adjusted R^2	X1 Coefficient	X2 Coefficient	X3 Coefficient	X4 Coefficient	X5 Coefficient	X6 Coefficient	X7 Coefficient	Intercept
ln(SPHI-DTSM_SLOW-DTSM_FAST-DTCO-GR)	0.42	0.00	-1.20	10.32	-10.08	7.89	-0.33			-35.39
ln(SPHI-DTSM_SLOW-DTSM_FAST-DTCO-GR-AF90-PE)	0.59	0.03	0.46	79.21	-57.72	30.53	-11.82	-1.42	3.14	-184.89
ln(SPHI-DTSM_SLOW-DTSM_FAST-DTCO-GR-AF90)	0.55	0.10	-0.03	46.25	-41.54	23.16	-6.86	-0.91		-89.90
ln(SPHI-DTSM_SLOW-DTSM_FAST-DTCO-GR-PE)	0.43	-0.14	-1.15	6.31	-10.54	8.27	0.07	-0.99		-15.17
ln(SPHI-DTSM_SLOW-DTSM_FAST-DTCO-AF90)	0.35	0.03	-0.76	12.78	-12.39	4.01				-20.07
ln(DTSM_SLOW-DTCO-GR)	0.06	-0.26	0.82	-0.72	0.04					-0.74
ln(SPHI-GR-AF90-PE)	0.29	-0.06	-1.16	1.75	0.28	0.16				-10.30
ln(PE-GR-AF90)	0.07	-0.24	-0.20	-0.06	-0.02					1.00

BI4 continued										
Variables (X1,X2,X3,X4,X5,X6,X7)	R^2	Adjusted R^2	X1 Coefficient	X2 Coefficient	X3 Coefficient	X4 Coefficient	X5 Coefficient	X6 Coefficient	X7 Coefficient	Intercept
ln(SPHI-PE)	0.06	-0.12	-0.04	-0.20						0.60
ln(SPHI-GR)	0.07	-0.11	-0.15	0.16						-0.63
ln(PE)	0.04	-0.04	-0.17							0.64
ln(SPHI)	0.01	-0.08	-0.03							0.29
BI5										
Variables (X1,X2,X3,X4,X5,X6,X7)	R^2	Adjusted R^2	X1 Coefficient	X2 Coefficient	X3 Coefficient	X4 Coefficient	X5 Coefficient	X6 Coefficient	X7 Coefficient	Intercept
ln(SPHI-DTSM_SLOW-DTSM_FAST-DTCO-GR)	0.89	0.81	0.15	29.17	-21.83	8.24	-2.20			-63.09
ln(SPHI-DTSM_SLOW-DTSM_FAST-DTCO-GR-AF90-PE)	0.95	0.87	0.43	103.34	-40.44	15.48	-11.92	-0.70	11.47	-340.04
ln(SPHI-DTSM_SLOW-DTSM_FAST-DTCO-GR-AF90)	0.90	0.81	-1.36	-17.08	18.68	-11.42	6.20	1.17		7.08
ln(SPHI-DTSM_SLOW-DTSM_FAST-DTCO-GR-PE)	0.94	0.89	-0.36	67.69	-17.36	4.60	-6.10	9.45		-257.03
ln(SPHI-DTSM_SLOW-DTSM_FAST-DTCO-AF90)	0.68	0.52	3.07	45.38	-37.10	-17.41				38.02
ln(DTSM_SLOW-DTCO-GR)	0.87	0.83	6.50	9.57	-2.27					-64.61
ln(SPHI-GR-AF90-PE)	0.89	0.84	-1.00	2.80	0.67	-0.79				-16.05
ln(PE-GR-AF90)	0.88	0.84	-1.10	1.24	0.41					-6.29
ln(SPHI-PE)	0.65	0.58	0.62	-1.43						1.90
ln(SPHI-GR)	0.58	0.49	1.39	-0.89						4.61
ln(PE)	0.31	0.25	-1.76							1.20
ln(SPHI)	0.45	0.40	0.71							-0.37

BI Correlations for Combined Well Data

Table C-60. Combined Correlation Data For All Wells

BI Parameter	Logging Parameter(s)	R^2	Adjusted R^2	X1	X2	X3	X4	Intercept
BI1	ln(Poro-GR-SP)	0.74	0.72	-0.13	-3.36E-02	-0.80		3.33
	ln(GR-SP)	0.74	0.72	-1.90E-02	-0.85			3.78
	ln(Poro-SP)	0.74	0.73	-0.12	-0.80			3.22
	ln(SP-PE)	0.74	0.72	-0.85	-7.52E-02			3.83
BI5	ln(PE-Res-Poro-GR)	0.28	0.23	-1.65	0.14	0.26	0.15	0.61
	ln(Poro-PE)	0.22	0.19	0.10	-1.56			1.26
	Poro-PE	0.18	0.16	-0.52	-8.84E-02			0.82
	ln(PE-Res-GR)	0.18	0.15	-1.15	0.15	0.28		-1.27
	PE-Res-Poro	0.18	0.14	-0.09	1.77E-05	-0.49		0.81
BI2	ln(PE-Res-Poro-GR)	0.18	0.11	-1.16	-0.42	-0.86	0.21	-0.70
	ln(Res)	7.71E-02	5.93E-02	-0.24				-0.50
BI3b	ln(Poro-GR)	0.11	7.16E-02	-0.49	-0.74			-3.51
	ln(PE-Res-Poro-GR)	0.14	7.10E-02	0.43	-0.25	-0.80	-0.78	-3.66
	ln(Res-Poro)	2.03E-02	4.46E-02	-7.81E-02	-0.55			-5.19
	ln(Poro)	4.36E-02	2.52E-02	-0.63				-6.64
BI3a	ln(SP)	2.53E-02	5.04E-03	0.54				-9.47
BI4	ln(PE)	2.21E-02	7.71E-03	-0.86				2.35
	ln(GR-PE)	3.22E-02	3.00E-03	-0.26	-1.10			3.67

Table C 61. Fracture Toughness vs. Brittleness

Core Depth	Log Depth	Value Using Sample Height for R	FT Value Using Half Sample D for R	BI1 (horizontal)	BI2 (horizontal)	BI3a (horizontal)	BI3b (horizontal)	BI4 (horizontal)	BI5 (horizontal)	BI1 (vertical)	BI2 (vertical)	BI3a (vertical)	BI3b (vertical)	BI4 (vertical)	BI5 (vertical)	Well ID
7617	7616.5	8253.5	6589.75	0.81	0.44	8.95E-04	-5.77E-03	1.17	0.27	1.56	0.03	8.23E-04	-6.63E-03	1.16	0.11	CS36-13
7594.7	7594.2	1571	1285.5	2.05	0.12	1.57E-03	-6.89E-03	1.22	0.10	2.46	0.31	3.65E-04	-1.52E-03	1.13	0.11	
7612	7611.5	563	476	1.30	0.24	2.28E-03	-1.10E-02	1.47	0.24	0.75	0.34	2.90E-04	-8.71E-04	1.20	0.35	
7622.5	7622	616	461	0.88	0.34	4.89E-03	-4.73E-02	1.34	0.08	0.49	0.42	4.82E-03	-3.29E-02	1.37	0.16	
7331.3	7321.1	935.2	831	0.23	0.00	2.88E-02	-1.94E-01	2.56	0.35	0.61	0.00	9.31E-04	-3.59E-02	25.37	0.61	BTR14-3-45
7356.8	7346.6	1356	1393	0.28	0.21	3.56E-04	-8.06E-04	1.27	0.08	0.74	0.61	5.72E-05	-3.23E-03	3.47	0.36	
7413.9	7408.9	1461	1291	5.51	0.95	6.00E-04	-1.21E-03	1.11	0.03	5.78	0.94	2.52E-04	-1.08E-03	1.06	0.03	CCU26-3
7433.6	7428.6	719	617	0.92	0.23	2.32E-03	-4.67E-03	1.42	0.21	0.98	0.67	7.01E-03	-6.50E-02	3.25	0.25	
6692.5	6685	1653.83	1468.91	0.14	0.28	1.29E-01	-3.93E-01	8.00	0.37	0.20	0.00	2.23E-03	-5.51E-02	2.49	0.14	BTR14-1-46

Table C 62. Nomenclature

FT1=	D/2=R
FT2=	h=R
D=	Sample Diameter
h=	Sample Height
H=	Horizontal Sample Orientation
V=	Vertical Sample Orientation
AVG=	Average of V&H
FT1V-FT1H	Difference between Vertical and Horizontal Fracture toughness at the same depth for method 1 of calculating Fracture toughness
FT2V-FT2H	Difference between Vertical and Horizontal Fracture toughness at the same depth for method 2 of calculating Fracture toughness
FT2V-FT1V	Difference between the correlations for the two methods of calculating Fracture Toughness with horizontal orientation and depth
FT2H-FT1H	Difference between the correlations for the two methods of calculating Fracture Toughness with vertical orientation and depth
FT2-FT1	Difference between the orientation averaged correlations for the two methods for calculating Fracture Toughness

Table C 63. Brittleness (see Table 62)

		R^2	FT1V-FT1H	FT2V-FT2H	FT2V-FT1V	FT2H-FT1H
BI vs. FT	BI1-H-FT1	0.0056	0.001	0.0012	-0.0003	-0.0005
	BI2-H-FT1	0.0453	0.0939	0.1026	0.0075	-0.0012
	BI3a-H-FT1	0.0051	0.0639	0.0511	-0.0111	0.0017
	BI3b-H-FT1	0.0143	0.0602	0.0534	-0.0047	0.0021
	BI4-H-FT1	0.0065	0.0256	0.0247	0.0011	0.002
	BI5-H-FT1	0.0458	0.0607	0.0643	0.0056	0.002
	BI1-V-FT1	0.0066				
	BI2-V-FT1	0.1392				
	BI3a-V-FT1	0.069				
	BI3b-V-FT1	0.0745				
	BI4-V-FT1	0.0321				
	BI5-V-FT1	0.1065				
	BI1-H-FT2	0.0051				
	BI2-H-FT2	0.0441				
	BI3a-H-FT2	0.0068				
	BI3b-H-FT2	0.0164				

		R^2	FT1V-FT1H	FT2V-FT2H	FT2V-FT1V	FT2H-FT1H
	BI4-H-FT2	0.0085				
	BI5-H-FT2	0.0478				
	BI1-V-FT2	0.0063				
	BI2-V-FT2	0.1467				
	BI3a-V-FT2	0.0579				
	BI3b-V-FT2	0.0698				
	BI4-V-FT2	0.0332				
	BI5-V-FT2	0.1121				

Table C 64 Statistics for Tables 61 and 62

		R^2	FT2-FT1
Average BI vs. FT	BI1-AVG-FT1	0.000002	0.000028
	BI2-AVG-FT1	0.0152	0.0019
	BI3a-AVG-FT1	0.0074	0.0018
	BI3b-AVG-FT1	0.0234	0.0019
	BI4-AVG-FT1	0.036	0.0023
	BI5-AVG-FT1	0.0149	0.0009
	BI1-AVG-FT2	0.00003	
	BI2-AVG-FT2	0.0171	
	BI3a-AVG-FT2	0.0092	
	BI3b-AVG-FT2	0.0253	
	BI4-AVG-FT2	0.0383	
	BI5-AVG-FT2	0.0158	

Table C 65. Brittleness

		R^2	FT1V-FT1H	FT2V-FT2H	FT2V-FT1V	FT2H-FT1H	
ln(BI) vs. ln(FT)	BI1-H-FT1	0.0042	0.0653	0.0734	0.0045	-0.0036	
	BI2-H-FT1	0.052	0.1681	0.1724	0.0093	0.005	
	BI3a-H-FT1	0.0455	0.0217	-0.0028	-0.0299	-0.0054	
	BI3b-H-FT1	0.0398	-0.0208	-0.013	-0.0039	-0.0117	
	BI4-H-FT1	0.0005	0.0334	0.0513	0.0191	0.0012	
	BI5-H-FT1	0.0116	0.1297	0.1515	0.0236	0.0018	
	BI1-V-FT1	0.0695					
	BI2-V-FT1	0.2201					
	BI3a-V-FT1	0.0672					
	BI3b-V-FT1	0.019					
	BI4-V-FT1	0.0339					
	BI5-V-FT1	0.1413					
	BI1-H-FT2	0.0006					
	BI2-H-FT2	0.057					
	BI3a-H-FT2	0.0401					
	BI3b-H-FT2	0.0281					
	BI4-H-FT2	0.0017					
	BI5-H-FT2	0.0134					
	BI1-V-FT2	0.074					
	BI2-V-FT2	0.2294					
	BI3a-V-FT2	0.0373					
	BI3b-V-FT2	0.0151					
	BI4-V-FT2	0.053					
	BI5-V-FT2	0.1649					

Table C 66. Statistics for Table 65

		R^2	FT2-FT1
ln(Average BI) vs. ln(FT)	BI1-AVG-FT1	0.0089	0.0053
	BI2-AVG-FT1	0.0692	0.011
	BI3a-AVG-FT1	0.0588	-0.0109
	BI3b-AVG-FT1	0.0641	-0.0107
	BI4-AVG-FT1	0.02	0.0138
	BI5-AVG-FT1	0.0136	0.0049
	BI1-AVG-FT2	0.0142	
	BI2-AVG-FT2	0.0802	
	BI3a-AVG-FT2	0.0479	
	BI3b-AVG-FT2	0.0534	
	BI4-AVG-FT2	0.0338	
	BI5-AVG-FT2	0.0185	

Appendix D

BI Results from Smoothed Processed Triaxial Stress-Strain Curves

Bill Barret 14-1-46

Sample	Brittleness Index	Measured Core Depth (feet)	Orientation	Confining Pressure (psi)	Peak Axial Stress Difference (psi)
BTR1-2	0.17	6684.40	Horizontal	2739.303	16995
BTR1-6	0.31	6684.40	Vertical	1336.557	20853
BTR2-1	0.12	6693.70	Vertical	1332.223	27773
BTR2-2	0.39	6693.45	Horizontal	2739.296	47185
BTR2-5	0.72	6693.45	Horizontal	2744.044	Unknown
BTR3-1	0.37	6698.25	Vertical	1340.309	22639
BTR3-2	0.38	6699.00	Horizontal	2745.591	49929
BTR4-2	0.46	6702.90	Horizontal	1347.193	24007
BTR4-4	0.06	6703.10	Vertical	1340.798	24998
BTR5-2	0.17	6706.65	Horizontal	2749.533	14495
BTR5-4	0.27	6706.50	Vertical	1340.617	13147

Bill Barret 14-3-45

Sample	Brittleness Index	Measured Core Depth (feet)	Orientation	Confining Pressure (psi)	Peak Axial Stress Difference (psi)
BTR1-2	0.52	6684.4	Horizontal	2739.303	16995
BTR1-6	0.72	6684.4	Vertical	1336.557	20853
BTR2-1	0.49	6693.7	Vertical	1332.223	27773
BTR2-2	0.31	6693.45	Horizontal	2739.296	47185
BTR2-5	0.67	6693.45	Horizontal	2744.044	Unknown
BTR3-1	0.76	6698.25	Vertical	1340.309	22639
BTR3-2	0.64	6699	Horizontal	2745.591	49929
BTR4-2	0.40	6702.9	Horizontal	1347.193	24007
BTR4-4	0.38	6703.1	Vertical	1340.798	24998
BTR5-2	0.75	6706.65	Horizontal	2749.533	14495
BTR5-4	0.74	6706.5	Vertical	1340.617	13147

Cane Creek 7-1

Sample	Brittleness Index	Measured Core Depth (feet)	Orientation	Confining Pressure (psi)	Peak Axial Stress Difference (psi)
Sample	Brittleness Index	Measured Core Depth (feet)	Orientation	Confining Pressure	Peak Axial Stress Difference (psi)
CCU1-1	0.429674433	7609.35	Vertical	3347.815	25407
CCU1-3	0.632039891	7609.15	Horizontal	3880.93	41065
CCU2-1	0.113820131	7614	Vertical	3350.04	28744
CCU2-3	0.11635919	7614.65	Horizontal	3882.521	29464
CCU3-1	0.35063765	7619	Vertical	3351.642	14868
CCU3-5	0.120162483	7619.2	Horizontal	3886.275	17802
CCU4-1	0.08972916	7620.8	Vertical	3354.322	10461
CCU4-5	0.288507271	7620.3	Horizontal	3884.219	14940
CCU5-1	0.261678576	7624.65	Vertical	3354.487	17448
CCU5-3	0.170423694	7624.9	Horizontal	3886.115	30056
CCU6-1	0.177902562	7630.25	Vertical	3356.698	12059
CCU6-3	0.181261257	7630.6	Horizontal	3891.498	16672
CCU7-1	0.143726125	7638.3	Vertical	3361.237	11584
CCU8-1	0.068836331	7645.3	Vertical	3364.428	24903
CCU8-3	0.049124151	7645.75	Horizontal	3898.354	26598
CCU9-1	0.158559223	7651.6	Vertical	3366.591	18005
CCU9-3	0.763277189	7651.25	Horizontal	3901.324	25785
CCU10-1	0.776492743	7657.5	Vertical	3368.457	25890
CCU10-5	0.163215834	7657.65	Horizontal	3903.633	36067

Cane Creek 26-3

Sample	Brittleness Index	Measured Core Depth (feet)	Orientation	Confining Pressure (psi)	Peak Axial Stress Difference (psi)
FDY1-1	0.286891578	7464.5	Vertical	3876.936	32820
FDY1-2	0.336271586	7464.3	Horizontal	4069.072	13632
FDY1-4	0.519139732	7464.3	Vertical	3880.792	32074
FDY2-1	0.1109027	7417.75	Vertical	3861.96	14677
FDY2-2	0.135871286	7417.85	Horizontal	4056.56	16656
FDY3-1	0.008901444	7413	Vertical	3855.909	7731
FDY3-2	0.0057679	7413.05	Horizontal	4038.899	10214

NewField Cesspooch

Sample	Brittleness Index	Depth (ft)	Orientation	Confining Pressure (psi)	Peak Axial Stress Difference (psi)
CSP1-1	0.213308109	8497.05	Vertical	1813	10685
CSP1-2	0.795182676	8497.05	Vertical	906	11335
CSP1-3	0.445017044	8497.3	Vertical	2719	21655
CSP2-1	0.953496472	8513.5	Vertical	2724	52725
CSP2-2	0.695346112	8513.5	Vertical	1816	46845
CSP2-3	0.204307334	8513.5	Vertical	908	34905
CSP3-1	0.266808726	8514.5	Vertical	2725	31100
CSP3-2	0.651816245	8514.35	Vertical	1816	23905
CSP3-3	0.636538159	8514.35	Vertical	910	20910
CSP4-1	0.418958382	8528.7	Vertical	910	23460
CSP4-3	0.53180482	8528.9	Vertical	2729	31754
CSP4-8	0.355191942	8528.75	Vertical	1819	29935
CSP5-1	0.127602546	8531.55	Vertical	2730	32685
CSP5-2	0.286343624	8531.55	Vertical	1820	31055
CSP5-3	0.119807594	8531.55	Vertical	910	24745
CSP6-1	0.492828793	8538.1	Vertical	1821	22495
CSP6-2	0.4906716	8538.1	Vertical	2732	25910
CSP6-3	0.155545826	8538.1	Vertical	911	16460
CSP7-1	0.197400793	8557.9	Vertical	1826	38985
CSP7-3	0.299706188	8557.9	Vertical	2739	42600
CSP7-11	0.216547939	8557.45	Vertical	913	38155
CSP8-1	0.269752014	8569.7	Vertical	914	14520
CSP8-2	0.721480247	8569.7	Vertical	1828	16900
CSP8-3	0.487803896	8569.7	Vertical	2742	18125
CSP9-1	0.398130409	8561.9	Vertical	2740	46530
CSP9-2	0.249985672	8561.9	Vertical	1827	52610
CSP9-3	0.324139087	8561.9	Vertical	913	17605
CSP9-8T	0.670921478	8560.3	Vertical	913	45865
CSP10-1	0.387758335	8590.1	Vertical	916	17865
CSP10-2	0.308805651	8590.1	Vertical	1833	21035
CSP10-3	0.471398348	8590.1	Vertical	2749	21435
CSP11-1	0.644728842	8549.3	Vertical	2736	15615
CSP11-2	0.575297005	8549.3	Vertical	1824	14415
CSP11-3	0.301973256	8459.3	Vertical	912	11460

Cisco State 36-13

Sample	Brittleness Index	Measured Core Depth (feet)	Orientation	Confining Pressure (psi)	Peak Axial Stress Difference (psi)
CSO1-1	0.186566	7588.8	Vertical	2739.3	15282
CSO1-2	0.120219	7588.9	Horizontal	3622.46	15476
CSO2-1	0.090147	7593	Vertical	2732.048	10100
CSO2-2	0.086437	7592.9	Horizontal	3606.303	12305
CSO3-1	0.453401	7559.75	Vertical	2735.652	17144
CSO3-2	0.328328	7559.85	Horizontal	3609.543	19719
CSO4-1	0.20816	7605.35	Vertical	2754.27	32602
CSO4-2	0.436386	7605.65	Horizontal	3612.739	19030
CSO4-4	0.388601	7605.65	Vertical	2738.263	16908
CSO5-1	0.111132	7615.4	Vertical	2742.393	11670
CSO5-2	0.28618	7615	Horizontal	3617.135	15480
CSO6-1	0.044851	7627.3	Vertical	2754.266	20916
CSO6-2	0.047093	7627.1	Horizontal	3637.43	25173

National Energy Technology Laboratory

626 Cochrans Mill Road
P.O. Box 10940
Pittsburgh, PA 15236-0940

3610 Collins Ferry Road
P.O. Box 880
Morgantown, WV 26507-0880

13131 Dairy Ashford Road, Suite 225
Sugar Land, TX 77478

1450 Queen Avenue SW
Albany, OR 97321-2198

Arctic Energy Office
420 L Street, Suite 305
Anchorage, AK 99501

Visit the NETL website at:
www.netl.doe.gov

Customer Service Line:
1-800-553-7681